

Proceedings of the 11th International Conference on Structures in Fire



**Editors: David Lange, Cristian Maluk, Kang Hai Tan, Dong Zhang, Yao Zhang,
Julian Mendez Alvarez, Juan Hidalgo, Felix Wiesner, Martyn McLaggan,
Abdulrahman Zaben, Wenxuan Wu, Hangyu Xu**

UQ Fire



**THE UNIVERSITY
OF QUEENSLAND**
AUSTRALIA

CREATE CHANGE

NETZSCH
Proven Excellence.

afac 

omnii
Consulting Fire Engineers

Proceedings of the 11th International Conference on Structures in Fire

Hosted by The University of Queensland

Proceedings of the 11th International Conference on Structures in Fire
(SiF 2020)

Hosted by The University of Queensland

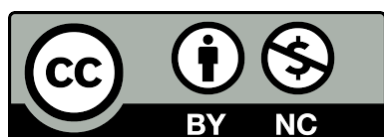
30 November to 2 December 2020

Editors: David Lange, Cristian Maluk, Kang Hai Tan, Dong Zhang, Yao Zhang, Julian Mendez Alvarez,
Juan Hidalgo, Felix Wiesner, Martyn Mclaggan, Abdulrahman Zaben, Wenxuan Wu, Hangyu Xu

Published by The University of Queensland, Australia © 2020

ISBN: 978-1-74272-343-3

All articles included in this collection are published under a Creative Commons Attribution Non-Commercial (CC BY 4.0) License



Sponsored by:

NETZSCH

Proven Excellence.



omnii
Consulting Fire Engineers

Organised by:

UQ Fire



TABLE OF CONTENTS

Table of contents	v
Preface	xii
Committees	xiv
 Applications of structural fire engineering	
A practical tool for evaluating fire induced failure probability of steel columns designed based on U.S. prescriptive standards <i>Ramla Qureshi; Ruben Van Coile; Danny Hopkin; Thomas Gernay; Negar Elhami Khorasani</i>	1
Fire performance of a steel open car park in the light of the recent development of the localised fire model "LOCAFI" <i>Mauro Sommavilla; Nicola Tondini</i>	12
The collapse of World Trade Center 7: revisited <i>Mhd Anwar Orabi; Liming Jiang; Asif Usmani; Jose L. Torero</i>	23
Steel sheet piles exposed to fire experimental tests and numerical modelling <i>Jean-Marc Franssen; João Martins</i>	34
Modelling concrete slabs subjected to localised fire action with OpenSees <i>Liming Jiang; Mhd Anwar Orabi; Jin Qiu; Asif Usmani</i>	46
A framework for reliability-based assessment of structures in post-fire conditions <i>Tom Molkens; Barbara Rossi</i>	55
Influence of time step on stability of the hybrid fire testing in a limited divergence zone <i>Bunthan Iea; Duc Toan Pham; Nicolas Pinoteau; Romain Mege; Jean-François Caron</i>	67
Real-time multi degrees of freedom hybrid fire testing using Pi control <i>Elke Mergny; Jean-Marc Franssen</i>	77
Lifetime economically optimum position of steel reinforcement in a concrete column exposed to natural fire <i>Shuna Ni; Ruben Van Coile; Negar Elhami Khorasani; Danny Hopkin; Thomas Gernay</i>	89

Composite structures

Evaluation of the fire performance of unprotected composite beams with fin-plate joints <i>N. Yotsumoto; T. Hirahisma; K. Toyoda</i>	101
Effect of steel-fiber reinforced concrete on the fire resistance of concrete-filled steel tubular columns under simultaneous axial loading and double curvature bending <i>Takuya Kinoshita; Yusuke Shintani; Tomohito Okazaki; Toshihiko Nishimura; J Y Richard Liew</i>	113
Applicability of the resistance integration method on bonded fasteners loaded in tension in uncracked concrete under ISO 834-1 fire <i>Omar Al-Mansouri; Romain Mège; Nicolas Pinoteau; Thierry Guillet; Sébastien Rémond</i>	124
Bond behaviour of elliptical concrete-filled steel tubes after fire exposure <i>Tianyi Song; Xialu Liu; Kai Xiang</i>	134
Bonding of grouted eccentric strands in duct at elevated temperatures <i>Xiqiang Wu; Francis Tat Kwong Au; Xinyan Huang</i>	146
Experimental study on fire resistance of a full-scale composite floor assembly in a two-story steel framed building <i>Lisa Choe; Selvarajah Ramesh; Xu Dai; Matthew Hoehler; Matthew Bundy</i>	158
The role of end conditions on the behaviour of steel-concrete composite beams in fire <i>Priya S. Natesh; Anil Agarwal</i>	171

Concrete structures

Effect of transverse and longitudinal confinement on the interlayer bond in 3D printed concrete at elevated temperatures: an experimental study <i>Antonio Cicione; Khanya Mazolwana; Jacques Kruger; Ricahrd Walls; Zara Sander; Gideon Van Zijl</i>	184
Predicting the fire rating of cantilever slab-wall connection with post installed rebar <i>Hitesh Lakhani; Jatin Aggarwal; Jan Hofmann</i>	196
Influence of spalling on the biaxial bending resistance of reinforced concrete columns exposed to fire <i>David L. Peña; Carmen Ibáñez; Vicente Albero; Ana Espinós; Antonio Hospitaler; Manuel L. Romero</i>	204
Effect of non-uniform heating and cooling on eccentrically loaded reinforced concrete columns <i>Jamie Maclean; Luke Bisby; Carmen Ibáñez</i>	212
Bond behavior between reinforcing steel bars and concrete at elevated temperatures <i>Ira Banoth; Anil Agarwal</i>	222
Post-earthquake fire assessment of reinforced concrete columns <i>Hemanth Kumar Chinthapalli; Anil Agarwal</i>	230

Damage assessment framework for tunnel structures subjected to fire <i>Nan Hua; Anthony Frederick Tessari; Negar Elhami Khorasani</i>	242
Comparative fire behavior of reinforced concrete beams made of different concrete strengths <i>Venkatesh Kodur; Srishti Banerji</i>	254
Modeling the structural behavior of reinforced concrete walls under ISO fire exposure <i>Mohsen Roosefid; Marie Helene Bonhomme; Pierre Pimienta</i>	262
Numerical investigation of the structural response of eccentrically loaded reinforced concrete columns exposed to non-uniform heating and cooling <i>Patrick Bamonte; Nataša Kalaba; Jamie Maclean; Luke Bisby</i>	271
Global resistance factor for the burnout resistance of concrete slabs exposed to parametric fires <i>Thomas Thienpont; Ruben Van Coile; Balsa Jovanovic; Wouter De Corte; Robby Caspeelee</i>	282
Bond strength between steel reinforcement and RCA concrete at elevated temperatures <i>Md. Abu Yusuf; Salah Sarhat; Hamzeh Hajiloo; Mark F. Green</i>	293
Evaluation of expected damage costs from fire in concrete building structures <i>Shuna Ni; Thomas Gernay</i>	301
Spalling of geopolymers concrete in ring-restrained specimens under high temperatures <i>Mitsuo Ozawa; Hiroyuki Ikeya; Koji Harada; Hiroki Goda</i>	313
Generalized fragility curves for concrete columns exposed to fire through surrogate modelling <i>Ranjit Kumar Chaudhary; Balša Jovanović; Thomas Gernay; Ruben Van Coile</i>	322
Critical fibre dimensions for preventing spalling of ultra-high performance concrete at high temperature <i>Dong Zhang; Kang Hai Tan</i>	333
Probabilistic models for thermal properties of concrete <i>Balša Jovanović; Negar Elhami Khorasani; Thomas Thienpont; Ranjit Kumar Chaudhary; Ruben Van Coile</i>	342
Effect of steel fibers on fire endurance of extruded hollow-core slabs <i>Hang T N Nguyen; Kang Hai Tan</i>	353
Experimental research and any other	
Retrofitting of fire damaged RC columns <i>Hemanth Kumar Chinthapalli; M. Chellapandian; Anil Agarwal; Suriya Prakash</i>	363
Developing real-time hybrid simulation to capture column buckling in a steel frame under fire <i>Ramla K Qureshi; Negar Elhami Khorasani; Mettupalayam Sivaselvan</i>	374
Thermal response and capacity of beam end shear connections during a large compartment fire experiment <i>Xu Dai; Lisa Choe; Erica Fischer; Charles Clifton</i>	386

Experimental study of concrete elements subjected to travelling fires <i>Camilo Montoya; David Lange; Cristian Maluk; Juan P. Hidalgo</i>	398
Robust circle tracking for deflection measurements in structural fire experiments <i>Felix Wiesner; Luke Bisby</i>	410
Alkali-activated sprayed concrete as a fire protection coating for tunnels inner lining: proof-of-concept study on the heat transfer <i>Anna-Lena Hammer; Christian Rhein; Thomas Rengshausen; Markus Knobloch; Götz Vollmann; Markus Thewes</i>	418
Evaluation of measuring methods for water vapor pressure in concrete at elevated temperature <i>Ye Li; Kang Hai Tan</i>	430
Travelling fire in full scale experimental building subjected to open ventilation conditions <i>Ali Nadjai; Naveed Alam; Marion Charlier; Olivier Vassart; Xu Dai; Jean-Marc Franssen; Johan Sjöström</i>	439
Shear resistance of sandwich panel connection to the substructure at elevated temperature <i>Kamila Cábová; Marsel Garifullin; Ashkan Shoushtarian Mofrad; František Wald; Kristo Mela; Yvonne Ciupack</i>	451
Near-limit burning of timber material under irradiation-assisted smoldering <i>Shaorun Lin; Xinyan Huang</i>	458
Rotational ductility of steel web-flange splice connections in fire <i>Paul Akagwu; Faris Ali; Ali Nadjai</i>	468
Fire experiments inside a very large and open-plan compartment: x-TWO <i>Mohammad Heidari; Egle Rackauskaite; Matthew Bonner; Eirik Christensen; Sébastien Morat; Harry Mitchell Panos Kotsovinos; Piotr Turkowski; Wojciech Wegrzynski; Piotr Tofilo; Guillermo Rein</i>	479
Assessment of a fire damaged concrete overpass: the Verona bus crash case study <i>Roberto Felicetti</i>	492
Numerical modelling	
Simple calculation method for the temperature profile in a circular concrete filled steel tubular column <i>Yusuke Shintani; Takuya Kinoshita; Tomohito Okazaki; Toshihiko Nishimura; Tamotsu Takao</i>	504
Simulation of pyrolysis and combustion of pine wood using two-step reaction scheme <i>Dharmit Nakrani; Tejas Wani; Gaurav Srivastava</i>	515
A simplified representation of travelling fire development in large compartment using CFD analyses <i>Marion Charlier; Olivier Vassart; Xu Dai; Stephen Welch; Johan Sjöström; Johan Anderson; Ali Nadjai</i>	526

Disproportionate collapse of steel-framed gravity buildings under fires with a cooling phase <i>Jian Jiang; Bowen Wang; Wenyu Cai; Guo-Qiang Li; Wei Chen; Jihong Ye</i>	537
Simple structural models for computational analysis of restrained columns under fire conditions <i>Pedro Dias Simão; João Paulo C. Rodrigues</i>	543
A static solver for hybrid fire simulation based on model reduction and dynamic relaxation <i>Patrick. Covi; Giuseppe Abbiati; Nicola Tondini; Oreste Salvatore Bursi; Bozidar Stojadinovic</i>	556
A thermo-mechanical stochastic damage perspective for concrete at elevated temperatures <i>Hao Zhou</i>	567
Linked CFD-thermo-mechanical simulation for virtual horizontal furnace <i>Stanislav Šulc; Kamila Cábová; Filip Zeman; Jakub Šejna; Vít Šmilauer; František Wald</i>	579
AI modelling & mapping functions: a cognitive, physics-guided, simulation-free and instantaneous approach to fire evaluation <i>M Z Naser; Haley Hostetter; Aditya Daware</i>	590
A numerical investigation of 3D structural behavior for steel-composite structures under various travelling fire scenarios <i>Zhuojun Nan; Xu Dai; Haimin Chen; Stephen Welch; Asif Usmani</i>	599
An improved implicit analysis method to model transient strain of high-strength concrete during unloading at elevated temperatures <i>Shan Li; J Y Richard Liew; Ming-Xiang Xiong</i>	611
The behaviour of bridge decks due to fire induced thermal expansion of protected stays cables <i>Panagiotis Kotsovinos; Egle Rackauskaite; Ryan Judge; Graeme Flint; Peter Woodburn</i>	622
Modelling Grenfell disaster: interactions between facades and apartments <i>Eric Guillaume; Virginie Dréan; Bertrand Girardin; Talal Fateh</i>	627
Steel structures	
Studies on bending strength and collapse temperature of a steel beam considering effects of steel strain rate and heating rate at elevated temperatures <i>Fuimnobi Ozaki; Takumi Umemura</i>	639
Experimental and numerical-analytical study on structural behavior of steel frames based on small-scale fire tests <i>Akinobu Takada; Tomohito Okazaki; Mami Saito</i>	650
Investigation of the performance of a novel ductile connection within bare-steel and composite frames in fire <i>Yu Liu; Shan-Shan Huang; Ian Burgess</i>	662
Behaviour of axially compressed angles and built-up steel members at elevated temperature <i>Luca Possidente; Nicola Tondini; Jean-Marc Battini</i>	673

Stability check of web-tapered steel beam-columns in fire <i>Elio Maia; Paulo Vila Real; Nuno Lopes; Carlos Couto</i>	685
Post-fire mechanical properties of TMCP high strength structural steel <i>Lin-Xin Song; Guo-Qiang Li; Qing Xu</i>	697
Prediction of fracture behavior for high-strength steel bolts at elevated temperatures <i>Wenyu Cai; Jian Jiang; Guo-Qiang Li</i>	708
New methodology for the calculations on steel columns with thermal gradients in contact with brick walls <i>António Moura Correia; João Paulo Rodrigues; Venkatesh Kodur</i>	715
OpenSees simulation of the collapse of Plasco tower in fire <i>Ramakanth Veera Venkata Domada; Aatif Ali Khan; Mustesin Ali Khan; Asif Usmani</i>	727
Fire resistance of stainless steel slender elliptical hollow section beam-columns <i>Flávio Arrais; Nuno Lopes; Paulo Vila Real</i>	739
Material properties of structural, high strength and very high strength steels for post-fire assessment of existing structures <i>Tom Molkens; Katherine A. Cashell; Barbara Rossi</i>	751
Fire fragility curves for steel pipe-racks exposed to localised fires <i>Jérôme Randaxhe; Olivier Vassart; Nicola Tondini</i>	763
A novel approach to model the thermal and physical behaviour of swelling intumescent coatings exposed to fire <i>Andrea Lucherini; Juan P. Hidalgo; Jose L. Torero; Cristian Maluk</i>	775
Experimental study of unloaded structural steel stay-cables under fire exposure <i>Benjamin Nicoletta; Scott Watson; Bronwyn Chorlton; John Gales; Panagiotis Kotsovinos</i>	783
Experimental investigation of the behavior of martensitic high-strength steels at elevated temperature <i>Xia Yan; Yu Xia; Hannah B. Blum; Thomas Gernay</i>	791
Effect of transient creep on stability of steel columns exposed to fire <i>Venkatesh Kodur; Svetha Venkatachari</i>	803
Timber structures	
Compressive strength and MoE of solid softwood at elevated temperatures <i>Abdulrahman Zaben; David Lange; Cristian Maluk</i>	811
A method for determining time equivalence for compartments with exposed mass timber, using iterative parametric fire curves <i>David Barber; Robert Dixon; Egle Rackauskaite; Khai Looi</i>	818

Calibration of a coupled post-flashover fire and pyrolysis model for determining char depth in mass timber enclosures <i>Colleen Wade; Danny Hopkin; Michael Spearpoint; Charles Fleischmann</i>	830
The behaviour of timber in fire including the decay phase - charring rates, char recession and smouldering <i>Joachim Schmid; Antonio Totaro; Andrea Frangi</i>	842
Design of timber-concrete composite floors for fire <i>Erica C. Fischer; Annabel B. Shephard; Arijit Sinha; Andre R. Barbosa</i>	852
Proposal for stress-strain constitutive models for laminated bamboo at elevated temperatures <i>Mateo Gutierrez Gonzalez; Cristian Maluk</i>	859
The use of research for the explicit consideration of self- extinction in the design of timber structures <i>Juan Cuevas; Cristian Maluk</i>	866
Fire performance of moment-resisting concealed timber connections reinforced with self-tapping screws <i>Oluwamuyiwa Okunrounmu; Osama (Sam) Salem; George Hadjisophocleous</i>	879
Deformation behaviour and failure time of glued laminated timber columns in fire <i>Takeo Hirashima; Heisuke Yamashita; Shungo Ishi; Tatsuki Igarashi; Shigeaki Baba; Tomoyuki Someya</i>	890
Comparative study on the fire behaviour of fire-rated gypsum plasterboards vs. thin intumescent coatings used in mass timber structures <i>Ambrosine Hartl; Qazi Samia Razzaque; Andrea Lucherini; Cristian Maluk</i>	901
The response of exposed timber in open plan compartment fires and its impact on the fire dynamics <i>Sam Nothard; David Lange; Juan P. Hidalgo; Vinny Gupta; Martyn S. McLaggan</i>	911

PREFACE

The Structures in Fire (SiF) series of conferences is an opportunity for researchers, practitioners and engineers to share and discuss their research related to structures in fire with their peers in an open, international forum. This is the book of proceedings for the 11th International Conference on Structures in Fire (SiF 2020) hosted by The University of Queensland between the 30 November and 2 December 2020. As a result of the global COVID-19 coronavirus pandemic it is the first SiF conference to be held completely online.

The organising committee received 251 extended abstracts for the conference, and each and every one of those was reviewed by at least 3 reviewers from the scientific committee. The quality was exceptionally high and of the nearly 250 abstracts which were submitted, we invited 147 of those to present during the conference and to be extended to a full paper for inclusion in the proceedings.

We are delighted that, having moved the conference to an online platform, we are ultimately able to include 87 papers in the proceedings and to deliver what is a very packed conference program over the usual three days of a SiF conference. It is testimony to the resilience and engagement of our global SiF community that we are able to offer such a full and interesting conference program.

Locally, it has taken very many of the PhD students at The University of Queensland's Fire Safety Engineering research group very many late nights and early mornings to get the proceedings ready for publication and to get to grips with and prepare the online platform for the conference. Equally, at Nanyang Technological University there has been significant support given to the work of the scientific committee by two other students. The contribution of these individuals is at least as important as those of us who have signed this preface and they are all listed as editors of this book of proceedings. You will no doubt be seeing and hearing much more of these very talented and dedicated researchers in the future.

Thanks must also go to our colleagues in the local organising committee including: Selina Weller and Lily Boström (The University of Queensland), Priyan Mendis (The University of Melbourne), Kate Nguyen (RMIT), Mahen Mahendran (Queensland University of Technology), Anthony Abu (The University of Canterbury); as well as Mary-Anne Marrington and Elena Danilova at the University of Queensland's library; Dong Zhang and Yao Zhang at the Nanyang Technological University and all of the members of the scientific and steering committee who are listed on the following pages.

Finally, this conference would not had been possible without the very generous support of our event sponsors Netzsch, AFAC and Omnii Consulting Fire Engineers; and our award sponsors the Journal of Structural Fire Engineering and the International Association for Fire Safety Science (IAFSS).

Organising and hosting Structures in Fire 2020 has been both a privilege and an exercise in agility. Over the past year we have both changed the date of the conference and moved the conference to an online event in response to the changing reality of a world in the grip of a pandemic. This pandemic has impacted on almost every aspect of our lives, and while Australia and Queensland in particular has had relatively low

numbers of infections we have looked on from our isolated position at the horrors of the situation which the rest of the world has faced.

As we look with hope towards a post-pandemic world, one thing is sure – the built environment will be crucial in many regions to enabling a strong and rapid economic recovery. This means that our collective work, the work to ensure that we are able to deliver structures which are able to withstand the effects of fire, will be as relevant and important as ever.

On behalf of the local organising committee:

Dr David Lange
The University of Queensland

Dr Cristian Maluk
The University of Queensland

On behalf of the scientific committee:

Professor Kang Hai Tan
Nanyang Technological University

COMMITTEES

Organising Committee

Dr David Lange (The University of Queensland)
Dr Cristian Maluk (The University of Queensland)
Dr Felix Wiesner (The University of Queensland)
Dr Juan P. Hidalgo (The University of Queensland)
Dr Martyn S. McLaggan (The University of Queensland)
Selina Weller (The University of Queensland)
Professor Priyan Mendis (The University of Melbourne)
Dr Kate Nguyen (RMIT)
Professor Mahen Mahendran (Queensland University of Technology)
Dr Anthony Abu (The University of Canterbury)

Scientific Committee

Professor Kang Hai Tan (Nanyang Technological University)

Applications of structural fire engineering

Jean-Marc Franssen
Anthony Abu
Lisa Broberg
Yong Du
Qianru Guo
Jiayu Hu
Timo Jokinen
Inka Kleiboemer
Susan Lamont
Linus Lim
Tom Molken
Eric Tonicello
Bernice Wong
Zhi Zhang

Timber structures

Andrea Frangi
David Barber
Andy Buchanan
Daniel Brandon
Steve Craft
Christian Dagenais
Massimo Fragiaco
Marc Janssens
Alar Just
Koji Kagiya
Michael Klippel
Birgit Östman
Pedro Palma
Joachim Schmid
Colleen Wade
Norman Werther

Numerical modelling

Asif Usmani
Pradeep Bhargava
Katherine Cashell
Suwen Chen
Mustesin Khan
Martin Gillie
Kazunori Harada
Ann Jeffers
Jian Jiang
David Lange
C.S. Manohar
Asif Usmani
Hamid Ronagh
Serdar Selamet
Ruben Van Coile
Chao Zhan

Steel structures

Paulo Vila Real
Florian Block
Ian Burgess
Carlos Couto
Michael Engelhardt
Leroy Gardner
Maria Garlock
François Hanus
Tomaž Hozjan
Michal Jandera
Markus Knobloch
Nuno Lopes
Paulo Piloto
Christophe Renaud
Peter Schaumann
Nicola Tondini
František Wald
Yong Wang
I Paya Zaforteza
Raul Zaharia
Bin Zhao

Composite structures

Guo-Qiang Li
Lisa Choe
Panwei Du
Shengxin Fan
Liming Jiang
Ali Nadjai
John Gales
Lou Guobiao
Shan-Shan Huang
João Paulo Rodrigues
Zhong Tao
Peijun Wang
Weiyong Wang
Yuzhuo Wang

Concrete and masonry structures

Venkatesh Kodur
Anil Agarwal
Faris Ali
Luke Bisby
Byong Choi
Mohammadreza Eslami
Roberto Felicetti
Pietro Gambarova
Thomas Gernay
Mark Green
Rami Hawileh
Vasant Matsagar
Priyan Mendis
M.Z. Naser
Ananth Ramaswamy
Luc Taerwe
Bernardo Tutikian
Bo Wu
Li Ye
Haiyan Zhang

Experimental research and any other

Cristian Maluk
Mariyana Aida Abk
Blanca Andres
Eleni Asimakopoulou
Antonio Bilotta
Piergiacomo Cancelliere
Iolanda del Prete
Richard Emberley
Ricardo Fakury
Erica Fischer
Carmen Ibanez Usach
Amar Khennane
Angus Law
Kathinka Leikanger Friquin
Cristian Maluk
Muhammad Masood Rafi
Kate Nguyen
Emidio Nigro
Aldina Santiago
Holly Warren
Felix Wiesner
Jochen Zehfuß

Steering Committee

Professor Jean-Marc Franssen (The University of Liege)
Professor Paulo Vila Real (The University of Aveiro)
Professor Venkatesh Kodur (Michigan State University)
Professor Kang Hai Tan (Nanyang Technological University)

Proceedings of the 11th International Conference on Structures in Fire

A PRACTICAL TOOL FOR EVALUATING FIRE INDUCED FAILURE PROBABILITY OF STEEL COLUMNS DESIGNED BASED ON U.S. PRESCRIPTIVE STANDARDS

Ramla Qureshi¹, Ruben Van Coile², Danny Hopkin³, Thomas Gernay⁴, Negar Elhami Khorasani⁵

ABSTRACT

Previous research has investigated and developed systematic probabilistic models for parameters involved in determining the reliability of a structure under fire. The established models have been summarized and applied in this paper to quantify and compare the reliability of steel columns protected based upon the US prescriptive approach. A set of columns with a range of section factors are selected to study the influence of utilization ratio, restraint conditions, and fuel load density on the probability of failure under fire. The results show a relatively large variation in the value of probability of failure for columns with similar fire protection rating but different section factors and utilization ratio. The influence of fuel load density is presented in the form of fragility functions, where the probabilities of failure for expected fuel load density values are discussed. In addition, the probability of failure for columns across different stories of a building is calculated, leading to the conclusion that further harmonization of safety levels can be achieved if reliability-based quantifications are introduced in the design process.

Keywords: Steel column; reliability; US prescriptive design; probability of failure

1 INTRODUCTION

The US fire protection industry is trained to design passive fire protection of steel buildings based on well-established prescriptive approaches. Alternatively, performance-based fire design can be adopted, where the engineer designs the structural system for fire as a demand. While performance-based fire engineering indeed provides a solution for exceptional structures and those with atypical consequences of failure or with complex geometry, the US industry will continue using prescriptive design for a range of simple and regular designs. To ensure consistency in safety requirements, there is a need to better comprehend the safety level (structural reliability) of such members designed following the prescriptive guidelines. The load combination for extraordinary events (i.e., for temperature effects in case of a fire) in the “ASCE 7: Minimum Design Loads for Buildings and Other Structures” assumes a conditional failure probability of approximately 0.1, given a structurally significant fire [1]. Yet, no study has been completed to systematically quantify the inherent safety of the prescriptive approach under realistic fire conditions, and when components or sub-assemblies become part of a structural system. To fill this gap, this paper presents the following two contributions:

¹ PhD Candidate, Department of Civil, Structural and Environmental Engineering, University at Buffalo
e-mail: ramlakar@buffalo.edu, ORCID: <https://orcid.org/0000-0002-8652-5726>

² Assistant Professor, Department of Structural Engineering and Building Materials, Ghent University
e-mail: Ruben.VanCoile@UGent.be, ORCID: <https://orcid.org/0000-0002-9715-6786>

³ Visiting Professor, Department of Civil and Structural Engineering, The University of Sheffield
e-mail: D.J.Hopkin@sheffield.ac.uk, ORCID: <https://orcid.org/0000-0002-2559-3581>

⁴ Assistant Professor, Department of Civil and Systems Engineering, Johns Hopkins University
e-mail: tgernay@jhu.edu, ORCID: <https://orcid.org/0000-0002-3511-9226>

⁵ Assistant Professor, Department of Civil, Structural and Environmental Engineering, University at Buffalo
e-mail: negarkho@buffalo.edu, ORCID: <https://orcid.org/0000-0003-3228-0097>

- A methodology to calculate probability of failure for steel columns and the assumed probabilistic models for the random variables: the majority of assumed probabilistic distributions, including thermal and mechanical properties of steel and insulating materials and applied gravity loads, are based on a series of previous reviews and research by the authors. In addition, the results of a recent fuel load survey from 3 office buildings in the US are included and the obtained distribution of fuel load density is provided. The procedure is implemented in a new integrated computer-based code that enables automatic calculation of the reliability of steel columns in fire.
- The sensitivity of the probability of failure of columns to a number of parameters, including section factor, utilization ratio, end restraint condition, and fuel load density: the procedure is applied to a cohort of steel columns protected according to the US standards and relevant to multi-story building designs. The probability of failure of columns across different stories of a building is also presented.

The results provide an assessment of the safety levels of the prescriptive design for steel columns. The quantification of safety levels allows a systematic evaluation of risk, which can be used to harmonize safety levels across designs with similar occupancy types.

2 METHODOLOGY

Quantifying the reliability of a structural member under fire involves capturing uncertainty in several variables. The assumed probability distributions for random variables affect the probability of failure, thus it is important to carefully examine and select relevant probabilistic models for input variables. In this paper, the probability of failure of a column is defined by a limit state where the load-carrying capacity of the member is less than the applied axial load (i.e., resistance domain). It should be noted that similar results were obtained for the steel columns when defining the probability of failure using the temperature domain (not shown in this paper). The considered random variables are dead and live loads (i.e., demand load), and thermal and mechanical properties of steel and insulating materials. The assumed distributions for the random variables are selected based upon rigorous evaluations of different models in the prior work of the authors (discussed in more detail in Section 2.0). In addition, column size, height, boundary conditions, hourly rating (under standard fire exposure) for the prescriptive approach (or thickness of the insulation), and fire scenario should be defined. This section provides a brief overview of the methodology and implemented random variables. Figure 1 shows the required inputs to calculate the probability of failure for a steel column.

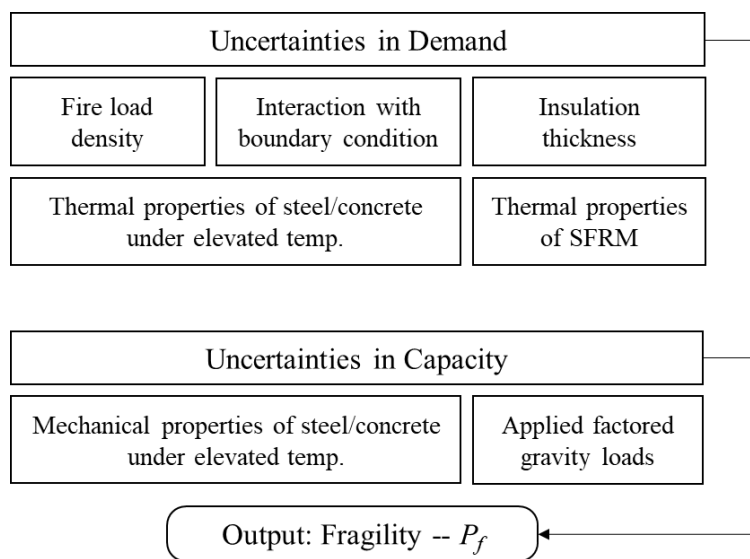


Figure 1. Overview of required inputs to calculate probability of failure for a steel column (note: parameters can be taken as deterministic or probabilistic)

2.1 Column capacity

The nominal compression strength of the column is calculated and compared using two approaches, namely: (1) the provisions of Appendix 4 in AISC SCM [2], and (2) the provision of EC3 [3]. These approaches capture global buckling as a limit state, but do not capture local instabilities of the plates; therefore, the studied columns are selected to be class 3 or above (based on the Eurocode classification of cross-sections). The AISC SCM Appendix 4 sets forward equations 1 and 2 for calculating the critical compressive stress as a function of temperature, where $k_{y,\theta}$ and $k_{E,\theta}$ are reduction factors for yield strength and modulus of elasticity at elevated temperatures, f_y is the yield stress (at ambient temperature), E is the modulus of elasticity (at ambient temperature), L_c is the effective length of the column, r is the radius of gyration, and $F_e(\theta)$ is the critical elastic buckling stress. L_c is determined as kL where k is the effective length coefficient considering the end restraints, and L is the length of the column. The compression capacity is obtained by multiplying the critical compressive stress with the cross-section area of the column. The AISC commentary of Appendix 4 provides an adjustment for the column slenderness ratio considering rotational restraints offered by cooler columns in stories above and below. The adjustment reduces the column slenderness as a function of temperature and having cooler columns both above and below or only on one side. The revised slenderness ratio improves the fire resistance capacity of the column. This adjustment is not directly considered in this paper, rather the column strength is calculated for a range of k values.

$$F_{cr}(\theta) = \left[0.42 \sqrt{\frac{k_{y,\theta} f_y}{F_e(\theta)}} \right] k_{y,\theta} f_y \quad (1)$$

$$F_e(\theta) = \frac{\pi^2 k_{E,\theta} E}{\left(\frac{L_c}{r}\right)^2} \quad (2)$$

The EC3 provisions for calculating the capacity of a column as a function of temperature are shown in equations 3-7, where χ_{fi} is the reduction factor for flexural buckling at elevated temperatures, A , and I are the area and moment of inertia of the column, $\gamma_{M,fi}$ is the partial factor for material property taken as 1.0 for properties of steel, and finally $\bar{\lambda}$ is the non-dimensional column slenderness at normal temperature.

$$N_{b,fi,t,Rd} = \chi_{fi} A k_{y,\theta} f_y / \gamma_{M,fi} \quad (3)$$

$$\chi_{fi} = \frac{1}{\varphi_\theta + \sqrt{\varphi_\theta^2 - \bar{\lambda}_\theta^2}} \quad (4)$$

$$\varphi_\theta = \frac{1}{2} [1 + \alpha \bar{\lambda}_\theta + \bar{\lambda}_\theta^2] \quad (5)$$

$$\alpha = 0.65 \sqrt{235/f_y} \quad (6)$$

$$\bar{\lambda}_\theta = \bar{\lambda} \sqrt{\frac{k_{y,\theta}}{k_{E,\theta}}} \quad (7)$$

$$\bar{\lambda} = \sqrt{\frac{A f_y}{\frac{\pi^2 E I}{L_c^2}}} \quad (8)$$

Based upon the AISC commentary notes of Appendix 4, the AISC equation (post 2010 edition) provides a relatively close prediction of strength when compared with finite element models validated by test data. The AISC equation, in comparison to the EC3 method, provides slightly smaller column strength values, which would result in larger probability of failure.

2.2 Fire scenario

Two fire exposure scenarios are considered in this paper: (1) the ASTM E119 fire, and (2) the parametric temperature-time curve. In the former case, the probability of failure is calculated for a given fire-resistance rating (e.g., 2 hours). In the latter case, the probability of failure is calculated as a function of fuel load density. Given the variability of fuel load density and its importance in determining the fire gas-phase temperature, the results are presented in terms of fragility curves as a function of fuel load density. A discussion on the distribution of fuel load density is provided in Section 2.3.3. The opening factor and size of the compartment are assumed as deterministic values when calculating the probability of failure for a given column. However, these variables can also be treated as random variables.

2.3 Random variables

Table 1 lists the random variables and associated probability distributions. The rest of this section provides a brief background for each parameter.

Table 1. Summary of random variables considered for calculating probability of failure of a steel column

Stochastic variable	Description	Ref
Thermal model: insulating materials		
Density [kg/m ³]	$\rho_i = \exp(-2.028 + 7.83 \times T^{-0.0065} + 0.122 \times \varepsilon)$	[4]
Thermal conductivity [W/m-K]	$k_i = \exp(-2.72 + 1.89 \times 10^{-3}T - 0.195 \times 10^{-6}T^2 + 0.209 \times \varepsilon)$	[4]
Specific heat [J/kg-K]	$c_i = 1700 - \exp(6.81 - 1.61 \times 10^{-3} \times T + 0.44 \times 10^{-6}T^2 + 0.213\varepsilon)$	[4]
Thickness	Lognormal with mean = nominal + 1.6 mm and COV=0.2	[5]
Structural model		
Steel yield strength at 20 °C [MPa]	Lognormal with mean= $f_y + 2\sigma$ and COV=0.07 where f_y is the yield strength at 20°C	[6]
Steel yield strength reduction factor	$k_{y,\theta} = \frac{1.7 \times \exp[r_{logit} + 0.412 - 0.81 \times 10^{-3} \times T + 0.58 \times 10^{-6} \times T^{1.9} + 0.43 \times \varepsilon]}{1 + \exp[r_{logit} + 0.412 - 0.81 \times 10^{-3} \times T + 0.58 \times 10^{-6} \times T^{1.9} + 0.43 \times \varepsilon]}$ with $r_{logit} = \ln \frac{(k_{y,EN} + 10^{-6})/1.7}{1 - (k_{y,EN} + 10^{-6})/1.7}$	[4]
Steel modulus of elasticity reduction factor	$k_{E,\theta} = 1.1 \times \frac{e^{(2.54 - 2.69 \times 10^{-3} \times T - 2.83 \times 10^{-6} T^2 + 0.36 \times \varepsilon)}}{e^{(2.54 - 2.69 \times 10^{-3} \times T - 2.83 \times 10^{-6} T^2 + 0.36 \times \varepsilon)} + 1}$	[4]
Applied load P [kN]	Permanent load G : Normal with mean of nominal value and COV=0.10 Live load Q : Gumbel distribution with mean of $0.2 \times$ nominal value and COV=0.95 Model uncertainty load effect K_E : Lognormal with mean 1.0 and COV = 0.10	[7]
Model uncertainty for capacity	K_R : Lognormal distribution, mean of 1.0 and COV = 0.15	[8]
Note: ε is the standard normal distribution and T is the temperature in [°C].		

2.3.1 Thermal model

The thermal properties of the insulating material, including density, thermal conductivity, and specific heat are modelled as temperature-dependent random variables. The models were derived in [4] considering data from three sprayed fire-resistive materials (Blaze-Shield DC/F, Blaze-Shield II, and Monokote MK-5). Density has a slightly decreasing trend with temperature while thermal conductivity and specific heat have

increasing trends with temperature. The increase in thermal conductivity with temperature is noticeable and should be considered as it leads to a larger rate of heat transfer to the section. The insulation thickness is also assumed as a random variable as defined in Table 1. The density and specific heat of steel are modelled as deterministic values, where density is taken as 7850 kg/m^3 and specific heat is taken as the deterministic EC3 (temperature-dependent) model [3].

2.3.2 Mechanical model

The uncertainty in yield strength both at the ambient temperature and at elevated temperatures is modelled. The uncertainty at 20°C follows the recommendation of [6]. The reduction factors for yield strength and modulus of elasticity of steel at elevated temperatures are taken from [4]. The authors completed a comprehensive study on the effect of model choice on the probability of failure of steel columns when the yield strength reduction factor is modelled using different approaches and based on different distributions [9]. The results showed that the model choice did not seem to have a considerable effect on the probability of failure, especially in the range of 1% to 10% failure quantiles. The applied model in this paper is a logistic model with strength defined at 2% strain. At temperatures below 500°C , the median values of this model have values larger than that of EC3, reflecting the effect of strain hardening. The resistance model uncertainty in calculating the capacity of the steel columns K_R is assumed as lognormal distribution with a mean of unity and coefficient of variation (COV) 0.15.

Jovanovic et al. [7] reviewed relevant literature on dead load, live load, and total load for application in probabilistic structural fire engineering. The study recommended modelling the total load as listed in Table 1 with K_E as the action model uncertainty, G as the dead load, and Q as the live load. The model uncertainty follows a lognormal distribution with a mean of 1.0 and COV of 0.10. The dead load is modelled as a normal distribution with the mean taken as the nominal value and a COV of 0.10. Live load follows a Gamma distribution with the mean equal to 0.2 times the nominal value and COV of 0.95. In determining the total load when studying the probability of failure for a series of columns, the load ratio χ is defined as the ratio of nominal live load to the total nominal load [$Q / (G+Q)$].

2.3.3 Fuel load density

EC1 [10] prescribes a Gumbel distribution for fuel load density with associated mean and 80% fractile values for different occupancy types. Figure 2 shows the distribution for office and library buildings according to the EC. Fuel load density is one of the major parameters influencing the gas-phase temperature-time distribution of fire in a compartment. Surveys of fuel load density are rare since existing surveying approaches are cumbersome. In a recent study supported by the National Fire Protection Association (NFPA), a new digitized surveying methodology was developed to collect fuel load density data by processing images of room contents using online databases [11]. Item weight and specifications are extracted through image matching within existing online search engines. The newly developed methodology was applied to 3 office buildings on a university campus in the US [12]. The obtained distribution from the collected data (34 closed offices and 161 cubicles within 12 large open plan offices) is shown in Figure 2.

The surveyed rooms had large quantities of paper, where the movable fuel load density composition was 54% paper, 30% wood, and 16% plastic, noting that no derating factor was applied for enclosed spaces. Breakdown of data in terms of furniture contribution to fuel load density consists of 36% furniture, 8% electronics, 54% paper, and 2% other. The resulting fuel load density distribution for moveable content lands in between EC1 office and library occupancy types, with a mean of 1115 MJ/m^2 and a standard deviation of 614 MJ/m^2 . The results are based on a limited number of surveyed offices located on a university campus. However, the difference between obtained values and the distribution from EC1 is significant. Thus, the results emphasize the need to conduct more surveys of modern buildings and potentially investigate occupancy sub-classifications to, for example, distinguish between different office types to account for the expected type of load (e.g., large loads of papers in offices on a university campus).

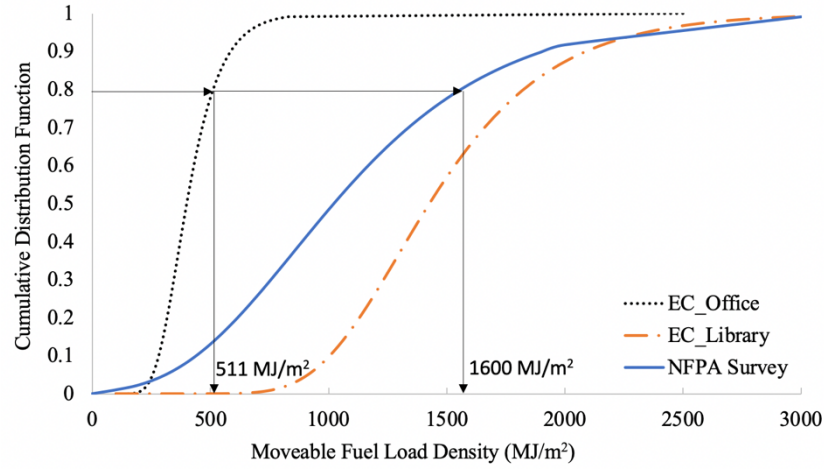


Figure 2. Fuel load density distributions from EC1 and recent survey of 3 office buildings in the US

3 APPLICATION

The probability of failure of a cohort of columns, with a range of section factors, is first calculated and compared for different utilization ratios and end restraint conditions when subjected to 2 hours of the ASTM E119 fire exposure. Considered column sizes are W10×60, W10×77, W10×100, W12×58, W12×65, W12×79, W12×106, W12×136, W12×152, W14×53, W14×68, W14×82, W14×109, W14×145, and W14×159. The covered range of section factors, reflecting the rate of temperature increase in the section as a function of mass and surface area exposed to fire, is 60.9 to 127.3 kg/m². The height of all columns is taken as 3692 mm. The characteristic values for steel yield strength and modulus of elasticity at ambient temperature are taken as 345 MPa and 200,000 MPa, respectively. The applied load is determined based on a load ratio χ (defined in Section 2.3.2) of 0.25 and the assumed utilization ratio for the case under study. The utilization ratio is defined as the ratio of demand to capacity where demand is defined as the factored design load at ambient temperature (based on load combinations in the US ASCE 7-16 code [13]) and the column capacity is calculated at ambient temperature using the AISC standard [2]. Both demand load and axial capacity are calculated using nominal values of variables.

In the second step, the probability of failure for the same set of columns is calculated as a function of fuel load density, assuming the EC parametric temperature-time curve. The compartment size is taken as 9.144 m × 6.096 m × 2.8 m (based on dimensions of a 9-story building explained next). The opening size is taken as 3.0 m × 1.5 m. In the last step, the probability of failure for columns from the gravity frame of a 9-story building, designed according to the US standards, are examined. The 9-story building requires a 2-hour fire rating for columns in the gravity frame. The column on the 1st story has a k value of 0.7 while the other floors have a k value of 0.5, given the end restraint conditions. Table 2 provides the list of columns for the 9-story frame (except for the 9th story where the column section is a class 4 at elevated temperatures and thus excluded from the analysis), the corresponding nominal dead and live loads used in the design process, and the utilization ratio at ambient temperature (UR). Details of the design and fire compartment dimensions can be found in [14].

Table 2. Column section sizes, applied load, and utilization ratio at ambient temperature

Story	Size	DL [KN]	LL [KN]	UR	Story	Size	DL [KN]	LL [KN]	UR
1	W14×109	3692	689	0.96	5	W14×68	2064	368	0.83
2	W14×109	3285	608	0.79	6	W14×68	1657	288	0.66
3	W14×82	2878	528	0.96	7	W14×53	1253	219	0.67
4	W14×82	2471	448	0.82	8	W14×53	849	148	0.45

4 RESULTS FOR PROBABILITY OF FAILURE OF COLUMNS

4.1 Sensitivity of probability of failure to various parameters

This section studies variation in the probability of failure for a cohort of columns listed in Section 3. The columns are assumed to be protected with Isolatek Blaze-Shield II insulation with the specified nominal thickness corresponding to the 2-hour rating (the 2-hour rating is selected to have comparable results with those of the 9-story building described in Section 3). The fire protection material specification and design aid tables for insulation thickness provided by the manufacturer can be found in [15]. The probability of failure is obtained by generating 5,000 parameter combinations using Latin Hypercube Sampling (LHS) with f_y , $k_{y,\theta}$, E , $k_{E,\theta}$, ρ_i , k_i , c_i , thickness of insulation, applied load, and model error taken as random variables. Figure 3 shows the variation in the probability of failure assuming 2 hours of the ASTM E119 fire, a load ratio χ of 0.25, and a k value of 1.0. For the same fire rating, columns with a larger W/D ratio have a smaller probability of failure. The performance criteria in determining the insulation thickness during standard furnace tests of columns in the prescriptive approach mainly relate to temperature limits in the cross section during the test (e.g., average temperature should remain below 538°C or temperature at no one location along the member should exceed 649°C). Depending on the available resources and capabilities of the laboratory conducting the standard test, the column may not be loaded. The variation in probabilities of failure presented in Figure 3 reflects the change in slenderness ratio of the columns as the section sizes change.

In addition, columns with a higher utilization ratio have a larger probability of failure, as the prescriptive approach does not take the utilization ratio into account. The selected utilization ratios are consistent with those listed in Table 2 for the 9-story building. As expected, when capacity is calculated using the AISC SCM provisions, a larger probability of failure is obtained compared to the EC3 calculation, given that the AISC SCM provides slightly lower capacity predictions. The calculated range of probability of failure is relatively large, varying between 0.1 and 0.6 for W/D values between 60 and 140 and the utilization ratio of 0.55.

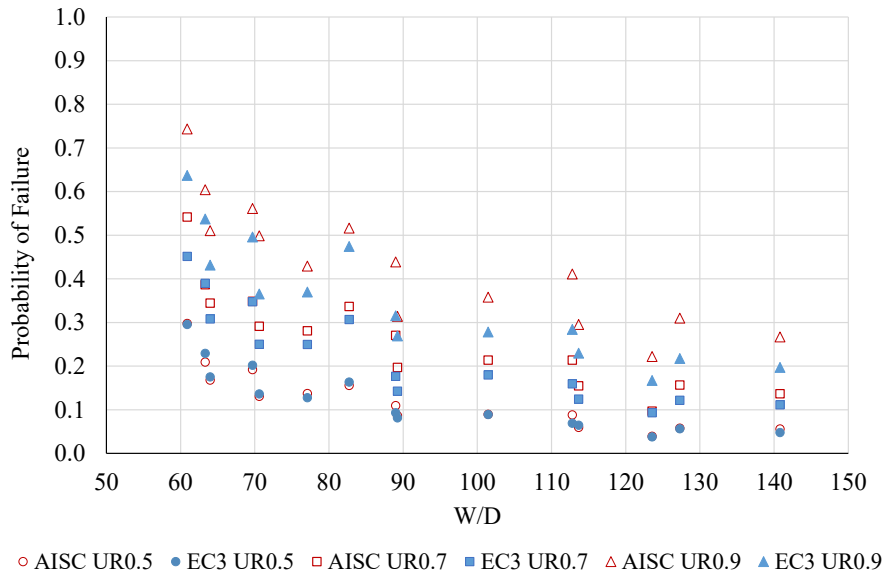


Figure 3. Probability of failure versus W/D ratio for different utilization ratios, assuming load ratio = 0.25, $k = 1.0$, and $H = 3962$ mm

Figure 4 shows the change in the probability of failure as a function of end restraint condition, calculated using AISC. The influence of end condition is more pronounced for columns with a lower W/D ratio. For example, a column with a W/D ratio of 60 has a probability of failure ranging from about 0.34 to about 0.55 by changing the end conditions from fixed to pinned at both ends. Such difference is not observed for columns with W/D ratio above 100 where the probability of failure is equal to or less than 0.2. For a given length, load ratio, and utilization ratio, the columns with smaller W/D ratio have larger slenderness ratio

(given a smaller radius of gyration). The larger variation in the probability of failure at lower W/D values can be explained by the higher sensitivity of cases that are more slender.

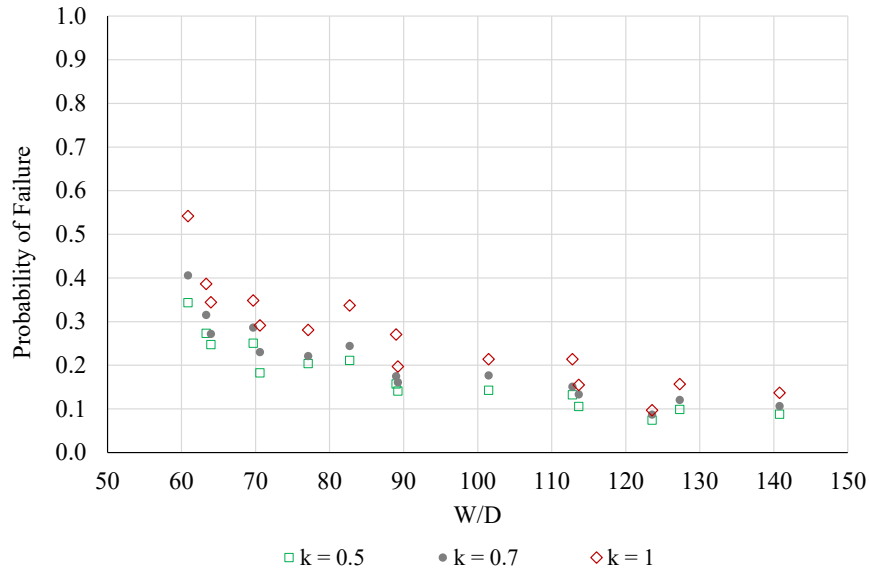


Figure 4. Probability of failure versus W/D ratio for different k values, assuming load ratio = 0.25, utilization ratio = 0.7, and H = 3962 mm

Figure 5 shows the probability of failure as a function of the (deterministic) fuel load density. In this case, the fire scenario is changed to the parametric temperature-time curve and the probability of failure is calculated considering the full duration of fire until burnout. Here, 10,000 LHS combinations (to ensure convergence in probability of failure at high values of fuel load density) were used to generate the probability of failure. The nominal insulation thickness is kept the same as that specified for the 2-hour rating.

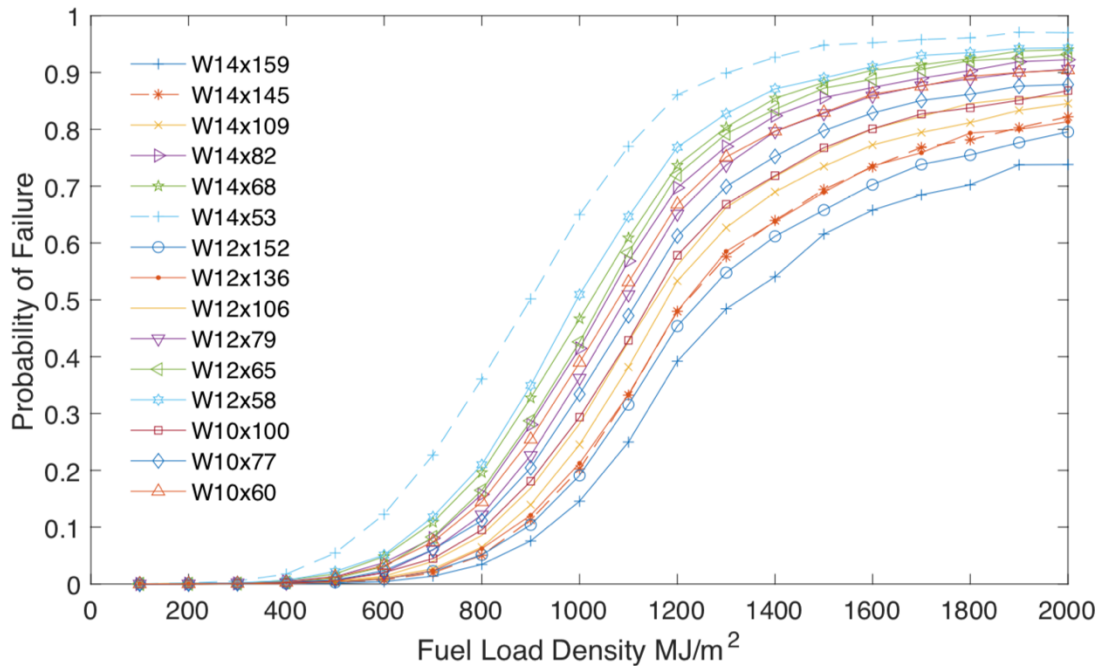


Figure 5. Probability of failure as a function of fuel load density, assuming load ratio = 0.25, utilization ratio = 0.7, k = 1.0, and H = 3962 mm

The fragility function representation of results provides an opportunity for the structural engineer to obtain the reliability of a design considering the distribution of fuel load density for the building under study. Based on the discussion in Section 2.3.3, the EC1 80% quantile fuel load density value for offices is 511 MJ/m², which implies a probability of failure ranging from 0.002 to 0.065, for this characteristic fire load density. The lower and upper bounds of the probability of failure change to 0.66 to 0.95 respectively, when considering the 80% quantile of fuel load density (1600 MJ/m²) from the 3 newly surveyed office buildings in the US. These results show that the fuel load density in a compartment significantly influences the fire severity, and hence the probability of failure. While a 2-hour prescriptive rating allowed most columns to survive until full burnout when adopting the EC1 office occupancy distribution with the assumed compartment characteristics, failure was much more likely when adopting the fuel load distribution from the recent survey. When considering the uncertainty in the fuel load density, the fragility curve of Figure 5 allows to obtain a single value failure probability for the column in function of the occupancy type.

4.2 Variation in the probability of failure within a building

The procedure of Section 4.1 is applied to columns of the 9-story building described in Section 3 to investigate the reliability level in a given structure. The structure requires a 2-hour fire rating, the associated insulation thickness is applied to the columns, and the probability of failure is calculated for 2 hours of ASTM E119 fire exposure. Figure 6 shows the results as a function of building story and based on both AISC SCM and EC3 capacity calculations. The figure shows that the column on the 8th story has the smallest probability of failure due to a smaller utilization ratio. The results also show the variation in the probability of failure with values in the range of 0.5 to 0.2 on the 1st and 8th stories where the design conditions (e.g., height, end restraint, load) are different.

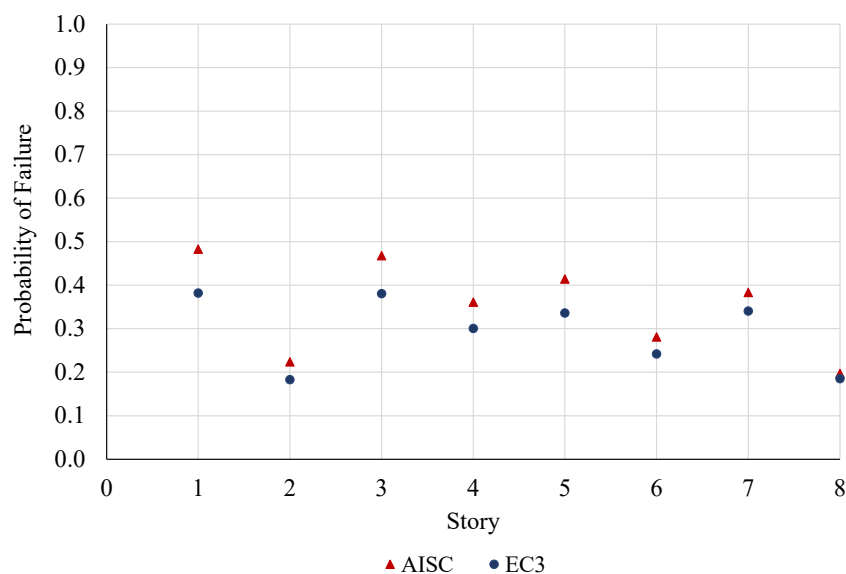


Figure 6. Probability of failure for columns in the gravity frame of a 9-story building

4.3 Discussion

The results presented in Sections 4.1 and 4.2 showed that the section factor and utilization ratio have a considerable influence on the probability of failure of steel columns protected based upon US prescriptive design approach. Another parameter that was not discussed earlier but could affect the probability of failure is the thermal conductivity of the fire protection. The properties of the insulating material, including thermal conductivity, specific heat, and density, are proprietary and typically listed by manufacturers at ambient temperature only. However, limited experimental data show that these properties change with temperature, more specifically, the thermal conductivity of insulating material changes from 0.065 to 0.378 W/mK on average at 25 and 1000 °C, respectively [16]. Thus, using the listed values at ambient temperature for properties of insulating material does not provide realistic results and leads to values of probability of failure

that are an order of magnitude smaller. The results presented in this paper include randomness as well as the temperature-dependent variation of thermal properties.

In terms of an acceptable threshold for the probability of failure of steel columns, Ellingwood assumed a conditional failure probability of approximately 0.1 for structural elements given a structurally significant fire to arrive at the design load combination when including fire. It is not the intent of this paper to discuss acceptable reliability thresholds and it should be mentioned that structural collapses due to fire in the US are considered to be rare. However, there are two discussion points to be considered when evaluating the reliability of structures under fire: (1) the probability of failure of elements should be quantified and guidance should be provided to ensure a harmonized safety level for structures of similar occupancy type, an approach that is not currently being followed, (2) the fire protection design of structural elements, designed based upon prescriptive or performance-based approaches, can be optimized if the design follows a target safety level.

5 CONCLUSIONS

This paper completed a systematic comparison of the probability of failure for a set of steel columns designed based upon the US prescriptive approach with varying section factor (60.9 to 127.3 kg/m²), utilization ratio (0.5, 0.7, and 0.9), and end restraint condition (k of 0.5, 0.7, and 1.0). The limit state was defined in the load domain, comparing axial demand load and capacity, where capacity was calculated using either AISC SCM or EC3 approaches. The columns were subjected to the ASTM E119 and parametric temperature-time curve considering a range of fuel load density (up to 2000 MJ/m²). The probability of failure was calculated with the yield strength of steel, modulus of elasticity of steel, density, thermal conductivity, specific heat, and thickness of insulation, applied load, and model error as random variables. The applied probabilistic models for the random variables were carefully selected based on the prior studies by the authors. The process was implemented in a code for future applications by engineers and researchers. The presented results in this paper showed a relatively large variation in the probability of failure when considering columns with different section factors. The US prescriptive approach also does not consider the effect of utilization ratio in the prescribed insulation thicknesses. Limiting the comparison to columns of a 9-story building designed according to current prescriptive codes, the probability of failure still varied between 0.2 and 0.5, where the largest difference occurred for first and last stories with different height, applied load, and end restraint conditions. One question that needs to be further investigated relates to the thermal properties of insulating materials that are proprietary. Values of the probability of failure are sensitive to the input properties, including thermal conductivity of insulation. In general, the level of safety of the US prescriptive approach practiced for decades can be acceptable, yet, the reliability level is not known and has not been established. Results presented in this paper demonstrate that a more harmonized safety level for more efficient and economic designs should be investigated, which will also ensure known, consistent, and quantified safety levels for structural fire design.

REFERENCES

1. Ellingwood, B., Load combination requirements for fire-resistant structural design. *Journal of Fire Protection Engineering*, 15, 2005, pp. 43-61.
2. American Institute of Steel Construction (AISC), Specification for structural steel buildings, ANSI/AISC 360-16, Chicago, IL, 2017.
3. CEN: European Committee for Standardization, General rules – structural fire design – EN1993-1-2, Eurocode 3, Brussels: Belgium, 2005.
4. Elhami Khorasani, N., Gardoni, P., Garlock, M., Probabilistic fire analysis: material models and evaluation of steel structural members. *Journal of Structural Engineering* 141, 2015, 12, 04015050.
5. Iqbal, S, Harichandran, R.S., Capacity reduction and fire load factors for design of steel members exposed to fire. *Journal of Structural Engineering*, ASCE, 136(12), 2010.

6. Holický, M., Sýkora, M., Stochastic models in analysis of structural reliability. Proceedings of the international symposium on stochastic models in reliability engineering, life sciences and operation management, Beer Sheva, 08-11/02, Israel, 2010.
7. Jovanovic, B., Van Coile, R., Hopkin, D., Elhami Khorasani, N., Lange, D., Gernay, T., Review of current practice in probabilistic structural fire engineering – permanent and live load modelling, *Fire Technology*, 2020, <https://doi.org/10.1007/s10694-020-01005-w>.
8. Van Coile, R., Hopkin, D., Elhami Khorasani, N., Gernay, T., Demonstrating adequate safety for a concrete column exposed to fire using probabilistic methods, *Fire and Materials*, 2020, <https://doi.org/10.1002/fam.2835>.
9. Qureshi, R., Ni, S., Elhami Khorasani, N., Van Coile, R., Hopkin, D., Gernay, T., Probabilistic models for temperature dependent strength of steel and concrete, *ASCE Journal of Structural Engineering*, 146(6), 2020. [https://doi.org/10.1061/\(ASCE\)ST.1943-541X.0002621](https://doi.org/10.1061/(ASCE)ST.1943-541X.0002621)
10. CEN: European Committee for Standardization, Actions on structures—Part 1-2: General actions—Actions on structures exposed to fire. Eurocode1, Brussels, Belgium, 2002.
11. Elhami Khorasani, N., Salado Castillo, J.G., Gernay, T., A digitized fuel load surveying methodology using machine vision, *Fire Technology*, 2020, <https://doi.org/10.1007/s10694-020-00989-9>
12. Elhami Khorasani, N., Salado Castillo, J.G., Saula, E., Josephs, T., Nurlybekova, G., Gernay, T., Application of a digitized fuel load surveying methodology to office buildings, *Fire Technology*, 2020, <https://doi.org/10.1007/s10694-020-00990-2>.
13. ASCE, Minimum Design Loads for Buildings and Other Structures (ASCE/SEI 7-16), American Society of Civil Engineers, Reston, VA, 2016.
14. Gernay, T., Elhami Khorasani, N., Garlock, M.E.M., Fire fragility functions for steel frame buildings: Sensitivity analysis and reliability framework, *Fire Technology*, 55, 1175–1210, 2019.
15. Isolatek, Isolatek international product manual, Isolatek International, Stanhope, NJ, 2020.
16. Carino, N.J., Starnes, M.A., Gross, J.L., Yang, J.C., Kukuck, S.R., Prasad, K.R., Bukowski, R.W., Passive fire protection, Federal building and fire safety investigation of the World Trade Center disaster, NIST NCSTAR 1–6A, 2005.

FIRE PERFORMANCE OF A STEEL OPEN CAR PARK IN THE LIGHT OF THE RECENT DEVELOPMENT OF THE LOCALISED FIRE MODEL “LOCAFI”

Mauro Sommavilla¹, Nicola Tondini²

ABSTRACT

The paper presents the results of a comprehensive finite element thermo-mechanical analysis conducted on a steel open car park subjected to localised fires. In particular, the LOCAFI model, a localised fire model recently developed in a European research project to estimate the radiative heat flux received by vertical members, was exploited to evaluate the fire performance of bare steel columns under the typical fire scenario of 4 vehicles burning around a column. The car park, to be built in Italy, was designed according to the Italian Building Code and the Eurocodes with steel grade S460M. Different column profiles were selected in order to optimise the structural fire performance, structural weight and related costs. The parametric analysis showed that, for this fire scenario and the selected profiles, the LOCAFI model was not the major governing factor of the column collapse. Indeed, when collapse occurred, it was mainly caused by material fracture in the column element just below the slab and subjected to the Hasemi model. As a result, it was observed that cross sections with thicker flanges and webs, i.e. HE of the M series are to be preferred with respect to cross sections with same area but higher inertia such as HE of the B series, that are characterised by thinner flanges and webs. Finally, no composite action and fireproofing are potentially needed for the vertical members by accounting for a profile with an adequate low section factor and higher strength, e.g. in this specific case an HE 260 M series S460M quality.

Keywords: Localised fires; LOCAFI model, steel structures; open car park; finite element modelling

1 INTRODUCTION

In the framework of the Fire Safety Engineering (FSE) approach, the fire behaviour of steel open car parks exposed to localised fires has been widely investigated in the last twenty years for which natural fire curves and fire scenarios have been derived. Full-scale tests were performed in France in the late ‘90s and recommendations about the rate of heat release (RHR) of typical Class 3 cars and commercial vehicles to be adopted in design are now available [1]³. Analytical models describing the effects of localised fires were included in the structural Eurocode EN1991-1-2 [1], i.e. Hasemi and Heskestad correlations. However, they have limited field of applicability, e.g. the Hasemi model is valid only for flame impacting the ceiling and it is typically employed for horizontal structural members located at the ceiling level, whereas the Heskestad model may be applied to vertical elements fully engulfed into the localised fire. Due to the absence in the code of a suitable model able to provide the thermal action on vertical members external to the fire, safe assumptions are usually taken. For instance, one common assumption is to take the heat flux computed at the top of the column by means of the Hasemi model and to apply it to all column cross sections or is to

¹ Senior Engineer, Arcelormittal Steligenca Italy
e-mail: mauro.sommavilla@arcelormittal.com

² Assistant Professor, Department of Civil, Environmental and Mechanical Engineering, University of Trento, Italy
e-mail: nicola.tondini@unitn.it, ORCID: <https://orcid.org/0000-0003-2602-6121>

It worth mentioning that a major event that occurred at the Liverpool Echo Arena car park fire that destroyed 1400 vehicles in 2018 was not in line with the proposed fire scenarios.

compute the Hasemi heat flux at each column cross section by using in the model correlation the height of the considered cross section, as indicated in the French guidelines [3]. Computational Fluid Dynamics can be a viable option but it is still rather computationally demanding and its use is not straightforward for engineers with typical structural background [4]. Therefore, by applying simplified and safe assumptions, the most severe scenario for the columns generally leads to the design of either fireproofed columns or steel-concrete composite columns (partially encased H-sections or concrete filled tubes) hindering the use of potentially more economical compact bare steel elements. This increases the costs of application and of maintenance, in the first case, or the complexity of joint detailing between the composite column and the unprotected steel-composite I-beams, in the second one. In the last few years, to overcome the lack of a simplified method that covers the computation of the radiative heat flux received by a column outside a localised fire, comprehensive research on localised fires at European level has been done [5,6] and it has led to the development of an analytical model [7], the LOCAFI model, able to predict the radiative heat flux in space and in time emitted by a fire of conical shape to vertical members exposed to localised fires. The LOCAFI model was implemented in the thermo-mechanical software SAFIR [8] that was thoroughly used in this work.

2 DESCRIPTION OF THE CASE STUDY

This work describes a detailed numerical investigation of an unprotected steel open car park to be built in Italy (see Figure 1), subjected to a fire scenario relevant for the column, i.e. 3 Class 3 vehicles and 1 commercial vehicle around it, as depicted in Figure 2a. This fire scenario is included in the Italian Fire Prevention Code [9] and others code in Europe, e.g. France [1]. The rate of heat release (RHR) is shown in Figure 2b, where Car 3 corresponds to the commercial vehicle. This fire scenario can be seen as four localised fires, which surround the column, but they do not engulf it. In more detail, the car park will be realised in the area of Turin. The structure is a 3 to 4-storey split-levels car park of dimensions 48 m x 40 m x 9/12 m (interstorey height = 3 m) with 16-m long IPE 500 steel-concrete composite beams and 220-mm deep steel decking spanning transversally over 5-m long beams and directly connected to the beam web by means of appropriate connectors so-called “wings”. In the transverse direction, between each column HE 120 B 5-m long profiles were employed. To minimise the impact on the structural weight the use of fine grain steel S460M according to EN10025-4:2019 was foreseen for both beams and columns. Concrete of class C35/45 inside the ribs and over the upper beam flange (plain slab of 8/10cm) was employed. Joints between columns and beams are pinned and horizontal loads are withstood either by appropriate steel bracings or concrete walls. The live load was taken equal to 2.5 kN/m². The car park was designed in accordance with the Italian Building Code and the relevant parts of the Eurocodes.

In the original project, partially encased columns were envisaged, which were composed of an HE 260 A S355 with 8 additional $\phi = 22$ mm reinforcement bars and concrete strength class C35/40 that filled the steel section between the two flanges. However, it was decided to also investigate a different solution by considering bare steel columns. In this respect, different profiles were considered in order to analyse their performance under the selected fire scenario and they are reported in Table 1. It is possible to observe that the utilisation ratio μ is in the order of 15%-20%; thus, about half of the maximum suggested by the French Guidelines [3], i.e. 35%. These μ values are due to the adopted philosophy that aims at the column overdesign to avoid fireproofing or a composite solution. Indeed, the partially encased solution would have entailed a higher utilisation ratio equal to 29%. Moreover, it is worth presenting the selection criteria of the column profiles. For instance, let us consider an HE 260 M and an HE 450 B. They have basically the same cross-sectional area (and consequently weight per unit length); therefore, the axial resistance $N_{pl,Rd}$ is pretty much the same. However, they differ in terms flexural properties for which the HE 450 B profile has more favourable properties by having larger height and width, which in turn entails thinner thicknesses of the flanges and the web with respect to the HE 260 M. Thus, if the axial force is governing, as it is case because, apart from bending moments caused by second order effects, the columns are predominantly axially loaded due to the pinned connections and an HE 260 M should then exhibit a more favourable behaviour since it has a smaller section factor. Similar observations can be made for the HE 240 M and the HD 320x158.

Moreover, an HP 320x184 was also selected. It has an increased cross-sectional area ($A = 234 \text{ cm}^2$) as well as enhanced flexural properties with respect to an equivalent HE 280 M profile ($A = 240.2 \text{ cm}^2$), by keeping at the same a reasonable size, with respect to an equivalent HE 500 B profile ($A = 238.6 \text{ cm}^2$), that it is important for a car park in order to maximise the available space for the parking spots.

Table 1. Column profiles

Profile	h (mm)	b (mm)	t _w (mm)	t _f (mm)	A (cm ²)	I _y (cm ⁴)	I _z (cm ⁴)	G (kg/m)	Section factor (m ⁻¹)	N _{Ed} /N _{pl} (-)	λ _y (-)	λ _z (-)
HE 240 M	270	248	18	32	199.6	24290	8153	157	73	0.192	0.41	0.70
HE 260 M	290	268	18	32.5	219.6	31310	10450	172	72	0.174	0.37	0.65
HE 450 B	450	300	14	26	218.0	79890	11720	171	93	0.176	0.23	0.61
HD 320x158	330	303	14.5	25.5	201.2	39640	11840	158	89	0.190	0.32	0.58
HP 320x184	329	317	25	25	234.5	42340	13330	184	78	0.163	0.33	0.59

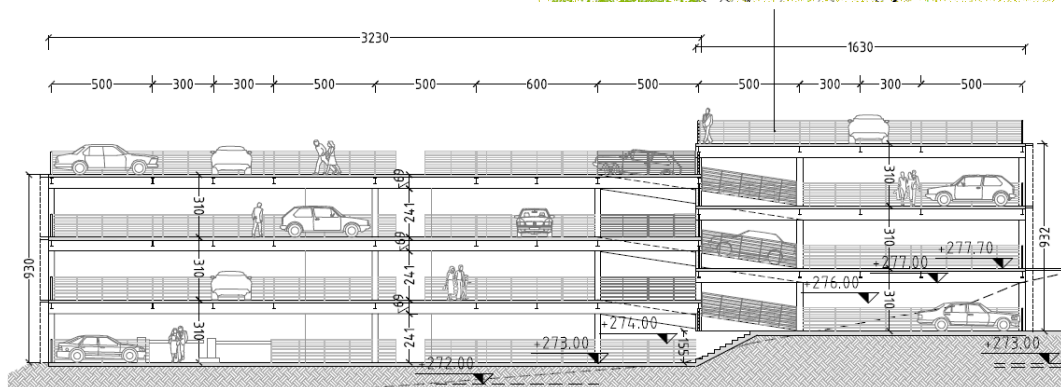


Figure 1 – Layout of the car park. Dimensions in cm.

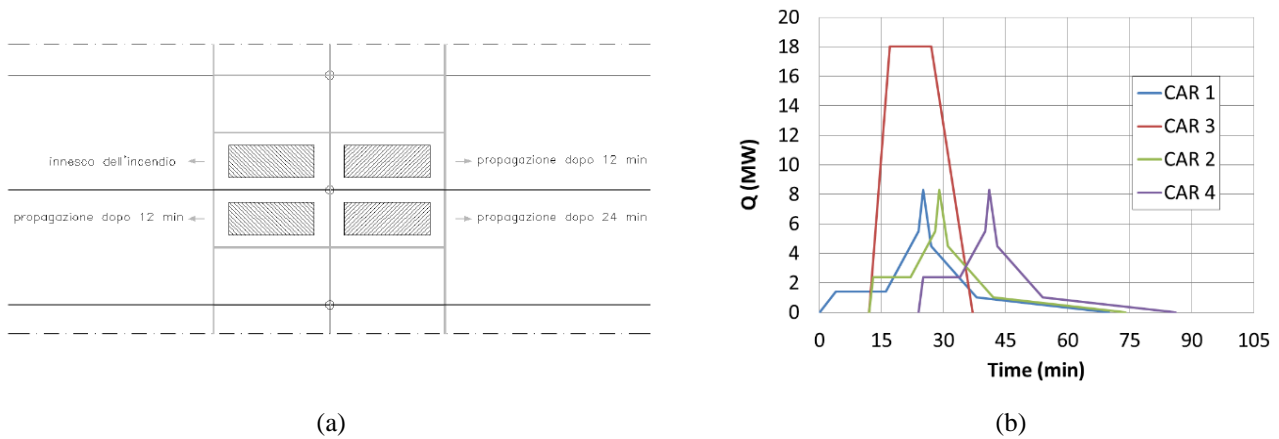


Figure 2 – a) Selected fire scenario according to the Italian Fire Prevention Code [9] and b) RHR of a 4-car scenario.

3 LOCAFI MODEL

Localised fires result from a liquid or solid fuel burning on a limited surface. Several models are available in literature to study localised fires and they can be classified among field/computational fluid dynamics (CFD) models and empirical/analytical models. Tondini et al. [7] showed how the analytical LOCAFI model compared with CFD models to predict the radiative heat flux emitted from localised fires and how it fared against experimental measurements. Among empirical/analytical models, solid flame models adopt a specific shape for the flame geometry, that may be a cylinder, an elliptical cylinder or a cone. These models consider that the radiative heat fluxes are emitted from the surfaces of the solid representing the fire and that the radiative heat flux received by an external element is the sum of the radiative heat fluxes emitted from each surface based on the computation of the configuration factor, which may be done analytically and/or numerically depending on the flame shape assumption. In the framework of this research, a solid flame model is adopted with the use of the LOCAFI model developed within the European LOCAFI Project. This model was developed and calibrated based on experimental tests and CFD numerical analyses [7]. A brief description is summarized herein.

The LOCAFI model represents the localised fire with a conical shape, as depicted in Figure 3. It means that the fuel is distributed in such a way that an equivalent circular representation of its distribution is still a reasonable assumption, i.e. when the ratio of the two sides of a hypothetical rectangular distribution is not greater than two. It has to be noted that LOCAFI model neglects wind effects, as it was done in this work. The fire model relies on the existing localised fire correlations provided in Annex C of EN1991-2 [2]. Thus, the length of the flame is defined in Equation (1) as a function of the fire diameter D and the rate of heat release Q .

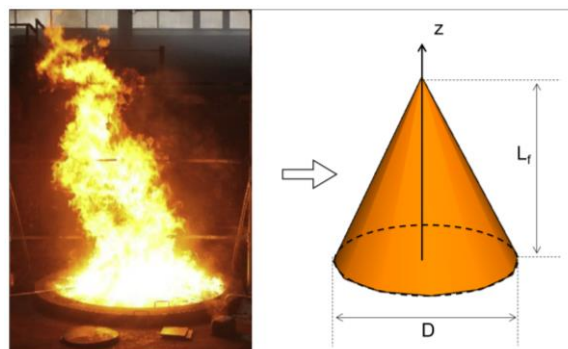


Figure 3. Solid flame modelled with conical shape in the LOCAFI model.

$$L_f = -1.02D + 0.0148Q^{2/5} \quad (1)$$

where D is the diameter (or its equivalent) of the localised fire (m) and Q is the RHR (W). The temperature along the vertical flame axis can be expressed with Equation (2) as a function of the height z

$$T(z) = 20 + 0.25Q_c^{2/3} (z - z_0)^{-5/3} \leq 900 \quad (2)$$

$$z_0 = -1.02D + 0.00524Q^{2/5}$$

where T is the temperature ($^{\circ}\text{C}$) along the centreline of the localised fire, Q_c is the convective part of the RHR Q in (W) taken as 0.8 times the RHR, z is the height along the fire centreline (m) and z_0 is the virtual origin (m) and D is the diameter (or its equivalent) of the localised fire (m).

Once a localised fire is defined with a conical shape and a temperature evolution along the flame axis, incident radiative heat fluxes can be computed for any external element considered. Equation (3) defines the incident radiative heat flux $\dot{q}_{inc.A \rightarrow B}''$ emitted by a surface A and received by a surface B .

$$\dot{q}_{inc.A \rightarrow B}'' = \phi_{A \rightarrow B} \varepsilon_A \sigma (T_A + 273.15)^4 \quad (3)$$

Where $\phi_{A \rightarrow B}$ is the configuration factor, ε_A is the emissivity of surface A , σ is the Stefan-Boltzmann constant ($\text{W}/\text{m}^2\text{K}^4$) and T_A the temperature ($^{\circ}\text{C}$) of surface A . The surface A is an element discretising the conical fire and the surface B is an element discretising the structural steel members. The emissivity of the flame ε_A , or ε_f , is conservatively taken equal to 1. The configuration factor can be determined analytically, if available, otherwise through numerical integration. In this work, the model implemented in SAFIR is based on numerical integration of the configuration factor. It discretizes the surfaces of the fire and the member with small elements. The temperature of each slice is calculated with Equation (2), by considering its average height. Steel members are represented with their actual cross section and shadows effects are considered. As explained in Section 4, the columns are modelled with beam elements with two points of integration each. At each integration point a 2D thermal analysis is performed with thermal boundary conditions that are representative of the position of the structural element with respect to the localised fire (or fires). In fact, SAFIR is able to compute at each time step and for each finite element located on the border of the cross section an incident radiative heat flux, which is calculated by summing all the radiative heat fluxes emitted by the surfaces discretizing the fire (or fires) and visible by the element according to a numerical procedure. Then, the net heat flux is expressed as the difference between the absorbed radiative heat flux and the heat fluxes reemitted by the surface B through radiation and convection at ambient temperature.

4 NUMERICAL MODELLING

The numerical was developed with the thermo-mechanical software SAFIR [8]. A 3D FE model of half of the ground floor (48 m x 20 m x 3 m) was developed with the steel beams and columns modelled with Bernoulli beam elements and the concrete slab with quadrangular shell elements, as illustrated in Figure 4. Since the columns were continuous, the ones above the floor under study were also modelled and kept cold. Each exposed column was divided into 6 finite elements, with the top one just below the slab subjected to the Hasemi model, whilst the other five subjected to the LOCAFI model. The beams and the slab were subjected to the Hasemi model. Typically, this is a conservative assumption since the flame does not impact the ceiling during the whole duration of the fire scenario. The selected fire scenario of the 4 vehicles burning around one column described in Section 2 was included in SAFIR. The parking spots 2.5 m x 5 m were defined as equivalent circular areas centred at the middle of the parking and whose diameter was taken equal to 3.91 m. The thermal and mechanical material properties were selected according to the relevant fire parts of the Eurocodes. Partial reversibility of the steel strength was considered when the steel temperature exceeded 600°C by allowing for a loss of $0.3 \text{ MPa}/^{\circ}\text{C}$. For the concrete slab a bi-axial plane stress element that included the explicit transient creep strain model developed was employed [10]. The concrete model is calibrated on the EN 1992-1-2 model and it is able to take into account the non-reversibility of transient creep strain when the stress and/or the temperature decrease. Thus, the use of an explicit transient creep model allowed a more accurate analysis. Plasticity is based on a Drucker-Prager

yield function in compression and a Rankine cut off in tension. Compressive strength equal to 35 MPa was considered. The fracture energy, that was set to approximate the tension-stiffening effect, was taken as 1500 N/m². This value was chosen based on the considerations made by Gernay et al. [11] to have a more robust numerical simulation. In this respect, the characteristic concrete tensile strength was lowered from 2.2 MPa, typical of a C35/40 concrete strength class, to 0.5 MPa. The other material parameters were considered as default values [8]. Concrete degradation at elevated temperature followed the EN 1992-1-2 provisions for siliceous aggregates. In the thermal analysis, the beam elements representing the IPE 500 were modelled with the slab on top of them only for thermal purposes as the slab acts as heat sink, as shown in Figure 4b, because in the mechanical analysis the slab was modelled with shell elements. Moreover, since the rib depth of the profiled steel sheet was significant (220 mm), in order to better model the slab, the ribs were represented by means of beam elements spanning transversely with section shown in Figure 4c, where only the rib is acting in the mechanical model, whereas the slab on the top was exploited only for the thermal analysis. Distributed loads were applied to the slab and point loads were applied at the top of the columns to simulate the load coming from the upper floors. After a sensitivity analysis on the mesh, the mechanical model was composed of 4581 nodes, 2347 beam elements and 1764 shell elements.

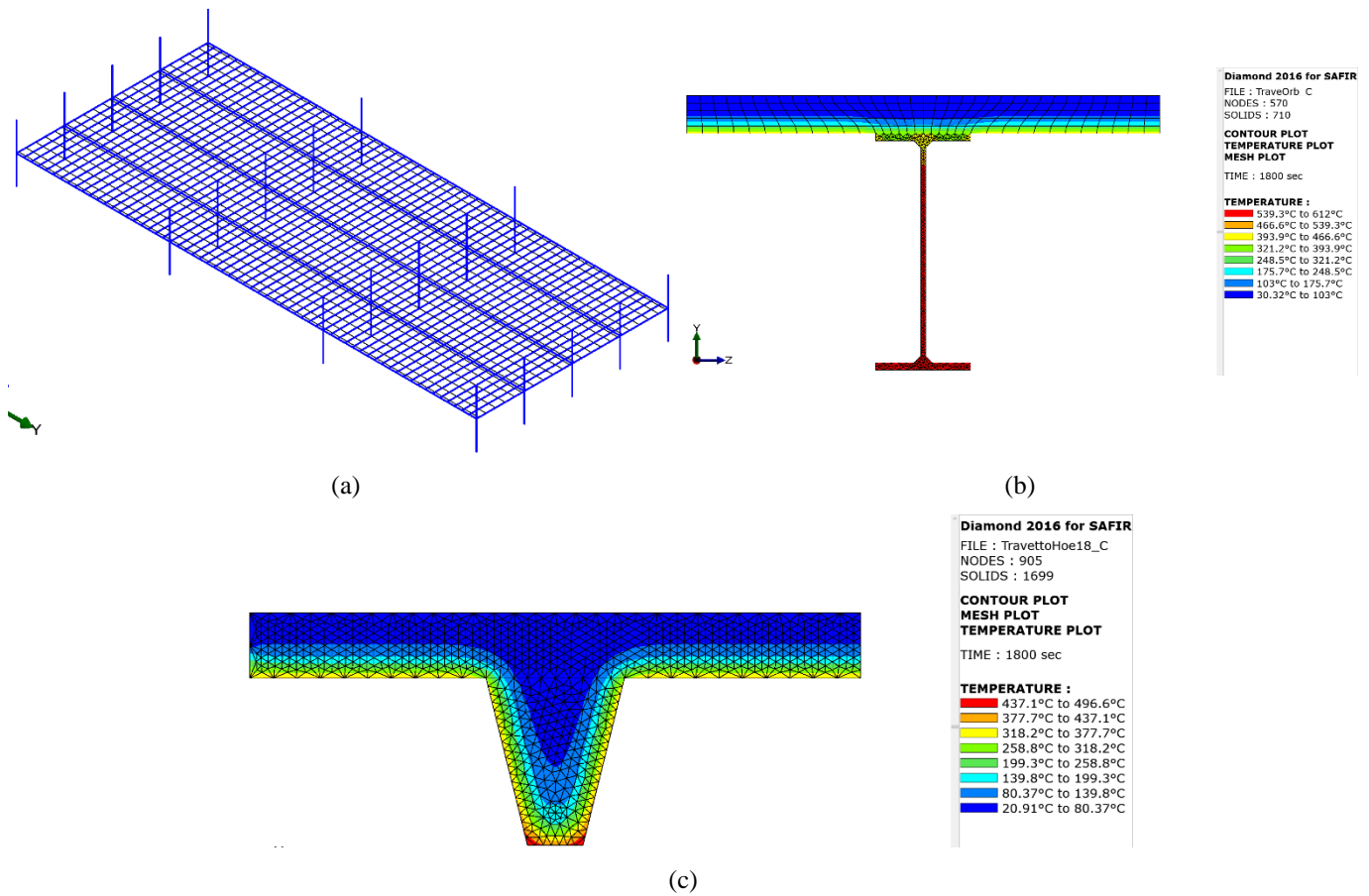


Figure 4. a) 3D finite element model; b) main beam modelling; c) slab rib modelling.

5 RESULTS AND DISCUSSION

The results of the thermo-mechanical analyses will mainly focus on the column surrounded by the burning vehicles since it is the objective of this work to investigate its fire behaviour. Moreover, it will be shown that the structural fire performance of the car park was governed by the column profile choice and failure, if it occurred, was indeed due to the loss of load-bearing capacity of the column.

5.1 Thermal analysis

The results of the thermal analysis relative to the selected columns are illustrated in Figure 5 and Figure 6. In particular, in Figure 5 the temperature distributions after 30 min of exposure to the fire scenario for three profiles (HE 260 M, HE 450 B, HP 320x184) are shown both for the Hasemi exposed element below the ceiling and for the LOCAFI most thermally impacted element at about 70 cm from the ground. It is possible to observe that, the Hasemi model is much more demanding in terms of thermal attack than the LOCAFI model. In fact, it causes peak steel temperatures in the order of 800-850°C. However, the temperature distributions in the three cross sections is markedly different (see Figure 5a, c and e). If we look at Figure 5c relative to HE 450 B, the entire web, i.e. about $\frac{1}{4}$ of the entire cross-sectional area, is at temperatures higher than 800°C, which corresponds to a steel retention factor for the effective yield strength $k_{y\theta} \leq 0.11$ [12]. Now, for the HE 450 B profile, as shown in Table 1, the utilisation ratio is 0.176 and this data already provides a hint that an HE 450 B may not be enough to support the applied axial load under the considered fire scenario. In this respect, the average temperature of the cross section after 30 min is beyond 750°C, which implies $k_{y\theta} < 0.17$. Conversely, looking at Figure 5a relative to the HE 260 M, which has about the same cross-sectional area as the HE 450 B, one may observe that, as expected, the temperature field is characterised by lower temperatures, with only about half of the web characterised by temperatures higher than 780°C. Moreover, the average section temperature can be roughly estimated in a value below 750°C; thus $k_{y\theta} > 0.17$ and being $\mu = 0.174$ this profile may have enough strength to survive the fire. The temperature field of the HP 320x184 is more uniform since the web and the flanges have the same thickness (Figure 5e) and similarly to the HE 260 M the average temperature in the cross section is less than 750°C with a utilisation ratio equal to 0.163. Figure 6a and b show the evolution in time of the temperature in the flange and in the web for each profile under the Hasemi model. It is possible to note that the HE 240 M and the HE 260 M have very similar temperature evolutions, which is consistent with their respective section factors and geometries, as shown in Table 1. However, the HE 240 M has a cross-sectional area, which is 10% less than the HE 260 M, and this may affect the ability of the profile to sustain the applied loads under the fire scenario.

As expected, the LOCAFI model caused a significant non-uniform temperature distribution in the cross sections and along the member. Here, only the most heated cross sections are shown. In particular, Figure 5b, d and f highlight that at 30 min, a time that corresponds to all 4 vehicles burning (see Figure 2b), one flange corner is hotter than the rest of the cross section. Indeed, that part of the cross section is oriented towards the burning commercial vehicle that produces higher heat fluxes. However, peak temperatures lie under 500°C (see also Figure 6c) with most of the cross section being below 400°C, that is the temperature at which $k_{y\theta}$ starts to decrease below 1.0. Therefore, the thermal impact of the LOCAFI model, despite causing thermal bowing and enhancing second order effects, should not govern the possible failure of the selected profiles. In sum, by analysing the results of the thermal analysis, a loss of the cross-section axial resistance of the column element subjected to the Hasemi model seems the main factor that can lead to the structural failure of the column.

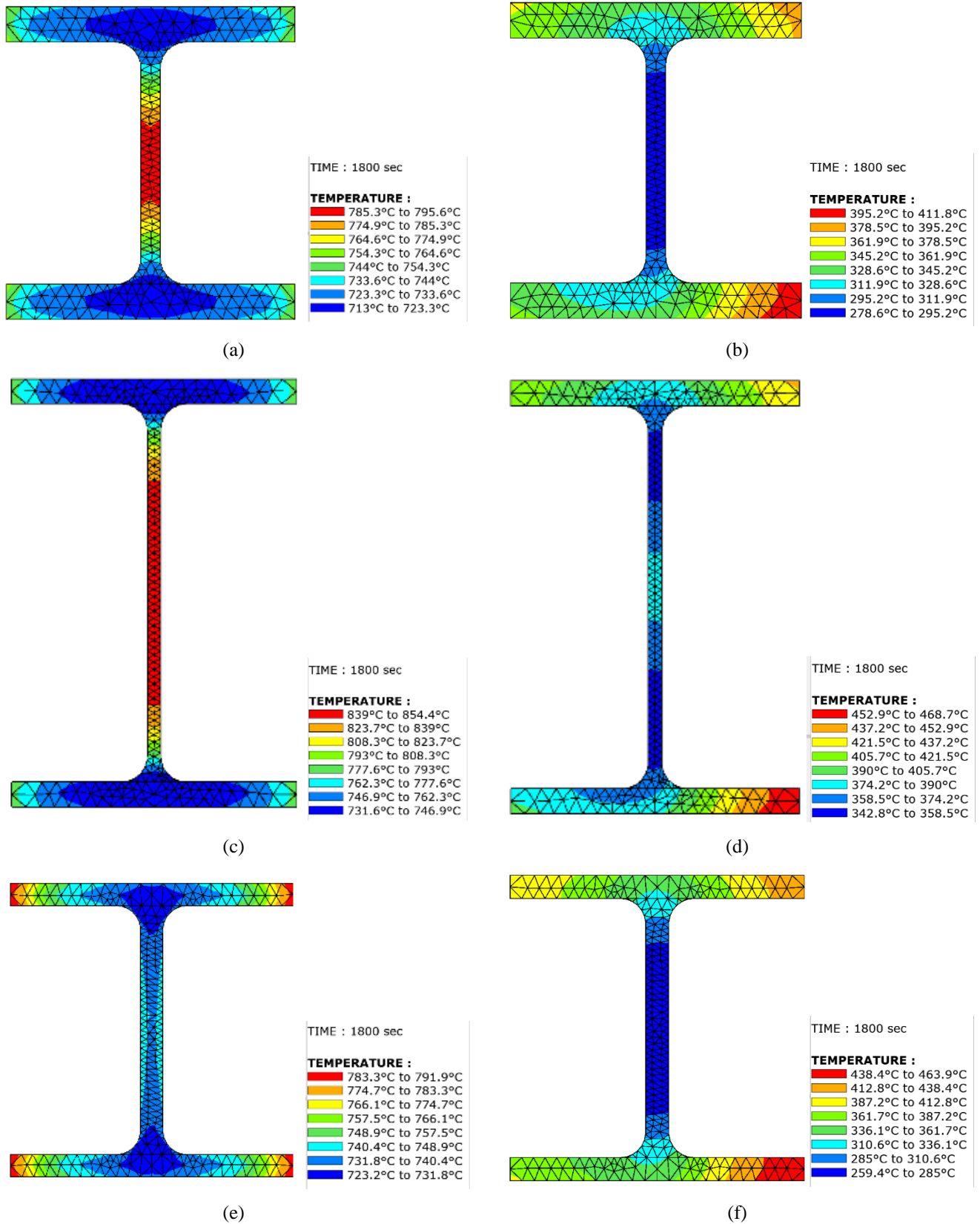


Figure 5. Column thermal analysis at 30 min: a) Hasemi HE 260 M; b) LOCAFI HE 260 M; c) Hasemi HE 450 B; d) LOCAFI HE 450 B; e) Hasemi HP 320x184; f) LOCAFI HP 320x184.

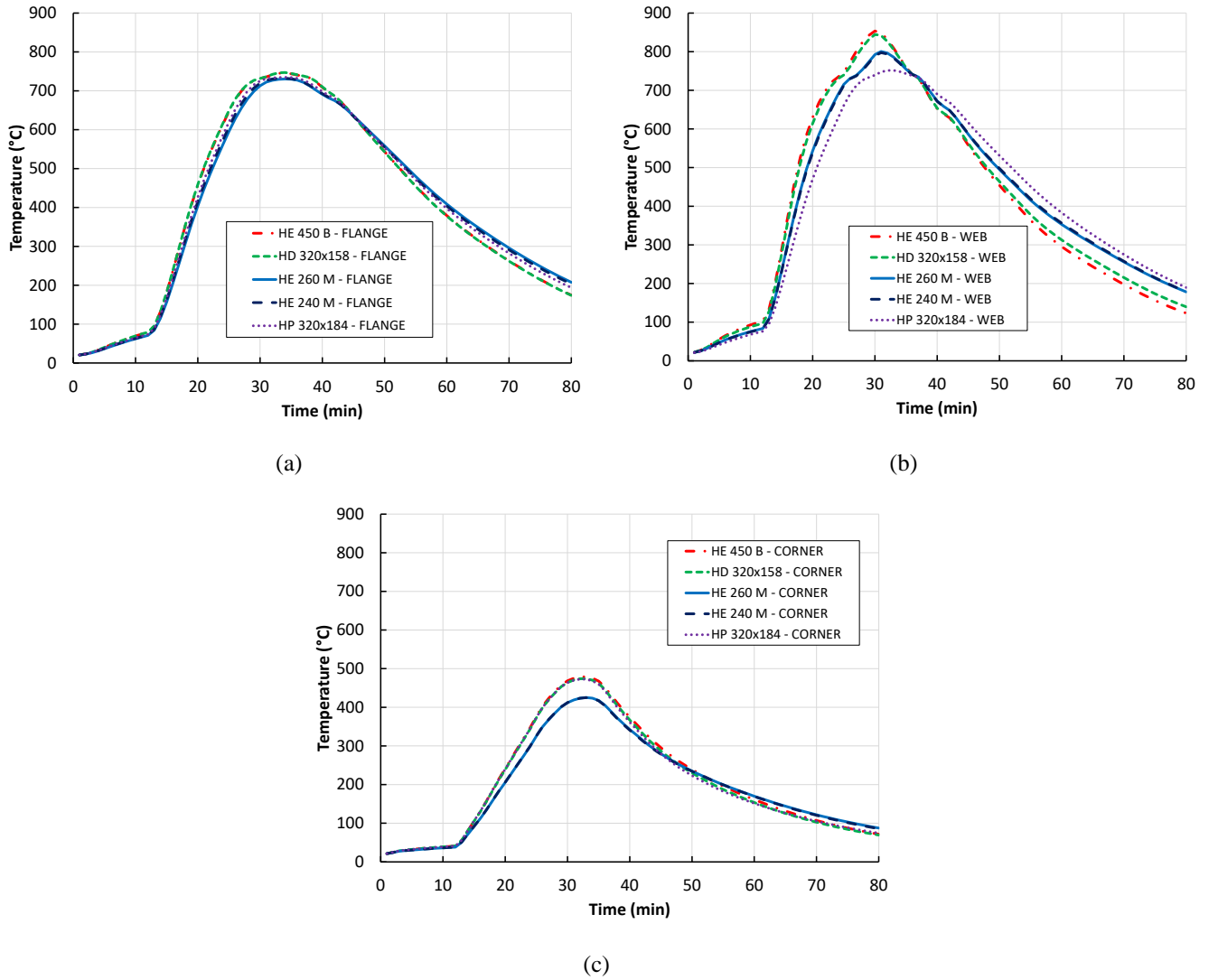


Figure 6. Column thermal analysis: a) Hasemi flange temperature; b) Hasemi web temperature; c) LOCAFI maximum temperature in the cross sections.

5.2 Mechanical analysis

All five mechanical responses were run based on the outcomes of the thermal analysis. Three out of five analyses did not converge and structural failure of the column was observed. Indeed, as hinted before by looking at thermal analysis results, the top column element heated by the Hasemi model was the cause of collapse owing to loss of load-bearing capacity under the applied forces, as shown in Figure 7 for the HE 450 B case. The analyses with the HE 260 M and the HP 320x184 profiles survived the whole duration of the fire with maximum vertical displacement of the slab above the commercial vehicle being in the order of 50 cm, as illustrated in Figure 8. Indeed, based on the thermo-mechanical outcomes that exploit the new available LOCAFI fire model that allows for the prediction of the heat fluxes along the height of the column, a design strategy that aims at the column overdesign could be a viable option for steel open car parks. Moreover, the use of a steel grade S460 revealed to be beneficial in sustaining the applied loads. Finally, the choice of columns made of profiles HE 260 M S460M was the most economical solution.

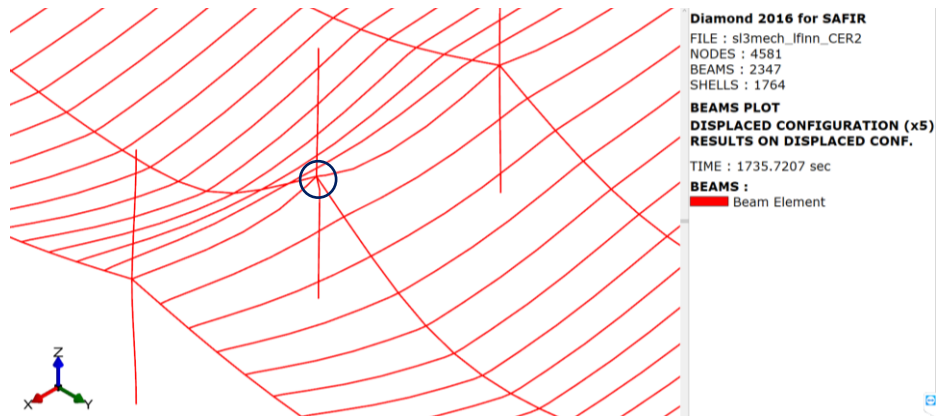
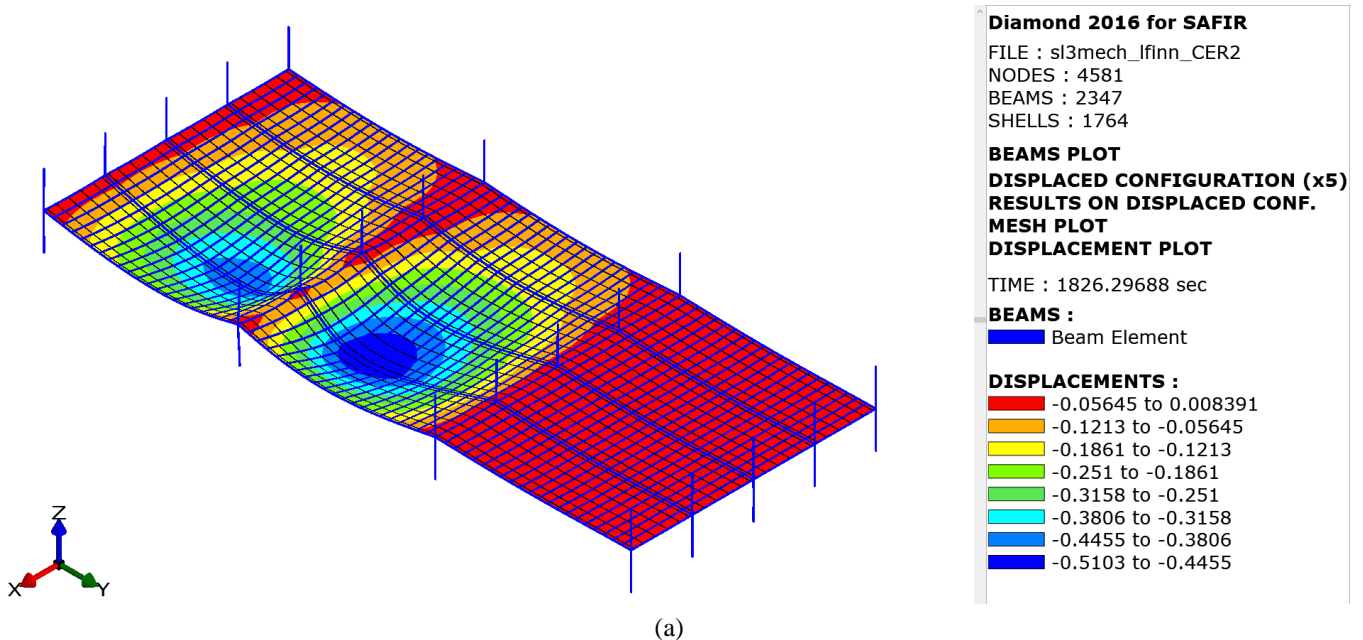
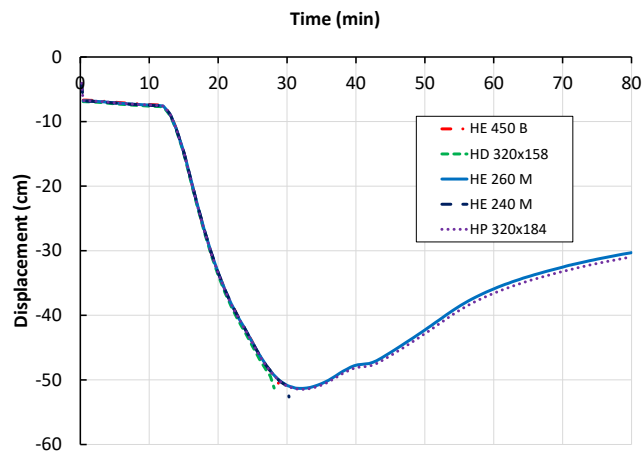


Figure 7. HE 450 B column failure owing to mainly crushing in compression.



(a)



(b)

Figure 8. a) Deformed shape (x5) and vertical displacements (m) of the car park at about 30 min with HE 260 M S460 column;
 b) maximum vertical displacement evolution of the slab.

6 CONCLUSIONS

The paper presented a refined finite element thermo-mechanical of a steel open car park to be built in Italy and subjected to a fire scenario relevant for the column, which is represented by 4 localised fire of burning vehicles that surrounds it. According to a design strategy of the column overdesign, a parametric analysis was performed with the aim to find a suitable bare steel column profile that could satisfy the requirements of structural fire performance by surviving the entire duration of the fire scenario without collapsing. The Hasemi model combined with a newly developed localised fire model, the LOCAFI model, were employed to predict the radiative heat fluxes along the height of the column. The analyses showed that the thermal impact caused by the Hasemi model is much more demanding than the one determined by the LOCAFI model. In particular, failure was attained by mainly crushing in compression of the cross section in the column element just below the ceiling and impacted by the Hasemi model. Moreover, as the axial load was the most significant action on the columns, compact profiles with low section factor, e.g. HE profiles of the M series, are more suitable than profiles with the same cross-sectional area but characterised by more slender flanges and web, e.g. HE profiles of the B series. Finally, an HE 260 M S460M with utilisation ratio of 0.174 in the fire situation was identified as a potential option that could avoid the use partially encased or fireproofed profiles.

ACKNOWLEDGMENT

This work was supported by the Italian Ministry of Education, University and Research (MIUR) in the frame of the ‘Departments of Excellence’ (grant L 232/2016). Moreover, the information about the structural design provided by design B&V Eng-Arch Office, Corso Novara 99, Turin, Italy, is also acknowledged.

REFERENCES

1. INERIS (2001) Parcs de stationnement en superstructure largement ventilés. Avis d’expert sur les scénarios d’incendie.
2. EN1991-1-2 (2002) Eurocode 1: Actions on structures – Part 1-2: General actions – Actions on structures exposed to fire, CEN, Brussels.
3. Roosefid M. and Zhao B. (2014) Guide pour la vérification du comportement au feu de parcs de stationnement largement ventilés en superstructure métallique, CTICM.
4. Tondini N., Morbioli A., Vassart O., Lechêne S., Franssen J.-M. (2016) An integrated modelling strategy between FDS and SAFIR: Methodology and application, *Journal of Structural Fire Engineering*, 7 (3), 217-233, [dx.doi.org/10.1108/JSFE-09-2016-015](https://doi.org/10.1108/JSFE-09-2016-015).
5. Vassart O., Hanus F., Brasseur M., Obiala, R., Franssen J.-M., Scifo A., Zhao, B., Thauvoye C., Nadjai A., Sanghoon H. (2016) LOCAFI: Temperature assessment of a vertical steel member subjected to localised fire – Final Report’, Research Fund for Steel and Coal.
6. Tondini N. and Franssen J.-M. (2017) Analysis of experimental hydrocarbon localised fires with and without engulfed steel members, *Fire Safety Journal*, 92:9–22, [dx.doi.org/10.1016/j.firesaf.2017.05.011](https://doi.org/10.1016/j.firesaf.2017.05.011).
7. Tondini N., Thauvoye C., Hanus F., Vassart O. (2019) Development of an analytical model to predict the radiative heat flux to a vertical element due to a localised fire, *Fire Safety Journal*, 105:227-243.
8. Franssen J.-M., Gernay T. (2017) Modeling structures in fire with SAFIR©: Theoretical background and capabilities. *Journal of Structural Fire Engineering*, 8 (3), 300-323.
9. Ministero dell’Interno, D.M. 3 agosto 2015 “Approvazione di norme tecniche di prevenzione incendi”, ai sensi dell’articolo 15 del decreto legislativo 8 marzo 2006, n. 139, Roma, 2015.
10. Gernay T., Millard A., Franssen J.M. (2013). A multiaxial constitutive model for concrete in the fire situation: Theoretical formulation, *Int J Solids Struct* 50(22-23), 3659-3673.
11. Nia S., Gernay T. (2020), Considerations on computational modeling of concrete structures in fire, *Fire Safety Journal*, [10.1016/j.firesaf.2020.103065](https://doi.org/10.1016/j.firesaf.2020.103065).
12. EN 1993-1-2 (2005). Eurocode 3: Design of steel structures - Part 1-2: General rules - Structural fire design, CEN, Brussels.

THE COLLAPSE OF WORLD TRADE CENTER 7: REVISITED

Mhd Anwar Orabi¹, Liming Jiang², Asif Usmani³, Jose Torero⁴

ABSTRACT

In structural fire engineering literature, the catastrophic events of Sept. 11 2001 stand out as a major reason and motivation for research on improving the understanding of structural behaviour in fire. These events included the first complete collapse of a tall steel framed structure solely due to fire. World Trade Center 7 (WTC 7) was a 47-storey office building within the WTC complex that was set alight by debris from WTC 1 collapse, and in turn also collapsed 7 hours later. In the following years, detailed investigations were carried out by the National Institute of Standards and Technology (NIST), Weidlinger Associates Inc. (WAI), Guy Nordenson Associates (GNA), Arup, and the BRE Centre for Fire Safety Engineering. Each of these teams analysed the fire and structure differently, and reached varying conclusions with regards to the mechanisms responsible for initiating and propagating the collapse of WTC 7. This paper will give an overview of how the various investigations were performed, what collapse hypotheses were made, and how it is possible that the building emergency power system may have been responsible for failure.

Keywords: finite element modelling; world trade center; progressive collapse; case study

1 INTRODUCTION

During the events of Sept. 11 2001, WTC 1 and WTC 2 were each struck by a commercial airliner. With all WTC buildings in relatively close proximity, the debris from the twin towers caused severe damage to the surrounding structures many of which collapsed. WTC 7 was located north of WTC 1 and suffered considerably little damage that did not directly jeopardise its structural integrity. The debris, however, set over ten floors alight within WTC 7 and diverted the attention of first respondents away from the building [1]. After seven hours of fire burning on consecutive floors and traversing the building perimeter, the structure finally gave in with what appeared to be a failure of the core where the penthouse on top of the building first sank into the building followed by the outside framing. As the first tall steel-framed building to collapse solely due to fire, WTC 7 has gained a reputation as a major incentive for bettering the community awareness of the risks fire poses to buildings. Despite this, the collapse of WTC 7 is not as well-understood as what one may think considering its importance to the field. After years of investigation by some of the world leading experts in both fire and structural engineering, there remains multiple possible hypotheses without any consensus on how the building behaved and failed because of the fire. The authors of this article believe that there is valuable scientific merit for the community in reviewing this case study more closely and considering the big picture when the worst-case scenario really takes place. This paper begins with introducing the WTC 7 structure, its unique backup energy systems, and the events that led to its complete collapse. An overview of previous expert investigations and their results is then presented, with focus on how they analysed the fire and the structure. Finally, a different hypothesis for the collapse

¹ Mr., Department of Building Services Engineering, The Hong Kong Polytechnic University,
e-mail: anwar.orabi@connect.polyu.hk, ORCID: <https://orcid.org/0000-0001-5083-3623>

² Dr., Department of Building Services Engineering, The Hong Kong Polytechnic University,
e-mail: liming.jiang@polyu.edu.hk, ORCID: <https://orcid.org/0000-0001-8112-2330>

³ Prof., Department of Building Services Engineering, The Hong Kong Polytechnic University,
e-mail: asif.usmani@polyu.edu.hk, ORCID: <https://orcid.org/0000-0003-2454-5737>

⁴ Prof., Department of Civil, Environmental and Geomatic Engineering, University College London,
e-mail: j.torero@ucl.ac.uk, ORCID: <https://orcid.org/0000-0001-6265-9327>

is proposed that explains the fate of the 12,000 gallons of diesel fuel that were unaccounted for after the incident, and the role of the large transfer structures of the building in initiating and progressing the collapse.

2 WTC 7 AND THE SEPTEMBER 11 DISASTER

2.1 Structural layout

WTC 7 was a rather unique structure in a prime location in one of the most expensive real estate markets in the world. Created as a later addition to the World Trade Center Complex, WTC 7 was erected atop an existing electrical substation that supplied power to lower Manhattan and had to make most efficient use of the trapezoidal plot it was located upon. The tower had 47 stories and was 186 m high making it the third tallest building in the complex after WTC1 and 2 respectively. Its footprint was larger than either of the twin towers with a trapezoidal plan with North, South, East and West dimensions of 100 m \times 75 m \times 43 m \times 45 m respectively as shown in Figure 1 which also highlights the eastern bay which would become the focus of many of the collapse hypotheses. The first four floors from the ground contained the power substation, the lobby of the building, as well as other functional space such as a cafeteria and a conference room. In addition, the first floor also contained the pumps for the emergency power system. The fifth and sixth floors were primarily mechanical spaces containing ventilation and other equipment. Eleven of the fifteen power generators that comprised a critical component of the building emergency system discussed in the next section were also located on the fifth floor along with a small diesel “day tank”. Floors above the sixth consisted mainly of both open-plan and traditional office spaces. The gravity system consisted of wide flange beams and columns supporting a 140 mm thick concrete-on-steel-deck slab composite with the floor framing using headed shear studs. Lateral load resistance was provided by moment resisting connections along the perimeter frame and by two-storey high belt truss systems between the 22nd and 24th floors and the 5th and 7th floors. Core bracing below the 7th floor resisted lateral loads transferred to it by the floor diaphragm. Most floor framing connections consisted of various types of shear connections including fin plate, knife, and multiple variants of seated connections [2]. SFRM (spray applied fire resistant materials) type fire protection was applied to the structural components with a 3-hour rating for the columns and 2-hour rating for the steel decking and beams, which exceeded the required fire protection of 2 and 1.5 hour-rating for the columns and beams respectively. The entire building was also covered with sprinklers fed from the city mains from the ground to the 20th floor, and complemented with water tanks that serviced the 21st floor and above. To transfer the load from the structure into the columns and foundation while bridging over the Con Edison power substation below, a transfer system was used which consisted of three trusses, eight cantilevered built-up girders, and three transfer girders all between floors 5 and 7 as shown in Figure 2.

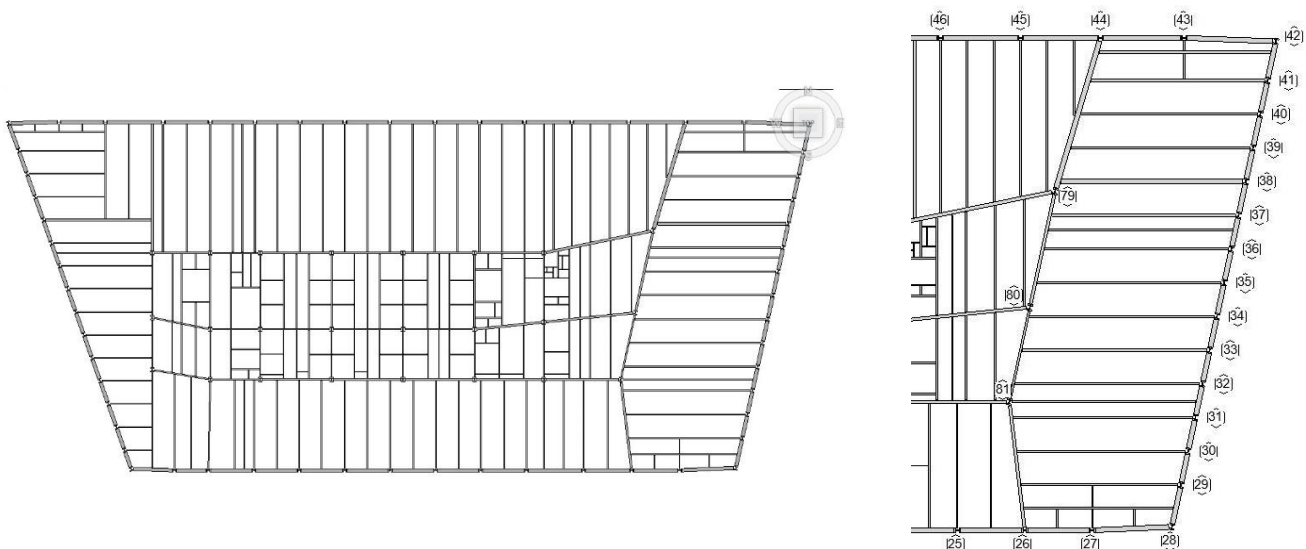


Figure 1. Typical floor layout of WTC 7

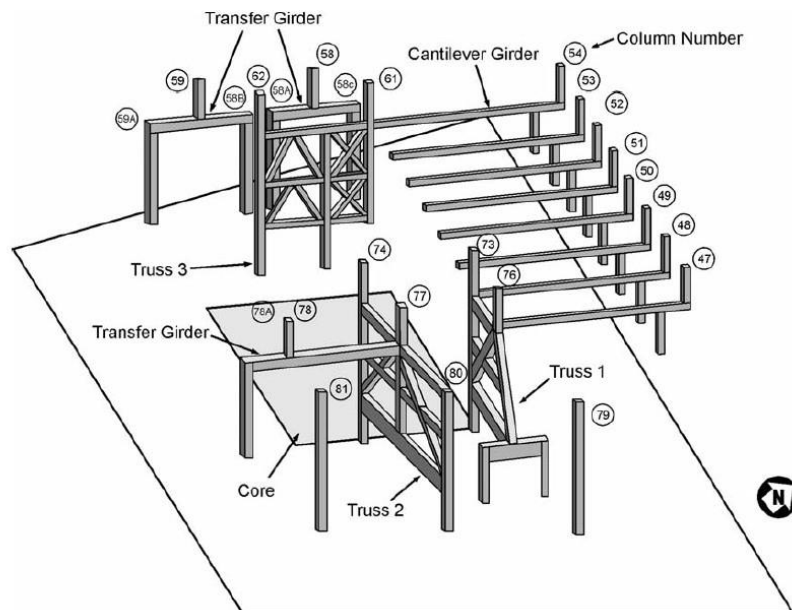


Figure 2. Transfer structure for WTC 7 [2]

2.2 Emergency fuel system

To ensure continuous operation of the primary functions of the building, an emergency power system was installed. This system had a diesel fuel capacity of about 117 m³ which fed through several pump sets that powered generators located on the 5th, 7th, 8th, and 9th floors. Separate from this system was the Salomon Brothers emergency power system which had its own subgrade diesel tanks with a capacity of 45 m³, and nine power generators all located on the 5th floor [3]. About 87 m³ of the fuel in the primary emergency system storage tanks was recovered a few months after the collapse, which is within the expected residual amount. None of the fuel within the Salomon Brothers system was recovered, however, and there were no traces of leaked residue within the proximity of the then-damaged tanks. Since there was a pre-existing 275-gallon day tank on the 5th floor as part of the primary emergency power system, the Salomon Brothers system had to be designed without a day tank. The system, therefore, was designed to supply fuel continuously to the generators as long as they were operational. The rate at which fuel was pumped to the generators was controlled by a regulator downstream from the generators. As long as the pressure downstream from the generators is kept low, fuel would continuously circulate to power up the generators which in turn powered up the pumps [3].

2.3 Fire and collapse

After WTC1, the Pentagon, and WTC2 were attacked, all 4,000 occupants of WTC 7 evacuated the building. When WTC1 began to collapse at 10:28 AM, debris launched by the collapse damaged and penetrated the south western face of WTC 7 severing the perimeter columns over floors 7 through 17 along the building corner. Large areas of the Southern façade glass were also broken. Nonetheless, the debris damage to the building and its structure did not pose an immediate threat to its stability. The water supply to the sprinklers from the city mains was disrupted due to the collapse of WTC1 and 2, and the early evacuation of building occupants made the building a low priority for the fire department which was preoccupied with rescue and firefighting operation elsewhere. Multiple fires erupted as a result of the burning debris that made it into the building, with visible fires over floors 7 through 9 and 11 through 13 burning uncontrolled for about 7 hours. The fires burned throughout the lower fire floors (floors 7, 8, and 9) spreading in a clockwise manner and travelled counter clockwise in the upper fire floors 11, 12, and 13 [4]. At 5:21 PM, a kink in the penthouse located on top of the building appeared followed immediately by the penthouse plunging into the building suggesting an implosion followed immediately by the progressive collapse of the entire structure beginning somewhere in the lower portion of the building.

3 PREVIOUS INVESTIGATIONS

The collapse of WTC 7 destroyed the electrical substation below it, for which the owners sued for damages. This resulted in several expert teams investigating the collapse and each providing a plausible scenario by which the building may have failed. Additionally, the National Institute of Standards and Technology (NIST) were commissioned to do an independent study for public interest. In this section, the various collapse scenarios are introduced and discussed starting with NIST, with particular attention paid to numerical modelling approaches.

3.1 NIST

Investigation by NIST commenced after WTC 7 debris was cleared, and so the primary investigation material was videos of the incident and the information known about the structure as per the drawings available [5,6]. To analyse the failure, NIST considered four major factors: 1. Structural damage from the debris of WTC 1, 2. Fire propagation as seen in the videos, 3. Computational Fluid Dynamics modelling of the fire calibrated with the videos, and 4. Nonlinear static and dynamic finite element models of the building.

3.1.1 Fire

According to the NIST investigation, the most severe fires were those occurring on floors 7 through 9 and 11 through 13 [1]. Fires on other floors may not have had a significant effect because they only burned briefly and are thus not visible on video. Floors 7 through 9 comprised mostly of open plan offices with a fuel load of 20 kg/m^2 mainly consisting of office equipment and paper. This fuel load was arrived at by considering the fire spread rate from the videos and comparing with the load-dependent calculated rate. The upper fire floors, 11 through 13, had more traditional offices separated by partitions and joined with false ceilings. The paper load on these floors was higher and so the fuel load NIST arrived at was 32 kg/m^2 [1]. With this data, NIST used Fire Dynamics Simulator (FDS) to produce a model of each of the fire floors individually. The models for floors 7, 8, and 12 were calibrated based on the visibility of flame and glass breakage in the videos. The models for the fire on the 9th floor was derived from the 8th floor model, and the models for floors 11 and 13 were based on the 12th floor model due to lack of sufficient footage for calibration of each individual model. Using FDS derived gas temperatures, NIST then calculated the structural temperatures in the structural members and varied them by $\pm 10\%$ to create three scenarios that envelope the potential building fires and account for uncertainties in the modelling to some extent [4,7].

3.1.2 Structural analysis

The structural analysis of the building was performed in two stages: stage 1. Implicit pseudo-static analysis of the bottom 16 floors of the building considering the heating effects, and 2. Dynamic explicit model of the entire building to investigate debris impact, heating damage, and collapse propagation. The first model was created in ANSYS and accounted for shear stud connection failure in the eastern part of the fire floors, lateral torsional buckling of floor beams, and removal of slab sections that had reached large strains. Connections were modelled as collections of springs in series or parallel depending on the type of connection modelled, and shear studs were modelled as 'break elements' that would be removed once they reached their capacity. The results of the first model analysis showed the same behaviour occurring but at slightly different time due to the variance in the heating scenario temperatures. The thermo-mechanical damage generally resulted from connection failure which led to loss of vertical support of several floor beams. Lateral torsional buckling also occurred in some members considering loss of shear studs and thus absence of lateral support. The analysis was stopped after 3.5 to 4 hours of heating, and results transferred over to a dynamic explicit model built in LS-DYNA [1].

The second model was analysed in incremental steps, starting with gradual application of dead load to avoid introducing undue vibrations into the structure. The impact and damage from the WTC1 debris was then added instantaneously, and then the model was allowed to stabilise. The addition of the debris impact indeed showed that the structure could redistribute its load-bearing capacity and avoid disproportionate damage or

collapse as was observed in reality. The temperature of the structure was then gradually increased up to the levels reached in the ANSYS model to induce secondary effects, before finally applying material and component damage instantaneously to the model. After the damage was applied, the model showed that the structure would undergo progressive collapse.

3.1.3 Collapse hypothesis

The collapse of WTC 7 according to the NIST models and investigation primarily initiated, because of connection failure. The connection between the internal column 79 and the girder linking it to perimeter column 44 failed by girder walk-off during the heating phase. To the east of column 79, many of the floor beams were lost to either loss-of-vertical-support or lateral torsional buckling. The severe heating and restrained expansion of the floor slab caused what remained of the floor to lose its stiffness by concrete crushing, and severely weakened the fire floors causing partial collapse which could not be impeded and resulted in cascading floor failure that left column 79 unsupported over 9 floors causing its buckling failure which caused the kink observed in the collapse video. The buckling of column 79 was followed by similar failures of columns 80 and 81, and then the progressive collapse of the adjacent column lines. The apparent implosion of the interior of the building was followed by perimeter failure starting at a location adjacent to the entry point of the majority of the WTC1 debris damage in the south west of the structure. The perimeter columns failed in quick succession and the complete failure of the building occurred [4].

3.2 Arup & Guy Nordenson and Associates

Arup and Guy Nordenson took a different approach to the analysis of the WTC 7 collapse. First, Arup performed an FDS and FE studies to predict the collapse initiation event. Then, GNA performed a series of nonlinear studies to study the progression of collapse from its initiation point.

3.2.1 Fire

Similar to NIST, Guy Nordenson Associates (GNA) performed a photographic study of the debris damage and fire in WTC 7 [8] and Arup performed a large scale FDS study of the 12th floor, which was one of the six floors (7th-9th, 11th-13th) where persistent potentially structurally damaging fires occurred. Arup's FDS model was calibrated with the observed fire behaviour on the day, and the window breakage was programmed following the photographs and videos. The fuel load used was 36.6 kg/m² which correlated well with the values provided in the NFPA Handbook for private and government office fuel loads [9,10]. No vertical fire spread was allowed, mechanical ventilation was assumed to have been off, and the building core was not breached and remained free from fire throughout the simulation [11]. The simulation results were in very good agreement with the observed fire in the north and east faces of the building, but less so with that in the west face. However, as Arup had determined that the critical fire space was to the east of the core, the FDS results were deemed acceptable [11]. In order to use the FDS simulation for structural analysis, an idealized but consistent heating regimen of 1 hour heating at 800 °C and 1 hour cooling at 20 °C was implemented [9]. This approach was based on the ceiling-level temperatures at multiple monitoring points throughout the area east of the core, and despite being simple, it accounted for the traveling nature of the fire, preheating, and conservation of energy. Considering the applied fire protection, particularly the assumption that the space between the ribbed floor slab and girders was left unfilled with SFRM, heat transfer analysis was performed at the University of Edinburgh. The scenario of unfilled 'flutes' presented with a unique temperature distribution in the floor girder where the top flange was the hottest, contrary to standard thermal exposure in fire where top flanges would be the coldest. Similarly, heat transfer analysis was performed considering filled flutes, and using an additional heating scenario where the ambient temperatures would peak at 700 °C instead of 800 °C.

3.2.2 Structural analysis

The structural model used by Arup was built in Abaqus/Explicit [12] and represented the east half of a typical floor, with symmetry boundary conditions representing the other side. The ribbed slab was abstracted with uniform-depth shell elements including the steel decking and using Concrete Damaged

Plasticity [13,14] to consider material nonlinearity. While most of the steel framing was idealised using beam elements, columns 44 and 79 as well as girders 79-80, 76-79, and 44-79 were modelled with a higher grid resolution using shell elements [15]. Likewise, both connections of girder 44-79 and all connections into column 79 were modelled in full detail using shell elements to represent the various plates, tie elements to model the bolts, and rigid links to represent the welds. Shear studs were only modelled in the north east corner of the floor, and assumed to be rigid elsewhere. Their force-slip relationship was temperature dependent, and ‘broke’ beyond a slip limit of 6 mm as proposed by [16]. Details of the model as built by Arup can be more clearly seen in Figure 3 [11]. Both mass and time scaling were used to ensure an efficient solution, while inertial forces were monitored to maintain reasonably accurate results [15]. The Arup analysis predicted that failure could indeed commence in the vicinity of column 79 in either heating or cooling and only if the flutes between the girder and slab were unfilled. The expansion of the beams in the north east, as well as the breakage of the studs over the girder, results in the girder severing its connection bolts and being pulled off of its seat. Given this initiating event assessed by Arup, GNA investigated collapse propagation using a full-scale elastic model built in SAP 2000 [17]. The model was supported by multiple nonlinear sub-models that would manually inform the progression of the analysis such as removing particular columns if they were prone to buckling. None of the models used by GNA were thermo-mechanically loaded and instead the analysis focused on collapse progression rather than assessment of thermal damage which was assumed to have been adequately addressed by the prerequisite Arup analysis.

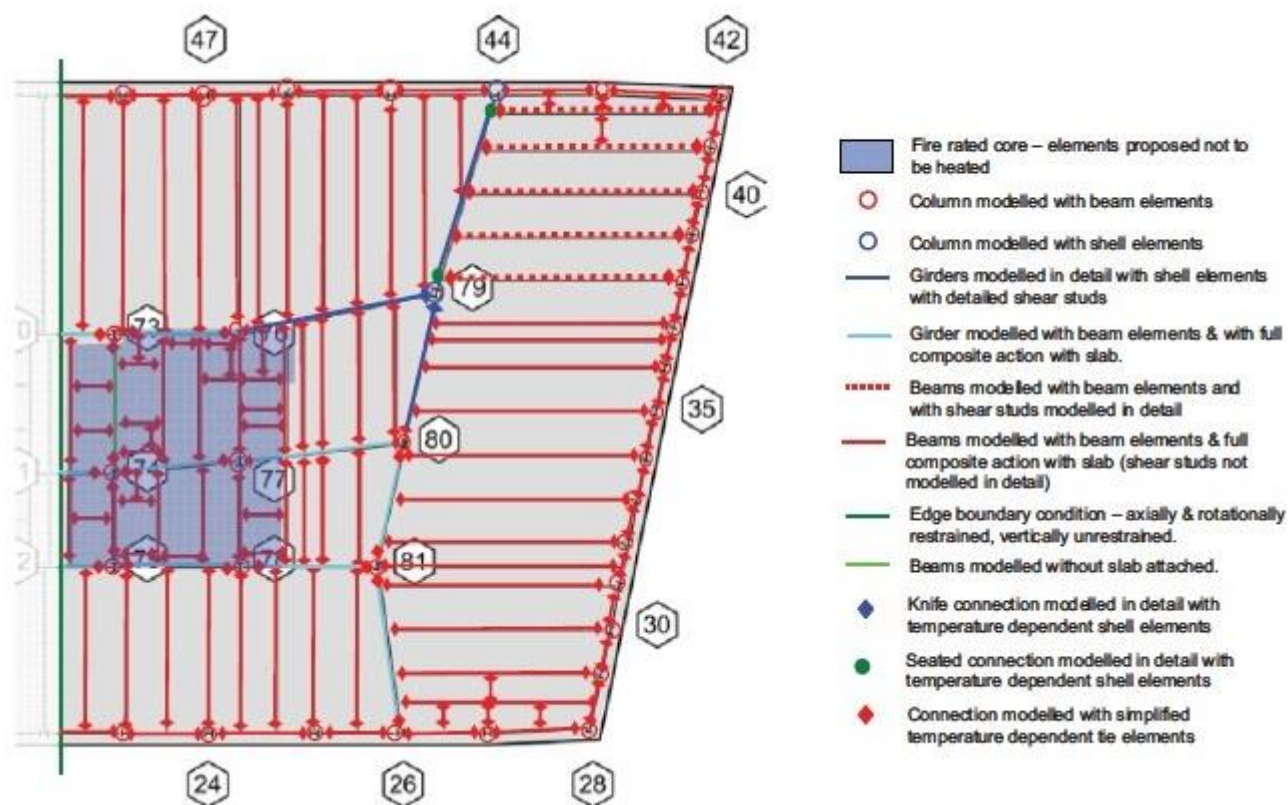


Figure 3. The Arup model and its details as built in Abaqus [11]

3.2.3 Collapse hypothesis

The Arup-GNA investigation concluded that several factors and defects contributed to the collapse of WTC 7. While the debris from WTC 1 contributed to the collapse by starting the fires, its actual impact and structural damage was largely inconsequential. Despite the fires burning uncontrollably for 7 hours throughout the structure, their effect seriously jeopardised the building only after reaching the eastern face. There, the high loads borne by column 79, the asymmetry of floor framing into girder 44-79, and most importantly the un-filled flutes (no fire protection for the top flange) caused the girder to be pulled off of

its seat [18]. From that initiating event, the analysis performed by GNA showed that a sequence of potentially stoppable events would lead to global collapse. Just after the failure of girder 44-79, the north eastern floor slab would collapse over multiple floors causing column 79 to also lose its west-facing connection and thus buckling. The failure of column 79 and its supported floor area leaves column 80 unbraced and its buckling then causes the kink observed in the penthouse as seen in the collapse videos. The falling debris then damages the transfer trusses and results in the failure of the next column line followed by pulling of the remaining core and causing the failure of interior of the building. Finally, the perimeter frame begins to buckle resulting in total collapse of the building.

3.3 Weidlinger & Associates and Hughes Associates

WAI and Hughes Associates were tasked to investigate the collapse of WTC 7 on behest of the defendants in the litigation over the power substation. Two reports were released based on their investigation, one regarding the fire and another dealing with the structural response. Unfortunately, the former, produced by Hughes Associates, was never made public and so little about it can be said.

3.3.1 Fire

Despite the WAI report adhering to the theme of thermo-mechanical response to thermal action presented in the Hughes Associates report, some important insight about the fire is given. First, it is assumed that the debris damage not only started the fires over multiple floors, but also inhibited the fire prevention measures in the building. It is assumed that most compartmentation was lost and that the sprinklers were destroyed due to the debris impact. It is also noted that the presence of widespread fires on affected floors resulted in a severely reduced ability to arrest potential progressive collapse by weakening the floor capacity to resist the local impact of a falling floor.

3.3.2 Structural analysis

Similar to Arup and NIST, WAI also used an explicit dynamic model to study the collapse of WTC 7. The analysis performed by WAI relied on one full building model, and two sub-models representing the eastern bay of one and two floors respectively. The sub-models were used to study the thermo-mechanical response of the east bay, while the full building model was used to study the collapse propagation. All models were built using WAI's inhouse nonlinear FE software 'FLEX', and included a high level of detail. All shear studs, welds, connections and slab-beam contact were modelled explicitly in the sub models. Moreover, all beams, girders and columns were modelled using shell elements. The global model was less complex with connections built as consolidations of uniaxial spring based on connection capacity estimation using the component method, and beam elements representing the steel framing.

Mechanical load was applied to the models by increasing the gravity and the density incrementally until full quasi static load was applied. Thermal loading was also a quasi-static phase employing time scaling and incurring few dynamic effects. The thermal loading continued until failure initiation, at which point dynamic analysis proceeds until re-stabilisation or total collapse.

3.3.3 Collapse hypothesis

WAI analysis also showed that the collapse initiated in the eastern part of the building. However, the initialising event did not occur in the vicinity of column 79 but in the proximity of column 80. Uncontrolled heating in the eastern bay had led to floor deflections in the order of 1/15 of the span, which resulted in high tensile forces in the floor beams. At the same time, the uncontrolled heating had resulted in high connection temperatures of which the nearest to column 80 would sever and lead to zipping off of adjacent connections. With this, the eastern portion of the floor would collapse impacting a similarly weakened floor resulting in progressive failure of the east section of the interior floor of WTC 7. Columns 79, 80, and 81 then unsupported over multiple floors would buckle and cause the kink in the penthouse. The collapsing debris severely damaged the transfer structure on the fifth and sixth floors, and also resulted in westwards internal collapse propagation. The unbraced perimeter columns then buckled and the total failure of the structure occurred [19].

4 MECHANICAL ROOM FIRE

As previously mentioned, the Salomon Brothers emergency power system was designed as a pressurised loop where fuel would continuously be pumped from the storage tanks as long as the generators were operational. It is possible that once a power outage was detected on 11 September, the Salomon Brothers power system would have started. Had there been a penetration in the double-walled fuel line anywhere away from the first few generators on the fifth floor, a low-pressure signal in the valve rig at the end of the system may have signalled to the pumps to continuously push fuel into the system [3]. There was no indication of any automatic leak-detection system in the Salomon Brothers system, and it is therefore possible for all available fuel to have been available at the fifth floor to feed a potential fire there. NIST did consider this scenario in their analysis but dismissed it based on three reasons:

1. A pool fire would have raised the temperature beyond the generators operational limit thus cutting power supply to the fuel pumps.
2. The fire would not have heated the structure to critical levels.
3. A critical fire in that location would have resulted in significant exhausted smoke visible from the outside of the structure but none were seen.

This assessment was based on FDS results assuming a pool fire occurring in the vicinity of column 79 just outside the mechanical room located on the 5th floor. It is possible that a breach in the fuel line and masonry wall of the mechanical room would have led to a pool fire inside the mechanical room, or a fire may have started just outside the mechanical room and propagated into it through damage in the partition. Both of these scenarios would have heated the large transfer trusses in the mechanical room resulting in potentially critical damage to the structural integrity of the building. Such a diesel fuel fire would likely generate large amounts of smoke that, if not all had exhausted through other openings in the building or its core, would have been visible outside the east face of the structure. As noted by Mowrer [9], petroleum-based smoke was indeed observed in the videos and witnessed by first responders after 3:30 PM just outside the north east corner of the building as seen in Figure 4 [8].



Figure 4: Smoke outside the north east corner of WTC7 between 4:15 and 4:38 PM [8]

4.1 Fire scenario

Assuming a pool fire in the mechanical room, an FDS analysis was run by the BRE Center for Fire Engineering [20]. Several ventilation conditions were assessed considering the opening of the mechanical room to the plenum east of the building, and the results were compared to the Thomas curve [21] since the fire had reached steady state burning within 300 – 600 seconds in all cases. All FDS simulations gave predictions below the Thomas curve indicating that the analyses were conservative and well-below experimental data and reality. By considering energy balance while neglecting re-radiation and conduction, and assuming a linear growth phase for the fire it was found that the column and truss-member temperatures would reach steady state with a small delay but are otherwise the same as the gas-phase temperatures. Considering the fire protection, a 20% lag in heat uptake may occur but would be inconsequential assuming that for the columns it was thermal degradation and so maximum attained temperatures that were most critical [20]. Similarly, a CFD analysis of a pool fire in the vicinity of column 79 was performed and it was found that the column temperatures would be very similar to the mechanical room fire scenario.

4.2 Structural analysis

The approach that the BRE Centre had taken towards the structural analysis of the collapse was unique as it had paid more attention to the global structural behaviour and focused on load redistribution rather than on localised failures of individual connections and elements. A 15-storey model was built in Abaqus using beam-column elements to represent the steel framing, shell elements to represent the concrete slab. Vertical load corresponding to the column forces from the upper floors was applied at the top of the columns which were allowed to translate vertically but not planarly. All elements were connected to one another rigidly; no connections were allowed to fail and composite action was maintained throughout the analysis. The rationale for this modelling approach is because the investigators believed that adding all the details entails making many assumptions most of which would complicate the problem and obscure what may be a global limit state. Unlike the other models, this particular approach did not aim to recreate the exact events but rather give insight into the global behaviour of the structure and unlock the many possible ways the buildings may have potentially failed.

An elimination analysis was performed where different collapse scenarios were modelled and checked for consistency with the observed collapse. Heating of only truss 1, heating of only truss 2, heating of both trusses, and heating of only column 79 were all tested. In each of the scenarios, load transfer played a critical role in overall deformation of the structure, and it was identified that it was most likely that a combination of heating both trusses were responsible for the collapse as will be discussed in the next section. This analysis also showed that heating of column 79 just outside the mechanical room would likely result in a similar global collapse.

4.3 Collapse hypothesis

A fire in the mechanical room would heat columns 77 and 80 as well as the diagonals of truss 2 which connects them. As these columns lose their capacity, their load is transferred to columns 76, 79, and 81. Likewise, the exposed and partially heated truss 1 is also losing capacity due to heating thus transferring its own capacity to the core and to column 79. Given that column 79 is likely to have been heated due to a diesel fire in its location, and that it also is the most heavily loaded column, it is likely that it would have failed. From this, it was clear that failure of any one of truss 1, truss 2, or column 79 would overload the other two and lead to their failure. It was, therefore, that combined heating of truss 1 and truss 2, and potential heating of column 79 was the primary factor for global collapse of WTC 7. The initiating failure could have been either failure of column 79 or of truss 2, because a collapse event beginning at either of these two points had the potential to manifest the kink observed in the penthouse and cause its sinking as was seen in the videos.

5 CONCLUSIONS

The collapse of WTC 7 remains to this day a unique event in the history of structural fire engineering. Despite occurring nearly twenty years ago, there is no real way to know what exactly caused its failure.

Multiple expert teams had investigated the disaster and tried to recreate the various events that led to the progressive failure of the structure. With most debris gone, the expert teams had to rely on photos, videos, and numerical modelling to piece together their different hypotheses. FDS and explicit FEM played a crucial role in each of the investigative teams' approaches, which shows a trend towards more computationally intensive methods for forensic analysis of fire-attacked structures. By reviewing the various modelling approaches and hypotheses of the investigators some important insights about the case can be gained:

1. There is consensus amongst the investigators regarding two main aspects of the collapse of WTC7: fire was the primary cause of the failure, and the failure initiated in the east side of the building somewhere in the lower 14 floors.
2. FDS simulations of affected floors 7-9 and 11-13 calibrated against videos produce comparable temperatures in the structural components. Even the small variations in temperature, however, may result in different outcomes depending on the nature of the structural model.
3. Despite the tremendous efforts of the various investigative teams, there is no consensus regarding the exact initiating mechanism. Arup's analysis showed that girder 44-79 would be pulled off of its seat, opposite to the prediction by NIST which show the girders pushed off of their seats. WAI's analysis points towards a floor beam connection failing followed by entire floor collapsing. Finally, the UoE mechanical room fire scenario predicts that the failure may have occurred due to a completely different fire caused by a breach of the emergency power system.
4. Numerical models are only idealisations of real events, and thus by nature they would be dependent on the decisions made by the analyst. There are many discrepancies between the different numerical models and outcomes for WTC 7, and each may be sensitive to different factors. There still remains a gap in the knowledge on the most suitable approach to modelling large structural systems in fire, and what is the right level of abstraction to capture the most important aspects of the behaviour without complicating the models beyond reasonable computational cost and pushing it outside its predictive capacity.

REFERENCES

1. NIST, NIST NCSTAR 1A: Final Report on the Collapse of the World Trade Center Building 7, 2008.
2. NIST, NIST NCSTAR 1-1: Design , Construction , and Maintenance of Structural and Life Safety Systems, 2005.
3. NIST, NIST NCSTAR 1-1J: Documentation of the Fuel System for Emergency Power in World Trade Center 7, 2005.
4. NIST, NIST NCSTAR 1-9: Structural Fire Response and Probable Collapse Sequence of the World Trade Centre Building 7, 2008.
5. Frankel Steel Limited, Erection Drawings: 7 World Trade Center, (1985).
6. Office of Irwin G. Cantor, Structural Design Drawings: 7 World Trade Center, (1985).
7. T. McAllister, R. MacNeill, O. Erbay, A. Sarawit, M. Zarghamee, S. Kirkpatrick, J. Gross, Analysis of structural response of WTC 7 to fire and sequential failures leading to collapse, J. Struct. Eng. (United States). 138 (2012) 109–117. [https://doi.org/10.1061/\(ASCE\)ST.1943-541X.0000398](https://doi.org/10.1061/(ASCE)ST.1943-541X.0000398).
8. Guy Nordenson and Associates, Photographic Analysis: Volume A Photographic Timeline, New York, 2009.
9. F. Mowrer, Expert Report by Frederick Mowrer, 2010.
10. National Fire Protection Association, Fire Protection Handbook, 20th edition, 2008.
11. Ove Arup & Partners Consulting Engineers PC, World Trade Center 7 Floor 12 Fire Effects Simulation, 2010.
12. Simulia, Abaqus, (2018).
13. J. Lee, G.L. Fenves, Plastic-damage model for cyclic loading of concrete structures, J. Eng. Mech. 124 (1998) 892–900. [https://doi.org/10.1061/\(ASCE\)0733-9399\(1998\)124:8\(892\)](https://doi.org/10.1061/(ASCE)0733-9399(1998)124:8(892)).
14. Dassault Systèmes, Abaqus Analysis User's Manual, (2012).
15. Arup, JA-3240: Master Assumptions List, 2009.

16. Z. Huang, I.W. Burgess, R.J. Plank, The influence of shear connectors on the behaviour of composite steel-framed buildings in fire, *J. Constr. Steel Res.* 51 (1999) 219–237. [https://doi.org/10.1016/S0143-974X\(99\)00028-0](https://doi.org/10.1016/S0143-974X(99)00028-0).
17. Guy Nordenson and Associates, WTC7 Global Collapse Analysis Report and Summary of Findings, 2010.
18. Arup, WTC -7 Structural Fire Analysis Report (Runs 1-4), 2010.
19. Weidlinger Associates Inc., WTC 7 Collapse Analysis and Assessment Report, 2010.
20. BRE Centre for Fire Safety Engineering, Analysis of the Impact of a Fire in the Mechanical Room (5th & 6th Floor) of the World Trade Center 7 Building, 2010.
21. P.. Thomas, A.J.M. Hseselden, Fully Developed Fires in Single Compartments: new correlations of burning rates, 1973.

STEEL SHEET PILES EXPOSED TO FIRE

EXPERIMENTAL TESTS AND NUMERICAL MODELLING

Jean-Marc Franssen¹, João Martins²

ABSTRACT

This paper deals with the behaviour under fire of vertical walls made of steel sheet piles in retaining walls close to, for example, a traffic road or an industrial facility or in underground structures such as car parks or cut and cover tunnels. For the latter situation, the sheet pile walls support not only the horizontal pressure from the ground but also the vertical loads induced by the different floors.

Four experimental tests have been performed in the fire lab of ULiege on a test setup where different soils were located at the back of a heated sheet pile wall, namely sand and clay, either saturated with water or not. Equivalent thermal properties have been derived that allow reproducing in a simple conductive model the temperature distributions measured on the steel piles.

Modelling the whole sequence of events from erection of the structure to failure under fire requires the successive application of 2 different software, RIDO that reproduces the evolution of the displacements and force distribution in the wall during the successive sequences of construction and SAFIR[®] that models the behaviour of the structure when it is subjected to fire. The links that have been established to transfer the results of the first simulation to be taken as initial conditions for the second software are described.

Finally, a specialised one node finite element that has been introduced in SAFIR to model the elasto-plastic behaviour of soil is described and an application example is briefly discussed.

Keywords: Steel; sheet piles; tests; modelling; soil

1 INTRODUCTION

Steel sheet piles are used extensively in the construction industry, as temporary as well as permanent structures, essentially for retaining the horizontal pressure of soil or water. In most applications and, generally speaking, in temporary structures, there is no requirement with respect to the fire resistance of such retaining walls.

There are some cases yet when the stability of a wall made of sheet piles must be ensured during a fire, such as retaining walls close to a traffic road, walls of cut and cover tunnels or underground car parks, see Figure 1. In the latter case, sheet pile walls support not only the horizontal pressure from the ground, the horizontal forces from eventual anchorages or from the floors that expand or pull on the walls, but also the vertical loads induced by the floors.

¹ Professor, Liege University,
e-mail: jm.franssen@uliege.be, ORCID: <https://orcid.org/0000-0003-2655-5648>

² Head of Technical & Marketing Department, ArcelorMittal
e-mail: joao.martins@arcelormittal.com, ORCID: <https://orcid.org/0000-0003-4987-115X>



Figure 1. Walls in an underground car park made of unprotected steel sheet piles [1]

2 THERMAL CALCULATIONS

2.1 General approach

It cannot be envisaged to make experimental tests for every project to be realised. Modelling has to be made and, because of the complexity of the problem, numerical modelling is the tool of choice.

The choice of the fire scenario is of course crucial but it should be made independent of the type of structure in the building (at least as long as non-combustible materials are used). It will therefore not be discussed here. The software SAFIR[®] [2] that has been developed namely by the first author and is used in the company of the second author can accommodate different representations of the fire attack such as time-temperature curves or different localised fire models such as the LOCAFI [3] solid flame model or results of CFD modelling [4].

On the base of the chosen fire scenario, the first step in the design is the computation of temperatures in the steel piles. If the attack from the fire on the exposed side and the conduction of heat in the eventually protected steel section is handled by nowadays traditional techniques, distribution of heat in the ground on the back of the wall is much more complex, especially if the soil is saturated with water the movements of which will participate to the distribution of heat. The idea was to make a series of full scale tests, with different soil compositions, in order to see whether the results of these tests could be reproduced with an acceptable level of approximation by a much simpler purely conductive model

2.2 Experimental tests

Four tests were conducted in the fire lab of Liege university. The gas furnace was closed on one of its vertical sides by a caisson made, on one side, of full scale PU 6 steel sheet piles that faced the furnace and contained a given soil for each test with a thickness in the order of 50 cm, see Figure 2. The steel wall was not loaded during the test and the top of the caisson was not closed, which left way for eventual vapour release to escape from the caisson. Two different types of soil were tested, namely sand and clay, each one in two different situations with regards to water, either saturated or not.

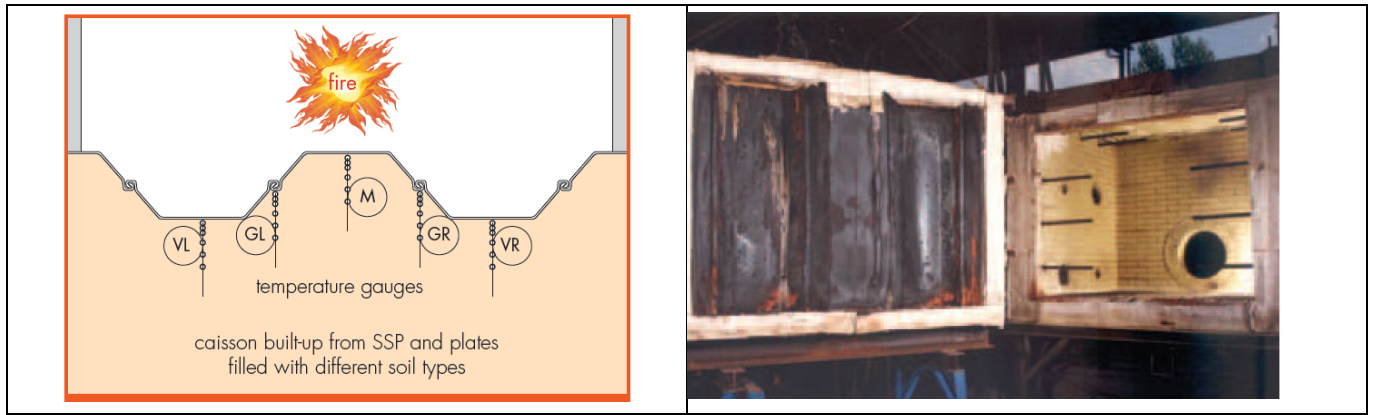


Figure 2. Schematic view of the test setup (left) - The caisson and the furnace after a test (right) [5]

The standard fire curve ISO 834 was applied for 3 hours, except for the test with water saturated sand in which a shortage of gas supply limited the test to 2 hours.

Nine temperature gauges were applied on the steel piles at different locations whereas 5 thermocouple trees of 6 gauges each were placed in the soil.

There was a marked influence of the soil on the steel temperatures that were observed to be the highest with non-saturated sand, then non saturated clay, saturated clay and, markedly colder with saturated sand. For the latter case, the significantly lower temperatures were likely due to recirculation of liquid water in this highly permeable soil. The evolution in time of temperatures with saturated soils was less regular than with non-saturated soils. There were also, for each soil, temperature differences in the steel piles that can be linked to the concave or convex side with respect to fire exposure (VL and VR compared to M on Figure 2 – left) or to a higher value of the local massivity at the interlocks between two adjacent piles (GL and GR on Figure 2 – left).

2.3 Thermal properties of soils

The tests have been recalculated and some equivalent thermal properties have been proposed for various soils as gravels, sand, sandy clays or clays, each saturated with water or not.

Values were proposed for thermal conductivity and specific heat but also for an equivalent water content that can be linked to the soil permeability. It may come as a surprise that water contents higher than 1000 L/m³ are proposed when the permeability is higher than 10⁻⁸ m/s, but it has to be understood that this equivalent water content is introduced here to take into account by water evaporation an energy dissipation that in reality takes place essentially by water movements.

All proposed thermal properties can be found in detail in reference [5] that can be downloaded from Internet.

3 LOADING FROM THE SOIL

3.1 Pressure from the soil

It is commonly accepted that the pressure from a soil on a vertical wall p_0 is proportional: to the vertical distance from the surface z ; to the specific weight of the soil γ ; and to a coefficient that takes into account mechanical properties of the soil (such as the friction angle ϕ) K_0 , see equation (1)

$$p_0 = K_0 \gamma z \quad (1)$$

A constant can be added if a vertical load is applied on the surface.

The specific weight of the soil is reduced in equation 1 by the specific weight of water γ_w for the zones of the wall that are under the water table, while the hydrostatic pressure from water has to be applied in such zones.

The beam finite element of SAFIR can accommodate trapezoidal distributed loads. They can be formulated in the global system of coordinates of the structure or in the local system of coordinates of the element but,

even in the latter case, these loads do not follow the element when it enters in the large displacement domain. The approximation is expected to be acceptable as the rotations of the retaining walls are usually limited, even in the near failure situations.

The hydraulic pressure from the water table has nevertheless been coded as a following pressure in the sense that the direction of this load will remain perpendicular to the axis of the element and its intensity is proportional to the vertical distance from the surface of the water table, taking into account large displacements. The following character of this load is expected to have very limited effects, as mentioned about the trapezoidal loads from the soil.

The pressure given by equation (1) is valid when the retaining wall is at rest, i.e. when it is not subjected to significant displacements. The wall may yet be moving away from the soil at certain levels, for example because of a global rotation induced by loss of stability of the wall. The pressure will then decrease as the displacement increases, down to a certain value that will remain constant, whatever the displacement. This value, called active pressure, is computed by an equation similar to equation (1) but with replacing the coefficient for the wall at rest K_0 by a coefficient for active pressure K_a . On the contrary, if the wall is subjected to a displacement toward the soil, the pressure will increase with the displacement up to a value characterised by a coefficient for passive pressure K_p .

During the course of a fire, horizontal movements of the retaining wall are to be expected, due to thermal expansion of the horizontal beams and slabs, to sagging of these elements at the time of failure and to thermal gradients on the depth of the steel sheet pile, see section 2.2.

As these displacements can develop in any direction and, at a given location, can change in direction during the course of the fire, the load cannot be predicted beforehand and a specific procedure had to be developed which is described in the section underneath.

3.2 Specific finite element

As the evolution of the pressure is directly dependent on the displacements and the displacements in the numerical model are computed for the nodes, these effects have been taken into account by a dedicated finite element that is attached to the nodes.

A specific finite element has been developed with the following characteristics.

- The element is linked to a single node, one node of the structure that is supposed to be in contact with the soil. It can thus be used in models made of beam finite elements, shell elements or even solid elements.
- The direction of the pressure is given by the angle related to the global axis X in 2D models or by a vector in 3D models. The direction is defined from the soil to the structure. If the element is used to model an elastic foundation under a beam, the vector will thus point upward, it will point to the left on the wall of a car park that is on the right side, and to the right for the wall on the left hand side.
- The constitutive relationship in the element is expressed in terms of force-displacement relationship $F-u$ that is elastic-plastic as shown on Figure 3 where F has the direction of the element and u is the component of the displacement of the node parallel to this direction. This relationship is characterised by a lower limit FI and an upper limit FS , as well as the stiffness used between both levels K . If the element is used to represent a foundation underneath a beam, the lower limit may be set to 0.
- The behaviour in case of reversal in the direction of the displacement is plastic; unloading follows the elastic stiffness until reaching the opposite level.
- As engineers are used to quantities of soil mechanics that are expressed in terms of kN/m^3 for stiffness and kN/m^2 for pressures, such units are used in the input data³ together with an area of influence of each element A that will multiply the input values in order to obtain, for the element, upper and lower limits in N and a stiffness in N/m.

³ In fact, N/m^3 and N/m^2

- In order to be consistent, a specific command has been introduced in the 2D model of the sheet pile used for the thermal analysis, see Section 2. This command gives the width B of the section that has been modelled; the section of all fibres of the section is then divided by B which will lead to the fact that all mechanical properties of the section are given for a width of the wall of 1 meter.

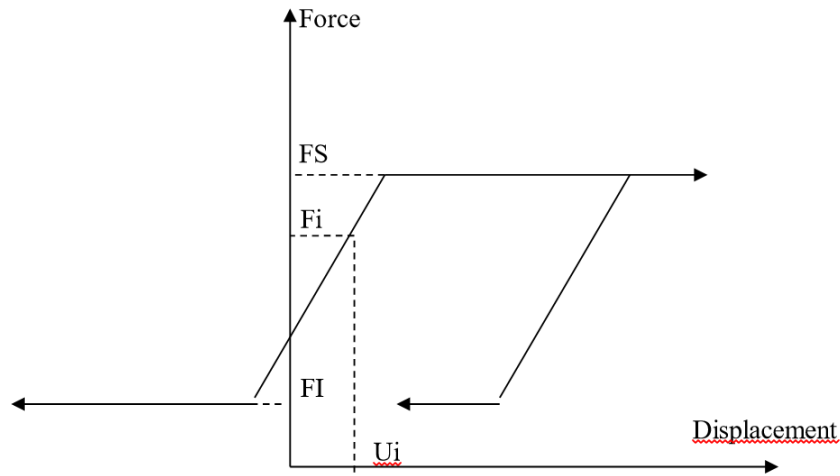


Figure 3. Force displacement relationship in the element

The meaning of F_i and U_i in Figure 3 will be explained in section 4.

4 SEQUENCES OF CONSTRUCTION

4.1 Introduction

For buildings that are erected above ground level, it is commonly accepted that the successive sequences in the building process need not be explicitly modelled; the numerical model is built completely and, when finished, is subjected to all the loads of the load combination that is considered. This is probably justified by the fact that, generally speaking, a building is designed in such a way that the behaviour remains in the elastic domain and does not lead to large displacements during the construction phases. It has also to be noted that the construction process is essentially from bottom to top in such a way that gravity loads are progressively applied on the elements which are already in place.

The building process of an underground car park with steel sheet piles walls, on the contrary, may involve different successive sequences that lead to non-linear effects. Because of that, the retaining walls with multiple supports that are present in these car parks are usually designed on the base of a subgrade reaction model or with a Finite Element method, taking into account the soil structure interaction and the execution phases. The deflections as well as the bending moments obtained at the end of the construction process are more realistic than those determined with a limit equilibrium method.

The software used to design the sheet pile structure in the normal case by ArcelorMittal is called RIDO and it is based on a subgrade reaction model. The user interface is not very attractive, but it is quite simple to use, versatile and powerful.

When designing a flexible retaining wall, it is vital to select adequate values for the stiffness of the springs that simulate the soil reaction (see Section 3) and those that eventually simulate the supports provided by the horizontal slabs if these members are not explicitly modelled; these values will influence the active and passive soil pressure, as well as the deformation of the sheet pile. The subgrade reaction modulus k_h of the soil layers, which represent the stiffness of the soil, can be estimated with different formulas. The French National Annex of EN 1997-1 [6] gives a formula that is well adapted for stiff structures. Sheet pile walls are rather flexible structures and it is common practice to use Chadeisson's abacus [7] that considers only

two parameters of the shear strength of the soil: the cohesion and the internal friction angle. The stiffness of the soil is simulated with a single slope.

It is recommended to check the influence of the selected parameters by performing a sensitivity analysis, mainly on the subgrade modulus coefficients, the stiffness of the supports, the shear strength of the layers, and the level of the groundwater, before choosing the design case that will be submitted to a fire scenario. If the retaining wall is anchored in the ground or supported by temporary struts, which is very common, the design of anchors and struts is usually performed by a structural engineer at a later stage, and although this is not common practice, it would be preferable to recheck the final design of the retaining wall with the stiffness of the optimized strutting system.

If the structure has several levels below ground, the fire design will be performed for each level separately. Theoretically, the cold case scenario associated to the fire analysis could be slightly different for each level but, in most projects, it is enough to consider the final stage of the construction process for all fire scenarios. After the analysis of the construction phase at room temperature, the software creates an input file that defines the structure and its initial condition to be used by SAFIR. In order to make the transition from RIDO to SAFIR transparent to the user, these two codes have been integrated in a module called SARI.

4.2 Numerical simulation of the structural behaviour

The position of the wall before the fire results from different phases that generated horizontal displacements which influence the behaviour of the soil, see Figure 3. The wall is considered as vertical in the initial configuration in the analysis by SAFIR. In order to take the preliminary displacements into account, the soil finite elements receive the initial condition of the soil, noted as U_i and F_i on Figure 3, determined from the preliminary analysis made with RIDO.

In the first iteration of the first time step of the fire analysis, SAFIR computes the force in the springs corresponding to a displacement of 0. These forces are applied as out of equilibrium forces and lead to incremental displacements. A few iterations are requested for the structure to find its equilibrium because of the non-linear behaviour of the springs. As the axial stiffness of the springs is significantly higher than the bending stiffness of the wall, the position of the wall at the end of the first step and the pressure in the springs are virtually equal to the values defined as F_i and U_i in the springs. The value of the first time step is short, typically 1 second, which ensures that the effects of temperature are negligible at this stage. The steel wall is designed in such a way that the load level, induced by the pressure from the soil and by the vertical loads of the slabs, does not induce plasticity in the material. The software has no difficulty to converge as the simulation is normally made in the quasi-static mode. The dynamic mode is indeed not necessary to model the failure mode by buckling that may develop. In case a simulation in the dynamic mode should be requested, it can be computed that a displacement of 0.050 m that develops in 1 second corresponds to an acceleration of 0.1 m/s^2 or 0.01 g which should be accommodated by the structure. If not, a simulation with an initial time step of 3 seconds would lead to an acceleration as low as 0.01 m/s^2 or 0.001 g .

After this initial step, the simulation can continue with a progressive increase of the steel temperature depending on the fire scenario leading, or not, to a failure by buckling of the heated level toward the inside of the car park.

5 CASE STUDY

This case study is based on a real project, see Figure 4, but the loads have been increased on order to obtain a collapse before the required fire resistance time of 90 minutes.

The steel sheet pile is 15 m high. All levels given hereafter are with respect to the top of the wall. The car park is on the right hand side with 4 slabs at levels $z = 0 \text{ m}$, -2.75 m , -5.35 m and -8.05 m . A vertical load of 740 kN/m is applied on the upper slab while the other slabs transfer a load of 250 kN/m .

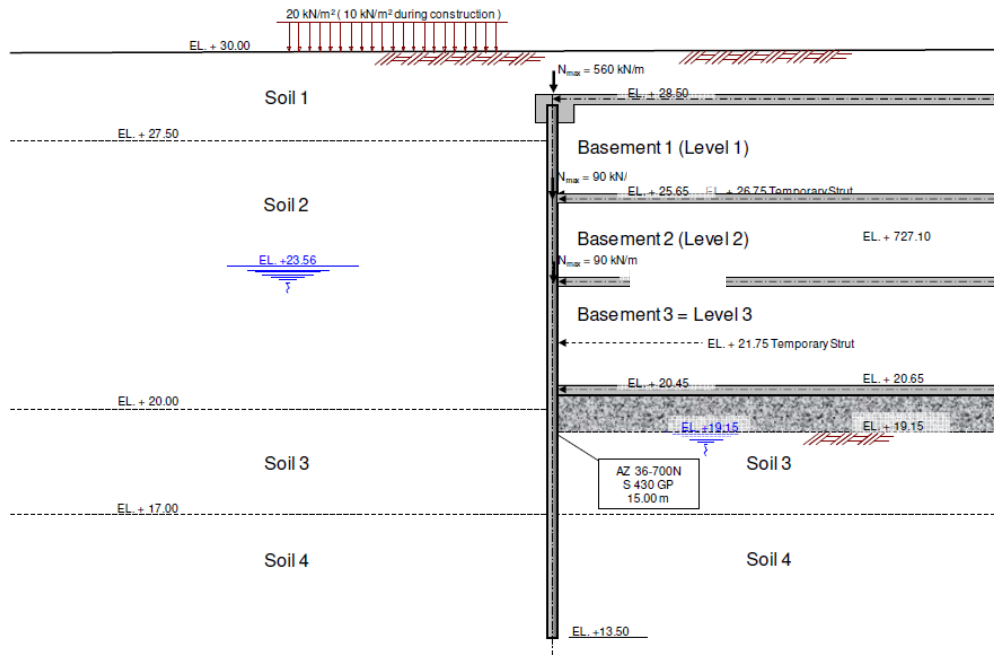


Figure 4. Sketch of the steel wall at the final stage

The sequence of events in the construction process after introducing the pile in the ground is:

- 1) Remove the soil down to $z = -4.25$ m.
- 2) Install a temporary strut at $z = -2.75$ m
- 3) Pump the water table down to -7.55 m and remove the soil to this level.
- 4) Install a second temporary strut at $z = -6.75$ m.
- 5) Pump the water table down to -9.35 m and remove the soil to this level.
- 6) Execute the 4 slabs.
- 7) Remove the temporary struts.
- 8) The water table goes back up to $z = -4.94$ m in the ground while it is maintained at -9.35 m below the lowest slab of the car park.

Figure 5 shows the situation at the end of the construction phase. On the left side are the pressures in the soil, on both sides of the wall, the reactions from the concrete slabs and, in red, the displaced position of the wall amplified by a factor of 50. In order to draw the diagram of pressures, the force in each spring element is divided by the area of influence of this spring. The bending moment diagram is shown on the right hand side where it can also be observed that the only imposed boundary condition is the vertical displacement at the foot of the wall. The rigid body movements of rotation or horizontal translation of the wall are prevented by the springs, which are not represented here⁴.

⁴ Each arrow on the Figure at the left indicates the presence of a spring element.

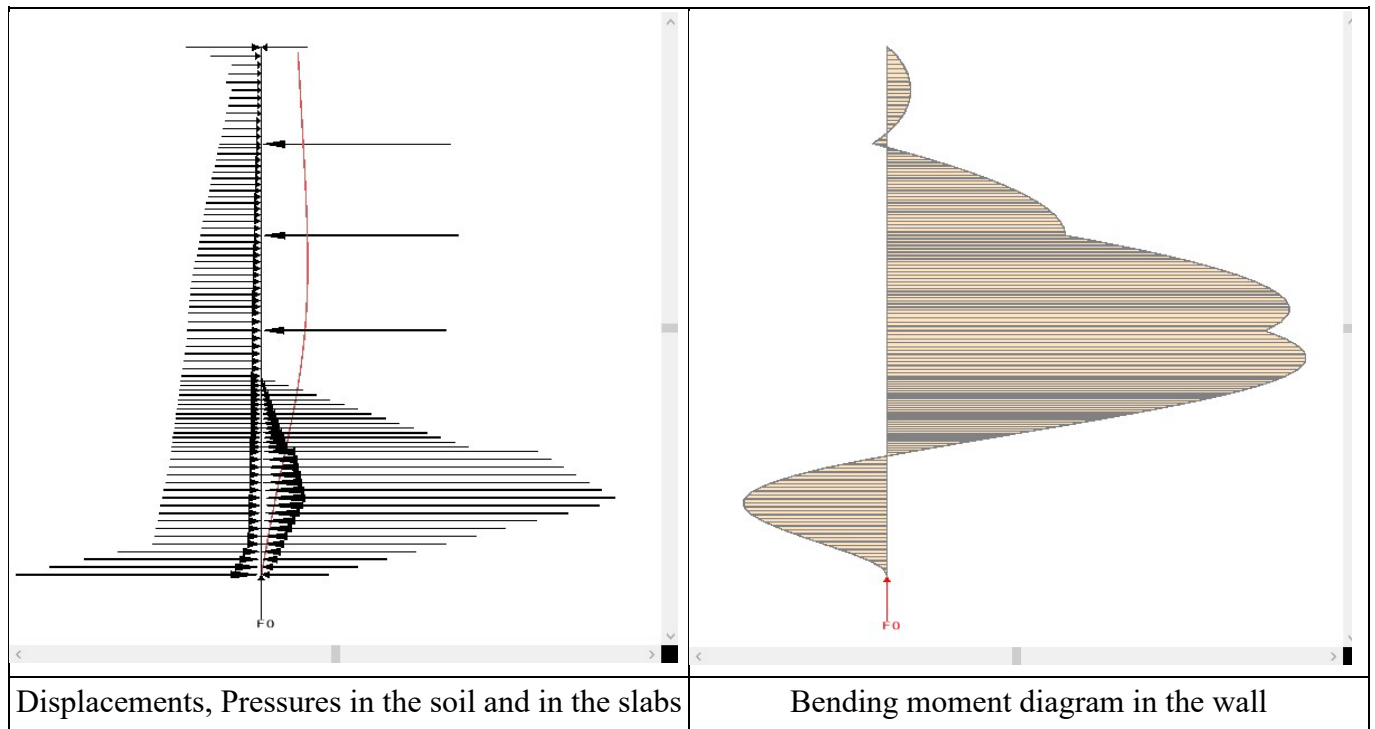


Figure 5. Situation before the fire

Figure 6 shows the isotherms in the steel sheet pile after 90 minutes of ISO fire. The steel pile is of the type AZ 36-700N – S 430⁵ GP. It has a depth of 499 mm. The total depth of the model is 1 meter with a cover of soil of 501 mm on the steel section which is enough to have the same temperatures as in a semi-infinite medium. The model has a width of 700 mm, owing to the two vertical axes of symmetry of the section. Water saturated sand with a water content of 200 kg/m³ has been considered for the thermal properties of the soil owing to the presence of water at the back of the wall. The temperatures in steel after 90 minutes of fire are in the range from 715°C to 925°C. Only the lowest level of the car park is subjected to the fire.

⁵ Yield strength = 430 MPa

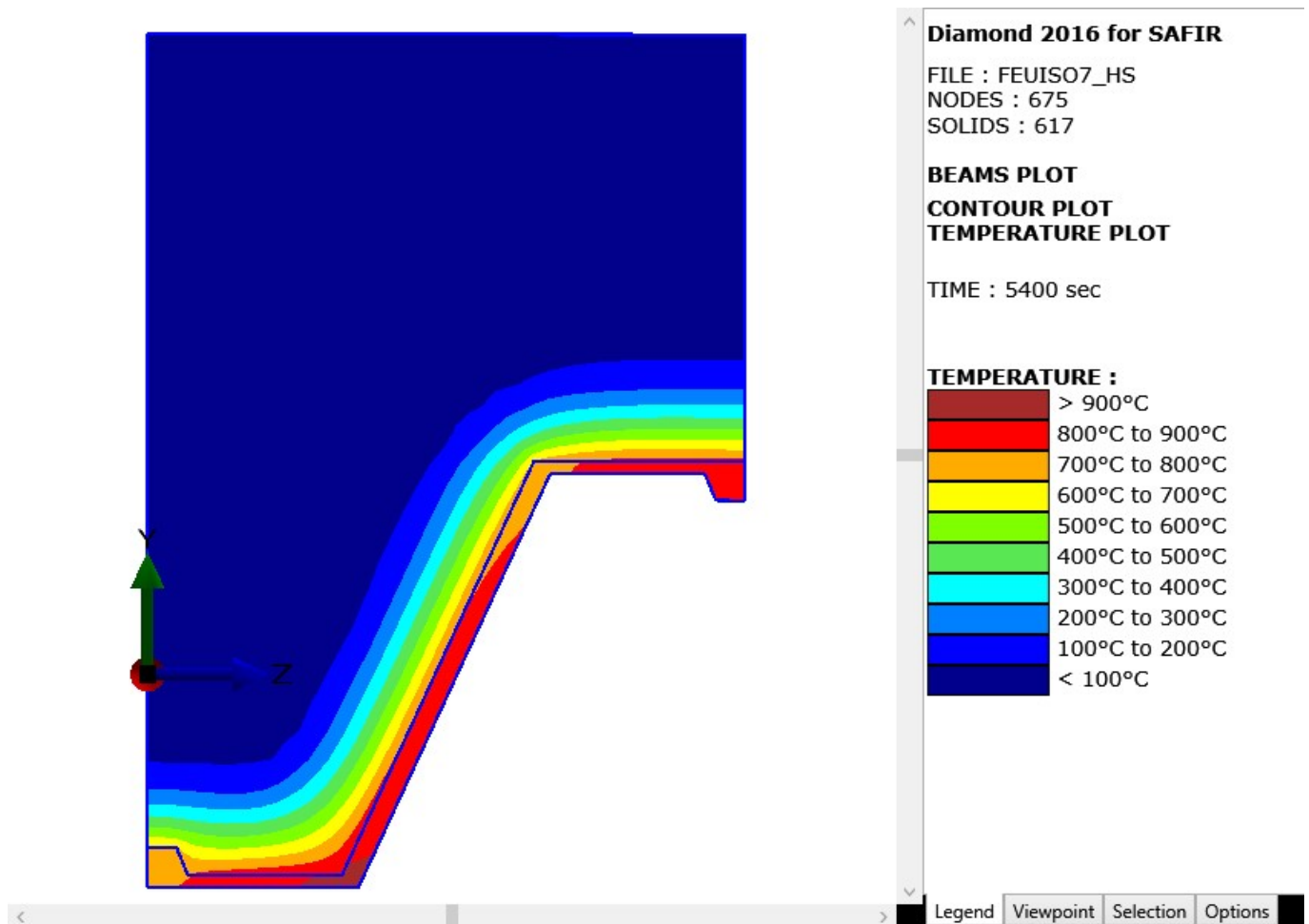


Figure 6. Isotherms after 90 minutes of ISO fire

Figure 7 shows the situation in the wall just before collapse which occurs just before 90 minutes by buckling of the wall at the level that is subjected to the fire.

It can be observed that the pressure diagram has changed significantly. More pronounced are the modifications in the reactions of the slabs and even more in the bending moment diagram.

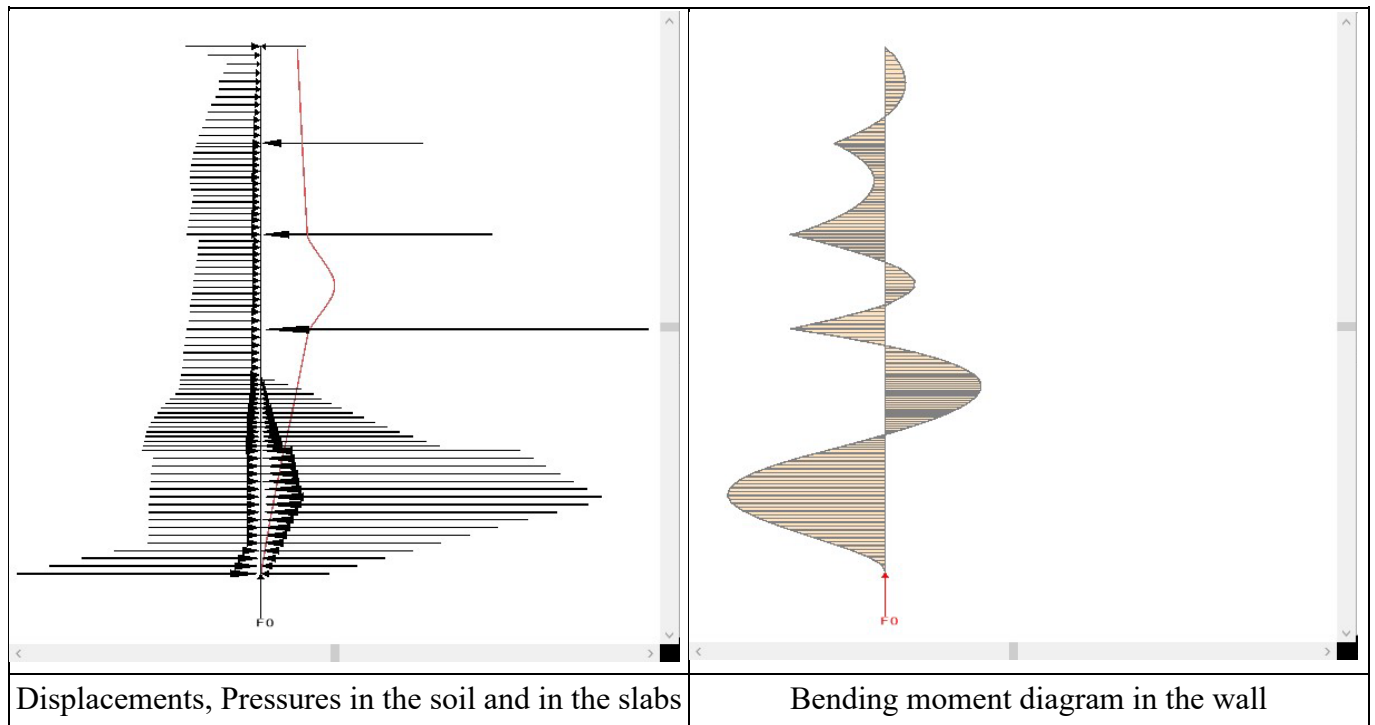


Figure 7. Situation just before failure

Figure 8 shows the evolution with time of the horizontal displacement at mid-level of the fire affected floor and Figure 9 shows the evolution with time of the vertical displacement at the top of the sheet pile. They clearly show the vertical asymptotes typical of run-away failures, which ensures that end of convergence in the simulations corresponds to the loss of load bearing capacity and not to a numerical failure.

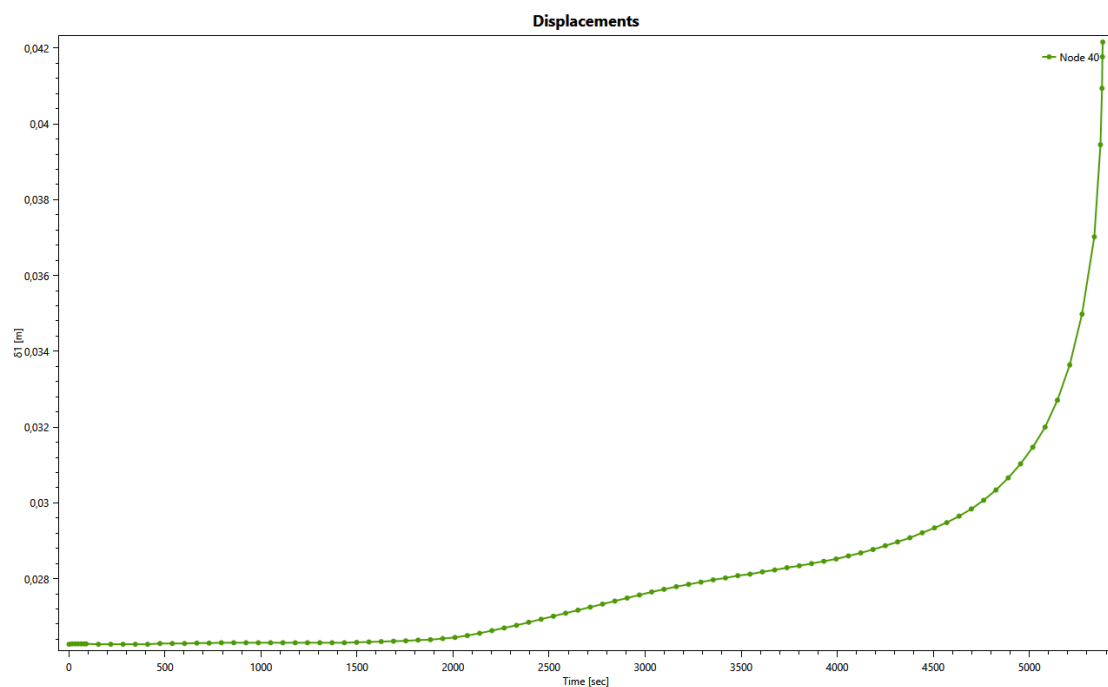


Figure 8. Horizontal displacement in the section on fire

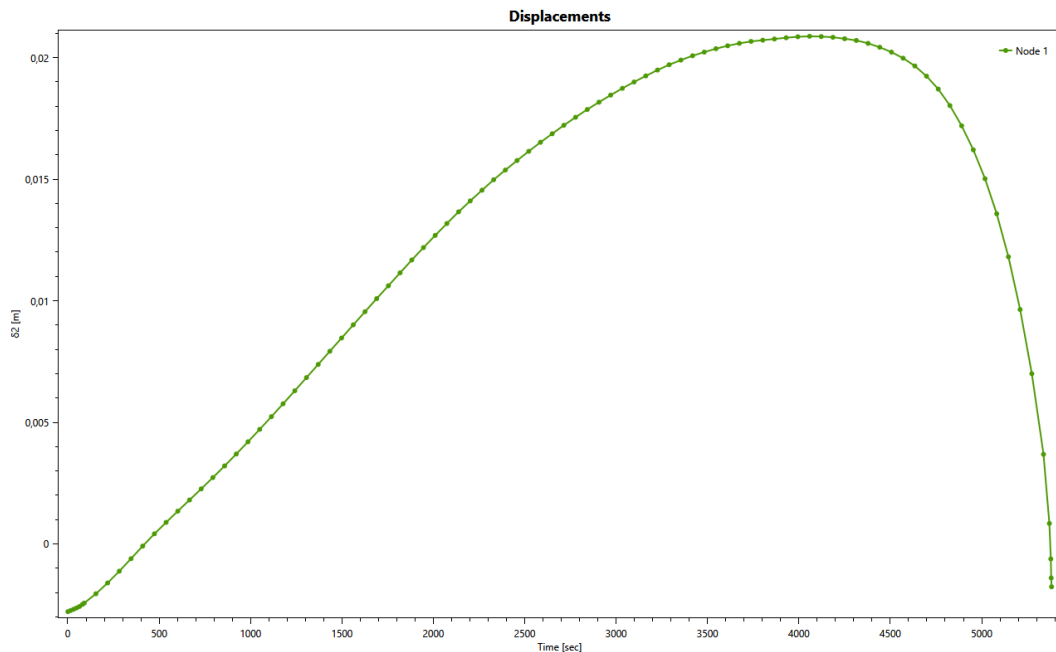


Figure 9. Vertical displacement at the top of the wall

6 CONCLUSIONS

The sequences of events involved in the construction process of buildings are very rarely taken into account in the numerical simulations performed to model the behaviour of the building structure subjected to a fire. This cannot be the case for retaining walls of underground car parks made of steel sheet piles. In such a construction, the quite flexible wall is subjected to various horizontal displacements produced by a succession of different operations that change the applied loads as well as the structural system.

A procedure has been established in order to link a software specialised in the analysis of these construction sequences at room temperature and a software that is specialised in the analysis of structures subjected to fire. The situation that prevails at the end of the construction process is transmitted from one software to the other one by the possibility to introduce an initial situation for the force F_i and the displacement U_i in the specialised 1 node elasto-plastic finite element that has been developed to represent the pressure of the soil as a function of the horizontal displacement of the wall.

Some experimental full scale tests have been performed on steel sheet piles backed by 2 different types of soils, either water saturated or not, in order to derive equivalent thermal properties of the soils to be used in thermal numerical simulations.

A case study has been presented where only the steel wall is modelled explicitly while the concrete slabs are represented by elastic springs. The door is yet open for modelling a whole frame made of the two walls of the car park, one on each side, with the concrete slabs also modelled explicitly, including the one that is subjected to the fire.

ACKNOWLEDGMENT

The experimental tests described in this paper have been undertaken in collaboration with J-B Schleich of ArcelorMittal. The interconnection between RIDO and SAFIR have been coded under the supervision of M. Meyrer and A. Schmit of ArcelorMittal.

REFERENCES

1. Underground car parks. Guide book for the Netherlands, ArcelorMittal Sheet Piling, Esch-sur-Alzette, Luxembourg, 2018
2. Franssen, J-M & Gernay T., Modeling structures in fire with SAFIR®: Theoretical background and capabilities. Journal of Structural Fire Engineering, 8(3), 300-323. (2017). <http://hdl.handle.net/2268/202859>

3. Brasseur, M, Zaharia, R, Obiala, R, Franssen, J-M, Hanus, F, Zhao, B, Pintea, D, Sanghoon, H, Vassart, O, Nadjai, A, Scifo, A et Thauvoye, C, Temperature assessment of a vertical steel member subjected to localised fire (LOCAFI), Publication Office of the EU, DOI 10.2777/67601,
4. Tondini, N, Morbiolo, A, Vassart, O, Lechêne, S & Franssen, J-M, An integrated modelling strategy between a CFD and an FE software: Methodology and application to compartment fires, J. Struct. Fire Engng, 7(3), 217-233 (2016). <http://hdl.handle.net/2268/206664>.
5. Steel Sheet Piles. Underground car parks. Fire resistance. ArcelorMittal, Esch-sur-Alzette, Luxembourg, https://sheetpiling.arcelormittal.com/wp-content/uploads/2018/03/AMCRPS_UCP_Fire_Resistance_EN.pdf
6. NF-EN 1997-1 juin 2005, Eurocode 7 : calcul géotechnique – Partie 1 : règles générales, AFNOR Editions, 2^{ème} tirage août 2011
7. Chadeisson, R, Parois continues moulées dans le sols, Proceedings of the 5th European Conf. on Soil Mechanics and Foundation Engineering, Vol. 2, Dunod, Paris, pp.563-568, 1961

MODELLING CONCRETE SLABS SUBJECTED TO LOCALISED FIRE ACTION WITH OPENSEES

Liming Jiang¹, Mhd Anwar Orabi², Jin Qiu³, Asif Usmani⁴

ABSTRACT

Reinforced concrete slabs in fire have been heavily studied over the last three decades. However, most experimental and numerical work focuses on long-term uniform exposure to standard fire. Considerably less effort has been put into investigating the response to localised fires that result in planarly non-uniform temperature distribution in exposed elements. In this paper, the OpenSees for Fire framework is presented, verified against benchmark solutions, and validated against experimental tests. The thermal wrapper developed within OpenSees is then presented and used to apply localised fire exposure to the validated slab models. It is seen that the deflections produced by the localised fire exposure are less than the standard fire exposure. It is also shown that by using the damage perimeter from the concrete damage plasticity model developed for OpenSees it is possible to predict the degree of cracking in the top layer each fire model is expected to produce.

Keywords: Structures; finite element modelling; localised fire; fire tests

1 INTRODUCTION

The Open System for Earthquake Engineering Simulation (OpenSees) is a powerful open source finite element framework primarily for seismic loading [1]. Its open source nature gives it a unique extensibility and reach not enjoyed by other expensive commercial software or in-house propriety codes. This was one of the crucial reasons why it was chosen to be a research platform for simulating structure interaction with various fire scenarios such as the post-flashover fires, localised fires, traveling fire scenarios, and Computational Fluid Dynamics (CFD) results. The behaviour of concrete slabs such as tensile membrane action has been recognised by previous research when studying the global response of composite floor systems to fires and especially the progressive collapse mechanism due to fire [2]. Recently, the ability to model slabs in fire with geometric nonlinearity was added to OpenSees by introducing the geometrically nonlinear shell element NLDKGQThermal. Material degradation and damage was also incorporated by the development of a 2D plane stress formulation of the thermo-mechanical Concrete Damage Plasticity (CDP) model for use with the shell elements. In OpenSees, reinforcement could be modelled within the section abstraction as either a continuous 2-dimensional layer of plane-stress steel material, or as a layer of uniaxial steel material representing rebars in a particular orientation. This paper introduces the OpenSees approach for modelling slabs in fire, including temperature calculation, thermo-mechanical materials, section abstractions, and shell elements. Validation against experimental work from literature is presented for ambient and high-temperature scenarios. Finally, a demonstrating example regarding the response of slabs to localised fire behaviour is presented showcasing the ability of this framework to capture the effects of

¹ Dr., Department of Building Services Engineering, The Hong Kong Polytechnic University,
e-mail: liming.jiang@polyu.edu.hk, ORCID: <https://orcid.org/0000-0001-8112-2330>

² Mr., Department of Building Services Engineering, The Hong Kong Polytechnic University,
e-mail: anwar.orabi@connect.polyu.hk, ORCID: <https://orcid.org/0000-0001-5083-3623>

³ Ms., Department of Building Services Engineering, The Hong Kong Polytechnic University,
e-mail: jinjin.qiu@connect.polyu.hk ORCID: <https://orcid.org/0000-0002-0603-854X>

⁴ Ms., Department of Building Services Engineering, The Hong Kong Polytechnic University,
e-mail: asif.usmani@polyu.edu.hk, ORCID: <https://orcid.org/0000-0003-2454-5737>

moderate fires which is different from the traditional uniform post-flashover fire scenarios. This work marks an important milestone for the OpenSees for Fire project, and is available for download here, where researchers and engineers from around the world are free to explore its features and use it for their study and research.

2 MODELLING ABSTRACTIONS IN OPENSEES FOR FIRE

2.1 Thermal action

OpenSees for Fire is equipped with a capable 3D heat transfer solver [3]. Within the heat transfer framework, the user specifies a ‘heat transfer entity’ and its mesh parameters, boundary conditions, and material type. There are predefined families of materials and entities covering the most common types used in structural engineering such as Hasemi’s model [4]. Likewise, for boundary conditions the user may either define temperatures, heat flux, or select from a family of fire models including the SFPE localised fire, natural temperature-time curve, and hydrocarbon curve [5]. For concrete slabs under the most common standard uniform heating scenarios, one dimensional heat transfer analysis is often sufficient to produce an accurate temperature history for thermo-mechanical analysis. For localised heating regimens, a series of one-dimensional heat transfer analysis would likely produce a sufficiently detailed temperature history map for structural analysis, as was shown in [6]. Three-dimensional heat transfer analysis is often unnecessary and may be reserved for more complicated thermal exposures such as those experienced in traveling fires. The results of the heat transfer analysis can then be applied to the structural model over 15 points in a beam element or 9 points through the depth of a shell element. To represent localised fire exposure in the structural model, temperatures from the heat transfer analysis are applied over a set of individual nodes. To facilitate this process for the user, temperature data is only required over three nodes with OpenSees interpolating the temperature histories and mapping them to all nodes within the radius specified by the selected nodes via a thermal action wrapper object as shown in Figure 1. The temperature interpolation performed by the wrapper considers smooth heat flux transition between the central region and the far point as shown in [7].

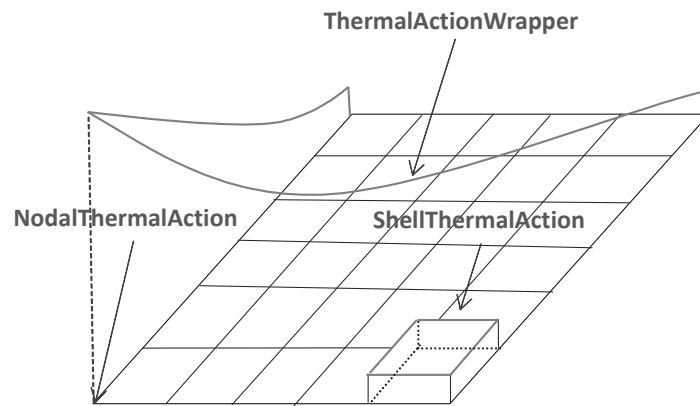


Figure 1. Thermal action wrapper in OpenSees

2.2 Shell element and section abstraction

Formerly, OpenSees for Fire was only capable of modelling slabs using plate sections with a limited number of fibres and only using a single material. That approach required at least two shell elements to represent the reinforcement and concrete layers of a typical steel reinforced concrete slab [8]. Recently, a thermo-mechanical NLDKGQ shell element was introduced to OpenSees for fire based on the work by Lu et al. [9], which enables geometric nonlinearity using updated Lagrangian approach. A layered section capable of representing slab sections with layers to represent the concrete and reinforcement at elevated temperature. As shown in Figure 2, the ShellNLDKGQThermal shell element has four nodes with six degrees of freedom and through-depth temperature profile for each node, which are interpolated for the four Gauss points to obtain section deformation and temperature distribution. Smeared steel reinforcement

is represented as a plane stress layer using uniaxial steel material oriented with respect to the element local axis as shown in Figure 2 (b). In a similar way, concrete is modelled as a plane stress layer of multi-axial Concrete Damage Plasticity (CDP) material which was developed by the authors particularly for slabs in fire as discussed in the next section.

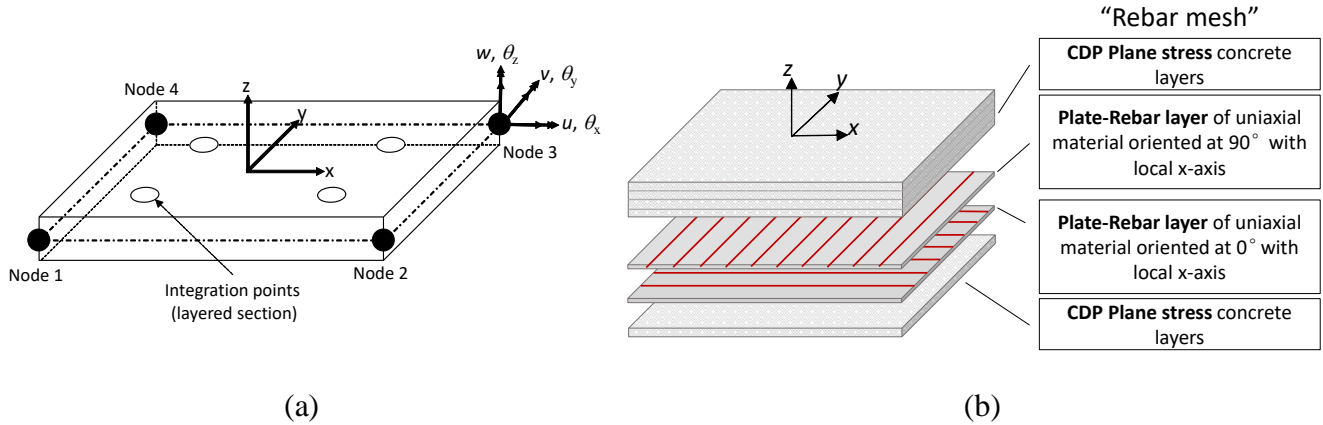


Figure 2. Abstractions for modelling reinforced concrete slabs in OpenSees for Fire. (a) element definition, (b) layered shell section definition

2.3 Concrete damage plasticity

Modelling concrete in fire is a difficult task because of the potential for stress reversal, thermal degradation, and especially the damage. Modelling such phenomena requires balance between computational expense and accuracy which is exactly what the CDP model provides. CDP was first introduced by Lubliner et al. [10] and then improved by Lee and Fenves [11] who decoupled the degradation damage from the elastoplastic state determination. Since then, it has been used successfully for analysing the behaviour of concrete slabs in fire [12,13]. A plane-stress variation of the CDP based on the return-mapping algorithm developed by Lee and Fenves [14] has been adopted in this work and uses the yield surface shown in Figure 3. Concrete thermo-mechanical properties based on the provisions of the EN 1992-1-2 [15] are incorporated with the damage plasticity formulation, with inclusion of load induced thermal strains as provided by Le et al. [16].

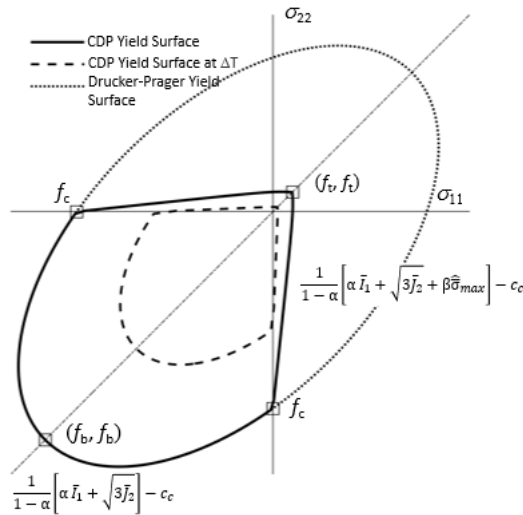


Figure 3. CDP and Drucker-Prager yield surfaces and degradation of CDP yield surface with temperature

3 VERIFICATION AND VALIDATION

3.1 Verification of geometric nonlinearity

Geometric nonlinearity is one of the primary complications that arise within nonlinear thermo-mechanical analysis. High axial forces due to expansion coupled with large deflections result in second order effects that may dominate the behaviour. These second-order effects are clearly evident in tensile-membrane action which occurs when a slab reaches a deformation in the same order of its thickness as demonstrated experimentally by Nguyen and Tan [17]. In this section, the aforementioned developments are verified against analytical solutions for a benchmark geometrically nonlinear elastic problem. The cantilever shown in Figure 4 (a) is modelled identically in OpenSees using corotational beam elements and both linear and nonlinear shell elements. The thin beam is tested for both mechanical loading alone and thermo-mechanical loading. In the first case, it is only subjected to an edge mechanical load P . In the second, it is also subjected to a uniform thermal gradient with bottom temperature of 1000°C and top temperature of 0°C . The vertical displacement of both cases is plotted in Figure 4 against the analytical solution and prediction by a beam element. In both cases, the linear shell elements give poor predictions compared to the nonlinear shell elements which agree very well with their respective benchmarks.

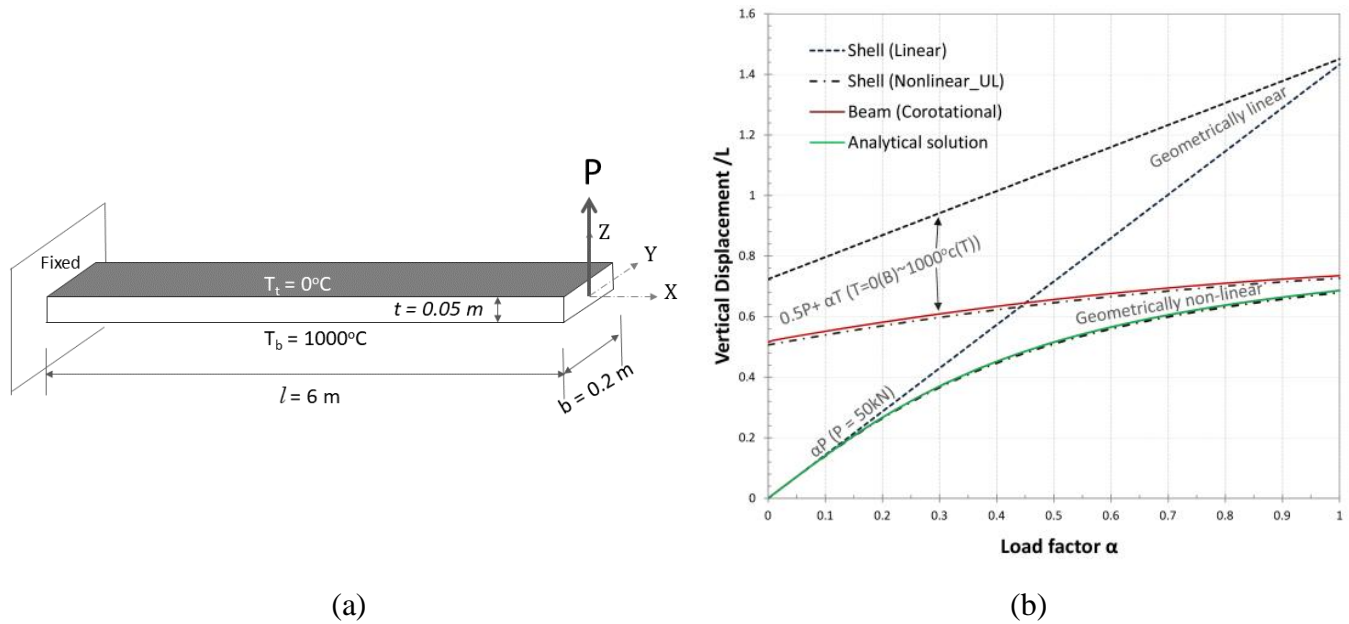


Figure 4. Verification of geometric nonlinearity (a) problem definition, (b) comparison of results

3.2 Validation against experimental results

A series of simply supported full-scale slab specimens were tested in New Zealand under uniform vertical load and three hour exposure to the ISO 834 standard fire [18]. Specimen D147 from [18] was modelled in OpenSees and is compared to the observed results and numerical predictions made by other researchers [13,19]. The slab was simply supported and had a foot print and thickness of $4.3 \text{ m} \times 3.3 \text{ m}$ and 100 mm respectively. It was loaded with a uniform load of 5.4 kN/m^2 and then heated from the bottom for three hours. The concrete had a compressive strength of 37 MPa , and was modelled as having a tensile strength of 4 MPa and a Young's modulus of 22.2 GPa . The reinforcement was a mesh of D147 cold formed bars with a yield strength of 565 MPa and had a 25 mm thick concrete cover. The bars were 8.7 mm in diameter and were spaced at 300 mm . One dimensional heat transfer analysis produced highly representative temperatures as shown in Figure 5 (a). The central deflection predictions by OpenSees showed an earlier 'failure' than the experiment as marked by the onset of runaway deflection and thus termination of the analysis. The results compare very well with the experimental observations and other numerical predictions up to about the termination of the analysis as shown in Figure 5 (b). Slab HD12 from the same experimental

series had the same dimensions, load, and thermal exposure. The reinforcement, however, had a larger diameter of 12 mm and was more densely spaced at 200 mm. Moreover, while the rebars in D147 were cold drawn, those in HD12 were hot rolled and had a yield stress of 468 MPa. The higher reinforcement ratio, ductility of the HD12 bars as well as the better-property retention of hot rolled steel at high temperatures contributed to the lower deflection of the slab at the end of the fire loading as shown by both the experimental results and numerical prediction presented in Figure 6 (a). Figure 6 (b) shows the predictions for traction vectors across the thickness of slab D147 at around two hours of heating with a clear compressive ring on the perimeter and a tensile central region as would be expected [20].

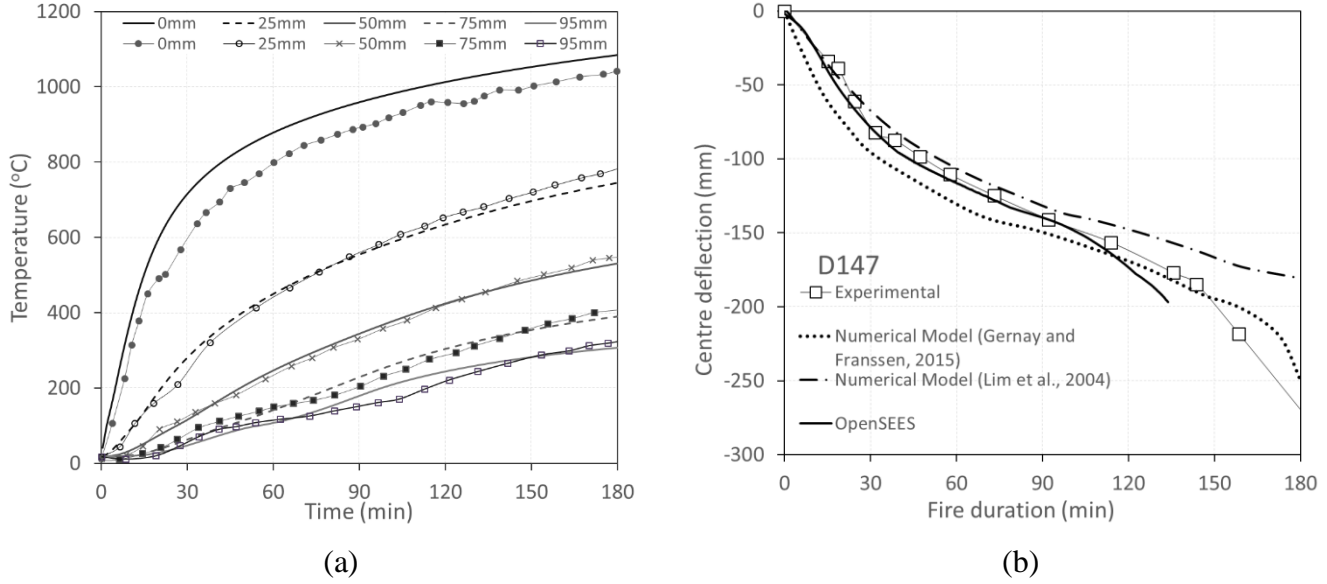


Figure 5. Comparison between experimental results and numerical predictions (a) Temperature, (b) central deflection

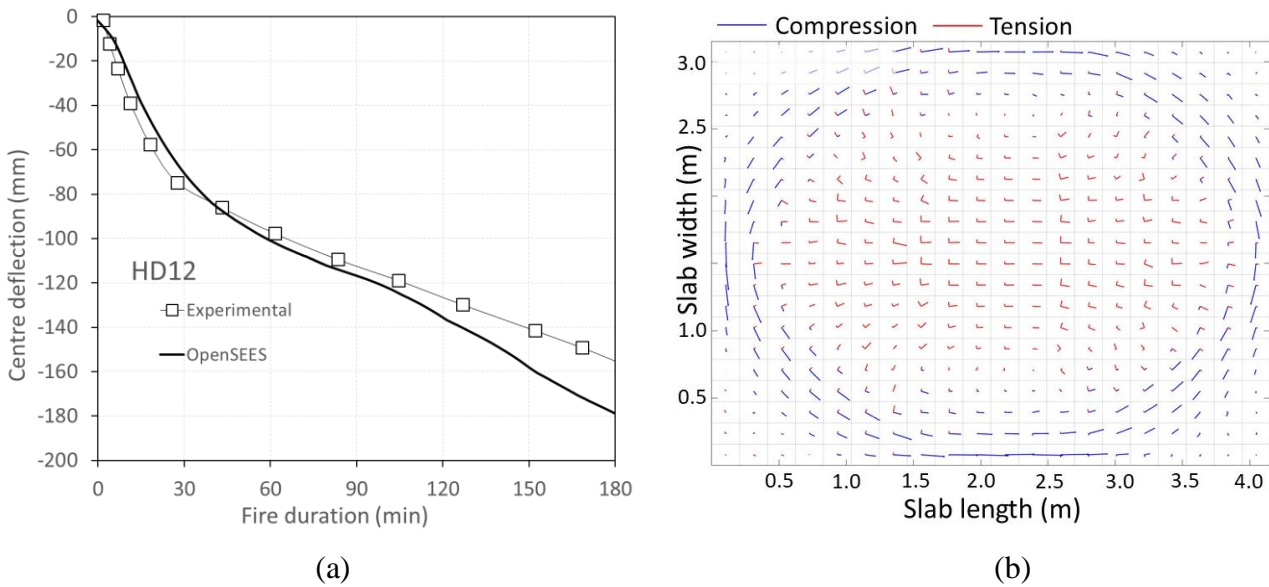


Figure 6. Numerical prediction for (a) deflections of slab HD12, and (b) traction vectors in principal space for slab D147

4 MODELLING LOCALISED FIRE

4.1 Fire scenario

To demonstrate OpenSees capabilities in modelling localised fire, two localised fire scenarios were considered and applied to the validated thermomechanical models for slabs D147 and HD12. The first fire

scenario was a modified localised fire with a heat release rate of 1.127 MW validated by the localised fire test with smoke layer [4,21], and the second was a EC1 localised fire but with an increased heat release rate of 2 MW (no smoke layer modification). Both of these scenarios were run to simulate a 30-minute fire as would be consistent with short-term localised fires in building structures. The fire scenarios were applied to a three-dimensional heat transfer model to produce thermal histories for the thermo-mechanical model. The temperature profile at three points was extracted from the heat transfer model corresponding to a point at the centre of the slab, half-way to the corner, and the corner point. The temperature profiles were then applied in the thermo-mechanical model via the thermal action wrapper discussed in section 2.1 which produced an interpolated three-dimensional temperature distribution to all shell elements within the slab. The temperature distribution at the bottom of the slab after 30 minutes of heating is shown for each fire scenario in Figure 7. It is clear from this figure that the 2 MW fire without the smoke layer would produce a larger zone with the maximum temperature but with more special discrepancy as evident by the cold edges as seen in Figure 7.

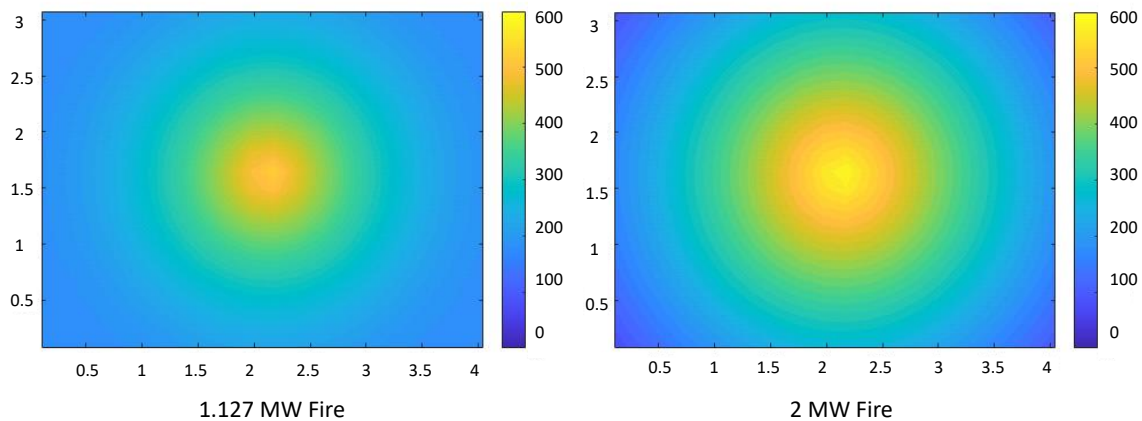


Figure 7. Layer temperature distribution near the exposed surface after 30 minutes of heating

4.2 Deflection

Thermo-mechanical analysis was performed for both slab D147 and HD12. The central deflection up to 30 minutes of heating is reported in Figure 8 (a) and (b) for specimen D147 and HD12 respectively. The experimental deflections and the deflections predicted by OpenSees for ISO 834 fire are also shown in the figure. In all cases, ISO 834 fire produces the highest deflections. This is to be expected because the entire slab is subjected to elevated temperatures that are significantly higher than the applied localised fires which heat the slabs less evenly and less severely. It is interesting to see that in this early stage of heating specimens show very similar levels of deflection for each applied fire scenario. This is because during the early stages of a fire, thermal expansion is the dominant factor governing deflection and the increments of temperature near the exposed surfaces in early period of heating are similar. The level of deflection observed for a 1.127 MW is less than the deflection observed under the 2 MW fire, which also produces less deflections than the ISO 834 fire at the end of the 30 minutes heating window. Note that the earlier stage of deflection development is overestimated for the localised fire because the model assumes the fire immediately reaches its peak heat fluxes as a steady state.

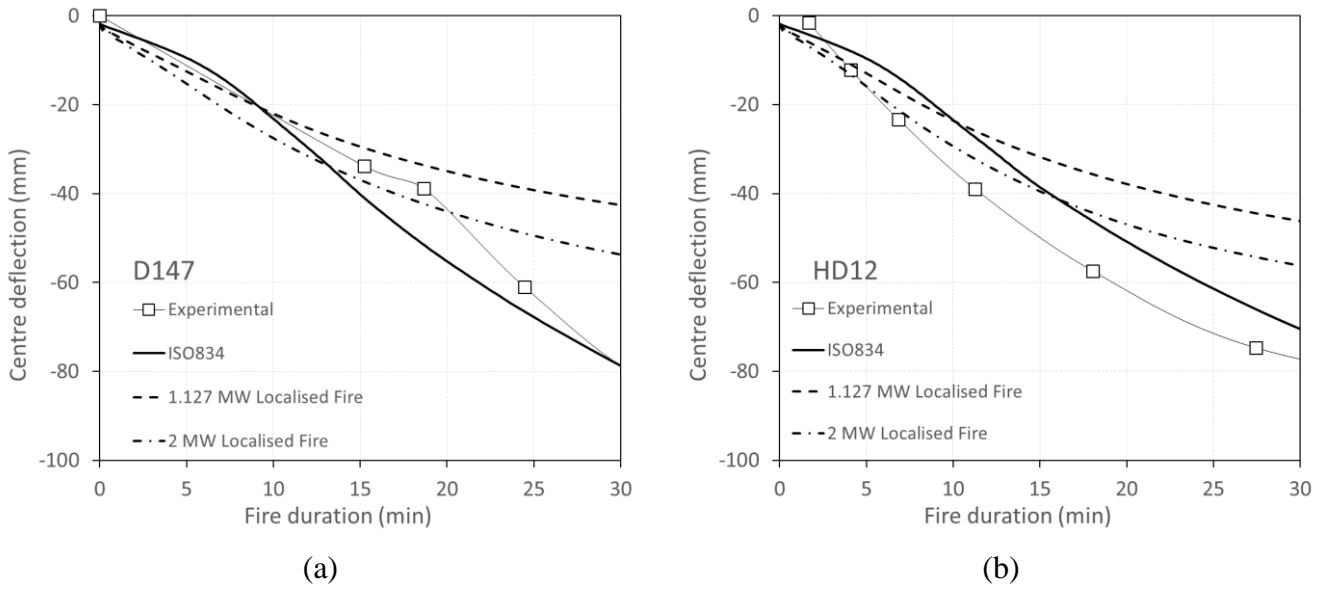


Figure 8. time-deflection curves for 30 minutes localised fire and standard fire exposure for (a) slab D147, and (b) slab HD12

4.3 Damage

It was mentioned in section 3.2 and shown in Figure 5 (b) that a compressive ring encompassing a tensile membrane region forms in the specimens by the end of the heating. By plotting the tractions in slab HD12 at the 30 minutes mark for each fire scenario in Figure 9 a clear pattern emerges. The localised fire scenarios produce less vertical deflection and heat the slab less severely and less evenly, which results in the emergence of the compression ring in the perimeter of the slab and the beginning of tensile action in the interior of the slab. As the centre of the slab is still the focal point of the heating, the midpoint is expanding relative the perimeter which puts it in compression. It is expected that if the localised fire is allowed to burn for longer, then the slab would go into full tensile membrane action. The pattern presented by the ISO 834 at 30 minutes is close to tensile membrane action even with limited vertical deflection of less than the slab thickness, which presents with a still-forming compressive ring supporting a developing central tensile region. The tractions for specimen D147 show the same pattern as those discussed for each fire scenario.

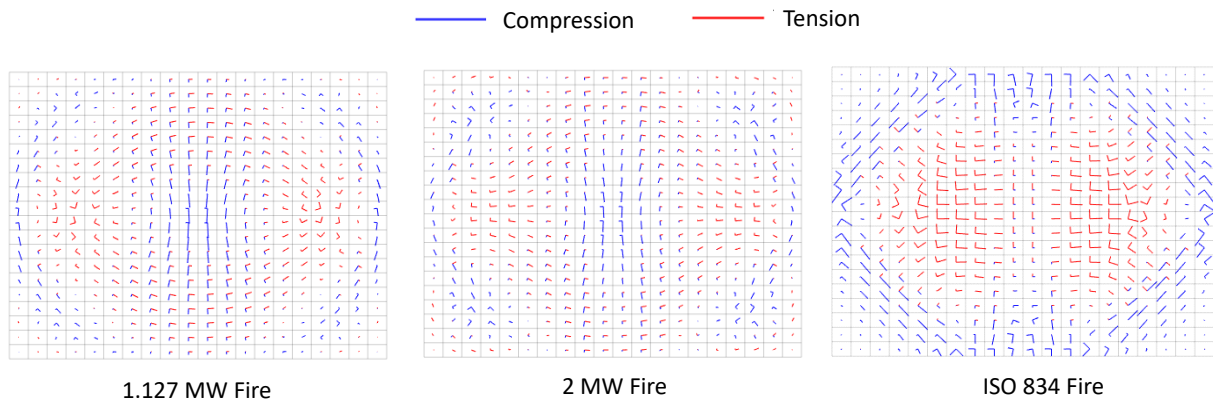


Figure 9. Traction vectors in slab HD12 after 30 minutes of fire exposure for each different fire scenario

The tensile damage variable D_t is shown for the top layer of slab D147 in Figure 10. The damage variable in this layer indicates the degree of surface cracking expected with $D_t = 1$ meaning the concrete is cracked and $D_t = 0$ indicating it is still intact. The ISO 834 fire predicts the most severe damage with the corners and a central strip across the short direction being fully cracked. This is consistent with the restraint provided to the slab preventing it from moving vertically at the perimeter, and with the longer direction being more flexible than the shorter direction. Similar damage is seen when the slab is subjected to the 2

MW localised fire, but to a lesser extent particularly in the middle of the slab. The 1.127 MW fire produces high tensile damage only in the corners with almost no damage across the short span in middle of the slab.

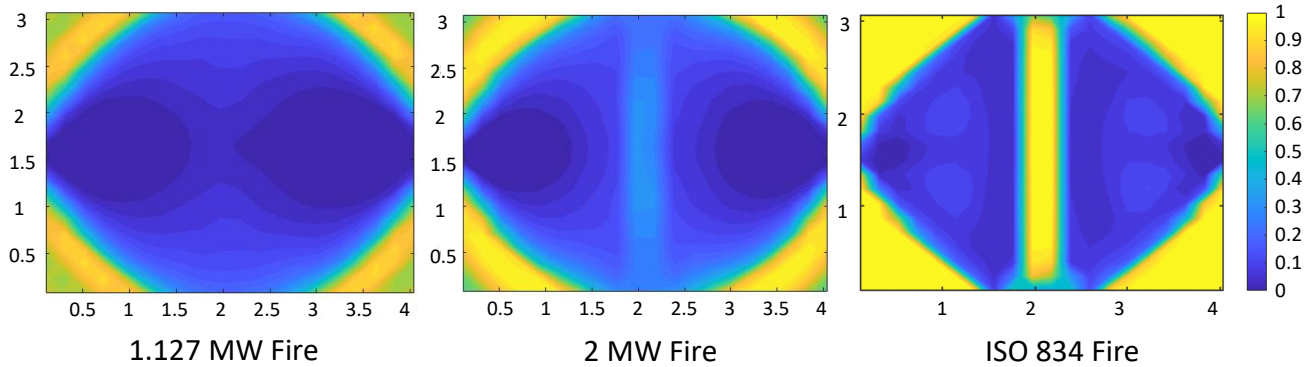


Figure 10. Tensile damage parameter D_t in top layer of D147

5 CONCLUSIONS

The OpenSees for Fire capabilities for representing concrete slabs under uniform and localised fire were presented. Validations against analytical solutions of a cantilever beam subject to thermal gradient show that the shell elements developed capture geometric nonlinearity well in thermo-mechanical analysis. Further validation against fire tests on slabs has also shown agreeable results. When subjected to two different intensities of localised fire as measured by their heat release rate, the model also produces the expected outcomes. Even the more severe localised fire with a heat release rate of 2 MW predicts lower deflections than an ISO 834 fire after 30 minutes of exposure. The tractions produced by the model show that the localised fires produce tractions that are approaching tensile membrane action as found in standard fire tests. By exporting the damage variable D_t from the CDP material in OpenSees it is possible to visualise potential top-surface cracks. The damage produced by the 1.127 MW fire is concentrated at the corners but indicating that cracks in the span may not necessarily develop after 30 minutes exposure to this fire. The 2 MW fire and the ISO 834 fire on the other hand produce prominent damage patterns with severe damage over the corners and across the short span in the middle of the slab. The work presented in this paper is to demonstrate the modelling of floor slabs in real fire behaviour with the thermo-mechanical model in OpenSees where the fire is generated as per engineering models (EC1) or CFD fire models representing real fires including the smoke layer. The fire induced damage patterns of slabs in these localised fire scenarios provides a more complete estimation of fire impact in addition to the uniform fire exposure defined by the standard fire curve.

REFERENCES

1. F. McKenna, Object-oriented finite element programming: frameworks for analysis, algorithms and parallel computing, University of California, Berkeley, 1997.
2. I. Burgess, M. Sahin, Tensile Membrane Action of Lightly-reinforced Rectangular Composite Slabs in Fire, Structures. 16 (2018) 176–197. <https://doi.org/10.1016/j.istruc.2018.09.011>.
3. Y. Jiang, Development and application of a thermal analysis framework in OpenSees for structures in fire, The University of Edinburgh, 2012.
4. T. Wakamatsu, Y. Hasemi, K. Kagiya, D. Kamikawa, Heating Mechanism of Unprotected Steel Beam Installed Beneath Ceiling and Exposed to a Localized Fire : Verification using the real-scale experiment and effects of the smoke layer, in: Fire Saf. Sci. Seventh Int. Symp., 2003: pp. 1099–1110.
5. M.A. Orabi, A.A. Khan, A. Usmani, An Overview of OpenSEES for Fire, in: Proc. 1st Eurasian Conf. OpenSEES OpenSEES Days Eurasia, Hong Kong, China, n.d.
6. L. Jiang, S. Chen, A. Usmani, Feasibility of dimensionally reduced heat transfer analysis for structural

- members subjected to localised fire, *Adv. Struct. Eng.* 21 (2018) 1708–1722. <https://doi.org/10.1177/1369433218754334>.
7. L. Jiang, Development of an integrated computational tool for modelling structural frames in fire considering local effects, University of Edinburgh, 2015.
8. J. Jiang, P. Khazaeinejad, A. Usmani, Nonlinear analysis of shell structures in fire using OpenSees, (2012).
9. X. Lu, L. Xie, H. Guan, Y. Huang, X. Lu, A shear wall element for nonlinear seismic analysis of super-tall buildings using OpenSees, *Finite Elem. Anal. Des.* 98 (2015) 14–25. <https://doi.org/10.1016/j.finel.2015.01.006>.
10. J. Lubliner, J. Oliver, S. Oller, E. Oñate, A plastic-damage model for concrete, *Int. J. Solids Struct.* 25 (1989) 299–326. [https://doi.org/10.1016/0020-7683\(89\)90050-4](https://doi.org/10.1016/0020-7683(89)90050-4).
11. J. Lee, G.L. Fenves, Plastic-damage model for cyclic loading of concrete structures, *J. Eng. Mech.* 124 (1998) 892–900. [https://doi.org/10.1061/\(ASCE\)0733-9399\(1998\)124:8\(892\)](https://doi.org/10.1061/(ASCE)0733-9399(1998)124:8(892)).
12. N. Wahid, L.A. Bisby, Modelling the deflection response of reinforced concrete flat slabs during heating, in: 15th Int. Conf. Fire Sci. Eng. (Interflam 2019), 2019.
13. T. Gernay, J.M. Franssen, A plastic-damage model for concrete in fire: Applications in structural fire engineering, *Fire Saf. J.* 71 (2015) 268–278. <https://doi.org/10.1016/j.firesaf.2014.11.028>.
14. J. Lee, G.L. Fenves, Return-mapping algorithm for plastic-damage models: 3-D and plane stress formulation, *Int. J. Numer. Methods Eng.* 50 (2001) 487–506. [https://doi.org/10.1002/1097-0207\(20010120\)50:2<487::AID-NME44>3.0.CO;2-N](https://doi.org/10.1002/1097-0207(20010120)50:2<487::AID-NME44>3.0.CO;2-N).
15. British Standards Institution, Eurocode 2 - Design of concrete structures Part 1-2: Structural fire design, (2004).
16. Q.X. Le, J.L. Torero, V.T.N. Dao, Understanding the effects of stress on the coefficient of thermal expansion, *Int. J. Eng. Sci.* 141 (2019) 83–94. <https://doi.org/10.1016/j.ijengsci.2019.05.016>.
17. T.T. Nguyen, K.H. Tan, Ultimate load of composite floors in fire with flexible supporting edge beams, *J. Constr. Steel Res.* 109 (2015) 47–60. <https://doi.org/10.1016/j.jcsr.2015.03.004>.
18. L. Lim, C. Wade, Experimental Fire Tests of Two-Way Concrete Slabs, 2002.
19. L. Lim, A. Buchanan, P. Moss, J. Franssen, Numerical modelling of two-way reinforced concrete slabs in fire, 26 (2004) 1081–1091. <https://doi.org/10.1016/j.engstruct.2004.03.009>.
20. N.S. Zhang, G.Q. Li, A new method to analyze the membrane action of composite floor slabs in fire condition, *Fire Technol.* 46 (2010) 3–18. <https://doi.org/10.1007/s10694-009-0086-8>.
21. L. Jiang, Y. Zhang, Z. Zhang, A. Usmani, Thermal analysis infrastructure in OpenSees for fire and its smart application interface towards natural fire modelling, *Fire Technol.* (2020 in-process).

A FRAMEWORK FOR RELIABILITY-BASED ASSESSMENT OF STRUCTURES IN POST-FIRE CONDITIONS

Tom Molken¹, Barbara Rossi^{2,3}

ABSTRACT

The actual codes on design procedures to assess the structural reliability in case of fire allows for a whole scope of methodologies to be used. At one end of the spectrum, the codes allow to simply combine design rules with member analysis using tabulated data or simplified calculation models. On the other extreme end of the spectrum, complex performance-based design approaches are proposed, the results of which are unique and highly dependent on the system's boundary conditions. Between those two extreme options, there are several other methodologies including the possibility to use probabilistic approaches. In this paper, reliability assessment of structures is based on the force-based method including temperature effects as well. This method is developed for single-bay portal frame and is based on the combined failure probability of 5 critical sections. All data needed to generate a probability density functions of the thermal actions on the structure is collected and described. Heat transfer equations of unprotected steel are used to calculate the profile temperature and reduction of mechanical characteristics during and after the fire. Coupling of the probabilistic-based thermal actions to the force-based method enables to create numerous simulations (Monte Carlo technique), and thus enable the system during and after a fire. This analysis is done for different load levels (self-weight), portal frame geometries and for several fire scenarios. Last, the post-fire behaviour of structural carbon steel single-bay portal frames is carefully investigated.

Keywords: Probabilistic analysis; steel portal frame; reliability assessment during fire; post-fire reliability

1 INTRODUCTION

While probability analyses have become common in structural engineering practice and form the basis of all structural codes at the component level [1, 2], their application to complete structural systems subjected to fire as well as the post-fire probabilistic assessment of structures is today a subject that has not yet been extensively researched. The subject became of interest in the last two decades, however it seems that the research is mainly focusing on concrete elements and remains limited to the component level rather than whole structures.

The need of a reliability-based assessment methodology for structures subjected to fire and in post-fire conditions is key to study the risks taken by fire brigades during a fire and the options available to building owners (and the society in general) when buildings have been submitted to a fire and are still standing. Ensuring adequate reliability is necessary if the reinstatement of buildings after a fire is being considered. To analyse a risk associated with a certain load (fire, gravity load, live load, etc.), the probability theory should be used to quantify uncertain processes and statistical distributions should be used to

¹ PhD researcher, KU Leuven, Belgium,

e-mail: tom.molken@kuleuven.be, ORCID: <https://orcid.org/0000-0002-3401-9047>

² Prof., KU Leuven, Belgium

e-mail: barabara.rossi@kuleuven.be, ORCID: <https://orcid.org/0000-0001-6228-0309>

³ Prof, New College Oxford, UK

e-mail: barabara.rossi@new.ox.ac.uk, ORCID: <https://orcid.org/0000-0001-6228-0309>

characterize the load, material, geometrical and thermal effects. The specified probability density functions (PDFs) giving the probability that the considered random variable falls within a specified range of values are different for all the mentioned statistical distributions and so Normal (N), lognormal (LN), Gumbel (GU) functions associated with determined parameters (such as the average and standard deviation) will have to be defined and combined. During and after the fire, the maximum reached (gas and steel) temperature will be needed, which is the reason why time-dependent Monte Carlo simulations will be used. This will then be coupled in a rather straightforward way to a simplified description of the limit state function g of the system established based on the force-based method (FBM).

2 OUTLINE OF THE PAPER

Different methodologies are available to achieve a parametric study where different probability functions are used for all variables. At the system level, four building types with a unique shape are treated in a fully probabilistic way in [7] however without fire. Twenty-two failure modes are investigated for the system collapse, each time involving attainment of the plastic bending capacity. The limit state function for each failure mode is expressed as the difference between the internal and the external work. From the analysis, it appears that one mode was governing the design, i.e. the failure probability P_f increased from $1.1 \cdot 10^{-7}$ to $1.16 \cdot 10^{-7}$, for an at the end almost equal reliability index β of 5.2.

Instead of spending a great deal of time finding all failure modes of the system frame, this study investigates if, due to fire, one dominant failure mode and a number of critical sections can be characterized. This will be described in Chapter 3 for three different shape ratios of the single bay portal frame (height-to-span H/L) and three vertical load levels. The fire development follows the nominal standard fire curve from [8] and thermo-plastic analysis of all frames is done with the finite element method software (FEM) SAFIR® [9].

Then, additional exploration of the possibilities of the FBM as is proposed by [10] is done in Chapter 4, which focusses on the inclusion of the influence of temperature effects in the system of equation that describes the frame's structural behaviour. This is done to establish a more general method of study of steel portal frames subjected to fire, in agreement with the conditions set in [11].

In the FBM, the equations of equilibrium are formulated in the undeformed state and are not updated with deformation taking place. Since the interest of this paper goes to structures that survive a fire and stay in the elastic range, it is deemed acceptable. During the fire, thermal and mechanical material properties can be obtained in, among others, the following codified document [11]. For the post-fire evaluation, a statistical evaluation of the stress-strain characteristics of carbon and stainless steel grades being exposed to fire and then cooled down can be found in [12].

The most recent publication related to statistical evaluation of structures submitted to fire [13] provides information on the appropriate PDFs and coefficients of variation (V) describing the thermal loads. However, information on the PDFs of the hot gas temperature evolution and subsequently the steel temperature developed under natural fires for industrial buildings is scarce. One single-bay portal frame is used as a case-study to illustrate the methodology and obtained results. In Chapter 6, the failure risk of the portal frame for some thermal scenarios is studied.

Post-fire conditions of the portal frame are discussed in Chapter 7. Partial (material) factors for steel structures that survived a fire, depending on the maximum reached temperature, are then proposed. The core question of this chapter is whether or not the proposed additional partial factors for material properties allow the assessment of a structure post-fire, guaranteeing a target reliability level of the existing real structure.

3 FAILURE MODES AND CRITICAL SECTIONS IN CASE OF FIRE

A single-bay portal frame as presented in Figure 1 (a) is considered. The basic variables and hypotheses of the problem are:

- The span between the centre lines of the columns L ;

- The height between the foundations and the centre line of the beam H ;
- The geometrical properties of the cross-sections: the gross cross-section area A , the second moment of area I_z , and a time-dependent temperature increment $\Delta\theta$ (considered uniform over the cross-section) due to the fire. Indexes are cL for the left column, b for beam, and cR for the right column on the figure (both columns can be different; however, this will not be the case in this paper);
- The mechanical properties are the same for all the profiles (same steel batch);
- Only in-plane displacements due to normal forces and bending moments are allowed and it is assumed that potential failures due to shear or instability will be eliminated by appropriate means;
- It is presumed that the global structural behaviour can be described in an elastic way and that imperfections will not have a major impact on the behaviour;
- The time history does not influence the mechanical behaviour of the portal frame; only the maximum temperature does;
- Columns and beam can have different properties and can be subjected to different maximum temperatures to simulate the effect of a local fire. However, the temperature is considered constant, per element along the whole length.

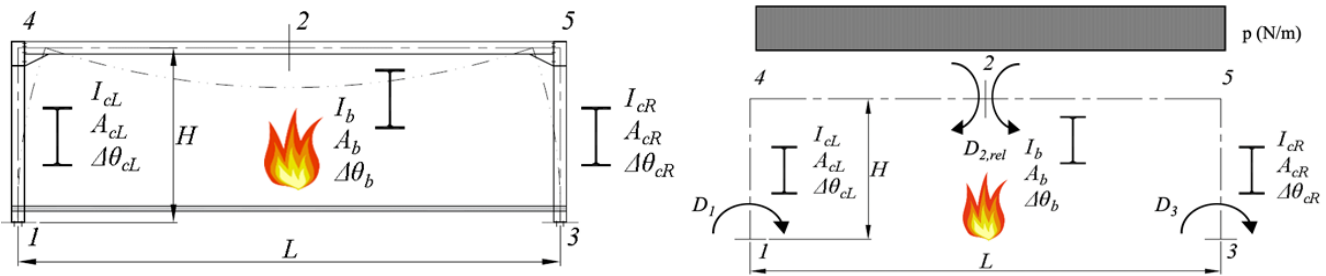


Figure 1. Typical single-bay portal frame of an industrial steel building (a) and a schematic version (b).

For rather simple structures, as the one presented in Figure 1 (a), the critical sections under ambient conditions can easily be based on the engineer's expertise, but can also be deduced from a FEM analysis until failure (subjected to a standard fire). However, in case of fire, the scenarios (the uniform or non-uniform application of heating in the compartment), H/L -ratio (shape factor) and load level investigated in this paper could lead to different failure modes as described in the following sub-sections.

All connections will be assumed to be perfectly rigid and, due to the presence of additional material, the thermal resistance will be higher than that of the connected elements. Standard European I-profile sections are used. Note that, in case of fire, the degree of indeterminacy can be higher than under ambient temperature. This is due to the possible and usual presence of concrete floor slabs that block the horizontal movements and rotations at the bottom level of the columns. Of course, this is only valid if the considered column passes through this concrete slab down to a lower level.

The failure modes depicted in Figure 2 are obtained by subjecting the presented portal frames to the mechanical load and a uniform compartment gas temperature (standard fire) that increases over the time and using the thermal-structural analysis software SAFIR® [9]. Load levels in the figure are the ones that include the self-weight of the chosen profiles that satisfy for the gives ratios both service and ultimate limit states following the partial factor method according to [16] ($H = 5$ or 10 m and $L = 15$ or 20 m). No wind load is considered acting on the portal frame as its effect was found neglectable, as also described in [7]. The failure is always initiated by the same mechanism as the one at ambient conditions. Plastic hinges initiate at nodes 4 and 5. When the cross-section at node 2 also starts to yield under catenary action, nodes 1 and 3 act as ends of a cantilever column and fail almost instantaneously which inevitably leads to global collapse of the system.

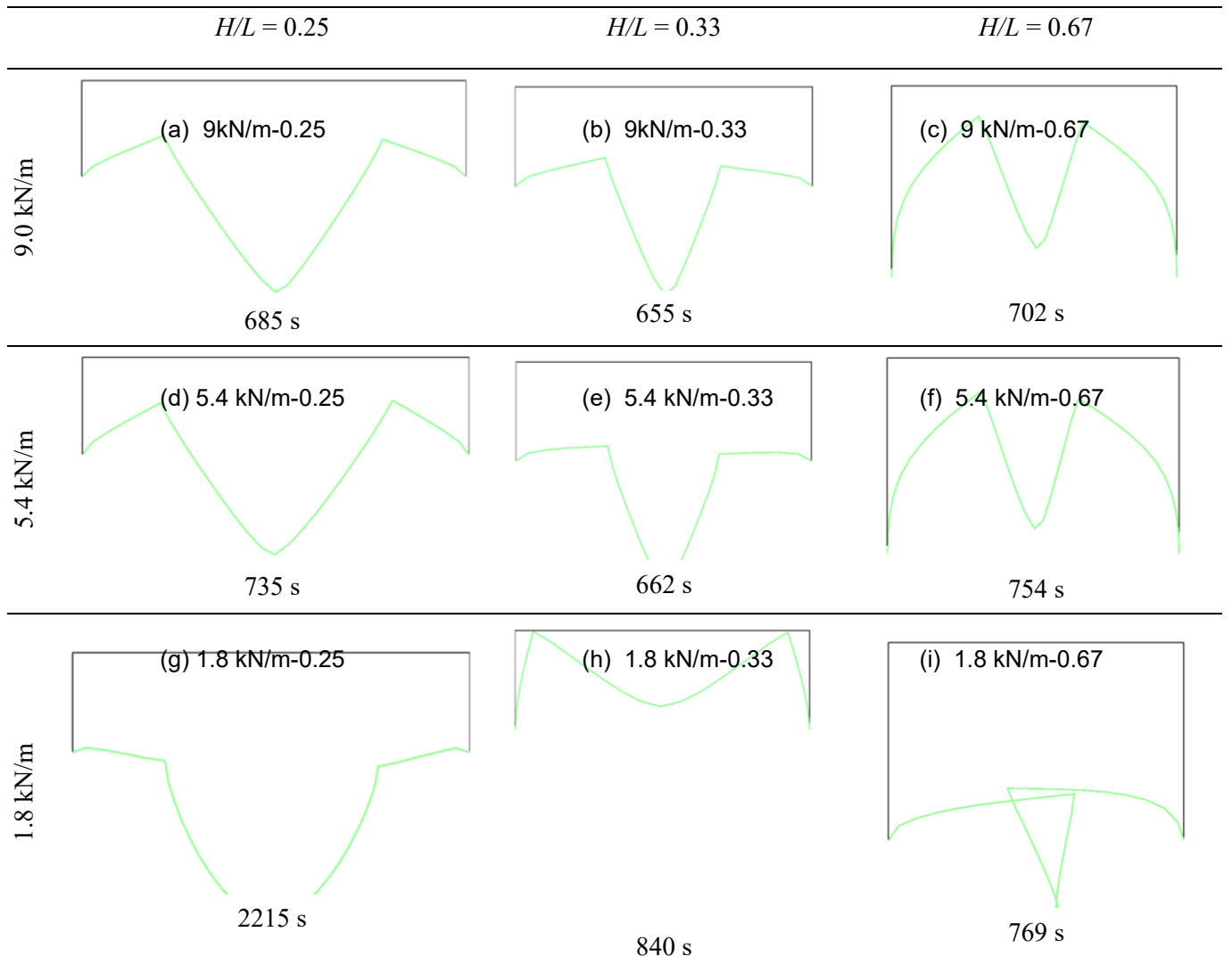


Figure 2. Failure modes and time of collapse due to uniform heating for several portal frames with H/L -ratio 0.25, 0.33, and 0.67 combined with 3 permanent load levels.

4 FORCE-BASED METHOD FOR A SINGLE-BAY STEEL PORTAL FRAME

The scope of the paper is limited to one type of structure i.e. a single-bay portal frame as shown in Figure 1 (b). The frame is composed of I-profile section members with their strong axis oriented in the plane. The unknown deformations (rotations) are located at the critical sections where failure is likely to occur (nodes 1 to 3). As previously mentioned, yielding is firstly initiated at nodes 4 and 5, which is the reason why the description of the mechanical behaviour is extended to 5 nodes (nodes 4 and 5 in addition to 1 to 3, see Figure 1 (b)). The moments at these locations can be calculated based on equilibrium equations; see [10].

In the case of the investigated portal frames, the 3 moments (M_1 , M_2 , and M_3) at the critical nodes can then be obtained using the matrix in Eq. (1). In this case, the flexibility coefficients will depend on the temperature through Young's modulus temperature dependency:

$$\begin{Bmatrix} M_1 \\ M_2 \\ M_3 \end{Bmatrix} = \begin{bmatrix} f_{11} & f_{12} & f_{13} \\ f_{21} & f_{22} & f_{23} \\ f_{31} & f_{32} & f_{33} \end{bmatrix}^{-1} \begin{Bmatrix} -D_{10} - D_{1,t} \\ -D_{20} - D_{2,t} \\ -D_{30} - D_{3,t} \end{Bmatrix} \quad (1)$$

The moments should then be compared to the bending moment capacity of the corresponding cross-section to verify if the system has reached failure, i.e. a unity check as provided in [16] is used for each node,

disregarding the contribution of normal and shear forces, resulting in a utilisation ratio η_j for each node j as in Eq. (2).

$$\eta_j = \frac{E_j}{R_j} = \frac{M_{Ed,j}}{M_{Rd,j}} \leq 1 \quad (2)$$

For Class 1 sections with a normal force lower than 25% of the plastic cross-sectional capacity as well as 50% of the web capacity [16]:

- $M_{Ed,j}$ is the considered internal moment as a result of the applied external factored loads;
- $M_{Rd,j}$ is the temperature-dependent design resting moment equal to the product of the section modulus by the yield strength for steel members.

5 STATISTICAL DATA

Statistical data required for reliability analyses are needed at 3 levels in ambient conditions: the mechanical load, the material and the geometrical properties. This kind of information can be found in [18, 19, 20, 13]. Natural fires will be modelled with an adjusted parametric fire model based on [8]. This will be processed for 3 typical design fires as described in [15] for industrial buildings. Based on the developed temperature-time curves, the steel temperature of unprotected elements is then calculated based on [11]. The coupling with the mechanical model using the FBM for different scenarios and the evaluation of the reliability level will be the topics of Chapter 6.

5.1 Reference statistical data to describe the thermal action

The structural response of a system will be highly dependent on the thermal action. A temperature-time curve can be evaluated based on the building characteristics such as wall thermal effusivity (with values for different materials mostly ranging between 100 and 2200 J/m²s^{1/2}K), opening factor, geometrical dimensions of the portal frame and as well as on the fire load. Those are characterized by distributions with specific averages and standard deviations as provided in Table 1 [5].

Table 1. PDFs according to [5].

Variable X	Distribution	Averages as fractile of the characteristic value X_k	Coefficient of variation V_X
Thermal characteristics of a wall $b = \sqrt{\rho c \lambda}$	Beta (B)	0.50	0.05
	Determined (D)	0.50	0
Opening factor $O = \frac{A_v \sqrt{h_{eq}}}{A_t}$	Lognormal (LN)	0.50	0.1
	D	0.50	0
Geometrical dimensions	Normal (N)	0.50*	0.005 → 0.03
	D		0
Fire load q_f	Gumbel (maxima)	0.80	0.3
	B		0.05 → 0.10

*This value comes from the reference document but is deemed to be erroneous

Most material properties follow a lognormal (LN) distribution however, in [5] it is recommended to use a beta (B) distribution or a determined parameter. With the rather low V of 0.05, the difference between the B and LN distribution is insignificant, which is why a LN distribution is presently selected. The distribution is applied on the thermal effusivity b (J/m²s^{1/2}K) which is the square root of the product of the density ρ

(kg/m³), the thermal capacity c (J/kgK), and the conductivity λ (W/mK). All other material constants will be assumed to be determined parameters.

A lognormal (LN) distribution is proposed for the opening factor O , composed of the product of the vertical openings A_v (m²), the square root of the surface weighted height h_{eq} (m) of the openings divided by the total surface of the surroundings A_t (m²) openings included.

The geometrical dimensions of the compartment are the width (B), length (L), and height (H) of a compartment expressed in (m). The range of possible V's for the geometrical overall system's dimensions is relatively high. In [21], a value of 0.022 was derived and will also be used here for sake of consistency. It should be noted that the recommended value of 0.5 as average fractile from [5] is probably a typing error and should be 1.0.

For the thermal load, Annex E of [8] refers to the Gumbel distribution, see Table E.4, with the fire load densities related to the floor area q_f . The same distribution will be applied to the fire load density q_t related to the total surface of the enclosure.

5.2 Temperature-time relationships

The temperature-time relationship of the gas (θ_g) will generate a thermal action on the surface of the structural members. With this information, the net heat flux can be determined by taking the heat transfer by convection and radiation into account [8]. For a four-sided heated unprotected profile, the equivalent uniform steel temperature can be calculated according to [11] as well as its mechanical response assessed. The coupling process between the thermal action calculation and mechanical response evaluation will be executed in time steps of 60 seconds.

Two types of models can be distinguished to set up the temperature-time relationship [18]. The first one is based on energy, mass balance equations, and gas properties (chemistry), while the second types of model are based on simplified semi-empirical equations. The last ones have the advantage that they can be worked out in an easy manner perfectly suited for multiple analyses and deliver still accurate results [22]. The Eurocode parametric-time (PF) curve from Annex A [8] is well-suited for this purpose, see [6]. However, for reliability analyses, preference is given to an analytical continuous function [5] capable of estimating the maximum temperature based on the fire duration [25]. In [23] it is suggested to use the adjusted parametric fire (APF) instead. A brief summary of the formulation and its adjustments, including those proposed in [23] leading to a continuous and more accurate curve is given in Table 2. Considering the ratio $\theta_{mod}/\theta_{test}$ of the maximum calculated temperature of the model (θ_{mod}) to the test temperature (θ_{test}), the best fit is obtained by a unique numerical parameter equalling $0.14 \cdot 10^{-3}$.

Table 2. Successive steps needed for the adjusted parametric fire (APF).

Step	APF [23]
Thermal characteristics of compartments at 20°C	$b = \sqrt{\rho c \lambda}$ and $b_{comp} = \frac{\sum(b_j A_j)}{(A_t - A_v)}$
Opening factor	$O = \frac{A_v \sqrt{h_{eq}}}{A_t}$
Fire load	$q_t = q_f \frac{A_f}{A_t}$
Severity factor Γ ($> 1 =$ worse than standard fire)	$\Gamma = \left(\frac{O/0.04}{b/1160} \right)^2$
Shortest duration time t_{lim} (hours)	$t_{lim} = 25/60$ for slow, $20/60$ for medium, and $15/60$ for fast growth rate
Duration heating phase t_{max} (hours)	$t_{max} = 0.14 \cdot 10^{-3} \frac{q_{t,d}}{O}$

If $t_{\max} > t_{\lim}$ (ventilation-controlled)	$\theta_{g,heating} = 20 + 1325(1 - 0.324e^{-0.2t^*} - 0.204e^{-1.7t^*} - 0.472e^{-19t^*})$
	With $t^* = \Gamma \cdot t$ until $t_{\max}^* = \Gamma \cdot t_{\max}$
	$\theta_{g,cooling} = \theta_{\max} - 625(t^* - t_{\max}^*)$ for $t_{\max}^* < 0.5$
	$\theta_{g,cooling} = \theta_{\max} - 250(3 - t_{\max}^*)(t^* - t_{\max}^*)$ for $0.5 < t_{\max}^* < 2.0$
$\theta_{g,cooling} \geq 20^\circ\text{C}$	$\theta_{g,cooling} = \theta_{\max} - 250(t^* - t_{\max}^*)$ for $2.0 < t_{\max}^*$
If $t_{\max} \leq t_{\lim}$ (fuel-controlled)	$O_{lim} = 0.14 \cdot 10^{-3} \frac{q_{t,d}}{t_{lim}}$
	$\Gamma_{lim} = \left(\frac{O_{lim}/0.04}{b/1160} \right)^2$
Correction to Γ_{lim} for large openings in a fuel-controlled situation	If $O > 0.04 \text{ m}^{1/2}$ and $q_t < 75 \text{ MJ/m}^2$ and $b < 1160 \text{ J/m}^2\text{s}^{1/2}\text{K}$
	$k = 1 + \left(\frac{O - 0.04}{0.04} \right) \left(\frac{q_t - 75}{75} \right) \left(\frac{1160 - b}{1160} \right)$
	$\theta_{g,heating} = 20 + 1325(1 - 0.324e^{-0.2t^*} - 0.204e^{-1.7t^*} - 0.472e^{-19t^*})$
	With $t^* = \Gamma_{lim} \cdot t$ until $t_{\max}^* = \Gamma_{lim} \cdot t_{lim}$
	$\theta_{g,cooling} = \theta_{\max} - 625(t^* - t_{lim}^*)$ for $t_{\max}^* < 0.5$
	$\theta_{g,cooling} = \theta_{\max} - 250(3 - t_{\max}^*)(t^* - t_{lim}^*)$ for $0.5 < t_{\max}^* < 2.0$
	$\theta_{g,cooling} = \theta_{\max} - 250(t^* - t_{lim}^*)$ for $2.0 < t_{\max}^*$

One of the limitations of the parametric fire model concerns the compartment geometry, the floor area of which should be limited to 500 m² and ceiling height to 4 m [8]. Nevertheless, scaling the parametric fire can be imagined as long as the ratio between the vertical openings and the total surface of the compartment, the equivalent height, the fire load versus the total surface as well as the thermal properties are kept constant.

The Belgian regulation [15] provides the dimension of a typical industrial building i.e. 60 m long, 12 m high, and L/B = 3 with the following building characteristics: gates of 5x5 m² combined with doors of 0.95x2.2 m² as well as square skylights of 1.2 m high in the roof, which leads to an opening factor O of 0.15 and an equivalent height h_{eq} of 3.35 m. All fires appear to be fuel-controlled with $t_{\max} = 20$ min due to a relatively high opening factor O . A summary of the fire load density as well as the gas and steel temperature can be found in Table 3.

Table 3. Gas and steel temperatures for a typical portal frame steel building

Temperature (°C)	Class A (225 MJ/m ²)	Class B (625 MJ/m ²)	Class C (1250 MJ/m ²)
θ_g with standard values	748	1035	1246
θ_a with standard values	711	1032	1246
$\theta_g, b_{comp} = 1742 \text{ J/m}^2\text{s}^{1/2}\text{K}$	492	838	1045
$\theta_a, b_{comp} = 1742 \text{ J/m}^2\text{s}^{1/2}\text{K}$	401	800	1042
$\theta_g, O = 0.05 \text{ m}^{1/2}$	748	979	1081
$\theta_a, O = 0.05 \text{ m}^{1/2}$	713	974	1080

Firstly, the gas and steel temperature under fuel-controlled conditions are high, and so is the failure risk. Secondly, for the Class C fire load, both the gas and steel temperatures reach 1200°C i.e. the maximum temperature used in [11]. To illustrate the capabilities of the APF, Table 3 also shows the values with an almost double effusivity b and one third of the opening factor O , where all other properties are kept constant.

6 EVOLUTION OF THE RELIABILITY INDEX DURING A FIRE

It was shown that the FBM as described in [10] is a good tool for comparative reliability-based assessment of portal frame and approximates well the results of the comprehensive probabilistic analysis from [7]. By including the temperature-dependent deformations in the matrix equation (Eq. (1)) of Chapter 4, the method enable to capture the effect of uniform temperature effects (along a member). The influence of heating on the reliability of a single-bay portal frame can be achieved by coupling the outputs of the simulations presented in Section 5 to the FBM analysis.

Out of the portal frames proposed in Chapter 3, the frame (c) is here chosen as case-study. Note that the results of sections 5.2 and 5.3 are independent of the building shape. They vary with the parameters of the fire i.e. the opening factor O , equivalent height h_{eq} and effusivity of the compartment b_{comp} . The most important statistical data are summarized in Table 4. Determined values are used for other parameters.

Table 4. Summary of statistical data for thermal and structural analysis of the chosen portal frame (c).

Subject	Property	Unit	Characteristic	Distribution	Mean μ	V
Resistance beam IPE360	A, W_{pl}	m ³	1019·10 ⁻⁶	N	804.3·10 ⁻⁶	0.02
	f_y	N/m ²	235·10 ⁶	LN	327·10 ⁶	0.08
	E	N/m ²	210·10 ⁹	N	210·10 ⁹	0.001
Resistance column IPE400	A, W_{pl}	m ³	1307·10 ⁻⁶	N	804.3·10 ⁻⁶	0.02
	f_y	N/m ²	235·10 ⁶	LN	327·10 ⁶	0.08
	E	N/m ²	210·10 ⁹	N	210·10 ⁹	0.001
Dimensions, fire	L and H	m	15 and 10	N	H and L	0.022
mechanical	L and H	m	15 and 10	N	0.95 H and L	0.022
Load	SW	N/m	568	N	568	0.02
	DL	N/m	9000	N	9000	0.10
Thermal	b_{comp}	J/m ² s ^{1/2} K	902	LN	902	0.05
	O	m ^{1/2}	0.15	LN	0.15	0.10
	L, B and H	m	$L, B,$ and H	N	$L, B,$ and H	0.022
	qt	MJ/m ²	1.22xA, B, C	GU+	A, B, or C	0.30

Using the data above, a reliability index β higher than 7.9 was found in ambient conditions (20°C). The different fire Classes highlighted in Table 3 do correspond to another use of the building but, since the steel temperatures rises (from Class A to Class C), this can also be seen as a developing fire in a compartment. All other parameters being kept constant, the calculated β is evaluating from bigger as 7.9 at 20°C to respectively 1.64, -2.52, -2.31 and -2.04 for temperatures of 395, 704, 1028 and 1242 °C. Based on those values it follows that the probability of system's failure P_f in the case of a compartment fire is only acceptable at relatively low temperatures (395°C) when the effusivity equals 1742 J/m²s^{1/2}K. In this case, a failure risk of 50% can be (backward-) calculated for a steel temperature of about 520 °C only.

7 POST-FIRE RELIABILITY OF SINGLE-BAY PORTAL STEEL FRAMES

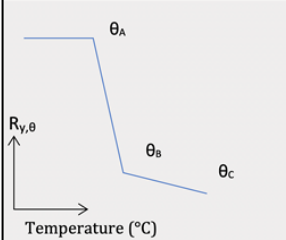
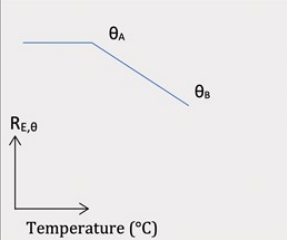
Where the evolution of the reliability level during a fire can be seen as an application example, the real added value of the method is the post-fire reliability assessment of structures. Based on the evaluation of 718 tests collected from 19 references, reliability-based, post-fire steel material properties and safety factors are calculated in [12]. The retention factor versus temperature can be found in Table 5, see [12]. They can be used in the assessment of existing steel structures that suffered and survived a fire. The data is

used to derive retention factors for each of the significant and characteristic material properties and adjusted safety factors (for post-fire assessment of structures) based on the detailed analysis. Both factors depend on the maximum temperature to which the steel is exposed. It is shown that, for traditional strength steel, the impact of fire on the post-fire mechanical properties remains reasonable up to temperatures approaching 1000°C. It is also proposed that the safety factor $\gamma_{M0,post,\theta}$ is increased to 1.15 starting from heating above 650°C for traditional strength carbon steel, with a modified reliability level β of 3.3 proposed for the assessment of existing structures. The work is based on a statistical evaluation of test data without dealing with the behaviour of a part of the structure.

Here, validation of the suggested additional partial factors will be done for the three load fire Class i.e. for averaged maximum steel temperatures of 704, 1028, and 1242°C as calculated in Chapter 3 on the nine portal frames i.e. with three different shape ratios H/L ranging from 0.25 to 0.67. And thus, three load ratios (superimposed dead load from 1.8 until 9 kN/m) will be considered. All factors and their appropriate PDFs can be found in Table 4. In this evaluation, only permanent loads will be considered ($V = 0.10$). Because the material safety factors for carbon steel is equal to 1.0, the effect on the reliability level can easily be considered by using an additional safety factor, where appropriate. Each random series of simulation is then repeated five times to increase accuracy. In total, this results in 9 portal frames with 3 fire loads, and 1000 repeated 5 times, i.e. 135000 simulations.

Table 5. Proposed simplified retention factors suitable for verification of normal structural steel (NSS).

Property	$R_{y,\theta}$			$R_{E,\theta}$	
θ (°C)/ R_θ	θ_A	θ_B	θ_C	θ_A	θ_B
All	400/ 1.00	750/ 0.40	1200/ 0.13	700/ 1.00	1200/ 0.65
NSS	600/ 1.00	750/ 0.75	1000/ 0.62	800/ 1.00	1000/ 0.90

Furthermore, for the reinstatement of (existing) buildings, the reliability level can be decreased to find an acceptable level taking into account economical and societal aspects [27], [28]. In accordance with ISO 2394 [29], and as is proposed in [12], a value of 3.3 for the post-fire reliability index β is proposed.

7.1 Compartment fire

A compartment fire was firstly investigated which is generally considered to be the most severe situation [22] for an industrial building and, due to the floor area, this scenario is generally assumed to be very unlikely to occur. In Figure 3 it is shown that only for low fire loads (Class A) i.e. after being submitted to relatively low temperatures the post-fire reliability level remains above an acceptable minimum target value.

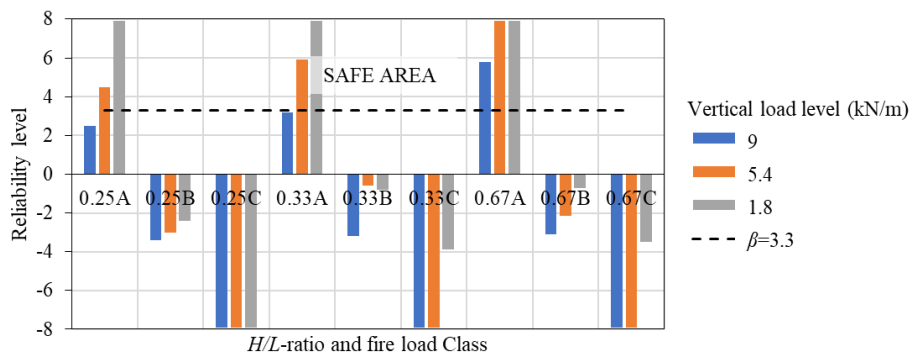


Figure 3 Reliability level in function of the H/L -ratio for different fire and vertical loads due to uniform heating.

7.2 Local fire against a column

The same analysis is here done on a portal frame where only one column is submitted to a local fire. The reliability level only slightly increases when only a single column is engulfed in the fire, however leading

to the same conclusions. Figure 4 compares the failure times for the case of a fire next to the left column. It is seen that the difference in reliability levels is not as pronounced as the difference in collapse time.

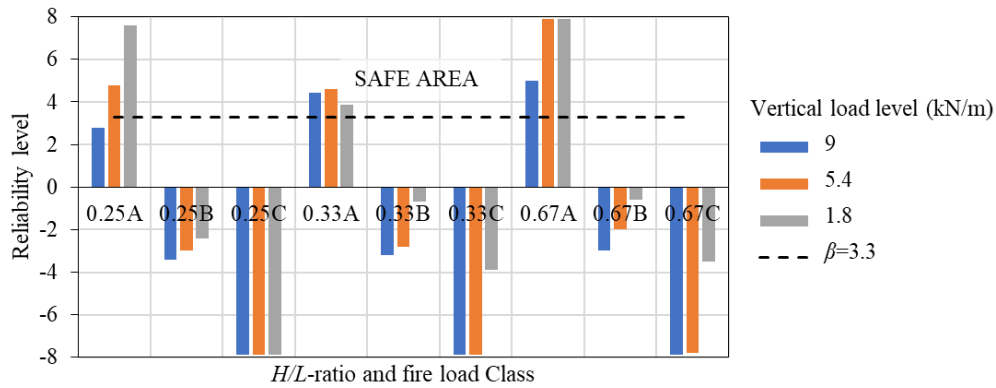


Figure 4 Reliability level in function of the H/L -ratio for different vertical loads due to local column heating (left column).

It is clear that the assumption made by [22] that a compartment fire is the most severe scenario can now be confirmed based on the outcomes of this reliability assessment, the differences are almost negligible.

7.3 Beam in the hot smoke layer

A common assessment question is what should be done with the structures when only the beam of the frame was engulfed in the hot smoke layer. This can happen in case of a local fire but, usually more often, in combination with a severe fire during which part of the structure collapsed and the interest lies in whether the remaining part can still be re-used in a reliable way. From Figure 5, it can be seen that if the beam does not fail during the fire, the reliability level can be guaranteed.

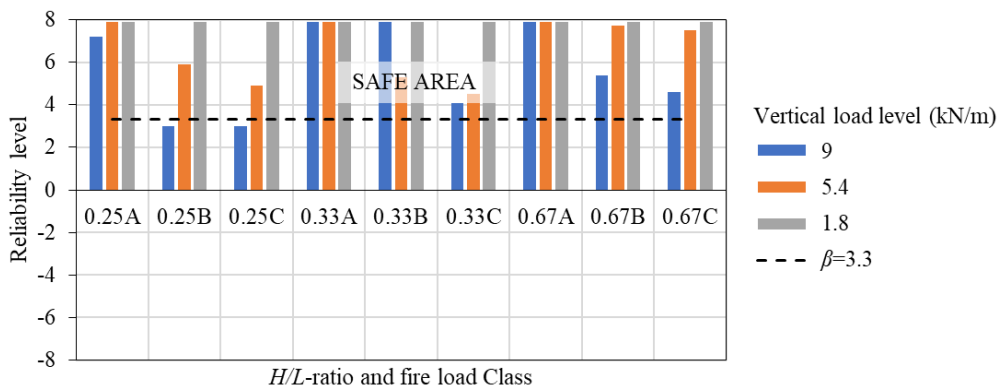


Figure 5 Reliability level in function of the H/L -ratio for different vertical loads and a beam in the hot smoke layer.

Only the combination of big span with high dead load, and a moderate to severe fire (Class B and C) could lead to a too low reliability index. This conclusion seems to be confirmed by several observations from practical cases investigated by the authors in the past years. References can be found in [25] of recent reinstated structures.

7.4 Reliability evaluation

In [12], a material additional safety factor of 1.15 was proposed to assess the post-fire resistance of structures having reached 650°C , in order to deal with the increased uncertainty level on the material properties. It is worth underlining that material reduction factors are only needed once heated above 1000°C i.e. most probably a point at which the structure has collapsed. It is worth recalling that only permanent loads are applied on the portal frame and that the (ambient temperature) material safety factor is equal to one which results in a clear link between the utilization ratio η (including the additional post-fire safety factor) and the reliability level (see Eqs. (3) and (4)).

$$\eta = \frac{E_d}{R_{d,post}} = \frac{\gamma_G G}{R/(\gamma_M \gamma_{M0,\theta,post})} = \frac{\gamma_{M0,\theta,post} \gamma_G G}{R} \quad (3)$$

$$\gamma_G = \gamma_{Ed,G} \cdot \gamma_g = \gamma_{Ed,G} \cdot \frac{\mu_G [1 - \alpha_E \beta V_G]}{\mu_G [1 + k \cdot V_G]} \approx 1.07 \cdot [1 - \alpha_E \beta V_G] \quad (4)$$

Those are based on the recommendations of [30], with a model uncertainty factor $\gamma_{Ed,G}$ of 1.07 for an unfavourable action, $k = 0$, which is commonly assumed for permanent actions, α_E is the sensitivity factor (-0.7 [31]), and V_G is the standard deviation for the permanent loads.

It is seen that where Classes B and C reach 1000°C (1028°C and 1242°C respectively) and thus do not reasonably survive the fire ($\beta < 0$ or $P_f < 0.5$); see Figure 3. However, Class A (with effusivity up to 1742 J/m²s^{1/2}K) works perfectly well up to 704°C.

For a Consequence Class 2 building, the safety factor on permanent action is equal to 1.35 [31], hence the product $\alpha_E \cdot \beta \cdot V_G$ is equal to -0.26. In post-fire conditions, this will therefore become -0.45 since an additional post-fire partial factor of 1.15 is used. Neither the sensitivity factor nor the standard deviation on permanent actions will be changed. Hence, this can only be explained by an increased reliability level β which is multiplied by a factor 0.45/0.26 = 1.72. The lowest value for a Class A fire from Figure 3 to Figure 5 is 2.5, and so will be increased up to 1.72 · 2.5 = 4.3, i.e. there is still some resistance reserve. This reserve is of prime importance to guarantee an adequate reliability level at higher exposure up to 1000°C. By the application of the proposed methodology, it is therefore proven that the adjusted partial factor method delivers safe results for single-bay portal frames.

8 CONCLUSIONS

By comparing the results of numerical analysis (SAFIR® [9]) to analytical solutions it was shown that reasonable evaluations of the structural failure modes of single-bay portal frames submitted to high temperatures can be achieved. The methodology based on the assessment of critical sections can be extended to structures subjected to fire as well as to assess them in post-fire situation.

To facilitate the reliability analysis, the adjusted parametric fire as proposed by [23] is well-suited to be coupled to the developed FBM equations. By including the time-dependent formulation of the heat transfer, it is possible to develop a methodology for a full probabilistic (analytical-) analysis of a single-bay portal frame during a fire and in post-fire conditions.

An evaluation of the reliability of single-bay portal frames is then performed for several fire load levels (during and after the fire) and 3 different length-to-height ratios. It was found that the reliability of structures during a fire is rapidly decreasing. Only buildings with a high thermal inertia (high effusivity) do deliver an acceptable level of safety if they remain under 400°C. Otherwise, entering the building should be prohibited. Starting from 520°C the failure and survival probability are equal.

Post-fire reliability calculations are then performed for a compartment fire as well as for various local fire scenarios such as a heated column, a column and a beam or only the beam engulfed in a hot smoke layer. When the beam only is engulfed in the fire, all the studied geometries can survive the fire (i.e. keeping reasonable reliability level). However, it is only if the temperature remains below an acceptable level (about 700°C i.e. for Class A fire) that the scenario involving heating of the beam provides satisfying reliability.

Finally, it is shown that the procedure developed in [12] for the post-fire verification of remaining structural parts having been submitted to fire and cooled down delivers safe results, encouraging the reinstatement of structures over their dismantling.

REFERENCES

- 1 M. H. Faber, „Risk assessment in engineering - Principles, system representation and risk criteria,” JCSS, Zürich, 2008.

- 2 H. Gulvanessian, J.-A. Calgaro en M. Holicky, Designers' guide to Eurocode: Basis of structural design EN 1990, 2nd red., London: ICE Publishing, 2012.
- 3 K. Sidibé, F. Duprat, M. Pinglot en B. Bourret, „Fire safety of reinforced concrete columns,” *ACI-journal*, 2000.
- 4 R. Van Coile, E. Annerel, R. Caspeepe en L. Taerwe, „Full-probabilistic analysis of concrete beams during fire,” *Journal of structural fire engineering*, vol. 4, pp. 165-174, 2013.
- 5 Handbook 5, Implementation of Eurocodes: Handbook 5 - Design of buildings for the fire situation, Luxembourg: European Commission, Joint Research Centre, CZ/02/B/F/PP-134007, Leonardo Da Vinci Pilot Project, 2005.
- 6 Q. Guo en A. E. Jeffers, „Finit-element reliability analysis of structures subjected to fire,” *Journal of structural engineering*, pp. 1-11, 2014.
- 7 EUR 21695, „Probabilistic quantification of safety of a steel structure highlighting the potential of steel versus other materials,” European Commission, Luxembourg, 2005.
- 8 EN 1991-1-2, Actions on structures - Part 1-2: General actions - Actions on structures exposed to fire, Brussels: CEN, 2002.
- 9 J. Franssen en T. Gernay, „Modelling structures in fire with SAFIR,” *Journal of Structural Fire Engineering*, vol. 8, nr. (3), pp. 300-323, 2017.
- 10 T. Molkens en B. Rossi, „Determination of the structural behaviour of single storey steel buildings in case of fire by a simplified force-based method,” in *IFireSS*, Ottawa, CA, 2019.
- 11 EN 1993-1-2, Design of steel structures - Part 1-2: General rules - Structural fire design, Brussels: CEN, 2004.
- 12 T. Molkens, K. A. Cashell en B. Rossi, „Post-fire mechanical properties of carbon steel and safety factors for the reinstatement of steel structures,” *Engineering structures*, p. Under review, 2020.
- 13 R. Van Coile, D. Hopkin, N. Elhami-Khorasani, D. Lange en T. Gernay, „Permanent and live load model for probabilistic structural fire analysis: a review,” Minneapolis, 2019.
- 14 S. Selamet en E. Akcan, „Reliability risk assessment in high rise buildings in case of fire,” Brisbane, 2015.
- 15 FPS Interior, „Annex 6 - Industrial buildings,” in *Royal decree to point out the regulations for the prevention of fire and explosions for new buildings*, Brussels, Moniteur Belge - Belgisch staatsblad, 2009, pp. 49369-49397.
- 16 EN 1993-1-1, Eurocode 3 - Design of steel structures: Part 1-1: General rules and rules for buildings, Brussels: CEN, 2003.
- 17 A. Ghali en A. M. Neville, Structural analysis a unified classical and matrix approach, 3rd red., London - New York: Chapman and Hall, 1989.
- 18 JCSS, „Probabilistic Model Code,” <https://www.jcss.byg.dtu.dk>, Denmark, 2001.
- 19 M. Holicky en M. Sykora, „Stochastic models in analysis of structural reliability,” Beer (Israel), 2010.
- 20 EUR 28906, „Standardization of safety assessment procedures across brittle to ductile failure modes,” European commission, Directorate-General for Research and Innovation, Luxembourg, 2017.
- 21 T. Molkens en B. Rossi, „Mode Based Reliability Approach for Single Bay Portal Frames,” *Journal*, p. To be submitted, 2020.
- 22 A. H. Buchanan en A. K. Abu, Structural design for fire safety, 2nd red., Chichester: John Wiley & Sons Inc., 2017.
- 23 S. Reitgruber, C. Pérez-Jimenez, C. Di Blasi en J.-M. Franssen, „Some comments on the parametric fire model of Eurocode 1,” Jordanstown, 2006.
- 24 J.-M. Franssen en R. Zaharia, Design of steel structures subjected to fire, Liège: Les éditions de l'université de Liège, 2005.
- 25 T. Molkens en B. Rossi, „On the simulation of real fire for post-fire resistance evaluation of steel structures,” *Fire Technology*, p. Under review, 2020.
- 26 C. Roberts, „Monte Carlo methods in statistics,” *Hal.archive-ouvertes.fr*, p. 00412639, 2009.
- 27 M. Sykora, D. Diamantidis, M. Holicky en K. Jung, „Target reliability levels for existing structures considering economic and societal aspects,” *Structure and Infrastructure Engineering*, nr. 13, pp. 181-194, 2017.
- 28 R. Caspeepe, M. Sykora, D. L. Allaix en R. Steenbergen, „The design value method and adjusted partial factor approach for existing structures,” *Structural Engineering International*, vol. 23, nr. (4), pp. 386-393, 2013.
- 29 ISO 2394, General principles on reliability for structures, Geneva: International standard organization, 2015.
- 30 fib bulletin 80, Partial factor methods for existing structures, Lausanne: Fédération internationale du béton, 2016.
- 31 EN 1990, Eurocode 0 - Basis of structural design, Brussels: CEN, 2002.

INFLUENCE OF TIME STEP ON STABILITY OF THE HYBRIDE FIRE TESTING IN A LIMITED DIVERGENCE ZONE

Bunthan IEA¹, Duc Toan PHAM², Nicolas PINOTEAU³, Romain MEGE⁴, Jean-François CARON⁵

ABSTRACT

The present contribution deals with an application of the displacement-controlled procedure in a hybrid fire test, taking into account the evolution of the stiffness ratio related to the degradation of local material stiffness properties due to the fire-induced temperature increase. In the previous work (Pinoteau *et al.* 2020, Development of Hybrid Fire Testing by real-time subdivision of physical and numerical substructures), an interface where data were exchanged between a finite element software and a hydraulic jack regulator using text files has been developed and applied to perform two experimental campaigns of nine tests on simple steel frame structures, with different thermal loading conditions. It has been observed that some hybrid fire tests did not show clear divergence results even though the theoretical convergence condition on the stiffness ratio was no longer respected. However, clear justification for such a phenomenon was still missed. It is for this reason that a new concept, called here after “limited divergence zone”, is introduced to reanalyse the quoted experimental results. In addition, a gap of compatibility is also introduced and discussed, making it possible to define another practical criterion for the stability of the Hybrid Fire Testing. For illustrative purpose, parametric studies are carried out in order to investigate the influence of time step on the convergence of the Hybrid Fire Testing in the limited divergence zone.

Keywords: Hybrid Fire Testing; limited divergence zone; gap of compatibility; time step; parametric study

1 INTRODUCTION

The Hybrid Fire Testing (HFT) (see among many others: Mostafaei [1]; Tondini *et al.* [2], Sauca *et al.* [3] or recently Grolimund *et al.* [4]; Wang *et al.* [5], Pinoteau *et al.* [6]) relies on the subdivision of a studied structure into two substructures: the tested specimen (noted here as Physical Substructure (PS)) and the remaining parts of the structure which are numerically simulated and noted as Numerical Substructure (NS). During a hybrid fire test, interaction between PS and NS is carried out by updating boundary conditions at the interface of the two substructures. This allows evaluating the fire behaviour of structural elements in an

¹ Mr., Laboratoire Navier (Ecole des Ponts ParisTech, IFSTTAR, CNRS UMR 8205), 6-8 avenue Blaise Pascal, Cité Descartes, Champs-sur-Marne, 77455 Marne-la-Vallée Cedex 2, France / Université Paris-Est, Centre Scientifique et Technique du Bâtiment (CSTB), 84 avenue Jean Jaurès, Champs-sur-Marne, 77447 Marne-la-Vallée Cedex 2, France
e-mail: bunthan.iaa@cstb.fr, ORCID: <https://orcid.org/0000-0002-3422-6791>

² Dr., Université Paris-Est, Centre Scientifique et Technique du Bâtiment (CSTB), 84 avenue Jean Jaurès, Champs-sur-Marne, 77447 Marne-la-Vallée Cedex 2, France
e-mail: ductoan.pham@cstb.fr, ORCID: <https://orcid.org/0000-0002-0130-9152>

³ Dr., Université Paris-Est, Centre Scientifique et Technique du Bâtiment (CSTB), 84 avenue Jean Jaurès, Champs-sur-Marne, 77447 Marne-la-Vallée Cedex 2, France
e-mail: nicolas.pinoteau@cstb.fr, ORCID: <https://orcid.org/0000-0001-9569-9835>

⁴ Dr., Université Paris-Est, Centre Scientifique et Technique du Bâtiment (CSTB), 84 avenue Jean Jaurès, Champs-sur-Marne, 77447 Marne-la-Vallée Cedex 2, France
e-mail: romain.mege@cstb.fr

⁵ Prof., Laboratoire Navier (Ecole des Ponts ParisTech, IFSTTAR, CNRS UMR 8205), 6-8 avenue Blaise Pascal, Cité Descartes, Champs-sur-Marne, 77455 Marne-la-Vallée Cedex 2, France
e-mail: jean-francois.caron@enpc.fr

environment closer to reality than traditional testing methods, without it being necessary to carry out delicate, expensive or even impossible full-scale tests.

This paper is a continuation of a previous one (Pinoteau *et al.* [6]) which has dealt with an application of the displacement-controlled procedure of the “first generation” method of the HFT (Sauca *et al.* [3]). An interface where data was exchanged between a finite element software and a hydraulic jack regulator using text files was developed to perform two experimental campaigns of nine tests on simple steel frame structures, with different thermal loading conditions. Such a procedure is direct and relatively simple to implement. The convergence of the algorithm (continuity of displacements or equilibrium of forces) is ensured as far as the stiffness k_P of the PS is lower than the stiffness k_N of the NS (see for example Sauca *et al.* [3]). However, while convergence of the HFT was conditioned by the stiffness ratio of the two substructures in the theoretical work of Sauca *et al.* [3], it has been observed that some hybrid fire tests in the experimental work of Pinoteau *et al.* [6] did not show clear divergence results even though the theoretical convergence condition was no more respected. These available experimental results suggest that the theoretical condition of convergence based only on the stiffness ratio of the two substructures is still questionable and may be improved for practical purpose.

In this context, the present paper focuses on the configuration where the stability of the HFT could be ensured even in when the stiffness k_P of the PS is higher than the stiffness k_N of the NS. It is shown that such results could be obtained when the curves representing the evolution of stiffness of the two substructures as functions of fire exposure time, cross each other twice, which in turn leads to a particular configuration where a divergence zone (where $k_P > k_N$) is limited by two convergence zones (where $k_P < k_N$) (see Fig. 1 for example). Such a zone is called hereafter “limited divergence zone”.

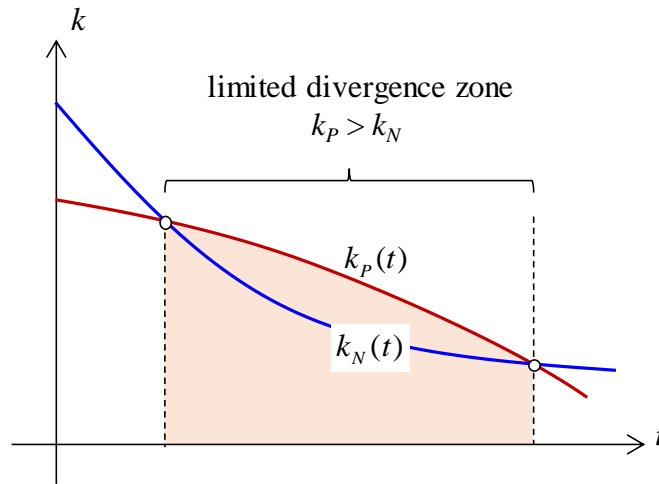


Figure 1. Illustration of a “limited divergence zone”

In order to assess the influence of time step on convergence of the HFT in the limited divergence zone, parametric studies have been performed, using a simplified one-dimensional (1D) model. This constitutes additional understandings to identify possible paths of improvements that might have been missed or could not be accessed through previous studies.

2 BACK TO THE CONCEPT OF CONVERGENCE AND DIVERGENCE OF THE HFT

2.1 Displacement-controlled procedure

During a hybrid fire test, physical and numerical substructures exchange data iteratively. The sequence in which the two substructures exchange data iteratively is sketched in Fig. 2 and described as follows.

- i. At the beginning of the test ($t = 0$), the furnace is first turned on while the hydraulic jack applies an initial displacement u_0 to the PS. As a direct consequence, the PS will react to the loading and the increase of the temperature increase (causing loss of stiffness and thermal displacement).
- ii. At $t = \Delta t$, the reaction force F_1 on the PS is measured, then sent to the NS to be applied as boundary conditions, Δt being the time step of the HFT and mostly conditioned by the calculation time of the numerical modelling (see for example Sauca *et al.* [3], Pinoteau *et al.* [6]) and the speed of the hydraulic jack. Thereafter, a new calculation is carried out on the NS with the new boundary conditions, resulting in the new displacement u_1 . Such a calculation may take a little time but should never exceed the time step Δt .
- iii. The displacement u_1 is sent to the control system of the hydraulic jack, to be applied again to the PS at $t = 2\Delta t$.

For the next steps, these previous steps ii and iii are repeated until the end of the test.

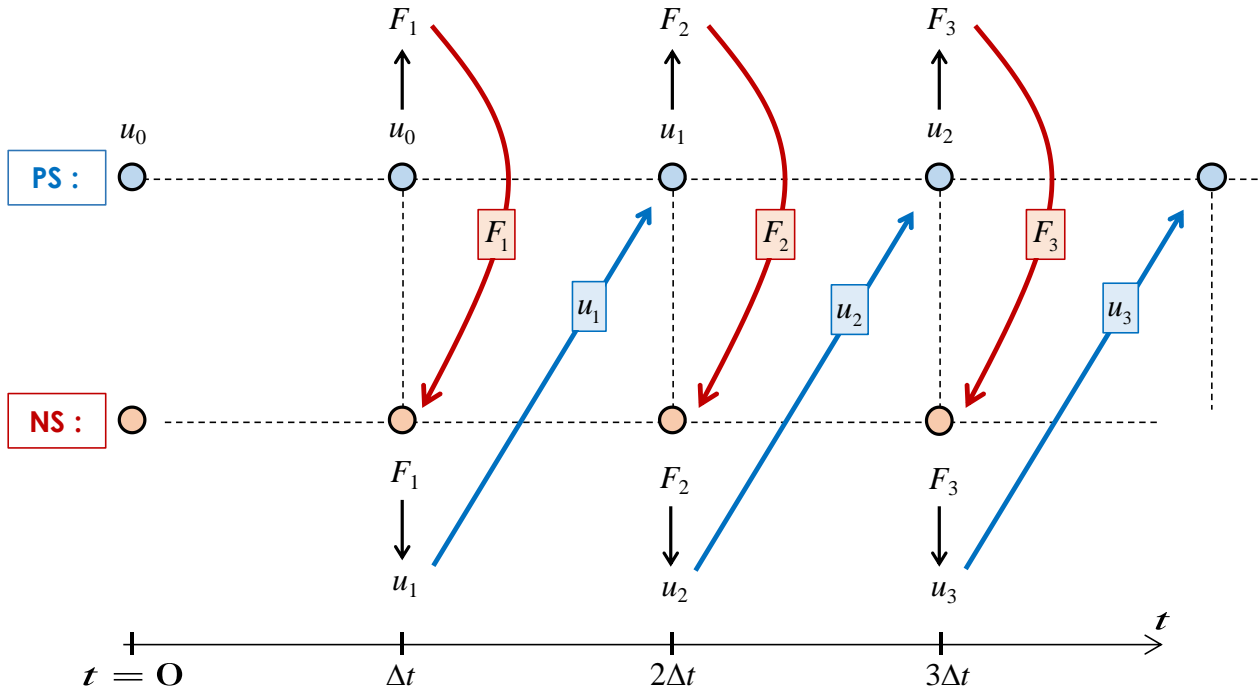


Figure 2. Iterations of HFT with displacement-controlled procedure

In the following, the displacement-controlled procedure is implemented in a simplified one-dimensional (1D) model. Such a linear elastic system has also been adopted for analysing the convergence of the HFT in the theoretical work of Sauca *et al.* [3].

2.2 A simplified 1D model and definition of the “gap of compatibility”

As it has been recalled above, the communication between the PS and the NS is carried out iteratively by successive measuring and applying load or displacement. The values of load, displacement and temperatures are expressed in discrete values along with stiffness and thermal displacements. In order to ensure the representativity of the HFT, it is necessary to guaranty identical boundary conditions at the

PS/NS interface. The mechanical equilibrium is defined as the position of the interface which satisfies both the load equilibrium between both substructures and the displacement compatibility.

Referring to an uniaxial Ou -axis, the PS and the NS are modelled as two springs (of stiffness $k_P(t)$ and $k_N(t)$ and of length $l_{0,P}$ and $l_{0,N}$) fastened to two fixed walls as sketched in Fig. 3. These two springs are both in their relaxed states (unstretched and uncompressed) at ambient temperature ($T = 20^\circ$):

$$u_P(T = 20^\circ C) = u_N(T = 20^\circ C) = 0 \quad (1)$$

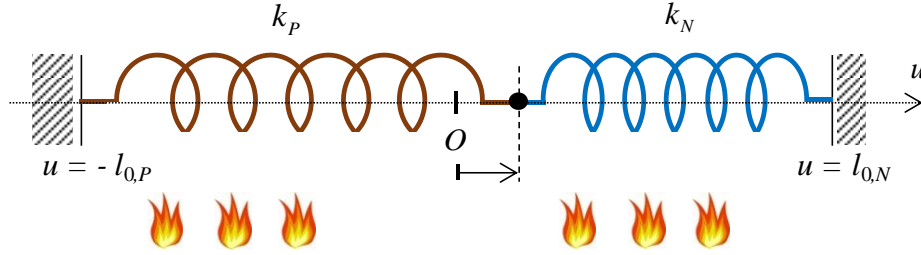


Figure 3. Simplified schematic interaction of the PS and the NS in a hybrid fire test

Assuming that an initial thermal perturbation is brought to the system by a temperature increase at the beginning (both the PS and the NS are uniformly exposed to fire), the length of the two substructures tends to expand, resulting in a new equilibrium.

For a given time, assuming that the displacement of the connected point is small enough, a linear thermo-elastic behaviour of the entire structure is expressed by the following static equilibrium relationship:

$$\underbrace{k_P(t)(u^{eq}(t) - u_P^{th}(t))}_{F_P(t)} + \underbrace{k_N(t)(u^{eq}(t) - u_N^{th}(t))}_{F_N(t)} = 0 \quad (2)$$

leads to the equilibrium position:

$$u^{eq}(t) = \frac{k_P(t)u_P^{th}(t) + k_N(t)u_N^{th}(t)}{k_P(t) + k_N(t)} \quad (3)$$

where u_P^{th} (resp. u_N^{th}) denotes the associated thermal expansion displacement of the PS (resp. the NS). The corresponding values of the loading parameters in the PS/NS interface are thus simplified to:

$$F^{eq}(t) = F_N(t) = -F_P(t) = \frac{k_P(t)k_N(t)}{k_P(t) + k_N(t)}(u_N^{th}(t) - u_P^{th}(t)) \quad (4)$$

The main objective of the HFT is to reproduce as faithfully as possible the equilibrium solutions of Eqs. (3) and (4). At each communication iteration (step) i of the HFT which corresponds to $t_i = i\Delta t$, the equations (3) and (4) become:

$$u_i^{eq} = \frac{k_{P,i}u_{P,i}^{th} + k_{N,i}u_{N,i}^{th}}{k_{P,i} + k_{N,i}} \quad ; \quad F_i^{eq} = F_{N,i} = -F_{P,i} = \frac{k_{P,i}k_{N,i}}{k_{P,i} + k_{N,i}}(u_{N,i}^{th} - u_{P,i}^{th}) \quad (5)$$

In this case, it is proven that the difference between the solution of force and displacement of the hybrid fire test and the equilibrium solutions (5) can be written as:

$$\begin{aligned}
u_{N,i} - u_i^{eq} &= \frac{k_{P,i}}{k_{P,i} + k_{N,i}} \Delta u_i \quad ; \quad F_{N,i} - (-F_i^{eq}) = \frac{k_{P,i} k_{N,i}}{k_{P,i} + k_{N,i}} \Delta u_i \\
u_{P,i} - u_i^{eq} &= -\frac{k_{N,i}}{k_{P,i} + k_{N,i}} \Delta u_i \quad ; \quad F_{P,i} - F_i^{eq} = -\frac{k_{P,i} k_{N,i}}{k_{P,i} + k_{N,i}} \Delta u_i
\end{aligned} \tag{6}$$

where $\Delta u_i = u_{N,i} - u_{P,i}$ is defined as the “gap of compatibility”. As a direct result, the solution of the hybrid fire test is equal to the equilibrium solution if and only if the gap of compatibility is equal to zero. Therefore, the gap of compatibility can be considered as the necessary and sufficient condition for the reproducibility of the equilibrium solution. In the following, it will be used as the main indicator to study the stability of the HFT.

By the communication layout presented in Fig. 2, the calculated displacement at iteration $i-1$ is applied to the PS in iteration i :

$$u_{N,i-1} = u_{P,i} \tag{7}$$

can be incorporated into equations (6), leading to the following relations:

$$\Delta u_i = -\frac{\alpha_{i-1}(1+\alpha_i)}{1+\alpha_{i-1}} \Delta u_{i-1} + (1+\alpha_i)(u_i^{eq} - u_{i-1}^{eq}) \tag{8}$$

where $\alpha_i = k_{P,i} / k_{N,i}$ is the stiffness ratio of the two substructures at iteration i .

The equation (8) could be written in the explicit form:

$$\Delta u_i = (1+\alpha_i) \sum_{k=0}^{i-1} \left[\prod_{j=k+1}^{i-1} (-\alpha_j) \right] (u_{k+1}^{eq} - u_k^{eq}) \tag{9}$$

Equation (9) points out that the gap of compatibility depends on two parameters: the stiffness ratio α_i and the progression of the theoretical solution of displacement u^{eq} at each time step (*i.e.*, $u_i^{eq} - u_{i-1}^{eq}$). The later should not be neglected because even when the stiffness ratio α_i is infinitely small (*i.e.*, when the NS is infinitely more rigid than the PS), the gap of compatibility can never be eliminated:

$$\Delta u_i \xrightarrow{\alpha \rightarrow 0} u_i^{eq} - u_{i-1}^{eq} \tag{10}$$

2.3 Discussions on the available experimental results of Pinoteau *et al.* [6]

Three hybrid fire tests were carried out on simple steel frame structures (Fig. 4) with different mechanical loading conditions and time steps. They were performed using different steel HEA120 beams exposed to fire on their lower surface for the PS and with the same NS. A fully detailed description of the PS as well as of the NS, the test setup and measurement devices (temperatures and displacements) may be found in Pinoteau *et al.* [6].

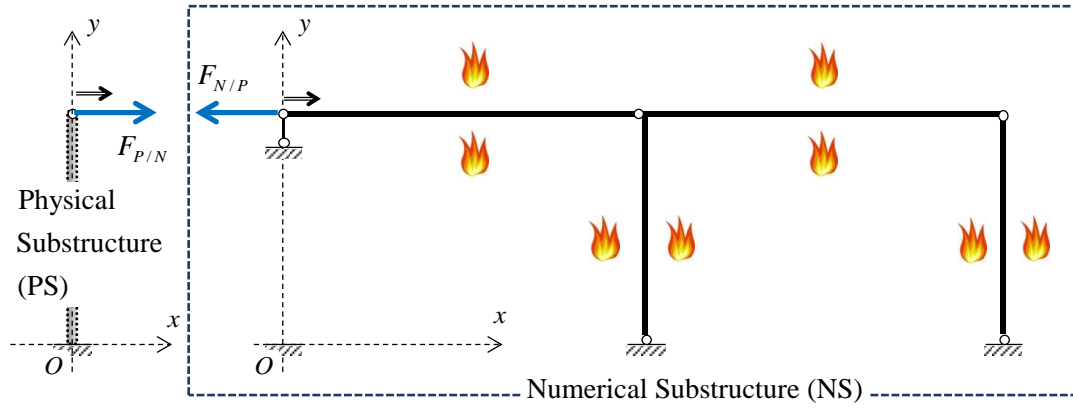


Figure 4. The PS and the NS in the hybrid fire tests of Pinoteau *et al.* [6]

Figure 5 where the evolutions of the stiffness of both the PS and the NS have been reported shows that:

- Before the tests, the stiffness $k_N(t=0)$ of the NS was higher than the stiffness $k_P(t=0)$ of the PS.
- Both $k_N(t)$ and $k_P(t)$ decreased with temperature increase. The two corresponding curves cross each other at $t = 14$ min. After this time, $k_N(t)$ was always lower than $k_P(t)$ but divergence did not occur.
- In the region where divergence was expected, $k_N(t)$ decreased faster than $k_P(t)$ before 16 min, but slower than $k_P(t)$ after 16 min. The two curves seem to cross again if the tests were not stopped for safety issues. It may turn out that $k_N(t)$ might be higher than $k_P(t)$ again if the tests would be continued, which in turns limit the divergence zone (the “limited divergence zone” previously defined) between two convergence zones.

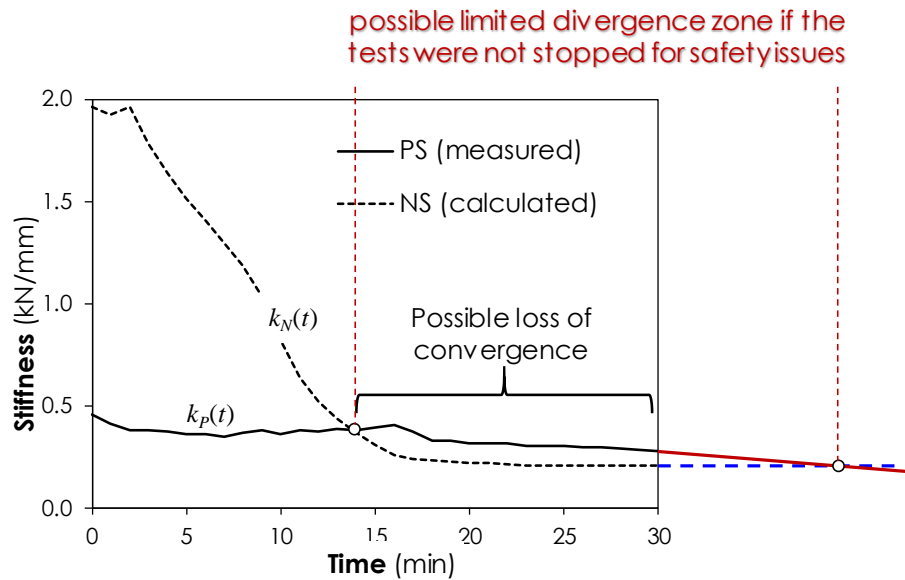


Figure 5. Evolution of the stiffness of PS and NS as functions of fire exposure time (Pinoteau *et al.* [6]) and the associated possible limited divergence zone (if the tests were not stopped for safety issues)

In order to provide further support for the later assumption, additional virtual hybrid fire tests are carried out on the simplified 1D model in the following section.

3 ADDITIONAL VIRTUAL HYBRID FIRE TESTS

Six examples corresponding to six configurations where the stiffness $k_P(t)$ of the PS is varied from one configuration to the other while the stiffness $k_N(t)$ of the NS is kept fixed, are displayed in Fig. 6. $k_N(t)$ is always represented by the same curve while $k_P(t)$ are represented by six parallel right curves. The first configuration (configuration n° 1) corresponds to the case where the size of the limited divergence zone is the smallest (the case where $k_P(t)$ is tangent to $k_N(t)$) while the configuration n° 6 corresponds to the configuration where its size is the largest, the second to the fifth case study being intermediate cases. In addition, six values of time step Δt , regularly varying from 10 s to 60 s, are considered for each case study.

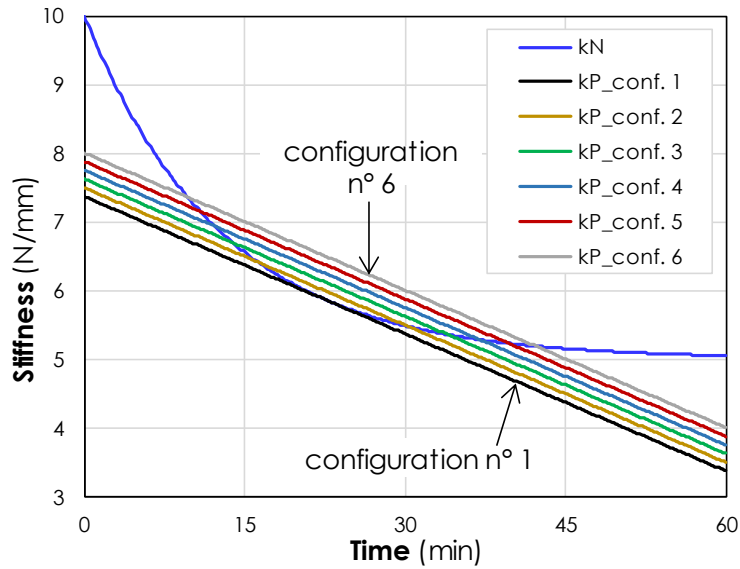


Figure 6. Evolution of the stiffness of the PS and the NS as functions of fire exposure time for the six configurations of virtual hybrid fire tests

For illustrative purpose, the resulting displacement and force of the two configurations n° 3 and n° 5 are shown in Fig. 7 and Fig. 8 respectively, with the same time step $\Delta t = 20$ s. It can be seen that the instability of the HFT occurs in the configuration n° 5 (Fig. 8) but not in configuration n° 3 (Fig. 7), showing that the stability of the HFT can depend on the width of the limited divergence zone. The stability of the HFT may be obtained if the limited divergence zone is small enough.

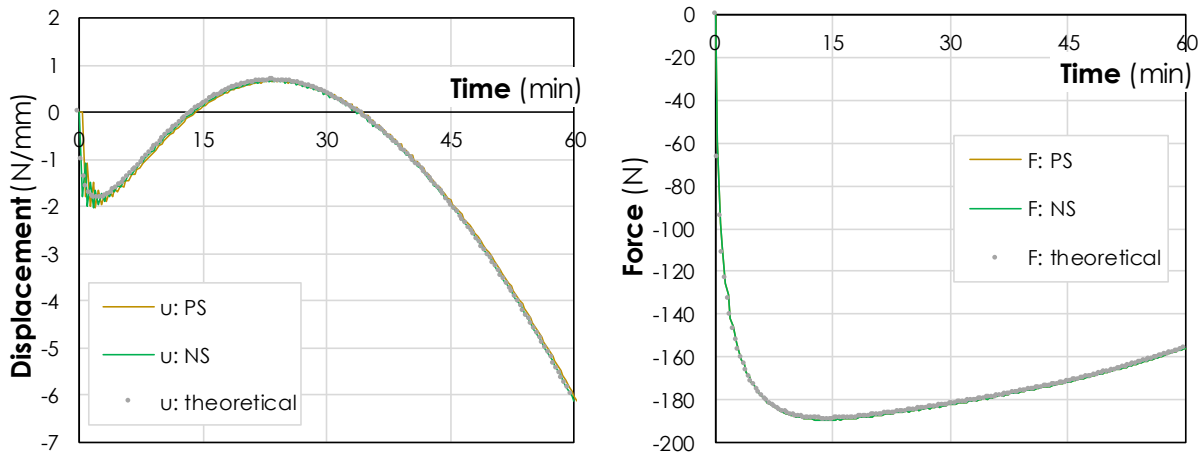


Figure 7. Evolution of displacement (left) and of force (right) for the configuration n° 3

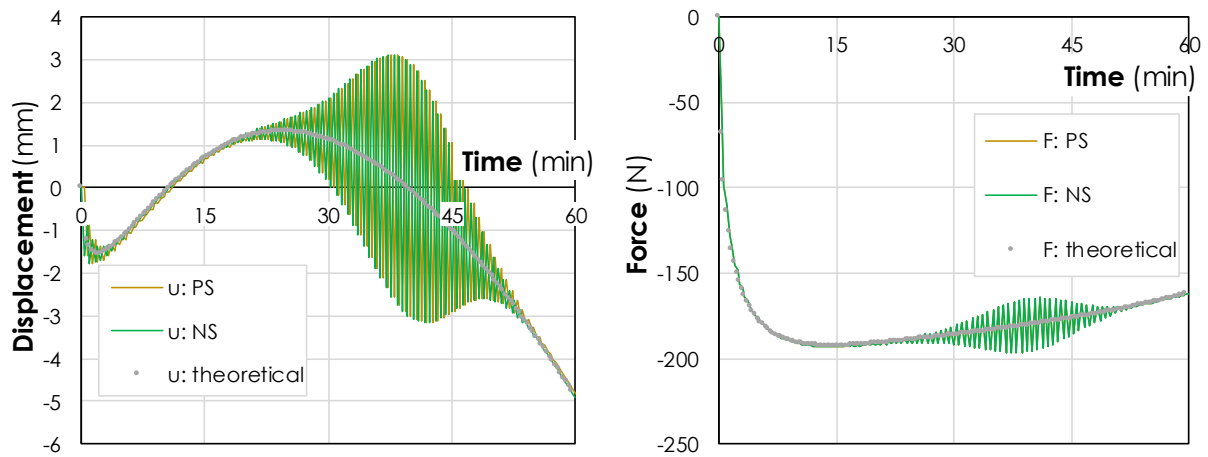


Figure 8. Evolution of displacement (left) and of force (right) for the configuration n° 5

The resulting gaps of compatibility as functions of fire exposure time for all the six case studies shown in Fig. 9, may call for some comments:

- For all the six configurations studied: the gap of compatibility changes its sign (positive to negative or vice versa) after each iteration.
- For the first four configurations: the highest values of the gap of compatibility (varying from -2 mm to +3 mm) are observed only in the first few minutes. This is due to the use of ISO 834 fire curve (EN 1991-1-2, [7]) which abruptly increases at the beginning of the test. When the test arrives at the limited divergence zone, the gap of compatibility increases with the time step increase but remains always very small. Stability is always ensured until the end of the tests. This is due to the fact that, according to Eq. (9), the gap of compatibility needs of some duration to accumulate to a critical value. However, since the limited divergence zone of these four cases are still slightly small, the tests arrive in the new convergence zone before the gap of compatibility reaches its critical value.
- For the last two configurations where the limited divergence zone is larger: contrary to the first four configurations, the gap of compatibility decreases with the time step increase. This is due to the fact that, even though in a single iteration small time step introduces less error (gap of compatibility) than high time step, more iterations must be carried out for an equal duration when small time step is used. It can be also seen that the gap of compatibility remains the same in the first few minutes (as in the first four configurations), then highly increases and reaches very high values. These values may exceed critical values (which are directly linked to the capacity of the actuator travel), leading then to the divergence of these tests. This is in fact the direct results of the accumulation of the gap of compatibility after each iteration in the limited divergence zones which are larger than those for the first four configurations.

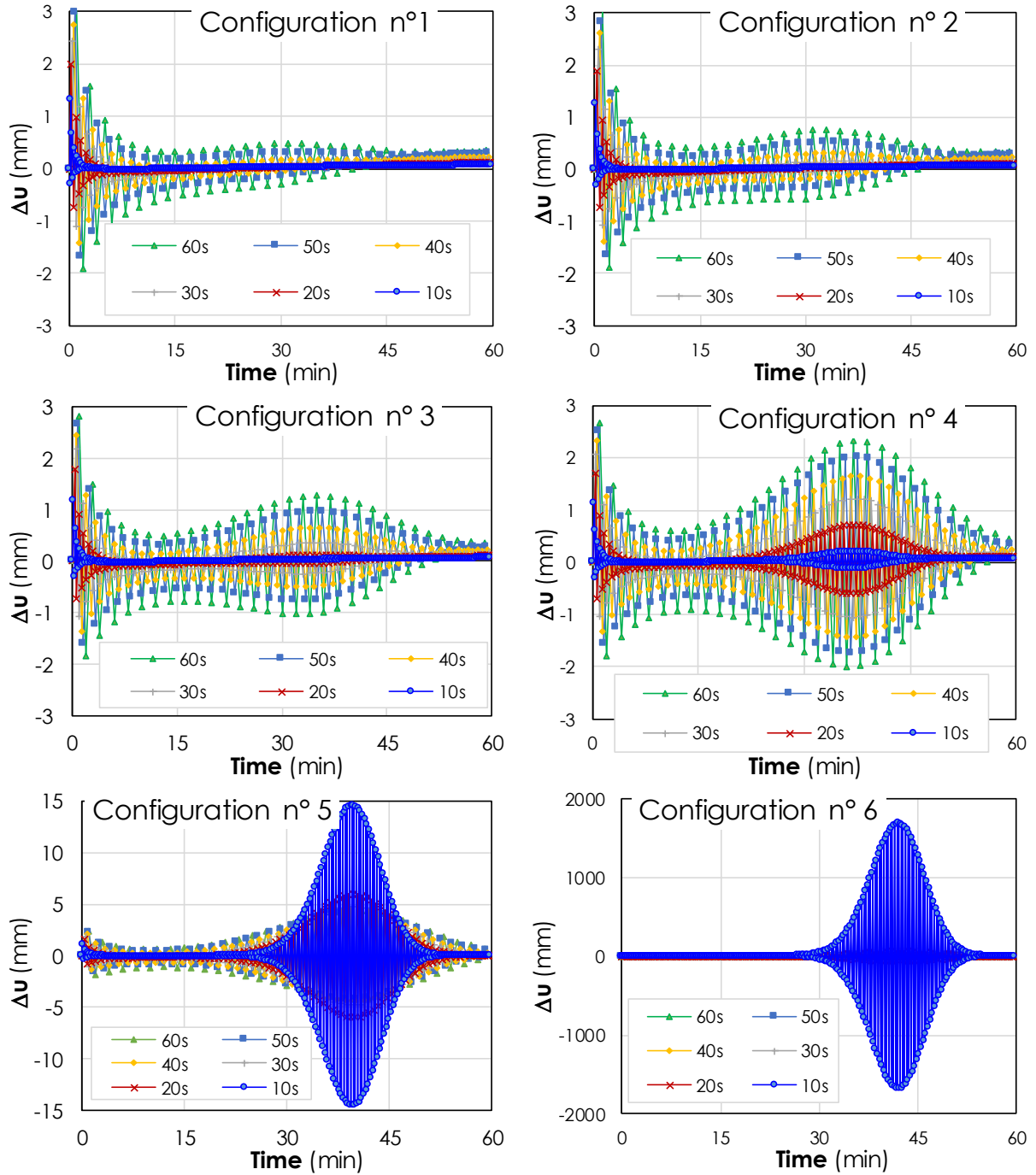


Figure 9. Gaps of compatibility as functions of time step for different configurations: (configuration n°1 to n°4) less than 3mm; (configuration n°5) peak at 15mm; (configuration 6) peak at 1687 mm

4 CONCLUSIONS

It has been shown in the present contribution that stability of a hybrid fire test may be ensured even in the case that the stiffness of the physical substructure (PS) is higher than the stiffness of the numerical substructure (NS), in some situations where the curves representing the evolution of the stiffness of the two substructures as a function of fire exposure time, cross each other twice, which in turn leads to a particular configuration where a divergence zone is limited by two convergence zones. The concept of convergence and divergence of the Hybrid Fire Testing (HFT) is recalled and discussed, showing the necessary to define a practical criterion which may be based on the gap of compatibility. Finally, parametric studies are carried out on six illustrative case studies in order to assess the influence of time step on the convergence of the

HFT in the limited divergence zone. For the first four case studies where the limited divergence zone remains small, the gap of compatibility increases when the time step increases but it is not the case for larger limited divergence zones. Even though in a single iteration a small time step introduces less error (gap of compatibility) than high time step, more iterations should be carried out for the same duration when small time step is used. The instability occurs when the accumulation of the gap of compatibility after each iteration exceeds critical values (which are directly linked to the capacity of the actuator travel).

REFERENCES

1. Tondini, N., Abbiati, G., Possidente, L., Stojadinovic, B., A Static Partitioned Solver for hybrid Fire Testing. Proceedings of the 9th International Conference on Structures in Fire, New Jersey, USA, 827-35 (2016)
2. Mostafei, H., Hybrid fire testing for assessing performance of structures in fire – Application. Fire Safety Journal 56, 30–38 (2013).
3. Sauca, A., Gernay, T., Robert, F., Tondini, N., Franssen, J. M., Hybrid fire testing: Discussion on stability and implementation of a new method in a virtual environment. Journal of Structural Fire Engineering 9(4), 319–341 (2017).
4. Grolimund, R., Fontana, M., Consolidated Fire Analysis – a coupled experimental and numerical framework for the analysis of steel structures subjected to fire. Proceedings of the 3rd International Fire Safety Symposium, Ottawa, Ontario, Canada (2019).
5. Wang, X., Kim, R. E., Kwon, O. S., Yeo, I., Hybrid Simulation Method for a Structure Subjected to Fire and Its Application to a Steel Frame. Journal of Structural Engineering 144(8), (2018). (doi:10.1061/(ASCE)ST.1943-541X.0002113).
6. Pinoteau, N., Pham, D. T., Nguyen, H. H., Mège, R., Hybrid fire testing: Development of hybrid fire testing by real-time subdivision of physical and numerical substructures. Journal of Structural Fire Engineering, (2020). (doi.org/10.1108/JSFE-07-2019-0026)
7. EN 1991-1-2. Eurocode 1: Actions on Structures. Part 1-2: General Actions-Actions on structures exposed to fire. (2002)

REAL-TIME MULTI DEGREES OF FREEDOM HYBRID FIRE TESTING USING PI CONTROL

Elke Mergny¹, Jean-Marc Franssen²

ABSTRACT

Hybrid testing has been successfully developed in earthquake engineering and begins to be applied to fire engineering (Hybrid Fire Testing or HFT) for coupling fire tests and numerical simulations. To this end, several tests have been performed since the 1990's but were limited to one-degree-of-freedom (DOF) systems.

This paper approaches MDOF tests. It presents fully automated HFT performed on half-scale steel specimens using proportional integral control procedure. Three tests were performed : a one DOF-test, a two-DOF test and a three-DOF test. The tested specimens are steel square hollow sections heated with electrical resistances. The numerical substructure of these tests are modelled with SAFIR® [1] and their behaviour is non-linear. The tests were performed successfully and replicate the numerical predictions to a large extent.

Keywords: Hybrid fire testing, Steel, Control theory, multi degrees of freedom.

1 INTRODUCTION

Hybrid Fire Testing (HFT) is a performance-based approach for structures in fire based on substructuring method. A complete structure is divided in two substructures, one being tested in a fire test laboratory (physical substructure [PS]), and one being numerically simulated (numerical substructure [NS]). By reducing the number of elements to be tested, this method overcome the huge costs of large-scale tests.

Although the research in HFT began in the 1990s, only a few tests have been performed. The first attempt was reported by Korzen et al. [2] and consisted in a proof-of-concept HFT of a steel frame with a column subjected to fire. The axial force in the specimen was adjusted as a function of the elastic response of the numerical substructure to the displacement of the heated column. In a similar way, a multi-degree-of-freedom (DOF) test was attempted by Robert et al. [3] but it encountered stability issues before failure. Later, Mostafaei [4] successfully coupled a concrete column and a multi-storey building modelled in SAFIR® [1]. Nevertheless, the axial force was controlled and adjusted every 5 minutes by a human operator. This limitation was overcome by Whyte et al. [5] and Schulthess et al. [6] that proposed fully automated Single Degrees of Freedom (SDOF) tests. However, these tests were carried out on small-scale elements (less than 10 cm). To date, the most advanced hybrid test was performed by Wang et al. [7], who tested a full-scale steel column (SDOF test) at the KICT testing facilities with a fully automated procedure. Previous research has been limited to SDOF tests. The present paper approaches SDOF and MDOF tests (two-DOF and three-DOF) performed on half-scale steel specimens. The procedure is a fully automated HFT, uses proportional integral (PI) control procedure developed and validated in Mergny et al. [8] and considers nonlinear NS.

¹ PhD Candidate, Urban and Environmental Engineering (UEE), Liège University, Belgium
e-mail: elke.mergny@uliege.be

² Professor, Urban and Environmental Engineering (UEE), Liège University, Belgium
e-mail: jm.franssen@uliege.be

2 PI CONTROL IN HFT

The test procedure is based on the algorithm developed in Mergny et al [8]. This displacement-controlled procedure consists in adjusting the interface displacements of the PS to equilibrate the interface forces of both substructures. It is based on the use of a PI controller. Considering a d -DOF test, the displacement vector at the interface of the PS, $\mathbf{u}_{PS} \in \mathbb{R}^{d \times 1}$ is corrected at every time step by means of a term proportional to the instantaneous error and an integral term that considers the history of this error. The basic equation is as follows:

$$\begin{aligned}\mathbf{u}_{PS_{i+1}} &= \mathbf{u}_{PS_i} + \mathbf{L}_P \mathbf{e}_i^{\text{inst}} + \mathbf{L}_J \mathbf{j}_i \\ \mathbf{j}_{i+1} &= \mathbf{j}_i + \mathbf{e}_i^{\text{inst}}\end{aligned}\quad (1)$$

$\mathbf{e}_i^{\text{inst}} \in \mathbb{R}^{d \times 1}$ is the instantaneous error at discrete time i and $\mathbf{j}_i \in \mathbb{R}^{d \times 1}$ is the sum of $\mathbf{e}_i^{\text{inst}}$ over time. $\mathbf{L}_P \in \mathbb{R}^{d \times d}$ and $\mathbf{L}_J \in \mathbb{R}^{d \times d}$ are the gain matrices of the PI controller that will be designed by the user. The error $\mathbf{e}_i^{\text{inst}}$ is equal to $-(\mathbf{F}_{NS_i} + \mathbf{F}_{PS_i})$. \mathbf{F}_{PS_i} and \mathbf{F}_{NS_i} are the interface forces of PS and NS when the interface displacements are compatible. The displacement vector is thus applied in parallel to PS and NS as shown on Figure 1(a). One considers in this section that NS and PS have the same number d of DOF at the interface. Otherwise, transformation matrices must be added, as it was shown in Schellenberg *et al.* [9] and will be considered during the tests. This assumption does not change the outcomes and simplifies the notations. Thus, the force vectors of PS and NS have the same size ($\mathbf{F}_{PS_i}, \mathbf{F}_{NS_i} \in \mathbb{R}^{d \times 1}$) and the compatibility of displacement can be written as :

$$\mathbf{u}_{PS_i} = \mathbf{u}_{NS_i} \quad (2)$$

\mathbf{L}_P and \mathbf{L}_J are designed using the state equation of the loop showed on Figure 1(a). This equation is obtained by substituting \mathbf{F}_{PS_i} and \mathbf{F}_{NS_i} in equation (1) with the interface static equations :

$$\mathbf{K}_{PS_i} \mathbf{u}_{PS_i} + \mathbf{F}_{PS_i}^{\text{TH}} = \mathbf{F}_{PS_i} \quad (3)$$

$$\mathbf{K}_{NS_i} \mathbf{u}_{NS_i} + \mathbf{F}_{NS_i}^{\text{TH}} = \mathbf{F}_{NS_i} \quad (4)$$

$\mathbf{K}_{PS_i} \in \mathbb{R}^{d \times d}$ and $\mathbf{K}_{NS_i} \in \mathbb{R}^{d \times d}$ stand for the interface stiffness. $\mathbf{F}_{PS_i}^{\text{TH}} \in \mathbb{R}^{d \times 1}$ and $\mathbf{F}_{NS_i}^{\text{TH}} \in \mathbb{R}^{d \times 1}$ are the thermal forces of the substructures. Considering the compatibility of displacement between the two substructures, the state equation can be established as follows [8]:

$$\begin{bmatrix} \mathbf{u}_{PS_{i+1}} \\ \mathbf{j}_{i+1} \end{bmatrix} = \begin{bmatrix} \mathbf{I} - \mathbf{L}_P(\mathbf{K}_{PS_i} + \mathbf{K}_{NS_i}) & \mathbf{L}_J \\ -(\mathbf{K}_{PS_i} + \mathbf{K}_{NS_i}) & \mathbf{I} \end{bmatrix} \begin{bmatrix} \mathbf{u}_{PS_i} \\ \mathbf{j}_i \end{bmatrix} + \begin{bmatrix} -\mathbf{L}_P(\mathbf{F}_{NS_i}^{\text{TH}} + \mathbf{F}_{PS_i}^{\text{TH}}) \\ -(\mathbf{F}_{NS_i}^{\text{TH}} + \mathbf{F}_{PS_i}^{\text{TH}}) \end{bmatrix} \quad (5)$$

The matrix of this system is the state matrix. \mathbf{L}_P and \mathbf{L}_J are designed based on the eigenvalues or poles of this matrix. The stability is ensured if the modules of the eigenvalues are lower than 1. As it will be shown in section 4, these eigenvalues are chosen depending on the desired value of the time parameters of the step response of the system: rise time, settling time and overshoot [10]. Initial stiffness, \mathbf{K}_{PS_0} and \mathbf{K}_{NS_0} are considered for the design. The stiffness of the NS is computed whereas the stiffness of the PS can only be estimated and will be noted as $\mathbf{K}_{PS_0}^{\text{EST}}$. This procedure has been validated numerically in [8] but faces three difficulties when translated into a real test.

First of all, as it is a displacement control procedure, the actuators must move continuously in order to avoid large thermal forces (especially in the axial direction of a member). This problem was observed by Wang et al. [7] and was eliminated by the implementation of a continuous movement of the jack, based on the compensation delay technique that was developed in seismic field.

Then, the procedure requires that the displacements of the two substructures are compatible. The actuators must therefore accurately apply the corrected displacement to PS. If this is not the case, the evaluation of the instantaneous error $\mathbf{e}_i^{\text{inst}}$ will be inaccurate. This problem is seen especially in the axial direction: small errors in displacement can lead to large errors in force when the test specimen is very stiff. Nevertheless, according to [8], the method is robust to this problem.

Finally, in case of MDOF tests, a displacement (elongation, rotation) in a specimen is not necessarily related to the movement of a single actuator. For instance, a rotation can correspond to the difference in position between two jacks. This can make displacement control quite complex. This latter difficulty required that equation (1) be reformulated for testing. Instead of the displacement of the PS \mathbf{u}_{PS_i} , the commanded displacement \mathbf{u}_{C_i} (or measured actuator's stroke) is used in the basic equation :

$$\begin{aligned}\mathbf{u}_{C_{i+1}} &= \mathbf{u}_{C_i} + \mathbf{L}_p \mathbf{e}_i^{inst} + \mathbf{L}_j \mathbf{j}_i \\ \mathbf{j}_{i+1} &= \mathbf{j}_i + \mathbf{e}_i^{inst}\end{aligned}\quad (6)$$

In this case, the instantaneous error must contain the force applied by each actuator instead of the interface force. If one considers that the resulting force is related to the interface forces via a transformation matrix noted \mathbf{T} , the error can thus be written as $\mathbf{e}_i^{inst} = -\mathbf{T}(\mathbf{F}_{NS_i} + \mathbf{F}_{PS_i})$. In the same way as before, the interface forces can be substituted with equations (3) and (4) and the displacement \mathbf{u}_{NS} with \mathbf{u}_{PS} according to (5). If one assumes that the displacement vector of the specimen is also linked to the one of the actuator by a transformation matrix \mathbf{T}' , the state equation can be rewritten as follows :

$$\begin{bmatrix} \mathbf{u}_{C_{i+1}} \\ \mathbf{j}_{i+1} \end{bmatrix} = \begin{bmatrix} \mathbf{I} - \mathbf{L}_p \mathbf{T}(\mathbf{K}_{PS_i} + \mathbf{K}_{NS_i}) \mathbf{T}' & \mathbf{L}_j \\ -\mathbf{T}(\mathbf{K}_{PS_i} + \mathbf{K}_{NS_i}) \mathbf{T}' & \mathbf{I} \end{bmatrix} \begin{bmatrix} \mathbf{u}_{C_i} \\ \mathbf{j}_i \end{bmatrix} + \begin{bmatrix} -\mathbf{L}_p \mathbf{T}(\mathbf{F}_{NS_i}^{TH} + \mathbf{F}_{PS_i}^{TH}) \\ -\mathbf{T}(\mathbf{F}_{NS_i}^{TH} + \mathbf{F}_{PS_i}^{TH}) \end{bmatrix}\quad (7)$$

The gain matrices \mathbf{L}_p and \mathbf{L}_j must be designed with the new state matrix with initial stiffness. The procedure is modified and showed on Figure 1(b). To ensure the compatibility of the displacement, the displacement \mathbf{u}_{PS} is measured and directly applied to the NS. Depending the studied structure, it will be necessary to add rigid body motion or to perform geometric transformations on \mathbf{u}_{PS} to obtain \mathbf{u}_{NS} .

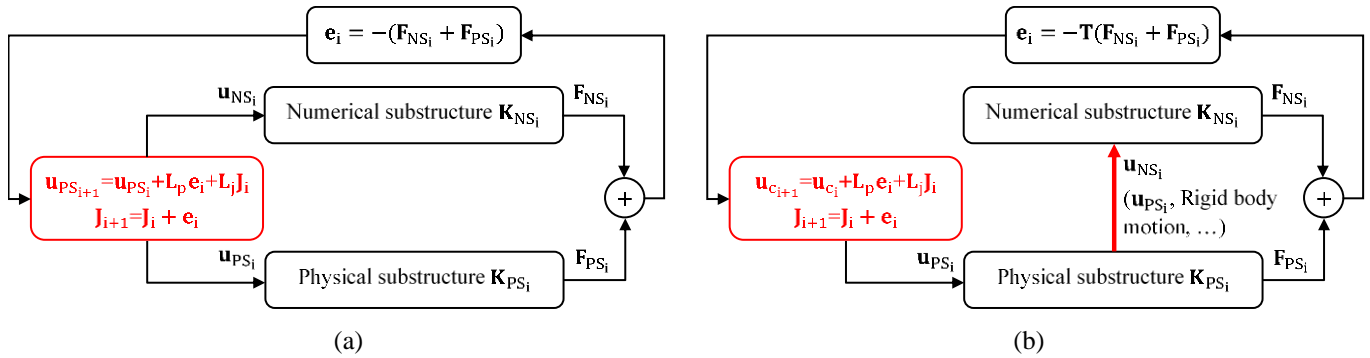


Figure 1. Simplified block diagram. Initial procedure (a) Modified procedure (b)

3 TESTING APPROACH

3.1 Experimental setup

An experimental setup was built in the Fire Test Laboratory of Liege University to perform hybrid fire tests. The setup is made of two steel frames bolted on two horizontal beams and braced by diagonal elements (Figure 2 (a)-(b)). Three electric jacks are mounted on supports and apply displacements through cross strut (Figure 2(c)). These actuators are 100 kN-capacity trapezoidal screw jacks. In these jacks, the rotation of the worm is transformed into axial translation of the screw using the rotation of the motor. The position of this threaded rod (\mathbf{u}_c) can be controlled accurately. Several sensors have been placed to measure different types of displacements and will be detailed in section 4 for each type of test.

Electrical resistances are used to heat the specimen. The power of these devices are adjusted in order to maintain a commanded temperature. The feedback variable of each electrical pad is the temperature of a thermocouple welded on the specimen.



(a)



(b)



(c)

Figure 2. (a), (b) Experimental setup (c) Electrical actuator

3.2 Test procedure

Based on section 2, the process shown on Figure 3 follows the following steps:

1. At the beginning of the time step, forces and displacements of the PS are measured by the datalogger of the laboratory and sent to the computer.
2. The measured displacements are imposed to the NS (considering geometrical transformations and rigid body motion if necessary). The NS is a FE model in SAFIR[®]. The interface forces are computed by SAFIR.
3. The forces of PS and NS are sent to an intermediate software that was developed in [8] to ensure the connections between PS and NS. The instantaneous error $\mathbf{e}_i^{\text{inst}}$ is calculated. The new commanded displacement \mathbf{u}_C and the integral term \mathbf{j}_i are then computed with equation (6).
4. The new command $\mathbf{u}_{C_{i+1}}$ is sent at the end of the time step.

During the time step, the actuators do not stop moving. If $\mathbf{u}_{C_{i+1}}$ is computed before the end of the time step, the displacement is interpolated between \mathbf{u}_{C_i} and $\mathbf{u}_{C_{i+1}}$. Otherwise, the position \mathbf{u}_C is extrapolated using previous positions.

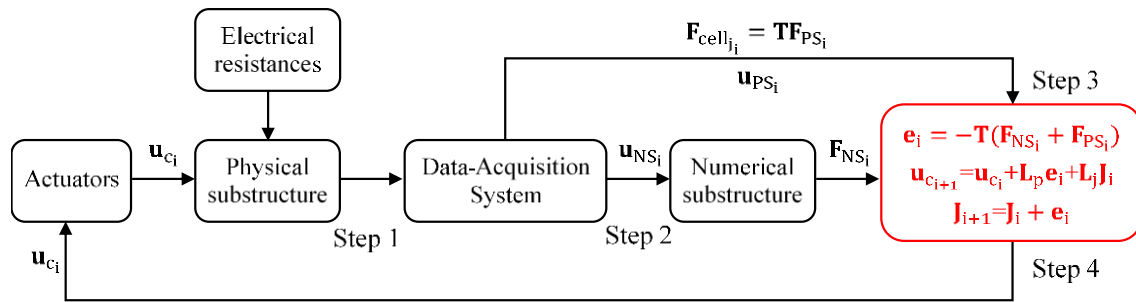


Figure 3. Test architecture

4 EXPERIMENTAL CASES

4.1 One-DOF Test

The reference structure for the one-DOF test is presented on Figure 4(a). It consists of two structural elements, a 1.5 m column and a 2 m loaded beam that are respectively the PS and the NS. The column is hinged at the top with a roller support and at the bottom with a pinned support. The NS has two roller supports.

The beam (NS) is made of a rectangular hollow section HS 150x50x5. Eurocode dependent material properties (CEN. EN 1993-1-2:2005) are used in the analysis of the NS that is performed in SAFIR®. The considered steel grade is S355. In the test presented here, one span of the beam NS is heated at a rate of 5°C/ minute.

The column (PS) is a squared hollow section HS 50x5. The extremities of the specimen are welded to steel plates and these are bolted to hinges. The top hinge is bolted to the steel frame of the test set-up and the bottom one is bolted to a cross strut. An electrical jack (actuator 1 in Figure 5) applies the displacement through this cross strut which can move up and down while the horizontal position is maintained. The yield strength of steel in this column has been measured at 382 N/mm² using standardized tests. The PS is heated at a rate of 6°C/minute, with four electrical resistances, shown on Figure 5(a).

The heating of the two substructures does not start immediately. The load of the NS is first applied linearly at 20 ° C in 20 minutes. Then the load is maintained for 5 minutes. Even if the substructures are not heated, the procedure described in section 3.2 is followed. Eventually, both substructures are heated at t=25 minutes and HFT begins.

The displacements at the interface between NS and PS are the axial elongation of the PS (\mathbf{u}_{ps}) and the vertical displacement at the middle of the NS (\mathbf{u}_{ns}). For this first test, the horizontal displacement at the top of the column is blocked in the reference structure to delete the rigid body motion and simplify the relationship between \mathbf{u}_{ns} and \mathbf{u}_{ps} . This simplification will not be applied in sections 4.2 and 4.3.

The elongation of the column \mathbf{u}_{ps} that will feed the NS at step 2 of the test procedure is obtained by the difference of the displacement of the cross strut and the displacement of the top beam of the set-up due to the force applied by the actuator. These displacements are obtained from four displacements sensors shown on Figure 5(a). A load cell is placed between the cross truss and the actuator (Load cell 1).

The gain matrices \mathbf{L}_p and \mathbf{L}_j must be designed using the state matrix of equation (7). The 1x1 transformation matrix \mathbf{T} and \mathbf{T}' are necessary. As the load cell directly measures the normal force in the column, \mathbf{T} is equal to 1. The matrix \mathbf{T}' would be also equal to 1 if the stiffness of the frame was infinite. Otherwise, the link between \mathbf{u}_{ps} and \mathbf{u}_c is as follow :

$$\mathbf{u}_c = \mathbf{u}_{ps} + \frac{\mathbf{F}_{ps}}{\mathbf{K}_f} = \left(1 + \frac{\mathbf{K}_{ps_0}}{\mathbf{K}_f}\right)^{-1} \mathbf{u}_{ps} \quad (8)$$

\mathbf{K}_f is the stiffness of the frame and is evaluated as being equal to 300 kN/m. The initial stiffness matrices that are necessary for calculating the gain matrices are given hereunder:

$$\mathbf{K}_{ps_0}^{EST} = \left[\frac{EA}{L}\right] = 126\,000\,000 \text{ N/m} \quad \mathbf{K}_{NS_0} = 9\,500\,000 \text{ N/m} \quad (9)$$

As equation (7) is 2x2 system, this HFT is a second order system. The relationship between the eigenvalues and the parameters of the step response of the system, that is the time behaviour of the outputs of a general system when its inputs change from zero to one in a very short time, has been widely developed in literature [10]. These parameters are called rise time, overshoot and settling time. They respectively represent the time to reach the final value, the occurrence of the function exceeding its target and the elapsed time to reach a stable value.

The hypothesis is made that the displacement and the forces of the system can be discretized with an interval of 12 s. The rise time is thus fixed to 12 s. Overshoot is set to 0, meaning that no deviation of system output from its final value is accepted. One assumes that the command \mathbf{u}_c is updated every 3 seconds. The value of the double eigenvalue λ is thus determined using usual equations of control theory [10]:

$$\lambda = \exp\left(-2.72 \frac{3}{12}\right) = 0,51 \quad (10)$$

The gain matrices can be directly determined with the equations developed in [8] for a SDOF system:

$$\mathbf{L}_p = 7.3801 \times 10^{-9} \quad \mathbf{L}_j = 1.8450 \times 10^{-9} \quad (11)$$

4.2 Two-DOF Test

The reference structure of the two-DOF test (see Figure 4(b)) also consists of two structural elements: a 1.4m column (PS) and a uniformly loaded 1.2m beam (NS). The column which is a squared hollow section HS 80x5 has a hinged support and is rigidly connected to the beam, made of a rectangular hollow section HS 160x80x5. The support of the NS is completely fixed. The PS and the NS are heated but at different rate as shown on Figure 4(b). The yield strength of the PS has been measured at 460 N/mm² and thus steel grade S460 is considered for the elements of the NS.

After substructuring, as the horizontal displacement of the top of the column is not blocked, there are three DOFs at the interface of the PS as the NS (two translations and one rotation). However, in the setup, rigid body motion must be avoided. It is thus necessary to block both horizontal DOFs and one vertical DOF of the PS. The column is thus tested with two supports, a roller support and a pinned support. Consequently, the interface displacements of the PS are the axial elongation and the rotation at one end. For the NS, they consist of the relative distance between the free extremity of the beam and the virtual position of the support of the column and of the rotation of the joint with the PS. This rotation is not equal to the one of the PS as the rigid body rotation must be taken into account (see Figure 4(b)).

The column is tested upside down as shown on Figure 5(b); the extremity with the support is at the top and the other one where the displacements are controlled is at the bottom. As in the SDOF test, the top of the specimen is welded to a steel plate bolted to a hinge. The bottom of the steel column that corresponds to the extremity that is rigidly connected to the beam is welded to a HEB100-lever arm that will allow applying a bending moment in addition to the normal force. The axial elongation of the column is measured as in section 4.1. An inclinometer is placed on the lever arm to measure the rotation (inclinometer 1 in Figure 5(b)). The load cells (load cell 1 and load cell 2) are between the cross struts and the actuators (actuator 1 and actuator 2).

The 2x2 transformation matrices \mathbf{T} and \mathbf{T}' must be determined in order to design of the gain matrices. The normal force is the sum of the two forces measured with load cell 1 and load cell 2. The bending moment also consists of two terms. First, the force of the load cell 2 multiplied by the lever arm. Then, due to assembly inaccuracies in the set-up, the first actuator is slightly offset by 2.5 mm towards the inside and as a result and a contribution from the force of the load cell 1 must thus also be considered. The matrix \mathbf{T} is thus as follow:

$$\mathbf{T} = \begin{bmatrix} 1 & 1 \\ a_1 & a_2 \end{bmatrix}^{-1} \quad (12)$$

With a_1 and a_2 , respectively, the eccentricity of actuator 1 and the length of the lever arm, equal to 0.0025 m and 0.61 m. The matrix \mathbf{T}' was also determined. The relationship between measured displacements and the actuator's strokes is more complex than in the SDOF system and consists of large expressions that will not be detailed in this paper.

To design the controller, the stiffness of the PS and NS are required and are then calculated/estimated. They are given hereunder. All the values presented are expressed in [N], [m] and [rad] :

$$\mathbf{K}_{PS_0}^{EST} = 10^3 \begin{bmatrix} 225000 & 0 \\ 0 & 846 \end{bmatrix} \quad \mathbf{K}_{NS_0} = 10^3 \begin{bmatrix} 229400 & 10400 \\ 10400 & 6040 \end{bmatrix} \quad (13)$$

The system contains four eigenvalues that have to be chosen. Nowadays, the behaviour of 4th order systems are not well-known in literature, as first- or second-order system. The controllers of such systems are thus hard to design. To get around this problem, the controller is designed in order to have a pair of non-null dominant eigenvalues. It allows to approximate a 4th order system to second order system, by setting a double eigenvalue with the others set to 0. The poles can thus be linked to the parameter of the step response as in section 4.1. If \mathbf{A} stands for the state matrix of equation (7) and $\lambda_1, \lambda_2, \lambda_3$ and λ_4 for the four eigenvalues of \mathbf{A} , the following equation must be solved to find the gain matrices:

$$|\mathbf{I}z - \mathbf{A}| = (z - \lambda_1)(z - \lambda_2)(z - \lambda_3)(z - \lambda_4) \quad (14)$$

With $\lambda_1, \lambda_2 = 0.51$ and $\lambda_3, \lambda_4 = 0$. The two polynomials are equal if their coefficients are equal. As the coefficient of the highest degree term is equal to 1, the system has four equations to solve. An automatic procedure was implemented in MATLAB[®] and the following gain matrices are obtained :

$$\mathbf{L}_P = 10^{-9} \begin{bmatrix} 4.520 & 0 \\ 0 & 52.99 \end{bmatrix} \quad \mathbf{L}_J = 10^{-7} \begin{bmatrix} 0.227 & 0 \\ 0 & 1.322 \end{bmatrix} \quad (15)$$

4.3 Three-DOF Test

The reference structure is a two-storey half scaled building with four longitudinal bays, as shown on Figure 4(c). It is composed of 1.3 m steel beams (HS160x80x5, S460) and 1.3 m columns (HS80x5, S460). The PS is a HS80x5 steel column located at the edge of the building in a heated compartment. NS is the remaining structure.

As in section 4.2, the specimen is tested with a roller support and a pinned support. The interface displacements of the PS are the elongation of the column and two rotations, at the top and at the end of the element. In the NS, these displacements consists of the relative distance between the two extremities of the column and two rotations to which rigid body rotations are added. The column is tested upside down as shown on Figure 5(c). The two extremities are welded to HEB100-lever arms. These beams are welded to plates bolted to hinges.

The 3x3 transformation matrix \mathbf{T}' and \mathbf{T} and the initial stiffness matrices, $\mathbf{K}_{PS_0}^{EST}$ and \mathbf{K}_{NS_0} were also determined, as in the previous cases. The matrix \mathbf{T} gives the following relationship between the interface forces and the forces measured by the load cells :

$$\mathbf{T} = \begin{bmatrix} 1 & 1 & 0 \\ a_1 & a_2 & 0 \\ 0 & 0 & b \end{bmatrix}^{-1} \quad (16)$$

With b equal to 0.61 m. The stiffness matrices are as follows (in [N], [m] and [rad]) :

$$\mathbf{K}_{PS_0}^{EST} = 10^3 \begin{bmatrix} 237461 & 0 & 0 \\ 0 & 885 & 442.5 \\ 0 & 442.5 & 885 \end{bmatrix} \quad \mathbf{K}_{NS_0} = 10^3 \begin{bmatrix} 4944 & 170 & -3895 \\ 170 & 4827 & -130 \\ -3895 & -130 & 4040 \end{bmatrix} \quad (17)$$

One obtains a 6th order system. As in section 4.2, it is approximated to a second order system with two dominant eigenvalues equal to 0.51. Using the MATLAB[®] procedure, the following gain matrices are computed:

$$\mathbf{L}_P = 10^{-9} \begin{bmatrix} 4.502 & 0 & 0 \\ 0 & 123.58 & 0 \\ 0 & 0 & 65.366 \end{bmatrix} \quad \mathbf{L}_J = 10^{-9} \begin{bmatrix} 0.186 & 0 & 0 \\ 0 & 57.778 & 0 \\ 0 & 0 & 15.352 \end{bmatrix} \quad (18)$$

5 RESULTS AND DISCUSSION

5.1 One-DOF Test

The test was performed on June 18, 2020. Results are shown in Figure 6. Displacements/forces are given as a function of time. The expected temperature of the column (6°C/min after t=25 min) is mentioned at the top of the graph. "u PS" and "N PS" stand for the axial displacement and the normal force measured during the HFT.

Before the test, the complete structure was simulated in SAFIR. The curves "u REF (predicted)" and "N REF (predicted)" were computed from the behaviour of the complete structure, assuming that steel in the PS behaves as foreseen by the Eurocode (CEN. EN 1993-1-2:2005) and that the temperature is uniform in the column. The buckling of the specimen was expected to occur around 130 minutes when the temperature would be around 550 °C. An initial geometrical imperfection of 1.5 mm was considered. During the loading phase at ambient temperature (from 0 to 25 min), the behaviour of the PS corresponds to the one that was predicted. When the column is heated, one notices that the curves are shifted and that PS seems to lag behind its predicted behaviour. Also, the failure occurs sooner, around 100 minutes.

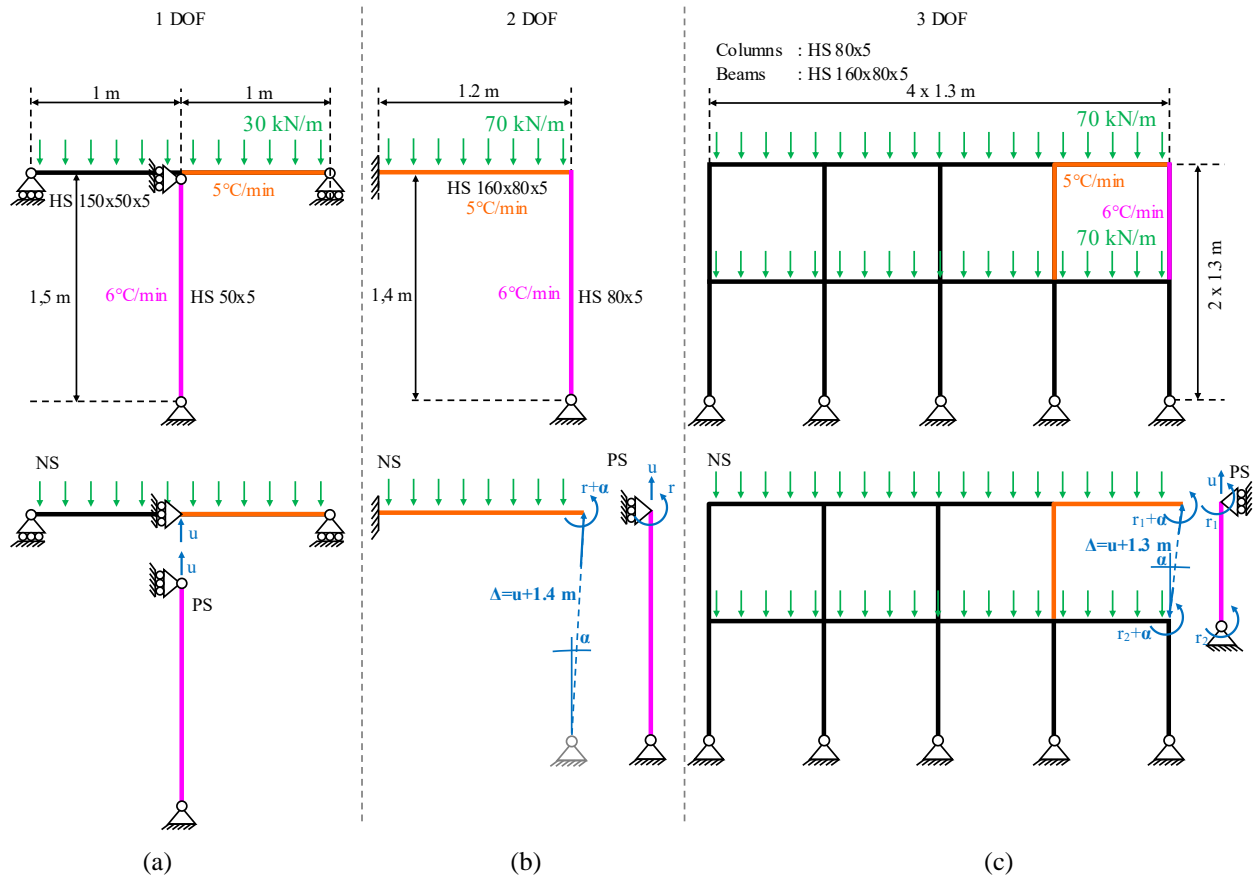


Figure 4. Test procedure

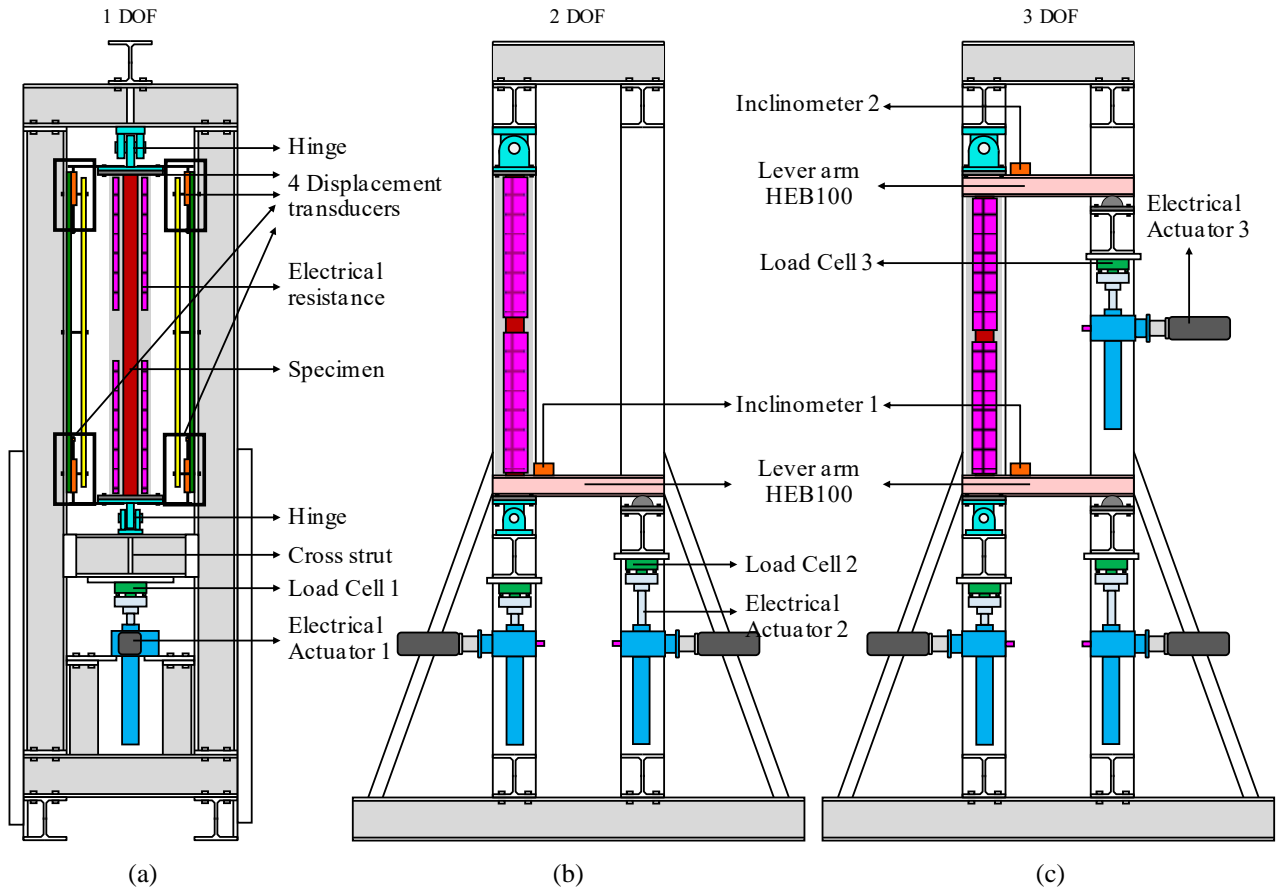


Figure 5. Experimental setup for the one, two and three DOF-tests

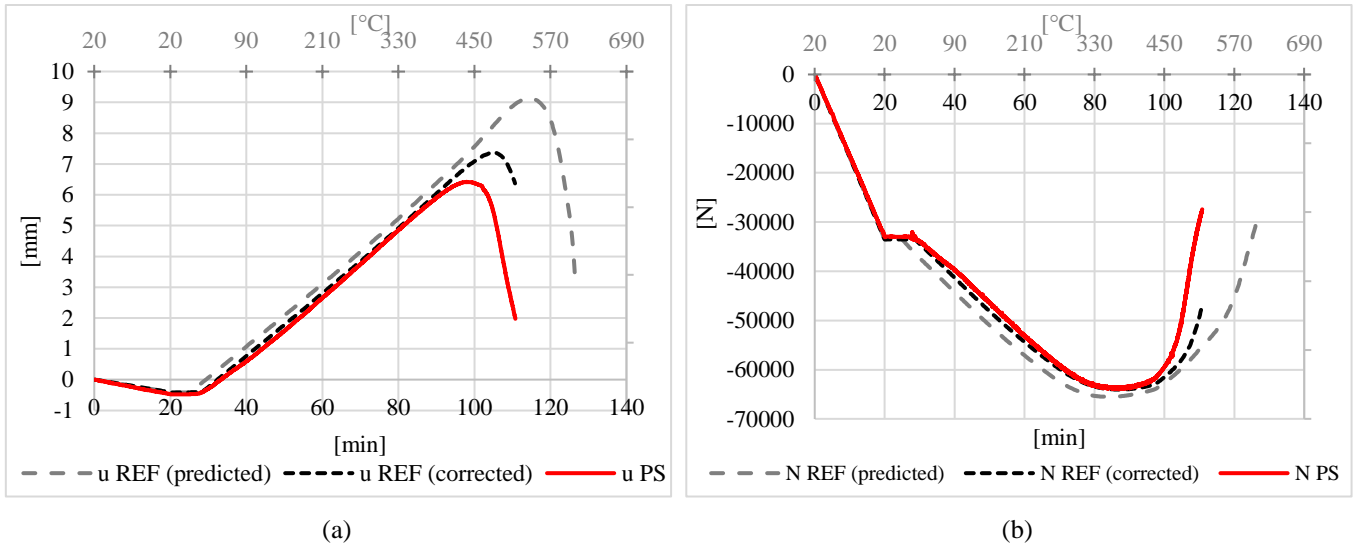


Figure 6. Results of the one-DOF test (a) Elongation u (b) Normal force N

These differences can be explained by the fact that the curve of the reference structure is calculated considering that the temperature is uniform in the PS, which is not the case during the test. Indeed, each electrical resistance that heats the columns is controlled with a single thermocouple. If the desired temperature is reached at this point, it is not necessarily reached in the other parts of the column. Some parts such as the bottom of the column are cooler and others may be warmer, especially the upper parts.

Sixteen thermocouples measured the temperature of the column during the test. These measurements made it possible to calculate a second curve after the test which takes into account the real temperatures of the column. These new curves are called " u REF (corrected)" and " N REF (corrected)" in Figure 6. The axial displacement and normal force are closer to this corrected curve although failure occurred earlier in the test than in the numerical simulation.

The hereunder graph (Figure 7) shows the relative instantaneous error between F_{PS} and F_{NS} in function of time. The relative error is high at the very start of the test but decreases very fast to reach equilibrium. The value is then under 2% during the loading. It increases again when the heating starts but is quickly stabilized by the algorithm. The value remains low (less than 1%) until failure. The fact that the error between the interface forces of NS and PS are low shows that the algorithm is working properly.

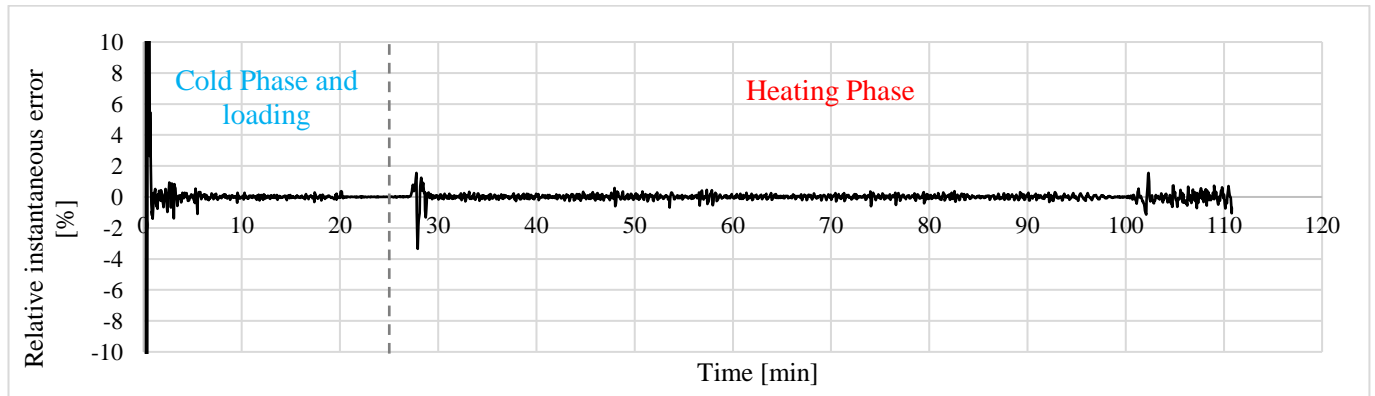


Figure 7. Results of the one-DOF test (a) Elongation u (b) Normal force N

Consequently, the observed differences with the reference curves must be put into perspective. The reference curves, even corrected, are calculated by making numerous assumptions about the behaviour of the steel and the geometric imperfections of the specimen. Only the trend and the orders of magnitude must be taken into account.

5.2 Two-DOF Test

The test was performed on September 18, 2020. The elongation and rotation of the column are shown on Figure 8 (a) and (c). The axial force and bending moment can be seen on Figure 7 (b) and (d).

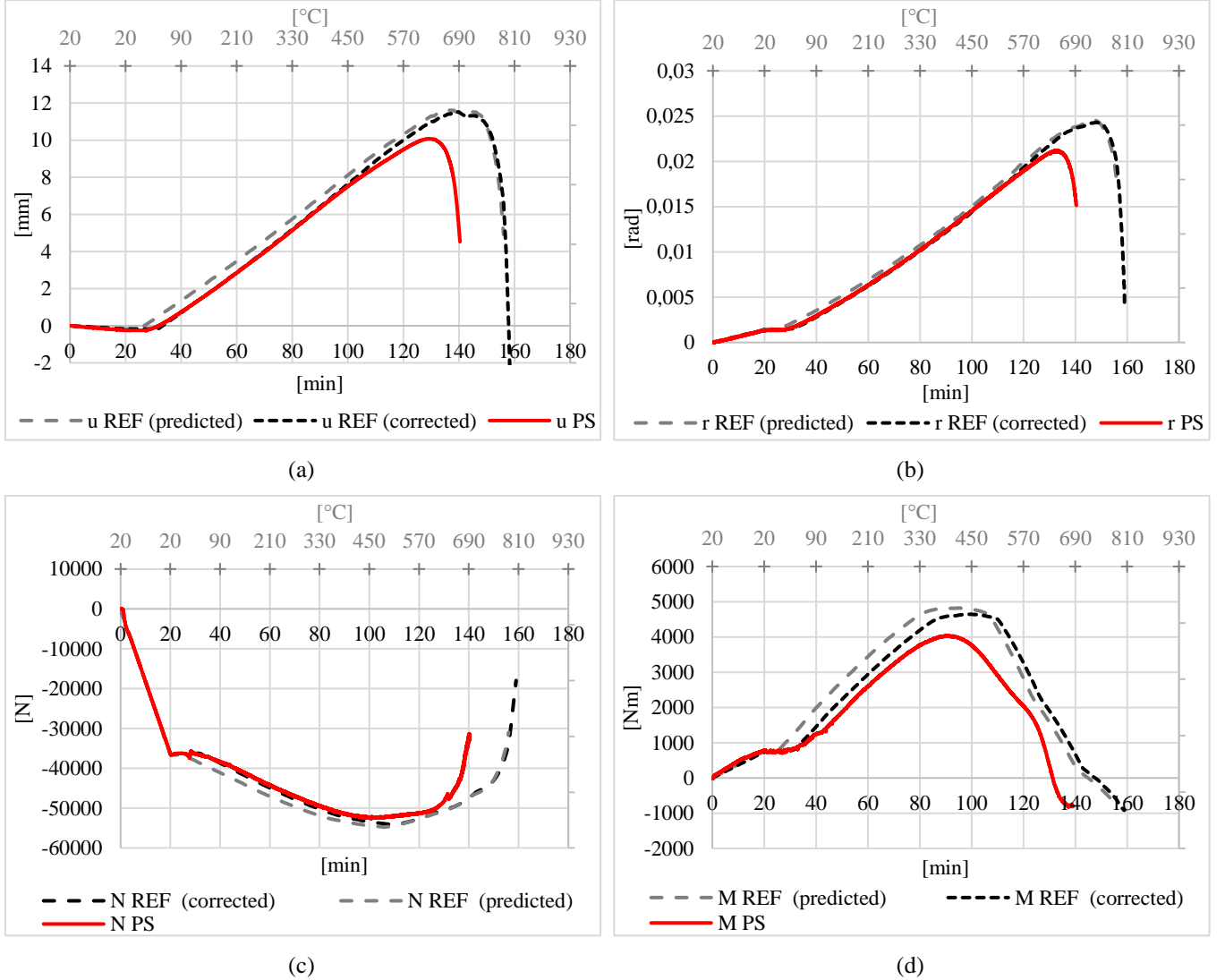


Figure 8. Results of the two-DOF test (a) Elongation u (b) Normal force N (c) Rotation r (d) Bending moment M

As in section 5.1, the curves “REF (predicted)” refers to a numerical simulation in SAFIR of the complete frame that was performed before the test. The buckling was predicted at a temperature of 792°C after approximatively 157 min. One can make similar observations as in the one-DOF test when the HFT curves (“U PS”, “r PS”, “N PS” and “M PS”) are compared with the ones predicted by numerical simulation: there is a lag and the failure occurs earlier. Moreover, the column buckled out of plane.

However, it is important to specify that the curves “REF (predicted)” were computed using a “plane frame” structure, whereas the column is tested in an imperfect environment that proved to display a three-dimensional character: the hinges are not completely rigid in the out-of-plane direction and allow a slight rotation that could cause this early failure.

The “corrected” numerical simulation was therefore performed, considering a three-dimensional column that is pinned in the direction perpendicular to the plane of the reference structure. An initial geometrical imperfection of 2.8 mm was added. The temperatures were also corrected. Under these conditions, a buckling in this direction was in fact observed. One can see in Figure 8 that the internal forces obtained during the test are closer to the corrected simulations although the failure still occurs earlier in the test. The general trend of the curve is nevertheless followed. The relative errors between PS and NS are of the same order of magnitude as for the one-DOF test, which shows the reliable performances of the algorithm.

5.3 Three-DOF Test

The test was performed on October 8, 2020. Results of the axial displacement and the rotations of the PS as a function of time are shown on Figure 9 (a), (c) and (e). The normal forces and bending moments of the specimen can be seen on Figure 9 (b), (d) and (f). The notations r_1 , r_2 , M_1 , and M_2 correspond to Figure 3 (c).

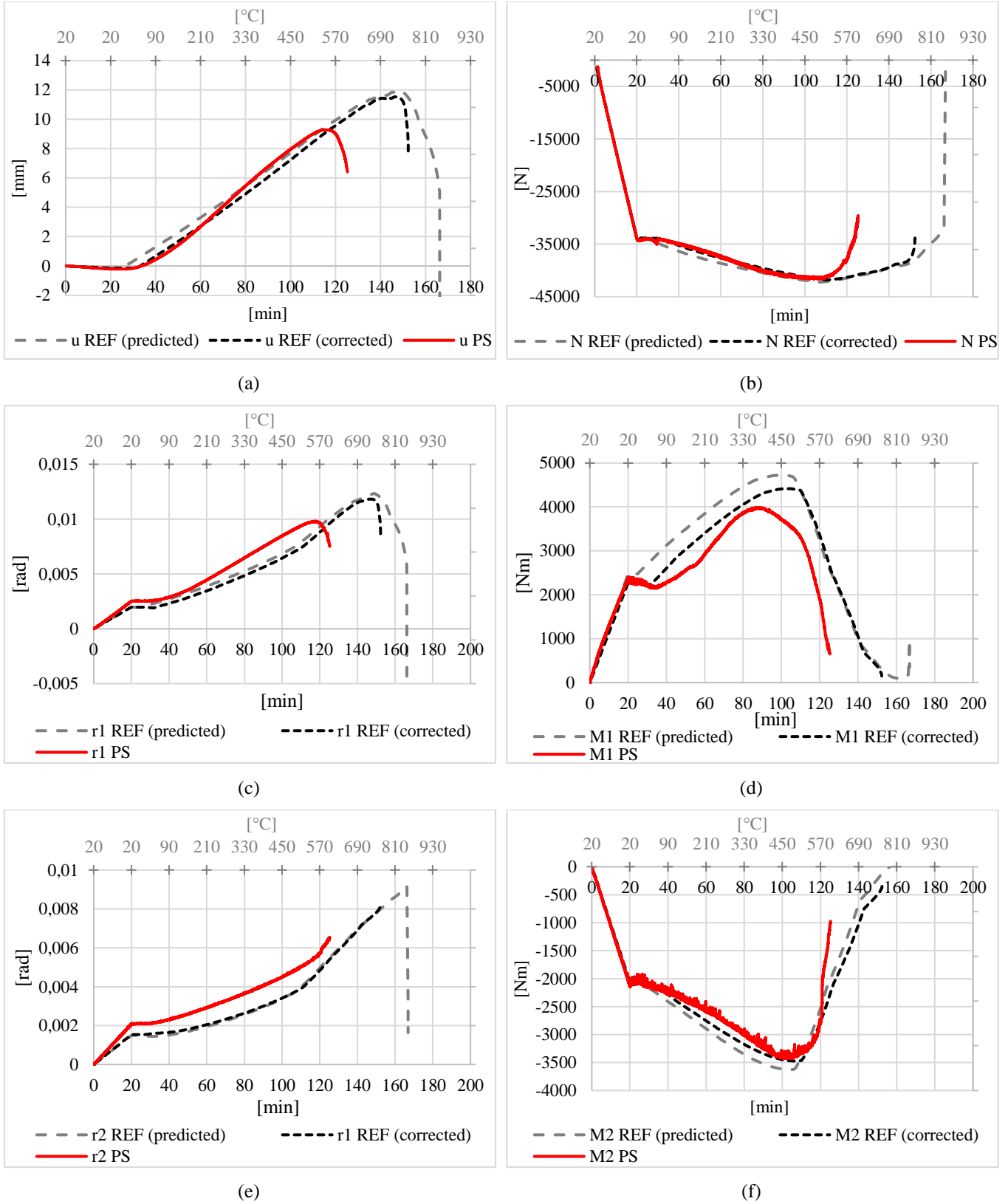


Figure 9. Results of the three-DOF test (a) Elongation u (b) Normal force N (c) Rotation r_1 (d) Bending moment M_1 (e) Rotation r_2 (f) Bending moment M_2

The failure was initially expected at 165 minutes with a temperature around 840°C. The test was stopped shortly after 120 minutes when the column buckled out of plane, as in the two-DOF test. A “corrected” numerical simulation of the reference structure was performed, considering a 3D structural model and the measured temperature during the test. After correction, the differences between the experimental results and the numerical behaviour are reduced but still remain for rotations and bending moments.

6 CONCLUSIONS

For the first time, MDOF hybrid tests were successfully performed in fire field. The proposed HFT method is reliable, ensures stability and equilibrium of the interface forces between the two substructures and reproduces the trend of the numerical predictions made on the complete structures.

Differences between numerical simulation and experimental results can be explained by the fact that numerical simulations of the complete structures are based on the hypothesis that the element of the structure that will become the PS in the test behaves in a perfect manner. This is of course not the case, partly due to some limitations of the experimental setup: the temperature of the tested column is not uniform and the hinges are not completely fixed in the out-of-plane direction.

ACKNOWLEDGMENT

This work was supported by the Fonds de la Recherche Scientifique - FNRS under Grant n° 31297790.

The authors would like to thank Mr. Fabien Dumont and Mr. Nicolas Mestre for their assistance and contribution in the implementation of the HFT and the building of the experimental setup.

REFERENCES

1. Franssen, J. M., and Gernay, T. (2017). *Modelling structures in fire with SAFIR®: Theoretical background and capabilities*, Journal of Structural Fire Engineering, 8(3):300-323.
2. Korzen, M., Magonette, G., and Buchet, P. (1999). *Mechanical Loading of columns in Fire Tests by Means of the Substructuring Method*, Zeitschrift für Angewandte Math. und Mech., Vol. 79, pp S617-S618.
3. Robert, F., Rimlinger, S., and Collignon, C. (2010). *Structure fire resistance: a joint approach between modelling and full-scale testing (substructuring system)*, 3rd fib International Congress.
4. Mostafaei, H., (2013). *Hybrid fire testing for assessing performance of structures in fire –Application*, Fire Safety Journal, 56, pp 30–38.
5. Whyte, C. A., Mackie, K. R., and Stojadinovici, B. (2016). *Hybrid Simulation of Thermomechanical Structural Response*, Journal of Structural Engineering, pp 142(2).
6. Schulthess, P., Neuenschwander, M., Mosalam, K.M., Knobloch, M. (2020). *A computationally rigorous approach to hybrid fire testing*, Computers & Structures, doi: 10.1016/j.compstruc.2020.106301.
7. Wang, X., Kim, R. E., Kwon, O.-S., and Yeo, I. (2018). *Hybrid Simulation Method for a Structure Subjected to Fire and its Application to a Steel Frame*, ASCE Journal of structural Engineering.
8. Mergny, E., Drion, G, Franssen JM (2020), *Stability in Hybrid Fire Testing Using PI Control*, Experimental Techniques, doi: 10.1007/s40799-020-00375-8.
9. Schellenberg, A. H., Mahin, S. A. and Fenves, G. L. (2009). *Advanced implementation of Hybrid Simulation*, PEER Report 2009/104, University of California, Berkeley.
10. Åström, J., Murray, R. (2008). *Feedback Systems: An Introduction for Scientists and Engineers*, Princeton University Press, 2nd edition, November 2008.

LIFETIME ECONOMICALLY OPTIMUM POSITION OF STEEL REINFORCEMENT IN A CONCRETE COLUMN EXPOSED TO NATURAL FIRE

Shuna Ni¹, Ruben Van Coile², Negar Elhami Khorasani³, Danny Hopkin⁴, Thomas Gernay⁵

ABSTRACT

This paper incorporates a probabilistic fire loss assessment method for reinforced concrete structures into a cost-benefit analysis to optimize a structural fire design. Economic losses in case of failure and survival of the structure are both quantified with, in the latter case, an estimate of the damage and repairs costs. As a case study, a cost-benefit optimization of the position of rebars in a concrete column is investigated. The column response in fire is evaluated using finite element simulations in SAFIR. Variations in cover thickness result in variations in failure probabilities and, for cases where no failure occurs, variations in repair costs due to heat penetration and residual out-of-plane deformation of the column. The optimum cover thickness is the one that offers the best trade-off between the various repair costs across the range of likely fire intensity levels. This optimum is sensitive to repair decisions such as the tolerance on the acceptable residual out-of-plane deformation after a fire. For the studied cases, the optimum cover thickness is smaller in slender columns than in stocky columns due to greater out-of-plane deformations in the former.

Keywords: Fire; probabilistic loss estimation; cost-benefit analysis; concrete columns; cover optimization

1 INTRODUCTION

Adequate fire safety requires that the building's risk profile with respect to fire exposure is tolerable, and that societally cost-effective safety measures are implemented [1]. The tolerability evaluation is best done holistically, taking into account the combined fire performance of all the building's fire safety features. In the end, an explicit tolerability evaluation elucidates the range of potential consequences and their occurrence frequencies for the design, and confirms that these are acceptable to the stakeholders under the condition that further investment is too costly. The consideration that further investment is not cost-effective is a direct implementation of the As Low As Reasonably Practicable (ALARP) requirement, demonstrating that the residual risk level is ALARP.

A case specific demonstration of tolerability and ALARP is however exceedingly rare. Most buildings are constructed through consideration of prescriptive design guidance, either directly or through engineered 'alternative solutions'. Achieving tolerability and ALARP for those buildings is assumed based on the application of the design guidance itself, placing great importance on the appropriateness of this guidance. The design guidance should result in a building for which the residual risk is approximately ALARP, i.e., further safety investments are suboptimal, provided that guidance is applied within its intended scope.

¹ Assistant Professor, Utah State University
e-mail: shuna.ni@usu.edu, ORCID: <https://orcid.org/0000-0002-8795-176X>

² Assistant Professor, Ghent University
e-mail: Ruben.VanCoile@UGent.be, ORCID: <https://orcid.org/0000-0002-9715-6786>

³ Assistant Professor, University at Buffalo
e-mail: negarkho@buffalo.edu, ORCID: <https://orcid.org/0000-0003-3228-0097>

⁴ Visiting Professor, University of Sheffield
e-mail: danny.hopkin@ofrconsultants.com, ORCID: <https://orcid.org/0000-0002-2559-3581>

⁵ Assistant Professor, Johns Hopkins University
e-mail: tgernay@jhu.edu, ORCID: <https://orcid.org/0000-0002-3511-9226>

The above observation is not restricted to fire engineering. As stated by Rackwitz, design optimization forms the basis of code calibration in structural engineering [2]. When adopting such an approach, the lifetime costs and benefits of safety investments are balanced to derive optimum values for the design. These optima can then be either listed directly in design guidance as part of prescriptive (tabulated) recommendations or can be generalized towards target safety levels. In fire safety engineering, efforts towards lifetime cost optimization (LCO) have only been explored recently. For example, De Sanctis and Fontana derived the optimum egress width for compartments in multi-story commercial premises with a single compartment exit [3]. In structural fire safety engineering, LCO based methods are applied by Hopkin et al. [10] to derive optimum insulation thicknesses for protected steel beams.

However, most current studies related to the design optimization calculate the lifetime costs, particularly the repair cost, only based on a binary damage criterion, failure or no failure [4–6], which may not be suitable for some scenarios where a finer degree of granularity in defining fire damage is required, e.g., for reinforced concrete (RC) structures that usually do not collapse under fire but require significant repair efforts for continued use. To overcome this limitation, this paper incorporates a recently developed fire loss estimation method [7] into a lifetime cost optimization. The loss estimation method addresses gradual levels of damage states and the corresponding repair efforts, in addition to a binary failure/no failure criterion, thus providing a more refined estimate of the repair costs. In this paper, the general formulation of the cost-benefit analysis is introduced first; then, the fire loss estimation method is described. The theory is then applied to the problem of cover thickness optimization of RC columns in the fire situation. Finally, the discussion is expanded to show the effects of occupancy types and column slenderness on the derived optimum cover thickness.

2 METHOD

2.1 Cost-benefit analysis for fire design optimization

Cost-benefit evaluations in structural engineering are commonly derived from [2], with further reference to [8]. These formulations were adapted to consider fire exposure in [4,9,10]. Following the formulation as described by Hopkin et al. [10], the lifetime cost is given by Eq. 1, with constituent terms including the total building construction and maintenance cost, C ; the obsolescence cost, A ; the adverse event (nonstructural) direct and indirect material damages, D_M ; the adverse event loss to human life and limb, D_L ; and the adverse event (structural) reconstruction and repair cost after fire, D_R . The lifetime cost and its constituent terms are functions of a vector \mathbf{p} of design parameters p_i . Minimizing the overall lifetime cost corresponds with finding the combination of design parameters for which the lifetime cost's partial derivatives are zero, i.e., Eq. 2. For completeness, Eq. 2 should be solved with considerations to avoid obtaining local minima or maxima. Furthermore, when considering physical constraints to the design parameters, the global minimum lifetime cost may correspond with the limiting values of the design parameters, which do not conform to Eq. 2. For simple cases in accordance with the current state-of-the-art, the above issues are generally not a concern as the lifetime cost function Y can readily be visualized, confirming the global minimum.

$$Y = C + A + D_M + D_L + D_R \quad (1)$$

$$\frac{\partial Y}{\partial p_i} = 0 \quad \forall i \quad (2)$$

The construction cost C is commonly modelled as the sum of a base construction cost C_0 and a safety-investment cost C_1 . Only the latter cost is considered as a function of the design parameter vector \mathbf{p} . The obsolescence cost A is commonly specified through an obsolescence rate ω , discounted to present net value through the continuous discount rate γ . Considering (from a practical perspective) an infinite time horizon for the optimization, the present net values for C and A are given by Eq. 3 and Eq. 4.

$$C = C_0 + C_1(\mathbf{p}) \quad (3)$$

$$A = C \frac{\omega}{\gamma} \quad (4)$$

The damage terms D_M , D_L , and D_R relate to damages incurred in case of adverse events. First of all, such damages can be incurred in case of structural failure in normal design conditions. Considering a yearly probability of structural failure $P_{f,0}$, the associated annualized costs are specified through Eq. 5-7, with $C_{M,0}$ the material damage incurred in case of normal design situation failure, and $C_{L,0}$ and $C_{R,0}$ the corresponding human losses and repair costs. These costs are here considered as deterministic (expected) values. The effect of variability in the incurred damages is considered through the tolerability assessment.

$$D_{M,0} = \frac{P_{f,0}}{\gamma} C_{M,0} \quad (5)$$

$$D_{L,0} = \frac{P_{f,0}}{\gamma} C_{L,0} \quad (6)$$

$$D_{R,0} = \frac{P_{f,0}}{\gamma} C_{R,0} \quad (7)$$

In the context of this paper, fire-induced damages are investigated. It is considered here that other damage terms (related to, for example, flooding) can be neglected, or more precisely: that these other damage terms are not p -dependent. The fire-related damage terms are specified below, where λ_{fi} is the occurrence rate of structurally significant fires, $P_{f,fi}$ is the (conditional) probability of structural failure (collapse) in case of fire. With respect to the incurred losses, a distinction can be made between situations where the structure collapses during fire and situations where the structure survives up to burnout. Hence, a distinction is made for the incurred costs as well, with the index ' f ' corresponding with failure and the index ' nf ' indicating the situation where the structure maintains stability up to and including burnout.

$$D_{M,fi} = \frac{\lambda_{fi}}{\gamma} (P_{f,fi} C_{M,fi,f} + (1 - P_{f,fi}) C_{M,fi,nf}) \quad (8)$$

$$D_{L,fi} = \frac{\lambda_{fi}}{\gamma} (P_{f,fi} C_{L,fi,f} + (1 - P_{f,fi}) C_{L,fi,nf}) \quad (9)$$

$$D_{R,fi} = \frac{\lambda_{fi}}{\gamma} (P_{f,fi} C_{R,fi,f} + (1 - P_{f,fi}) C_{R,fi,nf}) \quad (10)$$

Summation of Eq. 3-10 gives an extensive formulation of the total lifetime cost Y in accordance with Eq. 1, considering a vector \mathbf{p} of design variables. Depending upon the case, the vector of design parameters \mathbf{p} will influence the failure probabilities and/or the expected values of the incurred costs for Eq. 5-10. In agreement with current state-of-the-art applications, adoption of a number of simplifying assumptions allows a reduction in the equations considerably. Firstly, current LCO for structural fire engineering (SFE) considers only a single design variable p for the optimization. Secondly, the probability of structural failure in normal design conditions can be considered negligible, i.e., $P_{f,0} \approx 0$, or to the same effect, the failure probability and costs incurred in case of normal design failure can be considered independent of the fire design optimization parameter p . In that case, the contribution of normal design failure to the lifetime cost can be substituted by a constant value a . The lifetime cost now reduces to Eq. 11, where the index ' p ' has been introduced to denote p -dependency.

$$Y = a + C_0 \left(1 + \frac{\omega}{\gamma}\right) + C_{1,p} \left(1 + \frac{\omega}{\gamma}\right) + D_{M,fi,p} + D_{L,fi,p} + D_{R,fi,p} \quad (11)$$

Further assumptions can be made to simplify the formulation for specific cases. For example, where the design variable p applies to a member that is not critical to the stability of the entire structural assembly (e.g., due to redundancy and robustness of the structure), it may be assumed that incurred costs due to complete building failure are negligible. In other words, if structural stability up to burnout is readily ensured, the term $P_{f,fi} \approx 0$. Rebasing the lifetime cost to Y_{nl} , leaving only the p -dependent terms, results in Eq. 12.

$$Y_{nl} = C_{1,p} \left(1 + \frac{\omega}{\gamma}\right) + \frac{\lambda_{fi}}{\gamma} (C_{M,fi,nf,p} + C_{L,fi,nf,p} + C_{R,fi,nf,p}) \quad (12)$$

If, in addition to the above, the design parameter does not significantly affect the cost of the design, then $C_{1,p} \approx 0$. Rebased and renormalizing the cost to $Y_{n,2}$ results in Eq. 13.

$$Y_{n2} = C_{M,fi,nf,p} + C_{L,fi,nf,p} + C_{R,fi,nf,p} \quad (13)$$

If furthermore the fire is contained to the storey of origin, and knowing that stability up to burnout is maintained, the nonstructural material losses and human losses can reasonably be considered independent of structural fire design parameters. The lifetime cost can then be rebased to the basic formulation of Eq. 14, i.e., the lifetime cost of the design is in such cases fully dependent on the reconstruction and repair cost in the wake of a fire.

$$Y_{n3} = C_{R,fi,nf,p} \quad (14)$$

2.2 Fire loss estimation

The cost-benefit analysis requires the estimation of fire loss. A framework [7] has been proposed to estimate the direct fire loss in concrete structures. The framework considers different possible fire scenarios within the building, corresponding to different possible ignition locations. For a given fire location, the framework applies a four-step procedure, which parallels the PEER methodology [11], including fire hazard analysis, fire-thermo-mechanical analysis, damage analysis, and loss analysis.

The fire hazard analysis first calculates the probability of having a severe fire in a building and the conditional probability of fire occurrence in different compartments. These probabilities are used to integrate the losses associated with different fire locations, as shown by the loop in Figure 1. The fire hazard analysis then provides the associated distribution of the intensity measure (IM) of fire hazards that represents the hazard severity. The fire load density q_f in a compartment (in MJ/m² of floor area) is used as IM [12].

Given a location of fire fiL_i and a fire load q_f , a fire-thermo-mechanical analysis is conducted to obtain the engineering demand parameters (EDPs) that are used to quantify the damage. The analysis incorporates the uncertainties from the fire, heat transfer, and mechanical models. For each fire location, probabilistic fire-thermo-mechanical analyses of the building are conducted for different values of the fire load q_f . The analyses yield probability density distributions of the defined EDPs.

Based on the EDPs, the damage analysis quantifies the probability associated with failure, as well as the probability associated with each damage state for the building's components. This probability distribution for the damage measure (DM) is conditional on a specific fire load q_f and fire location fiL_i . Finally, the loss analysis estimates the replacement or repair cost. This estimation is based on loss functions that represent the probabilistic distributions of the repair costs for each component at each damage state, including structural components, nonstructural components, and content, in the fire exposed area and outside this area. The repair cost is estimated for each fire location. The total fire loss for a building is the weighted summation of the fire loss at each fire location, where the weights account for the probabilities of the different fire scenarios (i.e. allocation of the annual ignitions amongst compartments).

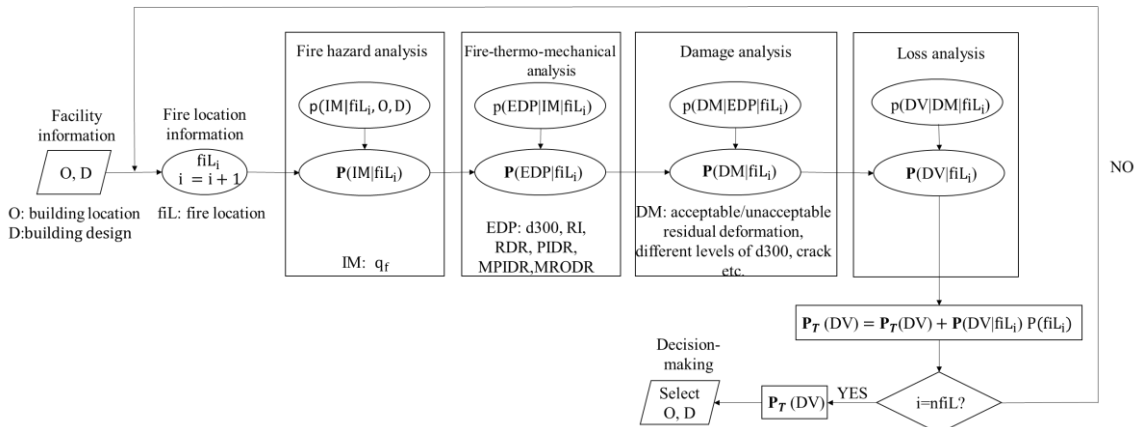


Figure 1. Probabilistic loss assessment for buildings under fire [7]

2.3 Optimization of the cover thickness of a column

The above described methods are implemented in this paper to optimize the cover thickness of RC columns. As the full fire-induced collapse of RC buildings is rare, it is assumed as a simplification that $P_{f,fi} \approx 0$. This assumes that the failure of a column in a fire compartment does not lead to the failure of the building. Meanwhile, the change of cover thickness by displacing the rebars (at constant section size) does not change the construction cost for a column, hence $C_{1,p} = 0$. Assuming that the fire is contained to the fire compartment where the target column is located and knowing that stability up to burnout is maintained, the nonstructural material losses and human losses can reasonably be considered independent of the column cover thickness. Therefore, the optimization of cover thickness could be conducted based on Eq. 14 that has been simplified to only include the expected repair cost, $C_{R,fi,nf,p}$. The framework described in Section 2.2 is used to estimate the expected repair cost in Eq. 14, but without considering the uncertainties in fire locations. The estimation of the expected repair cost for a single column includes both failure (of the column) and nonfailure cases.

The optimization is conducted using the numerical method, and the optimal design parameter is identified by visualizing the variation of the repair cost with the design parameter. The optimum cover thickness is the one that minimizes the repair cost.

3 ANALYSES

3.1 Description of the columns

The cover thickness of two columns (Column A and Column B) are optimized to illustrate how to use the method of Section 2. Columns A and B are assumed to be located in a 21 m x 21 m fire compartment, with maximum opening factor equal to $0.043 \text{ m}^{1/2}$. The mean compressive strength of concrete is 30 MPa, while the steel rebar's mean yield strength is 400 MPa. The dimension and reinforcement details of the two columns are shown in Figure 2a and 2b. The column height is 3.867 m. The reference cover thickness is 40 mm for Column A and 30 mm for Column B. The columns are assumed as pinned-pinned with an axial load at the top of the column, as shown in Figure 2c. Column A is exposed to natural fire on three sides, with a reference gravity load (Eurocode combination in the fire situation) of 992 kN. Column B is exposed to natural fire on four sides, with a reference gravity load of 1984 kN. A sinusoidal geometric imperfection with $1/400h$ at the middle height is imposed to the columns, where h is the height of the column.

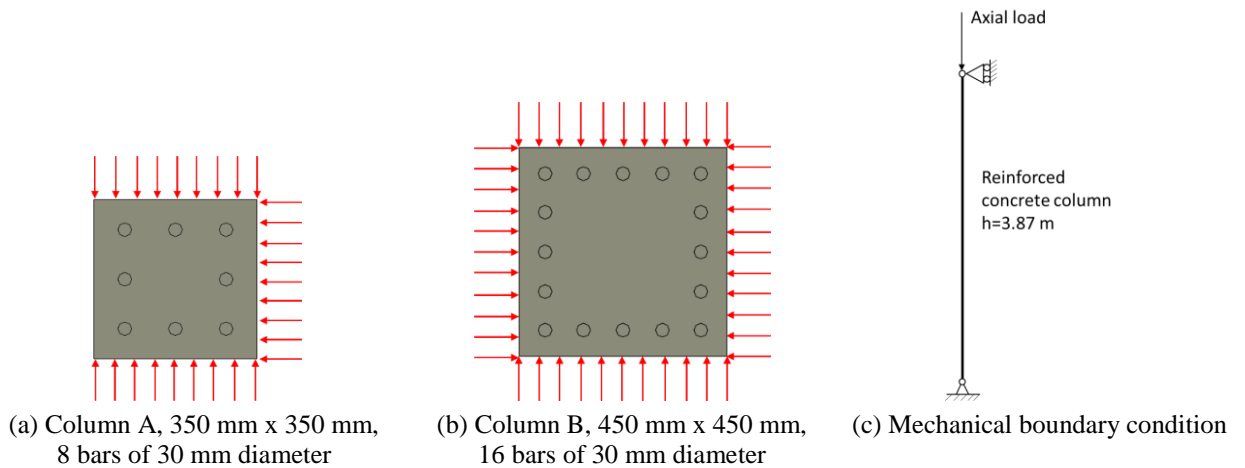


Figure 2. Dimension and thermal boundary condition of RC columns

3.2 Description of EDPs, DSs, fragility functions, and loss functions

The columns are subject to natural fires inclusive of a cooling phase. A failure criterion is first used to identify whether a column fails. Here, failure is characterized by the sudden and large increase in deformation. If the column fails, the cost of reconstruction of the column is adopted. If the column does not

fail, the repair cost related to each damage state of a column is calculated based on fire-specific EDPs, DSs, fragility functions and loss functions.

It is recognized that fire damage is caused by both thermal action (i.e., thermally-induced degradation of the material) and mechanical action (i.e., thermally-induced deformations and forces in the structure). Therefore, two EDPs are selected to assess the damage in the members. The first EDP is the heat penetration depth of the 300°C isotherm in the section, to address the material damage due to heat penetration [7]. Different repair actions are required as a function of the heat penetration. The second EDP is the maximum residual out-of-plane deformation ratio (MRODR), i.e., the ratio of the maximum residual out-of-plane deformation over column height, to address the fire damage related to residual deformations. A limit in the out-of-plane deformation could avoid the detrimental effects in terms of mechanical resistance and stability in transient and service stages, the service performance during the use of a building, and guaranteeing the compatibility for the erection of the structure and its nonstructural components. ENV 13670-1 [13] recommends that the structural deviation of a column should be less than the larger of $1/300 h$ and 15 mm. Such a threshold value may be different for different purposes; therefore, various threshold values ($1/300 h$, $1/500 h$, and $1/700 h$) are investigated in this paper. A column has to be replaced if its MRODR value is greater than the selected threshold value; otherwise, no repair actions are required.

The damage states of the column, corresponding to different levels of repair efforts, are mapped to different EDP thresholds. The damage related to the heat penetration of the 300 °C isotherm has four states, which has been described in details in [7]. The damage related to the residual out-of-plane deformation has only two states, i.e., MRODR exceeding the threshold value (replacement) or not (no action). To consider the uncertainties inherent to the post-fire evaluation, the threshold values are taken as probabilistic variables. The lognormal distribution of the lower threshold of each damage state, as a probabilistic function of the EPD, is the fragility function that represents the probability that a component reaches or exceeds a specified damage state [7].

The repair cost corresponding to each damage state is assumed to follow a lognormal distribution, with the mean value estimated from data in the Concrete & Masonry Costs (RSMeans, 2019 [14]) and the COV ranging from 0.6 to 0.8 based on earthquake engineering data [15]. Table 4 lists the mean repair cost of the two columns with the reference cover thicknesses for the damage related to heat penetration. As the cover thickness changes, the repair cost varies slightly for DS1, DS2, and DS3 while the costs for DS4 remain the same, corresponding to the reconstruction (demolition and replacement) of a column due to extensive damage from the heat penetration, which is also the cost for scenarios when a column fails or experiences extensive out-of-plane deformation leading to its replacement.

Table 1. Repair cost for the EDP of heat penetration (d300) for columns exposed to fire

	DS1 (\$)	DS2 (\$)	DS3 (\$)	DS4 (\$)
Column A, 40 mm	143	725	1,240	7,329
Column B, 30 mm	246	1,179	2,461	12,852

3.3 Identification of probabilistic parameters

This section studies the sensitivities of column damage to variables related to fire analysis, thermal analysis, and structural analysis, including opening factor of a fire compartment, concrete thermal conductivity, concrete density, dead load, live load, model effect, retention factor of concrete compressive strength at high temperature, and retention factor of steel yield strength at high temperatures.

The uncertainty in the opening factor is adopted from the JCSS model [16], $O = O_{\max}(1 - \zeta)$, where O_{\max} is the maximum possible opening factor assuming all the window glass is immediately broken when fire breaks out. $O_{\max} = 0.043 \text{ m}^{1/2}$ is assumed for the target compartment. ζ is a random variable following a truncated (cut off at 1.0) lognormal distribution with a mean of 0.2 and a standard deviation of 0.2.

The concrete thermal conductivity can be chosen between a lower ($\alpha=0$) and an upper ($\alpha=1$) limit, which follow the recommendation of Eurocode [17]. It is assumed that α follows a uniform distribution with a

range from 0 to 1. The characteristic range of normal-weight concrete density ranges from 2240 kg/m³ to 2400 kg/m³ [18]. For the thermal analysis, it is assumed that the density of normal-weight concrete follows a uniform distribution with a range from 2240 kg/m³ to 2400 kg/m³.

The total load effect is described by $K_E \cdot (G + Q)$, with K_E the model uncertainty for the load effect, G the permanent load, and Q the imposed load [19]. The model uncertainty K_E is described by a lognormal distribution with a mean equal to 1 and a COV of 0.10. The dead load is modelled by a normal distribution with a mean equal to the nominal dead load (G_{norm}), and a COV of 0.1. The live load effect Q is modelled by a Gamma distribution. For typical occupancies (office, residential), the mean live load can be taken as 0.2 times the nominal, with a COV of 0.60 for large load areas (> 200 m²). For the columns analysed in this paper, G_{norm} is equal to dead load plus superimposed dead load (6.9 kPa in total) while the Q_{norm} is equal to live load (3 kPa). The two columns are assumed to be located at the ground floor of a five story building. Column A is subject to a gravity load from a tributary area of 7 m x 3.5 m while Column B is subject to a gravity load from a tributary area of 7 m x 7 m.

The retention factor of concrete compressive strength at high temperatures, $k_{c,T}$, follows a weibull distribution, while the retention factor of steel yield strength at high temperatures, $k_{y,T}$, follows a lognormal distribution [20]. The parameters for the two distributions are temperature-dependent variables.

The scenarios with each variable equal to its mean value are taken as the reference cases. The column cover thickness remains as the reference values in the sensitivity studies. The parametric fire model in the Eurocode 1 [21] is used to calculate the gas temperature, with the fire load equal to 420 MJ/m². For the reference cases, the heat penetration depth d_{300} is 49 mm for Column A and 51 mm for Column B, and the maximum residual out-of-plane deformation is 3 mm for Column A and 0.8 mm for Column B. For each variable, two additional cases were run: one is the column with the target variable equal to its mean value minus one standard deviation and the other one is the column with the target variable equal to its mean value plus one standard deviation; all the other variables equal to their mean values. Table 2 summarizes the absolute value of the variation of the EDP values as the target variable changes from $\mu - \text{std}$ to $\mu + \text{std}$, relative to that of the reference case. The percentages listed in Table 6 are the average values for the two example RC columns.

According to Table 2, the opening factor is the most critical variable for d_{300} , while d_{300} is not very sensitive to the thermal conductivity and density of concrete, with the variation percentages less than 10%. The MRODR of the columns is sensitive to the retention factor of the yield strength of steel at high temperatures, model effect, dead load, and opening factor. The variation percentage of MRODR due to the uncertainties in live load is greater than 10%, although not as great as the other variables. Therefore, the following parameters will be included in the probabilistic fire-thermo-mechanical analysis: opening factor, dead load, live load, model effect, and retention factor of the yield strength of steel at high temperatures. The uncertainties from the other variables are ignored in this paper.

Table 2 Relative variation in EDP values associated with variable changes from $\mu - \text{std}$ and $\mu + \text{std}$

	d_{300} (%)	MRODR (%)
Opening factor	54.3	18.0
Concrete thermal conductivity	8.6	3.4
Concrete density	1.2	1.2
Model effect	-	29.6
Dead load	-	27.9
Live load	-	11.7
Concrete strength	-	8.6
Steel strength	-	37.7

4 RESULTS OF THE COVER THICKNESS OPTIMIZATION

The expected repair cost of a column is estimated for a cover thickness ranging from 10 mm to 70 mm, using the fire loss estimation framework described in Section 2.2. For each cover thickness, the probabilistic analysis is based on 500 calculations with SAFIR [22] for each level of fire load (ranging from 100 MJ/m² to 2300 MJ/m²). In addition, the optimum cover thickness of another relatively slender column is investigated in Section 4.3 to investigate the impacts of column slenderness on the optimum cover.

4.1 Fragility curves

Figure 3 shows the failure probabilities of the two columns, as a function of the fire load. The numerical data (dots in Figure 3) were fitted by lognormal distributions. The failure probability is almost zero for fire loads up to 1500 MJ/m². For fire loads greater than 1500 MJ/m², as the cover thickness increases, a column becomes less vulnerable to failure first but then may become more vulnerable if the cover thickness is as great as 70 mm. This is because a thick cover can provide adequate protection to the rebar but also decreases the distance between the rebar (lever arm) for bending behavior. Compared to Column A, the failure probability of Column B is lower due to its relatively large section and symmetrical fire exposure.

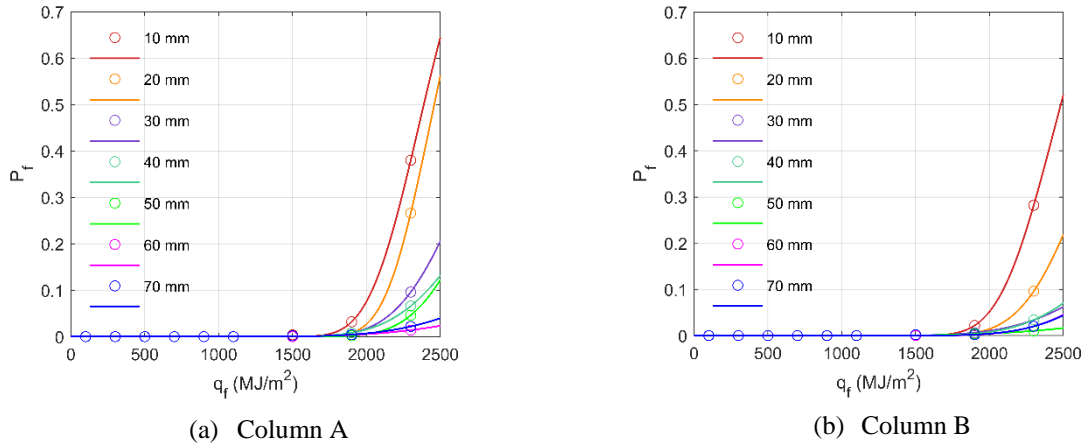


Figure 3. Failure probability of the two target columns

For nonfailure (nf) scenarios, the distributions of the two EDPs at different levels of fire loads are determined by the probabilistic fire-thermo-mechanical analysis, incorporating the variable uncertainties in opening factor, live load, dead load, model effect, and retention factor of steel yield strength at high temperature. The PDFs of d300 and MRODR are fitted by the modified gamma distribution and lognormal distributions, respectively. The convolution of the fragility function and the PDF of EDP yields the probability that a column reaches or exceeds a specified damage state (fragility curves). Figure 4 shows the fragility curves of Column A, related to the heat penetration of the 300 °C isotherm, for cover thickness of 10 mm, 40 mm, and 70 mm. The fragility curve of DS1 is unaffected by the change in cover because the lower threshold value of DS1 is a constant value of zero, independent of the cover thickness. Since the lower threshold value of DS2 is 1/10 of the cover thickness that is close to zero [7], the fragility curve of DS2 is close to that of DS1. However, as the cover thickness increases, the fragility curve of DS3 moves away from DS2 towards DS4, while the fragility curve of DS4 slightly shifts to the right side on the x axis.

Figure 5 shows the fragility curves of the two columns related to the maximum residual deformation, for different cover thicknesses. Those curves are from the damage analysis with the limit for the MORDR set as 1/700 h. As the cover thickness increases, the fragility curves move to the right since a thick cover protects the rebar from exposure to high temperature. Compared to Column B, Column A is more vulnerable to the out-of-plane deformation due to its relatively small section dimension and unsymmetrical fire exposure. As the cover thickness increases further up to 70mm, its probability of reaching or exceeding the threshold value is relatively high when the fire load is low (as shown in the blue curve in Figure 5a), since the bending stiffness of a section decreases when the distance between the rebars decreases. However, when the fire load increases further, the advantage of insulation from a thick cover prevails; thus, the probability decreases.

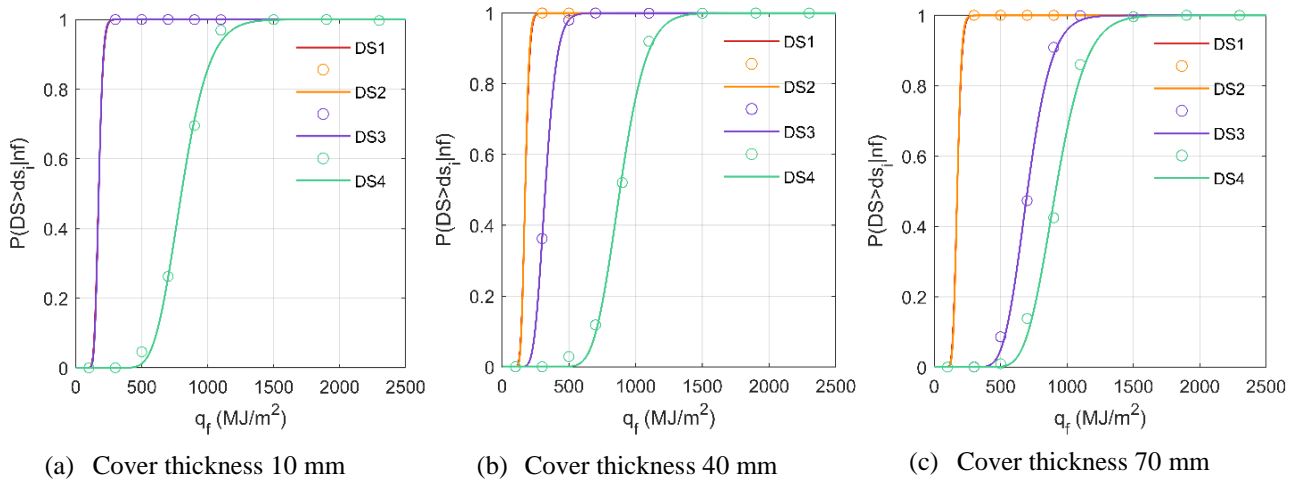


Figure 4. Fragility curves related to the heat penetration of the 300 °C isotherm (Column A)

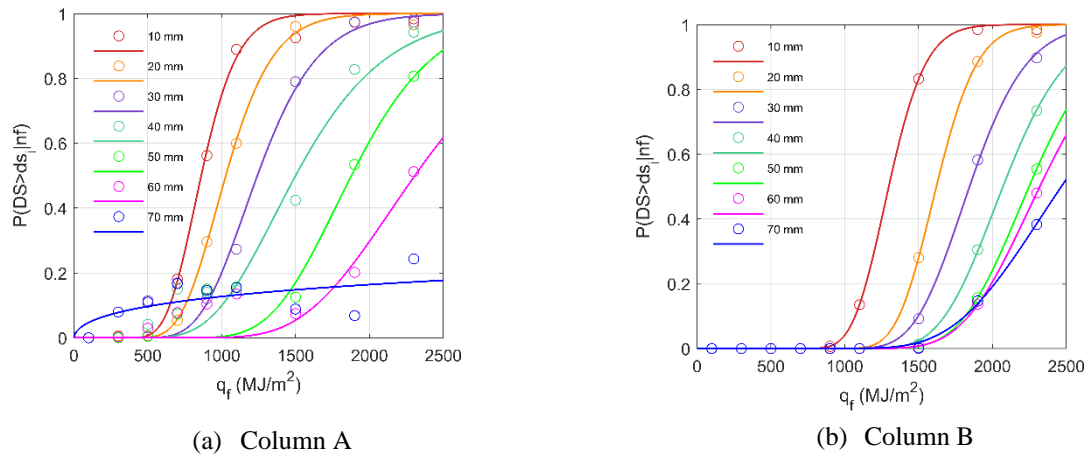


Figure 5. Fragility curves related to the maximum residual out-of-plane deformation

4.2 Optimum cover thickness

Figure 6 shows the variation of the two columns' expected repair cost with cover thickness, conditional on the threshold value for the out-of-plane deformation equal to $1/700$ h. These curves are calculated from the convolution of the probabilities of a column at different damage states and the PDF of the fire load density, taking into account the costs such as those listed in Table 1. Each curve in Figure 6 represents a level of fire load in a compartment, which depends on a compartment's occupancy type [21]. The fire load is assumed to follow the Gumbel type I distribution; the legends in Figure 6 are the mean values of the fire loads, ranging from 100 MJ/m^2 to 1100 MJ/m^2 .

As shown in Figure 6a, as the cover thickness increases up to 60 mm, the expected repair cost of Column A decreases. For further increase to 70 mm, the repair cost increases slightly. Thick concrete cover could protect the rebar from exposure to high temperatures, thus decreasing the probability that d300 reaches or exceeds DS3, as shown in Figure 4, and reducing the repair cost significantly since the repair efforts for DS3 requires the supplement rebars. However, as the cover thickness increases to 70 mm, the distance between the rebars decreases, resulting in relatively low bending stiffness of a section and thus a relatively high probability to reach or exceed the MRODR threshold value (as shown in the blue curve in Figure 5a); that is why the repair cost increases for the largest value of cover thickness. Moreover, the expected repair cost increases as the fire load level increases; however, this does not impact the value of the optimum cover thickness which equals to 60 mm for Column A, regardless of the fire load. It is noteworthy that this optimum is larger than the minimum cover thickness (40 mm) required for design [23].

Unlike Column A, Column B is heated from four sides and is of a relatively large section, leading to small out-of-plane deformations under fire. Most of the cost of Column B results from the repair efforts associated with the heat penetration of the 300 °C isotherm. As mentioned before, a thick cover could minimize the

probability that d300 reaches or exceeds DS3; that is why the repair cost decreases continuously as the cover thickness increases. However, it is reasonable to expect that the fire loss would increase at some point as the cover thickness increases further beyond 70 mm, due to a reduction in the lever arm.

For both columns studied in this section, the expected repair cost is the highest when the cover thickness is as low as 10 mm (which is, anyway, an unacceptably low value for other requirements as well, e.g., corrosion). A 10 mm-thick cover is unable to protect the rebar from exposure to high temperature. The degradation of the mechanical properties of rebar at high temperatures leads to a relatively higher failure probability, as shown in Figure 5, thus increasing the expected repair cost. The analyses suggest that the optimum cover thickness from the perspective of fire loss minimization is greater than the minimum cover thickness required for other purposes [23].

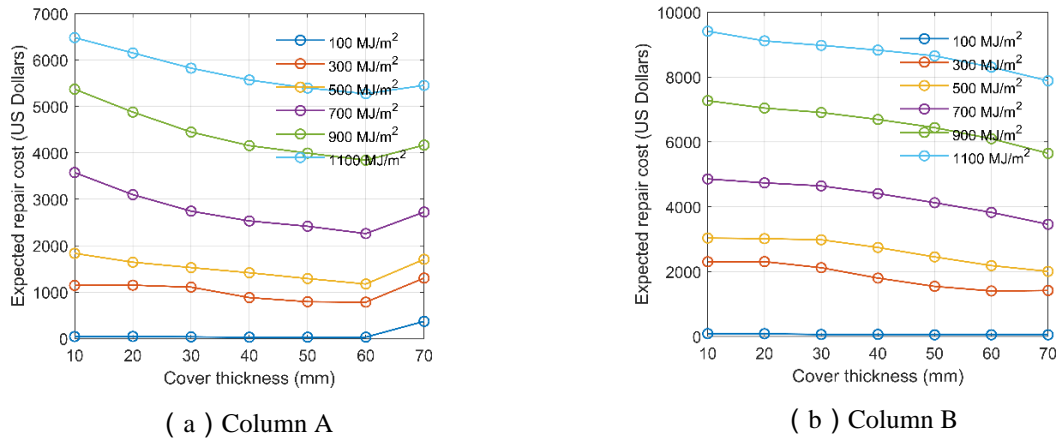


Figure 6. Variation of expected repair cost with cover thickness

The optimum cover thickness discussed above is conditional to a threshold value of MRODR equal to 1/700 h. As the threshold value increases to a higher level, the repair cost of Column A also decreases continuously as that of Column B due to the limited out-of-plane deformation of the two columns.

4.3 Effect of column slenderness on the optimum cover thickness

The studied columns A and B were relatively stocky. This resulted in a limited influence of the residual out-of-plane deformation damage state on the fire losses. In this section, another column was studied to investigate the effect of column slenderness on the optimum cover thickness. The column is 4.76 m high, simply supported. The section of the column is 300 mm x 300 mm, with 6 steel bars of 20 mm diameter and a reference cover thickness of 28 mm. The mean compressive strength of concrete is 31MPa, and the mean yield strength of steel is 462 MPa. It is assumed that the column is located in a fire compartment of 14 m x 14 m, with a maximum opening factor of 0.043 m^{1/2}. Similar to Column B, this column is exposed to fire on four sides. The fire severity is probabilistically assessed, assuming uncertainty in the opening factor, in addition to fire load being selected as the intensity measure. A stratified sampling method is adopted to select the opening factor for each fire load based on the probability density distribution of opening factor; ten opening factors are selected for each fire load. The axial load imposed at the top of the column remains the same, 650 kN, in all the analyses. Table 3 lists the mean repair cost of the column with the reference cover thickness (28 mm), for the damage related to heat penetration. As the cover thickness changes, the repair cost varies slightly for DS1, DS2, and DS3 while the costs for DS4 remain the same. The repair cost at DS4 is equal to the reconstruction cost of the column in the scenarios where the column has to be replaced due to failure, extensive heat penetration, or extensive out-of-plane deformation.

Table 3. Repair cost for the EDP of heat penetration (d300) for the slender column exposed to fire

Cover thickness	DS1 (\$)	DS2 (\$)	DS3 (\$)	DS4 (\$)
28 mm	202	905	1,184	3,451

Figure 7 shows the variation of the expected repair cost of the column with cover thickness under different fire load levels, for various threshold values of MRODR. If the threshold value of MRODR is equal to

1/300 h, the expected repair cost continuously decreases as the cover thickness increases, regardless of the fire load. This is because the importance of out-of-plane displacement is lesser when the tolerance on the threshold is more lenient. For a threshold value of MRODR of 1/500 h (meaning that the tolerated residual deflection becomes more stringent), a clear optimum cover can be observed for medium fire load levels (500 MJ/m² to 900 MJ/m²), as the expected repair cost decreases first and then increases slightly after an optimum of 49 mm. For fire load levels lower than 500 MJ/m² and higher than 900 MJ/m², the expected repair cost continuously decreases with the increase of the cover thickness. This is because low fire load limits the out-of-plane deformation while high fire load requires a thick cover to protect the rebars, thus the advantages of insulation from a thick cover prevail in both cases. As the threshold of MRODR decreases further to 1/700 h, the decreasing-increasing trend of the expected repair cost becomes more evident for the three fire load levels, 500 MJ/m², 700 MJ/m², and 900 MJ/m². The optimum cover thickness is 42 mm for the three levels of fire load. Similar to the slender column, Column B is also exposed to four side fire. However, due to its relatively large section dimension and relatively small height, the expected repair cost of Column B does not have a decreasing-increasing trend even when the threshold value of MRODR is equal to 1/700 h.

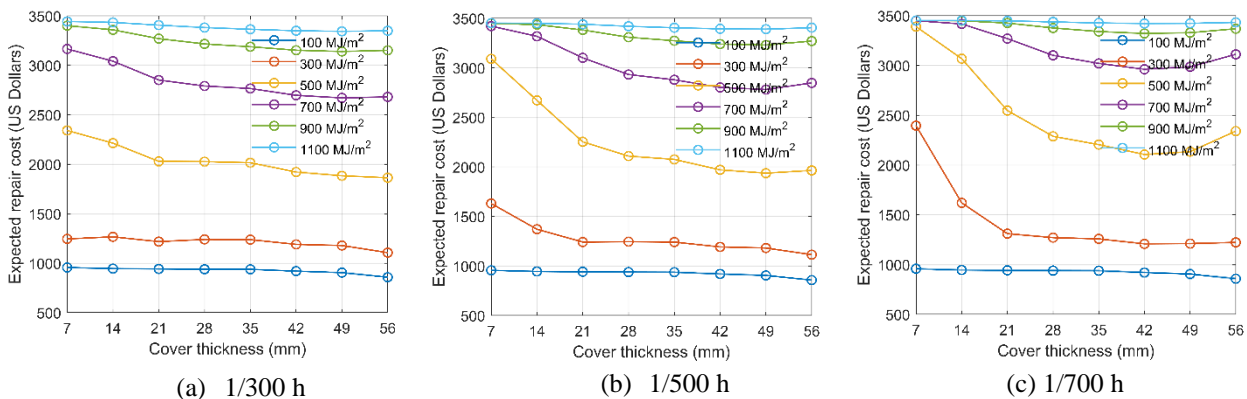


Figure 7. Variation of expected repair cost with cover thickness for the slender column

5 CONCLUSION

This paper incorporated a method for probabilistic fire loss estimation of reinforced concrete structures into a lifetime cost optimization framework to optimize the cover thickness with respect to fire response. Without considering the impact of other cost components in the cost-benefit analysis, the cover thickness of several columns was optimized based on the expected probability of failure and repair cost after a fire event. The expected repair cost accounted for the cost of repairs due to heat penetration in the section and residual out-of-plane deformations, as well as the cost for replacement in case of failure. These cost components vary with the variation of cover thickness. The optimum thickness is achieved by balancing the cost components across the range of expected fire events, as characterized by the fire load as the intensity measure. The optimum is also sensitive to assumptions on repair actions, such as on the tolerance for the acceptable residual out-of-plane deformation. For large values of this tolerance, the cost continuously decreased with an increase in cover thickness. Compared to stocky columns, a slender column that experiences more out-of-plane deformation has a smaller optimum cover thickness. The optimization in this paper only focuses on the repair cost of isolated columns. Future works will seek to include more damage characteristics, e.g., residual axial deformation will be incorporated into the fire loss estimation of a column; more cost components in Eq. (1); and to conduct the optimization of design parameters at the scale of a whole building, the importance of which has been emphasized in [24].

REFERENCES

1. Van Coile R, Hopkin D, Lange D, Jomaas G, Bisby L. The Need for Hierarchies of Acceptance Criteria for Probabilistic Risk Assessments in Fire Engineering. *Fire Technol* 2019;55:1111–46. <https://doi.org/10.1007/s10694-018-0746-7>.

2. Rackwitz R. Optimization — the basis of code-making and reliability verification. *Struct Saf* 2000;22:27–60. [https://doi.org/10.1016/S0167-4730\(99\)00037-5](https://doi.org/10.1016/S0167-4730(99)00037-5).
3. De Sanctis G, Fontana M. Risk-based optimisation of fire safety egress provisions based on the LQI acceptance criterion. *Reliab Eng Syst Saf* 2016;152:339–50. <https://doi.org/10.1016/j.ress.2016.04.001>.
4. Van Coile R, Caspeele R, Taerwe L. Lifetime cost optimization for the structural fire resistance of concrete slabs. *Fire Technol* 2014;50:1201–27. <https://doi.org/10.1007/s10694-013-0350-9>.
5. Van Coile R, Gernay T, Hopkin D, Elhami Khorasani N. Resilience targets for structural fire design: An exploratory study. 17th Int. Probabilistic Work., Edinburgh, UK: 2019.
6. Balogh T, Vigh L. Optimal Fire Design of Steel Tapered Portal Frames. *Period Polytech Civ Eng* 2017;61. <https://doi.org/10.3311/PPci.8985>.
7. Ni S, Gernay T. A framework for probabilistic fire loss estimation in concrete building structures. *Struct Saf* 2021.
8. Rosenblueth E, Mendoza E. Reliability Optimization in Isostatic Structures. *J Eng Mech Div* 1971;97:1625–42.
9. Fischer K. Societal decision-making for optimal fire safety. ETH Zürich, 2014. <https://doi.org/https://doi.org/10.3929/ethz-a-010243009>.
10. Hopkin D, Fu I, Van Coile R. Adequate fire safety for structural steel elements based upon life-time cost optimization. *Fire Saf J* 2020;103095. <https://doi.org/10.1016/j.firesaf.2020.103095>.
11. Moehle J, Deierlein G. A framework methodology for performance-based earthquake engineering. 13th World Conf. Earthq. Eng., Vancouver, B.C., Canada: 2004, p. No. 679.
12. Gernay T, Elhami Khorasani N, Garlock M. Fire fragility curves for steel buildings in a community context: A methodology. *Eng Struct* 2016;113:259–76. <https://doi.org/https://doi.org/10.1016/j.engstruct.2016.01.043>.
13. ENV 13670-1:2000. Execution of concrete structures - Part 1: Common. European Standard, 2000.
14. Gordon Group Inc. Concrete & masonry costs with RSMeans data 2019. 37th ed. Rockland, MA: RSMeans Co; 2018.
15. Applied Technology Council. Guidelines for the seismic rehabilitation of buildings: Example applications. Washington, D.C.: 1997.
16. JCSS PMC. JCSS probabilistic model code part 2: Load models. Joint Committee on Structural Safety; 2001.
17. BS EN 1992-1-2. Eurocode 2. Design of concrete structures - Part 1-2: General rules. Structural fire design. European Standard, 2004.
18. Harith IK. Study on polyurethane foamed concrete for use in structural applications. *Case Stud Constr Mater* 2018;8:79–86. <https://doi.org/10.1016/j.cscm.2017.11.005>.
19. Jovanović B, Van Coile R, Hopkin D, Elhami Khorasani N, Lange D, Gernay T. Review of Current Practice in Probabilistic Structural Fire Engineering: Permanent and Live Load Modelling. *Fire Technol* 2020. <https://doi.org/10.1007/s10694-020-01005-w>.
20. Qureshi R, Ni S, Elhami Khorasani N, Van Coile R, Hopkin D, Gernay T. Probabilistic models for temperature dependent strength of steel and concrete. *J Struct Eng* 2020;146:04020102. [https://doi.org/10.1061/\(ASCE\)ST.1943-541X.0002621](https://doi.org/10.1061/(ASCE)ST.1943-541X.0002621).
21. BS EN1991-1-2. Eurocode 1: Actions on structures - Part 1-2: General actions - Actions on structures exposed to fire. European Standard. 2002.
22. Franssen J-M, Gernay T. Modeling structures in fire with SAFIR®: theoretical background and capabilities. *J Struct Fire Eng* 2017;8:300–23. <https://doi.org/10.1108/JSFE-07-2016-0010>.
23. CSA A23.3-14. Design of concrete structures. Canadian Standards Association. Mississauga, Ontario, Canada. Can Stand Assoc 2014:109–70.
24. Ni S, Gernay T. Predicting residual deformations in a reinforced concrete building structure after a fire event. *Eng Struct* 2020;202:109853. <https://doi.org/10.1016/J.ENGSTRUCT.2019.109853>.

EVALUATION OF THE FIRE PERFORMANCE OF UNPROTECTED COMPOSITE BEAMS WITH FIN-PLATE JOINTS

N. Yotsumoto¹, T. Hirahisma², K. Toyoda³

ABSTRACT

When the load level of composite beams is relatively low, there exists a potential for the fire protection used for steel beams to be eliminated or reduced. In performance-based design, this can be considered in terms of the hogging moment resistance of the joints. In order to investigate the fire performance of composite beams when considering the hogging moment resistance of the fin-plate beam-to-girder joints including the effect of continuity of reinforcements, experiments on composite beams protected only at the beam ends with continuous floor slabs have been conducted. The main test parameter was the specification of reinforcement, which affects the rotational restraint of the beam ends. The test results indicated that the failure time of the beam is extended by the hogging moment resistance of the joints; this was particularly noticeable when using a reinforcing bar with a large plastic deformation capability. In addition, a simple method for predicting the failure time of the beam using an evaluation model based on the bending moment resistance of the beam considering the hogging moment resistance of the fin-plate joint and the reinforcement is also presented. The predicted failure times corresponded well with the test results.

Keywords: Composite beam; unprotected steel; fin-plate joint; load-bearing fire test; hogging moment resistance; heat transfer analysis

1 INTRODUCTION

Fin-plate joints in steel structures are generally designed as pinned. Even so, such joints have some rotational stiffness and exhibit considerable hogging bending resistance especially at elevated temperature (hereinafter referred to as ET), which can have a significant effect on the fire performance of beams [1]. When the load level is relatively low, there is a potential for the fire protection used for steel beams to be eliminated or reduced owing to the hogging moment resistance of the joints. During a fire, it has been reported that in the case of composite beams with concrete floor slabs arranged continuously over multiple spans, a greater hogging moment resistance is exhibited at the joint owing to the effect of the reinforcement in the floor slab at the beam end [2]. In order to consider such an effect in structural fire design, it is necessary to clarify the bending moment resistance and rotational capacity of the joint, including the effect of reinforcement.

Ding and Wang [3] conducted load-bearing fire tests of a rugby goalpost shaped steel frame with beam-to-column joints and clarified that the fin-plate joint has low resistance against catenary action but worked well up to the limit state of bending. Selden et al. [4] conducted load-bearing fire tests of one-span composite beams with beam-to-column joints and clarified their load-bearing capacity. Fischer et al. [5] simulated the behaviour of three-span composite beams with beam-to-column joints during fire using

¹ General Building Research Corporation of Japan, Osaka, Japan
e-mail: yotsumoto@gbrc.or.jp

² Professor, Graduate School of Engineering, Chiba University, Chiba, Japan
e-mail: hirashima@faculty.chiba-u.jp

³ General Building Research Corporation of Japan, Osaka, Japan
e-mail: toyoda@gbrc.or.jp

FEM model and clarified that the fire performance of the composite beam was improved by the continuous arrangement of mild steel reinforcements. Some experiments focusing on the fire performance of composite beams with continuous floor slabs during heating and cooling phases [6]-[8] has been conducted; however, the hogging moment resistance of composite joints has not yet been quantified based on experiments.

From the perspective of preventing joint fractures and ensuring resistance, composite beams protected only at the beam-end joints were the focus of the present study. By protecting the beam ends at the same time as the girders, the labour requirement can be reduced. When only a beam end is protected a non-negligible temperature difference occurs near the protection boundary, which causes heat transfer in the axial direction of the beam. These effects complicate heat transfer behaviour near the joint. To investigate the temperature of the joint when only the beam ends are protected, Dai et al. [9] conducted fire tests on beam-to-column joints using an intumescent coating and clarified that the joint temperature was the same as that when protecting the entire length of the beam by protecting only the region up of 400 mm from the joint. If the joint temperature can be accurately predicted including the influence of heat transfer in the axis direction, the range of protection can be further reduced.

In this study, load-bearing fire tests of composite beams protected only at the beam ends with continuous floor slabs were conducted. Moreover, the fire performance of the beam when considering the hogging moment resistance of the fin-plate joint including the reinforcement was examined. Furthermore, a heat transfer analysis using a finite difference method considering heat transfer in the axial direction and a prediction method of the failure time of the beam based on simple plastic theory are shown, with their validity confirmed by comparison with test results. In recent studies on the fire performance of steel-concrete composite structures, many experiments and analyses focusing on the catenary action of beams [10] or the membrane action of floor slabs [11], which occur after bending failure, have been carried out. They are superior in that the fire limit states in actual steel structures are accurately investigated. However, it is necessary to analyse the deflection behaviour by FEM in order to design the fire resistance in consideration of these actions; such methods are not always applicable in practice owing to costs and analysis complexity. The model proposed in this paper focused on up to the bending failure before the catenary action of beams and the membrane action of slabs, so that is a simpler evaluation method based on plastic theory without requiring deflection analysis by FEM.

2 EXPERIMENTAL PROGRAMME OF LOAD-BEARING FIRE TEST

2.1 Test parameters, specimens, test setup and measurements

Table 1 shows the test parameters of the load-bearing fire test; Fig.1 shows the specimen shape, loading equipment and measuring points. The test parameters are the reinforcement specifications (reinforcement type, arrangement and main rebar amount) that affect the hogging moment resistance of the joint. SB is a specimen used to investigate the fundamental fire performance of a steel beam with fin-plate joints. CB-CS is a partially composite beam using composite slab with single-stage wire mesh (WFP, $\Phi 6@150$ mm, main rebar amount 170 mm^2). CB-RC is a fully composite beam using reinforced concrete slab (RC slab) with two-stage deformed bar (SD295A, D6@200 mm, main rebar amount 253 mm^2). Flat deck plates of thickness 1.0 mm were used as the concrete formwork in CB-RC. Headed studs (tensile strength 400 N/mm^2 class, $\Phi 16\text{-L80}$) were used as shear connectors between the beam and the floor slabs. In CB-CS, one stud was placed in each deck valley (300 mm on average). In CB-RC, one stud was placed every 200 mm. The ratio of the number of studs placed to the number of studs required to perform the full plastic moment of the composite beam (composite rate) was 0.69 for CB-CS and 1.04 for CB-RC.

The load level in this test was $M_0 = 0.4M_a$, where M_0 is the total value of working moment cM at the mid-span and eM at the support, and M_a is the long-term allowable bending moment of the beam. The term $0.4M_a$ corresponds to about one-quarter of the yield moment of the beam. Based on prior failure prediction calculations, this load level was determined to provide 1 hour of fire resistance in composite beam specimens. The M_a of the composite beam specimens was calculated by the yield moment

considering the composite effect [12]. The design concrete was 24 N/mm^2 and that of the steel beam was 235 N/mm^2 .

Tests were carried out in a loading frame and furnace for horizontal elements at General Building Research Corporation of Japan. As shown in Fig.1(a), the specimen was placed on pin rollers and a constant load was applied using two hydraulic jacks at the centre of the beam such that $M_0 = 0.4M_a$. The load eP at the cantilever outside the girder beam restrained the rotation of the beam end and was controlled so that the deflection angle at the support was maintained at zero. The deflection angle at the support was obtained by dividing the difference between the horizontal displacements $Dh1$ and $Dh2$ by the distance between the measurement points (500 mm). Specimen SB has a pantograph-type buckling stopper installed on both sides at 900 mm from the mid-span in order to prevent lateral buckling of the beam.

Heating was in accordance with the ISO834 curve. As shown in Figs.1(a)-(c), the beam and the cantilevers were unprotected. To protect the beam ends and girders, a 12.5-mm alkaline-earth silicate wool blanket (AES blanket) offering an equivalent fire resistance of 1 hour was used. Protection materials were attached to the girders in a 'boxed' shape and to the beam ends in a 'profiled' shape. Figures 1(b) and (c) show the temperature measurement points at the mid-span and the joint, respectively.

In these tests, it was judged that the beam failed when the beam become unable to support the applied load; at this time, the test was terminated.

Table 1. Test parameters

Specimen	Floor slab	Reinforcement	Composite rate	Load ($0.4M_a$)
SB	ALC with slit	none	0 (No composite action)	30.1 kNm
CB-CS	Composite slab	Wire mesh (WFP) $\Phi 6@150$	0.69 (Partially composite)	44.1 kNm
CB-RC	RC slab	Deformed bar (SD295A) $D6@200$	1.04 (Fully composite)	45.0 kNm

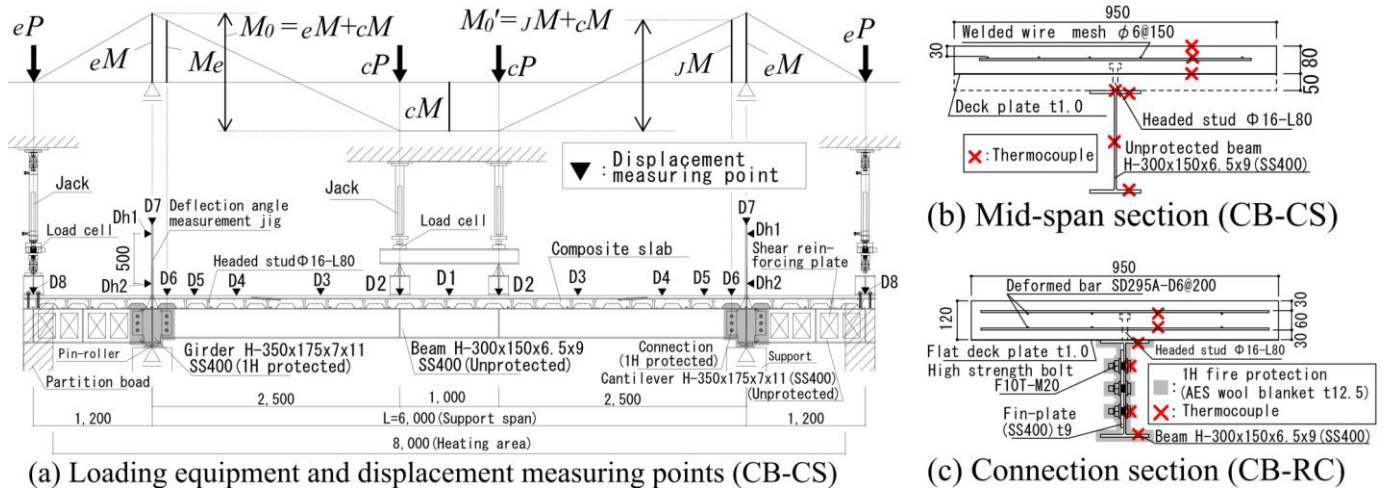


Fig. 1. Shape of specimen, loading equipment and measurement points (Dimension unit: mm)

2.2 Evaluation model of bending moment resistance

Figures 2(a)-(c) show the effective yield strength (stress at 1-% strain) of the steel beam (SS400), the tensile strength of the high strength bolt (F10T) and the tensile strength of the headed stud, respectively. The stress of the steel beam at 1-% strain decreased significantly from 400 to 700°C, after which it decreased more gradually. Since the load level in these tests was about one-quarter of the yield moment, it is expected that the load-bearing capacity is lost between 600 and 700°C in the case of simply supported steel beams. The tensile strength of high strength bolts decreased significantly above 300 °C, reaching about one-quarter of the initial value at 600 °C. The tensile strength of the headed studs decreased significantly above 300 °C, reaching about one-tenth of the initial value at 750 °C, after which it decreased gradually.

The upper reinforcement, which had a large influence on the hogging moment resistance of the joint, was located on the upper surface of the concrete slab; therefore, the temperature increase was expected to be small even after heating for 1 hour. For this reason, the tensile test of reinforcement at ET was not conducted; rather, it was conducted at ambient temperature (hereinafter referred to as AT). Figure 2(d) shows the stress-strain relationship of the reinforcement at AT. The deformed bar showed more than 15-% elongation, with strain hardening after yielding. On the other hand, in the welded wire mesh, no yield shelf appeared, the tensile strength was between 1- and 2-% strain and the fracture elongation was small. The plastic deformation capacity of the welded wire mesh was lower than that of the deformed bar.

The compressive strength of the concrete at AT was 34.8 N/mm² at 28 days of standard curing and 28.7 N/mm² at 67 days (near the test day) of site-sealed curing.

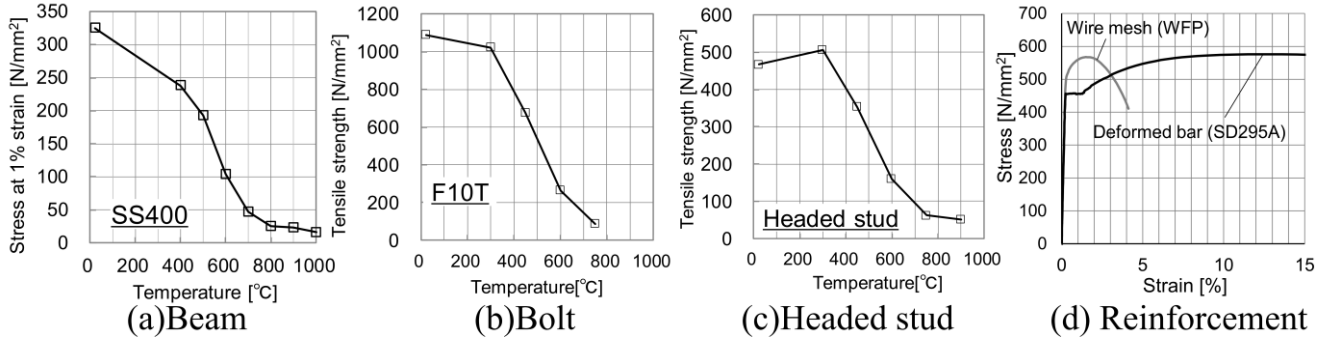


Fig. 2. Test results at elevated temperature (a–c) and ambient temperature (d)

3 PREDICTION METHOD FOR BENDING FAILURE OF BEAMS WITH FIN-PLATE JOINTS AT THEIR ENDS DURING FIRE

3.1 Evaluation model of bending moment resistance

(1) Process of bending failure

In this study, the failure time of the beam was predicted based on simple plastic theory. As shown in Fig.3(a), at the initial stage of heating, the hogging moment jM at the joint increases owing to the additional bending moment (referred to as thermal stress) to suppress thermal deflection. After that, the moment distribution changes while the total bending moment M_0' (sum of the bending moment cM at the mid-span and jM at the joint) remains constant. Then, when the total moment resistance (sum of the sagging moment resistance M_u^+ at the mid-span and the hogging moment resistance M_u^- at the joint) is reduced to M_0' , a three-hinge state is created and the beam collapses.

(2) Evaluation model of hogging moment resistance of the joint

In steel beam SB without reinforcement, only the bolts contribute to the hogging moment resistance of the joint. In the composite beam using composite slabs CB-CS (described in Section 4.2), the wire mesh at the beam ends fractured during the initial heating stage; therefore, only the bolts (and not the wire mesh at the joint) contributed to the hogging moment resistance of the joint. As shown in Fig.3(b), the evaluation model of the hogging moment resistance jM_u^- at the joint of both SB and CB-CS assumes that the upper and lower bolts reach maximum strength bN_u . In these tests, the bearing deformation of the bolt holes was relatively small compared with the shear deformation of the bolts; therefore, bN_u was determined by the shear fracture of the bolt. In addition, jM_u^- was calculated using Eq.(1).

$$jM_u^- = bN_u \cdot j \quad (1)$$

$$bN_u = -0.6a_{bs} \cdot F_{bu}(\theta_b)$$

where a_{bs} is the cross section of the bolt shaft and $F_{bu}(\theta_b)$ is the tensile strength of the bolt at ET.

The hogging moment resistance jRM_u^- for the joint considering the slab reinforcement of composite beam CB-RC using RC slabs assumes the force distribution shown in Fig.3(c). Here it is assumed that the state

in which the lower bolt reaches maximum strength lbN_u and the upper reinforcement reaches yield strength urN_y corresponds to the bending moment resistance. It also is assumed that the force distribution of bolts located between them is proportional to lbN_u and the distance from the neutral axis. The relationship between the force of the upper and lower reinforcements is assumed to exhibit the same proportional relationship as that of the bolts. The neutral axis position x_n where $\Sigma N = 0$ and each force are determined, and JRM_u^- is calculated using Eq.(2). The temperature of the upper reinforcement at the joint at the time of collapse was less than 200 °C, and the decrease in strength was considered to be small; therefore, the yield stress at AT (Fig.2(d)) was used as the strength of the upper reinforcement.

$$JRM_u^- = \sum (N \cdot t) \quad (2)$$

$$\begin{aligned} urN_y &= ura \cdot r\sigma_y && : \text{Yield strength of upper reinforcement} \\ lrN &= urN_u(x_n - lr t)/(x_n - ur t) && : \text{Force of lower reinforcement} \\ ubN &= lbN_u(x_n - ub t)/(x_n - lb t) && : \text{Force of upper bolt} \\ mbN &= lbN_u(x_n - mb t)/(x_n - lb t) && : \text{Force of middle bolt} \\ lbN_u &= -0.6a_{bs} \cdot F_{bu}(\theta_b) && : \text{Maximum strength of lower bolt} \end{aligned}$$

where ura is the total sectional area of the upper reinforcement and $r\sigma_y$ is the yield stress of the reinforcement at AT.

(3) Evaluation model of sagging moment resistance at mid-span

The sagging moment resistance $B M_u^+$ of steel beam SB was evaluated using the full plastic moment of the steel beam section [13][14]. The sagging moment resistance $CB M_u^+$ of composite beams CB-CS and CB-RC was evaluated using the full plastic moment of the composite beam section, considering the composite effect of the horizontal shear strength of the headed studs placed only in the sagging moment region. In these tests, the composite rate at the failure time was over 1.0, even for the partially composite beam CB-CS. This is because the strength of the unprotected steel beam was greatly decreased; as such, the shear strength required for the shear connector was also decreased. Therefore, $CB M_u^+$ of CB-CS was also evaluated as a fully composite beam. As an example, Fig.3(d) shows the evaluation model for $CB M_u^+$ of CB-RC when the plastic neutral axis is located between the upper and lower reinforcements. In this case, $CB M_u^+$ was calculated using Eq.(3). For the compressive strength of the concrete, the prediction equation of the compressive strength at ET obtained from the compressive strength at AT and the water-binder ratio effect [15] was used. For the effective yield stress of the steel beam, the stress at 1-% strain (shown in Fig. 2 (a)) was used.

$$CB M_u^+ = \sum (N \cdot t) \quad (3)$$

$$\begin{aligned} cN_u &= 0.85F_c(\theta_c) B_{ec}T && : \text{Maximum strength of concrete slab} \\ lrN_y &= lra \cdot r\sigma_y && : \text{Yield strength of lower reinforcement} \\ ufN_y &= ufa \cdot s\sigma_y(\theta_{uf}) && : \text{Yield strength of upper flange} \\ wnN_y &= wa \cdot s\sigma_y(\theta_w) && : \text{Yield strength of web} \\ lfN_y &= lfa \cdot s\sigma_y(\theta_{lf}) && : \text{Yield strength of lower flange} \end{aligned}$$

where $F_c(\theta_c)$ is the compressive strength of concrete at ET, $s\sigma_y(\theta_{uf})$, $s\sigma_y(\theta_w)$ and $s\sigma_y(\theta_{lf})$ are the yield stresses at ET of the upper flange, web and lower flange, respectively; lra , ufa , wa , lfa are the sectional areas of the lower reinforcement, upper flange, web and lower flange, respectively.

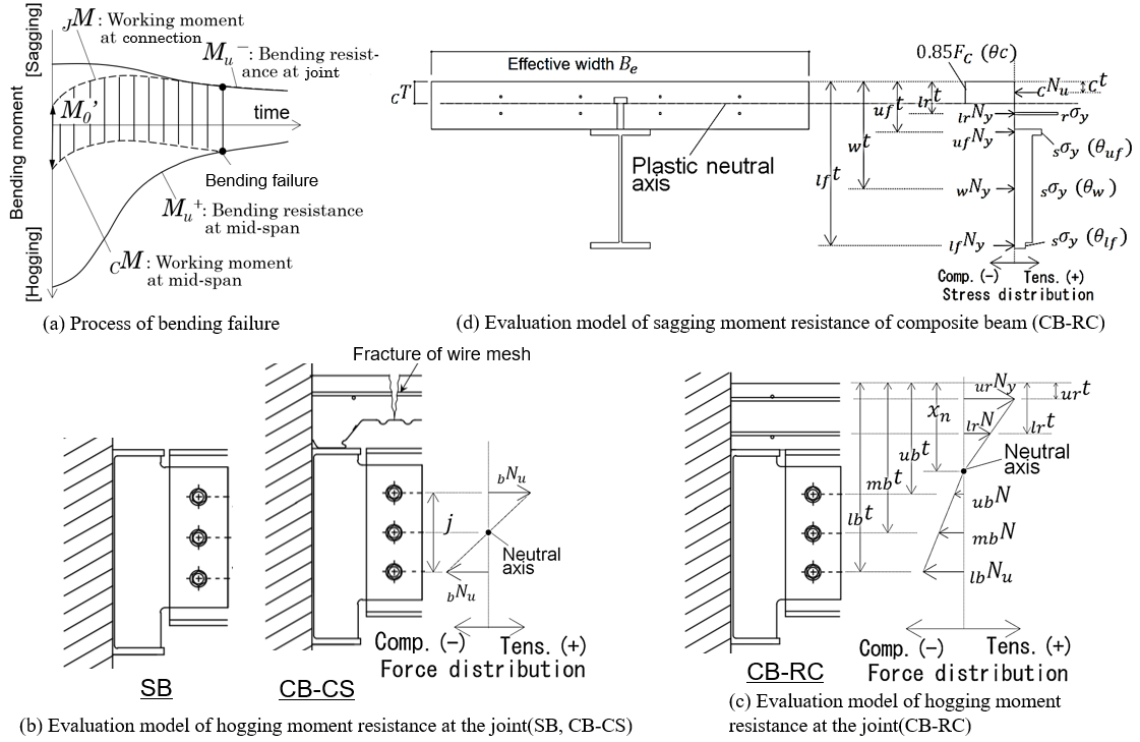


Fig. 3. Evaluation model of the bending moment resistance

3.2 Analysis model of temperature distribution of the unprotected beam and its protected joint

(1) Finite difference model and boundary condition

In order to predict beam failure time in a fire, it is necessary to obtain the cross-sectional temperature distribution of the unprotected beam at mid-span and the joint at the beam end. The heat capacity of the joint is larger than that of the beam owing to the effects of the bolts and fin-plate. When only the beam end is protected, a non-negligible temperature difference occurs near the protection boundary, causing heat transfer in the axial direction of the beam. In this study, three-dimensional heat transfer analysis considering these thermal behaviours was performed using the finite difference method, which is a relatively simple numerical solution.

As some examples, Figs.4(a)–(c) show the grid division model for CB-CS and CB-RC. Near the protection boundary, the temperature distribution in the axial direction becomes large; therefore, the grid at the beam end was divided more finely than that at the mid-span. The beam was divided into the lower flange, web and upper flange, whereas the concrete slab was divided every 5 mm in the height direction. Although the actual deck shape had inclinations, the slab shape was simplified to a rectangle. Considering that an air layer is formed when the deck is peeled from the concrete, the heat transfer from the deck to the concrete was set to radiation only in the analysis. Conduction occurred at the contact between the upper flange and the concrete; where these were not in contact, heat was transferred to the upper flange by radiation and convection from the fire. In steel beam SB using autoclaved lightweight concrete (ALC) for the floor slab, the thermal conductivity of the ALC was much lower than that of concrete; therefore, the upper surface of the upper flange was taken as the insulation boundary in the analysis. Owing to the increase in heat capacity of the web at the beam end due to the bolts and the fin-plate, their volumes were added to the grid of the web at the joint section. Test results were used for the fin-plate temperature of the girder, which was taken as the boundary condition at the end of the joint. Equations (4) and (5) were used for the convective heat flux q_{cv} and radiation heat flux q_{rd} , respectively, of the fire in the unprotected region.

$$q_{cv} = h(\theta_f - \theta_m) \quad (4)$$

$$q_{rd} = F\epsilon_{eff}\sigma(T_f^4 - T_m^4) \quad (5)$$

where θ_f , T_f is furnace temperature [°C], [K], θ_m , T_m is member temperature [°C], [K], h is the convective

thermal transfer coefficient, F is the view factor and ϵ_{eff} is the resultant emissivity. The value of h is $23 \text{ W/(m}^2\text{K)}$ on the exposed surface and $6.4 \text{ W/(m}^2\text{K)}$ on the unexposed surface. ϵ_{eff} is obtained using an emissivity value of 0.9 on the steel surface, 0.7 on the concrete surface and 1.0 for the fire.

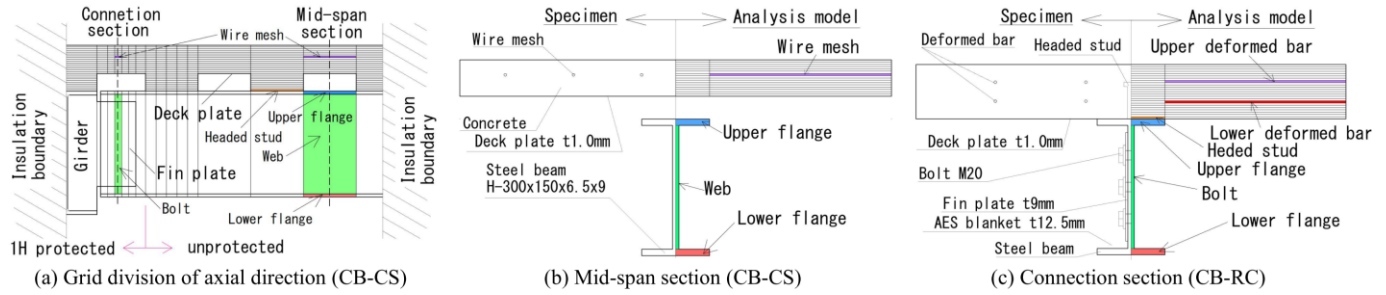


Fig. 4. Grid division model for the heat transfer analysis

(2) Thermal properties of materials

The effective specific heat and thermal conductivity of the steel and concrete used in the analysis were based on temperature dependent ones in Eurocode 4 [13]. The effect of the moisture in the concrete was considered by adding the latent heat of moisture to the specific heat of concrete at 95-105 °C based on Ref. [16] using the measured moisture content of the specimens (3.5%). The density was 7850 kg/m^3 for the steel and 2300 kg/m^3 for the concrete.

(3) Simple heat transfer model for fire protection

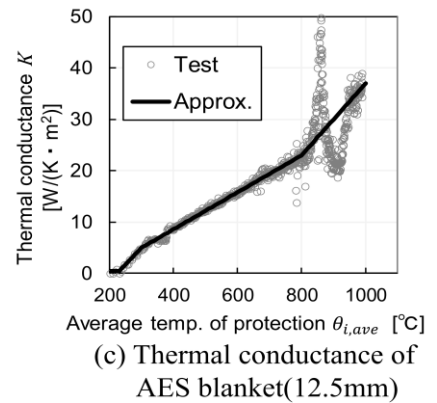
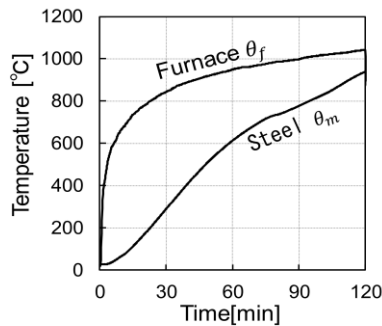
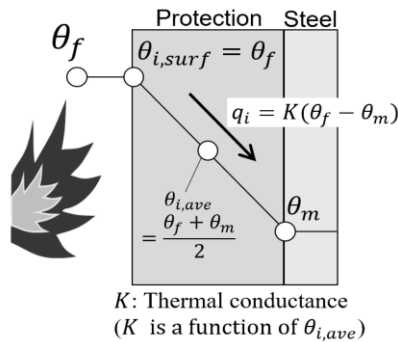
As shown in Fig.5(a), it is assumed that the internal temperature distribution of the AES blanket applied to the beam ends is instantaneously steady, and a simple heat transfer model using the thermal conductance K from the fire to the steel surface was applied to the protected regions. The value of K was calculated from Eq.(6) using the measured temperature (see Fig.5(b)) obtained in a heating test on a 200-mm square steel plate (9-mm thickness) protected with the same AES blanket as that used for the full-scale specimens.

$$K = \frac{\rho_s c_s}{H_s/A_s} \frac{d\theta_m/dt}{(\theta_f - \theta_m)} \quad (6)$$

where ρ_s is the density of the steel, c_s is the specific heat of the steel, H_s/A_s is the section factor, θ_f is the furnace temperature and $(d\theta_m/dt)$ is the rate of steel temperature increase.

For this method, Fig.5(c) shows the relationship between K and the protection average temperature $T_{i,ave}$. The disturbance in the test results after 800 °C is caused by the specific heat model of the steel. In the analysis, a polyline that approximates the test result was used. The heat flux q_i to the member in the protected region is calculated from Eq.(7) using the obtained value of K .

$$q_i = K(\theta_f - \theta_m) \quad (7)$$



(a) Heat transfer model of protection

(b) Measured temperatures from the fire test result

(c) Thermal conductance of AES blanket(12.5mm)

Fig. 5. Simple heat transfer model for fire protection

4 TEST RESULTS AND DISCUSSION

4.1 Temperature distribution at the mid-span and the joint

(1) Temperature at the mid-span

Figures 5(a)-(c) show comparisons between the test results and analytical results for the temperature in the unprotected mid-span section. In all the specimens, the measured temperatures of the web and lower flange reached about 800 °C in 30 min; whereafter, the difference between the furnace temperature and these components was less than 50 °C. The calculated temperatures of the lower flange, web and upper flange agreed well with the test results. The temperature of the upper flange followed the order: CB-CS (where the upper surface of the upper flange was directly heated) > SB (where the upper surface of the upper flange was insulated with ALC) > CB-RC (which exhibited an endothermic effect owing to the concrete). This feature was reproduced in the analysis. The temperature of the root of the headed stud that impacts the composite effect was almost the same for CB-CS and CB-RC, and no difference in relation to slab shape was found. The calculated temperature of the headed stud agreed well with the test result for CB-RC and was conservative for CB-CS.

At the end of heating, the measured temperatures of the reinforcements were about 100 °C for the wire mesh of CB-CS and about 150 °C for the upper deformed bar of CB-RC. Therefore, it is considered that decreases in the strength of the reinforcement and the concrete on the compression edge were small. The calculated temperature of the wire mesh of CB-CS was up to about 100°C higher than the test result. The calculated temperatures of the reinforcements of CB-RC agreed well with the test results.

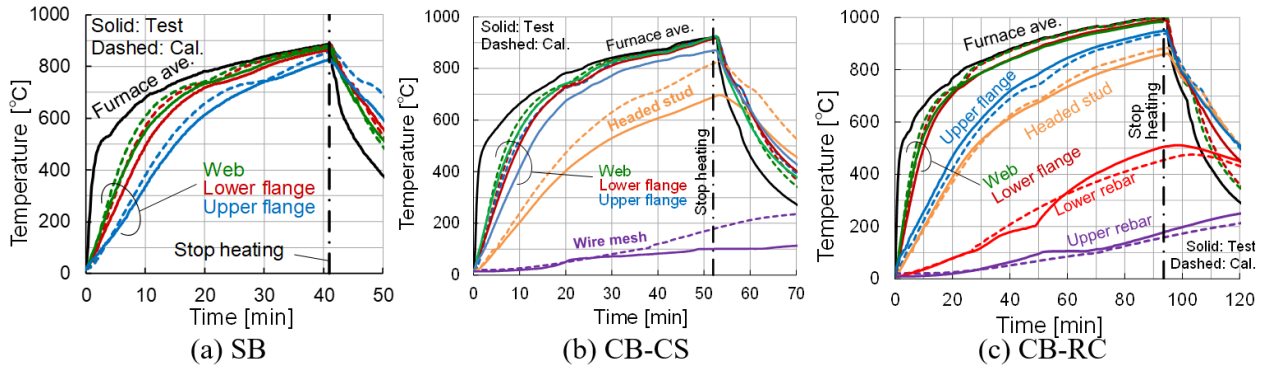


Fig. 6. Temperature of the beams at the mid-span

(2) Temperature at the joint

For the temperature in the protected joint section, Figures 6(a)-(c) show comparisons between the test results and the analytical results. The temperature of the web and the lower flange at the unprotected mid-span reached 800 °C in 30 min, whereas the bolts of all specimens were less than 400 °C within 30 min, demonstrating the effects of the protection and the large heat capacity. The temperatures of the bolts of CB-RC remained below 600 °C within 60 min owing to protection at the beam ends. The calculated bolt temperatures of all specimens agreed well with the test results.

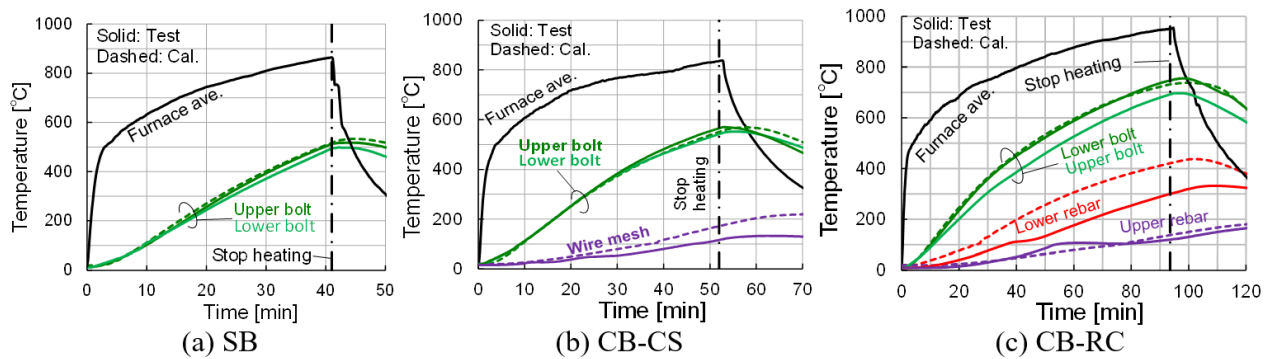


Fig. 7. Temperature of the joints at the beam end

4.2 Deflection behaviour and failure mode

(1) Deflection and damage to the specimen after the test

Figures 8(a)-(c) show the deflection and damage to the specimens after the tests. Deflection of the double curvature was observed in all specimens, indicating rotational restraint at the joint. At the mid-span, local buckling of the upper flange in SB and compressive collapse of the upper end of the slab in CB-CS and CB-RC were observed. Therefore, it is considered that the mid-span had reached the sagging moment resistance in all specimens. There was no noticeable damage to the headed stud and the surrounding concrete.

As shown in Fig.8(a), the joint rotated markedly, and the lower flange at the beam end and the fin-plate were in contact. No fracture of the bolt was observed in any of the specimens. Significant shear deformation was observed in the bolts, following the descending order of bolt temperature at collapse, as follows: CB-RC > CB-CS > SB. In all of the test specimens, the bolt holes of the web were expanded by about 2 mm due to the bearing. As shown in Fig.8(b), the wire mesh in the joint section of CB-CS was fractured. As shown in Fig.8(c), the upper deformed bar in the joint section of CB-RC was fractured. Therefore, it is considered that the joint had reached the hogging moment resistance in all specimens.

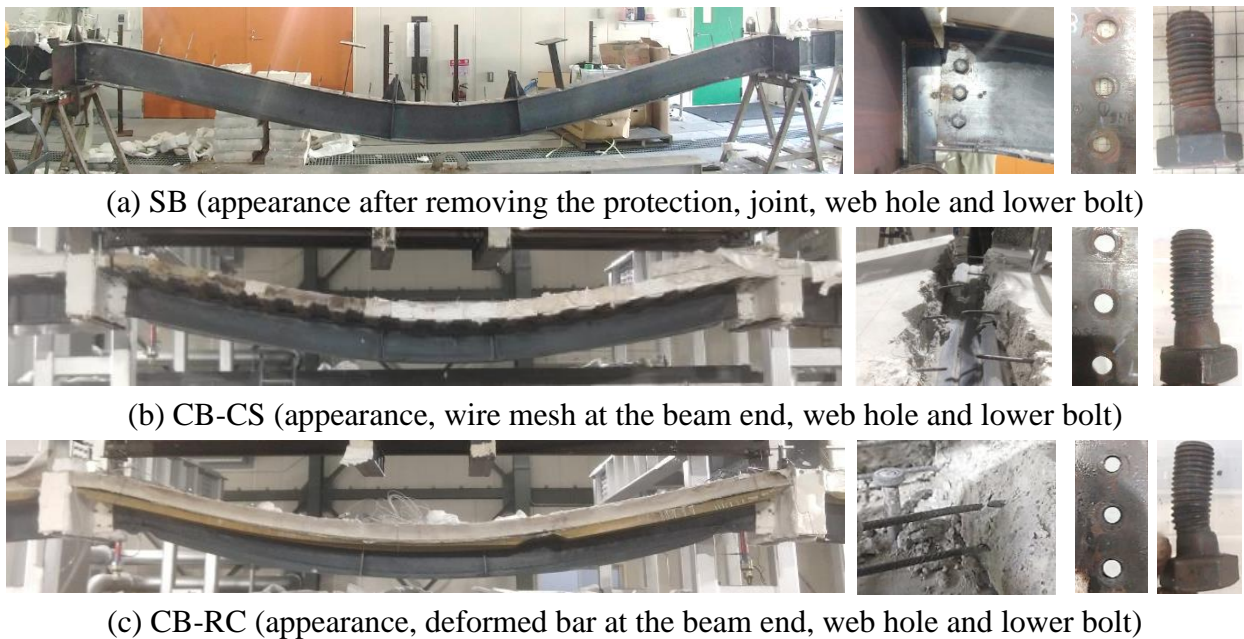


Fig. 8. Deflection and damage to the specimens

(2) Deflection at the mid-span and rotation angle at the joint

Figures 9(a) and (b) show the deflection at the mid-span and the rotation angle at the joint. The rotation angle at the joint was obtained by dividing the difference between the vertical displacements D5 and D6 (shown in Fig.1(a)) by the interval between each measurement position (275 mm). Figure 9(a) also shows the ISO834 limiting deflection ($L^2/400D = 300$ mm), where L is the support span (6000 mm) and D is the steel beam depth (300 mm). In the tests of SB and CB-CS, the beams could support the applied load until the loading jack reached its stroke limit (about 500 mm); however, the beams were judged to have almost lost their bending moment resistances from the observation of specimen damages (see Fig.8) and rapid increases in the deflection rate. In the test of CB-RC, the vertical displacements at the mid-span became unmeasurable before the specimen collapsed because of the displacement gauge failure. Therefore, the ultimate strength of CB-RC was confirmed by gradually increasing the load until the beam could not become able to support the applied load after 90 min.

In steel beam SB, the deflection due to the temperature difference between the upper and lower flanges (thermal deflection) increased until about 10 min. After that, the deflection stagnated until about 25 min. As shown in Fig.9(b), the deflection angle at the joint also stagnated, indicating that the rotational restraint effect was exerted at the joint. After 25 min, with the occurrence of slipping noise at the joint, the deflection and deflection angle increased rapidly. After reaching the limiting deflection at 36 min, the

deflection rate increased rapidly at 41 min; the test was then terminated based on the judgement that the beam had collapsed.

In the composite beam with deck composite slab (CB-CS), the thermal deflection behaviour up to about 10 min was the same as that of SB; however, the deflection and deflection angle at the joint continued to increase without stagnation thereafter. This is probably because the rotational restraint at the joints decreased owing to fracture of the wire mesh at the beam ends. Even after fracture of the wire mesh, the joints exhibited rotational resistance owing to the bolt components (as in SB); however, thermal deflection occurred not only due to the temperature difference between the upper and lower flanges but also due to the temperature difference between the lower flange and the top of the slab in the case of composite beams. These are the causes of the increased deflection after 10 minutes. After that, the deflection at the mid-span reached limiting deflection at 42 min and the deflection rate increased rapidly at 52 min, so the test was terminated. Owing to the composite effect with the concrete slab (the temperature increase of which is small), the decreases in bending stiffness and sagging moment resistance at the mid-span are moderate compared with the steel beam SB. However, in CB-CS, the wire mesh at the beam end fractured; therefore, the rotational resistance of the joints did not improve. This is the reason for the failure time of CB-CS being only about 10 min longer than that of SB.

In the composite beam using RC slab (CB-RC), the deflection behaviour up to about 25 min was almost the same as that of SB. After this time, the deflection and rotation of the joint were greatly suppressed as compared with the other specimens. The deflection at the mid-span reached the limiting deflection at 65 min and continued to support the applied load without increasing the deflection rate until 90 min. In CB-RC, the deflection was greatly suppressed compared with the steel beam SB, and the failure time was more than twice that of SB.

Based on elastic theory, the deflection angle at a beam end when reaching the limiting deflection of a simply supported beam is about 0.15 rad. As shown in Fig.9(b), the rotation angle at the joint exceeded 0.15 rad in all specimens. Prior to collapse, the fin-plate joint exhibited sufficient rotational capacity without fracture.

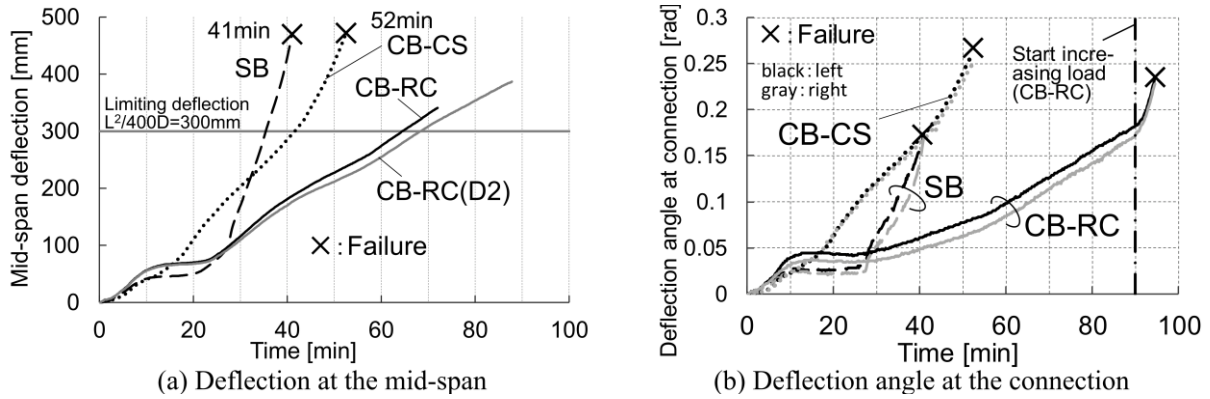


Fig. 9. Deflection behaviour

4.3 Bending moment resistance

Figures 10(a)-(c) show comparisons of the calculated bending moment resistance and the experimental bending moment. The bending moment resistance was calculated based on the evaluation model shown in Section 3 using the material strength shown in Section 2.2 and the calculated temperature shown in Section 4.1. The experimental bending moment was obtained using the measured load cP , eP .

4.3.1. Steel beam (SB)

As shown in Fig.10(a), jM (the hogging moment at the joint) increased to about 20 kNm owing to thermal stress in the initial stage of heating. After that, jM decreased to around 10-20 kNm. At the time when the beam collapsed, jM was almost equal to jM_u^- (the hogging moment resistance of the joint considering only the bolts). $B M_u^+$ (the sagging moment resistance of the steel beam) decreased to the applied load level (30.1 kNm) at 15 min. In the case of the simply supported beam, it is assumed that the

beam would have collapsed at this time. The predicted failure time (the time for the total bending moment resistance and the total bending moment to become equal) was 37.5 min, which almost corresponded with the experimental failure time. Owing to the effect of the rotational restraint at the joints, the failure time was more than twice that expected for the simply supported beam.

4.3.2. Composite beam using composite slab (CB-CS)

As shown in Fig. 10(b), jM increased to about 40 kNm owing to thermal stress in the initial stage of heating, but rapidly decreased to 10-20 kNm (equivalent to that of SB) at 7 minutes. It is considered that the wire mesh at the beam ends fractured at this time and only the bolts contributed to the subsequent rotational resistance of the joint. The low plastic deformation capacity of the wire mesh (as shown in Fig. 2(d)) caused fracture at the initial stage of heating. At the time when the beam collapsed, jM was almost equal to jM_u^- (the hogging moment resistance of the joint considering only the bolts) $_{CB}M_u^+$ (the sagging moment resistance of the composite beam) decreased to the applied load level (44.1 kNm) at 28 min; therefore, it is assumed that the simply supported beam would have collapsed at this time. The predicted failure time was 52 min, which corresponded well with the experimental failure time. The reinforcement at the beam ends did not work; however, owing to the rotational restraint effect of the bolts, the failure time was about twice that expected for the simply supported beam.

4.3.3. Composite beam using RC slab (CB-RC)

As shown in Fig. 10(c), jM increased owing to thermal stress in the initial stage of heating, and was maintained at 40-50 kNm, following $_{JR}M_u^-$ (the hogging moment resistance considering the reinforcement), until around 17 min. After that, jM gradually decreased. $_{CB}M_u^+$ decreased to the applied load level (45.0 kNm) at 35 min; therefore, it is assumed that the simply supported beam would have collapsed at this time. The predicted failure time was 90 min; however, in the test, the load-bearing capacity was not lost until 90 min. After 90 min, to confirm the ultimate strength of the beam, the applied load was gradually increased until the load-bearing capacity was lost. At 93 min, cM and jM decreased and the load could not be retained. At this time, $_{JR}M_u^-$ was equal to jM and it is considered that the upper deformed bar at the beam end fractured. In CB-RC, the reinforcement contributed to the hogging moment resistance of the joint until the beam collapsed, resulting in a failure time that was about three times longer than that assumed for the simply supported beam.

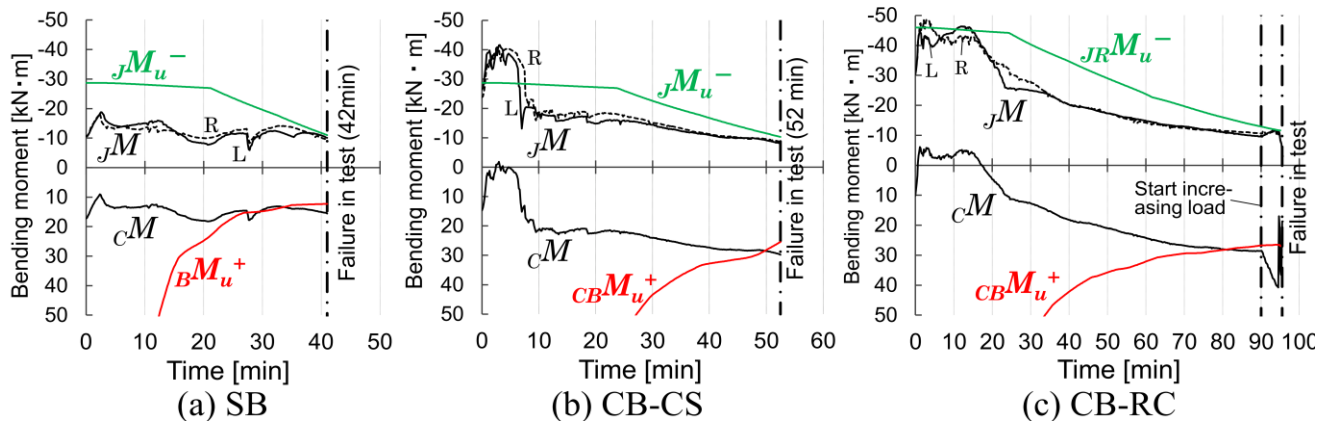


Fig. 10. Bending moment resistance

5 CONCLUSIONS

The main conclusions obtained from the load-bearing fire tests of composite beams protected only at the beam ends with continuous floor slabs were as follows:

1. The failure times in the tests were 41 min for the steel beam, 52 min for the composite beam using composite slab, and over 90 min for the composite beam using RC slab. Compared with the expected failure time for beams under simply supported condition, these values were approximately doubled for the steel beam and composite beam using composite slab, and more than tripled for the composite beam using RC slab, whose reinforcement contributed to the hogging moment resistance of the joints.

2. In the case of the cross section of the steel beam used in these tests, it was confirmed that the joint temperature during heating for 1 hour remained at about 600 °C when protecting only the beam ends using protection equivalent to a fire resistivity of 1 hour.
3. The joint temperatures calculated by the finite difference method, which considered conduction in the axial direction of the beam and used thermal conductance for the heat transfer model of the protected elements, corresponded well with the experimental values.
4. A simple method for predicting the failure time of the beams using an evaluation model of the bending moment resistance of the beam, which included the hogging moment resistance of the fin-plate joint and considered the reinforcement, was presented. The failure time predicted based on bending moment resistance, which was calculated based on the test results of the materials and calculated temperatures, corresponded well with the test results.

ACKNOWLEDGMENT

The authors would like to acknowledge Toa-rika Co., Ltd for producing the specimens.

REFERENCES

1. Khalifa S. Al-Jabri, J. Buick Davison, Ian W. Burgess: Performance of beam-to-column joints in fire—A review, *Fire Safety Journal* 43, 50–62, 2008.
2. Lawson RM: Behaviour of steel beam-to-column joints in fire, *Structural Engineer* 68(14), 263–271, 1990.
3. J. Ding, Y.C. Wang: Experimental study of structural fire behaviour of steel beam to concrete filled tubular column assemblies with different types of joints, *Engineering Structures* 29, 3485–3502, 2007.
4. Selden KL, Fischer EC, Varma AH: Experimental investigation of composite beams with shear joints subjected to fire loading. *Journal of Structural Engineering* 142(2), 04015118, 2016.
5. Erica C. Fischer, P.E., Amit H. Varma: Fire resilience of composite beams with simple joints: Parametric studies and design, *Journal of Constructional Steel Research* 128, 119–135, 2017.
6. X. H. Dai, Y.C. Wang, C.G. Bailey: Effects of partial fire protection on temperature developments in steel joints protected by intumescent coating, *Fire Safety Journal* 44, 376–386, 2009.
7. Emily I. Wellman, Amit H. Varma, Rustin Fike, Venkatesh Kodur: Experimental Evaluation of Thin Composite Floor Assemblies under Fire Loading, *Journal of Structural Engineering* 137(9), pp.1002-1016, 2011.
8. L. Choe, S. Ramesh, M. Seif, M.S. Hoehler, W. Grosshandler, J. Gross, M. Bundy: Fire performance of long-span composite beams with gravity connections, *Conference proceedings of the 10th International Conference on Structures in Fire* 2018, pp.601-608, 2018.
9. R. Dwiputra, N. Yotsumoto, T. Hirashima, F. Ozaki, Y. Murakami, K. Kimura: Load-bearing fire tests of unprotected composite beams pinned with steel girders, *Proceedings of 10th International Conference on Structures in fire*, 561-568, 2018.
10. T.C.H. Liu, M.K. Fahad, J.M. Davies: Experimental investigation of behaviour of axially restrained steel beams in fire, *Journal of Constructional Steel Research* 58, 1211-1230, 2002.
11. C. G. Bailey, D. B. Moore: The structural behaviour of steel frames with composite floorslabs subject to fire (1. Theory), *Structural Engineer* 78(11), 19-27, 2000.
12. Architectural Institute of Japan: Design Recommendations for Composite Constructions, 2010 (in Japanese).
13. Eurocode 4 Design of composite steel and concrete structures, Part 1-2: General rules, *Structural fire design*, EN 1994-1-2, European Committee for Standardization, 2005.
14. S. Yasuda, S. Michikoshi, Y. Tagawa: Study on Ultimate Strength of Composite Beam with Ends Restrained against Rotation in Fire, *Journal of Structural and Construction Engineering (Transactions of AIJ)*, 74(643), 1691–1698, 2009 (in Japanese).
15. Architectural Institute of Japan: Guide Book for Fire-Resistive Performance of Structural Materials, 2017 (in Japanese).

EFFECT OF STEEL-FIBER REINFORCED CONCRETE ON THE FIRE RESISTANCE OF CONCRETE-FILLED STEEL TUBULAR COLUMNS UNDER SIMULTANEOUS AXIAL LOADING AND DOUBLE CURVATURE BENDING

Takuya Kinoshita¹, Yusuke Shintani², Tomohito Okazaki³, Toshihiko Nishimura⁴, J. Y. Richard Liew⁵

ABSTRACT

Fire resistance of unprotected CFST columns under axial and horizontal loading is investigated. Furnace tests on CFST columns with large cross section (Over 600 mm diameter) are conducted. Specimens are heated while applying simultaneous axial loading and double curvature bending in order to simulate the actual behavior of building frames in fire. Mixing steel fibers into the filled concrete significantly improves fire resistance time. Finite element analysis is conducted to investigate the effect of steel fibers.

Keywords: Concrete-Filled Steel Tubular (CFST) column; double curvature bending; fire resistance; furnace test; multiple loading; steel fiber reinforced concrete

1 INTRODUCTION

Concrete-Filled Steel Tubular (CFST) columns are widely used in building construction, particularly in large and high-rise buildings, because of their high structural performance and workability. In terms of fire resistance, CFST columns also have higher performance than conventional steel columns because of the high heat capacity of the inner concrete. From the viewpoint of aesthetics and construction efficiency, there is a great demand to omit the fire-protection of CFST columns.

This paper focuses on a case in which the peripheral CFST columns of a relatively large building are stayed unprotected. In fire cases, the peripheral (outer) CFST column undergoes horizontal deformation due to thermal elongation of the girder as well as axial force (Figure 1). In addition, the column is supported by the unheated surrounding frame of the upper and lower floors, and its behaviour shows the double curvature bending in which the bending moments are reversed in the middle of the heated column. The moment distribution is shown on the right side in Figure 1.

A few other studies did investigate unprotected and protected CFST columns that had been subjected to such a double curvature bending due to the thermal elongation of their beams and the restraint provided by the connected cooler columns [1, 2]. Nishimura et al. [1] conducted a series of ten experiments on unprotected square hollow section columns filled with plain concrete. He varied the axial force, forced

¹ Associate Chief Researcher, Takenaka Corporation,
e-mail: kinoshita.takuya@takenaka.co.jp, ORCID: <https://orcid.org/0000-0002-2107-6704>

² Chief Researcher, Takenaka Corporation
e-mail: shintani.yuusuke@takenaka.co.jp

³ Senior Manager, Takenaka Corporation
e-mail: okazaki.tomohito@takenaka.co.jp

⁴ Chief Researcher, Takenaka Corporation
e-mail: nishimura.toshihiko@takenaka.co.jp

⁵ Professor, National University of Singapore
e-mail: ceeljy@nus.edu.sg, ORCID: <https://orcid.org/0000-0002-0078-9043>

horizontal displacement, and wall thickness. The columns bearing axial loads of approximately 30 % of the load-bearing capacities of their concrete fillings failed in approximately 1 hour.

Watada et al. [3] conducted a series of finite element analyses targeting the experiment by Nishimura et al., and confirmed the fact that the unprotected CFST column which is subjected to simultaneous axial loading and double curvature bending, bears the compressive force in a very limited area. This result suggests that a local crush of concrete may trigger early collapse of whole structure. There is a steel fiber mixing as a method to avoid local crush of concrete. Therefore, in this paper, we conduct experiments in two cases with and without steel fibers in the internal concrete for CFST column specimens which is subjected to simultaneous axial loading and double curvature bending in order to confirm the effect of steel fiber contamination. We also conduct a series of finite element analyses which are heat transfer analysis and structural analysis and investigate the mechanism that improves fire resistance.

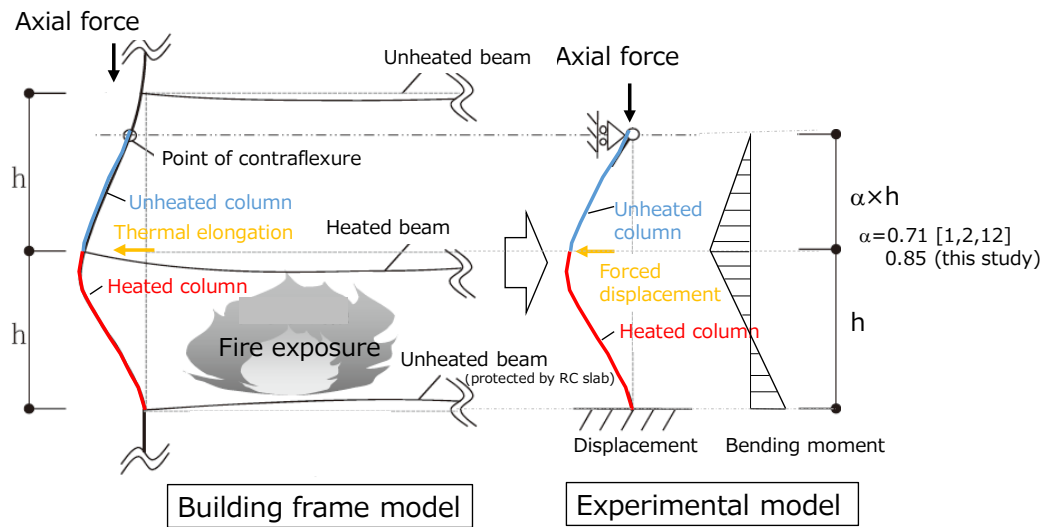


Figure 1. Experimental model for double curvature bending column

2 EXPERIMENTAL METHODS

2.1 Experimental setup and conditions

Furnace tests using CFST columns, considering the restraint provided by the upper columns and forced displacement by the heated beams, were conducted like those of a few earlier studies [1, 2, 4]. Figure 2 presents the whole experimental setup of the test in this study under multi-loading conditions. Specimens comprised a heated lower column, an unheated upper column, and the joint between these columns. The top of the upper column was supported by pin rollers and the bottom of the lower column was supported by fixation. The bottom endplate of the upper column, the joint, and the top endplate of the lower column were connected by a PC steel bar and these were protected by a ceramic fiber blanket. An axial load was applied using a vertical hydraulic jack, the capacity of which is 30 MN. The forced horizontal displacement on the joint was increased linearly by the horizontal hydraulic jack, the capacity of which is 3 MN, considering the thermal elongation of the heated beams. The lower columns were subjected to a standard ISO 834 fire. Experimental study by Shintani et al. [4] were conducted as same series of experiments to this study. Therefore, Reference [4] should be referred to for detailed information on the experimental setup and measurement conditions.

The upper part of Table 1 presents experimental conditions. Two tests (P-CFT, SF-CFT) were conducted under multi-loading conditions. The axial force ratio, which is the ratio of the axial load to the load-bearing capacity of the concrete filling in the columns, of both specimens was 0.24.

The forced horizontal displacement of the joints of both P-CFT and SF-CFT increased linearly and reached 1/50th of the length of the heated lower column after 2 hours because the temperature of the protected beam

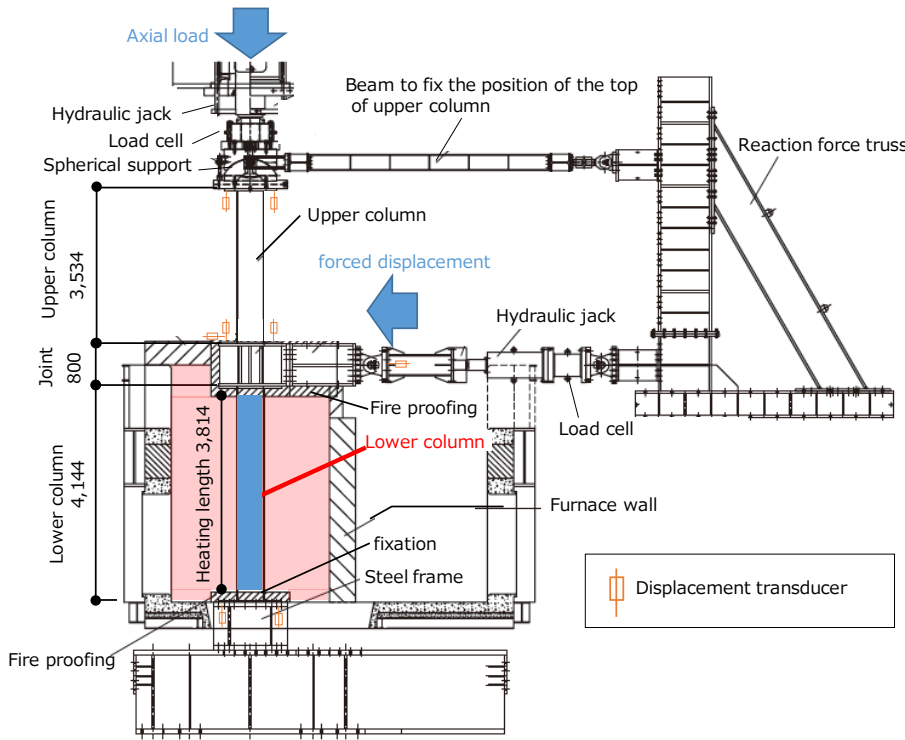


Figure 2. Experimental setup of the test with multi-loading conditions

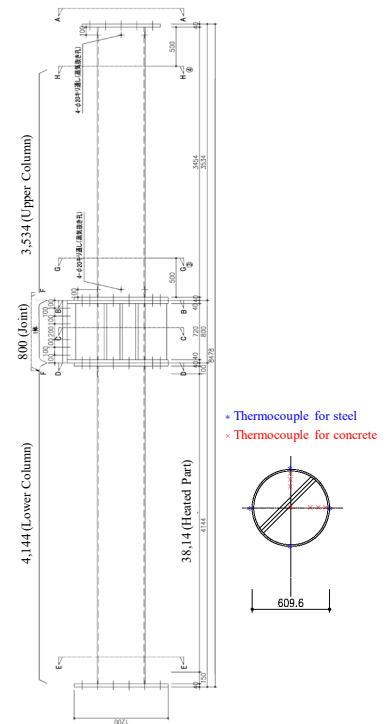


Figure 3. Specimen

increased almost linearly under ISO 834 fire. The Rate of forced horizontal displacement was determined in consideration of the amount of thermal elongation of the unrestrained beam, the temperature and length of which are 550 °C and 15 m, respectively. The estimated maximum horizontal displacement after 2-hour fire is 99 mm. When the length of the column is 5 m, the ratio of the horizontal displacement to the length of the column is approximately 1/50.

2.2 Specimens

The vertical and horizontal sections of P-CFT and SF-CFT are shown in Figure 3. The lower part of Table 1 describes details of the two specimens. The diameter of the steel tube was 609.6 mm. The length of lower column was 4,144 mm, the length of upper column was 3,534 mm, and the length of joint part was 800mm. Steel fiber with 1% of volume was mixed into concrete of SF-CFT specimen.

2.2.1 Steel

Hollow sections of cold-formed circular steel with outer diameters of 609.6 mm and wall thicknesses of 12.7 mm with two ventilation holes at the top and the bottom were used. The steel grade was STK 490 ($f_y = 315 \text{ N/mm}^2$, $f_u = 490 \text{ N/mm}^2$). Steel tensile coupon tests were carried out to determine the mechanical properties of the steel. Tensile coupons were cut from the steel tubes. From the resulting stress-strain curve, the mechanical properties, including the elastic modulus E_s , the yield strength f_y , and the ultimate stress f_u , were determined. Table 2 shows the average results of the steel tensile coupon tests.

2.2.2 Concrete

High strength concrete with siliceous aggregate was used for tests both with and without steel fibers. To determine the compressive strength of the concrete f_c , short CFST columns were also prepared and concrete cylinders were core drilled from the columns about 1 week before tests. All the cylinder samples were tested one day before furnace tests. The cylinder compressive strengths obtained are shown in Table 2. The

concrete moisture content, m_w , was also determined using the cylinder samples core drilled from the short columns. The moisture levels are also shown in Table 2.

2.2.3 Steel fiber

For concrete reinforcement, steel fibers with hooks on both ends were mixed into concrete of SF-CFT specimen. The fiber length was 30 mm, the diameter was 0.62 mm, and the tensile strength was 1,270 N / mm².

2.3 Measurements

The vertical displacements of four corners on the top endplate of the upper column, the bottom endplate of the upper column, the bottom endplate of the lower column, and the horizontal displacement of the horizontal hydraulic jack and the joint of columns were measured by displacement transducers as shown in Figure 2. The temperatures at four points on the steel tube, seven points on the concrete were also measured at the middle section of the heated part of the columns by type K thermal couples, as shown in Figure 3.

Table 2. List of experimental conditions and specimens

	P-CFT	SF-CFT
Axial load ratio ($N/A_c\sigma_c$)	0.24	0.24
Axial load (N)	5,427 kN	5,345 kN
Rate of forced horizontal displacement	39.5 mm/h	
Rotation angle of the lower column	1/50 at 2 h	
Steel tube	STK490 $\phi 609.6 \times t 12.7$	
	$f_y = 446 \text{ N/mm}^2$, $E_s = 197 \text{ GPa}$,	
	Lower column length: 4,144 mm (Heated: 3,814 mm) Upper column length: 3,534 mm	
Concrete	Portland cement 459 kg/m ³ , Water 170 kg/m ³ , Sand 811 kg/m ³ , Aggregate 906 kg/m ³ , Plasticizer 5.05 kg/m ³	
	$f_c = 84.3 \text{ N/mm}^2$, $m_w = 4.8\%$ (98 days)	$f_c = 83.1 \text{ N/mm}^2$, $m_w = 4.8\%$ (123 days)
	124 days at test	137 days at test
Steel fiber	-	1.0 vol.% (80 kg/m ³)

3 EXPERIMENTAL RESULTS

Table 3 lists the failure times of the columns and the forced horizontal displacement at the failure time. The failure time was determined based on the criteria used in the fire resistance test of the axially loaded elements (ISO834-1). The failure time of P-CFT and SF-CFT was 70 min and 121 min, respectively. Mixing steel fibers significantly improve the failure time of the columns.

The temperature of SF-CFT specimen, vertical deformation at the joint part between the upper column and lower column, and horizontal reaction force of both specimens are presented in Figure 4. The labels in the temperature history graph indicate the distance from the concrete surface. The temperature of the steel tube was approximately 1,000 °C, the temperature of concrete 10 mm away from the surface was approximately 700 °C when the heating was stopped after 121 min, which corresponded to the failure time of the SF-CFT specimen. There was no significant difference in temperature changes between P-CFT and SF-CFT.

The vertical deformations of the heated lower columns showed the same trend for both two specimens, and the same as that demonstrated by earlier studies. Espinos et al. [5] showed that the behaviour of CFST columns in fire can be divided into four stages. Initially, the vertical deformation increased because of the

thermal elongation of the steel tube which was directly exposed to fire (stage 1). This increase stopped after approximately 15 min; the vertical elongation then began to decrease because of the decrease in the stiffness of the steel tube (stage 2). After around 20 min, the rate of decrease in the vertical deformation became slow because the loading plate at the top of the lower column contacted the inner concrete and the compressive load was transferred to concrete (stage 3). Eventually the vertical deformation decreased rapidly because concrete lost its resistance, and the columns failed (stage 4).

The horizontal reaction forces also showed the same trend for both two specimens. They increased during stage 1 and decreased rapidly after 15 min because outer steel tube lost its resistance against bending. During stage 3, they increased again because the inner concrete became the main resistant element. After approximately 35 or 40 min, they reached the peak and then decreased gradually. Eventually the horizontal reaction force became negative, which mostly corresponded to the time when the vertical deformation decreased rapidly.

The heated columns after the tests and the direction of the loads are shown in Figure 5. As shown by the dashed red circle, large local buckling could be observed at the bottom part, about 400 mm away from the bottom plates of both columns. According to Reference 4, based on the observation with tearing off the steel plate after the test, the concrete inside the local buckling part especially in P-CFT specimen was crushed, which indicated that the loss of confined effect triggered the collapse of whole columns.

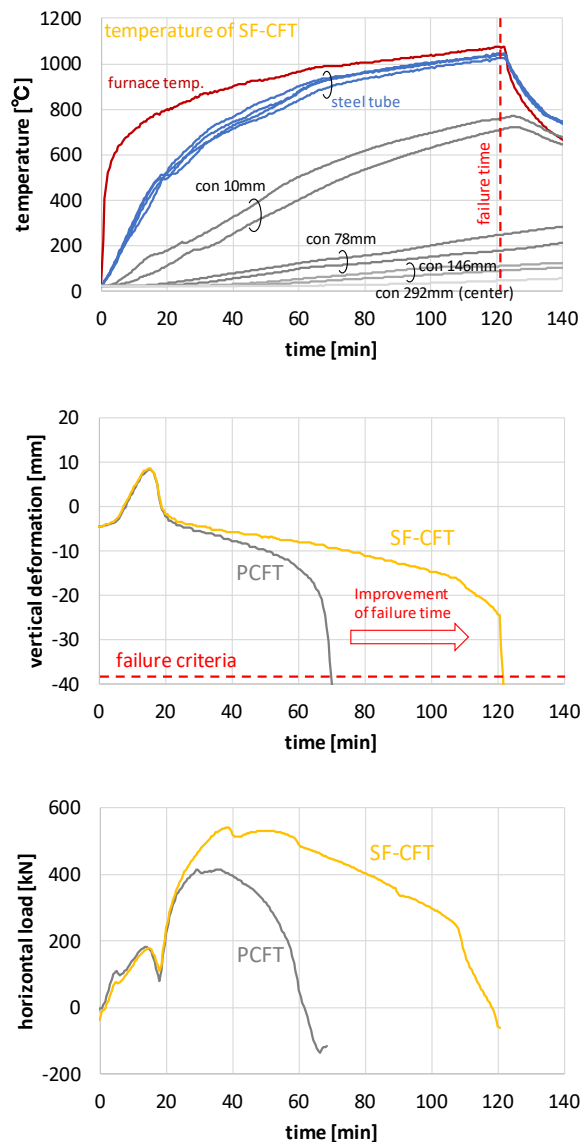


Figure 4. History of temperature, vertical deformation, and reaction force

Table 3. Experimental results

	P-CFT	SF-CFT1
Failure time	70 min	121 min
Horizontal deformation at failure time	47 mm	78 mm

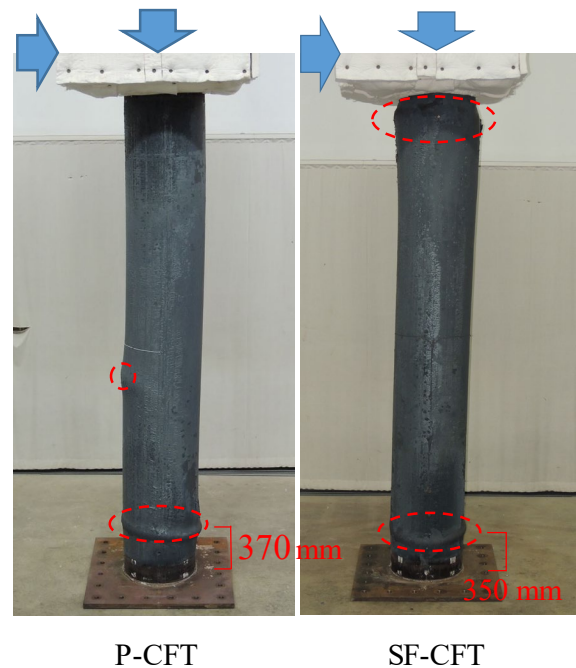


Figure 5. Failure modes of CFST columns

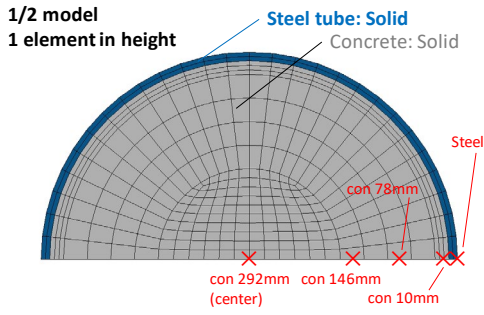
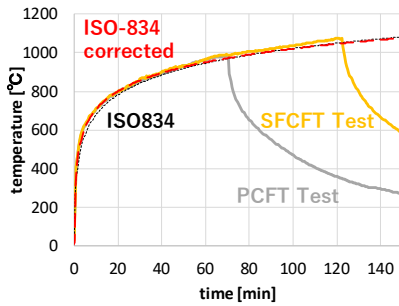


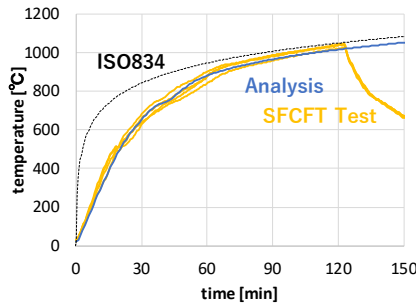
Figure 6. FE model for heat transfer analysis

Table 3. Parameters for heat transfer analysis

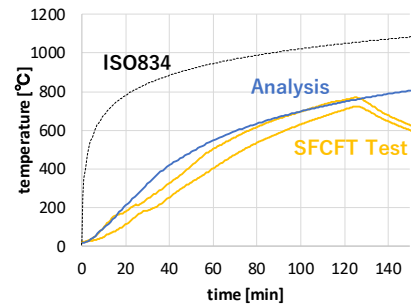
Ambient temperature (°C)	ISO-834 temperature value slightly corrected to match the test result	
Heat transfer coefficient (W/m ² K)	23.0	
Total emissivity	0.73	
	Steel tube	Concrete
Specific heat	EC4 [7]	EC4 with correction factor by Ref. [8]
Conductivity	EC4 [7]	
Density (ton/m ³)	7.85	2.3



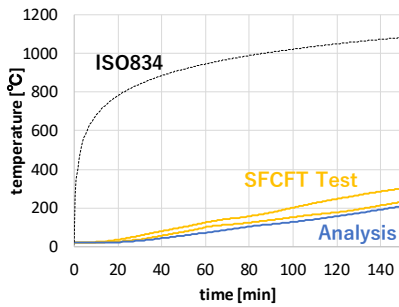
(a) Ambient temperature



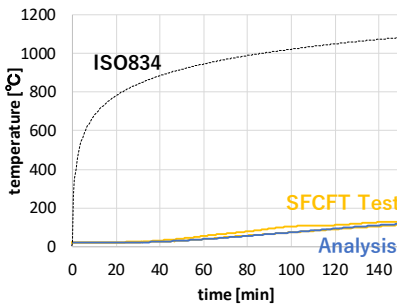
(b) Steel tube



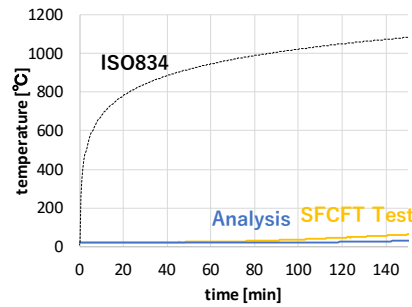
(c) Concrete 10 mm



(d) Concrete 76 mm



(e) Concrete 146 mm



(f) Concrete 292 mm (center)

Figure 7. Result of heat transfer analysis

4 NUMERICAL ANALYSES

In this section, we conducted a series of numerical analyses comprising heat transfer analysis and structural analysis using the three-dimensional finite element (FE) method. Abaqus 2018 [6] was used to conduct FE analysis. The purpose of the analysis is to investigate the mechanism how steel fibers improve the failure time of CFST columns by examining the stress changes in the inner concrete. Visual observation is severely limited in furnace tests. Additionally, CFSTs are surrounded by steel tubes. FE analysis is an effective approach to understand the mechanism.

4.1 Heat transfer analysis

The heat transfer analysis model is presented in Figure 6. Both steel tubes and inner concrete are as solid elements. We assumed that no temperature gradient along the axis of the vertical column direction, therefore we modeled only one element in height. Also, the half of cross section was modelled considering the symmetricity. The conditions for the heat transfer analysis are shown in Table 3. The ambient temperature was given based on ISO-834 fire temperature after slight correction to match the experimental result. Since there was no significant difference between the temperature histories of PCFT and SFCFT in the experimental results, the heat transfer analysis was performed for one case only. This allowed the

thermal conditions of two specimens to be equal for the later structural analysis. Figure 7 shows the time history of the temperatures. It shows that the analytical results of blue lines agree well with the experimental results of yellow lines.

4.2 Structural analysis

4.2.1 Analytical conditions

The model of structural analysis is shown in Figures 8 and 9. In the structural analysis, the Abaqus/Explicit solver [6] utilizing explicit finite element method was used in consideration of geometrical nonlinearity. Shell elements (S4R) were used for steel tube, solid elements (C3D8I) were used for inner concrete, and rigid bar elements were used to concentrate degrees of freedom at several nodes at the joint part. The half of cross section was modelled considering the symmetry.

Contact and friction between the steel tube and inner concrete were considered. The contact was given by the penalty method, and the coefficient of friction was uniformly set to 0.6. Adhesive behaviour that does not depend on contact pressure was not considered here.

Reference [3] should be referred for the material properties conditions. Nonlinearity model of steel tube is isotropic hardening and that of concrete is damage plasticity [6]. In addition to thermal expansion strain and stress strain, transient strain was also considered for concrete.

The analysis had two steps. The vertical load and the weight of the jack and jig were first given at a sufficiently slow speed in the step before heating. After that, horizontal forced displacement was given while applying the heat obtained by heat transfer analysis to each element. The temperature of the unheated part was kept constant at 20 degrees.

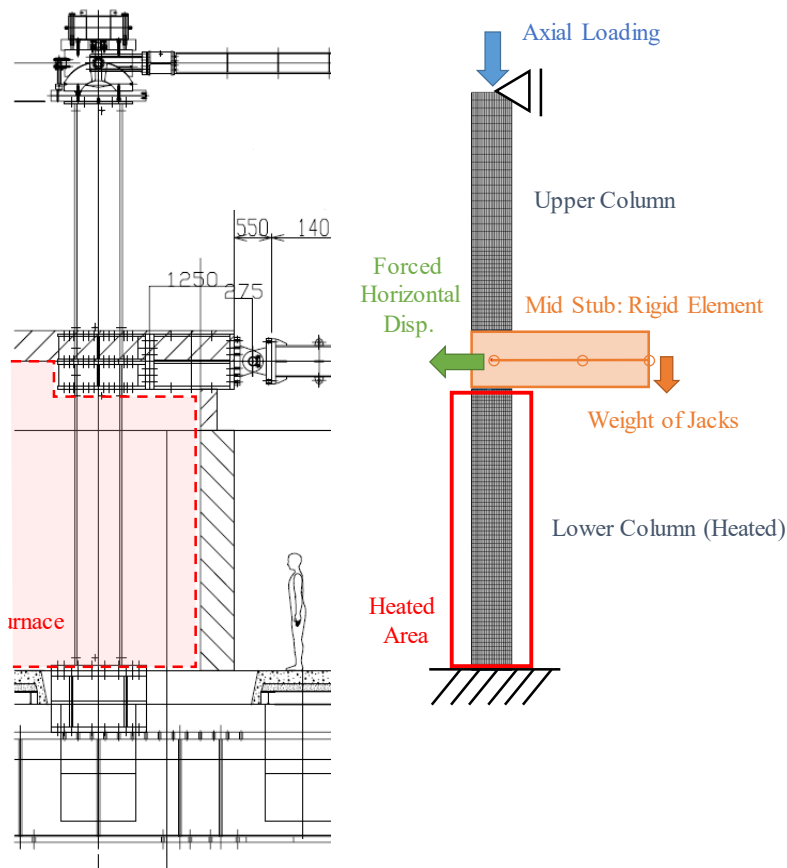


Figure 8. FE model for structural analysis (whole view)

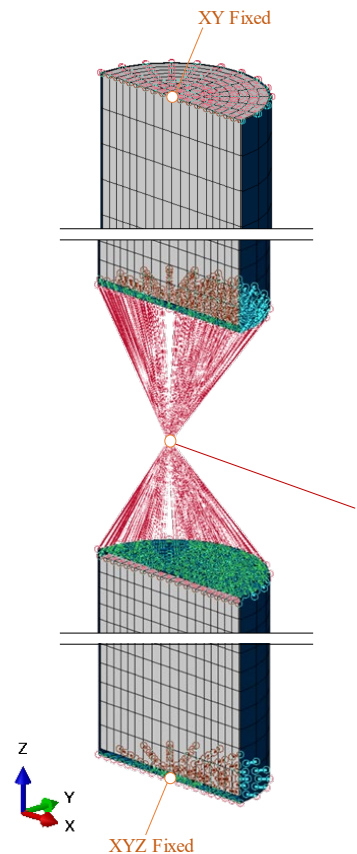


Figure 9. FE model (detailed)

4.2.2 Considering of steel fibers

In order to analytically express the effect when mixing steel fibers into concrete, the following changes were set to the stress-strain curves of concrete both in compressive and tensile direction.

Compressive direction: The compressive stress decreases after reaching the compressive strength, and here the strain ε_0 , at which the stress eventually became zero, was increased to increase the energy absorption capacity during compressive failure of concrete. According to Reference [9], the energy absorption capacity increased even in high temperature steel fiber reinforced concrete. Here, ε_0 for SF-CFT specimens was 1.75 times against that of P-CFT specimen.

Tensile direction: In Reference [10], regarding the tensile direction characteristics of steel fiber reinforced concrete, the tensile strength was increased and the curve after reaching the tensile strength was relaxed. Reference [10] examined those effect only at room temperature, but here the rate of change was applied uniformly to each temperature level.

The stress-strain curves in the compressive and tensile directions are shown in Figures 10 and 11, respectively.

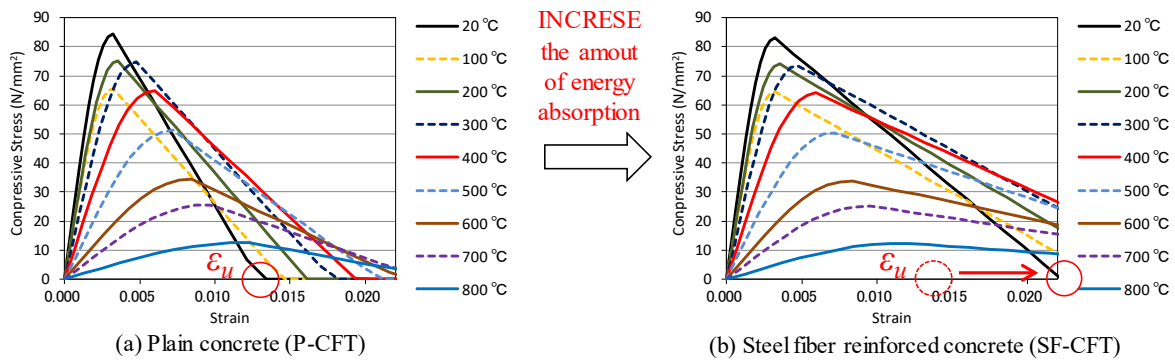


Figure 10. Modeling of steel fiber reinforced concrete (compressive direction)

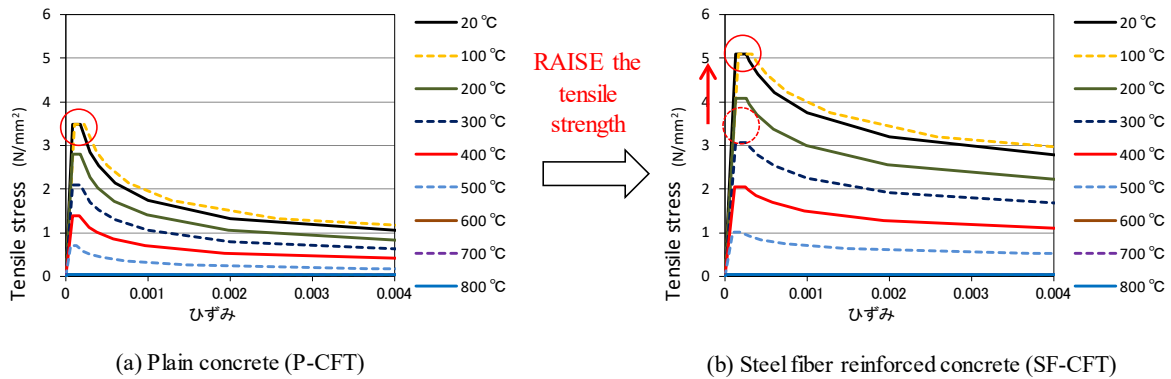
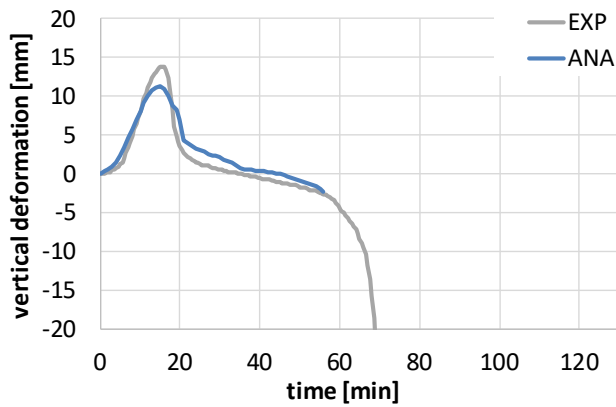


Figure 11. Modeling of steel fiber reinforced concrete (tensile direction)

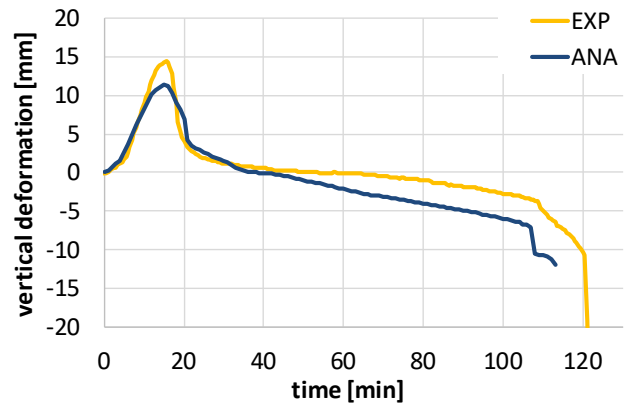
4.2.3 Analytical results

Figures 12 and 13 show the time history of vertical displacement of the joint and the time history of horizontal reaction force, respectively. From Figure 12, it can be seen that the analysis results agree well with the experimental results, and clearly show the deformation stage of Espinos et al. [5] described in Section 3. In addition, Figure 13 shows that the horizontal reaction force of analysis increase once, then decrease, and then increase again same as that of experiment. Overall, the analysis results are in good agreement with the experimental results.

Figure 14 is an elevation of FE model of P-CFT specimen with deformation and contour map of the vertical stress σ_z of the internal concrete drawn at four timeframes: 10 minutes, 20 minutes, 35 minutes, and 70 minutes immediately before the collapse. The deformation ratio is set to 50 times, and the minimum contour value is set to 90 N/mm², which is close to the compressive strength. It is well understood that horizontal deformation gradually progresses because forced displacement is given to the joint part as well as heating. In addition, until 20 minutes, the steel tube that exhibited rapid thermal elongation bears the axial force, and almost no compressive stress is generated in the concrete. However, 35 minutes after the start of heating, a large compressive stress is generated in a very narrow region of the internal concrete in a red circle. This is a typical phenomenon of a furnace test of CFST column under simultaneous axial loading and bending. The compressive region is halved by bending and the outer circumference is weakened by heat from the surroundings (See the right side of Figure 14). When the cross section is large as in this experiments, the transient strain (or Load Induced Thermal Strain, LITS) also has a large effect on stress localization. This behaviour may occur even in real buildings when connected beams exhibit thermal elongation. Eventually, at 70 minutes, the concrete undergoes extreme compressive deformation, leading to collapse. In such a region where stress was highly concentrated, the effect of modeling that enhances the energy absorption capacity of steel fiber reinforced concrete would contribute to the improvement of the failure time. Even inside the experimental specimen of SF-CFT, it is possible that steel fibers prevented local failure as well.

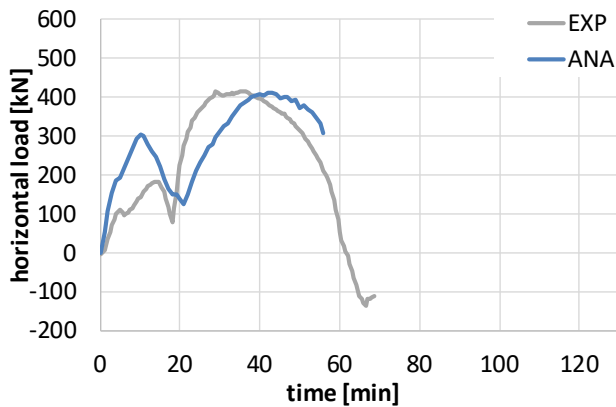


(a) P-CFT

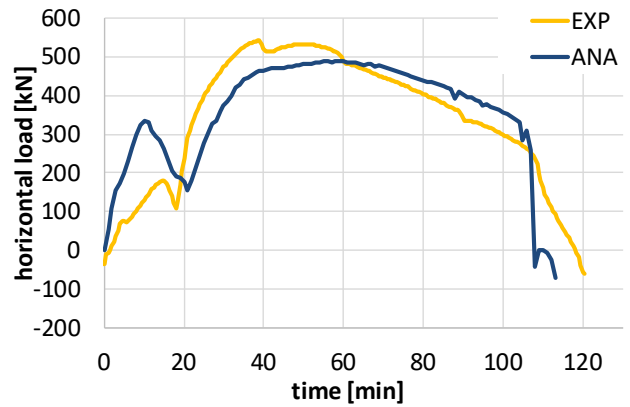


(b) SF-CFT

Figure 12. Vertical deformation history at the joint part

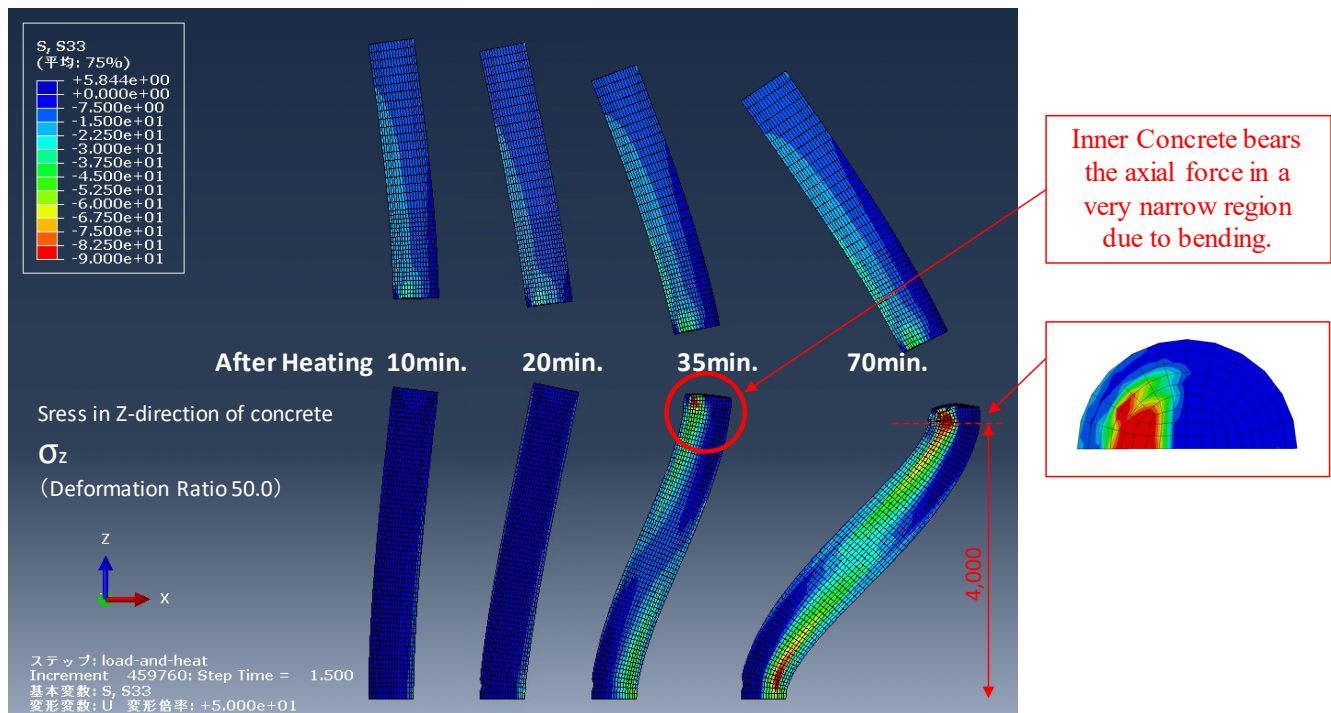


(a) P-CFT



(b) SF-CFT

Figure 13. Horizontal reaction force history at the joint part



REFERENCES

1. Nishimura, T., Kohno, M. and Nagaoka, T., Experimental study on fire resistance of unprotected concrete-filled tubular columns subjected to double curvature bending, *Journal of Structural and Construction Engineering (Transactions of AIJ)*, 78 (2013) 885-894, <https://doi.org/10.3130/aijs.78.885>
2. Working Group for Fire Resistance of Concrete-Filled Steel Tubular Columns Research Committee, Fire resistance of concrete-filled steel tubular long columns without fire protection, *AIJ J. Technol. Des.* 8 (2002) 145-150, <https://doi.org/10.3130/aijt.8.145>
3. Watada, R., Kinoshita, T., Nishimura, T. and Takada, A., Analytical study on fire resistance of unprotected concrete-filled tubular columns subjected to double curvature bending, *Journal of Structural and Construction Engineering (Transactions of AIJ)*, 84 (2019) 1355-1365, <https://doi.org/10.3130/aijs.84.1355>
4. Shintani, Y., Nishimura, T., Okazaki, T., Kinoshita, T., Ito, H. and Liew, J. Y. R., Experimental study on the fire resistance of unprotected concrete-filled steel tubular columns under multi-loading, *Fire Safety Journal*, 103174 (2020), <https://doi.org/10.1016/j.firesaf.2020.103174>
5. Espinos, A., Romero, M. L. and Hospitaler, A., Advanced model for predicting the fire response of concrete filled tubular columns, *Journal of Constructional Steel Research*, 66(8-9) (2010) 1030-1046 <https://doi.org/10.1016/j.jcsr.2010.03.002>
6. Abaqus 2018, Dassault Systèmes Simulia Corporation, 2018.
7. Eurocode4, Design of composite steel and concrete structures Part1-2: General rules - structural fire design, CEN EN 1994-1-2: 2005.
8. Saito, H., Morita, T. and Uesugi, H., Fire resistance of concrete-filled steel tube columns under constant axial loads, *Journal of Environmental Engineering (Transactions of AIJ)*, 69 (2004) 9-16, https://doi.org/10.3130/aije.69.9_6
9. Kikuchi, T., Shintani, Y., Hirashima, T. and Kohno, M., Mechanical properties of steel fiber reinforced concrete at high temperature, *Journal of Structural and Construction Engineering (Transactions of AIJ)*, 85 (2020) 169-176, <https://doi.org/10.3130/aijs.85.169>
10. Kake, S., Sakata, M., Tabei, M., Hoshino, M., Ohta, Y. and Ishikawa, Y., Seismic performance of a steel fiber reinforced concrete pile cap using headed main bars in foundation beams, *Journal of Structural and Construction Engineering (Transactions of AIJ)*, 84 (2019) 949-959, <https://doi.org/10.3130/aijs.84.949>

APPLICABILITY OF THE RESISTANCE INTEGRATION METHOD ON BONDED FASTENERS LOADED IN TENSION IN UNCRACKED CONCRETE UNDER ISO 834-1 FIRE

Omar Al-Mansouri¹, Romain Mège², Nicolas Pinoteau³, Thierry Guillet⁴, Sébastien Rémond⁵

ABSTRACT

European guidelines for fire design of post-installed anchor systems are limited to mechanical (e.g., expansive, undercut) mechanisms of load transfer and the steel failure mode, whereas the adhesive bond mechanism remains unaccounted for in bonded anchors. Furthermore, current design methods are not based on temperature profiles but rather give a specific resistance for a certain fire duration. This paper presents a study of the applicability of the Resistance Integration Method, proposed originally for Post-Installed Reinforcement (PIR) by Pinoteau, on bonded anchors. This method is validated from comparison of test results obtained from a research project conducted at CSTB on bonded anchors under fire, and calculation. The collected data include tests conducted on anchor sizes of M8 and M12 using epoxy adhesive. Design using Pinoteau's method can be tricky depending on the entry data (numerical calculation of temperature profiles and bond stress vs. temperature relationship adopted in the integration process) and may yield different results (sometimes too conservative) if the wrong parameters are adopted. This paper also presents a study on the influence of these parameters on the outcome of the method. Finally, recommendations are given to ensure good design values for bonded anchors under fire based on the assessment at high temperatures.

Keywords: adhesive resin, bonded anchor, fire tests, thermal distribution, numerical model

¹ PhD candidate, Centre Scientifique et Technique du Bâtiment (CSTB), 84 avenue Jean Jaurès, Champs-sur-Marne, 77447 Marne-la-Vallée Cedex 2, France

IMT Lille-Douai, Univ. Lille, EA 4515 – LGCgE, Département Génie Civil & Environnemental, F-59000 Lille, France
e-mail: Omar.ALMANSOURI@cstb.fr

² Head of division (Dr. Eng.), Centre Scientifique et Technique du Bâtiment (CSTB), 84 avenue Jean Jaurès, Champs-sur-Marne, 77447 Marne-la-Vallée Cedex 2, France
e-mail: Romain.MEGE@cstb.fr

³ Research Engineer (Dr. Eng.), Centre Scientifique et Technique du Bâtiment (CSTB), 84 avenue Jean Jaurès, Champs-sur-Marne, 77447 Marne-la-Vallée Cedex 2, France
e-mail: Nicolas.PINOTEAU@cstb.fr

⁴ Expert in fixings (Senior Eng.), Centre Scientifique et Technique du Bâtiment (CSTB), 84 avenue Jean Jaurès, Champs-sur-Marne, 77447 Marne-la-Vallée Cedex 2, France
e-mail: Thierry.GUILLET@cstb.fr

⁵ Professor, Univ Orléans, Univ Tours, INSA CVL, LaMé, EA 7494, France
e-mail: Sebastien.REMOND@univ-orleans.fr

1 INTRODUCTION

Post-installed bonded anchors are commonly used for steel to concrete connections and offer a great flexibility for construction and renovation projects thanks to their ease of installation and advantageous strength compared to classic cast-in place inserts. Bonded anchors transfer their load to concrete through bond and friction. Bonded anchors can be designed to ensure similar strengths to post-installed mechanical anchors at ambient temperature. However, they are sensitive to several environmental factors [1 – 4]. Indeed, the assessment of bonded anchors in European [5] and American guidelines [6] require tests on different anchor geometries in dry and wet concrete, minimum curing time, freeze/thaw conditions, high alkalinity, sulphurous atmosphere, installation in insufficiently clean holes, installation in freezing conditions, short and long-term temperatures...etc. Several accidents around the world happened due to the insufficient knowledge or of the behavior or poor design choices of bonded anchors at high temperatures. The collapse of the Big Dig Tunnel in the USA (2006) [7], the bridge fencing collapse in Atlanta [8] and the Sasago tunnel in Japan (2012) occurred because of the poor choice of adhesive, inadequate installation and increase of temperature inside the tunnels. The mechanical properties of adhesive resins are particularly temperature dependent [9]. Therefore, assessment and design criteria of bonded anchors in fire situations should be provided.

So far, assessment and design guidelines do not offer evaluation and design methods for bonded anchors under fire. Post-Installed Rebars however, have an existing guidelines allowing to assess the bond stress vs. temperature curve of a PIR connection at high temperature [10]. This curve is obtained by a minimum of 20 tests on a 12 mm rebar. The anchor (PIR) is installed in a steel coated cylinder with $10 \cdot d$ embedment depth. After curing of the adhesive, the test is conducted under constant load and increased temperature by electrical heating on the lateral sides of the cylinder. The obtained curve allows to design PIRs under fire using Pinoteau's method (Bond Strength Resistance Integration). The term "resistance" refers to the maximum bond stress obtained locally at the steel/adhesive interface. The load-bearing capacity of the anchor is calculated based on temperature profiles along the embedment depth. In order to determine the resistance profiles, two types of entry data are required. First, the thermal distribution along the embedment depth of the anchor at every time during heating (by numerical calculations). Secondly, a relationship between resistance and temperature is determined by pull-out tests.

Bonded anchors may fail in different failure modes under tensile loading (concrete cone failure, steel failure, pull-out failure of the anchor, splitting failure of concrete and combined concrete cone/pull-out failure) [11 – 12]. Under fire, research studies [13 – 14] have shown that pull-out failure occurs more frequently than other failure modes for common ranges of bonded anchor diameter and embedment.

The steps of resistance integration were established first by Pinoteau et al. [15] and validated on a large scale test at the fire resistance laboratory at CSTB on cantilever-wall connection using PIRs under ISO 843-1 fire [16]. Another large scale validation was also performed at CSTB on a slab-wall connection under ISO 843-1 fire by Lahouar et al [17]. Lahouar et al. [18] also proposed a non-linear shear-lag model taking into account the displacement compatibility of PIRs at high temperatures (unaccounted for in resistance integration). Both approaches yielded accurate predictions of fire resistance durations of cantilever connections. Reichert and Thiele [19] also attempted to adapt the method for bonded anchors under fire using axisymmetric thermal modelling of the anchors, but yielding too conservative design values compared to fire tests (i.e. for some configurations, the calculated design value was zero where the anchor was still resisting in the fire test). Lakhani and Hofmann [14,20] presented resistance integration results based on 2D thermal modelling of anchors yielding sometimes higher design values than fire tests (e.g. bonded anchors with insulated fixtures). Al-Mansouri et al. [21] validated this method for the design of bonded anchors. They investigated the parameters influencing fire tests on bonded anchors (fixtures, insulation, concrete member thickness...). The case of an anchor directly exposed to fire (with metallic fixture and without insulating material) was identified as the worst case scenario for which the anchor should be assessed [22]. Al-Mansouri et al. based the resistance integration method on 3D thermal modelling and the example of M12 rods with 110 mm embedment depth yielding conservative design values compared to fire tests.

In the framework of the research project (bonded anchors under fire) at CSTB, fire tests were conducted on bonded anchors in uncracked concrete using an epoxy adhesive on two sizes M8 and M12. The testing campaign was performed according to the general requirements of fire tests in [23]. This standard gives a heating curve to be applied inside the furnace (i.e. measured temperature of hot gas inside the furnace during heating). This curve is obtained from the ISO 834-1 standard [16].

The objectives of this paper is to evaluate the calculation method (based on 3D transient heat transfer and Eurocode material properties for steel [24] and concrete [25,26]) to test its sensitivity to the entry data (i.e. bond stress vs. temperature relationship adopted in the integration process). The aim is to extend the validity of Pinoteau's method for the design of bonded anchors under fire, and propose recommendations for the evaluation method in consistence with design requirements. Indeed, one of the main entry data for resistance integration method is the bond stress vs. temperature relationship obtained from confined tension tests on bonded anchors at high temperatures according to the guideline for PIRs. The bond stress vs. temperature curve is stopped at a maximum temperature (approximately 300°C for a maximum test duration of 3 hours). Unlike PIRs, bonded anchors are not protected by a concrete cover and are directly exposed to fire and exceed 300°C along the embedment depth very rapidly in fire situations. The evaluation method is therefore assessed in this paper for bond stress vs. temperature curves extended above this temperature. The extension of the curve should however be limited to another temperature. A new temperature limit is proposed based on the calculations presented in this paper.

2 DESCRIPTION OF TESTING CAMPAIGNS AND PROPERTIES OF USED MATERIALS

This section describes the configuration of fire tests on bonded anchors adopted by the fire resistance laboratory at CSTB. Also, the properties of used materials are presented.

2.1 Description of fire tests

Fire tests were conducted at CSTB according to the specifications of EOTA TR 020 [27]. Bonded anchors were installed according to manufacturers' instructions and loaded in tension (constant load) before the fire. The fire scenario applied in the furnace on test specimens was ISO 834-1 [16]. After a certain fire exposure time, due to the degradation of material properties of the bond, the constant load could not be supported by the anchors and pull-out failure occurred. Finally, a fire resistance in terms of load and time are reported for the failed anchor.

Fire test conditions of anchors at CSTB consisted of loading the anchors (installed in beams) using a metallic frame connected to the fixture of the anchor inside the furnace and to a hydraulic jack outside the furnace (Figure 1).

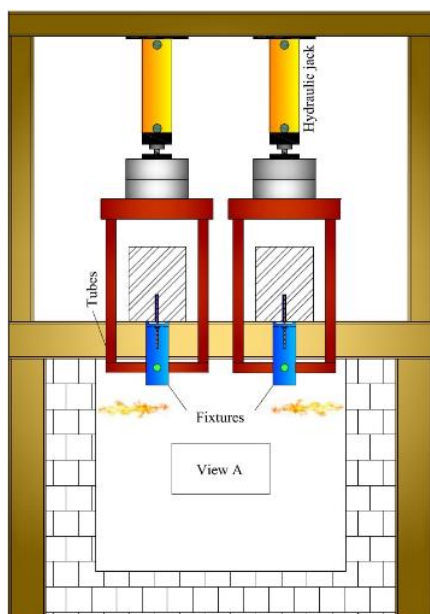


Figure 1: CSTB's furnace and loading system for fire tests on bonded anchors

In a previous experimental work [22] the current authors investigated the influence of the loading system on temperature profiles and resulting load-bearing capacity of bonded anchors and found it negligible. Details of used fixtures were adopted from EOTA TR 020 [27] depending on the applied load of the anchor.

2.2 Prediction of the load-bearing capacity using the Resistance Integration Method and 3D thermal modelling of the anchor

The numerical model presented in this paper observes the following characteristics

1. The bonded anchor resin is not modeled.
2. Steel threads are not modeled.
3. The concrete remains uncracked.
4. Concrete spalling is ignored.
5. The fire exposed surface of all elements is subjected to convective and radiative fluxes of ISO 834-1 fire temperatures on all sides.
6. The unexposed fire surface of concrete beams is subjected to convective and radiative fluxes of ambient air at 20°C.
7. Slip of anchors is ignored.

During a fire, heat transfer occurs between fire and exposed elements at the boundaries via convection and radiation. The heat propagates inside the members via conduction. ANSYS solves the governing differential equation for 3D transient heat conduction using implicit scheme and iterative solver (equation (1)).

$$\rho c \frac{\partial T}{\partial t} = k \left(\frac{\partial^2 T}{\partial x^2} + \frac{\partial^2 T}{\partial y^2} + \frac{\partial^2 T}{\partial z^2} \right) \quad (1)$$

By knowing the thermal distribution along the anchor at each moment of heating, it is possible to associate a resistance to each temperature using the resistance-temperature relationship. Hence, the resistance profiles are determined at every moment of fire exposure.

2.3 Bond stress capacity vs. temperature relationship

The bond stress capacity vs. temperature relationship was obtained from tests according to EAD 330087-00-0601 [10]. Figure 2 shows test results for the epoxy adhesive used in this study. It should be noted that the evaluation curve has a large gap between test 150 and 200 °C. This gap does not respect the maximum distance between neighbouring points in the guidelines of EAD 330087 (50 °C). However, the other criteria for maximum distance of 1 N/mm² is respected. The curves were therefore considered beyond this gap for better representability of the adhesive's behaviour at high temperature. Indeed, adding an additional point would fill the gap and have a negligible statistical weight on the fitting curve.

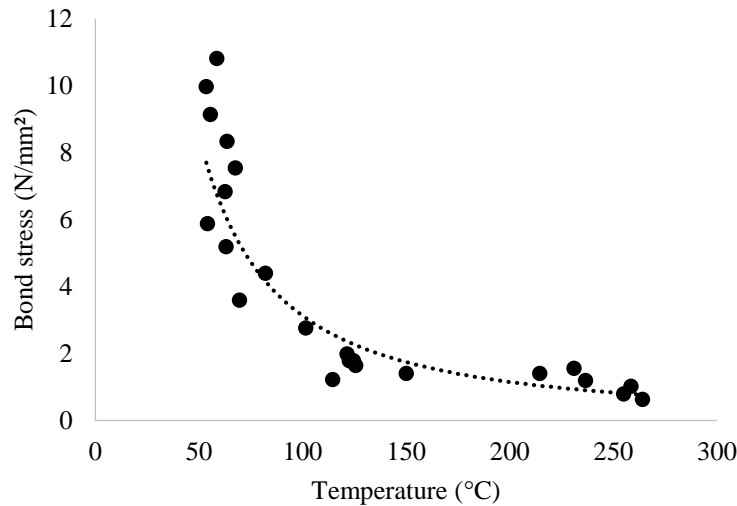


Figure 2: Bond stress vs. temperature relationship for Adhesive-3 according to EAD 330087-00-0601

3 VALIDATION OF PINOTEAU'S METHOD FOR FIRE DESIGN OF BONDED ANCHORS

To investigate the validity of Pinoteau's method, pull-out fire tests were selected from two projects (Table 1). Fig. 3 show a comparison between fire tests and the outcome of Pinoteau's method for the three products used in this study. The figures show calculated resistances using Pinoteau's method (Resistance Integration) at 15, 30, 60, 90 and 120 minutes in addition to the times where pull-out failure in fire tests occurred.

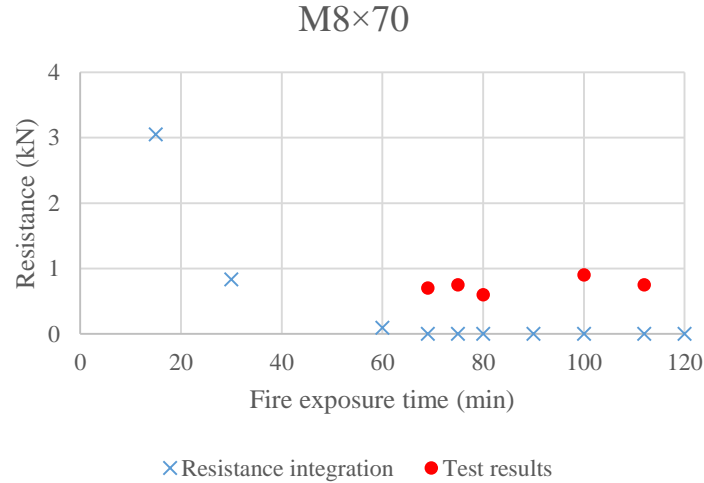


Fig. 3. Fire resistance of M8×70 bonded anchor

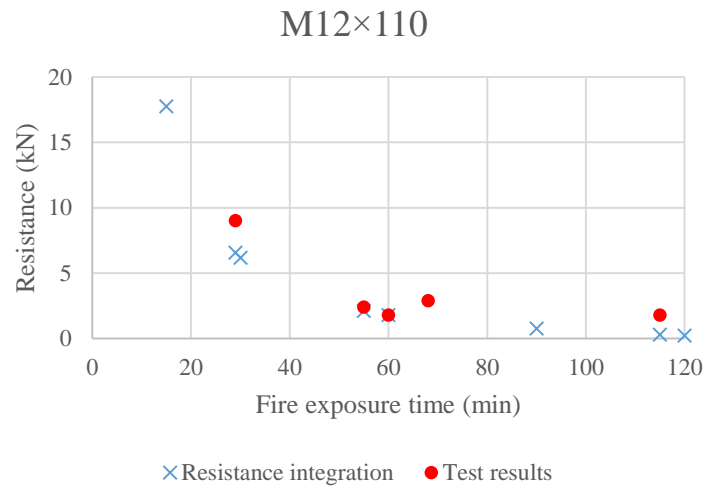


Fig. 4. Fire resistance of M12×110 bonded anchor

From the previous results it can be concluded that Pinoteau's method (Resistance Integration) can be used for the design of bonded anchors under fire. Indeed, the method yields conservative design values compared to fire tests. However, some calculated resistances are too conservative where the design method shows that the anchor possesses no resistance under fire. This is due to the fact that Resistance Integration is based on the bond stress vs. temperature curve. So far, this curve was only assessed through the approach in EAD 330087 up to a maximum temperature T_{\max} (around 300°C) for a maximum test duration of less than 3 hours, beyond of which no extrapolation is allowed. Therefore, in the Resistance Integration process, when the temperature of the anchor (in a segment or over the whole embedment depth) exceeds the maximum temperature of the bond stress vs. temperature curve, the segment is attributed zero bond stress hence no resistance. It should be noted that for an anchor exposed directly to fire, temperature profiles reach and exceed 300°C along the embedment depth very rapidly. This explains the difference between calculated

resistances and fire test results since in reality the anchor still holds a certain resistance at high temperatures T_{\max} (mostly by friction).

In order to minimize the difference between calculated resistances (Pinoteau's method) and fire test results, a parametric study was conducted to assess the influence of considering the remaining bond stress beyond T_{\max} in the Resistance Integration Method. This study is only informative and is not based on data points beyond T_{\max} , therefore for the design of anchors in reality, this extension of the bond stress vs. temperature curve should be based on test data. A parametric study was conducted and it was deduced that extending the bond stress vs. temperature curve up to 450°C was beneficial for the design values of the studied adhesives.

Figure 5 show the beneficial influence of considering the bond stress beyond T_{\max} in the design method, on the calculated design values (fire resistance of the anchor).

It should be noted that Pinoteau's method does not count as a predictive method for the fire resistance of bonded anchors. It contains several safety factors:

1. The method is based on evaluation of PIRs according to [10]. The resulting bond stress vs. temperature curve is slightly conservative compared to tests on bonded anchors (threaded rod inserts). Indeed, adopting a curve based on tests with rods could have a beneficial impact on the calculated design values.
2. The bond stress vs. temperature curve is obtained for a constant load and increased temperature applied on the anchor until failure. Failure temperature is obtained by the weighted average of measurements of two thermocouples (head and bottom of the anchor) = $1/3$ of the higher measured temperature and $2/3$ of the lower measured temperature, yielding a conservative failure temperature value.
3. The bond stress vs. temperature curve is stopped at an upper limit for PIRs of approximately 300°C . This limit should be reevaluated for bonded anchors since their temperature increases rapidly over short periods of time in fire situations. The conversion of temperature profiles to stress (resistance) profiles based on this curve is therefor cut beyond this maximum temperature (zero resistance) because the behavior of the anchor is unknown for higher temperatures.
4. The stress (resistance) profiles are obtained based on temperature profiles calculated according to Eurocode thermophysical properties of concrete and steel using numerical modelling. These material properties are design properties. Calculation based on these properties yield conservative design values and not physically representative values.

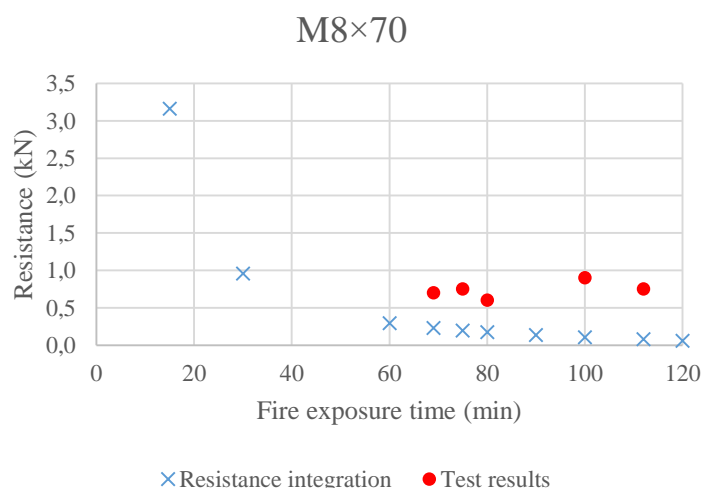


Figure 5. Fire resistance of M8×70 bonded anchor using Adhesive-3 after consideration of bond stress beyond T_{\max}

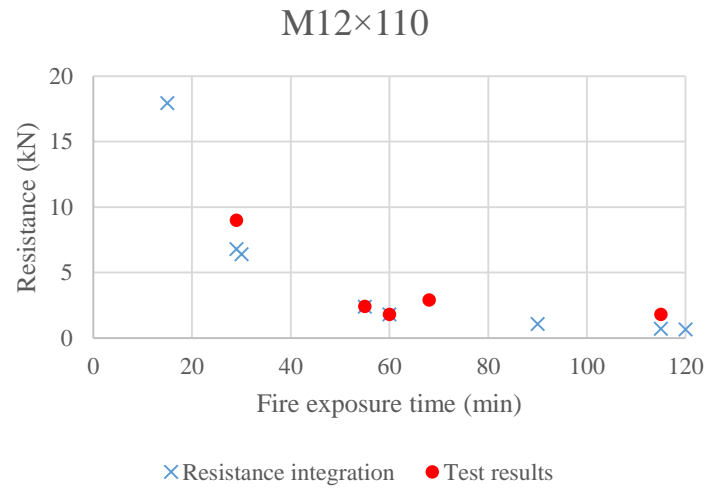


Figure 6. Fire resistance of M12×110 bonded anchor using Adhesive-3 after consideration of bond stress beyond T_{\max}

A summary of the results of fire tests and calculated design values from both campaigns is shown in Table 1.

Table 1. Summary of results of pull-out fire tests on bonded anchors

Anchor geometry (size × embedment [mm])	Applied load [kN]	Pull-out failure time under fire [min]	Calculated fire resistance at failure time [kN]	Calculated fire resistance at failure time after consideration of bond stress- temperature curve beyond T_{\max} [kN]
M8 × 70	0.75	112	0	0.08
	0.90	100	0	0.11
	0.60	80	0	0.17
	0.75	75	0	0.20
	0.70	69	0	0.23
M12 × 110	1.80	115	0.31	0.69
	1.80	60	1.80	1.80
	2.40	55	2.12	2.40
	2.90	68		
	9.0	29	6.57	6.78

4 CONCLUSIONS

This paper presents validation and parametric study of Pinoteau's method (Resistance Integration) for calculating the load-bearing capacity of bonded anchors in uncracked concrete under ISO 834-1 fire conditions [16]. The method employs 3D transient heat transfer equations to obtain temperature profiles along the embedment depth of anchors. The temperature profiles then serve as input for the bond Resistance Integration Method, in which bond strength contributions of discrete segments along the embedment depth of anchors is computed during fire exposure. In this study, the method was validated with experimental results obtained in a research project at CSTB on an epoxy based adhesive. The method yields conservative calculations of load-bearing capacities at various fire exposure times compared to experimental results for two common configurations and sizes of bonded anchors (M8×70 and M12×110).

A parametric study was also presented after experimental validation of the method. This study investigated the influence of considering the bond stress vs. temperature curve beyond the maximum temperature allowed for the assessment of Post-Installed Rebars in EAD 330087, resulting in the following conclusion:

- Extending the curve up to a temperature of 450°C yielded more advantageous and conservative design values (less conservative than stopping the curve at ~ 300°C) for bonded anchors under fire for the studied adhesives.

The authors recommend that the maximum temperature limit gets lifted for bonded anchors since anchors are directly exposed to fire and therefore reach much higher temperatures in a short period of time. The authors also recommend that the maximum bond stress limit of 10 MPa imposed on PIRs gets lifted for bonded anchors. Indeed, this limit corresponds to the minimum bond strength required for the evaluation of PIRs compared to cast-in rebars. This criterion is not required for bonded anchors and therefore the reference value (upper limit) should be established at the value of bond strength at ambient temperature.

ACKNOWLEDGMENT

The experimental research presented in this paper was conducted at the fire-resistance laboratory at CSTB (Centre Scientifique et Technique du Bâtiment). The authors would like to acknowledge Dr. Mhd Amine Lahouar, Dr. Duc Toan Pham and Eng. Paul Lardet, Mr. Romuald Avenel, Mr. Stéphane Charuel, Mr. Luntala Diafunana, Mr. Jean-François Moller, Mr. Paulo Pangia Ngani, Mr. Wissem Lassadi and Mr. Florian Demoulin at CSTB for their contribution to this work.

REFERENCES

1. Eligehausen R, Werner F. Recent developments and open problems in fastening technique. In: 2nd international symposium on connections between steel and concrete, Stuttgart, FIB, Germany; 2007.
2. Petit J, Nassiet V, Baziard YH-RB. Etude de la durabilité des assemblages collés. *Techniques de l'ingénieur*; 2005. p. COR160.
3. Zhang Y, Lou G, Chen K, Li G. Residual strength of organic anchorage adhesive for post-installed rebar at elevated temperatures and after heating. *Fire Technol J* 2016;52:877–95.
4. Muciaccia, G., Navarrete, D.D., Pinoteau, N., Mege, R. Effects of different test apparatus and heating procedures on the bond properties of post-installed rebar connections under elevated temperatures. *Mater Struct* (2019) 52: 47.
5. EOTA. EAD 330499-01-0601. Bonded fasteners for use in concrete. June 2019.
6. ICC-ES. AC308. Acceptance criteria for post-installed adhesive anchors in concrete elements. October 2017.
7. National Transportation Safety Board, 2006. Ceiling Collapse in the Interstate 90 Connector Tunnel Boston, Massachusetts.
8. Georgia Department of Transportation, 2012. 17th Street Bridge Canopy Failure Investigation, s.l.: WJE.
9. Reis J. Effect of temperature on the mechanical properties of polymer mortars. *Mater Res* 2012;15(4):645–9.
10. EOTA. EAD 330087-00-0601. Systems for post-installed rebar connections with mortar. May 2018.
11. Eligehausen R, Mallée R, Silva JF. Anchorage in concrete construction. Ernst & Sohn; 2006.
12. EN 1992-4. Eurocode 2 – Design of concrete structures – Part 4 : Design of fastenings for use in concrete. September 2018.
13. Reichert M, Thiele C. Qualification of bonded anchors in case of fire. Proceedings of the 3rd international symposium on connections between steel and concrete. Stuttgart, Germany. September 2017. p. 1191–9.
14. Lakhani H, Hofmann J. A numerical method to evaluate the pull-out strength of bonded anchors under fire. Proceedings of the 3rd international symposium on Connections between Steel and Concrete. Stuttgart, Germany. September 2017. p. 1179–90.
15. Pinoteau N [Ph.D thesis]: Behavior of post-installed rebars in concrete under fire, Lille: University of Lille (France). <https://ori-nuxeo.univ-lille1.fr/nuxeo/site/esupversions/de94303f-5d72-4f61-9183-515ff08b490b>; 2013.
16. ISO 834-1 International Standard. Fire-resistance tests – Elements of building construction – Part 1: General requirements. First edition, 15 September 1999.
17. Lahouar MA, Pinoteau N, Caron J-F, Forêt, Rivillon Ph. Fire design of post-installed rebars: full-scale validation test on a $2.94 \times 2 \times 0.15$ m³ concrete slab subjected to ISO 834–1 fire. *Eng Struct J* 2018;174:81–94.
18. Lahouar MA, Pinoteau N, Caron J-F, Forêt G, Mège R. A nonlinear shear-lag model applied to chemical anchors subjected to a temperature distribution. *Int J Adhe Adhes* 2018;84:438–50.
19. Reichert, M, Thiele, C, 2017. Verbunddübel im Brandfall-DIBt. Kaiserslautern, University of Kaiserslautern.
20. Lakhani H, Hofmann J. On the pull-out capacity of post-installed bonded anchors and rebars during fire. Proceedings of the 10th International Conference on Structures in Fire. Belfast, UK. June 2018. p. 165-71.
21. Al-Mansouri O, Mège R, Pinoteau N, Guillet T, Piccinin R, McBride K, Rémond S. Numerical investigation of parameters influencing fire evaluation tests of chemically bonded anchors in uncracked concrete. *Eng Struct J* 2020;209:110297.
22. Al-Mansouri O, Mege R, Pinoteau N, Guillet T, Rémond S. Influence of testing conditions on thermal distribution and resulting load-bearing capacity of bonded anchors under fire. *Eng Struct J* 2019;192:190-204.
23. EN 1363-1. Fire resistance tests Part 1: General requirements. February 2020.
24. EN 1993-1-2. Eurocode 3: Design of steel structures – Part 1-2: General rules – Structural fire design. November 2005.

25. EN 1992-1-2. Eurocode 2: Design of concrete structures – Part 1-2: General rules – Structural fire design. July 2008.
26. ACI 318-14, "Building code requirements for reinforced concrete" Detroit, Michigan: American Concrete Institute, 2014.
27. EOTA TR 020. Evaluation of anchorages in concrete concerning resistance to fire. European Organization for Technical Approvals Technical report no. 20. May 2005.

BOND BEHAVIOUR OF ELLIPTICAL CONCRETE-FILLED STEEL TUBES AFTER FIRE EXPOSURE

Song tianyi¹, Liu xialu², Xiang kai³

ABSTRACT

Concrete-filled steel tube (CFST) columns have been widely used in construction structures in recent years. Besides the traditional square and circular CFST columns, the elliptical concrete-filled steel tube (ECFST) columns are becoming more and more attractive to the architects and structural engineers because of their streamlined appearance and excellent structural performance. For the steel-concrete composite structures, the bond behaviour between steel and concrete is very important in terms of the forming of composite effect. Therefore, plenty of studies on the bond behaviour of square and circular CFSTs at ambient temperature and in fire condition have been conducted by previous researchers. However, very limited study on the bond behaviour in ECFSTs has been reported. In this paper, finite element analysis (FEA) model is developed to analyse the post-fire bond behaviour of ECFSTs. For comparison, the FEA models of circular and square CFSTs with the same interface contact area as the ECFST are established as well. Based on the proposed FEA models, the temperature distribution, post-fire bond stress-slip relationship and the bond strength of the three types of CFSTs are analysed. Finally, the influence of key parameters including target temperature (20 °C, 600 °C and 800 °C), high temperature duration time (30min, 90min, 120min and 180min) and section perimeter (388mm, 484mm, 630mm, 727mm) on the post-fire bond strength of ECFSTs is discussed and analysed.

Keywords: Elliptical concrete-filled steel tube; post-fire; bond behaviour; bond strength

1 INTRODUCTION

Concrete-filled steel tube (CFST) has been widely used in building structures because of its excellent structural performance [1-3]. Compared with traditional circular and square CFSTs, elliptical concrete-filled steel tube (ECFST) shows streamlined appearance, and can provide higher torsion stiffness and flexural stiffness. Therefore, it is becoming more and more attractive to architects and structural engineers. For CFST members subjected to external loads, the steel tube-core concrete interface should be able to provide enough bond strength to ensure the two parts work together, which is the basis of forming composite action in CFST members. Therefore, it is of great significance to study the bond behaviour of steel tube-concrete interface in CFSTs from the perspective of theoretical research or practical engineering design.

Existing studies focus on investigating the bond behaviour of CFSTs at ambient temperature, in fire and after fire conditions. Liu et al. [4] and Tao et al. [5] reported push-out tests of circular and square CFSTs at ambient temperature; Charles et al. [6] carried out 20 push-out tests on circular CFSTs, and the effect of concrete shrinkage on bond strength in CFSTs with large sections was identified; Lyu and Han [7] conducted a series of push-out tests on 56 circular and square CFSTs using recycled concrete, and the effect of section size, section shape and concrete strength on interfacial bond behaviour were investigated. Besides push-out tests of CFSTs at ambient, a few tests in fire and after fire conditions are conducted as

¹ Associate professor, College of Architecture and Civil Engineering, Beijing Univ. of Technology, Beijing 100124, P.R. China
e-mail: songty666@qq.com

² Postgraduate, College of Architecture and Civil Engineering, Beijing Univ. of Technology, Beijing 100124, P.R. China
e-mail: liuxialuu@163.com

³ Associate Researcher, Tianjin Fire Research Institute of MEM, Tianjin, 300381, P.R. China
e-mail: xiangkai@tfri.com.cn

well. Song et al. [8] reported the push-out test data of circular and square CFSTs in fire, and the test results indicated the bond strength of CFSTs with normal steel-concrete interface dropped significantly when the fire temperature was 200°C; Chen et al. [9] tested a series of push-out tests of circular and square CFSTs at 20°C - 900°C. It can be found that the influence trending of temperature on bond strength was not monotonical, and the bond strength of CFSTs showed a decreasing-increasing-decreasing trend as the increasing fire temperature; Tao et al. [10] conducted a series of post-fire push-out tests of circular and square CFSTs, and it can be found that the post-fire bond strength of CFSTs decreased with the increasing section size. On the basis of experimental studies, theoretical analysis on bond behaviour of CFSTs is conducted by researchers, and simplified bond stress (τ) - slip (S) models for circular and square CFSTs were developed by researchers [11-13]. However, very limited studies on the bond behaviour of ECFSTs have been reported so far.

To fill the above-mentioned research gap, the authors are devoted to experimentally and theoretically investigate the post-fire bond behaviour of ECFSTs. In this paper, the theoretical analysis part based on a proposed finite element analysis (FEA) model for capturing the post-fire bond behaviour of ECFSTs is presented.

2 ESTABLISHMENT OF FEA MODEL

To study the post-fire bond behaviour of ECFSTs, the commercial software ABAQUS [14] was employed to build the FEA model of ECFSTs subjected to push-out load after fire exposure. Generally speaking, the temperature analysis model of ECFSTs is established firstly to predict the historical maximum temperature of the ECFSTs, and then the structural analysis is conducted to capture the post-fire bond behaviour of ECFSTs, in which the post-fire material properties of steel and concrete, and bond stress-slip relationship of the steel tube-concrete interface are decided according to the historical maximum temperature data.

For the temperature analysis model, considerable numerical studies of CFSTs have been conducted, and very accurate numerical analysis results have been achieved [15]. In this paper, the same temperature modelling method as reference [15], including thermal properties models of steel and concrete, steel-concrete interface modelling method, element types, was adopted for ECFSTs. Figure 1(a) shows the boundary conditions and element division of the established FEA model for ECFST. The thermal convection coefficient was 25W/m², the thermal radiation coefficient was 0.5. The contact thermal resistance between the steel tube and core concrete was ignored for the steel-concrete interface. Solid element DC3D8 was used to model the steel tube and core concrete.

For the structural analysis model, Song and Han [15] has proposed post-fire material models of steel and core concrete for circular and square CFSTs. In this paper, the same post-fire stress-strain model of steel as [15] was adopted for ECFSTs. For the passively confined core concrete in ECFSTs, the existing post-fire stress-strain model of core concrete in circular and square CFSTs may not be suitable [16]. However, due to the limited study on ECFSTs, the post-fire stress-strain model of core concrete for circular CFSTs proposed by [15] was tentatively adopted for ECFSTs in this paper since the circular and elliptical sections are close to each other. The element division of structural analysis model was consistent with the temperature field analysis model as shown in Figure 1(a), and stress analysis element C3D8R was used for both the steel tube and core concrete. During the post-fire push-out stage, the bottom end of the steel tube was fixed, and axial push-out load (N) was applied at the top end of the core concrete. The UX and UY directions of the top end of core concrete were restrained, and the UZ direction was free to allow the core concrete can be pushed out from the steel tube as shown in Figure 1(a).

In terms of the post-fire bond behaviour analysis of ECFSTs, the key issue is how to model the interface between steel tube and core concrete. Two types of methods can be used to simulate the steel-concrete interface in CFSTs. One method is by adopting the Coulomb friction model, which is widely used in the analysis of CFST columns under pressure, bending, torsion and shear [17]. The other method is by adopting spring elements, which is fit for analysing the slippage between steel and concrete [18]. In order to evaluate the simulation method of steel-concrete interface in CFSTs after fire, the two types of methods

are used to simulate the circular CFST push-out test specimens after fire exposure in [13]. For the Coulomb friction model, the friction coefficient was taken as 0.6 in the tangential direction, and a "hard contact" was used in the normal direction of the steel-concrete interface. For the modelling method adopting spring elements, the nonlinear spring element SPRING2 with specified bond stress (τ) - slip (S) relationship can be used to connect the element nodes of core concrete and steel tube with the same geometric position at the steel tube-concrete interface. The relative slip between steel and concrete of CFSTs may be occurred in the circumferential, normal and longitudinal directions. For the circumferential and normal directions, a very large spring stiffness value of $1 \times 10^{18} \text{N/m}$ was adopted to ignore the slippage in these two directions. For the longitudinal direction, three nonlinear bond stress (τ)- slip (S) relationship models proposed by Song et al. [19], Xu [20] and Liu [13] were adopted. Detailed bond stress (τ)- slip (S) relationship equations corresponding to the three models are shown in Equations (1)-(3), respectively.

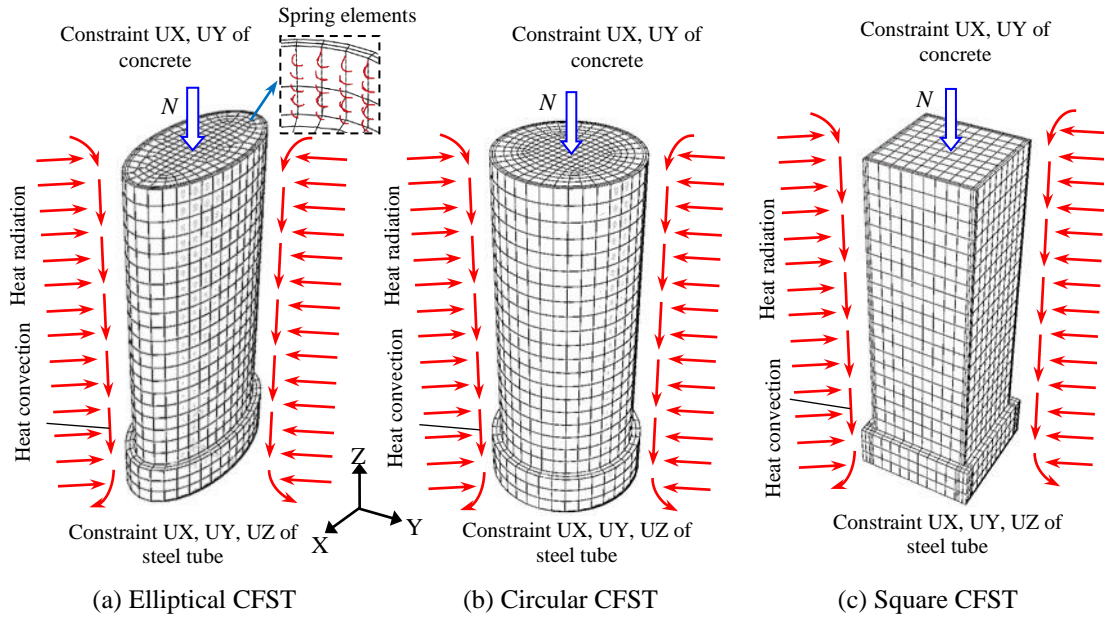


Figure 1. Element division and boundary conditions of FEA models

Song et al. [19] proposed a τ - S relation model to capture the bond behaviour of steel-concrete interface in steel reinforced concrete after exposed to high temperature. Equation (1) shows the details of Song et al.'s model.

$$\tau = \begin{cases} \tau_{oT} \sqrt[4]{S / S_{oT}} & (0 \leq S \leq S_{oT}) \\ k_{1T} + k_{2T}S + k_{3T}S^2 & (S_{oT} < S \leq S_{uT}) \\ \tau_{uT} - \frac{(S - S_{uT})(\tau_{uT} - \tau_{crT})}{(S_{crT} - S_{uT})} & (S_{uT} < S \leq S_{crT}) \\ \tau_{crT} & (S > S_{crT}) \end{cases} \quad (1)$$

where: $k_{\tau T}$ and k_{ST} = parameters to determine the characteristic bond stresses and slip values corresponding to different temperature phases.

$$k_{\tau T} = \begin{cases} 1 + 0.49 \times 10^{-3}T & (0 \leq T \leq 100^\circ\text{C}) \\ 1.326 - 2.767 \times 10^{-3}T & (100^\circ\text{C} < T \leq 400^\circ\text{C}) \\ 0.657 - 1.095 \times 10^{-3}T & (400^\circ\text{C} < T \leq 600^\circ\text{C}) \end{cases}; \quad k_{ST} = \begin{cases} 1 - 3.49 \times 10^{-3}T & (0 \leq T \leq 100^\circ\text{C}) \\ 0.239 + 4.12 \times 10^{-3}T & (100^\circ\text{C} < T \leq 400^\circ\text{C}) \\ 1.887 & (400^\circ\text{C} < T \leq 600^\circ\text{C}) \end{cases}$$

$$S_{oT} = 0.00018tk_{ST}; S_{uT} = 0.0525tk_{ST}; S_{crT} = 0.625tk_{ST}; \tau_{oT} = 0.252f_tk_{\tau T};$$

$$k_{1T} = \tau_{uT} - k_{2T}S_{uT} - k_{3T}S_{uT}^2; k_{2T} = 2S_{uT}(\tau_{uT} - \tau_{oT})/(S_{uT} - S_{oT})^2; k_{3T} = (\tau_{uT} - \tau_{oT})/(S_{uT} - S_{oT})^2;$$

$$\tau_{uT} = (0.378 + 0.096c/t_s' + 10\rho_{sv})f_tk_{\tau T}; \tau_{crT} = 0.171f_tk_{\tau T}; f_t = 0.23f_{cu}^{2/3}; \rho_{sv} \leq 0.01727; c/t_s' \leq 6.25$$

t_s' is the thickness of section steel plate (mm); ρ_{sv} is the area stirrup ratio; c is the thickness of reinforced concrete cover (mm); f_{cu} is the cube compressive strength of concrete at ambient temperature (MPa).

Xu [20] developed a τ - S relation model for the steel-concrete interface in circular CFSTs at ambient temperature, as shown in Equation (2). In this model, a total of six key parameters, including τ_u , S_u , τ_l , S_l , S_r , τ_r , should be obtained according to the test data. When the model is used to simulate the push-out test after fire, the values of the above six key parameters can be obtained from the corresponding post-fire test data.

$$\tau = \begin{cases} \frac{S}{aS + b} & (0 < S \leq S_u) \\ \tau_u + c(S - S_u) & (S_u \leq S \leq S_r) \\ \tau_r & (S > S_r) \end{cases} \quad (2)$$

where: $a = \frac{S_u - 2S_l}{\tau_u(S_u - S_l)}$; $b = \frac{S_u \cdot S_l}{\tau_u(S_u - S_l)}$; $c = \frac{\tau_r - \tau_u}{S_r - S_u}$

τ_u is the bond strength (MPa); S_u is the corresponding slip value of limit state (mm); $\tau_l = 0.5\tau_u$;

S_l is the slip value corresponding to the control point ($S_l, 0.5\tau_u$); S_r is the slip value corresponding to the starting point of horizontal residual stage; τ_r is the bond stress corresponding to the slip value S_r .

Liu [13] proposed a simplified τ - S relation model to capture the post-fire bond behavior in CFSTs as shown in Equation (3). This model can be applied to the circular and square sections directly. Herein, the τ - S model for circular CFSTs was adopted for ECFSTs.

$$\tau = \begin{cases} \frac{\tau_u}{S_u} \cdot S & (0 \leq S \leq S_u) \\ \tau_u \cdot \frac{\tau_r - \tau_u}{8 - S_u} \cdot (S - S_u) & (S_u \leq S \leq S_r) \\ \tau_r & (S > S_r) \end{cases} \quad (3)$$

where: $\tau_r = 0.74163\tau_u + 0.33608$; $S_r = 8\text{mm}$;

$$\tau_u = \begin{cases} \gamma[2.533 + 0.061f_{cu} - 0.16L/D - 0.056D/t_s - 0.008D] \\ \text{(circular concrete filled steel tube)} \\ \gamma[0.376 - 0.006B/t_s + 0.053L/B + 0.003f_{cu} + 0.001B] \\ \text{(square concrete filled steel tube)} \end{cases};$$

$$S_u = \begin{cases} \gamma[-0.637 + 0.086f_{cu} - 0.114L/D - 0.054D/t_s - 0.011D] \\ \text{(circular concrete filled steel tube)} \\ \gamma[0.601 - 0.029B/t_s + 0.144L/B + 0.006f_{cu} + 0.006B] \\ \text{(square concrete filled steel tube)} \end{cases};$$

γ is the reduction factor of fire action, and the expression is as follows:

$$\gamma = \begin{cases} 0.964 + 0.037R_T - 0.0024R_T^2 + t(-0.076 + 0.0134R_T - 6.712R_T^2) + t^2(7.464 - 1.315R_T + 0.0614R_T^2) / 10^{-4} \\ \text{(circular concrete filled steel tube)} \\ 0.978 + 0.051R_T - 0.0032R_T^2 + t(0.201 - 0.028R_T + 0.00126R_T^2) + t^2(-20.186 + 3.301R_T - 0.15R_T^2) / 10^{-4} \\ \text{(square concrete filled steel tube)} \end{cases}$$

t is the heating time corresponding to a standard fire; R_T is the cooling rate after the heating process.

It should be noted that the τ - S models in Equations (1) and (3) were developed based on the ISO-834 standard [21] fire curves. When these two models are used for a case with any specified fire curve, an equivalent fire exposure time corresponding to the ISO-834 standard fire should be calculated first.

Take the specimen C1-90-10 ($D=200\text{mm}$; $t_s=6\text{mm}$; $L=600\text{mm}$; $f_y=449\text{MPa}$; $f_{cu}=64\text{MPa}$) in [13] as an example, Figure 2 shows the comparison between the tested and predicted push-out load (N) - slip (S) relationship curves, in which the predicted results are from Coulomb friction model, Song et al.'s model [19], Xu's model [20] and Liu's model [13], respectively. It can be seen that the predicted curves according to Coulomb friction model and Song et al.'s model [19] are significantly lower than the test result because these two models are not developed for capturing the bond behavior in CFSTs. The predictions based on Xu's model [20] and Liu's model [13] are close to the measured N - S curve, and the predicted peak push-out load values are 99% and 91% of the measured value, respectively. It should be mentioned that the comparison between test and predicted results indicates that the prediction of Xu's model is better than the other models. However, as mentioned before, a total of six key parameters must be confirmed according to the test data when using Xu's model. So, this model cannot be used when the corresponding test data is absent. By contrast, the Liu's model can be used for the post-fire bond behaviour simulation of CFSTs easily, and the predicted N - S curve is basically consistent with the test result. Therefore, in this paper, the τ - S model proposed by [13] was adopted in the bond behavior simulation of ECFSTs after fire exposure.

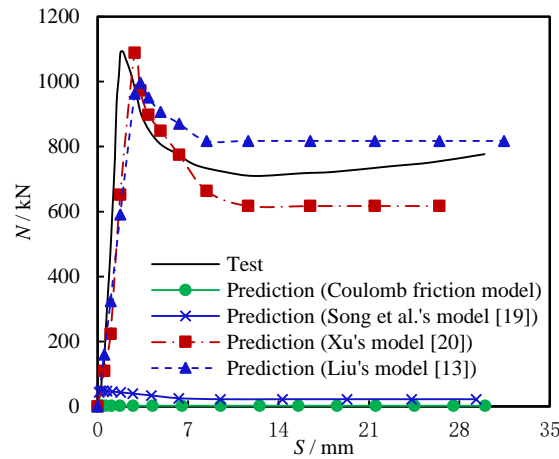


Figure 2. Predicted N - S curves corresponding to different interface simulation methods

For comparison, the FEA models of circular and square CFSTs are established as well. The same modelling method for ECFSTs was adopted, and the boundary conditions and element division of circular and square CFSTs can be seen in Figure 1(b) and (c).

3 VERIFICATION OF FEA MODEL

So far, no test data on post-fire push-out test of ECFSTs has been reported. Therefore, to validate the accuracy of the proposed modelling method, the push-out test data on circular and square CFSTs reported by [11-13, 20] are simulated in this section.

A total of six push-out tests on circular CFSTs in [11, 13, 20], including two ambient temperature tests and four post-fire tests, were simulated. Due to the page limit, only the predicted N - S curves of one ambient temperature test (CFST0-1) and one post-fire test (HCST-10) are shown in Figure 3(a) and (b), respectively. It can be seen that the predicted N - S curves are in good agreement with the test curves. For all the six circular specimens, the mean value of the ratio of predicted ultimate push-out load (N_{uc}) to measured value (N_{uc}) is 0.97 with a standard deviation of 0.006.

For the square CFSTs, two ambient temperature push-out tests and four post-fire push-out tests were simulated, and the comparisons between test and prediction for specimen S1-0-0 (ambient temperature test) and specimen HSCFST-17 (post-fire test) are shown in Figure 3(c) and (d), respectively. Similarly to

the circular one, the proposed FEA model is able to capture the N - S development very well, and the mean value of N_{uc}/N_{ue} is 1.09 with a standard deviation of 0.008.

Generally speaking, the proposed FEA model is able to predict the bond behaviour of circular and square CFSTs very well. It is acceptable to further analyse the post-fire bond behaviour of ECFSTs based on the proposed FEA model in this stage.

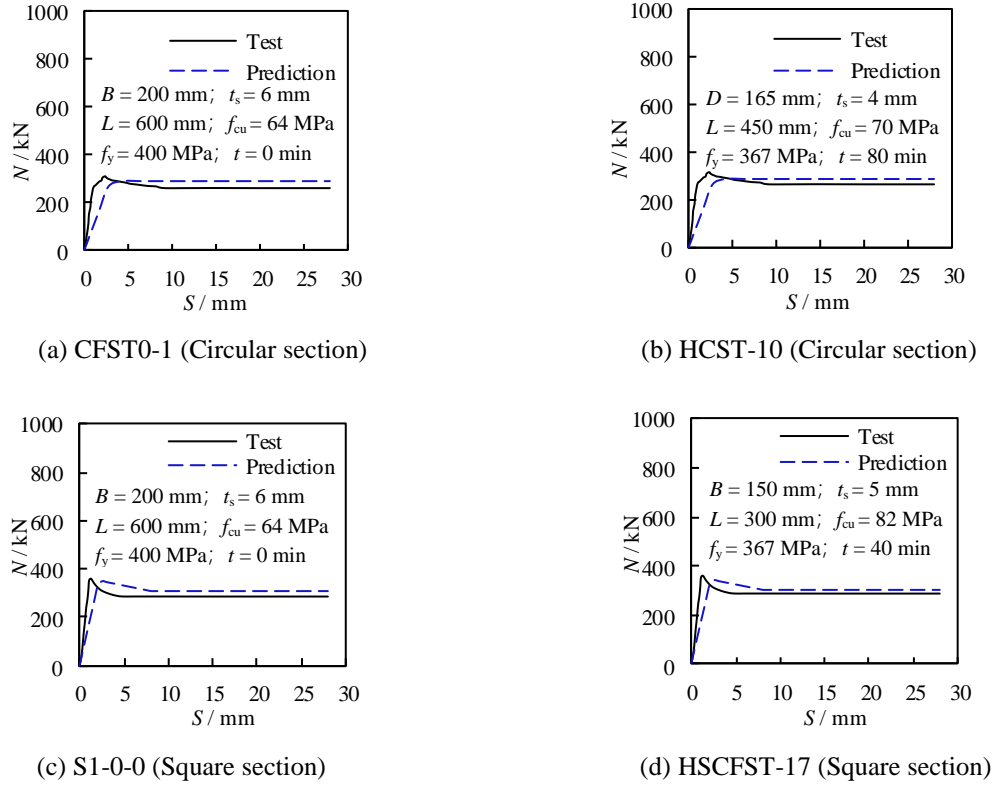


Figure 3. Comparison between test and predicted N - S curves of circular and square CFSTs

4 ANALYSIS ON THE POST-FIRE BOND BEHAVIOR OF STEEL TUBE-CONCRETE INTERFACE IN CFSTs

On the basis of the verified FEA model, the post-fire bond behaviour of ECFSTs is analysed and discussed in this section. The basic calculation conditions of ECFSTs are shown in Table 1, in which, $2a$ and $2b$ are the long axis and short axis dimensions of the elliptical section, respectively; t_s is the thickness of steel tube; L is the contact length of steel tube-concrete interface. The yield strength of steel tube is 345 MPa, and the cube compressive strength of concrete is 40 MPa.

In order to investigate the influence of section shape on the post-fire bond behaviour in CFSTs, FEA models of circular and square CFSTs with the same interface contact area as the ECFST one are established. The dimensions of circular and square CFSTs are listed in Table 1 as well, in which, D and B are the outer diameter and outer length of circular and square sections, respectively; “E”, “C” and “S” in the model label represent the elliptical, circular and square sections; respectively.

Table 1. Calculation conditions of FEA models

Section type	Model label	$2a, D$ or B (mm)	$2b, D$ or B (mm)	t_s (mm)	L (mm)	T_{tar} (°C)	t_d (min)
Elliptical	E200-600-30	200	100	5	400	600	30
Circular	C154-600-30	154	154	5	400	600	30
Square	S121-600-30	121	121	5	400	600	30

To analyse the post-fire bond behaviour of CFSTs, the CFSTs are heated first following a specified fire curve, and then after the temperature of CFSTs drops to ambient temperature, the push-out test is conducted. For the specified fire curve, the fire temperature is increased to a specified target temperature (T_{tar}) firstly at a heating rate of 20 °C/min, and after reaching the T_{tar} -value listed in Table 1, the fire temperature is kept constant until the specified high temperature duration time (t_d) listed in Table 1 is reached.

Based on the above-mentioned calculation conditions, the temperature distribution and development, post-fire bond stress-slip relationship and bond strength of elliptical, circular and square CFSTs are investigated.

4.1 Distribution and development of temperature

Figure 4 shows the temperature distribution of the three types of CFSTs at the end of heating ($t = 30$ min) and the end of high temperature duration ($t = 60$ min). It can be seen that the temperature of core concrete centre at the end of heating is only 45°C because of the effect of thermal inertia of concrete. At the end of high temperature duration, an evenly distributed temperature field is observed for the circular CFST, and the maximum temperature of the steel tube reaches 501°C. For the square CFST, the maximum temperature of the steel tube is formed at the corner of the square section, which is 532°C. The maximum temperature point of ECFST locates at the end of the long axis of the elliptical section, and the maximum temperature is 530°C. In terms of the temperature of core concrete centre at the end of high temperature duration, the maximum temperature values corresponding to elliptical, circular and square sections are 302°C, 274°C and 297°C, respectively. It can be concluded that the influence of section type on the temperature distribution becomes more and more significantly with the increasing fire duration time.

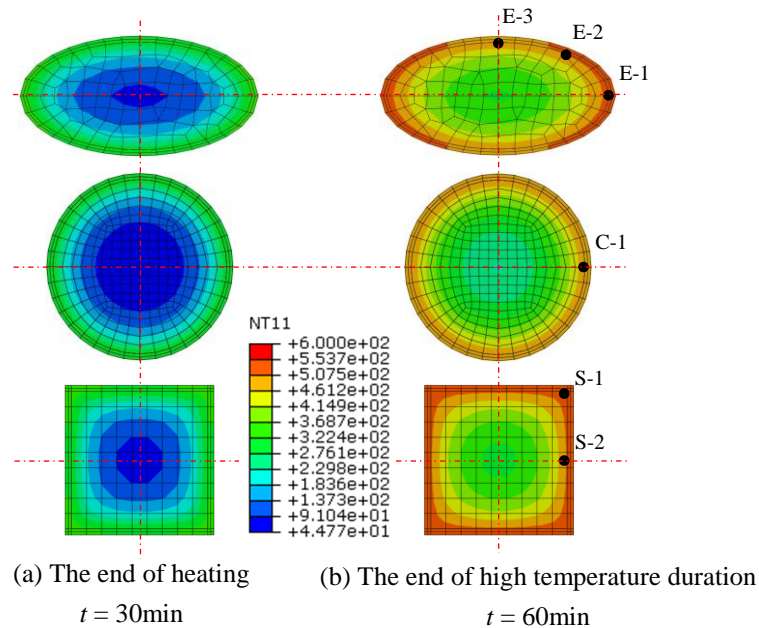


Figure 4. Temperature distribution of cross-sections in three types of CFSTs

In order to further analyze the influence of section type on the temperature of the steel tube-concrete interface in CFSTs, several characteristic points located at the steel tube - concrete interface are selected to investigate the temperature development. The locations of characteristic points, including E-1 ~ E-3 in elliptical section, C-1 in circular section and S-1 and S-2 in square section, are shown in Figure 4(b). The following conclusions can be drawn:

- (1) For the steel-concrete interface in elliptical CFST, the temperatures of points E-1~E-3 at the end of high temperature duration ($t = 60\text{min}$) are $T_{E-1}=528^\circ\text{C}$ 、 $T_{E-2}=512^\circ\text{C}$ and $T_{E-3}=501^\circ\text{C}$, respectively. It can be seen that the interface temperature at the end of the long axis of elliptical CFST is the highest, and gradually decreases from points E-1 to E-3 along the circumferential direction, the interface temperature reaches the lowest value at point E-3 (end of the short axis). For the circular CFST, the interface temperature is uniformly distributed along the circumferential direction, at $t = 60\text{min}$, the T_{C-1}

= 500°C. The interface temperature at the corner of square CFST (point S-1) is $T_{S-1}=530^{\circ}\text{C}$, which is higher than the temperature of point S-2 ($T_{S-2} = 515^{\circ}\text{C}$).

- (2) The average temperature at the steel-concrete interface corresponding to $t= 60\text{min}$ is extracted from the FEA model, which can better reflect the influence of section type on the interface temperature distribution in CFSTs. The average interface temperatures T_{E-AVG} , T_{C-AVG} and T_{S-AVG} corresponding to elliptical, circular and square CFSTs are 513°C , 500°C and 521°C , respectively. It can be seen that the T_{C-AVG} -value is lowest, and the T_{S-AVG} -value is highest. This can be explained by the influence of CFST's volume. The three types of CFSTs are designed to have the same steel-concrete interface contact area. That means the fire exposure areas of the three types of CFSTs are close to each other, but their volumes are significantly different. Under the predetermined calculation conditions in Table 1, the circular CFST has the largest volume, the second larger one is the elliptical CFST, and the smallest one is the square CFST. Therefore, when the fire exposure condition is identical, the large one in volume is able to absorb more heat, which leads to a lower average temperature. It should be pointed out that the size of CFSTs in this paper is small and the heating time is a little bit short, which leads to the fact that the average interface temperature difference caused by section type is not so significant. However, for the CFSTs with larger size and longer fire exposure time in practical engineering, the influence of section type on interface temperature should be concerned.

4.2 Post-fire bond stress versus slip relations

Figure 5 shows the post-fire bond stress (τ) - slip (S) curves of elliptical (E200-600-30), circular (C154-600-30) and square (S121-600-30) CFSTs with the same contact area. Herein, the bond stress (τ) is the average interface bond stress ($\tau= N/A_i$, A_i is the contact area of steel tube-concrete interface); slip (S) is the relative slip between the steel tube and concrete at the loading end.

It can be seen from Figure 5 that at the initial stage of the τ - S curve (when S is less than 1.5mm) the influence of section type on the bond stress of CFST interface is minor, and the post-fire τ - S curves of the three types of cross-sections basically coincide; With the increase of slip value, the influence of section type on bond stress becomes more and more significantly. When the slip value is the same, the bond stress of circular CFST is the largest, while that of square CFST is the smallest. When $S=2.8\text{mm}$, the bond stress of CFST with three types of cross-sections reaches the peak value; after the bond stress reaches the peak value, the bond stress of CFST begins to decrease with the increase of slip value. When $S=8.7\text{mm}$, the bond stress tends to be stable, and the bond stress of elliptical, circular and square CFSTs are 1.8, 1.9 and 1.7MPa, respectively.

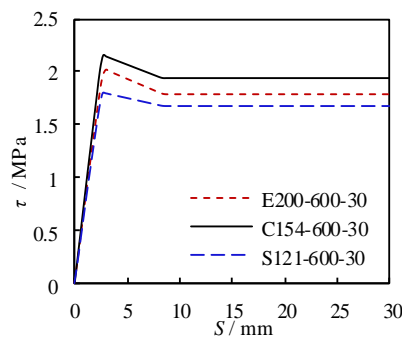


Figure 5. Post-fire τ - S curves of the three types of CFSTs

4.3 Post-fire bond strength

On the basis of the bond stress (τ)- slip (S) curve, the bond stress corresponding to the peak point is defined as the bond strength (τ_u) of CFSTs. From Figure 5, the post-fire bond strength of elliptical, circular and square CFSTs are 2.0, 2.2 and 1.8MPa, respectively. It can be seen that the section type has a moderate influence on the bond strength of CFSTs under the same fire condition and interface contact area. The τ_u -value of circular CFST is greater than that of the elliptical and square CFSTs. This may be explained by the influence of confinement effect of steel tube to core concrete in different CFST sections. The circular steel tube is able to provide better confinement to the core concrete, while the confinement

effect provided by the square steel tube is weaker than the circular one. For the ECFST, the confinement effect at the end of the long axis of the steel tube is better than that at the end of the short axis, but the total confinement effect in ECFST is intermediate between the circular and square ones.

When the bond stress of the steel tube-concrete interface reaches the bond strength, the push-out load reaches the maximum value, and this external load is borne by all the bond stress along the steel tube-concrete interface. In order to further analyse the contribution of different interface positions along the length direction of CFST to resist the external push-out load when the bond strength is reached, Figure 6 shows the distribution curve of bond stress (τ) along the longitudinal direction at the characteristic points when the peak push-out load is reached, in which, the fixed end of CFST is $L = 0$ mm, the loading end is $L = 400$ mm, and the bond stress is calculated by $\tau = F_s / A_s$ (F_s is the force of the spring element at any position of the steel tube-concrete interface, and A_s is the action area of spring element and equal to the A_i divided by the total number of spring elements). The positions of characteristic points are shown in Figure 4.

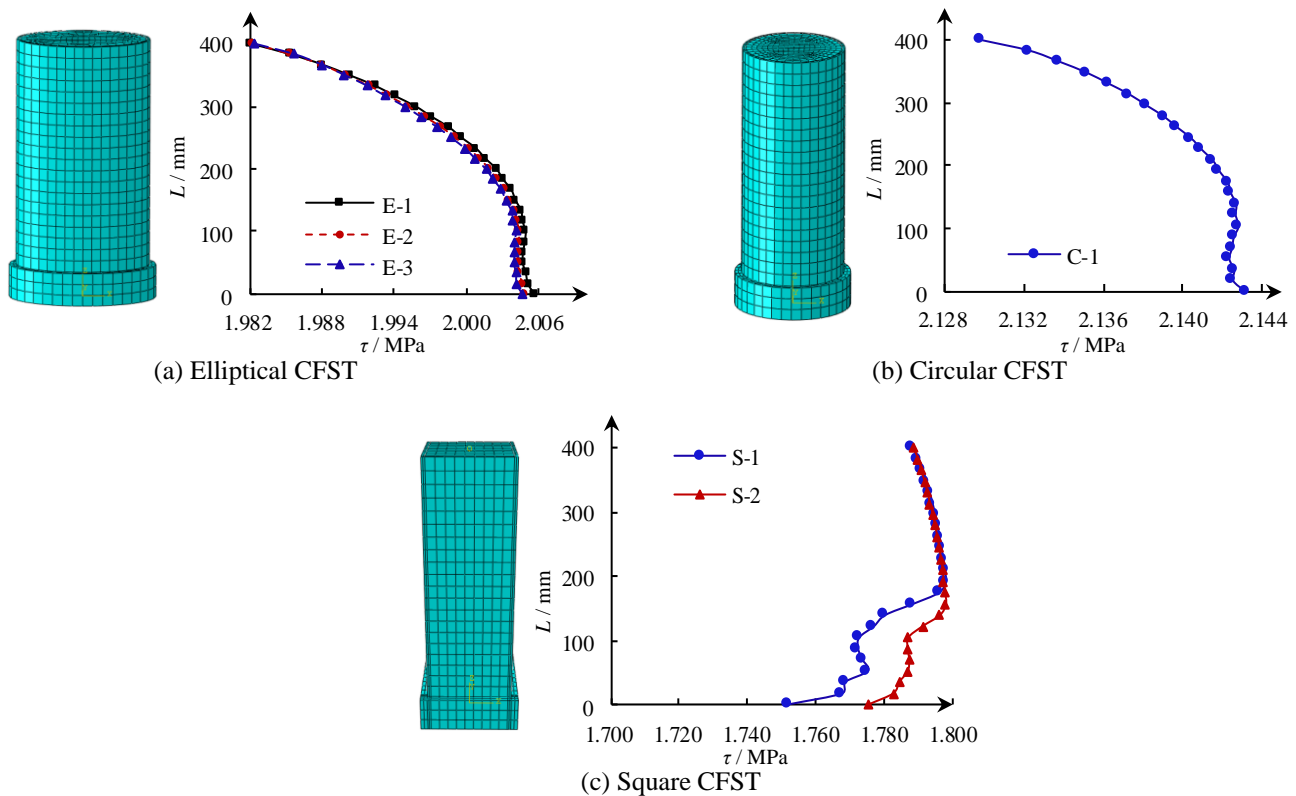


Figure 6. Bond stress distribution along the longitudinal direction corresponding to the maximum push-out load

The following conclusions can be drawn from Figure 6:

- (1) When the maximum push-out load in ECFST is reached, as shown in Figure 6(a), the bond stress increases gradually from the loading end ($L = 400$ mm) to the fixed end ($L = 0$ mm), the variation range of τ is 1.982~2.006 MPa. Corresponding to the same L -value, the difference of τ -values at points E-3 is minor. For example, at the long axis of the fixed end, the τ -value of point E-1 is 2.006 MPa, while that of the point E-3 at the short axis is 2.005 MPa.
- (2) Similar to the ECFST, the bond stress of circular CFST increases gradually from the loading end to the fixed end, and the variation range is $\tau = 2.130 \sim 2.143$ MPa as shown in Figure 6(b). In addition, because of the better confinement effect of the circular cross section, when the L -value is the same, the τ -value in circular CFST is greater than that in the ECFST with the same contact area.
- (3) As shown in Figure 6(c), the distribution of bond stress along the longitudinal direction of the square CFST is more complex compared with the elliptical and circular ones. When L is around 175 mm, the τ -value of points S-1 and S-2 reach the peak value ($\tau = 1.798$ MPa). When L ranges from 175 mm to 0 mm or 400 mm, the τ -value keeps decreasing, and the range of τ is from 1.752 MPa to 1.798 MPa.

In addition, Figure 6 also indicate that, within the research parameters of this paper, the bond stress corresponding to the length range of 0 ~ 175mm is greater than that at other length range for the elliptical and circular CFSTs, and the length range with greater bond stress for square CFST is 175 ~ 400mm. Therefore, to enhance the bond strength in CFSTs, it is more effective to adopt special methods, such as welding internal ring or stud onto the inner surface of the steel tube, in the above-mentioned length range.

5 EFFECTS OF VARIOUS PARAMETERS ON BOND STRENGTH IN ECFST

This section will discuss the influence of target temperature (T_{tar}), high temperature duration time (t_d) and section perimeter (C) on the bond strength of ECFST after fire. The calculation conditions of the standard model in parameter analysis are consistent with that of the ECFST model E200-600-30 in Table 1, which are $2a=200\text{mm}$, $2b=100\text{mm}$, $t_s=5\text{mm}$, $L=400\text{mm}$, $T_{tar}=600^\circ\text{C}$, $t_d=30\text{min}$, $a/b=2$, $C=484\text{mm}$ and $L/a=2$. Based on the standard model, the influence of the above three parameters is analyzed, and the variation range of each parameter is shown in Table 2. When the target temperature (T_{tar}) and high temperature duration time (t_d) change, other parameters are kept consistent with the standard model. The section perimeter (C) is changed by adjusting a and b , but the value of a/b remains as 2.

Table 2. Parameter variation range

Parameters	Lable	Unit	Range of variation
Target temperature	T_{tar}	$^\circ\text{C}$	20、600、800、1000
High temperature duration time	t_d	min	30、90、120、180
Section perimeter	C	mm	388、484、630、727 (160×80 、 200×100 、 260×130 、 300×150) *

* The values in brackets are the sizes of the major axis and minor axis of the ellipse corresponding to different section perimeter.

Figure 7 shows the influence of the three parameters on the post-fire bond strength of ECFSTs. It can be found that:

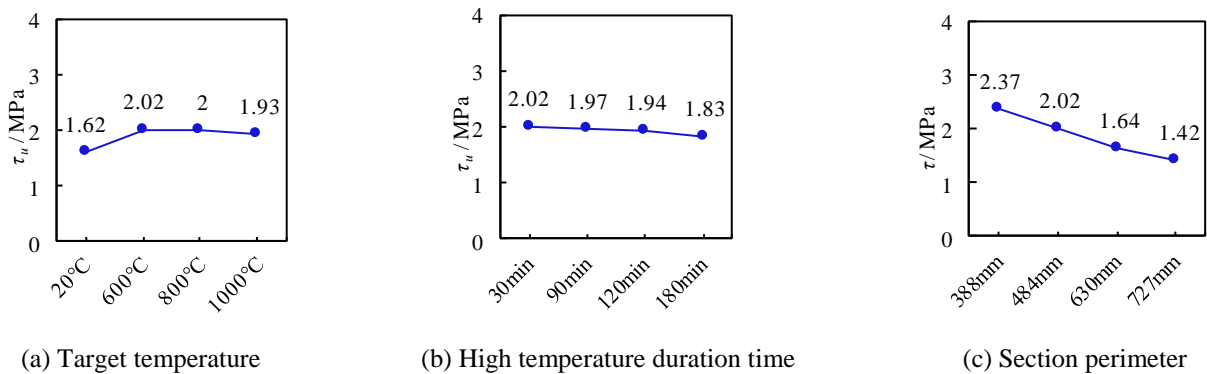


Figure 7. Influence of different parameters on post-fire bond strength

- (1) The bond strength increases first and then decreases slowly with the increase of target temperature. As shown in Figure 7(a), the value of τ_u at 20°C is the lowest (1.62MPa). When T_{tar} ranges from 600 to 1000°C , the value of τ_u is significantly higher than that at ambient temperature, and the T_{tar} -value decreases gradually with the increasing T_{tar} . The improvement of bond strength of CFSTs after subjected to high temperature has been proved by previous experimental studies. One main reason is that the roughness of concrete surface is increased after fire exposure, which leads to the improvement of bond strength.
- (2) As shown in Figure 7(b), the bond strength decreases slowly with the increase of high temperature duration time. The τ_u -value ranges from 1.83 to 2.02MPa when t_d -value increases from 30 to 180min. When t_d is equal to 30min, the interface temperature of ECFST is about 500°C . With the increase of t_d , the interface temperature gradually approaches the target temperature of 600°C . Therefore, when t_d ranges from 30 to 180min, the difference of corresponding interface temperatures in ECFSTs is

around 100°C, which induces to a minor effect of high temperature duration time on post-fire bond strength.

- (3) It is very clear that the post-fire bond strength of ECFSTs decreases significantly with the increasing section perimeter. The post-fire bond strength ranges from 2.37 to 1.42MPa when section perimeter increases from 388 to 727mm. This can be explained by the fact that the concrete shrinkage and creep can induce to the forming of gap between steel tube and core concrete, which can reduce the bond strength of the steel tube - core concrete interface, and the weakness effect can be enhanced with the increasing section size [8]. Therefore, the post-fire bond strength of ECFST decreases with the increase of section perimeter.

6 CONCLUSIONS

In this paper, the post-fire bond behaviour of ECFST are analysed and discussed, and the following conclusions can be drawn:

- (1) A finite element analysis model has been established to analyse the post-fire bond behaviour of elliptical CFSTs in this paper. The steel tube-core concrete interface behaviour in the proposed FEA model is simulated by using the spring elements with validated bond stress versus slip models. The modelling method has been validated by comparing with existing post-fire push-out tests of circular and square CFSTs. The accuracy of the FEA model is acceptable.
- (2) The temperature field analysis indicates that the average interface temperature of ECFSTs is lower than that of the square CFST and higher than that of the circular CFST with the same steel tube – core concrete contact area, but the difference of average interface temperature in the three types of CFSTs is minor in the research scope of this paper. However, for CFSTs in real structures, the influence of section type on interface temperature may be enhanced because of the larger section size and longer fire exposure time.
- (3) The influence of section type on the initial stage of post-fire bond stress - slip curves of CFSTs with the same contact area is minor, but with the increasing of slip between steel tube and core concrete, the influence becomes significantly, and different bond strength is obtained according to the simulation results. The predicted post-fire bond strength of elliptical, circular and square CFSTs are 2.0, 2.2 and 1.8MPa, respectively.
- (4) An unevenly distributed post-fire bond stress is observed along the longitudinal direction of CFSTs when the push-out load reaches the peak value. For the elliptical and circular CFSTs, the bond stress at $L=0\sim175\text{mm}$ is greater than that at other length range, and the length range is $175\sim400\text{mm}$ for square CFST. So, it may be more beneficial to adopt special methods within the above-mentioned length range in terms of improving the post-fire bond strength in CFSTs.
- (5) The parameter analysis indicates that the influence of section perimeter on the post-fire bond strength of ECFST is significant. It is clear that the bond strength at ambient temperature is lower than that after fire, but the effect of target temperature is minor when it ranges from 600 to 1000°C. The effect of high temperature duration time on post-fire bond strength of ECFST is minor.

REFERENCES

1. Han, L. H., Concrete Filled Steel Tubular Structures-Theory and Practice, Science Press, 2016, pp. 1-66.
2. Han, L. H., Mu, T. M. and Wang, F. C., Design Theory of CFST (Concrete-Filled Steel Tubular) Mixed Structures and Its Applications in Bridge Engineering, China Civil Engineering Journal, Vol. 5, 2020, pp. 1-24.
3. Han, L. H., Song, T.Y. and Zhou, K., Fire Safety Design Theory of Steel-Concrete Composite Structures, Science Press, 2017, pp. 356-370.
4. Liu, Y. J., Liu, J. P. and Chi, J. J., Shear Bond Behaviours at Interface of Concrete-Filled Steel Tube, Journal of Guangxi University, Vol. 35(1), 2010, pp. 17-23.
5. Tao, Z., Song, T. Y. and Uy, B., Bond Behaviour in Concrete-Filled Steel Tubes, Journal of Constructional Steel Research, Vol. 120, 2016, pp. 81-93.

6. Charles, W. R., Brad, C. and Colin, B. B., Composite Action in Concrete Filled Tubes, *Journal of Structural Engineering*, Vol. 125(5), 1999, pp. 477-484.
7. Lyu, W. Q., Han, L. H., Investigation on Bond Strength Between Recycled Aggregate Concrete (RAC) and Steel Tube in RAC-Filled Steel Tubes, *Journal of Constructional Steel Research*, Vol. 155, 2019, pp. 438-459.
8. Song, T. Y., Tao, Z. and Han, L. H., Bond Behaviour of Concrete-Filled Steel Tubes at Elevated Temperatures, *Journal of Structural Engineering*, Vol. 143(11), 2017, pp. 1-12.
9. Chen, J., Xue, Y.Y. and Tan, Q.H., Experimental Study on Bond Behaviour of Interface for Concrete-Filled Steel Tube Under Constant High Temperature, *China Civil Engineering Journal*, Vol. 51(3), 2018, pp. 11-17.
10. Tao, Z., Han, L. H. and Uy, B., Post-Fire Bond Between the Steel Tube and Concrete in Concrete - Filled Steel Tubes, *Journal of Constructional Steel Research*, Vol. 67(3), 2011, pp. 484-496.
11. Chen, Z. P., Liu, X. and Zhou, W. X., Interface Bond Behaviour Between Circle Steel Tube and High Strength Concrete After High Temperatures, *Engineering Mechanics*, Vol. 35(8), 2018, pp. 192-255.
12. Chen, Z. P., Liu, X. and Xu, J. J., Study on Interface Bond Behaviour of High Strength Concrete Filled Square Steel Tube After High Temperatures, *Journal of Building Structures*, Vol. 38(6), 2017, pp. 133-143.
13. Liu, Z. J., Experimental Investigation of Post-Fire Bond-Slip Performances of Interface for Concrete-Filled Steel Tubular Columns, Hunan University, 2016.
14. ABAQUS. ABAQUS/Standard Version 6.14 User's Manual: Volumes I-III. Dassault Systèmes Simulia Corp, Rhode Island, USA, 2014.
15. Song, T. Y., Han, L. H., Concrete Filled Steel Tube Stub Columns Under Combined Temperature and Loading, *Journal of Constructional Steel Research*, Vol. 66, 2010, pp. 369-384.
16. Yang, H., Lam, D. and Gardner, L., Testing and Analysis of Concrete-Filled Elliptical Hollow Sections, *Engineering Structures*, Vol. 30(2), 2008, pp. 3771-3781.
17. He, A., Liang, Y. T. and Zhao, O., Behaviour and Residual Compression Resistances of Circular High Strength Concrete-Filled Stainless Steel Tube (HCFSSST) Stub Columns After Exposure to Fire, *Engineering Structures*, Vol. 203, 2020, pp. 1-15.
18. Liu, B., Bai, G. L. and Xu, Z. H., Experimental Study and Finite Element Modelling of Bond Behaviour Between Recycled Aggregate Concrete and The Shaped Steel, *Engineering Structures*, Vol. 201, 2019, pp. 1-21.
19. Song, T. Y., Han, L. H. and Tao, Z., Structural Behaviour of SRC Beam-to-Column Joints Subjected to Simulated Fire Including Cooling Phase, *Journal of Structural Engineering*, Vol. 141 (9), 2015, 04014234.
20. Xu, K. C., Study on Bond-Slip Relationship of Concrete-Filled Steel Tube Base on Interface Damage , Nanchang University, 2013.
21. ISO-834-1. Fire-resistance tests-elements of building construction—Part 1: General requirements. International Standard ISO 834, Geneva, 1999.

BONDING OF GROUTED ECCENTRIC STRANDS IN DUCT AT ELEVATED TEMPERATURES

Xiqiang Wu¹, Francis Tat Kwong Au², Xinyan Huang³

ABSTRACT

Prestressing strands are often located eccentrically within ducts in post-tensioned structures due to curvature of profile. To investigate the bond performance of grouted tendons, pull-out tests are conducted on mono- and multi-strand tendons located eccentrically in grouted ducts in concrete at temperatures of 20°C to 600°C. Each specimen is first heated to the designated temperature and then loaded either immediately or after cooling down. Results show that the bond strength of eccentrically embedded tendons is lower than that of centrally embedded tendons. The bond strength and stiffness are found to decrease with increase of temperature, but the bond recovers certain strength after cooling down. The bond is enhanced by confinement steel surrounding the duct. However, specimens cooled by water behave almost the same as those cooled in air. A bond-slip model is proposed accordingly.

Keywords: Bond; Prestressing strand; Pull-out testing; Thermal effects

1 RESEARCH SIGNIFICANCE

In the fabrication of post-tensioned concrete (PC) members, tendons are often bonded in ducts by grouting after prestressing. The tendon force is primarily transferred to concrete through anchorages while the bonding between tendon and grout enhances the structural integrity. Upon exposure to fire, the structural response is influenced by the degradation of material properties. Half of its strength is lost for concrete, reinforcement and strand at temperatures 570°C, 600°C and 400°C respectively according to Eurocode 2 [1]. Cement grout was also found to lose half of its strength at temperature 440°C [2]. Studies have shown the significant influence of bond behaviour on the structural responses of bonded PC members under fire [3]. Failure to consider the bond degradation may overestimate the load-carrying capacity [4].

The bonding of strand embedded in cement-based materials at ambient temperature is often studied by pull-out tests. Tests of strand embedded in grout showed that the bond strength increased with lateral pressure, embedded length and grout strength [5]. Standard pull-out test [6] conducted on strand bonded in mortar gave bond strength increasing with the strand diameter. Even though the bonding of strand may differ from that of rebar due to their distinct surface geometry, the bond tests on rebars could provide valuable reference. The bond force was reported [7] to increase not only with the embedded length, strength of surrounding material and bar diameter, but also the concrete cover, bar spacing and transverse confining steel, indicating the influence of layout of strands, steel duct and additional reinforcement on the bond behaviour. Moreover, the eccentricity of tendon in duct due to the curvature of profile should also be considered.

¹ Research Assistant Professor. Department of Building Services Engineering, The Hong Kong Polytechnic University, Hong Kong.
e-mail: xiqiang.wu@polyu.edu.hk, ORCID: <https://orcid.org/0000-0003-2614-0530>

² Professor and Head. Department of Civil Engineering, The University of Hong Kong, Hong Kong.
e-mail: francis.au@hku.hk, ORCID: <https://orcid.org/0000-0002-2163-3531>

³ Assistant Professor. Department of Building Services Engineering, The Hong Kong Polytechnic University, Hong Kong.
e-mail: xy.huang@polyu.edu.hk, ORCID: <https://orcid.org/0000-0002-0584-8452>

Limited pull-out tests have been conducted at elevated temperatures [8]. The bond behaviour of rebars is influenced by various factors including elevated temperatures as well as heating and cooling mechanisms [9]. Tests on rebars showed that a longer fire exposure would result in more reduction of bond strength [10]. Pull-out tests of strand embedded in concrete at elevated temperatures showed that the bond strength decreased with the increase of temperature and strand diameter [11]. As cement grout may be more sensitive to elevated temperatures [1], the bonding of grouted strand at elevated temperatures needs further study.

In this study, pull-out tests are conducted to investigate the bond behaviour of grouted tendons considering the influence of eccentricity and number of strands in a duct, elevated temperature, cooling method and confinement steel. The bond-slip relationship and failure modes of specimens are studied for development of an analytical model for predicting their bond behaviour at elevated temperatures.

2 EXPERIMENTAL PROGRAMME

The pull-out tests conducted in this study are designed based on recommendations for pull-out tests at ambient temperature [6,12].

2.1 Specimen geometry

Figure 1 shows a typical specimen comprising strands, cement grout, corrugated steel duct and concrete. To achieve even heating at the interface between strands and grout, the specimen is cylindrical in shape and the tendon is bonded only near the middle of specimen. The concrete cylinder has a length of 240 mm and outside diameter of 150 mm, which are restricted by the inner space of furnace. The nominal diameter of 7-wire strand d_b is 15.2 mm. The outside diameter of concrete cylinder is thus approximately $10 d_b$, which falls into the range of specimen diameter 82 – 172 mm often adopted [9]. The bonded length l_b is 80 mm, which is about $5 d_b$ as adopted by Diederichs and Schneider [13]. PVC pipes with inner diameter slightly larger than the tendon are used as bond breaker at both ends of specimen. The grouted tendon is placed inside a corrugated steel duct 50 mm in diameter. Helical confinement steel located concentrically with the concrete cylinder is also used to study its influence on the bond behaviour.

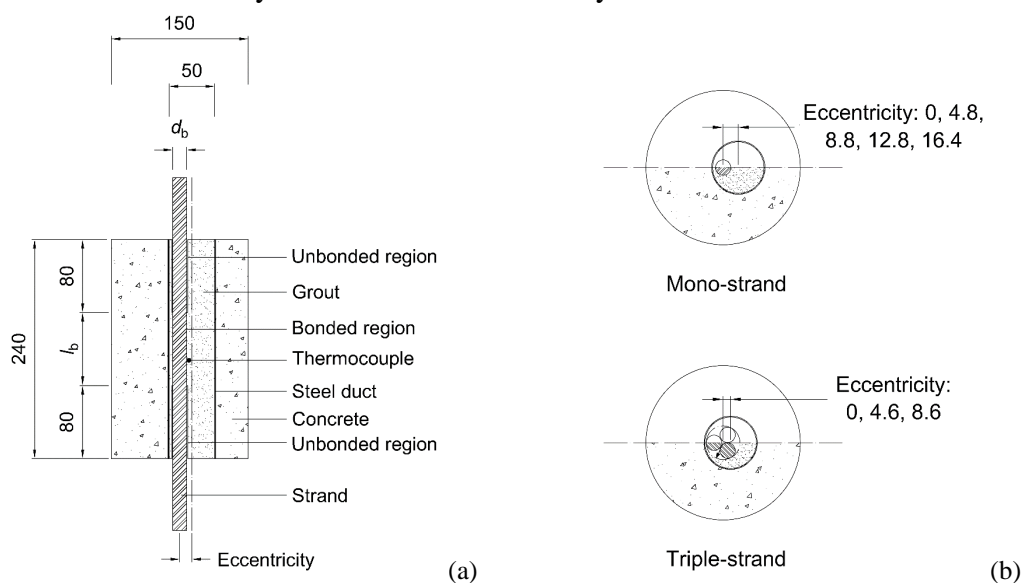


Figure 1. Test specimen (unit: mm): (a) vertical cross section for mono-strand tendon; (b) horizontal cross sections

Figure 1(b) shows the tendon eccentricity defined as the distance between the centre of duct and the centroid of tendon. Assuming the cross section of triple-strand tendon to possess rotational symmetry of order 3, its centroid can be taken as the centre of rotational symmetry. The eccentricities tested are 0 mm, 4.8 mm, 8.8 mm, 12.8 mm and 16.4 mm for the mono-strand specimens, and 0 mm, 4.6 mm and 8.6 mm for the triple-strand specimens. The maximum eccentricities of 16.4 mm and 8.6 mm for the mono- and triple-strand tendons respectively are those when the tendon of assumed cross section is in contact with

the duct. The tendon eccentricity is varied for the tests conducted at ambient temperature, while those tested at elevated temperatures or after cooling down are those having maximum eccentricities. This is a realistic arrangement for testing. The tendon eccentricity within duct is achieved by varying the duct position while keeping the tendon and concrete cylinder concentric as shown in Figure 1(b).

2.2 Material, mix and fabrication

Grade 52.5R ordinary Portland cement is used for the grout. A water-cement ratio of 0.4 is adopted considering its workability and fluidity, which is in the recommended range of 0.35-0.45. The designed cylinder strength of concrete is 50 MPa. The granitic coarse and fine aggregates are of sizes 20 mm and 10 mm respectively. Three cement grout cylinders 100 mm (diameter) by 200 mm (height) and three concrete cylinders 150 mm (diameter) by 300 mm (height) are prepared for each test series for quality control of compressive strength. Low-relaxation 7-wire strands of 15.2 mm nominal diameter conforming to BS 5896 are used, which have Young's modulus and ultimate tensile strength of 200 GPa and 1860 MPa respectively at ambient temperature [14]. The confinement reinforcement, where applicable, is provided by 6 mm steel wire in helical form throughout the length of concrete cylinder having a coil diameter of 86 mm and a pitch of 10 mm with the axis of helical coil aligned with the centreline of concrete cylinder.

2.3 Heating procedure

An electrical furnace capable of reaching 1400°C is used. A heating rate of 1.6°C/minute was determined by heat transfer analysis to ensure that the thermal condition in the bonded area of the specimen agreed with that of a structural member exposed to standard fire [15]. The target temperatures at the bonded area are 20°C for tests at ambient temperature, and 100°C, 200°C, 300°C, 400°C, 500°C and 600°C for tests at elevated temperatures and after cooling down. As the pull-out test lasts around 3 minutes, during which the temperature measured at the bonded area keeps rising with the furnace temperature, the pull-out test is started slightly earlier such that the difference between the temperature measured at the bonded area and the target temperature is less than 5°C during the pull-out test. For the tests conducted after cooling down, the furnace is opened before the temperature measured at the bonded area has reached the target value as the temperature would continue increasing slightly afterwards. temperature or by spraying with water, followed by further pull-out tests.

2.4 Pull-out Testing

The key information of the tests is summarised in Table 1. The influence of tendon eccentricity in a duct at ambient temperature is studied in Series 1, where the eccentricity of mono-strand tendon varies from 0 mm to 16.4 mm, and that triple-strand tendon varies from 0 mm to 8.6 mm. Two tests are conducted for each eccentricity. The specimens in the other series are fabricated with the maximum eccentricity to simulate realistic conditions, i.e. eccentricities of 16.4 mm and 8.6 mm for mono- and triple-strand tendons respectively. The bond performance of mono- and multi-strand tendons are studied in Series 2 and 3 respectively, covering both tests at elevated temperature and after air-cooling. Tests in Series 4 are to study the influence of water cooling after heating, while those in Series 5 address the effect of helical confinement steel. The specimens in Series 2 to 5 are exposed to elevated temperatures of 100°C, 200°C, 300°C, 400°C, 500°C and 600°C. A specimen is tested at the elevated temperature specified or after cooling from it. Totally, 52 specimens are tested.

Figure 2 shows the test setup consisting of a furnace, a loading system (including a hydraulic jack, two drawbars, a reaction frame, a tendon anchor and several steel plates), two insulating firebricks, a bearing cylinder, and measuring devices comprising thermocouples adjacent to the surface of specimen, a load cell and a linear variable differential transformer (LVDT).

The pull-out process is carried out by gradually pulling the anchor up while holding back the upper surface of specimen with the bearing cylinder. The test is conducted at a displacement rate of 2.6 mm/minute (mean value), which falls into the range of 2.5 ± 0.13 mm/minute as specified in ASTM [6].

The load, displacement and temperature are measured by load cell, LVDT and thermocouple with accuracies of 0.1 kN, 0.01 mm and 0.1°C respectively. A test is terminated when the displacement exceeds the range 20 mm of LVDT.

Table 1. Parameters in each test series

Test series	No. of specimens	No. of strands	Tendon eccentricity	Confinement	Thermal conditions
1	10	1	Varies	No	Ambient
	6	3	Varies	No	Ambient
2	12	1	Max.	No	Elevated; air-cooled
3	12	3	Max.	No	Elevated; air-cooled
4	6	1	Max.	No	Water-cooled
5	6	3	Max.	Yes	Elevated

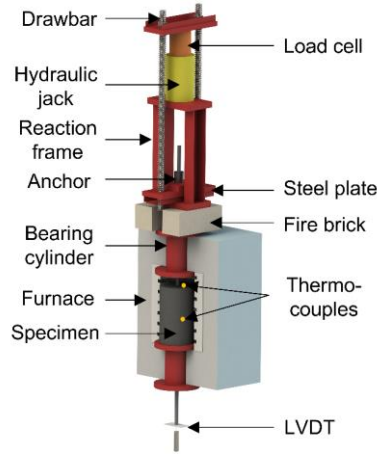


Figure 2. Test setup

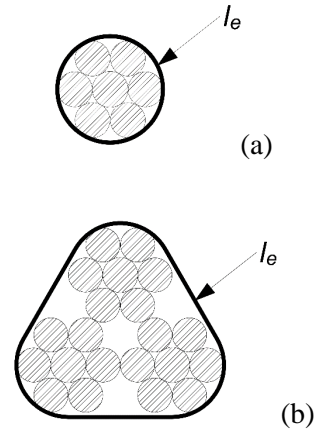


Figure 3. Envelope perimeter of tendon: (a) mono-strand; (b) triple-strand

2.5 Evaluation of bond stress

During the pull-out process, the parts of grout between adjacent wires or strands will be gradually detached, possibly creating failure surfaces approximated by the envelope surfaces as shown in Figure 3 for both mono- and triple-strand tendons. Assuming that the equivalent bond stress t_b is uniformly distributed along the embedded length, t_b can then be calculated by pull-out force P over the failure surface as

$$t_b = \frac{P}{l_e \cdot l_b} \quad (1)$$

where l_e is the envelope perimeter as shown in Figure 3, which equals $(\pi \cdot d_b)$ and $(\pi+3)d_b$ for mono- and triple-strand tendons respectively, and l_b is the bonded length.

3 TEST RESULTS AND DISCUSSIONS

3.1 Failure modes

As the specimens are enclosed in the furnace during test, making it inconvenient to observe the failure process visually, they are only checked afterwards. The fracture of steel duct is inspected by cutting each specimen into parts.

Pull-out failure occurs under high confinement and low embedded length while splitting failure is more frequently observed in practical engineering. Besides, splitting failure is more likely at elevated temperatures [16]. Pull-out failure is not observed in the current tests, but only splitting failure is observed. Two kinds of splitting failure modes are observed as shown in Figure 4: (a) partial splitting with a few splitting cracks formed in the concrete while duct is intact; and (b) through splitting with concrete broken into pieces and the duct fractured. The triple-strand specimens tested at elevated temperatures or after cooling down from temperatures not higher than 300°C are observed to fail in through splitting mode due to insufficient confinement provided by the duct, while all the other specimens are observed to fail in partial splitting mode.

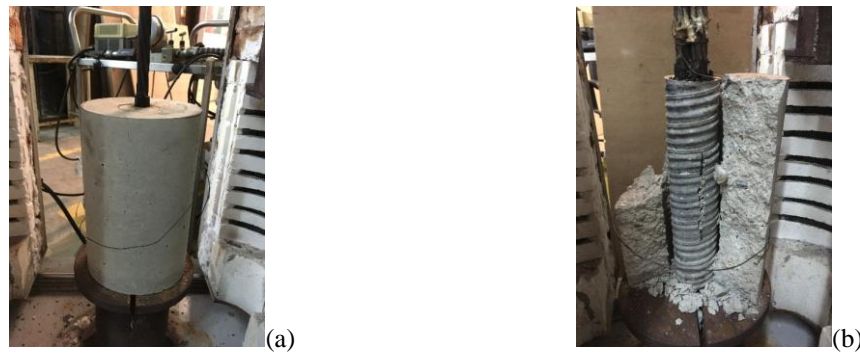


Figure 4. Typical failure modes: (a) partial splitting; (b) through splitting

3.2 Effect of tendon eccentricity

The bond-slip curves for different eccentricities from tests at ambient temperature in Figure 5 show that the general trend of bond behaviour is hardly influenced by eccentricity. However, the bond strength is weakened with the increase in tendon eccentricity inside duct, which gives rise to non-uniform distribution of bond stresses around the tendon. Because of the profiles used in PC structures, the tendons are often positioned eccentrically inside ducts. Adopting the bond strength of tendons positioned concentrically inside the ducts for analysis could overestimate the structural strength. To keep the total number of tests to a reasonable amount, the remaining tests involving elevated temperatures are conducted on specimens with maximum eccentricities inside duct.

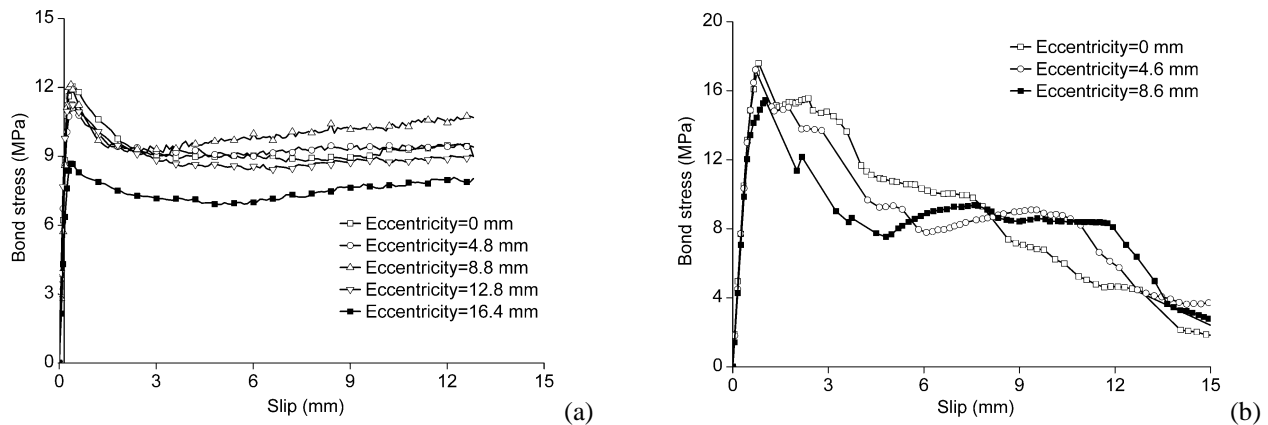


Figure 5. Bond-slip curves for different eccentricities at ambient temperature: (a) mono-strand; (b) triple-strand

3.3 Bond-slip curves of mono- and triple-strands

Figure 6 presents the bond-slip curves of mono-strand specimens at elevated temperatures and after cooling from elevated temperatures, while Figure 7 shows those for triple-strand specimens. They show that the temperature has major effect on the bond behaviour due to degradation of mechanical properties of grout, concrete, and duct at elevated temperatures. Initially, the bond stress increases almost linearly with slip. For specimens failing in partial splitting mode at elevated temperatures, the bond stress decreases after the initial increase, which is possibly associated with the fracture of concrete due to insufficient confinement. After then, the bond stress remains almost unchanged. The friction resistance at the interface may dominate at this stage.

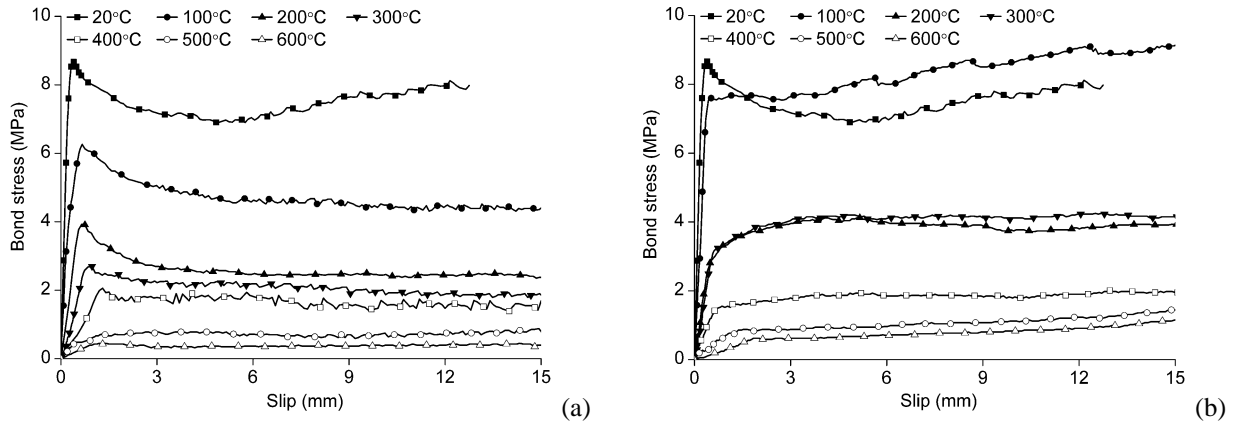


Figure 6. Bond-slip curves for mono-strand tendons: (a) at elevated temperatures; (b) after air-cooling from elevated temperatures

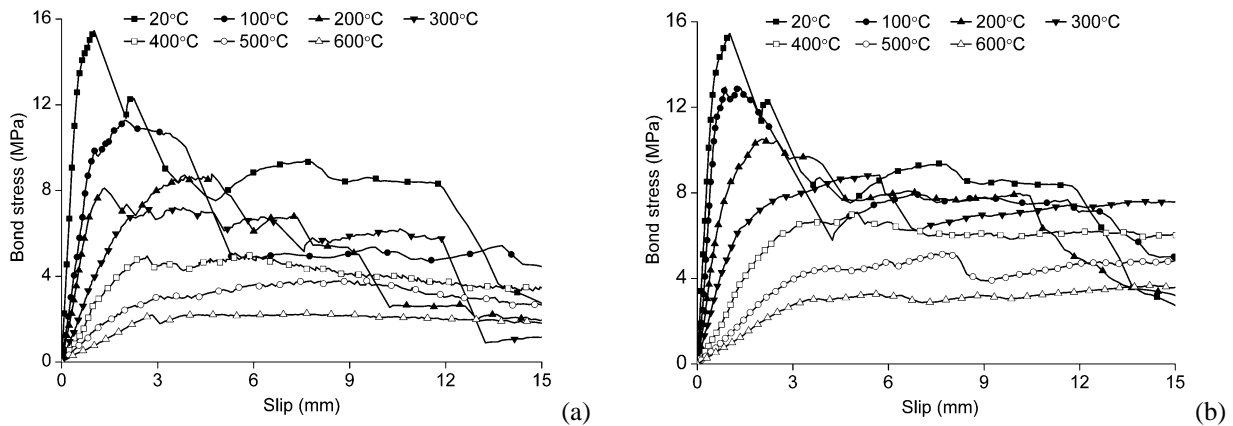


Figure 7. Bond-slip curves for triple-strand tendons: (a) at elevated temperatures; (b) after air-cooling from elevated temperatures

For specimens failing in partial splitting mode after air-cooling from elevated temperatures, the slope of bond-slip curve diminishes gradually with the evolvement of slip and no apparent reduction in bond stress after the initial increase is observed, as the grout is well confined by the steel duct, leading to gradual crushing of grout at interface and gentle development of cracks in grout and concrete. This confinement is more effective after cooling down since, unlike concrete, steel can regain most of its mechanical properties.

For specimens failing in through splitting mode, the bond behaves in a brittle manner with the bond stress decreasing abruptly after reaching the peak value and eventually resulting in minor residual bond strength. Post-test examination shows that the corrugated steel duct has already fractured. These distinct bond-slip curves reaffirm the important role of confinement offered by the duct in bond behaviour.

Test results show that water cooling has insignificant effect on the bonding of tendon, while helical confinement steel enhances the bond behaviour of triple-strand tendons. This indicates that the inner part of concrete is confined effectively during the pull-out process. If sufficient confinement reinforcement is

provided, the bond behaviour of tendon is improved, and no apparent reduction of bond stress occurs after attaining the bond strength.

4 ANALYTICAL BOND-SLIP MODEL

Figures 6 and 7 show that the duct and additional confinement reinforcement play a key role in the bond behaviour after attaining the bond strength and the failure mode. After the initial linear increase of bond stress with slip, the bond behaviour depends on the confinement conditions. The confinement provided can be inferred from the test results and failure mode observed. The mono-strand specimens all fail in partial splitting mode, although the bond-slip curves vary for different conditions. The mono-strand tendons tested at elevated temperatures can be regarded to have medium confinement by the steel ducts since the bond stress decreases after attaining the respective bond strength. The mono-strand tendons tested after cooling down from elevated temperatures can be regarded to have high confinement by the steel ducts.

Under low confinement conditions, multi-strand tendons at temperatures not higher than 300°C or upon cooling down from such temperatures will fail in through splitting mode and the bond stress drops abruptly after reaching the peak strength. Under medium confinement conditions, mono-strand tendons at elevated temperatures or multi-strand tendons at temperatures above 300°C will fail in partial splitting mode with a slight drop of bond stress after reaching the peak strength. Under high confinement conditions, mono-strand tendons cooled down from elevated temperatures, multi-strand tendons cooled down from temperatures above 300°C, or multi-strand tendons provided with sufficient additional transverse reinforcement will fail in partial splitting mode with no obvious reduction of bond stress after reaching the peak strength.

Following the rationale of the previous bond models [3,17], an analytical model is proposed for the bond behaviour of tendons at elevated temperatures as shown in Figure 8. The tri-linear bond-slip relationship is defined by a few characteristic parameters, including the bond strength t_{bmax} , initial bond stiffness E_b , ratio of residual strength to bond strength η , and slip s_1 , which can be obtained from experimental results by regression. For cases of high confinement that do not show any brittle behaviour, the middle line segment and the parameters η , and s_1 can be omitted thereby degenerating to a bi-linear model.

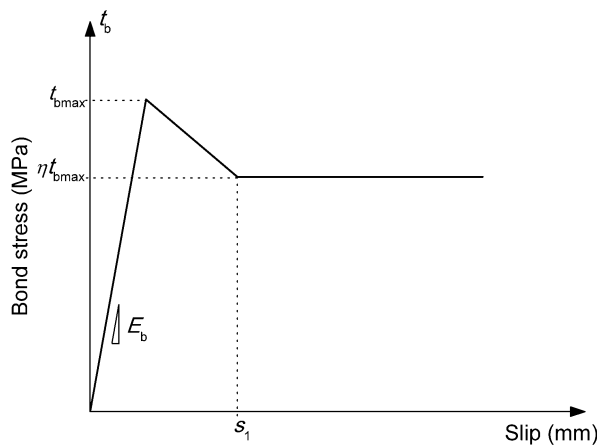


Figure 8. Analytical bond model for grouted tendons

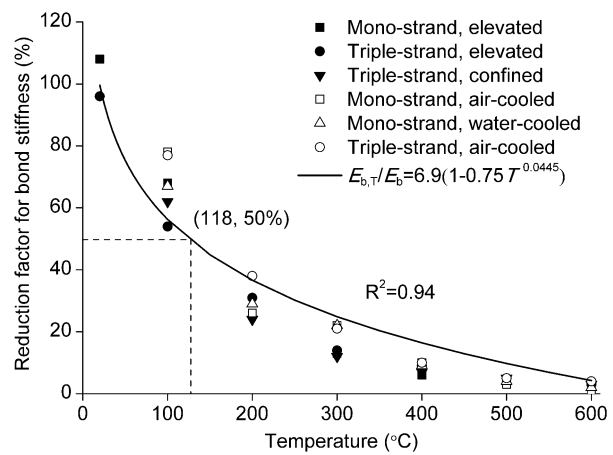


Figure 9. Regression for bond stiffness at various temperatures

4.1 Initial bond stiffness

The initial bond stiffness E_b is taken as the tangent modulus of bond-slip curve at zero slip, which is given an average value of 25 MPa/mm for both mono- and triple-strand tendons at ambient temperature. Its corresponding value $E_{b,T}$ at elevated temperature T °C is similarly defined with the help of reduction factor $E_{b,T}/E_b$. Figure 9 presents the reduction factor for bond stiffness for each test series. The bond

stiffness decreases drastically with increase in temperature primarily due to the degradation of mechanical properties. Higher values of bond stiffness are obtained for specimens tested after cooling down from elevated temperatures as compared with those tested at the corresponding elevated temperatures. This is mainly because of the better confinement provided by the steel duct that has recovered its mechanical property after cooling down from fire exposure according to Eurocode 4 [1]. The slight recovery of bond stiffness is neglected however. In general, the reduction factor for bond stiffness at elevated temperatures can be obtained from regression as a power relation

$$\frac{E_{b,T}}{E_b} = 6.9 (1 - 0.75T^{0.0445}) \quad (2)$$

Figure 9 compares of the test results with the fitted curve. The value of R^2 for regression 0.94 is close to unity, representing a good fitting with the experimental results.

4.2 Definition of bond strength

The bond strength can be calculated from the maximum load measured during a pull-out test according to ASTM standard [6]. While the peak load for specimens with low or medium confinement can be easily identified at the end of initial linear increase of load, it is relatively difficult to identify the peak load for specimens with high confinement. For consistency, the bond strength t_{bmax} is taken as the stress when the tangent stiffness drops to $0.1 E_b$. Similarly, $t_{bmax,T}$ is the bond strength at elevated temperature T °C.

4.3 Bond strength at elevated temperatures

Figure 10 shows the variations of bond strength of mono- and triple-strand tendons at various temperatures. The bond strength is significantly affected by the peak temperature T °C experienced whether it is tested immediately after reaching it or after cooling in air or by water from it. Although a disproportionate loss of bond strength at temperature around 100°C is often observed because of loss of moisture content near the interface [18], this phenomenon is not found in Figure 10 since the moisture at the bonded area has hardly evaporated after exposing to a temperature around 100°C for several minutes. Like that of bond stiffness, the bond strength recovers slightly after cooling down to ambient temperature. After exposure to the same peak temperature, specimens have similar bond strength whether cooled in air or by water.

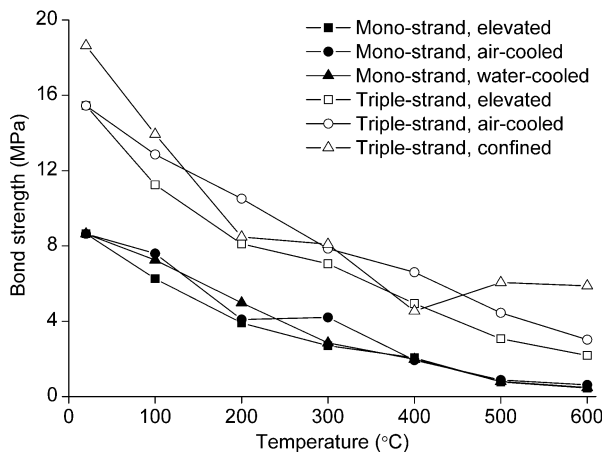


Figure 10. Bond strength at various temperatures

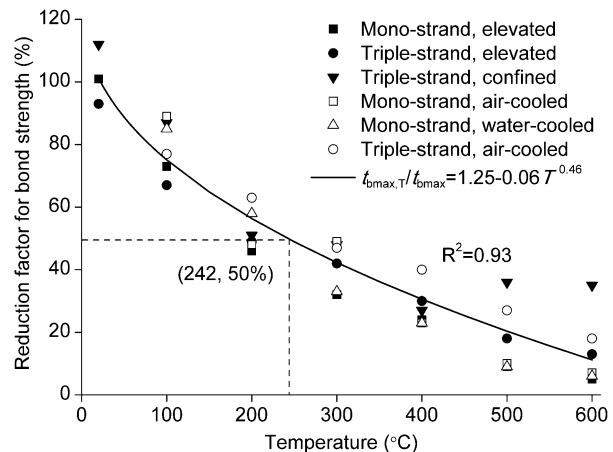


Figure 11. Regression for bond strength at various temperatures

Figure 10 shows that additional helical steel improves the bond strength at ambient temperature but has minor effect at higher temperatures of 100-300°C, during which the helical steel is directly exposed to furnace temperature after spalling of outer concrete cover. A higher bond strength is apparently obtained at temperatures above 400°C since the outer concrete cover has not spalled incidentally, still protecting the helical steel from the furnace temperature and maintaining effective confinement.

4.4 Regression for bond strength at ambient temperature

The average bond strengths of mono- and triple-strand tendons at ambient temperature are 8.7 MPa and 17.1 MPa respectively. On condition that a specimen is confined by stirrups and potentially failing in splitting mode, the bond strength t_{max} can be calculated using the formula proposed in the FIB code [17] as

$$t_{max} = 8.0 \left(\frac{f_c}{25} \right)^{0.25} \quad (3)$$

where f_c is compressive strength of embedding material that is cement grout in the current tests. Based on the average compressive strength of grout of 40 MPa from tests, the bond strength calculated using Equation 3 is 9.0 MPa for mono-strand tendons, showing good agreement with the test results.

For a given degree of confinement, the bond strength of a rebar increases linearly with its size. The bond strength of triple-strand tendons obtained confirms this. However, the exact formula for the bond strength incorporating the influence of bar diameter and transverse reinforcement cannot be established based on the limited test data. An approximate approach is therefore adopted. The equivalent diameter $d_{b,e}$ of the bundle can be expressed as (l_e / π) in terms of the envelope perimeter l_e defined in Figure 4. Assuming that the bond strength is proportional to $d_{b,e} (f_c/25)^{0.25}$ in the light of Equation 3, the proportionality constant can be determined by regression from available test results as 0.5, giving

$$t_{max} = 0.5 d_{b,e} \left(\frac{f_c}{25} \right)^{0.25} \quad (4)$$

The bond strength of triple-strand tendons calculated with Equation 4 is 17.4 MPa, which is consistent with the bond strength obtained from tests.

4.5 Regression for bond strength at elevated temperatures

The reduction of bond strength at elevated temperatures can be calculated based on the bond strength [3,9] or the reduction of compressive strength of embedding material [10]. As the bond strength of tendon is influenced by not only the embedding grout but also the confinement offered by the steel duct and concrete, the correlation between bond strength and the strength of grout is complicated. It is more convenient to correlate the bond strength with the corresponding temperature direct. The reduction factor of bond strength for both mono- and triple-strand tendons can be fitted with a power relationship as

$$\frac{t_{bmax,T}}{t_{bmax}} = 1.25 - 0.06T^{0.46} \quad (5)$$

The comparison of experimental and fitted results are shown in Figure 11, giving a value of R^2 for regression approaching 1.0, indicating good fitting of the test results.

4.6 Residual strength and slip

Distinct bond behaviour is observed for specimens with high, medium and low levels of confinement. Negligible strength is left after formation of through splitting cracks across the whole specimen provided with low confinement. There is also a drop in bond stress after attaining the bond strength for specimens with medium confinement. However, the bond stress remains almost unchanged after attaining the bond strength for specimens with high confinement. To evaluate the level of residual bond strength $t_{bf,T}$, the ratio η of residual bond strength to the corresponding bond strength is defined. The ratio η at various temperatures for specimens with medium confinement as shown in Figure 12 is averaged as 0.7, which is almost double of that for ribbed bars as given in the FIB code [17]. The ratios of residual bond strength are 0 and 1.0 for specimens with low and high levels of confinement, respectively.

Based on the analytical bond model shown in Figure 8, the bond stress for cases of low to medium levels of confinement is assumed to decrease linearly from the bond strength to the residual strength between two points selected from the post-peak branch of bond-slip curve from experiment, including the peak

point and another point where the slope of curve has dropped to 0.1 of that at the peak point. The slip s_1 at which the bond stress has dropped to the residual bond strength can then be obtained as shown in Figure 13, where s_1 barely changes with temperature. The average slip for mono- and triple-strand tendons are 2.5 mm and 5.1 mm respectively, which are approximately equal to the characteristic value of $(1/6) d_{b,e}$.

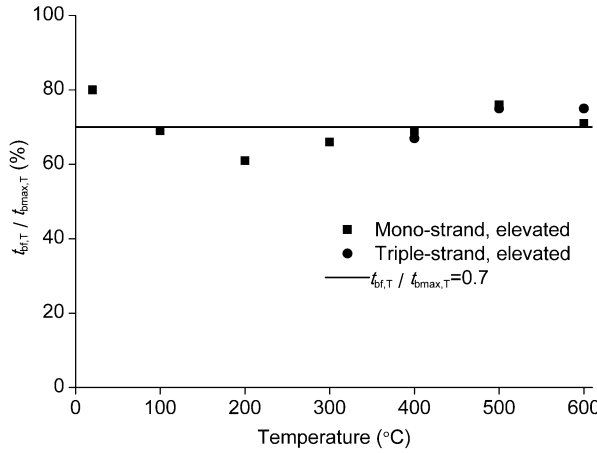


Figure 12. Regression for residual strength ratio at various temperatures

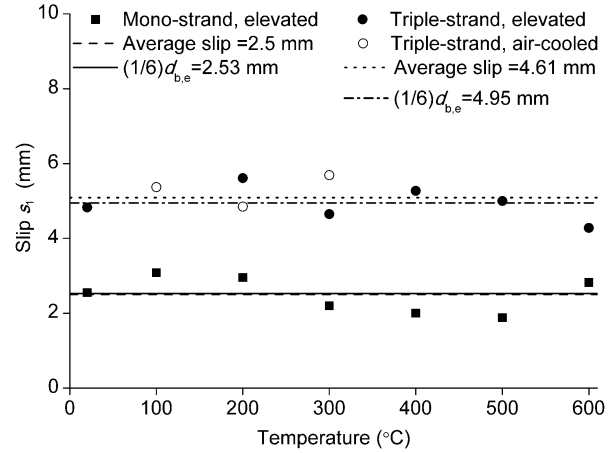


Figure 13. Regression for slip s_1 for mono- and triple-strand tendons

4.7 Summary of characteristic parameters

The analytical bond model is used to predict the bond-slip relationship of mono- or multi-strand tendons located eccentrically in grouted ducts at temperatures 20°C - 600°C. Table 2 summarizes the parameters obtained from regression. Before applying this model, the confinement condition should be determined first for calculation of various parameters.

Table 2. Parameters of bond-slip relationship at temperatures 20 °C - 600 °C

Parameter	Value
t_{bmax} (MPa)	$0.5 d_{b,e} (f_c/25)^{0.25}$
$t_{bmax,T}$ (MPa)	$(1.25 - 0.06 T^{0.46}) t_{bmax}$
$t_{bf,T}$ (MPa)	$\eta t_{bmax,T}$
s_1 (mm)	$(1/6) d_{b,e}$
$E_{b,T}$ (MPa/mm)	$172.5 (1 - 0.75T^{0.0445})$
Note: η is 0, 0.7, and 1.0 for low, medium and high confinement respectively.	

5 CONCLUSIONS

Pull-out tests have been conducted on mono- and multi-strand tendons in grouted ducts at elevated temperatures and after cooling. The effects of eccentricity, cooling and confinement on the bond behaviour are also investigated. An analytical model is developed from the experimental data. Based on the test results, the following conclusions can be drawn:

- The bond strength is lower for eccentrically embedded tendons compared with that of concentrically embedded tendons, indicating the need for considering the eccentricity of tendon in grouted duct.
- The bond strength and initial stiffness are severely affected by elevated temperatures. About half of the values of strength and stiffness at ambient temperature are lost at temperatures of 242°C and 118°C respectively.

- After attaining the bond strength at each temperature, at least 70% of its bond strength will remain if the duct does not split; otherwise the bond stress will drop suddenly to almost zero eventually.
- Multi-strand tendons normally have higher bond capacities, but their bond behaviour tends to be more brittle unless sufficient transverse confinement is provided to avoid brittle splitting.
- Cooling in air or by water has similar effect on the bond behaviour. The bond strength will recover slightly after cooling down from elevated temperature.
- While confinement steel tends to enhance the bond strength of tendons, the effectiveness of confinement steel at elevated temperature should be viewed with caution as spalling of outer concrete cover may expose the confinement steel to the direct effect of fire thereby reducing this contribution.
- An analytical tri-linear model is proposed to predict the bond behaviour of grouted tendons exposed to elevated temperatures considering the confinement conditions.

Acknowledgment

The work presented here was partially supported by the Ministry of Science and Technology, China (project no. 2019YFB1600702).

REFERENCES

1. CEN (European Committee for Standardisation), Eurocode 2: EN 1992-1-2: Design of Concrete Structures. Part 1-2: General Rules - Structural Fire Design. CEN, Brussels, Belgium, 2004.
2. Dias, W., Khoury, G. and Sullivan, P., Mechanical properties of hardened cement paste exposed to temperatures up to 700 C (1292 F). *ACI Mater J* 87(2), 160-166 (1990).
3. Khalaf, J. and Huang, Z. H., Analysis of the bond behaviour between prestressed strands and concrete in fire. *Constr Build Mater* 128, 12-23 (2016). <https://doi.org/10.1016/j.conbuildmat.2016.10.016>.
4. Panedpojaman, P. and Pothisiri, T., Bond characteristics of reinforced normal-strength concrete beams at elevated temperatures. *ACI Structl J* 111(6), 1351-1362 (2014).
5. Laldji, S., Bond Characteristics of Prestressing Strand in Grout. MPhil Thesis. University of Leicester, Leicester, UK (1987).
6. ASTM, A1081/A1081M: Standard Test Method for Evaluating Bond of Seven Wire Steel Prestressing Strand. ASTM International, West Conshohocken, PA, USA (2012).
7. ACI (American Concrete Institute) committee 408, Bond and Development of Straight Reinforcing Bars in Tension. Report No. 408R-03. American Concrete Institute, Farmington Hills, MI, USA (2003).
8. Naus, D. J., The Effect of Elevated Temperature on Concrete Materials and Structures: A Literature Review. Office of Nuclear Regulatory Research, Washington, DC, USA, 90–130 (2006).
9. Aslani, F. and Samali, B. Predicting the bond between concrete and reinforcing steel at elevated temperatures. *Struct Eng Mech* 48(5), 643-660 (2013). <https://doi.org/10.12989/sem.2013.48.5.643>.
10. Haddad, R. H. and Shannis, L. G., Post-fire behavior of bond between high strength pozzolanic concrete and reinforcing steel. *Constr Build Mater* 18(6), 425-435 (2004). <https://doi.org/10.1016/j.conbuildmat.2004.03.006>.
11. Moore, W. L., Performance of Fire-damaged Prestressed Concrete Bridges. Master's Thesis. Missouri University of Science and Technology, Rolla, Missouri, USA (2008).
12. RILEM/CEB/FIP, Bond Test for Reinforcing Steel 2: Pullout Test. E & FN SOPN, London, U.K (1983).
13. Diederichs, U. and Schneider, U., Bond strength at high temperatures. *Mag Concrete Res* 33(115), 75-84 (1981). <https://doi.org/10.1680/mac.1981.33.115.75>.
14. Zhang, L., Wei, Y., Au, F. T. K. and Li, J., Mechanical properties of prestressing steel in and after fire. *Mag Concrete Res* 69(8), 379-388 (2017). <https://doi.org/10.1680/jmacr.15.00267>.
15. CEN (European Committee for Standardisation), Eurocode 1: EN 1991-1-2: Actions on Structures. Part 1-2: General Actions - Actions on Structures Exposed to Fire. CEN, Brussels, Belgium (2002).
16. Hertz, K., The anchorage capacity of reinforcing bars at normal and high temperatures. *Mag Concrete Res* 34(121), 213-220 (1982). <https://doi.org/10.1680/mac.1982.34.121.213>.

17. FIB (International Federation for Structural Concrete), Model Code for Concrete Structures 2010. Ernst & Sohn, Berlin, Germany (2013).
18. Morley, P. and Royles, R., Response of the bond in reinforced concrete to high temperatures. Mag Concrete Res 35(123), 67-74 (1983). <https://doi.org/10.1680/mac.1983.35.123.67>

EXPERIMENTAL STUDY ON FIRE RESISTANCE OF A FULL-SCALE COMPOSITE FLOOR ASSEMBLY IN A TWO-STORY STEEL FRAMED BUILDING

Lisa Choe^{1,*}, Selvarajah Ramesh², Xu Dai³, Matthew Hoehler⁴, Matthew Bundy⁵

ABSTRACT

This paper presents the first of four planned fire experiments of a full-scale two-story steel framed building constructed at the National Fire Research Laboratory. This first experiment was aimed to quantify the fire resistance and behaviour of the steel composite floor system commonly built in the United States, incorporating prescriptive approaches for a 2-hour fire resistance rating. The 9.1 m × 6.1 m composite floor assembly, situated in the edge bay on the first floor of the prototype building, was tested to failure under a natural gas fuelled compartment fire and simultaneously applied mechanical loads. The test showed that the protected floor beams and girders of the test assembly achieved matching or superior fire resistance based on the acceptance criteria of standard furnace testing. However, the test floor slab exhibited a potential fire hazard within a specified fire rating period because of the use of a minimum code-compliant shrinkage reinforcement (59 mm²/m). The heated slab cracked around the interior edges of the test bay less than 30 min into heating, followed by centre cracks along the secondary beam at 70 min. This centre breach, accompanied by ruptures of wire reinforcement, was caused by tension (due to catenary action) developed along the shorter span of the test floor assembly. This result suggests that the minimum slab reinforcement prescribed for normal conditions may not be sufficient to activate tensile membrane action of a composite floor system under the 2-hour standard fire exposure.

Keywords: Composite floors; steel buildings; fire resistance; compartment fire experiments

1 INTRODUCTION

There is lack of experimental data quantifying the fire performance of full-scale composite steel frames designed in accordance with United States (U.S.) building codes and specifications. Standard fire testing of the full-scale composite floor assemblies, incorporating both steel member connections and slab continuity, are extremely rare due to the size limitations of testing furnaces. The National Institute of Standards and Technology (NIST) is conducting a multi-year experimental test program to quantify the behaviour and limit states of full-scale structural steel frames with composite floors under compartment fire conditions. This test program consists of two parts: Phase 1 covers 12.8 m long composite beams with

¹ Research Structural Engineer, National Institute of Standards and Technology (NIST)
e-mail: lisa.choe@nist.gov, ORCID: <https://orcid.org/0000-0003-1951-2746> (corresponding author)

² Foreign Guest Researcher, National Institute of Standards and Technology (NIST)
e-mail: selvarajah.ramesh@nist.gov, ORCID: <https://orcid.org/0000-0002-9525-6767>

³ Foreign Guest Researcher, National Institute of Standards and Technology (NIST)
e-mail: xu.dai@nist.gov, ORCID: <https://orcid.org/0000-0002-9617-7681>

⁴ Research Structural Engineer, National Institute of Standards and Technology (NIST)
e-mail: matthew.hoehler@nist.gov, ORCID: <https://orcid.org/0000-0002-6049-7560>

⁵ Supervisory Mechanical Engineer, National Institute of Standards and Technology (NIST)
e-mail: matthew.bundy@nist.gov, ORCID: <https://orcid.org/0000-0002-1138-0307>

simple shear connections [1] and Phase 2 covers 9.1 m by 6.1 m composite floor assemblies in a two-story structural steel gravity frame. This paper presents the first experiment of the Phase 2 study conducted at NIST's National Fire Research Laboratory (NFRL) [2] on November 14, 2019. The test floor assembly was located on the first floor south-edge bay of the two-story prototype building and tested to failure under combined mechanical loads and a standard fire exposure simulated using natural gas burners. The objective of this test was to measure the structural and thermal responses of the composite floor assembly designed and constructed following the current U.S. prescriptive approach and to evaluate its system-level fire resistance based on the American Society of Testing and Materials (ASTM) standard E119 criteria [3]. The experimental results presented herein will serve as baseline to compare with the remaining experiments in Phase 2 and be used to guide the validation of computational models and design tools.

2 TEST STRUCTURE

The two-story structural steel frame was constructed to conduct a series of single-bay compartment fire experiments; see Figure 1(a). This test frame consisted of three bays by two bays in plan with a total floor area of 18 m × 11 m. The total height was approximately 7.2 m. The composite floor assembly was constructed on the first floor (3.8 m above the ground floor), whereas on the second floor a beam framing was erected without concrete slab. The same sizes of wide-flange steel shapes were used for both the first and second floor frames. Figure 1(b) shows the plan view of the prototype building. All steel columns were W12×106 shapes typically used for reaction frames in the NFRL and anchored to the laboratory strong floor. The perimeter columns were continuous over two stories, whereas the two interior columns were spliced 92 cm above the concrete slab on the first floor. The 9.1 m long W16×31 beams in the fire test bay were connected to the column flange or at midspan of the 6.1 m long W18×35 girder using standard shear tabs; see Figure 2(a). Extended shear tabs were used at the ends of W18×35 girders; see Figure 2(b). All other beams and girders were connected using bolted angles and extended shear tabs, respectively. All structural steel shapes and shear tabs were rolled from A992 steel (a minimum specified yield strength of 345 MPa) and A36 steel (a minimum specified yield strength of 250 MPa), respectively.

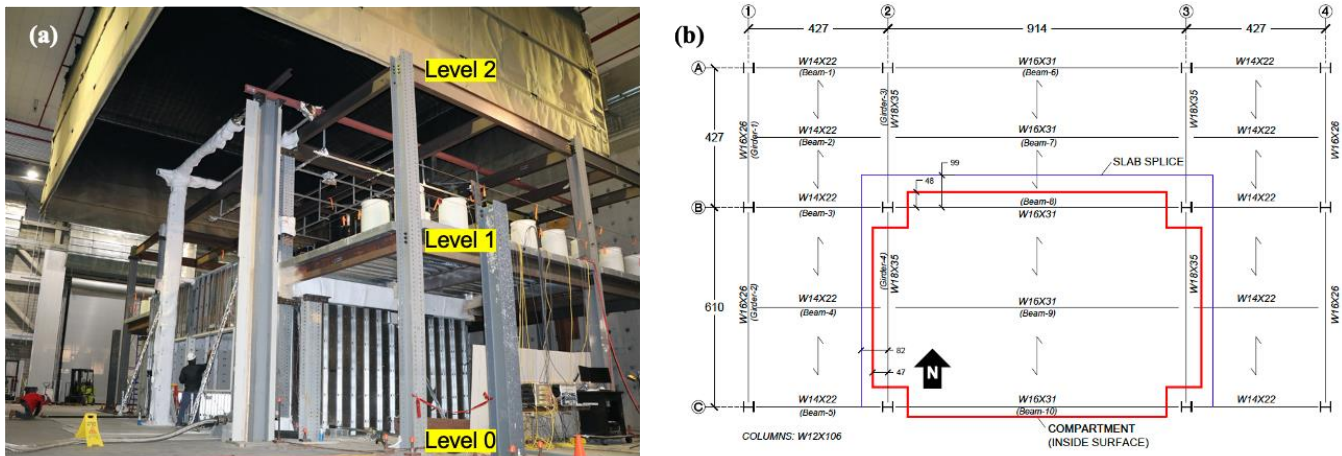


Figure 1. (a) Two-story prototype steel framed building; (b) Floor plan view (dimensions in cm).

The concrete slab was lightweight concrete (a minimum specified compressive strength of 28 MPa) cast on 76 mm deep formed steel decking. The concrete mixture included polypropylene fibres to minimize thermally induced spalling as suggested by Maluk et al. [4], which was also used for the Phase 1 composite beam study [5]. The concrete slab was cast approximately 5 months prior to fire testing. The moisture content of the concrete at time of fire testing was 7.6 % when measured according to ASTM C642-13 [6]. As shown in Figure 2(c), the slab thickness was 83 mm required for the 2-hour fire resistance rating with exposed steel deck. The cold-formed welded wire reinforcement of 59 mm²/m, spaced at 152 mm, was embedded 41 mm below the top surface of the concrete slab. This is the minimum shrinkage reinforcement prescribed in the relevant U.S. design standard [7]. The floor slab was acting partially composite with steel beam assemblies through headed stud anchors (shaft Ø19 mm). For the W16×31 beams, a single headed

stud anchor was spaced at 305 mm; a pair of the same size stud anchors were welded atop the W18×35 girders at spacing of 356 mm, as shown in Figure 2(c). The corresponding degree of composite action was about 65 % of the ambient yield strength of the steel beams. In addition, the 77 cm long No. 4 hooked reinforcing bars (Ø13 mm) were placed perpendicular to the south edge beam under each stud to prevent separation of the heated concrete slab during the test. The slab splices along the interior edges of the test bay, shown in Figure 1(b), incorporated No. 4 bars and screw anchors so that the surrounding floor assemblies can be reused for subsequent fire tests. This splice design allows the full slab continuity (i.e., moment and shear transfer) between the test floor and the surrounding floor assemblies at ambient temperature. The construction detail at the northwest corner of the test bay is shown in Figure 3(a).

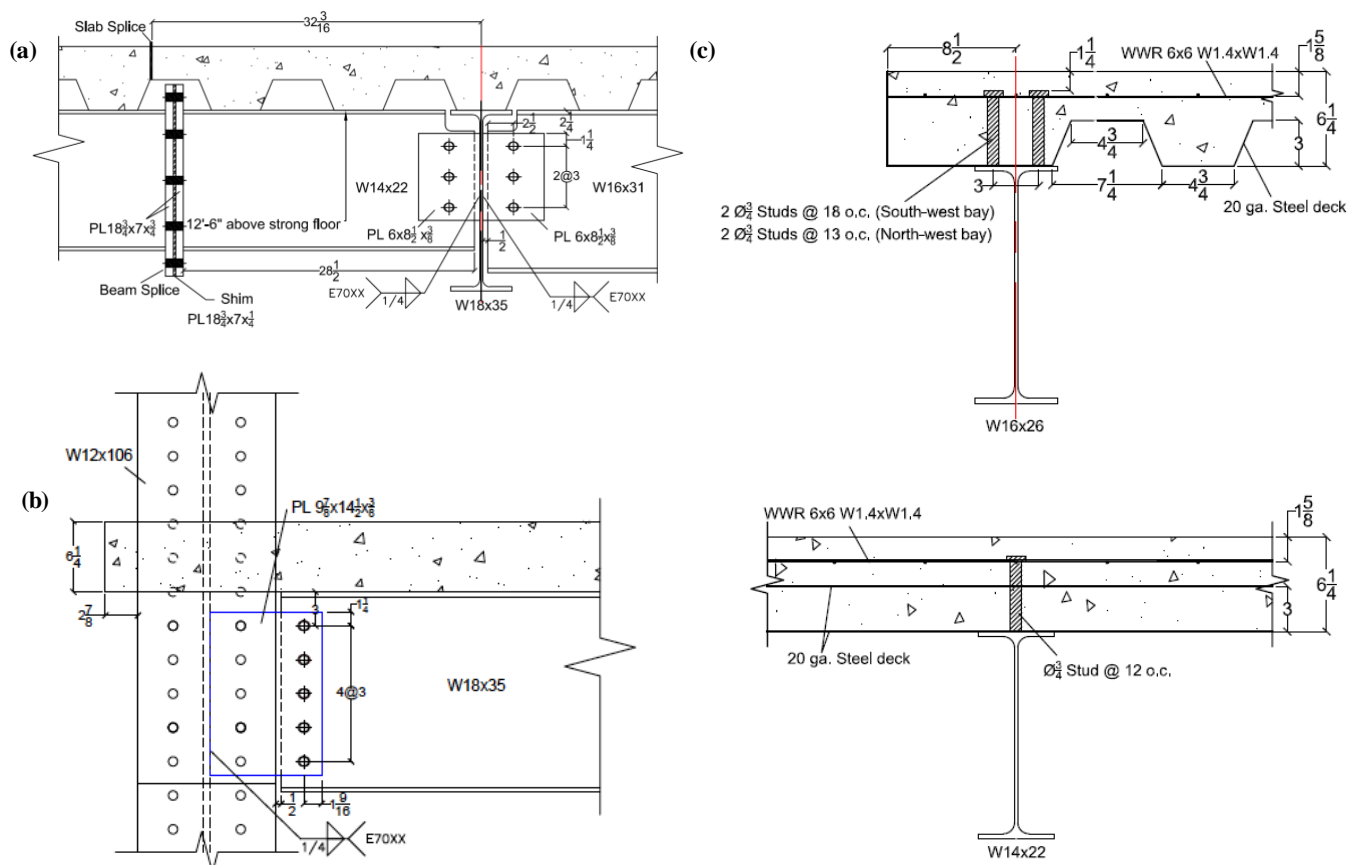


Figure 2. Details of (a) Standard shear-tab connection; (b) Extended shear-tab connection; (c) Composite sections. Dimensions in inch (1 in. = 2.54 cm)

Figure 3(b) shows a photograph of the fire test compartment, approximately 10 m long and 7 m wide. The height of the composite floor soffit was 377 cm above the compartment floor. The enclosing walls were constructed with 3 m tall sheet steel metals and a 48 mm thick gypsum board liner on the exposed wall surface. The 0.8 m gap between the compartment ceiling and the top edges of the three internal walls was lined with two layers of 25 mm thick ceramic blankets. Four natural gas burners (1.5 m × 1 m each) were distributed across the floor of the test compartment. The main vent was on the south wall, approximately 150 cm tall × 582 cm wide. There was a 30 cm tall × 582 cm wide slit on the north wall, designed for air intake only. The height of the windowsill on both the north and south walls was 100 cm above the strong floor.

The exposed steel frame within the test compartment, shown in Figure 1(b), was sprayed with a gypsum-based cementitious material (average specified density of 295 kg/m³) for the 2-hour fire resistance rating. The average measured thickness of sprayed fireproofing prior to fire testing was 18 mm for both primary W16×31 beams and W18×35 girders and 13 mm for the secondary W16×31 beam. The coefficient of variation in thickness measurements was approximately 15 %. The exposed steel connections and columns were over sprayed with the same fireproofing material, with the thickness ranging from 25 mm to 28 mm.

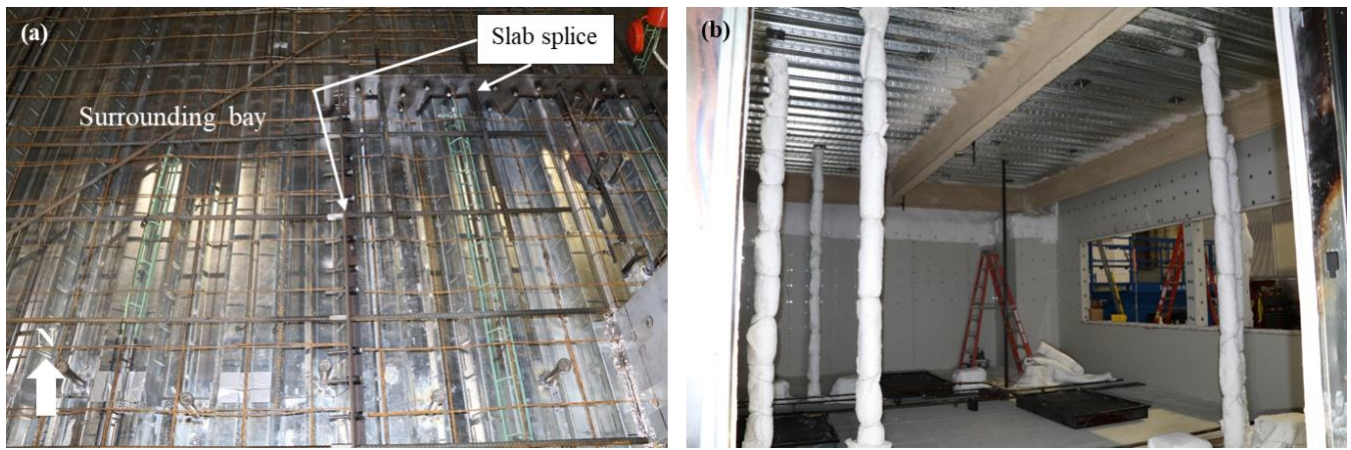
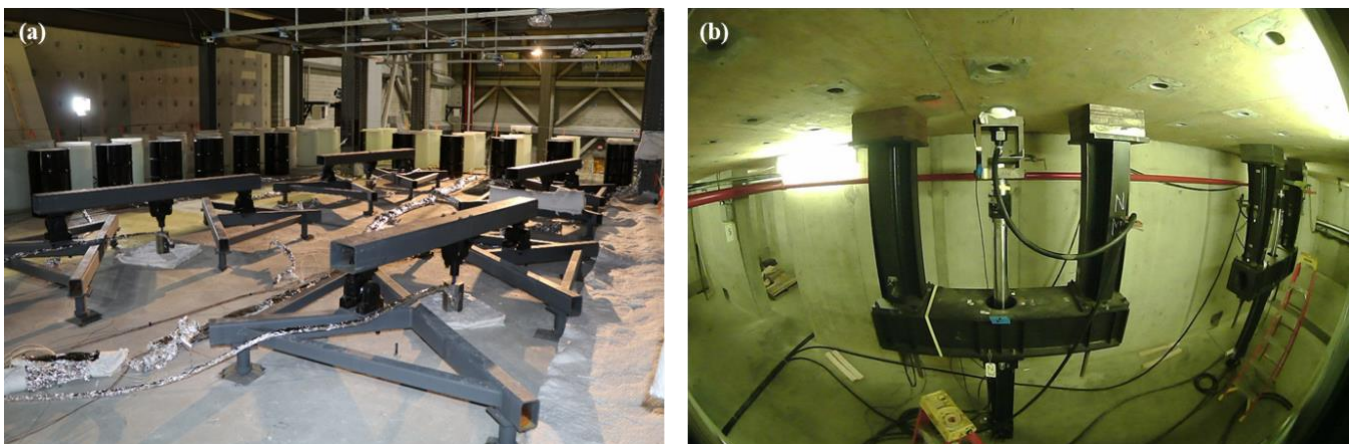


Figure 3. (a) Reinforcement details of slab splice; (b) Fire test compartment with the main vent on the south wall.

3 TEST CONDITIONS

The total mechanical load imposed on the $9.1 \text{ m} \times 6.1 \text{ m}$ test floor assembly was approximately 150 kN (or 2.7 kPa), conforming to the American Society of Civil Engineers (ASCE) gravity load combination [8] of $1.2 \times \text{dead load} + 0.5 \times \text{live load}$. This load was distributed at twenty-four points across the test floor using water-cooled loading frames connected to four hydraulic actuators mounted in the basement, Figures 4(a) and 4(b). The total floor load including the assembly self-weight was approximately 5 kPa. The surrounding floors were loaded by water-filled drums, simulating a uniformly distributed mechanical load about 1.3 kPa. The load ratio (i.e., total load normalized by the ambient design capacity) of the test assembly was approximately 0.3 for both the secondary composite beam and the standard shear tabs of the same beam. The load ratio of the steel members and connections in the surrounding bays was less than 0.2.

The hydraulically loaded test floor assembly was exposed to a natural gas fuelled compartment fire, Figure 4(c), simulating the ASTM E119 time-temperature curve. Figure 4(d) shows the burner heat release rate (HRRburner) versus time relationship used in this test. This relationship was verified through a series of mock-up tests [10] conducted prior to this experiment. It should be noted that, as shown in Figure 4(d), there was a short loss ($< 3 \text{ min}$) of the HRRburner data at 102 min due to network disruption of the natural gas delivery system. The fire and mechanical loads were removed at approximately 107 min. The total expanded uncertainty (with a coverage factor of 2 as defined in [11]) in measurements of the burner heat release rate and mechanical load is estimated 1.4 % at 10 MW [12] and 2 % at 150 kN, respectively.



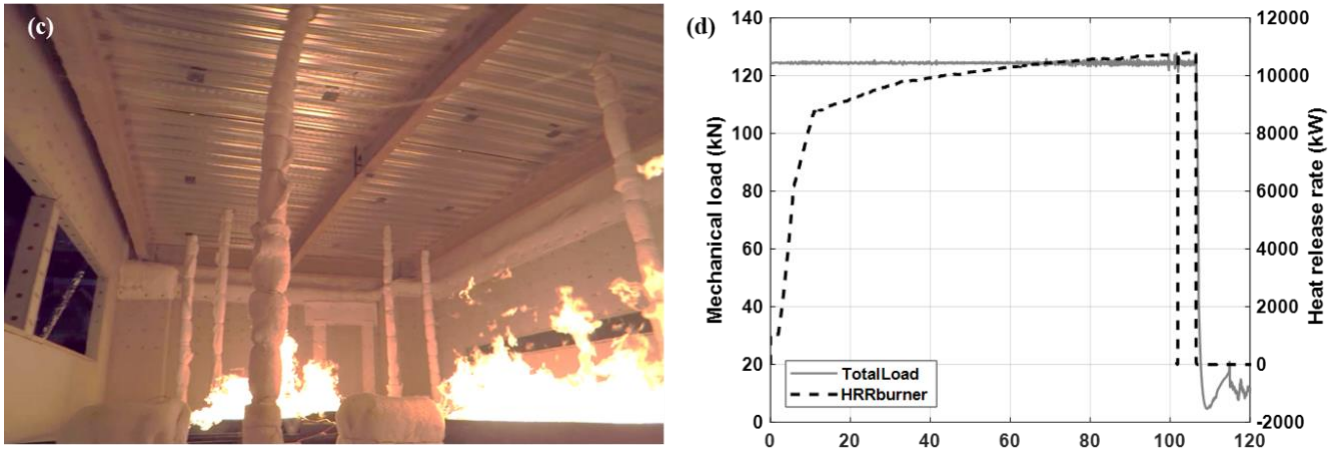


Figure 4. (a) Mechanical loading atop the test assembly; (b) hydraulic actuators mounted beneath the test compartment using yoke [9]; (c) compartment fire growth simulated with natural gas burners; (d) time history of total mechanical load (TotalLoad) and heat release rate of burners (HRRburner).

4 RESULTS AND OBSERVATIONS

4.1 Thermal response

Over two-hundred type K thermocouples (bead \varnothing 0.5 mm) were deployed at various locations across the test assembly. The average upper layer gas (ULG) temperature within the test compartment was measured using twelve Inconel-sheathed thermocouple probes hanging 305 mm below the steel deck. The average ULG temperature exceeded 700 °C at 11 min and reached a peak value of 1060 °C at 107 min. After 15 min from the burner ignition, the increase in the average ULG temperature resembled the International Organization for Standardization (ISO) standard 834 [13] temperature and was about 2 % higher than the ASTM E119 temperature. The standard deviation of temperatures measured using these thermocouples was less than 50 °C, indicating practically uniform temperatures below the test floor assembly.

Figure 5 illustrates the measured temperature rise in the midspan composite sections of the test assembly, Figure 2(c). For the W16 \times 31 composite beams, the average temperature of the web and bottom flange of the protected steel beams reached 600 °C at 60 min and exceeded 800 °C at 107 min, Figure 5(a). The average concrete temperature at 0.5 mm above the top rib of the steel decking along the beam centrelines increased to 270 °C at 107 min. Temperatures of headed stud anchors at 38 mm above the top flange and welded wire reinforcement (WWR) remained below 400 °C and 200 °C, respectively.

For the W18 \times 35 composite girders, as shown in Figure 5(b), the lower portion of the protected steel girders heated to 450 °C at 60 min and 700 °C at 107 min. The top flange steel temperature increased to 400 °C. The bottom concrete temperature in the shallow section next to the steel girder, Figure 2(c), increased to 600 °C at 80 min but significantly influenced by combined effects of concrete fractures and debonding of steel decking afterwards. The average temperatures of headed studs (at 2.5 cm above the steel decking) and WWR atop the girders never exceeded 300 °C and 200 °C, respectively, during and after fire exposure.

The standard deviation in temperatures of the three heated W16 \times 31 beams ranged from 60 °C to 110 °C, as indicated by error bars in Figure 5(a). This temperature variation might be caused by thermally induced fissures and degradation in coated insulation as the beams were undergoing severe thermal elongation and bending under fire loading. Unlike W16 \times 31 beams, one can observe a smaller temperature difference (30 °C to 60 °C) between the east and west W18 \times 35 girders, Figure 5(b). These girders seldom physically deformed, and thereby the applied fireproofing appeared to maintain relatively good integrity during fire loading.

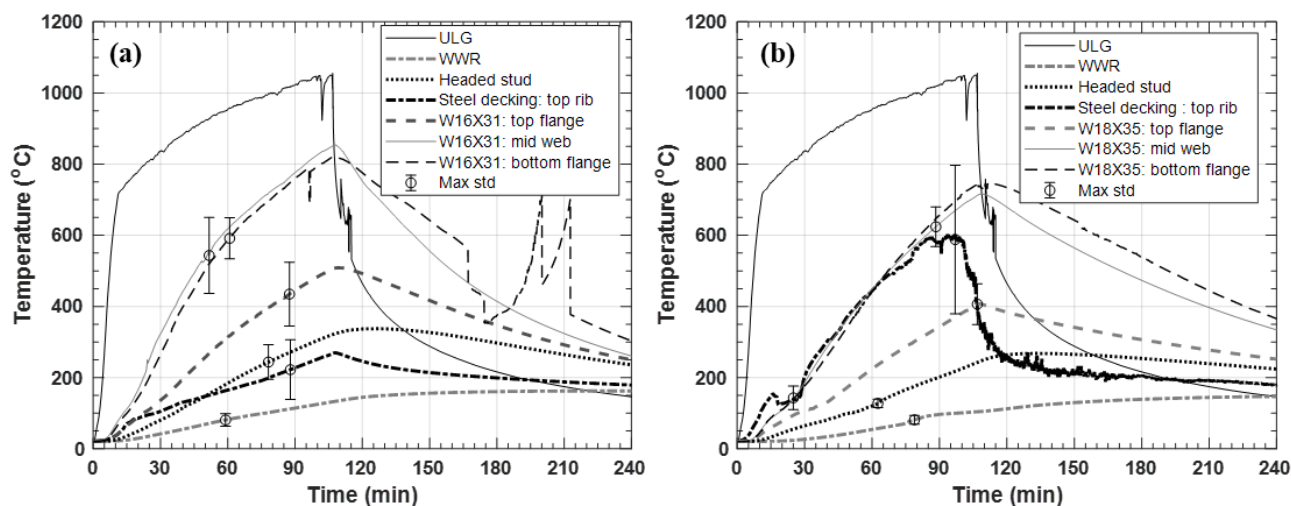


Figure 5. (a) Measured temperatures of (a) W16×31 composite beam and (b) W18×35 composite girder. Plotted with the average values of three W16×31 beams or two W18×35 girders in the test compartment.

A total of thirty-six thermocouples were mounted inside of the 9.1 m by 6.1 m test floor slab at various locations that were not thermally shaded by the steel framing underneath. Figure 6 shows the average concrete temperature in the deep (thickness = 159 mm) or shallow (thickness = 83 mm) sections of the concrete slab. Thermocouples installed at the steel decking (TST-5*) measured the hottest temperature, reaching nearly 900 °C during fire loading. The peak temperature of the concrete near the bottom rib of the steel decking (TST-4) was about 100 °C higher than the concrete temperature near the top rib (TST-7). However, the spatial temperature variation of TST-5* and TST-7 was quite high (> 110 °C), as indicated by the large error bars. These temperatures could be sensitive to debonding of the concrete from the steel decking. Temperatures of the WWR were affected by varying thickness of the concrete slab. At 107 min, for example, TST-1 (at deep sections) and TST-6 (at shallow sections) was 120 °C and 380 °C, respectively. In addition, the concrete temperatures towards the top surface (TST-1, TST-5, and TST-6) or at the centroid of the deep section (TST-2) were affected by moisture, as evidenced by the temperature plateau at 100 °C, over a longer period.

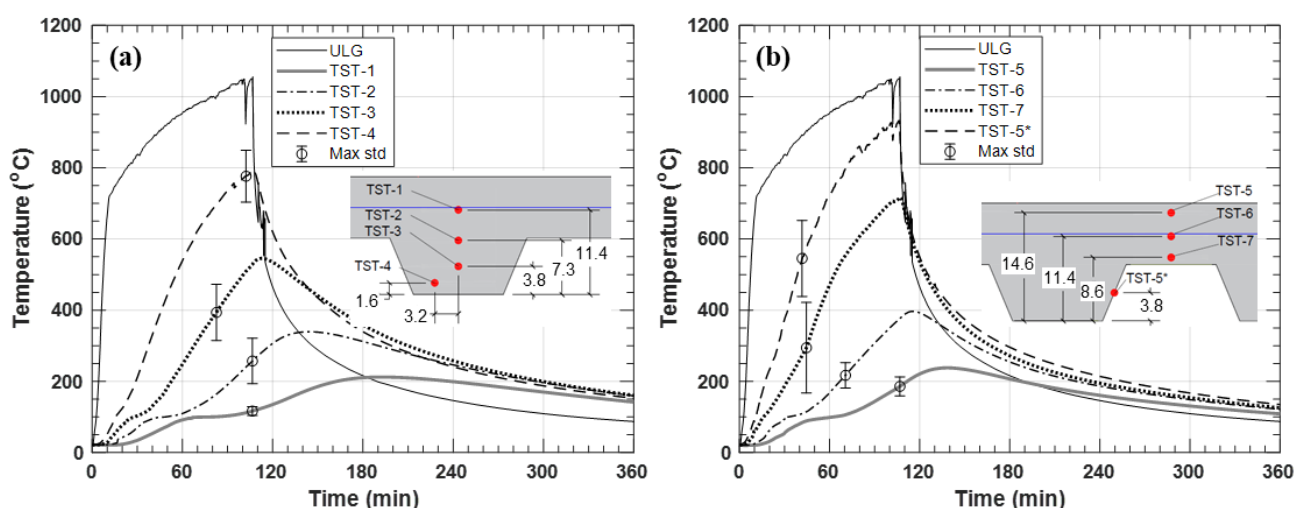


Figure 6. Measured temperatures of (a) deep section and (b) shallow section of the concrete floor slab. Plotted with the average values of six deep sections or four shallow sections across the test floor; thermocouple locations are in cm.

Although the data are not presented in this paper, the top (unexposed) surface temperature continued to rise during the cooling phase (up to 1 hour following extinguishment), ranging from 140 °C to 180 °C. Temperatures of the beam-to-girder shear-tab connection reached over 600 °C, whereas that of the shear-tab connections to columns were below 400 °C due to the thicker insulation sprayed on those regions. Detailed discussions and results of the connection temperatures are presented in the companion paper [14].

Estimates of total expanded uncertainty (with a coverage factor of 2) in measurements of the gas-phase, steel, and concrete temperatures are 8 % at 1110 °C, 4 % at 970 °C, and 6 % at 310 °C, respectively.

4.2 Structural response

The loaded test floor assembly continuously sagged during heating, while sequentially developing concrete fractures at various locations. No explosive spalling of the concrete was visible during or after the experiment, however, small ‘popping’ sounds continued during heating indicating that (micro) spalling was occurring between the bottom of the slab and the steel deck. Concrete surface cracks first appeared along the east and west girders as well as the north edge beam of the test bay about 20 min to 30 min after ignition. Around 40 min into heating, the southeast corner of the heated floor slab fractured making a loud noise. After 70 min, tensile fracture of the concrete was visible near the longitudinal (east-west) centreline of the test floor. Reaching 100 min in fire, small flames were intermittently visible above the top of the heated slab towards the east and west ends of this longitudinal crack, indicating failures of some screw joints of steel deck units in those locations. From this point forward, the mechanical loads on the south side of the test slab appeared to be supported by the steel deck and the south edge beam with concrete hanging cantilever, Figure 7(a). The fire and mechanical loading were removed at 107 min due to safety concerns.

A total of thirty displacement transducers were deployed to characterize the displacement of the two-story steel frame and the 9.1 m by 6.1 m test floor assembly during and after fire exposure. Figure 7(b) shows locations of the selected vertical and horizontal displacement sensors (labelled VD and HD, respectively) of the test assembly. All VD sensors in Figure 7(b) were located at the transverse (north-south) centreline of the test assembly. HD4 and HD6 sensors were used to measure thermal expansion at the perimeter of the heated floor assembly in the east-west direction and the north-south direction, respectively. HD9 measured the lateral displacement of the southeast column at the first story level. These horizontal displacement measurements were made at 15 cm above the top surface of the test floor slab. The total expanded uncertainty (with a coverage factor of 2) in measurements of the vertical and horizontal displacements is estimated 1 % at 580 mm and 5 % at 35 mm, respectively.

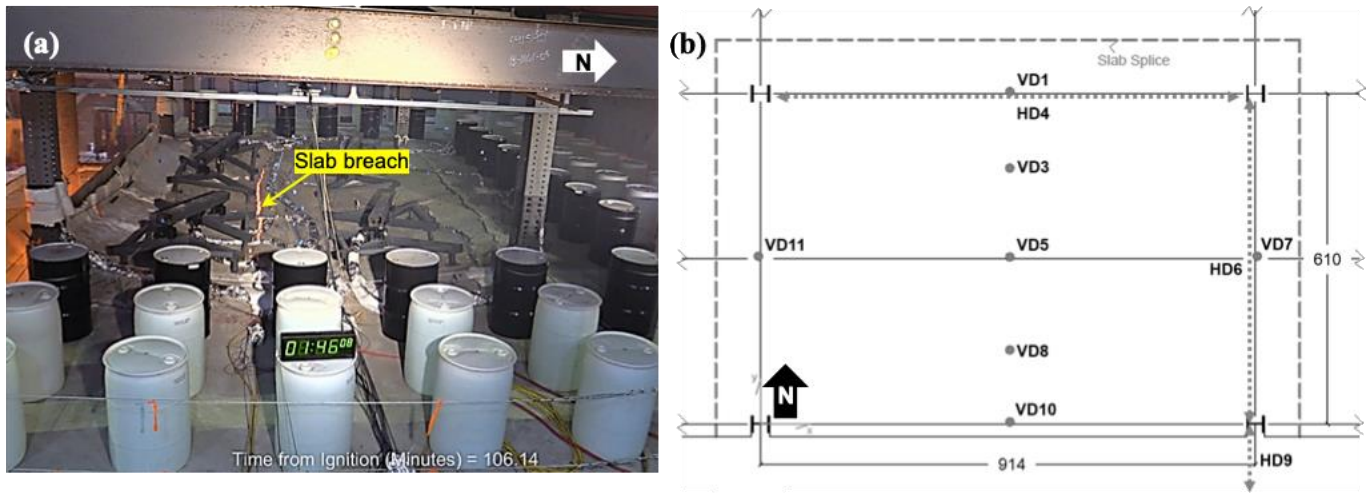


Figure 7. (a) Breach of the test floor slab; (b) Locations of displacement measurements with dimensions in cm.

As shown in Figure 8, the vertical displacement of the test floor assembly continuously increased during heating (until 107 min) and partly recovered during cooling; however, collapse did not occur. Until 60 min after ignition the values of VD5 and VD8 were similar. However, after the test floor slab began to breach (wide longitudinal crack) around 70 min, VD5 surpassed VD8 and reached 460 mm at 92 min. This displacement was approximately equal to the ratio of $L/20$ where L is the east-west span of 9.1 m. While VD5 finally reached the $L/16$ ratio at 107 min, there was no indication of ‘runaway’ deformation. Conversely, the vertical displacements of the perimeter steel members (VD1, VD7, VD10, and VD11) were relatively small, ranging from 65 mm to 210 mm. Also, VD7 and VD11 appeared to be less affected by the longitudinal concrete fractures. These perimeter members exhibited some degree of twisting and lateral deformations, discovered during the post-test inspections.

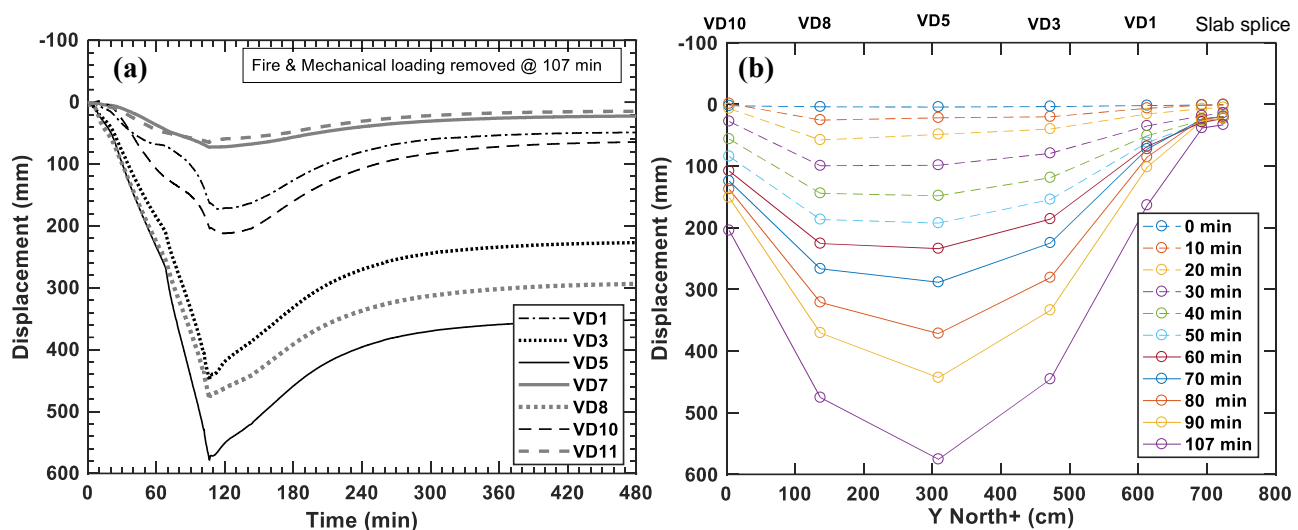


Figure 8. (a) Vertical displacements after the burner ignition at 0 min; (b) Vertical displacement profile varying with fire exposure time.

Figure 9(a) shows the midspan vertical displacements of fireproofing protected steel beams and girders as a function of the bottom flange temperatures. When the bottom flange temperature exceeded 700°C , the vertical displacement of the secondary beam (VD5) increased much more rapidly from $0.4\text{ mm}/^{\circ}\text{C}$ to $1.4\text{ mm}/^{\circ}\text{C}$. This change could be caused by several factors, such as initiation of a longitudinal breach of the test floor slab and continuous degradation of flexural strength and stiffness of support beams at higher temperatures. In the early stage of fire, on the other hand, the increase in displacements of the east and west girders (VD7 and VD11, respectively) was affected by smaller applied load ratios than the secondary beam. Furthermore, the heating rate of these members was relatively slow due to larger heat capacity and any heat loss associated with their close proximity to the upper wall lining with ceramic blankets or concrete fractures above these members. The vertical displacement of the south edge beam (VD10) was more responsive to the temperature change than other three perimeter members due to its free slab edge allowing less resistance to lateral-torsional buckling of this beam.

The horizontal (axial) displacements of the test assembly were measured using the lateral displacements of the columns at the first-story level. Figure 9(b) shows the time-varying horizontal displacement of the north primary beam (HD4) and the east girder (HD6) of the test assembly as well as the lateral displacement of the southeast column. The positive values in this figure represent the displacements due to thermal expansion of the heated test assembly. The values of HD6 and HD9 were similar throughout the test, indicating that the east girder expanded in single direction, towards the south due to a much larger restraint provided by the north surrounding frame. These displacements increased continuously to a peak value ranging from 32 mm to 34 mm until the fire test was terminated. The value of HD4 increased at a similar rate but began to decrease after 70 min when the longitudinal fracture of concrete occurred. The maximum axial displacement due to thermal expansion in the east-west direction was approximately 22 mm.

Figure 10 shows the final fracture pattern of the test floor slab after cooling. As mentioned earlier, concrete cracks developed along the north, east, and west edges of the test bay, followed by the longitudinal cracks 530 mm or less south of the secondary beam. Most of WWR ($59\text{ mm}^2/\text{m}$) across the thicker lines of fractures visible in Figure 10 completely ruptured. Neither concrete failures along the south (free) edge (i.e., separation from the south edge beam) nor slab splice failures were witnessed. Based on crack openings of the concrete, the east and west edge cracks were initiated near the flanges of the southeast and southwest columns, whereas the north edge crack was propagated from the midspan or its vicinity. No through-depth fractures were observed around the northeast and northwest columns.

The middle breach of the test floor slab appeared to be occurred due to catenary action in the north-south direction where the steel decking was continuous into the north adjacent bay. It is believed that the tensile membrane action of the test floor slab was not achieved or developed in a limited fashion because of the early formation of concrete fractures and ruptures of welded wire reinforcement along the east and west

edges. These through-depth cracks located 100 mm or less inside of the test-bay column grid, which formed shortly after fire ignition and continued to widen unchecked during heating. Thus, the headed stud anchors on the east and west girders were ineffective to induce tension in the concrete in the east-west direction as the heated floor slab continued to deflect downward. In contrast, the north edge crack formed 370 mm or less north of the north primary beam (i.e., outside of the test-bay column grid) and thereby the headed stud anchors on all three 9.1 m long beams appeared to provide anchorage of the concrete and steel decking against tension developing in the north-south direction. As the vertical displacement of the test floor increased in fire, the excessive tension would develop more effectively in the north-south direction than in the east-west direction until WWR finally ruptured at critical locations. This WWR rupture would happen in the concrete where the vertical displacements were greater, i.e., south of the secondary beam as shown in Figure 8(b).

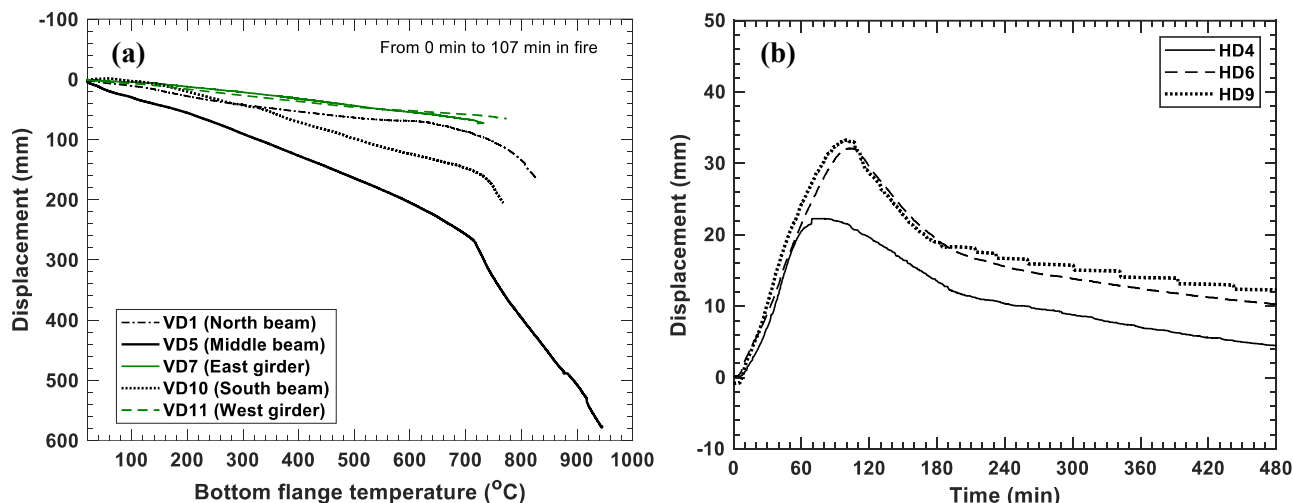


Figure 9. (a) Vertical displacement data as a function of bottom flange temperatures during heating; (b) Horizontal displacements measured at 15 cm above the test floor slab during heating (until 107 min) and cooling.

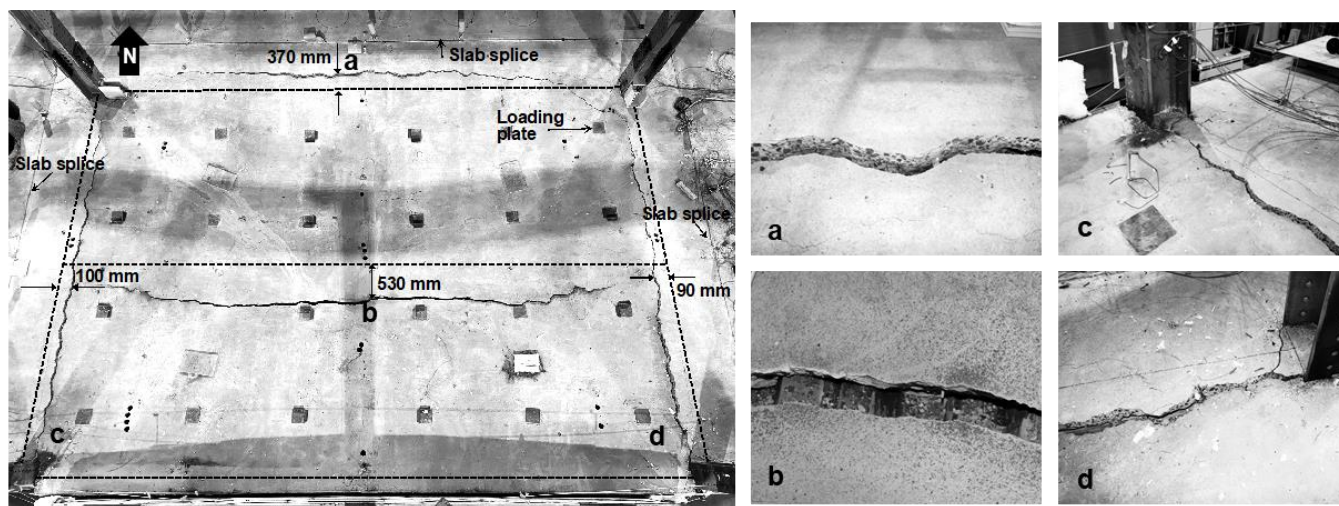


Figure 10. Top of the test floor slab after cooling. Dashed lines define the test-bay column grid. The four photographs on the right (a through d) show close-ups of concrete fractures.

Figure 11 shows the underside of the test floor assembly after cooling. The steel deck below concrete fractures (Figure 10) mostly maintained its integrity with good ductility. Only a local rupture was found in the deck unit below the east end of the mid-panel longitudinal crack, i.e., near the west edge of the top flange of the east girder. All three 9.1 m long W16×31 beams exhibited permanent strong axis bending deformation and local buckling near the beam ends. Furthermore, the north and south primary beams also exhibited twisting and lateral deformations. The end connections of these beams, however, maintained their structural integrity. The east and west W18×35 girders showed little residual vertical deflection and exhibited minor out-of-plane deformations in the webs near the end connections. The extended shear tabs

welded to the northeast and the northwest columns exhibited noticeable out-of-plane deflection but no bolt failures. The extended shear tabs welded to the southeast and the southwest columns deflected little, whereas there were partial shear ruptures in the lower bolts of the southeast connection. The sprayed fireproofing on the beams and girders mostly remained intact, although fissures were evident on the beam web near the end connections and at the lower beam web of the secondary beam at midspan.

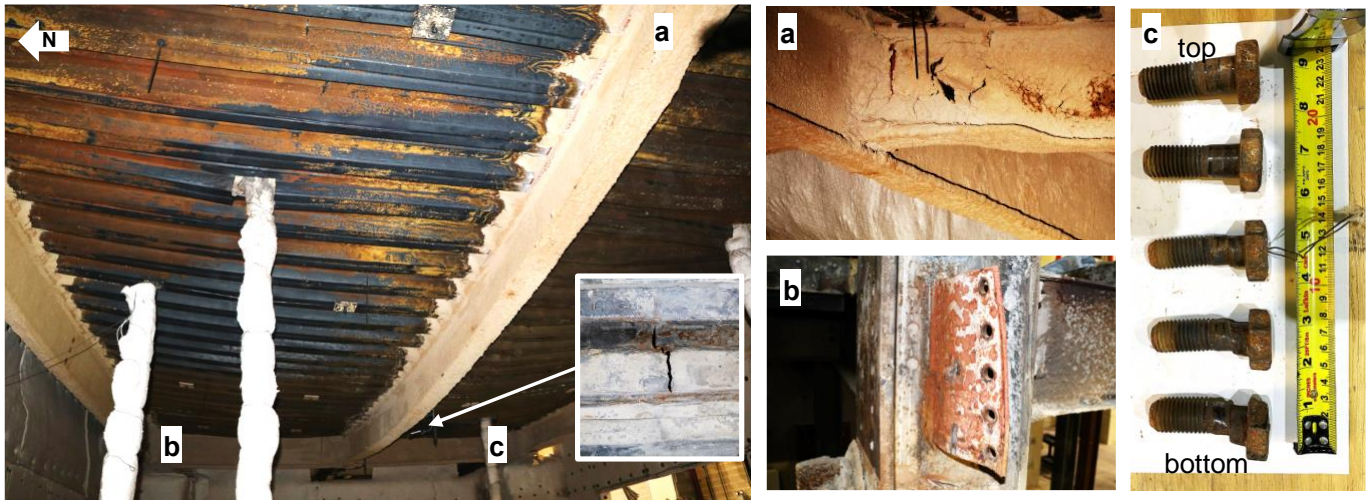


Figure 11. Fire-exposed steelwork of the test floor assembly after cooling. Close-ups of some deflected steel parts are shown in a through c.

4.3 Comparison with ASTM E119 criteria

The intent of standard fire testing, mostly performed using a purpose-built furnace, is to provide a consensus-based method to evaluate the duration for which an *isolated* floor assembly contains a fire while retaining its structural stability, the so-called *fire resistance rating* expressed in minutes or hours. This testing is typically performed using a test assembly with limited size (e.g., a minimum floor area of 16.7 m² and a minimum beam span of 3.7 m [3]) with two end support conditions, either *restrained* or *unrestrained* as explained in LaMalva et al [15]. A test assembly is required to resist its maximum load for normal conditions (e.g., $1.2 \times \text{dead load} + 1.6 \times \text{live load}$ per ASTM E119 standard) while subjected to standard furnace heating. The fire resistance rating of a test assembly is usually determined based on limiting temperatures and displacements as discussed below.

Figure 12 summarizes the test results in comparison with ASTM E119 acceptance criteria. For the 2-hour *restrained* fire resistance rating, the test specimen must meet the following conditions: (i) sustaining the applied loads with no ignition of cotton waste placed on the top of the heated concrete slab during the full rating period, (ii) the average temperature on unexposed surface less than 139 °C above its initial temperature during the first hour, (iii) a peak temperature of structural steel members below 704 °C during the first hour, and (iv) the average temperature at any section of structural steel members below 593 °C during the first hour, and (v) the maximum total displacement less than the value of $Lc^2/400d$ where Lc = beam clear span, d = depth of composite beam, and the corresponding displacement rate less than the value of $Lc^2/9000d$. As shown in Figure 12, the protected individual W16×31 beams and W18×35 girders of the test assembly successfully met the limiting temperature and displacement criteria. The average concrete surface temperature measured by eight thermocouples distributed across the test assembly was approximately 120 °C prior to extinguishment of the fire. Although the maximum total displacement of the secondary beam exceeded the ASTM E119 displacement limit, the measured displacement rate of this beam was 40 % less than its specified value. It is important to note that this condition was achieved at the total floor load from the load combination of $1.2 \times \text{dead load} + 0.5 \times \text{live load}$, approximately 60 % of the maximum load condition (e.g., $1.2 \times \text{dead load} + 1.6 \times \text{live load}$) as prescribed in ASTM E119 [3].

Furthermore, this test has revealed some potential issues related to the integrity of a composite floor assembly as part of compartmentation under fire loading. As shown in Figure 13, the centre breach in the test floor slab, initiated prior to the specified rating period of 120 min, was accompanied by ruptures of the wire reinforcement in tension at the mid-panel displacement of 350 mm ($L/26$) or greater. A minimum

code-required amount of shrinkage reinforcement ($59 \text{ mm}^2/\text{m}$) used in the test assembly was insufficient to resist thermally induced tension during the investigated fire. Although the steel deck continuously running in the transverse (north-south) direction of the test assembly appeared to be ductile at large vertical displacements, failure of side deck joints (screws failure at the decking overlap), local deck ruptures, exposure of the heated decking units within concrete cracks allowed the penetration of flames and hot gases beyond the test compartment. This condition could have potentially ignited cotton waste placed on the unexposed surface, failing to meet the standard fire testing criterion (i) as mentioned above.

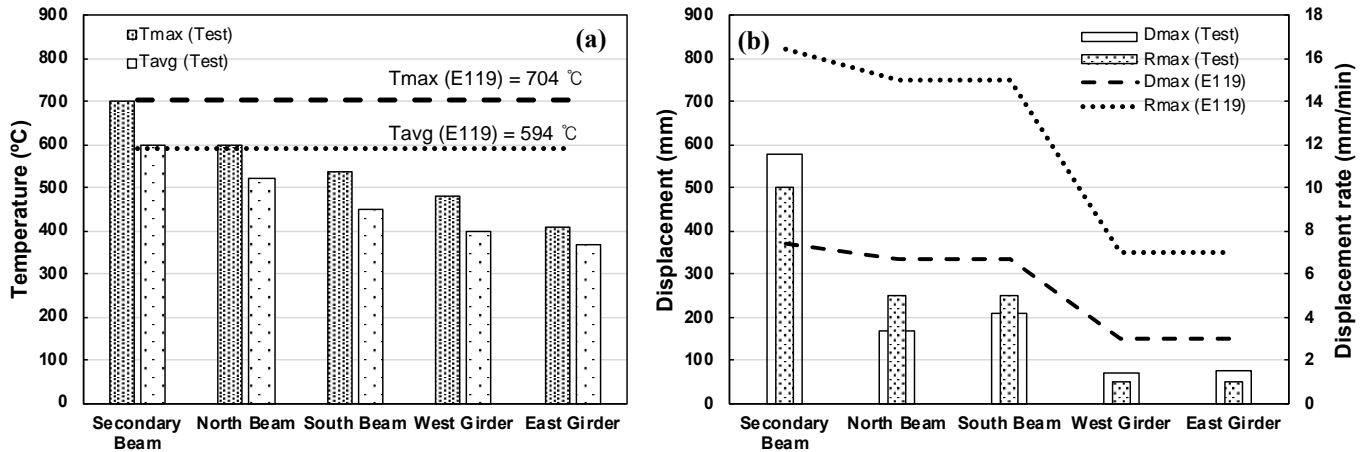


Figure 12. Comparisons of the test results with (a) limiting temperatures and (b) limiting displacements and displacement rates, where D_{max} = maximum displacement and R_{max} = maximum displacement rate.

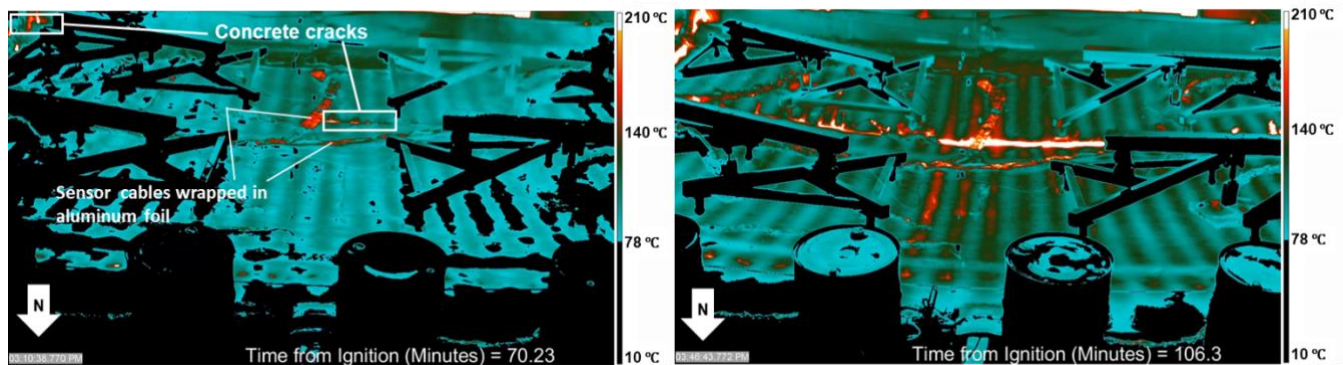


Figure 13. Thermal images of the top of the test floor slab at 70 min and 106 min after fire ignition.

5 SUMMARY & CONCLUSIONS

This paper presented the results of the first fire experiment on the 9.1 m by 6.1 m composite floor assembly situated on the first floor, south-edge bay of the two-story steel building designed and constructed following the current U.S. construction practice. The test floor assembly was subjected to a simulated compartment fire environment and mechanical loads conforming to the ASCE 7 load combination for extraordinary events (approximately 5 kPa including the assembly self-weight). The fire test conditions as well as thermal and structural responses of the test assembly to the combined effects of fire and mechanical loading are discussed and compared with the ASTM E119 acceptance criteria.

This test demonstrated that all fire-protected floor beams and girders met the ASTM E119 limiting temperatures. Also, these steel members never reached runaway at large vertical displacements (up to the ratio of $L/16$). The test floor assembly did not collapse after fire exposure, although some partial shear ruptures of connecting bolts were discovered after the test. However, the heated floor slab, during fire loading, exhibited a potential fire hazard before reaching a specified rating period, because of the use of the minimum code-compliant shrinkage reinforcement of $59 \text{ mm}^2/\text{m}$. The test floor slab began to crack along the interior edges (hogging moment regions) of the test column grid less than 30 min after ignition of the

fire. The centre cracks appeared around the midspan of the secondary beam at 70 min, which continued to propagate in the east-west direction. The glowing hot deck was exposed on the top of the slab through enlarged concrete cracks. This main breach was caused by ruptures of wire reinforcement in tension (due to catenary action) parallel with formed steel decking. Membrane action of the floor slab appeared not to be effective due to ruptures of the wire reinforcement across the east and west edges of the test-bay column grid and the subsequent loss of the east and west vertical supports of the concrete slab. This initial experiment suggests that the minimum required slab reinforcement currently allowed in the U.S. practice may not be sufficient to maintain the structural integrity of the composite floor assembly during structurally significant fire events.

Further study is recommended to evaluate the fire hazard of relatively ‘thin’ concrete slab details permitted in steel building constructions. As future work, the second test in this experimental program will study the influence of enhanced slab design (for both strength and ductility) on the fire performance of composite floor systems and the effectiveness of tensile membrane action, which is believed to significantly improve the fire safety of steel-framed buildings. The influence of slab reinforcement on the fire performance of composite floor systems is discussed in Choe et al. [16], which is the basis of the experimental design of the second test being planned in 2021.

ACKNOWLEDGMENT

This work was conducted as part of the project “Measurement of Structural Performance in Fire” under the NIST Engineering Laboratory’s Fire Risk Reduction in Building Programs. The authors thank William Baker (Skidmore, Owings, and Merrill), Craig Beyler (Jensen Hughes), Luke Bisby (University of Edinburgh), Ian Burgess (University of Sheffield), Charles Carter (AISC), Charles Clifton (University of Auckland), Michael Engelhardt (University of Texas), Graeme Flint (Arup), Nestor Iwankiw (Jensen Hughes), Kevin LaMalva (Warringtonfire), Roberto Leon (Virginia Tech.), and Amit Varma (Purdue University) for their expert consultation. The authors also thank the NIST colleagues including Brian Story, Anthony Chakalis, Philip Deardorff, Laurean DeLauter, Marco Fernandez, Artur Chernovsky, Rodney Bryant, William Grosshandler, John Gross, Mina Seif, Ana Sauca, Fahim Sadek, Joseph Main, Chao Zhang, and Jonathan Weigand for their significant contributions to design, construction, and execution of this test program.

REFERENCES

1. Choe, L., Ramesh, S., Grosshandler, et al. Composite floor beams with simple shear connections subject to compartment fires: experimental evaluation, *Journal of Structural Engineering*, vol. 146, pp. 1-14, 2020. [https://doi.org/10.1061/\(ASCE\)ST.1943-541X.0002627](https://doi.org/10.1061/(ASCE)ST.1943-541X.0002627)
2. Bundy M., Hamins, A., Gross, J., Grosshandler, W., Choe, L., Structural fire experimental capabilities at the NIST national fire research laboratory, *Fire Technology*, vol. 52 (4), pp. 959-966, 2016. <https://doi.org/10.1007/s10694-015-0544-4>
3. ASTM, Standard methods of fire test of building construction and materials, ASTM E119–19, ASTM International, West Conshohocken, PA, 2019.
4. Maluk, C., Bisby, L., Terrasi, G.P., Effects of polypropylene fibre type and dose on the propensity for heat-induced concrete spalling, *Eng. Struct.*, vol. 141, pp. 584–595, 2017. <https://doi.org/10.1016/j.engstruct.2017.03.058>
5. Ramesh, S., Choe, L., Seif, M., et al. Compartment fire experiments on long-span composite beams with simple shear connections Part 1: experimental design and beam behavior at ambient temperature, Technical Note (NIST TN) - 2054, p141, 2019. <https://dx.doi.org/10.6028/NIST.TN.2054>
6. ASTM, Standard Test Method for Density, Absorption, and Voids in Hardened Concrete, ASTM C642 - 13, ASTM International, West Conshohocken, PA, 2013. <https://doi.org/10.1520/C0642-13>
7. SDI, C-2017 Standard for composite steel floor deck-slabs, Steel Deck Institute (SDI), 2017. <http://www.sdi.org/wp-content/uploads/2017/02/ANSI-SDI-C-2017-Standard.pdf>
8. ASCE, Minimum Design Loads and Associated Criteria for Buildings and Other Structures, ASCE/SEI 7-16, American Society of Civil Engineers, Reston, VA, 2016.

9. Choe, L., Ramesh, S., Hoehler, M. National fire research laboratory commissioning project: testing steel beams under localized fire exposure, Technical Note (NIST TN) – 1983, p117, 2018.
<https://dx.doi.org/10.6028/NIST.TN.1983>
10. Zhang, C., Grosshandler W., Sauca A., and Choe L. Design of an ASTM E119 fire environment in a large compartment, Fire Technology, pp. 1–23, 2019. <https://doi.org/10.1007/s10694-019-00924-7>
11. Taylor B. and Kuyatt, C. Guidelines for Evaluating and Expressing the Uncertainty of NIST Measurement Results, Technical Note (NIST TN) – 1297, p24, 1994.
<https://doi.org/10.6028/NIST.TN.1297>
12. Bryant, R. and Bundy, M. The NIST 20 MW calorimetry measurement system for large-fire research, Technical Note (NIST TN) – 2077, p68, 2019. <https://doi.org/10.6028/NIST.TN.2077>
13. ISO, ISO 834-2:2019 Fire-Resistance Tests – Elements of Building Construction (ISO, Geneva), 2019. Available at <https://www.iso.org/standard/75137.html>
14. Dai, X., Choe, L., Fischer, E., Clifton, C. Thermal response and capacity of beam and shear connections during a large compartment fire experiment. Proceeding of the 11th International Conference on Structures in Fire (SiF' 20), November 30 – December 02, 2020, University of Queensland, Australia (accepted for publication)
15. LaMalva, K., Bisby, L., Gales, J. et al. Rectification of “restrained vs unrestrained”. Fire and Materials, pp 1-11, 2020. <https://doi.org/10.1002/fam.2771>
16. Choe, L., Ramesh, S., Zhang, C., Clifton, C. Behaviour of composite floor assemblies subject to fire: Influence of slab reinforcement. Proceeding of 2021 Eurosteel Conference, September 1-3, 2021, University of Sheffield, United Kingdom (in production)

THE ROLE OF END CONDITIONS ON THE BEHAVIOUR OF STEEL-CONCRETE COMPOSITE BEAMS IN FIRE

Priya S Natesh¹, Anil Agarwal²

ABSTRACT

There are several knowledge gaps to be addressed in the behaviour of composite beams under fire conditions. Some of the critical ones are: (i) the role of negative reinforcement near beam ends in controlling the beam deformation failure behaviour and (ii) the effect of the axial restraint stiffness on the performance of composite beam in heating and cooling phases of fire.

In the present work, a detailed three-dimensional FE based model of a long-span continuous composite beam was developed by using Abaqus, a commercially available finite element modelling and analysis software. The analysis method was calibrated and validated against the test data. Various structural responses such as beam deflection, rebar axial force, time of beam web buckling were predicted accurately. A parametric study was conducted to understand the effect of additional hogging moment reinforcement in the beam ends, and effect of support conditions for the rebar and beam. The axial restraint condition of the beam has a significant role in the behaviour of beam under fire loading. Stiff connections are not preferable during cooling phase of loading.

Keywords: Composite beam, fire, continuity, end conditions

1 INTRODUCTION

The composite beam optimises the material by making use of concrete slab in the compression zone and structural steel beam in the tension zone of the member. The shear tab connection in the beam provides an adequate bond between the concrete slab and steel beam. The concrete slab can be of flat or trapezoidal in cross-section. Currently, there is a significant need to understand the behaviour of long span composite beams under various critical loading conditions such as earthquake, fire, impact loading. There are a few experimental investigations on the behaviour of composite beams and connections under elevated temperatures [1- 5]. The experimental investigation of the behaviour of any structural members under fire loading and post-fire loading is costly, which demand alternative methods such as simulations using powerful software tools. Numerical model validated with experimental data can be used for such extensive study.

Wainman and Kirby [1] studied the behaviour of the simply supported composite beam of effective span 4.58m under fire loading. The width and depth of the flat slab in the experimental setup were 0.642m and 0.130m, respectively. The authors concluded that at elevated temperature, the flexural failure happened once it reaches its plastic capacity. Zhao & Kruppa [2] focused on the importance of steel protection and slab width in composite beam behaviour by carrying out experimental investigation on 4.9 m long beams. Steel beam IPE300 were connected to flat concrete slabs using 19 mm diameter headed shear studs. They observed that the crushing of concrete leads to the failure of protected composite beams and plasticisation of the steel beam leads to the failure of unprotected beams.

¹ Assistant Professor, Faculty of Science and Technology, ICFAI Foundation for Higher Education
(Declared as Deemed to be University u/s 3 of the UGC Act 1956), Hyderabad- 501 203, India
e-mail: priyas@ifheindia.org

² Assistant Professor, Indian Institute of Technology, Hyderabad - 502 285, India
e-mail: anil@iith.ac.in

Agarwal et al. [3-6] studied on the importance of shear tab connection in the stability of 10 storey office building subjected to a corner compartment fire. Selden et al. [7] investigated fire behaviour of composite beams and associated simple shear beam to column connections. A series of partial composite beams of span 3.65 m were tested. The authors observed that if the beams are overloaded, concrete compression failure is a potential failure mode for composite beams with flat slabs exposed to medium temperature levels. Prediction of behaviour of composite beams during the cooling phase makes it challenging, as the fracture of shear tab connection observed in the cooling period of loading. Fischer et al. [8-10] developed a numerical model and studied the behaviour of composite beams and connections in single-bay and three-bay systems. The connections considered were shear tab, single-angle and double angle. The fire protection, cooling rates were some of the parameters considered. With two-hour fire protection on steel beam, there was no tensile axial force developed in the member and no damage was observed. The connections with slotted hole and coped beam had large rotation and midspan deflections.

Choe et al. [11] carried out an experimental investigation on steel-concrete composite beam with double angle connections. They considered 12.3 m long span simply supported and continuous beams (Test 3) subjected to combined structural and thermal loading. The beam tested by Choe et al. [11] had very detailed instrumentation set up. The test program provides a very useful data such as the axial force in negative reinforcement and axial restraint force on the beam throughout the testing. Very few experiments provide such detailed data. Using the test data from this experiment, a detailed parametric study has been conducted to understand the roles of various parameters on the behaviour of the long-span continuous composite beam. The effect of slab continuity was one of the parameters under consideration. Authors observed that local buckling of steel beam near the connection leads to an increase in tensile force demand in continuity bars of the concrete slab.

In the present paper, the fire and post-fire behaviour of a complex continuous composite beam using Abaqus software is studied. The modelling procedure is validated with experimental data available in literature.

2 MODELLING APPROACH

For simulation purpose, finite element-based computer programme Abaqus software was used. While studying the behaviour of structural members under fire load, the member is subjected to 45 % of its design capacity along with fire load. Therefore, the analysis was conducted in two parts. i) Nonlinear heat transfer analysis performed independently to obtain nodal temperature histories, ii) Dynamic explicit stress analysis by incorporating nodal temperature histories from heat transfer analysis.

2.1 Heat Transfer Analysis Modelling

The 3D model was developed using 8-node linear heat transfer brick elements (DC3D8), and a 3D heat transfer analysis was conducted on the entire system. Through mesh convergence study, mesh size of 35mm have been finalised. For validation purpose, the fire scenarios were adopted from respective pieces of literature. The same fire scenario and loading conditions were followed for parametric study as well. The default option available in the software for conducting heat transfer analysis was conduction. To integrate the effect of convection and radiation, user-defined subroutine from Cedeno et al. [12] was adopted. All parts of the composite beam such as steel beam, metal deck, concrete slab, insulation materials, shear studs, wire mesh, rebars angles and bolts were modelled using 3D brick elements.

2.2 Stress Analysis Modelling

The structural analysis was carried out in two steps. In the first step, gravity load was applied, and the second step was of thermal loading. The thermal load included heating and cooling phases. To incorporate the elevated temperature in the analysis, the output file of heat transfer analysis was defined as a predefined load in thermal load step. To achieve it, the structural and heat transfer analysis models need to be compatible. C3D8R, a 3D 8-node linear brick elements with reduced integration and hourglass control were used for the modelling the assembly. Dynamic Explicit analysis procedure was adopted to predict this time-dependent behaviour of composite beam under fire loading. The welding between the steel beam and shear

stud was modelled using tie and shear stud- concrete bond was defined using embedded constraint in the interaction module unit of Abaqus. Contact between surfaces such as steel- concrete, connection-beam, connection angle and sacrificing plates, etc. was modelled by using penalty contact. Rebars and welded wire mesh were embedded in concrete. Welded connections of the sacrificing plate with column were represented by giving displacement boundary conditions. Isometric view of the modelling the literature Choe et al. [11] with shear studs and wire mesh highlighted is shown in Figure 1.

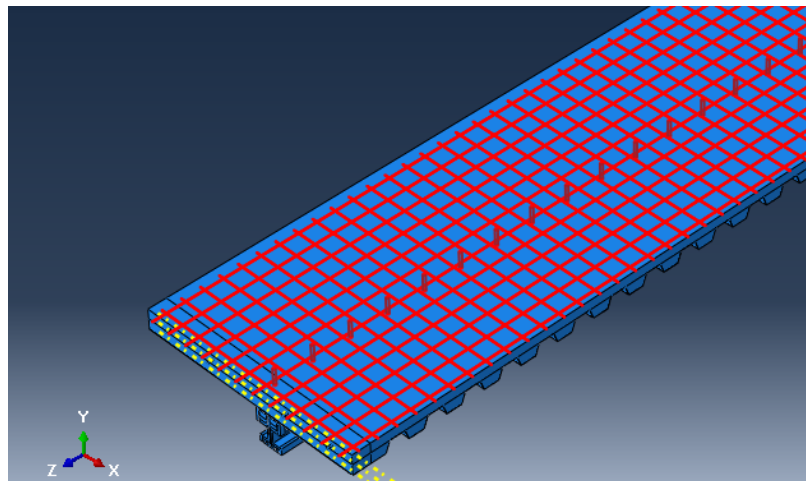


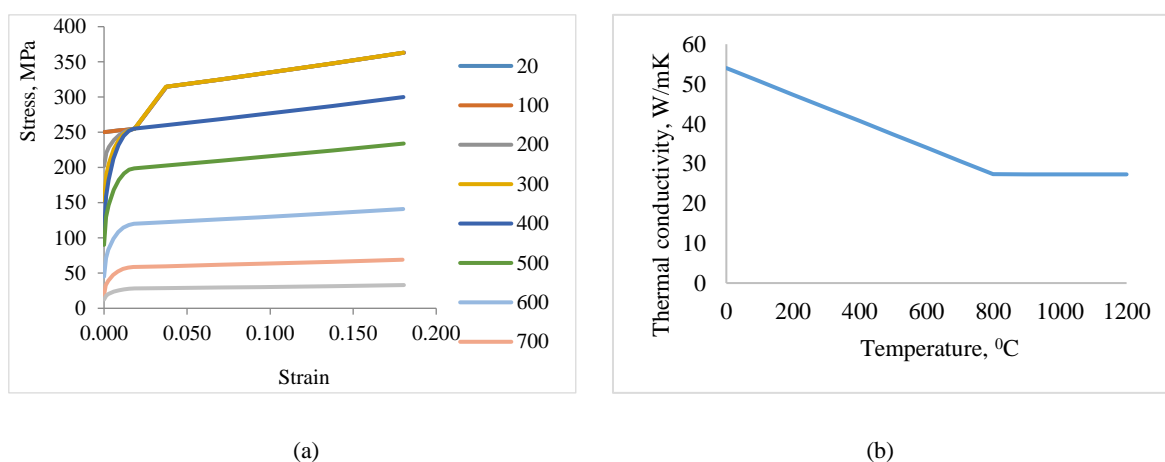
Figure 1. Isometric view of the sample model

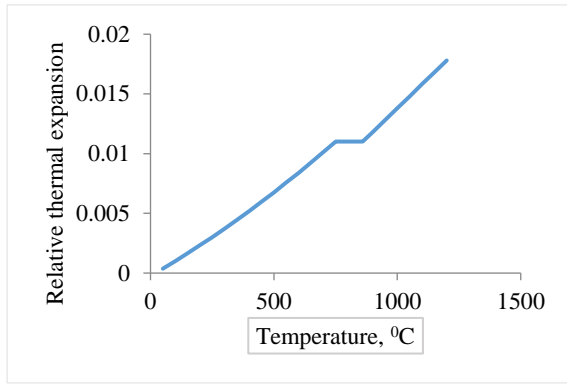
2.3 Material Properties

Eurocode [13,14] defined temperature dependant material properties were adopted in the analysis. Thermal property such as conductivity, specific heat, thermal expansion, etc. were also taken from the Eurocode.

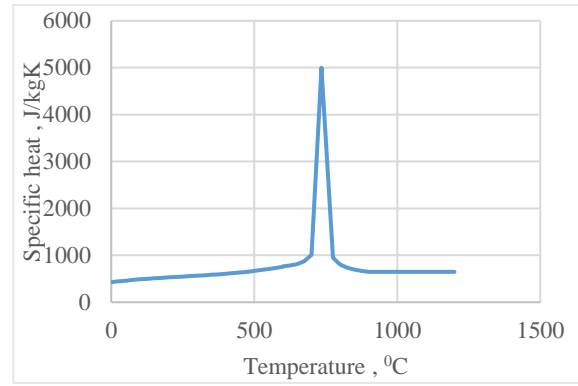
2.3.1 Steel

From the published experimental works of literature, the yield strength of taken as the inputs for Eurocode distinct relationships for mechanical properties. For both steel and concrete models, temperature-dependent strength reduction factors from the code taken care of reduction in strength at elevated temperature. Figure 2 shows the Eurocode defined temperature dependent mechanical and thermal properties of steel.





(c)

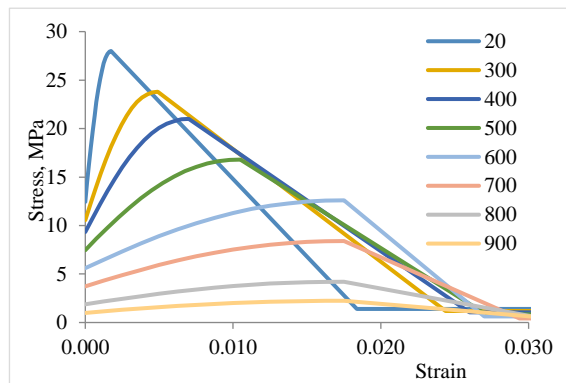


(d)

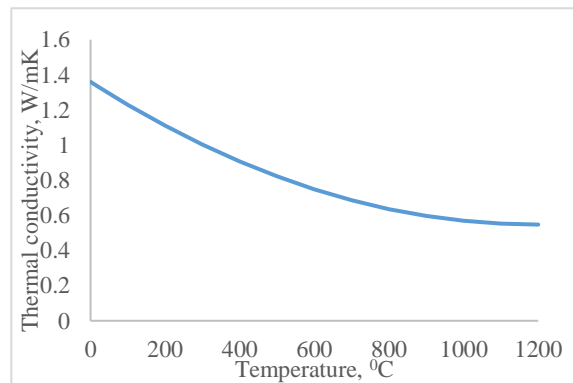
Figure 2. (a) Typical Eurocode stress-strain curve for steel with yield strength 350 MPa as a function of temperature (b) Thermal conductivity of steel as a function of temperature (c) Relative thermal expansion of steel as a function of temperature (d) Specific heat of steel as a function of temperature

2.3.2 Concrete

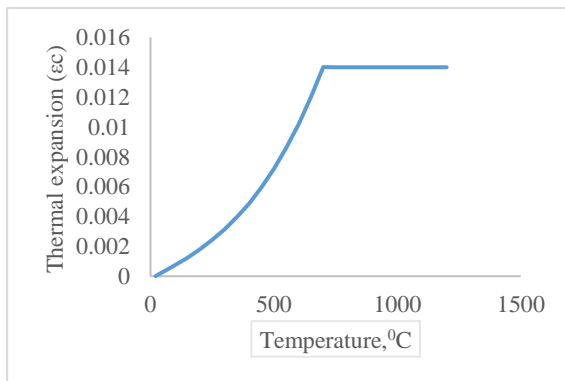
Drucker Prager plasticity model was used for simulating damage in concrete. Characteristic compressive strength of concrete for various models was taken from experimental data provided in the literature. Figure 3 (a) to (d) show the typical Eurocode stress-strain curve for concrete with characteristic compressive strength of 28 MPa, thermal conductivity, thermal expansion and specific heat as a function of temperature. Specific heat of concrete with 3% moisture content adopted for modelling purpose as shown in Figure 3(c).



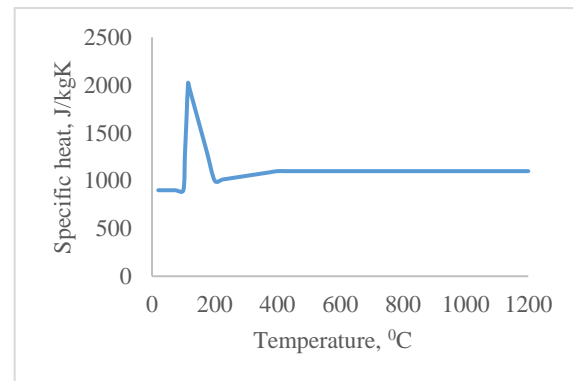
(a)



(b)



(c)



(d)

Figure 3. (a) Typical Eurocode stress-strain curve for concrete with yield strength 350 MPa as a function of temperature (b) Thermal conductivity of concrete as a function of temperature (c) Thermal expansion of concrete as a function of temperature (d) Specific heat of concrete as a function of temperature

3 BENCHMARKING OF THE ANALYSIS PROCEDURE

The analysis procedure adopted in this numerical investigation was benchmarked with the literature data. Experiments conducted by Wainman & Kirby [1], Zhao and Kruppa [2], and Choe [11] were considered for this purpose and successfully validated the modelling techniques.

3.1 Wainman and Kirby [1]

From Wainman and Kirby test series, Test 15 from Wainman and Kirby [1] was considered for validation. Figure 3 shows the isometric view of the model in Abaqus. User subroutine was adopted to incorporate the temperature in each and every node of the beam, and it was coupled with the subsequent stress analysis. The temperature distribution on the steel bottom flange and midspan deflection of the composite beams were compared with the literature data, as shown in Figure 4(a) and (b), respectively, which shows a very good agreement.

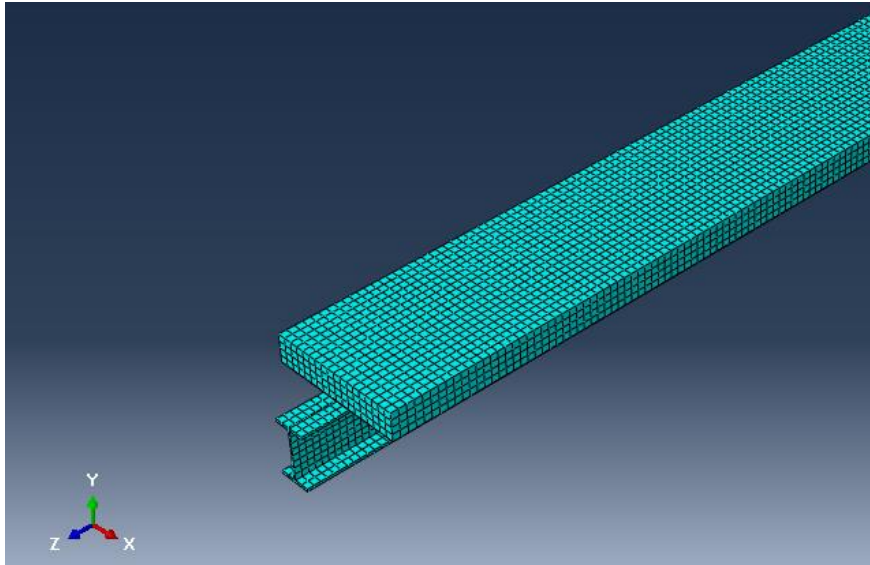


Fig 3. Isometric view of the model

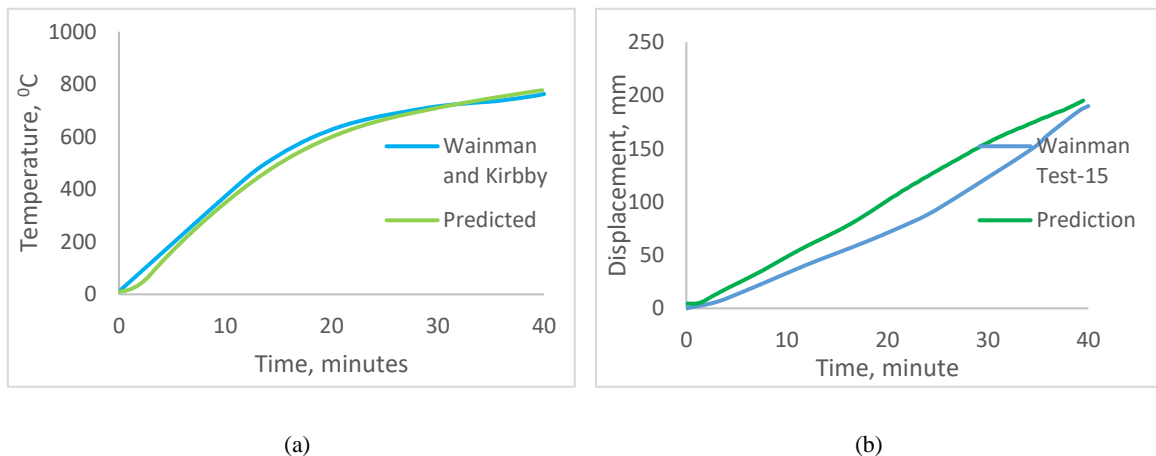


Figure 4. Comparison of (a) steel bottom flange temperature (b) mid span deflection of prediction with Literature

3.2 Zhao and Kruppa [2]

Out of fourteen experiment test specimens of Zhao and Kruppa [2], Test 1 was adopted for the validation purpose. The details of the composite beam are IPE 300 steel beam with 25mm thick mineral wool used as fire protection. Figure 5 shows a comparison of deflected shape of the experimental model and numerical model. The figure 6(a) and (b) shows the comparison of the steel bottom flange temperature and midspan deflection of the model with experimental results.

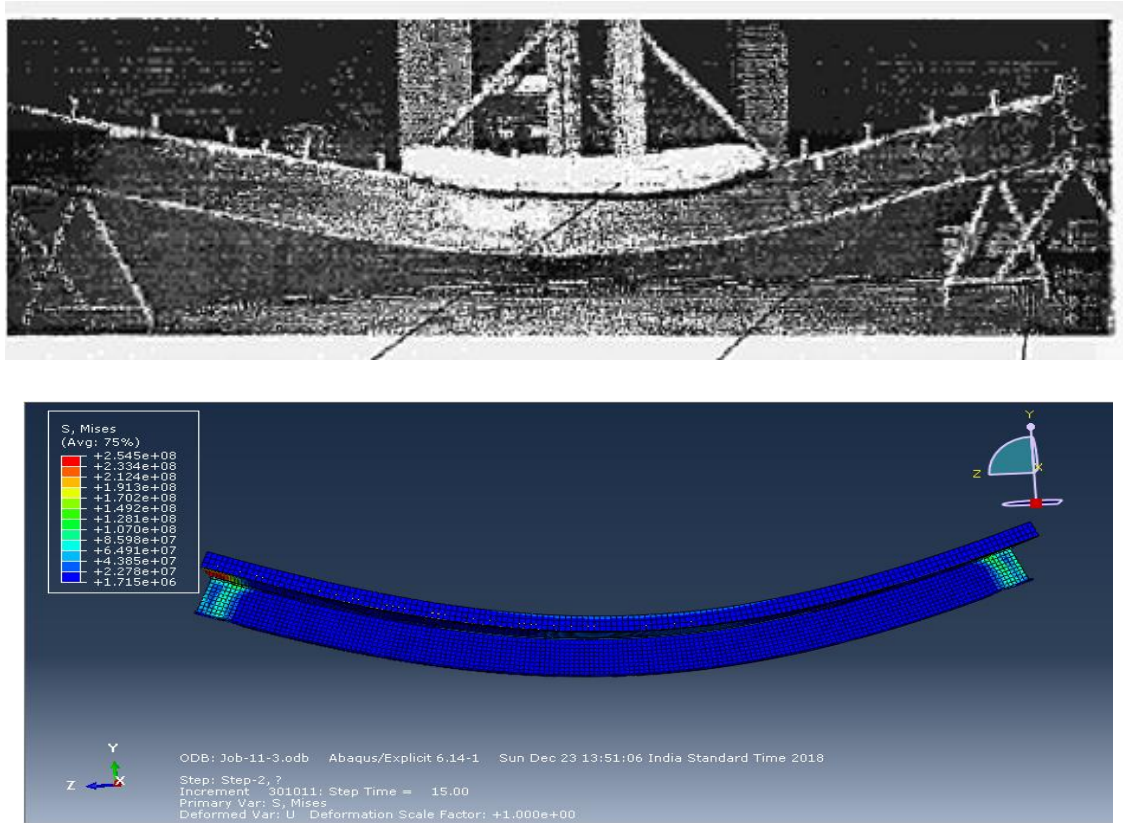


Figure 5. Comparison of deflected shape of specimen in (1) experiment and (2) simulation

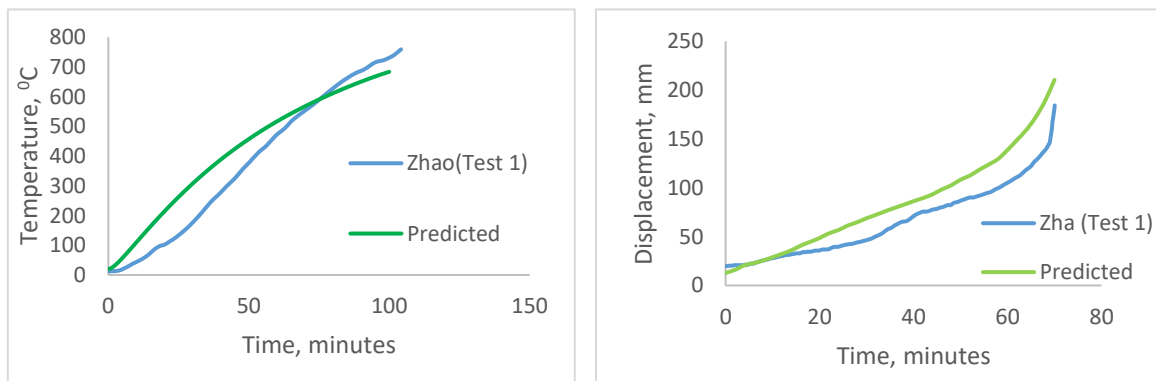


Figure 6. Comparison of (a) steel bottom flange temperature and (b) mid span deflection of predictions with Literature values

3.3 Choe et al. (2018)

Choe et al. (2018a & b) conducted a series of fire test on a 12.8 m long composite beam with different parameters. Test-3 from this experiment series was considered for validation purpose. The steel beam was

of size W18x35 used in the experiment. Lightweight profiled concrete slab of width 1.83 m with metal deck modelled. At both ends of the beam, four 12.7 mm diameter reinforced bars of yield strength 415 MPa was there in the experiment. These reinforcements were extended beyond the slab and tied to the supporting system to simulate the continuity of rebar. Cementitious gypsum-based fire protection of thickness 16 mm was used throughout the steel beam length. The isometric view of the beam and the close view of the connection are shown in Figure 7(a) and (b). To achieve the nodal temperature history during elevated temperature, a subroutine was adopted while executing heat transfer analysis. Figure 8 shows the comparison of the temperature distribution of steel beam and concrete slab of the model with literature.

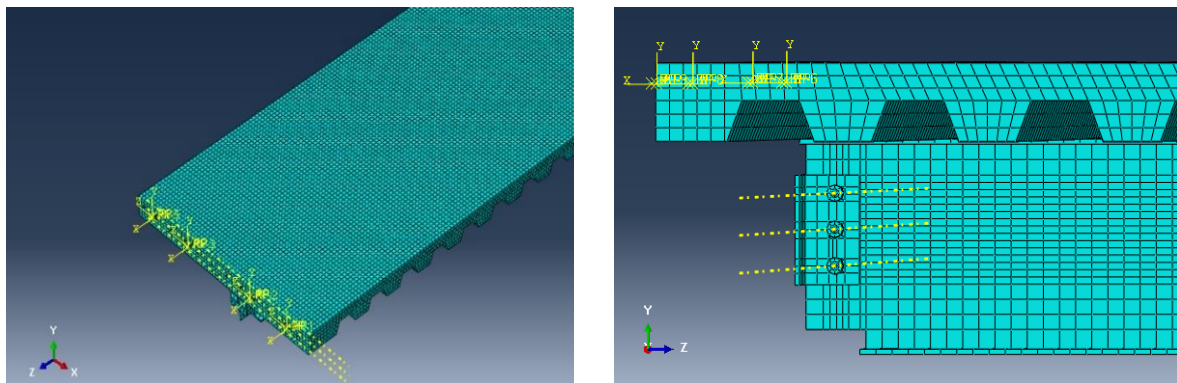


Figure 7(a) Isometric view of the model (b) Close view of connection (Choe Test 3)

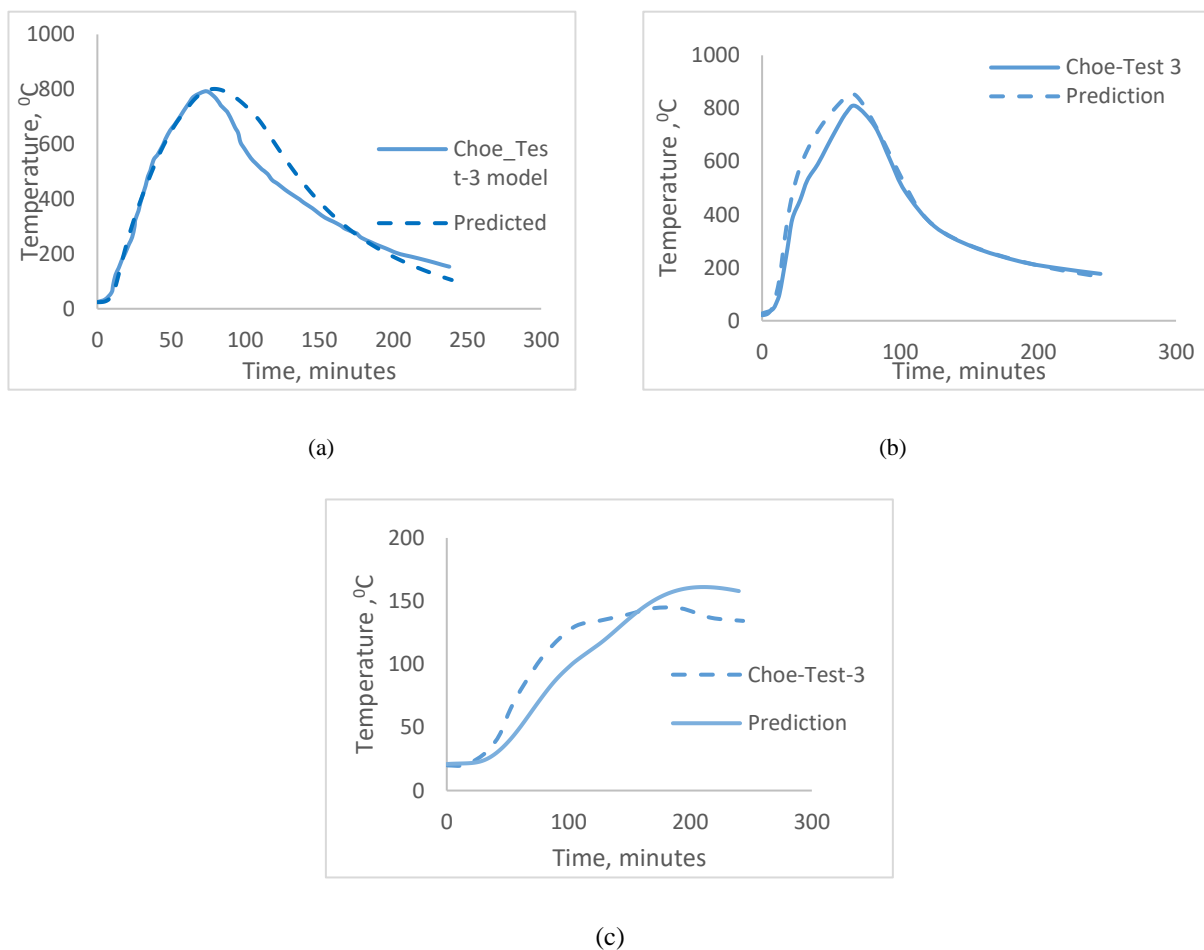


Figure 8. (a) Comparison of bottom flange temperature distribution (b) Bottom concrete slab temperature distribution (c) Top concrete slab temperature distribution (Choe Test 3)

In stress analysis, gravity load was given in the first step. A total gravity load of 106 kN at six equally distributed points was applied. In the second step, the thermal load was applied. At around 30 minutes after fire started, local buckling of steel beam near the connection lead to an increase in tensile force demand in continuity bars of the concrete slab. In the numerical model, axial restraint offered by the support was modelled using connector elements available in the interaction module of Abaqus. Figure 9 shows the comparison of the buckled shape of experimental test specimen and prediction. In the experiment, the gravity load was removed once the midspan deformation exceeds the allowable limit of $L/20$. The similar procedure was adopted in the numerical model as well. Figure 10 (a), (b) and (c) shows the comparison of the prediction with the experimental results of midspan deflection Vs. Time and Rebar force Vs. Time.

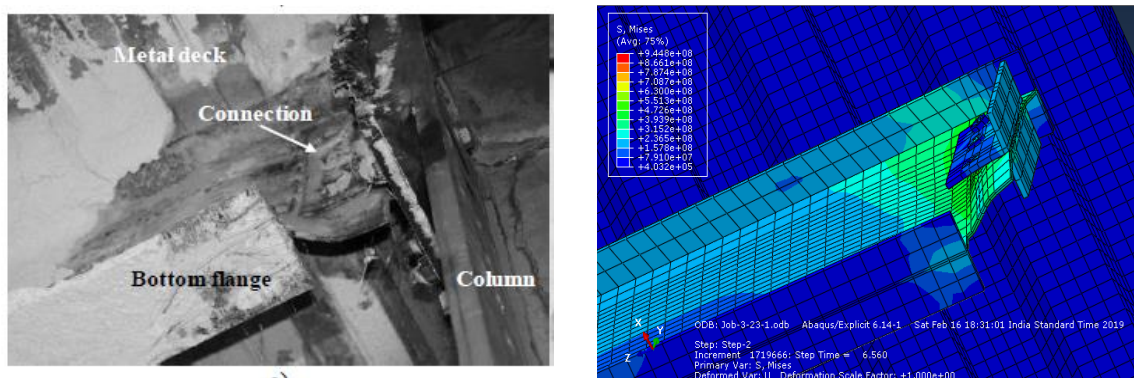


Figure 9. Comparison of buckled shape of experimental test Specimen and prediction (Choe Test-3)

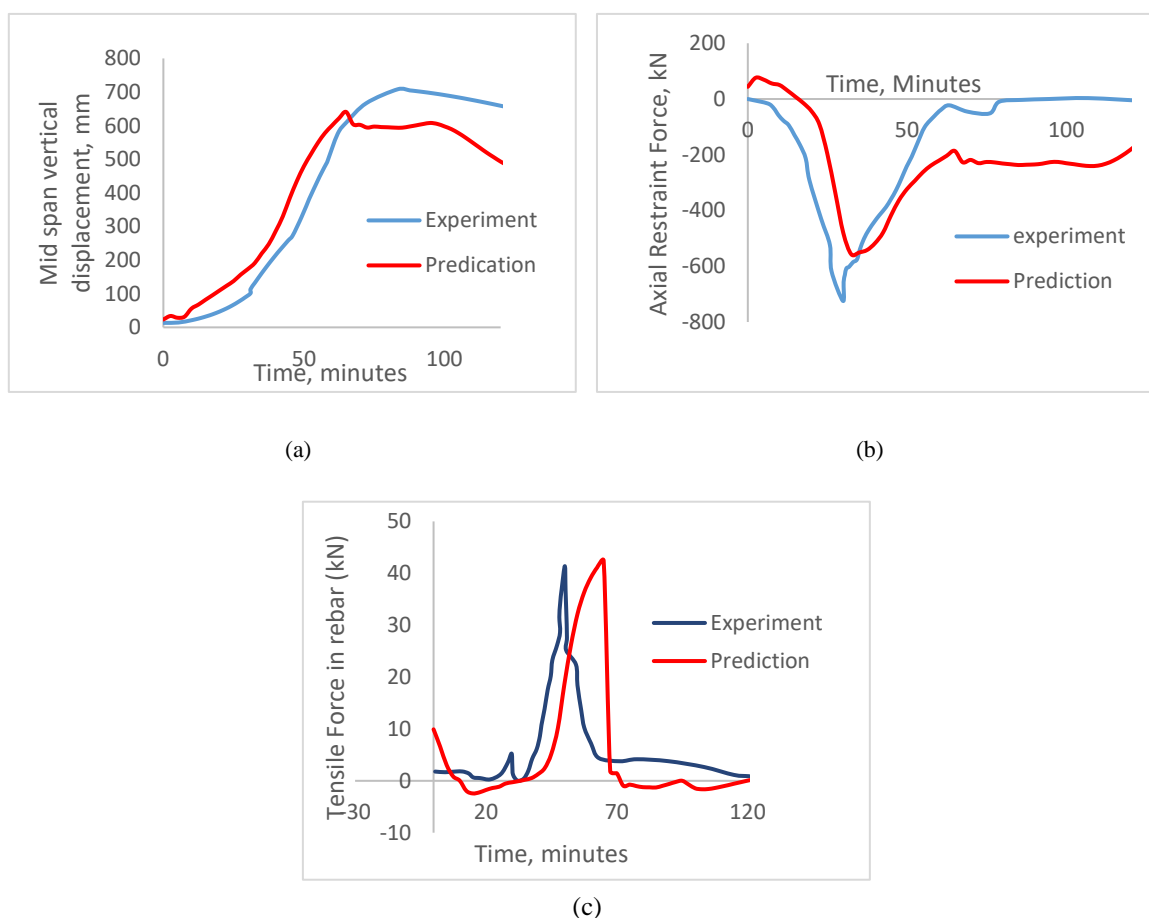


Figure 10. Comparison of (a) Mid span deflection Vs time (b) Axial restraint force Vs time at the connection (c) Tensile Force in rebar Vs Time (Choe Test-3)

4 PARAMETRIC STUDY

A detailed parametric study has been conducted to understand the roles of various parameters on the behaviour of the long-span continuous composite beam. The details of the various parameters considered in this paper are listed in table 1.

Table 1: Models details considered for the analysis

S.No.	Model Name	Parameters
1	CBLS1	Lateral Stiffness of the supporting system: 22 kN/mm
2	CBLS2	Lateral Stiffness of the supporting system: 110 kN/mm
3	CBLS3	Lateral Stiffness of the supporting system: 220 kN/mm
4	CBLS4	Lateral Stiffness of the supporting system: 2200 kN/mm
5	CBLS5	Lateral Stiffness of the supporting system: Infinity
6	CBP	Composite beam without any rebar in hogging moment region
7	CBHR	Composite beam with rebar in hogging moment region and no bond failure was modelled
8	CBRS1	Stiffness of Rebar support 14 kN/mm
9	CBRS2	Infinity

4.1 Effect of Stiffness of the supporting system

In the experiment of Choe et al. [3], the axial restraint stiffness of the supporting system, which includes column and supporting braces was found to be 220 kN/mm. However, a significantly broad range of end-conditions may prevail in real-time structures. To understand the effect of the axial restraint on the behaviour of the member, five models with different stiffness values as listed in table 1 (Serial Numbers 1 to 5) have been modelled and studied the behaviour under fire loading. CBLS3 was assigned with stiffness used in the experimental setup. In models CBLS1, CBLS2 and CBLS4 the stiffness was $1/10^{\text{th}}$, half and 10 times of stiffness in the experiment. Whereas in the model CBLS5, the hypothetical rigid condition was considered. The supporting system stiffness was incorporated in the model with the help of connectors. In the model CBLS5 with infinite axial restraint stiffness at support, the buckling of the web and bottom flanges occurred at around 17.5 minutes after fire loading started whereas in the other models, with stiffness 2200 kN/mm, 220 kN/mm, 110 kN/mm and 22 kN/mm the buckling took place at around 23 minutes, 30 minutes, 32.5 minutes and 40 minutes respectively. By reducing the axial restraint stiffness of the supporting system, the buckling can be delayed in the beam-web or bottom flange, thereby, potentially increasing the fire resistance of the beam.

The comparison of midspan deflection of various models considered is shown in the figure 11. It was assumed that the beam fails when the midspan deflection in the beam reaches 620mm ($L/20$). In models CBLS1, 2, 3 and 4, the failure of the beam was observed in between 60 minutes to 65 minutes. Whereas in the model CBLS5, the maximum deflection observed was around 600 mm at around 65 minutes. The restraint force developed in the supporting system increases with the axial restraint stiffness. In the heating phase of the analysis, the beams with more axial restraint stiffness behaved in a better way. The running out failure can be delayed in the members by increasing axial restraint stiffness of the supporting system.

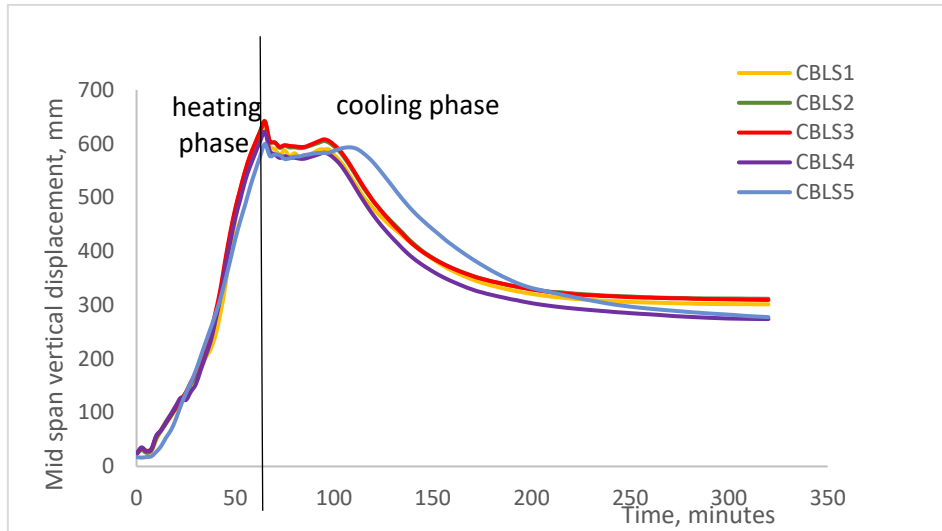


Figure 11. Mid span deflection Vs time

The stress plots at the connection at around 325 minutes after starting the analysis is shown in the figure 11. In model CBL55 with rigid connection, during the cooling phase, it was observed that, at around 125 minutes, the web started yielding near the connection and axial force demand in the connection increased in a faster way compared to other models, which leads to changing of the nature of force demand from compression to tension. The axial restraint force at the connection is shown in the Figure 12. It may cause the failure of the connection in the cooling phase. Whereas the models with less lateral stiffness, the tensile force demand in the connection during cooling phase was negligible. However, a more detailed parametric study is required by changing various parameters to understand the behaviour.

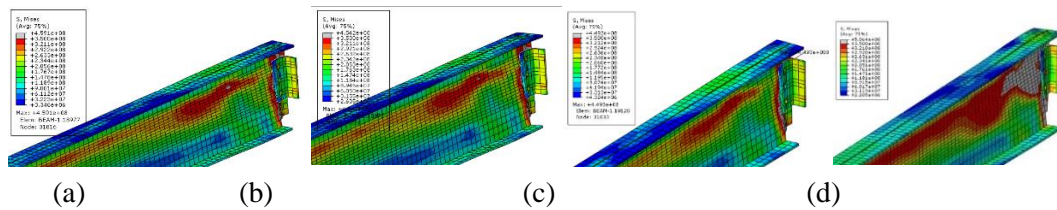


Figure 13: Stress fields for models (a) CBL51 (b) CBL52 (c) CBL53 and (d) CBL55 at 325 minutes

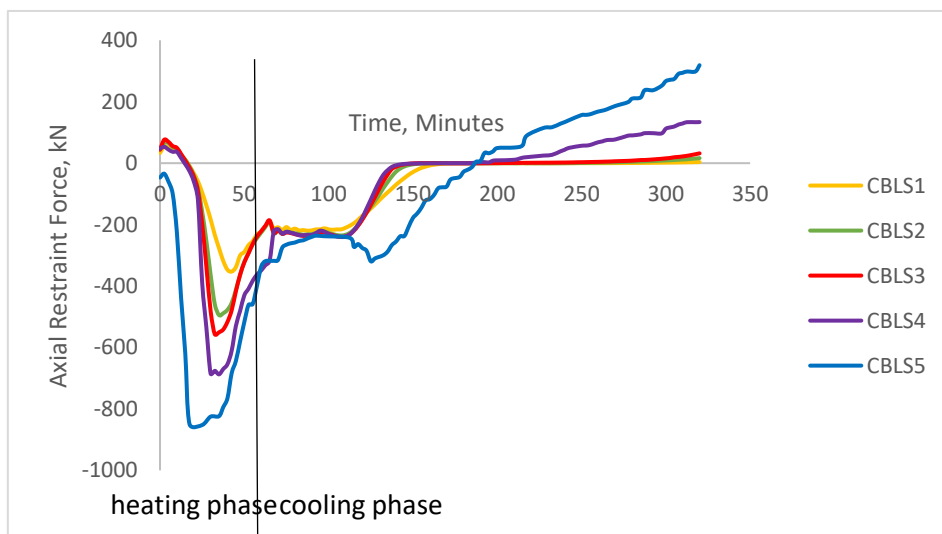


Figure 12. Axial restraint force Vs time at the connection

4.2 Effect of bond strength of negative Reinforcement at support

In the experiment, it is reported that the rebar bond with concrete was lost during heating phase itself. Furthermore, the failure of the bond in the experiment happened well before reaching its theoretical bond strength. In this paper, the authors attempted to understand the behaviour of the beam, assuming the bond failure is not happening in the member. Analyses listed in serial numbers 6 and 7 studied the effect of negative reinforcement at the support. The model CBP was without any additional reinforcement in the hogging moment region, and the model CBHR was with some reinforcement in the hogging side. The comparison of midspan deflection of the beam is shown in figure 14(a). It is evident that the beam with hogging moment reinforcement at the support, the peak deflection has reduced from 866 mm to 640mm. The axial force developed at the support is shown in figure 14(b). The behaviour is more or less the same until 50 minutes. At around 50 minutes, there was a sudden rise in the deflection for the model CBP. Whereas in the beam CBHR, the rate of increase of deflection is comparatively slow, and it is due to the presence of reinforcement bars in the hogging side of the member. If we compare the axial force demand in the cooling phase, the tensile force in the connection is more for CBP compared to CBHR, which may cause the welded connection failure by rupture of the weld.

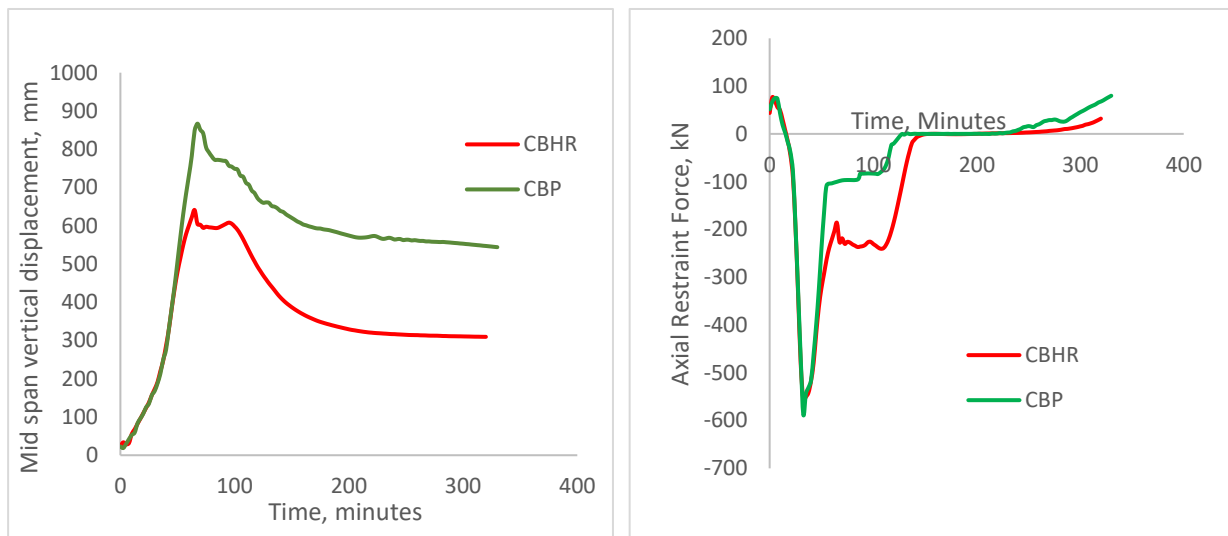


Figure 14(a). Mid span deflection Vs time (b) Axial restraint force Vs time at the connection

4.3 Effect of continuity of negative moment reinforcement at the support

The beam models listed in table 1 with serial numbers 8 and 9 were analysed to study the effect of continuity of negative reinforcement in the long span composite beam. In the beam CBRS1, the experimental support condition was given. In the experiment, to simulate the continuity condition, the rebars were extended beyond the slab ends and tied to a hollow beam. In numerical modelling, the support condition was modelled with the help of connectors. The stiffness of the supporting system was calculated and assigned to the connector. In real-time, the rebar will be embedded in concrete, and it will be continued in the adjacent concrete slab. Therefore, specimen CBRS2 was modelled with the axial stiffness of supporting member as infinity. Remaining all parameters such as dimensions of various parts, boundary conditions, fire loading, gravity loading pattern were kept as same as mentioned in the literature. It was found that in the beam CBRS2, the peak midspan deflection gets reduced to 610mm in comparison to 645 mm with the beam CBRS1 as shown in the figure 15(a). Axial forces developed in the rebar of various models are plotted in the figure 15(b). During the cooling phase, the compressive force was developed in the rebars of model CBRS2, which further slowdown the deflection recovery of the beam.

The axial restraint force developed at the support is plotted in figure 16. At around five minutes after the thermal loading, the steel beam expands, and it comes in contact with the supporting system. Further, the

expansion is stopped by the support by offering compressive force induced at the support. The peak axial force developed at the support gets reduced from 556 kN to 505kN when the stiffness of the rebar end support changed from 14kN/mm to infinity. It is due to the additional compressive force developed in the rebar.

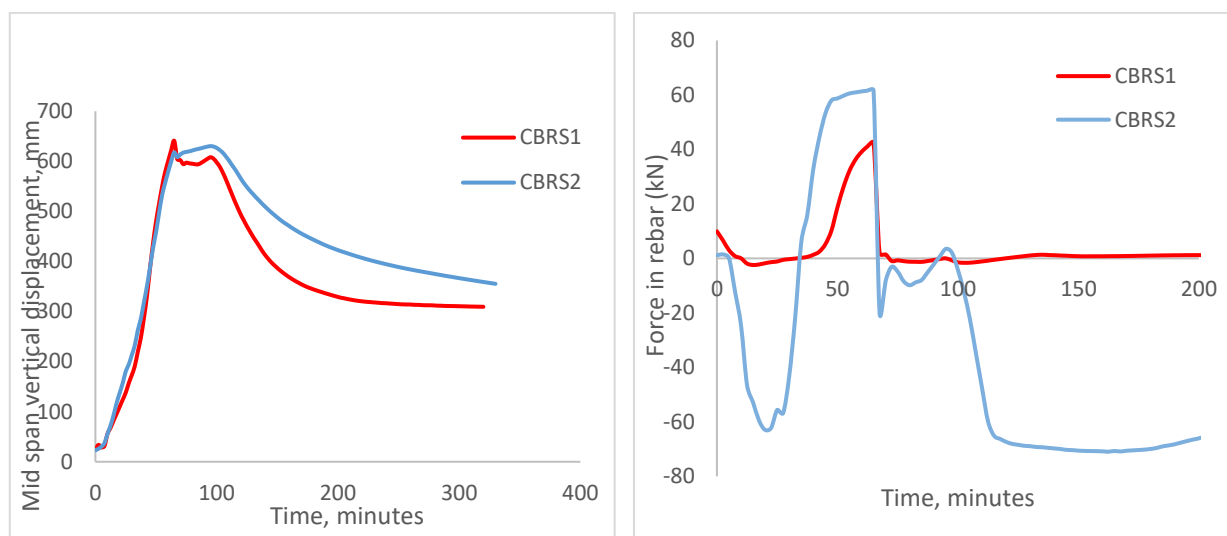


Figure 16(a). Mid span deflection Vs time (b) Tensile Force in rebar Vs Time

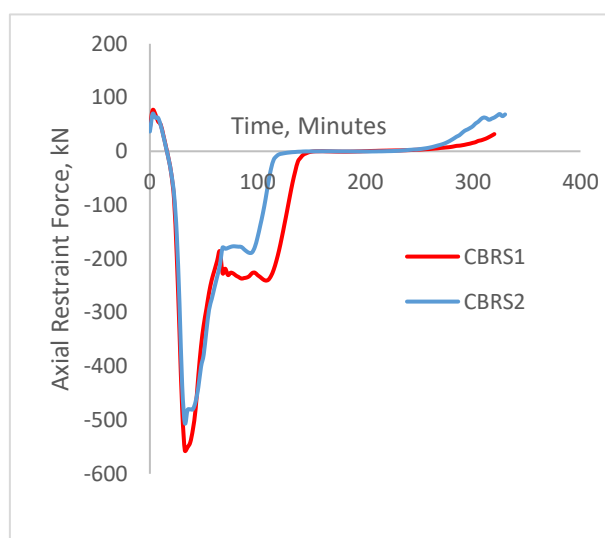


Figure 17. Axial restraint force Vs time at the connection

5 CONCLUSIONS

A three-dimensional model of long span composite beam for predicting the behaviour under fire loading was modelled successfully. Even though the analysis is very much time consuming, it can predict the behaviour in an accurate way. The modelling and analysis procedure was validated with Wainman and Kirby [1], Zhao and Kruppa[2] and Choe et al. [3] experimental values. A parametric study was conducted to understand the behaviour of beam during the heating and cooling phase of fire loading. The parameters considered were the presence of reinforcement in hogging zone of the beam, stiffness offered by supporting system and the stiffness offered by the rebar due to its continuity. The double angle connection was considered for all analyses. The angles were bolted to the beam and welded to the column. The stiffness of the beam end support plays a major role in the behaviour during the cooling phase. In the beam with more

end stiffness develop comparatively high tensile force in the cooling phase, which may even cause the failure of weld. The provision of additional reinforcement in the hogging portion of the member increases the stiffness of the member and thereby prevent running out the failure of the structure. Detailed studies are required to confirm the findings.

REFERENCES

1. Wainman, D.E. and Kirby, B.R. (1987) Compendium of UK standard fire test data, unprotected structural steel – 1. Reference Number RS/RSC/S10328/1/98/B, British Steel Corporation (now Corus), Swinden Laboratories, Rotherham.
2. Zhao, B., and Kruppa, J. (1997) Fire Resistance of Composite Slabs with Profiled Steel Sheet and of Composite Steel Concrete Beams, Part 2: Composite Beams. ECSC – agreement No. 7210 SA 509, CTICM, France.
3. Agarwal, A., Selden, K. L., and Varma, A. H. (2014) Stability behaviour of steel building structures in fire conditions: Role of composite floor system with shear-tab connections. *J. Struct. Fire Eng.*, 5(2), 77–96. doi:10.1260/2040-2317.5.2.77
4. Agarwal, A., and Varma, A. H. (2014) Fire induced progressive collapse of steel building structures: The role of interior gravity columns. *Engineering Structures*, 58, 129-140. doi: 10.1016/j.engstruct.2013.09.020
5. Agarwal A. (2011) Stability of steel building structures under fire loading. PhD dissertation. School of Civil Engineering, Purdue Univ.; 2011.
6. Agarwal, A., Varma, A. H. (2011) Design of steel columns at elevated temperatures due to fire: effects of rotational restraints. *Eng J*, AISC.
7. Selden, K. L., Fischer, E. C., & Varma, A. H. (2015) Experimental investigation of composite beams with shear connections subjected to fire loading. *Journal of Structural Engineering*, 142(2), 04015118. doi: 10.1061/(ASCE)ST.1943-541X.0001381
8. Fischer, E. C., and Varma, A. H. (2016) Fire resilience of composite beams with simple connections: Parametric studies and design. *J. Constr. Steel Res.*, 119–135. doi: 10.1016/j.jcsr.2016.08.004
9. Fischer, E. C., and Varma, A. H. (2015) Fire behaviour of composite beams with simple connections: Benchmarking of numerical models. *J. Constr. Steel Res.*, 111, 112–125. doi: 10.1016/j.jcsr.2015.03.013
10. Fischer, E. C., Selden, K. L., & Varma, A. H. (2017) Experimental Evaluation of the Fire Performance of Simple Connections.” *Journal of Structural Engineering*. 143(2), 04016181. doi: 10.1061/(ASCE)ST.1943-541X.0001664
11. Choe, L., Ramesh, S., Seif, M., Hoehler, M., Grosshandler, W., Gross, J., Bundy, M. (2018a) Fire Performance of Long-Span Composite Beams with Gravity Connections. *Proc. of the 10th International Conference on Structures in Fire Fire SERT*, Ulster University, Belfast, UK, June 6-8, 2018.
12. Cedeno, G., Varma, A.H. and Agarwal, A. (2009) Behaviour of floor systems under realistic fire loading, *Proceedings on CD-ROM of the ASCE Structures Congress*, ASCE, Reston, VA, pp. 1-10. doi: 10.1061/41031(341)224
13. European Committee for Standardization (CEN) (2005) Eurocode 4: Design of Composite Steel and Concrete Structures, Part 1-2: General Rules – Structural Fire Design, European Committee for Standardization, Brussels.
14. European Committee for Standardization (CEN) (2002) Eurocode 1: Actions on Structures, Part 1.2: General Actions –Actions on Structures Exposed to Fire. European Committee for Standardization.
15. ABAQUS (2012) ABAQUS/Standard Version 6.12 User’s Manuals, ABAQUS, Providence, RI.

EFFECT OF TRANSVERSE AND LONGITUDINAL CONFINEMENT ON THE INTERLAYER BOND IN 3D PRINTED CONCRETE AT ELEVATED TEMPERATURES: AN EXPERIMENTAL STUDY

Cicione A.¹, Mazolwana K.², Kruger J.³, Walls R.⁴, Sander Z.⁵, Van Zijl G.⁶

ABSTRACT

In the last decade, the study of three-dimensional concrete printing (3DCP) has become extremely popular, with a number of researchers studying the behaviour of 3DCP at ambient conditions. The interest in 3DCP has been aroused by its ability to facilitate the realization of geometrically complex objects at reduced construction time, and potentially cost, compared to conventional construction techniques. However, it is crucial to understand the effects of this new layer-wise construction technique on the fire performance of 3DPC elements, especially since negligible research is available on the behaviour of 3DPC samples in fire. In 2019 one of the first experimental studies of 3DCP at elevated temperatures was conducted by the authors, which highlighted a new failure mechanism, i.e. self-equilibrating stresses causing tension exceeding the interfacial bond strength, as opposed to dominating spalling failure in cast concrete. It is with the above mentioned in mind that the paper seeks to investigate the effect of boundary conditions on the interlayer bond behaviour of 3DPC at elevated temperatures. Six 3DPC samples were tested by exposing the samples to an incident heat flux via radiant panels, along with an additional 5 samples to obtain ambient strength properties. The temperatures were measured at various positions within the 3DPC samples. It was found that restraining the samples from movement perpendicular to the interlayer direction, can reduce the tendency of the samples to delaminate and as a result increase the post-fire flexural capacity.

Keywords: 3D concrete printing; heating rate; structural fire experiments; filament delamination; boundary conditions.

1 INTRODUCTION

Three-dimensional printing of concrete (3DPC) is an innovation of the 4th industrial revolution. 3DPC is an additive manufacturing process where a three-dimensional object is built from a computer-aided design model by successive deposition of concrete in a layer-wise manner. It is postulated that the construction industry will significantly benefit from automation through additive manufacturing, compared to the traditional method of mixing and casting concrete on site, by reducing construction time, material required, labour, possibly costs and environmental impact [1]. 3DPC was first introduced in 1986 as a means of rapid prototyping [2]. Figure 1 depicts the cumulative number of additive manufacturing projects from Pegna [3]

¹ Stellenbosch University, Department of Civil Engineering, Stellenbosch, South Africa,
e-mail: acicione@sun.ac.za, ORCID: <https://orcid.org/0000-0002-1368-4718>

² Stellenbosch University, Department of Civil Engineering, Stellenbosch, South Africa
e-mail: 20764944@sun.ac.za

³ Stellenbosch University, Department of Civil Engineering, Stellenbosch, South Africa
e-mail: pjkruger@sun.ac.za, ORCID: <https://orcid.org/0000-0003-0090-423X>

⁴ Stellenbosch University, Department of Civil Engineering, Stellenbosch, South Africa
e-mail: rwalls@sun.ac.za, ORCID: <https://orcid.org/0000-0002-0913-3200>

⁵ Stellenbosch University, Department of Civil Engineering, Stellenbosch, South Africa
e-mail: zaras@sun.ac.za

⁶ Stellenbosch University, Department of Civil Engineering, Stellenbosch, South Africa
e-mail: gvanzijl@sun.ac.za, ORCID: <https://orcid.org/0000-0001-8066-7750>

to 2019, along with two examples of large-scale construction making use of 3DCP. The reader is referred to Labonnote et al. [4] and Paul et al. [1] for recent contemporary reviews of the literature.

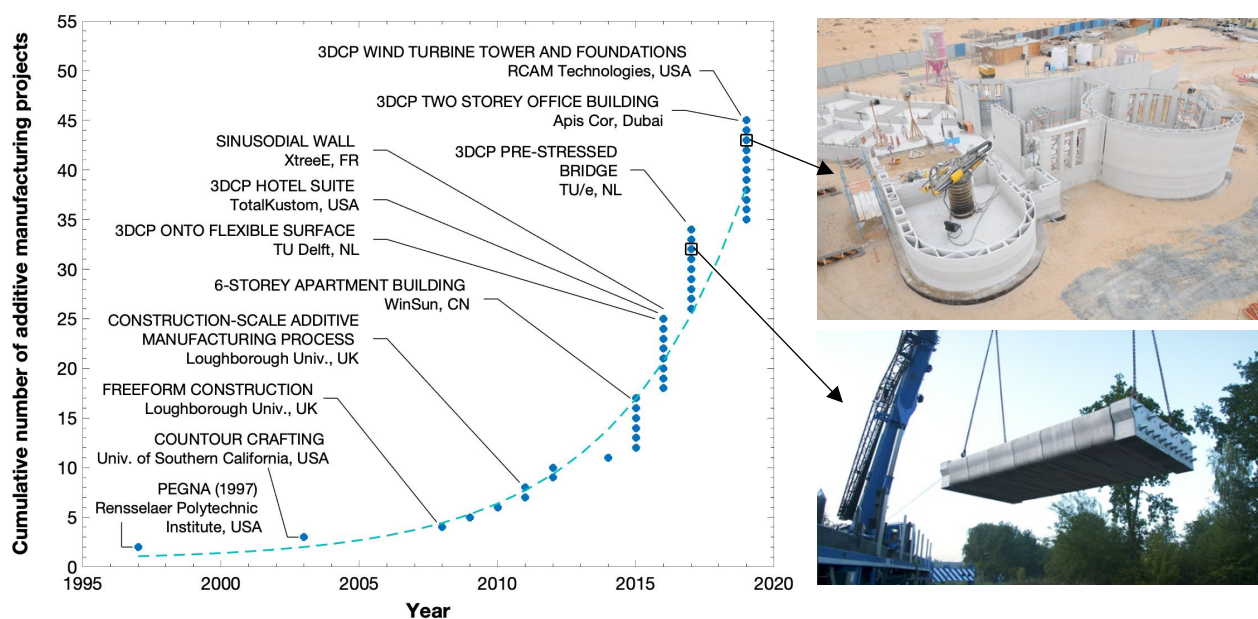


Figure 1. The rise in additive manufacturing for construction applications from the seminal work of Pegna (1997) to 2019 (left image). The graph (left image) was reproduced from [5]. Two storey 3DCP office in Dubai [6] (top right image) and a 3DCP pre-stressed cycle bridge in Netherlands [7] (bottom right image).

This revolutionary innovation of additive manufacturing (i.e., 3DCP) within the construction realm does however come with some challenges. A pertinent disadvantage of 3DCP is the inability to automatically include steel reinforcement to the additive manufacturing process [8]. Another challenge with extrusion based additive manufacturing that attracts significant attention, is that the mechanical properties of 3D printed concrete (3DPC) have a reduction in flexural capacity as a result of a weaker bond between filament layers [9]. This anisotropic behaviour is common for 3DCP and is typically referred to as lack of fusion, which is a similar phenomenon to that of a cold joint in conventionally cast concrete. Recent studies found that as a result of this lack of fusion, 3DPC samples can have a reduction of up to 36% in flexural strength compared to their mould-cast counterparts [10]. A number of researchers are investigating the above-mentioned challenges and the behaviour of 3DPC samples at ambient temperature.

Until 2019, negligible research has been conducted on the behaviour of 3DPC samples at elevated temperatures. In 2019, Cicione et. al [11] conducted one of the first experiments of 3DPC samples at elevated temperatures. The authors heated six 3DPC samples and three conventionally casted samples by means of radiant panels, and found that the 3DPC samples were less prone to thermal-hygral spalling, but rather experienced thermal-mechanical spalling (in the form of the interlayer delamination) as a result of a thermal gradient, which caused self-equilibrating tension stresses that exceeded the 3DPC samples' interlayer tensile capacity. By equating the expected thermally induced tension stresses (calculated using beam theory [12]) to the expected flexural strength of the samples at a given temperature, Cicione et. al [11] showed that the stresses resulting from the thermal gradient were sufficient to cause interlayer bond delamination. Kruger et. al [13] repeated the experiments conducted by ref. [11] as baseline experiments for their study, but added additional samples to investigate the effect of orthogonally included steel fibres between filament layers on the interlayer delamination behaviour at elevated temperatures. The authors found that the steel fibres did not prevent the samples from delaminating, but did however improve the samples' post-fire/post-cracking mechanical performance.

Typically, 3DPC wall elements consist of a number of interconnected filaments, meaning that in plan view they have a truss-like geometry. When exposed to a fire, the outer, fire-exposed filament, will be restrained by the interior infill filaments at certain intervals. Depending on the geometry of the section, expansion perpendicular or parallel to the interlayer orientation may occur. Hence, the geometry must be designed to

resist flexural forces induced by thermal effects to improve the flexural fire performance of the interlayers to avoid multiple cracks that can potentially expose the steel reinforcement to a significant amount of heat. It is with this backdrop in mind that this paper seeks to investigate the effect of boundary conditions on the interlayer bond behaviour of 3DPC at elevated temperatures. Six 3DPC samples were tested by exposing the samples to an incident heat flux ($40\text{--}50\text{ kW/m}^2$) via radiant panels (similar to what was done by [11,13]), along with an additional five samples to obtain ambient strength properties. The hypothesis before these experiments were conducted was that by restraining the samples from expanding, there will be no/reduced interlayer delamination, since the samples will be in compression when restrained and thus not experience any tensile stress. Although full compression was not entirely achieved, novel insight is provided by the experimental work.

2 EXPERIMENTAL SETUP

In order to be consistent with past experimental work [11,13] and to ensure a one-dimensional heat conduction scenario, the experimental setup was kept relatively simple, as depicted in Figure 2. Not shown in Figure 2, for aesthetic reasons, is the fact that the sides of the 3DPC samples were covered with ceramic blanket to ensure a one-dimensional heat transfer scenario, with the back of the samples exposed to the environment and the front face to the radiant panels, as depicted in Figure 2. Six samples, with dimensions as shown in Figure 2, were tested. The samples were cut from a larger 3D printed rectangle whilst still in the plastic concrete state. Two samples were unrestrained (hence the hydraulic press was not used to restrain these samples), two samples were restrained perpendicular to the interlayers (denoted as RH) by applying a 1 kN preload with the hydraulic press (Figure 3), and two samples were restrained parallel to the interlayers (denoted as RV) by applying a 1 kN preload with the hydraulic press (Figure 4). The samples were heated via radiant panels with an approximate heat flux received of $40\text{--}50\text{ kW/m}^2$. The samples were heated to a point where the thermocouples placed in the centre of the samples reached 300°C (similar to [11,13]) or once the force transducer reached 50°C (the force transducer is rated to 60°C).

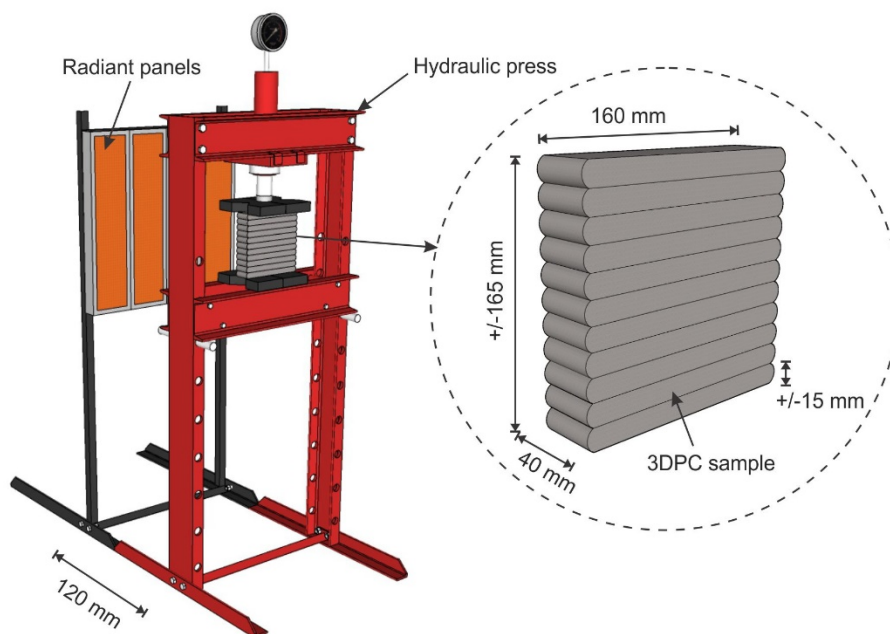


Figure 2. Experimental setup and approximate sample dimensions (see measured sample dimensions below)



Figure 3. Restrained with layers orientated horizontally (restrained perpendicular to layers - referred to as RH)



Figure 4. Restrained with layers orientated vertically (restrained parallel to layers - referred to as RV)

2.1 Instrumentation

During these experiments, six temperature measurements were recorded per sample using Type K thermocouples (1.5 mm tip diameter). Two readings were recorded 3 mm from the front face of the sample (Figure 5), two readings were recorded in the centre of the sample, i.e. approximately 20 mm into the sample (Figure 5), and two readings were recorded 3 mm from the back face of the samples (Figure 5). It should be mentioned here that the layer width does change slightly from layer to layer due to the nature of over extrusion. The current nozzle size of the 3D printer at Stellenbosch University is 25 mm in diameter and in order to perform four-point bending tests on the printed samples (discussed in a later section), it was necessary to over extrude to obtain samples that are 40 mm wide. Hence, the positions of the thermocouples mentioned above are approximate and may vary slightly from layer to layer. All thermocouples were fixed by drilling a 2 mm hole from the back of the sample and pushing the thermocouple flush against the concrete. The thermocouples were fixed in place with a small amount of fire sealant placed into the back part of the hole. In addition to the temperature readings, a 10 kN force transducer was used to measure the load induced by the heating, i.e. as a result of the restrained samples wanting to elongate at elevated temperatures. The force transducer was placed between two rigid steel plates below the sample, as depicted in Figure 5. The force transducer, steel plates and hydraulic press were protected from heating with ceramic blanket and aluminium foil. The aim of the hydraulic press' inclusion is to simulate restraint, as introduced above.

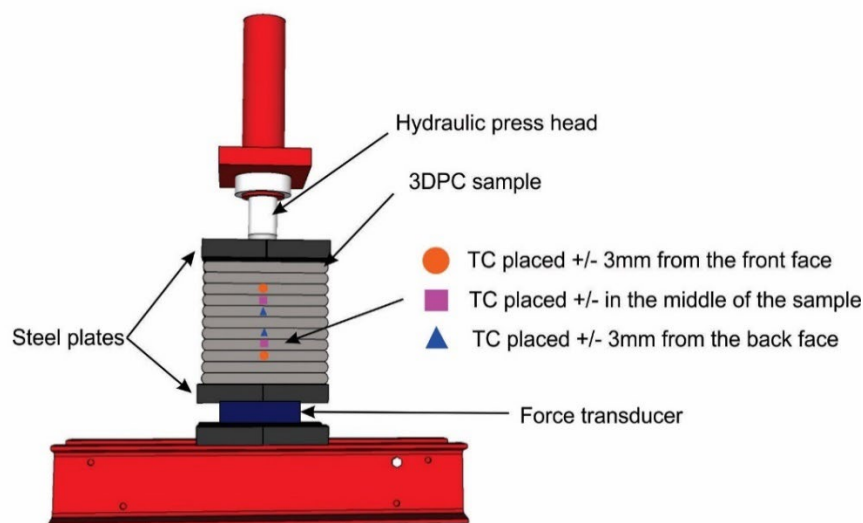


Figure 5. Instrumentation setup

2.2 Material composition and properties

The standard high-performance 3D printable concrete employed at Stellenbosch University was utilised in this research. The concrete mixture, given in Table 1, has a water to cement ratio of 0.45 and a 28-day compressive strength of 70 MPa. A CEM II 52.5 N cement that contains between 6 and 20 % limestone as extender is employed. Class F fly ash together with Chryso densified silica fume (DSF) are utilized as extenders to obtain appropriate rheological properties for 3D printing. A locally mined natural quarry sand with a well-graded particle size distribution and 4.75 mm maximum particle size is employed as the fine aggregate. Common potable tap water is used together with a modified polycarboxylate ether superplasticizer, Chryso Premia 310, to obtain high thixotropy for pumping and placement purposes.

Table 1: Printable concrete mix constituent quantities

Constituent	Description	Mass (kg)
Cement	PPC SureTech 52.5 N	579
Fly Ash	DuraPozz Class F	165
Silica Fume	Chryso DSF	83
Fine Aggregate	Local Malmesbury (4.75 mm max. size)	1167
Water	Potable Tap Water	261
Superplasticizer	Chryso Premia 310	5.75

This high-performance 3D printable concrete's flexural strength is determined in four-point bending according to EN 196-1 [14] at the age of sample fire testing, namely 185 days. All flexural tests were conducted at ambient temperature, with filament interlayers orientated vertically (i.e., orientation III), as depicted in Figure 6. Samples are $40 \times 40 \times 160$ mm (w \times h \times l) in size, cut from a larger 3D printed rectangle whilst still in the plastic concrete state. All specimens were cured in climate-controlled conditions at 23 ± 2 °C and 65 ± 5 % relative humidity. The physical testing was conducted using a Zwick Z250 material testing machine. The results are given in Table 2. It was determined that this 3D printable material has a 3.3 MPa flexural strength at 185 days concrete age. High variability is obtained (29.1 %), which although might seem significantly high for concrete in general, is actually reasonable for 3D printed concrete [15].

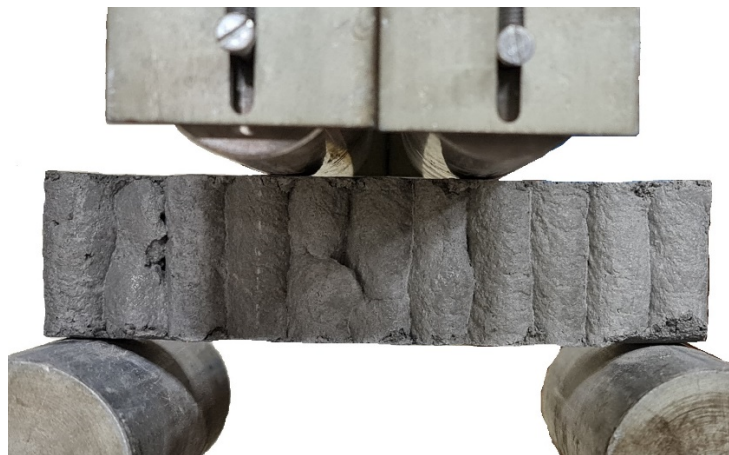


Figure 6. Four-point bending test of a $40 \times 40 \times 160$ mm 3D printed concrete specimen at ambient temperature with interlayers orientated vertically

Table 2: Flexural strength of the 3D printed concrete used in this study

Sample	Breaking Force (N)	Cross-Sectional Height (mm)	Cross-Sectional Width (mm)	Flexural Strength (MPa)	Average Flexural Strength (MPa)	Coefficient of Variation (%)
A1	434	38	18	2.5	3.3	29.1
A2	1780	40	32	5.2		
A3	1271	42	33.5	3.2		
A4	1024	39.5	32	3.1		
A5	904	40	31.5	2.7		

3 EXPERIMENTAL RESULTS

Figure 7 a) and b) depict the average temperatures measured during the unrestrained experiments at the front face of the samples, centre of the samples and the back face of the samples for sample 1 and sample 2, respectively.

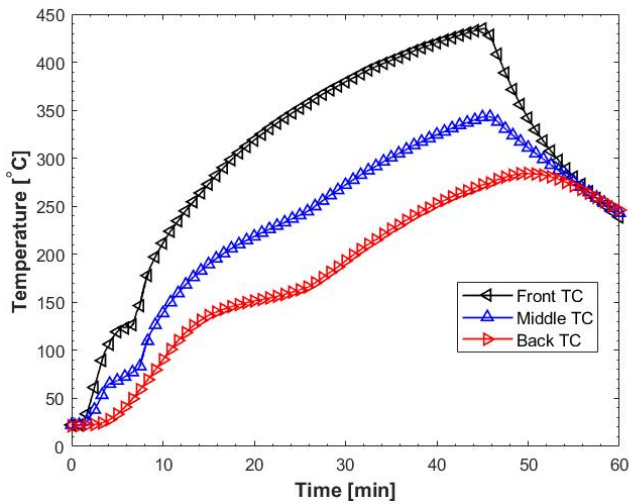


Figure 7 a) Temperatures of unrestrained Sample U1

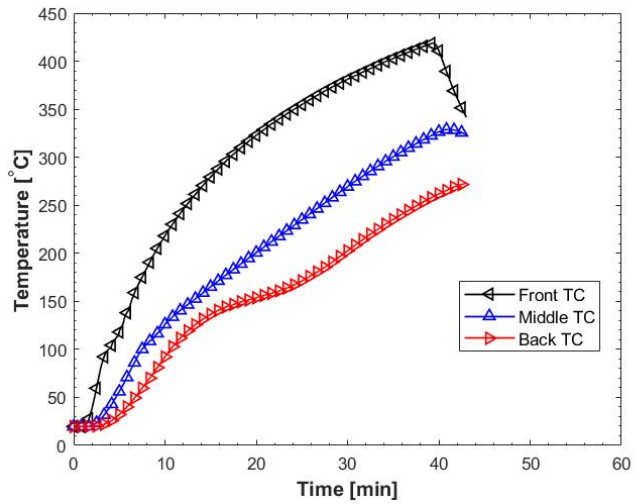


Figure 7 b) Temperatures of unrestrained Sample U2

Figure 8 a) and b) depict the average temperatures measured during the vertically restrained (perpendicular to interlayers) experiments at the front face of the samples, centre of the samples and the back face of the samples for sample RH1 and sample RH2, respectively.

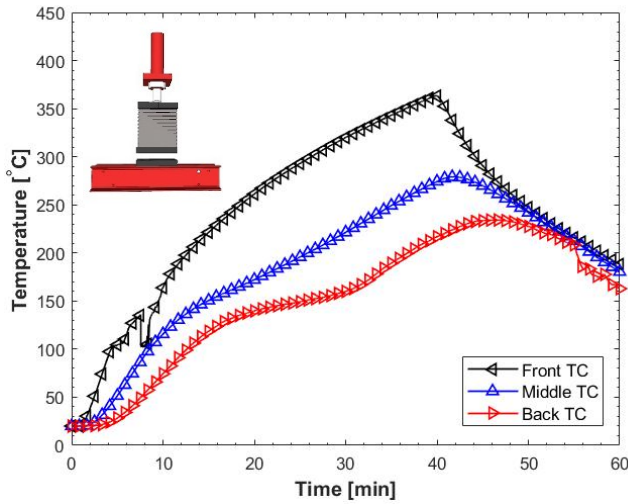


Figure 8 a) Temperatures of Sample RH1 restrained perpendicular to interlayer

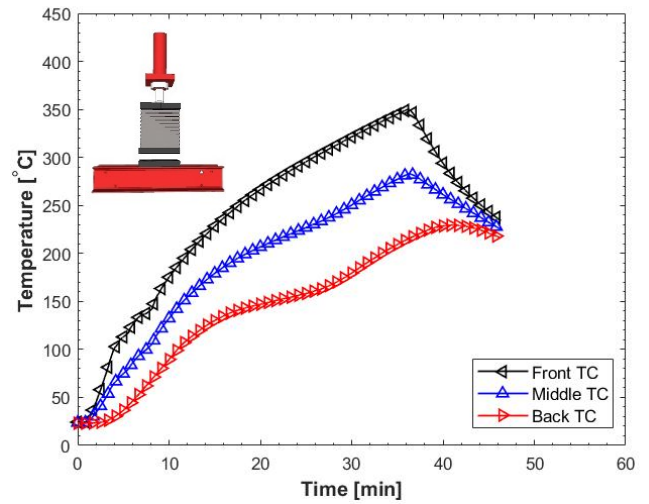


Figure 8 b) Temperatures of Sample RH2 restrained perpendicular to interlayer

Figure 9 a) and b) depict the average temperatures measured during the horizontally restrained (parallel to interlayers) experiments at the front face of the samples, centre of the samples and the back face of the samples for sample RV1 and sample RV2, respectively.

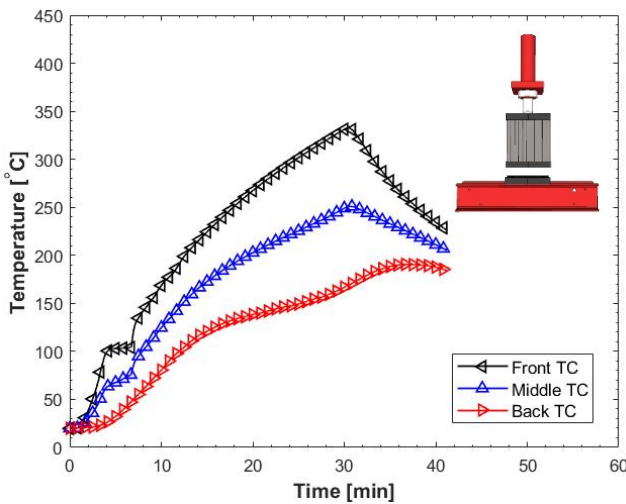


Figure 9 a) Temperatures of Sample RV1 restrained parallel to interlayer

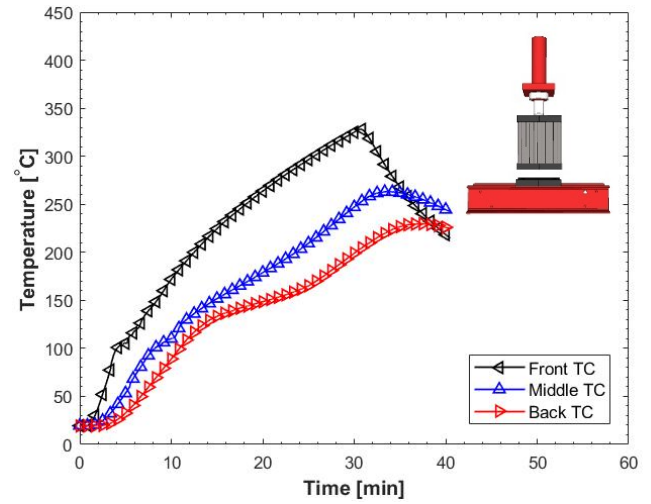


Figure 9 b) Temperatures of Sample RV2 restrained parallel to interlayer

The load applied by the press increased as the samples tried to elongate. Unfortunately, the setup was more flexible than initially expected. However, results obtained do then show that tensile forces developed appear to govern the delamination process which is important (discussed below), as this process can be numerically investigated more readily than processes such as spalling. Table 3 presents the maximum restraint force induced by the hydraulic press experimental setup as the samples expanded, which will be discussed further below. Note that there were no restraints for samples U1 and U2, hence the restrained forces are 0 kN. The load cell malfunction for sample RV2 and hence no force is listed for RV2 in Table 3.

Table 3: Maximum compressive restraint forces exerted by hydraulic press

	U1	U2	RH1	RH2	RV1	RV2
Max restraint force	0 kN	0 kN	5.8 kN	3.5 kN	4.7 kN	-

Considering Figures 7 and 8, it is evident that the heating rate for the samples restrained perpendicular to the interlayers (Figure 8) was slightly lower compared to the unrestrained samples (Figure 7), i.e. between 38-40 minutes the restrained samples (Figure 8) reached 350°C where the unrestrained samples (Figure 7) reached approximately 400°C in the same time period. Similarly, the heating rate for the samples restrained parallel to the interlayers (Figure 9) was slightly lower compare to the unrestrained samples (Figure 7), but was similar to the heating rate of the samples restrained perpendicular to the interlayers (Figure 8). This is unfortunate since a lower heating rate implies a smaller temperature gradient between the front and back face of the samples, meaning lower self-equilibrating tensile stresses are induced. However, the delamination behaviour results (discussed in detail below) does show that the slightly lower heating rates were still sufficient to cause interlayer delamination. Additionally, for the samples restrained sufficiently from in-plane movement, the heating rate should also not affect the results related to the interlayer delamination behaviour (i.e. since the samples would be completely in compression), which is the focus of this preliminary study.

4 EFFECT OF BOUNDARY CONDITIONS ON INTERLAYER BEHAVIOUR

In addition to the ambient flexural strength determined with the four-point bending tests (Table 2), the full $160 \times 40 \times 160$ mm ($w \times h \times l$) restrained samples were also tested under four-point bending (after the samples were cooled to ambient temperatures) to give an indication of the residual flexural strength of the samples. The authors did attempt to cut the unrestrained samples to 40 mm widths in order for the sample size to comply with EN 196-1 [14] and be comparable to the ambient four-point bending tests, however the cutting led to the samples breaking at the interlayer positions. Hence, for the restrained samples it was decided to use the full samples, although not entirely correct, but to give some indication of the residual flexural strength of the samples. The flexural strength of the heated samples and average of the ambient condition samples (unheated samples) are listed in Table 4.

Table 4: Flexural strength of the average ambient samples (unheated samples) and the post-fire restrained samples (approximately $160 \times 40 \times 160$ mm)

Sample	Breaking Force (N)	Cross-Sectional Height (mm)	Cross-Sectional Width (mm)	Flexural Strength (MPa)	Average Flexural Strength (MPa)	Coefficient of Variation (%)
A1-A5	1082.6	39.9	29.4	2.5-5.2	3.3	29.1
RV1	389.39	34	147	0.34	0.25	38.4
RV2	172.17	34	146	0.15		
RH1	2667.3	37	153	1.91	1.91	-

A: Average ambient samples of 5 tests, RV: Restrained with layers orientated vertically, RH: Restrained with layers orientated horizontally

Similar to the findings of [11,13], the unrestrained samples in this work delaminated, i.e. the samples cracked along the interlayers, during heating. As mentioned above, Cicione et al. [11] showed that as a result of the differential heating, the thermal gradient developed in the samples induce self-equilibrating tensile stresses that are greater than the flexural capacity of the samples at the relevant elevated temperature. For these unrestrained samples this has also been calculated using the beam theory method proposed by [16], with material models being based upon EN 1992-1-2. For a detailed explanation and a parametric study on the beam theory method used to calculate the internal stress and strains the reader should refer to [12]. Further research is required to characterize elevated temperature-stress-strain behaviour of 3DPC (specifically for the interlayer bond), but this calculation provides an estimate of stresses experienced. Figure 10 shows the calculated stress and stain profile for sample U1, where the initial flexural capacity of the sample was assumed to be 3.3 MPa (i.e. the flexural capacity of the unheated samples in Table 4) and

it was assumed that the flexural strength reduced at the same rate as tensile stresses according to EN 1992-1-2. The graph was obtained at the peak front face temperature which occurred at approximately 42.5 minutes (Figure 7). From Figure 10 it can be observed that for approximately 8 mm from the exposed face to 8 mm from the unexposed face, the sample failed as a result of the sample's expected strain exceeding the failure strain (which is based on EN 1992-1-2). Hence, this is likely why the unrestrained samples broke during cutting since there would have been no residual capacity left in the samples. Cracks were also visible for the unrestrained samples at the interlayer positions after testing.

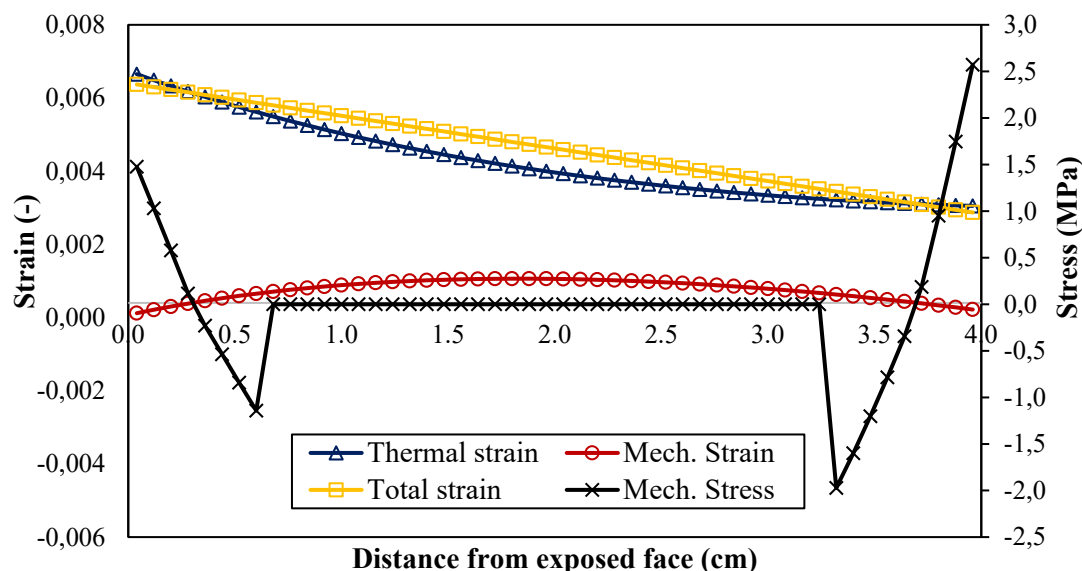


Figure 10. Strains and mechanical stress in sample U1 (Note: negative here indicates a tension stress)

Considering Table 4, it is clear that the residual flexural capacity of the samples restrained parallel to the interlayers (RV1 and RV2) are negligible, which is very similar to what was found for unrestrained 3DPC samples. However, the residual flexural capacity of the one sample restrained perpendicular to the interlayers (RH) was still relatively strong (1.91 MPa), although this is still significantly less than the unheated samples (3.3 MPa). An analysis of sample RH1 (carried out using the methodology presented in [16,17] as done to obtain Figure 10), which is the only sample that retained significant post-fire flexural strength, is presented in Figure 11. This analysis was done at around 39 minutes when the maximum temperature gradient and restraint force were present. From the stress and strain profile through the sample, it can be observed that the sample was almost fully in compression, with stresses ranging between -1.9 MPa (tension) and 8.2 MPa (compression). Hence, as a result of the thermally-induced axial force of 5.8 kN (Table 3) due to restraint, sample RH1 did not fail in the middle of the sample as seen for the unrestrained samples (Figure 10).

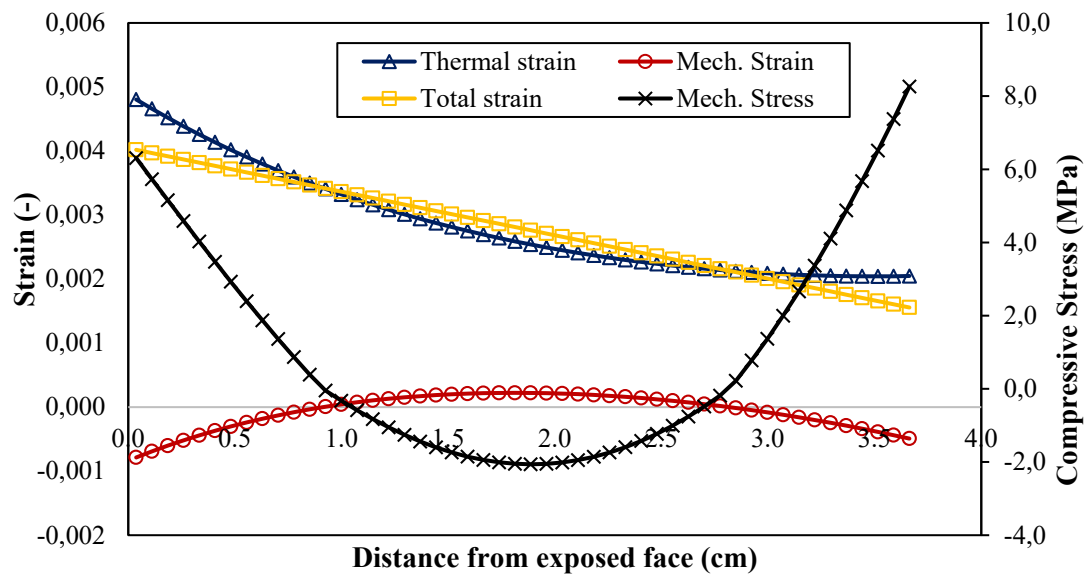


Figure 11. Strains and mechanical stress in sample RH1 (Note: negative here indicates a tension stress)

Although sample RH2 was also restrained, sample RH2 did however break post-testing under light hand pressure, as depicted in Figure 13. This indicates that sample RH2 had virtually no residual capacity. Similar to above an analysis was done to determine the stress and stain profile during heating for sample RH2, which experienced a maximum restraining force of 3.5 kN (i.e. 2.4 kN less than sample RH1). From Figure 12 it can be observed that for approximately 11 mm from the exposed face to 15 mm from the unexposed face, the sample failed as a result of the sample's expected strain exceeding the failure strain (which is based on EN 1992-1-2). This indicate that the 3.5 kN force induced by the hydraulic press was not sufficient to avoid cracking, as observed for sample RH1. Hence, this is presumably why sample RH2 broke under light hand pressure (while handling the sample). Thus, this does suggest that the primary mechanism of failure is due to the stress profiles induced exceeding tensile limits, and not thermal-hygral spalling or similar mechanisms at the interlayer location. However, these samples are not enough to make any assertive conclusions and complementary research is required.

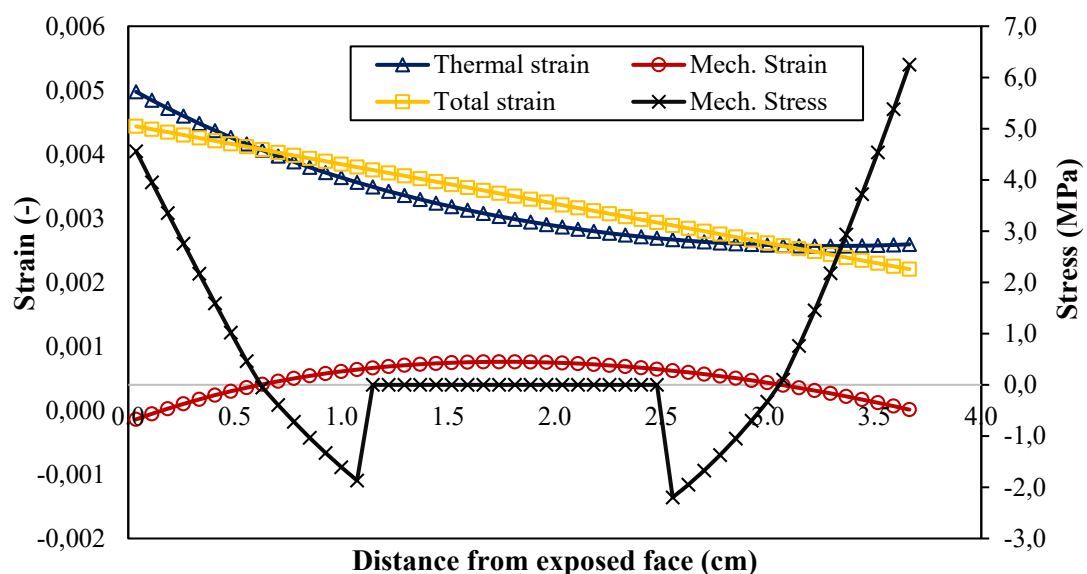


Figure 12. Strains and mechanical stress in sample RH2

Samples RV1 and RV2 retained a small post-fire flexural strength of 0.15-0.34 MPa, i.e. less than 10% of the ambient temperature results, but more than the unrestrained samples (which simply broke while handling). The platens of the hydraulic press may have prevented horizontal elongation through friction-induced shear stresses, thereby inducing some compressive stresses to counteract Poisson effects. However, this counteracting force was likely significantly less than the axial forces in sample RH1 and RH2, hence the samples would also have experienced some cracking in the middle of the sections, similar to samples U1, U2 and RH2. Figure 14 depicts sample RV1 after the 4-point bending test, which clearly shows the samples breaking at the interlayers.



Figure 13. Sample RH2 of horizontally restrained test breaking under hand pressure



Figure 14. Sample RV1 of vertically restrained test after 4-point bending test

5 CONCLUSION

This paper presented a simple, yet novel, preliminary experimental study on the effect of boundary conditions on interlayer bond behaviour at elevated temperatures. In the work, six three-dimensional concrete printed (3DCP) samples were tested. Two samples were left unrestrained during heating and four samples were restrained from in-plane movement. The samples were heated via radiant panels and temperature readings were measured at the front face, centre and back face of the samples during the experiments. Additionally, after the heated samples were cooled back to ambient conditions, the samples were tested in four point-bending to determine the post-fire flexural capacity of the samples. It was found that only one of the six sample (sample RH1) retained some post-fire flexural capacity, i.e. 1.9 MPa for sample RH1 versus 3.3 MPa for the unheated samples. Based on beam theory analyses it was found that sample RH1 was the only sample which was sufficiently restrained for axial movement (perpendicular to the interlayers) to avoid the self-equilibrating tensile stresses (resulting from the differential heating) from causing interlayer delamination. The preliminary results indicate that if sufficient restraint perpendicular to the interlayers is present the tendency of the interlayers to delaminate can be overcome. However, only a small number of samples were tested in this work and more tests and research is required before any assertive conclusions can be made.

ACKNOWLEDGMENT

The authors would like to acknowledge the financial support of the Royal Academy of Engineering / Lloyd's Register Foundation Engineering X programme under grant "A Fire Safe Africa" (Grant ESMN1921\1\141). The support by The Concrete Institute of South Africa is gratefully acknowledged.

REFERENCES

1. S.C. Paul, G.P.A.G. van Zijl, M.J. Tan, I. Gibson, A Review of 3D Concrete Printing Systems and Materials Properties: Current Status and Future Research Prospects, *Rapid Prototyp. J.* 24 (2017) 784–798. <https://doi.org/10.1108/RPJ-09-2016-0154>.
2. C.W. Hull, C. Arcadia, Apparatus for production of three-dimensional objects by stereo thography. US Patent 4575330, 1896.
3. J. Pegna, Exploratory investigation of solid freeform construction ', 1997.
4. N. Labonnote, A. Rønnquist, B. Manum, P. Rüther, Additive construction: State-of-the-art, challenges and opportunities, *Autom. Constr.* 72 (2016) 347–366. <https://doi.org/10.1016/j.autcon.2016.08.026>.
5. R.A. Buswell, W.R. Leal de Silva, S.Z. Jones, J. Dirrenberger, 3D printing using concrete extrusion: A roadmap for research, *Cem. Concr. Res.* 112 (2018) 37–49. <https://doi.org/10.1016/cemconres.2018.05.006>.
6. <https://www.dezeen.com/2019/12/22/apis-cor-worlds-largest-3d-printed-building-dubai/> (accessed March 22, 2020).
7. World's first 3D printed reinforced concrete bridge opened, (n.d.). <https://www.tue.nl/en/our-university/departments/built-environment/news/17-10-2017-worlds-first-3d-printed-reinforced-concrete-bridge-opened/> (accessed March 22, 2020).
8. V. Mechtcherine, J. Grafe, V.N. Nerella, E. Spaniol, M. Hertel, U. Füssel, 3D-printed steel reinforcement for digital concrete construction – Manufacture, mechanical properties and bond behaviour, *Constr. Build. Mater.* 179 (2018) 125–137. <https://doi.org/10.1016/j.conbuildmat.2018.05.202>.
9. R.J.M. Wolfs, F.P. Bos, T.A.M. Salet, Hardened properties of 3D printed concrete: The influence of process parameters on interlayer adhesion, *Cem. Concr. Res.* 119 (2019) 132–140. <https://doi.org/10.1016/cemconres.2019.02.017>.
10. T.T. Le, S.A. Austin, S. Lim, R.A. Buswell, R. Law, A.G.F. Gibb, T. Thorpe, Hardened properties of high-performance printing concrete, *Cem. Concr. Res.* 42 (2012) 558–566. <https://doi.org/10.1016/cemconres.2011.12.003>.
11. A. Cicione, P.J. Kruger, R.S. Walls, G. van Zijl, An experimental study of the behavior of 3D printed concrete at elevated temperatures, *Fire Saf. J.* (2020).
12. R.S. Walls, C. Viljoen, H. de Clercq, Parametric investigation into the cross-sectional stress-strain behaviour, stiffness and thermal forces of steel, concrete and composite beams exposed to fire, *J. Struct. Fire Eng.* (2019). <https://doi.org/10.1108/JSFE-10-2018-0031>.
13. P.J. Kruger, A. Cicione, F. Bester, M. van den Heever, R.S. Walls, G. van Zijl, Facilitating ductile failure of 3D printed concrete elements in fire, in: *Digit. Concr. 2020 - 2nd RILEM Int. Conf. Concr. Digit. Fabr.*, 2020.
14. EN 196-1, Cement - Determination of Strength, *Build. Mater.* 10 - Test. Methods. (n.d.) 66–71.
15. P.J. Kruger, G.P.A.G. van Zijl, A compendious review on lack-of-fusion in digital concrete fabrication, *Addit. Manuf. J.* In press (2020).
16. R.S. Walls, C. Viljoen, H. de Clercq, Analysis of Structures in Fire as Simplified Skeletal Frames Using a Customised Beam Finite Element, *Fire Technol.* (2018). <https://doi.org/10.1007/s10694-018-0762-7>.
17. R.S. Walls, A beam finite element for the analysis of structures in fire, Stellenbisch University, 2016.

PREDICTING THE FIRE RATING OF CANTILEVER SLAB-WALL CONNECTION WITH POST INSTALLED REBAR

Hitesh Lakhani¹, Jatin Aggarwal², Jan Hofmann³

ABSTRACT

It is known that the chemical adhesives used as bonding material for Post Installed Rebars (PIRs) are very sensitive to temperature. Due to this reason the bond strength of PIRs decreases drastically with increase in temperature. Hence, the connections in Reinforced Concrete (RC) structures built using PIRs may lead to structural safety issues in an event of fire. There exists in literature, methods to compute the pull-out capacity of PIRs. But the fire resistance of PIR systems cannot be obtained only using the information related to the pull-out capacity. Rather, additional information is needed about the demands imposed on the rebar due to fire exposure, which depends on the structural system built using PIR. The paper presents a design procedure and its validation against experimental results available in literature. It has been shown that conventional modelling assumption of ignoring reinforcement during thermal analysis may not be suitable for analysing the PIR systems. The main reason being the axial heat flow along the rebar, thus, transporting more heat into the joint/end anchorage zone. Hence, the paper recommends conducting a 3D transient thermal analysis to compute the temperatures along the embedment depths of PIR, which are then used for calculating the pull-out capacities.

Keywords: Post installed rebar, Slab-wall connection, Adhesive mortar, Fire rating

1 INTRODUCTION

The use of Post Installed Rebars (PIRs) has increased in various structural engineering application. Due to the practical and economical advantages offered by this technique to add new structural components / members to existing structures [1,2]. But at the same time, the (polymeric) adhesive mortars are known to be sensitive to temperature [3–5], which can cause safety issues [6–8]. There are a variety of different adhesive materials (mortars) available in market and the bond-strength degradation is different for each product depending on its chemical composition [4,9]. Therefore, an objective design procedure would be one which requires the least amount of product dependent parameters.

The paper presents an improved and extended version of the design procedure proposed by Lakhani and Hofmann (2018) [7]. The study by Lakhani and Hofmann (2018) had shown that for a realistic calculation of the pull-out capacity of PIR, reinforcement should be considered during the heat transfer analysis. Because the reinforcement, due to its high conductivity, acts as a heat transfer path and carries heat into the connection region, which may not be exposed to fire directly. The study predicted a significantly reduced failure time for the slab-wall connection when steel is considered explicitly. But it should be noted that the results were based on 2D heat transfer analysis, which is an assumption commonly made in practice [1,10].

¹ Scientific Associate, Institute of Construction Materials, University of Stuttgart, Germany
e-mail: hitesh_lakhani06@rediffmail.com, hitesh.lakhani@iwb.uni-stuttgart.de, ORCID: <https://orcid.org/0000-0003-2988-9264>

² Student, Department of Civil Engineering, Indian Institute of Technology, Roorkee, India
e-mail: jatinaggarwal2106@gmail.com

³ Professor, Institute of Construction Materials, University of Stuttgart, Germany
e-mail: jan.hofmann@iwb.uni-stuttgart.de

But a 3D heat transfer analysis is needed, if reinforcement is to be considered explicitly, as the correct volume/contact surface of reinforcement with the surrounding concrete cannot be modelled correctly in a 2D analysis. This was the reason that Lakhani and Hofmann (2018) predicted a substantially huge difference between the predicted failure time with and without considering steel. Hence, improved results based on 3D heat transfer analysis are presented in this paper.

2 CALCULATION / DESIGN PROCEDURE

Basically, the verification/design of PIR connections, has two aspects associated with it. The first being the capacity of the PIR system, which would be product dependent. The second aspect being the demand imposed on the PIR, which changes due to stress-redistribution at sectional level and load redistribution at structural level. Hence, the steps involved in the design procedure can be grouped under two broad categories:

1. Computing the pull-out capacity of the PIR system
2. Computing the demand imposed on the PIR, using sectional analysis or member analysis or structural analysis, depending on the complexity of the case being analysed.

2.1 Assumptions

Following assumptions were made for the first step of computing the pull-out capacity of the PIR:

1. The thin mortar layer between rebar and concrete is neglected during the heat transfer analysis.
2. Perfect contact is assumed between concrete and reinforcement.

The assumptions for the second step would vary depending on the complexity of the structural analysis undertaken for computing the demand on the PIR. For example: for the presented case of cantilever slab-wall connection, a sectional analysis was sufficient to calculate the variation

2.2 Design steps

The proposed design procedure consists of the following steps:

1. Conducting a transient heat transfer analysis of the structural system/component using temperature dependent thermal properties for concrete and steel.
2. The computed variation of temperature along the embedment length of the PIR at various time instances is converted to corresponding bond strength variation along the length using the product dependent degradation of bond strength.
3. Compute the pull-out capacity of the PIR at various time instances by integrating the bond strength variation along the embedment length. Thus, obtaining the capacity curve for the PIR.
4. In this step the demand imposed on the PIR is computed. The demand on the PIR changes with exposure time due to redistribution of internal stresses and forces within the connected structural members, due to the fire exposure. Hence, a structural analysis (thermal stress analysis) needs to be conducted to determine the demand imposed on the PIR. Depending on the complexity of the structural configuration being designed structural analysis with various levels of complexity can be performed.
5. The failure time for PIR due to pull-out failure is obtained as the point of intersection of the capacity and the demand curve computed in step 3 & 4, respectively.

3 CASE STUDY: CANTILEVER SLAB-WALL CONNECTION

To demonstrate the design procedure presented in Section 2, the full-scale cantilever slab-wall connection tested by Lahouar et al., (2017, 2018) [1,10] was selected from the literature. The loading setup used by Lahouar et al., (2017, 2018) is shown in Figure 1. For further details about the test, the readers may refer

to the original references [1,10], but for the completeness of this paper important information are given below.

The cantilever slab tested by Lahouar et al., (2017, 2018) was $2.94 \text{ m} \times 2 \text{ m} \times 0.15 \text{ m}$ large, made of normal strength concrete with propylene fibers (to avoid spalling). The cantilever slab was connected to the wall using $8 \times 16 \text{ mm}$ rebars with an embedment length of 135mm. The rebars were installed in the wall using epoxy resin-based mortar. The slab was loaded with a superimposed dead load of 325 kg at 2.2 m from the wall-connection end. The total applied moment (self-weight + imposed dead load) at the slab-wall connection was $\approx 32 \text{ kN m}$. The slab was exposed standard fire exposure as per ISO834 [11]. The slab-wall connection was reported to fail at 117 minutes.

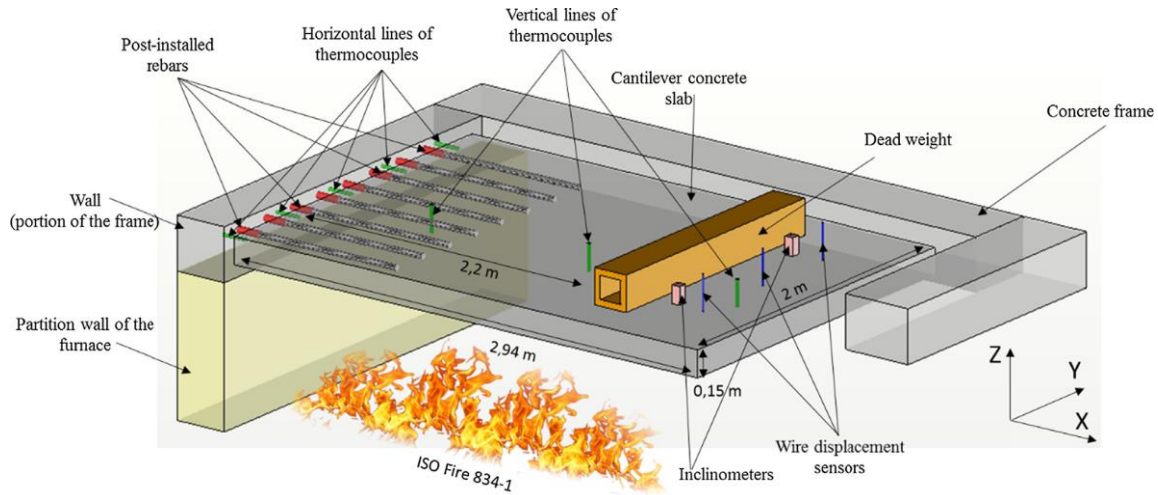


Figure 1. Fire test configuration for slab-wall connection with PIR tested by Lahouar et al., (2017, 2018)

3.1 Input data

The thermal results report in this paper were obtained using the thermal properties for concrete and steel as recommended by EN1992-1-2 [12] and EN1993-1-3 [13], respectively. Figure 2 shows graphically the thermal properties used for heat transfer analysis. The heat transfer from the hot gases to slab surface was modelled using convective and radiation boundary conditions with convection heat transfer coefficient $h_c = 25 \text{ W/m}^2 \text{ K}$ and emissivity $e = 0.8$.

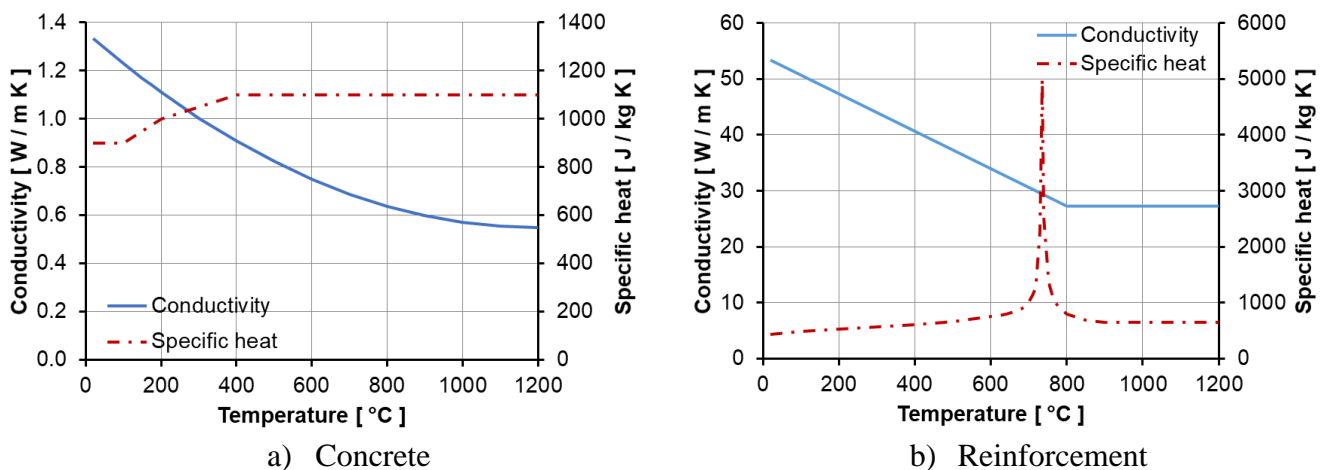


Figure 2. Thermal properties of concrete and reinforcement

The bond strength degradation as function of temperature for the adhesive mortar used for making the slab-wall connection using PIR, was also obtained experimentally in accordance to EAD 330087-00-0601 [14],

by Lahouar et al., (2017, 2018) and is shown in Figure 3. The bond strength of the mortar was not affected by temperature up to 31°C and was zero for temperature above 115°C.

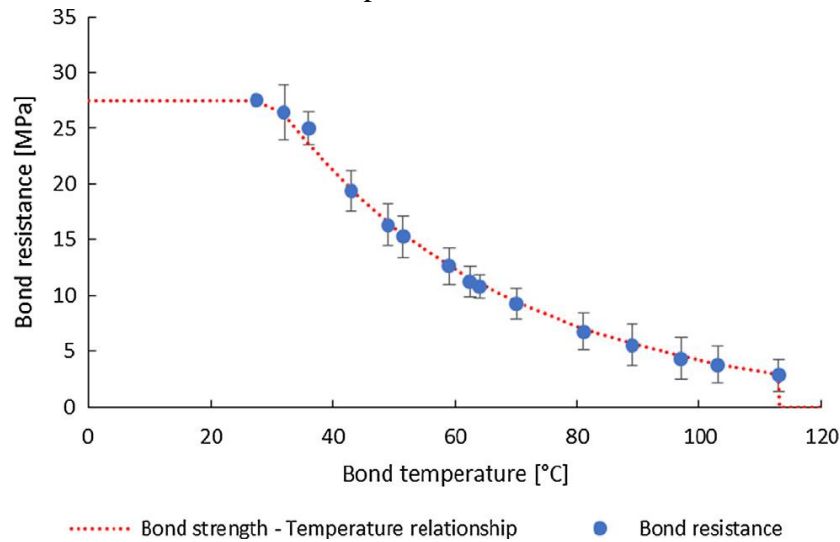


Figure 3. Bond-strength variation with temperature for the adhesive mortar [1]

The demand on the PIR was predicted by conducting a sectional analysis assuming the concrete to be made of siliceous aggregates ($f_c=23\text{ MPa}$) and reinforcement to be cold rolled ($f_y = 460\text{ MPa}$). The constitutive material laws & the degradation of mechanical properties with temperature were taken from EN1992-1-2 [12]. This implies that the load induced thermal strain for concrete was considered implicitly.

3.2 Results and discussion

Comparison of the predicted temperature variation along the embedment depth of PIR based on the 3D analysis is shown in Figure 4. Due to the presence of steel the predicted temperatures at the junction of the slab-wall connection (denoted as location 0 along the x-axis) reduces slightly with increase in exposure duration. Whereas, the temperature at the end of the embedment lengths are always higher, due to the heat being transported by the reinforcement. To further support this statement the temperature contours on a section along the reinforcement at exposure durations of 30, 60, 90 and 120 minutes are shown in Figure 5. The legend for these contours was deliberately set to a maximum of 115 °C (temperature beyond which bond strength is zero), to read qualitatively the length of rebar which has completely lost its bond strength. The contours also clearly show the heat path along the rebar which leads to higher temperature at the end of the PIRs.

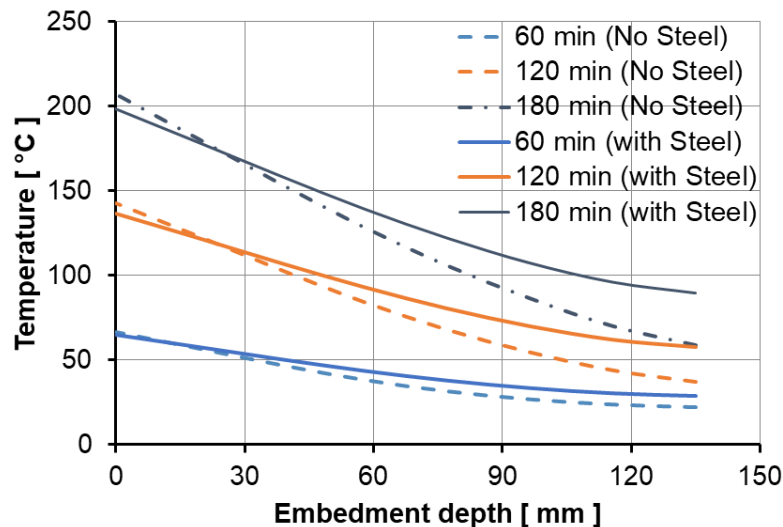


Figure 4. Predicted temperature along the rebar embedment depth (Location 0 corresponds to face of the wall)

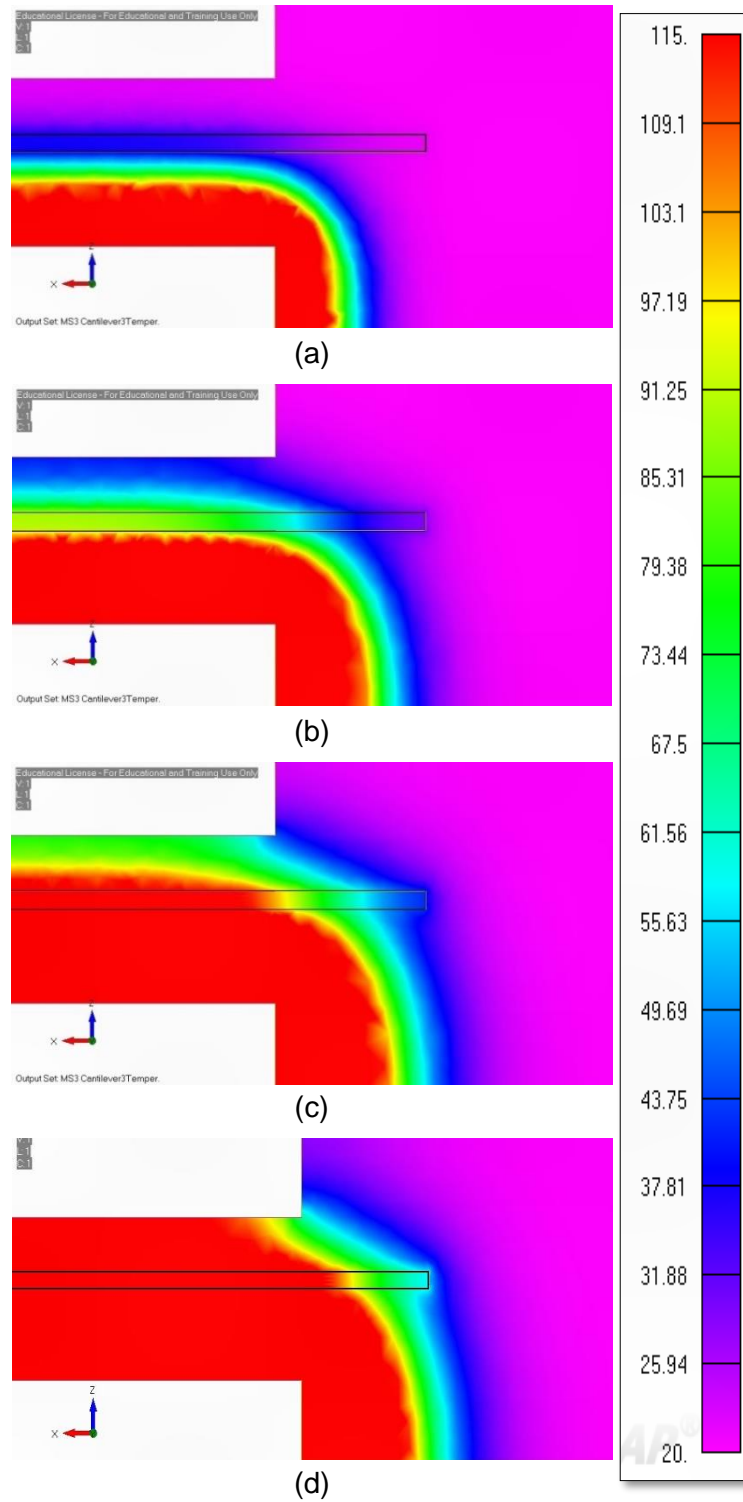


Figure 5. Temperature contours on the section along the rebar at a) 30 min, b) 60 min, c) 90 min and d) 120 min

Using the computed temperature along the embedment depth of the rebar (shown in Figure 4) and the bond strength degradation with temperature (shown in Figure 3), bond strength variation along the embedment depth is obtained. The bond strength variations for cases with and without steel at 60 and 120 minutes of fire exposure are shown in Figure 6 and 7. The figure clearly shows the reduction in the area under the bond strength curves (the pull-out capacity) for cases with reinforcement.

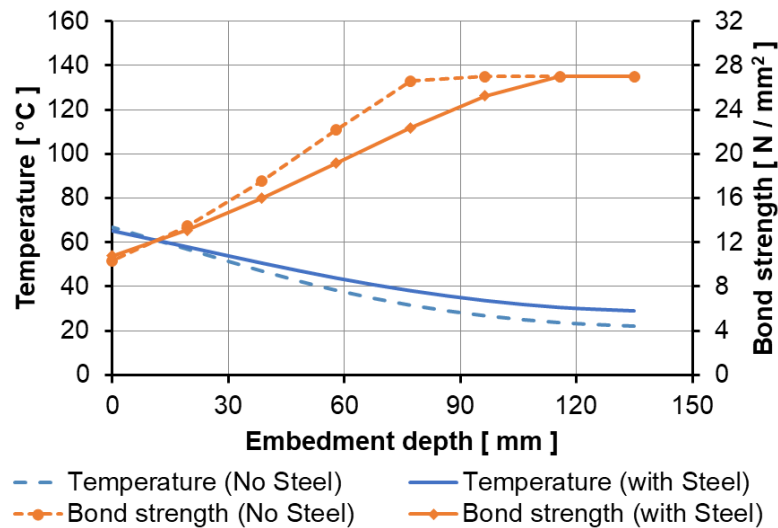


Figure 6. Temperature and bond strength variation along the embedment depth of PIR at 60 minutes.

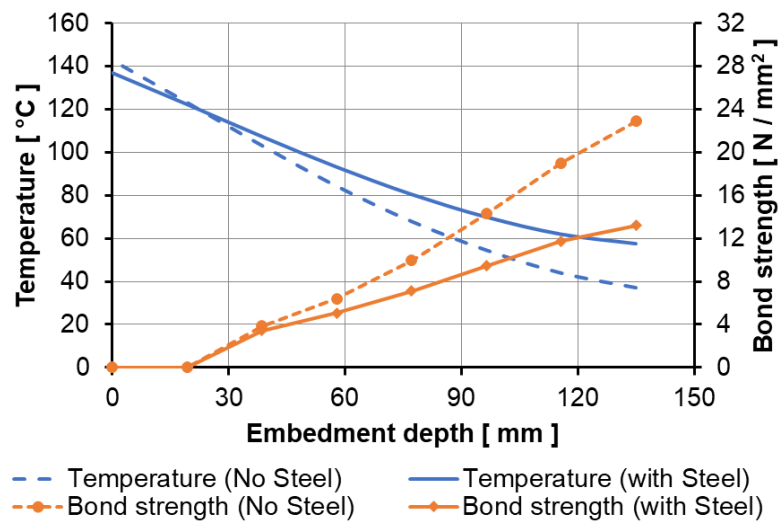


Figure 7. Temperature and bond strength variation along the embedment depth of PIR at 120 minutes.

The pull-out capacity of the PIR is obtained by integrating the bond strength variation along its embedment depth. Figure 8 shows the computed capacity curves for the cases with and without steel (during heat transfer analysis). The capacity curve based on 2D heat transfer analysis (with steel), from the previous study [7], is also shown in Figure 8, to show the improvements in the results obtained using 3D heat transfer analysis. The computed demand curve using sectional analysis is also shown in Figure 8. Since, the sectional analysis was conducted for the cross-section at the slab-wall interface, and at this section the temperatures were not influenced by the presence of steel. Hence, the computed demand curve remains the same and can be used to obtain the failure time for all the capacity curves plotted on Figure 8.

The large difference between the failure time with and without steel, reported in the previous study was a result of incorrect representation of the steel volume and contact surface between steel and concrete, in a 2D model. This difference reduced based on more realistic 3D model. The case with steel predicts a failure time $\approx 12\%$ less than the case without steel.

It is still interesting to note that the failure time predicted by case without steel is the closest to the experimentally obtained failure time of 117 minutes. This can be attributed to several factors like the actual thermal properties of fiber reinforced concrete (are the thermal properties given in EN1992-1-2 also

applicable to concrete with poly propylene fibers ?), effect of moisture content or moisture migration etc., which needs to be further investigated.

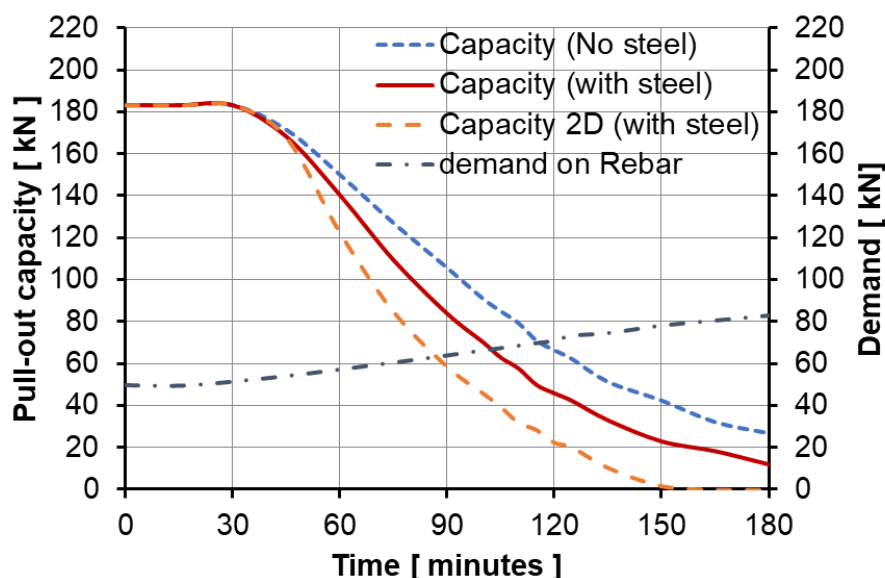


Figure 8. Capacity and demand curves for each PIR

4 CONCLUDING REMARKS

- The paper discussed a simple design procedure which can be used for determining the fire rating of PIR connections. The design procedure was demonstrated, with the help of a case study of cantilever slab-wall connection.
- The design procedure recommends conducting a 3D heat transfer analysis to correctly model the heat flow/transfer along the rebar, which has been ignored by researchers.
- The predicted failure time were 12% less when the heat flow along the rebar was correctly modelled.
- Since there are very limited experimental studies available in literature, more experiments on different PIR connections are needed for further verification of the design procedure.

REFERENCES

1. Lahouar MA, Pinoteau N, Caron J-F, Foret G, Rivillon P. Fire design of post-installed bonded rebars: Full-scale validation test on a $2.94 \times 2 \times 0.15$ m³ concrete slab subjected to ISO 834-1 fire. *Engineering Structures* 2018; 174: pp. 81–94. <https://doi.org/10.1016/j.engstruct.2018.07.069>.
2. Hofmann J, Lakhani H, Aggarwal J. Post installed rebars - Pull-out capacity during fire. *Otto-Graf-Journal* 2019; 18: pp. 141-152.
3. Pinoteau N, Pimienta P, Guillet T, Rivillon P, Rémond S. Effect of heating rate on bond failure of rebars into concrete using polymer adhesives to simulate exposure to fire. *International Journal of Adhesion and Adhesives* 2011; 31: pp. 851–61. <https://doi.org/10.1016/j.ijadhadh.2011.08.005>.
4. Pinoteau N, Pimienta P, Guillet T, Rivillon Ph, Remond S. Effect of heat on the adhesion between post-installed bars and concrete using polymeric mortars. Volume 2: Bond in new materials and under severe conditions, Brescia, Italy: 2012, pp. 573–80.
5. Muciaccia G, Navarrete DD, Pinoteau N, Mége R. Effects of different test apparati and heating procedures on the bond properties of post-installed rebar connections under elevated temperatures. *Materials and Structures* 2019; 52. <https://doi.org/10.1617/s11527-019-1337-x>.
6. Pinoteau N, Heck JV, Rivillon Ph, Avenel R, Pimienta P, Guillet T, et al. Prediction of failure of a cantilever-wall connection using post-installed rebars under thermal loading. *Engineering Structures* 2013; 56: pp. 1607–19. <https://doi.org/10.1016/j.engstruct.2013.07.028>.

7. Lakhani H, Hofmann J. On the pull-out capacity of post-installed bonded anchors and rebars during fire. Proceedings of 10th International Conference on Structures in Fire, Belfast, United Kingdom: 2018, pp. 165–71.
8. Al-Mansouri O, Mege R, Pinoteau N, Guillet T, Rémond S. Influence of testing conditions on thermal distribution and resulting load-bearing capacity of bonded anchors under fire. *Engineering Structures* 2019; 192: pp. 190–204. <https://doi.org/10.1016/j.engstruct.2019.04.099>.
9. Zhang Y, Lou G, Chen K, Li G. Residual Strength of Organic Anchorage Adhesive for Post-installed Rebar at Elevated Temperatures and After Heating. *Fire Technology* 2016; 52: pp. 877–95. <https://doi.org/10.1007/s10694-015-0510-1>.
10. Lahouar A, Pinoteau N, Caron J-F, Guillet T, Mege R. Chemically bonded post installed steel rebars in a full-scale slab-wall connection subjected to standard fire (ISO834-1). Proceedings of 3rd International Symposium on Connections between Steel and Concrete, Stuttgart. Germany: 2017, p. 1119–30.
11. ISO 834-1:1999, Fire-resistance tests - Elements of building construction - Part 1: General requirements. International Organization for Standardization; 1999.
12. EN1992-1-2:2004. Eurocode 2: Design of concrete structures - Part 1-2: General rules - Structural fire design. Brussels: European Committee for standardization; 2004.
13. EN1993-1-2:2005. Eurocode 3: design of steel structures - Part 1-2: General rules — Structural fire design. Brussels: European Committee for standardization; 2005.
14. EAD 330087-00-0601. Systems for post-installed rebar connections with mortar. Brussels: European organisation for technical assessment; 2018.

INFLUENCE OF SPALLING ON THE BIAXIAL BENDING RESISTANCE OF REINFORCED CONCRETE COLUMNS EXPOSED TO FIRE

Peña David L.¹, Ibáñez Carmen², Alberó Vicente³, Espinós Ana⁴, Hospitaler Antonio⁵,
Romero Manuel L.⁶

ABSTRACT

Concrete exposed to fire can experience spalling when the pore pressure increases due to water evaporation and that results in the surface sloughing off. This work evaluates the consequences that spalling has on the biaxial bending resistance of reinforced concrete columns exposed to fire by means of a sequential model. In this case, it is a sectional model with fibres integration. The model is able to generate the interaction surfaces of the columns subjected to biaxial bending and 4-sided uniformly exposed to the standard fire curve ISO 834.

Keywords: Reinforced concrete; spalling; columns; biaxial bending; fire resistance

1 INTRODUCTION

Reinforced concrete (RC) exposed to fire can experience spalling when the internal pore pressure increases due to water evaporation, resulting in loss of concrete to a certain depth. Spalling can be grouped into four categories: (a) aggregate spalling; (b) explosive spalling; (c) surface spalling and (d) corner spalling [1]. Mechanisms (a), (b) and (c) are highly influenced by the heating rate whereas (d) tends to be a function of the maximum temperature and, unlike the others, is non-violent.

Spalling produces a relevant loss of the resistant cross-section of RC elements. The probability of spalling appearances as well as the causes producing it are still up for debate. Parameters affecting spalling occurrence are: concrete moisture content, heating rate, previous stress state, permeability, concrete compressive strength, concrete cover and bars spacing, or concrete vibration technique [2-4].

Most of the knowledge about spalling comes from the observation of the phenomenon on buildings and other structures exposed to fire [5].

This paper presents a study into the effects of corner spalling on reinforced concrete columns [6]. When spalling occurs at the corners of a RC structural member, the core and reinforcing bars may become exposed to fire after the loss of the concrete cover. This may lead to a rapid increase in temperature and a reduction in the fire resistance of the column, resulting in a decrease in the level of safety of the column when designed using the prevailing fire resistance design framework [5].

¹ PhD student, Concrete Science and Technology Institute (ICITECH), Universitat Politècnica de València, Spain
e-mail: dapeman1@posgrado.upv.es, ORCID: <https://orcid.org/0000-0003-2236-1774>

² Associate Profesor, Concrete Science and Technology Institute (ICITECH), Universitat Politècnica de València, Spain
e-mail: caribus@upv.es, ORCID: <https://orcid.org/0000-0002-9354-5637>

³ Assistant Profesor, Department of Mechanical Engineering and Construction, Universitat Jaume I, Spain
e-mail: valbero@uji.es, ORCID: <https://orcid.org/0000-0001-7193-9232>

⁴ Associate Profesor, Concrete Science and Technology Institute (ICITECH), Universitat Politècnica de València, Spain
e-mail: aespinos@mes.upv.es, ORCID: <https://orcid.org/0000-0001-7335-4676>

⁵ Full Profesor, Concrete Science and Technology Institute (ICITECH), Universitat Politècnica de València, Spain
e-mail: ahospitaler@cst.upv.es, ORCID: <https://orcid.org/0000-0001-7108-3104>

⁶ Full Profesor, Concrete Science and Technology Institute (ICITECH), Universitat Politècnica de València, Spain
e-mail: mlromero@mes.upv.es, ORCID: <https://orcid.org/0000-0001-5247-4767>

Therefore, some researchers have developed models focused on predicting the occurrence of spalling. Dwaikat y Kodur [7] developed a one-dimensional model based on pore pressure calculation. Lottman et al. [8] presented a model based on two coupled finite elements models where the first one finds the temperature and pore pressure evolution and the second defines the fracture mechanism causing spalling. Specifically regarding RC columns, Buch and Sharma [9] pointed out in a recent paper the importance of studying the fire resistance of structures subjected to eccentric loads combined with spalling. After performing a series of experiments, it was observed that load eccentricity increases the occurrence of spalling. As with Khoury [1], they proved the effectiveness of reinforcing bars in limiting spalling, particularly if these are distributed along the sides of the cross-section.

This work does not model the time to occurrence of spalling. It is instead assumed that spalling occurs, and the effects that this has on the performance of the columns are analysed after the fact. To this end, a sectional model for evaluating the effect of spalling on the biaxial bending resistance of RC columns exposed to fire is presented.

2 MODEL DESCRIPTION AND VALIDATION

In practice, one of the most common loading conditions for RC columns is compression combined with biaxial bending due to load transfer from adjacent beams and slabs. Nevertheless, most studies deal with the behaviour of RC columns subjected to uniaxial bending only. Among the scarce number of publications on RC columns subjected to biaxial bending, attention must be paid to the works by Wang et al. [10] and Kodur and Raut [11] who numerically studied RC columns non-symmetrically exposed to fire. It is noteworthy that EN 1992-1-2 [12] does not include a specific design model that considers spalling. To date, no experimental data has been located by the authors on the fire resistance of RC columns subjected to biaxial bending. Considering all, in this work a sectional model to consider the effect of spalling on the biaxial bending resistance of RC columns exposed to fire is developed.

2.1 Description

The model presented in this work is a sectional model with fibre integration (Figure 1a) developed in MatLab [13]. A sequentially coupled thermal-stress analysis is conducted: first, a thermal analysis (finite difference) is carried out and then a mechanical problem is solved.

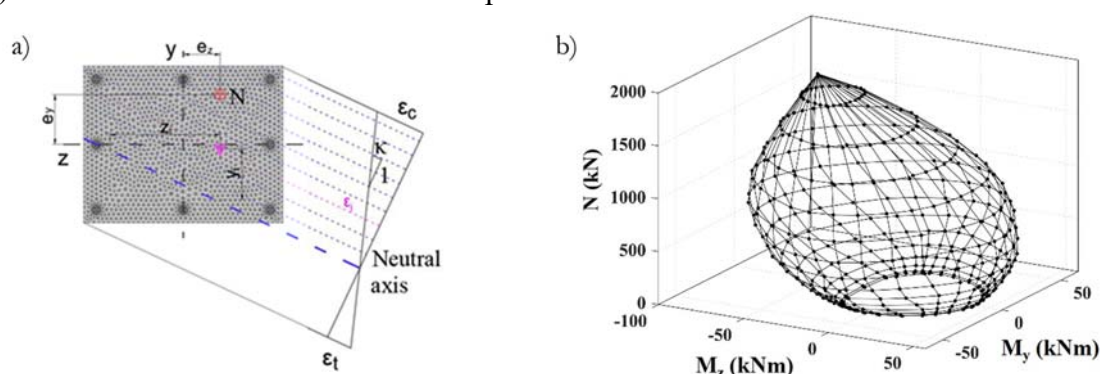


Figure 1. a) Discretization and strain distribution; b) 3D view of an interaction surface

The cross-section is discretised (Figure 1a) and each cell is characterised by its position, temperature and corresponding material properties. In this case, for both steel and concrete, the thermal mechanical properties given by EN 1992-1-2 [12] are used. The Navier-Bernoulli assumption is adopted, which states that a plane section remains plane and normal to the neutral axis (Figure 1a) after bending. Therefore, the curvature of the cross-section (κ) can be derived from the linear distribution of total strains (in this work, mechanical strains are equal to total strains minus thermal strains). The stress state of each cell is obtained

from the constitutive equation of the material at the corresponding temperature. For a given applied load N and through an iterative process, the location of the neutral axis is determined based on the force balance equation given in equation (1).

$$\sum_{i=1}^n A_i \sigma_i - N = 0 \quad (1)$$

where A_i is the area of cell i (mm^2),
 σ_i is the stress of cell i (N/mm^2),
 N is the axial load applied (N).

The bending capacity in each axis is determined by solving equation (2) and (3) by increasing gradually the value of the curvature of the cross-section in order to generate the $M-\kappa$ curve.

$$\sum_{i=1}^n A_i \sigma_i z_i - M_y = 0 \quad (2)$$

$$\sum_{i=1}^n A_i \sigma_i y_i - M_z = 0 \quad (3)$$

where y_i are the y-axis position of the centroid of cell i (mm),
 z_i are the z-axis position of the centroid of cell i (mm),
 M_y is the applied bending moment in y-axis (Nmm),
 M_z is the applied bending moment in z-axis (Nmm).

To obtain the interaction surface, the balance equations are solved for all the loading situations generated by rotating the neutral axis and increasing the axial load from 0 up to the value of the cross-sectional plastic resistance (N_{pl}). In the example of Figure 1b, an interaction surface generated by means of the described numerical model for a RC column with 3-sides exposed to the ISO 834 [14] fire curve is shown.

2.2 Thermal validation

The thermal model was validated with the experimental temperatures recorded in the tests carried out by Lie and Irwin [15] and Kodur et al. [16]. In the validation, the predictions given by the model for the inner points of the concrete cross-section at different fire exposure times were compared with experimental values. To illustrate this process, in Figure 2 it is shown the validation for one of the columns. The points lie mainly in the inner part of the $\pm 15\%$ boundaries and the precision of the model increases for temperatures higher than 400°C . More details about the model and its validation can be found in Peña et al. [17].

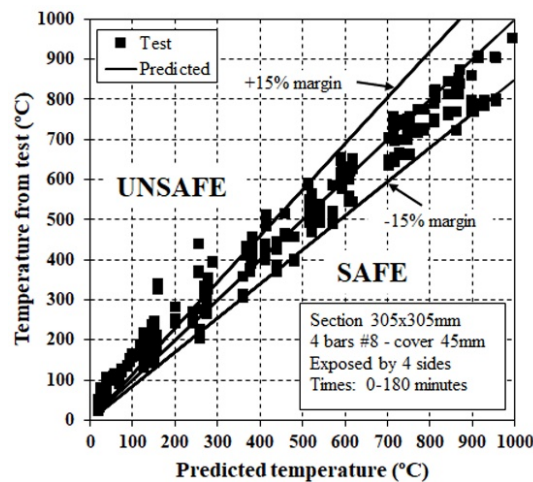


Figure 2. Tests vs. predictions. Col. 1 Lie and Irwin [15]

2.3 Mechanical validation

Given the lack of experiments on columns subjected to biaxial bending in fire, the validation of the mechanical model is completed by parts: (1) validation at ambient temperature for biaxial bending and (2) validation at high temperatures under uniaxial bending. For the ambient temperature validation, experimental results from different published works are used as can be consulted in [17]. Figure 3 shows the good agreement that exists between tests and predicted results for the 61 cases used in validation (Mean=0.99, SD=0.17).

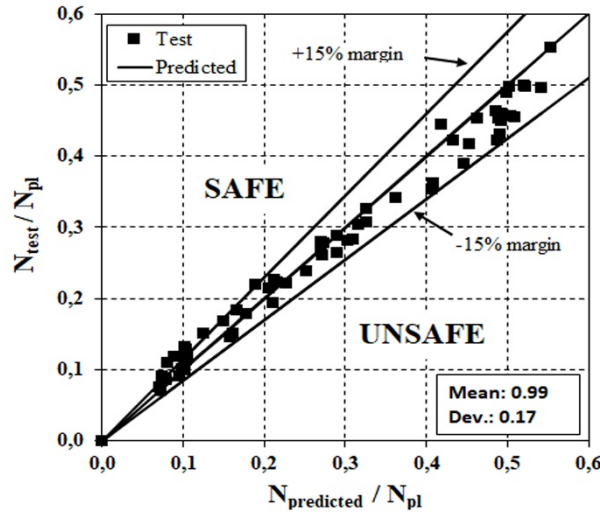


Figure 3. Tests vs. predictions [17]

For the validation at high temperatures under uniaxial bending, the model predictions have been validated against those given by the model presented by Law and Gillie [18]. The specimen taken as reference (300x500mm, 6 ϕ 20) is a ISO 834 3-sides exposed column. The predictions given by both models are identical as can be seen in Figure 4. Thus, the prediction capacity of the model is proven to be satisfactory.

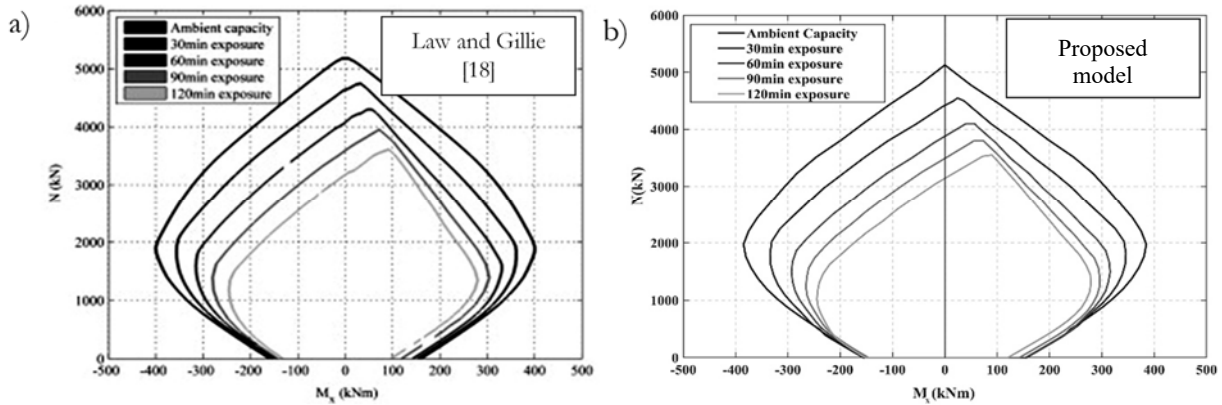


Figure 4. Uniaxial interaction diagrams for different times of fire exposure.

3 APPLICATION OF THE MODEL FOR THE EVALUATION OF SPALLING EFFECTS

In this work, RC columns 4-sided exposed to the ISO834 standard fire curve are considered. The parameters governing the model regarding the moment of occurrence and the depth affected are set according to the conclusions obtained after the study of the most relevant literature. In this case, it has been considered that the half of the perimeter of the corner reinforcing bar is directly exposed to fire.

First, the evolution in time of the cross-sectional temperatures is obtained and when spalling occurs its effect is evaluated by eliminating the fibres of concrete affected (Figure 5a). This leads to the loss of the

initial cross-sectional symmetry, both thermal and geometrical. Therefore, the cross-sectional temperatures must be updated for the new boundary conditions, as shown in Figure 5b and 5c. This non-symmetrical geometry leads to what is, in essence, a biaxial bending problem.

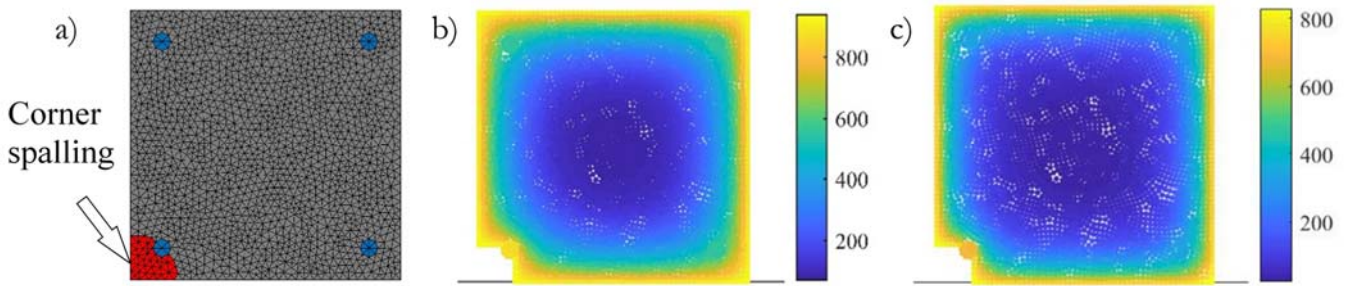


Figure 5. a) Spalling modelling; b) Temperatures at 60 minutes; c) Temperatures at 90 minutes

A cross-section measuring 300x300mm with 4 ϕ 16 reinforcing bars and a concrete cover of 35mm is taken as reference. A concrete strength of C30 is used. The column is 4-sided exposed to the standard fire curve ISO834. The parameter varied is the time of spalling occurrence. The times considered are 10, 15, 20 and 30 minutes from the start of heating. In Figure 5b and 5c the cross-sectional temperatures for 60 and 90 minutes of fire exposure are shown in case of a corner spalling. The temperature in the reinforcing bar that now is exposed directly to fire is much higher than the other three as expected.

In the graph of Figure 6 it is shown the evolution of the temperature of the corner reinforcing bar that is left directly exposed to fire after spalling for different times of spalling occurrence (10, 20 and 30 minutes). In varying the time of spalling it is observed that the effect of this parameter decreases as the exposure time increases. For fire exposure times higher than 45 minutes, the time of spalling has no effect. This highlights that, at least for the case studied, the time of spalling occurrence has no influence unless the fire behaviour is evaluated for a time higher than 45 minutes.

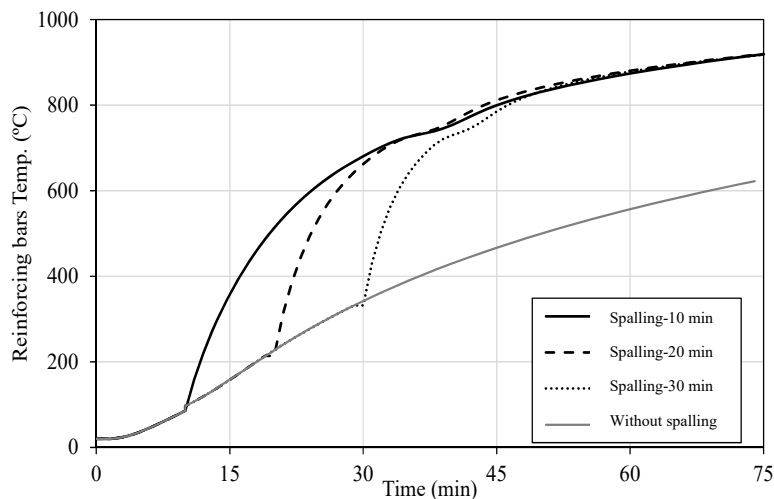


Figure 6. Temperature of directly fire exposed corner reinforcing bar

This observation is corroborated by the modeled mechanical response shown in Figure 7. In this figure several interaction surfaces for columns exposed to 60 minutes for different spalling times are shown and it can be seen that they are identical. This is likely a result of the fact that, after 60 minutes of exposure, the temperature of the concrete on the surface has surpassed the point of being structurally viable and does not therefore contribute to the performance of the column. The temperature gradient within the column is the dominating factor (in this specific corner spalling scenario) in the performance of the column.

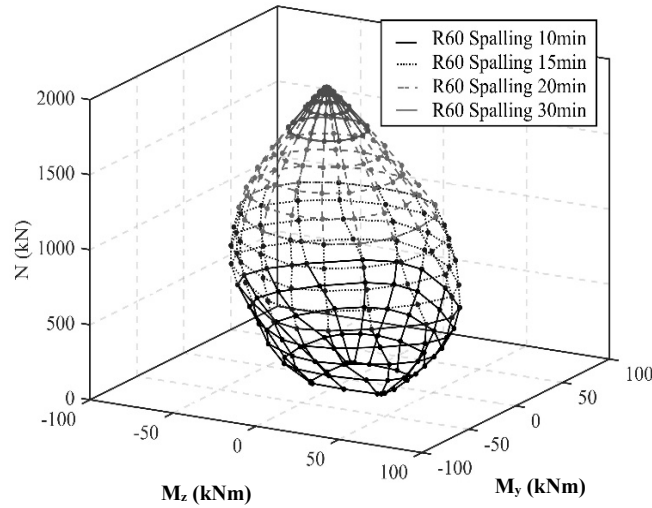


Figure 7. Superposition of interaction surfaces for 60 minutes of fire exposure.

From the interaction surfaces, the M_y - M_z interaction diagrams for certain load ratios can be obtained by taking slices. Thus, for the same load ratio, it is possible to compare diagrams of columns with and without spalling. The decrease in the fire resistance due to spalling can be quantified by finding the diagram modelled without spalling that, in the most critical quadrant, coincides with the diagram modelled with spalling.

In Figure 8 it is shown with a dashed line the 30-minute interaction diagram for a RC cross-section where spalling has occurred. This diagram is obtained by taking a slice of the 3D interaction surface at the plane of the axial load corresponding to a load level of 0.4 (1080 kN in this case). In the same graph of Figure 8, with a continuous line, it is also plotted the diagram for the same section without spalling (same load level) and a fire exposure of 50 minutes. Since spalling has not appeared, in this case the diagram is symmetric.

As can be seen, in the first quadrant both diagrams coincide in the most critical part of the 30-minute diagram (with spalling). This means that the most serious situation for a 30-minute fire exposure with spalling is equivalent to the situation where the RC cross-section is 50-minute exposed to fire without spalling. Therefore, the spalling effect is comparable to extend the heating of the cross-section for another 20 minutes.

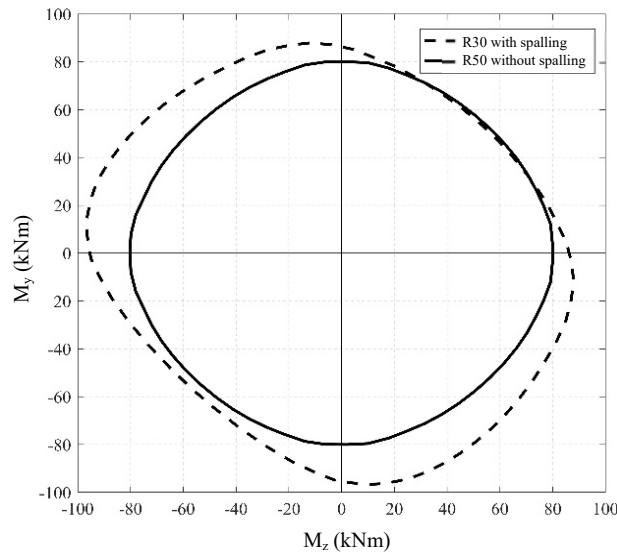


Figure 8. 30-minute interaction diagram $\mu=0.4$.

Another example is displayed in Figure 9, where the 60-minute diagram with spalling (dashed line) is shown together with the 80-minute diagram without spalling (solid line) for a load ratio of 0.4. In the most critical quadrant both match. This means that the occurrence of spalling, in this case, results in a loss of 20 minutes of fire exposure.

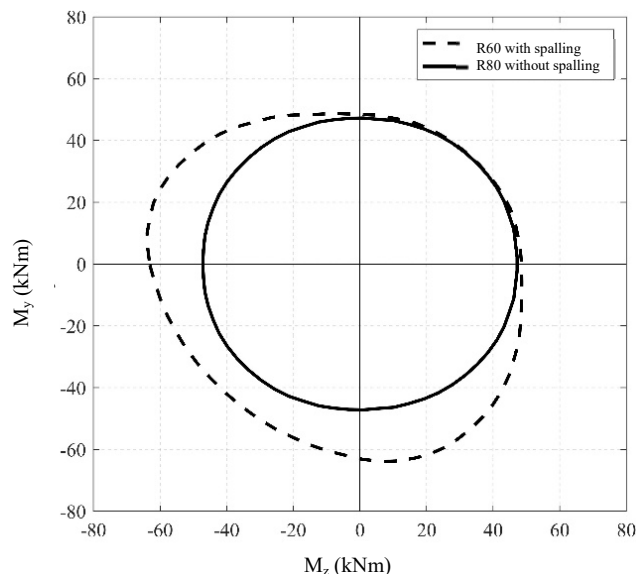


Figure 9. 60-minute interaction diagram $\mu=0.4$.

4 CONCLUSIONS

In this work, a sectional model for evaluating the effect of corner spalling on the biaxial bending resistance of RC columns exposed to fire is presented. From this study, the next conclusions can be drawn:

- The sequentially coupled model presented is able to generate the interaction surfaces to represent the mechanical capacity of biaxially loaded RC column when spalling occurs.
- When a corner spalling occurs, the temperature of the directly exposed reinforcing bar increases much quicker than when the concrete cover is maintained.
- Both the mechanical capacity and the temperature of the reinforcing bar affected by the spalling are influenced by the spalling occurrence time. From 45 minutes on, the influence of this parameter disappears.
- For a given load level and fire exposure time of a RC cross-section with spalling, it is possible to find the diagram of the same section without spalling that is equivalent in the most critical quadrant.
- The negative effect of spalling in a RC cross-section is equivalent to extending for another 20 minutes the heating of a section without spalling.

ACKNOWLEDGMENT

The authors gratefully acknowledge the financial support given by the Chilean Doctoral Fellowship Programme: CONICYT PFCHA/ DOCTORADO BECAS CHILE/2018– 72190104 for the first author's doctoral fellowship at Universitat Politècnica de València.

REFERENCES

1. G.A. Khoury, Effect of fire on concrete and concrete structures. Progress in Structural Engineering and Materials. 2, 429-447 (2000).
2. J.C. Dotreppe, J.M. Franssen, Y. Vanderzeipen, Calculation Method for Design of Reinforced Concrete Columns under Fire Conditions. American Concrete Institute. 96(1) 9-18 (1999).

3. A.M. Gil, B. Fernandes, F.L. Bolina, B.F. Tutikian, Experimental analysis of the spalling phenomenon in precast reinforced concrete columns exposed to high temperatures. *Revista IBRACON de Estruturas e Materiais*, 11(4) 856-875 (2018).
4. R. Jansson, Fire spalling of concrete – A historical overview, *MATEC Web of Conferences*. 6, 01001 (2013).
5. CEB-FIB: Fire design of concrete structures-materials, structures and modelling, State-of-the-art, Bulletin 38. International Federation for Structural Concrete (fib) (2007).
6. K.D. Hertz, Limits of spalling of fire-exposed concrete. *Fire Safety Journal* 38, 103-116 (2003).
7. M.B. Dwaikat, V. Kodur, Hydrothermal model for predicting fire-induced spalling in concrete structural systems. *Fire safety Journal*. 44(3) 425–434 (2009).
8. B.B.G. Lottman, E.A.B. Koenders, C.B.M. Blom, J.C. Walraven, Spalling of concrete due to fire exposure: A coupled fracture mechanics and pore pressure approach. *MATEC Web of Conferences* 6, 05002 (2013).
9. S.H. Buch, U. K. Sharma, Fire resistance of eccentrically loaded reinforced concrete columns. *Fire Technology* 55, 1517-1552 (2019).
10. L. Wang, R. Van Coile, R. Caspeele, L. Taerwe, Simplified method for evaluating the biaxial capacity of rectangular reinforced concrete columns during fire, *Materials and Structures*, 50, 1–13 (2017).
11. V. Kodur, N. Raut, A simplified approach for predicting fire resistance of reinforced concrete columns under biaxial bending, *Engineering Structures*, 41, 428–443 (2012).
12. CEN., 2004b. EN 1992-1-2, Eurocode 2: Design of concrete structures, Part 1.2: General rules – Structural fire design, Brussels Belgium: Comité Européen de Normalisation.
13. MATLAB, 2018. Natick: The MathWorks Inc.
14. CEN., 2002. EN 1991-1-2, Eurocode 1: Actions on structures, Part 1.2- Actions on structures exposed to fire, Brussels, Belgium: Comité Européen de Normalisation.
15. T.T. Lie, R.J. Irwin, Evaluation of the fire resistance of reinforced concrete columns with rectangular cross-sections, Internal Report, Institute for Research in Construction, National Research Council of Canada (NRCC), Ottawa, Canada (1990).
16. V. Kodur, F. Cheng, T. Wang, J. Latour, P. Leroux, Fire Resistance of High-Performance Concrete Columns, Internal Report, Institute for Research in Construction, National Research Council of Canada (NRCC), Ottawa, Canada (2001).
17. D. Peña, V. Alberro, A. Hospitaler, C. Ibañez, A. Espinos, M. L. Romero, Reinforced concrete columns exposed to fire: evaluation of the fire resistance under biaxial bending conditions, *Applications of Structural Fire Engineering*, (2019).
18. A. Law, M. Gillie, Interaction diagrams for ambient and heated concrete sections, *Engineering Structures*, 32(6) 1641–1649 (2010).

EFFECT OF NON-UNIFORM HEATING AND COOLING ON ECCENTRICALLY LOADED REINFORCED CONCRETE COLUMNS

Jamie Maclean¹, Luke Bisby², Carmen Ibañez³

ABSTRACT

A range of experiments are available within the literature interrogating the response of reinforced concrete columns when exposed to standard heating conditions. By and large, such experiments have been performed on concentrically loaded columns, uniformly heated on all four sides, and are therefore of only limited value for developing a deep understanding of concrete column response to real fires, or for validation of material and structural fire models. To begin to fill the resulting gaps in knowledge, an experimental programme was performed involving carefully-controlled heating experiments on reinforced concrete columns subjected to differing mechanical and thermal boundary conditions. These experiments generated a range of data that can be used by engineers to begin to validate complex structural fire models of realistic concrete structures. In total, 46 nominally identical reinforced concrete columns were constructed and exposed to an approximately constant incident radiant heat flux for 90 minutes while under sustained eccentric axial compression. Data were collected through both the heating and cooling phases of the experiments, and every column that survived heating and cooling whilst under load was subsequently tested to destruction 24 hours later, to determine its residual capacity after cooling back to ambient temperature. The results provide a wealth of unique data and have further demonstrated the potential importance of the cooling phase as regards possible progression of structural elements to failure during cooling under sustained load.

Keywords: Reinforced concrete; column; fire; experiments

1 INTRODUCTION

It is generally accepted that reinforced concrete performs well in fire [1], and a significant body of research is available regarding the thermal and mechanical performance of concrete elements at elevated temperatures (e.g. [2-4]). However, the performance of concrete structural elements (notably columns) and assemblies thereof at elevated temperature, and in particular when subjected to realistic, as opposed to standard, fire exposures, has not been extensively studied. With the advent of complex numerical tools for structural fire engineering analysis and design, there is a paucity of experimental results from experiments on fire-exposed concrete columns that capture the necessary thermal and mechanical actions; such experiments are badly needed for credible validation and benchmarking of complex computational analysis packages.

¹ Senior Software Developer, UFirstGroup, Spain

e-mail: jamie.maclean@ufirstgroup.ch

² Personal Chair of Fire and Structures, School of Engineering, University of Edinburgh, UK

e-mail: luke.bisby@ed.ac.uk, ORCID: <https://orcid.org/0000-0001-8293-4322>

³ Associate Profesor, Concrete Science and Technology Institute (ICITECH), Universitat Politècnica de València, Spain

e-mail: caribus@upv.es, ORCID: <https://orcid.org/0000-0002-9354-5637>

The vast majority of research in this to date has concentrated on testing reinforced concrete columns in an unrealistic arrangement within a fire testing furnace, and uniformly exposed to a cellulosic standard heating curve [5]. In general, such research has been primarily concerned with defining the standard ‘fire resistance’ times of the tested elements; such an approach has rather limited utility from a research perspective.

For example, Dotreppe et al. [6] performed a series of tests aiming to validate Method A for the structural ‘fire resistance’ design of concrete columns given in EN 1992-1-2 [7]. This provides evidence that parameters other than the dimensions of the cross section and of the concrete cover could affect the ‘fire resistance’ of concrete columns. However, neither detailed in-depth temperature data nor lateral displacements of the columns during heating have been presented, and hence it is a challenge to interpret the testing outcomes when seeking to carefully interrogate and understand the responses of the columns tested. Such testing permits the generation of semi-empirical relationships, but does little to support credible validation of complex computational structural fire models.

Various other experiments to study the performance of reinforced concrete columns are available in the literature, for example [8-11]. These test series have collected limited data on internal temperatures and structural displacements; however, the conclusions are again related to the standard ‘fire resistance’ times observed. Other research has been more useful, for example research by Kodur et al. [12] which, despite applying standard heating conditions, does provide some data for limited model validation.

However, the clear recognition that data beyond loading ratio and ‘fire resistance’ time is critical for fire testing of concrete elements appears not to be universal, and even more recent studies continue to neglect the importance of more considered data collection and presentation (e.g. [13, 14]).

Regarding the residual performance of concrete columns *after* a fire, Jau and Huang [15] performed experiments on six two-side exposed specimens. These were heated in a furnace and were subsequently eccentrically loaded to failure investigate their post-heating *residual* capacity. Recent work by Kodur et al. [16] has also investigated the residual performance of reinforced concrete columns exposed to specified design fires, with both displacements and internal temperature data presented, albeit with only two specimens tested. The authors of the current paper are unaware of any available studies that have seriously considered the structural response of concrete columns *during* cooling and whilst under sustained load.

The above campaigns *have* informed the structural fire engineering community; however, the conclusions drawn are typically related to ‘fire resistance’ (i.e. time to failure), a criterion that lacks physical meaning and provides very few genuine insights. Standard ‘fire resistance’ testing cannot significantly underpin an understanding of structural response under more complex thermal and mechanical situations, as are to be expected in real concrete structures. More and higher fidelity data need to be collected during structural fire experiments, and loading conditions need to interrogate the parameters of interest in real structures. Research concentrating on times to failure or other non-physical criteria, despite holding a valuable place in construction practice, have little value in helping to develop understanding.

Most of the available experimental programs are on reinforced concrete columns which are axially (and effectively concentrically) loaded, and essentially uniformly heated following a standard fire curve (e.g. [5]). Few experiments interrogate heating, cooling, and/or post-heating residual states, due to the predominant – and outdated – regulatory focus on ‘fire resistance’, rather than real structural performance in fires. This paper presents selected results from experiments on 46 reinforced concrete columns, maintained under sustained eccentric compressive loading through cycles of heating, cooling, and (in some cases) post-heating residual loading. The variables investigated in this campaign were; the concrete compressive strength, the sustained loading magnitude and initial eccentricity, the imposed incident radiant heat flux, the length of the column exposed to elevated temperatures, and the number of heat-exposed column faces.

Due to the volume of data collected it is not possible to provide an exhaustive summary here; a fulsome description is given in the first author’s doctoral thesis [17].

2 EXPERIMENTAL METHODOLOGY

Forty six geometrically identical reinforced concrete columns were constructed to investigate the influence of different loading/heating conditions on their response during heating, cooling, and residually. Figure 1 shows the dimensions of the columns as well as a schematic of the bespoke experimental setup used. The loading frame was designed to impose a load at predefined initial eccentricities of 5, 15, or 25 mm, with pinned supports at both ends, whilst simultaneously exposing the columns to elevated temperatures on one or more column faces.

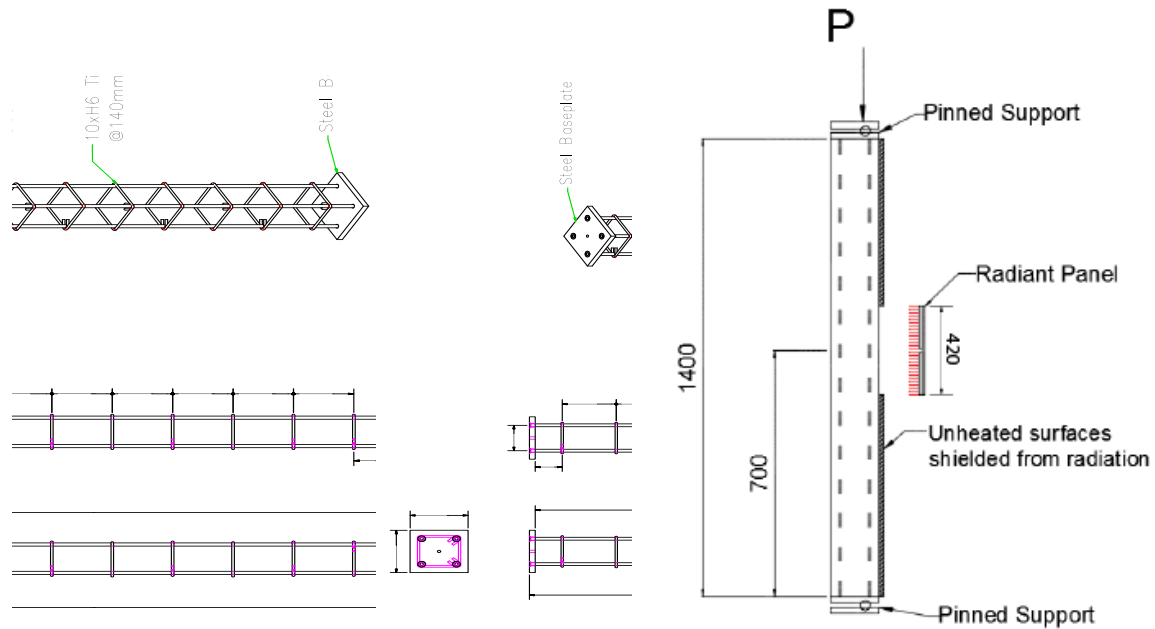


Figure 1. Details of column specimens and schematic of experimental setup (dimensions in mm)

2.1 Column design and construction

The columns were designed in accordance with Eurocode 2 [18]. They were roughly 1/3 scale and symmetrically reinforced with four deformed steel reinforcing bars, as shown in Figure 1. All columns were 150 mm x 150 mm in cross-section and 1400 mm long (1430mm pin-to-pin, including end plates), longitudinally reinforced with four 10 mm diameter deformed reinforcing bars and 6mm diameter deformed steel ties spaced at 140 mm on centre. Half of the columns were cast using 24 MPa (28-day measured) cylinder strength, and second set was cast using 40 MPa concrete. Both mixes included 2 kg/m³ of polypropylene (PP) fibres with the intention of mitigating concrete cover spalling during heating. All columns were cast vertically and cured at 20 °C and 50 % RH for a minimum of 12 months before performing the experiments. Even load transfer from the loading frame to the columns to avoid stress concentrations was ensured by the addition of steel end plates welded to the longitudinal reinforcing bars.

2.2 Load application

In addition to the steel end plates, steel caps were manufactured to provide a repeatable method of applying sustained eccentric axial compressive load to the columns during heating, cooling, and residually. The caps were designed such that they could be slipped over the top of the end plates and secured with a single M10 positioning bolt, thus allowing them to be reused. The steel caps allowed for carefully controlled pinned-pinned end conditions with precise initial loading eccentricities.

2.3 Data collection and instrumentation

Due to the localised thermal exposures used in these experiments, it was crucial that temperatures within the columns were measured at a sufficient number of locations to provide a sufficiently detailed spatial distribution of heating, and to quantify the relevant temperature gradients throughout the heating and cooling phases of the experiments. Thermocouples (TCs) were therefore cast in place within the columns

using three thermocouple “trees” that were cast into each column at heights of 700 mm (mid-height), 900 mm (top of the heated zone, see Figure 1), and 950 mm (just above heated zone) from the base of the column. Figure 2 shows the thermocouples (TCs) cast within the concrete columns.

To capture the vertical and lateral deflections of the columns during the experiments, it was possible (for most cases) to use linear potentiometers connected to a data logger for data collection. Deflections were measured at four locations on/within the columns, as shown in Figure 2, namely:

- at the base of the column measuring the stroke displacement of the hydraulic jack (vertical displacement at the base of the column);
- the lateral displacement at 350 mm from the base;
- the lateral displacement at 700 mm from the base (mid-height); and
- the lateral displacement at 1050 mm from the base.

In order to determine the deflections of the columns when subjected to heating on both faces, a digital image correlation (DIC) software, *GeoPIV-RG*, was used [19]. Given a series of photos taken from the same location throughout the experiment, the software was able to track selected patches of pixels in the images to determine their displacement. This technique is typically used when the photographs obtained are taken perpendicular to the plane being measured (i.e. the plane being measured within photos is at a fixed distance and at right angles to the columns). However, due to the specific configuration of the loading frame constructed, perpendicular photos that resulted in only in-plane photos could not be obtained in this specific scenario. As the images were captured at an angle other than perpendicular, the true in-plane deflection could not be easily determined using conventional analysis. To convert the pixel values obtained from the DIC software into real in-plane measurements, additional MATLAB scripts were written to correct for the angle of the photographs taken and for lens distortion.

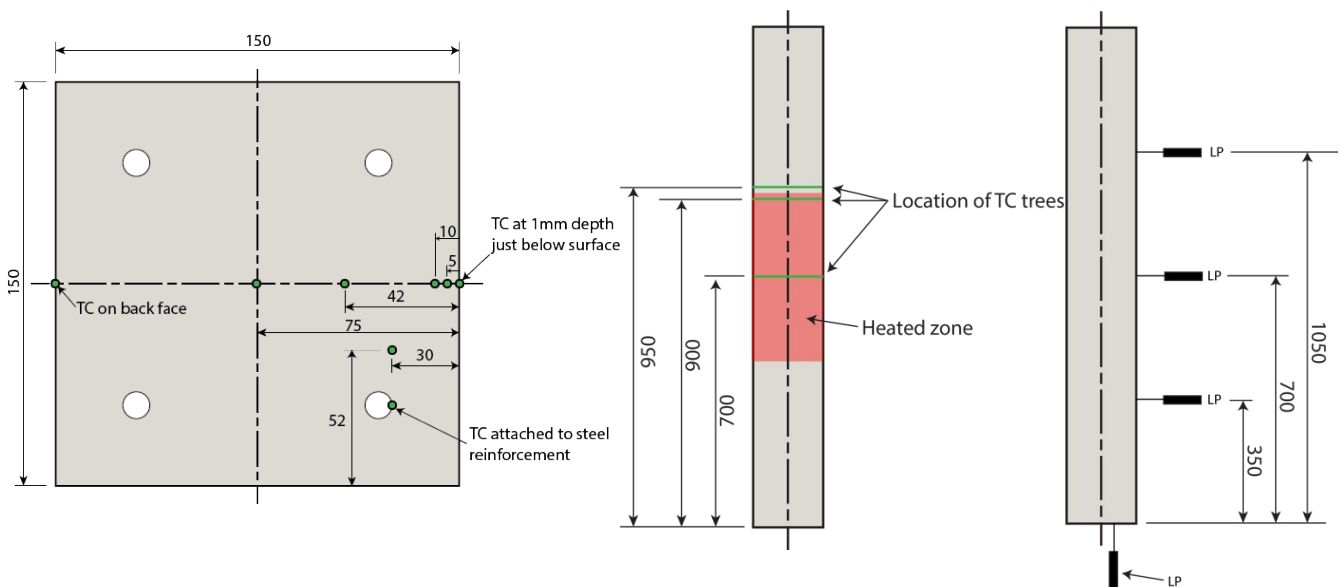


Figure 2. Instrumentation in (left) cross section and (right) over column height (dimensions in mm)

2.4 Experimental matrix

The experimental programme varied a range of parameters between columns, including:

1. the magnitude of sustained load (1 % or 60% of ambient temperature capacity);
2. the initial eccentricity of the load (5 mm, 15 mm, or 25 mm);
3. the ambient temperature concrete compressive strength (24 MPa or 40 MPa);
4. the applied initial incident radiant heat flux (50 kW/m² or 70 kW/m²);
5. The side(s) heated (less compressed (tension) face, more compressed (compression) face, or both); and
6. The length of the heated area (33 % and 66 % of the length of the column).

A limited number of experiments were performed in duplicate to verify repeatability. Space limitations prevent full presentation of the experimental matrix here; only parameters 1-3 are presented in this paper. Interested readers should consult Maclean's doctoral thesis [17].

3 SELECTED RESULTS

Data were collected during the loading, heating, *and* cooling stages of the experiments (where relevant) and, in addition, columns that survived the heating and cooling cycles were allowed to cool for 24 hours before being loaded to failure residually. The residual performance of the columns is not discussed here, and only the most interesting experiments have been selected for presentation in this paper. In what follows, when referring to the side(s) heated, the terminology “compression heated” or “tension heated” is used to allow the reader to quickly identify which side(s) of the column has been directly exposed to elevated temperatures. It is noteworthy that despite being referred to as the “tension face”, the concrete may indeed be subjected to compressive stresses (particularly at low eccentricities).

3.1 Response at ambient temperature

Before conducting any heated experiments, two control experiments were conducted for each column strength and loading eccentricity at ambient temperature. Columns were loaded at a rate of about 12 kN/min until failure. The load versus midspan deflections for each control experiment is shown in Figure 3.

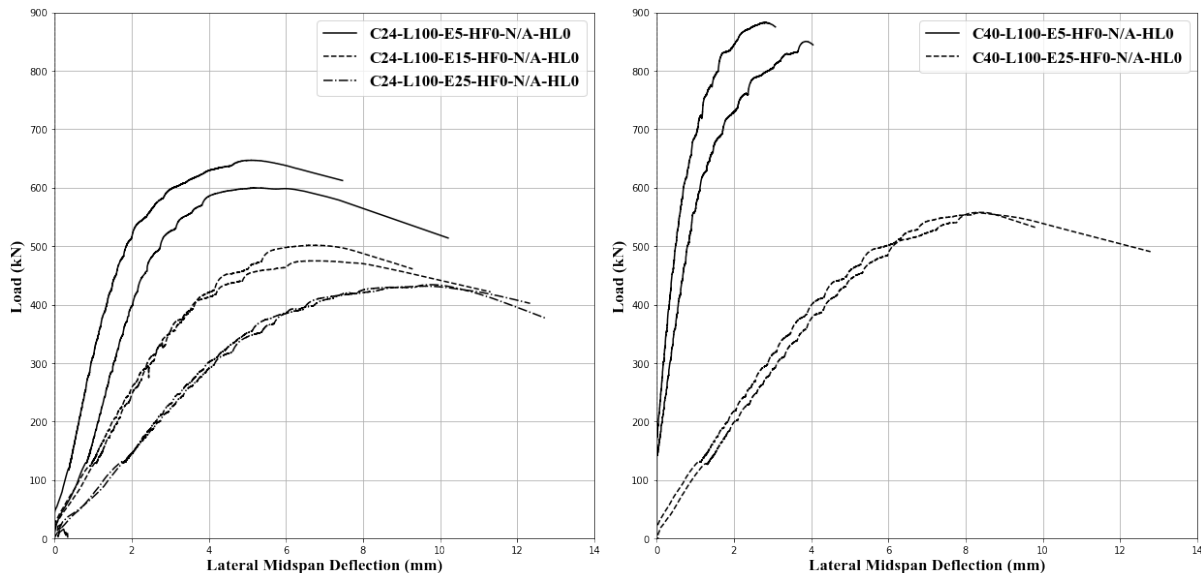


Figure 3. Load versus displacement from control experiments on (left) C24 columns and (right) C40 columns

The objectives of the ambient temperature loading experiments were to determine the ambient temperature axial-flexural and load-deflection responses of the columns, and also to ensure that the experimental rig designed could provide adequately repeatable experimental conditions. It is clear from the load-deflection responses in Figure 3 that the duplicate experiments demonstrated very good repeatability. Experiments with larger initial loading eccentricities were most repeatable; as should be expected given their lesser inherent sensitivity to small instabilities and imperfections.

3.2 Response at elevated temperature

3.2.1 ‘Low’ load experiments

Specimens of both the 24 and 40 MPa concrete strength columns were first maintained under a sustained load of 10 kN to study their deflection history under nominally identical heating conditions. 10 kN was chosen as this was the minimum value that could be applied to the columns by the hydraulics whilst holding the specimens within the loading frame. Four conditions were investigated for each concrete strength: (1) 5 mm load eccentricity, heated on the tension face, (2) 5 mm load eccentricity, heated on the compression

face, (3) 25 mm load eccentricity, heated on the tension face, and (4) 25 mm load eccentricity, heated on the compression face.

Selected results from the unloaded experiments are shown in Figure 4. All columns exposed to heating under low load conditions at a 5 mm eccentricity displayed similar deflection responses during heating and cooling phases. The 10kN load was applied at -20 mins, and at 0 mins, the columns were locally exposed to a 70kW/m² incident radiant heat flux on one face for a total of 90 mins. Almost immediately upon being exposed to heating the columns began to bow thermally due to differential thermal expansion through their cross sections. Lateral deflections increased to about 6-6.5 mm after 90 mins of heating, after which the heaters were removed and the columns allowed to slowly cool back to ambient temperature, during which time the column deflections recovered almost entirely to their pre-heating condition.

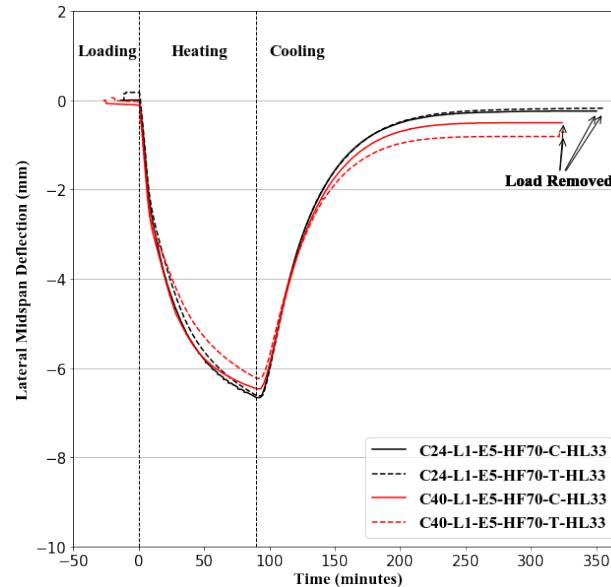


Figure 4. lateral deflections with time for the control experiments on (left) C24 columns and (right) C40 columns

No major differences were evident between the “tension heated” and “compression heated” experiments at 5 mm eccentricity, as expected. There were also no clear differences between the deflection histories of the columns cast from different strength concretes. Considering that the columns were subjected to nominally identical thermal exposures, this suggests that the thermal properties of the two concrete mixes were similar.

At 25 mm load eccentricity and under a load of 10 kN the “tension heated” experiments deflected more than those that were “compression heated” experiments, and did not fully recover their lateral deflections after cooling. It should be noted that, despite being subjected to the same (low) load, the bending moment in the sections was now five times higher than for the 5 mm eccentricity experiments. Considering thermal bowing, the expansion of the heated surface in the “tension heated” experiments would work alongside the moment induced in the section by loading eccentricity, thus increasing the deflection in the column. This increase in the deflection induced even greater secondary moments, and so on. This is in comparison to the “compression heated” experiments where thermal bowing decreased the moments in the section thus resulting in smaller deflections.

The above results show that differing the experimental conditions by changing the side heated or the load eccentricity had no great effect on the response of columns at low load levels, as expected. All of the columns experienced lateral deflections in the same direction (i.e. bowing towards the heat source) and these were largely recovered upon cooling.

3.2.2 Effect of severity of sustained loading

A comparison of the low load experiments and selected “compression heated” experiments conducted under loads of 60% of the ambient temperature load bearing capacity is given in Figure 5. The increase in loading severity resulted in drastically different structural responses.

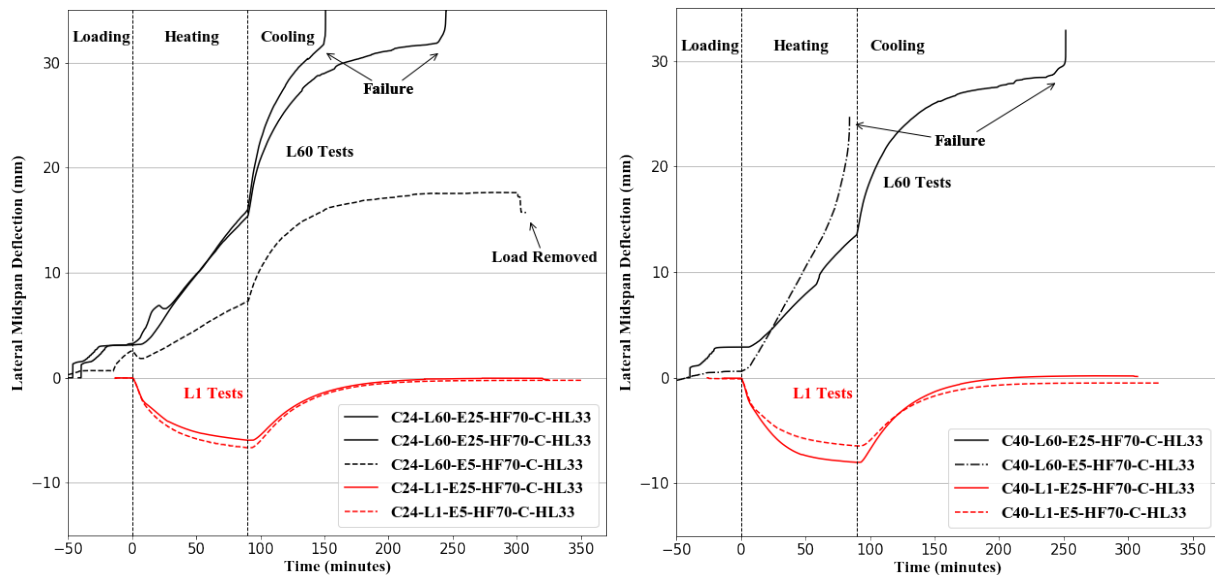


Figure 5. Lateral deflections with time for the “compression heated” experiments on (left) C24 columns and (right) C40 columns

At the beginning of the “compression heated” experiments, as a result of the increased (60 %) load, the columns bowed away from the heat source (positive deflection), as expected. The load was then maintained for a minimum period of 20 mins and the heat source was turned on at 0 mins. Upon exposure to heating the columns continued to deflect *away* from the heat source (positive deflection), and did not display any thermal bowing whatsoever. This may be attributed to thermal creep and weakening of the concrete at elevated temperatures.

After 90 mins of heating the radiant panels were switched off and the columns cooled back to ambient temperature. Upon the onset of cooling, the columns continued to deflect away from the heat source (more rapidly, in fact) due in part to thermal contraction. This continued for the remainder of the experiments until either the column failed, or a new equilibrium was achieved with irrecoverable lateral deflections.

A notable aspect of these experiments is that several of the columns failed under sustained load *during the cooling phase*. Both the high load experiments and the low load experiments deflected away from the heat source upon the onset of cooling due to rapid thermal contraction. The thermal wave within the concrete, however, continues to penetrate the section and the concrete in depth achieves its maximum temperature at some later time. This behaviour, combined with creep under load at high temperature, results in increased deflections, accompanying increased secondary moments, and – eventually – structural failure in some cases. Such behaviours, however, are poorly understood and rarely – if ever – explicitly considered in the structural fire engineering assessment or design of reinforced or prestressed concrete structures. These data therefore provide a unique opportunity for concrete structural fire modellers to assess their models’ abilities to simulate the necessary, and complex, responses.

Figure 6 and Figure 7 give comparisons of responses of columns heated on the “compression face” and columns heated on the “tension face” with differing initial loading eccentricities. Varying the side heated had a marked effect on the responses of the columns. In addition, changing the eccentricity with the side heated produced a range of different behaviours. Unlike the “compression heated” columns, each different load eccentricity resulted in a markedly different response.

Looking at the “tension heated” columns with a load eccentricity of 25mm, the columns deflected toward the heat source during the heating phase and only slightly recovered these deflections during the cooling phase. This behaviour is expected and may be explained in terms of thermal bowing and contraction, along with the degradation of the concrete at elevated temperature.

Looking at the “tension heated” column with a load eccentricity of 5 mm, the behaviour is substantially different to the 25 mm eccentricity cases. Upon heating, the column began to deflect towards the heat source, again due to thermal bowing. After roughly 15 mins of heating, the column began to recover and

deflect in the opposite direction. This trend continued until the column recovered its lateral deflection entirely and began to deflect in the opposite direction, away from the heat source; thus deflection increases further during the cooling phase of the experiment, as for the “compression heated” cases.

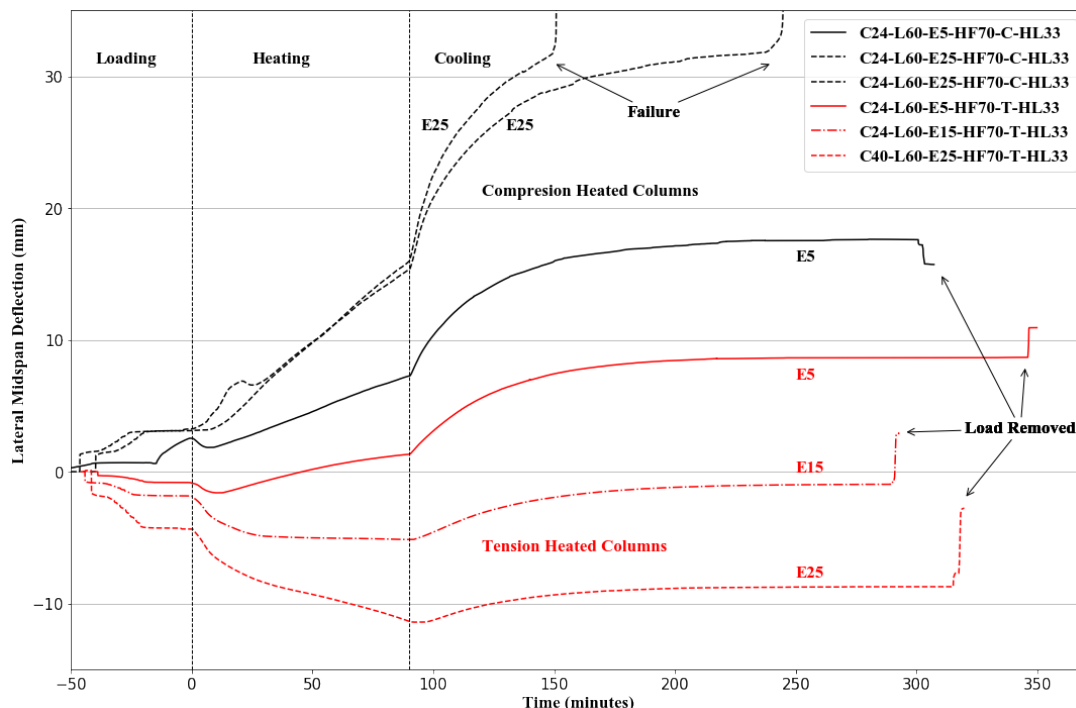


Figure 6. Load versus displacement for the “compression heated” experiments on (left) C24 columns and (right) C40 columns

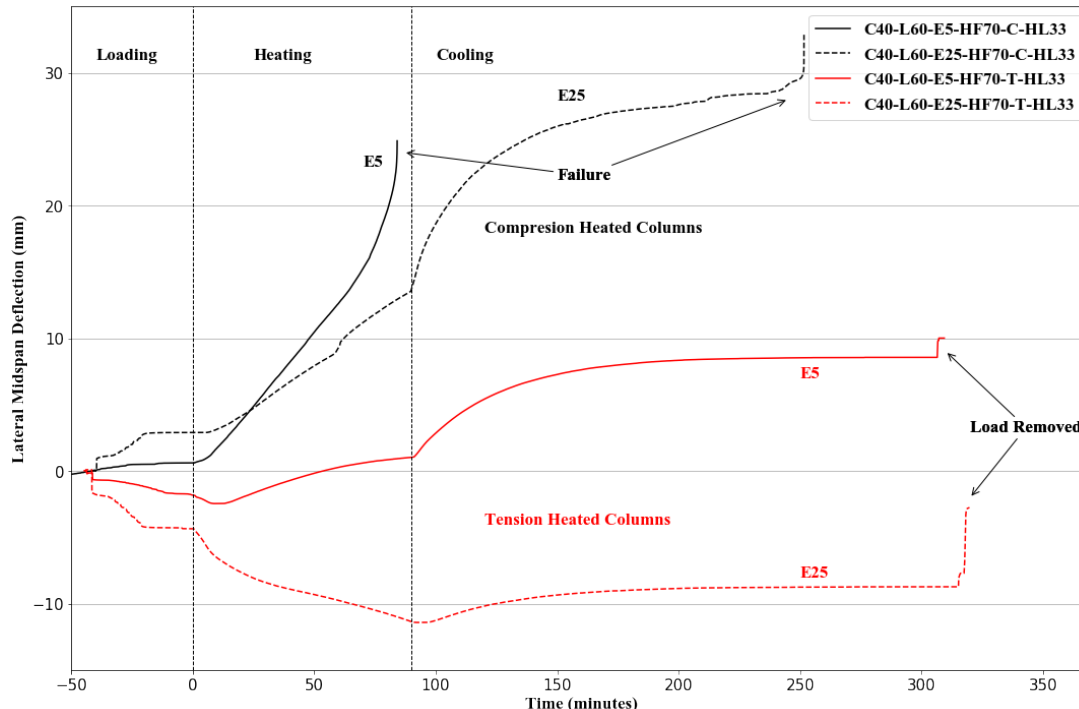


Figure 7. Load versus displacement for the “compression heated” experiments on (left) C24 columns and (right) C40 columns. The above behaviour was not foreseen prior to these experiments, and illustrates the need for a detailed, mechanics-based approach when considering the structural fire response of concrete compression elements in particular.

Taking this behaviour into account, a decision was taken to investigate an intermediate load eccentricity of 15 mm for the “tension heated” columns. The 15 mm load eccentricity experiment behaved in such a manner that, when heated, it bowed toward the heat source for the first 30 mins of heating. It then reached a plateau where, despite the temperatures continuing to rise within the column, no further deflections were observed during the final 60 mins of heating. Much like the 25 mm load eccentricity, the concrete stress at the extreme fibre of the “tension face” of the column was insufficient for significant creep to occur. This resulted in thermal bowing of the extreme fibre of the column for the first 20 mins of heating, much like the 25 mm load eccentricity scenario. However, after 50 mins, the thermal wave within the concrete had travelled deeper into the section, reaching the more highly stressed concrete. This concrete began to compress via creep and the column stopped deflecting towards the heat source. Between 50 and 90 mins after the start of heating, the column was still being subjected to a 70 kW/m^2 heat flux and the thermal wave continued to travel through the section while the load was held constant. However, no additional lateral movement from the column was observed during this period. Therefore, the combination of the aforementioned parameters can be assumed to have been counteracting each other and preventing the column from experiencing increased lateral deflections, despite the concrete within the column necessarily sustaining additional damage.

It is clear from these experiments that a number of complex and interrelated mechanisms are at play within the concrete under the experimental conditions presented: reductions in strength, reductions in stiffness, thermal expansion, creep, and transient thermal creep. All of these will contribute to the various behaviours observed.

4 CONCLUSIONS

This paper has presented, with only cursory discussion and analysis, selected results from an extensive experimental programme conducted on non-uniformly heated reinforced concrete columns under sustained eccentric compressive loading. A brief discussion of some of the most interesting responses observed has been provided, from which the following conclusions can be made:

- Predicting the structural fire response of reinforced concrete columns under non-uniform heating and eccentric compressive loading is clearly not as simple as predicting the reduction in the strength of the material due to elevated temperatures. In order for structural fire safety engineers to accurately predict the response of reinforced concrete compression elements exposed to elevated temperatures, the full mechanical behaviour must be considered, since a number of interrelated factors and mechanisms occur which may greatly affect the response of such elements in real structures.
- Interactions between losses in strength and stiffness, thermal bowing, creep, transient thermal creep, thermal contraction, and secondary moments, can contribute to vastly different structural responses under conditions which at first glance may appear similar. Current. Prescriptive approaches to predicting the structural ‘fire resistance’ of concrete compressive elements are inadequate to provide a credible understanding of such elements’ response both during, and importantly *after*, real fires.
- The current design methodology of quoting ‘fire resistance’ in terms of minutes of standard fire exposure may need adaptation in order to take account of the cooling phase responses presented in this paper; behaviours which are not currently explicitly considered in design but which may be important under certain conditions from a life safety perspective – particularly in multi-storey residential buildings with higher strength reinforced concrete compression elements.
- Given the findings of this work, and the novel data set that has been created as regards to the performance of reinforced concrete columns subjected to non-uniform heating and cooling regimes, fire engineering modellers now have the capability to begin to credibly validate complex finite element models against this series of experiments on 46 reinforced concrete columns through the full range of heating, cooling, and post-cooling residual structural performance.

ACKNOWLEDGMENTS

The authors gratefully acknowledge the support of the UK Engineering and Physical Sciences Research Council (EPSRC) and the School of Engineering at the University of Edinburgh.

REFERENCES

1. Bailey CG, Khoury G. Performance of concrete structures in fire. 2011. MPA The Concrete Centre, UK.
2. Ma Q, Guo R, Zhao Z, Lin Z, He K. Mechanical properties of concrete at high temperature-A review. *Construction and Building Materials* 2015; 93: 371-383.
3. Kodur V. Properties of Concrete at Elevated Temperatures. *ISRN Civil Engineering* 2014; 2014: 1-15. <http://dx.doi.org/10.1155/2014/468510>.
4. Torelli G, Gillie M, Mandal P, Tran VX. A multiaxial load-induced thermal strain constitutive model for concrete. *The International Journal of Solids and Structures* 2016; 108: 1-11.
5. ISO (International Standards Organization). ISO 834: Fire resistance tests, elements of building construction. Switzerland: International Standards Organisation; 1980.
6. Dotreppe IC, Franssen JM, Bruls A, Baus R, Vandeveld P, Minne R, Nieuwenburgt DV, Lambottet H. Experimental research on the determination of the main parameters affecting the behaviour of reinforced concrete columns under fire conditions. *Magazine of Concrete Research* 1997; 49(179):117-127.
7. CEN. EN 1992-1-2, Eurocode 2: design of concrete structures, Part 1.2: General rules – structural fire design. Brussels, Belgium: Comité Européen de Normalisation; 2004.
8. Zhu HL, Lie, TT. Fire Resistance Evaluation of Reinforced Concrete Structures. Internal Report (National Research Council Canada. Institute for Research in Construction)1993-03; 45-49.
9. Ali F, Nadjai A, Glackin P, Silcock G, Abu-tair A. Structural performance of high strength concrete columns in fire. *Fire Safety Science* 2003; 7: 1001-1012.
10. Gaithersburg, MD, Phan LT, Carino NJ, Duthinh D, Garboczi E. Fire test on normal and high-strength reinforced concrete columns. NIST International Workshop on Fire Performance of High Strength Concrete 1997. Proceedings. Appendix B: 109-124.
11. Buch SH, Sharma UK. Fire resistance of eccentrically loaded reinforced concrete columns. *Fire technology* 2019; 55: 1517-1552.
12. Kodur V, Mcgrath R. Fire Endurance of High Strength Concrete Columns. *Fire Technology* 2003; 39: 73–87. <https://doi.org/10.1023/A:1021731327822>
13. Mohamed Bikhiet M, El-Shafey NF, El-Hashimy HM. Behavior of reinforced concrete short columns exposed to fire. *Alexandria Engineering Journal* 2014; 53: 643-653.
14. Xu YY, Wu B. Fire resistance of reinforced concrete columns with L-, T-, and +-shaped cross-sections. *Fire Safety Journal* 2009; 44 (6): 869-880.
15. Jau WC, Huang KL. A study of reinforced concrete corner columns after fire. *Cement and Concrete Composites* 2008; 30: 622-638.
16. Kodur V, Hibner D, Agrawal A. Residual response of reinforced concrete columns exposed to design fires. *Procedia Engineering* 2017; 210: 574-581.
17. Maclean, JW. 2018. The structural response of reinforced concrete columns during and after exposure to non-uniform heating and cooling regimes (doctoral dissertation). The University of Edinburgh, Scotland, UK. <https://era.ed.ac.uk/handle/1842/35515>.
18. CEN. EN 1992-1-1: Eurocode 2: Design of concrete structures, Part 1-1: General rules and rules for buildings. Brussels, Belgium: Comité Européen de Normalisation; 2004.
19. Stanier S, Blaber J, Take W, White D. Improved image-based deformation measurement for geotechnical applications. *Canadian Geotechnical Journal* 2016; 53(5): 727-739.

BOND BEHAVIOR BETWEEN REINFORCING STEEL BARS AND CONCRETE AT ELEVATED TEMPERATURES

Ira Banoth¹, Anil Agarwal²

ABSTRACT

This study focuses on the bond behaviour between steel rebars and concrete at elevated temperatures. The steel-concrete interface temperature values included in this study varied between 20°C and 500°C, the concrete strength of 25 MPa and, the steel diameters varied between 12 mm and 20 mm, and two different heating rates, namely 2°C/min, standard fire curve (ISO-834) were used for the experimental program. After reaching the desired temperature at the steel-concrete interface, pull-out tests were conducted on a cubical specimen of size 200 x 200 x 200 mm with eccentrically embedded rebar. The results showed significant reduction of bond strength at elevated temperatures.

The reduction in bond strength is found to depend very significantly on the rate of heating. The strength reduction with respect to the increase in interface temperature is most rapid in case of following the standard fire curve followed by 2°C/ min heating rate protocol. This significant effect of heating rate on the bond behaviour is probably due to the thermal gradients present in concrete in case of a rapid rate of heating.

Keywords: Concrete; Rebar; Heating rate; Pull-out; Elevated temperatures.

¹ Ira Banoth, Research scholar, Department of Civil Engineering, Indian institute of Technology Hyderabad, India-502285
e-mail: ce16resch11003@iith.ac.in

² Anil Agarwal, assistant professor, Department of Civil Engineering, Indian institute of Technology Hyderabad, India-502285
e-mail: anil@iith.ac.in

1 INTRODUCTION

The bond behaviour between steel rebars and concrete in RC structure is one of the significant factors to be considered for the structural integrity. The bond behaviour between steel and concrete becomes very critical for structures at elevated temperatures.

In the past, many researches have studied material properties of different types of construction materials at elevated temperatures. Several studies are available for the bond behaviour between steel rebars and concrete in post fire scenario. However, very few detailed studies are available at elevated temperatures conditions.

Diederichs et al. [1] studied the bond behaviour between steel and concrete of different types of rebars. The conclusions drawn from these studies are that (1) bond strength reduces with the increase of temperatures, (2) and bond strength not only depends on the temperatures level but also depends on the shape of the rebar and test procedure. Morley et al. [2] studied the bond behaviour in different test condition namely: stressed residual, unstressed residual, stressed hot and unstressed hot. They have concluded that the bond stress in residual condition is more up-to the temperature of 250°C than the tested in hot due to the additional thermal stresses.

Some researchers have studied the bond behaviour between the steel rebars and different fibre reinforced concrete at ambient temperature conditions or in the post-fire scenario. Hadad et al. [3] studied the bond behaviour between steel rebars and fibre reinforced concrete (hooked end steel polypropylene and basalt coated fibres and the hybrid combinations of fibres). The study concluded that incorporation of fibres increased steel concrete ductility of the bond. Eva Lubloy et al. [4] studied the bond behaviour by using the concrete prepared with different types of aggregates and different fibres with different composition. They concluded that the reduction of bond strength is more significant after the elevated temperatures of 400°C and above. This phenomenon can be explained by the decomposition of portlandite at 450°C. Varona et al. [5] studied the post-fire bond behaviour with concrete of two different strengths (normal and high strength concrete) and different polypropylene fibres and hooked end steel fibres with 2 different aspect ratios. Inclusion of hybrid fibres increase the peak bond strength. This effect is more in the case of high strength concrete.

Ranade et al. [6] studied the post-fire bond behaviour with different type of concrete: concrete strength (35 MPa, and 60 MPa, and HFR-SHCC (Hybrid fibre-strain hardening cementitious composites, PVC-SHCC (Polyvinyl chloride- strain hardening cementitious composites), HFA-SHCC (High fly ash - strain hardening cementitious composites) the bond strength is more in the case of conventional concrete than the SHCC due to the interlocking of coarse aggregate with the steel rebar ribs. At elevated temperatures of more than 200°C, HFR-SHCC showed more bond strength due to higher tensile properties which can prevent the splitting failure along the length of the rebar.

Ferhat et al. [7] studied the bond behaviour between steel rebars and concrete by varying different parameters such as concrete strength (25 MPa and 30 MPa), cooling conditions (water cooling, air cooling), and different embedment length (60mm ,100 mm, 160 mm). the bond strength increased with the increase of concrete strength. The cooling conditions did not play a significant role in the

case of 60 mm embedment length. But in other two cases the reduction of bond strength was more in the case of water cooling this is due to rapid temperature changes.

Lee et al. [8] studied the post-fire bond behaviour between steel rebars and concrete for epoxy coated and uncoated rebar, different heating rates, and different cooling conditions (water cooling and natural cooling). The bond strength was higher in the case of epoxy coated rebars up to the temperature of 200°C, due to the melting of epoxy can improve the bond between steel and concrete. Bond strength decreased with increases of temperatures. Higher heating rate has higher thermal gradient so it can cause the reduction in bond strength. The effect of cooling condition is more significant in the case of coated rebar than the un-coated rebar.

Two types of tests [9] were recommended to study the bond behaviour between steel and concrete: Pull-out test and beam test. the pull-out test is handier than the beam test. So, in this study the pull-out test is adopted to study the steel concrete interface behaviour. The aim of this study is to find the role of heating rate on significant bond strength reduction.

2 EXPERIMENTAL PROGRAMME

2.1 Materials

Ordinary Portland cement of grade 53, crushed angular gravel coarse aggregate and fine aggregate river sand and steel rebars of grade Fe500 were used.

2.2 Concrete mix design

Concrete is designed according to the code IS 10262 [10]. The following mix proportions were used for 1 m³ of concrete: cement: 379, sand: 828, coarse aggregate: 1173, water: 162 and superplasticizers: 4.43 kg/m³. Concrete was mixed in a drum mixer of capacity 0.5 m³. Concrete was cast in plywood moulds, then left for 24 hours to dry, then demoulded and placed in curing tank for 15 days, and then specimens were removed from the curing tank and kept in dry and shaded environment for 15 days.

2.3 Specimen details

The cubical specimens of size 200x200x200 mm were prepared for the pull-out test. The rebar is placed at the cover of 20 mm. The rebars were bonded with concrete for a length of four times the diameter of rebar in the middle and the remaining length at the top and bottom was un-bonded with PVC pipes. Specimen details is shown in Figure 1.

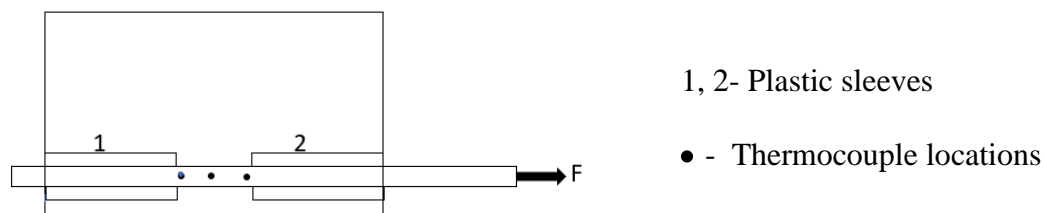


Figure 1. specimen details

3 TEST PROCEDURE AND SETUP

3.1 Test procedure

Specimen were heated from the 3 sides to replicate the beam behaviour by following 2 different heating rates $2^{\circ}\text{C}/\text{min}$ and ISO-834 [11]. The time-temperature plots as measured in the furnace and at the steel-concrete interface are shown in Figure 2. Specimens were gradually heated until the temperature at the interface reaches the desired value. After the desired temperature was achieved, a pull-out load was applied on the rebar at the rate of $1.25\text{ mm}/\text{min}$. This rate of loading allows us to make sure that the temperature at the interface does not change significantly during the loading period and the conditions during the load test can be classified as isothermal.

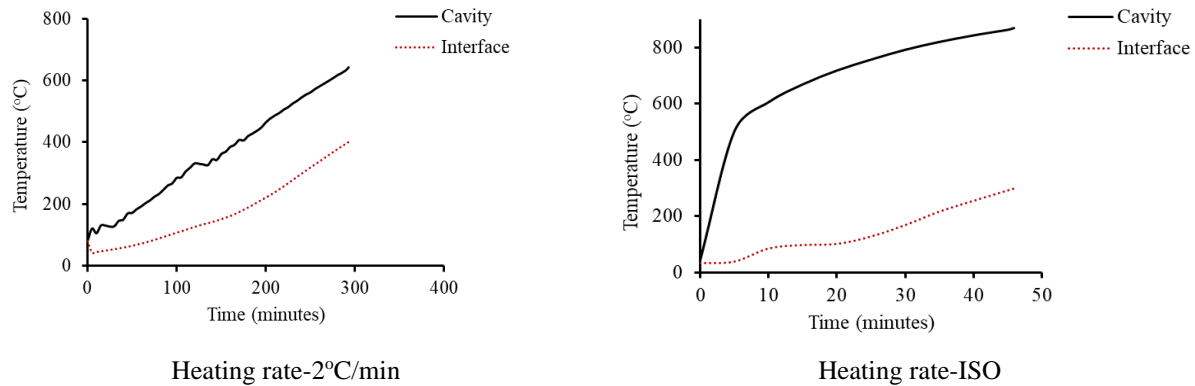


Figure 2. Time temperature

3.2 Test setup

The test setup mainly consisted of a steel beam that held the concrete cube inside the furnace as the rebar is pulled out. Two threaded steel rods were anchored to the platform of the bottom and were holding the steel beam in place. Two LVDTs were used to measure the slip of the rebar as shown in Figure 3.

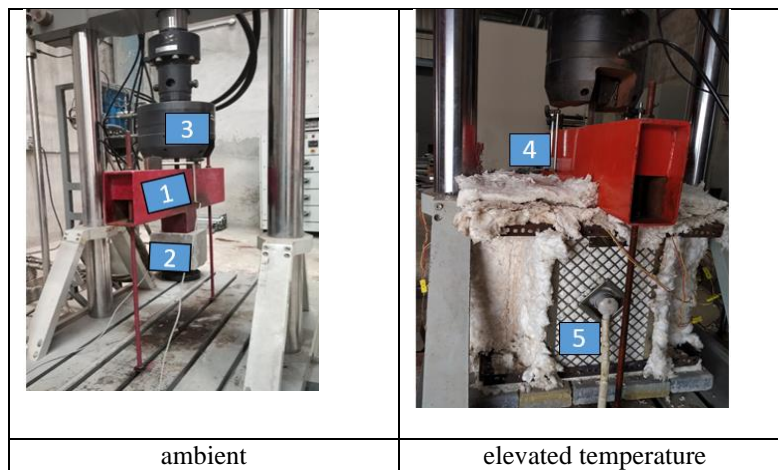


Figure 3. Test set up (1 - beam resisting against the pullout specimen, 2 – Specimen, 3 – Loading actuator, 4 – LVDT, 5 – electric heating panel)

4. TEST RESULTS

4.1 Bond strength versus slip behaviour

The bond stress and slip of 12 mm rebar at the loaded are as shown in Figure 4. The bond strength at 20°C is 10.4 MPa and at the elevated temperature of 100, 200 and 300°C by following heating rate of 2°C/min and iso 834 are: 4.4, 2.7, 0.6 MPa and 3.9, 3, 1 MPa, as sown in Table 1. The bond strength decreased with increasing temperatures. At all the temperatures specimens failed by pull-out failure. Typical failure patterns are shown in Figure 5.

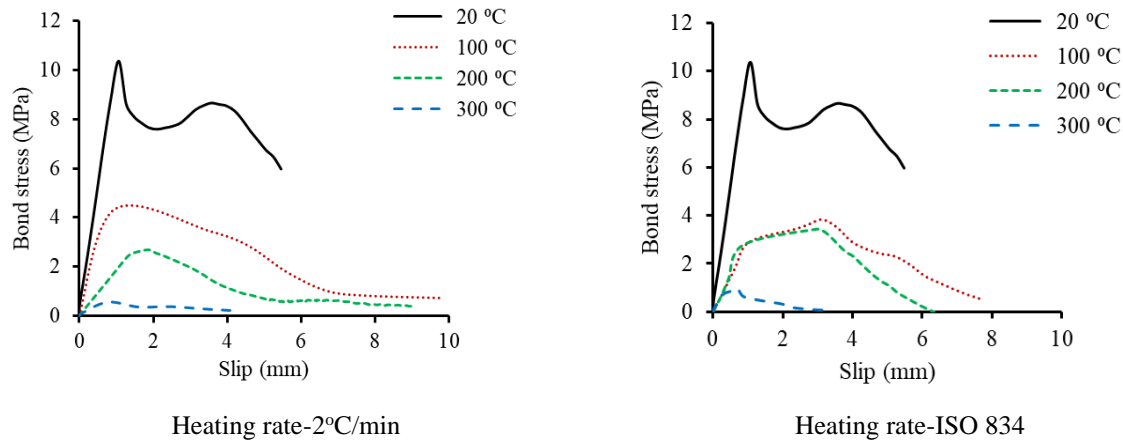


Figure 4. Bond stress and slip of 12 mm rebar

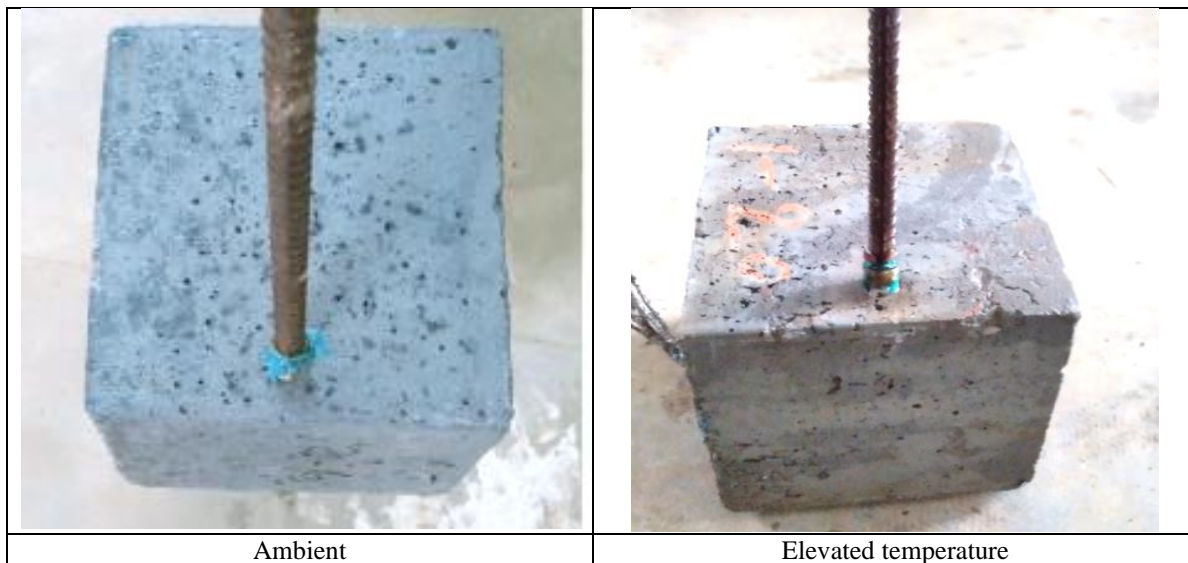


Figure 5. Failure patterns of 12 mm rebar

Table 1. Test results

specimen	Temperature	Bond Strength (kN)	Bond Strength (MPa)	Slip (mm)	Bond Strength (% of 20°C)
D12-ambient	25	18.8	10.4	1.07	100
D12-it100-hr2	100	7.9	4.4	0.97	42
D12-it200-hr2	200	4.9	2.7	1.87	26
D12-it300-hr2	300	1.0	0.6	0.76	6
D12-it100-hriso	100	6.9	3.9	3.74	37
D12-it200-hriso	200	6.2	3.0	3.13	29
D12-it300-hriso	300	1.7	1.0	0.71	9
D20-ambient	25	57.4	11.4	2.43	100
D20-it100-hr2	100	35.0	7.0	1.80	61
D20-it200-hr2	200	42.2	8.4	2.20	74
D20-it300-hr2	300	32.6	6.5	3.30	57
D20-it400-hr2	400	30.4	6.0	2.69	53
D20-it500-hr2	500	22.7	4.6	1.65	40
D20-it100-hriso	100	7.4	1.5	1.06	13
D20-it200-hriso	200	4.1	0.8	1.52	7
D20-it300-hriso	300	2.0	0.4	2.75	3

The bond stress and slip of 20 mm rebar as shown in Figure 6. Bond strength at temperatures of 20,100,200,300,400 and 500 °C by following heating rate of 2°C/min are: 11.4, 7, 8.4, 6.5 and 4.6, respectively. At the temperatures of 100, 200, and 300°C by following ISO-834 heating rate, the bond strength was found to be 1.5, 0.8 and 0.4 MPa, respectively as shown in Table 1. At the temperature of 200°C the specimen failed by splitting failure and all other specimens failed by bond-slip failure. Typical failure patterns are shown in Figure 7. And the role of heating rate is having more significant effect on the reduction of bond strength in the case of 20 mm rebar.

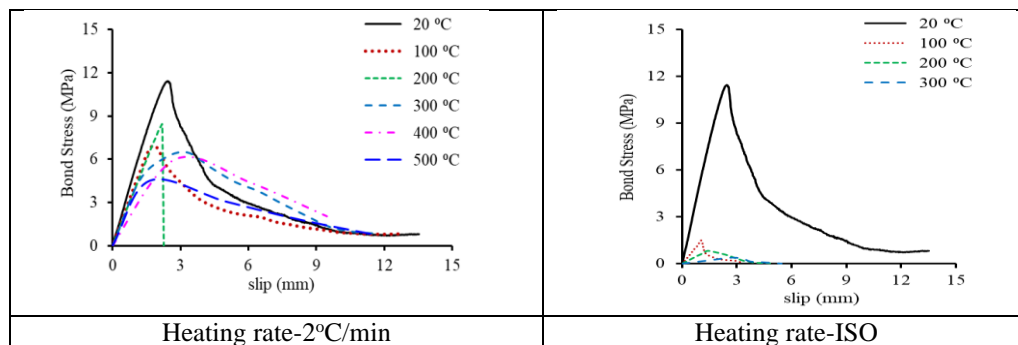


Figure 6. Bond stress versus slip of 20 mm rebar

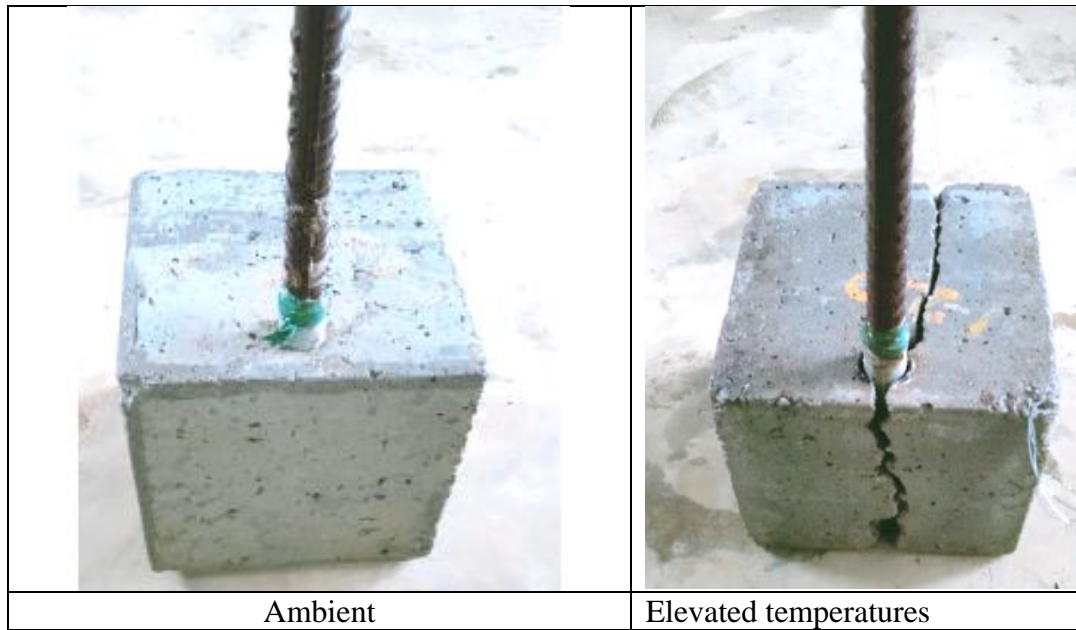


Figure 7. Failure patterns of 20 mm rebar

4.2 Residual bond strength (RBS)

Residual bond strength against temperature is shown in Figure 8. The residual bond strength at the elevated temperatures of 100, 200, 300°C by following heating rate of 2°C /min and ISO 834 are: 42, 26, 6 and 37, 29, 9% for the 12 mm rebar, and for the 20 mm rebar RBS at the temperature of 100, 200, 300, 400, 500°C by following heating rate of 2°C/min are: 61, 74, 57, 53, 40 and by following ISO heating rate the bond strength varied from 13 to 3% in the temperature range of 100-300°C. Bond strength at 200°C is more than the bond strength at 100°C in the case of 20 mm rebar. Similar has also been reported by earlier researchers.

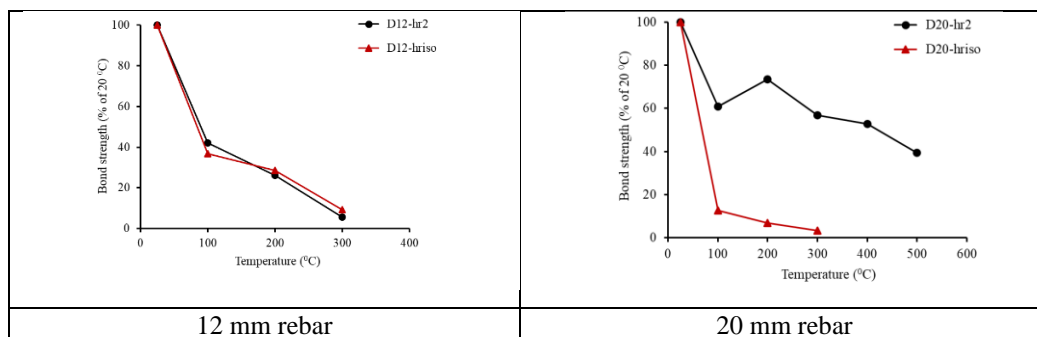


Figure 8. normalized Bond strength against temperature

5 CONCLUSIONS

- Bond behaviour between the steel and concrete studied at the elevated temperature in the range of 20-500°C by conducting pull-out test.
- Bond strength decreases with increasing of temperatures. The heating rate has significant effect on the bond strength reduction. With the increase of heating rate bond strength decreased due to larger thermal gradients in the case of higher heating rate. The reduction of bond strength is more in the case of heating rate followed by ISO than the heating rate followed by 2°C/min in the case of 20 mm rebar. Although, this effect in the case of 12 mm rebar is not very significant.

REFERENCES

1. Diederichs, U., Schneider, U., Bond strength at high temperatures. *J Mag Concr Res* 33(115), 75–84 (1981). <https://doi.org/10.1680/mac.1981.33.115.75>.
2. Royles, R., Morley, P.D., Response of the bond in reinforced concrete to high temperatures. *J Mag Concr Res* 35(124), 157–163 (1983). <https://doi.org/10.1680/mac.1983.35.124.157>.
3. Haddad, R.H., Al-Saleh, R.J., & Al-Akhras N.M., Effect of elevated temperature on bond between steel reinforcement and fibre reinforced concrete. *J Fire Saf* 43(5), 334–343 (2008). <https://doi.org/10.1016/j.firesaf.2007.11.002>.
4. Lubloy, É, Hlavička, V., Bond after fire. *J Constr Build Mater* 132, 210–218 (2017). <https://doi.org/10.1016/j.conbuildmat.2016.11.131>.
5. Varona, F.B., Baeza, F.J., Bru, D., Ivorra, S., Evolution of the bond strength between reinforcing steel and fibre reinforced concrete after high temperature exposure. *Constr Build Mater*, 176, 359–370 (2018). <https://doi.org/10.1016/j.conbuildmat.2018>.
6. Deshpande, A., Kumar, D., Ranade, R., Temperature effects on the bond behavior between deformed steel reinforcing bars and hybrid fiber-reinforced strain-hardening cementitious composite. *Constr Build Mater* 176, 117337 (2019) <https://doi.org/10.1016/j.conbuildmat.2019.117337>
7. Bingöl, A.F., Gül, R., Residual bond strength between steel bars and concrete after elevated temperatures. *J Fire Saf*. 44(6), 854–859 (2009). <https://doi.org/10.1016/j.firesaf.2009.04.001>.
8. Lee, J., Sheesley, E., Jing, Y., Xi, Y., Willam, K., The effect of heating and cooling on the bond strength between concrete and steel reinforcement bars with and without epoxy coating. *J Constr Build Mater* 177, 230–236 (2018). <https://doi.org/10.1016/j.conbuildmat.2018.05.128>.
9. IS: 10262-2009, Concrete Mix Proportioning – Guidelines.
10. ENV 10080:1995, Steel for the reinforcement of concrete- Weldable reinforcing steel – General
11. ISO: 834-11:2014, Fire Resistance Tests – Elements of Building Construction – Part 11: Specific Requirements for assessment of fire Protection to Structural Steel Elements.

POST-EARTHQUAKE FIRE ASSESSMENT OF REINFORCED CONCRETE COLUMNS

Hemanth Kumar Chinthapalli¹, Anil Agarwal²

ABSTRACT

The earthquake tremors not only increase the chances of fire ignition but also hinders the fire-fighting efforts due to the damage to the lifelines of a city. Most of the international codes provide provisions for structural design against earthquake and fire. However, the possibility of a multi-hazard event, such as fire following an earthquake is seldom addressed. The buildings designed using these codes may be vulnerable when exposed to such an event.

This paper presents an experimental study of RC columns in post-earthquake fire conditions. An experimental approach is proposed that allows the testing of columns instead of the entire structural frame. This approach allows us to control the loading and boundary conditions individually and facilitates the testing under a variety of these conditions. Also, it allows the structure to be tested until failure. The role of parameters such as earthquake intensity, axial load, and the ductile detailing of the column on the earthquake damage and subsequently the fire resistance of the structure is studied in this research. Six RC column specimens are tested under a sequence of quasi-static earthquake loading, fire loading, and axial compression loading conditions.

Ductile detailed columns subjected to 4% or less lateral drift did not lose significant load-carrying capacity in fire conditions. However, a lateral drift of 6% caused significant damage to the column and reduced the load-carrying capacity in fire conditions. The columns that were not detailed for a ductile behavior observed a more significant reduction in axial load carrying capacity in fire conditions. The level of the axial load acting on the column at the time of earthquake loading was found to have a very significant effect on the extent of damage and reduction in column load capacity in fire conditions.

Keywords: Structures; finite element modelling; compartment fires; fire tests

1 INTRODUCTION

The earthquake shaking not only increases the chances of fire ignition but also hinders the fire-fighting efforts due to the damage to the lifelines of a city. Some of the essential infrastructure such as bridges, water pipelines, sprinkler systems, etc. may get damaged during the earthquake. Similarly, the communication networks are likely to be overcrowded during an earthquake, and fire departments and aid workers are likely to be preoccupied with helping rescue the victims of the earthquake. As a result, some of the fires can grow to the extent that they can affect structural health. The post-earthquake fire (PEF) can grow, intensify, and spread out of control, in one or more neighborhoods. This is often referred to as a conflagration. Some of the major PEFs across history have occurred during the San Francisco earthquake (1906), Great Kanto earthquake (1923), Niigata earthquake (1964), Fukui earthquake (1948),

¹ Research Scholar, Indian Institute of Technology Hyderabad,

e-mail: ce15resch11006@iith.ac.in,

² Assistant Professor, Indian Institute of Technology Hyderabad,

e-mail: anil@ce.iith.ac.in

Coalinga earthquake (1983), Loma Prieta earthquake (1989), Northridge earthquake (1994), Kobe earthquake (1995), Turkey Marmara earthquake (1999), Chile earthquake (2010), Great Tohoku earthquake (2011) and Christchurch earthquake (2011). Therefore, besides satisfying structural design requirements for normal loads, such as dead and live loads, including the seismic hazard, buildings should also be designed to withstand the fire following earthquakes for a certain minimum duration as required for a desired level of performance. In fact, according to current seismic codes, ordinary structures are designed to suffer damage or plastic deformation to some extent during a severe earthquake. Structural members were typically designed to satisfy the requirements of serviceability and safety limit states for various environmental conditions. Fire represents one of the most severe undesired conditions, and hence the provision of appropriate fire safety measures for structural members is a significant safety requirement in building design. The basis for this requirement can be attributed to the fact that, when other measures for containing the fire fail, structural integrity is the last line of defense. In general, structural members or systems are designed for a required fire-resistance rating, which is defined as the duration in which a structural member or system exhibits adequate structural integrity, stability, and heat resistance. The occurrence of fire following an earthquake can understandably produce a disastrous effect. Although shaking is the major concern in most earthquakes which results in cracks, spalling, material degradation. Subsequent fire can pose a major risk to structural members. The risk is also increased by the delayed fire response due to extreme traffic congestion, collapsed structures like buildings, bridges, and electrical structures. The fire-resistance rating depends on several factors including the features of the building and the occupancy type. But, after an earthquake, the fire-resistance rating of the members subjected to fire may decrease significantly due to spalling, exposure of reinforcement to fire, permanent drift, degradation of material strength and stiffness properties due to large plastic deformations, and also on the extent of the above factors [1–4]. Some researchers have recommended that fire safety codes should distinguish between structures located in seismic and non-seismic areas, with more stringent fire resistance provisions for those buildings potentially subjected to seismic actions [5,6].

Post-earthquake, the fire resistance of structures depends on a large number of factors, and its evaluation is affected by large uncertainties such as the mechanical behavior of structural components and the intensity of external loads. Assessment of the changes to the structure's physical state (e.g., inter-story drift, cracks, decrease in cross-section area due to spalling, buckling of reinforcement, etc.) after an earthquake is one of the major challenges. In particular, structural damage has been schematized as the combination of two damage types: geometric damage and mechanical damage. Geometric damage consists of residual deformation or permanent drift due to plastic deformations and changes to the cross-section dimensions. Mechanical damage consists of degradation in the main mechanical properties such as stiffness and strength of the structural components. Vitorino et.al., [1,2] analyzed RC elements and frames with different levels (such as Immediate Occupancy (IO), Life Safety (LS), Collapse Prevention (CP)) of earthquake damage using SAFIR. The damage was incorporated by reducing the clear cover of the cross-section. The influence of the cracking of the concrete is not considered in the thermal analysis and mechanical properties during the cyclic load. Evrine et.al. [7] conducted a study on damaged RC beams and concluded that the effect of tensile cracking on the thermal propagation through concrete is less compared to the uncracked section but the difference is very small and therefore, the effect of cracks on the heat transfer analysis can be ignored. The finding implies that the heat transfer analysis can be conducted on the undamaged cross-section disregarding the effects of cracks during the earthquake loading. However, the studies conducted by Wu et.al. [8] contradict this, and instead demonstrate that the cracks will decrease the conductivity of the concrete significantly when the cracks are wider than 3 mm and deeper than 100 mm.

Behnam and Ronagh [4] conducted numerical analyses to simulate the PEF behavior of two RC frames. The frames were designed to the ACI 318-08 code and were simulated in SAP19 to a spectral Peak Ground Acceleration of 0.35g. The results showed that the structures previously damaged by the earthquake and exposed to PEF are more vulnerable than those that are undamaged.

Wen et.al. [9,10] studied the PEF performance of RC columns and beams by testing the frames of 1:8 scale and derived equations to predict the length of spalling. This equation is further used to simulate the spalling in the numerical model developed using Abaqus without considering the permanent deformation, stiffness,

and strength degradation of the members. Finally, they concluded that the load-bearing capacity reduces with an increase in spalling width and is independent of the length of spalling.

Several studies [11–16] on the PEF behavior of RC frames were conducted at IIT Roorkee. Full-scale one-story RC frames were tested under PEF conditions. The frames were subjected to LS (2% drift) and CP (4% drift) levels of earthquake damage followed by fire loading. All the frames were subjected to the desired damage level with the following cyclic load protocol. The test frame was subjected to push-pull cycles starting with a 10-mm cycle and then each successive cycle was increased with an increment of 10 mm until the target displacement was achieved. All the frames were subjected to a 1-hour kerosene pool fire. The columns were located at the four corners of the compartment and therefore, were partially heated. Two different levels of reinforcement detailing, i.e., ductile detailing as per IS13920:1993 [17] and non-ductile detailing as per IS 456:2000 [18], were used. After the fire was extinguished, the residual permanent drifts were measured and compared. For example, a frame that was not detailed for ductile behavior had a permanent drift of 1.09%, whereas a comparable frame detailed for ductile behavior had a permanent drift of 0.05%. Therefore, it was concluded that ductile detailing improves the PEF behavior of RC frames. These very elaborate experiments indicated that ductile RC frames perform better in PEF conditions.

As discussed above, there are only a handful of experimental studies investigating the PEF behavior of RC structures. Some of these studies use permanent drift after a post-earthquake fire to assess PEF performance of the structure. From the structural safety point of view, however, quantification of the reduction in the load-carrying capacity is more important. The structural damage during an earthquake also depends on one other important parameter, namely, the level of axial load on the member, which is not studied in the earlier research. While testing a frame system, it is difficult to separately account for the damage in columns and beams. For a given inter-story drift the damage to individual members may differ depending on their relative flexural strengths. Therefore, it is difficult to relate the inter-story drift of the frame to column damage. In some of the studies, the columns are heated only from two or three sides leading to an unconservative estimate of the thermal loading. In some of the studies, tests are conducted on scaled specimens.

Considering the above limitations of the earlier research, there is a need to develop a test protocol wherein (i) the specimens are tested until failure so that the reduction in load capacities can be compared directly, (ii) full-scale structural systems are tested, (iii) various member level parameters such as damage caused to an individual member, and axial load during the earthquake can be controlled directly.

2 EXPERIMENTAL STUDY

The earthquake response of RC frame structures is controlled by the hinge formation at member ends. The formation of hinges at beam ends is desirable. The columns may, however, undergo severe plasticization if (i) the strong column weak beam design philosophy is not followed or (ii) if the earthquake load is beyond the design earthquake level. Columns are the most critical components that control the ability of the frame to resist the gravity loads. If columns undergo severe damage, it threatens the ability of the structure to resist the gravity loads. Therefore, instead of testing the entire frame system, one may test individual columns under appropriate boundary conditions and predict the failure load of the frame under the gravity loads. This method will not be suitable where the global stability of the frame system is in question. However, fire is a local phenomenon and the structural collapse in fire conditions typically starts with the failure of one column [19,20]. A similar approach for studying the PEF behavior of Concrete-Filled Double-Skinned Tube (CFDST) columns has been adopted by Imani et al. [21]

As discussed above, individual columns can be tested under the PEF conditions to assess the reduction in the fire resistance of RC structures after an earthquake. A set of six columns were tested under PEF conditions. The study includes testing the ductile and non-ductile columns at different levels of earthquake damage and axial load ratio. Among the six columns, two were designed as per the ductile detailing requirements of IS 13920 [17] and four were designed as per the requirements of IS 456 [18].

2.1 Column Specifications and Test Matrix

Six RC square columns of 230 mm size and 1800 mm length were cast. The columns are reinforced with four longitudinal bars of 12 mm diameter, which corresponds to 0.86% of the cross-section area. Out of the

six columns, four columns were designed as a part of an Ordinary Moment Resisting Frame (OMRF) following the requirements of IS 456 [18] and the other two were designed as a part of a Special Moment Resisting Frame (SMRF) following the requirements of IS 13920 [17]. The non-ductile columns are provided with 8 mm dia. lateral ties at 200 mm center to center distance. The ductile detailed columns were provided with 10 mm dia. lateral ties at 75 mm center to center spacing up to a distance of 475 mm from one end, and then at 150 mm center to center spacing throughout the remaining length. All lateral ties were bent at 135°. A clear cover of 25 mm was provided to the confining reinforcement. All the reinforcement steel is of grade Fe500. The specimens are cast with an M25 concrete mix. The specimen details and loads applied to each specimen are presented in Table 1. The schematic of the reinforcement details in plan and elevation details were presented in Figure 1 and the location of the thermocouples in the cross-section at the heating region were presented in Figure 2.

Table 1: Test matrix with specimen details

S.No.	Specimen	Ductile Detailing	Earthquake Damage (Drift %)	Axial Load (kN)
1	ND-E0-A0	No	0	0
2	ND-E6-A350	No	6	350
3	ND-E6-A500	No	6	500
4	ND-E6-A621	No	6	621
5	D-E4-A350	Yes	4	350
6	D-E6-A350	Yes	6	350

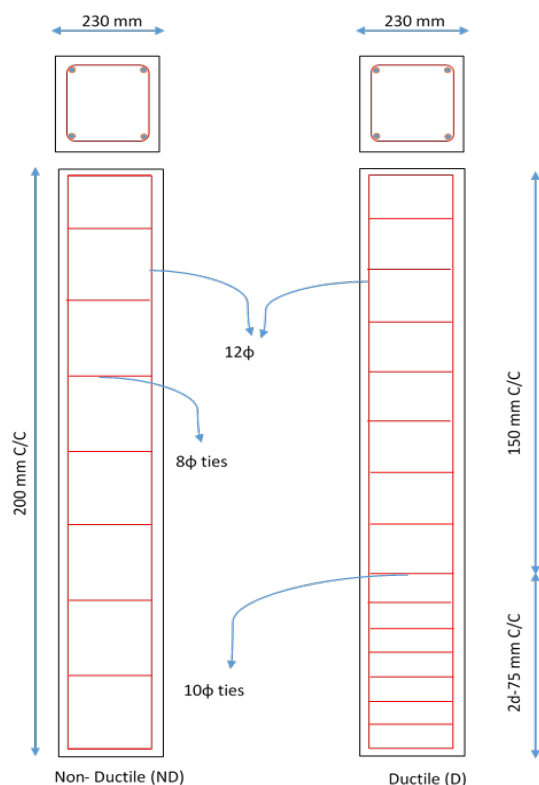


Figure 1: Schematic of the cross-section and reinforcement detailing of the columns

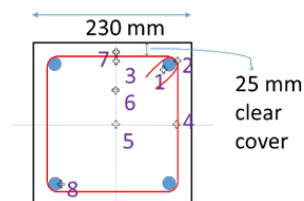


Figure 2: Location of thermocouples in the specimen

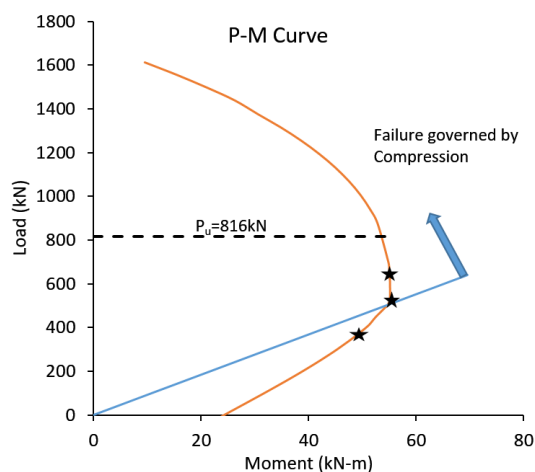


Figure 3: P-M interaction curve of the column section

Three different axial load levels were considered in the test matrix to understand the effect of the axial load ratio during the earthquake loading on the PEF behavior. The loads were considered based on the behavior of the column under combined axial load (P) and bending moments (M). Figure 3 shows the P-M interaction curve of the RC column cross-section described in the previous paragraph. Failure strain of concrete in compression was considered as 0.003. The yield strength of steel and the corresponding strain were considered as 520 MPa and 0.0025, respectively. Whitney stress block was considered for calculating the stresses in the concrete for developing the P-M interaction curve. Based on the P-M interaction curve, it was observed that when the axial compressive load is less than 500kN (balanced point), the column fails in tension dominant mode, and when the axial load is above 500kN, the column fails in compression dominant mode. Therefore, in the test matrix, one axial load value corresponded to the tension dominated failure (350kN), one value corresponded to the balanced point (500kN), and one value corresponded to the compression dominated failure (621kN). These axial load values correspond to 40%, 60%, and 76% of the design load-carrying capacity ($P_u = 861\text{kN}$) of the column, respectively. The design load capacity (P_u) value is calculated according to IS 456 [18].

As per the numerical and the experimental studies [4,10–14,22–25] available in the literature, the ductile detailing and the earthquake intensity are likely to affect the fire-resistance rating of RC members in the PEF scenarios. To simulate those behaviours, the columns in the test matrix were subjected to three different levels of earthquake damages. The loading protocol described in FEMA 461:2007 [26] was used to apply the cyclic lateral loading on the columns. Maximum drift ratios of 4% and 6% were applied in different specimens. The collapse prevention level story drift limit is 4% as per FEMA356 [27]. The different combinations of these parameters used for individual specimens are presented in Table 1.

2.2 Loading Sequence

One possible approach to test the post-earthquake fire response of RC columns would be to follow the following sequence. Step 1: Apply the axial compression load (representing the gravity load) on the column. Step 2: Apply the lateral cyclic load (representing the earthquake load) to reach the expected damage level. Step 3: Apply the thermal loading until failure. It should be noted that in this approach, the axial load applied in step 1 is maintained during steps 2 and 3. This approach directly provides the fire resistance value in terms of fire duration. However, this sequence of loading makes it difficult to understand the role of axial load during the earthquake loading as the same axial load will be acting during the fire test. Therefore, it would be impossible to differentiate the two effects. Therefore, a slightly different testing approach, as presented below was adopted.

The approach adopted for this research had the following steps: Step 1: First, the column was loaded statically in pure compression up to the desired load level and the load is maintained for minimum 45 min before the application of the cyclic loading to make sure that the axial load is constant and that there are no settlements or deformations in the setup or specimen. Step 2: Maintaining the axial load at a constant level, the lateral cyclic load was applied up to the desired maximum drift level. The details of the earthquake loading protocol are presented in the subsequent section. Step 3: After damaging the column to the desired level of maximum drift, the lateral and axial loads on the column were removed slowly. Subsequently, the column was removed from the earthquake loading setup and placed in the compression testing machine for a load-bearing test under fire conditions. Step 4: The damaged portion of the column was subjected to the standard ISO fire conditions [28] for one-hour duration without loading the column mechanically. Step 5: After 1 hour of heating, the column was immediately loaded in axial compression until it failed. The loading was applied in a displacement-controlled manner at a constant rate of 2 mm/min. The temperature change during Step 5 was small and therefore, it can be approximated as testing under adiabatic conditions. The graphical representation of the loading sequence for the fire test is presented in Figure 4 in following steps 1 to 5.

2.3 Cyclic Loading Protocol

FEMA 461: 2007, section 2.9 [26] describes a loading history for testing RC structures under quasi-static seismic conditions. The loading history consists of repeated cycles with stepwise increasing deformation amplitudes. The targeted smallest deformation amplitude (D_0) of the loading history must be safely smaller

than the amplitude at which the lowest damage state took place and a minimum of six cycles must be executed before the first initiation of the damage. The amplitude a_{i+1} (not of each cycle since each step has two cycles) is 40% greater than a_i , where a_i is the amplitude of the i^{th} step. Beyond a maximum drift value of 4%, the subsequent steps were applied at 20% increment. Figure 5 illustrates the deformation-cycles adopted for simulating the earthquake load on the column. The distance between the support and the loading point was measured as 765 mm. Lateral deformation in the first step (a_1) was taken as 0.86 mm. The maximum drift values of 4% and 6% correspond to lateral deformations of 32.4 mm and 46.7 mm, respectively. After the final cycle, the column is pushed in the opposite direction to achieve zero permanent deformation.

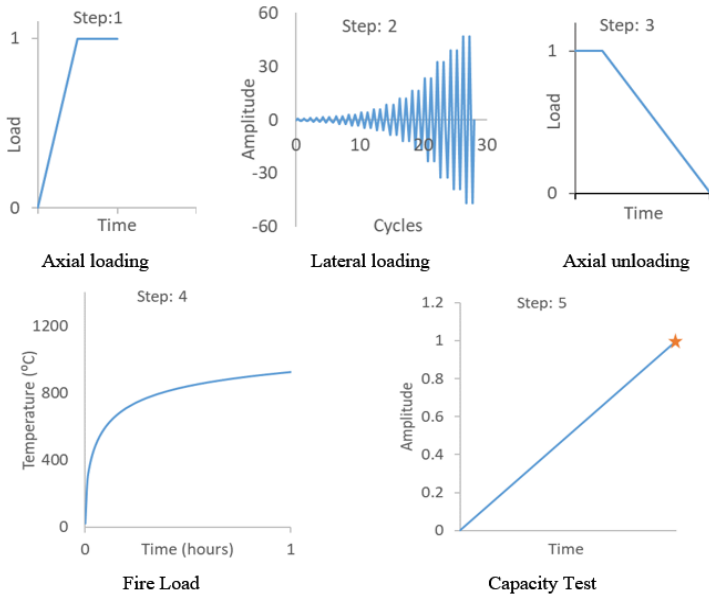


Figure 4 : Loading and testing sequence adopted in this study

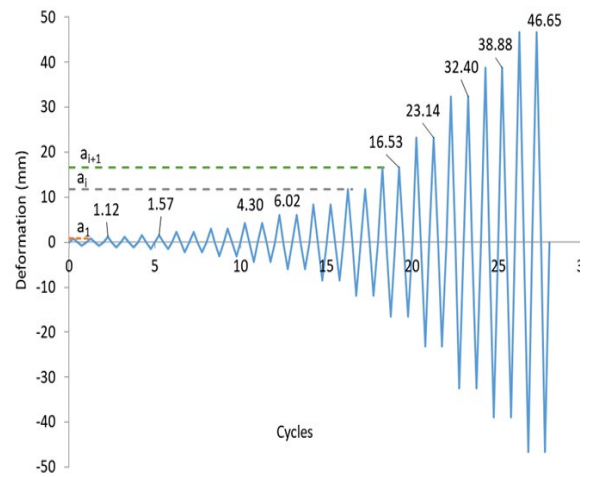


Figure 5: Loading Protocol as per FEMA 461

3 RESULTS

3.1 Behavior during the Cyclic Earthquake Loading

Specimen ND-E0-A0 was a control specimen and was not subjected to any earthquake loading. The load vs deformation curves for the cyclic tests on the remaining specimens are presented in Figure 6 and the details of the spalled concrete are presented in Table 2. When the hysteresis behavior of two identical specimens subjected to different axial loads such as ND-E6-A350 and ND-E6-A500 are compared, one may notice that after reaching the peak lateral force value, specimen ND-E6-A500 undergoes a more significant decline in comparison to ND-E6-A350. Specimen ND-E6-A621 had a very sudden failure after it reached the maximum lateral force value. This clearly shows that an increase in the axial load value reduces the ductility of the member in cyclic loading conditions. As the axial load increased from 350 kN to 500 kN, the maximum lateral load resisted by the column also increases from 74 kN to 88 kN. This can be explained from the P-M interaction curve for this column shown in Figure 3. No significant increase was observed when the axial load increases from 500 kN to 621 kN. The volume of concrete spalled during cyclic loading also increases with an increase in the axial load. As the axial load during the cyclic loading was increased from 350 kN to 500 kN to 621 kN, the amount of volume loss of concrete increased from 605 cm³ to 2090 cm³ to 6835 cm³.

The specimens with ductile detailing underwent less damage in comparison to the specimens that were not designed to meet the ductility requirements. Specimens ND-E6-350 and D-E6-350 are identical except that the latter meets ductility requirements of IS 13920 [17]. From the hysteresis plots, specimen ND-E6-350

has a more significant post-peak drop in comparison to ND-E6-350. The volume of concrete spalled during the cyclic loading for ND-E6-350 was 605 cm³ in comparison to 485 cm³ for ND-E6-350.

Table 2: Concrete spalled during the earthquake loading and load resistance after one-hour fire.

Specimen	Spalled Concrete			Fire Capacity
	Length (mm)	Depth (mm)	Volume Loss (cm ³)	Max. Load (kN)
ND-E0-A0	0	0	0	1110
ND-E6-A350	150	20	605	709.8
ND-E6-A500	250	35	2090	611.7
ND-E6-A621	350	80	6835	0
D-E4-A350	0	0	0	1369
D-E6-A350	120	15	485	1108

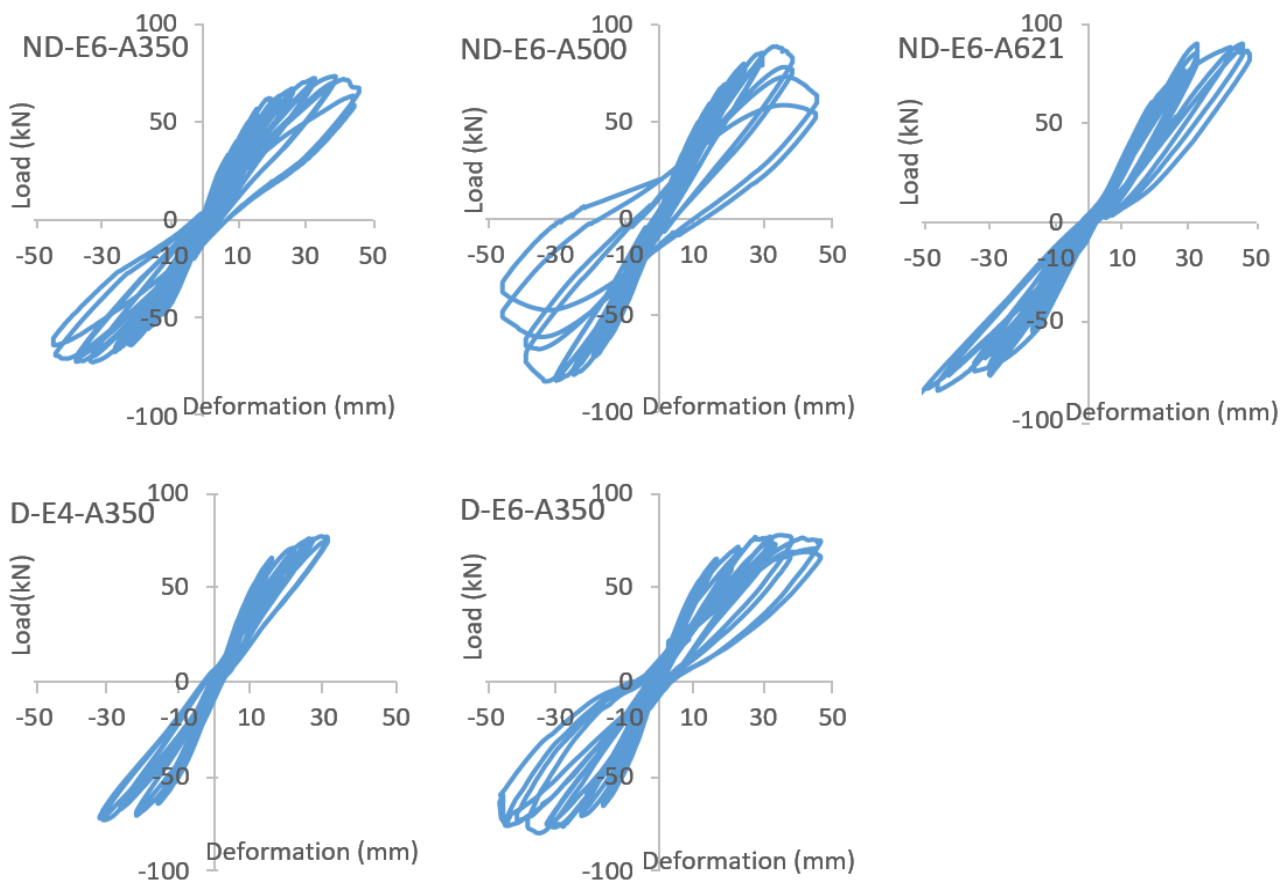


Figure 6: Load-deformation curves measured during the horizontal cyclic testing.

3.2 Thermal Response

After the earthquake loading, the columns were placed on the CTM and were heated for 1 hour duration under the ISO standard fire conditions [28]. Eight thermocouples were placed inside the cavity to measure furnace temperatures. The average readings of the eight thermocouples from each test are presented in Figure 7. The measured temperatures are also compared with the target standard fire curve. The heat output

lagged behind the standard fire curve slightly during the initial few minutes. However, the deviations are within the permissible limits of the standard fire test protocol and the temperature distribution inside the furnace was uniform and consistent among all the tests. The location of the thermocouples in the specimen furnace [29,30] are followed as per the standards.

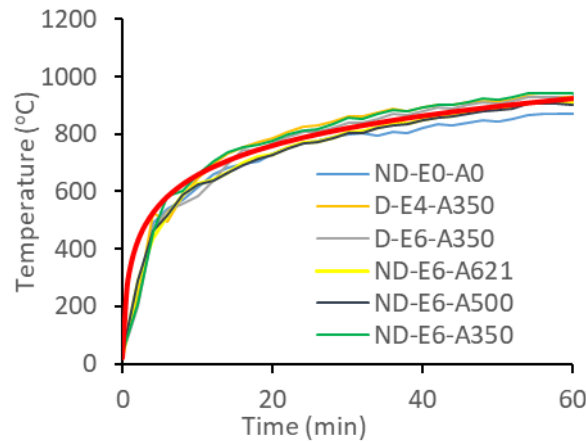


Figure 7: Average time-temperature plots measured from the furnace thermocouples.

Temperatures measured at different locations in the column cross-section A-A marked in Figure 2 were plotted against time in Figure 8 for all the specimens. The temperature values vary significantly depending on the volume loss in the cross-section during the cyclic loading test. The plateau associated with the vaporization of water at 100°C is visible in all specimens at the core. While the temperature rise in the outer layer of the concrete columns is not significantly affected by the presence of moisture in the concrete, the temperature rise in the inner layers is very slow during the initial 60 minutes of heating due to the moisture present in the concrete. It can be observed that the temperatures rise more rapidly for the specimens that had more severe spalling and volume loss during the earthquake damage. For example, D-E6-A350 and ND-E6-A350 were identical specimens except the ductile detailing specifications. The temperatures in specimen ND-E6-A350 were higher than those in specimen D-E6-A350 as the latter had less spalling (Table 2). Similarly, specimens ND-E6-A350 and ND-E6-A621 were subjected to axial loads of 350 kN and 621 kN, respectively. As a result, ND-E6-A621 was damaged more severely during the cyclic loading and observed more rapid temperature rise during the heating. Specimens D-E4-A350 and D-E6-A350 were subjected to lateral deformations of 4% and 6%, respectively. As a result, the temperatures in the former specimen were lower than the latter specimen.

3.3 Axial Compression Response of the Damaged and Heated Columns

The earthquake-damaged specimens were heated for a 1-hour duration and then were immediately subjected to axial compressive loading until failure, which was marked by at least a 20% drop from the peak resistance value. The compressive load on the columns was increased in displacement-controlled mode at a rate of 2.0 mm per minute. After the completion of each test, the damage in each column was studied. Photographs of the damaged columns after the tests are presented in Figure 9. All specimens suffered failure within the heated zones. It was noticed that the lateral reinforcement had undergone plastic deformation and the longitudinal reinforcement bars had buckled. The load-deformation curves of all the six specimens are presented in Figure 10. The maximum axial load resistance and the initial stiffness values of the load-deformation curves were presented in Table 2.

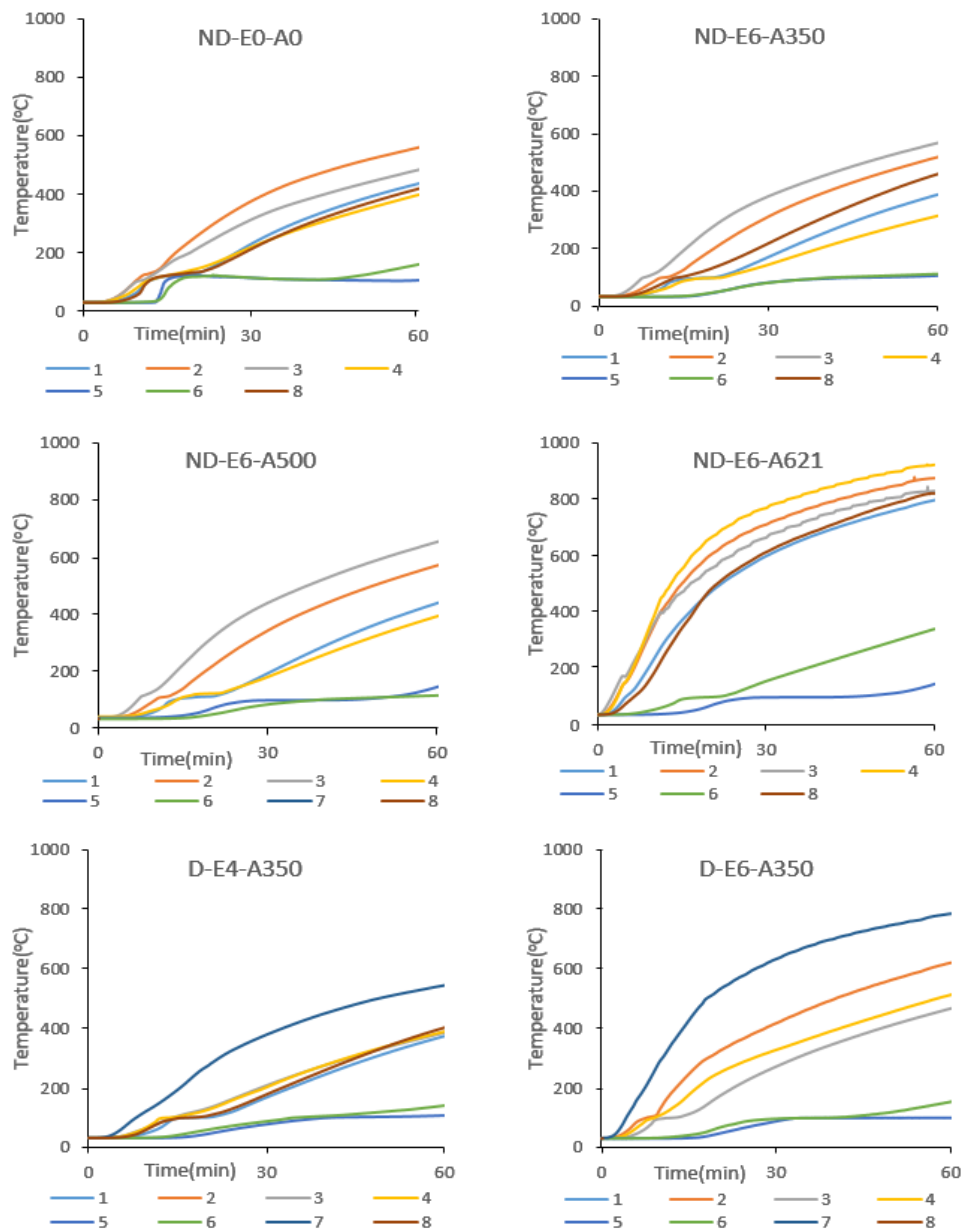


Figure 8. Time-temperature plots measured from the thermocouples in the damaged specimens.

The extent of the earthquake damage has significant effect on the load-carrying capacity of columns in fire conditions. This may be illustrated by the following observations: specimens D-E4-A350 and D-E6-A350 are identical but were subjected to the maximum drift values of 4% and 6%, respectively. D-E6-A350 had a more significant spalling than D-E4-A350 therefore, resisted 23% less axial load than D-E4-A350 in fire conditions.

Axial load acting on the column during the cyclic loading significantly controls the ductility and damage of the column. As the axial load on the column is increased, the failure mode changes from tension controlled to compression controlled. As a result, the likelihood of concrete crushing and spalling increases. This leads to a very significant drop in the load-carrying capacity of the column in fire conditions. As the axial load during the cyclic loading was increased from 350 kN to 500 kN and subsequently to 621 kN, the amount of volume loss of concrete due to spalling was 605 mm³, 2090 mm³, and 6835 mm³, respectively. As a result, the column capacity in fire conditions reduced from 710 kN to 612 kN to almost zero.

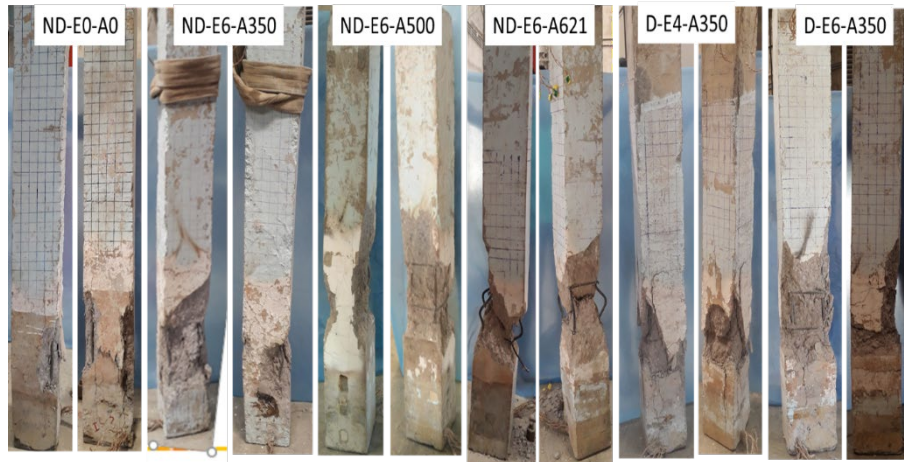


Figure 9: Photographs of the damaged specimens after the fire test.

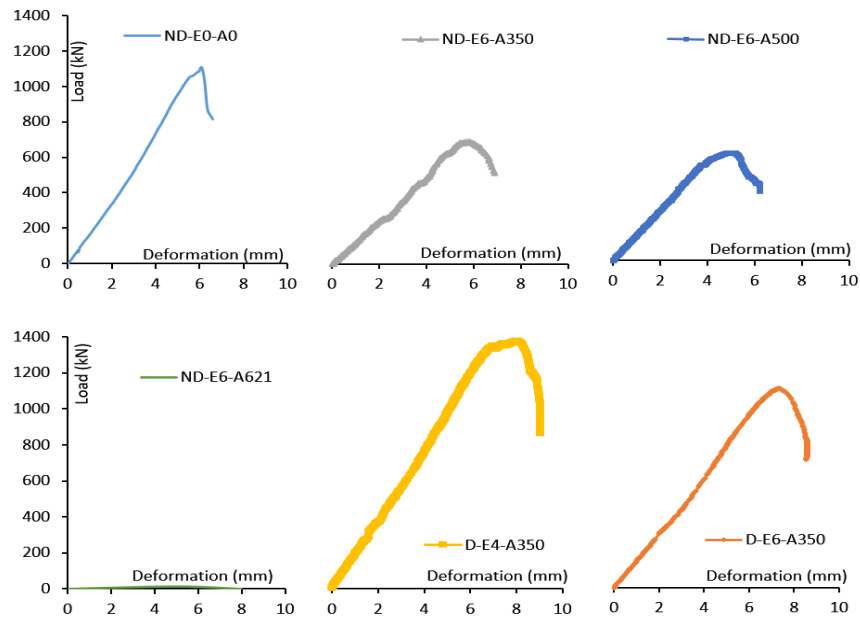


Figure 10: Load-deformation curves of PEF-tests.

The PEF performance of RC columns depends very significantly on whether the column is ductile detailed or not. A ductile detailed column subjected to a cyclic load of 4% lateral drift (D-E4-A350) resisted 23% more load under the subsequent fire conditions than a similar nonductile column without any earthquake damage (ND-E0-A0). A ductile column even with a 6% drift (D-E6-A350) resisted almost the same load as a nonductile column with no earthquake damage (ND-E0-A0). This behavior is understandable as effect of the amount of confining reinforcement on the load carrying capacity in fire conditions has been discussed in detail by Chinthapalli and Agarwal [29].

The fire performance was significantly affected only for those columns that had undergone significant volume loss during the cyclic loading. Some of the specimens that had developed cracks without any spalling, e.g., D-E4-A350, resisted greater load than some of the undamaged columns.

4 SUMMARY AND OBSERVATIONS

Six full-scale RC columns were tested to study the PEF response of RC structures. The study focused on the column behavior as they are the most critical elements for the stability of the structure in fire conditions.

The testing procedure involved first damaging the columns to a predetermined level of cyclic earthquake loading in presence of an axial compressive load followed by heating the columns for 1-hour duration and again subjecting them to pure axial compressive load until failure. The study revealed some interesting observations:

- Cracks alone during the cyclic earthquake loading did not significantly reduce the load capacity of the column in the subsequent fire conditions. Volume loss due to spalling, however, had a significant effect on the load capacity in fire conditions.
- The level of axial load on the column during the cyclic earthquake loading significantly changed the nature of the damage in the column. Under a small axial load, the column behavior was governed by yielding of the reinforcement marked by tension cracks in concrete. Under a large axial load, the column behavior was governed by crushing of concrete in compression marked by spalling of concrete. The members that underwent only tensile cracking did not lose the axial load capacity in fire conditions as much as the column that underwent concrete crushing and spalling.
- Columns with ductile detailing performed significantly better than the column not detailed for ductile behavior.
- The experimental procedure proposed in this paper offers an alternative to testing of a complete structural frame system for post-earthquake fire behavior. In addition to the ease of conducting the tests, the procedure also allows a much better control over the heating, structural loading, and boundary conditions.

REFERENCES

1. Vitorino H, Rodrigues H, Couto C. Evaluation of post-earthquake fire capacity of a reinforced concrete one bay plane frame under ISO fire exposure. *Structures* 2020;23:602–11. <https://doi.org/10.1016/j.istruc.2019.12.009>.
2. Vitorino H, Rodrigues H, Couto C. Evaluation of post-earthquake fire capacity of reinforced concrete elements. *Soil Dynamics and Earthquake Engineering* 2020;128:105900. <https://doi.org/10.1016/j.soildyn.2019.105900>.
3. Mousavi S, Bagchi A, Kodur VKR. Review of post-earthquake fire hazard to building structures. *Can J Civ Eng* 2008;35:689–98. <https://doi.org/10.1139/L08-029>.
4. Ronagh HR, Behnam B. Investigating the Effect of Prior Damage on the Post-earthquake Fire Resistance of Reinforced Concrete Portal Frames. *Int J Concr Struct Mater* 2012;6:209–20. <https://doi.org/10.1007/s40069-012-0025-9>.
5. Della Corte G, Landolfo R, Mazzolani FM. Post-earthquake fire resistance of moment resisting steel frames. *Fire Safety Journal* 2003;38:593–612. [https://doi.org/10.1016/S0379-7112\(03\)00047](https://doi.org/10.1016/S0379-7112(03)00047).
6. Jelinek T, Zania V, Giuliani L. Post-earthquake fire resistance of steel buildings. *Journal of Constructional Steel Research* 2017;138:774–82. <https://doi.org/10.1016/j.jcsr.2017.08.021>.
7. Ervine A, Gillie M, Stratford TJ, Pankaj P. Thermal Propagation through Tensile Cracks in Reinforced Concrete. *J Mater Civ Eng* 2012;24:516–22. [https://doi.org/10.1061/\(ASCE\)MT.1943-5533.0000417](https://doi.org/10.1061/(ASCE)MT.1943-5533.0000417).
8. Wu B, Xiong W, Wen B. Thermal fields of cracked concrete members in fire. *Fire Safety Journal* 2014;66:15–24. <https://doi.org/10.1016/j.firesaf.2014.04.003>.
9. Wen B, Zhang L, Wu B, Niu D. Structural Performance of Earthquake-damaged Beams in Fire. *KSCE J Civ Eng* 2018;22:5009–25. <https://doi.org/10.1007/s12205-017-1001-3>.
10. Wen B, Wu B, Niu D. Post-earthquake fire performance of reinforced concrete columns. *Structure and Infrastructure Engineering* 2016;12:1106–26. <https://doi.org/10.1080/15732479.2015.1085883>.
11. Shah AH, Sharma UK, Bhargava P. Outcomes of a major research on full scale testing of RC frames in post earthquake fire. *Construction and Building Materials* 2017;155:1224–41. <https://doi.org/10.1016/j.conbuildmat.2017.07.100>.

12. Kamath P, Sharma UK, Kumar V, Bhargava P, Usmani A, Singh B, et al. Full-scale fire test on an earthquake-damaged reinforced concrete frame. *Fire Safety Journal* 2015;73:1–19. <https://doi.org/10.1016/j.firesaf.2015.02.013>.
13. Sharma UK, Bhargava P, B Singh B, Y Singh Y, Kumar V, Kamath P, et al. Full-scale testing of a damaged reinforced concrete frame in fire. *Proceedings of the Institution of Civil Engineers - Structures and Buildings* 2012;165:335–46. <https://doi.org/10.1680/stbu.11.00031>.
14. Shah AH, Sharma UK, Kamath P, Bhargava P, Reddy GR, Singh T. Fire performance of earthquake-damaged reinforced-concrete structures. *Mater Struct* 2016;49:2971–89. <https://doi.org/10.1617/s11527-015-0699>.
15. Shah AH, Sharma UK, Kamath P, Bhargava P, Reddy GR, Singh T. Effect of Ductile Detailing on the Performance of a Reinforced Concrete Building Frame Subjected to Earthquake and Fire. *Journal of Performance of Constructed Facilities* 2016;30:04016035. [https://doi.org/10.1061/\(ASCE\)CF.1943-5509.0000881](https://doi.org/10.1061/(ASCE)CF.1943-5509.0000881).
16. Kumar V, Sharma UK, Singh B, Bhargava P, Singh Y, Kamath P, et al. Behaviour of Full-Scale Reinforced Concrete Frame Under Simulated Post-Earthquake Fire. 15 WCEE, Lisboa.
17. BIS (Bureau of Indian Standards). IS 13920 (2003): Ductile detailing of reinforced concrete structures subjected to seismic forces - Code of practice, New Delhi, India; 2003
18. BIS (Bureau of Indian Standards). IS 456 (2000) : Plain and reinforced concrete - Code of practice, New Delhi, India ; 2000
19. NIST (National Institute of Standards and Technology). Final Report on the collapse of world trade center building 7, Federal building and fire safety investigation of the world trade center disaster. Washington, D.C.;2008
20. BIS (Bureau of Indian Standards). IS 13920 (2003): Ductile detailing of reinforced concrete structures subjected to seismic forces - Code of practice, New Delhi, India; 2003
21. BIS (Bureau of Indian Standards). IS 456 (2000) : Plain and reinforced concrete - Code of practice, New Delhi, India ; 2000
22. NIST (National Institute of Standards and Technology). Final Report on the collapse of world trade center building 7, Federal building and fire safety investigation of the world trade center disaster. Washington, D.C.;2008
23. Behnam B, Ronagh HR. Firewalls and post-earthquake fire resistance of reinforced-concrete frames. *Proceedings of the Institution of Civil Engineers - Structures and Buildings* 2016;169:20–33. <https://doi.org/10.1680/stbu.14.00031>.
24. Behnam B, Ronagh HR. Post-earthquake fire resistance of CFRP strengthened reinforced concrete structures: using caron fiber polymers to improve post-earthquake fire resistance. *Struct Design Tall Spec Build* 2014;23:814–32. <https://doi.org/10.1002/tal.1084>.
25. Chen Y-H, Chang Y-F, Yao GC, Sheu M-S. Experimental research on post-fire behaviour of reinforced concrete columns. *Fire Safety Journal* 2009;44:741–8. <https://doi.org/10.1016/j.firesaf.2009.02.004>.
26. Federal Emergency Management Agency. FEMA 461 (2007) Interim testing protocols for determining the seismic performance characteristics of structural and nonstructural components. Washington, D.C.;2007.
27. Federal Emergency Management Agency. FEMA 356 (2000) Prestandard and commentary for the seismic rehabilitation of buildings. ASCE, Washington, D.C.; 2000.
28. ISO. 1980. Fire resistance tests - Elements of building construction. ISO 834, Geneva; 1980.
29. Chinthapalli HK, Agarwal A. Effect of Confining Reinforcement on Fire Behavior of Reinforced Concrete Columns – An Experimental and Numerical Study. *Journal of Structural Engineering* 2019.
30. Chinthapalli HK, Chellapandian M., Agarwal A., Prakash SS. Effectiveness of hybrid fibre-reinforced polymer retrofitting on behaviour of fire damaged RC columns under axial compression. *Engineering Structures* 2020.

DAMAGE ASSESSMENT FRAMEWORK FOR TUNNEL STRUCTURES SUBJECTED TO FIRE

Nan Hua¹, Anthony Frederick Tessari², Negar Elhami-Khorasani³

ABSTRACT

Fire hazards are a major threat to tunnel structures. The rapid rise of gas temperatures exceeding 1000 °C inside a confined tunnel space as well as long fire durations due to limited emergency responder access necessitate special analyses and design considerations. Intense lining damage, mostly due to concrete spalling, has been observed after major tunnel fires. Although collapse of the tunnel structure is rare, the serviceability and resilience of the tunnel structure are challenged, as major fire events could lead to months of downtime and millions of dollars of losses from repair and affected operations. This research will propose an assessment methodology to quantify tunnel fire damage to tunnel linings. While the framework is applied to railway tunnels, the approach is general and can be extended to roadway tunnels. The ultimate goal is to minimize economic losses and improve resilience of the transportation network by ensuring that individual structures, such as tunnels within the network, are resilient when subjected to extreme events.

Keywords: Tunnel fire; fire scenarios; concrete spalling; damage assessment

1 INTRODUCTION

Fire hazards are major threats and can cause severe damage to tunnel structures. There is a long list of historical tunnel fires, including some extreme events with a large number of fatalities, injuries, and significant socioeconomic impacts. On May 29, 1999, a truck crash resulted in a major fire in the Tauern Tunnel connecting the industrial areas of southern Germany and northern Italy. A total of 24 cars and 16 trucks were completely burnt. Severe concrete spalling was observed on the tunnel ceiling and sidewalls. In the area that underwent the highest temperatures, the concrete lining spalled to a depth of 400 mm over a 100 m tunnel length. Around 600 m³ of chip-size spalled concrete had to be removed after the fire. The downtime of the tunnel was three months and 6.5 million US dollars were spent on the repair work, while another 19.5 million US dollars were lost via uncollected toll fees [1]. Similar lessons can be learned from other major tunnel fire events, such as the Mont Blanc Tunnel fire in 1999 and the multiple Channel Tunnel fires that occurred in 1996, 2006 and 2008. Among the long list of tunnel fire events, although collapse or local failure of the tunnel structures due to fire are rarely observed, the serviceability and resilience of the tunnel structures are impacted, as major fire events could lead to months of downtime and millions of dollars of losses from repair and affected operations.

Tunnel fires have become a growing concern and received increasing attention in recent decades. On one hand, an increasing density in the transport of goods, especially of flammable materials, increases the amount of potential fuel, and the likelihood for a fast fire spread in the case of a fire within a tunnel space.

¹ Ph.D. Candidate, University at Buffalo
e-mail: nanhua@buffalo.edu, ORCID: <https://orcid.org/0000-0002-3046-9331>

² Assistant Professor, University at Buffalo
e-mail: atessari@buffalo.edu, ORCID: <https://orcid.org/0000-0003-0231-345X>

³ Assistant Professor, University at Buffalo
e-mail: negarkho@buffalo.edu, ORCID: <https://orcid.org/0000-0003-3228-0097>

On the other hand, modern tunnel design uses higher strength concrete and thinner linings. Although the use of high-strength concrete saves cost for materials, it may lead to severe spalling, and consequently loss of a large fraction of lining sections in the case of a fire. While the historical events identified the disastrous consequences of tunnel fires with respect to conventional materials, the newly raised concerns associated with modern tunnels further emphasize the need to design tunnels for fire.

In the existing research areas of tunnel fires, there is a relatively large body of literature on fire propagation and smoke control inside tunnels, as well as relevant provisions on evacuation routes in tunnel spaces to ensure passenger safety. However, very little focus has been placed on the damage assessment of tunnel structures due to fire. Meanwhile, fire is not widely considered in the current engineering practice of tunnel design. There are limited official documents providing guidance on designing tunnels for fire, most of which focus mainly on the design of emergency ventilation systems. No performance-based framework exists in the guidelines to design tunnel liners for loss of functionality following a fire event.

The performance-based design (PBD) method provides improved engineered solutions based on realistic characterization of fire hazards and allows higher design flexibility and a better understanding of the fire performance of tunnel structures. A comprehensive performance-based approach requires a clear definition of design objectives, assessment of performance, and demonstration of compliance with the required performance objectives. Developing an understanding for tunnel fire damages, by investigating the influences of the key parameters, provides references for PBD for fire in tunnels based on performance requirements, such as the acceptable cost (for damage repair) given a fire demand.

The objective of this paper is to propose a framework to quantify fire damage to tunnel linings considering the uncertainties in fire scenarios. While the following paper focuses on the implementation of the framework on a rail tunnel, the methodology is general and can be extended to roadway tunnels. The outcome can be used to assess downtime and decide on proper mitigation measures, such as the design of passive fire protection of tunnel linings to minimize life cycle costs and improve resilience of the tunnel structure subjected to fire.

2 METHODOLOGY

The framework for fire damage assessment of tunnels follows the three typical steps of solving structural fire engineering problems: (1) determining the fire scenario (temperature-time curve), (2) performing thermal (heat transfer) analysis, and (3) performing structural analysis that considers the thermal load. The rest of this section will introduce the three steps for tunnel fire damage assessment using a case study of a prototype rail tunnel. The geometry of the prototype cross-section is adapted from the Howard Street Tunnel in Baltimore, Maryland, which serves as an integral part of CSX operations on the eastern coast of the US [2]. As shown in Figure 1(a), the cross-section is horseshoe-shape, 6.7-meters tall and 8.2-meters wide. The real Howard Street Tunnel was built in 1895 and is made of thick masonry. In this study, it is assumed that the tunnel is instead made of concrete with a thickness of 0.3 m to reflect a modern design.

2.1 Computational fluid dynamics modelling of fire scenarios

A tunnel fire scenario describes the evolution of gas temperatures over time during a fire event, which is primarily influenced by the tunnel geometry, fire size (i.e., energy released), ventilation conditions, and characteristics of fire spread. Although the procedure of defining the fire scenario involves a high level of uncertainty due to variation of the influencing factors, the design fire curves currently being used are deterministic [3], which do not consider the fire duration, spread of fire within the tunnel, and the unique environmental conditions during a tunnel fire. Limited studies are available in the literature on quantifying uncertainties in tunnel fire demand (e.g. heat release rate) [4-6]. However, the uncertainty in temperature-time evolution of a tunnel fire has not been investigated. In addition, the evolving spatial distribution of fire temperatures within the tunnel space has not been widely studied, which impedes a realistic quantification of fire damage to the whole structure.

While experimental studies are necessary to capture the real response of engineered systems, they are costly in terms of both monetary value and time to successful execution. Numerical modelling can be used to run

a series of simulations with a range of input parameters, the results of which can be used for making design recommendations and assisting with the decision-making process. Computational fluid dynamics (CFD) modelling, though costly, provides a feasible approach to obtain both temporal and spatial fire temperatures within the tunnel and to predict traveling fire scenarios when multiple railway cars are involved in a fire. In this paper, a series of railway tunnel fire scenarios, considering the uncertainties in the heat release rate, ventilation velocity, tunnel slope, ignition point, and ignition criteria for fire spread, are modelled using Fire Dynamics Simulator (FDS), a CFD software package developed by the National Institute of Standards and Technology [7]. The modelling approaches have been verified using the experimental data from the SP small-scale test and the MTFVT program [8].

2.1.1 Tunnel model

The cross-section of the modelled tunnel in FDS is shown in Figure 1(b), where the curved ceiling is constructed using rectangular obstructions. Thermal properties of the tunnel lining were defined in the FDS model to capture the influence of thermal conduction of tunnel lining on the surface gas temperature. The thermal conductivity of concrete is taken as 1 W/m-K, specific heat as 1000 J/Kg-K, and density as 2400 kg/m³. The model includes 260 m of the tunnel in length. The ambient temperature and background pressure are set as 20 °C and 101325 Pa in the simulations.

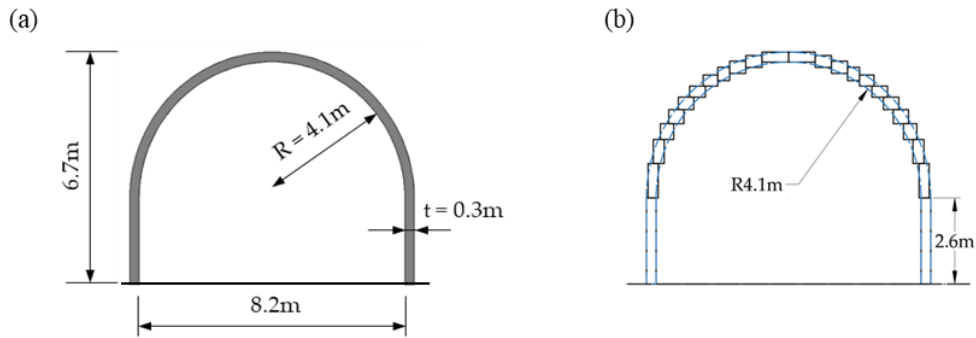


Figure 1. (a) Cross-sectional geometry of the prototype tunnel, and (b) modeled tunnel lining in FDS

Tunnel slope affects the buoyancy force of the smoke flow and back-layering length, and consequently alters the fire demand by influencing ventilation [9, 10]. Three different tunnel slopes are considered in this study to investigate the influence of slope on fire gas temperature: upward 2.2%, downward 2.2%, and zero. The selected values cover the range of practical and allowable slopes: 2.2% slope corresponds to the steepest section of the Cascade Tunnel in Washington State, which serves both passenger and freight trains.

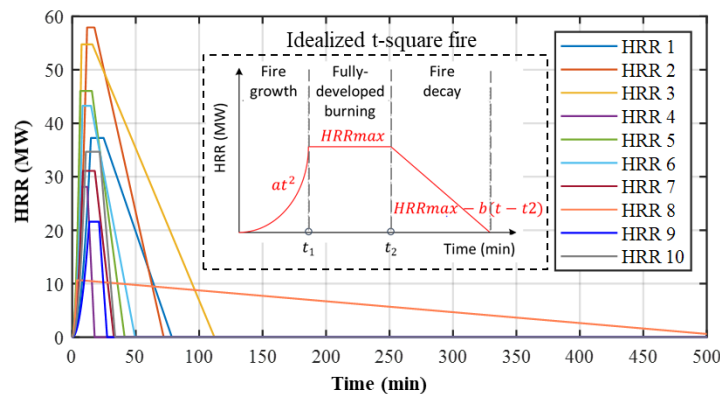


Figure 2. Randomly generated HRR curves based on available experimental data

2.1.2 Heat release rate

Heat Release Rate (HRR) describes the rate of energy released during a fire and reflects the magnitude and development of a fire. For train fires, the HRR largely depends on the combustion load of carriages while

it can also be influenced by the tunnel geometry, ventilation conditions, and fire propagation. A variety of train body types, geometry of windows and openings, and the amount of combustible material in the interior introduces a large uncertainty in determining the combustion load of a carriage. To capture the uncertainties in HRR and establish the HRR demands for passenger train fires, 10 HRR curves are generated using Latin Hypercube Sampling (LHS) [8], based on the distributions of available experimental data [6, 11]. The ten generated HRR demands, as Figure 2 shows, will be used as inputs to the FDS parametric study to investigate a series of potential fire scenarios.

2.1.3 Ventilation velocity

Ventilation of a tunnel can be achieved by either natural or mechanical (forced) means. Mechanical ventilation systems are generally classified as longitudinal or transverse based on the direction of airflow in the traffic space. Longitudinal systems ensure a longitudinal flow along the axis of the tunnel with fans at portals or distributed along the tunnel, whereas transverse systems use air ducts to circulate polluted and fresh air perpendicular to the tunnel axis [12, 13]. Practically, longitudinal ventilation systems are easier to adopt and cheaper compared to transverse systems [14]. This research only investigates tunnel fires under longitudinal ventilation.

NFPA 502 [15] requires emergency ventilation in tunnels with lengths exceeding 1000 m. For life safety concerns in tunnels operating with passenger trains, the ventilation system should be designed to create an air velocity exceeding the critical velocity (V_c). The critical velocity is defined as “the minimum steady-state velocity of the ventilation airflow moving towards the fire, within a tunnel or passageway, that is required to prevent back-layering at the fire site” [15]. The critical ventilation velocity (V_c) has been widely studied in terms of influencing factors (e.g. HRR, tunnel height, slope, etc.) and predictive models [16-21]. The critical velocity (V_c) of 2.65 m/s is calculated for the tunnel under study using Li’s equation [16], assuming HRR curves of Figure 2 (limiting to HRR values larger than 20 MW) and tunnel slope of zero.

In practice, fans may be controlled by the tunnel operator, adding uncertainty in the process due to the human-element. Given the lack of data to quantify the uncertainty in the ventilation velocity during a tunnel fire, and given the variation in detection time, operator reaction, and time needed to change a fan’s operation mode, a uniform distribution with a range of $0.8 V_c$ to $1.5 V_c$ is assumed for the ventilation velocity. The realizations of ventilation velocity are generated using LHS, as 2.45 m/s, 3.08 m/s and 3.70 m/s, based on a uniform distribution between 2.1 m/s ($0.8 V_c$) and 4.0 m/s ($1.5 V_c$). The air flow is assumed to blow at a constant velocity from the left entrance of the tunnel, while the right portal is set to be open to ambient air.

2.1.4 Modelling of the train and fire spread criteria

The size of a railcar influences the distance between the fire source and the ceiling, resulting in different blockage ratios. Considering that passenger railcar dimensions are relatively standard, the dimension of an Amtrak “Superliner” railcar [22] was adopted in this study for the train model, which is 25.9 meters long, 4.9 meters tall, and 3.1 meters wide. Five identical railcars are aligned longitudinally inside the tunnel to study the fire spread pattern (Figure 3). The distance between two adjacent railcars is 1 m. The distance from the left portal of the tunnel to the first train carriage is 50 m. The surface material of the train cars is assumed to be stainless steel, with a thermal conductivity of 15 W/m-K, specific heat of 500 J/Kg-K, and density of 7800 kg/m³. The applied HRR values are normalized by the surface areas of each railcar (except for the bottom surface), and the evolution of HRR over time is applied using piecewise linear functions.

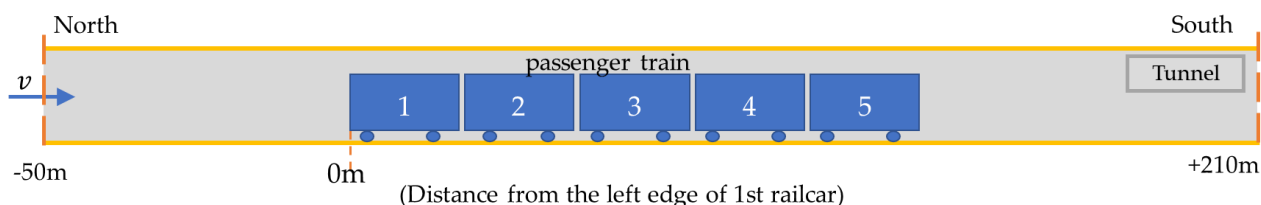


Figure 3. Schematic graph of the FDS model

When a fire occurs in a tunnel, the fire spread between railcars will exacerbate the fire size and the potential damage. Extreme fire spread has been observed in almost all of the major tunnel fires, however, research on tunnel fire spread is quite limited. Characterize the ignition condition for a real passenger carriage, due to the varying ignition sources, paths and train materials, is a complex process. Andreini et al. [23] provided ignition temperatures of the main components of a typical Italian passenger rail carriage, obtained from a series of cone calorimeter tests. The test result shows that the ignition temperatures of the seat, floor curtain, headrest, wall and ceiling material of the carriage ranges from 352-462 °C. In this study, a train carriage is considered as a lumped mass and modelled as an object with bulk thermal properties and an ignition temperature. When the surface of an object reaches the ignition temperature, it will ignite and follow one of the HRR evolution curves as defined earlier. To cover the potential range and investigate the influence of ignition conditions, three values of 300 °C, 400 °C, and 500 °C are selected as ignition temperatures. The ignition temperature is also assigned to the surfaces of train carriages. The fire can start from either the first or third car from the north portal to capture the fire initiation from one end and the middle of the train. In summary, a total of 540 simulations, considering 10 HRR demands, three ventilation velocities, three tunnel slopes, three ignition temperatures, and two fire initiation locations are conducted in FDS. For each simulation, the fire temperature-time histories were recorded at 1) different cross-sections (10m interval) to reflect temperature distribution along tunnel length, and 2) three different heights (6.4 m, 3.9 m and 1.3 m) at each cross-section to account for potential non-uniform fire damage within a cross-section.

2.2 Spalling incorporated heat-transfer analysis

The second step for damage assessment is to determine the temperatures within the tunnel lining sections. The damage level of a certain tunnel location can be evaluated based on the maximum temperature reached in a fire event. In case of a tunnel fire, different locations of the lining would be exposed to different fire temperatures, and hence undergo varied levels of damages. To investigate the total damage of the 260m length of the investigated tunnel, the fire temperature-time histories measured across the tunnel (from FDS simulations) are transferred as input data to SAFIR heat transfer analysis [24].

2.2.1 Proposed concrete spalling model

Heat-induced spalling is a major and common issue for fire performance of concrete structures [25]. This phenomenon is still not well-understood because of the complex mechanisms and large uncertainties involved. The research focusing on the subject is mostly experimental and has shown that factors such as the geometry of concrete elements, fire duration and temperature, boundary and restraint conditions, and the externally applied loads could influence spalling (more details and references are provided in [26]). Different spalling prediction models have been developed by studying macro- and micro- behaviours of concrete [27-29], yet they are unable to accurately predict spalling for a given concrete mix under certain mechanical and heating protocols, and cannot be applied to mainstream finite element software packages.

To incorporate spalling in the heat transfer analysis of SAFIR, a simplified spalling model is proposed. This paper considers that, for a given location of tunnel lining, concrete spalling is a gradual and uniform process with a constant spalling rate (i.e., describes spalling depth vs. time, with a unit of mm/min). Thus, a spalling process can be characterized using three factors: spalling start time (t_{start}), spalling rate (R_s), and the end time (t_{end}) of the process. The determination of t_{start} , R_s and t_{end} is based on the collected data from published experiments. While the large-scale experiments provide the most reliable data on potential spalling of tunnel segments, the number of investigated specimens is quite limited. This paper also investigates small- and intermediate- scale tests to expand the data pool. Figure 4 shows the spalling process from the collected data, where the tests using hydrocarbon fire curves (HC or RWS) are shown in red, and those using ISO 834 fire curve (with lower heating rate) are shown in black. The details of collected data and references are provided in Hua et al. [26]. Figure 4 shows that specimens tested under Hydrocarbon (HC) or RWS fire curves start spalling within the first five minutes of the fire because of the high heating rate. These specimens also have a higher spalling rate (2-5 mm/min). Specimens under less-intense fire conditions (e.g., ISO 834) mostly start to spall after 5-10 minutes and have a relatively mild spalling rate (1 to 3 mm/min).

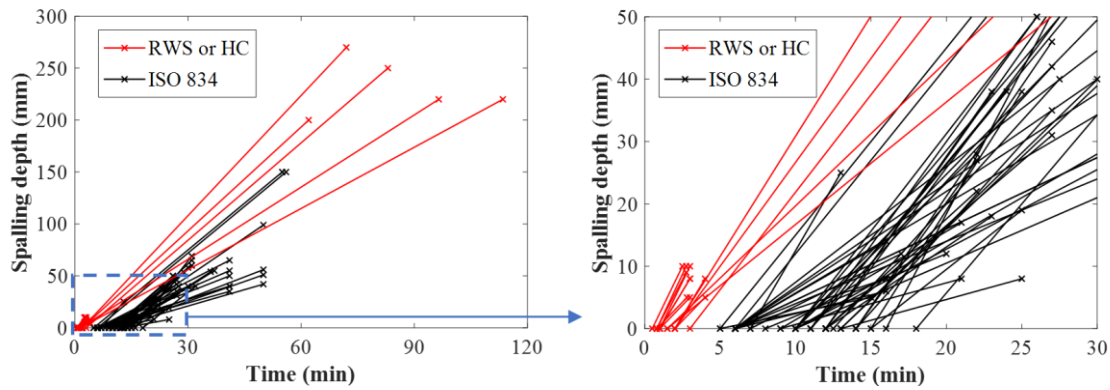


Figure 4. Experimental data for concrete spalling [26]

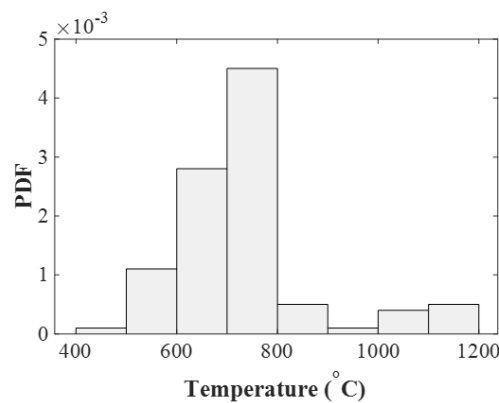


Figure 5. Probability density function of spalling start temperature [26]

This paper characterizes the spalling starting time as a function of gas temperature. That is, when the gas temperature in proximity of the tunnel lining reaches the spalling starting temperature, the concrete lining will begin to spall. Figure 5 shows the distribution of the spalling start temperatures calculated by on the spalling start time and fire curves reported from the published experiments. Most test specimens start to spall when fire temperatures reach 600-800 °C. For a practical implementation and a starting point, this paper takes the spalling start temperature as 740 °C and the spalling rate as 2.6 mm/min, which are the mean values of the collected data. However, data that could be used to determine the endpoint of the spalling process is quite limited, as many experiments were terminated shortly after the first indication of spalling (Figure 4). For modeling purposes, this paper assumes that spalling ceases when the first reinforcement layer is exposed. The assumption can be adjusted by integrating additional future experimental results.

2.2.2 MATLAB/SAFIR interactive code

To incorporate the described fire spalling model within the thermo-mechanical finite element analysis, a fine mesh has been created in SAFIR, for which the concrete cover of the reinforced concrete section is composed of relatively fine layers of concrete fibres to enable proper removal of concrete when spalling occurs. A program has been coded in MATLAB to control and update the input files of SAFIR over the duration of fire as spalling occurs. The code automatically generates input files for the SAFIR thermal analysis, decides whether spalling occurs, removes concrete layers based on the spalling rate, updates the input file (and finite element mesh) with the removed nodes and elements, restarts SAFIR to continue the thermal analysis, and finally reads output files from SAFIR for damage quantification.

In this paper, damage is defined as the volume of concrete that requires repair and replacement. While there is no consensus on how to quantify fire damage to a tunnel lining, similar statements can be found in existing standards where 300°C is recommended as a threshold for discolouring and reduced residual

strength of concrete [30–32]. Hence, the damaged volume of concrete is calculated as the volume of concrete that experiences temperatures above 300 °C. This temperature threshold is also consistent with existing experiments and observations, showing permanent material degradation above 300 °C [33, 34].

2.3 Coupled thermal-structural analysis

The third step in the framework is to investigate the structural performance of the tunnel under elevated temperatures. This section focuses on the SAFIR thermo-mechanical analysis of a 2D model of the cross-section of the prototype tunnel. The tunnel lining is constructed using 26 beam elements, and the earth resistance is modelled using 25 compression-only spring elements, as Figure 6(a) shows. The tunnel base is located 11 m below the grade and is modelled as fixed-fixed. One of the most intense temperature profiles from the 540 FDS simulations is selected to study stability of the structure. If structural stability of the tunnel is verified for an extreme fire scenario, it can be assumed that the tunnel structure will not collapse in less severe cases. As Figure 6(b) shows, the tunnel section is divided into three regions and assigned with different temperature boundaries to account for the variance in gas temperature across the height.

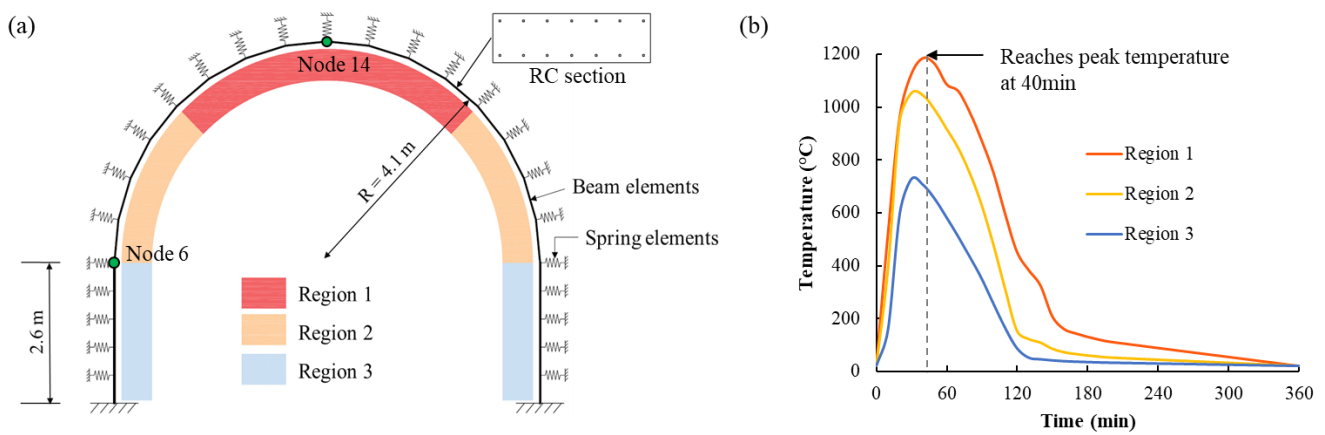


Figure 6. (a) Beam spring model of the tunnel for structural analysis, and (b) an extreme fire scenario

As for the material properties, at ambient temperature, the compressive strength of concrete is 45 MPa and the tensile strength is assumed to be zero. The tensile yield strength of the reinforcement is 414 MPa. The temperature-dependent material properties from EN 1992-1-2 [35] are applied to both concrete and steel. The applied loads on the tunnel include self-weight, vertical earth pressure, horizontal earth pressure, and surcharge. The stiffness of the compression-only springs is calculated based on Eq. 1, as a function of tunnel radius R , modulus of elasticity E , and Poisson's ratio ν of the surrounding soil [36]. Assuming a clay soil, E and ν are taken as 30 MPa and 0.4, respectively.

$$k_s = \frac{E}{1+\nu} \cdot \frac{1}{R} \quad (1)$$

The structural analysis is performed considering “with spalling” and “no spalling” cases, to obtain lower and upper bound responses. The spalled layers cannot be removed from the finite element mesh during the structural analysis in SAFIR. Thus, the spalling-induced section losses within the structural model is represented by assigning a fibre temperature of 1200 °C to spalled layers – the temperature at which concrete loses all material strength and stiffness [36] – to effectively remove the material from the analysis.

3 RESULTS

3.1 Fire scenarios

The results from the 540 FDS simulations of this study are organized and presented in two parts. The first part focuses on capturing the control fire demand and providing design recommendations. The second part investigates the spatial temperature distribution along the length and across sections of the prototype tunnel for fire damage assessment.

3.1.1 Critical fire demand

This section investigates the temperature-time curve at the critical section of the prototype tunnel, where the critical section is defined as the tunnel section that experiences the highest temperatures. Based on the distributions of the maximum temperature (T_{\max}) data, the 540 fire scenarios have been divided into three categories as a function of HRR to observe clear trends: low intensity fires ($HRR_{\max} \leq 30\text{MW}$), intermediate intensity fires ($30\text{MW} < HRR_{\max} \leq 40\text{MW}$) and high intensity fires ($HRR_{\max} > 40\text{MW}$). The mean of T_{\max} data of low and high intensity fires are 245°C and 1007°C , respectively. The distribution of T_{\max} data and the Weibull fits of low and high intensity fires are shown in Figure 7. While the distribution of T_{\max} data of low and high intensity fires show distinct peaks, no clear trends are observed in the intermediate intensity fires (not shown here), as the temperatures tend to be controlled by other parameters, such as ventilation velocity.

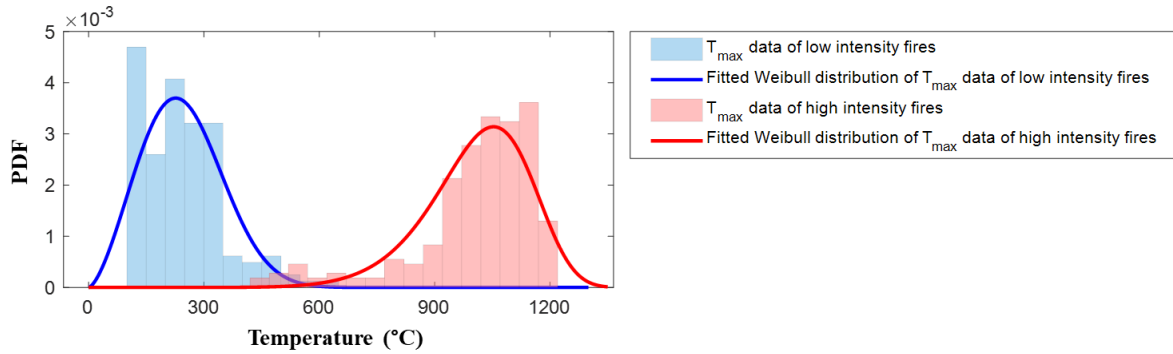


Figure 7. T_{\max} data and the Weibull fits of low intensity and high intensity fires

Table 1 provides the quantiles of T_{\max} for low and high intensity fires based on the Weibull distribution fits (values are within $\pm 10\%$ of the generated data). More results of this study, such as the data on fire growing rate and duration, can be found in Hua et al. [8]. The study provides insight on the distribution of expected fire temperature-time scenarios and demonstrates a clear trend among the proposed low and high intensity fires. For design purposes, the intermediate-intensity fires with HRR values between 30 and 40 MW can be conservatively assumed as high intensity fires.

Table 1. Quantiles of T_{\max} for low and high intensity fires

Quantile	T_{\max} ($^{\circ}\text{C}$) for low intensity fires	T_{\max} ($^{\circ}\text{C}$) for high intensity fires
80th	333	1125
85th	356	1145
90th	384	1170
95th	426	1204

3.1.2 Spatial distribution of temperature

The spatial and temporal distributions along the length and across sections of the prototype tunnel are also studied. This part focuses on the unique features of the tunnel fire scenario and provides a basis to quantify fire damage to the whole tunnel structure. The results are directly transferred as the input to the heat-transfer analysis in SAFIR. Figure 8 shows the boxplots of peak temperatures across the tunnel length. The spatial distribution pattern of the modelled tunnel fire scenarios can be summarized as follows: (1) fire temperatures in low-intensity fires are mostly below 300°C , while temperatures in high-intensity fires can be as high as 1200°C ; (2) when studying temperatures at different heights, the tunnel ceiling ($H = 6.4\text{m}$) is expected to have the most fire damage; and (3) upstream of the fire ($x \leq 0$) remains at ambient temperature in almost all the fire scenarios. Overall, the critical section with the highest temperatures, considering the potential for fire spread, is 120 m downstream of the fire ignition point ($x = 120\text{ m}$).

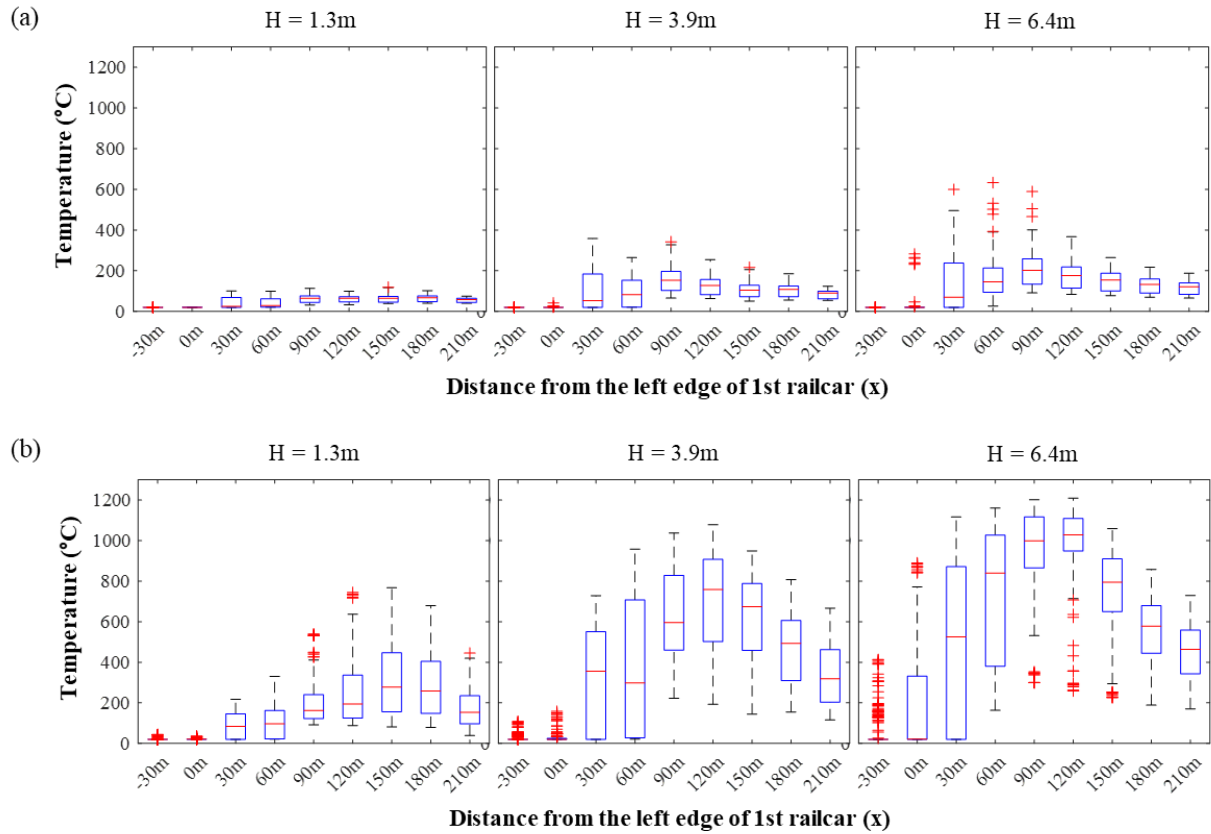


Figure 8. Boxplots of peak temperatures at different locations for (a) low- and (b) high- intensity fires

3.2 Damaged volume of concrete

This section studies the volume of concrete loss for the 540 fire scenarios based on the results of heat-transfer analyses using SAFIR and incorporating spalling. The section losses can originate from two criteria: spalling induced concrete losses and heat-induced losses where concrete temperature exceeds 300 °C, as discussed in Section 2.2. From the analysis, all the low intensity fires cause no damage to concrete lining. Figure 9(a) shows the distribution of damaged volume of concrete for high intensity fires, and Figure 9(b) shows damage when not considering spalling.

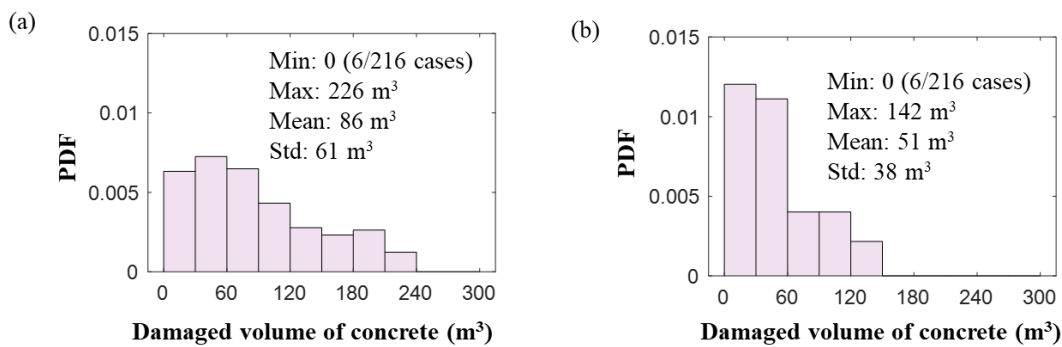


Figure 9. Damaged volume of concrete (a) considering spalling and (b) not considering spalling

The results show that extensive repair work is needed after high intensity fires. The normalized damaged volume of concrete for the worst-case scenario (226 m³), with respect to the total volume of concrete within the affected 260 m of the tunnel section, is 16%. The volume of damaged concrete provides an understanding of how much material should be replaced after a fire, as well as a reference for predicting the potential labour cost, downtime, and economic losses from service interruptions. Comparing the results with and without spalling shows that occurrence of spalling significantly increases damage. The observation emphasizes the necessity of incorporating spalling into fire damage analyses for more realistic assessment.

3.3 Structural stability

The considered extreme fire scenario does not result in a structural failure of the tunnel, as the load is redistributed within the cross section to the cooler side of the concrete lining. The arch shape of the tunnel section transfers loads in compression and prevents a tensile failure of the structure. Displacements over time for two locations have been recorded to understand the deformation of the tunnel structure under fire: one is the vertical displacement of the crown (node 14 marked in Figure 6), and the other is the horizontal displacement of the spring-line (node 6 marked in Figure 6). Figure 10 shows that the structure moves upwards at the crown and bends inward at the spring-line during the heating phase. The delayed response and propagation of heat within the section due to low thermal conductivity of concrete should be noted. The FDS fire scenario in Figure 6(b) reaches peak temperatures at approximately 40 minutes, while the maximum deflection occurs after 1 hour, during the cooling phase. Understanding the delayed response of the concrete structure is significant when considering life safety of emergency responders.

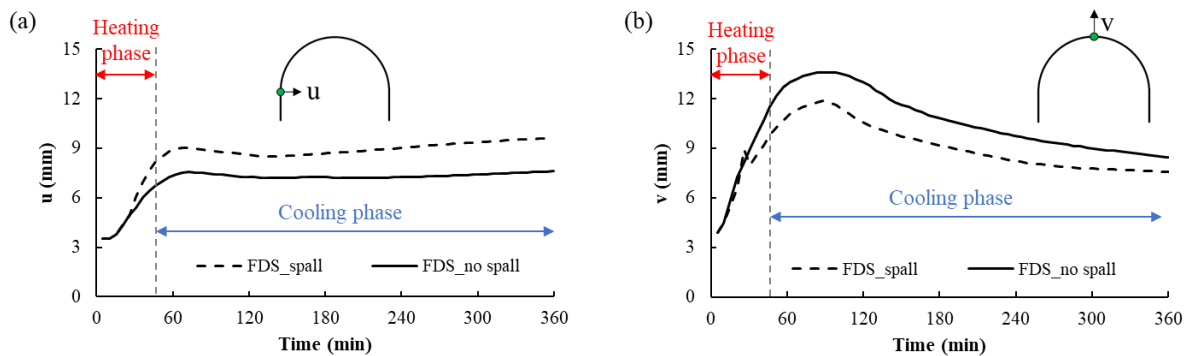


Figure 10. Displacements at (a) spring-line and (b) crown under an extreme fire scenario

4 CONCLUSIONS

This paper provides a framework to quantify fire damage to concrete tunnel linings considering the uncertainties of fire scenarios, with a spalling model incorporated. The fire scenarios were modelled using FDS including five random variables: the heat release rate (HRR), ventilation, tunnel slope, starting ignition point among the railcars, and fire spread criteria between the railcars. The spatial and temporal distributions of fire temperature within the tunnel were recorded. Damage was defined as any concrete exceeding a temperature of 300 °C. Spalling-incorporated heat transfer analyses were conducted to calculate the damaged volume of concrete. Finally, the stability of the tunnel was evaluated based on structural analyses of the tunnel section subjected to extreme fire scenarios.

Based on the results of the sample study conducted on a passenger rail tunnel, the maximum damaged volume of concrete was calculated as 226 m³, meaning that 37 concrete trucks are needed to repair the damaged sections of the tunnel. Structural analysis of the tunnel section confirmed stability of the tunnel structure under an extreme fire scenario, as was also observed in historical events, where collapse has rarely occurred. However, it was noted that the maximum demand within the tunnel section was not observed until the fire entered into the cooling phase, due to the low thermal conductivity of concrete. The proposed framework in this paper can be integrated within probabilistic risk-assessment methods to guide the design of fire protection for concrete linings. The first step is to quantify the probability of a high intensity fire based on the type of railcars passing through the tunnel. Given said probability (i.e., frequency of the fire scenario and its intensity), concrete damage (as discussed in this paper) and consequently the corresponding downtime of the tunnel can be evaluated. Combining the probability of hazard with the associated consequences (i.e., losses) provides an assessment of risk. The decision to incorporate fire protection (if any) and the corresponding design should be based on the comparison of the calculated risk versus the acceptable risk that is agreed upon with the stakeholders.

ACKNOWLEDGMENT

The authors gratefully acknowledge the CAIT Region 2 UTC Consortium and the Institute of Bridge Engineering at the University at Buffalo for their generous support. The views and conclusions contained in this document are those of the authors and should not be interpreted as representing the opinions or policies of the CAIT Region 2 UTC Consortium. Mention of trade names or commercial products does not constitute their endorsement by the CAIT Region 2 UTC Consortium.

REFERENCES

1. Leitner, A., The fire catastrophe in the Tauern Tunnel: experience and conclusions for the Austrian guidelines. *Tunnelling and Underground Space Technology*, 2001. 16(2001): p. 217-223.
2. McGrattan, K. and Hamins, A., Numerical simulation of the Howard Street Tunnel fire. *Fire Technology*, 2006. 42(4): p. 273-281.
3. EFNARC, Specification and guidelines for testing of passive fire protection for concrete tunnels linings. 2006, EFNARC.
4. Meng, Q. and Qu, X., A probabilistic quantitative risk assessment model for fire in road tunnels with parameter uncertainty. *Int. J. of Reliability and Safety*, 2011. 5: p. 285-298.
5. Cheong, M.K., Spearpoint, M., and Fleischmann, C., Design fires for vehicles in road tunnels. 2008.
6. Li, Y. and Ingason, H., A new methodology of design fires for train carriages based on exponential curve method. *Fire Technology*, 2015. 52.
7. McGrattan, K., Hostikka, S., McDermott, R., Floyd, J., Weinschenk, C., and Overholt, K., Fire dynamics simulator user's guide. NIST special publication, 2013. 1019(6).
8. Hua, N., Tessari, A., and Elhami-Khorasani, N., Quantifying uncertainties in the temperature-time evolution of railway tunnel fires. *Fire Technology*, 2020.
9. Atkinson, G.T. and Wu, Y., Smoke control in sloping tunnels. *Fire safety journal*, 1996. 27(4): p. 335-341.
10. Chow, W., Wong, K., and Chung, W., Longitudinal ventilation for smoke control in a tilted tunnel by scale modeling. *Tunnelling and Underground Space Technology*, 2010. 25(2): p. 122-128.
11. Lattimer, B.Y. and McKinnon, M., A review of fire growth and fully developed fires in railcars. *Fire and Materials*, 2018. 42(6): p. 603-619.
12. Fire and smoke control in road tunnels. 1999, PIARC Committee on Road Tunnels: Paris, France.
13. Road tunnels: operational strategies for emergency ventilation. 2011, PIARC Committee on Road Tunnels: Paris, France.
14. Design fire characteristics for road tunnels 2017, PIARC Committee on Road Tunnels: Paris, France.
15. NFPA, NFPA 502: Standard for road, tunnels, bridges, and other limited access highways 2017.
16. Li, Y.Z. and Ingason, H., The maximum ceiling gas temperature in a large tunnel fire. *Fire Safety Journal*, 2012. 48: p. 38-48.
17. Lee, S.R. and Ryou, H.S., An experimental study of the effect of the aspect ratio on the critical velocity in longitudinal ventilation tunnel fires. *Journal of Fire Sciences*, 2005. 23(2): p. 119-138.
18. Lee, Y. and Tsai, K., Effect of vehicular blockage on critical ventilation velocity and tunnel fire behavior in longitudinally ventilated tunnels. *Fire Safety Journal*, 2012. 53: p. 35-42.
19. Tanaka, F., Takezawa, K., Hashimoto, Y., and Moinuddin, K.A., Critical velocity and backlayering distance in tunnel fires with longitudinal ventilation taking thermal properties of wall materials into consideration. *Tunnelling and Underground Space Technology*, 2018. 75: p. 36-42.
20. Weng, M., Lu, X., Liu, F., Shi, X., and Yu, L., Prediction of backlayering length and critical velocity in metro tunnel fires. *Tunnelling and Underground Space Technology*, 2015. 47: p. 64-72.
21. Wu, Y. and Bakar, M.A., Control of smoke flow in tunnel fires using longitudinal ventilation systems—a study of the critical velocity. *Fire Safety Journal*, 2000. 35(4): p. 363-390.
22. Superliner(railcar).Access date: Dec. 2018; Available from: [https://en.wikipedia.org/wiki/Superliner_\(railcar\)](https://en.wikipedia.org/wiki/Superliner_(railcar)).
23. Andreini, A., Da Soghe, R., Facchini, B., and Giusti, A. Fire scenarios modelling for the safe design of a passenger rail carriage. in 9th World Congress of Railway Research. 2011. Lille, France.

24. Franssen, J.-M. and Gernay, T., Modeling structures in fire with SAFIR®: Theoretical background and capabilities. *Journal of Structural Fire Engineering*, 2017. 8.
25. Bisby, L., Mostafaei, H., and Pimienta, P., White paper on fire resistance of concrete structures. 2014, US Department of Commerce, National Institute of Standards and Technology.
26. Hua, N., Tessari, A., and Elhami-Khorasani, N., Characterizing damage to a concrete liner during a tunnel fire. Submitted to *Tunnelling and Underground Space Technology*, in revision.
27. Gawin, D., Pesavento, F., and Schrefler, B., Towards prediction of the thermal spalling risk through a multi-phase porous media model of concrete. *Computer methods in applied mechanics and engineering*, 2006. 195(41-43): p. 5707-5729.
28. Ožbolt, J. and Bošnjak, J. Modelling explosive spalling and stress induced thermal strains of HPC exposed to high temperature. in *MATEC Web of Conferences*. 2013. EDP Sciences.
29. Zeiml, M., Lackner, R., and Mang, H.A., Experimental insight into spalling behavior of concrete tunnel linings under fire loading. *Acta Geotechnica*, 2008. 3(4): p. 295-308.
30. Concrete Society, Assessment, design and repair of fire-damaged concrete structures. 2008: Camberley, UK.
31. Federal Highway Administration, Tunnel Operations, Maintenance, Inspection, and Evaluation (TOMIE) Manual. 2015: Washington DC, USA.
32. International Federation for Structural Concrete (*fib*), Fire design of concrete structures – structural behavior and assessment. 2008: Lausanne, Switzerland.
33. Du, S., Zhang, Y., Sun, Q., Gong, W., Geng, J., and Zhang, K., Experimental study on color change and compression strength of concrete tunnel lining in a fire. *Tunnelling and Underground Space Technology*, 2018. 71: p. 106-114.
34. Hager, I., Colour change in heated concrete. *Fire Technology*, 2013. 49.
35. European Committee, Eurocode 2: Design of concrete structures, in Part 1-2: General rules-structural fire design. 2004.
36. Savov, K., Lackner, R., and Mang, H.A., Stability assessment of shallow tunnels subjected to fire load. *Fire safety journal*, 2005. 40(8): p. 745-763.

COMPARATIVE FIRE BEHAVIOR OF REINFORCED CONCRETE BEAMS MADE OF DIFFERENT CONCRETE STRENGTHS

Venkatesh Kodur¹, Srishti Banerji²

ABSTRACT

This paper presents results from fire resistance tests to illustrate the comparative fire performance of reinforced concrete (RC) beams made with concretes of different strength. Four RC beams made of normal strength concrete (NSC), high strength concrete (HSC), and ultra-high performance concrete (UHPC) beams (with two different fibre combinations) were subjected to structural loading and tested under fire conditions. Results from the fire resistance tests show that UHPC beams undergo severe fire-induced spalling and exhibit lower fire resistance as compared to HSC and NSC beams. Additionally, inclusion of polypropylene (PP) fibres in UHPC beams aids in reducing spalling and increasing fire resistance in UHPC beams.

Keywords: Fire resistance; fire-induced spalling; fire tests; reinforced concrete beams; ultra-high performance concrete.

1 INTRODUCTION

Significant research in concrete technology over the last four decades has led to the development of newer concretes with enhanced strength, durability, and sustainability properties as compared to conventional concretes. The concretes utilized currently for construction is broadly grouped under normal strength concrete (NSC), high strength concrete (HSC), and ultra-high performance concrete (UHPC) based on compressive strength range. Generally, concrete below a compressive strength of 70 MPa is referred to as NSC, concrete with compressive strength in the range of 70 to 150 MPa is classified as HSC, while concrete with compressive strength above 150 MPa is designated as UHPC [1]. Recent studies have indicated that the structural members made of higher strength concretes, such as HSC and UHPC, exhibit lower fire resistance, unlike conventional NSC [2–4]. The lower fire resistance in these concrete members is mainly due to faster degradation of strength at elevated temperatures and also due to increased susceptibility to fire-induced spalling resulting from reduced permeability in higher strength concretes [5].

Numerous experimental and numerical studies on fire behaviour of structural members made of NSC, and to a lesser extent on HSC members, have been carried out. With regard to UHPC structural members, very few experimental and numerical studies have been reported, and these limited studies are mostly at material level to evaluate degradation of compressive strength of UHPC with temperature. Previous studies carried out on HSC members, have indicated addition of steel or polypropylene (PP) fibres to the concrete mix to be an effective strategy to mitigate fire-induced spalling [3]. The increased tensile strength facilitated by the presence of steel fibres, or enhanced permeability resulting from the melting of PP fibres at around 160°C during a fire event is effective in minimizing fire-induced spalling in HSC members. However, there is not much information on the fire performance of members made of UHPC incorporating steel and PP fibres. Further, there is a lack of data on comparative fire response of concrete members made of different concrete types.

¹ University Distinguished Professor, Dept. of Civil and Environmental Eng., Michigan State Univ., East Lansing, MI, USA.
e-mail: kodur@egr.msu.edu

² Ph.D. Student, Dept. of Civil and Environmental Eng., Michigan State Univ., East Lansing, MI, USA.
e-mail: banerjis@msu.edu

To evaluate comparative fire performance of different concretes, fire resistance experiments were carried out on reinforced concrete (RC) beams fabricated with different concrete types and having varying strengths. Data generated in fire resistance tests is utilized to illustrate the variations in fire performance of UHPC beams, as compared to those of NSC and HSC beams.

2 FIRE RESISTANCE TESTS

Fire resistance tests were carried out on four reinforced concrete beams, designated as NSC (plain – without fibres), HSC (plain – without fibres), UHPC-St (with steel fibers), and UHPC-StPP (with steel and polypropylene fibers).

2.1 Design and fabrication of test beams

The dimensions of the tested beams were dictated by the size of the furnace and loading equipment. The NSC and HSC beams were designed as per ACI 318 specifications [6], whereas the UHPC beams were designed based on the available best practice recommendations as no specific design provisions for UHPC members are currently available [7]. The UHPC beams had only tensile reinforcement (no shear and compression reinforcements) to take advantage of high compressive and high tensile strength provided by UHPC. Figure 1 shows the elevation and cross-sectional details of the tested RC beams.

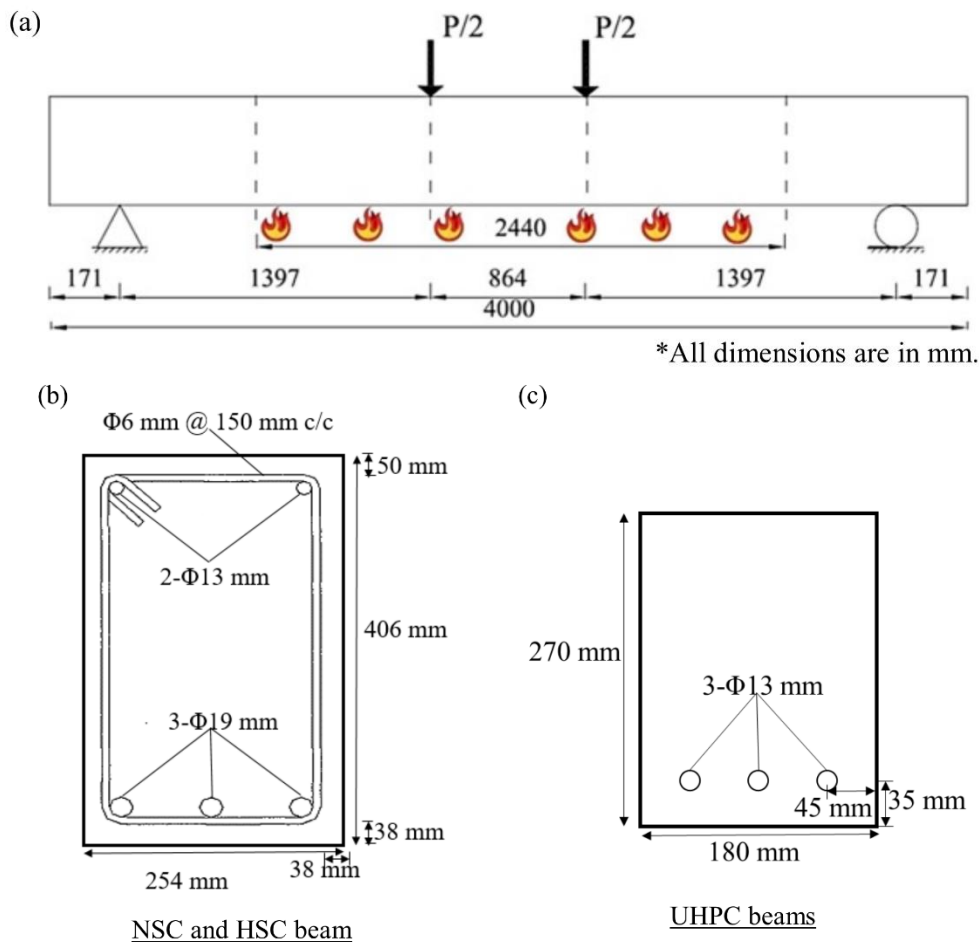


Figure 1. Elevation and cross-section of the tested RC beams.

Four batches of concrete were used for fabricating these beams and the details of mix proportions are given in Table 1. All the batches were prepared with general purpose, Type I ordinary Portland cement, and carbonate (calcareous) coarse aggregate. To optimise the density and strength, only a controlled amount of coarse aggregates were included in the UHPC mixes as compared to NSC and HSC mix. High volumes of fine mineral admixtures such as silica fume and chemical admixtures were added to UHPC batch mixes to attain the target compressive strength and workability properties in concrete. For both the UHPC mixes,

1.5% by volume fraction of steel fibres were added. The steel fibres were of straight type (without hooks) with 0.2 mm diameter and 13 mm length (aspect ratio of 65), and had tensile strength in the range of 900 to 1000 MPa. Additionally, MONOFILAMENT polypropylene fibres (0.11% by volume) with a length of 13 mm and a melting point of 160°C were added to the UHPC-StPP batch mix.

All the beams were cured in the forms for 7 days and stored in ambient conditions, maintained at about 25°C temperature and 40% relative humidity. The compressive strength of concrete were evaluated periodically during curing stage, and the measured values at 28 days and on the day of the testing is listed in Table 1. The test beams were instrumented with thermocouples, high-temperature strain gauges, and displacement transducers [4, 8]. Thermocouples were installed to monitor temperatures in steel reinforcement and concrete at different depths in cross-sections along the span of the beam. The deflection of each beam was measured by placing displacement transducers at mid-span and two point loads. Strain gauges were mounted at rebar level to supplement the data obtained through displacement transducers.

Table 1. Concrete batch mix proportions used in fabrication of RC beams.

Ingredients (kg/m ³)	NSC	HSC	UHPC-St	UHPC-StPP
Cement	390	513	472	510
Coarse aggregate	1037	1078	478	517
Fine aggregate	830	684	951	1027
Water	156	130	136	121
Water reducing agent	2	15	43	48
Silica fume	-	43	208	224
Steel fibers	-	-	118	127
Polypropylene fibers	-	-	-	1.6
Compressive strength-28th day (MPa)	52	93	145	160
Compressive strength-Test day(MPa)	58	106	167	173

St-Steel, PP-Polypropylene

2.2 Test conditions and procedure

The fire resistance tests on the beams were conducted in the structural fire testing furnace at Michigan State University (MSU) Civil Infrastructure Laboratory. This furnace is specifically designed to simultaneously apply thermal and structural loading, to which a typical beam might be subjected to when exposed to fire. Full details on the furnace can be found elsewhere [4]. The fire resistance tests were carried out by exposing the middle 2.44 m length of the beam as illustrated in Figure 1 (a). Each beam was exposed to fire from three sides (bottom and two side surfaces), while the top surface of the beam was insulated to simulate practical conditions, wherein a concrete slab is present on the top surface of the beam. The plain NSC and HSC beams were exposed to ASTM E119 [9] standard fire exposure and both the UHPC beams (UHPC-St and UHPC-StPP) were exposed to design fire (DF) exposure simulating ventilation controlled office fire, comprising of 120 min of heating phase followed by a cooling phase as shown in Figure 2.

All the RC beams were tested under simply-supported end conditions and were subjected to two point loads, each of which was placed at about 1.4 m from the end supports to simulate pure flexural loading in the portion between the two loading points as shown in Figure 1 (a). The NSC and HSC beams were subjected to two point loads of 50 kN each, which is about 55% of the beam capacity according to ACI 318 design provisions. UHPC-St and UHPC-StPP beams were subjected to two point loads of 19 kN and 22 kN each respectively, which was 40% and 45% of the ultimate flexural capacity of a UHPC-St control beam tested at room temperature. The load was applied on each beam approximately 30 minutes before the start of the fire resistance test and was maintained constant until the beam failed under fire exposure. The beams were considered to have failed when the actuator could no longer maintain the load. The test parameters are summarized in Table 2.

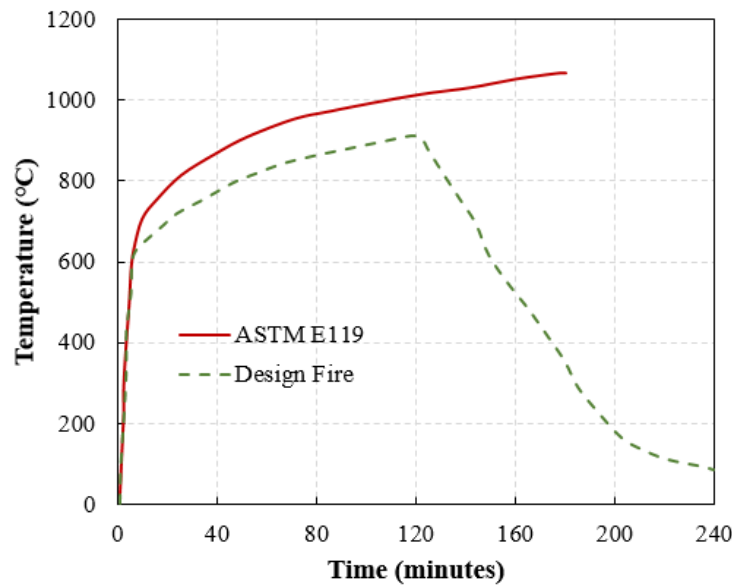


Figure 2. Time-temperature curves for fire scenarios used in the fire tests.

Table 2. Concrete batch mix proportions used in fabrication of RC beams.

Concrete type	Fire exposure	Applied load ratio (% of capacity)	Fire resistance (minutes)	Spalled volume ratio (%)	Extent of spalling
NSC	ASTM E119	55%	180	1.7	minor
HSC	ASTM E119	55%	160	3.3	moderate
UHPC- St	Design fire	40%	75	11.5	severe
UHPC- StPP	Design fire	45%	114	7.3	severe

St-Steel, PP-Polypropylene

3 RESULTS AND DISCUSSION

Data generated from the above fire tests is utilized to evaluate the comparative fire behaviour of RC beams by analysing the thermal response, structural response, spalling patterns, as well as fire resistance time.

3.1 Thermal response

The thermal response of the tested beams is compared by plotting the temperature progression in corner rebar and concrete (at mid-depth) with fire exposure time in Figure 3. While NSC and HSC beams were exposed to ASTM E119 standard fire exposure, UHPC-St and UHPC-StPP were exposed to a design fire of slightly lesser severity. The influence of cooling phase on sectional temperature progression in UHPC-StPP beam could not be assessed due to failure of the beam in the heating phase. In all four beams, the measured temperatures in concrete (at mid-depth) increase less rapidly than that in corner rebar. This can be attributed to low thermal conductivity and high specific heat of concrete that delays heat penetration to the inner concrete layers.

From the comparison of thermal response trends in Figure 3, it can be seen that although the UHPC beams were subjected to a fire scenario with lesser intensity, the sectional temperatures in both the UHPC beams increase at a faster pace as compared to HSC and NSC beams. As shown in Figure 1, UHPC-St and UHPC-StPP beams were designed to have reduced cross-sectional area to utilize high compressive strength of UHPC [10]. This smaller sectional dimensions contributed to reduction in thermal mass and utilization of more heat for temperature rise in both the UHPC beams as compared to beams made of NSC and HSC. Moreover, severe spalling occurred in UHPC-St and UHPC-StPP beams (see Table 2), which led to a loss of concrete section and in turn resulted in rapid temperature rise. In addition, UHPC has slightly higher

thermal conductivity as compared to NSC and HSC, which further resulted in faster progression of sectional temperatures in the UHPC-St and UHPC-StPP beams [11].

The rebar temperature rise in UHPC-StPP beam (with PP fibres), occurs at a slower rate than UHPC-St beam due to mitigation of spalling facilitated by the presence of PP fibres. The temperature progression at concrete mid-depth follows closely in UHPC-St and UHPC-StPP beams due to the increase in distance of the inner concrete layers from the exposed surface which reduces the adverse effect of spalling on the temperature distribution in the beam. Similarly, the rebar temperatures in HSC beam raise at a faster pace as compared to NSC beam. This trend in temperature progression can be directly attributed to the higher levels of spalling and slightly higher thermal conductivity of HSC as compared to that of NSC [12].

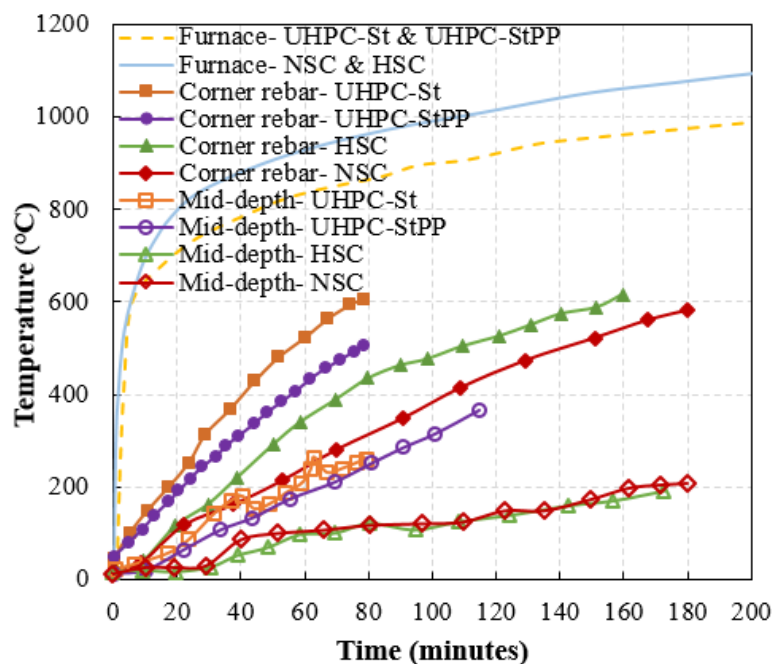


Figure 3. Comparative temperature progression in NSC, HSC, and UHPC beams.

3.2 Structural response

The relative structural response of tested beams is illustrated by plotting progression of mid-span deflection as a function of time in Figure 4. For all the beams, deflection increases with fire exposure time as a result of thermal gradients developed within the beam cross section, applied loading, and deterioration of strength and stiffness properties of concrete and reinforcing steel with temperature. In the later stages of fire exposure, the effect of creep becomes pronounced due to higher temperatures in concrete and steel.

It can be seen from Figure 4 that although the UHPC beams were subjected to lower load level and lesser fire severity, they experienced rapid rise in deflections as compared to a gradual increase in deflection in NSC and HSC beams. This trend can be attributed to the higher rebar (and concrete) temperatures in UHPC beams and also due to the faster degradation of strength and stiffness properties of UHPC at elevated temperatures, as compared to NSC and HSC [13]. Although, UHPC-StPP beam was subjected to a fire scenario with a cooling phase, this beam failed before the rebar and concrete temperatures could possibly lower in the cooling phase and thus no strength recovery was possible in this beam. Among the two UHPC beams, the UHPC-St beam experienced a more rapid increase in deflections due to higher capacity degradation that resulted from the removal of concrete due to severe spalling. In comparison, the rate of deflection increase in UHPC-StPP beam was at a moderate pace as compared to the case of UHPC-St beam without polypropylene fibres. This can be attributed to slower deterioration of stiffness owing to reduced loss of cross-section through spalling mitigation facilitated by the melting of polypropylene fibres present in UHPC-StPP.

Furthermore, the deflection-time curves in Figure 4 show that under similar load level and fire exposure, the mid-span deflection of NSC beam is lower than that of HSC beam throughout the entire duration of fire exposure. The slower progression in deflections in NSC beam than other beams can be attributed to slower

degradation of strength and stiffness properties of NSC and negligible extent of spalling, which in turn resulted in lower rebar temperatures.

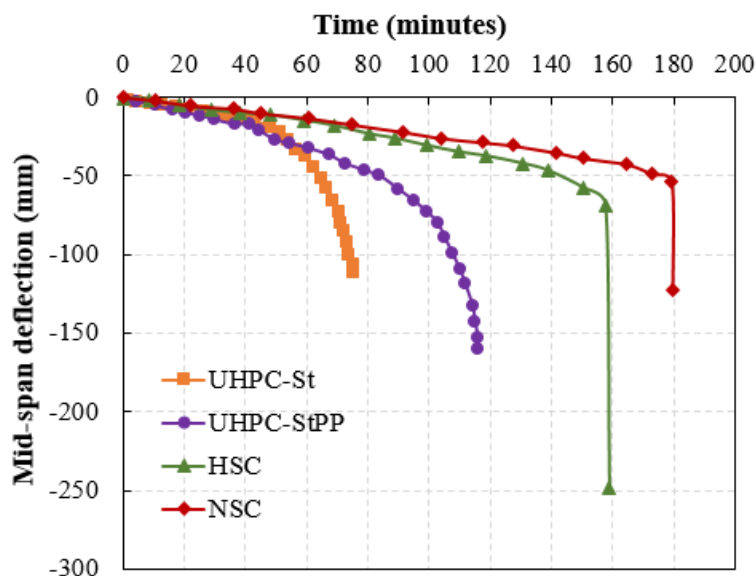


Figure 4. Comparative structural response in NSC, HSC, and UHPC beams.

3.3 Fire-induced spalling and failure mode

The extent of spalling during the fire test was recorded by taking observations made through the glass panes of the furnace. Additionally, volumetric measurements of spalling in beams, as well as visual observations, after fire exposure were made to determine the extent of spalling. Figure 5 shows the state of NSC, HSC, UHPC-St, and UHPC-StPP beams after fire resistance tests and Table 2 provides comparative extent of spalling (volumes) measured after the fire tests.

In both the UHPC beams, spalling started after 10 min into fire exposure which resulted in the loss of concrete cross-section, leading to higher sectional temperatures and faster strength degradation. The severe spalling in UHPC beams can be attributed to their dense microstructure and low permeability that impeded the pore pressure from escaping. Additionally, much of the spalling in the UHPC beams occurred in the compression zone (upper portions) of the beams (see Figure 5) and not in the bottom surface (as experienced in NSC and HSC beams). This phenomenon is due to release of pore pressure through tensile cracking in bottom portions of the UHPC beams. Both the UHPC beams failed in flexural mode exhibiting a distinct tensile cracking pattern consisting of formation of multiple micro-cracks, together with the progression of a single macro-crack in the beam mid-span. The development of numerous micro-cracks in the tension zone of the beam is owing to the bridging effect facilitated by steel fibres present in UHPC [14]. The macro-crack at mid-span in UHPC-StPP beam propagated gradually to the top surface of concrete and led to breaking up of the beam in two parts as shown in Figure 5. The extent of spalling in UHPC-StPP beam was lower (7.3%) than that in the UHPC-St beam without PP fibres (11.5%), due to enhanced permeability and partial dissipation of pore pressure through melting of polypropylene fibres at about 160 °C [4, 15].

In contrast, the extent of spalling was moderate in HSC beam (3.3%) and was almost negligible in the NSC beam (1.7%). Majority of the spalling in the NSC and HSC beams occurred in the form of surface scaling [8]. Loss of concrete can be observed in Figure 5 around the mid-span at bottom surface in HSC and NSC beams. The NSC and HSC beams failed in flexural mode followed by a longitudinal crack along the length of the tensile reinforcement, which resulted in spalling at the bottom surface of the beam prior to failure, unlike spalling in upper portions in UHPC beam during early stages of fire exposure. The spalling in NSC and HSC did not significantly impact the fire response of the RC beams as it occurred in later stages of fire exposure and closer to failure time.

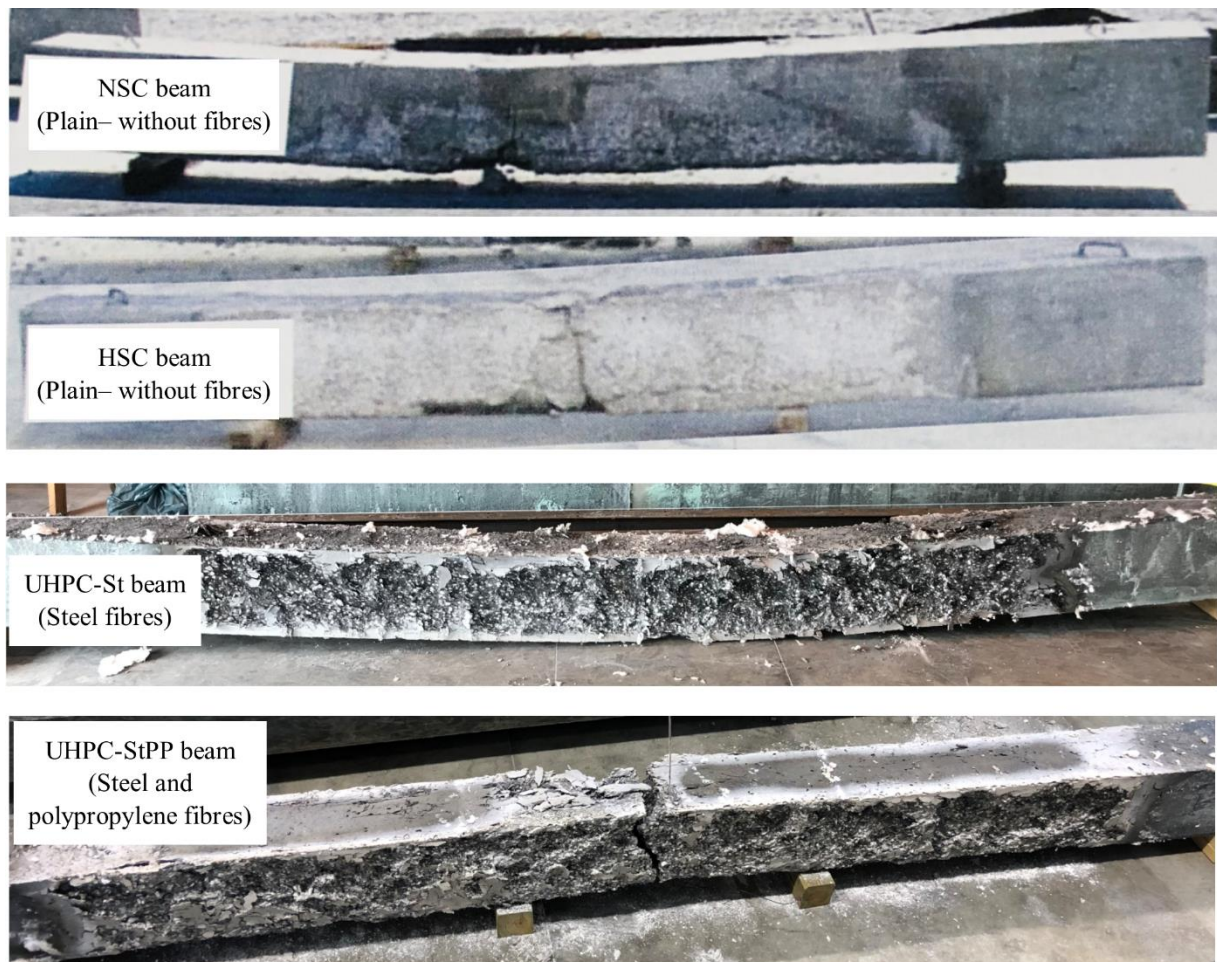


Figure 5. State of NSC, HSC, and UHPC beams after the fire resistance tests.

3.4 Fire resistance

A comparison of fire resistance of the four beams is given in Table 2. Fire resistance is the time to failure and failure is said to occur when the beam cannot sustain the applied loading. It can be seen from the tabulated results that the UHPC-St beam failed in only 75 min, while UHPC-StPP beam failed in 114 min. This shows that a significant increase in fire resistance of UHPC beams can be achieved by lowering the extent of spalling through the addition of polypropylene fibres to UHPC mix. The presence of steel fibres alone in UHPC, could not yield any considerable reduction in spalling in the tested UHPC beam. Even though fire resistance was higher in UHPC-StPP beam, the beam failed in the heating phase of the design fire (DF) exposure, 6 min before entering the cooling phase.

The UHPC beams (UHPC-St and UHPC-StPP) failed earlier than the NSC and HSC beams due to severe spalling, thinner cross-sections, and faster deterioration in mechanical properties. The HSC beam failed in 160 min, which is much higher than that of the UHPC beams but less than the NSC beam. The NSC beam had the highest fire resistance (180 min) among the four tested beams and this can be mainly attributed to minimal spalling and slower degradation of strength properties of NSC.

4 SUMMARY

Results from the experimental study show that UHPC beams exhibit lower fire resistance as compared to NSC and HSC beams. The fire resistance of UHPC beams was significantly lower due to higher spalling levels resulting from their lower permeability, than NSC and HSC beams, where permeability is high. Besides, in comparison to NSC and HSC beams, the extent, location, and time of spalling are distinct in the UHPC beams. Spalling in UHPC beams occurs in the upper portion (compression zone) during early stages of fire exposure, whereas spalling in NSC and HSC beams takes place predominantly in bottom part of the beam and in later stages of fire exposure. The fire resistance tests also showed that the presence of

polypropylene fibres in UHPC beam helps in lowering fire-induced spalling by relieving the pore pressure, and thereby increasing its fire resistance. These results clearly infer that strength (or type) of concrete has a major influence on fire performance of RC beams, including spalling. Therefore, this aspect has to be given consideration in fire resistance design of RC beams.

REFERENCES

1. Kodur, V., & Naser, M. (2020). Structural fire engineering. McGraw Hill Professional London.
2. Kahanji, C., Ali, F., & Nadjai, A. (2016). Explosive spalling of ultra-high performance fibre reinforced concrete beams under fire. *Journal of Structural Fire Engineering*, 7(4), 328–348.
3. Khaliq, W., & Kodur, V. (2018). Effectiveness of polypropylene and steel fibers in enhancing fire resistance of high-strength concrete columns. *Journal of Structural Engineering*, 144(3), 04017224. [https://doi.org/10.1061/\(ASCE\)ST.1943-541X.0001981](https://doi.org/10.1061/(ASCE)ST.1943-541X.0001981)
4. Banerji, S., Kodur, V., & Solhmirzaei, R. (2020). Experimental behavior of ultra high performance fiber reinforced concrete beams under fire conditions. *Engineering Structures*, 208, 110316. <https://doi.org/10.1016/j.engstruct.2020.110316>
5. Kodur, V. K. R. (2000). Spalling in high strength concrete exposed to fire: concerns, causes, critical parameters and cures. In *Advanced Technology in Structural Engineering* (pp. 1–9). Presented at the Structures Congress 2000, Philadelphia, Pennsylvania, United States: ASCE. [https://doi.org/10.1061/40492\(2000\)180](https://doi.org/10.1061/40492(2000)180)
6. Committee, A. C. I. (2019). Building code requirements for structural concrete (ACI 318-19) and commentary (ACI 318R-19). Farmington Hills, MI: American Concrete Institute.
7. Banerji, S., Kodur, V. K. R., & Solhmirzaei, R. (2019). Fire response of ultra high performance concrete beams. In *International Interactive Symposium on Ultra-High Performance Concrete* (Vol. 2(1)). Albany, New York, USA: Iowa State University Digital Press. Retrieved from https://www.extension.iastate.edu/registration/events/2019UHPCPapers/UHPC_ID53.pdf
8. Dwaikat, M. B., & Kodur, V. K. R. (2009). Response of restrained concrete beams under design fire exposure. *Journal of Structural Engineering*, 135(11), 1408–1417. [https://doi.org/10.1061/\(ASCE\)ST.1943-541X.0000058](https://doi.org/10.1061/(ASCE)ST.1943-541X.0000058)
9. ASTM E119-19. (2019). Standard Test Methods for Fire Tests of Building Construction and Materials. West Conshohocken, PA: American Society of Testing Materials.
10. Sritharan, S. (2015). Design of UHPC Structural Members: Lessons Learned and ASTM Test Requirements. *Advances in Civil Engineering Materials*, 4(2), 113–131. <https://doi.org/10.1520/ACEM20140042>
11. Kodur, V., Banerji, S., & Solhmirzaei, R. (2020). Effect of Temperature on Thermal Properties of Ultrahigh-Performance Concrete. *Journal of Materials in Civil Engineering*, 32(8), 04020210. [https://doi.org/10.1061/\(ASCE\)MT.1943-5533.0003286](https://doi.org/10.1061/(ASCE)MT.1943-5533.0003286)
12. Kodur, V. (2014). Properties of Concrete at Elevated Temperatures. *ISRN Civil Engineering*. Review Article. <https://doi.org/10.1155/2014/468510>
13. Abid, M., Hou, X., Zheng, W., & Hussain, R. R. (2019). Effect of Fibers on High-Temperature Mechanical Behavior and Microstructure of Reactive Powder Concrete. *Materials*, 12(2), 329. <https://doi.org/10.3390/ma12020329>
14. Yoo, D.-Y., Banthia, N., & Yoon, Y.-S. (2016). Flexural behavior of ultra-high-performance fiber-reinforced concrete beams reinforced with GFRP and steel rebars. *Engineering Structures*, 111, 246–262.
15. Li, Y., Tan, K. H., & Yang, E.-H. (2018). Influence of aggregate size and inclusion of polypropylene and steel fibers on the hot permeability of ultra-high performance concrete (UHPC) at elevated temperature. *Construction and Building Materials*, 169, 629–637. <https://doi.org/10.1016/j.conbuildmat.2018.01.105>

MODELING THE STRUCTURAL BEHAVIOR OF REINFORCED CONCRETE WALLS UNDER ISO FIRE EXPOSURE

Mohsen Roosefid¹, Marie Helene Bonhomme², Pierre Pimienta³

ABSTRACT

Despite a century of experience and a great deal of effort, considering the risk of thermal instability of concrete when exposed to fire is still in many cases a very difficult task as it includes many uncertainties in real practice. Moreover, there is lack of validated numerical models for predicting realistic behaviour of concrete structural elements under fire exposure.

In the framework of the international benchmark “Vulcain tests on 3 Walls”, three full scale ISO fire tests on a reinforced concrete wall, simultaneously subjected to a constant uniaxial compressive load, were conducted in CSTB in Paris, France. The duration of these tests exceeded 120 minutes. In order to assess the capability of available finite elements (FE) models to represent reinforced concrete structural behaviour under fire exposure, IRSN, within the scope of the Vulcain benchmark, developed a concrete model with help of Mazars isotropic continuum damage mechanical model [1] ran with the CAST3M software [2]. Also, the numerical simulation of three full scale ISO fire tests of Vulcain was carried out with the help of a FE model that takes into account the values of the concrete thermomechanical parameters previously identified. The numerical model is composed of two different parts, one for heat transfer analysis and the other one for structural analysis based on a 3D FE model including concrete and reinforcing steel meshes. It is illustrated through this numerical investigation that the proposed model can predict the thermomechanical behaviour of reinforced concrete walls under fire exposure.

Keywords: Concrete structures; finite element modelling; damage model; reinforced concrete walls; transient strain

1 INTRODUCTION

Fire is a major risk for the safety of the nuclear facilities that can act on the building structures as an external and internal aggression. Reinforced concrete structures are widely used in the nuclear facilities, in which fire can induce severe damages (cracks, fissures and spalling etc.), and therefore the impact of fire needs to be considered carefully through a combined structural and fire engineering assessment. The reinforced concrete bearing walls in the nuclear facilities have to be designed for minimum two hours of fire resistance according to the regulations of the French “Autorité de Sûreté Nucléaire” (Nuclear Safety Authority), especially due to their effective role in the fire sectorization. Moreover, the nuclear requirements e.g. the confinement of radioactivity impose additional constraints on the fire safety provisions in order to limit the concrete cracking or spalling risk. However, more evidence is still necessary to confirm such fire

¹ PhD, Civil Engineer, Nuclear Safety Division, Equipement ans Struture Assessment Departement, Civil Engineering Assessment Section, IRSN
e-mail: mohsen.roosefid@irsn.fr

² Head of Section, Nuclear Safety Division, Equipement ans Struture Assessment Departement, Civil Engineering Assessment Section, IRSN
e-mail: marie-helene.bonhomme@irsn.fr

³ Vice head of Division, Fire Studies and Tests Division, Safety, Structures and Fire Direction, CSTB, Université Paris Est
e-mail: pierre.pimienta@cstb.fr, ORCID: <https://orcid.org/0000-0002-9087-5657>

performance of concrete structures because there are limited data available, especially regarding to the degradation of concrete structures due to ageing related phenomena.

In order to gain a deeper understanding, three full-scale reinforced concrete wall tests were carried out in CSTB in the framework of the International benchmark “Vulcain tests on 3 Walls”. The aim of this work is to provide the possibility to check the validity of the advanced modelling which is more and more widely applied to investigate such type of structure system in fire safety engineering. In consequence, a numerical model developed on the basis of a finite element (FE) computer code has been applied to these tests. The calculated results were then compared to experimental ones, from which one can get an accurate idea about the precision of the numerical model.

2 VULCAIN FIRE TESTS

Three full-scale reinforced concrete walls of section 1.2 m width, 0.2 m thick and 3.0 m height were exposed on one side to ISO 834-1 fire with 3 different levels of uniaxial mechanical loading (0, 100 and 1100 kN). Each wall involved an ordinary concrete (f_c 28 days = 32 MPa) and was reinforced by a steel mesh (rebar \varnothing 5.5 mm, mesh 11.9 x 11.9 mm²) positioned at 5 cm from the shuttered surface. All the walls were tested at the age of 2 years. The wall specimens were loaded before the fire test and then the load was maintained constant throughout the fire test. The boundary conditions at the top and the bottom of the walls were pivot connections centred on the thickness allowing only rotation along the length horizontal axis. No spalling was observed on any of the 3 walls [8].

3 NUMERICAL INVESTIGATION OF THE FIRE TESTS

Within the scope of the Vulcain benchmark, it is intended to conduct a numerical study on the basis of advanced calculation models validated against the fire tests in order to develop appropriate design guidelines on the stability of concrete walls when exposed to fire and external mechanical loading [8]. The three fire tests described above constitute then ideal experimental evidence to check the validity of numerical design tools. In consequence, Vulcain fire tests have been subjected to a specific numerical investigation with help of a 3D structural FE model. The numerical model is composed of two different parts, one for heat transfer analysis and another one for mechanical analysis. In the mechanical analysis, the modelling of fire behaviour of concrete involves the use of damage models that have the ability to compute time to failure. For this purpose, Mazars’ damage model was used in which an elasticity model and damage theory are coupled. As far as reinforcing steel mesh is concerned, its behaviour was modelled as elastic-perfectly plastic according to EN 1992-1-2 [10].

3.1 Modelling

Experiments have brought to light the complex mechanical behaviour of concrete structures in fire conditions. Few models describe this behaviour and their implementation in a finite elements method is scarce.

The present analysis is based on elasticity coupled with Mazars’ damage model. In this regard, a number of comments need to be made. Firstly, a suitable model should respect the non-symmetry of behaviour between tension and compression. Secondly, the concrete presents a strong heterogeneity characterised by the presence of many defects (pores, micro-cracks...). Damage mechanics is particularly suitable to describe materials containing micro defects such as porosity, cavities, cracks that alter the rigidity of the macro material. Moreover damages have been evidenced in the fire tests and should be taken into account. In consequence, we decided to model the concrete behaviour with a damage mechanics model.

Additionally, one important choice is that the model must allow the finite element calculation of concrete structures in fire. Moreover, its final industrial use imposes robustness and easy implementing. In general the finer the description of the material behaviour, the bigger the problems of numerical convergence are in concrete structures simulation, thus in practice limiting utility of the modelling. All these considerations

brought us to model the concrete behaviour thanks to an elastic damage mechanics model (Mazars model), which is implemented in CAST3M finite element code.

3.1.1 Mazars's elastic damageable model

The Mazars's constitutive model is an elastic model that includes damage theory that is based on the concept of effective stress [9]. The concrete is supposed to behave elastically and to remain isotropic, and it is assumed that only the elastic properties of the concrete are affected by damage. The coupling of elasticity and damage processes is achieved by substituting the nominal stress tensor, σ , by the effective stress tensor, $\tilde{\sigma}$, in accordance with the strain equivalence principle. This leads to:

$$\sigma = (1 - D) \cdot \tilde{\sigma} \quad (1)$$

where D is the damage parameter.

The damage parameter D is defined as a combination of two damaging modes defined by D_t and D_c , for tensile and compressive states of stress, respectively, and ranges between 0 and 1 ($0 < D < 1$).

When D is 0, the concrete is undamaged, whereas a value close to 1 indicates a rupture of the concrete.

The damage is controlled by the equivalent deformation, $\tilde{\varepsilon}$, who takes into account only the positive value of the principal strain:

$$\tilde{\varepsilon} = \sqrt{\langle \varepsilon_1 \rangle_+^2 + \langle \varepsilon_2 \rangle_+^2 + \langle \varepsilon_3 \rangle_+^2} \quad (2)$$

where $\langle \varepsilon_i \rangle_+$ are defined as follows:

$$\langle \varepsilon_i \rangle_+ = \varepsilon_i \quad \varepsilon_i \geq 0 \quad (3)$$

$$\langle \varepsilon_i \rangle_+ = 0 \quad \varepsilon_i < 0$$

According to the damage model, damage occurs when the state of tension in the material reaches a certain threshold K . The damage occurrence criterion is expressed:

$$f(\varepsilon, D) = \tilde{\varepsilon} - K(D) = 0 \quad (4)$$

with $K(D) = \varepsilon_{D0}$ if $D = 0$ in which ε_{D0} is the strain threshold.

The parameters D_t and D_c are explicitly related to the equivalent strain, $\tilde{\varepsilon}$, and the strain threshold, ε_{D0} . The associated equations are, respectively, for tension and compression:

$$D_t = 1 - \frac{\varepsilon_{D0}(1-A_t)}{\tilde{\varepsilon}} - \frac{A_t}{\exp[B_t(\tilde{\varepsilon}_M - \varepsilon_{D0})]} \quad (5)$$

$$D_c = 1 - \frac{\varepsilon_{D0}(1-A_c)}{\tilde{\varepsilon}} - \frac{A_c}{\exp[B_c(\tilde{\varepsilon}_M - \varepsilon_{D0})]} \quad (6)$$

The parameters A_t , A_c , B_t , and B_c , describe the shape of the stress-strain curve and can be identified on the basis of the uniaxial monotonic loading in tension and compression tests.

3.1.2 Parameters calibration

The identification of the evolution of the damage parameters of the Mazars model has been performed on the basis of tests results carried out within the framework of Mindeguia's thesis [3]. The procedure of identification of the Mazars' model parameters will not be reported in the present paper.

Figure 1 presents the evolution of the concrete compressive damage parameters of the Mazars model.

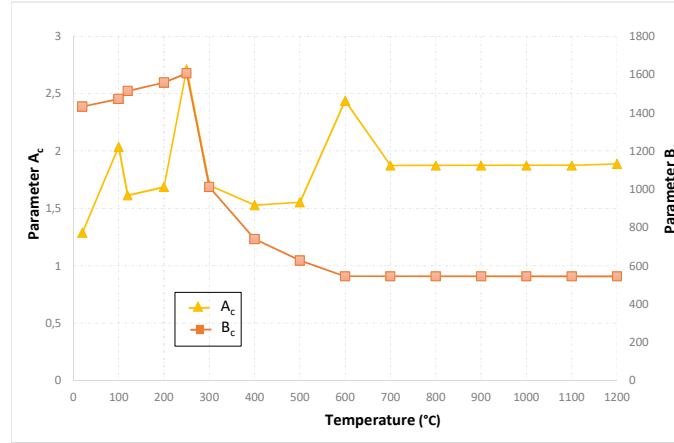


Figure 1. Parameters A_c et B_c as a function of temperature

In tension, the concrete behaviour is considered elastic up to the peak. Thus, the damage threshold in equation (5) was expressed in strain at peak, i.e., ($\varepsilon_{D0} = \frac{f_t}{E}$) where E is the Young modulus of elasticity, and f_t the tensile strain at peak.

The post-peak in tension is calibrated using the energetic-regularization technique based on the so-called Hillerborg method [5] in which it was demonstrated that damage is typically diffuse for reinforced concrete structures. The Mazars' model parameter B_t , driving the shape of the strain softening, can be written as follows:

$$B_t = \frac{h f_t}{G_f} \quad (7)$$

where G_f is the fracture energy and h corresponds to the size of the finite element.

In this framework, identification of numerical values of the constitutive equations in tension has been performed with the Hillerborg approach. In a second approach, the calculations ran to identify the parameter values were also performed assuming a non-local application of the Mazars model in order to avoid mesh dependency at the structural level.

The Mazars' model parameter A_t is taken constant and equal to 0.8 and -10 for nonlocal technique and Hillerborg approach, respectively. Moreover, the use of the non-local formulation of Mazars model requires the introduction of a characteristic length which is estimated at three times the maximum aggregate size [4]. However, this technique tends to smoothen the discontinuities and thus makes the study of the cracks harder, as shown in Figure 2.

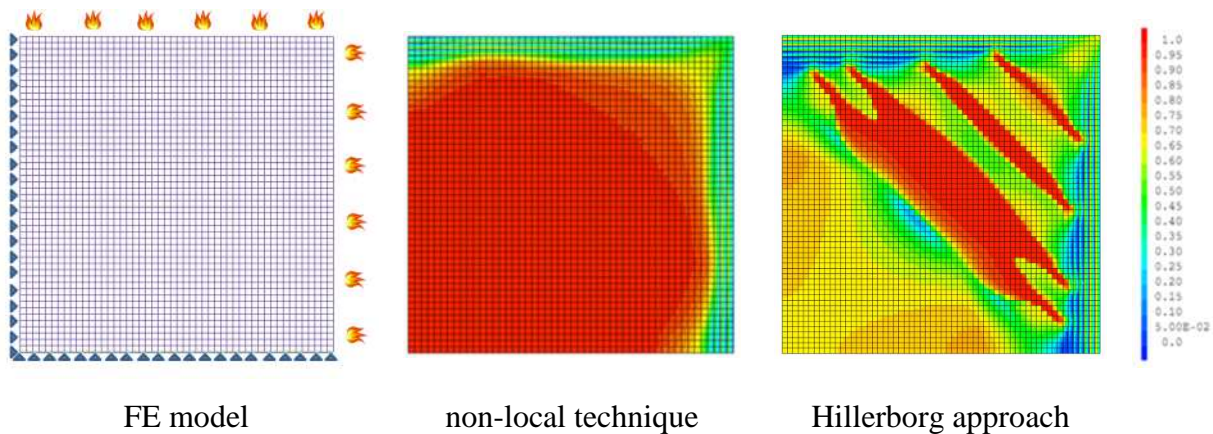


Figure 2. Damage comparison between two regularization techniques used

In order to evaluate the quality of identification and the pertinence of the model, a 3D Finite Element model is developed under computer code CAST3M, and is validated against the fire tests carried out within the framework of the thesis of Miah [7]. An example of modelling for a concrete slab subjected to ISO 834-1 fire under 1.5 MPa biaxial compressive loading is given in terms of vertical displacement versus time with respect to both nonlocal technique and Hillerborg approach, as shown in Figure 3. The comparison of the experimental curve with the adapted model using Hillerborg approach appears to be in good agreement. The remaining difference between predicted with Hillerborg approach and measured displacement can be explained by the reduction of thickness due to spalling which has not been considered in the model.

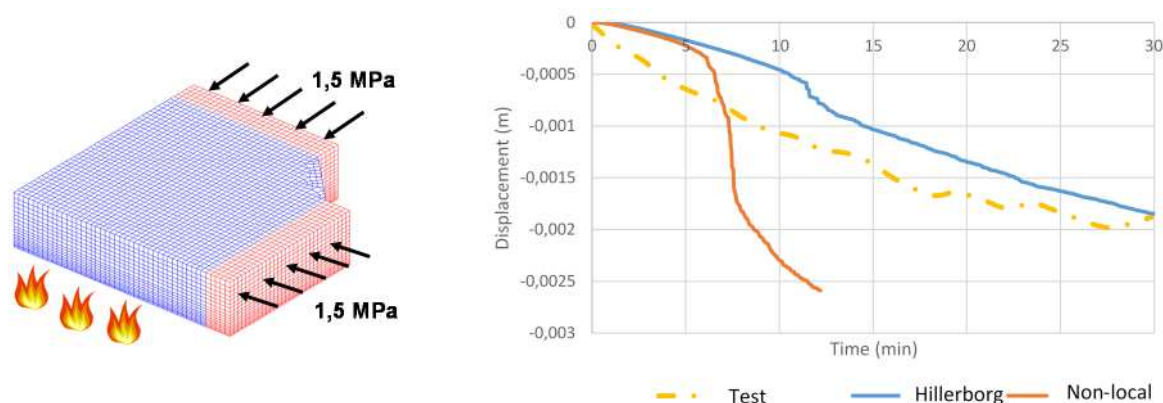


Figure 3. Detail of the structural modelling (left) and comparison between predicted and experimentally measured out of plane displacement (right)

3.2 Heat transfer analysis

In the heat transfer analysis, the heating of all of the walls was predicted with help of a 2D model using the cross section of the walls. Their thermal properties are those given in EN 1992-1-2 [10].

On the exposed side of the walls the net heat flux is based on heat transfer by convection and radiation. The coefficient of heat transfer by convection on the exposed face is taken as $\alpha_c = 25 \text{ W/m}^2\text{K}$ according to EN 1991-1-2 [11] for a member exposed to the standard temperature–time curve.

A comparison of calculated temperatures with test temperatures for different distance from exposed face in cross section through the walls is illustrated in Figure 4.

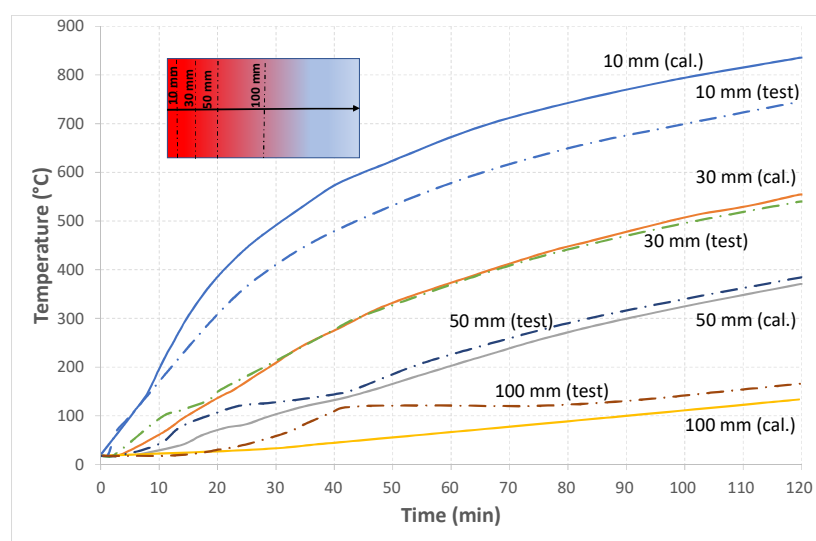


Figure 4. Comparison between numerical and experimental temperatures of the studied walls

From this comparison, a good agreement between test and numerical modelling is evidenced, which constitutes also a good basis for mechanical analysis.

3.3 Mechanical behaviour of the walls

The structural analysis is based on a structural model that takes into account concrete wall and reinforcing steel mesh (Figure 5).

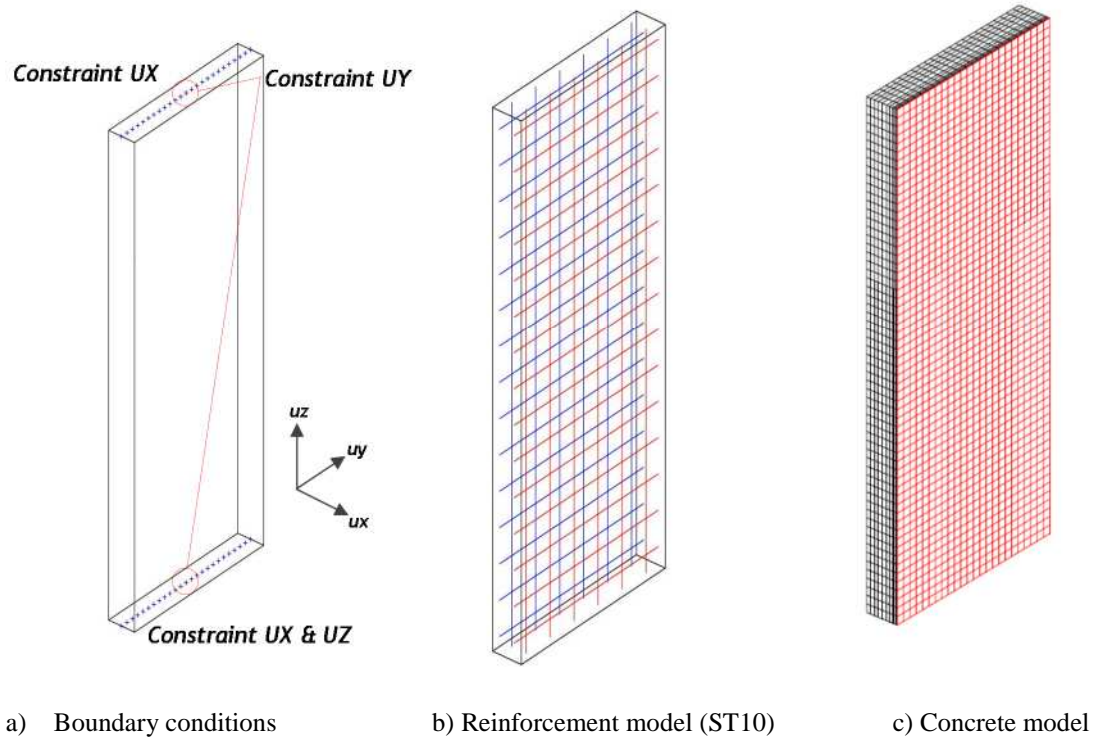


Figure 5. Detail of the structural modelling

The global structural behaviour of the walls is analysed on the basis of previously calculated temperature field. The simulated results of the walls were compared to the experimentally measured deflection by the ratio of deflection (w) to maximal experimentally measured deflection of the walls ($w_{\max, \text{test}}$), versus time, as shown in Figure 6. It can be observed that globally the numerical simulations follow quite closely the experimental results, except for the wall loaded at 1100 kN in which the difference between predicted and measured displacement appears significant. This behaviour can be explained by the fact that the elaborated model does not take into account transient thermal strain, observed in the experiments where the concrete is submitted simultaneously to mechanical and thermal loads, which has an influence on the structural response. As a consequence, the wall loaded at 1100 kN induces more transient thermal strain which leads to lower thermal expansion than the other walls, thus creating a lower thermal curvature. Moreover, it can be seen that the predicted deflections using Hillerborg approach are generally in good agreement with the experimentally measured deflection. However, this observation is not confirmed with the measured lower deflection of the wall loaded at 1100 kN.

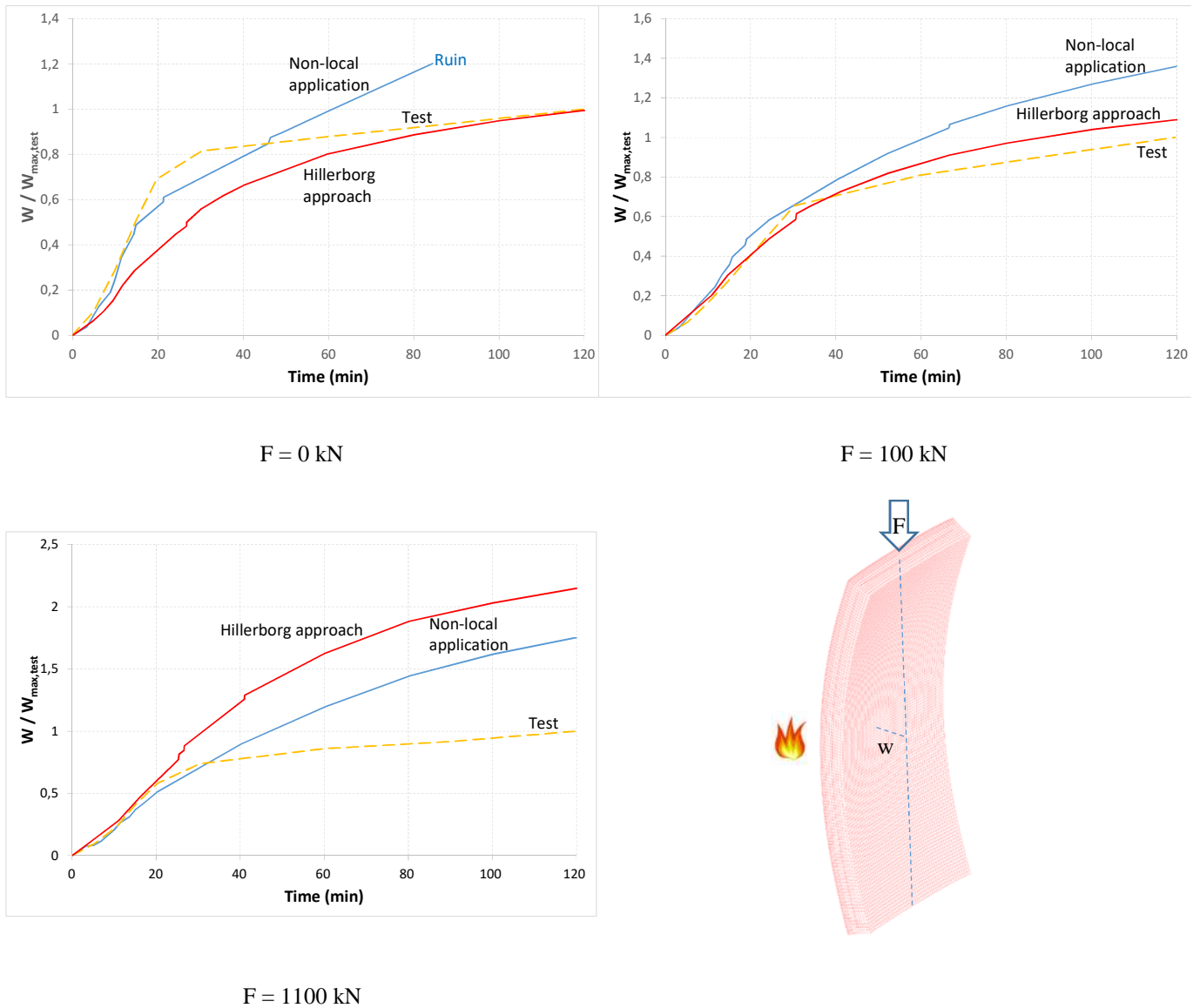


Figure 6. Comparison between numerical and experimental measured deflections, w , of the 3 walls loaded at 0, 100 and 1100 kN

Figure 7 displays maps of damage in transverse section at the mid-height of the wall loaded at 100 kN determined from calculations run using Hillerborg approach at 5, 15, 30 et 120 minutes of fire exposure. These results are in good agreement with the results reported in the literature. Indeed, the reason that concrete damage occurs near the exposed surface is due to the stress redistribution through the wall thickness. This behaviour is mainly explained by the differential thermal dilatation and that of the loss of stiffness, caused by the temperature gradient through the thickness of the wall. At the beginning of the analysis, the concrete inside the wall is cold so a tensile load is applied by the exposed surface. At this time the compressive stress is therefore increasing in the exposed surface and decreasing in the middle, becoming tensile stresses; the compressive stress increases in the hot and cold surfaces with the increasing applied compressive loading.

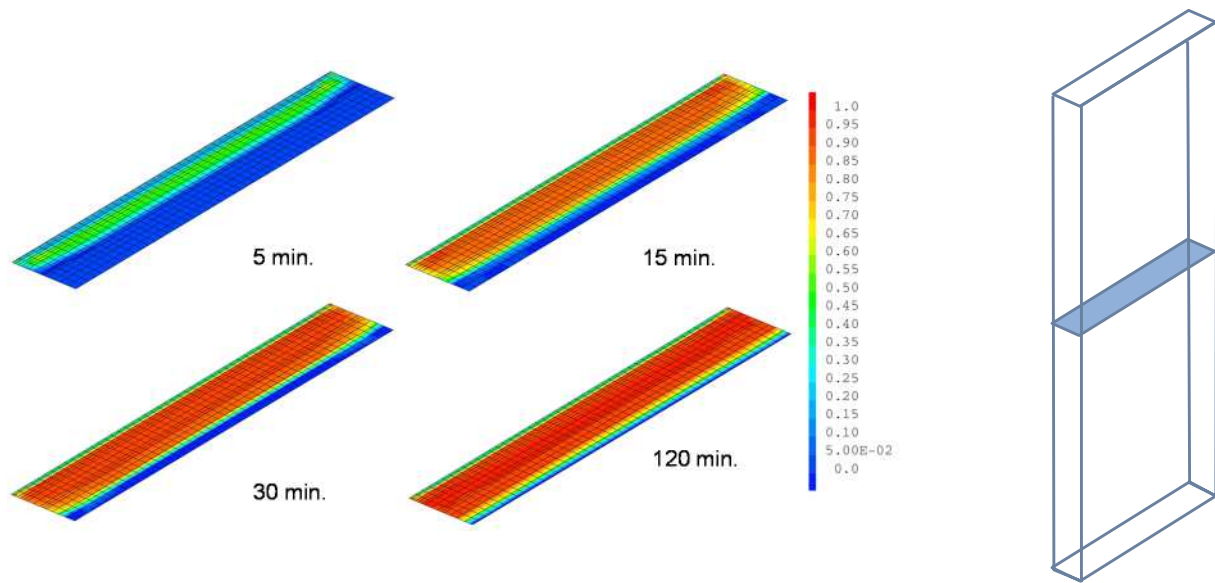


Figure 7. Distribution of the modelled damage in transverse section at the mid-height of the wall loaded at 100 kN

4 CONCLUSIONS

Numerical simulations of fire behaviour of reinforced concrete bearing walls demonstrate that the Mazars' elastic damageable model can be relevant for predicting the global structural behaviour of reinforced concrete structures exposed to fire but thermo-mechanical modelling of concrete has to take into account transient thermal strain. These improvements are currently undertaken by adding a new parameter in the thermo-mechanical behaviour law.

However, the local behaviour such as deshydration processes and strain incompatibility effects between cement paste and aggregates cannot be taken into account in an accurate way. In consequence, the numerical simulations would need to be adapted when such type of conditions have a significant contribution to the global structure behaviour.

REFERENCES

1. Mazars, J., Application de la mécanique de l'endommagement au comportement non linéaire et à la rupture du béton de structure, PhD Thesis. Univ. Paris 6, ENS Cachan. France, 1984.
2. Verpeaux P., Charras T. and Millard A., CASTEM 2000 : une approche moderne du calcul des structures, Calcul des Structures et Intelligence Artificielle, ed. par Fouet J-M., Ladevèze P. et Ohayon R, Pluralis, 1988, pp. 261–271.
3. Mindeguia, J. C., Contribution Expérimental a la Compréhension des risqué d'Instabilité Thermiques des Béton, PhD Thesis, Université de Pau et des Pays de l'Adour, France, 2009.
4. Bazant, Z. P. and Oh, B. H., Crack band theory for fracture of concrete, Materials and Structures, Vol. 16, 1983, pp. 155-177.
5. La Borderie, C., Stratégies et modèles de calculs pour les structures en béton, HDR Thesis, Université de Pau et des pays de l'Adour, France, 2003.
6. Bamonte, P., Felicetti, R., Kalaba, N., and Monte, F., Modelling the structural behaviour of R/C walls exposed to fire, 2016.
7. Jihad, M., M., The Effect of Compressive Loading and Cement Type on the Fire Spalling Behaviour of Concrete, PhD Thesis, Université de Pau et des pays de l'Adour, France, 2017.
8. Jihad, M., M., Pinoteau N. and Pimienta. P, A thermomechanical experimental investigation on 3 loaded concrete walls exposed to ISO 834-1 fire, 2019.

9. Kachanov, M., Effective elastic properties of cracked solid: critical review of some basic concepts. *Applied Mechanics Reviews* 45, 304–335. 1959.
10. CEN, EN 1992-1-2, Eurocode 2: Design of concrete structures, Part 1–2: General rules - structural fire design, European Committee for Standardisation, 2005.
11. CEN, EN 1991-1-2, Eurocode 1: Actions on structures, Part 1-2: General actions - Actions on structures exposed to fire, European Committee for Standardisation, 2003.

NUMERICAL INVESTIGATION OF THE STRUCTURAL RESPONSE OF ECCENTRICALLY LOADED REINFORCED CONCRETE COLUMNS EXPOSED TO NON-UNIFORM HEATING AND COOLING

Patrick Bamonte¹, Nataša Kalaba², Jamie Maclean³, Luke Bisby⁴

ABSTRACT

This paper explores the applicability of advanced numerical models to the complex structural behaviour observed when symmetrically reinforced and eccentrically loaded concrete columns are subjected to non-uniform heating regimes. To this end, attention is focused on a recently completed experimental campaign specifically aimed at providing a novel data set on the performance of reinforced concrete members subjected to several combinations of loading, heating, and cooling conditions. The structural behaviour of the columns was studied using 3D finite element models developed using commercial software by means of sequentially-coupled thermomechanical analyses. A user subroutine was developed to model the mechanical properties as irrecoverable in the cooling phase. The results obtained show that, on the whole, the structural behaviour can be adequately represented by the numerical model. Moreover, the roles of thermal and transient deformations are correctly captured, as well as the possibility of failure in the cooling phase.

Keywords: Reinforced concrete columns; finite element modelling; cooling

1 INTRODUCTION

Concrete modelling at high temperature is not an easy task due to the highly nonlinear material and structural behaviour. When irrecoverable deformations at the material level take place, it is required to perform plastic analyses and, consequently, to resort to advanced constitutive models implemented in finite element codes. When beams and columns are at issue, numerical modelling via beam finite elements (Bamonte and Lo Monte, 2015; Gernay, 2019) can be carried out by means of uniaxial constitutive laws, such as those provided in the pertinent standards (e.g. EN 1992-1-2, 2004). On the other hand, when more complex structural members (such as slabs, walls and tunnel linings) are considered, 2D or 3D finite elements analyses must be carried out, thus requiring the definition of concrete behaviour for multiaxial states of stresses. Numerical models that use 3D Finite Elements are the most complex models for structural analysis. They require significant computational and modelling effort and should be used with care. In the case where the local behaviour of RC structures exposed to fire is the main goal of the investigation, a 3D finite elements model can be a very efficient tool. In addition, non-

¹ Associate Professor of Structural Analysis and Design, Politecnico di Milano, Milan, Italy
e-mail: patrick.bamonte@polimi.it, ORCID: <http://orcid.org/0000-0002-4967-1089>

² Structural Fire Engineer, CERIB, Epervan, France
e-mail: N.KALABA@cerib.com

³ Structural Engineer
e-mail: jwmaclean@gmail.com

⁴ Chair of Fire and Structures, School of Engineering, University of Edinburgh, Edinburgh, UK
e-mail: Luke.Bisby@ed.ac.uk, ORCID: <https://orcid.org/0000-0001-8293-4322>

uniform heating (e.g. localized heating), when the heat transfer along the length of the member is important, modelling bond-slip or localized spalling (if possible) requires considering the whole volume of the structural member and modelling it in the 3D space.

This paper explores the applicability of advanced numerical models to the complex structural behaviour observed when symmetrically reinforced and eccentrically loaded concrete columns are subjected to non-uniform heating regimes. To this end, attention is focused on a recently completed experimental campaign specifically aimed at providing a novel data set on the performance of reinforced concrete columns subjected to several combinations of loading, heating, and cooling conditions. The structural behaviour of the columns was studied using 3D finite element models developed using ABAQUS by means of sequentially-coupled thermomechanical analyses. Attention will be focused on the role played by different parameters, which were varied during the tests, namely load magnitude, eccentricity of the applied load, concrete compressive strength, magnitude of applied initial incident radiant heat flux, overall length of the heated area, and fire exposure.

2 EXPERIMENTAL CAMPAIGN

2.1 General description

The reference experimental database considered consists of 46 nominally-identical reinforced concrete columns tested at the University of Edinburgh (Maclean, 2018; Maclean and Bisby, 2020). The dimensions of the specimens are shown in Figure 1a. All the tested columns had identical geometry, with dimensions of the cross section $150 \times 150 \text{ mm}^2$ and overall length of 1400 mm. The columns were all pinned-pinned and reinforced with 4H10 longitudinal bars (distance between the axes = 90 mm) and 10H6 closed stirrups (spacing = 140 mm). 36 columns have been tested while exposed to fire, while 10 columns have been tested at ambient temperature, to determine the reference load capacity. Concrete strength at the test day was 30 and 50 MPa for the two mixes considered. Both mixes contained 2 kg/m^3 of polypropylene fibres, to minimize the likelihood of spalling.

In the experimental campaign, the influence of various parameters on the columns' performance during heating and during/after cooling has been investigated:

- load magnitude: severe loading and low loading were considered – 60 % of the ambient load capacity or a constant load of 10 kN (equivalent to 1-2% of the columns ambient capacity), respectively;
- eccentricity of the applied load: 5, 15 or 25 mm;
- concrete compressive strength: 30 or 50 MPa;
- magnitude of applied initial incident radiant heat flux: 0, 50 or 70 kW/m^2 ;
- overall length of the heated area – 33% of the length (middle third) or 66% of the column length;
- number and sides exposed to fire (one side or two sides) – the heated sides were front and back of the columns;

Before presenting the results, it is important to explain denomination of the tested columns (MacLean, 2018). For instance, the test HF70-F30-L60-E25-C stands for the column exposed to a heat flux of 70 kW/m^2 (HF70), having a compressive strength $f_c = 30 \text{ MPa}$ (F30), loaded with an axial force equal to 60% of its axial capacity (L60) applied with eccentricity of 25 mm (E25). Finally, C denotes the side heated – compression (C) or tension (T) heated side.

2.2 Heating of the columns

The columns were heated by using radiant panels (Figure 1a and b). The panels could be placed at a specified distance from the member, in order to achieve the desired value of the incident radiant heat flux. Only a portion of the column was directly heated, while in the areas of the member away from the heated surface area, heat transfer was governed by conduction through the concrete itself, rather than radiation from the panels (as well as convective losses from exposed surfaces). It is worth observing that such setup leads to a non-uniform distribution of incident heat flux over the exposed surface of the column, which is

due to the variation of the view factor at any particular location on the heated surface and the interaction of the surface with convective currents generated both by the radiant panels themselves and by the heated face of the column. The radiant panels had a rectangular shape; therefore, the plane of incident radiant heat flux, which represents a specific desired peak value (for example, 50 kW/m^2 or 70 kW/m^2 in the experimental campaign) at the location of maximum heat flux at a specified offset distance will actually represent a variable incident radiant heat flux distribution over the target surface.

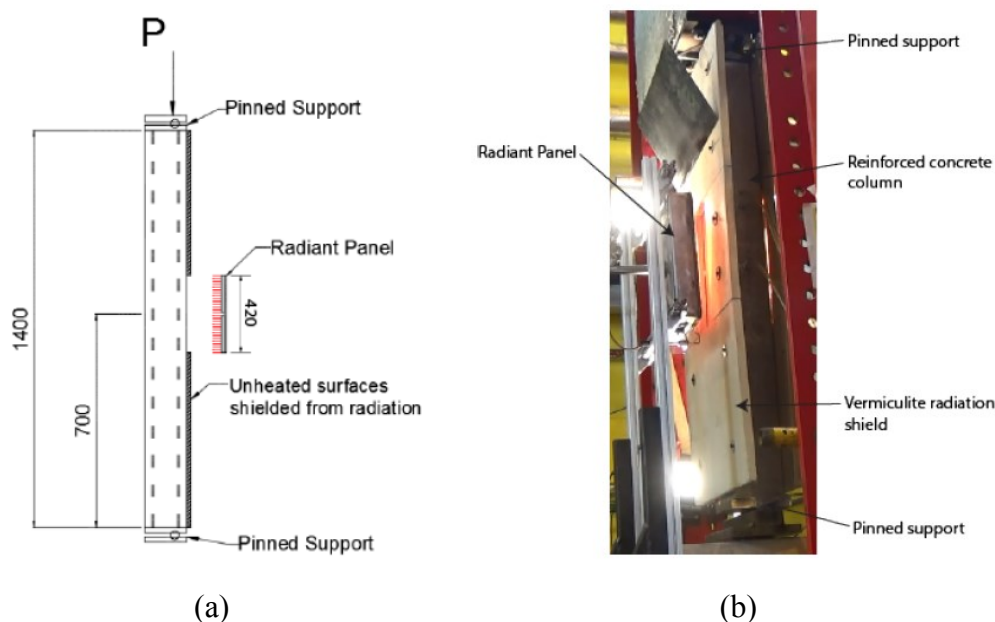


Figure 1. (a) Geometry of a typical column specimen; (b) photo of test set-up

3 NUMERICAL MODELLING

3.1 General

The columns tested at the University of Edinburgh were analysed by means of sequentially-coupled thermo-mechanical analyses performed by means of the commercial finite element software ABAQUS 6.19. The first step consists in solving the heat transfer problem. Afterwards, the temperature output is used in a mechanical analysis as a predefined field. Therefore, two sub-models are built: a model for the thermal analysis and a model for the mechanical analysis. Nodal temperatures are stored as a function of time in the output results. The temperatures in the member act as thermal body-load in the structural model, and are applied together with the mechanical loading in the subsequent mechanical analysis. Longitudinal reinforcing bars and stirrups were included in both models.

3.2 Thermal analysis

Linear brick elements with eight nodes (DC3D8) are used for concrete, while reinforcing bars are discretized using linear elements with two nodes (DC1D2). These elements have the nodal temperature as the only active degree of freedom. Concrete-rebar interface is modelled using a tie constraint, to enforce a unique temperature at the nodes shared between steel and concrete.

In order to properly model the heat exposure, a user subroutine (DFLUX) was used to calculate the net incident heat flux on the heat-exposed surface of the member as a function of time, while in the cooling phase the applied heat flux is equal to zero. The subroutine is called at each integration point whenever a surface-based non-uniform distributed heat flux is defined in the analysis. The net incident heat flux is calculated according to the provisions of EN 1991-1-2 (2002). The subroutine DFLUX requires the definition of two values: FLUX(1) is the value of the applied heat flux, namely the magnitude of the flux flowing into the point as a function of time and space, while FLUX(2) is the derivative of the heat flux

with respect to surface temperature. In the case under consideration, the incident heat flux varies over the exposed surface. The maximum values of the incident radiant heat fluxes to which the columns were exposed are 50 and 70 kW/m², but these values are not constant over the exposed surface. This variable spatial distribution of the heat flux on the exposed surface was not taken into account. For this reason, the two reference values of the heat flux, 50 and 70 kW/m², were reduced to 42 and 60 kW/m², respectively, to obtain a reasonably accurate fit between the predicted temperature at the heat-exposed side and the experimentally measured value.

Heat transfer inside the member takes place through conduction. At the boundaries of the heat-exposed surfaces, convection with convective coefficient of 25 W/(m²·K) is assumed, while for the unexposed surfaces the convective coefficient is set to 9 W/(m²·K), accounting for the radiation. Radiation with emissivity $\varepsilon = 0.7$ was assumed for all the heat exposed concrete surfaces. Thermal properties of concrete and steel are assumed as per EN 1992-1-2 (2004). An exemplary temperature distribution in the column at the end of the heating phase (90 minutes) is shown in Figure 2.

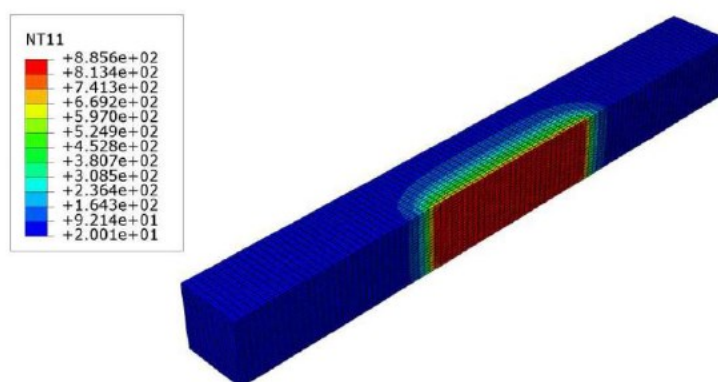


Figure 2. Temperature distribution in the column at 90 minutes of heat exposure

3.3 Mechanical analysis

The model for the mechanical analysis was built using 3D stress-displacements elements for the discretization of concrete and steel rebars. Concrete is discretized using 8-node linear-brick elements (C3D8), with translations in the three directions as active degrees of freedom at each node. This element type can be used for modelling of solids with or without reinforcement, and it is capable of accounting for cracking of concrete in tension and crushing of concrete in compression, creep and large strains. Steel rebars are discretized with 2-noded linear displacement truss elements (T3D2), which deform by axial elongation only. When the strains are large, the formulation is simplified by assuming that the trusses are made of incompressible material. This approach has been used to model the reinforcement where the nodes of reinforcement are coincident with the nodes of concrete. Concrete-rebar interface is modelled with embedded region constraint, i.e. no slip is allowed (perfect bond is assumed).

Decay of the mechanical properties at elevated temperature for concrete and reinforcing steel is taken as per EN 1992-1-2. In the cooling phase, the properties are considered as irrecoverable, to account for the irreversible thermal damage in the material. This has been done by implementing a FORTRAN user subroutine – UFIELD, which allows updating the mechanical properties only in the heating phase, when the temperature in the current time increment is higher than the temperature in the previous time increment. If the material is in the cooling phase, its mechanical properties retain the value they had at the maximum temperature, i.e. the behaviour is governed by the maximum temperature reached and not by the current temperature. Finally, definition of material properties in the software requires the definition of temperature dependent elastic properties as well as the definition of the plastic model (Kalaba, 2019).

Regarding the boundary conditions, two reference points are created, at a small distance from the column member, and then kinematically coupled with the surface of the column. Restraint conditions (pinned ends) and external loads are then applied directly to the two reference points (Figure 2).

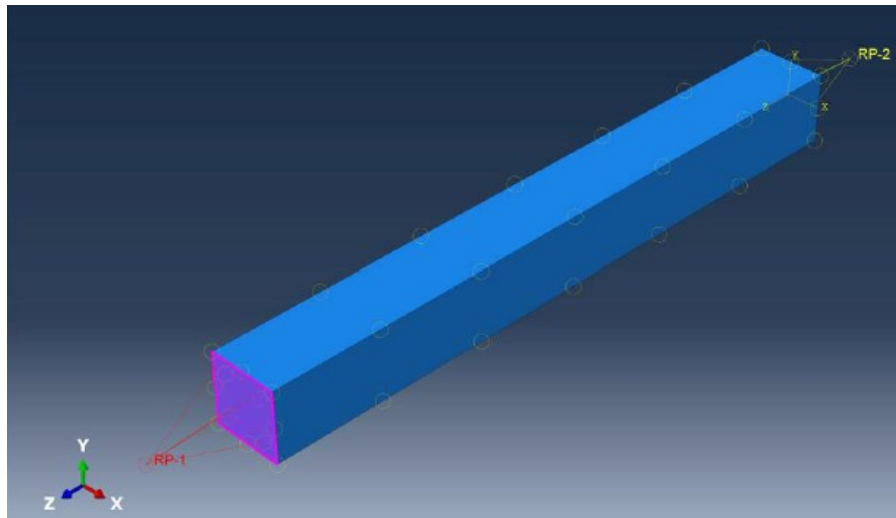


Figure 3. Definition of the mechanical boundary conditions for the columns: reference points kinematically coupled with the column surface

4 NUMERICAL RESULTS

4.1 Columns of the 1st Group

All the columns that belonged to this group had a compressive strength $f_c = 30$ MPa and were exposed to a heat flux 70 kW/m^2 . Load level, side exposed to fire and eccentricity of the applied load varied.

Applying the lower load on the columns helps to understand the extent of the irrecoverable deformation that takes place upon cooling back to ambient temperature. In case that a low load, equal to 1-2 % of the load capacity, is applied, it would be expected that the thermal expansion governs the deflection response. In case of low load eccentricity, lateral deflection and bowing take place due to thermal expansion.

Looking at Figure 4, the displacement response can be divided into three stages: initial bowing towards the heat source, governed by the thermal expansion, followed by the contraction of the columns, and the ensuing bowing direction reversal. The last stage of the cooling phase brings in some stabilization of the deflections, when the values keep almost constant values (from around 200 minutes onwards). The maximum deflection is reached soon after the heating phase has ended (after 90 minutes). Slight differences in the response can be observed for a varying eccentricity (Figure 4b). For a 25 mm load eccentricity, tension-heated columns deflect more than compression-heated columns.

There is no full recovery to the initial values upon cooling: the measured residual deflection is around 1 cm. While the overall trend is well reproduced by the numerical model, the displacements are very conservative in the later stages of the heating phase and then in the subsequent cooling phase of fire. The numerical model predicts a certain amount of irrecoverable deformation which was not measured in the tests. As pointed out by MacLean (2018), thermal expansion of tension-heated columns together with the moment induced by the eccentric load, increases the deflection of the column. This increase in deflection would then induce secondary moments, increasing the moment in the section even farther. In compression-heated columns the opposite is valid: deflections due to thermal expansion reduce the moment in the section, resulting in smaller deflections in comparison to tension-heated columns. Still, the fact that tension-heated columns deflect more than compression-heated columns might have been caused by the higher temperatures experienced in those members, given that during the fire they deflect towards the heat source, thereby increasing the heat flux on the exposed side with respect to compression-heated columns. This effect is not captured in the numerical analyses, as the basic premise of the sequentially-coupled thermo-mechanical analyses is that the thermal field is not dependent on the displacement/stress field.

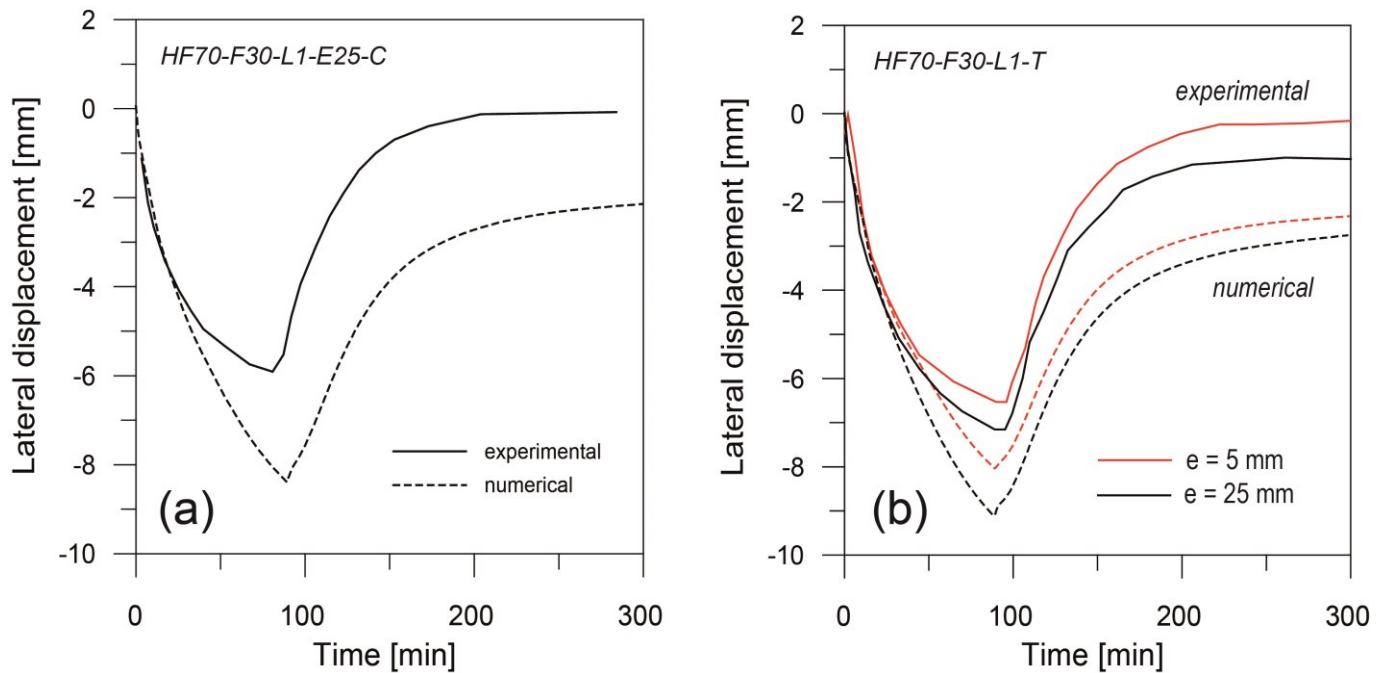


Figure 4. Comparison between experimental and numerical midspan deflection evolution in: (a) compression-heated columns with $e = 25$ mm and (b) tension-heated columns with $e = 25$ mm and $e = 5$ mm (continuous lines = experimental results; dashed lines = numerical results)

Columns tested under higher loads exhibit a different structural response than the columns tested under low loads (Figure 5). At the beginning of the test, compression-heated columns bow away from the heat source, as the effect of the load dominates the response (Figure 5a). Unexpectedly, the column continues to deflect away from the heat source even after the end of the heating phase. This can be explained with the effect of transient creep strain, resulting in contraction rather than expansion. Upon removal of the heating panels (after approximately 90 minutes), the columns deflect rapidly away from the heat source, until failure or attainment of a new state of equilibrium. Deflections are not recovered during cooling. Instead, after around 180 minutes into the fire, the deflections stabilized and kept almost a constant value until the end of the test. Numerically, the general trend is well reproduced. The column failed for the eccentricity $e = 25$ mm, after around 260 minutes (in the cooling phase of fire), which is just slightly non conservative in comparison to the failure time measured during the test. On the other hand, the column survived the fire for lower eccentricity, thanks to the smaller bending moments and thus smaller deflections and less pronounced second-order effects; the predicted displacements follow closely the experimental curve. Residual deflection obtained numerically is around 16 mm while experimentally measured value was 14.7 mm.

Tension-heated columns with lower eccentricity (Figure 5b) behave in a similar way to compression-heated columns (Figure 5a). The behaviour during the heating phase and the stabilization of the deflection in the later stages of the cooling phase is correctly captured by the model. However, the same cannot be said for the tension-heated column with the higher load eccentricity (Figure 5c): the effect of thermal expansion prevails, due to low compressive stresses at the heated face, resulting in overall smaller deflections than for the lower eccentricity case. Numerical model was not able to capture the experimentally observed behaviour during the cooling phase, where there was almost no recovery in the deflections. The numerical model underestimated the residual deflections measured during the test, while the maximum deflection measured at the end of the heating phase was somewhat conservative.

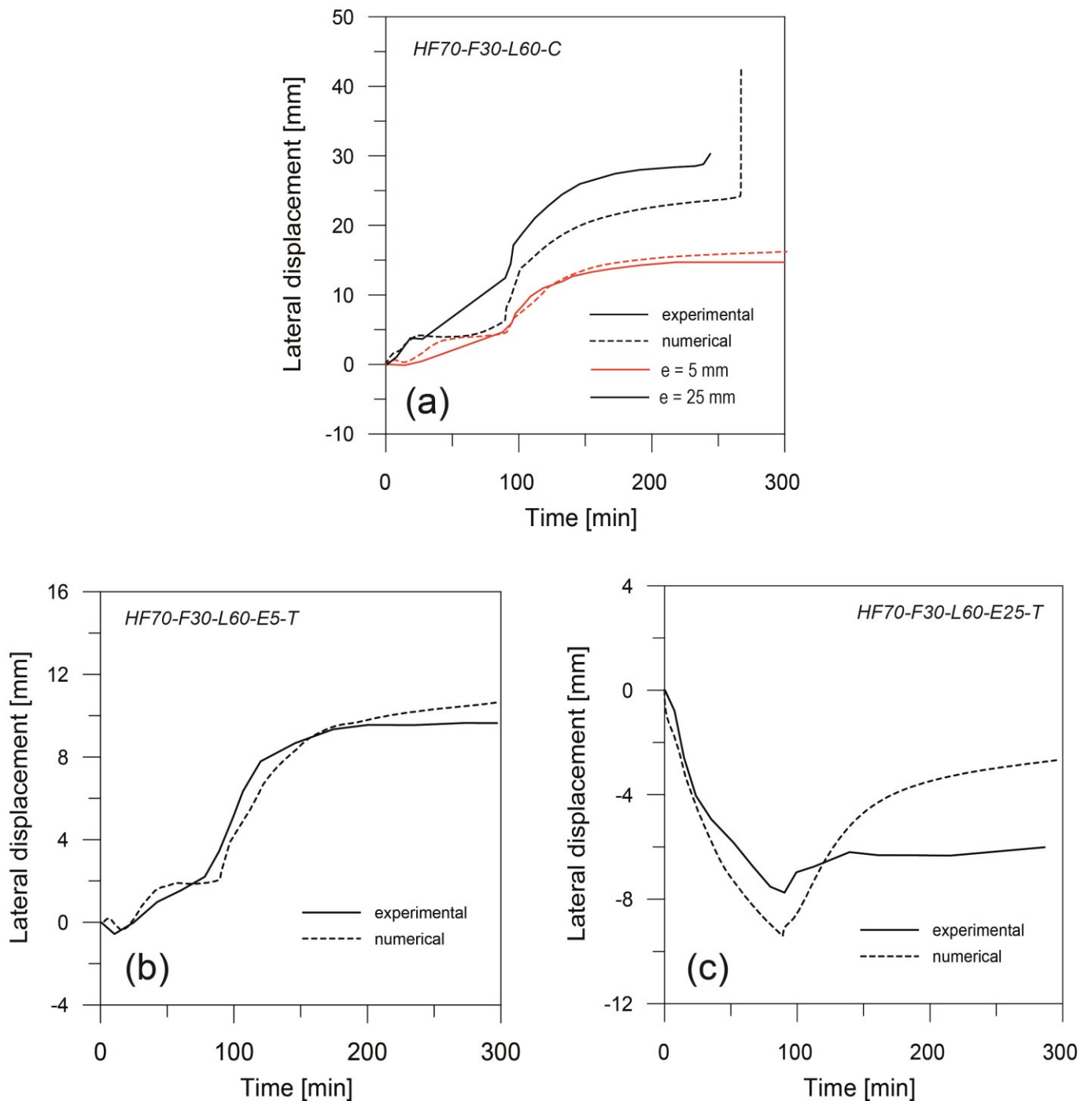


Figure 5. Comparison between experimental and numerical midspan deflection evolution for heavily loaded columns: (a) tension-heated, $e = 5$ mm; (b) tension-heated, $e = 25$ mm and (c) compression-heated, $e = 5$ mm and $e = 25$ mm

4.2 Columns of the 2nd Group

All the columns that belong to this group had a compressive strength $f_c = 30$ MPa, were exposed to a heat flux 50 kW/m^2 and loaded with an axial force equal to 60% of their axial load capacity. The side exposed to fire and load eccentricity varied.

During the tests, it was observed that decreasing the heat flux to 50 kW/m^2 did not change the general trend in the deflection evolution: it produces similar but less severe and less pronounced response compared to a higher heat flux of 70 kW/m^2 . This is expected because decreasing the heat flux will lead to a similar thermal field inside the member, with lower values of the maximum temperature and thus less significant damage inside the member.

Tension-heated specimen bows towards the heat source in the first 20 minutes of fire, and then the deflection trend reverses, and the columns bow away from the heat source for the remaining duration of fire. Displacement of tension heated columns is overestimated by the model. General trend suggests that the displacements are monotonically increasing (though at a lower rate during cooling phase, i.e. after 150 min) while during the test displacements were almost constant after 150 min of fire.

Compression-heated columns deflect away from the heat source during the whole fire duration (Figure 6b). Columns from Group 1, exposed to a heat flux of 70 kW/m^2 , exhibited more significant damage and deflections than columns from Group 2. This is probably due to transient thermal creep caused by the higher temperatures at the exposed side. The predicted displacement is slightly underestimated in the case of compression-heated columns loaded with the eccentricity of $e = 25 \text{ mm}$, while in the case of lower eccentricity, the displacements are well predicted, during both heating and cooling phase of the fire (Figure 6b).

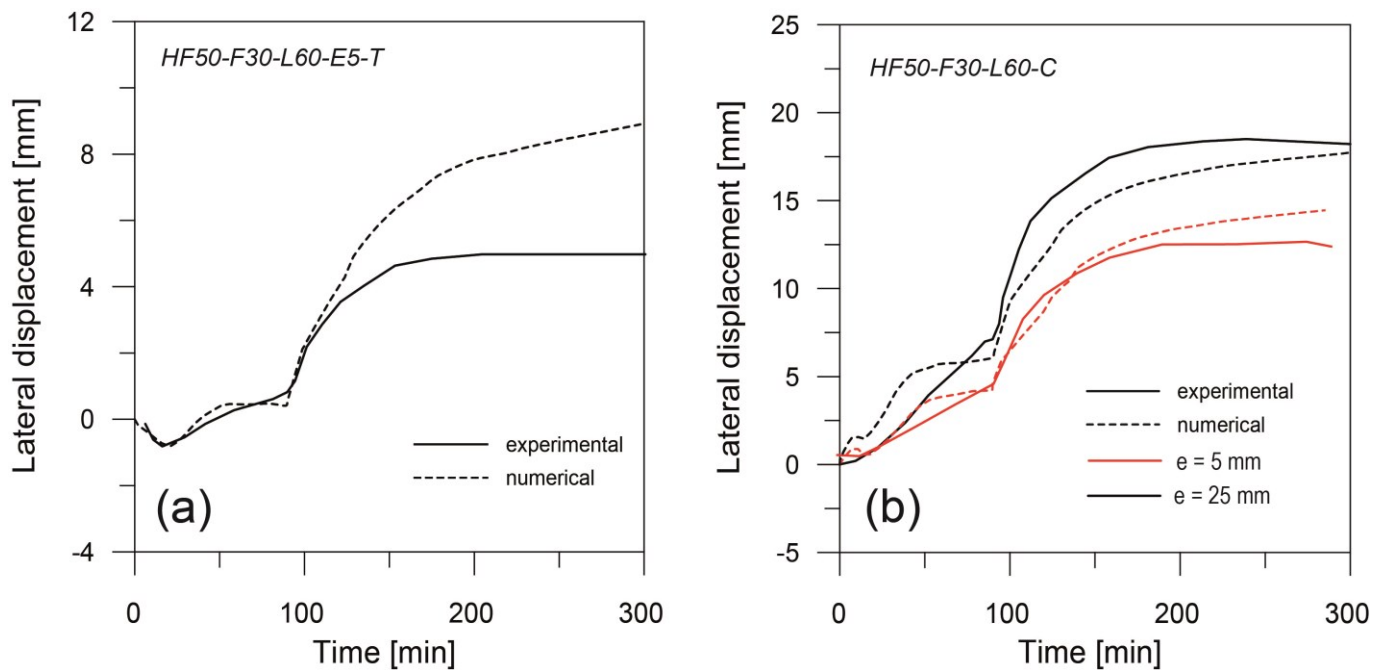


Figure 6. Comparison between experimental and numerical midspan deflection evolution for heavily-loaded columns, with heat flux of 50 kW/m^2 : (a) tension-heated columns with $e = 5 \text{ mm}$ and (b) compression-heated columns with $e = 5 \text{ mm}$ and $e = 25 \text{ mm}$

4.3 Columns of the 3rd Group

All the columns that belonged to this group had a compressive strength $f_c = 50 \text{ MPa}$ and were exposed to a heat flux of 70 kW/m^2 . Load level, side exposed to fire and eccentricity of the applied load varied.

The columns deform towards the heat source for the whole duration of the heating-cooling cycle. In the first 90 minutes of heating, the displacement is increasing towards the heat source. Upon cooling, the deflection trend reverses, and the columns deform away from the heat source. Both compression-heated and tension-heated columns behave in a similar way, except that compression-heated columns recovered the deflections to the initial values, while tension-heated columns had some residual deflection left. Comparing the response of the columns with different compressive strength shows significant differences, as expected.

The comparison is first carried out for columns loaded with low load, where its influence is minimal and the deflections are expected to be fully recovered upon cooling (transient strain is not taking place). In the tests, columns with compressive strength $f_c = 30 \text{ MPa}$ deflected less than columns with compressive strength $f_c = 50 \text{ MPa}$, which is somewhat counter-intuitive, especially given the fact that same low load

was applied to all the columns. This may suggest that stronger columns suffered more pronounced thermal expansion but this could not be verified during the experimental campaign. However, an opposite trend is obtained in the model – stiffer and stronger columns indeed deformed less, both in terms of peak deflection and also in the residual stage (Figure 7).

Columns exposed to low load exhibited lateral deflections and bowing almost immediately after being exposed to fire, due to thermal gradients developing through the depth of the column section. While the numerical model has been able to capture the general trend as well as to predict the maximum deflection at the end of the heating phase, it proved to be more conservative during the cooling phase. It predicted certain amount of residual deflections in compression-heated columns, while in the tests an almost complete deflection recovery was observed (Figure 7a). On the other hand, deflections during cooling for tension-heated columns are well predicted, while during heating phase they are slightly underestimated (Figure 7b).

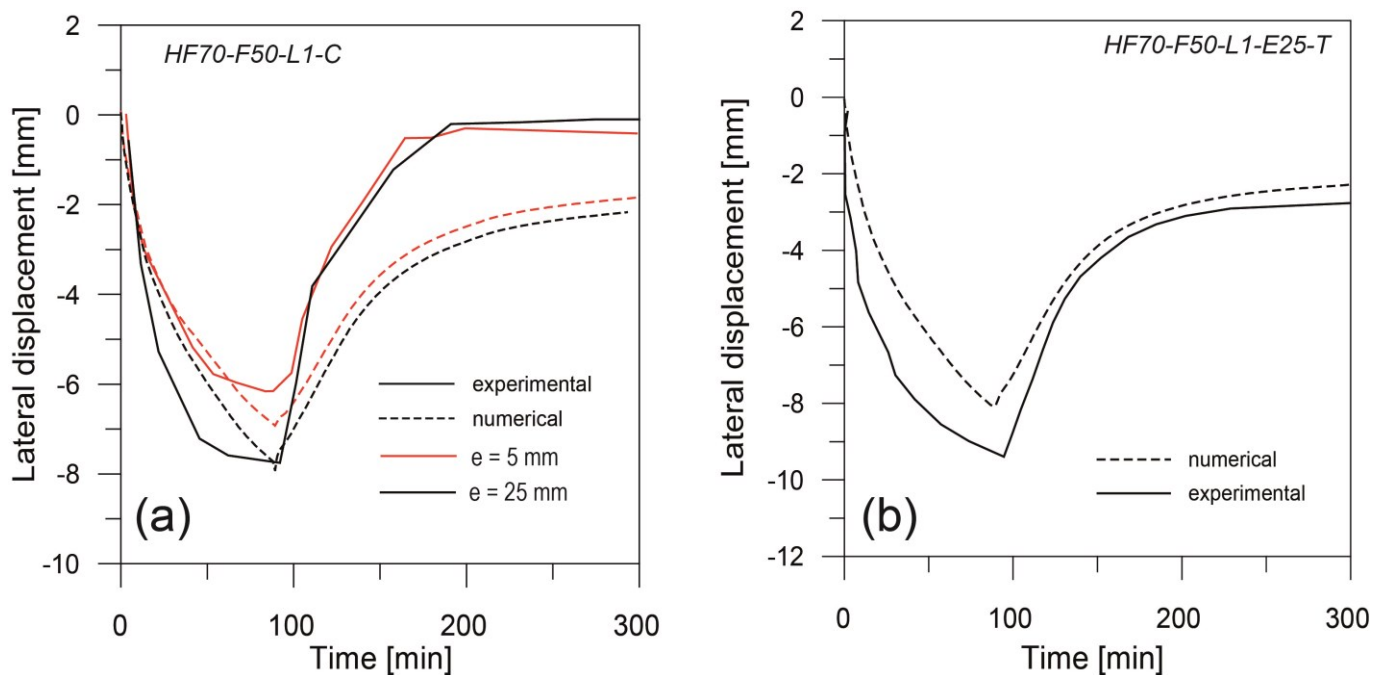


Figure 7. Comparison between experimental and numerical lateral midspan deflection evolution for low-loaded columns, with compressive strength $f_c = 50$ MPa: (a) compression-heated, $e = 5$ mm and $e = 25$ mm and (b) tension-heated, $e = 25$ mm

While the load level proved to be a significant factor, compressive strength proved to play less important role in view of the deflection evolution. It is true that the columns of different strength deform to a different extent but this is in part due to the different load applied. Compression-heated specimens deflect away from the heat source due to the transient creep strain while tension-heated specimens bend towards the heat source due to thermal expansion of the extreme fibre of the heated face. The behaviour of compression-heated columns is well simulated and failure time is predicted well, only slightly on the non-conservative side (Figure 8).

Deflection of the tension-heated column is predicted accurately for lower eccentricity, when the columns bows away from the heat source, due to the influence of applied load and stresses on the heated side. On the other hand, for higher eccentricity the influence of thermal expansion dominates the response, because compressive stresses in the heat exposed side are low and cannot counteract the thermal expansion. Thus, the column bows towards the heat source.

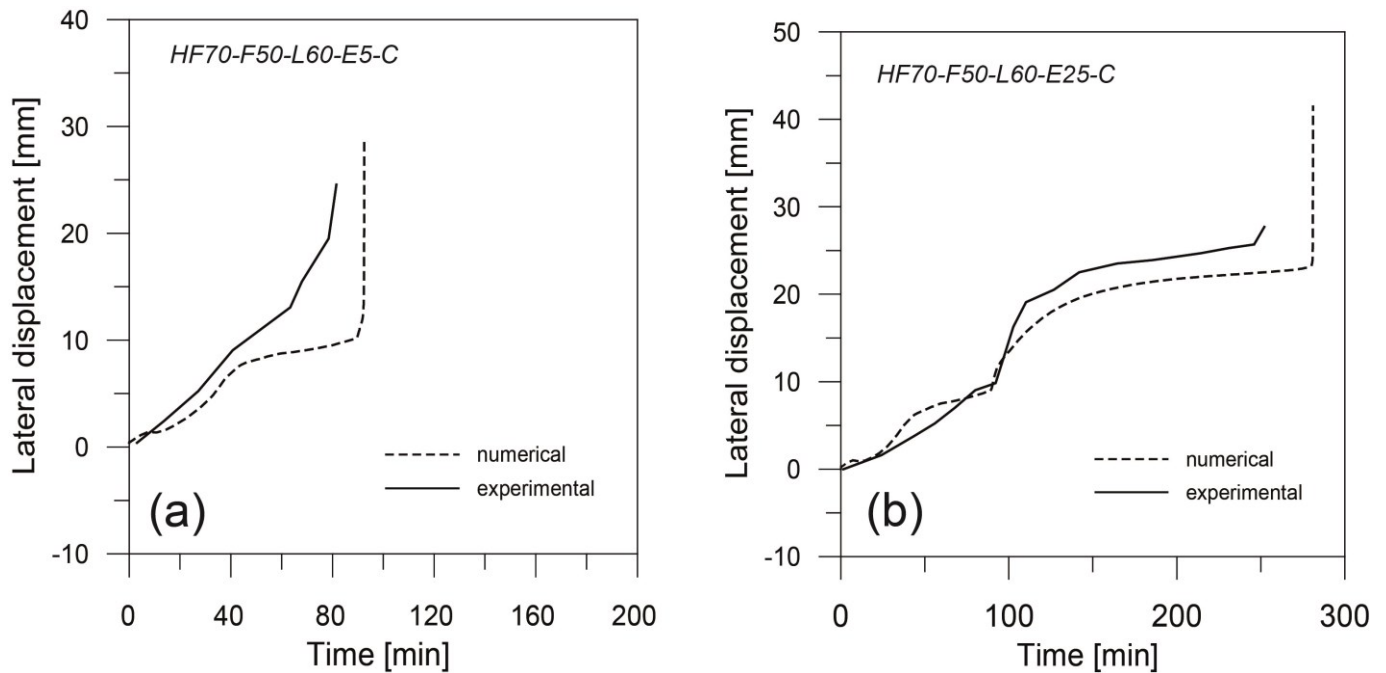


Figure 8. Comparison between experimental and numerical midspan deflection evolution for heavily loaded columns with compressive strength $f_c = 50$ MPa: (a) compression-heated, $e = 5$ mm, and (b) compression-heated, $e = 25$ mm

The general trend is well predicted by the model, but the displacements in the cooling phase are somewhat underestimated (Figure 9). Compression-heated columns are heated on the most stressed section, the extent of the transient creep and therefore the magnitude of the deflections depends on the magnitude of the load - higher loads lead to higher compressive stresses and thus to higher deflections (away from the heat source) due to transient thermal creep strain. Being exposed to higher loads than the corresponding columns from the 1st Group (with $f_c = 30$ MPa), they deflect more and their deflection response is more sizable. Tension-heated columns are subjected to elevated temperatures on the less stressed section of the column, thus the columns deflect toward the heat source. In the case of $e = 25$ mm, the compressive stresses are not enough to counteract the effect of thermal expansion through the development of transient thermal creep. Still, the heat transfer inside the section may play a role, since as the heat reaches to the compressed fibres, where the compressive stresses are higher, transient thermal creep develops, thereby influencing the evolution of the deflections. Finally, higher loads in tension-heated columns result in lower stresses on the “tension face”, thereby reducing the deflections.

5 CONCLUSIONS

From the extensive experimental campaign examined and the numerical analyses of the selected tested columns, several meaningful conclusions can be drawn about the structural behaviour of eccentrically loaded columns exposed to a localized heating. It was concluded, or to say confirmed, that the thermal gradient and stress state within the section are the two most important factors governing the response. In that regard, the most significant investigated parameters are:

- increasing the eccentricity of the applied load increases the moment induced by the load: as a result, if the stress on the heated face is large enough to cause transient thermal creep, the column will deflect away from the heat source during the whole fire duration. Otherwise, the influence of thermal expansion will dominate the response and the columns will bow towards the heat source;
- the magnitude of the imposed load will determine the stress state within the section and this will determine the extent of transient thermal creep through the depth of the section. This directly influences the direction in which the column will deflect: towards the heat source, in case the thermal expansion governs the problem (low compressive stresses at the exposed sides) or away

from the heat source (when the compressive stresses at the exposed sides are large enough to counteract the effect of thermal expansion);

- heat flux is a parameter of utmost importance, as it determines the temperature gradient within the structural member and thus it has a strong impact on the structural response. The higher the temperature inside the member, the more the concrete will be weakened and the greater non-recoverable deformations as a result of increased transient thermal creep resulting both from the elevated temperature and stress distribution through the section;
- the structural response can be very different depending on which side of the member is heated - the most stressed side or the least stressed side. This can even determine if the column will survive heating and cooling or will collapse.

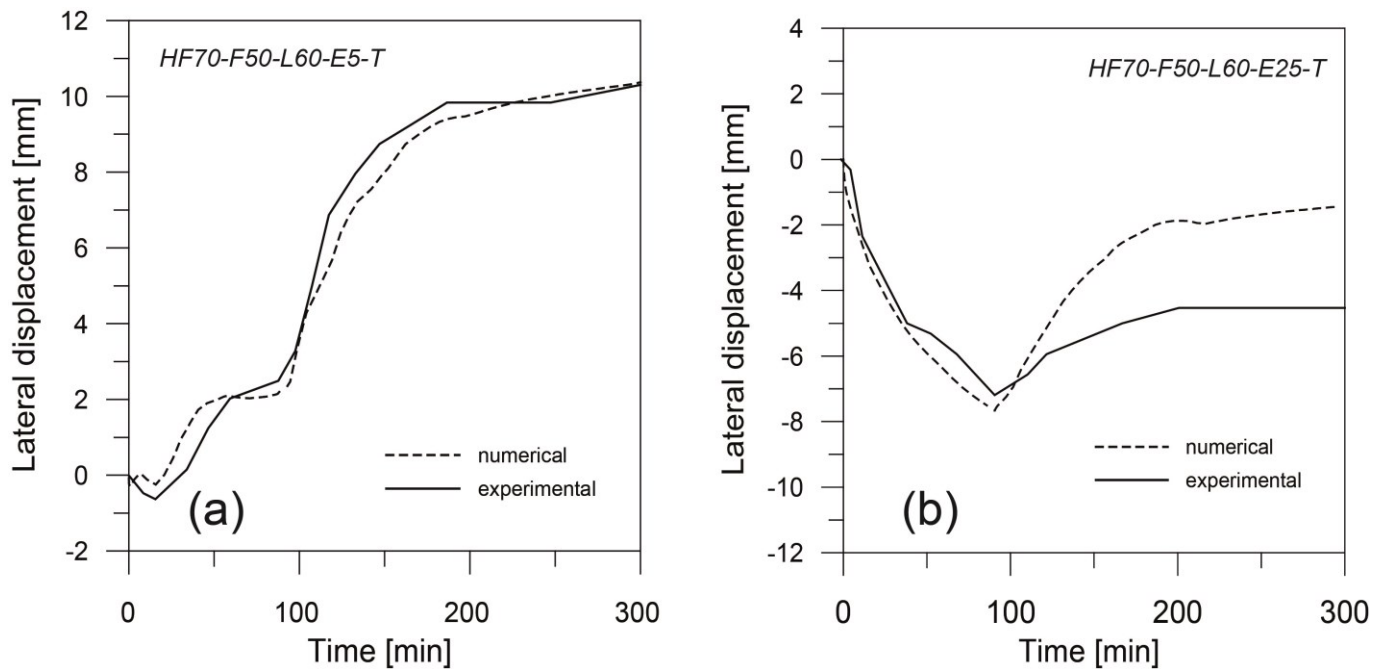


Figure 9. Comparison between experimental and numerical midspan deflection evolution for heavily-loaded columns with compressive strength $f_c = 50$ MPa: (a) tension-heated, $e = 5$ mm and (b) tension-heated, $e = 25$ mm

REFERENCES

1. Bamonte, P. and Lo Monte, F., Reinforced concrete columns exposed to standard fire: comparison among different constitutive models for concrete at high temperature, *Fire Safety Journal*, Vol. 71, 2015, pp. 310-323.
2. EN 1991-1-2, Eurocode 1: Actions on structures – Part 1-2: General actions - Actions on structures exposed to fire, European Committee for Standardization, Brussels (Belgium), 2002.
3. EN 1992-1-2, Eurocode 2: Design of concrete structures – Part 1-2: General rules - Structural fire design, European Committee for Standardization, Brussels (Belgium), 2004.
4. Gernay, T., Fire resistance and burnout resistance of reinforced concrete columns, *Fire Safety Journal*, Vol. 104, 2019, pp. 67-78.
5. Kalaba, N., On the role of materials properties and structural context in reinforced concrete members exposed to natural fires, PhD Thesis, Politecnico di Milano (Milan, Italy), 2019.
6. Maclean, J., The Structural Response of Reinforced Concrete Columns During and After Exposure to Non-Uniform Heating and Cooling Regimes, PhD Thesis, University of Edinburgh (Edinburgh, UK), 2018.
7. Maclean, J. and Bisby, L., Effect of non-uniform heating and cooling on eccentrically loaded reinforced concrete columns, *Proceedings of the 11th International Conference on Structures in Fire – SiF 2020*, hosted online by the University of Queensland (Brisbane, AUS), 30th November – 2nd December 2020.

GLOBAL RESISTANCE FACTOR FOR THE BURNOUT RESISTANCE OF CONCRETE SLABS EXPOSED TO PARAMETRIC FIRES

Thomas Thienpont¹, Ruben Van Coile², Balsa Jovanovic³, Wouter De Corte⁴, Robby Caspee⁵

ABSTRACT

Although traditionally the fire resistance rating of concrete elements is determined through standardized tests or tabulated data, there is a growing trend towards the use of performance-based approaches to evaluate structural behaviour during or after a fire. The safety format to be applied with these advanced numerical evaluations is however unclear. In this paper, the applicability of the concept of a global resistance factor (GRF) safety format is explored for simply supported concrete slabs exposed to the Eurocode parametric fire curve for a wide range of parameters. The safety of the slab is evaluated in relation to its ability to withstand a complete burnout scenario, i.e. its ability to resist the applied loads throughout the entire duration of a fire including the cooling phase. Using a full-probabilistic model, the required GRF is numerically derived for a specified target safety level in case of fire. Additionally, a calculation method is provided which allows to determine the GRF of fire exposed slabs for any given compartment through the use of a reference compartment and equivalency equations.

Keywords: Structural fire safety; Burnout resistance; Concrete slab; Global resistance factor

1 INTRODUCTION

Traditional structural fire design typically employs the fire resistance time R as the primary metric to evaluate whether a structural member can maintain its functionality in a predefined fire exposure scenario. Typically, this fire scenario is defined by the ISO 834 [1] or ASTM E119 [2] time-temperature relationship. This principle forms the basis of many design practices, and is applied in several design codes such as EN 1992-1-2:2004 [3]. However, recent investigations have highlighted that designing concrete structures using these traditional methods has some major shortcomings.

Firstly, these methods fail to encompass essential information about the structural behaviour in a realistic fire scenario. Apart from a heating phase, real compartment fires are also characterized by a cooling phase. Herein, as the available fuel in the compartment is used up, the temperature decreases back to ambient conditions. Research has shown that, in a design, considering a complete burnout scenario with a cooling phase is indispensable to identify (delayed) failure modes that would otherwise remain undetected [4, 5]. In the case of reinforced concrete (RC) members, such a delayed failure can occur due to the fact that the

¹ PhD Student, Department of Structural Engineering and Building Materials, Ghent University, Ghent, Belgium.
e-mail: thomas.thienpont@ugent.be, ORCID: <https://orcid.org/0000-0003-1466-3377>

² Professor, Department of Structural Engineering and Building Materials, Ghent University, Ghent, Belgium.
e-mail: ruben.vancoile@ugent.be, ORCID: <https://orcid.org/0000-0002-9715-6786>

³ PhD Student, Department of Structural Engineering and Building Materials, Ghent University, Ghent, Belgium.
e-mail: balsa.jovanovic@ugent.be, ORCID: <https://orcid.org/0000-0001-5200-5848>

⁴ Professor, Department of Structural Engineering and Building Materials, Ghent University, Ghent, Belgium.
e-mail: wouter.decorte@ugent.be, ORCID: <https://orcid.org/0000-0002-9416-3593>

⁵ Professor, Department of Structural Engineering and Building Materials, Ghent University, Ghent, Belgium.
e-mail: robby.caspee@ugent.be, ORCID: <https://orcid.org/0000-0003-4074-7478>

maximum temperatures in the section can be reached a significant time after the beginning of the cooling phase [6]. In contrast to steel members, due to the high thermal capacity and relatively low thermal conductivity of concrete, it takes quite some time for the inner layers of a section to heat up. As a consequence, the highest temperatures in the embedded steel reinforcement are reached long after the onset of the cooling phase. This is especially relevant in RC beams and slabs loaded in bending, which rely heavily on the steel tensile strength to maintain their load bearing capacities. To avoid delayed failure of RC slabs it is indispensable to evaluate the change in carrying capacity throughout the entire duration of the fire scenario. Therefore this article discusses the concept of burnout resistance of RC slabs, as it allows for designing structural members to survive the total duration of the fire until complete burnout, thus providing clarity on the expected performance of the structure in case of a real fire.

A second shortcoming stems from the fact that the input values for the material properties and loads used in structural design are usually based on characteristic values, combined with partial factors. This approach, which is commonly referred to as being semi-probabilistic, ensures an appropriately low probability of failure, while limiting the complexity of the analysis. It provides a trade-off between simplicity and accuracy, and has proven very useful in normal design situation. However, for fire safety engineering applications, no generally accepted safety targets and semi-probabilistic design methodologies based on such explicit target levels currently exist. In search of a suitable safety format, several methods have been proposed. For the case of structural fire design, which nowadays typically involves the use of computationally demanding finite element (FE) models, a full-probabilistic approach quickly becomes unfeasible. The application of these FE models requires the definition of a safety format which relies on a limited (ideally a single) evaluation of the computationally expensive model. Therefore several studies have proposed the use of a global resistance factor (GRF) safety format for numerically expensive models [7–10]. In a GRF based safety format, the design resistance R_d is obtained from a single evaluation with mean values for the stochastic input parameters. This constitutes a (first-order Taylor) approximation for the average resistance μ_R and which is then divided by a GRF γ_R , to obtain the design value for the structural resistance R_d , see Eq. (1).

$$R_d = \frac{\mu_R}{\gamma_R} \quad (1)$$

Considering the above, the main objective of this article is to evaluate and calibrate the GRF for the burnout resistance of simply supported RC slabs. The methods presented in this article are intended as a stepping stone towards the development of more elaborate GRF based safety formats, for complex geometries and advanced numerical tools.

2 BURNOUT RESISTANCE OF A RC SLAB

In the following, a method is presented to evaluate the burnout resistance of simply supported RC slabs exposed to natural fires. First, an analytical equation for the bending capacity during fire is introduced. Subsequently, in Section 2.2, the concept of burnout resistance is summarily discussed and illustrated for a reference compartment exposed to several natural fires.

2.1 Resistance of RC slab during fire

The load bearing capacity of a simply supported RC slab exposed to fire at the bottom side, can be expressed in terms of the bending moment capacity at the mid-span of the slab. In this article, the evolution of the bending moment capacity $M_{R,fi}$ during the course of a fire is calculated using a two-step procedure.

First, the temperature evolution inside the slab is calculated using a numerical 1D-temperature ingress model. The details on the temperature calculation procedure are described in detail in a previous study by the authors [6]. Figure 1 depicts the temperature evolution in a 200 mm concrete slab exposed to a Eurocode parametric fire (red curve) [11]. This time-temperature curve corresponds to a fire in a 10 m × 10 m × 3 m compartment, with an opening factor $O = 0.05 \text{ m}^{1/2}$ (a measure for the ventilation properties), fire load density $q_f = 800 \text{ MJ/m}^2$ (the amount of combustibles in the compartment) and thermal effusivity $b =$

1450 J/m²s^{0.5}. From the graph it is evident that the maximum temperature inside the solid slab (e.g. at depth = 50 mm) is reached long after the onset of the cooling phase. The highest temperatures in a rebar at that location, and the corresponding lowest strength, are thus reached during (or after) the fire's decay phase.

The temperature data obtained in the first step is subsequently used as input to estimate the bending moment capacity $M_{R,fi,t}$ of a RC slab section with a single layer of bottom reinforcement using a simplified expression. The expression (2) is based on Van Coile et al. [12] and was validated against more detailed numerical simulations [13].

$$M_{R,fi,t}(a) = A_s k_{fy}(\theta) f_{y,20^\circ C} (h - a) - 0.5 \frac{(A_s k_{fy}(\theta) f_{y,20^\circ C})^2}{w f_{c,20^\circ C}} \quad (2)$$

Herein, A_s is the area of reinforcement, k_{fy} is the strength retention factor for reinforcement yield stress at temperature θ , $f_{y,20^\circ C}$ is the steel strength at 20°C, h is the slab thickness, a is the rebar axis distance (i.e. concrete cover + ½ rebar diameter), w is the slab section width and $f_{c,20^\circ C}$ is the concrete compressive strength. Note that expression (2) takes into account the temperature dependent strength reduction of the steel reinforcement (through the factor $k_{fy} \leq 1$), but not for concrete. Since the slab is only exposed to elevated temperatures at the bottom, the temperature increase in the concrete at the compression side has negligible effect on the overall strength reduction for the 200 mm thick slab. When combining the above expression with temperature calculations for exposure to natural fire, the burnout resistance can be obtained.

2.2 Burnout resistance

Considering the previously presented methodology, the evolution of the bending moment capacity $M_{R,fi}$ as it changes through time during a fire scenario can be evaluated. Figure 2(b) and 3(b) each depict the bending moment resistance of an example slab, as defined in Table 1, for three Eurocode parametric fire scenarios. Figure 2(a) lists three fires curves for a compartment with a fixed opening factor $O = 0.05 \text{ m}^{1/2}$. From the combination of Figure 2(a) and (b) it is clear that when the density of combustible material q_f in the compartment increases, a certain threshold is reached at which the capacity of the slab during fire become smaller than the moments due to the self-weight and loads (i.e. demand), which ultimately means that the structure does not maintain its load-carrying capacity up to burnout. Similarly, in Figure 3, decreasing the opening factor O ultimately leads to a scenario where the carrying capacity reaches a critical value and is unable to survive the entire duration of the fire scenario. A more in-depth discussion on the burnout resistance of RC slabs, along with an easily applicable design method is presented in Thienpont et al. [6]. In this article, burnout resistance $M_{R,burnout}$ is defined as the combination of parameters O and q_f for which the slab is able to withstand the entire duration of the fire.

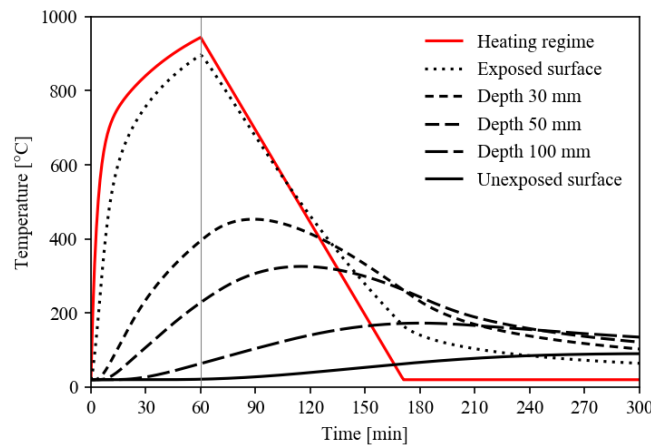


Figure 1: Temperature evolution in a 200 mm solid concrete slab, exposed from below to a Eurocode parametric fire

Table 1. Properties of example RC slab.

height h	width w	Rebar axis distance a	Area of reinforcement A_s	f_{ck}	f_{yk}
200 mm	1000 mm	35 mm	785 mm ²	30 MPa	500 MPa

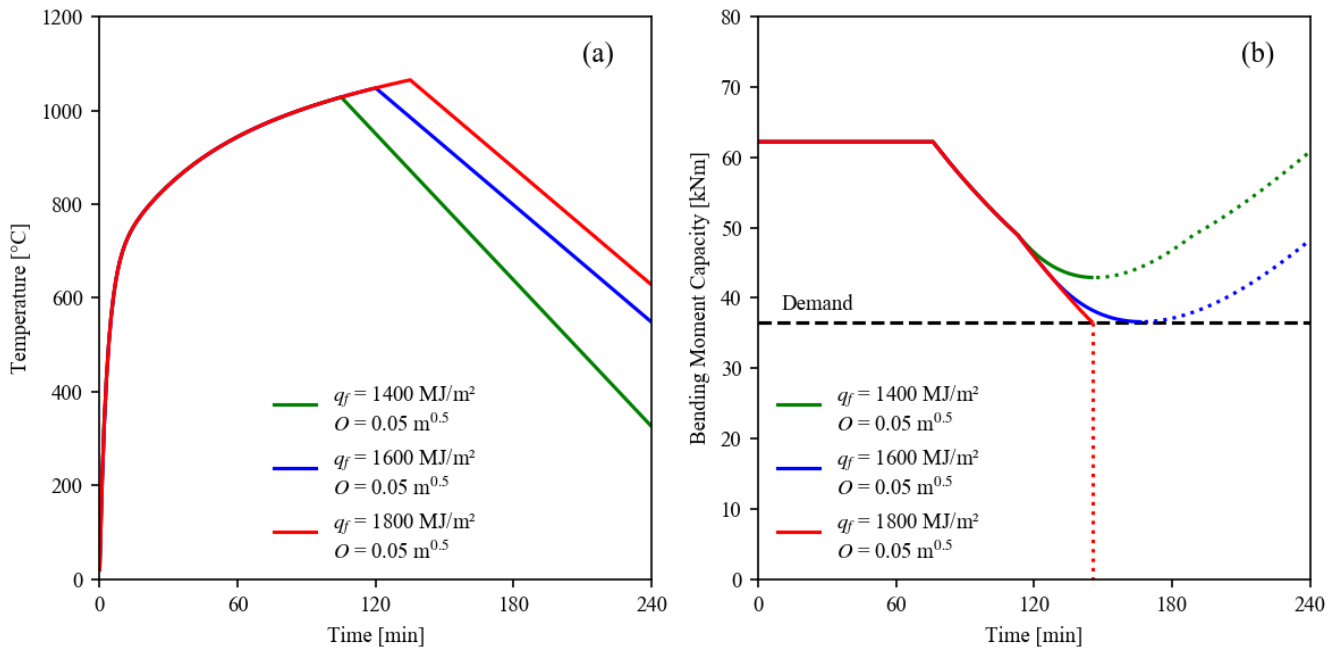


Figure 2: a) Time temperature curves for natural fires with opening factor $O = 0.05$ and variable fire load density; b) evolution of bending moment capacity for the RC slab defined in Table 2, exposed to said natural fires.

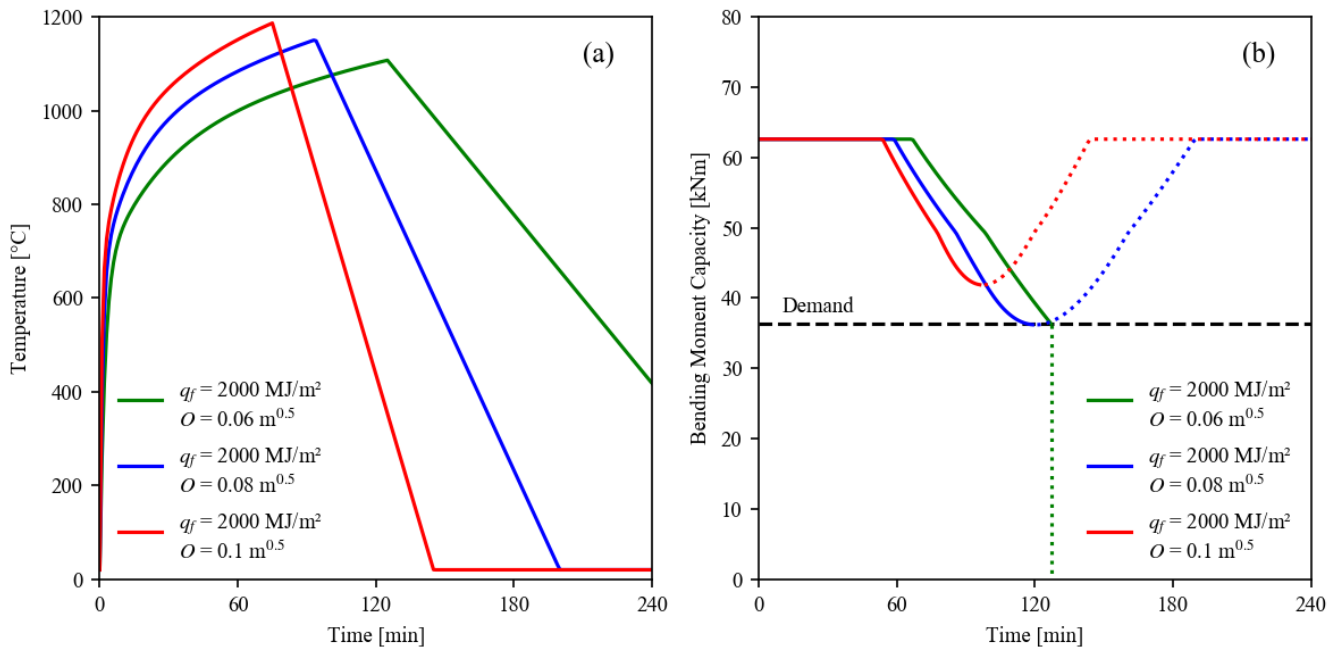


Figure 3: a) Time temperature curves for natural fires with fire load density $q_f = 2000 \text{ MJ/m}^2$ and variable opening factor; b) evolution of bending moment capacity for the RC slab defined in Table 2, exposed to said natural fires.

3 PROBABILISTIC BENDING RESISTANCE OF FIRE EXPOSED RC SLABS

In this section, the concept of burnout resistance is applied in a probabilistic evaluation of the bending moment capacity, thus taking into account the uncertain nature of the material properties and geometry. Next, in section 3.2, the consequences of also considering the uncertainties on the amount of combustible material, i.e. the fire load density, is discussed. Lastly, in Section 3.3, which also takes into consideration the uncertain nature of the permanent and variable loads, a set of fragility curves for the burnout resistance of RC slabs are derived.

3.1 Probabilistic burnout bending resistance of RC slabs for deterministic fire exposure

The burnout evaluation presented in the previous section is based on deterministic modelling assumptions, in accordance with the Eurocode design methodology (EN 1991-1-2:2002 and EN 1992-1-2:2004). However, in contrast to the Eurocode guidance for normal design conditions, the target safety level for accidental design situations is not well-specified. To address this issue, Van Coile et al. [14] proposed target safety levels for structural fire design, based on a simplified cost-optimization model. Moreover, probabilistic methods are increasingly applied in fire safety engineering as a modification of more traditional design approaches, since these methods can more thoroughly take into account the uncertainties associated with the design and explicitly demonstrate the attainment of an adequate safety level [9]. Taking into account the uncertainties related to structural fire design is indispensable for evaluating the structural fire response of RC members. For example, it has been experimentally observed that both steel and concrete show considerable scatter in the value of their respective structural strengths at room temperature. Moreover, for both materials an even larger scatter is observed at the high temperatures typically associated with a building fire [15]. Indicative values for the uncertainties on the dimensions of concrete elements can be found in [16, 17].

To study the influence of the uncertainties related to the material properties and the geometry of fire exposed RC slabs, the burnout bending moment distribution is evaluated using Monte Carlo (MC) simulations. Figure 4.a and b depict the probability density function (PDF) and cumulative density function (CDF) for the burnout bending moment resistance $M_{R,burnout}$ of a RC slab, at ambient temperatures and for exposure to three Eurocode parametric fires regimes with a fixed fire load density q_f and varying opening factor O . These graphs are obtained through repeated evaluation of Eq. (2) for 10^5 MC samples. In each sample, the slab configuration is characterized by a vector X of randomly generated values of the probabilistic parameters listed in Table 2, with a reinforcement area $A_s = 785 \text{ mm}^2$. By generating many variable vectors X , calculating $M_{R,burnout}$ for each X and analysing the results, the PDF and CDF of $M_{R,burnout}$ are obtained [18].

From these figures, it can be concluded that the mean bending moment resistance decreases with increasing fire load density and decreasing opening factor. Moreover, when lognormal curves are fitted to the obtained resistance distributions, the lognormal approximations are found to be an imperfect fit. In some cases, the lognormal approximation underestimates the frequency of low $M_{R,burnout}$ values, while in other cases it gives a crude overestimation. This phenomenon has been shown to be caused by the variability in the rebar axis distance σ_a [12]. Moreover, the lognormal approximation appears to be worse for larger σ_a and/or for lower rebar axis distances to the exposed surface.

Table 2. Stochastic models for RC slab variables.

Property	Distribution	μ_x	COV_x	Ref.
Concrete compressive strength $f_{c,20^\circ C}$ at $20^\circ C$	lognormal	42.9 MPa ($f_{ck} + 2\sigma$)	0.15	[17]
Reinforcement yield stress $f_{y,(\theta)}$ at $\theta^\circ C$ (variation incorporated in $k_{fy(\theta)}$)	Deterministic	560 MPa	-	-
Retention factor $k_{fy(\theta)}$ for the steel yield stress at $\theta^\circ C$	Logistic	temperature dependent	temperature dependent	[15]
Slab height h	Normal	200 mm	0.025 ($\sigma = 5 \text{ mm}$)	[17]
Slab width w	Deterministic	1000 mm	-	-
Bottom reinforcement area A_s	Normal	1.02 A_s	0.02	[17]
Rebar axis distance a	Beta [$\mu \pm 3\sigma$]	35 mm	0.143 ($\sigma_a = 5 \text{ mm}$)	[16, 17]

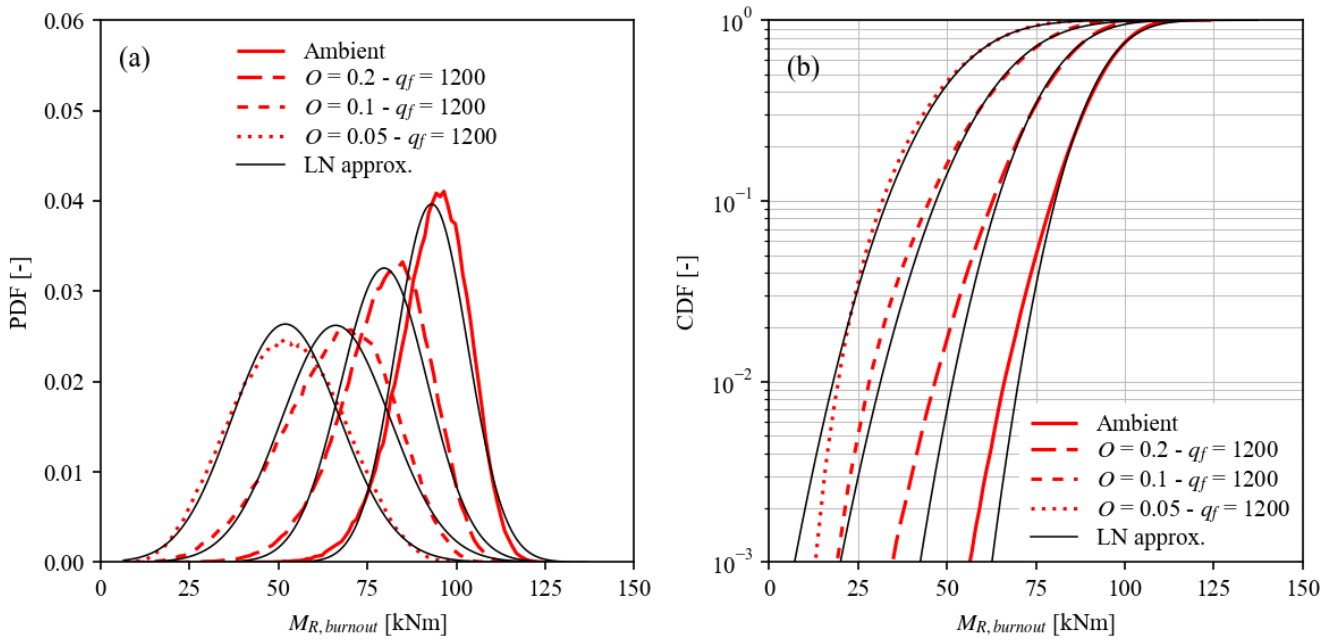


Figure 4: Burnout bending moment capacity $M_{R,burnout}$ and lognormal fitting curves for the RC slab specified in Table 2, for exposure to Eurocode parametric fires with varying opening factor O .

3.2 Probabilistic burnout bending resistance of RC slabs, with stochastic fire load density

The previous Section 3.1 only considers the uncertain nature of the material properties and geometry of the slab. However, as no two compartments in a building are identically furnished, also the fire load density should be considered as a stochastic variable. Therefore, the above calculation is repeated with explicit consideration of the fire load density as defined in Annex E of EN 1991-1-2, see Table 3. Figure 5 depicts the PDF for the bending moment resistance of a slab as defined in Table 2, for a dwelling for a number of opening factors. In Figure 6, similar graphs are presented for office compartments.

Similar to the graphs in Figure 4, the results show that in compartments with a smaller opening factor, the average carrying capacity tends to be smaller. When comparing Figure 5a and b, it is also evident that the average bending moment capacity reduces more in the case of a dwelling compared to an office compartment, as the average fire load density $\mu_{q,f}$ of the latter is higher, see Table 3. Like the figures in the previous section, the lognormal approximations are found to be an imperfect fit.

Table 3. Stochastic models for Eurocode parametric fire variables.

Property	Distribution	μ_x	COV_x	Ref.
Fire load density for a dwelling $q_{f,dwelling}$	Gumbel	780 MJ/m ²	0.3	[11]
Fire load density for an office $q_{f,office}$	Gumbel	420 MJ/m ²	0.3	[11]
Opening factor O	Deterministic	-	-	-

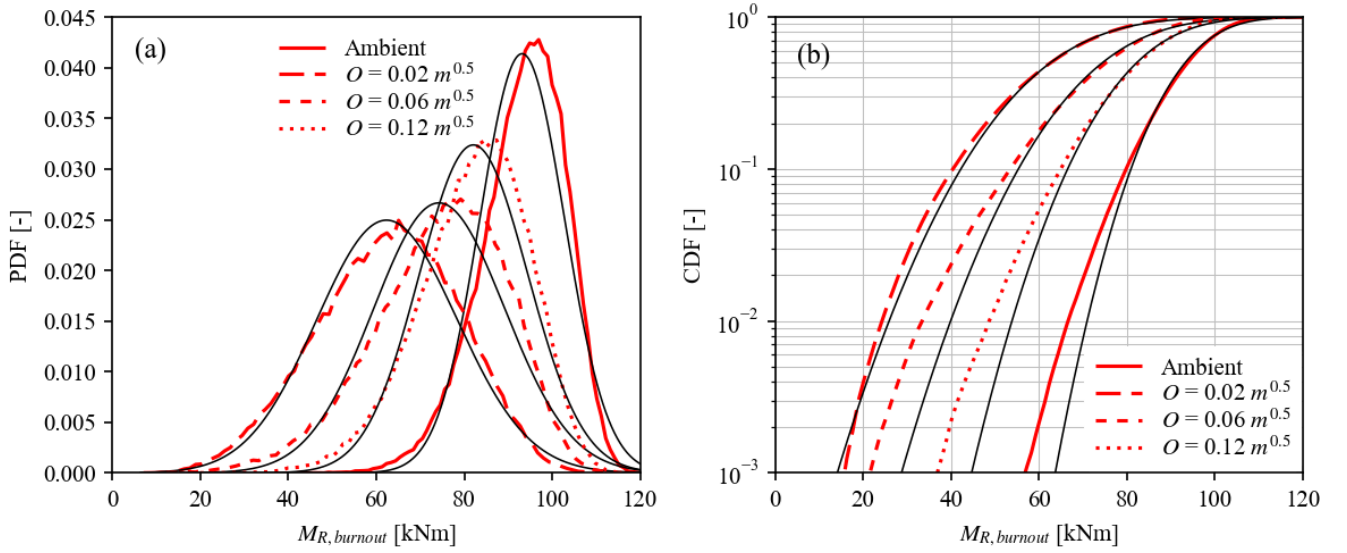


Figure 5: Burnout bending moment capacity $M_{R, burnout}$ and with lognormal fitting curves for the RC slab specified in Table 2, for exposure to Eurocode parametric fires in dwelling compartments.

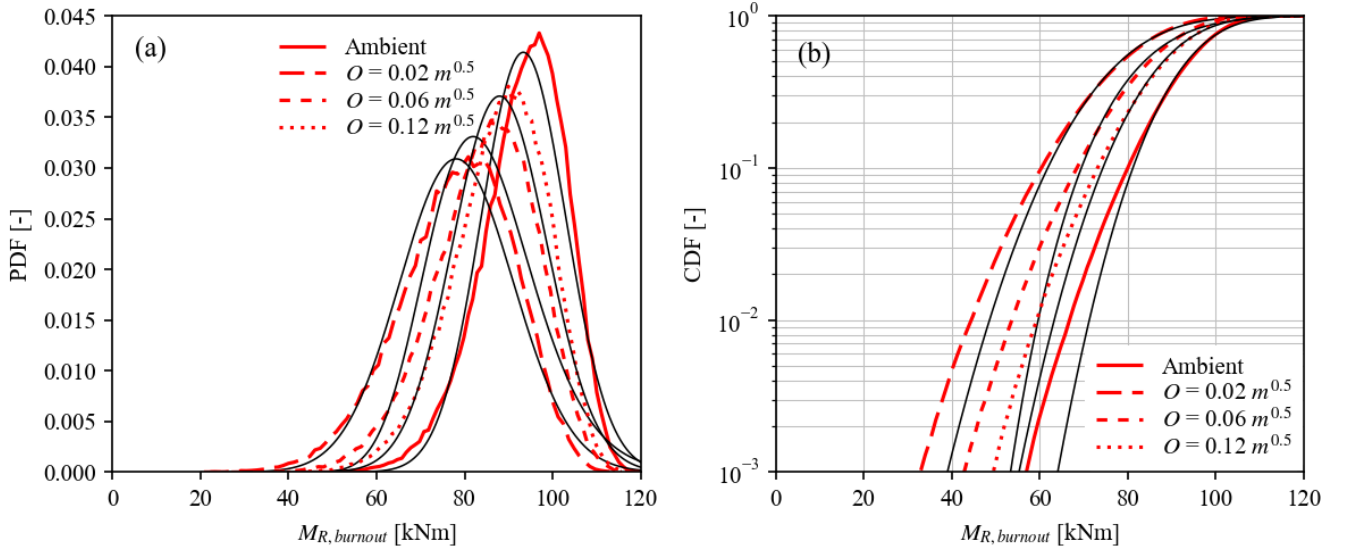


Figure 6: Burnout bending moment capacity $M_{R, burnout}$ and with lognormal fitting curves for the RC slab specified in Table 2, for exposure to Eurocode parametric fires in office compartments.

3.3 Failure probability of fire exposed RC slabs

The stochastic formulation for the bending capacity must be combined with appropriate load models and model uncertainties to demonstrate a high reliability with respect to the attainment of burnout resistance. Then, the performance of the design can be demonstrated by comparing the obtained probability of failure P_f to a specified target failure probability $P_{f,t}$. Previous studies investigating the failure probability of concrete slabs [19, 20] showed that in determining the capacity of the structure, the mechanical properties of steel at elevated temperatures cause large variations in the response.

Applied to the case of a simply supported fire exposed RC slab subjected to bending, and considering a functional requirement of structural resistance up to and including burnout, the probability of failure P_f is defined as the probability of the bending moment due to load effect $M_{E,fi}$ exceeding the burnout bending moment capacity $M_{R, burnout}$ of the slab:

$$P_f = P\left(K_R M_{R, burnout} < K_E (M_G + M_Q)\right) \quad (3)$$

Herein, the load effect is considered as a combination of the moment M_G induced by the permanent loads and the moment M_Q induced by the applied variable load. K_E and K_R in this expression are the model

uncertainties for respectively the load effect and the resistance effect. The probabilistic models for the model uncertainties and load effects are given in Table 4. By performing 10^6 Monte Carlo simulations, and counting for which the realization of the resistance effect $K_R \cdot M_{R,burnout}$ is smaller than the realization of the load effect $K_E \cdot (M_G + M_Q)$, fragility curves for the burnout resistance of the slab as defined in Table 2 are obtained, as shown in Figure 7. Herein fragility curves are presented for three load ratios χ , which defines the relation between the characteristic values M_{Gk} and M_{Qk} :

$$\chi = \frac{M_{Qk}}{M_{Gk} + M_{Qk}} \quad (4)$$

The fragility curves are plotted as a function of the fire design utilization u_{fi} , which for a RC slab in bending is defined as the ratio between the design load $M_{Ed,fi}$ and design resistance $M_{Rd,fi}$ in case of fire evaluated at ambient temperatures (i.e. $k_{fy} = 1$):

$$u_{fi} = \frac{M_{Ed,fi}}{M_{Rd,fi(20^\circ C)}} = \frac{M_{Gk} + \psi_{fi} M_{Qk}}{M_{Rd,fi(20^\circ C)}} \quad (5)$$

The partial factors in the expression for $M_{Ed,fi}$ are equal to unity and the combination factor $\psi_{fi} = 0.3$ for the variable load, i.e. the recommended value for residential and office buildings. From the graphs it is clear that both the opening factor O and load ratio have a significant influence on the failure probability of RC slabs exposed to Eurocode parametric fires.

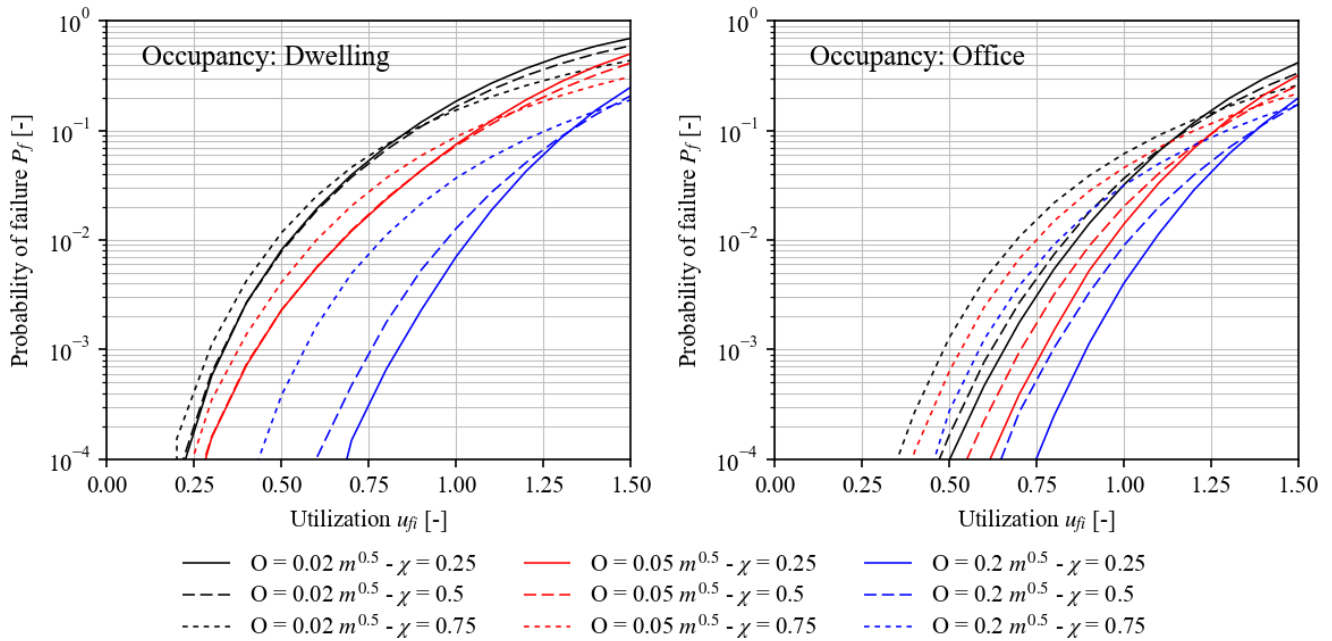


Figure 7: Fragility curves for RC slabs exposed to natural fires with varying opening factor O , for Dwellings and Offices

Table 4. Stochastic models for load variables and model uncertainties.

Property	Distribution	μ_x	COV_x	Ref.
Moment M_G induced by the permanent load	Normal	M_{Gk}	0.1	[21]
Moment M_Q induced by the variable load (arbitrary point in time)	Gamma	$0.2 M_{Qk}$	0.95	[21]
Model uncertainty K_E for the load effect	Lognormal	1	0.1	[21]
Model uncertainty K_R for the resistance effect	Lognormal	1.2	0.15	[17]

4 GLOBAL RESISTANCE FACTOR FOR RC SLABS EXPOSED TO NATURAL FIRE

As specified in the introduction, the global resistance factor (GRF) γ_R allows to perform a reliability-based evaluation, considering a single model evaluation using mean values for the stochastic variables. The design value for the resistance effect R_d is then obtained through eq. (1). Applied to the situation of RC slabs subject to bending, the attainment of the target safety level is then confirmed through eq. (6), where $\mu_{R,burnout}$ is the evaluation of eq. (2) considering the expected values for the stochastic variables.

$$\frac{\mu_{R,burnout}}{\gamma_R} = M_{Rd,fi} > M_{Ed,fi} = M_{Gk} + \psi_{fi} M_{Qk} \quad (6)$$

In case the resistance effect R_d can be neatly approximated by a lognormal distribution, the GRF γ_R can be approximated directly using a simple expression based on the coefficient of variation V_R as applied in [8]. However, as shown in Figure 4, 5 and 6 a lognormal approximation is not appropriate for the burnout resistance of RC slabs exposed to parametric fires. Therefore, this article applies an alternative calculation method, which uses a large number of Monte Carlo simulations and a full-probabilistic analysis to determine directly the actual value of the GRF for the bending moment capacity of concrete slabs exposed to fire.

Figure 8 depicts the calculated values of the GRF for the slab configuration in Table 2, exposed to several Eurocode parametric fire regimes, for various target failure probabilities $p_{f,i}$ and load ratios χ . In accordance with the Eurocode, for dwellings and offices, the combination factor for the variable load was set to $\psi_{fi} = 0.3$.

Overall, the graphs show that the highest values for the GRF are obtained for the case of a dwelling; compared to the case for offices, the GRF is higher over the entire range of studied opening factor values. For both compartment types, the GRF reduced significantly with increasing opening factor. Furthermore, the load ratio is shown to have a significant influence on the GRF. This is especially the case for $\chi = 0.75$ (i.e. $M_{Qk} = 3 \cdot M_{Gk}$), where consistently higher GRF values are observed over the entire range of opening factor values.

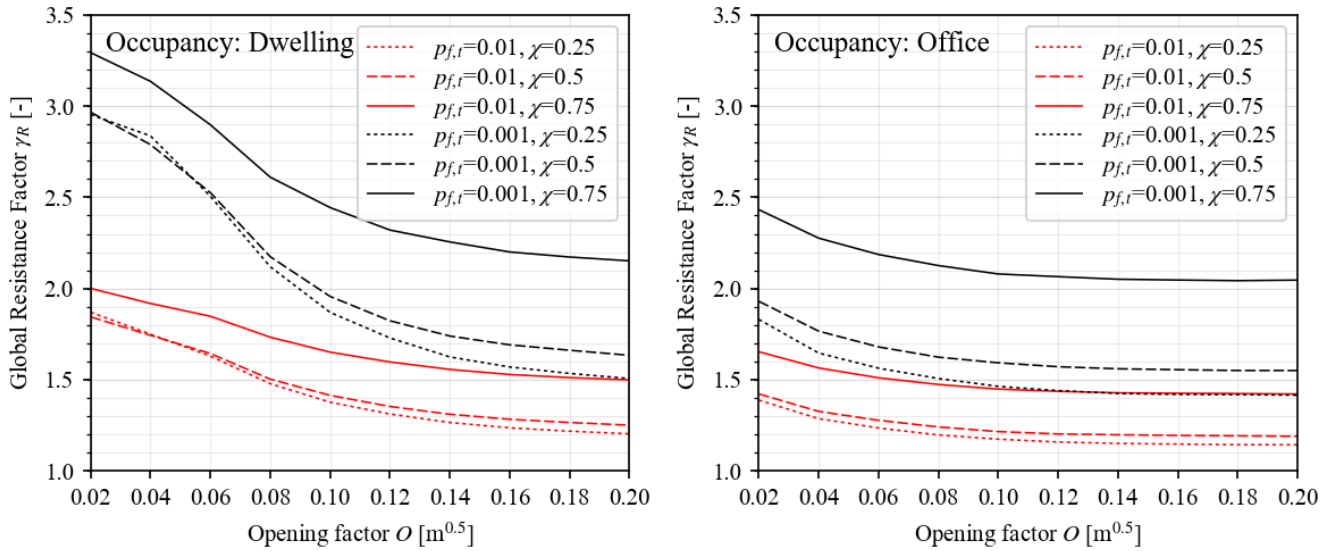


Figure 8: GRF for simply supported RC slabs exposed to natural fire, for various load ratios and target failure probabilities, over a range of fire opening factors.

5 EQUIVALENCY EXPRESSION

The above calculations were obtained assuming a $10 \text{ m} \times 10 \text{ m} \times 3 \text{ m}$ reference compartment with an opening factor $O = 0.05 \text{ m}^{1/2}$, fire load density $q_f = 800 \text{ MJ/m}^2$ and thermal effusivity $b = 1450 \text{ J/m}^2\text{s}^{0.5}$. However, as shown in [6], these results can be generalized for any compartment within the boundaries defined in EN1991-1-2 annex A, using the following scaling expressions (7) and (8).

$$O_{eq} = O \cdot \frac{b_{eq}}{b} \quad (7)$$

$$q_{f,eq} = q \cdot \frac{A_f}{A_{f,eq}} \cdot \frac{A_{t,eq}}{A_t} \cdot \frac{b_{eq}}{b} \quad (8)$$

These expressions are based on the fact that any parametric fire in a generic compartment with a given set of geometric and thermal properties is identical to the temperature-time curve in a reference compartment with an invariant geometry and invariant thermal properties when considering appropriate equivalent values for the fire load density $q_{f,eq}$ and opening factor O_{eq} for this equivalent compartment [22]. The suffix ‘eq’ refers to the equivalent compartment with fixed geometry and thermal inertia, while the other parameters refer to the generic compartment.

Using the above expressions, the calculated values presented in Figure 8 are applicable to any compartment within the Eurocode parametric fire framework. They can therefore easily be implemented as part of a more elaborate GRF based design method, as presented in [6].

6 CONCLUSIONS

The concept of a global resistance factor (GRF) for concrete slabs exposed to Eurocode parametric fire, including a cooling phase, was presented and the GRF values were computed for different target failure probabilities and for a several compartment types, over the entire range of opening factor values defined in the Eurocodes. Application of the determined GRF allows for explicit safety evaluations for fire exposed concrete slabs, without requiring the application of expert probabilistic methods. Lastly, a procedure for scaling these results to a compartment of different dimensions and thermal properties was presented. Through this procedure, the obtained GRF values can be incorporated in a simple design check for a wide range of compartment configurations.

ACKNOWLEDGMENT

The authors wish to thank the Research Foundation of Flanders (FWO) for the financial support on the research project “Performance-based analysis and design for enhancing the safety of prestressed concrete hollow-core slabs in case of fire and unforeseen events”.

REFERENCES

1. Organization International for Standardization, (1975). ISO 834-1975. Fire resistance tests- elements of building construction
2. American Society for Testing and Materials, (2008). ASTM Standard methods of fire test of building construction and materials. Test Method E119a -08. West Conshohocken, PA
3. CEN, (2004). EN 1992-1-2. Eurocode 2 – design of concrete structures. Part 1–2: general rules – structural fire design. Brussels
4. Gernay, T, (2019). Fire resistance and burnout resistance of reinforced concrete columns. Fire Safety Journal 104:67–78. <https://doi.org/10.1016/j.firesaf.2019.01.007>
5. Salah Dimia, M, Guenfoud, M, Gernay, T, Franssen, JM, (2011). Collapse of concrete columns during and after the cooling phase of a fire. Journal of Fire Protection Engineering 21:245–263. <https://doi.org/10.1177/1042391511423451>
6. Thienpont, T, Van Coile, R, Caspeele, R, De Corte, W, Burnout resistance of concrete slabs: probabilistic assessment and global resistance factor calibration. Fire Safety Journal (in review)
7. Cervenka, V, (2008). Global Safety Format for Nonlinear Calculation of Reinforced Concrete. Beton- und Stahlbetonbau 103:37–42. <https://doi.org/10.1002/best.200810117>
8. Van Coile, R, Caspeele, R, Taerwe, L, (2012). Global Resistance factor for concrete slabs exposed to fire. In: Fontana M, Frangi A, Knobloch M (eds) 7th International Conference on Structures in Fire. Zurich
9. Thienpont, T, Van Coile, R, De Corte, W, Caspeele, R, (2019). Determining a Global Resistance Factor for

- simply supported fire exposed RC slabs. In: Proceedings of the fib Symposium 2019. Krakow, pp 2191–2197
10. Allaix, DL, Carbone, VI, Mancini, G, (2013). Global safety format for non-linear analysis of reinforced concrete structures. *Structural Concrete* 14:29–42. <https://doi.org/10.1002/suco.201200017>
 11. CEN, (2002). EN 1991-1-2. Eurocode 1: actions on structures – Part 1-2: general actions – actions on structures exposed to fire. Brussels
 12. Van Coile, R, Caspeelee, R, Taerwe, L, (2013). The mixed lognormal distribution for a more precise assessment of the reliability of concrete slabs exposed to fire. In: *Safety, Reliability and Risk Analysis*. pp 2693–2699
 13. Van Coile, R, (2015). *Reliability-Based Decision Making for Concrete Elements Exposed to Fire*. Ghent University
 14. Van Coile, R, Hopkin, D, Bisby, L, Caspeelee, R, (2017). The meaning of Beta: Background and applicability of the target reliability index for normal conditions to structural fire engineering. *Procedia Engineering* 210:528–536. <https://doi.org/10.1016/j.proeng.2017.11.110>
 15. Qureshi, R, Ni, S, Khorasani, NE, Van Coile, R, Gernay, T, Hopkin, D, (2020). Probabilistic models for temperature dependent strength of steel and concrete. *Journal of Structural Engineering* 146:
 16. The Joint Committee on Structural Safety, (2001). Probabilistic Model Code - Part 3.10: Dimensions. JCSS
 17. Holicky, M, (2009). *Reliability analysis for structural design*. SUN MeDIA Stellenbosch
 18. Ang, AHS, Tang, WH, (2007). *Probability concepts in engineering*, 2nd ed. John Wiley & Sons, New York
 19. Ioannou, I, Aspinall, W, Rush, D, Bisby, L, Rossetto, T, (2017). Expert judgment-based fragility assessment of reinforced concrete buildings exposed to fire. *Reliability Engineering and System Safety* 167:105–127. <https://doi.org/10.1016/j.ress.2017.05.011>
 20. Gernay, T, Khorasani, NE, Garlock, M, (2019). Fire Fragility Functions for Steel Frame Buildings: Sensitivity Analysis and Reliability Framework. *Fire Technology* 55:1175–1210. <https://doi.org/10.1007/s10694-018-0764-5>
 21. Jovanović, B, Van Coile, R, Hopkin, D, Elhami Khorasani, N, Lange, D, Gernay, T, (2020). Review of Current Practice in Probabilistic Structural Fire Engineering: Permanent and Live Load Modelling. *Fire Technol.* <https://doi.org/10.1007/s10694-020-01005-w>
 22. Thienpont, T, Van Coile, R, Caspeelee, R, De Corte, W, (2019). Comparison of fire resistance and burnout resistance of simply supported reinforced concrete slabs exposed to parametric fires. In: *Proceedings of CONFAB 2019*. London

BOND STRENGTH BETWEEN STEEL REINFORCEMENT AND RCA CONCRETE AT ELEVATED TEMPERATURES

Md. Abu Yusuf¹, Salah Sarhat², Hamzeh Hajiloo³, Mark F. Green⁴

ABSTRACT

The exposure of reinforced concrete structures to elevated temperatures during a fire can have a detrimental impact on the bond between steel reinforcement and concrete. This can endanger the integrity of reinforced concrete structures under fire conditions because the transfer of tensile stresses from concrete to steel can decrease significantly. In addition, coarse aggregates play an essential role in the behaviour of concrete under fire exposure because aggregate types vary widely in their response to elevated temperatures. Replacing natural aggregate with recycled concrete aggregate (RCA) represents a promising solution to the growing construction and demolition waste challenge and helps in reducing excessive aggregate extraction from natural resources. The behaviour of RCA concrete under different loading types is a well-studied topic at both material and structural levels. However, relatively few investigations have been conducted on the bond strength between steel reinforcement and RCA concrete, especially when subjected to elevated temperatures. This paper aims at presenting the bond strength tests between steel reinforcement and RCA concrete at various steady-state temperatures. The results demonstrate that the bond strength between the steel and both types of concretes decreased with the increase of heating temperature, with splitting of the concrete block being the primary mode of failure. Lower bond strengths were observed at 200°C, 300°C, and 550°C because of the reduced tensile strength of concrete. The bond between the steel and the RCA concrete during exposure to high temperature performs better than that of the natural aggregate concrete.

Keywords: Bond strength; pullout test; RCA concrete; elevated temperature; steady-state temperature test

1 INTRODUCTION

Demolishing, renovation or retrofitting after or within the design life of the buildings, roads will create a large number of waste materials. Simultaneously it will require Virgin aggregate for new construction. The per capita per annum aggregate use is more than 16 tons in Ontario [1]. The extraction of virgin aggregate destroys the natural habitats of the organisms and environmental flow of the streams and water bodies. In addition, different organisms are vulnerable in the region of quarries and pits of aggregates due to the extraction [2]. It is widely recognized that the coarse aggregates play an essential role in the behavior of concrete under fire exposure as aggregate types vary widely in their response to elevated temperatures. Replacing natural aggregate with Recycled Concrete Aggregate (RCA) represents a promising solution to the growing construction and demolition waste challenge and helps in reducing excessive aggregate extraction from natural resources. The behaviour of RCA concrete under different loading types is a well-studied topic at both material and structural levels. However, relatively few investigations have been conducted on the bond strength between steel reinforcement and RAC concrete, especially when subjected

¹ Ph.D. Candidate, Dept. of Civil Engineering, Queen's University at Kingston, Ontario, Canada.

e-mail: md.yusuf@queensu.ca.

² Visiting Assistant Professor, Purdue University Fort Wayne, Indiana, USA.

e-mail: ssarhat@pfw.edu.

³ Assistant Professor, Dept. of Civil & Environmental Engineering, Carleton University, Ottawa, Ontario, Canada.

e-mail: hamzeh.hajiloo@carleton.ca.

⁴ Professor, Dept. of Civil Engineering, Queen's University at Kingston, Ontario, Canada.

e-mail: greenm@queensu.ca.

to elevated temperatures. Work has been done at the materials lab at Queen's University to study the bond strength between steel reinforcement and RCA concrete during and after exposure to elevated temperatures. Tests are being conducted according to three heating scenarios: steady-state temperature tests (20, 200, 300, 400 and 550°C), transient temperature tests (after preloading to 30% and 60% of the reference bond stress), and residual (after 550°C exposure) bond strength tests.: steady-state temperature tests (20, 200, 300, 400 and 550°C), transient temperature tests (after preloading to 30% and 60% of the reference bond stress), and residual (after 550°C exposure) bond strength tests.

The bond is the grip in the interface of reinforcement bar with the adjacent concrete to transmit the axial load from one element to another. The Bond stress will ensure the combined action of steel and concrete along to ensure the strain compatibility [3]. Bond between steel and concrete is the most important structural property to act together as composite materials. Through the bond between steel and concrete, load is being transferred from one to another and the reinforced concrete will act as composite material. The bond stress is being calculated from the shear stress per unit area of the bar surface [3]. The bond stress between the reinforcement and concrete interface has direct influence on the behavior of the reinforced concrete structure [4]. In the reinforced concrete design, the strain in steel is considered as same as the strain in the surrounding concrete [5]. But it is totally depending on the bond between steel and concrete. Darwin et al. [6] observed that the bond strength will increase with the use of higher aggregate strength. They found higher value of bond strength due to having high fracture energies of the aggregate. The development requirement is larger for the lightweight concrete than that of the normal weight concrete [3].

Sindy Seara-Paz et al. [7] investigated the bond strength of RAC with respect to replacement ratio of RCA (20%, 50% and 100%). They found less bond strength with the increase of RCA in concrete and reported the same thing for the compressive strength of the concrete. Sun-Woo Kim and Hyun-Do Yun [8] made RAC with different replacement ratio using two different aggregate size to observe the effect of RCA in concrete bond strength and concluded with the higher strength for the concrete made of aggregate maximum size of 20 mm than that for the concrete with maximum aggregate size of 25 mm. The compressive strength was being decreased with the increase of replacement ratio. However, the change of bond strength was not dependent with the ratio of RCA used in the concrete.

It is clear that relatively few investigations have been conducted on the bond strength between steel reinforcement and RCA concrete, especially when subjected to elevated temperatures. This paper aims at presenting the initial results of this experimental program conducted at Queen's university focusing on the bond strength tests at various steady-state temperatures.

2 EXPERIMENTAL PROGRAM

2.1 Test matrix

The main focus of this experimental work is to assess the effect of elevated temperatures on the bond strength between steel reinforcement and RCA concrete. Pull-out specimens were prepared with 15M deformed steel bars embedded into 150mmx150mmx150mm concrete blocks with an embedment length of 64 mm the remaining length was covered with high-temperature resistant epoxy coating to leave it unbonded shown in Figure 13. Two different types of concrete were utilized in this study. These are the control concrete made of natural crushed limestone aggregate (100%CL0%RCA), and the concrete made with 100% coarse RCA (0%NA100%RCA). This paper reports the test results of 30 pull-out specimens tested in steady-state scenario under five different temperatures (20°C (ambient), 200 °C, 300 °C, 400 °C and 550°C). In addition to the pull-out specimen, twenty concrete cylinders were cast, exposed to same temperature levels as their corresponding pull-out specimens. The concrete cylinders were tested to measure the compressive and the splitting tensile strengths. Table 1 shows the experimental test matrix covered in this paper.

Table 1. Experimental Test Matrix

Concrete Type		100%CL-0%RCA			0%CL-100%RCA		
Type of Specimen		Cylinder		Pullout Sample	Cylinder		Pullout Sample
Test Type	Temperature (°C)	Compressive Strength	Splitting Tension	Bond strength	Compressive Strength	Splitting Tension	Bond strength
Steady-state test	20°C	3	3	3	3	3	3
	200°C			3			3
	300°C			3			3
	400°C	2		3	2		3
	550°C	2		3	2		3

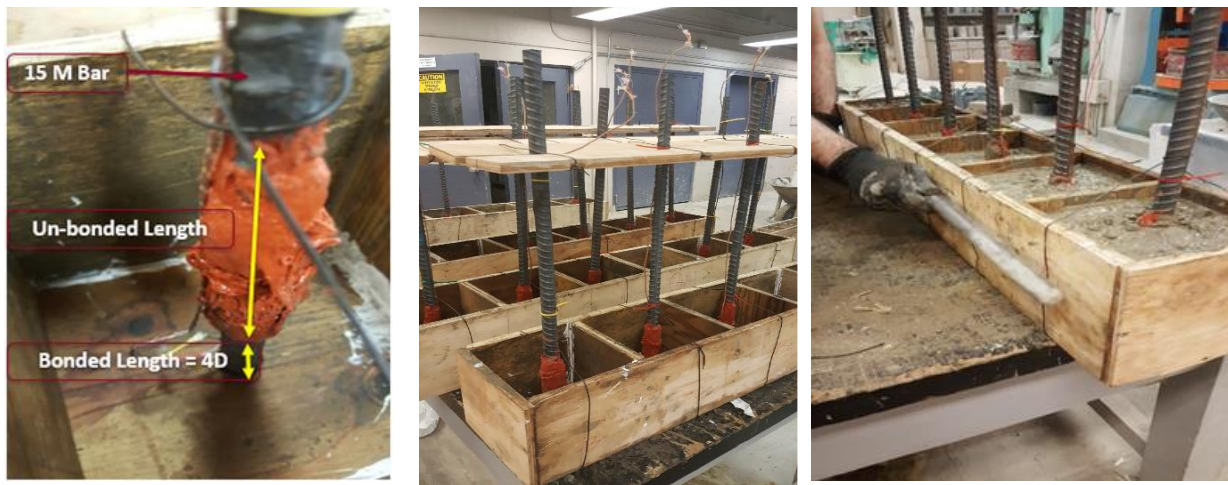


Figure-1: Preparation of 150mm cube moulds with a concentric 15M reinforcing bars

2.2 Materials and mixes

Portland limestone cement produced in Canada was used in all mixes. Natural river sand with a fineness modulus of 2.66 was used as fine aggregate. Crushed limestone was used as natural aggregate. The Recycled Aggregate was originated from the demolition of the large chunks of concrete curb sides of roads. There was a layer of natural aggregate attached to back of these curb side chunks which accounted for 12% of natural aggregate particles mixed with the RCA (See Figure 2 for samples of both types of aggregates). For consistency, each aggregate was separated into different size fractions using a sieve shaker and recombined to a predetermined gradation (33% passed 19 mm and retained on 12.5 mm sieve, 33% passed 12.5 mm and retained on 9.5 mm sieve and 34% passed 9.5 mm and retained on 4.75 mm sieve). To rationally evaluate the effects of each type of coarse aggregate on the bond between concrete and steel rebars during exposure to elevated temperatures, the coarse aggregate volume was kept constant in both mixes. Water-cement ratio was kept constant for both mixes as well. Mixes were designed using the absolute volume method. The physical properties of the coarse aggregates are summarized in Table 1. It can be seen in Table 1 that RCA has a lower density and greater water absorption than the natural aggregates due to the presence of cement mortar.



Figure 2. Coarse aggregates types, a) Natural crushed limestone aggregate, b) Recycled concrete aggregate

Table 2. Details of aggregate properties

Aggregate Properties	Aggregate Types		
	Natural Crushed Limestone Aggregate	Recycled Concrete Aggregate	Natural Sand
Max. Size (mm)	19	19	4.75
Unit Weight (kg/m ³)	1762.7	1440.6	1756.7
Relative Density (OD)	2.64	2.34	2.60
Relative Density (SSD)	2.65	2.49	2.67
Water absorption (%)	1.15	4.5	1
Crushing value (%)	21.5	24.5	-
Residual Mortar (%)	0	27	0

All aggregates were introduced into the mixing process in a saturated-surface dry condition. They were weighted and stored in plastic containers, 24 hours before mixing, together with the exact amount of water needed to achieve their saturated surface-dry condition. A small amount of superplasticizer (SP) was used in the RCA concrete to maintain a slump value of 90-100 mm. As shown in Figure 1, one type K thermocouple was attached to the middle of bonded length to measure the temperature rise inside the sample. Proper compaction was achieved by vibrating the sides of the wooden mould using a needle vibrator (Fig. 3b). Casted specimens were kept wrapped with polythene sheets for one week. The specimens were then demolded and stored in a room maintained at a temperature of 22°C and relative humidity of 65% for 28 days.

Table 3. Mixing proportion (kg/m³)

Concrete type	Replacement ratio (%)	Natural Crushed Limestone (CL)	Recycled Concrete Aggregate (RCA)	Sand	Cement	Water	Super plasticizer
100%CL-0%RCA	0	1024	0	743	410	205	0
0%CL-100%RCA	100	0	903	743	410	205	0.75

2.3 Test setup

An Instron SATEC testing machine (Figure 3 a) was used for the pullout tests. In the current experiments, the displacement rate was set to 1.0 mm/minute. In this machine, loading and heating of the samples can be conducted

simultaneously based on the type of test. In the steady-state temperature tests, the specimens were heated to the specified temperature and then kept in the furnace for 3 hours until the temperature rise inside concrete reaches a steady-state condition. After that, pullout specimens were loaded until failure at high temperature. To simulate a representative fire condition, the heating rate was chosen close to the rate of temperature rise during a real fire in concrete which was estimated 5 °C/min [9,10]. Figure 3b illustrates the furnace air temperature and inside temperatures of the pull-out specimens during heating. All tests for unheated and heated specimens and cinders, were carried out in the materials laboratory of Queen's University at age ranging from of 70 days to 77 days. Bond strength was calculated on the basis of load required to pullout the bar divided by the surface area of the bonded length shown in equation 1.

$$\text{Bond stress, } \tau = \frac{P_{failure}}{\pi D * 4D} \quad \text{----- (1)}$$

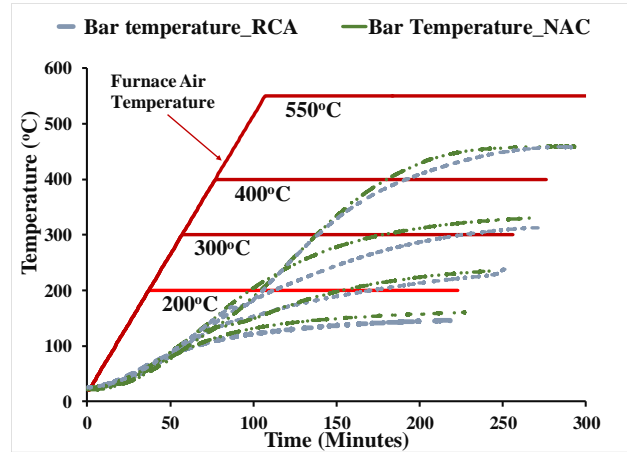
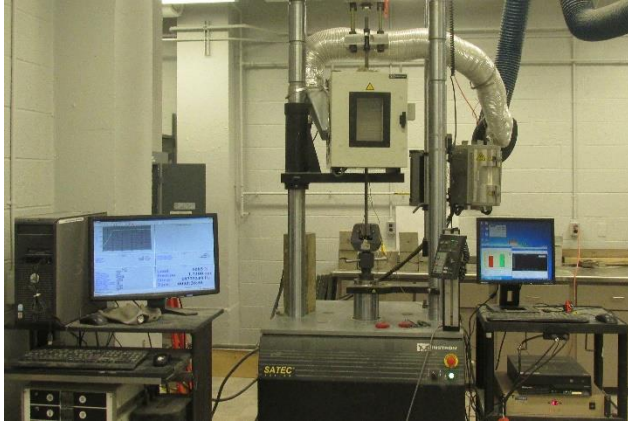


Figure 3. a) Test setup (Instron-SATEC testing machine) , b) Temperature rise in the rebar inside the concrete of pullout specimens during heating Results and discussion

3 RESULTS AND DISCUSSION

3.1 Failure modes

Four types of bond failure were observed in the pullout specimens of both types of concretes at different exposure temperatures. These are: pure end-slip, block splitting, diagonal splitting, and radial splitting. Most of the pullout failures included splitting and crushing of concrete grips (bearing of concrete) as shown in Figure 4. The failure patterns of the interface between concrete and reinforcement are listed in Figure 5. At temperature within 200°C-300°C, there was no destruction in the rib faces as the pullout specimens were failed by splitting of concrete. When the temperature reaches more than 400°C, the failure was initiated with shearing/crushing of concrete under the ribs and then failed by splitting of concrete.



Figure 4: (From left) Pure End-Slip, Block Splitting, Diagonal Splitting, and Radial Splitting

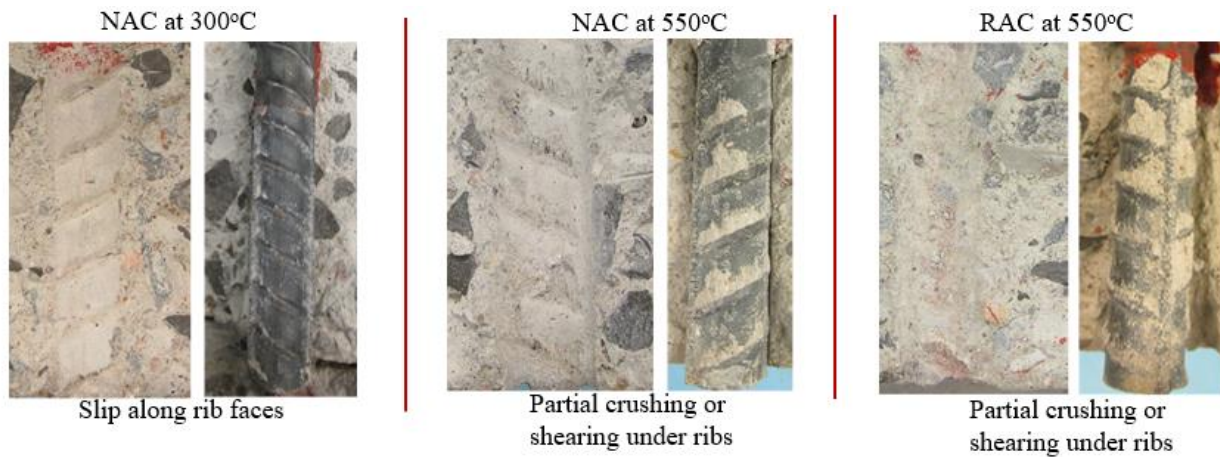


Figure 5. Failure patterns: Slip along rib faces and partial crushing or shearing under ribs.

3.2 Bond Strength between steel rebar and concrete

Figure 6 represents a summary of the bond strength of RCA concrete and natural aggregate concrete at different temperature. Bond strength of Recycled Aggregate Concrete (RAC) was smaller than that of Natural Aggregate Concrete at ambient temperature by an average of 10%. Figure 6 shows that exposure to elevated temperatures effects caused significant reductions in bond strength between steel rebars and both types of concrete. Lower bond strengths were observed at 200°C, 300°C, and 550°C because of the reduced tensile strength of concrete. This can be supported by the test results of compressive strength during exposure to elevated temperatures (See figure 7). It can be clearly seen in Figure 9 that the compressive strength decreased significantly with the increase of exposure temperatures. Splitting tensile strength which is dependent on copressive strength can be expected to decrease significantly with the increase of exposure temperatures as well.

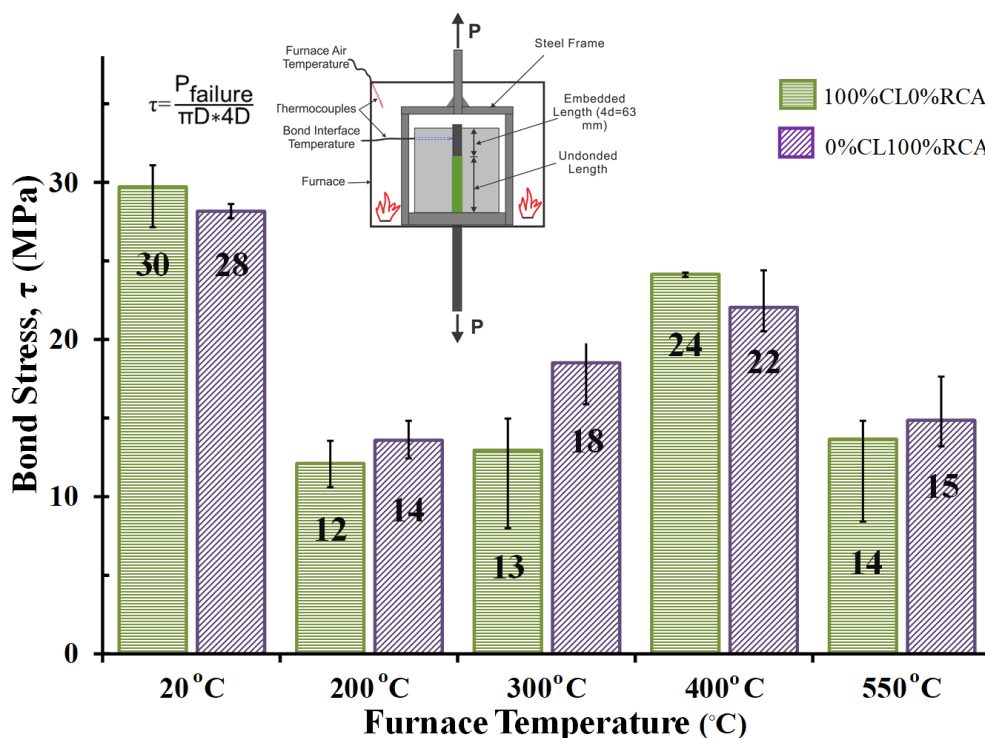


Figure 6. Bond strength between steel reinforcement and concrete during exposure to different elevated temperatures

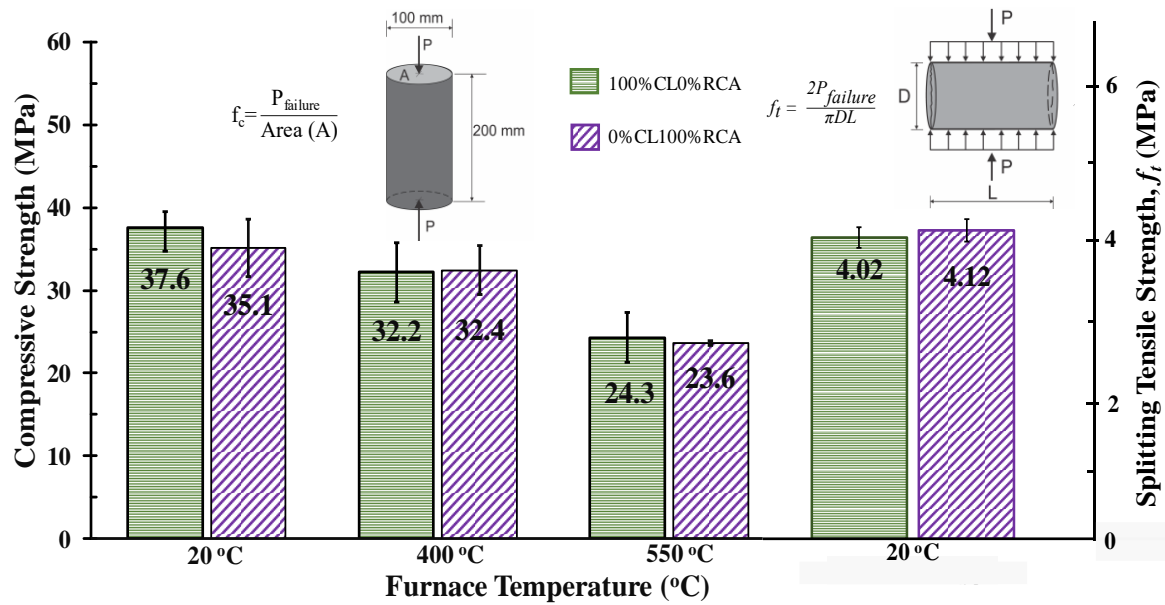


Figure 7. Compressive strength of concrete at different steady-state temperatures and splitting tensile strength at ambient temperature.

It is interesting to note that the bond strength improved between 300°C and 400°C compared to 200°C and 550°C. This can be explained by softening in steel, which limited the effect of decreased concrete splitting strength. It is also interesting to note that the bond between steel rebars and RCA concrete during exposure to different elevated temperatures performs better than that of natural aggregate concrete. This improvement in bond strength of RCA concrete can be attributed to the better match in mechanical properties and thermal expansions of RCA and cement paste [11]. The improvement in bond strength of RCA concrete compared to that of natural aggregate concrete was also evident from the load versus stroke displacement behaviors at both ambient and during exposure to 550 °C (see Figure 8).

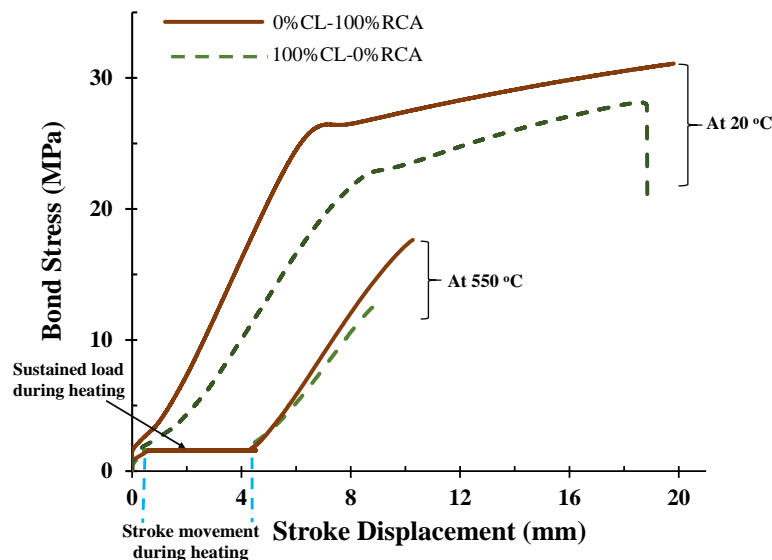


Figure 8. Bond strength vs stroke displacements for both concretes at ambient and during exposure to 550°C

4 CONCLUSIONS

Based on the experimental results, the following conclusions can be derived:

- Behaviour of bond strength between steel reinforcement and RCA concrete is quite similar to that of NAC. Test results of this paper indicate that the bond strength between the steel and both types of concretes (NAC and RCA) decreased with the increase of heating temperature, with RCA concrete showing smaller reductions in bond strength compared to that of natural aggregate concrete during exposure to elevated temperatures of up to 550°C. This improvement in bond strength of RCA concrete can be explained by referring to the better match in mechanical properties and thermal expansions of RCA and cement paste.
- The reduction in bond strength between the steel and concrete during exposure to 400 °C is smaller than those at 200°C, 300°C, and 550°C. This trend can be attributed softening of steel, which limited the effect of decreased concrete splitting strength.

REFERENCES

1. APAO (Aggregate Producers Association of Ontario), Importance of Aggregate: The About Aggregate Series, Aggregate Producers Association of Ontario, Mississauga, Ontario, 2004, pp. 1-4.
2. Winfield, M.S., Taylor, A. Replacing the load: The need for an aggregates conservation strategy for Ontario, Report published by Pembina Institute for Appropriate Development, 2005. ISBN 0-921719-71-x
3. ACI Committee 408, 2003, “Bond and Development of Straight Reinforcing Bars in Tension”, ACI 408R-03, ACI Committee 408 Report, American Concrete Institute, Farmington Hills, Michigan, 2003.
4. Hussain L., Analytical Modelling of Bond stress at steel-concrete interface due to corrosion, MASc. thesis, Civil Engineering, Ryerson University, pp 109-110, 2011.
5. Nilson A.H., Darwin D., Dolan C.W. 2004, Design of Concrete Structure, Thirteenth edition, The McGrawHill Company, 2004.
6. Darwin, D., Barham, S., Kozul, R., and Luan, S. Fracture Energy of High-Strength Concrete, ACI Materials Journal, Vol. 98, No. 5, 2001, pp. 410 – 417.
7. Sindy Seara-Paz, Bele’n González-Fontebao, Javier Eiras-Lo’pez, Manuel F. Herrador, Bond behavior between steel reinforcement and recycled concrete, published on Materials and Structures (2014) 47:323–334 DOI 10.1617/s11527-013-0063-z
8. Kim, S.W. and Yun, H.D., Influence of Recycle Coarse Aggregates on the bond behavior of deformed bars in concrete, Engineering Structures journal, 48:133-143(2013).
9. Katz, A., Berman, N. and Bank, L. C., Effect of high temperature on bond strength of FRP rebars.” J. Compos. Constr. 3 (2): 73–81 (1999). [https:// doi.org/10.1061/\(ASCE\)1090-0268\(1999\)3:2\(73\)](https://doi.org/10.1061/(ASCE)1090-0268(1999)3:2(73)).
10. Hajiloo, H., and Green, M. F., Bond strength of glass fibre reinforced polymer bars in concrete at high temperature, Building on our Growth Opportunities: Proceedings of CSCE Annual Conference, Regina, May 2015.
11. Sarhat, S.R. and Sherwood, E.G., Residual Mechanical Response of Recycled Aggregate Concrete after Exposure to Elevated Temperatures, Journals of Materials 25 (11): 1721-1730 (2013). DOI:10.1061/(ASCE)MT.1943-5533.0000719

EVALUATION OF EXPECTED DAMAGE COSTS FROM FIRE IN CONCRETE BUILDING STRUCTURES

Shuna Ni¹, Thomas Gernay²

ABSTRACT

This paper proposes a framework for estimating annual economic losses due to fire in concrete building structures, considering the uncertainties in the occurrence and growth of a fire and the response of the building. The loss assessment follows four steps for each possible fire location, including fire hazard analysis, response analysis, damage analysis, and loss analysis. The expected loss for the building is the weighted summation of the expected losses under fires in different locations. Two sets of fire-specific engineering demand parameters (EDPs) are proposed for structural components to address the damage related to both the temperature penetration in the section and the deformation of the component. Components are characterized in damage states depending on threshold values of the EDPs, based on which the fragility and consequence functions are defined. As a case study, the expected fire loss was estimated for a five-story RC frame building. Direct losses from single-compartment fire scenarios were evaluated at about 188 k\$, conditional to the occurrence of a severe fire. However, losses from structural components amounted to only 14% of this total, highlighting the need for more studies on nonstructural components and content. The method discussed herein could be generalized for other types of buildings and expanded to cover indirect fire losses. This framework can serve to support cost-benefit analyses of fire safety measures and hazard vulnerability assessments of communities.

Keywords: Fire; resilience; concrete structures; PEER; probabilistic loss estimation; performance-based

1 INTRODUCTION

While methodologies exist to probabilistically estimate annual losses caused by natural hazards such as earthquake [1–3], such a well-developed methodology is not available for fire hazards, due to challenges from the unique spatial-temporal evaluation of fire hazard, the complexity of assessing structural fire damage, and the scarcity of empirical data to construct fragility and consequence functions. However, communities can suffer great loss following a fire due to direct damage, content loss, and loss of functionality of the damaged buildings and infrastructures at the scales of both individual structures and communities [3–5]. A systematic framework to estimate probabilistic fire losses is required to evaluate the aftermath of a fire hazard, which is also desirable for engineers to enable performance-based design optimization and cost-benefit analysis of fire safety measures [6,7].

Existing studies about the fire loss estimation mainly focused on either individual structural components or 2D frames [8–11], rather than a whole structure system, ignoring the significant interaction between structural components within a building when it is exposed to fire. Moreover, existing studies generally used a binary criterion of failure/no failure to classify damage states, which works for some cases but is not the case for the fire damage of concrete structures. Most RC structures do not collapse under fire [12,13];

¹ Assistant Professor, Utah State University,
e-mail: shuna.ni@usu.edu, ORCID: <https://orcid.org/0000-0002-8795-176X>

² Assistant Professor, Johns Hopkins University
e-mail: tgernay@jhu.edu, ORCID: <https://orcid.org/0000-0002-3511-9226>

however, the damage related to heat penetration or deformation may require significant repair efforts, hence influencing the loss assessment.

To fill the gaps mentioned above, this paper proposes a framework for the probabilistic estimation of annual direct economic losses due to fire, applied to reinforced concrete building structures [14]. Building on the PEER methodology [15], the framework consists of four steps: fire hazard analysis, fire-thermo-mechanical analysis, damage analysis, and loss analysis (Figure 1). Yet unlike an earthquake, the damage caused by a fire to a building depends on the location of fire ignition and spread within the building. Therefore, the assessment considers a multiplicity of scenarios within the building, corresponding to different locations of ignition of the fire, captured by the outer loop in Figure 1. For a given fire location, the fire load (q_f) is used as the intensity measure. The methodology calculates the expected annual loss due to fire as a weighted sum (conditional probabilities) of estimated losses for different fire locations.

In addition to incorporating the uncertainties in fire occurrence, location, and growth, this framework addresses the multi-physic characteristics of fire damage by defining fire-specific engineering demand parameters, based on which fire-specific damage states were classified, and fire-specific fragility and loss functions were developed. Unlike previous works [8,10,11], this framework addresses gradual levels of repair efforts of the building components, thereby providing a finer degree of granularity in defining fire damage as required for RC structures that often do not collapse under fire [12,13] but require repair efforts for re-use.

In the following sections, this paper first describes the framework and then presents a case study estimating the annual expected fire loss of a five-story RC building. The case study uses finite element analysis to quantify the response of the entire structural system to capture the three-dimensional interactions between frame members and floors due to thermally-induced effects, which corroborated at the scale of an entire building that the PEER seismic engineering methodology can be adapted to conduct fire loss assessment through the sequential four-step analyses using new EDPs.

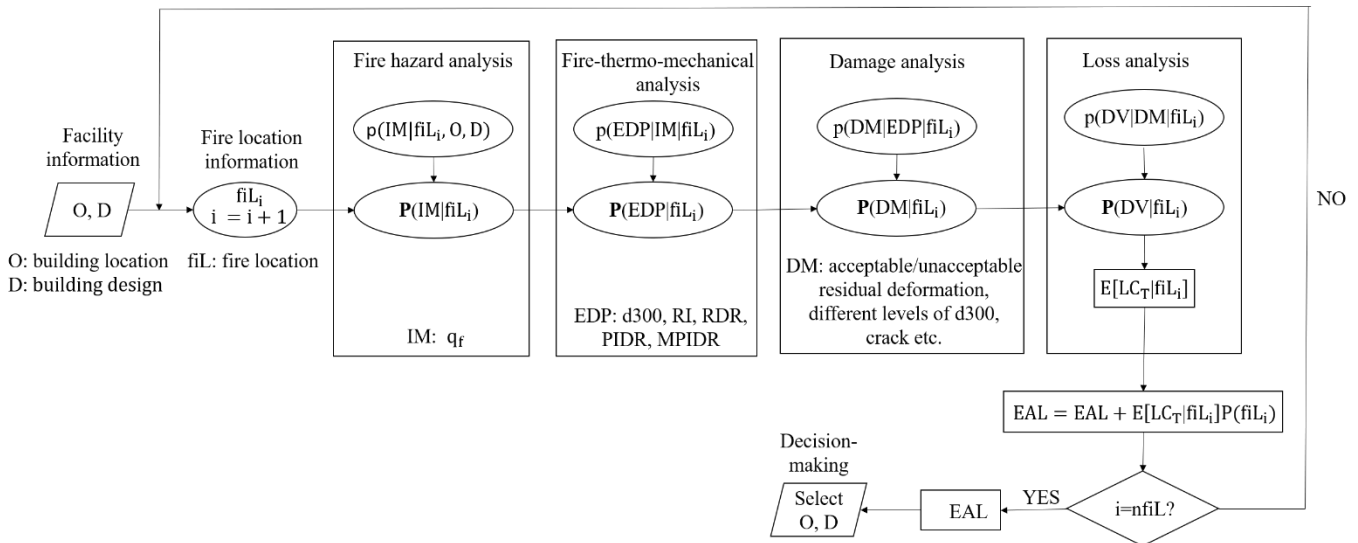


Figure 1. Probabilistic loss assessment for buildings under fire, adapted from PEER [14]

2 DEMAND PARAMETERS (EDP), DAMAGE STATES (DS) AND FRAGILITY FUNCTIONS

The framework of Figure 1 requires EDPs, DSs, and fragility functions to assess the damage caused by fire in a RC building. These parameters are defined for each type of component potentially damaged by fire exposure, including structural/nonstructural components and content in both fire and non-fire regions.

Structural members in the fire-exposed area are damaged both by direct exposure to elevated temperature (e.g. irreversible loss of strength) and by the deformations generated in the structure. Therefore, for heated structural members, two sets of EDPs are adopted: (1) one based on heat penetration depth, and (2) one based on residual deformations. Figure 2 shows the definition of the EDPs from the global finite element

model. The EDP for heat penetration is based on the 300°C isotherm in the concrete section (noted d300) because existing research on the degradation of concrete under fire has shown that a considerable reduction in material properties occurs during a fire and after cooling [16]. The EDP for residual deformation is taken as the residual inclination (RI) for columns and as the residual vertical deflection ratio (RDR) for the floors, including beams and slabs. The RI is defined as the ratio of residual deformation at the column top (Δ_c) over the height of the column (h). The RDR is defined as the ratio of the residual vertical deformation at the center of the slab (Δ_s) over the square root of the product of spans in x and y directions ($l = \sqrt{l_1 l_2}$).

The damage states (DS) corresponding to different levels of repair efforts are classified as a function of predefined threshold values of these EDPs. The thresholds are based on repair actions defined in codes and bulletins. For the EDP of heat penetration, the DS listed in Table 1 correspond to different levels of repairs needed for concrete sections as described in [16–18]. Regarding the residual deformation of columns, the research done by McCormick et al. for earthquake [19] has proposed a threshold of 0.005 rad, considering functionality, construction tolerance, and safety. They noted that no structural realignment is required for a column with a residual inclination up to 0.5%, while repairs are required beyond this value. Therefore, two DS are adopted, as shown in Table 2. The first level corresponds to the scenario where RI is less than 0.5%, and no repair efforts are needed; the second level corresponds to the scenario where RI is equal to or greater than 0.5%. Since it is difficult to straighten an RC structural component, a column at the second level of damage state should be replaced. For a floor system (slabs and beams), the thresholds can be based partly on the serviceability limiting values in design codes. For instance, the CSA A23.3-14 [20] includes a limit of $L/360$ for the immediate deflection of a floor under the live load, and a limit of $L/240$ for the long-term deflection of a floor under the dead load and the sustained live load. Those limits are adopted as the threshold values of the residual vertical deflection of a floor system in classifying DS that are listed in Table 3. The repair actions corresponding to the four DS are no repair, levelling the floor surface, replacing the slab, and replacing the whole floor system.

The DS thresholds are taken as probabilistic variables to incorporate the uncertainties inherent to the post-fire evaluation process. Data is lacking to quantify these probabilistic variables and further research is required. Here, it is assumed that those variables follow a lognormal distribution with mean values equal to the threshold values listed in Tables 1-3 and coefficients of variation equal to 0.1. The lognormal distribution of the lower threshold of each DS (as shown in Tables 1-3), as a probabilistic function of the EDP, is the fragility function that represents the probability of a component to reach or exceed the damage state, as shown in Figure 2.

Nonstructural components and content in the fire-exposed area are assumed to be irreversibly damaged. Therefore, the loss assessment assumes a total loss for the content and the nonstructural components in the fire area.

Components outside the fire area, albeit cold, may also be damaged as they may be subject to forces and displacements exerted by the surrounding heated members. Their level of damage is evaluated using displacement-based EDPs, and corresponding DSs and fragility functions that are adapted from earthquake literature [21,22]. The content outside the fire area is assumed to remain intact from fire damage.

Table 1. Damage states for the EDP of 300°C isotherm penetration depth in the RC sections [16–18].

Damage states	EDP: Penetration depth of the 300°C isotherm (d300)
DS0	The temperature did not exceed 300°C in concrete
DS1	$0 < d300 < c/10$
DS2	$c/10 \leq d300 < c$
DS3	$c \leq d300 < d/4$; d is the side dimension of the cross-section
DS4	$d/4 \leq d300 \leq d/2$

Note: c is the concrete cover to the edge of the rebar

Table 2. Damage states based on the residual inclination of RC columns [19][16].

Damage state	EDP: Residual inclination (RI)
DS0	$\Delta_c/h < 0.5\%$
DS1	$\Delta_c/h \geq 0.5\%$

Table 3. Damage states based on the residual vertical deflection of RC slabs [20].

Damage state	EDP: Residual vertical deflection (RDR)
DS0	$\Delta_s/l < 1/240$
DS1	$1/240 \leq \Delta_s/l < 1/120$
DS2	$1/120 \leq \Delta_s/l < 1/60$
DS3	$1/60 \leq \Delta_s/l$

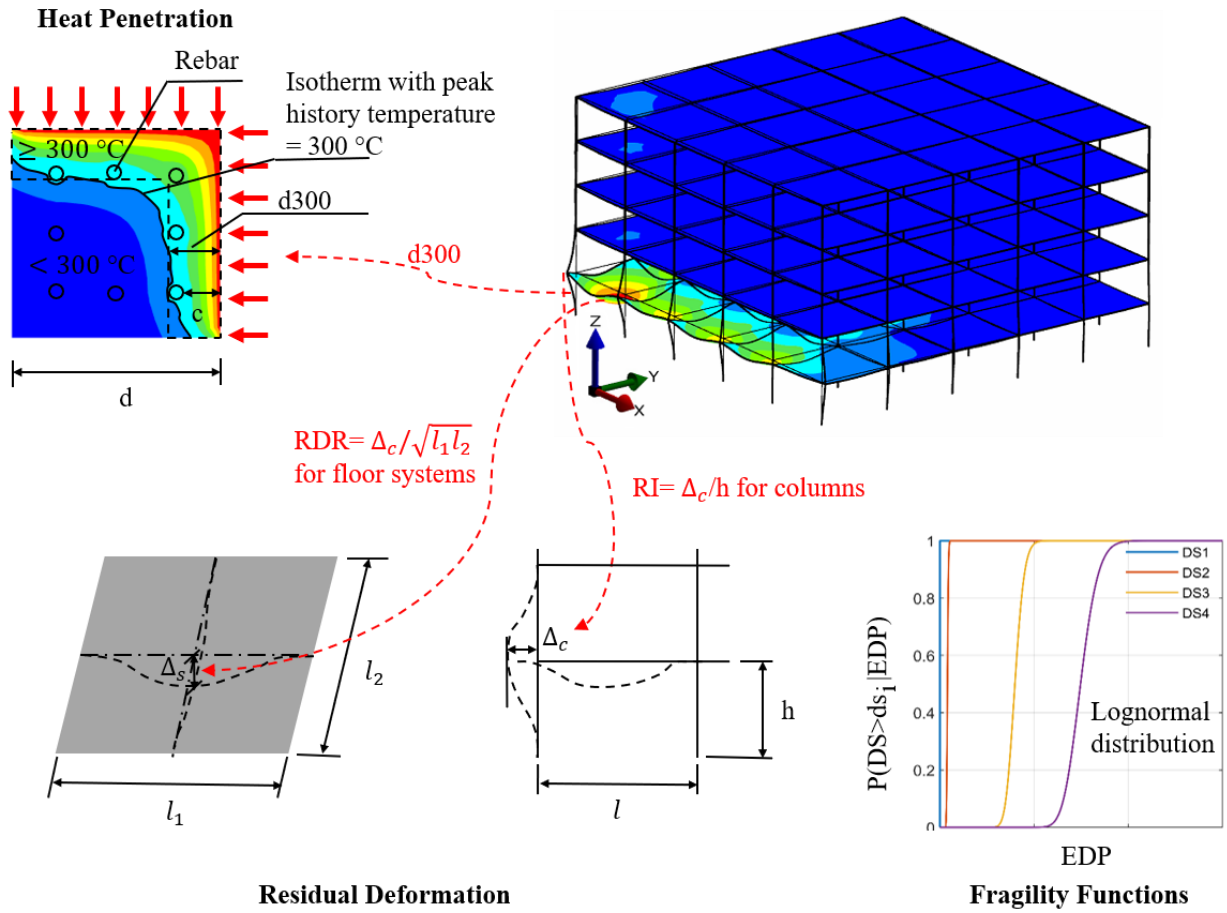


Figure 2. Definition of the engineering demand parameters from the global structural model.

3 DESCRIPTION OF THE ASSESSMENT PROCEDURE

The damage caused by a fire depends on the fire location of ignition and development within the building. Therefore, the assessment considers different possible fire scenarios within the building corresponding to different locations of ignition of the fire. Four analysis steps, including fire hazard analysis, fire-thermo-mechanical analysis, damage analysis, and loss analysis are repeated for each fire location, as shown in Figure 1. The assessment allows evaluating expected annual fire losses of a building.

3.1 Fire hazard analysis

The fire hazard analysis aims at determining the conditional probability applicable to each loss scenario and the associated distribution of intensity measure of the hazard. The probability to have a severe fire in a building that grows uncontrolled and challenges the structure despite the possible presence of sprinklers or other active fire protection measures is noted $P(fi)$. Given this occurrence, the probability to have the fire in a specific compartment i is noted $P(fiL_i|fi)$. The calculation of the probabilities $P(fi)$ and the distribution between compartments $P(fiL_i|fi)$ can rely on statistics or recommendations from guidance documents such as [23]. These conditional probabilities are used to integrate the losses associated with different scenarios as shown by the loop in Figure 1.

The hazard severity is characterized through the PDF of an intensity measure (IM) for this hazard. For structures in fire, the fire load density q_f in a compartment (in MJ/m² of floor area) has been proposed as IM [10], because it is one of the main parameters affecting the intensity of fire [24], it varies over a wide range, and it has a straightforward definition that is easily understood by all stakeholders. The Eurocode proposes to adopt Gumbel type I distributions for the fire load and provides the parameters of the distribution as a function of the occupancy [23] [25]. For example, for an office, the parameters are $\sigma = 126 \text{ MJ/m}^2$ and $\mu = 420 \text{ MJm}^2$. A PDF of the IM can thus be associated to each given fire location fiL_i considered in the loss assessment of Figure 1 as a function of the compartment occupancy.

3.2 Fire-thermo-mechanical analysis

Given a location of fire fiL_i and a fire load q_f , a fire-thermo-mechanical analysis is conducted to evaluate the EDPs in the structure (left part of Figure 3). This step is completed using numerical FE analysis, as it requires estimation of section isotherms and global displacements. The analysis incorporates the uncertainties from the fire, heat transfer, and mechanical models. The analysis can be run using Monte Carlo simulations that is an unbiased method but requires a large number of model evaluations. The computational effort can be reduced through the use of efficient techniques, such as surrogate models, stratified sampling, maximum entropy methods [26], etc. For each fire location, probabilistic fire-thermo-mechanical analyses of the structure are conducted for different values of the fire load q_f to get the probability density distributions of EDPs at different values of the IM.

3.3 Damage analysis

The damage analysis relates the distributions of the EDPs to the DM (right part of Figure 3). As part of the damage analysis, cases of complete collapse are identified; the probability of building collapse as a function of fire load, conditional to a certain fire location i , is noted $P(C|q_f, fiL_i)$. For cases where no global collapse occurs, the damage analysis quantifies the probability associated with each damage state for the building's components, i.e. the fragility functions. The convolution of the PDF of the EDPs with the fragility functions yields the probability that a component reaches or exceeds a specified damage state. The procedure is repeated for different levels of intensity measures; thus, different points relating the fire load and the probability that the component reaches and exceeds a certain damage state are obtained and are fitted. The probability of the component at one specific damage state when it is subjected to a specified fire load under a certain fire location, $P(ds_{j,k}|NC, q_f, fiL_i)$, is estimated as the difference between two successive damage states. Here, k refers to a specific damage state while j refers to a specific component.

3.4 Loss analysis

The loss analysis includes two parts. The first part is to determine the loss functions for each component at each damage state. Loss functions are assumed to follow a cumulative lognormal distribution to estimate the probability of a certain level of loss in a component when a certain damage state has been observed [21,22]. The expected mean repair cost, $E[LC_j|ds_{j,k}]$, has to be evaluated for each damage state. Data about repairs costs are given in the RSMeans data book [17]. The cost evaluated from the RSMeans database is used as the mean value of a loss function corresponding to each damage state. The coefficient of variation (COV) ranges from 0.6 to 1.1 for typical construction cost [27]; according to FEMA 276, the COV of the cost of rehabilitation for typical structural components ranges from 0.6 to 0.8 [28].

Once the loss function is determined for each component at different damage states, the repair cost of a building can be estimated. The estimation is conducted for each fire location. The repair cost is first evaluated for the cases where the building has survived the fire (non-collapse in Figure 3). The estimates include structural/nonstructural components and content in both fire and non-fire regions. The repair cost is evaluated by summing the products of the expected repair cost of a component at each damage state, $E[LC_j|ds_{j,k}]$, by their corresponding probabilities $P(ds_{j,k}|NC, q_f, fiL_i)$. The total repair cost, $E[LC_T|NC, q_f, fiL_i]$, is the summation of that for each component, conditional to the non-collapse of the building. Then, the repair cost is evaluated for the cases where the building collapses, as the cost of demolishing and reconstructing the building $E[LC_T|NC, q_f, fiL_i]$, conditional to the collapse of the building (NC). Assuming that $P(C|q_f, fiL_i)$ is the conditional probability that the building collapses, the expected total cost for the building is given by equation (1). These estimates are conditional on a specific scenario (fire occurrence at location fiL_i) and IM (fire load q_f).

$$E[LC_T|q_f, fiL_i] = E[RE_T] \times P(C|q_f, fiL_i) + E[LC_T|NC, q_f, fiL_i] \times (1 - P(C|q_f, fiL_i)) \quad (1)$$

By adopting a PDF for the IM (i.e. the fire load), it can be integrated into the cost estimation. The cost estimates are convoluted with the PDF of q_f to yield the probabilistic loss of the building given the fire occurrence in the considered fire location, see equation (2).

$$E[LC_T|fiL_i] = \int_0^\infty E[LC_T|q_f, fiL_i] p(q_f) dq_f \quad (2)$$

The procedure is repeated for multiple fire locations, as shown in the outer loop of Figure 1. The expected annual fire loss for the building is finally estimated by considering the different fire locations in the building and their associated probabilities $P(fiL_i|fi)$, i.e. the conditional probability of fire occurring in the compartment i provided a structurally significant fire starts in the building. This is expressed by Eq. (3), where $nfiL$ is the total number of fire locations where the estimation is made.

$$E[LC_T|fi] = \sum_{i=1}^{nfiL} E[LC_T|fiL_i] P(fiL_i|fi) \quad (3)$$

Finally, it remains to account for the probability to have a structurally significant fire. The expected annual loss (EAL) can be calculated as the product of the annual frequency of a structurally significant fire for the overall building, $P(fi)$, with the expected loss conditional on fire occurring $E[LC_T|fi]$, as shown in Eq. (4), where the factors C_I and C_L account for inflation and location, respectively [21][17].

$$EAL = C_I C_L E[LC_T|fi] P(fi) \quad (4)$$

4 CASE STUDY

4.1 Description of the prototype building

A benchmark code-conforming five-story reinforced concrete frame building is used as a prototype to illustrate the application of the methodology. This building is adapted from [29] but redesigned by the authors for a less severe seismic zone. The frame building consists of moment-resisting frames in both orthogonal directions with 5 bays in each direction, having a 7 m span length, resulting in a 35 m by 35 m square floor plan (as shown in Figure 4). The story height is 4 m. The building was designed based on the 2010 NBCC seismic requirements with accompanying CAS Standard A23.3-04 “Design of Concrete Structures” used for proportioning and detailing of members [29–31]. The design load included member self-weight, a superimposed dead load of 1.33 kPa as well as a live load of 2.4 kPa. The characteristic compressive strength of concrete is 30 MPa, and the characteristic yield strength of the steel rebar is 400 MPa. The IBC classifies the building as a Type II A construction [32]. The fire-resistance rating requirements are one hour for the primary structural frame, the floor construction and associated secondary members, and the roof construction and associated secondary members. No requirements are specified for exterior and interior partition walls. The design concrete cover thickness for the primary members and slab meets the fire resistance requirements. The interior partition wall is a gypsum panel with steel studs (with both top and bottom fixed) and the exterior wall system is the 11.5 cm-thick precast concrete panel.

4.2 Response analysis and damage analysis

The nonlinear finite-element software SAFIR [34] is used to conduct the heat transfer analysis in the structure, followed by the transient structural analysis. Modelling of the building in SAFIR is described in [33]. Analyses were conducted for several levels of fire load (IM) ranging from 200 MJ/m² to 1000 MJ/m², to cover the range of realistic fire loads in an office building. The fire load multiplied by a combustion factor 0.8 is the one used to calculate the gas temperature. The fire compartment is 7 m by 7 m (Figure 4). To reduce the number of computations, the symmetrical layout is taken advantage of, meaning that at a given floor only one scenario is studied for the corner compartments (highlighted in blue in Figure 4), for the exterior non-corner compartments (in green), and for the interior compartments (in yellow). This reduces the number of (single-compartment) fire locations from 125 to 15.

The opening factor is adopted as a random parameter in the fire-thermo-mechanical analysis. This is in addition to the fire location and fire load (IM). Uncertainty in the opening factor is taken from the JCSS model [34], $O = O_{max}(1 - \zeta)$. O_{max} is the maximum possible opening factor assuming all the window glass is immediately broken, adopted here as $O_{max} = 0.0439 m^{1/2}$ for each fire compartment. ζ is a random variable that follows a truncated (cut off at 1.0) lognormal distribution with a mean of 0.2 and a standard deviation of 0.2. A stratified sampling method is adopted to select the opening factor for each fire scenario based on the PDF of opening factor; five opening factors are selected for each fire scenario. The gas temperature curve is calculated according to the parameter fire model in EN 1991-1-2 [25].

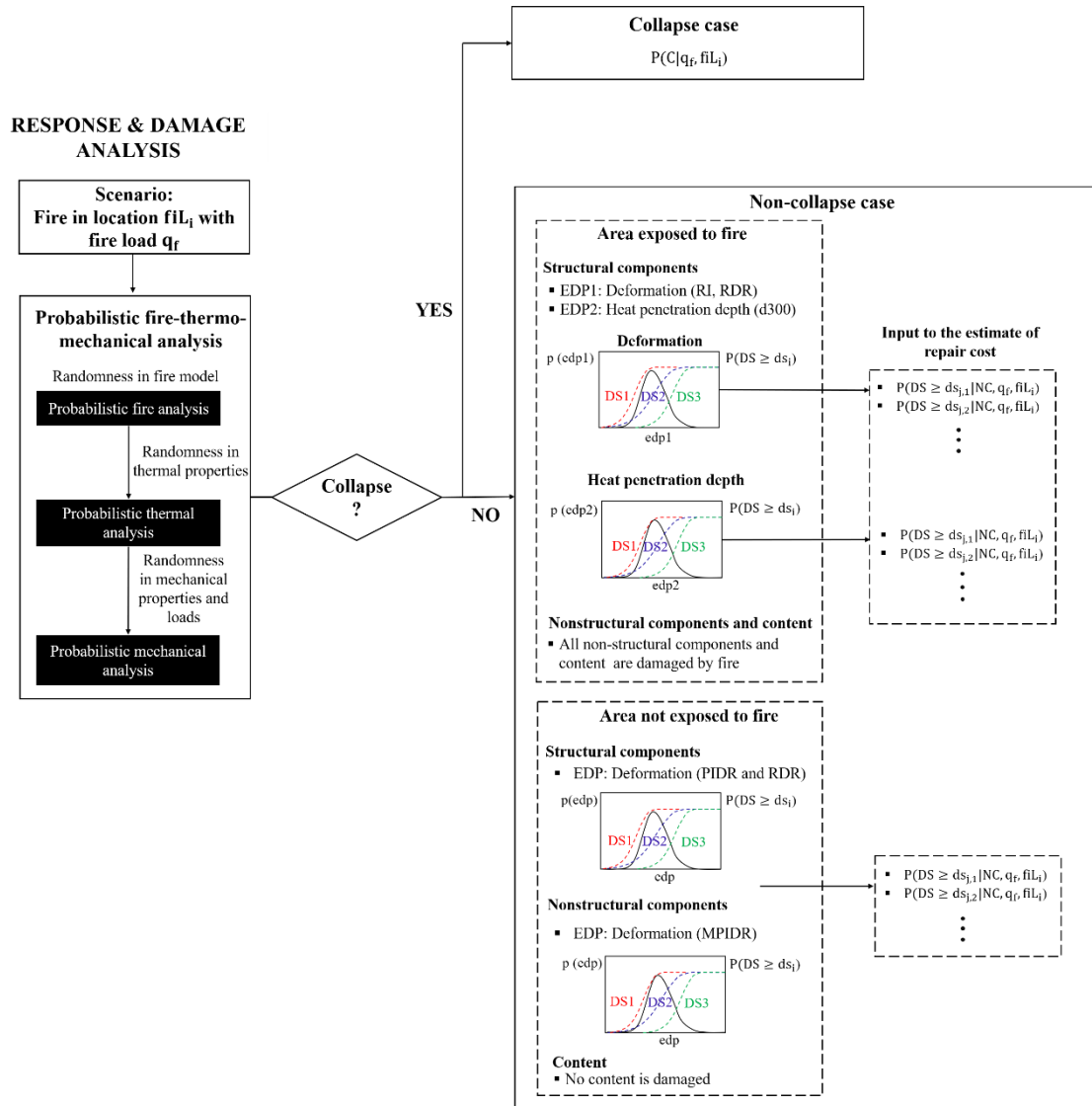


Figure 3. Overview of the response analysis and damage analysis

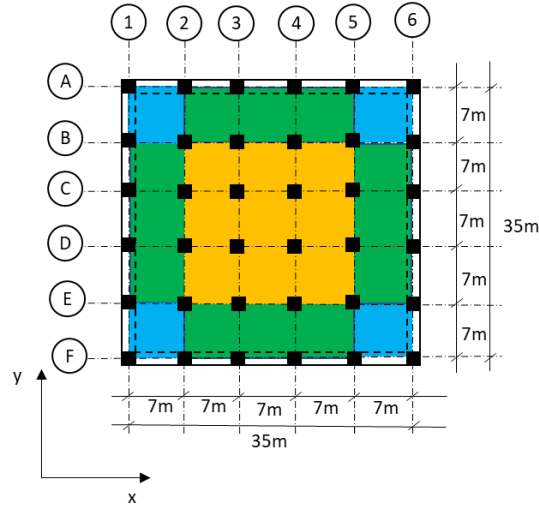


Figure 4. Floor plan and different areas exposed to fire

Given the fire occurrence in the compartment, The PDFs of the EDPs are determined from the numerical simulations for each compartment i and fire load q_f . The PDFs of the EDPs are fitted using lognormal distributions. According to the fitted PDF curves of the EDPs and their corresponding fragility functions, the conditional probability of one component reaching or exceeding a specified damage state is calculated. By varying the fire load, the relationship between the fire load (q_f) and the probability of reaching or exceeding one specified damage state ($P(DS \geq ds_{j,i} | NC, q_f, fiL_i)$) is identified and then fitted by lognormal cumulative distribution functions, as shown in Figure 5a-5c. None of the analyses yields to global building collapse. Therefore, the probability of building failure in fire is assumed negligible in this case study (this is supported by the conclusions in [12,35–37] for similar buildings) and the loss estimate is based on non-collapse cases.

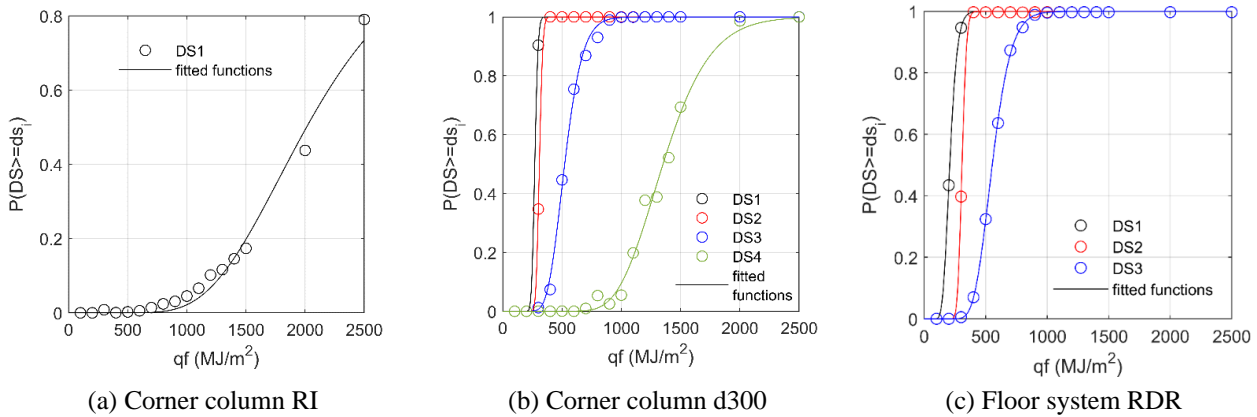


Figure 5. Probability of reaching or exceeding the DS associated with different EDPs for the corner columns and floor system under a fire scenario in the corner compartment of the first story.

4.3 Loss assessment for the building

The total replacement cost of the building is estimated according to the data in the Square Foot Costs (RSMeans, 2019) [38]. The mean cost per square foot is \$176 according to the occupancy and size of the building [39], inclusive of both structural and nonstructural components. Therefore, the total replacement cost of the building is \$11,607,628, with 38% of this cost from structural components and 62% from nonstructural components. The demolishing cost of the building is \$358,686, estimated from data in the Concrete & Masonry Costs (RSMeans, 2019 [17]). The replacement cost for the content in a building is assumed to be equal to the total construction cost (\$11,607,628) of all structural and nonstructural components in the building [40]. It is further assumed that each of the 125 fire compartments in the building

has the same nonstructural components and content. Therefore, the replacement cost is \$57,574 for all nonstructural components in one compartment and \$92,861 for all content in one compartment.

For structural components exposed to fire, the repair costs by component for each damage state are estimated from the repair actions, based on the Concrete & Masonry Costs (RSMMeans, 2019 [17]) and FEMA 58 [41], including labor, materials, equipment, overhead and profit. If a component has to be replaced, the cost includes demolition and reconstruction (accounting for scaffolding and forming). For nonstructural components and content in the area where a fire developed, their total replacement costs is considered.

The loss amount for a 7 m x 7 m compartment fire in the building is calculated for each possible location. The final calculated loss of the building is the summation of the weighted estimated losses for different fire locations, summarized in Table 4. Given the occurrence of a structurally significant fire, the expected loss for the building is \$187,900, including the damage loss of structural components (\$27,100), damage loss of nonstructural components (\$67,900), and damage loss of content (\$92,900). This assumes that the fire remains in a 7 m x 7 m compartment (other fire scenarios, including spread, could be included following the same method).

Most of the loss is due to the fire damage to content (50%) in the fire region. Damage to structural components amount to 14% of the losses, while nonstructural components amount to 36%. It is noteworthy that assumptions were made regarding the content, including about the value of the content in a room, and its complete loss in case of fire. In an actual event, the content and nonstructural components exposed to fire might not be totally damaged, which may decrease the losses associated with these items and proportionally increase the losses due to structural fire damage. Nevertheless, it is notable that structural damage accounts for such a limited part of the fire losses in the studied RC building.

Regarding the fire losses due to structural damage, 89% comes from the floor systems while 11% is from the columns. Most of the damage cost comes from the floor above the fire compartment. Another distinction can be made in terms of EDP. The damage cost to structural components in the fire-exposed area is at 71% related to the EDP of heat penetration (d300), while 29% is due to the EDPs of deformations. In cases with large fire load, the slab or the whole floor system had to be replaced due to the severe heat penetration, which contributed a lot to the final cost.

The compartment in which the fire develops did not have any significant influence on the estimated loss. Fires in interior compartments lead to slightly higher losses than exterior and corner compartments. In terms of floor, fires occurring in the fifth floor lead to slightly lower losses than for the lower floors, because in the latter case some damage develops in the upper stories.

Table 4. Results of loss estimation for the fire scenarios within 7 m x 7 m compartments in the building. The estimated loss is conditional to the occurrence of a structurally significant fire.

E[LC_T fi] \$ 187,900	Inside the fire compartment	Structural components	\$ 19,600
		Non-structural components	\$ 58,700
		Content	\$ 92,900
	Outside the fire compartment	Structural components	\$ 7,500
		Non-structural components	\$ 9,200

The numbers above are conditional to fire occurrence. One can evaluate the estimated yearly losses for a community, using the likelihood of structurally significant fires and the number of buildings in the community. According to an NFPA report [42], the U.S. fire department responded to an average of 3,340 fires in office buildings per year during the five years of 2007-2011. For the sake of the discussion, let assume that 20% of those office buildings are RC frame buildings with compartments similar to those of the studied prototype. Further, according to NFPA 557, the average fraction ratio of fires that are “structurally significant” in office occupancies for fire-resistive construction is 6.75% [43]. Therefore, the total yearly direct loss due to structurally significant fires could be estimated as $188 \text{ k\$} \times 3340 \times 20\% \times$

6.75% = 8.5 M\$ for RC frame office buildings in the U.S. According to the NFPA, the annual average cost associated to direct property damage from fires in offices (from any material and structural type) was 112 M\$ from 2007 to 2011 (without including inflation). This simple estimation at the national level illustrates the interest of the method, but more data is needed to refine the estimates.

5 CONCLUSION

This paper proposed a framework for probabilistically estimating the yearly economic losses in concrete buildings due to fire events. Unlike for seismic or wind hazards, no unified loss assessment framework currently exists for fire. The PEER framework was adopted as a basis for the work, but was modified to address the unique spatial-temporal evaluation of fires within a building and the multi-physics nature of structural fire damage. The former was accounted for by iterating the sequence of analyses for multiple fire scenarios to cover the range of possible events. The latter was addressed by defining a dual set of engineering demand parameters, damage states, fragility functions, and loss functions, with one in the thermal domain and the other in the structural domain. Unlike most previous studies, the fire loss estimation is conducted at the scale of an entire building and accounts for the response of the 3D structural system.

The expected yearly direct fire loss of a five-story RC frame building was estimated as a case study. To capture thermally-induced deformations and restraints, the response analysis of the building was conducted using nonlinear FE modelling with SAFIR. Direct fire losses for single-compartment (49 m²) fire scenarios was evaluated as 188 k\$, consisting mostly of content losses (50%) and nonstructural components damage (36%), with structural components damage accounting for 14%. The majority of the 14% fire loss for structural components was associated with floors (rather than columns) and with the thermal EDP (rather than the deformation EDP). Adopting NFPA statistics and simplifying assumptions for the ratio of RC buildings in the U.S. building stock and the layouts of these buildings, the case study estimates yearly direct fire losses in concrete office buildings of about 8.5 M\$ for the U.S.

This work is seen as a first step toward establishing a performance-based approach to evaluate the expected cost of fire and the optimum investments in fire safety for structures. As such, it currently has the following limitations: 1) the lack of data about repairs cost for quantifying fragility functions for the fire damage of structural components; 2) the limited ability to predict complex fire scenarios (including compartmentation failure and fire spread), and 3) the lack of data about nonstructural and content value, which was addressed here through a conservative estimate of expected losses for nonstructural components and content. The latter point is particularly important since the case study showed that content and nonstructural components contributed the most to the direct fire losses. Another drawback relates to the high computational cost associated with nonlinear thermo-mechanical analyses. Advances in reduced-order modelling for structures in fire (e.g., surrogate models) could support broader application of this methodology.

REFERENCES

1. Botzen WJW, Deschenes O, Sanders M. The Economic Impacts of Natural Disasters: A Review of Models and Empirical Studies. *Rev Environ Econ Policy* 2019;13:167–88. <https://doi.org/10.1093/reep/rez004>.
2. Estrada F, Botzen WJW, Tol RSJ. Economic losses from US hurricanes consistent with an influence from climate change. *Nat Geosci* 2015;8:880–4. <https://doi.org/10.1038/ngeo2560>.
3. Badger SG. Large-loss fires in the United States 2017. Quincy, MA: 2018.
4. Kousky C, Greig K, Lingle B, Kunreuther H. Wildfire costs in California: the role of electric utilities 2018.
5. Vitorino H, Rodrigues H, Couto C. Evaluation of post-earthquake fire capacity of reinforced concrete elements. *Soil Dyn Earthq Eng* 2020;128:105900. <https://doi.org/10.1016/j.soildyn.2019.105900>.
6. Fragiadakis M, Lagaros ND, Papadrakakis M. Performance-based multiobjective optimum design of steel structures considering life-cycle cost. *Struct Multidiscip Optim* 2006;32:1–11. <https://doi.org/10.1007/s00158-006-0009-y>.
7. Hopkin D, Fu I, Van Coile R. Adequate fire safety for structural steel elements based upon life-time cost optimization. *Fire Saf J* 2020:103095. <https://doi.org/10.1016/j.firesaf.2020.103095>.
8. Lange D, Devaney S, Usmani A. An application of the PEER performance based earthquake engineering

- framework to structures in fire. *Eng Struct* 2014;66:100–15. <https://doi.org/10.1016/j.engstruct.2014.01.052>.
9. Memari M, Mahmoud H. Framework for a performance-based analysis of fires following earthquakes. *Eng Struct* 2018;171:794–805. <https://doi.org/10.1016/j.engstruct.2018.05.099>.
10. Gernay T, Elhami Khorasani N, Garlock M. Fire fragility curves for steel buildings in a community context: A methodology. *Eng Struct* 2016;113:259–76. <https://doi.org/10.1016/j.engstruct.2016.01.043>.
11. Shrivastava M, Abu A, Dhakal R, Moss P. State-of-the-art of probabilistic performance based structural fire engineering. *J Struct Fire Eng* 2019;JSFE-02-2018-0005. <https://doi.org/10.1108/JSFE-02-2018-0005>.
12. Bailey C. Holistic behaviour of concrete buildings in fire. *Proc Inst Civ Eng - Struct Build* 2002;152:199–212. <https://doi.org/10.1680/stbu.2002.152.3.199>.
13. Molkens T, Van Coile R, Gernay T. Assessment of damage and residual load bearing capacity of a concrete slab after fire: Applied reliability-based methodology. *Eng Struct* 2017;150. <https://doi.org/10.1016/j.engstruct.2017.07.078>.
14. Ni S, Gernay T. A framework for probabilistic fire loss estimation in concrete building structures. *Struct Saf* 2021;88. <https://doi.org/10.1016/j.strusafe.2020.102029>.
15. Moehle J, Deierlein G. A framework methodology for performance-based earthquake engineering. 13th World Conf. Earthq. Eng., Vancouver, B.C., Canada: 2004, p. No. 679.
16. Schneider U, Nagele E. Repairability of fire damaged structures: CIB W 14 report. CIB; 1989.
17. Gordon Group Inc. Concrete & masonry costs with RSMeans data 2019. 37th ed. Rockland, MA: RSMeans Co; 2018.
18. ACI Committee 706. RAP-12: Concrete repair by shotcrete application. ACI RAP Bulletin 12, American Concrete Institute; 2011.
19. McCormick J, Aburano H, Ikenaga M, Nakashima M. Permissible residual deformation levels for building structures considering both safety and human elements. 14th World Conf. Earthq. Eng., Beijing, China: 2008.
20. CSA A23.3-14. Design of concrete structures. Canadian Standards Association. Mississauga, Ont., Canada. Can Stand Assoc 2014;109–70.
21. Haselton C, Goulet C, Mitrani-Reiser J, Beck J, Deierlein G, Porter K, et al. An assessment to benchmark the seismic performance of a code-conforming reinforced-concrete moment-frame building. Berkeley, CA: 2008.
22. Aslani H. Probabilistic earthquake loss estimation and Loss disaggregation in buildings. Department of Civil and Environmental Engineering, Stanford University; 2005.
23. Vassart O, Zhao B, Cajot LG, Robert F, Meyer U, Frangi A. Eurocodes: Background and applications - Structural fire design - Worked examples. Luxembourg: 2014. <https://doi.org/10.2788/85432>.
24. Zalok E. Validation of methodologies to determine fire load for use in structural fire protection, Fire Protection Research Foundation, NFPA mission; 2011.
25. BS EN1991-1-2. Eurocode 1: Actions on structures - Part 1-2: General actions - Actions on structures exposed to fire . European Standard. 2002.
26. Gernay T, Van Coile R, Elhami Khorasani N, Hopkin D. Efficient uncertainty quantification method applied to structural fire engineering computations. *Eng Struct* 2019;183:1–17. <https://doi.org/10.1016/j.engstruct.2019.01.002>.
27. Touran A, Suphot L. Rank correlations in simulating construction costs. *J Constr Eng Manag* 1997;123:297–301. [https://doi.org/10.1061/\(ASCE\)0733-9364\(1997\)123:3\(297\)](https://doi.org/10.1061/(ASCE)0733-9364(1997)123:3(297)).
28. Applied Technology Council. Guidelines for the seismic rehabilitation of buildings: Example applications. Washington, D.C.: 1997.
29. Al Mamun A, Saatcioglu M. Seismic fragility curves for reinforced concrete frame buildings in Canada designed after 1985. *Can J Civ Eng* 2017;44:558–68. <https://doi.org/10.1139/cjce-2016-0388>.
30. NBCC 2010. National building code of Canada. National Research Council of Canada. Ottawa, Canada., 2010.
31. CSA A23.3-04. Design of concrete structures. Canadian Standards Association. Mississauga, Ont., Canada., 2004.
32. IBC 2018. International building code. International Code Council. Country Club Hills, IL, USA, 2018.
33. Ni S, Gernay T. Predicting residual deformations in a reinforced concrete building structure after a fire event. *Eng Struct* 2020;202:109853. <https://doi.org/10.1016/J.ENGSTRUCT.2019.109853>.
34. JCSS. JCSS Probabilistic Model Code: Part 2: Load Models. 2001. <https://doi.org/10.1016/B978-185718029-9/50001-9>.
35. Fire resistance of concrete structures. Report of a Joint Committee of the Institution of Structural Engineers and the Concrete Society. 1975.

36. Bate SCC. Concrete for fire resistant construction. vol. 1. 1979. [https://doi.org/10.1016/0262-5075\(79\)90016-2](https://doi.org/10.1016/0262-5075(79)90016-2).
37. Mistri A, Pa RD, Sarkar P. Condition assessment of fire affected reinforced concrete shear wall building - A case study. *Adv Concr Constr* 2016;4:89–105. <https://doi.org/10.12989/acc.2016.4.2.089>.
38. Gordon Group Inc. Square foot costs with RSMeans data 2019. 40th ed. Rockland: RSMeans Co; 2018.
39. Federal Emergency Management Agency (FEMA). Hazus flood model: User guidance. Washington, D.C.: Federal Emergency Management Agency; 2018.
40. Federal Emergency Management Agency (FEMA). Multi-hazard loss estimation methodology - earthquake model, Hazus-MH MR4: Technical Manual. Washington, D.C.: FEMA; 2003.
41. Federal Emergency Management Agency. FEMA P-58-3: Seismic performance assessment of buildings, Volume 3: Supporting electronic materials and background documentation. Washington, D.C.: Federal Emergency Management Agency; 2018.
42. Campbell R. U.S structure fires in office properties. Quincy, MA: 2013.
43. NFPA. NFPA 557: Standard for determination of fire loads for use in structural fire protection design. 2020th ed. 2012.

SPALLING OF GEOPOLYMER CONCRETE IN RING-RESTRAINED SPECIMENS UNDER HIGH TEMPERATURES

Mitsuo Ozawa¹, Hiroyuki Ikeya², Koji Harada³, Hiroki Goda⁴

ABSTRACT

Recent studies have reported that geopolymer concrete has the advantage of being fire-resistant, in addition to being eco-friendly, as geopolymers do not employ Portland cement; hence, they can serve as an alternative to Portland cement in the future. However, few studies have assessed the fire spalling behaviour of geopolymer concrete while measuring the vapour pressure and thermal stress during heating tests. Ring-restraint heating tests are commonly used to measure thermal stress and vapour pressure, and the Japan Concrete Institute standard method is adopted for these tests. In the present study, ring-restraint heating tests were conducted on geopolymer concrete and normal-strength concrete to evaluate the fire spalling behaviour of geopolymer concrete. The relationships between restraint stress, from ring strain measurements, and vapour pressure and temperature were also examined.

Keywords: geopolymer concrete; fire spalling; ring-restraint heat test

1 INTRODUCTION

Generally, concrete is a fire-resistant material. However, when subjected to high temperatures, its mechanical properties deteriorate owing to the thermal decomposition of cement hydration products, especially calcium hydroxide [1], and explosive spalling occurs in concrete during a fire. The mechanism of explosive spalling follows vapour pressure theory [2], thermal stress theory [3], and its combined theory.

However, recent studies have reported the fire resistance properties of geopolymer concrete (GPC) [4–6]. As GPC does not use cement, its mechanical properties do not decrease due to the thermal decomposition of cement hydration products like ordinary concrete during a fire. However, certain studies have reported on the behaviour of thermal stress, vapour pressure, and explosive spalling behaviour of GPC under high-temperature environments.

Therefore, in this study, the fire spalling behaviour of a geopolymer at high temperature was evaluated using the ring restraint specimen test method: Method A of the “fire spalling test of concrete” [7], which is standardized by the Japan Concrete Institute.

This method has proven to be successful in the evaluation of high-strength concrete [8–10]. In the present study, the internal temperature, restraint stress, and vapour pressure were measured, and the fire spalling.

¹ Dr.Eng., Gunma University
e-mail: ozawa@gunma-u.ac.jp, ORCID: <https://orcid.org/0000-0002-6207-7180>

² Graduate student, Gunma University
e-mail: t201c002@gunma-u.ac.jp

³ Dr.Eng., Nishimatsu Construction Co.,Ltd.
e-mail: koji_harada@nishimatsu.co.jp

⁴ Ph.D, Kyusyu Institute of Technology
e-mail: goda-h@civil.kyutech.ac.jp

behaviour during heating was observed. Furthermore, core samples were taken from the heated specimens, and the internal damage was evaluated using internal observations and ultrasonic (US) methods.

2 OUTLINE OF THE EXPERIMENT

2.1 Ring specimen

Figure 1 shows the outline of the ring restraint specimen used in this study. The restraint rings consisted of two layers of steel rings with an outer diameter of 300 mm, a height of 50 mm, and a thickness of 8 mm, filled with concrete. A thermocouple was installed inside the restraint ring to measure the temperature. Strain gauges (heat-resistant temperature: 80 °C) were installed on the outer circumference of the ring at positions of 5, 10, 25, and 40 mm from the heating face to calculate the restraint stress of concrete. Stainless-steel pipes (inner diameter: 2 mm, outer diameter: 5 mm, and length: 180 mm) were similarly installed at positions of 5, 10, 25, 40 mm from the bottom surface to measure the vapour pressure inside the concrete. Before conducting the heating test, the inside of the stainless-steel pipe was filled with silicone oil and connected to the pressure sensor (allowable value: 10 MPa).



Figure 1. Ring specimen

2.2 Mixture proportion and mechanical and fresh properties

Table 1 and 2 shows a mixture of GPC and normal strength concrete (NSC). The materials used included an alkali-silica solution (GPW, density: 1.40 g/cm³), fly ash II (FA-II, density: 2.21 g/cm³, JIS II standard), blast furnace slag fine powder (BFS, density: 2.91 g/cm³), sea sand (S, density: 2.58 kg/cm³ from Kitakyushu), and crushed stone (Ga, density: 2.70 kg/cm³ from Kitakyushu).

The ring-restraint specimens were filled with the GPC and NSC, respectively, and then surface coated with a curing material, moulded, and covered with a wrap to be sealed. The curing was conducted for 3 h before the temperature was raised to 70 °C over 3 h, kept at 70 °C for 24 h, and then lowered to 20 °C over 3 h. After curing, the specimens were removed from the mould and allowed to stand in the indoor environment for 33 days until the fire resistance test was conducted. Table 3 shows the GPC and NSC each fresh property, water content, compressive strength, and elastic modulus. The measurement of water content ratio was diameter 50 mm × Height 100 mm, and two cylinders each were used. The water content was calculated using the change in mass before and after drying, in which the water content was put into a drying oven at 105 °C to evaporate the water and render the water content constant. The compressive strength test was performed by using three cylinders with dimensions of diameter 100 mm × Height 200 mm, each of which was based on the JIS standards.

2.3 Heating tests

One ring-restraint specimen was prepared for each of the GPC and NSC mixtures. The ring-restraint specimen method was standardized as a JCI test method, and reproducibility was ensured for each specimen. A horizontal gas furnace (Figure 2) with a heating area of 900 mm × 900 mm was used for the heating test.

Figure 3 shows the RABT 30 heating curve, according to which the heating conditions were tested. The heating time was set from the beginning of the test up to 30 min.

Table 1 Mixture of Geopolymer Concrete (GPC)

kg/m ³				
Alkali silica solution	Fly ash	Blast furnace slag	Fine aggregates	Coarse aggregates
330	353	152	559	875

Table2 Mixture of Normal strength Concrete (NSC)

kg/m ³					
Water	Cement	Fine aggregates	Coarse aggregates	AE water reducing agent	Ae agent
160	296	848	985	444	18

Table 3 Fresh property, water content, compressive strength, and elastic modulus.

Type	Compressive strength (MPa)	Elastic modulus (GPa)	Air (%)	Water content ratio (mass %)
GPC	34.2	33.5	6	3.6
NSC	26.2	13.4	1.4	5.0



Figure 2. Horizontal gas furnace

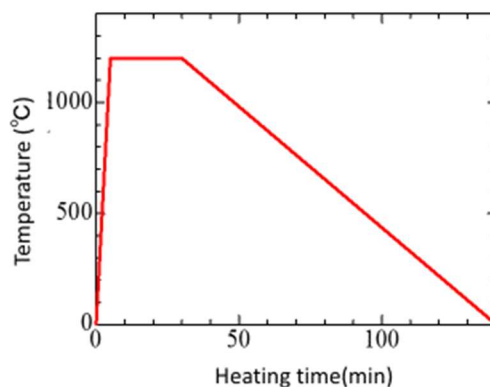


Figure 3. RABT30 heating curve

2.4 Calculation of restraint stress

The restraint stress was calculated using the measured circumferential strain of the steel ring. The calculation method is shown in equation (1).

$$\sigma_{re} = \varepsilon_{\theta} \cdot E_s \cdot t / R \quad (1)$$

where σ_{re} is the restraint stress generated in concrete (N/mm²),

ε_{θ} is the ring circumferential strain,

E_s is the elastic modulus of ring material (N/mm²),

t is the ring material thickness (mm), and

R is the ring material inner diameter (mm).

2.5 US wave velocity test

An US wave propagation velocity test (Figure 4) was performed on the core extracted from the ring-restraint specimen after the heating test. The US velocity was calculated using the propagation time and the distance between the probes. Two cores of each type were measured, and the measurement positions were 20, 50, and 70 mm from the heating surface.



Figure 4. US test

3 RESULTS AND DISCUSSION

3.1 Condition of the heated surface after the heating test

Figures 5 and 6 depict the condition of the heated surface of the GPC and NSC specimens after the heating test and the condition of the side surface of the specimens after being cored, respectively. It was observed that fire spalling did not occur in both GPC and NSC, and that microcracks in the heating face were confirmed in the NSC specimen. Furthermore, the concrete near the heated surface was damaged during core removal. Additionally, when the side surface was observed, discolouration occurred up to a depth of 40 mm from the heated surface, and cracks were confirmed at the aggregate interface. This is thought to be the result of thermal decomposition and discolouration of the cement hydration product owing to heating and the effect of microcracks.

However, traces of the geopolymer being fired and expanded by heating were observed in the GPC. When the side surface of the core sample was confirmed, the geopolymer was baked, solidified, and turned black to a depth of 20 mm from the heated surface.

3.2 Internal temperature

Figure 7 shows the change in the internal concrete temperature over time. It can be observed that the internal temperature of both GPC and NSC increases with heating time. It confirms that the two test specimens had

almost the same degree of temperature rise for each measurement. The temperatures at 5 mm and 10 mm were $\sim 870^\circ\text{C}$ and 700°C , respectively, at 30 min.



Figure 5. Results of heating face

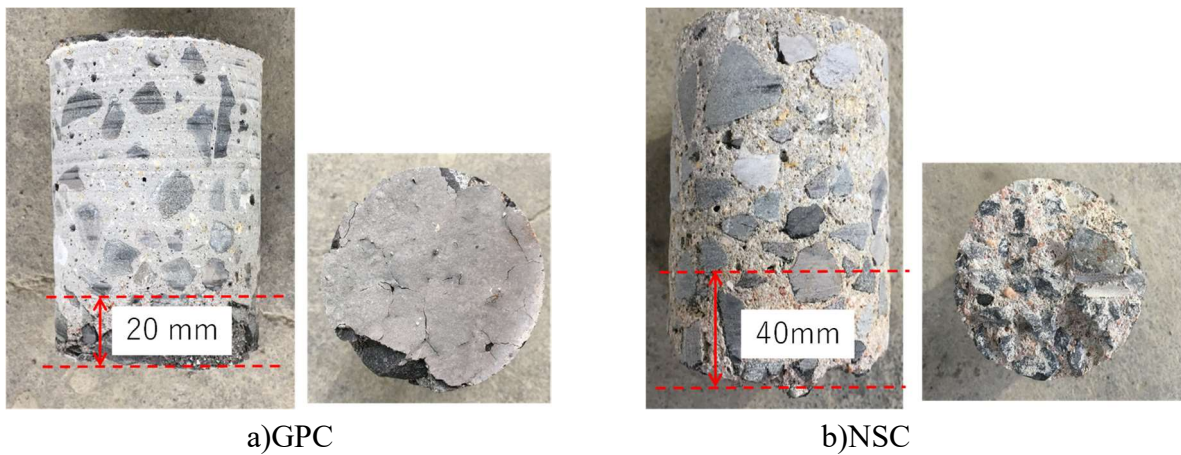


Figure 6. Cored concrete after heating test

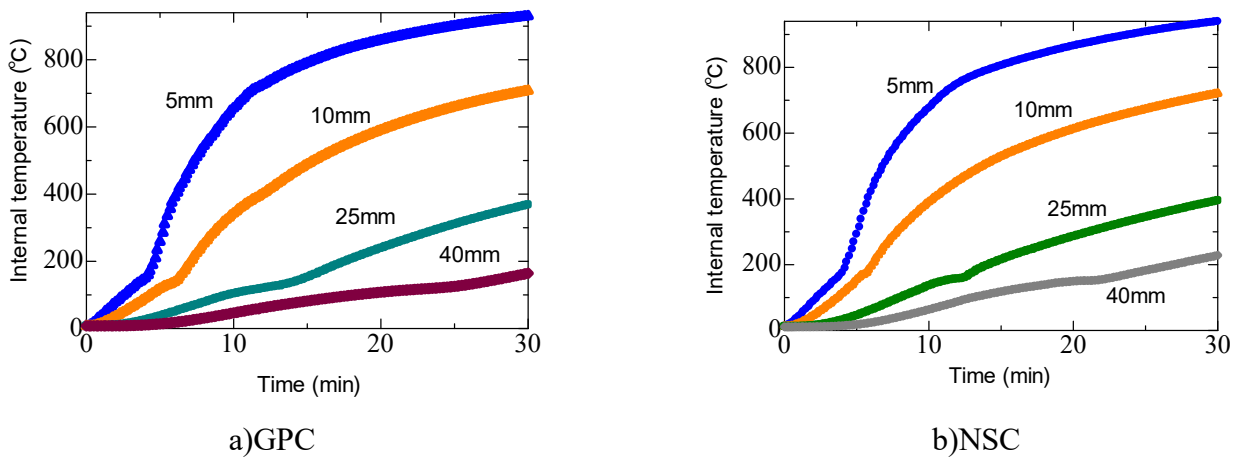


Figure 7. Internal temperature

3.3 USV measurement

Figure 8 shows the relationship between the distance from the top of the measurement position and UV velocity (USV). The USV of the NSC was found to be faster than that of the GPC. This is because the elastic modulus of the NSC is larger than that of the GPC. Additionally, the USV of both the NSC and GPC reduced as measurement positions approached the heated surface. This indicates that the core is more damaged near the heated surface. The reduction in USV for the NSC and GPC from the upper edge was 36.6% and 16.8%, respectively.

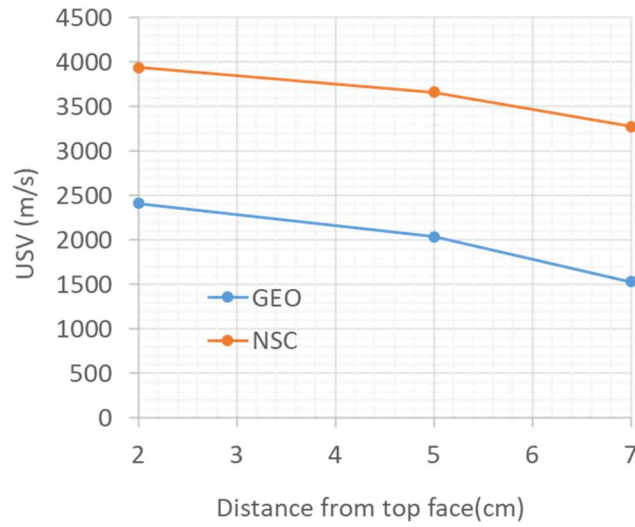


Figure 8. the relationship between the distance from the top of the measurement position and UV velocity (USV)

3.4 Restraint stress

Figure 9 shows the change in restraint stress over time. The restraint stress of NSC increase with heating, and a maximum value of 11 MPa was observed at 5 mm. The restraint stress of the GPC increased for approximately 6 min from the start of the heating but tended to decrease. A maximum value of 1.6 MPa was observed at the 5 mm position.

On comparing the NSC and GPC, it can be observed that the maximum value of the restraint stress of the GPC is approximately 15% of that of the NSC, which is small. This is thought to be because the static elastic modulus is 33 GPa for the NSC and 13 GPa for the GPC, which is approximately 50%.

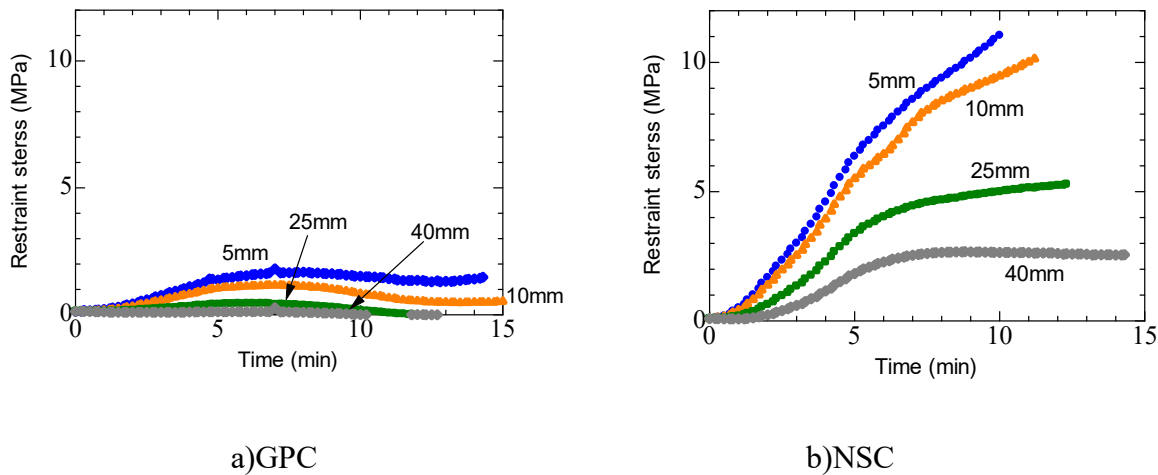


Figure 9. Restraint stress

3.5 Vapour pressure

Figure 10 shows the change in vapour pressure over time. For NSC, water vapour sharply increases at the 5 mm and 10 mm positions and then, sharply decreases. The maximum values are 13 MPa and 4.7 MPa at 5 mm and 10 mm, respectively. It can be confirmed that in GPC as well as NSC, the vapour sharply increases at the 5 mm and 10 mm positions and then sharply decreases. The maximum values are 5.5 MPa and 4.7 MPa for 5 mm and 10 mm, respectively. The maximum value of vapour pressure was larger in NSC at 5 mm. In both NSC and GPC, the vapour pressure increased at 25 mm and 40 mm positions but decreased gradually compared to 5 mm and 10 mm. This is because the vapour pressure drops more rapidly at the 5 mm and 10 mm positions close to the heated surface as the vapour inside is released to the outside from the minute cracks generated on the surface because of heating.

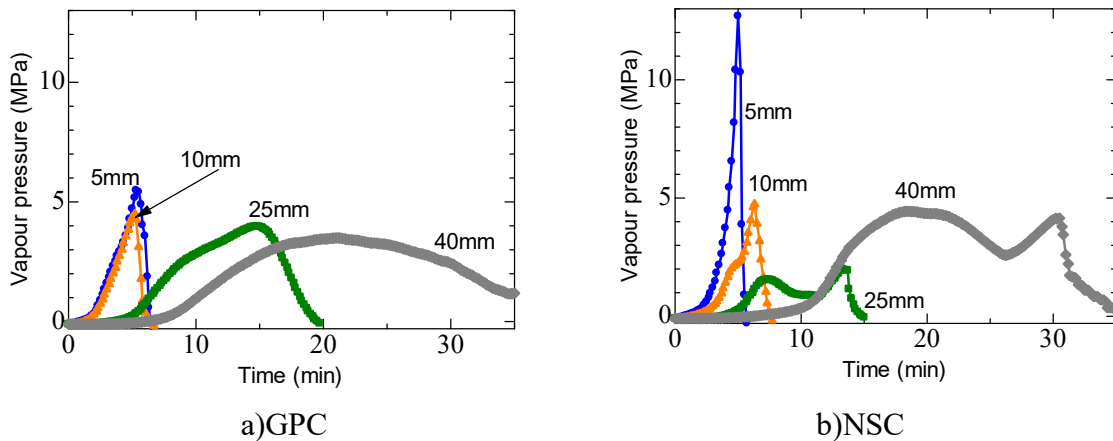


Figure 10. Vapour pressure

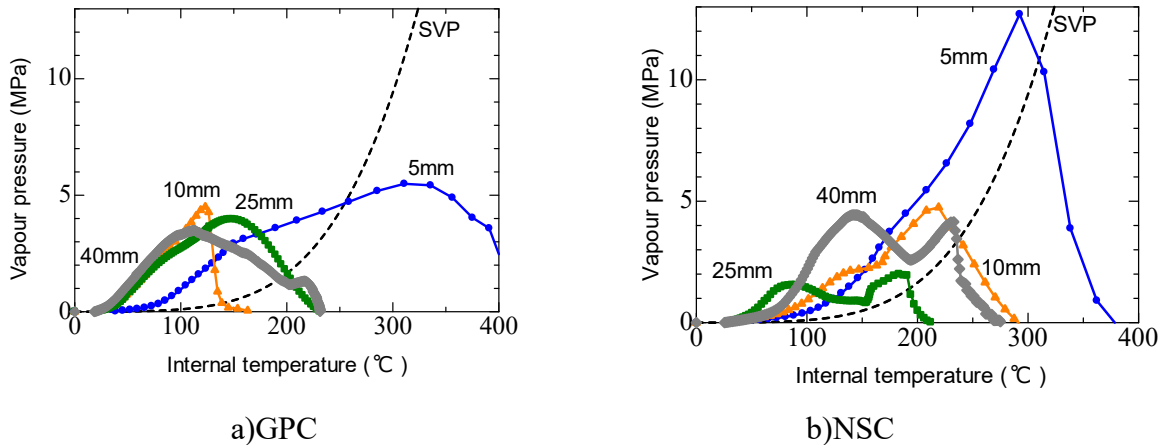


Figure 11. Relationship between vapour pressure and internal temperature

3.6 Relationship between vapour pressure and internal temperature

Figure 11 shows the relationship between vapour pressure and the internal temperature of NSC and GPC specimens. Ichikawa et al. [11] discussed the changes in vapour pressure and temperature inside the concrete. At the boundary of the saturated vapour pressure (SVP) curve, the low-temperature side is the supersaturated zone (Saturated zone), and the high-temperature side is the unsaturated zone (Dry zone).

It can be observed that the measured values change near the SVP curve for both NSC and GPC in this study. In both cases, the vapour pressure changes from the supersaturated region to the unsaturated region. This is considered to be related to the increase in vapour pressure and transition from the supersaturated region to the unsaturated region owing to the movement of water inside the concrete because of heating. The maximum value at 5 mm in NSC was 13 MPa, which rapidly increased with heating and decreased near

280 °C. At the 10 mm position, an inflexion point was displayed at approximately 220 °C, and the vapour pressure decreased in the supersaturation region. The maximum value at the 5 mm position in GPC was 5.5 MPa but remained constant up to the unsaturated region. The 10 mm position showed an inflexion point at approximately 140 °C. At the inflexion point, it is observed that the vapour pressure decreased due to the formation of voids caused by microcracks due to heating or alteration of the material.

3.7 Relationship between restraint stress, vapour pressure, and internal temperature

A comparison was made between GPC and NSC with the ring-restrained specimen test results [10] of high-strength concrete (HSC), in which fire spalling occurred during the heating test.

The focusing position was 5 mm from the heating surface. Figure 12 shows the relationship between vapour pressure, restraint stress, and internal temperature. The restraint stress of NSC showed an inflexion point near 180 °C but increased gradually thereafter. The vapour pressure increased in the supersaturated region and decreased near 280 °C, and fire spalling did not occur in NSC. The restraint stress of GPC was approximately 1.6 MPa, and no clear inflexion point was found. The maximum vapour pressure was 5 MPa at 300 °C in the unsaturated region. Fire spalling also did not occur in GPC and occurred at 180 °C in HSC. The restraint stress of HSC monotonically increased up to 5.2 MP at 180 °C, but then showed an inflexion point and became constant. It can be observed that the vapour pressure increased from approximately 100 °C and dropped sharply to 2.5 MPa at 180 °C. This is considered to indicate that the vapour pressure was released owing to the occurrence of fire spalling. Table 4 shows the mechanical properties, water content, and air content of HSC to compare NSC with GPC and HSC.

The fire spalling mechanism has been discussed using Tables 3 and 4. It is considered that the mechanism of fire spalling is related to the occurrence of cracks in the horizontal direction on the heating surface and the increase in vapour pressure owing to the increase in restraint stress because of heating. HSC has a compressive strength of 80 MPa and air content of 0.6%vol, which is low. Moreover, the water content is 4.5%, which is a large value. As can be observed from the results, vapour pressure increased rapidly in HSC. However, NSC has a higher restraint stress and vapour pressure than HSC, although its compressive strength is small at 24 MPa; hence, microcracks are likely to occur inside the specimen. The results showed that the vapour pressure can be released to the outside, and as such, fire spalling does not occur. In the case of GPC, the vapour pressure increases to the same level as NSC, but the restraint stress decreases owing to the melting of the geopolymer accompanying heating. Furthermore, the vapour pressure in the voids does not increase locally owing to changes in the internal structure. As the compressive strength and the static elastic modulus of GPC are also smaller than those of HSC, localized failure and fire spalling are considered to not occur. In the future, we plan to accumulate more data and proceed with the study.

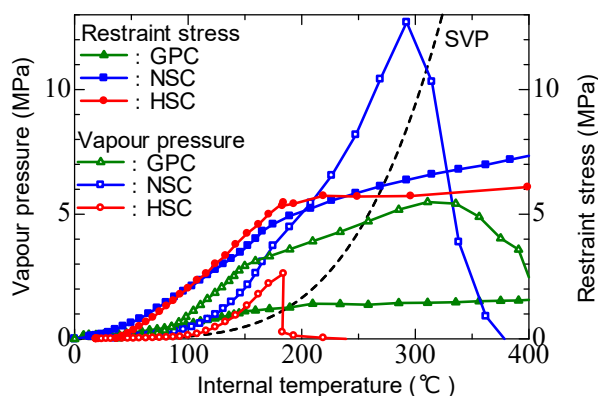


Figure 12. Relationship between vapour pressure, restraint stress, and internal temperature

Table 4. Fresh property, water content, compressive strength, and elastic modulus (HSC).

Type	Compressive strength (MPa)	Elastic modulus(GPa)	Air (%)	Water content ratio(mass %)
HSC	80	45	0.6	4.5

4 CONCLUSION

The findings of this study are shown below:

- (1) As a result of the heating test conducted according to the RABT 30 curve by the ring specimen heating test, neither NSC nor GPC exploded.
- (2) Concerning the restraint stress, it was found that GPC was smaller than NSC. It was also found that the maximum vapour pressure was smaller in GPC than in NSC.
- (3) A core sample was taken from the specimen after heating, and an US wave propagation velocity test was performed. As a result, USV of NSC and GPC decreased as they approached the heated surface. This indicates that the core was more damaged near the heated surface. Additionally, the reduction rate of US wave propagation velocity in the upper surface near the heated surface was 36.6% for GPC and 16.8% for NSC.

REFERENCES

1. Bailey, C. & Khoury, G.A., Performance of Concrete Structures in Fire, MPA, The Concrete Centre, 2011
2. Bazant, Z.P. Analysis of pore pressure, thermal stress and fracture in rapidly heated concrete, In: Phan, L.T., Carino, N.J., Duthinh, D. & Garboczi, E. (Eds) Proceedings of the international workshop on fire performance of high-strength concrete. NIST, Gaithersburg, Maryland, Feb 13–14, 1997, pp. 155–164. https://tsapps.nist.gov/publication/get_pdf.cfm?pub_id=916655
3. Anderberg, Y., Spalling phenomena in HPC and OC, In: Phan, L.T., Carino, N.J., Duthinh, D. & Garboczi, E., (Eds.) Proceedings of the international workshop on fire performance of high-strength concrete. NIST, Gaithersburg, Maryland, 1997, pp. 69-73. <https://nvlpubs.nist.gov/nistpubs/Legacy/SP/nistspecialpublication919.pdf>
4. Faiz, U.A.S. & Anwar, H., Mechanical properties of steel fibre reinforced geopolymer concretes at elevated temperatures. Constr Build Mater 114, 15-28 (2016). <https://doi.org/10.1016/j.conbuildmat.2016.03.158>
5. Hosan, A., Haque, S. & Shaikh, F.U.A., Compressive behaviour of sodium and potassium activators synthesized fly ash geopolymer at elevated temperatures: A comparative study. J Build Eng 8, 123–130 (2016). <https://doi.org/10.1016/j.job.2016.10.005>
6. Assaedi, H., Shaikh, F.U.A. & Low, I.M., Effect of nano-clay on mechanical and thermal properties of geopolymer. J Asian Ceram Soc 4, 19-28 (2016). <https://doi.org/10.1016/j.jascer.2015.10.004>
7. Japan concrete Institute, Test Method for Spalling of Concrete under High Temperature Exposure, JCI-S-014-2018 (2018) (in Japanese). http://www.jci-net.or.jp/j/jci/study/jci_standard/JCI-S-014-2018.pdf
8. Ozawa, M., Tanibe, T., Kamata, R., Uchida, Y., Rokugo, K. & Parajuli, S.S., Behavior of ring-restrained high-performance concrete under extreme heating and development of screening test. Constr Build Mater 162, 215–228 (2018). <https://doi.org/10.1016/j.conbuildmat.2017.11.144>
9. Ozawa, M., Tanibe, T., Kanematsu, M. & Morita, T., Screening-test analysis of fire spalling behavior with various concrete samples, Proceeding of 5th International Workshop on Concrete Spalling due to Fire Exposure. Boras, Sweden, October 12-13, pp. 315–326 (2017).
10. Ozawa, M., Akashi, K., Kamata, R., Tanibe, T. & Sirjana, S.P., Effects of curing ages on spalling failure under ring restraint test of high strength concrete during fire, Proceedings of the 7th International Conference of Asian Concrete Federation - Sustainable Concrete for now and the Future, Hanoi, Vietnam, Oct 30–Nov 2, (2016).
11. Ichikawa, Y. & England, G.L., Prediction of moisture migration and pore pressure build-up in concrete at high temperature. Nucl Eng Des 228, 245–259 (2004). <https://doi.org/10.1016/j.nucengdes.2003.06.011>

GENERALIZED FRAGILITY CURVES FOR CONCRETE COLUMNS EXPOSED TO FIRE THROUGH SURROGATE MODELLING

Ranjit Kumar Chaudhary¹, Balša Jovanović², Thomas Gernay³, Ruben Van Coile⁴

ABSTRACT

Common structural fire design relies on recommendations from design codes, or (a single or small set of) more advanced numerical analyses. When applying such procedures to the design of structures under normal loading conditions, adequate safety is ensured through calibrated safety factors and ample experience with structural failures. This is however not the case when considering accidental fire loading, where the stochasticity in the structural fire behaviour is rarely fully acknowledged. Therefore, a significant interest in the use of probabilistic approaches to evaluate structural fire performance, which take into account the uncertainty associated with model parameters, can be observed among researchers, with a special focus on the development of fragility curves. The calculation of fragility curves is, however, a laborious task, demanding huge computational expense, mainly attributed to the adoption of advanced calculation procedures and the need for a large number of model evaluations. The present study contributes to addressing the limitations imposed by these computational requirements through the development of surrogate models for fire exposed structural members. To achieve this, a framework for carrying out probabilistic studies of structures under fire through the use of surrogate modelling is presented. The framework is applied to a concrete column subjected to a standard fire and proves efficiency and accurateness for the selected simple example. Future studies will investigate the applicability of the framework to structural assemblies under physically-based fires.

Keywords: Fire safety; probabilistic approach; surrogate modelling; concrete columns; machine learning.

1 INTRODUCTION

Traditionally, the structural fire design is carried out based on prescriptive guidelines and code-based recommendations. These recommendations refer to a standard building type, in a specific region, serving a specific purpose, which undermines the idea of its application to a wide range of structural configurations. Thus, the structural fire design based on traditional approaches appears to result in case-dependent outcomes in terms of prescribed safety level. To demonstrate adequate structural fire safety, whether for developing more uniform guidance or for designing exceptional structures, the risk profile for the structures should explicitly be considered. When evaluating the risk profile, all the influential conditions of possible fires and their probabilities, together with the uncertainty associated with structural system, are taken into account [1-2]. Acknowledging this, there has recently been an increase in the use of probabilistic methodologies for structural fire design. Several probabilistic frameworks can be found in the literature for

¹ Ph.D. researcher, Ghent University, Belgium.

e-mail: ranjitektumar.chaudhary@ugent.be, ORCID: <https://orcid.org/0000-0002-1104-5859>

Ph.D. researcher, Ghent University, Belgium.

e-mail: balsa.jovanovic@ugent.be, ORCID: <https://orcid.org/0000-0001-5200-5848>

³ Assistant professor, Johns Hopkins University, United States.

e-mail: tgernay@jhu.edu, ORCID: <https://orcid.org/0000-0002-3511-9226>

⁴ Assistant Professor, Ghent University, Belgium.

e-mail: ruben.vancoile@ugent.be, ORCID: <https://orcid.org/0000-0002-9715-6786>

probabilistic assessment of fire exposed structures. For example, Shrivastava et al. [3] applied performance based earthquake engineering (PBEE) framework for probabilistic studies in structural fire engineering (SFE), where annual rates of exceedance of hazard intensity and structural response were estimated. At the same time, Heidari et al. [4] estimated the failure probability of a fire exposed concrete slab to assess its reliability adopting a Monte-Carlo (MC) method, and Gernay et al. [5] developed fragility curves to assess the performance of steel building under fire hazard. Out of the available probabilistic approaches, the development of fragility curves has been found to be popular among researchers as it is conceptually easy to understand and allows faster design iterations [5].

Although available probabilistic methodologies, such as the development of fire fragility curves, can contribute to enable a safe and reliable design for fire exposed structures [2-6], their implementation has been found arduous and computationally challenging. The commonly large computational demand can mainly be attributed to the multi-step calculation procedure required for fire analysis of structures, together with the need for a large number of structural evaluations for probabilistic estimations. For instance, the Monte Carlo approach adopted for reliability assessment of reinforced concrete (RC) slabs by Van Coile et al. [6] involves about 10,000 structural evaluations, demonstrating substantial computational demand. A similar difficulty can be observed in the probabilistic studies carried out by Guo et al., and Hopkin et al. [7-8] for the probabilistic evaluation of protected steel elements. To address this limitation, some studies adopt simplified structural fire models (simply supported beam considered by Guo et al.; uniform steel temperature assumption by Hopkin et al.), while others limit the number of structural evaluations through efficient stochastic modelling procedures [5, 7]. Although these more advanced approaches managed to reduce the computational expense in the above cases, their execution requires careful error analysis and added expert knowledge. Furthermore, the above-mentioned probabilistic studies have a drawback that they are limited to a specific case, where any alteration in the design parameter involves re-assessment of the entire probabilistic evaluation.

Therefore, there is a need for a technique which can reduce the computational effort significantly and allow quick iterations for alteration in design parameters. In this regard, Machine learning (ML) algorithms, which can mimic a complex high-fidelity model [9] (here, SFE models), could be a promising technique for probabilistic analysis of structures in fire. Additionally, such models allow rapid generation of fragility curves at limited computational expense when design parameters are altered (within the range of applicability). Recent applications of ML algorithms in the field of fire safety engineering can be found in Dexters et al. [10], where lasso-regression based surrogate models were adopted to predict the flashover in a compartment. Likewise, Naser [11-12] carried out a series of investigations based on ML algorithms in the field of SFE. Based on this available literature, it can be hypothesized that ML algorithms can efficiently be used to predict the response of fire exposed structures and thereby allow computationally efficient probabilistic analysis for SFE models.

The present study intends to present a computationally efficient methodology for probabilistic analysis of a fire exposed structure through the use of ML algorithms. The methodology is demonstrated through application to a RC column under standard fire exposure. The structure of the paper is as follows. Initially the methodology for development of surrogate model is discussed (Section 2). Section 3 presents the considered fire exposed column and the development of the surrogate model. Finally, the probability distribution functions based on actual and surrogate models are evaluated and compared in Section 4. Section 4 further demonstrates the application of the surrogate model for developing generalized fragility curves applicable to design changes with respect to the ISO834 exposure duration.

2 METHODOLOGY: SURROGATE MODELING

The surrogate models developed through ML algorithms can be found in a wide variety of fields for evaluating the response of physical systems [9, 10, 13]. Similarly, in the field of SFE, ML algorithms such as regression, GA and ANN have demonstrated promising performance [10-12]. However, the use of ML techniques in fire safety engineering remains hardly explored. In this regard, the current study explores the potential of regression based surrogate models for approximating the response of SFE models. Regression based surrogate models are simple and interpretable compared to algorithms such as ANN and GA and thus

allow to evaluate the effect of model parameters on the response of the physical system. Here, polynomial regression-based surrogate models are adopted to predict the response of fire exposed structures. The methodology for the development of a regression-based surrogate model is discussed hereafter.

2.1 Training data generation

The first step for the training data generation is the identification of model variables on which the response of the high-fidelity model depends. If $x = [x_1, x_2, x_3, \dots, x_{r-1}, x_r]$ represents a vector of model variables, then the response, y of the high-fidelity model, $h(x)$ is given by:

$$y = h(x) \quad (1)$$

A sampling scheme for the considered parameters is then developed (e.g. Latin hypercube sampling (LHS) can be used [14]), accounting for a range of possible design configurations. Finally, the response of the high-fidelity model, i.e. in this case the finite element simulation of the structural system or element in fire, is evaluated for each of the points in the sampling scheme. The sample space of the model variables, x and the response, y of the high-fidelity model forms the training data for the surrogate model.

2.2 Model hypothesis and fitting

A hypothesis for the surrogate model is assumed based on the complexity of the high-fidelity model. In the present study, a polynomial model is adopted. Eq. (2) illustrates a first order polynomial hypothesis ($m = 1$) to represent the surrogate model for the high-fidelity model.

$$\hat{y} = \hat{h}(x) = \theta_0 + \sum_{i=1}^r \theta_i x_i \quad (2)$$

where, $\hat{y} = \hat{h}(x)$ represents the surrogate model approximation, and $\theta = [\theta_0, \theta_1, \dots, \theta_r]$ represents the regression coefficients, where θ_0 refers to the bias term and θ_1 to θ_r refers to the weights of the respective polynomial terms of the surrogate model.

The regression coefficients of the surrogate model are obtained through minimization of the cost of prediction (i.e. the divergence between the high-fidelity evaluations and the surrogate predictions for the training samples) using an optimization algorithm. Here, a gradient descent technique is adopted [15]. The cost of prediction is here referred to as cost function, $J(\theta)$, which is given by:

$$J(\theta) = \frac{1}{2n} \sum_{i=1}^n (\hat{h}(x_i) - y_i)^2 \quad (3)$$

where n refers to the size of the training sample. The gradient descent is an optimization algorithm following downhill approach, where regression coefficients are obtained iteratively in the reverse direction to the positive gradient of the cost function. The regression coefficients at each iteration of the optimization procedure are given by:

$$\theta_r = \theta_r - \alpha \frac{\partial}{\partial \theta_r} J(\theta) \quad (4)$$

where, α is the learning rate for the surrogate model optimization. The regression coefficients are changed iteratively in each step until the cost function reaches a specified tolerance value. Based on the estimated regression coefficients and polynomial surrogate model, i.e. Eq. (2), the response of the high-fidelity model can be predicted straightforwardly.

2.3 Fitting issues, optimization of hyperparameters and performance evaluation

In the procedure of Section 2.2, it can be difficult to achieve the recommended tolerance value for the cost function because the input variables have different orders of magnitude (and dimensions), which results in unequal weighting of the features during updating of regression coefficients. To address this issue, the features (model variables) need to be scaled before the regression optimization. In the present study, the features are scaled based on the standardization technique, where the normalized values are given by:

$$x_{\text{norm}} = \frac{x - \mu_x}{\sigma_x} \quad (5)$$

where x refers to a particular feature, while μ_x and σ_x are the mean and standard deviation of the feature values used for training the model.

Another issue in training a regression model is underfitting or overfitting of data. This issue is related to the training parameters of the surrogate model, namely size of the training set (n) and order of polynomial (m). Adoption of a lower order polynomial as surrogate model hypothesis might lead to an underfitting of the model, while there is an overfitting of data if higher order polynomials are adopted. Likewise, an insufficient sample size is incapable of mapping the entire sample space of the model variables, leading to a surrogate model which is limited in application scope. Thus, an appropriate polynomial order and sample size are needed for training a surrogate model to achieve accurate response prediction. The issue of overfitting of a surrogate model can be addressed by adopting a regularized cost function as shown in Eq. (6), where the regularization parameter λ penalizes the regression coefficients by artificially increasing the cost function if polynomials are adopted with more significant (non-zero) coefficients.

$$J_{\text{learn}}(\theta) = \frac{1}{2n} \sum_{i=1}^n \left(\hat{h}(\mathbf{x}_i) - y_i \right)^2 + \frac{\lambda}{2n} \sum_{l=1}^r \theta_l^2 \quad (6)$$

In Eq. 6, $J_{\text{learn}}(\theta)$ is the regularized cost function. However, it is necessary to determine a proper value of regularization parameter (λ). Similarly, an appropriate (minimum) sample size (n) and order of polynomial (m) should also be chosen to address the issue as a whole. These parameters can also be called hyperparameters and can be determined through the development of ‘learning curves’. In order to develop the learning curves, three input data sets are considered, namely a training set, a cross-validation set and a test set. The learning curves then refer to the plot of the cost-function evaluated from the training (J_{train}) and cross-validation data set (J_{cv}), i.e.:

$$J_{\text{train}}(\theta) = \frac{1}{2n_{\text{train}}} \sum_{i=1}^{n_{\text{train}}} \left(\hat{h}(\mathbf{x}_{\text{train},i}) - y_{\text{train},i} \right)^2 \quad (7)$$

$$J_{\text{cv}}(\theta) = \frac{1}{2n_{\text{cv}}} \sum_{i=1}^{n_{\text{cv}}} \left(\hat{h}(\mathbf{x}_{\text{cv},i}) - y_{\text{cv},i} \right)^2 \quad (8)$$

The approach for estimating hyperparameter involves developing learning curves by varying training parameters, each at a time and evaluating the prediction errors. After, the desired accuracy has been achieved, the surrogate model is considered sufficiently trained to predict the response of the high-fidelity model. Finally, the accuracy of the developed surrogate model with the particular combination of hyperparameters is evaluated based on the test data set. Here, the coefficient of determination, R^2 [16] is evaluated for estimating the prediction efficiency of the surrogate model:

$$R^2 = 1 - R_{\text{res}} / R_{\text{tot}} \quad (9)$$

where, $R_{\text{res}} = \sum_{i=1}^{n_{\text{test}}} \left(\hat{h}(\mathbf{x}_{\text{test},i}) - y_{\text{test},i} \right)^2$ and $R_{\text{tot}} = \sum_{i=1}^{n_{\text{test}}} \left(y_{\text{test},i} - \bar{y}_{\text{test}} \right)^2$ refers to the residual and total sum of squares, respectively. The R^2 ranges from 0 to 1, where ‘1’ represents a perfectly fitted surrogate model.

3 APPLICATION TO REINFORCED CONCRETE COLUMN

In this study, the methodology for the development of a regression-based surrogate model is demonstrated by considering the assessment of the fire-resistance rating of a RC column. The high-fidelity model is a finite element model in SAFIR [17], which involves a computational cost to solve the nonlinear thermal-structural computation. The probabilistic studies have been presented in [18] and incorporated in [19]. The cross-section of the considered column is 500 mm × 500 mm, reinforced with 12 bars of 20 mm diameter, which is shown in Figure 1(a). The height of the column is 4 m, with pinned support at the bottom, and roller support at the top (restraining lateral movement). The grade of the concrete used is C30/37 and the

reinforcing steel is of grade 500. The column is subjected to the ISO834 fire from all sides. Figure 1(b-c) shows the thermal and mechanical response of the considered concrete column with an axial loading of 6000 kN. Based on Figure 1, the column is observed to have the fire-resistance of 140 min.

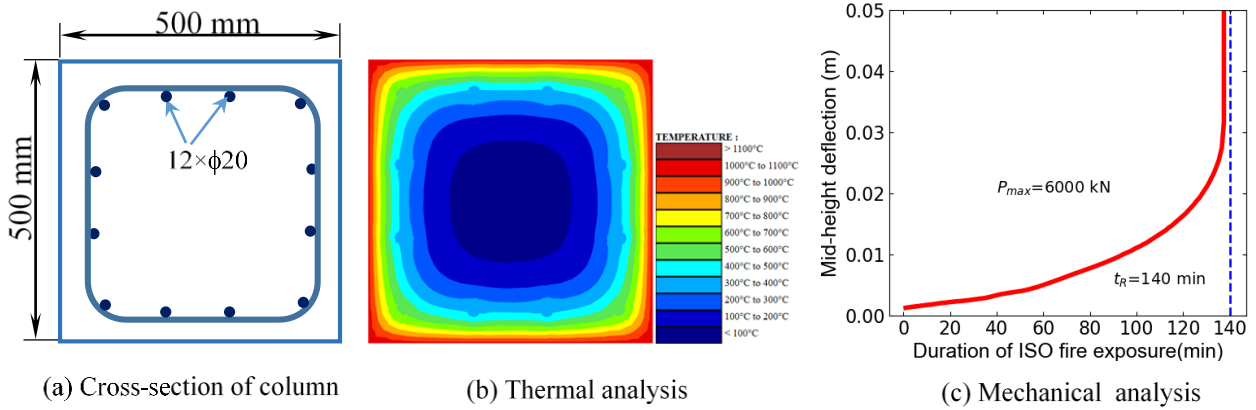


Figure 1. Response of RC column exposed to ISO834 fire, with an axial load of 6000 kN

3.1 Development of surrogate model

For the development of the surrogate model, the model variables for the high-fidelity model need to be selected first. For the RC column, seven variables are identified, namely: the retention factor parameters for the compressive strength of concrete (ϵ_{kfc}) and yield strength of reinforcing bars (ϵ_{kfy}), the concrete cover (c), average eccentricity (e), out of straightness (f), out of plumbness (Φ) and the applied load (P). The variables ϵ_{kfc} and ϵ_{kfy} define the quantile of the retention factors at elevated temperature based on the strength retention models by Qureshi et al. [20]. The model variables e , f and Φ are the three eccentricities of the column, as listed in the JCSS probabilistic model code [21]. The considered model variables along with the ranges for the sample space are shown in Table 1. An LHS scheme is adopted for developing the sample space for training the surrogate model. The generated training data initially contains a training set of 10^4 realizations (LHS set) and a cross-validation 1250 realizations (MC). Finally, the high-fidelity model is evaluated for each of these generated training and cross-validation sample points. In the present study, to allow comparison with the results by Van Coile et al. [18], the surrogate model is trained to predict the maximum axial load bearing capacity of the column (P_{max}) for a specified duration (240 min) of ISO 834 fire exposure. In order to achieve this, the numerically obtained fire resistance for the RC column is considered as input parameter for the surrogate model, while the axial load on the column is considered as response of the surrogate model.

Table 1. Model variables and their distribution for development of surrogate model

Independent variables	Lower limit	Upper limit	Unit	Sampling distribution
Concrete strength retention factor parameter, ϵ_{kfc}	-4.00	4.00	-	Uniform
Rebar yield strength retention factor parameter, ϵ_{kfy}	-4.00	4.00	-	
Concrete cover, c	16	96	mm	
Average eccentricity, e	-0.03	0.03	mm	
Out of straightness, f	-0.03	0.03	mm	
Out of plumbness, Φ	-0.01	0.01	mm	
Maximum applied load, P_{max}	1000	10500	kN	

Next, the surrogate model hypothesis is defined and the model is trained based on the developed sample space and evaluated response from SAFIR analyses (the high-fidelity model). Subsequently, the learning curves are developed to assess the optimum value of the hyperparameters by evaluating J_{train} and J_{CV} for different sets of the hyperparameters. Figure 2 shows the learning curves for the surrogate model of the RC column considered in the study, which allows to determine optimized hyperparameters.

Figure 2 (a) allows to determine the optimum order of polynomial to be adopted for the surrogate model to work precisely. The J_{cv} shows significant improvement in prediction error for polynomials with $m \leq 3$, while there is no further decrease in error for polynomial with $m \geq 5$. Thus, a 4th order polynomial hypothesis is adopted for the surrogate model hypothesis.

Similarly, Figure 2(b) helps to determine the optimum training sample size of the surrogate model. Based on the Figure, a training set of 10^4 LHS samples is considered to be adequate to develop the surrogate model as the learning curves shows a sign of convergence. Figure 2(c) is developed considering estimated optimum order of polynomial and training sample size, where J_{train} and J_{cv} are evaluated for varying regularization parameter values. The figure shows that the regularization parameter is not required for the considered surrogate model, as the cost function monotonously increases with increasing value of the regularization parameter. The learning curves indicate that J_{train} is higher than J_{cv} . This may seem unexpected, but the LHS scheme adopted for the training set ensures sampling evenly across the entire input space, necessarily including many low probability (outlier) parameter combinations, while the MCS samples directly from the parameter distributions, without ensuring that also low probability combinations are included in the set. It is thus hypothesized that the higher J_{train} results from a higher proportion of low “extreme” cases which are less well captured by the surrogate model.

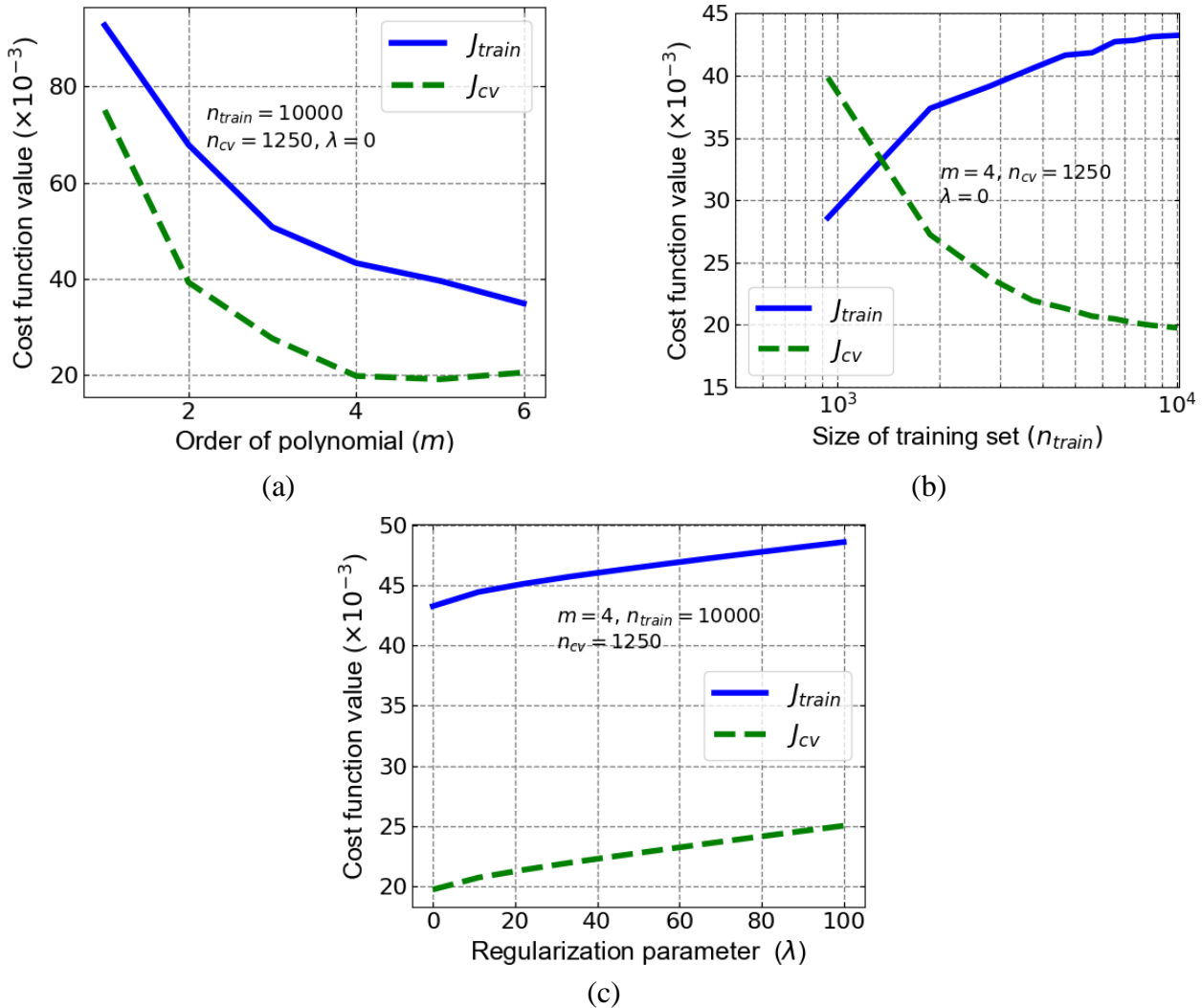


Figure 2. Learning curves for development of surrogate model

3.2 Performance evaluation of surrogate model

To evaluate the performance of the developed surrogate model in Section 3.1, a Monte-Carlo test set of 1250 sample points is considered. Figure 3(a) shows the comparison of the response for the test data set based on the high-fidelity model (i.e. SAFIR) and the surrogate model. The coefficient of determination (R^2) for the surrogate model is found to be 0.95. Similarly, Figure 3(b) shows the absolute normalized error

(for the test data set, indicating that more than 90% of the test samples are predicted by the surrogate model with an error of less than 20%. The absolute normalized error (ANE) for the test data set is given by:

$$ANE = \left| \frac{y_{test} - \hat{h}(\mathbf{x}_{test})}{y_{test}} \right| \quad (10)$$

A mean ANE value of 0.0506 is observed for the predicted capacity for the column. As the FE model for the RC column considered in the present study involves complex structural calculations, the evaluated error is considered reasonable. Thus, the surrogate model is implemented to predict the response of the RC column. The evaluation of the FE model for all the test samples took 60 core-hour on a state-of-the-art personal computer, while the evaluation is quasi-instantaneous for the surrogate model.

Considering the trained surrogate model, the regression coefficient for the duration of fire exposure (t_E) has the highest absolute value and thus can be considered as the most influencing parameter of the surrogate model. In contrast, there is negligible influence of the bias term on the response of surrogate model and thus this term can be neglected.

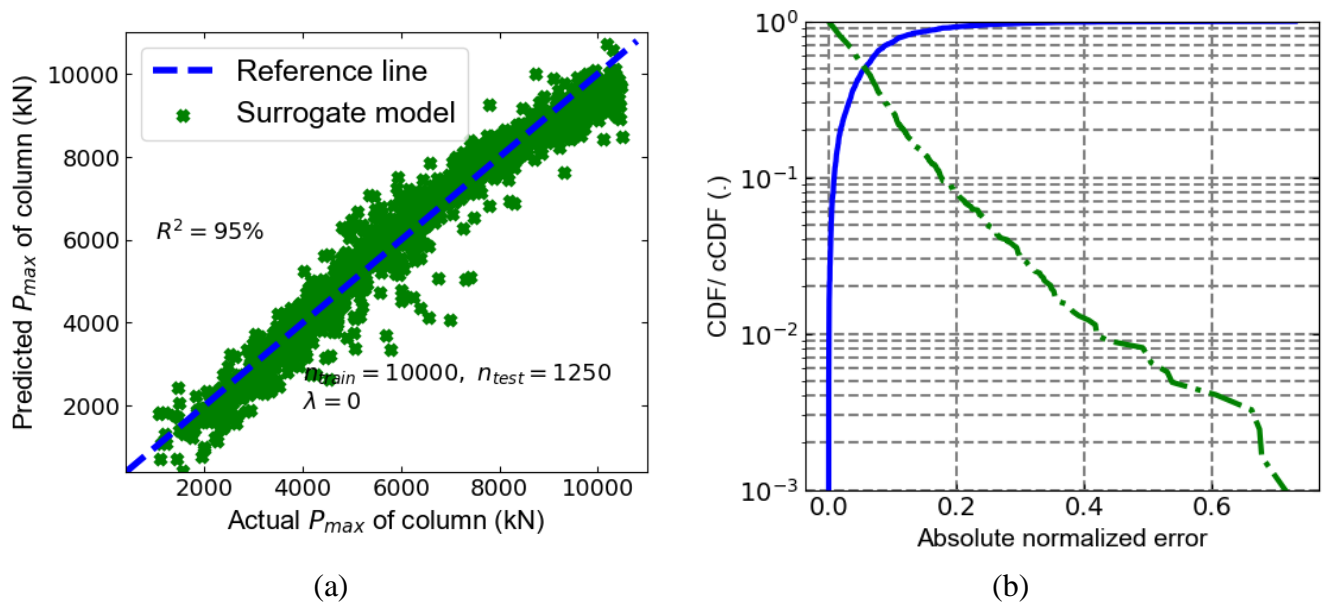


Figure 3. Performance of the surrogate model for the RC column. The output P_{max} is the column axial capacity after 240 min of ISO fire exposure. Actual value is obtained with SAFIR. Predicted value is obtained by the surrogate model.

4 SURROGATE MODEL BASED PROBABILISTIC STUDIES

Figure 4 shows the framework proposed for probabilistic studies of fire exposed structures based on the regression-based surrogate models. For the probabilistic studies, initially a surrogate model needs to be developed for the high-fidelity model (SAFIR model here). Section 2 above elaborates the steps for developing a surrogate model, which has been implemented in Section 3 for the RC column. Once the surrogate model with the desired accuracy is developed, the probabilistic distributions of the model variables can be considered for the specific design to carry out a probabilistic evaluation. In this regard, a sample space is developed based on the assumed probabilistic distribution through a sampling scheme (LHS considered here) and subsequently, the response of the structure is evaluated considering the surrogate model for each of the sample points. Finally, fragility curves are developed based on the estimated responses. As the surrogate model involves significantly lower computational cost, the probabilistic estimations can be done at limited computational expense, also considering design changes.

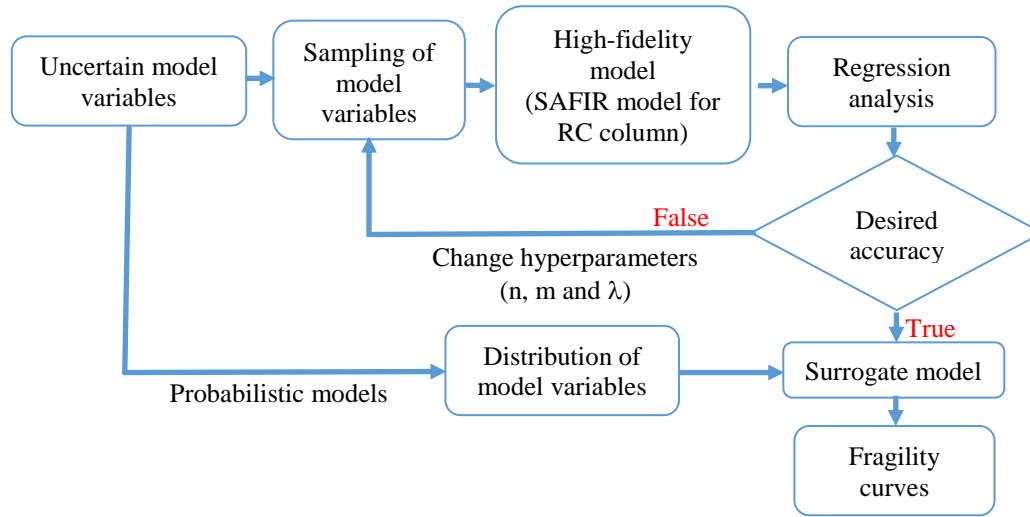


Figure 4. Framework for probabilistic studies of fire exposed structures based on surrogate modelling methodology

4.1 Concept validation

To validate the proof-of-concept, the probability density function (PDF) and cumulative density function (CDF) for the considered RC column, developed based on the proposed framework is compared against that obtained by a traditional direct Monte Carlo approach. The validation is carried out for maximum axial load for the considered RC column exposed to 4 hours of ISO834 fire, as presented in [18]. Table 2 shows the uncertain model variables along with their probabilistic distributions [18, 21] for the probabilistic evaluation. A set of 10^4 LHS samples are developed for the considered stochastic variables. Finally, the PDF and CDF for the RC column can easily be evaluated based on the surrogate model developed in Section 2. On the other hand, the development of PDF and CDF based on the traditional Monte Carlos method involves direct evaluation of the complex high-fidelity model and is computationally expensive, notably due to a need to apply an iterative search algorithm to determine the maximum allowable axial load to achieve 240 min standard fire resistance for each RC column realization.

Table 2. Stochastic variables and their distributions for probabilistic evaluation of RC column

Stochastic variables	Distribution	Mean	Standard deviation
Yield strength of rebars, $f_{y,T}$ ($f_{yk,20} = 500$ MPa; $\mu_{f_{y,20}} = 560$ MPa)	Logistic model [20]	Temperature-dependent	Temperature-dependent
Concrete compressive strength, $f_{c,T}$ ($f_{ck,20} = 30$ MPa; $\mu_{f_{y,20}} = 42$ MPa)			
Concrete cover, c [mm]	Beta [$\mu-3\sigma$; $\mu+3\sigma$]	42+5=47	5
Average eccentricity, e [–]	Normal	0	0.001
Out of straightness, f [–]	Normal	0	0.001
Out of plumbness, Φ [–]	Gumbel	0	0.0015

Figure 5 shows the comparison of the PDF and CDF for the RC column, evaluated based on direct estimation from the high-fidelity model (10^4 evaluations) and the surrogate model. Based on Figure 5(a), the PDF are quite in agreement. The mean predicted value for the load capacity of the column for 4 hours of ISO834 exposure is 5137 kN based on the surrogate model, which is quite close to the actual capacity of 5038 kN, evaluated through the SAFIR Monte-Carlo approach. Likewise, Based on Figure 5(b), it can be determined that the CDF based on application of the surrogate model agrees reasonably well with the CDF evaluated through SAFIR Monte Carlo computations, especially with respect to the lower quantile of P_{max} . The comparison of the capacity quantiles is shown in Table 3, where a prediction error of less than 5 % can be observed. In the Table, the 10^{-2} capacity quantiles for RC column based on actual model is 2931 kN, which is predicted as 3010 kN by the surrogate model, indicating an error of 2.7 %.

Table 3. Capacity quantiles for load capacity of RC column exposed to ISO 834 fire

S.N	CDF (.)	M_R of slab (kN) for RC column		
		Surrogate model (ML)	Actual model (SAFIR)	ANE (%)
1.	10^{-1}	3987	3805	4.7
2.	10^{-2}	3010	2931	2.70
3.	10^{-3}	2475	2414	2.52

These results suggest that the surrogate modelling methodology can be used for probabilistic studies of fire exposed structures (provided adequate training data has been generated), thereby validating the proof-of-concept. From the perspective of computational cost, the probabilistic estimation of capacity of column based on the trained surrogate model is instantaneous, while the same evaluation required approximately 7 days through a traditional Monte-Carlo approach. Thus, the surrogate modelling methodology being computationally efficient is considered promising for the probabilistic studies of fire exposed structures.

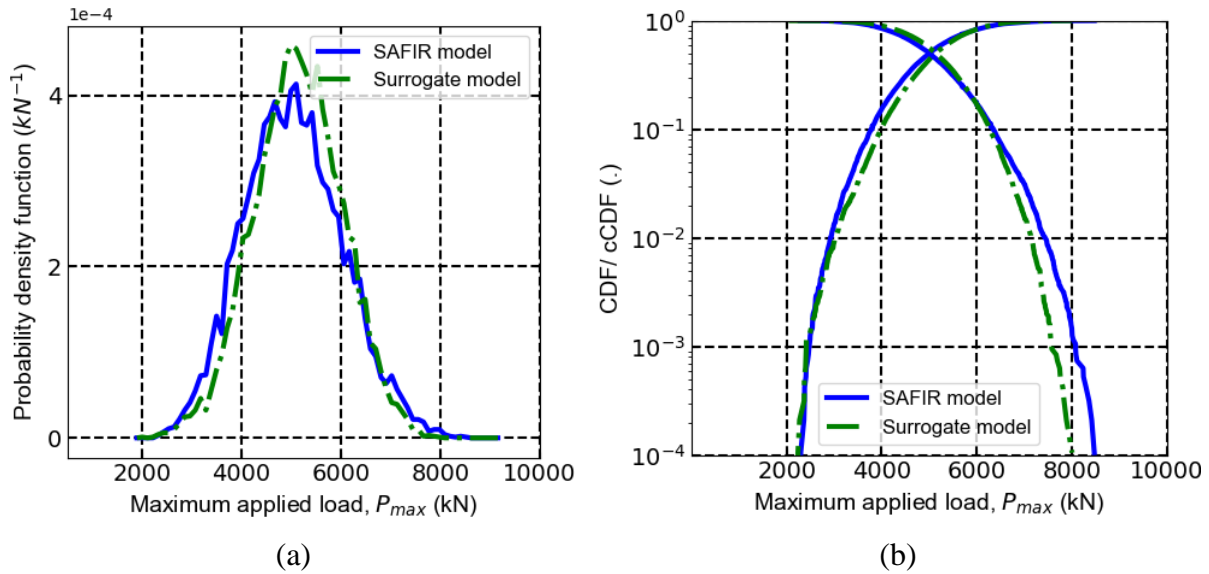


Figure 5. PDF and CDF for the concrete column based on actual and surrogate model

4.2 Generalized fragility curves

The direct Monte-Carlo approach for the probabilistic evaluation involves an iterative evaluation of the high-fidelity system in order to evaluate P_{max} for a given ISO834 fire duration, which is a computationally expensive task. Thus, it is impractical to perform probabilistic evaluations in case of a change in the design variables. In this regard, the surrogate model can be most helpful as it allows quasi-instantaneous prediction of the structural response for any alteration in design variables (within the parameter range for which the model has been trained). This concept is demonstrated through the application of the developed surrogate model to different ISO834 exposure durations in Figure 6. Based on the evaluations, the mean load carrying capacities of the RC column for 1, 2, 3 and 4 hours of ISO834 exposure are 8547 kN, 7290 kN, 6210 kN and 5137 kN, respectively. The 10^{-2} capacity quantiles for the RC column are predicted as 6513 kN, 4944 kN, 3852 kN and 3010 kN, respectively. The results of Figure 6 for P_{max} , can be understood as fragility curves, where the intensity measure is the maximum applied load on the column. This allows an engineer to swiftly evaluate the probability of failure of the column at different times of exposure, given its applied load in the fire situation. For example, if the RC column is subjected to an applied load of 4500 kN, the failure probability under ISO exposure is 0.3 % after 2h, 4.30 % after 3h, and 24.53 % after 4h. The failure probability is virtually null after 1h. These fragility curves can be generated efficiently for any alteration in design parameters through the surrogate modelling methodology.

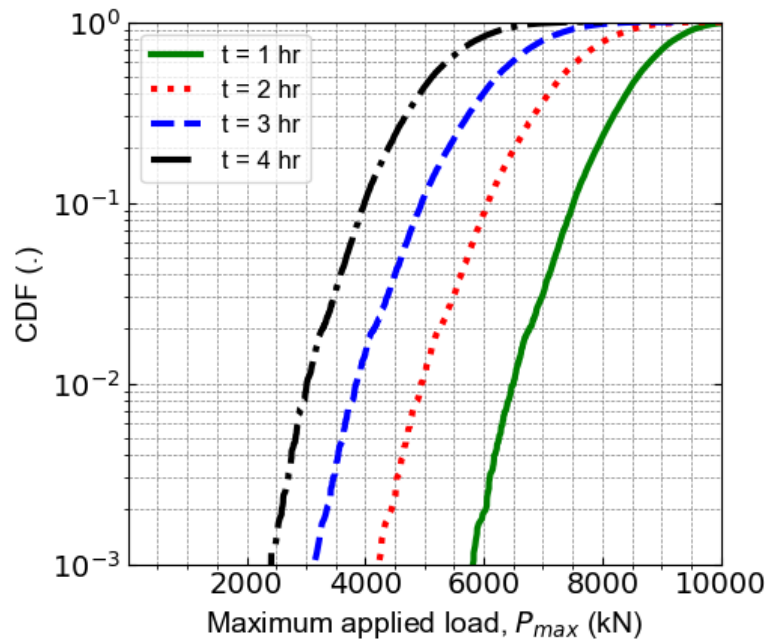


Figure 6. CDF for the RC column exposed to ISO834 fire of different durations

5 CONCLUSIONS

Available prescriptive guidelines and code-based recommendations are at times insufficient for the design of structures under fire exposure. In certain cases, the use of probabilistic approaches, where the important uncertainties in the model evaluation are taken into account, is required to explicitly assess the risk profile of the fire hazard on structures. However, probabilistic evaluations are complex and computationally demanding, and as most structural fire analysis involves complex structural calculations, it is impractical to adopt direct probabilistic approaches. To address this issue, this study has proposed adopting regression-based surrogate models for the probabilistic evaluation of fire exposed structures. The surrogate models can simulate the behaviour of a complex high-fidelity model precisely and can predict the response of the model quasi-instantaneously. The current study acts as a proof-of-concept.

In the present study, the basic case of a fire exposed reinforced concrete (RC) column is considered. Initially, a surrogate model was developed for the RC column, which can predict the maximum load carrying capacity for a given ISO834 exposure duration. The coefficient of determination for the surrogate model was found to be 0.95. The developed surrogate model was then adopted for probabilistic studies, where the probability density functions (PDF) and cumulative distribution functions (CDF) were evaluated. These PDF and CDF are quite in agreement with those obtained through the direct evaluation of the computationally more expensive high-fidelity model. The 0.1%, 1% and 10% capacity quantiles show a maximum error of 5 %. The probabilistic study based on the surrogate model is quasi-instantaneous while the direct estimation through a Monte Carlo approach involves significant computational cost (approximately 7 days). This observation makes it possible for design iterations (changes in design parameters) to be considered in a probabilistic analysis, harnessing the surrogate modelling approach. Thus, based on the current study, surrogate modelling seems a promising methodology to advance probabilistic studies in the field of structural fire engineering, allowing computationally efficient probabilistic evaluations during structural fire design.

REFERENCES

1. Van Coile, R., Hopkin, D., Lange, D., Jomaas, G., and Bisby, L. (2019). The need for hierarchies of acceptance criteria for probabilistic risk assessments in fire engineering. *Fire Technology*, 55(4), 1111-1146.
2. Gernay, T., Van Coile, R., Khorasani, N.E. and Hopkin, D., (2019a). Efficient uncertainty quantification method applied to structural fire engineering computations. *Engineering Structures*, 183, 1-17.

3. Shrivastava, M., Abu, A. K., Dhakal, R. P., and Moss, P. J. (2019). Severity measures and stripe analysis for probabilistic structural fire engineering. *Fire Technology*, 55(4), 1147-1173.
4. Heidari, M., Robert, F., Lange, D. and Rein, G. (2019). Probabilistic study of the resistance of a simply-supported reinforced concrete slab according to eurocode parametric fire. *Fire Technology*, 55(4), pp.1377-1404.
5. Gernay, T., Khorasani, N.E. and Garlock, M., (2019b). Fire fragility functions for steel frame buildings: sensitivity analysis and reliability framework. *Fire Technology*, 55(4), pp.1175-1210.
6. Van Coile, R., Caspeelee, R., and Taerwe, L. (2014). Reliability-based evaluation of the inherent safety presumptions in common fire safety design. *Engineering structures*, 77, 181-192.
7. Guo, Q., Shi, K., Jia, Z., and Jeffers, A. E. (2013). Probabilistic evaluation of structural fire resistance . *Fire technology*, 49(3), 793-811.
8. Hopkin, D., Van Coile, R., and Fu, I. (2018). Developing fragility curves and estimating failure probabilities for protected steel structural elements subject to fully developed fires. *Proceedings of the 10th International Conference on Structures in Fire*. 06-08/06, Belfast, UK.
9. Forrester, A., Sobester, A. and Keane, A., (2008). *Engineering design via surrogate modelling: a practical guide*. John Wiley & Sons.
10. Dexters A., Leisted R. R., Van Coile R., Welch S., Jomaas, G. (2019). Testing for Knowledge: Maximising Information Obtained from Fire Tests by using Machine Learning Techniques. *Proceedings of the 15th International Interflam conference*, 1.
11. Seitllari, A. and Naser, M.Z. (2019). Leveraging artificial intelligence to assess explosive spalling in fire-exposed RC columns. *Comput. Concr*, 24, pp.271-282.
12. Naser, M. Z., (2019). Fire resistance evaluation through artificial intelligence-A case for timber structures. *Fire safety journal*, 105, 1-18.
13. James, G., Witten, D., Hastie, T. and Tibshirani, R. (2013). *An introduction to statistical learning*. New York: springer, 112, 3-7.
14. Olsson, A., Sandberg, G. and Dahlblom, O. (2003). On Latin hypercube sampling for structural reliability analysis. *Structural safety*, 25(1), 47-68.
15. Du, S.S., Lee, J.D., Li, H., Wang, L. and Zhai, X. (2018). Gradient descent finds global minima of deep neural networks. *arXiv preprint arXiv:1811.03804*.
16. Draper, N. R. and Smith, H. (1998). *Applied Regression Analysis*. Wiley-Interscience, 326.
17. Franssen, J.M. and Gernay, T., 2017. Modeling structures in fire with SAFIR®: Theoretical background and capabilities. *Journal of Structural Fire Engineering*, 8(3), 300-323.
18. Van Coile, R., Hopkin, D., Elhami Khorasani, N. and Gernay, T., (2020). Demonstrating adequate safety for a concrete column exposed to fire, using probabilistic methods. *Fire and Materials*. <https://doi.org/10.1002/fam.2835>.
19. ISO/CD TR 24679-8: 2020. Fire safety engineering — Performance of structures in fire — Part 8: Example of a probabilistic fire design of structures. ISO Technical Report. International Organization for Standardization, Geneva, Switzerland.
20. Qureshi, R., Ni, S., Elhami Khorasani, N., Van Coile, R., Hopkin, D. and Gernay, T., (2020). Probabilistic Models for Temperature-Dependent Strength of Steel and Concrete. *Journal of Structural Engineering*, 146(6), 04020102.
21. JCSS. (2013). Probabilistic Model Code. Joint Committee on Structural Safety. Available online at <http://www.jcss.byg.dtu.dk/>.

CRITICAL FIBRE DIMENSIONS FOR PREVENTING SPALLING OF ULTRA-HIGH PERFORMANCE CONCRETE AT HIGH TEMPERATURE

Dong Zhang¹, Kang Hai Tan²

ABSTRACT

This paper presents an experimental study that investigates the effect of fibre geometry on preventing spalling of ultra-high performance concrete (UHPC). UHPCs with different dimensions of polypropylene (PP) fibres were prepared for permeability test at different temperatures and spalling test under ISO834 fire curve. Scanning electron microscope (SEM) observation was also conducted focusing on the fibre of a UHPC sample at the same location after it was subjected to an elevated temperature. The results of permeability tests and spalling tests showed that longer fibres of 12 mm and 18 mm and finer fibres of 28 μm and 33 μm were more beneficial for increasing the permeability of UHPC at high temperature, resulting in higher effectiveness on spalling prevention. Permeability measurements indicated a significant increase occurred at 150 °C regardless of fibre dimensions; this increase plays an important role in spalling prevention. SEM results further testify that this increase can be attributed to the formation of microcracks caused by expansion of PP fibres.

Keywords: ultra-high performance concrete (UHPC); permeability; spalling; high temperature

1 INTRODUCTION

Ultra-high performance concrete (UHPC) is considered as a promising material due to its high compressive strength and excellent durability. There is widespread utilization of UHPC in structures such as bridges and nuclear waste storage facilities, for the last two decades [1]. However, due to its dense microstructure, UHPC is susceptible to explosive spalling when exposed to fire[2], which limits its applications to building construction.

It should be noted that explosive spalling results in a rapid loss of concrete, exposing deeper layers of concrete to fire condition. As a consequence, spalling increases the transmission rate of heat to inner layers of a member as well as embedded reinforcement, thereby compromising its load-carrying capacity[3]. Conventional wisdom has it that thermal gradient and high vapour pressure are two main causes of spalling[4-7]. To prevent spalling, one of the most widely accepted methods is the addition of polypropylene (PP) fibre that is supposed to relieve vapour pressure by creating interconnected paths in concrete at high temperature [8, 9].

According to extensive studies on using PP fibres to prevent spalling, many researchers focused on its efficiency on spalling protection. PP fibres of different dimensions, ranging from 15 to 300 μm in diameter and 3 to 38 mm in length, have been adopted in the existing studies[10, 11]. Results of literature on the performance PP fibres of different dimensions can appear to be contradictory at times. It was mentioned by

¹ PhD, School of Civil and Environmental Engineering, Nanyang Technological University, 639798, Singapore,
e-mail: zhangdong@ntu.edu.sg, ORCID: <https://orcid.org/0000-0002-0138-3416>

² Professor, School of Civil and Environmental Engineering, Nanyang Technological University, 639798, Singapore,
e-mail: ckhtan@ntu.edu.sg, ORCID: <https://orcid.org/0000-0003-1500-6643>

Bilodeau, Kodur [12] that finer PP fibres of 12mm in length were more efficient than thicker PP fibres with a length of 20 mm. However, Bangi and Horiguchi [13] reported that longer and finer PP fibres had better performances than shorter and thicker ones. Furthermore, the experimental results by Jansson [14] supported that thick PP fibres had higher effectiveness on preventing spalling than the finer ones.

In spite of the above conflicting findings, there are also insufficient experimental evidences to extrapolate the research findings from high performance concrete (HPC) to UHPC [9]. In fact, hardly any studies have been carried out on spalling resistance of UHPC. Xiong and Liew [15] claimed that a dosage of 0.1 vol. % of PP fibre with diameter of around 30 μm and length of 13mm was effective in preventing spalling for temperature up to 800 $^{\circ}\text{C}$. But in a report by Klingsch, Frangi [16], it was observed that only fibre with diameter of 18 μm and length of 6 mm could prevent spalling of UHPC, while fibres of 32 μm and 15.4 μm in diameter could only minimize spalling to some extent even with a high dosage of more than 0.3 vol. %.

Clearly, from the existing studies, fibre geometry plays an important role on spalling prevention [17]. However, the above contradictory findings are far from satisfactory to account for the effect of fibre geometry on spalling mitigation. This is largely because there has not been a systematic and extensive study on the effect of fibre geometry on spalling protection. In addition, there is a lack of testing on the role of PP fibres in concrete at high temperature.

In this experimental investigation, PP fibres of different geometries (different diameters and lengths) were chosen to study the effect of fibre dimensions on spalling prevention of UHPC. Permeability, a vital parameter describing the capacity of moisture transportation in concrete, was measured at different temperatures. Spalling tests were also conducted on concrete cylinders to evaluate the effectiveness of PP fibre of different dimensions. Microstructures of UHPC at different temperatures were investigated through scanning electron microscope (SEM). The first author subjected the same PP fibre on the UHPC sample to different temperatures and studied its behaviour.

2 DESIGN OF EXPERIMENT

2.1 Material

The materials used for UHPC in this study included Portland cement (ASIA@ CEM II 52.5 R), silica sand, silica fume, fine aggregate, tap water, superplasticizer and PP fibre, and the mix proportion is shown in Table 1. The mean size of the silica sand was 110 μm . Natural river sand with the maximum size of 0.6 mm was used as fine aggregate. All the PP fibres, with the specifications shown in Table 2, were from Wuhan Zhongding Economical Development Ltd., China. A third generation polycarboxylic type superplasticizer Sika ViscoCrete-2044 was applied in all concrete mixtures.

The specimens were demoulded after being cast for 1 day and were stored in lime-saturated water at ambient temperature to 28 days. The specimens were named by the size of the PP fibre contained. For example, U28/06/0.33 denoted the UHPC containing PP fibre with 28 μm diameter and 6 mm length and the fibre content was 0.33 vol.%. The number of specimens and their mean compressive strength at 28 days are presented in Table 3. The compressive strengths of all the specimens were around 150 MPa. Although addition of PP fibre slightly affected the compressive strength of UHPC, this influence was beyond the objective of this study and will not be discussed here.

Table 1. Mix proportions

W/B*	Cement	Silica fume	Silica sand	Superplasticizer	Aggregate	PP fibre (vol.%)
0.2	1	0.25	0.25	0.04	1.1	0.33

*W/B: water to binder ratio.

Table 2. Property of PP fibres

Density (kg/m ³)	Tensile strength (MPa)	Melting point (°C)	Elastic modulus (MPa)
910	552	170	3800

Table 3. Number of specimen and compressive strength

No.	Diameter (μm)	Length (mm)	f_c 28day (MPa)
U28/06/0.33	28	6	137
U28/09/0.33	28	9	137
U28/12/0.33	28	12	140
U28/18/0.33	28	18	158
U33/06/0.33	33	6	141
U33/09/0.33	33	9	150
U33/12/0.33	33	12	149
U33/18/0.33	33	18	147
U100/06/0.33	100	6	144
U100/09/0.33	100	9	135
U100/12/0.33	100	12	152
U100/18/0.33	100	18	150

2.2 Testing procedure

The specimens used for permeability test were cast in cake-shape polyester moulds with a depth of 45 mm and a diameter of 150 mm. To study the gas permeability of UHPC subjected to high temperature, four target temperatures were chosen, viz. 105 °C, 150 °C, 200 °C and 300°C, with 150 °C and 200 °C representing the temperatures just before and after melting point of PP fibre, respectively. The samples were kept in the target temperature until the mass reached equilibrium. Residual permeability of the specimen was measured using Torrent permeability tester[16, 18].

Cylinders with 50 mm diameter and 100 mm height were used in spalling test. Three cylinders were tested for each mix design. The cylinders were heated in the electrical furnace for 1 h in accordance with the standard heating curve of ISO 834.

To get a flat surface and avoid initial microcracks, samples for SEM observation were carefully prepared following a series of grinding and polishing procedure. A SEM of JSM 6360 was used for observing the evaluation of microstructure at different temperatures. The same magnification of 500× with an accelerating voltage of 5 kV and a working distance of 10 mm was used for all the observation.

3 RESULT AND DISCUSSION

3.1 Gas permeability test

The evolutions of permeability with increasing temperature are plotted in Figure 1 for specimens with different dimensions of fibres. The permeability values of all the specimens exposed to 105 °C were very close, mostly in the range of 10^{-19} m², which were similar with the value reported in literature [19]. Generally, permeability of UHPC increased with increasing temperature. For example, as can be observed

in Fig. 1a, UHPC with PP fibres of 28 μm showed a significant increase on permeability of several orders of magnitudes at 150 °C. The increase of permeability in concrete before melting of PP fibre was also reported in other literature[20-22]. After 150 °C, permeability kept increasing but with a lower rate. When the temperature increased to 200 °C, one order of increase in permeability could be observed, while the permeability only increased slightly when temperature rose from 200 °C to 300 °C. It can also be found in Figure.1a that permeability of UHPC with fibres of 9, 12 and 18 mm in length showed a much larger increase compared to the one with 6 mm fibres. At 150 °C, the permeability of U28/12/0.33 and U28/18/0.33 were slightly larger than that of U28/09/0.33, with all the values hovering around $0.8 \times 10^{-16} \text{ m}^2$, while the permeability of U28/06/0.33 was about 2 orders of magnitude less. Interestingly, regardless of the fibre length, the increasing rate of permeability, either from 150 °C to 200 °C or from 200 °C to 300 °C, was quite similar at each stage. Consequently, permeability of U28/06/0.33 was always much less than those of other specimens.

In the case of UHPC with PP fibres of 33 μm in diameter, a significant increase, as shown in Figure.1b, can be observed at 150 °C. Permeability of U33/12/0.33 and U33/18/0.33 were around $0.6 \sim 1 \times 10^{-16} \text{ m}^2$ the highest point. Permeability of U33/09/0.33 was around $0.5 \times 10^{-16} \text{ m}^2$, while permeability of U33/06/0.33 was significantly less than that of U33/09/0.33. After 150°C, the rate of increase in permeability also reduced for all the specimens, similar with the specimens containing PP fibres of 28 μm .

Likewise, as presented in Figure.1c, a similar trend was found in the permeability of UHPC with 100 μm PP fibres. However, the permeability of UHPC with 100 μm PP fibres was smaller, with all the values around $1 \times 10^{-17} \text{ m}^2$ at 150 °C and around $1 \times 10^{-16} \text{ m}^2$ after exposed to 300 °C. As to fibres with 12 mm and 18 mm length, UHPC with fibres of 28 μm and 33 μm had a much larger permeability than those with fibres of 100 μm when subjected to 150 °C. However, the reduction of diameter did not show much improvement on the increase of permeability of UHPC containing shorter fibres of 6 mm, indicating fibre length makes an important influence on permeability of UHPC. When the temperature increased further, the benefit of finer fibres on increasing the permeability of UHPC became more and more obvious. After exposure to 200 °C and 300 °C, permeability of UHPC with finer fibre (28 μm and 33 μm in diameter) was 1 order larger than those of UHPC containing 100 μm fibres. Consequently, finer fibres were more beneficial for increasing permeability of UHPC at high temperature. For thicker fibres with a diameter of 100 μm , there was negligible effect on increasing permeability.

On the other hand, indications show that the increasing of fibre length led to an increase on the permeability of UHPC. For UHPC with PP fibre of 28 μm , the permeability of UHPC increased more than 1 order when the length of fibre increased from 6 mm to 12 mm at every target temperature. Comparing the permeability of UHPC containing 12 mm PP fibre with that of 18 mm PP fibre, the increase was slight. The effect of fibre length on the permeability reduced when the exposed temperature increased. A similar result could be obtained for UHPC with fibres of 33 μm and 100 μm in diameter.

3.2 Spalling test

The results of spalling test of UHPC with different dimensions of PP fibres are presented in Table 4. Obviously, dimensions of fibres played a critical role in preventing spalling of UHPC. It can be seen that thicker fibres could rarely help prevent spalling of UHPC, regardless of the fibre length. All the specimens with the fibres of 100 μm diameter suffered severe spalling after being subjected to ISO834 fire curve for 1 h. Finer fibres of 28 μm and 33 μm diameter showed better performance on spalling protection, but shorter fibres were less efficient than longer fibres. Fibres with the length of 6 mm did not contribute to spalling protection significantly, as specimens with fibres of 6 mm length all spalled served. When the length of fibre increased to 9 mm, the effectiveness of fibres on preventing spalling showed a significant improvement in UHPC with fibres of 28 μm and 33 μm in diameter. Only partially spalling occurred in U33/09/0.33 and spalling was eliminated in U28/09/0.33. In addition, no spalling occurred in the UHPC containing finer PP fibres (28 μm and 33 μm) with the length of 12mm and 18mm, indicating finer and longer fibres were beneficial for spalling prevention of UHPC. This is also evident in Figure 2, which illustrates the weight loss of specimens with different dimensions of fibres. Serious weight losses on the

UHPC containing 100 μm fibre or 6mm fibre showed PP fibre in these sizes were not efficient in spalling prevention.

The result also confirms that permeability is an important factor that is related to spalling resistance. When exposed to high temperature, UHPC with higher permeability exhibited higher spalling resistance. As shown in Figure 1 and Table 4, fibres of 100 μm diameter could not increase permeability of UHPC significantly at high temperature, thereby failing to enhance spalling resistance. On the contrary, adding PP fibre with the diameter of 28 μm or 33 μm and length of 12 mm and 18 m resulted in high permeability in UHPC, leading to high spalling resistance in these specimens. In addition, as the increasing rate of permeability was quite similar in all the specimens when the temperature was above 200 $^{\circ}\text{C}$, the sudden increase of permeability at 150 $^{\circ}\text{C}$ showed a critical influence on explosive spalling prevention.

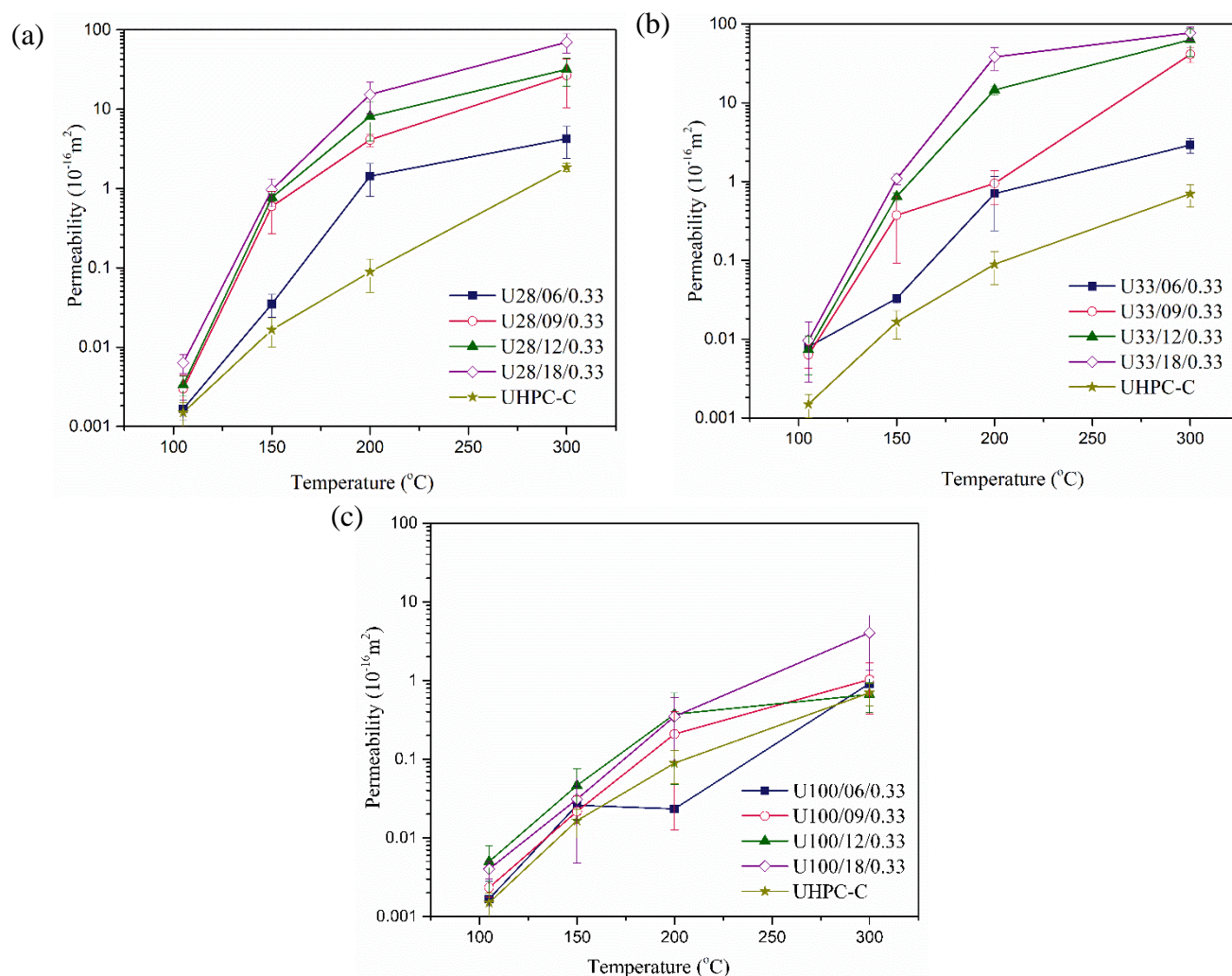





Figure 1. Permeability with increase temperature: (a) UHPC with 28 μm PP fibres, (b) UHPC with 33 μm PP fibres and (c) UHPC with 100 μm PP fibres (UHPC-C denoted UHPC without fibres and the data could be referred to [23]).

Table 4. Results of spalling test.

Length	Diameter		
	28 μm	33 μm	100 μm
6 mm			
9 mm			
12 mm			
18			

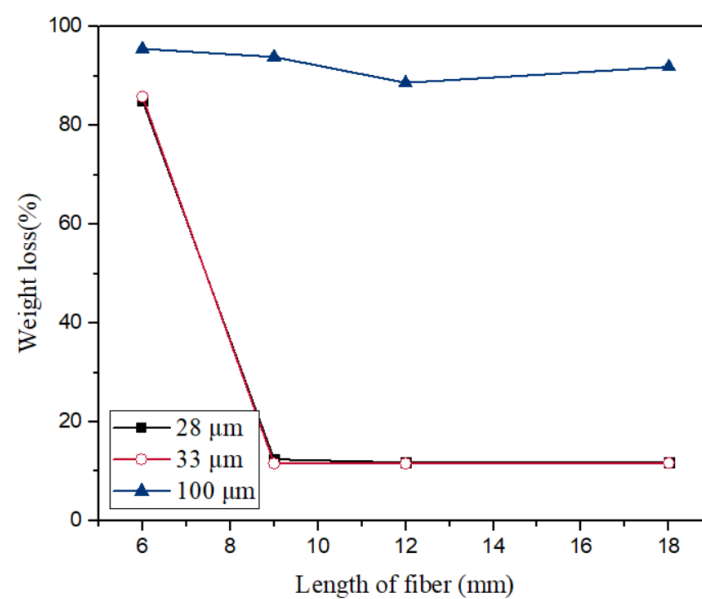


Figure 2. Weight loss of UHPC with different dimension of PP fibres after heated.

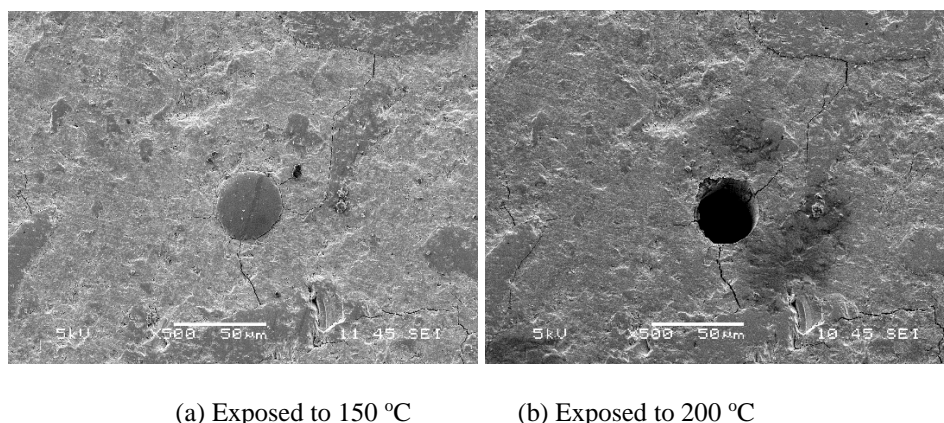


Figure 3. Morphology of UHPC with PP fibres (U33/12/0.33) exposed to different temperatures.

3.3 Microstructural observation

The SEM images of UHPC with PP fibres after exposure to high temperatures are shown in Figure 3. As presented in Figure 3a, after being heated to 150 °C, the interface of PP fibres and cement matrix became loose and some microcracks were formed around PP fibres, showing a radial pattern from fibres to cement matrix. The formation of these microcracks can be attributed to the high thermal mismatch between PP fibre and cement matrix [23, 24]. After being subjected to 200 °C (Figure 3b), PP fibres disappeared in the initial channels. The molten fibres might flow to the surface or flow into the air bubbles connected to the fibre channels. However, it is interesting to find that the disappearance of fibres and the creation of empty channels did not contribute significantly to the permeability of concrete at these temperatures (Figure 1). As evident, the microcracks caused by the expansion of PP fibres before melting played a critical role in enhancing the permeability of UHPC.

With a same fibre content, reducing fibre diameter increases the number of PP fibres significantly, leading to a higher possibility of interconnecting of fibres. In addition, increasing numbers of fibres can also reduce the distance between individual fibres. Therefore, the possibility of forming interconnecting network by radial microcracks is increased. On the contrary, due to the dramatic decreasing in the number of fibres, increasing fibre diameter negatively affected the formation of interconnecting network of microcracks. Consequently, fibres with large diameter (100 μm) showed low effectiveness in increasing permeability and preventing spalling (Figure 1 and Table 4). On the other hands, large fibre length may be more beneficial for forming microcrack network, as long fibres are easier to connect with each other. Furthermore, shorter fibres usually disperse better in concrete [25], which also increases the distance between individual fibres. As a result, short fibres (6 mm) were not efficient in increasing permeability and preventing spalling, as shown in Table 4.

Since both length and diameter of PP fibres affected the effectiveness of spalling prevention, aspect ratio (L/D ratio) of fibres is used to describe the relationship between fibre dimensions and spalling prevention of UHPC. The relationships between permeability and aspect ratio of fibres at 150 °C and 200 °C are plotted in Figure 4. As can be seen, at the aspect ratio of 273, permeability showed a significant increase at 150 °C. However, partially spalling occurred in UHPC with PP fibres of an aspect ratio of 273. With further increasing in aspect ratio of PP fibres, the permeability of UHPC increased and spalling was completely eliminated. At the aspect ratio of 300, permeability of UHPC showed relatively high permeability at both 150 °C and 200 °C. Besides, according to Table 4, spalling of UHPC could be eliminated when the aspect ratio of fibres was larger than 321 (U28/09/0.33). Therefore, with the content of fibre used in this study, an aspect ratio of ~300 may be required for spalling protection. However, the critical aspect ratio can be different when the fibre content changes. The fibre dimensions used in this study may be not enough to cover all the cases and to study the effect of fibre content. A numerical study will be conducted in the future.

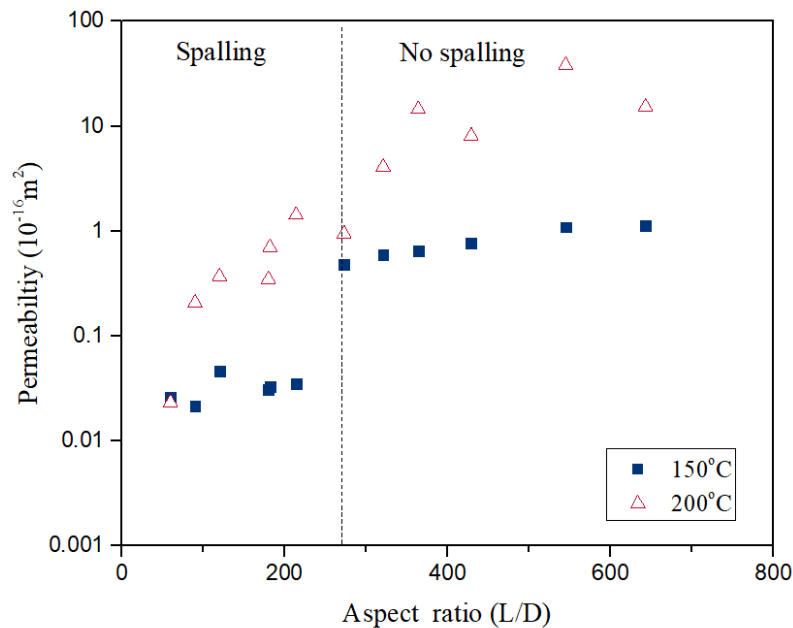


Figure 4. Relationship between permeability and aspect ratio of fibre (L/D ratio).

4 CONCLUSIONS

In this study, the effect of PP fibres dimensions on spalling prevention were studied experimentally, the following conclusions can be drawn:

1. Permeability of UHPC with PP fibres started increasing significantly at 150 °C. It can be attribute to the formation of microcracks around PP fibres. Beyond 150 °C, permeability kept increasing as temperature increased, but at a slower rate.
2. Longer fibres appeared to be more helpful on spalling protection of UHPC. The permeability of UHPC increased when the length of fibre changed from 6 mm to 12 mm. But there was no obvious difference between 12 mm and 18 mm on spalling prevention in this study. PP fibres of 6 mm length were ineffective on spalling prevention of UHPC, while fibres of 12 mm and 18 mm length could eliminate spalling of UHPC when the diameters of fibres were either 28 µm or 33 µm.
3. Finer fibres were more beneficial to preventing spalling of UHPC at high temperature, while thicker fibres were hardly helpful. All the specimens with PP fibres of 100 µm, regardless of length, suffered severe explosive spalling and their permeabilities were at a relatively low level as well. However, finer fibres with 28 µm and 33 µm in diameter and 12 mm and 18 mm in length can prevent spalling of UHPC by providing a significant increase on permeability at high temperature.
4. Aspect ratio of PP fibres is an important factor that determine the effectiveness spalling prevention. Aspect ratio of ~300 is a critical value for spalling protection of UHPC, when 3 kg/m³ of PP fibres are used.

ACKNOWLEDGMENT

This material is based on research/work supported by the Land and Livability National Innovation Challenge (L2NIC) Award No. L2NICCFP1-2013-4.

DISCLAIMER

Any opinions, findings, and conclusions or recommendations expressed in this material are those of the author(s) and do not necessarily reflect the views of the L2NIC.

REFERENCES

1. Shi, C., et al., A review on ultra high performance concrete: Part I. Raw materials and mixture design. *Construction and Building Materials*, 2015. 101: p. 741-751.
2. Zhang, D., et al., Effect of natural fibers on thermal spalling resistance of ultra-high performance concrete. *Cement and Concrete Composites*, 2020. 109: p. 103512.
3. Kodur, V.K.R. and L. Phan, Critical factors governing the fire performance of high strength concrete systems. *Fire Safety Journal*, 2007. 42(6-7): p. 482-488.
4. Ozawa, M. and H. Morimoto, Effects of various fibres on high-temperature spalling in high-performance concrete. *Construction and Building Materials*, 2014. 71: p. 83-92.
5. Khoury, G.A., Effect of fire on concrete and concrete structures. *Progress in Structural Engineering and Materials*, 2000. 2(4): p. 429-447.
6. Ma, Q., et al., Mechanical properties of concrete at high temperature—A review. *Construction and Building Materials*, 2015. 93: p. 371-383.
7. Liu, J.-C. and K.H. Tan, Fire resistance of strain hardening cementitious composite with hybrid PVA and steel fibers. *Construction and Building Materials*, 2017. 135: p. 600-611.
8. Lee, G., et al., Combining polypropylene and nylon fibers to optimize fiber addition for spalling protection of high-strength concrete. *Construction and Building Materials*, 2012. 34: p. 313-320.
9. Kalifa, P., G. Chene, and C. Galle, High-temperature behaviour of HPC with polypropylene fibres: From spalling to microstructure. *Cement and concrete research*, 2001. 31(10): p. 1487-1499.
10. Heo, Y.-S., et al., Critical parameters of nylon and other fibres for spalling protection of high strength concrete in fire. *Materials and Structures*, 2010. 44(3): p. 599-610.
11. Ding, Y., et al., Influence of different fibers on the change of pore pressure of self-consolidating concrete exposed to fire. *Construction and Building Materials*, 2016. 113: p. 456-469.
12. Bilodeau, A., V.K.R. Kodur, and G.C. Hoff, Optimization of the type and amount of polypropylene fibres for preventing the spalling of lightweight concrete subjected to hydrocarbon fire. *Cement and Concrete Composites*, 2004. 26(2): p. 163-174.
13. Bangi, M.R. and T. Horiguchi, Effect of fibre type and geometry on maximum pore pressures in fibre-reinforced high strength concrete at elevated temperatures. *Cement and Concrete Research*, 2012. 42(2): p. 459-466.
14. Jansson, R., *Fire Spalling of Concrete: Theoretical and Experimental Studies*. 2013, KTH Royal Institute of Technology in Stockholm: Sweden.
15. Xiong, M.-X. and J.Y.R. Liew, Spalling behavior and residual resistance of fibre reinforced Ultra-High performance concrete after exposure to high temperatures. *Materiales de Construcción*, 2015. 65(320): p. e071.
16. Klingsch, E., A. Frangi, and M. Fontana, *Explosive spalling of concrete in fire*. 2013, Institut für Baustatik und Konstruktion, ETH Zürich.
17. Khoury, G.A., Polypropylene fibres in heated concrete. Part 2: Pressure relief mechanisms and modelling criteria. *Magazine of Concrete Research*, 2008. 60(3): p. 189-204.
18. Liu, J.-C., et al. Experimental study on thermal spalling of ductile fibre reinforced cementitious composites. in *4th International Symposium on Ultra-High Performance Concrete and High Performance Materials*. 2016. Kassel, Germany.
19. Teichmann, T. and M. Schmidt. Influence of the packing density of fine particles on structure, strength and durability of UHPC. in *First international symposium on ultra high performance concrete*, Kassel. 2004.
20. Li, Y. and K.H. Tan, Effects of Polypropylene and Steel Fibers on Permeability of Ultra-high Performance Concrete at Hot State, in *Structures in Fire (Proceedings of the Ninth International Conference)*, M.E.M. Garlock and V.K.R. Kodur, Editors. 2016, DEStech Publications: Princeton University. p. 145-152.
21. Hager, I. and T. Tracz, The impact of the amount and length of fibrillated polypropylene fibres on the properties of HPC exposed to high temperature. *Archives of Civil Engineering*, 2010. 56(1): p. 57-68.
22. Bošnjak, J., J. Ožbolt, and R. Hahn, Permeability measurement on high strength concrete without and with polypropylene fibers at elevated temperatures using a new test setup. *Cement and Concrete Research*, 2013. 53: p. 104-111.
23. Zhang, D., A. Dasari, and K.H. Tan, On the mechanism of prevention of explosive spalling in ultra-high performance concrete with polymer fibers. *Cement and Concrete Research*, 2018. 113: p. 169-177.
24. Zhang, D. and K.H. Tan, Effect of various polymer fibers on spalling mitigation of ultra-high performance concrete at high temperature. *Cement and Concrete Composites*, 2020: p. 103815.
25. Heo, Y.-S., et al., Synergistic effect of combined fibers for spalling protection of concrete in fire. *Cement and Concrete Research*, 2010. 40(10): p. 1547-1554.

PROBABILISTIC MODELS FOR THERMAL PROPERTIES OF CONCRETE

Balša Jovanović¹, Negar Elhami Khorasani², Thomas Thienpont³, Ranjit Kumar Chaudhary⁴, Ruben Van Coile⁵

ABSTRACT

Thermal conductivity and specific heat of concrete are highly influential parameters for the heat transfer into the material during fire exposure. Reviewing the available literature has shown that there is a large scatter in the data for these thermal parameters. To quantify that uncertainty, novel probabilistic models for thermal conductivity and specific heat of concrete at elevated temperatures are developed.

Analysis of available experimental data indicates that a temperature-dependent Gamma distribution can be recommended for both thermal properties. Closed-form equations for the temperature-dependent mean and standard deviation are derived. Thus, for both the thermal conductivity and the specific heat, a continuous probability distribution as a function of temperature is obtained, which can be easily implemented in numerical simulations. Using the example of the probabilistic analysis of a simply supported concrete slab exposed to the standard fire, the models are compared with the commonly used deterministic representation of the thermal properties. It is shown that the calculated probabilities of failure using the deterministic models are an order of magnitude lower and therefore unconservative. This analysis suggests that accounting for the uncertainty in thermal properties for concrete slabs can have a significant effect on evaluating the safety and therefore should not be ignored in cases of high importance.

Keywords: Fire; specific heat; thermal conductivity; uncertainty; failure probability

1 INTRODUCTION

Fire is a rare event that can have a significant negative impact on people's safety. Luckily many fires are extinguished or suppressed early on by the occupants of the building or active measures (e.g. sprinklers). However, when fires progress beyond this level, they can cause serious damage to the structure. The effects of these, often referred to as 'structurally significant', fires are analysed in structural fire engineering (SFE). The main task of SFE is to produce a design solution that provides an adequate safety level, more precisely a solution with the failure probability below an explicit or implicit acceptable value.

¹ Corresponding author, Ghent University
e-mail: balsa.jovanovic@ugent.be, ORCID: <https://orcid.org/0000-0001-5200-5848>

² University at Buffalo
e-mail: negarkho@buffalo.edu, ORCID: <https://orcid.org/0000-0003-3228-0097>

³ Ghent University
e-mail: thomas.thienpont@ugent.be, ORCID: <https://orcid.org/0000-0003-1466-3377>

⁴ Ghent University
e-mail: ranjatkumar.chaudhary@ugent.be, ORCID: <https://orcid.org/0000-0002-1104-5859>

⁵ Ghent University
e-mail: ruben.vancoile@ugent.be, ORCID: <https://orcid.org/0000-0002-9715-6786>

In most design situations, the combination of prescribed fire resistance ratings and standardized calculation methods is sufficient to prove that the structure has an adequately low, although unquantified, failure probability. In special cases of high importance, however, adequate safety needs to be demonstrated explicitly. In those situations, (semi-)probabilistic calculations are required which directly take into account the stochastic nature of the input parameters. Even though the appropriate probabilistic models for some of these input variables are well-defined, others are often regarded as deterministic due to the lack of the appropriate models.

Probabilistic structural fire engineering (PSFE) is traditionally conducted using a large number of calculations with varying parameters and using numerical simulations. As the probabilistic approach is much more developed in classical structural engineering, the stochastic description of a large number of input variables needed for the structural analysis is well defined. This involves the geometry [1], loads [2] and material strength at ambient and elevated temperatures [3]. However, concerning the heat transfer part of the calculation, there is not much information available on the stochastic description of needed inputs.

Heat transfer has three modes: convection, radiation, and conduction. When conducting the heat transfer analysis for the temperature within structural members, the first two modes can be considered as a boundary condition and the last, conduction, as the main mode of temperature propagation through the concrete element. Conduction represents the diffusion of thermal energy (heat) within the material.

Thermal conductivity, k describes the material's ability to conduct heat, and specific heat, c_p represents the amount of energy needed to heat up a unit mass of the material by a unit temperature. Both of these properties are highly material and temperature dependant. Their influence on the thermal gradient within an element is defined by Fourier's law of (1D) conduction:

$$\frac{\partial T}{\partial t} = \frac{k}{\rho c_p} \nabla^2 T \quad (1)$$

where $\frac{\partial T}{\partial t}$ represents the change of temperature with time, $k \left[\frac{W}{m \cdot K} \right]$ is the thermal conductivity, $c_p \left[\frac{J}{kg \cdot K} \right]$ is the specific heat and ρ is the material density.

The heat transfer analysis in SFE in its essence represents the numerical solution of the multidimensional version of equation (1). The most commonly used approach is to use the deterministic models for these thermal properties as provided in guidance documents. For concrete, some of the most widely used models are those presented in Eurocode [4]. Thermal conductivity is defined by two limits (upper and lower) that are given as quadratic functions of the temperature T :

$$k_{upper} = 2.00 - 0.2451 \cdot (T/100) + 0.0107 \cdot (T/100)^2 \quad \text{for } 20^\circ C \leq T \leq 1200^\circ C \quad (2)$$

$$k_{lower} = 1.36 - 0.1360 \cdot (T/100) + 0.0057 \cdot (T/100)^2 \quad \text{for } 20^\circ C \leq T \leq 1200^\circ C \quad (3)$$

where the choice of the exact value between these two limits is left to the user, but the lower values are recommended

On the other hand, specific heat is given as a single piecewise function:

$$\begin{aligned} c_p &= 0.9 & \text{for } 20^\circ C \leq T \leq 100^\circ C \\ c_p &= 0.9 + (T - 100)/1000 & \text{for } 100^\circ C \leq T \leq 200^\circ C \\ c_p &= 1.0 + (T - 200)/2000 & \text{for } 200^\circ C \leq T \leq 400^\circ C \\ c_p &= 1.1 & \text{for } 400^\circ C \leq T \leq 1200^\circ C \end{aligned} \quad (4)$$

Both of these definitions are graphically presented in Figure 1.

Review of the available literature has shown that a significant scatter exists in the values of these thermal properties of concrete. In order to conduct a valid probabilistic calculation of the behaviour of a concrete structure exposed to fire, the uncertainty in the heat transfer analysis should be considered. In doing so, probabilistic models for the thermal properties of the material (i.e., thermal conductivity and specific heat) are needed.

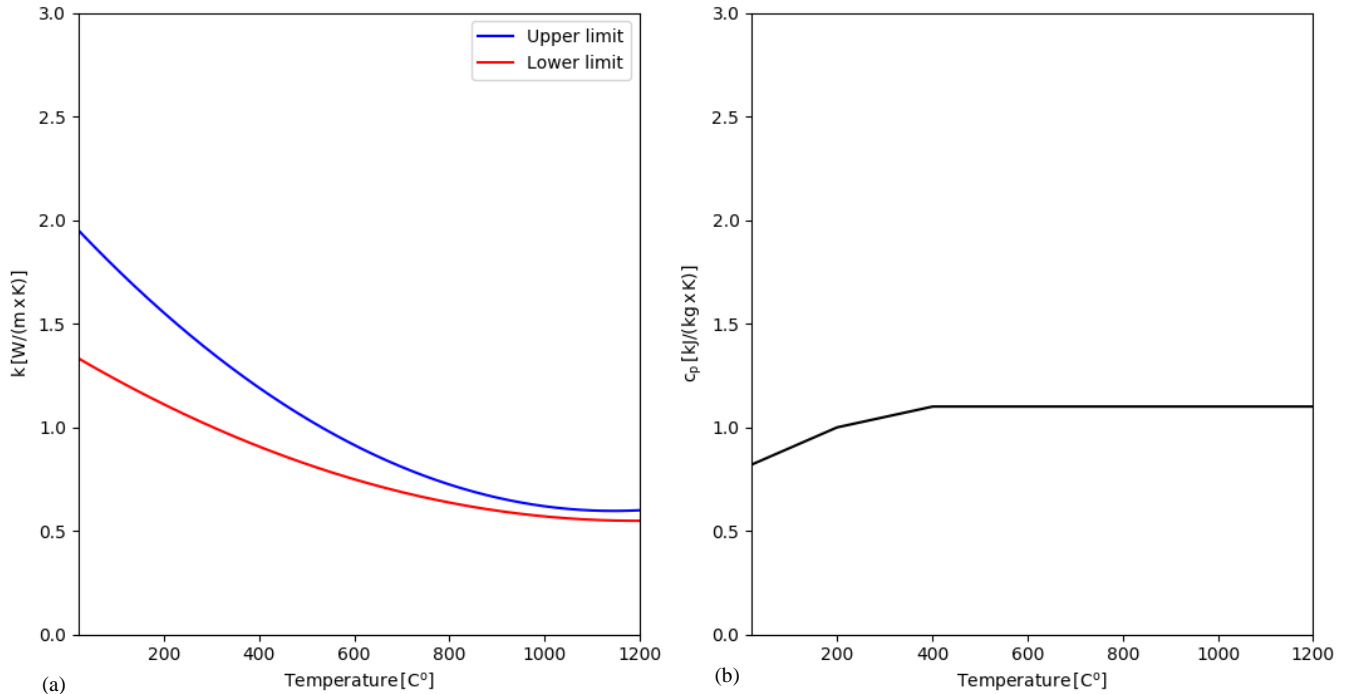


Figure 1. a) thermal conductivity k and b) specific heat c_p of concrete as a function of temperature as defined by the Eurocode [4]

2 METHODOLOGY

Probabilistic models in this study are developed with the intention of being used in numerical simulations. For that purpose, (i) the models have to be continuous functions across the appropriate temperature range, and (ii) there should be a closed-form function for each specific quantile value to facilitate implementation in the numerical simulations. The methodology for the model development is based on the one presented by Qureshi et al. [3], but with few modifications that are highlighted in the further text.

To obtain a closed-form function for each specific quantile value, the thermal conductivity and the specific heat are each individually considered to be described by the same probability distribution type (e.g. normal distribution, lognormal distribution) at any fixed temperature. The parameters that govern the probability distribution at a given temperature are then considered to be a continuous function of temperature. To obtain those parameters the first step is to organize the data in bins. More precisely, all the data points in the relatively narrow range around chosen temperature values are grouped into one bin and the mean and standard deviation of each bin are calculated. This way the closed-form equation for the mean and standard deviation as a function of temperature can be obtained by fitting a polynomial curve to these values. In order to take into account the different number of data points inside each bin and to capture the different amount of information each bin carries, each mean and standard deviation value is weighted with a number proportional to its size in the fitting process.

After both the mean value and standard deviation are fitted in the form of a polynomial function, the appropriate probability distribution must be determined. This is done based on the Akaike Information Criteria (AIC) [5]:

$$AIC = 2m - 2\ln(L) \quad (5)$$

where m represents the number of estimated parameters in the model and L is the likelihood of the model for the given data. It must be noted that the AIC value can only be used as a comparative measure, more precisely, a single absolute value of AIC on its own does not contain any useful information. It can only be used to compare two or more models in a way that the model with the lowest AIC value represents the best fit.

The procedure to find the most appropriate distribution is as follows: Firstly, for each data point, the corresponding model mean and the standard deviation are calculated, based on the data point's temperature and the previously fitted polynomial functions. Based on those two values a specific theoretical distribution is defined and the likelihood of the data point is calculated. Lastly, the total likelihood is calculated by multiplying the values for each data point, and the AIC for a specific theoretical distribution is then obtained through (5). Using all the AIC values the best distribution is chosen.

It should be highlighted that even though the methodology described here is based on the work presented in [3] it has a couple of distinctive differences. First, the choice of adequate theoretical distribution is done more holistically, using the AIC for every data point based on the fitted curves for the governing parameters, instead of fitting the distribution for each bin separately, summing the AIC for each bin and then fitting a curve on the parameters. As its direct consequence, the second difference is fitting of the polynomial functions on mean and standard deviation values instead of the specific chosen distribution's parameters. The main advantage of this modified approach is that the best candidate distribution is chosen based on the final model and all the data points instead of only the data in the bins.

3 RESULTS AND DISCUSSION

The temperature range of $20 - 1200^{\circ}\text{C}$ is chosen based on three factors, firstly the available data for constructing the model, secondly the fact that damage to the concrete at temperatures higher than 1000°C is large enough that it loses all of its mechanical properties, and finally the range of the commonly used Eurocode models.

Based on the available literature data, it is evident that the thermal properties differ significantly based on the type of concrete, whether its lightweight, normal strength (NSC) or high strength concrete (HSC). The focus in this paper is on the NSC as it is the most commonly used type. When considering the type of aggregate used in the concrete, it is decided to not make the distinction between siliceous and calcareous, in order to be in sync with the widely used Eurocode models for thermal properties [4].

Data needed for the creation of the models have been collected from the literature. Some data was found as tabulated values, but the majority had to be extrapolated from figures. The thermal conductivity dataset collected in this study consists of 382 points taken from 12 sources [6–17]. On the other hand, the specific heat data consists of 343 points taken from 9 sources [6, 8, 9, 12, 14–16, 18, 19].

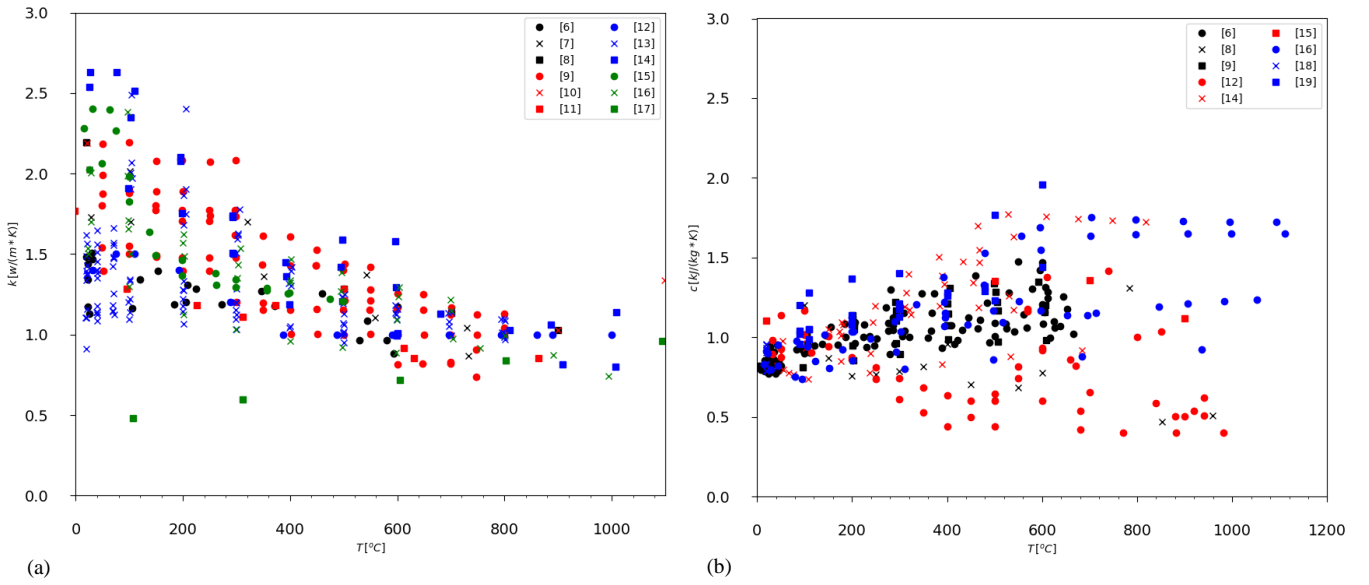


Figure 2. Acquired data points for a) thermal conductivity k and b) specific heat c_p of concrete at elevated temperature

From Figure 2, which presents all the acquired data points for both thermal conductivity and specific heat, it is evident that there is a large scatter, which implies considerable uncertainty. It is also clear that almost all of the data points are measured at a temperature that is close to a multiple of 50°C . Thus, the data is grouped in bins with $50^\circ \pm 5^\circ\text{C}$ temperature intervals. A minimum number of 5 data points are considered to form a bin (for example, there were only 4 points in the $350 \pm 5^\circ\text{C}$ range for specific heat and therefore that bin was omitted). This concept is illustrated using a box plot in Figure 3, where it can also be observed that the lack of data at higher temperatures implies that no bins are created at temperatures higher than 800°C and 700°C for thermal conductivity and specific heat respectively.

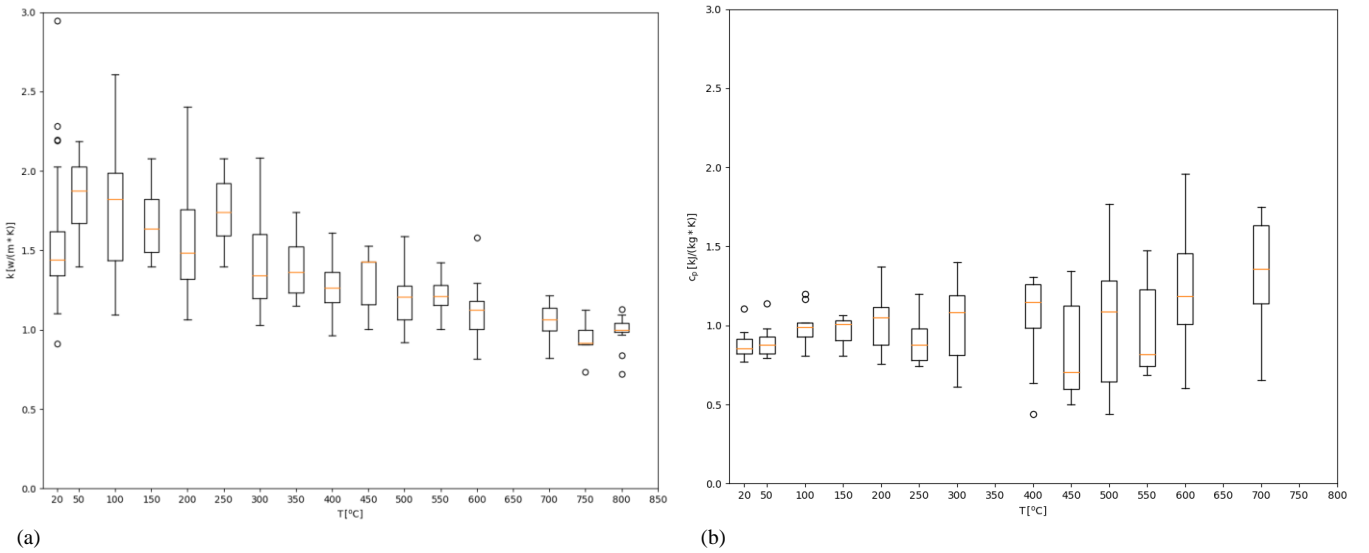


Figure 3. Box plot representing the variation of the a) thermal conductivity k and b) specific heat c_p of concrete data inside the bins

The fitting of the mean and standard deviation of the bins described earlier shows that the second order polynomial function is an appropriate fit. Because of the lack of data at temperatures higher than 800°C , one condition is added to the fitting process. Namely, in the case of the thermal conductivity, the functions are defined as monotonically decreasing in the range $20\text{--}1200^\circ\text{C}$ based on the global trends of the data and physical considerations. Similarly, the functions for the specific heat are considered as monotonically

increasing in the same domain. The resulting equations are graphically presented in Figure 4 and are the following:

$$mean_k = 6.627 \times 10^{-7} \times T^2 - 1.458 \times 10^{-3} \times T + 1.772 \quad (6)$$

$$std_k = 3.139 \times 10^{-7} \times T^2 - 0.691 \times 10^{-3} \times T + 0.434 \quad (7)$$

$$mean_{c_p} = -2.953 \times 10^{-7} \times T^2 + 6.498 \times 10^{-4} \times T + 0.872 \quad (8)$$

$$std_{c_p} = -3.500 \times 10^{-7} \times T^2 + 7.700 \times 10^{-4} \times T + 0.042 \quad (9)$$

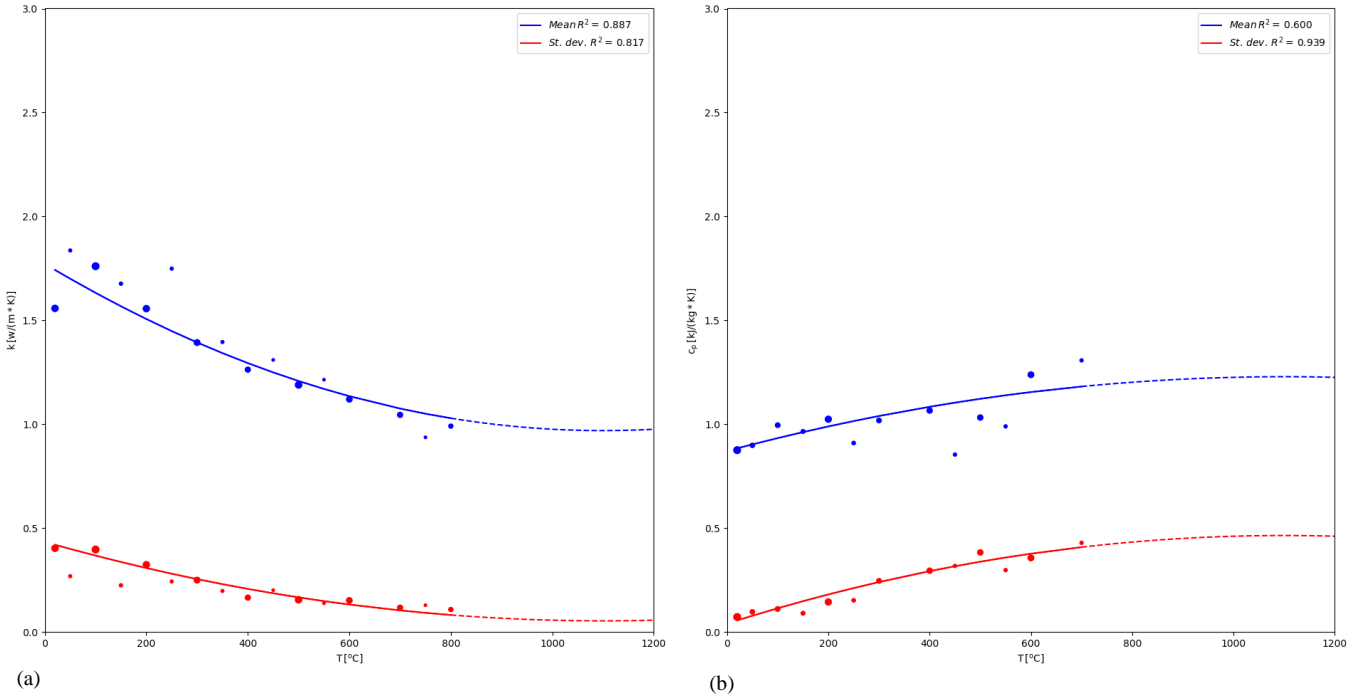


Figure 4. Polynomial function fit for the mean and standard deviation values for a) thermal conductivity k and b) specific heat c_p of concrete

Numerous two parameter theoretical distributions have been fitted in order to find the most adequate one for the models. More precisely, the fitted distributions were: Normal, Lognormal, Gamma, Gumbel, Beta44, Weibull, Inverse Gaussian, Logistic, Log-logistic, Rician, Nakagami and Birnbaum Saunders. Figure 5 shows the AIC values obtained for different distributions (for clarity only the five best fits are presented, as the values for the others were an order of magnitude larger). Both in the case of thermal conductivity and specific heat, the best fits (i.e., the lowest AIC score) are obtained by Normal and Gamma distributions. From the two, the Gamma distribution is chosen given that, on the contrary to the Normal distribution, it has zero probability for negative values (which are theoretically impossible for these thermal properties).

Figure 6 presents the obtained models alongside with the data points and Eurocode models. In the case of the specific heat, it can be seen that the 50% quantile values are close to those prescribed in Eurocode, however, that is not the case for thermal conductivity where the overlap between the two is minimal, especially at higher temperatures. Also, it can be seen that even though the data points for temperatures higher than 800°C were not used for the fitting of polynomial functions due to the lack of data, the overall model behaviour describes them relatively well.

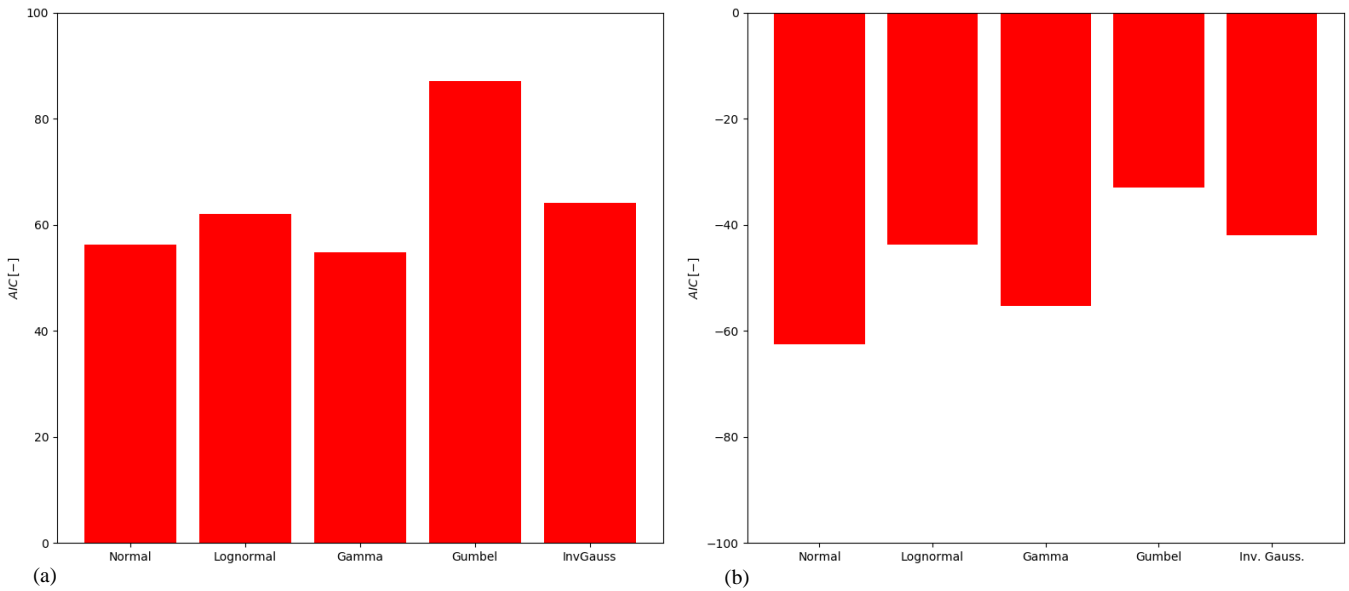


Figure 5. Akaike information criteria (AIC) comparison of a few theoretical distributions for a) thermal conductivity and b) specific heat of concrete

For the specific heat, the Eurocode [4] recommends an additional peak between 100°C and 200°C , as a function of the moisture content, to take into account the moisture inside the concrete and the needed energy for moisture evaporation. Due to the great similarities of the 50% quantile curve, the same approach with the same values is recommended when using the probabilistic model for the specific heat of concrete. More precisely, the same moisture peak values are added to the specific heat curve for the desired quantile value. Even though the models do not provide a direct closed-form equation for any quantile value, the needed value can be easily calculated in two steps. Firstly the mean and the standard deviation are calculated for a given temperature and then based on the two calculated values and the desired quantile, the thermal property is evaluated using the well-known equations defining the Gamma distribution.

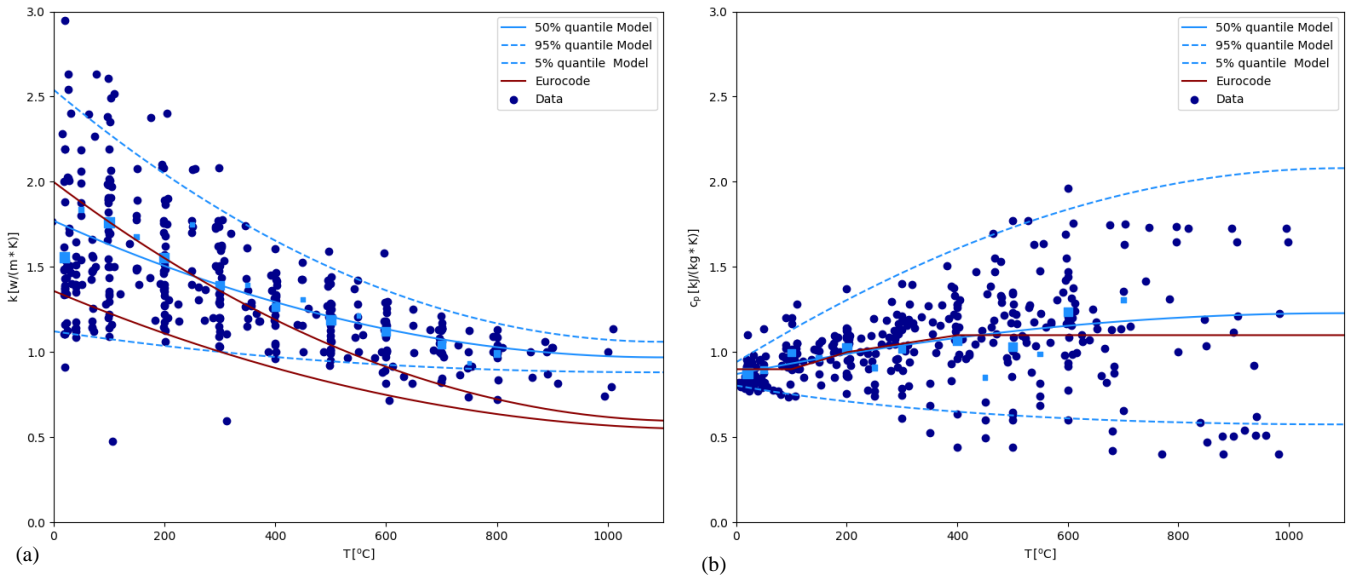


Figure 6. Probabilistic models for (a) thermal conductivity and (b) specific heat of concrete at elevated temperatures: 5%, 50%, and 95% quantiles, together with the model from Eurocode and the raw data.

4 EXAMPLE

An example of a simply supported concrete slab exposed to the standard fire will be used to demonstrate the influence of stochasticity in concrete thermal properties on the probability of failure. This example, but

with deterministic thermal properties, in accordance with the Eurocode, was used in [20]. The slab in question is exposed to the fire only on the bottom side, while the top side is subjected to the ambient conditions. Thus, for the considered slab thickness, it is safe to assume that the temperatures on the top (i.e., the compression side) will not achieve values high enough to cause considerable strength reduction. For those reasons, it is justifiable to use the following equation to calculate the resisting moment of the slab, M_R :

$$M_R = k_{fy} \cdot f_{y,20} \cdot A_S \cdot \left(h - \phi/2 - c\right) - \frac{(k_{fy} \cdot f_{y,20} \cdot A_S)^2}{2 \cdot b \cdot f_c} \quad (10)$$

where b is the slab width (taken as 1 m) and all the other parameters, along with their distributions, are presented in Table 1.

A probabilistic analysis based on 10^4 Latin Hypercube Samples (LHS) is conducted in three parts: (i) first the heat transfer analysis using finite difference method and newly presented probabilistic models for thermal conductivity and specific heat are conducted in order to obtain the temperature distribution inside the slab; (ii) next, taking into account the temperature of the reinforcements inside the slab and Eqn. (10), the moment capacity of the slab is calculated; and (iii) finally, the probability of failure is calculated based on the loads and model uncertainties presented in Table 2 and using the limit state equation:

$$Z = R - E = K_R \cdot M_R - K_E \cdot (G + Q) \quad (11)$$

Figure 7 (a) shows the results of the heat transfer analysis, specifically the temperature gradient inside the slab after 120 and 180 minutes of standard fire exposure. In the figure, also the temperature gradient obtained using the Eurocode equations (lower limit) for thermal properties is presented. The most notable observation is that the temperatures are higher when calculated using the probabilistic models. The Eurocode temperature gradient is on the level of the 5% quantile of the probabilistic model for both fire exposure times, and only close to the top surface of the slab, where the temperature is close to ambient condition, does the Eurocode temperature gradient come closer to the median results obtained with the probabilistic model.

Table 1. Stochastic input parameters used for the moment capacity calculation

Parameter	Distribution	Mean μ	Standard deviation σ	Ref
20°C concrete compressive strength, $f_{c,20}$ [MPa]	Lognormal	42.9 ($f_{ck} = 30MPa$)	6.44	[21]
20°C reinforcement yield strength, $f_{y,20}$ [MPa]	-	560 ($f_{yk} = 500MPa$)	-	-
Steel yield stress retention factor, k_{fy} [-]	Lognormal	Temperature dependent	Temperature dependent	[3]
Reinforcement area, A_S [mm^2/m]	Normal	785	16	[21]
Reinforcement diameter, ϕ [mm]	-	10	-	-
Slab height, h [m]	-	0.2	-	-
Concrete cover, c [mm]	Beta [$\mu \pm 3\sigma$]	30+5 = 35	5	[1]

Figure 7 (b) shows the Probability Density Function (PDF) of moment capacity of the slab. It can be seen that an analysis using the Eurocode thermal properties overestimates the slab capacity compared to an analysis using the probabilistic models for thermal properties. This indeed can be explained by the higher temperatures in the reinforcement. The difference is even better illustrated in Figure 8, which shows the Cumulative Distribution Function (CDF) of the limit state from the Eqn. 11. The CDF value at 0 kNm represents the probability of failure. Probabilities of failure in the case where the probabilistic model for the

thermal properties is used are an order of magnitude higher compared to those obtained using the Eurocode thermal models, more precisely $2.82 \cdot 10^{-4}$ vs $2.37 \cdot 10^{-5}$ and $7.32 \cdot 10^{-2}$ vs $3.07 \cdot 10^{-3}$ for 120 and 180 min respectively. This difference in the probability of reaching the limit state illustrates how important it is to take into account the uncertainties in the thermal properties of concrete, especially since using the deterministic model is unconservative.

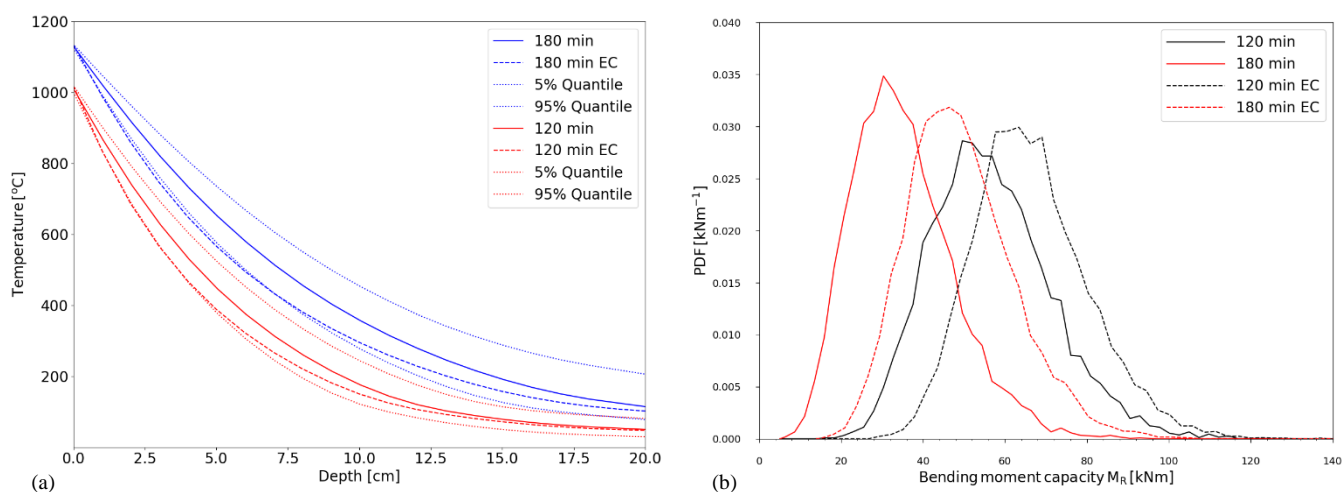


Figure 7. a) Temperature gradient inside of the concrete slab after 120 and 180 minutes of standard fire exposure at the bottom side, b) PDFs of the slab bending capacity calculated using the probabilistic and deterministic models for the thermal properties of concrete

Table 2. Stochastic input parameters used for calculation for the probability of failure

Parameter	Distribution	Mean μ	Standard deviation σ	Ref
Dead load, G [kNm]	Normal	15	1.5	[2]
Live load, Q [kN/m ²]	Gamma	1.875	1.78	[2]
Model uncertainty for the load effect, K_E [-]	Lognormal	1	0.1	[2]
Model uncertainty for the resistance effect, K_R [-]	Lognormal	1	0.15	[2]

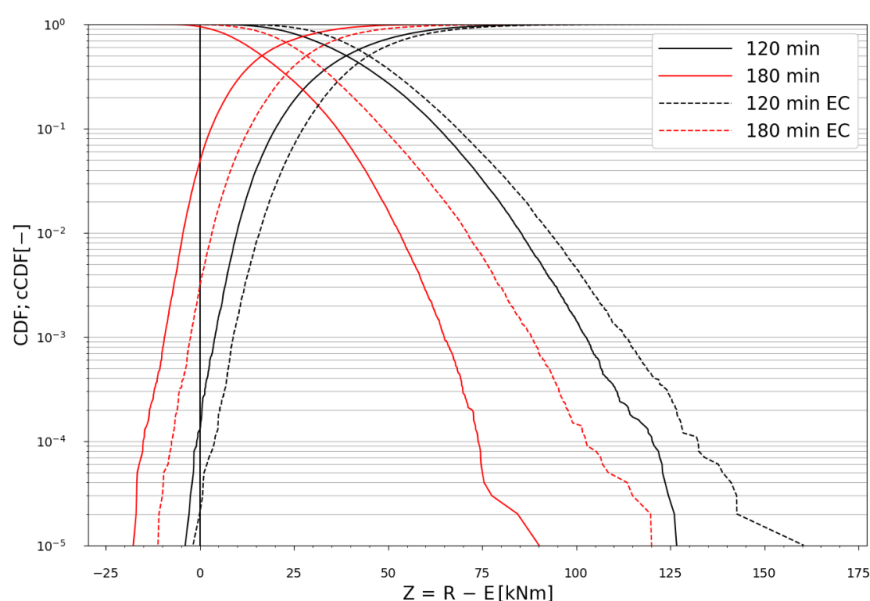


Figure 8 CDFs of the limit state calculated using the probabilistic and deterministic models for the thermal properties of concrete

5 CONCLUSION

Novel probabilistic models for thermal conductivity and specific heat of concrete are developed. The motivation for this study is the large uncertainty in the thermal properties of concrete that is evident from the large scatter in data reported in the literature. The models provide an efficient way to define the value of the thermal property at a specific temperature for the required quantile value, which is highly suitable for numerical simulations.

Models for both thermal parameters are defined using two steps. First, the mean and standard deviation are calculated for a specific temperature using Eqn. (6)-(9). Afterwards, the thermal property value can be generated based on the mean, standard deviation and the specified quantile value using the Gamma distribution.

In the case of the specific heat, the median, 50% quantile, values are similar to those prescribed in Eurocode, but the overall model still shows considerable variation. For thermal conductivity, however, the values are much larger and show a relatively small overlap with the Eurocode models. The influence of such differences is demonstrated using the probabilistic structural fire engineering analysis of a simply supported concrete slab. It was shown that a considerable difference in the temperature gradient, moment capacity and finally probability of failure could be expected when using the developed models as opposed to existing deterministic relationships.

Using the traditional deterministic models for thermal properties is justified for simple design situations, but the uncertainty of the thermal properties values cannot be neglected for special cases where the probabilistic calculations are needed, as traditional models could lead to unconservative results.

REFERENCES

1. JCSS, (2001). Probabilistic Model Code. Part 3.10 Dimensions. Joint Committee on Structural Safety
2. Jovanović, B, Van Coile, R, Hopkin, D, Elhami Khorasani, N, Lange, D, Gernay, T, (2020). Review of Current Practice in Probabilistic Structural Fire Engineering: Permanent and Live Load Modelling. *Fire Technol.* <https://doi.org/10.1007/s10694-020-01005-w>
3. Qureshi, R, Ni, S, Elhami Khorasani, N, Van Coile, R, Hopkin, D, Gernay, T, (2020). Probabilistic models for temperature dependent strength of steel and concrete. *Journal of Structural Engineering* 146:04020102. [https://doi.org/10.1061/\(asce\)st.1943-541x.0002621](https://doi.org/10.1061/(asce)st.1943-541x.0002621)
4. CEN, (2004). EN 1992-1-2:2004: Eurocode 2: Design of concrete structures - Part 1-2: General rules. Structural fire design. European Standard
5. Akaike, H, (1974). A new look at the statistical model identification. *IEEE Transactions on Automatic Control* 19:716–723
6. Harmathy, T, Allen, L, (1973). Thermal properties of selected masonry unit concretes. *Journal of The American Concrete Institute* 70:132–142
7. Harada, T, Takeda, J, Yamane, S, Furumura, F, (1972). Strength, Elasticity and Thermal Properties of Concrete Subjected to Elevated Temperatures. *ACI Structural Journal* 34:377–406
8. Schneider, U, (1988). Concrete at high temperatures - A general review. *Fire Safety Journal* 13:55–68. [https://doi.org/10.1016/0379-7112\(88\)90033-1](https://doi.org/10.1016/0379-7112(88)90033-1)
9. Adl-Zarrabi, B, Boström, L, Wickström, U, (2006). Using the TPS method for determining the thermal properties of concrete and wood at elevated temperature. *Fire and Materials* 30:359–369. <https://doi.org/10.1002/fam.915>
10. Banerjee, DK, (2016). An analytical approach for estimating uncertainty in measured temperatures of concrete slab during fire. *Fire Safety Journal* 82:30–36. <https://doi.org/10.1016/j.firesaf.2016.03.005>
11. Kodur, KR, Dwaikat, MMS, Dwaikat, MB, (2009). High-temperature properties of concrete for fire resistance modeling of structures. *ACI Materials Journal* 106:390
12. Shin, K-Y, Kim, S-B, Kim, J-H, Chung, M, Jung, P-S, (2002). Thermophysical Properties and Transient Heat Transfer of Concrete at elevated temperature. *Nuclear Engineering and Design* 212:233–241
13. Anderberg, Y, (1976). Fire-exposed concrete structures. An experimental and theoretical study. *Bull Div*

14. Lie, TT, Kodur, VKR, (1995). Thermal properties of fibre-reinforced concrete at elevated temperatures. National Research Council Canada, Institute for Research in Construction
15. Kakae, N, Miyamoto, K, Momma, T, Sawada, S, Kumagai, H, Ohga, Y, Hirai, H, Abiru, T, (2017). Physical and thermal properties of concrete subjected to high temperature. *Journal of Advanced Concrete Technology* 15:190–212. <https://doi.org/10.3151/jact.15.190>
16. Hu, XF, Lie, TT, Polomark, GM, Maclaurin, JW, (1993). Thermal properties of building materials at elevated temperatures. Intern report/National Res Counc Canada, Inst Res Constr no 643
17. Marechal, J, (1972). Conductivity and Thermal Expansion Coefficients of Concrete as a Function of Temperature and Humidity. Special Publication 34:1047--1058
18. T.T. Lie, (1980). Structural Fire Protection
19. Naus, DJ, (2006). The effect of elevated temperature on concrete materials and structures-A literature review. Oak Ridge National Laboratory (United States)
20. Thienpont, T, Van Coile, R, De Corte, W, Caspeepele, R, (2019). Determining a global resistance factor for simply supported fire exposed RC slabs. In: *Concrete : innovations in materials, design and structures: fib Symposium 2019*. pp 2191–2197
21. Holický, M, Sýkora, M, (2010). Stochastic models in analysis of structural reliability. In: *International symposium on stochastic models in reliability engineering, life sciences and operation management*, Beer Sheva, Israel

EFFECT OF STEEL FIBERS ON FIRE ENDURANCE OF EXTRUDED HOLLOW-CORE SLABS

Hang T. N. Nguyen¹, Kang Hai Tan²

ABSTRACT

This paper presents an experimental program, test results, and failure modes of two precast/prestressed concrete hollow core (PCHC) slabs with and without hooked steel fibers tested under elevated temperatures. The main objectives of this experimental investigation were to study the effect of steel fibers on fire endurance of PCHC slabs and to examine the potential use of steel fibers to enhance shear performance of PCHC slabs. Full-scale shear tests were conducted on two PCHC slabs, namely, F.HC1.0 and F.HC4.H.40 under elevated temperatures. While F.HC1.0 was a control specimen without any fibers, hooked steel fibers with a mass content of 40 kg/m³ (a volumetric content of 0.51 %) were used in F.HC4.H.40. The experiments showed that it was feasible to include hooked steel fibers with a content of 0.51 % in zero slump concrete in the extrusion method. In addition, results from the fire tests demonstrated that resistance to load and elevated temperatures of PCHC slabs was substantially increased with the use of hooked steel fibers. Furthermore, while web-shear failure (brittle mode) was observed in the control specimen without fibers (F.HC1.0), flexural failure (a more favorable mode) occurred in F.HC4.H.40 with hooked steel fibers. The research showed a potential use of hooked steel fibers in extruded PCHC slabs in practice to avoid shear failure and to enhance their ductility and toughness in case they are subjected to fire.

Keywords: Prestressed concrete; hollow core slabs; shear capacity; hooked steel fibers; fiber-reinforced concrete; fire conditions.

1 INTRODUCTION

Extruded precast/prestressed concrete hollow core (PCHC) slabs with a reduction in cross sections and without stirrups are susceptible to shear failure as reported in previous studies [1-5]. Data collected by Jansze et al. [4] showed that although PCHC slabs were commonly designed to resist at least 1 h fire rating based on the prescriptive method specified in Eurocode 2 [6], in 27 out of 42 tests, the test slabs failed prematurely in web-shear mode before achieving their design fire resistance (Figure 1). It raised some concerns about fire safety of hollow-core slabs.

¹ Lecturer, National University of Civil Engineering, 55 Giai Phong Street, Hanoi, Vietnam.
e-mail: hangntn@nuce.edu.vn.

² Professor, Nanyang Technological University, Singapore
e-mail: ckhtan@ntu.edu.sg

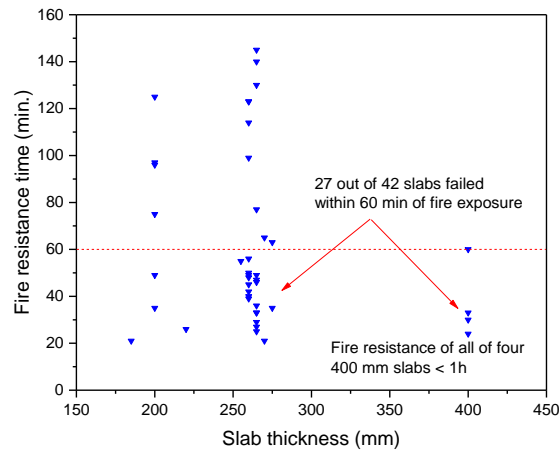


Figure 1. Fire resistance time of 42 fire tests (from Jansze *et al.* [4])

It is generally accepted that the inclusion of steel fibers into concrete could help to transform brittle behavior to ductile [7]. The main benefit of steel fibers in steel-fiber-reinforced concrete (SFRC) members is to bridge the cracks induced by tensile stresses in the concrete, redistribute them, and slow down propagation of cracks [8]. For this reason, there have been a number of studies on incorporating steel fibers to improve shear response of SFRC members [9-15]. These studies showed that the use of steel fibers with volumetric contents within a range of 0.5 to 1 % significantly enhanced ultimate shear capacity and ductility of concrete members. Moreover, substantial improvements in resistance to the formation and growth of cracks were also observed. Therefore, while shear reinforcement could not be incorporated in PCHC slabs due to the production process of the extrusion method (the most popular practice to cast hollow-core slabs), the use of steel fibers shows potentials to improve the low shear endurance of PCHC slabs under elevated temperatures. With this motivation, this research (full version of this has been published in Nguyen *et al.* [16]) experimentally investigates the use of fibers to enhance shear capacity of fire-exposed PCHC slabs. This paper presents the experimental program, test results, and failure modes of two deep PCHC slabs with and without hooked steel fibers tested under elevated temperatures.

2 EXPERIMENTAL INVESTIGATIONS

To study effect of steel fibers on fire behavior of PCHC slabs, full-scale shear tests were conducted on two hollow-core specimens with and without hooked steel fibers named as F.HC1.0 and F.HC4.H.40. The former slab was the control specimen without any fibers and the latter was the slab incorporating hooked steel fibers with a content of 40 kg/m^3 . The hooked steel fibers used were Dramix RC-80/60-BN type (60 mm long and a diameter of 0.75 mm with an aspect ratio of 80) with tensile strength of 1345 MPa. The extrusion method was used to cast both specimens with and without fibers. Table 1 presents summary of the test program while Figure 2 shows the type of hooked steel fibers used. Figure 3 illustrates casting F.HC4.H.40 (the specimen with steel fibers) using the extrusion method. It is shown that it was feasible to include hooked steel fibers with a content of 0.51 % in very dry (nearly zero-slump) concrete in the extrusion process.

Table 1. Overall test program

Slab ID.	Slab depth (mm)	Hooked fiber content in kg/m ³	Fiber content in volume fraction, %	Shear span (shear-span-to-depth ratio)	Failure load at ambient (kN)*	Applied load (kN) (load level (%), % of ambient capacity)
F.HC1.0	400	0	0	1000 (2.5)	365	146 (40)
F.HC4.H.40	400	40	0.51	1000 (2.5)	520	208 (40)

* Defined by tests (details can be found in Nguyen *et al.* [17])

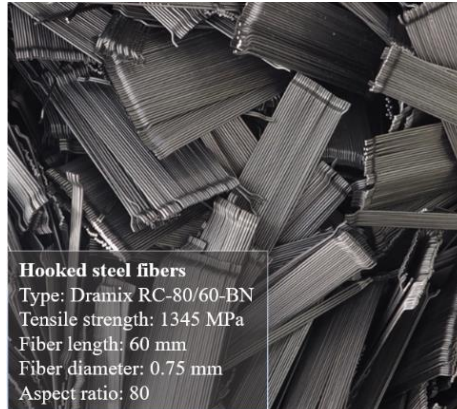


Figure 2. Hooked steel fibers used

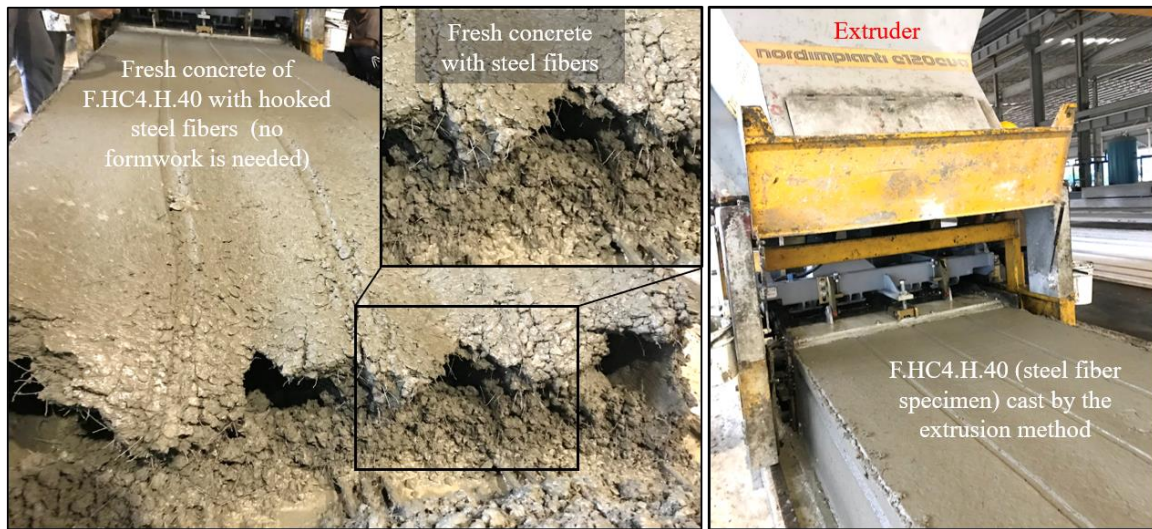


Figure 3. Casting hollow core specimen with steel fibers using the extrusion method

2.1 Test specimens and material properties

The two specimens were 4.15 m long, 1.2 m wide with depth of 400 mm, consisting of 4 non-circular voids. Figure 4 shows nominal cross section of the two specimens. Two types of prestressing strands were incorporated in the hollow-core specimen, i.e. 9.6 mm in diameter with an area of 54.8 mm² and 12.9 mm in diameter with an area of 98.7 mm². The prestressing strands were 7-wire, low relaxation type with an ultimate strength of 1860 MPa. They were prestressed to 1150 MPa which corresponded to 62 % of their ultimate capacity.

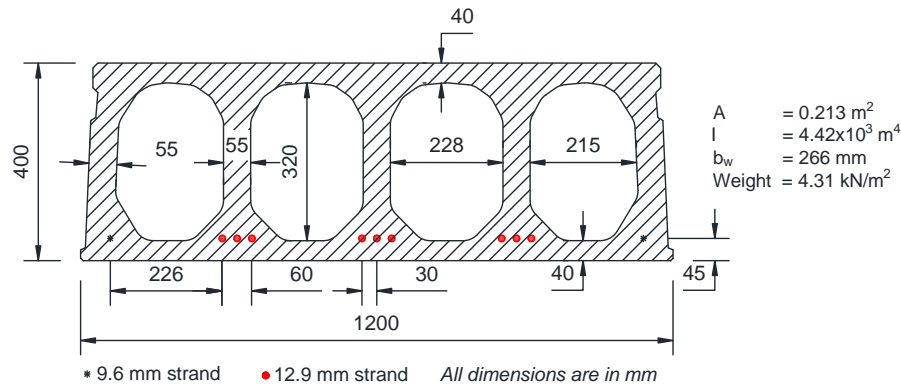


Figure 4. Nominal cross section of the specimens

Concrete compressive strength of F.HC1.0 and F.HC4.H.40 was determined from 150 mm cube samples (shown in Figure 5(a)) while tensile strength of the two specimens was defined using three cylindrical cores with dimensions of 50 x 100 mm. It should be noted that the cube strength results obtained from concrete compressive tests were then converted to cylinder strength using Table 3.1 in Eurocode 2 [6]. Besides, flexural tensile strength was conducted for the specimen with hooked steel fibers (F.HC4.H.40). Details of the flexural tensile strength test is presented in Nguyen *et al.* [17]. Table 2 shows the measured values of the compressive, the tensile splitting and flexural tensile strengths of the two test slabs.

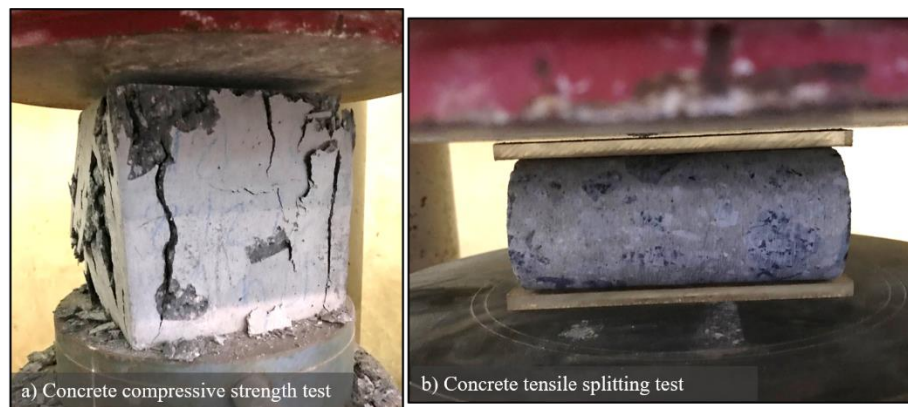


Figure 5. Concrete compressive and tensile splitting tests

Table 2. Concrete properties

Slab ID.	Mean compressive cylinder strength (SD) (MPa)*	Mean tensile strength (SD) (MPa)**	Flexural tensile strength (MPa)			
			$f_{R,1}$	$f_{R,2}$	$f_{R,3}$	$f_{R,4}$
F.HC1.0	66.8 (1.0)	4.5 (0.1)	n.a	n.a	n.a	n.a
F.HC4.H.40	65.3 (3.5)	7.2 (0.9)	8.7	10.6	10.6	9.4

SD: Standard Deviation; * mean values of two samples; ** mean values of three samples.

2.2 Test rig and instrumentation

Figure 6 shows an overall test setup adopted in the experimental program. The two specimens were placed on top of an electrical furnace with interior dimensions of 3 m wide, 3 m long with depth of 0.75 m and were simply supported at their ends by two A-frames. They were loaded by an *unsymmetrical line load* with regard to the center line of slab, following a three-point loading scheme, which is in accordance with shear-test setup specified in EN-1168:2005+A3 [18]. As a result, shear span was 1000 mm, resulting in a

shear-span-to-depth ratio of 2.5 for both specimens. Thermal wool was used to cover opening parts of the furnace top to prevent heat loss.

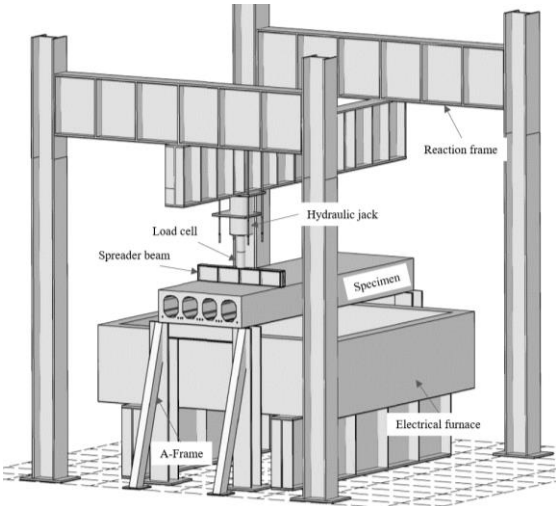
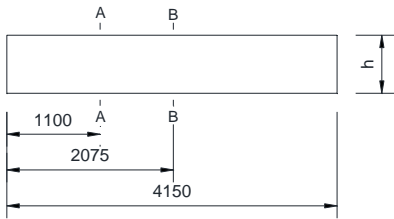
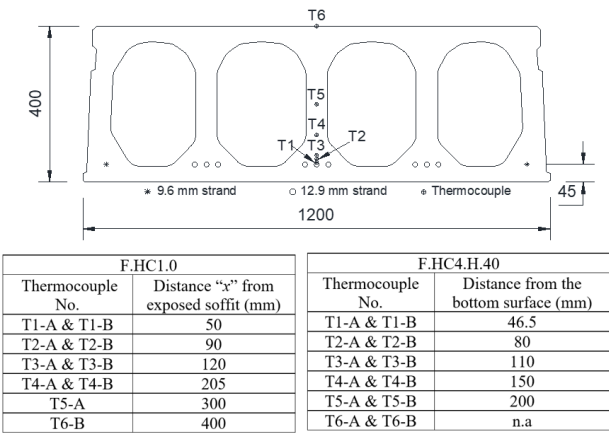


Figure 6. 3-D view of the test setup

The instrumentation of the fire tests included type K thermocouples (T), one load cell, and linear variable displacement transducers (LVDTs). Thermocouples were used to monitor temperature development inside the hollow-core specimens. They were embedded in the specimens through drilled holes which were subsequently filled using cement paste, around three months before testing. Along the specimen length, thermocouples were installed at two different sections named as Section A and Section B. In vertical direction, there were 5 or 6 thermocouples placed over the slab depth at one section. Besides thermocouples, in each fire test, one load cell and 12 LVDTs were used to representatively measure load transferred from a 100-ton hydraulic jack to the specimen and development of deflection in vertical direction and longitudinal thermal expansions. Arrangement of thermocouples are shown in Figure 7 while load cell and LVDT arrangements are shown in Figure 8.



a) Thermocouples in longitudinal direction (at Sections A and B)



Notation: T1-A represents for Thermocouple 1 at Section A. Similarly, T2-B denotes Thermocouple 1 at Section B, and etc.

b) Thermocouples in vertical direction

Figure 7. Thermocouple arrangement

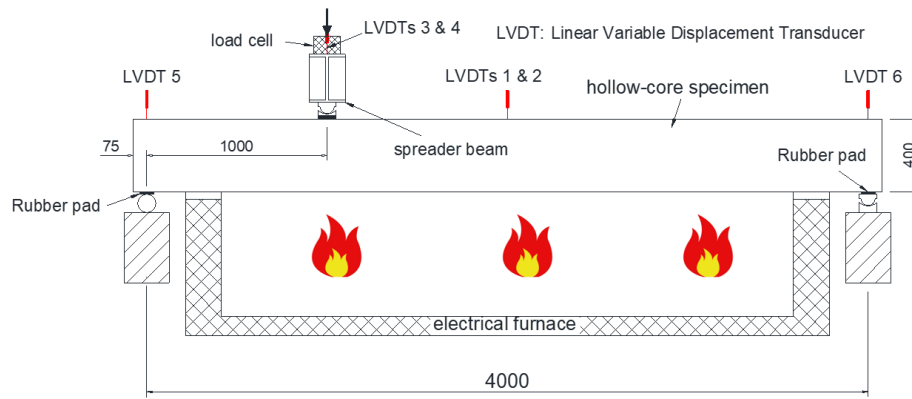


Figure 8. Load cell and LVDT arrangements

2.3 Testing procedure and heating curves

The two fire tests were conducted following a transient-state regime, of which the specimens were first loaded up to 40 % of their ambient capacity (Table 1) and temperatures were subsequently applied. The hollow-core specimens were heated under a programed curve (shown in Figure 9) up to failure while the applied loads were maintained constant during the fire tests. It should be noted that temperature curves used in this program was not ISO 834. Therefore, results from the tests were used to investigate structural behavior of the two slabs with and without steel fibers under elevated temperatures and measured failure times could not be interpreted as their fire resistance.

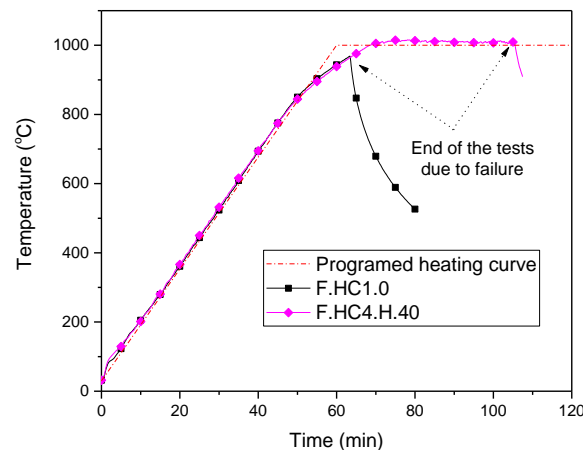


Figure 9. Programed heating curve and measure furnace temperatures in each test.

3 TEST RESULTS AND DISCUSSIONS

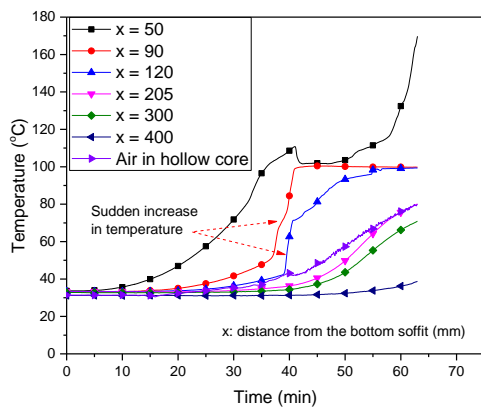
Table 3 shows results from the tests. Test results will be presented and discussed in terms of temperature and deflection evolutions, cracks developed and failure modes. It should be noted that the fire tests were stopped when failure occurred. Exposure times were then determined although these values could not be considered to be “fire resistance”.

Table 3. Test results

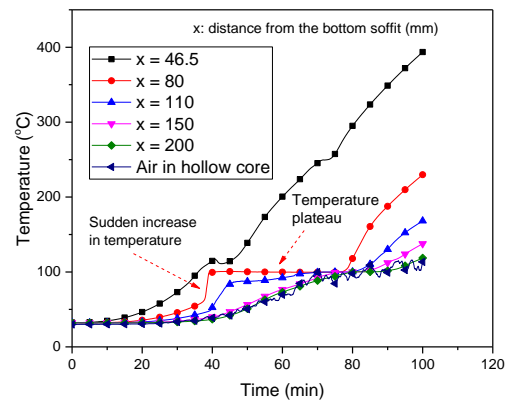
Test ID.	Shear-span-to-depth ratio (a/d)	Applied load (kN)	Furnace temperature at failure (°C)	Total exposure time (min)	Mid-span deflection at failure (mm)	Failure mode*
F.HC1.0	1000 (2.5)	146	956	62	24.3	Web-shear
F.HC4.H.40	1000 (2.5)	208	1008	100	58.9	Flexural

3.1 Temperature distribution

Temperature development inside the specimens is shown in Figure 10 where x is the distance (mm) from the bottom slab (the exposed soffit) to the measured level. It is noteworthy that temperature readings from installed thermocouples at the same level at Section A and Section B were highly consistent. Therefore, only the mean values of the two sets of measured temperatures were presented. As shown, results from thermocouples exhibit reasonable readings since concrete cross-sectional temperatures over slab height decreased as x increased. This is because low thermal conductivity and high specific heat of concrete delayed heat transfer over the cross section [19]. Figure 10 shows that concrete temperatures at measured levels gradually increased from ambient to 100 °C as time of fire exposure increased from beginning to about 40 min. From 40 min onwards, at several measured layers, there was an abrupt increase in concrete temperature. Such a sudden increase in temperature could be due to occurrence of longitudinal cracks which will be discussed in great detail in Nguyen [5]. In addition, there was a plateau at concrete temperature of 100 °C was observed.



a) F.HC1.0

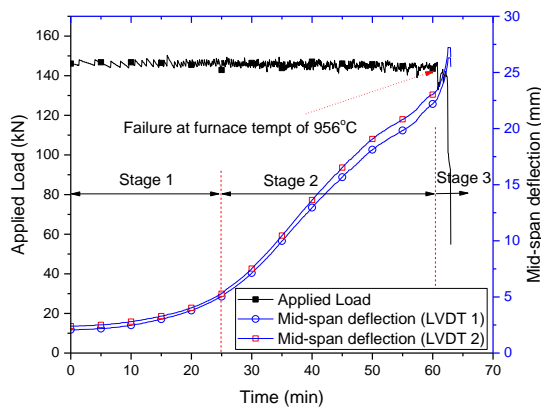


b) F.HC4.H.40

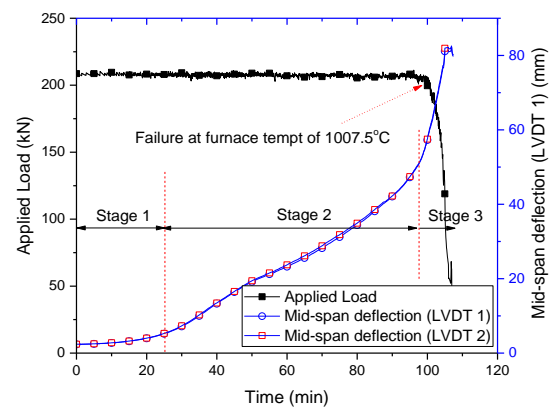
Figure 10. Temperature development inside the test specimens

3.2 Structural behavior

Figure 11 shows applied loads and development of mid-span displacement with time. As can be seen, the fire tests were about to be ended once the specimens showed “runaway” deflections. At these moments, the test slabs were unable to sustain the imposed loads due to a substantial drop in load-bearing capacity.



a) F.HC1.0



b) F.HC4.H.40

Figure 11. Imposed load and mid-span displacement development vs. time

As can be seen from Figure 11, the two specimens experienced three stages before failure took place. In tentatively first 25 min of fire exposure (Stage 1), due to thermal-bowing effect, the slabs deflected

downwards at a slow rate. Displacements of the two specimens at the end of Stage 1 were about 5 mm at furnace temperature of about 430 °C. Stage 2 started with a greater deflection rate due to combined effect of degradation in strength and stiffness of the concrete and strands and thermal bowing as temperatures continually increased. The duration of Stage 2 varied from one slab to another, from 35 min in F.HC1.0 to 74 min in F.HC4.H.40. The slab with hooked steel fibers sustained longer durations in Stage 2 compared to F.HC1.0. Stage 3 emerged when slab deflection increased at a much faster rate due to a significant decrease in load-bearing capacity and stiffness of the specimens as a result of elevated temperatures. Stage 3 occurred in a short duration (commonly less than 5 min), and very soon failure occurred.

Figure 11 also shows that F.HC1.0 failed at gas temperatures lower than 1000 °C and displacement of about 24 mm. However, with the inclusion of steel fibers, displacement of F.HC4.H.40 reached about 60 mm which was more than two times compared to that of H.HC1.0. Furthermore, F.HC4.H.40 was able to resist higher applied load (208 compared to 146 MPa as shown in Table 1) for a longer duration (100 compared to 62 min) before failure. The test results show enhanced resistance in terms of strength and ductility of the slab with steel fibers (F.HC4.H.40) compared to the control specimen without any fibers (F.HC1.0).

3.3 Failure modes and development of crack patterns

Failure modes of the two specimens are shown in Figure 12. As can be seen, F.HC1.0 without fibers failed in web-shear mode with the formation of web-shear cracks. In this mode of failure, cracks initially occurred in concrete webs due to excessive tensile strength caused by applied loads and temperatures. Once occurred, the cracks immediately propagated towards the bearing and loading regions, forming diagonal web-shear cracks (Figure 12(a)) and causing a sudden failure. In contrast, with the inclusion of hooked-steel fibers, shear failure was completely avoided in F.HC4.H.40. The slab with steel fibers failed in ductile flexural mode of which cracks emerged in the bottom slab in the vicinity of loading regions. As temperatures increased, vertical cracks propagated upwards and widened up, exposing prestressing strands to high temperatures. As a result, strand strength reduced considerably, and the slab failed with yielding or rupture of prestressing strands, exhibiting ductile failure mode. The test results showed that when steel fibers were used, F.HC4.H.40 could be able to sustain higher applied loads for a longer duration and experienced larger displacement before failure and collapsed in ductile failure mode. Obviously, fire endurance of hollow-core slabs with steel fibers was significantly improved.

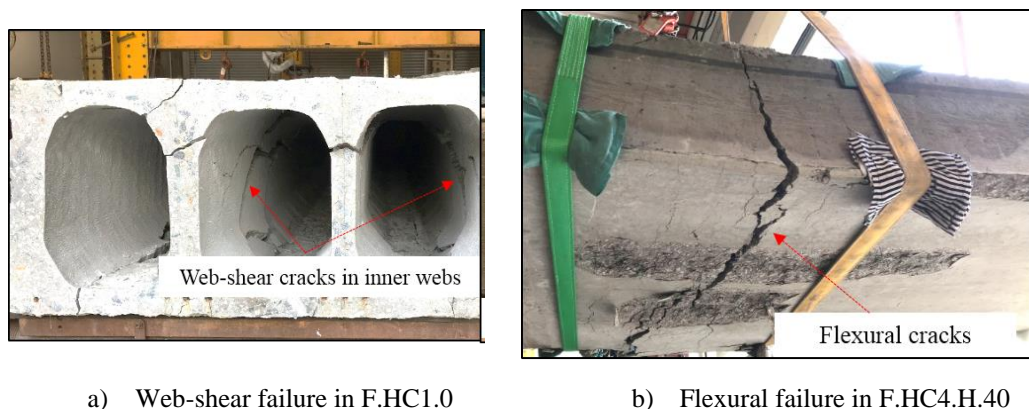
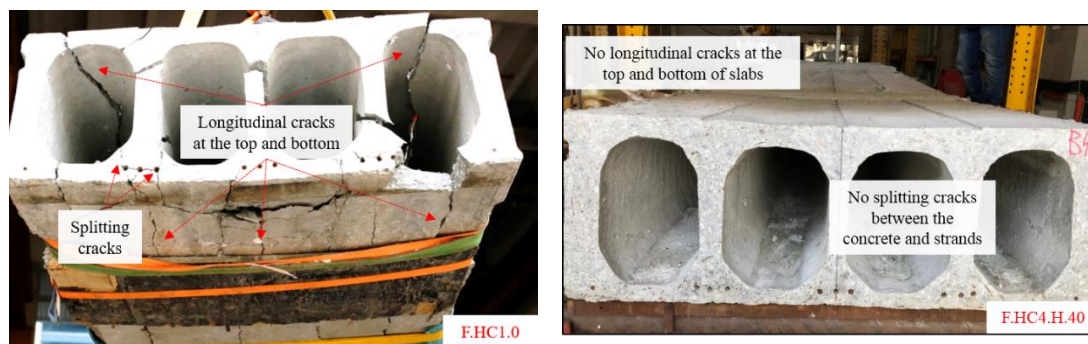


Figure 12 Failure-mode comparison

During the fire tests, five types of cracks were sequentially observed, *namely*, splitting, longitudinal, thermal, web-shear, and flexural cracks (discussions for each type of cracks can be found in Nguyen [5]). It is worth mentioning that while the first four cracks occurred in F.HC1.0, only two types of cracks, i.e. thermal and flexural cracks were observed in F.HC4.H.40 (Figure 13). This was because tensile strength of fiber-reinforced concrete was significantly enhanced (as shown in Table 2) and therefore, splitting,

longitudinal and web-shear cracks could not be able to develop. However, it should be noted that during the fire tests, temperature-induced spalling was observed in both slabs with and without steel fibers.



a) Splitting and longitudinal cracks in F.HC1.0

b) No splitting and longitudinal cracks in F.HC4.H.40

Figure 13 Crack-pattern comparison

4 CONCLUSIONS

Two full-scale fire tests were conducted on hollow-core specimens with and without hooked steel fibers under elevated temperatures. They were tested to examine fire endurance of fiber-reinforced hollow-core slabs. On the basis of the experimental results, the following conclusions are drawn:

1. It was feasible to include hooked steel fibers with an aspect ratio of 80 and a volumetric content up to 0.51 % in very dry (zero or nearly zero slump) concrete in the extrusion method.
2. Resistance to applied load and elevated temperatures and ductility of PCHC slabs were substantially increased with the use of hooked steel fibers. Hollow-core slabs with hooked steel fibers could sustain higher imposed loads for a longer duration and experienced much larger deformation before failure compared to slabs without steel fibers.
3. With the inclusion of steel fibers, web-shear failure mode (brittle type) in PCHC slabs was completely avoided.
4. The study shows a potential use of steel fibers to enhance shear capacity of hollow-core slabs subjected to elevated temperatures. However, it should be noted that temperature-induced spalling of concrete was observed in both slabs with and without steel fibers. Therefore, techniques should be considered to enhance spalling resistance of steel-fiber-reinforced concrete before they are applied in practice.

ACKNOWLEDGMENT

This material is based on research/work supported by the Singapore Ministry of National Development and National Research Foundation under L2 NIC Award No. L2NICCFP1-2013-4. Any opinions, findings, and conclusions expressed in this material are those of the authors and do not necessarily reflect the views of L2 NIC.

REFERENCES

1. Hawkins, N.M. and S. Ghosh, Shear strength of hollow-core slabs. *PCI journal*, 2006. 51(1): p. 110-114.
2. Walraven, J.C. and W.P.M. Merckx, The bearing capacity of prestressed hollow core slabs. *Heron*, 1983. Vol. 28 (No. 3).
3. Nguyen, T.N.H., K.-H. Tan, and T. Kanda, Investigations on web-shear behavior of deep precast, prestressed concrete hollow core slabs. *Engineering Structures*, 2019. 183: p. 579-593.
4. Jansze, W., A.V. Acker, and R. Klein-Holte, Fire resistance of hollow core floors regarding shear and anchorage capacity, in *Structures in Fire*. 2012: Zurich, Switzerland. p. 709-718.

5. Nguyen, H.T.N., Shear behavior of deep precast/prestressed concrete hollow-core slabs with and without fibers at ambient and under fire conditions, PhD Thesis 2020.
6. EN-1992-1-2, Eurocode 2: Design of concrete structures, in Part 1-2: General rules - Structural fire design. 2004: Brussels.
7. Narayanan, R. and I.Y.S. Darwish, Use of Steel Fibers as Shear Reinforcement. ACI Structural Journal, 1987. **84**(3).
8. Dinh, H.H., Shear Behavior of Steel Fiber Reinforced Concrete Beams without Stirrup Reinforcement. 2009, PhD Thesis, The University of Michigan, USA.
9. Yoon-Keun Kwak, M.O.E.W.-S.K. and K. Jubum, Shear Strength of Steel Fiber-Reinforced Concrete Beams without Stirrups. ACI Structural Journal, 2002. **99**(4).
10. Hai H. Dinh, G.J.P.-M. and K.W. James, Shear Behavior of Steel Fiber-Reinforced Concrete Beams without Stirrup Reinforcement. ACI Structural Journal, 2010. **107**(5).
11. Victor C. Li, R.W. and M.H. Ali, Steel and Synthetic Fibers as Shear Reinforcement . Materials Journal, 1992. **89**(5).
12. Palmer, K.D. and A.E. Schultz, Experimental investigation of the web-shear strength of deep hollow-core units. 2011, PCI Journal. p. 83-104.
13. Peaston, K.E. and K. Paine, Steel Fiber Reinforcement for Extruded Prestressed Hollow Core Slabs . ACI Symposium Publication, 1999. **182**.
14. Cuenca, E. and P. Serna, Failure modes and shear design of prestressed hollow core slabs made of fiber-reinforced concrete . Composites Part B: Engineering, 2013. **45**(1): p. 952-964.
15. Simasathien, S. and S.-H. Chao, Shear strength of steel-fiber-reinforced deep hollow-core slabs. PCI Journal, 2015: p. 85-101.
16. Nguyen, H.T.N., Y. Li, and K.H. Tan, Shear behavior of fiber-reinforced concrete hollow-core slabs under elevated temperatures (*accepted on Oct 06, 2020*). Construction and Building Material.
17. Nguyen, H.T.N., K.H. Tan, and T. Kanda, Effect of polypropylene and steel fibers on web-shear resistance of deep concrete hollow-core slabs . Engineering Structures, 2020. **210**: p. 110273.
18. EN-1168:2005+A3, European Standard, in Precast concrete products - Hollow core slabs . 2011: Brussels.
19. Nguyen, H.T.N. and K.H. Tan, Experimental studies on shear behavior of deep prestressed concrete hollow core slabs under fire conditions, in 10th International Conference on Structures in Fire, Belfast, Northern Ireland, UK, 6-8 June , A. Nadjai, et al., Editors. 2018. p. 51-59.

RETROFITTING OF FIRE DAMAGED RC COLUMNS

Hemanth Kumar Chinthapalli¹, Chellapandian M², Anil Agarwal³, Suriya Prakash⁴

ABSTRACT

The post fire (residual) capacity of Reinforced Columns (RC) members descends drastically due to degradation of concrete strength, permanent deformation and damage (spalling or buckling of rebar's) in the column. The restoration of such members is essential immediately after the fire event in case of important structures and /or where some part of the structure damaged to fire or fire event may have suppressed after short time which may partially damage the members, where the cost of demonization and reconstruction is very high than retrofitting. The present study have been trying to shed light in restoring the fire-damaged columns back to its service state.

The present study focuses to understand the effectiveness of hybrid strengthening technique for retrofitting the fire-damaged columns. The test matrix consists of five short columns in which three were damaged only under fire and two were damaged under fire cum axial load. The parameters considered in this study are concrete strength, duration of fire exposure, damage due to axial load during fire. Experimental results reveal that the hybrid technique restores the original capacity when subjected up to 2 hours fire. The column damaged beyond 2 hours restores to the original capacity. Depending on duration of fire exposure and initial ambient capacity of the column with more than 100% restoration in ductility levels.

Keywords: Retrofitting; Fire tests; Re-habitation; Fire damage; Hybrid strengthening

1 INTRODUCTION

FRP strengthening techniques such as near surface mounting (NSM) and external bonding (EB) has been successfully used in the past for improving the overall performance of reinforced concrete elements under different load combinations such as axial compression, bending, shear, torsion and their combinations [1-3]. Repair and strengthening of damaged RC columns for restoring the axial strength and displacement ductility using FRP confinement has been extensively investigated by the researchers [4-7]. Dalgic et al. [8] studied the effect of FRP confinement on the behavior of pre-damaged RC columns under axial compression. They concluded that FRP confinement was able to restore the strength and ductility completely for the pre-damaged RC columns. Ilki et al. [9] studied the effect of pre-damage on the behavior of FRP confined RC columns under cyclic compression loads. Similar investigations on the effect of different levels of pre-damage and the effect of compressive strength on the pre-damaged RC columns were also carried out [10]. FRP strengthening on the post-fire performance of RC columns are relatively less studied. Zhou and Wang [11] presented a state-of-the-art review on the repair of fire-damaged RC members

¹ Research Scholar, Indian Institute of Technology Hyderabad,
e-mail: ce15resch11006@iith.ac.in,

² Post doctoral fellow, Indian Institute of Technology Hyderabad,
e-mail: : ce15resch11005@iith.ac.in,

³ Assistant Professor, Indian Institute of Technology Hyderabad,
e-mail: anil@ce.iith.ac.in,

⁴ Associate Professor, Indian Institute of Technology Hyderabad
e-mail: suriya@ce.iith.ac.in,

using techniques such as concrete section enlargement strengthening, steel jacketing method, externally bonded reinforcement strengthening. Al-Nimry and Ghanem [12] and Al-Nimry et.al,[13] investigated the effectiveness of FRP confinement in improving the performance of RC columns heated up to 500°C for 2 and 3 hour duration under axial compression. They reported that a single layer of the CFRP fabric managed to restore the original axial resistance of the columns heated for 2 hours. However, two layers were essential in restoring the axial resistance of circular columns subjected to 3-hour heating. In addition, they showed that the use of Glass FRP sheets were found to be less effective and the number of plies required for restoring the original capacity of heat damaged columns is twice than the CFRP. In case of rectangular columns the two layers are not sufficient to restore the original axial resistance of the columns heated to 3 hours. Some researchers [14-16] also investigate the effect of FRP strengthening on the fire performance of RC elements under different load combinations. In addition, the behavior of FRP confined RC columns after damage under fire was an emerging topic, and investigations have been done by some researchers.

Review of literature works clearly indicates that no studies in the past have focused on accessing the post-fire behavior of severely damaged RC columns strengthened using hybrid FRP composites, which were damaged due to fire beyond 500°C. Limited studies in the past have focused on understanding the behavior of RC columns initially damaged under elevated temperatures and further strengthened using FRP composites. Damage of concrete due to fire can be catastrophic leading to partial/complete collapse. Therefore, it is essential to repair and strengthen the fire damaged RC members to their original load levels. It is worth mentioning that the suitability of Hybrid FRP strengthening technique on the post-fire performance of RC columns is not well understood.

2 EXPERIMENTAL STUDY

2.1 Preparation of Column Specimen

Seven RC square columns were cast with cross section dimensions of 230 mm and height of 860 mm. All the specimens were reinforced with four longitudinal bars, the diameter of the bars and percentage of the reinforcements were presented in Table 1 columns 4 and 5 respectively. The volume of hoop reinforcement (stirrups) were also presented in Table 1 and the cross-sectional dimensions are shown in Fig.1. The specimen ID : MxxLzHtt were used to denote the specimen. In MxxSyyHtt, xx denotes the cylindrical strength of the concrete used to cast the Member, yy denotes the diameter of the Stirrup, and ttt denotes Heating duration in minutes. For example : M30S10H140, which consists of member cast with concrete of 30 MPa cylindrical strength, stirrups made of 10mm diameter bar and heated for a duration of 140 min. All the columns had a clear cover of 25 mm to the transverse reinforcement. Both the longitudinal and transverse reinforcement ratio used in this study resemble that of mid-rise building columns.

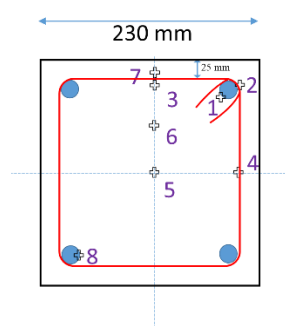


Figure 1. Cross-section details and location of thermocouples in the specimen

Table 1: Test matrix and specimen details

S.No.	Specimen ID	Reinforcement Details			Duration of Heating (min)	Loaded to Failure (Yes/No)
		Volumetric ratio of shear reinforcement (%)	Diameter of Longitudinal bars (mm)	Longitudinal Reinf. (%)		
1	M30S08H060	0.87	16	1.52	60	No
2	M30S12H120	0.87	16	1.52	120	No
3	M30S10H180	0.87	16	1.52	180	No
4	M30S06H200	0.25	16	1.52	200	Yes
5	M25S10H000	1.43	12	0.86	0	Yes
6	M25S10H120	1.43	12	0.86	120	Yes
7	M25S10H180	1.43	12	0.86	180	Yes

2.2 Thermal and Structural Loading Systems and procedure

Inorganic cement-based mortar with high initial strength was used to cap the top and bottom surfaces of the specimen. Capping ensured that the columns were standing plumb on the loading platen and were loaded uniformly in pure axial compression through the cross-section. The following procedure was used to test the column specimens during fire combined with axial loading conditions. First, the column was centered in the loading frame, the ceramic radiant heating panel heaters were then assembled around the column maintaining a clear distance of 90 mm on all sides of the column as shown in figure 2. Eight thermocouples were placed in the cavity of the furnace to measure the cavity temperatures. Then, all the openings were packed with ceramic glass wool. The reinforced concrete columns were heated using ceramic radiant heating panels. Fig. 2 shows the photographs of the electric furnace designed for conducting these high-temperature tests. The test setup used in this experiment consists of four heater panels. Each heater consists of a heated surface area of 305 mm x 450 mm and can achieve a maximum surface temperature of 1050°C.

As shown in figure 2, a set of four heaters were arranged such that it forms a rectangular tube with internal dimensions of 420 mm x 420 mm. The openings in the furnace were closed with ceramic glass wool blankets of density 128 kg/m³. These heaters were placed in such a way that the four sides of the column are at equal distances from the respective heaters. A clearance of 90 mm was maintained between the surfaces of the column and the heater to avoid any damage to the heater from spalled concrete pieces during loading. This heating zone controller consists of a proportional-integral-derivative (PID) controller to control the furnace temperature and a limit controller to prevent accidental overheating. A data acquisition system with two modules, each consisting of 16-thermocouple channels, is used to acquire temperature data from the specimen and the furnace cavity at the desired time intervals. This data acquisition system allows recording of high-resolution temperature data at the rate of 1 sample/second from each thermocouple. Each specimen was 860 mm long, and the specimen was heated over mid-length of 450 mm. The ends of the column specimens were kept outside the furnace to avoid heating of the loading platens and the hydraulic system. It was observed that the maximum temperatures at the column ends did not exceed 50°C during the experiment.

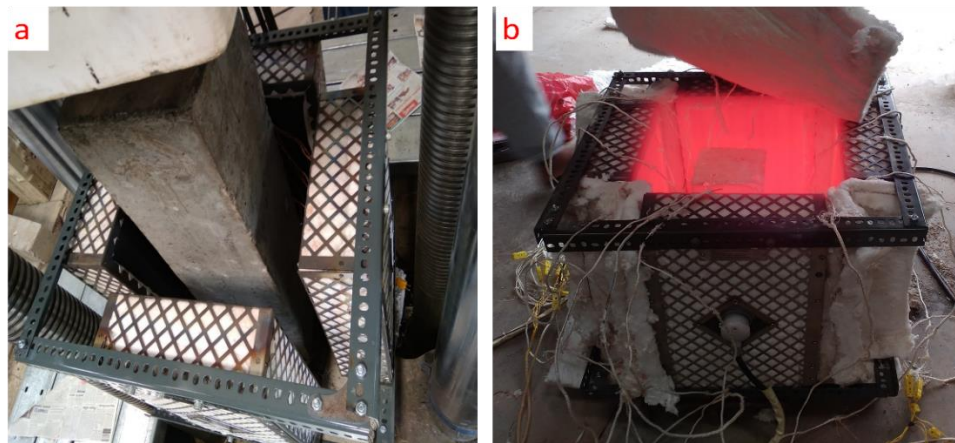


Figure 2. Thermal Loading System (a) Arrangement of the heaters around the specimen (b) Furnace during trial testing.

Figure 3(a) shows the photograph of total experimental setup, which includes the RC column specimen, the heating panels, and the loading system. Figure 3(b) schematically illustrates the instrumentation layout used for measuring the axial deformations of the columns at elevated temperatures. Fig. 1 shows the layout of the K-type thermocouples (0.65 mm diameter) embedded in the column cross-section A-A. Additional thermocouples (8 No's) installed in the furnace cavity for measuring the furnace temperatures were connected to the data acquisition system for the record. Moreover, two additional thermocouples were installed in the furnace cavity as well. One of these was connected to the process controller, and the other was connected to the limit controller. Three 50-mm linear variable differential transformers (LVDTs) were used to measure the axial deformations of the column specimens. After that, all the openings were packed with ceramic glass wool and placing the LVDT's at desired locations. The heaters were then switched on and controlled to follow the ISO-834 standard fire curve [17]. Even though the furnace is set to follow the standard fire curve carefully for the desired duration, the maximum temperature in the furnace is restricted to 950°C due to the limitation of the radiant heating system. The temperature profiles and load-deformation curves of the specimens during a fire when subjected to the desired time duration are presented in the following section.

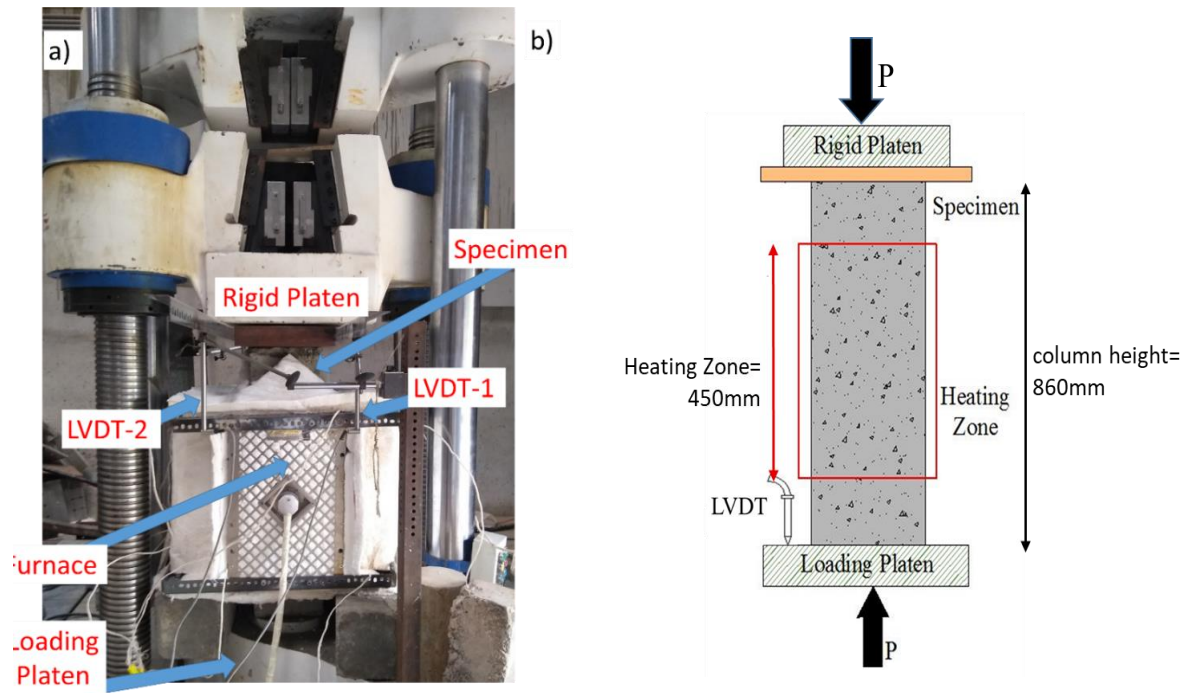


Figure 3. Test Setup for Fire Loading under Compression (a) Experimental setup (b) Heating zone of specimen

3 TEST RESULTS UNDER COMBINED COMPRESSION AND THERMAL LOADING

The average temperature (T) versus time (t) curves of the furnace during each test are presented in Figure 4, along with the ISO standard fire curve.

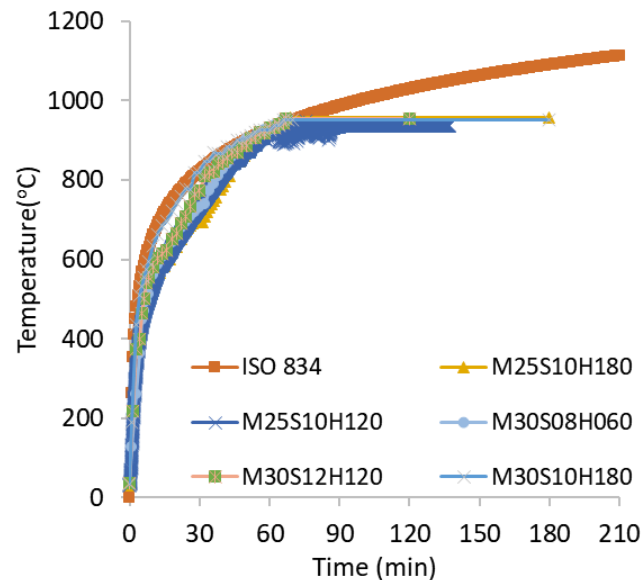


Figure 4. Average temperature vs time curves of the furnace during the test.

During the heating process, the columns were not subjected to any axial load and were allowed to expand freely. After heating the columns for the desired duration (as mentioned in Table 1), the compressive load on the columns was increased in displacement control mode at a rate of 2.0

mm per minute until the columns failed (isothermal loading). The columns were considered to be failed when the axial load resistance of the columns dropped by 20% of the maximum load value. The column (M25S10H000) tested at room temperature (RT) were also loaded using the same loading frame without the heating system. All the axially loaded RC columns underwent severe damage, including the buckling of longitudinal bars and the crushing of concrete. Both the longitudinal and confining steel reinforcement yielded during the process of testing.

The load-displacement behaviour of the two control specimens and the corresponding heated specimens are presented in figure 5. It is evident that with an increase in fire exposure duration, the strength and axial stiffness of the specimen decreases. Also, the columns exhibited greater ductility at elevated temperatures (FD) than at room temperature (RT). It is to be noted that the specimens M30S08H060, M30S10H180 and M30S12H120 were tested only under fire damaged conditions. More detailed explanation about the failure mechanism and behavior of specimens under elevated temperatures along with the numerical modelling can be found from the other paper of authors [26].

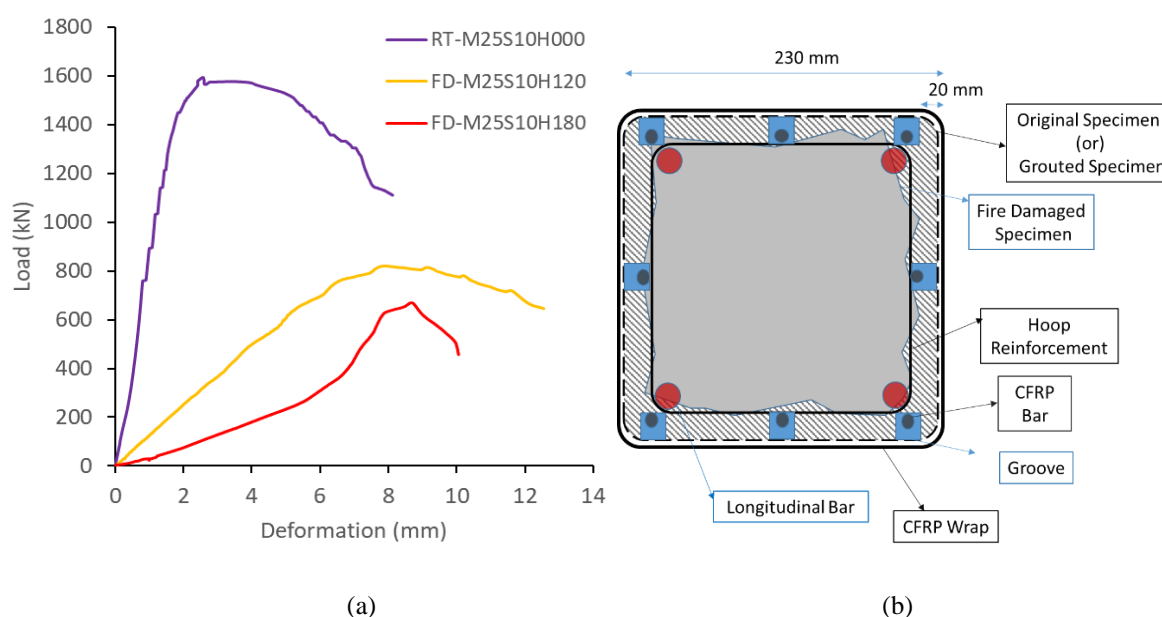


Figure 5.(a) Load – axial displacement behaviour of original and fire-damaged RC columns (b) Cross-section of repaired columns

4 STRENGTHENING DETAILS AND THEIR PERFORMANCE

4.1 Strengthening of Damaged Columns

Before strengthening of columns, all the columns were air cured to achieve room temperature in the specimen. Then all the loose concrete cover was chipped off, dust and debris on the damaged surfaces were removed by the application of air pressure and water spray. Thereafter, these specimens were placed in the molds and high strength cementitious grout was filled under pressure to fill the chipped of concrete in the damaged specimen. The grout was quick setting type and had a good bond strength with the old damaged concrete specimen. The specimens were demoulded after 24 hours. Thus, the final specimens obtained using quickset cementitious grout were obtained with neat and even surface. The specimens are strengthened with hybrid techniques [18-21].

All the damaged columns were initially repaired with quick setting cement mortar as mentioned above. In hybrid strengthening, NSM strengthening was carried out initially followed external bonding of CFRP fabric. After NSM strengthening, the corners of columns were grind to achieve round edges with a minimum radius of 15 mm to avoid possible stress concentrations [22-25]. A primer coating was applied on the surfaces of the column elements for the

improved bond. Thereafter, the CFRP fabric was wrapped around the column using the two component based epoxy. The cross-section of the repaired columns were presented in figure.5 (b). Possible air bubbles present during FRP wrapping were removed with the help of a hand roller. The step-by-step procedure was presented in figure 6 A tapping test using a plastic hammer was done to observe any hollow sound for the indication of air gap. No hollow sound indicated a perfect bond of FRP with the concrete.

4.2 Loading System for Repaired Columns

The fire damage retrofitted RC Columns were tested in micro-test compression testing machine of capacity 3000 kN. The rate of loading was fixed at 2 mm/min to enable better capture of post-peak behavior. The column elements were attached with five LVDT's of 20 mm stroke (180 mm gauge length); four LVDT's to capture the surface strains and displacements, one LVDT to capture the lateral surface deformation at the mid height of the specimen. Additionally one 50mm LVDT to capture the loading platen deformation. DAQ (Data Acquisition System) was used for acquiring all the data like strain and displacement measurements.

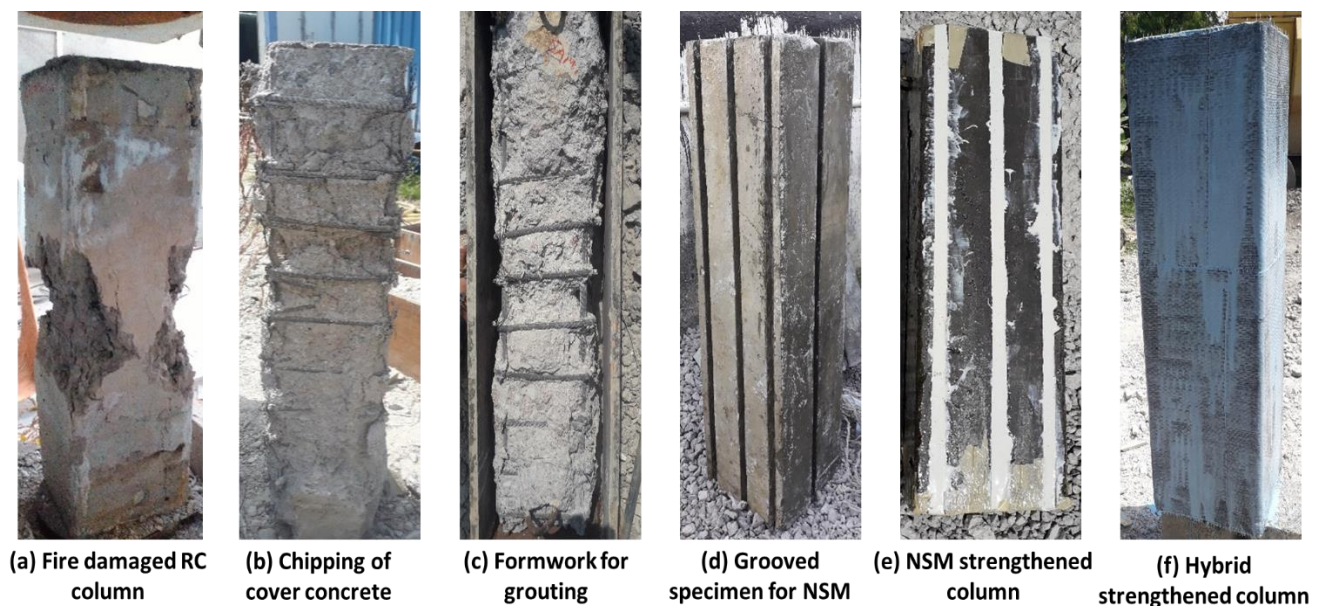


Figure 6. Procedure of hybrid retrofitting procedure

5 TEST RESULTS OF RETROFITTED COLUMNS

In the seven columns, three columns damaged under combined axial load and fire, three damaged only by fire and one column under pure axial load were damaged prior to retrofitting. All the damaged columns were retrofitted using the hybrid CFRP scheme mentioned in detail in above section 4. The load bearing capacities of the specimens after retrofitting were presented in Table 2 and the load deformation curves are presented in Fig. 4. The nomenclature and strengthening details of repaired specimens are given in Table 1. To differentiate the load deformation curves tested at Room Temperature (RT), Fire Damage (FD) and Rapid Retrofitted (RR) the load deformation curves are designated as RT-,RD- and FD- respectively before the sample name, suppose the RR-S08L2H180 in the graph indicates the curve of sample S08L2H180 after Rapid Retrofitting.

Table 1: Test matrix and specimen details

S.No.	Specimen ID	Longitudinal Reinf. (%)	Loaded to Failure (Yes/No)	Load Resistance after Retrofitting (kN)	Strength Index (SI)
1	M30S08H060	1.52	No	1809	1.1
2	M30S12H120	1.52	No	1715	0.99
3	M30S10H180	1.52	No	1525	0.87
4	M30S06H200	1.52	Yes	1796	0.9
5	M25S10H000	0.86	Yes	2189	1.16
6	M25S10H120	0.86	Yes	1978	1.1
7	M25S10H180	0.86	Yes	1743	0.96

5.1 Strength Indices

Strength index (SI) can be defined as the ratio of peak load of repaired column (P_r) to the peak load of control column (P_0) as shown in equation 1.

$$SI = \frac{P_r}{P_0} \quad (1)$$

The load bearing capacity of the columns obtained at room temperature M25S10H000 was used as reference for comparison of high temperature and retrofitted columns. The experimental load bearing capacity of the columns M25S10H000 is 1593 kN. The horizontal dotted line in the graphs presented in figure 7 are the axial load carrying capacity of the column at room temperature.

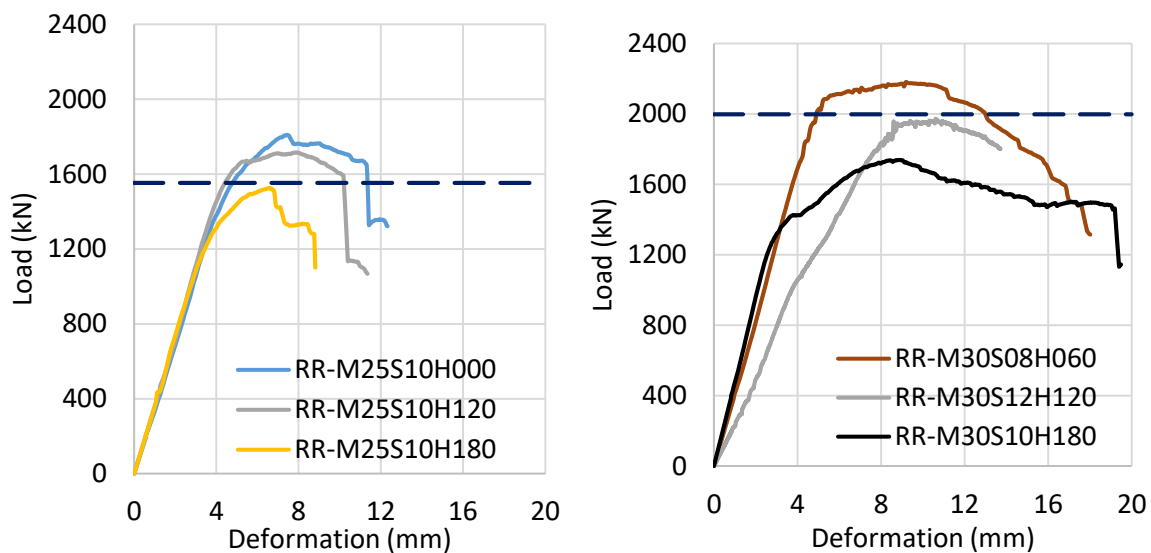


Figure 7. Load-deformation curves of retrofitted columns

5.2 Comparison between Room Temperature and High Temperature behaviour of Specimens

The comparison between the column capacity at Room Temperature (RT), Rapid Retrofitting (RR) columns and Fire Damage (FD) were presented in figure 8. During fire temperatures the load bearing capacity of the columns are very less compared to the pre-damaged and retrofitted columns, because at high temperature the material strength and stiffness are very less which results in less axial load capacity and higher deformations. The ductility of the retrofitted columns are far better than the ambient temperature, this is due to confining pressure provided by CFRP

fabric. The columns damaged under combined 2 hour ISO-Fire curve and axial load after retrofitting able to achieve its full capacity but incise of 3 hour heated columns 85% was achieved with higher ductility in both the cases.

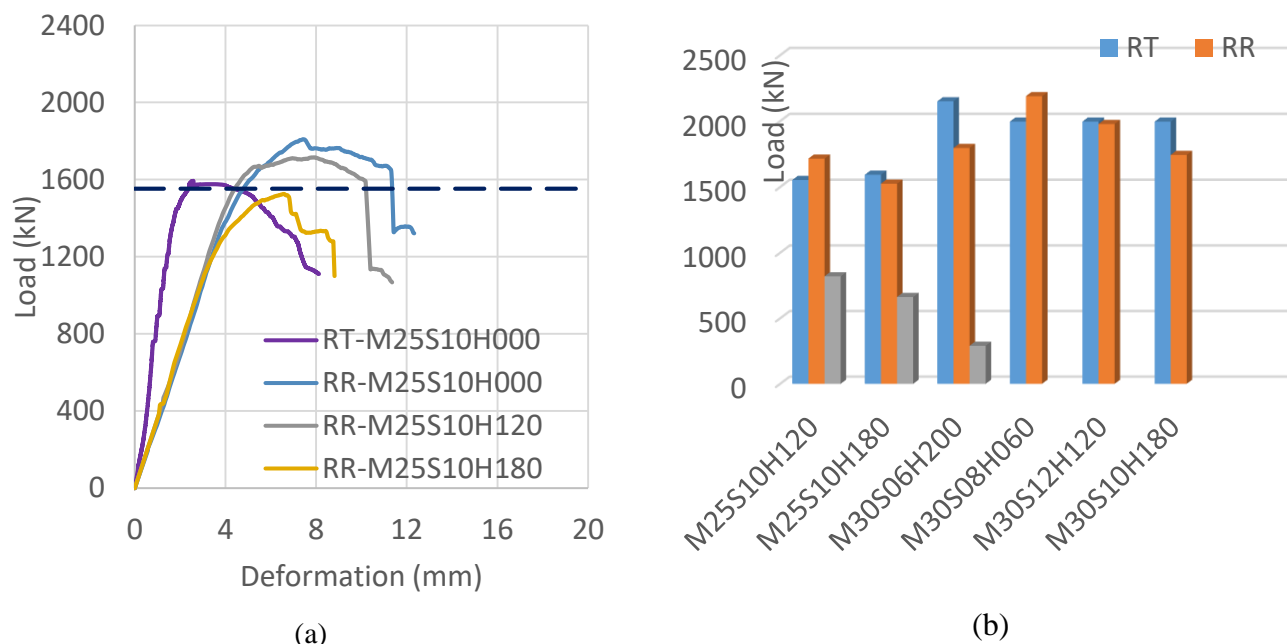


Figure 8. (a) Load-deformation curves of retrofitted columns with ambient test (b) Peak load comparison of RT, RR and FT.

6 SUMMARY AND CONCLUSIONS

This paper presented the results of RC columns severely damaged under fire under axial compression and strengthened with hybrid technique. The efficiency of strengthening techniques to restore the actual capacity of the column is evaluated for different strengths and fire exposure conditions. Same amount of CFRP material used both in hybrid CFRP technique, from the present study columns subjected to 2 hour fire duration and fully damaged under gravity loads can be restored to original capacity using the hybrid technique. The strengthening procedure involved removing the concrete cover and replacing it with high strength cementitious grout, CFRP-NSM strengthening followed by CFRP-EB strengthening. The adopted repair procedure is easy to implement in the field for emergency repair applications. Results suggest that the hybrid strengthening technique can restore strength, stiffness and ductility of fully damaged columns under fire and axial compression. The following major conclusions can be drawn from the limited results presented in this study:

- Thermal exposure increased the deformation capacity by double due to creep of materials at high temperature.
- The hybrid strengthening technique was found to be one of the efficient scheme to restore the fire damaged RC columns to its full capacity when RC Columns damaged due to 2-hour ISO fire combined with axial load.
- The damaged RC columns subjected to 3-hour under combined ISO fire and axial load can be restored by 85% of its original capacity.
- The ductility of the fire damaged retrofitted columns is higher than the ambient case columns.

REFERENCES

1. Triantafyllou GG, Rousakis TC, Karabinis AI. Effect of patch repair and strengthening with EBR and NSM CFRP laminates for RC beams with low, medium and heavy corrosion. *Compos. Part B: Eng.* 2018; 133: 101-111.
2. Wu RY, Pantelides CP. Rapid seismic repair of reinforced concrete bridge columns. *ACI J. Struct.* 2017; 114(5): 1339-1350.
3. Triantafyllou GG, Rousakis TC, Karabinis AI. Corroded RC beams patch repaired and strengthened in flexure with fiber-reinforced polymer laminates. *Compos. Part B: Eng.* 2017; 112(1): 125-136.
4. Karantzikis M, Papanicolaou CG, Antonopoulos CP, and Triantafyllou TC. Experimental investigation of nonconventional confinement for concrete using FRP. *J. Compos. Constr.* 2005; 9(6): 480-487.
5. Triantafyllou GG, Rousakis TC, and Karabinis AI.: Axially loaded reinforced concrete columns with a square section partially confined by light GFRP straps. *J. Compos. Constr.* 2015; 19(1): 04014035.
6. Ilki A. and Kumbasar N. Behavior of damaged and undamaged concrete strengthened by carbon fiber composite sheets, *Structural Engineering and Mechanics* 2002; 13(1): 75-90.
7. Kalyoncuoglu A, Ghaffari P, Gosku C, Ilki A. Rehabilitation of corrosion damaged substandard RC columns using FRP sheets. *Adv. Mater. Res.* 2013; doi:10.4028/www.scientific.net/AMR.639-640.1096.
8. Dalgic K.D, Ispir M, Binbir E. and Ilki A. Effects of pre-damage on axial behavior of CFRP jacketed non-circular members. *Proceedings of Conference on Civil Engineering Infrastructure based on Polymer Composites* 2012; Poland, 22nd – 23rd November.
9. Ilki A, Demir C. and Kumbasar N. Effects of pre-damage and cyclic compression on axial behavior of FRP jacketed concrete. *Asia-Pacific Conference on FRP in Structures (APFIS 2007)*, Hong-Kong, China.
10. Ferroto MF, Fischer O, Niedermeier R. Experimental investigation on the compressive behavior of short-term preloaded carbon fiber reinforced polymer-confined concrete columns. *Struct. Concrete* 2017;1–14.
11. Zhou, J., & Wang, L. (2019). Repair of fire-damaged reinforced concrete members with axial Load: A review. *Sustainability*, 11(4), 963.
12. Al-Nimry, H. S., & Ghanem, A. M. (2017). FRP confinement of heat-damaged circular RC columns. *International Journal of Concrete Structures and Materials*, 11(1), 115-133
13. Al-Nimry, H., Haddad, R., Afram, S., & Abdel-Halim, M. (2013). Effectiveness of advanced composites in repairing heat-damaged RC columns. *Materials and structures*, 46(11), 1843-1860.
14. Bisby, L.A.; Kodur, V.K.R.; Green, M.F. Fire endurance of fiber-reinforced polymer-confined concrete columns. *Aci. Struct. J.* 2005, 102, 883–891
15. Bisby, L.A.; Green, M.F.; Kodur, V.K.R. Modeling the behavior of fiber reinforced polymer-confined concrete columns exposed to fire. *J. Compos. Constr.* 2005, 9, 15–24.
16. Kodur, V.K.R.; Baolin, Y. Evaluating the Fire Response of Concrete Beams Strengthened with Near-Surface-Mounted FRP Reinforcement. *J. Compos. Constr.* 2013, 17, 517–529.
17. ISO. (1980). Fire resistance tests - Elements of building construction. ISO 834, Geneva.
18. ASTM D3039. Standard Test Method for Tensile Properties of Polymer Matrix Composite Materials, ASTM, West Conshohocken, PA 2009.
19. ASTM D 6484M. Standard test method for open-hole compressive strength of polymer matrix composite laminates 1999.
20. Chellapandian M, Prakash S.S. and Sharma A. Strength and Ductility of Innovative Hybrid NSM Reinforced and FRP Confined Short Reinforced Concrete Columns under Axial Compression. *Composite Structures Elsevier* 2017; 176: 205-216. DOI: 10.1016/j.compstruct.2017.05.033.
21. ACI 440.2R. Guide for the design and construction of externally bonded FRP system for strengthening concrete structures. ACI committee 440. Farmington Hills (MI): American Concrete Institute 2017: 45.
22. Galati, D., & De Lorenzis, L. (2009). Effect of construction details on the bond performance of NSM FRP bars in concrete. *Advances in Structural Engineering*, 12(5), 683-700.
23. Soliman, S. M., El-Salakawy, E., & Benmokrane, B. (2010). Bond performance of near-surface-mounted FRP bars. *Journal of Composites for Construction*, 15(1), 103-111

24. Jiang, S. F., Zeng, X., Shen, S., & Xu, X. (2016). Experimental studies on the seismic behavior of earthquake-damaged circular bridge columns repaired by using combination of near-surface-mounted BFRP bars with external BFRP sheets jacketing. *Engineering Structures*, 106, 317-331.
25. Ding, L., Wu, G., Yang, S., & Wu, Z. (2013). Performance advancement of RC columns by applying basalt FRP composites with NSM and confinement system. *Journal of Earthquake and Tsunami*, 7(02), 1350007.

DEVELOPING REAL-TIME HYBRID SIMULATION TO CAPTURE COLUMN BUCKLING IN A STEEL FRAME UNDER FIRE

Ramla K. Qureshi¹, Negar Elhami-Khorasani², Mettupalayam Sivaselvan³

ABSTRACT

In typically conducted real-time hybrid simulation, the behaviour of an element in the physical test is observed and monitored while servo-hydraulic actuators apply loading and interfacing boundary condition in real time by receiving feedback from a numerical model of the rest of the structure. When applied to structural fire engineering, this approach enables cost-effective fire experiments while capturing the interaction of the sub-assembly being tested with the rest of the structure. This paper describes the application of a control strategy for real-time hybrid fire simulation that decouples the physical substructure response from the control design. The proposed strategy is to add a new control input to the transfer system (i.e., the servo-hydraulic actuator and a controller) to tune the internal dynamics of the actuator and have the transfer system mimic the behaviour of the numerical substructure, independent of the physical substructure. The mathematical formulation of the proposed strategy is presented for an example of a steel moment frame with one column under fire. It is shown that the formulation for the transfer system and the control input results in a displacement history that matches the expected response from the numerical substructure.

Keywords: Hybrid simulation; structural fire testing; real-time hybrid fire simulation; hybrid fire testing; dynamic buckling; active boundary conditions; control strategy; servo-hydraulic actuator; column

1 MOTIVATION

Real-time hybrid simulation (RTHS), or dynamic substructuring, is an innovative technology only recently introduced to the domain of structural fire testing, where it promises more realistic response evaluation as opposed to currently available element-level “standard” fire tests. Typically, this technique couples physical and computational sub-models of a structural system to emulate static and dynamic interactions at the boundary that may be present during a fire scenario. The physical substructure (hereon denoted as PS) is a laboratory test specimen, and the numerical substructure (or NS) is a finite element computational model of the remaining structure. Servo-hydraulic actuators operating in feedback control function as “active boundaries”, and are used to apply interfacing force-displacement conditions to the PS. The corresponding response is measured and then fed back to the NS, providing a continuously updating response history throughout the duration of the fire test in real-time.

Consider the conventionally used RTHS feedback loop depicted in Figure 1. In this particular schematic, the boundary interaction between the NS and PS is realized with the help of an actuator in displacement control. Hereon referred to as transfer system, or TS, the actuator in this setup applies the interface

¹ PhD Candidate, Department of Civil, Structural and Environmental Engineering, University at Buffalo
e-mail: ramlakar@buffalo.edu, ORCID: <https://orcid.org/0000-0002-8652-5726>

² Assistant Professor, Department of Civil, Structural and Environmental Engineering, University at Buffalo
e-mail: negarkho@buffalo.edu, ORCID: <https://orcid.org/0000-0003-3228-0097>

³ Associate Professor, Department of Civil, Structural and Environmental Engineering, University at Buffalo
e-mail: mvs@buffalo.edu, ORCID: <https://orcid.org/0000-0001-6661-5567>

displacement on the PS, and sensors measure the corresponding force conjugate to be communicated back to the NS. As shown in the figure, some interaction between the TS and the PS specimen can be expected in the form of natural physical feedback. This is also termed as control-structure interaction and can lead to instability in the feedback loop if it is left unaccounted in the experimental control strategy [1]. Often in conventional RTHS experiments, the TS and the PS archetype are considered together as a single-input single-output system, and experimental controls are then designed accordingly to mitigate errors or disturbance introduced due to the PS feedback. This is not an easy task, as PS properties such as resonance, inertial effects, stiffness changes, etc. can lead to issues of equipment time lag, inexact tracking, and may require complicated time-integration schemes.

Specifically, for the case of real-time hybrid fire simulation (RTHFS), it has been established in previous literature [2-5] that constantly increasing furnace temperatures and the resulting degradation of PS stiffness under high temperatures can introduce errors in equilibrium and compatibility at the PS-TS interface node, requiring strict control techniques and advanced computational methods that cost time and might be susceptible to induced time lag. Therefore, in the big picture, RTHFS requires a comprehensive strategy that limits drastic errors from being induced in control design for the experiment due to changes in PS properties, while simultaneously accounts for actuator dynamics, and maintains equilibrium at the interface node in real-time.

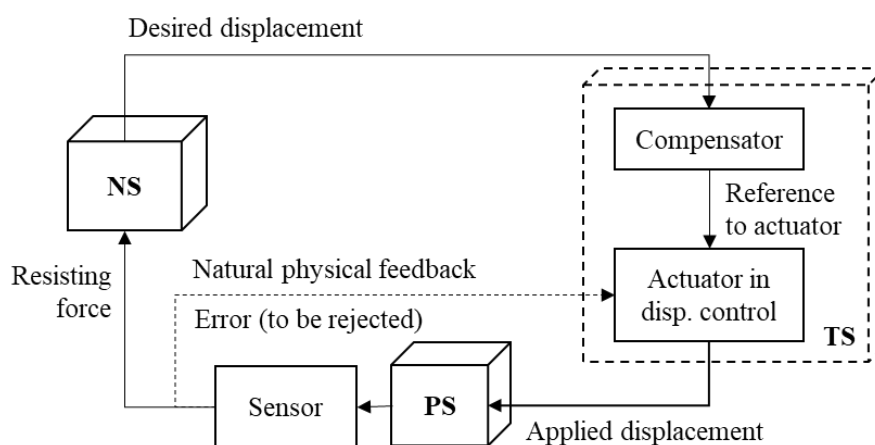


Figure 1. Conceptual block diagram for a conventionally used RTHS feedback loop

2 A DIFFERENT CONTROL STRATEGY FOR REAL-TIME HYBRID FIRE SIMULATION

This research applies a newly developed control strategy [6-7] to the proposed RTHFS, with the aim to resolve issues previously encountered in maintaining the numerical and experimental stability of the hybrid fire simulation test. This control strategy decouples the PS response completely from control design, and is designed by addressing the question: “How should the TS be controlled, if it were to enforce the exact same boundary condition on the PS as the NS would have done, were the boundary conditions intrinsic (such as is the case in an undivided structure)?” From this perspective, the accuracy of the RTHFS now directly depends on how closely the TS response can be made to resemble the NS behaviour. To achieve this, the proposed scheme introduces an additional “control input” to tune the internal dynamics of the actuator; the addition of which can adjust the output work conjugate to match the corresponding NS behaviour regardless of PS properties. Now, the TS becomes a two-input one-output system, where input no. 1 is the PS boundary condition feedback, and input no. 2 is the control input, denoted here as u . Note that in this setup, u is not a reference command, rather it is an “adjustment” that enables the TS to transfer the required boundary condition onto the PS, resembling the NS behaviour.

Such a decoupled control design is represented schematically in Figures. 2a and b, where PS is taken as a steel column within a moment frame for an example application. In Figure 2b, target displacements (as outputs) corresponding to both NS and TS are represented using transfer functions. Mostly used within control systems engineering, transfer functions are mathematical representations that can theoretically

associate the output of any modelled system to each plausible input; generally defined as the ratio of an output to an input of the considered system.

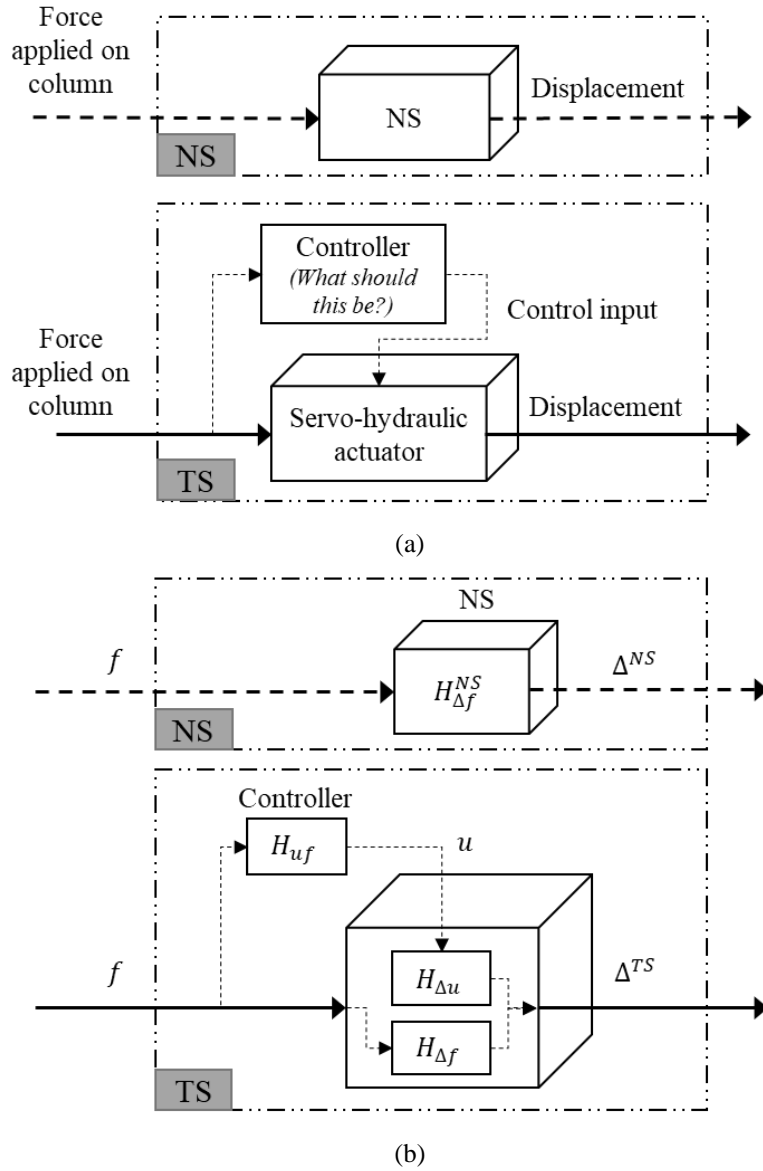


Figure 2. a) Conceptual representation, and b) block diagram with transfer function representation of proposed RTHFS strategy

In Figure 2, $H_{\Delta f}^{NS}$ is the transfer function for the NS taking input force (f) and giving output displacement (Δ^{NS}), such that;

$$\Delta^{NS} = H_{\Delta f}^{NS} f \quad (1)$$

For the purpose of this research and initial implementation, the NS model is considered to be stable and linear. Similarly, $H_{\Delta f}$ and $H_{\Delta u}$ are transfer functions for the TS taking two inputs, force f and control input u , respectively, and giving one output displacement, Δ^{TS} , such that;

$$\Delta^{TS} = H_{\Delta f} f + H_{\Delta u} u \quad (2)$$

The new strategy dictates that the controller be designed such that the output of the TS is as similar to the NS output as possible, i.e., theoretically, the aim is to ensure that $\Delta^{NS} = \Delta^{TS}$. From Figure. 2b, the control input u can be mathematically defined as:

$$u = H_{uf} f \quad (3)$$

Therefore, equations 1 to 3 can be rearranged to give:

$$H_{\Delta f}^{NS} f = H_{\Delta f} f + H_{\Delta u} H_{uf} f \quad (4)$$

Implying that a controller can be designed as H_{uf} , such that from the inversion approach:

$$H_{uf} = H_{\Delta u}^{-1} (H_{\Delta f}^{NS} - H_{\Delta f}) \quad (5)$$

Equation 5 defines the working principle of the new control strategy. Here, the PS does not appear in the design of the controller; and as the PS response is completely decoupled from the feedback path, no explicit tracking compensator is required, and no advanced numerical integration schemes seem to be necessary to maintain equilibrium and compatibility at the interface node. Because of this characteristic, PS can also be tested for nonlinear behaviour. What is important though, is to have thorough confidence in NS and TS transfer functions, so that the designed controller model H_{uf} is not sensitive to parameter variations and nonlinearities. This includes an in-depth understanding of the actuator properties such as fluid pressure difference, friction, valve error, etc. Simultaneously, it is important to note that the inverse model, $H_{\Delta u}^{-1}$ can be noncausal, i.e., its present response may depend on future values of inputs, making it impossible to be practically implemented. Stefanaki [6] and Verma et al. [8] have presented various approaches for fixing causality, and these will be discussed in subsequent sections. Overall, a meaningful inverse model $H_{\Delta u}^{-1}$ implies that the new strategy is simple to implement and yet highly robust.

3 FORMULATION OF A BENCHMARK STUDY FOR APPLICATION IN STRUCTURAL FIRE ENGINEERING

As shown in the previous sections, the presented control strategy for dynamic substructuring appears promising for adaptation to structural fire testing, and the process is hereinafter referred to as RTHFS. In order to develop and validate this strategy and create a framework for RTHFS, this section presents a benchmark problem which will be used to later test and validate the hybrid simulation procedures for fire. Consider the large-scale steel moment frame that was tested by Jiang et al. [9], where buckling of a hollow steel column exposed to fire and the subsequent progressive collapse of the full frame was investigated. This frame was also extensively discussed in [10], where the conventional RTHS feedback loop and error mitigation schemes were established for this frame within a virtual framework. The middle column on the first floor was considered as PS, while the remaining frame was considered as NS (as schematically shown in Figure 3).

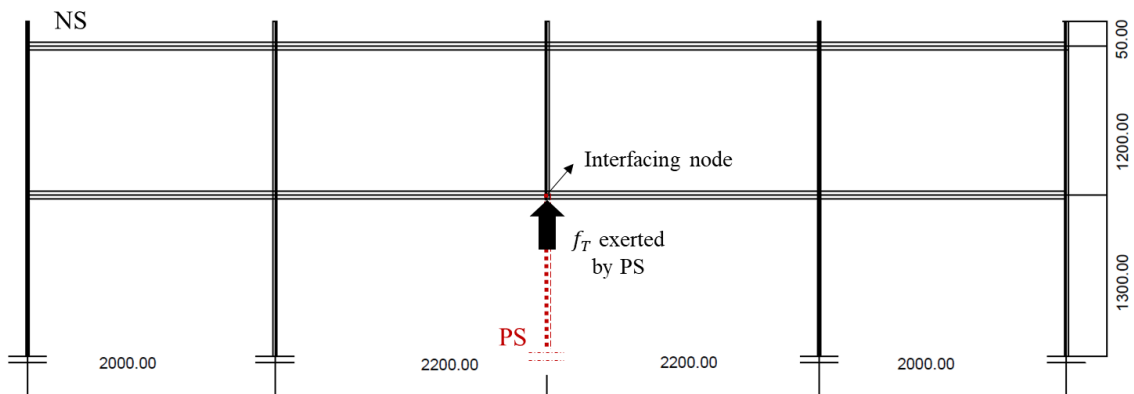


Figure 3. Substructuring configuration for the benchmark study (all dimensions are in mm)

This section applies the control strategy discussed in Section 2 in order to demonstrate the application of the framework on the global behaviour of the frame. The intention is to communicate force-displacement interactions throughout the test as well as at the time of failure. It is assumed that the surrounding NS frame

remains at ambient temperature, and that no heat transfer occurs between the NS and the PS column. As can be seen from Figure 3, the interfacing node is expected to face a thermal force from the heated (and therefore expanding) PS column. In the RTHFS framework, the tip of the actuator (representing the interface of the NS) is required to transfer the work conjugate displacement to resist the thermal expansion of PS. This can now be achieved through the new controller, which should ensure the stability of the RTHFS.

The PS is subjected to the loading protocol of the experiment conducted in [9] and explained for RTHFS in [10], so that the failure load maps to prior observed results. A detailed discussion on the dimensions, thermal and mechanical properties of the steel moment frame can be found in [9,10]. The following subsections provide a concise explanation of the NS, TS, and the control strategy for this benchmark problem.

3.1 Numerical substructure

At the interfacing node in the NS, it is expected that the PS will exert a thermal force f_T during the fire, resulting in vertical displacement, κ . The equation of motion for this virtual frame is presented as:

$$M\ddot{\kappa} + C\dot{\kappa} + K\kappa = \Omega_{in}f_T - f_{FEF} \quad (6)$$

where M is the nodal mass matrix,

C is the Rayleigh damping matrix with damping ratio = 5%,

K is the global stiffness matrix;

Ω_{in} is a vector considering all degrees of freedom (DOF) other than the vertical translation at the interfacing node as zero, implying only a unit multiplier at the vertical DOF in consideration, and;

f_{FEF} is the vector of nodal fixed end forces originating from the element self-weight and applied dead load.

M , C and K are all 30×30 matrices capturing all 3 degrees of freedom for each node on the portal frame, whereas Ω_{in} and f_{FEF} are both 1×30 vectors. Simultaneously, the output displacement response at the interfacing node is given by:

$$y = [\Omega_{in}] \times \kappa \quad (7)$$

Following equations 6 and 7, NS dynamics can also be represented in state-space form as:

$$\dot{\kappa} = A^{NS}\kappa + B_1^{NS}f_T + B_2^{NS}f_{FEF} \quad (8)$$

$$y = C\kappa \quad (9)$$

with

$$\kappa = \begin{bmatrix} \kappa_1 \\ \kappa_2 \end{bmatrix} \quad (10)$$

$$A^{NS} = \begin{bmatrix} 0 & I \\ -M^{-1}K & -M^{-1}C \end{bmatrix} \quad (11)$$

$$B_1^{NS} = \begin{pmatrix} 0 \\ M^{-1}\Omega_{in} \end{pmatrix} \quad (12)$$

$$B_2^{NS} = \begin{pmatrix} 0 \\ -M^{-1}f_{FEF} \end{pmatrix} \quad (13)$$

$$C = [\Omega_{in}^T \quad 0] \quad (14)$$

Where the state variables κ_1 , κ_2 represent the displacement κ , and velocity $\dot{\kappa}$ respectively, and I is a 30×30 identity matrix. Using above relations and NS properties, two 60th order transfer functions are

obtained associating output displacement with: (1) dead load, i.e., $H_{\Delta f_{FEF}}$, and (2) applied thermal load exerted by the PS, i.e., $H_{\Delta f_T}$, can be calculated in MATLAB as:

$$H_{\Delta f_T} = \text{tf}(\text{ss}(\mathbf{A}^{NS}, \mathbf{B}_1^{NS}, \mathbf{C}, [])); \quad (15)$$

$$H_{\Delta f_{FEF}} = \text{tf}(\text{ss}(\mathbf{A}^{NS}, \mathbf{B}_2^{NS}, \mathbf{C}, [])); \quad (16)$$

where `ss` is the MATLAB command for constructing a state-space model from system (\mathbf{A}^{NS}), input ($\mathbf{B}_1^{NS}, \mathbf{B}_2^{NS}$), and output (\mathbf{C}) state matrices, and `tf` is used to construct the transfer function of this state space model.

Understandably, these transfer functions cover many high frequency modes that may not be necessarily observable within the likely range of frequencies at which the RTHFS is set to operate. For this purpose, the first six modes of the NS frame that participate in the vertical direction are calculated and then verified by modelling the same frame in SAP2000 and conducting a modal analysis. Frequencies and mode shapes associated with these modes as obtained from SAP2000 are tabulated in Table 1. Bode plots in Figure 4 show the magnitude (in decibel scale) and phase angle plots for the frequency response of the 60th order system calculated above. It can be seen that the peak frequencies map to those obtained previously from SAP2000, indicating a robust NS model up until 1000 Hz. Next, to reduce the effect of higher modes, both the 60th order transfer functions are reduced to 6th order transfer functions. This reduced model is mapped in a dotted line in Figure 4 and can be seen to match the full-system model exactly through to 1000 Hz.

Table 1. Time periods and frequencies for considered NS mode shapes from SAP2000

Mode number	Period [s]	Circular Frequency [rad/s]	Frequency [Hz]
2	0.531	11.827	1.882
5	0.03194	196.720	31.309
7	0.0246	255.201	40.616
9	0.019682	319.229	50.806
11	0.0143	438.210	69.743
13	0.0112	556.781	88.614

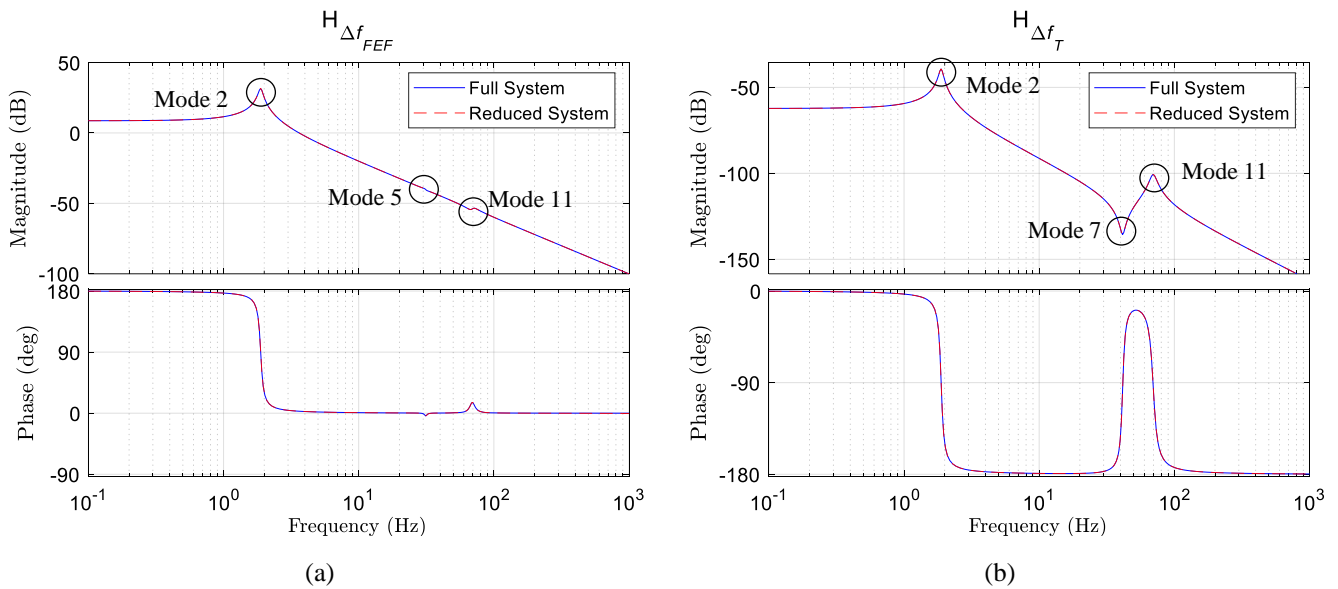


Figure 4. Bode plots depicting frequency response of NS for a) $H_{\Delta f_{FEF}}$ and b) $H_{\Delta f_T}$

3.2 TS modelling

Accuracy of the RTHFS depends on how closely the tuned actuator resembles the NS response. For this purpose, it is necessary to understand the internal dynamics of the actuator (such as oil column frequency and damping, etc.) and develop a robust mathematical model of the TS to assemble transfer functions based on the internal physics of the actuator, especially within the range of concerned structural resonant frequencies. Especially important to this study is the response of TS when the physical specimen buckles (i.e., a fast process compared to temperature effects during fire). To capture this fast process in real-time, a high-speed servo-controlled actuator teamed with a three-stage electro-hydraulic servovalve is considered. This section briefly discusses the mathematical modelling of this servo-hydraulic system.

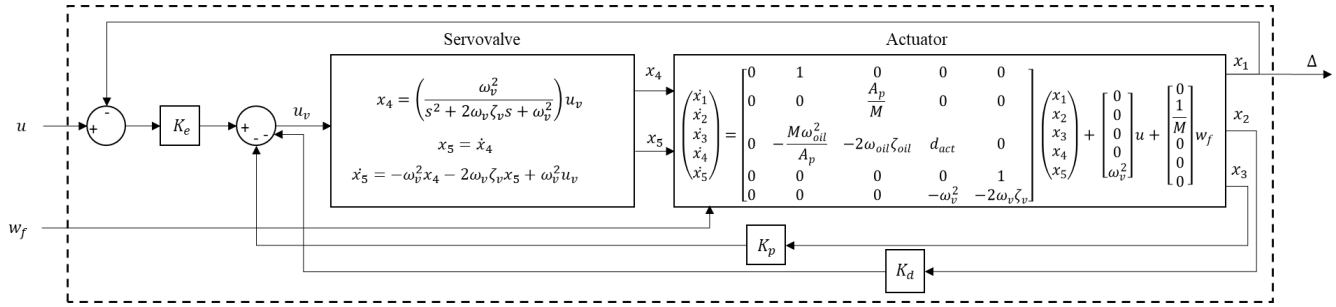


Figure 5. Block diagram representation of linearized TS model

Consider the block diagram presented in Figure 5. Here, the state variables x_1 and x_2 are the displacement and velocity of the actuator piston respectively, and x_3 represents the pressure difference ΔP between the two main chambers of the actuator (which regulates the flow and direction of hydraulic fluid entering the actuator from pressurized orifices, and is the main principle that allows for such high-flow, high-response tests). A hydraulic controller employs a proportional-integral-derivative (PID) control algorithm in closed-loop displacement mode, and with it the command to the controller, u leads to the following feedback:

$$u_v = K_e(u - x_1) - K_d x_2 - K_p x_3 \quad (17)$$

where u_v is input to the servovalve in the form of electric current, and;
 K_e, K_d, K_p are the proportional, derivative and differential pressure gains for the hydraulic controller.

In the case of this benchmark study, an exogenous input in the form of NS dead load also exists, and is here represented as w_f . On the other hand, exact properties of the three stage servovalve are difficult to obtain, and therefore, for the purpose of this research, it is modelled as a generic second-order system as:

$$x_v = \left(\frac{\omega_v^2}{s^2 + 2\omega_v\zeta_v s + \omega_v^2} \right) u_v \quad (18)$$

$$\dot{x}_4 = x_5 \quad (19)$$

$$\dot{x}_5 = -\omega_v^2 x_4 - 2\omega_v\zeta_v x_5 + \omega_v^2 u_v \quad (20)$$

where x_v is the position of the 3rd stage spool, and is also equal to the state variable x_4 , and;
 ω_v, ζ_v are the servovalve dynamics signifying the cutoff frequency and damping inherent to the servovalve, and;
 x_5 is the first derivative of x_v .

Using the equation of motion, flow equations, and continuity equations, as well as the block diagram presented in Figure 5, a linearized analytical model of the actuator and servovalve is identified as:

$$\begin{pmatrix} \dot{x}_1 \\ \dot{x}_2 \\ \dot{x}_3 \\ \dot{x}_4 \\ \dot{x}_5 \end{pmatrix} = \begin{bmatrix} 0 & 1 & 0 & 0 & 0 \\ 0 & 0 & \frac{A_p}{M} & 0 & 0 \\ 0 & -\frac{M\omega_{oil}^2}{A_p} & -2\omega_{oil}\zeta_{oil} & d_{act} & 0 \\ 0 & 0 & 0 & 0 & 1 \\ -K_e\omega_v^2 & -K_d\omega_v^2 & -K_p\omega_v^2 & -\omega_v^2 & -2\omega_v\zeta_v \end{bmatrix} \begin{pmatrix} x_1 \\ x_2 \\ x_3 \\ x_4 \\ x_5 \end{pmatrix} + \begin{bmatrix} 0 \\ 0 \\ 0 \\ 0 \\ K_e\omega_v^2 \end{bmatrix} u + \begin{bmatrix} 0 \\ \frac{1}{M} \\ 0 \\ 0 \\ 0 \end{bmatrix} w_f \quad (21)$$

where A_p is the area of actuator piston,
 M is the moving mass of the actuator,
 d_{act} is a coefficient associated with the bulk modulus of oil, area of the piston and other physical properties of the actuator [6], and;
 $\omega_{oil}, \zeta_{oil}$ are the oil column frequency and damping of the actuator.

Using equations 17 – 21, the TS transfer functions $H_{\Delta u}$ and $H_{\Delta f}$ introduced in Section 2 can be calculated from the control input u , and the applied static dead load, f , to the actuator displacement, $x_1 = \Delta$.

3.3 Parametric identification for the servo-hydraulic TS system

For this research, an MTS 244.31 series actuator is considered; which is a high-speed, servo-controlled model with an effective piston area, A_p equal to 19.6 in² (12650 mm²) and total static stroke equal to 12 in (304.8 mm). The nominal force capacity of this actuator is 55 kips (250 kN), and it is fitted with an MTS 256.09 series three-stage electro-hydraulic servovalve having a rated flow of 90 gpm in order to achieve a peak velocity of 90 [gpm] \times 3.85 [in³/s/gpm] / A_p [in²] = 17 in/s (431.8 mm/s). Once the mathematical model is ready; values of mass, oil column dynamics, valve dynamics, and gain coefficients are experimentally calibrated. A full list of TS properties based on this parametric identification is presented in Table 2.

Table 2. Parameters to be used for linearized TS model

Parameters	Value
Mass, M	1.52 lb s ² /in (587.5 lb or 266 kg)
Actuator piston area, A_p	19.6 in ² (12650 mm ²)
Oil column frequency, ω_{oil}	104.3 Hz
Oil column damping, ζ_{oil}	0.16
Input coefficient, d_{act}	14 \times 10 ⁴ psi/s/V (965 MPa/s/V)
Servovalve cutoff frequency, ω_v	30 Hz
Servovalve damping, ζ_v	0.78

The identified model is then compared with experimentally obtained frequency response transfer function for the TS from displacement command to the displacement response. Figure 6 shows one such comparison (in good agreement), where a Bode plot maps the experimentally obtained transfer function $H_{\Delta u}$ versus one obtained from the linearized analytical model. It is noted that in the absence of significant moving mass within the TS (as is in the case of large shake tables used in the field of earthquake engineering), the dynamic properties of the three-stage servovalve largely dominate the overall actuator dynamics (i.e., the peak magnitude of the experimental frequency response plot in Figure 6 shows a resonant frequency close to 30 Hz instead of expected oil column resonant frequency at \approx 100 Hz, indicating more influence of servovalve).

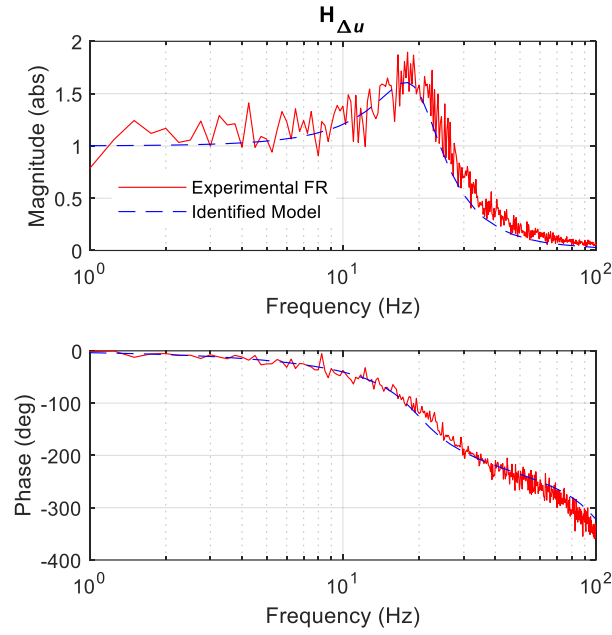


Figure 6. Bode plots depicting experimental frequency response for the TS transfer function $\mathbf{H}_{\Delta u}$ (when running multi-sine displacement containing content up to 100 Hz with max. amplitude = 0.2 in) versus identified parametric model

3.4 Controller model

The new control strategy explained in Section 2 is now applied to the benchmark problem. Figure 7 presents a decoupled control design for this benchmark problem. Building on equations 1 – 5, the addition of a concurrent exogenous input from the static dead load changes the control equations previously discussed:

$$\Delta^{NS} = H_{\Delta f_T}^{NS} \cdot f_T + H_{\Delta f_{FEF}}^{NS} \cdot f_{FEF} \quad (22)$$

$$\Delta^{TS} = (H_{\Delta f_T} + H_{uf_T} \cdot H_{\Delta u}) f_T + (H_{uw_f} \cdot H_{\Delta u}) w_f \quad (23)$$

The control input for this setup is:

$$u = H_{uf_T} \cdot f_T + H_{uw_f} \cdot w_f \quad (24)$$

If, $w_f = f_{FEF}$, then the decoupled control strategy model becomes:

$$H_{uf_T} = H_{\Delta u}^{-1} (H_{\Delta f_T}^{NS} - H_{\Delta f_T}) \quad (25)$$

$$H_{uf_{FEF}} = H_{\Delta u}^{-1} (H_{\Delta f_{FEF}}^{NS}) \quad (26)$$

To be able to apply the developed model to the RTHFS experiment, it is necessary that H_{uf_T} and $H_{uf_{FEF}}$ are stable, and causal, requiring that the order of the polynomial in the numerator of each of these transfer functions be less than or equal to the order of the denominator polynomial (i.e., the transfer functions are *proper*). Using the NS transfer functions obtained in Section 3.1 and TS parameters discussed in Section 3.2 and taking state-space matrices \bar{A} , \bar{B}_u , and \bar{B}_w from equation 21 and $\bar{C} = [1 \ 0 \ 0 \ 0 \ 0]$, equations 25 and 26 are calculated. Figure 8 shows the Bode frequency magnitude and phase angle plots obtained from the tuned actuator model using these controller model transfer functions. It can be seen that the tuned actuator model (TS+C) mimics the NS mode at 1.88 Hz (or 11.8 rad/s) exactly. This is the first mode engaging vertically (as presented in Table 1), which implies that the TS response can be expected to match the NS response quite well within the expected frequency range.

[6] presented a robust controller using simple inversion and applied the new strategy to RTHS for soil-structure interaction testing. A detailed examination was conducted on the influence of actuator properties,

NS dynamics, and any nonlinearities incurred in the TS model, and it was shown that the presented controller was stable and accurate for dynamic substructuring.

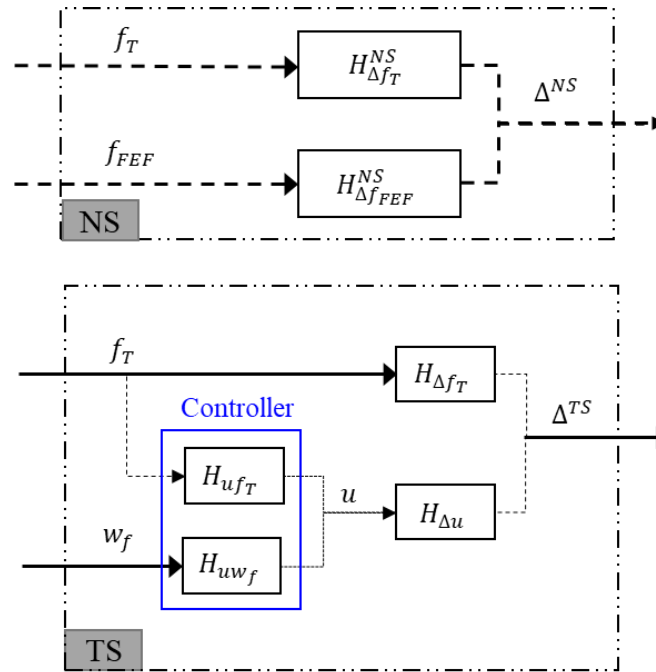


Figure 7. Block diagram of proposed RTHFS strategy applied to benchmark problem

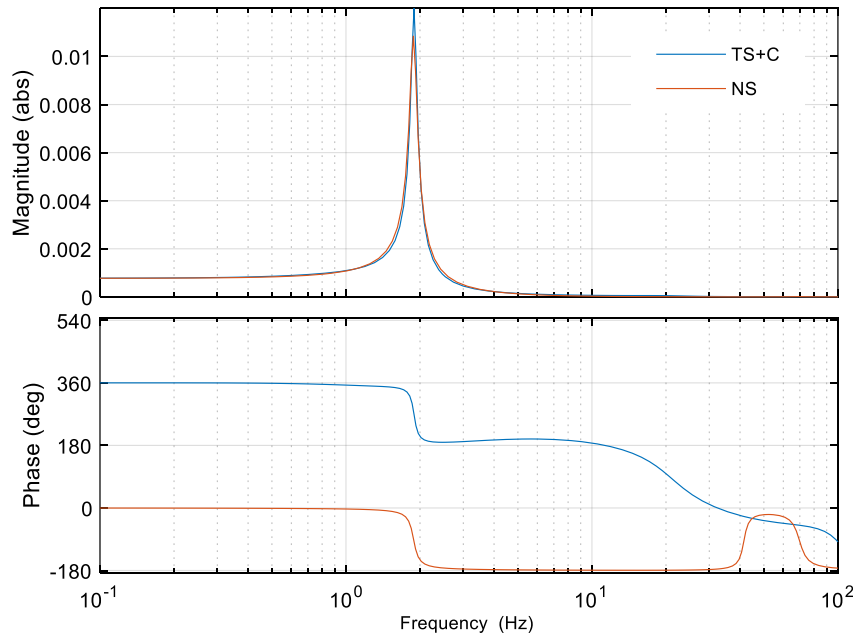


Figure 8. Bode plots depicting frequency response comparison between tuned actuator model (TS+C) and NS model

4 EXPECTED BENEFITS OF THE PROPOSED FRAMEWORK

Figure 10 plots the displacement time history for the vertical movement of the interface node between the PS and NS (as shown in Figure 3) under simulated dead load followed by the PS response to the thermal load due to the fire scenario presented in [9]. The steel column under study (the PS) is subjected to increasing temperatures until failure occurs in the form of column buckling. The abrupt numerical application of dead load causes the interface node to undergo some oscillation at the beginning (capturing

the inherent dynamics of the NS). This is presented in the zoomed-in graph in Figure 10b. In a lab application of this framework, this issue can be resolved by applying dead load using a ramp loading protocol. Aside from that, it can be seen from Figure 10 that the tuned actuator model (TS+C) follows the NS displacements very closely for the duration of fire. Simulation results presented in this figure also indicate that this strategy holds the potential to capture the dynamic response under sudden buckling of the PS (at approximately 50 minutes) quite well, as the tuned actuator model follows the NS at the time that the PS fails. Note that the buckling of steel column does not cause the frame to collapse but to experience large deflections at the interface node. The proper tuning of the actuator model in the proposed framework and its application to the benchmark study confirms a robust controller that eliminates the need for error compensator and specialized numerical schemes.

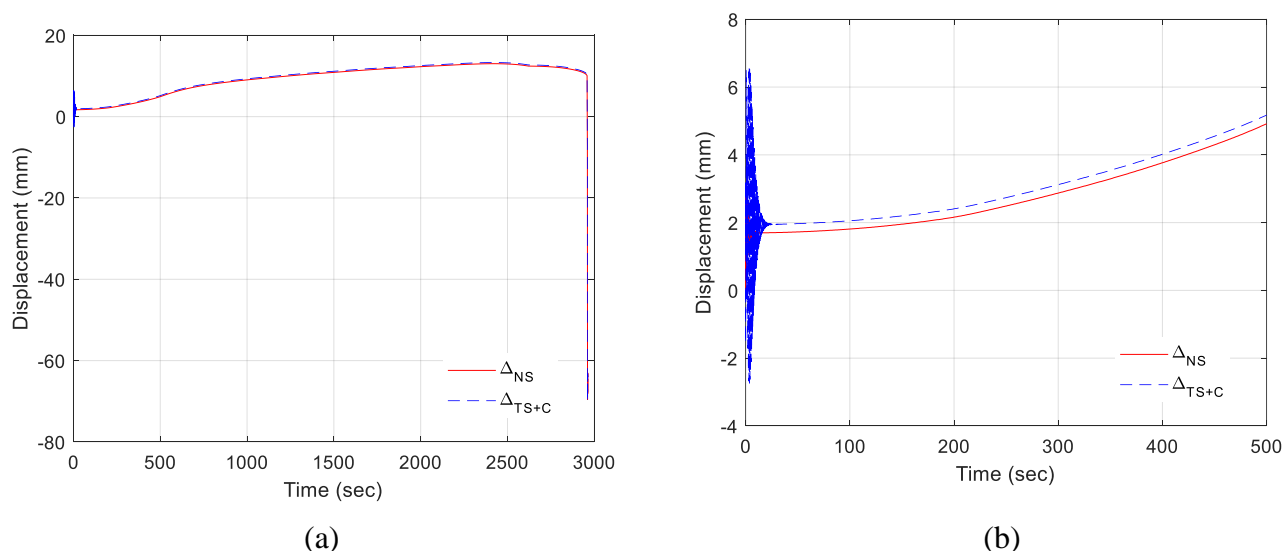


Figure 10. a) Displacement history at interface node from tuned actuator model (TS+C) plotted versus that from NS model when subjected to loading protocol from [9], b) Zoomed in view captures oscillation due to abrupt dead load application

5 CONCLUSIONS

The application of hybrid simulation in the field of structural fire engineering has gained momentum in recent years. Large scale fire testing of structures is expensive and requires special facilities. Meanwhile, the well-established element level fire tests do not capture the interaction of the structural component being tested with the rest of the structure and thus cannot be used to study the real behaviour of a structure under fire. In real-time hybrid fire simulation, the behaviour of an element in the physical test is observed and monitored while servo-hydraulic actuators apply loading and interfacing boundary condition in real-time by receiving feedback from a numerical model of the rest of the structure. This approach can provide realistic failure modes by considering the behaviour of the surrounding structure throughout the duration of a fire event, is a cost-effective alternative to full-scale testing of structures and is in line with advancing performance-based fire engineering. Recent experiments presented in the literature show that constantly increasing furnace temperatures and the resulting degradation in stiffness of the physical substructure under high temperatures can introduce errors in equilibrium and compatibility at the interface between physical and numerical substructures.

This paper presents a control strategy for real-time hybrid fire simulation that decouples the physical substructure response from the control design. A transfer system (consisting of a servo-hydraulic actuator and a controller) is designed to mimic the behaviour of the numerical substructure independent of the physical substructure. In doing so, a control input is added to the transfer system to tune the internal dynamics of the actuator and adjust the output work conjugate to match the corresponding numerical substructure behaviour. The mathematical formulation for the behaviour of the numerical substructure, parametric identification of a servo-hydraulic actuator, and their integration to arrive at a controller model are presented for an example case of a steel frame with one column under fire. It is shown that the

formulation for the transfer system and the control input results in a displacement history that matches the expected response from the numerical substructure when the response of the physical substructure is used as an input. The next step of this research will test the developed control strategy in the laboratory to capture the failure mode of a steel column under fire as part of a frame system.

ACKNOWLEDGMENT

The first author acknowledges the guidance and direction provided by Dr. Mohit Verma, Senior Scientist, CSIR- Structural Engineering Research Centre, Chennai, India. The authors acknowledge the help and support provided by the staff at the Structural Engineering and Earthquake Simulation Laboratory (SEESL) at the University at Buffalo.

REFERENCES

1. Dyke, S., Spencer Jr, B., Quast, P., and Sain, M. (1995). "Role of control-structure interaction in protective system design." *Journal of Engineering Mechanics*, 121(2), 322-338
2. Whyte, C. A., Mackie, K. R., and Stojadinovic, B. (2015). "Hybrid simulation of thermomechanical structural response." *Journal of Structural Engineering*, 142(2), 04015107
3. Sauca, A., Gernay, T., Robert, F., Tondini, N., and Franssen, J.-M. (2018). "Hybrid fire testing: Discussion on stability and implementation of a new method in a virtual environment." *Journal of Structural Fire Engineering*, 9(4), 319-341
4. Wang, X., Kim, R. E., Kwon, O.-S., and Yeo, I. (2018). "Hybrid Simulation Method for a Structure Subjected to Fire and Its Application to a Steel Frame." *Journal of Structural Engineering*, 144(8), 04018118
5. Schulthess, P. (2019). "Consolidated Fire Analysis-Coupled Numerical Simulation and Physical Testing for Global Structural Fire Analysis." ETH Zurich
6. Stefanaki, A. (2017). "A simple strategy for dynamic substructuring and its application to soil-foundation-structure interaction." State University of New York at Buffalo.
7. Stefanaki, A., and Sivaselvan, M. (2018). "A simple strategy for dynamic substructuring: I. Concept and development." *Earthquake Engineering & Structural Dynamics*, 47(9), 1801-1822
8. Verma, M., Sivaselvan, M., and Rajasankar, J. (2019). "Impedance matching for dynamic substructuring." *Structural Control and Health Monitoring*, 26(11), e2402
9. Jiang, B., Li, G.-Q., Li, L., and Izzuddin, B. (2017). "Experimental studies on progressive collapse resistance of steel moment frames under localized furnace loading." *Journal of Structural Engineering*, 144(2), 04017190
10. Qureshi, R., Elhami-Khorasani, N. and Gernay, T. (2019), "Adaption of active boundary conditions in structural fire testing", *Journal of Structural Fire Engineering*, Vol. 10 No. 4, pp. 504-528. <https://doi.org/10.1108/JSFE-12-2018-0042>

THERMAL RESPONSE AND CAPACITY OF BEAM END SHEAR CONNECTIONS DURING A LARGE COMPARTMENT FIRE EXPERIMENT

Xu Dai^{1,*}, Lisa Choe², Erica Fischer³, Charles Clifton⁴

ABSTRACT

The role of steel connections is essential in structural fire design and analysis for steel-framed composite structures. The current structural design provisions provide strength reduction factors of load-carrying members and their end-connection elements (e.g. bolts) at elevated temperatures, based on small-scale experiments under uniform heating conditions. The realistic temperature evolution in member connections, especially as part of full-scale floor assemblies exposed to a large compartment fire, has not been well characterized. A large compartment fire experiment was recently conducted on a 9.1 m by 6.1 m composite floor assembly as part of a two-story steel framed building. The test assembly had a total of ten shear-tab (fin-plate) connections subjected to combined fire and mechanical loading. This paper presents the measured thermal response of these connections in comparison with the corresponding Eurocode 3 predictions with two methods (1) incorporating the beam bottom flange temperature at midspan and (2) the section factor method. The results show that the Eurocode 3 methods conservatively predict the maximum temperature during heating and the cooling rate but overestimate the high-temperature strength of connections while using the section factor method. The predicted thermal responses are highly influenced by the fire protection sprayed on the connection region which was actually at least 43% thicker than the protection on the beams used in this test program. However, partial shear failure of bolts was witnessed in the test. This suggests that designing connections solely through temperature provisions may not guarantee a safe structural fire design. The axial load demand of the shear connection due to restraints to thermal elongation or contraction should be considered in future design guidance.

Keywords: Connections; fire test; Eurocodes; temperatures; capacity; shear tab

1 INTRODUCTION

In fire safety design of buildings, the structure is required to meet the desired performance objectives. At a minimum these include maintaining structural integrity such that compartmentalization is not compromised [1]. However, the accurate quantification of fire severity in a structure has been challenging due to lack of design tools validated against experimental data. Particularly, the thermal response of composite beam connections to a large compartment fire is one of such examples [2-4]. Currently in Eurocode 3 [5] and other similar provisions used in many other countries including the United States, the thermal gradient of the beam end connections is estimated using the empirical equations based upon the bottom flange temperature of composite floor beams. However, the bottom flange beam temperature utilized in these

¹ Foreign Guest Researcher, National Institute of Standards and Technology (NIST)
e-mail: xu.dai@nist.gov, *corresponding author, ORCID: <https://orcid.org/0000-0002-9617-7681>

² Research Structural Engineer, National Institute of Standards and Technology (NIST)
e-mail: lisa.choe@nist.gov, ORCID: <https://orcid.org/0000-0003-1951-2746>

³ Assistant Professor, Oregon State University
e-mail: erica.fischer@oregonstate.edu, ORCID: <https://orcid.org/0000-0002-7653-2068>

⁴ Associate Professor, University of Auckland
e-mail: c.clifton@auckland.ac.nz, ORCID: <https://orcid.org/0000-0003-0723-1699>

methods are assumed to be remote from the connection. The thermal gradient across the beam-end connections is then used to calculate the connection capacity incorporating strength reduction factors for bolts and welds. The reliability of those Eurocode 3 predictions is unknown especially for the fire-protected connections and full-scale typical beam sizes and spans within a large compartment fire [6, 7] due to lack of such experimental temperature data. Furthermore, even if the thermal response of the steel connection components was within the range predicted by Eurocode 3 methods, to what extent this will ensure a robust structural fire design is also uncertain, based on the lack of supporting experimental data and analysis.

The work presented in this paper aims to: (1) enrich the experimental data library for thermal and structural response of the shear-tab (fin-plate) connections with fire protection subjected to a full-scale large compartment fire; (2) examine the Eurocode 3 connection design (temperature and strength) utilizing experimental data [8] with a large compartment fire; and (3) identify gaps in knowledge or data for structural design of shear connections under fire conditions.

2 FIRE TEST

2.1 The test building and fire compartment

A two-story steel frame with composite floors has three by two bays in plan ($18\text{ m} \times 11\text{ m}$) with a total building height of 7.2 m , and the fire was in a large compartment at the south-central bay having dimensions of $9.1\text{ m} \times 6.1\text{ m}$ with a 3.8 m ceiling height (Figure 1). The composite floor assemblies were designed to resist an ambient design gravity load of 8.6 kPa . The test floor assembly was subjected to a floor load of 5.3 kPa following the ASCE 7 [9] load combination for extraordinary events ($1.2 \times \text{dead load} + 0.5 \times \text{live load}$).



Figure 1. NIST large compartment fire experiment [8] on a steel-composite building. (a). Photo taken during the experiment; (b). Plan view of the test building and test bay location; and (c). Plan view of composite connection instrumentation locations in the experimental compartment, ten in total, from connection 1-10 (abbrev. as C1-C10).

For passive fire protection of exposed steel members, a medium density (ranging from 240 kg/m³ to 350 kg/m³ [10]) gypsum-based cementitious material, was sprayed on beams and connections exposed to fire. The design thickness of insulation on both south and north primary W16×31 beams, as well as on the west and east primary W18×35 beams inside the fire test compartment was 17.5 mm (11/16 inch) determined using the Underwriter Laboratory (UL) directory N791 [11] for the 2-hour restrained beam rating. Insulation thickness of the secondary W16×31 beam was 13 mm (7/16 inch), slightly thinner than the primary beams, determined using UL D949 [12] for the 2-hour restrained assembly rating. The exposed connection regions and columns were over sprayed with the same insulation material with the thickness of 25 mm or greater, i.e. 43% thicker than the primary beams, to ensure the 3-hour rating of columns.

2.2 The connections and relevant instrumentations

Two types of simple shear connections were used in this test program: standard shear tabs for the beam-to-column flange and beam-to-beam web connections; extended shear tabs for the beam-to-column web connections. All shear tabs were 9.5 mm in thickness and made of ASTM A36 [13] steel (the minimum yield stress of 245 MPa). The size of fillet welds was 6.3 mm. All structural bolts (Gr. A325 specified in the ASTM F3125 [14]) had a diameter of 19 mm. The dimensions of the short-slot holes (21 mm in width and 25 mm in length) drilled on the shear tabs conform to the AISC 360 specification [1]. Examples of the connections and mounted thermocouples⁵ are demonstrated in Figures 2(a) and 2(b).

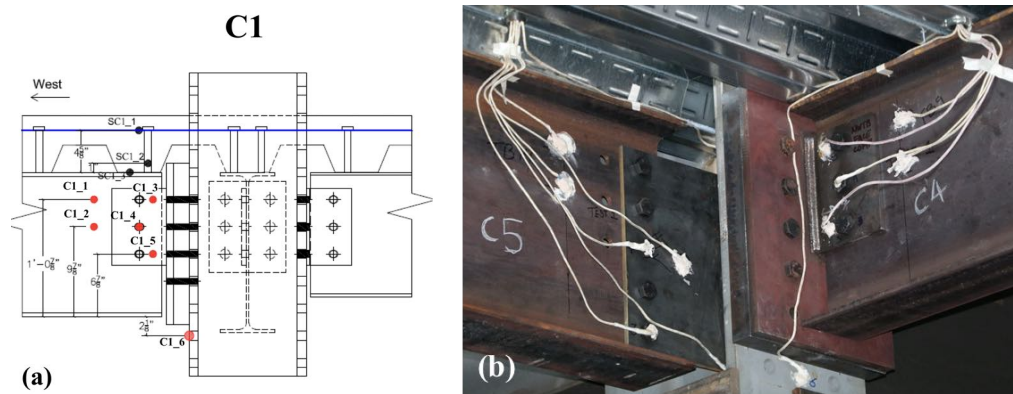


Figure 2. (a). Thermocouple instrumentation locations at connection C1, tagged as C1_1 to C1_6; and (b). Thermocouple instrumentation locations at connection C4 (standard shear tab) and connection C5 (extended shear tab), prior to SFRM installation.

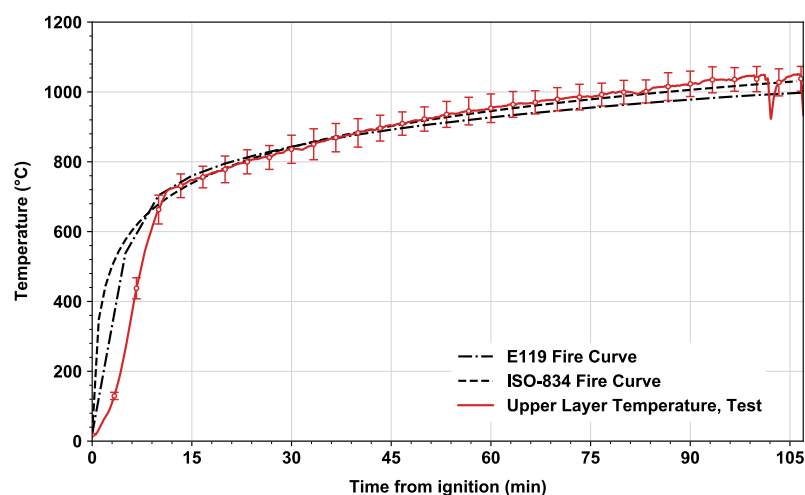


Figure 3. A comparison between measured⁶ upper layer gas temperature within the test compartment, and standard fire curves (i.e. the ASTM E119 fire curve, and the ISO-834 fire curve)

⁵ An expanded uncertainty of thermocouple locations is estimated to be ± 6 mm with a coverage factor of 2 (95% confidence interval)

⁶ An expanded uncertainty of measured gas temperatures is estimated to be $\pm 8\%$ at 1100 °C with a coverage factor of 2

2.3 Mechanical and fire loading

The vertical shear load imposed on the connections was in the range of 0.2 to 0.4 of their ambient design capacities during the fire experiment. The fire load (or exposure) was applied using natural gas burners [15-17] following the ASTM E119 temperature-time curve [18] lasting 107 mins equivalent to 921 MJ/m^2 with $\pm 1.5 \text{ MJ/m}^2$ uncertainty (95 % confidence interval) as the applied fire load density. At 107 min the heat release rate reached to its maximum value of 10.8 MW. As demonstrated in Figure 3, the test revealed that the measured time-temperature curve matched better with the ISO Standard Fire curve [19] (which is more severe than the ASTM E119 curve) after 45 mins. The maximum standard deviation of the upper layer gas temperature was around 70°C throughout the heating regime. This standard fire environment was to ensure that the whole structural assembly was being challenged to a severe fire impact and for the research interest of steel connections. This impact included a large compressive force induced by the restraint to thermal expansion during the heating phase, a tensile force due to catenary action during heating, and a tensile force by the restraint to thermal contraction during cooling.

2.4 Gas temperature and steel temperatures

An example of the temperature comparison is presented in Figure 4, including upper layer gas temperature and temperatures of the west primary beam bottom flange (average of thermocouple TBi_5 and TBi_6) and connection C5. This comparison considers seven hours of testing duration including the natural cooling phase. After the burner was switched off at 107 min, the upper layer gas temperature decreased sharply from 1040°C to 490°C within approximately 10 mins into cooling. This drastic temperature decrease would likely induce large tension forces on the connections, due to the restraint to thermal contraction of the steel beam during the cooling stage.

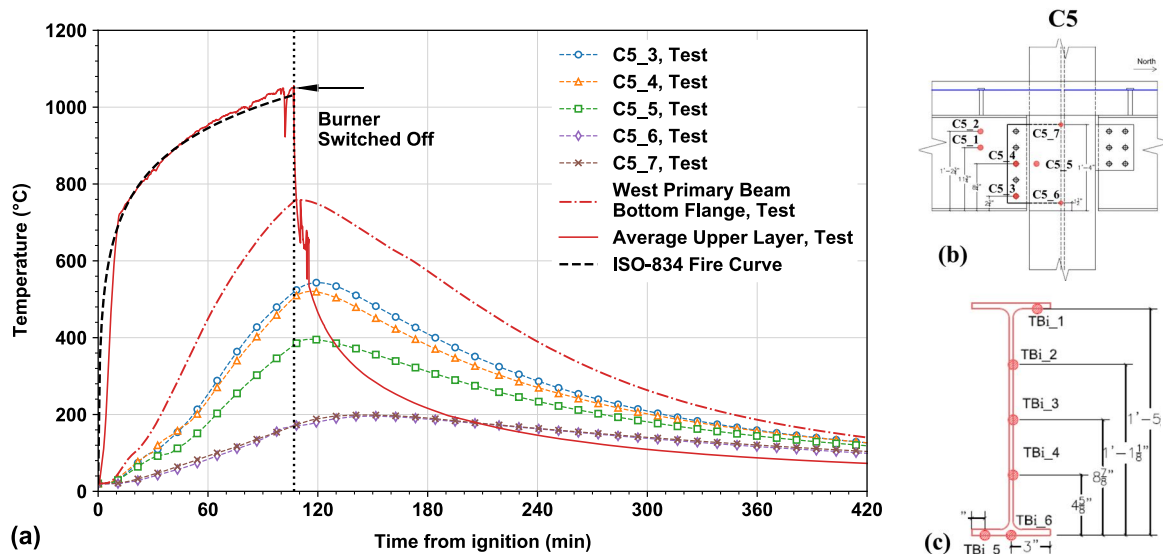


Figure 4. (a). Comparison of the time temperature curves for the compartment upper layer gas, west primary beam bottom flange, and steel connection⁷ C5; (b). Thermocouple instrumentation locations at connection C5, tagged as C5_1 to C5_7; and (c). Thermocouple instrumentation locations at west primary beam midspan, tagged as TBi_1 to TBi_6.

The bottom flange temperature of the west primary beam reached its measured maximum value of 760°C and cooled off gradually due to the presence of the fire protection. The connection temperatures followed a similar tendency but with relatively lower maximum values (e.g. 540°C at C5_3) and a time delay to their peaks, provided that thicker SFRM was applied. The test showed that C5_3 and C5_4 (bolts) indicated higher component temperatures, compared to the measured temperatures at C5_6 and C5_7 (welds). This is believed to be because C5_6 and C5_7 were affected by the thermal shadow effect or the heat conduction loss to the connected column at this region. Those relative relationships of temperatures were further evaluated using Eurocode 3 methods, as detailed in the subsequent section.

⁷ An expanded uncertainty of measured steel temperatures is estimated to be $\pm 4\%$ at 970°C with a coverage factor of 2

3 CONNECTION TEMPERATURES

3.1 Eurocode 3 method

According to the Eurocode 3, for beam-to-beam and beam-to-column connections where concrete floors are atop the beams, temperatures of the connections can be estimated based upon the bottom flange temperature of the connected steel beam at midspan. Considering the depths of the steel members used in the experiment (i.e. W16×31 and W18×35), are both greater than 400 mm, hence two equations are used:

when h is less or equal than $D/2$:

$$\theta_h = 0.88\theta_o \quad (1)$$

when h is greater than $D/2$:

$$\theta_h = 0.88\theta_o [1 + 0.2(1-2h/D)] \quad (2)$$

where θ_h is the temperature at height h (mm) of the steel beam, see Figure 5;

θ_o is the bottom flange temperature of the steel beam remote from the connection;

h is the height of the component being considered above the bottom of the beam in (mm);

D is the depth of the beam in (mm).

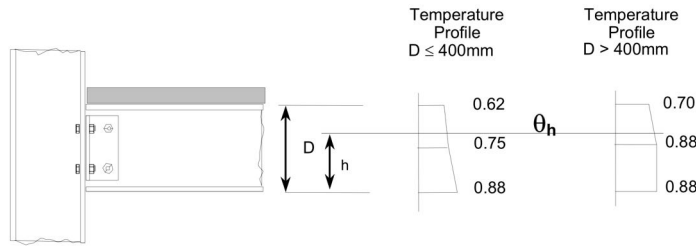


Figure 5. Thermal gradient within the depth of a composite connection (figure adapted from Eurocode 3 [5]).

If the gas temperature is known, the Eurocode 3 step-by-step section factor method can be used to estimate the steel beam bottom flange temperature θ_o as follows:

$$\Delta\theta_{a,t} = \frac{\lambda_p A_p/V(\theta_{g,t} - \theta_{a,t})}{d_p c_p \rho_a (1 + \phi/3)} \Delta t - (e^{\phi/10} - 1) \Delta\theta_{g,t} \quad (3)$$

$$\phi = \frac{c_p \rho_p}{c_a \rho_a} d_p A_p/V \quad (4)$$

where A_p/V is the section factor for steel members insulated by fire protection material in (m^{-1});

c_a is the temperature dependant specific heat of steel in (J/kgK);

c_p is the temperature independent specific heat of the fire protection material in (J/kgK);

d_p is the thickness of the fire protection material in (m);

λ_p is the thermal conductivity of the fire protection in (W/mK);

ρ_a is the unit mass of steel in (kg/m^3);

ρ_p is the unit mass of the fire protection in (kg/m^3);

$\theta_{a,t}$ is the steel temperature at time t in ($^{\circ}C$);

$\theta_{g,t}$ is the ambient gas temperature at time t in ($^{\circ}C$);

Δt is the time interval in (seconds);

As detailed above, theoretically two analytical methods can be used to estimate temperatures of connection components: if the steel beam bottom flange temperature at midspan is known, then equations (1) and (2) can be employed directly; if the gas temperature within the compartment is known, then equation (3) can be used to estimate the steel beam temperature which is a main variable of equations (1) and (2). The following section will examine those two methods, utilizing the experimental data to evaluate the applicability of the Eurocode 3 provisions.

3.2 Comparison between the measurements and Eurocode 3 predictions - method 1

Following the Eurocode 3 convention, see Figure 5, dimensionless thermal gradients of all the test connections are summarized in Figure 6. These gradients were estimated when the connected structural beam members reached to their maximum deflections, at around 107 min. At this time, as summarized in Table 1, temperatures of the end connections of the secondary and primary W16×31 beams were in excess of 500 °C, whereas the end connections of the primary W18×35 beams were heated below 400 °C. The temperature discrepancy between the primary and secondary beam-end connections is mainly due to the difference in applied SFRM thickness, see Table 1. As shown in Figure 5, for components of the standard shear tabs connecting W16×31 beams, the dimensionless experimental temperatures vary from 0.35 to 0.7, less than the values calculated using the Eurocode 3 (0.7 to 0.88). For those of the extended shear tabs at the ends of W18×35 beams, moreover, the measured dimensionless temperatures range from 0.5 to 0.86, which remain below 0.88 calculated using equations (1) and (2). This comparison demonstrates that the Eurocode 3 provisions, estimating temperatures of the standard shear tabs as a function of the beam bottom flange temperatures at midspan, are conservative. It is also anticipated that under a natural fire (rather than in a standard fire), the temperature difference between the connections and the beam flange at midspan is greater. If a natural fire is fuelled by array of wood cribs, e.g. [3], the upper layer gas temperature is expected to be less uniform and highly influenced by other factors (e.g. distribution of fuel, ventilation, wood properties) when compared with the conditions in which the test fire is controlled by natural gas burners.

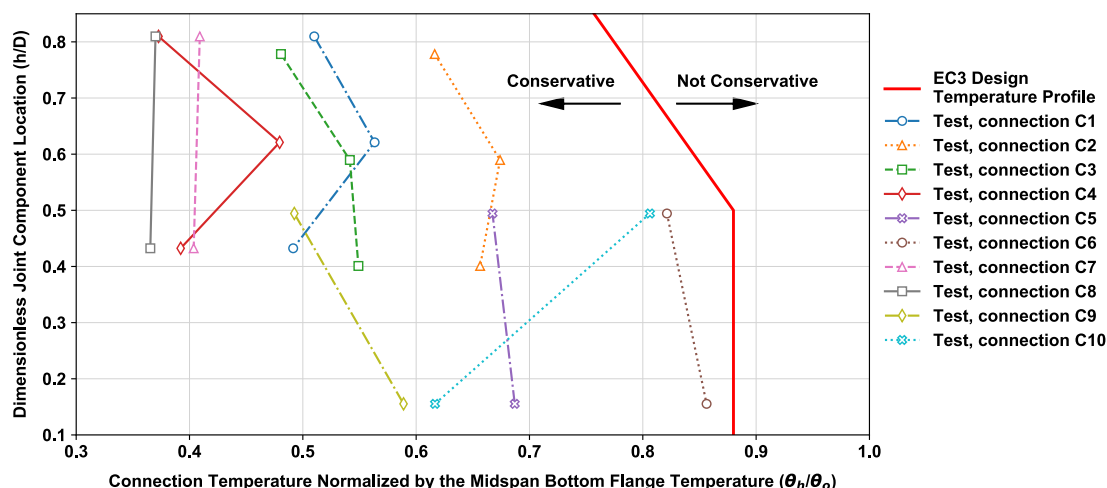


Figure 6. Thermal gradient within the depth of the composite connections, test vs. Eurocode 3

Table 1. Summary of the connections: connected members, types, SFRM thickness (\pm represented as standard deviation), and measured max component temperature.

Connection Tag	C1	C2	C3	C4	C5	C6	C7	C8	C9	C10
Connected Members	primary beam - column flange	secondary beam - primary beam	secondary beam - primary beam	primary beam - column flange	primary beam - column web	primary beam - column web	primary beam - column flange	primary beam - column flange	primary beam - column web	primary beam - column web
Member Dimension	W16×31	W16×31	W16×31	W16×31	W18×35	W18×35	W16×31	W16×31	W18×35	W18×35
Shear Tab Type	Standard	Standard	Standard	Standard	Extended	Extended	Standard	Standard	Extended	Extended
Fire Protection Thickness (mm)	28 ± 2	31 ± 3	29 ± 3	26 ± 2	27 ± 3	25 ± 1	29 ± 6	28 ± 4	24 ± 3	25 ± 2
Maximum Temperature (°C)	400	660	570	380	530	590	300	310	500	580

3.3 Comparison between the measurements and Eurocode 3 predictions - method 2

An example of comparison between the measured and predicted temperatures based upon the step-by-step section factor method (method 2) is presented in Figure 7. In this example, the connection components C1_4 and C4_4 were situated at the diagonal locations of the test compartment.

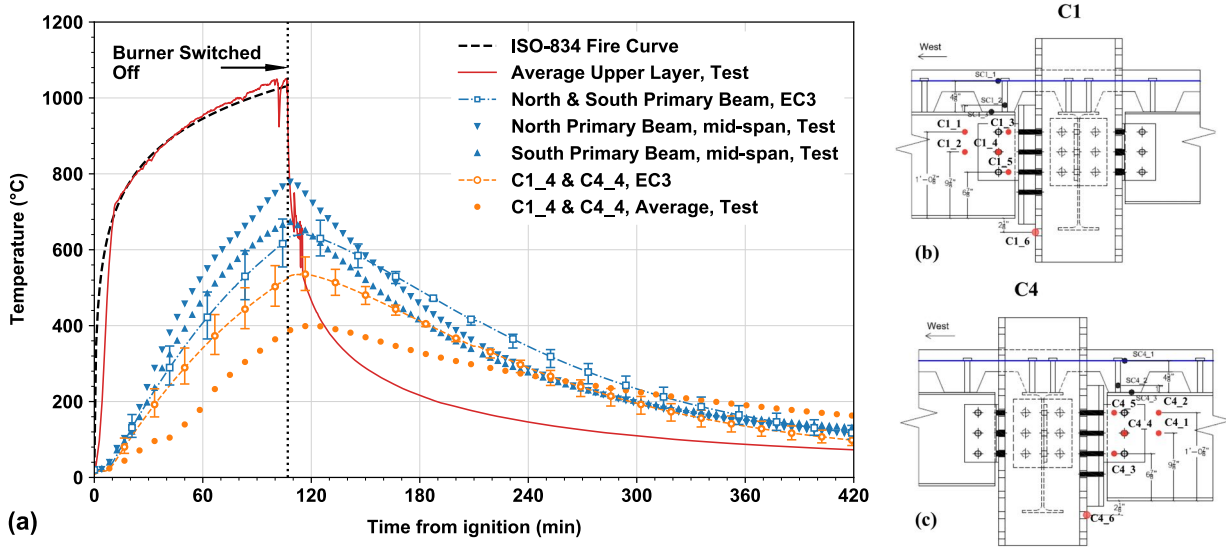


Figure 7. (a). Comparison between predicted temperatures with the measured temperatures: north and south primary beams at midspan, and steel bolt temperatures at same height C1_4 & C4_4; (b). Thermocouple instrumentation locations at connection C1, tagged as C1_1 to C1_6; and (c). Thermocouple instrumentation locations at connection C4, tagged as C4_1 to C4_6.

The measured upper layer gas temperature, $\theta_{g,t}$, is used as the input variable of equation (3) with a 5 s time interval for calculation. Note that the measured gas temperature during the heating phase of the experiment, closely matching with the ISO-834 standard fire curve, provides a good benchmark to examine the applicability of Eurocode 3 since standard fire curves (e.g. the ISO-834 fire curve) are a common fire situation considered for design. In addition, this study utilized the steel member density ρ_a of 7850 kg/m³, and the temperature-dependent specific heat of the steel c_a according to Eurocode 3. The section factor of the W16×31 shape, A_p/V , was taken to be equal to 203 m⁻¹ with a three-sided fire exposure. The SFRM thermal conductivity λ_p is 0.086 W/mK [20], and its specific heat c_p is assumed to be 1200 J/kgK [21]. There are also two SFRM-related parameters used for estimating uncertainties, including the unit mass, ρ_p , ranging from 240 kg/m³ to 350 kg/m³; and the applied thickness d_p . The measured value of d_p was 18 mm on average for the north primary beam, with 3 mm standard deviation and was 19 mm for the south primary beam with 2 mm standard deviation. The average temperatures of the north and south primary beams reached a maximum value of 780 °C and 670 °C, respectively, approximately 2 mins after the fire was extinguished (i.e., at 109 min). The Eurocode 3 prediction, incorporating the step-by-step method, on these primary beams suggests a maximum value ranging from⁸ 580 °C to 690 °C at 115 min. The steel beam temperature predicted using the same method (equation (3)) appears to be lower than the corresponding values of measured temperatures, and yet the connection temperatures of the components C1_4 and C4_4 are conservative when calculated using equations (1) and (2). The predicted maximum temperature of those two connection components is approximately 540 °C, i.e. higher than their measured value of 400 °C on average.

The step-by-step section factor method using equation (3) is a preliminary step for calculating the steel connection component temperatures using equation (1) and (2). Therefore, it is worth investigating the accuracy of the section factor method in a more extensive manner, as presented in Figure 8 and further summarized in Table 2. For all steel beams, with an exception of the east primary beam, the predicted maximum temperatures of steel members are approximately 6% lower than the measured values on average.

⁸ This range is due to the SFRM input property uncertainties: unit mass and thickness.

Furthermore, the average cooling rate⁹ of all beams in the experiment is 110 °C/hour, about 9% greater than the predicted rate. One possible reason for the discrepancy between the prediction and the measurement, is due to the fire conditions achieved during the experiment. In the experiment, natural gas was used as the fuel which seldom generated smoke, applying cumulative radiation to the surface of the passive fire protection; however, in a real building fire, this situation is highly unlikely. The sooty smoke within the compartment upper layer, generated from a real fire, would obscure some of the radiation from the flames to the fire protection.

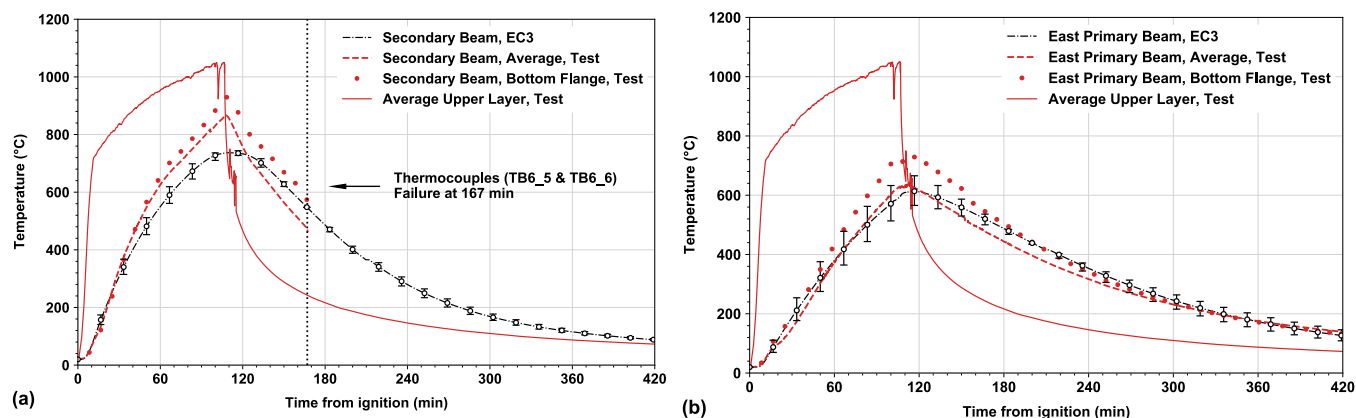


Figure 8. Comparison of the predicted with measured temperatures: (a). Secondary beam (thermocouples at the bottom flange of beam midspan, TB6_5 and TB6_6 failed at 167 min); and (b). East primary beam.

Table 2. Comparison between the test and the Eurocode 3 prediction on steel beam temperatures (for maximum temperature, Eurocode 3 method considers the upper bound prediction for comparison except for east primary beam; for cooling rate, Eurocode 3 method considers the mean value)

Beam at midspan	Maximum Temperature (°C)		Cooling Rate (°C/hour)	
	Test (Average)	Eurocode 3	Test (Average)	Eurocode 3
Secondary Beam	870	750	/	120
South Primary Beam	670	650	105	95
North Primary Beam	780	690	130	100
West Primary Beam	690	650	105	90
East Primary Beam	640	560 - 660	100	90
Average All Beams	730	680	110	100

Figure 9(a) and (b) present the predicted and measured values of maximum temperatures as well as cooling rates respectively, for all the measured connection components on the ten connections considered in this study. In Figure 9(a), the error bar of the test measured maximum temperature represents the standard deviation of two connection components on the same beam at two different ends; and the error bar of the Eurocode 3 predicted maximum temperature refers to the temperature variation due to the range of SFRM input variables, i.e. unit mass and thickness. Figure 9(a) suggests that Eurocode 3 tends to overpredict maximum temperatures of the connection components when actually heated to 400 °C or lower. However, the predicted temperatures (using Eurocode 3) become comparable to the measured temperatures of the connection components when actually heated in excess of 400 °C. It is important to repeat herein that this comparison is made under the situation where the SFRM thickness on the connection region was at least 43% thicker than the SFRM on the beams. To further examine the impact of SFRM thickness varying between the beam midspan and the connection region, Figure 9(a) also includes the comparison with

⁹ The average cooling rate is calculated from the time of steel member at peak temperature, lasting five hours during the cooling phase.

another data from the long-span composite beam fire test carried out at NIST [22]. In this test, the SFRM thickness on the connection region was at least 68% greater than that on the steel beam. For this case, Eurocode 3 method overestimates the connection temperatures of which measured values were actually lower than 300 °C. Figure 9(b) explores the comparison between the measured and predicted cooling rates. It suggests that in most cases Eurocode 3 predicts much rapid cooling rates, from 70 °C/hour to 120 °C/hour for the connections used in this study, whereas the measured cooling rates significantly vary from 10 °C/hour to 110 °C/hour. This difference would be influenced by several factors, including the Eurocode 3 overestimation on maximum temperatures leading to a higher slope, the thicker SFRM applied on the connection region resulting in slow cool-down, or both.

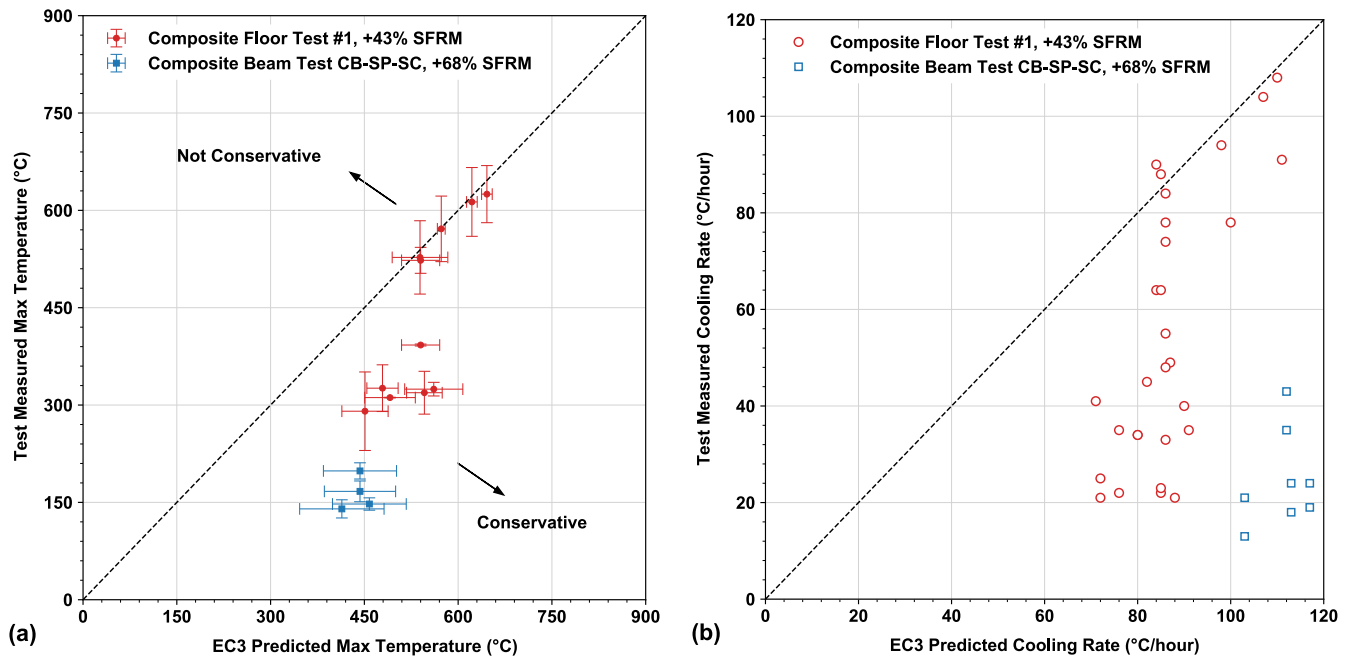


Figure 9. Comparison of the measured against Eurocode 3 predicted temperatures on all ten connections, i.e. 30 connection components in total plus another 8 connection components from composite beam test CB-SP-SC [22]: (a). Maximum temperature; and (b). Cooling rate within five hours.

4 CAPACITY OF THE CONNECTIONS

The shear capacity of welds and bolts used in the connection C2 was estimated using the Eurocode 3 reduction factors and experimentally measured temperatures. Figure 10(a) demonstrates that C2 would have failed at 575 °C (around 100 mins after the gas burner ignition). However, this behaviour was not witnessed during the experiment, see Figure 10(b) and (c).

Figure 11 illustrates the overestimation of connection temperature C2 predicted using the Eurocode 3 bolt strength reduction factor¹⁰. As shown, at 90 min, the bolt reduction factor decreases to as low as 0.11 when calculated using the measured bottom flange temperature of the steel beam at midspan or ranges from 0.20 to 0.31 when the Eurocode 3 step-by-step section factor method is used. Those two predictions are conservative, as compared to the actual 0.46 estimated via the temperature measurement at bolt C2_4.

However, in the case of C6 connection, the Eurocode 3 prediction of bolt strength reduction factor is less conservative, see Figure 12 at 90 min. This bolt reduction factor (based on the thermocouple measurement at this bolt) decreases to 0.53. This result is within the predictive range of 0.48 to 0.74 based upon the Eurocode 3 step-by-step section factor method but higher than the reduction factor 0.35 predicted using the measured beam bottom flange temperature at midspan. Although these predictions still imply no bolt failures, the post-fire inspection of the experiment discovered that three of five bolts from the connection C6 middle row to lower row experienced partial shear rupture failure, Figure 13. This was due to the

¹⁰ Reduction factor: a ratio (≤ 1) between the steel bolt strength at high temperature and the strength at ambient temperature

combined large axial force and bending moment, induced by the thermal restraint and thermal bowing effects during the heating phase.

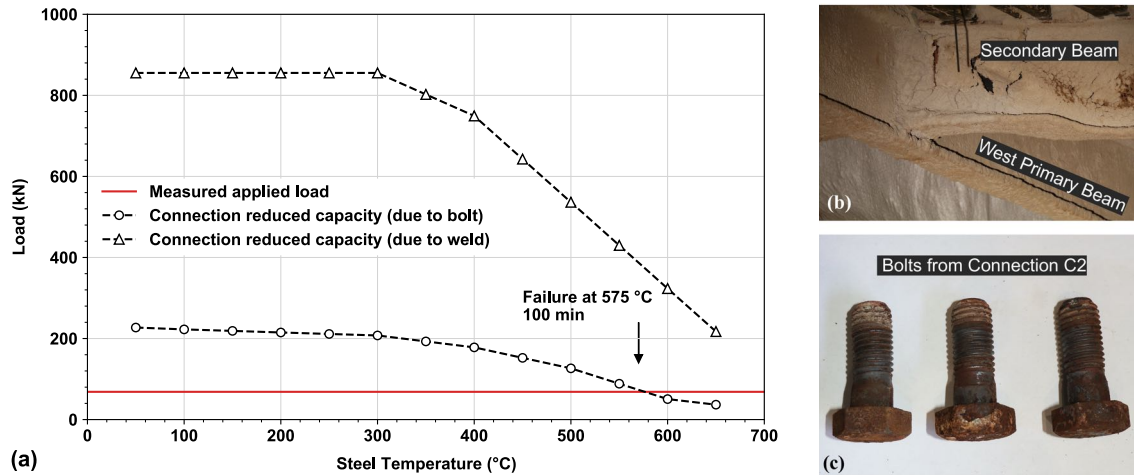


Figure 10. (a). Reduction of connection capacity with experimental increasing temperature at connection C2, against the corresponding measured applied load; (b). Post-fire inspection on connection C2 (before SFRM removed); and (c). Post-fire inspection on the bolts from connection C2.

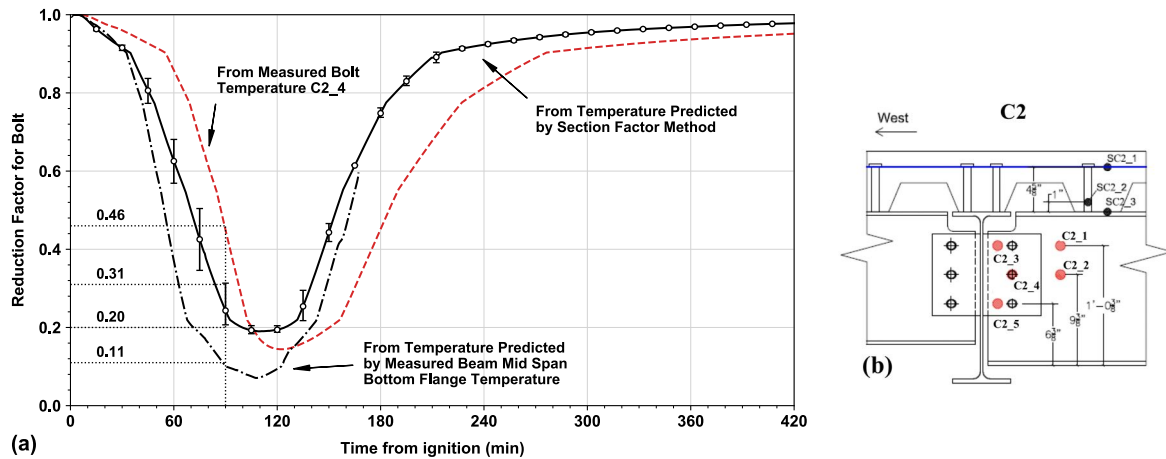


Figure 11. (a). Reduction factor of the bolt based on different methods and measured temperature at the C2 middle row, C2_4 (beam thermocouples at bottom flange failed at 167 min); and (b). Thermocouple instrumentation locations at connection C2, tagged as C2_1 to C2_5.

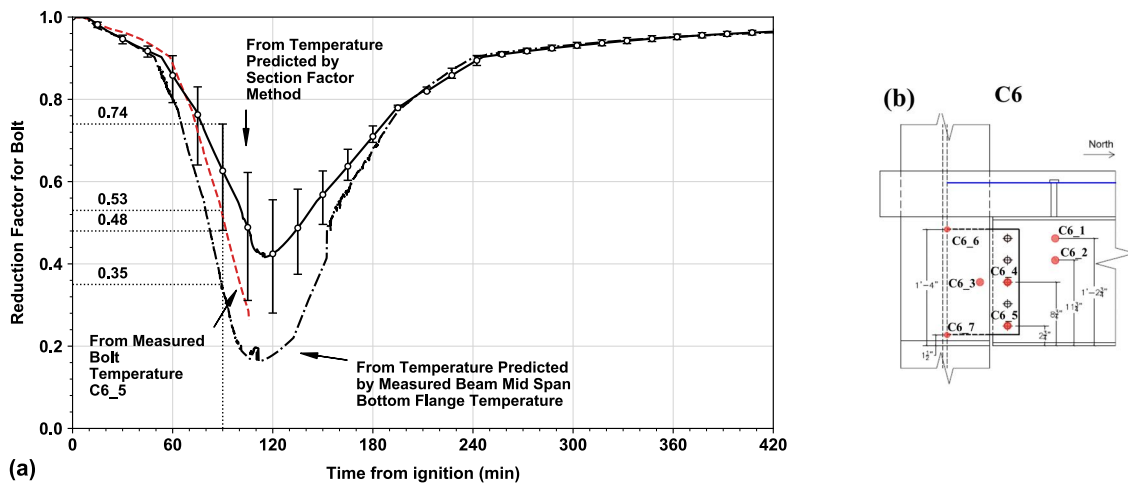


Figure 12. (a). Reduction factor of the bolt based on Eurocode 3 methods and measured temperature at the C6 lower row, C6_5 (bolt thermocouple failed at 106 min); and (b). Thermocouple instrumentation locations at connection C6, tagged as C6_1 to C6_7.



Figure 13. Post-fire inspection on the bolts from connection C6.

The findings in this section shows that Eurocode 3 method does not account for (1) additional sources constituting the capacity of a connection, such as the presence of slab and slab continuity to adjacent bays and (2) additional sources for the demand, such as thermally-induced axial forces due to the restraint to thermal expansion or contraction as well as catenary action. All these factors are needed to be incorporated for reliable estimation of the connection integrity.

5 CONCLUSIONS

The experimental results presented in this paper enrich the database that can be used for validation of computational models predicting beam end shear connections with fire protection under large compartment fires. The data acquisition of the measurements was successful, only 3 out of 45 thermocouple measurements on the total ten connection regions failed during the 7 hours (including cooling phase) of this structural fire test duration. This work demonstrates that the Eurocode 3 provision on the temperature prediction of connection components is conservative, provided that the fire protection at the connection region is at least 43% thicker than the protection on the beams. Finally, designing shear connections through temperature provisions may not guarantee a safe structural fire design. It is strongly recommended that the influence of the axial load demand (i.e. compressive/tensile load demands) of the connection *must also* be taken into account in future design guidance. This test indicated that the connection region can be subjected to varying axial forces during a fire event, such as a compressive force induced by the restraint of thermal expansion in the heating phase, followed by a tension force by catenary action and the contraction of beam members during cooling. The combined effects from high temperatures and fire-induced forces can lead to failure of connections designed only through Eurocode temperature provisions.

ACKNOWLEDGMENT

The support of numerous NIST colleagues on this project is acknowledged and greatly appreciated: Matthew Hoehler, Matthew Bundy, Selvarajah Ramesh, Brian Story, Tony Chakalis, and Philip Deardorff.

DISCLAIMER

Certain commercial entities, equipment, software, or materials may be identified in this paper in order to describe an experimental procedure or concept adequately. Such identification is not intended to imply recommendation or endorsement by the National Institute of Standards and Technology, nor is it intended to imply that the entities, materials, or equipment are necessarily the best available for the purpose.

REFERENCES

1. AISC, Specification for Structural Steel Buildings, ANSI / AISC 360-16. American Institute of Steel Construction (AISC), Chicago, Illinois, 2016.
2. Clifton, G. C., Meng, F., Mohammadjani, C. and Abu, A., Importance of Concrete Floor Slabs in Composite Beam to Column Connections during Severe Fires, ASFE, 2019, Singapore.

3. Chloubá, J., Wald, F. and Sokol, Z., Temperature of connections during fire on steel framed building, *International Journal of Steel Structures*, vol. 9, pp. 47–55, 2009. <https://doi.org/10.1007/BF03249479>
4. Fischer, C. E., Varma, H. A., Fire resilience of composite beams with simple connections: Parametric studies and design, *Journal of Constructional Steel Research*, vol. 128, pp. 119-135, 2017. <https://doi.org/10.1016/j.jcsr.2016.08.004>
5. Eurocode 3. Design of Steel Structures - Part 1-2: General rules — Structural fire design. European Standard EN 1993-1-2, CEN, Brussels, 2005.
6. Wang, Y., Burgess, I., Wald, F., Gillie, M., Performance-based Fire Engineering of Structures, CRC Press, Taylor & Francis Group, p363, 2013.
7. da Silva, L.S., Santiago, A., Real, P.V., Moore, D., Behaviour of steel connections under fire loading. *Steel and Composite Structures*. Vol. 5, No. 6, pp. 485-513, 2005. <https://doi.org/10.12989/SCS.2005.5.6.485>
8. Choe, L., Ramesh, S., Dai, X., Hoehler, M., Bundy, M., Experimental study on fire resistance of a full-scale composite floor assembly in a two-story steel framed building. *Proceeding of the 11th International Conference on Structures in Fire (SiF' 20)*, Nov. 30 – Dec. 02, 2020, University of Queensland, Australia
9. ASCE, Minimum Design Loads and Associated Criteria for Buildings and Other Structures. ASCE/SEI 7-16, American Society of Civil Engineers, Reston, VA., 2016.
10. Southwest Type 5MD, Product Data Sheet, Carboline, 2019.
11. Underwriter Laboratory (UL), Fire Resistance Ratings – ANSI/UL 263. Design NO. N791, 2011
12. Underwriter Laboratory (UL), Fire Resistance Ratings – ANSI/UL 263. Design NO. D949, 2015
13. ASTM, Standard Specification for Carbon Structural Steel. ASTM A36/A36M - 19, ASTM International, West Conshohocken, PA., 2019.
14. ASTM, Standard Specification for High Strength Structural Bolts and Assemblies, Steel and Alloy Steel, Heat Treated, Inch Dimensions 120 ksi and 150 ksi Minimum Tensile Strength, and Metric Dimensions 830 MPa and 1040 MPa Minimum Tensile Strength. ASTM F3125/F3125M - 19, ASTM International, West Conshohocken, PA., 2019.
15. Zhang, C., Grosshandler W., Sauca A., and Choe L., Design of an ASTM E119 fire environment in a large compartment, *Fire Technology*, pp. 1–23, 2019. <https://doi.org/10.1007/s10694-019-00924-7>
16. Sauca, A., Zhang, C., Grosshandler, W., Choe, L., and Bundy, M., Development of a Standard Fire Condition for a Large Compartment Floor Assembly, *Technical Note (NIST TN) - 2070*, pp 62, 2019. <https://doi.org/10.6028/NIST.TN.2070>
17. Bryant, R. and Bundy, M. The NIST 20 MW Calorimetry Measurement System for Large-Fire Research, *Technical Note (NIST TN) - 2077*, pp 68, 2019. <https://doi.org/10.6028/NIST.TN.2077>
18. ASTM, Standard Test Methods for Fire Tests of Building Construction and Materials. ASTM E119–19, ASTM International, West Conshohocken, PA., 2019.
19. Eurocode 1. Actions on Structures - Part 1-2: General Actions - Actions on Structures Exposed to Fire. European Standard EN 1991-1-2, CEN, Brussels, 2002.
20. Fire Protection Systems, Southwest Fireproofing Type 5 MD, 2008.
21. Franssen, J.M., Vila Real, P., Fire Design of Steel Structures, 2nd Edition, ECCS – European Convention for Constructional Steelwork, p450, 2016.
22. Choe L.Y., Ramesh S., Hoehler M.S., Seif M.S., Bundy M.F., Reilly J., Glisic B., Compartment Fire Experiments on Long-Span Composite-Beams with Simple Shear Connections Part 2: Test Results, *Technical Note (NIST TN) - 2055*, pp 144, 2019. <https://doi.org/10.6028/NIST.TN.2055>

EXPERIMENTAL STUDY OF CONCRETE ELEMENTS SUBJECTED TO TRAVELLING FIRES

Camilo Montoya¹, David Lange², Cristian Maluk³, Juan P. Hidalgo⁴

ABSTRACT

Fires in open plan compartments are known to result in a non-homogeneous temperature distribution. Large compartment geometries allow the fire to move around a floor plan as it spreads while fuel is consumed. The Travelling Fire Methodology (TFM) was developed to address these scenarios during design and analysis. This methodology describes the fire exposure to a structure as a function of the total floor area that is burning at any one time. In this article, a testing methodology is developed to study the behaviour of concrete elements subjected to travelling fires. As described in this methodology, the experimental series utilised the H-TRIS (Heat Transfer Rate Induced System) to reproduce a family of fires from the TFM. This paper reports on the results from this study as well as the development of the experimental technique which allowed the reproduction of the travelling fires, characterised by very long burning durations and high temperatures in this equipment.

Keywords: Travelling fires; concrete; fire testing; H-TRIS; numerical models.

1 INTRODUCTION

Models of fire scenarios for structural design are often based on an assumption of a well-mixed reactor, such as the parametric temperature-time curves in [1], or the standard fire in [2] and [3]. In the event of a fire in a compartment, these approaches describe an assumption of uniform burning and homogeneous temperature through a room. Nevertheless, a variety of events around the world have demonstrated the fact that this assumption does not account for the real behavior of fires in large open plan compartments, in which fire travels along the floor as flames spread and fuel is consumed [4, 5].

To understand the impact of these types of fires, a procedure was developed called Travelling Fire Methodology (TFM) [6]. This method assumes that the size of the burning region will remain constant while the location will change as the fuel is consumed at a constant rate. The procedure separates the temperature inside the compartment into two regions, a near field (flaming region) with a temperature of 1200 °C and a far field (cooler region), (Figure 1); this substitutes the assumption of simultaneous and uniform burning inside of a compartment from the design codes.

Based on the temperature, size of the compartment and duration of burning, the size of the near field region fires can vary as a percentage of the whole floor area and be divided in bays to account for different fire scenarios (Figure 2). The family of fires inside the compartment provides the designer with a tool to systematically evaluate the response of a structure exposed to a range of different thermal boundary conditions. Computational modelling of travelling fires in a concrete frame reported in the literature suggests that critical travelling fires for the compartment in the cited study are between the 10 % and 25 %

¹The University of Queensland,
e-mail: c.montoyagiraldo@uqconnect.edu.au

² Senior Lecturer, The University of Queensland
e-mail: d.lange@uq.edu.au, ORCID: <https://orcid.org/0000-0002-4551-1045>

³ Senior Lecturer, The University of Queensland
e-mail: c.maluk@uq.edu.au, ORCID: <https://orcid.org/0000-0002-1662-6943>

⁴ Senior Lecturer, The University of Queensland
e-mail: j.hidalgo@uq.edu.au, ORCID: <https://orcid.org/0000-0002-2972-5238>

of the floor area [6]. Nevertheless, the real impact on concrete elements has not been validated because the analysis was computational.

In the work described in this article, a testing methodology for reinforced concrete subjected to these types of fires was developed. The study is based on the same compartment as is described in [6], shown schematically in Figure 2. The aim of this paper is to present the process of preparation and testing of concrete elements exposed to travelling fires using the Heat Transfer Rate Induced System (H-TRIS). Moreover, the paper discusses the specific issues encountered through the development of the experimental program and the approach to account for these variables while testing and validating the TFM.

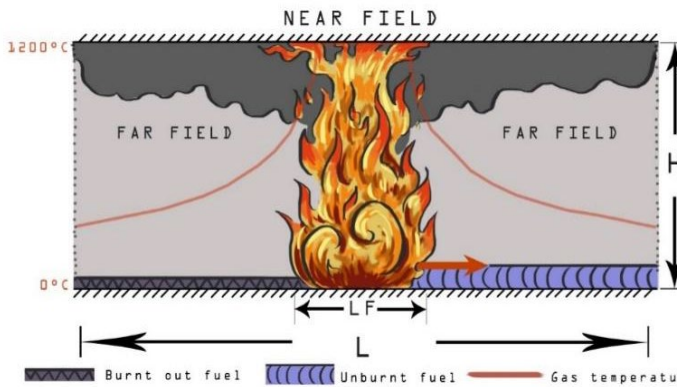


Figure 1. Travelling fire methodology (adopted from [6]).

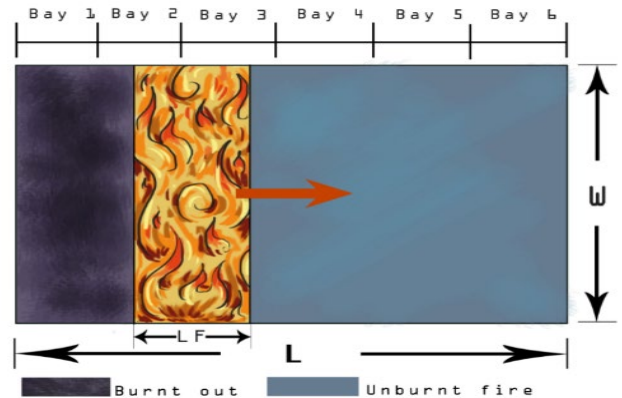


Figure 2. Compartment division for TFM.

2 METHODOLOGY

The H-TRIS Test Method in this experimental program is used to recreate the thermal boundary condition for concrete elements exposed to travelling fires. This approach requires the use of an inverse heat transfer model to calculate the net heat flux at the surface of a specimen exposed to the TFM – the surface boundary condition for the heat diffusion equation. This net heat flux is then converted to an equivalent boundary condition at the surface, expressed as an incident radiant heat flux from a radiant panel in an ambient temperature environment which results in the same temperature profile being developed through the depth of the sample being tested. The incident radiant heat flux to the surface of the sample is controlled by adjusting the distance between the surface of the panel and the specimen being exposed. The inverse heat transfer model and experimental methodology are validated for this application through the exposure of rectangular concrete blocks with embedded thermocouples to compare with the results of the heat transfer model.

2.1 Heat Transfer Induced System (H-TRIS)

The H-TRIS (Figure 3) is used to reproduce the fire conditions from the travelling fire that covers 25 % of the total floor area. To recreate the fires, H-TRIS utilises a propane fuelled radiant panel array [7]. The incident radiant heat flux on the surface of a sample is controlled when testing using H-TRIS by continually adjusting the distance between the specimen and the panel. By adjusting the linear distance throughout testing, thus adjusting the view factor between the panel and the exposed sample, a range of heat flux time histories can be applied to different specimens. The radiant panels on the linear motion system of the H-TRIS with the input values of incident heat flux calculated to recreate the boundary conditions of the travelling fire are used to simulate the fire conditions of travelling fires. In addition to the features described in this methodology, the radiant panels are protected with a steel mesh to eliminate any possible damage from concrete spalling during testing.

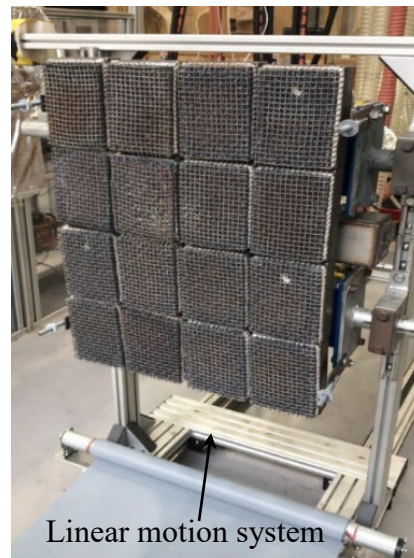


Figure 3. H-TRIS (Heat Transfer Rate Induced System) on the linear motion system.

2.2 Travelling Fire Methodology (TFM)

The initial task is the implementation of the travelling fire methodology on concrete elements with a finite difference method to define the initial boundary conditions of the experiment. These are represented by a heat transfer model calculated based on the temperature history calculated according to the methodology described in [6]. The heat transfer model requires as a boundary condition the incident radiative heat flux and the gas temperature derived from the temperature curves of travelling fires inside the compartment combined with the radiative losses and convective exchange at the surface of the concrete. The convective heat transfer coefficient is assumed to be $25 \text{ W/m}^2\text{K}$. All of these temperature values vary as a function of time and space inside of the compartment as the fire moves around. Material properties for the heat transfer model are taken from the Eurocode [1].

The calculation process of the TFM follows the equations from [8] to calculate the far field temperature inside the compartment and of [9] cited in [6] to calculate the boundary condition for the heat diffusion equation. For the studied compartment of 7×42 meters divided in six (6) bays (B) the temperature distribution from the TFM is calculated (Figure 4) and is used to describe the thermal boundary condition, the net heat flux, to the structure in the different bays. In the analysis presented, the net heat flux to the surface of a concrete element in the different bays is shown by the dashed lines in Figure 5; along with the incident radiative heat flux that must come from the radiant panels to produce the same temperature profile in the specimens during testing (note that this is not the incident radiant heat flux in the TFM). The travelling fires used for the testing covered the family of fires with a size 25% of the total compartment area, the upper most of the range of critical scenarios based on the numerical model presented in [7]. The values of the incident radiant heat flux are used as input to the H-TRIS to enable the recreation of the design fires and apply those to the concrete samples.

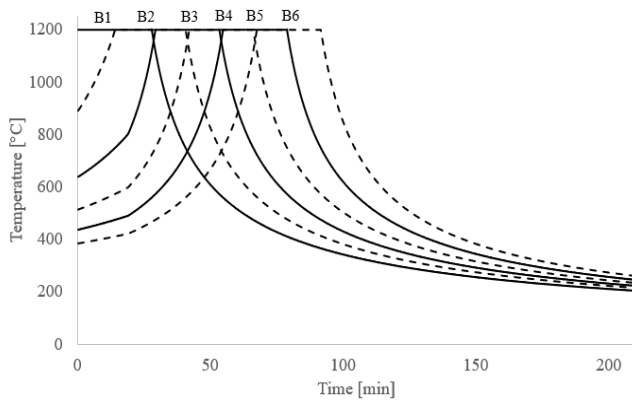


Figure 4. Compartment temperature for travelling fire 25 %; bay 1, 3 and 5 (solid) and bay 2, 4, 6 (dashes).

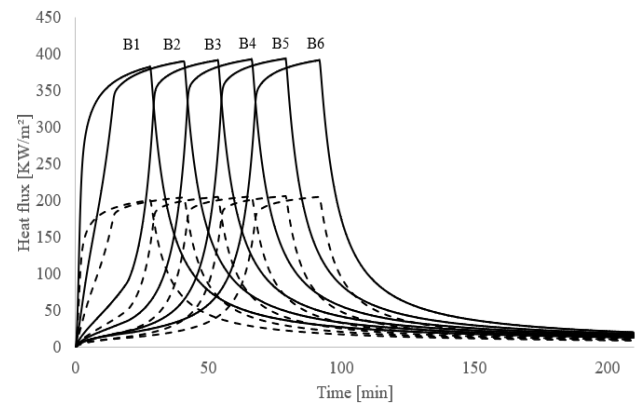


Figure 5. Incident (solid) and Net (dashes) heat flux for travelling fire 25%; bay 1 to 6 (B1 to B6).

The initial testing methodology comprised unreinforced concrete blocks with a compressive strength of 40 MPa. The blocks had dimension of 300 mm (width), 300 mm (height) and 150 mm (depth), allowing a single person to manipulate them.

Thermocouples were installed inside the blocks to measure the temperature distribution through the depth of the elements. To assure that sensors maintained their position during the casting process, holes were drilled in the sides of the timber formwork and thermocouples were anchored across the width with Dyneema thread to keep them secure (Figure 6). The position of thermocouples in the depth are: surface (covered with a thin layer of cement after de-moulding), 3 mm, 5 mm, 10 mm, 15 mm, 20 mm and 25 mm.

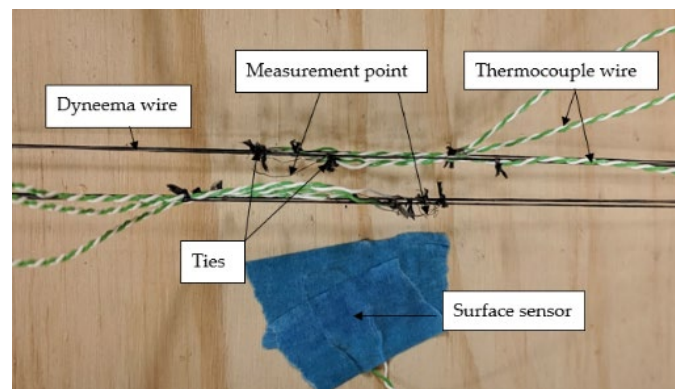


Figure 6. Location of thermocouples.

2.3 Calibration

The calibration process consisted of measurements of incident heat flux from the radiant panels at different locations. The values are recorded with a water-cooled heat flux gauge [10]. The gauge is located at the same height and distance that the centre of concrete blocks are to be located during the testing. This stage consisted of different calibrations to determine functionality, repeatability and capacity of the H-TRIS to reproduce heating conditions associated with the travelling fire. The calibration process covered a path of 720 to 20 mm between the panels and the sample's surface and the maximum incident heat flux reached at 20 mm varied between 250 and 275 kW/m².

2.4 Limitations

One of the main assumptions for the travelling fires is a temperature in the near field of 1200 °C. H-TRIS in the configuration used in these tests was unable to recreate this type of fire using an array of 16 panels.

The maximum incident heat flux during calibration is in average 265 kW/m² at a location of 20 mm from the surface measured using a water-cooled heat flux gauge; this value corresponds to a temperature in the near field of up to 1000 °C for this family of fires (recall that the incident heat flux required from H-TRIS is not the incident radiant heat flux in the fire environment but is the incident radiant heat flux required to provide an equivalent boundary condition at the surface of the sample in an otherwise ambient temperature environment). Furthermore, the minimum capacity with all panels on is nearly 30 to 40 kW/m² at a location of 750 mm, which is higher than the lowest required heat fluxes in the far field. Table 1 presents the maximum required incident heat flux from H-TRIS for different near field temperature assumptions.

The maximum values of incident heat flux from the numerical model for the family of fires of 25 % are compared against the calibration. Conditions to reproduce travelling fires with a near field temperature assumption of 1200 °C cannot be reached. This type of fire requires an incident heat flux of 394 kW/m² in order to be able to represent the boundary condition from the TFM based on the inverse model. Therefore, the assumption of near field temperature is reduced based on the maximum capacity of the panels to 1000 °C.

Table 1. Maximum incident heat flux to be required for testing travelling fires of 25 %.

Near field temperature [°C]	Radiant incident heat flux required [kW/m²]
1200	393.82
1100	300.98
1000	226.53
900	167.94

3 RESULTS AND DISCUSSION

The subsequent experimental process is divided in three stages:

- Similar concrete blocks are tested under conditions equivalent to the TFM fire in bays 1 and 2 from the 25 % travelling fire with a near field temperature assumption of 1000 °C;
- A study was carried out to determine the impact of concrete blocks on radiant panels and variability of results during testing and calculation of modification factors; and
- Tested bays 1, 3 and 6 from the 25 % travelling fire with near field temperature assumption of 900 °C and application of modification factors to adjust data.

3.1 First stage

The first stage of testing covered the bays 1 and 2 fire curves for the travelling fire of 25 % with a near field temperature assumption of 1000 °C. The full set of panels (16) were used during the experiments. Variables recorded were temperature inside the samples and the heat flux next to the concrete block to compare against measurements taken from the same location during calibration to confirm that the boundary conditions were reproduced correctly.

This first stage was subject to some issues with regards to the repeatability of testing, largely as a result of loss of data and difficulty in control and verification of the thermocouple placement in the concrete blocks. The heat flux gauge adjacent to the concrete blocks also recorded higher heat fluxes than the heat flux gauge in the same location during calibration, suggesting that the position of the sample relative to the panels was affecting the panel output. This can be explained due to the exchange of radiant energy reflected between these surfaces as well as convective exchange in close proximity.

Further, there was significant variability in the response of the concrete to fire, with some samples cracking at the surface while others spalled and others melting once exposed to the maximum values of incident heat flux according to the model (Figure 7). The melting phenomenon occurs at temperatures in excess of

1300 °C which is not consistent with the prescribed near field temperature of 1000 °C. Initial results revealed that experimental conditions varied from the conditions that were required to represent the TFM. The measured incident heat flux values were higher than the input model (Figure 8). The gauge, which was not located in front of the centre of the samples recorded higher values than were recorded by the calibration heat flux gauge which was measured at the centre of the samples. Bearing in mind the reproducibility of results from the same test method described in [11] these factors suggest that there was some issue with the casting of the blocks that impacted on the concrete quality; and further support the issue highlighted around proximity between sample and panel.



Figure 7. Melted concrete sample.

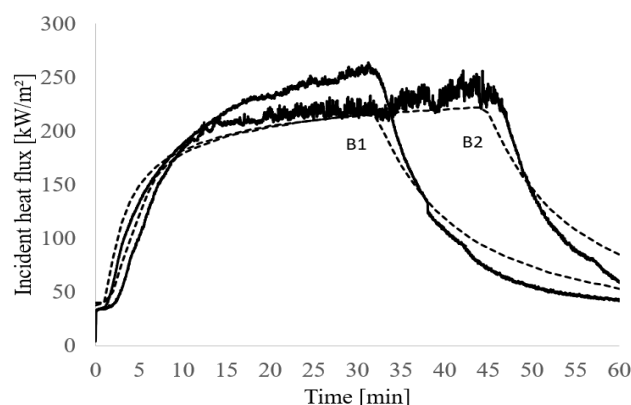


Figure 8. Radiant incident heat flux for bay 1 and 2; experimental (solid) and model (dashes).

3.2 Second stage

A new approach to improve the testing methodology and address the variability of results was implemented. This study focused on understanding the behaviour of the radiant panels in the H-TRIS and the measurement equipment during testing of concrete samples. To avoid overheating of panels during the experimental work, this stage only used half of the radiant panels (8). These changes resulted in a reduction of maximum temperature at the near field zone from 1000 to 900 °C reflected in a maximum incident radiant heat flux from 227 to 168 kW/m² (Table 1).

The revised study comprised the following:

- A determination of the difference in incident heat flux measurements during testing from what was expected based on the calibration. Heat flux gauges were positioned at two different locations in front of the panels. The first gauge was located at the position of the centre of the blocks. The second gauge was located at the side of the position of the blocks. The difference between the measurements of the heat flux gauge located adjacent to the sample position and the heat flux gauge used for calibration located at the centre of the sample is attributable to the view factor. The ratio of the two heat fluxes measured at these locations is therefore the ratio of the view factors, suggesting that a correction factor can be derived to correct the expected heat flux based on the calibration for the effects of the sample being present.
- The values of incident heat flux for two conditions were measured and compared; with and without concrete blocks present (Figure 9). Results reflected that the concrete samples have no significant impact on measurements in distances up to 100 mm. As a result of this, the minimum distance between the H-TRIS and sample's surface was increased to 100 mm from 20 mm.

- The difference between the measurements of the heat flux gauge located adjacent to the sample position and the heat flux gauge used for calibration located at the centre of the sample is attributable to the view factor. The ratio of the two heat fluxes measured at these locations is therefore the ratio of the view factors, suggesting that a correction factor can be derived to correct the expected heat flux based on the calibration for the effects of the sample being present.

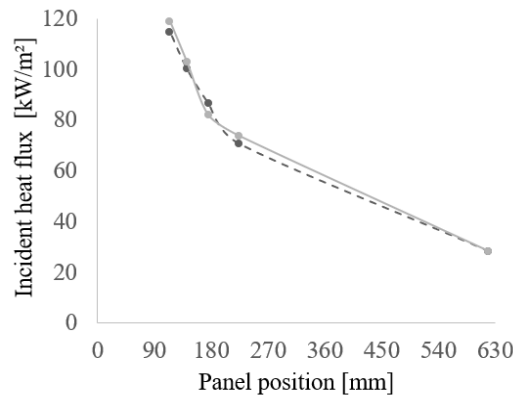


Figure 9. Values of incident heat flux measured adjacent to the corner of the sample from different testing conditions; sample (solid) and no sample (dashes).

- A determination of the approximate variation of temperature in the radiant panels during a test with and without a sample being present was also attempted. A shielded thermocouple was positioned inside the panels located at the same position that the centre of the panels will have during testing recorded the temperature values (Figure 10). To avoid damage of the sensor, the test stopped after reaching temperatures higher than 1200 °C. The temperature at the panel without a sample stabilizes at 1168 °C, however the presence of concrete samples led to an increase in temperature at the surface of the panel. After passing the range of 200 mm (between the sample and panels), the exchange of energy between the blocks and the panels generated higher temperatures in the panels than without the concrete block. Note that this measurement is likely to be prone to significant error as a result of the difficulty in measuring the temperature of the radiant panels, however it gives an indication of the potential impact of the concrete blocks on the panels.

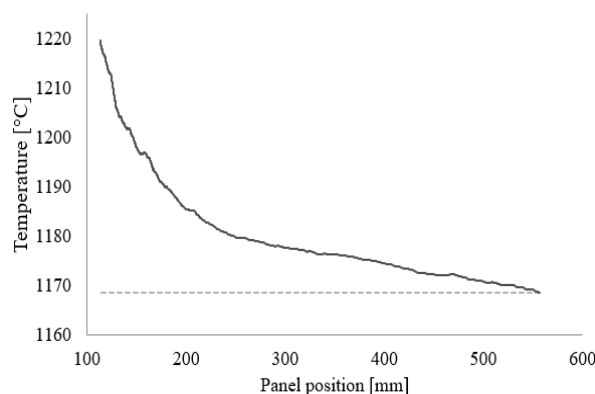


Figure 10. Radiant panels temperature; with sample (solid) and no sample (dashes).

- Results of incident heat flux measured at the position of the centre of the surface of the concrete blocks were higher in comparison to the incident heat flux measured at the side (Figure 11).

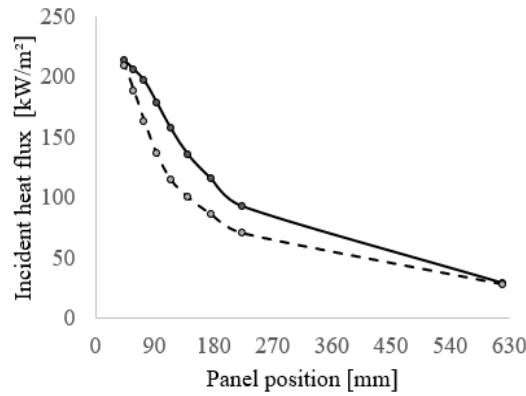


Figure 11. Incident heat flux due to different view factors with no sample; middle (solid) and corner (dashes).

Initial results from the study provide a better understanding of the impact of concrete testing on radiant panels and measurement equipment. Likewise, the outcome confirms the assumption of experiment temperature increments which led to instability in results during the initial stage. A modification factor was calculated to incorporate the results from the three previous phases (Table 2). The factor is then used in subsequent studies to recalculate the heat flux from the panels to the blocks based on the measured incident heat flux from the gauge located adjacent to the blocks.

Table 2. Radiant incident heat flux modifier factor.

Position of Radiant Panels [mm]	Factor	Position of Radiant Panels [mm]	Factor	Position of Radiant Panels [mm]	Factor
620	1.03	440	1.18	260	1.33
600	1.04	420	1.19	240	1.35
580	1.06	400	1.21	220	1.36
560	1.08	380	1.23	200	1.39
540	1.09	360	1.25	180	1.42
520	1.11	340	1.26	160	1.45
500	1.13	320	1.28	140	1.49
480	1.14	300	1.30	120	1.55
460	1.16	280	1.31	100	1.55

3.3 Third stage

The third stage of testing covered the bays 1, 3 and 6 from Figure 2 for the travelling fire of 25% with a near field temperature assumption of 900 °C.

Incident heat flux data from the adjacent heat flux gauge was used to correct the predicted response of the concrete blocks. The modification factor was implemented to adjust values of incident heat flux for bays 1, 3 and 6 (Figure 12). The results reflect a similarity in the tendency and values of the curves in bays 1 and 6, contrary to bay 3 where values are larger than the model. Although the incident heat flux does not present a similar tendency in all cases, it provides a guide to understanding the heating conditions during testing that must be compared to the temperature profiles.

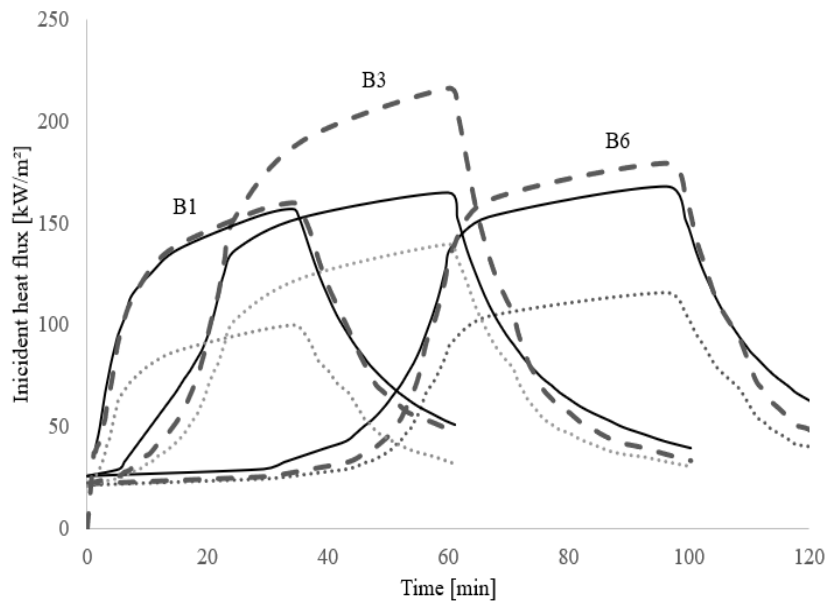


Figure 12. Incident heat flux during experiment (dots), model (solid) and fitted (dashes) values.

Measurements of temperature inside the samples were compared with the numerical values recalculated from the fitted conditions. Because incident heat flux for bay 3 does not fit the adjusted data, only the temperature measurements are used as a reference for this bay. Although values of temperature at the surface are higher than the model, temperature measurements presented similarities in a depth of 20 mm (Figure 13). This reflects that the heating conditions during the experiments are still larger than the input values. Further comparison to the model with a higher near field temperature assumption of 950 °C is presented in Figure 14. In this case, the temperature at the surface in all bays presented a better fit but higher values to a depth of 20 mm.

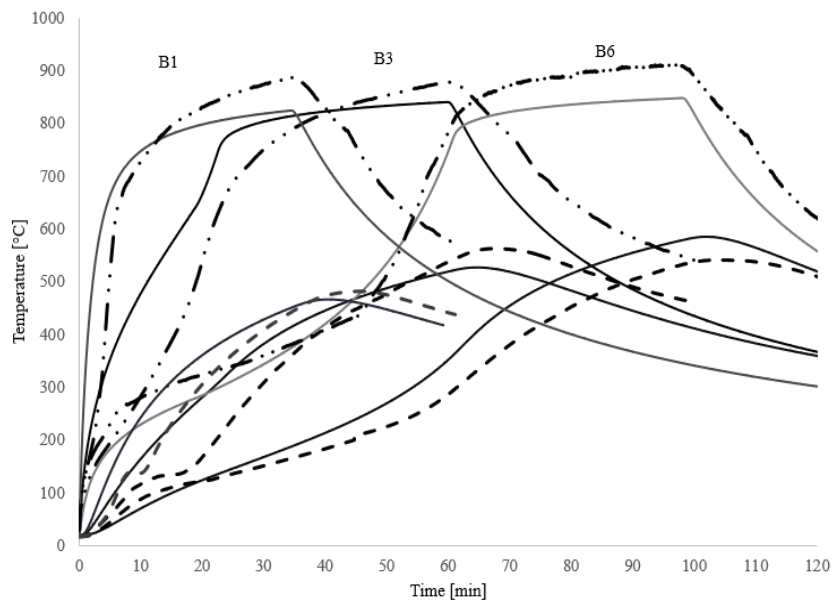


Figure 13. Temperature distribution at surface and 20 mm depth; experiment (near field temperature = 900 °C) (dots and dashes) and model (solid).

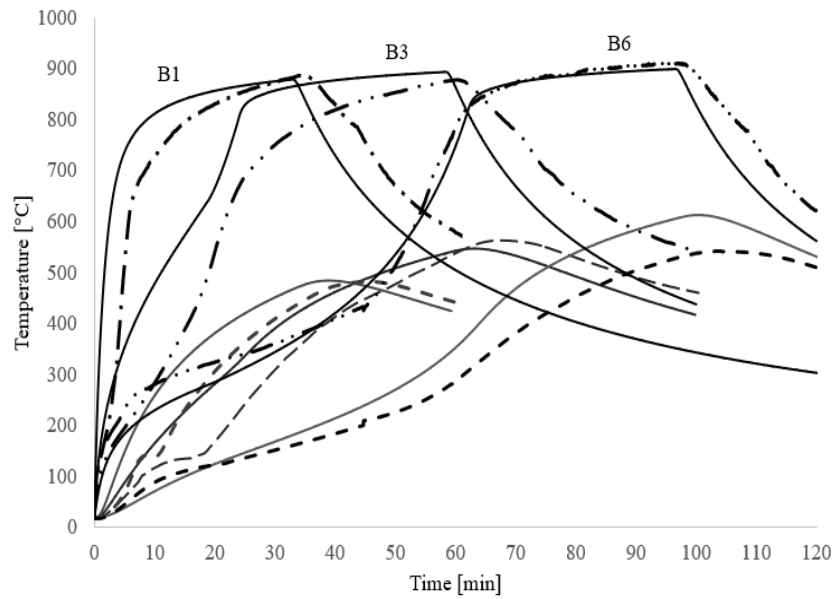


Figure 14. Temperature distribution at surface and 20 mm depth; experiment (near field temperature = 950 °C) (dots and dashes) and model (solid).

The predicted temperature gradient away from the heated surface was also adjusted using a near field assumption of 950 °C for a better fit. The adjusted and un-adjusted temperatures are shown in Figure 15 and in Figure 16. The corrected near field conditions used in the model result in a reasonable correlation, however there remain significant differences. These are in this instance attributed to movement in the thermocouple position during the casting.

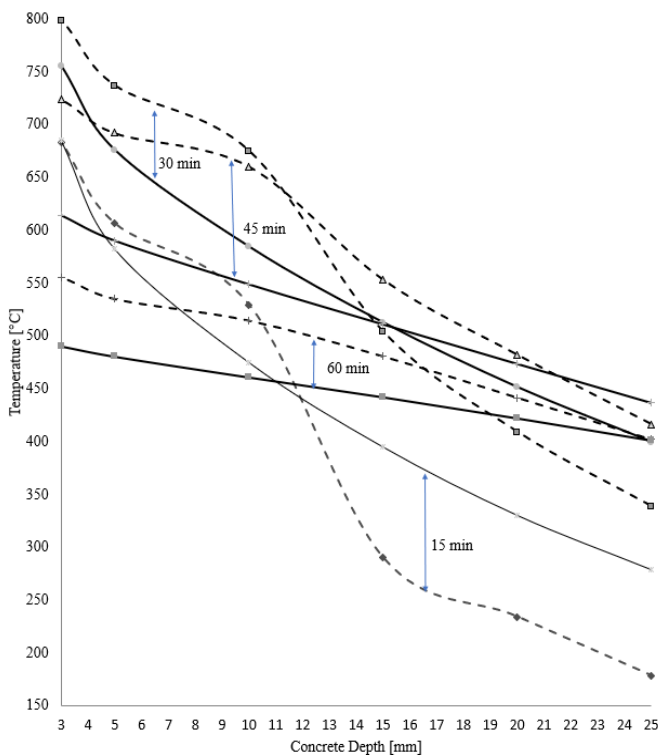


Figure 15. Gradient temperature distribution for bay 1; model (solid) experiment (dashes).

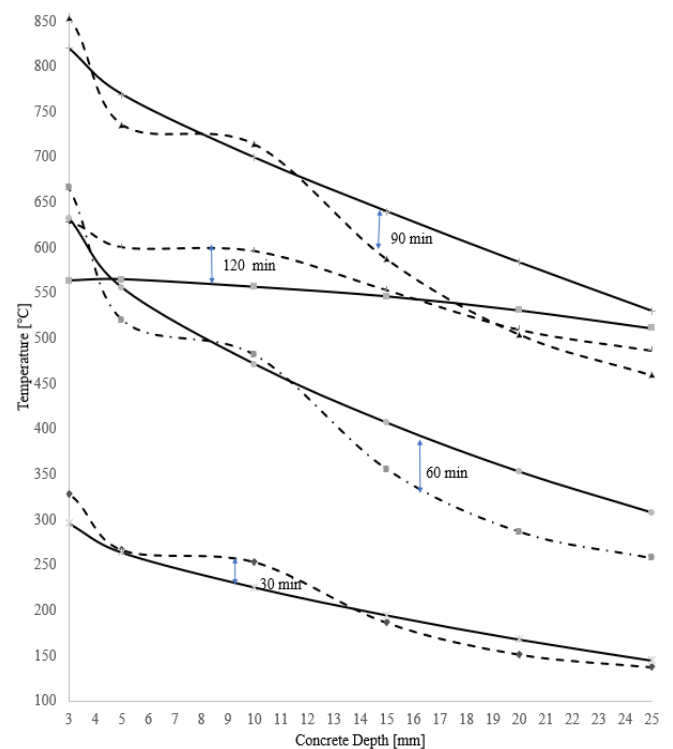


Figure 16. Gradient temperature distribution for bay 6; model (solid) experiment (dashes).

The H-TRIS was capable of reproducing travelling fires with an assumption of maximum compartment temperature of 900 °C with acceptable results. The increased minimum distance between the sample and radiant panels reduced the impact of energy exchange between surfaces of the panels and the concrete. Recorded data presented stable tendencies and repeatability through the whole testing. For the case of concrete samples, once subjected to travelling fires fractures appeared on the surface with no melting or spalling in the final configuration of the test setup.

The fitted results from experiments contrasted against the values from the heat transfer model allowed to confirm the applicability of the modifier factors. This allowed reaching a more accurate approximation of the fire conditions that the H-TRIS was reproducing. Moreover, results from the experiments presented similar tendencies which indicate that the methodology was repeatable. With the adjusted incident heat flux and temperature results, the numerical model was validated, meaning that the TFM can be implemented to calculate the temperature distribution in concrete samples.

4 CONCLUSIONS

This article has reported on the development of a testing methodology to study the response of concrete elements to travelling fires using the H-TRIS test method. During the first stage, the boundary conditions from the TFM could not be reproduced with the H-TRIS because of a limiting maximum incident radiant heat flux achieved with the radiant panel array used herein. Moreover, the interaction between the panels and the concrete elements, especially at small proximity, resulted in an increased net heat flux to the concrete and various other issues, including the melting of concrete and overheating of panels.

The study to understand the impact of concrete blocks during experimentation with the H-TRIS led to the development of a modified experimental methodology using a modification factor to estimate the actual incident heat flux at the exposed surface of concrete. The new methodology improved stable operation of the radiation panels, specially when used with high inlets of air flow and proximity to the heated surface of the concrete sample. The modification factors determined herein were used to recalculate incident heat flux at the heated surface of concrete samples, resulting in a better heating condition replicating the heating scenarios based on the TFM. Experimental outcomes from the third stage (bays 1, 3 and 6 for the travelling fire of 25% with a near field temperature assumption of 900 °C) demonstrated that H-TRIS is capable of reproducing the heating conditions for concrete exposed to a travelling fires; assuming a maximum near field temperature of 900 °C. From this, temperature distribution inside concrete elements due to travelling fires can be compared to numerical models for further study of the response of concrete elements to fires derived from the TFM.

In the future, these modification factors could be used to mitigate potential experimental errors arriving from an inaccurate control of the heating conditions at the exposed surface of heated specimens tested H-TRIS or similar apparatus. For example, through running a calibration with and without a dummy sample and recording the modification factors thus for each specific case. More experimentation is required to be carried out, reproducing the boundary conditions of the travelling fires. The H-TRIS method provides a good approximation to the travelling fires from numerical models with suitable modifications to account for limitations in the panels and the effect of the sample on the panel temperatures in instances where testing requires a close proximity between the two.

REFERENCES

1. Eurocode 1: Actions on structures – Part 1-2: General actions – Actions on structures exposed to fire, European standard EN 1991-1-2, 2002. CEN, Brussels.
2. BS476:1987, Fire Tests on Buildings Materials and Structures. London, British Standards Institution, 1987.3.
3. ISO 834-1, Fire-resistance tests — Elements of building construction — Part 1: General requirements.
4. Law, A., Stern-Gottfried, J., Gillie, M. & Rein, G., The influence of travelling fires on a concrete frame, *Engineering Structures*, Vol. 33, 2011, pp. 1625-1642.
5. Rackauskaite, E., Hamel, C., Law, A. & Rein, G, Improved formulation of travelling fires and application to concrete and steel structures, *Structures*, Vol. 3, 2015, pp. 250-260.
6. Stern-Gottfried, J., Travelling fires for structural design, 2011, The University of Edinburgh.
7. Maluk, C., Bisby, L., Krajcovic, M. & Torero, J. L., A Heat-Transfer Rate Inducing System (H-TRIS) test method, *Fire Safety Journal*, Vol. 105, 2016, pp. 307-319.
8. Alpert, R., L., Calculation of Response Time of Ceiling-Mounted Fire Detectors, *Fire Technology*, Vol. 8, 1972, pp. 181–195.
9. Incropera, F., DeWitt, D., Bergman, T., & Lavine, A., *Fundamentals of Heat and Mass Transfer*, John Wiley & Sons, 2007.
10. Wickstrom, U., Heat transfer by radiation and convection in fire testing, *Fire and Materials*, Vol. 18, 2004, pp. 411-415.
11. Maluk, C., Development and application of a novel test method for studying the fire behaviour of CFRP prestressed concrete structural elements, PhD Thesis, 2014, The University of Edinburgh.

ROBUST CIRCLE TRACKING FOR DEFLECTION MEASUREMENTS IN STRUCTURAL FIRE EXPERIMENTS

Felix Wiesner¹, Luke Bisby²

ABSTRACT

Measuring movements and deflections in structural fire experiments can yield critical information to generate the knowledge required to further understanding of the behaviour of structural systems in fire. However, due to the influence of flames, smoke, and heat, detailed deflection measurements can be difficult to install and maintain during experiments involving fire or heat exposure. This paper describes the concept and functionality of a simple tracking mechanism for robust image analysis of structural elements heated from one side. The concept and its potential applications are demonstrated for a set of cross-laminated timber wall strips which were exposed to one-sided radiant heating whilst being subjected to sustained imposed loads. The deflected shape of the specimens was measured using a circle tracking technique, and the results then used to estimate and analyse the stresses within the wall strips' cross-sections.

Keywords: Image analysis; measurement techniques; deflected shape; curvature; engineered timber; fire safety research

1 INTRODUCTION

The detailed investigation of mechanical properties and behaviour of structural elements in fire requires the measurement of deflections and deformations in response to loads applied. These measurement data can then be used for research or testing outputs, either as performance criteria – as is often done for standardised testing procedures [1] – or to deduce the influence of fire and heat on changing mechanical properties (e.g. the structural stiffness from increasing deflections under sustained loads).

Cross-laminated timber panels are increasingly used as loadbearing walls in residential buildings. In a fire, these mass timber wall elements can act as compartment boundaries and will therefore be subjected to one-dimensional heating from one side. Thermal exposure will lead to charring, which will reduce the available cross-sectional area, causing asymmetrical loading conditions; this in turn will lead to bending moments and shear forces being developed due to P-Delta effects, which may ultimately culminate in a buckling failure [2-4]. Knowledge of the deflection history is therefore critical in correctly assessing the structural fire behaviour of CLT walls under sustained loading. It should be noted that this concept is equally applicable to other materials that are used for wall construction (e.g. concrete or encapsulated timber stud walls); CLT walls are used herein since this was the specific material for which the deflection measurements reported herein were required as part of a larger study [5].

¹ School of Civil Engineering, The University of Queensland, Brisbane, Australia
e-mail: f.wiesner@uq.edu.au, ORCID: <https://orcid.org/0000-0002-0231-4244>

² School of Engineering, The University of Edinburgh, Edinburgh, Scotland
e-mail: Luke.Bisby@ed.ac.uk, ORCID: <https://orcid.org/0000-0001-8293-4322>

A common method to measure deflections is to use linear potentiometers or string pot gauges, however these sensors require physical contact with the tested specimens. In addition, when using these sensors, it must be ensured that they are supported by a structural system that is independent from both the tested specimen and the structural loading frame; this must be done to avoid any influence from deformations of the specimen or loading frame on the absolute positioning of the sensor, otherwise the measurements will be corrupted by relative movements between these systems. It must also be thermally isolated so as to avoid thermal deformations. From these considerations it follows that each physical sensor requires a support system, which can be cumbersome to provide in an experimental set-up. In addition, these physical measurements can be limited by the travel that the sensors allow, imposing a physical cap on the range of deflections that can be measured. Another potential issue that arose for the testing described below was that linear potentiometers were not able to accurately measure movement in two directions. If an LP is placed onto a wall to measure the lateral deflections (the main point of interest for instability failure), then there is a non-negligible probability that the tip of the LP will stick to the specimen, causing bending in the LP as vertical movements are induced.

Physical measurements and sensors can be supported, supplemented, or replaced by visual observations and measurements. Most careful researchers who have undertaken measurements using the aforementioned physical sensors is likely to have implicitly confirmed their measurements visually; if a sensor states negative deflections but the observed movement is in the other direction, the accuracy of the sensor will have to be reassessed. If images are taken from a fixed frame of reference (i.e. the camera is not moved between images) then the movement of objects between frames can be identified from successive frames. This process can be digitized to measure the movement of objects in pixels, which can then be translated into real length scales through calibration images. These techniques are known as digital image correlation (DIC) and have been successfully used in multiple engineering disciplines [6,7] to measure strains and deflections. Image correlation technology has also been successfully used to study timber elements at ambient and/or elevated temperatures [8,9]. When fire exposure is considered (as would be expected for a combustible product such as timber) DIC will often experience challenges, since it relies on the detection of very small movements and can easily be disrupted by the presence of smoke or flames which cause problems in correlating between successive images [10]. The application of blue light, for example, to mask flames from images is a promising way to deal with this problem; however it is still in development [10].

The current paper introduces a method that sacrifices the high fidelity of common DIC techniques to employ a more robust method that can be implemented without the need for sophisticated equipment to measure spot deflections on specimens where smoke and flames might be present. The opportunities for this method are highlighted through demonstration of how multiple deflections can be used to measure curvature and to estimate stress profiles in fire-exposed cross-laminated timber walls.

2 METHODOLOGY

2.1 Experimental set-up

The measurements presented herein are of pinned-pinned CLT wall strips under sustained axial compressive load that were heated, using radiant panels, from one side at their centre portion. A drawing of the experimental set-up is shown in Figure 1. These experiments were part of a wider experimental campaign to study the load bearing capacity of CLT compression elements in fire [5]. The results presented herein are used to demonstrate the concept of novel deflection measurements and their use in analysis. The actual deflection outputs and failure times for the specimens (and their specific production parameters) are out of the scope of this paper and are therefore not explicitly addressed or discussed.

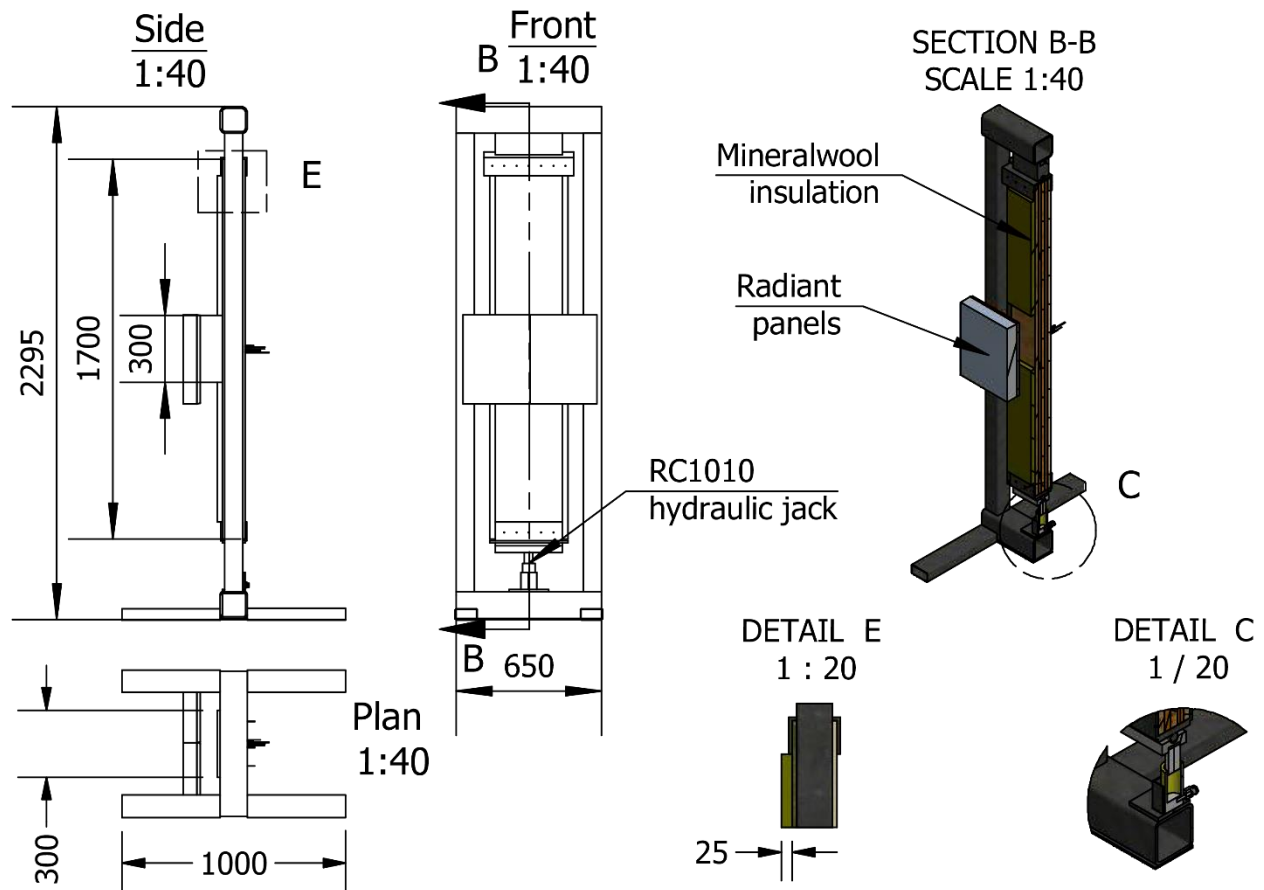


Figure 1. Schematics of the experimental set-up showing the CLT wall strip within the reaction loading frame, and faced by radiant panels.

2.2 Circle tracking

The methodology proposed in this paper relies on the detection of circular objects. For the tested CLT elements this was achieved through the simple application of circular adhesive targets to the fire unexposed side of the specimens. A camera was placed facing the side of the wall strips with a clear view on the targets. Images were taken every five seconds and circles in each image were detected through a Hough transformation [11,12] which relies on the parametrisation of each point that can be distinguished in the image based on its brightness (or lack thereof); this functioned well, as the chosen targets were black and the underlying surface was spruce, with a yellowish brown colour.

The basic principle to detect circular targets via Hough Transformation is described by Duda and Hart [11]. The centre coordinates and radii of circles are parametrised and transformed into three axial space, where each point is represented as a circular cone shape. Intersection of these cones by common points indicated that these points were located on the same circle, which can be identified by a high point count with shared coordinate parameters. Interested readers are advised to look into Duda and Hart's description [11], offering an interesting explanation of early computer vision methods. The actual implementation of the Hough Transformation varies; herein the MATLAB *imfindcircle* function [13], which employs a 2D array of point (pixel) count to speed up computations, was used.

This procedure enabled the determination of the position of each circle at each time step, and from this the movement of each circle relative to its original position could be deduced. This concept is visualised in Figure 2, showing detected and traced circles along the unexposed edge for a CLT wall strip at the beginning of an experiment, along with the deflected shape when buckling failure is imminent.

Smoke was observed to flow through the frame of reference and across the traced circles in some of the experiments. This was observed to not influence the measurements, highlighting the robustness of this method (at least for the experiments performed to date).

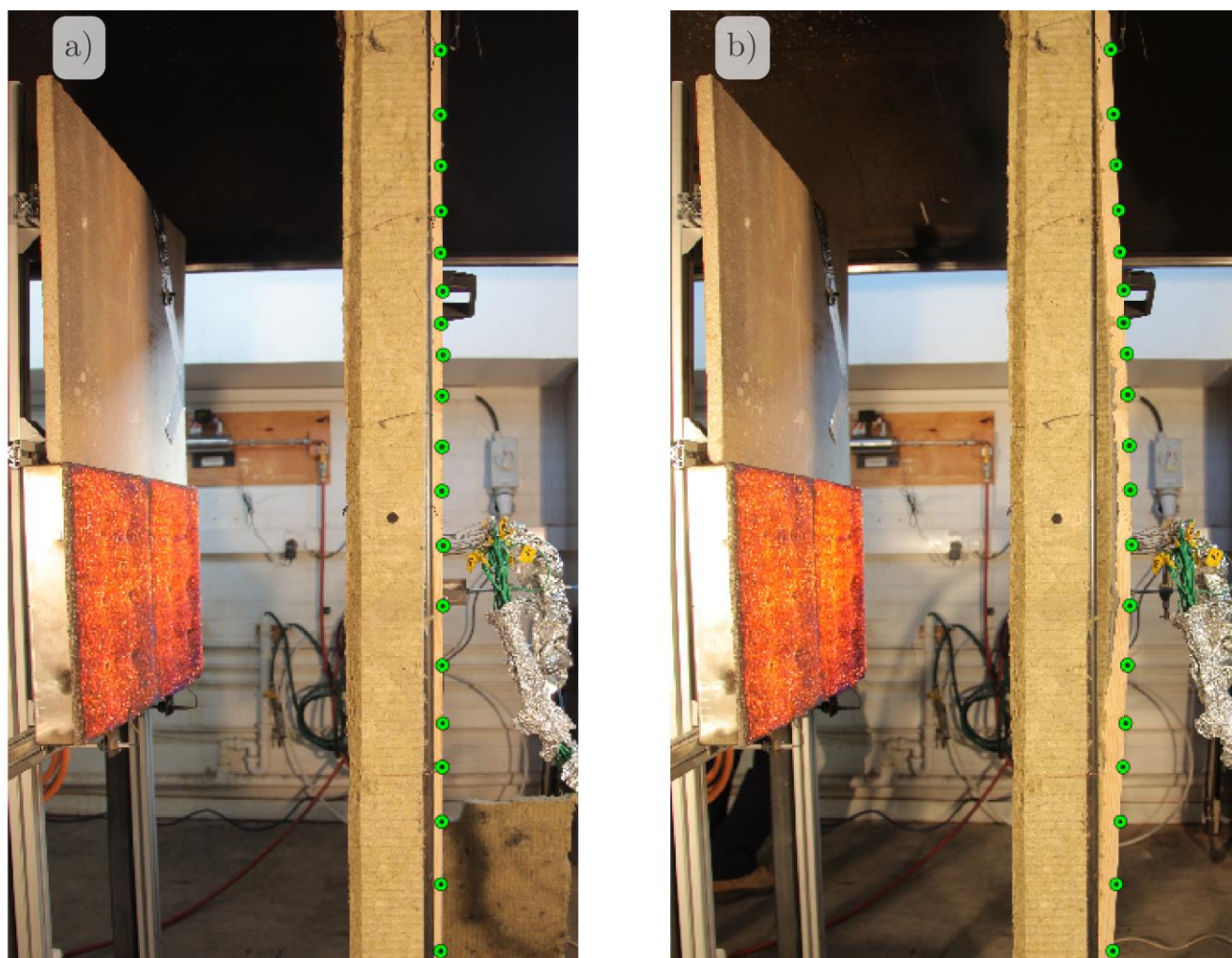


Figure 2. Highlighted circles for deflection measurements along the unexposed edge of a CLT wall strip at a) start of an experiment and b) approaching buckling failure of the specimen.

2.3 Validation

The image-based deflection measurements of the lateral deflections can be compared against simultaneous measurements from a linear potentiometer (LP) that was placed at midspan on the unexposed side of the wall strips in these experiments. A comparison of these two measurements is shown in Figure 3 to validate principles of the image tracking; it can be seen that the image-based measurements closely align with the LP measurements. Some minor deviations can be observed in Figure 3 a) and b): (1) the LP measurements are delayed, highlighting that the image-based tracking is capable of registering smaller deflection changes. Since the LP has some stiffness itself and timber is a rather soft material, where force is applied perpendicular to the cross-wise direction. As the timber moves the tip of the LP causes a local indentation in the timber surface rather than measuring the deflection. This issue does not arise for the image-based tracking, as it does not rely on any physical contact with the samples. (2) The indentation of the tip of the LP in the timber results in curvature of the LP shaft if the wall strips deflect vertically – this influences the measurements and can cause sudden shifts and discontinuities when elastic energy in the bent LP means it shifts position, as shown in Figure 3 b).

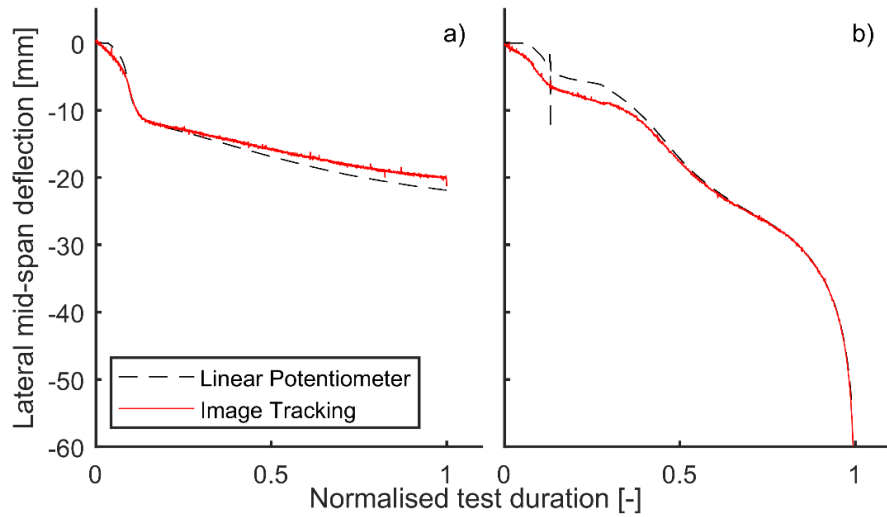


Figure 3. Comparison of the lateral midspan deflection between a linear potentiometer and the proposed image tracking methodology for two wall strip experiments.

3 DEFLECTION TRACKING – WHAT IS IT GOOD FOR?

The proposed measurement technique is not entirely novel in itself, and many prior researchers have presumably used similar techniques in their research without explicitly reporting on it. The following section explores the possibilities of this methodology to gain further insights into the structural performance of a material or structural element.

One advantage of the proposed methodology is that multiple deflection points can be created and traced throughout an experiment; this allows for the determination of the deflected shape of the specimen. The position of the points can be used to fit a sinusoidal curve fit of deflected points against the height of the wall strips. This is shown in Figure 4, where it can be observed that reasonably accurate fits can be achieved.

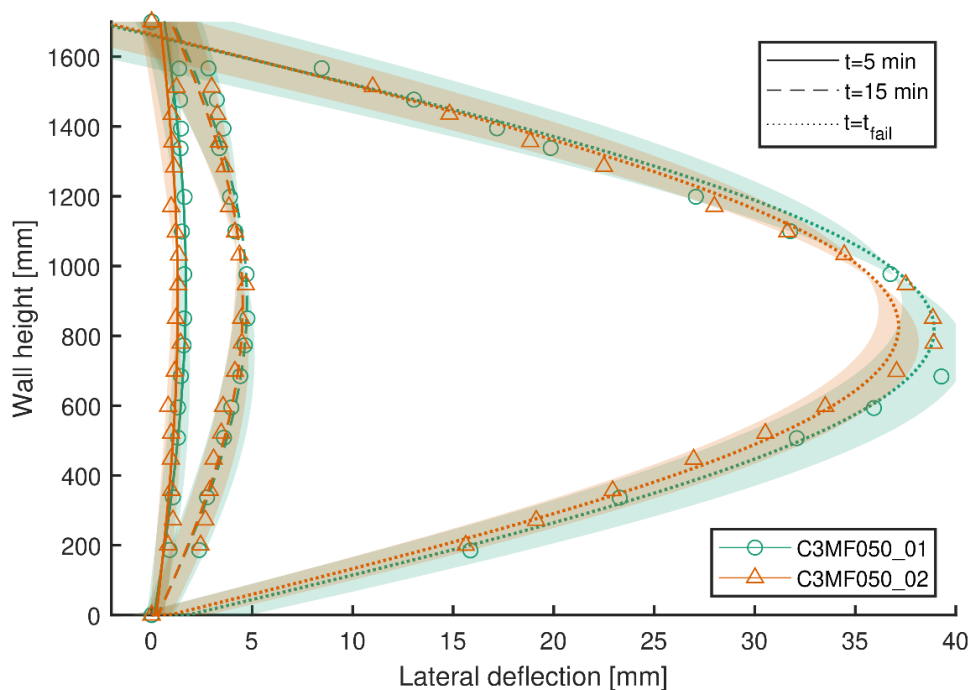


Figure 4. Vertical and horizontal position of tracked points on two repeat experiments for CLT wall strips and fitted Sine curves at selected time steps. Shaded areas show the 95 % confidence interval of the fitted curves.

4 DISCUSSION

The obtained sinusoidal functions of the deflected shapes were subsequently used to differentiate the horizontal deflection, v , twice with respect to height, x , to yield an expression for the curvature, κ , as highlighted in Equation (1). To assess the effects of a thermal gradient in the samples, the assessed wall strip could then be divided into a number of slices along its width. Each slice, numbered i , was attributed a value corresponding to its estimated elastic modulus, E_i , which depends on its temperature, and, for CLT, the orientation of its wood fibres with respect to the main loading direction. The stress, σ_i , in each slice was then calculated as the product of the elastic modulus and the strain, which is the product of curvature and the distance to the neutral axis position within the cross-section, na , as shown in Equation (2).

$$\kappa = \frac{d^2 v}{dx^2} \quad (1)$$

$$\sigma_i = \kappa \cdot (na - y_i) \cdot E_i \quad (2)$$

This procedure could then be used to determine the stress profiles throughout the CLT cross-section at all timesteps throughout the experiments. One unknown variable when analysing the stress profile of timber with a thermal gradient is the neutral axis position. The reduction in elastic modulus for timber at elevated temperatures varies for timber in tension and compression [14,15]. To find the neutral axis location through force equilibrium, as shown in Equation (3), where A_i is the cross-sectional area of slice i and P is the applied force, it must be known which parts of the cross-section are in tension and which are in compression. However, this must be determined from knowledge of the neutral axis position; thus, an iterative approach is required to approximate the location of the neutral axis position.

$$\sum_{i=1}^{n_s} \sigma_i \cdot A_i - P = 0 \quad (3)$$

The measured temperature profile and the estimated stress profiles arising from the procedure outlined above are shown for a three ply CLT wall system at selected times in Figure 5. The wall can be observed to be in compression for the majority of the test duration, before a sharp increase in tensile stresses on the unexposed face occurred with progressing lateral deflections, leading to buckling failure.

The results and analysis highlighted above can be used to better understand the mechanical response and failure behaviour of wall systems that are subjected to one-sided heat exposure and sustained loads. From Figure 5 it can be seen that tensile stresses only reach structurally relevant values in the later stages of the experimental duration. In design, the assessment and grading of timber is heavily focused on its modulus of rupture (also sometimes denoted as bending ‘strength’), which is characterised by its tensile properties. These results show that more knowledge on the mechanical properties of timber in compression and the effects of elevated temperatures is needed to correctly assess failure criteria for engineered timber in fire.

The ideas outlined in this paper demonstrate how simple image correlation methods can be utilised to test assumptions and validate theories through the combination of measurements and simple analytical expressions based on first principles.

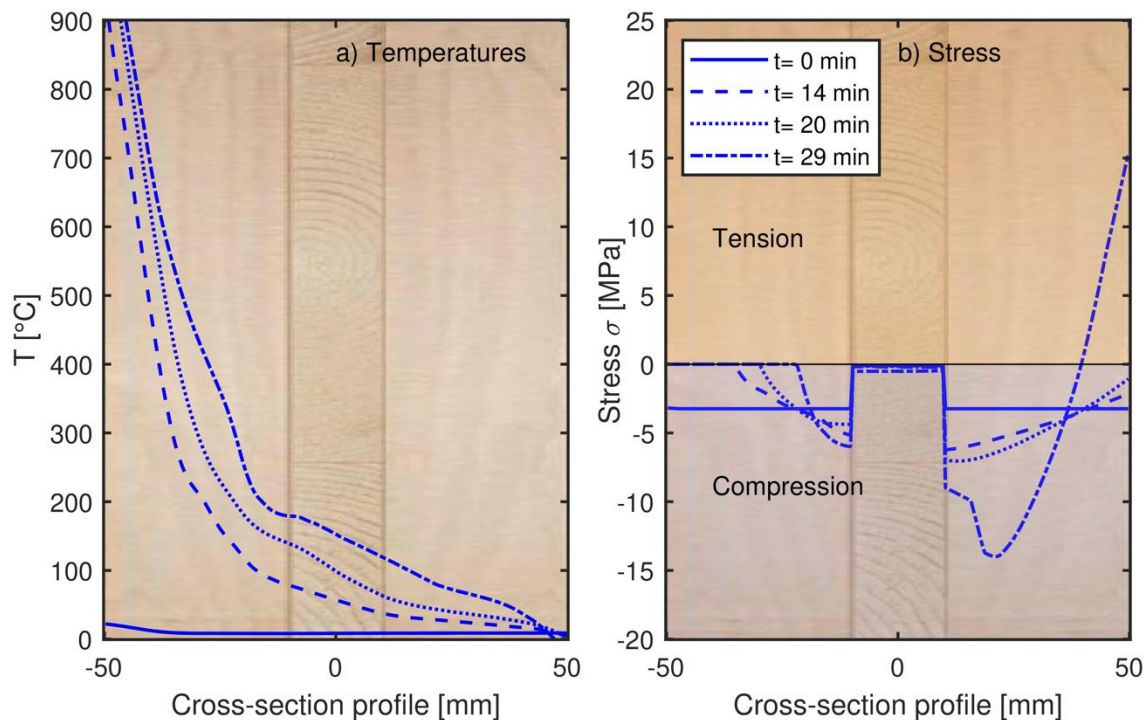


Figure 5. (a) Temperature and (b) estimated stress profiles at selected temperatures to failure for a three ply CLT wall strip.

5 CONCLUSIONS

A novel but simple technique for image-based deflection measurements is proposed and demonstrated for cross-laminated timber wall strips subjected to one sided heat exposure. The technique utilises circle tracking of adhesive targets that were placed on the edge of wall samples that were subjected to one sided fire exposure. A validation of the robust circle tracking method is provided using physical measurements from a linear potentiometer. The usefulness of this technique has been highlighted via assessment of the curvature from measured deflected shapes.

The resulting assessment of the stress profiles in the timber walls has been used to highlight that tensile stresses in cross laminated timber walls exposed to fire from one side only become relevant when deflections are considerable and failure is imminent.

The work presented herein suggests novel opportunities for better and more robust assessment of deflections, leading to improved insights into structural behaviour.

ACKNOWLEDGMENT

The authors gratefully acknowledge support from Arup and the University of Edinburgh to undertake the experiments from which this paper draws its primary data. The authors would also like to acknowledge support from the UK Engineering and Physical Sciences Research Council (EPSRC, EP/M508032/1) and the National Centre for Timber Durability and Design Life. Mayr-Melnhof Holz are acknowledged for their generous contribution of materials.

REFERENCES

1. CEN (2014) EN 1365-2 Fire resistance tests for loadbearing elements. Floors and roofs. European Committee for Standardisation, Brussels
2. Suzuki J-i, Mizukami T, Naruse T, Araki Y (2016) Fire Resistance of Timber Panel Structures Under Standard Fire Exposure. *Fire Technol* 52 (4):1015-1034. doi: <https://doi.org/10.1007/s10694-016-0578-2>

3. Wiesner F, Randmael F, Wan W, Bisby L, Hadden RM (2017) Structural response of cross-laminated timber compression elements exposed to fire. *Fire Safety Journal* 91 (Supplement C):56 - 67. doi:<https://doi.org/10.1016/j.firesaf.2017.05.010>
4. Kippel M, Leyder C, Frangi A, Fontana M (2014) Fire tests on loaded cross-laminated timber wall and floor elements. *Fire Safety Science* 11:626-639
5. Wiesner F (2019) Structural behaviour of cross-laminated timber elements in fires. Thesis, The University of Edinburgh, Edinburgh
6. Stanier SA, Blaber J, Take WA, White DJ (2015) Improved image-based deformation measurement for geotechnical applications. *Canadian Geotechnical Journal* 53 (5):727-739. doi:10.1139/cgj-2015-0253
7. White D, Take W, Bolton M (2003) Soil deformation measurement using particle image velocimetry (PIV) and photogrammetry. *Geotechnique* 53 (7):619-631
8. Wiesner F, Deeny S, Bisby LA (2020) Influence of ply configuration and adhesive type on cross-laminated timber in flexure at elevated temperatures. *Fire Safety Journal*. doi:10.1016/j.firesaf.2020.103073
9. Quiquero H, Chorlton B, Gales J (2018) Performance of Adhesives in Glulam After Short Term Fire Exposure. *International Journal of High Rise Buildings* 7 (4)
10. Smith CM, Hoehler MS Application of Digital Image Correlation to Structures in Fire. In: Lamberti L, Lin M-T, Furlong C, Sciammarella C, Reu PL, Sutton MA (eds) *Advancement of Optical Methods & Digital Image Correlation in Experimental Mechanics, Volume 3*, Cham, 2019// 2019. Springer International Publishing, pp 129-131
11. Duda RO, Hart PE (1972) Use of the Hough transformation to detect lines and curves in pictures. *Communications of the ACM* 15 (1):11-15
12. Atherton TJ, Kerbyson DJ (1999) Size invariant circle detection. *Image and Vision computing* 17 (11):795-803
13. MATLAB (2019) `imfindcircles` 9.7.0.1190202 (R2019b). The MathWorks Inc, Natick, USA
14. König J, Walleij L (2000) Timber frame assemblies exposed to standard and parametric fires: part 2: a design model for standard fire exposure. *Institutet för Träteknisk Forskning* (0001001):1-76.
15. Gerhards CC (1982) Effect of moisture content and temperature on the mechanical properties of wood: an analysis of immediate effects. *Wood and Fiber Science* 14 (1):4-36

ALKALI-ACTIVATED SPRAYED CONCRETE AS A FIRE PROTECTION COATING FOR TUNNELS' INNER LINING: PROOF-OF-CONCEPT STUDY ON THE HEAT TRANSFER

Anna-Lena Hammer¹, Christian Rhein², Thomas Rengshausen³, Markus Knobloch⁴, Götz Vollmann⁵,
Markus Thewes⁶

ABSTRACT

Existing road and railway tunnels in Europe are characterised by progressive ageing. Due to dramatic events, such as the Montblanc and Gotthard Tunnel fires [1] and novel research findings, European authorities have reviewed and revised several guidelines for the design of tunnel structures in recent years. The resulting requirements for the construction – as they are defined by the German authorities – are the consideration of the closed fire curves according to ZTV-ING and EBA guidelines [2, 3] for the design process of the structural fire protection. The German authorities ask for applying these rules even if the current state of an existing tunnel construction causes repair or upgrading, which often brings up problems of conformity. Within the national research project KOINOR [4] a sprayable alkali-activated concrete (AAC) is currently being developed, which should fulfil these requirements, especially in terms of heat transfer and spalling avoidance. A proof-of-concept study has confirmed good fire resistance properties of AAC. This paper presents this first of its kind study on the heat transfer of the developed material. The material-technological development is outlined and investigations on heat transfer are analysed. In order to optimise the heat transfer behaviour, various additives were compared as an extension of the basic AAC recipe. The test results have shown that sprayable AAC withstands the temperature loading without obvious damages. Additionally, the use of an air polymer has a positive influence on the heat transfer behaviour.

Keywords: tunnel fires; tunnel repair; tunnel refurbishment; sprayed concrete; alkali-activated concrete; geopolymer; cement free concrete; fire tests

1 INTRODUCTION

The building stock of tunnels for road, rail and public underground transport in Germany corresponds to the Central European tunnel age characteristic. That said, the infrastructure is progressively ageing. The oldest road tunnels were built in the 1970s and are therefore more than 50 years old. Railway tunnels in Germany were built since 1850, accordingly about 15% of the German railway tunnels are more than 150 years old. Hence, there will be an increased need for maintenance and structural improvements in the future. [5, 6]

¹ Dr.-Ing., Institute for Tunnelling and Construction Management, Ruhr University Bochum
e-mail: anna-lena.hammer@rub.de, ORCID: <https://orcid.org/0000-0003-2399-6149>

² M.Sc., Institute for Tunnelling and Construction Management, Ruhr University Bochum
e-mail: christian.rhein@rub.de, ORCID: <https://orcid.org/0000-0001-9174-7158>

³ M.Sc., PORR GmbH & Co. KGaA
e-mail: thomas.rengshausen@porr.de, ORCID: <https://orcid.org/0000-0001-9846-7650>

⁴ Univ.-Prof. Dr., Chair of Steel, Lightweight and Composite Structures, Ruhr University Bochum
e-mail: markus.knobloch@rub.de, ORCID: <https://orcid.org/0000-0002-1289-0691>

⁵ Dr.-Ing., Institute for Tunnelling and Construction Management, Ruhr University Bochum
e-mail: goetz.vollmann@rub.de, ORCID: <https://orcid.org/0000-0002-6284-524X>

⁶ Prof. Dr.-Ing., Institute for Tunnelling and Construction Management, Ruhr University Bochum
e-mail: markus.thewes@rub.de, ORCID: <https://orcid.org/0000-0003-1777-2616>

Dramatic tunnel fire events such as Montblanc (1999) and Gotthard (2001) [1] showed that, in addition to operational improvements, upgrades in structural fire protection are also necessary. Consequently, the applicable standards and regulations were amended to this effect by the German authorities by setting higher requirements for constructive measures of tunnel infrastructure. [7]

However, the vast majority of existing traffic tunnels were built according to specifications that can be considered obsolete today. This means that in case of severe fire exposures, potentially large amounts of damage are to be expected due to outdated design properties. A repair or structural improvement up to today's safety levels is therefore necessary in a timely manner, but becomes mandatory when the structure needs to be repaired due to ageing and deterioration problems, for instance as a result of chloride migration phenomena. Internationally, there are no uniform temperature-time curves for the fire design of tunnels; therefore, many authorities refer to their national guidelines. For Germany, the decisive requirements for the constructions are a minimum concrete cover of 6 cm and the maximum steel rebar temperature is limited to 300 °C in case of fire. With that in mind, closed fire curves were developed and are regulated via the ZTV-ING and EBA guidelines [2, 3].

However, a tunnel with a need for a substantial refurbishment has also to comply with these structural guidelines, which might lead to an interference with regulations for the safe operation, especially in terms of available clearance gauge and other constraints. Actually, there exist several tunnels in Germany that cannot be safely refurbished due to such impasses.

The national research project KOINOR aims to develop new concepts for the repair and retrofitting of underground infrastructures, especially with fire scenarios in mind. With this setup, the partners currently are developing an alkali-activated cementless concrete for the structural improvement of traffic tunnels. This material shall comply with the described requirements while also allowing a quick and easy rehabilitation process with minimum disturbance of the regular tunnel operation due and with no substantial interference with safety regulations and an overall safe operation of infrastructure tunnels.

2 REQUIREMENTS AND CONSTRAINTS FOR THE STRUCTURAL FIRE PROTECTION OF TRAFFIC TUNNELS

2.1 Fire curves

Internationally, there are different fire curves for the design of structural fire protection of tunnels available, depending on the responding authorities and the transport carrier of the tunnel. In principle, the individual curves follow the pattern of rapid temperature development and a subsequent full fire phase in a similar way. The main differences occur in the determination of the duration of the full fire phase and the consideration of a cooling phase.

For the design process in international building construction the unit temperature-time curve (UTC) is generally used. Since there are no uniform temperature-time curves available, that could be used for the fire design of tunnels; many authorities developed their own national guidelines. In Germany, these are the fire curves according to ZTV-ING and EBA guidelines [2, 3]. Due to a high linear temperature increase of 240 K/min, the maximum temperature of 1,200 °C is reached in both curves after a heating phase of only 5 minutes. This is followed by a full burning phase on an identical course, except for the overall duration. While the full fire phase takes only 25 minutes according to ZTV-ING [3], the EBA curve [2] prescribes a full burning phase with a duration of 55 minutes. A subsequent cooling phase of 110 minutes is prescribed in both curves. In contrast to the UTC defined in [8], both German tunnel-specific curves presented are so-called closed fire curves. This means that after the firing phase at maximum temperature a cooling phase is considered. In contrast, open curves can be extended in the fire duration to be applied and thus typify a fire with a constant supply of fuel and oxygen and without effective extinguishing action [9]. Figure 1 shows the course of the described German tunnel fire curves together with the UTC and other international tunnel fire curves.

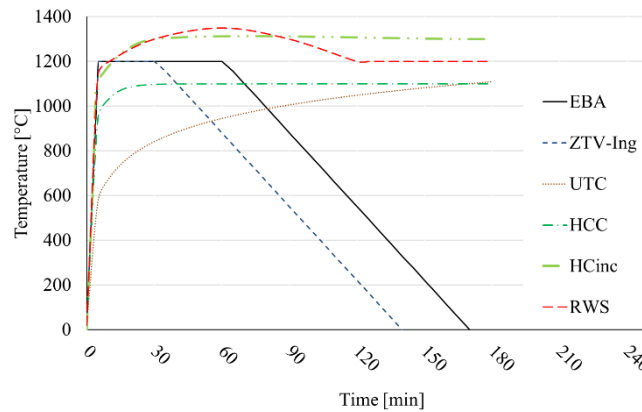


Figure 1. Comparison of normative fire curves

Since the KOINOR research project is a national project funded by the German Federal Ministry of Education and Research (BMBF), the EBA curve was selected as a national worst case scenario and as the decisive specification of German guidelines for the investigations.

The EBA curve was designed based on the fire of a single passenger coach. The fire of an entire passenger train or a freight train fire with significantly higher fire loads was classified as a negligible risk due to the low probability of occurrence as a result of measures to prevent a burning train to stop inside a tunnel, according to the European regulations for the safe operation of train tunnels [10]. [11]

2.2 Concrete spalling

With cement-based concrete, the development of spalling can be observed in almost all cases of fire [12]. Concrete spalling in the event of fire depends on a variety of influencing factors such as fire development and temperature, component geometry as well as moisture content, porosity, density and strength of the concrete [13–15]. According to Kordina and Meyer-Ottens [16], a classification is made between aggregate spalling, the sloughing off of concrete layers, and explosive spalling. According to this classification, concrete spalling as a result of cracking or splintering aggregates poses the least [11] and explosive spalling, that involves sudden spalling of concrete layers close to the edges, represents the greatest potential danger to the stability of a tunnel in the event of fire [13].

As a result of concrete spalling, either the reinforcement is directly exposed to the thermal action or the remaining layer thickness is heated up so that the requirements on the reinforcement temperature discussed in Section 2.3 are exceeded. Both can lead to failure of the reinforcement, to partial structural failure of the tunnel lining, combined with loss of serviceability, up to complete loss of the structure.

The occurrence of concrete spalling can be reduced by adding polypropylene (PP) fibres to the fresh concrete mixture, although the exact mechanisms of the accompanying effects that PP fibres provide are research subjects that are widely and controversially discussed [17–20]. However, according to German regulations [2, 21], the addition of polypropylene (PP) fibres is mandatory for the concrete of tunnel inner linings. Accordingly, in Switzerland [22] and Austria [23, 24] the use of PP fibres as a fire protection measure for tunnel linings is also regulated by various standards and directives.

In addition to the prescribed use of PP fibres, railway tunnels in Germany are required to minimise the expected concrete spalling depending on the expected risk of fire [21]. In Austria, for instance, expected spalling of more than 1 cm must be taken into account in the dimensioning of components [24]. In the USA spalling must be minimised or avoided completely [25].

Practical experience shows, however, that despite the addition of PP fibres, spalling of the inner shell can occur in the event of fire [26]. In addition, the workability of the fresh concrete is considerably poorer if large quantities of PP fibres are used.

2.3 Rebar temperature

In addition to the specifications on fire loads and possible concrete spalling, the national and international guidelines contain specifications on either maximum permissible temperatures of the steel reinforcement or maximum concrete surface temperature. In a comparison of international guidelines for structural fire protection of road tunnels, the USA, the Netherlands and Austria have the strictest specifications with a maximum reinforcement temperature of 250°C [24, 25, 27]. The maximum temperature of the concrete surface in the USA and the Netherlands is limited to 380°C [25, 27]. In Austria, 350°C is defined as the maximum value for the concrete surface temperature, while Swiss regulations allow a maximum temperature of 450°C [22, 24]. Furthermore, a minimum concrete cover of 50 mm is prescribed in Austria for road and railway tunnels, even without taking into account a possible attack by de-icing agents [24]. In Germany, the value of the minimum concrete cover for road tunnels according to ZTV-ING [2] is 60 mm. According to ZTV-ING [2], the structural fire protection of road tunnels must be based on the fact that the supporting reinforcement is not heated above 300 °C in case of fire. This can usually be ensured by maintaining a sufficient concrete cover. If the design specifications of a minimum thickness of the permanent lining of 35 cm in total and a 6 cm thick concrete cover are fulfilled, no further structural fire protection measures are required. In the German guidelines there is no specification for a maximum concrete surface temperature.

3 CHARACTERISTICS OF ALKALI-ACTIVATED CONCRETE

In alkali-activated concrete (AAC), alternative binders are used to replace the cement. These binders form a durable three-dimensional network, which makes such concretes particularly resistant to sulphate and chloride attacks. Furthermore, these materials are considered to have good fire resistance. [28–30] In addition to these technological advantages of AAC, another positive property is the absence of cement in the concrete matrix. Global cement production currently accounts for about 5-7 % of global CO₂ emissions [31, 32]. Considering this, the use of alternative, cementless binders is becoming environmentally increasingly important.

3.1 Application

Compared to common cements, alkali-activated binders only generate about 70% of the CO₂ emissions of an equal cement production [33]. Moreover, the production of cement consumes more natural resources than the production of alkali-activated binder [30].

The mentioned fire resistance of AACs compared to cement-based concretes [30, 33] is mainly due to the lower proportion of water in the matrix, which in addition has stronger bonds in AACs than in cement. Cement-based concretes generally have a bound water content of about 15 %. When exposed to high temperatures, this water passes into the gaseous phase, which can lead to spalling as described above. [33]

Due to their advantages, alkali-activated concretes have already been successfully implemented in various areas of the international construction industry. Alkali-activated slags have been used for constructive purposes in building constructions in the Ukraine and Russia whilst alkaline-activated mixing systems of fly ash and granulated blast furnace slag have been applied for sewer construction and infrastructure works in Australia. Moreover, in Australia the use of AACs is successfully established as an approved alternative building material [34]. The approved AAC product based on fly ash and granulated blast furnace slag as well as fine and coarse aggregates, was already tested for its fire resistance [35].

Alkali activated concretes have so far only been used for the production of in-situ concrete or precast concrete elements. An application as shotcrete has not yet been published. Despite numerous successful international applications, they are still considered a niche product in Europe and are not widely used in practice. The often occurring problem is that – compared to “classical” concrete – no reliable design principles and accompanying recipe designs are currently available. That said, a full compliance with EN 1992 or other comparable codes is currently not a given.

3.2 Composition

In alkali-activated concrete (AAC), alternative binders such as fly ash or slag sand replace the cement. An alkaline activator controls the hardening process of the concrete. Positive properties of the alkali-activated concrete are its high sulphate and chloride resistance and in particular its high fire resistance [28–30]. Compared to common concrete, few water molecules are dissolved and are very strongly integrated into the resistant three-dimensional aluminosilicate network, as shown in Figure 2 [33]. The proportion of chemically bound water within the concrete matrix is therefore a decisive factor for the resistance to the effects of fire and leads to a very low or even no tendency to spalling of the alkali-activated concrete.

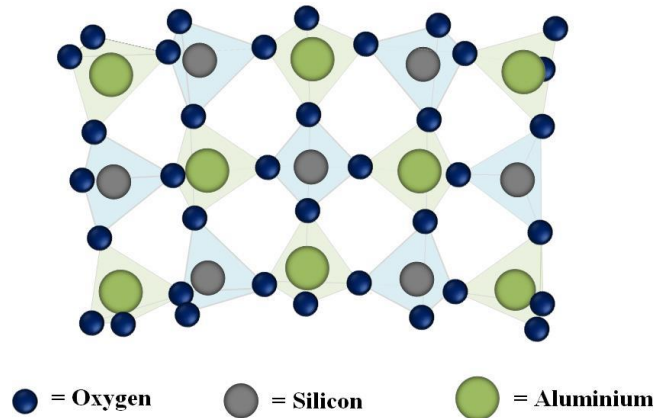


Figure 2: Three-dimensional aluminosilicate network of AACs

AACs can generally be characterized as inorganic binders consisting of a reactive powdery solid and an alkaline activator solution [36]. During the geopolymerisation – the chemical reaction of these two components – the mixture hardens and forms a water resistant and spatially stable three-dimensional aluminosilicate network (Figure 2) [33]. Metakaolins and fly ashes are used as reactive solids [37], whilst alkali hydroxides and silicates such as sodium and potassium are frequently used for the activator solution [38]. In principle, all raw materials with sufficient SiO_2 and Al_2O_3 in reactive form can be used for alkaline activation [36]. However, the choice of reactive raw materials as well as the alkaline activator solution influences the course of the reaction processes and thus the resulting concrete properties to a high extend [37].

Alkali-activated concretes are also often referred to as "geopolymers" [37, 39]. More recent observations, however, have pointed out that geopolymers are a subgroup of AACs with a particularly low calcium content of less than 10 M-% [36, 37, 40]. As the calcium content of the solids increases, the strength-forming reaction products change. If the limit value of the Ca content of 10 M-% is exceeded, the formation of cement clinker phases is increasingly observed [36]. This leads to improved mechanical properties [36], but also to cement-like workability and durability properties [37].

3.3 Fire resistance and heat transfer

In contrast to cement-based components with PP fibres, fire tests on AAC components are not widespread and there are few reliable results from such tests, despite the described fire safety properties that can be expected.

The fire tests carried out in Australia as part of the approval of the AAC building material (see section 3.1) were based on the unit temperature curve with a full fire phase of 4 hours, whereby maximum fire temperatures of 1150 °C were reached [35]. During the tests, neither concrete spalling nor other damage patterns on the surface of the test specimens were detected. However, it should be taken into account that the UTC specifies a significantly slower temperature rise and lower maximum temperature for the fire phase than the EBA curve.

The heat transfer through large scale reinforced wall panels and small scale cubes and cylinders made of fly ash based AA mortar without aggregates were investigated by Ali [41] with respect to the HC curve. Due to the higher specific heat capacity, the thermal conductivity of the investigated material was lower

than with cement-based mortar. No spalling on the surface of the material could be detected in these tests although the HC curve applied is characterised by a rapid rise of temperature similar to the EBA curve. However, even in this case the maximum temperature is not comparable with the specifications of the EBA curve.

In order to be able to estimate the spalling tendency of AACs when exposed to high temperatures, the partners in the KOINOR project carried out preliminary investigations. Therefore, two concrete slabs were equipped with state-of-the-art repair coatings. On the one hand, a cement-based coating was used, which was developed for use under the conditions of the RWS curve and on the other hand an AA mortar. As shown exemplary in Figure 3 (A), a metal block at about 1,300 °C was stored on both test specimens for about 10 minutes. According to figure 3 (B and C), concrete spalling could be observed on the cement-based material, while only fine cracks were visible on the surface of the AA coating. Furthermore, the cracks in the AA mortar were merely cracks that had propagated from the concrete substructure into the coating. [4]

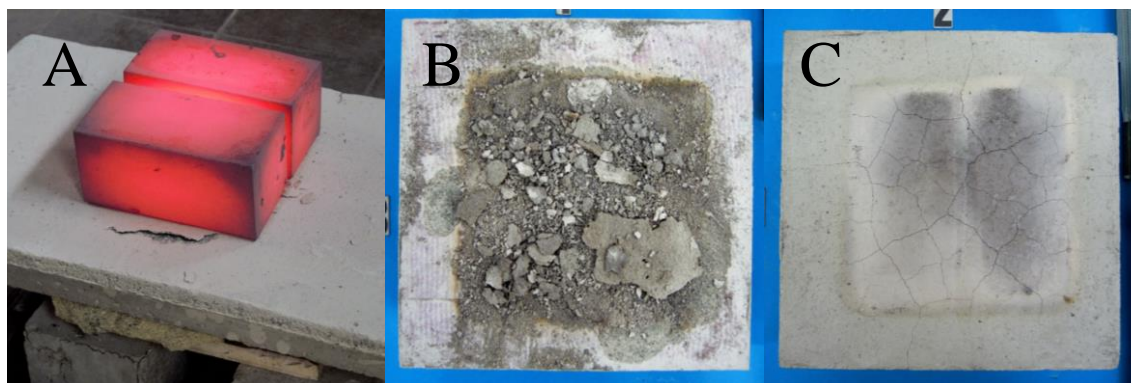


Figure 3. Heat exposure investigations carried out in the KOINOR research project | A: example of heat exposure | B: cement coated specimen after heat exposure | C: AA mortar coated specimen after heat exposure [4]

4 PROOF-OF-CONCEPT STUDY ON HEAT TRANSFER

During a comprehensive study the behaviour and overall performance of different recipes were observed and a preferred mixture was selected. In order to achieve this, ten recipe variations were initially developed using different basic materials. Test specimens of these recipes were then placed in a muffle furnace at a maximum temperature of 1,200 °C for 60 minutes. The recipe of the test specimen that showed the least deformation was selected as the basic recipe for the study presented here. In this context, a eutectic at about 1,150 °C was found for most of the test specimens investigated. The study on recipe development is not part of this publication. The authors refer to [4] and [42] for further consideration.

For a subsequent Proof-of-concept study, the selected basic recipe is modified for the investigations of its heat transfer properties. That said, a total of five different variations are available. For the different variations, additives are used which have already proven their worth in reducing the heat transmission with cement-based concrete technology.

Since the studies presented here are intended to be a proof-of-concept study in preparation for further material investigations and to provide initial insights into the material behaviour, some deviations from the standardised test procedure are accepted. These deviations in particular relate to the production of the test specimens, the choice of the maximum furnace temperature and the application of the temperature-time curve.

4.1 Composition

In concrete technology, some additives serve to reduce the density of the building material and thus delay the heat transfer. The additives used in this case are in detail micro hollow spheres and air-entraining agents (AEA).

Hollow microspheres with an elastic plastic shell are lightweight aggregates. They are used in cement-based concretes to reduce capillary suction and increase freeze-thaw resistance. Due to the ball bearing effect, the addition also improves the workability. MC Bauchemie's micro hollow spheres are known as air polymer. Their plastic shell dissolves during the hardening of the concrete, leaving voids of the appropriate size in the concrete. The air polymer is used to modify the recipe to determine whether the fire protection properties of the AAC are improved by the addition, due to the reduced thermal conductivity of the voids.

AEAs are used to create uniformly distributed, spherical air voids in concrete. The size of the air-filled pores usually remains below 0.3 mm. Since an increased air void content can reduce the thermal conductivity of a concrete, different recipes with varying AEA content are to be used in the planned fire tests.

Table 1 shows the recipe variations due to the additives to be used, with the basic recipe remaining unchanged in order to compare the results.

Table 1. AAC recipes to be used in heat transfer tests; all data in [g]

Recipe	Basic	Variation 1	Variation 2	Variation 3	Variation 4
Water demand	2000	2000	2000	2000	2000
Blast furnace slag	1800	1800	1800	1800	1800
Filler EFA (fly ash)	3600	3600	3600	3600	3600
Silica Fume	300	300	300	300	300
Activator	550	550	550	550	550
F36 quartz sand	3440	0	3440	3440	3440
Sand 0,2-0,6	2680	2680	2680	2680	2680
Sand 1,0-2,0	4500	4500	4500	4500	4500
Sand 2,0-3,0	3730	3730	3730	3730	3730
Air polymer	-	259	-	-	-
AEA	-	-	19,28	38,52	57,84

4.2 Experimental setup

When dimensioning the test specimens for the heat exposure tests, various boundary conditions must be taken into account. The maximum specimen size is determined by the internal size of the muffle furnace to be used, which is about 50 x 50 x 50 cm for the largest available furnace within the scope of these investigations. The muffle furnace chosen can be seen in Figure 4 A. A minimum sample size is also given by the use of the thermocouples. These sensors must be mounted at a defined distance from each other. Nevertheless, the sensors should be installed in a sufficient amount to obtain a reliable temperature profile. An additional factor influencing the dimensioning of the samples is the required storage time, which must be sufficiently long to ensure an equilibrium regarding the moisture content within the samples. Due to the factors described above and since the production of sprayed concrete test specimens represents a disproportionate effort within the framework of a proof-of-concept study, the AAC specimens are poured into conventional cube moulds of 15 x 15 x 15 cm according to DIN EN 12390-2, as no significant influence on the results is expected. After casting, the test specimens are stored and covered with a vapour-tight film for 24 h and then stripped. After a subsequent storage time of 72 h in a water bath, the samples are stored dry for 24 d before the tests are carried out.

In order to obtain a temperature profile for the respective sample cubes, a total of six measuring points are defined. The type K thermocouples are arranged in five layers inside the sample and another sixth layer is located on the upper surface of the cube. The arrangement is made at symmetrical distances from the centre of the sample, with the middle layer being in the centre of gravity of the cube. In this way a reliable temperature profile can be determined over the entire thickness of the cube. Since a common cube formwork was used, a non-destructive insertion of the measuring technique into the test specimens during the casting process was not possible. Due to the small vertical distance between the holes, which is further reduced by the hole diameter, holes two and four for the sensor insert are drilled from the back of the test specimen as shown in Figure 4 B. In this way, non-destructive drillings can be achieved. After the insertion of the thermocouples, the boreholes are sealed with an approved heat resistant adhesive.

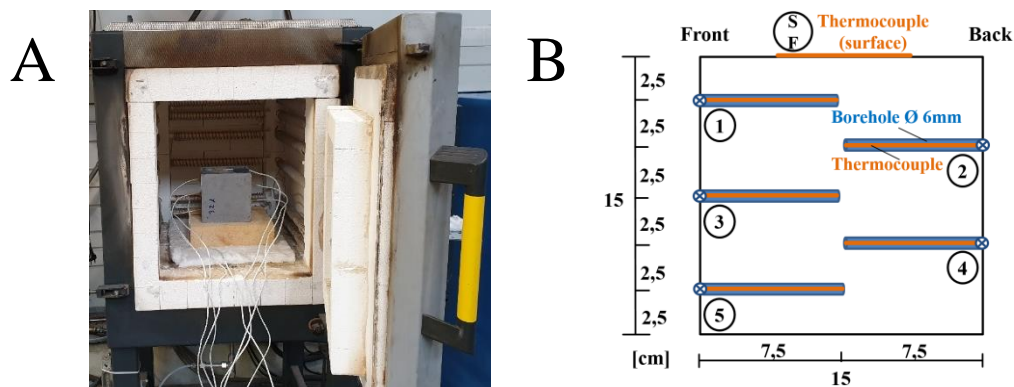


Figure 4. A: AAC test specimen with measuring technology in the test furnace | B: Schematic representation of the arrangement of the thermocouples in the test specimen

The selection of the muffle furnace is based on local availability and feasibility. Despite an attainable maximum temperature of up to 3,000 °C, none of the previously presented design fire curves (Section 2.1) can be reproduced with this electric furnace. Due to the required lengthy heating phase the prescribed test temperature can only be reached after several hours. Even placing the samples in a preheated furnace as in the previous investigations (see [4, 42]) is no longer possible for these tests due to the high heat, the large furnace opening and the complex measuring technology built into the specimens. The test specimens must remain in the furnace during the entire heating and cooling phases. Although the normative time temperature curve cannot be represented in its course within the context of the presented investigations, the full firing phase of 55 minutes at maximum temperature is maintained. Due to the longer durations of the heating and cooling phase relative to the EBA curve and the full firing phase of the same length, a higher temperature load can be assumed overall, even though an overall lower maximum temperature is applied.

Based on the experience gained from the small-format tests presented in [4] and [42], a maximum furnace temperature of 1,100 °C is chosen for this proof-of-concept study. Although this does not meet the requirements of the EBA curve, it was decided not to exceed a possible eutectic in the initial heat transfer tests with new recipes.

It is to be expected, however, that the described tests in the muffle furnace lead to evaluable and meaningful results and findings on the behaviour of the test formulations under high-temperature loading.

4.3 Test performance and analysis of the test results

The heat transfer investigations are carried out on two test specimens from the basic recipe and also for one specimen of each recipe variation (Table 1). Thermocouples 3 and 4 of one specimen of the basic recipe were defective, which is taken into account in the evaluation. None of the test specimens examined showed signs of spalling or melting after exposure to the temperature. After the tests, some of the test specimens showed fine cracks, which in some cases even led to breakage during removal from the furnace. However, the cracks recorded occurred exclusively in the plane of the holes drilled for the thermocouples. No differences in the cracking behaviour of test specimens of different AAC formulations were observed. An influence of the duration of the cooling phase on crack formation was found. A rapid drop in temperature led to a fracture along the plane of the thermocouples. It can be concluded that these cracks resulted from the weakening of the material in the drill hole area. Cracks outside the plane of the drill holes were not found in any test specimen.

Table 2 shows the time required to reach the 300 °C criterion (Section 2.3) in the respective depth positions of the thermocouples. It can be seen that varying the recipe with air polymer (Variation 1) led to a delay in heating in all depth levels. The shorter heating time of the sample surface in case of variation 1 (23 min) must be taken into account. Variations 2 to 4, which were modified with air entraining agents, did not show a delay of heating compared to the basic formulation. The time intervals between thermocouples 3, 4 and 5 until 300 °C was reached are very short in all cases, which is due to the furnace used. In all tests, the test specimens were exposed to heat from five sides. That said, the distance between the heated surface and one of the thermocouples never exceeded 7.5 cm in any case. However, thermocouples 4 and 5 were closer to

the only non-heated surface than the other sensors. This can be derived from the test data. A setup with one-sided heating could not be realised within the scope of these investigations, due to the constraints of the test setup.

Table 2. Times until a temperature of 300 °C is reached at the level of the installed thermocouples

Time to reach 300° C [min]		Specimen				
Thermocouple	Distance to Specimen Surface [cm]	Basic	Variation 1	Variation 2	Variation 3	Variation 4
SF	0	29	23	28	25	22
1	2,5	62	62	51	48	59
2	5	75	77	75	69	74
3	7,5	82	98	82	87	90
4	10	89	102	87	81	87
5	12,5	90	104	90	86	89

Figure 5 A shows the temperature development for the thermocouple 5 exemplary within the different test specimens alongside with the actual furnace. Figure 5 B shows this actual furnace temperature in comparison with the specifications of EBA and ZTV-ING as well as the unit temperature-time curve to which the furnace temperature during the tests most closely corresponded.

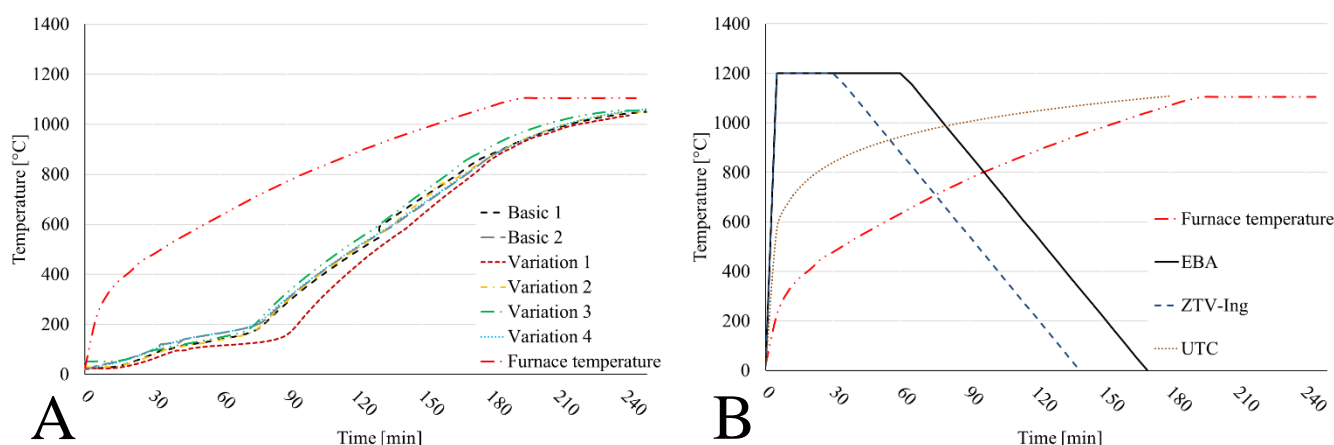


Figure 5. A: Temperature time curves for thermocouples 5 of all tested recipes | B: Furnace temperature in relation to normative specifications

Together with Table 2 it can be seen that variations 2, 3 and 4 show a similar temperature increase compared to the two test specimens made of the basic recipe. Only Variation 1 – with the air polymer as an additive – shows a temperature development with a significantly lower heating gradient. The measured curves of the other thermocouples show a similar course. During a heating phase of about 80 to 90 minutes, the temperatures measured in the test specimens increase with a flat gradient, thereafter they develop approximately parallel to the furnace temperature until they correspond to it in the full firing phase. The overview in table 2 shows that this heating phase corresponds approximately to the period of time from which the temperatures of all thermocouples of a specimen have nearly the same temperature. The curves of the measured data of the other thermocouples also describe this pattern.

4.4 Conclusion for proof-of-concept study

The overall results of this study have shown that alkali-activated sprayed concrete withstands the temperature loading without obvious deterioration. Apart from minor cracks, which can be traced back to previous weakening of the material, no deterioration as a result of heat exposure is detected. This corresponds well with additional test that have been conducted in our laboratory but are not part of this publication. For all tested specimen evaluable temperature profiles could be determined. These profiles indicate that the use of an air polymer has a significant influence on the heat transfer, which is shown by a delay in heating of about 15 minutes at the lowest measuring point. A conventional air-entraining agent

does not produce the desired effect in combination with the activator. The chosen test setup has known limitations that make it rather challenging to evaluate the results. The position of the measuring points is suitable to record the course of the heat transport in the test specimen. However, the long heating phase of the furnace favours an even, slow heating of the material. Effects which can result from the prescribed rapid temperature development of the EBA curve are therefore not recorded. The prescribed maximum temperature was also not obtained. Furthermore, the heating of the test specimens from all sides is unfavourable for the determination of a thermal transmittance profile with the selected measuring geometry. Nevertheless, the obtained findings provide a good basis for further investigations of the developed material.

5 CONCLUSIONS AND OUTLOOK

The basic steps in the development of an alkali-activated sprayed concrete as a fire protection coating are shown within this publication. In order to improve the material behaviour with regard to the heat transfer, possible optimisation of the recipe with further additives is needed. Further formulations with air polymer and other additives are being developed and investigated. After the development of new formulations, investigations have to be carried out which represent the realistic load situation of a shotcrete coating. These include the one-sided temperature exposure with simultaneous mechanical load of the coated shell, like shown in Figure 6 A and the testing of the material under the prescribed conditions of the EBA curve. For the purpose of realising the load situation shown in Figure 6 A in a laboratory environment a new furnace was installed at RUB laboratories. This furnace – as it is illustrated in Figure 6 B – is modular and fully customisable. In addition to heatable and non-heatable elements, it will in future be possible to provide passages in the furnace shell that allow mechanical loading of heated test specimens.

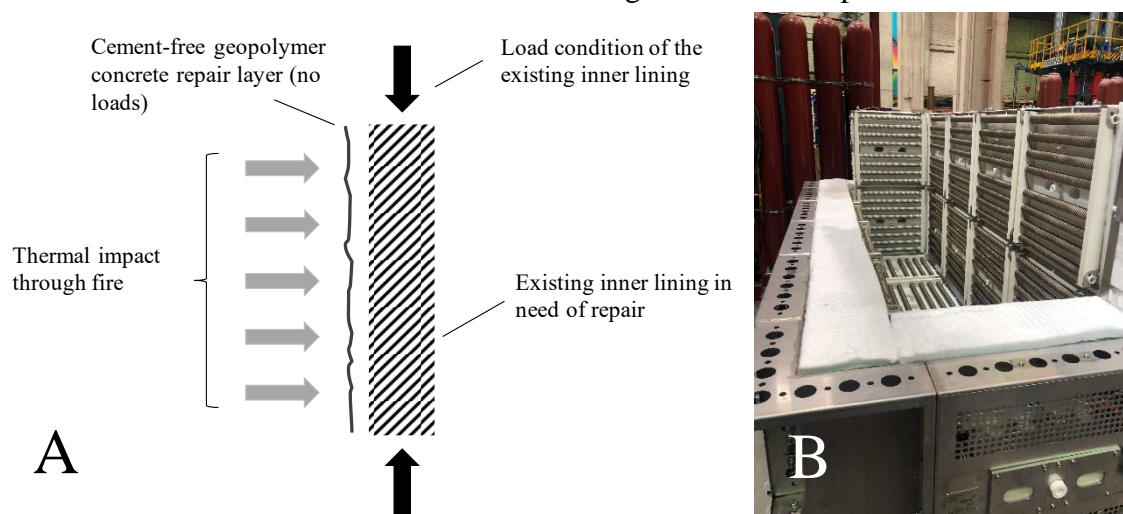


Figure 6. A: Load situation of a coated tunnel inner shell in case of fire | B: Erection of the modular furnace for large-scale tests at RUB laboratories

At present, experiments are being carried out to examine the material on the in situ bedrock of the existing Kuckuckslay tunnel of Deutsche Bahn. Mechanical tests before and after the temperature exposure are carried out. In the future, tests on conventional concrete will be necessary to compare the knowledge gained about the new material with the parameters of conventional materials. The aim of these further research is to obtain approval for the application of alkali activated sprayed concrete in tunnelling.

ACKNOWLEDGMENT

The KOINOR research consortium consists of the Institute for Tunnelling and Construction Management of the Ruhr-University Bochum, the Studiengesellschaft für Tunnel und Verkehrsanlagen – STUVA - e. V., the MC-BAUCHEMIE MÜLLER GmbH & Co. KG and the PORR GmbH & Co. KGaA.

The Federal Ministry of Education and Research (BMBF) provided financial support in the framework of this research project. This support is gratefully acknowledged. We would also like to thank the Department

of Energy Plant Technology and the Chair of Materials Engineering of the Faculty of Mechanical Engineering at the Ruhr University Bochum for providing the furnaces.

REFERENCES

1. Almand K. Safety & Security in Roadway Tunnels: Final Report. American Association of State Highway and Transportation Officials, Quincy, MA, United States. 2008.
2. Bundesanstalt für Straßenwesen. Zusätzliche Technische Vertragsbedingungen und Richtlinien für Ingenieurbauten. ZTV-ING, Teil 5 Tunnelbau. 2018.
3. Eisenbahn Bundesamt (EBA). Richtlinie Anforderungen des Brand- und Katastrophenschutzes an den Bau und Betrieb von Eisenbahntunneln. 2008.
4. Hammer A-L, Vollmann G, Kleen E, Uhlmann D, Thienert C, Klaproth C, et al. KOINOR – Improvement of Fire Safety and Upgrading of Underground Transport Tunnels. tunnel. 2019;6:27–39.
5. Haack A. ASFINAG, DB Netz AGSTUVA Sachstandbericht 2017: Instandsetzungsstrategien und -verfahren für Verkehrstunnel. Forschung + Praxis 50. 2018:1–3.
6. DB Netz AG. Tunnel- und Erdbau Technik. I.NPF 23(T). 2019.
7. Goj, K., Fischer, O., Ettelt, B. Instandsetzung und Nachrüstung, Tunnel Pfaffenstein – Nachrechnung eines Straßentunnels im Bestand. Taschenbuch für den Tunnelbau (DGGT, Hrsg.). 2018:pp. 76-81.
8. DIN EN 1991-1-2:2010-12: : Eurocode 1: Einwirkungen auf Tragwerke - Teil 1-2: Allgemeine Einwirkungen - Brandeinwirkungen auf Tragwerke: Deutsche Fassung EN 1991-1-2:2002 + AC:2009.
9. Blofeld J. Brandkurven für den baulichen Brandschutz von Straßentunneln. Bundesanstalt für Straßenwesen. Bremerhaven (Berichte der Bundesanstalt für Strassenwesen B, Brücken und Ingenieurbau). 2009.
10. THE EUROPEAN COMMISSION. COMMISSION REGULATION (EU) No 1303/2014 concerning the technical specification for interoperability relating to ‘safety in railway tunnels’ of the rail system of the European Union: TSI SRT; 18 November 2014.
11. Peter C. Tragverhalten von Verkehrstunneln im Brandfall mit einer Innenschale aus PP-Faserbeton [Dissertation]. Wuppertal: Bergischen Universität Wuppertal.
12. Janson R. Fire Spalling of Concrete [Dissertation]. Stockholm, Sweden: KTH Architecture and the Built Environment; 2013.
13. Bundesministerium für Verkehr, Innovation und Technologie. Österreichische Forschungsgesellschaft Straße-Schiene-Verkehr. Brandbeständigkeit von Faser-, Stahl- und Spannbetonbau. 2004.
14. Horvath J. Beiträge zum Brandverhalten von Hochleistungsbetonen [Dissertation]. Wien: TU Wien; 2003.
15. Schneider U, König G, Dehn F, Horvath J. Versuche zum Brandverhalten von Tunnelinnenschalenbeton mit Faserzusatz. Bautechnik. 2001;78:pp. 795-804.
16. Kordina, K., Meyer-Ottens, C. K. Beton Brandschutz Handbuch: Beton-Verlag; 1981.
17. Pistol K. Wirkungsweise von Polypropylen-Fasern in brandbeanspruchtem Hochleistungsbeton [Dissertation]. Berlin, Germany: Bundesanstalt für Materialforschung und -prüfung (BAM); 2016.
18. Lo Monte, F., Miah, M., Shamima, A., Negri, R., Rossino, C., Felicetti, R., editor. Experimental study on the explosive spalling in high-performance concrete: Role of aggregate and fiber types; 2014.
19. Zhang, H., Cao, L., editor. Bond Strength of Geopolymer Mortars after exposure to high temperatures; 2014.
20. Khoury GA. Polypropylene fibres in heated concrete. Part 2: Pressure relief mechanisms and modelling criteria. Magazine of Concrete Research. 2008;60:189–204. doi:10.1680/mac.2007.00042.
21. DB Netz AG. Richtlinie 853: Eisenbahntunnel planen, bauen und instand halten 09/2018. Frankfurt am Main.
22. SIA 198 - 2004: Untertagebau – Ausführung; Schweizerische Normen-Vereinigung.

23. ÖNORM EN 13051-2:2016 11 01: Klassifizierung von Bauprodukten und Bauarten zu ihrem Brandverhalten - Teil 2: Klassifizierung mit den Ergebnissen aus den Feuerwiderstandsprüfungen, mit Ausnahme von Lüftungsanlagen.
24. Österreichische Bautechnik Vereinigung - ÖBV. Richtlinie: Erhöhter baulicher Brandschutz für unterirdische Verkehrsbauwerke aus Beton; 2015.
25. NFPA 502 – 2017: Standard for Road Tunnels, Bridges, and Other Limited Access Highways; National Fire Protection Association.
26. Ring B. Auswirkungen eines Brandes während der Bauausführung im Tunnel Follo – Untersuchungen zum Brandschaden an der Tübbingschale, Standsicherheitsberechnungen und Instandsetzung. Forschung + Praxis 53: STUVA Tagung. 2019;pp. 183-189.
27. Richtlijnen Ontwerp Kunstwerken ROK 1.4, RTD 1001:2017.
28. Lyon R, Sorathia U, Balaguru PN, Foden A, Davidovits J, Davidovits M. Fire Response of Geopolymer Structural Composites. . Proceedings of the First International Conference on Fiber Composites in Infrastructure (ICCI' 96). 1996:972–81.
29. Giancaspro, J., Balaguru, P., Lyon, Richard. Fire protection of flammable materials utilizing geopolymer. SAMPE Journal 40. 2004:42–9.
30. Dehn, F., Koenig, A., Wüstemann, A. Alkalisch-aktivierte Bindemittel und Geopolymer-Bindemittel als Alternative zu Zement. 2017.
31. García-Lodeiro, I., Palomo, A., Fernández-Jiménez, A. An overview of the chemistry of alkali-activated cement-based binders. Handbook of Alkali-Activated Cements, Mortars and Concretes. 2015;pp. 19-47.
32. Pacheco-Torgal F, editor. Handbook of Alkali-activated Cements, Mortars and Concretes; 2015.
33. Vogt, O., Ukrainczyk, N., Koenders, E. Geopolymere als Spezialbaustoff. Nachr. Chem. 65 (12). 2017:1198–202.
34. Glasby, T., Day, J., Genrich, R., Aldred, J., editor. EFC geopolymer concrete aircraft pavements at Brisbane West Wellcamp Airport; 2015.
35. Provis J. Fire Resistance of Geopolymer Concretes. 2010:8.
36. Buchwald A. Geopolymere Bindemittel - Teil 1: Was sind Geopolymere? Zement, Kalk, Gips International. 2007;60:pp. 78-84.
37. Wüstemann, A., Koenig, A., Dehn, F. Vorschlag zur Klassifizierung von alkalisch-aktivierten Bindemitteln und Geopolymer-Bindemitteln. Beton. 2015;64:pp. 236-239.
38. Mohajerani A, Suter D, Jeffrey-Bailey T, Song T, Arulrajah A, Horpibulsuk S, Law D. Recycling waste materials in geopolymer concrete. Clean Techn Environ Policy. 2019;21:493–515. doi:10.1007/s10098-018-01660-2.
39. Davidovits J. Geopolymers. Journal of Thermal Analysis. 1991;37:1633–56. doi:10.1007/BF01912193.
40. Provis, J., van Deventer, Jannie S. J. Alkali Activated Materials. State-of-the-Art Report. RILEM TC 224-AAM. 2014.
41. Ali A. Performance of geopolymer concrete in fire [Dissertation]. Melbourne, Australia: Swinburne University of Technology; 2018.
42. Vollmann, G., Kleen, E., Hammer, A.-L., Uhlmann, D., Weiner, T., Budnik, J., Thewes, M., Thienert, C., Leismann, F., Klaproth, C. KOINOR – Development of a sprayable geopolymer concrete for fire protection improvement and upgrading of underground traffic structures. ITA-AITES World Tunnel Congress - WTC, Kuala Lumpur, Malaysia: 11.-17. September 2020.

EVALUATION OF MEASURING METHODS FOR WATER VAPOR PRESSURE IN CONCRETE AT ELEVATED TEMPERATURE

Ye LI¹, Kang Hai TAN²

ABSTRACT

Build-up of water vapor pressure is a main trigger leading to explosive spalling of concrete in fire scenario. However, there is no available standard for measurement of pore pressure inside concrete specimens. This paper summarised three main differences on pore pressure measurement techniques *viz.*, medium to transfer pore pressure, type of pressure gage head, and placement of thermocouples. One-dimensional heating test of concrete slabs including twelve pore pressure gages were conducted to evaluate effectiveness of all the gage design factors. The test results showed that filling steel tubes with rods or leaving the tubes empty would weaken build-up of vapor pressure. On the contrary, filling it with silicon oil has the risk to create extra hydraulic pressure. The use of sintered metal as a gage head could compensate the hydraulic pressure by introducing free volume. By placing thermocouples outside the steel tube, the complexity of the measurement system could be greatly reduced. At last, two requirements are proposed for correctly measuring vapor pressure: (1) expansion of filled oil should be compensated by introducing a certain amount of free volume; (2) the free volume should not be too large to interfere with vapor pressure build-up.

Keywords: Explosive spalling; pore pressure; measurement techniques; elevated temperature

1 INTRODUCTION

Fire is one of the most detrimental hazards for underground structures, high-rise buildings, and tunnels, etc. [1]. Under fire exposure, one of the most violent phenomena for concrete structures is explosive spalling, which causes cracking of concrete, a sudden loss of concrete cover, and subsequent exposure of steel reinforcement to fire [2-5]. With occurrences of explosive spalling, load-carrying capacity of reinforced concrete (RC) structures will be dramatically reduced. Explosive spalling is a complicated phenomenon caused by a combination of thermal, hydral, and mechanical processes [5]. The two main triggers causing failure of concrete in explosive spalling are thermal stress and water vapor pressure [6-8]. Between them, migration of moisture and build-up of pore pressure in porous concrete are considered as the governing factors for explosive spalling of concrete with dense microstructure and high strength [9-11]. For high strength concrete (HSC) and ultra-high performance concrete (UHPC), the densely packed microstructure restrains migration of water vapor and hinders release of vapor pressure. To achieve a better understanding of the mechanism of explosive spalling so as to evaluate risk of explosive spalling, it is essential to accurately measure pore pressure during fire exposure.

¹Dr., School of Civil and Environmental Engineering, Harbin Institute of Technology, Shenzhen, Shenzhen 518055, PR China

School of Civil and Environmental Engineering, Nanyang Technological University, Singapore 639798, Singapore

e-mail: liye@hit.edu.cn, ORCID: <https://orcid.org/0000-0002-2379-5497>

²Professor, School of Civil and Environmental Engineering, Nanyang Technological University, Singapore 639798, Singapore

e-mail: ckhtan@ntu.edu.sg

Measuring pore pressure and temperature simultaneously is particularly challenging because the elevated temperature would damage installed pressure sensors. While many efforts have been made to measure these two parameters accurately, techniques used by different researchers are nonstandard, which led to inconsistent pore pressure measurements. The basic concept adopted to prevent pressure transducers from being damaged by elevated temperature is to transfer pore pressure out of the heated concrete specimen by a steel tube [9, 12-20]. To capture the pore pressure in an area larger than the head of the steel tube and in an evenly manner, porous sintered metal was welded on top of the steel tube [1, 11, 21-34]. However, the porous sintered metal may alter local properties of the concrete matrix. Moreover, the empty steel tube introduces free volume of air, which promotes vaporization of condensed water and delays build-up of pore pressure [13, 14]. To solve this issue, steel rods [9, 12] or thermocouples [1, 11, 20-23, 27], silicon oil [18, 19, 24-26, 28, 30-34], or jack oil [15-17] were filled into the steel tube to minimize the free volume and to transfer pressure more effectively [31]. However, expansion of oil may cause additional hydraulic pressure, which may lead to a wrong pressure result. In summary, the techniques to measure pore pressure of concrete at elevated temperature are differentiated on the basis of: (i) type of gage heads, (ii) placement of thermocouples, and (iii) fillers inside the tube.

To determine a reliable technique to measure pore pressure of concrete at elevated temperature, pore pressure measurements of UHPC at elevated temperature were conducted by using twelve designs of pore pressure gage considering all possible combinations of the different gage heads, placement of thermocouple, and fillers in the tube. The mix proportion, the curing condition of the specimens, and the heating rate were kept constant. The maximum pore pressure measured was selected as the evaluation criterion. Comparison between pore pressure measurements and saturated vapour pressure (SVP) were also made to evaluate reliability of pore pressure measurement.

2 EXPERIMENTAL PROCEDURE

2.1 Mix proportions and specimen preparation

Table 1 shows the mix proportion of the concrete used in the present study. Portland cement ASIA® CEM I 52.5 N, natural river sands with a maximum diameter of 600 µm, micro silica sands with median particle size of 130 µm, silica fume Grade 940 from Elkem Microsilica®, polycarboxylate-based superplasticizer ADVA® 181N, and monofilament cylindrical PP fibers with 12 mm length and 30 µm diameter were used to prepare the UHPC samples. Water-to-binder ratio was kept at 0.2 and compressive strength of the UHPC sample is 148.7±3.3 MPa (mean value of three 50 mm cubes). The cement, silica fume, fine aggregates, and silica sand were dry-mixed for 2-3 min. Then the premixed water and superplasticizer was added. After mixing for 3 to 5 min when the fresh mortar became consistent, PP fibers were slowly added and the mixture was stirred for another 3-5 min. Thereafter, the fresh UHPC mixture was poured into a plastic (200×200×120 mm³) mould placed on a shake table. The pore pressure gages were fixed on a steel frame and slowly inserted into the specimens during casting. After 24 h of hardening, the specimens were demoulded and stored in lime-saturated water for 13 days and in air for another 14 days before pore pressure measurements began.

Table 1. Mixture proportion of UHPC (kg/m³)

Mix Design	Cement	Fine aggregates	Silica sand	Silica fume	Superplasticizer	Water	PP fiber
UHPC	833	917	208	208	25	208	3

2.2 Experimental setup

Figure 1 shows the schematic experimental setup. The specimens were placed at the opening of an electric heating furnace. Unidirectional heating was applied on front face of the specimen at a heating rate of 10 °C/min. After reaching 600 °C, the furnace temperature was kept constant. Totally 24 gages were prepared for the 12 gage designs with 2 gages for one design. Six specimens were prepared with four gages

on each specimen. The gage heads were 25 mm from the heated surface. During the test, an additional thermocouple was placed 2 cm in front of the heated surface to monitor the temperature.

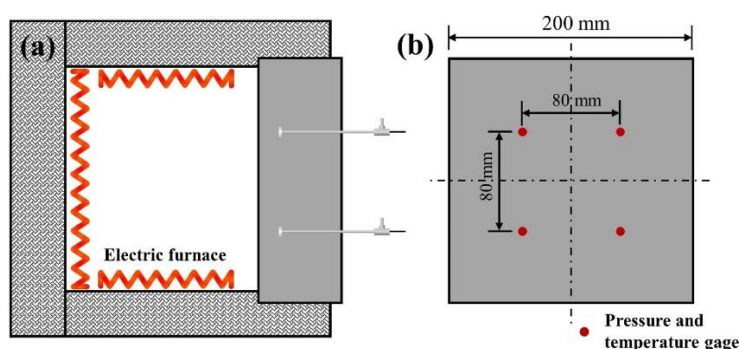


Figure 1. (a) schematic experimental setup (b) locations of gages.

Figure 2 shows different configurations of the experimental setup including the twelve measurement techniques. The letters used in the sequential naming of gage designs indicate placements of K-type thermocouples (Inside or Outside of the tubes), type of gage head (Sintered metal encapsulated into a steel cup or Tube without sintered metal), and type of filler inside the tube (Silicon Oil, Steel Rod, or Air). As an example, I-S-O represents a gage with a thermocouple inside the tube, with a sintered metal head, and with oil as a filler. For gages with a thermocouple inside the tube, a connector was installed at the outer end of the tube to connect the thermocouple to a data-logger and the tube to a pressure transducer. For gages with a sintered metal head, a sintered metal plate was encapsulated onto a steel cup ($\varnothing 12 \times 2$ mm), which was welded to the 5 mm steel tube with 4 mm inner diameter. Figure 3 shows a photo of the sintered metal. The steel tubes were filled with silicon oil, a steel rod, or air. The silicon oil used was PM-125 silicone transfer fluid from CLEARCO. Thermal expansion coefficient of the silicon oil is $7.5 \times 10^{-4} \text{ }^{\circ}\text{C}^{-1}$. To verify if expansion of the silicon oil can induce overpressure, an additional test was conducted by heating a sealed steel tube with fully-filled silicon oil. The pressure was measured at the end of the tube.

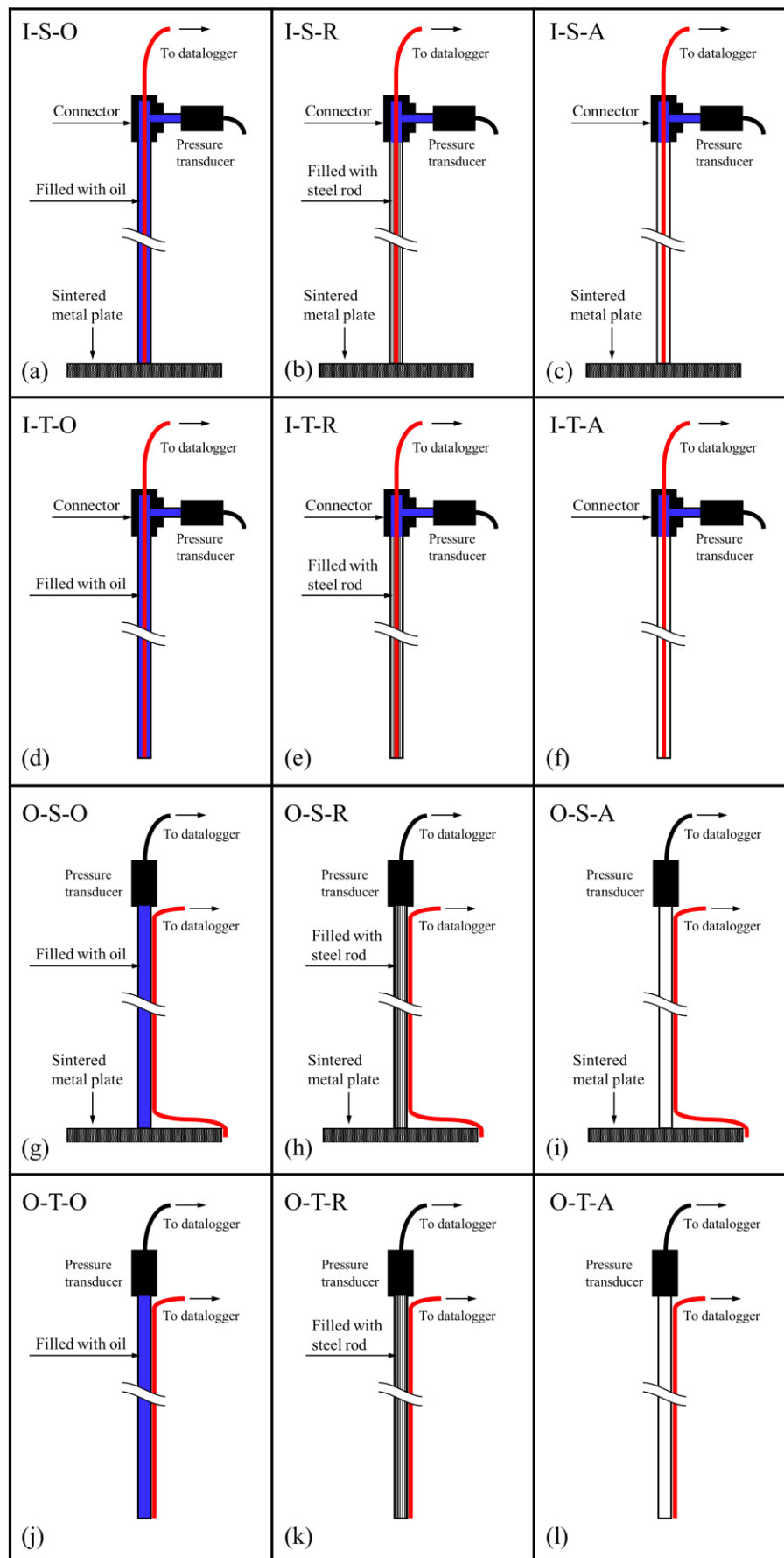


Figure 2. Configuration of pressure gages (I or O: thermocouples Inside or Outside of the tube. S or T: Sintered metal gage head or Tube gage head. O, R, or A: use Oil, Rod, or Air to fill the tube).

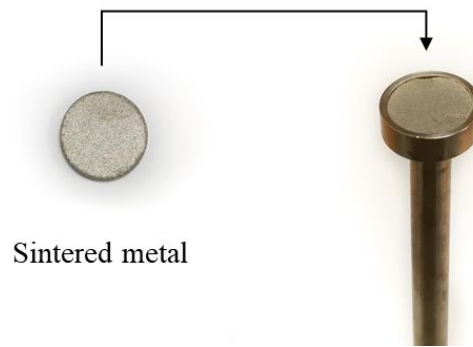


Figure 3. Sintered metal plate.

3 RESULTS

3.1 Build-up of pore pressure

Figure 4 summarises the maximum pore pressure recorded of each measurement technique. The maximum recorded pore pressure of the measuring techniques with oil filling (i.e., I-S-O, I-T-O, O-S-O, and O-T-O) is higher than their counterparts filled with a steel rod or air. This is because filling the tube with either a steel rod or air leaves too much free volume for vaporisation of moisture. As a consequence, build-up of pore pressure at high temperature in the concrete was affected. Placing a thermocouple inside the tube and using the sintered metal plate (Figure 3) as a gage head seemed to reduce the pore pressure reading.

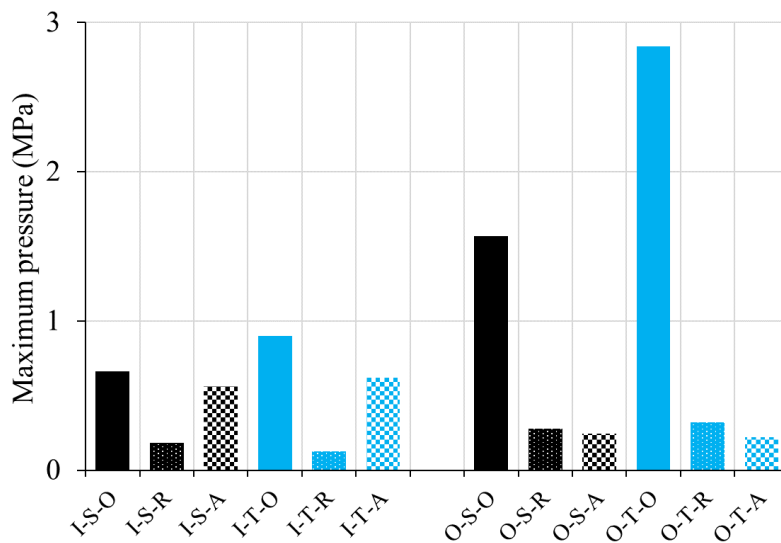


Figure 4. Maximum pore pressure of each technique.

To have a clearer view of the significance of each factor, the results were analysed statistically. Figure 5a gives a plot of the LogWorth values. A value of LogWorth exceeding 2 (p -value<0.01) shows that the corresponding factor is significant. It can be seen that the type of fillers has very high influence on the pore pressure measurement followed by its interaction with the other two factors. On the other hand, the thermocouple location inside or outside the steel tube and the type of gage head are not as significant on pore pressure measurements. Figure 5b shows the effects of detailed gage design factors on the measured maximum pore pressure. The coefficients indicate that filling the tube with silicon oil can measure pore pressure more effectively, which is in accordance with the finding made in Figure 4. In comparison, the effects of placement of thermocouple and the type of gage head are not as critical.

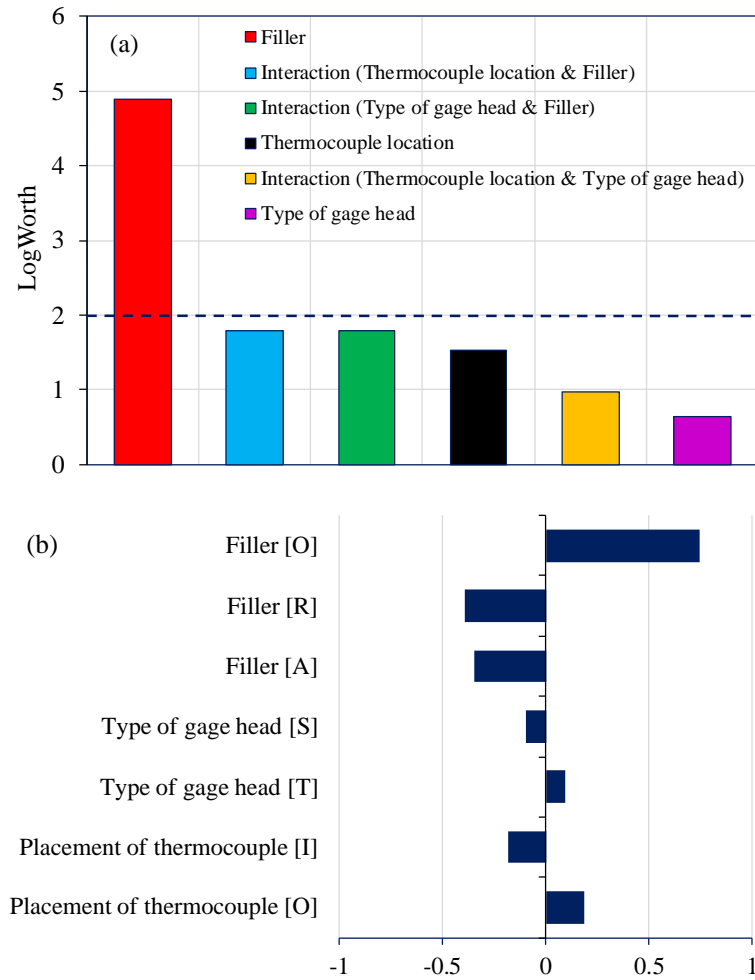


Figure 5. Effect of factors on maximum pore pressure.

The pore pressure profiles are compared with saturated vapor pressure (SVP - P_{sat}) to analyse the saturation state and the reliability of gage design. Figure 6 presents the evolution of pore pressure as a function of temperature. Each line is an averaged value of two repeated tests with the same gage design. For all the gage designs with the thermocouple placed inside the steel tube, pore pressure increased with elevated temperature, but was lower than the P_{sat} curve. One possible reason is the inaccuracy caused by the complex connections for placing the thermocouple inside the tube.

In Figure 6b, the dashed line represents pressure development inside a sealed tube fully filled with silicon oil. It is obvious that the hydraulic pressure created by expansion of oil cannot be neglected. It can be seen that the pore pressure of O-T-O (red line) shows a similar increasing trend with the dashed line and it clearly exceeds the P_{sat} curve. From previous studies [1, 11, 16, 23, 31], the measured overpressure was explained by partial pressure of the air within the porous network. When the degree of saturation is high, the partial pressure of the dry air is superimposed onto water vapor pressure, thus exceeding the P_{sat} curve. However, the present study shows the risk of build-up of misleading overpressure caused by the oil filler. In Figure 6b, the pore pressure of O-S-O correlates with the P_{sat} curve very well. This shows that the sintered metal evenly collects pore pressure from a larger contact area and its porosity somewhat compensates the expansion of silicon oil. Placing thermocouple outside the steel tube will not compromise the accuracy of temperature measurement, and at the same time the complexity of the measuring system can be greatly reduced.

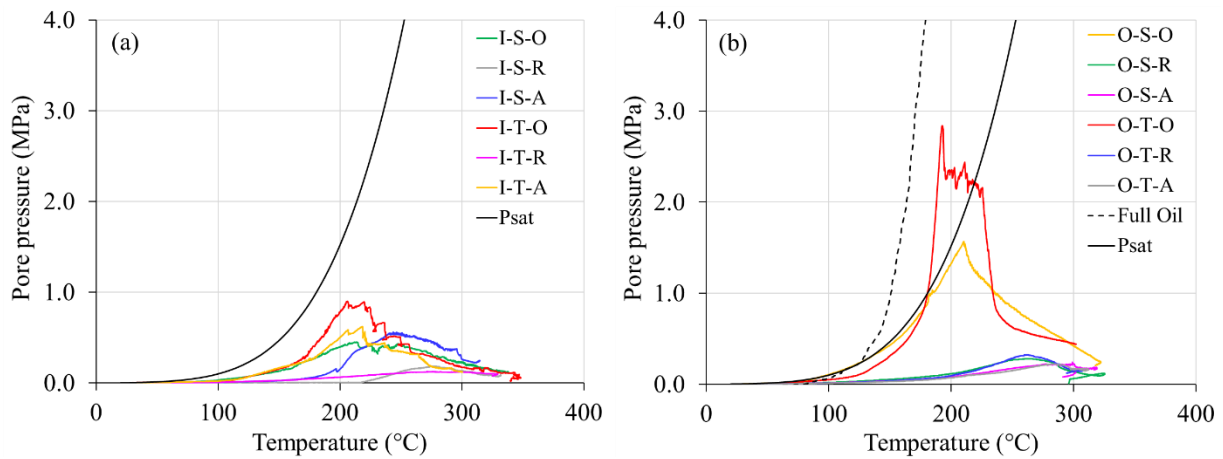


Figure 6. (a, b) Pore pressures as a function of temperature plotted with the SVP curve.

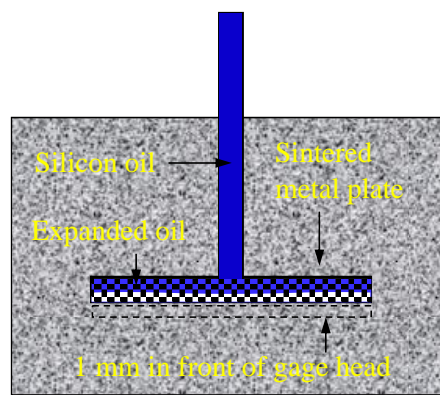


Figure 7. Schematic illustration for expansion of oil.

4 CONCLUSIONS AND RECOMMENDATION

This paper presents an experimental study to seek to reconcile inconsistency of measurement methods and to accurately monitor pore pressure in concrete specimens during fire exposure. A full factor experimental analysis was conducted to consider all the possible combination of factors (i.e., type of gage heads, placement of thermocouples, and type of fillers inside the tube). Twelve designs of pore pressure gages were evaluated by conducting one-dimensional heating tests on UHPC specimens. Evolution of pore pressure and temperature were analysed in terms of the maximum pore pressure and agreement with SVP. The results showed that for pressure measurements, either filling the steel tube with a steel rod or leaving it empty will affect build-up of pore pressure. On the other hand, filling silicon oil has the risk of building up addition hydraulic pressure, which may lead to misleading results. The use of the sintered metal gage head can collect pore pressure over a larger surface area and its porosity somewhat compensated the expansion of silicon oil. Placing the thermocouple outside the steel tube will not compromise the accuracy of pressure measurement. At the same time the complexity of the system can be greatly reduced. Furthermore, two requirements are proposed for accurate pore pressure measurements, namely, (1) expansion of oil should be compensated to avoid misleading hydraulic pressure; (2) free volume should not interfere with moisture accumulation and vapor pressure build-up.

ACKNOWLEDGMENT

This material is based on research/work supported by the Land and Liveability National Innovation Challenge under L2 NIC Award No. L2NICCFP1-2013-4.

REFERENCES

1. Mindeguia, J.-C., et al., Temperature, pore pressure and mass variation of concrete subjected to high temperature — Experimental and numerical discussion on spalling risk. *Cement and Concrete Research*, 2010. 40(3): p. 477-487.
2. Klingsch, E.W.H., *EXPLOSIVE SPALLING OF CONCRETE IN FIRE*. 2014, ETH: Zurich.
3. Kodur, V. and L. Phan, Critical factors governing the fire performance of high strength concrete systems. *Fire Safety Journal*, 2007. 42(6): p. 482-488.
4. Ma, Q., et al., Mechanical properties of concrete at high temperature—A review. *Construction and Building Materials*, 2015. 93: p. 371-383.
5. Gawin, D., et al., Effect of damage on permeability and hygro-thermal behaviour of HPCs at elevated temperatures: Part 1. Experimental results. *Computers and Concrete*, 2005. 2(3): p. 189-202.
6. Khoury, G.A., Effect of fire on concrete and concrete structures. *Progress in Structural Engineering and Materials*, 2000. 2(4): p. 429-447.
7. Jansson, R., L. Boström, and J. Silfwerbrand, *Fire spalling of concrete*. 2013.
8. Li, Y., *Material properties and explosive spalling of ultra-high performance concrete in fire*. 2018.
9. Debicki, G., R. Haniche, and F. Delhomme, An experimental method for assessing the spalling sensitivity of concrete mixture submitted to high temperature. *Cement and Concrete Composites*, 2012. 34(8): p. 958-963.
10. Zeiml, M., et al., How do polypropylene fibers improve the spalling behavior of in-situ concrete? *Cement and Concrete Research*, 2006. 36(5): p. 929-942.
11. Kalifa, P., F.-D. Menneteau, and D. Quenard, Spalling and pore pressure in HPC at high temperatures. *Cement and concrete research*, 2000. 30(12): p. 1915-1927.
12. Schneider, U. and H. Herbst. Pressure development in heated concrete members. in *Transactions of the 10th international conference on structural mechanics in reactor technology*. 1989.
13. Choe, G., et al., Effect of moisture migration and water vapor pressure build-up with the heating rate on concrete spalling type. *Cement and Concrete Research*, 2019. 116: p. 1-10.
14. Ko, J., T. Noguchi, and D. Ryu, The spalling mechanism of high-strength concrete under fire. *Magazine of Concrete Research*, 2011. 63(5): p. 357-370.
15. Ozawa, M., et al., Behavior of ring-restrained high-performance concrete under extreme heating and development of screening test. *Construction and Building Materials*, 2018. 162: p. 215-228.
16. Ozawa, M. and H. Morimoto, Effects of various fibres on high-temperature spalling in high-performance concrete. *Construction and Building Materials*, 2014. 71: p. 83-92.
17. Jansson, R. and L. Boström, The Influence of Pressure in the Pore System on Fire Spalling of Concrete. *Fire Technology*, 2009. 46(1): p. 217-230.
18. Jochen, R. and M. Christoph. The influence of the pore size distribution and the chemical composition of cement paste on the explosive spalling of concrete. in *5th International Workshop on Concrete Spalling due to Fire Exposure*. 2017. RISE Research Institutes of Sweden.
19. Dal Pont, S., et al., An experimental relationship between complete liquid saturation and violent damage in concrete submitted to high temperature. *Magazine of Concrete Research*, 2005. 57(8): p. 455-461.
20. Kalifa, P., G. Chene, and C. Galle, High-temperature behaviour of HPC with polypropylene fibres: From spalling to microstructure. *Cement and concrete research*, 2001. 31(10): p. 1487-1499.
21. Mindeguia, J.-C., et al., Experimental analysis of concrete spalling due to fire exposure. *European Journal of Environmental and Civil Engineering*, 2013. 17(6): p. 453-466.
22. Mindeguia, J.-C., et al. Influence of water content on gas pore pressure in concretes at high temperature. in *2nd International RILEM Workshop on Concrete spalling due to fire exposure*. 2011.
23. Li, Y., et al., Effect of aggregate size and inclusion of polypropylene and steel fibers on explosive spalling and pore pressure in ultra-high-performance concrete (UHPC) at elevated temperature. *Cement and Concrete Composites*, 2019. 99: p. 62-71.
24. Bangi, M.R. and T. Horiguchi, Effect of fibre type and geometry on maximum pore pressures in fibre-reinforced high strength concrete at elevated temperatures. *Cement and Concrete Research*, 2012. 42(2): p. 459-466.
25. Mugume, R.B. and T. Horiguchi, *Prediction of fire spalling in fibre-reinforced high strength concrete*. 2013.
26. Bangi, M.R. and T. Horiguchi, Pore pressure development in hybrid fibre-reinforced high strength concrete at elevated temperatures. *Cement and Concrete Research*, 2011. 41(11): p. 1150-1156.

27. Huismann, S., et al. Concrete spalling due to fire exposure and the influence of polypropylene fibres on microcracking. in 2nd International RILEM Workshop on Concrete Spalling due to Fire Exposure. 2011. RILEM Publications SARL.
28. Ding, Y., et al., Influence of different fibers on the change of pore pressure of self-consolidating concrete exposed to fire. *Construction and Building Materials*, 2016. 113: p. 456-469.
29. Ye, G., G. De Schutter, and L. Taerwe. Spalling behaviour of small self-compacting concrete slabs under standard fire conditions. in 5th International RILEM Symposium on Self-Compacting Concrete (SCC 2007). 2007.
30. Phan, L.T., Pore pressure and explosive spalling in concrete. *Materials and Structures*, 2008. 41(10): p. 1623-1632.
31. Felicetti, R., F. Lo Monte, and P. Pimienta, A new test method to study the influence of pore pressure on fracture behaviour of concrete during heating. *Cement and Concrete Research*, 2017. 94: p. 13-23.
32. Monte, F.L. and R. Felicetti, Heated slabs under biaxial compressive loading: a test set-up for the assessment of concrete sensitivity to spalling. *Materials and Structures*, 2017. 50(4): p. 192.
33. Monte, F.L., R. Felicetti, and C. Rossino, Fire spalling sensitivity of high-performance concrete in heated slabs under biaxial compressive loading. *Materials and Structures*, 2019. 52(1): p. 14.
34. Miah, M.J., et al. Experimental investigation on fire spalling behaviour of concrete: effect of biaxial compressive loading and cement type. in 5th International Workshop on Concrete Spalling. 2017. RISE Research Institutes of Sweden.

TRAVELLING FIRE IN FULL SCALE EXPERIMENTAL BUILDING SUBJECTED TO OPEN VENTILATION CONDITIONS

Ali Nadjai¹, Naveed Alam², Marion Charlier³, Olivier Vassart⁴, Xu Dai⁵, Jean-Marc Franssen⁶, Johan Sjöström⁷,

ABSTRACT

In the frame of the European RFCS TRAFIR project, three large compartment fire tests involving steel structure were conducted by Ulster University, aiming at understanding in which conditions a travelling fire develops, as well as how it behaves and impacts the surrounding structure. During the experimental programme, the path and geometry of the travelling fire was studied and temperatures, heat fluxes and spread rates were measured. Influence of the travelling fire on the structural elements was also monitored during the travelling fire tests. This paper provides details related to the influence of a travelling fire on a central structural steel column. The experimental data is presented in terms of gas temperatures recorded in the test compartment near the column, as well as the temperatures recorded in the steel column at different levels. Because of the large experimental data, only the fire test n°1 results are discussed in this paper.

Keywords: Structures; compartment fires; fire tests

1 INTRODUCTION

The response of a structure in fire is dependent on the fire exposure scenario. Small compartment fires behave in a relatively well understood manner, usually defined as a post-flashover fire, where the temperatures within the compartment are considered to be uniform. However, with modern architecture there is an important increase of open large-floor plan spaces, for which the assumption of post-flashover fire does not hold and there is instead a smaller localised fire that moves across the floor with time. The current design methods were developed using extrapolation of existing fire test data. These data come from small compartments tests for which a uniform distribution of gases and temperatures fit well. But as soon as large compartments are involved, this assumption does not hold anymore. After inspecting fires in large compartments that occurred the past two decades, the conclusion is that such fires have a great deal of non-uniformity. They generally burn locally and move across entire floor plates over a period of time. This

¹ FireSERT, Ulster University, School Built Environment
a.nadjai@ulster.ac.uk, ORCID: <https://orcid.org/0000-0002-9769-7363>

² FireSERT, Ulster University, School Built Environment
n.alam@ulster.ac.uk, ORCID: <https://sandbox.orcid.org/0000-0003-3637-1113>

³ ArcelorMittal Global R&D (Luxembourg)
marion.charlier@arcelormittal.com, ORCID: <https://orcid.org/0000-0001-7690-1946>

⁴ ArcelorMittal Steligençe®, Esch/Alzette, Luxembourg
olivier.vassart@arcelormittal.com, ORCID: <https://orcid.org/0000-0001-5272-173X>

⁵ School of Engineering, BRE Centre for Fire Safety Engineering, The University of Edinburgh, Edinburgh, United Kingdom
x.dai@ed.ac.uk, ORCID: <https://orcid.org/0000-0002-9617-7681>

⁶ Liege University, Civil Engineering Department, Liege, Belgium
jm.franssen@ulg.ac.be, ORCID: <https://orcid.org/0000-0003-2655-5648>

⁷ RISE Research Institutes of Sweden
johan.sjostrom@ri.se, ORCID: <https://orcid.org/0000-0001-8670-062X>

phenomenon generates non-uniform temperatures and transient heating of the structure. This type of fire scenario is currently idealized as travelling fires [1].

In the EN1991-1-2 [2], only two models consider a non-uniform temperature distribution: the localised fire model and the advanced fire models (zone models and computational fluid dynamic models). Nevertheless, the localised fire method considers a static fire which do not translate the effect of a travelling fire (Figure 1a). For zone models, the situation starts as a two-zones model based on the the assumption of accumulation of combustion products in a layer beneath the ceiling, with a horizontal interface. Uniform characteristics of the gas may be assumed in each layer and the exchanges of mass, energy and chemical substance are calculated between these different zones. Although this model considers a non-uniform temperature distribution within the compartment, it does not translate the possible travelling nature of a fire. The CFD (computational fluid dynamic) models enable to solve numerically the partial differential equations giving in all points of the compartment, the thermo-dynamic and aero-dynamic variables. This tool is consequently complex (Figure 1b) and implies a high computational cost.

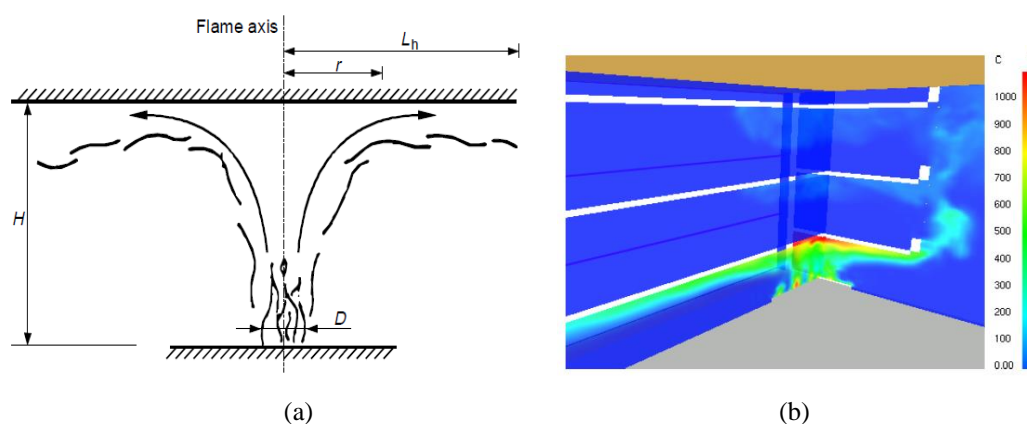


Figure 1. (a) Localised fire [2], (b) use of CFD in a case study with an atrium [1]

Travelling fires have been observed in several structural failures especially from 2000: The World Trade Center Towers [3] in New York City in 2001, the Windsor Tower [4] in Madrid in 2005, and the Faculty of TU Delft Architecture building [5] in Netherlands in 2008. The recent years have seen growing interest in investigating travelling fires which underlined the inadequacy of uniform heating in large compartments [6-12]. Further research effort is still needed, especially to extend the experimental results of such fire scenario.

2 EXPERIMENTAL PROGRAMME

During the experimental programme, three large-scale fire tests were conducted in a compartment with different boundary conditions having similar fire load (which can be observed on Figure 2a). The floor plan between the outer gridlines of the test structure was 15 m x 9 m as shown in Figure 3. The level of the ceiling from the floor finish surface was 2.90 m. The test compartment is a representative of a modern office building and represents a part of the entire office layout. The test compartment consisted of steel beams and columns as the main structural frame while hollow-core precast slabs were used for the construction of ceiling.. The fire load used for the three tests is also representative of an office building following references [2,10].



(a) Test 1: Opening area= 85.2 m²



(b) Test 2: Opening area= 30 m²



(c) Test 3: Opening area= 10 m²

Figure 2 Different opening layouts were used for the three tests.

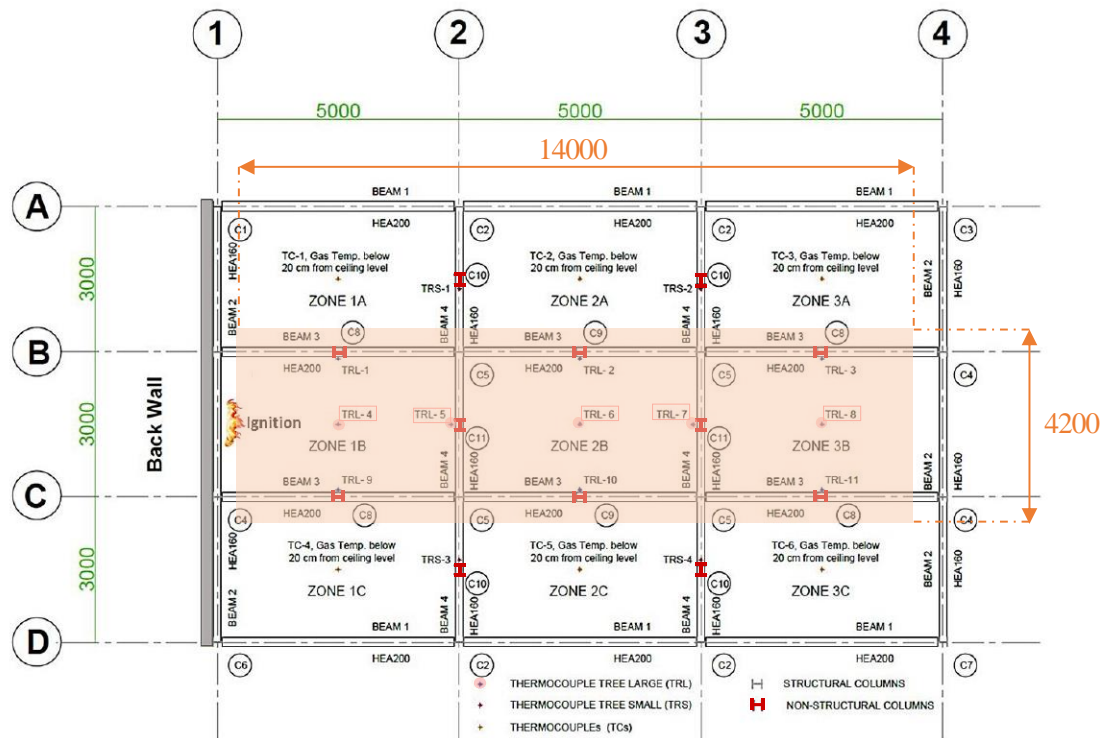


Figure 3. Layout plan of the structure and location of the fuel load (dimensions given in mm)

2.1 Outline and formal structure

The structural steel frame of the test compartment was erected by Saverfield Ltd, local partner to FireSERT. The steel columns were separated into two categories, the structural columns and the dummy columns. The structural columns were part of the steel frame transmitting the loads to the foundation while the dummy columns were not part of the structural steel frame.

Table 1 Description of the steel structure

Description	Sections	Section Factor (m ⁻¹)	Length Height (m)	Protection Applied
Structural columns	HEA 200	209.5	3.5	Yes: R60
Dummy columns	HEA 200	209.5	2.7	No
Long beams	HEA 200	172.3	4.8	No
Short beams	HEA 160	138.0	3.0	No

All columns were fixed to the pre-existing reinforced concrete flooring via anchorage bolts. For the structural columns, four anchorage bolts were used while for the dummy columns, only two anchorage bolts were used for fixing purposes. The connections between the structural columns and beams were designed as fin-plates. The distance amongst the structural columns along the longer direction of the test compartment was 5000 mm while the same along the shorter direction was 3000 mm. The structural frame was laterally restrained using four diagonal bracings, two each along the longer and the shorter directions. The dummy columns provided for data acquisition purposes were anchored to the bottom flanges of the steel beams. The structural steel used for the construction of the test compartment was grade S355. Both the structural and dummy columns, as well as the beams provided along the longer direction, consisted for HEA 200 steel sections (see Table 1). On the other hand, the beams in the shorter direction consisted of HEA 160 steel sections. The ceiling consisted of 120 mm thick hollow-core precast concrete slabs spanning between the beams along the shorter direction of the test compartment. Keeping in view the usage of the test compartment, the main structural columns of the steel frame were protected using intumescent coating in order to maintain the structural integrity during the three fire tests. It can be seen in Figure 4, that only the structural columns are protected while the dummy columns are kept unprotected for data acquisition purposes.

2.2 Details of the fire load

The fuel wood source consisted of the species “*Picea abies*” with an average density 470 kg/m^3 having a moisture content of 15.22%. As the test compartment was a representative of an office building, Eurocodes propose a medium fire growth rate for such occupancy. In the frame of TRAFIR RFCS project, Gamba et al. [10] performed a series of fire tests with uniformly distributed cellulosic fire loads, aiming at defining an arrangement representative of an office building according to Eurocode 1. This work led to devise a well-established methodology, used to define the fuel load for the experimental campaign described in this paper. To achieve a medium fire growth rate for the office building, 9 layers of wooden sticks with an axis distance of 120 mm (90 mm intervals) were provided in three different directions. The wood sticks were 30 mm wide and 35 mm deep. The first layer of the wooden sticks was laid at 60° angle while the second was laid at an angle of 120° . The third layer was at 0° or 180° and the process was repeated in such a way the 6th layer of the sticks laid at 0° or 180° had a lateral offset of 60 mm with respect to the third layer as shown in Figure 4. The final layer, the ninth layer, of the fuel wood was at 0° or 180° , such an arrangement helped to visually observe the travelling behaviour of fire from one stick to another. The fuel load arrangement was kept same during all three tests while the boundary conditions were varied from one test to another.

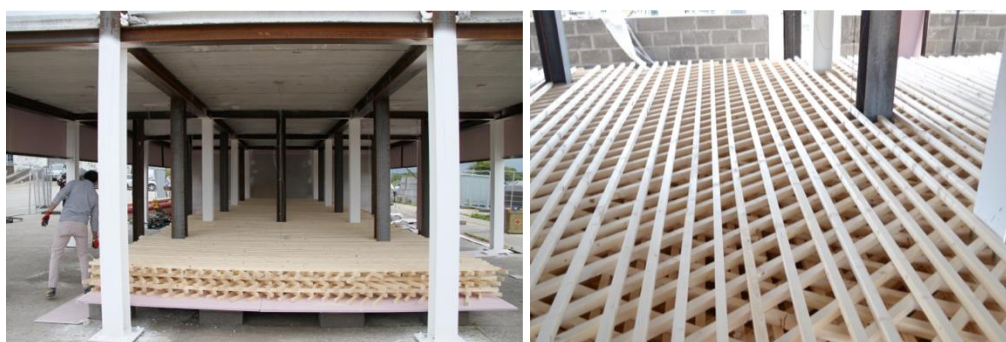


Figure 4. Fuel load arrangement and steel columns (with and without fire protection)

The fuel wood was provided along the centre of the test compartment, as shown in Figure 4. The fire load was 14 m long stretching from wall to wall along the longer dimension of the test compartment. For convenience, a gap of 500 mm was maintained between the walls and the edge of the fuel bed at both ends. The width of the fuel bed was 4.2 m and was aligned with the centre line of the compartment. Such an arrangement of the fire load resulted in a distance of 2.4 m from the edge of the fuel bed to the centreline

of the columns provided along in the longer dimension along gridline A and D. The wood sticks were provided on a platform constructed using concrete blocks and gypsum fireboards as shown in Figure 4. The top surface of the platform was at a distance of 325 mm from the floor finish level.

3 DETAILS OF THE INSTRUMENTATION

The purpose of these large-scale tests was to investigate the dynamics of the travelling fires and to record fire related data. The recorded data included the compartment temperatures, temperatures in the structural steel components, the heat fluxes and the mass loss of the wooden fuel. For the purpose of data acquisition, intensive instrumentation was applied, which consisted of thermocouples, heat flux gauges, thin-skinned calorimeters, anemometer and the load cells (see detail of the large thermocouple trees, placed in the centreline of the compartment, in Figure 5, labelled TRL-1 to TRL-11)

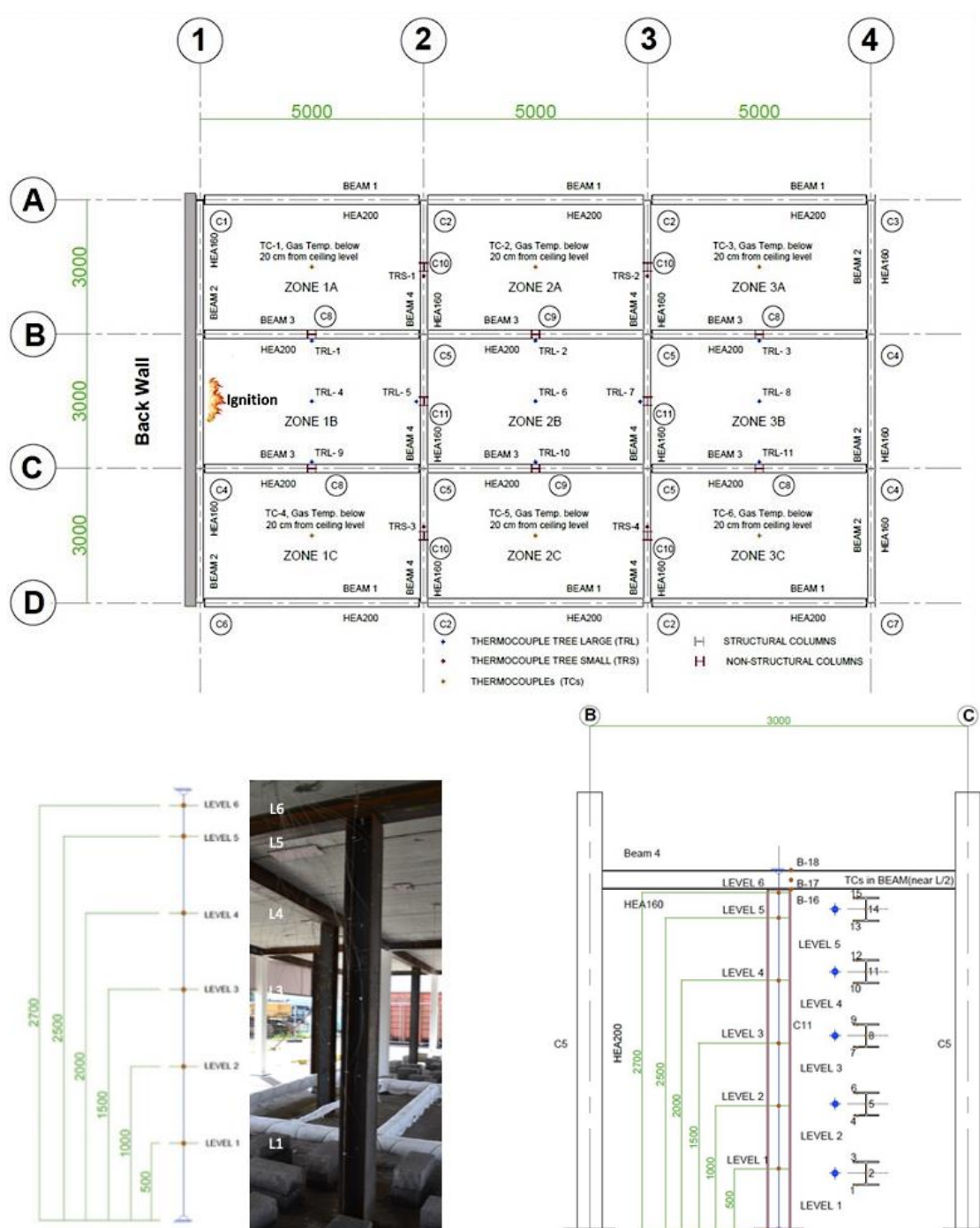


Figure 5. Location of the thermocouple trees in the test compartment and detail of the different levels of the thermocouples for the central zone

In addition to the data recorded in the compartment, temperatures were also recorded in the steel frame during the tests. Temperatures in the steel frame were recorded in the non-structural columns and the selected beams. All thermocouples were provided at 3 mm depth from the surface of the flanges and the steel web. The heat fluxes were monitored via Gordon Gauges (GGs) and the thin-skinned calorimeters (TSCs).

3.1 Mass loss recording

The mass loss was monitored in the middle of the test compartment between gridlines 2 and 3 using a steel platform as shown in Figure 6. The steel platform was 3 m long x 5 m wide and was supported using four load cells as shown in Figure 6. To avoid any damage to the platform during the fire tests, fire blanket was wrapped around the steel elements. The load cells were also protected using the fire blanket to avoid any damage resulting from rise in temperatures. On top of the steel platform, two layers of gypsum fire board were provided to support 4.2 m x 3.6 m of the wooden fuel. The layers of the fire board were placed 325 mm from the floor finish level and were aligned with other fire board panels used to support the fuel wood. Although the fire boards supporting the fuel wood above the steel platform were at the same level, these were kept segregated from the rest of the floorboards to ensure separation of the fuel wood for accurate measurement of the mass loss during the fire tests.

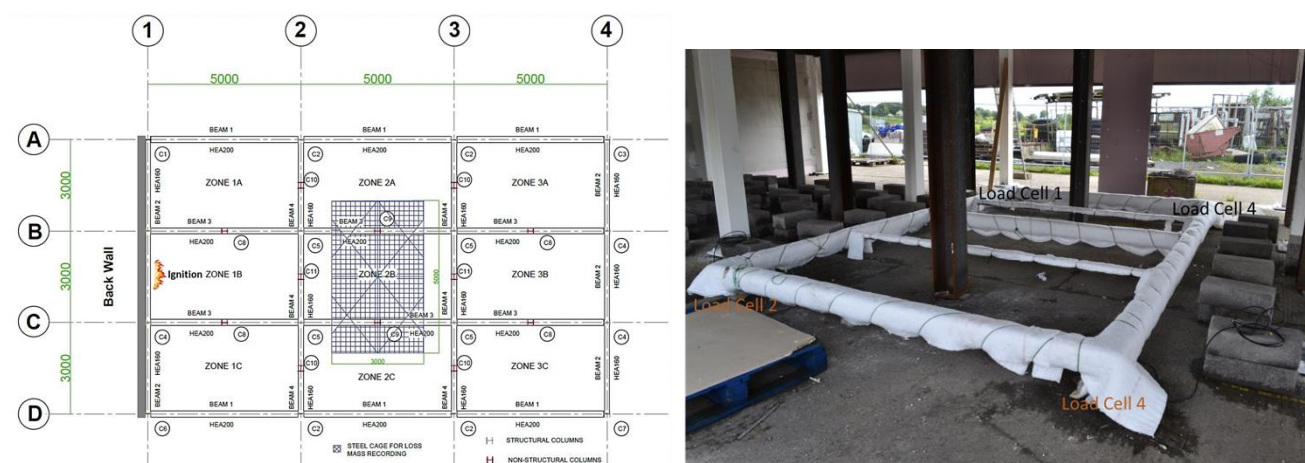


Figure 6. Position and arrangement of the mass loss recording through four load cells

3.2 Data logging system

All the assigned sensors were connected to the data logging system through extension cables. The extension cables were stretched along the roof and were connected with the data loggers stationed in the site office as shown in Figure 7. A layer of fire blanket was laid under these cables to evade any damage from the heat during the tests. Due to higher number of sensors applied, multiple data loggers were employed during the tests.



Figure 7. Extension cables for data sensors and data loggers

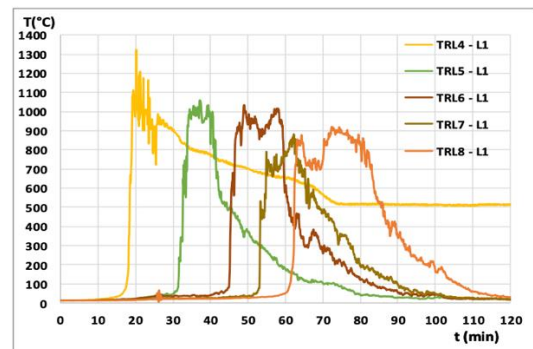
4 RESULTS AND DISCUSSION

In this paper only the first fire test results are presented. Figure 8 illustrates the travelling fire taking place along the length of the compartment through photographs and graphs plotting the evolution of gas temperatures in the compartment along the longer dimension, parallel to the path of the travelling fire, in five thermocouple trees (TRL-4 to TRL-8) equipped with six sensors each (as described in Figure 5). The first thermocouple tree was positioned in the middle of zone 1B at 1.5 m from the source of ignition. The remaining thermocouple trees (TRL-5 through TRL-8) along the centreline of the compartment were equidistant and positioned at 2500 mm centres.

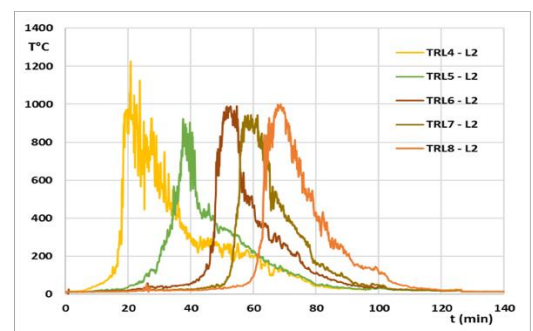
The maximum temperatures recorded in TRL-4 were more than 1000°C after 20 mins from ignition but were measured for a very limited period of time, the gas temperatures quickly decreasing to reach the interval $[800^{\circ}\text{C}-900^{\circ}\text{C}]$. It is interesting to note that the plateau of the maximum recorded temperatures is longer at upper levels as compared to the lower levels. With the fire band travelling towards the next thermocouple tree, TRL-5, the temperatures recorded at TRL-4 reduce while the temperatures at TRL-5 increase. Temperatures recorded at TRL-5 reached the 900°C after 38 mins of the ignition. Similarly, the maximum recorded temperatures using TRL-6, TRL-7 and TRL-8 at level 2 were 995°C , 975°C and 1000°C after 50 mins, 57 mins and 70 mins from ignition respectively as shown in Figure 8. It can be observed that the recorded temperatures vary along the height of the compartment, and that the TRL-6 to TRL-8 (placed in the second half of the compartment) present a shorter temperature peak than TRL-4 and TRL-5 (placed close to the ignition) from 2 m height.



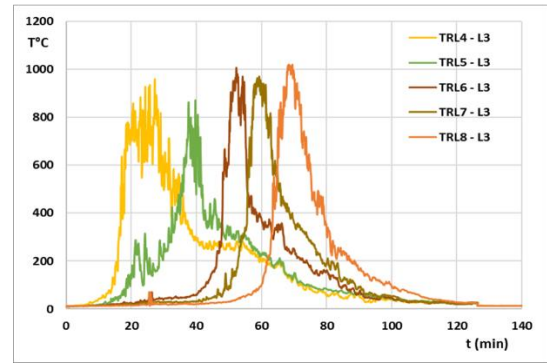
Time :12 min



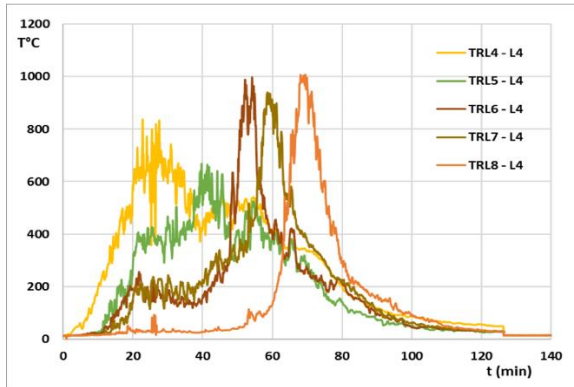
Height = 0.5 m



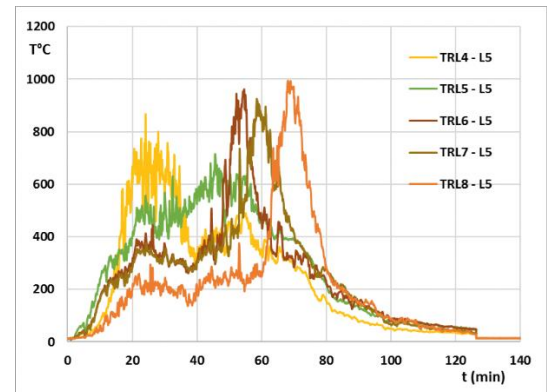
Height = 1.0m



Height = 1.5 m



Height = 2.0 m



Height = 2.5 m

Figure 8. Photographs of the fire and evolution of gas temperatures measured in TRL-4 to TRL-8 at 5 different levels

The maximum flame thickness (i.e. length of the fire along the longer dimension of the compartment) could be observed and is shown in Figure 9. The square markers correspond to a translation of the observations during the test, while the triangle markers correspond to inspection made from the video recording. The “travelling” behaviour of the fire (i.e. when the back end of the fire begins to travel) starts at 28 minutes from ignition for test n°1. This evolution suggests a fairly constant flame thickness of around 3.5 meters, with the lowest value occurring when the fire reaches the central bay of the compartment.

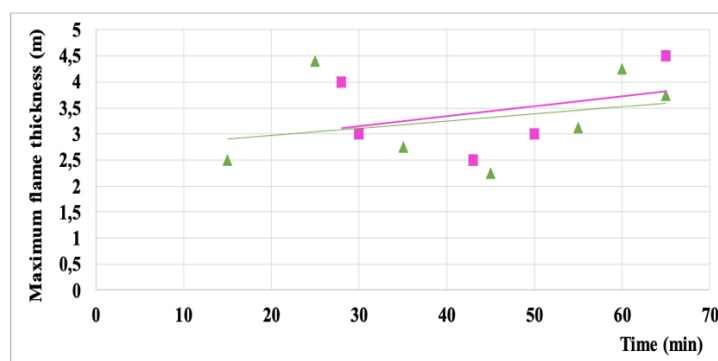


Figure 9. Evolution of the maximum flame thickness

4.1 Results of temperatures in the steel structure

Temperatures were recorded in the selected beams and the unprotected dummy columns. In this paper the column and beam along gridline 3 positioned between gridlines B and C have been selected for data presentation purposes, and thermocouples were placed as shown in Figure 5. During the test, it was observed that the fore end of the travelling fire reached the wooden fuel beneath the selected beam after 52 mins from ignition. The temperatures recorded at the ceiling level along the centre of the compartment (zone B) and the temperatures recorded in the compartment adjacent to the selected column using thermocouple tree TRL-7 are presented in Figure 10 and Figure 11, respectively. The temperature rises at higher levels L5 and L6 initiates earlier as compared to that at the lower levels. The temperature rise at L4 is earlier as compared to the remaining lower levels while it is slower in comparison with levels L5 and L6. This could be explained by the hot gases rising in the compartment, establishing in the upper part. For the bottom three levels, the increase in temperature is rapid as temperatures rise from 1000°C to 950°C within a few mins, translating the direct contact with the flames.

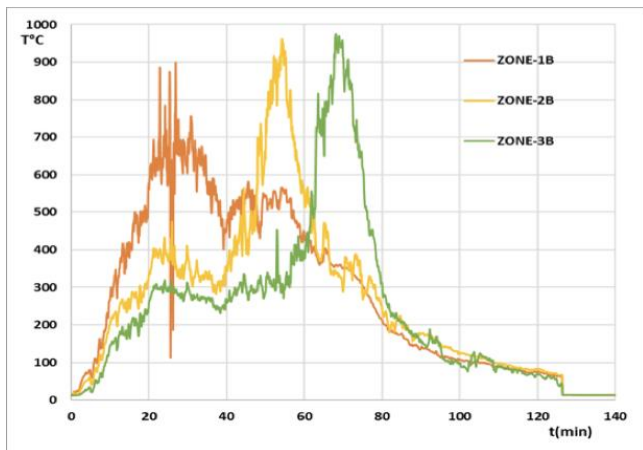


Figure 10. Recorded temperatures at the ceiling level along the centre of the compartment (zone B)

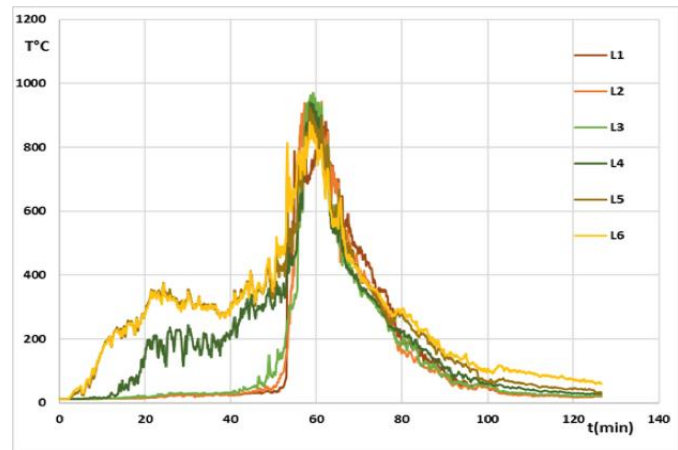


Figure 11. Recorded gas temperatures in the thermocouple tree near the selected column and beam – TRL-7

The temperatures recorded in the flanges and the web of the column at level 3 are presented in Figure 12. Temperatures at level 2 rise after 52 mins from ignition while those at level 4 rise after 15 mins. For the first 50 mins from ignition, the rise in temperature at level 4 is slow while it rises significantly as the wooden fuel near the column starts to burn. The temperatures recorded across the section of the column at each level can be considered as uniform.

The temperatures recorded in the flanges and the web of the column (close to TRL-7) are presented in Figure 12. The label “LHS-F” corresponds to the flange closer to gridline C (i.e. those whose thermocouple number are 1, 4, 7, 10, 13 in Figure 5), “WEB-L” corresponds to the web and “RHS-F” corresponds to the flanges closer to gridline B (i.e. those whose thermocouple number are 3, 6, 9, 12, 15 in Figure 5). It can be seen that the steel temperature profiles are similar to the gas ones, with the following differences:

- The maximum steel temperature is 803°C at 63 minutes (versus 937°C at 58 minutes for gas temperature: this decrease, and delay translate the effect of the steel thermal inertia).
- The steel temperature descending branch is less steep than the gas temperature one (it reaches 500°C after around 80 minutes while the gas temperature one reaches this value after around 67 minutes).
- Also, the temperatures recorded across the section of the column at each level can be considered as uniform.

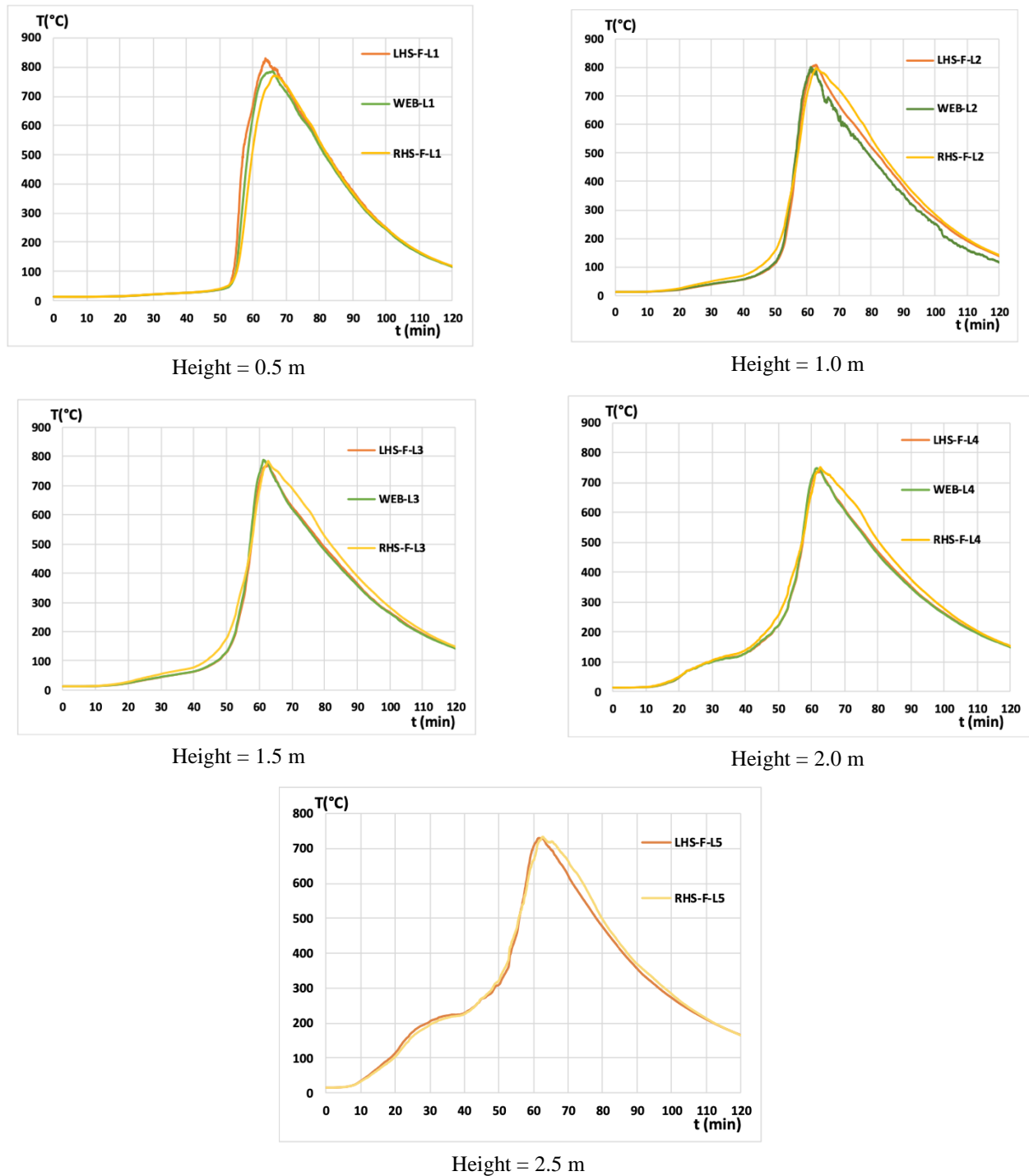


Figure 12. Steel temperatures at different locations along the height of the column close to TRL-7

4.2 Mass loss of the burning fuel

The mass loss data recorded during the test is presented in Figure 13. As observed during the test, a decrease in the mass of the fuel wood supported on the platform is seen once it catches fire after 37 mins from ignition. After 39 min, a uniform decrease in the wooden fuel mass is recorded. After 58 min from ignition, a slow reduction in the mass loss is recorded due to non-uniformity of the burning fuel. The mass loss recordings also comply with the observations during the test where most of the fuel wood provided on the platform was consumed after 64 minutes recorded in the selected column next to TRL-7.

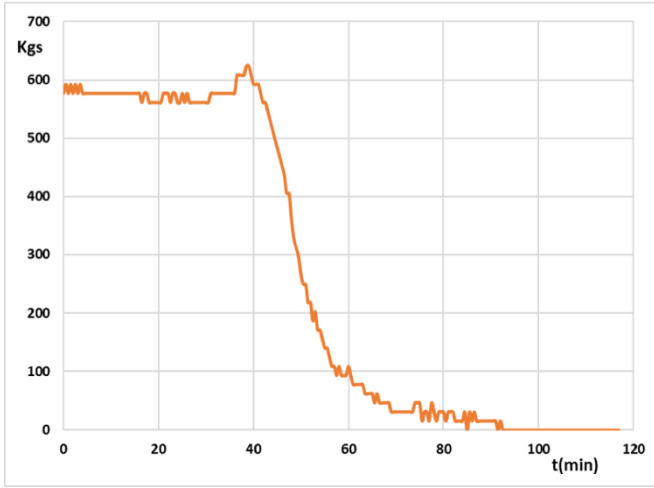


Figure 13. Recorded mass loss

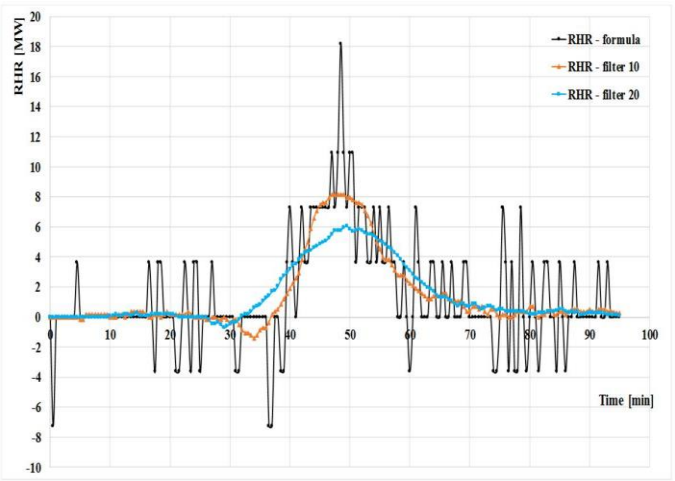


Figure 14. RHR derived from the mass loss measurements

The mass loss rate [kg/s] is the variation of the solid fuel mass during the combustion process. It is possible to deduce the rate of heat release from the mass loss rate, since these two parameters are linked by the equations (1) and (2), H_u being the net calorific value [MJ/kg] and m being the combustion factor (considered equal to 0.8, following Eurocode 1). To evaluate the mass loss rate from the continuously measured mass, a backward finite difference scheme must be applied, which requires the definition of a fixed time step. There is no unique correct value for this time step; but the following consequences should be considered: a more important time step implies a smoother curve, while a less important time step translates in a more precise way the measurements but might provide unrealistic peaks (noise and outliers). Finally, a time step $\Delta t = 60$ seconds was considered as an acceptable compromise.

$$RHR(t) = H_u \cdot m \cdot MLR(t) \quad (1)$$

$$RHR(t) = -H_u \cdot m \cdot \frac{dm}{dt} = -H_u \cdot m \cdot \frac{\Delta m}{\Delta t} \quad (2)$$

As the mass loss rate is the derivative of an experimental signal, noise and outliers (for example negative values) are quickly generated. One method to cope with this is to filter the curve using, for example, a Savitzky–Golay filter. This digital filter that can be applied to a set of digital data points for the purpose of smoothing the data, that is, to increase the precision of the data without distorting the signal tendency. This is achieved, in a process known as convolution, by fitting successive sub-sets of adjacent data points with a low-degree polynomial. The simplest form of this approach, called running average, consists in computing the average for each subset. This approach is commonly used with time series data to smooth out short-term fluctuations and highlight longer-term trends or cycles. The RHR [kW] obtained by derivative of the mass loss using a time step of 60 seconds, the filtered RHR obtained with smoothing parameters of 10 and 20 are depicted in Figure 14. The filtered RHR with parameters 10 and 20 show maxima values of 8140 kW and 5850 kW, respectively. It also has to be noted that some discrepancies can be noticed with wooden fuel load, at the end of the combustion process. Indeed, the heat of combustion of wood is not perfectly constant: it is higher at the end of a test when only embers are left.

8 CONCLUSIONS

Three large scale tests were performed in real building dimensions were conducted to represent a realistic fire the travelling fire as realistic as possible. Instrumentation was installed to measure atmospheric

temperatures, surface temperatures, heat fluxes and temperature within the steel columns, beams and boundaries conditions of the surrounding compartment. In this paper only of the first of the three conducted tests is described and the evolution of the following results were presented: gas temperatures recorded in the central part of the compartment, along its length, maximum flame thickness, steel temperatures in a central beam and a central column, as well as mass loss data. The results obtained from the fire test demonstrated the non-uniform temperature distribution, leading to the heating of the nearby structural steel elements, resulting in a reduction of individual members' resistance, which could influence the global structural stability. The walls and precast slabs forming the boundary of the compartment retained its integrity despite a significant thermal gradient across the wall and slabs. In addition, all the connections and steel members performed very well and showed no signs of failure during the three conducted fire tests.

ACKNOWLEDGMENT

This work was carried out in the frame of the TRAFIR project with funding from the Research Fund for Coal and Steel (grant N°754198). Partners are ArcelorMittal, Liège University, the University of Edinburgh, RISE Research Institutes of Sweden and the University of Ulster. The authors also wish to acknowledge the supporting of companies Sean Timoney & Sons Ltd, FP McCann Ltd, Saverfield Ltd and Crossfire Ltd.

REFERENCES

1. J. Stern-Gottfried, G. Rein (2012). *Travelling fires for structural design – Part I: Literature review*. Fire Safety Journal 54. pp 74- 85.
2. EN1991-1-2 (2002). Eurocode 1: Actions on structures – Part 1- 2: General Actions on structures exposed to fire. CEN, Brussels.
3. R. G. Gann, A. Hamins, K. McGrattan, H. E. Nelson, T. J. Ohlemiller, K. R. Prasad, and W. M. Pitts, (2013) Reconstruction of the fires and thermal environment in World Trade Center buildings 1, 2, and 7, Fire Technol., vol. 49, pp. 679–707.
4. I. Fletcher, A. Borg, N. Hitchen, and S. Welch, (2005) Performance of concrete in fire: A review of the state of the art, with a case study of the Windsor Tower fire,” in 4th International Work- shop in Structures in Fire, pp. 779–790.
5. D. M. Zannoni, J. G. H. Bos, D. K. E. Engel, and P. dr. U. (2008) Rosenthal, Brand bij Bouwkunde.
6. G. Rein, X. Zhang, P. Williams, B. Hume, A. Heise, A. Jowsey, B. Lane, and J. L. Torero, (2007) Multi-storey fire analysis for high- rise buildings, in Proceedings of the 11th International Inter- flam Conference, London, UK, pp. 605–616.
7. K. Horová, T. Jána, F. Wald (2013). Temperature heterogeneity during travelling fire on experimental building. Advances in En- gineering Software 62-63. pp 119-130.
8. J.P. Hidalgo, A. Cowlard, C. Abecassis-Empis, C. Maluk, A.H. Maj- dalani, S. Kahrman, R. Hilditch, M. Krajcovic, J.L. Torero (2017). An experimental study of full-scale open floor plan en- closure fires. Fire Safety Journal 89. pp 22-40.
9. J. P. Hidalgo, T Goode, V. Gupta, A. Cowlard, C Abecassis-Empis, J. Maclean, A. Barlett, C. Maluk, J.M. Montalva, A. F. Osorio, J. L. Torero (2019). The Malveira fire test: Full-scale demonstration of fire modes in open-plan compartments. Fire Safety Jour- nal vol.108 No 102827.
10. A. Gamba, M. Charlier, J.M. Franssen (2020). Propagation tests with uniformly distributed cellulosic fire load. Fire Safety Journal 117, 103213.
11. J. Degler, A. Eliasson, A. Anderson, D. Lange, D. Rush (2015). A- priori modelling of the Tisova fire test as input to the experimental work. Proc. 1st Int. Conf. on Struct. Safety under Fire & Blast, Glasgow, UK.
12. M. Charlier, A. Gamba, X. Dai, S. Welch, O. Vassart, J.M. Franssen (2018). CFD analyses used to evaluate the influence of compartment geometry on the possibility of development of a travelling fire. Proceedings of the 10th International Conference on Structures in Fire (Ulster University, Belfast, UK). pp 341-348.

SHEAR RESISTANCE OF SANDWICH PANEL CONNECTION TO THE SUBSTRUCTURE AT ELEVATED TEMPERATURE

Kamila Cábová¹, Marsel Garifullin², Ashkan Shoushtarian Mofrad³,
František Wald⁴, Kristo Mela⁵, Yvonne Ciupack⁶

ABSTRACT

Sandwich construction has developed and has become an integral part of lightweight construction. In the recent projects it has been shown that by using sandwich panels as stabilizing members, a considerable amount of savings of steel can be achieved for structural members at ambient temperature. These stabilizing effects may also help to achieve similar savings in case of fire. The response of a single panel as well as the behaviour of the whole structure is influenced by joints between the sandwich panels and the sub-structure. The fastenings used to fix the sandwich panels to a sub-structure may be loaded by shear forces caused by self-weight, live loads or diaphragm action. Therefore, an experimental investigation was conducted to investigate the shear behaviour of sandwich panel joints in fire. This paper summarised briefly the experimental results, numerical simulations and analytical models on the shear behaviour of sandwich panel joints at ambient and elevated temperatures.

Keywords: Steel structures; stabilization; fire design; sandwich panels; connections; shear resistance.

1 INTRODUCTION

Sandwich panels, which are used as a building envelope, usually comprise two layers of thin steel faces and a thick core layer of lightweight insulation materials. They have long span capability and a high insulation standard, which allows them to be used as wall or roof cladding. The four most commonly used insulation materials are the products based on polyurethane foams (PUR), polyisocyanurate foams (PIR), extruded polystyrene, and mineral wool (MW). In recent years, the use of lightweight sandwich panels for both industrial and civil buildings is becoming more and more popular. When sandwich panels are used as a cladding wall, they contribute to structural behaviour of the building in addition to aesthetic effects. If a suitable connecting system is adopted, such panels may, in fact, provide a remarkable increase of both lateral stiffness and energy dissipative capacities of the whole structure [1].

In the recent projects [2-5] it has been shown that by using sandwich panels and trapezoidal sheeting as stabilizing members, a considerable amount of savings of steel can be achieved for structural members at ambient temperature. However, the previously performed investigations did not cover the fire limit state. Therefore, in order to fill this gap, a research project “Steel cladding system for stabilization of steel

¹ Ing., Ph.D., Czech Technical University in Prague,

e-mail: kamila.cabova@fsv.cvut.cz

² Postdoctoral Research Fellow, Tampere University, Finland

e-mail: marsel.garifullin@tuni.fi, ORCID: <https://orcid.org/0000-0001-6744-9249>

³ M.Sc., Brandenburg University of Technology, Cottbus, Germany

e-mail: ashkan.shoushtarianmofrad@b-tu.de, ORCID: <https://orcid.org/0000-0002-1570-6298>

⁴ prof. Ing., CSc., Czech Technical University in Prague,

e-mail: wald@fsv.cvut.cz, ORCID: <https://orcid.org/0000-0003-2416-8951>

⁵ Assistant Professor (tenure track), Tampere University, Finland

e-mail: kristo.mela@tuni.fi, ORCID: <https://orcid.org/0000-0002-8411-8625>

⁶ Dr.-Ing., Brandenburg University of Technology, Cottbus, Germany

e-mail: yvonne.ciupack@b-tu.de, ORCID: <https://orcid.org/0000-0002-4276-1356>

buildings in fire” (STABFI) was prepared. The project approved that savings could be achieved in fire due to the stabilizing effect of sandwich panels and trapezoidal sheeting similar to ambient temperature design. The programme was divided into several objectives. This paper covers the short information about the shear resistance of sandwich panel connections at elevated temperature.

2 SHEAR RESISTANCE TEST

2.1 Test set up and specimens

The testing arrangement consists of a sandwich specimen of size 300 mm × 500 mm (width × length) connected to a steel plate using a self-tapping stainless-steel screw with the diameter of 5.5 mm. The steel plates are considered equivalent to the flange thicknesses of the steel profiles to which the sandwich panels are connected in practice. Two types of sandwich panels were used for the tests: with mineral wool (MW) core and polyurethane foam (PIR) core, which consists of a combination of urethane and isocyanurate with polyester polyols into annular structure. The variables of the test include the thickness of 8 mm and 10 mm for the steel plate and sandwich panel thicknesses of 100 mm (MW and PIR), 160 mm (PIR) and 230 mm (MW). The tests were conducted both at ambient and elevated temperatures of 250°C, 300°C and 450°C for panels with PIR core and 300°C, 450°C and 600 °C for panels with MW core. The material properties of the specimens are given in Table 1.

Table 1. Material properties and dimensions of the sandwich panel connection

Parts	Material	Yield strength (MPa)	Thickness (mm)
MW panel			
Inner/outer sheet	S280	280	0.5/0.6
Insulation	Mineral wool	0.086 (Tension) 0.06 (Compression)	100/230
PIR panel			
Inner/outer sheet	S250	250	0.4/0.5
Insulation	PIR	0.05 (Tension) 0.1 (Compression)	100/160
Screw	Stainless steel A2/AISI 304	450	Ø 5.5
Supporting steel	S355	355	8/10

The sandwich panels were connected to the steel plates from both sides, but the interest was to determine the shear resistance of a single connection from one end. Therefore, only elongation of the screw connection from the lower end was measured and three screws were used from the other end in order to minimize the shear displacement of the connection from that end, as shown in Figure 1.

A displacement-controlled testing machine was used for the experiment. The displacement was increased monotonically until failure. A loading rate of 1 mm/min was used for the experiments according to the ECCS recommendation of "The testing of connections with mechanical fasteners in steel sheeting and sections, ECCS No.124" [6]. The displacement of the fastening was measured using an optical extensometer, with optic sensors placed at the central axis of the connection.

At elevated temperatures, the tests were carried out in two steps. Firstly, the specimens were heated to the designed temperatures by Manning's heating pads at the rate of 16.67°C per min. Then the specimen was loaded at a rate of 1 mm/min, and the temperature was kept constant until the end of the experiment. According to the "Preliminary European Recommendations for the Testing and Design of Fastenings for Sandwich Panels, ECCS No.127" [7], the maximum load is reached at a displacement of 3 mm for serviceability limit state. However, in case of fire the large deformation is an alternative mechanism to

prevent the failure of the structure. Thus, the tests were stopped when a displacement of 20 mm was reached both at room and elevated temperatures.

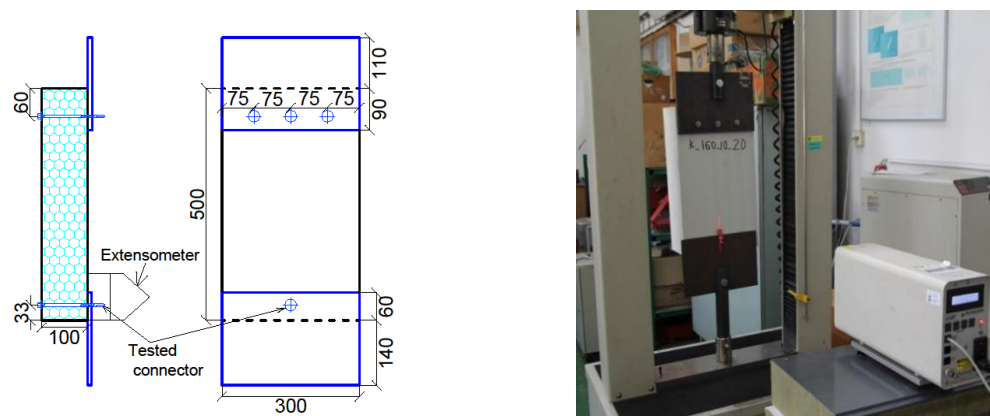


Figure 1. Scheme and experimental setup for shear resistance of sandwich panel joint

2.2 Sandwich connection failure modes

Figure 2 shows the failure modes observed for the sandwich panel connection in the experimental tests. For all the experiments, the major failure was a bearing failure of the inner face of the sandwich panel near the hole of the screw connection. For most of the experiments at ambient temperature, the tearing of the sheet was in a narrow path, approximately equivalent to the screw diameter with a small stacking (folding) of the steel sheet during tearing off. However, for the experiments at elevated temperature, the steel sheet tore off in a wider area and also experiencing stacking (folding) of the steel sheet near the end of the opening. This folding of the steel sheet strengthens the steel sheet further after the initial peak and enables it to carry more load, which is represented by further peak values.

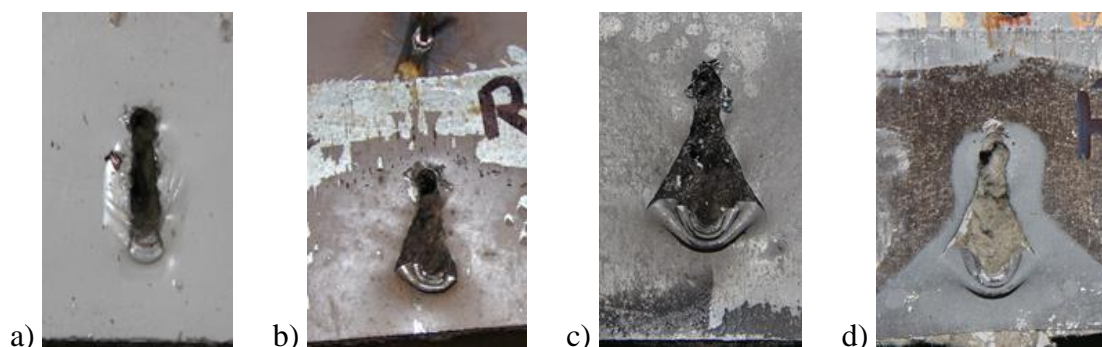


Figure 2. Bearing failure of the inner steel sheet for MW core thick 230 mm, a) at 20°C, b) at 300°C c) at 450°C, d) at 600°C.

2.3 Heating and temperature distribution on a sandwich panel

As a sample, the temperature distribution for the experiments at 300°C is given in Figure 3 for both MW and PIR.

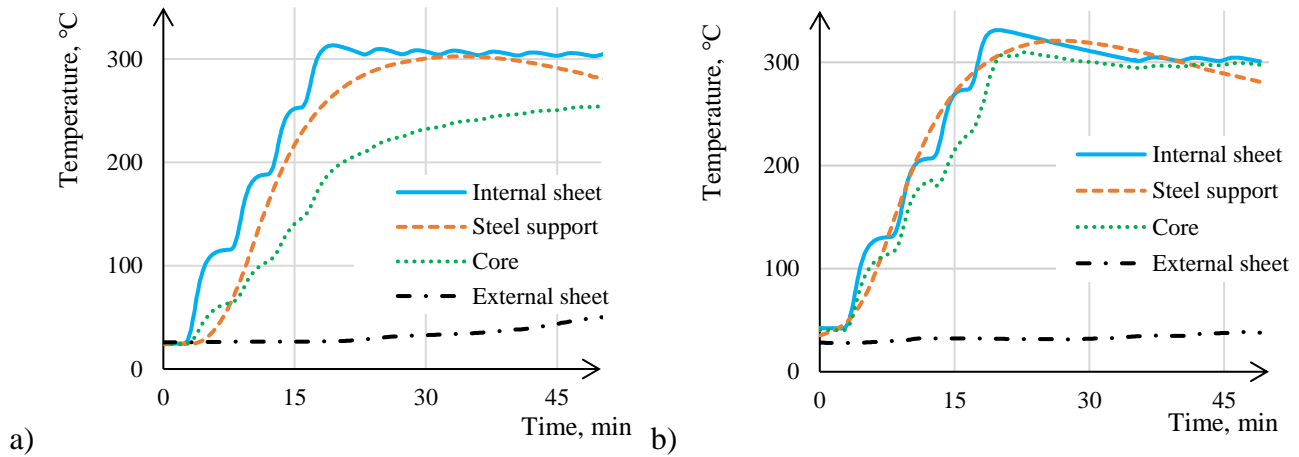


Figure 3. Temperature distribution for the 100 mm thick panel with a) MW and b) PIR core in the middle of the specimen

2.4 Force-displacement curves

The force-displacement curves of the connections at ambient and elevated temperatures with 8 mm steel support are shown in Figure 4. Because fire is an accidental action, the design requires that the structure does not collapse in case of fire. In addition, catenary action of sheeting occurred in the large deformation. From these two points, the specimens were loaded until the displacement reached 20 mm.

It can be seen that with the increase of temperature, both strength and stiffness of the connections are reduced. The stiffness of connection starts to reduce when the slip is initiated at the inner steel sheet because of the spreading of yielding zone. At elevated temperatures, the stiffness reduced further due to the degradation of the material properties. It can be observed that the folding of the steel sheet after the first peak strengthens the steel sheet further and enables it to carry more load, which can be represented by other peaks after the first one, as shown in Figure 4.

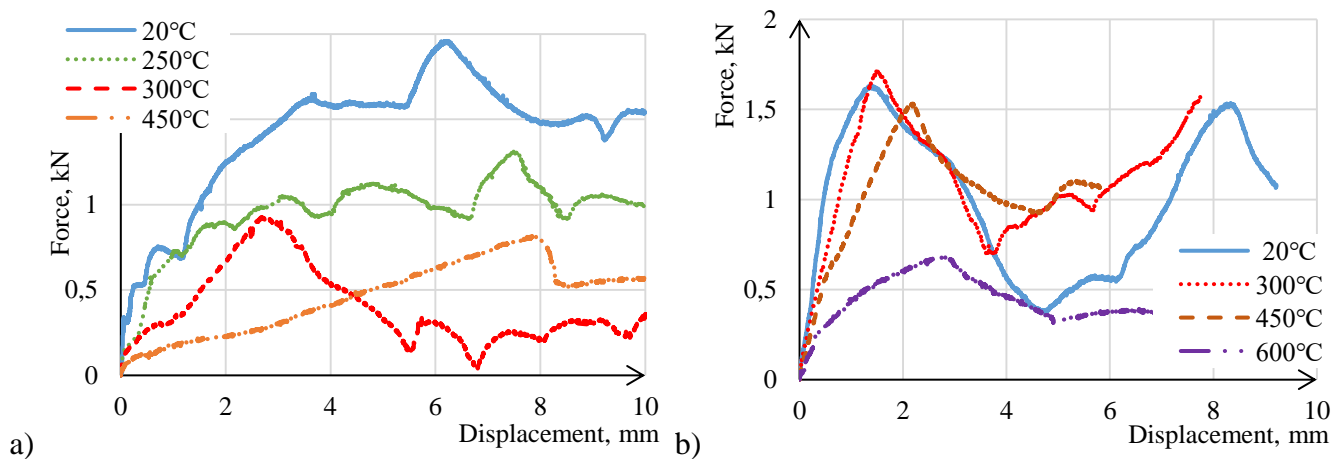


Figure 4. Force-displacement curves for 100 mm thick panels with a) PIR and b) MW core.

3 NUMERICAL SIMULATION

The ABAQUS program [9] is applied to simulate the tests. The model considers material nonlinearity, geometric nonlinearity and contact behaviour. Although the used core materials, PIR and MW, are anisotropic (orthotropic) materials, their behaviour in the numerical model is regarded as isotropic with sufficient accuracy. The density of MW and PIR core is 85 and 40 kg/m³, respectively. To simulate thermal effects, the specific heat for MW and PIR core of 840 and 1300 kJ/(kg·°C) respectively and the thermal conductivity is assumed depending on the temperature in accordance with [10,11].

The material of facing is steel S280, with a density of 7850 kg/m³. The reduction factors for the stress-strain diagram at elevated temperatures are selected in accordance with EN 1993-1-2:2005 [8].

Replicating the experimental set-up, A two-step thermo-mechanical analysis is employed. On the first step, the test specimen is heated until the stationary limit temperature is reached; on the second step, a mechanical load is applied until the required displacement is reached. The tie constraint is applied between the core and facings. The interaction between the screws and the core and supporting members are modelled by the surface-to-surface contact. The boundary conditions of the FE model follow those in the tests. In particular, the lower side of the first supporting member is fully constrained ($U_x = U_y = U_z = 0$), where U is displacement. In contrast, the upper side of the second supporting member is free in the Y direction and fixed in the lateral directions ($U_x = U_z = 0$). According to the tests, the temperature is assigned to the surface of one supporting member and half of the inner facing, as shown in Figure 5.

The connections of sandwich panels with mineral wool core (thickness 100 – 230 mm) and PIR core (thickness 100 – 160 mm) with different sheets thicknesses ($t = 0,5 - 0,7$ mm) on supports 8 and 10 mm exposed to temperatures from 20 °C till 700 °C, and with self-tapping screws $\varnothing 5.5$ were studied.

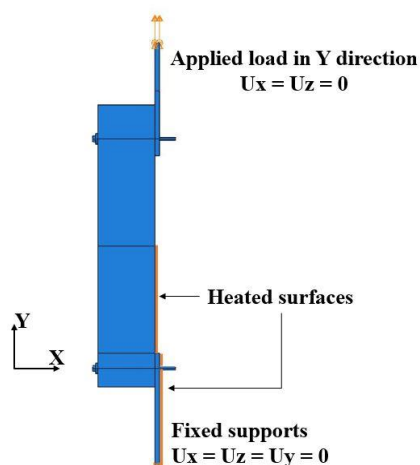


Figure 5. Boundary conditions and loading of FE model.

Figure 6 compares the load-displacement curves of the MW and PIR panels at ambient temperature, where the thicknesses of the panels and supporting members are 100 mm and 8 mm, respectively. As can be seen, the FE model shows slightly stiffer behaviour with a higher resistance compared to the test results, which can be explained by the specimen imperfections (initial cracks, imperfect installation, etc.) in the test set up. However, the differences between the numerical and experimental results are not substantial, and the load-bearing capacity, as well as the initial stiffness for the PIR panel, demonstrate good agreement with the test results.

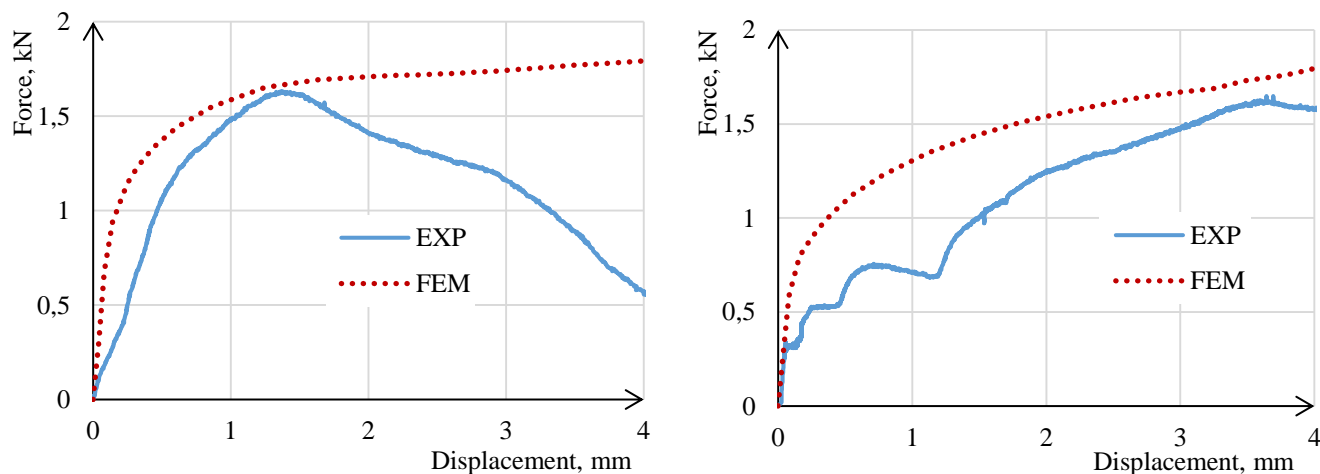


Figure 6. Validation of numerical simulation at room temperature,
a) MW panel, b) PIR panel

4 ANALYTICAL MODEL

The analytical resistance at elevated temperature is calculated employing the equation for the resistance at ambient temperature provided in the ECCS manual [3]:

$$V_{\theta} = 4.2 \sqrt{t_{cor,F2}^3 \cdot d_1 \cdot f_{u,F2,\theta}} \quad (1)$$

where $t_{cor,F2}$ is the core thickness of internal face, d_1 is the minor diameter of the threaded part of the fastener, $f_{u,F2,\theta}$ is the tensile strength of the internal face at elevated temperature, which is found according to Annex A of EN 1993-1-2 [8] as:

$$f_{u,F2,\theta} = \begin{cases} 1.25 f_{y,F2,\theta}, & T < 300^{\circ}\text{C} \\ f_{y,F2,\theta} (2 - 0.0025T), & 300^{\circ}\text{C} \leq T < 400^{\circ}\text{C} \\ f_{y,F2,\theta}, & T \geq 400^{\circ}\text{C} \end{cases} \quad (2)$$

In Eq. (2), $f_{y,F2,\theta}$ is the yield strength of the internal face at elevated temperature, which is calculated according to Table 3.1 of EN 1993-1-2 [8]. The analytical stiffness at elevated temperature is calculated as:

$$k_{v,\theta} \approx k_v \cdot k_{p,\theta} \quad (3)$$

where k_v is the stiffness at ambient temperature calculated according to the ECCS manual [3] and $k_{p,\theta}$ is the reduction factor for the proportional limit according to Table 3.1 of EN 1993-1-2 [8].

The presented analytical solutions for resistance and stiffness are validated with the obtained FE results. The results of the verification are presented separately for the PIR and MW panels in Figure 7, where the analytical values $V_{\theta,theory}$ and $k_{v,\theta,theory}$ are plotted against the numerical ones $V_{\theta,FEM}$ and $k_{v,\theta,FEM}$. For convenience, the two black lines correspond to the equality between the analytical and numerical values, and the cases above and below the black lines correspond to safe and unsafe cases, respectively.

As can be seen, the resistance is safe for all the PIR panels and most of the MW panels, only three MW cases are unsafe. It should be noted that Eq. (1) presents the characteristic value of the resistance; the design value will be safe for all the considered cases. For stiffness, the term safety is not applicable, and the validation/verification is evaluated by the accuracy of the analytical prediction. It can be seen that the analytical values are equal or slightly smaller than the numerical ones, although the underestimation seems to be significant for some cases. In addition, the prediction of stiffness for the MW panels is more conservative than for the PIR panels.

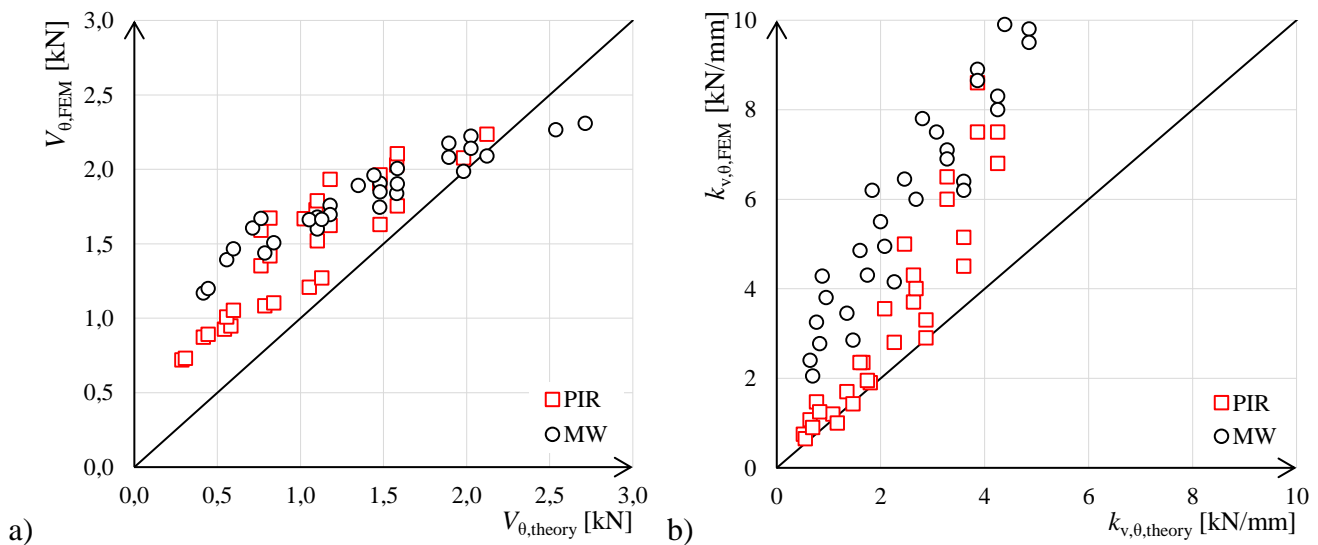


Figure 7. Verification of the analytical model with FE results; a) shear resistance; b) shear stiffness

5 CONCLUSIONS

The STABFI project investigated the stabilizing effect of sandwich panels and trapezoidal sheets for structural buildings in fire. Under the mentioned project, this paper presents the experimental, numerical and analytical results on the shear behaviour and resistance of sandwich panel fasteners both at ambient and elevated temperature. The conclusions of the paper are the following:

- The major failure of the tested connections was a bearing of the inner face of the sandwich panel. The bearing of the steel sheet at ambient temperature was insignificant with small folding of the face, while at elevated temperature it tore off in a wider area with pronounced folding of the sheet. This folding strengthened the sheets and enabled them to carry additional load.
- With the increase of temperature, both the strength and stiffness of the connections decreased. The stiffness of the connection started to reduce when the slip was initiated at the inner sheet because of the spreading of the yielding zone. At elevated temperatures, the stiffness reduced further due to the degradation of the material.
- The developed FE model was validated against the experimental results. The numerical model allowed to enlarge the scope of physical experiments for the successful development of the analytical models.
- The proposed analytical solutions show good correlation with the numerical results, providing safe resistance and accurate stiffness for the connections of the considered MW and PIR panels.
- In the STABFI project were obtained the temperature development in sandwich panels and its connections, the bending stiffness and resistance of panels at elevated temperature, the shear and torsional resistance connections and in total of the stabilization contribution to the whole industrial hall and its compressed members at elevated temperature. The obtained results will be offered to future development of EN1993-1-2.

ACKNOWLEDGMENT

The research reported under this paper was supported by the European Commission for the Research Fund for Coal and Steel under the Grant Agreement Number: 751583 – STABFI – RFCS-2016.

REFERENCES

1. De Mattes & G., Landolfo, R. Structural behaviour of sandwich panel shear walls. An experimental analysis. *Materials and Structures*, Vol. 32, 1999, pp. 331-341.
2. EASIE. Ensuring advancement in sandwich construction through innovation and exploitation. Project final report, 2013.
3. ECCS/CIB. European recommendations on the stabilization of steel structures by sandwich panels. Publication 379, ECCS TC7 and CIB W056, 2013.
4. Hedman-Petursson, E. Column buckling with restraints from sandwich wall elements. Doctoral thesis, Steel Structure Division, Department of Civil and Mining Engineering. Luleå, Sweden, 2001.
5. Misiek, T., Käßlein, S., Saal, H. & Ummenhofer, T. Stabilization of beams by sandwich panels –Lateral and torsional restraint. Eurosteel, August 31-September 2, 2011. Budapest, Hungary.
6. ECCS. The testing of connections with mechanical fasteners in steel sheeting and sections, ECCS publication No. 124, 2009.
7. Preliminary European recommendations for the testing and design of fastenings for sandwich panels - ECCS publication No. 127, 2009.
8. EN1993-1-2, Eurocode3. Design of steel structures. Part 1-2: General rules. Structural fire design, 2005.
9. ABAQUS, 2017. Abaqus Programme..
10. Liu, F., Fu, F., Wang, Y. & Liu, Q., 2017. Fire performance of non-load-bearing light-gauge slotted steel stud walls. *Journal of Constructional Steel Research*, Vol. 137, pp. 228-241.
11. Wang, Y. & Foster, A., 2017. Experimental and numerical study of temperature development in PIR core sandwich panels with joint. *Fire Safety Journal*, pp. 1-14.

NEAR-LIMIT BURNING OF TIMBER MATERIAL UNDER IRRADIATION-ASSISTED SMOLDERING

Shaorun Lin¹, Xinyan Huang²

ABSTRACT

The environmental-friendly timber buildings have sprung up rapidly in the world, but their fire safety is still a significant concern. In this work, we investigate the burning behaviors of different types of woods and their self-extinction mechanism under external radiation. A unique near-limit flame is observed when the irradiation is above a critical value of about 40 kW/m². Such a near-limit flame is weak, blue, and discrete that tends to attach to the wood residue surface, different from the normal buoyancy-controlled sooty yellow flame. If the irradiation is low, the yellow flame extinguishes and transits directly to smoldering at the mass flux of about 4 g/m²·s. However, above the critical irradiation level, the yellow flame transits to the blue flame that does not extinguish until the mass flux of around 1 g/m²·s, extending the flame extinction limit of timber materials. The near-limit blue flame appears only if the char surface temperature exceeds 700 °C. Two critical conditions are hypothesized for this unique blue flame, (I) in-depth pyrolysis sustained by the internal smoldering combustion, and (II) the hot surface maintained by large external radiation to extend the flammability limit. This newly observed blue flame may play an essential role in the transition between flaming and smoldering and help evaluate the fire risk of timber structure under real fire scenarios.

Keywords: extinction limit; external radiation; flaming-to-smoldering transition; timber

1 INTRODUCTION

In the last few decades, timber materials have been reconsidered as a favored construction material for high-rise buildings because of its abundance in nature, high stiffness, and the high strength-to-weight ratio [1, 2]. Many environmental-friendly high-rise timber buildings have sprung up rapidly all around the world, e.g., the 18-story timber building (85 m) in Brumunddal, Norway. Attributed to innovative timber materials like the cross-laminated timber (CLT) [3, 4], Sumitomo made a plan to build a 70-story (350 m) timber skyscraper in Tokyo by 2041 [5]. However, the fire risk of timber is still the primary concern, and the application of high-rise timber building is highly controversial [1], because of its flammable nature and large fuel load in structures [6]. For example, a recent fire in Notre Dame Cathedral burnt out its wooden frame that was made of oak about 800 years ago [7]. Thus, it is urgent to fully understand the fire dynamics and combustion limits of timber materials to guide the fire safety design of timber-based buildings [2].

In the literature, the ignition of various timbers or wooden materials has been studied extensively to understand the initiation and growth of the timber-structured building fire [8–14]. Like most flammable materials, the combustion limits and fire behaviors of timber materials can be influenced by both environmental (e.g., heating source, oxygen concentration, and wind velocity) and material (e.g., density, composition, moisture, and age) factors [15–18]. Moreover, timber, as a typical charring material, can sustain both flaming and smoldering combustion [11]. Flaming is a homogeneous combustion process, while smoldering is the slow, low-temperature, and flameless burning of porous fuels and is the most

¹ Ph.D. student, Research Centre for Fire Safety Engineering, The Hong Kong Polytechnic University
e-mail: flynn.lin@connect.polyu.hk, ORCID: <https://orcid.org/0000-0003-4090-1148>

² Assistant Professor, Department of Building Services Engineering, The Hong Kong Polytechnic University
e-mail: xy.huang@polyu.edu.hk, ORCID: <https://orcid.org/0000-0002-0584-8452>

persistent type of combustion phenomenon [19]. In general, the difficulty of igniting wood and other charring materials is found to increase from the self-ignition, the piloted flaming ignition, to flaming autoignition, and to smoldering (or glowing/surface) ignition [10, 11]. This is different from low-density and high-porosity foam materials, for which smoldering ignition is the easiest [19–21].

On the other hand, a flame is sometimes found not to be able to sustain above the timber material after ignition, i.e., the self-extinction may occur [8, 22, 23]. The self-extinction of timber flame is a crucial concept that supports the fire safety of high-rise timber building and its fast-growing market [22, 24]. However, very few studies have investigated the extinction mechanisms of timber and quantified its combustion limits. Previously, Babrauskas [25] used a flame to ignite a timber material for several minutes and found the self-extinction occurred once the igniting flame was removed. Emberley *et al.* [13, 26] further studied the self-extinction of flaming timber and CLT under external radiation and found the minimum irradiation of $43.6 \pm 4.7 \text{ kW/m}^2$ and the minimum mass flux of $3.93 \pm 0.45 \text{ g/m}^2 \cdot \text{s}$ were required to sustain the flame. Vermesi *et al.* [27] found that for engineered wood, the critical mass flux for flameout varied in a wide range ($1.4\text{--}17 \text{ g/m}^2 \cdot \text{s}$). Nevertheless, extinction of the flame is not the end of a fire, as it may be followed by the stable smoldering [28]. Moreover, under specific conditions, smoldering may transition to the flaming, i.e., the smoldering-to-flaming (StF) transition [19, 29]. Therefore, in a real timber fire, the ignition (and re-ignition) and extinction of the flame, as well as smoldering combustion, could repeatedly occur several times until the eventual burnout, during which the timber structure loses its stability or even collapses [13].

In our recent wood fire tests, a thin layer of weak blue flame (Figure 1a) was observed floating above the wood surface near the flaming extinction limit. A similar blue flame is also widely observed in the burning charcoal (Figure 1b). Such a near-limit blue flame may play an important role in defining the true extinction limit of timber flame and the transition between flaming and smoldering, while to the best of authors' knowledge, the combustion mechanism dominating this unique phenomenon has not been systematically studied yet, posing a knowledge gap. In this work, we will quantify the extinction limits of timber flame and its near extinction fire behaviors using both laboratory experiments and theoretical analysis.

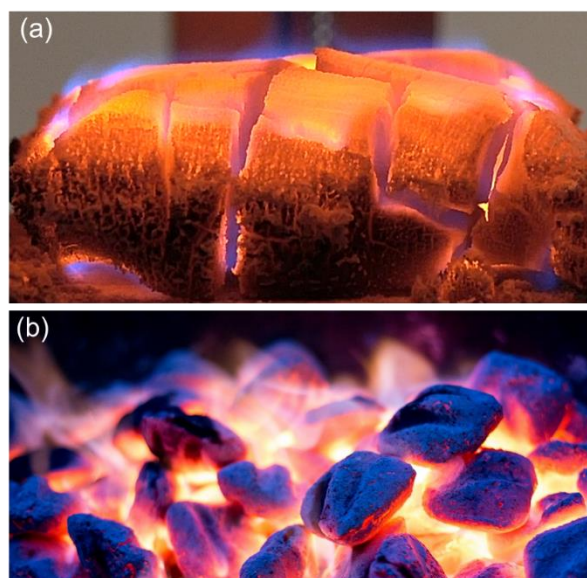


Figure 1 the blue flame above the (a) timber (cc by S. Lin), and (b) charcoal (cc by M. Simon).

2 EXPERIMENTAL METHOD

Six different types of natural woods, which have the same dimension of $10 \text{ cm} \times 10 \text{ cm} \times 3 \text{ cm}$ and different densities, were tested (Figure 2a). Before the experiments, all wood samples were first oven-dried at 70°C for 48 h, and then, placed into an electronic dry cabinet to avoid the re-absorption of moisture from the air. Their dry bulk densities from low to high are listed in Table 1.

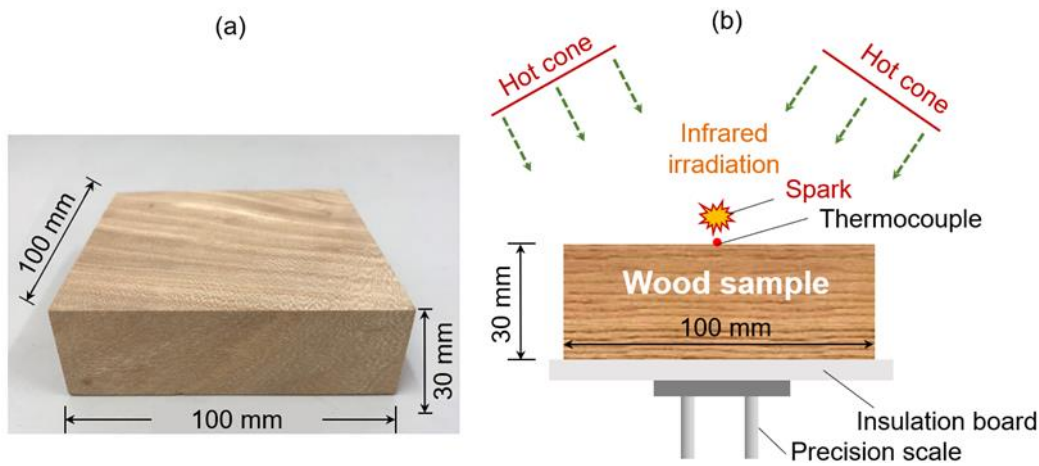


Figure 2. (a) A photo of the wood sample, and (b) a schematic diagram of the experimental apparatus.

All experiments were conducted under the cone calorimeter (FTT iCone Plus), which mainly includes a conical heater, spark igniter, sample holder, and precision scale, as illustrated in Figure 2(b). The conical heater could provide relatively constant and uniform irradiation (\dot{q}_e'') to the sample area of 10 cm \times 10 cm, so that the whole top surface of the wood sample would have uniform irradiation [30]. Before the test, the temperature of the conical heater was calibrated with the irradiation level, which was measured by a radiometer. The test section, including the wood sample, sample holder, and cone heater, was partially open to ensure a sufficient air supply and smoke ventilation.

Table 1. The dry bulk density (ρ), ignition mass flux at 50 kW/m² (\dot{m}_{ig}''), minimum irradiation ($\dot{q}_{B,crt}''$) for near-limit blue flame, and extinction mass flux for yellow flame ($\dot{m}_{ex,Y}''$) and blue flame ($\dot{m}_{ex,B}''$) for different wood types, where the standard error of repeating tests is within 5%.

Wood sample	ρ (kg/m ³)	\dot{m}_{ig}'' (g/m ² ·s)	$\dot{q}_{B,crt}''$ (kW/m ²)	$\dot{m}_{ex,Y}''$ (g/m ² ·s)	$\dot{m}_{ex,B}''$ (g/m ² ·s)
A	406	7.4	52	3.9	0.91
B	560	8.4	37	4.0	1.08
C	570	9.6	37	3.9	0.89
D	588	10.5	37	4.2	0.93
E	781	12.5	32	4.0	0.96
F	816	12.8	32	3.9	0.92

The piloting spark was placed at 5 mm above the top surface of the wood sample. Once the flame was piloted, the spark was removed, while heating was continued until the sample mass no longer changed or the wood sample completely turned into white ashes (i.e., burnout). The test process was recorded by a camera, and the sample mass was monitored by the precision scale (± 0.1 mg). The surface temperature of wood was carefully monitored using a K-type thermocouple (0.5 mm junction bead diameter) that was contacted with the wood top surface. During the test, the ambient temperature was 22 ± 2 °C, the relative humidity was $50 \pm 10\%$, and the ambient pressure was 1 atm. For each test, at least two repeating experiments were conducted to ensure the experimental repeatability and quantify the experimental random uncertainty.

3 EXPERIMENTAL RESULTS

3.1 Fire phenomena and critical heat flux

Figure 3 shows the examples of the fire phenomena of Wood C under different external radiation (\dot{q}_e'') of 30 kW/m² and 60 kW/m², respectively. The critical mass fluxes and time moments of transitioning to different stages are also indicated in Figure 3. Before the piloted flaming ignition, smoke was always observed, likely the pyrolysis gases [20, 31]. Continuing the heating, a strong buoyancy-controlled yellow flame was piloted by the spark and maintained.

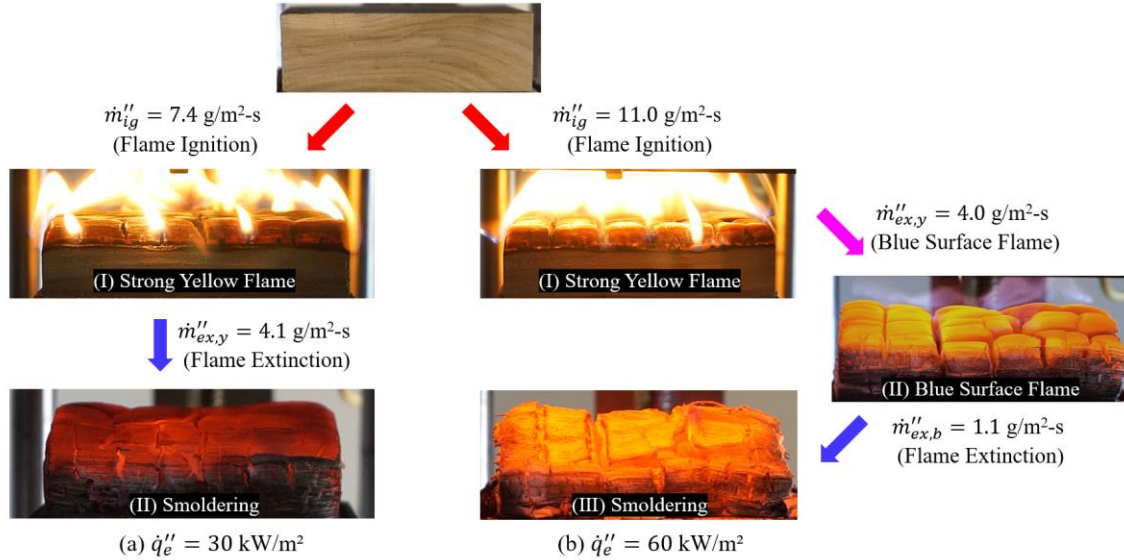


Figure 3. Different burning phenomena of Wood C under the external radiation (\dot{q}_e'') of (a) 30 kW/m², and (b) 60 kW/m².

Under the lower irradiation of 30 kW/m², a two-stage burning process was observed (Figure 3a). After the extinction of the initial strong yellow flame, a stable smoldering fire in the solid phase occurred and sustained until burnout. On the other hand, under the higher irradiation of 60 kW/m², a three-stage burning process was observed (Figure 3b). After the extensive burning of yellow flame, a near-limit blue flame appeared and lasted for more than 20 min before transitioning to smoldering. This blue flame is weak, blue, flat, discrete above parts of the wood residue surface, and lacks buoyancy effect, all of which are quite different from the regular yellow flame.

In the real fire scenarios, wood materials may receive high irradiation from nearby hot smokes or flames ($> 80 \text{ kW/m}^2$ in post-flashover compartment fires and wildland fires) [26]. Therefore, one can expect that after the disappearance of intense yellow flame, this kind of blue flame can still be sustained on timber for an extended period, although it may be too weak to be visible. Also, as the blue flame does not entirely cover the wood surface, oxygen molecules may diffuse into the charred wood, so that smoldering may co-exist with the flame. Thus, this newly observed blue flame may not only help evaluate the fire risk of timber structure under real fire scenarios, but also play an essential role in the transition between flaming and smoldering.

Moreover, the experiments have quantified the critical (minimum) irradiation level for the appearance of this near-limit blue flame (\dot{q}_b'') and the three-stage combustion processes. As showed in Table 1, the required minimum external radiation is found to increase as wood density decreases, where the average value is about $40 \pm 10 \text{ kW/m}^2$. Specifically, Wood F with the highest bulk density of 816 kg/m³ can maintain the blue flame at the lowest critical irradiation of 32 kW/m², while the Wood A with the lowest density of 406 kg/m³ requires the highest critical irradiation of 52 kW/m².

3.2 Critical mass flux and surface temperature

The mass flux (\dot{m}'') is the mass-loss rate (or burning rate) per unit area, which is considered as one of the most important parameters to quantify different forms of combustion [32]. During the flaming combustion, the increasing thickness of the char layer can reduce the amount of the heat the pyrolysis front receives like a thermal insulator, and extinction occurs when heating is too small to maintain the minimum mass flux (\dot{m}_{ex}'') [13, 14]. Figure 4 illustrates the evolution of mass flux of Wood C (570 kg/m³) under external radiations of (a) 30 and (b) 60 kW/m².

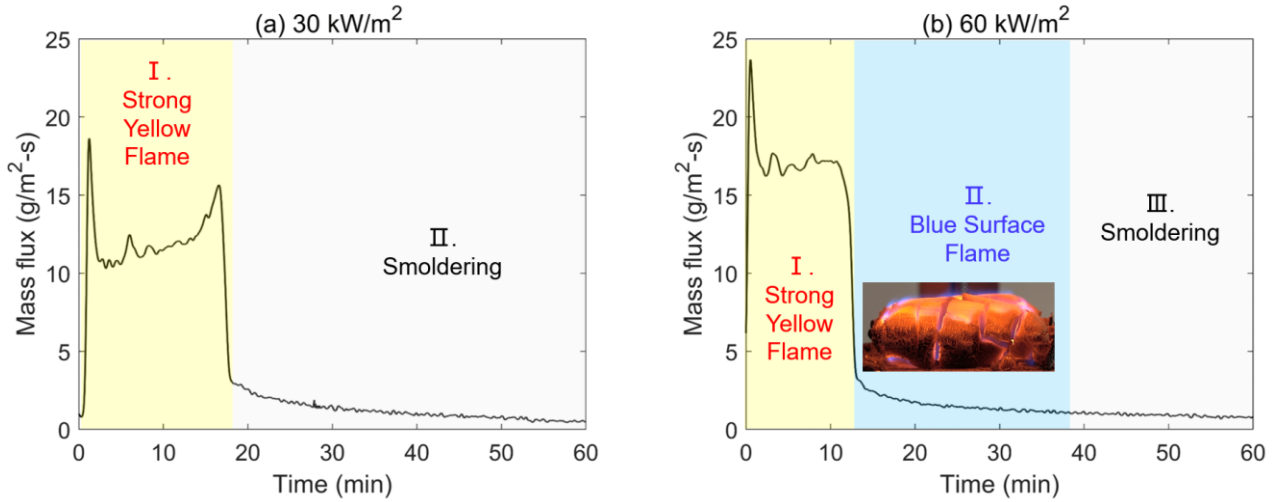


Figure 4. Time evolution of mass flux of Wood B under the radiant heat flux of (a) 30 kW/m² and (b) 60 kW/m².

At the lower irradiation of 30 kW/m² (Figure 4a), the mass flux curve is similar to the typical evolution in [10]. Once exposed to the irradiation, the mass flux increases dramatically to a peak value, and then, it decreases gradually due to the build-up of the char layer. Continuing the heating, the pyrolysis front eventually reaches the bottom of the wood sample and approaches to the top of the insulation board, so that the downward heat conduction into the wood is reduced. As a result, the pyrolysis is accelerated and results in the second peak of the mass loss curve. Afterward, the whole sample is mostly charred, and the mass flux goes through a sharp drop. Eventually, the self-extinction of the yellow flame occurs when the mass flux decreases to about 4 g/m²·s. This value is consistent with previous studies on the critical mass flux for flaming extinction [13, 26, 33, 34].

On the other hand, under the higher irradiation of 60 kW/m², as shown in Figure 4(b), extinction of the yellow flame also occurs when the mass flux decreases to about 4 g/m²·s. Afterward, a blue flame closely attached to the sample surface occurs and maintains for nearly 30 minutes at a lower mass flux (1~4 g/m²·s), rather than directly transitioning to smoldering. In this circumstance, the self-extinction of the flame should be the extinction of this blue flame, rather than the traditional buoyancy-controlled yellow flame. Therefore, the existence of this blue flame may have extended the extinction limit. Eventually, the near-limit blue flame extinguishes and transitions to smoldering at the critical (minimum) mass flux around $\dot{m}_{ex}'' \approx 1$ g/m²·s, re-defining the flame extinction limit of timber materials.

As the external irradiation increases, the sample top-surface temperature (T_s) will increase as well, as measured and shown in Figure 5(a). As expected, the near-limit blue flame can only be sustained when the surface temperature is sufficiently high, that is, $T_s > T_B \approx 700$ °C at $\dot{q}_e'' > \dot{q}_b'' \approx 40$ kW/m². Considering typical irradiation in a compartment fire can easily go up to 80 kW/m² [35], it is likely to sustain a long-term blue flame on timber materials before flame extinction. Figure 5(b) further summarizes the true critical mass flux for the flame extinction (\dot{m}_{ex}'') under real fire scenarios with the external irradiation. When the external irradiation is lower than 40 kW/m², the yellow flame extinguishes at about 4 g/m²·s, agreeing with the literatures [13, 26]. When the external irradiation is above 40 kW/m², the persistent blue flame can be maintained until $\dot{m}_{ex}'' \approx 1$ g/m²·s. Moreover, this redefined flame-extinction limit is insensitive to the wood type, as shown in Table 1, thus, helping evaluate the fire risk of timber materials in real fire scenarios.

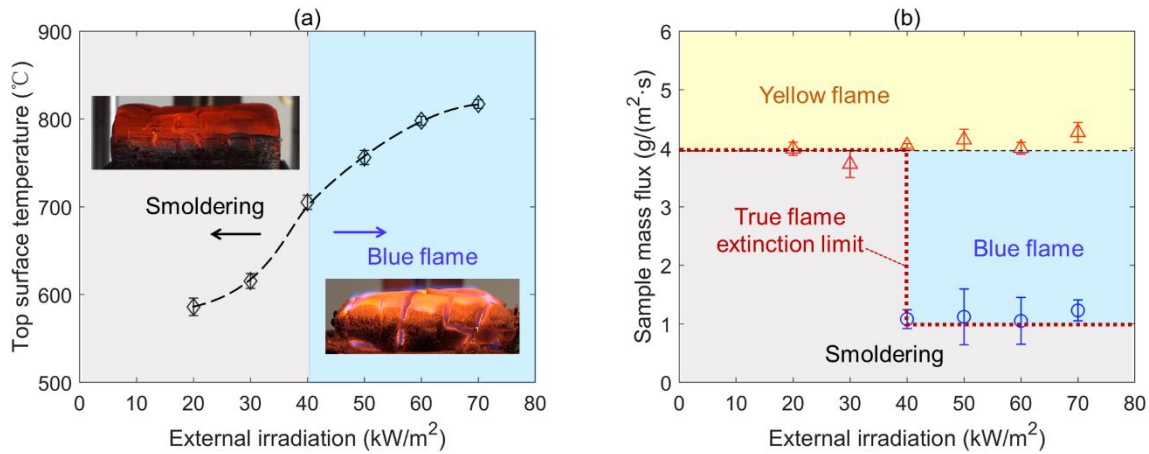


Figure 5. (a) Surface temperature (T_s) as a function of external irradiation (\dot{q}_e'') for Wood B, and (b) mass flux (\dot{m}'') boundary for different combustion behaviors and extinction limits.

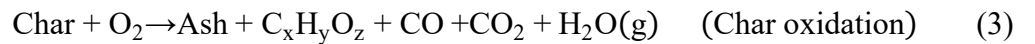
3.3 Theoretical analysis of near-limit blue flame

Considering the blue flame is never observed in PMMA regardless of the irradiation level, the decomposition chemistry and charring tendency of wood fuels are expected to play an important role in this near-limit flame behavior. To maintain a wood flame, at least two kinds of reactions are needed, namely, the pyrolysis of solid fuel to release pyrolyzates and the subsequent oxidation reaction of the pyrolyzates in the gas phase:

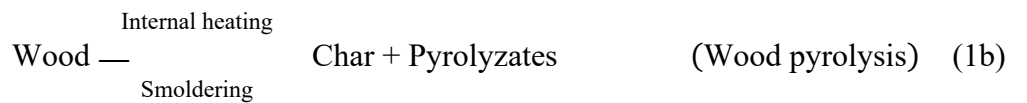


Pyrolysis is maintained by the heating from flame and external irradiation, and a robust sooty flame will persist until the pyrolysis is weakened by the thick char layer (Figure 6a). In contrast, for non-charring fuels like PMMA, there will always be a yellow flame until burnout. Compared to the low-temperature solid-phase oxidation, gas-phase flame reactions are much faster. Thus, almost all ambient oxygen will be consumed within the flame sheet, whereas little oxygen can diffuse into the porous char to sustain robust smoldering combustion.

As the char layer builds up to weaken the effectiveness of the heating, less fuel is produced to support the flame. Under such a negative feedback, eventually, the yellow flame extinction occurs at $\dot{m}_{ex}'' \approx 4 \text{ g/m}^2\cdot\text{s}$, leaving undecomposed wood in-depth and unburned char near the surface. Afterward, without the blockage of flame, oxygen can diffuse into the cracked and porous char layer to sustain smoldering combustion, which is sustained by the char oxidation.



This heterogeneous char oxidation is incomplete, which could produce a fuel mixture of hydrocarbons and CO [36, 37]. Moreover, the internal heat release from the char oxidation can further pyrolyze the wood in-depth as



Especially, the lignin component, which has a higher pyrolysis temperature (400-500 °C) than the cellulose and hemicellulose components [38], continues to produce a small amount of flammable gas fuel before being oxidized to ash.

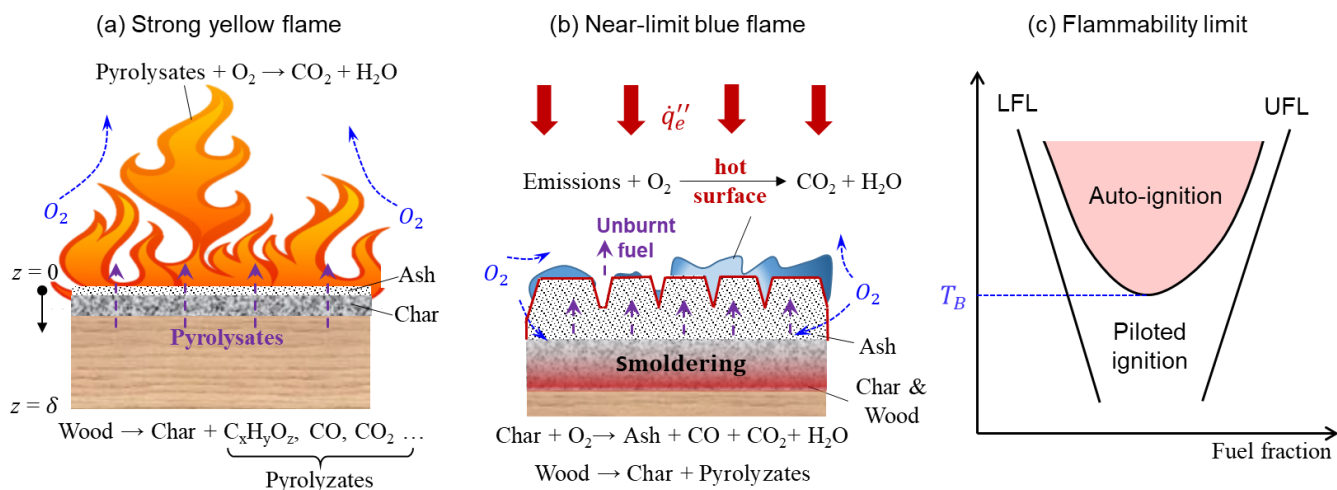
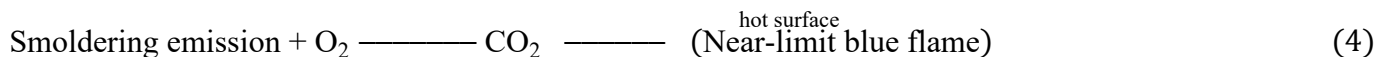


Figure 6. Schematic diagrams of (a) strong yellow flame, (b) weak blue flame, and (c) the flammability limit for piloted and auto-ignition.

As the surface temperature increases with the external radiation, eventually, it becomes hot enough (>700 °C) to either pilot the flame or supports an auto-ignition of the fuel/air mixture. As illustrated in Figure 6(b), it is hypothesized that the near-limit blue flame is maintained by the mixture produced from both char-oxidation and wood-pyrolysis reactions of smoldering combustion



There are two pieces of supporting evidence, (1) the color of a fuel-lean near-limit flame is pale blue like those in microgravity [21, 39–41], and (2) the discrete blue flame partially covers the char and allows the oxygen diffusion inside to maintain the in-depth char oxidation.

The critical surface temperature of $T_B \approx 700$ °C to sustain the blue flame may be the minimum auto-ignition temperature (AIT) of the mixed hydrocarbons and CO produced from smoldering, as illustrated in Figure 6(c). Below this temperature, the flammable mixture cannot be ignited without a pilot source. Above this temperature, the auto-ignition of the fuel-lean mixture not only ensures the existence of flame but also acts as a piloted source to ignite the nearby lean mixture. Because the release of smoldering emission is not uniform across the wood sample, the random ignition and flame propagation on the fuel surface makes the flame flicker around. In other words, the surface flame is a combination of premixed flame and diffusion flame. As the flame reaction takes place near the hot surface, and the fuel mass flux is small, the role of buoyancy is too small to create a conical shape.

In short, two necessary conditions are hypothesized for this unique blue flame,

The robust in-depth pyrolysis should be sustained by the internal smoldering combustion and external heating; and

A hot surface temperature (>700 °C) over the auto-ignition temperature should be maintained by the external radiation.

Further decreasing the fuel mass flux to about $1 \text{ g/m}^2\cdot\text{s}$, the composition of the fuel-lean mixture near the hot surface may become lower than the lean flammability limit, giving rise to extinction.

4 CONCLUSIONS

In this study, a unique wood combustion mode showing a near-limit blue flame was identified as an intermediate combustion mode between the buoyancy-controlled yellow flame and the smoldering combustion. The blue flame appears only if the external radiation exceeds a critical value of about 40 kW/m^2 and the surface temperature higher than 700°C . This near-limit flame tends to attach to the hot charring and smoldering surface and is almost free of buoyancy effect. Below the critical irradiation, the intense yellow flame directly transitions to smoldering when the mass flux decreases to about $4.0 \text{ g/m}^2\cdot\text{s}$ for all wood samples. Above the critical irradiation, on the other hand, the near-limit blue flame can still

survive at the mass flux until $1.0 \text{ g/m}^2\cdot\text{s}$. Thus, it redefines the flame extinction limit of timber materials under external radiation.

The analysis shows two necessary conditions for the occurrence of near-limit blue flame, (I) in-depth pyrolysis sustained by the internal smoldering combustion, and (II) the hot surface maintained by large external radiation to extend the flammability limit or achieve autoignition. The future work will focus on emission gas compositions from different combustion stages, as well as numerical simulations coupling gas-phase and solid-phase processes. This newly observed blue flame may play an essential role in the transition between flaming and smoldering and help evaluate the fire risk of timber structure under real fire scenarios.

ACKNOWLEDGMENT

This work is supported by the National Natural Science Foundation of China (No. 51876183, 51806230), HK PolyU Startup Fund (1-BE04), and the SKLFS Open Fund (No. HZ2019-KF02).

REFERENCES

1. Barber D (2015) Tall Timber Buildings: What's Next in Fire Safety? *Fire Technology* 51:1279–1284. <https://doi.org/10.1007/s10694-015-0497-7>
2. Richter F, Atreya A, Kotsovinos P, Rein G (2019) The effect of chemical composition on the charring of wood across scales. *Proceedings of the Combustion Institute* 37:4053–4061. <https://doi.org/10.1016/j.proci.2018.06.080>
3. Crielaard R, van de Kuilen JW, Terwel K, et al (2019) Self-extinguishment of cross-laminated timber. *Fire Safety Journal* 105:244–260. <https://doi.org/10.1016/j.firesaf.2019.01.008>
4. Song J, Chen C, Zhu S, et al (2018) Processing bulk natural wood into a high-performance structural material. *Nature* 554:224–228. <https://doi.org/10.1038/nature25476>
5. Boarin P, Calzolari M, Davoli P (2018) Two timber construction models: tradition without innovation or innovation without tradition?
6. Drysdale D (2011) *An Introduction to Fire Dynamics*, 3rd ed. John Wiley & Sons, Ltd, Chichester, UK
7. Prior R (2019) The entire wooden interior of Notre Dame Cathedral has been lost. *CNN*
8. Bilbao R, Mastral JF, Aldea ME, et al (2001) Experimental and theoretical study of the ignition and smoldering of wood including convective effects. *Combustion and Flame* 126:1363–1372. [https://doi.org/10.1016/S0010-2180\(01\)00251-6](https://doi.org/10.1016/S0010-2180(01)00251-6)
9. Bartlett AI, Hadden RM, Bisby LA (2019) A Review of Factors Affecting the Burning Behaviour of Wood for Application to Tall Timber Construction. *Fire Technology* 55:1–49. <https://doi.org/10.1007/s10694-018-0787-y>
10. Boonmee N, Quintiere JG (2002) Glowing and flaming autoignition of wood. *Proceedings of the Combustion Institute* 29:289–296. [https://doi.org/10.1016/S1540-7489\(02\)80039-6](https://doi.org/10.1016/S1540-7489(02)80039-6)
11. Boonmee N, Quintiere JG (2005) Glowing ignition of wood: The onset of surface combustion. *Proceedings of the Combustion Institute* 30 II:2303–2310. <https://doi.org/10.1016/j.proci.2004.07.022>
12. Richter F, Atreya A, Kotsovinos P, Rein G (2017) The effect of chemical composition on the charring of wood across scales. *Proceedings of the Combustion Institute* 000:1–9. <https://doi.org/10.1016/j.proci.2018.06.080>
13. Emberley R, Do T, Yim J, Torero JL (2017) Critical heat flux and mass loss rate for extinction of flaming combustion of timber. *Fire Safety Journal* 91:252–258. <https://doi.org/10.1016/j.firesaf.2017.03.008>
14. Moghtaderi B, Novozhilov V, Fletcher DF, Kent JH (2006) A New Correlation for Bench-scale Piloted Ignition Data of Wood. *Fire Safety Journal* 29:41–59. <https://doi.org/10.1016/j.firesaf.2006.03.004>
15. Shi L, Chew MYL (2012) Influence of moisture on autoignition of woods in cone calorimeter. *Journal of Fire Sciences* 30:158–169. <https://doi.org/10.1007/s12648-015-0783-8>
16. Huang X, Li K, Zhang H (2017) Modelling bench-scale fire on engineered wood: Effects of transient flame and physicochemical properties. *Proceedings of the Combustion Institute* 36:3167–3175. <https://doi.org/10.1016/j.proci.2016.06.109>

17. Richter F, Rein G (2019) Heterogeneous kinetics of timber charring at the microscale. *Journal of Analytical and Applied Pyrolysis* 138:1–9. <https://doi.org/10.1016/j.jaap.2018.11.019>
18. Richter F, Rein G (2020) A multiscale model of wood pyrolysis to study the role of chemistry and heat transfer at the mesoscale. *Combustion and Flame* 216:316–325. <https://doi.org/10.1016/j.combustflame.2020.02.029>
19. Rein G (2014) Smoldering Combustion. *SFPE Handbook of Fire Protection Engineering* 2014:581–603. https://doi.org/10.1007/978-1-4939-2565-0_19
20. Lin S, Sun P, Huang X (2019) Can peat soil support a flaming wildfire? *International Journal of Wildland Fire* 28:601–613. <https://doi.org/10.1071/wf19018>
21. Huang X, Gao J (2020) A review of near-limit opposed fire spread. *Fire Safety Journal* 103:141. <https://doi.org/10.1016/j.firesaf.2020.103141>
22. Bartlett AI, Hadden RM, Hidalgo JP, et al (2017) Auto-extinction of engineered timber: Application to compartment fires with exposed timber surfaces. *Fire Safety Journal* 91:407–413. <https://doi.org/10.1016/j.firesaf.2017.03.050>
23. Richter F, Jervis FX, Huang X, Rein G (2020) Burning rate of wood pyrolysis, smouldering, and flaming: Effect of oxygen. *Combustion and Flame* (under review)
24. Cuevas J, Torero JL, Maluk C (2020) Flame extinction and burning behaviour of timber under varied oxygen concentrations. *Fire Safety Journal* 103:087. <https://doi.org/10.1016/j.firesaf.2020.103087>
25. Babrauskas V (2002) Journal of Fire Protection Ignition of Wood : A Review of the State of the Art. *Journal of Fire Protection Engineering* 12:163–189. <https://doi.org/10.1106/104239102028711>
26. Emberley R, Inghelbrecht A, Yu Z, Torero JL (2017) Self-extinction of timber. *Proceedings of the Combustion Institute* 36:3055–3062. <https://doi.org/10.1016/j.proci.2016.07.077>
27. Vermesi I, Richter F, Chaos M, Rein G (2020) Ignition and Burning of Fibreboard Exposed to Transient Irradiation. *Fire Technology*. <https://doi.org/10.1007/s10694-020-01017-6>
28. Smucker BD, Mulky TC, Cowan DA, et al (2019) Effects of fuel content and density on the smoldering characteristics of cellulose and hemicellulose. *Proceedings of the Combustion Institute* 37:4107–4116. <https://doi.org/10.1016/j.proci.2018.07.047>
29. Wang S, Huang X, Chen H, Liu N (2017) Interaction between flaming and smoldering in hot-particle ignition of forest fuels and effects of moisture and wind. *International Journal of Wildland Fire* 26:71–81. <https://doi.org/10.1071/WF16096>
30. Babrauskas V (2016) The Cone Calorimeter. In: Hurley M (ed) *SFPE Handbook of Fire Protection Engineering*, 5th Editio. Springer, London, pp 952–980
31. Lin S, Huang X, Urban J, et al (2019) Piloted ignition of cylindrical wildland fuels under irradiation. *Frontier in Mechanical Engineering* 5:54. <https://doi.org/10.3389/fmech.2019.00054>
32. Rich D, Lautenberger C, Torero JL, et al (2007) Mass flux of combustible solids at piloted ignition. *Proceedings of the Combustion Institute* 31:2653–2660. <https://doi.org/10.1016/j.proci.2006.08.055>
33. Delichatsios MA, Delichatsios MM (1997) Critical Mass Pyrolysis Rates for Extinction of Fires over Solid Materials. *Fire Safety Science-Proceedings of The Fifth International Symposium* 153–164
34. Delichatsios MA (2005) Piloted ignition times, critical heat fluxes and mass loss rates at reduced oxygen atmospheres. *Fire Safety Journal* 40:197–212. <https://doi.org/10.1016/j.firesaf.2004.11.005>
35. Welch S, Jowsey A, Deeny S, et al (2007) BRE large compartment fire tests-Characterising post-flashover fires for model validation. *Fire Safety Journal* 42:548–567. <https://doi.org/10.1016/j.firesaf.2007.04.002>
36. Rein G, Cohen S, Simeoni A (2009) Carbon emissions from smoldering peat in shallow and strong fronts. *Proceedings of the Combustion Institute* 32 II:2489–2496. <https://doi.org/10.1016/j.proci.2008.07.008>
37. Wu D, Schmidt M, Huang X, Verplaetsen F (2017) Self-ignition and smoldering characteristics of coal dust accumulations in O₂/N₂ and O₂/CO₂ atmospheres. *Proceedings of the Combustion Institute* 36:3195–3202. <https://doi.org/10.1016/j.proci.2016.08.024>
38. Stefanidis SD, Kalogiannis KG, Iliopoulou EF, et al (2014) A study of lignocellulosic biomass pyrolysis via the pyrolysis of cellulose, hemicellulose and lignin. *Journal of Analytical and Applied Pyrolysis* 105:143–150. <https://doi.org/10.1016/j.jaap.2013.10.013>
39. Gollner MJ, Huang X, Cobian J, et al (2013) Experimental study of upward flame spread of an inclined fuel surface. *Proceedings of the Combustion Institute* 34:2531–2538. <https://doi.org/10.1016/j.proci.2012.06.063>
40. Link S, Huang X, Fernandez-Pello C, et al (2018) The Effect of Gravity on Flame Spread over PMMA

Cylinders. Scientific Reports 8:120. <https://doi.org/10.1038/s41598-017-18398-4>

41. Wu C, Sun P, Wang X, et al (2020) Flame Extinction of Spherical PMMA in Microgravity: Effect of Fuel Diameter and Conduction. Microgravity Science and Technology. <https://doi.org/10.1007/s12217-020-09829-5>

ROTATIONAL DUCTILITY OF STEEL WEB-FLANGE SPLICE CONNECTIONS IN FIRE

Paul Akagwu¹, Faris Ali², Ali Nadjai³

ABSTRACT

In this paper, the results of an experimental and a numerical study on the rotational ductility of bolted web-flange splice connections in fire are presented. This class of connections are a prominent feature in column tree moment frames where they enable efficient shop welding of the column stubs and a convenient on-site bolting of the link beams. A total of four connections were tested in a furnace and observations on their resistance under elevated temperatures are reported. The specimens were subjected to a four-point loading arrangement. The parameters investigated in the tests were connection load ratio and bolt diameter. A finite element model was developed and validated with results from the experiments to further examine the effect of the relationship between bolt diameter and splice plate thickness on the rotational ductility of the connection in fire. Average maximum rotations of between 85 to 100 millirad were recorded for the tested specimens. Results in the form of temperature versus rotation curves are presented and failure modes are discussed to provide useful insights on the performance of these connections in fire. Observations show that increasing plate thickness might be detrimental to the rotational capacity while the use of bigger sized bolts was found to be beneficial.

Keywords: Bolted splice connection; fire tests; finite element modelling.

1 INTRODUCTION

Forensic data from investigations on previous failures in steel structures triggered by fire, impact or blast loadings seem to suggest that steel connections are the components most susceptible to failure in a structural assembly [1]. This explains in part why significant effort has been channelled into investigating resistance of steel connections when subjected to such extreme loading events.

Two common types of connections exist for fastening beams to each other in steel construction and they are end-plate connection and web-flange splice connections - in which the splices are either bolted or welded to the beam. These two variations of splice connections differ in that in the former the fasteners are subjected to both axial and shear forces while in the latter, only shear forces are present [2]. Bolted web-flange connections generally have a broader application in the industry as attested by their wide usage in countries such as the USA, Japan, and South Korea particularly in column-tree steel frames, bridges and industrial buildings [3]. The disastrous Northridge failures provided an impetus to the rise in the adoption of bolted web-flange connections in the industry. These connections eliminated the major limitations of the pre-Northridge connections amongst which was poor quality control arising from the fact that welding was done on site. In contrast, the use of bolted web-flange connections enables column-tree connections to be

¹ PhD Researcher, Ulster University, Belfast, United Kingdom,
akagwu-p@ulster.ac.uk

² PhD, FireSERT Ulster University, Belfast, United Kingdom.
f.ali@ulster.ac.uk

³ PhD, FireSERT Ulster University, Belfast, United Kingdom.
a.nadjai@ulster.ac.uk

conveniently welded in the shop under better conditions and greater quality control and then assembled afterwards on the site with the web-flange splice plates.

While there is currently no scarcity of published works on the response of beam to column connections in fire, this is not the case with beam to beam connections. There is very limited information in the literature [4], [5] on the behaviour of beam to beam connections such as the bolted web-flange connections. Experimental tests in which these connections are subjected to the scale of the rotational demands and deformations triggered by fire exposure are few. Hence, the primary aim of this paper is to investigate the rotational ductility of bolted web-spliced connections by means of experimental testing and numerical analysis. Finite element models validated with the results from the experiments have been used to extend the scope of the investigations to incorporate the impact of bolt diameter on the ductility of the connection.

2 FIRE TESTS

2.1 Connection specimen

Four 203 x 102 x 23 I-beam specimens with central splices were tested in a medium sized furnace as part of the study. Each specimen had a total length of 2000 mm with a clear span of 1750 mm. Other geometrical details on the tested specimens are provided in Figure 1 and Table 1. It should be remarked that whilst bolted web-flange connections are conventionally designed as slip critical for moment frame applications, the connections were designed as non-slip critical in the present study, since the ultimate fire resistance was the focus of the study. However, to ensure a uniform load distribution in the bolts, all the bolts were carefully aligned and tightened to a nominal torque of 150 Nm using a torque wrench. Such an alignment was thought necessary to prevent or minimise differential loadings on the bolts which could potentially result in premature bolt failure during the tests.

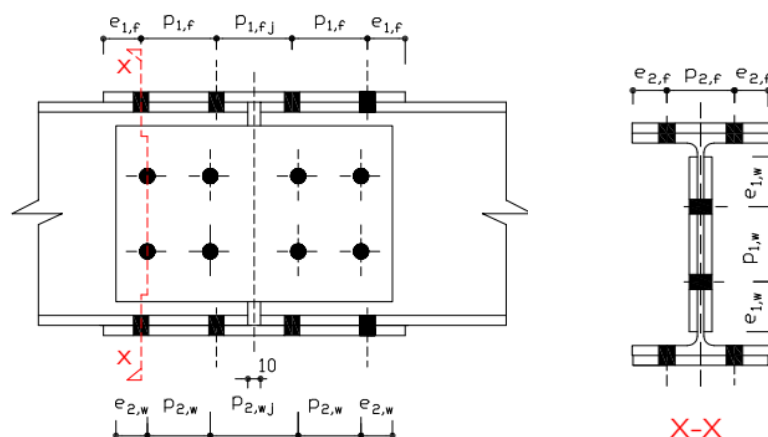


Figure 1 Connection elevation and section details

Table 1 Specimen geometrical details

Test	Splice plates		Bolt	End and edge distances									
	Flange	Web		$e_{1,f}$	$e_{2,f}$	$p_{1,f}$	$p_{2,f}$	$p_{1,f,j}$	$e_{1,w}$	$e_{2,w}$	$p_{1,w}$	$p_{2,w}$	$p_{2,w,j}$
1	230 x 100 x 10	220 x 130 x 6	M16	30	25	60	50	60	30	30	70	50	70
2	230 x 100 x 10	220 x 130 x 6	M16	30	25	60	50	60	30	30	70	50	70
3	230 x 100 x 10	220 x 130 x 6	M16	30	25	60	50	60	30	30	70	50	70
4	240 x 100 x 10	250 x 150 x 6	M20	30	25	60	50	60	40	25	70	60	70

2.2 Test programme

Four tests were conducted in the study using the four point loading configuration shown in Figure 2. The loads were applied at a distance of 732.5 mm from each support. Load ratios of 0.2, 0.4 and 0.6 were investigated. Furthermore, Grade 8.8 M16 and M20 bolts have been used in the splice connections. The order of the whole test is detailed in Table 2.

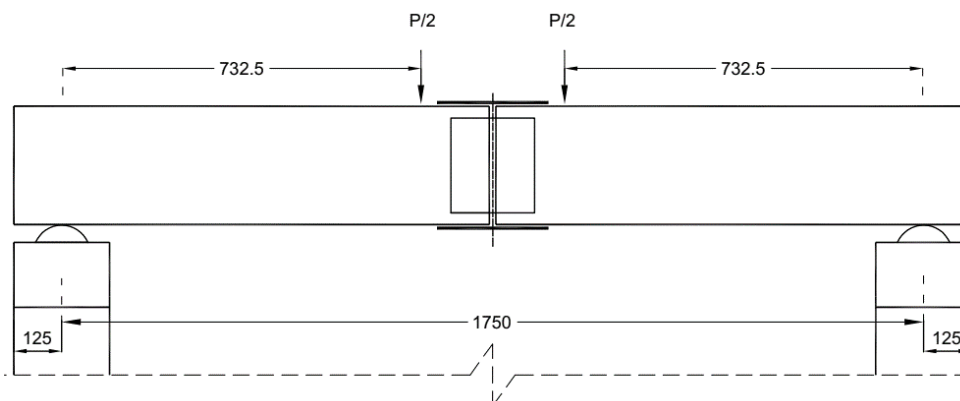


Figure 2 Four - point loading arrangement

Table 2 Test details

Test	Loading	Bolt		Load ratio
		Dia. (mm)	Grade	
1	4Pt	16	8.8	0.2
2	4Pt	16	8.8	0.4
3	4Pt	16	8.8	0.6
4	4Pt	20	8.8	0.6

2.3 Test instrumentation & procedure

In order to obtain the temperature profiles in each connection specimen during the test, Type K Cromel-Almel thermocouples were installed at 13 locations. See Information on the location and designations of the thermocouple are provided in Figure 3 and Table 3. Deflections were measured by two linear variable differential transformers (LVDTs) installed at a distance of 120mm from either side of the loading ram. To obtain the midspan deflection from the tests, the readings from the two LVDTs were averaged.

Electronic load and deflection monitors enabled the load and deflection values to be displayed in real-time during the test. The temperature, loading and deflection readings from the monitoring devices were directly fed into an electronic data acquisition system and conveyed to a central laptop for logging and monitoring during the tests.

Clinometers can be used to directly obtain the rotations at connections, however, in the absence of clinometers, it is possible to express connection rotation in terms of the vertical deflection readings obtained from the LVDTs. Both approaches have been shown to produce consistent results. [6]. The second option was used to obtain the rotations as shown in equation (1) as no clinometers were installed during the test.

$$\phi = \text{Arctan} \left(\frac{2\Delta_{\text{avg}}}{L} \right) \times 1000 \quad (1)$$

where ϕ - rotation,

Δ_{avg} - average midspan vertical deflection and

L - beam free span.

The test procedure entailed initially loading the specimen incrementally to a predefined load value and then heating to the point of failure which in the context of the study is the point at which the connection loses most of its capacity to resist the mechanical loading. A gradual or abrupt shear failure of the bolts or significant yielding of the bolt holes which may trigger tensile fracture of the plate occur at this point.

The transient loading methodology implemented here is a close approximation of the true load application sequence in a real structure exposed to fire.

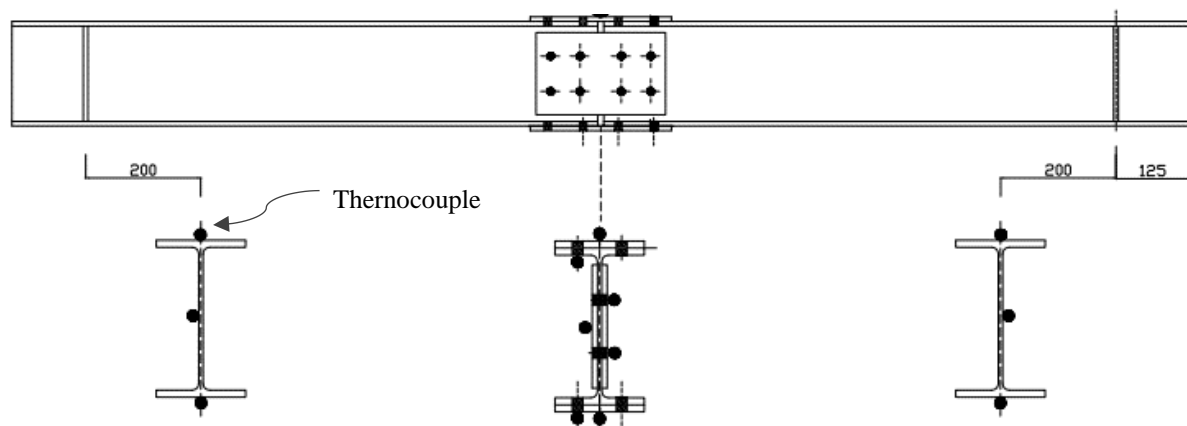


Figure 3 Thermocouple locations.

Table 3 Thermocouple designation details

S/No	Thermocouple ID	Location
1	T1_TFR	Right span top flange
2	T11_TFL	Left span top flange
3	T2_WR	Right span web
4	T12_WL	Left span web
5	T03_BFR	Right span bottom flange
6	T13_BFL	Left span bottom flange
7	T04_TP	Top plate
8	T10_BP	Bottom plate
9	T05_TFB	Top flange bolt
10	T09_BFB	Bottom flange bolt
11	T06_WTB	Web top bolt
12	T08_WBB	Web bottom bolt
13	T07_WP	Web plate

A single cylinder Enerpac hand-operated hydraulic pump was used to apply the loading quasi – statically for each case. A load cell with a maximum capacity of 100 kN placed between the loading ram and a load transfer beam equipped with two rollers welded at the base for transferring the load symmetrically to the connection, enabled the applied loading to be measured and logged during the duration of the test. See Figure 4a. The load was applied incrementally up to the full test load followed by a brief stabilisation period prior to starting the furnace.

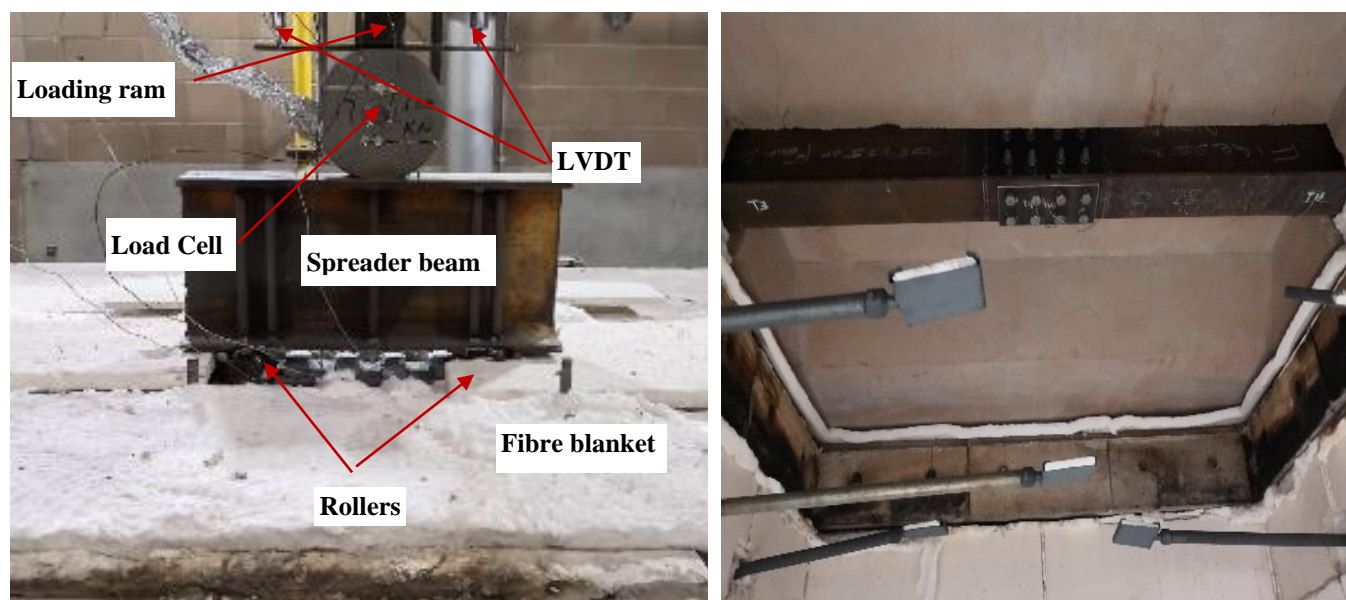


Figure 4 a) Load application. b) Specimen set up in furnace

In real fires scenarios, beams are often heated from three sides as the top flange in most circumstances supports a concrete slab which provides some degree of shielding from the heat resulting in a non-uniform temperature distribution. Hence, three-sided heating with ISO 834 fire curve was applied to the specimens at the bottom flange and the webs by means of five burners in a furnace with two custom-made demountable concrete roof covers and internal compartment dimensions of 1500mm x 500mm x 1500 mm. Lateral restraint was provided by the concrete covers which were positioned with sufficient clearance to prevent any potential interference with the downward movement of the of the beam during the test. See Figure 4b. The top flanges were covered with ceramic fibre blanket to prevent any damage to the instrumentation from escaping hot gases. Furthermore, fire retardant foil was used to wrap the LVDT and load cell signal cables to prevent damage during the tests. Consistent readings were obtained over the entire duration of the tests from the ambient up to the elevated temperature phases showing that the direct contact of the load cell with the load transfer beam had no detrimental effect on the integrity of the test results.

3 EXPERIMENTAL TEST RESULTS

3.1 Connection ductility and failure modes

An indication of the rotational ductility of the specimens is provided in the temperature - rotation history plots presented here in Figure 5 covering the full ambient and elevated temperature ranges. The early stages of the structural response were controlled primarily by the friction caused by the nominal torque earlier applied to the specimens and once the frictional forces were overcome, a full transition to bearing resistance occurred. It can be observed that the plot contains three major distinct segments with the first phase depicted by a linear curve starting from ambient up to a temperature of circa 500 °C. Only very minimal deformation in strength and stiffness occurred at this stage since steel generally retains up to two – third of its ambient capacity at temperatures up to 500 °C. From this point onward, a second rather brief transient stage occurred

in the specimen terminating at a temperature of around 700 °C at which point significant degradation in the steel material had occurred.

In the last phase of the response, a total loss of capacity occurred resulting in a noticeable increase in the rate and magnitude of the deflection up to the point of test stoppage.

Failure for specimens one to three which were all fastened with M16 grade 8.8 bolts occurred exclusively by shear fracture in the bottom flange bolts with different levels of bearing deformation recorded in the splice plates. The web splice plate bolts were largely intact with minor deformations along their shearing plane. For the fractured bolts, total erosion of the shearing plane was observed.

In specimen four, the M16 bolts were replaced with M20 bolts of the same grade to check if the observed failure mode would be altered. The test results showed that significant deformation occurred in the bottom flange plates as well as in the bolts. A more ductile behaviour was observed for the connection fastened with the M20 bolts as the abrupt shear fracture observed in the M16 bolts did not occur. For this specimen, some degree of bearing deformation was also noticed in the beam web with some ovalisation of the bolt holes. For the M20 bolts specimen, the test was intentionally ended at some point after runway displacement ensued to prevent any damage to the furnace. Selected photos of the damaged connection components are presented below in Figure 6 and Figure 7 for specimens three and four to provide a visual appreciation of the extent of the deformations observed.

Plots of the temperature versus rotation histories shown in Figure 5 reveal that the average maximum rotation achieved was up to around 85 millirad for the M16 group and 100 millirad for the M20 specimen. A close inspection of the failed connection components however revealed that the connection fastened with M20 bolts was capable of further rotation before fracture.

The plots suggest that the load ratio applied had an inverse correlation with the temperature at which the connections failed. This is expected since lower stresses are induced in the connection subjected to lower load ratios and vice versa. For instance, for the 0.2LR case, failure occurred at a temperature of around 803 °C in contrast with the 0.6LR case where failure occurred at 653°C, a difference in failure temperature of around 19%.

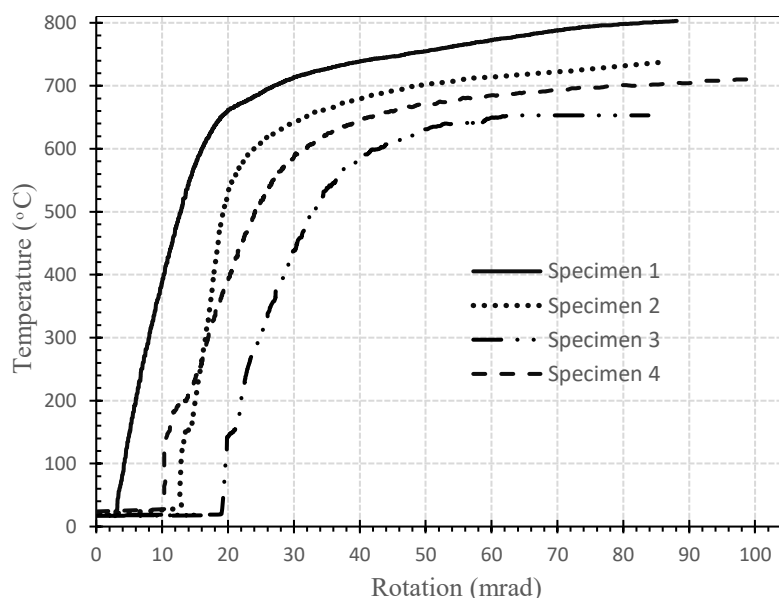


Figure 5 Temperature versus rotation plots for specimens 1 to 4.



a) Bottom flange plate



b) Fractured lower flange M16 bolts

Figure 6 Specimen 3 post-test connection components



a) Bottom flange plate



b) Shear deformed lower flange M20 bolts

Figure 7 Specimen 4 post-test connection components

4 FINITE ELEMENT MODELLING

4.1 Model description

In order to investigate the effect of the relationship between bolt diameter and splice plate thickness on the ductility of bolted web-flange connections, finite element analyses incorporating material and geometrical nonlinearities were performed with the general purpose finite element software Abaqus Standard which implements an implicit integration scheme in solving for the required displacement fields. Whilst Abaqus explicit can and has been used for such analyses previously, the difficulties associated with ascertaining the results obtained in this way are well known. A detailed description of the modelling methodology and approach has been provided in a separate paper [7] and hence only a brief summary will be presented here. A three-dimensional modelling technique was implemented using a combination of 3-D reduced integration eight-node brick elements C3D8R for the irregular profiles like the holes, fillets, etc, and the 3-D incompatible mode eight-node brick element C3D8I which is generally recommended for bending dominated problems [8]. A fine mesh was utilised in areas of high stress as shown in Figure 8.

The material properties of the beams and plate were obtained from a coupon test performed as part of this study and reported elsewhere [7]. No tests were conducted for the bolts, therefore, nominal yield and ultimate strength values of 640 MPa and 900 MPa were adopted for the Grade 8.8 bolts with a young's modulus value of 210 GPa. The material properties obtained from the tests were converted to true stress and strain accordingly for input into the software. The material strength and stiffnesses of the components were degraded as per the Eurocode degradation factors for elevated temperatures.

Since fracture strains based on uniaxial test specimen elongation grossly underestimate the real strains at fracture within the necking region for ductile materials [9], a strain-controlled failure criteria was employed for the numerical simulations undertaken herein.

The complex geometries in the model with irregular profiles like the holes, fillets, etc., were meshed with the 3-D reduced integration eight-node brick elements C3D8R, while the sections with more regular profiles were meshed with the 3-D incompatible mode eight-node brick element C3D8I which is generally recommended for bending dominated problems [8]. Tangential and normal interactions occur at the different interfaces between the individual connection components and these must be accurately modelled

to achieve realistic simulation results. A hard contact algorithm was implemented via the non-linear penalty enforcement method which permits a little penetration between surfaces in contact without compromising the accuracy of the results. The isotropic coulomb friction penalty model was defined for the tangential interactions.

The loading was applied in three steps. Contact between the interacting components was carefully established in the first step, in the second step the load was applied under ambient conditions and in the final step thermal loading was applied with the load kept constant. The thermal loading was applied from the thermocouple readings obtained from the experiments.

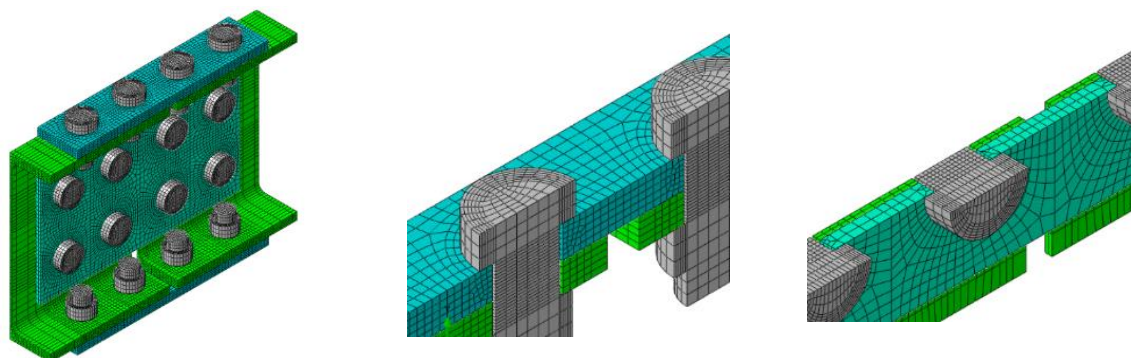


Figure 8 FE model details

4.2 Model validation

The experimental results and the FE simulations for specimens three and four are compared in this section to provide confidence in the FE model. The FE model's ability to accurately simulate the response observed in the tests can be seen in the close agreement between the experimental and numerical temperature versus rotation plots shown in Figure 9. The small disparity in the results can be explained by such factors as modelling simplifications, variation between the nonlinear constitutive law adopted in the model and the actual material properties of the specimens especially considering that only uniaxial results for the stress strain behaviour of the material were available etc. The damaged connection components from the experiments and the FE simulations are also presented in Figure 10.

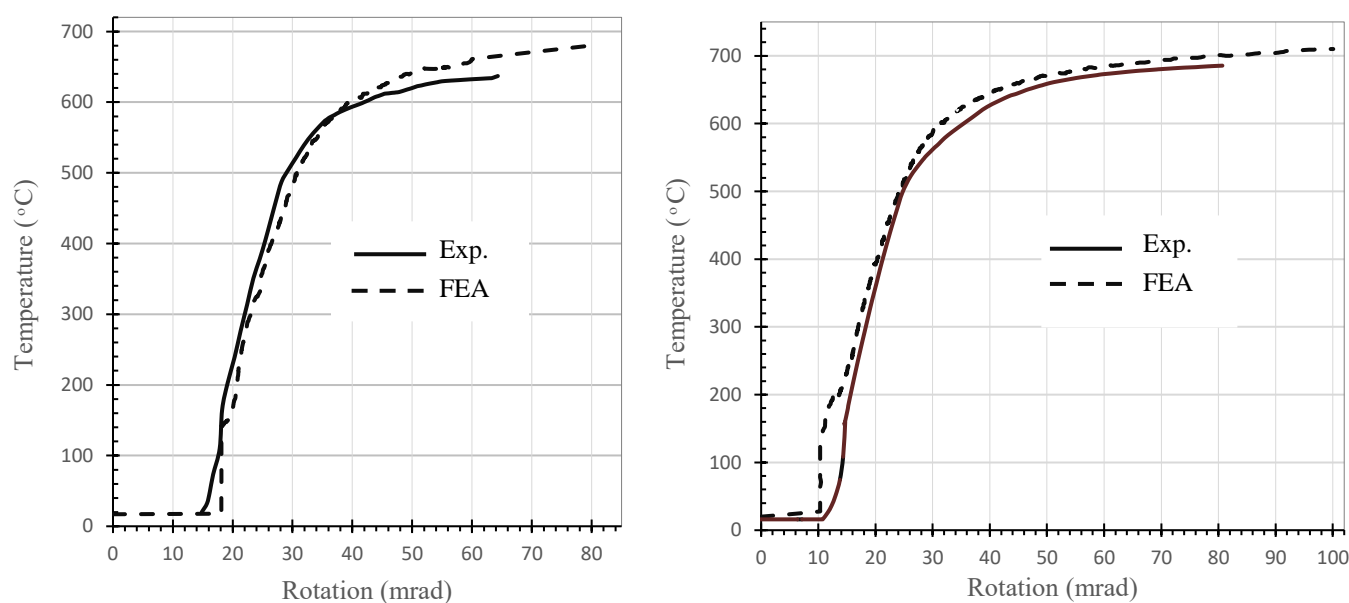


Figure 9 Experimental vs FE results for a) Specimen 3. b) Specimen 4

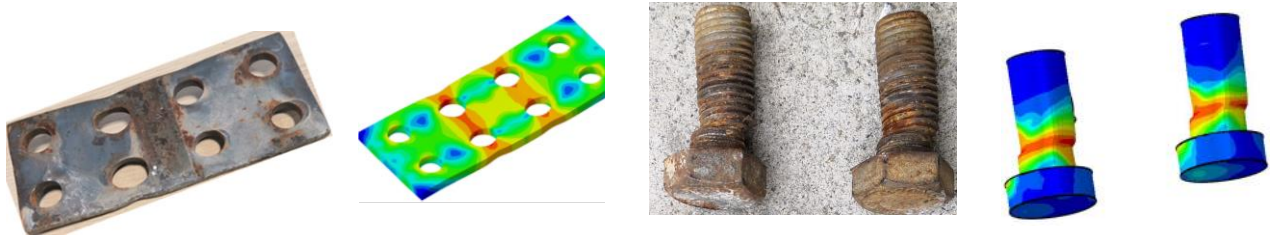


Figure 10 Experimental vs FE damaged bottom splice plates and bolts (Specimen 4)

4.3 Effect of flange plate thickness and bolt diameter on rotational ductility.

Following the validation of the finite element modelling strategy presented above, a parametric study was performed to provide further insight into the effect of plate thickness and bolt diameter on the rotational capacity of bolted web flange connections. It is imperative to remark that due to the small size of the furnace and the limited loading capacity available, a relatively small I-beam section was employed for the specimen used in the experiments. The use of such an I-beam section in the parametric study will invariably limit the range of the geometrical properties of the bolts and plates that can be investigated therefore in order to allow the consideration of a wider scope of plate and bolt geometries a bigger section i.e. 457x191x98 was selected. Further details are provided elsewhere [10]. Plate thicknesses ranging from 8 to 19mm in combination with bolt diameters ranging from M12 to M24 were investigated in the simulations.

Grade 8.8 bolts were used in combination with S275 beam and plates for the analyses. The results from FE analyses performed at 450 and 700 °C are presented in Figure 11 and Figure 12. Since the objective was to study the influence of plate thickness and bolt diameter at different temperatures, the numerically obtained rotational capacities ϕ , were normalised against the maximum rotation ϕ_m recorded for each temperature group.

In all cases, increasing the plate thickness from 8 to 19mm had no noticeable effect on the rotational capacity of the connection for the specimens fastened with M12 bolts. Over this range of plate thicknesses bolt shearing failure accompanied by very minimal bolt hole bearing deformation was observed. For the M16 bolts, at 450 °C, increasing the plate thickness from 8mm to 12mm was accompanied by a reduction of about 13% in the rotational capacity. This can be explained by the fact that with the 8mm plate thickness, some bearing deformation occurred in the bolt hole before the bolts sheared. This increase had no effect on the rotational capacity at 700 °C because the bolt to plate strength ratio at this temperature based on strength degradation factors is lower than at 450 °C meaning failure was governed by pure shear without bearing deformation in the plate. Increasing the plate thickness further had no real impact on the rotational capacity. For the M20 bolts, at 450 °C, increasing the plate thickness from 8 to 12 mm was accompanied by a drop in rotational capacity of about 40%. This substantial reduction is attributed to the change in failure mode between the two thicknesses. With the 8mm plate, plate failure preceded with significant bearing deformation in the bolt holes occurred. Whereas, with the 12mm plate, bolt shearing failure with minimal bearing occurred resulting in a reduction in ductility. This behaviour was not fully replicated at 700 °C because failure was caused by bolt shear for the entire range of plate thicknesses at that temperature. Observations show that increasing the plate thickness further had little impact at both 450 and 700°C.

For the M24 bolts, increasing the plate thickness from 8mm to 16mm resulted in an improvement in the ductility of the connection of about 22% and 8% at 450 and 700 °C respectively followed by a reduction of around 42% and 20% at 450 and 700 °C respectively as the plate thickness increased to 19mm. This reduction was caused by the decrease in the contribution to the connection ductility by bolt hole bearing deformation.

In general, whilst it can be observed from these plots that increasing the splice plate thickness reduced the rotational capacity of the connection, for bolt diameter, the reverse is true, i.e. increasing the bolt diameter enhanced the rotational capacity for all the cases studied, and the improvement was most noticeable for plate thicknesses of up to 16mm.

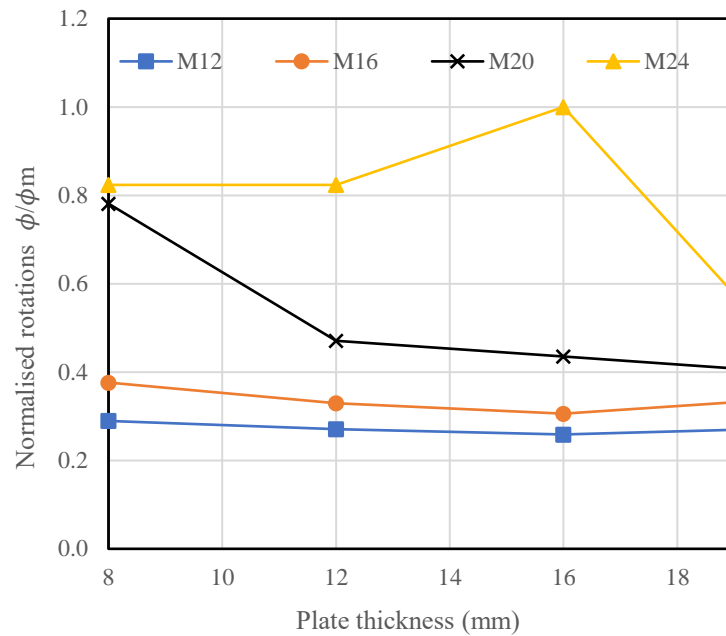


Figure 11 Plate thickness vs normalised rotations @ 450 °C for different bolt diameters

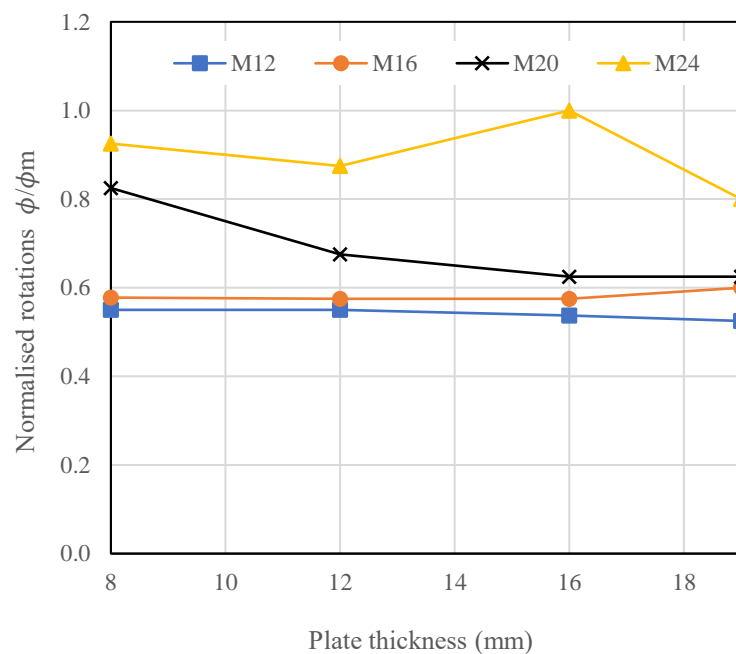


Figure 12 Plate thickness vs normalised rotations @ 700 °C for different bolt diameters

5 CONCLUSIONS

The results from a series of fire tests and numerical analyses on bolted web-flange connections have been reported in this paper to provide an insight into their rotational capacity. Results from the tests showed that the specimens were capable of achieving average maximum rotations of between 85 to 100 millirad. Observations from the finite element simulations performed revealed that using thicker splice plates has a detrimental effect on the rotational capacity of the connections but the reverse is true with using bigger bolts which resulted in significant improvements in the magnitude of rotations achieved, mainly because bolt shear dominates at higher temperatures.

REFERENCES

1. I. Burgess, J. B. Davison, G. Dong, and S.-S. Huang, 'The role of connections in the response of steel frames to fire', *Structural Engineering International: Journal of the International Association for Bridge and Structural Engineering (IABSE)*, vol. 22, no. 4, pp. 449–461, Jan. 2012, doi: 10.2749/101686612X13363929517811.
2. G. L. Kulak, J. W. Fisher, and J. H. Struik, 'Guide to Design Criteria for Bolted and Riveted Joints Second Edition', 2001.
3. A. Astanteh, 'Seismic design of steel column-tree moment-resisting frames', *Structural Steel Education Council, Steel TIPS Report*, 1998.
4. T. Hirashima, K. Okuwaki, X. Zhao, Y. Sagami, and K. Toyoda, 'An Experimental Investigation of Structural Fire Behaviour of a Rigid Steel Frame', *Fire Safety Science*, vol. 11, pp. 677–690, 2014.
5. M. Yahyai and A. Rezaeian, 'Behavior of beams in bolted column-tree frames at elevated temperature', *Fire and Materials*, vol. 40, no. 3, pp. 482–497, Apr. 2016, doi: 10.1002/fam.2305.
6. K. Al-Jabri, 'The behaviour of steel and composite beam-to-column connections in fire. Ph.D. Thesis', University of Sheffield, 1999.
7. P. Akagwu, F. Ali, and A. Nadjai, 'Behaviour of bolted steel splice connections under fire', *Journal of Constructional Steel Research*, vol. 170, p. 106103, 2020.
8. D. Simulia, 'Abaqus 2017 documentation', 2017.
9. E. Dowling Norman, 'Mechanical Behaviour of Materials Prentice Hall', New Jersey.
10. P. Akagwu, "Experimental and numerical study of bolted web-flange steel connections in fire" PhD Thesis, Ulster University 2020.

FIRE EXPERIMENTS INSIDE A VERY LARGE AND OPEN-PLAN COMPARTMENT: x-TWO

Mohammad Heidari^{1,3}, Egle Rackauskaite², Eirik Christensen³, Matthew Bonner³, Sébastien Morat¹, Harry Mitchell³, Panos Kotsovinos², Piotr Turkowski⁴, Wojciech Wegrzynski⁴, Piotr Tofilo⁵, Guillermo Rein³

ABSTRACT

The most common design fires used in structural fire engineering are the ISO standard and Eurocode parametric temperature-time curves, both of which were derived from fire experiments inside small compartments with less than 100 m² of floor area. Application of these parametric temperature-time curves necessarily assumes flashover and that the temperature and burning conditions are uniform in the whole compartment regardless of size. However, modern office buildings often have large open-plan floors, like the Shard in London with up to 1600 m², which would lead to non-uniform temperature and burning conditions during a fire. This paper presents observations from two travelling fire experiments, x-TWO Part 1 and Part 2, conducted inside a compartment with a floor area of 380 m², the largest fire compartment studied to date. The compartment is 10.8 m wide, 35.5 m long and 3.19 m high, well ventilated with openings representing 20% of the compartment walls. This concrete building in Poland was also used in the 2017 experiment x-ONE as reported in literature. The fuel load is a continuous wood crib of load densities 355 MJ/m² in Part 1, and 250 MJ/m² in Part 2 (within appropriate values for office buildings). In both experiments, the fire was observed to travel with clear leading and trailing edges. Flashover was not observed, despite complete burn out of the entire fuel load. In Part 1, flame spread rate was observed not to be constant, instead with both the leading and trailing edges accelerating across the compartment and reaching the far end 32 min after ignition. In x-TWO Part 2, the leading and the trailing edges quickly reached steady state and travelled at nearly constant spread rate, and reached the end of compartment 180 min after ignition. The observed distributions of temperatures are remarkably different from the conditions typically assumed in structural fire engineering and could lead to different failure times and mechanisms. The findings from large-scale experiments x-ONE and x-TWO contribute to a better understanding of fire dynamics and develop improved design tools for structural engineering.

1 INTRODUCTION

Past small compartment fire experiments (area<100m²) [1]–[5] have provided the knowledge to formulate and validate the fully developed fire models [6]–[10] that determine severity and thermal load of fires for structural fire design purposes. These models, including parametric fires, are a challenged [11] but convenient tool for practitioners, which typically assume a uniform and homogeneous temperature inside the compartment. The Eurocode 1-1-2 parametric fire is applicable for circumspective usage for compartments with a floor area of 500 m² and ceiling height of 4 m [7], [11]. However, the small compartment fire experiments and the few available large compartment fire

¹ CERIB, Fire testing Centre, France

² Arup, UK

³ Imperial College, Department of mechanical Engineering
e-mail: g.rein@imperial.ac.uk, ORCID: <https://orcid.org/0000-0001-7207-2685>

⁴ Instytut Techniki Budowlanej (ITB), Poland

⁵ The Main School of Fire Service, Poland

parametric fire [11]. Thus, the validity of models with uniform temperature assumption needs to be examined [11], particularly for large open space compartments, where travelling fires with heterogeneous temperatures [16] can be structurally the most severe fire scenario [17], [18] and cause a major structural collapse [16].

Large-scale travelling fire experiments [15], [19]–[22] have been conducted to identify and understand the dynamics of travelling fires and improve theoretical travelling fire models. The experiments provided a set of valuable data and confirmed the spatial and temporal temperature distributions. A review of classic literature and the description of some recent experimentation [23] showed the need for more high-resolution experimental data to provide insight on the fire dynamics of large compartment and complex geometries. This further enriches the application of robust state-of-the-art fire safety engineering to complex geometries and modern buildings and will enhance the development of modern future cities with increased resilience to fire.

The most recent fire experiment campaign is the largest compartment fire carried out to date (384 m²); this consisted of x-ONE (September 2017) [15] and x-TWO (May 2019). The experiments were carried out to capture and understand the fire dynamics of a very large compartment and measure basic fire characteristics such as temperature and spread rate. In x-ONE, the fire was ignited at one end of the compartment and allowed to develop naturally. The experiment captured a fast and accelerating fire travelling with 25 min fire duration, having a spread rate gradually increasing and accelerating from 3 to 167 mm/s over the uniform fuel load of wood cribs along the length of the compartment. The experiment showed that flashover does not always occur in a large compartment, but instead the fire can spread and generate a non-uniform temperature distribution across the compartment. In comparison to the EC1-1-2 parametric fire, some structural elements experienced more onerous thermal conditions [24].

x-ONE concluded that additional experiments with a different fuel load arrangement would bring more insights into the travelling behaviour of fire and its spread rate. Consequently, this chapter presents the x-TWO experiment series, and observations and experimental measurements made during the experiments. x-TWO consisted of two experiments (Part one and Part two) in the same compartment of x-ONE, but with a comparatively reduced fuel load to exhibit a longer travelling fire duration.

One of the main objectives of the x-TWO experiment was to understand the key characteristics of travelling fires due to the variation of fuel load density in a large compartment and minimise the level of complexity of travelling fire scenarios and models. More precisely, to understand the impact of fuel load variation (the most important parameter in fire) on the temperature, fire duration, spread rate, and flame height, since the volume of the compartment and the size of the openings are already known. The x-TWO experiments attempted to support the technical justification to introduce travelling fire in the current design methodologies and fire safety engineering codes.

2 X-TWO EXPERIMENT

2.1 The building

The x-TWO experiment was carried out in a farm building located near Golaszew, 20 km west of Warsaw, Poland. The building has one floor that is mostly open plan with thick external masonry walls. The beam and block concrete slab ceiling is supported by reinforced concrete columns, beams and external masonry walls. The experiment was carried out in the open plan section of the building which has a floor plan of approximately 384 m². The floor is 10.8x35.5 m and 3.24 m high (Fig. 1). Two doors of 2.51x2.50 m are located at each end of compartment and two doors of 1.81x2.50 m are in the middle of each wall in the length of the compartment. There are 29 window openings (1x1 m). Sketch of the floor plan of the section of the building is shown in Fig. 1.

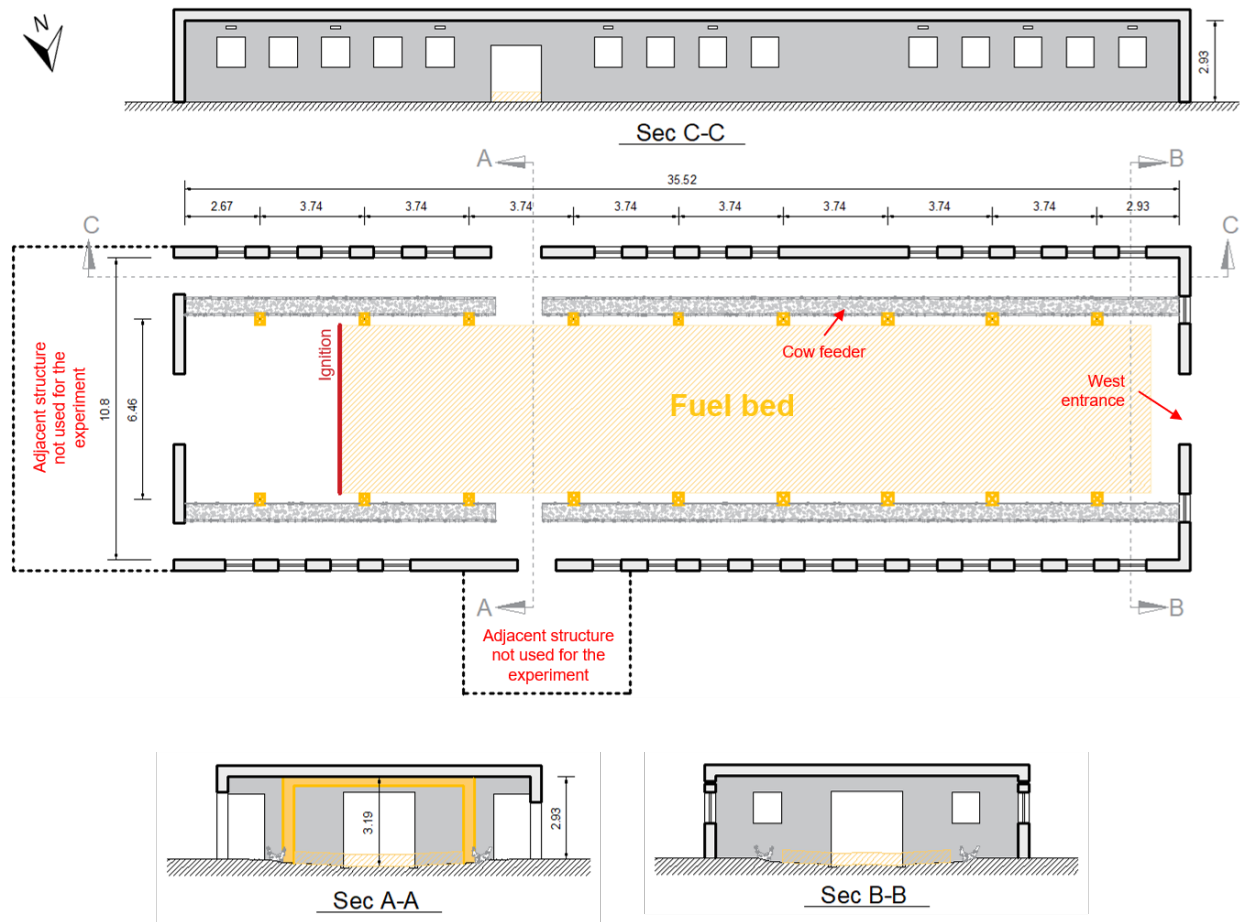


Figure 1. Floor plan and sections of the compartment used for x-ONE [15] and x-TWO experiments.

2.2 Protection

The structure was thermally protected to avoid significant structural damage and reduce the risk of collapse during the experiment. Ceiling, beams, and columns were protected using CONLIT 150 P slabs with the density of 165 kg/m³. CONLIT 150 System used had a fire resistance for 240 minutes. HILTI IDMS fasteners were used to bolt the Rockwool slabs to concrete elements.

2.3 Ventilation

6 doors and 31 windows (1.00 × 1.09 m) openings are available around in the building (Fig. 1 and Table 1). All openings were left open to represent the conditions of an open plan compartment with large ventilation and to minimise the likelihood of a ventilation-controlled fire. The ventilation condition was unchanged compared to x-ONE experiment [15].

Only 1 door and 1 window opening to the adjacent structure along the South elevation of the building, and all the openings to the attic were closed. The aforementioned openings were closed to eliminate any potential influence of the adjacent compartment on the fire dynamics within the main compartment, that is, to keep the fire compartment simple and only maintain ventilation openings directly to outside.

In total, 20% of the compartment walls (i.e. $A_w=56 \text{ m}^2$) are the openings with an opening factor of 0.0621 $\text{m}^{1/2}$ ($A_w h^{0.5}/A_{total}$) and weighted average opening height of 1.34 m, as stated in Annex A of Eurocode 1-1-2 [7]. Opening factor represent the amount of compartment ventilation in fire. The large opening factor increase the possibility of a fuel-controlled fire compartment. Window breakage during the fire were not of interest in this experiment to minimise the level of complexity, potential variables, and to allow a simple experiment.

Table 1. Opening dimensions along different elevations of the building used for the x-TWO experiment (the same as x-ONE).

Building Elevation	Door openings (m) (Number × Width × Height)	Window openings (Number × Width × Height)
East (<i>Sec A-A in Fig. 3</i>)	1 × 2.54 m × 2.66 m 2 × 1.31 m × 2.34 m	<i>None</i>
South (<i>Sec C-C in Fig. 3</i>)	1 × 1.80 m × 20.3 m	14 × 1.00 m × 1.09 m
West (<i>Sec B-B in Fig. 3</i>)	1 × 2.54 m × 2.66 m	2 × 1.00 m × 1.09 m
North	1 × 1.37 m × 2.38 m (<i>closed</i>)	15 × 1.00 m × 1.09 m (<i>1 opening closed</i>)

2.4 Fuel load

x-TWO used an arrangement of continuous wood crib to encourage a natural spatial and temporal fire growth. The wood crib arrangement was based on the fuel design of x-ONE experiment in September 2017 (for more details see [15]). Prior to the x-ONE experiment, 9 small-scale exploratory experiments were carried out to investigate different wood crib arrangements, materials to be combined with wood, and ignition methods for the optimum fuel load design. The fuel load of x-ONE was approximately 370 MJ/m² (19.4 kg/m²) and covered a floor area of 174 m² (6 m × 29 m). The fuel set up consisted of 11,5 layers of continuous wood crib (4 sticks each layer), mixed with two layers of 4mm fibreboard to facilitate a faster flame spread and higher heat release rates than in the previously identified travelling fire experiments. This fuel load was chosen to limit the risk of damage to the structure but to still be within the range of typical fuel load densities in office buildings [7], [25], [26]. A fast and accelerating fire was observed with the total fire duration of x-ONE was 21 min.

In x-TWO, fuel load was the only parameters that was changed compared to x-ONE to understand the impact of the changes in the fire dynamics of travelling fires due to fuel load variation. The same type of wood and the same arrangement as in x-ONE without two layers of the fibreboard in the whole surface of wood cribs was used, to have a longer fire duration compared to x-ONE. Fire board was assumed to accelerate the flame spread of the x-ONE.

For x-TWO, Wood cribs were softwood sticks with the dimensions of 3 cm × 3cm × 100 cm, density of ~450 kg/m³, heat of combustion of 18.94 ± 0.14 MJ/kg, and moisture content of 9.3 ± 0.3%. The fuel bed area was 174 m² (6 m × 29 m) as illustrated Fig. 1. The fuel bed was placed 5.40 m from the East entrance and 1 m from the West entrance. Cribs were lifted from the ground by placing bricks every 1 m to reduce heat losses to the concrete floor and enable air circulation below the crib.

x-TWO Part 1 had the fuel load of approximately 353 MJ/m² (18.63 kg/m²), which was within the range of typical fuel load densities in office buildings [26]. Cribs were arranged to have 11,5 stick layers with 4 sticks/m per layer as shown in Fig. 2. The total duration of x-TWO Part 1 was about 35 min, so it was decided to reduce the fuel load by 30% in order to have a slow spread travelling fire with longer fire duration compared to previous experiments. The fire load was approximately 261 MJ/m² (13.95 kg/m²) in x-TWO Part 2, which was within the range of typical fuel load densities in sparsely loaded office buildings [26]. The wood crib was arranged with 8,5 stick layers with 4 sticks/m per layer.

In Part 1 and 2 experiments, 2 layers of 4 mm thick wood fibreboard was added to the first meter of the wood cribs to assure the uniform flame spread path as illustrated in Figure 225. The wood fibreboard (i.e. BARLINEK grey underfloor board) was chosen for the experiment. The summary of the fuel load of x-TWO, x-ONE and the office fuel load density of Eurocode 1-1-2 are presented in Table 2.



Figure 2. Photos of the final wood crib arrangement used as fuel for the x-TWO experiment. Wood sticks dimensions were 3 cm × 3 cm × 1m. The left image shows a uniform initial linear fire forming and starting to naturally progress. The right image shows completed wood crib at the moment of ignition.

Table 2. The summary of the fuel load densities in x-ONE, x-TWO and Eurocode 1-1-2

Experiment/Code	x-ONE [15]	x-TWO Part 1	x-TWO Part 2	Eurocode 1-1-2
Fuel load MJ/m ²	370	355	249	285-420
Wood crib layers	11,5	11,5	8,5	-
Fibreboard layers	2 covered 6m x 29m	2 covered 6m x 1m	2 covered 6m x 1m	-
Design Consideration	-Natural fire - Save the building -Not a very slow spread -Flame impinging ceiling	Same as x-ONE but a slower fire spread than x-ONE	Same as x-TWO Part 1 but a slower fire spread than x-TWO Part 1	-

A uniform initial linear fire along the width of the one end of wood cribs (i.e. East entrance) was used to study the flame spread along the compartment. To achieve this, 6 pans (15 cm x 25 cm) each filled with 0.5 litres of methanol were located below the one end of wood cribs (i.e. East entrance). The methanol pans were ignited simultaneously using a torch, a uniform line of fire formed as illustrated in Fig 2.

2.5 Instrumentations and data collection

39 Type-K thermocouples of 1.5 mm bead were used to capture spatial and temporal fields of compartment temperature. 15 thermocouples were attached to 9 columns (TC). At all columns, thermocouples were attached at the height of 2.4 m above the floor with 6 columns having an additional thermocouple at the height of 1 m above the floor. 18 thermocouples were placed 5 cm below the soffits of beams (T), at mid-span and 3.5 m distance from the side walls at the height of approximately 2.9 m. 6 thermocouples (TP) were installed between blocks of mineral wool (Rockwool), in contact with the ceiling to measure the ceiling surface temperature and ensure that the structure is not exposed to severe heat, leading to collapse. Finally, three plate thermocouples (PT) were installed at the mid-span of the ceiling at the East end, middle, and West end of the compartment.

Thermocouples measurements were corrected for radiation error following the radiation correction (α -method) implemented in x-One [15]. This correction assumes the thermocouple is in thermal (quasi steady-state) equilibrium by equating the convective and radiative heat fluxes.

13 cameras (Cam) recorded the test series and captured the fire size and flame spread rates. Cameras were positioned in the windows and the openings in the west and east ends, looking into the compartment, and were pre-programmed to take time-lapse photos every 4 s. Fig 3 shows the location of the instrumentation used to measure the flame spread rate and the thermal exposure in the compartment.

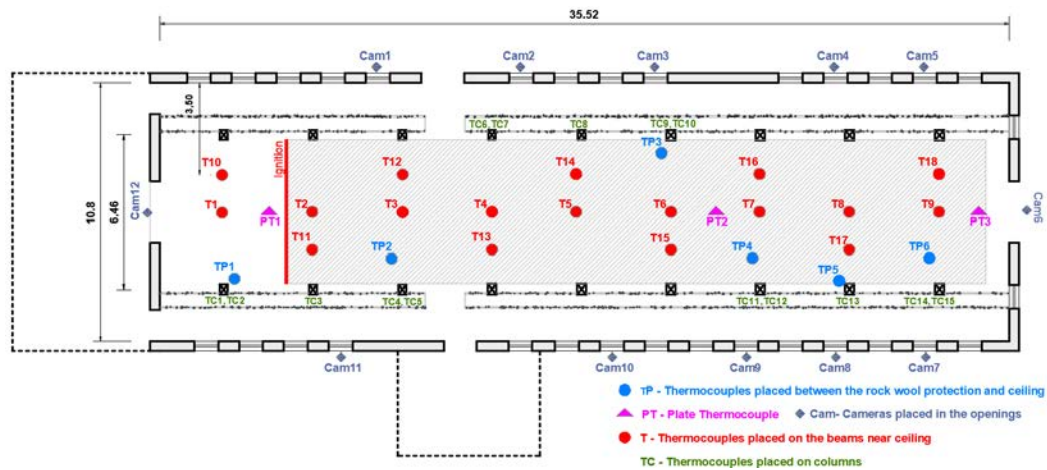


Figure 3 Thermocouple and camera locations in the compartment. thermocouples (T) were placed at the soffits of beams at a height of ~2.9 m from the floor. Where there are two thermocouples (TC) at the same column, they are located at heights of 1 m and 2.4 m, while single thermocouples are located at a height of 2.4 m from the floor.

3 EXPERIMENT RESULTS

3.1 Observations and fire characteristics

After ignition a fire developed naturally along the width of the wood cribs. The fire travelled over the surface of the fuel along the length of the compartment without rapid transition to a state of total fuel surface involvement in fire (flashover definition as identified by [11]). The experiment demonstrated that flashover does not always occur in a large compartment, but instead the fire can travel. Fire burned out after about 35 min and 180 min, in Part 1 and 2 respectively. The travelling fire and the burn out area behind the fire at different locations of the compartment and at different times are presented in Fig. 4 (x-TWO Part 1) and Fig. 5 (x-TWO Part 2).



Figure 4. Fire photos taken from different locations (i.e. North entrance and West entrance) at four different times during the Part 1 experiment indicating fire development and progress. An accelerating travelling fire of 32 min duration was observed.



Figure 5. Fire photos taken from different locations at four different times during the Part 2 experiment indicating fire development and progress. A steady state travelling fire of 180 min was observed.

In x-TWO Part 1, the spread rate of the fire was observed as not constant during the whole burning time. Initially, the fire grew and spread relatively slowly (i.e. ~ 1 m in 5.5 min). Flames have been observed to impinge on the ceiling at 7 approx. 9 min after the ignition. The leading edge had a steady spread rate until the time the fire reached the North entrance door (i.e. ~ 14 min), then the fire accelerated (i.e. 25 m in 8 min) to the West end of the compartment. The increase in the spread rate of fire is likely due to a combination of change of air flows within the compartment (more oxygen available to the fuel bed) as the flames approached the larger North side opening and an increase of radiation from the flames impinging on the ceiling and the smoke layer as the fire grew in size, thus, facilitating a faster ignition of fuel ahead of the flames and accelerated fire growth as also observed in x-ONE. It is difficult to establish which of the latter is the governing factor as the North entrance door is located only ~ 6 m from ignition location. The leading edge of the fire reached the far end of the compartment (i.e. West entrance) at ~ 22 min.

A clear trailing edge is observed at approximately 5 min after ignition. The spread velocity of the trailing edge of the fire increased with time but slower compared to the trailing edge. The fire burned out approximately 32 min after ignition. A thick smoke layer started to form in the compartment from the moment of ignition and grew quickly (see Fig 4). At 14 min, the flame was partially visible from the West entrance due to build-up of the thick smoke layer. Smoke was mainly exhausted via the windows adjacent to the location of the flame and the North and West entrances with fresh air coming in through the remaining windows and below the neutral plane of the North and West entrances. An external flaming was only observed locally due to the flame extension under the ceiling. This is more representative of a fuel-controlled fire rather than a typical ventilation-controlled fire where external flaming is typically observed from all the windows due to the lack of fresh air.

In x-TWO Part 2, the line fire along the width of the compartment grew and covered one meter of the wood cribs along the length of the compartment after 4 min. Then, the leading and the trailing edges of the fire had almost the same spread rates and travelled with a uniform accelerating rate until reached the end of compartment after 174 min and 180 min after the ignition respectively. The fire size changed and grew slightly about 2m in the length of wood cribs when the fire passed 1.5 the North entrance. The reason can be the air flow to the fuel bed from the North entrance. The flame did not impinge on the ceiling. The flame height was varying between 1 m and 1.30 m above the floor during the fire. A thin layer of smoke was accumulated under the ceiling.

There was limited involvement from the fire service who watered the exterior of the building and the external flaming to prevent fire spread to the attic, which was supported by and contained timber framing.

No fire damage to the building fire was observed. The mineral wool applied as protection to the ceiling, beam and columns was not observed to fall-off during the fire in x-TWO Part 1.

3.2 Fire characteristics

A travelling fire is a limited burning area of the compartment floor that move across the floor plate [26]–[30]. Along a single axis of travel, the burning area is constrained by the leading edge (front of fire) and the trailing edge (fuel burn out takes place) of the fire (Fig 6), both of which progress through the compartment until the total available fuel is consumed. Location and spread rates of the leading and trailing edges from the point of ignition at discrete time intervals was achieved using image data from an array of cameras positioned at all windows across the compartment (Fig. 3), and using camera calibration and ray tracing theory to map the 2D fire images onto a 3D space [15]. Fig 6 shows the extracted locations and spread rates of the flames on the floor, as well the best fit curves for each set of data, for Part 1 and Part 2, respectively.

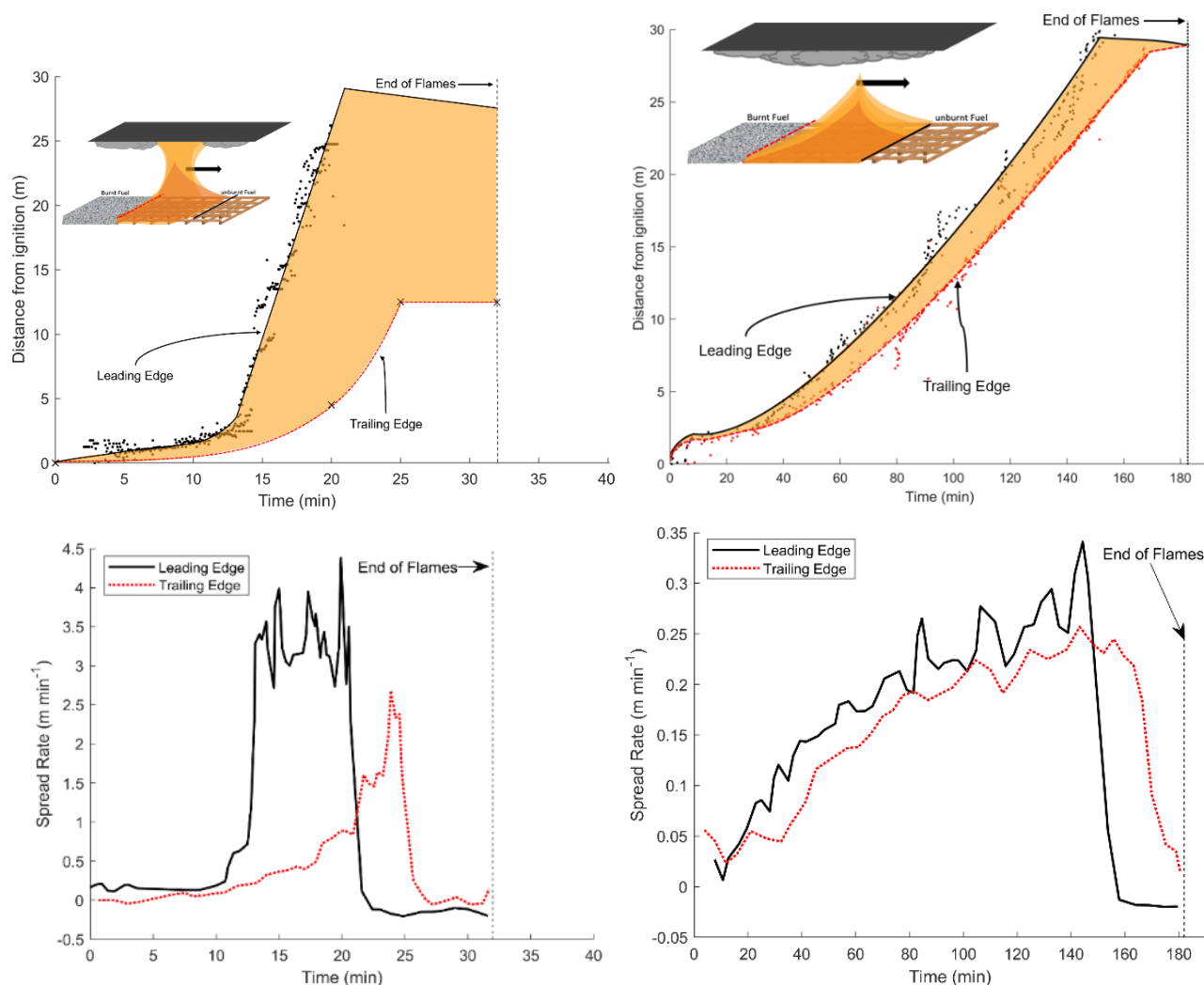


Figure 6 Distance (top) and spread rates (bottom) of leading and trailing edges from the ignition point for x-TWO Part 1 (Right) and Part 2 (Left).

As discussed in the x-TWO Part 1 the flame spread rate increased during the experiment as illustrated in Fig. 6. The fire had an initial spread rate of 0.25 m/min until arriving to the North entrance at about 13 min. The flame spread rate then increased significantly to an average value of almost 3.5 m/min until reaching the end of the end of wood cribs near the West entrance. After 5 min from the ignition a clear trailing edge of fire started to move along the compartment, with the spread rate of ~ 0.25 m/min almost the same as the leading edge. The spread rate increased from 13 min after the ignition the fire, with a maximum value of 2.5 m/min. Therefore, different spread rates of the leading and trailing edges have resulted in a continuously growing fire during the experiment. This means that the front of the fire was travelling at a different speed

compared to the trailing edge of the fire, and the fire size was not steady in size as assumed in TFM methodology.

The visualisation for x-TWO Part 2 shows after a brief period until fire reaches the North entrance at after 25 min, then the leading and trailing edges had a uniform acceleration with an average spread rate of 0.22 m/min. The trailing edge spread rate was consistently ~0.02 meters per minute less than the leading edge, where the fire size slightly increases from 40min-140min. The flames travelled across the compartment, finally extinguishing at the other end 180 min after ignition and without flashover.

Compared to x-ONE, both x-TWO part 1 and 2 lasted longer in fire duration, as x-ONE reached extinguishment 25 min after ignition, and the leading edge reaching the end of the compartment after 12 mins. Similarly, the peak rates of spread of both the leading and trailing edges of x-ONE were significantly higher than those for x-TWO part 1 and 2, with maximum spread rates of 13.5 m/min and 6 m/min for the leading and trailing edges respectively. This, considering the similarity in ventilation conditions between x-ONE and x-TWO, further shows that the spread rate of a travelling fire is a function of the fuel load density.

The experiments showed that the spread rate of travelling fire is a function of the fuel load density when the ventilation condition is unchanged. It is confirmed that for the same ventilation conditions the lower fuel load density results in a smaller fire size, lower flame height, and thinner smoke layer, therefore less radiation from the flame and smoke arrives to the fuel bed thus. Consequently, lower flame spread, and longer fire duration is reached.

3.3 Gas Temperature

Temperatures throughout the compartment were measured with thermocouples recording gas temperature as the fire travelled in the compartment. Fig. 7 show the spatial and temporal evolution of the gas phase temperature at the beam soffit level at a height of 2.90m from the floor (near the ceiling) along the fire path for x-ONE, x-TWO Part 1, and x-TWO Part 2. The first and the last set of thermocouples were located at (-2.8) m and 27.1 m from the ignition location towards the West entrance (See TCS location in Fig 3).

The shaded region in the Fig. 7 describes the region of correction bounded by correction coefficients of $3 \leq \alpha \leq 4$, following the radiation correction methodology (α -method) implemented in x-One [15]. The radiation

error of the Part 2 result was near zero, as the thermocouples were about 1.50m above the flame height and measured the plume temperature.

Location of near-field and far-field exposures at different times of fire can be clearly identified along the length of compartment. In Part 1 (Fig. 7), near-field represents flames directly impinging on and extending under the ceiling, while far-field represents cooler smoke further away from the flames. In Part 2, where the fuel load was decrease by 30% compared to Part 1, the maximum flame height was 1.3 m (1.60 m below the ceiling). As such, the maximum temperatures of curves for x-TWO Part 2 in Fig 7, represent the plume temperature at the centre line of the burning area (near-field), which was travelling though the compartment floor.

In x-ONE, during the first 13 min after ignition just the leading edge of fire was spreading, so the near field was increasing in size. After 14 min both leading and trailing edge were moving along the length of the compartment, as illustrated in Fig 7.

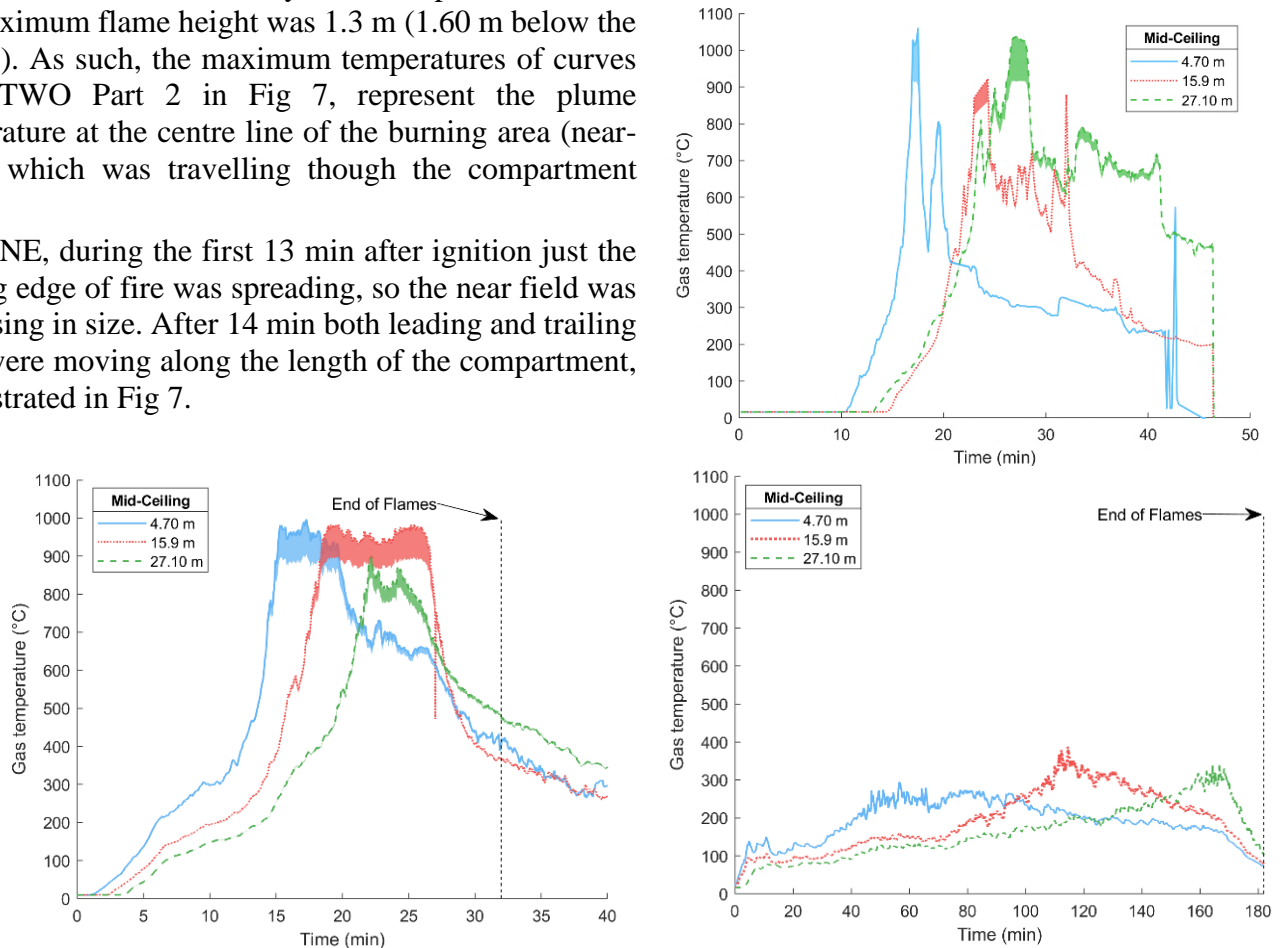


Figure 7. Corrected gas temperature for radiation error from thermocouples at the beam soffit level at 3 locations (at 4.70 m (T3), 15.90 m (T6), and 27.10 m (T9) from ignition location towards the West entrance, for x-ONE (Top), x-TWO Part 1 (Left) and Part 2 (Right). The shaded region describes the region of correction bounded.

Maximum corrected gas temperatures in the near-field region reached temperatures up to $\sim 1000^{\circ}\text{C}$ and $\sim 325^{\circ}\text{C}$, in Part 1 and Part 2 of x-TWO, respectively. Part 1 reached similar maximum corrected gas temperatures compared to x-ONE, which also reached up to $\sim 1000^{\circ}\text{C}$. Each thermocouple in the compartment (except for T1 which was not located above the fuel bed) was subjected to near-field region. Once the near-field has passed and fire has burned out, the temperatures at that location (i.e. far-field) dropped to below 900°C in Part 1 and below 250°C in Part 2. The total durations of fire were 32 min in Part 1 and 182 min in Part 2. The lower temperature and longer burning duration of Part 2 was due to 30% lower fuel load compared to Part 1.

By looking at the temperature at the near end of the compartment, shown in Fig 7, it can be seen how the temperature has a small variation until the fire is approaching this point. As a reference for x-TWO Part 1 in Fig 7, at 18 min, where for the first third of the compartment peak temperatures have almost been reached, the temperature near the far end of the compartment is still below 450°C . The temperature near the end of compartment then reaches a peak value of 900°C around 23min while the temperature in the beginning of the compartment is quickly cooling down to temperatures below 800°C . The spatial evolution of the gas temperature throughout the compartment confirms the non- uniform temperature with pre-heating associated with the travelling fire methodology [26].

Vertical temperature variations for two different locations in the beginning of the compartment (i.e. at 3.90 m along the fire path from the ignition point) are shown in Fig 8. At different times of the experiment

vertical temperature variations are in the range of approx. 50-400°C. The temperatures near the bottom of columns (i.e. 1 m above the floor) are lower than those recorded at the top of column (i.e. 2.4 m above the floor). Temperature variations are more obvious prior to arrival of the flame front (i.e. the leading edge) and after the trailing edge has spread past it. In addition, thermocouples at the column bottom mainly capture the flame temperatures as the flames approached and spread past it, whereas thermocouples at the column top were also exposed to and captured temperatures within the smoke layer.

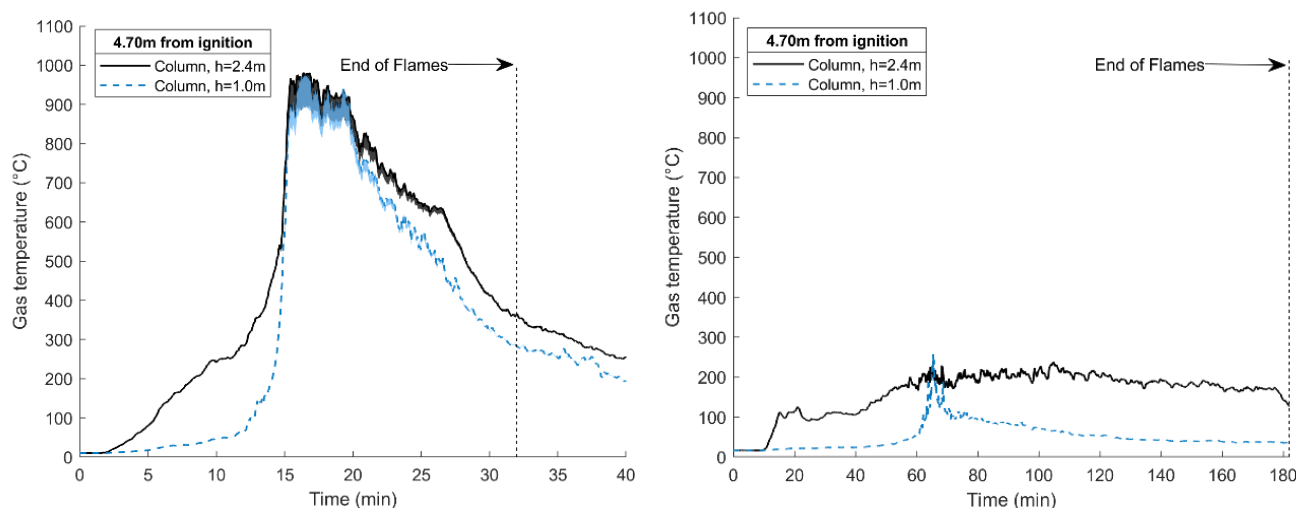


Figure 8 Vertical temperature variations within the compartment from x-TWO Part 1 (left), Part 2 (right). For each bay, thermocouples were located at the top of the column (~2.4 m), and the bottom of the column bottom (~1 m), respectively. Temperature are corrected for the radiation error.

Fig 8 illustrates that when the flames are burning in proximity of the column at 27.1 m from the ignition point along the fire path, the temperature at the bottom of column is lower than the top of the columns, because the fresh air entering the compartment cooled down the air in the bottom of the column. As identified previously, the difference can go up to 200°C. In Part 2, fresh air from the West entrance cooled down the bottom column thermocouple, which was exposed to flame, as such, the temperature of the bottom of column was equal to the recorded at top of column in the fire plume.

The results confirm the high special variation of the gas temperature inside the compartment with pre-heating associated with the travelling fire methodology. It is in contrary to the uniform temperature assumption of the current codes. Therefore, the experiment confirms the results of previous studies [17], [31] that showed travelling fires with non-uniform temperature should be considered for the structural fire design along with the Eurocode parametric fire with uniform temperature assumption.

4 CONCLUSION

x-TWO consisted of two large scale travelling fire experiments (Part 1 and Part 2), conducted in Poland in September 2019 to capture experimentally a natural travelling fire inside a large real compartment and measure its spread characteristics. Part 1 had a fuel load density of 355 MJ/m² and Part 2 had 30% less fire load compared to Part 1 (i.e. 249 MJ/m²). The aim was to understand the impact of fuel load changes on travelling fire dynamics and to reduce other uncertainties that could affect the fire behaviour since the compartment and ventilation were fixed. The fire was allowed to develop naturally, and the experiment successfully managed to capture a fast and accelerating fire travelling of 32 min duration in Part 1 and a steady state spread travelling fire of 180 min in Part 2, over a 380 m² compartment. Maximum radiation corrected gas temperatures were about 1000 °C in part 1 and used in travelling fire methodology is correct. The maximum recorded near-field temperature was ~1200 °C. The observations and results of the experiment further confirm that flashover does not always occur in large compartments, but fire can travel across the compartment, meaning that non-uniform heating associated with travelling fire methodology is valid in large compartments. From a design perspective, this paper concludes that both uniform and non-uniform fires need to be considered during design, as recent research [17], [31] has shown that both the uniform and the non-uniform heating can challenge a structure.

The spread rate of the fire was not constant in Part 1 (and to some degree in Part 2), and is assumed in travelling fire methodology to be constant, but was in fact gradually increasing. The experiment can be used for validation, and further development of the travelling fire methodology (as part of future research). Future research should include complementary experiments, changing ventilation conditions, compartment size, and fuel load density to improve the travelling fire methodology which is an essential for open plan structural fire safety design.

ACKNOWLEDGEMENT

This research has been funded by Centre d'Études et de Recherches de l'Industrie du Béton (CERIB, France), Ove Arup and Partners Limited (UK), the Engineering and Physical Sciences Research Council (EPSRC, UK), and Educational & Scientific Foundation of the Society of Fire Protection Engineers (SFPE, USA) in collaboration with Imperial College London (UK), Instytut Techniki Budowlanej (ITB, Poland), and The Main School of Fire Service (Poland).

REFERENCES

1. K. Kawagoe, "Fire behaviour in rooms," Rep. No. 27, Build. Res. Institute, Tokyo, 1958.
2. P. H. Thomas and A. Heselden, "Fully developed fires in single compartments; a co-operative research programme of the Conseil international du bâtiment," Conseil Internationale du Bâtiment Report No. 20, Fire Research Note No. 923. <https://catalog.princeton.edu/catalog/SCSB-8466674> (accessed Oct. 16, 2020).
3. K. D. Steckler, J. G. Quintiere, and W. J. Rinkinen, "Flow induced by fire in a compartment," Symp. Combust., vol. 19, no. 1, pp. 913–920, Jan. 1982, doi: 10.1016/S0082-0784(82)80267-1.
4. J. M. Franssen, "Improvement of the parametric fire of Eurocode 1 based on experimental test results," in Fire Safety Science, 2000, pp. 927–938, doi: 10.3801/IAFSS.FSS.6-927.
5. L. T. and M. D., "The natural fire safety concept--full-scale tests at Cardington," Fire Saf. J., vol. 38, no. 7, pp. 623–643, 2003.
6. "ISO 834-1:1999(en), Fire-resistance tests — Elements of building construction — Part 1: General requirements." <https://www.iso.org/obp/ui/#iso:std:iso:834:-1:ed-1:v1:en> (accessed Feb. 06, 2019).
7. "Eurocode 1: Actions on structures – Part 1-2: General actions – Actions on structures exposed to fire, Annex B," European Committee for Standardization, 2002.
8. O. Pettersson, S.-E. Magnusson, and J. Thor, "Fire Engineering Design of Steel Structures, Publication 50," Stockholm:Swedish Institute of Steel Construction, 1976.
9. V. Babrauskas and R. B. Williamson, "Post-flashover compartment fires: Basis of a theoretical model," Fire Mater., vol. 2, no. 2, pp. 39–53, Apr. 1978, doi: 10.1002/fam.810020202.
10. J. F. Cadorin and J. M. Franssen, "A tool to design steel elements submitted to compartment fires - OZone V2. Part 1: Pre- and post-flashover compartment fire model," Fire Saf. J., vol. 38, no. 5, pp. 395–427, Sep. 2003, doi: 10.1016/S0379-7112(03)00014-6.
11. D. Drysdale, An Introduction to Fire Dynamics. Chichester, UK: John Wiley & Sons, Ltd, 2011.
12. B. Bohm and S. Hadvig, "Nonconventional Fully Developed Polyethylene and 564 Wood Compartment Fires," Combust. Flame, vol. 44, pp. 201–221, 1982.
13. G. Rein, C. . Empis, and R. Carvel, "The Dalmarnock Fire Tests: Experiments and Modelling | Fire Safety Engineering Applied To," The School of Engineering and Electronics, University of Edinburgh, 2007. <https://www.fireseat.eng.ed.ac.uk/dalmarnock-fire-tests-experiments-and-modelling> (accessed Oct. 16, 2020).
14. J. Gales, "Travelling Fires and the St. Lawrence Burns Project," Fire Technol., vol. 50, no. 6, pp. 1535–1543, Oct. 2014, doi: 10.1007/s10694-013-0372-3.
15. E. Rackauskaite and Et. al, "Fire Experiment inside a Very Large and Open-Plan Compartment : x-ONE," Fire Technol. Press, pp. 1–29.
16. J. Stern-gottfried, "Travelling Fires for Structural Design.Ph.D thesis," School of Engineering, The university of Edinburgh, 2011.
17. E. Rackauskaite, P. Kotsovinos, A. Jeffers, and G. Rein, "Structural analysis of multi-storey steel frames exposed to travelling fires and traditional design fires," Eng. Struct., 2017, doi: 10.1016/j.engstruct.2017.06.055.

18. A. Law, J. Stern-Gottfried, M. Gillie, and G. Rein, "The influence of travelling fires on a concrete frame," *Eng. Struct.*, vol. 33, no. 5, pp. 1635–1642, May 2011, doi: 10.1016/j.engstruct.2011.01.034.
19. K. Horová, T. Jána, and F. Wald, "Temperature heterogeneity during travelling fire on experimental building," *Adv. Eng. Softw.*, vol. 62–63, pp. 119–130, 2013, doi: 10.1016/j.advengsoft.2013.05.001.
20. J. P. Hidalgo et al., "An experimental study of full-scale open floor plan enclosure fires," *Fire Saf. J.*, vol. 89, pp. 22–40, Apr. 2017, doi: 10.1016/j.firesaf.2017.02.002.
21. D. RUSH, D. LANGE, J. MACLEAN, and E. RACKAUSKAITE, "Modelling the Thermal and Structural Performance of a Concrete Column Exposed to a Travelling Fire – Tisova Fire Test," *Struct. Fire*, vol. 0, no. 0, 2016, Accessed: Oct. 16, 2020. [Online]. Available: <http://www.dpi-proceedings.com/index.php/structures-in-fire/article/view/21506>.
22. J. P. Hidalgo et al., "The Malveira fire test: Full-scale demonstration of fire modes in open-plan compartments," *Fire Saf. J.*, vol. 108, p. 102827, Sep. 2019, doi: 10.1016/J.FIRESAF.2019.102827.
23. J. Stern-Gottfried, G. Rein, L. a. Bisby, and J. L. Torero, "Experimental review of the homogeneous temperature assumption in post-flashover compartment fires," *Fire Saf. J.*, vol. 45, no. 4, pp. 249–261, Jun. 2010, doi: 10.1016/j.firesaf.2010.03.007.
24. E. Rackauskaite et al., "x-ONE Fire Experiment in a Very Large and Open-Plan Compartment," 2018.
25. P. H. Thomas, "Design Guide: Structural Fire Safety - Workshop Cib W14."
26. J. Stern-Gottfried and G. Rein, "Travelling fires for structural design-Part II: Design methodology," *Fire Saf. J.*, vol. 54, pp. 96–112, Nov. 2012, doi: 10.1016/j.firesaf.2012.06.011.
27. E. Rackauskaite, C. Hamel, A. Law, and G. Rein, "Improved Formulation of Travelling Fires and Application to Concrete and Steel Structures," *Structures*, vol. 3, pp. 250–260, 2015, doi: 10.1016/j.istruc.2015.06.001.
28. M. Heidari, P. Kotsovinos, and G. Rein, "Flame extension and the near field under the ceiling for travelling fires inside large compartments," *Fire Mater.*, vol. 44, no. 3, pp. 423–436, 2020, doi: 10.1002/fam.2773.
29. X. Dai, S. Welch, and A. Usmani, "A critical review of 'travelling fire' scenarios for performance-based structural engineering," *Fire Saf. J.*, vol. 91, pp. 568–578, Jul. 2017, doi: 10.1016/j.firesaf.2017.04.001.
30. C. Mayfield and D. Hopkin, "Design fires for use in fire safety engineering," BRE Trust, FB29, 2011.
31. E. Rackauskaite, P. Kotsovinos, A. Jeffers, and G. Rein, "Computational analysis of thermal and structural failure criteria of a multi- storey steel frame exposed to fire," *Eng. Struct.*, vol. 180, no. November 2018, pp. 524–543, 2019, doi: 10.1016/j.engstruct.2018.11.026.

ASSESSMENT OF A FIRE DAMAGED CONCRETE OVERPASS: THE VERONA BUS CRASH CASE STUDY

Roberto Felicetti¹

ABSTRACT

The assessment of fire damaged infrastructures entails the implementation of quick diagnostic techniques and reliable interpretation procedures to determine the residual safety margin and any possible need for repair works. In this perspective, several tailored Non-Destructive Test methods have been developed in the last two decades, providing immediate results, with no need for time consuming laboratory analyses. Moreover, matching their indications with the calculated effects of a tentative fire scenario allows harmonizing distinct evidences in the coherent physical framework of fire dynamics and heat transfer. This approach was followed in the investigations on a concrete overpass in Verona (Italy) after a coach violently impacted one supporting pillar and caught fire in 2017. Technical specifications of the vehicle made possible to bound the acceptable ranges for fire load and maximum Rate of Heat Release, while surveillance video footage indicated the duration of the burning stage. Some established NDT methods (evaluation of discoloration, de-hydroxylation, rebar hardness) were implemented, together with advanced ultrasonic tests based on pulse refraction and pulse-echo tomography. The results clearly showed the extension of the most damaged area at the intrados of the box girders and validated the maximum heating depth, as predicted by numerical analysis of the heat transient ensuing from the localized fire model.

Keywords: fire damage assessment; fire scenario models; Non-Destructive Testing; ultrasonic testing

1 INTRODUCTION

Bridge fires are becoming an increasing concern, due to the development of ground shipping and the high incidence of hazardous transports [1]. Though far less frequent than fires in buildings, such events imply a remarkable risk, because of the high costs of service disruption and structural rebuilding or repair. The most severe cases reported in the literature [2] were caused by accidents involving tanker trucks transporting highly flammable fuels, leading to collapse or demolition of the structure due to excessive deformation (steel and composite decks) or generalized spalling (concrete decks). Less severe damage is generally observed when fire is fed by just the vehicle components and its fuel.

This was the case of a dramatic collision happened on January 20, 2017 night on the E70 motorway near Verona, Italy. A coach transporting Hungarian high-school students crashed into one pillar of a concrete overpass and caught fire [3]. Despite of the considerable mass of the vehicle (more than 20t) and the high speed at impact (the pillar penetrated 8m into the chassis) the structure didn't exhibit any visible mechanical damage ascribable to the high impulsive load. This evidence was corroborated by numerical stress analyses of the pillar base, showing that in the worst possible scenario the maximum exerted thrust was close to the onset of shear cracking, namely about 80% of the shear capacity [4].

As concerns fire, the visible signs of damage include spalling on one side of the impacted pillar (with direct exposure of some rebars) and diffuse surface cracking and cover delamination of the above portal.

¹ Associate Professor, Politecnico di Milano,
e-mail: roberto.felicetti@polimi.it, ORCID: <https://orcid.org/0000-0001-8658-0461>

Due to the considerable thickness of these element, there was no question they could still resist the design loads and be easily repaired. A more cryptic condition was recognized in the box girders, due to the significant heating of the thin bottom flange in the region sustaining hogging bending moment. The possible damage to post-tensioning cables in the lateral web of the first girder was also at issue.

The preliminary survey suggested a deeper analysis of the heating depth and a reassessment of the residual bearing capacity of the deck. To this purpose, a coordinated procedure was implemented, based on validation of a tentative fire scenario by way of specialized Non-Destructive Testing techniques [5]. The objectives of in-situ inspections and the adopted techniques can be listed as follows:

- general survey of crack patterns and delaminated/spalled areas (visual inspection and hammer tapping);
- mapping of damage levels at the deck intrados (Ultrasonic Pulse Velocity, pulse-echo tomography);
- assessment of damage depth in the most impacted regions (UP refraction, alkalinity and colour checks);
- evaluation of residual response of exposed rebars (Leeb dynamic hardness tests);
- condition check on the elastomeric bearing pads on top of the portal (visual inspection and lab test).

An account of the above activities and the conclusions that were drawn is given in the following sections.

2 STRUCTURE DESCRIPTION AND POST-FIRE VISUAL INSPECTION

The impacted structure is a semi-integral concrete bridge built in 1992 (Figure 1). The deck includes 5 post-tensioned box girders sustained by two intermediate precast portals and restrained by sets of 6 columns at the abutments. Each girder is made of 4 precast segments assembled with wet joints and post-tensioned with 6 concordant cables (7 x 0.6" strands each). Adjacent girders are connected with shear keys obtained by filling two lateral recesses with non-shrink grout. To be mentioned is a note on the original drawings prescribing the addition of polypropylene fibre to the C40/50 concrete mix (possibly to control early age cracking). As will be discussed, this may explain why no spalling was observed on these elements.

The precast portals consist of two inverted tapered pillars (cross section 0.6x1.1m to 0.7x1.5m) and a transverse beam with 1.5m deep trapezoidal cross-section (width 0.7 to 1.0m). The moment resisting connections are obtained by grouting groups of 7x26mm rebars protruding from each corner of the pillars.

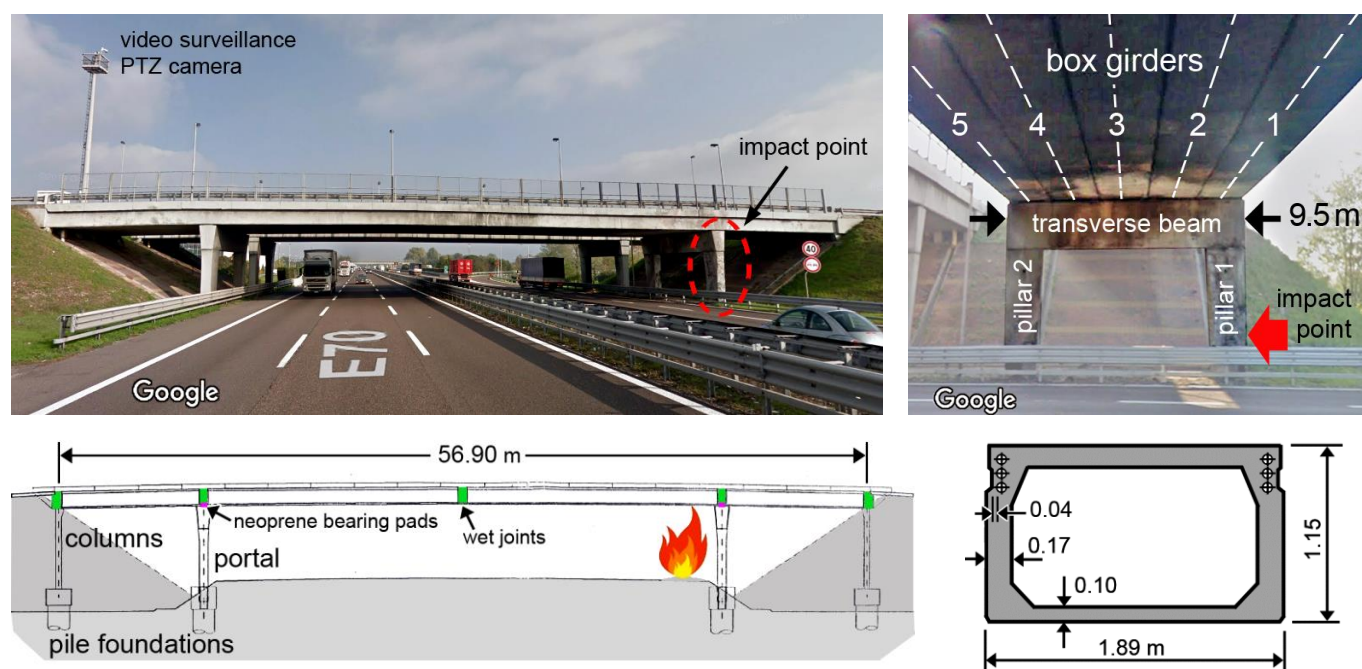


Figure 1. General views of the overpass under study, elements nomenclature and size.

In all elements, fire protection of the reinforcement is provided by a rather thick cover (axis distance of stirrups = 35mm, minimum surface distance of cables at the lateral recess = 40mm, see Figures 1 and 6).

The visible damages observed during preliminary inspection (Figure 2) include spalling on the upper half of pillar 1, with direct exposure of two longitudinal rebars and some stirrups (then, a small share of the member reinforcement). A stable delamination of large plates (10-15mm thick) was recognized at the top of pillar 2. Here the fractured debris could be easily removed and inspected for discoloration. Extensive incipient delamination was detected by hammer tapping also at the intrados of the transverse beam, together with regularly spaced vertical cracks with the same pitch as the stirrups. In summary, no lack of rebar protection affected these latter two elements.

Despite of the direct impact of flames, the intrados of the box girder showed no sign of spalling and just limited delamination, exhibiting a sound response to the tap test. Structural analysis under dead loads showed that the compressive stress borne by the bottom flange next to the support was 5N/mm^2 , outlining a worse condition than the top section of the pillars (average sustained stress 2N/mm^2). This highlights the likely benefit brought in by polypropylene fibre in the most critical part of the structural system.

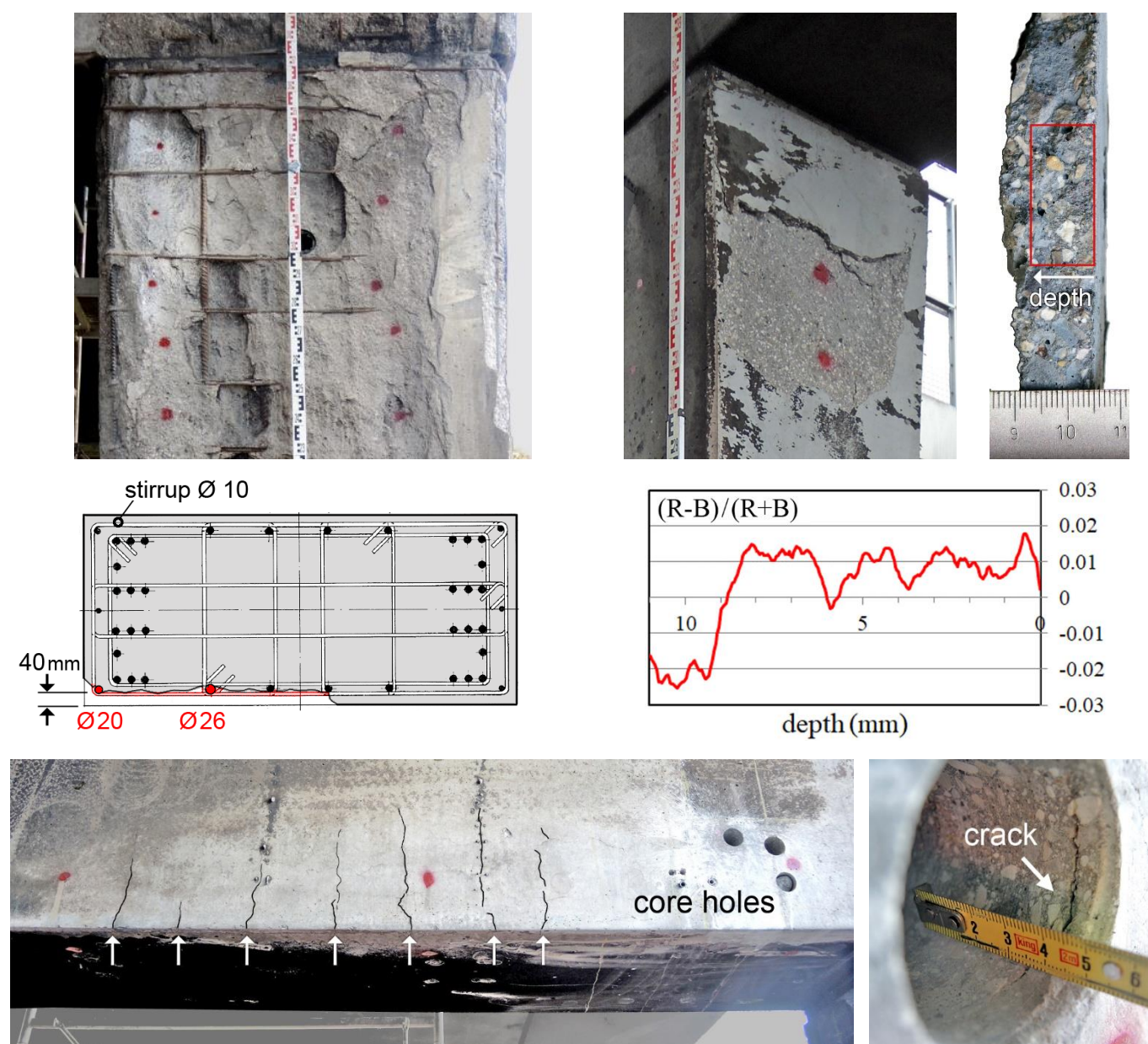


Figure 2. Observed damage patterns: spalling at the top of pillar 1, stable delamination at the top of pillar 2 and discoloured detached plate, equally spaced cracks and incipient delamination at the bottom chord of the transverse beam.

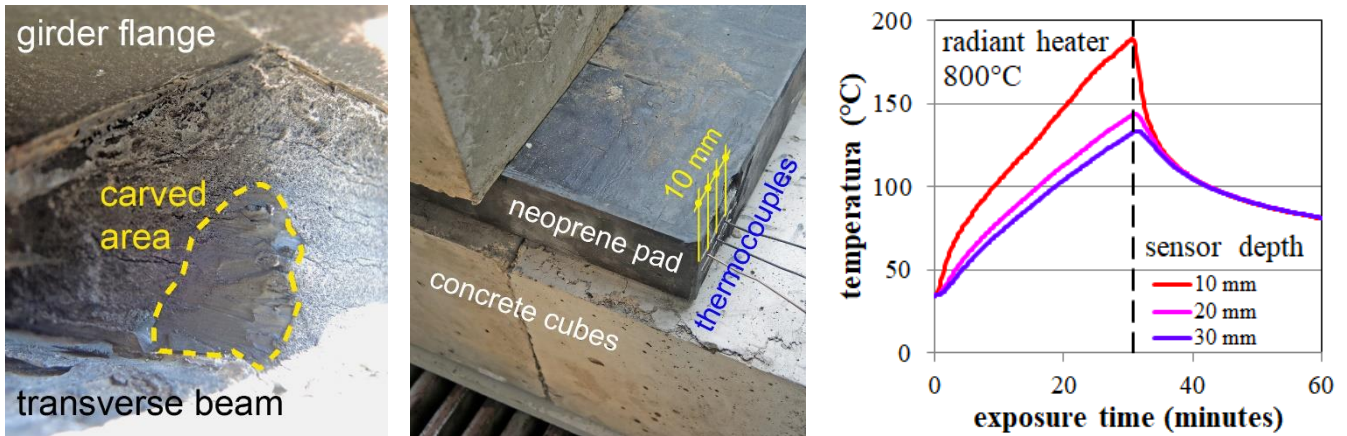


Figure 3. Charred skin removal from a neoprene bearing pad and heating curves resulting from the radiant heater test.

A last aspect deserving attention was the possible damage undergone by the elastomeric bearing pads laid between the transverse beam and the box girders. Visual inspection showed a charred surface on the most exposed sides (Figure 3). However, carving a thin slice was sufficient to expose an intact material with rubbery consistency. In a laboratory test, a like pad was stacked between concrete cubes and exposed to 30min intense radiant heating (about 50kW/m^2). The specimen showed limited charring depth (4mm) and decreasing heating rate, due to the protective effect of the charred layer and the high conductivity of the reinforcing metal shims. The maximum temperature at 10mm depth was below the onset of decomposition as indicated by thermogravimetric analysis [6], confirming the good fire endurance of this component.

3 ACCIDENT DETAILS, FIRE SCENARIO AND THERMAL ANALYSES

The technical specifications of the burnt coach are summarized in the table of Figure 4. The diesel fuel was contained in two tanks anterior to the front wheels, one of which was destroyed by the impact. A supplementary tank was also installed in the central part of the chassis. The surveillance camera installed across the highway (see Figure 1) was not framing the accident area, but the impact instant was indicated by image blurring due to vibration of the supporting pole. Later the camera was directed towards the vehicle, though the view was obstructed by the overpass deck. Nonetheless, it was possible to spot some smoke 3 minutes after the impact and long flames sticking out the parapets one minute later. Pictures and videos shot by witnesses recorded the flame height (Figure 5). Two fire engines reached the place 16 minutes after the accident and flame extinction was completed about 15 minutes later.

vehicle specifications	
brand/model:	Setra S317 GT-HD
	(3 axles, High Decker, 17 seat rows)
length:	13.850 m
width:	2.500 m
height:	3.615 m
gross mass:	24000kg
additional ski box:	650kg
tank capacity:	480 + 370 litres
occupants:	54 passengers + 2 drivers

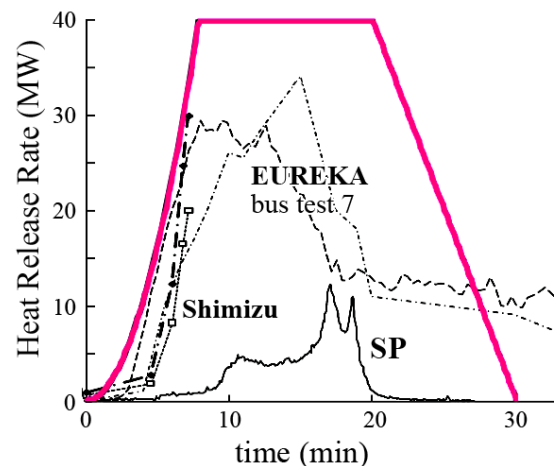


Figure 4. Technical specifications of the coach and assumed HRR curve compared against results from the literature.



Figure 5. Pictures showing the flame height in the fully developed stage of the fire.

Based on the above indications and data from the literature [7], a possible trend of the Heat Release Rate curve was sketched, according to the following assumptions:

- ultra-fast parabolic growth (t-squared model, 1MW in 75s);
- 40MW maximum power (by scaling literature data to the larger number of seats and fire load);
- 30 min total duration of the fire event (video footage).

The total released energy entailed by this scheme adds up to nearly 50GJ.

The HRR curve was introduced in the Hasemi's model of the localized fire [8] (equivalent diameter 5m, fire-to-soffit height 4m). Due to the high thermal power, the condition where flames directly impinge the structure was met for 80% of the fire duration and the received heat flux approached the maximum value allowed by the model. This made the results insensitive to possible adjustments of the HRR curve.

The ensuing heat flux was then used to implement the thermal analysis of the key parts of the structure: a 100mm thick plate representing the box girder flange at the intrados and the recess zone on the lateral side of the first girder. The recess zone was analysed by way of a 2D Finite Element model (Figure 6) where the cable was regarded as a homogeneous disk whose thermal properties were a weighed average of steel and grout properties. The beam intrados was also modelled by means of a 1D finite difference routine, as a starting point for the following reconstruction of ultrasonic refraction ray paths (see section 5).

The analyses were continued until all nodes in the discretized models had reached the cooling stage [11], so to determine the maximum temperature ever experienced at each point, to be related to the unrecoverable damage observed by way of Non-Destructive inspections. It can be observed that this rather intense but short fire is expected not to causes a very deep heating of the exposed members. Moreover, the thermal bridge produced by a cable fosters the gradient in the cover and keeps the most exposed side of the duct colder compared to a plain concrete element (the rebar-centre rule applies also to thicker reinforcement).

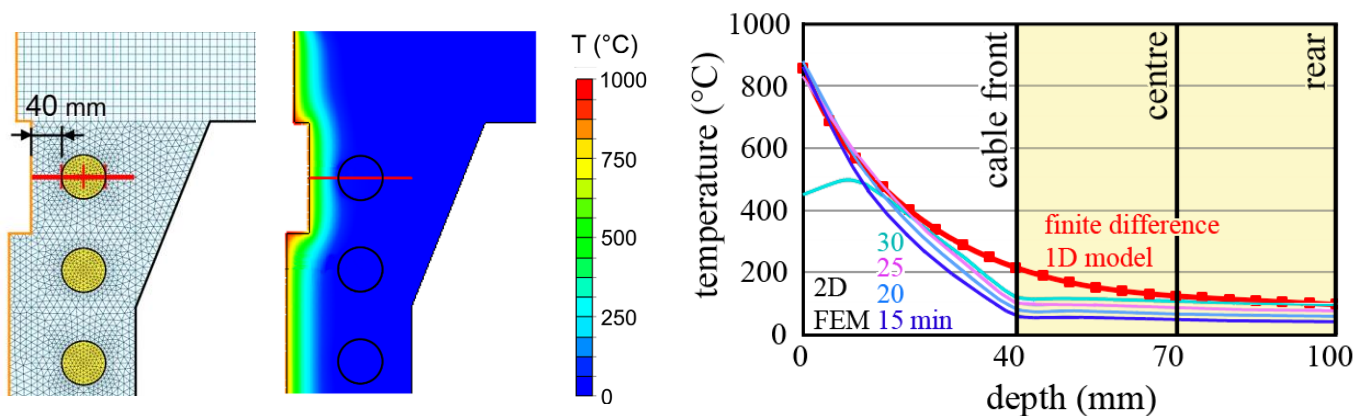


Figure 6. FE model of the recess region of the girder and maximum temperature envelope profiles in the cable and its cover.

4 GENERAL MAPPING OF DAMAGE AT THE DECK INTRADOS

The first task in the framework of onsite inspections was recognizing the most heated zones of the bottom flange of the box girders, which were directly impinged by the flames but experienced just minor delamination. This aspect looked not crucial in the precast portal, since extensive cracking affected the members surface, requiring a complete reinstatement of the concrete cover.

The option of surface hardness survey by means of the rebound hammer was discarded, due to the limited thickness of the plates and the poor sensitivity to fire damage of this method [5]. A definitely more responsive material property is the velocity of ultrasonic pulses (UPV), to be monitored with the probes side by side on the exposed face of the elements (indirect method [9]), being the hollow core of the girders not accessible. To this purpose, a rubber template was devised (Figure 7), so to keep the ultrasonic probes at 150mm centre-to-centre distance, with negligible crosstalk and full adaptability to any surface unevenness. In actual fact, the effective distance was 13.7mm less, due to the not negligible probe size (30mm diameter), which implies an inherent offset [9]. As will be more deeply discussed in the next section, this distance allows an optimal balance between sensitivity to thermal damage and signal strength.

This setup was used to scan the central axis of the girders flange (0.5m step) and several vertical alignments along the pillars (0.25m step) and horizontal sections along the transverse beam (0.5m step). The results pertaining to the deck intrados were collected in the form of a map (Figure 7), clearly illustrating the remarkable pulse velocity reduction in the area right above the burnt coach. Damage tends to vanish at a distance exceeding 8m from the portal edge and in the farthest beam. It has to be stressed that the minimum indicated values represent the mean pulse velocity along a curved ray path plunging to about 20mm in the damaged cover (see the wavefront trajectories in Figure 10).

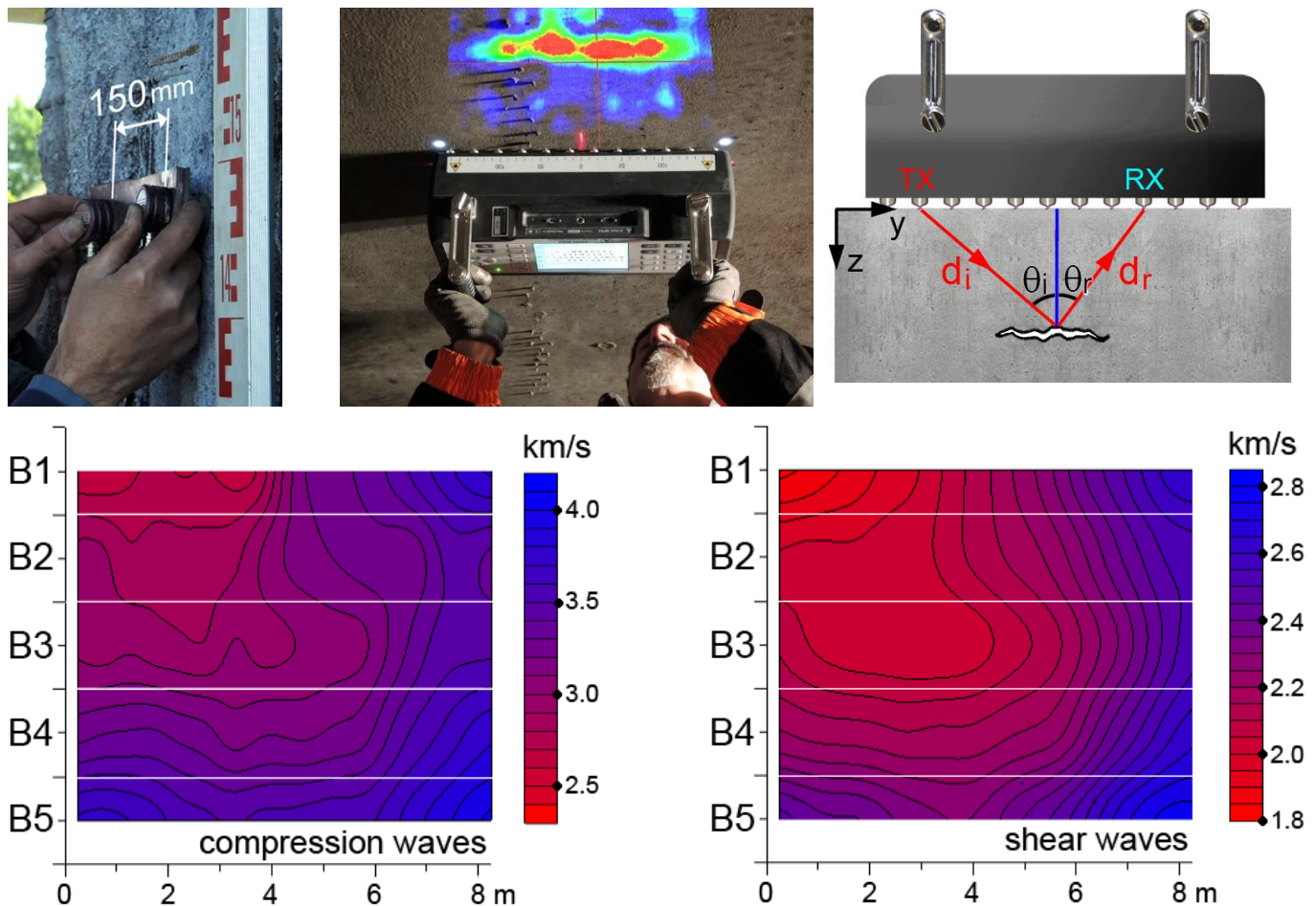


Figure 7. Setup for fast UPV mapping via the indirect method and the A1040 MIRA tomograph; their respective pulse velocity maps detected at the intrados of the 5 box girders composing the deck (abscissa measured from the portal edge).

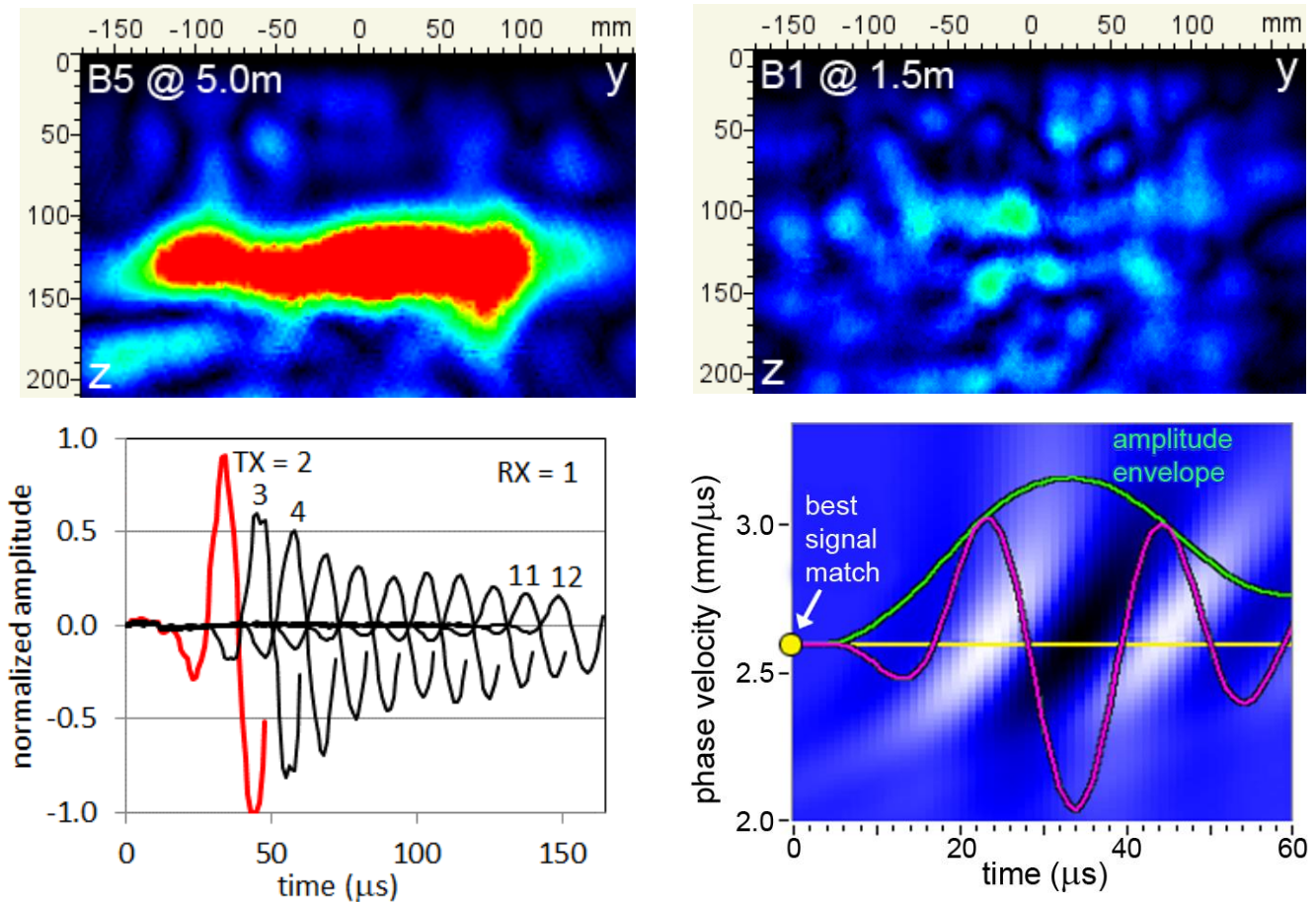


Figure 8. Different strength of the bottom-echo in case of pristine and damaged concrete flanges, regular increase of arrival time at increasing transmitter-receiver distance, assessment of surface wave velocity by optimization of the pulse alignment.

An alternative way to map the surface condition is represented by an innovative ultrasonic tomograph (A1040 MIRA by Acoustic Control Systems, Figure 7) based on the pulse-echo principle. The equipment is fitted with an array of 12 sensors working in turn as transmitters (TX) or receivers (RX). The transmitter sends a short ultrasonic pulse which is reflected by any void or strong inhomogeneity in the material and then is detected by a receiver. Under the assumption of a uniform propagation velocity, the delay of the received pulse indicates the total distance ($d_i + d_r$) covered by the incident and the reflected waves. The process is repeated for all possible combinations of sensors pairs (66 waveforms collected in about 2 seconds) and the signals are processed according to the Synthetic Aperture Focusing Technique [10], so to produce an image of reflectors across a section orthogonal to the tested surface (B-scan). Other peculiar features of this instrument are the spring loaded dry-point contact sensors, not requiring any coupling medium to adapt to the surface unevenness, and the use of shear wave pulses, characterized by a lower velocity and not suffering any mode conversion when reflected.

In the application at issue, the steep gradients of pulse velocity tend to invalidate the SAFT algorithm and the strong bottom-echo produced by the inner cavity of the girders progressively vanishes as fire damage increases (Figure 8). Nonetheless, the slower surface layer tends to guide horizontally polarized shear waves (Love waves), which propagates along the surface with milder decay compared to other modes. This mode governs the first received signal, whose time shift goes with the sensor spacing divided by the surface wave velocity. The latter parameter is determined by optimizing the pulse realignment (max waveform sum).

Besides the different magnitude (shear waves are slower than compression waves), the resulting map (Figure 7) is very similar to the one obtained by means of the traditional UPV method. However, merging 66 waveforms in one measurement allows offsetting the local disturbance due to cracks, rebars and other defects, producing a smoother output. To be mentioned is that both mapping techniques were implemented at the pace of 25 test points per hour, minimizing the traffic disruption in this strategic highway.

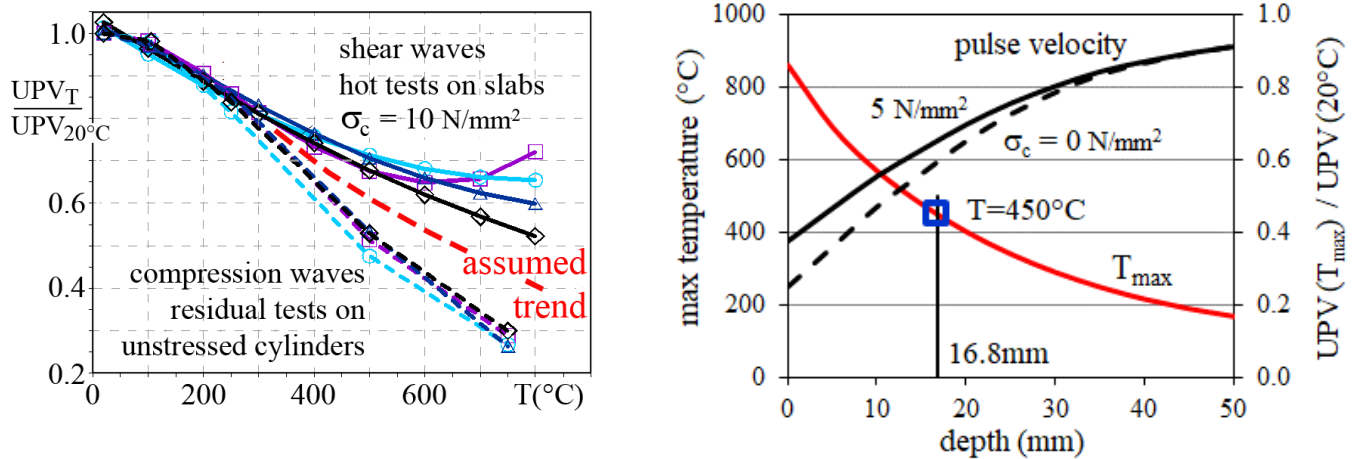


Figure 9. Decay of Ultrasonic Pulse Velocity with temperature as a function of the sustained stress [12]; profiles of the max temperature and corresponding UPV for a 100mm thick plate submitted to the localized fire discussed in section 3.

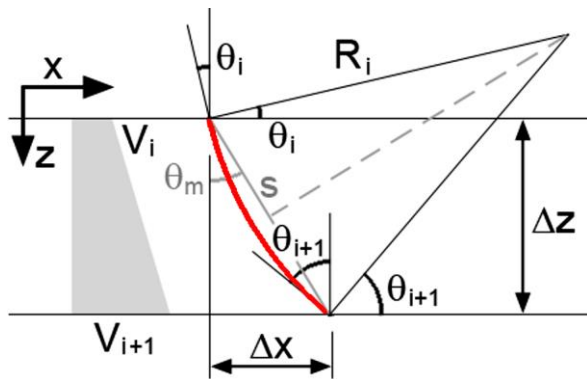
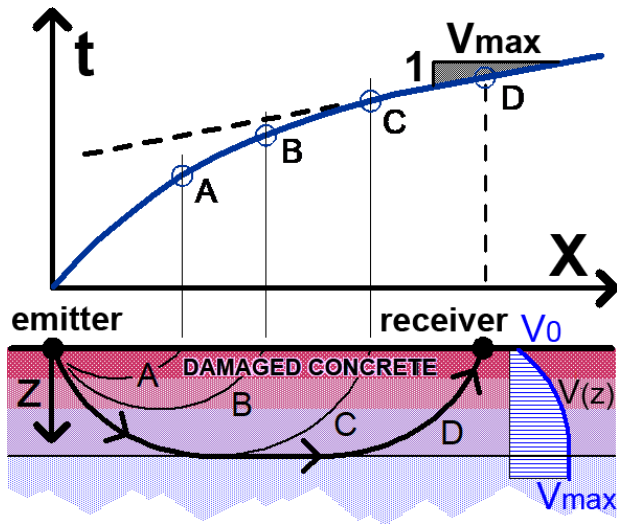
5 VALIDATION OF DAMAGE DEPTH BY ULTRASONIC PULSE REFRACTION

The velocity of elastic waves is one of the most responsive indicators of concrete thermal damage, due to the pronounced temperature sensitivity of the Young's modulus and to the synergistic effect of drying [11]. Nonetheless, a mild compressive loading may mitigate this effect, due to reduced meso-scale damage at the aggregate-cement interface (Figure 9 [12]). This aspect should be duly considered when dealing with columns or the compressed chord of beams, since a more severe temperature exposure may be inferred from the observed response.

Due to the steep temperature variations induced by fire, remarkable velocity gradients develop in the concrete cover, which behaves like a strongly layered medium. Though scaled down by 3-4 orders of magnitude, the problem resembles a natural soil whose mechanical properties improve with depth. Taking inspiration from Geophysics, the velocity profile can be characterized via the the refraction of ultrasonic compression (P) waves implemented by way of the indirect Ultrasonic Pulse Velocity technique. In this method the measurement of the pulse time-of-flight is performed by applying both the emitting and receiving probes on the same face of the investigated element (Figure 10). When the material velocity rises with depth, the first wave front detected by the receiver follows a curved ray path representing the best compromise between a shallow trajectory of shorter length and a deeper route involving faster undamaged layers [13]. As a consequence, the maximum explored depth is a function of the probe distance X. A series of repeated time-of-flight measurements at increasing probe distance allows to sound deeper and deeper layers in the cover. The outcome is a X-t plot whose shape has been the object of several studies in the literature [14]. To be recalled among its properties:

- A monotonically increasing velocity profile implies a convex shape. Any exception indicates the presence of cracks, which should be avoided by preliminary visual inspection and hammer tapping.
- The local slope at any point equals the slowness of the deepest layer crossed by the corresponding minimum-time ray path (slowness = 1 / velocity). Then, the curve asymptotically tends to a linear trend whose slope is the slowness of the deepest undamaged layer (maximum velocity, minimum slope).
- The rate of convergence to the final linear trend denotes the thickness of the damaged layer: a higher asymptote intercept indicates a delayed convergence and then a deeper damage.

A systematic series of numerical simulations of different thermal transients involving a broad range of concretes allowed to derive some correlations [13] between these geometrical features and the underlying material damage (inverse problem). As an alternative, the theoretical X-t curve can be easily plotted once a guess velocity profile is determined by combining the material decay curve (Figure 9) and the maximum temperature experienced at each depth, as results from the analysis of the thermal transient ensuing from a tentative fire scenario (cooling stage included).



Snell's law: $\sin(\theta)/V = p = \text{ray parameter (constant)}$
for any p in the range $1/V_{\max} \leq p \leq 1/V_0$ find θ_i and θ_{i+1}
 $\Delta x = \Delta z \cdot \tan[(\theta_{i+1} + \theta_i)/2] = \Delta z \cdot \tan(\theta_m)$
 $R_i = \Delta z / [\sin(\theta_{i+1}) - \sin(\theta_i)] = \Delta z / [p \cdot (V_{i+1} - V_i)]$

propagation time:
 $\Delta t_i = \int R_i/V d\theta = R_i \cdot p \cdot \int 1/\sin(\theta) d\theta$
 $= R_i \cdot p \cdot \{\ln[\tan(\theta_{i+1}/2)] - \ln[\tan(\theta_i/2)]\}$
if $V_i = V_{i+1}$ then $R_i = \infty$ and $\Delta t_i = 2 \Delta z \cdot p / \sin(2\theta)$

Figure 10. Basic principle of the pulse refraction method, application to the intrados of a box girder, circular ray path in a generic layer with linear velocity trend and formulas for the incremental construction of the X-t curve.

To this purpose, the cover is discretized in a series of layers with linearly changing velocity through their thickness Δz (Figure 10). In each layer, a ray path obeying the Snell's law of wave refraction takes the shape of a circular arc whose radius depends on the velocity gradient [14]. The increments of covered distance Δx and time-of-flight Δt are expressed in closed form and can be summed across the explored thickness. The following hints should be considered in the implementation of this scheme:

- If $V(z)$ is not monotonically increasing the formulae in Figure 10 are still valid, with $R < 0$.
- A ray path of initial angle θ_0 can re-emerge if $\arcsin(V_0/V_{\max}) \leq \theta_0 \leq \pi/2$, and then $1/V_{\max} \leq p \leq 1/V_0$.
- For any ray parameter p in the above range the inversion point $\theta = \pi/2$ is at the depth where $V=1/p$.
- Ray paths of gradually increasing initial slope (decreasing θ_0 and p) lead to deeper inversion points and milder slopes on the X-t curve. However, X and t are monotonically increasing functions of $1/p$ only in the case of a convex velocity profile ($d^2V/dz^2 \leq 0$). If this condition is not met, multiple arrival times are obtained for the same distance X (triplication) and the shortest time envelope should be considered.

The above procedure was implemented with reference to the localized fire scenario depicted in section 3. The maximum temperature envelope profile [11] within the 100mm thick bottom flange of the box girders was calculated via a 1D finite difference procedure, which was continued until all terms in the temperature vector had reached the cooling stage. The velocity profile was then obtained, based on the expected decay for slightly compressed concrete (reference pulse velocity for pristine concrete $V_{20^\circ\text{C}} = 4.3\text{km/s}$). The intermediate curve in Figure 9 was adopted, being about 5 N/mm^2 the average compressive stress sustained by the bottom flange under dead loads. Finally, the refracted ray paths and the corresponding X-t curve were traced by keeping the same discretization as the thermal model (Figure 11).

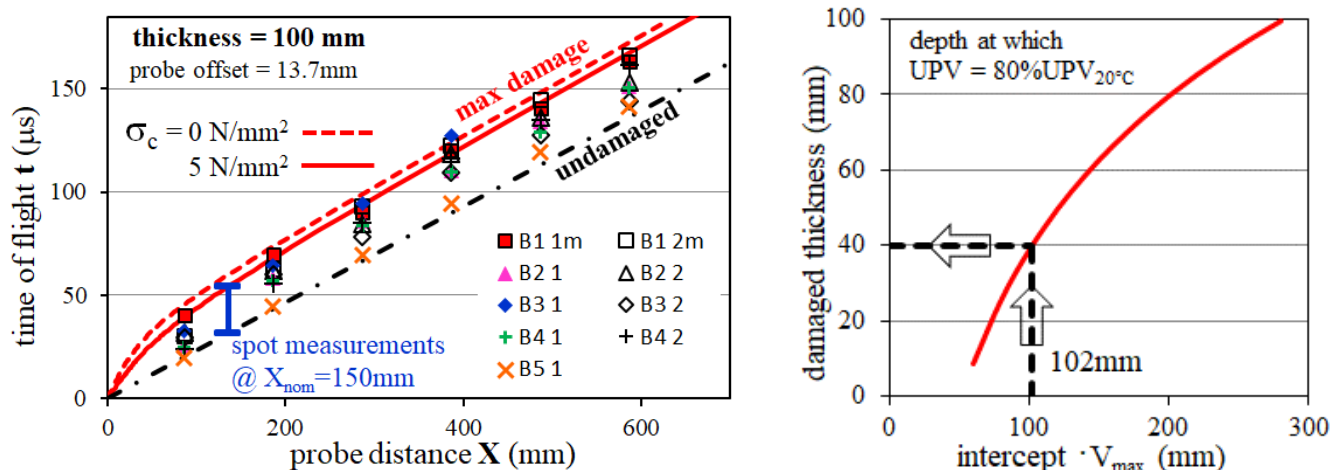


Figure 11. Comparison between experimental pulse refraction measurements and the theoretical X-t curve descending from the assumed fire scenario; quick assessment of damage depth according to the semi-empirical correlation proposed in [13].

In-situ measurements were taken along the central axis of each box girder, at 1m and 2m distance from the edge of the supporting transverse beam. The comparison against the theoretical trends (Figure 11) shows that all results lie between the plots pertaining to undamaged concrete (a straight line of slope $1/V_{20^\circ\text{C}}$) and to the maximum expected damage above the localized fire source. A good correspondence is observed between damage depth and the location in the general velocity maps of Figure 7, with smoothly decreasing effects in beams 4 and 5. The effectiveness of spot measurements at $X=150\text{mm}$ nominal probe distance in discriminating damage levels in this range is also highlighted.

It has to be remarked that the theory of waves refraction allows establishing a direct connection between velocity profiles (and then mechanical damage) and field results. This is the basis behind the semi-empirical correlation proposed in [13], providing an indication of the damaged thickness, with no specific assumptions on the fire scenario and the inherent material sensitivity to fire. However, the limited thickness of the flanges under study would require to adapt the proposed relation, since the depth at which a 20% decay of pulse velocity is assigned is overestimated by about 10mm (see Figures 9 and 11).

6 FURTHER CHECKS AND EVALUATION OF RESIDUAL CAPACITY

The maps of ultrasonic velocity at the deck intrados and the validation of the tentative fire scenario by way of ultrasonic pulse refraction already allowed forming a clear picture of the fire impact on the box girders, whose support region was recognized as the most critical part of the structure. Nonetheless, other inspection techniques were implemented to corroborate this appraisal.

Colorimetry. Some discoloration was visible across the thickness of delaminated plates of pillar 2 and inside the holes remaining on the transverse beam from former cores extraction (see Figure 2). This shift to pink was objectively recognized on digital images by computing the normalized difference between the red and blue colour planes $(R-B)/(R+B)$. This parameter is equivalent but easier to obtain than the strict analysis proposed in [11]. The alteration (ascribable to heating above 470°C) was found not to exceed 9mm depth, which indicates a less severe heating of these two elements compared to the girder intrados, as could be inferred from their smaller view factor.

De-hydroxylation depth. Calcium hydroxide is the main source of alkalinity in concrete pores. It is decomposed by heating above 450°C , leading to the formation of calcium oxide, which is a highly hygroscopic product. For this reason, the reaction is reversible and can be recognized only if no water is used while sampling, as is made possible by collecting drilling powder via the Carbondest[®] kit [13]. Tests performed on the portal confirmed the lower impact of fire, as anticipated by colour analysis. Checks on the exposed web of the first girder (Figure 12) gave slightly lower values than expected ($<15\text{mm}$ vs. 16.7mm in Figure 11), confirming the assumed fire scenario as a cautious description of the event.

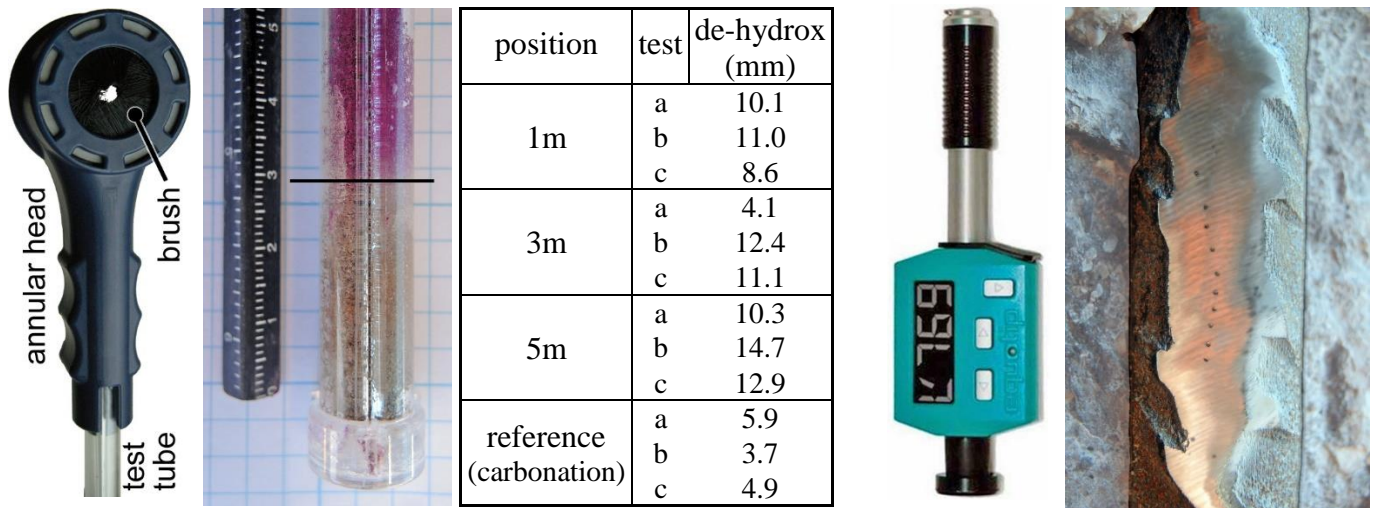


Figure 12. The Carbontest[®] kit, a de-hydroxylated powder sample (scale factor 2.25) and results collected on the exposed web of the 1st girder; Leeb dynamic hardness tester and resulting indentations on the smoothed face of an exposed rebar of pillar 1.

Dynamic hardness tests on rebars. Steel rebars may recover a significant share of their initial strength during cooling, though this strongly depends on their metallurgical features (alloying elements, thermal and mechanical working process [15]). The dynamic hardness test (Leeb method) is a viable tool to assess their residual performance regardless of original quality [5]. Tests were performed on one rebar exposed by spalling in pillar 1 and a reference piece uncovered by chiselling on the opposite side. The results (mean rebound index / std deviation = 515/6 and 536/8, respectively) showed a marginal decay of the rebar response (-4%), which corresponds to an almost double loss of yield strength. Given also the minor contribution to sectional capacity (see Figure 2), this confirms the little impact of fire on this element. A permanent loss of strength about 10% can be ascribed to heating up to about 700°C [15], which seems coherent with the other observations.

Going back to the most critical part of the structure, it can be concluded that the post-tensioning cables underwent a not significant heating (< 120°C, Figure 6), whereas temperature exceeded 300°C in the first 30mm of the most exposed cover. Though concrete is expected to retain most of its strength at this temperature, stability in presence of possible fractures and durability in case of increased porosity were also of concern. Then, a check on the residual capacity was performed by neglecting any contribution from this layer. The results showed that the extra capacity in the hogging bending moment region dropped from +30% to +10% relative to the design bending moment (Figure 13). Even though the safety check were passed, the sizeable loss of resisting area caused a rise of the neutral axis at the Ultimate Limit State from 20% to 50% of the cross-section depth, significantly affecting the rotation capacity of the weakest cross-section in this redundant scheme. Some strengthening works were then recommended to the highway management to reinstate the original sectional ductility as well as cover stability.

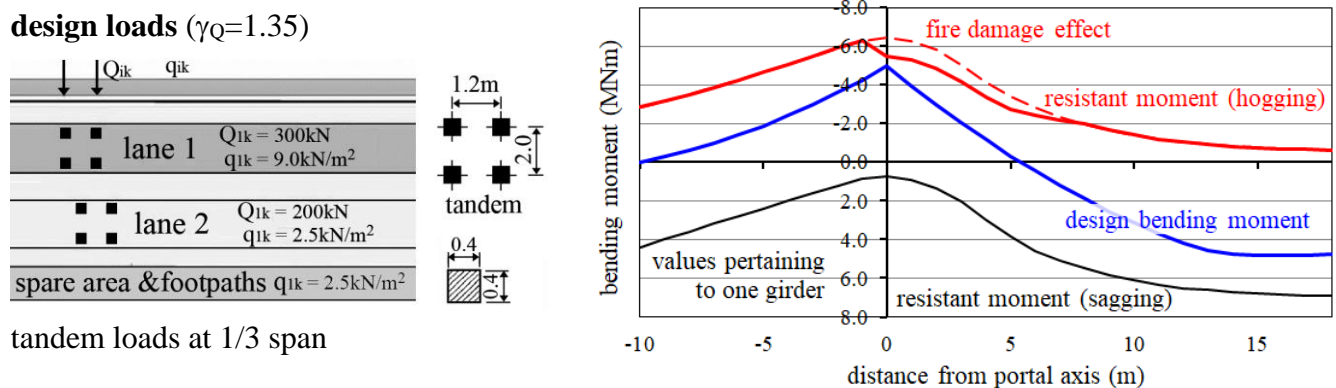


Figure 13. Design loads and diagrams of the design and resistant bending moments for the most fire damaged girders

7 CONCLUDING REMARKS

Case studies in post-fire damage assessment represent an essential opportunity to validate the operational strategies and to verify the viability and effectiveness of both established and innovative inspection tools. The lessons learnt in the analysis of a fire damaged concrete bridge are briefly summarized here.

Depicting a tentative scenario, and then the ensuing thermal output and the consequent temperature profiles in the exposed members allows a consistent and harmonized interpretation of many distinct indications ensuing from visual inspection and Non-Destructive Test results. A sensitivity analysis is advisable in case of possible alternative assumptions and uncertain parameters.

Several specialized inspection techniques are available, providing immediate indications on some mechanical or chemo-physical features of the material. The alkalinity analysis of drilling powder samples stands out for affordability. Ultrasonic pulse refraction and pulse-echo tomography are to be cited among the advanced tools for a deeper analysis, at the cost of more sophisticated equipment and data processing.

Besides the residual capacity of some critical sections, other features may be at issue, like durability, cover stability, sectional ductility and global robustness of the structural system.

ACKNOWLEDGMENT

The author wishes to acknowledge Marco Cucchi for the valuable support during onsite inspections and Nicola Bettini for the cooperative working on the numerical analyses. A sincere thought goes to the students who lost their lives in this tragic accident and to their families.

REFERENCES

1. Garlock, M., Paya-Zaforteza, I., Kodur, V. and Guc, L., Fire hazard in bridges: Review, assessment and repair strategies, *Engineering Structures* 35, 89-98 (2012).
2. G. Peris-Sayol, G., Paya-Zaforteza, I., Balasch-Parisi, S. and Alós-Moya, J., Detailed analysis of the causes of bridge fires and their associated damage levels, *J. of Performance of Constructed Facilities*, 31(3), (2017).
3. 2017 Verona bus crash, https://en.wikipedia.org/wiki/2017_Verona_bus_crash, last visited October 2020.
4. Belleri, A., Bettini, N. and Felicetti, R., Evaluation of the impact and fire damage of a highway bridge, *Proc of the Italian Concrete Days, Lecco (Italy)*, 8p (2018), in Italian, <http://hdl.handle.net/10446/125455>
5. Felicetti, R., Assessment of fire damage in concrete structures: new inspection tools and combined interpretation of results, *Proc. 8th Int. Conf. Structures in Fire - SIF 14, Shanghai (China)*, 1111-1120 (2014).
6. Caballero, J.A., Conesa, J.A., Martín-Gullón, I. and Font, R., Kinetic study of the pyrolysis of neoprene, *Journal of Analytical and Applied Pyrolysis*, 74, 231-237, (2005).
7. Beard, A. and Carvel, R., *The handbook of tunnel fire safety*, 2nd edition, ICE, London (2012).
8. EN 1992-1-2, Eurocode 1: Actions on structures - Part 1-2: General actions - Actions on structures exposed to fire, Annex C: Localised fires, (2002).
9. Bungey, J.H., Millard, S.G. and Grantham, M.G., *Testing of concrete in structures*, Taylor & Francis, 4th edition, 353 p, 2006.
10. Schickert, M., Krause, M. and Muller, W., Ultrasonic Imaging of Concrete Elements Using Reconstruction by Synthetic Aperture Focusing Technique, *ASCE J. Materials in Civil Engineering*, 235-246, (2003).
11. Colombo, M. and Felicetti, R., New NDT techniques for the assessment of fire-damaged concrete structures, *Fire Safety Journal*, 42, 461-472, (2007).
12. Felicetti, R. and Lo Monte, F., Pulse-Echo Monitoring of Concrete Damage and Spalling during Fire, *Proc. 9th Int. Conf. Structures in Fire 2016 - SIF16, Princeton (USA)*, 851-858 (2016).
13. Felicetti, R., Assessment Methods of Fire Damages in Concrete Tunnel Linings, *Fire Technology*, 49 (2), 509-529, (2013).
14. Greenhalgh, S.A. and King, D.W., Curved raypath interpretation of seismic refraction data, *Geophysical Prospecting*, 29, 853-882, (1981).
15. Felicetti, R., Gambarova, P.G. and Meda, A., Residual behaviour of steel rebars and R/C sections after a fire, *Construction and Building Materials*, 23 (12), 3546-3555 (2009).

SIMPLE CALCULATION METHOD FOR THE TEMPERATURE PROFILE IN A CIRCULAR CONCRETE FILLED STEEL TUBULAR COLUMN

Yusuke Shintani¹, Takuya Kinoshita², Tomohito Okazaki³, Toshihiko Nishimura⁴, Tamotsu Takao⁵

ABSTRACT

A hand calculation method was proposed for the prediction of temperature profile of inner concrete of concrete filled steel tubular column based on the heating experiment. The proposed method was validated by comparing it with the experimental results of concrete filled steel tubular (CFST) columns with different diameter. The temperature profiles were predicted well by the proposed method. The effect of shear studs placed in the steel tube on the temperature profile of inner concrete was also studied by heating test. The shear studs acted as heat bridge, and the temperature of inner concrete, especially near the interface between steel tube and concrete, were higher than that without shear studs. This worsened the fire resistance performance of CFST column. The proposed hand calculation method was extended to predict the temperature profile of the column with shear studs. The temperature near concrete interface could be predicted well by using weight average thermal diffusivity.

Keywords: Concrete filled steel tubular columns; temperature profile of inner concrete; heat transfer analysis; hand calculation method

1 INTRODUCTION

Concrete filled steel tubular (CFST) columns have been widely used in building construction, particularly high-rise buildings, because of their high structural performance and high fire resistance. Their fire resistance considerably depends on the temperature profile of the inner concrete, as reported in previous studies [1]. In addition, shear studs, which are designed to be placed inside the steel tube to transmit shear force from the connected beam to the column, act as heat bridges to the inner concrete and affect the temperature profile of the inner concrete. These effects can be estimated using heat transfer analysis. However, a simpler calculation method is desirable for design trials.

Simple calculation method of circular and rectangular reinforced concrete column was proposed based on the heat transfer analysis [2]. However, the method was not verified by the comparison with the experimental result and the effect of shear studs could not be estimated.

¹ Chief researcher, Research and Development Institute, Takenaka Corporation, Chiba 270-1395, Japan
e-mail: shintani.yuusuke@takenaka.co.jp, ORCID: <https://orcid.org/0000-0002-5488-2761>

² Associate Chief researcher, Research and Development Institute, Takenaka Corporation, Chiba 270-1395, Japan
e-mail: kinoshita.takuya@takenaka.co.jp

³ Senior Manager, Takenaka Corporation
e-mail: okazaki.tomohito@takenaka.co.jp

⁴ Chief researcher, Research and Development Institute, Takenaka Corporation, Chiba 270-1395, Japan
e-mail: nishimura.toshihiko@takenaka.co.jp

⁵ Senior Manager, Takenaka Corporation
e-mail: takao.tamotsu@takenaka.co.jp

Therefore, this study proposes a simple calculation method for the temperature profile of the inner concrete of CFST columns with and without shear studs based on the results of heating experiments of CFST column exposed to ISO-standard fire. The method was verified by the comparing it with other experimental results.

2 EXPERIMENT

2.1 Experimental method

Heating experiments were conducted on CFST columns with and without shear studs. Three 1,000-mm long steel tubes of $\square 609.6 \times t12.7$ were used as specimens, as shown in Fig. 1. One (S0) did not contain shear studs, whereas the other two (S10, S20) did. S10 had 10 shear studs in circumferential direction and S20 had 20 shear studs inside the steel tube as shown in the cross-section diagram in Fig.1. Normal weight concrete was filled in the steel tubes.

The temperatures of the steel tube surface and inner concrete at 10 mm, 78 mm, 146 mm, 292 mm (centre) away from the concrete surface were measured using thermocouples, as shown in Fig. 1. The temperature of the edge of two shear studs were also measured as shown in Fig.1.

The top surface of the specimens were insulated by ceramic fibre blankets, and the specimens were exposed to ISO834-standard fire for 4 h continuously as shown in Fig.2. The concrete moisture content of specimen was estimated using the cylinder samples core drilled from the short columns, and the section size was equal to the specimen. The moisture content was 4.7 %.

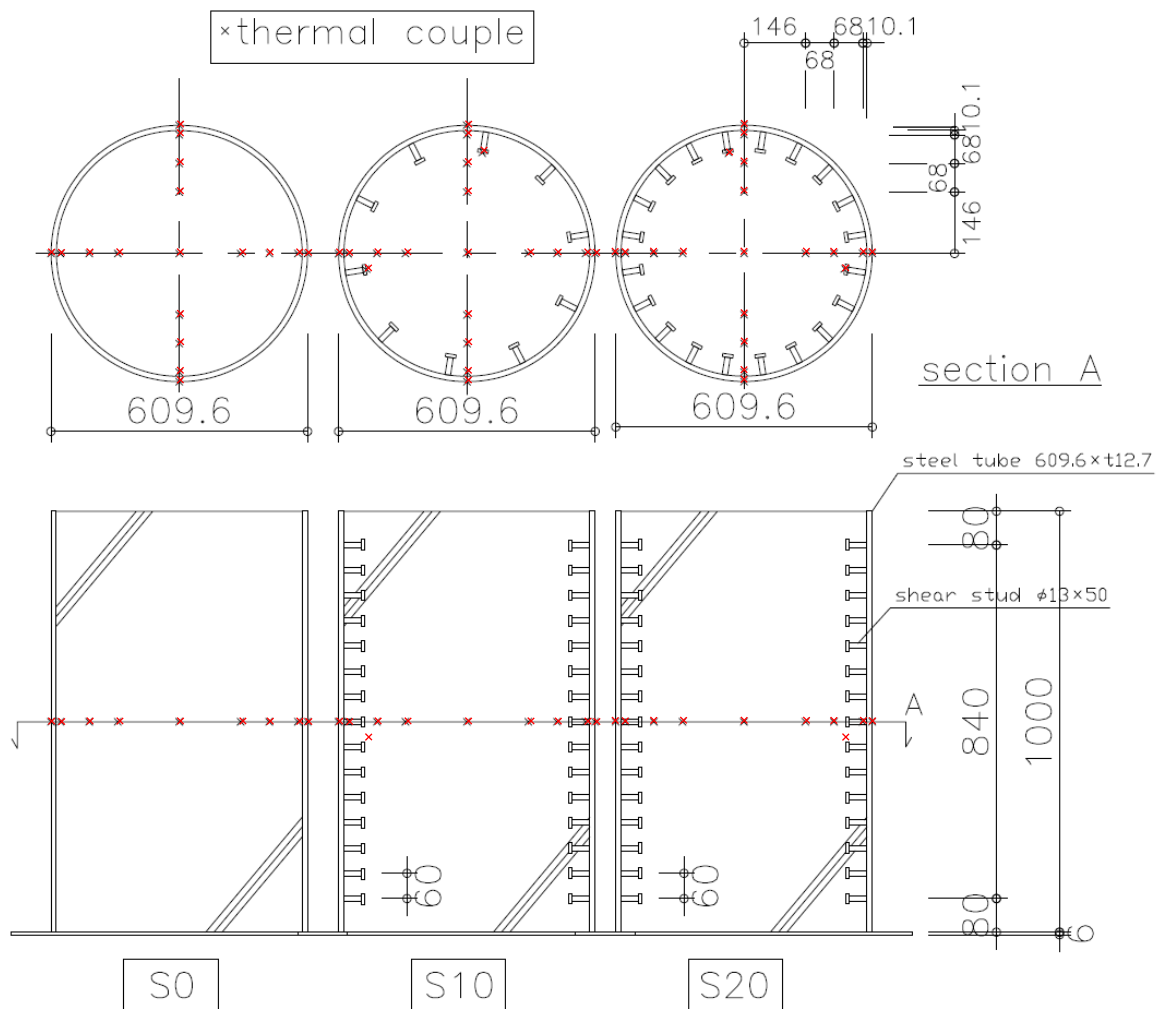


Fig. 1 Sectional views of specimens and measurement points of temperature.



Fig. 2 Experimental setup.

2.2 Experimental result

The histories of the heating temperature and the temperature of the steel tube, shear studs and inner concrete in S0 are shown in Fig.3. The temperatures of steel tube surface increased rapidly and were almost equal to the heating temperature after 240 min. The temperature of inner concrete at 10 mm away from the concrete surface (interface between steel tube and concrete) were 200 –300 °C lower than that of the temperature surface. The temperature of centre of concrete was almost constant at approximately 100 °C during 120 to 240 min; subsequently, the temperature increased gradually. The difference of the temperature were small when the distance from the surface of specimen was same.

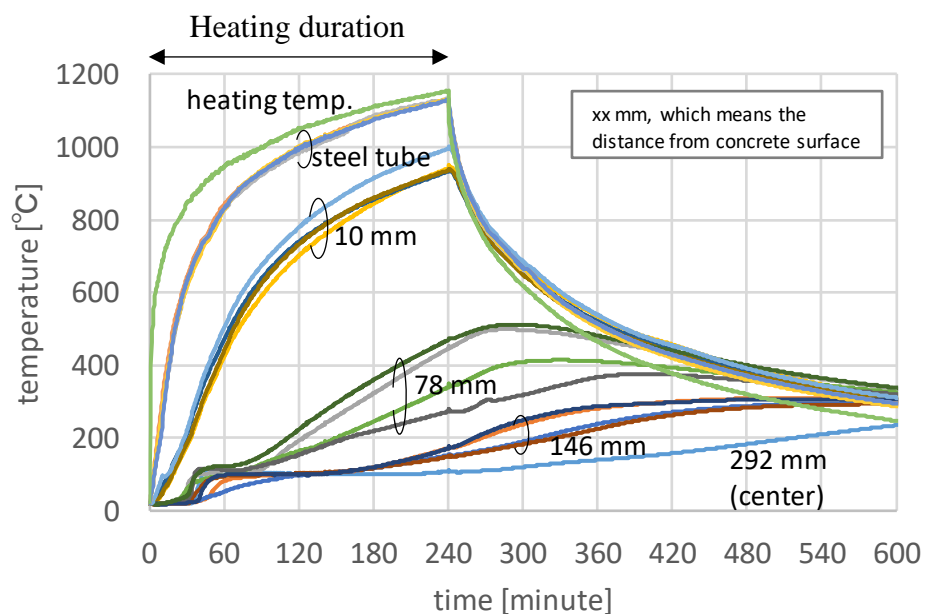


Fig. 3 Temperature history of steel tube, inner concrete (S0)

The average temperature histories of the steel tube, inner concrete, and shear studs are shown in Fig.4. The temperature of steel tube surface and the centre of inner concrete were similar regardless of the number of shear studs. In contrast, the temperature of inner concrete of the specimen with shear studs (S20, S10) were higher than that without shear studs (S0). This difference was larger near concrete surface. This shows that shear studs acts as heat bridge to inner concrete. Therefore, shear studs worsen the fire resistance performance of CFST column. The experimental results are described in APPENDIX.

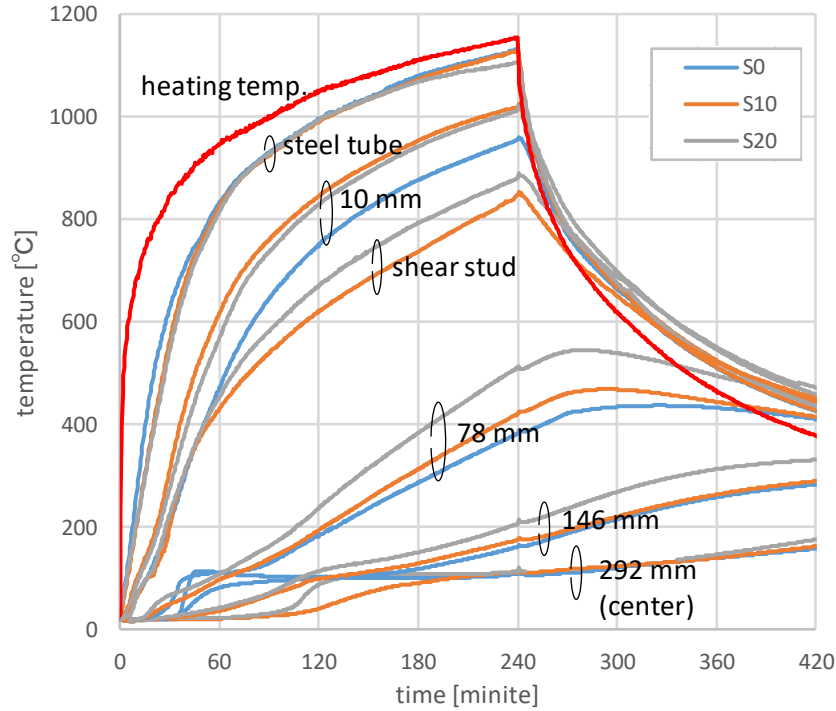


Fig. 4 Average temperature history of steel tube, shear studs, inner concrete

3 ANALYSIS

Simple calculation method for temperature profile in the inner concrete was derived from heat conduction equation. When the effect of internal heat generation is ignored, one dimensional heat conduction equation can be represented as:

$$\frac{\partial T}{\partial t} = \alpha \frac{\partial^2 T}{\partial x^2} \quad (1)$$

where T is the temperature rise of the solid [K],

T is temperature [K],

α is the thermal diffusivity [m^2/s],

t is time [s].

When the column is assumed to be thermally thick, equation(2) could be used to estimate the temperature profile of the CFST column because the heat capacity of the inner concrete was large. When the surface temperature is known, the temperature profiles of semi-infinite one-dimensional solids can be calculated using the following equation[2, 3] :

$$\Delta T / \Delta T_s = \text{erfc}(x / 2\sqrt{\alpha t}), \quad (2)$$

where ΔT is the temperature rise of the solid [K],

ΔT_s is the temperature rise of the surface [K],

x is the distance from the surface [m].

Considering the temperature dependability of thermal diffusivity of concrete and the cylindrical coordinates system of the columns, Equation (2) was replaced with the following equation:

$$\Delta T / \Delta T_s = \operatorname{erfc}(x / 2k\sqrt{\alpha t}), \quad (3)$$

where k is the experimental coefficient ($k = 1$) in theory for one dimensional semi-infinite solid),

x is the distance from concrete surface [m],

α is the thermal diffusivity [$= 0.78 \times 10^{-6} \text{ m/s}^2$].

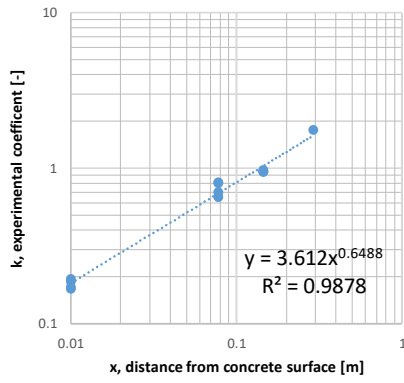
Because thermal conductivity of steel tube was high, the temperature difference between front and back of the steel tube was ignored and x was set as the distance from concrete surface and not steel tube surface. The value of k was determined by the fitting to the experimental results. Equation (3) could be transformed to the following equation:

$$k = (1/\operatorname{erfc}^{-1}(\frac{\Delta T}{\Delta T_s})) \left(\frac{x}{2\sqrt{\alpha t}} \right). \quad (4)$$

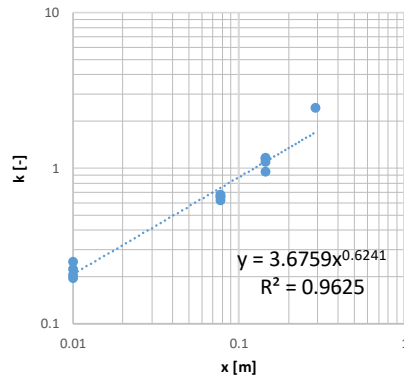
k was calculated by substituting the experimental result of the specimen without shear studs (S0) to Equation (4). Fig. 5 shows the relationship between k and x . If the CFST column could be assumed as one-dimensional thermally thick solid, theoretically the value of k can change to 1. However, the calculation results of k were smaller than 1 when the distance from concrete surface is small because the thermal diffusivity of concrete at high temperature was larger than that at normal temperature. The value of k was determined by fitting all the parameters to the all experimental data, and the value was found to be equal to $1.8x^{2/5}$ as shown in Fig. 5i).

The nondimensional temperature rise, represented by the left-hand side of Equation (3), and nondimensional distance, represented by the term in parentheses on the right-hand side of Equation (3), are shown in Fig. 6. The black solid line represents the error function, $Y = \operatorname{erfc}(X)$. The experimental coefficient was determined such that the experimental results of specimen S0 were in good agreement with the error function (Fig. 6a)).

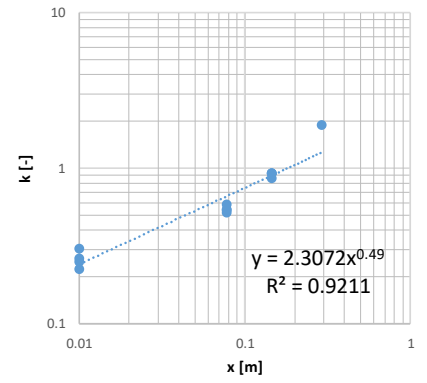
The experimental results of the specimen with shear studs (S10, S20) were slightly higher than the error function because of the heat bridge effect of shear studs as shown in Fig 6b), 6c). Fig. 7a) and 7b) show the relationship between nondimensional temperature rise and nondimensional distance when thermal diffusivity of the specimen with shear studs (α_{10} , α_{20}) were calculated by weight average of the section area of concrete and shear studs as listed Table 1. The results were in good agreement with the error function when the nondimensional distance was small where there are shear studs. However, the difference between the experimental results and error function equation were larger when nondimensional distance was large because the effect of shear studs is lower in this area.



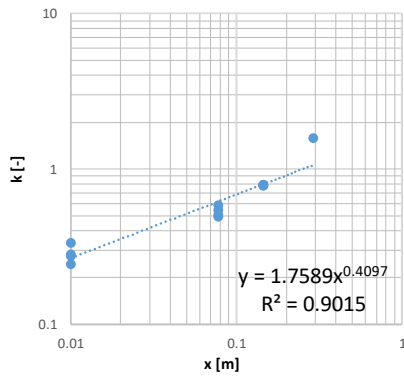
a) 30 minutes



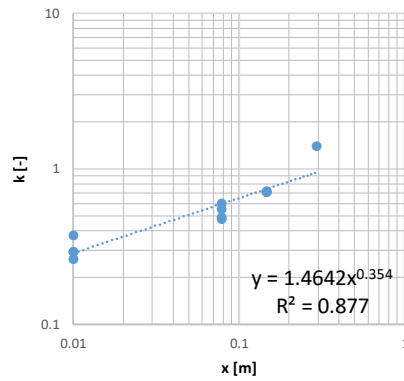
b) 60 minutes



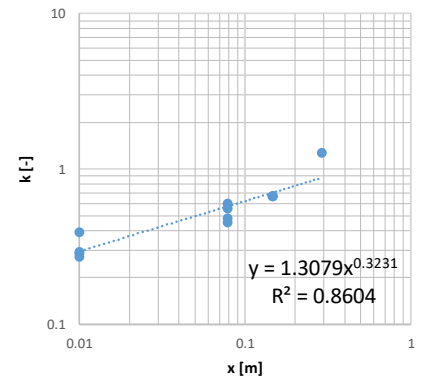
c) 90 minutes



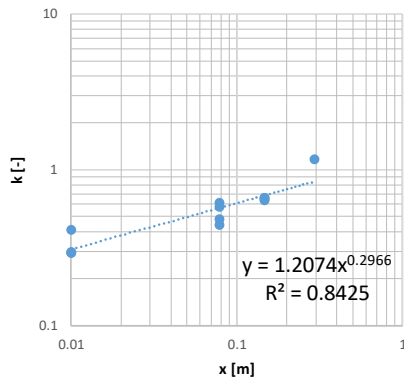
d) 120 minutes



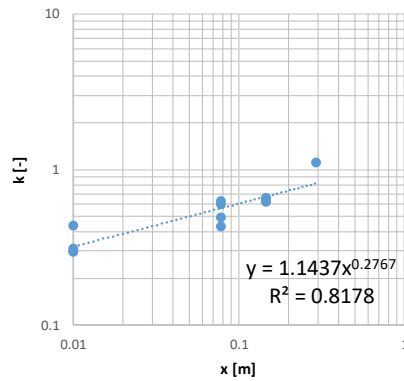
e) 150 minutes



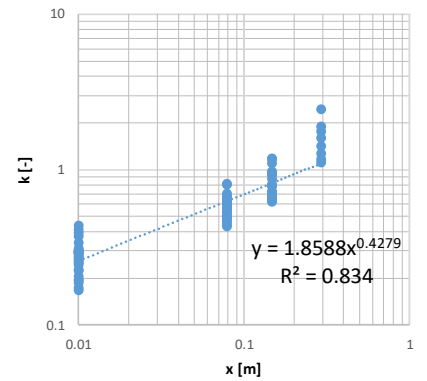
f) 180 minutes



g) 210 minutes



h) 240 minutes



i) all

Fig. 5 Relationship between k and x

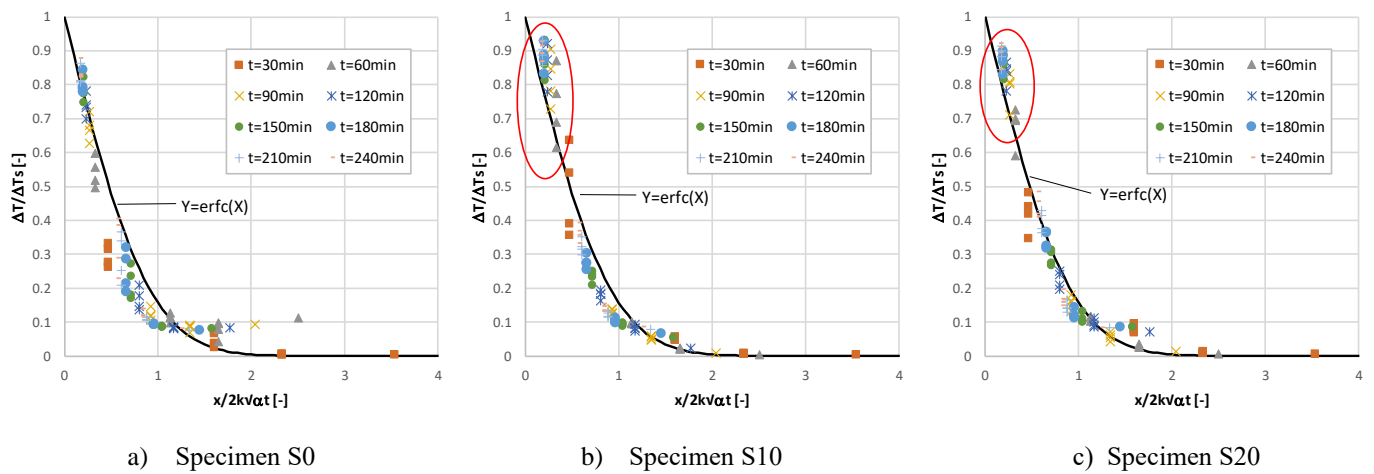


Fig. 6 Nondimensional temperature profile of inner concrete.

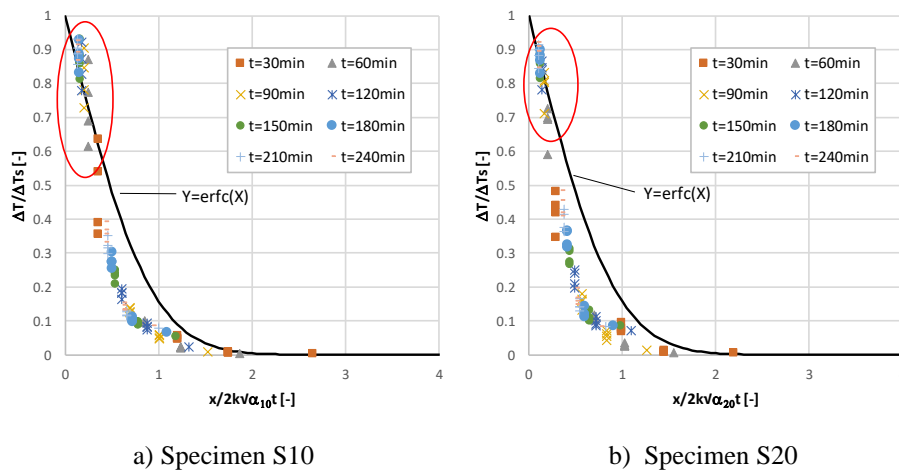


Fig. 7 Modified nondimensional temperature profile of inner concrete.

Table 1. weight average thermal diffusivity of specimen

Specimen	A_c [mm ²] Section area of concrete	A_s [mm ²] Section area of shear stud	α Thermal diffusivity
S0	268,048	0	$\alpha_0 = 0.78 \times 10^{-6} (= \alpha_c)$
S10	260,588	7,460	$\alpha_{10} = 1.40 \times 10^{-6}$
S20	253,128	14,920	$\alpha_{20} = 2.02 \times 10^{-6}$

* concrete: $\alpha_c = 0.78 \times 10^{-6}$ [m²/s], shear studs (steel): $\alpha_s = 23.08 \times 10^{-6}$ [m²/s]

4 VALIDATION

Equation (3) ($k = 1.8x^{2/5}$) was validated by comparison with the other experimental results as shown in Table 2. Fig. 8 and 9 show the experimental results for the temperature profile of the inner concrete in the unprotected steel tube with a diameter of 406.4 mm and the results for the temperature profile of inner concrete in the protected steel tube every 10 min, respectively. The figures show that when the experimental coefficient was employed, Equation (3) could predict the temperature profile regardless of the steel tube diameter and the fire protection.

Table 2. Specimen and Experimental condition for validation

	specimen	Steel tube	Concrete	Fire protection	Heating duration [min]
Fig.8 [4]	LF0.2	$\phi 406.4 \times t9$ mm	Steel fibre reinforced concrete	-	176
	LF0.3				91
	L0.2		Normal weight concrete		176
Fig.9 [5]	PCFT (in Table A1)	$\phi 457.2 \times t16$ mm	Normal weight concrete	Ceramic FP (1 H rated)	173

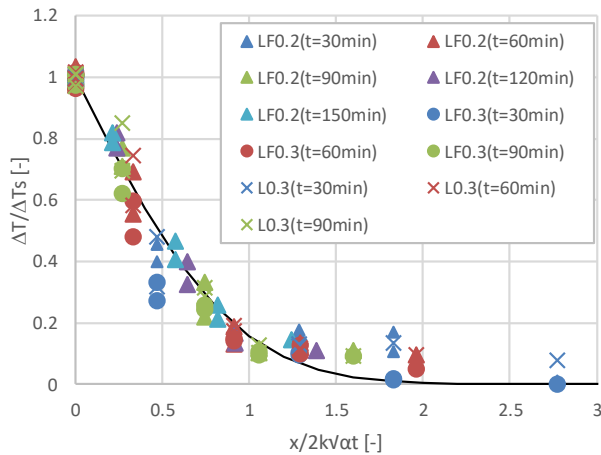


Fig. 8 Unprotected CFST column [4].

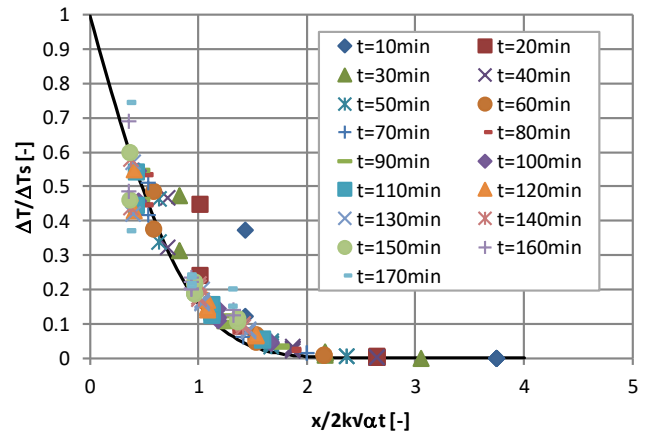


Fig. 9 Protected CFST column [5].

5 CONCLUSIONS

A hand calculation method was proposed for predicting the temperature profile of the inner concrete of CFST columns based on the thermal conduction theory of semi-infinite solids. The equation was corrected by using the results of heating tests conducted on unprotected CFST columns without shear studs. The equation was validated through comparison with other experimental results of previous studies on protected and unprotected CFST columns. The equation could accurately predict the temperature profile when the diameter is in the range of 400–600 mm and the column is heated according to ISO standard fire. The temperature profile of protected CFST columns were also predicted well. This indicates the equation might be applied to the column exposed the other heating curve. Further studies are needed to expand the scope of the equation.

The effects of shears studs on the temperature profile in inner concrete were also studied. The concrete temperature near the steel tube with shear studs were higher than that without shear studs. This worsens the fire resistance performance of the CFST column, especially when the axial force is large. The proposed hand calculation method was revised for columns with shear studs by using weight average thermal diffusivity. The revised method could predict the temperature profile near the concrete surface, but it overestimated the profile when the distance from concrete surface was large.

ACKNOWLEDGMENT

The authors would like to thank N. Igarashi, N. Odajima, and K. Yamazaki for suggesting the topic of research pursued in this paper and for years of collaboration and advice. We would like to thank Editage (www.editage.com) for English language editing.

REFERENCES

1. EN1994-1-2, Design of Composite Steel and Concrete Structures. Part 1-2: General Rules – Structural Fire Design. CEN –European Committee for Standardization, 2005.
2. Ministry of Land, Infrastructure, Transport and Tourism et al., Explanation of the 2001 Fire Resistance Verification Method and the Explanation of the Calculation Examples, 2001 (in Japanese)
3. SFPE Handbook of Fire Protection Engineering, Vol.1, 5th edition.
4. Shintani Y. et al., Fire Resistance of Unprotected CFT Columns, Summaries of Technical Papers of Annual Meeting, Archit Inst Japan, 43–46, 2019. (in Japanese)
5. Kinoshita T. et.al., Analytical Study of Fire Resistance of Axially Loaded Concrete Filled Steel Tubular Columns, Summaries of Technical Papers of Annual Meeting, Archit Inst Japan, 339–340, 2018. (in Japanese)

APPENDIX

The four tests conducted are listed in Table 1. The specimens with fire protection were tested to investigate the effects of shear stud when the temperature of steel tube increased slowly, and the specimens without fire protection were tested to investigate the effects when the temperature of steel tube increased rapidly.

The column was 3,600 mm long; however, only 2,710 mm was exposed to fire inside the furnace. Further, 160 shear studs (20×8 rows) were welded at the top and the bottom of heating part of inner steel tube. The specimen with shear studs is shown in Figure A1.

The temperatures of the steel tube, inner concrete, shear studs, and axial deformation were measured. The concentrically loaded and pin-supported specimens were exposed to ISO 834 standard fire until they met the ISO failure criteria.

Table A1. Specimen, experimental conditions, and experimental results

	Steel tube	Concrete	Shear stud	Fire protection	Applied axial load [kN]	Test FRR [min]
PCFT	$\bigcirc 457.2 \times t16 \text{ mm}$ $\sigma_y = 469 \text{ N/mm}^2$	$\sigma_c =$ 64 N/mm^2	-	Ceramic FP (1 H rated)	9,939 ($=1/3 \sigma_c A_c$ $+2/3 \sigma_y A_s$)	173
PCFT+S			$\phi 13 \times$ L40mm			140
UCFT	$\bigcirc 457.2 \times t9.5 \text{ mm}$ $\sigma_y = 437 \text{ N/mm}^2$	$\sigma_c =$ 70 N/mm^2	-	-	5,281 ($=0.5 \sigma_c A_c$)	40
UCFT+S			$\phi 13 \times$ L40mm			36

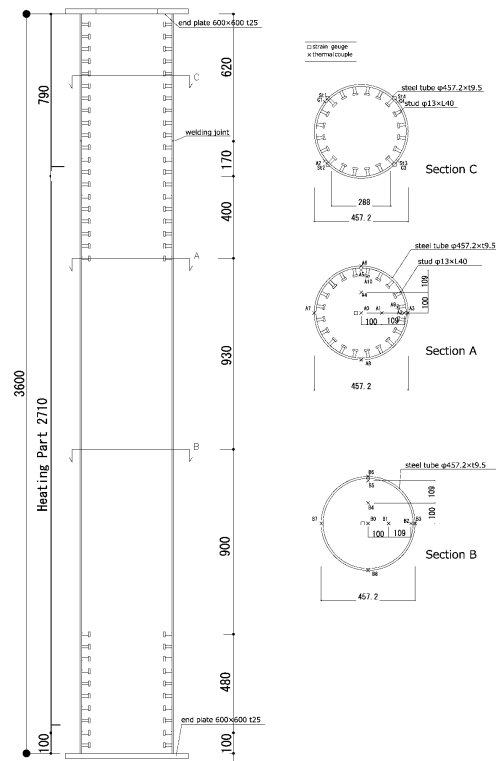


Figure A1. Specimen with shear studs (UCFT+S)

Figure A2 shows the histories of axial deformation, and Table 1 summarizes the corresponding data for the resulting fire resistance time (FRR), obtained according to ISO834. The trends of axial deformation of all specimens were similar to those in previous studies; the specimens expanded owing to initial heating, and then they started shrinking because of the reduction in the stiffness of the steel tube and inner concrete. The FRR of the protected and unprotected specimens with shear studs were shorter than that of the specimen without shear studs.

The unprotected specimens reached their failure criteria when the inner concretes were crushed, as proved by the axially directed cracks observed when a part of the steel tube was removed after test. In contrast, the protected specimens reached their failure criteria when the local buckling of the steel tube occurred at the position of the cracks of the fire protection material. Therefore, the effects of the shear studs on the FRR of the protected specimen is not completely clear. However, the shear studs will cause early failure of the protected specimen because the axial deformation of the specimen with shear studs was larger than that of the specimen without shear studs.

Figure A3 shows the temperature profile in the inner concrete plotted against the distance from the concrete surface. The temperatures of the inner concrete with shear studs were higher than that of the concrete without shear studs, especially near the surface because the shear studs acted as a heat bridge to the inner concrete. Kikuta [A1] showed that the strength of a heated column decreased significantly below its plastic strength because of transient strain when the axial force was large and the difference in the temperature in the inner concrete was large. The shear studs cause a larger temperature difference. Therefore, the shear studs worsen the fire resistance performance, especially when the axial force was large.

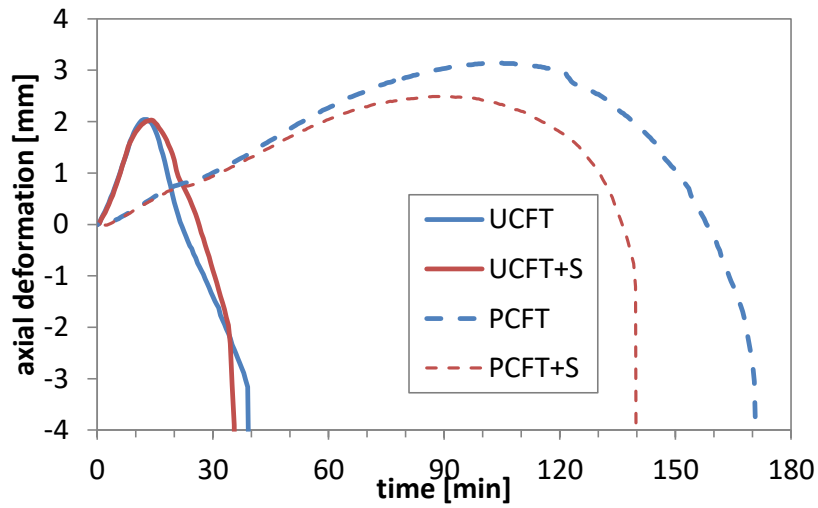


Figure A2. History of axial deformation

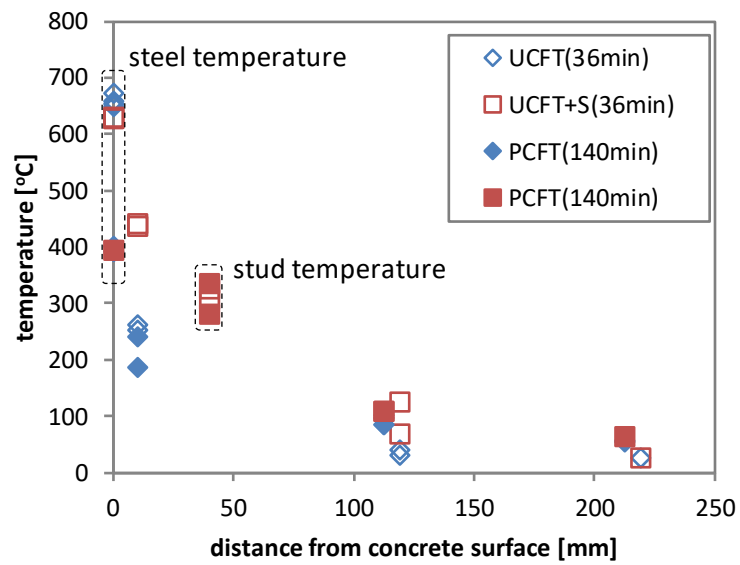


Figure A3. Temperature profile in inner concrete

Reference

- A1. Kikuta, S. and Suzuki, H., Study on Fire Resistance of Concrete Filled Tubular Columns - Influence of Transient Strain on Axial Compressive Strength, J Struc Construc Eng AIJ .76 (664), 1171–1180, 2011 (in Japanese)

SIMULATION OF PYROLYSIS AND COMBUSTION OF PINE WOOD USING TWO-STEP REACTION SCHEME

Dharmit Nakrani¹, Tejas Wani², Gaurav Srivastava³

ABSTRACT

This study developed a simulation framework employing a two-step decomposition model approach in Fire dynamic Simulator (FDS). The kinetic parameters for the two-step decomposition approach were determined through experimental thermogravimetry analysis (TGA). TGA in the temperature range of 298–1073K at four different heating rates of 5, 10, 15 and 20 K/min were performed. Two regions were detected from the iso-conversional plot of pine indicating with average activation energy E_a values of 171 kJ/mol and 251 kJ/mol in the conversion range of 1–25% and 25–85% respectively were obtained. The activation energy values were used to determine the material degradation mechanism using the Criados masterplots. The results showed that the pyrolysis process of pine wood can be described by three-dimensional diffusion reaction mechanism (Jander equation). Corresponding values of pre-exponential factors were calculated using compensation effect with $\ln A$ values ranging from 12–23 s⁻¹.

The kinetic parameters determined from TGA were subsequently utilized to simulate the TGA experiments in FDS. The proposed simulation approach demonstrated better agreement of simulation and experimental data of TGA when compared to the traditional single-step approach. Single-step reaction scheme did not accurately reproduce the required attributes of the DTG curve i.e., onset of decomposition, peak location and peak magnitude when compared with two-step reaction scheme. In order to further validate the proposed model, a cone calorimeter simulation model was developed wherein kinetic parameters obtained through single-step and two-step decomposition were simultaneously studied with corresponding experimental data for three different irradiation levels. It was observed that single-step reaction scheme predicts early time to ignition and underestimates the second peak HRR than two-step reaction scheme. The proposed simulation approach results in better predictions and is expected to lead to improved simulation-based research in the area of fire engineering.

Keywords: pinewood; pyrolysis; combustion; Fire dynamics simulation; two-step kinetics

¹ PhD Scholar, Indian Institute of Technology Gandhinagar,
e-mail: nakrani.dharmit@iitgn.ac.in, ORCID: <https://orcid.org/0000-0002-4125-6833>

² Sabarmati Bridge Fellow, Indian Institute of Technology Gandhinagar
e-mail: wani.tejas@iitgn.ac.in, ORCID: <https://orcid.org/0000-0002-7666-0238>

³ Associate Professor, Indian Institute of Technology Gandhinagar
e-mail: gauravs@iitgn.ac.in, ORCID: <https://orcid.org/0000-0002-4946-694X>

1 INTRODUCTION

Timber is one of the structural materials currently used in the construction of large structures, along with steel and reinforced concrete. Modern timber engineering has been largely based around use of hardwood (maple, oak, teak, etc.) and softwood (yellow pine, douglas fir, cedar, etc.) species [1][2]. Since timber is combustible in nature, research groups have identified the key research needs to be addressed for the next generation of large timber buildings [3][4]. They address the performance of system behaviour at all levels including bench scale material behaviour and full-scale behaviour under real fire scenarios. As with all structural materials, any advanced modelling of the fire resistance of timber structures must include both thermal modelling (pyrolysis and combustion models) and structural modelling, integrated as far as possible. For example, combustion properties obtained through the cone-calorimeter provides data which are used to (1) determine the characteristic parameters such as peak HRR or total heat evolved (2) develop pyrolysis and burning models (3) derive the material parameters needed as input to mathematical models for full-scale room/corner assessment and (4) compare the fire response of materials to assess their fire performance. [5][6].

One of the charring softwood materials used in timber construction is pine wood [2]. Use of pinewood has been central to fire research as most standardized experiments utilize cribs and fire loads of other forms made from pinewood. With the increasing use of high fidelity simulations in the area of fire engineering, robust and accurate pyrolysis and combustion models for pinewood are also needed. Consequently, the study of pyrolysis and combustion processes of pinewood has been a matter of active research in the past.

A single-step decomposition model [7] has been traditionally utilized in the past for modelling the pyrolysis of pinewood. Atreya [8] presented a comprehensive description of wood pyrolysis in the context of fire spread calculation, including a one-dimensional numerical model for pyrolysis. However, the actual reaction mechanism of wood pyrolysis is complex due to the formation of multiple intermediate products and hence, it is generally modelled on the basis of apparent kinetics [9]. Multi-step decomposition model to effectively characterize the pyrolysis kinetics for wooden polymeric samples has also been proposed [10]. However, all of the computer simulations (oftentimes in Fire Dynamic Simulator (FDS)) of pinewood decomposition have been limited to using single-step kinetics only.

The aim of this study was to develop a simulation framework for Pine wood employing a two-step decomposition reaction scheme approach in FDS. The kinetic parameters were determined through analytical methods (direct/isoconversional) from thermogravimetric experiments for both single-step and two-step decomposition approaches. The model validity was investigated by developing a cone calorimeter simulation model wherein kinetic parameters obtained through single-step and two-step decomposition reaction schemes were simultaneously studied with corresponding experimental data for different irradiation levels.

2 MATERIAL AND METHODS

2.1 Material

The experiments were conducted using the samples of pine wood. The dry density of samples was $535 \pm 20 \text{ kg/m}^3$. The moisture content of the material was about $8 \pm 1 \%$ when samples were conditioned at 28°C and 50% relative humidity.

2.2 Methods

2.2.1 Experimental Program

Thermo-gravimetric analysis (TGA) of the pine samples was carried out using NETZSCH STA 449 F3 Jupiter equipment in Nitrogen (N_2) atmosphere with a flow rate of 60ml/min (40ml/min as purge and 20

ml/min as protective gas) at four heating rates 5, 10, 15 and 20 K/min from room temperature to 800°C. The initial sample mass was about 10 ± 5 mg and it was tested in powder form (sample crushed with hammer into small fragments). Constant N₂ flow rate and initial sample mass were maintained for all the experiments. The samples were dried before the experiment but they absorbed 2-3% moisture from air before the experiments started.

Cone-calorimeter experiments were carried out in air at 30, 50 and 75 kW/m² irradiation levels (two runs at each flux level) to determine the burning characteristics of pine wood using Fire Testing Technology (FTT) iCone Calorimeter mini model (compliant to ISO 5660-1). Sample size was 10cm × 10cm × 1cm for all the experiments. Samples were dried in an oven at 105°C and were then tested after being wrapped in aluminium foil and insulated from the bottom by mineral wool.

2.2.2 Reaction Schemes

Two different reaction schemes were considered for modelling of pyrolysis and combustion of pinewood (Figure 1). The simplest possible approach is a single-step reaction that converts virgin wood to char and flammable gas. It allows the calculation of pre-exponential factor and activation energy analytically, assuming first order reaction. In the second scheme, the reacting wood is constructed from the two main components that decompose independently. Since the cellulose and hemicellulose components together form about 75% of the pine wood material [11] [12], it is considered to model the independent decomposition of these two components to determine the pyrolysis kinetics and combustion parameters of pinewood more effectively than single-step reaction scheme [13]. The two-step reaction scheme also used first-order reactions for independent decomposition of components and determined the kinetic parameters analytically from TGA data by various iso-conversional methods. A similar approach was recently used by Li.et.al. [14] and Ding et.al. [15] to predict the pyrolysis kinetics of Medium density fibreboard and beech respectively.

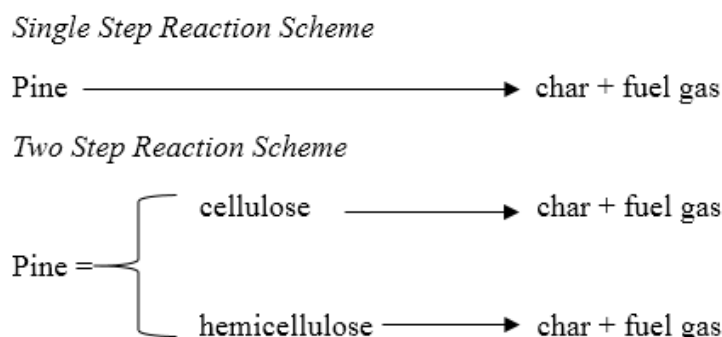


Figure 1. Reaction Schemes considered for thermal decomposition of pine wood

2.2.3 Kinetic parameters estimation and model selection

Iso-conversional methods are most reliable tools to calculate the kinetic parameters like activation energy. Isoconversional methods calculate E_a at progressive degrees of conversion without modelistic assumptions. In the current study, after considering different differential and integral methods, the Kissinger-Akahira-Sunose (KAS) integral method [16][17] was used to calculate the activation energy through the following expression

$$\ln\left(\frac{\beta}{T^2}\right) = -\frac{E_a}{RT} + \ln\left[\frac{AR}{Eg(\alpha)}\right], \quad (1)$$

where β is the heating rate (dT/dt), R is the universal gas constant, A is the pre-exponential factor, α is the degree of conversion and $g(\alpha)$ is the reaction model. At different degrees of conversion, the graph of $\ln(\beta/T^2)$ versus $(1/T)$ can be utilized to calculate the activation energy.

The kinetic model of the process was determined by the Criado Masterplots [18]. The following equation is obtained using reaction rate expression and Coats –Redfern equation [19].

$$\frac{Z(\alpha)}{Z(0.5)} = \frac{f(\alpha)g(\alpha)}{f(0.5)g(0.5)} = \left(\frac{T_\alpha}{T_{0.5}} \right)^2 \frac{(d\alpha / dt)_\alpha}{(d\alpha / dt)_{0.5}} \quad (2)$$

where 0.5 refers to the conversion in $\alpha = 0.5$ and $f(\alpha)$ and $g(\alpha)$ are the differential and integral functions for some of the common mechanisms operating in solid state reactions. The purpose of dividing by 50% condition is to normalize $Z(\alpha)$ function.

Table 1. Expressions for $f(\alpha)$ and $g(\alpha)$ functions for some of the common mechanisms operating in solid state reactions

Reaction Model	Model Code	$f(\alpha)$	$g(\alpha)$
Contracting Sphere	R2	$2(1 - \alpha)^{1/2}$	$[1 - (1 - \alpha)^{1/2}]$
Contracting Cylinder	R3	$3(1 - \alpha)^{2/3}$	$[1 - (1 - \alpha)^{1/3}]$
One-dimensional diffusion	D1	$1 / 2\alpha$	α^2
Two-dimensional diffusion	D2	$[-\ln(1 - \alpha)]^{-1}$	$[(1 - \alpha)\ln(1 - \alpha)] + \alpha$
Three-dimensional diffusion, Jander equation	D3	$3(1 - \alpha)^{2/3} / [2(1 - (1 - \alpha)^{1/3})]$	$[1 - (1 - \alpha)^{1/3}]^2$
Ginstling-Brounshtein	D4	$3 / 2((1 - \alpha)^{-1/3} - 1)$	$1 - (2\alpha / 3) - (1 - \alpha)^{2/3}$
First-order	F1	$(1 - \alpha)$	$-\ln(1 - \alpha)$
Second-order	F2	$(1 - \alpha)^2$	$(1 - \alpha)^{-1} - 1$
Third-order	F3	$(1 - \alpha)^3$	$[(1 - \alpha)^{-2} - 1] / 2$

The left side of Eqn. (2) associates with a reduced theoretical curve, which is a characteristic of each reaction mechanism, whereas the right side of the equation is associated with the reduced rate which can be obtained from experimental data. The Criado method compares experimental TGA results with established frequently used reaction models as mentioned in Table 1. For multi-heating rate data, Criado plots were obtained for all the heating rates and the most suitable model was selected by comparing the linearity coefficient (R^2) between theoretical and experimental plots.

Finally, Constable plots [20], also known as compensation method, was used to determine the pre-exponential factor (A). For a particular degree of conversion, logarithmic form of the rate equation can be written as,

$$\ln(Af(\alpha)) = \frac{E_a}{RT} + \ln\left(\frac{d\alpha}{dt}\right) \quad (3)$$

Generalized form of Eqn. (3) can be written as

$$y = \ln(Af(\alpha)) - xE_a \quad (4)$$

where $x = 1/RT$ and $y = \ln(d\alpha/dt)$. At different degree of conversion α , the values of x and y can be calculated. Then the values of $\ln(Af(\alpha))$, can be determined from the intercept of a linear plot of y and x using iso-

conversion principle. From the known reaction model $f(\alpha)$ predicted by Criado masterplots, the values of a pre-exponential factor at various degree of conversion is possible to calculate from $\ln(Af(\alpha))$.

2.2.4 TGA Modelling using FDS

To confirm the efficacy of the kinetic parameters determined experimentally which serves as input parameters, numerical simulation of pyrolysis was carried out in FDS. In these simulations, FDS was tasked to simulate the solid phase only using the kinetic parameters obtained considering both single and two-step reaction approaches. For these simulations, the sample was modelled as an obstruction of 2m length, 1m width and 0.00001m thick placed horizontally at the bottom of a two-dimensional domain of size 4m x 1m and the sample was heated by radiation only.

2.2.5 Cone Calorimeter Modelling using FDS

For the cone calorimeter simulations, the burning of an appropriate sized sample is simulated with a specified heat flux irradiances of 30, 50 and 75 kW/m² to represent the effect of the cone heater. The fuel-pan was modelled as an obstruction with dimensions same as the actual size. The top face of the obstruction was used to simulate the fuel surface and the other faces were modelled as steel sheet. In all cases the back of the sample was considered to be insulated as they were encased during the experiments with only the sample face exposed. For these simulations, the sample was modelled as an obstruction of 100mm × 100mm × 10mm for pine wood placed horizontally at lower end with overall domain size of 200mm × 200mm × 1000mm being open from all sides.

To model the coupled pyrolysis and combustion process, various input parameters are required for the FDS. These include combustion parameters (from the cone calorimeter), thermo-physical properties and derived pyrolysis parameters (from TGA and DSC discussed in 3.1). Some of these parameters were measured experimentally and others were taken from the literature and are given in Table 2. Moreover, in single step reaction scheme, it is taken 89% pine and 11% char as residue, whereas in two-step reaction scheme, pine wood is assumed to be composed of 26.7% hemicellulose content and 62.3% cellulose content [12] and 11% char is produced as residue.

Table 2. Combustion and thermo-physical properties for both reaction schemes used in cone-calorimeter simulations of pine-wood

Property/Parameter	Value
<i>Combustion Parameters</i>	
Heat of Combustion (kJ/kg)	12210
Soot Yield (kg/kg)	0.006
CO Yield (kg/kg)	0.017
CO ₂ Yield (kg/kg)	1.140
<i>Thermo-physical parameters</i>	
Density (kg/m ³)	550
Thermal Conductivity* (k) (W/m-K)	T = 20°C, k = 0.168; T = 225°C, k = 0.2; T = 600°C, k = 0.3
Specific heat* (c) (kJ/kg-K)	T = 20°C, c = 1.1; T = 60°C, c = 1.23; T = 225°C, c = 1.7; T = 600°C, c = 2.0

* Values are taken from [21]

3 RESULTS AND DISCUSSION

3.1 Evaluation of Reaction Scheme using TG data

The TG and DTG curves of pine wood in inert atmosphere of nitrogen at different heating rates are shown in Figure 2 (a) and (b) respectively. TG curves shows that three zones can be identified for the pyrolysis process of pine wood. In the first zone, with a temperature range from ambient to 150°C, a slight weight loss of 9.52% can be seen. This weight loss is due to moisture loss and some light volatile compounds. The second stage is the one where major decomposition occurs and corresponds to the temperature range of 150°C to 400°C. The deconvolution of DTG curve shows two visible peaks in this zone with peak maxima temperatures of 328°C and 362.1°C which can be related to hemicellulose and cellulose decomposition, respectively [22]. The merged peaks of hemicellulose and cellulose form a broader peak for the second zone. The third zone, also referred as passive pyrolysis zone, corresponds to the temperature range of 400 - 800°C and involves lignin decomposition as the most prominent reaction in this region. Lignin decomposes slowly over a wide temperature range (in both second and third zone) and is responsible for long tailing of the DTG curve [23].

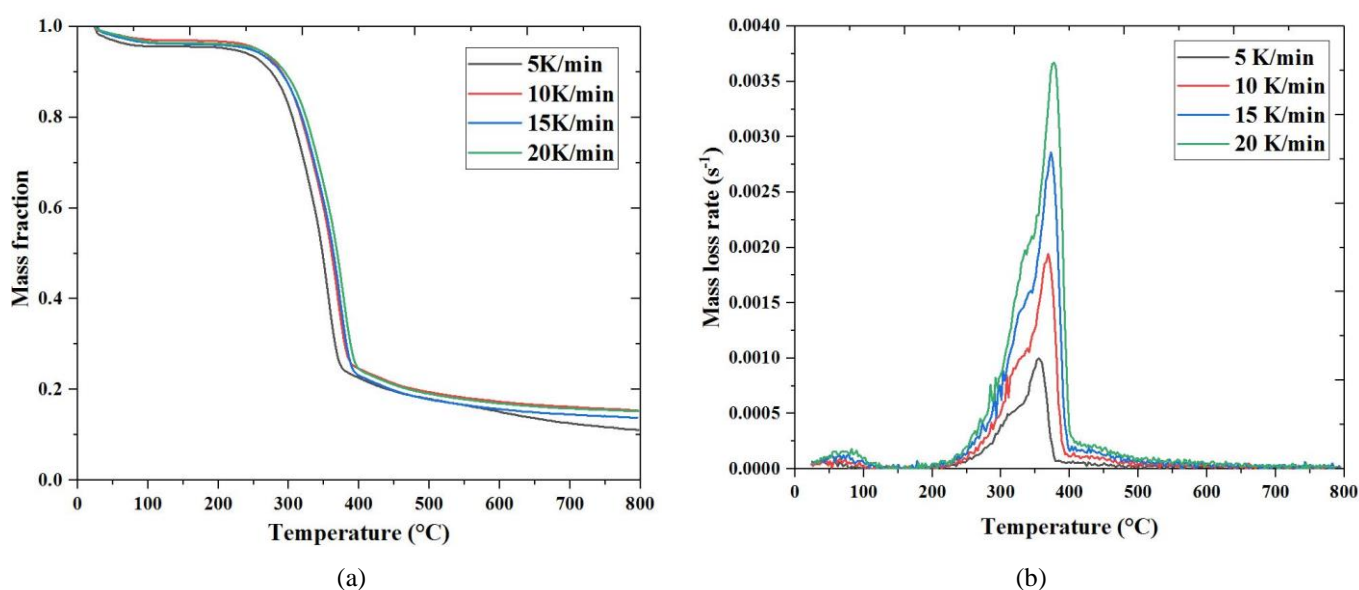


Figure 2. (a) TG curves and (b) DTG curves of pine at different heating rates

The thermograms recorded at different heating rates were used to calculate activation energy. The conversion range up to 80% was taken as the kinetic analysis range to obtain the isoconversion plot of activation energy E_a with conversion α . As can be seen from Figure 3, the activation energy varies with conversion but the variation is relatively modest. The variation of activation energy with conversion indicates occurrence of a complex multistep mechanism for pine-wood pyrolysis. Two regions were detected from the isoconversional plot of pine wood with average activation energy E_a values of 207 kJ/mol and 240 kJ/mol in the conversion range of 1–25% and 25–85%, respectively. The activation energy values were used to determine the material degradation mechanism using the Criados masterplots. The results showed that pyrolysis process of pine wood can be described by three-dimensional diffusion reaction mechanism (Jander equation) ($R^2=0.9816$) which was found to be in concurrence with Bojan and Marija [24]. Corresponding values of the pre-exponential factors were calculated using compensation effect with $\ln A$ values ranging from 12–23 s⁻¹.

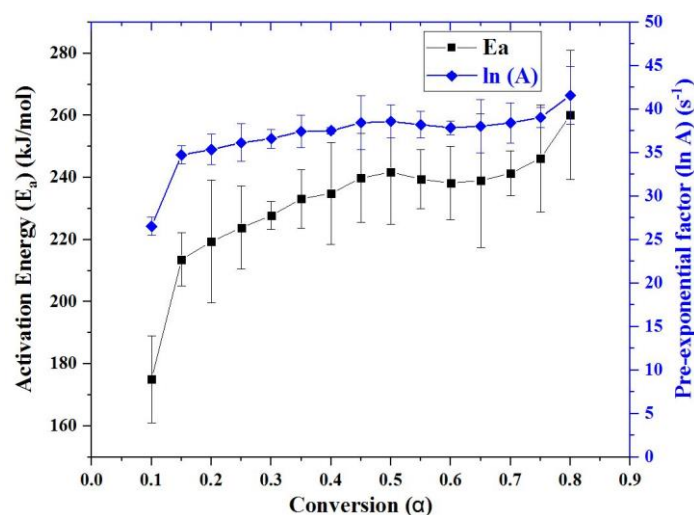


Figure 3. Activation energy and Pre-exponential factor for various degree of conversion

The kinetic parameters determined from TGA were subsequently utilized to simulate the TGA experiments in FDS. The proposed simulation approach demonstrated better agreement of simulation and experimental data of TGA when compared to the traditional single-step approach (see Figure 4). It can be seen from Figure 4, the peak temperatures were correctly reproduced but the initiation around 250°C was not captured by the single step reaction scheme, as the overall reaction ranges were shifted towards high temperatures. Also, the model seemed to exaggerate the influence of the heating rate on the reaction temperatures. In the two-step reaction scheme, the model reproduced two important aspects of the experimental MLR curve: (1) the shoulder of the reaction, i.e., the initiation of pyrolysis and (2) the location and magnitude of the cellulose degradation peaks (in the range of 300-350°C).

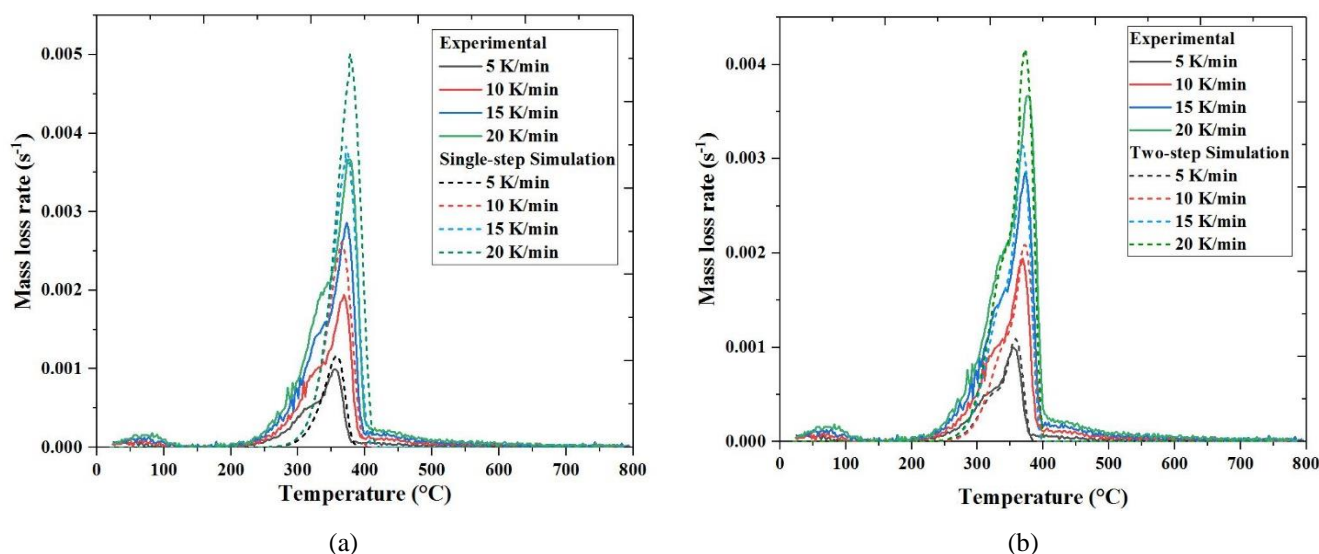


Figure 4. DTG results for experiments (solid lines) and simulations (dashed lines) with (a) single-step and (b) two-step reaction scheme

3.2 Evaluation of Reaction Scheme using Cone Calorimeter data

In order to further validate the proposed model, a cone calorimeter simulation model was developed wherein the kinetic parameters obtained through single-step and two-step decomposition were simultaneously studied with corresponding experimental data for different irradiation levels of 30, 50 and 75 kW/m². The key combustion parameters as obtained from the experiments and as predicted by the

simulations are summarized in Table 3. The variation of HRR at different irradiation levels is shown in Figure 5.

It can be seen from Figure 5 and Table 3 that both the models reproduced the main characteristics of the HRR curve, including the ignition and burn-out times, the burning rate reduction due to formation of insulating char layer, and the second peak at the end. However, it needs to be pointed out that the single-step reaction model predicts early time to ignition as compared to two step reaction at all irradiance flux levels. Also, it can be observed that the single-step reaction model underestimated the second peak HRR compared to the two-step reaction model. During the final stages of burning, the differences between the two models were found to be greater.

Table 3. Characteristics of HRR and MLR curves observed from experiments and both reaction models at different heat flux levels

Irradiance heat-flux (kW/m²)	Experimental/ Reaction step	Time to ignition (s)	1st Peak HRR (kW/m²)	2nd Peak HRR (kW/m²)	1st peak MLR (g/s)	2nd peak MLR (g/s)
30	Experimental	58	205.96	207.09	0.1876	0.1654
	Single-step	48	185.87	152.59	0.1533	0.123
	Two-step	55	172.72	210.84	0.1402	0.167
50	Experimental	21	265.83	285.63	0.2035	0.2116
	Single-step	11	278.76	162.38	0.246	0.1425
	Two-step	22	264.09	300.52	0.2109	0.249
75	Experimental	7	386.08	344.31	0.3059	0.2548
	Single-step	3	427.30	185.12	0.378	0.163
	Two-step	11	402.98	360.34	0.3143	0.2876

At 30 kW/m² heat flux, both models predicted lower first peak HRR compared to the experimental results. At 50 and 75 kW/m² heat flux levels, the two-step reaction scheme predicted the first peak HRR better as compared to the single-step reaction model which over-predicted the first peak HRR. Overall, the two-step reaction model produced better results as compared to the single-step model. The experimental tail of the HRR curves represents the glowing oxidation of the char layer. As the oxidation reactions were not included in the reaction schemes, both the models failed to reproduce it. The oxidation is also believed to contribute to the height of the second peak.

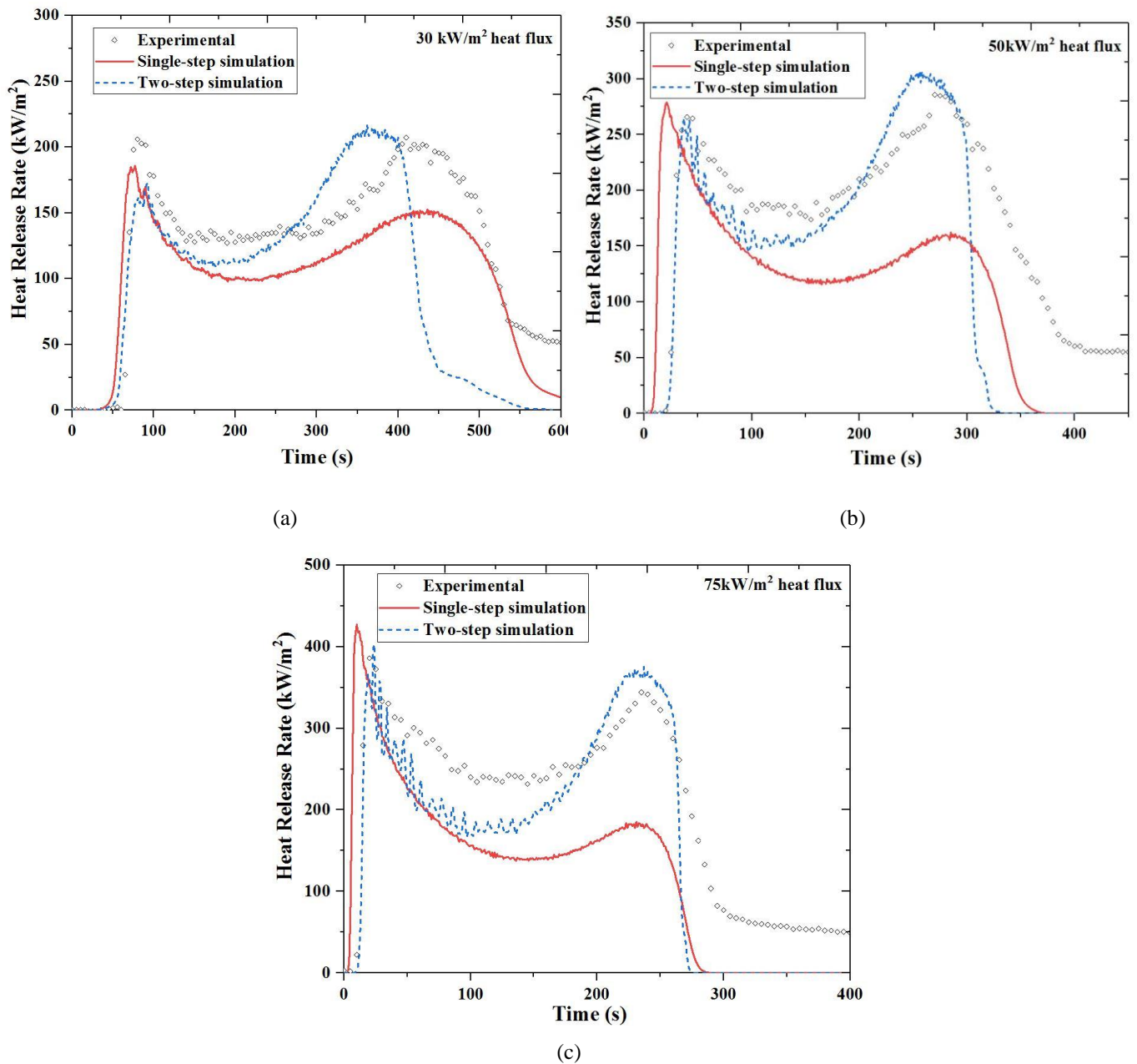


Figure 5. Experimental and simulated HRR using both reaction models at (a) 30kW/m² (b) 50kW/m² and (c) 75kW/m² irradiance flux levels.

4 CONCLUSIONS

The current work developed a simulation approach for combustion of pine wood considering a two-step reaction scheme. Extensive TGA of pine wood samples was carried out at different heating rates and the reaction kinetic parameters were determined using the KAS integral method for both single and two-step mechanisms. A number of cone calorimeter experiments at different irradiation levels were also carried out for the validation of the proposed simulation approach.

Computer simulations of the TGA and the cone calorimeter experiments were carried out in FDS with both, the commonly used single-step reaction scheme as well as the proposed two-step reaction mechanism. In both the cases, it was observed that the two-step reaction scheme demonstrated better behaviour compared to that of the single-step scheme, primarily due to its ability to consider the decomposition of cellulose and hemicellulose individually. Both the models, however could not capture the oxidation of the char layer,

observed towards the end of the cone calorimetry experiments, due to non-inclusion of the oxidation reaction in either of the models. This aspect can be included in the model to further enhance the accuracy.

ACKNOWLEDGEMENTS

The authors would like to thank Centre for Safety Engineering at IIT Gandhinagar for providing support to perform the experiments. The authors also acknowledge the generous support from IIT Gandhinagar through Sabarmati Bridge Fellowship to one of the authors.

5 REFERENCES

1. M. H. Ramage *et al.*, “The wood from the trees: The use of timber in construction,” *Renew. Sustain. Energy Rev.*, vol. 68, no. October 2015, pp. 333–359, 2017.
2. A. I. Bartlett, R. M. Hadden, and L. A. Bisby, “A Review of Factors Affecting the Burning Behaviour of Wood for Application to Tall Timber Construction,” *Fire Technol.*, vol. 55, no. 1, 2019.
3. A. Buchanan, B. Ostman, and A. Frangi, “Fire resistance of solid timber structures,” 2014.
4. R. Gerard, D. Barber, and A. Wolski, “Fire Safety Challenges of Tall Wood Buildings - Phase 1: Final Report,” 2013.
5. M. A. Dietenberger, O. Grexa, and R. H. White, “Reaction-to-Fire of Wood Products and Other Building Materials : Part II , Cone Calorimeter Tests and Fire Growth Models,” 2012.
6. B. Scharrel and T. R. Hull, “Development of fire-retarded materials—Interpretation of cone calorimeter data,” *Fire Mater.*, vol. 31, no. May 2007, pp. 327–354, 2007.
7. F. Shahfzadeh and P. P. S. Chin, “Thermal Deterioration of Wood,” *ACS Symp. Ser. 43, Am. Chem. Soc.*, pp. 57–81, 1977.
8. A. Atreya, “Fire Growth on Horizontal Surfaces of Wood,” Ph.D. Thesis, Harvard University, 1983.
9. C. Di Blasi, “Modeling chemical and physical processes of wood and biomass pyrolysis,” *Prog. Energy Combust. Sci.*, vol. 34, no. 1, pp. 47–90, 2008.
10. A. C. Y. Yuen *et al.*, “Establishing pyrolysis kinetics for the modelling of the flammability and burning characteristics of solid combustible materials,” *J. Fire Sci.*, vol. 36, no. 6, pp. 494–517, 2018.
11. C. Di Blasi, “Physico-chemical processes occurring inside a degrading two-dimensional anisotropic porous medium,” *Int. J. Heat Mass Transf.*, vol. 41, no. 24, pp. 4139–4150, 1998.
12. J. Yu, N. Paterson, J. Blamey, and M. Millan, “Cellulose, xylan and lignin interactions during pyrolysis of lignocellulosic biomass,” *Fuel*, vol. 191, pp. 140–149, 2017.
13. E. Moukhina, “Determination of kinetic mechanisms for reactions measured with thermoanalytical instruments,” *J. Therm. Anal. Calorim.*, vol. 109, no. 3, pp. 1203–1214, 2012.
14. K. Y. Li, X. Huang, C. Fleischmann, G. Rein, and J. Ji, “Pyrolysis of medium-density fiberboard: Optimized search for kinetics scheme and parameters via a genetic algorithm driven by Kissinger’s method,” *Energy and Fuels*, vol. 28, no. 9, pp. 6130–6139, 2014.
15. Y. Ding, C. Wang, M. Chaos, R. Chen, and S. Lu, “Estimation of beech pyrolysis kinetic parameters by Shuffled Complex Evolution,” *Bioresour. Technol.*, vol. 200, pp. 658–665, 2016.
16. H. E. Kissinger, “Reaction Kinetics in Differential Thermal Analysis,” *Anal. Chem.*, vol. 29, no. 11, pp. 1702–1706, 1957.
17. T. Akahira and T. Sunose, “Trans joint convention of Four Electrical Institutes,” *Chiba Inst. Technol. Sci Technol*, vol. 16, pp. 22–31, 1971.
18. J. M. Criado, “Kinetic analysis of DTG data from master curves,” *Thermochim. Acta*, vol. 24, no. 1, pp. 186–189, 1978.
19. A. W. Coats and J. P. Redfern, “Kinetic parameters from thermogravimetric data [12],” *Nature*, vol. 201, no. 4914, pp. 68–69, 1964.
20. F. H. Constable, “Mechanism o f Catalytic Decomposition. 355,” *Proc. R. Soc. London*, vol. 108, pp. 355–378, 1925.

21. A. S. A. Bakar and A, "Characterization of Fire Properties for Coupled Pyrolysis and Combustion Simulation and Their Optimised Use," Ph. D. Thesis Victoria University, 2015.
22. G. Mishra, J. Kumar, and T. Bhaskar, "Kinetic studies on the pyrolysis of pinewood," *Bioresour. Technol.*, vol. 182, pp. 282–288, 2015.
23. S. Hostikka and A. Matala, "Pyrolysis model for predicting the heat release rate of birch wood," *Combust. Sci. Technol.*, vol. 189, no. 8, pp. 1373–1393, 2017.
24. B. Janković and M. M. Janković, "Pyrolysis of pine and beech wood under isothermal conditions: The conventional kinetic approach," *Res. Chem. Intermed.*, vol. 41, no. 4, pp. 2201–2219, 2015.

A SIMPLIFIED REPRESENTATION OF TRAVELLING FIRE DEVELOPMENT IN LARGE COMPARTMENT USING CFD ANALYSES

Marion Charlier¹, Olivier Vassart², Xu Dai³, Stephen Welch⁴, Johan Sjöström⁵, Johan Anderson⁶, Ali Nadjai⁷

ABSTRACT

Fires in open large-floor plan spaces do not always reach a post-flashover fire state and recently, the “travelling fire” terminology has been used to define fires burning locally and moving across entire floor plates over a period of time [1]. Several studies have been presented about the behavior of a structure when it is subjected to this fire scenario [2-5]. Due to their limited number, fire tests are not enough to cover all possible configurations encountered in practice, but this limitation can potentially be overcome with help of CFD. In the frame of the European RFCS TRAFIR project, a simplified representation of the fire load was developed to calibrate an FDS model representing large scale travelling fire tests. The numerical and experimental results have been compared in terms of gas and steel temperatures (the radiative intensities and gas temperatures calculated by FDS have been used by SAFIR® to calculate the temperatures in a steel column). The approach provides acceptable representations of fire spread and steel temperatures within reasonable computational demands.

Keywords: CFD; travelling fire; fire load; link CFD-FEM

1 INTRODUCTION

The development of knowledge concerning the appropriate representation of the fire load for large compartments in CFD is required to be able to further analyze the influence of compartment geometry on the development of a travelling fire, to perform numerical analyses of the temperature development and of resulting mechanical behavior of structures that considers comprehensively the travelling nature of the fire. The FireSERT (Ulster University) performed three natural fire tests involving steel structure within the context of the European RFCS TRAFIR project [6]. The aim of this experimental campaign was to perform uncontrolled tests based on a well-established fire load, to evaluate the influence of the ventilation conditions on the development of the fire, and to assess the impact on steel structural elements. A

¹ ArcelorMittal Global R&D (Luxembourg)

marion.charlier@arcelormittal.com, ORCID: <https://orcid.org/0000-0001-7690-1946>

² ArcelorMittal Stelience®, Esch/Alzette, Luxembourg

olivier.vassart@arcelormittal.com, ORCID: <https://orcid.org/0000-0001-5272-173X>

³ School of Engineering, BRE Centre for Fire Safety Engineering, The University of Edinburgh, Edinburgh, United Kingdom

x.dai@ed.ac.uk, ORCID: <https://orcid.org/0000-0002-9617-7681>

⁴ School of Engineering, BRE Centre for Fire Safety Engineering, The University of Edinburgh, Edinburgh, United Kingdom

s.welch@ed.ac.uk, ORCID: <https://orcid.org/0000-0002-9060-0223>

⁵ RISE Research Institutes of Sweden

johan.sjostrom@ri.se, ORCID: <https://orcid.org/0000-0001-8670-062X>

⁶ RISE Research Institutes of Sweden

johan.anderson@ri.se, ORCID: <https://orcid.org/0000-0001-7524-0314>

⁷ FireSERT, Ulster University, School Built Environment

a.nadjai@ulster.ac.uk, ORCID: <https://orcid.org/0000-0002-9769-7363>

parametrical study using FDS software was conducted to calibrate the three tests using a simplified representation of the fire load. Simplification was targeted, to afterwards reproduce a broader range of scenarios encompassing different fires and end-use situations, to generate an extended virtual experimental dataset, as well as to facilitate analyses of real building dimensions. A few previous attempts defining a simplified representation of a continuous fuel bed have been carried through [7,8], and this paper suggests that such approach can allow for both an acceptable representation of the travelling fire in terms of fire spread and steel temperatures and an acceptable computation time. On the other hand, there are therefore inevitable limitations inherent to the simplification made, and these are also discussed. This paper presents the setup of the CFD simulations and its corresponding assumptions, and the calibration of one of the three TRAFIR natural fire tests while focusing on gas temperatures measured at mid-width, along the length of the compartment (at several levels) and on steel temperatures measured on a central column. For the latter, two methods are presented: one based on the incremental formula from EN1993-1-2 (considering a constant temperature through the section for a given height) and other one linking CFD (FDS software) and FEM (SAFIR® software).

2 EXPERIMENTAL CAMPAIGN

2.1 Travelling fire in full scale experimental steel building

For the natural fire tests undertaken at Ulster University, the test compartment was designed to represent a part of an entire office layout, consisting of steel beams and columns for the main structural frame, while hollow-core precast slabs were used for the construction of ceiling. The layout of the structure (see Figure 1) and fire load were identical for the three tests. Only the openings were modified to assess the influence of the ventilation conditions on the development of the fire. This paper considers the test n°2, for which concrete walls were constructed along the shorter dimensions of the compartment. In addition, down-stands made of gypsum fire board panels were provided along the longer dimension of the compartment. A concrete block wall was also constructed along the longer dimensions of the compartment such that the distance between the top of the wall and the lower edge of the down-stands was 1 meter. Such configuration provided openings with a total area of 30 m². These openings were equally distributed along gridlines A and D with an area of 15 m² each. Photographs of the test n°2 compartment can be seen on Figure 2 (a) and (b).

2.2 Characterization of the fire load

Within the TRAFIR project, Franssen et al. performed a series of fire tests with uniformly distributed cellulosic fire loads [9], aiming at defining an arrangement representative of an office building according to Eurocode 1 [10]. This work led to devise a well-established methodology [11], used to define the fuel load arrangement for the three natural fire tests undertaken at Ulster University. For the latter, the wood species consisted of “*Picea abies*” with an average density of 470 kg/m³. To achieve a medium fire growth rate, 9 layers of wooden sticks with an axis distance of 120 mm (90 mm intervals) were provided in three different directions (alternation of 60°-120°-180°) as shown in Figure 2 (c), resulting in 511 MJ/m². The fuel wood was provided along the centre of the test compartment. The fire load was 14 m long stretching from wall to wall along the longer dimension of the test compartment (a gap of 0.5 m was kept between the short walls and the edge of the fire load). The width of the fuel bed was 4.2 m and was aligned with the centerline of the compartment. The wood sticks were provided on a platform constructed using concrete blocks and gypsum fireboards: the top surface of the platform was placed at 325 mm from the floor finish level. For the three tests, the ignition was punctual and located at mid-width of the fire load, 0.5 m from its edge (i.e. at a distance of 1 m from the back wall). The fire started to grow close to gridline 1 and then travelled from gridline 1 to gridline 4.

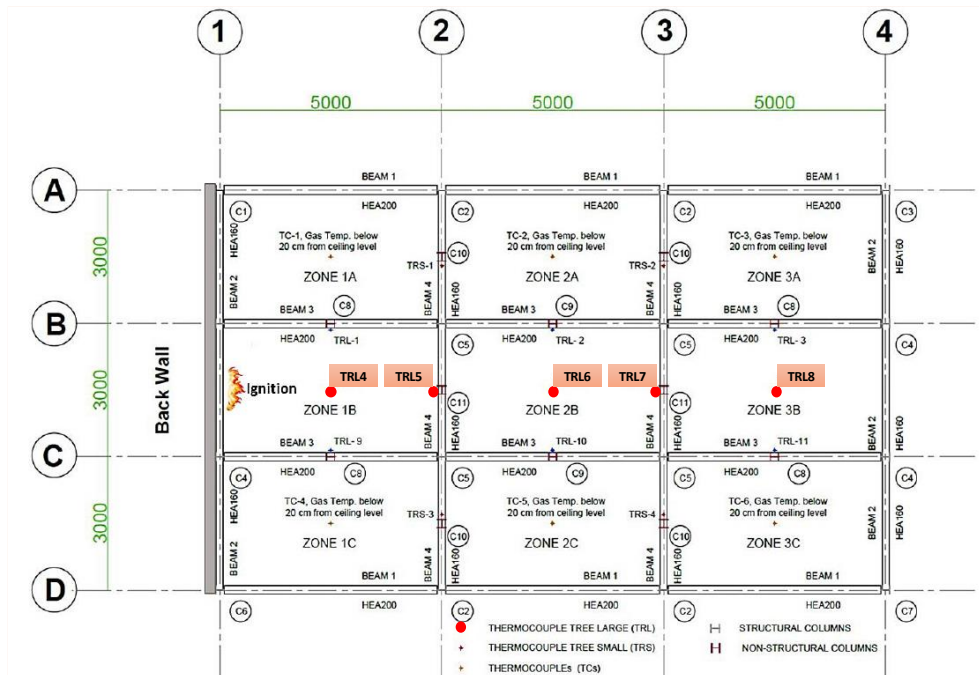


Figure 1. Layout plan of the test compartment and location of TRL4 to TRL8 (dimensions in mm)



Figure 2. Photographs of the experimental campaign carried out by Ulster University in the frame of TRAFIR project:
(a) compartment for test n°2 ; (b) fire at the beginning of test n°2 ; (c) continuous fire load made of wood sticks

3 THE SETUP OF CFD SIMULATIONS AND ITS CORRESPONDING ASSUMPTIONS

Several CFD simulations were launched with the FDS software [12] to calibrate the model for these natural fire tests, and the paper presents the comparison between numerical and experimental results in terms of gas and steel temperatures. These CFD simulations consider a simplified representation of the continuous fire load consisting of discrete volumes (cubes) based on a regular arrangement (no detailed representation of a wood crib involving alternation of sticks and air gaps was used). This approach is based on the work done by Horová [7] (a similar chessboard pattern was used to calibrate the Veselí fire test), Degler et al. [8] (a similar pattern was used to perform *a priori* numerical analysis of the Tisova fire test) and Charlier et al. [13] (a similar approach to perform numerical works in the frame of TRAFIR project to explore the conditions leading to the development of a travelling fire). Simplifications were targeted, as the modelling of the real wood stick size in CFD requires a very fine mesh and therefore a very significant computational time for real building geometries. The simulation detailed below, using 24 cores (6 MPI processes with 4 OpenMP threads per process), required 41.6 hours to complete.

3.1 Representation of the fire load

The cell size used in the FDS models depends highly on the situation that is modelled and on the purpose of the simulation. Several attempts are considered: having cell size equal to 0.16 m or 0.32 m and cube size equal to 0.16 m, 0.32 m or 0.64m. Concerning the cube size, Horová [7] advises to define cell size at least

two times smaller than the object size. Indeed, no proper fire spread was achieved for the simulations where the cell size equals the cube size. The calibrated model considers 0.16m cell size and 0.32 m cube size, which lead to an acceptable computation time. The overall heat release rate was used as input to VENTs, with each VENT representing a cube face (the lower face excluded). The wood constituting the cubes (*Picea abies*, the Norway spruce or European spruce) has the following chemical composition: $C_{1.0}H_{3.584}O_{1.55}$ with an assumed soot yield of 0.015 [g/g] (adopted from the SFPE Handbook [14]) and a heat of combustion of 1.684 MJ/kg (obtained from a bomb calorimeter test conducted by the University of Edinburgh). The modelled compartment and fire load are depicted on Figure 3.

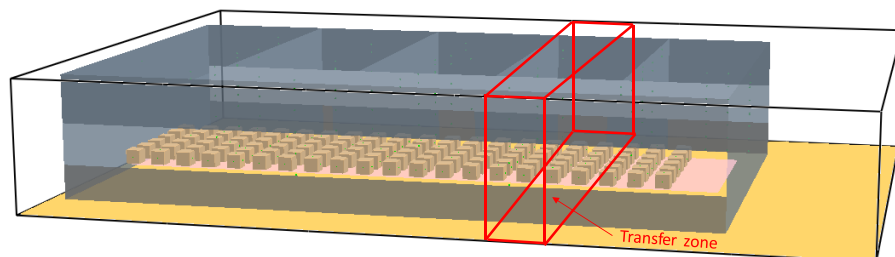


Figure 3. FDS model for the UU fire test n°2, with the transfer zone for SAFIR® highlighted

3.2 Fire spread and rate of heat released

The overall heat release rate per unit area is used as an input and the spread mechanism is determined using planar devices on each face of the cubes (except the lower one) to measure the temperatures on the solid surfaces. If the surface temperature reaches 250°C on at least one face of the cube, then all five surfaces are set to start burning following the prescribed heat release rate per unit area curve. This ignition temperature was chosen based upon cone calorimeter testing which found a critical heat flux for ignition of 13 kW/m². The RAMP function, function describing the evolution of heat release rate per unit area (HRRPUA) with time, presents a symmetric profile: a growing phase, a plateau, a peak, a plateau and finally a decay phase. For clarity sake, the HRRPUA parameter is redefined here via two parameters: HRRPUA_floor refers to the HRR per unit area of floor, while HRRPUA_assigned refers to the HRRPUA assigned on the cubes (i.e. per unit area of cube surface, side facing the floor excluded). The calibrated model has a plateau HRRPUA_floor equal to 250 kW/m² (corresponding to HRRPUA_assigned equal to 217 kW/m²) and a peak HRRPUA_floor equal to 500 kW/m² (corresponding to HRRPUA_assigned equal to 434 kW/m²). Indeed, the fire load consists in 21 columns and 6 rows of cubes (i.e. a total burning surface of 64,5 m²) placed on a floor area of 56 m². The surface below the RAMP function (and indirectly the duration of this function) can be evaluated from a given HRRPUA and a given fire load. A fire load of 511 MJ/m², representative of an office building according to Eurocode 1, was set up.

3.3 Boundaries and materials

The FDS domain's VENTs are all defined as OPEN, except the lower limit (representing the floor) which is set as INERT. The ceiling is made of 15 cm of concrete. The short wall along gridline 1 is made as a succession of 3 layers: concrete (8 cm), insulation type 1 (10 cm), concrete (15 cm). The insulation type 2 material is used to represent the down-stands (1,5 cm thickness) and the platform (3 cm thickness) on which the fire load lies. The concrete block walls along the longer dimensions are made of 15 cm of manufactured concrete blocks. Finally, the other short wall (along gridline 4) is defined with two layers: 1.5 cm of insulation type 2 and 15 cm of manufactured concrete blocks. As in the test, the platform on which the fire load lies is elevated from the floor. Table 1 summarizes the thermal properties defined for the different materials.

Table 1. Thermal properties of the different materials defined in the CFD model

	Conductivity [W/m/K]	Specific heat [kJ/kg/K]	Density [kg/m ³]	Emissivity [-]
Concrete	1.6	1.0	2400	0.8
Insulation type 1	0.09	0.66	45	0.9
Insulation type 2	0.24	1.25	900	0.89
Manufactured concrete blocks	0.92	1.05	1973	0.8

4 CALIBRATION OF THE CFD MODEL – GAS TEMPERATURES

Gas temperatures in the test compartment were recorded at different locations and levels using thermocouples. This section focuses on thermocouple trees TRL4 to TRL8, placed within the central zones along the length of the compartment, between gridlines B and C, as depicted on Figure 1. The first thermocouple tree (TRL4) is positioned at 2.5m from the back wall (gridline 1), i.e. at 1.5 m from the source of ignition. These thermocouple trees are equidistant, with 2.5m between each of them. Each tree was equipped with thermocouples provided at six different levels: at 0.5 m (Level 1), at 1 m (Level 2), at 1.5 m (Level 3), at 2 m (Level 4), at 2.5 m (Level 5) and at 2.7 m (Level 6) from the ground floor. Measurements from TRL4 to TRL8 are detailed for Level 2, Level 4 and Level 6 in Figure 4 to Figure 6 (some of the test data is missing due to thermocouple deficiency). These figures also present the corresponding FDS outputs from THERMOCOUPLE devices.

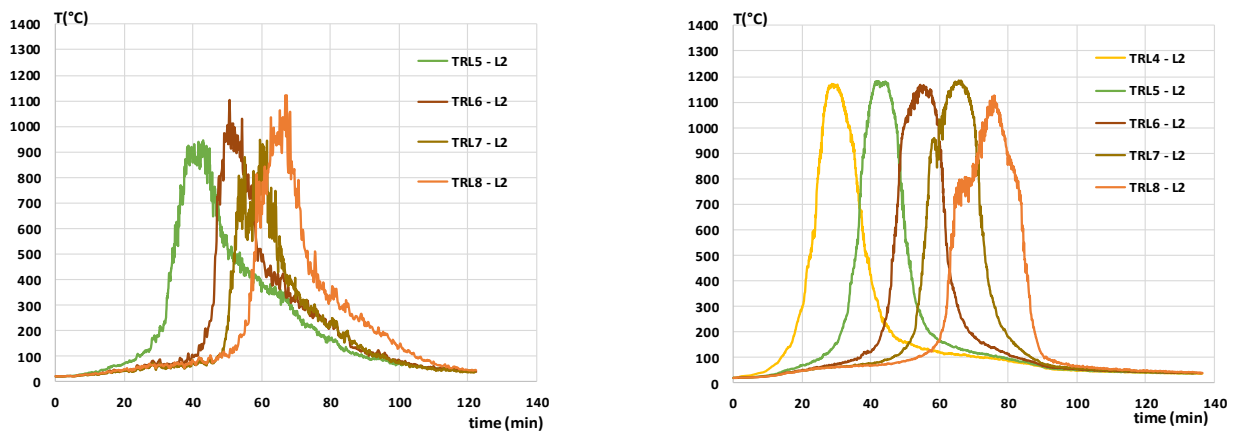


Figure 4. Comparison of gas temperatures for test n°2 at Level 2 (a) test measurements ; (b) FDS outputs

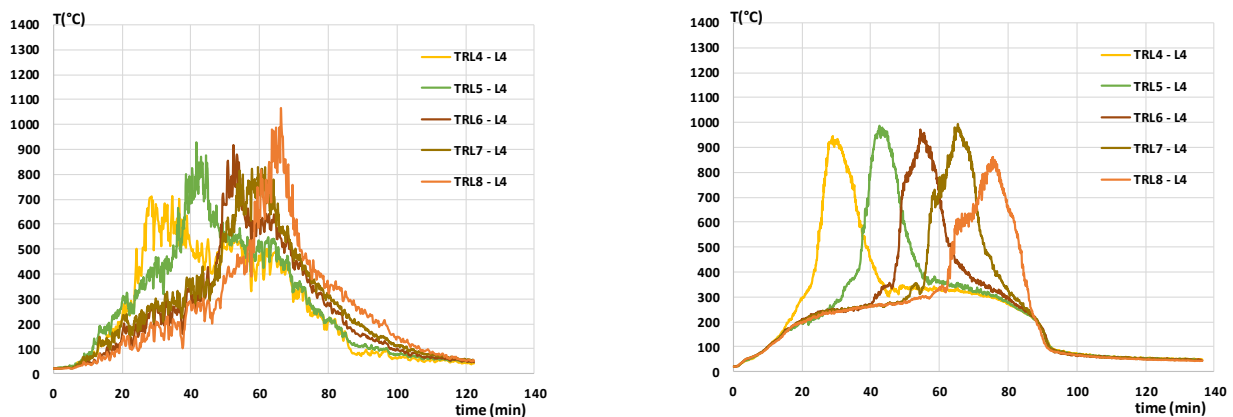


Figure 5. Comparison of gas temperatures for test n°2 at Level 4 (a) test measurements ; (b) FDS outputs

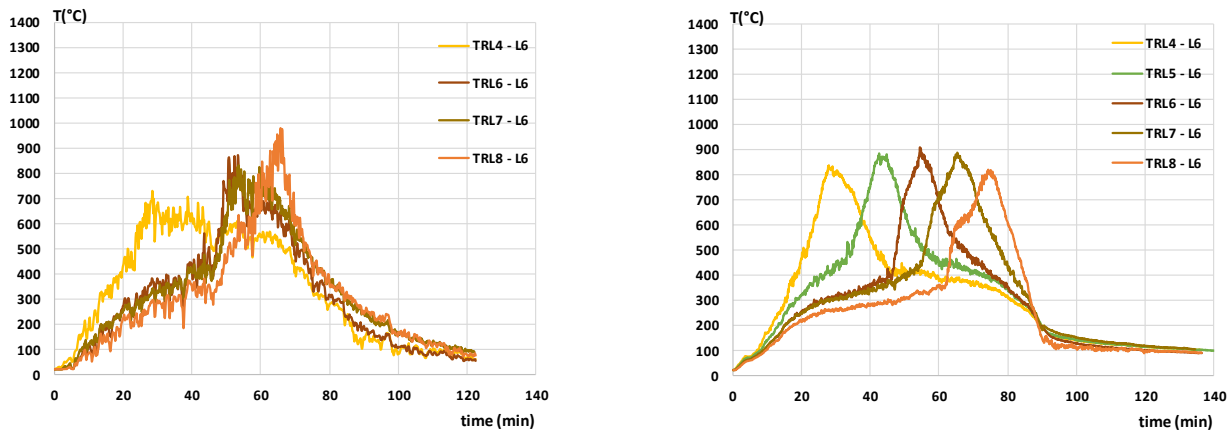


Figure 6. Comparison of gas temperatures for test n°2 at Level 6 (a) test measurements ; (b) FDS outputs

It can be observed that the global fire spread is well captured, as well as main tendency in terms of temperatures. The temperatures generated by FDS for level 2 are higher than the ones measured, while the temperatures generated for level 4 and level 6 are close to the ones measured. Nevertheless, the FDS model is not able to capture the different temperature profile of TRL4 (closer to ignition location) for which lower temperatures are met, as well as the small acceleration which can be seen from the test curves TRL6, TRL7 and TRL8 being slightly closer in time.

5 CALIBRATION OF THE CFD MODEL – TEMPERATURES OF A STEEL COLUMN

The steel temperatures comparison is performed for the unprotected steel column (hot rolled profile HE 200 A) positioned just next to the thermocouple tree TRL7. Three thermocouples were provided at five levels along the height of the column: at 0.5 m (Level 1), at 1 m (Level 2), at 1.5 m (Level 3), at 2 m (Level 4) and at 2.5 m (Level 5) from the ground floor. All thermocouples were provided at 3 mm depth from the surface of the flanges and the steel web, on parts of the column facing the source of ignition. Thermocouples provided in the web were positioned in the middle while the thermocouples provided in the flanges were at 20 mm distance from their edges.

This experimental data is compared with numerical results using two different methods. In a first step, the CFD output “thermocouple” was used to evaluate the related steel temperature using subsequently, in a simplified manner, the incremental formula from EN1993-1-2 section 4.2.5.1 [15]. This method considers a constant temperature through the section for a given height. In a second step, a coupling between CFD (FDS software) and FEM (SAFIR® software) was used. As of version 6.7.3 (used for the present analysis), FDS allows for the creation of a new file in which particular results are written to be used by the subsequent structural analysis by SAFIR® [13]. Radiative intensities and gas temperatures calculated by FDS have been used by SAFIR® (version 2019b0) to calculate the temperatures in the steel column. This coupling generates a non-uniform temperature distribution across one section of the steel column.

5.1 Evaluation of steel temperatures using FDS outputs and EN1993-1-2

The steel temperature of a steel structural element can be obtained, in a simplified manner, from the incremental formula from EN1993-1-2 section 4.2.5.1 providing the increase of temperature $\Delta\theta_{a,t}$ in an unprotected steel member during a time interval Δt , see equation (1). The unprotected column is a hot rolled steel profile HE 200 A, therefore having a section factor of 211 m^{-1} , and the correction factor for the shadow effect was considered equal to 1. The temperature is calculated for a column corresponding to the TRL7 position, at 5 heights: Level 1 to Level 5. The analysis was carried out using the FDS outputs from THERMOCOUPLE devices. These outputs take into account the radiation effect, which is evaluated from all directions as the thermocouple is modelled as a sphere. They also consider convection with environment gas.

$$\Delta\theta_{a,t} = k_{sh} \frac{A_m/V}{c_a \rho_a} \dot{h}_{net} \Delta t \quad (1)$$

Where k_{sh} is the correction factor for the shadow effect;
 A_m/V is the section factor for unprotected steel elements [1/m];
 A_m is the surface area of the member per unit length [m²/m];
 V is the volume of the member per unit length [m³/m];
 c_a it is the specific heat of steel [J/kgK];
 \dot{h}_{net} is the design value of the net heat flux per unit area [W/m²];
 Δt is the time interval [s];
 ρ_a is the unit mass of steel [kg/m³].

5.2 Evaluation of steel temperatures using a link between CFD and FEM

When launching the FDS simulation, a specific command is introduced to request the creation of a transfer file in which particular results are written to be used by the subsequent FEM analysis by SAFIR [16-19]. The FDS command RADF allows to save the radiation intensities I_{ijk}^l , for each cell with indices ijk that is bounded by the transfer zone and for each solid angle l [12]. Linear interpolations are performed by SAFIR when reading the transfer file to compute the relevant values at the requested positions in time and in space. Using this data as input, a series of 2D transient thermal analyses are performed along the structural members and the results are stored in appropriate files. A temperature distribution is calculated for each longitudinal point of integration of each beam finite element; in this case two points of Gauss are defined along the BEAM elements. In these 2D thermal analyses, the impinging flux is computed for each boundary (in the sense of finite element discretization) of the section, depending on its orientation. A hypothesis that was present in SAFIR versions prior to 2019b0 was that, when computing temperatures in a beam section or a shell section heated by a CFD fire, the flux at the different boundaries of the section was calculated at the position of the node line (for beams) or at mid-level of the shell (for shell elements), for all boundaries of the section. As of version 2019b0, the flux is computed at the precise position of the boundary, for each boundary of the section. For the boundaries on concave parts of the section, impinging radiative intensities from certain direction are discarded if there is an obstruction by other parts of the section. Mutual radiation between different boundaries of the section in the concave regions is not considered.

The zone for which a transfer file is created is highlighted in Figure 3. This zone covers the full width of the CFD domain and a portion of 1.6 m of its length. The upper coordinate (in height) of this zone was set equal to the height of the lower face of the ceiling, to avoid englobing in the thermal analysis the colder temperatures from the concrete ceiling. The column is divided into 17 BEAM elements of the same length (0.16m) and two integration points are defined per BEAM element. Since the temperatures are computed at each integration point, the heights at which SAFIR provides results slightly differ from the heights at which steel temperatures were measured during the test (maximum discrepancy of 5 cm). The Figure 7 depicts five points of interest within the steel profile: points 1, 2, 4, 5 in the flanges and point 3 in the web. These will be used to compare the measured and computed (with SAFIR) steel temperatures of the column.

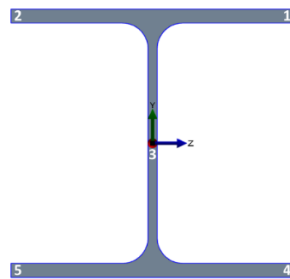


Figure 7. Location of the five points of interest for steel temperature in SAFIR

5.3 Comparison of the results

Figure 8 (a) and (b) depict the steel temperature distribution obtained across the section located at level 5 with SAFIR at 50 minutes and 80 minutes respectively. At 50 minutes (i.e. before the temperatures peak), a gradient can be observed in the flanges from left (higher steel temperatures towards gridline 1) to right (lower temperatures towards gridline 4). At 80 minutes, the reverse effect can be observed (i.e. higher steel temperatures towards gridline 4), and this reflects the spread of the fire in the compartment from left to right. Figure 8 (c) provides the evolution of the steel temperatures across the section located at level 5, as a function of time and at the five points of interest highlighted in Figure 7. From the start of the fire till around 50 minutes: steel temperatures are below around 300°C and all five curves follow a similar evolution. From around 50 minutes till around 67 minutes: steel temperatures rise up to around 750°C, with points n°2, 3 and 5 heating slightly faster, as these points corresponds to the left part of the profile (facing gridline 1). From around 67 minutes until around 90 minutes: steel temperatures decays to around 300°C, with points n°2 and 5 cooling slightly faster. Globally, the temperatures at the five points of interest present a similar evolution, the temperature gradient within the section being quite limited, and the same tendency is observed for the different levels of the column. The evolution of the steel temperatures resulting from the SAFIR analysis presented below will therefore be presented as the average of the steel temperatures from the five points of interest.

The Figure 9 and Figure 10 present the steel temperatures in column close to TRL7 during test n°2, from level 2 (1 m from the floor level) to level 5 (2.5 m from the floor level). The following results are presented: steel temperatures directly measured during the test (“TEST – measure”), the steel temperatures evaluated considering the FDS output from “thermocouple” devices and applying the formula from EN1993-1-2 (“FDS tmc – via EC3”) and the steel temperatures computed by SAFIR, using the radiation intensities and gas temperatures from FDS as input (“SAFIR”). The results obtained through coupling FDS and SAFIR are quite similar to the ones obtained through the application of EN1993-1-2 formula, the main difference being the maximum temperatures (the temperatures obtained via FDS-SAFIR are lower and closer to the ones measured during the test).

As the temperatures obtained via FDS-SAFIR are closer to the ones measured during the test, these results are considered to draw the following conclusions (but these remain valid if considering “FDS tmc – via EC3” since results are quite similar):

- Steel temperatures from lower levels (1 and 2) are too high in comparison to the ones of the test (the results for level 1 are not shown but the tendency is similar to the one at level 2);
- Steel temperatures from higher levels (from level 3 to level 5) show a very good correspondence with the ones of the test;
- The global profile versus time is well captured;
- There is an important difference in the descending branch: the ones obtained numerically being sharper than the ones measured. This could be explained by the CFD model’s inability to properly capture glowing embers as well as the heat accumulated within the compartment.

The fact that temperatures are too high at lower levels (close to the cubes) can be explained by the simplified representation of the fire load. With the wooden cubes, it is prescribed that the heat is released at each cube’s frontier, while in reality (continuous wood crib) some burning sticks are hidden by other sticks, implying that some heat is contained inside the crib and not directly impinging the exterior of the crib.

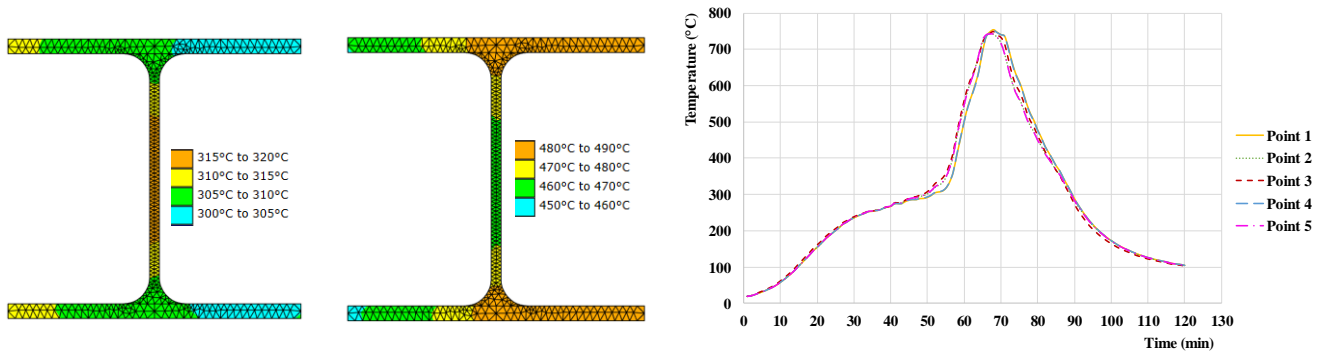


Figure 8. Steel temperature distribution across the section located at level 5 at (a) 50 mins ; (b) 80 mins ; (c) Steel temperatures evolution at level 5 from SAFIR at different locations of the section

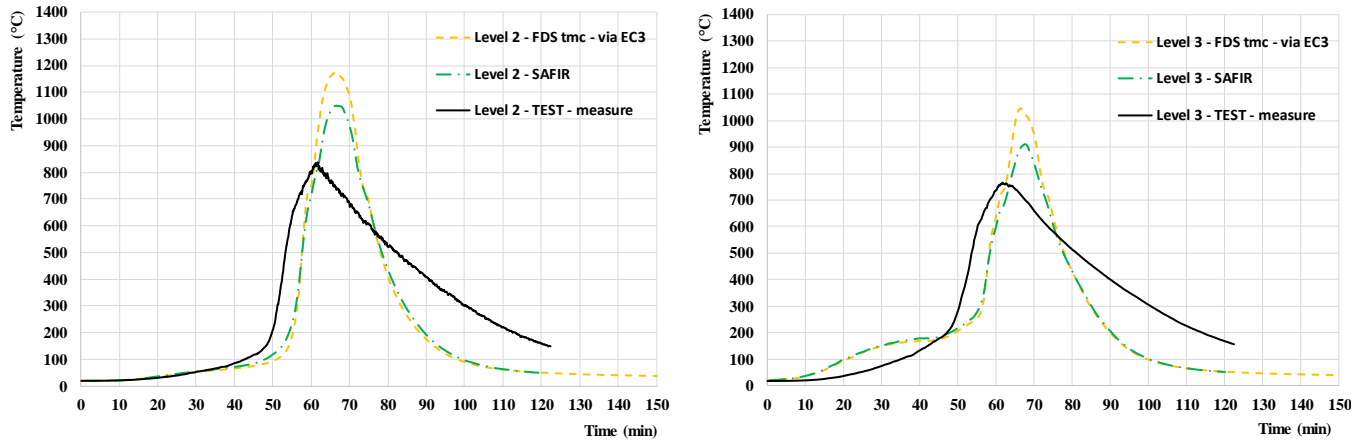


Figure 9. Steel temperatures in column close to TRL7 during test n°2 (a) at level 2 ; (b) at level 3

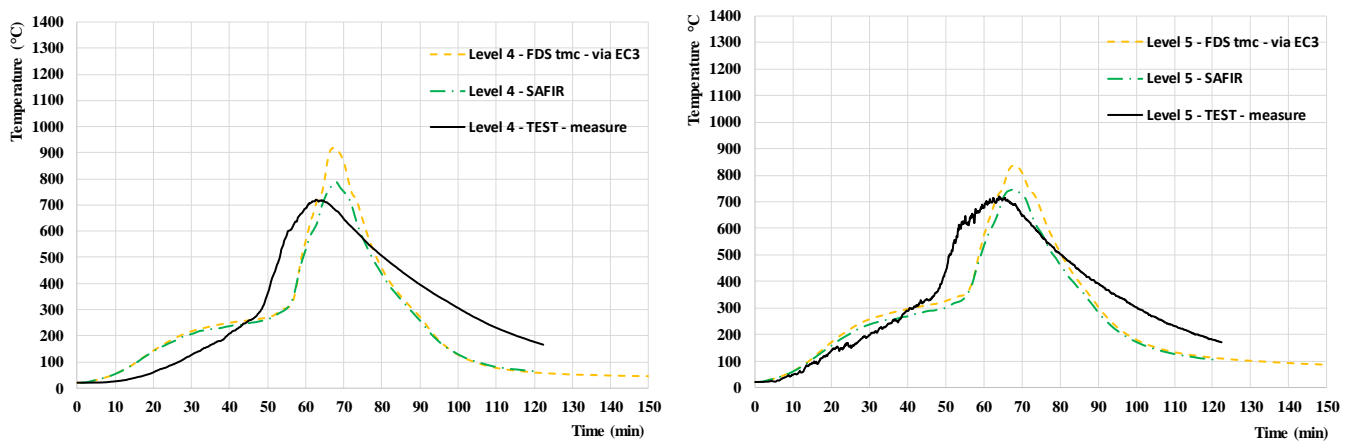


Figure 10. Steel temperatures in column close to TRL7 during test n°2 (a) at level 4; (b) at level 5

6 CONCLUSIONS

This article presents a simplified representation of the fire load for travelling fire development in large compartments using CFD analyses with FDS software. The potential benefit of such representation is shown while modelling one of the three TRAFIR natural fire tests and comparing gas temperatures measured at mid-width, along the length of the compartment and steel temperatures measured on a central column. The steel temperatures resulting from the CFD model were evaluated using two methods: one based on the incremental formula from EN1993-1-2 and other one linking CFD (FDS software) and FEM (SAFIR® software). The results obtained through these two methods are quite similar, the main difference being the maximum temperatures: the temperatures obtained via FDS-SAFIR are closer to the ones measured during the test. The steel temperature profiles globally showed a very good correspondence with the ones of the test. Nevertheless, the approach yields higher steel temperatures at lower levels, which could be inherent to the simplified representation of the fire load (the heat is released at each cube's frontier,

which is not the case in reality). It also leads to a non-negligible difference in the descending branch, which could be explained by the CFD model's inability to properly capture glowing embers as well as the heat accumulated within the compartment, and such aspects could be improved in future research. Although it implies some simplifications, the proposed approach can allow for both an acceptable representation of the travelling fire in terms of fire spread and steel temperatures while being less computationally demanding (the simulation detailed in this paper required around 40 hours to complete), making it more desirable for practical applications.

ACKNOWLEDGMENT

This work was carried out in the frame of the RFCS TRAFIR project with funding from the European Commission (grant N°754198). Partners are ArcelorMittal Belval & Differdange, Liège University, the University of Edinburgh, RISE Research Institutes of Sweden and the University of Ulster.

REFERENCES

1. J. Stern-Gottfried, G. Rein (2012). Travelling fires for structural design – Part I: Literature review. *Fire Safety Journal* 54. pp 74-85.
2. K. Horová, T. Jána, F. Wald (2013). Temperature heterogeneity during travelling fire on experimental building. *Advances in Engineering Software* 62-63. pp 119-130.
3. J.P. Hidalgo, A. Cowlard, C. Abecassis-Empis, C. Maluk, A.H. Majdalani, S. Kahrmann, R. Hilditch, M. Krajcovic, J.L. Torero (2017). An experimental study of full-scale open floor plan enclosure fires. *Fire Safety Journal* 89. pp 22-40.
4. D. Rush, D. Lange, J. Maclean, E. Rackauskaite (2015). Effects of a Travelling Fire on a Concrete Column – Tisova Fire Test. *Proceedings of the 2015 ASFE Conference*.
5. J.P. Hidalgo, T. Goode, V. Gupta, A. Cowlard, C. Abecassis-empis, J. Maclean, A. Barlett, C. Maluk, J.M. Montalva, A. F. Osorio, J. L. Torero (2019). The Malveira fire test: Full-scale demonstration of fire modes in open-plan compartments. *Fire Safety Journal* 108 No 102827.
6. A. Nadjai, N. Alam, M. Charlier, O. Vassart, X. Dai, J.-M. Franssen, J. Sjöström (2020). Travelling fire in full scale experimental building subjected to open ventilation conditions. Accepted for the 11th Intl. Conf. on Structures in Fire, 2020.
7. K. Horová (2015). Modelling of Fire Spread in Structural Fire Engineering. PhD thesis, Czech Technical University in Prague.
8. J. Degler, A. Eliasson, J. Anderson, D. Lange, D. Rush (2015). A-priori modelling of the Tisova fire test as input to the experimental work. *Proc. 1st Int. Conf. on Struct. Safety under Fire & Blast*, Glasgow, UK.
9. J.-M. Franssen, A. Gamba, M. Charlier (2019). Toward a standardized uniformly distributed cellulosic fire load. *Proceedings of the 3rd International Fire Safety Symposium* (Ottawa, Canada).
10. EN1991-1-2 (2002). Eurocode 1: Actions on structures – Part 1-2: General actions-Actions on structures exposed to fire. CEN, Brussels.
11. A. Gamba, M. Charlier, J.-M. Franssen (2020). Propagation tests with uniformly distributed cellulosic fire load. *Fire Safety Journal* 117, 103213
12. K. McGrattan, S. Hostikka, R. McDermott, J. Floyd, C. Weinschenk, K. Overholt (2017). *Fire Dynamics Simulator User's Guide*. Sixth Edit. National Institute of Standards and Technology (NIST) Special Publication 1019.
13. M. Charlier, A. Gamba, X. Dai, S. Welch, O. Vassart, J.-M. Franssen (2018). CFD analyses used to evaluate the influence of compartment geometry on the possibility of development of a travelling fire. *Proceedings of the 10th International Conference on Structures in Fire* (Ulster University, Belfast, UK). pp 341-348.
14. SFPE Handbook of Fire Protection Engineering (2002). Third Edition. NFPA.
15. N1993-1-2 (2005). Eurocode 3: Design of steel structures - Part 1-2: General rules – Structural fire design. CEN, Brussels.

16. J.-M. Franssen, T. Gernay (2017). Modeling structures in fire with SAFIR®: Theoretical background and capabilities. *Journal of Structural Fire Engineering*, 8(3), pp 300-323.
17. N. Tondini, A. Morbioli, O. Vassart, S. Lechêne, J.-M. Franssen (2016). An integrated modelling strategy between a CFD and an FE software: Methodology and application to compartment fires. *Journal of Structural Fire Engineering* 7(3), pp 217-233.
18. S. Welch, S. Miles, S. Kumar et al. (2008). FIRESTRUC – Integrating advanced three-dimensional modelling methodologies for predicting thermo-mechanical behaviour of steel and composite structures subjected to natural fires. *Fire Safety Science* 9, pp 1315-1326.
19. N. Tondini, O. Vassart, J.-M. Franssen (2012). Development of an interface between CFD and FE software. *Proceedings of the 7th International Conference on Structures in Fire (Zurich, Switzerland)*.

DISPROPORTIONATE COLLAPSE OF STEEL-FRAMED GRAVITY BUILDINGS UNDER FIRES WITH A COOLING PHASE

Jian Jiang¹, Bowen Wang², Wenyu Cai³, Guo-Qiang Li⁴, Wei Chen⁵ and Jihong Ye⁶

ABSTRACT

This paper investigates the progressive collapse behavior of 3D steel-framed gravity buildings under fires with a cooling phase. The effect of fire protections and bracing systems on whether, how, and when a gravity building collapses is studied. It is found that the duration of the heating phase of a fire has a great effect on whether a building collapse or not, and the building may collapse during its cooling phase. A “long-cool” fire is more dangerous than mild and “short-hot” fires since the former causes a higher temperature in the structure. It is also found that the application of a higher level of fire protection may prevent the collapse of a building, but may also lead to its collapse in the cooling phase due to the delayed temperature increment in the heated members. It is recommended for practical design that hat bracing systems should be arranged on the whole top floor, and vertical bracing systems at perimeter be used to mitigate the fire-induced collapse of gravity buildings.

Keywords: progressive collapse; gravity building; parametric fire; cooling phase; fire protection; bracing system.

1 INTRODUCTION

A standard fire (e.g. ISO 834 fire) are traditionally conducted in a furnace on simply supported members with a failure criterion of either failure of the member, limit of deformation, rate of deformation or limiting temperature. Since the Broadgate Phase 8 fire and the subsequent Cardington fire tests [1] in the 1990s, the global behavior of steel framed structures in fire has received growing concern [2-3]. It has been confirmed that steel members in real multi-story buildings have significantly greater fire resistance than isolated members in standard fire tests. From then on, the research focus moves from simply supported structural members to restrained members [4-6]. Especially since the collapse of World Trade Tower (WTC) under the terrorist attack on September 11, 2001, there have been growing interests in understanding progressive (or disproportionate) collapse behavior of structures under accidental loads such as blast, impact or fire [7-11]. An important lesson from the collapse of WTC is that prescriptive fire resistance ratings of individual structural members do not guarantee the adequate performance of a whole building system [12]. Since then, the research focus further moves to the global collapse behavior of buildings under fire conditions and performance-based design for structures in fire [13].

¹ Professor, School of Mechanics and Civil Engineering, China University of Mining and Technology, Xuzhou 221116, China.
e-mail: jiangjian_0131@163.com

² PhD student, School of Mechanics and Civil Engineering, China University of Mining and Technology, Xuzhou 221116, China.
e-mail: 760927240@qq.com

³ Post-doctor, College of Civil Engineering, Tongji University, Shanghai 200092, China.
e-mail: wenyucan@tongji.edu.cn

⁴ Professor, College of Civil Engineering, Tongji University, Shanghai 200092, China.
e-mail: gqli@tongji.edu.cn

⁵ Associate professor, School of Mechanics and Civil Engineering, China University of Mining and Technology, Xuzhou 221116, China.
e-mail: chenweiseu@163.com

⁶ Professor, School of Mechanics and Civil Engineering, China University of Mining and Technology, Xuzhou 221116, China.
e-mail: yejihong@seu.edu.cn

Previous studies on fire-induced disproportionate collapse of structures have three main issues: (1) using standard fires rather than compartment fires with a cooling phase, localized fires or travelling fires; (2) using moment-resisting frames rather than gravity frames. NIST research [14] has demonstrated the vulnerability of steel gravity framing systems with shear connections to collapse under column loss scenarios; (3) focusing on collapse modes rather than measures to mitigate or prevent structural collapse. The objective of this paper is to investigate the collapse behavior of 3D gravity frames under parametric fires with a cooling phase, and to propose effective mitigation measures for practical structural fire design.

2 LAYOUT AND NUMERICAL MODEL OF PROTOTYPE STRUCTURE

A 10-story, 5-bay gravity building published by NIST [15] was selected as the prototype structure. The dimension, section size and material properties of the prototype building is shown in Figure 1. The lateral loads are resisted by seismically designed intermediate moment frames located on the exterior of the building (rigid connections). Pinned beam-to-column connections were used for all interior frames which were designed to sustain gravity loads only. The building had one-hour fire-resistance rating. A numerical model of this prototype building was created in LS-DYNA, with modelling details and validation in the reference [16]. Flat reinforced concrete slabs in a thickness of 120 mm were simulated in the model to equivalently represent the composite slabs used in the original design.

A fire was assumed to occur in an interior compartment on Floor 2, as shown in Figure 1a. Three parametric fires with a cooling phase, representing a “short-hot” fire, mild fire, and “long-cool” fire, respectively, were chosen in this study, with parametric temperature-time curves as shown in Figure 2. They were calculated according to Annex A of EN1991-1-2, depending on the fire load density ($q_{t,d}$), enclosure property (b) and opening factor (O).

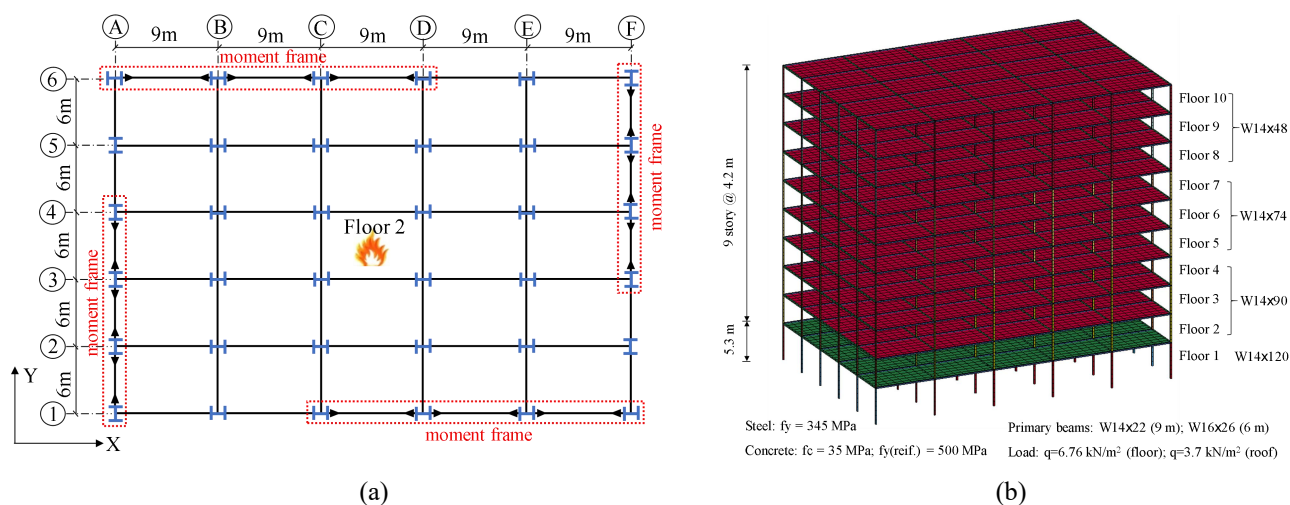


Figure 1. Modeling of a 3D 10-storey gravity building: (a) plan view; (b) finite element model

3 COLLAPSE OF PROTECTED GRAVITY FRAMES UNDER COMPARTMENT FIRES WITH A COOLING PHASE

The frame withstood Fire 1, but collapsed under Fire 2 after 60min and under Fire 3 after 90min, as shown in Figure 3. The collapse was triggered by the buckling of the heated columns in the fire compartment, followed by the buckling of the adjacent columns along the short span. Afterwards, the surrounding frame moved laterally towards the fire compartment driven by the large deflection of beams and slabs.

For all the fires, the top of the heated columns rapidly moved upwards due to the thermal expansion effect, and the upward movement slowed down when the column temperature reached 400 °C, above which the yield strength of steel started to degrade at elevated temperatures as pre-defined in the material properties. As the material properties continued to degrade, the heated columns buckled at 60 min and 90 min for Fire 2 and Fire 3, respectively. The survival of the frame in Fire 1 is because of the early cooling down of

the fire, where the temperature of the heated columns started to decrease before reaching its critical temperature. For Fire 2 and Fire 3, the buckling of the heated and adjacent columns led to generation of large tensile forces in the heated beam, about one-third of the yielding capacity of the beam.

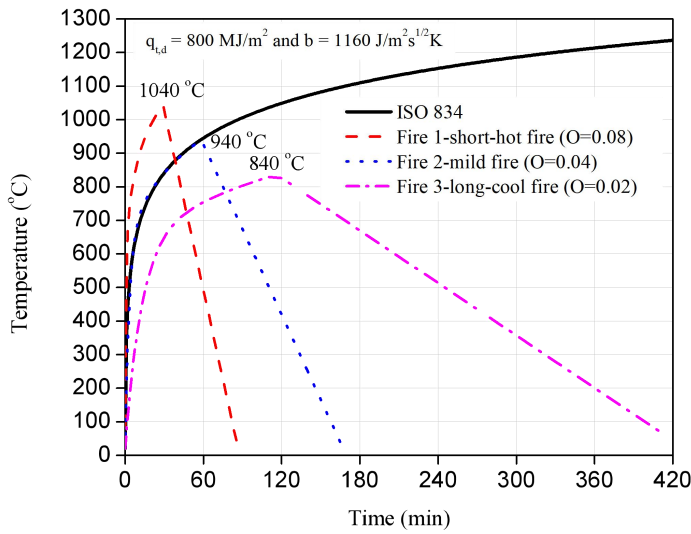


Figure 2. Parametric temperature-time curves

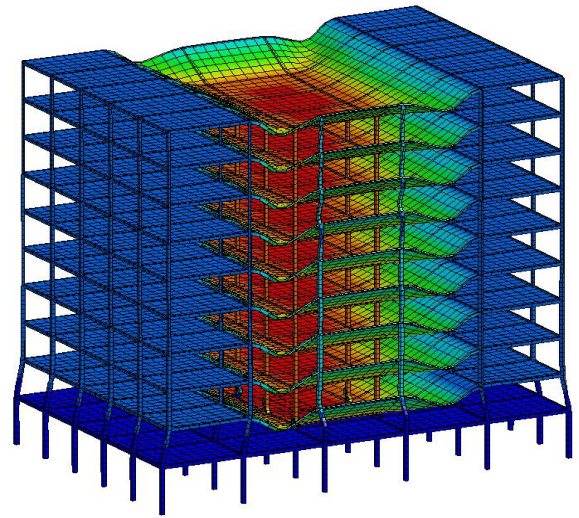


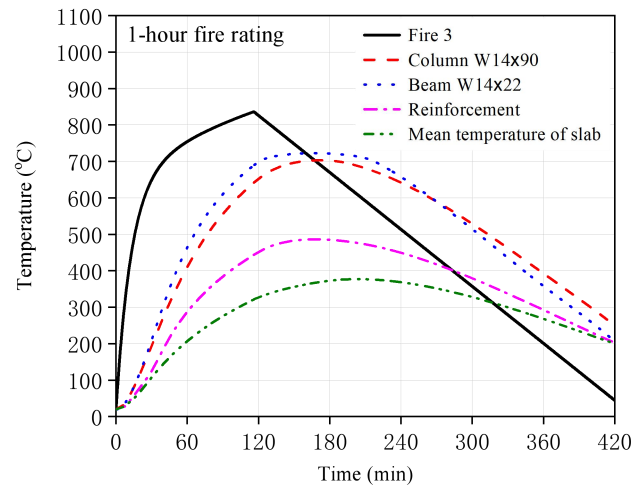
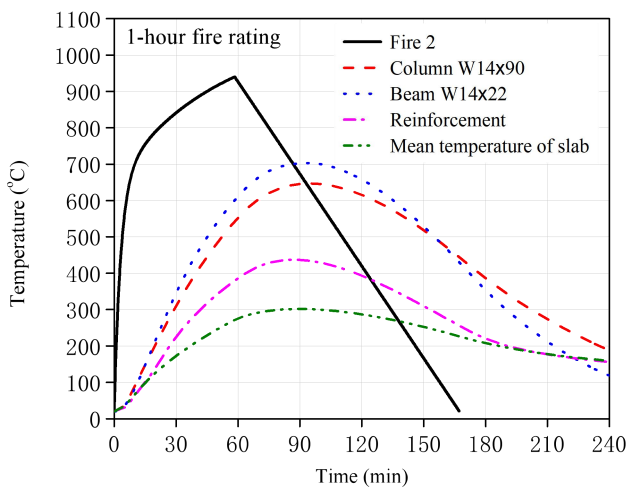
Figure 3. Collapse of the gravity frame

4 MITIGATION MEASURES FOR PRACTICAL DESIGN

Strategies to mitigate collapse can be proposed based on the three collapse stages. Firstly, the buckling of the heated columns can be prevented by increasing the fire protection level. Secondly, the buckling of the adjacent columns can be mitigated by a more uniform load redistribution in them by adding hat braces on the top floor of the frame. Thirdly, the lateral drift of the surrounding frame can be mitigated by using vertical braces along the height of the frame. The feasibility of using these methods was investigated.

4.1 Enhancement of fire protection levels

For a standard fire with a heating phase alone, the enhanced fire-resistance rating can only delay the failure of a heated column, rather than preventing its failure. However, for a realistic fire with a cooling phase, a higher fire-resistance rating may lead to a lower temperature in a structural member than its critical temperature. It was found that for a higher level of fire protection such as two-hour FRR, Fire 3 (long-cool fire) became severer than Fire 2 (mild fire) since the frame collapsed in Fire 3 but survived in Fire 2 (for one-hour FRR, Fire 2 was severer than Fire 3), as shown in the Figure 4. This indicates that the severity of fires depends on the fire protection level on the structural members.



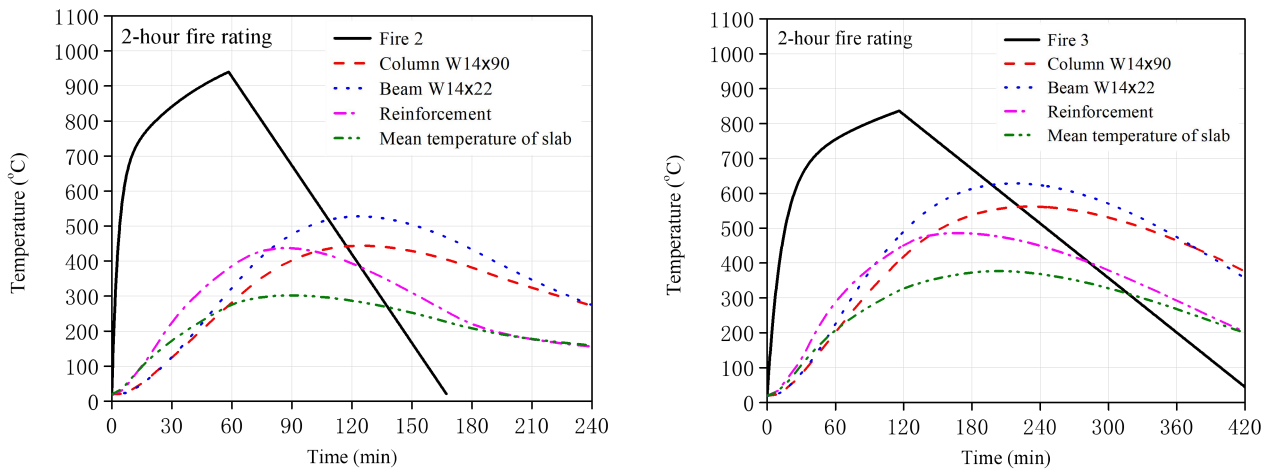


Figure 4. Temperature-time curves of steel and concrete members for 1-hour or 2-hour fire-resistance rating

4.2 Use of horizontal or vertical bracing systems

Increasing the fire protection level alone cannot effectively guarantee the stability of buildings since the protected heated columns can still buckle as long as the fire fuel is sufficient. The application of hat or vertical bracing systems can effectively mitigate or prevent the collapse of gravity buildings. Two arrangements of hat braces were considered: hat braces along perimeter alone (Hat-perimeter) and hat braces on the whole floor (Hat-wholeFloor). Figure 5 shows a comparison of behavior of the frames in Fire 2, where the frame with Hat-perimeter collapsed but that with Hat-wholeFloor withstood the fire. It was found that the perimeter arrangement of hat braces had little effect on the buckling of the heated and adjacent columns, and also on the load redistribution among the internal columns. The braces along the long span buckled due to the significant lateral drift of the frame after the buckling of the adjacent columns. For the frame with hat braces on the whole floor (Hat-wholeFloor), no buckling of braces occurred and the brace uniformly redistributed the load to the surrounding columns.

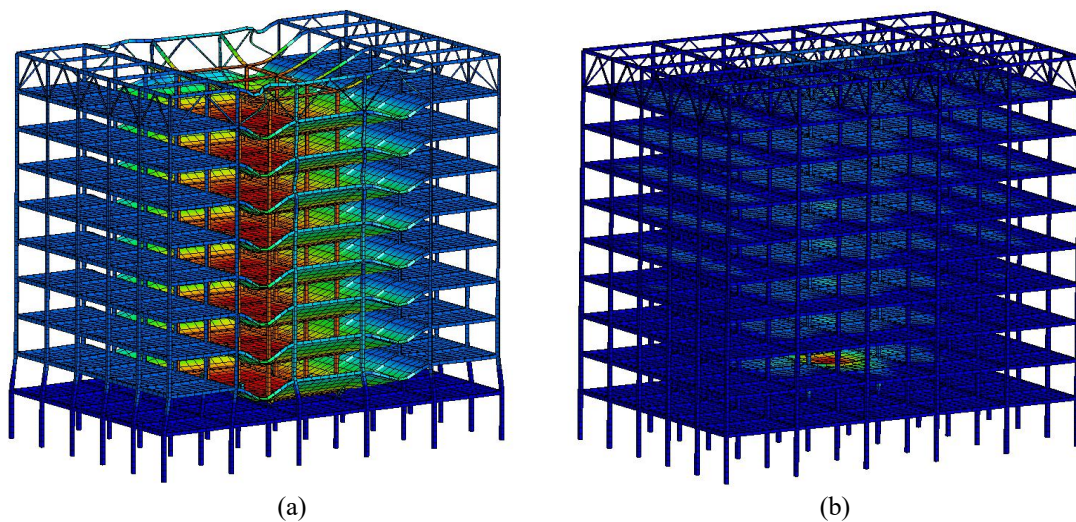


Figure 5. Behavior of the frame in Fire 2 with: (a) Hat-perimeter (collapse); (b) Hat-wholeFloor (withstand)

A layout of braces arranged in two edge bays along the perimeter of the frame (i.e. Vertical-perimeter as shown in Figure 6). The frame with vertical bracing systems withstood the fire, as shown in Figure 7. For the frame with Vertical-perimeter, the heated and adjacent columns buckled, but the lateral drift of surrounding frame was mitigated by the vertical braces. The floors experienced large deflection, but the building did not globally collapse. However, this large deflection of slabs is somewhat unacceptable because the building cannot be used after the fire although it survives in the fire.

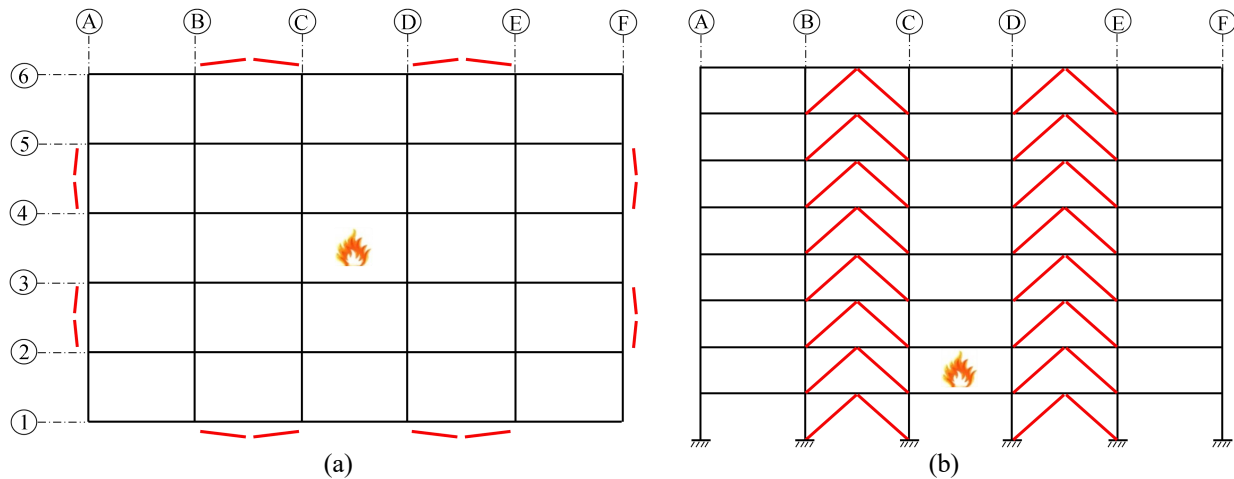


Figure 6. Layout of vertical bracing system: (a) plan view; (b) elevation view

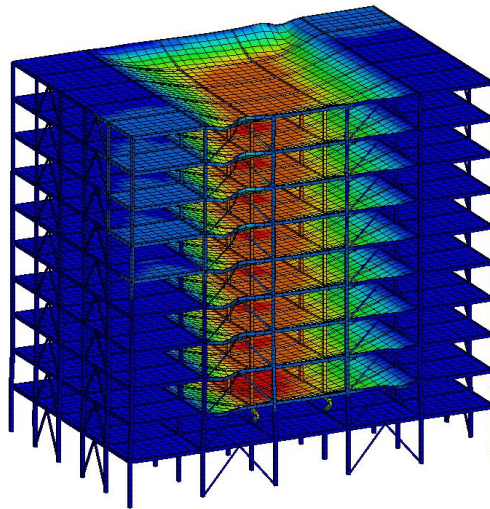


Figure 7. Behavior of the frame in Fire 2 with Vertical-perimeter braces (withstand)

5 CONCLUSIONS

Gravity buildings may collapse during the cooling phase of a fire, and they can withstand a “short-hot” fire, but collapse under a mild fire or “long-cool” fire. It is recommended to consider the potential fire scenario when determining the fire-resistance rating in addition to the importance of buildings. A “long-cool” fire was more dangerous, and it is suggested to increase the fire-resistance rating determined according to the importance of a structure to prevent its collapse under a “long-cool” fire. It is recommended to arrange hat bracing systems on the whole top floor of a building, and to use a perimeter vertical bracing systems.

ACKNOWLEDGEMENT

The work presented in this paper was supported by the National Natural Science Foundation of China with grant 52078478.

REFERENCES

1. Kirby, B.R., British steel technical European fire test program design, construction and results. Fire, static and dynamic tests of building structures. London. (1997).
2. Shahabi, S.E.M., Sulong, N.H.R. and Shariati, M., Performance of shear connectors at elevated temperatures-A review. Steel and Composite Structures, 20(1), 185-203 (2016).
3. Ye, Z.N., Jiang, S.C., Heidarpour, A., et al., Experimental study on cyclically-damaged steel-concrete composite joints subjected to fire. Steel and Composite Structures, 30(4), 351-364 (2019).

4. Pantousa, D. and Mistakidis, E., Rotational capacity of pre-damaged I-section steel beams at elevated temperatures. *Steel and Composite Structures*, 23(1), 53-66 (2017).
5. Davoodnabi, S.M., Mirhosseini, S.M., and Shariati, M., Behavior of steel-concrete composite beam using angle shear connectors at fire condition. *Steel and Composite Structures*, 30(2), 141-147 (2019).
6. Lim, O.K., Choi, S.K., Kang, S.W., et al., Experimental studies on the behaviour of headed shear studs for composite beams in fire. *Steel and Composite Structures*, 32(6), 743-752 (2019).
7. Menchel, K., Massart, T., Rammer, Y., and Bouillard, P., Comparison and study of different progressive collapse simulation techniques for RC structures. *Journal of Structural Engineering*, 135(6), 685-697 (2009).
8. Tian, L.M., Wei, J.P., Hao, J.P. et al., Dynamic analysis method for the progressive collapse of long-span spatial grid structures. *Steel and Composite Structures*, 23(4), 435-444 (2017).
9. Huang, Y., Wu, Y., Chen, C.H., Dynamic increase factor for progressive collapse of semi-rigid steel frames with extended endplate connection. *Steel and Composite Structures*, 31(6), 617-628 (2019).
10. Ferraioli, M., Evaluation of dynamic increase factor in progressive collapse analysis of steel frame structures considering catenary action. *Steel and Composite Structures*, 30(3), 253-269 (2019).
11. Cowlard, A., Bittern, A., Abecassis-Empis, C., and Torero, J., Fire safety design for tall buildings. *Proceedings of the 9th Asia-Oceania Symposium on Fire Science and Technology*, *Procedia Engineering*, 62, 169-181 (2013).
12. Cesarek, P., Kramar, M., Kolsek, J., Effect of creep on behaviour of steel structural assemblies in fires. *Steel and Composite Structures*, 29(4), 423-435 (2018).
13. Sadek, F., El-Tawil, S., and Lew, H.S., Robustness of composite floor systems with shear connections: modeling, simulation, and evaluation. *Journal of Structural Engineering*, 134(11), 1717-1725 (2008).
14. Main, J.A., and Sadek, F., Robustness of steel gravity frame systems with single-plate shear connections. *NIST Technical Note 1749*, National Institute of Standards and Technology, Gaithersburg, MD. (2012).
15. Jiang, J., and Li, G.Q., Progressive collapse analysis of 3D steel frames with concrete slabs exposed to localized fire. *Engineering Structures*, 149, 21-34 (2017).

SIMPLE STRUCTURAL MODELS FOR COMPUTATIONAL ANALYSIS OF RESTRAINED COLUMNS UNDER FIRE CONDITIONS

Pedro Dias Simão¹ and João Paulo C. Rodrigues²

ABSTRACT

In advanced structural engineering, two distinct types of computational strategies can be used to analyse the structural behaviour of a frame under the action of forces. Focusing on the analysis of structural elements under fire conditions, the first type applies to any general structure and opts to incorporate all involved complexities in the mathematical model, representing as accurate as possible all involved phenomena. This strategy leads usually to very heavy and complex numerical models, such as the FEM, and for a specific example it delivers a large amount of numerical data, hard to interpret. On the other hand, in the second type of strategies simple but representative mathematical models are created, aimed to analyse a specific phenomenon in a specific structural system. Despite of their restricted range of application, these latter models enable a much easier and deeper analysis of the phenomena they are devoted to, owing to their simplicity, and bring out coherent physical interpretations without significant deterioration of the accuracy. Within this latter context, this work presents two simplified structural models devoted to the analysis of restrained columns under fire conditions that complement each other: an adapted Shanley model, for elastic and elasto-plastic analysis, and a two rods model joined by a plastic hinge devoted to the analysis in the plastic range. Only uniform heating is considered, for reference, and all nonlinear aspects are taken into account, namely the degradation of the steel's properties with heating and the instability effects provoked by the thermal elongation.

Keywords: restrained columns; nonlinear analysis; Shanley model; plastic-hinge model

1 INTRODUCTION

In the present work, two simple structural models that represent the behaviour of restrained columns in fire conditions are developed. Usually, a generic column is a part of a global frame but its design is performed on an individual basis. Therefore, the restrained column model [AB] proposed in [1] and depicted in Fig. 1-a) is adopted: it is simply supported, because it is the reference case in Structural Stability [2], and comprises an axial spring at the top edge section B that simulates the restraining effects to thermal elongation caused by the surrounding structure. Its thorough analysis accounting for all involved nonlinearities requires advanced numerical methods, which leads to very heavy mathematical models with great computational complexity, whether these are based on Finite Elements [3] or on meshless methods [4]. The column is submitted to uniform heating, here taken as reference case and which, in the engineering practice, corresponds to a column completely engulfed in fire. At the onset of heating, it is assumed that the column is in static equilibrium under an axial load N_{Ed} , which represents the force resultant provoked by the external loading applied to the global frame, and also that the spring B is at rest, since it pretends

¹ Assistant Professor, Coimbra University– Civil Engineering Department and INESC–Coimbra (Institute of Computers and Systems Engineering of Coimbra), Portugal

e-mail: pedro@dec.uc.pt, ORCID: <https://orcid.org/0000-0002-5197-5989>

² Associate Professor with Habilitation, Coimbra University – Civil Engineering Department, Portugal

e-mail: jpaulocr@dec.uc.pt, ORCID: <https://orcid.org/0000-0002-6865-7995>

simply to model the thermal restraint effects of the surrounding structure. Instead of analysing this column by means of advanced numerical techniques, we concern ourselves here with the development of two simplified models that enable the analysis of all involved phenomena, with much less mathematical effort but without unacceptable loss of accuracy. These models comprise the Shanley model [5] depicted in Fig. 1-b), and the two rigid rods model joined by a plastic hinge depicted in Fig. 1-c), both used in the past for plastic column analysis [2,6]. These models are broadened here to the analysis of the restrained Euler column under fire and, at the present stage, it is important to underline a crucial difference between column design for load capacity at isothermal conditions and for fire resistance: for load capacity, the strategy adopted in [7] is based simply on an elastic limit analysis [8], while the design for fire conditions requires exploring deeply the plastic range, in order to compute the so called “critical temperature” that determines the column’s strength under fire, defined by the temperature at which the restraining force at spring B returns to zero [1]. This critical temperature clearly occurs when the most stressed fibres along the column are deep in plastic regime and so, since our goal is to compute this critical temperature, all models to be developed must deal with plasticity, together with the degradation of the relevant mechanical properties with temperature.

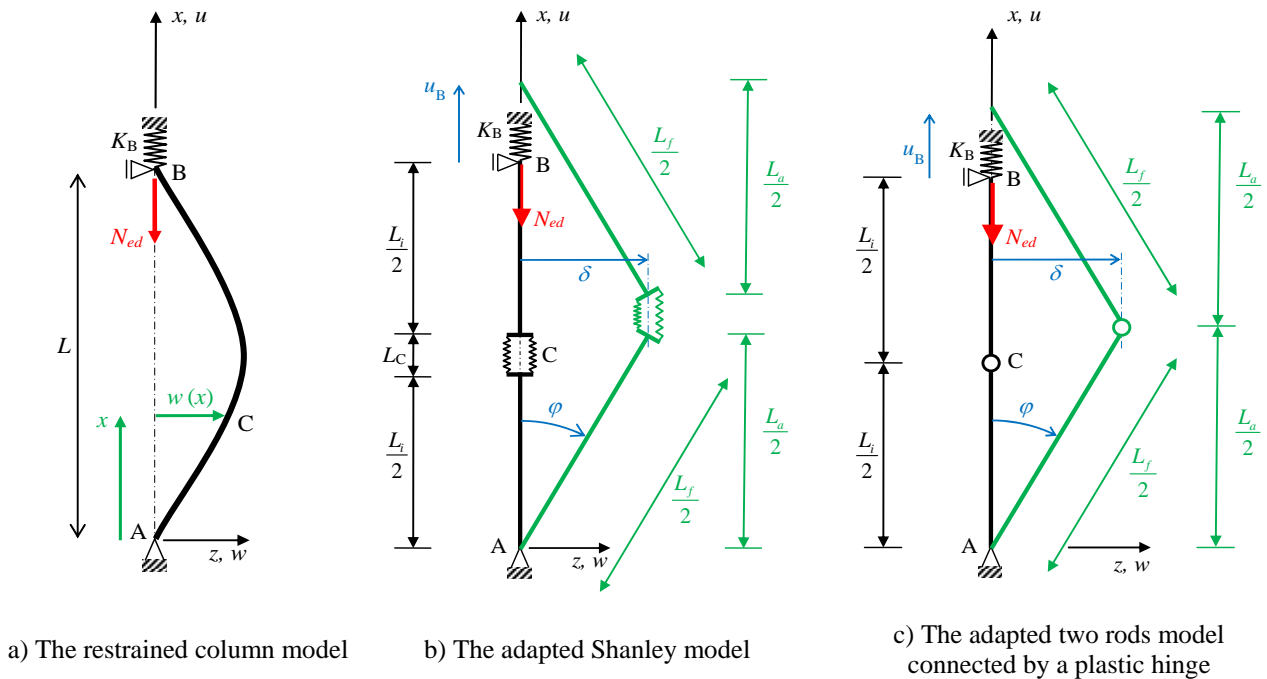


Figure 1. The adopted models for the analysis of restrained columns under fire

As mentioned above, we consider only the uniform temperature case, assumed as reference, meaning that the temperature θ along the whole member rises uniformly from the initial ambient temperature $\theta_{amb} = 20^\circ\text{C}$. We assume as well that the heating transfer problem is solved prior to the mechanical one, so that both problems can be split and are thus independent one from the other. We consider also that the material’s relevant mechanical properties, namely the yield stress f_y , the Young’s modulus E and the linear thermal elongation coefficient α , depend on the column’s temperature θ . Starting by the steel’s thermal elongation coefficient $\alpha(\theta)$, it is written in the form $\alpha(\theta) = \alpha k_\alpha(\theta)$, where α is the linear thermal elongation coefficient at ambient temperature and $k_\alpha(\theta)$ is a factor that describes the coefficient’s evolution with temperature [9] – instead of the piecewise form presented in [9], we adopt here the following continuous and smooth function:

$$k_{\alpha}(\theta) = \frac{14102.979563 - 17.939725 \theta}{\theta^2 - 1620.218697 \theta + 665880.448493} + 0.000266668 \theta + 0.972984 \quad (1)$$

Turning now our attention to the evolution of the Young's modulus E with temperature, we assume once again it is given by $E(\theta) = E k_E(\theta)$, where E is its value at ambient temperature and $k_E(\theta)$ is the reduction factor that computes the degradation of E with heating, here approximated by:

$$k_E(\theta) = \frac{134630.820652 - 201.611600 \theta}{\theta^2 - 687.773186 \theta + 274552.641013} + \frac{201.611600 \theta + 126566.356641}{\theta^2 + 607.773186 \theta + 248641.713574} \quad (2)$$

Finally, the yield stress f_y also degrades with temperature. It is given as $f_y(\theta) = f_y k_y(\theta)$, f_y being the yield stress at ambient temperature, and the reduction factor $k_y(\theta)$ is approximated by:

$$k_y(\theta) = \frac{100423.074478 - 137.995255 \theta}{\theta^2 - 973.682703 \theta + 299579.347708} + \frac{137.995255 \theta + 52699.605531}{\theta^2 + 214.078581 \theta + 80400.979938} \quad (3)$$

All coefficients in formulae (1) to (3) equal to 1 when $\theta = \theta_{amb}$, were fitted to the corresponding piecewise function presented in [9] and are continuous and smooth along the range of interest. Fig. 2 compares them with the corresponding piecewise formulae given in [9], and an excellent agreement occurs in all cases.

In the following, both structural systems depicted in Figures 1-b) and 1-c) are enhanced for fire behaviour. All computations were performed within the context of the algebraic symbolic manipulator Mathematica [10] and a set of conclusions ends the paper.

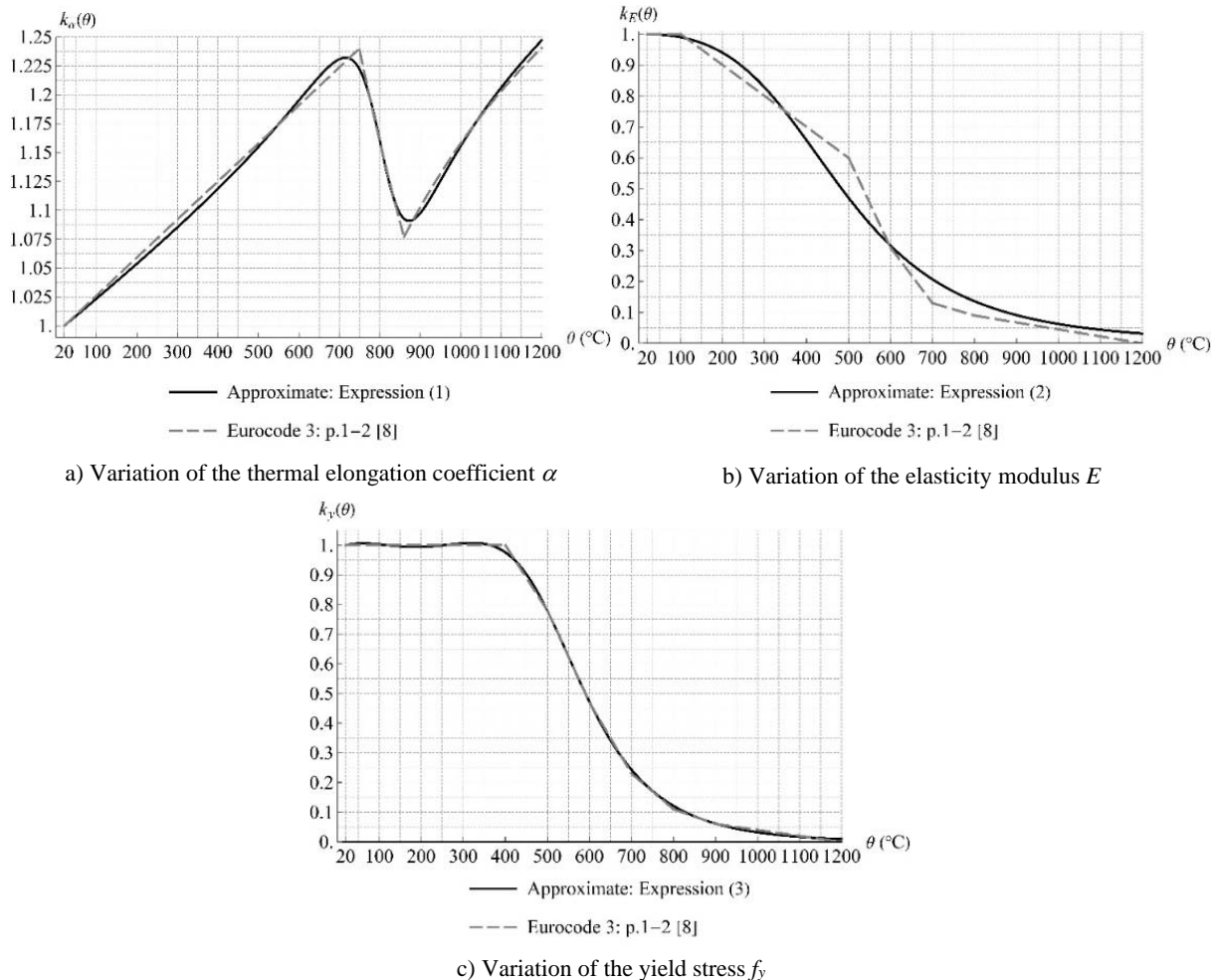


Figure 2. Evolution of the relevant mechanical properties with the temperature θ

2 THE SHANLEY MODEL ADAPTED TO THE ANALYSIS OF THERMAL RESTRAINED COLUMNS IN CASE OF FIRE

2.1 Introduction and kinematic description

The Shanley model was a major step forward in column's stability analysis because it provided, for the first time, a comprehensive explanation on the column's stability behaviour in the plastic range [5]. It is adapted in Fig. 1-b) in order to represent a restrained Euler column in fire. This adaptation consists merely in replacing the column in Fig. 1-a) by two rigid rods, [AC] and [CB], joined by a deformable cell at the mid-height section C. The rods have equal length and are fully rigid with respect to the application of forces and bending moments, but elongate when heated, with thermal elongation coefficient $\alpha(\theta)$. The whole system has an initial length L_i and, at the mid-height section C, these two rods are connected by a load cell, with negligible length. The cell's length is infinitesimal and is thus neglected, but the cell captures all deformations due the action of forces and moments in the system. These deformations comprise the average longitudinal deformation ε_m and the deformation due to the rods finite rotations ε_r , being all deformations positive for elongation and negative otherwise. The load cell, depicted in Fig. 3-a), is composed by two similar springs placed symmetrically with respect to the system's longitudinal axis, being b_{Sh} the distance between them, much smaller that the column's length: $b_{Sh} \ll L_i$. Due to the uniform heating $\theta - \theta_{amb}$, each rod [AC] and [CB] expands to the following length:

$$\frac{L_f}{2} = \frac{L_i}{2} [1 + \alpha k_\alpha(\theta)(\theta - \theta_{amb})] \quad (4)$$

From Fig. 1-b) the cell's transverse displacement δ is related to the rods rotation angle φ by:

$$\sin \varphi = \frac{\delta}{\frac{L_f}{2}} \Rightarrow \varphi = \arcsin \frac{2\delta}{L_f} \quad (5)$$

and the projection of each deformed rod along the longitudinal axis xx has the following length:

$$\frac{L_a}{2} = \frac{L_f}{2} \cos \varphi = \frac{L_f}{2} \sqrt{1 - \left(\frac{2\delta}{L_f}\right)^2} \quad (6)$$

Hence, point B is forced to move upwards, along the xx -axis, a distance u_B given by:

$$u_B = L_a - L_i + \varepsilon_m = \sqrt{\left\{L_i [1 + \alpha_{amb} k_\alpha(\theta - \theta_{amb})]\right\}^2 - 4\delta^2} - L_i + \varepsilon_m \quad (7)$$

Turning now our attention to cell C, whose deformed shape is described in Fig. 3-a), the total deformations $\varepsilon_{C,1}$ and $\varepsilon_{C,2}$ at springs 1 and 2 respectively are from the cell's average deformation ε_m and from the cell's deformation due to the rotation of the rigid rods ε_r by:

$$\begin{cases} \varepsilon_{C,1} = \varepsilon_m - \varepsilon_r \\ \varepsilon_{C,2} = \varepsilon_m + \varepsilon_r \end{cases} \quad (8)$$

Observing Fig. 3-a) yields the relation between the deformation ε_r and the transverse displacement δ :

$$\sin \varphi = \frac{\varepsilon_r / 2}{b/2} = \frac{\varepsilon_r}{b} \Rightarrow \frac{2\delta}{L_f} = \frac{\varepsilon_r}{b} \Rightarrow \varepsilon_r = \frac{2b}{L_f} \delta \quad (9)$$

All in all, the deformed shape of the structural system is fully described by means of two kinematic coordinates only: the average cell's deformation ε_m and the transverse displacement δ .

2.2 The equilibrium system

Due to the rods elongation caused by the temperature's rising $\theta - \theta_{amb}$, point B moves upwards, being this displacement u_B given by expression (7). Consequently, spring B applies a force F_B to the upper rod:

$$F_B = K_B (u_B - u_{ref}) \quad (10)$$

where K_B is the spring's stiffness coefficient, assumed to be constant along the heating process, and u_{ref} is a displacement needed to comply with the assumption of null force at spring B at the onset of fire, in order to force spring B to model solely the restraining effects of the surrounding structure during fire. u_{ref} is simply given by the shortening of the frame before fire due to N_{Ed} :

$$u_{ref} = -\frac{N_{Ed}}{K_C} \quad (11)$$

where the minus sign is used to impose an axial shortening for a (positive) compressive force N_{Ed} , and K_C is the total elastic axial stiffness coefficient of cell C. The equilibrium analysis for both rods [AC] and [CB] requires the inclusion of all relevant forces acting on the model's deformed shape, as illustrated in Fig. 3-b). Denoting by $F_{C,1}$ and $F_{C,2}$ the forces developed in the cell's springs 1 and 2, respectively, the equilibrium of the whole system is fully described by imposing equilibrium to the upper rod [CB] as follows:

$$\begin{cases} F_B + N_{Ed} + F_{C,1} + F_{C,2} = 0 \\ (F_B + N_{Ed})\delta + \frac{b_{Sh}}{2}(F_{C,1} - F_{C,2}) = 0 \end{cases} \quad (12)$$

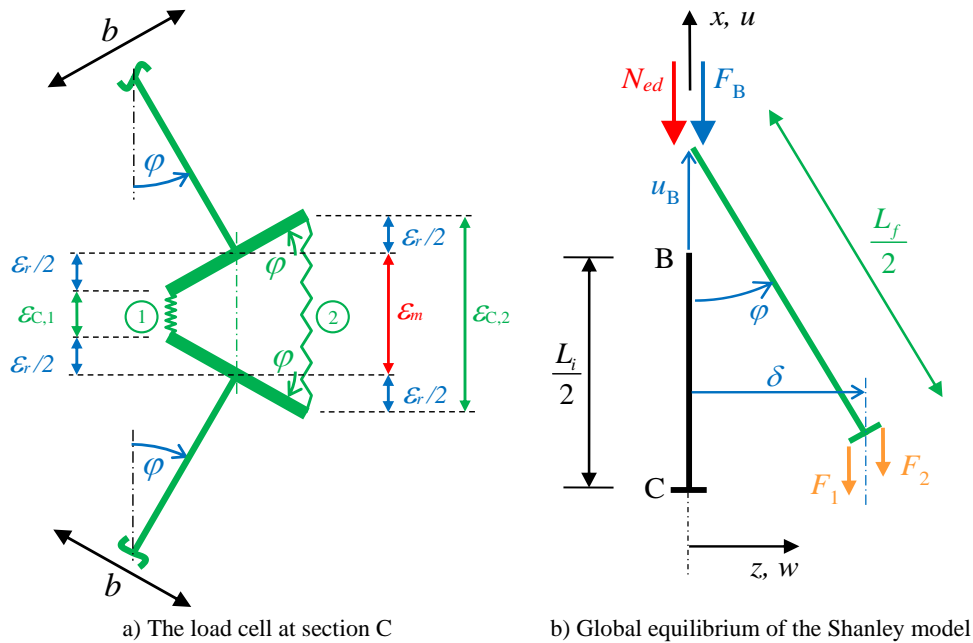


Figure 3. Global equilibrium of the adapted Shanley model

In expression (12) it is considered that forces F_B and N_{Ed} are positive if of compressive type, while each of the forces $F_{C,1}$ and $F_{C,2}$ are positive if pointing downwards, corresponding to tension at the springs and in order to agree with the sign convention adopted for the strains ϵ_m and ϵ_r , related to the deformations of both springs through expression (8). On the other hand, in the second member of the moments equilibrium equation in the system (12), we use the arm b_{Sh} and not $b_{Sh} \cos \phi$. In fact, this model aims to represent the

true behaviour of real restrained columns as close as possible, in many cases with class 1 [7] cross sections of I or H type. For these sections and due to the Bernoulli assumptions for bending [11], the arm between the resulting axial forces at both flanges does not vary in the plastic range because the cross section does not distort in its own plane. Consequently, we assume that the distance between both springs at cell C remains constant as the frame deforms. The analysis of equilibrium proceeds with the definition of forces $F_{C,i}$ that follow a pre-established constitutive behaviour. For both the elastic and the elasto-plastic cases presented in the following sections, the equilibrium system (12) has three unknowns – ε_m , δ and θ – and the task is, at the present stage and for any adopted constitutive behaviour, to input one of these unknowns and to compute the remaining two by any appropriate continuation method [12], accounting for the relevant stability effects [13].

2.3 Equilibrium analysis for elastic behaviour and calibration against the Euler column

When cell C behaves elastically, both forces $F_{C,i}$ in expression (12) take the following form:

$$F_{C,i} = \frac{K_C}{2} k_E(\theta) \varepsilon_{C,i} = K_i k_E(\theta) \varepsilon_{C,i}, \quad i=1,2 \quad (13)$$

where both $\varepsilon_{C,i}$ are given by formula (8), K_C is the cell's total elastic stiffness coefficient at the onset of fire and $k_E(\theta)$ is the reduction factor given by expression (2). The equilibrium system becomes given by:

$$\begin{cases} K_B \left\{ \sqrt{L_i^2 [\alpha k_\alpha(\theta)(\theta - \theta_{amb}) + 1]^2 - 4\delta^2} + \frac{N_{Ed}}{K_C} - L_i + \varepsilon_m \right\} + K_C \varepsilon_m k_E(\theta) + N_{Ed} = 0 \\ \delta \left\{ K_B \left\{ \sqrt{L_i^2 [\alpha k_\alpha(\theta)L_i(\theta - \theta_{amb}) + 1]^2 - 4\delta^2} + \frac{N_{Ed}}{K_C} - L_i + \varepsilon_m \right\} - \right. \\ \left. - \frac{b_{Sh}^2 K_C k_E(\theta)}{L_i [\alpha k_\alpha(\theta)(\theta - \theta_{amb}) + 1]} + N_{Ed} \right\} = 0 \end{cases} \quad (14)$$

and it has a fundamental solution that emanates from the initial resting state, denoted by subscript FP :

$$\begin{cases} \varepsilon_{m,FP} = - \frac{K_B [\alpha k_\alpha(\theta) K_C L_i (\theta - \theta_{amb}) + N_{Ed}] + K_C N_{Ed}}{K_C [K_B + K_C k_E(\theta)]} \\ \delta_{FP} = 0 \end{cases} \quad (15)$$

In addition to this solution, an alternative post-buckling one exists, denoted by subscript PB and given by:

$$\begin{cases} \varepsilon_{m,PB} = - \frac{b_{Sh}^2}{L_i [1 + \alpha k_\alpha(\theta)(\theta - \theta_{amb})]} \\ \delta_{PB} = \pm \frac{1}{2K_B K_C L_i [\alpha k_\alpha(\theta)(\theta - \theta_{amb}) + 1]} \times \sqrt{\left\{ -b_{Sh}^4 K_C^2 [K_B + K_C k_E(\theta)]^2 - \right.} \\ \left. - 2b_{Sh}^2 K_C L_i [K_B + K_C k_E(\theta)] [\alpha k_\alpha(\theta)(\theta - \theta_{amb}) + 1] [K_B K_C L_i - N_{Ed} (K_B + K_C)] + \right.} \\ \left. + L_i^2 [\alpha k_\alpha(\theta)(\theta - \theta_{amb}) + 1]^2 \{ (K_B K_C L_i [\alpha k_\alpha(\theta)(\theta - \theta_{amb}) + 2] - K_B N_{Ed} - K_C N_{Ed}) \} \times \right.} \\ \left. \times \{ K_B [\alpha k_\alpha(\theta) K_C L_i (\theta - \theta_{amb}) + N_{Ed}] + K_C N_{Ed} \} \right\} \end{cases} \quad (16)$$

This solution corresponds to a symmetric post-buckling behaviour and the switch from the fundamental path (15) to the post-buckling one (16) occurs at the thermal critical state, where both paths intersect the other [13]. At this state, the determinant of the Jacobean matrix of the equilibrium system (14) must vanish,

and this condition is used to compute the correspondent temperature, henceforth denoted by “thermal buckling temperature” θ_B . In elastic systems, it corresponds to the so-called “peak temperature” and is obtained by solving the following nonlinear equation in θ :

$$b_{Sh}^2 K_B K_C + b_{Sh}^2 K_C^2 k_E(\theta) - L_i N_{ed} (K_B + K_C) - \alpha L_i (\theta - \theta_{amb}) k_\alpha(\theta) \times \\ \times [\alpha K_B K_C L_i (\theta - \theta_{amb}) k_\alpha(\theta) + K_B K_C L_i + N_{Ed} (K_B + K_C)] = 0 \quad (17)$$

The general Euler column depicted in Fig. 1-a) with cross sectional area A and second moment of area I has a buckling load similar to the Shanley model's when:

$$K_C = \frac{EA}{L_i} \quad \wedge \quad b = \pi \sqrt{\frac{I}{A}} \quad (18)$$

Henceforth, we refer to the Shanley model obeying to relations (18) as “calibrated”, denoted by subscript cal , and the restraining force F_B along the post-buckling range is equal to:

$$F_{B,PB,cal} = \frac{\pi^2 EI}{L_i^2} \cdot \frac{k_E(\theta)}{1 + \alpha k_\alpha(\theta)(\theta - \theta_{amb})} - N_{Ed} = P_{Euler} \frac{k_E(\theta)}{1 + \alpha k_\alpha(\theta)(\theta - \theta_{amb})} - N_{Ed} \quad (19)$$

where P_{Euler} denotes the traditional Euler critical load [2]. Expression (19) is an elastic enveloping curve along the post-buckling range and shows that the restraining force always decreases with increasing temperatures, even for the elastic case. Moreover, his curve matches exactly the corresponding ones obtained by alternative methods applied to the analysis of columns [4] and, although the real behaviour of columns under fire is elasto-plastic, due to its simplicity this expression is quite useful as an upper bound to real problems and to check alternative methodologies. It is also a simpler alternative to equivalent formula developed in the literature that lays behind us [14].

2.4 Elasto-plastic thermal analysis and bending moment – axial force interaction in the plastic range

Slender columns buckle in elastic regime, even when buckling is provoked by heating. However, even for very slender columns plasticity is triggered immediately after the critical state [4]. Furthermore, in fire analysis we are mainly interested in the so-called “critical temperature” [1] that defines the column fire resistance, which shall be computed obviously in the plastic range. To this end and in order to enable a more realistic behaviour, the calibrated Shanley model must adopt an elasto-plastic constitutive law for both springs. Since the springs elastic stiffness coefficient K_C and the cell's width b_{Sh} are both already defined by expression (18) for elastic conditions, the remaining property yet to be defined is the yield force at each spring, henceforth denoted by $F_{Cy,M-N}$. The starting point is the bending moment – axial force ($M-N$) interaction curve in the plastic range (see section 6.2.9 of [7]) which, despite of having been developed for isothermal conditions, we suppose it applies also to heating problems as long as the degradation of the yield stress f_y with temperature is accounted for, in the present work by means of expression (3), and also by considering that $F_{Cy,M-N}$ is a function of the axial force ratio κ_N defined by:

$$\kappa_N = \frac{F_B + N_{Ed}}{A f_y k_y(\theta)} = \frac{N_{total}}{N_y(\theta)} \quad (20)$$

Focusing only on class 1 cross sections with I or H shape bending about the weak axis, the $M-N$ interaction curve must comply with the following conditions:

- For pure bending: $\kappa_N = a \Rightarrow \begin{cases} F_{Cy,M-N} = \frac{W_{pl} f_y k_y(\theta)}{b_{Sh}} \\ \frac{\partial F_{Cy,M-N}}{\partial \kappa_N} = 0 \end{cases} \quad (21)$

- For pure axial force: $\kappa_N = 1 \Rightarrow F_{Cy,M-N} = \frac{A f_y k_y(\theta)}{2} = \frac{N_y(\theta)}{2} \quad (22)$

where W_{pl} is the cross section plastic modulus, a is a parameter depending on the ratio between the cross sectional area A and the area of the flanges: $a = \frac{A - 2 b t_f}{A} \leq 0.5$, b is the cross section's width and t_f is the flange's thickness [7]. The resulting $M-N$ interaction curve to define the springs yield force $F_{Cy,M-N}$ is defined by means of the non-dimensional interaction factor $\kappa_{M-N,i}$ in the following form

$$\begin{cases} \kappa_N \leq a \Rightarrow \kappa_{M-N} = k_y(\theta) \frac{2 W_{pl}}{A b_{Sh}} \\ \kappa_N > a \Rightarrow \kappa_{M-N} = k_y(\theta) \frac{A b_{Sh} (a - \kappa_N)^2 + 2 W_{pl} (\kappa_N - 1) (2a - \kappa_N - 1)}{A (a - 1)^2 b_{Sh}} \end{cases} \wedge F_{Cy,M-N} = \kappa_{M-N} \frac{A f_y}{2} \quad (23)$$

For the HEB 200 section, whose properties will be presented thoroughly in section 4, the interaction factor κ_{M-N} takes the form described in Fig. 4. The nonlinear constitutive law for each spring in cell C is appropriately modelled by adapting the Richard formula [15] as follows:

$$F_{C,i} = \frac{\frac{K_c}{2} k_E(\theta) \varepsilon_{C,i}}{\left\{ 1 + \left[\left(\frac{\frac{K_c}{2} k_E(\theta) \varepsilon_{C,i}}{F_{Cy,M-N}} \right)^2 \right]^{\frac{n}{2}} \right\}^{\frac{1}{n}}}, \quad i = 1, 2 \quad (24)$$

For slender systems, the critical state occurs still in elastic regime but from this point onwards an elasto-plastic analysis is strictly necessary to obtain a realistic behaviour, since plasticity is triggered immediately after buckling [4]. Therefore, expression (24) shall be adopted to analyse the problem along the post-buckling range and to compute the critical temperature. Due to the high nonlinearity of the problem, analytical formulae, such as expression (19) for elastic analysis, are no longer possible and an appropriate numerical method must be applied, in the context of the symbolic manipulator Mathematica [10].

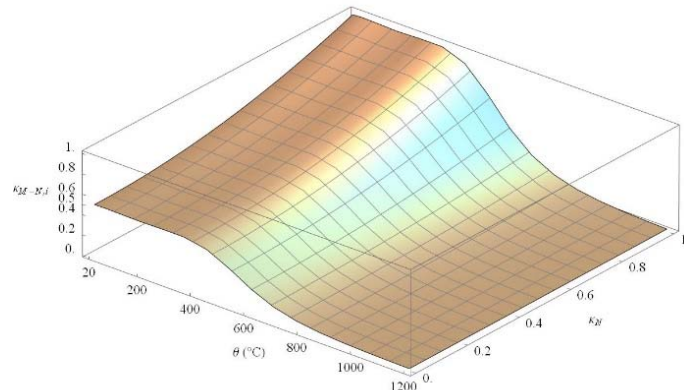


Figure 4. Factor κ_{M-N} for the calibrated Shanley model related to an HEB 200 cross section

2.5 The effects of initial imperfections

In Structural Stability, the analysis of the perfect column is of major relevance because it is the case for which all real systems tend when their imperfections tend to zero, regardless their shape [2,6,13]. Hence, the perfect column is always the reference case and, for the problem under observation, it corresponds to a Shanley frame perfectly straight at the onset of loading and heating, with no residual forces neither at spring B nor at cell C. However, imperfections are unavoidable, play a major role in the column's load capacity and are usually represented by a geometrical initial bow of the column's longitudinal axis. This imperfect shape represents many mechanical properties all together that lead to "imperfect" behaviour, such as residual stresses, real out-of-straightness of the longitudinal axis, off-centred axial loading, material heterogeneities and the variation of the cross section's geometrical form [2,6,8,13,16]. For fire conditions, it is therefore important to analyse their role on the critical temperature, in order to assess their effect on the column's fire resistance. Within this context, the Shanley model just described can be quite easily adapted in order to incorporate geometrical imperfections: it suffices, in expression (12), simply to replace the transverse displacement of cell C, δ , by $\delta_0 + \delta$, where δ_0 denotes, for the unloaded state at ambient temperature, the initial distance of cell C to the longitudinal axis xx .

3 A SIMPLIFIED MODEL FOR THE ANALYSIS OF RESTRAINED COLUMNS UNDER FIRE IN THE PLASTIC RANGE

3.1 Introduction and the kinematic description

The post-buckling behaviour of compressed columns in the plastic range at ambient temperature can be approximately described by a simple two rods model connected by a rotational plastic hinge [6], where the plastic bending moment arises from the column's cross section and material properties. Although the spread of plasticity along the longitudinal direction is quite relevant in restrained structural members under fire conditions [17], it is still worth to broaden this model to the analysis of restrained columns in fire, depicted in Fig. 1-c). For the uniform heating case, taken once again as the reference, the analysis just requires the inclusion of the plastic moment degradation with temperature, in addition to its degradation with the axial force. Starting by the kinematic description of the model, when heated the two rods system depicted in Fig. 1-c) enlarges to the following total length:

$$L_f = L_i [1 + \alpha k_\alpha(\theta)(\theta - \theta_{amb})] \quad (25)$$

The bars rotation φ is related to the transverse displacement of the plastic hinge at section C, denoted by δ :

$$\varphi = \arcsin \frac{2\delta}{L_f} \quad (26)$$

Due to heating, point B moves upwards the following quantity:

$$u_B = L_f \cos \varphi - L_i \quad (27)$$

3.2 Equilibrium analysis for the plastic range

Due to the elongation u_B , spring B applies a compressive force F_B to the column:

$$F_B = K_B (u_B - u_{ref}) \quad (28)$$

where u_{ref} is a reference displacement used to provoke a null force at spring B at the onset of heating:

$$u_{ref} = -\frac{N_{Ed} L_i}{EA} \quad (29)$$

Thus, the total axial force acting on the model is $N_{total} = F_B + N_{Ed}$ and the system is in equilibrium when

the bending moment provoked by the total axial force equals the plastic bending moment at section C:

$$M_{pl}(\theta, \kappa_N) = \delta(F_B + N_{Ed}) \quad (30)$$

where M_{pl} is the plastic bending moment at section C that degrades with temperature θ and with the axial force axial force ratio κ_N . Instead of modelling the plastic zone as complex plastic hinge-piston mechanism that imposes the incremental plastic deformation to be normal to the yield surface, as in [18], in fact the effects of rotations are far more important than the shortening ones in the plastic zone, and it is therefore legitimate to adopt the simplified method that models the plastic zone as a purely rotational hinge and simply reduces the plastic bending moment due to the presence of the axial load, in order do not violate the yield curve [19]. Taking into account one again the M - N interaction formulae for class 1 cross sections with I of H shape presented in [7], it is assumed that the yield stress degrades with heating by means of expression (3). This leads to the following definition of the plastic bending moment:

$$\begin{cases} \kappa_N \leq a \Rightarrow M_{pl}(\theta, \kappa_N) = W_{pl} f_y k_y(\theta) \\ a < \kappa_N \leq 1 \Rightarrow M_{pl}(\theta, \kappa_N) = W_{pl} f_y k_y(\theta) \frac{(\kappa_N - 1)(2a - \kappa_N - 1)}{(a - 1)^2} \end{cases} \quad (31)$$

At the present stage, the equilibrium equation (30) has two unknowns, δ and θ , and the plastic behaviour is appropriately described by solving this equation by means of any appropriate continuation method [12], determining the temperature θ for a given δ that varies along a range of interest. From these results the restraining force F_B can be computed and the critical temperature θ_c is easily found when F_B reaches zero.

3.3 Imperfection sensitivity for thermal plastic limit analysis

In line with the Shanley model, the two rods model depicted in Fig. 1-c) can be easily adapted to include the effect of initial imperfections as well. Once again, it suffices simply to replace the transverse displacement δ of the plastic hinge at section C by $\delta_0 + \delta$, where δ_0 is the initial distance between cell C and the longitudinal axis xx , when the frame is still at rest and at ambient temperature.

4 ILLUSTRATIVE EXAMPLE

The two simplified structural models just developed are now validated by means of a representative example of a restrained Euler column under fire, which is now compared to the results arising from an exact plastic zones meshless method [4] and from the commercial FEM package Abaqus [20]. The column is made of grade S355 steel:

- $E = 210 \text{ GPa}$, $\alpha = 12.16 \times 10^{-6}$ and $f_y = 355 \text{ MPa}$

and the adopted cross section is a HEB 200 bending about the weak axis:

- area: $A = 78.1 \text{ cm}^2$, weak axis moment of inertia: $I_z = 2003 \text{ cm}^4$
- cross section's height: $h = 200 \text{ mm}$ and width: $b = 200 \text{ mm}$; flange thickness: $t_w = 15 \text{ mm}$
- weak axis plastic bending modulus: $W_{pl,z} = 305.8 \text{ cm}^3$

The adopted length is $L_i = 7.739 \text{ m}$ to which corresponds the reduced slenderness coefficient at ambient temperature [2,7]:

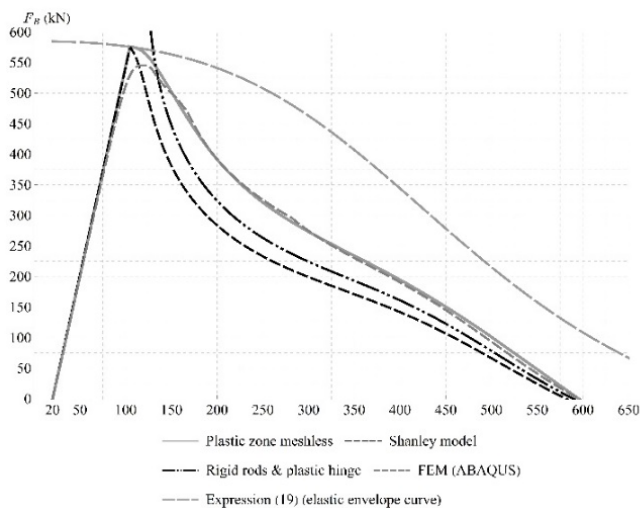
$$\bar{\lambda} = L \sqrt{\frac{A}{I}} \cdot \pi \sqrt{\frac{f_y}{E}} = 2 \quad (32)$$

Since $\bar{\lambda}$ is significantly larger than 1, the column can be considered as slender and buckling occurs clearly in the elastic range. The plastic bending moment at ambient temperature is $M_{pl} = 108.559$ kNm and the column's design buckling load [7] is $N_{b,Rd} = 543.929$ kN. The Euler buckling load [2,6] is $N_{Euler} = 693.137$ kN and, for all cases, an initial compressive force is applied before the fire event, equal to 20 % of $N_{b,Rd}$: $N_{Ed} = 108.786$ kN. For the restraining spring at the edge section B, three cases for its stiffness coefficient K_B are analysed, listed in Table 1 in dimensionless form as a function of the column's axial stiffness: $K_B = k_{adim} \frac{EA}{L_i} = k_{adim} \times 211.924 \times 10^3$ kN/m. The analyses are completely described by plotting the

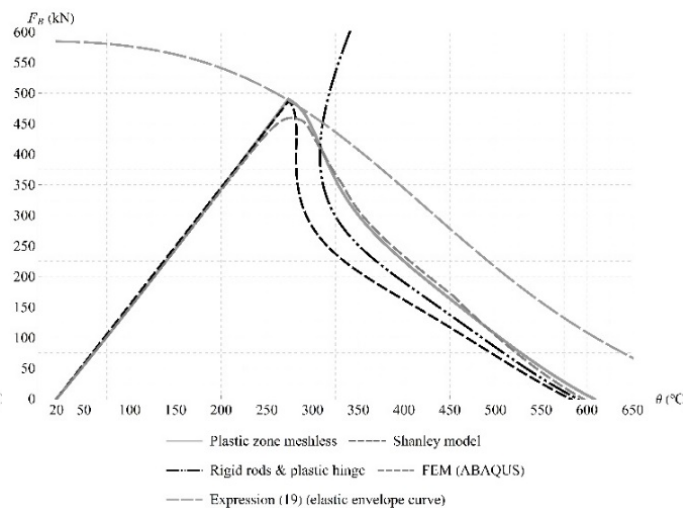
restraining force at section B, F_B , against the applied temperature θ , and the critical temperature is simply defined by the temperature at which force F_B returns to zero [1]. The computed critical temperatures for all cases are also listed in Table 1 as well and it is worth to highlight that, despite of being mere simplified models, both the Shanley model and the two rods model joined by a plastic hinge are still capable of computing the critical temperature with a minimum error, in all analysed cases less than 5% and always on the safe side, which is quite remarkable. In fact, when it is needed to compute the column's critical temperature, it is much easier at the engineering office to solve just the nonlinear equation (29) along a range of interest, which is easily programmable in any computer, than to perform a cumbersome nonlinear geometrically and materially analysis using a complex numerical method such as the FEM [20].

Table 1. The analysed cases

Case	k_{adim}	K_B (kN/m)	θ_b (°C)	θ_c (°C)					
			Shanley model	Plastic zones GBT&R-R	Shanley model		Two rods & plastic hinge		FEM (Abaqus)
					θ_c (°C)	Error (%)	θ_c (°C)	Error (%)	
A	0.5	105961.973	104.867	595.280	581.454	2.36	590.038	0.92	595.528
B	0.1	21192.395	274.102	607.276	581.449	2.37	590.036	0.93	595.563
C	0.05	10596.197	379.878	600.808	581.446	2.40	590.035	0.96	595.733



a) Case A



b) Case B

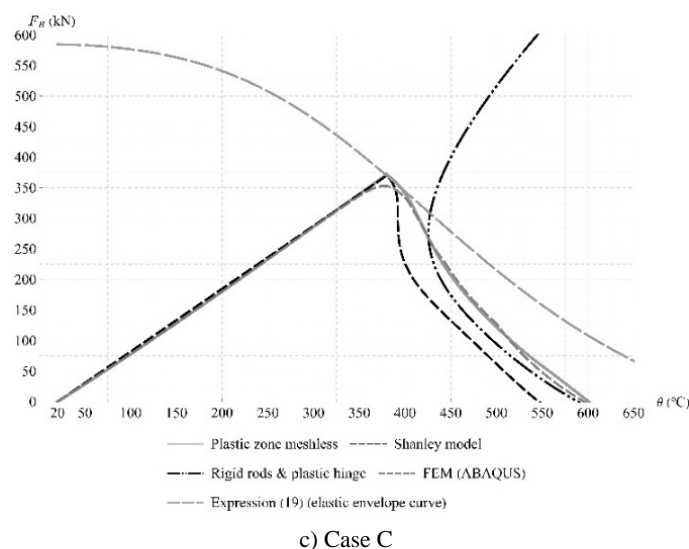


Figure 5. Plot of the restraining force F_B versus the applied temperature for all analysed cases A to C (see Table 1)

5 FINAL REMARKS

In the present work two simple structural systems, usually used to perform simplified buckling analyses of compressed columns, were revisited and adapted to the analysis of restrained Euler columns under fire. Noting that it is completely different to design a column for load capacity at isothermal conditions or for fire behaviour, which is governed by the critical temperature, these simplified models, namely the traditional Shanley model and the two rigid rods joined by a plastic hinge, provided a methodology capable to predict, with a minimum error, the critical temperature for a column submitted to uniform severe heating. This task requires usually highly nonlinear cumbersome numerical methods, in order to deal with all nonlinearities of the problem, namely the geometrical effects related to stability, the degradation of the mechanical properties with heating and plasticity, but the developed strategies were capable of predicting θ_c within a minimum and completely acceptable error. The findings presented here are clearly of great interest at the engineering office and shall be enhanced to other structural systems, such as plates and cold-formed structures, by means of adapting the yields line method [21].

ACKNOWLEDGMENT

This work was supported by FCT – Portuguese Foundation for Science and Technology under project grants UIDB/00308/2020 and PCIF/MOS/0129/2018.

REFERENCES

1. Neves, I.C., The critical temperature of steel columns with restrained thermal elongation. *Fire Safety Journal* 24, 211-227 (1995).
2. Chen, W.F., Lui, E.M., *Structural stability – Theory and implementation*. Prentice Hall; 1987.
3. Franssen, J.-M., “SAFIR: A thermal/structural program for modelling structures under fire”, *Engineering Journal – American Institute of Steel Construction*, V. 42, 2005, N. 3 (Third Quarter), p. 143-158.
4. Simão, P.D, Rodrigues, J.P.C., GBT Rayleigh-Ritz analysis of slender elasto-plastic steel columns under fire conditions. H. Barros, C. Ferreira. J. M. Adam and N. Delatte (Eds), *CoRASS 2019 – 3rd Int. Conf. on Recent Advances in Nonlinear Design, Resilience and Rehabilitation of Structures*. Coimbra 16th-18th October, 2019, p. 436-447.

5. Shanley, F.R., Inelastic column theory. *Journal of the Aeronautical Sciences* 14 (N. 5 – May), 261-268 (1947).
6. Allen, H.G., Bulson, P.S., *Background to buckling*. McGraw Hill, London; 1980.
7. European Committee for Standardization (CEN), Eurocode 3: Design of Steel Structures – Part 1-1: General rules and rules for buildings, EN 1993-1-1, Brussels; 2004.
8. Rondal, J., Maquoi, R., Single equation for SSRC column-strength curves. *Proceedings of the American Society of Civil Engineers (ASCE) – Journal of the Structural Division* 105 (ST1 – January), 247-250 (1979).
9. European Committee for Standardization (CEN), Eurocode 3: Design of Steel Structures – Part 1-2: General rules – Structural fire design, EN 1993-1-2, Brussels, 2005.
10. Wolfram Corp. (2020), *Mathematica*, version 12.1, Wolfram Corp. Inc, USA.
11. Silva, V. D., *Mechanics and strength of materials*. Springer-Verlag, Berlin-Heidelberg; 2006.
12. Allgower, E.L., Georg, K., *Numerical continuation methods*. Springer-Verlag, Berlin-Heidelberg; 1990.
13. Thompson J.M.T., Hunt, G.W., *A general theory of elastic stability*. John Wiley and Sons; 1973.
14. Shepherd, P.G., Burgess, I.W., On the buckling of axially restrained steel columns in fire. *Engineering Structures* 33, 2832-2838 (2011).
15. Richard, R.M., Abbott, B.J., Versatile elastic-plastic stress-strain formula. *ASCE Journal of the Engineering Mechanics Division – Proceedings of the American Society of Civil Engineers* 101 (EM4 – August), 511-515 (1975).
16. Hirt, M., Bez, R., *Construction Métallique – Notions fondamentales et methods de dimensionnement, Traité de Génie Civil de l'Ecole Polytechnique Fédérale de Lausanne (EPFL) – Vol. 10*. Presses Polytechniques et Universitaires Romandes, Lausanne; 2001.
17. Ravi Prakash, P., Srivastava, G., Distributed plasticity model for analysis of steel Structures subjected to fire using the direct stiffness method. *Fire Safety Journal* 105, 169-187 (2019).
18. Orbison, J.G., McGuire, W., Abel, J.F., Yield surface applications in nonlinear steel frame analysis. *Computer Methods in Applied Mechanics and Engineering* 33, 557-573 (1982).
19. de Luca, A., Faella, C., Mele, E., Advanced inelastic analysis: numerical results and design guidelines for rigid and semirigid sway frames. In: White, D.W., Chen, W.F., *Plastic hinge based methods for advanced analysis and design of steel frames*. Structural Stability Research Council; 1993.
20. Dassault Systèmes – Simulia Corp., *ABAQUS/CAE Standard User's Manual*, version 6.14-1. Providence (RI); 2014.
21. Zhao, X.-L., Yield line mechanism analysis of steel members and connections. *Progress in Structural Engineering and Materials* 5, 252-262; 2003.

A STATIC SOLVER FOR HYBRID FIRE SIMULATION BASED ON MODEL REDUCTION AND DYNAMIC RELAXATION

P. Covi¹, G. Abbiati², N. Tondini³, O.S. Bursi⁴, B. Stojadinovic⁵

ABSTRACT

Large-scale tests of an entire structure are generally prohibitively expensive, both in terms of finances and time, because of the need for expensive specialized facilities. As a result, most of the research regarding the behavior of structures subjected to fire has been carried out on partial subassemblies or single components subjected to standard heating curves. Standard fire tests use simplified mechanical boundary conditions for the tested structural element. However, for some elements, these conditions can lead to results that are overly conservative. Hybrid fire simulation emerged as a viable solution for performing component level experiments that account for the interaction between the tested specimen and a realistic yet virtual subassembly instantiated in a finite-element software. On these premises, this work presents a virtual hybrid fire simulation campaign conceived for a steel braced frame. Numerical experiments demonstrate the effectiveness of a newly conceived hybrid fire simulation algorithm. Finite-element simulations performed with the software SAFIR are used as a reference for verification.

Keywords: Hybrid fire simulation; dynamic relaxation; partitioned time integration; steel structures

1 INTRODUCTION

Hybrid Simulation (HS) is an online dynamic simulation paradigm that combines classical experimental techniques with online computer simulation for cost-effective large-scale testing of the structure under simulated loads, as comprehensively reviewed in [1]. Hybrid simulation of the response of a structure to a fire load was also investigated [2-7]. In this context, Hybrid Fire Simulation (HFS) utilizes sub-structuring: the part of the structure, whose behavior is difficult to simulate, is modeled physically, i.e., the physical substructure (PS); all other parts are simulated numerically, i.e., the numerical substructure (NS). Many tools for hybrid testing are coming from earthquake engineering, and in most the fire scenarios, there is exactly a complementary situation. For instance, the axial force in columns is variable during the fire development caused by the axial force redistribution due to the restrained thermal expansion, and the structural response is static because the temperature variation is slow compared to the mechanical frequency of the system. Conversely, in the seismic case, the inertia plays a substantial role, and the response is governed by the dynamic amplification. Axial degrees of freedom of the columns are typically activated by

¹ Ph.D. student, Dept. of Civil, Mechanical and Environmental Engineering, Univ. of Trento, 77 via Mesiano, Trento 38123, Italy
e-mail: patrick.covi@unitn.it, ORCID: <https://orcid.org/0000-0002-0570-4061>

² Assistant Professor, Dept. of Engineering, Univ. of Århus, 10 Inge Lehmanns Gade, Århus C 8000, Denmark
e-mail: abbiati@eng.au.dk, ORCID: <https://orcid.org/0000-0002-5048-8505>

³ Assistant Professor, Dept. of Civil, Mechanical and Environmental Engineering, Univ. of Trento, 77 via Mesiano, Trento 38123, Italy
e-mail: nicola.tondini@unitn.it, ORCID: <https://orcid.org/0000-0003-2602-6121>

⁴ Professor, Dept. of Civil, Mechanical and Environmental Engineering, Univ. of Trento, 77 via Mesiano, Trento 38123, Italy
e-mail: oreste.bursi@unitn.it, ORCID: <https://orcid.org/0000-0003-3072-7414>

⁵ Professor, Chair of Structural Dynamics and Earthquake Engineering, Dept. of Civil, Environmental and Geomatic Engineering, Institute of Structural Engineering, 5 Stefano-Francini Platz, Zürich 8093, Switzerland
e-mail: stojadinovic@ibk.baug.ethz.ch, ORCID: <https://orcid.org/0000-0002-1713-1977>

high modes associated with low participating masses. Therefore, in the seismic scenario, those degrees of freedom (DOFs) are usually removed from the hybrid simulation loop, but the same DOFs cannot be removed in the fire case. Another difference is that in most of the seismic engineering cases, the structural response can be assumed as rate-independent, which means that experiments can be performed with an extended time scale. Materials at a high temperature usually exhibit creep and stress relaxation, which entail a time-dependent structural response. These effects prohibit the adoption of an extended time scale, thus enforcing the use of real-time hybrid simulation.

2 HYBRID FIRE SIMULATION ALGORITHM

The Real-Time Hybrid Fire Simulation (RT-HFS) algorithm presented in this paper [7] relies on the Finite Element Tearing and Interconnecting (FETI) approach to couple PS and NS [8]. In particular, the Gravouil and Combescure (GC) algorithm [9] and the Localized Lagrange Multipliers (LLM) method [10] are used in combination to solve the coupled equation of motion of the hybrid model. Since the structural response to fire is quasi-static, the Dynamic Relaxation (DR) algorithm [11] is adopted to build an equivalent dynamic system that mimics the static response of substructures. The basic idea behind DR is to obtain the displacement solution of a static structural problem,

$$\mathbf{r}(\mathbf{u}) = \mathbf{f}(t) \quad (1)$$

by computing the transient response of an equivalent dynamic system, whose equation of motion reads,

$$\mathbf{M}\ddot{\mathbf{u}} + \mathbf{C}\dot{\mathbf{u}} + \mathbf{r}(\mathbf{u}) = \mathbf{f}(t) \quad (2)$$

where \mathbf{r} is the internal restoring force vector, which depends on the displacement vector \mathbf{u} (and, possibly, to its past time history) while $\mathbf{f}(t)$ represents a time varying external loading; \mathbf{M} and \mathbf{C} are fictitious mass and damping diagonal matrices, respectively. Expressions for diagonal entries of both fictitious mass and damping matrices read,

$$M_{ii} = \frac{(1.1\Delta t)^2}{4} \sum_j |K_{ij}|, C_{ii} = 2\omega_0 M_{ii} \quad (3)$$

which are derived to maximize the convergence rate of the DR algorithm, where K_{ij} is a generic element of the initial tangent stiffness matrix $\mathbf{K} = \partial \mathbf{r} / \partial \mathbf{u}$; ω_0 is the lowest undamped frequency of equation (2) after linearization of $\mathbf{r}(\mathbf{u})$ at zero displacement and velocity; Δt is the time step size of the equivalent transient analysis solved using the Central Difference (CD) algorithm, which is equivalent to the Newmark scheme with $\gamma = \frac{1}{2}$ and $\beta = 0$.

The LLM-GC algorithm proposed in this paper relies on the coupling scheme of the GC method [9] adapted to the LLM method [10] to couple the equations of motion of PS and NS, both represented by equivalent dynamic systems computed with DR. For the sake of simplicity, the LLM-GC algorithm is described for a hybrid model comprising a single PS and a single NS,

$$\begin{cases}
\mathbf{M}^N \ddot{\mathbf{u}}_{k+1}^N + \mathbf{C}^N \dot{\mathbf{u}}_{k+1}^N + \mathbf{r}^N(\mathbf{u}_{k+1}^N, \theta_{k+1}^N) = \mathbf{f}_{k+1}^N + \mathbf{L}^{N^T} \boldsymbol{\Lambda}_{k+1}^N \\
\mathbf{L}^N \dot{\mathbf{u}}_{k+1}^N + \bar{\mathbf{L}}^N \dot{\mathbf{u}}_{k+1}^g = \mathbf{0} \\
\mathbf{M}^P \ddot{\mathbf{u}}_{k+1}^P + \mathbf{C}^P \dot{\mathbf{u}}_{k+1}^P + \mathbf{r}^P(\mathbf{u}_{k+1}^P, \theta_{k+1}^P) = \mathbf{f}_{k+1}^P + \mathbf{L}^{P^T} \boldsymbol{\Lambda}_{k+1}^P \\
\mathbf{L}^P \dot{\mathbf{u}}_{k+1}^P + \bar{\mathbf{L}}^P \dot{\mathbf{u}}_{k+1}^g = \mathbf{0} \\
\bar{\mathbf{L}}^{N^T} \boldsymbol{\Lambda}_{k+1}^N + \bar{\mathbf{L}}^{P^T} \boldsymbol{\Lambda}_{k+1}^P = \mathbf{0}
\end{cases} \quad (4)$$

where superscripts N and P indicates NS and PS, respectively. In detail, $\boldsymbol{\Lambda}$ vectors represent interface forces used to enforce velocity compatibility between NS and PS. \mathbf{L} and $\bar{\mathbf{L}}$ are Boolean matrices used to collocate these interface forces on both substructures' degrees-of-freedom. For a detailed description of how those matrices are defined, the reader is addressed to the paper of Abbiati and co-workers [7]. It is important to remark that both fictitious damping matrices \mathbf{C}^N and \mathbf{C}^P are computed based on the lower eigenvalue of the coupled equations of equilibrium, as defined in equation (2), which is estimated with a linearized monolithic version of the partitioned hybrid model. The LLM-GC algorithm is presented in algorithmic form to integrate equation (4) from time t_k to t_{k+1} with a time step Δt :

1. Solve the NS free problem at t_{k+1} ,

$$\begin{cases}
\tilde{\mathbf{u}}_{k+1}^{N,free} = \mathbf{u}_k^N + \dot{\mathbf{u}}_k^N \Delta t + \left(\frac{1}{2} - \beta\right) \Delta t^2 \ddot{\mathbf{u}}_k^N \\
\tilde{\dot{\mathbf{u}}}_{k+1}^{N,free} = \dot{\mathbf{u}}_k^N + (1 - \gamma) \Delta t \ddot{\mathbf{u}}_k^N \\
\ddot{\mathbf{u}}_{k+1}^{N,free} = \mathbf{D}^{N^{-1}} \left(\mathbf{f}_{k+1}^N - \mathbf{C}^N \tilde{\dot{\mathbf{u}}}_{k+1}^{N,free} - \mathbf{r}_{k+1}^N(\tilde{\mathbf{u}}_{k+1}^{N,free}) \right)
\end{cases} \quad (5)$$

$$\begin{cases}
\mathbf{u}_{k+1}^{N,free} = \tilde{\mathbf{u}}_{k+1}^{N,free} + \ddot{\mathbf{u}}_{k+1}^{N,free} \beta \Delta t^2 \\
\dot{\mathbf{u}}_{k+1}^{N,free} = \tilde{\dot{\mathbf{u}}}_{k+1}^{N,free} + \ddot{\mathbf{u}}_{k+1}^{N,free} \gamma \Delta t
\end{cases}$$

with,

$$\mathbf{D}^N = \mathbf{M}^N + \mathbf{C}^N \gamma \Delta t + \mathbf{K}^N \beta \Delta t^2$$

In detail, the displacement predictor $\tilde{\mathbf{u}}_{k+1}^{N,free}$ is sent to the FE software that computes the corresponding restoring force \mathbf{r}_{k+1}^N . According to equation (3), mass \mathbf{M}^N and damping \mathbf{C}^N matrices are computed based on the initial tangent stiffness matrix $\mathbf{K}^N = \frac{\partial \mathbf{r}^N}{\partial \mathbf{u}^N} \big|_{u_0, \dot{u}_0}$ once at the beginning of the simulation.

2. Solve the PS free problem at t_{k+1} ,

$$\begin{cases}
\tilde{\mathbf{u}}_{k+1}^{P,free} = \mathbf{u}_k^P + \dot{\mathbf{u}}_k^P \Delta t + \left(\frac{1}{2} - \beta\right) \Delta t^2 \ddot{\mathbf{u}}_k^{P,free} \\
\tilde{\dot{\mathbf{u}}}_{k+1}^{P,free} = \dot{\mathbf{u}}_k^P + (1 - \gamma) \Delta t \ddot{\mathbf{u}}_k^{P,free} \\
\ddot{\mathbf{u}}_{k+1}^{P,free} = \mathbf{D}^{P^{-1}} \left(\mathbf{f}_{k+1}^P - \mathbf{C}^P \tilde{\dot{\mathbf{u}}}_{k+1}^{P,free} - \mathbf{r}_{k+1}^P(\tilde{\mathbf{u}}_{k+1}^{P,free}) \right)
\end{cases} \quad (6)$$

$$\begin{cases}
\mathbf{u}_{k+1}^{P,free} = \tilde{\mathbf{u}}_{k+1}^{P,free} + \ddot{\mathbf{u}}_{k+1}^{P,free} \beta \Delta t^2 \\
\dot{\mathbf{u}}_{k+1}^{P,free} = \tilde{\dot{\mathbf{u}}}_{k+1}^{P,free} + \ddot{\mathbf{u}}_{k+1}^{P,free} \gamma \Delta t
\end{cases}$$

with

$$\mathbf{D}^P = \mathbf{M}^P + \mathbf{C}^P \gamma \Delta t + \mathbf{K}^P \beta \Delta t^2$$

Similarly to the NS, at each step t_{k+1} , the displacement predictor $\tilde{\mathbf{u}}_{k+1}^{P,free}$ is imposed to the PS by means of servo-controlled actuators and the corresponding restoring force vector \mathbf{r}_{k+1}^P is measured with load cells. Mass \mathbf{M}^P and damping \mathbf{C}^P matrices are computed based on the initial tangent stiffness matrix $\mathbf{K}^P = \frac{\partial \mathbf{r}^P}{\partial \mathbf{u}^P} \big|_{u_0, \dot{u}_0}$, which is measured from the PS with small displacement perturbations once before the experiment. It is noteworthy that displacement control errors affect the measured restoring force $\mathbf{r}_{k+1,mes}^{P,free}$ and may bias the emulated system response. Accordingly, the method proposed by Bursi and Shing (1996)[12] is suggested to compensate for control errors,

$$\mathbf{r}_{k+1}^{P,free} = \mathbf{r}_{k+1,mes}^{P,free} + \mathbf{K}^P (\mathbf{u}_{k+1}^{P,free} - \mathbf{u}_{k+1,mes}^{P,free}) \quad (7)$$

where $\mathbf{u}_{k+1,mes}^{P,free}$ and $\mathbf{r}_{k+1,mes}^{P,free}$ are measured displacement and restoring force vectors.

3. Calculate the interface Lagrange multiplier vectors as,

$$\begin{bmatrix} \Lambda_{k+1}^N \\ \Lambda_{k+1}^P \\ .g \\ \mathbf{u}_{k+1} \end{bmatrix} = -\mathbf{G}^{-1} \begin{bmatrix} \mathbf{L}^N \dot{\mathbf{u}}_{k+1}^{N,free} \\ \mathbf{L}^P \dot{\mathbf{u}}_{k+1}^{P,free} \\ \mathbf{0} \end{bmatrix} \quad (8)$$

It is important to point out that the Steklov-Poincare' operator \mathbf{G} is computed only once based on the initial tangent stiffness of both PS and NS and inverted before the simulation starts. A full derivation of \mathbf{G} is reported in Abbiati et al. (2020) [7]. As a result, the calculation of link solutions requires only a few matrix multiplications.

$$\begin{cases} \ddot{\mathbf{u}}_{k+1}^{N,link} = \mathbf{D}^{N-1} \mathbf{L}^{N^T} \Lambda_{k+1}^N \\ \ddot{\mathbf{u}}_{k+1}^{P,link} = \mathbf{D}^{P-1} \mathbf{L}^{P^T} \Lambda_{k+1}^P \end{cases} \quad (9)$$

4. Calculate the coupled velocities and accelerations,

$$\begin{cases} \ddot{\mathbf{u}}_{k+1}^N = \ddot{\mathbf{u}}_{k+1}^{N,free} + \ddot{\mathbf{u}}_{k+1}^{N,link} \\ \ddot{\mathbf{u}}_{k+1}^P = \ddot{\mathbf{u}}_{k+1}^{P,free} + \ddot{\mathbf{u}}_{k+1}^{P,link} \end{cases} \quad (10)$$

$$\begin{cases} \dot{\mathbf{u}}_{k+1}^N = \dot{\mathbf{u}}_{k+1}^{N,free} + \dot{\mathbf{u}}_{k+1}^{N,link} \gamma \Delta t \\ \dot{\mathbf{u}}_{k+1}^P = \dot{\mathbf{u}}_{k+1}^{P,free} + \dot{\mathbf{u}}_{k+1}^{P,link} \gamma \Delta t \end{cases}$$

Consistently with DR, $\gamma = \frac{1}{2}$ and $\beta = 0$ for both PS and NS. Accordingly, link displacements are null and coupled displacements are equal to free displacements.

The LLM-GC algorithm inherits second-order accuracy from the GC method [9]. Figure 1 provides a detailed representation of the procedure for integrating the coupled equation of motion of the hybrid model between times t_k and t_{k+1} .

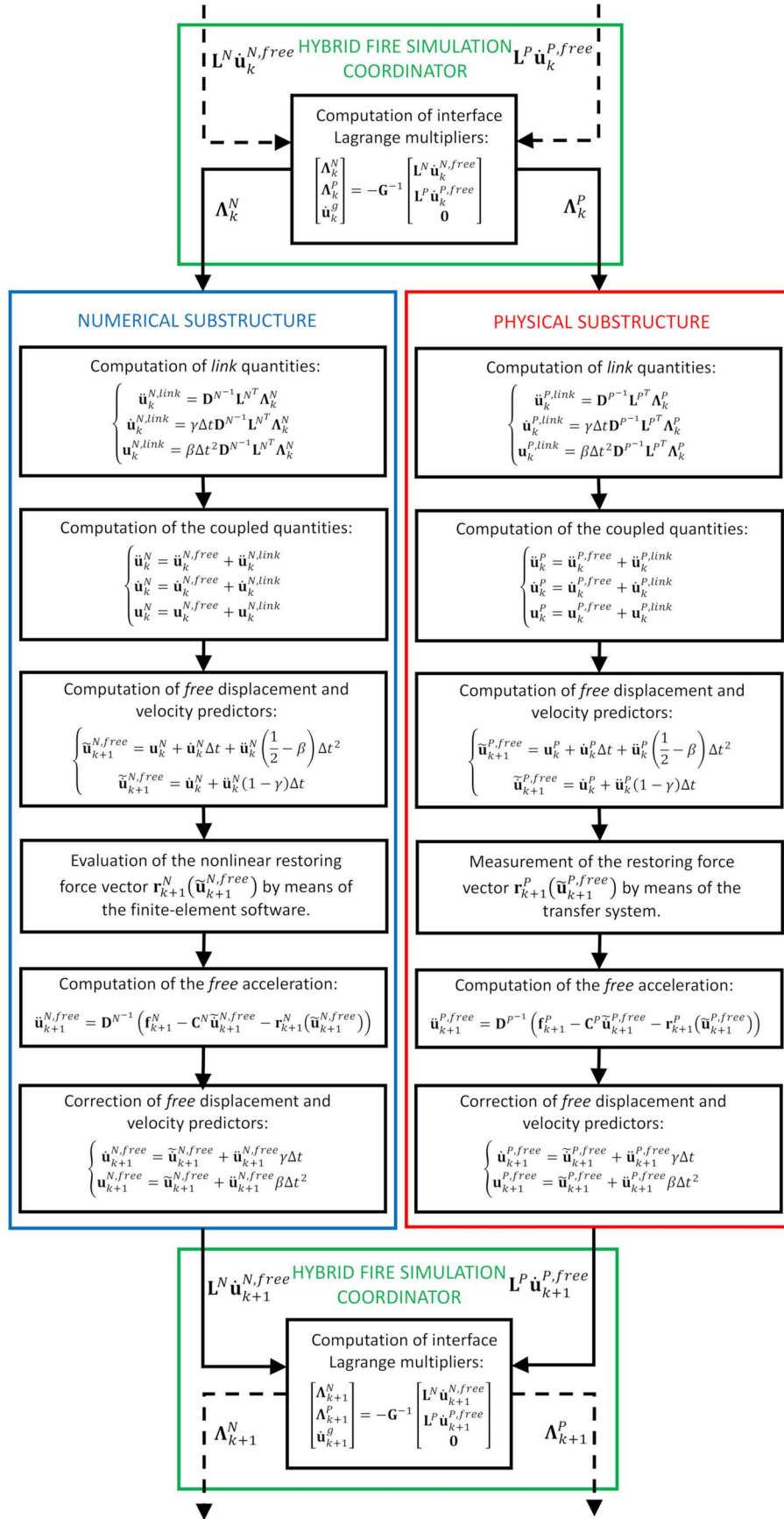


Figure 1. Architecture of the implementation of RT-HFS method based on the LLM-GC algorithm reproduced from Abbiati et al. (2020) [7].

As can be appreciated from Figure 1, one-step free solutions of PS and NS are parallel processes. In fact, the PS approaches the target boundary conditions while a FE software evaluates the restoring force of the NS, possibly with a Newton-Raphson algorithm. The computation of interface forces Λ_k^N and Λ_k^P , which determine the link solution, requires only interface velocities $\mathbf{L}^N \dot{\mathbf{u}}_k^{N,free}$ and $\mathbf{L}^P \dot{\mathbf{u}}_k^{P,free}$ and relies solely on the matrix-vector product defined in equation (8). The computational cost (and the related time overhead) of the latter is negligible compared to the computation of the one-step free solution of the NS and the PS responses. As long as the number of interface DoFs is determined by the number of actuation points of the PS and not on the total number of DoFs of the hybrid model, the LLM-GC algorithm enables RT-HFS with realistic nonlinear FE models used as NSs. Limited data exchange, as well as minimal computational overhead, make the proposed LLM-GC algorithm suitable for being implemented as a coordinator in existing HFS middleware thus facilitating reusing of existing verified FE software (e.g., OpenFresco [13-14]).

In order to maximize the convergence rate of DR, Component-mode synthesis (CMS) [15] can be used to derive reduced-order matrices for both PS and NS.

3 VIRTUAL REAL-TIME HYBRID FIRE TEST

In order to demonstrate the effectiveness of the framework with the RT-HFS method [7] and to illustrate the implementation of a real test, a virtual HFS campaign was conceived for the case study selected in the EQUFIRE project [16], which is part of the Transnational Access activities of the SERA project (www.sera-eu.org). The case study is represented by a steel braced frame, and both NS and PS are simulated numerically. Results of the virtual real-time hybrid test were then verified against the monolithic solution developed in the thermo-mechanical software SAFIR [17].

3.1 EQUFIRE case study description

The EQUFIRE project [16] aims at investigating the post-earthquake fire performance of steel braced frames endowed with passive fire protection. In particular, a four-story three-bay steel frame with concentric bracing in the central bay was selected as a case study, as illustrated in Figure 2. The building is an office with a square plan of 12.5 m x 12.5 m. It is located in Lisbon, Portugal, in an area of medium-high seismicity. The story height is 3 m with the exception of the first floor, which is 3.6 m high. Each frame is endowed with a lateral force-resisting system. The columns are continuous, and all connections are regarded as pinned. Two different steel grades were used, namely S275 and S355. The S275 was adopted for the bracing system, which acts as a structural fuse during the seismic event according to the capacity design philosophy. Steel grade S355 was selected for columns and beams that are intended to remain elastic during a seismic event. The frame was designed according to the relevant parts of EN 1993 and according to EN 1998-1 [18] relative to the seismic action.

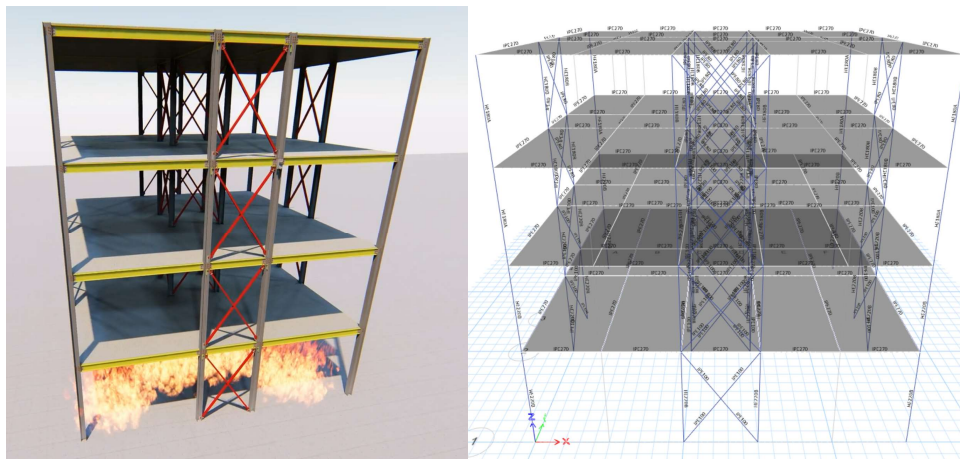


Figure 3. EQUFIRE case study

3.2 FE models and Substructuring

Figure 3a shows the member sizes and the magnitude of the gravity loads acting simultaneously with the fire action that for this case study was located at the base floor, whereas the remainder of the structure was kept cold. Figure 3b shows the location of the test frame. For the fire action, a prescriptive approach was chosen, and, in particular, the standard ISO 834 [19] heating curve was employed. This choice was made because it is easy to reproduce in a furnace. In this respect, Figure 3c illustrates the temperature evolution in time of the compartment and of the steel temperature in the unprotected members subjected to fire, i.e., IPE 100, IPE 270, and HEB 220, calculated according to a lumped mass approach and 4-side exposure. The IPE 100 profiles composing the bracing system were oriented according to the weak axis in the plane of the frame in order to force in-plane buckling so that a 2D modeling was representative.

As shown in Figure 4, it was decided to couple the PS and NS at translational DoFs, whilst continuity of the rotational DoFs was neglected. Figure 4 also illustrates the possible subdivision between the NS and PS by highlighting the controlled DoFs with an actuator. It is possible to observe that, since it is difficult to directly control rotations, only translational DoFs are controlled. Moreover, it was decided to consider as a PS both the base and the first floor in order to accurately simulate the base floor behavior under fire by guaranteeing the continuity of the column at the top of the base floor. Nonetheless, if the budget does not allow only the base floor could be physically modeled in the laboratory by accepting a lower degree of accuracy. Each column and beam element were discretized using six elements, while each brace element was discretized using eight elements. The partitioned simulation was then verified against nonlinear a thermomechanical FE analysis of the whole frame performed in SAFIR [17], which employs fiber-based thermomechanical Bernoulli beam elements. In order to reduce the frequency bandwidth of the NS, which deteriorates the convergence rate of the RT-HFT-FETI method, CMS was applied to condense NS matrices to the translational DoFs of the nodes numbered in Figure 4.

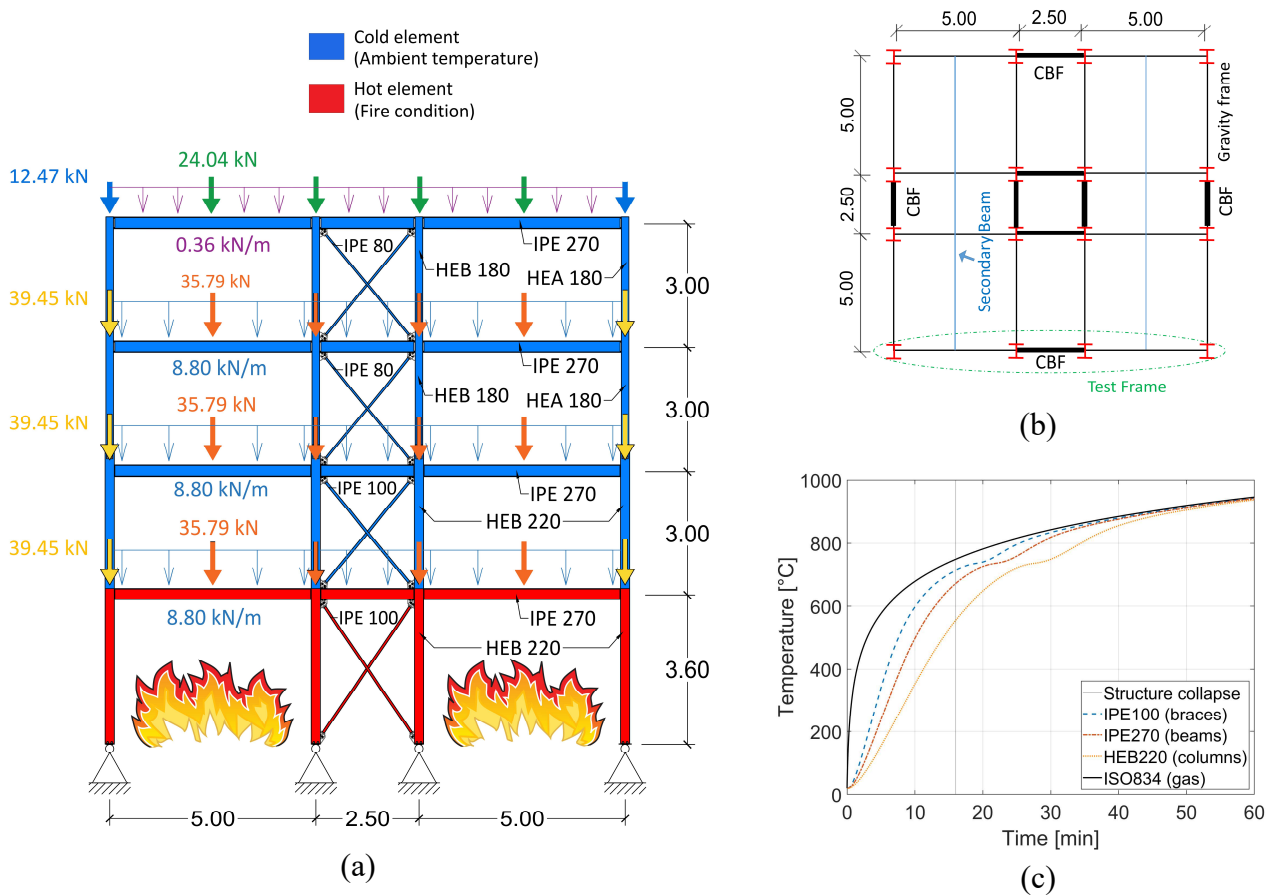


Figure 2. (a) Emulated steel frame; (b) plan view of the building (c) time-temperature heating curves. (dimensions in m)

As anticipated, the RT-HFS of the steel braced frame is numerically simulated. The proposed LLG-GC algorithm is implemented into a MATLAB thermomechanical FE environment developed in house by some

of the authors. Such a simulation environment comes with a nonlinear beam element, which accounts for geometric nonlinearity and temperature-dependent nonlinear material behavior. The beam element is based on large deformation theory (corotational formulation) under the assumption of small strains [20-21]. The beam cross-section is treated such that a non-uniform temperature distribution can be simulated. Degradation in material strength and stiffness at increasing temperature is represented by steel retention factors for effective yield strength, elastic modulus, and proportional limit, and the material constitutive law is defined according to EN 1993-1-2 stress-strain curve [22]. Structures subjected to increasing loads or temperatures are analyzed using an incremental Newton-Raphson iterative procedure. The analysis provides a complete load-deformation and temperature-deformation history for two-dimensional steel frames.

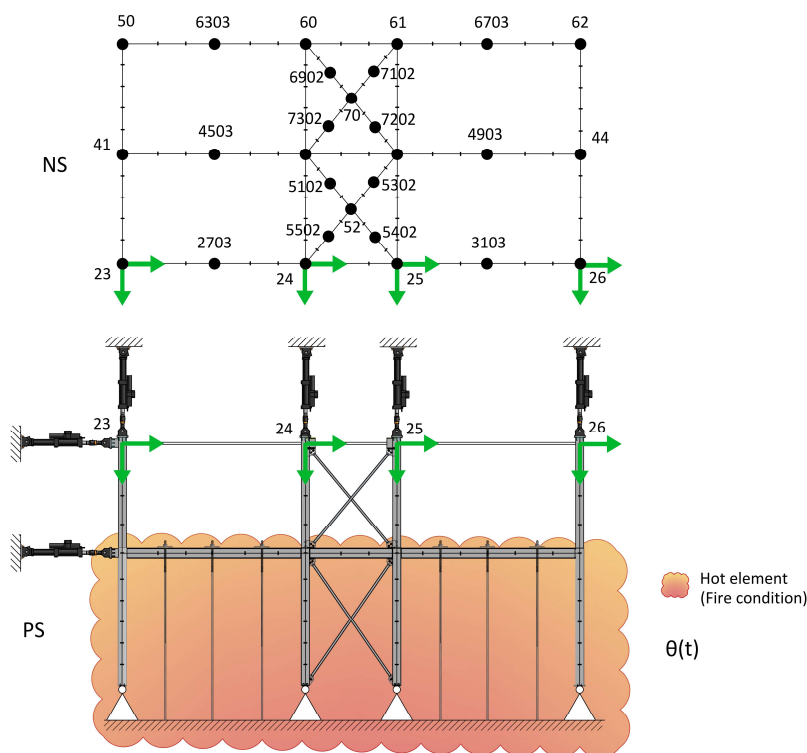


Figure 4. Substructuring scheme adopted for HFS.

4 RESULTS AND COMPARISON

The results of the virtual RT-HFS campaign are summarized herein. In order to assess the effect of experimental errors, the same simulation was performed by including noise on the restoring force of the PS and bias of the PS tangent stiffness matrix estimate. In particular, in the PS restoring force, a Gaussian noise of zero mean and 100 N standard deviation was superimposed, while all terms of the PS tangent stiffness matrix were perturbed by a random multiplicative factor that followed a uniform distribution bounded between 0.8 and 1.2. Figure 5a and Figure 5b compare the deformed configuration of the steel braced frame after 700 s and at the end of the simulation when the failure of beams occurred at time=1001 s. As can be appreciated in Figure 5a, the static response of the frame obtained via HFS well matches the reference SAFIR solution after 700 s, which represents the onset of the beam runaway. Conversely, since in the HFS continuity of rotation was not enforced at the interface between PS and NS, some discrepancies are visible at failure, as depicted in Figure 5b. In fact, the location of the hinge at the top of the column of the first floor was a good approximation at the beginning of the fire and during its first phases. However, as the fire progressed and the loss of strength and stiffness of the heated elements became significant, the load redistribution determined a variation of the bending moment diagram that was not compatible with the choice of the DoFs to control during the HFS, as highlighted in Figure 6. A comparison with and without the effect of experimental errors can be appreciated in Figure 7a and b. The error propagation analysis

provides satisfactory results, in fact, the variability of the system response is small, and the RT-HFS method results robust to measurement errors. Figure 7c-f compares the horizontal and vertical displacement responses measured at Node 1303 of the beam midspan and at Node 8 of the external right column of the PS measured at the top end of the base floor. Again, it is possible to observe a very good degree of accuracy between the partitioned and the monolithic solution, with some discrepancies occurred after the onset of the beam runaway owing to the lack of continuity of the rotational DoFs between the PS and the NS.

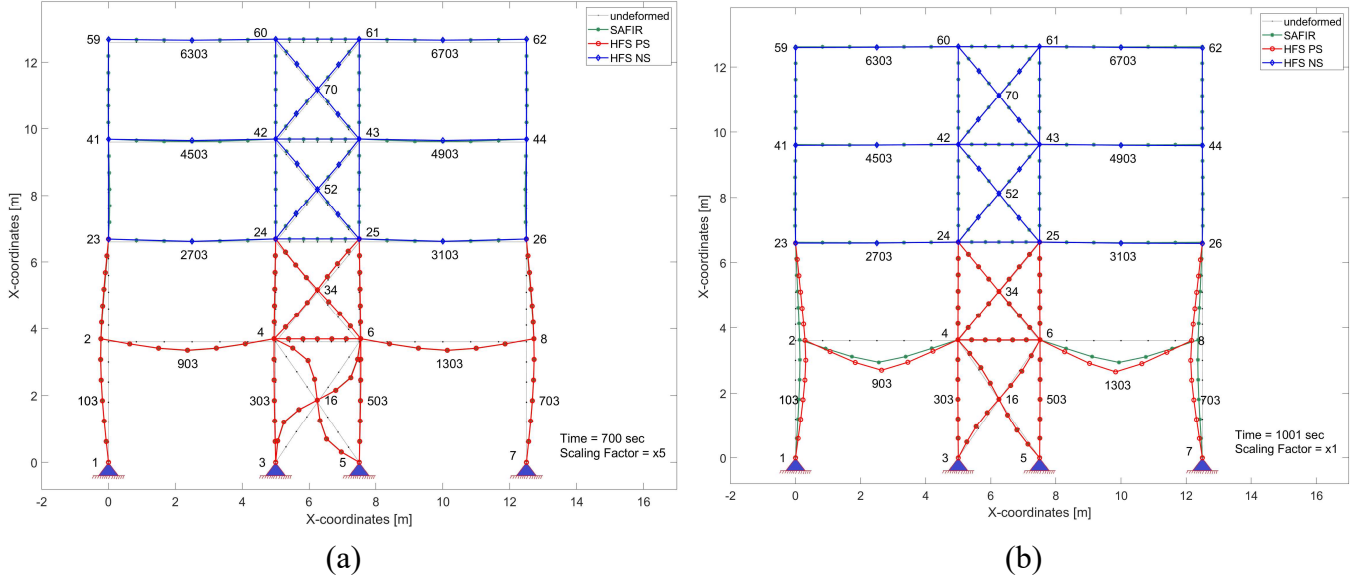


Figure 5. (a) Deformed configuration of the case study at 700 s; (b) deformed configuration of the case study 1001 s at failure.

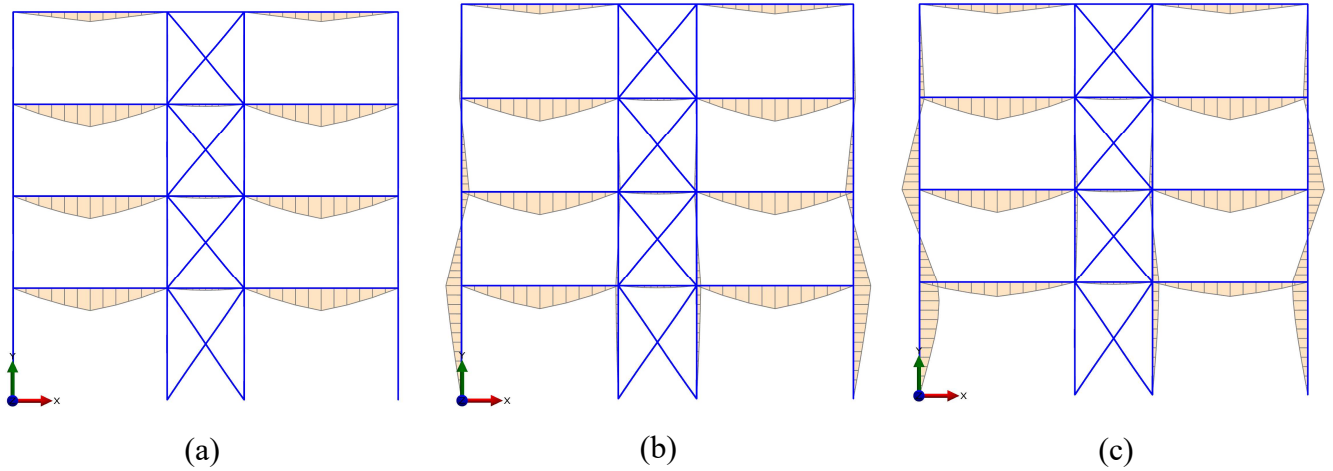
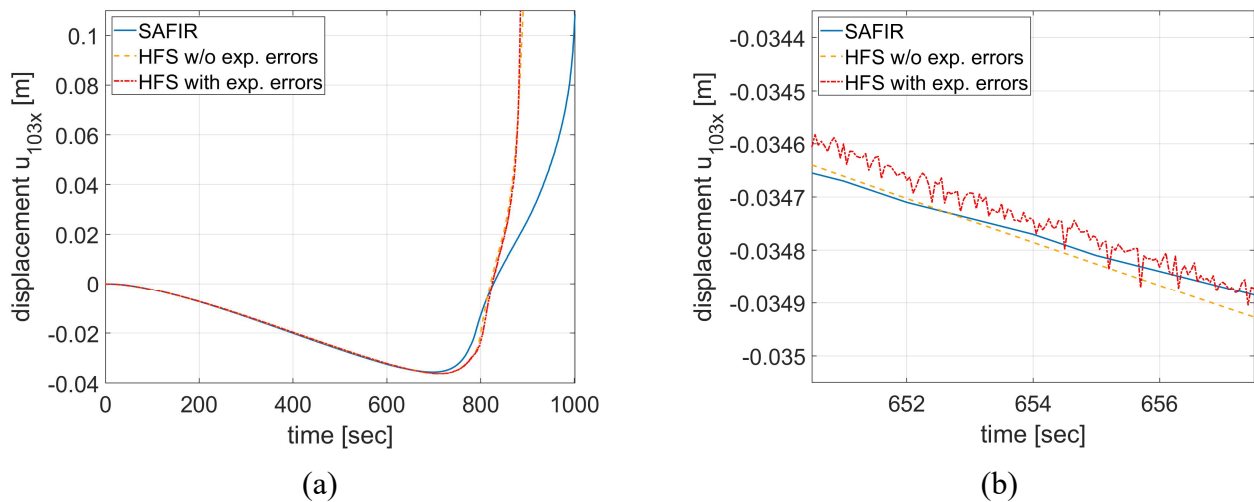
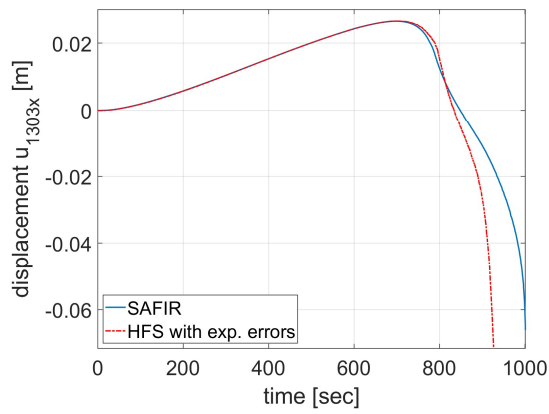
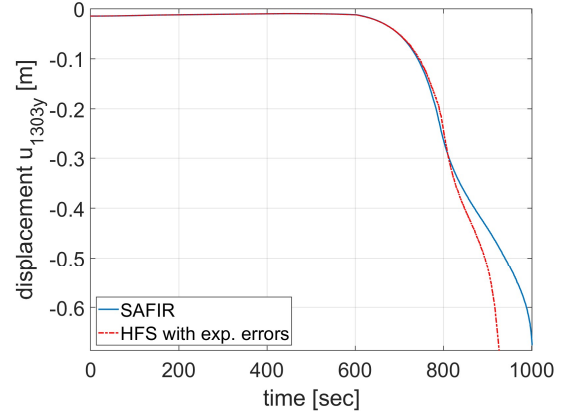


Figure 6. Bending moment diagram in the SAFIR model of the case-study steel frame at (a) $t = 0$ s; (b) $t = 700$ s; (c) $t = 1001$ s

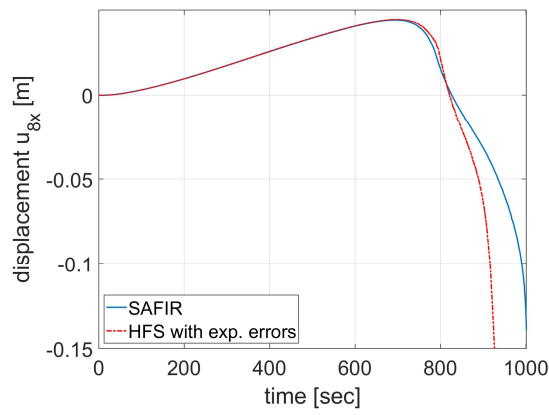




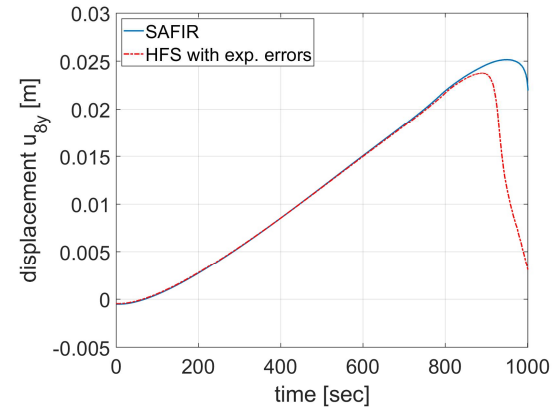
(c)



(d)



(e)



(f)

Figure 7. (a) Comparison of the horizontal displacement at Node 103; (b) comparison of the horizontal displacement at Node 103 zoomed plot; (c) comparison of the horizontal displacement at beam midspan Node 1303; (d) comparison of the vertical displacement beam midspan Node 1303; (e) comparison of the horizontal displacement measured at Node 8; (f) comparison of the vertical displacement measured at Node 8.

5 CONCLUSIONS

The results presented in this paper showed the effectiveness of the proposed RT-HFS method, which combines dynamic relaxation and partitioned time integration to compute the static response of a virtual hybrid fire test. In fact, it was found that to obtain compatibility and equilibrium at the interface DoFs, the partitioned algorithm LLM-GC based on the FETI algorithm class is suitable to couple the PS with the NS. Indeed, the proposed method is robust to error propagation. With regard to the specific application case study, the substructuring scheme was conceived, accounting for experimental limitations associated with control or rotational degrees-of-freedom. The time-history response produced by virtual hybrid fire simulations showed good agreement with the monolithic references obtained from SAFIR. The validation carried out in a fully numerical framework is promising for forthcoming experimental implementations.

ACKNOWLEDGMENT

This work has received funding from the European Union's Horizon 2020 research and innovation program under the SERA Grant Agreement No. 730900 and the related TA project EQUFIRE. This work was also supported by the Italian Ministry of Education, University and Research (MIUR) in the frame of the 'Departments of Excellence' (grant L 232/2016).

REFERENCES

1. Schellenberg A., Mahin S.A., Fenves G.L. (2009) Advanced Implementation of Hybrid Simulation, PEER Report 2009/104, Pacific Earthquake Engineering Center, University of California, Berkeley.
2. Korzen M., Magonette G., Buchet P. (1999) Mechanical loading of columns in fire tests by means of the substructuring method, *Zeitschrift für Angewandte Mathematik und Mechanik*, 79: S617-S618.
3. Sauca, A., Gernay, T., Robert, F., Tondini, N. and Franssen, J.-M. (2018), "Hybrid fire testing: Discussion on stability and implementation of a new method in a virtual environment", *Journal of Structural Fire Engineering*, Vol. 9 No. 4, pp. 319-341. <https://doi.org/10.1108/JSFE-01-2017-0017>.
4. Wang, X., Kim R.E., Kwon O.-S., Yeo I.-H. and Ahn J.-K. (2019) Continuous real-time hybrid simulation method for structures subject to fire. *J. Struct. Eng.* Vol. 145 (12). [https://doi.org/10.1061/\(ASCE\)ST.1943-541X.0002436](https://doi.org/10.1061/(ASCE)ST.1943-541X.0002436).
5. Memari M., Wang, X., Mahmoud, H., Kwon O.-S. (2020) Hybrid Simulation of Small-Scale Steel Braced Frame Subjected to Fire and Fire following Earthquake, *Journal of Structural Engineering*, 146(1), 04019182
6. Schulthess P., Neuenschwander M., Mosalam K.M., Knobloch, M.A. (2020) Computationally rigorous approach to hybrid fire testing, *Computers and Structures*, Vol. 238, <https://doi.org/10.1016/j.compstruc.2020.106301>.
7. Abbiati, G., Covi, P., Tondini, N., Bursi, O.S., Stojadinovic, B (2020) A Real-Time Hybrid Fire Simulation Method Based on Dynamic Relaxation and Partitioned Time Integration. *Journal of Engineering Mechanics* Vol. 146 (9). [https://doi.org/10.1061/\(ASCE\)EM.1943-7889.0001826](https://doi.org/10.1061/(ASCE)EM.1943-7889.0001826).
8. Farhat, C. and Roux, F.-X. (1991). A method of finite element tearing and interconnecting and its parallel solution algorithm. *Int J Num Meth Engng*, 32: 1205–1227.
9. Gravouil, A., and A. Combescure. (2001). Multi-time-step explicit–implicit method for nonlinear structural dynamics. *Int. J. Numer. Methods Eng.* Vol. 50 (1): 199–225.
10. Park K. C., Felippa C. A., Gumaste U. A. (2000). A localized version of the method of Lagrange multipliers and its applications, *Computational Mechanics* Vol. 24 (6) 476-490
11. Underwood P. G. (1983). *Computational Methods for Transient Analysis*, North-Holland, Amsterdam, 1983, Ch. Dynamic relaxation techniques: a review.
12. Bursi, O. S., & Shing, P.-S. B. (1996). EVALUATION OF SOME IMPLICIT TIME-STEPPING ALGORITHMS FOR PSEUDODYNAMIC TESTS. *Earthquake Engineering & Structural Dynamics*, Vol. 25, 333–355.
13. Whyte, C. A., Mackie, K. R., & Stojadinovic, B. (2016). Hybrid Simulation of Thermomechanical Structural Response. *Journal of Structural Engineering*, 142(2), 04015107.
14. Khan, M. A., Jiang, L., Cashell, K. A., & Usmani, A. (2018). Analysis of restrained composite beams exposed to fire using a hybrid simulation approach. *Engineering Structures*, 172, 956–966.
15. Craig R. R., Kurdila A. J. (2006). *Fundamentals of structural dynamics*, John Wiley & Sons, 2006
16. Lamperti Tornaghi M., Tsionis G., Pegon P., Molina J., Peroni M., Korzen M., Tondini N.; Covi P., Abbiati G., Antonelli, M., Gilardi, B. (2020) Experimental study of braced steel frames subjected to fire after earthquake. 17th World Conference on Earthquake Engineering - Sendai International Centre, Sendai, Japan.
17. Franssen, J-M, Gernay, T. (2017): Modeling structures in fire with SAFIR©: Theoretical background and capabilities. *Journal of Structural Fire Engineering*, 8 (3), 300-323.
18. CEN (2004): EN 1998-1 Eurocode 8: Design of structures for earthquake resistance - Part 1: General rules, seismic actions and rules for buildings, European Committee for Standardization, Brussels.
19. ISO (1999): ISO 834-1:1999, Fire-resistance tests -Elements of building construction- Part 1: General requirements. International Organization for Standardization.
20. Morbioli, A., Tondini, N., Battini J.-M. (2018). A branch-switching procedure for analysing instability of steel structures subjected to fire, *Structural Engineering and Mechanics* 67 (6) 629–641.
21. Battini J.M. (2002). Corotational beam elements in instability problems, PhD thesis (2002), Department of Structural Engineering KTH, Stockholm, Sweden.
22. CEN (2005). Eurocode 3: Design of steel structures - Part 1-2: General rules - Structural fire design, European Committee for Standardization Brussels.

A THERMO-MECHANICAL STOCHASTIC DAMAGE PERSPECTIVE FOR CONCRETE AT ELEVATED TEMPERATURES

Hao Zhou¹

ABSTRACT

Concrete under/after fire attacks has been widely evidenced to exhibit strong nonlinearities with striking randomness. To represent fully the behaviors of concrete exposed to elevated temperatures, a thermo-mechanical stochastic damage model is presented. Emphasis is placed on the effect of temperature on the mechanical constitutive law of concrete coupled with the influence by the randomness in material micro-properties. Transient creep and thermal strains are included to account for the thermal response. The proposed model captures the stiffness degradation and strain softening of concrete due to both thermal and mechanical loadings via the formulation of the gradient enhanced damage theory with temperature dependency. A novel positive/negative projection operator of the effective stress tensor is introduced to maintain the major symmetry of the secant stiffness tensor and exhibit orthotropic behavior under uniaxial tension and mixed tension/compression using the thermodynamically consistent unilateral damage model. Random damage evolution is represented by a fiber bundle model in which a set of brittle linear-elastic micro-springs of equal stiffness are joined in parallel. The failure strengths of the springs are modelled as a correlated random field such that the statistics of the random stress-strain and damage-strain functions are analytically derived for the specific structural element. Several illustrative examples will be presented in a forthcoming journal paper to verify the effectiveness and applicability of the proposed model.

Keywords: Concrete; high temperature; thermo-mechanical damage; constitutive model; random damage evolution; strain softening

1 INTRODUCTION

Modelling of concrete behavior under high temperatures provides an important basis for predicting structural performance under fire attack. During heating, the inner structure of concrete changes due to complicated physical and chemical transformations [1 – 3], causing a dramatic influence on the material properties. The stress-strain behavior of concrete in such conditions is highly nonlinear and random. In recent years, the stochastic damage model [4,5] developed within the framework of continuum damage mechanics reveals the profound mechanism of damage initiation and propagation of concrete. A comprehensive representation of nonlinearity and randomness in mechanical behavior of concrete is achieved with the stochastic damage model. However, a significant decrease appears in material properties as the dehydration and crack development of concrete at elevated temperatures. In the meantime, the variability of mechanical properties is more pronounced, making it so difficult to predict accurately the fire-resistant performance of concrete structures.

Since the 1980s, systematic theoretical and experimental research has been carried out for modelling the constitutive relation of concrete under high temperatures. Quite a few promising models provided the

¹ Postdoctoral Research Fellow, Department of Civil Engineering, South China University of Technology, Guangzhou 510641, China
e-mail: hzhou@scut.edu.cn, ORCID: <https://orcid.org/0000-0002-0146-5518>

foundation for fire-resistance analysis and design of concrete structures. Within the framework of irreversible thermodynamics, the coupling thermo-mechanical damage was introduced to capture the softening and degradation behavior of concrete under high temperature, resulting in some excellent elastic damage constitutive models [3,6,7]. By introducing the Willam-Warnke yield criterion, the chemical plastic damage constitutive model was formulated to represent the burst-induced softening and degradation behavior of concrete exposed to fire [8,9]. The burst and flaking behavior of concrete shear wall was reproduced by the isotropic elastic damage model [10]. Taking the influence of plastic deformation and instantaneous thermal strain into consideration, several elastic-plastic damage constitutive models were proposed for concrete at elevated temperatures [11 – 13]. Also, some elastic-plastic constitutive models for concrete at ambient temperatures [14] were generalized for high temperature ones [15 – 17]. Based on the temperature-dependent micro-plane model, the anisotropic damage constitutive model was formulated and applied to simulate the fire behavior of four-point bending concrete beam [18]. Due to lack of large sample of multiaxial constitutive tests, most existing models can hardly represent both the nonlinearity and randomness of concrete under high temperatures, which have severely restricted the development of fire resistance reliability analysis and design methods for concrete structures.

This paper presents a new random damage constitutive model for concrete exposed to fire situations. The model extends recent developments on constitutive modelling of concrete at ambient temperature to high temperatures. Coupling with the probabilistic nonlocal damage model of the model allows for the effects of material degradation and softening to be captured. Some numerical simulations are presented for validating the applicability of the concrete model to structural fire engineering applications.

2 STRAIN DECOMPOSITION UNDER THERMO-MECHANICAL INTERACTIONS

Deformation of concrete under combined heating and loading is dependent on both the thermal and the mechanical properties of concrete. The corresponding total strain $\boldsymbol{\varepsilon}$ is recognized to be decomposed into four additive components, namely, the free thermal strain $\boldsymbol{\varepsilon}^{\text{ft}}$, the transient creep strain $\boldsymbol{\varepsilon}^{\text{tr}}$, and the mechanical elastic strain $\boldsymbol{\varepsilon}^{\text{e}}$ and plastic strain $\boldsymbol{\varepsilon}^{\text{p}}$ [19 – 21]. This can be mathematically expressed in the rate form as

$$\dot{\boldsymbol{\varepsilon}} = \dot{\boldsymbol{\varepsilon}}^{\text{ft}}(T) + \dot{\boldsymbol{\varepsilon}}^{\text{tr}}(\boldsymbol{\sigma}, T) + \dot{\boldsymbol{\varepsilon}}^{\text{e}}(\boldsymbol{\sigma}, T) + \dot{\boldsymbol{\varepsilon}}^{\text{p}}(\boldsymbol{\sigma}, T) \quad (1)$$

where $\boldsymbol{\sigma}$ is the corresponding stress and T is the temperature.

It should be noted that the basic creep strain is neglected here because it is minor compared with the other thermo-mechanical strains in concrete under practical test or disaster conditions due to the short period of the fire [15,21]. In the case of long-term scenarios with loading and heating, the temperature dependent creep strain should be added to the strain decomposition in Eq. (1).

2.1 Free thermal strain

The free thermal strain is caused by thermal expansion which is recognized to be relevant to the rate of temperature change and the material thermal property. It is therefore empirically expressed as

$$\dot{\boldsymbol{\varepsilon}}^{\text{ft}}(T) = \alpha \dot{T} \times \mathbf{I} \quad (2)$$

with the postulation of isotropy for multiaxial stress states, in which \mathbf{I} is the second-order unit tensor; α is the coefficient of thermal expansion which, in this paper, assumes as constant: $\alpha = 1.2 \times 10^{-5}$ for siliceous aggregate and $\alpha = 0.8 \times 10^{-5}$ for calcareous aggregate at elevated temperatures [17]. Since the free thermal strain is strongly influenced by the type of aggregate employed, alternative linear or nonlinear functions may be used to capture the behaviors of other aggregate types [20 – 23].

The free thermal strain of concrete is recognized to be partly irreversible due to a widely observed residual dilatation or contraction after cooling down to ambient temperature. Therefore, the residual free thermal strain is taken as a function of the maximum temperature ever reached during the whole loading history [15,20].

2.2 Transient creep strain

The transient creep strain is stipulated as the difference between the total strain during first heating of a concrete specimen under sustained load and the free thermal strain measured on an analogous unstressed specimen [25]. This strain component is recognized to appear only during first heating and not during subsequent cooling or heating process [19]. The mechanisms behind can hardly be explained solely by the thermo-mechanical degradation of the elastic properties nor by the plastic flow. It seems that the drying of the cement matrix at 100-200 °C and the change of the chemical structure of the hydrates at higher temperatures are primarily responsible for the presence of the transient creep strain [24,25]. Torelli et al. [26] provided a comprehensive review on the experimental evidence and the numerical modeling of the transient thermal creep.

A simple uniaxial formula for calculation of the transient creep strain was first proposed by Anderberg & Thelandersson [27]. Then the model was further generalized to a multiaxial stress state separately by Thelandersson [28] and by de Borst & Peeters [24] under the postulation that the multiaxial creep rate depends linearly on the stress vector and does not induce anisotropy. Based on the work above, Gernay et al. [15] proposed the following explicit formula to compute the transient creep strain

$$\dot{\epsilon}^{\text{tr}}(T) = \dot{\phi}(T) \mathbb{H} : \frac{\bar{\sigma}^-}{f_c^0} \quad (3)$$

in which the effective stress has been considered, because this mechanism occurs in the undamaged part of concrete; $\dot{\phi}$ is the rate of the transient creep function which is generally related to the current temperature T and the material properties such as the coefficient of thermal expansion α [7,15,17,24,28]; A detailed parameter table for the transient creep function $\phi(T)$ is provided by Gernay et al. [15] for reference; $\bar{\sigma}^-$ is the negative component of the total effective stress tensor, which will be presented in the following section. f_c^0 is the uniaxial compressive strength of concrete at room temperature (e.g., 20 °C); and \mathbb{H} is the fourth-order tensor given by [24]

$$H_{ijkl} = -\gamma \delta_{ij} \delta_{kl} + \frac{1}{2} (1 + \gamma) (\delta_{ik} \delta_{jl} + \delta_{il} \delta_{jk}) \quad (4)$$

where δ_{ij} is the Kronecker symbol; the material parameter γ can be taken equal to the transient creep Poisson's ratio [7,11], in conformity to the multiaxial transient creep test data [28].

In the numerical implementation of a general elastoplastic constitutive law in rate form, the transient creep strain can be calculated through an explicit scheme as [15]

$$\dot{\epsilon}_{(s+1)}^{\text{tr}} = \dot{\epsilon}_{(s)}^{\text{tr}} + [\dot{\phi}(T_{(s+1)}) - \dot{\phi}(T_{(s)})] \mathbb{H} : \frac{\bar{\sigma}_{(s)}^-}{f_c^0} \quad (5)$$

where the irreversibility of the transient creep strain at unloading and cooling is postulated and s signifies the time step.

2.3 Mechanical elastic and plastic strains

The sum of the elastic strain and the plastic strain is referred to as the instantaneous stress-related strain which is a function of the stress and temperature. Note that the instantaneous stress-related strain is also stress history dependent, which means that the stress-strain relation is elastoplastic. When a material becomes plastic the strain states corresponding to two identical stress states may be different if the two stress states have different loading histories.

3 THERMO-MECHANICAL STOCHASTIC DAMAGE MODEL

3.1 Temperature-dependent effective stress

For concrete under combined heating and loading, the effective stress tensor $\bar{\sigma}$ holds an isotropic linear elastic relation with the elastic strain ϵ^e invoking the hypothesis of strain equivalence [29], i.e.,

$$\bar{\sigma}(T) = [1 - \chi(T)] \mathbb{E}_0 : \varepsilon^e \quad (6)$$

where the thermal damage parameter $\chi(T)$ is introduced to link the temperature T to the current elastic modulus $E(T)$ [7,10,11,30], i.e.,

$$\chi(T) = 1 - \frac{E(T)}{E_0} \quad (7)$$

and the initial fourth-order elasticity tensor at room temperature \mathbb{E}_0 reads [29,31]

$$\mathbb{E}_0 = \frac{E_0}{1 + \nu_0} (\mathbb{I} + \hat{\nu}_0 \mathbf{I} \otimes \mathbf{I}) \quad (8)$$

where \otimes signifies a tensor product, e.g., $(\mathbf{A} \otimes \mathbf{B})_{ijkl} = A_{ij} B_{kl}$; E_0 and ν_0 are the Young's modulus and Poisson's ratio at room temperature, respectively; $\hat{\nu}_0$ is the modified Poisson's ratio which is defined as $\hat{\nu}_0 = \nu_0 / (1 - 2\nu_0)$ in general 3-D and plane strain cases, and $\hat{\nu}_0 = \nu_0 / (1 - \nu_0)$ for plane stress condition; \mathbb{I} is the fourth-order unit tensor.

3.2 Positive/negative decomposition of effective stress in energy norm

To represent the different behavior of concrete in tension and in compression, the effective stress tensor $\bar{\sigma}$ is decomposed into positive (tensile) and negative (compressive) components [29,32,33]. The decomposition is generally achieved by introducing the fourth-order positive/negative projection (PNP) tensors \mathbb{P}^\pm , i.e.,

$$\bar{\sigma} = \bar{\sigma}^+ + \bar{\sigma}^-, \quad \bar{\sigma}^\pm = \mathbb{P}^\pm : \bar{\sigma}, \quad \mathbb{P}^+ + \mathbb{P}^- = \mathbb{I} \quad (9)$$

where the indices (+) and (-) will be extensively used hereafter, to point out tensile and compressive entities, respectively.

There exist multiple options to determine the PNP operators \mathbb{P}^\pm , resulting in distinct expressions of the positive/negative effective stress tensors $\bar{\sigma}^\pm$ [31]. A classical alternative is to impose additionally an orthogonal condition [29,32,34,35]

$$\bar{\sigma}^+ : \bar{\sigma}^- = \bar{\sigma}^- : \bar{\sigma}^+ = 0 \quad (10)$$

such that the corresponding positive/negative effective stress tensors $\bar{\sigma}^\pm$ can be determined uniquely.

In this case, the PNP operators \mathbb{P}^\pm can be derived analytically as [32]

$$\mathbb{P}^+ = \sum_{n=1}^3 H(\bar{\sigma}_n) \mathbf{P}_{nn} \otimes \mathbf{P}_{nn}, \quad \mathbb{P}^- = \mathbb{I} - \mathbb{P}^+ \quad (11)$$

where the second-order symmetric tensor $\mathbf{P}_{nn} := \mathbf{P}_n \otimes \mathbf{P}_n$. Herein, $\bar{\sigma}_n$ and \mathbf{P}_n are respectively the n th ($n = 1, 2, 3$) principal value and principal vector of the effective stress tensor $\bar{\sigma}$, and $\bar{\sigma}_n = \mathbf{P}_{nn} : \bar{\sigma}$.

The PNP operators in Eq. (11) are of both major and minor symmetries through, the resulting secant stiffness and compliance of the bi-scalar damage constitutive model [14] are not universally symmetric. Thus, the postulation of a well-defined Gibbs or Helmholtz free energy potential can hardly be guaranteed. Moreover, excessive lateral deformations under uniaxial tension are prone to be predicted by the classical PNP operators. To overcome these deficiencies, a closest-point PNP scheme in energy norm was developed by imposing on Eq. (9) the following orthogonal condition [31]

$$\bar{\sigma}^+ : \mathbb{C}_0 : \bar{\sigma}^- = \bar{\sigma}^- : \mathbb{C}_0 : \bar{\sigma}^+ = 0 \quad (12)$$

where the initial fourth-order compliance tensor \mathbb{C}_0 reads [36]

$$\mathbb{C}_0 = \frac{1}{E_0} [(1 + \nu_0) \mathbb{I} - \nu_0 \mathbf{I} \otimes \mathbf{I}] \quad (13)$$

Considering that the positive/negative components $\bar{\sigma}^\pm$ are coaxial to the parent effective stress tensor $\bar{\sigma}$, the second-order symmetric tensor \mathbf{P}_{nn} expanded by the principal vector \mathbf{P}_n of the effective stress tensor $\bar{\sigma}$ can also be decomposed into positive/negative parts such that

$$\bar{\sigma}_n^\pm = \mathbf{P}_{nn}^\pm : \bar{\sigma}, \quad \mathbf{P}_{nn}^+ + \mathbf{P}_{nn}^- = \mathbf{P}_{nn} \quad (14)$$

Combing Eqs. (9), (12), and (14), an explicit solution to the second-order symmetric tensor \mathbf{P}_{nn}^+ associated with the principal values $\bar{\sigma}_n$ was derived as [31]

$$\begin{cases} \mathbf{P}_{11}^+ = \mathbf{P}_{11}, \mathbf{P}_{22}^+ = \mathbf{P}_{22}, \mathbf{P}_{33}^+ = \mathbf{P}_{33} & \text{Case I : } \bar{\sigma}_1 \geq 0, \bar{\sigma}_2 \geq 0, \bar{\sigma}_3 \geq \nu_0(\bar{\sigma}_1 + \bar{\sigma}_2) \\ \mathbf{P}_{11}^+ = \mathbf{P}_{11}, \mathbf{P}_{22}^+ = \mathbf{P}_{22}, \mathbf{P}_{33}^+ = \nu_0(\mathbf{P}_{11} + \mathbf{P}_{22}) & \text{Case II : } \bar{\sigma}_1 \geq 0, \bar{\sigma}_2 \geq 0, \bar{\sigma}_3 \leq \nu_0(\bar{\sigma}_1 + \bar{\sigma}_2) \\ \mathbf{P}_{11}^+ = \mathbf{P}_{11}, \mathbf{P}_{22}^+ = \mathbf{P}_{33}^+ = \frac{\nu_0}{1-\nu_0} \mathbf{P}_{11} & \text{Case III : } \bar{\sigma}_1 \geq 0, \bar{\sigma}_3 \leq \bar{\sigma}_2 \leq \frac{\nu_0}{1-\nu_0} \bar{\sigma}_1 \\ \mathbf{P}_{11}^+ = \mathbf{P}_{22}^+ = \mathbf{P}_{33}^+ = \mathbf{0} & \text{Case IV : } \bar{\sigma}_3 \leq \bar{\sigma}_2 \leq \bar{\sigma}_1 \leq 0 \end{cases} \quad (15)$$

Then the novel PNP operators in energy norm can be given by

$$\mathbb{P}^+ = \sum_{n=1}^3 \mathbf{P}_{nn} \otimes \mathbf{P}_{nn}^+, \quad \mathbb{P}^- = \mathbb{I} - \mathbb{P}^+ \quad (16)$$

both of which possess the minor and major symmetry. And the resulting secant stiffness and compliance tensors are always major symmetric [31].

3.3 Continuum bi-scalar thermo-damage formulation

As different mechanisms are involved in the damage evolution of concrete under tension/compression, two scalars $d^+ \in [0, 1]$ and $d^- \in [0, 1]$ associated with the positive/negative components $(\bar{\sigma}^+, \bar{\sigma}^-)$ are introduced to model the tensile and compressive damage, respectively. In accordance with the double scalar damage theory [14,36], the tensile damage d^+ only affects the positive component $\bar{\sigma}^+$ whereas the compressive damage d^- only affects the negative component $\bar{\sigma}^-$. Therefore, the thermo-damage constitutive relationship can be given by

$$\boldsymbol{\sigma} = (1-d^+) \bar{\sigma}^+ + (1-d^-) \bar{\sigma}^- = \mathbb{E}^{\text{sec}} : \boldsymbol{\varepsilon}^c \quad (17)$$

for the secant stiffness tensor \mathbb{E}^{sec}

$$\mathbb{E}^{\text{sec}} = [1 - \chi(T)] [(1-d^+) \mathbb{P}^+ + (1-d^-) \mathbb{P}^-] : \mathbb{E}_0 = [1 - \chi(T)] (\mathbb{I} - \mathbb{D}) : \mathbb{E}_0 \quad (18)$$

where the fourth-order damage tensor $\mathbb{D} = d^+ \mathbb{P}^+ + d^- \mathbb{P}^-$ is symmetric invoking the novel PNP operators in energy norm in Eq. (16). And the major symmetry of the resulting secant stiffness \mathbb{E}^{sec} is naturally guaranteed as well.

To further derive the tangential stiffness tensor, the effective stress tensor in rate form is also split into positive and negative parts as

$$\dot{\bar{\sigma}} = \dot{\bar{\sigma}}^+ + \dot{\bar{\sigma}}^-, \quad \dot{\bar{\sigma}}^\pm = \mathbb{Q}^\pm : \dot{\bar{\sigma}}, \quad \mathbb{Q}^+ + \mathbb{Q}^- = \mathbb{I} \quad (19)$$

for the fourth-order PNP tensors \mathbb{Q}^\pm [14,31,35,36]

$$\mathbb{Q}^+ = \mathbb{P}^+ + 2 \sum_{n=1}^3 \sum_{m>n}^3 \frac{\langle \bar{\sigma}_n \rangle - \langle \bar{\sigma}_m \rangle}{\bar{\sigma}_n - \bar{\sigma}_m} \mathbf{P}_{nm} \otimes \mathbf{P}_{nm}, \quad \mathbb{Q}^- = \mathbb{I} - \mathbb{Q}^+ \quad (20)$$

where the symbols $\langle \cdot \rangle$ are the Macaulay brackets returning the enclosed quantity if positive, and setting zero if negative.

Taking derivative of the stress in Eq. (17) with respect to time gives the thermo-damage constitutive relationship in rate form

$$\dot{\boldsymbol{\sigma}} = (1-d^+) \dot{\bar{\sigma}}^+ + (1-d^-) \dot{\bar{\sigma}}^- - (\dot{d}^+ \bar{\sigma}^+ + \dot{d}^- \bar{\sigma}^-) = (\mathbb{I} - \mathbb{Q} - \mathbb{R}) : \dot{\bar{\sigma}} = \mathbb{E}^{\text{tan}} : \dot{\boldsymbol{\varepsilon}}^c \quad (21)$$

for the tangent stiffness tensor \mathbb{E}^{tan}

$$\mathbb{E}^{\text{tan}} = [1 - \chi(T)](\mathbb{I} - \mathbb{Q} - \mathbb{R}) : \mathbb{E}_0 \quad (22)$$

where the fourth-order tensors \mathbb{Q} and \mathbb{R} are given by [14,31,35,36]

$$\mathbb{Q} = d^+ \mathbb{Q}^+ + d^- \mathbb{Q}^-, \quad \mathbb{R} = h^+ \bar{\boldsymbol{\sigma}}^+ \otimes \boldsymbol{\Lambda}^+ + h^- \bar{\boldsymbol{\sigma}}^- \otimes \boldsymbol{\Lambda}^- \quad (23)$$

for the second-order tensors $\boldsymbol{\Lambda}^\pm := \partial Y^\pm(\bar{\boldsymbol{\sigma}}) / \partial \bar{\boldsymbol{\sigma}}$ and the damage hardening functions $h^\pm := \partial d^\pm / \partial r^\pm \geq 0$; $Y^\pm(\bar{\boldsymbol{\sigma}})$ are the damage driving forces expressed in terms of the effective stress $\bar{\boldsymbol{\sigma}}$; and the damage thresholds r^\pm are given by

$$r^\pm = \max_{\tau \in [0, t]} [r_0^\pm, Y^\pm(\bar{\boldsymbol{\sigma}}, \tau)] \quad (24)$$

where r_0^\pm is the initial damage thresholds and τ denotes time.

In the bi-scalar damage theory, the damage driving forces $Y^\pm(\bar{\boldsymbol{\sigma}})$ are defined as the following damage energy release rates [14]

$$Y^+ = \frac{1}{2[1 - \chi(T)]} \bar{\boldsymbol{\sigma}}^+ : \mathbb{C}_0 : \bar{\boldsymbol{\sigma}}^+, \quad Y^- = b_0 \left(a_0 \bar{I}_1^- + \sqrt{3 \bar{J}_2^-} \right)^2 \quad (25)$$

where \bar{I}_1^- is the first invariant of $\bar{\boldsymbol{\sigma}}^-$; \bar{J}_2^- is the second invariant of the deviatoric component of $\bar{\boldsymbol{\sigma}}^-$; a_0 and b_0 are material parameters related to the ratio of uniaxial and multiaxial strengths [4,14].

The foregoing thermo-damage formulation is driven by the evolution laws of the internal variables d^\pm . In the effective stress space, the damage criteria can be expressed as [29]

$$g(Y^\pm, r^\pm) \equiv Y^\pm(\bar{\boldsymbol{\sigma}}) - r^\pm \leq 0 \quad (26)$$

with the Kuhn-Tucker damage loading/unloading conditions

$$g^\pm(Y^\pm, r^\pm) \leq 0, \quad \dot{d}^\pm \geq 0, \quad \dot{d}^\pm g^\pm(Y^\pm, r^\pm) = 0 \quad (27)$$

As can be seen, the stiffness degradation of concrete under coupled heating and loading is represented by the multiplicative combination of the thermo and mechanical damage evolutions, rather analogous to the manipulations by other scholars [3,7,15,17,25].

3.4 Probabilistic nonlocal damage evolution laws

It is well known that the damage process of concrete is notably affected by the randomness inherent to the material properties. The pre-existing microcracks and microdefects of concrete under loading propagate randomly, resulting in considerable variability of structural responses. Even the structural failure modes may be biased merely due to the presence of randomness in concrete [37]. The variability is even more pronounced under coupled heating and loading scenarios, making it rather difficult to predict accurately the responses of structures subjected to high temperatures.

However, deterministic analysis methods fail to fully characterize the multiscale uncertainties coupled with nonlinearities of concrete and products under thermo-mechanical damage. Therefore, quantitatively representing these complex mechanical behaviors allows for a better approximation of the actual responses at both the material level and the structural level, and further a more accurate assessment of the overall reliability of structures under/after fire attack.

The micromechanics-based stochastic damage models (also known as the idealized fiber-bundle models or the parallel element models) [4,38] provide feasible alternatives to represent the variability as well as nonlinearity of concrete structures. A representative volume element (RVE) of concrete with characters of multi-scale and random distribution can be idealized as a sequence of springs (fibers, or micro-elements) with elastic-brittle behavior, joined in parallel, as shown in Figure 1. The micro- and macro-level properties of concrete are represented severally by responses of the individual springs and the bundle. The fracture strain of the fibers is then randomized to allow the formulation of an analytical stochastic damage model for predicting the mean, variance, and probability distribution of the structural responses [4,5].

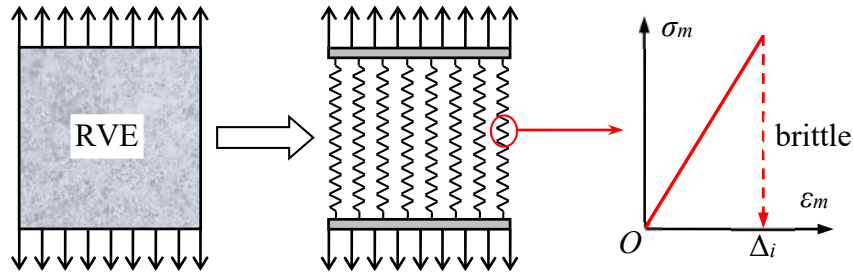


Figure 1. Idealized fiber-bundle model for random damage of quasibrittle materials

The RVE may exhibit degradation and softening behaviors due to random fracture of the fibers. Thus, the stochastic damage evolution function of the RVE under loading can be given by [4]

$$d^{\pm}(\varepsilon^{\pm}) = \int_0^1 H[\varepsilon^{\pm} - \Delta^{\pm}(x)] dx \quad (28)$$

where $H(\cdot)$ denotes the Heaviside function; ε^{\pm} are the uniaxial elastic strains; $\Delta^{\pm}(x)$ are the one-dimensional fracture strain random field at position x , which can be generated numerically by several different approaches [39 – 41]. In this paper, the stochastic harmonic function representation of the stochastic processes [41] will be employed for achieving a small number of random variables.

Assuming that $\Delta^{\pm}(x)$ follow the lognormal distribution inheriting the previous studies [4,5,38,42], the mean and variance of the damage evolution functions (28) can be derived respectively as

$$\mu_{d^{\pm}} = \Phi\left(\frac{\ln \varepsilon^{\pm} - \lambda^{\pm}}{\zeta^{\pm}}\right) \quad (29)$$

$$V_{d^{\pm}}^2 = 2 \int_0^1 (1 - \gamma) \Phi\left(\frac{\ln \varepsilon^{\pm} - \lambda^{\pm}}{\zeta^{\pm}}, \frac{\ln \varepsilon^{\pm} - \lambda^{\pm}}{\zeta^{\pm}} \middle| \rho_{Z^{\pm}}(\gamma)\right) d\gamma - \mu_{d^{\pm}}^2 \quad (30)$$

where $\Phi(\cdot)$ signifies the cumulative distribution function (CDF) of the standard normal distribution; λ^{\pm} and ζ^{\pm} are the mean and standard deviation of $Z^{\pm}(x) = \ln[\Delta^{\pm}(x)]$, respectively; $\gamma = |x_1 - x_2|$; and $\rho_{Z^{\pm}}(\gamma)$ are the correlation functions of $Z^{\pm}(x)$ assumed to be

$$\rho_{Z^{\pm}}(\gamma) = \exp(-\gamma/\zeta^{\pm}) \quad (31)$$

in which the correlation parameters ζ^{\pm} equal to half of the fluctuation scales of $Z^{\pm}(x)$ [5,40]. As the correlation parameters ζ^{\pm} approach to zero, $\Delta^{\pm}(x)$ tend towards uncorrelated random fields.

The damage consistent condition states that the rates of damage evolutions under uniaxial and multiaxial stress states are equal on condition that their initial damage states and damage energy release rates are the same [4]. Under this postulation, the uniaxial random damage evolution laws (28) can be generalized to the multiaxial stress states by introducing the following energy equivalent strains

$$\varepsilon_{\text{eq}}^{\pm} = \sqrt{\frac{2Y^{\pm}}{[1 - \chi(T)]E_0}}, \quad \varepsilon_{\text{eq}}^{\pm} = \frac{1}{(1 - a_0)[1 - \chi(T)]E_0} \sqrt{\frac{Y^{\pm}}{b_0}} \quad (32)$$

Referring to Eq. (28), the multi-dimensional random damage evolution laws can be given by

$$d^{\pm}(\varepsilon_{\text{eq}}^{\pm}) = \int_0^1 H[\varepsilon_{\text{eq}}^{\pm} - \Delta^{\pm}(x)] dx \quad (33)$$

Considering the relations between Y^{\pm} and $\varepsilon_{\text{eq}}^{\pm}$ as shown in Eq. (32), the damage criteria in Eq. (26) can be equivalently expressed as

$$g(\varepsilon_{\text{eq}}^{\pm}, r_e^{\pm}) \equiv \varepsilon_{\text{eq}}^{\pm} - r_e^{\pm} \leq 0, \quad r_e^{\pm} = \max_{\tau \in [0, t]} [\varepsilon_{\text{eq}}^{\pm}(\tau)] \quad (34)$$

It is recognized that the mesh sensitivity and strain localization phenomena are frequently encountered in the finite element analyses of the strain-softening materials, like concrete, rock, and ceramic, etc. In this

regard, the gradient enhanced damage model [43] approximately equivalent to the nonlocal damage model [44] is introduced to regularize the above damage-equivalent strains. Specifically, the local equivalent strains $\varepsilon_{eq}^{e\pm}$ should be replaced by its nonlocal counterparts $\tilde{\varepsilon}_{eq}^{e\pm}$, and they satisfy

$$\tilde{\varepsilon}_{eq}^{e\pm} - c\nabla^2 \tilde{\varepsilon}_{eq}^{e\pm} = \varepsilon_{eq}^{e\pm}, \quad \nabla \tilde{\varepsilon}_{eq}^{e\pm} \cdot \mathbf{n} = 0 \quad (35)$$

where ∇^2 is the Laplacian operator; c is a positive constant of unit length squared, which implicates the dimension of the localization zone; ∇ is the gradient operator and \mathbf{n} is the outer normal unit vector, which together constitute a natural boundary condition [43].

The foregoing probabilistic damage evolution laws provide a rational approach towards exploring the statistics of concrete behaviors. Random stress-strain relationships for concrete under coupled heating and loading conditions can be generated given the mean, variance, and fluctuation scale of the random fields for the microscopic fracture strains. As regards the stochastic finite element analysis of a certain component or a structure, the correlation of the generated random samples in spatial domain must be considered properly under the constraint of the fluctuation scale from the upper-level of concrete, say, the correlation of strength distribution. More details refer to [5].

3.5 Empirical evolution model for plastic strain

Under the postulation of strain equivalence, it is recognized that the effective stress space plasticity (ESP) can be established by [14,42,45]

$$\begin{cases} \dot{\varepsilon}^p = \dot{\lambda}^p \frac{\partial F^p(\bar{\sigma}, \kappa)}{\partial \bar{\sigma}} \\ \dot{\kappa} = \dot{\lambda}^p \mathbf{h}(\bar{\sigma}, \kappa) \\ F(\bar{\sigma}, \kappa) \leq 0, \quad \dot{\lambda}^p \geq 0, \quad \dot{\lambda}^p F(\bar{\sigma}, \kappa) = 0 \end{cases} \quad (36)$$

where F^p and F are the plastic potential and the plastic yield function, respectively; $\dot{\lambda}^p$ is the plastic consistency parameter; κ is the hardening parameter; and \mathbf{h} is the vectorial hardening function.

The ESP provides a rigorous framework for determining the plastic evolution of concrete undergone damage. A wide variety of models have been developed to represent the plastic behaviors of concrete [4,11,14,15,17,36,45,56]. However, a unified conclusion in selecting the plastic potential and the plastic yield function has not been achieved yet due to multiple physical considerations. The associated parameters are difficult to be identified by test data. Moreover, the models are intricate and time-consuming in numerical implementations. The convergence problem occurs inevitably in solving the complex systems especially while the thermal effect is considered. To overcome these deficiencies, a phenomenological plastic model catering for the ESP was proposed for practical applications with sound experimental support [42]. The evolution of plastic strain was postulated dynamically proportional to the evolution of elastic strain relating to the effective stress.

To characterize the different plastic behaviors of concrete in tension/compression, the plastic strain rate is also split into positive/negative parts, i.e.

$$\dot{\varepsilon}^p = \dot{\varepsilon}^{p+} + \dot{\varepsilon}^{p-} \quad (37)$$

for the phenomenological plastic evolution

$$\dot{\varepsilon}^{p\pm} = H(\dot{d}^\pm) \xi_p^\pm (d^\pm)^{n_p^\pm} \dot{\varepsilon}^{e\pm} = \frac{1}{1 - \chi(T)} H(\dot{d}^\pm) \xi_p^\pm (d^\pm)^{n_p^\pm} \mathbb{C}_0 : \dot{\bar{\sigma}}^\pm = \frac{1}{1 - \chi(T)} H(\dot{d}^\pm) \xi_p^\pm (d^\pm)^{n_p^\pm} \mathbb{C}_0 : \mathbb{Q}^\pm : \dot{\bar{\sigma}} \quad (38)$$

where ξ_p^\pm and n_p^\pm are test parameters [42].

Solving iteratively the simultaneous Eqs. (37) and (38) gives the plastic strain rate tensors $\dot{\varepsilon}^{p\pm}$.

It is seen that the plastic evolutions are coupled straightforwardly with the damage evolution processes, resulting in an implicit thermal-damage constitutive model.

3.6 Reformulation of the material tangent

Considering all the deformations induced by the thermal-mechanical interactions, the material tangent in Eq. (22) needs to be reformulated. Combining Eqs. (1), (21), (37), and (38), the complete thermo-mechanical stochastic damage constitutive relation in rate form for concrete under coupled loading and heating can be derived as

$$\dot{\boldsymbol{\sigma}} = (1 - \chi)(\mathbb{I} - \mathbb{Q} - \mathbb{R}) : \left[\mathbb{I} + H(\dot{d}^+) \xi_p^+(d^+)^{n_p^+} \mathbb{Q}^+ + H(\dot{d}^-) \xi_p^-(d^-)^{n_p^-} \mathbb{Q}^- \right]^{-1} : \mathbb{E}_0 : (\dot{\boldsymbol{\varepsilon}} - \dot{\boldsymbol{\varepsilon}}^{\text{ft}} - \dot{\boldsymbol{\varepsilon}}^{\text{tr}}) \quad (39)$$

where the characters of temperature dependence are implied as regards some related internal variables.

Considering that the free thermal strain $\boldsymbol{\varepsilon}^{\text{ft}}$ in Eq. (2) and the transient creep strain $\boldsymbol{\varepsilon}^{\text{tr}}$ in Eq. (3) can be addressed in an explicit manner in numerical implementation, the tangential stiffness tensor of the constitutive equation (39) can be expressed as

$$\mathbb{E}^{\text{tan}} = (1 - \chi)(\mathbb{I} - \mathbb{Q} - \mathbb{R}) : \left[\mathbb{I} + H(\dot{d}^+) \xi_p^+(d^+)^{n_p^+} \mathbb{Q}^+ + H(\dot{d}^-) \xi_p^-(d^-)^{n_p^-} \mathbb{Q}^- \right]^{-1} : \mathbb{E}_0 \quad (40)$$

It is noted that most of the material properties of concrete change with the variation in temperature. Accounting fairly for the temperature-dependencies of the attribute parameters is of crucial importance for representing the degradations of concrete under thermal-mechanical interactions. Various empirical models are already available for this purpose in the literatures [15,47]. Also, there exists considerable experimental data working on this aspect [20,27,48 – 51]. In the present paper, the elastic moduli, peak strengths and strains of concrete changing with temperature are taken from Eurocode-2 [52]. The temperature-dependencies of the Poisson's ratio, strength ratio between uniaxial and multiaxial loadings, and other related material parameters are treated referring to the elaborate contributions by Gernay et al. [15].

4 NUMERICAL IMPLEMENTATION

The above model is programmed with the user defined material (UMAT) subroutine in ABAQUS for numerical implementations. At time step n , the stress tensor $\boldsymbol{\sigma}_n$, the total strain tensor $\boldsymbol{\varepsilon}_n$, and the basic state variables $(\bar{\boldsymbol{\sigma}}_n, \boldsymbol{\varepsilon}_n^{\text{p}}, \boldsymbol{\varepsilon}_n^{\text{tr}}, d_n^{\pm}, r_n^{\pm})$ for each integration point are assumed to be known. After a given increment $(\Delta T_{n+1}, \Delta \boldsymbol{\varepsilon}_{n+1})$, the stress tensor $\boldsymbol{\sigma}_{n+1}$, the total strain tensor $\boldsymbol{\varepsilon}_{n+1}$, and the basic state variables $(\bar{\boldsymbol{\sigma}}_{n+1}, \boldsymbol{\varepsilon}_{n+1}^{\text{p}}, \boldsymbol{\varepsilon}_{n+1}^{\text{tr}}, d_{n+1}^{\pm}, r_{n+1}^{\pm})$ at time step $n+1$ for each integration point can be updated by the UMAT subroutine. The Newton-Raphson method is adopted to solve the nonlinear implicit Eq. (38) for the elastic strain $\boldsymbol{\varepsilon}^{\text{e}}$ with a given total strain tensor $\boldsymbol{\varepsilon}$. The mean values of the damage scalars $\mu_{d^{\pm}}$ are calculated at each iteration, along with the evaluation of the damage variance $V_{d^{\pm}}^2$. Then the mean and variance curves of the random stress-strain relations can be determined.

As is known, the laboratory tests with large samples of concrete specimen at elevated temperatures are rare and hard-conducted. The mean and variance curve of the one-dimensional stress-strain relation can be verified by small sample randomized tests. However, it is very tough to carry out the multi-axial loading tests of concrete with the randomness and the thermal effect taken into consideration. Therefore, the multi-dimensional stress-strain relation in the mean level is to be numerically examined by both the elementary tests and some case studies in the structural scale. Further, the variance curve of the multi-dimensional constitutive laws for concrete under high temperatures can be deduced theoretically. Due to space limitation, all these will be presented in a forthcoming journal paper where the effectiveness and applicability of the proposed model is to be illustrated as stated above.

5 CONCLUSIONS

A thermo-mechanical stochastic damage model is developed to represent the random degradation and softening behavior of concrete exposed to elevated temperatures. The model reveals physically the damage evolution law of concrete based on a theoretical fiber bundle model. The thermal damage and the mechanical damage as well as their coupling effect are integrated into a unified framework for capturing

the actual response of concrete under fire situations. In the mean and variance sense, the present model takes fully care of the randomness exists in concrete and its propagation with the development of the mechanical nonlinearity. The consideration of uncertainties makes for the assessment of actual concrete structures under/after fire attacks.

ACKNOWLEDGMENTS

Financial support from the National Natural Science Foundation of China (Grant No. 51908224) and the Postdoctoral Science Foundation of China (Grant Nos. 2018M640783 and 2020T130211) is gratefully appreciated.

REFERENCES

1. Bažant, Z.P., Kaplan, M.F. Concrete at High Temperatures: Material Properties and Mathematical Models, Longman, Harlow, 1996.
2. Khoury, G.A., Majorana, C.E., Pesavento, F., Schrefler, B.A. Modelling of heated concrete, Magazine of Concrete Research, 2002, Vol. 54, pp. 1-25.
3. Gawin, D., Pesavento, F., Schrefler, B.A. Modelling of hygro-thermal behaviour of concrete at high temperature with thermo-chemical and mechanical material degradation. Computer Methods in Applied Mechanics and Engineering, 2003, Vol. 192, No. 13-14, pp. 1731-1771.
4. Li, J., Ren, X.D. Stochastic damage model for concrete based on energy equivalent strain. International Journal of Solids and Structures, 2009, Vol. 46, No. 11-12, pp. 2407-2419.
5. Zhou, H., Li, J., Spencer Jr., B.F. Multiscale random fields-based damage modeling and analysis of concrete structures. Journal of Engineering Mechanics, 2019, Vol. 145, No. 7, pp. 04019045.
6. Stabler, J., Baker, G. On the form of free energy and specific heat in coupled thermo-elasticity with isotropic damage. International Journal of Solids and Structures, 2000, Vol. 37, No. 34, pp. 4691-4713.
7. Pearce, C.J., Nielsen, C.V., Bićanić, N. Gradient enhanced thermo-mechanical damage model for concrete at high temperatures including transient thermal creep. International Journal for Numerical and Analytical Methods in Geomechanics, 2004, Vol. 28, No. 7-8, pp. 715-735.
8. Ulm, F., Coussy, O., Bažant, Z.P. The “chunnel” fire. i: Chemoplastic softening in rapidly heated concrete. Journal of Engineering Mechanics, 1999, Vol. 125, No. 3, pp. 272-282.
9. Li, R.T., Li, X.K. A coupled chemo-elastoplastic-damage constitutive model for plain concrete subjected to high temperature. International Journal of Damage Mechanics, 2010, Vol. 19, No. 8, pp. 971-1000.
10. Davie, C.T., Zhang, H.L., Gibson, A. Investigation of a continuum damage model as an indicator for the prediction of spalling in fire exposed concrete. Computers & Structures, 2012, Vol. 94-95, pp. 54-69.
11. Nechnech, W., Meftah, F., Reynouard, J.M. An elasto-plastic damage model for plain concrete subjected to high temperatures. Engineering Structures, 2002, Vol. 24, No. 5, pp. 597-611.
12. Luccioni, B.M., Figueroa, M.I., Danesi, R.F. Thermo-mechanic model for concrete exposed to elevated temperatures. Engineering Structures, 2003, Vol. 25, No. 6, pp. 729-742.
13. Tenchev, R., Purnell, P. An application of a damage constitutive model to concrete at high temperature and prediction of spalling. International Journal of Solids and Structures, 2005, Vol. 42, No. 26, pp. 6550-6565.
14. Wu, J.Y., Li, J., Faria, R. An energy release rate-based plastic-damage model for concrete. International Journal of Solids and Structures, 2006, Vol. 43, No. 3-4, pp. 583-612.
15. Gernay, T., Millard, A., Franssen, J.M. A multiaxial constitutive model for concrete in the fire situation: Theoretical formulation. International Journal of Solids and Structures, 2013, Vol. 50, No. 22-23, pp. 3659-3673.
16. Gernay, T., Franssen, J.M. A plastic-damage model for concrete in fire: Applications in structural fire engineering. Fire Safety Journal, 2015, Vol. 71, pp. 268-278.
17. Yao, Y., Wang, K.M., Hu, X.X. Thermodynamic-based elastoplasticity multiaxial constitutive model for concrete at elevated temperatures. Journal of Engineering Mechanics, 2017, Vol. 143, No. 7, pp. 04017039.
18. Ožbolt, J., Bošnjak, J., Periškić, G., Sharma, A. 3D numerical analysis of reinforced concrete beams exposed to elevated temperature. Engineering Structures, 2014, Vol. 58, pp. 166-174.

19. Khoury, G.A., Grainger, B.N., Sullivan, P.J.E. Transient thermal strain of concrete: Literature review, conditions within specimen and behavior of individual constituents. *Magazine of Concrete Research*, 1985, Vol. 37, No. 132, pp. 131-144.
20. Schneider, U. Concrete at high temperatures-a general review. *Fire Safety Journal*, 1988, Vol. 13, pp. 55-68.
21. Li, L.Y., Purkiss, J. Stress-strain constitutive equations of concrete material at elevated temperatures. *Fire Safety Journal*, Vol. 40, pp. 669-686.
22. Terro, M.J. Numerical modelling of the behaviour of concrete structures. *ACI Structural Journal*, 1998, Vol. 95, No. 2, pp. 183-193.
23. Nielsen, C.V., Pearce, C.J., Bićanić N. Theoretical model of high temperature effects on uniaxial concrete member under elastic restraint. *Magazine of Concrete Research*, 2002, Vol. 54, No. 4, pp. 239-249.
24. de Borst, R., Peeters, P. Analysis of concrete structures under thermal loading. *Computer Methods in Applied Mechanics and Engineering*, 1989, Vol. 77, pp. 293-310.
25. Nechnech, W., Meftah, F., Reynouard, J.M. An elasto-plastic damage model for plain concrete subjected to high temperatures. *Engineering Structures*, 2002, Vol. 24, pp. 597-611.
26. Torelli, G., Mandal, P., Gillie, M., Tran, V.X. Concrete strains under transient thermal conditions: A state-of-the-art review. *Engineering Structures*, 2016, Vol. 127, pp. 172-188.
27. Anderberg, Y., Thelandersson, S. A constitutive law for concrete at transient high temperature conditions. *ACI Special Publication SP-55-8*, Detroit, 1978, pp. 187-205.
28. Thelandersson, S. Modeling of combined thermal and mechanical action in concrete. *Journal of Engineering Mechanics*, 1987, Vol. 113, No. 6, pp. 893-906.
29. Simó, J.C., Ju, J.W. Strain-and stress-based continuum damage models—I. Formulation. *International Journal of Solids and Structures*, 1987, Vol. 23, No. 7, pp. 821-840.
30. Gawin, D., Pesavento, F. An overview of modeling cement based materials at elevated temperatures with mechanics of multi-phase porous media. *Fire Technology*, 2012, Vol. 48, No. 3, pp. 753-793.
31. Wu, J.Y., Cervera, M. A novel positive/negative projection in energy norm for the damage modeling of quasi-brittle solids. *International Journal of Solids and Structures*, 2018, Vol. 139, pp. 250-269.
32. Ortiz, M. A constitutive theory for the inelastic behavior of concrete. *Mechanics of Materials*, 1985, Vol. 4, No. 1, pp. 67-93.
33. Mazars, J., Pijaudier-Cabot, G., Continuum damage theory—application to concrete. *Journal of Engineering Mechanics*, 1989, Vol. 115, No. 2, pp. 345-365.
34. Carol, I., Willam, K. Spurious energy dissipation/generation in stiffness recovery models for elastic degradation and damage. *International journal of Solids and Structures*, 1996, Vol. 33, No. 20-22, pp. 2939-2957.
35. Wu, J.Y., Xu, S.L. Reconsideration on the elastic damage/degradation theory for the modeling of microcrack closure-reopening (MCR) effects. *International Journal of Solids and Structures*, 2013, Vol. 50, No. 5, pp. 795-805.
36. Faria, R., Oliver, J., Cervera, M. A strain-based plastic viscous-damage model for massive concrete structures. *International Journal of Solids and Structures*, 1998, Vol. 35, No. 14, pp. 1533-1558.
37. Li, J., Zhou, H., Ding, Y.Q. Stochastic seismic collapse and reliability assessment of high-rise reinforced concrete structures. *The Structural Design of Tall and Special Buildings*, 2018, Vol. 27, No. 2, pp. e1417.
38. Kandarpa, S., Kirkner, D.J., Spencer Jr., B.F. Stochastic damage model for brittle materials subjected to monotonic loading. *Journal of Engineering Mechanics*, 1996, Vol. 126, No. 8, pp. 788-795.
39. Shinozuka, M., Deodatis, G. Simulation of stochastic processes by spectral representation. *Applied Mechanics Reviews*, 1991, Vol. 44, No. 4, pp. 191-204.
40. Vanmarcke, E. *Random Fields: Analysis and Synthesis*. World Scientific, 2010.
41. Chen, J.B., Sun, W.L., Li, J., Xu, J. Stochastic harmonic function representation of stochastic processes. *Journal of Applied Mechanics*, 2013, Vol. 80, No. 1, pp. 011001.
42. Ren, X.D., Zeng, S.J., Li, J. A rate-dependent stochastic damage-plasticity model for quasi-brittle materials. *Computational Mechanics*, 2015, Vol. 55, No. 2, pp. 267-285.
43. Peerlings, R.H., de Borst, R., Brekelmans, W.M., de Vree, J.H.P. Gradient enhanced damage for quasi-brittle materials. *International Journal for Numerical Methods in Engineering*, 1996, Vol. 39, No. 19, pp. 3391-3403.

44. Pijaudier-Cabot, G., Bažant, Z.P. Nonlocal damage theory. *Journal of Engineering Mechanics*, 1987, Vol. 113, No. 10, pp. 1512-1533.
45. Lee, J., Fenves, G.L. Plastic-damage model for cyclic loading of concrete structures. *Journal of Engineering Mechanics*, 1998, Vol. 124, No. 8, pp. 892-900.
46. Sarikaya, A., Erkmen, R.E. A plastic-damage model for concrete under compression. *International Journal of Mechanical Sciences*, 2019, Vol. 150, pp. 584-593.
47. Guo, Z.H., Shi, X.D. *Experiment and Calculation of Reinforced Concrete at Elevated Temperatures*. Beijing: Tsinghua University Press, 2011.
48. Poon, C.S., Azhar, S., Anson, M., Wong, Y.L. Comparison of the strength and durability performance of normal- and high-strength pozzolanic concretes at elevated temperatures. *Cement and Concrete Research*, 2001, Vol. 31, pp. 1291-1300.
49. Chen, B., Li, C.L., Chen, L.Z. Experimental study of mechanical properties of normal-strength concrete exposed to high temperatures at an early age. *Fire Safety Journal*, 2009, Vol. 44, pp. 997-1002.
50. Netinger, I., Kesegic, I., Guljas, I. The effect of high temperatures on the mechanical properties of concrete made with different types of aggregates. *Fire Safety Journal*, 2011, Vol. 46, pp. 425-430.
51. Wu, Y.P., Wu, B. Residual compressive strength and freeze-thaw resistance of ordinary concrete after high temperature. *Construction and Building Materials*, 2014, Vol. 54, pp. 596-604.
52. Eurocode 2. *Design of concrete structures - Part 1-2: General rules - Structural fire design*, European Standards, London, 2004.

LINKED CFD-THERMO-MECHANICAL SIMULATION FOR VIRTUAL HORIZONTAL FURNACE

Stanislav Šulc¹, Kamila Cábová², Filip Zeman³, Jakub Šejna⁴, Vít Šmilauer⁵, František Wald⁶

ABSTRACT

The article presents a weakly-linked computational approach, employing the concept of adiabatic surface temperature. The simulation comprises computational fluid dynamics, heat transport and solid mechanics. Application programming interfaces in linked codes define methods for steering, data storage, visualization or fields mapping. The linked simulation is successfully validated on timber and concrete structural elements exposed to fire.

Keywords: Computational fluid dynamics; object-oriented finite element method package; linking; adiabatic surface temperature.

1 INTRODUCTION

Numerical models address in fire design the questions of new materials, complex geometries and joint details, large deformations of fire protection and/or the assessment of structural reliability to a large extent. Computational fluid dynamics (CFD) brings solutions of Navier-Stokes equations, supplemented often with mass and species transport. The Fire Dynamics Simulator (FDS) represents such a widely-used, open source code, which was developed at NIST [15]. The code has been validated on a variety of simulation scenarios [1,16,18].

A weak and discretized form of heat balance and equilibrium equations provides the framework for thermo-mechanical analysis using the finite element method (FEM) [14,19]. It may address thermal boundary conditions, non-linear material stress-strain laws, finite strains, changes of static boundary conditions, temperature-dependent material properties, etc. Today, thermo-mechanical simulations are well established in the majority of finite element codes using at least a staggered solution strategy.

Linking CFD and thermo-mechanical analysis presents a relatively new approach to tackling multi-physical problems of fire-exposed structural behaviour [7,9,13,22,23]. The first linked version assumed that heat transfer from CFD to a thermal problem occurred through radiation only [17]. At the same time, Wickström coined the term Adiabatic Surface Temperature (AST) as a field which allows transferring heat fluxes

¹ Ing., Czech Technical University in Prague,
e-mail: stanislav.sulc@fsv.cvut.cz,

² Ing., Ph.D., Czech Technical University in Prague,
e-mail: kamila.cabova@fsv.cvut.cz,

³ Ing., Czech Technical University in Prague,
e-mail: filip.zeman@address,

⁴ Ing., Czech Technical University in Prague,
e-mail: jakub.sejna@address,

⁵ Ing., Czech Technical University in Prague,
e-mail: firstname.lastname@address,

⁶ doc. Ing., Ph.D., DSc.

e-mail: vit.smilauer@fsv.cvut.cz, ORCID: <https://orcid.org/0000-0002-0465-7443>

⁶ prof. Ing., CSc., Czech Technical University in Prague,
e-mail: frantisek.wald@fsv.cvut.cz, ORCID: <https://orcid.org/0000-0003-2416-8951>

composed of radiative and convective components [21,23]. Such a linking was successfully demonstrated using FDS and ANSYS codes [9,23], later extended with the Fire-thermo-mechanical interface [13].

This article shows a more versatile approach to CFD-thermo-mechanical linking using the object-oriented multi-physics integration framework abbreviated as MuPIF [3,4,]. MuPIF is written in Python 3.x and defines abstract base classes for individual components, e.g. data, application, or networking. The abstract classes define generic interface in terms of provided methods. Derived classes representing particular components implement the interface. The generic interfaces allow to manipulate all the derived classes (implementing particular components) using the same generic interface. Moreover, as the simulation data are represented by objects as well, the platform is independent on particular data format(s), as the simulation data (such as microstructures, fields or properties) can be manipulated using the generic interfaces.

The data exchange is based on exchange of the corresponding data components, embedding raw data and operations. This way, the models receive data with methods how to interpret the data. Therefore, the focus on services is provided by objects (object interfaces) and not on underlying data itself. In this way, the MuPIF platform is not standardizing the structure of data, it is standardizing the fundamental, core operations on the data.

The generic interfaces for applications allow to initialize and terminate application, to set data components as inputs, to get data components, e.g. receive the outputs from the application, and to execute a single time step of a particular model. Even though the platform can be used locally on a single computer orchestrating individual applications, the real strength of the platform is its distributed design, allowing to execute simulation scenarios involving remote applications. MuPIF provides a transparent distributed object system, which takes care of the network communication between the objects when they are distributed over different machines on the network.

MuPIF has been used for linking heterogeneous commercial and in-house codes written in Fortran, C, C++, Python and Matlab, running locally or remotely over a network, simulating CFD, nonstationary thermo-mechanical tasks, phase field models for CIGS microstructure formation, light-scattering models, etc. [5].

This article describes a new API for FDS, passing an AST field in selected timesteps to the thermo-mechanical model in OOFEM [2]. Its validation on timber and concrete members proved efficient computation, robustness, and stability using built-in features from MuPIF such as field mapping algorithms and network support.

2 CFD AND THERMO-MECHANICAL LINKING

Adiabatic surface temperature, T_{AST} , corresponds to the temperature of a perfect insulator's surface with zero conduction, flux to this surface is set to zero. The total heat flux from the fire model to the thermal model can be expressed using T_{AST} as [21,23]:

$$q_{tot} = \varepsilon\sigma(T_{AST}^4 - T_{TM}^4) + h(T_{AST} - T_{TM}) \quad (1)$$

where T_{TM} is the temperature of a surface in the thermal model, h is the heat transfer coefficient, σ is the Stefan-Boltzmann constant and ε is the emissivity of the exposed surface.

2.1 CFD task

The Fire Dynamics Simulator (FDS) [15], developed by the National Institute of Standards and Technology (NIST), is frequently used for simulating building fires. It is an open-source numerical solver written in Fortran to simulate a flow of gas during burning. FDS numerically solves a form of the Navier-Stokes equation appropriate for low-speed, thermally-driven flow with an emphasis on the transport of heat and smoke from fires. It has been used for several studies and applications in recent years, such as room fire simulation, liquid fire simulation, smoke characteristics, see a review of recent applications [1].

For the purpose of linked simulation, the FDS code version 6.5.2 has been modified in such a way that each computational time-step can be called individually and the resulting AST field obtained. Those API functions, exposed to Python, facilitate the necessary operations:

- *initASTMesh()* - initializes a MuPIF mesh and field with the coordinates of all points registered in FDS to export adiabatic surface temperatures.
- *updateASTField()* - updates all the AST values from FDS in the MuPIF field of node values on a MuPIF mesh.
- *getASTField()* - returns the MuPIF field with AST.
- *saveASTField()* - saves the field of AST into a file.
- *loadASTField()* - loads the field of AST from a file.
- *solveStep()* - solves a computational time-step with an undefined length, where FDS determines the length itself. It returns the time of the end of the time-step.

FDS needs an explicit definition of AST points of interest. They should be located slightly above an element surface so FDS knows they are in a gas phase. FDS fortran code has been compiled as a shared library and imported to Python. Exposure of important functions to Python is realized using the `iso_c_binding` library.

2.2 Thermo-mechanical task

The thermo-mechanical analysis of structural elements takes place in an object-oriented finite element method package called OOFEM [2]. The thermal analysis represents a general non-stationary problem with temperature-dependent material properties.

Radiative and Cauchy boundary conditions are used according to Eq. 1 with the help of the AST field. The thermal analysis passes the temperature field to the mechanical analysis, introducing thermal strain and modifying material properties such as yield strength and elastic modulus. The mechanical solution is generally non-linear.

The OOFEM code implements the BOOST [7] wrapper, which exposes important functions to Python. Particularly, the exposed functions are

- *setASTField(Field f)* - copies the values of *f* into the field of AST registered in OOFEM.
- *solveStep(double targetTime)* - solves a thermo-mechanical time step defined by the target time.

2.3 Multi-physics integration platform

The Multi-physics integration platform MuPIF provides an effective gluing framework between FDS and OOFEM, written in Python 3.x [3]. It offers several useful tools such as field mapping, exporting data to the VTK format, parallel computations and steering of particular models. APIs for FDS and OOFEM were developed. A top-level, steering script imports them as shared libraries, controls the execution of both codes and data synchronization, see Figure 1.

First, FDS is called to process several computational steps until the length of our defined time-step of the thermo-mechanical task is reached. The FDS application determines its time-step itself and it is usually much shorter than the OOFEM time-step. Once finished, the MuPIF field representation of temperature and AST fields from FDS are created. The AST field has no underlying mesh and the value in the closest point is returned. Thus, AST points need to be located close to surfaces with defined boundary conditions according to adiabatic temperature. The MuPIF field of AST values is passed to OOFEM as an AST field (using *setField* method). OOFEM solves the computational step of the thermal task and passes the computed temperature field to the mechanical model. Temperature-dependent material parameters are updated. The global time step ends with computing the resulting mechanical response.

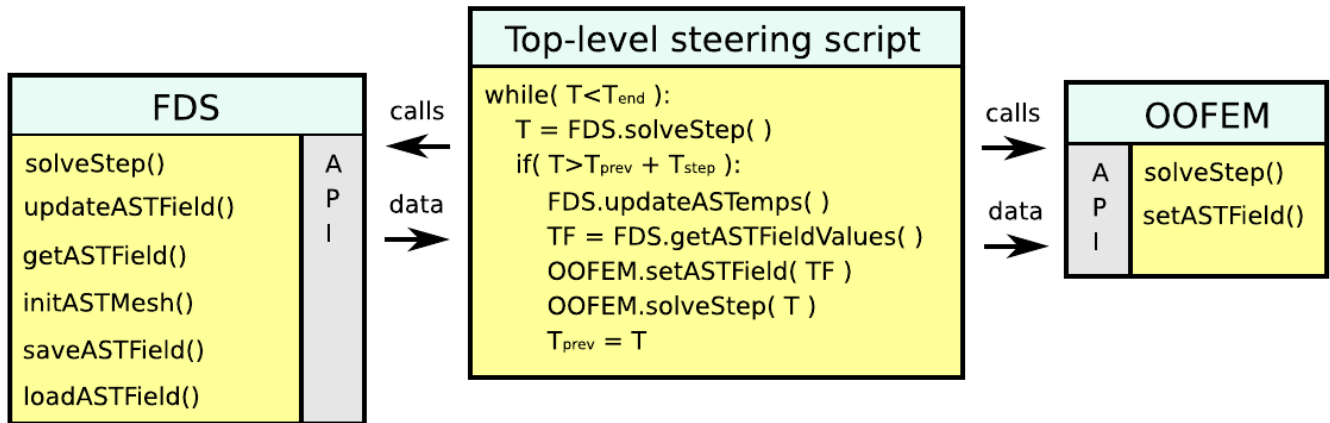


Figure 1. API implementation for FDS and OOFEM

Figure 2 shows the linking methodology. The left subfigure displays a part of the FDS mesh with a gray block for subsequent thermo-mechanical analysis. The middle subfigure zooms the block with black dots which represent AST locations. They are positioned slightly above each finite element's face exposed to fire. AST points are defined in the FDS input file, prior to computation. The right subfigure presents the temperature field which is further used for mechanical analysis.

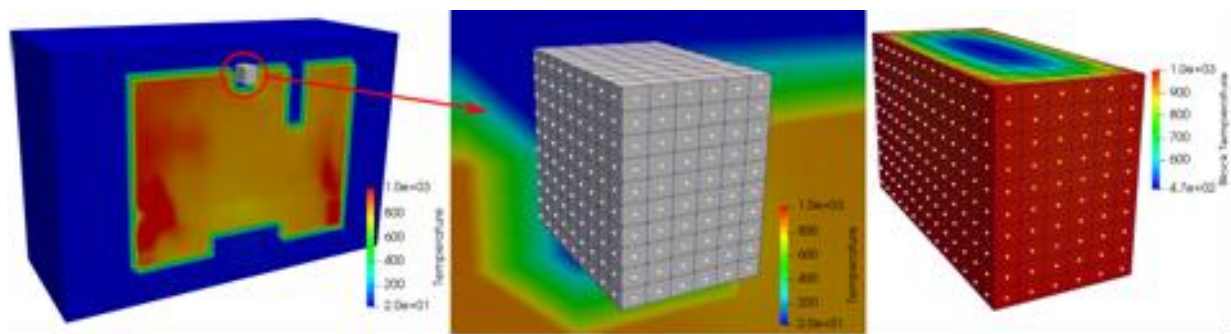


Figure 2. Linking methodology between CFD and thermo-mechanical models. CFD Temperature field (left), AST locations (middle) and block's temperature field (right)

The thermal boundary conditions are evaluated in Gauss points on each element's surface exposed to fire. Figure 3 shows characteristic locations of AST points together with locations of the Gauss integration points. It shows that Gauss point takes temperature from the nearest AST point and integrates the contribution into power density.

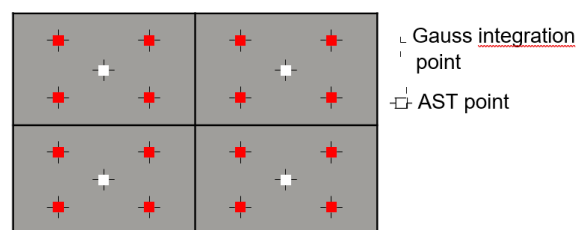


Figure 3. Characteristic locations of AST points and Gauss integration points on four element surfaces

The FDS analysis is generally a time-consuming process and the computations can take several days. MuPIF stores temperature and AST fields at specific times to files. In this regard, it is possible to run the FDS simulation first and compute the thermo-mechanical task afterwards.

The testing occurred in the fire laboratory of PAVUS, a.s. The furnace inner dimensions were 4.0×3.0×2.57 m (length×width×height). The furnace was heated by eight natural gas burners. The flue gas exhaust system used a frequency-controlled fan placed in a conduit connected to the opening 500×800 mm in the floor. In

both cases, the temperature in the furnace followed the standard temperature curve [11]. Input parameters in the FDS analysis play a key role for accuracy. The parameters with the highest influence on AST are the material properties of furnace linings, gas fuel composition, ventilation system, calculation time step and meshing. FDS models for both simulations proved successful performance in validation.

3 VALIDATION ON CONCRETE BLOCK

This validation focuses on a concrete block $0.35\text{ m} \times 0.15 \times 0.2\text{ m}$ placed below the furnace ceiling. Mineral wool insulates its top side, see Figure 4. The experiment involved concrete elements, which were a part of another R&D project. Concrete class C30/37 with cement's amount of 370 kg/m^3 constituted the block. In order to avoid spalling of the surface, the concrete contained 1.5 kg m^3 of PP fibers. Indeed, no spalling had occurred as evident from Figure 5.

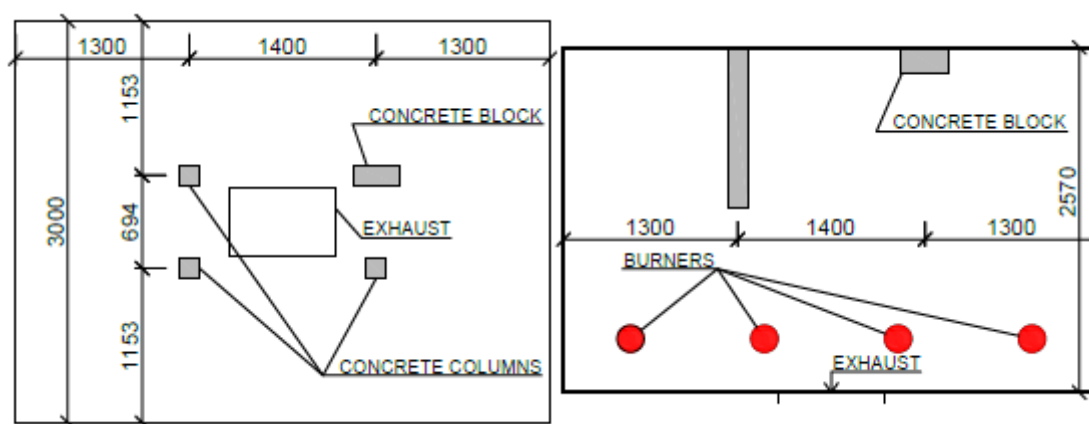


Figure 4. Horizontal a) and vertical b) layout of the furnace



Figure 5. Concrete block after fire exposure

The heat power of gas burners followed the nominal standard fire curve with the maximum output of 258 kW, see Figure 6. FDS used this curve for explicit control of the burners. Figure 6 validates the average gas temperature. The experiment lasted 120 mins and the initial temperature of the whole furnace was $10\text{ }^{\circ}\text{C}$.

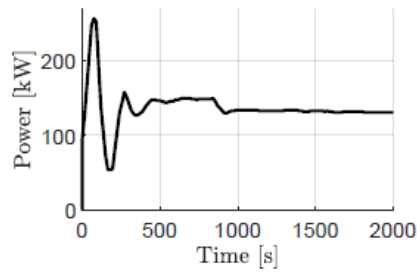


Figure 6. Total heat power of gas burners

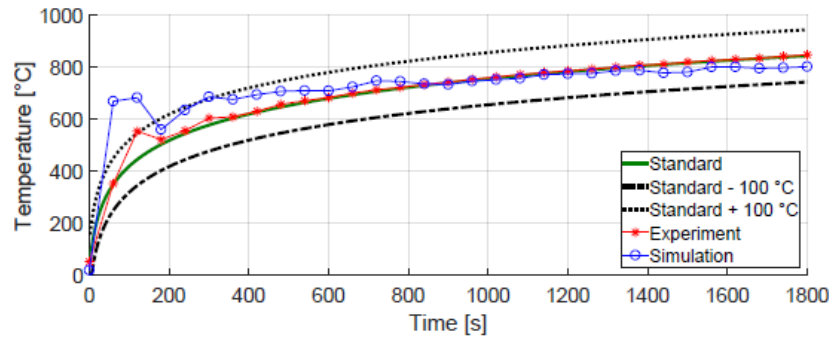


Figure 7. Validation of average gas temperature in the furnace

The FDS task used a global mesh consisting of $36 \times 36 \times 24$ elements, see Figure 8. The FDS simulation took 72 hours on 4 CPU cores.

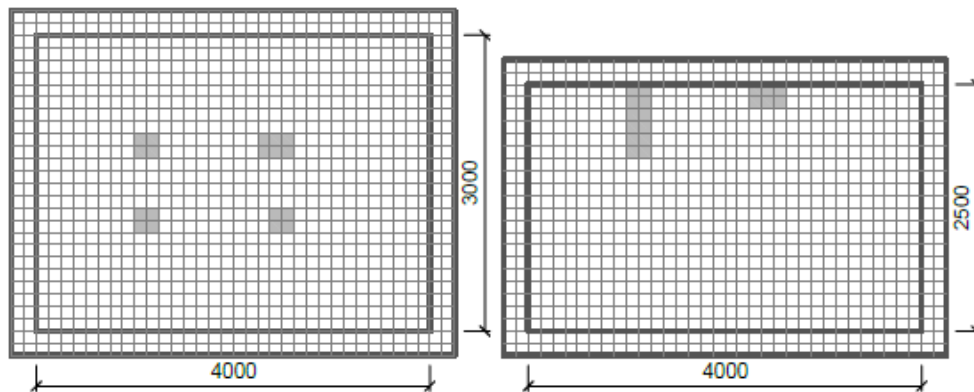


Figure 8. Meshing in the FDS model, horizontal and vertical cut through the block

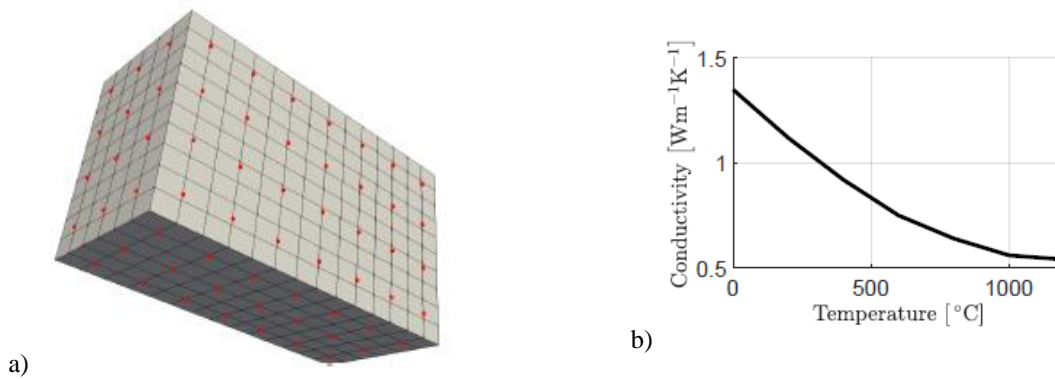


Figure 9. OOFEM mesh with AST points a) and Thermal conductivity of concrete b)

A regular mesh in OOFEM contained $14 \times 6 \times 8$ quadratic brick elements, see Figure 9. AST sampling was 2 s, corresponding with the time step of OOFEM. Standard concrete properties followed EN1992-2:2005, particularly thermal conductivity and heat capacity. The isotropic damage model served for demonstrating the mechanical behaviour, while the damaged material stiffness tensor $K = (1 - \omega)K_e$ describes material softening. K_e is the elastic undamaged stiffness tensor and ω is the damage parameter, related to the largest previously reached equivalent strain level. We used Mazar's definition, defining the equivalent strain as the sum of the maximum principal strains $\varepsilon = \sqrt{\sum_{l=1}^3 \langle \varepsilon_l \rangle^2}$, where $\langle \varepsilon_l \rangle$ are positive parts of the principal values of the strain tensor ε . Mechanical material properties were assumed as Young's modulus $E = 30$ GPa, density $d = 2400$ kgm³, Poisson's ratio $\nu = 0.25$, coefficient of thermal expansion $\alpha = 12 \times 10^{-6}$ K⁻¹, constant tensile strength 2.1 MPa and fracture energy 250 Jm². The emissivity of the concrete surface was assumed as 0.85. The heat transfer coefficient was set to zero since it has a small impact on the results. Thermocouples followed the vertical line at the centre of the block, see Figure 10.

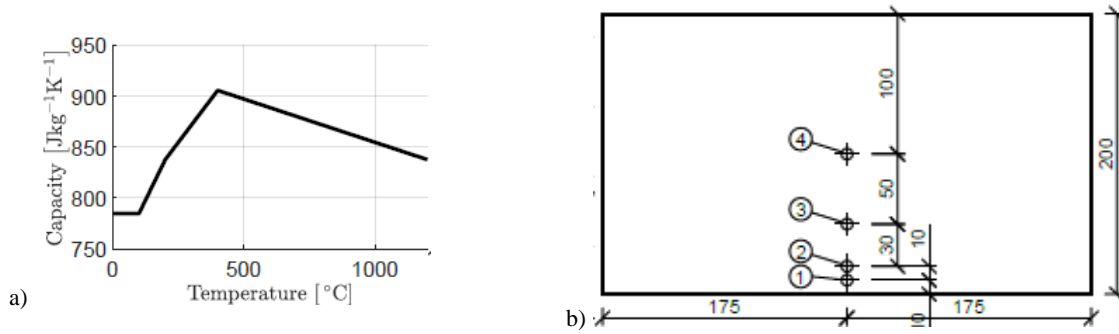


Figure 10. Model of heat capacity of concrete a) and Cross-section of the concrete block with positions of thermocouples b)

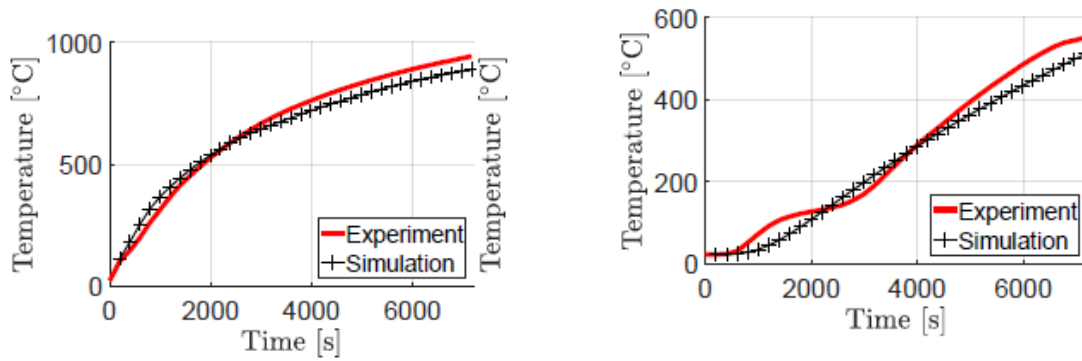


Figure 11. Validation of temperature in #3 a) and in #3 b)

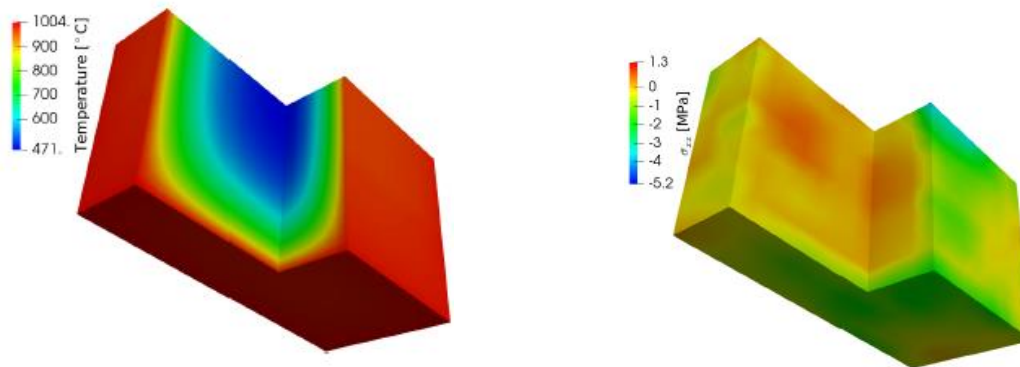


Figure 12. Distribution of temperature and stress σ_{xx} in time $t = 7200$ s

The simulation results in Figure 11 present a very good match with the experimental data. There are some discrepancies, which can be caused by the assumed standard material parameters. The maximum relative error of the presented graphs is 10.4 %. It occurs in point #4 with 57.5 °C out of the maximum temperature of 554 °C Figure 12 provides the visualization of the temperature field at the time of 7200 s. The mechanical task computes corresponding stresses; an example of the σ_{xx} field from the isotropic damage model is presented in Figure 12 . 4.8×10^{-4} .

4 VALIDATION ON TIMBER BEAM

This validation considers glued timber beams made of spruce wood. Figure 13 illustrates the layout of the beams in the furnace. The beams with dimensions of 120×320×3000 mm were placed under the ceiling and were instrumented with coated thermocouples, see Figure 14. High surrounding temperatures led to the burning of the beams. The experiment lasted 30 mins and the initial temperature in the whole furnace was 10 °C.

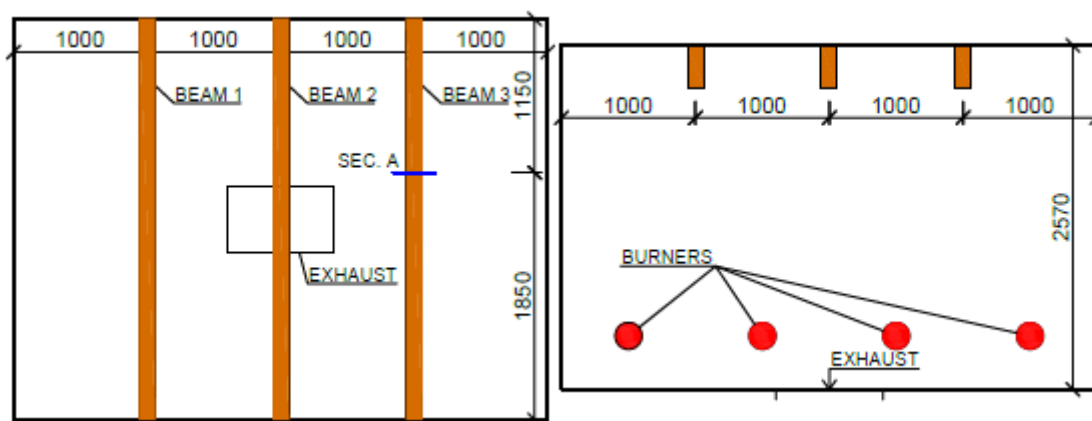


Figure 13. Horizontal and vertical layout in the furnace



Figure 14. Cross-section of beam 3 and wiring to sensors

Preliminary analysis found that the thermal conductivity of thermocouples' wiring significantly influenced the measured temperature, see Figure 15 For this reason, only temperatures in points #1 and #2 from Figure 11 were validated. The FDS task is composed of one global mesh consisting of $18 \times 18 \times 12$ elements and three finer meshes around the beams, each consisting of $4 \times 24 \times 8$ elements, see Figure 15. The mesh densities were designed in order to complete the computation in approximately 24 hours.

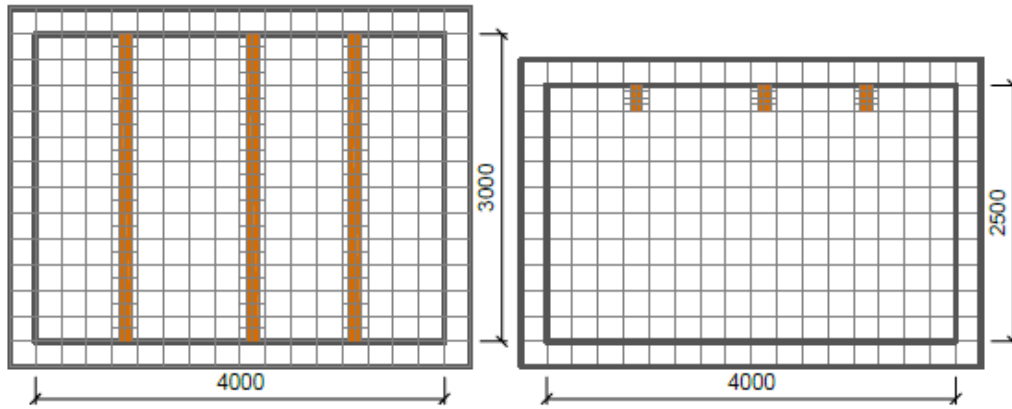


Figure 15. Meshing in the FDS model, horizontal and vertical cut through beams

For simplicity, OOFEM considered only a 0.1 m long section of the beam. The regular mesh was composed of $24 \times 1 \times 64$ finite quadratic elements, mimicking 2D heat transport. The AST field around the beam was exported every 0.5 s, which was the time-step in OOFEM, found for good numerical stability. Temperature-dependent wood properties followed standard curves from Eurocode 6, which describes the overall thermal behaviour. EN 1996-2 assumes that using these properties is relevant only for the first 30 mins of fire exposure. More precise simulation would need explicit implementation of timber burnout, which is beyond the scope of this article. Figure 16 shows timber thermal conductivity and timber density, assuming initial moisture content of 13.5 %. The timber heat capacity was modelled including a high peak due to water evaporation around 100 °C Those functions were smoothed to stabilize the numerical solution.

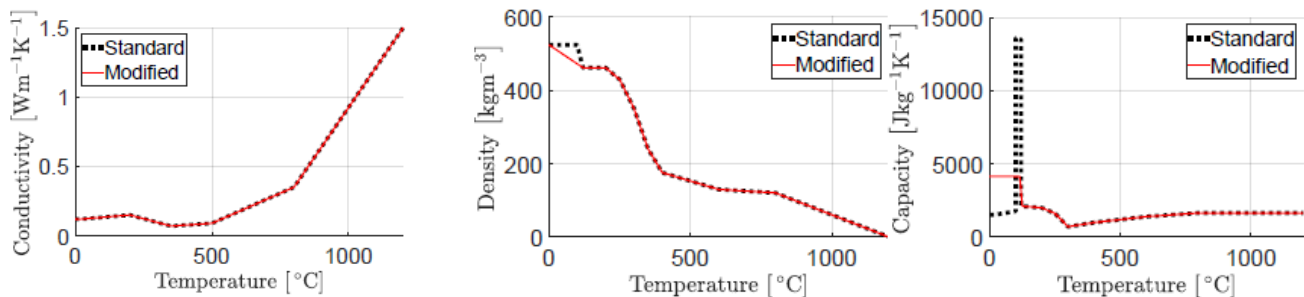


Figure 16. Timber thermal conductivity, density and heat capacity

The emissivity of the timber surface was set to 0.95, assuming a fully carbonized surface. It was found that the radiation term has the largest impact while the convection term can be neglected in this case. The validation of the temperature field occurred on beam #3, cross-section A and points 1, 2 #1, #2, see Figure 17 the temperature field at 1800 s and the distribution in time.

Results in points #11 and #22 are less affected by wiring conductivity. The maximum absolute error yields 111.1 °C from the measured temperature range 10 – 757 °C, which leads to the relative error of 14.7 % with regards to the maximum temperature. The reasons for these differences are i) using standard parameters instead of measuring parameters of the used material and ii) the capacity and density were modified in the interval (0, 120 °C) for better numerical stability. Considering these simplifications and the complexity of the whole simulation, the temperatures from the simulation agree reasonably well with the experiment. The simulation also yields temperatures in points #3 #6, which are showed in Figure 18. It points to a rapid increase of temperatures in the surface layer of finite elements (#3) compared with almost no temperature change at depth of 40 mm (#6) during the 30 mins simulation, which manifests strong insulating behaviour of timber. The figure also shows temperature offset due to heat diffusion into the member.

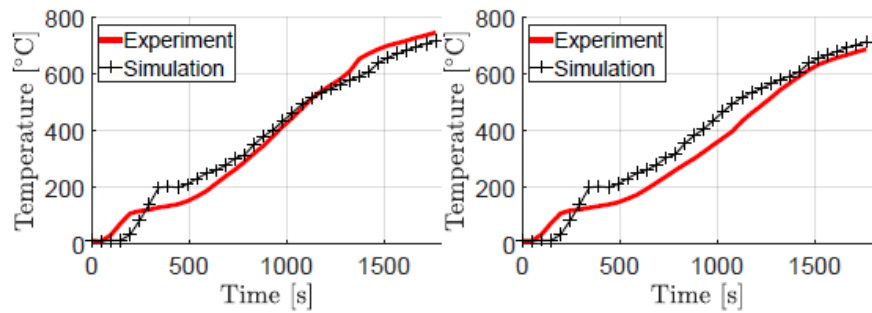
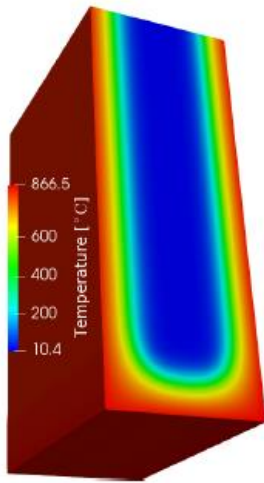


Figure 17. Temperature in the cross-section of the beam at time $t = 1800$ s, and in #1 and #2

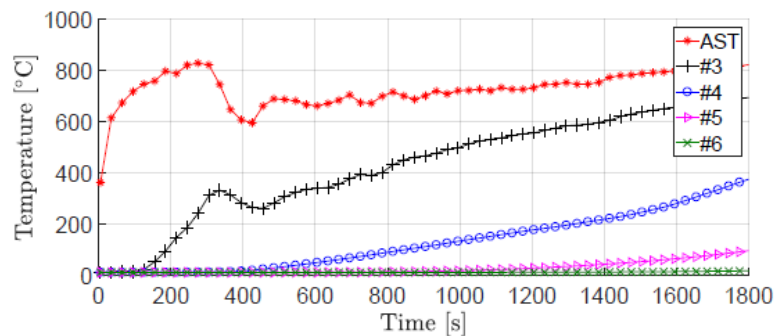


Figure 18. Temperatures predicted in measured points in timber member exposed to the fire based on predicted adiabatic surface temperature (AST)

5 CONCLUSIONS

The work presents the linking of two computational codes for a complex multi-physical problem; a CFD simulation with a FDS code and a thermo-mechanical simulation using OOFEM. The approach leads to the following conclusions:

1. Adiabatic surface temperature (AST) presents a suitable and accurate concept of heat transfer between both codes, capturing radiation and convection effects.
2. MuPIF provided an effective gluing Python framework for field mapping, exporting data and orchestrating both codes. Modified FDS code with MuPIF's API is publicly available on <https://github.com/mupif/APIs> under FDS for further development.
3. Validations of the thermal response showed good accuracy for timber and concrete elements exposed to fire in a furnace. A mechanical analysis can be linked easily, as demonstrated on stress and crack state of concrete element. Computation times for presented analyses take approximately a few days.
3. Multi-physical simulation allows performing fire-safety analysis of key elements of larger structures, mechanical analysis, or approximate simulation of wood charring. Larger structures can be analysed using the same approach, requiring for example parallel processing.

ACKNOWLEDGMENT

We appreciate our collaborators Dr. Lukáš Blesák and Dr. Radek Štefan for their help with experiments and Martin Benýšek and Filip Zeman for FDS models. We gratefully acknowledge financial support from the Czech Science Foundation, grant 19-22435S Performance of structures with timber fire protection – multi-physics modelling.

REFERENCES

1. Byström, A., et al. Full-scale experimental and numerical studies on compartment fire under low ambient temperature. *Building and Environment*, 2012, Vol. 51, pp. 255-262.
2. Patzák, B. OOFEM—an object-oriented simulation tool for advanced modeling of materials and structures. *Acta Polytechnica*, 2012, pp. 52.6.
3. Patzák, B., RYPL, Daniel; KRUIS, Jaroslav. MuPIF—A distributed multi-physics integration tool. *Advances in Engineering Software*, 2013, Vol. 60, pp. 89-97.
4. Patzák, B., et al. Multi-Physics Integration Framework - MuPIF 2.0. 2017. url: <http://mupif.org>.
5. PATZÁK, Borek; RYPL, Daniel; KRUIS, Jaroslav. MuPIF—A distributed multi-physics integration tool. *Advances in Engineering Software*, 2013, Vol. 60, pp. 89-97.
6. Patzák, B., et al. Multi-Physics Integration Framework MuPIF—design, operation and application to simulate CIGS thin film growth for photovoltaics ICME 2016.
7. BOOST, url: <https://www.boost.org/>
8. Zhang, CH.; Li, G.-Q.. Wang, R., Using adiabatic surface temperature for thermal calculation of steel members exposed to localized fires. *International Journal of Steel Structures*, 2013, Vol. 13.3, pp. 547-556.
9. Duthinh, D., Structural design for fire: A survey of building codes and standards. US Department of Commerce, National Institute of Standards and Technology, 2014.
10. Duthinh, D., McGrattan, K.; Khaskia, A., Recent advances in fire–structure analysis. *Fire safety journal*, 2008, Vol. 43.2: 161-167.
11. EN 1363-1 Fire resistance tests - Part 1: General Requirements, 2012
12. EN 1991-1-2: Eurocode 1: Actions on structures - Part 1-2: General actions - Actions on structures exposed to fire, 2002.
13. Hadjisophocleous, G. V.; Bénichou, N., Development of performance-based codes, performance criteria and fire safety engineering methods. *International Journal on Engineering Performance-Based Fire Codes*, 2000, 2.4, pp. 127-142.
14. Silva, J.G., Landesmann, A., Ribeiro, F., Luz, B., Fire-thermomechanical interface model for performance-based analysis of structures exposed to fire. *Fire Safety Journal*, 2016, Vol. 83, pp. 66-78.
15. Bathe, K.-J., Finite element procedures. Prentice Hall, 1995.
16. McGrattan, K., Hostikka S., McDermott R., Floyd J., Weinschenk C., Overholt, K., Fire Dynamics Simulator (Version 6) - User's Guide. NIST special publication, National Institute of Standards and Technology, 2019.
17. McGrattan, K., and S., Hostikka S., McDermott R., Floyd J., Vanella M., Weinschenk C., Overholt, K., Fire Dynamics Simulator Technical Reference Guide, Volume 3: Validation, National Institute of Standards and Technology, 2017.
18. Prasad, K., Baum, H.R., Coupled fire dynamics and thermal response of complex building structures. *Proceedings of the Combustion Institute*, 2005, Vol. 30.2, pp. 255-2262.
19. Beata, P.A., Jeffers, A.E., Spatial homogenization algorithm for bridging disparities in scale between the fire and solid domains. *Fire Safety Journal*, 2015, Vol. 76, pp. 19-30.
20. Hughes, Thomas J.R., The finite element method: linear static and dynamic finite element analysis. Courier Corporation, 2012.
21. The European Materials Modelling Council - MODA, homepage, <https://emmc.info/moda/>
22. Wickström, U., Heat transfer by radiation and convection in fire testing. *Fire and Materials*, 2004, Vol. 28.5, pp. 411-415.
23. Wickström, U., Temperature calculation in fire safety engineering. Cham, Switzerland: Springer, 2016.
24. Wickström, U; Duthinh, D., McGrattan, K., Adiabatic surface temperature for calculating heat transfer to fire exposed structures. In: *Proceedings of the Eleventh International Interflam Conference*. Interscience Communications, London. 2007.
25. Šulc S., Šmilauer V., Patzák B., Cábová K., Wald F., Linked simulation for fire-exposed elements using CFD and thermo-mechanical models. *Advances in Engineering Software*, 2019, Vol. 131, pp.12-22.

AI MODELLING & MAPPING FUNCTIONS: A COGNITIVE, PHYSICS- GUIDED, SIMULATION-FREE AND INSTANTANEOUS APPROACH TO FIRE EVALUATION

M.Z. Naser¹, Haley Hostetter², Aditya Daware³

ABSTRACT

Artificial intelligence (AI) is a computational technique that exploits hidden patterns between seemingly unrelated parameters to draw solution(s) to a given phenomenon. From this view, we believe that AI has the highest potential to deliver unique and modern solutions to the fire engineering community, noting that: 1) fire spans multiple fields (i.e. engineering, materials science, etc.) and hence its effects on structures require a holistic understanding, and 2) in a given fire engineering problem, a large number of variables exist with high variability and varying degrees of interdependency. The above clearly infers how structural fires represent a complex phenomenon in which traditional assessment methods struggle to resolve and hence an attempt to integrate AI could be promising. As a proof-of-concept, this paper showcases how AI can be used to develop a cognitive, simulation-free and instantaneous approach to evaluate fire response of reinforced concrete (RC) beams by using Artificial Neural Networks (ANN) and surrogates of Genetic Algorithms (GA). The presented approach is expected to open the door for new opportunities in fire engineering-related research, practice and education in the years to come.

Keywords: Artificial intelligence; Machine learning; structural fire engineering; modern analysis techniques.

1 INTRODUCTION

Early efforts at understanding fire response of structures started through standard fire tests. In such tests, a structural element is subjected to a “standard” temperature-time fire curve [1] to examine its fire performance through a series of instrumentations. The test continues until the fire weakens the tested element; whether by exceeding a certain temperature or deformation limit. The point in time at which a structural element fails, is referred to as fire resistance [2].

Throughout the years, outcomes of systematic standard fire tests were collected into fire rating tables, and also used to arrive at correlations that can be applied to estimate fire resistance of elements (of similar features to those tested earlier) [3]. Nowadays, researchers and practitioners started to utilize finite element (FE) simulation to evaluate fire response of structures. Although such techniques provide comparable and affordable means to evaluate fire performance, the open literature continues to lack guidance on proper

¹ Assistant professor, Clemson University,
e-mail: mznaser@clemson.edu, ORCID: <https://orcid.org/0000-0003-1350-3654>

² Graduate student, Clemson University
e-mail: hhostet@g.clemson.edu,

³ Graduate student, Clemson University
e-mail: adaware@g.clemson.edu

application and standardization of FE simulation process (e.g. required inputs for material properties, heat transfer boundaries etc.). Perhaps most notably is that such FE simulations require the use of special software (which implies the need for explicit licenses, expertise, and computing resources). One should still note, it should be noted that fire testing, correlation methods, fire rating tables and FE simulations have been extensively used over the past decades, and been shown to be effective in evaluating fire response of structural members [4, 5].

From this view, this work does not aim at critiquing existing methodologies but rather seeks to introduce AI as a modern technique to evaluate fire response of structures, in lieu of currently adopted methodologies. This work builds on the fact that AI has been widely and successfully used in various engineering disciplines, i.e. structural health monitoring [6], seismic [7], and wind design [8], yet has not been fully embraced by our community despite early attempts [9, 10]. For example, Chan et al. [9] developed an ANN able of tracing losses in concrete compressive strength under elevated temperatures by examining published data points. The same ANN was also applied to understand how concrete mix proportions influence property degradation in temperature range of 25-1200°C. In another work, McKinney and Ali [10] built a series of ANNs to predict fire-induced spalling in concrete. These researchers reported that it took the ANNs about 1500 training iterations to achieve a 0.5% error rate.

More recently, Erdem [11] developed and trained an ANN using 294 data points to examine flexural capacity of RC slabs under fire conditions by analysing compressive and yield strength properties, effective depth of slab, and fire exposure duration. Erdem reported that the newly developed ANN is capable of achieving an accuracy of 99.7% as compared to hand calculation methods – effectively solidifying the role of AI in predicting capacity loss under fire conditions. In parallel, this research group have also developed a number of AI-based techniques to evaluate fire response of construction materials and structural members. Findings from our works have generated design charts and AI-derived expressions capable of: 1) evaluating thermal response in insulated FRP-retrofitted RC beams, 2) developing material models for construction materials, and 3) predicting the intensity of fire-induced spalling [12–15].

This study aims to develop a cognitive framework to realize the complex thermal and structural behaviour of RC beams under fire conditions. More specifically, this framework seeks to derive expressions that can be used to evaluate temperature-time and temperature-deformation history of fire-exposed RC beams; thus minimizing the need to carry out fire tests or full-scale FE simulations. In our approach, high temperature properties of concrete and steel, and associated fire phenomena (i.e. creep) will be implicitly accounted for. Once completed, the proposed approach can be applied through a spreadsheet (i.e. Excel) interface and does not require special software, coding experience or dedicated computing resources, which will further expedite the fire evaluation process into about 1 member per second. Finally, the outcome of this work will demonstrate the potential of AI in modernizing fire resistance evaluation noting how AI has high degree of perception (i.e. learn from past mistakes) and improve through independent learning.

2 HYPOTHESIS AND RATIONALE

2.1 Hypothesizes

This paper hypothesizes that to obtain temperature rise or deformations (say in a RC beam), all that is needed is to identify key features responsible for such effects in a given RC beam, in addition to the governing relation that tie these features to “temperature rise” or “deformation” patterns. As engineers, we know that fire response of a structural member is primarily a function of this member’s geometric dimensions (i.e. width, span, etc.), material properties (strength, stiffness etc.), loading action (type, magnitude etc.), restraint conditions (viz. simply supported etc.), fire conditions (intensity, heating rate, duration etc.) and so on. The interaction of these features determines how a structural member or assembly will experience temperature rise or deformation under fire [16]. This paper will answer the following

questions: 1) how can we identify the aforementioned key features? And 2) if we do, how can we arrive at a governing relation to enable cognitive, simulation-free and instantaneous evaluation of thermal and mechanical response of structural members?

2.2 Rationale

This section summarizes the thermal and structural behavior of RC beams under fire conditions as a mean to showcase the rationale followed in this paper.

In the event of a fire, cross-sectional temperature slowly rises as a result of the insulating thermal properties of concrete. With extended exposure time, a thermal gradient develops in which the temperature at the exposed surface of the beam is much higher than that at the inner layers of concrete. In parallel, and for the sake of this discussion, a simply supported beam will first expand a bit to in response to the thermal expansion arising from heating. However, such expansion is minute due to the small coefficient of thermal expansion of concrete [17]. With the continued rise in cross sectional temperature, the mechanical properties (strength and modulus) of both concrete and steel reinforcement start to degrade; causing losses in sectional capacity. This, combined with stresses developed from gravity loads, induce further property degradation causes the beam to soften. As the beam weakens, it experiences faster rise in deflection and fails once its sectional capacity drops below the level of applied loading (see Figure 1).

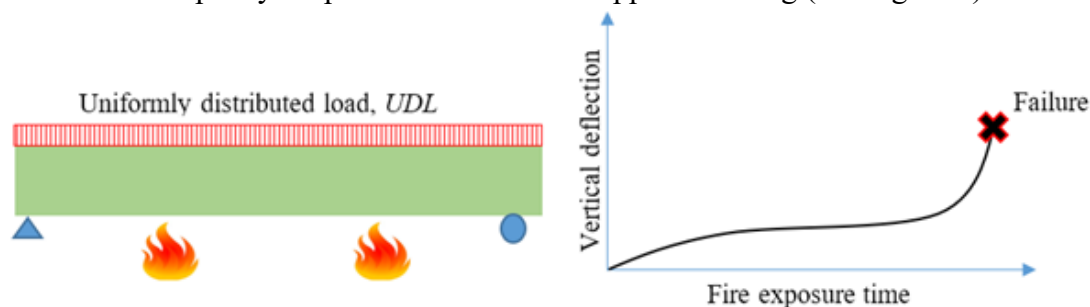


Figure 1. Typical response of a RC beam under fire

The above described phenomena are true for the majority of RC beams that happen to have similar features to that of the beam in question. As a result, one but to ask, if the physical phenomena can be properly understood, then would it be possible to train an AI algorithm to capture these phenomena? And if so, then, use the AI understanding to develop new tools for fire resistance evaluation?

3 AI MODEL DEVELOPMENT

3.1 Background to AI

The earliest reference to artificial intelligence (AI) was noted at Dartmouth College [18]. From this view, AI is but a computational technique that has the ability to mimic the cognition capability of the brain to construct conclusions from observations as a mean to represent a solution (or set of solutions) to a given phenomenon. From this view, AI is suitable for engineering problems wherein a large number of random variables exist with an unclear relationship between such variables and expected output. In this pursuit, AI tries to learn concealed patterns through systematic valuation, adaptive learning, or probabilistic discovery.

This study utilizes ANN as the primary AI technique to be employed. Existing ANNs are often labeled as “Blackbox” tools due to their intricate inner structure. As such, a surrogate model will be developed using genetic algorithms (GA) to provide an interpretable layer to the ANNs understanding of the examined two phenomena herein.

In general, the topology of an ANN algorithm is selected to mimic the functionality of the brain. Such a topology is characterized through layers; 1) first layer receives the information required for analysis, 2) subsequent “hidden” layers utilize neurons (processing units) to learn and recognize relevant patterns in inputs through transformative operations (i.e. training process), and 3) final layer to represent the output of the ANN analysis [12]. The above learning/training process in ANN continues until satisfying a set of fitness metrics (i.e. mean square error (MSE) and correlation coefficient (R) etc.). The most commonly used optimization method is called Leveberg-Marquard which, evaluates the error in terms of MSE (see Eq. 1) [12, 19].

$$MSE = \frac{1}{z} \sum_{i=0}^z (e_i)^2 = \frac{1}{z} \sum_{i=0}^z (m_i - p_i)^2 \quad (1)$$

where, z = the total number of datasets, e_i = the error for each input set, m_i = the measured output, and p_i = the estimated output.

Recent advancements in AI now allow converting ANN’s inner structure from hundreds of code lines into a systematic design procedure (i.e. mathematical expression of a mapping function) through a genetic algorithm (GA) surrogate model. In general, GA is an evolutionary search technique that tries to find a series of suitable mathematical expressions to represent AI’s understanding of a certain phenomenon. The GA analysis starts by creating a random population of expressions. An expression can hold mathematical operations (+, × etc.), power functions (^, log, exp), conditional and logic functions (>, OR etc.) etc. (see Figure 2). Each expression is then examined for fitness. The fitness of an expression is defined as a metric that best reflects how far an expression’s predictions are far from that in real observations. The fittest expression of AI’s understanding of thermo-structural phenomena in steel beams and columns is then selected and integrated into a spreadsheet.

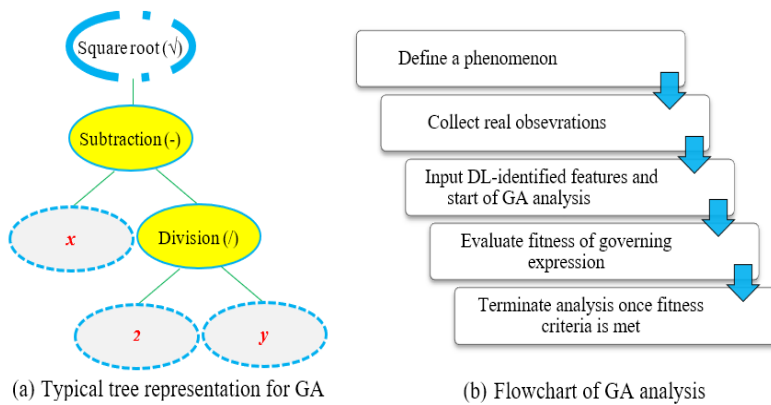


Figure 2. Details on GA

3.2 Proposed AI model

The proposed ANN will be trained to trace temperature-time history and temperature-deformation history RC beams when exposed to standard fires. Table 1 lists the identified inputs and outputs to the AI analysis (e.g. geometric properties etc.). These parameters were selected through close examination of published fire tests together with physics-guided engineering judgment [20–24].

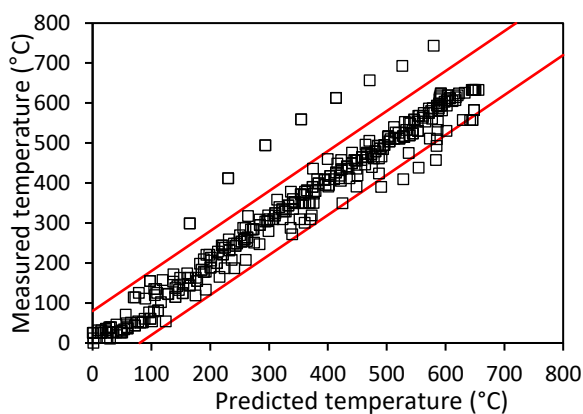
Table 1 Selected input parameters for the ANN

Parameter/Case	Input parameters						Output parameters		
	Fire exposure time (t)	Compressive strength of concrete (f_c')	Yield strength of steel (f_y)	Steel reinforcement ratio (ρ)	Load level (P)	Bottom cover to steel reinforcement (C_b)	Side cover to steel reinforcement (C_s)	Temperature (°C)	Mid-span deflection (mm)
	Thermal response	✓	-	-	-	-	✓	✓	-
	Structural response	✓	✓	✓	✓	✓	✓	-	✓

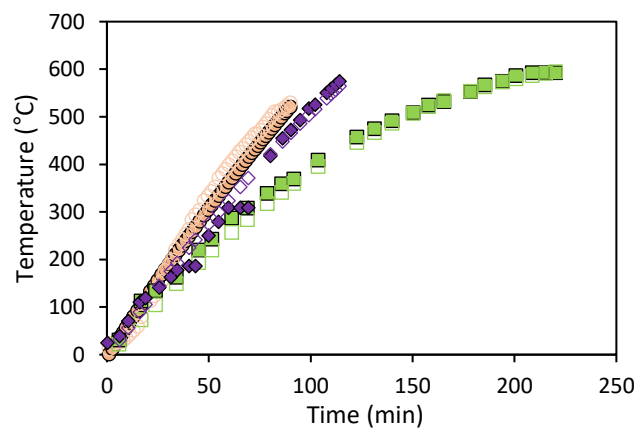
Noting the above, temperature rise in steel rebars in a RC beam during fire exposure time is said to be a function of duration of fire exposure, t , bottom and side cover to steel reinforcement, C_b and C_s , respectively. Other parameters that do not essentially contribute to temperature rise (i.e. restraint conditions) can be safely neglected. Through the above rationale, the developed ANN can tie temperature rise in steel rebars to t , C_b and C_s and then this relation can be augmented through GA through a simple expression. A more in depth discussion on selected inputs can be found in our earlier works [20, 25].

4 PERFORMANCE AND VALIDATION OF AI MODEL

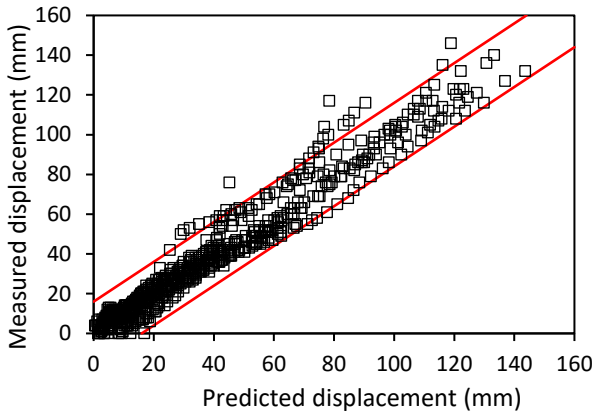
In total, two-thirds of the collected data is used in training the ANN and the final third was used to validate and test the AI-derived expressions. A ten-fold cross-validation method was also employed as an additional validation measure. The derived expressions are tested via fitness functions (see Table 3). For completion, Figure 3. plots the performance of the ANN and GA surrogate models (against specific fire test results).



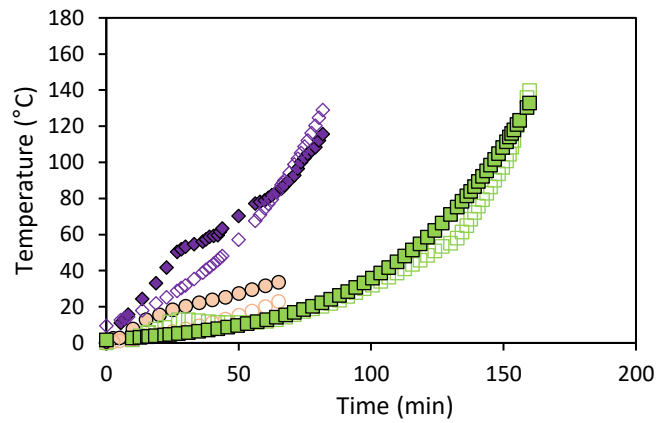
(a) Temperature in rebars (beams)



(b) Validation against fire tests (top to bottom: [26–28])



(a) Deflection of RC beams



(b) Validation against fire tests (top to bottom: [24, 29, 30])

Figure 3. Validation of the ANN model

Table 2 GA derived expressions to surrogate the ANN model

Derived expressions	$R^2(\%)$	$R(\%)$	MAE
$T = 0.0169tC_b + \frac{182.64t}{C_s} + t \sin(5.21C_b) - 6.43 - 0.0098t^2$	95.1	97.5	24.6°C
$\Delta = 36.2 \exp(0.023t) \cos(\sin(23040 P)) \cos(\sin(2.28 \times 10^{-8} P)) - 0.206C_b - 9.28\sin(f_y) - 12.59\exp(0.0236t) + 4.5 + 0.105t + 2.299 \times 10^{-6}t^{f_c \rho^P}$	95.6	97.8	4.8 mm

*In some instances, the second expression might unexpectedly yield relatively high values for initial deflection. In this case, all that is needed is to normalize this deflection through subtraction.

It can be seen from above table, as well as Fig. 2 that there is a strong correlation between predicted and measured points (both R^2 and R exceeds 95%). Given the fact that these expressions trace the temperature-time and temperature-deformation histories to few degrees and millimeters show that AI-based expressions are of adequate accuracy.

The tabulated expressions can be input into an excel spreadsheet (see Figure 4) to evaluate temperature rise of deformation magnitude at a specific point in time (i.e. $t = 60$ min, or 73 min etc.), or from fire initiation ($t = 0$ min) till failure of the beam. As a result, a fire practitioner will be able to trace temperature-time or temperature-deformation histories of a RC beam in orders of magnitude less time than current methods (expected at 1 member per second).

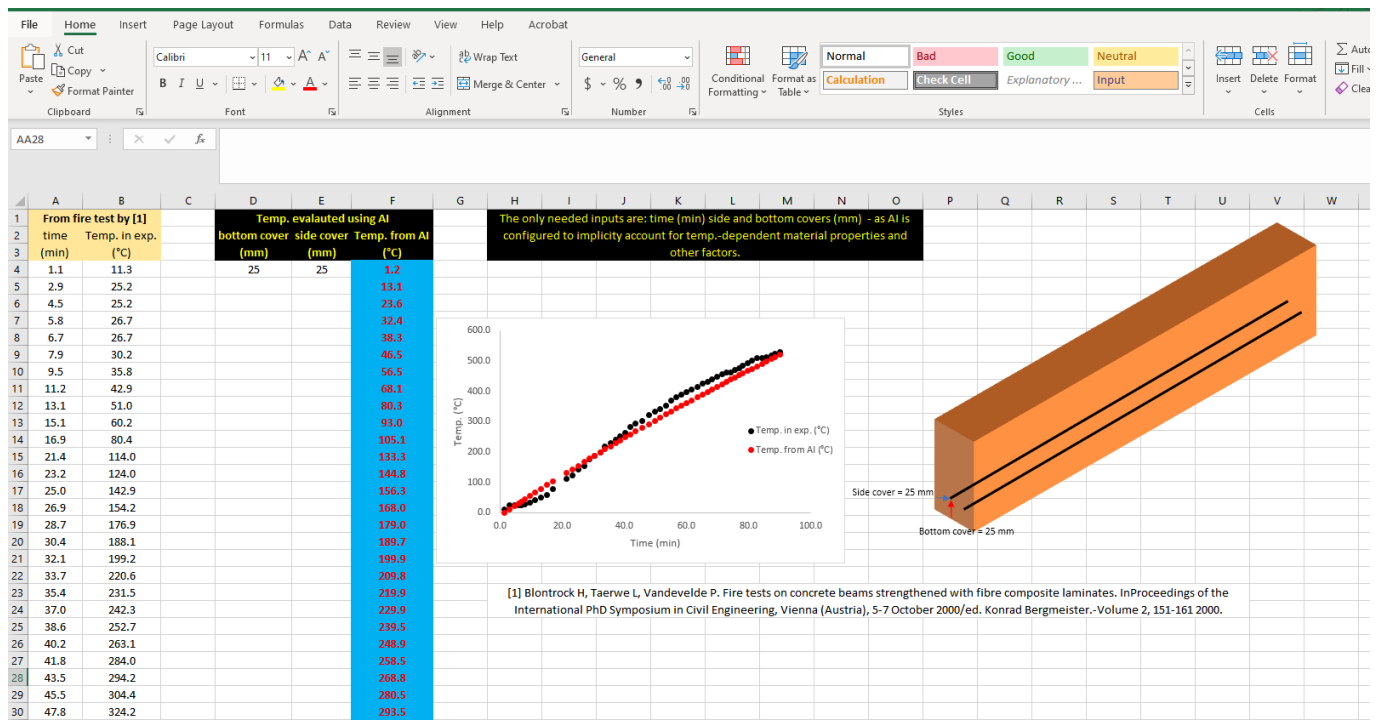


Figure 4. Proof of concept using Excel interface

5 CHALLENGES AND FUTURE NEEDS

This study builds upon our observations that AI and machine learning continue to evolve at a much faster pace than that in fire testing or FE simulation which favors integrating AI into fire engineering. However, one must realize adopting AI-based approaches comes with challenges and limitations. For example, the prediction capability of an AI-model depends, to a certain extent, on the number and quality of inputs. From this point of view, the available data on fire tests can be thought of as limited. Luckily, recent advancements in AI seem to be on the path to developing solutions to overcome such limitation (i.e. augmentation of data). The authors hope that upcoming works will develop improved cognitive approaches. Future AI generations are expected to accommodate construction materials (at the microstructure levels), complex geometries, fire scenarios (e.g. realistic fire), restraints conditions etc. which will be imperative in realizing cognitive and autonomous structures [31].

6 CONCLUSIONS

This work introduces AI as a contemporary tool that can augment fire evaluation of structures. A case study on RC beams is discussed and showcased the merit of utilizing AI in structural fire assessment. In addition, the following points could also be drawn from the findings of this study:

- Developing simple and automated fire assessment methods through AI can indeed modernize structural fire engineering.
- ANNs and GA surrogates are shown to be competent of accurately predicting thermal and structural response of RC beams under standard fire conditions.
- As with other methods, a few challenges continue to hinder the use of AI, e.g. limited data. Luckily, these challenges can be overcome through future advancements in AI.

ACKNOWLEDGMENT

We would like to acknowledge the start-up funds allocated to this research by Clemson University. The support of Clemson University is greatly appreciated it.

REFERENCES

1. Gales, J., Chorlton, B., Jeanneret, C.: The Historical Narrative of the Standard Temperature–Time Heating Curve for Structures. *Fire Technol.* 1–30 (2020). <https://doi.org/10.1007/s10694-020-01040-7>.
2. Kodur, V., Naser, M.: *Structural Fire Engineering*. McGraw Hill Professional (2020).
3. Buchanan, A., Abu, A.: *Structural design for fire safety*. (2017).
4. Franssen, J.M., Gernay, T.: Modeling structures in fire with SAFIR®: Theoretical background and capabilities. *J. Struct. Fire Eng.* (2017). <https://doi.org/10.1108/JSFE-07-2016-0010>.
5. Lie, T., Woollerton, J.: *Fire Resistance of Reinforced Concrete Columns - NRC Publications Archive - National Research Council Canada*. (1988). <https://doi.org/http://doi.org/10.4224/20386656>.
6. Gul, M., Necati Catbas, F.: Statistical pattern recognition for Structural Health Monitoring using time series modeling: Theory and experimental verifications. *Mech. Syst. Signal Process.* 23, 2192–2204 (2009). <https://doi.org/10.1016/J.YMSSP.2009.02.013>.
7. Zhang, Y., Burton, H. V., Sun, H., Shokrabadi, M.: A machine learning framework for assessing post-earthquake structural safety. *Struct. Saf.* (2018). <https://doi.org/10.1016/j.strusafe.2017.12.001>.
8. Jiménez, A.A., García Márquez, F.P., Moraleta, V.B., Gómez Muñoz, C.Q.: Linear and nonlinear features and machine learning for wind turbine blade ice detection and diagnosis. *Renew. Energy.* (2019). <https://doi.org/10.1016/j.renene.2018.08.050>.
9. Chan, Y.N., Jin, P., Anson, M., Wang, J.S.: Fire resistance of concrete: Prediction using artificial neural networks. *Mag. Concr. Res.* (1998). <https://doi.org/10.1680/mac.1998.50.4.353>.
10. McKinney, J., Ali, F.: Artificial Neural Networks for the Spalling Classification & Failure Prediction Times of High Strength Concrete Columns. *J. Struct. Fire Eng.* (2014). <https://doi.org/10.1260/2040-2317.5.3.203>.
11. Erdem, H.: Predicting residual moment capacity of thermally insulated RC beams exposed to fire using artificial neural networks. *Comput. Concr.* 19, 711 (2017). <https://doi.org/10.12989/CAC.2017.19.6.711>.
12. Naser, M., Abu-Lebdeh, G., Hawileh, R.: Analysis of RC T-beams strengthened with CFRP plates under fire loading using ANN. *Constr. Build. Mater.* 37, 301–309 (2012). <https://doi.org/10.1016/j.conbuildmat.2012.07.001>.
13. Naser, M.Z.: Properties and material models for modern construction materials at elevated temperatures. *Comput. Mater. Sci.* 160, 16–29 (2019). <https://doi.org/10.1016/J.COMMATSCI.2018.12.055>.
14. Naser, M.Z.: Heuristic machine cognition to predict fire-induced spalling and fire resistance of concrete structures. *Autom. Constr.* 106, 102916 (2019). <https://doi.org/10.1016/J.AUTCON.2019.102916>.
15. Naser, M.Z.: Autonomous Fire Resistance Evaluation. *ASCE Journal Struct. Eng.* (2020). [https://doi.org/10.1061/\(ASCE\)ST.1943-541X.0002641](https://doi.org/10.1061/(ASCE)ST.1943-541X.0002641).
16. Dong, W., Huang, Y., Lehane, B., Ma, G.: XGBoost algorithm-based prediction of concrete electrical resistivity for structural health monitoring. *Autom. Constr.* (2020). <https://doi.org/10.1016/j.autcon.2020.103155>.
17. Kodur, V.: Properties of concrete at elevated temperatures, (2014). <https://doi.org/10.1155/2014/468510>.
18. Russell, S., Norvig, P.: *Artificial Intelligence A Modern Approach Third Edition*. (2010). <https://doi.org/10.1017/S0269888900007724>.
19. Naser, M.Z., Alavi, A.: *Insights into Performance Fitness and Error Metrics for Machine Learning*. (2020).
20. Naser, M.Z.: AI-based cognitive framework for evaluating response of concrete structures in extreme conditions. *Eng. Appl. Artif. Intell.* 81, 437–449 (2019). <https://doi.org/10.1016/J.ENGAPPAI.2019.03.004>.
21. Dwaikat, M.B., Kodur, V.K.R.: Response of Restrained Concrete Beams under Design Fire Exposure. *J. Struct. Eng.* (2009). [https://doi.org/10.1061/\(asce\)st.1943-541x.0000058](https://doi.org/10.1061/(asce)st.1943-541x.0000058).
22. Kodur, V.K.R., Dwaikat, M.: Performance-based fire safety design of reinforced concrete beams. *J. Fire Prot. Eng.* (2007). <https://doi.org/10.1177/1042391507077198>.
23. Lin, I., Chen, S., Lin, C.: The Shear Strength of Reinforcing Concrete Beam after Fire Damage. In: *Structure Safety Evaluation after Fire Damage*. pp. 117–136 (1999).
24. Zhu, H., Wu, G., Zhang, L., Zhang, J., Hui, D.: Experimental study on the fire resistance of RC beams strengthened with near-surface-mounted high-Tg BFRP bars. *Compos. Part B Eng.* 60, 680–7 (2014).

<https://doi.org/10.1016/j.compositesb.2014.01.011>.

25. Seitllari, A., Naser, M.Z.: Leveraging artificial intelligence to assess explosive spalling in fire-exposed RC columns. *Comput. Concr.* (2019). <https://doi.org/10.12989/cac.2019.24.3.271>.
26. Blontrock, H., Taerwe, L., The, P.V.-P. of, 2000, U.: Fire tests on concrete beams strengthened with fibre composite laminates. *biblio.ugent.be.* (2000).
27. Ellingwood, B., Lin, T.D.: Flexure and Shear Behavior of Concrete Beams during Fires. *J. Struct. Eng.* 117, 440–458 (2007). [https://doi.org/10.1061/\(asce\)0733-9445\(1991\)117:2\(440\)](https://doi.org/10.1061/(asce)0733-9445(1991)117:2(440)).
28. Dotreppe, J.-C., Franssen, J.-M., Bruls, A., Baus, R., Vandeveld, P., Minne, R., van Nieuwenburg, D., Lambotte, H.: Experimental research on the determination of the main parameters affecting the behaviour of reinforced concrete columns under fire conditions. *Mag. Concr. Res.* (1997). <https://doi.org/10.1680/mac.1997.49.179.117>.
29. Palmieri, A., Matthys, S., Taerwe, L.: Experimental investigation on fire endurance of insulated concrete beams strengthened with near surface mounted FRP bar reinforcement. *Compos. Part B Eng.* 43, 885–895 (2012). <https://doi.org/10.1016/j.compositesb.2011.11.061>.
30. Choi, E.G., Shin, Y.S.: The structural behavior and simplified thermal analysis of normal-strength and high-strength concrete beams under fire. *Eng. Struct.* 33, 1123–1132 (2011). <https://doi.org/10.1016/J.ENGSTRUCT.2010.12.030>.
31. Naser, M.Z.: Autonomous and resilient infrastructure with cognitive and self-deployable load-bearing structural components. *Autom. Constr.* 99, 59–67 (2019). <https://doi.org/10.1016/J.AUTCON.2018.11.032>.

A NUMERICAL INVESTIGATION OF 3D STRUCTURAL BEHAVIOR FOR STEEL-COMPOSITE STRUCTURES UNDER VARIOUS TRAVELLING FIRE SCENARIOS

Zhuojun Nan¹, Xu Dai^{2,*}, Haimin Chen³, Stephen Welch⁴, Asif Usmani⁵

ABSTRACT

In the recent development of the performance-based structural fire design, the “travelling fire” methodology has been gradually accepted as a necessary fire boundary condition. However, its application is still limited by uncertainties in the selection of different design travelling fire parameters, which result from the lack of relevant experimental data and corresponding validated structural finite element models which can be used in advanced travelling fire methodologies, e.g. the extended travelling fire methodology (ETFM) framework. This paper aims to fill this gap through modelling a prototype steel-composite floor structure (regarded as a 'slice' of a large open-plan office), to investigate its true structural response under a wide range of travelling fire scenarios, with an emphasis on considering the effect of concrete slabs in a 3D finite element model, using LS-DYNA. To ensure the credibility of this numerical study, the model was validated against the experimental data from the Veseli Travelling Fire Test, and comparisons made with similar modelling efforts using Vulcan. In the parametric studies, eight cases were examined to investigate the structural response and the failure criteria, related to the selection of different key design parameters for the travelling fire within the ETFM framework, i.e. fire spread rate and inverse opening factor. It was found that solely satisfying the critical temperature (e.g. 550 °C for steel) and deflection criteria (e.g. beam span over 20) for the structural members might not guarantee a safe structural design for travelling fire scenarios, and it is suggested that the steel yielding stress status during the cooling phase in tension should also be examined. Compared to the inverse opening factor, it appears that the selection of fire spread rates is likely to be more critical in identifying the worst travelling fire scenario for the structural response with fire protection.

Keywords: Performance-based design; travelling fires; finite element analysis; fire resistance

1 INTRODUCTION

For structural fire design, appropriate fire boundary conditions are required for fire severity calculations, which may differ significantly from those in standard tests. Usually, when design compartments are very large, there is a significant challenge in representing the fire exposures in a manner which is accessible for practitioners. This kind of problem has been tackled using ‘travelling fire’ methodologies in recent years, a concept which invokes fires that may burn locally and spread by “travelling” across entire floor plates over a period of time, in larger compartments [1]. By the same token, a poor structural model cannot

¹ PhD Student, Hong Kong Polytechnic University; Graduate Fire Engineer, Arup, Shanghai; MSc Student, University of Edinburgh
e-mail: zhuojun.nan@connect.polyu.hk, ORCID: <https://orcid.org/0000-0001-8189-5448>

² Postdoctoral Research Associate, University of Edinburgh
e-mail: x.dai@ed.ac.uk, xudai1987@gmail.com, *corresponding author, ORCID: <https://orcid.org/0000-0002-9617-7681>

³ MSc Student, University of Edinburgh
e-mail: chenhaimin@sinochem.com, ORCID: <https://orcid.org/0000-0002-7090-879X>

⁴ Senior Lecturer, University of Edinburgh
e-mail: s.welch@ed.ac.uk, ORCID: <https://orcid.org/0000-0002-9060-0223>

⁵ Professor and Head of Building Services Engineering, Hong Kong Polytechnic University
e-mail: asif.usmani@polyu.edu.hk, ORCID: <https://orcid.org/0000-0003-2454-5737>

compensate for a rigorous fire model, as is the prevailing situation for travelling fires for performance-based structural engineering. For instance, Bailey *et al.* in 1996 [2], and Moss & Clifton in 2004 [3] systematically investigated the behaviour of steel-framed buildings under ‘spreading fires’ (i.e. so-called “travelling fires” nowadays). However, the travelling fire model applied in those studies was rather crude, essentially a series of parametric fires with a time lag (i.e. Clifton’s travelling fire model [4]). More recently Rezvani & Ronagh in 2015 [5] and Rackauskaite *et al.* in 2017 and 2019 [6–8] have performed extensive numerical studies on structural response of steel-framed buildings, using 2D generic frame structures under another travelling fire model which considers a fire near-field and far-field (i.e. Rein’s travelling fire model [9]). These studies are practically of limited value, as a travelling or spreading fire is by its nature a 3D phenomenon and 2D structural models simply cannot represent the complexity of behaviours presented in a realistic structure, such as the membrane behaviour of floor systems. The Cardington fire tests clearly showed that the concrete slabs carried most of the load at very high temperatures [10]. Martinez and Jeffers [11] performed a computational investigation using a 3D structural model with slabs, however with only one travelling fire scenario applied. Lastly, it is worth noting that the majority of the previous numerical studies on travelling fires [2, 5-8, 11] lacked structural model validation under a travelling fire scenario. This was due to the limited availability of experimental data, i.e. that which well characterised both the travelling fire behaviour (e.g. thermocouple temperatures at various locations of the large compartment, fire spread rates, heat release rate) and the resultant structural response (e.g. deflectometers) [1].

This paper presents the outcomes of research targeted at filling this gap, i.e. identifying the importance of concrete slab inclusion with a 3D structural model for steel-composite structures under travelling fires; and applying a *validated* structural model using a more advanced travelling fire model (which considers both the fire energy and mass balance within the large compartment, i.e. an extended travelling fire methodology (ETFM) framework [12]), via various travelling fire scenarios, to identify which travelling fire design parameters (e.g. fire spread rates, opening factor, etc.), or related structural design parameters (e.g. fire resistance time, etc.), are most critical to fulfilling the design goals.

2 VALIDATION OF A STRUCTURAL MODEL - VESELÍ TRAVELLING FIRE TEST

According to the literature, there are very few full-scale structural fire experiments aimed at the characterization of both the structural response and the travelling fire behaviour; one notable exception is the Veselí Travelling Fire Test carried out in 2011 in the Czech Republic [13].

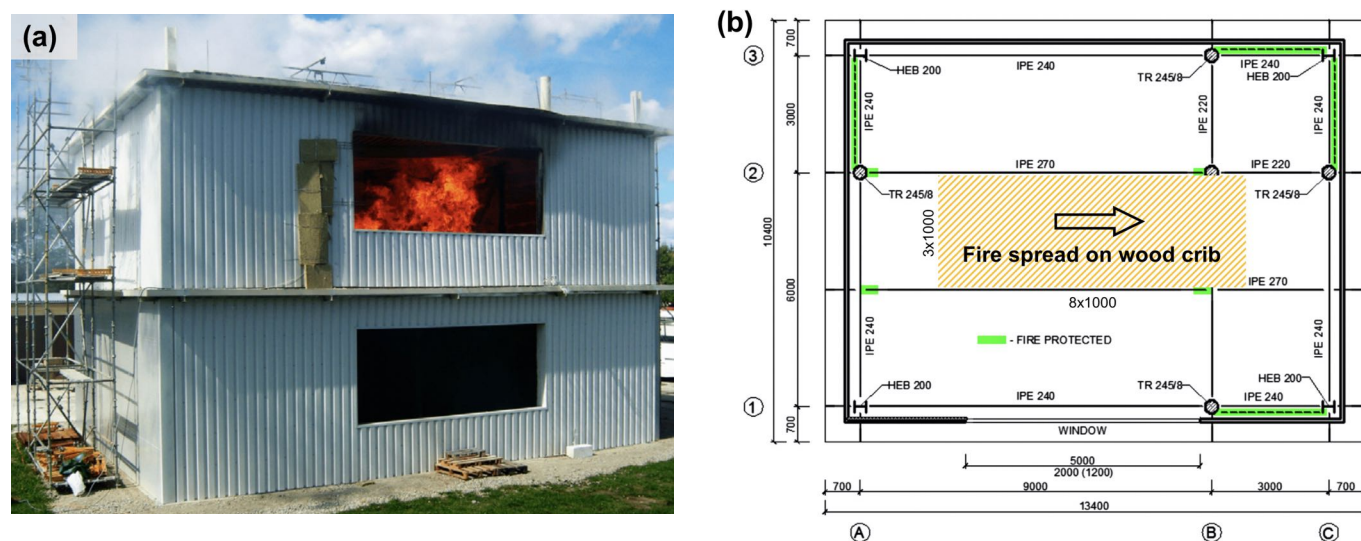


Figure 1. (a). Photo of the fire progression during the Veselí Travelling Fire Test on the upper floor; and (b). Plan view of upper floor structural layout and wood crib distribution (unit in mm). (both figures adapted from Cábová *et al.* [13])

The two-story steel framed building, with composite floors, had two by three bays in plan (13.4 m × 10.4 m) with a total building height 9 m, see Figure 1 (a). The columns of the upper floor used HEB 200 and TR 245/8 filled with concrete C30/37, and the steel beams had dimensions of IPE 220, IPE 240, and IPE 270

(steel S355) respectively, see Figure 1 (b) for their exact locations. The ceiling floor was composite with trapezoidal steel sheets (thickness 0.75 mm, S350), and the total thickness of the ceiling slab was 100 mm in the upper floor. The composite ceiling floor had steel wires \varnothing 1 mm length of 60 mm with average tensile strength of 1450 N/mm², in quantities 30 kg/m³ [14]. It is important to note that the ceiling floor was not subject to any other mechanical loading except for its self-weight, which is equivalent to approximately 1.6 kN/m². Fin plates and reverse channel connections were designed to resist shear forces. Two cross bracings were used for providing building horizontal stiffness. The wood crib fuel bed was uniformly distributed in a rectangular shape, with dimension 3 m \times 8 m, at the centre of the test compartment. Its equivalent fire load density on the whole floor area was 173.5 MJ/m². The wood crib was ignited with a linear source on the left end, hence the fire could develop naturally in a “travelling” fire manner. More details of the Veseli Travelling Fire Test can be found in reference 14.

In the LS-DYNA finite element structural model [15], the formulation of steel structural elements is Hughes-Liu type with cross section integration and the number of beam integration points for output is 10 and the number of integration points in the cross-section is 14. The Young’s modulus and yield strength of steel elements were taken to be 210 GPa and 355 MPa, respectively. The material of steel beams used MAT_202: Steel_EC3, and thermal properties for MAT_202 were defined according to EC3 [16]. Different from the experiment, the concrete filled steel internal columns with a profile of TR245/8, were modelled as circular steel columns instead. The Cofraplus 60 composite slab in the upper floor was simplified as the equivalent self-weight of flat concrete slab with a continuous depth of 70 mm, reinforced by two layers of reinforcement mesh \varnothing 5 mm 196 mm²/1000 mm placed 30mm from the top of the cross-section [17]. The strength of reinforcements was 420 N/mm². The shell formulation of slabs was *PART_COMPOSITE. The material type of C30/37 concrete slabs was MAT_172: CONCRETE_EC2. The thermal properties of concrete were defined according to EC2 [18]. Two different types of connections, rigid and pinned, were considered to demonstrate the effects of connections on determining the validity of this LS-DYNA finite element model. The shell element size was 0.5 m \times 0.5 m, and 1.0 m \times 1.0 m for the upper floor slab and lower floor slab respectively. The beams and columns were discretized with 8 elements (Figure 2(a)). Lastly, to reduce the computational time using LS-DYNA, temperature evolution within heated members was speeded up by a factor of 1000.

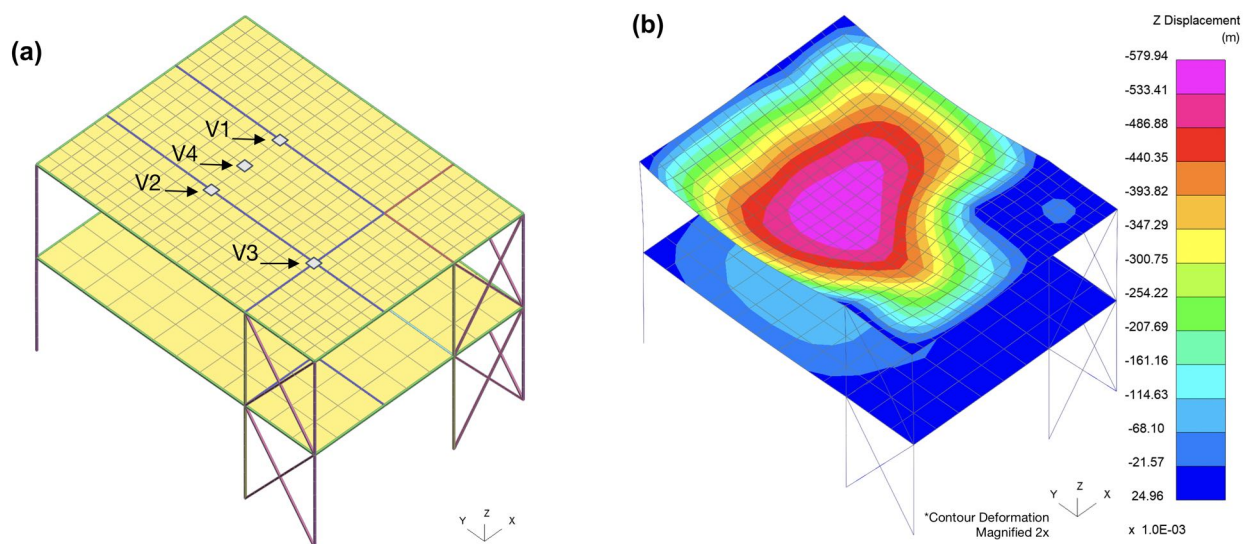


Figure 2. (a). 3D finite element model of the Veseli Travelling Fire Test building (tags V1 to V4 are monitored locations referred to Figure 3); and (b). Displacement contour of the model while reaching its maximum deflection (2x scaled).

The unfactored design loads were applied as the mechanical loading according to the experiment setup [14]. A total self-weight of 1.68 kN/m² from the concrete slab was applied on the upper floor. A uniformly distributed load of 5.54 kN/m² was imposed on the lower floor, where the dead load was 2.54 kN/m² including the self-weight 2.04 kN/m² and partition 0.5 kN/m², and the live load was 3.0 kN/m². To minimise the comparison uncertainty between the structural model prediction and the experimentally measured structural response, the measured thermocouple time-temperatures of TG2-TG4, TG6-TG13, and TG14-

TG20, from the gas phase, were applied to the related parts of the structural elements close to the locations of these sensors. Those time-temperature histories were *multiplied* with certain reduction ratios to consider the heat transfer within the structural member cross-sections following the assumptions by Horová and Wald in 2015 [17]. For example, the temperature reduction ratio 0.7 and 0.6, were applied on the fire exposed surface and the unexposed surface of protected steel beams.

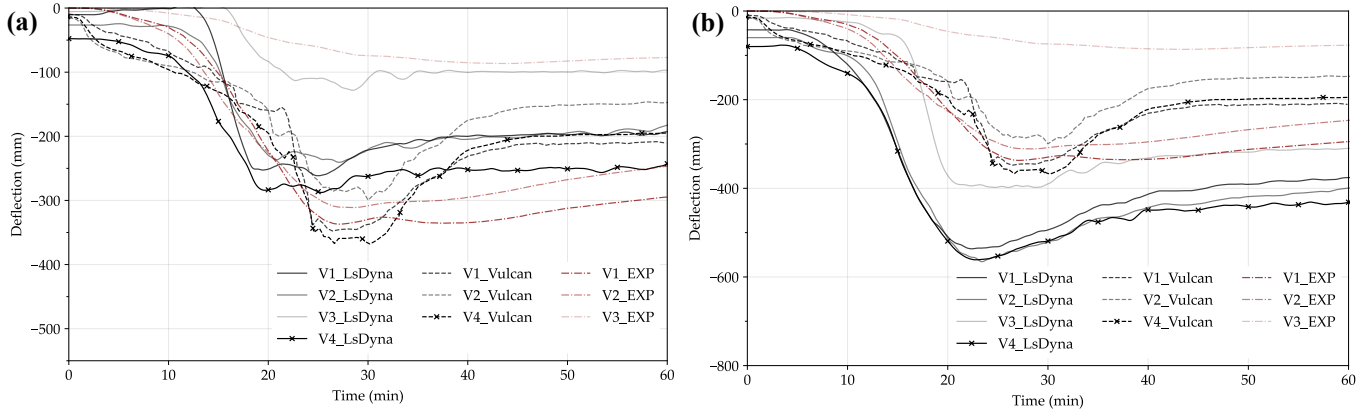


Figure 3. Deflection comparison between the Veseli Travelling Fire Test data, Vulcan modelling data based upon Horová and Wald in 2015 [17], and the LS-DYNA finite element modelling results, at various locations V1 to V4, when assuming: (a). Connection rigidity - fixed; and (b). Connection rigidity - pinned.

Figure 3 presents the validation of the LS-DYNA structural finite element model against the experimentally measured steel beam deflections, and the Vulcan modelling results [17]. For simplification purposes, the fin plates and reverse channel connections were simplified as either rotationally fixed (Figure 3(a)), or pinned (Figure 3(b)) to represent the connection rigidity. It can be seen that both models well capture the structural deflection sequence when the fire travels, i.e. V1, V2, and V4 start to deflect as a group first as they are closer to the travelling fire ignition source, and displacement of V3 at the far end of the compartment starts to increase with approx. 5 mins time delay. This deflection sequence was also captured by the experiment. It is worth noting that V1 of the LS-DYNA model reached its maximum 265 mm at 25 mins with the rigid connection, and 540 mm at 22 mins with the pinned connection, and V1 from the experiment showed that its maximum value at 27 mins with 340 mm, which lies in-between the two LS-DYNA model predictions. This is consistent with the expectation that in reality the connections should have a certain level of rotational stiffness, although the fin plates and the reverse channel connections were designed to resist the shear force only [19]. The structural residual deflection during the cooling phase was also properly reproduced by the two LS-DYNA models.

3 A PROTOTYPE STEEL FRAMED BUILDING UNDER VARIOUS TRAVELLING FIRES

Although the finite element structural model was validated against the Veseli Travelling Fire Test [13-14] and other similar modelling efforts [17], it is important to note that the aspect ratio of the test compartment was close to 1, i.e. approx. 1.3 obtained by 13.4 m over 10.4 m. This low aspect ratio is not ideal for carrying out parametric studies for travelling fire scenarios, as both the thermal and structural response of the structural members along the fire travelling trajectory were not very distinguishable in terms of time lag [12-13, 17]. Hence, it is of value to further adapt the validated LS-DYNA 3D finite element structural model for the Veseli Travelling Fire Test to a prototype steel framed building which has a much higher compartment aspect ratio, i.e. a long slim shape. Inspired by the structural layout of the BST/FRS 1993 travelling fire test (performed within a ‘slice’ of the large open-plan office compartment, see Figure 4(a)) [20], the adapted new LS-DYNA 3D numerical model represents a one-story prototype steel framed building with composite floors, having structural dimensions of 23 m length \times 6 m width \times 2.75 m height, see Figure 4(b). This prototype steel framed building has three bays: the first bay and third bay have the same length of 7.5 m, which are slightly shorter than the length of the second bay, i.e. 8 m. This prototype structure was designed following the Eurocode [21] to resist an ambient design load on the floor ($1.35 \times \text{dead load} + 1.5 \times \text{live load} = 1.35 \times 4.11 + 1.5 \times 2.5 = 9.30 \text{ kN/m}^2$). The cross-section of all floor beams

and columns were chosen as UB 406×178×54 with steel grade S235, and 140 mm thickness concrete slab with two ribbed mesh Ø 8 mm 490 mm²/1000 mm with the strength of 420 N/mm². The two layers of reinforcement were placed 30 mm from the top and the bottom of the slab cross-section, respectively. The steel beams and columns were designed for one-hour fire protection, using mineral fibre spray with thermal conductivity 0.12 W/(m·K), density 300 kg/m³ and specific heat 1200 J/(kg·K) following the recommendations from Franssen et. al. in 2009 [22]. During the fire simulation, the load imposed on the beams was in the range of 0.4 of their ambient design capacities. The unfactored design loads were applied as the mechanical loadings along with various travelling fire scenarios. Both the travelling fire modelling and subsequent heat transfer analysis were carried out using OpenSees [12]. Note that all the connections are modelled as pinned instead of rigid, as the former provides a more conservative structural response.

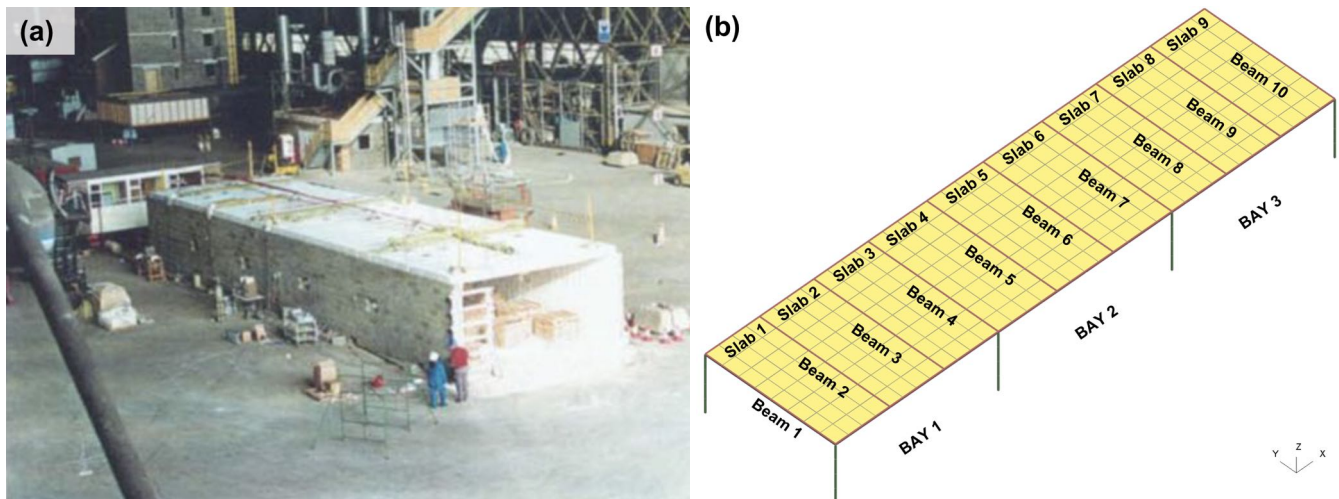


Figure 4. (a). Test compartment of the BST/FRS 1993 Fire Test Series [20]; and (b). 3D finite element model of the new adapted prototype building (beams and slabs tagged in the following sections).

3.1 The baseline travelling fire scenario

As mentioned, a more advanced travelling fire model, i.e. the ETFM framework [12] considering both the energy and mass balance of the fire compartment, was applied to this prototype steel framed building. To carry out the parametric studies of the structural response under various travelling fire scenarios, a baseline case has to be defined first. The selection of this baseline travelling fire scenario follows the rules that the relevant design parameters are from common design practice (e.g. fuel load density, heat release rate per unit area). Meanwhile, it is required that this selected baseline fire scenario can challenge the prototype steel framed building close to its “failure”, i.e. either following the critical temperature criteria, or the maximum deflection (rate) criteria. Hence, a well distributed “spectrum” of the structural response can be explored in the subsequent parametric studies.

Fuel load density 511 MJ/m², and heat release rate per unit area (HRRPUA) 250 kW/m², were selected for office buildings following the Eurocode 1 [23]. Fire spread rate was assumed to be a constant 2.5 mm/s, which was close to the findings from the Tisova Travelling Fire Test [24]. In addition, the total heat loss fraction 0.85 was adopted including a constant radiative heat loss fraction of 0.35 following the suggestions by Janssens [25]. Two openings with dimension 14 m × 1 m were assumed on the two “long” sides of this large compartment, having sill height 1 m and soffit height 2 m. This opening assumption is equivalent to an inverse opening factor 9.6, which is a suggested intermediate value in the region between fuel-controlled and ventilation controlled burning following Thomas & Heselden [26]. The fire was assumed to start at the one short end of the compartment, travelling along the longitudinal direction.

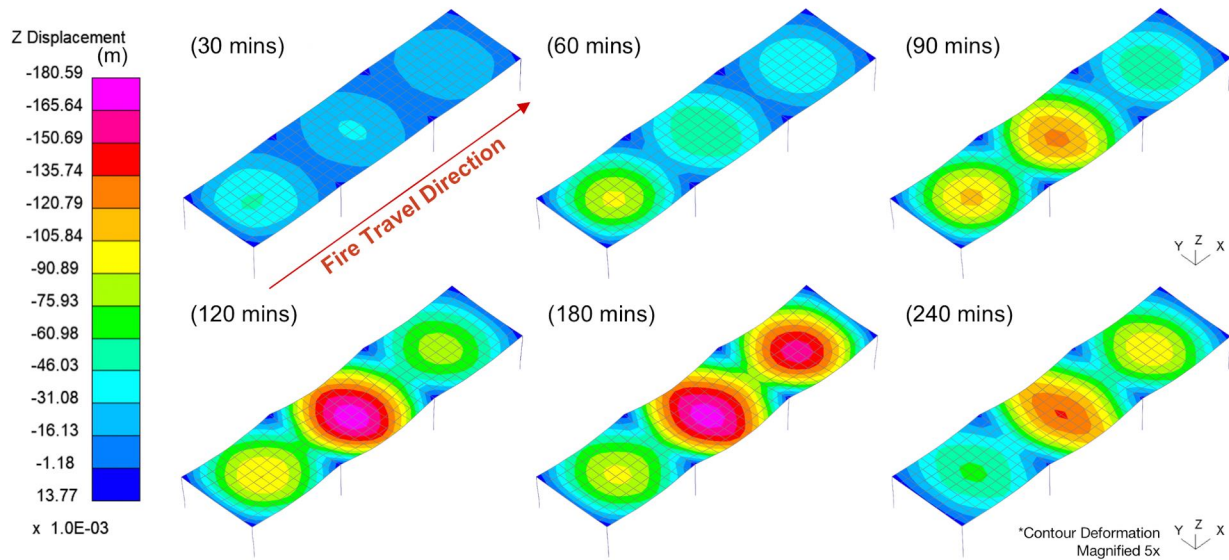


Figure 5. The displacement development under the baseline travelling fire scenario, 5x scaled (fire spread rate: 2.5 mm/s, fuel load density: 511 MJ/m², HRRPUA: 250 kW/m², and inverse opening factor: 9.6).

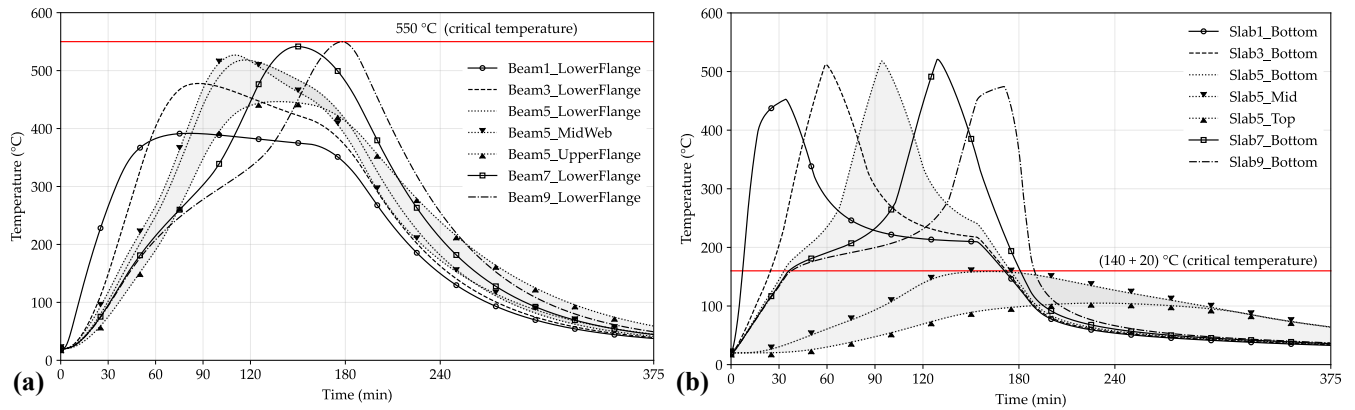


Figure 6. Temperature development of the structural elements under the baseline travelling fire scenario: (a). steel Beam1 - Beam10; and (b). concrete Slab1 - Slab10 (location of the structural member tags is referred in Figure 4).

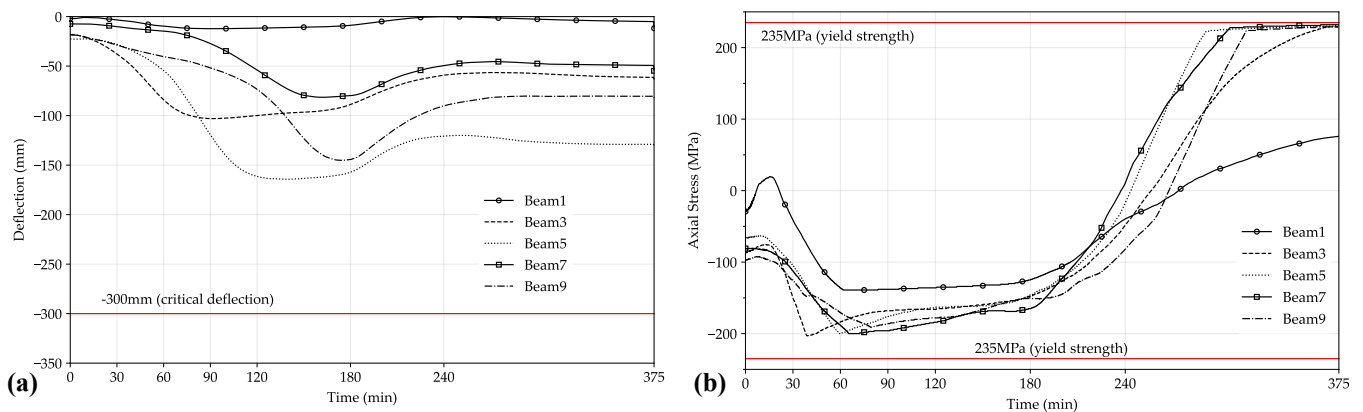


Figure 7. Structural response of the steel beams under the baseline travelling fire scenario: (a). Deflection of the steel beams, and (b). Maximum axial stress at the beam mid-span.

Figure 5 presents the slab deflection contour development under the baseline travelling fire scenario at every 30 mins. Generally, the deflection sequence of the steel beams in those three bays followed the fire travelling trajectory, i.e. as the fire travelled through each bay it would have the largest deflection compared to the other two bays; and as the fire travelled away from it, deflection would decrease due to cooling. Interestingly, the second bay, which has a slightly longer length, 8 m, had the largest residual deflection

compared to the other two bays which are 7.5 m in length. This is because the longer primary beams of the second bay generated larger deflections in the heating phase due to their thermal expansion being restrained by the neighbouring cooler bays, and hence relatively larger residual deflection occurred during the cooling phase. Figure 6 summarises the time-temperature histories of the steel beams and slabs along the travelling fire path. In Figure 6 (a), it can be seen that Beam9, located at the far end of this longitudinal compartment, experienced the maximum member temperature 550 °C at 178 mins. This is due to the effect of the far-field smoke temperature, which preheated the steel member for a long time, allowing the heat to penetrate through the fire protection, eventually reaching its maximum value, when the near-field fire reached the third bay. In contrast, Beam1 had a lower peak steel member temperature, i.e. 390 °C, as this beam was close to the travelling fire ignition location. When the near-field travelling fire left the first bay, only far-field smoke was left to heat this structural element. Figure 6 (b) shows the temperatures in the concrete slabs, and it is worth noting that none of the slab top surface reached its 160 °C critical temperature. The structural deflection history of the beams followed the same trend, i.e. Beam1 had the lowest deflection, 15 mm at 90 mins, in contrast Beam5 had the largest deflection 170 mm at 142 mins due to the larger deflection of the primary beams in the second bay. In addition, none of the beam members reached their critical deflection 300 mm, i.e. $L/20$, where L is the beam member length of 6 m, as shown in Figure 7 (a). More importantly, as presented in Figure 7 (b), most of the steel beams (except for Beam1 close to the fire ignition location) failed due to their maximum axial stresses reaching the steel yield stress 235 MPa, as the large tensile force was inevitably induced during the travelling fire cooling phase. This finding implies that in the design practice, solely satisfying the critical temperature and deflection for the structural members might not guarantee a safe design for travelling fires, and the yielding stress status of the structural members during the cooling phase should also be considered.

3.2 Thermal and structural response under different travelling fire spread rates

Travelling fire spread rates are among the most important design parameters for the thermal analysis of the structural members in a large compartment [12], however, their structural impact is still unclear, though pioneering work had been carried out [5-9], especially while the structural elements are supplied with a certain level of fire protection (i.e. one hour fire protection in our case) and concrete slab is carrying the majority of the loading at high temperature.

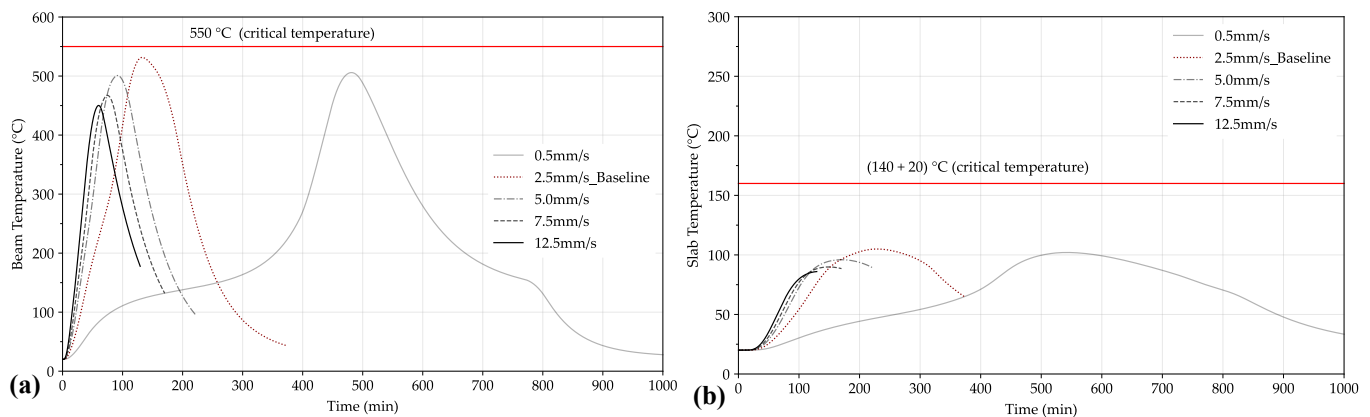


Figure 8. Temperature development of the structural elements under various travelling fire spread rates - 0.5 mm/s, 2.5 mm/s (baseline), 5.0 mm/s, 7.5 mm/s, and 12.5 mm/s on: (a). steel Beam6 bottom flange; and (b). concrete Slab5 top surface.

Figure 8 presents the thermal response of the steel Beam6 bottom flange and concrete Slab5 top surface, respectively, under various travelling fire spread rates, i.e. 0.5 mm/s, 2.5 mm/s (baseline), 5.0 mm/s, 7.5 mm/s, and 12.5 mm/s. The selection of the travelling fire spread rates followed the literature summary by Dai *et. al.* in 2020 [12]. Beam6 and Slab5 are both at the second bay, which tends to have the largest structural deflections according to the findings in the aforementioned baseline travelling fire scenario. All the setup of the design travelling fire parameters were kept the same as the baseline scenario, except for changing the fire spread rates. The thermal impact of the fire spread rates on the protected steel members' bottom flange, as well as on the concrete slabs' top surface, are not distinguishable on their peak temperatures (i.e. 450 °C to 530 °C for the steel members, 85 °C to 105 °C for the concrete slabs). Instead,

their predominant impact was mainly reflected on the total durations of one heat-cooling cycle, which is inversely proportional to their corresponding fire spread rates. The “non-distinguishable” peak member temperatures are mainly due to the “combination effect” of the presence of fire protection/concrete slab, and the travelling fire spread rate. When a fast travelling fire (e.g. 12.5 mm/s) approaches a structural member with a very high resultant heat release rate (HRR), i.e. 38 MW (the calculation of resultant heat release rate based upon the fire spread rates can be found in Dai *et al.* in 2020 [12]), it will also rapidly move away from the structural member reducing the total near field exposure time for that member. By contrast, when a slow travelling fire (e.g. 0.5 mm/s) approaches a structural member even with a modest total HRR, i.e. 1.5 MW, the longer near field exposure will enable the fire a lot more time to ‘heat up’ the structural member, which may result in more energy being absorbed by the structural member.

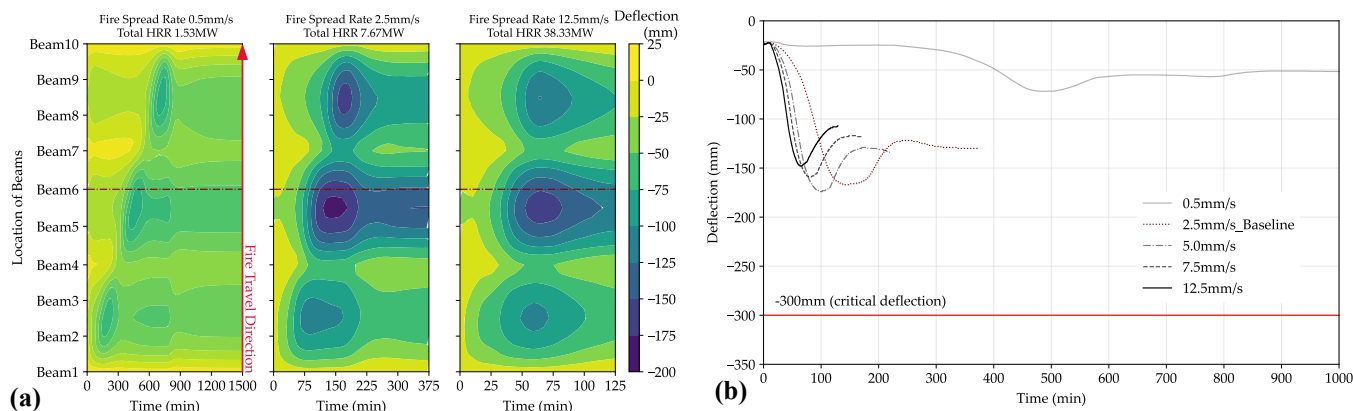


Figure 9. Deflection of the steel beams under various travelling fire spread rates: (a). contour of the Beam1 - Beam10 deflection with time under 0.5 mm/s, 2.5 mm/s (baseline), and 12.5 mm/s travelling fires; (b). Beam6 deflection with time.

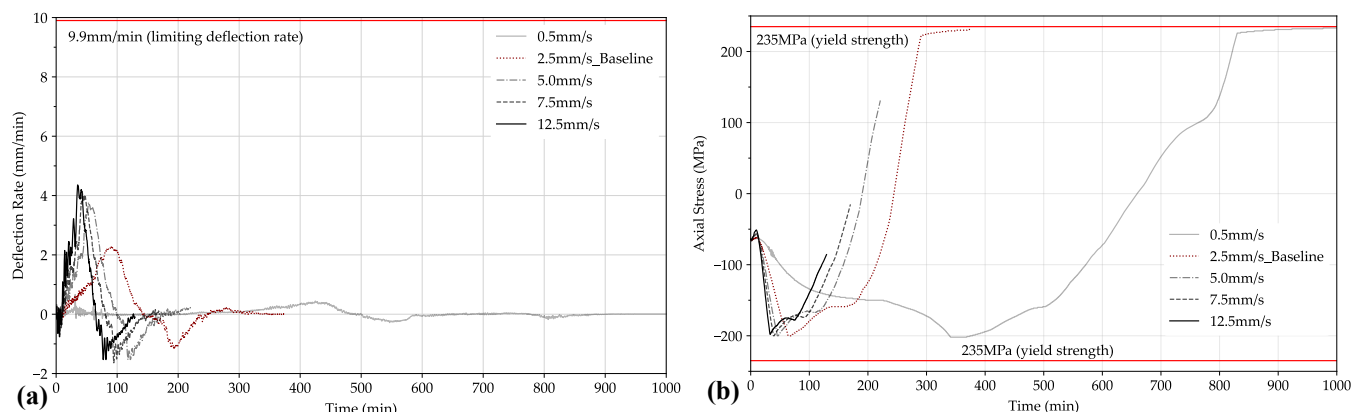


Figure 10. Determination of failure criteria for steel Beam6 under various travelling fire spread rates - 0.5 mm/s, 2.5 mm/s (baseline), 5.0 mm/s, 7.5 mm/s, and 12.5 mm/s on: (a). Deflection rate; and (b). Maximum axial stress at beam mid-span.

Figure 9 (a) demonstrates the structural deflections along the travelling fire trajectory, from Beam1 to Beam10, as time evolves. Among the three cases with fire spread rates of 0.5 mm/s, 2.5 mm/s (baseline), and 12.5 mm/s, it was found that 2.5 mm/s resulted in the largest structural deflection in the concrete slab between Beam5 and Beam6, i.e. Slab5. Again, the reason behind this is due to the aforementioned “combination effect”, between the presence of fire protection/concrete slab, and the travelling fire spread rate. An exemplar of this deflection result is presented in Figure 9 (b), that in the group of travelling fire cases with increasing fire spread rates 5.0 mm/s, 7.5 mm/s, and 12.5 mm/s, the maximum deflections of those cases were decreasing, i.e. to 175 mm, 160 mm, and 150 mm, respectively. The smallest deflection was 75 mm, related to the slowest travelling fire, 0.5 mm/s, and is probably due to the fact that only a limited number of the structural elements were heated by this smaller 1.5 MW fire. This fire could only impact a limited area of the structure while the remainder of the structural bays stay at a relatively low temperature, and still provide high stiffness and load redistribution paths to prevent the heated part of the structure from deflecting significantly. Further, the presence of the concrete slab increases the continuity of the whole structure, compared to a 2D steel framed structural analysis. Figure 10 (a) illustrates the

deflection rates of Beam6, that fire spread rates have limited impact on this value. More importantly, as shown in Figure 10 (b), the slow travelling fires (i.e. 0.5 mm/s, 2.5 mm/s) led to failure of the structure in the cooling phase due to the large tensile stresses reaching the steel yield stress, 235 MPa. This implies that slow travelling fire scenarios cannot be ignored in structural design for travelling fire scenarios.

3.3 Thermal and structural response under various opening factors

According to Dai *et. al.* in 2020 [12], another important travelling fire design parameter is the inverse opening factor (i.e. size of the compartment openings), which mainly affects the accumulated smoke temperature for preheating the structural elements at the far-field of the large compartment. This section investigates the impact of this parameter, while maintaining the values of all other parameters the same as the baseline scenario. This is done by changing the large compartment window height, resulting in equivalent inverse opening factors of 2.5, 5.0, 9.6 (baseline), and 28.6 accordingly.

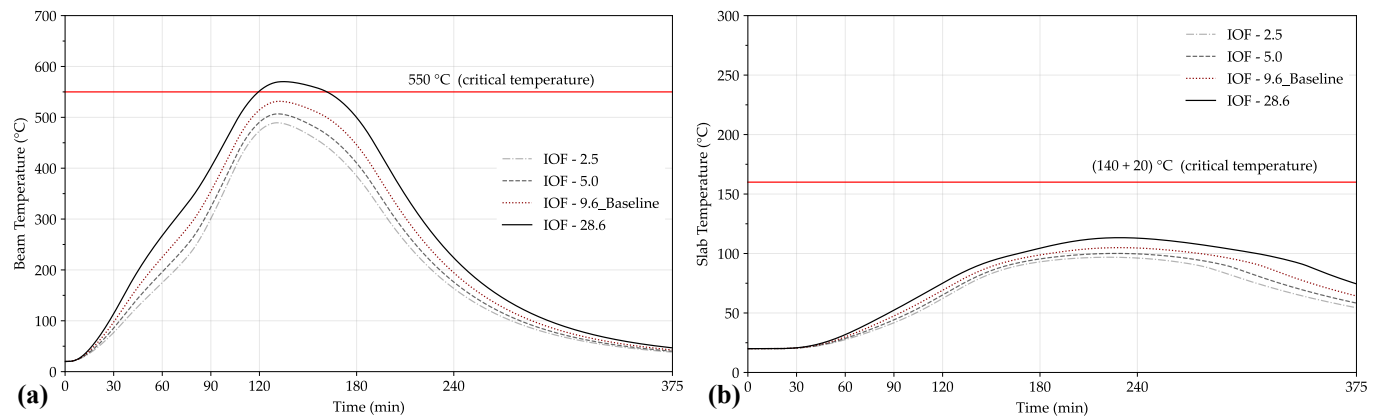


Figure 11. Temperature development of the structural elements under travelling fire scenarios with different inverse opening factors (abbrev. IOF), 2.5, 5.0, 9.6 (baseline), and 28.6: (a). steel Beam6 bottom flange; and (b). concrete Slab5 top surface.

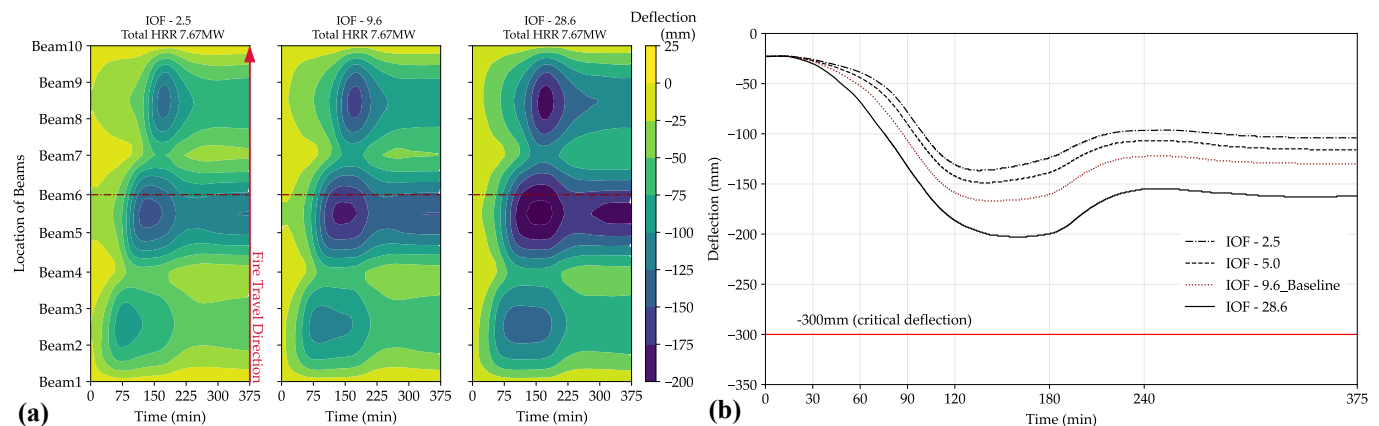


Figure 12. Deflection of the steel beams under travelling fire scenarios with different compartment inverse opening factors (abbrev. IOF): (a). contour of the Beam1 - Beam10 deflection with time with inverse opening factor 2.5, 9.6 (baseline), and 26.8 respectively; and (b). Beam6 deflection with time.

Unlike the structural response sensitivities due to various travelling fire spread rates, the impact of the opening factor displays a very linear relationship with the resultant thermal and structural response of the structural members, as presented in Figure 11 and Figure 12. For example, with increasing inverse opening factor (i.e. decreasing opening size), 2.5, 5.0, 9.6 (baseline), and 28.6, the maximum steel member bottom flange temperatures were also increasing, to 480 °C, 500 °C, 525 °C, and 575 °C respectively. This is due to more energy being confined within the large compartment as the opening size was reduced, hence higher gas phase temperatures were predicted by the ETFM framework. Figure 13 shows that the inverse opening factor has a limited impact on the structural deflection rate, as well as the maximum axial stress at beam mid-span.

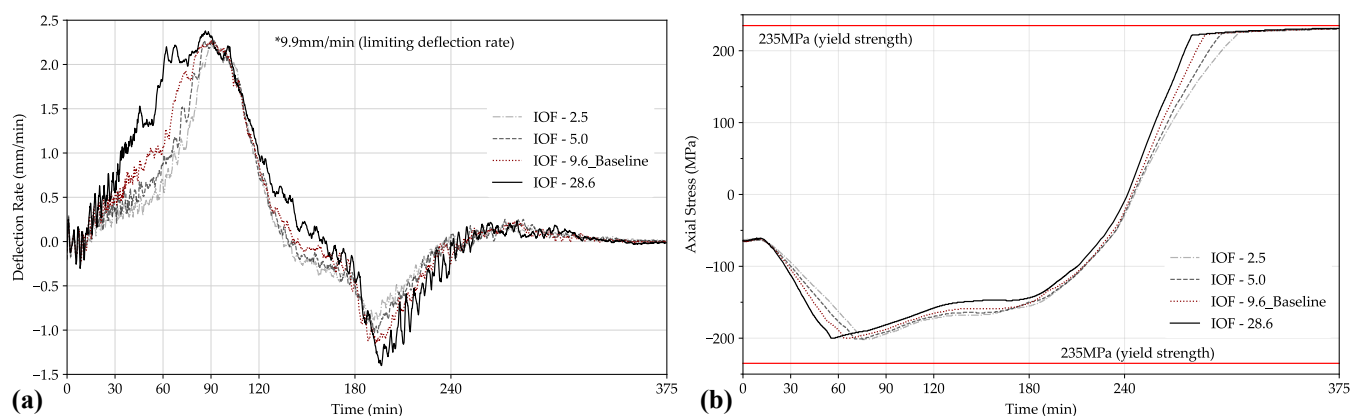


Figure 13. Determination of failure criteria for steel Beam6 under with different inverse opening factors (abbrev. IOF), 2.5, 5.0, 9.6 (baseline), and 28.6: (a). Deflection rate; and (b). Maximum axial stress at beam mid-span.

4 DISCUSSIONS AND CONCLUSIONS

This paper began with presenting the validation of a 3D finite element structural model against the Veseli Travelling Fire Test using LS-DYNA. Following this, a model for a one-story prototype steel-framed building with composite floors was adapted based on the structural layout of the BST/FRS 1993 travelling fire test. The established model investigated the structural response of a 'slice' of the large open-plan office compartment to a range of travelling fire scenarios (i.e. different fire spread rates and inverse opening factor) using the ETFM framework, as summarized in Table 1.

Table1: Summary of the case studies for the thermal and structural response and corresponding failure criteria, under various travelling fire scenarios (cells in grey for highlighting failure)

Case No.	Fire Spread Rate (mm/s)	Inverse Opening Factor (IOF)	Total HRR (MW)	Fire Duration (min)	Critical Temperature (°C)		Critical Deflection L/20 (mm)		Max Axial Stress (MPa)	
					Beam (550)	Slab unexposed (140+20)	Beam (-300)	Slab (-300)	Beam (Yield Stress 235)	
1*	2.5	9.6	7.67	375	550	105	-167	-181	232	-207
2	0.5	9.6	1.53	1600	506	102	-73	-78	233	-205
3	5.0	9.6	15.33	220	531	97	-174	-189	218	-208
4	7.5	9.6	23.00	170	492	91	-159	-180	202	-207
5	12.5	9.6	38.33	130	451	86	-148	-163	193	-204
6	2.5	2.5	7.67	375	505	97	-137	-148	230	-208
7	2.5	5.0	7.67	375	524	100	-149	-161	231	-208
8	2.5	28.6	7.67	375	590	114	-203	-218	233	-206

* Case 1 is the baseline scenario.

This parametric study assessed the structural fire performance under various travelling fire scenarios considering different failure criteria, including the maximum structural member temperatures, deflections, deflection rates, and maximum axial stresses. According to Table 1, the failure of structural steel beams, under different fire spread rates (key parameter for the travelling fire near-field) for case 1 and 2, as well as the inverse opening factors (key parameter for travelling fire far-field smoke) for case 6, 7, and 8, both have direct impact on the heating and cooling stages of the structural member failure. The travelling fire spread rate is directly related to the total HRR and fire duration, in a proportional and inversely proportional relationship, respectively.

It is instructive to see that the structural global behaviour could be fundamentally changed due to the selection of different travelling fire spread rates. As presented in Table 1, when the fire spread rates were 2.5 mm/s and 5.0 mm/s, the structural element peak temperature, deflection, and axial stress were generally larger than the other cases with 0.5 mm/s, 7.5 mm/s and 12.5 mm/s. This is mainly due to the “combination effect” of the presence of fire protection/concrete slab, and the travelling fire spread rate. Hence, it is recommended while applying the travelling fires for structural design, various travelling fire scenarios should be considered. The slow travelling fires (e.g. 0.5 mm/s, 2.5 mm/s) are also necessary travelling fire scenarios to be considered in design.

Furthermore, most of the failure cases were due to the structural beam members exceeding their steel material yield stress, mainly caused by the large tensile axial force during the cooling phase. Although the inverse opening factor has limited impact on the structural member deflection rate and the maximum axial stress, the inverse opening factor still directly affects the smoke layer (thickness and temperature of the far-field accumulated smoke layer), i.e. dominating the tensile axial force of the beam members during the cooling phase.

Ultimately, a single criterion cannot ensure a safe structural fire design under travelling fires. It can be seen from the above table that failure could be determined by different criteria. Therefore, when performing structural response analysis under travelling fires, the three criteria: critical temperature, critical deflection (deflection rate), and maximum axial stress should be considered altogether for judgment and the necessary overall structural analysis should also be performed.

ACKNOWLEDGMENT

The authors would like to express their sincere thanks to Kamila Cábová and František Wald from Czech Technical University, for providing access to the experimental data of the Veselí Travelling Fire Test.

REFERENCES

1. Dai, X., Welch, S. and Usmani, A., A critical review of ‘travelling fire’ scenarios for performance-based structural engineering, *Fire Safety Journal*, vol. 91, pp. 568–578, 2017. <https://doi.org/10.1016/j.firesaf.2017.04.001>
2. Bailey, C. G., Burgess, I. W. and Plank, R. J., Analyses of the effects of cooling and fire spread on steel-framed buildings, *Fire Safety Journal*, vol. 26, pp. 273–293, 1996. [https://doi.org/10.1016/S0379-7112\(96\)00027-6](https://doi.org/10.1016/S0379-7112(96)00027-6)
3. Moss, P. J. and Clifton, G. C., Modelling of the Cardington LBTF steel frame building fire tests, *Fire and Materials*, vol. 28, no. 2–4, pp. 177–198, 2004. <https://doi.org/10.1002/fam.868>
4. Clifton, C. G., *Fire Models for Large Firecells*. HERA Report R4-83. HERA publications, New Zealand, 1996.
5. Rezvani, F. H. and Ronagh, H. R., Structural response of a MRF exposed to travelling fire, *Proceedings of the Institution of Civil Engineers - Structures and Buildings*, vol. 168, no. SB9, pp. 619–635, 2015. <https://doi.org/10.1680/jstbu.14.00046>
6. Rackauskaite, E., Kotsovinos, P., Jeffers, A. and Rein, G., Structural analysis of multi-storey steel frames exposed to travelling fires and traditional design fires, *Engineering Structures*, vol. 150, pp. 271–287, 2017. <https://doi.org/10.1016/j.engstruct.2017.06.055>
7. Rackauskaite, E., Kotsovinos, P. and Rein, G., Structural response of a steel-frame building to horizontal and vertical travelling fires in multiple floors, *Fire Safety Journal*, vol. 91, pp. 542–552, 2017. <https://doi.org/10.1016/j.firesaf.2017.04.018>
8. Rackauskaite, E., Kotsovinos, P., Jeffers, A. and Rein, G., Computational analysis of thermal and structural failure criteria of a multi-storey steel frame exposed to fire, *Engineering Structures*, vol. 180, pp. 524–543, 2019. <https://doi.org/10.1016/j.engstruct.2018.11.026>
9. Rackauskaite, E., Hamel, C., Law, A. and Rein, G., Improved formulation of travelling fires and application to concrete and steel structures, *Structures*, vol. 3, pp. 250–260, 2015. <https://doi.org/10.1016/j.istruc.2015.06.001>

10. Gillie, M., Usmani, A. S. and Rotter, J. M., A structural analysis of the Cardington British steel corner test, *Journal of Constructional Steel Research*, vol. 58, no. 4, pp. 427–442, 2002. [https://doi.org/10.1016/S0143-974X\(01\)00066-9](https://doi.org/10.1016/S0143-974X(01)00066-9)
11. Martinez, J. and Jeffers, A. E., Global structural behaviour of steel-concrete composite floor systems under travelling fires, the 9th International Conference on Structures in Fire, pp. 967–974, 2016.
12. Dai, X., Welch, S., Vassart, O., Cábová, K., Jiang, L., Maclean, J., Clifton, C. and Usmani, A., An extended travelling fire method framework for performance-based structural design, *Fire and Materials*, vol. 44, pp. 437–457, 2020. <https://doi.org/10.1002/fam.2810>
13. Horová, K., Jána, T. and Wald, F., Temperature heterogeneity during travelling fire on experimental building, *Advances in Engineering Software*. vol. 62–63, pp. 119–130, 2013. <https://doi.org/10.1016/j.advengsoft.2013.05.001>
14. Simões da Silva, L. et al. Design of Composite Joints for Improved Fire Robustness, RFCS Compfire project-final report (RFSR-CT-2009-00021), Luxembourg: European Commission; 2014. DOI: 10.2777/76889
15. LSTC, LS-DYNA. Keyword User's Manual. Livermore: Livermore Software Technology Corporation (LSTC), 2007.
16. Eurocode 3. Design of Steel Structures - Part 1-2: General rules — Structural fire design. European Standard EN 1993-1-2, CEN, Brussels, 2005.
17. Horová, K. and Wald, F., Temperature heterogeneity of travelling fire and its influence on composite steel concrete floor, *Civil Engineering Journal*, vol. 24 (1), pp. 1–10, 2015. DOI: 10.14311/CEJ.2015.01.0006
18. Eurocode 2. Design of concrete Structures - Part 1-2: General rules — Structural fire design. European Standard EN 1992-1-2, CEN, Brussels, 2008.
19. Huang, S., Burgess, I. and Davison, B., A Structural Fire Engineering Prediction for the Veselí Fire Tests, *Journal of Structural Fire Engineering*, vol. 4 (1), pp. 1–8, 2013.
20. Kirby, B.R., Wainman, D.E. and Tomlinson, T.L., Natural Fires in Large Scale Compartments. *International Journal on Engineering Performance-Based Fire Codes*. 1999;1(2):43-58
21. Eurocode 1. Actions on structures - part 1-1: General actions - Densities, self-weight, imposed loads for buildings. European Standard EN 1991-1-1, CEN, Brussels, 2002.
22. Franssen, J., Kodur, V. and Zaharia, R., *Designing Steel Structures for Fire Safety*, Taylor & Francis, 2009.
23. Eurocode 1. Actions on Structures - Part 1-2: General Actions - Actions on Structures Exposed to Fire. European Standard EN 1991-1-2, CEN, Brussels, 2002.
24. Rush, D., Dai, X. and Lange, D., Tisova Fire Test – fire behaviours and lessons learnt. *Fire Safety Journal*, 2020.
25. Janssens. M.L., *An Introduction to Mathematical Fire Modeling*, 2nd edition, Lancaster, PA, USA, CRC Press, 2000.
26. Thomas, P.H. and Heselden, A.J., Fully developed fires in single compartments, CIB Report No 20, Fire Research Note 923. Borehamwood, UK, Fire Research Station, 1972.

AN IMPROVED IMPLICIT ANALYSIS METHOD TO MODEL TRANSIENT STRAIN OF HIGH-STRENGTH CONCRETE DURING UNLOADING AT ELEVATED TEMPERATURES

Shan Li¹, J. Y. Richard Liew², Ming-Xiang Xiong³

ABSTRACT

The stress-strain relationships of concrete at elevated temperatures given in EN1992-1-2 is found to result in partial recovery of the transient strain of concrete upon unloading. Consequently, numerical models that adopt these stress-strain relationships to predict the response of concrete structures under fire conditions will underestimate their deformations and might result in unsafe predictions. Therefore, this paper proposes a modified-elastic modulus (Modified-E) method to correctly model the compressive behaviour of C120 concrete at elevated temperatures. The proposed method is implemented in a three-dimensional (3-D) finite element model to predict the fire performance of a high-strength concrete encased steel (CES) column under ISO834 fire condition. Results from the numerical analysis show that compared to the conventional method in the current EN1992-1-2, the Modified-E method reduces the error in the modelled transient strain of concrete by 55%. It also enables the 3-D finite element model to better capture the axial displacement of the CES column specimen under fire conditions.

Keywords: stress-strain relationship ; high-strength concrete; finite element model; concrete encased steel column;

1 INTRODUCTION

In a thermal-mechanical analysis using finite element methods, the unknowns are usually the nodal displacements. It is commonly accepted that the corresponding total strain of concrete consists of five parts, namely the free thermal strain $\varepsilon_{th,\theta}$ caused by the change of temperature, the basic creep strain $\varepsilon_{cr,\theta}$ caused by the dislocation of microstructures of the material, the transient strain $\varepsilon_{tr,\theta}$ caused by the change of chemical composition and the instantaneous stress-related elastic strain, $\varepsilon_{el,\theta}$ and inelastic strain $\varepsilon_{in,\theta}$ caused by externally applied stresses [1-3]. Among them, elastic strain and inelastic strain are determined by steady-state test and their sum are referred as instantaneous stress-related strain $\varepsilon_{\sigma,\theta}$. Steady-state test is carried out by increasing the compressive stress on the concrete specimen under a constant temperature [4]. Such test condition eliminates the transient strain component in the measured strain. Transient strain is determined by transient-state test where the concrete specimens are subject to increasing temperature under a constant compressive stress [5]. For concrete material, transient strain only occurs during first-time heating and is irrecoverable [6-8]. For common values of fire duration, the creep strain plays a minor role compared to the transient strain, and is often either neglected or lumped into the transient strain [9]. Free thermal strain can be separately determined by fire test on unloaded specimens. Mathematically, the strain components can be expressed using Eq. (1) where the basic creep strain is omitted.

¹ PhD candidate, National University of Singapore
e-mail: ceelis@nus.edu.sg, ORCID: <https://orcid.org/0000-0001-9381-5599>

² Professor, National University of Singapore
e-mail: ceeljy@nus.edu.sg

³ Assistant Professor, Guangzhou University
e-mail: cvexmx@gzhu.edu.cn

$$\varepsilon_{tot,\theta} - \varepsilon_{th,\theta} = \varepsilon_{\sigma,\theta} + \varepsilon_{tr,\theta} = (\varepsilon_{el,\theta} + \varepsilon_{in,\theta}) + \varepsilon_{tr,\theta} \quad (1)$$

where $\varepsilon_{tot,\theta}$ is total strain of concrete, $\varepsilon_{th,\theta}$ is free thermal strain, $\varepsilon_{\sigma,\theta}$ is instantaneous stress-related strain, $\varepsilon_{tr,\theta}$ is transient strain, $\varepsilon_{el,\theta}$ is instantaneous stress-related elastic strain and $\varepsilon_{in,\theta}$ is instantaneous stress-related inelastic strain.

The terms implicit and explicit are used to differentiate the two approaches that are commonly adopted in numerical analysis for the strain components in equation (1). A graphical representation of the stress-strain curve described by implicit and explicit schemes is shown in Figure 1, where the strain components in equation (1) are depicted. The main distinction between these two schemes is that the implicit scheme is based on the total strain, whereas the explicit scheme requires the individual components of the total concrete strain to be computed. Such a difference may lead to different predictions on the axial deformation of concrete at elevated temperatures. In an explicit model, the components in equation (1) are distinctively formulated and are separately programmed into the numerical model, making it possible to calculate the transient strain of concrete incrementally based on its temperature and stress history. Hence, modelling the strains of concrete using an explicit scheme is the most accurate. Implicit model is known to be more straightforward for implementation in numerical analysis since it only requires a lumped term that combines instantaneous stress-related strain and transient strain. The generic implicit model proposed in EN1992-1-2 [10] is widely used in numerical analysis. However the implicit formulation in EN1992-1-2 [10] is believed to only includes partial creep effects [11], and is accurate only when the concrete element is subject to increasing temperature under constant stress [3], which is unlikely to take place under real fire conditions. For instance, when flexural buckling occurs in a concrete column, the concrete elements near the edge may undergo strain reversal and hence a reduction in compressive stress. Therefore, it is essential to ensure that the stress-strain relationships capture the realistic behavior of concrete upon strain reversal.

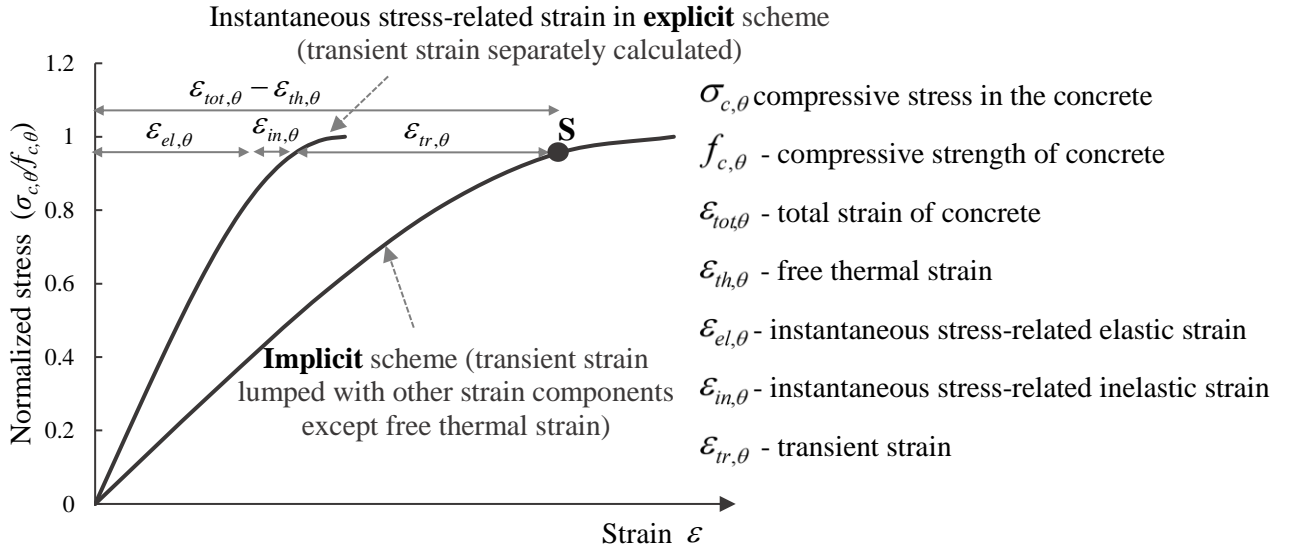


Figure 1. Normalised stress-strain relationship from explicit and implicit schemes showing the strain components of concrete at elevated temperatures

In the 3-D finite element model the constitutive relation for concrete was modelled by the concrete damaged plasticity (CDP) model available in ABAQUS software package [12]. In the concrete damaged plasticity model, the constitutive relationship for concrete at different temperatures adopts the implicit scheme where all strain components except free thermal strain are lumped into one term. It is defined by inputting the elastic modulus that describes the initial elastic range of the stress-strain curve and a set of stress and strain values that describe the inelastic range of the stress-strain curve. Secondly, the unloading modulus is taken as the initial tangent modulus of the stress-strain curve. Thirdly, the concrete strain is calculated based on the current stress state of the concrete elements. With these assumptions, the mechanism of calculating concrete strain upon strain reversal can be exemplified by Figure 2. At a given temperature, the stress-strain

curve generated using implicit scheme is shown in Figure 2. When the stress state of concrete element reaches state S and undergoes unloading to state S_1 , the stress-strain relation follows the “Path-Implicit” where the slope is identical to the initial tangent modulus of the stress-strain curve E_{imp} . By using this method, the transient strain component $\varepsilon_{tr,II}$ is assumed to be recoverable, resulting in a partially recoverable transient strain and consequently an incorrectly stiffer unloading behavior of concrete [3]. As a comparison in explicit scheme, when the concrete element undergoes unloading after stress state S to S_2 in Figure 2, the stress-strain relation follows the “Path-Explicit” where the slope is the elastic modulus E_{exp} obtained from the steady-state test. In this way, only the elastic strain of the concrete is recoverable upon unloading, which reflects the real behavior of concrete in fire situations. However, in order to correctly calculate the stress history-dependent transient strain, subroutine programs have to be developed to retrace the temperature and stress history of the concrete elements. Instead of developing a subroutine program, this study proposes the modified-elastic modulus (Modified-E) method to realistically predict the unloading behavior of concrete and to improve the accuracy of predicting the concrete strains under fire conditions. The features of implicit and explicit schemes discussed in this study are summarized in Table 1. A quantitative analysis is carried out to investigate the consequences of using an implicit and an explicit model for modelling concrete strains under fire conditions.

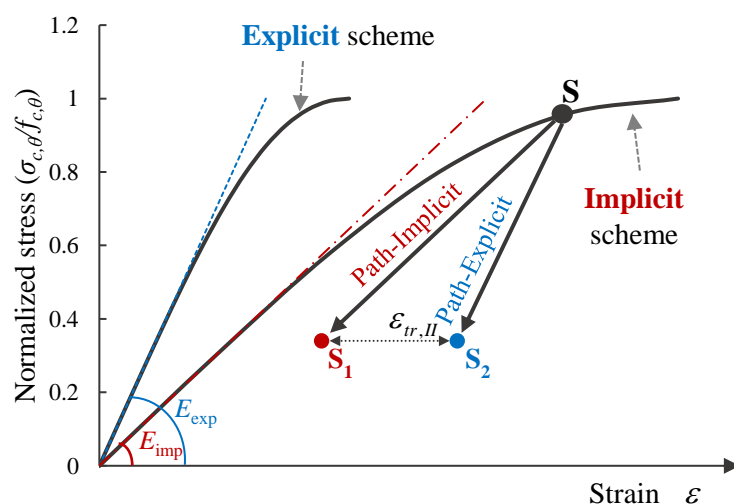


Figure 2. The unloading paths of concrete obtained using explicit and implicit schemes

Table 1. Features of the implicit and explicit schemes used for the constitutive relationship of concrete subject to compression under fire conditions

Schemes	Explicit scheme	Conventional method without modifying the initial tangent modulus (implicit scheme)	Modified-E method (implicit scheme)
Features			
Calculation for the total strain of concrete	The components of total strain are separately calculated	The total strain is calculated using a lumpsum term	The total strain is calculated using a lumpsum term
Model for the elastic range of concrete stress-strain curve	Linear	Linear	Trilinear
Modelling technique in ABAQUS	CDP model & Subroutine programs	CDP model	CDP model

*CDP = concrete damage plasticity

2 DEVELOPMENT OF MODIFIED ELASTIC MODULUS MODEL

In order to realistically predict the unloading behavior of concrete at elevated temperatures, a Modified-E method is developed to improve the current implicit stress-strain relationships of concrete under compression at elevated temperatures. Since at room temperature only the instantaneous stress-related strain develops, the stress-strain relationship for concrete at room temperature remains unchanged. Thus, the Modified-E method does not affect the structural response of concrete at room temperature. At elevated temperature θ , the stress-strain relationship for concrete follows Schneider's material law [13] and is defined by the peak strain $\varepsilon_{c1,\theta}$ corresponding to the compressive strength $f_{c,\theta}$ using equation (2). The same model is adopted in the current EN1992-1-2 [10]. When $\varepsilon_{c1,\theta} = \varepsilon_{\sigma,\theta}$, this equation describes the stress-strain relationship obtained in steady-state tests. When $\varepsilon_{c1,\theta} = \varepsilon_{\sigma,\theta} + \varepsilon_{tr,\theta}$, this equation describes the actual stress-strain relationship for concrete at elevated temperatures. The derivation for instantaneous stress-related strain $\varepsilon_{\sigma,\theta}$ is introduced in this section, and the procedures for calculating the peak strain $\varepsilon_{c1,\theta}$ is illustrated using the flowchart shown in Figure 3.

$$\sigma_{c,\theta} = \frac{3\varepsilon f_{c,\theta}}{\varepsilon_{c1,\theta} \left(2 + \left(\frac{\varepsilon}{\varepsilon_{c1,\theta}} \right)^3 \right)} \quad (2)$$

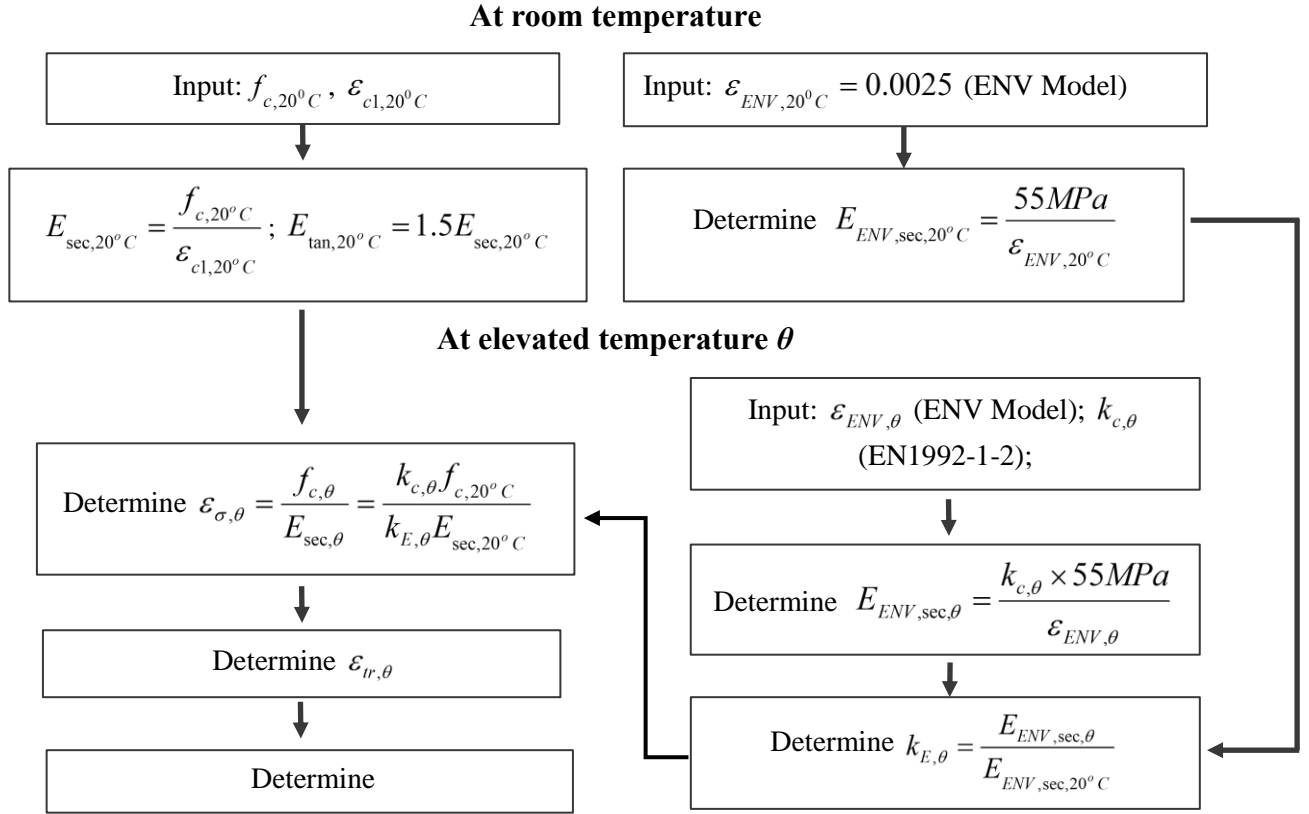


Figure 3. Calculation procedures for the peak strain of concrete at elevated temperatures

In order for the Modified-E method to be applicable to concrete up to grade C120, the values of instantaneous stress-related strain need to be derived according to the grade of concrete. Reduction factors of elastic modulus at elevated temperatures also need to be defined and are calculated based on the ENV model [14]. At 20°C, the peak strain $\varepsilon_{c1,20^\circ C}$ for different grades of concrete have been tabulated in EN1992-1-1 [15]. For concrete grade between C90 and C120, the peak strains are provided in Model Code 2010 [16]. Secant modulus at room temperature $E_{sec,20^\circ C}$ can be calculated by dividing compressive

strength at room temperature $f_{c,20^{\circ}C}$ by the peak strains $\varepsilon_{c1,20^{\circ}C}$, while initial tangent modulus $E_{tan,20^{\circ}C}$ is calculated as 1.5 times the secant modulus $E_{sec,20^{\circ}C}$.

At elevated temperatures, the minimum values of peak strain $\varepsilon_{ENV,\theta}$ provided in ENV model [14] represent the instantaneous stress-related peak strain determined from steady-state tests [3]. These values are used as the reference value to calculate the peak strain for concrete of different grades. The peak strain at room temperature is given as 0.0025 in ENV model [14], corresponding to the peak strain for grade C55/67 in room temperature design. Hence the minimum peak strain values at elevated temperatures provided in ENV model are deemed corresponding to concrete of grade C55/67. The secant modulus defined using equation (3) and retention factors for secant modulus $k_{E,\theta}$ defined using equation (4) can be subsequently calculated for C55/67 concrete at elevated temperatures.

$$E_{ENV,sec,\theta} = \frac{k_{c,\theta} \times 55 \text{ MPa}}{\varepsilon_{ENV,\theta}} \quad (3)$$

$$k_{E,\theta} = \frac{E_{ENV,sec,\theta}}{E_{ENV,sec,20^{\circ}C}} \quad (4)$$

where $E_{ENV,sec,20^{\circ}C}$ is the secant modulus at 20°C as calculated in Figure 3.

The instantaneous stress-related strain $\varepsilon_{\sigma,\theta}$ at elevated temperatures is calculated as

$$\varepsilon_{\sigma,\theta} = \frac{f_{c,\theta}}{E_{sec,\theta}} = \frac{k_{c,\theta} f_{c,20^{\circ}C}}{k_{E,\theta} E_{sec,20^{\circ}C}} \quad (5)$$

Equations (3) to (5) involves the retention factors for compressive strength $k_{c,\theta}$ and elastic modulus $k_{E,\theta}$. For concrete below grade C90/105, the compressive strength reduction factors provided in EN1992-1-2 [10] can be used for $k_{c,\theta}$. The retention factor for elastic modulus obtained from ENV model calculated by equation (4) is adopted. To plot the full stress-strain curve, $\varepsilon_{c1,\theta}$ in equation (2) is calculated as the sum of instantaneous stress-related strain $\varepsilon_{\sigma,\theta}$ and transient strain $\varepsilon_{tr,\theta}$. Since the unloading modulus is taken as the initial tangent modulus of the stress-strain curve, the initial tangent modulus of the stress-strain curve in implicit scheme is modified to initial tangent modulus $E_{tan,\theta}$ obtained in steady-state test. $E_{tan,\theta}$ is calculated as 1.5 times the secant modulus $E_{sec,\theta}$ shown in Figure 3. Therefore, the initial segment of the stress-strain curve in implicit scheme is altered to follow the instantaneous stress-related strain in explicit scheme as shown in Figure 4. Ideally, this segment using the modified initial tangent modulus should be sufficiently short because it does not truly reflect the elastic behaviour of concrete. On the other hand, this segment cannot be too short in order not to cause convergence difficulties in numerical calculations. In this study the segment in stress-strain curve with stress below 5% of the peak stress is modified as shown in Figure 4. Sensitivity analysis was carried out and demonstrated that the calculation results were not affected by further shortening this segment. To divert the stress-strain curve back to that in implicit scheme, a transitional linear curve is also proposed. In this way, the elastic range of the stress-strain curve in implicit scheme is modified to the Modified-E model shown in Figure 4. To implement the Modified-E model in ABAQUS, the inelastic strain corresponding to the peak stress is calculated using equation (6). Inelastic strain below peak strain is calculated using equations (7a) to (7c) in which $E_{tan,\theta} = \frac{3}{2} E_{sec,\theta}$.

$$\varepsilon_{in,\theta,peak} = (\varepsilon_{\sigma,\theta} + \varepsilon_{tr,\theta}) - \varepsilon_{el,\theta} = \left(\frac{f_{c,\theta}}{\frac{2}{3} E_{tan,\theta}} + \varepsilon_{tr,\theta} \right) - \frac{f_{c,\theta}}{E_{tan,\theta}} = \frac{1}{2} \frac{f_{c,\theta}}{E_{tan,\theta}} + \varepsilon_{tr,\theta} \quad (6)$$

When $\varepsilon \leq \frac{0.05 f_{c,\theta}}{E_{tan,\theta}}$,

$$\frac{\partial \sigma_{c,\theta}}{\partial \varepsilon} = E_{tan,\theta} \quad (7a)$$

When $\frac{0.05f_{c,\theta}}{E_{tan,\theta}} \leq \varepsilon \leq \frac{0.2f_{c,\theta}}{E_{tan,\theta}}$,

$$\sigma_{c,\theta} = 0.05f_{c,\theta} + \left(\frac{\varepsilon E_{tan,\theta}}{0.15f_{c,\theta}} - \frac{1}{3} \right) (\beta - 0.05f_{c,\theta}) \quad (7b)$$

In Eq. (5.7b), $\beta = \frac{0.6\beta_1 f_{c,\theta}}{2+0.008\beta_1^3}$, $\beta_1 = \frac{f_{c,\theta}}{\varepsilon_{c1,\theta} E_{tan,\theta}}$ and $\varepsilon_{c1,\theta} = \varepsilon_{\sigma,\theta} + \varepsilon_{tr,\theta}$.

When $\frac{0.2f_{c,\theta}}{E_{tan,\theta}} \leq \varepsilon$,

$$\sigma_{c,\theta} = \frac{3\varepsilon f_{c,\theta}}{\varepsilon_{c1,\theta} \left(2 + \left(\frac{\varepsilon}{\varepsilon_{c1,\theta}} \right)^3 \right)} \quad (7c)$$

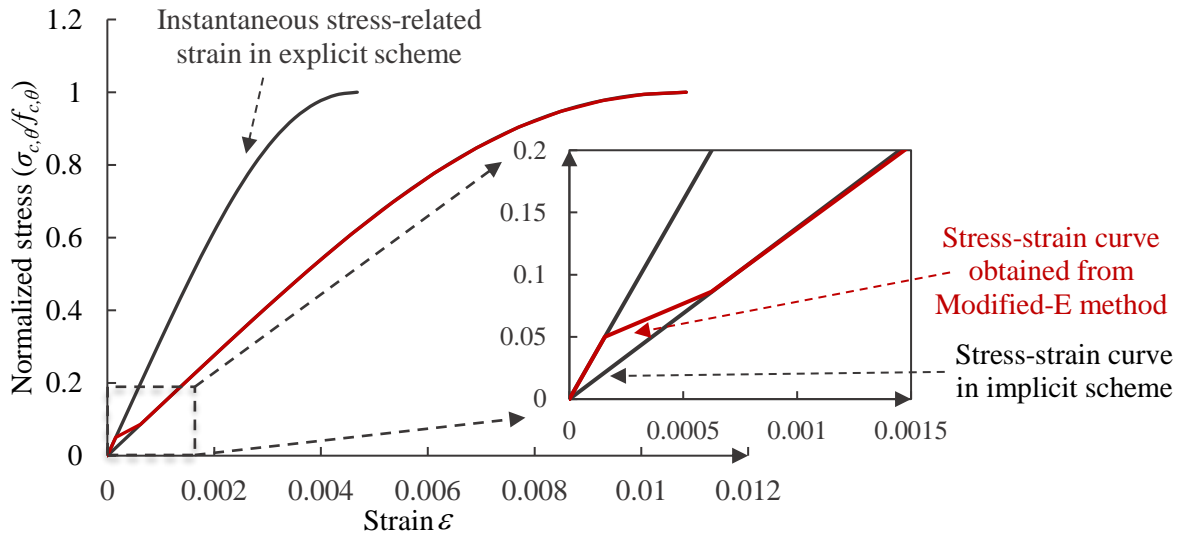


Figure 4. The stress-strain curve obtained from Modified-E method

3 3-D FINITE ELEMENT MODEL

The proposed Modified-E method for the stress-strain relationships of concrete under compression at elevated temperatures is implemented in a 3-D finite element model to predict the axial deformation of a concrete encased steel (CES) column tested under ISO834 fire condition. The CES column specimen comprises of the encased H-shaped steel section, concrete, steel rebars and stirrups as shown in Figure 5(a). The yield strength of the steel section and steel rebars are 590MPa and 527MPa respectively. The test-day compressive cylinder strength of the concrete is 128MPa. To prevent explosive spalling of HSC under fire conditions, 2kg/m³ polypropylene fibre is added in the concrete mix. This specimen has a clear height of 1.6m and is subject to a pinned-pinned end condition provided by knife-edge supports. The total pin-pin length of the specimen is 2.15m. The cross-sectional dimension of this column is 300mm×300mm. This column is tested under a concentric load with a load level of 0.45 calculated according to EN1994-1-2. This column was tested in an electric furnace specifically configured to reproduce the ISO834 fire curve. It lasted 174 minutes in the fire test before the applied load can no longer be sustained.

The 3-D finite element model is established using ABAQUS [17] software and is capable of performing sequentially coupled thermal-stress analysis. The components of the model and boundary conditions are shown in Figure 5(b). The calculation consists of heat transfer analysis and structural analysis and will be discussed separately.

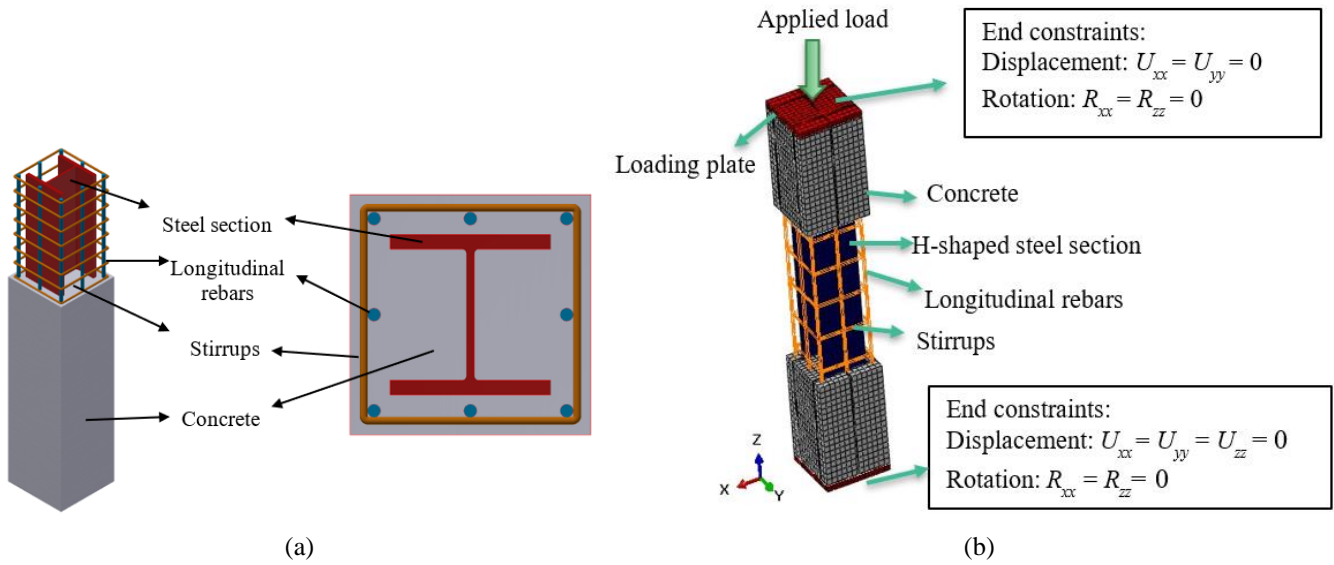


Figure 5. (a) structural components of CES columns; (b) Components and loading conditions in finite element model for the CES column

3.1 Heat Transfer Analysis

Heat transfer analysis is carried out to obtain the temperature distribution in the CES column specimens during fire tests. Steel section and concrete are modelled using the 8-node linear heat transfer brick elements. Steel rebars and stirrups are modelled using the 2-node heat transfer link elements [12]. The heating temperature uses the furnace temperatures measured by the thermocouples.

The following values are adopted in thermal analysis. Coefficient of convective heat transfer at exposed surfaces: $h = 25 \text{ W/m}^2\text{K}$; configuration factor for radiation at exposed surfaces: $\phi = 1$; Stephan-Boltzmann constant $5.67 \times 10^{-8} \text{ W/m}^2\text{K}^4$. Different values in the range from 0.2 to 0.7 are investigated for the resultant emissivity coefficient. It is found that the value of 0.3 generates the closest temperature prediction compared with fire tests therefore is used in the finite element analysis. The thermal resistance at the interface between concrete and steel section is modelled by adopting a constant value of $200 \text{ W/m}^2\text{K}$ for the gap conductance [18]. By varying the value of thermal conductivity of concrete between the lower and upper limits given in EN1994-1-2 [19], it is found that the lower limit of thermal conductivity generates closer predictions for the temperatures of CES columns in this study. Thermal conductivities and specific heats of steel components follow the values recommended in EN1992-1-2 [10] and EN1993-1-2 [20].

The predicted temperatures in the cross section of CES column are compared with the measured temperatures in Figure 6, which show a reasonable accuracy. A larger discrepancy is observed at TC4 because its location might be shifted during the casting of concrete.

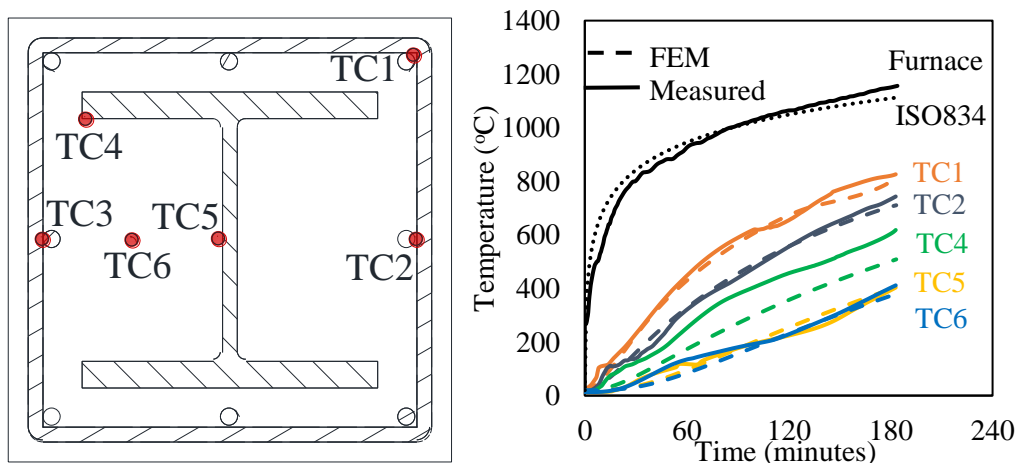


Figure 6. (a) location of thermocouples; (b) Temperature-time curves obtained from fire test and heat transfer analysis for the CES column specimen

3.2 Structural Analysis

The results from the heat transfer analysis are used as input in the structural analysis. The mechanical properties of steel section and steel rebars, including constitutive relationship and thermal expansion coefficients, adopt the values in EN1993-1-2 [20]. The effects of high-temperature creep have been implicitly included in this model. The Poisson's ratio is input as 0.3 for steel.

The compressive behavior of concrete is modelled through the Modified-E method. For the C120 concrete used in this study, the strength retention factors below 600°C followed those obtained by Li, Liew [21]. The transient strain $\varepsilon_{tr,\theta}$ in equation (6) and Figure 3 is calculated using the Anderberg & Thelandersson model [7] with the dimensionless material factor $k_{tr} = 3.8$. The tensile behavior of concrete is modelled using the crack band theory proposed by Bazant and Oh [22] in which the softening branch of the stress-strain diagram can be approximated by a linear curve. The area under this curve can be defined as fracture energy divided by the crack band width according to Ellobody and Ben [23]. The fracture energy and tensile strength are calculated as a function of the compressive strength of concrete according to Model Code 2010 [16]. The interfaces between steel rebars and concrete are modelled by the embedded constraint option in ABAQUS [12] assuming there is no debonding. The interfaces between steel section and concrete are modelled as surface-to-surface contact. The value of friction coefficient is determined as 0.25 according to Ellobody and Young [24]. The contacting steel section and concrete surfaces are assumed to undergo relatively small sliding relative to each other compared with their large overall motions. The initial geometrical imperfection is taken as $L/1000$ where L is the height of CES column specimens [25]. Steel section and concrete are modelled using C3D8R solid elements while steel rebars are modelled using T3D2 truss elements. In order to reduce the computational time without compromising the reliability of results, sensitivity analysis is carried out and determines mesh size as 25mm with an average aspect ratio of 1(length): 1(width): 1.5(depth). Refinement of mesh is needed in the joints between the flange and web of steel section. The load is applied above the loading plate at the same height of the knife-edge support used in fire tests.

In Figure 7 the axial displacement response predicted by finite element analysis is compared with the value obtained from the fire tests. Reasonable agreement is achieved between the predicted (with proposed Modified-E method) and measured axial displacements.

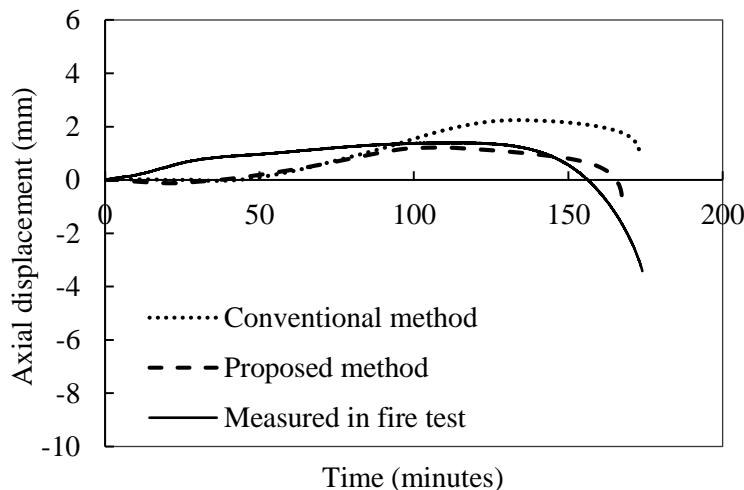


Figure 7. Predicted axial displacement curve using the conventional method and proposed Modified-E method

4 EFFECT OF USING MODIFIED-E METHOD FOR THE STRESS-STRAIN RELATIONSHIPS OF CONCRETE

The main features of explicit scheme, conventional method adopting the implicit scheme and the Modified-E method proposed in the current study are compared in Table 1. Modelling the strains of concrete using an explicit scheme is the most accurate because the calculation of concrete strain has considered its stress history, but it relies on developing subroutines in ABAQUS to account for the stress history. The conventional method that adopts the implicit scheme for the stress-strain relationship for concrete is straightforward to be implemented in numerical analysis but tends to underestimate the concrete strain at elevated temperatures. Therefore, the Modified-E method is proposed to improve the accuracy of prediction in the meanwhile preserving the simplicity of the conventional method. In this section, the verified 3-D finite element model is used to quantify the percentage improvement in the accuracy of predicted transient strain of concrete after adopting the Modified-E method. To achieve this, the finite element model for the CES column specimen is replicated and modified using the conventional method for the stress-strain curve of concrete. Concrete is assumed to retain its elastic behavior until around 40% of its compressive strength. The evaluation process starts with retrieving the axial stress and temperature of each concrete element at all time steps from the numerical analysis output file. The transient strain is assumed to be function of stress level and free thermal strain according to the Anderberg & Thelandersson model [7]. By adopting a constant value of $k_{tr} = 3.8$, the transient strain of concrete elements predicted by the conventional method at each time step can be calculated using the current-time step stress and temperature. On the other hand, the transient strain predicted using explicit scheme, which is also the true transient strain, can be calculated incrementally obeying its irreversible nature after considering its maximum stress in history. Then the percentage difference between the transient strain predicted using explicit scheme and conventional method, explicit scheme and Modified-E method can be separately calculated at each time step and are shown in Figure 8. Throughout the entire heating duration, the conventional method underestimates the actual transient strain by 50.4% in average, with a maximum error of 78.6%. This is because the conventional method cannot correctly calculate the transient strain of concrete elements when they undergo strain reversal due to temperature change or flexural buckling of CES column. Using the Modified-E method, the error in predicted transient strain of concrete is reduced to 22.6% in average with a maximum value of 43.7%. Hence the error in the modelled transient strain is reduced by 55%. The rest of the discrepancy is due to the inherent limitation of the finite element model that it is unable to calculate the transient strain in the current analysis step based on the temperature and stress history, which can only be realised by developing subroutine programs.

The effect of using Modified-E method is further evaluated by comparing the axial displacement-time curve predicted by conventional and Modified-E method. As shown in Figure 7, after correctly modelling the unloading modulus using the Modified-E method, the axial contraction of CES column increases significantly. The difference between the predicted axial displacements becomes particularly significant when flexural buckling accelerates and concrete elements start to undergo strain reversal at around 94 minutes. Therefore, the axial displacement of CES columns during the fire test can be better captured using the Modified-E method.

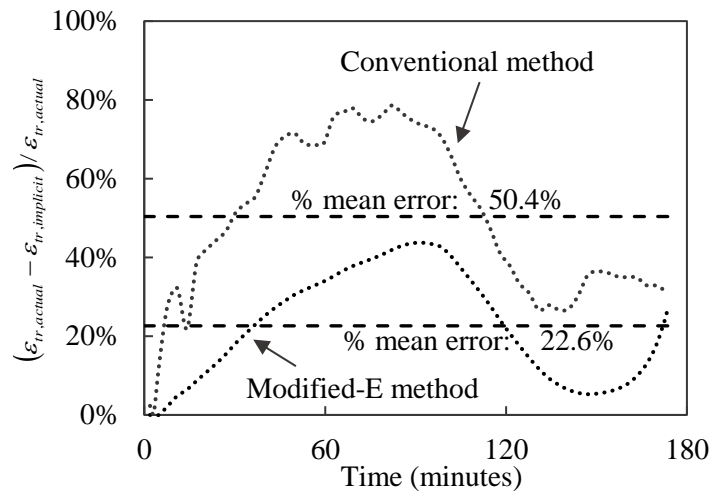


Figure 8. Discrepancies between the transient strains of concrete predicted by conventional method and Modified-E method compared with explicit scheme (actual value)

5 CONCLUSIONS

This paper proposes a modified-elastic modulus (Modified-E) method to improve the implicit stress-strain relationships of concrete under compression at elevated temperatures given in current EN1992-1-2. The proposed method overcomes the limitation of the current method that results in partial recovery of transient strain of concrete upon unloading at elevated temperatures. The Modified-E method is implemented in a three-dimensional (3-D) finite element model to predict the fire performance of a high-strength concrete encased steel (CES) column under ISO834 fire condition. The CES column is made of C120 concrete and S500 steel section. The 3-D finite element model is shown to predict the temperatures and axial displacement of the CES column specimen in good agreement with those obtained from the fire test.

Comparative studies show that the 3-D finite element model adopting the conventional stress-strain relationships of concrete under compression at elevated temperatures provided in EN1992-1-2 underestimates the transient strain of the concrete section in a CES column by 50%. By adopting the proposed Modified-E method, this error can be reduced by 55% and enables the 3-D finite element model to better capture the axial displacement of the CES column specimen under fire conditions.

ACKNOWLEDGMENT

The research is supported by the National Research Foundation Singapore, Sembcorp Industries Ltd and National University of Singapore under the Sembcorp-NUS Corporate Laboratory.

REFERENCES

1. Bamonte, P. and F.L. Monte, Reinforced concrete columns exposed to standard fire: Comparison among different constitutive models for concrete at high temperature. *Fire Safety Journal*, 2015. 71: p. 310-323.
2. Schneider, U., M. Schneider, and J.M. Franssen. Consideration of nonlinear creep strain of siliceous concrete on calculation of mechanical strain under transient temperatures as a function of load history. in *The Fifth International Conference on Structures in Fire*. 2008. Singapore.
3. Gernay, T. and J.M. Franssen, A formulation of the Eurocode 2 concrete model at elevated temperature that includes an explicit term for transient creep. *Fire Safety Journal*, 2012. 51: p. 1-9.
4. RILEM, Recommendation of RILEM TC 200-HTC: mechanical concrete properties at high temperatures—modelling and applications. Part 2: Stress-strain relation. *Materials and Structures*, 2007. 40(9): p. 855-864.

5. RILEM, RILEM TC 129-MHT: Test methods for mechanical properties of concrete at high temperatures. Recommendation: Part 7: Transient creep for service and accident conditions Materials and Structures, 1998. 31(June 1998): p. 290-295.
6. Anderberg, Y. and S. Thelandersson, Stress and Deformation Characteristics of Concrete at High Temperatures. 2. Experimental Investigation and Material Behaviour Model (Bulletin of Division of Structural Mechanics and Concrete Construction). 1976, Lund Institute of Technology.
7. Li, L.Y. and J. Purkiss, Stress-strain constitutive equations of concrete material at elevated temperatures. Fire Safety Journal, 2005. 40: p. 669-686.
8. Torelli, G., et al., Concrete strains under transient thermal conditions: A state-of-the-art review. Engineering Structures, 2016. 127: p. 172-188.
9. Anderberg, Y. The impact of various material models on structural fire behaviour prediction. in The fifth International Conference on Structures in Fire - SiF'08. 2008. Singapore.
10. European Committee for Standardization, Eurocode 2: Design of concrete structures-Part 1-2: General rules-structural fire design. 2004: European Committee for Standardization, Brussels, Belgium.
11. Kodur, V.K.R. and S.M. Alogla, Effect of high-temperature transient creep on response of reinforced concrete columns in fire. Materials and Structures, 2017. 50(27).
12. ABAQUS, ABAQUS Theory Guide. 2014: SIMULIA, Providence, RI, USA.
13. Schneider, U., Concrete at high temperatures — A general review. Fire Safety Journal, 1988. 13(1): p. 55-68.
14. European Committee for Standardization, Eurocode 2: Design of concrete structures-Part 1-2: General rules-structural fire design. 1995: European Committee for Standardization, Brussels, Belgium.
15. European Committee for Standardization, Eurocode 2: Design of concrete structures-Part 1-1: General rules and rules for buildings. 2004: European Committee for Standardization, Brussels, Belgium.
16. International Federation for Structural concrete (fib), Model Code 2010, Volume 1. 2010: Lausanne, Switzerland.
17. ABAQUS, ABAQUS 6.14 Analysis User's Guide. 2014: SIMULIA, Providence, RI, USA.
18. Espinos, A., M.L. Romero, and A. Hospitaler, Advanced model for predicting the fire response of concrete filled tubular columns. Journal of Constructional Steel Research, 2010. 66(8): p. 1030-1046.
19. European Committee for Standardization, Eurocode 4: Design of composite steel and concrete structures-Part 1-2: General rules-structural fire design. 2005: European Committee for Standardization, Brussels, Belgium.
20. European Committee for Standardization, Eurocode 3: Design of steel structures-Part 1-2: General rules-structural fire design. 2005: European Committee for Standardization, Brussels, Belgium.
21. Li, S., J.Y.R. Liew, and B.L. Lai. Constitutive model for steel-fibre-reinforced concrete in compression at elevated temperatures. in Applications of Structural Fire Engineering 19'. 2019. Singapore.
22. Bazant, Z.P. and B.H. Oh, Crack Band Theory for Fracture of Concrete. Materials et constructions, 1983. 16(93): p. 155-177.
23. Ellobody, E. and Y. Ben, Numerical simulation of concrete encased steel composite columns. Journal of Constructional Steel Research, 2011. 67(2): p. 211-22.
24. Ellobody, E. and B. Young, Investigation of concrete encased steel composite columns at elevated temperatures. Thin-Walled Structures, 2010. 48: p. 597-608.
25. Lai, B., J.Y.R. Liew, and T. Wang, Buckling behaviour of high strength concrete encased steel composite columns. Journal of Constructional Steel Research, 2019. 154: p. 27-42.

THE BEHAVIOUR OF BRIDGE DECKS DUE TO FIRE INDUCED THERMAL EXPANSION OF PROTECTED STAYS CABLES

Panagiotis Kotsovinos¹, Egle Rackauskaite², Ryan Judge³, Graeme Flint⁴, Peter Woodburn⁵

ABSTRACT

This research investigates the global structural response due to thermal expansion of a cable stayed bridge when subjected to fire assuming that the cables have been protected in accordance with the PTI DC45.1-12 standard and therefore would not experience any direct cable loss. It is found that thermal expansion of long span cables even at temperatures associated with cables provided with fire protection could significantly affect the resulting bending moments and axial forces in the deck. However, for the case study considered it is determined that, if the structural design considers the redundancy of a loss of a cable the resulting structural capacity would be adequate.

Keywords: Cable stayed bridges; finite element modelling; cable fire protection;

1 INTRODUCTION

The testing procedure described in the PTI DC45.1-12 standard is based on the principle of limiting the temperature of the cables below a critical threshold of 300 degrees to prevent structural failure [1-3]. As a result it does not capture the effect of thermal expansion of the cable. Therefore, the standard implicitly assumes that for the structures where the cables are protected in accordance to its recommendations, structural failure due to the thermally induced forces would not occur throughout the assumed fire exposure [1-3].

Using a generic cable stayed bridge with a steel-concrete composite deck as a case study, this research investigated the impact of the heating of single or multiple cables on the increase of bending moments and axial forces of the deck and therefore the potential for global instability of the bridge deck. The cables are assumed to be protected to not exceed a critical temperature of 300⁰C. This change in demand will also be assessed against a bridge that has been designed accounting for the loss of a single cable.

2 CASE STUDY

The case study of this paper is based on a commercial project in the USA designed by Arup appropriately.

¹ Senior Fire Engineer, Arup
e-mail: panos.kotsovinos@arup.com, <https://orcid.org/0000-0003-2234-0420>

² Fire Engineer, Arup
e-mail: Egle.Rackauskaite@arup.com

³ Senior Consultant, Resilience Consulting, Arup
e-mail: firstname.lastname@address

⁴ Associate, Fire Engineering, Arup
e-mail: firstname.lastname@address

⁵ Director, Fire Engineering, Arup
e-mail: firstname.lastname@address

The Main Span Bridge is a cable stayed bridge with an ~600m (1,000 ft) main span which comprises a steel-concrete composite ladder beam superstructure supported from hollow reinforced concrete mono-pole towers by multi-strand stay cables.

The Approach Bridges are single cell prestressed concrete box girders with a maximum span up to ~70m (230 ft). Each of the two roadways has three lanes and a clear width of ~17m (56ft).

The concrete deck is of 34MPa (5ksi) light weight concrete supported by steel edge girders and floor beams. A cross-sectional and an orthogonal plan view of the Main Span superstructure deck are shown in Figure 1 a and b respectively. As shown in Figure 1b, a bikeway is also provided on one side of the deck.

The bridge deck is connected to two 48MPa (7ksi) concrete A-shaped pylons by 10 cables at each side and orientation (40 cables per pylon). The concrete pylons have a tapered profile.

For the purposes of this study only the cable stayed component of the bridge is studied without the inclusion of the approach viaducts. The structure below the composite deck including the foundations is also outside the scope of this study.

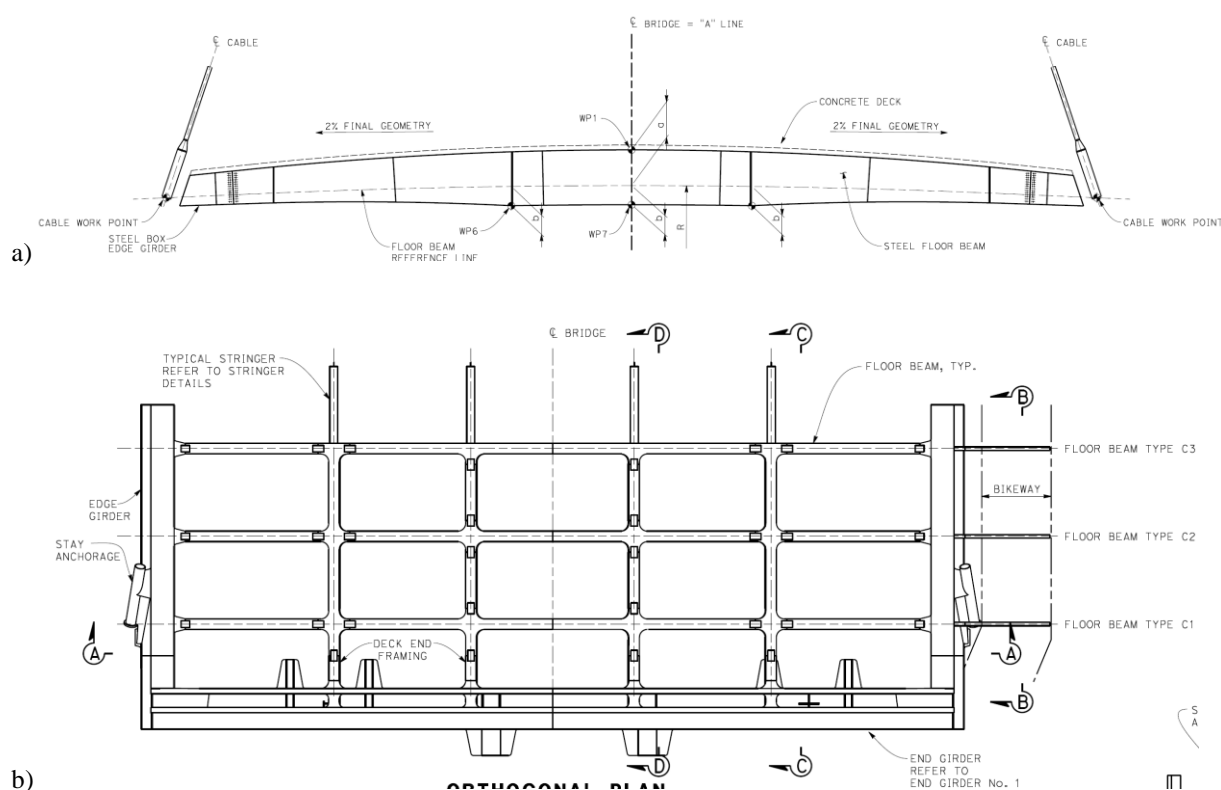


Figure 1 Main Span superstructure a) section view b) orthogonal plan view

3 NUMERICAL MODELLING

3.1 Thermal exposure

For the purposes of this work and to derive fire scenario independent conclusions, thermal exposure is simplistically considered and not based on specific fire scenarios. Selected cables are heated to 300°C over the length of 20m as a representative heated region of a heavy goods vehicle fire. The cables are assumed to expand on one side of the deck only. A parametric study is conducted on number and location on fire affected cables (1, 3 and 5 outer cables).

3.2 LS-DYNA model

The non-linear finite element software LS-DYNA is used for the analysis. Structural cables are represented through a series of linear inelastic beam elements. The cables are assumed to be protected and therefore cable rupture due to the applied axial load exceeding the elastic capacity or breaking load of the cable is not expected. The bridge deck is considered to be elastic. Perfect connection between the terminals and the deck and the steel girders to the concrete slab.

The change in demand (bending moments and axial forces) is considered before and after induced thermal expansion.

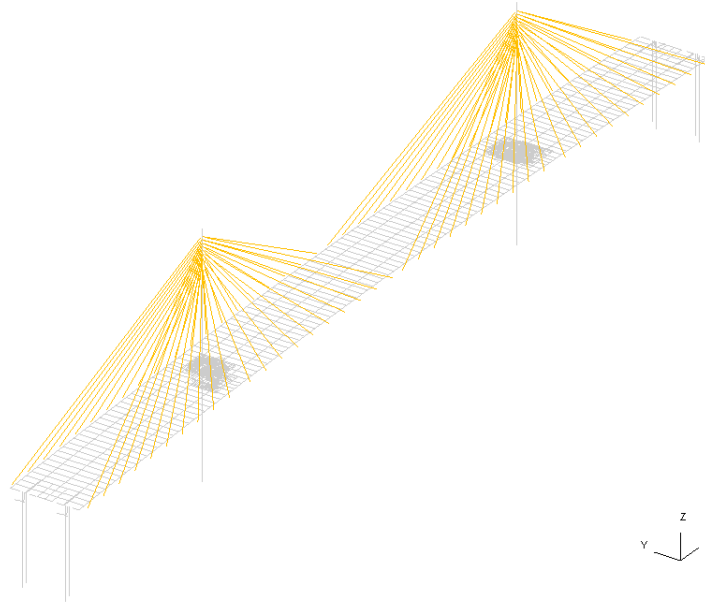


Figure 2. The LS-DYNA model of the bridge

4 RESULTS AND DISCUSSION

The bending moment profile and axial force profile across the deck of the bridge are shown in figure 3a and 3b respectively for ambient conditions and when 1,3 and 5 cables in the centre of the bridge are assumed to thermally expand. It can be seen that in comparison to ambient conditions an increase in bending moments of up to 160%, 360% and 245% for 1,3 and 5 heated cables respectively. Axial forces reduce locally in the locations where the cables expand.

The change in demand is also compared against a bridge that has been designed accounting for the loss of a single cable. This is because many long span bridges consider such a scenario in their structural design for robustness purposes. From the results illustrated in Figure 4a it can be seen that the increase in bending moments due to a potential cable loss is over two times greater from the increase in demand incurred by the thermal expansion of the cables. a result, if the structural design of the case study analyses considers the redundancy of a loss of a cable the resulting structural capacity would be adequate. However, further research is necessary for other bridge designs to investigate whether the same conclusion would apply.

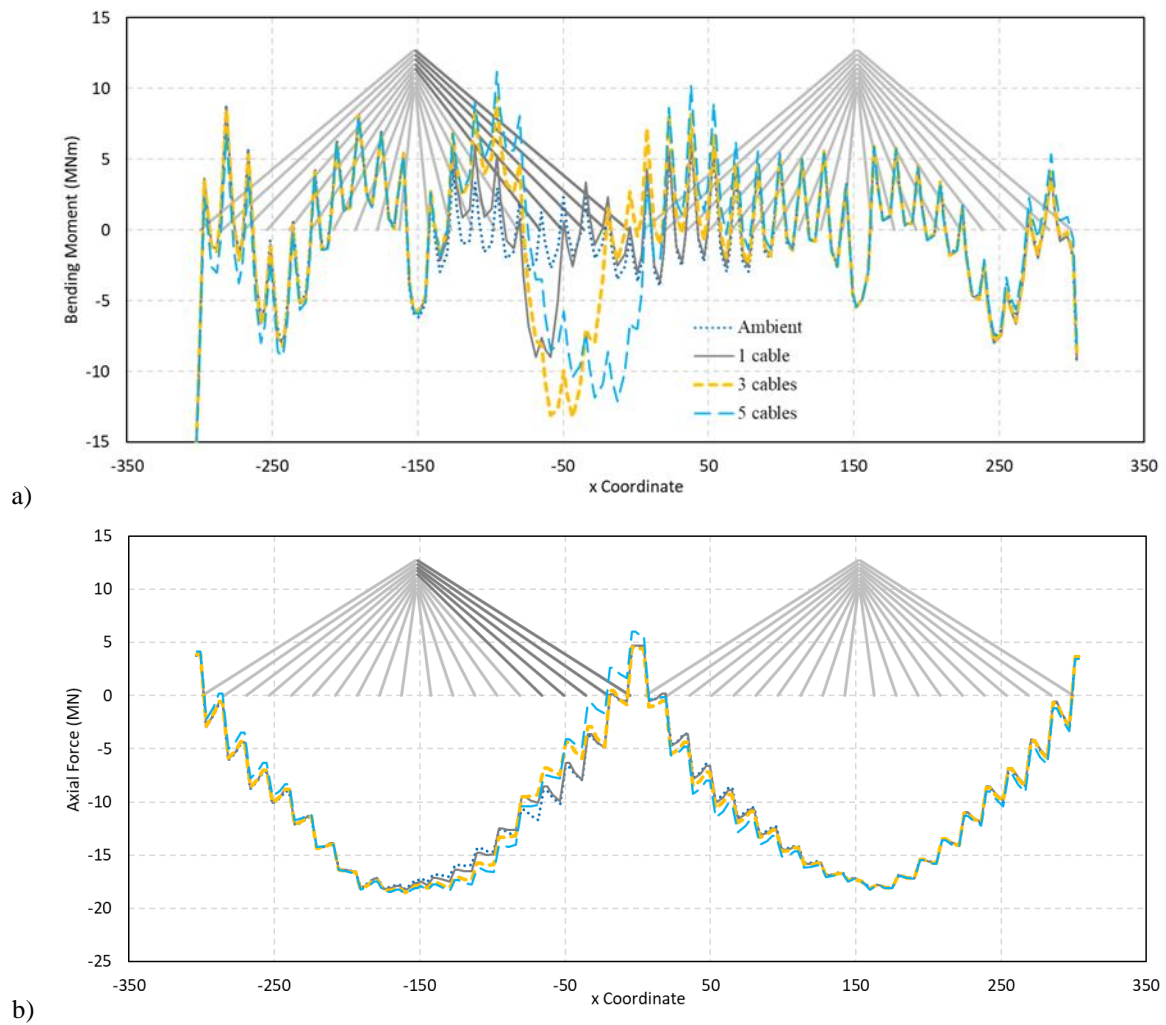


Figure 3. a) bending moments b) axial forces

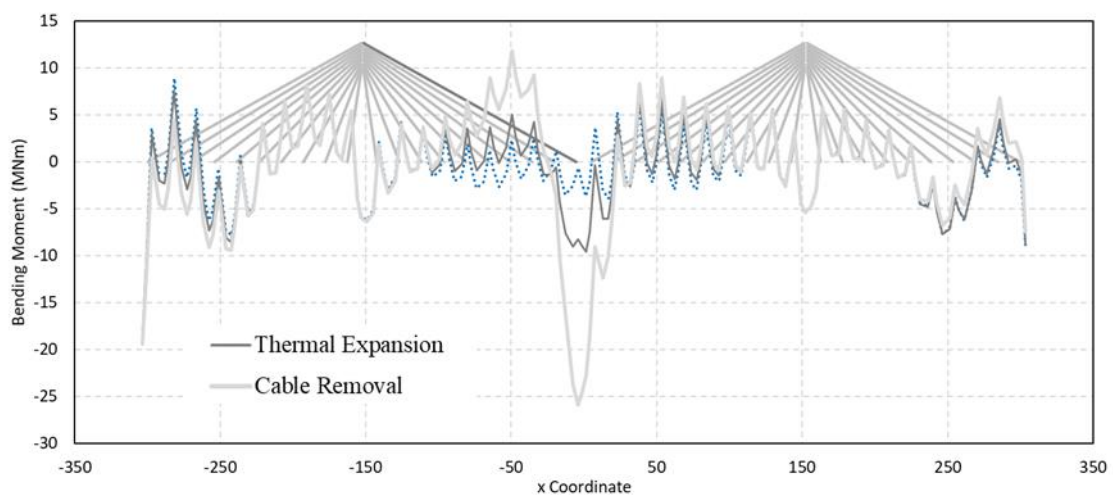


Figure 4. Change in bending moments due to cable loss and thermal expansion of a cable

5 CONCLUSIONS

This paper investigated the global structural response due to fire thermal expansion of a cable stayed bridge with fire protected cables. Initial finite element modelling has been undertaken based on a simplified

approach that is fire scenario independent. It is shown that a significant increase in demand occurs for bending moments on the side of the deck affected by the fire. The location and number of affected cables has a significant influence on the resulting moments. However, it was also shown that this increase in demand is less than the increase necessary to be accommodated if redundancy of a single cable is considered for the bridge considered in this study.

The response of the bridge to fire-generated thermal expansion is expected to be dependent on the layout and spacing of the cables as well as the deck structure; Therefore, further research is required to assess other type of bridges that may have different structural responses. In addition, the capacity of terminal connections to withstand the expansion of the cables should be assessed.

REFERENCES

1. Kotsovinos, Panagiotis, Ryan Judge, Gary Walker, and Peter Woodburn. "Fire Performance of Structural Cables: Current Understanding, Knowledge Gaps, and Proposed Research Agenda." *Journal of Structural Engineering* 146, 8, (2020).
2. Kotsovinos, Panagiotis, Athina Ataloti, Neil McSwiney, Francesca Lugaesi, Guillermo Rein, and Adam J. Sadowski. "Analysis of the thermomechanical response of structural cables subject to fire." *Fire Technology* 56, no. 2 (2020): 515-543.
3. Nicoletta, Benjamin, Panagiotis Kotsovinos, and John Gales. "Review of the fire risk, hazard, and thermomechanical response of bridges in fire." *Canadian Journal of Civil Engineering* 47, no. 4 (2020): 363-381.

MODELLING GRENFELL DISASTER: INTERACTIONS BETWEEN FACADES AND APARTMENTS

Eric Guillaume¹, Virginie Dréan², Bertrand Girardin³, Talal Fateh⁴

ABSTRACT

On June 14th, 2017, a fire occurred in the Grenfell Tower in London. With 71 fatalities, it has been one of the largest fire tragedy of the last decades. Among other causes such as a rapid fire propagation, one of the key points of Grenfell disaster is also the fire penetration from the façade into the apartments through windows. To investigate the behaviour of Grenfell fire, a reconstruction of this disaster using step-by-step numerical methods based on experimental fire tests has been proposed. The first steps of reconstruction of this disaster were recently published. After this first phase of analysis, updated results are addressed. The thermomechanical modelling of window frames and assemblies confirm that this point was probably one of the dominant way of fire penetration. Further simulations of the horizontal fire propagation clockwise and anticlockwise around the tower allowed an analysis of the interactions between apartments and façade fires, highlighting the importance of furniture from the apartments themselves as main contributor to the loss of tenability conditions (either thermal or toxic) inside the tower. Further analysis of tenability conditions were made for the last four storeys where the most fatalities have been observed and where several data exist on occurrence of openings and closing of the doors, as well as on evolution of the tenability conditions. This analysis is consistent with the observed events and helps understanding the conditions inside the tower during the whole period of the fire.

Keywords: Façade fire; CFD; thermomechanical behaviour; toxicity analysis; fire tests

1 INTRODUCTION

Fire events in building façades involving aluminium composite material (ACM) claddings in combination with various insulations have recently received attention [1-3]. On June 14th, 2017, a fire occurred in the Grenfell Tower in London. With 71 fatalities, it has been one of the largest fire tragedy of the last decades [4]. Consequences of this fire are due, among other causes, to a rapid vertical fire propagation via the East face in a first phase, and to both clockwise and anticlockwise horizontal spread around the tower in a second phase. One of the key points of Grenfell disaster is also the fire penetration from the façade into the apartments through windows.

To investigate the behaviour of Grenfell fire, a reconstruction of this disaster using step-by-step numerical methods based on experimental fire tests has been proposed [5-12]. The first steps of reconstruction were recently published. The initial step consisted in the validation of a façade numerical model for upscaling

¹ Dr, Efectis France,
e-mail: eric.guillaume@efectis.com, ORCID: <https://orcid.org/0000-0002-3055-2741>

² Dr, Efectis France,
e-mail: virginie.drean@efectis.com, ORCID: <https://orcid.org/0000-0002-3216-1808>

³ Dr, Efectis France,
e-mail: bertrand.girardin@efectis.com, ORCID: <https://orcid.org/0000-0003-2206-9626>

⁴ Dr, Efectis UK-Ireland & Ulster University, FIRECERT
e-mail: talal.fateh@efectis.com, ORCID: <https://orcid.org/0000-0002-4204-0540>

[6-7] using a multi-scale approach. The CFD code FDS was used to assess the fire performance of the refurbished façade system used on the Grenfell tower based on intermediate scale ISO 13785-1 [5-6] and large scale BS 8414-2 [7] reaction to fire tests. The results of these simulations closely matched the experimental results and showed that the ACM cladding was one of the main element driving the overall fire behaviour of this kind of façade constructions. In particular, systems that featured ACM cladding made with a polyethylene core (ACM-PE) showed extensive fire propagation regardless of the insulant used. Then, data from Grenfell disaster were collected and analysed [8]. The reconstruction of Grenfell fire consisted into visualizing all data available from observations, in terms of pictures and movies, of the disaster, in order to establish a full 3D model of the observations of the tower into a database, and then to determine flame spread rates, flames duration and fire location at each time. The development of the initial fire, inside the kitchen of the apartment of origin at Grenfell, and its behaviour at the kitchen window were investigated in reference [9]. This showed a very high probability that any limited fire in the kitchen could have led to the ignition of the façade system, even in absence of flashover, and confirmed initial hypotheses formulated by Torero [13]. Fire spread over the façade was also explored numerically. The initial vertical spread modelling is fully detailed in reference [10]. A very good agreement between simulated and observed flame spread was obtained and showed the importance of constructive details and materials.

After this first phase of analysis, the fire reconstruction progressed. The intention is to present the updated results with an emphasis on:

- Analysis and hypotheses from the disaster showed the importance of window failures in the propagation from the façade fire to the inside of the apartments. The results of thermomechanical modelling of window frames and assemblies confirm this point as probably one of the dominant way of fire penetration [11].
- Further simulations of the horizontal fire propagation clockwise and anticlockwise around the tower showed a good agreement with the observations [12]. Propagation rate is driven in a large proportion by the behaviour of ACM-PE itself, even considering the limitations from modelling tools to capture all aspects of this propagation.
- Analysis of the interactions between apartments and façade fires allows future studies of contributors to the loss of tenability conditions (either thermal or toxic) inside the tower.

2 VERTICAL FIRE SPREAD ALONG THE FAÇADE

In a previous work [8], the observational data from the Grenfell Tower disaster were synthesized to provide an analysis of the vertical and horizontal fire propagation over the whole Tower. The development of the fire, inside the kitchen of the apartment of origin at Grenfell, its behaviour at the kitchen window, and the fire propagation over the façade and from the façade to apartments through windows were also explored numerically [9]. The numerical simulations are performed with the Computational Dynamics (CFD) code Fire Dynamics Simulator (FDS) version 6.7.0 [14].

Then, the full height of the Grenfell façade was modelled to determine its fire behaviour [10] (Figure 1). In this 3D model, the thermal and combustion characteristics of the façade system are those validated in [6] and [7]. The HRRs from the combustion of apartment furniture, detailed in [9] are used at each floor of the Tower. The comparison between the numerical results and the video and photographic records of the real fire [8] was used to validate the modelling of the vertical fire spread over the east face of the Tower. The results highlighted that the installed cavity barriers were effective in limiting fire propagation during the short time period of integrity of the cavity. This previous study as well as observations, showed limited horizontal propagation of the fire during this initial phase of 30 minutes. The furniture in the kitchens and living rooms of “X6” flats above the initial compartment fire (Flat 16) contributed to the fire and enhanced the external flames. Almost all the kitchen and adjacent (east face) living room windows of “X6” flats have failed by 01:29 am. A summary of the results is indicated in Figure 2 and shows that the observed fire propagation is well reproduced by the numerical model.

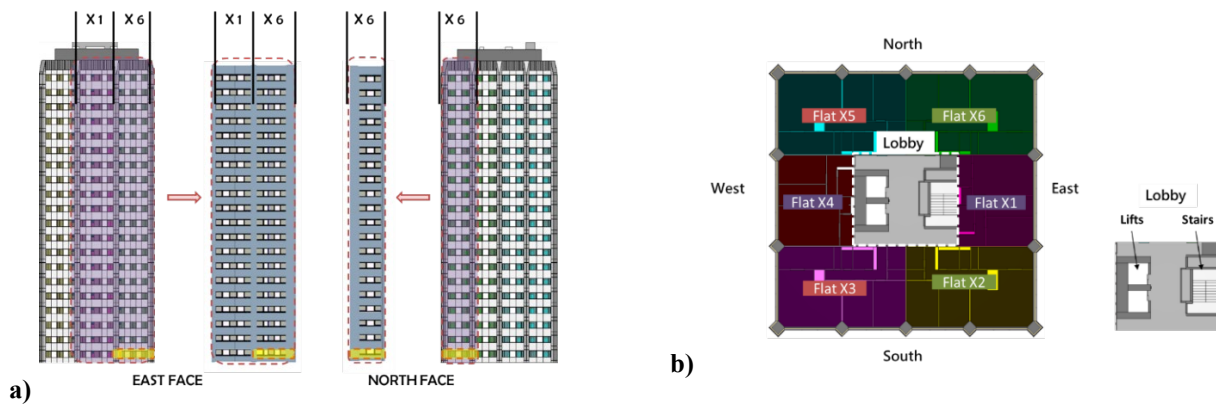


Figure 1. View of the numerical model of the Grenfell tower – a) East face with “X6” and “X1” flats – part of the north face with the living room of flats “X6” – Flat 16 is highlighted in yellow – b) Schematic of floor arrangement

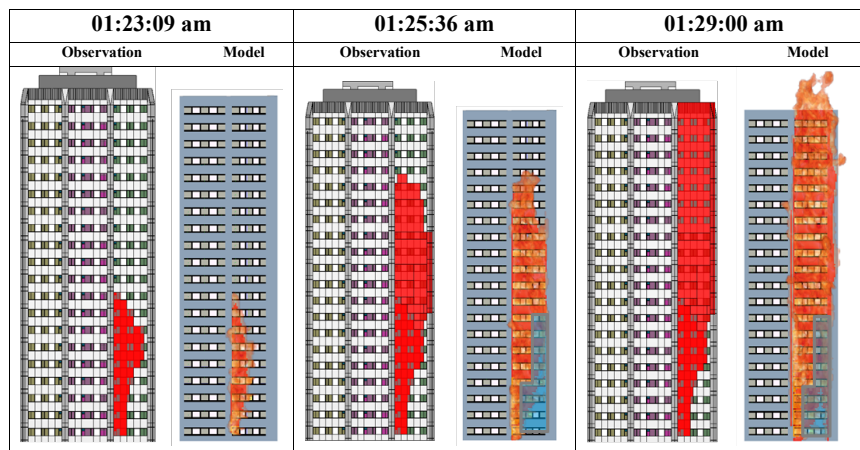


Figure 2. Comparison of observations and the output of the numerical simulation of fire propagation over the east face - third phase of propagation (01:23 to 01:29 am) [10]. Blue regions indicate areas where firefighting was efficient, not considered in the simulation. Red areas figure flame extension.

3 THERMOMECHANICAL ANALYSIS OF THE WINDOW FAILURE

In the global model of the Tower, it is assumed that there is no fire propagation path between floors, e.g. via ducts, HVAC systems, or holes in ceilings or walls. The fire propagation from one apartment to another (horizontally or vertically) occurs only via propagation over the façade, followed by window failure.

During the Grenfell disaster, the refurbished windows were not designed to present any performance against thermal action. In association with the combustible cladding mounted on the façade, it may have facilitate the spread of fire between the interior and exterior of the building. Furthermore, the fallout and deformation of windows and surrounding elements seems to be one of the main element that has led to the fire spread to the cladding at early stage of the façade fire spread. Later, when the fire was fully developed, the heat fluxes imparted to the windows were high enough to break the windowpanes whatever the surrounding materials were [4]. However, window failure was probably not the only way of flame exit and re-entry, and the window failure mode is probably not unique during the Grenfell disaster. The scenario leading to one of the earliest massive inflow of fire effluents appears to be the deformation of the window frame and is thus investigated in the present work.

3.1 Window structure

The details for the the window structure according to [15] is addressed in Figure 3. The window frame sized 1241 mm x 1285 mm [39], and is equipped with 26 mm thickness glass units in double pane. The window glass is set inside a two-shell (double-wall) extruded powder-coated aluminium frame structure, composed with polyamide thermal breaks (Figure 1 b). In some location, in particular in kitchens, extract fan units

fitted within aluminium faced polymer foam filled composite window infill panels were present. Different opening configurations are allowed: close, open, and in-tilt.

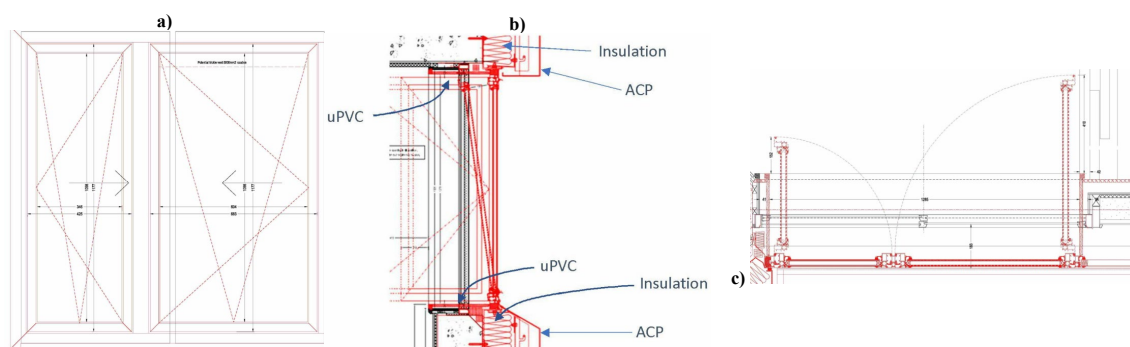


Figure 3: Details of the window system used in the refurbishment of Grenfell Tower a) front view b) side view (from J. Torero's expert report [4]) c) top view

The glass and polyamide material properties corresponding to the one implemented in Grenfell Tower are based on literature [16]. In general, the loss of thermal properties of polyamide materials varies between 182°C and 290°C [19]. Polyamide material is modelled with a thermal conductivity of 0.3 W/m.K and a specific heat of 1600 J/kg.K. The density of polyamide is 1490 kg/m³. In absence of any available database, the sealing gaskets are assumed to be made from the same polyamide material. According to the product datasheet, aluminium alloy types 6060T6, T5 or T4 are used to fabricate the window. The current analysis are performed for aluminium alloy types 6060T6. The thermal properties for 6xxx aluminium alloy are given in [17-18]. A non-linear isotropic hardening law is used to model the aluminium material behaviour. The melting point for 6060T6 alloy is of 650°C [17]. The yield stress (proof stress) for this material is of 150 MPa for plates thinner than 3mm-thick. Aluminium alloy is modelled as a multi-linear perfectly plastic and isotropic material with the rate dependent plasticity (viscoplasticity), based on the Perzyna model. The surface emissivity is 0.7 for the aluminium parts [19] and 0.85 for polyamide materials [21]. The surface emissivity for glass varies between 0.86 and 0.92 [20].

3.2 Failure modes

Post-disaster observations have shown different failure modes of the window frames: inward, outward and partial failures exist at several locations on the tower (Figure 4). However, all the failure modes are quite binary since we observe either a window still in place or no more window.

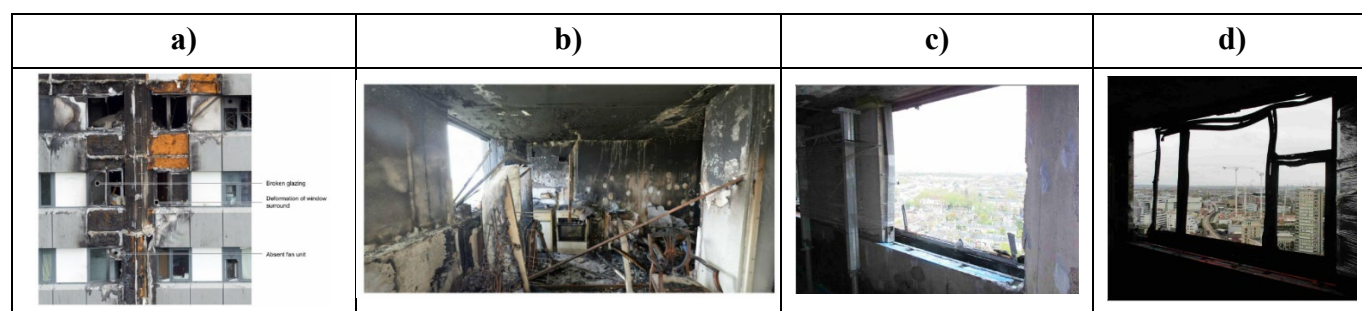


Figure 4. a) Failure mode of window frame [4], L. Bisby's expert report, Fig. 11, p. 166 – b) Inward failure of window frame, J. Torero's expert report, Fig. 54, p. 91 - c) Outward failure of window frame, B. Lane's expert report, Appendix C, Table 11C, p. 94 – d) Partial failure of window frame, B. Lane's expert report, Appendix C, Table 11C, p. 95

The relation between the initial position of the window during the disaster (close, in-tilt) and its fallout mode can be questioned, as well as the time to failure depending on a given opening configuration. Open or in-tilt configurations are probable because the Grenfell disaster happened during summer, and temperatures close to 20°C were recorded during the night of the disaster [25]. The present work only investigates the frame failure due to the thermal loads induced by the façade fire, and cannot claim to take into account all the events that led to the window failure.

3.3 Thermal analysis of the window frame

The initial fire, before spreading outside from the building, was localized close to the wall and window, in the scornor of the kitchen of Flat 16, located on the 4th floor of the East façade of the Tower. The analysis performed in [9] addressed the fire development inside the initial apartment, and its spread through the façade to the upper one (Flat 26, 5th floor). It allowed evaluating the thermal loads in terms of gauge heat fluxes (GHF) imparted to each part of the window frame. These are applied as boundary conditions on the exposed parts of the thermal analysis performed with ANSYS Mechanical APDL [23] using two-dimensional (2D) PLANE55 thermal planar elements. Both frame and casement sections of the window are modelled. A part of the glass is also modelled. Figure 5 shows the geometry used in the thermal model.

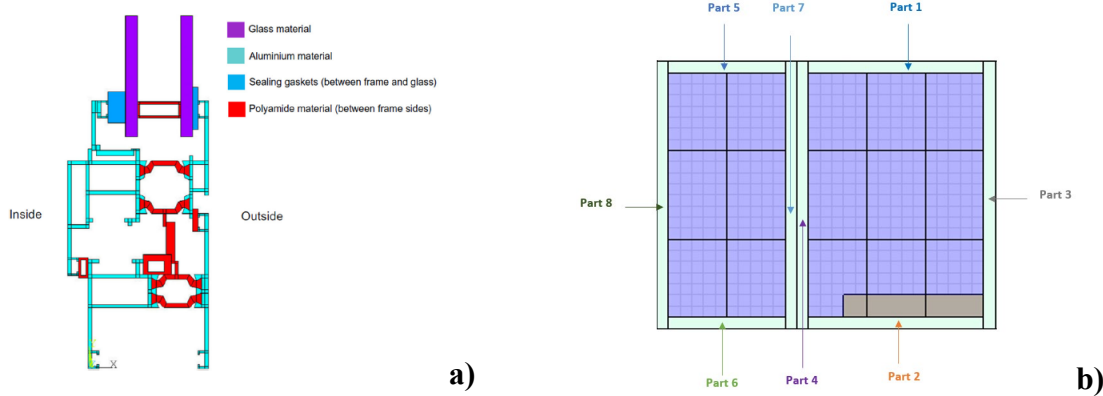


Figure 5. a) Geometry of the window frame addressed for the thermal model – b) Position of each window section defined for the applied thermal actions [10]

For the exposed and non-exposed faces of the window, the heat transfer coefficient is evaluated from the CFD simulation, and ranges between 10 and 15 W/m²/K for the exposed side, where the flow is turbulent, and is about 4 W/m²/K at unexposed side of the window. In the window cavities, the flow is quasi-laminar, and the coefficient is then set to 4 W/m²/K [22]. A sensitivity analysis was addressed in [11]. The thermal simulations are setup in 2D, because the out-of-plane distribution of boundary conditions applied at each part on window is uniform. Therefore, out-of-plane heat flow is insignificant. Two layers of SURF151 elements are modelled and superposed on the exposed faces of the windows, to apply both heat flux and temperature conditions at the surface of the materials. The unexposed face is modelled with surface layer elements to apply in-room (ambient) temperature condition. Convective heat exchange and surface-to-surface radiation are modelled for the cavities inside the frame using link elements (LINK34) connected to a node, which presents the cavity temperature.

Temperatures at four locations A, B, C and D, located close to the polyamide connectors, are indicated in Figure 7. Temperatures are up to 80°C between 1.5 minutes (on parts 4 and 8) and 2.5 minutes (on part 3) of external fire exposure, and up to 200°C between 2 minutes (on parts 4 and 8) and 4.5 minutes (on part 3) of exposure on the polyamide bridges. This is consistent with the numerical observations in [9] where the external fire first breaks the left window part first. Therefore, the thermal failure of the window frame is expected before 5 minutes of external fire exposure. This is consistent with the criterion of 4 minutes for the partial window failure considered in the fire model. The thermal fields at all sides of the window frame at 180 seconds (3 minutes) of fire exposure are addressed in Figure 6. The temperatures is about the melting point (650°C) at exposed side of part 4, 7 and 8. The results show also that the exposed side of the window melted at all parts except part 3 before about 4 minutes. However, the failure time of the aluminium frame is defined as the instant from which the temperature in the insulating strips used for the thermal bridge break has reached the temperature of melting as indicated in [16].

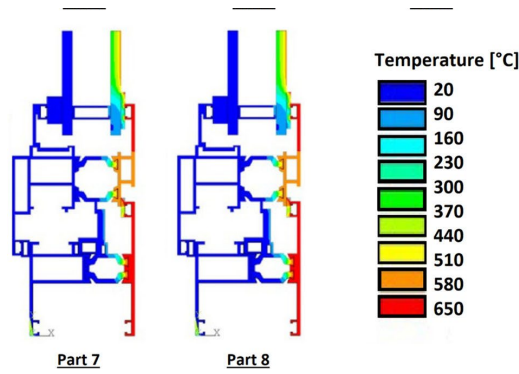


Figure 6. Temperature fields for different locations in the window frame at 180 s of fire exposure

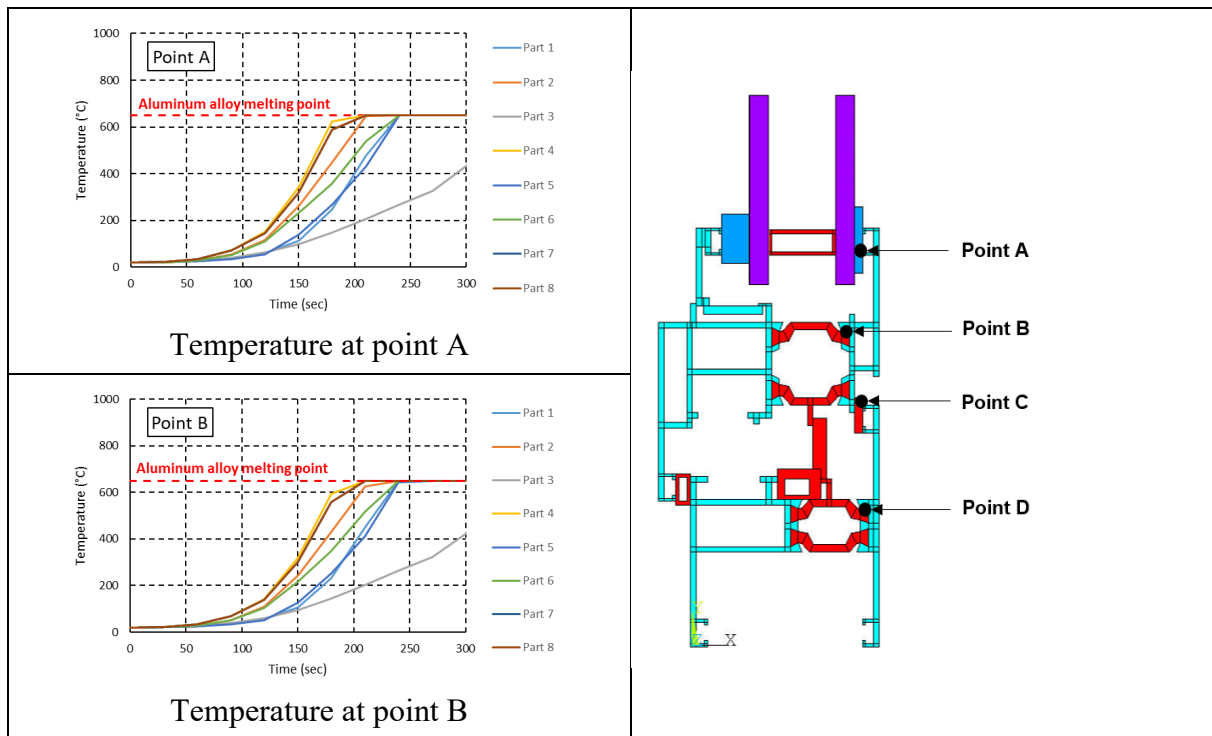


Figure 7. Time history for the temperature evaluated at four locations A, B, C and D of the window frame

The results of the thermal analysis (called type 1) on exposed face shows that the exposed side of window melted partially or totally at about 3 minutes (for parts 4 and 8. Therefore, a new thermal analysis is set up (called type 2) where the outside window frame wall is deactivated. Surface boundary elements and conductive elements are removed (so called killed) during analysis. Then, the new boundary surface elements are created (so called birth) on inner face of internal frame wall at 3 minutes. The result of temperatures show that the external wall may resist for some window parts until 4 to 5 minutes.

3.4 Thermomechanical analysis of the window frame

The structural behaviour of the window frame is investigated when subjected to thermal loads from the fire model. The thermomechanical model used is purely non-linear because of geometrical, material and contact between the different surfaces. The structural model proposed uses SHELL 181 elements. These elements are compatible for layered structures and may produce the plate buckling effect during the analysis. The frame cross section is modelled with 56 nodes in order to obtain an accurate shape and temperature distribution for mechanical analysis. The temperature of the aluminium frame at each position is mapped from the thermal analysis. Polyamide bridges are not modelled in the mechanical computation due to their poor rigidity resistance at any temperature with respect to the aluminium alloy, and negligible fire performance. Therefore, the structural modelling of this material does not carried out additional information to failure mode. Both frame and casement window sections are modelled. The numerical model consists of

the following element types: SHELL181 to model aluminium material, SOLID185 to model a semi-rigid part for the around studs, CONTA174 and TARG170 to model the contact surfaces between the frame and the wall, LINK180 used for in-tilt window condition. Two opening configurations of the window are investigated (closed and in-tilt position). Glass materials are not modelled in the structural analysis.

The model boundary conditions and loads are summarised in Figure 8. Each two nodes, one located on the frame and another one located on the casement of the window, which are along the line over the vertical jambs (for side hang) or horizontal jamb (for bottom hang), are coupled and used to model the hinges. The coupling of the nodes between the frame and the casement at position of window hardware generate the closing condition for the closed window configuration. The effect of wind on the window is neglected because the wind was coming from SSW direction the night of the disaster.

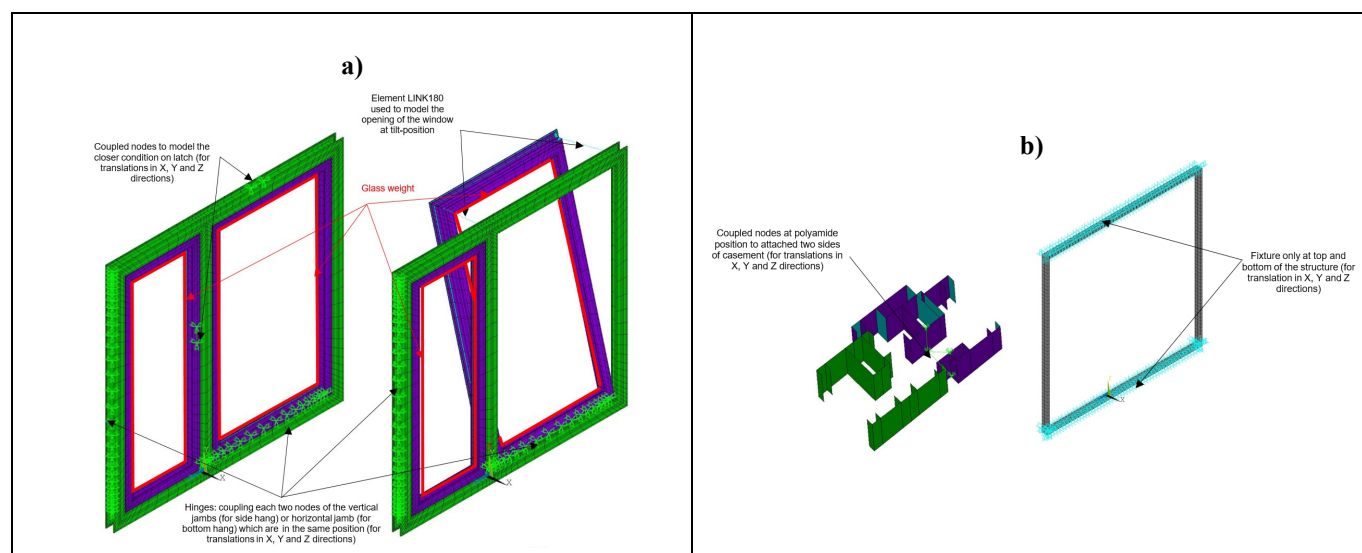


Figure 8. Loads and boundary conditions for the closed (a) and the in-tilt (b) opening configurations of the window

For the closed window, the thermomechanical computations give high values of deformation for the external face of the window at about 3 minutes (173 s). Figure 9-a gives the temperature at different sides of window, computed in 2D thermal analysis. The temperature at middle and left vertical jambs of the window (parts 4, 7 and 8) are about 600°C at this time, whereas the temperature at the right side jamb (part 3) is lower than 200°C. The vertical jambs of the frame are deformed and may be detached from the rest of the structure because of the large deflections as shown in Figure 9-b. The left side of the exposed frame plasticised because of the thermal stress (Figure 9-c). Aluminium alloy's yield stress decreases at high temperature. The material resistance is totally removed at the bottom and left side of the window (Figure 9-d). At this moment, the outer profile of the frame detaches from the rest of the window and falls outward. The dynamic force due to the weight of the outer profile and casement may lead to its outward failure. Thus, even if a part of the window frame stays in place, the glass breakage is almost certain at this moment, due to its fall when the frame does not maintain it anymore. If the external profile of the window collapses without pulling the whole window out, the inner profile will fail inward. The numerical results show the collapse of the inner profile of the frame at about 4 minutes (238 s) of fire exposure. The maximum temperature evaluated at the internal profile is up to 600°C when the failure occurs for the external side. At this time, almost all of the left side of the structure plasticised, which leads the window collapse.

The structure is also set-up to simulate the window in tilted condition. For this configuration, the hardware for the side turn casement is unlock, in order to see the effect of opening in the failure. Temperature loads are applied to the window except to the tilted sash. The outer face detaches from the rest of the window and falls outward approximately after 3 minutes (174 s) of fire exposition. The failure mode of the outer side for the in-tilt window is the same as the failure mode for the closed window configuration. The maximum temperature at failure time is about 610°C on the central window jamb. Figure 10 shows that the vertical jambs are deformed and may be detached from the rest of the structure because of the large deflections. The left side of the exposed frame plasticised because of the thermal stress. However, the failure of the

outer wall of the window does not cause the failure toward outside because the in-tilt casement weight stabilizes the frame and prevents this mode of failure. Thus, even if a part of the window frame stays in place, the glass breakage is almost certain at this moment, due to the large deformation of the frame leading to mechanical stress, or due to its fall when the frame does not maintain it anymore. In this case, the inner frame will collapse toward inside. Numerical results show that the window is deformed and the side turn casement opens toward inside at about 3.5 minutes (203 s) of fire exposure.

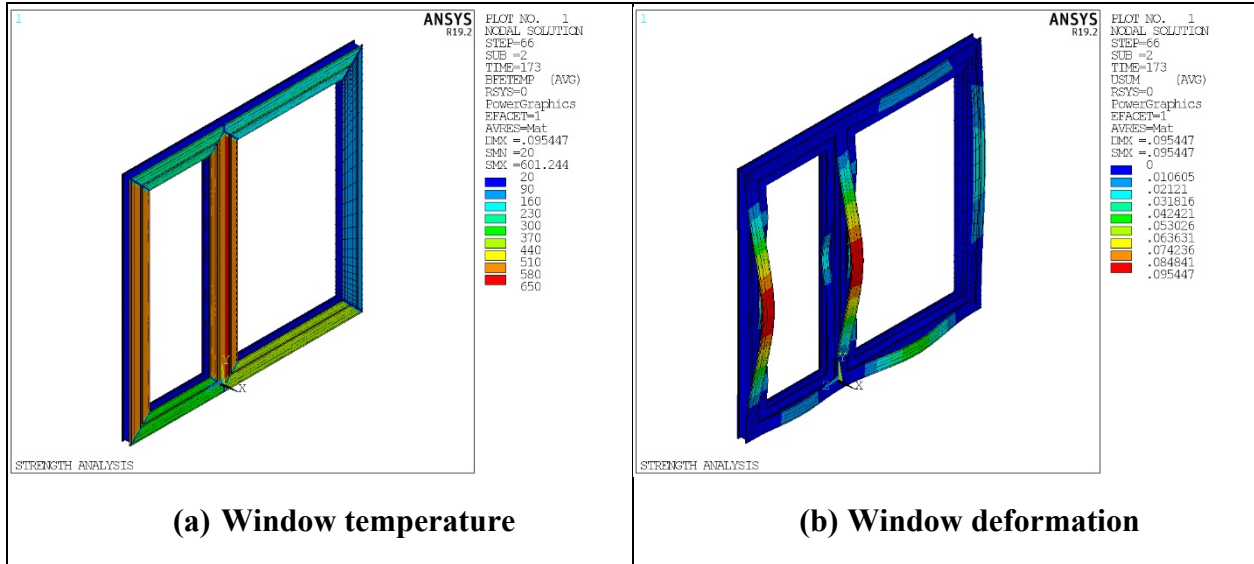


Figure 9. Frame temperature (a), deformation (b) before the failure of the outer frame at 173 seconds of fire exposure for the closed window configuration

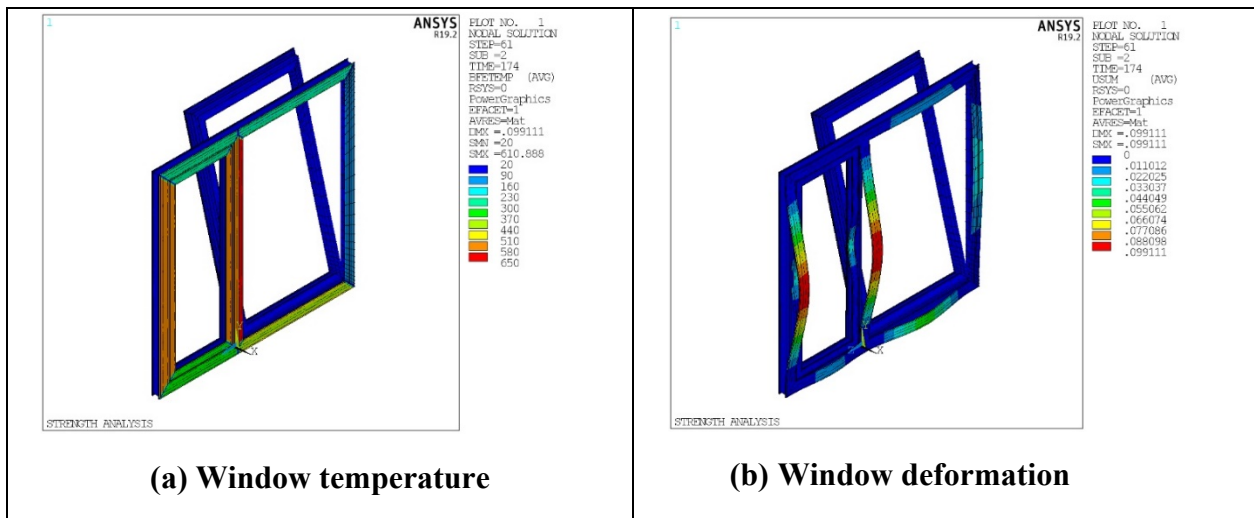


Figure 10. Frame temperature (a) and deformation (b) before failure of outer frame at 174 seconds of fire exposure for the in-tilt window configuration

4 HORIZONTAL FIRE SPREAD ALONG THE FAÇADE

After 01:29 am during Grenfell disaster, when the fire had reached the top of the Tower, observations showed that strongly enhanced horizontal fire propagation occurred, especially via the Tower's architectural crown. The fire spreads across the four faces of the Tower from 01:29 up to 04:09 am, due to the combustion of the insulated façade system and the apartment contents. The modelling of horizontal fire propagation for the whole Grenfell Tower considering both façade and apartments is then addressed based on the initial vertical fire spread [12] linked with the window failure criteria assessed [11] and used for each apartment opening. Therefore, depending on local window breakage, the numerical model takes into account the contributions of all the apartments' contents [8]. This modelling reflects the full-scale fires on the east, north, south and west faces of the Grenfell Tower, and provides a better understanding of fire

behaviour and the role of architectural details in fire spread. Additionally, the numerical model allows further investigation into the effect of changing the insulant material used in the cladding system.

Because the east and west faces, and the north and south faces, respectively, are identical, two different numerical models were built to simulate fire propagation over the faces of the Tower. The total dimensions of each numerical domain were four times 40 x 20 x 87 m (l x w x h), with open boundary conditions for pressure. Mesh size was uniform and taken as 0.25 x 0.25 x 0.25 m. About 4.5 million cells were used per face, for a total close to 18 million cells. Each face model integrates the related flats. The numerically modelled vertical fire spread over the east face of the Tower was validated until the fire reached the top of the east face at 01:29 am. The fire conditions at this time, in terms of burning surfaces, contributing flats, and heat release rate, are thus known at every location on the façade and in the apartments and are used as boundary conditions for each independent horizontal fire spread model including face and next corner. Thus, the third phase of the vertical fire spread describes in [12] is used as the starting point of the present calculation.

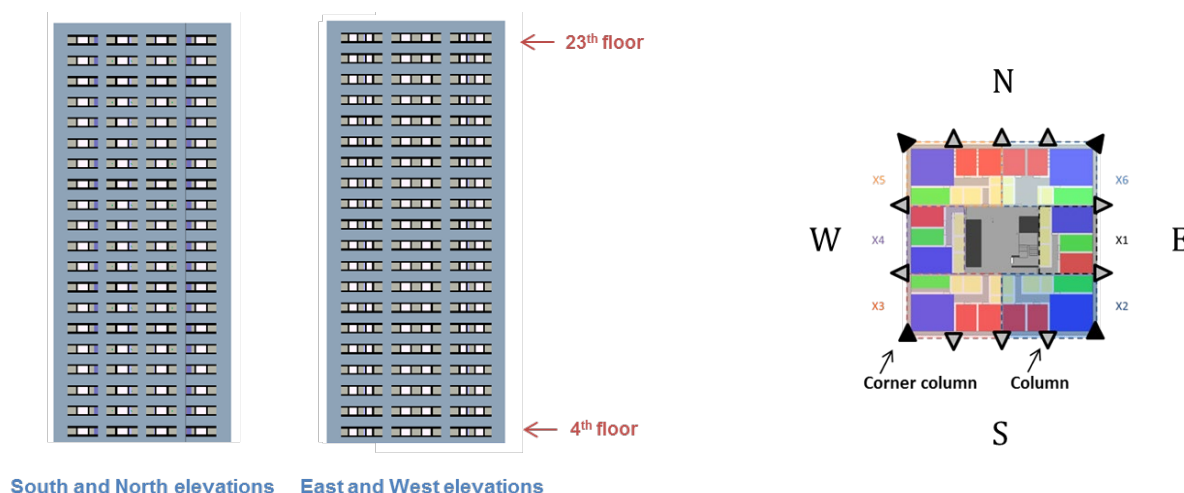


Figure 11. Numerical models of the south / north and east / west faces of the tower – Overview of the flats and columns disposition

The fire spread over the four faces of the Tower was modelled from 01:29 to 04:30 am. Results of the numerical simulation of horizontal fire spread along the east, north, south and, later, west faces are shown in Figure 12. Regarding the global fire behaviour along the four faces of the Tower, the fire spread is well reproduced by the numerical model for each face. At 3:53 am, the fire continues to spread only on the west face. The clockwise and anticlockwise fire paths merge close to south-west corner at 4:09 am. After this time, some parts of each façade remain unburnt.

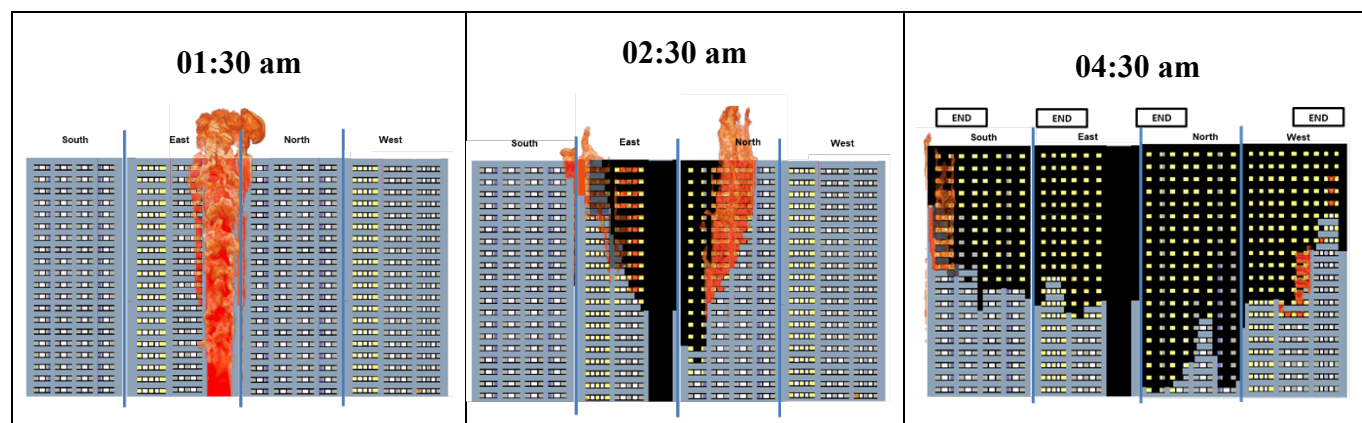


Figure 12. Numerical simulation for the fire propagation over the four faces of the tower between 01:30 am and 04:30 am [12]

The numerical model for horizontal fire spread across the whole allows the analysis of the horizontal rate of flame spread for several floors of the Tower as done in [8]. This analysis for the crown level shows that the rate of flame spread at the crown is similar for both the clockwise (from east face to south face) and anticlockwise (from east face to north face) spread. An average flame spread rate was estimated at about 0.29 m/min. This value is consistent with that evaluated in reference [8] and close to 0.3 m/min. The numerical prediction agrees with the observations of the real fire at each time recorded. The numerical simulations show that the fire propagates to the north, south and west faces respectively at 1:36 am, 2:30 am and 2:37 am. Although the average spread rate for both clockwise and anticlockwise directions are similar, the local values at specific flats or at columns are quite different. Indeed, the average spread rate at corner columns is 60% higher for the clockwise direction than for anticlockwise. However, the local effect of the columns included in the façade tends to decrease the average spread rate for the clockwise direction but to increase it for the anticlockwise one.

During the horizontal spread across the east, north, south and west faces, after 01:30 am, the fire is clearly propagating in a V-shape with an average angle close to $0.7^\circ/\text{min}$, as shown in Figure 13. This angle (α) corresponds to the angle between the maximum extent of horizontal propagation at the crown level and the local origin of the V-shape, considered in the east-north corner column at 4th floor. The average values are summarized in Table 3. Numerically, the angle of the V-shape is higher for the east face, and then decreases for north, south and west faces. Following observations, a similar angle is found for the east and north faces, while a lower value is evaluated for the south and west faces. The angle related to the establishment of the V-shape seems to decrease with the order of the faces involved in the fire (east then north, south and west) and thus follows the horizontal spread around the Tower. This can be related to the fire being more intense during its first phase (vertical spread and horizontal spread along the east face) mainly driven by the combustion of the cladding.

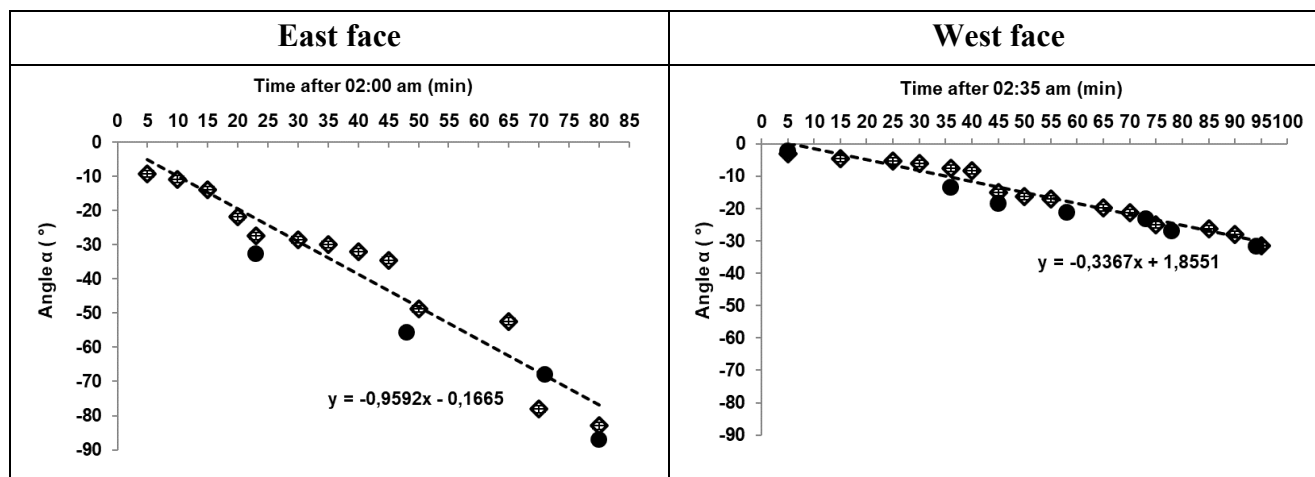


Figure 13. Horizontal fire propagation – Establishment of the V-shape for the east, north, south and west faces from observations [8] (black circles) and simulations (diamonds)

5 CONCLUSION

A reconstruction of the Grenfell fire using step-by-step numerical methods based on experimental fire tests was addressed. This provides a better understanding of the façade fire behaviour, and of the contribution of architectural details and their impact on fire spread, as well as the conditions inside the tower during the whole period of the fire.

From a façade numerical model for upscaling [6-7] using a multi-scale approach, the fire performance of the refurbished façade system used on the Grenfell tower were assessed based on intermediate and large scale reaction to fire tests. Then, the reconstruction of Grenfell fire consisted into visualizing all data available from observations, in terms of pictures and movies, of the disaster [8], in order to establish a full 3D model of the observations of the tower into a database, and then to determine flame spread rates, flames

duration and fire location at each time. The development of the initial fire, inside the kitchen of the apartment of origin at Grenfell, and its behaviour at the kitchen window [9] showed a very high probability that any limited fire in the kitchen could have led to the ignition of the façade system, even in absence of flashover. Fire spread over the façade was also explored numerically during the initial vertical spread and later horizontal spread [10][12]. A very good agreement between simulated and observed flame spread was obtained and showed the importance of constructive details and materials, and that propagation rate is driven in a large proportion by the behaviour of ACM-PE itself.

Analysis and hypotheses from the disaster showed the importance of window failures in the propagation from the façade fire to the inside of the apartments. The results of thermomechanical modelling of window frames and assemblies confirm this point as probably one of the dominant way of fire penetration [11].

As a perspective, these step by step simulations allow the analysis of the interactions between apartments and façade fires. This lead to further research on relative contribution to tenability from contents and from construction products. This further analysis will help understanding the conditions inside the tower during the whole period of the fire.

ACKNOWLEDGMENT

This reconstruction only uses public data available on Grenfell reports or published in the scientific literature. This work has been partially financed by Kingspan. Sponsor has not been involved in the results and the conclusions of this paper.

REFERENCES

1. J. Valiulis. Building Exterior Wall Assembly Flammability: Have we forgotten the past 40 Years? In Fire Engineering Magazine, November 2015.
2. N. White, M. Delichatsios. Fire Hazards of Exterior Wall Assemblies Containing Combustible Components. FPRF final report, project FE2568, Quincy, MA, USA, 2004.
3. N. White, M. Delichatsios, M. Ahrens, A. Kimball. Fire hazard of exterior wall assemblies containing combustible components. Proceedings of 1st International Seminar for Fire Safety of Facades., Paris, 2013.
4. Collection: Grenfell Tower. UK Department for Communities and Local Government, <https://www.gov.uk/government/collections/grenfell-tower>
5. E. Guillaume, T. Fateh, R. Schillinger, R. Chiva, S. Ukleja. Study of fire behaviour of façade mock-ups equipped with aluminium composite material-based claddings, using intermediate-scale test method. Fire and Materials, 2018;1-17. <https://doi.org/10.1002/fam.2635>
6. Dréan, V., Girardin, B., Guillaume, E., Fateh, T. Numerical simulation of the fire behaviour of façade equipped with aluminium composite material-based claddings—Model validation at intermediate scale. Fire and Materials 2019. <https://doi.org/10.1002/fam.2745>
7. Dréan, V., Girardin, B., Guillaume, E., Fateh, T., Numerical simulation of the fire behaviour of facade equipped with aluminium composite material-based claddings-Model validation at large scale. Fire and Materials 2019. <https://doi.org/10.1002/fam.2759>
8. Guillaume, E., Dréan, V., Girardin, B., Benameur, F., Fateh, T., Reconstruction of Grenfell Tower fire. Part 1: Lessons from observations and determination of work hypotheses. Fire and Materials 2019. <https://doi.org/10.1002/fam.2766>
9. Guillaume, E., Dréan, V., Girardin, B., Koohkan, M., Fateh, T., Reconstruction of Grenfell Tower fire. Part 2: A numerical investigation of the fire propagation and behaviour from the initial apartment to the façade. Fire and Materials 2019. <https://doi.org/10.1002/fam.2765>
10. Guillaume, E., Dréan, V., Girardin, B., Benameur, F., Koohkan, M., Fateh, T., Reconstruction of Grenfell Tower fire. Part 3—Numerical simulation of the Grenfell Tower disaster: Contribution to the understanding of the fire propagation and behaviour during the vertical fire spread. Fire and Materials 2019. <https://doi.org/10.1002/fam.2763>
11. Koohkan M., Dréan V., Guillaume E., Girardin B., Fateh T., Duponchel X. (2020) Reconstruction of Grenfell tower fire - Thermomechanical analysis of window failure during the Grenfell Tower disaster, Fire Technology, <https://doi.org/10.1007/s10694-020-00980-4>

12. Guillaume E., Dréan V., Girardin B., Fateh T. (2020). Reconstruction of Grenfell tower fire - Part 4: Contribution to the understanding of the fire propagation and behaviour during the horizontal fire spread, <https://doi.org/10.1002/fam.2911>
13. Torero J., Grenfell Tower: Phase 1 report. GFT 1710-OC-001-DR-01 – May 23rd 2018. <https://www.grenfelltowerinquiry.org.uk/evidence/professor-jose-l-toreros-expert-report>
14. Fire dynamics simulator FDS, <https://www.nist.gov/>
15. Kensington and Chelsea TMO, Reduced window opening in ware opening leafs, Grenfell tower regeneration project, Drawing NO. 1279 SK112 01
16. PN ISI - Comportement au feu des vitrages non résistants au feu, A14-G14-rapport d'action, 30 octobre 2010
17. Eurocode 1 (EN 1991), Part 1-2: Design of aluminium structures - Structural fire design
18. Eurocode 1 (EN 1991), Part 1-1: Design of aluminium structures - General structural rules
19. Okada T., Ishige R., Ando S. (2016) Analysis of Thermal Radiation Properties of Polyimide and Polymeric Materials Based on ATR-IR spectroscopy, Volume 29 Issue 2: 251-254
20. BS EN 755 Part 2 (April 2016), Aluminium and aluminium alloys - Extruded rod/bar, tube and profiles - Part 2 : Mechanical properties - Aluminium and aluminium alloys – Mechanical characteristics
21. Raman R., Thakur A. (1982), Thermal emissivity of materials, Applied Energy Volume 12, Issue 3: 205-220
22. Eurocode 1 (EN 1991), Part 1-2: Actions on structures - Actions on structures exposed to fire
23. ANSYS 17.2, August 2016, <https://www.ansys.com/>
24. Carrière J.F., Sekiguchi H. (1976) Thermal properties of aminoacid type polyamides, Chem. Zvesti, 30(3): 281-291
25. Weather in London, England, United Kingdom, www.timeanddate.com/weather/uk/london
26. ISO 13943:2017. Fire safety – Vocabulary
27. ISO/TR 20118:2019. Plastics - Guidance on fire characteristics and fire performance of PVC materials used in building applications.
28. Purser, D.A. (2016) Toxic Combustion Product Yields as a Function of Equivalence Ratio and Flame Retardants in Under-Ventilated Fires: Bench-Large-Scale Comparisons, Polymers 2016, 8, 330; doi:10.3390/polym8090330
29. Babrauskas V., Harris R.H., Braun E., Levin B.C., Paabo M., Gann R.G. (1991) The role of bench-scale test data in assessing real-scale fire toxicity, Technical Note 1284, National Bureau of Standards and. Technology, Gaithersburg MD
30. Marsh N.D., Gann R.G. (2013) Smoke Component Yields from Bench-Scale Fire Tests: 4. Comparison with Room Fire Results, NIST Technical Note 1763, NIST, Gaithersburg, MD
31. Forell B, Hosser D. (2007) The Relationship Between Ventilation Conditions And Carbon Monoxide Source Term In Fully-Developed Compartment Fires, Proceedings of the 5th International Seminar on Fire and Explosion Hazards, Edinburgh, UK, 23-27 April 2007
32. Marquis D.M., Hermouet F., Guillaume E. (2016) Effects of reduced oxygen environment on the reaction to fire of a poly(urethane-isocyanurate) foam, Fire Mater. 2016, DOI: 10.1002/fam.2378
33. Pitts, W.M. (1995). The Global Equivalence Ratio Concept And The Formation Mechanisms Of Carbon Monoxide In Enclosure Fires, Prog, Energy Combust. Sci. Vol.21, pp.197-237
34. Cuesta A., Abreu O., Alvear D. (2016) Evacuation Modeling Trends, DOI 10.1007/978-3-319-20708-7

STUDIES ON BENDING STRENGTH AND COLLAPSE TEMPERATURE OF A STEEL BEAM CONSIDERING EFFECTS OF STEEL STRAIN RATE AND HEATING RATE AT ELEVATED TEMPERATURES

Fuimnobu OZAKI¹ and Takumi UMEMURA²

ABSTRACT

In this paper, effects of strain and heating rates on fire resistance of a steel beam are examined by tests using a small specimen, and numerical analyses for a cantilever beam under the steady and transient state conditions, respectively, to clarify those bending strengths and collapse temperatures. The validity of the numerical analysis is verified by the test results. From both parametric tests and analytical results, it was clarified that the numerical results approximately agreed with the test results, and the bending strength and collapse temperature of the heated steel beam under the various heating and loading rates were quantified by the effective strength obtained from the coupon tests.

Keywords: steel beam, fire resistant test under steady and transient state condition, numerical analysis using two-dimensional beam element, bending strength, collapse temperature

1 INTRODUCTION

Stress and strain relationships of steel materials at elevated temperatures are evaluated from the coupon tests under the steady state condition. For the coupon test, a constant value on the strain rate [1/sec. or 1/min.] standardized in each country/area is generally used, for instance, the value of 0.003 [1/min.] based on the JIS (Japan Industrial Standard) code is usually used in Japan. It is, on the other hand, known that the steel strength at the elevated temperature is strongly affected by the strain rate, and that becomes larger with increasing the value of strain rate [1-3]. Furthermore, the heating rate for the steel members at the transient state condition possesses the same effect as the strain rate [4]. The value of strain rate for the heated steel member under the transient state condition changes every moment, in particular, that becomes larger when the steel member exhibits the collapse mode, because the large deflection or deformation at the collapse state occurs in a short time around the collapse time. The verification of the effect of the strain and heating rates are of importance, to clarify the actual load-bearing capacity, collapse time and collapse temperature for the steel member at the fire.

The main purpose of this paper is to examine the effects that the strain and heating rates cause to the fire resistance of a simple supported steel beam, by both steady and transient state tests using the small steel rectangular specimen. Furthermore, the validity of numerical analysis which has been proposed by the past study [4] is verified by the test results. From the test and numerical results, the bending strength and collapse temperature of the heated steel beam at the steady and transient states under various heating and loading rates were quantified by using the reduction factors on effective strengths of the steel material under the various strain rates.

¹ Associate Professor, Nagoya University, Japan
e-mail: ozaki@nuac.nagoya-u.ac.jp

² Former Graduate Student, Nagoya University, Japan
e-mail: takumi.dora2112@gmail.com

2 BENDING TESTS FOR SMALL STEEL BEAM SPECIMENS UNDER STEADY AND TRANSIENT STATE CONDITIONS

2.1 Test details

To examine the effects of loading and heating rates for the steel beam at the elevated temperature, the bending test using the small beam specimen under either steady or transient state condition was conducted. The loading rate of the steel beam for the steady state test is denoted by the loading speed of the bending moment applied to the specimen, which is the main test parameter that possesses the same effect as the strain rate under the steady state condition.

Figure 1 show the overview of the bending test using the simple supported beam specimen. The cross section of specimen is a rectangular (the depth $d = 12$ mm, and width $b = 18$ mm), and the support span length L is 150 mm. The steel grade of specimen is JIS SN 400B, which is the same steel lot as the specimen of coupon test reported in the past study [4]. The behavior of the actual steel beam size with a wide flange shape under the steady and transient states will be examined by the numerical analysis in the following chapter. A concentrated load P is applied at the center of the specimen, through steel jigs with the steel round bar at the loading point.

The test parameters are given by the heating rate α_θ of the specimen and the loading ratio γ_m of the constant bending moment for the transient state test, on the other hand, the loading rate α_L and test temperature θ for the steady state test, respectively. Table 1 shows the specimen details for each test parameter.

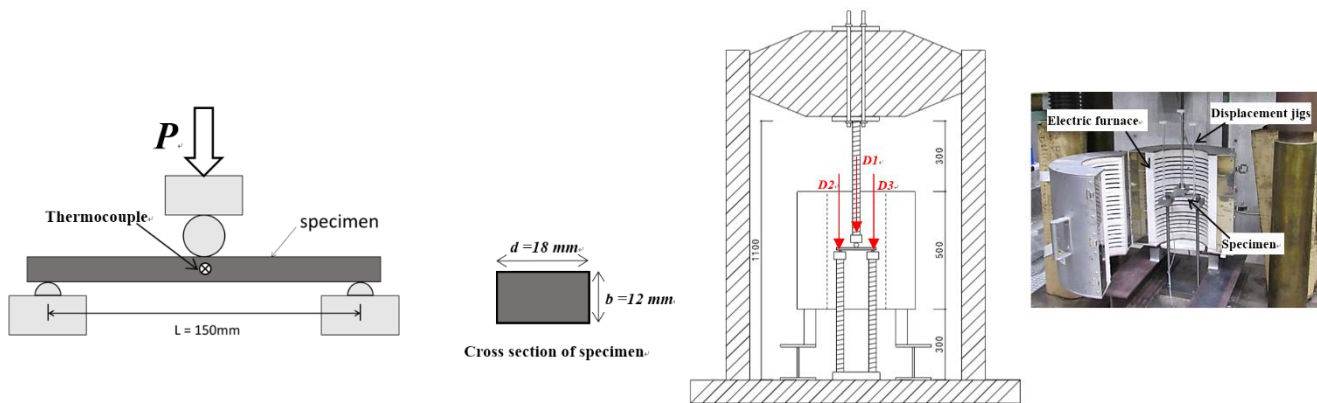


Figure 1. Specimens and test details

Table 1 Test parameters

Specimen	Heating rate α_T (°C/min.)	Load ratio ($\gamma_m = M/M_{y20}$)	Specimen	Temperature (°C)	Loading rate α_L (mm/min.)
L030F	40	0.3	T020	20	-
L045F	40	0.45	T500F	500	34
L060F	40	0.6	T700F	700	55
L075F	40	0.75	T500S	500	1
L030M	13	0.3	T700S	700	2
L045M	13	0.45			
L060M	13	0.6			
L075M	13	0.75			
L030S	4	0.3			
L045S	4	0.45			
L060S	4	0.6			
L075S	4	0.75			

temperature
 \downarrow
T 700 S
 \uparrow
 constant Temperature

load ratio
 \downarrow
L 075 S
 \uparrow
 constant Load

heating rate
 E: Fast
 M: Middle
 S: Slow

loading rate
 E: Fast
 M: Middle
 S: Slow

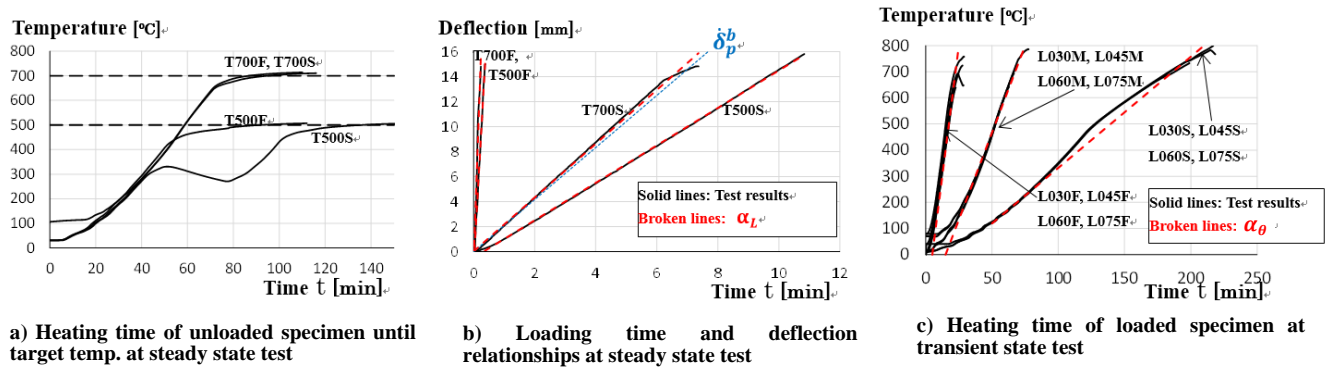


Figure 2. Time - temperature and time - deflection relationships

[Transient state tests (Figure 2c)]

The loading ratio γ_m for the transient state test is denoted by the following equation, to evaluate the various collapse time and temperature at the steady state tests.

$$\gamma_m = \frac{M_{const}}{M_{y20}} \quad (1)$$

Where,

M_{const} : Constant bending moment applied at the center of the specimen ($= \frac{PL}{4}$, P : constant load)

M_{y20} : Yield bending moment of the specimen at the ambient temperature in case of using the yield point f_{y20} (=270 MPa) evaluated from the coupon test [4].

The heating rate α_θ of the specimen was determined from the value of specimen temperature measured by a thermocouple attached at the center (Figure 1). Figure 2 c) show the heating duration time and specimen temperature relationships. The solid lines in Figure 2 c) are the test results measured by the thermocouple, on the other hand, the broken straight lines mean the approximate values of heating rate α_θ calculated from those. The maximum heating rate ($\alpha_\theta = 40$ [°C/min.]) listed in Table 1 was the limit-value in the case when inside-air temperature of an electric furnace can be raised by the maximum heating output.

[Steady state tests (Figure 2 a) and b)]

The steady state tests were conducted under the ambient temperature, 500 and 700 [°C], respectively. The specimen temperature and time relationships during the heating stages before the loading are shown in Figure 2 a). For the T500S test, the furnace temperature when the heating time was from 60 to 80 [min.] was not well controlled, because thermal insulation treatments for the opening of the furnace were insufficient. However, the specimen temperature reached to about 500 [°C] after improving those. The loading started after the specimen temperature was kept for 30 min. after reaching to the target test temperature. The loading rate α_L used as the test parameter at the 500 and 700 °C tests was denoted based on the value of the deflection rate [mm/min.] measured at the center of the specimen, which corresponds to the rate of vertical displacement at the loading point on the specimen.

The loading duration time and the deflection relationships are shown in Figure 2 b). The deflection of the specimen was measured by displacement meters (D1, D2, and D3 as shown in Figure 1) set outside of the furnace, respectively, though the displacement jigs made by quartz rod materials (the diameter is 4.5 mm) with a small coefficient of the thermal expansion (0.5×10^{-6} [1/°C]). The solid lines and broken straight lines in Figure 2 b) mean the test results and the approximate value of loading rate α_L calculated from those, respectively. The 700 °C test showed the larger loading rate than the 500 °C test for both fast and slow loading tests. In the steady state test, the deflection rate of specimen was actually not controlled, but the displacement rate of cross-head of a loading test machine was controlled. The displacement of cross-head at the 700 °C test proceeded a little faster than the 500 °C test, because the bending stiffness of the former specimen became smaller than the latter. In Figure 2 b), the collapse deflection rate of the simple supported steel beam $\delta_p^b (= L^2 / (9000d)$ [mm/min.]), which is the maximum standard values judged as the collapse state at Japanese general fire resistance performance-test using the ISO-834 standard fire curve under the transient state, is shown for reference. That performance-test is usually conducted to evaluate the fire

resistance performance of fire protection material regarding the Building Standard Low of Japan, and the protected beam specimen under the test is required to possess the lower deflection rate than the above $\dot{\delta}_p^b$ during the fire test time (1, 2 or 3 hours). It is, furthermore, known that the collapse deflection rate $\dot{\delta}_p^b$ gives the safety side evaluation in comparison with that at the actual collapse state of the heated steel beam, in order to include the large safety factor for the legal fire resistance performance. As shown from Figure 2 c), it was confirmed that the deflection rates at the fast tests (T500F and T700F) of the steady state test were larger than the maximum standard value $\dot{\delta}_p^b$ used at the fire resistant performance-test.

2.2 Test results

Figure 3 show the bending test results under the steady state condition, which are the relationships between the deflection δ and bending moment M of the specimen. The δ and M as shown in Figure 3 are divided by the collapse deflection value δ_p^b of steel beam at the above-mentioned Japanese legal fire performance-test and the full plastic moment M_{p20} of specimen at the ambient temperature, respectively. The δ_p^b is estimated by

$$\delta_p^b = \frac{L^2}{400d} \quad (2).$$

The collapse deflection δ_p^b is given by the two time values of the limit deflection value ($= \frac{L^2}{800d}$) proposed by Lyan R. et al [5], and the beam specimen applied to the fire performance test is judged as the collapse state when the maximum deflection exceeds the δ_p^b , based on the criterion regarding the maximum deflection value. It is know that the heated steel beam exhibits the plastic collapse mechanism when the maximum deflection approximately reached to the above value δ_p^b , and the collapse time and collapse temperature of steel beam are evaluated by each value at that time [6]. In this study, both collapse time and collapse temperature of steel beam are evaluated by each value at that time [6]. In this study, both collapse time and collapse temperature at the bending test were estimated when the maximum deflection reached to δ_p^b . The full plastic moment M_{p20} at the ambient temperature is evaluated by using the plastic section modulus Z_p and the yield point $f_{y20}(=270 \text{ MPa})$, that is, $M_{p20} = Z_p f_{y20}$.

The test results under the steady states were measured by intervals of one second for a data logger device, and those are shown by each mark in Figure 3. The test result at the ambient temperature (T020) shows the clear stiffness change around the full plastic moment M_{p20} . For the 500 and 700 [°C] tests, the results (T500F and T700F) with the fast loading rate show the larger bending moment than those with the slow loading rate (T500S and T700S), because of increasing the strain rate of specimen during the loading.

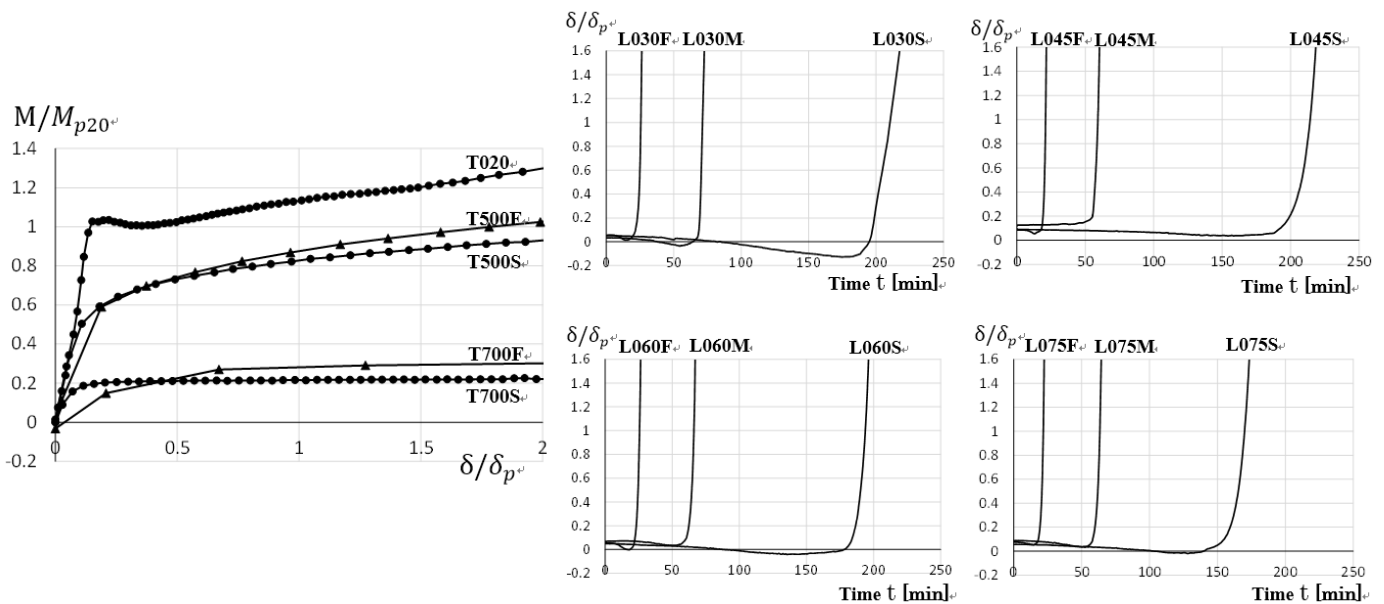


Figure 3. Test results for steady and transient state conditions

On the other hand, the elastic bending stiffness of the specimens of T500F and T700F was smaller than those of T500S and T700S, respectively. This is because the accurate elastic deflection of the former specimens might not be measured, because those specimens plasticized after just 1-2 seconds from stating the loading and the accurate measuring of the elastic bending stiffness was practically very difficult.

Figure 3 (right side figures) show the test results under the transient state conditions, which are the heat during time and deflection relationships. Each test result was measured by intervals of five seconds. All the beam specimens under the transient states sustained the constant loading bending moment M at the collapse deflection δ_p^b , after that, the specimen with the fast heating rate immediately exhibited the collapse state when the vertical load P rapidly decreased, on the other hand, that with the slow heating rate sustained the constant loading bending moment M until the deflection was equal to about $2.0 \times \delta_p^b$, because of slowly forming of the bending collapse mechanism with the slow heating rate. As shown from Figure 3 (right side figures), the collapse time of specimen decreases with increasing the load rate, understandably. The specimen with the fast heating rate possesses the shorter heating time and exhibits the rapid deflection increase at the collapse time.

2.3 Comparisons of test results with analytical results

Figure 4 show the analytical results evaluated by the numerical analyses considering the effect of strain rate [4] and the test results. The loading moment M and deflection δ relationships and the heating time t and deflection δ relationships are shown, respectively. The analytical model of simple supported beam are shown in Figure 4 which is a left half model considering the symmetry. For the analytical model, the actual heating and loading rates measured at the tests are used, respectively. As shown in Figure 4, the analytical results on both steady and transient state analyses approximately agree with the test results,

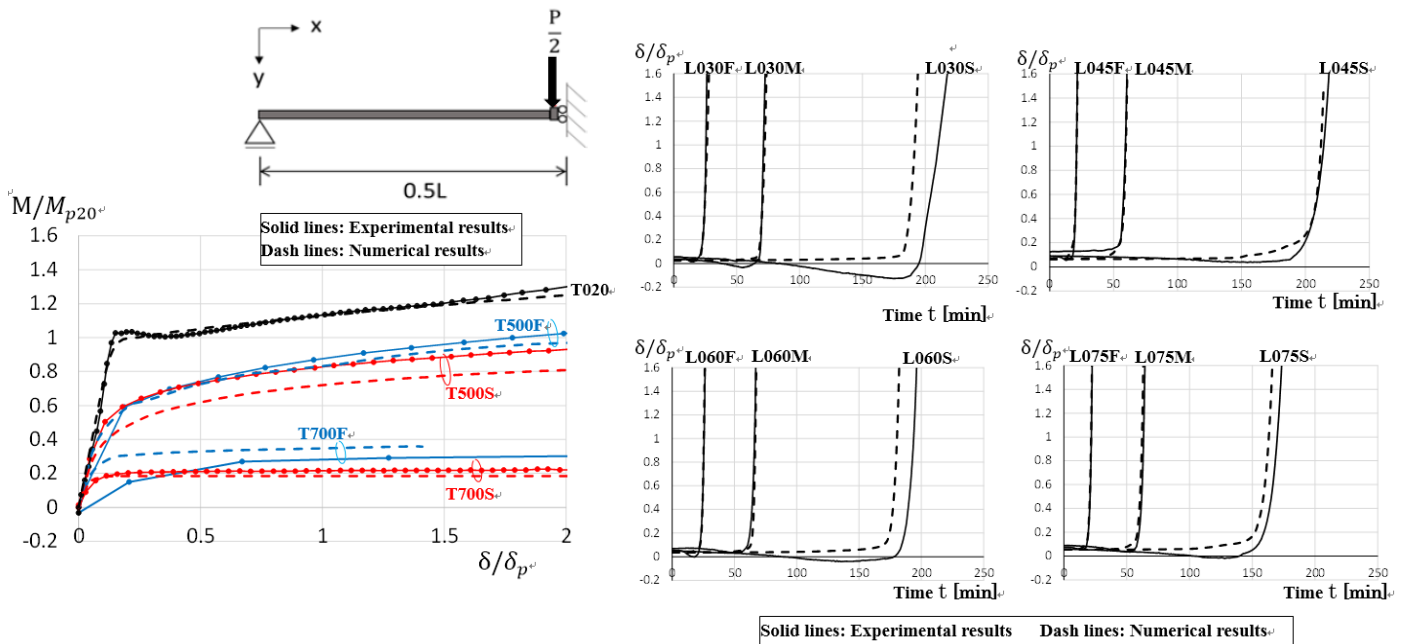


Figure 4. Test and analytical results for steady and transient state conditions

therefore, the validity of analytical model can be confirmed. On the other hand, according to the test result of T700F specimen at the fast loading condition, the elastic stiffness is the smaller than the analytical results. This is because the measurement interval at the T700F test was set as one second, however, the accurate measurement after the start of the test could not been obtained even if the above measurement interval was used, because of the very fast loading rate (55 [mm/min.]) at the T700F test. However, the analytical results on bending strength for the T700F specimen approximately agree with the test result.

3 PARAMETRIC ANALYSES OF THE CANTILEVER STEEL BEAM UNDER BOTH STEADY AND TRANSIENT STATE CONDITIONS

3.1 Analytical model

The parametric analyses for a cantilever steel beam under both steady and transient state conditions are conducted. The analytical model is shown in Figure 5. The cross section of beam is the wide flange shape (depth:400, width:200, web thickness:10, flange thickness:15 [mm]) and the beam length L is 3500 [mm]. The heating rate α_θ and the loading rate $\gamma_m (=M_{const}/M_{y20}$, M_{const} : the end moment owing to the constant vertical force P , M_{y20} : the yield bending moment at the ambient temperature) for the transient state analyses, on the other hand, the loading rate (loading speed) α_L and member temperature θ for the steady state analyses are used as the analytical parameters, respectively. Figure 5 (right figures) show the analytical parameters. The analytical case [1] (the heating rate α_θ : ISO-834 curve) assumes the fast heating situation, such as the unprotected steel beam after the start of fully developed compartment fire. Furthermore, the loading rate of the analytical case [4] is the same value as the collapse deflection rate $\dot{\delta}_p^b$ ($= (0.5L)^2/(9000d)$ [mm/min.]) which has been explained in the above chapter.

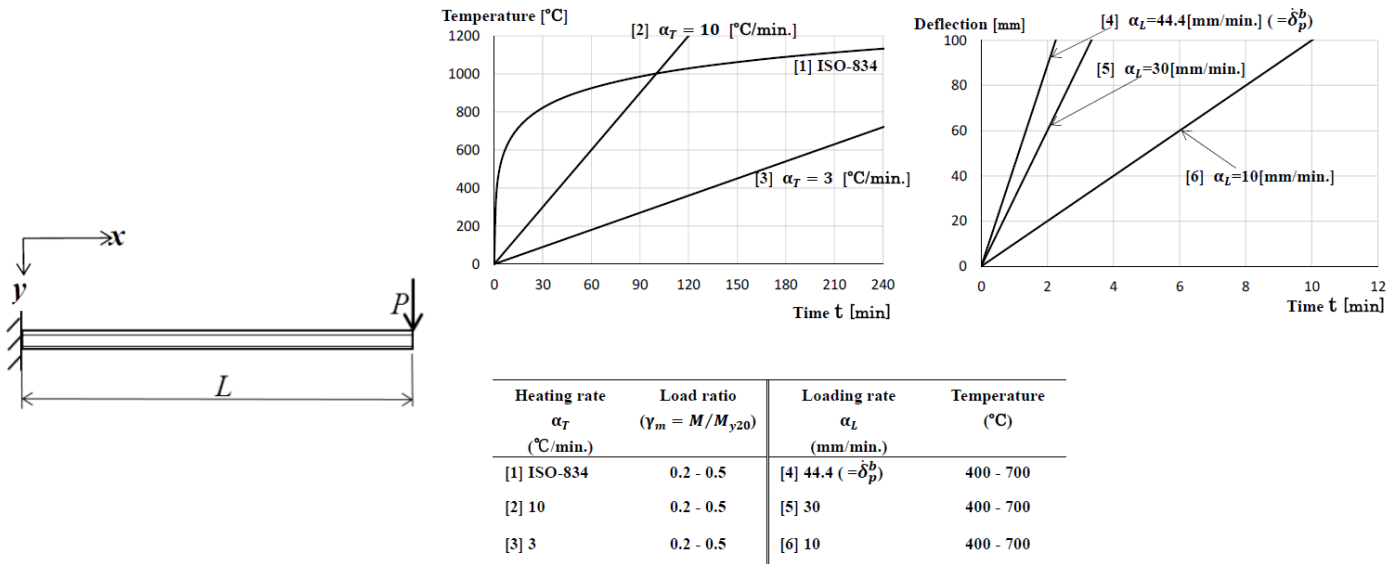


Figure 5. An Analytical model and analytical parameters

3.2 Analytical results

Figure 6 show the analytical results on the transient state [1-3] and the steady state [4-6] conditions, respectively. For the transient state analyses [1-3], the relationships between the time and the deflection at the free end, the strain ϵ , and the strain rate $\dot{\epsilon}$ of the upper flange at the fixed end, respectively. For the steady state analyses [4-6], the end moment M and the deflection δ relationships, and the relationships between the temperature θ and the strain ϵ , the strain rate $\dot{\epsilon}$ of the upper flange at the fixed end are shown, respectively. The strain ϵ and strain rate $\dot{\epsilon}$ for the analytical cases [4-6] as shown in the bottom figures of Figure 6 are the analytical results when the deflection reached to the collapse deflection δ_p . By using the numerical analysis, the behavior of strain rate for the steel beam at the elevated temperatures, which are difficult to measure at the actual fire test, can be evaluated.

From the analytical results of the transient state analyses, it was clarified that the strain rate of the fixed end sharply increased and exceeded 0.01 [1/min.] at the collapse time when the deflection was reached to δ_p . Furthermore, the strain rate at the collapse deflection δ_p for the steady state analyses exceeded 0.003 [1/min.] which is the standard value of the strain rate used for the coupon test at the elevated temperature.

On the other hand, the stress degradation for the stress and strain relationships used in this analysis has been considered, which has been observed in the case of the coupon test with the slow strain rate above 600 [°C] in the past study[4]. The strain at the steady state condition exhibited the large value over 0.01,

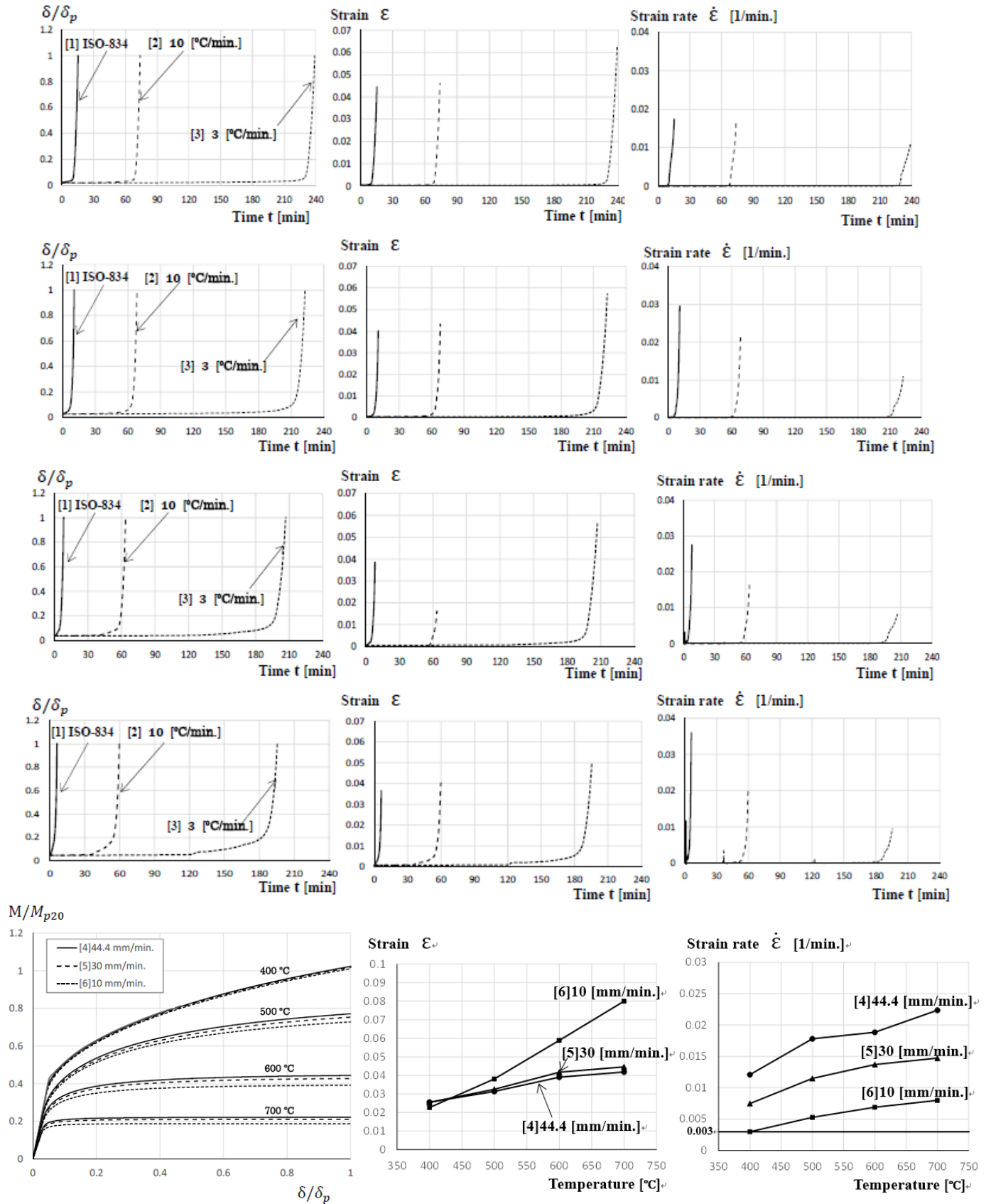


Figure 6. Analytical results for cantilever steel beam

however, the degradation of the bending moment was not observed, because the stress in the cross section increased with increasing the strain rate even if the loading rate was relatively slow such as the analytical case[6]. On the other hand, for the transient state analyses, the stress in the cross section at the fixed end increased, because of rapidly increasing the strain rate near at the collapse time. In general, the stress

degradation phenomenon for the stress and strain relationship triggers the degradation of load bearing capacity, however, the effect of the strain rate at the elevated temperature contributes to being the stable structural resistance without the degradation, and the stable numerical analysis at the fire. This is because the strain hardening of the stress and strain relationship continues with increasing the strain rate even if the strain exceed the uniform elongation. This is the importantly indicated point to consider the effect on strain rate at the elevated temperature.

4 EVALUATION OF BENDING STRENGTHS AND COLLAPSE TEMPERATURES BY USING EFFECTIVE STRENGTH UNDER VARIOUS STRAIN RATE

The bending strengths under the steady states, and the collapse temperatures under the transient states are evaluated by using the effective strength obtained from the past coupon tests [4], respectively. In this paper, the 0.002 off-set yield strength f_{02p} , the effective yield strengths f_{1y} and f_{2y} (see below) based on the coupon test results under the three kinds of strain rates ($\dot{\epsilon}=0.003, 0.03, \text{ and } 0.07$ [1/min.]) were used for those evaluations.

Figure 7 (upper side figures) show the test results (marks) using the small beam specimens under the steady and transient states, and the evaluated values on the bending strengths (three kinds of polygonal lines) in the case of using f_{02p} (0.002 offset yield stress), f_{1y} (stress when the strain is equal to 0.01), and f_{2y} (stress when the strain is equal to 0.02) obtained from the past coupon tests. The same lot steel has been used for both bending and coupon tests. The white and black marks mean the test results at the steady and transient state test results, respectively. On the other hand, Figure 7 (lower side figures) show the analytical results, which have been obtained from the above parametric analyses.

Regarding the evaluated values (three kinds of polygonal lines in Figure 7), the bending strength $M_{max}(\theta)$ at the temperature θ is given by,

$$M_{max}(\theta) = Z_p f_e(\theta). \quad (3)$$

Where,

$f_e(\theta)$: Effective strength of steel at the temperature θ , which is given by either f_{02p} , f_{1y} , or f_{2y} based on the coupon test result.

Dividing both sides of the above equation by the full plastic moment at the ambient temperature M_{p20} , the non-dimensional bending strength \bar{m} is obtained.

$$\begin{aligned} \bar{m} &= \frac{M_{max}(\theta)}{M_{p20}} = \frac{Z_p f_e(\theta)}{Z_p f_{y20}} \\ &= \frac{f_e(\theta)}{f_{e20}} \frac{f_{e20}}{f_{y20}} \\ &= \frac{f_{e20}}{f_{y20}} k_e(\theta) = r_{e20} k_e(\theta) \end{aligned} \quad (4)$$

Where,

f_{e20} : Effective strength of steel at the ambient temperature, which is given by either f_{y20} , f_{1y20} , or f_{2y20} at the ambient temperature

$k_e(\theta)$: Reduction factor regarding either f_{02p} , f_{1y} , or f_{2y} at the elevated temperature, which is estimated by either strength rate $k_{02p}(\theta) = f_{02p}(\theta)/f_{y20}$, $k_{1y}(\theta) = f_{1y}(\theta)/f_{1y20}$, or $k_{2y}(\theta) = f_{2y}(\theta)/f_{2y20}$

r_{e20} : Correction factor on the effective strength at the ambient temperature, which is estimated by either strength rate $r_{y20} = f_{y20}/f_{y20}(=1)$, $r_{1y20} = f_{1y20}/f_{y20}(=1.01)$, or $r_{2y20} = f_{2y20}/f_{y20}(=1.03)$

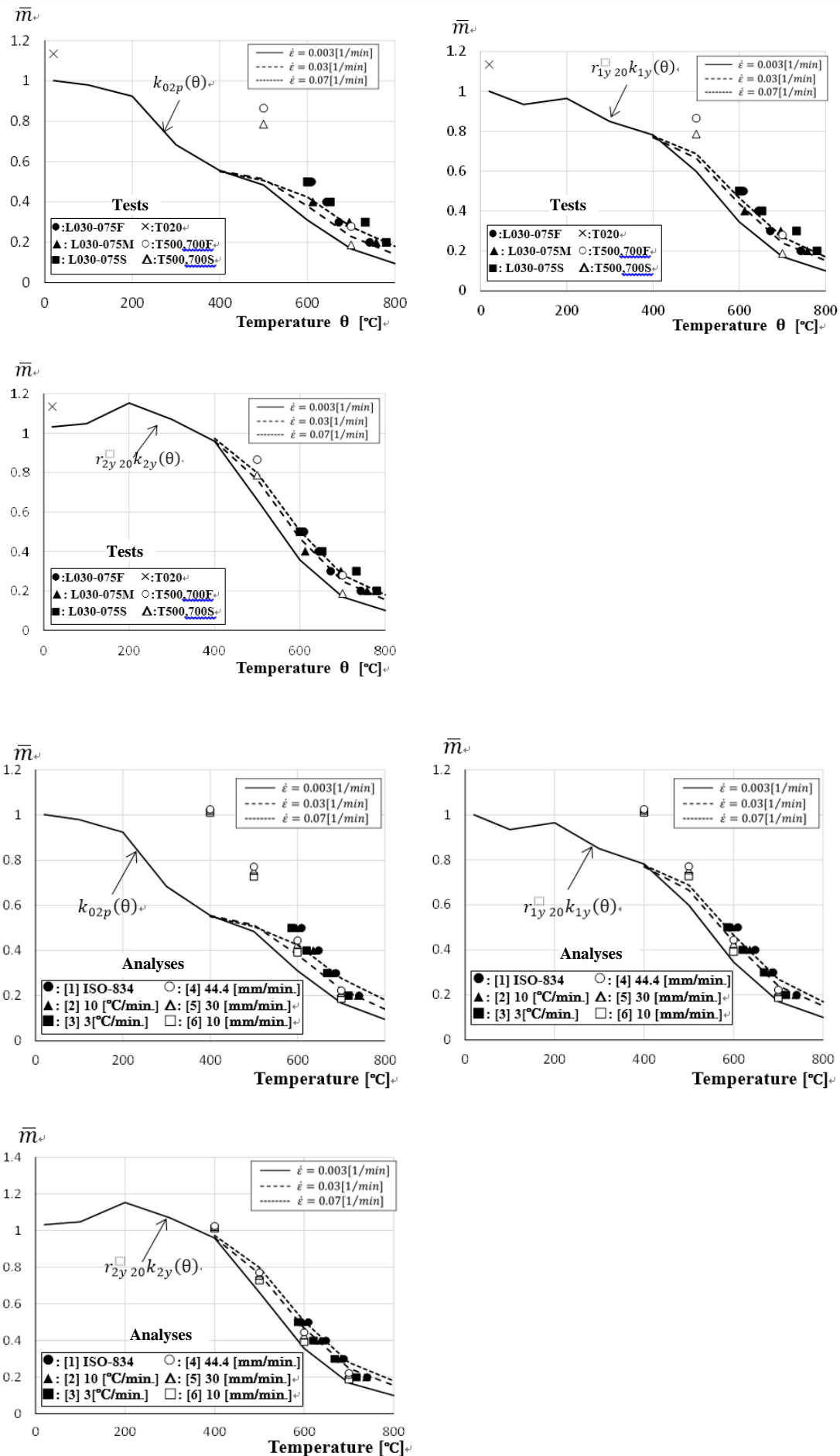


Figure 7. Bending strengths and collapse temperatures for test and analytical results

The polygonal lines as shown in Figure 7 mean the above equation (4), $\bar{m} = r_{e20}k_e(\theta)$ in the case of using the effective strengths under $\dot{\epsilon}=0.003, 0.03, 0.07$ [1/min.]

As for the test and analytical results (marks in Figure 7), the vertical and horizontal axes \bar{m} and θ are denoted by the following equations, respectively.

$$[\text{Steady state condition}] \quad \bar{m} = \frac{M_{max}}{M_{p20}}, \quad \theta = \theta_{const} \quad (5)$$

$$[\text{Transient state condition}] \quad \bar{m} = \frac{M_{const}}{M_{p20}}, \quad \theta = \theta_{ult} \quad (6)$$

Where,

M_{max} : The bending strength at $\delta^b = \delta_p^b$ at the steady state condition

M_{p20} : The full plastic moment at the ambient temperature

θ_{const} : The temperatures at the steady state condition

θ_{ult} : The collapse temperature at $\delta^b = \delta_p^b$ the transient state condition

From the comparison between the test results and the evaluated values (upper figures in Figure 7), the evaluated values using the reduction factor $k_{02p}(\theta)$ on the 0.002 off-set yield strength f_{02p} are a little smaller than both steady and transient test results (Figure 10(a)). On the other hand, the evaluated values using $k_{1y}(\theta)$ or $k_{2y}(\theta)$ under both strain rates of $\dot{\epsilon} = 0.03$ and 0.07 [1/min.] approximately correspond to the test results. It is considered that the steel beams at the collapse time ($\delta^b = \delta_p^b$) under the transient state possessed the higher the strain rate than $\dot{\epsilon} = 0.003$ [1/min.], and the bending strength and collapse temperature can be evaluated by the evaluated values using the effective strength f_{1y} or f_{2y} .

The analytical results exhibit the same tendency of the test results. The evaluated values (the lines in Figure 7 (lower side figures)) of the bending strength or collapse temperatures in the case of using the reduction factor $k_{1y}(\theta)$ or $k_{2y}(\theta)$ under both strain rates of $\dot{\epsilon} = 0.03$ and 0.07 [1/min.] approximately correspond to the analytical results.

On the other hand, the unstable behaviours such as the local buckling and lateral-torsional buckling of the heated steel beam, which have the influence on the bending strength and collapse temperature, were not considered for both analytical and test results, because those were obtained from the two dimensional beam element and rectangular cross section specimen, respectively. This paper focuses on the fundamental behaviour of the heated steel beam considering the effect of the strain and heating rate, and the various buckling behaviours of the heated steel member in the case of considering the effect of the strain and heating rates must be examined in the future research.

5 CONCLUSIONS

The steady and transient state tests using the small beam specimens at the elevated temperatures were conducted, to examine the effects that the loading and heating rates cause to the bending strengths and collapse temperatures. Furthermore, the validity of the numerical analysis using the two dimensional beam elements considering the effect of strain rate was verified by the test results. The numerical results approximately agreed with the test results, and it was reported that the bending strength and collapse temperatures with the effects of the loading and heating rates could be quantified by the effective strength obtained from the coupon tests under the various strain rates.

REFERENCES

1. Luecke, W. et. al. (2011), High-temperature tensile constitutive data and models for structural steels in fire, *NIST Technical Note 1714*, NIST

2. Knobloch, M. et al. (2013), Influence of the strain-rate on the mechanical properties of mild carbon steel at elevated temperatures, *Materials and Design* 49, 553–565
3. Alvarez Gonzalez, C. and Okabe, T. (2017), Identification of Multiplicative Viscoplasticity Model by the Date of Strain-controlled Tensile Test, *J. Structural and Construction Eng., AIJ*, 734, 605-611, *(in Japanese)*
4. Ozaki, F. and Umemura, T. (2019), Effects that Change in Strain Rate Causes to Structural Fire Resistance of a Steel Member - Formulation of Stress-Strain Relationships considering Effects of Strain Rate and Verification based on In-plane Analyses -, *the Proceedings of SEMC 2019, 1932-1937*
5. Ryan, J.V. and Robertson, A.F. (1959), “Proposed Criteria for Defining Load Failure of Beams, Floors and Roof Constructions during Fire Test”, *Journal of Research of the National Bureau of Standards-C, Engineering and Instrumentation*, Vol. 63C, No. 2
6. Architectural Institute of Japan (2018), AIJ Recommendation for Fire Resistant Design of Steel Structures *(in Japanese)*

EXPERIMENTAL AND NUMERICAL–ANALYTICAL STUDY ON STRUCTURAL BEHAVIOR OF STEEL FRAMES BASED ON SMALL-SCALE FIRE TESTS

Akinobu Takada¹, Tomohito Okazaki², Mami Saito³

ABSTRACT

This paper presents the results of an experiment involving a constant load and an elevated steel frame temperature, focusing on the redistribution of column axial force to unheated members and the results of numerical analysis to reproduce it. The specimens are steel moment-resisting frames of three stories and 2×2 spans. It is a small-scale model that is approximately 1/7 of an actual building scale. One specimen is heated only in one row of a column and beams, and the other is heated in three rows of columns and beams. Comparing the results of the two experiments, the temperature when collapse occurred is higher in the case of heating only one row of a column and beams than in the case of heating three rows. Moreover, in the case of heating only one row of a column and beams, it is confirmed that the column axial force redistributed to the unheated members. A finite element method with shell elements is used to reproduce the experiment. The results of the numerical analysis show that the collapse modes and the collapse temperature agree well with the experimental results. Furthermore, similar to the experimental results, the redistribution of the column axial force to the unheated members is confirmed in the case of heating only one row of a column and beams.

Keywords: Steel frame; finite element method; fire tests; redistribution of column axial force

1 INTRODUCTION

When a local fire occurs in a building, the collapse temperature of an entire building becomes higher than that of a single column because the axial force of heated columns is redistributed to unheated members in the building. The behaviour was observed and investigated via numerical analysis in [1, 2]. In a study that estimated the fire resistance performance of a frame using numerical analysis, the members in the frame were modelled as beam elements [1 – 6]. However, it is well known that local buckling is one of the collapse modes of a heated column [7]; therefore, using elements that enable local buckling to be reproduced is recommended such that a numerical analysis can be conducted with high accuracy. The behaviour of an entire building under fire was investigated experimentally in [6, 7]. However, few experimental studies have focused on the redistribution of column axial force.

In this study, experiments involving a constant load and an elevated temperature were conducted using two steel moment-resisting frames that have three stories and 2×2 spans. This paper focuses on the redistribution of the column axial force. One specimen was heated only one row of a column and beams, whereas the other was heated in three rows of columns and beams. The specimens were small-scale models that were approximately 1/7 of an actual building scale. In addition, the experiments were numerically

¹ Takada Akinobu, TAKENAKA Corporation
e-mail: takada.akinobu@takenaka.co.jp

² Tomohito Okazaki, TAKENAKA Corporation
e-mail: okazaki.tomohito@takenaka.co.jp

³ Mami Saito, TAKENAKA Corporation
e-mail: saitou.mamia@takenaka.co.jp

simulated via the finite element method using shell elements. The accuracy of the numerical analysis was verified by comparing it with the experimental results.

2 FIRE TEST OF STEEL FRAMES: WITH REDISTRIBUTION OF COLUMN AXIAL FORCE

2.1 Specimen specifications and experimental conditions

The elevation views of the specimens are shown in Fig. 1. The specimens were a steel moment-resisting frame of three stories and 2×2 spans. An overview of the experiments is shown in Fig. 2. The specimens were small-scale models whose floor height was approximately 1/7 that of a full-scale building, the floor height was 0.6 m, and the span length was 1 or 1.5 m. Table 1 shows the cross-sectional properties. The cross-sectional sizes of the column and beam were selected to be the smallest in their weldable range. Therefore, the cross-sectional size of the beam was larger than that of the column in comparison with that of actual-scale buildings. This means that the deformation restraint effect by the beam on the column was higher comparison with that of actual-scale buildings. Moreover, the ratio of the cross-section width to the plate thickness of the column was 16.7, which is lower than that of actual-scale buildings. This means that the local buckling of the column in the specimen will not occur easily compared with actual-scale buildings. Therefore, although the experimental results in this study cannot be directly used as a reference for the design of an actual-scale building, it can quantitatively confirm the column axial force redistribution by experiments. The materials of the specimens were STKR400 for columns and SS 400 for beams, which are steel materials based on the Japanese Industrial Standards. STKR is a cold-formed steel, whereas SS is a hot rolled steel. Table 2 shows the material test results for the steel at room temperature. Fig. 3 shows the stress–strain relationship from material tests. In this study, material tests were performed on three test pieces, and the mean values are shown in Table 2. The beam–column joint was manufactured to be of the diaphragm type with steel plates of thickness 9 mm (SS400). Steel base plates of thickness 25 mm were welded to the bottom of the specimens and fixed on the test bed with steel rods. As shown in Fig. 4, two specimens were used for two experiments with different heating areas. In the first step of both experiments, constant vertical loads (as shown by yellow arrows in Fig. 4) were subjected to the top of the three columns. In the second step, the area represented in red in Fig. 4 was heated. In the experiment termed ‘Three-frame heating’, three columns of the second floor and the beams around the columns were heated, as shown in Fig. 4(a). Under this heating condition, no unheated members were available to redistribute the axial force of the heated column through the X-axis beam. In the experiment termed ‘One-frame heating’, only one column of the second floor and the beams around the column were heated, as shown in Fig. 4(b). Under this heating condition, the axial force of the heated column is expected to be redistributed to the unheated columns through the X-axis beam. The load per column was 385 kN, which is equivalent to 75% of the column yield strength of 421 N/mm². Such a high axial force was used to collapse the specimens below 600 °C, which is the performance limit of the electric furnace. The electric furnace was a silver box, as shown in Fig. 2. The details of the electric furnace are shown in Fig. 1. The electrically heated wire to heat the beams was placed 140 mm below the bottom flange of the beams, and that to heat the columns was placed 148 mm from the column surface of the inner side of the specimen. The heating area of the columns was 340 mm from the bottom flange surface of the upper beams. The heating area of the beams is shown in Fig. 1. The electric furnace was supported by frames that were separate from the specimens. To prevent the electric furnace from interfering with the deformation of the specimen, a clearance was provided around the electric furnace wall where the specimen penetrated, and it was filled with alkaline earth silicate (AES) wool. The specimens did not have a concrete slab nor fire protection; however, only the upper surface of the heated beams was coated with AES wool of thickness 50 mm. In this condition, the beam in the presence of the concrete slab and the beam of the specimen have approximately the same temperature distribution. The heating control was manual, and it was controlled such that all heated members exhibited a uniform temperature. Because the specimen did not have fire protection and the plate was thin, it was assumed that the velocity of the temperature increase did not significantly affect the collapse behaviour. The temperature measurement point is shown by × in Fig. 1. K-type thermocouples were installed in the centre of the heating length of the column and in the centre of the span of the beams. Displacement was measured in each beam–

column joint. In the heating area, the measuring point was on the quartz glass tube extended from the beam–column joint to the outside of the electric furnace.

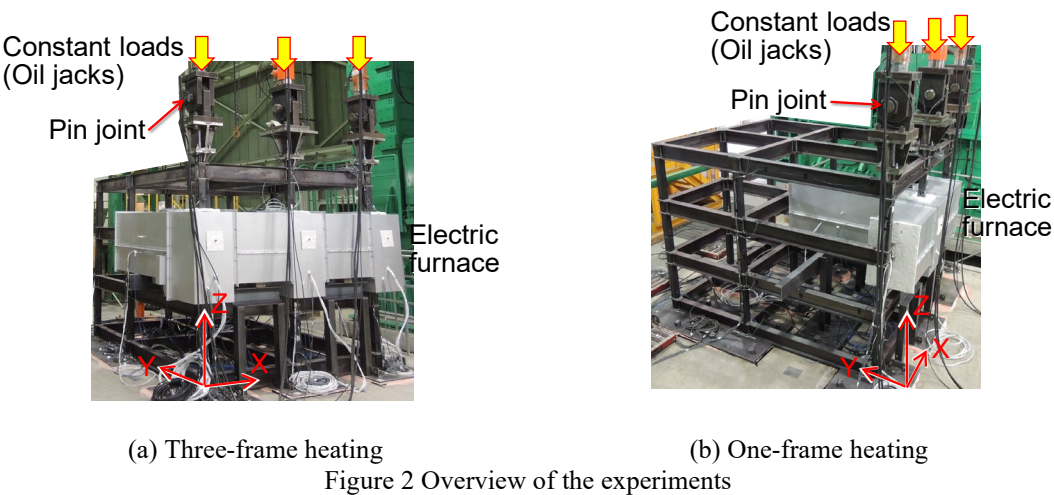
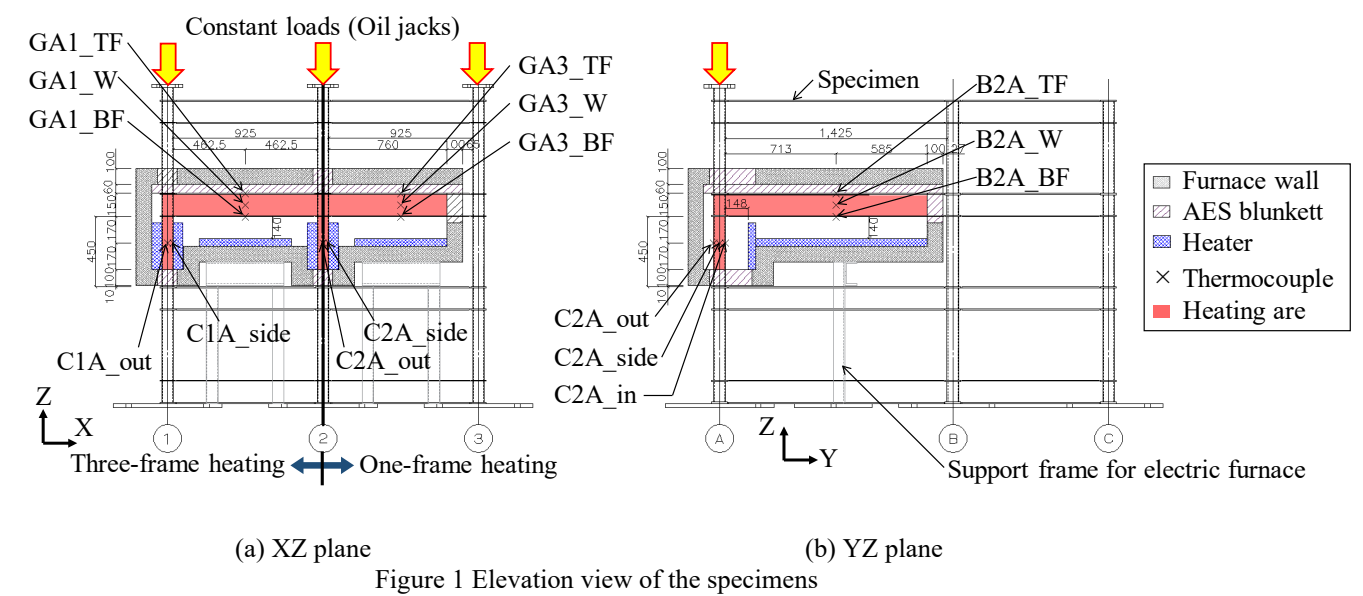


Table 1 Cross-sectional properties

Element	Shape (mm)	Cross-section area (mm ²)	Second moment of area (mm ⁴)		Radius of gyration (mm)		Product standard name
Column	Box-75×75×4.5	1,217	98.6×10 ⁴		28.5		STKR400
Beam	H-150×75×5×7	1,785	666×10 ⁴	49.5×10 ⁴	61.1	16.6	SS400

Table 2 Mechanical properties of steel at room temperature (mean value of material test results)

Element	Young’s modulus (GPa)	Yield stress (MPa)	Tensile strength (MPa)
Column	200	421	477
Web (Beam)	195	321	417
Flange (Beam)	201	288	404

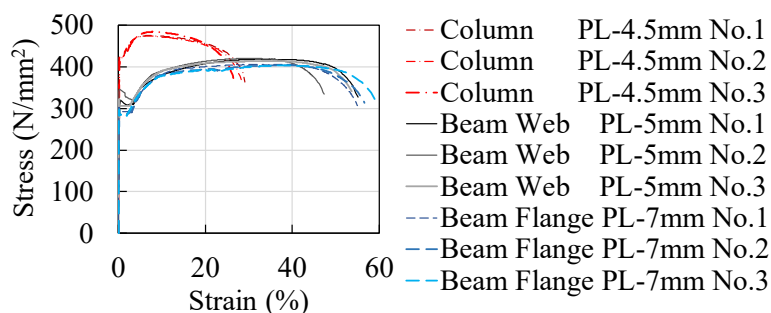
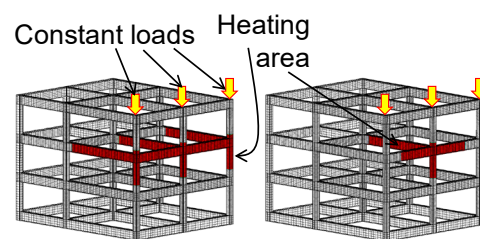


Figure 3 Results of material tests at room temperature

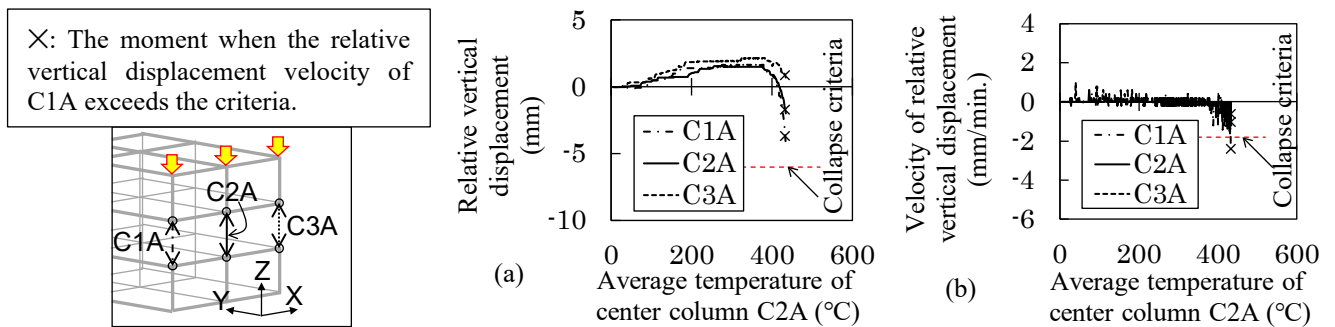
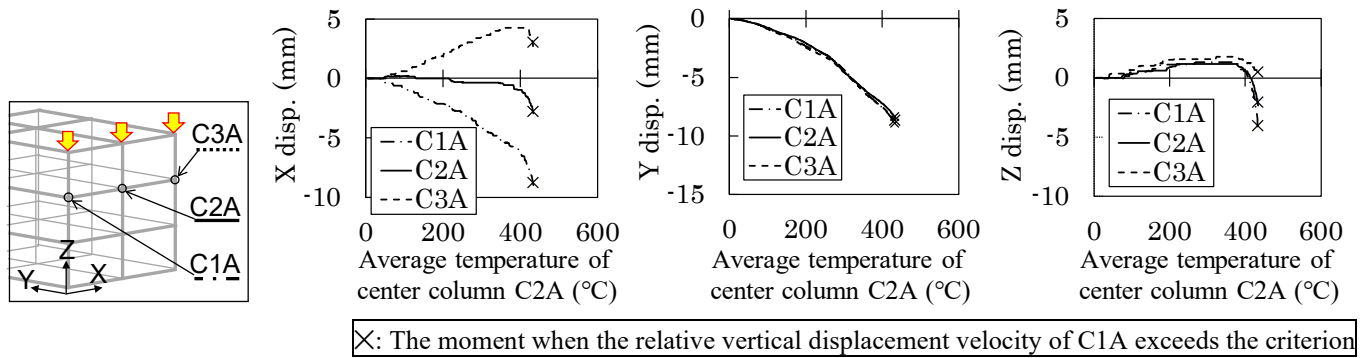
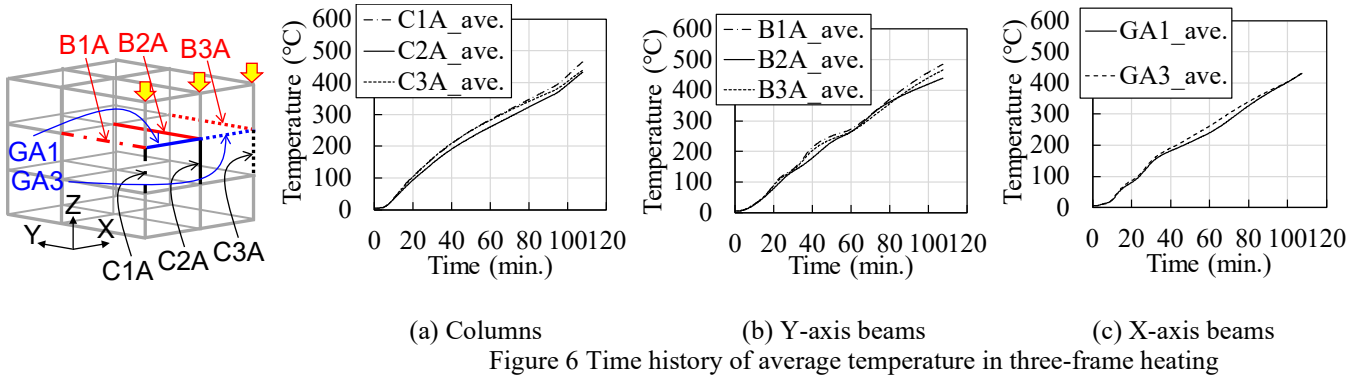
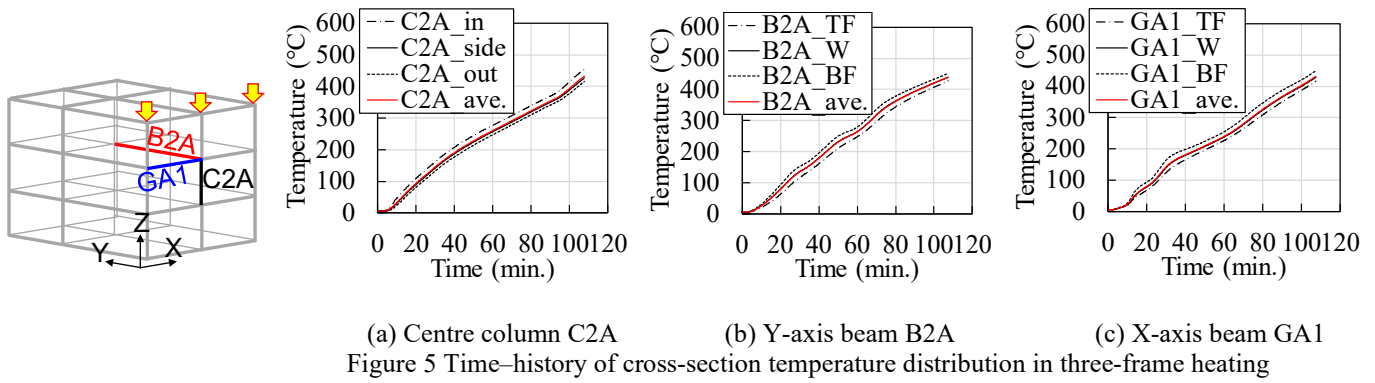


(a) Three-frame heating (b) One-frame heating
Figure 4 Heating area

2.2 Experiments results

2.2.1 Experimental results of three-frame heating

Fig. 5 shows the results of the temperature–time history in the cross-section of some heated members. Fig. 5 (a) shows the temperature–time history of a heated column. The column temperature decreases in the order of the heated surface (C2A_in), side surface (C2A_side), and rear surface (C2A_out) of the heater, and the temperature difference between the heated and rear surfaces was approximately 50 °C, which was the maximum value. Figs. 5 (b) and (c) show the temperature–time history of a heated beam. The beam temperature decreased in the order of bottom flange (BF), web (W), and top flange (TF), and the temperature difference between the BF and TF was approximately 50 °C, which was the maximum value. Fig. 6 shows the average temperature of the three temperature measurement points of the cross-section of each member. As shown in Fig. 6 (a), the temperature of the centre column (C2A) was slightly lower than that of the other two columns. Fig. 7 shows the relationship between the absolute displacement of the top of the second-storey columns and the average temperature of the centre column. The displacement at the start of heating was denoted as 0. The legend of Fig. 7 is shown on the extreme left; however, the × symbol is explained in Fig. 8. As shown in Fig. 7 (a), the thermal expansion of the heated beam in the X-axis direction increased the X-axis displacement of the top of the second-storey corner columns symmetrically (in the positive and negative directions). However, from approximately 400 °C, the top of all three heated columns began to rapidly displace in the negative direction of the X-axis. This behaviour was due to the formation of plastic hinges at the ends of the columns and beams, where the yield stress decreased with elevated temperature; hence, the formation of a storey collapse mode in the XZ plane was expected. As shown in Fig. 7 (c), the Z-axis displacement increased rapidly downward from approximately 400 °C for all three heated columns. Fig. 8 shows the relative vertical displacement and relative vertical displacement velocity of the top and bottom of the second-storey column subjected to load and heating. The horizontal axis of Fig. 8 represents the average temperature of the centre column. Because only the second storey was heated in the frame, it is appropriate to judge the collapse not by the absolute displacement, but also by the relative vertical displacement corresponding to the elongation of the second-storey column. The dashed red line in Fig. 8 shows the column collapse criterion according to ISO 834-1 [8], where the criterion of the vertical displacement is ($h/100 = 6$ mm) and the vertical displacement velocity is ($3h/1000 = 1.8$ mm/min), where h is the storey height. When the centre column temperature was 433 °C, the relative vertical displacement velocity exceeded the collapse criteria in the corner column C1A. The same time is indicated by the black cross mark ‘×’ in Figs. 7 and 8. In the three-frame heating, because the jig that connected the top of the specimen with the hydraulic jack was broken (see Fig. 9) immediately after the × mark, the experiment was terminated. Fig. 10 shows the relationship between the average axial strain at the column bottom of the specimen and the average temperature of the centre column. In the column at the bottom of the specimen, each of the strain gauge was adhered to four planes of a square steel pipe column 50 mm above the upper flange of the lowermost beams. In Fig. 10, the strain at the start of heating is denoted as 0. As shown in Fig. 10, the average axial strain of the lowermost column did not change significantly from the start of heating to the end of the experiment. This means that the redistribution of the column axial force was slight until the vertical displacement velocity of the column reached the collapse criteria.



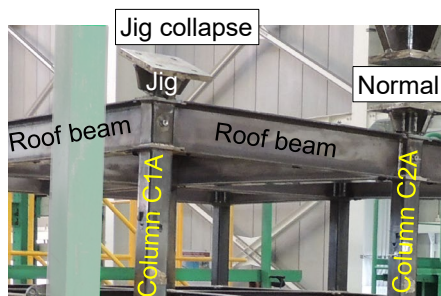


Figure 9 Jig collapse of three-frame heating

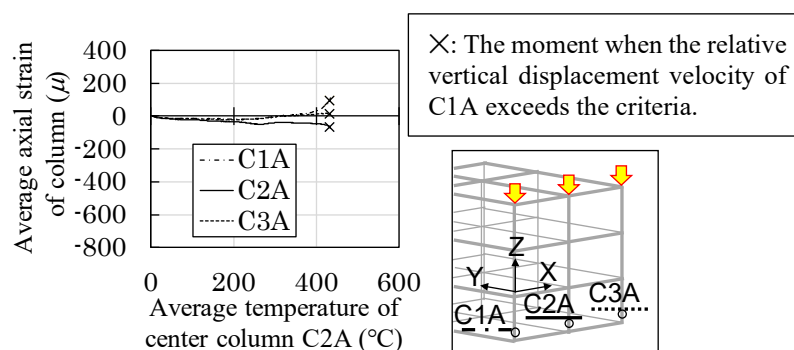


Figure 10 Relationship between column axial strain and average temperature of mid-span column of three-frame heating

2.2.2 Experimental results of one-frame heating

In Fig. 11, the average values of the temperatures measured using three thermocouples installed in the central cross-section of the heating area of each member are shown for the one-frame heating case. Although not shown in the graph, similar to the three-frame heating, a maximum temperature difference of approximately 50 °C was observed on the surface facing the heater and on the opposite surface at the temperature before averaging was performed. The arrangement of the heaters is shown in Fig. 1, and the heating area is shown in Fig. 4 (b). As shown in Fig. 11, the temperature difference between the column and beam in the X-axis direction was small, but the temperature of the beam in the Y-axis direction was not as stable as those of the other members. Furthermore, at certain times, the temperature was approximately 50 °C higher than that of the column. Fig. 12 shows the relationship between the absolute displacement of the top of the second-storey column subjected to load and the average temperature of the centre column C2A under heating. Fig. 13 shows the relative vertical displacement and relative vertical displacement velocity of the top and bottom of the second-story column subjected to load. The horizontal axis of Fig. 13 represents the average temperature of the centre column C2A. In the one-frame heating, when the centre column temperature was 469 °C, the velocity of the relative vertical displacement (shrinkage) of the second-story centre column, which was subjected to load and heating, exceeded the collapse criteria of 1.8 mm/min. The collapse time is indicated by the × mark in Figs. 12 and 13. Similar to the case of three-frame heating, as shown in Fig. 12(a), the top of the corner columns spread symmetrically according to the thermal expansion of the beam in the X-axis direction. However, the storey collapse mode, which is similar to the three-frame heating, did not occur, and the displacement in the X-axis direction of the top of the three columns did not rapidly increase after the displacement velocity exceeded the criterion. Comparing Figs. 8(a) and Fig. 13(a), the thermal expansion of the column from the one-frame heating was smaller than that from the three-frame heating. This occurred because, since only the centre column was heated, thermal expansion was suppressed by the unheated members in the one-frame heating. Fig. 13 (a) shows that at the centre column C2A, the relative vertical displacement changed from elongation to shrinkage before the velocity reached the collapse criteria. This was due to the occurrence of local buckling at the centre column, as shown in Fig. 14. Fig. 15 shows the relationship between the average axial strain of the columns at the bottom of the specimen and the temperature of the centre column C2A under heating. The strain at the beginning of heating was denoted as 0. Fig. 15 shows that the compressive strain of the centre column increased owing to thermal expansion until the temperature of the centre column reached 400 °C. However, when the temperature exceeded 400 °C, the tensile strain increased in the centre column and the compressive strain increased in the two corner columns before the collapse criterion was reached. This means that the axial force of the centre column was redistributed into two corner columns. However, this does not imply that all the compressive axial forces of the centre column were redistributed to the corner columns, because the magnitude of the strain if the load per column (385 kN) becomes 0 with elastic unloading is approximately 1500 μ. Comparing the three- and one-frame heating based on the graphs of axial strain of three columns subjected to loads, as shown in Figs. 10 and 15, it is clear that the column axial force did not redistribute significantly in the three-frame heating, whereas it occurred more significantly in the one-frame heating. Furthermore, when the shrinkage velocity of the column reached the collapse

criterion, the temperature of one-frame heating (469 °C) was higher than that of three-frame heating (433 °C).

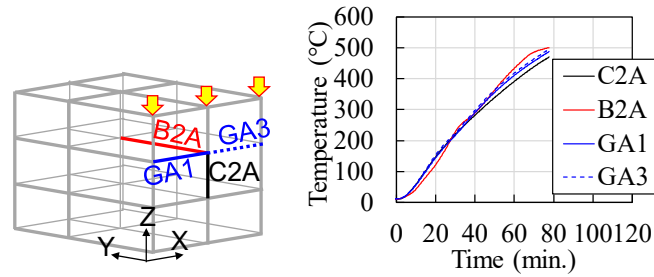


Figure 11 Time history of average temperature in one-frame heating

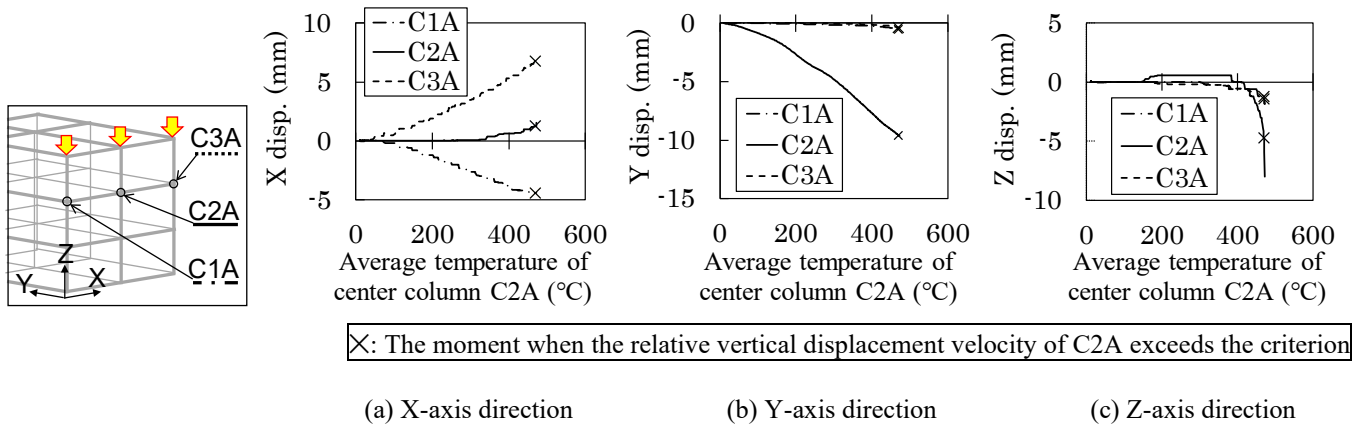


Figure 12 Relationships between displacement and average temperature of centre column (C2A) in one-frame heating

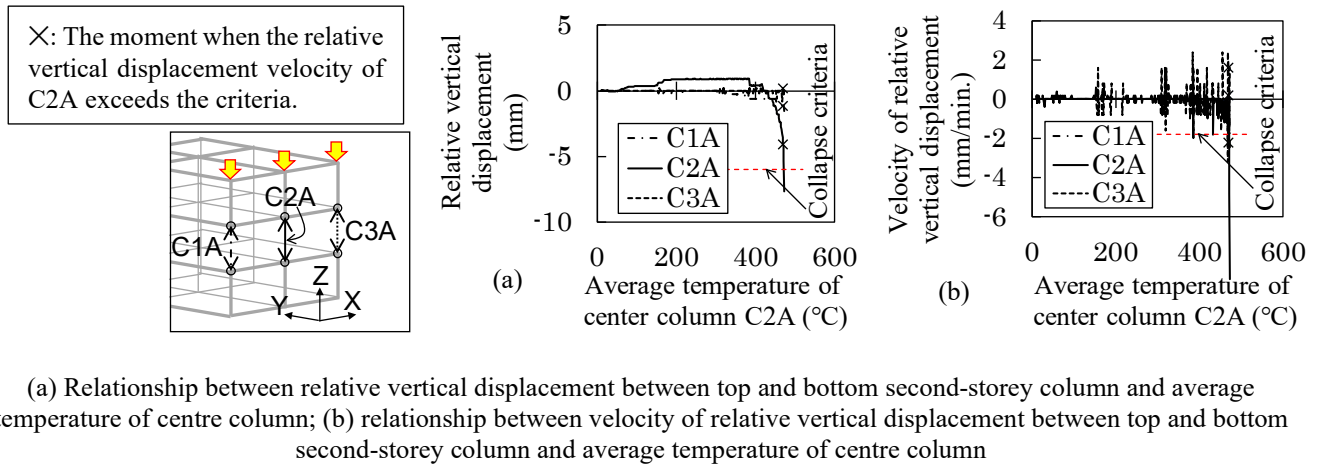


Figure 13 Comparison between collapse criterion of column and experiment results in one-frame heating

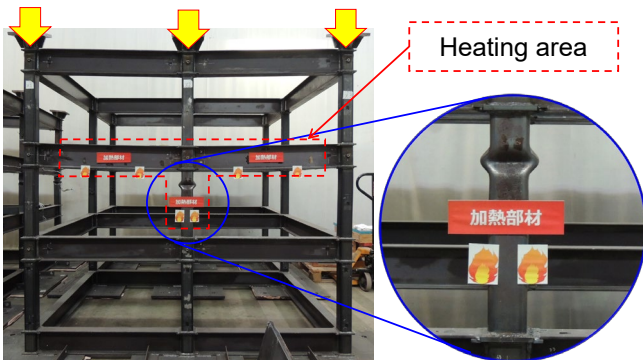


Figure 14 Specimen of one-frame heating after cooling

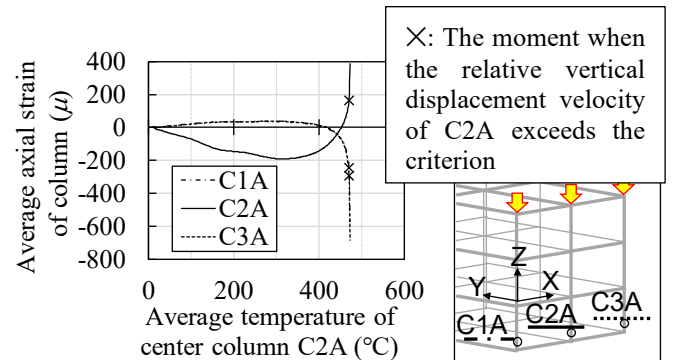


Figure 15 Relationship between average column axial strain and average temperature of centre column in one-frame heating

3 NUMERICAL ANALYSIS

3.1 Numerical analysis models and conditions

The finite element method and the static implicit solver (Abaqus/Standard) of Abaqus ver. 2018 were used for numerical analysis to reproduce the experimental results. The numerical analysis considered large deflections and the elasto–plastic behaviour. In the numerical analysis, as in the experiment, heating was started after loading three concentrated loads, as shown in Fig. 16. Fig. 16 shows the numerical analysis models. The specimens were modelled as shell elements (element name is S4R), and they were segregated into five elements in the plate thickness direction. The columns were segregated into four elements in the width direction to accurately reproduce the local buckling waveform. However, some members that were not heated had a lower mesh density compared with the previous description. Although the initial imperfection was not intentionally assigned to the numerical models, the mesh segregation was asymmetrical when the mesh was automatically segregated; consequently, it became the numerical initial imperfection. However, this occurred only in the unheated members, and the degree of asymmetry was slight. The floor height, span length, and member section size were defined to be the same as in the experiment, but the rounded corners of the column cross-section were not modelled. The load per column was set such that the stress obtained by dividing the load by the column cross-sectional area of the numerical analysis model was 75% of the yield stress. All nodes at the bottom of the numerical analysis model were fixed to all degrees of freedom. The red parts in Fig. 16 represent the heating area in the numerical analysis and correspond to the heating area shown in Fig. 1. Heat transfer analysis was not conducted, and the temperature in the heating area increased uniformly. The temperature of the unheated area was constant at 20 °C.

Fig. 17 shows the reduction factors of the mechanical properties with reference to Eurocode [9]. Beams were modelled using hot-rolled properties, whereas columns were modelled using cold-worked properties. Fig. 18 shows the stress–strain relationship at elevated temperatures in the numerical analysis. Similarly, the stress–strain relationship was set with reference to Eurocode [9]. The material test results shown in Fig. 2 were used as the mechanical values at room temperature. Because the column was a cold-worked material, strain hardening was not considered. It was assumed that strain hardening occurred in the web and flange of the beam. The degradation of strength due to material destruction was not considered. The coefficient of thermal expansion, shown in Fig. 19, was also referenced from Eurocode [9]. The values shown in Fig. 19 were obtained by defining the reference temperature at 20 °C and converting the equation of thermal strain shown in [9]. The conversion formula is expressed as shown in Equation (1).

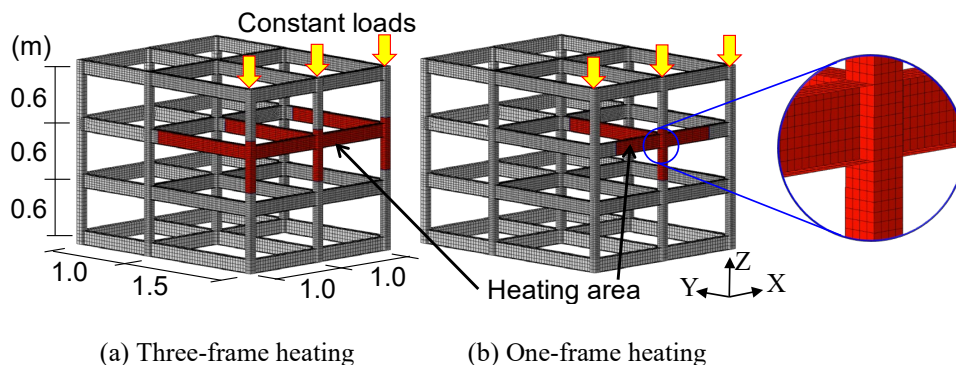
$$\alpha = \frac{\Delta l/l}{\theta - 20} = \frac{-2.416 \times 10^{-4} + 1.2 \times 10^{-5} \theta + 0.4 \times 10^{-8} \theta^2}{\theta - 20}, \quad (1)$$

where α is the coefficient of thermal expansion for $20\text{ }^{\circ}\text{C} < \theta \leq 750\text{ }^{\circ}\text{C}$,

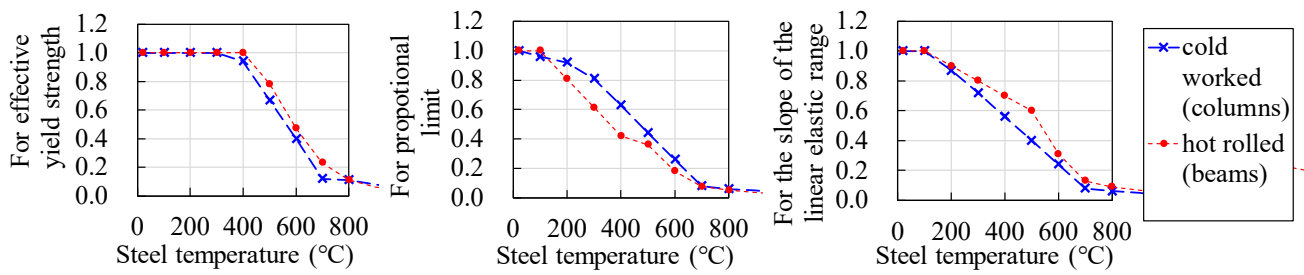
l is the length at 20 °C of the steel member;

$\Delta l/l$ is the temperature-induced elongation of the steel member;

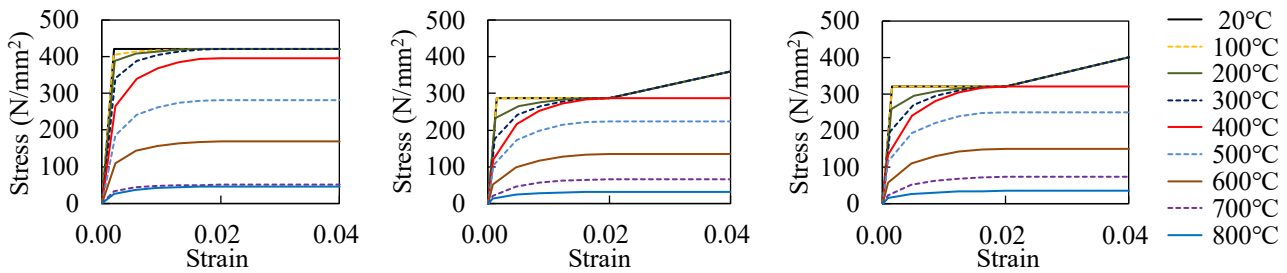
θ is the steel temperature (°C).



(a) Three-frame heating (b) One-frame heating
Figure 16 Overview of numerical analysis models



(a) Effective yield strength (b) Proportional limit (c) Slope of linear elastic range
Figure 17 Reduction factors of mechanical properties with reference to Eurocode [9]



(a) Column (b) Flange of beam (c) Web of beam
Figure 18 Stress-strain relationship for numerical analysis with reference to Eurocode [9]

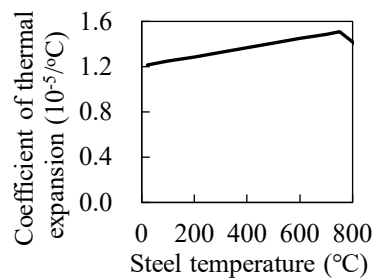


Figure 19 Coefficient of thermal expansion for numerical analysis

3.2 Results of the numerical analysis

Fig. 20 shows contour diagrams of the Mises stress at the end of the numerical analysis. The drawing magnification of the deformation was 5X. The numerical analysis was terminated because a convergent solution could not be obtained. This was due to unstable phenomena such as buckling. From the deformation diagram of the three-frame heating shown in Fig. 20 (a), it was confirmed that the columns were sloped owing to the thermal expansion of the heated beams. However, as shown by the deformation diagram in Fig. 20 (a), a clear collapse mode could not be confirmed. From the deformation diagram of the one-frame heating shown in Fig. 20 (b), it is clear that the heated centre column of the second storey buckled, similar to the experimental results shown in Fig. 14. The characteristic stress distribution in the bending yield beam can be confirmed from Fig. 20 (b), i.e., by observing the Mises stress contour diagram of the X- and Y-axis direction beams at the roof floor. This indicates that the axial force of the centre column subjected to the load and heating was redistributed to the unheated columns through the unheated uppermost beams in the one-frame heating.

Figs. 21 and 22 show the relationship between the absolute displacement of the second-storey column subjected to load and the average temperature of the heated centre column. The displacement at the start of heating is denoted as 0 in Figs. 21 and 22. The displacement output points in the numerical analysis are the centre of the column-beam joint of the second-storey column head. The numerical analysis of the three-frame heating ended when the vertical displacement reached -4.2 mm at C2A, and that of the one-frame heating ended when the vertical displacement reached -14.3 mm at C2A. As shown in Fig. 21, in both the three- and one-frame heating, the results of the numerical analysis approximately reproduced the experimental results. Because the shape of the numerical models was symmetrical, it was not a significant

problem that the displacement in the X-direction in the numerical analysis appeared in the opposite direction to that of the experiment. As shown in Figs. 21 and 22, a comparison between the experimental and numerical results shows a slight difference in the following two aspects: the temperature at which the displacement in the X-direction began to increase, and the manner in which the Z-axis displacement increased after the displacement began to increase suddenly. These differences were affected by the uniform temperature in the heating area and the lack of modelling of the rounded corners of the column cross-section. Fig. 23 shows the relationship between the average stress in the column axial direction and the heated column temperature in the numerical analysis. Compression is denoted as negative in the graph. The average stress is the mean value of the stress at the integration point in the shell element of the column one mesh above the beam–column joint at the bottom of the specimen. The corner column is the leftmost column in Fig. 20. Because the load corresponding to 75% of the yield stress was applied to the column head, the average stress at the start of heating was approximately $421 \times 0.75 = 316 \text{ N/mm}^2$. In the one-frame heating shown in Fig. 23 (b), the compressive stress of the centre column increased from the start of heating until the temperature exceeded 400°C because of the thermal stress generated with temperature elevation, whereafter the compressive stress of the centre column decreased, and the compressive stress of the corner column increased. This occurred because the X-axis direction beam of the top layer of the specimen connecting the centre column and the corner column redistributed the axial force of the centre column to the corner column by bending and shearing. Meanwhile, the average stress of the three-frame heating (as shown in Fig. 23 (a)) indicated a slight change with temperature elevation. The relationship between the average axial stress of the column and the temperature of the heating area in the numerical analysis shown in Fig. 23 is similar to the relationship between the average axial strain of the column and the average temperature of the centre column in the experiments shown in Figs. 10 and 15.

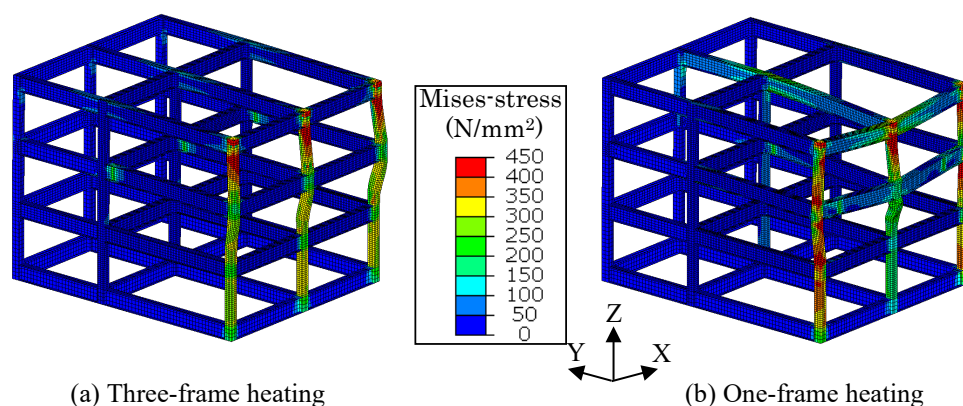


Figure 20 Mises stress and 5X deformation diagram at the end of numerical analysis

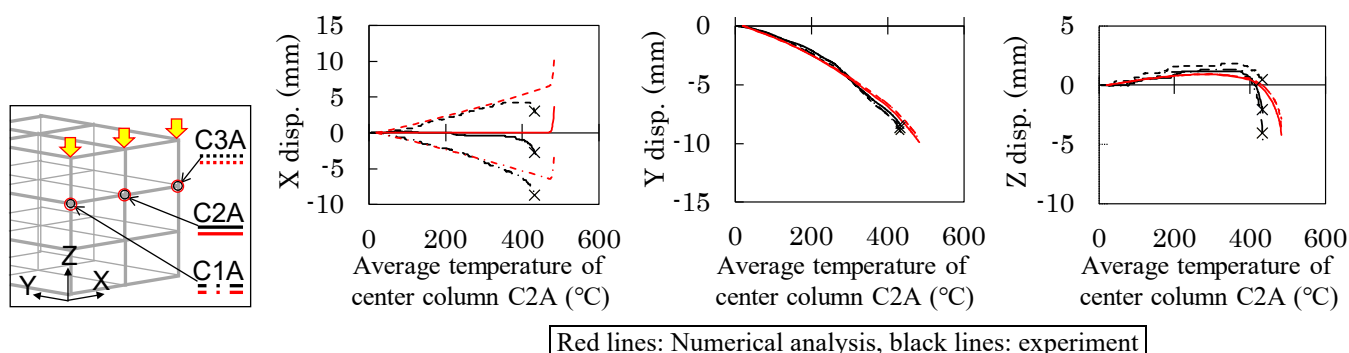
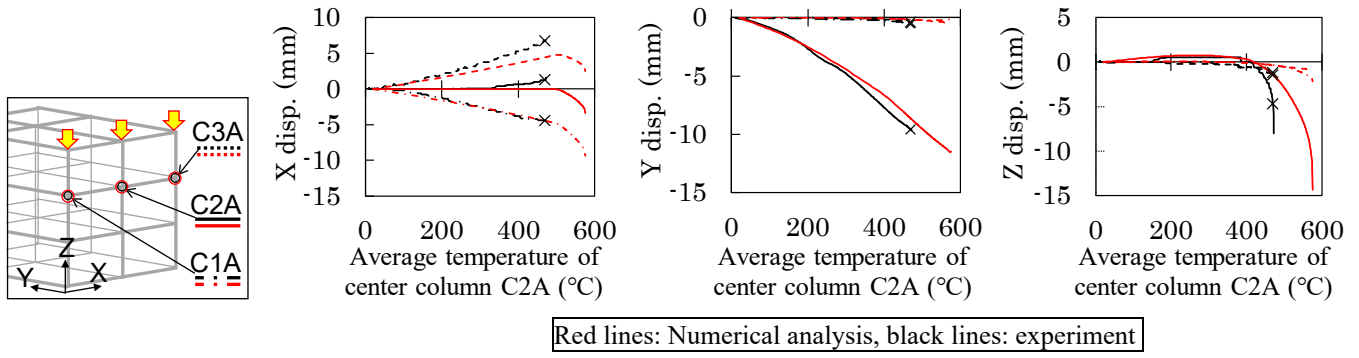


Figure 21 Verification of numerical analysis (relationships between displacement and average temperature of centre column (C2A) in three-frame heating)



(a) X-axis direction (b) Y-axis direction (c) Z-axis direction
Figure 22 Verification of numerical analysis (relationships between displacement and average temperature of centre column (C2A) in one-frame heating)

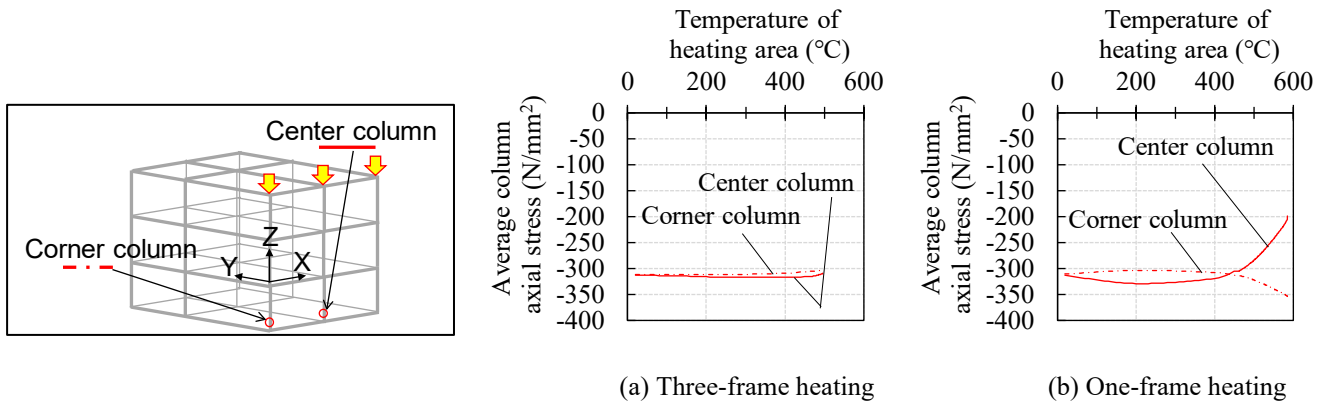


Figure 23 Relationship between average column axial stress and temperature of centre column in numerical analysis

4 CONCLUSIONS

This study focused on the redistribution of the axial force of heated columns to unheated members. The results of an experiment involving a constant load and the heating of steel frames were provided. The specimens used were steel moment-resisting frames of 3 stories and 2×2 spans, and they were small-scale models of approximately 1/7 the actual building scale. Two experiments were conducted: one in which one column and the beams around it were heated (one-frame heating), and the other in which three columns and the beams around them were heated (three-frame heating). The conclusions obtained from the experiment are as follows:

1. In the one-frame heating, the redistribution of the column axial force corresponding to a strain of a few hundred micrometres was confirmed with the temperature elevation of the heated column; however, it was barely confirmed in the three-frame heating
2. By comparing the temperatures of the one- and three-frame heating when the shrinkage velocity of the column reached the collapse criterion, it was shown that the temperature of the one-frame heating (469°C) was higher than that of the three-frame heating (433°C).

Furthermore, numerical analyses were conducted via a finite element analysis using shell elements to reproduce the experimental results. The results of the numerical analysis demonstrated that the deformation of the specimen agreed well with the experimental results. Moreover, the redistribution of the axial force of the heated column to the unheated members was confirmed from the one-frame heating and experimental results.

ACKNOWLEDGMENT

The authors would like to acknowledge Dr. Kohno, Professor, Tokyo University of Science, for his advice regarding the experimental design.

REFERENCES

1. Flint, G., Usmani, A., Lamont, S., Lane, B., & Torero, J., Structural response of tall buildings to multiple floor fires, *Journal of Structural Engineering*, Vol. 133, Issue 12, pp. 1719-1732, 2007.
2. Sun, R., Huang, Z., & Burgess, I. W., The collapse behaviour of braced steel frames exposed to fire, *Journal of Constructional Steel Research*, 72, pp. 130-142, (2012). doi:10.1016/j.jcsr.2011.11.008
3. Cheng, W., & Mak, C. K., Computer analysis of steel frame in fire, *Journal of the Structural Division*, 101(4), pp. 855-867, (1975). Retrieved from www.scopus.com
4. Najjar, S. R., & Burgess, I. W., A nonlinear analysis for three-dimensional steel frames in fire conditions, *Engineering Structures*, 18(1), pp. 77-89, (1996). doi:10.1016/0141-0296(95)00101-5
5. Huang, Z., Burgess, I. W., & Plank, R. J., Three-dimensional analysis of composite steel-framed buildings in fire, *Journal of Structural Engineering*, 126(3), pp. 389-397, (2000). doi:10.1061/(ASCE)0733-9445(2000)126:3(389)
6. Pyl, L., Schueremans, L., Dierckx, W., & Georgieva, I., Fire safety analysis of a 3D frame structure based on a full-scale fire test, *Thin-Walled Structures*, 61, pp. 204-212, (2012). doi:10.1016/j.tws.2012.03.023
7. British Steel Plc., The behaviour of multi-storey steel framed buildings in fire, Retrieved from https://www.steelconstruction.info/images/0/0d/The_Behaviour_of_Multi-storey_Steel_Framed_Buildings_in_fire.pdf
8. ISO 834-1: 1999(E). Fire-resistance tests – Elements of building construction – Part 1: General requirements.
9. EN 1994-1-2 (2005): Eurocode 4: Design of composite steel and concrete structures – Part 1-2: General rules – Structural fire design, CEN, 2005.

INVESTIGATION OF THE PERFORMANCE OF A NOVEL DUCTILE CONNECTION WITHIN BARE-STEEL AND COMPOSITE FRAMES IN FIRE

Yu Liu¹, Shan-Shan Huang², Ian Burgess³

ABSTRACT

In order to improve the performance of connections and enhance the robustness of structures in fire, a novel, axially ductile connection has been proposed. The component-based models of bare-steel ductile connection and composite ductile connection have been proposed, and incorporated into the software Vulcan to facilitate global frame analysis. These component-based models are validated against detailed Abaqus FE models. A series of 2-D bare-steel frame models and composite frame models with ductile connections, rigid connections, and pinned connections, have been created using Vulcan to compare the fire performance of ductile connection with other connection types in bare-steel and composite structures.

Keywords: Fire; component-based model; ductility; steel connection; composite connection

1 INTRODUCTION

The Cardington full-scale fire tests [1] in 1995-96 indicated that standard connections were potentially the weakest parts of a steel-framed or composite structure. Connection failures subsequently occurred in the collapse of the World Trade Centre buildings [2] in 2001. Failure of connections in a fire accident may lead to the detachment of connected beams, causing collapse of floor panel and the spread of fire into adjacent compartments, buckling of columns, and even the progressive collapse of the entire building. Connections play a crucial role in maintaining structural integrity, by tying structural members together. However, current commonly-used connection types lack the push-pull ductility required to accommodate either the compressive effects due to the constraint of thermal expansion of connected beams in the early stages of a fire, or the tensile effects caused by the catenary action of the connected beams when most of the steel strength has been lost at high temperatures. In order to improve the performance of connections and enhance the robustness of structures in fire, a novel ductile connection has been proposed by the authors [2-6]. Additional axial ductility is provided to a connection which is essentially a web-cleat by the inclusion of a semi-cylindrical zone in the connection leg which is attached to the beam web.

Traditional research on connection behaviour is largely limited to moment-rotation characteristics, which has been shown to be almost irrelevant to full structures in fire conditions. Connections undergo different combinations of loading at different stages of a fire. Numerical modelling is a most accessible way of reproducing these complex loading combinations, because experiments need to cover a large range of combinations of axial force and rotations over a range of temperatures, and are expensive to conduct. However, due to the time-consuming nature of model building and computational runtimes, detailed finite element approaches using solid elements are not suitable to be used, particularly where global frame

¹ Mr. Yu Liu, University of Sheffield
e-mail: yliu230@sheffield.ac.uk, ORCID: <https://orcid.org/0000-0001-7468-1089>

² Dr. Shan-Shan Huang, University of Sheffield
e-mail: s.huang@sheffield.ac.uk, ORCID: <https://orcid.org/0000-0003-2816-7104>

³ Prof. Ian Burgess, University of Sheffield
e-mail: ian.burgess@sheffield.ac.uk, ORCID: <https://orcid.org/0000-0001-9348-2915>

analysis needs to be conducted. An alternative, and more economical, strategy for conducting large structural frame analyses in fire conditions is the use of a high-temperature component-based method to simulate the connection behaviour within a structural finite element program. Component-based modelling strategies, and component models of traditional steelwork connections, have been proposed as a result of studies [7-16] over many years by researchers at the University of Sheffield. Leston-Jones [7] developed a component-based model, including components representing the column flange in bending, bolts in tension, endplate in bending and column web in compression to simulate the high-temperature rotational behaviour of flush end-plate connection. Block [9] used an analytical model of a T-stub developed by Spyrou [8] to represent the tension bolt rows, and a simplified analytical model of the column web in compression to represent the compression zone of the connection in his component-based model for end-plate connections. Sarraj [10, 11] conducted a series of finite element simulations, and proposed equations to describe the bearing and shearing behaviour of fin-plate connections. Yu [12] proposed and validated a yield-line based model for end-plate connections. Yu [13] also developed a component-based model for web-cleat connections including a mechanical model based on simple plastic theory to predict the behaviour of web cleats subjected to tying forces. Continuing Block and Yu's work, Dong [14] further developed a used-defined connection model, a flush end-plate connection model and a reverse-channel connection model, all for elevated temperatures. In addition, Hu [15] developed a flexible end-plate connection model, and Taib [16] developed a model for fin-plate connections based on the equations previously proposed by Sarraj [10]. The component-based model of the novel ductile connection has been developed by the authors [4-6] in the context of steel-framed buildings, as the most recent stage of this progression. It has been incorporated into the software Vulcan, which is used to carry out 3D modelling and robustness assessment of structures in fire.

The structural behaviour of composite connections is quite different from that of bare-steel connections, due to the continuity of the composite slab and its reinforcing mesh across the connection. At elevated temperatures, the composite slab acts as insulation to the reinforcement, reducing its temperature to very low levels compared with the steel-to-steel part, and thus enhancing its performance. Apart from this, the composite slab restrains the thermal expansion of steel beam in the initial stage of the fire, leading to thermal bowing, which also affects the deformation of connection. Up to now, only limited researches can be found on the structural performance of composite connections in fire. Leston-Jones [7, 17] carried out tests on composite flush end-plate connections to obtain their moment-rotation characteristics. Continuing his work on rotational behaviour, Al-Jabri [18] conducted high-temperature tests on composite flexible end-plate connections and developed component-based models of these connections. Li et al. carried out tests [19] to investigate the fire-resistance of flush end-plate composite joints, and developed a simplified component-based model [20] to calculate the initial stiffness and ultimate moment capacity of flush end-plate composite joints at elevated temperatures.

In this paper, the design of the novel ductile connection, and the component-based models of bare-steel and composite ductile connection are introduced. Sub-frame models of 2-D bare-steel and composite versions of the new ductile connection have been used to verify whether the component-based models of the bare-steel and composite connection have been correctly incorporated into Vulcan, by comparing the results with those from detailed finite element modelling using Abaqus. Finally, the structural performance of the ductile connection in steel-framed and composite structures is compared with that when conventional rigid or pinned connections are specified.

2 DESIGN AND COMPONENT-BASED MODELS OF THE DUCTILE CONNECTION

2.1 Detail of the ductile connection

The proposed novel connection consists of two identical parts, each of which may be characterised as a fin-plate which is bolted to the beam web, a face-plate which is bolted to either the column flange or web, and a semi-cylindrical section between these, as shown in Figure 1. The basic part of this ductile connection can be manufactured by simply bending a steel plate. The function of the semi-cylindrical section is to

provide additional push-pull ductility by allowing the fin-plate to move towards and away from the face-plate. The radius of this section should not be too small, otherwise, the ductility of connection will be reduced and the axial force generated in the adjacent structural components will be increased. Therefore, the semi-cylindrical section radius should be determined according to the ductility demand of the connected beam during a fire event, which can be calculated by equations proposed in the previous papers [2, 6].

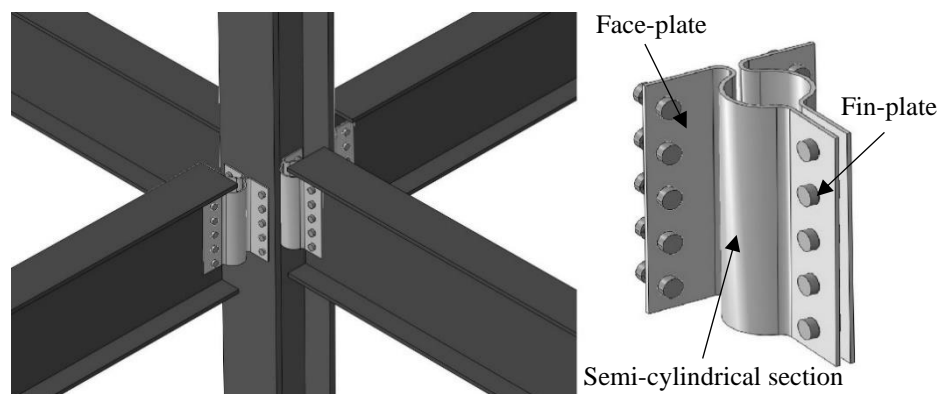


Figure 1. The proposed novel connection

2.2 Component-based models of the ductile connection

The component-based model of the bare-steel ductile connection has been proposed by the authors [4], as shown in Figure 2 (a). The basic structural actions of the component-based model include bolt pull-out, column web in compression, fin-plate in bearing, beam web in bearing, bolt in shear, and face-plate-semi-cylindrical component. The gap between the column web in compression and the vertical “rigid bar” represents the maximum axial compressive displacement before the beam bottom flange contacts the column flange. The two end nodes of the component-based model locate at the intersection points between the reference axes of the beam and column. The component-based model is assumed to be rigid in the vertical direction. Therefore, the vertical shear behaviour, which represents the slip between the beam end and the column flange, has not been taken into consideration. Design of this aspect of the connection uses the standard process for simple connections. The force-displacement curves of the fin-plate in bearing, beam web in bearing and bolt in shear are generated using the curve-fit equations proposed by Sarraj [10] based on a series of finite element parametric studies. The limiting strength of the bolt pull-out component is calculated using the simplified ‘plastic cone’ model developed by Dong [14]. Block [9] derived some equations for calculating the force-displacement curves of column web in compression, which have been directly applied to the current component-based model. As for the face-plate-semi-cylindrical component, the analytical models, based on simple plastic theory, developed by the authors [4] can be used to generate its characteristics.

The complete force-displacement relationship of a spring row under a complete axial load cycle in the component-based model of a bare-steel ductile connection is shown in Figure 3. The blue loop starts in pulling, and then the spring row is unloaded and pushed-back to its original state. The red loop starts in pushing, and the spring row is then unloaded and pulled back to its original shape. It is assumed that the stiffness of the unloading curve is the same as that of the initial elastic loading curve, for both tensile and compressive unloading. It can be seen from Figure 3 that the stiffness of tension and compression unloading is very large, resulting in a sudden change of spring row force when unloading occurs.

The component-based model of the composite ductile connection has been established by adding a reinforcement component to the bare-steel connection model [6], as shown in Figure 2 (b). The reinforcement component, which considers the pull-out of reinforcing bars and the influence of the anchorage and fracture of weld points in the mesh, is developed on the basis of the simple rebar slip model created by Sezen and Setzler [21]. It is further assumed that a discrete concrete crack occurs at the outer surface of the column flange, according with the experimental results obtained by Al-Jabri [18]. On one side of the crack, the development length is limited by the first three weld points, while on the other side of

the crack, the development length is limited by the first weld point and the centre line of the column section. Therefore, the slip of reinforcing bars on both sides of the concrete crack should be calculated separately, and the sum of the slips on both sides is the total displacement of reinforcement component.

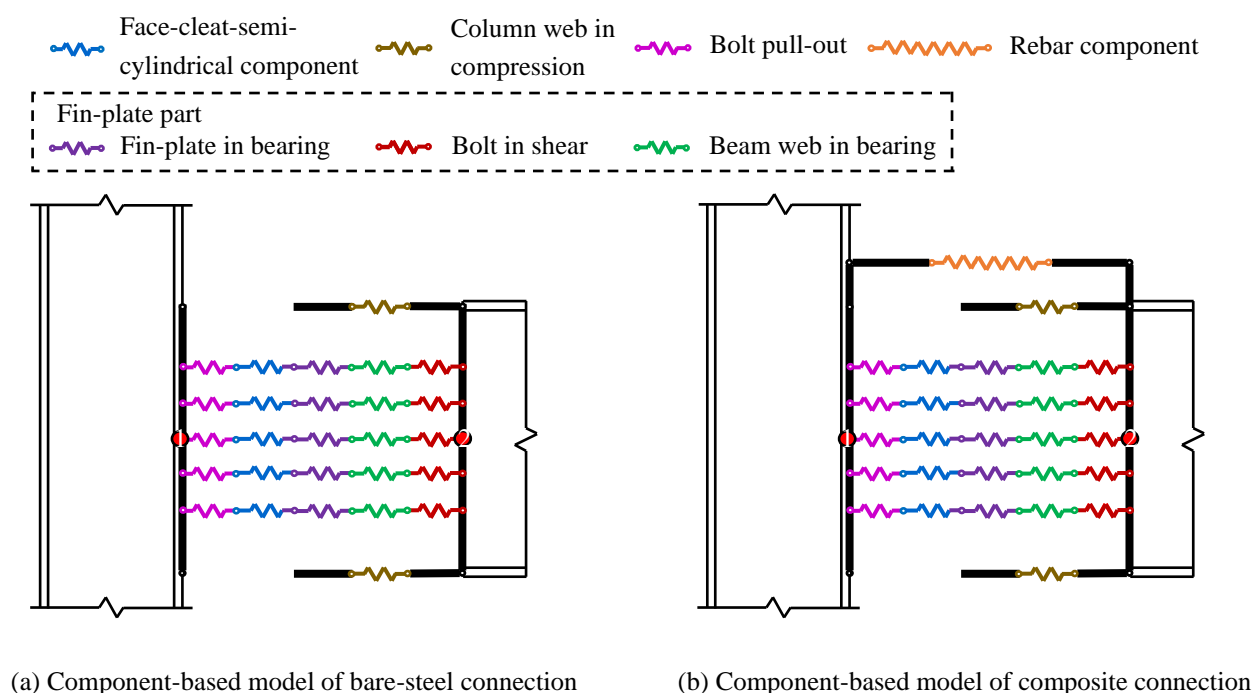


Figure 2. Component-based models of the ductile connection

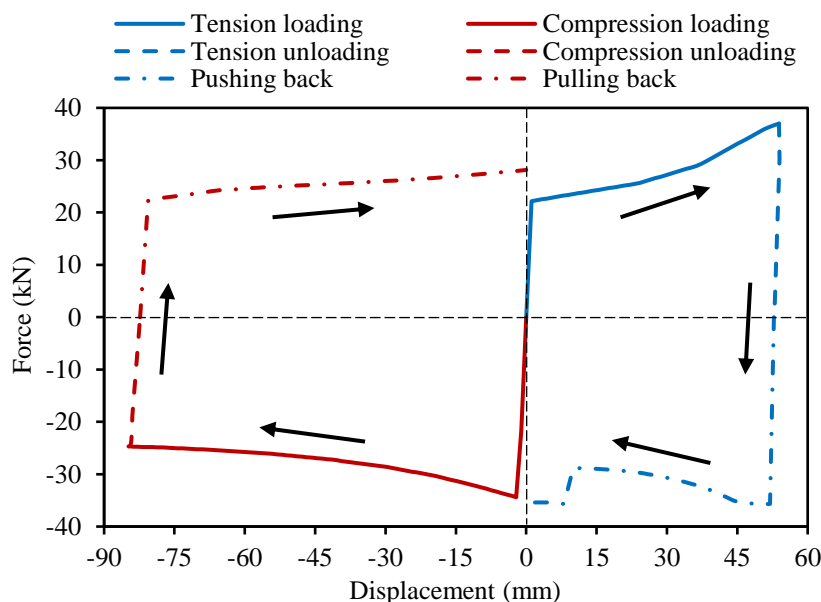


Figure 3. Loading and unloading process for a spring row

3 VALIDATION AGAINST DETAILED ABAQUS FE MODELS

3.1 Validation of the bare-steel connection model

According to the principles of the finite element method, the component-based model of the bare-steel ductile connection has been converted into a two-noded connection element located between the beam-end and the column, which has been incorporated into the software Vulcan [5]. In this section, a 2-D bare-steel

sub-frame model, shown in Figure 4 (a), is created using both Vulcan and Abaqus to check whether the connection element has been correctly incorporated into Vulcan. In order to save computational cost, only half of the model is built, and symmetric boundary conditions are applied at the mid-span of the beam. It is further assumed that fire only occurs on the lower floor, and the temperatures of the connection and the lower column are set to be half of the beam temperature. The detailed dimensions of the ductile connection used in the sub-frame model are listed in Table 1. The results from the Vulcan and Abaqus models are compared and shown in Figures 5 (a) and (b). It can be seen from these figures that Vulcan results are in good agreement with Abaqus results. The temperature-force and temperature-displacement curves of each spring row in the Vulcan model are shown in Figures 5 (c) and (d). At the start of heating, all the spring rows undergo compressive displacements, due to the thermal expansion of the connected beam. When the beam temperature reaches around 600°C, the compressive displacement of each spring row decreases gradually, and eventually changes into tensile displacement, as the connected beam enters its catenary action stage. It can be seen from Figure 5 (d) that, compared with other spring rows, Spring row 1 (the top spring row) experiences the largest tensile displacement, and is the first row to fail due to the pull-out of the bolt at that level. After the failure of Spring row 1, other spring rows fail row-by-row in the same manner. Once all the spring rows have failed, the connection element is considered as having failed, and will be removed from the model, leading to detachment of beam from the column face.

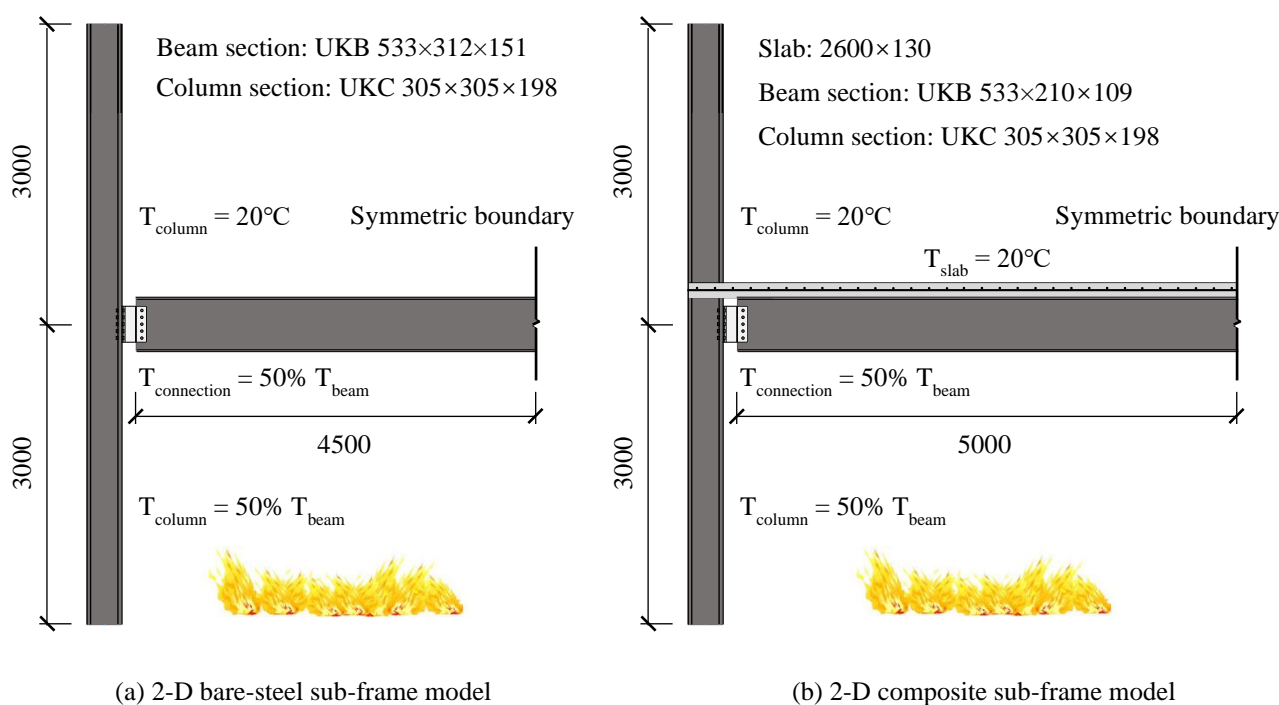


Figure 4. 2-D sub-frame model (units in mm)

Table 1. Connection size

Inner radius of semi-cylindrical section (mm)	50
Plate thickness (mm)	6
Fin-plate width (mm) × depth (mm)	100×360
Face-plate width (mm) × depth (mm)	100×360
Number of bolt rows	5

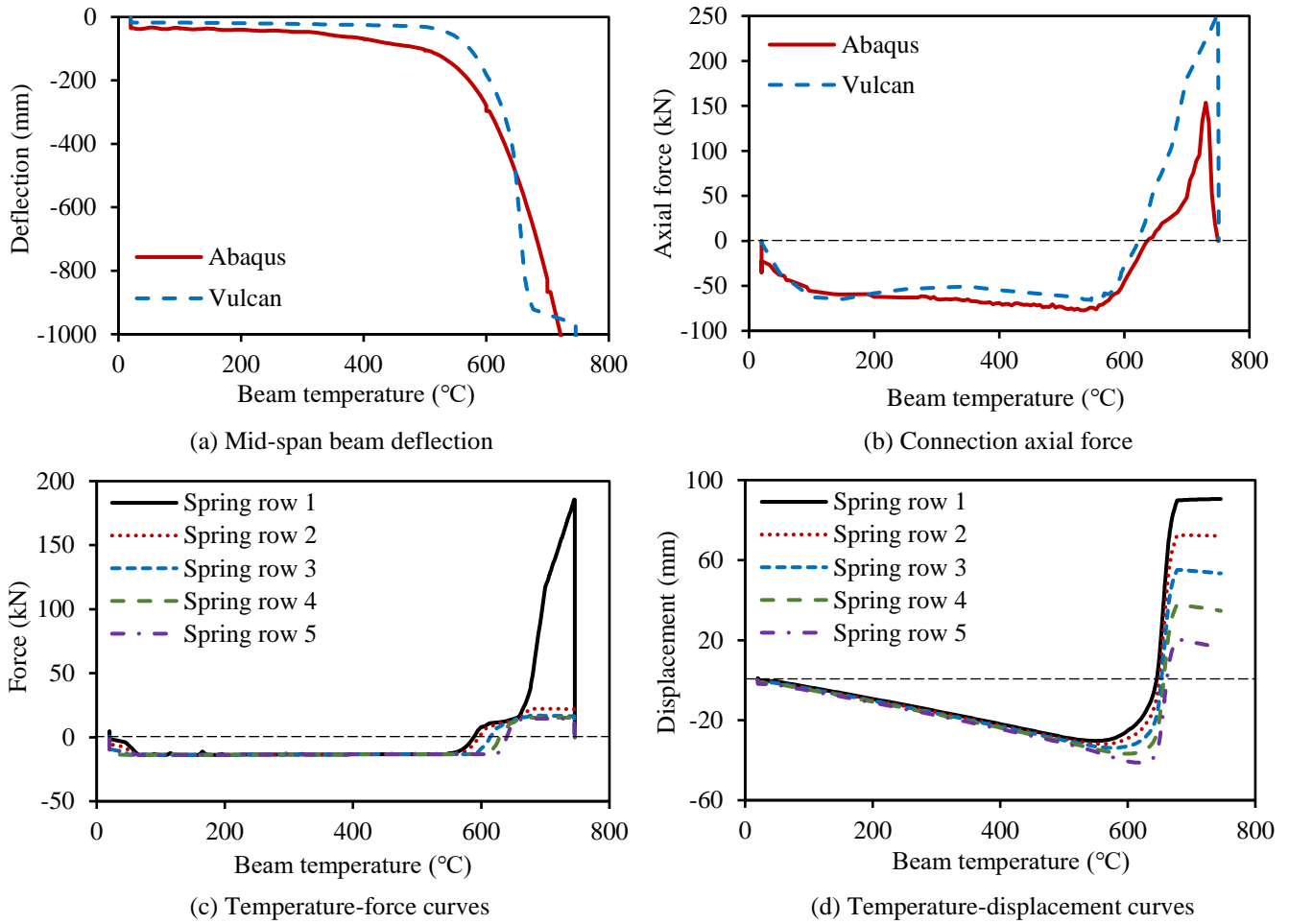


Figure 5. Results of the 2-D bare-steel sub-frame model

3.2 Validation of the composite connection model

The component-based model of the composite ductile connection has been converted into a connection element and incorporated into Vulcan [6]. The 2-D composite sub-frame shown in Figure 4 (b) has been modelled using Vulcan and Abaqus to test the performance of the composite connection element. The dimensions of the ductile connection used in the composite frame model are the same as those used in the bare-steel frame model, as listed in Table 1. The ductile connection is modelled in detail using solid elements in the Abaqus model, while the developed composite ductile connection element is used in the Vulcan model. The models adopt different methods to simulate the ductile connection. There are two key differences between the models are:

1. Concrete cracking and the pull-out of reinforcing bars are not considered in Abaqus model.
2. In the developed composite connection element, if the displacement of a spring row changes its direction, then unloading occurs. The force of the spring row changes its sense rapidly (Figure 3). This elastic unloading property is not considered in the detailed Abaqus model.

Figure 6 shows a comparison of the results of Vulcan model with those of Abaqus model. Above 200°C, the mid-span deflection and connection rotation of Abaqus model are smaller than those of Vulcan model, indicating that Abaqus model appears to be stiffer than Vulcan model. This is due to the fact that the Abaqus model does not take into account the concrete cracking and the pull-out of reinforcing bars, which makes the composite slab of Abaqus model stronger than that of Vulcan model. At about 686 °C, the mid-span deflection of Vulcan model increases rapidly, which is due to the change of spring row displacement direction. This will be further explained below. The mid-span beam axial forces of the Vulcan model and Abaqus model are compared in Figure 6 (c). As can be seen from the figure, with the increase of temperature, the initial tensile mid-span beam axial force decreases gradually due to the restraint of beam thermal

expansion. The decrease of the tensile mid-span beam axial force of the Abaqus model is larger than that of the Vulcan model (the mid-span beam axial force of the Abaqus model can reach -407kN around 211°C), which is because the composite slab of Abaqus model has stronger constraint on the beam thermal expansion than that of Vulcan model. Under the influence of thermal bowing, the mid-span beam axial force increases again at about 200°C. When the steel beam finally enters the catenary action stage, the mid-span beam axial force decreases again around 700°C. The comparison of the connection axial forces obtained from the Vulcan and Abaqus models is shown Figure 6 (d). The changes of the connection axial force are affected by the combined effects of beam thermal expansion and material degradation. It can be seen from the figure that the compressive axial force of the connection in the Vulcan model decreases rapidly at around 686°C, and changes temporarily into tension at about 800 °C. Above this temperature, the connection axial force becomes compressive again. It must be remembered that the Vulcan connection component assembly has the ability to reverse the direction in which each spring row moves; when this happens the row component unloads elastically and then changes the sense of its force. The Abaqus model does not have this capability. This explains the very marked divergence between the Vulcan and Abaqus curves shown in Figures 6 (a) and (d). It can be seen from Figure 7 that the displacement direction of all the five spring rows changes around 686 °C, resulting in a sudden decrease in the compressive force of all the spring rows. This is manifested in the sudden increase of beam mid-span deflection, as shown in Figure 6 (a), and the sudden decrease of connection compressive axial force as shown in Figure 6 (d). When the beam temperature reaches about 838 °C, the displacement direction of all the five spring rows changes again, leading to reversal of the connection axial force to compression. In general, the performance of the Vulcan connection element is in good agreement with the detailed Abaqus model, until the connection components' axial displacements change direction; beyond this stage the Vulcan model is more representative of the real behaviour, although this is not directly validated by Abaqus at this time. The current indication is that the Vulcan composite connection element can be used to investigate the effect of applying the ductile connection within a composite structure in fire conditions.

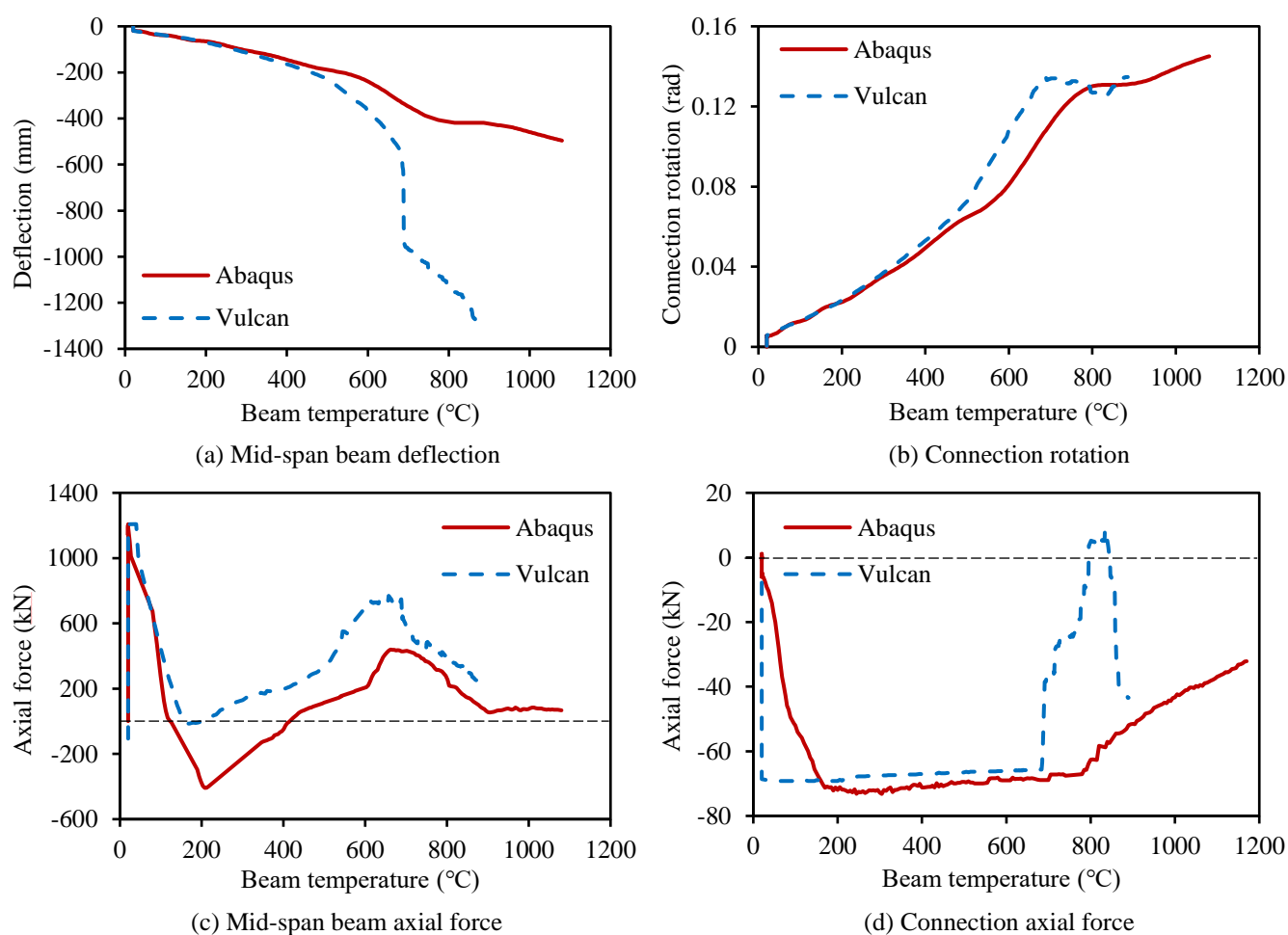
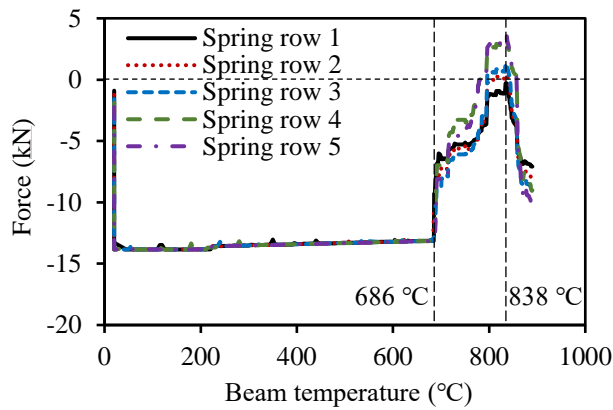
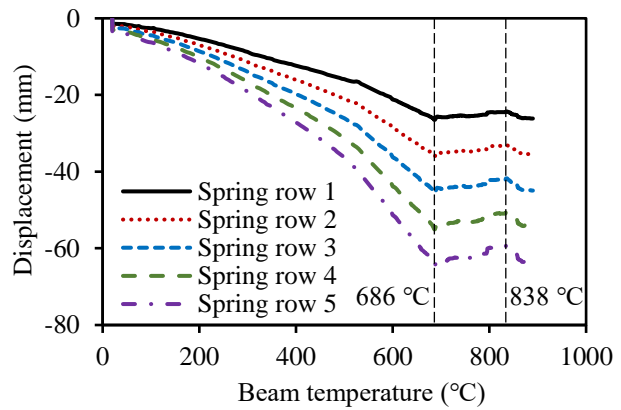


Figure 6. Results of the 2-D composite sub-frame model



(a) Temperature-force curve of each spring row



(b) Temperature-displacement curve of each spring row

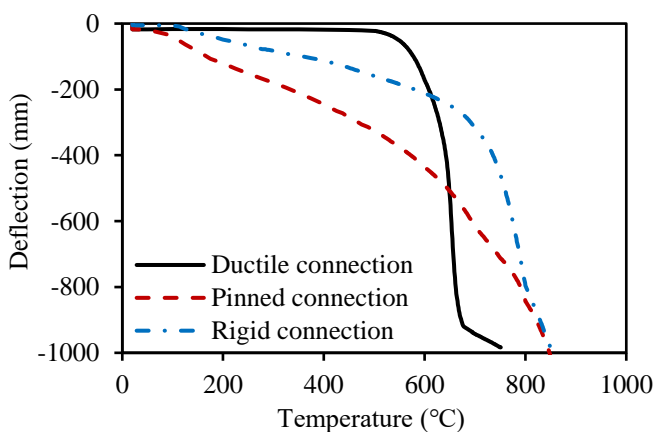
Figure 7. Temperature-force and temperature-displacement curves of each spring row

4 COMPARISON OF THE DUCTILE CONNECTION WITH OTHER CONNECTION TYPES

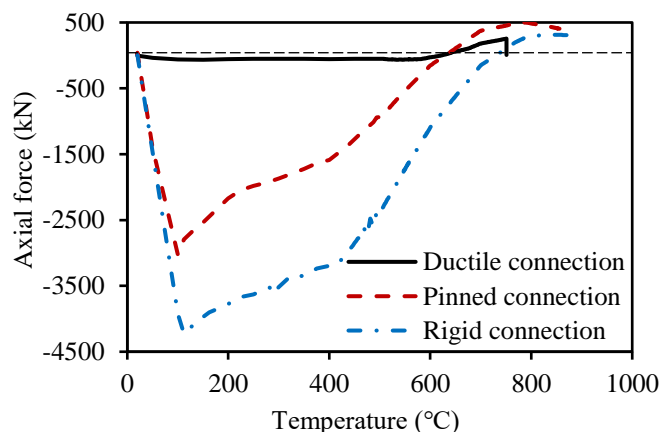
4.1 Performance comparison within bare-steel frame

In this section, the 2-D bare-steel sub-frame models shown in Figure 4 (a) are used to compare the performance of ductile connection with that of idealised pinned and rigid connection types. The comparison results are shown in Figure 8. As can be seen from Figure 8 (a) the mid-span deflection of the beam with the ductile connection is lower than those of the beams with the idealised connections up to around 600 °C. After that temperature, the deflection of the beam with ductile connection increases rapidly, and finally exceeds those of beams with idealised connections. The mid-span axial force generated in the heated beam with the ductile connection is significantly reduced compared with the beams with pinned and rigid connections, as shown in Figure 8 (b).

This phenomenon indicates that the ductile connection can provide additional ductility to accommodate the axial deformation of connected beam generated in fire conditions. The ductility of the ductile connection can also contribute to the reduction of axial forces to which the surround structural elements are subjected.



(a) Mid-span beam deflection



(b) Mid-span beam axial force

Figure 8. Performance comparison within bare-steel frame

4.2 Performance comparison within composite frame

The structural behaviour of connections within composite structures is quite different from that of connections within bare-steel frames, due to the existence and continuity of the composite slab. Two-dimensional composite sub-frame models with different connection types, including the ductile connection, the pinned and rigid connection, as shown in Figure 4 (b), are created using Vulcan in this section to compare the performance of the ductile connection with other connection types in composite structures. The comparison results are shown in Figure 9. As can be seen from Figure 9 (a) the mid-span deflection of the beam with ductile connections is basically the same as that of the beam with the idealized pinned connection up to about 680 °C. Within this temperature range, the rotation of the ductile connection is also almost equal to that of the pinned connection, as depicted in Figure 9 (b). After that, the rotation of the ductile connection continues to increase, while the rotation of the pinned connection begins to decrease. This is manifested in the rapid increase of the mid-span deflection of the beam with ductile connections above 680 °C (Figure 9 (a)). The mid-span and end axial forces of the beams with different connection types are compared in Figures 9 (c) and (d). The axial force generated in the beam with ductile connections is almost the same as that in the beam with pinned connections. However, rigid connections restrain the thermal expansion of the beam to a great extent, resulting in a very large compressive axial force in the beam. Once again, the ductile connection exhibits its good axial deformation capacity to accommodate the deformation of connected beam, thus reducing the compressive axial force generated.

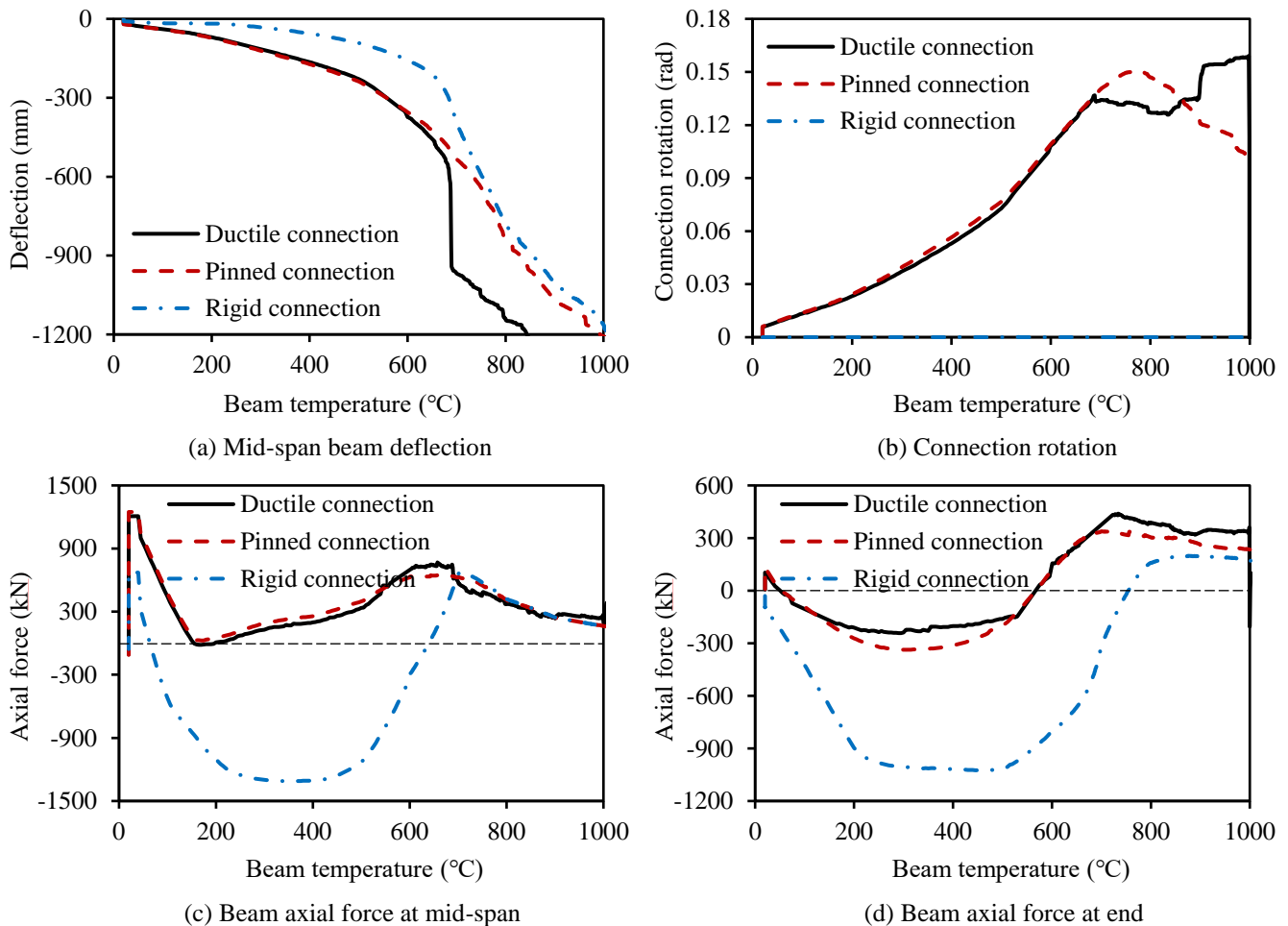


Figure 9. Performance comparison within composite frame

5 CONCLUSIONS

Connections are potentially the weakest part of a structure. In order to improve the ductility of connections and enhance the robustness of structures in fire, a ductile connection has been proposed by the authors. In

this paper, the design and the component-based models of the bare-steel and composite ductile connections have been introduced.

A 2-D bare-steel sub-frame with ductile connections was modelled using Vulcan and Abaqus. Vulcan results are in good agreement with Abaqus results, indicating that the component-based model of the bare-steel ductile connection has been correctly incorporated into Vulcan. Through the analysis of Vulcan model results, it is found that Spring row 1 (the top spring row) experiences the largest tensile displacement and is the first to fail due to bolt pull-out. After this, other spring rows fail row by row in the same manner. A 2-D composite subframe was used to check the performance of the component-based model of the composite ductile connection by comparing the results of Vulcan and Abaqus models. Comparison of the results shows that the Vulcan model is in good agreement with the detailed Abaqus model, up to the point where the connection components' axial displacements change direction. In the proposed connection element, the direction change of the spring row displacement leads to a rapid change of spring row force. This characteristic is not taken into consideration in the Abaqus model. The current indication is that the Vulcan composite connection element can be used to facilitate global frame analysis to investigate the effect of adopting the ductile connection in composite structures under fire conditions.

Performance of the ductile connection within bare-steel and composite frames has been compared with that of conventional connection types including idealized pinned and rigid connections. Results show that the compressive axial force generated in the heated bare-steel beam can be significantly reduced when the ductile connection is used. The axial force of the composite beam with ductile connection is basically the same as that when an ideal pinned connection is used. However, compared with the composite beam with rigid connections, the axial force in the composite beam with ductile connections is still greatly reduced. These comparison results demonstrate the axial deformation capacity of the proposed ductile connection.

REFERENCES

1. Lennon T, Moore D. The natural fire safety concept—full-scale tests at Cardington. *Fire Safety Journal*. 2003;38:623-43.
2. Liu Y, Huang S-S, Burgess I. Investigation of a steel connection to accommodate ductility demand of beams in fire. *Journal of Constructional Steel Research*. 2019;157:182-97.
3. Liu Y, Huang S-S, Burgess I. Ductile connections to improve structural robustness in fire. *Proceedings of the 6th Applications of Structural Fire Engineering Conference (ASFE'19)*: Sheffield; 2019.
4. Liu Y, Huang S-S, Burgess I. Component-based modelling of a novel ductile steel connection. *Engineering Structures*. 2020;208:110320.
5. Liu Y, Huang S-S, Burgess I. Performance of a novel ductile connection in steel-framed structures under fire conditions. *Journal of Constructional Steel Research*. 2020;169:106034.
6. Yu Liu S-SH, Ian Burgess. Fire performance of axially ductile connections in composite construction. *Fire Safety Journal*. 2020.
7. Leston-Jones LC. The influence of semi-rigid connections on the performance of steel framed structures in fire: University of Sheffield; 1997.
8. Spyrou S. Development of a component based model of steel beam-to-column joints at elevated temperatures: University of Sheffield; 2002.
9. Block FM. Development of a component-based finite element for steel beam-to-column connections at elevated temperatures: University of Sheffield Sheffield, UK; 2006.
10. Sarraj M. The behaviour of steel fin plate connections in fire: University of Sheffield; 2007.
11. Sarraj M, Burgess I, Davison J, Plank R. Finite element modelling of steel fin plate connections in fire. *Fire Safety Journal*. 2007;42:408-15.
12. Yu H, Burgess I, Davison J, Plank R. Development of a yield-line model for endplate connections in fire. *Journal of Constructional Steel Research*. 2009;65:1279-89.
13. Yu H, Burgess I, Davison J, Plank R. Tying capacity of web cleat connections in fire, Part 2: Development of component-based model. *Engineering structures*. 2009;31:697-708.

14. Dong G. Development of a General-Purpose Component-based Connection Element for Structural Fire Analysis: University of Sheffield; 2016.
15. Hu Y, Davison B, Burgess I, Plank R. Component modelling of flexible end-plate connections in fire. *International Journal of Steel Structures*. 2009;9:1-15.
16. Taib M, Burgess I. A component-based model for fin-plate connections in fire. *Journal of Structural Fire Engineering*. 2013;4:113-22.
17. Leston Jones L, Burgess I, Lennon T, Plank R. Elevated-temperature moment-rotation tests on steelwork connections. *Proceedings of the Institution of Civil Engineers-Structures and Buildings*. 1997;122:410-9.
18. Al-Jabri KS. The behaviour of steel and composite beam-to-column connections in fire: University of Sheffield; 1999.
19. Li J-T, Li G-Q, Lou G-B, Chen L-Z. Experimental investigation on flush end-plate bolted composite connection in fire. *Journal of Constructional Steel Research*. 2012;76:121-32.
20. Li G-Q, Chen L-Z, Li J-T, Lou G-B. Modeling of end-plate bolted composite connection in fire considering axial force effects. *Journal of Constructional Steel Research*. 2012;76:133-43.
21. Sezen H, Setzler EJ. Reinforcement slip in reinforced concrete columns. *ACI Structural Journal*. 2008;105:280.

BEHAVIOUR OF AXIALLY COMPRESSED ANGLES AND BUILT-UP STEEL MEMBERS AT ELEVATED TEMPERATURE

Luca Possidente¹, Nicola Tondini², Jean-Marc Battini³

ABSTRACT

Angles and built-up steel sections are widely employed in structures as members in bracing systems or in truss structures and are mainly designed to withstand axial loads. Torsional and flexural-torsional buckling might affect angles and built-up members subjected to compressive stresses. Great interest has been shown by researchers relative to the instability of steel elements in fire, but there is a lack of studies on the buckling behaviour of angles and built-up steel members in compression and this topic is not explicitly treated in the current version of Eurocode EN 1993-1-2. In order to provide new insights, a comprehensive numerical investigation of the behaviour of concentrically compressed angles, tee and cruciform steel members at elevated temperature was performed. A parametric study was carried out on Class 1 to 3 profiles with three different steel grades, namely S235, S275, S355, subjected to uniform temperature distribution. More than 41000 geometrically and materially nonlinear imperfect analyses (GMNIA) were performed on columns with different length and temperature by means of 3D beam and shell elements. Results showed that the buckling curve given in EN 1993-1-2 provides unconservative predictions for a range of slenderness of practical interest. To better predict the behaviour of the investigated steel members, an improved buckling curve was proposed, which allows for safer predictions, as also confirmed by statistical investigation.

Keywords: Steel structures; Flexural-torsional buckling; Torsional buckling; Fire; finite element modelling; Buckling curve

1 INTRODUCTION

Steel angular, cruciform and tee sections are frequently employed in bracing systems or in truss structures, in which they are mainly axially loaded. Thus, when subjected to compressive actions their resistance can be affected by instability phenomena. Local effects are negligible for compact sections and global buckling modes govern the behaviour of the steel elements. Unless flexural buckling is prevented by lateral restraints, in typical hot-rolled or welded I or H profiles that are axially compressed, torsional effects are rare. However, for angles, tee and cruciform steel sections, torsional or flexural-torsional buckling can be relevant, in particular, in a low slenderness range. Hereafter angles, tee and cruciform sections are referred to as L, T and X sections respectively. Prescriptions for the design of compressed steel members at both ambient and elevated temperature are given in EN 1993-1-1 [1] and EN 1993-1-2 [2], respectively. The resistance is reduced according to the slenderness of the element and buckling curves are provided. These curves were based on experimental and numerical results for H- and I-profiles and later, were calibrated

¹ PhD student, University of Trento; Department of Civil, Environmental and Mechanical Engineering, Via Mesiano 77, 38123, Trento, Italy & KTH, Royal Institute of Technology - Department of Civil and Architectural Engineering, SE-10044 Stockholm, Sweden
e-mail: luca.possidente@unitn.it, ORCID: <https://orcid.org/0000-0002-4179-1860>

² Assistant Professor, University of Trento; Department of Civil, Environmental and Mechanical Engineering, Via Mesiano 77, 38123, Trento, Italy
e-mail: nicola.tondini@unitn.it

³ Professor, KTH, Royal Institute of Technology - Department of Civil and Architectural Engineering, SE-10044 Stockholm, Sweden
e-mail: jean-marc.battini@byv.kth.se

and extended to other profiles, such as L profiles. In EN 1993-1-2 [2] flexural buckling is considered according to the model presented by Franssen et al. [3]. Then, researchers investigated the effects of other instability phenomena on the resistance of steel elements at elevated temperature such as lateral-torsional buckling [4]-[6] and its interaction with local instabilities [7]-[11]. However, axially compressed steel members in fire may be also prone to torsional and flexural-torsional buckling. Such buckling phenomena have been particularly studied for cold-formed steel profiles at both ambient and elevated temperatures [12]-[16]. Indeed, owing to the shape and the small thickness, an interaction of local, distortional and global buckling influences the resistance of L, T and X thin-walled members at ambient temperature, as shown by Dinis et al. [17]. Further considerations on X sections were provided in [18]-[20]. The work presented in this paper aims at providing indications about the torsional and flexural-torsional buckling of compressed L, T and X steel profiles, obtained by coupling L sections or by cutting H or I hot rolled profiles. Dedicated buckling curves were proposed based on the results of a numerical investigation. Statistical investigation was employed to compare the proposed model and the one prescribed in EN 1993-1-2 [2].

2 EUROCODE PROVISIONS

The resistance of steel members should be reduced to account for the effect of temperature. According to EN 1993-1-2 [2], for compressed elements with a uniform temperature θ_a and Class 1, Class 2 or Class 3 cross-sections, the resistance is determined as follows:

$$N_{b,fi,t,Rd} = \frac{\chi_{fi} A k_{y,\theta} f_y}{\gamma_{M,fi}} \quad (1)$$

where $\gamma_{M,fi}$ is the safety factor for the fire design situation, A is the area of the cross-section, $k_{y,\theta}$ is the retention factor for the yield strength of steel at temperature θ_a and f_y is the yield strength. χ_{fi} is the flexural buckling coefficient in the fire design situation, and is obtained according to the following equation:

$$\chi_{fi} = \frac{1}{\varphi_{\theta} + \sqrt{\varphi_{\theta}^2 - \bar{\lambda}_{\theta}^2}} \quad (2)$$

with

$$\varphi_{\theta} = \frac{1}{2} \left[1 + \eta_{EC3.1-2} + \bar{\lambda}_{\theta}^2 \right] \quad (3)$$

The generalised imperfection factor $\eta_{EC3.1-2}$ is defined as

$$\eta_{EC3.1-2} = \alpha \bar{\lambda}_{\theta} \quad (4)$$

the imperfection factor α depends on the yield strength f_y expressed in MPa

$$\alpha = \beta \sqrt{\frac{235}{f_y}}; \quad \beta = 0.65 \quad (5)$$

While the non-dimensional slenderness $\bar{\lambda}_{\theta}$ at the temperature θ_a , is given by:

$$\bar{\lambda}_{\theta} = \bar{\lambda} \left[\frac{k_{y,\theta}}{k_{E,\theta}} \right]^{0.5} \quad (6)$$

$k_{y,\theta}$ and $k_{E,\theta}$ are the reduction factors for the yield strength and Young's modulus at steel temperature θ_a , $\bar{\lambda}$ is the non-dimensional slenderness at ambient temperature. Further explanations about the design procedure and the definition of $\bar{\lambda}$ are not provided in the code for steel structures in fire situation. Instead, the definition of the non-dimensional slenderness at ambient temperature can be found in EN 1993-1-1 [1], which prescribes that for Class 1, 2 and 3 cross-sections at ambient temperature $\bar{\lambda}$ is determined as follows

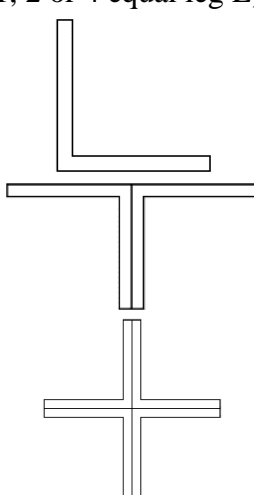
$$\bar{\lambda} = \bar{\lambda}_{cr} = \sqrt{\frac{A f_y}{N_{cr}}} \quad (7)$$

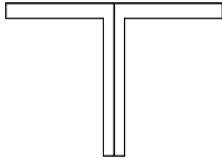
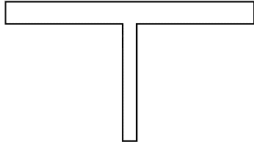
N_{cr} is the lowest elastic critical load at ambient temperature. Hence, the slenderness $\bar{\lambda}$ is associated with the lowest relevant buckling mode, that in some cases might be torsional or flexural-torsional. However, in EN 1993-1-2 [2] χ_{fi} is defined as the smaller between the flexural buckling coefficients $\chi_{y,fi}$ and $\chi_{z,fi}$, and thus, flexural-torsional buckling is not considered. The two different approaches might be in contrast and lead to confusion. Indeed, following the philosophy of EN 1993-1-2 [2], N_{cr} should be defined as the lowest pure flexural mode ($N_{cr,F} = \min(N_{cr,y}, N_{cr,z})$) but, in order to account for torsional effects, the value of N_{cr} associated to the lowest relevant buckling mode should be employed as in prescribed EN 1993-1-1 [1].

3 PARAMETRIC ANALYSIS

The behaviour of concentrically compressed members subjected to fire that may be sensitive to torsional or flexural-torsional buckling was investigated, performing a large number of Finite Element Analysis (FEA). Results in terms of resistance were compared with the EN 1993-1-2 provisions, and the accuracy and safety of the predictions were discussed. The analysed members consisted of L, T or X cross-sections, defined by coupling L sections back-to-back in case of T and X sections or by cutting in two halves H or I hot rolled steel profiles for additional T sections. In the case of coupled sections, it was assumed that, if the spacing of the connections is short enough, closely built-up members can be checked for buckling as single integral members [1]. Meaningful predictions of the behaviour of coupled members were obtained with this assumption in several papers [17]-[20]. Nevertheless, connecting plates or battens could be considered in more refined numerical models. 3D beam and shell elements were used in more than 41000 geometrically and materially imperfect nonlinear analyses (GMNIA). The length and the temperature of the columns were varied. Columns subjected to five different uniform temperatures were studied: 400°C, 500°C, 600°C, 700°C, 800°C. The temperature range 400°C-800°C is the most relevant temperature range for columns subjected to uniform temperature. This was proved for columns that buckle flexurally [3] and preliminary analyses showed that it holds true for the cross-sections studied in this work. For each temperature about 8200 columns were analysed with a length-to-width ratio higher than 3, in order to limit the analyses to columns of practical interest. 45 different equal leg L profiles of commercial dimensions were studied. 68 T section and 45 X sections were obtained by coupling 2 and 4 L sections respectively. 129 T sections were obtained by dividing into two halves hot rolled H- or I-sections. The different section types are summarised in Table 1. Classes in fire situation were defined according to EN 1993-1-2 [2] and the steel grade of each column was selected so that only cross-sections of Class 1, Class 2 or Class 3 were investigated.

Table 1. Investigated sections - •S235; #S275; +S355

Section type	Dimensions of the angles composing the sections (Flange depth x web height x flange thickness x web thickness in mm)			
L, T and X section (1, 2 or 4 equal leg L) 	45x45x7x7	#+	150x150x20x20	• +
	50x50x9x9	#+	150x150x18x18	•#
	60x60x10x10	#+	160x160x17x17	•
	65x65x11x11	+	180x180x19x19	•
	65x65x10x10	#+	200x200x28x28	#+
	70x70x9x9	#+	200x200x26x26	•#+
	90x90x16x16	•#+	250x250x34x34	#+
	100x100x16x16	•#+	250x250x33x33	#+
	100x100x15x15	•#+	250x250x32x33	+
	110x110x12x12	•	250x250x27x27	•
	120x120x15x15	•#	300x300x33x33	•
	120x120x13x13	•	300x300x32x32	•
	140x140x16x16	•#		

T sections (2 unequal leg L) 	65x100x9x9	•	90x130x12x12	•		
	65x100x10x10	•#	90x130x14x14	•#+		
	65x100x12x12	•#+	90x140x12x12	•		
	70x110x10x10	•#	90x140x14x14	•#		
	70x110x12x12	•#+	100x150x14x14	•#		
	80x120x12x12	•#	100x200x16x16	•		
T sections (half H or I) 	<i>From half</i>		<i>From half</i>			
	120x54,5x4,2x5,5	HE 120 AA	•#+	248x135x18x32	HE 240 M	•#+
	120x57x5x8	HE 120 A	•#+	280x140x10,5 x18	HE 280 B	•#+
	64x60x4,4x6,3	IPE 120	#+	268x145x18x32,5	HE 260 M	•#+
	120x60x6,5x11	HE 120 B	•#+	300x150x11x19	HE 300 B	•#+
	140x64x4,3x6	HE 140 AA	#+	288x155x18,5 x33	HE 280 M	•#+
	140x66,5x5,5x8,5	HE 140 A	•#+	300x160x11,5x20,5	HE 320 B	#+
	126x70x12,5x 21	HE 120 M	•#+	310x170x21x39	HE 300 M	•#+
	140x70x7x12	HE 140 B	•#+	300x170x12x21,5	HE 340 B	#+
	160x74x4,5x7	HE 160 AA	+	309x179,5x21x40	HE 320 M	•#+
	160x76x6x9	HE 160 A	•#+	300x180x12,5x22,5	HE 360 B	#+
	146x80x13x22	HE 140 M	•#+	309x188,5x21x40	HE 340 M	•#+
	160x80x8x13	HE 160 B	•#+	308x197,5x21x40	HE 360 M	•#+
	180x85,5x6x9,5	HE 180 A	#+	300x200x13,5x24	HE 400 B	+
	166x90x14x23	HE 160 M	•#+	307x216x21x40	HE 400 M	•#+
	180x90x8,5x14	HE 180 B	•#+	307x239x21x40	HE 450 M	•#+
	200x95x6,5x10	HE 200A	#+	306x262x21x40	HE 500 M	•#+
	186x100x14,5x24	HE 180M	•#+	306x286x21x40	HE 550 M	#+
	200x100x9x15	HE 200B	•#+	305x310x21x 40	HE600M	#+
	220x105x7x11	HE 220A	#+	310x316x25,5x46	HE600x337	•#+
	206x110x15x25	HE 200M	•#+	315x324x30x54	HE600x399	•#+
	220x110x9,5x16	HE 220B	•#+	309x340x25x46	HE650x343	#+
	240x115x7,5x12	HE 240A	#+	314x348x29,5x54	HE650x407	•#+
	226x120x15,5 x26	HE 220M	•#+	308x364x25x46	HE700x352	+
	240x120x10x17	HE 240B	•#+	313x372x29,5 x54	HE700x418	#+
	260x125x7,5x12,5	HE 260A	+	313x421x30x54	HE800x444	+
	260x130x10x17,5	HE 260 B	•#+			

3.1 Finite element modelling

Linear eigenvalue analyses were performed to determine the shape of the initial geometric imperfection to be introduced in each analysis. These imperfections were scaled so that the maximum nodal displacement along the column equalled 1/1000 of the length. The elasto-plastic behaviour of steel was modelled based on the Von Mises yield function and on the uniaxial stress-strain relationship given in EN 1993-1-2 [2]. Residual stresses were neglected since it was found that their effect on the resistance of steel member in fire is not significant [3], [7], [15], [24], [25]. Three steel grades were selected, i.e. namely S235, S275, S355. The Young's modulus value at ambient temperature was set to 210 GPa and the Poisson ratio was equal to 0.3. The monosymmetric sections (L and T sections) were investigated by means of the 3D beam finite elements developed in [22], whereas for the X section the shell element proposed in [23] was

employed. Indeed, shell elements were used as the introduction of imperfections associated to a pure torsional buckling would not be possible in beam elements-based analyses. However, beam elements were preferred for the monosymmetric cross-sections since they enable faster analyses and an easier definition of the boundary conditions, allowing for the investigation of simply supported columns, with the rotational degree of freedom along the longitudinal axis blocked. Instead, columns with clamped end conditions were analysed when shell elements were used. In detail, the lateral displacements were blocked only at the centroids of the two clamped ends, to allow for thermal expansion. The axial displacement was fixed on one end and free conditions were imposed at the opposite one, which was loaded. The axial load was applied to the centroid and master-slave constraints allowed for a uniform axial displacement of all the other nodes of the loaded end. Preliminary convergence analyses showed that 30 elements were sufficient for accurate solutions regarding beam models, while in the shell-based simulation it was necessary to vary the mesh with the length of the column. A minimum of 6 elements in each dimension of the section were always used.

3.2 Validation of the numerical models

The ability of beam and shell models to capture flexural-torsional buckling was validated numerically, since no experimental tests were available in literature. The behaviour of a compressed T section consisting of two 150x150x20x20 L sections (see Table 1) at elevated temperature was studied by means of both the shell and beam elements. Both ends of the column were clamped, except for the axial displacement that was free on the loaded side. In order to study a column that exhibits flexural-torsional behaviour, the length of the column was set to $L=1.67$ m. This was confirmed by a linear buckling analysis at ambient temperature, which identified flexural-torsional buckling as the lowest buckling mode for both the shell and the beam models (see Figure 1a). In terms of the associated buckling loads, a difference of only 3.2% was registered between the analyses ($N_{cr,BEAM}=12150$ kN and $N_{cr,SHELL}=12550$ kN). Then, the column was studied under a uniform and constant temperature of 600°C and an increasing compressive load N . The buckling mode shapes obtained in the previous linear buckling analyses were scaled and introduced as initial geometric imperfection in the numerical models. Figure 1b shows the load-displacement path of the loaded node. The load N is expressed with respect to the yield load $N_{yield} = Ak_{y,600^{\circ}\text{C}}f_y$. The results are in excellent agreement with the outcomes of the same analysis performed with a shell model developed in SAFIR [37]. An almost identical load level with a maximum difference of 3.7% was achieved.

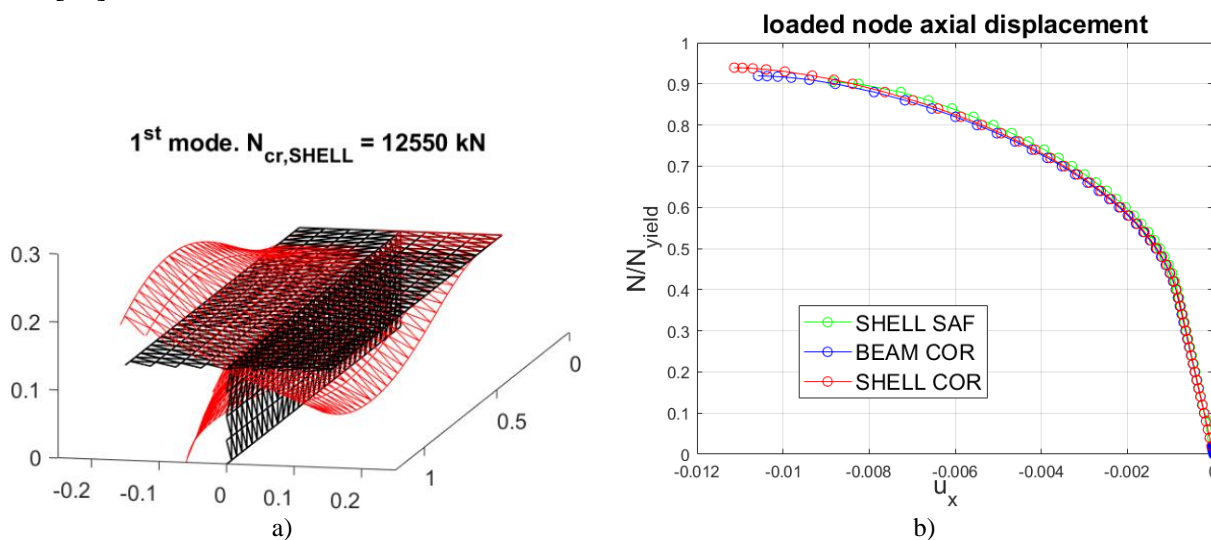


Figure 1. Validation test. Lowest buckling mode of the shell analysis; b) Load vs axial displacement of the loaded node

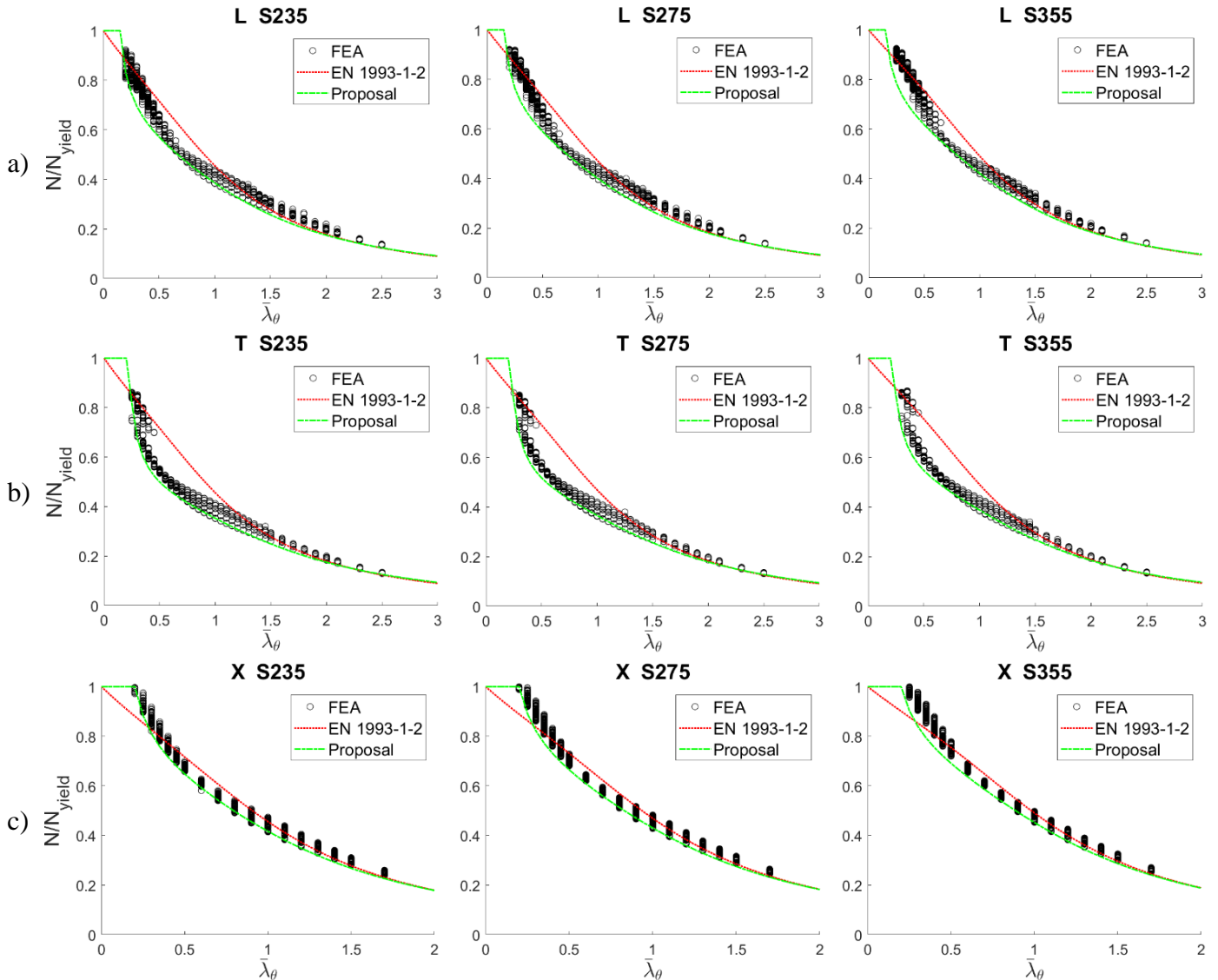
3.3 Description and discussion of the numerical results

The numerical outcomes of the parametric analysis are illustrated in Figure 2, where the numerical failure load N is expressed with respect to the yielding load at elevated temperature $N_{yield} = Ak_{y,\theta}f_y$ in order to compare the numerical outcomes with the buckling coefficient χ_{fi} from EN 1993-1-2 [2]. Since it was

found that a better representation of the results is obtained with buckling curves expressed with respect to the pure flexural buckling slenderness, $\bar{\lambda}$ in Eq. (6) was defined as follows

$$\bar{\lambda} = \bar{\lambda}_{cr,F} = \sqrt{\frac{Af_y}{N_{cr,F}}} = \sqrt{\frac{Af_y}{\min(N_{cr,y}, N_{cr,z})}} \quad (8)$$

Where $\bar{\lambda}_{cr,F}$ instead of $\bar{\lambda}_{cr}$ was used. Analogously, Taras and Greiner [21] and Popovic et al. [14] observed that when the torsional or flexural-torsional mode is the relevant lowest buckling mode, the length of a column l may not be well represented by the non-dimensional slenderness $\bar{\lambda}_{cr}$. Figure 2 shows that the actual design buckling curve well represents the numerical results and provides safe predictions only for very slender columns ($\bar{\lambda}_\theta > 1.5$). For all the sections and steel grades the buckling coefficient χ_{fi} ($=N/N_{yield}$) is overestimated for a medium slenderness range, in particular in the range $0.4 \leq \bar{\lambda}_\theta < 1.2$, in which the load-bearing capacity obtained with the EN 1993-1-2 buckling curves attain values significantly higher than the ones from the numerical simulation. Over-conservative predictions might be obtained for very stocky columns. Results for stocky columns with T sections obtained from dividing into two halves a H or I section are more spread, and the actual buckling curve is both conservative and non-conservative. However, since it seems difficult to obtain very accurate predictions in this case, a buckling curve on the safe side should be preferred. Summarising, for a large slenderness range of practical interest the buckling curve from EN 1993-1-2 provides inaccurate and non-conservative results. It would be beneficial to provide a different formulation for buckling curves, to improve the accuracy and safety of the predictions.



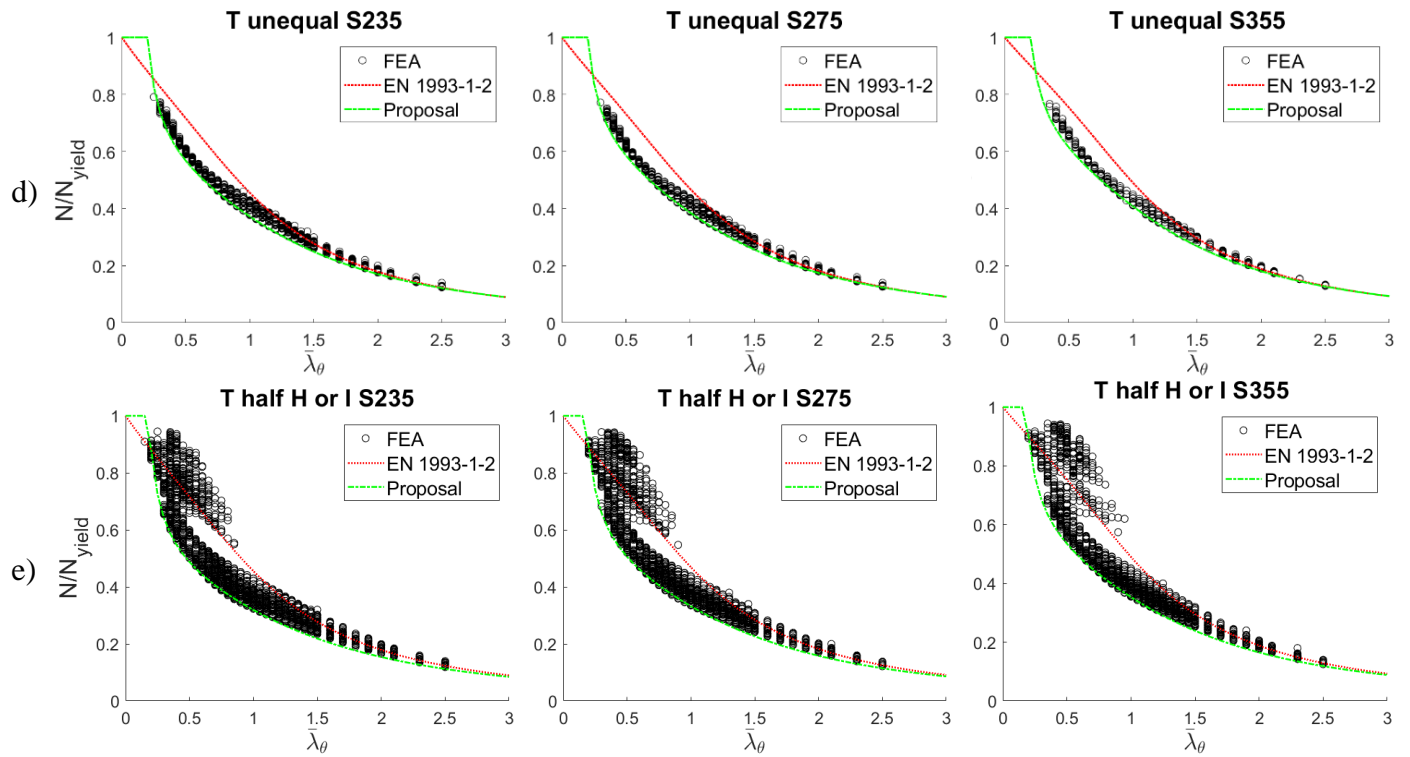


Figure 2. Buckling curves for S235, S275 and S355 steel grade. a) L, b) T and c) X made of coupled equal leg L sections, d) T obtained from unequal leg L sections and e) T obtained from half H or I section

It should be noted that in almost all the analyses of the X sections buckling occurred in its pure flexural form. Moreover, few very stocky columns attained failure loads higher than the yielding load ($N > N_{yield}$) and the associated results are not shown in Figure 2, as they would imply buckling coefficients $\chi_{fi} > 1$, while χ_{fi} should never exceed the value of 1. Failure loads exceeding the yielding load in shell analyses were also found in several works about the fire behaviour of steel elements subjected to lateral-torsional buckling and of cold-formed steel beams with open cross-sections [8]-[10], [16].

T sections obtained from hot-rolled H or I profiles need a separate discussion since, as evident from Figure 2, numerical results are more spread compared with the ones of the other sections. This is mainly due to the fact that these sections have very different geometric dimension, especially when it comes to the depth-to-thickness ratio of the flanges and of the web. Moreover, in some cases the strong axis of the section is directed along the web, but in the others, it has the same orientation of the flanges. This is not the case for T sections obtained by coupling L profiles. Indeed, coupling equal leg profiles the strong axis is always directed along the web, while for T sections obtained by coupling unequal leg profiles the strong axis is directed along the flange. A further difference consists in the fact that in sections obtained from H- or I-profiles, the web thickness is smaller than the flange thickness, while for the other T sections, the web thickness is always two times the flange thickness.

4 NEW BUCKLING CURVE PROPOSAL

Buckling curves that allow for a better representation of the results of numerical simulation were defined, based on the curves provided in EN 1993-1-2 [2]. In detail, to improve the buckling curve formulation it was decided to modify the generalised imperfection factor η by embracing the same philosophy of the buckling curves as defined in EN 1993-1- [1] and in EN 1993-1-2 [2]. The generalised imperfection factors for the different curves are summarised in Table 2.

Table 2. Generalised imperfection factors. EN 1993-1-1 [1], EN 1993-1-2 [2] and proposal

$\eta_{EC3.1-1}$	$\eta_{EC3.1-2}$	η_{PROP}
$\alpha(\bar{\lambda} - \bar{\lambda}_0)$	$\alpha\bar{\lambda}_\theta$	$\frac{\alpha}{\bar{\lambda}_\theta^\gamma} \left(\bar{\lambda}_\theta - \frac{\bar{\lambda}_0^2}{\bar{\lambda}_\theta} \right)$

The new generalised imperfection factor η_{PROP} introduces a plateau up to slenderness $\bar{\lambda} = \bar{\lambda}_0$, while the shape of the curve depends on the parameters γ and α . The imperfection factor α is defined according to Eq. (5) and thus, the parameters β , γ and $\bar{\lambda}_\theta$ allow for the complete description of the buckling curve. Since a plateau was introduced, Eq. (2) should be replaced by

$$\chi_{fi} = 1 \quad \bar{\lambda}_\theta \leq \bar{\lambda}_0$$

$$\chi_{fi} = \frac{1}{\varphi_\theta + \sqrt{\varphi_\theta^2 - \bar{\lambda}_\theta^2}} \quad \bar{\lambda}_\theta > \bar{\lambda}_0 \quad (9)$$

The values of β , γ and $\bar{\lambda}_0$ were calibrated to propose curves on the safe side. The selected values are given in Table 3. The obtained buckling curves are compared with numerical results and the EN 1993-1-2 buckling curve in Figure 2. Predictions from the proposal are safer and the introduction of a plateau ($\bar{\lambda}_0$) together with the change of the shape of the curve (β and γ), allow for a better representation of the numerical outcomes.

Table 3. Selected values for the parameters of the proposed buckling curve

	L	T (2 equal leg L)	T (2 unequal leg L)	T (half H or I)	X (4 equal leg L)
β	1.00	1.25	1.10	1.50	0.85
γ	0.50	0.80	0.50	0.50	0.35
$\bar{\lambda}_0$	0.15	0.22	0.20	0.18	0.20

In order to provide safe predictions, an additional check on the generalised imperfection factor was performed. For this purpose, the data relative to the envelope of the minimum values of the numerical results N_{FEA}/N_{yield} in Figure 2 were selected. An equivalent numerical generalised imperfection factor η_{FEA} was obtained from these data and compared with $\eta_{EC3.1-2}$ and η_{PROP} . Since the actual and the proposed buckling curves all derive from the equations in the following form

$$\chi_{fi} + \eta \frac{\chi_{fi}}{1 - \chi_{fi} \bar{\lambda}_\theta^2} = 1 \quad (10)$$

the imperfection factor η_{FEA} was obtained by substituting the reduction factor at elevated temperature χ_{fi} with the one obtained from the data relative to the envelope of the minimum values of the numerical results $\chi_{fi,FEA} = N_{FEA}/N_{yield}$ in Eq. (10). Hence, it holds

$$\eta_{FEA} = \left(\frac{1}{\chi_{fi,FEA}} - 1 \right) \left(1 - \chi_{fi,FEA} \bar{\lambda}_\theta^2 \right) \quad (11)$$

In Figure 3 the generalised imperfection factors over the slenderness are compared for L sections with a steel grade of 235 MPa. Generalised factors η higher than η_{FEA} entail safe results for the design curves. Since the generalised imperfection factor $\eta_{EC3.1-2}$ is proportional to the slenderness $\bar{\lambda}_\theta$ it does not represent well the non-linear behaviour exhibited by η_{FEA} . Conversely, the η_{PROP} factor is in good agreement with the η_{FEA} for slenderness lower than 1. Better agreement could be found for higher slenderness by introducing further terms in the expression of η_{PROP} , but this would introduce an unnecessary complexity in the model. In fact, the higher the slenderness, the lesser the difference between the generalised

imperfection factor η and η_{FEA} affects the buckling coefficient χ_{fi} . This is confirmed in Figure 2, in which for slenderness higher than 2, the actual and the proposed buckling curve are almost superimposed, though their generalised imperfection values are significantly different in Figure 3. Similar considerations can be drawn for all the section types and steel grades.

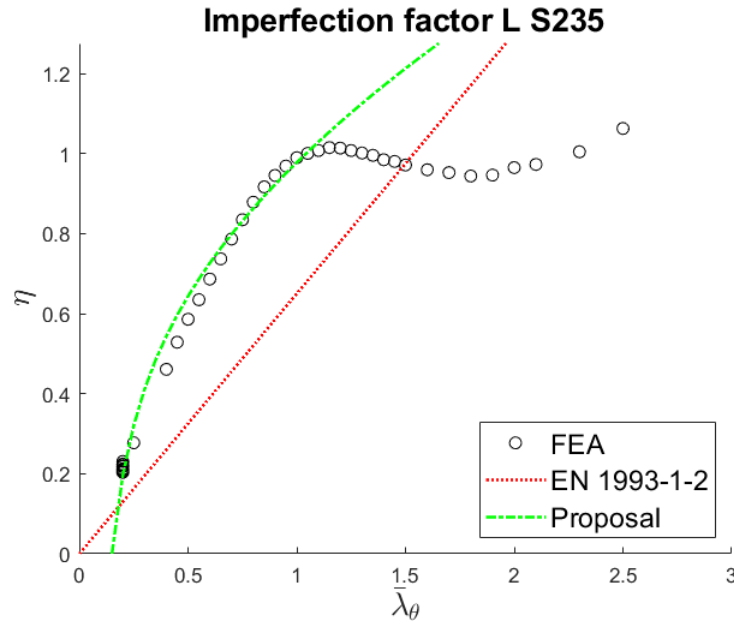
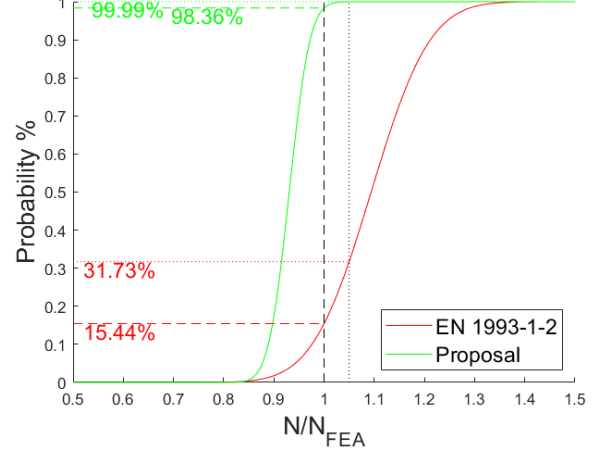
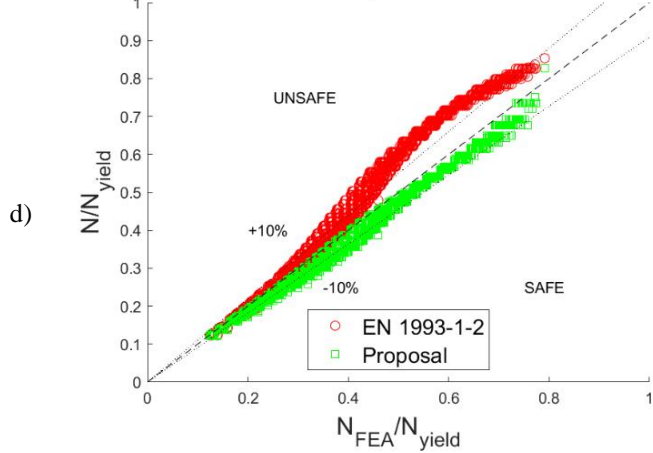
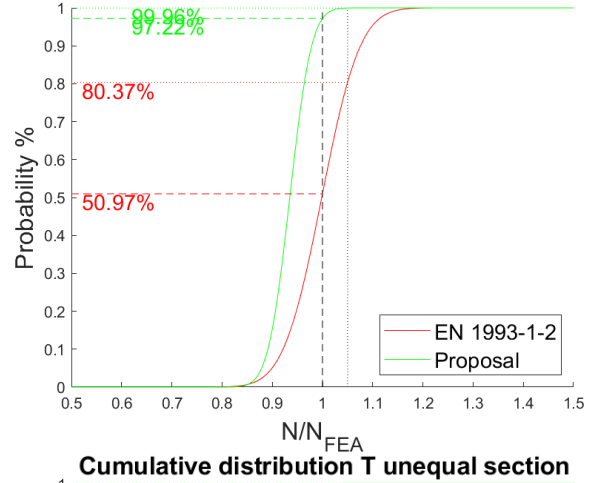
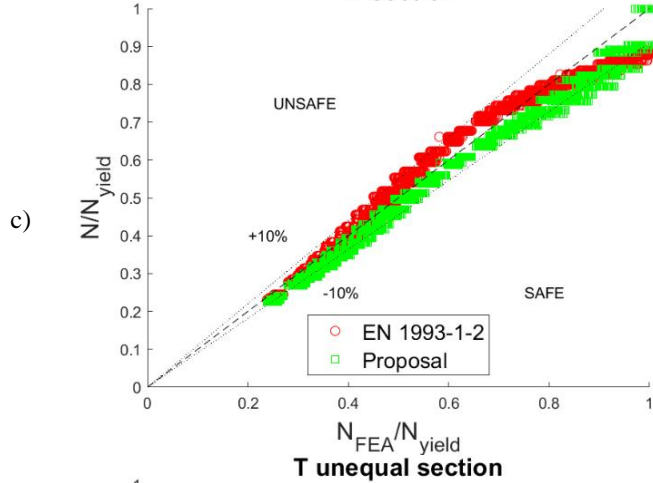
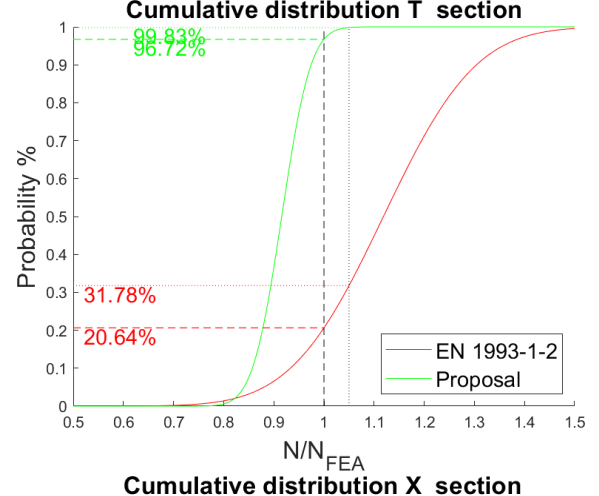
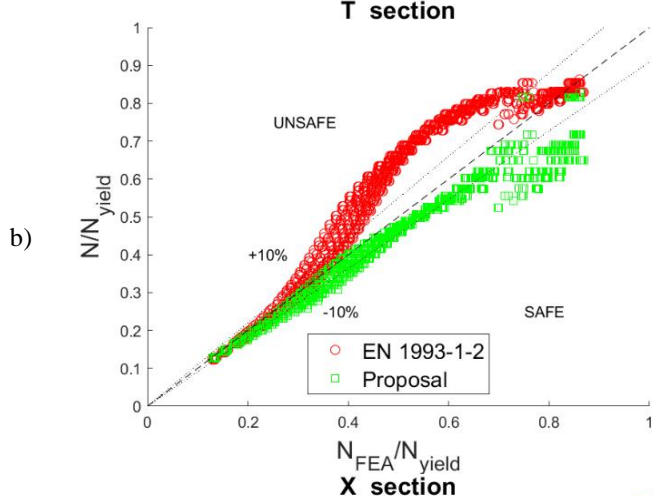
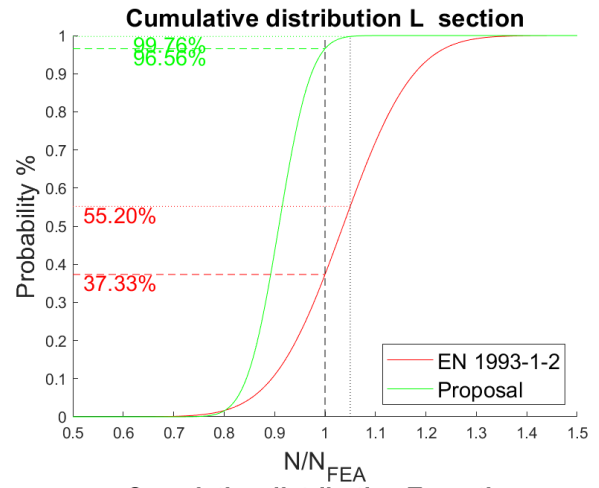
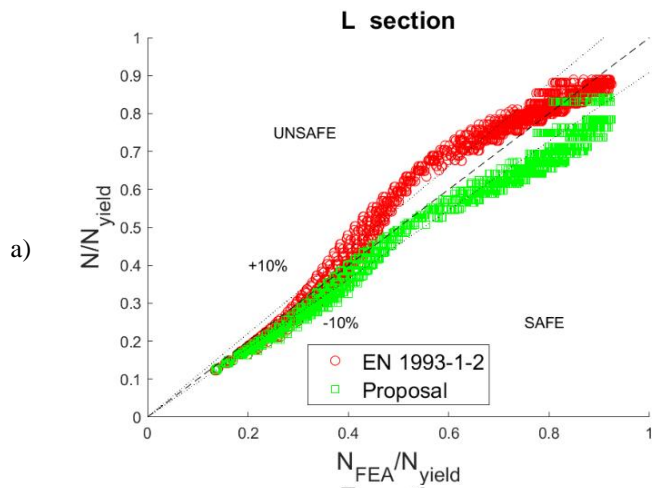


Figure 3. Generalised imperfection factors: evolution with the relative slenderness at elevated temperature for L sections and steel S235

4.1 Statistical analysis

The degree of safety of the buckling curves was assessed by comparison with the results from numerical simulation. For each non-dimensional slenderness $\bar{\lambda}_\theta$ employed in the numerical analyses, the predictions from the buckling curves were plotted against the numerical failure load N_{FEA} (Figure 4). The loads were normalised by means of the yield load N_{yield} . In Figure 7, the safe-unsafe limit is identified by the first quadrant bisector line ($N = N_{FEA}$). The EN 1993-1-2 design buckling attains values significantly higher than the ones from the numerical simulation ($>10\%$). Conversely, the proposed buckling curve is safer, and results are better distributed along the bisector line direction, especially for sections made of single or coupled L sections. The results of a statistical investigation are also presented in Figure 4, in which the safe-unsafe limit is drawn at $N/N_{FEA} = 1$ and data are shown assuming a normal distribution. Lower standard deviations and higher frequency were obtained for the proposal. The proposal provides a probability of safe predictions higher than 96% for sections made of single or coupled L sections, and higher than 94% for the T sections obtained from half H or I section. These probabilities of non-exceedance of the safe-unsafe limit are significantly higher compared to the ones from the EN 1993-1-2 design curve. Introducing a safety margin of 5% the probabilities of non-exceedance raise to more than 98%.



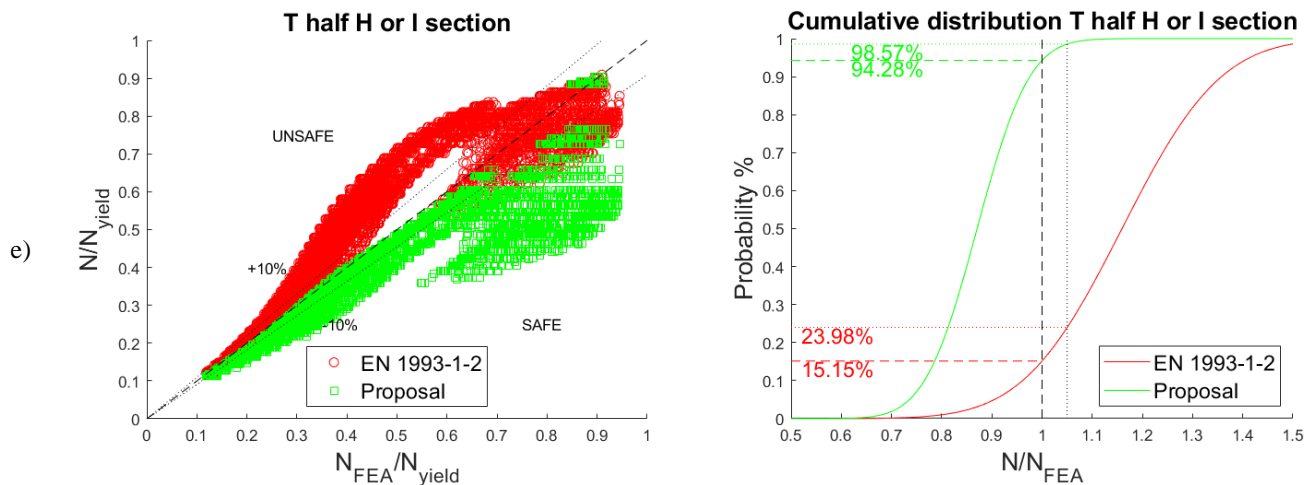


Figure 4. Numerical results vs predictions and statistical investigation. a) L, b) T and c) X made of coupled equal leg L sections, d) T obtained from unequal leg L sections and e) T obtained from half H or I section

5 CONCLUSIONS

A parametric analysis consisting of more than 41000 analysis was carried out to investigate the behaviour of axially compressed steel elements prone to torsional and flexural-torsional buckling at elevated temperature. It was found that flexural and flexural-torsional buckling may affect the resistance to compression of L, T and X sections in fire situation in the low slenderness range. Compared with numerical outcomes, the actual provisions of EN 1993-1-2 lead to both conservative and unconservative predictions. In detail, for a large range of medium slenderness, i.e. $0.4 \leq \bar{\lambda}_\theta < 1.2$, the load-bearing capacity is significantly overestimated by the EN 1993-1-2 buckling curve. In order to obtain safer and more reliable predictions, a new buckling curve was proposed. The latter differs from the formulation provided in EN 1993-1-1 and EN 1993-1-2 only in the definition of the generalised imperfection factor η_{PROP} , which is determined by three parameters, namely β , γ and $\bar{\lambda}_0$. The values assumed by these parameters were given for each investigated cross-section shape. The proposal was shown to be safer and more accurate. A statistical investigation was performed as well, and assuming a normal distribution, probabilities of safe predictions higher than 94% were reached. For T sections obtained from half an H or I section, the proposal was less accurate, but still safer and more reliable than the EN 1993-1-2 curve. It was found that a better representation of the results was obtained with buckling curves expressed with respect to the pure flexural buckling slenderness because the length of a column l may not be well represented by the non-dimensional the torsional or flexural-torsional slenderness. In future research, more refined finite element models could be employed to account for the influence of connecting plates or battens in elements made of coupled L sections. Moreover, experimental investigation would be beneficial.

ACKNOWLEDGMENTS

The authors acknowledge funding from the Italian Ministry of Education, University and Research (MIUR) in the frame of the Departments of Excellence Initiative 2018–2022 attributed to DICAM of the University of Trento

REFERENCES

1. European Committee for Standardisation (2005). Eurocode 3 Design of steel structures - Part 1-1: General rules and rules for buildings.
2. European Committee for Standardisation (2005). Eurocode 3 Design of steel structures - Part 1-2: General rules - Structural fire design
3. J.-M. Franssen, J.-B. Schleich, L.-G. Cajot (1995). A simple Model for the Fire Resistance of Axially-loaded Members According to Eurocode 3. Journal of Constructional Steel Research, Vol 35, pp. 49-69.

4. C.G. Bailey, I.W. Burgess, R.J. Plank, The lateral-torsional buckling of unrestrained steel beams in fire, *J. Constr. Steel Res.* 36 (2) (1996) 101–119
5. P. Vila Real, J.-M. Franssen, Lateral Torsional Buckling of Steel - Beams in Case of Fire – Numerical Modelling. First International Workshop Structures in Fire, Copenhagen, 2000.
6. P. Vila Real, N. Lopes, L.S. da Silva, J.-M. Franssen, Lateral-torsional buckling of unrestrained steel beams under fire conditions: improvement of EC3 proposal, *Comput. Struct.* 82 (20) (2004) 1737–1744
7. P. Vila Real, R. Cazeli, L. S. da Silva, A. Santiago, e P. Piloto (2004), The effect of residual stresses in the lateral-torsional buckling of steel I-beams at elevated temperature. *J. Constr. Steel Res.*, Vol. 60, No. 3–5, pp. 783–793.
8. C. Couto, P. Vila Real, N. Lopes, B. Zhao (2016), Numerical investigation of the lateral-torsional buckling of beams with slender cross section for the case of fire. *Engineering Structures*, Vol. 106, pp. 410-421.
9. C. Couto, P. Vila Real, N. Lopes, B. Zhao (2016), Local buckling in laterally restrained steel beam-columns in case of fire. *J. Construct. Steel Res.*, Vol. 122, pp. 543-556.
10. C. Couto, E. Maia, P. Vila Real, N. Lopes (2018), The effect of non-uniform bending on the lateral stability of steel beams with slender cross-section at elevated temperatures. *Engineering Structures*, Vol. 163, pp. 153-156.
11. J.-M. Franssen, F. Morente, P. Vila Real, F. Wald, A. Sanzel, B. Zhao (2016). Fire Design of Steel Members with Welded or Hot-rolled Class 4 Cross-sections (FIDESC4).
12. N. Silvestre, P. B. Dinis, D. Camotim (2013). Developments on the Design of Cold-Formed Steel Angels. *J. Struct. Steel Res*, Vol 139, No. 5, pp. 680-694.
13. B. W. Schafer (2008). Review: The Direct Strength Method of cold-formed steel member design. *J. Construct. Steel Res*, Vol 64, pp. 766-778.
14. D. Popovic, G. J. Hancock, K. J. R. Rasmussen (2001). Compression tests on cold-formed angles loaded parallel with a leg. *J. Struct. Steel Res*, Vol 127, No. 6, pp. 600-607.
15. T. Ranawaka, M. Mahendran (2010). Numerical modelling of light gauge cold-formed steel compression members subjected to distortional buckling at elevated temperatures. *Thin-Walled Structures*, Vol 48, No. 4-5, pp. 334-344.
16. L. Laim, J. P. C. Rodrigues (2018). Fire design methodologies for cold-formed steel beams made with open and closed cross-sections. *Engineering Structures*, Vol. 171, pp. 759-778.
17. P. B. Dinis, D. Camotim, N. Silvestre (2010). On the local and global buckling behavior of angle, T-section and cruciform thin-walled members, *Thin-Walled Structures*, Vol 48, pp. 786-797.
18. R. Dabrowski (1988). On Torsional Stability of Cruciform Columns, *J. Constr. Steel Res.*, Vol. 9, pp. 51-59.
19. G. Chen, N. S. Trahir (2006). Inelastic torsional buckling strengths of cruciform columns, *Engineering Structures*, Vol. 16, No. 2, pp. 83-90.
20. N. S. Trahir (2012). Strength design of cruciform steel columns. *Engineering Structures*, Vol. 35, pp. 307-313.
21. A. Taras, R. Greiner (2007). Torsional and flexural torsional buckling – A study on laterally restrained I-sections, *J. Constr. Steel Res.* Vol. 64, pp. 725-731.
22. L. Possidente, N. Tondini, J.-M. Battini (2019). Co-rotational 3D beam element for torsional problems of steel structures in fire. *Proceedings of the 7th International Conference on Structural Engineering, Mechanics and Computation (SEMC 2019)*, September 2-4, 2019, Cape Town, South Africa.
23. L. Possidente, N. Tondini, J.-M. Battini (2018). Branch-switching procedure for post-buckling analyses of thin-walled steel members in fire. *Thin-Walled Structures*, Vol 136, pp. 90-98.
24. S. E. Quiel, M. E. M. Garlock (2010), Calculating the buckling strength of steel plates exposed to fire. *Thin-Walled Structures.*, Vol. 48, No. 9, pp. 684-695.
25. C. Couto, P. Vila Real, N. Lopes, B. Zhao (2015), Resistance of steel cross-sections with local buckling at elevated temperatures. *J. Construct. Steel Res.*, Vol. 109, pp. 101-114.
26. J. Jönsson, T.-C. Stan (2017), European column buckling curves and finite element modelling including high strength steels. *J. Construct. Steel Res.*, Vol 128, pp. 136-151
- Thomas, P. H., Webster, C. T. and Raftery, M. M., Experiments on Buoyant Diffusion Flames, *Combustion & Flame*, Vol. 5, 1961, pp. 359

STABILITY CHECK OF WEB-TAPERED STEEL BEAM-COLUMNS IN FIRE

Élio Maia¹, Paulo Vila Real², Nuno Lopes³, Carlos Couto⁴

ABSTRACT

The General Method (GM) (clause 6.3.4 of EN 1993-1-1) covers the safety check of structural elements with complex support conditions and/or of non-prismatic members. However, the fire part of Eurocode 3 provides no specific guidelines regarding its applicability at elevated temperatures, apart from considering reduced material mechanical properties. Moreover, previous works by the authors have shown that the adaptation of the GM for tapered columns and beams provides unreliable results, motivating new proposals. With that in mind, current design procedures for tapered beam-columns at normal temperature (GM and Marques et al.'s proposal) were adapted to fire situation in the scope of the present investigation. Although the latter became unsafe at elevated temperatures, three approaches have been considered for the GM.

Provided that the GM is adapted using an interpolation between appropriate reduction factors, the present work validates this procedure for the safety check of tapered beam-columns at elevated temperatures. Yet, significant room for improvement on the flexural/lateral-torsional buckling interaction has been identified and should be the focus of future scientific efforts.

Most importantly, this work reinforces the need of deeper investigation on the stability of tapered beam-columns and non-uniform members in general, as adapting normal temperature methodologies to fire is not enough to produce accurate and reliable predictions of resistance for these members.

Keywords: Tapered beam-columns; Fire; General Method; FEM

1 INTRODUCTION

Non-uniform (tapered) steel members are widely used in steel construction due to their structural efficiency, as material savings can be achieved by optimizing member geometry to withstand non-uniform loads. At normal temperature, the out-of-plane stability check of non-uniform members should be performed using the General Method (GM) [1], as the variation in member geometry precludes the use of the usual stability verification clauses, namely clause 6.3.3 for uniform beam-columns. However, the existing fire design methods of Part 1-2 of Eurocode 3 (EC3) [2] are limited to uniform members and no specific rules are provided for their non-uniform counterparts.

At normal temperature, some of the limitations/inconsistencies of tapered member design have been addressed in the scope of project TaperSteel [3], leading to the proposal of new design methodologies by Marques et al. for non-uniform columns [4], beams [5] and beam-columns [6]. The latter [6] focuses on the

¹ PhD Student, RISCO – University of Aveiro,
e-mail: eliomaia@ua.pt, ORCID: <https://orcid.org/0000-0002-2445-3421>

² Full Professor, RISCO – University of Aveiro
e-mail: pyreal@ua.pt, ORCID: <https://orcid.org/0000-0002-7221-410X>

³ Associate Professor, RISCO – University of Aveiro
e-mail: nuno.lopes@ua.pt, ORCID: <https://orcid.org/0000-0003-0634-8991>

⁴ Assistant Researcher, RISCO – University of Aveiro
e-mail: ccouto@ua.pt, ORCID: <https://orcid.org/0000-0003-0865-2225>

extension of the EN 1993-1-1 [1] interaction formulae, originally developed for prismatic members, for the design of tapered beam-columns and its reliability for fire design will be investigated in this work.

At elevated temperatures, the safety check is unclear since no specific guidelines for the implementation of the GM are given in the fire part of the Eurocode 3, apart from using the standard reduction factors for steel material properties at elevated temperatures. However, previous investigations by the authors have demonstrated that the standard adaptation of the GM according to the EN 1993-1-2 [2] yields unsafe results for columns [7] and overly conservative results for beams [8]. In addition, these works [7,8] have also shown that adapting other normal temperature methodologies, namely the LTB procedure of the DIN 18800-2 [9] and Marques' et al. methodologies for columns [4] and beams [5] revealed to be unsafe. Still, room for improvement for the GM was identified in both publications [7,8], resulting in calibrations of the buckling curves for tapered columns [7], and also for tapered beams in a follow-up investigation [10].

As such, given the scarcity of design methodologies for fire situation, the purpose of this paper is to evaluate the reliability of the General Method, as well as Marques et al.'s [6] proposal for the out-of-plane stability check of tapered beam-columns in fire. Regarding the GM, three approaches were considered for its adaptation to fire: i) standard adaptation with the single buckling curve of EN 1993-1-2; ii) considering the out-of-plane reduction factor χ_{op} equal to the minimum value of χ_z and χ_{LT} , obtained according to the author's proposals for tapered columns [7] and beams [10] and iii) using the reduction factor χ_{op} obtained from an interpolation of the same coefficients χ_z and χ_{LT} from [7,10].

For that purpose, a parametric study is defined for two reference cross-sections with varying height taper ratios, for different temperatures and loading cases. The adaptation of the methodologies to fire is done by accounting for the reduction in steel material properties with the temperature, according to the EN 1993-1-2 [2]. The capacity predicted by the procedures is then compared with the numerically obtained ultimate bearing capacity of the members at elevated temperatures, based on geometrically and materially non-linear analyses with imperfections (GMNIA) using shell finite elements in the computer code SAFIR [11].

2 METHODOLOGIES

2.1 General Method

2.1.1 Normal temperature

The stability of uniform beam-columns in EC3-1-1 [1] is checked by the application of clause 6.3.3. Regarding the stability of a non-uniform member, however, this clause is not applicable as the evaluation of the buckling resistance of such members lies outside the range of application of the interaction formulae. For those cases, verification should be performed using clause 6.3.4 (denoted as General Method or GM). According to the GM, the stability of members is verified by ensuring that condition (1) is verified.

$$\frac{\chi_{op} \cdot \alpha_{ult,k}}{\gamma_{M1}} \geq 1 \quad (1)$$

where χ_{op} is the reduction factor for out-of-plane ("op") buckling phenomena, corresponding to the relative slenderness $\bar{\lambda}_{op}$ obtained with expression (2), with γ_{M1} being the partial safety factor.

$$\bar{\lambda}_{op} = \sqrt{\frac{\alpha_{ult,k}}{\alpha_{cr,op}}} \quad (2)$$

$\alpha_{cr,op}$ is the minimum amplifier for the in-plane design loads to reach the elastic critical resistance of the structural component in regards to the flexural/lateral-torsional buckling, and could be determined with the Finite Element Method by performing a Linear Buckling Analysis (LBA). $\alpha_{ult,k}$ is the minimum load amplifier of the design loads in order to reach the characteristic resistance of the most critical cross-section

of the structural component, considering only the in-plane behaviour of the member. It is taken as the minimum value given by the cross-sectional verification of expression (3) along the length of the member.

$$\alpha_{ult,k} = 1 / \left(\frac{N_{Ed}}{N_{Rk}} + \frac{M_{y,Ed}}{M_{y,Rk}} \right) \quad (3)$$

where N_{Ed} and $M_{y,Ed}$ correspond to the design value of the axial load and the in-plane moment, while N_{Rk} and $M_{y,Rk}$ are the characteristic values of the axial and bending moment resistances, respectively, at the most critical cross-section. For class 1 or 2 cross-sections, $M_{y,Rk}$ should be determined according to section 6.2.9 [1] for combined bending and axial force, if applicable.

The out-of-plane buckling reduction factor χ_{op} can be determined for the relative slenderness $\bar{\lambda}_{op}$ defined in expression (2) by choosing the appropriate buckling curves. Clause 6.3.4 of the EN 1993-1-1 [1] provides the following two methods:

- χ_{op} is taken as the minimum value between the reduction factor χ_z for flexural buckling (clause 6.3.1 of EN 1993-1-1) and the reduction factor χ_{LT} for lateral-torsional buckling (clause 6.3.2), each calculated for the relative slenderness $\bar{\lambda}_{op}$. In practice, this procedure considers that the most adverse out-of-plane buckling phenomena (flexural or lateral-torsional buckling) singlehandedly covers the stability of the member. This method will be explored throughout the work and will be referred to as “**Minimum**”;
- χ_{op} is interpolated between χ_z and χ_{LT} and obtained with expression (4). This method will be referred to as “**Interpolation**”.

$$\chi_{op,int} = \frac{\frac{N_{Ed}}{N_{Rk}} + \frac{M_{y,Ed}}{M_{y,Rk}}}{\frac{N_{Ed}}{\chi_z \cdot N_{Rk}} + \frac{M_{y,Ed}}{\chi_{LT} \cdot M_{y,Rk}}} \quad (4)$$

2.1.2 Adaptation to fire

The adaptation of this methodology to fire is done by accounting for the reduction in steel material properties with the temperature, namely the yield strength $f_{y,\theta}$ and Young's Modulus $E_{a,\theta}$, with the reduction factors $k_{y,\theta}$ and $k_{E,\theta}$, respectively. Given the direct proportionality of the critical load amplifier to the Young's Modulus, the following expression can be deduced:

$$\alpha_{cr,\theta,op} = k_{E,\theta} \cdot \alpha_{cr,op} \quad (5)$$

The load amplifier of the in-plane design loads is obtained with a similar process as described for normal temperatures, but considering both the characteristic resistances in fire situation $N_{fi,\theta,Rk}$ and $M_{y,fi,\theta,Rk}$, as well as the acting axial load $N_{fi,Ed}$ and bending moment $M_{y,fi,Ed}$. The cross-sectional resistances of class 1 and 2 cross-sections are obtained following the EN 1993-1-1 [1] procedures for normal temperature design (including clause 6.2.9 [1] for combined bending and axial force, if applicable), with the reduced mechanical properties given in Part 1-2 [2]. Class 3 and 4 cross-sections are calculated according to the guidelines of FIDESC4 [12], as proposed in [13].

$$\alpha_{ult,\theta,k} = 1 / \left(\frac{N_{fi,Ed}}{N_{fi,\theta,Rk}} + \frac{M_{y,fi,Ed}}{M_{y,fi,\theta,Rk}} \right) \quad (6)$$

The relative slenderness at elevated temperatures $\bar{\lambda}_{op,\theta}$ comes:

$$\bar{\lambda}_{op,\theta} = \sqrt{\frac{\alpha_{ult,\theta,k}}{\alpha_{cr,\theta,op}}} \quad (7)$$

The final condition to be fulfilled in fire situation for the General Method is thus

$$\frac{\chi_{op,fi} \cdot \alpha_{ult,\theta,k}}{\gamma_{M,fi}} \geq 1 \quad (8)$$

with $\gamma_{M,fi}$ being the partial safety factor, taken as 1.0. The reduction factor $\chi_{op,fi}$ in fire situation can be calculated with Eq. (9) following the guidelines of the EN 1993-1-2 [2]:

$$\chi_{op,fi} = \chi_{z,fi} = \chi_{LT,fi} = \frac{1}{\phi_{\theta} + \sqrt{\phi_{\theta}^2 - \bar{\lambda}_{op,\theta}^2}} \quad (9)$$

$$\phi_{\theta} = \frac{1}{2} \cdot \left(1 + \alpha \bar{\lambda}_{op,\theta} + \bar{\lambda}_{op,\theta}^2 \right) \quad (10)$$

$$\alpha = 0.65 \cdot \sqrt{235/f_y} \quad \text{where } f_y \text{ is the yield strength in } N/mm^2 \quad (11)$$

It should be noted that imperfection factor α is the same irrespective of member type, geometry or loading conditions. In practice, EN 1993-1-2 [2] provides a single buckling curve for both columns and beams, the stability of which is governed by different buckling phenomena, highlighting a limitation of the norm explored already explored by the authors [7,8]. Consequently, both methods – minimum and interpolation – for calculating χ_{op} yield the same results.

2.1.3 Improved out-of-plane reduction factors [7,10]

The shortcoming of the EN 1993-1-2 [2], which was discussed in the previous sub-section, motivated proposals of improved buckling curves by the authors for web-tapered columns [7] and beams [10]. For tapered columns [7], the coefficient of α in expression (11) was changed to 0.85 (from 0.65).

$$\alpha_{z,new} = 0.85 \cdot \sqrt{235/f_y} \quad \text{where } f_y \text{ is the yield strength in } N/mm^2 \quad (12)$$

For tapered beams [10], expression (10) was modified as per (13) and (14) by adding a slenderness plateau $\bar{\lambda}_{op,0,\theta}$, which takes into account the height taper ratio γ_h and loading conditions. Despite the addition of the slenderness plateau, χ_{op} should not be higher than 1.0.

$$\phi_{LT,\theta} = \frac{1}{2} \cdot \left(1 + \alpha (\bar{\lambda}_{op,\theta} - \bar{\lambda}_{op,0,\theta}) + \bar{\lambda}_{op,\theta}^2 \right) \quad (13)$$

$$\bar{\lambda}_{op,0,\theta} = \begin{cases} 0.1 \cdot \gamma_h + 0.2 & \text{for } \psi = -1 \\ 0.14 & \text{for } \psi = 0 \\ 0.2 \cdot \gamma_h - 0.2 & \text{for } \psi = 1 \\ 0.05 \cdot \gamma_h + 0.08 & \text{for Uniformly distributed load} \end{cases} \quad (14)$$

where $M_1 = \psi \cdot M_2$, with M_1 and M_2 corresponding to $M_{y,fi,Ed}$ at the smallest and tallest ends, respectively

These improvements to the buckling curves for non-uniform columns and beams will be compared to the standard adaptation of the General Method for beam-columns according to the two methods suggested in [1] for the calculation of χ_{op} : “Minimum” and “Interpolation”.

2.2 Extension of the EN 1993-1-1 interaction formulae [6]

A design procedure for the out-of-plane stability of tapered beam-columns at normal temperature has been proposed by Marques et al. [6] and validated against numerical data. This methodology is an extension of the EN 1993-1-1 [1] interaction formulae for prismatic beam-columns, together with an implementation of two methodologies previously proposed in the scope of the author’s PhD thesis for tapered columns [4] and beams [5]. Similar to the original interaction formulae, the stability is checked as long as conditions (15) and (16) are fulfilled.

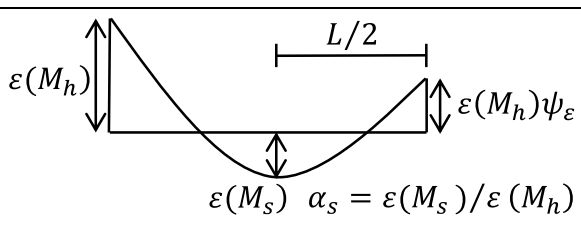
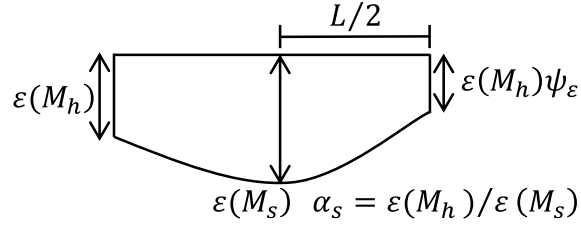
$$\frac{N_{Ed}(x_{c,N}^I)}{\chi_y(x_{c,N}^I)N_{Rk}(x_{c,N}^I)/\gamma_{M1}} + k_{yy} \frac{M_{y,Ed}(x_{c,M}^I)}{\chi_{LT}(x_{c,M}^I)M_{y,Rk}(x_{c,M}^I)/\gamma_{M1}} \leq 1.0 \quad (15)$$

$$\frac{N_{Ed}(x_{c,N}^I)}{\chi_z(x_{c,N}^I)N_{Rk}(x_{c,N}^I)/\gamma_{M1}} + k_{zy} \frac{M_{y,Ed}(x_{c,M}^I)}{\chi_{LT}(x_{c,M}^I)M_{y,Rk}(x_{c,M}^I)/\gamma_{M1}} \leq 1.0 \quad (16)$$

where χ_y , χ_z are reduction factors for the in-plane and out-of-plane flexural buckling of tapered columns, respectively, obtained with a modified methodology originally proposed in [4] for in-plane buckling, and likewise for χ_{LT} [5], which is the reduction factor for lateral-torsional buckling. It should be noted that the axial and bending components are calculated individually at the respective first-order critical cross-sections $x_{c,N}^I$ and $x_{c,M}^I$, respectively. Further details regarding the calculation of the reduction factors can be found in the original work [6].

The interaction factors k_{yy} and k_{zy} are calculated according to Method 2 of Annex B [1]. In order to adapt this methodology to tapered beams-columns, the author demonstrated that the diagram of Table B.3 of the norm could be used by taking the first-order utilization diagram instead of the bending moment diagram, as illustrated in Table 1. Essentially, the utilization $\varepsilon(x) = M_{y,Ed}(x)/M_{Rd}(x)$ of a tapered beam subjected to a linear bending moment distribution can be compared to the diagram of a prismatic beam subjected to a uniformly distributed loading and end moments. However, this approach is less accurate for the uniformly distributed load (UDL) case.

Table 1. Adaptation of the equivalent uniform moment factors C_m – edited version of Table 3.2 from [6].

Moment utilization diagram	Range		C_{my} and C_{mLT}
 <p>$\varepsilon(M_h)$ $L/2$ $\varepsilon(M_h)\psi_\varepsilon$ $\varepsilon(M_s)$ $\alpha_s = \varepsilon(M_s)/\varepsilon(M_h)$</p>	$0 \leq \alpha_s \leq 1$	$-1 \leq \psi_\varepsilon \leq 1$	$0.2 + 0.8\alpha_s \geq 0.4$
	$-1 \leq \alpha_s < 0$	$0 \leq \psi_\varepsilon \leq 1$	$0.1 - 0.8\alpha_s \geq 0.4$
		$-1 \leq \psi_\varepsilon < 0$	$0.1(1 - \psi_\varepsilon) - 0.8\alpha_s \geq 0.4$
 <p>$\varepsilon(M_h)$ $L/2$ $\varepsilon(M_h)\psi_\varepsilon$ $\varepsilon(M_s)$ $\alpha_s = \varepsilon(M_h)/\varepsilon(M_s)$</p>	$0 \leq \alpha_s \leq 1$	$-1 \leq \psi_\varepsilon \leq 1$	$0.95 + 0.05\alpha_h$
	$-1 \leq \alpha_s < 0$	$0 \leq \psi_\varepsilon \leq 1$	$0.95 + 0.05\alpha_h$
		$-1 \leq \psi_\varepsilon < 0$	$0.95 + 0.05\alpha_h(1 + 2\psi_\varepsilon)$

3 NUMERICAL MODEL

The Geometrically and Materially Non-Linear Analyses with Imperfections (GMNIA) were performed using the finite element computer code SAFIR [11]. The capability of SAFIR to model local buckling with shell elements was initially validated by Talamona and Franssen [14] and, specifically for web-tapered I-section members, the numerical model used in this work has been validated against experimental data at normal and elevated temperatures by the authors [7].

Based on sensitivity analyses, it was concluded that utilizing a mesh with 12 elements in the flange, 18 in the web and 100 along the length was sufficient for the range of models analysed in the parametric study.

The members were discretized into quadrangular shell elements with four nodes with six degrees of freedom. The integration on the shell element follows a Gauss scheme with 2x2 points on the surface and 4 points through the thickness.

The steel material law is a two-dimensional constitutive relation with the von-Mises yield surface, according to the non-linear stress-strain formulae of the EN 1993-1-2, as well as the respective reduction factors at elevated temperatures given in the EN 1993-1-2. Steel grade S235 was used in the parametric

investigation – yield strength of 235 MPa, modulus of elasticity of 210 GPa and Poisson’s ratio of 0.3 were adopted. The temperature was considered uniform along the section and along the member as this effect has shown to not have a negative impact on the stability of tapered members in the studied conditions [15].

The fork-support conditions were reproduced by restraining the vertical displacements (U_z) of the bottom flanges, as well as the horizontal displacements (U_y) of the web, at the ends. As the x-axis displacements (U_x) at the supports were not restrained, the rigid-body movement along the axis of the member was blocked by restraining the x-axis displacement (U_x) at mid-length. Due to the nature of load application, thicker elements (end plates) have been added at the supports in order to avoid numerical (local) instabilities. The thickness of these elements was taken as ten times the thickness of the web ($10 \times t_w$).

The geometric imperfections, both global (member) and local (plate) ones, have been introduced in the model by changing the nodal coordinates to represent the worst scenario for the assessment of member resistance. This has been considered as the shape given by the eigen modes of a linear buckling analysis (LBA) calculated with the software Cast3M [16]. In addition, the recommendations given in the Annex C of EN 1993-1-5 [17] were followed: i) a combination of local and global (Figure 1) modes was considered by taking the lowest mode as the leading imperfection and the other one reduced to 70%; ii) the amplitude of the imperfections was chosen as 80% of the fabrication tolerances given in the EN 1090-2:2011 [18] and presented in Table 2.

Table 2. Fabrication tolerances according to EN 1090-2:2011 [18].

Mode		Imperfection amplitude	
Local	Flange	$b_f/150$	for $b_f/t_f \leq 20$
		$b_f^2/(3000 \times t_f)$	for $b_f/t_f > 20$
	Web	$h_w/200$	for $h_w/t_w \leq 80$
		$h_w^2/(16000 \times t_w)$	for $80 < h_w/t_w \leq 200$
Global	-	$L/750$	for $h_w/t_w > 200$

For the material imperfections, the pattern of residual stresses for welded cross-sections illustrated in Figure 2 was included in the numerical simulations, following the recommendations of the ECCS [19,20]. It’s worth mentioning that, from the different patterns in the literature for welded sections, this has been identified as the most detrimental one when member failure is governed by lateral-torsional buckling. [21]

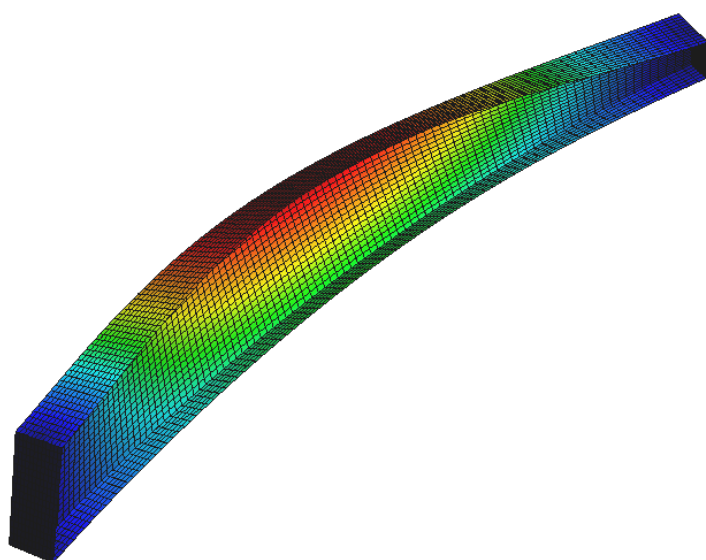


Figure 1. Global mode of a $\gamma_h = 3$ HEB300w beam-column.

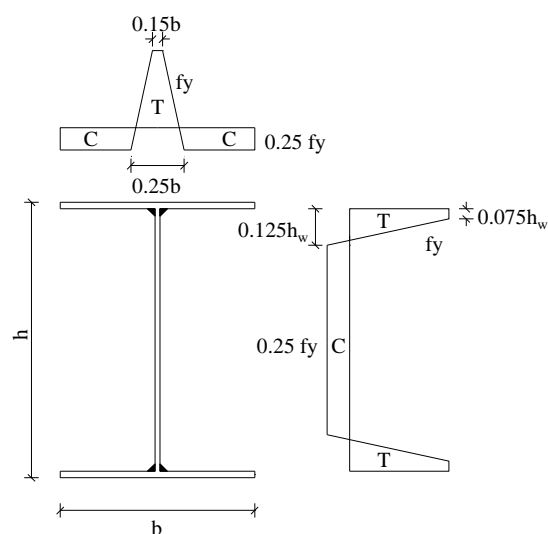


Figure 2. Residual stress pattern.

4 NUMERICAL STUDY

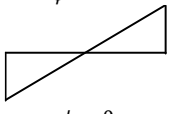
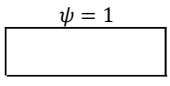
4.1 Parameters considered

The parametric study evaluated the out-of-plane behaviour of beams, columns and beam-columns according to the parameters presented in Table 3. The IPE200 and HEB300 were considered as reference sections and S235 was the chosen steel grade for the investigation and the web-tapering was centre-aligned, meaning that the line defined by the cross-sectional centres of mass was horizontal. The temperatures 350°C, 450°C, 550°C and 700°C were considered. These are typical temperatures reached in steel members during a fire and, therefore, are considered to be representative in the scope of this study. On this regard, this numerical framework is limited to uniformly distributed temperatures along the member. Although the influence of non-uniform temperature distributions has not been studied in this work, this effect was shown to not have a negative impact on the stability of tapered members [15]. Three taper ratios and prismatic beam-columns ($\gamma_h = 1$) were studied and the lengths were varied to obtain a representative set of slendernesses. Although prismatic members are not the main focus of the work, these data points cannot be ignored due to the risk of compromising the generality of the methodology.

For the loading ratios, in addition to the compression ($\beta = 0$) and bending ($\beta = 1$) cases, four different load ratios were used pertaining to the compression and bending cases, while uniform, triangular and bi-triangular bending diagrams were considered.

Members with an angle of taper higher than 15° have been removed from the parametric study due to common production limitations, which accounts for approximately 200 results. Moreover, since the focus of this work is on the study of flexural/lateral-torsional instability phenomena, the numerical simulations whose resistance was compromised due to shear were not considered. A numerical case was disregarded if, upon visual inspection, its collapse shape showed clear signs of shear buckling or if the theoretical acting shear force was higher than half of the shear resistance ($V_{fi,Ed} > 0.5V_{fi,\theta,Rd}$). A total of 4150 cases were studied.

Table 3. Parameters considered.

Reference cross-section ($h_w \times t_w + b \times t_f$)	Length		Temp.	Taper ratio $\gamma_h = h_2/h_1$	Load ratio β (*)	Bending diagram
-	(m)		(°C)	-	-	-
IPE200 (183 × 5.6 + 100 × 8.5) HEB300 (262 × 11 + 300 × 19)	1	6	350	1	0.0	Not applicable
		7			0.2	$\psi = -1$
	2	8	450	2	0.4	
	3	9		3	0.6	
	4	10	700	4	0.8	$\psi = 1$
	5				1.0	

* β has been defined as $N_{fi,Ed}/M_{y,fi,Ed} = (1 - \beta)/(\beta M_{y,fi,\theta,Rd}/N_{fi,\theta,Rd})$ and taking $\beta = 0$ for columns and $\beta = 1$ for beams

4.2 Accuracy of the General Method

The accuracy of the standard adaptation of the General Method following the guidelines of the EN 1993-1-2 [2] is assessed by analysing the GM safety criterion $\alpha_{ult,\theta,k} \cdot \chi_{op,fi}$ in Figure 3.

Since the General Method relies on the concept of load factors, a methodology to compare the accuracy of the method against GMNIA results must be established. The most direct approach is to evaluate the methodology against numerical data under the assumption that the ultimate resistance obtained via GMNIA simulations (N_{ult} and M_{ult}) corresponds to the maximum acting loads $N_{fi,Ed}$ and $M_{y,fi,Ed}$ the member can withstand. Under these conditions, if the theoretical load factor $\alpha_{ult,\theta,k} \cdot \chi_{op,fi}$ is greater than 1.0, this

means that the methodology predicts a resistance higher than the numerically obtained ultimate loads (N_{ult} and M_{ult}), therefore being considered unsafe.

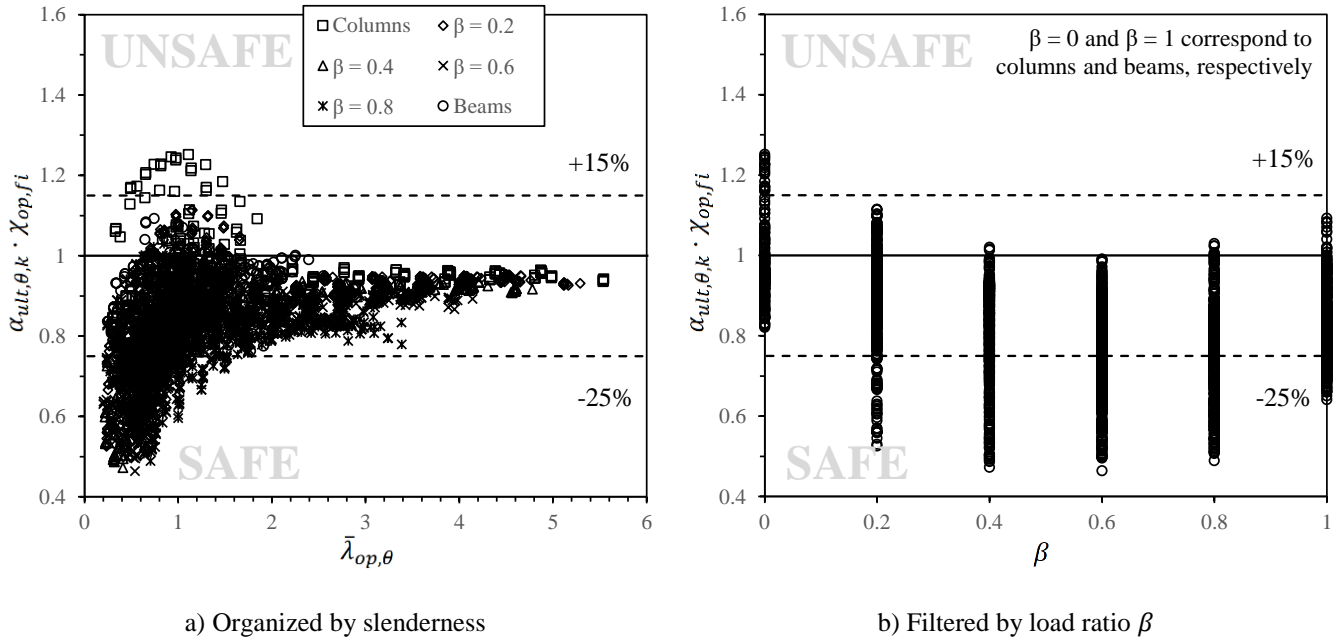


Figure 3. Comparison of the standard implementation of the General Method against numerical results.

The standard adaptation to elevated temperatures of the GM produces overestimations of resistance over 15% for $\beta = 0$ (columns), which is in line with the conclusions drawn in [7] but, on the other hand, is overly conservative for tapered beams (as demonstrated in [8]), which reinforces the hypothesis that utilizing a single buckling curve for the design of columns, beams and beam-columns is a shortcoming of the EN 1993-1-2 [2].

Most importantly, regarding the intermediate values of β (beam-columns), Figure 3b shows that the interaction between column and beam behaviours is not being correctly accounted for. Not only do intermediate values of β produce increasingly conservative predictions but the scatter of results is also higher, although the most conservative results are produced by stockier members ($\bar{\lambda}_{op,\theta} \leq 1.5$).

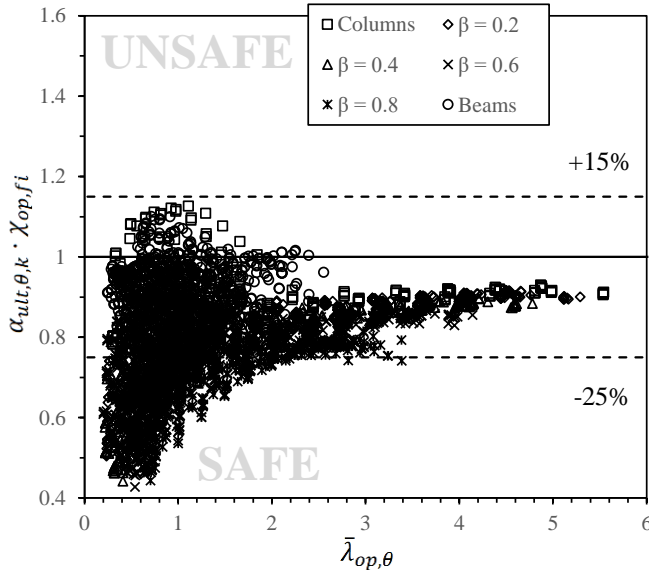
4.3 Accuracy of the General Method with improved reduction factors

4.3.1 Minimum reduction factor

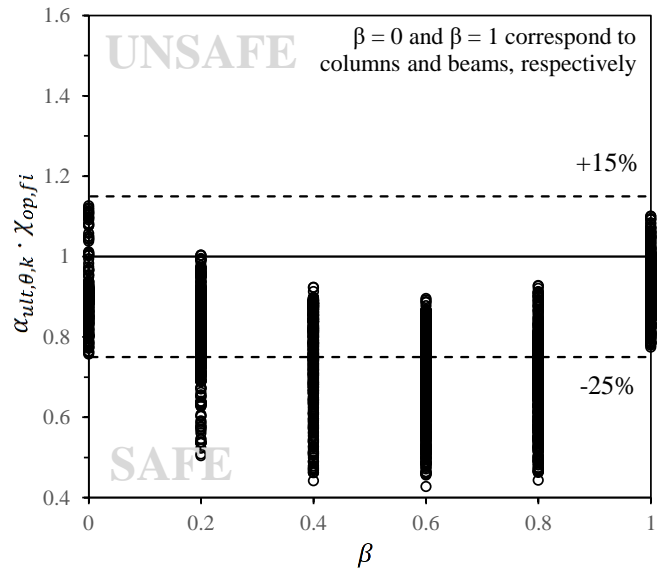
In order to improve the limitation of the EN 1993-1-2 [2] regarding the consideration of a single buckling curve irrespective of the loading conditions, as well as its inability to accurately and safely predict the stability of tapered columns and beams, improved buckling curve for these members have been proposed by the authors [7,10].

As described in sub-section 2.1, these enhanced reduction factors can be implemented in the General Method by using the out-of-plane reduction factor χ_{op} corresponding either the minimum coefficient between $\chi_{z,fi}$ [7] and $\chi_{LT,fi}$ [10] or an interpolation between the two, according to expression (4).

The first approach ("Minimum") is analysed in Figure 4. Understandably, columns ($\beta = 0$) and beams ($\beta = 1$) now show an improved correlation to numerical data with the new calibrated reduction factors. However, it should be noted that the reduction factor $\chi_{op,fi}$ of the intermediate members is calculated with the smallest coefficient, which generally corresponds to $\chi_{z,fi}$. Although the latter is an improvement over the standard EN 1993-1-2 curve, using a buckling curve calibrated only for columns with the goal of predicting the behaviour of beam-columns mostly subjected to bending (such as $\beta = 0.8$) seems counterintuitive and leads to the overly conservative data points of Figure 4.



a) Organized by slenderness

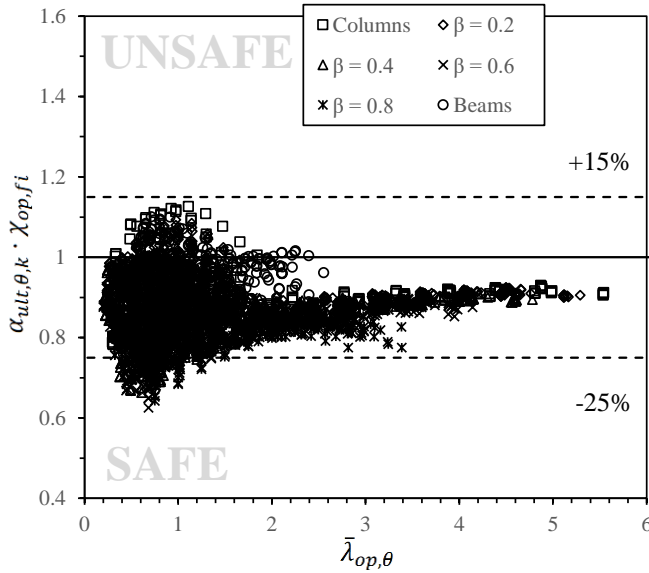


b) Filtered by load ratio β

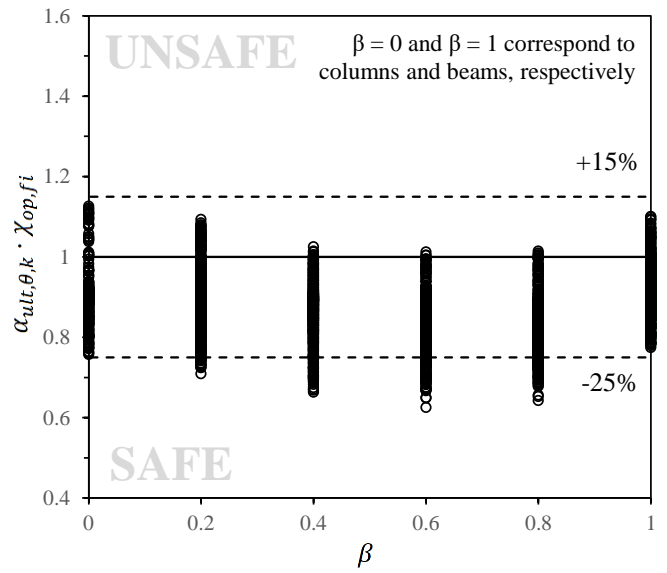
Figure 4. Comparison of the General Method against numerical results – “Minimum”.

4.3.2 Interpolated reduction factor

Similarly, Figure 5 evaluates the GM safety criterion following the “Interpolation” method described in expression (4), but using the improved reduction factors $\chi_{z,fi}$ [7] and $\chi_{LT,fi}$ [10] proposed by the authors.



a) Organized by slenderness



b) Filtered by load ratio β

Figure 5. Comparison of the General Method against numerical results – “Interpolation”.

By interpolating both reduction factors according to the critical cross-section utilization, the limitation of the “Minimum” method is alleviated, resulting in significantly better correlation against numerical data for beam-columns. Although the interpolation appears to be a more reasonable approach for the safety check of these members, the combined behaviour of flexural and lateral-torsional buckling phenomena is still not correctly accounted for (as shown by the evolution of $0.2 \leq \beta \leq 0.8$ data points).

In spite of the “Interpolation” method returning more accurate predictions of resistance, the proposal of a novel interaction factor, which is outside the scope of this work, appears to be the next step going forward.

4.4 Extension of the EN 1993-1-1 interaction formulae [6]

The adapted Marques et al. [6] methodology is analysed in a similar way as the General Method. However, in order to provide a more accurate visual representation/comparison of the results, the inverse of the minimum value of expressions (15) and (16) will be analysed. That way, a data point above 1.0 is considered unsafe and vice-versa. Figure 6 shows the comparison of this methodology against numerical results.

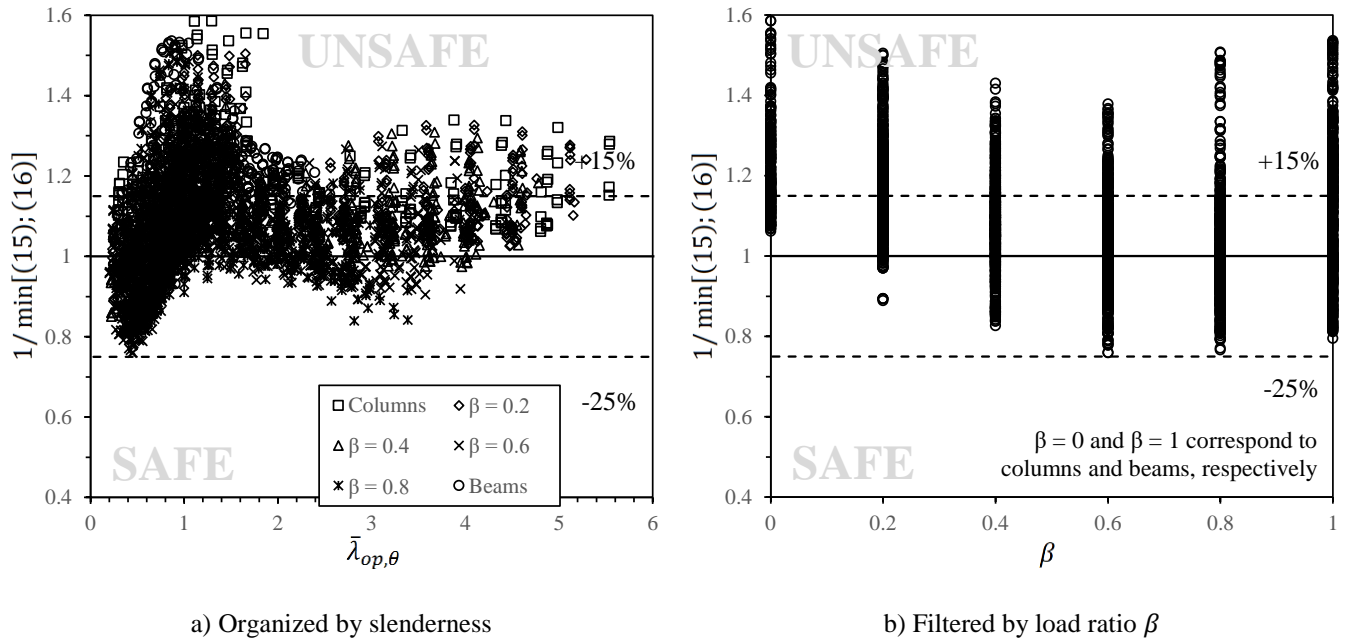


Figure 6. Comparison of the adapted Marques et al. [6] methodology against numerical results.

As was the case for the adaptation of normal temperature methodologies from the literature [7,8], the proposal of Marques et al. [6] returned unsafe results, which was understandable considering that it was developed for normal temperature design. Also, the novel interaction factor proposed in the work proved to be ineffective at describing the out-of-plane behaviour at elevated temperatures.

4.5 Statistical analysis

In order to better understand the significance and the variability of the numerical data, a general comparison between the adapted Marques et al. [6] methodology and the three implementations of the General Method is presented and organized in Table 4.

The accuracy of the methodologies is assessed by analysing the safety criterion of the General Method $\alpha_{ult,\theta,k} \cdot \chi_{op,fi}$ and the equivalent safety coefficient for Marques et al. [6] methodology, corresponding to the inverse of the minimum of expressions (15) and (16), using the reliability criteria of Kruppa [22].

Table 4. Statistical evaluation of the four methodologies.

Methodology	N. of cases	Mean	St. dev.	Min.	Max	%Unsafe	%(>1.15)
General Method (section 4.2)	4150	0.84	0.12	0.46	1.25	3.57%	0.48%
General Method + minimum (section 4.3.1)	4150	0.80	0.12	0.43	1.13	2.55%	0.00%
General Method + Interpolation (section 4.3.2)	4150	0.87	0.07	0.63	1.13	4.31%	0.00%
Marques et al. [6] (section 4.4)	4150	1.09	0.13	0.76	1.59	75.69%	29.73%

As previously discussed, a value equal or below 1.0 implies a safe data point, while a value higher than 1.15 (representing a 15% overestimation of the member resistance) is not acceptable [22] – see “Max” column. Moreover, a methodology is considered unsafe if more than 20% of values are above the safety threshold (see “%Unsafe” column) or if the mean value is on the unsafe side (see “Mean” column) [22].

Regarding the extension of the EN 1993-1-1 interaction formulae for tapered beam-columns (Marques et al. [6]), more than 75% of data points were unsafe, rendering the methodology inadequate for fire design.

Although the General Method is, on average, overly conservative (especially for beams), some column data points render it unsafe, which motivated the proposal of new calibrations by the authors [7,10]. In spite of the improvement on these new buckling curves for their respective member types, using the minimum reduction factor (“Minimum” approach) has demonstrated to be ineffective and too conservative. Applying an interpolated approach to the General Method (“Interpolation”) is not only safer but also more accurate than using the standard EN 1993-1-2 buckling curve.

A more detailed analysis on the GM with interpolated reduction factors (Table 5) shows that similar safety levels are obtained for all taper ratios, with all sub-sets fulfilling the safety criteria of Kruppa [22].

Table 5. Statistical evaluation of the “Interpolation” approach – analysis by sub-sets.

GM + Interpolation sub-set	N. of cases	Mean	St. dev.	Min.	Max	%Unsafe	%(>1.15)
$\gamma_h = 1$	1109	0.90	0.08	0.69	1.13	10.10%	0.00%
$\gamma_h = 2$	1064	0.87	0.06	0.65	1.07	1.97%	0.00%
$\gamma_h = 3$	1015	0.85	0.07	0.63	1.01	0.20%	0.00%
$\gamma_h = 4$	962	0.86	0.08	0.65	1.10	4.57%	0.00%

5 CONCLUSIONS

The present investigation describes a numerical and parametric study on the adaptation to fire of existing approaches for the out-of-plane stability of web-tapered beam-columns, namely the General Method and Marques et al. [6] methodology.

The majority of data points for the proposal of Marques et al. [6] in fire were deemed unsafe, which is expectable considering that it was calibrated to closely fit numerical data at normal temperature.

Regarding the GM [1], it was demonstrated that a standard adaptation with the EN 1993-1-2 [2] single buckling curve is unsafe for columns and overly conservative for beams. This observation is in line with previous conclusions by the authors [7,8], which have motivated the proposal of improved buckling curves for tapered columns [7] and beams [10]. Although these calibrated curves were an improvement for their respective member types, it was shown that considering the minimum of the out-of-plane reduction factor χ_{op} , corresponding to the most severe buckling phenomena of the two, leads to overly conservative estimations of resistance. On the other hand, interpolating the same coefficients according to the respective axial and bending moment utilizations has demonstrated to lead to increased reliability and thus it is the recommended approach for the application of the GM.

To conclude, this work reinforces the need of deeper investigation on the stability of tapered beam-columns in fire as numerical evidence confirms that adaptations to fire of existing methods at normal temperature are not enough to produce accurate and reliable representations of resistance by themselves. Overall, the stability of intermediate beam-columns, with important combined axial and bending utilization ratios, was underestimated, which suggests that the proposal of an interaction factor should be the next step in future investigations.

ACKNOWLEDGMENTS

This research work was funded by the Portuguese Government through the FCT (Foundation for Science and Technology) under the PhD grant SFRH/BD/114838/2016 awarded to the first author. Carlos Couto thanks the financial support of FCT – Fundação para a Ciência e a Tecnologia, I.P., under the Scientific Employment Stimulus – Institutional Call – CEECINST/00026/2018.

REFERENCES

1. CEN. EN 1993-1-1, Eurocode 3: Design of steel structures - Part 1-1: General rules and rules for buildings. Belgium: 2005.
2. CEN. EN 1993-1-2, Eurocode 3: Design of steel structures - Part 1-2: General rules - Structural fire design. Belgium: 2005.
3. FCT. TaperSteel, Stability design of non-uniform steel members - PTDC/ECM-EST/1970/2012 (2012-2014) 2012.
4. Marques L, Taras A, Simões da Silva L, Greiner R, Rebelo C. Development of a consistent buckling design procedure for tapered columns. *J Constr Steel Res* 2012;72:61–74.
5. Marques L, Simões da Silva L, Greiner R, Rebelo C, Taras A. Development of a consistent design procedure for lateral-torsional buckling of tapered beams. *J Constr Steel Res* 2013;89:213–35.
6. Marques L, Simões da Silva L, Rebelo C, Santiago A. Extension of EC3-1-1 interaction formulae for the stability verification of tapered beam-columns. *J Constr Steel Res* 2014;100:122–35.
7. Maia É, Vila Real P, Lopes N, Couto C. The General Method for the fire design of slender I-section web-tapered columns. *Thin-Walled Struct* 2020;155.
8. Couto C, Maia É, Vila Real P, Lopes N. Stability check of tapered steel beams in fire. *J Struct Fire Eng* 2019;10:373–98.
9. DIN. DIN 18800-2, Steel structures - Part 2: Stability - Buckling of bars and skeletal structures. Germany: 2008.
10. Maia É, Couto C, Vila Real P, Lopes N. Fire design of class 4 tapered steel beams with the General Method. *SDSS 2019 - Int. Colloq. Stab. Ductility Steel Struct.*, Prague, Czech Republic: 2019.
11. Franssen J-M, Gernay T. Modeling structures in fire with SAFIR® : Theoretical background and capabilities. *J Struct Fire Eng* 2017;8:300–23.
12. FIDESC4. Fire Design of Steel Members with Welded or Hot-rolled Class 4 Cross-sections - RFSR-CT-2011-00030 (2011-2014) 2014.
13. Couto C, Vila Real P, Lopes N, Zhao B. Effective width method to account for the local buckling of steel thin plates at elevated temperatures. *Thin-Walled Struct* 2014;84:134–49.
14. Talamona D, Franssen J-M. A Quadrangular Shell Finite Element for Concrete and Steel Structures Subjected to Fire. *J Fire Prot Eng* 2005;15:237–64.
15. Maia É, Couto C, Vila Real P, Lopes N. Influence of non-uniform temperature distributions on the behaviour of I-shaped beams subjected to elevated temperatures (In Portuguese). C. 2019 - Congr. Métodos Numéricos em Eng., Guimarães, Portugal: 2019.
16. CEA. CAST3M <<http://www-cast3m.cea.fr/>>. 2015.
17. CEN. EN 1993-1-5, Eurocode 3: Design of steel structures - Part 1-5: General rules - Plated structural elements. Belgium: 2006.
18. CEN. EN 1090-2:2008+A1, Execution of steel structures and aluminium structures - Part 2: Technical requirements for steel structures 2011.
19. ECCS. Manual on Stability of Steel Structures. Publication No. 22. European Convention for Constructional Steelwork Technical Committee No. 8; 1976.
20. ECCS. Ultimate limite state calculation of sway frames with rigid joints. Publication No. 33. European Convention for Constructional Steelwork Technical Committee No. 8; 1984.
21. Couto C, Vila Real P. Numerical investigation on the influence of imperfections in the lateral-torsional buckling of beams with slender I-shaped welded sections. *Thin-Walled Struct* 2019;145:106429.
22. Kruppa J. Eurocodes - Fire parts: Proposal for a methodology to check the accuracy of assessment methods. CEN TC 250, Horizontal Group Fire, Document No. 99/130: 1999.

POST-FIRE MECHANICAL PROPERTIES of TMCP HIGH STRENGTH STRUCTURAL STEEL

Lin-Xin Song¹, Guo-Qiang Li², Qing Xu³

ABSTRACT

According to the manufacturing process, high strength structural steel (HSSS) can be divided into TMCP (Thermo-Mechanical Controlled Process) and QT (Quenched and Tempered) types. Most previous studies on the post-fire mechanical properties of HSSS were conducted on QT HSSS and rarely on the TMCP HSSS. To investigate the influence of manufacturing process on the post-fire mechanical properties of HSSS, an experimental study was carried out on TMCP Q550 HSSS. The specimens were heated at nine temperature levels from 200 to 900°C and then cooled in air and water respectively before conducting static tensile tests at ambient temperature. Comparisons are made between the test results and the previous results on QT Q550 HSSS at different heating and cooling conditions. It can be found that the heating and cooling process had little influence on elastic modulus but significant effect on strength and ultimate elongation if the heated temperature exceeded 600°C, and the cooling method and manufacturing process became critical once the heated temperature exceeded 700°C. In general, the post-fire yield and ultimate strength of TMCP Q550 HSSS decreased but ultimate elongation increased in air cooling cases, while the opposite results occurred in water cooling cases. Moreover, TMCP Q550 HSSS generally performed worse than QT Q550 HSSS in post-fire mechanical properties. Based on the test results, predictive formulas were proposed to determine the post-fire mechanical properties of TMCP Q550 HSSS.

Keywords: TMCP Q550 HSSS; post-fire mechanical properties; cooling methods; manufacturing process; microstructure; predictive formulas

1. INTRODUCTION

The application of high strength structural steel (HSSS) in construction industry has great advantages in terms of safety, reliability, economy and environmental benefits. However, the mechanical properties of steel, especially for HSSS, may reduce significantly after fire [1-2]. Since fire is a frequent disaster, identifying the post-fire mechanical properties of HSSS is important for evaluating the safety of continuing use of the HSSS structures after fire.

Up to now, the research on the post-fire mechanical properties of HSSS mainly focused on QT (Quenched and Tempered) HSSS [3-6], which improves its strength by traditional quenching and tempering techniques. However, according to the manufacturing process, there is another category of HSSS named TMCP (Thermo-Mechanical Controlled Process) HSSS, which improves its strength by controlling rolling

[†] Ph.D. Candidate. College of Civil Engineering, Tongji University, Shanghai, China

e-mail: linlinslx@126.com

² Professor. State Key Laboratory for Disaster Prevention in Civil Engineering, Tongji University, Shanghai, China

e-mail: gqli@tongji.edu.cn

³ Ph.D. Candidate. College of Civil Engineering, Tongji University, Shanghai, China

e-mail: xuqing36@tongji.edu.cn

process and the speed of cooling [7]. Few studies have been conducted on the post-fire mechanical properties of TMCP HSSS. However, previous studies found that there are obvious distinctions of the mechanical properties after welding between TMCP and QT HSSS [8-9]. To some extent, the post-weld condition is similar to the post-fire condition, under which the HSSS is cooled down from a high temperature. Therefore, it is necessary to investigate the post-fire mechanical properties of TMCP HSSS.

This paper presents the details of the experimental study on the post-fire mechanical properties of TMCP Q550 HSSS, which is Chinese grade of structural steel with nominal yield strength of 550 MPa. The results of post-fire superficial characteristics, stress-strain relationship and mechanical properties, including elastic modulus, yield strength, ultimate strength and ultimate elongation after experiencing various elevated temperatures were compared with the original ones without being heated to understand the degeneration of mechanical properties of HSSS after fire. The effect of cooling methods, cooling in air and in water, was comparatively investigated. Based on the test results, predictive formulas were proposed to determine the post-fire mechanical properties of TMCP Q550 HSSS. Comparisons of post-fire mechanical properties were made between TMCP Q550 HSSS and normal strength steel as Q345 steel and S355 steel. Comparisons were also made between TMCP Q550 HSSS and QT Q550 HSSS to study the effect of manufacturing process.

2. EXPERIMENT PROCEDURE

The experimental study was conducted on the post-fire mechanical properties of TMCP Q550 HSSS, and was designed according to the similar previous studies on QT Q550 HSSS [4] for the purpose of comparison. The test operation was in accordance with GB/T 228.1-2010 [10] and GB/T 228.2-2015 [11].

2.1 Steel Specimens

The steel specimens were cut from a TMCP Q550 HSSS plate with a nominal thickness of 20mm. The chemical constitution of the steels is shown in Table 1. The geometry of the specimens is shown in Fig. 1.

Table 1 Chemical constitution of TMCP Q550 HSSS

Chemical constitution	C	Si	Mn	P	S	Nb	Ti	Cr	Ni	Mo	B	Alt	CEV	Pcm
wt%	0.06	0.24	1.56	0.01	0.001	0.032	0.015	0.19	0.02	0.005	0.0016	0.036	0.36	0.17

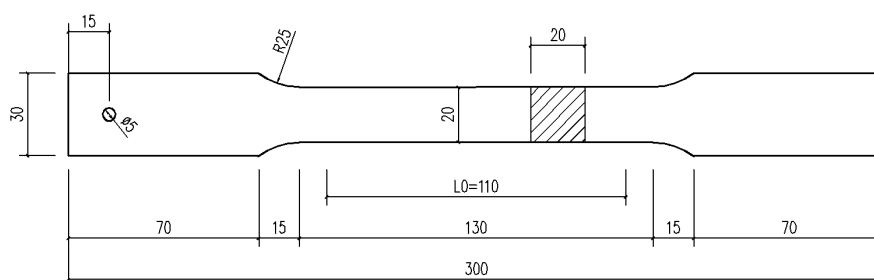


Fig. 1. Geometry of the specimens

2.2 Test setup and test program

Three procedures were included in the experiments, including heating, cooling and static tensile test at ambient temperature.



(a) MTS 653 Furnace



(b) Universal Testing Machine

Fig. 2 Test setup

The specimens were heated from ambient temperature to nine pre-selected temperatures at 200, 300, 400, 500, 600, 700, 750, 800 and 900°C in the MTS 653 Furnace shown in Fig. 2(a). After reaching each pre-selected temperature, kept the temperature constant for 15min to make sure the temperature distributed uniformly over the whole specimen. After maintaining 15min at the pre-selected temperatures, the specimens were then cooled down to ambient temperature by one of the two cooling methods. One method is cooling in air (CIA), i.e., the heated specimens were cooled in the open air to simulate the situation of the fire burning out naturally. The other is cooling in water (CIW) by dropping the heated specimens into a water tank to simulate the extreme case of extinguishing fire by water. After cooling down to ambient temperature, the specimens were left for two weeks before being carried out the static tensile tests conducted with the Universal Testing Machine shown in Fig. 2(b) at ambient temperature. The tensile tests were performed under displacement control at a constant rate of 2mm/min. For comparison, tensile tests were also conducted on the specimen without being heated.

3. EXPERIMENTAL RESULTS

3.1 Visual observations

After cooling down to ambient temperature from various elevated temperatures with different cooling methods, the superficial colors of TMCP Q550 HSSS were different, as shown in Fig. 3. The number marked on the specimens indicates the experienced temperature and the letter “CIA” or “CIW” denotes the method of cooling in air or in water. For example, the specimen marked with “900-CIA” indicates that it was heated up to 900°C and then cooled in air. The specimen marked with “30” refers to the specimen not being heated.



Fig. 3 Superficial color changing of specimens experiencing various heated temperatures

It can be found that the superficial characteristics of TMCP HSSS almost maintained the metal color and gradually changed into slightly reddish-brown and yellow when the heated temperature did not exceed 400°C for CIW cases or 600°C for CIA cases. However, silver-white appeared within a certain length range of the specimens after cooling from 600°C in both air and water. When the heated temperature exceeded 600°C, the superficial color gradually became darker with increasing of the heated temperatures, changing into dark blue for CIA cases or charcoal black for CIW cases. Meanwhile, reddish-brown can be obviously observed for CIA cases when the heated temperature was 800°C.

3.2 Stress-strain relationships

The post-fire stress-strain curves of TMCP Q550 HSSS are shown in Fig. 4. It can be found that the curves were relatively close and exhibited yield plateau at ambient temperature and for the scenarios with the heated temperature up to 600°C. However, when the heated temperature exceeded 600°C, the yield plateau disappeared.

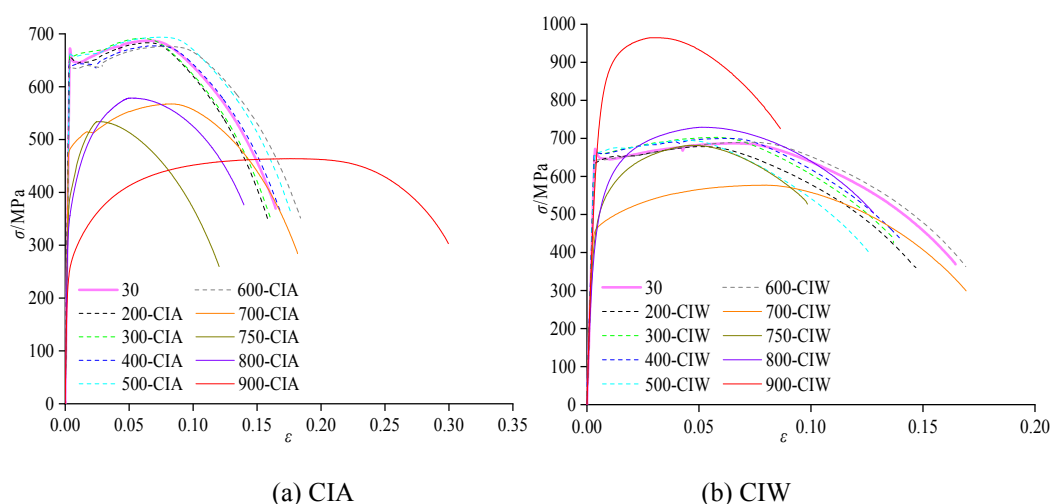


Fig. 4 Stress-strain curves of TMCP Q550 HSSS after heating

When the experienced temperature was 700°C, the stress-strain curves of the specimens, either in the CIA or CIW case, was lower than that without being heated, which represents the strength of the steel decreased. However, when the heated temperature ranged between 700°C and 750°C, the stress-strain curves were affected significantly by cooling methods, as shown in Fig. 4 and Fig. 5. It can be seen that when the heated temperature was above 700°C, the curves for CIA cases were lower than the corresponding ones for CIW cases. The most significant difference for the stress-strain curves between the two cooling methods was observed when the heated temperature was 900°C. In this situation, the curve for the CIA case was still lower than the corresponding one without being heated, while the curve for the CIW case was higher than that without being heated.

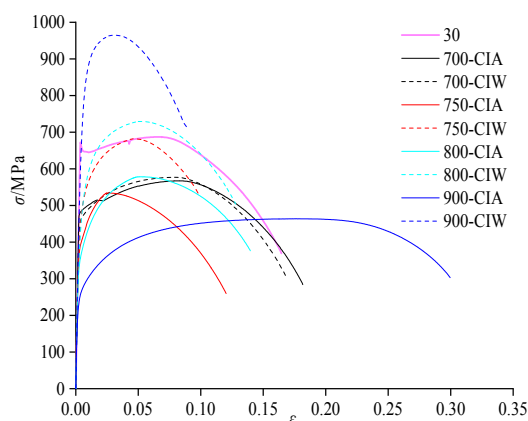


Fig. 5 Effects of cooling method on post-fire stress-strain curves of TMCP HSSS

3.3 Mechanical properties

The post-fire mechanical properties, including elastic modulus, E_T , yield strength, $f_{y,T}$, ultimate strength, $f_{u,T}$, and ultimate elongation, A_T , were investigated. The symbols without and with the subscript T indicate the mechanical properties before and after fire respectively. The reduction factor, calculated as the ratio of the post-fire mechanical properties to the corresponding original ones without experiencing any heating, was used to indicate the degeneration degree of the mechanical properties of TMCP Q550 HSSS after being subjected to various high temperatures and cooling methods. And if the reduction factor is greater than 1, it is actually the amplifying factor. The post-fire mechanical properties and corresponding reduction factors of TMCP Q550 HSSS are shown in Table 2. The variation of reduction factors of post-fire mechanical properties of TMCP Q550 HSSS are presented in Fig. 6.

Table 2 Post-fire mechanical properties and corresponding reduction factors of TMCP Q550 HSSS

$T/^\circ\text{C}$	E_T/GPa (E_T/E)		$f_{y,T}/\text{MPa}$ ($f_{y,T}/f_y$)		$f_{u,T}/\text{MPa}$ ($f_{u,T}/f_u$)		$A_T/\%$ (A_T/A)	
	CIA	CIW	CIA	CIW	CIA	CIW	CIA	CIW
30	199 (1.00)	199 (1.00)	643 (1.00)	643 (1.00)	682 (1.00)	682 (1.00)	19.77 (1.00)	19.77 (1.00)
200	197 (0.99)	197 (0.99)	649 (1.01)	636 (0.99)	687 (1.01)	674 (0.99)	19.98 (1.01)	19.13 (0.97)
300	193 (0.97)	199 (1.00)	652 (1.01)	642 (1.00)	690 (1.01)	686 (1.01)	20.00 (1.01)	19.18 (0.97)
400	199 (1.00)	195 (0.98)	620 (0.96)	661 (1.03)	667 (0.98)	701 (1.03)	20.58 (1.04)	18.95 (0.96)
500	199 (1.00)	197 (0.99)	669 (1.04)	647 (1.01)	704 (1.03)	682 (1.00)	19.19 (0.97)	18.92 (0.96)
600	196 (0.99)	198 (0.99)	624 (0.97)	644 (1.00)	662 (0.97)	683 (1.00)	20.07 (1.02)	19.61 (0.99)
700	190 (0.96)	176 (0.88)	510 (0.79)	507 (0.79)	568 (0.83)	577 (0.85)	20.93 (1.06)	17.62 (0.89)
750	175 (0.88)	182 (0.91)	402 (0.62)	479 (0.74)	534 (0.78)	682 (1.00)	17.07 (0.86)	13.75 (0.70)
800	179 (0.90)	196 (0.98)	365 (0.57)	445 (0.69)	587 (0.86)	718 (1.05)	20.51 (1.04)	9.70 (0.49)
900	193 (0.97)	194 (0.97)	251 (0.39)	766 (1.19)	466 (0.68)	957 (1.40)	31.53 (1.59)	12.86 (0.65)

As shown in Fig. 6, the reduction of the post-fire elastic modulus was not serious, except for the situations experiencing heated temperatures between 700 and 800 $^\circ\text{C}$, and the reduction factors reached the minimum, about 0.88 at 750 $^\circ\text{C}$ for the CIA case and 700 $^\circ\text{C}$ for the CIW case. For both the yield strength and ultimate strength, they may almost completely recover to the original values without being heated if the experienced temperature did not exceed 600 $^\circ\text{C}$. However, the two strengths dropped sharply when the heated temperature was about 700 $^\circ\text{C}$. The reason is that the coarsening of the microstructure and the decrease of dislocation density became more significantly above 600 $^\circ\text{C}$ [12-13]. When the heated temperature exceeded 700 $^\circ\text{C}$, the cooling method became the critical influence on the post-fire yield strength and ultimate strength. Both yield strength and ultimate strength continued to decrease in CIA cases. However, in CIW cases, the yield strength began to increase in the 800 $^\circ\text{C}$ case and became greater than the original values in the 900 $^\circ\text{C}$ case, and the ultimate strength began to increase in 700 $^\circ\text{C}$ case and became greater than the original values starting from the 800 $^\circ\text{C}$ case. For the post-fire ultimate elongation, it remained almost the same with the original values without being exposed to fire until the experienced temperature exceeded 600 $^\circ\text{C}$, and it decreased significantly at around 750 $^\circ\text{C}$ of the heated temperature. When the heated temperature was above 800 $^\circ\text{C}$, the post-fire ultimate elongation increased prominently and even became much larger than the original values for CIA cases, while it increased slightly and was still less than the original ones for CIW cases.

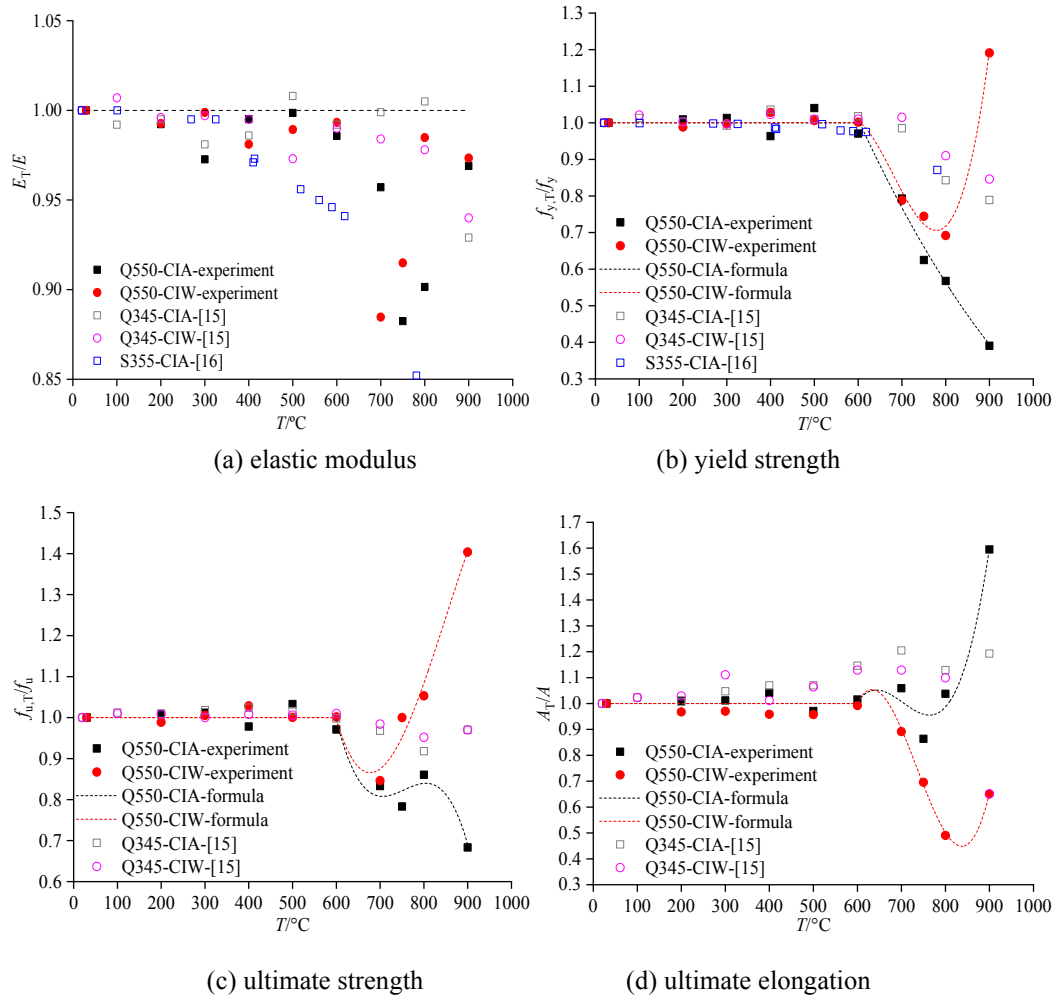


Fig. 6 Reduction factors of post-fire mechanical properties of TMCP Q550 HSS

When the experienced temperature was as high as 900°C, the post-fire yield strength and ultimate strength maintained 39% and 68% of the original values respectively for the CIA case, while were 119% and 140% of the original ones respectively for the CIW case. As for the post-fire ultimate elongation, the values were 159% of the original values for the CIA case, while were 65% of the original ones for the CIW case. The reason for that different cooling methods led to different trends of post-fire mechanical properties is the quenching effect. When the heated temperature exceeded the microstructural transformation temperature, generally about 700°C, the quenching effect occurs in the water cooling cases due to the rapid cooling rate, and thus the corresponding strength exceeds the original value but the ultimate elongation becomes smaller [12-14].

3.4 Predictive formulas

Based on the above discussion, it can be found that the heating and cooling process had little influence on post-fire elastic modulus of TMCP Q550 HSS up to 900°C, and thus the post-fire elastic modulus can be taken as the original one without being exposed to fire. The post-fire yield strength, ultimate strength and ultimate elongation did not change much and can be taken as the original ones when the heated temperature did not exceed 600°C. When the heated temperature exceeded 600°C (strength) or 700°C (ultimate elongation), the remarkable reduction happened. When the temperature exceeded 700°C the influence of the cooling method became obvious.

Considering the above regulations varied with the experienced temperatures, formulas for predicting the reduction factors of the post-fire mechanical properties of TMCP Q550 HSS are proposed, as shown in Table 3 and illustrated in Fig. 6.

Table 3 Formulas for calculating the post-fire strength reduction factors of TMCP Q550 HSSS

Factor	Formula of reduction factors		
	$30^{\circ}\text{C} \leq T \leq 600^{\circ}\text{C}$	$600^{\circ}\text{C} < T \leq 900^{\circ}\text{C}$	
	CIA or CIW	CIA	CIW
E_T/E	1	1	1
$f_{y,T}/f_y$	1	$1.7678 \times 10^{-6} T^2 - 0.0047 T + 3.1920$	$7.9946 \times 10^{-8} T^3 - 1.6304 \times 10^{-4} T^2 + 0.1085 T - 22.6692$
$f_{u,T}/f_y$	1	$-6.6565 \times 10^{-8} T^3 + 1.5074 \times 10^{-4} T^2 - 0.1133 T + 29.0873$	$-3.6214 \times 10^{-8} T^3 + 9.2529 \times 10^{-5} T^2 - 0.0755 T + 20.8071$
A_T/A	1	$1.0971 \times 10^{-7} T^3 - 2.3148 \times 10^{-4} T^2 + 0.1616 T - 36.3177$	$1.4222 \times 10^{-7} T^3 - 3.1370 \times 10^{-4} T^2 + 0.2262 T - 52.5067$

3.5 Comparison with normal strength steels

Comparisons of the reduction factors of post-fire mechanical properties among TMCP Q550 HSSS, Q345 steel [15] and S355 steel [16] are shown in Fig. 6. Q345 steel and S355 steel are commonly used structural steels with nominal yield strength of 345 MPa and 355 MPa respectively. Except for few CIW cases that the strength of TMCP Q550 HSSS exceeded the original ones without being heated, the strength of TMCP Q550 HSSS reduced more significantly than Q345 steel and S355 steel when the heated temperature exceeded 600°C . The reason for that the HSSS suffered greater strength loss than the normal strength steel after cooling down from elevated temperatures is the different microstructure changes. The initial microstructure of HSSS is finer than the normal strength steel, but will turn to coarser structure when exposed to relatively high temperatures [12-14]. Therefore, after cooling down to ambient temperature, the strength of HSSS may become close to the normal strength steel, but the corresponding reduction factors of HSSS will become smaller because the ratio is based on the original strength values.

4. EFFECT OF MANUFACTURING PROCESS

To identify the effect of manufacturing process on post-fire mechanical properties of HSSS, the comparative study was conducted between the experimental results of TMCP Q550 HSSS hereinabove and those of previous study on QT Q550 HSSS [4].

4.1 Elastic modulus

The comparison of the reduction factors of post-fire elastic modulus between TMCP Q550 HSSS and QT Q550 HSSS are shown in Fig. 7. It can be seen that the reduction degree of TMCP HSSS was slightly more severe than that of QT HSSS. However, the reduction for the two types of HSSS was not much, within 12% overall.

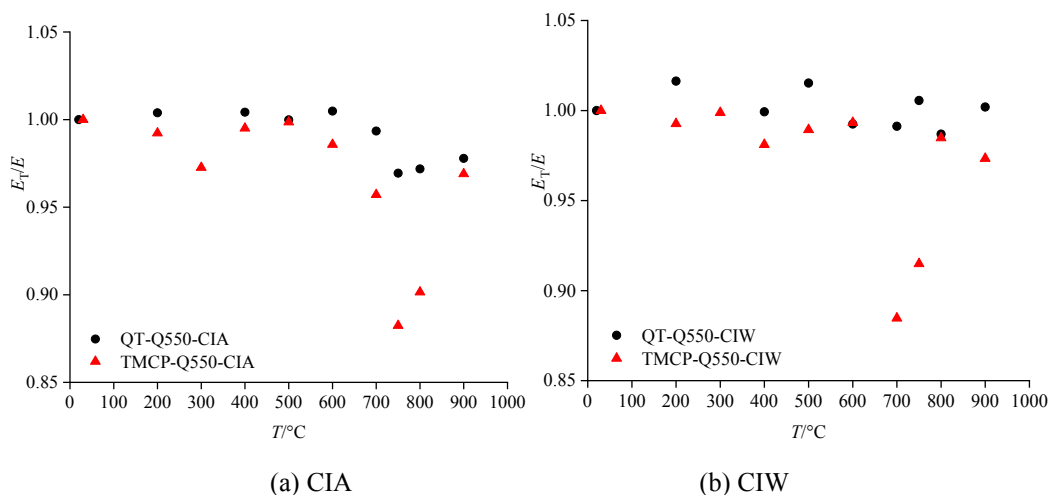


Fig. 7 Effect of manufacturing process on reduction factors of post-fire elastic modulus of Q550 HSSS

4.2 Yield strength

The variation of the reduction factors of post-fire yield strength of TMCP Q550 HSSS and QT Q550 HSSS are compared in Fig. 8. It can be found that the reduction of the post-fire yield strength for both TMCP HSSS and QT HSSS was minor when the heated temperature did not exceed 600°C but became significant when the heated temperature was above 600°C. However, the post-fire yield strength for TMCP HSSS generally reduced more severely than that of QT HSSS. The difference of the reduction between TMCP and QT HSSS became significantly with the heated temperature rising above 700°C.

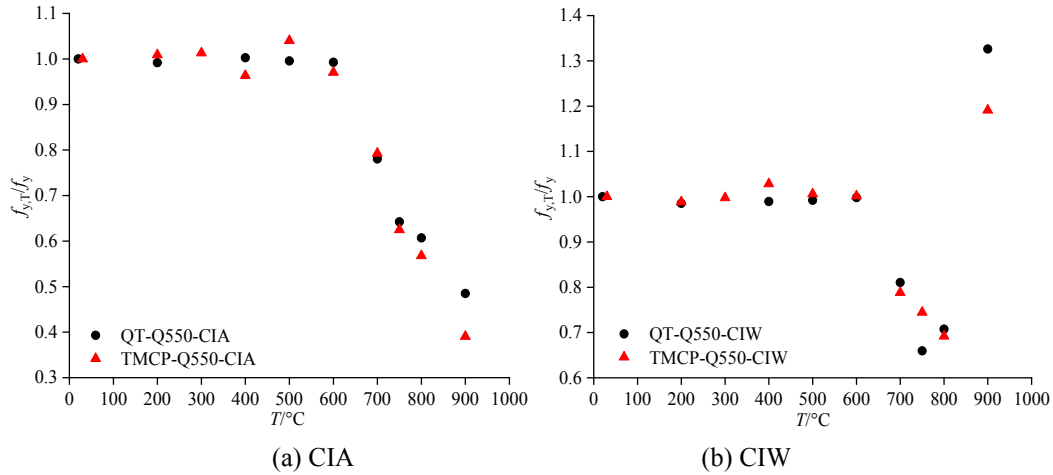


Fig. 8 Effect of manufacturing process on reduction factors of post-fire yield strength of HSSS

4.3 Ultimate strength

The variation of the reduction factors of post-fire ultimate strength of TMCP Q550 HSSS and QT Q550 HSSS are compared in Fig. 9. Consistent with the post-fire yield strength, there are two critical temperatures on the post-fire ultimate strength for both processed HSSS.

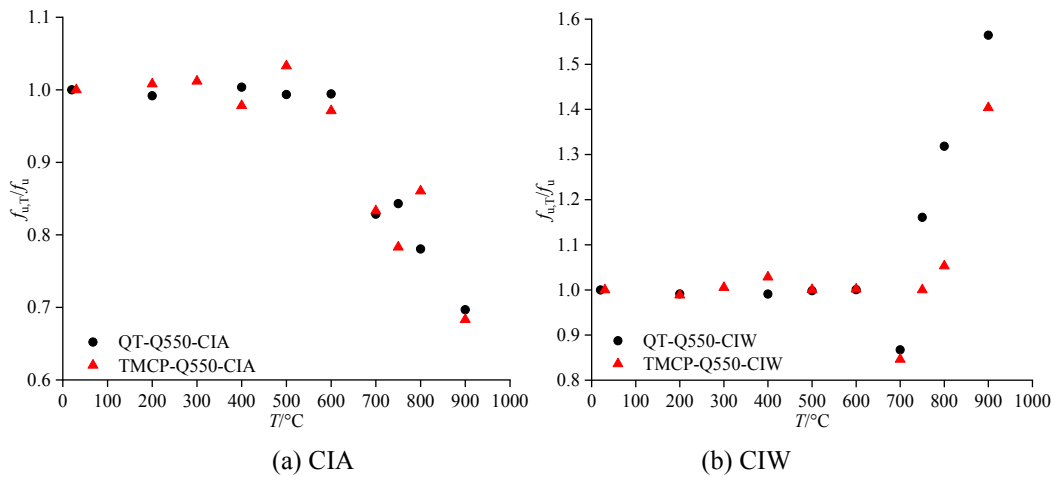


Fig. 9 Effect of manufacturing process on reduction factors of post-fire ultimate strength of HSSS

The first critical temperature is 600°C. When the heated temperature exceeded 600°C, the post-fire strength of both TMCP and QT HSSS began to decrease. The other critical temperature is 700°C. When the heated temperature exceeded 700°C, the post-fire strength of HSSS was affected significantly with the cooling method and manufacturing process. The post-fire strength of TMCP HSSS reduced more significantly in CIA cases and increased less prominently in CIW cases than that of QT HSSS. Therefore, the post-fire strength of TMCP HSSS was generally less than that of QT HSSS.

4.4 Ultimate elongation

The comparison of the reduction factors of post-fire ultimate elongation between TMCP Q550 HSSS

and QT Q550 HSSS are presented in Fig. 10. It can be found that the post-fire ultimate elongation of both processed HSSS fluctuated slightly around the original ones without being exposed to fire with the heated temperature up to 600°C. However, when the heated temperature exceeded 600°C, the post-fire ultimate elongation of TMCP HSSS increased much less significantly in CIA cases and decreased much more prominently in CIW cases than that of QT HSSS. Therefore, the post-fire ultimate elongation of TMCP HSSS was generally less than that of QT HSSS.

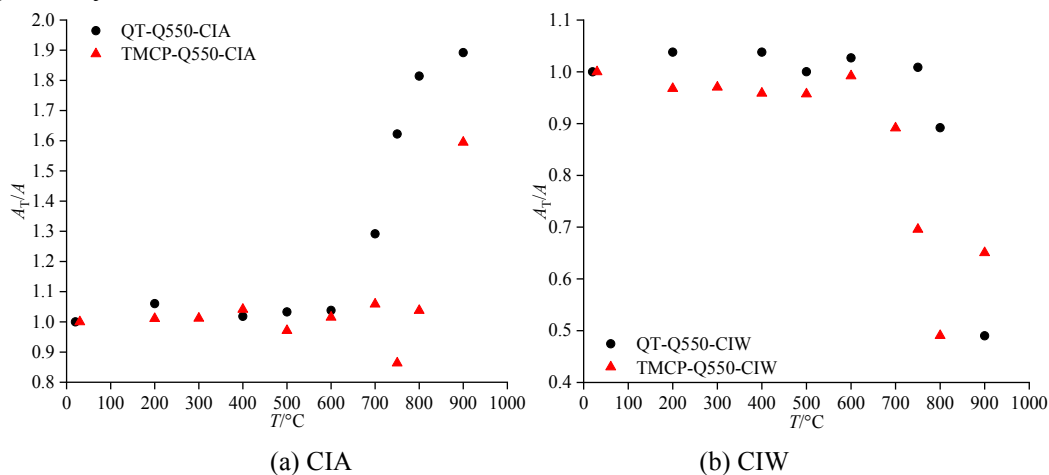


Fig. 10 Effect of manufacturing process on reduction factors of post-fire ultimate elongation of HSSS

4.5 Mechanism discussion

It can be found from the experimental study that the manufacturing process began to affect the post-fire mechanical properties of HSSS when the experienced temperature exceeded about 700°C. Overall, the mechanical properties of TMCP Q550 HSSS exhibited more significant reduction when experienced high temperatures than that of QT Q550 HSSS due to the following reasons [7, 12, 14, 17]. In terms of microstructure, TMCP HSSS is dominated by tempered bainite, which is a softer microstructure compared with that of QT HSSS dominated by tempered martensite. In addition, the different quantity of alloying elements also makes the difference. The quantity of alloying elements is one of the important factors to improve the strength of HSSS. The strength improvement on QT HSSS is mainly achieved by adding more quantity of alloying elements. However, the strength of TMCP HSSS is achieved by adding alloying elements and controlling cooling process during the production as well, which may be affected more significantly when the heated temperature is high enough to cause recrystallization and weaken the strengthening effects such as dislocation.

5. CONCLUSIONS

The results of a detailed experimental study on the post-fire mechanical properties of TMCP Q550 HSSS is presented in this paper and also compared with that of the corresponding QT Q550 HSSS. The effects of manufacturing process on the mechanical properties of HSSS after experiencing high temperatures is investigated. The conclusions are listed as follows.

- (1) The yield plateau of stress-strain curves of TMCP Q550 HSSS remained if the heated temperature did not exceed 600°C, while it would disappear once the heated temperature reached 700°C or higher.
- (2) The heating and cooling process had little influence on the post-fire elastic modulus of both TMCP Q550 HSSS and QT Q550 HSSS.
- (3) The post-fire yield strength, ultimate strength and ultimate elongation of TMCP Q550 HSSS did not change much when the heated temperature did not exceed 600°C. But they changed differently for different

cooling methods when the heated temperature exceeded 700 °C, i.e., the post-fire yield and ultimate strength decreased but ultimate elongation increased in CIA cases, while the opposite results occurred in CIW cases.

(4) The effect of manufacturing process on the post-fire mechanical properties of HSSS became significant when the heated temperature exceeded 700 °C. In general, the reduction factors of the post-fire strength and ultimate elongation were always lower for TMCP Q550 HSSS than QT Q550 HSSS.

ACKNOWLEDGEMENTS

The research work presented in this paper is supported by the National Natural Science Foundation of China through the contract 51878506. The support is gratefully acknowledged.

REFERENCES

1. Reidar Bjorhovde. Performance and design issues for high strength steel in structures. *Advances in Structural Engineering*, 2010, 13(3): 403-411. <https://doi.org/10.1260/1369-4332.13.3.403>.
2. W.Y. Wang, G.Q. Li. Research progress of fire resistance design theory of high strength steel structures. *Industrial Construction*, 2016, 46(7): 61-67. <https://doi.org/10.13204/j.gyjz201607010>.
3. W.Y. Wang, T.Z. Liu, J.P. Liu. Experimental study on post-fire mechanical properties of high strength Q460 steel. *Journal of Constructional Steel Research*, 2015, 114: 100-109. <https://doi.org/10.1016/j.jcsr.2015.07.019>.
4. G.Q. Li, H.B. Lyu, C. Zhang. Post-fire mechanical properties of high strength Q550 structural steel. 11th Pacific Structural Steel Conference. Shanghai, China, 2016.
5. G.Q. Li, H.B. Lyu, C. Zhang. Post-fire mechanical properties of high strength Q690 structural steel. *Journal of Constructional Steel Research*, 2017, 132: 108-116. <https://doi.org/10.1016/j.jcsr.2016.12.027>.
6. X.H. Qiang, Frans S.K. Bijlaard, Henk Kolstein. Post-fire mechanical properties of high strength structural steels S460 and S690. *Engineering Structures*, 2012, 35: 1-10. <https://doi.org/10.1016/j.engstruct.2011.11.005>.
7. Jin JIANG, W. Bao, Z.Y. Peng, Y.B. Wang, J. Liu, X.H. Dai. Experimental investigation on mechanical behaviours of TMCP high strength steel. *Construction and Building Materials*, 2019, 200: 664-680. <https://doi.org/10.1016/j.conbuildmat.2018.12.130>.
8. Franz Hochhauser, Wolfgang Ernst, Rudolf Rauch, Rudolf Vallant, Norbert Enzinger, Influence of the soft zone on the strength of welded modern HSLA steels, *Welding in the World*. 56(5-6) (2012) 77-85.
9. Mingming Ran, Feifei Sun, Guoqiang Li, Amit Kanvinde, Yanbo Wang, Robert Y. Xiao, Experimental study on the behavior of mismatched butt welded joints of high strength steel, *Journal of Constructional Steel Research*. 153(2019) 196-208. <https://doi.org/10.1016/j.jcsr.2018.10.003>.
10. Metallic materials: tensile testing: part 1: method of test at room temperature: GB/T 228.1-2010. Beijing: Standard Press of China, 2010.
11. Metallic materials: tensile testing: part 1: method of test at elevated temperature: GB/T 228.1-2010. Beijing: Standard Press of China, 2015.
12. X.Y. Zhu. Handbook of steel heat treatment [M]. Beijing: Standard Press of China, 2013.
13. Fatemeh Azhari, Amin Heidarpour, X.L. Zhao, Christopher R. Hutchinson. Mechanical properties of ultra-high strength (Grade 1200) steel tubes under cooling phase of a fire: An experimental investigation. *Construction and Building Materials*, 2015, 53: 841-850. <https://doi.org/10.1016/j.conbuildmat.2015.05.082>.

14. X. Song, H.F. Yang, C. Wang, Z.G. Qu, X.Y. Li, D.M. Wang. Microstructures and properties of 1100MPa grade ultra-high strength steel after heat treatments. *Journal of Iron and Steel Research*, 2019, 31(6): 592-599. <https://doi.org/10.13228/j.boyuan.issn1001-0963.20180279>.
15. J. Lu, H.B. Liu, Z.H. Chen, X.W. Liao. Experimental investigation into the post-fire mechanical properties of hot-rolled and cold-formed steels. *Journal of Constructional Steel Research*, 2016, 121:291-310. <http://dx.doi.org/10.1016/j.jcsr.2016.03.005>.
16. X. Lyu. Residual load capacity and experimental research on short steel tube infilled with high strength concrete column post-fire. Ph. D. Thesis, Southeast University, Nanjing, 2018.
17. F. Hochhauser, W. Ernst, R. Rauch, R. Vallant, N. Enzinger. Influence of the soft zone on the strength of welded modern HSLA steels. *Welding in the World*, 2012, 56(5-6): 77-85. <https://doi.org/10.1007/BF03321352>.

PREDICTION OF FRACTURE BEHAVIOR FOR HIGH-STRENGTH STEEL BOLTS AT ELEVATED TEMPERATURES

Wenyu Cai¹, Jian Jiang², Guo-Qiang Li³

ABSTRACT

High-strength bolts have been widely used for bolted beam-to-column connections in steel structures. In fire events, they are normally designed to tolerate fire-induced tensile forces caused by thermal expansion and catenary effect of steel beams. However, fracture of high-strength bolts dominated the failure mode of a steel bolted connection exposed to a temperature higher than 400 °C. This may result in a collapse of entire structure. To ensure fire safety for steel structures, it is required to accurately predict the fracture behavior of key components (e.g. beam-to-column connection) in steel structures. Thus, in this study, the fracture behavior of A325 steel bolt was investigated within the range of 400-700°C. To simulate fracture in A325 steel bolts, the three-stage fracture model parameters are calibrated at elevated temperatures by using standard tension tests and double shear tests. The calibrated fracture model parameters are further validated against the tension tests on shear tab connections at elevated temperatures which were dominated by fracture failure of bolts.

Keywords: Fracture behavior; high-strength bolts; fracture prediction; elevated temperatures

1 INTRODUCTION

High-strength bolts have been widely used for bolted beam-to-column connections in steel structures. For fire safety design, they are usually designed to tolerate fire-induced tensile forces caused by thermal expansion and catenary effect of steel beams. However, it was found that fracture of high-strength bolts usually dominates the failure mode of a steel bolted connection exposed to a temperature higher than 400 °C [1]. This can undermine the integrity of key components, and even lead to the collapse of entire structures. Therefore, to accurately predict the fracture behavior of high-strength steel bolts at elevated temperatures becomes particularly essential for fire safety of steel framed structures. Due to insufficient test data, computational predictions of fracture behavior of high-strength steel bolts at elevated temperatures are still lacking. Thus, the purpose of this study is to propose an approach to accurately predict fracture behavior of typical high-strength steel bolts in bolted connections at elevated temperatures. Computationally predicting fracture behavior of steel bolts requires an appropriate fracture model together with accurate model parameters. From several elevated-temperature experiments on steel shear tab connections [1], it was observed that shear fracture may be the dominant fracture mode in the steel bolts at high temperatures (≥ 400 °C). Therefore, the fracture model derived by Bao [2] with consideration of fracture caused by both tension and shear may be suitable to perform fracture prediction for steel bolts. However, parameters for the Bao's fracture model have not been reported for steel bolts at elevated temperatures. Thus, in this study, the Bao's fracture model parameters are calibrated at elevated temperatures by using results from tension and shear tests and numerical simulations in ABAQUS.

¹ Postdoctoral Researcher, College of Civil Engineering, Tongji University, Shanghai 200092, China,
e-mail: wenyucai@tongji.edu.cn

² Professor, School of Mechanics and Civil Engineering, China University of Mining and Technology, Xuzhou 221116, China,
e-mail: jian.jiang@cumt.edu.cn

³ Professor, College of Civil Engineering, Tongji University, Shanghai 200092, China,
e-mail: gqli@tongji.edu.cn

2 THEORETICAL FRACTURE MODEL

Bao's three stage fracture model, predicts the equivalent plastic strain at the initiation of ductile fracture ($\varepsilon_{p,critical}$) as a function of the stress triaxiality (η) which is defined as the ratio of mean stress σ_m to von-Mises stress (σ_e) at the location of ductile fracture initiation. The simplified Bao's fracture model function [2] is shown in Eq. (1).

$$\varepsilon_{p,critical} = \begin{cases} \infty & \eta \leq -1/3 \\ D_0 / (1 + 3\eta) & -1/3 \leq \eta \leq 0 \\ D_0 + (D_c - D_0)(3\eta)^2 & 0 \leq \eta \leq 1/3 \\ D_c / (3\eta) & \eta \geq 1/3 \end{cases} \quad (1)$$

The parameters D_0 and D_c in Eq. (1) is the parameters depending on material properties. As illustrated in Figure 1, within the zone one, defined as shear fracture zone, the range of stress triaxiality is negative and the equivalent strain at fracture initiation decreases with the stress triaxiality and reaches a minimum value D_0 at the stress triaxiality ($\eta = 0$), which corresponds to the stress state under pure shear; within the zone two, defined as the combined shear and tensile fracture zone, the range of stress triaxiality is positive and the equivalent strain at fracture initiation increases with the stress triaxiality and reaches a peak value D_c at the stress triaxiality ($\eta = 1/3$), which corresponds to the stress state under pure tension; and within the zone three, tension fracture zone, the equivalent strain at fracture initiation again decreases with the stress triaxiality.

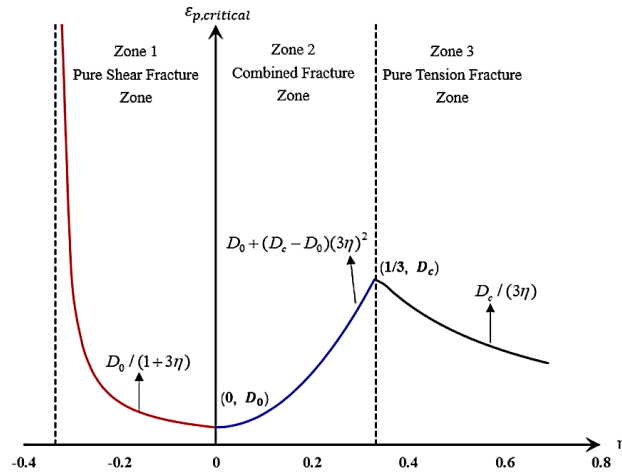


Figure 1. Bao's Three-stage fracture model [2]

3 CALIBRATION OF FRACTURE MODEL PARAMETERS FOR HIGH-STRENGTH STEEL BOLTS

3.1 Calibration of fracture parameter D_c

The tensile coupon tests [3] were used to determine the fracture parameter (D_c) in pure tension fracture zone. The tension in the fracture model together with parameter was then used as a fracture criterion for predicting the fracture behavior of high-strength steel bolt tension specimen to verify the accuracy of the calibrated parameters.

According to Yu and Jeong [4], at room temperature, fracture parameter (D_c) can be preliminarily estimated from the reduction of cross-sectional area of steel tension specimen after fracture, as shown in Eq. (2). However, this assumption has not been validated at elevated temperatures. In this study, from 400 °C to 700 °C, D_c was first calibrated based on Eq. (2) and then adjusted if the predicted results including the fracture failure mode and engineering stress-strain curves were not in good agreement with measured results.

$$D_c = -\ln(1 - A_g) \quad (2)$$

where, A_g is the reduction of cross-sectional area of steel tension specimen after fracture.

The reduction of the cross-sectional area of high-strength steel bolt after tension test was reported in Ref [3]. The estimated D_c was obtained using Eq. (2) and shown in Table 1. To validate the estimated fracture parameter, the tested tension specimen recorded by Kodur et al. [3] were modelled in ABAQUS using Solid element C3D8R. Based on the mesh sensitivity study, the minimum mesh size was 1 mm. The true stress-strain curves of A325 bolts which were required in finite element analysis was calibrated based on the approach reported in Ref [5]. The simulated model and boundary condition were shown in Figure 2. The predicted results were then compared with the test results.

Table 1. Estimated fracture parameters D_c

Temperatures	400 °C	500 °C	600 °C	700 °C
D_c	1.61	1.90	2.30	2.30

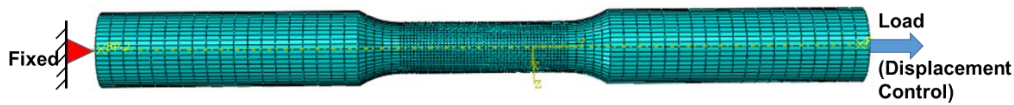


Figure 2. Load and boundary condition for A325 steel bolt material in tension

Figure 3 shows the comparison between the measured engineering stress-strain curves of A325 bolts in tension tests and the predicted results by ABAQUS using the three-stage model in tension zone with the estimated parameter (D_c) listed in Table 1. It is found that the differences between the measured maximum engineering stress and engineering strain at fracture and the predicted ones are within 10%. This comparison indicates that Eq. (2) is also valid for calibration of fracture model parameter (D_c) at elevated temperatures.

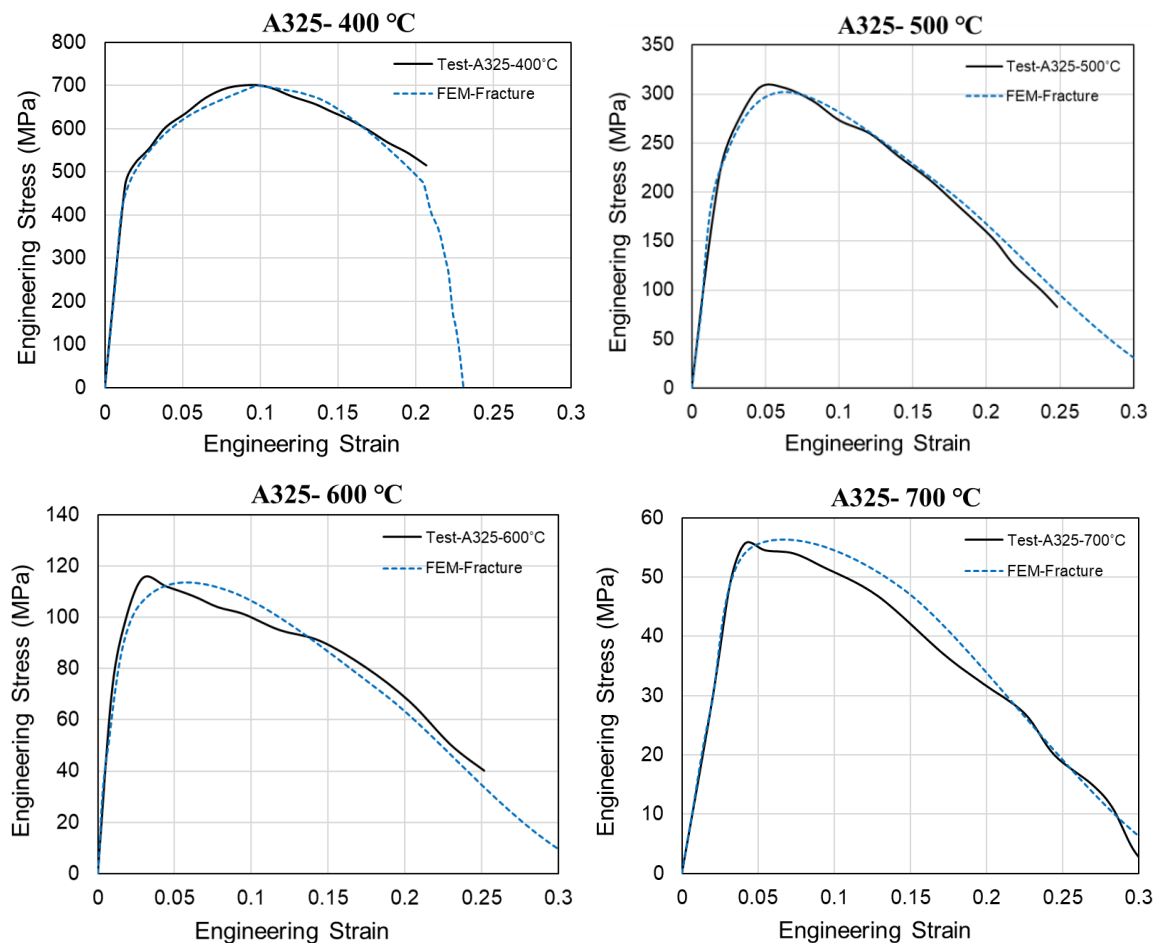


Figure 3. Comparison of predicted results and measured results for A325 bolts in tension

3.2 Calibration of fracture parameter D_0

The parameters D_0 in the shear zone of the three-stage model were calibrated in ABAQUS using results from double shear tests [6] on A325 steel bolts at elevated temperatures ranging from 400 °C to 700 °C. The tested specimens were modeled in ABAQUS and the fracture model in shear zone was input as fracture criterion. The boundary and load conditions of the simulated model are shown in Figure 4. The minimum mesh size was determined as 2 mm. Note that the input stress-strain behavior of A325 bolts were calibrated from test results reported in Ref [3] using the approach reported in Ref [5]. The plates were made of Grade 50 steel and the material properties were determined from Ref [6]. Different sets of fracture model curves with various parameters D_0 were input into ABAQUS to predict the behavior of A325 bolts in double shear tests at elevated temperatures. The parameter D_0 was then determined once the predicted load vs. displacement curve and fracture failure mode match the measured results best. Table 2 lists the calibrated parameters D_0 .

Table 2. Estimated fracture parameters D_0

Temperatures	400 °C	500 °C	600 °C	700 °C
D_0	0.38	0.45	0.38	0.21

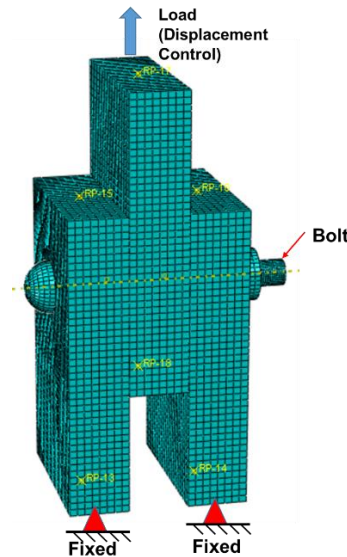
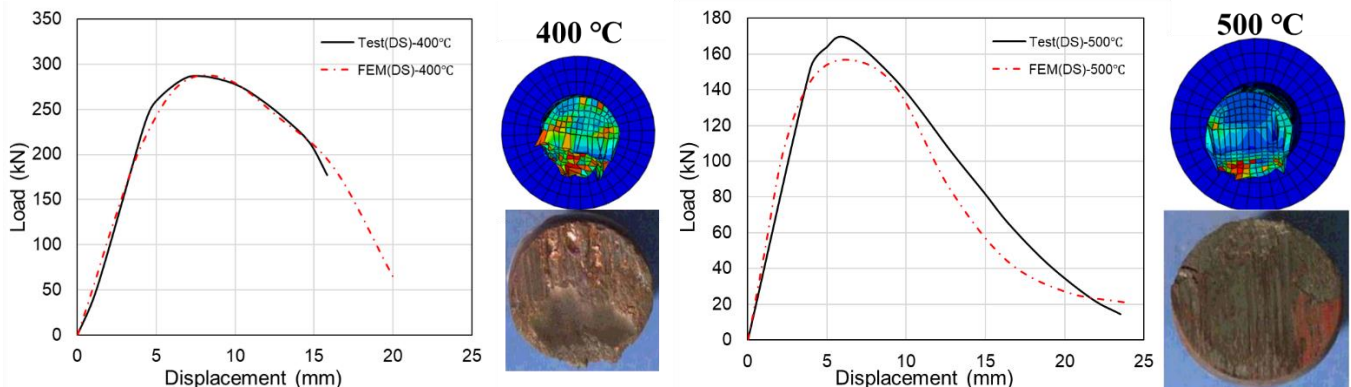


Figure 4. Load and boundary condition for A325 bolts in double shear tests

Figure 5 shows the comparison between the measured load vs. displacement curves and failure mode of A325 bolts from double shear tests and the predicted results by ABAQUS using the three-stage model in shear zone with the estimated parameter (D_0) listed in Table 2. The difference between the measured and predicted peak load is within 5% and that for maximum displacement is within 15%. The predicted failure modes dominated by shear fracture are also close to those from tests.



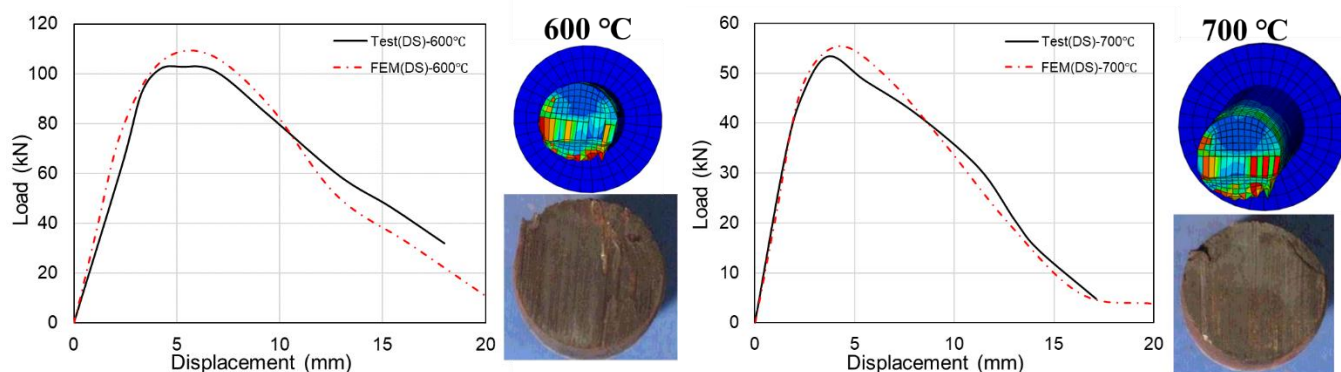


Figure 5. Comparison of predicted results and measured results for A325 bolts in double shear tests

3.3 Observations of three-stage fracture model parameters at elevated temperatures

Figure 6 illustrates the curves of calibrated three-stage fracture model for A325 bolts at elevated temperatures. In the tension zone, with the increase of the temperature, the parameter D_c increases. For the same stress triaxiality level, the larger the parameter D_c , the larger the equivalent plastic strain $\varepsilon_{p,critical}$ would be. This indicates that fracture resistance of A325 bolt improves with increase of temperature. However, the variation trends of the parameter D_c with temperature is quite different. Once the temperature is higher than 500 °C, the parameter decreases with temperature, which indicates that the shear fracture resistance degrades with increasing temperature.

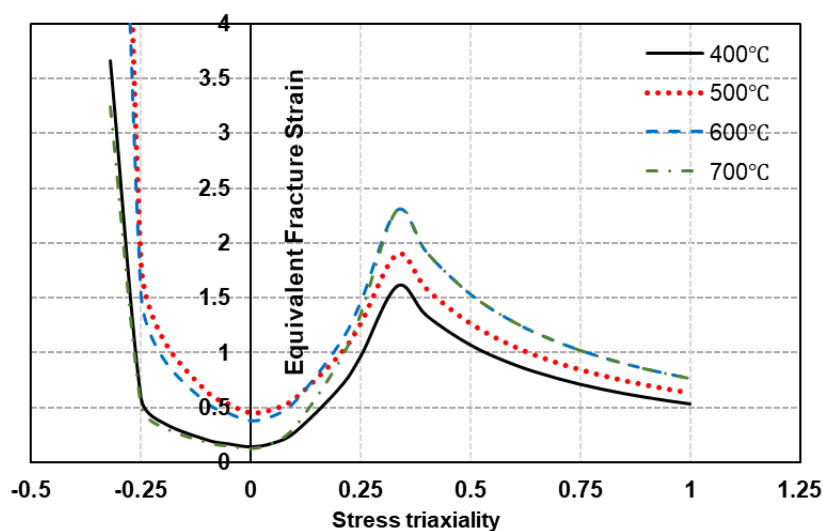


Figure 6. Calibrated three-stage fracture model for A325 bolts

4 NUMERICAL PREDICTION OF FRACTURE BEHAVIOR FOR HIGH-STRENGTH STEEL BOLTS

The calibrated fracture model and fracture parameters shown in Figure 6 were further validated against steel bolted connection tests reported by Hu [1] at temperature of 400 °C, 500 °C and 700 °C. The tested specimens were modeled in ABAQUS together with the calibrated three-stage fracture model for A325 model. The beam in the connection assembly was made from ASTM A992 steel, for which the input true stress-strain behavior can be derived from the results from Ref [5]. Material properties of the ASTM A325 bolts were derived from the test results by Kodur et al. [3]. The shear tab was made from ASTM A36 steel and its input true stress strain behavior was developed from the engineering stress strain curves obtained from Harmathy and Stanzak [7]. Fracture criterion for the other components was referred to [8]. Solid element C3D8R was used in ABAQUS with a minimum mesh size of 0.5 mm based on mesh sensitivity studies. For the boundary conditions, one end of the specimen was fixed for all degrees of freedom while the other end was assigned a target displacement of 70 mm.

Figure 7 shows a comparison of the fracture failure mode and load-deformation curve at elevated temperatures from test and numerical simulation. This comparison shows that the fracture of high-strength steel bolts can be predicted with reasonable accuracy using the calibrated fracture model.

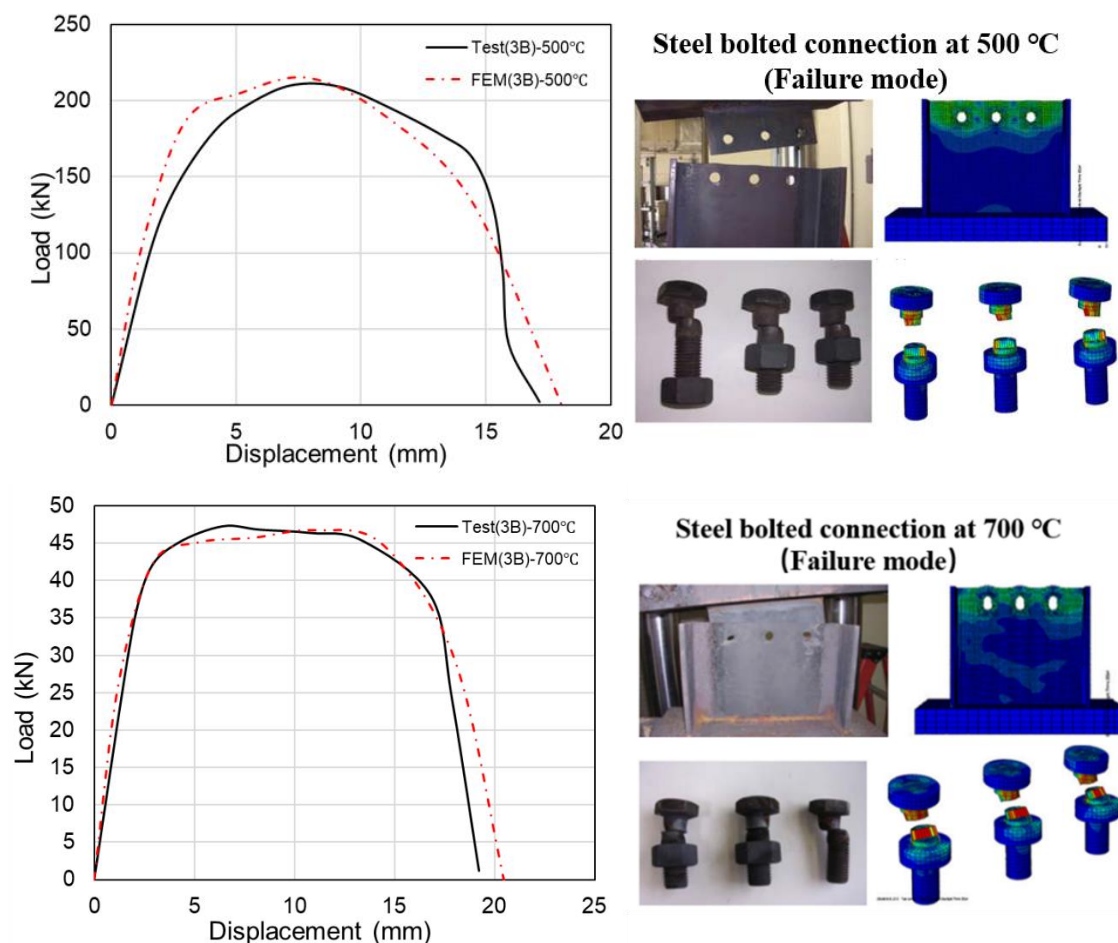


Figure 7. Comparison of the fracture mode and load-displacement curve of A325 bolts in shear tab connections between test and simulation

5 CONCLUSIONS

This paper presented fracture prediction for high-strength steel bolts in bolted connections at elevated temperatures. It was found that the calibrated three-stage fracture model was capable of predicting, with reasonable accuracy, the observed fracture behavior of high-strength steel bolts in experiments. The calibrated parameters in the fracture model were dependent on the material properties of steel at different temperatures. Fracture parameters in the three-stage fracture model was proposed for fracture simulation of high-strength steel bolts at elevated temperatures from 400 °C to 700 °C.

REFERENCES

1. Hu, G. "Behavior of Beam Shear Connections in Steel Buildings Subject to Fire." Ph.D. Dissertation. The University of Texas at Austin, 2011.
2. Bao, Y.B. "Prediction of ductile crack formation in uncracked bodies". PhD Dissertation, Massachusetts Institute of Technology, 2003.
3. Kodur, V., Kand, S., Khaliq, W. "Effect of temperature on thermal and mechanical properties of steel bolts." Journal of Materials in Civil Engineering, 2011, 24(6), 765-774.
4. Yu, H., Jeong, D. "Application of a stress triaxiality dependent fracture criterion in the finite element analysis of unnotched Charpy specimens." Theoretical and Applied Fracture Mechanics, 2010, 54, 54-62.
5. Cai, W., Morovat, M. A., & Engelhardt, M. D. "True stress-strain curves for ASTM A992 steel for fracture simulation at elevated temperatures." Journal of Constructional Steel Research, 2017, 139, 272-279.

6. Yu, L. "Behavior of bolted connections during and after a fire." Ph.D. Dissertation. The University of Texas at Austin, 2006.
7. Harmathy, T., Stanzak, W. "Elevated-Temperature Tensile and Creep Properties of Some Structural and Prestressing Steels." Fire Test Performance, ASTM STP 464, American Society for Testing and Materials, 1970, 186-208.
8. Cai, W. "Steel Fracture Modeling at Elevated Temperature for Structural-Fire Engineering Analysis." Ph.D. Thesis. The University of Texas at Austin, Austin, TX, 2015.

NEW METHODOLOGY FOR THE CALCULATIONS ON STEEL COLUMNS WITH THERMAL GRADIENTS IN CONTACT WITH BRICK WALLS

António Moura Correia¹, João Paulo Rodrigues², Venkatesh Kodur³

ABSTRACT

The study of the temperatures in steel elements with thermal gradients provoked by the contact with brick walls, has been carried out by several researchers in the past years. This research has proved that there are huge differences of temperature within the transversal cross-section of the profiles [1, 2, 3].

The study of the phenomenon of “Thermal Bowing” has now reached to a point at which it is important to determine the detrimental or beneficial role of the thermal gradients in steel columns of buildings, and this can only be made by an accurate determination of temperatures [4, 5]. Recent research have allowed to quantify the thermal gradients along the web and along the flanges, for cases with the column oriented with the web perpendicular or parallel to the adjacent walls.

However, the design Eurocodes for steel columns under fire situation [6], are based on the assumption that the temperature distribution is uniform, despite the fact that this assumption is very far from reality, and thermal gradients cannot be neglected.

Keywords: Steel, columns, walls, section factor, fire

1 INTRODUCTION

Most generally, it has been considered that in case of fire, a steel column experiments a uniform temperature distribution along the cross-section, due to the great thermal conductivity of the steel.

However, this assumption is not accurate, and in recent years several studies have been conducted to obtain a better understanding of this phenomenon. In 1988, Cooke [3] developed a study about the gradients in the cross-sections of building elements, and observed that important deflections occur on steel elements, because of this uneven heating of the elements. Valdir Silva [4] has carried out studies with the aim of calculating the temperature of thermally unprotected steel members under fire situations, with particular focus on the Section Factor parameter. In the University of Coimbra, a great amount of studies has been conducted, regarding these topics such as thermal gradients in cross-sections embedded on walls [5-7], section factor [8], determination of temperatures in cases of columns partially embedded in walls [9], and thermal bowing [10]. In 2016, Lopes presented some proposals for Section Factor calculation, for columns in contact with walls [11]. Moreover EN 1993-1-2 [1] considers a uniform temperature evolution in these elements, in case of fire, and does not contemplate all cases of embedment of steel columns in the partition walls.

Thus, based on many laboratory and numerical studies, it was found that this phenomenon should be considered in the fire design of buildings, even because it may create unfavorable situations in the structure

¹ Professor, Polytechnic Institute of Coimbra, Superior School of Engineering of Coimbra, Portugal
e-mail: antonio.correia@isec.pt, ORCID: <https://orcid.org/0000-0001-9199-7659>

² Professor, Department of Civil Engineering, University of Coimbra, Portugal
e-mail: jpaulocr@dec.uc.pt

³ Professor, Department of Civil and Environmental Engineering, Michigan State University, U.S.A.
e-mail: kodur@egr.msu.edu

due to the degradation of the material properties of steel, and the inversion of bending moments that create a marked curvilinear deformation in the element, best known as the phenomenon of "thermal bowing". The purpose of this study is the introduction of reduction coefficients in the formulae of the aforementioned Eurocode data for the calculation of the real temperatures in different parts of the steel sections embedded on walls.

2 METHODS OF MODELLING THE TEMPERATURE EVOLUTIONS IN STEEL PROFILES AND DETERMINATION OF SECTION FACTORS

This work presents a study based on a geometric and nonlinear material finite element analysis of 26 different steel profiles, with two different brick wall thicknesses of 7cm and 15cm and with two orientations of the web in relation to the walls, giving a total of 94 cases. In each of these cases, four methodologies were adopted to calculate the section factors. For each case it was identified which method most closely approximates the temperatures obtained by the numerical models.

2.1 Case studies

For each profile studied, temperature values are presented in four different methods, which consist no more than different ways of calculating the section factor, that is, different methodologies to obtain the temperatures in the profile.

Figure 1 depicts the 4 different cases of geometry target of the present study.

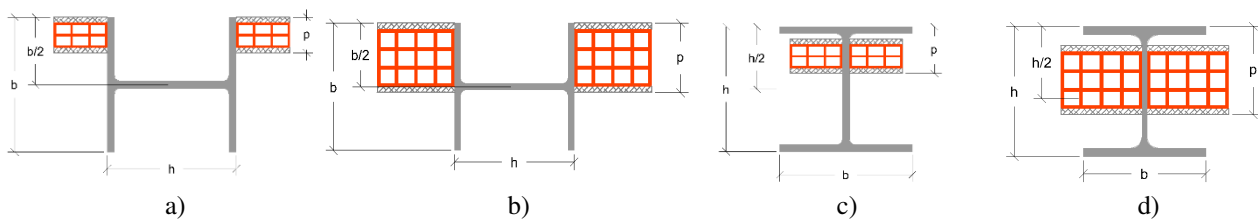


Figure 1. Visualization of the method to obtain the temperatures in the different zones: a) web parallel to walls and $p < 0.5b$ b) web parallel to walls and $p > 0.5b$ c) web perpendicular to walls and $p < 0.5h$ d) web perpendicular to walls and $p > 0.5h$

For each of the different configurations depicted in Figure 1, four different approaches were used to calculate the temperatures in the steel cross sections. Figure 2 intends to show these four approaches, for the case of the web parallel to the walls and $p < 0.5b$.

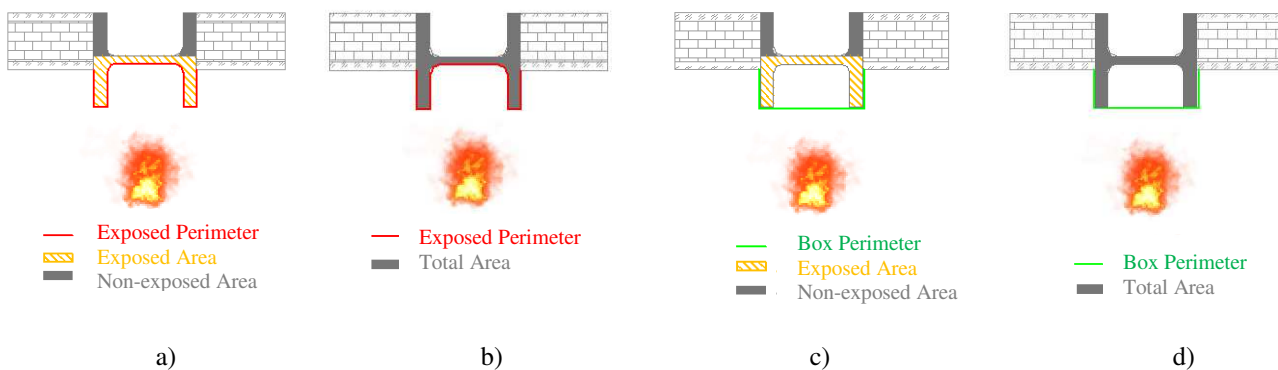


Figure 2. Different approaches to the calculation of temperatures in the steel profiles a) Case 1 b) Case 2 c) Case 3 d) Case 4

In these figures, we considered P_{exp} represented with a red line, A_{exp} with orange diagonal line, P_{box} with green line, and the unexposed area is dark gray as well as the total area of the profile.

In table 1 a list of the simulations programme is shown. For each combination of wall thickness and orientation of the web profile to the wall, the list of steel profiles adopted in the study is presented [12].

Table 1. Steel Profiles used in the numerical simulation models

Walls 7cm thick		Walls 15cm thick	
Web parallel to walls	Web perpendicular to walls	Web parallel to walls	Web perpendicular to walls
-	HD 320x127	HD 320x127	HD 320x127
HD 320x127	IPE 180	HE 450 AA	HE 450 AA
IPE 180	HE 160 A	HE 450 A	HE 450 A
HE 160 A	HE160 AA	HE 450 M	HE 450 M
HE160 AA	HE160 M	HP 260x52	HP 260x52
HE160 M	HE 450 M	HP 360x152	HP 360x152
HE 450 M	HP 360x174	HP 360x174	HP 360x174
HP 360x174	HP 250x62	HP 305x79	HP 305x79
HP 250x62	HP 360x152	HP 305x110	HP 305x110
HP 360x152	HP 305x79	HP 400x194	HP 400x194
HP 305x79	HP 400x194	HP 400x231	HP 400x231
HP 400x194	IPEO 180	IPEA 400	IPEA 400
IPEA 100	IPE 400	IPEA 270	IPEA 270
IPE 400	IPEA 180	IPE 400	IPE 400
IPEA 180	IPEO 270	IPEO 270	IPEO 270
IPEO 270	UBP 356x368x133	UBP 356x368x133	UBP 356x368x133
UBP 356x368x133	UB 254x102x28	UB 254x102x28	UB 254x102x28
UB 254x102x28	UB 406x178x54	UB 406x178x54	UB 406x178x54
UB 406x178x54	UC 254x254x107	UC 254x254x107	UC 254x254x107
UC 254x254x107	UC 356x406x551	UC 356x406x551	UC 356x406x551
UC 356x406x551	W 250x250x131	-	W 250x250x131
W 250x250x131	W 460x280x235	W 250x250x167	W 250x250x167
W 460x280x235	W 920x420x390	W 460x280x235	W 460x280x235
W 920x420x390	HD 320x127	W 920x420x344	W 920x420x344

For each of these profiles, the four approaches used to calculate the temperatures according the Eurocode 3 part 1-2 [1], are described next:

Case 1, $\frac{Am}{V} = \frac{P_{exp}}{A_{exp}}$, is shown in Figure 1 a). Case 1 e is related to the quotient between the exposed perimeter, which is in red and the exposed area, which is illustrated with orange dashes. The exposed perimeter corresponds to the profile boundary that is in contact with fire, while the exposed area reflects which surface is exposed to it.

In Case 2, $\frac{Am}{V} = \frac{P_{exp}}{A_{tot.profile}}$, the quotient between the exposed perimeter and the total profile area, shown in full and gray, representing the entire surface of the profile, is determined.

Case 3, $\frac{Am}{V} = \frac{P_{box}}{A_{exp}}$, is obtained dividing the perimeter of the box, represented by a green line, by the exposed area designating the surface in contact with fire.

The box designation refers to a box that surrounds the profile only from the exposed side. This box concept is intended to consider the perimeter that will be heated in the profile by entering the flame into a concave surface.

Case 4, $\frac{Am}{V} = \frac{P_{exp}}{A_{tot.profile}}$, refers to the division between the perimeter of the box, already mentioned, and the total profile area.

The parameters $A_{tot.profile}$, P_{box} , A_{exp} , and P_{exp} were calculated, in such a way to obtain for each case, the section factor calculated by different approaches.

With the above approaches, temperatures were estimated according to Eurocode 3 - part 1-2 [1] for 15 min, 60 min and 120 min.

With the ABAQUS finite element program [2], the temperatures were then calculated in the various cross-section zones of the profiles at different instants of time (15, 60 and 120 minutes). Temperatures were taken in different finite elements at half height, in the heated-flange (HF) or heated half-flange (HHF), web (W), and unheated flange (UF) or unheated half-flange (UHF). An average value was adopted, considering the total finite elements in each of the mentioned zones.

Subsequently, the reduction coefficients were determined by dividing the temperatures calculated by the Eurocode, and the temperatures obtained by the ABAQUS finite element analysis.

The cases mentioned above are:

- **Case 1:**
$$\frac{Am}{V} = \frac{P_{exp}}{A_{exp}} \quad (1)$$

- **Case 2:**
$$\frac{Am}{V} = \frac{P_{exp}}{A_{tot.profile}} \quad (2)$$

- **Case 3:**
$$\frac{Am}{V} = \frac{P_{box}}{A_{exp}} \quad (3)$$

- **Case 4:**
$$\frac{Am}{V} = \frac{P_{box}}{A_{tot.profile}} \quad (4)$$

2.2 Modelling with the ABAQUS program

Figures 3a and 3b represent the construction of the 3D models of the HE 160A profile with the web parallel to the wall and another with the web perpendicular to the wall, respectively.

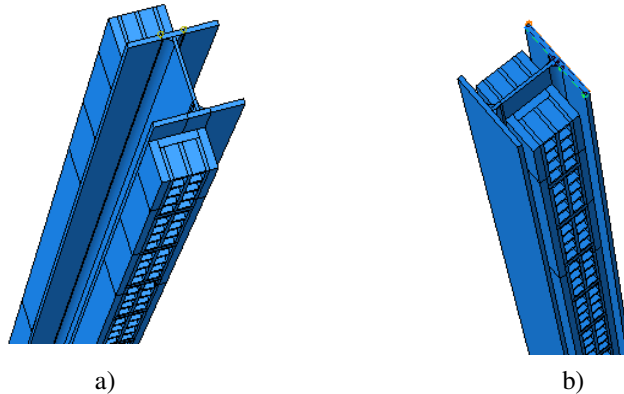


Figure 3. HE160A assembly with the web a) parallel to the wall b) perpendicular to the wall

The following figure (Figure 4) represents the assembly steps of the model and relate to the definition of the master and slave surfaces. The master face is represented in red and the slave face in pink.

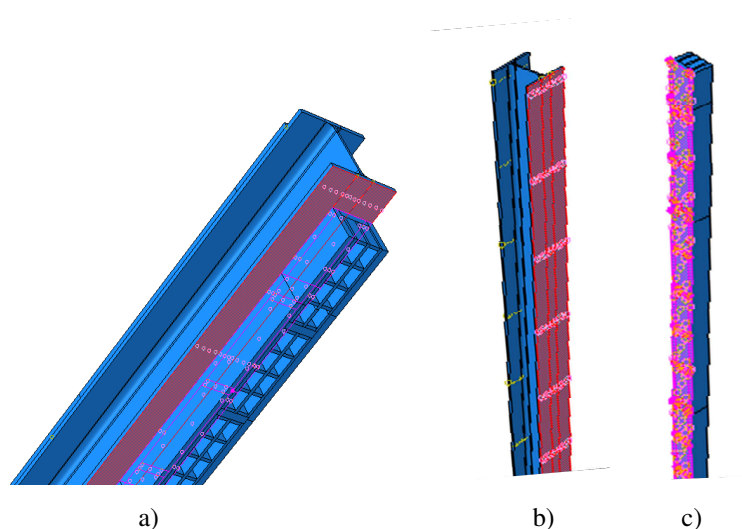


Figure 4. Surface definition demonstration a) master b) master c) slave

The following figures (Figure 5a and 5b) are examples of numerical models used in the finite element analysis of the thermal behavior of steel columns embedded in walls. These also show how the surfaces that were analyzed to obtain the temperatures of the finite elements were selected, that is, the results on the web and half-flanges of the profile. For the representation we used the HE 160A profile, 7cm wall with the web parallel to the wall. In this case, as in the others where the web is parallel to the wall, the wall creates a kind of fire protection and divides the flanges by their "half". So we refer to heated half-flanges and unheated half-flanges. The same does not apply to situations where the web is perpendicular to the wall.

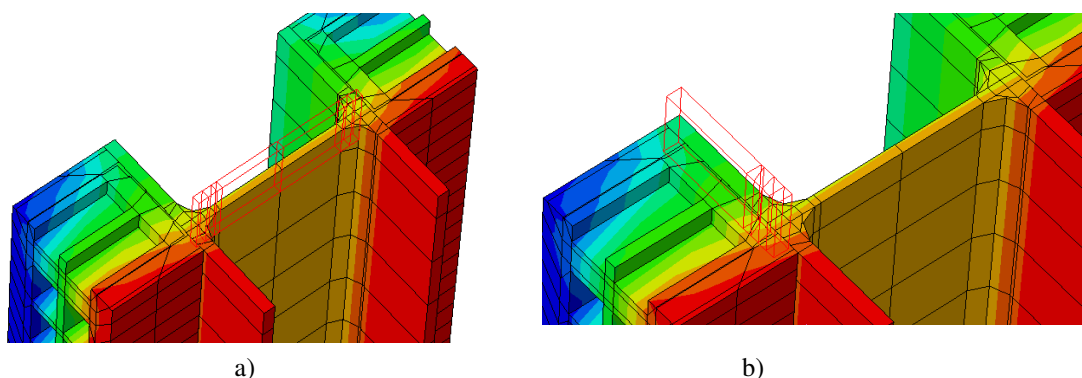


Figure 5. Visualization of the method to obtain the temperatures in the different zones of the profile a) web b) unheated flange

3 RESULTS

From the numerical simulations, temperature fields in the web and heated (HF) and unheated (UF) flanges were obtained, in the case of the columns with the web perpendicular to the walls, and in the heated and unheated half-flanges and web, in case of profiles with the web parallel to the walls. Tables 2, 3, 4 and 5 are related to the HE 160M profile with a web positioned perpendicular to the wall of 7 cm thickness.

Table 2. Temperatures obtained by Eurocode and ABAQUS, and their quotient - Case 1

Time (min)	Eurocode	ABAQUS			ABAQUS/EUROCODE		
		HF	WEB	UF	HF	WEB	UF
15	549	484.450	271.399	50.240	0.882	0.494	0.530
60	938	912.660	626.422	250.370	0.973	0.668	0.696
120	1046	1030.800	744.852	372.990	0.985	0.712	0.710
AVERAGE					0.947	0.625	0.691

Table 3. Temperatures obtained by Eurocode and ABAQUS, and their quotient - Case 2

Time (min)	Eurocode	ABAQUS			ABAQUS/EUROCODE		
		HF	WEB	UF	HF	WEB	UF
15	328	484.450	271.399	50.240	1.477	0.827	0.153
60	901	912.660	626.422	250.370	1.013	0.695	0.278
120	1042	1030.800	744.852	372.990	0.989	0.715	0.315
AVERAGE					1.160	0.746	0.249

Table 4. Temperatures obtained by Eurocode and ABAQUS, and their quotient - Case 3

Time (min)	Eurocode	ABAQUS			ABAQUS/EUROCODE		
		HF	WEB	UF	HF	WEB	UF
15	432	484.450	271.399	50.240	1.121	0.628	0.116
60	926	912.660	626.422	250.370	0.986	0.676	0.270
120	1045	1030.800	744.852	372.990	0.986	0.713	0.314
AVERAGE					1.031	0.672	0.234

Table 5. Temperatures obtained by Eurocode and ABAQUS, and their quotient - Case 4

Time (min)	Eurocode	ABAQUS			ABAQUS/EUROCODE		
		HF	WEB	UF	HF	WEB	UF
15	236	484.450	271.399	50.240	2.053	1.150	0.213
60	843	912.660	626.422	250.370	1.083	0.743	0.297
120	1038	1030.800	744.852	372.990	0.993	0.718	0.316
AVERAGE					1.376	0.870	0.275

For different time instants, 15, 60 and 120 seconds, the relationship between the temperature values estimated by the Eurocode calculation methods and the values obtained by the finite element numerical modeling was calculated.

4 NEW EXPRESSIONS FOR THE CALCULATION OF SECTION FACTOR

In this chapter, calculation methods have been developed to obtain new expressions for the calculation of the section factor. This factor, although present in EN 1993-1-2 [1], is not adapted to some real situations, as it assumes that the temperature distribution occurs evenly along the steel profile cross-section.

Parametric studies were used in 94 different cases, in steel profiles inserted, either in 7 cm wall or 15 cm wall, and with the position of parallel or perpendicular web to the wall. They were modeled in the ABAQUS program [2], as already mentioned previously, applying a thermal finite element analysis, in which the temperatures for each situation were obtained.

The problem was subdivided into four distinct cases where the perimeter of the box, the exposed perimeter, the exposed area and the total area of the profile under study were considered. The obtained temperatures were compared with those provided by the EN 1993-1-2 [1], thermal reduction coefficients were obtained for three time periods, being 15, 60 and 120 min for the heated flange, web and unheated flange (in the case of the web perpendicular to the wall), or heated half-flange, web and unheated half-flange (in case of the profile with web parallel to the wall).

After calculating the coefficients, we used the least squares method, performed for each case and situation studied, so that it was possible to verify which of the studied cases has the lowest error. For this evaluation we used the cases where the box perimeter was considered versus cases where it was not considered. Thus we analyzed case I versus case II and case III versus case IV.

The situations were further distributed in four new cases. These concern the dimensions of the wall and the dimensions of the profile as well as the position of the profile relative to the wall, subdivided into cases A, B, C and D which will be detailed next. Thus for each case two tables were constructed where the situations described in the previous paragraph are verified.

In cases with lower errors, which suggest to be the most accurate, coefficients k_1 , k_2 and k_3 were taken, which represent the heated flange, web and unheated flange, respectively (in the case of the web perpendicular to the wall) and heated half-flange, web and half unheated half-flange (in the case of the web parallel to the wall). These represent the correction coefficients to be applied in EN 1993-1-2 [1] formulas to obtain the most accurate approximation of temperatures during the occurrence of a fire.

The EN 1993-1-2 [3] formula to be used is:

$$\Delta\theta_{a,t} = k_{sh} \frac{A_m/V}{c_a \rho_a} \dot{h}_{net,d} \Delta t \quad (5)$$

Where:

- $\Delta\theta_{a,t}$ is the variation of temperature, for instant t [°C];
- k_{sh} is the correction of the shadow effect factor;
- A_m/V is the section factor for unprotected steel members;
- A_m is the surface area of the limb per unit length [m²];
- V is the member volume per unit length [m³];
- c_a is the specific heat of steel [J/kgK];
- $\dot{h}_{net,d}$ is the effective flow calculation value per unit area [W/m²];
- Δt is the time interval [seconds];
- ρ_a is the unit of mass of steel [kg/m³].

The proposal consists on implementing a correction coefficient, k_c , in the previous formula, so that it provides non-uniform temperatures throughout the section, and consequently, more realistic in the different zones of the section.

$$\Delta\theta_{a,t} = k_{sh} \frac{k_c}{c_a \rho_a} \frac{A_m}{V} \dot{h}_{net,d} \Delta t \quad (6)$$

The parameters involved in this new expression are the same as previously described with the introduction of k_c which corresponds to the correction coefficients obtained.

4.1 Reduction coefficients for Case A: $p > 0.5 \times b$

This subsection leads us to situations where the profile web is parallel to the wall (p) and the wall thickness is greater than half the flange dimension (b), meaning $p > 0.5 \times b$.

Table 6 presents the best fit performing the calculation with the calculation based on the box perimeter. It is possible to conclude that, after 120 seconds, the temperatures in the unexposed zone of the profile are about 63% of the temperature estimated by the EN 1993-1-2 [1].

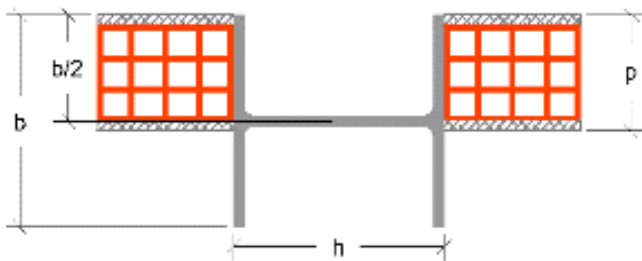
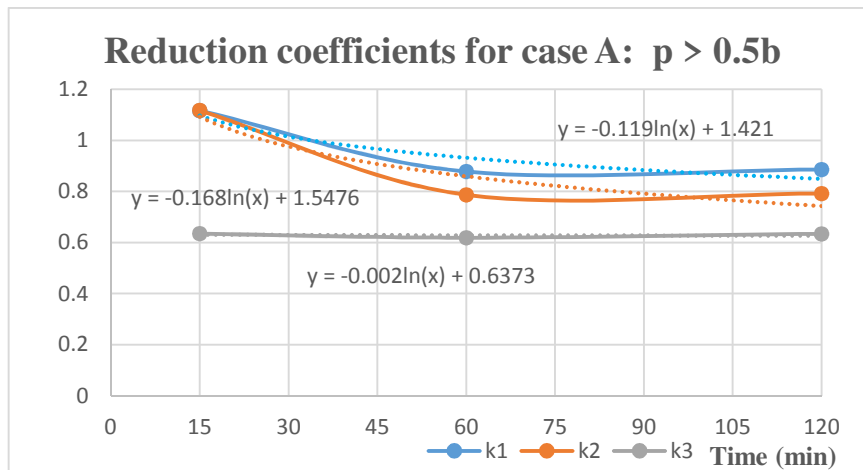


Table 6 - Reduction coefficients - Case 4

Time (min)	k_1	k_2	k_3
15	1.116	1.117	0.635
60	0.878	0.787	0.619
120	0.886	0.792	0.634

Figure 6. Profile subject to case A: $p > 0.5 \times b$

Figure 7 depicts the values of k_1 , k_2 and k_3 of table 6, and logarithmic regressions to the values of these coefficients along the time, between 15 to 120 minutes of fire exposure. With these regressions, it was possible to derive expressions (7) (8) and (9), which allow the calculation of these reduction coefficients for different instants of time.



$$k_1 = -0.119 \ln(t) + 1.421 \quad (7)$$

$$k_2 = -0.168 \ln(t) + 1.548 \quad (8)$$

$$k_3 = -0.002 \ln(t) + 0.637 \quad (9)$$

Figure 7. Logarithmic regression for case A: $p > 0.5 \times b$

4.2 Reduction coefficients for Case B: $p < 0.5 \times b$

This sub-chapter is intended for situations where the web of the steel profiles is parallel to the wall (p) and the wall width, in turn, is less than half the flange dimension (b), $p < 0.5 \times b$.

Table 7 presents the best fit performing the calculation based on the box perimeter. Again, the best calculation procedure was using the total area of the profile (cases 2 and 4). It was observed that the differences are not negligible.

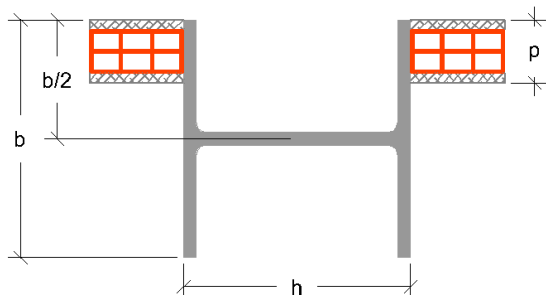
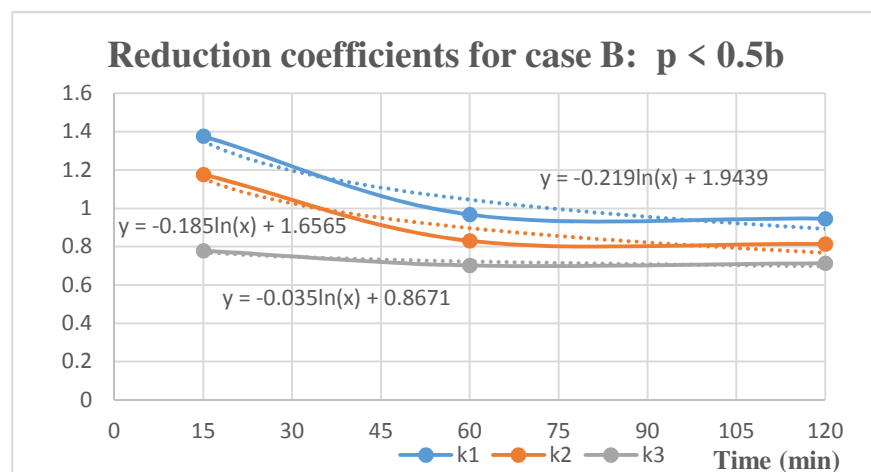


Table 7 - Reduction coefficients - Case 4

Time (min)	k ₁	k ₂	k ₃
15	1.376	1.177	0.779
60	0.967	0.830	0.702
120	0.946	0.814	0.713

Figure 8. Profile subject to case B: $p < 0.5 \times b$

The same methodology was used in this case. Figure 9 depicts the values of k_1 , k_2 and k_3 of table 7, and logarithmic regressions were applied. With these regressions, it was possible to derive expressions (10) (11) and (12), which allow the calculation of these reduction coefficients for case B, in which $p < 0.5b$.



$$k_1 = -0.219 \ln(t) + 1.944 \quad (10)$$

$$k_2 = -0.185 \ln(t) + 1.657 \quad (11)$$

$$k_3 = -0.035 \ln(t) + 0.867 \quad (12)$$

Figure 9. Logarithmic regression for case B: $p < 0.5 \times b$

4.3 Reduction coefficients for Case C: $p > 0.5 \times b$

For situations where the profile web is perpendicular to the wall and the wall (p) is greater than half of the total profile height (h), $p > 0.5 \times h$, a case C was defined.

Again table 8 presents the results for case 4. It is worth mentioning that on the unheated part of the column (k_3), the temperatures are now about 22% of the values estimated by the EN 1993-1-2 [1], after 120 seconds of heating.

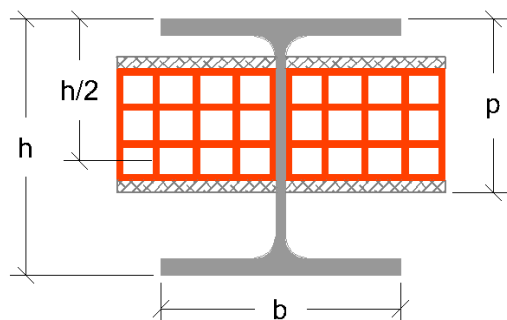
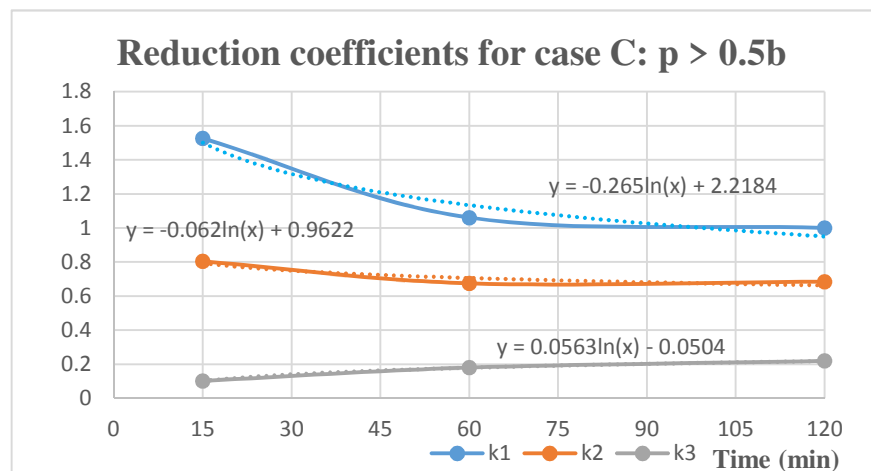


Table 8 - Reduction coefficients - Case 4

Time (min)	k ₁	k ₂	k ₃
15	1.526	0.804	0.102
60	1.061	0.675	0.180
120	1.000	0.685	0.219

Figure 10. Profile subject to case C: $p > 0.5 \times b$

The values of k_1 , k_2 and k_3 and the logarithmic regressions to the values of these coefficients are now depicted in figure 11. With these regressions, expressions (13) (14) and (15) were derived, to make possible the calculation of these reduction coefficients, for case C ($p > 0.5b$).



$$k_1 = -0.265 \ln(t) + 2.218 \quad (13)$$

$$k_2 = -0.062 \ln(t) + 1.657 \quad (14)$$

$$k_3 = 0.056 \ln(t) + 0.050 \quad (15)$$

Figure 11. Logarithmic regression for case C: $p > 0.5 \times b$

4.4 Reduction coefficients for Case D: $p < 0.5 \times b$

The methodology presented in 4.4 is used when the profile web is perpendicular to the wall and the wall dimension (p) is less than half of the total profile height (h), $p < 0.5 \times h$. Table 9 presents the reduction coefficients for this case, for times of 15, 60 and 120 minutes.

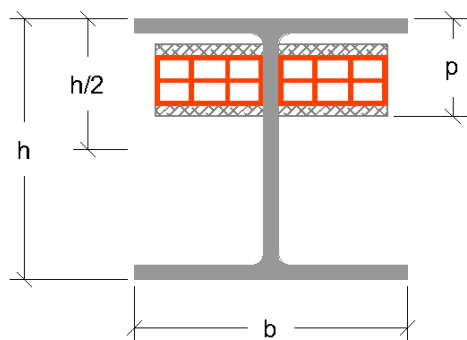


Table 9 - Reduction coefficients - Case 4

Tempo (min)	k_1	k_2	k_3
15	1.508	1.091	0.100
60	1.026	0.788	0.167
120	1.003	0.804	0.212

Figure 12. Profile subject to case D: $p < 0.5 \times b$

The same conclusions are applicable to this case D: both approaches 2 and 4 are more suitable for calculating the temperatures, i.e. using the total area of the profile. Another conclusion worth of notice is that the unheated flanges are much colder (k_3 equal do 0.212) than the heated flange and web.

The logarithmic regressions for the values of the reduction coefficients are shown in figure 13, and the corresponding formulae derived from these regressions are (16), (17) and (18).

As expected, the curves for k_1 and k_3 , are considerably more distanced for cases C and D, for the cases with the profile oriented with the web perpendicular to the walls, than in cases A and B, for the situations in which the profile is oriented with the web parallel to the walls.

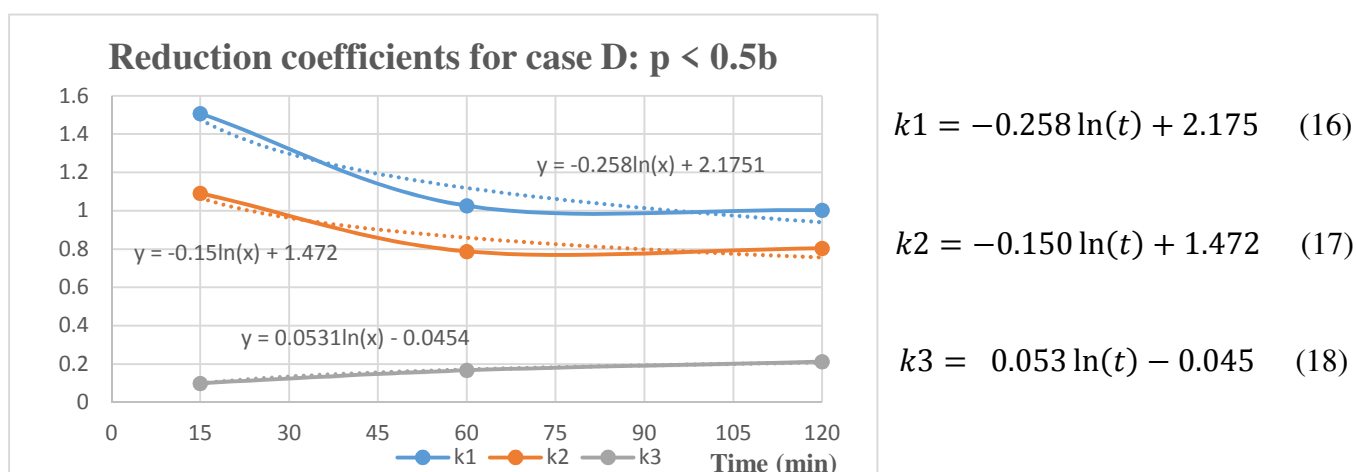


Figure 13. Logarithmic regression for case D: $p < 0.5 \times b$

5 CONCLUSIONS

In this study, proposals for calculations of the section factor, for cases not included in table 4.2 of the referred EN 1993-1-2 [1] were presented. These proposals were obtained using finite element numerical models with the ABAQUS program [2], varying the cross section of the steel profiles, the orientation of the web of the profiles in relation to the walls, and the position and thickness of the brick walls, in relation to the columns to allow obtaining a correction of the section factor calculations, with the largest possible field of validity. The methodology proposed makes very easy the determination of real temperatures in unevenly heated steel profiles in contact with walls. It is expected that, in the future, steel structures designers may take into consideration more real temperatures in the assessment of the fire safety of steel buildings.

REFERENCES

1. EN 1993-1-2 (2005). "Eurocode 3 - Design of steel structures - Part 1.2: General rules - Structural fire design". CEN, Brussels.
2. ABAQUS. ABAQUS/standard version 6.7 user's manual: volumes I-III. Pawtucket, Rhode Island: Hibbit, Carlsson & Sorensson, Inc.; 2005.
3. Cooke, G. M. E., (1988a). *Thermal Bowing and how it affects the design of fire separating construction*, Proceedings of the Interflamm'88, 230-236, London.
4. Silva, V. (2006). *Determination of the Temperature of Thermally unprotected Steel Members under Fire Situations: considerations on the Section Factor*. Latin American Journal of Solids and Structures, vol. 3, pp 113-125.
5. Correia A.M., Rodrigues J.P.C., Silva V.P. (2009a). *Experimental research on the fire behaviour of steel columns embedded on walls*. Application of Structural Fire Engineering, Prague, Czech Republic.
6. Correia, A.M., Rodrigues, J.P.C., Silva, V. P. (2009e). *Influence of Brick walls on the Temperature Distribution in Steel Columns in Fire*, Acta Polytechnica – Journal of Advanced Engineering, vol.49 No.1/2009, ISSN 1210-2709.
7. Correia; António Moura (2011). *Fire Resistance of Steel and Composite Steel-Concrete Columns*, PhD Thesis, University of Coimbra.
8. Correia, A. M., Rodrigues, J. P., Silva, V. P., Laim, L. (2009b). *Section factor and steel columns embedded in walls*; Nordic Steel – Construction Conference, Malmö, Sweden.
9. Correia, A. M., Rodrigues, J.P.C., Silva V.P. (2010). *A Simplified Calculation Method for Temperature Evaluation of Steel Columns Embedded in Walls*; Fire and Materials, DOI:10.1002/fam.1063.

10. Correia, A. J., Rodrigues, J. P., Vila Real, P., (2014). *Thermal bowing on steel columns embedded on walls under fire conditions*. Fire Safety Journal, Volume 67, pp. 53-69, 2014. <https://doi.org/10.1016/j.firesaf.2014.05.001>.
11. Lopes, Paula Cristiana Ribeiro (2016). Proposta de Novas Expressões para o Cálculo do Fator de Massividade para Elementos Estruturais de Aço em Contacto com Paredes, Dissertação de Mestrado em Engenharia Civil – Especialização em Construção Urbana, Instituto Superior de Engenharia de Coimbra.
12. Correia, A. J., Lopes, P., Rodrigues, J. P., Correia, J., (2019). *Proposal of new expresisons for the calculation of section factor on structural steel columns in contact with walls*. Fire Research, Volume 3:73, [doi:10.4081/fire.2019.73](https://doi.org/10.4081/fire.2019.73)

OPENSEES SIMULATION OF THE COLLAPSE OF PLASCO TOWER IN FIRE

Ramakanth Veera Venkata Domada¹, Aatif Ali Khan², Mustesin Ali Khan³, Asif Usmani⁴

ABSTRACT

The Plasco Building, built in 1962, was the tallest building with 17 stores in Iran at the time of its construction and was considered as an iconic high-rise dominating the Tehran skyline. On 19th January 2017, a fire started on the 10th floor and travelled horizontally within the floor and vertically to upper floors, eventually leading to the collapse of Plasco Building. Sixteen firefighters and ten civilians were killed in this accident. In this paper, an attempt has been made to understand the mechanism of the collapse of Plasco Building. A detailed finite element model is prepared using OpenSEES software. This paper discusses the insights obtained from preliminary stage analysis carried out considering a standard fire exposure. It is found that to accurately understand the behaviour of Plasco Building collapse, a realistic fire scenario is required to be generated. Therefore, FDS modelling capabilities have been used to arrive at the required fire scenario. The paper will also introduce a new framework (OpenFIRE) to link FDS and OpenSEES so that a seamless thermomechanical analysis can be performed. In this paper, only a part of the Plasco Building has been modelled using FDS to generate the fire scenario. The results obtained using OpenFIRE framework are significantly different and more close to reality compared to considering a standard fire exposure. In future study, the whole Plasco Building will be modelled using FDS to achieve a most accurate fire scenario and simulating the Plasco Building collapse.

Keywords: OpenSEES, structures in fire, FDS, heat transfer, finite element modelling.

1 INTRODUCTION

Fire accidents are usually a tragic phenomenon because of the associated loss of life and property but at the same time, it also offers engineers an opportunity to learn and improve fire safety design.

Investigation of the collapse of the three towers of the World Trade Centre (WTC), New York Buildings in 2001 following the terrorist attack also provided valuable lessons on fire safety and structural stability of tall buildings. The behaviour of structures in fire involves many counterintuitive and subtle phenomena in the thermo-mechanical response of large frame structures which are not well understood, even by experts in the profession. Structural fire resistance design relies heavily on the behaviour of materials at high temperatures which has skewed the attention of professionals towards seeking explanations of structural phenomena primarily in material response. While not wrong, this over-reliance on the material aspects often make engineers lose sight of structural system response. This was generally true of the multiple explanations for the WTC collapses that surfaced after the event. Usmani [1,2] and his research team at the

¹ PhD student, Building Services Engineering, The Hong Kong Polytechnic University,
e-mail: ramakanth.domada@connect.polyu.hk, ORCID: <https://orcid.org/0000-0001-9523-4472>

² PhD student, Building Services Engineering, The Hong Kong Polytechnic University,
e-mail: alikhan.aatif@connect.polyu.hk, ORCID: <https://orcid.org/0000-0001-9181-4795>

³ Research Assistant Professor, Building Services Engineering, The Hong Kong Polytechnic University,
e-mail: mustesin.khan@polyu.edu.hk, ORCID: <https://orcid.org/0000-0002-0806-3167>

⁴ Professor, Building Services Engineering, The Hong Kong Polytechnic University,
e-mail: asif.usmani@polyu.edu.hk, ORCID: <https://orcid.org/0000-0003-2454-5737>

University of Edinburgh found that the WTC towers had an unusual vulnerability to large fires. The team was able to produce a credible collapse mechanism, which did not depend upon any gross assumptions about the fire or failure of connections or even structural damage. A clear stability failure mechanism was established by conducting a simple computational analysis. The analysis was entirely consistent with the fundamental principles developed previously during the simulation of Cardington tests led by Usmani et al. [3].

On 19th January 2017, a fire accident occurred on the 10th floor and spread to other parts of the building which eventually resulted in the collapse of the building within four hours as shown in Figure 1. It was believed that the fire was initiated by a short circuit in the electrical system. The accident resulted in loss of many lives including residents and firefighters. In addition, hundreds of businesses were destroyed, and thousands of workers lost their employment. For these reasons, the fire incident and its consequence drew a lot of attention amongst fire engineering community globally.



Figure 1: Plasco Tower at different stages of the event (a) before the accident (d) during fire accident (c) at collapse (all images courtesy of IRNA NEWS Agency)

The overall aim of this paper is to discuss about the results obtained from preliminary thermo-mechanical analysis of the Plasco Building and introduce a newly developed OpenFIRE framework to generate a realistic fire scenario and carry out sequential heat transfer and thermomechanical analysis sequentially.

1.1 Plasco Tower description

The Plasco tower had two separate structural blocks; the 17-storey main tower standing beside a 5-storey building. The 17-storey building was $30\text{m} \times 30\text{m}$ in plan with two floors below the ground level and fifteen floors above the ground level. The height of the ground floor was 6.3m compared to 3.8m for other floors. The 5-storey building was a 105m long shopping mall along the North-South direction and had 3200 m² floor area approximately. Weaker section columns were placed along the periphery to resist the lateral loads such as wind and earthquake loads. Whereas stocky columns were placed in the centre to safely transfer the gravity loads to the foundation. Altogether, there were 50 columns in the building. The corner columns and two perimeter columns at the centre of each face were double in size of the other thinner 34 perimeter columns. The double-sized perimeter columns near the middle of each face were aligned with the four stocky interior core columns. The perimeter columns on the south side were not connected to the

foundation to provide free access to the adjoining 5-story part of the structure. Due to the lack of structural drawings and other information during the fire incident, many field inspections were conducted by researchers and engineers to establish the details of all structural members. All the structural members were welded built-up sections, meaning that they were made by welding multiple steel profiles such as U and L-shaped profiles. The flooring system comprised of a concrete slab with a thickness of 120 mm, which was supported by a series of ceiling trusses in both perpendicular directions forming a dense steel grillage structure. The structure details have been discussed in depth by Behnam [13].

2 OPENSEES MODELLING

2.1 General modelling philosophy and aims and scope of the simulation

The aim of this work is to understand the reasons for the total collapse of the Plasco Building through subjecting a reasonably comprehensive 3D finite element model of the building to the type of fire loading it experienced during the incident that caused its collapse. The long-term aim is to simulate the progressive collapse of the building with respect to the travelling fire phenomenon as observed during the fire disaster. The fire started on the 10th floor and was observed to have travelled along the floor horizontally and through the staircase and windows vertically. By analysing the visual evidence from different sides of the building during the fire, various potential trajectories of the fire were identified, and will eventually be implemented in the analysis enabled by OpenSEES. OpenSEES is an open source software which was originally developed for simulating the seismic response of structural and geotechnical systems. Later, the fire module of OpenSEES was developed by research group of Usmani at the University of Edinburgh [7–11], and Brunel University London [12–13] UK. Currently, the development of thermal OpenSEES is being carried out by fire research group at Hong Kong Polytechnic University [14].

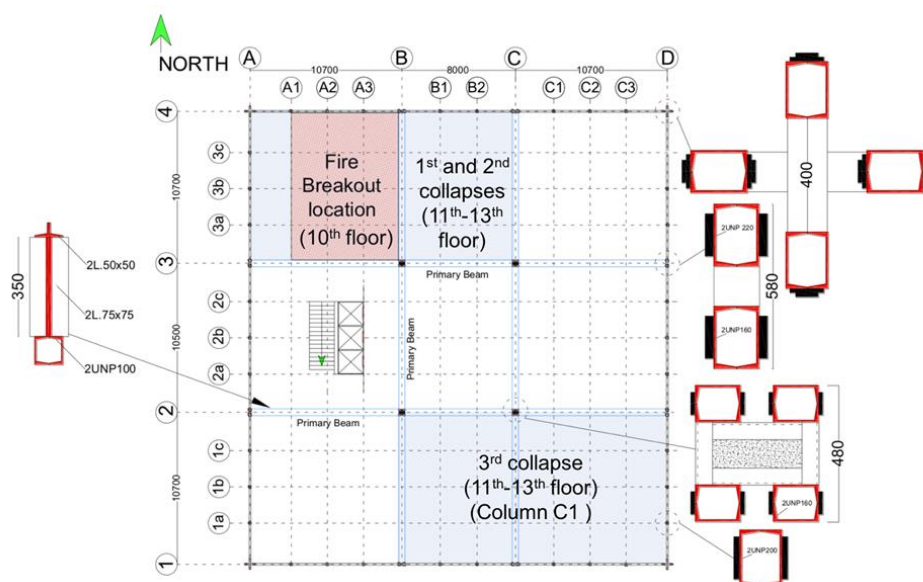


Figure 2 The plan view of Plasco tower and collapse locations [18]

2.2 Structural details of the building

The plan of the Plasco tower is shown in Figure 2. Four internal columns carried the loads transferred by the primary beams, and box columns were constructed along the perimeter of the building. All the steel sections were fabricated by welding standard European channel or angle profiles and no fire protection was applied. OpenSEES fibre-based sections and displacement-based beam-column elements are used to model the frames, while shell elements are used for concrete slabs. The material properties of the steel at room temperature were taken from experiments performed on the coupons gained from the crumbled structural elements [19].

2.3 Structural model of the floor system

In our investigation of the Plasco Building structural system we could not find a definitive answer to the question about whether the concrete floor slab was composite with the supporting grillage or simply rested on top of it. In this preliminary study therefore, a composite grillage floor system is assumed with simply supported primary trusses and continuous secondary floor beams spanning over the primary beams. The plan looks almost square except that the length along the North-South direction is slightly longer.

All the members in the structure were modelled using displacement-based beam column elements available in the OpenSEES library (*dispBeamColumnThermal*). The fiber section approach is followed while modelling the sections where each Fiber Section object is composed of multiple fibers. A uniaxial thermal material is assigned to all the fibres. The *fiberSecThermal* object class enables the user to apply thermal load at 2, 5 or 9 points across the depth of the section. Since the thickness of sections used in the Plasco Building was small, no temperature variation across the depth of sections is assumed; in other words, the temperature gradient across the section is assumed to be zero.

A gravity dead load of 5.3 kN/m^2 is assumed which includes load coming from composite floor and partition walls. A storage live load of 6.0 kN/m^2 was assumed for these floors. Generally, only a part of live load is assumed to be present in the building during the event of the fire but in this particular case, due to its usage as storage space, the whole live load is assumed to be active in the analysis.

3 PRELIMINARY ANALYSIS

A composite slab model of the Plasco Building has been created as shown in Figure 3 – (a) by creating shells on the plane of the truss members and merging the nodes on the shells with nodes of top chord members of the truss. The shells elements are made of *ShellMITC4Thermal* element class present in the OpenSEES which are sensitive for thermal load. Trusses have been modelled using OpenSEES ‘*Steel02Thermal*’ material class. *Steel02Thermal* is a non-linear material model with temperature dependent degradation of Elastic modulus. The material for shell elements in the model is modelled using Concrete Damage Plasticity with temperature dependent degradation of Elastic modulus.

A standard fire exposure has been assumed for conducting this analysis. The temperature histories for all FE elements, both truss and shells, have been generated using heat transfer modules present in the OpenSEES library. Heat transfer analysis in OpenSees is based on the finite element method to solve the transient governing equations. The modelling part involves creation of a separate heat transfer model consisting of material models and entities with relevant thermal material properties. The model will then be given appropriate heat flux boundary conditions such as coefficient of convection to or from ambient,

ambient air temperature etc. After describing the heat loss to the ambient environment, fire exposure definitions are specified as standard fire model, the analysis is then carried out.

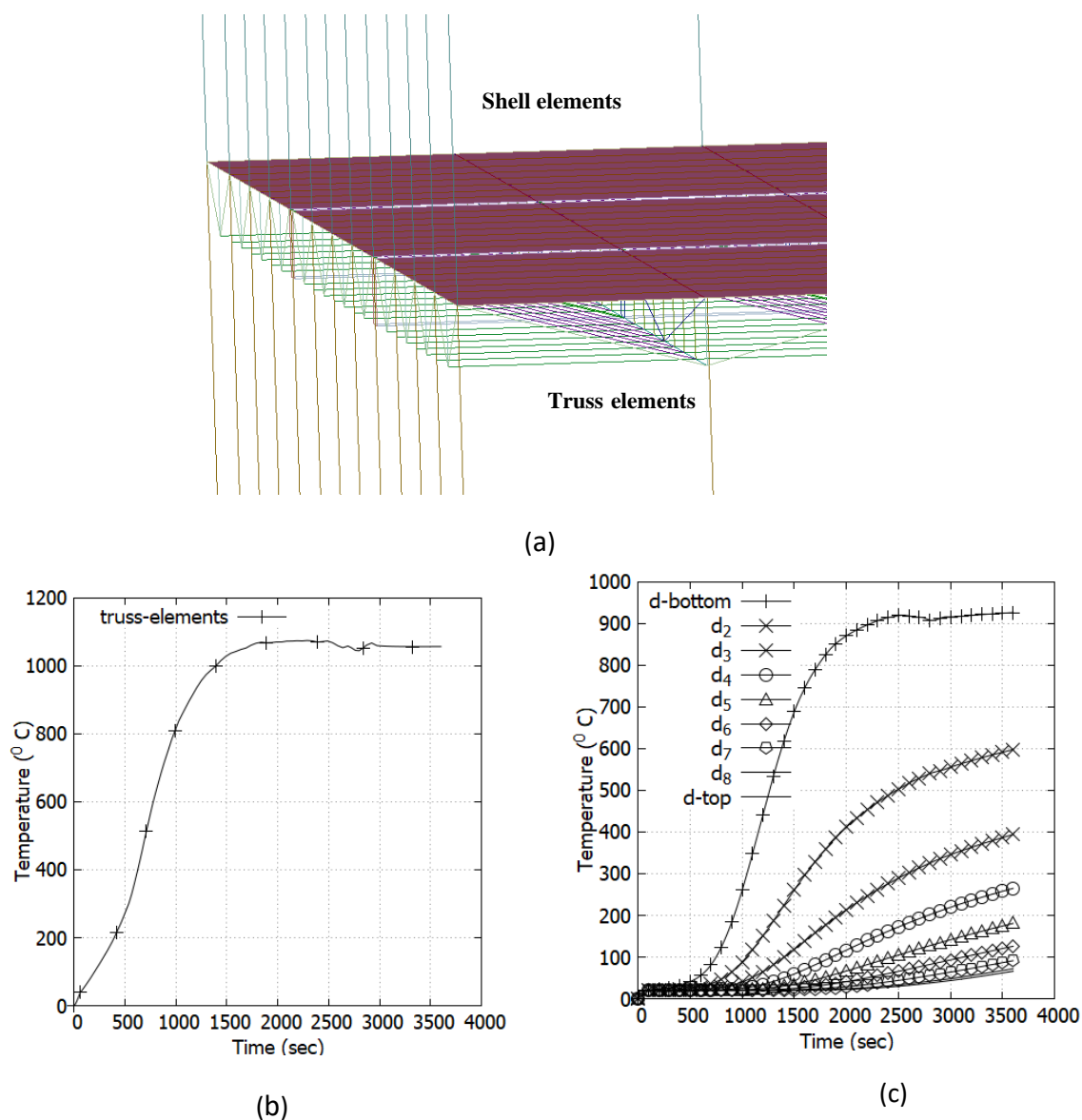


Figure 3 Picture (a) shows the building floor system comprised of truss beams and shell elements (visualized using GiD + OpenSEES interface); (b) and (c) shows the temperature vs time histories of truss members and at different locations across the slab depth

Figure 4 represent the temperature distribution for both steel truss members and concrete slab obtained after conducting the heat transfer analysis. The temperature history will then be applied as a load in the thermo-mechanical model to simulate the nonlinear structural response to the fire.

In these analyses, the rebars when modelled with elastic material model yielded almost the same results as when the same nonlinear material model as truss elements and with better analysis stability. It is because

the temperatures so high at the bottom face upto 20mm inside the cover depth. Hence the former material model has been chosen for the preliminary thermo-mechanical analysis.

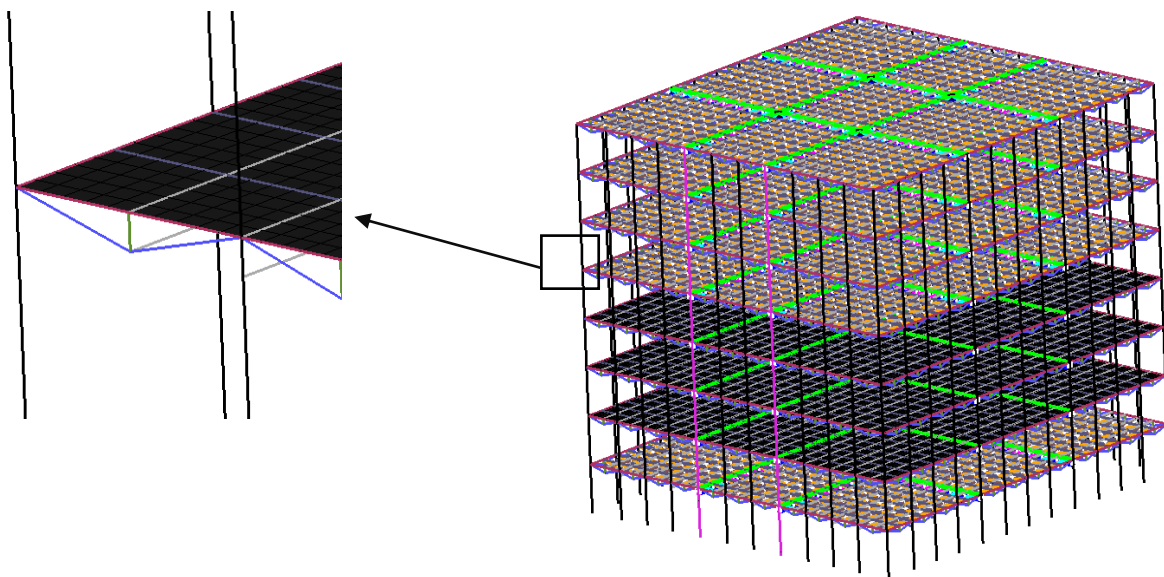


Figure 4 Visualization of OpenSEES model with composite slab modelled (three floors only) using GiD+OpenSEES interface

The entire floor has been modelled with 9 structurally independent zones, the slab crossing over parallel trusses of primary beams is fully cracked because of its age and hogging bending action as seen in Figure 4

3.1 Observations

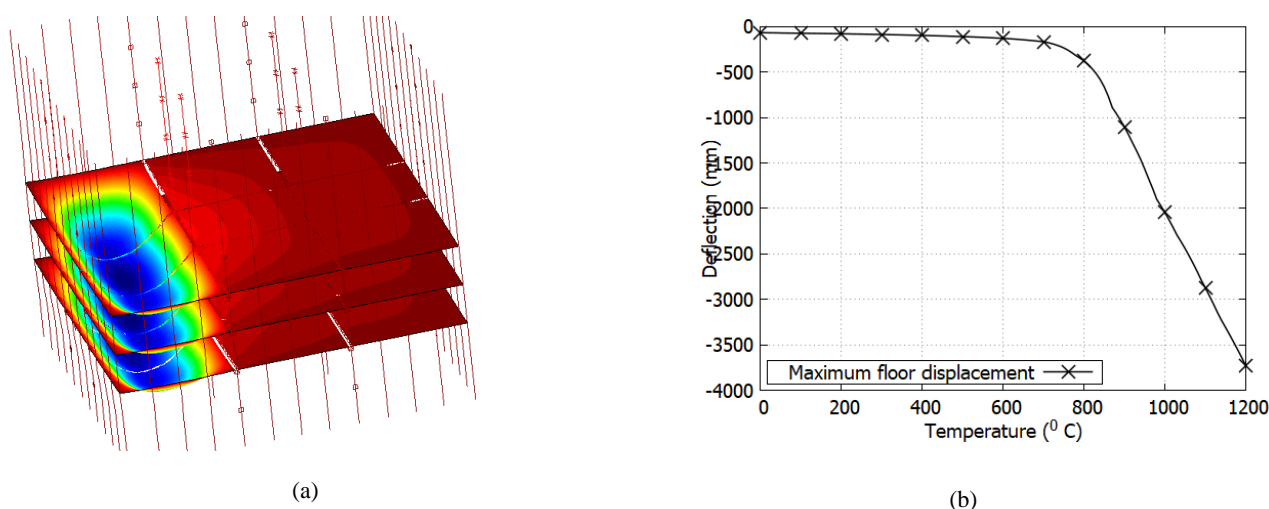


Figure 5 (a) Plot showing maximum floor displacement against steel truss temperature; (b) response of the three heated floors.

The work conducted so far has shown that the corner slabs experienced a partial 2-way bending moment whereas the edge slab is under one way bending action as seen in Figure 5–(a). Since, as per the model, it is evident that slabs at the corners have column supports along two edges, four edge slabs have column

supports on two sides and interior slab has columns at four corners. The response of individual slabs is also accordingly different.

Huge floor displacements have been observed as seen in Figure 5 –(b). Maximum deformations have seen in the middle floor which was supported by the Primary beam on either side. The rate of deformation started increasing after steel temperatures reaching 500°C and rapid rate of downwards displacements are seen after 660°C . The temperatures shown in the plot represent steel truss temperatures. The corresponding temperature at the bottom face of the concrete is 530°C whereas steel truss members is 660°C .

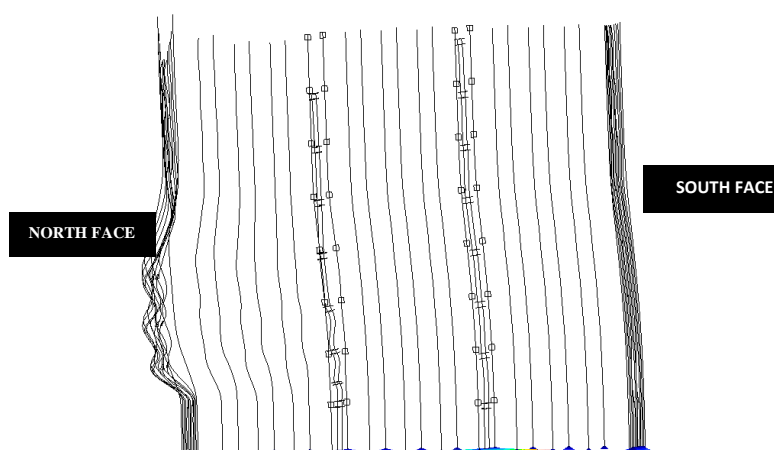


Figure 6 Global column response with North face on the left side and South face on the right.

The global response of the column at the end of thermo-mechanical analysis can be seen in Figure 6. The floor system has been hidden for clarity. The tops of central core columns can be seen at a position much lower than the edge and corner columns (left side of the image). This differential vertical column displacement caused the redistribution of the column loads. As the two North side central core columns are rapidly losing their strength than the edge and core columns. The load carried, up to that point, is redistributed to edge columns present on the East and West side of the tower. The edge and corner columns due to the additional load coming from the floor are further sinking thereby causing a side way displacement of the building globally. The columns on the North face (left side of the image) moving slightly away from the core at the same time sinking. This in turn causing edge and corner columns on the South face to drift inwards i.e., towards the core. Both these actions together are facilitating greater increase in displacements on the North side.

The collapsing two core columns seem to have put sufficient load on every North facing peripheral columns to reach buckling state even under the assumption of non-failure of floor/truss connections with columns.

The global lateral response indicated that the columns on the North face moving outwards from the beginning whereas the columns on the South face moved outwards till 500°C and started moving inwards after that.

It has been observed during the thermomechanical analysis that the core columns are losing the strength rapidly which caused the redistribution of the load towards the edge columns present on the East and West faces. The core columns on the South side also seem have been taking some additional redistributed load.

The material model used for the steel members follows the Elastic modulus deterioration against temperature as specified by the Eurocode 1993 [24]. As per the Eurocode, the loss of elastic modulus majorly occurs between temperatures 400°C and 500°C . It has been noticed in the analysis that the core columns are reaching its maximum load carrying capacity at 300°C - 400°C under thermal load conditions. Beyond 400°C the column seems to be losing its load carrying capacity by 50% i.e. a drop from 9000kN to 4500kN.

It is known that the standard fire applies uniform temperature and does not cater to increased fire load demand due to the change of occupancy of the building. The standard fires also do not have a cooling

branch which can affect connect behavior while cooling. The Plasco tower since it has huge floor area so travelling fires should be the rational choice. Hence in the next step of this research work FDS is included simulated realistic fires.

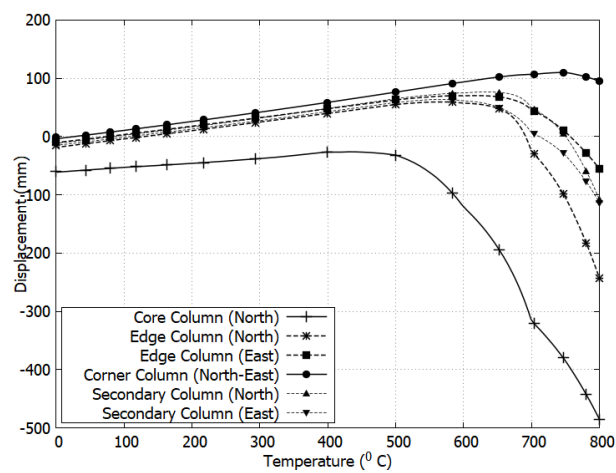


Figure 7 Plot showing the column vertical displacements in all types of columns as shown.

Figure 7 highlights the vertical displacements of all columns on the North-East corner of the building involving in fire load. This explains how dependent building’s global stability on the core columns.

4 APPROACH FOR DETAILED ANALYSIS

The analysis which has been conducted until now considered non-realistic (standard fire) fire scenario. For accurate analysis, CFD model with appropriate dimensions and fire loads of the Plasco Building are required. This would raise the data volume transfer by multiple folds hence a proper data transfer automation is required between CFD and FE models.

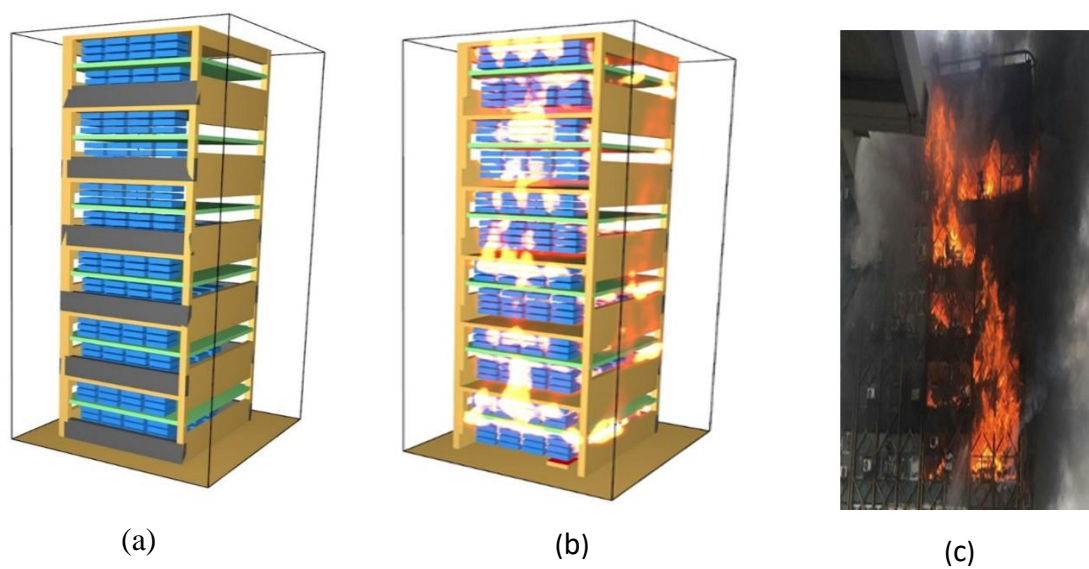


Figure 8 The above pictures (a) and (b) show the FDS model of 8 x 8m North West corner; (c) shows the an instant when the N-W corner was engulfed in the fire.

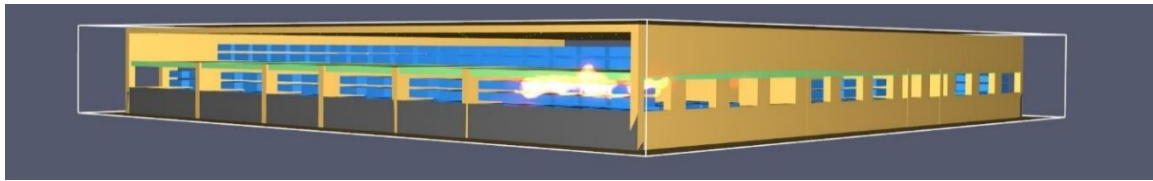


Figure 9 Shows the FDS model for 10th floor of Plasco tower.

For full-scale structural analysis, fire simulation needs to be performed for all the floors which were exposed to the fire. In further study, using the calibrated CFD model based on the visual evidence, realistic thermal boundary condition will be used to stimulate the structural collapse of the Plasco Building.

Before advancing towards the full-scale model with complete vertical and horizontal fire travel cases, the authors have decided to conduct two small scale analyses representing the fire event at two different stages, see Figure 8 and Figure 9.

To verify the vertical fire spread, the North-West corner (8×8m²) of the Plasco Building from the 10th to 15th floors is simulated where the fire could be seen to reach the top floor at the early stages of the fire as shown in Figure 8. The vertical fire spread can be verified with the photographic evidence of the Plasco Building (Figure 8-(c)), it was found from the testimonies of the witnesses that the fire reached to the top floor within 20 minutes of fire. This simulation is performed to represent the vertical fire spread and to predict the estimated time to reach the upper floor from the floor of fire origin. Whereas, to reconstruct the whole fire incident of the Plasco Building, authors recommend performing a detailed forensic study. A full-floor (30×30m²) is simulated to obtain the realistic temperatures from the CFD analysis. As primary combustible in the Plasco Building was clothes, therefore nylon is considered as fuel in the simulation and its properties are taken from the SFPE handbook [22].

Based on the gas temperatures obtained with a reasonable spatial resolution, heat transfer analysis will be carried out using OpenSEES Heat Transfer capabilities. This analysis would yield temperature-time histories for elements in the FE model. This is a three-step sequential analysis wherein the data transfer from one model to the other, in future, will be automated. This automation work named as OpenFIRE is another project being developed at The Hong Kong Polytechnic University fire team.

The OpenFire is an integrated computational framework to carry out CFD, Heat Transfer and Thermo-mechanical analysis sequentially. In detail, the first stage of OpenFire involves the generation of the geometry of the fire compartment by writing input code in FDS. After the fire simulation, FDS gives the output of the simulation as Adiabatic surface temperature.

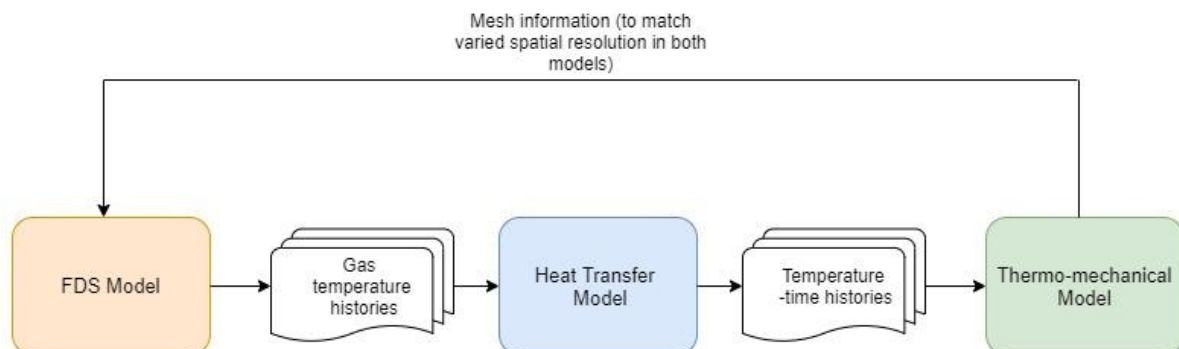


Figure 10 A broad view of data from FDS to FE models

The transient temperatures output from FDS analysis are used for performing heat transfer analysis of the structural members. A concrete slab of 130 mm thick and 400 mm deep truss are considered in this paper. The temperatures in the form of Adiabatic Surface temperatures (AST), a concept proposed by Wickström, are used as the boundary condition for heat transfer analysis. Figure 11 – (a), (b) and (c) shows the surface temperature obtained after heat transfer analysis for steel truss and sectional temperatures for concrete slab near the location where the fire was broke out (North-west corner of the building). The heat transfer analysis was performed to get the structural temperature due to both convective and radiative heat transfer. The heat transfer analysis was performed in OpenSEES software [7].

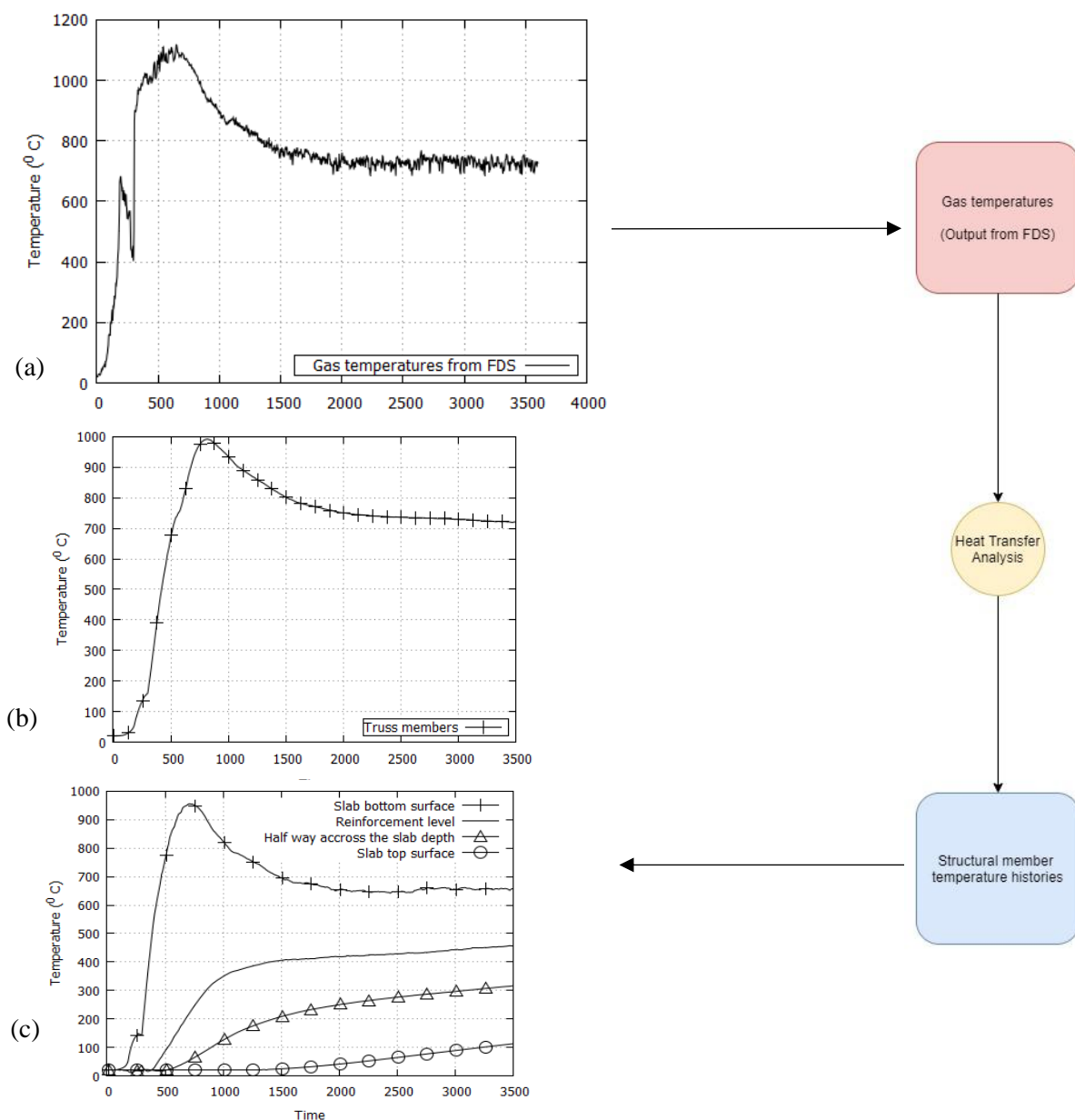


Figure 11 Shows (a) Output from FDS analysis; (b) and (c) shows output from heat transfer analysis for truss elements and slab at different location across the depth.

Figure 11 represent the time-temperature behaviour for both structural members i.e., steel truss and concrete slab, respectively. The overall surface temperatures reached in steel are slightly higher compared to concrete due to its higher conductivity and lower specific heat. After 12 minutes of the fire exposure, the surface temperature for both structural members started to decrease representing the travelling behaviour of fire. This decrease in surface temperature due to the travelling nature of the fire cannot be replicated

using the fire models available in design codes such as standard Time-temperature code e, Eurocodes parametric curves and so on [23]. Therefore, a CFD simulation is carried out to accurately estimate the fire load in this case. It is noteworthy that a significant thermal gradient can be observed across the slab depth as shown in the figure. Though the surface temperatures for the slab are relatively high, the temperatures at the reinforcement level are significantly low due to high specific heat and lower conductivity of the concrete. The current analysis is performed for one-hour fire duration where temperatures on the top surface of the slab are still in the range of 100 °C.

The data at this stage will be post processed to comply with the OpenSEES Heat Transfer requirements. The mapping of data to the right location in the heat transfer entities will be achieved using appropriate modules using the same global coordinate system as the FDS model. After the completion of heat transfer analysis, a middleware will then transfer temperature time histories to a FE model for final thermo-mechanical analysis.

5 CONCLUSIONS

The authors have obtained crucial insights from the preliminary tests carried out the Plasco Building model. The analyses have indicated that the building's global stability is highly sensitive to the stability of core columns. The core columns are susceptible to rapid sinking when temperatures cross 500°C thereby overloading the other columns in the building. This redistribution of vertical loads would result in sway of the structure, predominantly at 11 to 15th floors.

The authors believe that the non realistic temperatures which have been used until now cannot convincingly answer the question why the Plasco tower collapsed.

Hence the future work on this topic will be concentrated towards the modelling of fire loads extracted from FDS and heat transfer analysis. The full scale FDS model for Plasco building and related automation works are a part of OpenFire framework which is developed by the research team. Simultaneously the connection modelling in order to simulate floor collapse will be considered in future work.

ACKNOWLEDGEMENT

The authors gratefully acknowledge the support from the Department of Building Services and Engineering, FCE, The Hong Kong Polytechnic University for providing PhD funding.

The authors are grateful towards Chinese National Engineering Research Centre for Steel (CNERC)-Hong Kong Branch for providing the grant to carry out research into this project.

REFERENCES

1. Newman G. Structural fire engineering investigation of Broadgate phases 8 fire. Steel Construction Industry Forum. 1991.
2. British Steel Plc. The behaviour of multi-storey steel framed buildings in fire. Swinden Technology Centre, Rotherham: 1999.
3. Usmani A, Chung YC, Torero J. How did the WTC towers collapse: a new theory. *Fire Safety Journal*. 2003;38:501–33.
4. Lange, D., Roben C., Usmani, A. Tall building collapse mechanisms initiated by fire: Mechanisms and design methodology, *Engineering Structures*, 2012;36:90-103.
5. Usmani AS, Rotter JM, Lamont S, Sanad AM, Gillie M. Fundamental principles of structural behaviour under thermal effects. *Fire Safety Journal*. 2001;36:721–44.
6. McKenna FT. Object-oriented finite element programming: Frameworks for analysis, algorithms and parallel computing. ProQuest Dissertations and Theses. 1997.
7. Jiang J, Jiang L, Kotsovinos P, Zhang J, Usmani A. OpenSEES Software Architecture for the Analysis of Structures in Fire. *Journal of Computing in Civil Engineering*. 2015;29:04014030.
8. Jiang J, Usmani A, Li G-Q. Modelling of Steel-Concrete Composite Structures in Fire Using OpenSEES. *Advances in Structural Engineering*. 2014;17:249–64.
9. Jiang J, Li G-Q, Usmani A. Analysis of Composite Steel-concrete Beams Exposed to Fire using OpenSEES. *Journal of Structural Fire Engineering*. 2015;6:1–20.
10. Jiang J, Li G-Q, Usmani A. Progressive Collapse Mechanisms of Steel Frames Exposed to Fire. *Advances in Structural Engineering*. 2014;17:381–98.
11. Usmani A, Zhang J, Jiang J, Jiang Y, Kotsovinos P, Zhang J, et al. Using OpenSEES for structures in fire. *Structures in Fire*. 2010;3:919–26.
12. Khan MA, Jiang L, Cashell KA, Usmani A. Analysis of restrained composite beams exposed to fire using a hybrid simulation approach. *Engineering Structures*. 2018;172:956–66.
13. Zhou M, Cardoso RPR, Bahai H. A new material model for thermo-mechanical steels in fire. *International Journal of Mechanical Sciences*. 2019;159:467–86.
14. Yarlagadda T, Hajiloo H, Jiang L, Green M, Usmani A. Preliminary modelling of Plasco Tower collapse. *International Journal of High-Rise Buildings*. 2018;7:397–408.
15. Behnam B. Fire Structural Response of the Plasco Building: A Preliminary Investigation Report. *International Journal of Civil Engineering*. 2019;17:563–80.
16. Hajiloo H, Adelzadeh M, Green MF. Collapse of the Plasco Tower in Fire. *Second Int. Conf. Struct. Saf. under Fire Blast*, London, United Kingdom: 2017.
17. Hajiloo, H., Adelzadeh, M., and Green, M. F. (2017). "Collapse of the Plasco Tower in Fire." *Proc., The Second International Conference on Structural Safety under Fire & Blast*, London, UK.
18. Shakib, H., Dardaei, S., and Zaker Salehi, M. (2017). "Final Report on the Technical, Management, and Legal Aspects of the Plasco Fire." Commissioned by Tehran's City Council, Tehran.
19. Plasco Investigation committee (2017). "Plasco Fire's National Report." Tehran, Iran.
20. Shakib, Hamzeh, et al. "Technical and administrative assessment of Plasco building incident." *International Journal of Civil Engineering* 16.9 (2018): 1227-1239.
21. Iranian National Building Codes Compilation Office (2013) Iranian National Building code, part 22: care and maintenance of buildings. Ministry of Housing and Urban Development (MHUD)
22. Hurley, M. J., Gottuk, D. T., Hall Jr, J. R., Harada, K., Kuligowski, E. D., Puchovsky, M., ... & WIECZOREK, C. J. (Eds.). (2015). *SFPE handbook of fire protection engineering*. Springer.
23. Standard, B. (2006). Eurocode 1: Actions on structures.
24. Eurocode, C. E. N. (1993). 3: Design of steel structures.

FIRE RESISTANCE OF STAINLESS STEEL SLENDER ELLIPTICAL HOLLOW SECTION BEAM-COLUMNS

Flávio Arrais¹, Nuno Lopes², Paulo Vila Real³

ABSTRACT

Stainless steel has different advantages when compared to conventional carbon steel. The corrosion resistance and aesthetic appearance are the most known, however its better behaviour under elevated temperatures can also be important in buildings design. In spite of the initial cost, stainless steel application as a structural material has been increasing. Members with elliptical hollow sections integrate the architectural attributes of the circular hollow sections and the structural advantages of the rectangular hollow sections. They have a better torsional behaviour than open sections and, due to their shape, a higher bending strength when compared to circular hollow profiles. Hence, the application of stainless steel material combined with these elliptical hollow profiles stands as an interesting design option. This work presents a numerical study on the behaviour of slender stainless steel members composed of elliptical hollow sections, subjected to axial compression plus bending about the strong axis at elevated temperatures. This parametric investigation considers different stainless steel grades, member slenderness, cross-section slenderness, bending moment diagrams and elevated temperatures. With the ultimate bearing capacities, obtained from material and geometric non-linear analysis with imperfections, using the finite element software SAFIR, the safety and accuracy of different design procedures, such as Eurocode 3 rules, are analysed.

Keywords: Fire resistance; stainless steel; slender sections; elliptical hollow sections; beam-columns; numerical analysis

1 INTRODUCTION

The application of stainless steel in construction as a structural material has been increasing, due to a number of desirable qualities such as its durability, resistance to corrosion and aesthetic appearance [1,2]. Despite having a high initial cost, stainless steel can be a competitive material in a life cycle cost analysis, due to its low maintenance needs. Moreover, it has a higher fire resistance when compared to carbon steel [3] allowing in some cases the absence of thermal protection.

The austenitic stainless steel is generally the most used group for structural applications but, due to specific advantages, some interest has been recently shown for increasing the use of ferritic and austenitic-ferritic (Duplex) steels for structural purposes. Some of those advantages are the very good resistance to wear and stress corrosion cracking of the duplex grade and the lower percentage of Nickel of the ferritic grade, which reduces its price. These stainless steel groups' applications can range from buildings, to towers, domes and bridges (footbridges and road bridges) [1, 4-6].

¹ Assistant researcher, RISCO, Dep. of Civil Engineering, University of Aveiro, Campus Universitário de Santiago, 3810-193 Aveiro, Portugal, e-mail: arraais.f@ua.pt, ORCID: <https://orcid.org/0000-0001-8256-9185>

² Associate professor, RISCO, Dep. of Civil Engineering, University of Aveiro, Campus Universitário de Santiago, 3810-193 Aveiro, Portugal e-mail: nuno.lopes@ua.pt, ORCID: <https://orcid.org/0000-0003-0634-8991>

³ Full professor, RISCO, Dep. of Civil Engineering, University of Aveiro, Campus Universitário de Santiago, 3810-193 Aveiro, Portugal e-mail: pyreal@ua.pt, ORCID: <https://orcid.org/0000-0002-7221-410X>

The application of profiles with elliptical hollow section (EHS) has been occurring due to different characteristics, such as their aesthetic nature or better performance under torsion, when compared to the I-profiles. Recent studies on stainless steel beam-columns under fire conditions have been focusing on members with I-sections [7] or square and circular hollow sections [8,9], and there is still a lack of knowledge on the fire behaviour of stainless steel beam-columns with elliptical hollow sections.

Regarding fire design rules, Eurocode 3 (EC3) [3] recommends that stainless steel structural elements should be verified using the same calculation formulae developed for carbon steel, which has been found to be inaccurate and sometimes unsafe [7]. According to EN 1993-1-4 [10], the cross-section resistance is calculated considering gross cross-section properties for Class 1, 2 and 3 sections and effective cross-section properties for Class 4 sections, applying the effective width method. In addition, for Class 1, 2 and 3 cross-sections at elevated temperatures the strength at 2% total strain should be considered as the yield strength and for Class 4 cross-sections it should be applied the 0.2% proof strength [3].

A parametric study, with the purpose of analysing the EC3 calculation formulae accuracy and safety for stainless steel members subjected to bending plus axial compression with slender EHS in case of fire, is here presented. A recent proposal for Class 4 carbon steel beam-columns [11], which resulted from the European research project FIDESC4 [12] is also tested. The parametric study considers different: i) stainless steel grades (austenitic, ferritic and austenitic-ferritic grades); ii) element slenderness (from 0.15 to 2.00); iii) cross-sections slenderness; iv) bending moment diagrams (uniform bending, triangular and bi-triangular bending diagrams); and v) elevated temperatures (350 °C to 700 °C).

The fire resistance of stainless steel elliptical beam-columns is obtained by means of geometrical and material non-linear analysis with imperfections (GMNIA), applying the finite element software SAFIR [13]. The different instability modes and corresponded critical loads are analysed using the software CAST3M, developed at French Atomic Energy Commission [14]. With the obtained local and global instability modes they were used to define the geometrical imperfection shapes in SAFIR, by applying the interface RUBY, developed at the University of Aveiro in Portugal [15].

2 FIRE DESIGN SIMPLIFIED CALCULATION METHODS

The analysed simplified design formulae for the fire resistance of stainless steel beam-columns are presented in this section. The design methodologies considered are the one prescribed in EN1993-1-2 and a recently proposed design approach from Couto et al. (2016) [11].

2.1 Prescribed design formulae from EN 1993-1-2

According to EN 1993-1-2 [3], the cross-section fire resistance of a stainless steel member is calculated in the same way as for carbon steel, changing only the material mechanical properties (yield strength and modulus of elasticity). Regarding the cross-section classification, equation (1) is used to determine the parameter ε , needed for the determination of the EC3 classification limits. The corresponding classification limits are given in Table 1.

$$\varepsilon_{fi} = 0.85 \left[\frac{235}{f_y} \frac{E}{210000} \right]^{0.5} \quad (1)$$

Table 1. EC3 recommended classification limits for EHS [16]

Cross-section classification	$D_e/t \varepsilon_\theta^2$
	Compression and bending
Class 1	50
Class 2	70
Class 3	$\frac{2520}{5\psi + 23}$

Equation (2) presents the design expression for the cross-section resistance of slender profiles, obtained from EN1993-1-1 [17] and to be adapted to fire conditions.

$$\frac{N_{Ed}}{N_{c,Rd}} + \frac{M_{y,Ed}}{M_{c,y,Rd}} \leq 1.0 \quad (2)$$

Under fire situation $N_{c,Rd}$ corresponds to $N_{fi,t,Rd}$, the design resistance value of axially compressed members with a uniform temperature θ_a , and according to Annex E of EN 1993-1-2 the effective area (A_{eff}) should be considered for Class 4 sections.

$$N_{fi,t,Rd} = A_{eff} f_{y,\theta} / \gamma_{M,fi} \quad (3)$$

In this work the effective area (A_{eff}) was calculated according to Chan and Gardner [18] proposal for EHS:

$$A_{eff} = A \left[\frac{90}{D_e/t} \frac{235}{f_y} \right]^{0.5} \quad (4)$$

Considering the equivalent diameter $D_e = H^2/B$, whose variables are represented in Figure 1.

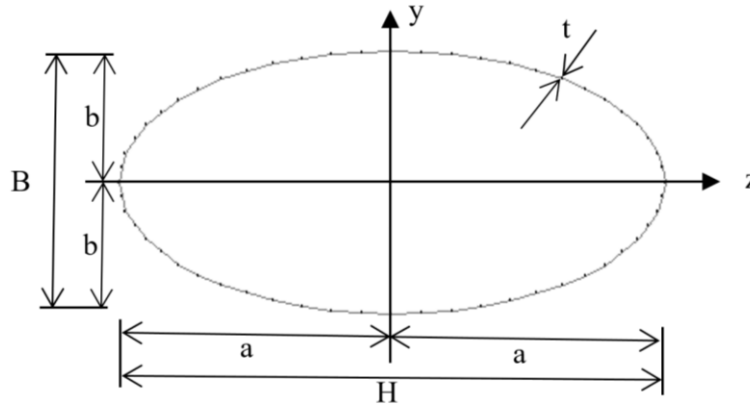


Figure 1. EHS dimensions

On the same way, the design resistance for bending about the major axis, $M_{c,y,Rd}$, corresponds to the design value of the bending moment resistance of a cross-section with a uniform temperature θ_a , $M_{fi,\theta,Rd,y}$, obtained by equation (4).

$$M_{fi,\theta,Rd,y} = W_{eff,y} f_{y,\theta} / \gamma_{M,fi} \quad (5)$$

Being the effective section modulus (W_{eff}) calculated according to Chan and Gardner [19] proposal:

$$W_{eff} = W_{el} \left[\frac{140}{D_e/t} \frac{235}{f_y} \right]^{0.25} \quad (6)$$

considering the equivalent diameter in bending about the strong axis, for $H/B > 1.36$, $D_e = 0.4H^2/B$.

In fire situation, higher strains are acceptable when compared to normal temperature design. Therefore, instead of 0.2% proof strength usually considered at normal temperature, for cross-section of Class 1, 2 and 3, at elevated temperatures the stress corresponding to 2% total strain should be adopted for the yield strength [3], as presented by equation (7).

$$f_{y,\theta} = f_{2,\theta} = k_{2,\theta} f_y \quad (7)$$

Nevertheless, for Class 4, according to EN 1993-1-2 Annex E, the 0.2% proof strength should be used, being the yield strength reduction factors for stainless steel presented in Annex C of the same standard.

$$f_{y,\theta} = f_{0.2p,\theta} = k_{0.2p,\theta} f_y \quad (8)$$

The interaction formulae for beam-columns in case of fire of EN 1993-1-2 [3] were developed based on carbon steel members with I-sections of Class 1 and 2 [20]. The proposed formulae for laterally restrained steel beam-columns subjected to bending about the major axis were used.

$$\frac{N_{fi,Ed}}{\chi_{y,fi} A_{eff} f_{y,\theta} / \gamma_{M,fi}} + k_{y,fi} \frac{M_{y,fi,Ed}}{W_{eff,y} f_{y,\theta} / \gamma_{M,fi}} \leq 1.0 \quad (9)$$

The reduction factor χ_{fi} value can be obtained according to equation (10):

$$\chi_{fi} = \frac{1}{\phi_{\theta} + \sqrt{[\phi_{\theta}]^2 - [\bar{\lambda}_{\theta}]^2}} \leq 1.0 \quad (10)$$

with

$$\phi_{\theta} = \frac{1}{2} [1 + \alpha \bar{\lambda}_{\theta} + (\bar{\lambda}_{\theta})^2] \quad (11)$$

and α an imperfection factor determined by:

$$\alpha = 0.65 \sqrt{\frac{235}{f_y}} \quad (12)$$

The recommended interaction factor, for Class 4 cross-sections, is:

$$k_{y,fi} = 1 - \frac{\mu_{y,\theta} N_{fi,Ed}}{\chi_{y,fi} A_{eff} k_{0.2p,\theta} \frac{f_y}{\gamma_{M,fi}}} \leq 3 \quad (13)$$

μ (for the strong axis) is given by:

$$\mu_{y,\theta} = (2\beta_{M,y} - 5)\bar{\lambda}_{y,\theta} + 0.44\beta_{M,y} + 0.29 \leq 0.8 \quad (14)$$

with $\bar{\lambda}_{y,20^\circ\text{C}} \leq 1.1$ and considering $\beta_{M,y}$, which is in function of the bending diagram shape, for end moments obtained with:

$$\beta_{M,y} = 1.8 - 0.7\psi \quad (15)$$

ψ is the ratio between the end moments ($-1 \leq \psi \leq 1$).

2.2 Proposal for laterally restrained steel beam-columns in case of fire [20]

As a result of the European research project on Class 4 members under fire [12], Couto et al. [11] presented a new proposal based on the EN 1993-1-2 formulae for laterally restrained steel beam-columns in case of fire, applying the elevated temperature strength at 2% total strain $f_{2,\theta} = k_{2,\theta} f_y$ and changing the interaction factor $\mu_{y,\theta}$:

$$\mu_{y,\theta} = (2\beta_{M,y1} - 5)\bar{\lambda}_{y,\theta} + 0.44\beta_{M,y2} + 0.7 \leq 0.6 \quad (16)$$

with $\bar{\lambda}_{y,20^\circ\text{C}} \leq 1.1$ and $\beta_{M,y1} = \beta_{M,y2} = \beta_{M,y}$, since only end moments are applied in this work.

$$\beta_{M,y} = 1.8 - 0.9\psi \quad (17)$$

According to Couto et al. [11], applying this approach there is a significant gain in accuracy and cost-effective design for Class 4 carbon steel beam-columns without lateral torsional buckling. However, this proposal was developed based only on members with I-sections.

3 CASE STUDY NUMERICAL MODELLING

3.1 Case study

Class 4 EHS under compression and bending with the dimensions and H/B ratios from Table 2 are analysed. The members lengths of 1, 3, 7 and 10 m, corresponded to different slenderness from 0.15 to 2.00, were considered. The stainless steel grades used were 1.4301 (Austenitic grade also known as 304), 1.4401 (Austenitic grade also known as 316), 1.4003 (Ferritic grade), and 1.4462 (Austenitic-ferritic grade also known as Duplex). Different bending moment diagrams (non-uniform, $\psi = -1$ and 0, and uniform, $\psi = 1$) are studied. And the uniform elevated temperatures of 350 °C (being the EC3 proposed critical temperature for slender sections when no calculation is made), 600 °C and 700 °C (common critical temperatures in this type of structural elements) are considered.

Table 2. Elliptical hollow sections analysed and respective dimensions

Designation	H [mm]	B [mm]	t [mm]	H/B [-]
EHS_140x85x2.0	140	85	2.0	1.65
EHS_150x75x2.0	150	75	2.0	2.00
EHS_200x100x2.5	200	100	2.5	2.00
EHS_200x100x4.0	200	100	4.0	2.00
EHS_300x150x4.0	300	150	4.0	2.00
EHS_150x50x3.0	150	50	3.0	3.00

3.2 Numerical model

The finite element software SAFIR [13], considering shell elements with four nodes with each six degrees of freedom (three translations and three rotations), is applied. Doubled hinged conditions are applied at both ends, preventing lateral zz axis displacements throughout the member length and, at mid-span, preventing longitudinal (xx axis) displacement to ensure the element and load symmetry. The loads are applied parallel to the element axis, at the member extremities, distributed over the cross-section surface to avoid local instability phenomena (Figure 2). The end-plates were considered to be at normal temperature and had 10 times the thickness of the element's wall.

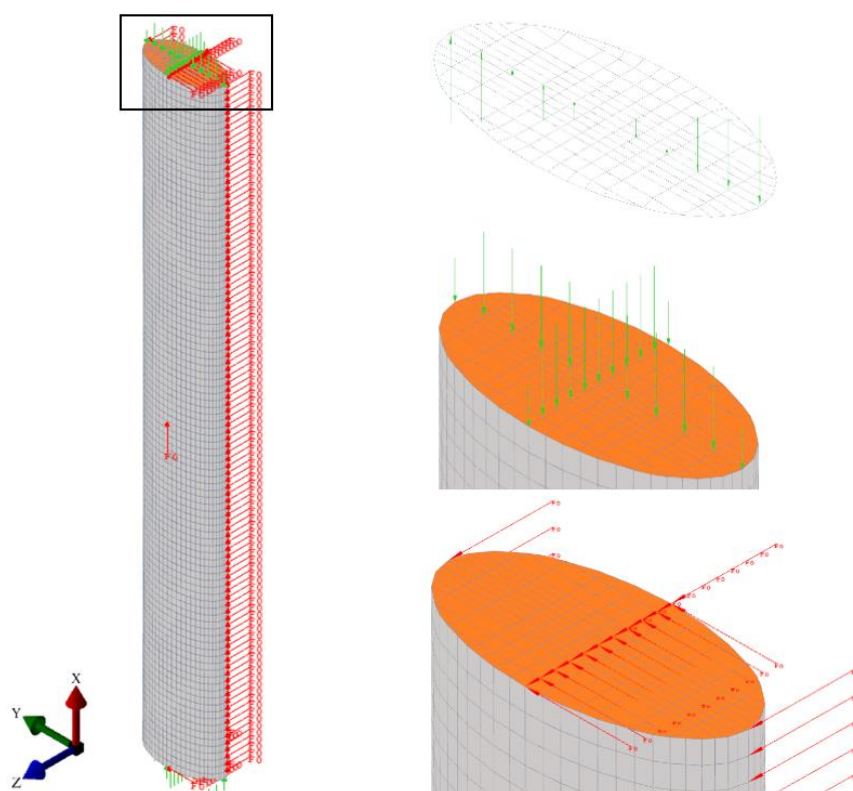


Figure 2. Numerical model for a column with 3 m length

Geometric imperfections were introduced into the numerical model by changing the nodal coordinates affine to the buckling mode shapes obtained with the software CAST3M [14] (applying the RUBY [15] interface) as presented in Figure 3.

For the imperfections' amplitude, 80% of $(a \text{ or } b)/100$ is considered for local imperfections and 80% of $L/750$ for global imperfections, following the recommendations of Annex C of EN 1993-1-5 [21] and the geometric fabrication tolerances from D.1 of Annex D of EN 1090-2+A1 [22] and EN 10219-2 [23], where a and b represent the dimensions in both directions y and z from elliptical sections and L the element length. The initial imperfections were combined adding the leading imperfection to 70% of the accompanying imperfections.

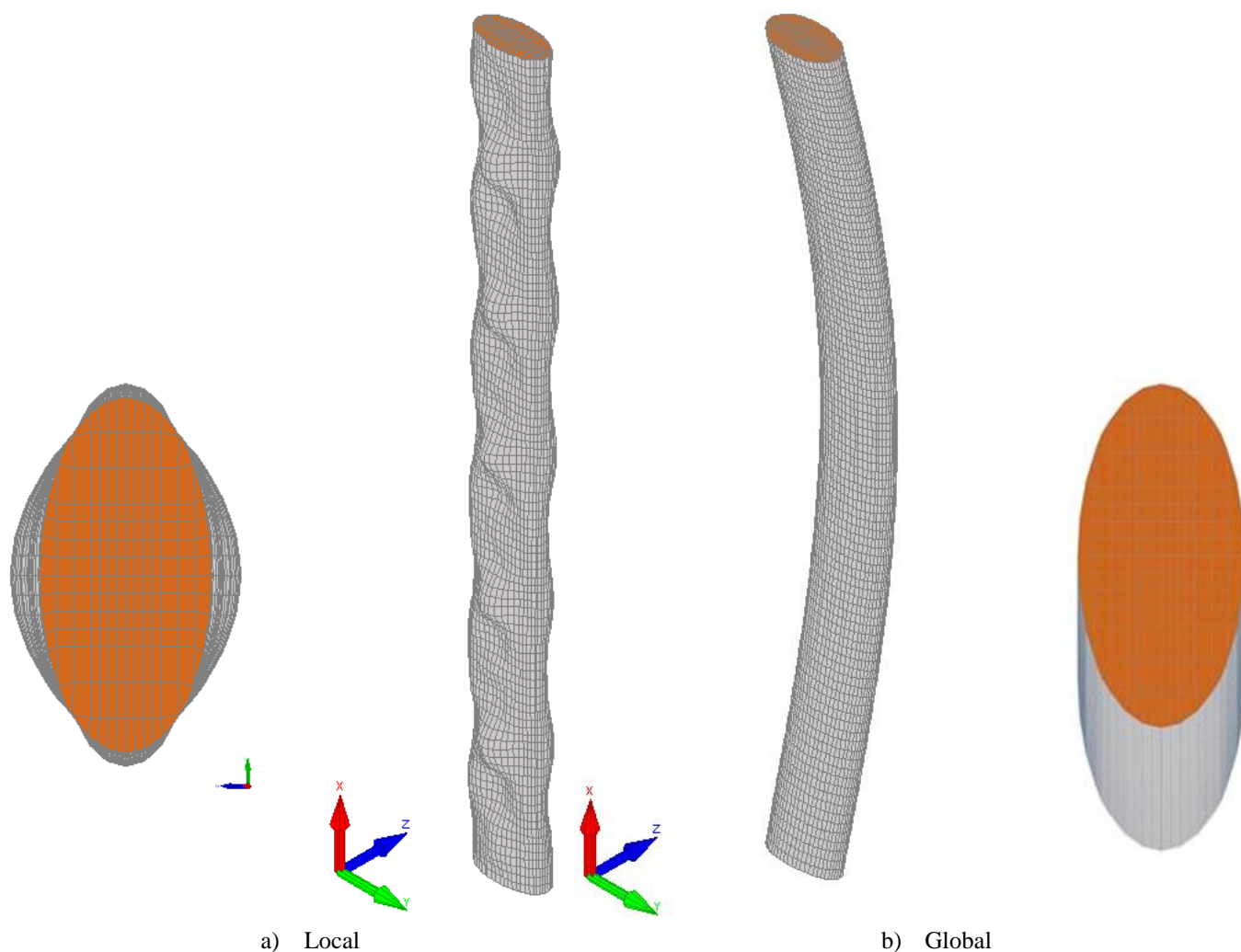


Figure 3. Amplified geometric imperfections of EHS elements: a) local and b) global

4 NUMERICAL STUDY

The design expressions described in Section 2, are here compared to the numerical results of stainless steel beam-columns with elliptical hollow sections at elevated temperatures. On these comparisons, the flexural buckling curve influence on the interaction curves was eliminated considering the numerical axial compression resistance results on those interaction curves.

4.1 Parametric analysis

With the purpose of better understanding the behaviour of EHS stainless steel beam-columns in case of fire, the following figures (Figure 4 - Figure 7) illustrate the influence of each parameter on the interaction curves, analysing also the accuracy of EC3 formulation, which is named “EN 1993-1-2”. Figure 4 presents the results for beam-columns of different lengths subjected to uniform bending at 600 °C, for the stainless steel grade 1.4301.

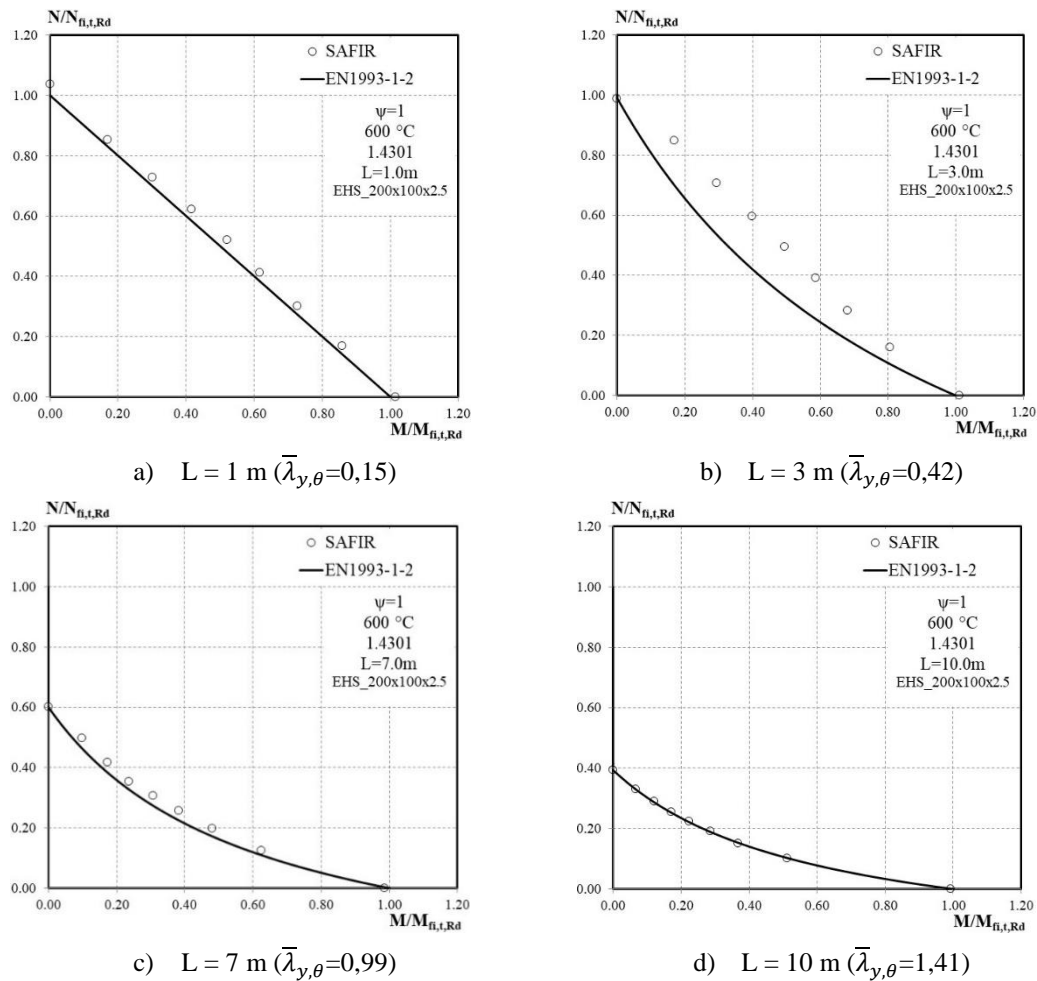


Figure 4. Comparison of EN 1993-1-2 interaction curves with the numerical results for Class 4 beam-columns of different lengths subjected to uniform bending at 600 °C, for stainless steel grade 1.4301

It is visible the influence of the member slenderness on the interaction curve shape of the numerical results that should be reproduced by the design formulae, by equations (14) and (16).

Figure 5 shows the results obtained for beam-columns of different stainless steel grades subjected to uniform bending at 600 °C, with 3 m length.

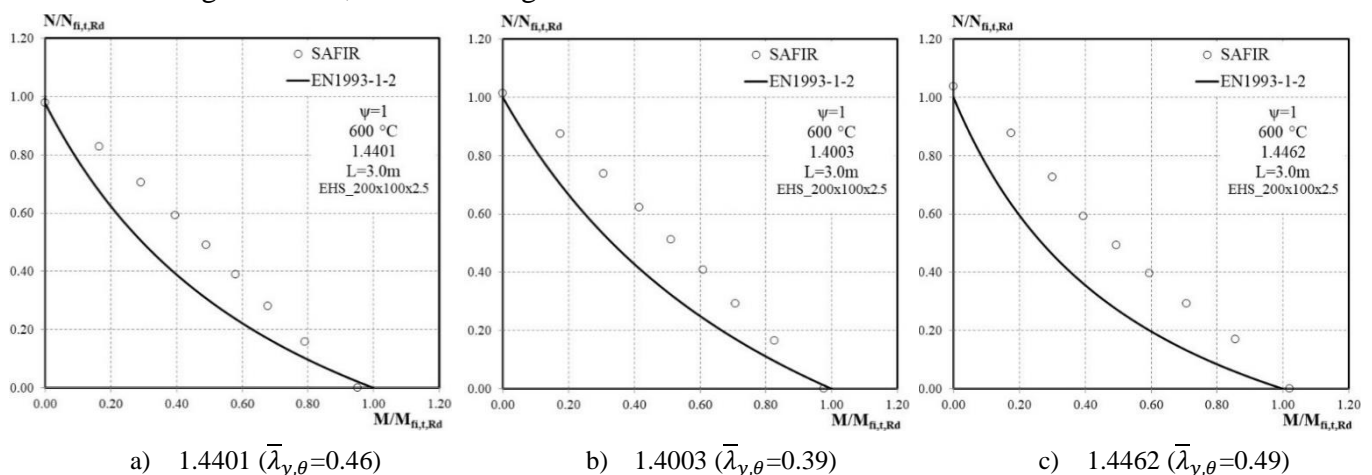
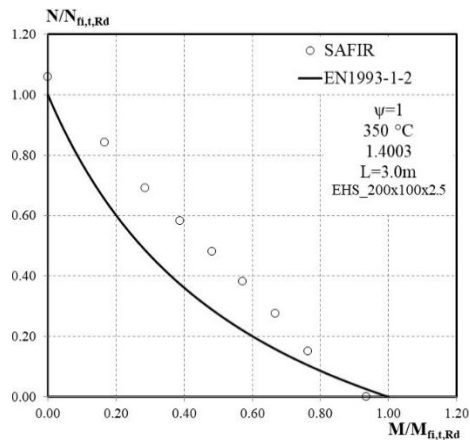


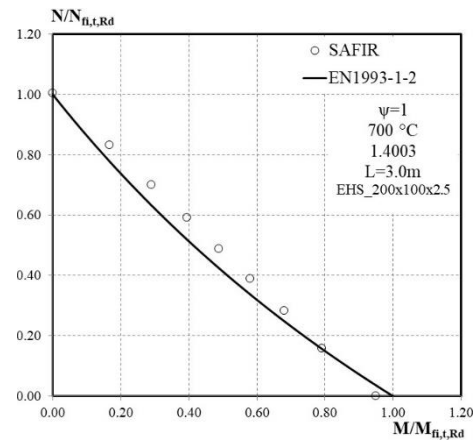
Figure 5. Comparison of EN 1993-1-2 interaction curves with the numerical results for Class 4 beam-columns of different stainless steel grades subjected to uniform bending at 600 °C, for 3 m length

The observed interaction behaviour did not present significant changes in function of the steel grade.

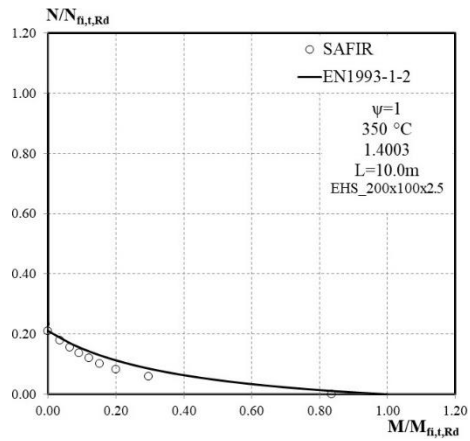
The charts from Figure 6 present the results for beam-columns subjected to uniform bending at 350 °C and 700 °C, for ferritic stainless steel grade 1.4003. This steel was chosen for this analysis due to the existing relevant difference between its mechanical properties' reduction factors for this range of temperatures.



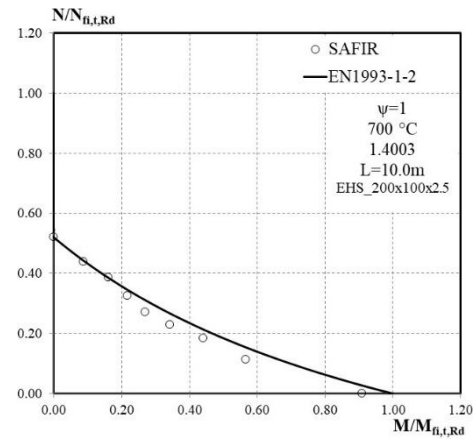
a) 350 °C ($\bar{\lambda}_{y,\theta}=0.52$)



b) 700 °C ($\bar{\lambda}_{y,\theta}=0.28$)



c) 350 °C ($\bar{\lambda}_{y,\theta}=1.60$)

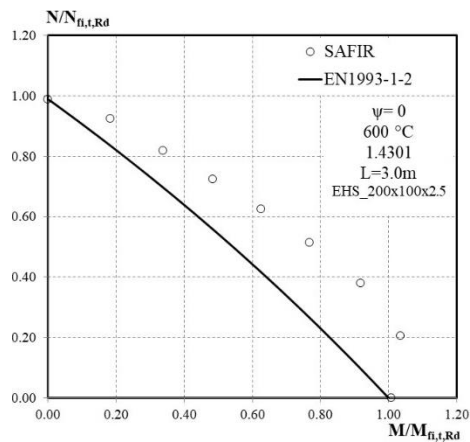


d) 700 °C ($\bar{\lambda}_{y,\theta}=0.79$)

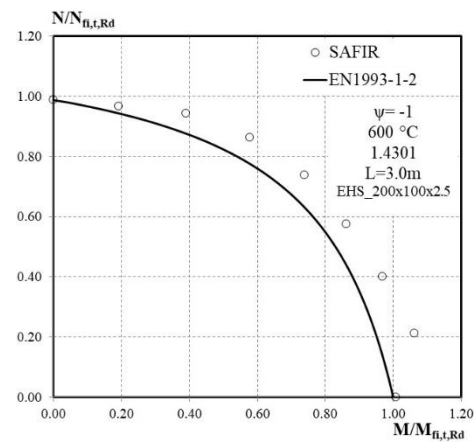
Figure 6. Comparison of EN 1993-1-2 interaction curves with the numerical results for Class 4 beam-columns of 3 m and 7 m lengths subjected to uniform bending at different temperatures, for stainless steel grade 1.4003

The chosen temperatures did not impose significant differences on the N-M interaction behaviour of the 3 m tested members. However, for 10 m members the N-M interaction SAFIR results demonstrated to be in the unsafe side.

Analysing beam-columns with non-uniform bending moments, Figure 7 shows the results for beam-columns of 3 m length, with $\psi=0$ (triangular diagram) and $\psi=-1$ (bi-triangular diagram), at 600 °C, of stainless steel grade 1.4301.



a) $\psi=0$ ($\bar{\lambda}_{y,\theta}=0.42$)



b) $\psi=-1$ ($\bar{\lambda}_{y,\theta}=0.42$)

Figure 7. Comparison of EN 1993-1-2 interaction curves with the numerical results for Class 4 beam-columns of 3m length subjected to non-uniform bending at 600 °C, for stainless steel grade 1.4301

Non-uniform bending moments induced higher resistance interaction between axial force and bending moment when compared to uniform bending ($\psi = 1$), which should be predicted by equation (15).

In Figure 8 are presented different collapse modes obtained with software SAFIR for the different cases analysed of bending moments.

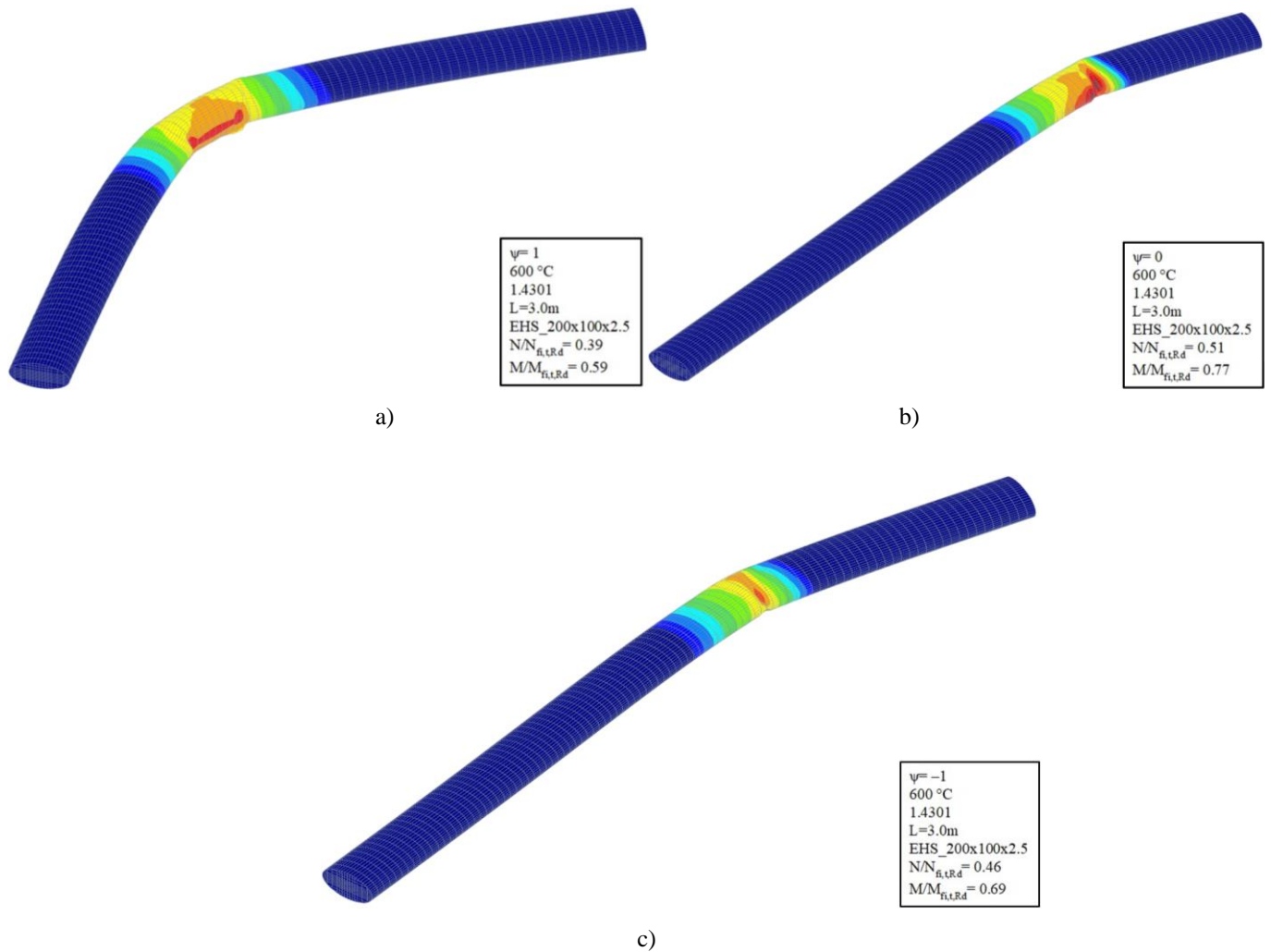


Figure 8. Collapse modes for Class 4 beam-columns of 3m length subjected to a) uniform ($\psi = 1$), b) non-uniform bending with triangular diagram ($\psi = 0$) and c) non-uniform bending with bi-triangular diagram ($\psi = -1$) for stainless steel grade 1.4301

4.2 Design methodologies validation

For a detailed analysis of the obtained numerical results, a statistical evaluation of the different methodologies is performed, following the three criteria of the validation procedure proposed by Kruppa [24]: i) The average of the ratio between the analytical values and the FE results (in this case the SAFIR results) should be on the safe side (lower than 1); ii) The percentage of the number of unsafe results should be less than 20%; iii) The design values must not be on the unsafe side by more than 15% of the FE results.

Table 3 presents the statistical results (average value – μ , standard deviation – s , maximum unsafe and percentage of unsafe results) for slender EHS considering the EN 1993-1-2 interaction curves and Table 4 shows the statistical evaluation for slender EHS taking into account the Couto et al. [20] proposal. The number of considered numerical simulations for Class 4 cross-sections is 5832 analysis.

Figure 9 and Figure 10 details the statistical analysis.

Table 3. Statistical evaluation of EN 1993-1-2 interaction curves considering the different bending moment diagrams and stainless steel grades

EN 1993-1-2	Austenitic				Ferritic				Duplex			
	μ	s	Max. Unsafe	% Unsafe	μ	s	Max. Unsafe	% Unsafe	μ	s	Max. Unsafe	% Unsafe
$\psi = 1$	0.92	0.21	1.25	28.32	0.94	0.19	1.26	37.34	0.84	0.25	1.25	30.80
$\psi = 0$	0.86	0.11	1.05	10.20	0.89	0.10	1.06	9.74	0.88	0.13	1.05	7.47
$\psi = -1$	0.93	0.17	1.15	29.59	0.94	0.11	1.15	26.30	0.96	0.14	1.16	39.94

Table 4. Statistical evaluation of Couto et al. [13] proposal considering the different bending moment diagrams and stainless steel grades

Couto et al. [23]	Austenitic				Ferritic				Duplex			
	μ	s	Max. Unsafe	% Unsafe	μ	s	Max. Unsafe	% Unsafe	μ	s	Max. Unsafe	% Unsafe
$\psi = 1$	0.98	0.29	1.79	24.24	1.01	0.36	1.79	57.79	1.12	0.25	1.79	52.60
$\psi = 0$	1.06	0.25	1.80	49.49	1.04	0.25	1.80	47.40	1.11	0.26	1.80	55.20
$\psi = -1$	1.02	0.21	1.66	45.15	0.98	0.22	1.56	44.81	1.01	0.21	1.52	36.36

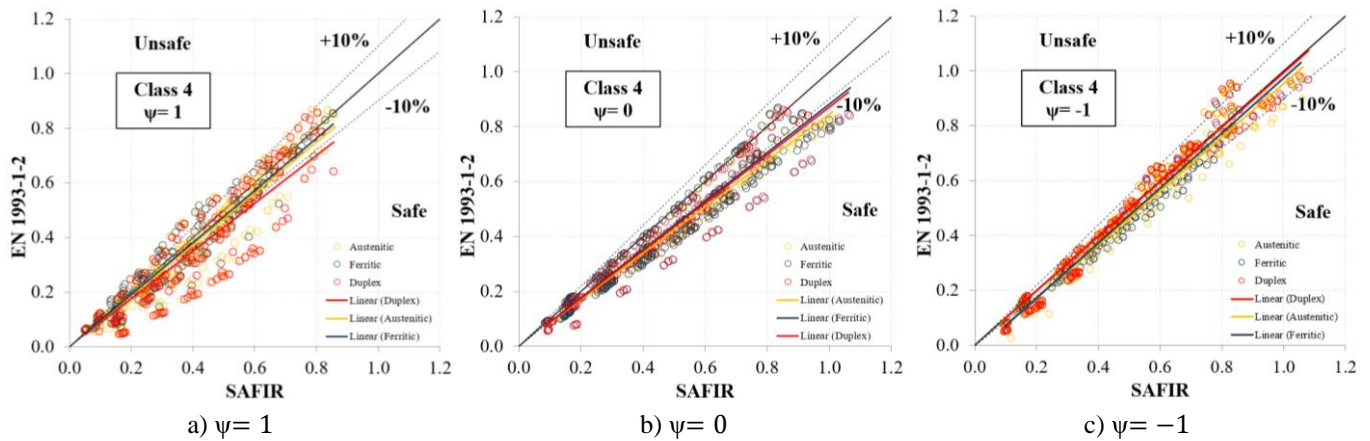


Figure 9. Comparison between EN 1993-1-2 and SAFIR results for Class 4 cross-sections

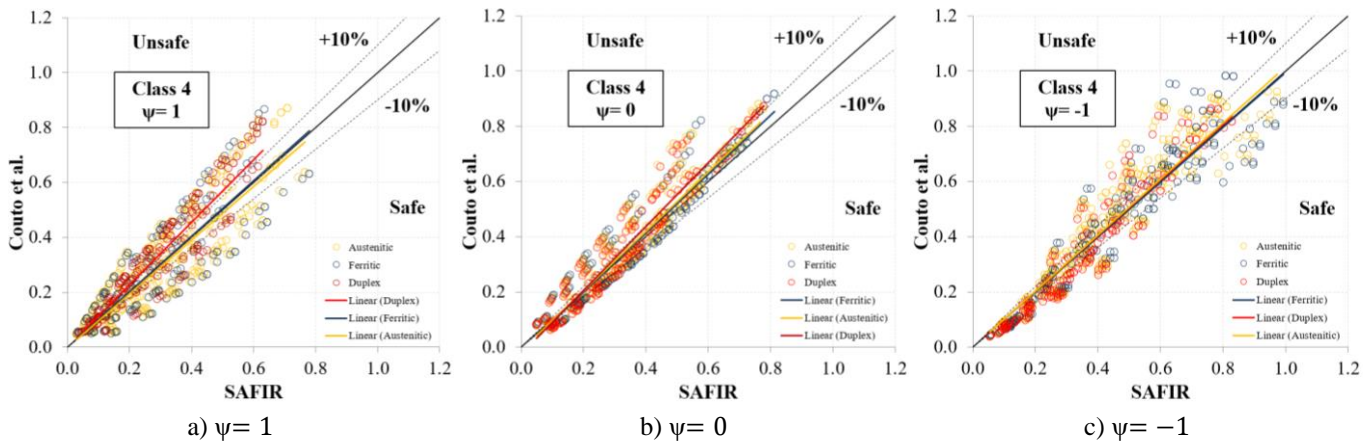


Figure 10. Comparison between Couto et al. [13] proposal and SAFIR results for Class 4 cross-sections

It is possible to observe that the EN 1993-1-2 methodology do not complies with the validation criteria, being however too conservative on several cases, with results that are far from the EC3 interaction curves.

Carlos et al. proposal presents less conservative values (average values closer to 1), but with high percentage of unsafe results (more than 40%) and very scattered values (high standard deviations).

5 CONCLUSIONS

A numerical parametric study on the fire behaviour of beam-columns with stainless steel elliptical hollow section was presented. The accuracy of the current Part 1-2 of Eurocode 3 prescriptions was evaluated against numerically obtained ultimate bearing capacities. Also, a proposal developed for Class 4 carbon steel members developed by Couto et. al [11] was here analysed.

The influence of different cross-section slenderness, element lengths, stainless steel grades, loading types and temperatures, was considered and analysed. It was possible to conclude that:

- i) the increase of member slenderness influences the interaction curve shape, which should be reproduced on the design expressions;
- ii) the interaction, between the numerically obtained axial force and bending moment ultimate capacities, did not presented big differences in function of the steel grade, leading to believe that a unique expression for the interaction factor could fit all grades; and
- iii) the temperature did not influence the N-M interaction behaviour of the tested members for intermediate slenderness, however for high slenderness values the results were on the unsafe side of the interaction N-M curve.

Regarding the overall estimations of the tested design interaction curves, none of them were in compliance with the adopted validation procedure [24]:

- i) the current EN1993-1-2 rules [3] provide generally safe approximations, existing however still some tests on the unsafe side, which reveals a high dispersion of the estimations; and
- ii) Couto et. al methodology [11] applied to stainless steel presents interaction curves less conservatives but still too insecure.

The main conclusion was that the existing calculation rules do not provide accurate approximations for stainless steel beam-columns with elliptical hollow section. Hence, new formulation should be developed specifically for these members, considering the different parameters studied in this work.

ACKNOWLEDGMENT

This research was performed within the framework of the project “StaSteFi - Fire design of stainless steel members”, POCI-01-0145-FEDER-030655, supported by the Portuguese Operational Programme “Competitividade e Internacionalização”, in its FEDER/FNR component, and the Portuguese Foundation for Science and Technology (FCT), in its State Budget component (OE).

REFERENCES

1. Gardner, L. “The use of stainless steel in structures”, Progress in Structural Engineering and Materials, vol. 7, 2005, pp 45-55.
2. Euro Inox, SCI, Steel Construction Institute. Design Manual for Structural Stainless Steel, 3rd edition, 2006.
3. CEN, European Committee for Standardisation, EN 1993-1-2, Eurocode 3: Design of Steel Structures - Part 1–2: General rules - Structural fire design, Brussels, Belgium, 2005.
4. Gardner, L. “Aesthetics, economics and design of stainless steel structures”, Advanced Steel Construction, vol. 4, no. 2, 2008, pp 113-122.
5. Gardner, L. “Stability and design of stainless steel structures – Review and outlook”, Thin-Walled Structures, vol. 141, 2019, pp 208-216.
6. Baddoo, N. R. “Stainless steel in construction: A review of re-search, applications, challenges and opportunities”, Journal of Constructional Steel Research, vol. 64, no. 11, 2008, pp 1199-1206.
7. Lopes, N.; Vila Real, P.; Simões da Silva, L.; Franssen, J.M., Numerical analysis of stainless steel beam-columns in case of fire, Fire Safety Journal, Vol. 50, 2012, 35-50.

8. Lopes, N.; Vila Real, P., Fire resistance of stainless steel structural elements with class 4 square hollow sections subject to combined bending and axial compression, 8th Int. Conf. on SiF, Shangai, China, 2014.
9. Lopes, N.; Manuel, M.; Sousa, A. R.; Vila Real, P., Parametric study on austenitic stainless steel beam-columns with hollow sections under fire, *Journal of Constructional Steel Research*, Vol. 152, 2019, 274-283.
10. CEN, European Committee for Standardisation, EN 1993-1-4, Eurocode 3: Design of Steel Structures - Part 1-4: General rules – Supplementary Rules for Stainless steels, Brussels, Belgium, 2006
11. Couto C., Sanzel A., Vila-Real P., Lopes N., Zhao B., Beam-columns with thin wall cross-sections in case of fire, 9th International Conference Structures in Fire, 2016.
12. FIDESC4. Fire Design of Steel Members with Welded or Hot-Rolled Class 4 Cross-Section, RFCS-CT-2011-00030, 2011-2014. 2014.
13. Gernay, T., Franssen, J.M. (2017), "Modeling structures in fire with SAFIR®: Theoretical background and capabilities", *Journal of Structural Fire Engineering*, Vol. 8, issue 3, pp. 300-323.
14. CAST3M, development sponsored by French Atomic Energy Commission; 2012. <http://www-cast3m.cea.fr/>
15. Couto, C., Vila Real, P., Lopes, N., RUBY – an interface software for running a buckling analysis of SAFIR models using Cast3M, University of Aveiro, 2013.
16. Gardner, L., Chan, T.M., Abela, J. M., Structural behaviour of elliptical hollow sections under combined compression and uniaxial bending. *Advanced Steel Construction*, Vol. 7, No.1, 2011, 86-112
17. CEN, European Committee for Standardisation, EN 1993-1-1, Eurocode 3: Design of Steel Structures - Part 1-1: General rules and rules for buildings, Brussels, Belgium, 2005.
18. Chan, T. M. and Gardner, L., Compressive resistance of hot-rolled elliptical hollow sections, *Engineering Structures*, Vol. 30 (2), 2008, 522-532.
19. Chan, T. M., Gardner, L., Bending strength of hot-rolled elliptical hollow sections, *Journal of Constructional Steel Research*, Vol. 64, 2008, 971-986.
20. Talamona, D., Flambement de Poteaux Métalliques Sous Charge Excentrée, à Haute Température (in French), PhD Thesis University Blaise Pascal, Clermont–Ferrand, France, 1995.
21. CEN, European Committee for Standardisation, EN 1993-1-5, Eurocode 3: Design of Steel Structures - Part 1-5: Plated structural elements, Brussels, Belgium, 2006.
22. CEN, European Committee for Standardisation, EN 1090-2+A1, Execution of steel structures and aluminium structures - Part 2: Technical requirements for steel structures, Brussels, Belgium, 2008.
23. CEN European Committee for Standardisation, EN 10219-2, Cold Formed Welded Steel Structural Hollow Sections - Part 2: Tolerances, Dimensions and Sectional Properties, Belgium, 2019.
24. Kruppa, J. Eurocodes – fire parts, proposal for a methodology to check the accuracy of assessment methods, CEN TC 250, Horizontal Group Fire, Document n° 99/130, 1999.

MATERIAL PROPERTIES OF STRUCTURAL, HIGH STRENGTH AND VERY HIGH STRENGTH STEELS FOR POST-FIRE ASSESSMENT OF EXISTING STRUCTURES

Tom Molken¹, Katherine A. Cashell², Barbara Rossi^{3,4}

ABSTRACT

This paper provides guidance on the post-fire material properties and associated safety factors for structural carbon steel which are required for the assessment and retrofitting of existing steel buildings which have suffered and survived a fire. Carbon steel can survive a fire with temperatures rising up to 600°C, even more if the elements have been designed with sufficient overstrength. In the past decade, a number of researchers have published test data and there is more information available on the mechanical properties of steel following a fire. Nevertheless, a statistical evaluation of these results has yet to be conducted although design codes generally adopt a reliability-based approach for the analysis and assessment of buildings. To fill this gap of knowledge, a statistical evaluation of 718 tests collected from 19 peer-reviewed articles and doctoral theses. The presented results concerns low-alloy normal structural, high strength and very high strength steels. By focusing on the effect of a fire on the mechanical properties after cooling, which is mostly related to how the coefficient of variation of their distribution increases, adjusted safety factors are proposed together with a reduced reliability index based on economic and social considerations. It is contended that by following this method, possible misunderstandings can be avoided and decisions on the salvage and rehabilitation of structures can be based on performance data and technical analysis.

Keywords: Carbon steel; post-fire; retention factor; existing buildings; statistical approach; reliability.

1 INTRODUCTION

This paper is concerned with the mechanical behaviour of structural carbon steel following exposure to elevated temperature and subsequent cooling. For the majority of structures that survive a fire and can be reinstated afterwards, it is necessary to ensure that they have sufficient strength and stability to survive for the rest of their projected lifetime. The influence of fire on the mechanical material characteristics of the structural elements depends on the material itself, the maximum temperature reached during the fire, the soak time at high temperature and the cooling regime. In the past, there has been considerable research effort devoted to the behaviour of structural materials following a fire, and many researchers have published performance data and even predictive formulae. However, the available data has never been assessed using a reliability-based approach. Even the most recent publications [1], [2], [3] which provide very useful information and are based on extensive literature surveys, do not include statistical data analysis.

¹ PhD researcher, KU Leuven, Belgium

e-mail: tom.molken@kuleuven.be, ORCID: <https://orcid.org/0000-0002-3401-9047>

² Dr., Brunel University London, UK

e-mail: katherine.cashell@brunel.ac.uk, ORCID: <https://orcid.org/0000-0003-2804-4542>

³ Prof., KU Leuven, Belgium

e-mail: barbara.rossi@kuleuven.be, ORCID: <https://orcid.org/0000-0001-6228-0309>

⁴ Prof, New College Oxford University, UK

e-mail: barbara.rossi@new.ox.ac.uk, ORCID: <https://orcid.org/0000-0001-6228-0309>

In this context, the current paper aims to fill this gap by using the available information from the literature and conducting a reliability-based assessment which can then be used in the analysis of structures following a fire to make informed decisions on their future service life. Probabilistic-based codes require that, by preference, uncertainties should be presented based on an array of available, measured, data. Herein, a meta-analysis is used to generate more general applicable retention factors R_θ and to identify and quantify the most salient influential factors. The study comprises carbon steels of various strengths (Table 1), cold-worked or cold-formed steel and cast or wrought irons. Currently, steel grades with a yield strength of up to 2020 MPa are available but the very high strength grades are mainly limited in application to the automotive and aerospace sectors. This investigation is limited to grades ranging from normal strength steels to the very high strength steel grades used in structural applications, i.e. grades with a yield strength of up to a maximum value of 960 MPa.

Table 1. Names of steel grades used in this article

Name of subsets	Abbreviation	Yield strength (MPa)	European reference standards
Normal structural steel	NSS	≤ 420	EN 10025-2 to 5 EN 1993-1-1 Table 6.2
High strength structural steel	HSS	> 420 and ≤ 700	EN 10025-6 EN 1993-1-1 and -1-12
Very high strength structural steel	VHSS	> 700 and ≤ 960	EN 10025-6

For the mechanical properties, the main focus is given to the yield (f_y) and tensile strength (f_u), the ultimate strain (ϵ_u) and Young's modulus (E). In the design of most new buildings, the yield strength and Young's modulus are of most significance as these are used in the strength and stability checks, as well as in the determination of deformations.

In this context, the current paper proceeds with a detailed description of the methodology which is employed for the statistical analyses. Then, the available test data is presented together with the statistical analyses to assess the post-fire mechanical properties. A methodology is proposed based by the application of a retention and additional safety factor. A more extensive explanation can be found in [4].

2 METHODOLOGY FOR THE STATISTICAL EVALUATION OF TEST DATA

A significant amount of test data has become available in the last decade on the mechanical behaviour of carbon steel in the post-fire condition, which provides an ideal basis for the current statistical evaluation. In this section, the procedures that are used in this article to determine the characteristic values of the mechanical properties are first discussed, followed by an overview of the experimental dataset which is used in the analysis. Then, the methodology to derive the post-fire characteristic values taking into account the variability that cannot be assigned to the post-fire situation are explained.

2.1 Characteristic values

This section explains the procedure for obtaining a material property value from test data, in accordance with Eurocode 0 [5] and also elsewhere [6]. The characteristic value of a single property X_k is typically used in combination with an appropriate partial factor (γ_M) from the relevant material code, to determine the design value of the property (X_d). Reference is made to [4] for the assumptions made.

In most of the experimental programmes from which results are employed in the current work, tests on the virgin material (i.e. without heating and cooling) are also reported. These results are used as the reference value at 20°C, namely $X_{i,amb}$. However, in some specific cases, this information is not available in the literature and then the relation between the nominal (or code specified) yield strength ($f_{y,n}$) and the mean

value of the yield strength according to EN 10025, is determined in accordance with the expression given in Eq. (1) which is taken from the JCSS code of practice (2000):

$$\mu = f_{y,n} \cdot \alpha' \cdot \exp(-u \cdot V_{amb}) - C \quad (1)$$

where $f_{y,n}$ is the specified (or nominal) yield strength, α' is the spatial position factor, \exp is the natural exponential function and u is a factor related to the fractile of the distribution used to describe the distance between the nominal and mean value, typically found to be in the range of -1.5 to -2.0 for EN 10025 steels. V_{amb} is the coefficient of variation at ambient conditions and C is a constant which reduces the yield strength as given in mill certificate to the static yield strength; a value of $C = 20$ MPa is recommended [7]. Generally, α' is taken as equal to 1.05 for webs and 1.0 otherwise, to include the additional effect of the rolling direction. A value of 1.05 may be used for plates with a thickness which is less than 10 mm.

An upper estimate for the coefficient of variation V_{test} cannot be derived based on mathematical considerations and therefore some engineering judgement and professional expertise are usually needed [6]. Some guidance is provided by the JCSS code of practice and a series of coefficients of variation based on tests executed under ambient conditions (V_{amb}) are proposed, as given in Table 2. However, as previously mentioned, these mean values and coefficients of variation are only valid for low alloy structural steel without heat treatment and which adhere to the product standard EN 10025 [8]. The values are relevant for the nominal material properties given in Table 2, where B is a factor equal to 1.5 for structural carbon steel, 1.4 for low alloy steel and 1.1 for quenched and tempered steels.

Table 2. Mean values and coefficients of variation for the main material properties according to JCSS [7]

Property	Mean value μ	V_{amb}
f_y	$f_{y,n} \cdot \alpha' \cdot \exp(-u \cdot V_{amb}) - C$	0.07
f_u	$B \cdot f_{u,n}$	0.04
ε_u	$\varepsilon_{u,n}$	0.06
E	$E_n = 210$ GPa	0.03

According to the classification procedures for carbon steels, when a particular structural steel does not meet all of the specified mechanical conditions for a particular grade, it is downgraded to the next classification which can result in remarkable overstrength for some materials. The codified nominal values are therefore the minimum values, and many carbon steel grades exhibit considerable overstrength. That has been extensively demonstrated through a number of testing programmes (e.g. [9, 10, 11, 12]).

2.2 Reduction of mechanical properties during fire and recovery following subsequent cooling

A large data set comprising the results in 19 peer-reviewed journal papers and doctoral theses are included in the current study, and these are summarized in Table 3. This includes a total of 718 individual tests on with different grades of carbon steel, mostly used in structural applications, including materials from Europe (S grades), Australia (also known as S grades), China (Q grades) and North America (A grades). Each reference is characterised by a set number, its year of publication, a subset number, the corresponding steel grade, soak time during which the specimen is kept at elevated temperature and the cooling regime. A number of different cooling regimes are employed including specimens that are cooled in air (CIA), cooled in the furnace (CIF), cooled in blanket (CIB) and cooled in water (CIW). The labels LPG and Elec indicate if the specimens were heated in a liquefied petroleum gas furnace or an electrical furnace, respectively, where this information is available.

Table 3. Details of the test data

Authors	Set number	Year	Subset reference	Corresponding steel grade (MPa)	Soak time (h)	Cooling regime
---------	------------	------	------------------	------------------------------------	------------------	----------------

Smith et al. [14]	1	1981	0	Wrought		CIA
			1	S235-355JR		CIA
			2	S235-355JR	1.00	CIA
			3	S235-355JR	4.00	CIA
Outinen, [15]	2	2007	4a	S355J2H		CIF
			4b	G350Z		CIF
J. Lee, [16]	3	2012	5	A992 = S345	1.00	CIA
			6	A992 = S345	1.00	CIB
			7	A992 = S345	1.00	CIW
Qiang et al. [17]	4	2012	8	S460NL	0.17	CIA
			9	S690QL	0.17	CIA
Qiang et al. [18]	5	2013	10	S960QL	0.17	CIA
S.P. Chiew et al. [19]	6	2014	11	S690RQT	0.17	CIA
Gunalan et al. [20]	7	2014	12	G300	1.00	CIA
			13	G500-550	1.00	CIA
W. Wang et al. [21]	8	2018	14	Q460	0.33	CIA
			15	Q460	0.33	CIW
Lu et al. [22]	9	2019	16	Q235-420	0.50	CIA
			17	Q235-420	0.50	CIW
H.T. Li, B. Young's [23]	10	2019	18	S690	0.33	CIF
			19	S960	0.33	CIF
H Zhou et al. [24]	11	2019	20	Q690	0.50	CIA
			21	Q690	0.50	CIW
Y. Cai, B. Young's [3]	12	2019	22	G450-550	0.25	LPG/CIF
			23	G450-550	0.25	Elec/CIF
X-Q Wang et al. [2]	13	2020	24	S690QT	0.5 -4	CIA
			25	S1070QT	0.5 -4	CIA
			26	S690QT	0.5 -4	CIF
			27	S1070QT	0.5 -4	CIF
			28	S690QT	0.5 -4	CIW
			29	S1070QT	0.5 -4	CIW
F. Azhare et al. [25]	14	2017	30	S1200		CIA
F. Azhare et al. [26]	15	2018	31	S1200		CIW
C. Siwei et al. [27]	16	2017	32	Q690		CIA
Z. Chen et al. [28]	17	2016	33	Q460-650	0.33	CIA
			34	Q835	0.33	CIA
			35	Q460-650	0.33	CIW
			36	Q835	0.33	CIW
			37	G20Mn5N	0.33	CIA
J. Lu et al. [29]	18	2017	38	G20Mn5QT	0.33	CIW
C. Maraveas et al. [30]	19	2015	39	Cast		CIA
			40	Cast		CIW

The graphs presented in section 3 represent the retention factors $R_{y,\theta}$, $R_{u,\theta}$, $R_{\epsilon u,\theta}$ or $R_{E,\theta}$ for yield strength, ultimate strength, ultimate strain and Young's modulus, respectively, at a temperature θ ($^{\circ}\text{C}$), given as the value of the considered property after a full cycle including heating to a temperature θ ($^{\circ}\text{C}$) and then cooling down, normalized by its value at ambient temperature before the cycle. R_{θ} is the product of the reduction factor $k_{y,\theta}$ (or $k_{E,\theta}$) and a new factor named herein as the recovery factor $r_{y,\theta}$ (or $r_{E,\theta}$) (i.e. $r_{\theta} = R_{\theta}/k_{\theta}$).

The coefficient of variation V_{amb} of the virgin material without having yet been subjected to heating and cooling is not negligible. To evaluate the modification of this coefficient after being exposed to fire, namely $V_{post,\theta}$, it is assumed that both V_{amb} and $V_{post,\theta}$ are related as expressed in Eq. (2). This leads to an expression for the characteristic value of the considered property, as given in Eq. (3). Clearly, $V_{post,\theta}$ cannot be lower than zero and V_{amb} is limited to the previously chosen value of 0.07 from the JCSS code [7].

$$V_{test,\theta}^2 = V_{amb}^2 + V_{post,\theta}^2 \quad (2)$$

$$X_{k,post,\theta} = X_{k,\theta} = \exp\left(\mu_{post,\theta} \pm k_n \sqrt{(V_{test,\theta}^2 - V_{amb}^2)}\right) \quad (3)$$

However, a very limited number of tests can lead to unrepresentative deviations. To avoid this, the proposed retention factor R_{θ} is adjusted by an operator in accordance with Eq. (4) where $\theta-1$ and $\theta+1$ are the preceding and following temperature intervals which has the effect of (i) forcing a decrease in the retention factor and (ii) removing the influence of outlying values, by comparing it to the averaged value of its neighbouring intervals. The maximum of both is retained.

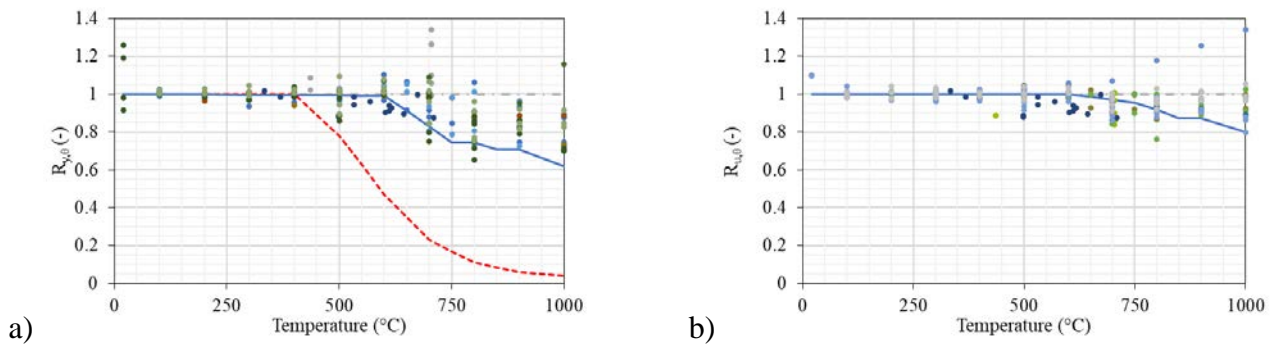
$$R_{\theta,i} = \min\left(R_{k,\theta-1,i}; \text{MAX}\left(R_{k,\theta,i}; \frac{R_{k,\theta-1,i} + R_{k,\theta+1,i}}{2}\right)\right) \quad (4)$$

3 RETENTION FACTORS

In this section, each classification of carbon steel is discussed in terms of its recovery of strength and stiffness following exposure to elevated temperature and subsequent cooling. In the following figures, the retention factor R_{θ} is presented as a solid line (with an additional subscript denoting the considered mechanical property). Additionally, the reduction factors for the yield strength $k_{y,\theta}$ and elastic modulus $k_{E,\theta}$ in accordance with Eurocode 3 Part 1-2 [31] are also presented as a dashed line.

3.1 Normal strength structural steel

Normal strength structural steel (NSS) is defined as steel with a yield strength between 235 and 420 MPa, as defined in Eurocode 3 Part 1-1 [32]. The set of available data is limited to 184 tests in total, from which 11 tests in ambient conditions are available. A significant degree of scatter is observed on V_{amb} which is the coefficient of variation of the virgin material and therefore it is concluded that not all steels included in these test programmes satisfy the EN 10025 product standard. The retention factors for the yield strength, ultimate tensile strength, ultimate strain and Young's modulus are presented in Figure 1.



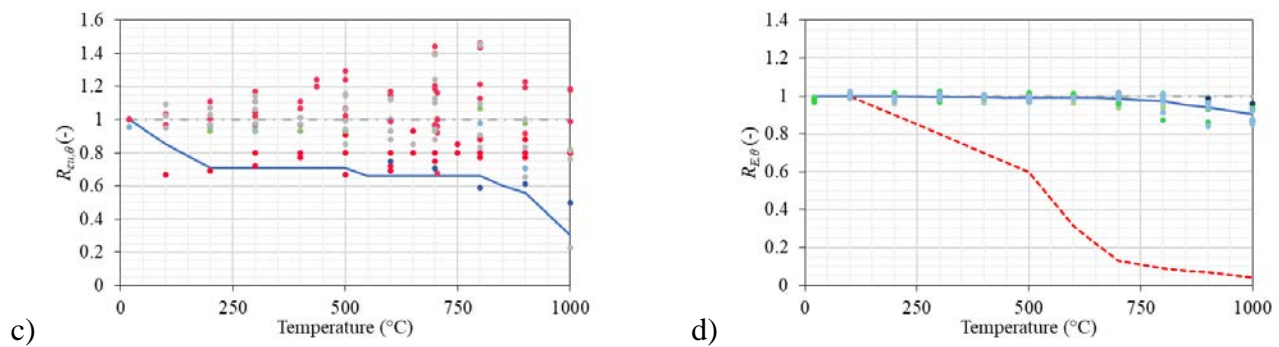


Figure 1 Summary of normal strength structural steel test results including a) yield strength, b) tensile strength, c) ultimate strain and d) Young's modulus after cooling down (dots).

With reference to the data presented in Figure 1, the following observations and conclusions are deduced:

- **Yield strength:** The yield strength retention factor $R_{y, \theta}$ as shown in Figure 1(a) shows a clear descending trend from approximately 600°C to 0.75 at 750°C. All of the subsets show similar general behaviour including a stepwise function which can be approximated by a linear function starting from 600°C, with a retention factor of unity, reducing to a value of 0.62 at 1000°C.
- **Ultimate strength:** It is observed in Figure 1(b) that the influence of exposure to elevated temperature on the post-fire ultimate tensile strength is rather limited. The retention factor for the tensile strength $R_{u, \theta}$ remains equal to unity until about 700°C and then slightly decreases to a minimum value of 0.82 at 1000°C.
- **Ultimate strain:** One of the ductility requirements in Eurocode 3 Part 1-1 [32] stipulates that the ratio of f_u/f_y should be greater than 10%. As stated before, the influence of heating and cooling is quite limited on the ultimate strength and therefore it is generally concluded that if the Eurocode 3 ductility criteria are fulfilled in the virgin material before the fire, these will be maintained even after fire and subsequent cooling.
- **Young's modulus:** The influence of the fire on Young's modulus is very limited. The retention factor $R_{E, \theta}$ has a value of unity until a temperature of 700°C and then decreases linearly to a value of 0.90 at 1000°C.

As a general conclusion to this section on normal strength carbon steels, it can be stated that for a post-fire assessment, the verification of the resistance criteria is likely to be the most important factor. Therefore, if a structure survives a fire, it is only necessary to re-check the ultimate limit states before a structure can return to service life.

3.2 High strength steel

High strength steels (HSS) can be produced in a number of different ways, typically involving either heat treatment or cold-working, and therefore the influence of the temperature that is reached during a fire as well as the soak time and cooling regime are likely to be important to the post-fire mechanical properties. In the last decade, there has been a reasonable body of research published on this material including a total of 259 test results. The retention factors for the yield strength, ultimate tensile strength, ultimate strain and Young's modulus are presented in Figure 2 and are discussed hereafter.

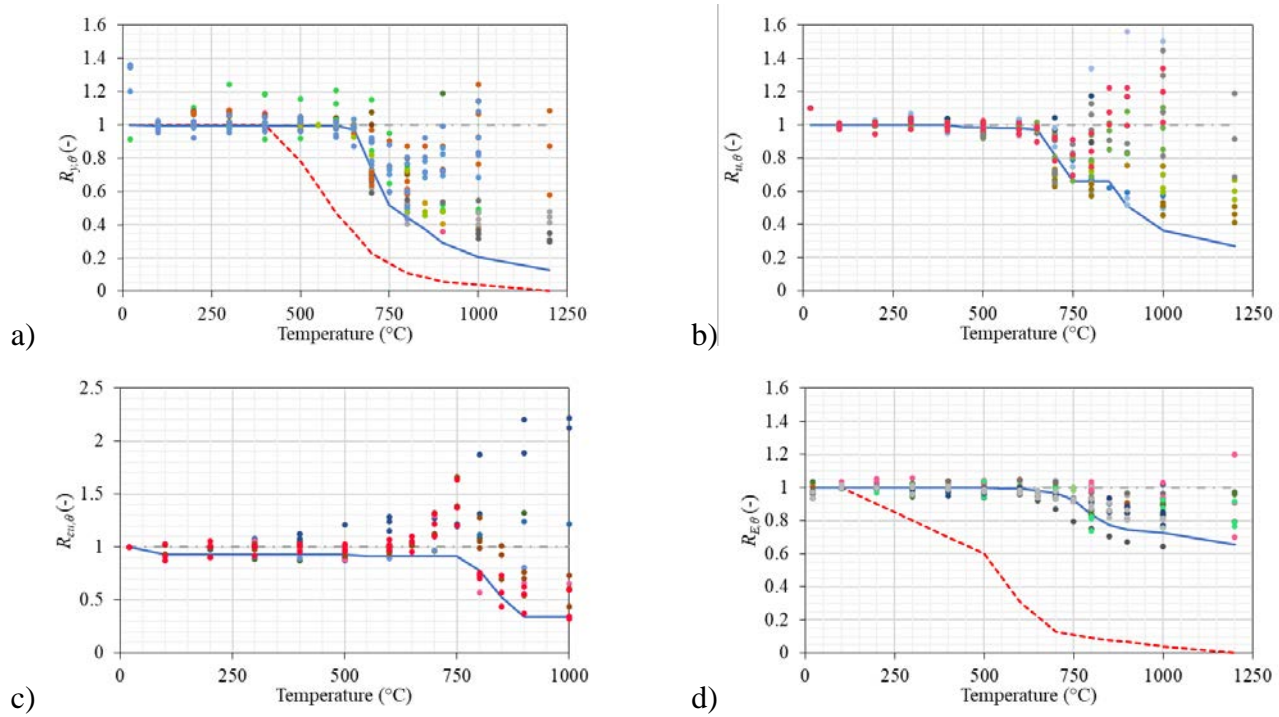


Figure 2 Summary of high strength steel test results including a) yield strength, b) tensile strength, c) ultimate strain and d) Young's modulus after cooling.

- **Yield strength:** As for the normal strength steels previously discussed, there is a degree of scatter for the yield strength, as shown in Figure 2(a), which is mostly as a result of the Bisalloy® samples in subsets 24, 26 and 28. These were cooled in air, furnace and in water, respectively. The yield strength retention factor $R_{y,\theta}$ follows the same trend as the reduction factor ($k_{y,\theta}$) but with a change which is noticeably from around 650°C.
- **Ultimate strength:** For the ultimate strength, between ambient and 650°C, $R_{u,\theta}$ has a value of 1.0, between 650°C and 750°C $R_{u,\theta}$ reduces linearly to 0.66 and then remains at this value until around 850°C after which it again decreases to a value of 0.27 at 1200°C.
- **Ultimate strain:** With reference to Figure 9(c), it is observed that the retention factor for ultimate strain $R_{\epsilon_{u,\theta}}$ slowly decreases to 0.91 at around 750°C, and then drops to around 0.34 at 900°C, and remains almost constant at this value as the temperature increases (0.30 at 1200°C). Subset 18 (Optim 700™ steel) also shows increased ultimate strains in terms of the retained values.
- **Young's modulus:** While for normal strength steel the effect of heating and subsequent cooling on the Young's modulus was very limited, a more significant reduction is observed for higher strength steels. Between ambient and 700°C, $R_{E,\theta}$ has a value of 1.0 then followed by a linear reduction to 0.66 at 1200°C. The values of subset 9 always time below the characteristic value.

3.3 Very high strength steel

This range of very high strength structural steel (VHSS) is covered by Eurocode 3 Part 1-12 [33] and EN 10025-6 [34]. Very high strength steels cover grades with a yield strength between 700 MPa and 960 MPa. These are generally still quite novel in the construction sector but are growing in popularity as the attraction to lighter and more bespoke designs increases. Of the database given in Table 3, only 4 research papers include tests on these grades resulting in a total of 54 experiments, with 4 in ambient conditions. Figure 3 presents the retention factors for yield strength, tensile strength, ultimate strain and Young's modulus, based on these data. As with the high strength steels, it is noteworthy that the production route for these grades can influence their behaviour under both elevated temperature, and post-fire conditions.

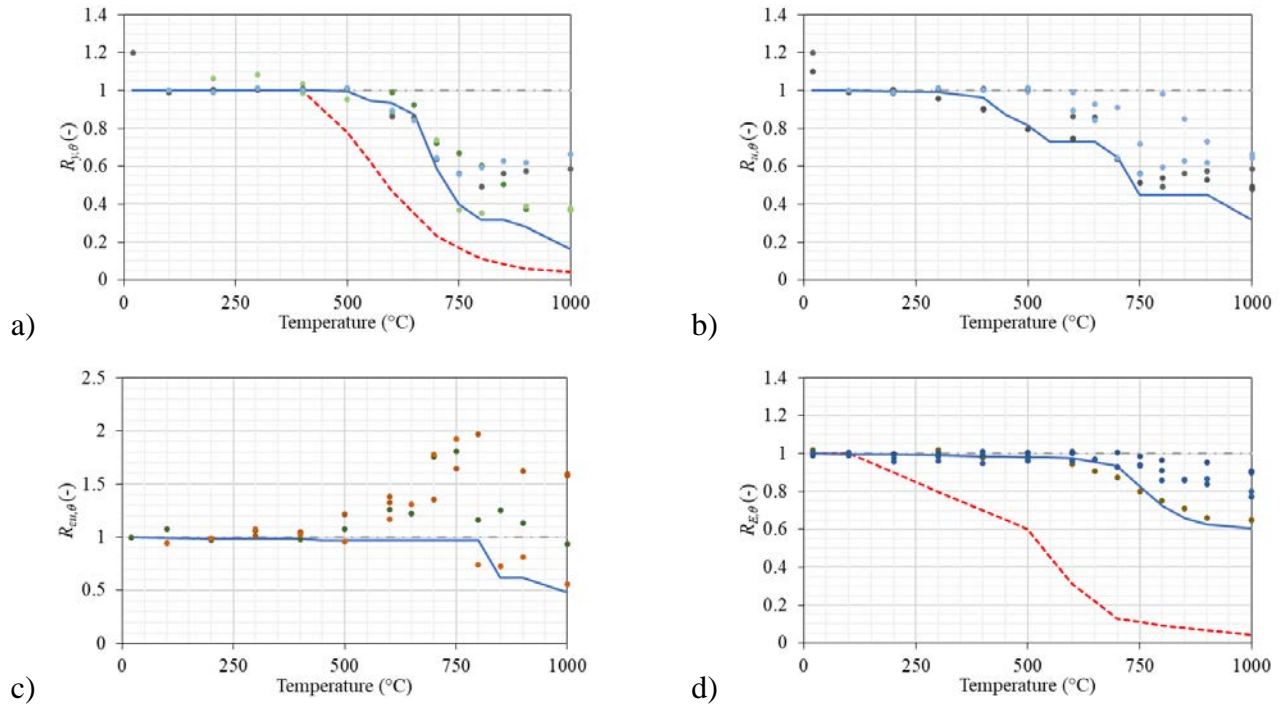


Figure 3 Summary of very high strength steel test results including a) yield strength, b) tensile strength, c) ultimate strain and d) Young's modulus after cooling.

The shape of all curves is, in general, almost the same as for the high strength steel grades. The following observations are made from the data presented in Figure 10.

- **Yield strength:** The yield strength follows, again, almost the same trend as the reduction factor ($k_{y,\theta}$). The retention factor is 1.0 between ambient temperature and 500°C, and this is followed by a linear reduction to a value of 0.84 at 650°C and then a further linear reduction to a value of 0.32 at 850°C and 0.16 at 1000°C.
- **Ultimate strength:** For the ultimate strength $R_{u,\theta}$, a lower scatter is generally observed, as for the HSS-grade. After exposure to temperatures higher than 250°C, the retention factor decreases. Starting from about 400°C, an almost linear decrease is observed to 0.45 at 750°C and then up to a retention factor of 0.32 at 1000°C.
- **Ultimate strain:** With reference to Figure 10(c), for the ultimate strains, after heating up to 500°C and then cooling, all tests deliver higher ultimate strains, the steel is relaxed and regains its initial ductility. Starting from 800°C however, a higher scatter is found which leads to a quick drop of the retention factor to 0.62 at 850°C, then descending to 0.48 at 1000°C.
- **Young's modulus:** The retention factor for Young's modulus exhibits a significant reduction (almost linear) from 600°C and has a value of 0.66 at 850°C, as shown in Figure 10(d). It then shows a less significant decrease to 0.61 at 1000°C. It is noteworthy that subset 10 is largely responsible for the lower values in the higher temperature range.

3.4 Summary of all the results

The characteristic temperatures θ and an overview of the accompanying retention factors R_θ can be found in Table 4 for each material group and individual mechanical property. In the table, for each data set, the temperature/retention factor (θ (°C)/ R_θ) is provided. More detailed information can be found in [4].

Table 4. Proposed simplified retention factors suitable for design

Property	$R_{y,\theta}$			$R_{u,\theta}$			$R_{eu,\theta}$			$R_{E,\theta}$	
θ (°C)/ R_θ	θ_A	θ_B	θ_C	θ_A	θ_B	θ_C	θ_A	θ_B	θ_C	θ_A	θ_B
All	400/ 1.00	750/ 0.40	1200/ 0.13	400/ 1.00	750/ 0.48	1200/ 0.27	200/ 0.78	750/ 0.70	1200/ 0.30	700/ 1.00	1200/ 0.65
NSS	600/ 1.00	750/ 0.75	1000/ 0.62	650/ 1.00	1000/ 0.82	-	200/ 0.71	800/ 0.66	1000/ 0.31	800/ 1.00	1000/ 0.90
HSS	650/ 1.00	750/ 0.52	1200/ 0.13	650/ 1.00	750/ 0.66	1200/ 0.27	750/ 0.91	900/ 0.34	1200/ 0.30	700/ 1.00	1200/ 0.66
VHSS	600/ 1.00	800/ 0.32	1000/ 0.16	400/ 1.00	750/ 0.45	1000/ 0.32	800/ 1.00	850/ 0.62	1000/0. 48	600/ 1.00	1000/ 0.61

4 UNCERTAINTY ASPECTS

The recommended material safety factor $\gamma_{M0,amb}$ for carbon steel equals 1.0, which corresponds to a very high certainty of the material characteristics and proven overstrength. This was extensively demonstrated in a recent European project [11] and is out of the scope of this article. An increasing uncertainty has an impact on the design values used in the assessment procedure. But, since this article deals with existing structures for which the remaining lifetime might be reduced, adjustments of the reliability level are also considered.

A simple method to obtain the relevant partial factor is to divide the design value of a resistance variable by its characteristic value, as described in annexes C and D of Eurocode 0 [5]. The derivation of a material property contributing to the resistance of a material should be carried out by (i) assessing a characteristic value which is divided by a partial factor or (ii) direct determination of the design value. Thus, the appropriate safety factor will be equal to the ratio of the characteristic to the design value, as given in Eq. (5). The sensitivity factor α_R for resistance effects has a value of 0.8 in accordance with Eurocode 0 [5] and the reliability factor β for new structures in Consequence Class 2 (CC2), is equal to 3.8 [5]. A CC2 refers to medium consequence for loss of human life, while economic, social or environmental consequences are considerable. Examples of CC2 are residential and office buildings, as well as public buildings with a medium consequence of failure.

$$\gamma_{M0,\theta} = \frac{X_{k,\theta}}{X_{d,\theta}} = \frac{\exp\left(-1.645\sqrt{\ln(V_{test,\theta}^2 + 1)}\right)}{\exp\left(-\alpha\beta\sqrt{\ln(V_{test,\theta}^2 + 1)}\right)} \quad (5)$$

In the previous section, Eqs. (2) and (3) gave the coefficient of variation resulting from a test $V_{test,\theta}$ as a combination of the coefficient of variation from the virgin material ($V_{amb} = 0.07$) and the corresponding post-fire value ($V_{post,\theta}$) depending on the temperature exposure. Regarding safety factors however, the final assessment in the post-fire condition should use the product of both safety factors i.e. one factor linked to the material properties in ambient conditions ($\gamma_{M0,amb}$) and another related to the post-fire conditions ($\gamma_{M0,post,\theta}$). All of these safety factors can be derived based on Eqs. (2) and (5).

There are two challenges with this approach which need to be considered:

1. Given the chosen conservative upper value of the coefficient of variation (i.e. 0.07), the safety factor at ambient temperature V_{amb} based on the collated data is 1.10. Nevertheless, the more comprehensive recommendations of a recent European project [11] and implemented in Eurocode 3 Part 1-1 [35] recommend using a $\gamma_{M0,amb}$ factor of 1.0. Therefore, the product of $\gamma_{M0,amb}$ and $\gamma_{M0,post,\theta}$ gives $\gamma_{M0,post,\theta}$ or ($\gamma_{M0,\theta}$), where $\gamma_{M0,post,\theta}$ is the safety factor based on $V_{post,\theta}$ with a sensitivity factor α_R of 0.8.
2. Due to the variation of the coefficient of variation based on tests $V_{test,\theta}$, the calculated safety factor $\gamma_{M0,test,\theta}$ varies depending on the temperature. It is observed that the data sometimes leads to lower safety

levels for steel exposed to higher temperatures which is perhaps counterintuitive. It is therefore necessary to include an operator which ensures that the safety factor does not decrease, and this is implemented using Eq. (6). The variables marked with an asterisk (*) symbol are those before the application of the operator.

$$V_{test,i,\theta} = MAX(V_{test,i,\theta-1}^*; V_{test,i,\theta}^*) \quad (6)$$

For buildings categorized in normal Consequence Class 2 [5], the reliability index β corresponding to a probability of failure of $7.23 \cdot 10^{-5}$ equals 3.8 [6]. It has previously been shown by a number of researchers [36], [37] that there should be a distinction between new, existing and even temporary structures regarding their reliability indexes. In accordance with ISO 2394 [38] it is proposed to limit β to a lower limit of 3.3 for an existing building in the post-fire condition, for which societal and human risks are still satisfactory [36]. Eq. (5) demonstrates that there is a direct impact of a lower β factor on the safety factor $\gamma_{M0,post,\theta}$, and this has been calculated and is depicted in Figure 4 and summarized in Table 5. The loss in material strength is still visible through the new safety factors but its effect is decreasing.

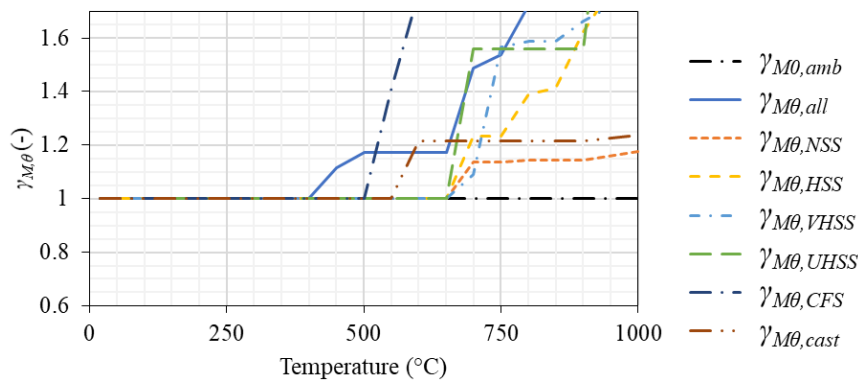


Figure 4 Summary of safety factor with a reliability index $\beta = 3.3$ for the different steel grades considered in this study.

Table 5. Critical temperatures and additional safety factors for steel grades discussed in this article, with $\beta=3.3$

Name of subsets	Abbreviation	θ (°C)	Safety factor $\gamma_{M0,post,\theta}$
Structural steel	NSS	> 650	1.15
		$\theta_{lim} > 1000$	
High strength structural steel	HSS	> 650	1.25
		> 750	> 1.40
		$> 850 = \theta_{lim}$	> 1.60
Very high strength structural steel	VHSS	> 650	1.10
		$> 700 = \theta_{lim}$	> 1.60

5 CONCLUSIONS

This paper deals with the determination of the post-fire steel material properties and safety factors used in the assessment and retrofitting of existing steel buildings which suffered and survived a fire. It is the first reliability-based approach for the reinstatement of structures based on the available information in the literature. The data is used to derive (i) retention factors for each of the significant and characteristic material properties i.e. directly providing an easy-to-use information on how a specific property changes in value when steel is subjected to a fire and subsequently cooled down and (ii) adjusted safety factors based on the details analysis reflecting the increase of variation in results after being heated and cooled down. Both factors depend on the maximum temperature to which the steel is exposed.

It is shown that, for normal strength steel and cast or wrought iron, the impact of fire on the post-fire properties remains reasonable until up to temperatures of 1000°C. For other steel grades, however, there exists a critical temperature above which reinstatement after the occurrence of a fire is economically unfeasible. In these cases, $\gamma_{M0,post,\theta}$ is greater than 1.60 when this critical temperature is reached during the fire.

Following this work, it is recommend that the following procedure is followed in the post-fire assessment of carbon steel structures: depending on the maximum temperature reached during the fire, the retention factor is taken from Table 4 and the additional safety factor taken from Table 5.

REFERENCES

- 1 Y. Yu, L. Lan, F. Ding en L. Wang, „Mechanical properties of hot-rolled and cold-formed steels after exposure to elevated temperature: a review.,” *Construction and Building Materials*, nr. 213, pp. 360-376, 2019.
- 2 X.-Q. Wang, Z. Tao en M. K. Hassan, „Post-fire behaviour of high-strength quenched and tempered steel under various heating conditions,” *Journal of Constructional Steel Research*, nr. 164, 2020.
- 3 Y. Cai en B. Young, „Mechanical properties of thin sheet steel after exposure to high temperatures,” *Thin-Walled structures*, nr. 142, pp. 460-475, 2019.
- 4 T. Molken, K. Cashell en B. Rossi, „Post-fire mechanical properties of carbon steel and safety factors for the reinstatement of steel structures,” *Engineering Structures*, vol. 2020, p. Under review, 2020.
- 5 EN 1990, Eurocode 0 Basis of structural design (consolidated version including A1:2005 and AC:2010), Brussels, Belgium: CEN, 2015.
- 6 H. C. Gulvanessian, J. Calgaro en M. Holicky, *Designers' Guide to Eurocode: Basis of Structural Design - 2nd Ed.*, Croydon, UK: Thomas Telford Ltd., 2012.
- 7 JCSS, Probabilistic model code: Part 3 - Resistance models, Copenhagen, Denmark: DTU, 2000.
- 8 EN 10025, Hot rolled products of structural steels, Brussels: CEN, 2005.
- 9 EUR 20344, „Partial safety factors for resistance of steel elements to EC3 and EC4 - Calibration for various steel products and failure criteria,” European commission, Directorate-General for Research and Innovation, Luxembourg, 2002.
- 10 EUR 25893, Optimizing the seismic performance of steel and steel-concrete structures by standardizing material quality control, Brussels: European commission, Directorate-General for Research and Innovation, 2013.
- 11 EUR 28906, „Standardization of safety assessment procedures across brittle to ductile failure modes,” European commission, Directorate-General for Research and Innovation, Luxembourg, 2017.
- 12 L. Simões da Silva, C. Rebelo, D. Nethercot, L. Marques, R. Simões en P. Vila Real, „Statistical evaluation of the lateral-torsional buckling resistance of steel I-beams, Part 2: Variability of steel properties,” *Journal of Constructional Steel Research*, pp. 832-849, 2009.
- 13 T. Molken, K. A. Cashell, M. Malaska, F.-U. Rehman, M. Alanen en B. Rossi, „Performance of stainless steel structures following a fire,” in *9th Eurosteel 2020*, Sheffield, UK, 2020.
- 14 C. I. Smith, B. R. Kirby, D. G. Lapwood, K. J. Cole, A. P. Cunningham en R. R. Preston, „The Reinstatement of Fire Damaged Steel Framed Structures,” *Fire Safety Journal*, vol. 4, pp. 21-62, 1981.
- 15 J. Outinen, Mechanical properties of structural steels at high temperatures and after cooling down, Helsinki, Finland: PhD dissertation, Helsinki University of Technology, 2007.
- 16 J. Lee, Elevated-Temperature Properties of ASTM A992 Steel for Structural-Fire Engineering Analysis, Austin, US: PhD dissertation, Univesity of Texas at Austin, 2012.
- 17 X. Qiang, F. S. Bijlaard en H. Kolstein, „Post-fire mechanical properties of high strength structural steels S460 and S690,” *Engineering Structures*, nr. 35, pp. 1-10, 2012.
- 18 X. Qiang, F. S. Bijlaard en H. Kolstein, „Post-fire performance of very high strength steel S960,” *Journal of Constructional Steel Research*, nr. 80, pp. 235-242, 2013.
- 19 S. Chiew, M. Zhao en C. Lee, „Mechanical properties of heat-treated high strength steel under fire/post-fire conditions.,” *Journal of Constructional Steel Research*, nr. 98, pp. 12-19, 2014.

- 20 S. Gunalan en M. Mahendran, „Experimental investigation of post-fire mechanical properties of cold-formed steels,” *Thin-Walled structures*, nr. 84, pp. 241-254, 2014.
- 21 W. Wang, T. Liu en J. Liu, „Experimental study on post-fire mechanical properties of high strength Q460 steel,” *Journal of Constructional Steel Research*, nr. 114, pp. 100-109, 2015.
- 22 J. Lu, H. Liu, Z. Chen en X. Liao, „Experimental investigation into post-fire mechanical properties of hot-rolled and cold-formed steels,” *Journal of Constructional Steel Research*, nr. 121, pp. 291-310, 2016.
- 23 H.-T. Li en B. Young, „Residual mechanical properties of high strength steels after exposure to fire,” *Journal of Constructional Steel Research*, nr. 148, pp. 562-571, 2018.
- 24 H. Zhou, W. Wang, K. Wang en L. Xu, „Mechanical properties deterioration of high strength steels after high-temperature exposure,” *Construction and Building Materials*, nr. 199, pp. 664-675, 2019.
- 25 F. Azhari, A. Heidarpour, X.-L. Zhao en C. R. Hutchinson, „Post-fire mechanical response of ultra-high-strength (Grade 1200) steel under high temperatures: Linking thermal stability and microstructure,” *Thin-Walled Structures*, nr. 119, pp. 114-125, 2017.
- 26 F. Azhari, A.-A. H. Apon, A. Heidarpour, X.-L. Zhao en C. R. Hutchinson, „Mechanical response of ultra-high-strength (Grade 1200) steel under extreme cooling conditions,” *Construction and Building Materials*, nr. 175, pp. 790-803, 2018.
- 27 C. Siwei, J. Shaokun, G. Houzuo, C. Huixuan, L. Yifeng en L. Kang, „Mechanical and ductile fracture performances of high strength structural steel Q690 after a fire: experimental investigation,” in *Protect2017*, Guangzhou, China, 2017.
- 28 Z. Chen, J. Lu, H. Liu en X. Liao, „Experimental study on the post-fire mechanical properties of high strength steel tie rods,” *Journal of Constructional Steel Research*, nr. 121, pp. 311-329, 2016.
- 29 J. Lu, H. Liu, Z. Chen en L. Bisby, „Experimental investigation of the residual mechanical properties of cast steels after exposure to elevated temperature,” *Construction and Building Materials*, nr. 143, pp. 259-271, 2017.
- 30 C. Maraveas, Y. Wang, T. Swailes en G. Sotiriadis, „An experimental investigation of mechanical properties of structural cast iron at elevated temperatures and after cooling down,” *Fire Safety Journal*, nr. 71, pp. 340-352, 2015.
- 31 EN 1993-1-2, Eurocode 3 : Design of steel structures - Part 1.2 : General rules Structural Fire Design, Brussels, Belgium: CEN, 2005.
- 32 EN 1993-1-1, Eurocode 3: Design of steel structures - Part 1-1: General rules and rules for buildings (includes AC:2006, AC:2009), Brussels: CEN, 2005.
- 33 EN 1993-1-12, Eurocode 3 - Design of steel structures - Part 1-12: Additional rules for the extension of EN1993 up to steel grades S700 + corrigendum 2009, Brussels: CEN, 2007.
- 34 EN 10025-6, Hot rolled products of structural steels - Part 6: Technical delivery conditions for flat products of high yield strength structural steels in the quenched and tempered condition, Brussels: CEN, 2009.
- 35 EN 1993-1-1, Design of steel structures - Part 1-1: General rules and rules for buildings, Brussels, Belgium: CEN, 2005.
- 36 M. Sykora, D. Diamantidis, M. Holicky en K. Jung, „Target reliability levels for existing structures considering economic and societal aspects,” *Structure and Infrastructure Engineering*, nr. 13, pp. 181-194, 2017.
- 37 R. Caspeele, M. Sykora, D. L. Allaix en R. Steenbergen, „The design value method and adjusted partial factor approach for existing structures,” *Structural Engineering International*, vol. 23, nr. (4), pp. 386-393, 2013.
- 38 ISO 2394, General principles on reliability for structures, Geneva: International standard organization, 2015.

FIRE FRAGILITY CURVES FOR STEEL PIPE-RACKS EXPOSED TO LOCALISED FIRES

Jérôme Randaxhe¹, Olivier Vassart², Nicola Tondini³

ABSTRACT

This paper proposes a new method to build a probabilistic fire demand model (PFDM) to investigate the structural behaviour of a steel pipe-rack located within an industrial installation and exposed to a localised fire. The PFDM will serve to develop fire fragility functions to be used either in a fire risk assessment or in a fully probabilistic structural fire engineering (PSFE) framework. The cloud analysis (CA) was exploited to build a PFDM based on different engineering demand parameters (EDP) – intensity measures (IM) pairs. In particular, the analysis was applied to a prototype steel pipe-rack integrating an industrial plant in Italy. In order to cover a wide range of plausible fire scenarios and to introduce uncertainties in the fire model, 539 fire scenarios were examined by varying the fire diameter, the fire-structure distance and the fuel. The selection of the fire diameters was based on parametric analyses quantifying liquid flow through orifices and pipes. The thermal impact of the pool fires on the structure was analysed using the LOCAFI localised fire model and the thermo-mechanical response of the pipe rack was evaluated by means of finite element analysis. Based on the structural analysis outcomes, it was found that the interstorey drift ratio (ISDR) – maximum average heat flux impinging the structure (HF_{avg}) EDP-IM pair was the most efficient. Moreover, it has to be noted that for this type of case study, the CA revealed to be a suitable and versatile tool to build a PFDM.

Keywords: probabilistic fire demand model; cloud analysis; pool fires; LOCAFI model; fire fragility functions; steel pipe-rack structure

1 INTRODUCTION

In industrial and petrochemical plants, piping systems are used to transport flammable material, liquid or gas fuel, on long distances. They are usually supported by pipe-rack steel structures, passing between other industrial components, e.g. tanks, distillation tower, etc. These structures usually unprotected due to their significant length, are components among the most exposed to natural hazards, such as earthquakes, hurricanes or tsunamis. It appears in plants that under certain conditions, these events can trigger severe structural damages, leading a pipe or a tank to lose its containment. Furthermore, petrochemical plants are locations where a releasing flammable material is more likely to ignite than anywhere else due to activities and operations taking place in industrial environments. Even if the probability of occurrence is low, the consideration of such scenarios cannot be ignored, given their catastrophic consequences. Numerous studies have recently highlighted the exposure of petrochemical plants, piping systems to natural hazards generating technological issues, also named NaTech events. Among the wide research work which has been undertaken, Zheng and Chen ¹ investigated storage tank fire accidents due to maintenance and management problems. Chan and Lin ² reviewed 242 accidents involving storage tanks and analysed their causes to

¹ Research Engineer, Global R&D Center of ArcelorMittal, Esch-sur-Alzette, Luxembourg
e-mail: jerome.randaxhe@arcelormittal.com

² Chief Executive Officer Steligenz at ArcelorMittal, Luxembourg
e-mail: olivier.vassart@arcelormittal.com

³ Assistant Professor, Department of Civil, Environmental and Mechanical Engineering, University of Trento, Italy
e-mail: nicola.tondini@unitn.it, ORCID: <https://orcid.org/0000-0003-2602-6121>

identify that 85% of accidents impacting petrochemical facilities are due to fires and explosions. Pantousa³ investigated the behaviour of steel storage tanks when exposed to the thermal radiation from surrounding burning tanks. Numerous seismic analyses were performed on petrochemical piping systems and their support structure by Paolacci et al.⁴⁻⁸.

Specifically, this work adopts a performance-based approach to investigate the thermo-mechanical response of a steel pipe-rack subjected to a number of meaningful fire scenarios, characterised by a pool fire located beside it, with the aim to build a probabilistic fire demand model from which deriving fire fragility functions. For that purpose, a pool fire model has to be selected, allowing the simulation of a burning tank resulting from leakage and loss of containment. It is worth pointing out that the governing heat transfer mechanism of a localised fire impacting a structure that is not engulfed into the fire, is radiation. In this respect, the LOCAFI model, developed in the framework of a European research project was exploited.⁹⁻¹⁴.

Fragility functions are convenient tools when decisions are to be taken in structural design considering uncertainties. More specifically, for a given structure exposed to fire, a fragility function computes the probability that a structure reaches a predefined damage state (e.g. beam deflection level, interstorey drift ratio, critical temperature, ...) depending on an intensity measure characterising the fire (e.g. fire load, fire geometry, ...). There are few research works addressing the development of fragility functions in fire field. In particular, Gernay et al.^{15, 16} proposed a methodology to define fire fragility functions for a steel building exposed to compartment fires considering different fire loads. If this approach is relevant for buildings intended for offices and dwellings, it cannot be applied for a steel pipe-rack exposed to a localised fire. Lange et al.¹⁷ and Shrivastava et al.¹⁸ modified and adapted to fire engineering the widely used Performance-Based Earthquake Engineering (PBEE) approach from the Pacific Earthquake Engineering Research Center (PEER) probabilistic framework¹⁹. The use of fragility functions, considering efficient intensity measures to characterise the fire severity, allows the mitigation of fire risks when petrochemical plants are designed. However, there is a lack of work related to the study of probabilistic fire demand models relative to the structural fire behaviour of supporting structures in industrial plants.

2 CASE STUDY: PROTOTYPE STEEL PIPE-RACK

2.1 Description of the structure

The prototype steel pipe-rack considered for this work is defined in Figure 1. That structure is inspired from a reference steel pipe-rack operational in an existing petrochemical plant located in Italy. The structure is composed of several steel frames with rigid beam-to-column joints and pinned column-base joints in the transversal direction, whose distance from each other is 6 m; whereas, in the longitudinal direction, the structure is braced, with repeated modules composed of seven bays and only one endowed with bracings. Horizontal braces are used to limit relative displacements between the frames and the pipe supports. For the interest of the analyses addressed in this paper, only the supporting steel pipe-rack was considered while the structural contribution of the piping system was neglected. Furthermore, since a pipe-rack is, by definition, a structure intended for carrying pipes on kilometres, it was decided to focus the analyses on a limited and regular part. The steel grade is an S275. The columns are HEA 340, the longitudinal beams are HEA 200 and the transversal beams are HEA- and HEB 300 steel profiles, respectively. The self-weight of the pipe and their content is evaluated to 75 kN/m. This load corresponds to a pipe arrangement as depicted in Figure 1(d), considering 22" DN550 SCH140 pipes characterised by a diameter of 559 mm with a wall thickness of 47 mm, and filled with a fuel with density equal to 780 kg/m³. The horizontal load is equal to 2 kN/m, considering the friction of the pipes, that are uniformly distributed on the transversal beams. Vertical contingency operating point loads of 15 kN and horizontal contingency friction point loads of 7.5 kN are applied at mid-span of the longitudinal beams. Wind loads acting on the structure are not considered during the fire. The loads applied on the pipe-rack are detailed in Figure 2. It has to be noted that this load combination represents about 50% of the structure vertical bearing capacity.

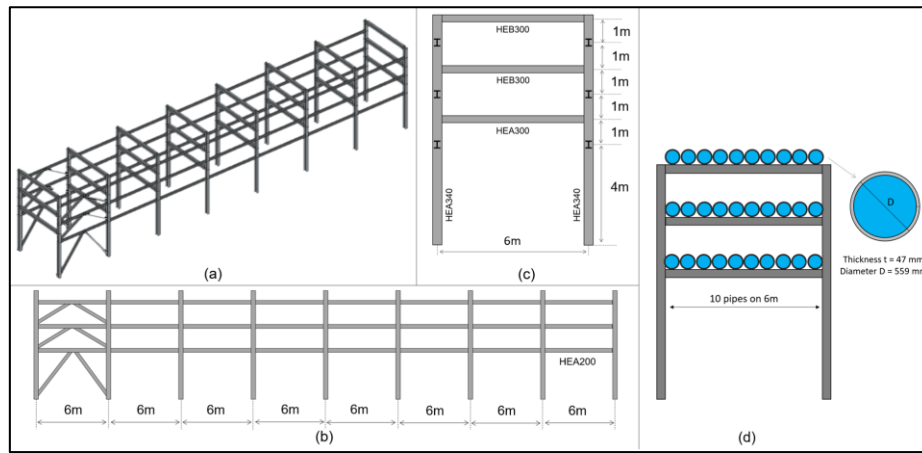


Figure 1. Prototype steel pipe-rack: (a) 3D view; (b) Longitudinal view; (c) Transversal view; (d) 22'' DN550 SCH140 pipe arrangement

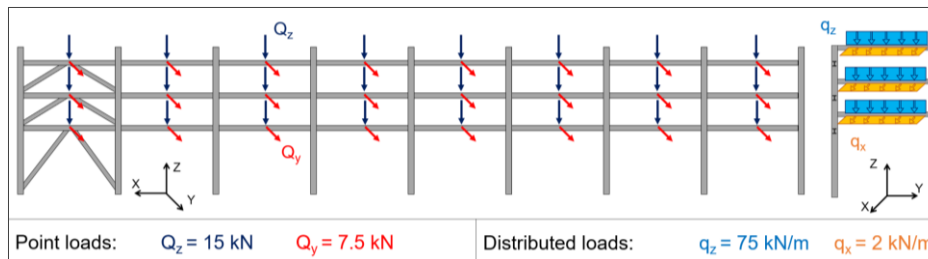


Figure 2. Loads applied on prototype pipe-rack

2.2 Numerical model

The pipe rack described in Section 2.1 was modelled with the thermo-mechanical non-linear finite element software SAFIR²⁰. This software includes the LOCAFI model, as described in Section 3.1. The structural response of the pipe-rack exposed to a localised fire was investigated by means of a 3D model that exploited 3D Bernoulli fibre-based beam elements. Thus, at each integration point 2D thermal analyses were performed with heat flux boundary conditions obtained from the application of the LOCAFI model. The entire structure was discretized with beam elements having length of 50 cm and containing two points of integration each. That represents a total of 936 beam elements to model the prototype pipe-rack. The properties of steel at elevated temperature were taken as the ones provided in EN 1993-1-2²¹. The boundaries conditions assigned to the structural model comply with the assumptions formulated in Section 2.1. As described in Figure 3, the columns HEA340 are continuous and pinned at their base in both principal directions. The transversal beams HEA- and HEB300 are both end fixed to the columns, while the longitudinal beams, HEA200 are pinned to the columns. At both longitudinal ends of the pipe-rack, horizontal restraints were applied to allow for the bracing system that was not modelled to limit the computational burden. This modelling was justified by the fact that based on the fire scenarios described in Section 3.2, the heating of the bracing system was not enough to significantly change its degree of restraint. Moreover, the major thermal impact and the consequent structural failure occurred in the transverse direction. It may be noted that longitudinal thermal expansion joints were not considered in the structural module under study.

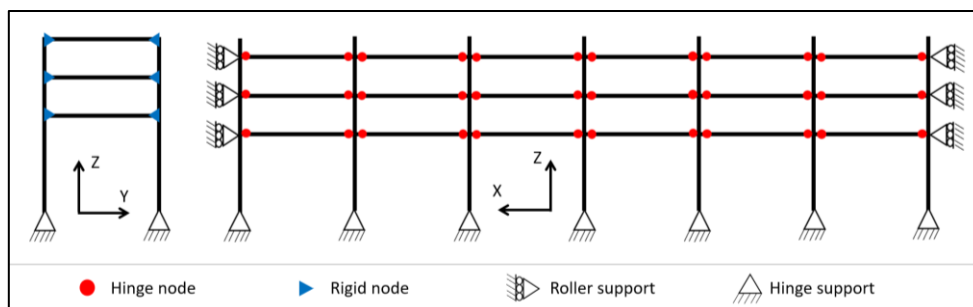


Figure 3. Boundary conditions of the 3D FE model of the prototype steel pipe-rack

3 LOCALISED FIRE SCENARIOS

In this work, emphasis was put on the thermal demand, whose definition for this case study is highly uncertain. Thus, for the derivation of the fire fragility curves, only the uncertainty related to the fire input was considered, but of course other forms of uncertainty can be found, e.g. steel mechanical properties, steel thermal properties, applied loads^{15, 16, 22, 23}.

3.1 LOCAFI Model

Localised fires results from a liquid or solid fuel burning on a limited surface. Several models are available in literature to study localised fires and they can be classified among field/computational fluid dynamics (CFD) models and empirical/analytical models. Tondini et al.¹⁰ showed how the analytical LOCAFI model compared with CFD models to predict the radiant heat flux emitted from localised fires and how it fared against experimental measurements. Among empirical/analytical models, solid flame models adopt a specific shape for the flame geometry, that may be a cylinder, an elliptical cylinder or a cone^{24, 10}. These models consider that the radiative heat fluxes are emitted from the surfaces of the solid representing the fire and that the radiative heat flux received by an external element is the sum of the radiative heat fluxes emitted from each surface based on the computation of configuration factor, which may be done analytically and/or numerically depending on the flame shape assumption. In the framework of this research, a solid flame model is adopted with the use of the LOCAFI model developed within the European LOCAFI Project⁹. This model was developed and calibrated based on experimental tests and numerical analyses performed with a CFD model¹⁰ and it is based on the existing localised fire correlations provided in Annex C of EN1991-2²⁵. Once a localised fire is defined with a conical shape and a temperature evolution along the flame axis, incident radiative heat fluxes can be computed for any external element considered. Equation (1) defines the incident radiative heat flux $\dot{q}_{A \rightarrow B}$ emitted by a surface A and received by a surface B.

$$\dot{q}_{A \rightarrow B} = \phi_{A \rightarrow B} \varepsilon_A \sigma (\theta_A + 273)^4 \quad [\text{W/m}^2] \quad (1)$$

Where $\phi_{A \rightarrow B}$ is the configuration factor, ε_A is the emissivity of the surface A, σ is the Stefan-Boltzmann constant and θ_A is the temperature of the surface A. In this research context, as depicted in Figure 4a, the surface A is an element discretising the conical fire and the surface B is an element discretising the structural steel members. The emissivity of the flame ε_A , or ε_f , is conservatively taken equal to 1. The configuration factor can be determined analytically, if available, otherwise through numerical integration. The configuration factor is calculated considering sizes and orientations of surfaces A and B and the distance separating them. This calculation complexity is function of the discretization level adopted for the fire and for the structure. Two models are available to compute the radiative heat fluxes impacting a structural element; the analytical model¹⁰ and the numerical model²⁰. In this work, the model implemented in SAFIR is based on numerical integration of the configuration factor. It discretizes the surfaces of the fire and the member with small elements, as shown in Figure 4b. SAFIR is able to compute at each time step and for each finite element located on the border of the cross section, as depicted in Figure 4c, an incident radiative heat flux that is calculated by summing all the radiative heat fluxes emitted by the surfaces discretizing the fire and visible by the element according to a numerical procedure. Then, the net heat flux is expressed as the difference between the absorbed radiative heat flux and the heat fluxes reemitted by the surface B through radiation and convection, as shown in Equation (2), where the first term is the absorbed radiative heat flux by the surface, the second and third terms are the heat fluxes reemitted by the surface through radiation and convection at ambient temperature, i.e. 20°C.

$$\dot{q}_{\text{net}} = \varepsilon_B \dot{q}_{A \rightarrow B} - \varepsilon_B \sigma [(\theta_B + 273)^4 - 293^4] - \alpha_c (\theta_B - 20) \quad [\text{W/m}^2] \quad (2)$$

As an example, Figure 4d shows the temperature field observed within the cross section of an HEA340 steel column at a height of 5 m after 1 h of exposure to a heptane localised fire characterised by a diameter of 20 m and located 2 m away.

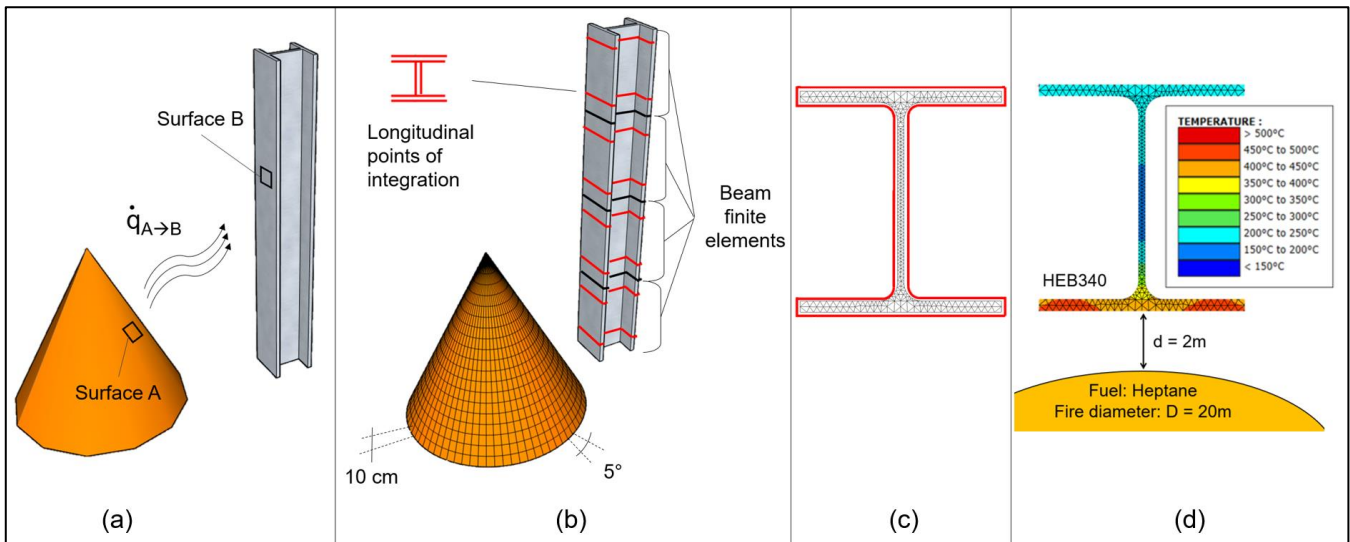


Figure 4. (a) Steel column exposed to localised fire; (b) LOCAFI numerical model; (c) Cross-section discretization; (d) Temperature field within the cross section observed with numerical model

3.2 Selection of fire scenarios

To study the behaviour of the steel pipe-rack exposed to localised fires in a probabilistic way, a meaningful set of fire scenarios must be defined. The objective is to encompass plausible fire scenarios, that impact the structure with different levels of intensity. It was decided to define fire scenarios by varying three parameters: the pool fire diameter, the fuel and the fire-structure distance. As analysed by Randaxhe et al ²⁶, in petrochemical plants, pool fires can result from the ignition of a fuel contained in a cylindrical tank or from the ignition of a leaking fuel. Resulting fires are likely to present a diameter varying between 5m and 30m. Therefore, 11 fire diameters, denoted D , varying between 5 m to 30 m with a step of 2.5 m were selected. Since petrochemical plants deal with various flammable products, 7 liquid fuels were selected to cover a wide range of different fire loads. These 7 fuels are namely listed in Table 1 that defines 77 different localised fires and summarizes the rate of heat release (RHR) computed for each of them.

Table 1. Rate of heat release depending on fuels and fire diameters

Fuel	Rate of heat release [MW]										
	Diameters [m]										
	5	7.5	10	12.5	15	17.5	20	22.5	25	27.5	30
Pentane	91	205	364	569	819	1115	1456	1843	2276	2754	3277
Heptane	71	160	284	443	638	869	1135	1436	1773	2146	2554
Benzene	67	151	268	418	602	820	1071	1355	1673	2025	2409
Kerosene	53	120	213	332	479	652	851	1077	1330	1609	1915
Gasoline	47	106	189	295	425	578	755	956	1180	1428	1699
Fuel Oil	26	60	106	166	239	325	424	537	663	802	954
Acetone	19	43	77	120	173	236	308	390	481	582	693

As explained in Section 3.1, the distance separating a structure and a fire has a direct influence on the magnitude of the radiative heat flux received by the structure. For the definition of the fire scenarios, 7 distances separating the edge of the fire and the structure. The 7 distances, denoted d , are: 0.5 m, 1 m, 2 m, 3 m, 4 m, 5 m and 6 m. It has to be noted that the localised fires were positioned on the axis of the central moment resisting frame in order to have the most important impact on the structure. Fire scenarios with distances d close to 0 m have a significant impact on the structure while the ones close to 6m are definitely less demanding, which explains why no further distance was considered. Eventually, by varying the values of the three parameters: fire diameter, fuel, and distance, 539 fire scenarios were defined and 539 thermo-mechanical analyses with the LOCAFI localised fire model as thermal input were performed in SAFIR.

4 PROBABILISTIC FIRE DEMAND ANALYSIS

4.1 Cloud analysis method

A fragility function expresses the probability that an engineering demand parameter (EDP) exceeds a structural limit state (LS) as a function of an intensity measure (IM). That probability is usually written in the following form.

$$P(\text{EDP} > \text{LS} | \text{IM}) \quad (3)$$

The aim is to develop fire fragility functions to be used in a probabilistic framework that will serve as a means for practitioners to probabilistically assess/design a pipe-rack structure subjected to localised fires. To build up fragility functions and to define the probability expressed in Equation (3), it is necessary to develop a probabilistic demand model. In literature, several probabilistic seismic demand models (PSDM) can be found, whereas only few probabilistic fire demand models (PFDM) have been developed so far¹⁵⁻¹⁸. Most PSDMs characterise the relation between EDP and IM based on results obtained through non-linear dynamic analysis. In the framework of this research, the cloud analysis (CA) method appeared to be the most appropriate for the development of a probabilistic fire demand model. In the CA all fire scenarios are run and based on thermo-mechanical results a cloud of points is plotted on an EDP vs IM chart. Assuming that the EDP follows a lognormal distribution when conditioned on the IM, which is a common assumption, it is possible to write the median EDP, i.e. $\widehat{\text{EDP}}$, as expressed in Equation (4). Therefore, the conditional median of EDP given IM is linear in log-log space, as shown in Equation (5), whereas the conditional dispersion of EDP given IM is constant. Thus, the resulting probabilistic demand model can be represented in linear and logarithmic forms as in Equations (4) and (5), respectively, where $a = \exp(A)$ and $b = B$. A and B are parameters that can be determined from linear regression. With coefficients a and b , the standard deviation of the linear regression error can be defined with Equation (6). This term is also defined $\beta_{\text{EDP}|\text{IM}}$ as the dispersion of the EDP conditioned on IM. Considering the lognormal assumption and Equations (4) and (6), Cornell et al.²⁷ defined the fragility function with the use of a lognormal cumulative distribution function as expressed in Equation (7).

$$\widehat{\text{EDP}} = a \text{IM}^b \quad (4)$$

$$\ln(\widehat{\text{EDP}}) = A + B \ln(\text{IM}) \quad (5)$$

$$\sigma_{\ln(\text{EDP})|\text{IM}} = \beta_{\text{EDP}|\text{IM}} = \sqrt{\frac{\sum_{i=1}^n [\ln(\text{EDP}_i) - \ln(\widehat{\text{EDP}}_i)]^2}{n-2}} \quad (6)$$

$$P(\text{EDP} > \text{LS} | \text{IM}) = 1 - \Phi \left(\frac{\ln(\text{LS}/(a \text{IM}^b))}{\beta_{\text{EDP}|\text{IM}}} \right) \quad (7)$$

Eventually, different EDP-IM pairs can be considered and for each of them fire fragility functions can be derived considering different LS. Therefore Sections 4.2 and 4.3 aim at identifying relevant IMs and EDPs to build PFDMs through CA.

4.2 Intensity measures

An intensity measure (IM) aims at characterising the severity of a fire scenario. Thus, 7 IMs are here proposed in Table 2 to characterise in an efficient way the impact of the localised fire. 3 IMs are the parameters defining the fire scenarios, i.e. D , d and q , while 4 IMs are functions of them. The parameter q is referred to as the RHR density. That is appropriate to characterise the power associated to a fuel. The fire position L in the ratio L/D corresponds to the distance separating the structure from the centre of the fire and it is simply derived from distance d and fire diameter D . The maximum average radiative heat flux impinging the structure HF_{avg} considered here as IM was evaluated for each of the 539 fire scenarios with the analytical LOCAFI model¹⁰. It was computed as the weighted average heat flux impinging the four sides of the cross section impinged by maximum radiative heat flux computed with the LOCAFI model.

Table 2. Intensity measures

IM	Name	Unit	Function
D	Fire diameter	m	f(D)
d	Structure fire distance	m	f(d)
q	Equivalent RHR density of the fuel	MW/m ²	f(q)
L/D	Fire position-fire diameter ratio	-	f(D,d)
L _{FI}	Flame length	m	f(D,q)
HF _{avg}	Maximum average heat flux impinging the structure	kW/m ²	f(D,d,q)
d/L _{FI}	Structure fire distance - flame length ratio	-	f(D,d,q)

4.3 Engineering demand parameters

The selection of appropriate engineering demand parameters (EDP) that are able to describe the structural response is paramount to build a probabilistic demand model. Thus, in order to identify suitable EDPs considering localised fire located beside the structure, 130 analyses out of the 539 scenarios, were deeply investigated. These 130 cases are among the ones causing major internal actions and displacements. For 59 cases, the structure failed within 60 minutes of analysis, whereas for the 71 other cases, the structure survived the whole analysis. Based on these analyses, 5 possible EDPs for the case under study were identified and reported in Table 3.

Table 3. Engineering demand parameters

EDP	Name	Unit
ISDR	Interstorey drift ratio	%
N _Z	Axial load	kN
M _X	Bending moment	kNm
T _{MAX}	Maximum average temperature	°C
T _{AVG}	Average temperature	°C

For each of the 130 analyses, ISDR, N_Z and M_X were respectively the maximum interstorey drift ratio, axial load and bending moment observed within the structure. T_{MAX} was the maximum average temperature computed within the whole structure, while T_{AVG} was the average temperature within the highly stressed structural element. These EDPs were evaluated and compared based on their ability to characterise the structural response and it appeared that the ISDR was the most suitable EDP. In fact, it offers several advantages: i) it only considers the structural response, independently from the fire scenario and it is representative of the fire scenarios that cause significant lateral displacement; ii) it is straightforward to evaluate and to compare with other structural and load configurations and iii) it can be associated with specific structural damage states as referred in literature. In this respect, the American seismic rehabilitation prestandard²⁸ associates, for steel moment resisting frames, an ISDR equal to 5% and an ISDR equal to 2.5% that are representative of a near collapse limit state and life safety limit state, respectively. Differently from the seismic case where the ISDR is widely used as EDP, some care might have to be taken for structural fire applications. Nevertheless, in this study, the ISDR can be assumed as global EDP because it can be related to damage and collapse of a significant part of the pipe-rack. Therefore, ISDR values of 5% and 2.5% were adopted in the probabilistic fire demand model framework as limit states.

4.4 Results of the numerical analyses

As explained in Sections 2.2 and 3.1, numerical analyses were performed with SAFIR. The analyses were run for 60 minutes, a time during which the different structural members received a constant heat flux so that they could reach their thermal equilibrium as for steel temperature. The impact of the localised fire on structural members was investigated for the entire pipe-rack. Figure 5a depicts the pipe-rack after a 60 min exposure to a heptane pool fire characterised by a diameter of 20 m and located 2 m away from the structure. The thermal effect of the localised fire and the horizontal loads applied in the positive y-direction induced significant horizontal displacements. These horizontal displacements increased during the fire owing to thermal bowing and loss of stiffness of steel and consequently second order effects became not negligible.

As expected, the fire scenarios under consideration induced significant non-uniform heating in the cross sections, as shown in Figure 5b and 5c, that depict the temperature fields within the cross sections located at an height of 5 m of columns A4 and A3, that are respectively 2 m and 3.41 m distant from the fire. Among the 539 fire scenarios investigated, 59 cases led the pipe-rack to collapse. In this respect, Figure 5d depicts the failure mechanism of the structure, which involves the loss of stability of the central frame. The displacements were maximal at the top of the structure (9 m high) but the highest interstorey drift ratios (ISDR) were observed transversally at the first level of the columns. Table 4 reports on the maximum ISDRs observed for each of the 539 analyses and provides an overview of the influence of the basic fire parameters D , d and q on the structural response. As expected, the increase in ISDR is generally related to an increase in fire diameter D and/or to a reduction in the fire-structure distance d and/or to a more hazardous fuel in terms of higher mass burning rate or heat of combustion. In Table 4, green cells indicate ISDR values between 2.5% and 5% and red cells indicate values greater than 5%. Based on the 539 results of the numerical analysis, using the ISDR as EDP, and by considering the IM candidates listed in Table 2, PFDMs were developed through CA. For brevity here only the 2 best IM candidates, i.e. HF_{avg} and L/D , will be considered and for a more comprehensive analysis refer to Randaxhe et al.²⁶.

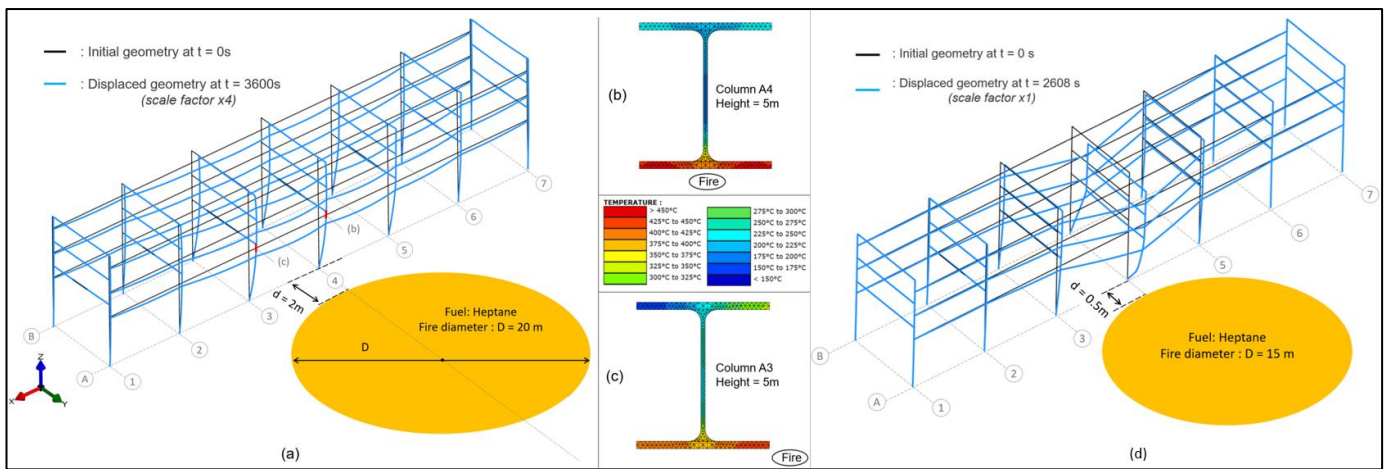


Figure 5. - Steel pipe-rack exposed to fire scenario “ $D=20\text{m} - d=2\text{m} - \text{Fuel}=\text{Heptane}$ ” for 60 min: (a) Initial and displaced shape of the structure; (b) Temperature field in cross section of column A4 ($h=5\text{m}$); (c) Temperature field within in cross section column A3 ($h=5\text{m}$); (d) Steel pipe-rack exposed to fire scenario “ $D=15\text{m} - d=0.5\text{m} - \text{Fuel}=\text{Heptane}$ ”: Failure of the structure after 2608 s

4.5 Fire fragility functions

An IM is qualified efficient if it generates low variations between actual and predicted EDP values for a given IM value. That variation is characterised by the dispersion $\beta_{EDP|IM}$ of the EDP conditioned on the IMs, as expressed in Equation (6), which is satisfying when its value is low. Usually a value lower than 0.3 is considered efficient²⁹. For both IM candidates, the values of dispersion $\beta_{EDP|IM}$ were computed and reported in Figure 6. Eventually, it appeared that both IM candidates are efficient since they exhibit dispersion values lower than 0.3. In particular, the most efficient candidate IM is the maximum average heat flux imping the structure HF_{avg} . Based on the definition of the probabilistic fire demand models, fragility functions were derived considering the maximum average heat flux impinging the structure HF_{avg} as IM, since it was found to be the most efficient. The ISDR was used as EDP and the two limit states (LS) defined in Section 4.3 were considered. Applying the CA, fragility functions could be derived for both LS using Equation (7). As illustrated in Figure 6a, when HF_{avg} was taken as IM, coefficients a and b were found to be equal to 0.007 and 0.620, respectively, and they yielded the dispersion value $\beta_{EDP|IM}$ of 0.09. Fragility curves are plotted in Figure 7a that show the probability of the interstorey drift ratio ISDR exceeding 5% and 2.5% conditioned on the maximum average heat flux impinging the structure HF_{avg} . These functions can be used to quantify the probability that a steel pipe-rack exposed to localised fire exceeds a predefined LS. It is possible to note that when $HF_{avg} > 30 \text{ kW/m}^2$ the probability of exceeding an ISDR value of 5% becomes larger than 80%, whereas it occurs for $HF_{avg} > 10 \text{ kW/m}^2$ when considering the life safety limit state, i.e. $ISDR = 2.5\%$.

Table 4. Maximum interstorey drift ratios observed for the 539 fire scenarios

Distance d [m]	Fuels	Interstorey drift ratios										
		Fire diameters D [m]										
		5	7.5	10	12.5	15	17.5	20	22.5	25	27.5	30
6	Pentane	1.79%	2.43%	2.89%	3.21%	3.43%	3.58%	3.70%	3.77%	3.83%	3.87%	3.90%
6	Heptane	1.68%	2.31%	2.77%	3.10%	3.33%	3.49%	3.62%	3.70%	3.77%	3.81%	3.85%
6	Benzene	1.66%	2.27%	2.74%	3.07%	3.30%	3.47%	3.60%	3.68%	3.75%	3.80%	3.84%
6	Kerosene	1.56%	2.14%	2.61%	2.95%	3.19%	3.36%	3.49%	3.59%	3.67%	3.72%	3.77%
6	Gasoline	1.51%	2.07%	2.53%	2.87%	3.11%	3.29%	3.42%	3.53%	3.61%	3.67%	3.72%
6	Fuel Oil	1.27%	1.69%	2.09%	2.40%	2.65%	2.84%	2.98%	3.10%	3.19%	3.26%	3.32%
6	Acetone	1.16%	1.48%	1.81%	2.09%	2.31%	2.48%	2.62%	2.73%	2.81%	2.88%	2.94%
5	Pentane	2.03%	2.71%	3.16%	3.46%	3.66%	3.79%	3.88%	3.93%	3.96%	4.00%	4.04%
5	Heptane	1.91%	2.58%	3.04%	3.35%	3.57%	3.71%	3.81%	3.87%	3.92%	3.96%	4.00%
5	Benzene	1.88%	2.55%	3.01%	3.32%	3.54%	3.69%	3.79%	3.86%	3.90%	3.94%	3.99%
5	Kerosene	1.76%	2.41%	2.88%	3.20%	3.43%	3.59%	3.70%	3.78%	3.83%	3.88%	3.92%
5	Gasoline	1.70%	2.33%	2.80%	3.13%	3.36%	3.53%	3.64%	3.73%	3.79%	3.83%	3.88%
5	Fuel Oil	1.40%	1.91%	2.33%	2.66%	2.90%	3.08%	3.21%	3.32%	3.40%	3.46%	3.52%
5	Acetone	1.25%	1.65%	2.02%	2.32%	2.55%	2.72%	2.85%	2.95%	3.03%	3.09%	3.14%
4	Pentane	2.33%	3.00%	3.44%	3.73%	3.90%	4.00%	4.05%	4.08%	4.11%	4.25%	4.32%
4	Heptane	2.20%	2.88%	3.33%	3.63%	3.82%	3.94%	4.00%	4.04%	4.08%	4.11%	4.20%
4	Benzene	2.16%	2.85%	3.30%	3.61%	3.80%	3.92%	3.99%	4.03%	4.06%	4.09%	4.16%
4	Kerosene	2.03%	2.71%	3.17%	3.49%	3.70%	3.83%	3.91%	3.96%	4.01%	4.04%	4.07%
4	Gasoline	1.95%	2.63%	3.09%	3.41%	3.63%	3.77%	3.86%	3.92%	3.97%	4.00%	4.04%
4	Fuel Oil	1.57%	2.17%	2.61%	2.94%	3.18%	3.34%	3.46%	3.55%	3.62%	3.67%	3.72%
4	Acetone	1.38%	1.87%	2.28%	2.58%	2.81%	2.98%	3.10%	3.19%	3.26%	3.32%	3.36%
3	Pentane	2.66%	3.33%	3.76%	4.03%	4.17%	4.21%	4.22%	4.28%	4.54%	4.68%	4.86%
3	Heptane	2.53%	3.21%	3.66%	3.94%	4.10%	4.16%	4.19%	4.20%	4.35%	4.49%	4.62%
3	Benzene	2.50%	3.18%	3.63%	3.91%	4.07%	4.15%	4.18%	4.19%	4.31%	4.44%	4.58%
3	Kerosene	2.35%	3.04%	3.50%	3.80%	3.98%	4.07%	4.12%	4.15%	4.16%	4.27%	4.40%
3	Gasoline	2.27%	2.96%	3.42%	3.73%	3.92%	4.02%	4.08%	4.12%	4.14%	4.17%	4.30%
3	Fuel Oil	1.81%	2.47%	2.93%	3.25%	3.48%	3.63%	3.72%	3.80%	3.85%	3.89%	3.92%
3	Acetone	1.56%	2.14%	2.57%	2.89%	3.11%	3.26%	3.37%	3.46%	3.51%	3.56%	3.60%
2	Pentane	3.02%	3.69%	4.15%	4.40%	4.46%	4.41%	4.47%	5.02%	5.39%	5.31%	5.54%
2	Heptane	2.89%	3.57%	4.04%	4.31%	4.40%	4.39%	4.35%	4.70%	5.10%	5.56%	5.45%
2	Benzene	2.85%	3.53%	4.00%	4.28%	4.38%	4.38%	4.34%	4.63%	5.00%	5.31%	5.34%
2	Kerosene	2.71%	3.39%	3.87%	4.16%	4.30%	4.33%	4.32%	4.29%	4.68%	4.86%	4.89%
2	Gasoline	2.62%	3.31%	3.79%	4.09%	4.24%	4.29%	4.30%	4.28%	4.53%	4.70%	4.74%
2	Fuel Oil	2.12%	2.81%	3.28%	3.61%	3.82%	3.94%	4.02%	4.07%	4.10%	4.13%	4.16%
2	Acetone	1.81%	2.45%	2.90%	3.22%	3.44%	3.59%	3.68%	3.76%	3.81%	3.85%	3.89%
1	Pentane	3.37%	4.10%	4.65%	5.33%	4.96%	4.55%	5.47%	5.29%	5.28%	5.27%	5.27%
1	Heptane	3.24%	3.97%	4.51%	4.86%	4.84%	4.58%	5.27%	5.41%	5.20%	5.38%	5.41%
1	Benzene	3.20%	3.93%	4.47%	4.81%	4.81%	4.59%	5.09%	5.31%	5.26%	5.19%	5.20%
1	Kerosene	3.06%	3.79%	4.32%	4.64%	4.72%	4.59%	4.67%	5.37%	5.37%	5.24%	5.33%
1	Gasoline	2.97%	3.70%	4.23%	4.56%	4.66%	4.58%	4.48%	5.16%	5.38%	5.40%	5.30%
1	Fuel Oil	2.46%	3.16%	3.67%	4.03%	4.24%	4.32%	4.34%	4.33%	4.32%	4.57%	4.67%
1	Acetone	2.09%	2.77%	3.26%	3.60%	3.83%	3.97%	4.04%	4.09%	4.12%	4.12%	4.14%
0.5	Pentane	3.50%	4.28%	5.35%	5.14%	5.10%	5.50%	5.39%	5.39%	5.23%	5.06%	5.45%
0.5	Heptane	3.38%	4.15%	4.88%	5.16%	5.13%	4.77%	5.39%	5.34%	5.09%	5.33%	5.40%
0.5	Benzene	3.34%	4.11%	4.81%	5.27%	5.14%	4.67%	5.23%	5.12%	5.32%	5.25%	5.19%
0.5	Kerosene	3.20%	3.97%	4.58%	5.34%	5.25%	4.62%	5.43%	5.32%	5.25%	5.36%	5.53%
0.5	Gasoline	3.12%	3.88%	4.48%	4.95%	5.01%	4.64%	4.39%	5.31%	5.40%	5.22%	5.43%
0.5	Fuel Oil	2.60%	3.34%	3.89%	4.26%	4.45%	4.48%	4.44%	4.39%	4.77%	5.07%	5.58%
0.5	Acetone	2.23%	2.93%	3.44%	3.81%	4.03%	4.15%	4.20%	4.22%	4.21%	4.21%	4.19%

Finally, fragility curves considering L/D as IM were also derived and plotted in Figure 7b, because it is an IM commonly used in practice. Furthermore, the L/D IM was found to be the most efficient and sufficient after the maximum average heat flux impinging the structure HF_{avg} ²⁶. The PFDM provided, through linear regression a and b coefficients to be equal to 0.026 and -0.976 and dispersion $\beta_{EDP|IM}$ equal to 0.13, as illustrated in Figure 6b. It can be observed that these fragility curves are meaningful if $L/D \geq 0.5$, because when the L/D decreases below 0.5 it means that part of the structure is engulfed into the localised fire and consequently a different structural response is expected with the ISDR no longer being the most appropriate EDP. Therefore, a grey shade for L/D values < 0.5 was included in Figure 7b to highlight the validity range of the fire fragility curves. It may be observed that when L/D is larger than 0.75 the probability of exceeding an ISDR value of 5% becomes very low and only from $L/D < 0.75$ the probability increases. For $L/D = 0.5$ it attains almost 60%. When $L/D > 1.5$ the probability of exceeding an $ISDR = 2.5\%$ becomes almost zero, whereas it overcomes 80% when $L/D < 0.9$.

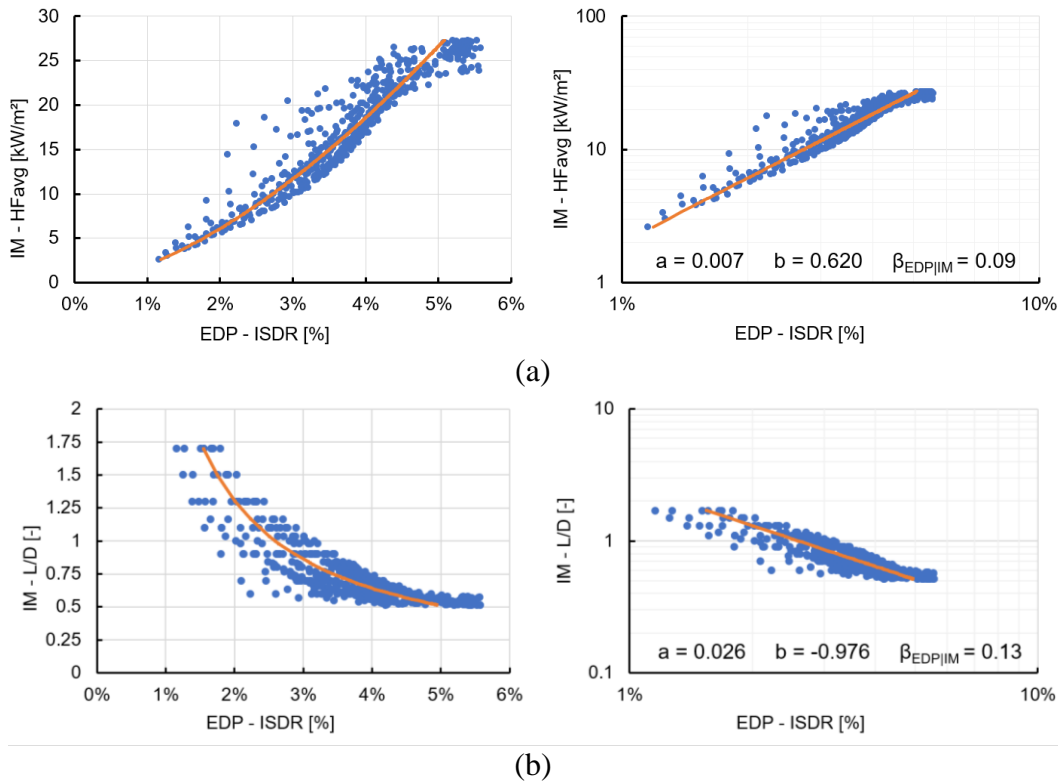


Figure 6. Cloud analysis and linear regression for IMs: (a) HF_{avg} ; (b) L/D

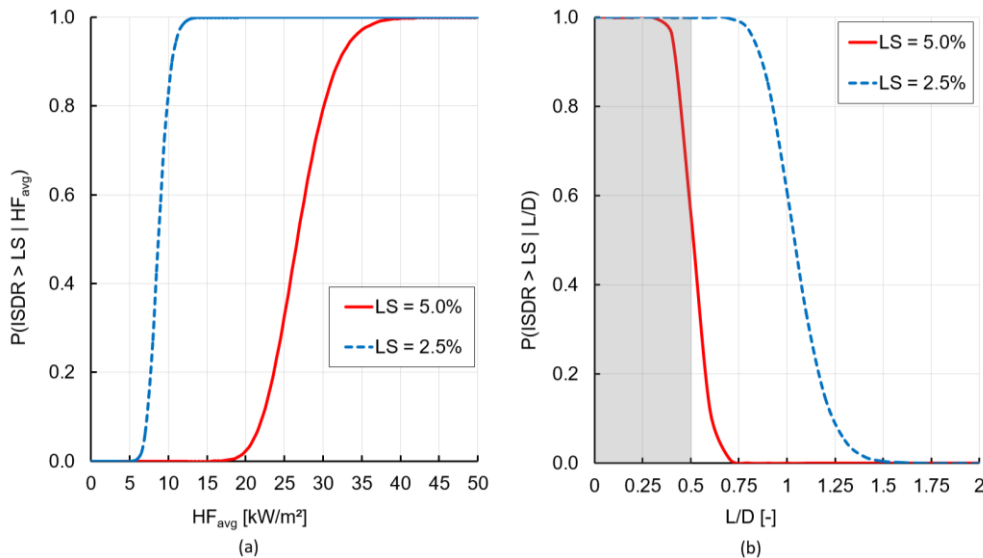


Figure 7. (a) Fragility curves based on CA for near collapse- and life safety preventions with HF_{avg} as IM; (b) Fragility curves based on CA for near collapse- and life safety preventions with L/D as IM

5 CONCLUSION

This paper presented the development of a probabilistic fire demand model for a steel pipe-rack exposed to localised fires. Considering 539 localised plausible fire scenarios in industrial/petrochemical plants, thermo-mechanical analyses were performed with the FE software SAFIR that includes the LOCAFI localised fire model. Based on numerical analyses, probabilistic analyses were conducted to derive fire fragility functions by adopting the cloud analysis (CA) method. The maximum transversal interstorey drift ratio (ISDR) was found to be the most suitable EDP for this case study, because it provides a global measure of the structural response as it can be related to damage and collapse of a significant part of the pipe rack. In this respect, two structural ultimate limit states, near collapse and life safety, were defined for ISDR exceeding 5% and 2.5%, respectively. Two intensity measures (IM) were here considered and compared based on their efficiency. The maximum average heat flux impinging the structure HF_{avg} and the ratio between fire position and fire diameter L/D appeared to be efficient IMs to characterise the localised fire severity. Thus, fire fragility functions were derived considering these two EDP-IM pairs, i.e. ISDR- HF_{avg} and ISDR- L/D . Focusing on the near collapse limit state, fragility functions showed that localised fires generating HF_{avg} lower than 20 kW/m^2 have low probability of exceedance. Conversely, when HF_{avg} is higher than 35 kW/m^2 , it is close to 1. For L/D values higher than 0.75 the probability of exceedance an ISDR of 5% is very low. Regarding the life safety limit state, fragility functions showed for HF_{avg} higher than 15 kW/m^2 the probability of exceedance is very high, as well as when the L/D value varies between 0.5 and 0.75. In sum, the CA can be considered an appropriate and versatile method to develop PFDMs from which building fire fragility functions to be used in fire risk assessment or in a fully probabilistic structural fire engineering (PSFE) framework of steel pipe-rack design. Future works will be addressed to consider the uncertainty in the structural capacity, multiple burning pool fires and the presence of the wind.

ACKNOWLEDGMENTS

This research has been funded by the European H2020 Marie Skłodowska- Curie XP-RESILIENCE project through the grant agreement number 721816. This work was also supported by the Italian Ministry of Education, University and Research (MIUR) in the frame of the ‘Departments of Excellence’ (grant L 232/2016).

REFERENCES

1. Zheng B, Chen G. Storage Tank Fire Accidents. *Process Saf Prog.* 2011;30(3). doi:10.1002/prs
2. Chang JI, Lin C. A study of storage tank accidents. *J Loss Prev Process Ind.* 2005;19:51-59. doi:10.1016/j.jlp.2005.05.015
3. Pantousa D. Thin-Walled Structures Numerical study on thermal buckling of empty thin-walled steel tanks under multiple pool- fire scenarios. *Thin Walled Struct.* 2018;131(January):577-594. doi:10.1016/j.tws.2018.07.025
4. F.Paolacci, O.Bursi, Md.S.Reza, A.Kumar, A.M.Gresnigt. Main Issues On The Seismic Design Of Industrial Piping Systems And Components. In: *ASME 2013 Pressure Vessels & Piping Division Conference.* ; 2013:1-10.
5. Paolacci F. Structural safety of industrial steel tanks; pressure vessels and piping - Basic seismic structural design of a typical piping system. 2010;(February 2010).
6. Bursi O, Paolacci F, Reza MS, Alessandri S, Tondini N. Seismic Assessment of Petrochemical Piping Systems Using a Performance-Based Approach. *J Press Vessel Technol.* 2010.
7. Paolacci F, Bursi OS, Md.Shahin R. SEISMIC ANALYSIS AND COMPONENT DESIGN OF REFINERY. In: *Conference on Computational Methods in Structural Dynamics and Earthquake Engineering.* ; 2011:26-28.
8. Bursi OS, Paolacci F, Reza MS. Performance-Based Analysis of Coupled Support Structures and Piping Systems. In: *ASME 2015 Pressure Vessels & Piping Division Conference.* ; 2015. doi:10.1115/PVP2015-45123
9. Francis P, Baddo N, Hanus F, Thauvoye C. Design of columns subject to localised fires. 2018.
10. Tondini N, Thauvoye C, Hanus F, Vassart O. Development of an analytical model to predict the radiative heat flux to a vertical element due to a localised fire. *Fire Saf J.* 2019;105(March):227-243. doi:10.1016/j.firesaf.2019.03.001

11. Kamikawa D, Hasemi Y, Wakamatsu T, Kagiya K. Experimental flame heat transfer correlations for a steel column adjacent to and surrounded by a pool fire. In: *Fire Safety Science - Seventh International Symposium*. ; 2000:989-1000.
12. Santiago A, Ferraz G, Rodrigues JP, Barata P. Thermal analysis of hollow steel columns exposed to localised fires. *Fire Technol*. 2016;52:663-681. doi:10.1007/s10694-015-0481-2
13. Hanus F, Vassart O, Tondini N, Nadjai A, Franssen J. Temperature assessment of a vertical steel member subjected to localised fire: Experimental tests. In: *Proceedings of the 9th Conference on Structures in Fire*. Princeton (NJ) USA; 2016.
14. Tondini N, Franssen J-M. Analysis of experimental hydrocarbon localised fires with and without engulfed steel members. *Fire Saf J*. 2017;92(May):9-22. doi:10.1016/j.firesaf.2017.05.011
15. Gernay T, Khorasani NE, Garlock M. Fire fragility curves for steel buildings in a community context : A methodology. *Eng Struct*. 2016;113:259-276. doi:10.1016/j.engstruct.2016.01.043
16. Gernay T, Khorasani NE, Garlock M. Fire Fragility Functions for Steel Frame Buildings: Sensitivity Analysis and Reliability Framework. *Fire Technol*. 2019;55(4):1175-1210. doi:10.1007/s10694-018-0764-5
17. Lange D, Devaney S, Usmani A. An application of the PEER performance based earthquake engineering framework to structures in fire. *Eng Struct*. 2014;66:100-115.
18. Shrivastava M, Abu AK, Dhakal RP, Moss PJ. Severity measures and stripe analysis for probabilistic structural fire engineering. *Fire Technol*. 2019;55(4):1147-1173. doi:10.1007/s10694-018-0799-7
19. Cornell CA, Krawinkler H. Progress and challenges in seismic performance assessment. *Peer Cent News*. 2000;3(2):1-3.
20. Franssen JM, Gernay T. Modeling structures in fire with SAFIR®: Theoretical background and capabilities. *J Struct Fire Eng*. 2017;8(3):300-323. doi:10.1108/JSFE-07-2016-0010
21. European Committee for Standardization CEN. Eurocode 3: Design of steel structures – Part 1–2: General rules – structural fire design. EN 1993-1-2. 2005.
22. Khorasani NE, Gardoni P, Garlock M. Probabilistic Fire Analysis: Material Models and Evaluation of Steel Structural Members. *J Struct Eng*. 2015;141(12). doi:10.1061/(ASCE)ST.1943-541X.0001285
23. Qureshi R, Ni S, Elhami Khorasani N, Van Coile R, Hopkin D, Gernay T. Probabilistic Models for Temperature-Dependent Strength of Steel and Concrete. *J Struct Eng*. 2020;146(6). doi:10.1061/(ASCE)ST.1943-541X.0002621
24. Shokri M, Beyler CL. Radiation from large pool fires. *SFPE Handb Fire Prot Eng*. 1989;4(1):141-150.
25. European Committee for Standardization C. Eurocode 1: Actions on structures – Part 1–2: General actions – actions on structures exposed to fire. EN 1991-1-2. 2002.
26. Randaxhe J, Popa N, Tondini N. Probabilistic fire demand model for steel pipe-racks exposed to localised fires. *Eng Struct*. 2021;226(March 2020). doi:10.1016/j.engstruct.2020.111310
27. Cornell CA, Jalayer F, Hamburger RO, Foutch DA. Probabilistic Basis for 2000 SAC Federal Emergency Management Agency Steel Moment Frame Guidelines. *J Struct Eng*. 2002;(April):526-533. doi:10.1061/(ASCE)0733-9445(2002)128
28. FEMA, ASCE. FEMA 356 - Prestandard and commentary for the seismic rehabilitation of buildings. 2000;(November).
29. Tondini N, Stojadinovic B. Probabilistic seismic demand model for curved reinforced concrete bridges. *Bull Earthq Eng*. 2012. doi:10.1007/s10518-012-9362-y

A NOVEL APPROACH TO MODEL THE THERMAL AND PHYSICAL BEHAVIOUR OF SWELLING INTUMESCENT COATINGS EXPOSED TO FIRE

Andrea Lucherini¹, Juan P. Hidalgo², Jose L. Torero³, Cristian Maluk⁴

ABSTRACT

The research study presented herein proposes a finite-difference heat transfer model aimed at simulating the thermal and physical response of swelling intumescent coatings during heating. The numerical model is based on the outcomes of a previous experimental study which analysed the effectiveness of thin intumescent coatings for a range of heating conditions and initial coating thickness. The model solves the one-dimensional heat conduction problem using the finite-difference Crank-Nicolson method, and it assumes that the effectiveness of intumescent coatings is mainly dependent on their ability to develop swelled porous char. Accordingly, the coating swelling is implemented by adding finite elements in the proximity of the substrate-coating interface following empirical correlations, and the intumescent coating is modelled as swelled porous char with constant material properties. The described model offers a performance-based design engineering tool able to characterise the heat transfer through swelling intumescent coatings (i.e. thermal gradient) by predicting the evolution of the coating surface and substrate steel temperatures, and the evolution of the swelled coating thickness. Based on its assumptions, the numerical model defines a quasi-steady-state thermal problem: more accurate for conditions close to steady-state (e.g. high heat fluxes), but it loses accuracy for cases characterised by transient phenomena.

Keywords: intumescent coatings; fire safety; finite-difference modelling; heat transfer; fire-safe structures; steel; H-TRIS; swelling

1 INTRODUCTION

In recent times, in order to ensure the stability and integrity of structural systems in the event of a fire, the utilisation of various fire safety solutions have become a common practice. For example, the application of different thermal barriers characterised by low thermal conductivity, such as gypsum plaster-boards or cementitious spray-on systems, is a widely used method to limit the rate of temperature increase within load-bearing structural elements [1]. Fundamentally different from conventional applications, intumescent coatings (also known as reactive coatings) represent a worldwide dominant fire safety solution for protecting load-bearing structural steel systems during fire. At ambient temperature, these systems appear as a pigmented thin coating, applied to a dry film thickness (DFT) in the order of few millimetres (thin intumescent coatings) or few centimetres (thick intumescent coatings). When exposed to sufficient heat,

¹ Research Fellow, School of Civil Engineering, The University of Queensland, Australia.
e-mail: a.lucherini@uq.edu.au, ORCID: <https://orcid.org/0000-0001-8738-1018>

² Senior Lecturer, School of Civil Engineering, The University of Queensland, Australia.
e-mail: j.hidalgo@uq.edu.au, ORCID: <https://orcid.org/0000-0002-2972-5238>

³ Professor and Head of Department, Department of Civil, Environmental & Geomatic Engineering, University College London, UK.
e-mail: j.torero@ucl.ac.uk, ORCID: <https://orcid.org/0000-0001-6265-9327>

⁴ Senior Lecturer, School of Civil Engineering, The University of Queensland, Australia.
e-mail: c.maluk@uq.edu.au, ORCID: <https://orcid.org/0000-0002-1662-6943>

they swell to form a thick low-density and highly-insulating porous char that prevents the substrate material from reaching high temperatures that can cause structural instability and possibly progressive failure. The success of intumescent coatings is associated with their unique advantages over conventional solutions: attractive appearance of visible structures, lightweight, ease and flexibility for both on- and off-site applications [2-5].

Within the structural fire safety engineering practice, the insulating capacity of intumescent coatings is typically assessed based on the exposure to the standard temperature-time fire curve in furnaces [6-7]. From the temperature evolutions experienced by coated samples, simplified engineering methods (e.g. tabulated fire ratings and effective thermal conductivity method) are commonly adopted for the structural and fire safety design [8]. However, the research community has widely demonstrated that the swelling and the effectiveness of intumescent coatings are influenced by several factors, such as the heating exposure, the substrate thermal conditions and the applied initial thickness [9-16]. Consequently, the performance assessment based on the unique standard fire exposure does not represent a comprehensive design practice. The professional and scientific communities are requesting performance-based engineering solutions that enable explicit understanding and quantification of the effectiveness of intumescent coatings for the fire-safe design of structures [5,17].

In the last decades, several researchers have been attempting to overcome the shortcomings of the current design framework by performing various experimental studies and proposing numerical models [5]. However, due to the significant complexity and the wide range of products available in the market, researchers followed different approaches and adopted various experimental methodologies to investigate this topic. Consequently, several models and engineering tools have been proposed. However, the research outcomes have not been universally generalised or internationally regulated because of their limited application, the high complexity or the contrasting results [5]. In general, the available literature offers numerous numerical models and design methods aimed at simulating the temperature evolution of structural elements protected with intumescent coatings. However, there is a lack of a standard methodology and generalised understanding for rigorous and systematic testing and a design framework that explicitly quantifies the effectiveness of intumescent coatings for a wide range of conditions.

Recent research studies proposed an experimental methodology aimed at analysing the effectiveness of thin intumescent coatings through a detailed characterisation of their thermal and physical response using the Heat-Transfer Rate Inducing System (H-TRIS) test method [18]. The experimental results showed how the heating conditions, the substrate thermal conditions and the applied initial coating thickness affect the behaviour of a commercial solvent-based thin intumescent coating [13,15,19]. Based on these experimental outcomes, the research study presented herein proposes a comprehensive heat transfer model able to simulate the thermal and physical response of swelling intumescent coatings during heating. The numerical model offers a performance-based design engineering tool able to predict the thermal gradient within swelling intumescent coatings and the temperature evolution of the coating surface and the protected substrate (e.g. steel) for a range of conditions and scenarios (e.g. heating conditions and applied initial coating thickness).

2 RELEVANT EXPERIMENTAL OUTCOMES

A recently published research study [19] presented an experimental methodology aimed at analysing the effectiveness of intumescent coatings through detailed characterisation of their thermal and physical response. This was possible by measuring the evolution of the swelled coating thickness, the steel substrate and the coating surface temperatures, and the transient in-depth temperature profile within the intumescent coating [19]. Numerous carbon steel plates (200x200 mm², 10 mm thick: section factor $A_p/V = 100 \text{ m}^{-1}$) were coated with a solvent-based thin intumescent coating, selected as an exemplar commercially available product. According to material characterisation and the available literature, it was found that the tested product has similar characteristics to typical intumescent formulations based on the APP-PER-MEL system [19-21]. The Heat-Transfer Rate Inducing System (H-TRIS) test method, consisting of movable high-performance radiant panels, was used to test the coated plates under a range of constant incident radiant

heat fluxes (10-90 kW/m²) [18]. The influence of the applied initial coating Dry Film Thickness (DFT) (1-3 mm) was also investigated.

Experimental results emphasised how the swelling process and the resulting swelled thickness govern the thermal and physical response of intumescent coatings, thus their effectiveness. During swelling, the coated steel plates tended to the temperature range 300-350°C, which corresponds to the temperatures at which the intumescent coating typically undergoes the swelling reaction (300-400°C) [19-21]. Once the swelling process is completed, the substrate temperature increases above this threshold. This close relationship between the substrate temperature and the swelling of intumescent coatings is explained by the location of the swelling reaction: it occurs at the virgin coating located behind the swelled porous char, close to the interface between the applied coating and the substrate material. Accordingly, the coating protects the substrate by displacing the already-swelled coating towards the direction of the heat source [15,19].

The experimental study also highlighted that the intumescent porous chars obtained from different heating conditions have similar thermo-physical properties and the thermal gradient within the swelling intumescent coating is mainly governed by the swelling process and the resulting swelled thickness [19]. In particular, the evolution of the swelled coating thickness is influenced by various factors in different manners: the heating conditions govern the swelling rate of the intumescent coating, while the applied initial coating thickness governs the maximum thickness that the coating can achieve during thermal exposure [19].

3 HEAT TRANSFER MODEL: GENERAL APPROACH AND ASSUMPTIONS

The development of a numerical model able to simulate the heat transfer through swelling intumescent coatings represents a crucial aspect for performance-based design engineering methods. Indeed, it aims at quantifying the thermal and physical properties of thermal barriers developed by thin intumescent coatings to protect substrate materials. The phenomenon of intumescence is very challenging to model due to the complex thermo-physical response of reactive coatings. As a consequence, the heat transfer model involves several assumptions and simplifications, which are derived in accordance with the above-mentioned experimental campaign and outcomes [19]:

- The model focuses on solving the *one-dimensional heat conduction problem* by resolving energy-balance equation based on fundamental physical principles, following the main direction of the heat flow: from the coating surface, through the swelling coating and towards the protected substrate. Conventional formulas and correlations from the literature are adopted [22].
- The model is defined as a *finite-difference numerical model* based on the *Crank-Nicolson method*, a finite-difference method able to solve the one-dimensional heat conduction equation: implicit in time, numerically stable and computationally efficient [23-24]. The intumescent coating is discretised as a single-layer material into N finite elements, corresponding to N nodes (refer to Figure 1).
- The model relies on the accurate definition of the *thermal conditions at the coating boundaries*. The thermal boundary condition at the exposed surface is defined by the time-history of incident heat flux imposed by the H-TRIS test method (\dot{q}_{inc}'') with convective and radiative heat flux losses (\dot{q}_{conv}'' and \dot{q}_{rad}'') to the surrounding environment [18]. Adiabatic conditions are assumed at the unexposed surface, and the substrate steel plate is lumped into a thermal mass connected to the coating end element (refer to Figure 1).
- The model assumes that the effectiveness of the thermal barrier provided by the intumescent coating is mainly dependent on the *ability to develop swelled porous char*. Following the experimental outcomes from the material characterisation of coating porous chars [21], the intumescent coating is approximated with the following constant material properties: thermal conductivity $\lambda_c = 0.16$ W/mK, density $\rho_c = 50$ kg/m³, specific heat capacity $c_{p,c} = 1550$ J/kgK and emissivity $\varepsilon_c = 0.90$.
- The *swelling of thin intumescent coatings* is modelled by increasing the thickness of the protective thermal barrier by adding finite elements to the coating discretisation, in particular at the substrate-coating interface. In this way, the protective thermal barrier developed by the intumescent coating

increases its thickness during thermal exposure (refer to Figure 2). Empirical correlations are introduced to predict the evolution of the swelled coating thickness during thermal exposure [19,21].

From the energy-balance equation, the heat transfer model aims at quantifying the effectiveness of the tested intumescent coating for a wide range of potential conditions, in terms of heating exposure and applied initial coating thickness. The detailed derivation of the model solving equations can be found in [21].

The numerical model provides an estimation of the evolution of the substrate temperature during thermal exposure, which is the key aspect to study the structural behaviour of load-bearing elements protected with thin intumescent coatings.

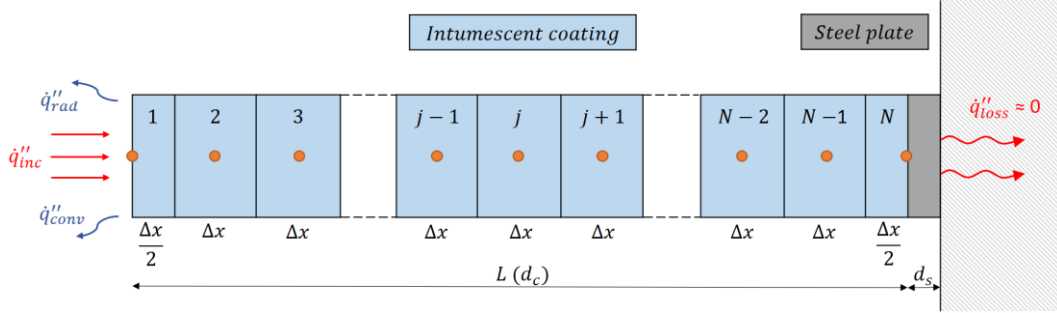


Figure 1. Schematic illustration of the single-layer material heat transfer model, including the thermal boundary conditions.

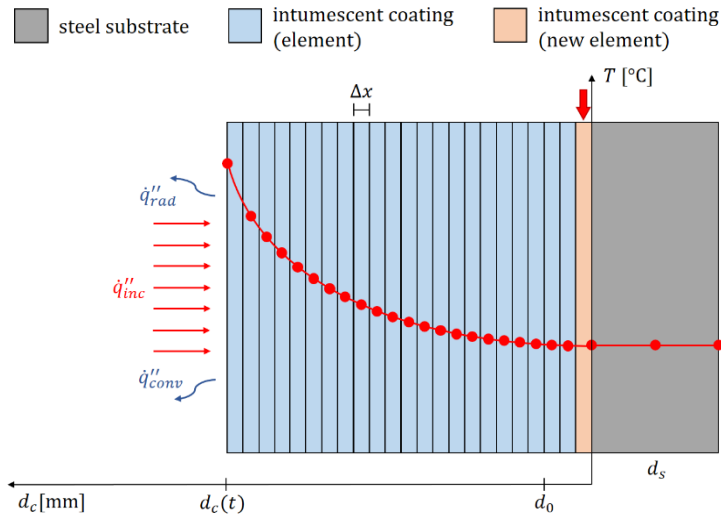


Figure 2. Schematic illustration of the heat transfer model formulated for swelling intumescent coatings.

4 MODELLING RESULTS

Starting from the assumptions, simplification and material properties described above, the numerical model was implemented in order to solve the heat transfer problem for all the experimental scenarios, involving a range of heating conditions and applied initial coating thicknesses [19]. Within the current manuscript, the exemplar modelling case of constant incident radiant heat fluxes of 50 kW/m² and an applied initial coating thickness of “*Medium DFT*” (1.80 mm) is presented. The full version of all the modelling results can be found in [21].

4.1 Model characteristics

Following the described approach, the modelling of swelling intumescent coatings mainly becomes a *physical problem*, largely driven by an accurate prediction of the evolution of the swelled coating thickness. The model focuses on solving *quasi-steady-state heat transfer problem* due to the highly-insulating properties of the intumescent coating (high Biot number), the applied constant incident heat flux and the

relatively-high swelling speed, compared to the penetration speed of the heat wave within the swelling intumescent coating. In this way, the transient thermal states become secondary (e.g. short transient phase), the thermo-physical properties of the intumescent porous char have minor influence and linear quasi-steady-state thermal gradients within swelled coating thickness are obtained. As a consequence, the heat transfer model is more accurate for conditions close to steady-state, for example, high heat fluxes: the intumescent coating has high swelling rates, and it rapidly develops its insulating properties (low density and low thermal conductivity). On the contrary, the model loses accuracy for cases characterised by transient phenomena. This is the example of low heat fluxes: the intumescent coating slowly swells and the transient thermal phenomena (e.g. change in density and specific heat capacity) control the problem.

4.2 Swelled coating thickness

Employing empirical correlations [19,21], the evolution of the swelled thickness of the tested intumescent coating during thermal exposure can be calculated for all the experimental cases. Figure 3 provides an exemplar comparison between the experimentally-measured and predicted swelled coating thickness. Under the same heating conditions, the swelling rate (i.e. slope of the thickness-time curve) is fixed and the maximum swelled thickness that the coating can achieve during thermal exposure is controlled by the initial coating thickness (*DFT*). The empirical model occasionally under- or over-estimates the swelled coating thickness, but the overall trend for predicting the evolution of the swelled coating thickness for different applied initial *DFT*s and different constant incident heat fluxes is correctly captured by using the described model.

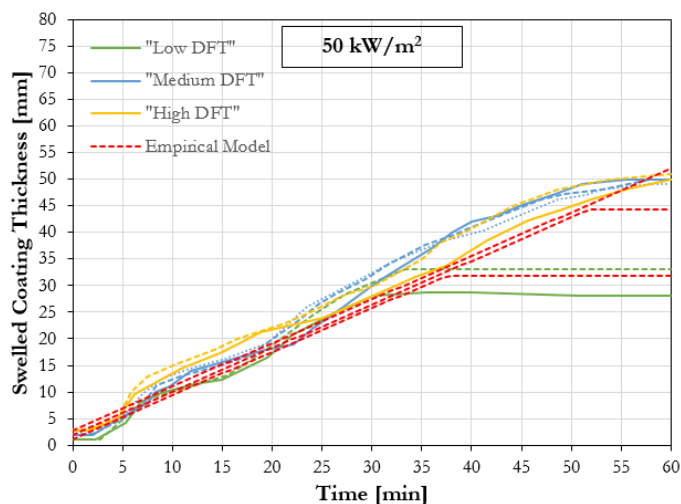


Figure 3. Comparison between the evolution of the experimentally-measured swelled coating thickness and the one predicted using empirical correlations for different applied initial *DFT*s (50 kW/m² and 70 kW/m²).

4.3 Coating surface and substrate steel temperatures

Employing the simplified heat transfer model, it is possible to study the temperature evolution within swelling intumescent coatings, applied to a well-defined initial coating thickness and exposed to a well-defined incident heat flux at the coating surface. Figure 4 provides an exemplar comparison between the evolution of the experimentally-measured coating surface and steel temperatures to the ones predicted using the described heat transfer model.

Regarding the steel substrate, the model is able to correctly predict the evolution of the steel temperature for the shown case. However, the prediction accuracy varies for different cases and, generally, the steel temperatures are over-predicted for low heat fluxes and under-predicted for high heat fluxes. This is the results of the optimisation process carried out on the thermal conductivity of the intumescent coating: this value can be changed in order to control the model accuracy (over-prediction or under-prediction). In this case, the thermal conductivity of the intumescent coating was set in order to obtain the best overall model fitting (lowest total discrepancy), considering all the experimental cases.

Figure 4 also compares the temperature evolution at the coating surface. The general steady-state trend is captured, but the surface temperatures are generally under-predicted, and the model is not able to capture

the initial transient phase, as already discussed. The temperature under-prediction can be related to several aspects. In the authors' opinion, the main reason may be related to the fact that the model does not consider the coating oxidation (exothermic reaction). Experimental results have highlighted that oxidation usually takes place at the coating surface in the oxygen-rich environment of the H-TRIS test method [19,21]. Consequently, the surface temperature may be under-estimated. Other reasons may be related to the accuracy of the imposed thermal boundary conditions and the analysis of the surface temperatures based on IR camera measurements.

In general, the heat transfer model is capable of describing the heat transfer within the swelling intumescent coating because it is able to restrict the problem by correctly defining the two edges of the thermal gradient: coating surface and protected substrate. Accordingly, in accordance with the experimental outcomes, the thermal gradient within the intumescent coating is primarily governed by the swelled coating thickness and the thermal boundary conditions at the coating boundaries. The surface coating temperature is primarily dependent on the heating conditions (i.e. external heat flux) and the coating swelling results in stretching the thermal gradient between the substrate and the coating surface.

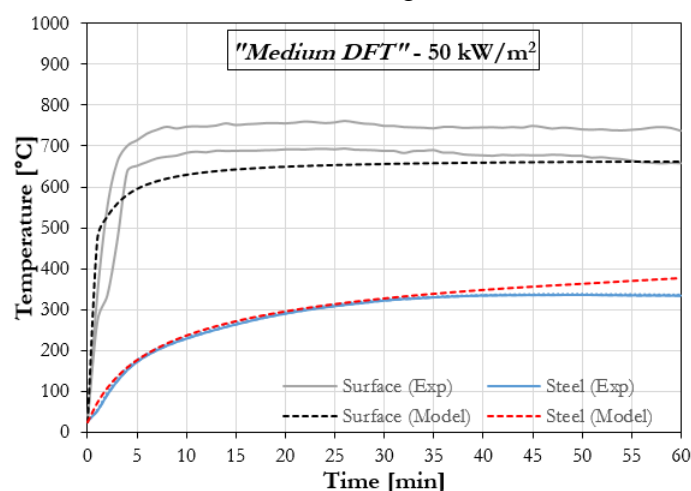


Figure 4. Comparison between the experimentally-measured coating surface and steel temperatures and the ones predicted using the described heat transfer model (50 kW/m², "Medium DFT").

4.4 Coating in-depth temperatures

Using the experimental measurements and adopting the described heat transfer model, it is also possible to investigate the evolution of the in-depth temperature profiles within the swelling coating during thermal exposure. Figure 5 provides an exemplar comparison between the experimentally-measured and predicted in-depth temperature profiles, plotted after 10, 30 and 60 minutes of thermal exposure.

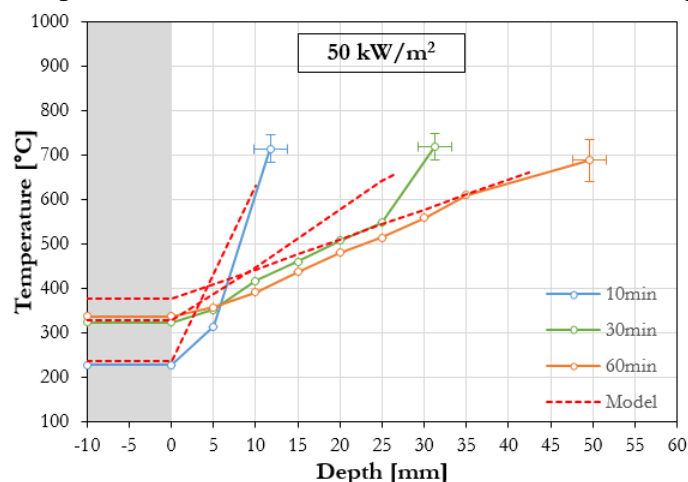


Figure 5. Comparison between the experimentally-measured in-depth temperature profiles and the ones predicted using the described heat transfer model at different instants during the heating exposure (50 kW/m², "Medium DFT").

Due to its quasi-steady-state nature, the plot in Figure 5 confirms the linearity of the in-depth temperature profiles obtained from the numerical model. The discrepancy between the experimentally-measured and predicted in-depth temperature profiles is foreseeably more significant for the cases in which transient phenomena are more relevant: the first part of the thermal exposure and for lower constant incident heat fluxes. Despite the shape, the thermal gradient within the intumescent coating is generally captured: this is the direct consequence of a good prediction of the temperature evolutions at the coating surface and steel substrate and the swelled coating thickness.

5 CONCLUSIONS

The modelling study presented herein proposes a heat transfer model aimed at simulating the thermal and physical behaviour of thin intumescent coatings under thermal exposure. The heat transfer model is formulated according to the experimental outcomes obtained by testing steel plates coated with a commercially available solvent-based thin intumescent coatings using the Heat-Transfer Inducing System (H-TRIS) test method. The model solves the one-dimensional heat conduction problem by resolving the energy-balance equation using the finite-difference Crank-Nicolson method.

In accordance with the experimental outcomes, the model assumes that the effectiveness of the thermal barrier provided by the intumescent coating is mainly dependent on the ability to develop swelled porous char, defined with specific constant material properties. The coating swelling is predicted using empirical correlations and implemented by adding finite elements in the proximity of the substrate-coating interface.

From the results obtained from the heat transfer model, the following concluding remarks can be drawn:

- The modelling of swelling intumescent coatings becomes a physical problem, largely driven by an accurate prediction of the evolution of the swelled coating thickness (i.e. swelling rate) and the thermo-physical properties of the intumescent porous char have minor influence.
- Based on the model assumptions and simplifications, the formulated model defined a quasi-steady-state thermal problem: the highly-insulating swelled coating achieves a quasi-steady surface temperature in equilibrium with the external heat source, the duration of transient phases are minimised, and linear thermal gradients are obtained.
- The heat transfer model is capable of characterising the heat transfer through swelling intumescent coatings by predicting the evolution of coating surface and substrate steel temperatures, and the evolution of the swelled coating thickness. In this way, the thermal gradient within the swelling intumescent coating is correctly predicted, despite the profile shape.
- The heat transfer model is more accurate for conditions close to steady-state, for example, high heat fluxes, characterised by high swelling rates (high Biot number). On the contrary, the model loses accuracy for cases characterised by transient phenomena: phases prior to the onset of swelling (low Biot number), low heat fluxes (longer transient phase and low swelling rates), and heating conditions characterise by varying incident heat flux.

This study aims at building the principles for developing engineering methods for the performance-based design of steel structures protected by intumescent coatings, taking into account their effectiveness for a wide range of potential conditions, such as fire scenarios or applied initial coating thickness.

ACKNOWLEDGMENT

The authors would like to gratefully acknowledge the Fire Safety Engineering Research Group at The University of Queensland, for the continuous inspiration, feedback and technical support. In particular, all students, academics, researchers and technical staff who collaborated on the research projects related to intumescent coatings. The authors are also grateful for the collaboration and continuous support kindly offered by Remedial Building Services Australia Pty Ltd.

REFERENCES

1. Buchanan A.H. and Abu A.K. "Structural design for fire safety". John Wiley & Sons, 2nd Edition, 2017.

2. Mariappan T. "Recent developments of intumescent fire protection coatings for structural steel: A review". *Journal of Fire Sciences*, vol. 34, no. 2, pp. 1-44, 2016.
3. Weil E.D. "Fire-protective and flame-retardant coatings – A state-of-the-art review". *Journal of Fire Science*, vol. 29, pp. 259-296, 2011.
4. Puri E.G. and Khanna A.S. "Intumescent coatings: a review on recent progress". *Journal of Coatings Technology and Research*, vol. 14, pp.1-20, 2017.
5. Lucherini A. and Maluk C. "Intumescent coatings used for the fire-safe design of steel structures: A review". *Journal of Constructional Steel Research*, vol. 162, no. 105712, 2019.
6. International Organization for Standardization (ISO). "ISO834-1:1999 Fire resistance tests - Elements of building construction - Part 1: General requirements for fire resistance testing". Geneva, Switzerland, 1999.
7. Comité Européen de Normalization (CEN). "EN 1363-1:2012 Fire resistance tests - Part 1: General Requirements". Brussels, Belgium, 2012.
8. Comité Européen de Normalization (CEN). "EN 13381-8:2013 Test methods for determining the contribution to the fire resistance of structural members - Part 8: Applied reactive protection to steel members". Brussels, Belgium, 2013.
9. Lucherini A., Giuliani L. and Jomaas G. "Experimental study of the performance of intumescent coatings exposed to standard and non-standard fire conditions". *Fire Safety Journal*, vol. 95, pp. 42-50, 2018.
10. Li G.Q., Lou G.B., Zhang C., Wang L. and Wang Y. "Assess the fire resistance of intumescent coatings by equivalent constant thermal resistance". *Fire Technology*, vol. 48, pp. 529-546, 2012.
11. Wang L., Dong Y., Zhang D., Zhang D. and Zhang C. "Experimental study of heat transfer in intumescent coatings exposed to non-standard furnace curves". *Fire Technology*, vol. 51, no. 1, pp. 627-643, 2015.
12. Elliott A., Temple A., Maluk C. and Bisby L. "Novel testing to study the performance of intumescent coatings under non-standard heating regimes". *Fire Safety Science – Proceedings of the 11th International Symposium*, University of Canterbury, New Zealand, pp. 652-665, 2014.
13. Lucherini A. and Maluk C. "Assessing the onset of swelling for thin intumescent coatings under a range of heating conditions". *Fire Safety Journal*, vol. 106, pp. 1-12, 2019.
14. Zhang Y., Wang Y., Bailey C.G. and Taylor A.P. "Global modelling of fire protection performances of an intumescent coating under different furnace conditions". *Journal of Fire Science*, vol. 31, no.1, pp. 51-72, 2012.
15. Lucherini A., Torero J.L. and Maluk C. "Effects of substrate thermal conditions on the swelling of thin intumescent coatings". *Fire and Materials*, Article in press.
16. de Silva D., Bilotta A and Nigro E. "Experimental investigation on steel elements protected with intumescent coating". *Construction and Building Materials*, vol. 205, pp. 232-244, 2019.
17. Kolsek J. and Cesarek P. "Performance-based fire modelling of intumescent painted steel structures and comparison to EC3". *Journal of Constructional Steel Research*, vol. 104, pp. 91-103, 2015.
18. Maluk C., Bisby L., Krajcovic M. and Torero J.L. "A Heat-Transfer Inducing System (H-TRIS) Test Method". *Fire Safety Journal*, vol. 105, pp. 307-319, 2019.
19. Lucherini A., Hidalgo J.P., Torero J.L. and Maluk C. "Influence of heating conditions and initial thickness on the effectiveness of thin intumescent coatings". *Fire Safety Journal*, no. 103078, Article in press.
20. Wang Z., Han E. and Ke W. "Effects of nanoparticles on the improvement in fire-resistant and anti-ageing properties of flame-retardant coating". *Surface & Coatings Technology*, vol. 200, pp. 5706-5716, 2006.
21. Lucherini A. "Fundamentals of thin intumescent coatings for the design of fire-safe structures". PhD Thesis, School of Civil Engineering, The University of Queensland, 2020.
22. Incropera F.P., DeWitt D.P., Bergman T.L. and Lavine A.S. "Fundamental of heat and mass transfer". John Wiley & Sons, 6th Edition, 2006.
23. Crank J. and Nicolson P. "A practical method for numerical evaluation of solutions of partial differential equations of the heat-conduction type". *Advances in Computational Mathematics*, vol. 6, pp. 207-226, 1996.
24. Hidalgo J.P. "Performance-based methodology for the fire safe design of insulation materials in energy efficient buildings". PhD thesis, School of Engineering, The University of Edinburgh, 2015.

EXPERIMENTAL STUDY OF UNLOADED STRUCTURAL STEEL STAY-CABLES UNDER FIRE EXPOSURE

Benjamin Nicoletta ¹, Scott Watson ¹, Bronwyn Chorlton ¹, John Gales ², Panagiotis Kotsovinos ³

ABSTRACT

Cables-supported structures have seen a dearth of research attention towards their expected performance in realistic but non-standard fire exposures. Herein the authors perform novel fire tests on multiple stay-cable members of various size, coil configuration, and steel type to quantify the thermal response. Cables are subjected to a 30 minute methanol pool fire and instrumented to record temperature and thermal strain data. Temperature data is collected at different cross-sections along the cables' length using thermocouples in order to measure thermal gradients in fire-exposed and insulated regions. Experimental results are presented to compare various cable configurations. A preliminary two-dimensional computational model is presented using LS-DYNA which shows good agreement across both spiral strand and fully locked coil cables. Although preliminary in nature, the model can reliably predict maximum core wire temperatures.

Keywords: Stay-cables, steel, heat transfer, finite element modelling

1 INTRODUCTION

Structural cables are extensively used in a variety of building types forming tension or coupled reactions. These can be seen in bridges, stadia, and other important structures (see Figure 1). Although fire safety in these structures is critical, the fire performance of cables has not been adequately characterized in contemporary literature. The characterization of cross-sectional and longitudinal heat transfer in steel cable members is becoming more relevant in performance-based fire design. Information on the heat transfer within cable members is valuable and necessary for assessing the global response of cable systems. Therefore, the goal of this research is to identify the response of steel stay-cables during exposure to open-air fire and to quantify the thermal response in terms of temperature distributions and thermal expansion.



Figure 1. A cable-supported structure in Winnipeg, Canada (author's photo).

¹ Graduate Researchers, York University, Canada:

e-mail: bnico@yorku.ca, <https://orcid.org/0000-0001-9115-4969>

e-mail: scott.watson@uwaterloo.ca

e-mail: bronwyn1@yorku.ca

² Assistant Professor, York University, Canada:

e-mail: jgales@yorku.ca, <https://orcid.org/0000-0003-2843-2924>

³ Fire Engineer, ARUP, UK:

e-mail: panos.kotsovinos@arup.com ORCID: <https://orcid.org/0000-0003-2234-0420>

There has been limited research conducted in studying structural cable elements with respect to their performance in fire scenarios, let alone efforts to form computational modelling techniques. Existing research attempting to model stay-cables in fire have done so based on experiments with approximated cable members (bundled bars of mild steel) and/or standard fire heating in furnaces, not open-air fire exposure. This study attempts to model commercially available stay-cable members exposed to an open-air pool fire.

An early model by Bennetts and Moinuddin [1] presented one of the first modelling attempts of a stay-cable exposed to a uniform fire. These authors consider a stay-cable cross-section as concentric lumped masses separated completely by air gaps, where larger-diameter strands have more concentric layers to represent more wire layers. Although this method ignores conduction between concentric layers which may increase heat transfer to internal layers, it is one of the first studies to consider the radiation between wire layers that occurs in cable void spaces. Main and Luecke [2] create a three-dimensional thermo-mechanical model of a parallel-wire strand and treat the cable structure as an exterior layer composed of a paint, wire-wrap layer, and a corrosion inhibiting paste, surrounding a solid metal interior representative of the steel wire structure. This approach therefore does not consider the role of air voids in the cable structure. Various heating exposures, including non-uniform heating with boundary gas temperatures of 800°C, were studied to determine specific wire temperatures which later informed the same model in a thermo-mechanical setting.

Similarly to Main and Luecke [2], Liu et al. [3] apply ANSYS to model a stay-cable cross-section by considering no internal discretization of wires or voids. This solid tube model was used to determine the temperature development in the cable cross-section during uniform exposure to a tanker truck fire, represented by a uniform convective and radiative thermal boundary with a predefined time-temperature curve.

The first experimentally validated modelling effort in modelling steel stay-cables in fire was presented by Fontanari et al. [4]. These authors consider a 60 mm diameter full locked-coil strand in addition to a six-strand rope consisting of six 38 mm strands wrapped around a polymeric core. Experimental furnace heating tests were conducted at ambient and elevated temperatures, considering uniform heating to the ISO 834 standard fire curve. A parametric thermal finite element model in ANSYS was validated based on the furnace tests and considered the specific contact area between adjacent wires in the heat transfer analysis. This model was used to produce a time-temperature history for all elements which was later applied to the thermo-mechanical model to inform material properties based on the experimental wire tests. The developed model was found to replicate the experimental results with good accuracy and this methodology is suggested by the authors to be the basis for thermo-mechanical cable models moving forward.

Du et al. [5] develop analytical equations to consider the role of cavity radiation in the heat transfer of a steel cable cross-section and make a comparison to a similarly sized solid steel bar. The developed analytical equations found that the cable member, approximated to a concentric cylinder model separated by an air gap, developed slightly warmer temperatures than the solid bar due to an increased external surface area for heat transfer and a reduced outer layer density. These authors develop ABAQUS models for both a parallel-wire strand and a similarly-sized solid bar under exposure to the ISO 834 standard fire to assess the role of cavity radiation and validate the analytical equations; it was found there was good agreement between the methods.

Most recently, Kotsovinos et al. [6] developed an analytical approach that considers both wire-to-wire conduction and cavity radiation in a two-dimensional cross-sectional thermal analysis. The developed analytical approach was applied in an ABAQUS thermo-mechanical model to investigate the effect of cross-sectional heat transfer on load shedding between wires under non-uniform heating. This model was idealized such that out-of-plane wire movements were restrained, in addition to the thermal dilation of the cable and rotation of individual wires. Thermal moment development based on the elongation of wires was permitted and monitored. These authors conclude that lumped capacitance models which consider no internal wire/void discretization are and less accurate than the developed analytical approach for some thermal exposures.

2 METHODOLOGY

The research programme herein includes the combination of an experimental approach and a preliminary numerical modelling endeavour which ultimately attempts to describe the thermal transfer of heating through various cable coil configurations, steel alloys, and cable diameters.

2.1 Experimental

Experimentation was performed at the York University High Bay Fire Lab following strict safety and environmental testing protocols. Nicoletta et. al [7] illustrates a methodology for testing materials within a repeatable but non-standard methanol fire exposure. The choice of pool fire was considered as this procedure can be repeatable, quantified in terms of characterized heat release, and also facilitated optical measurements using narrow spectrum illumination and digital image correlation (DIC). In these tests a temperature in excess of the standard fire is considered, with average gas temperatures ranging from 800-900°C on the soffit of the cable specimens. Methanol was chosen because it generally burns more completely compared to other available fuels and therefore soot production is reduced. Table 1 provides the eight stay-cables examined herein. Both fully locked and spiral coil types are considered as well as stainless and high strength galvanized carbon steel.

Table 1. Cable specimen test matrix.

Coil Type	Material	Nominal Diameter (mm)	Name	Quantity
Spiral Strand	Galvanized Steel	44.5	S-GS-44.5-A	1
		74	S-GS-74-A	1
	Stainless Steel	22	S-SS-22.6-A	1
		50	S-SS-50-A	1
Locked Coil	Galvanized Steel	70	L-GS-70	1
		100	L-GS-100-A/B	2
		140	L-GS-140-A	1

This study exposes eight structural steel stay-cables to a localised methanol pool fire of dimensions 0.6 m x 0.49 m and measures the thermal gradient in multiple locations throughout the cable structure using K-Type thermocouples. The fire duration was approximately 30 minutes for each test. The cables were allowed to cool in air post fire until temperatures in the insulated region (see Figure 2) were observed to maximize. The specimens were supplied by stay-cable manufacturers and are heated without load to collect information solely on the thermal response of the cable which can later inform loaded experiments and the development of thermomechanical models as introduced herein. The test configuration is provided in Figure 2.

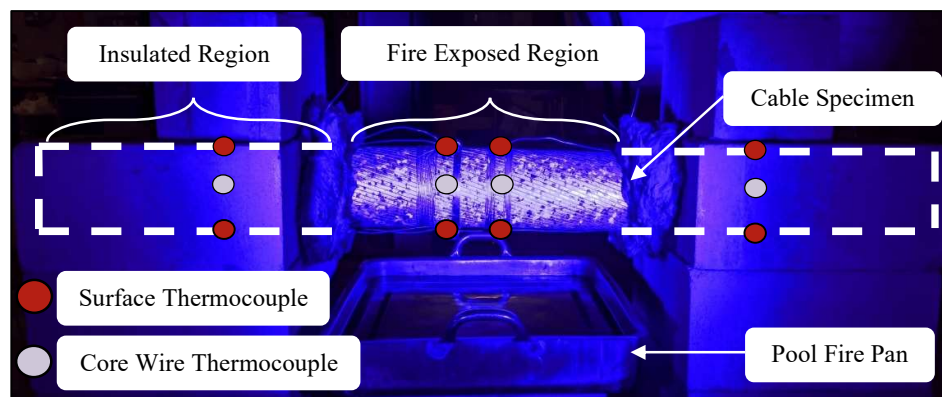


Figure 2. Experimental cable heating configuration and thermocouple placement.

Cross-sectional gradients are measured ± 50 mm from the centreline in the fire exposed region and ± 550 mm from the centreline in the outer insulated regions. The central fire exposed region has a length of 500 mm. Core wire thermocouples were installed by milling holes through half the cable diameter at each location of interest. An optical filtering technique known as narrow-spectrum illumination is also applied to enable the use of digital image correlation (DIC) on the cable surface without flame obstruction. DIC analysis post-fire allows enables the calculation of thermal strains during heating and cooling.

2.2 Preliminary Numerical Modelling

The modelling herein represents the authors current progress at the time of writing and focuses on predicting heat transfer through the cable cross-section in attempt to establish a best practice framework. At this stage, the modelling is limited to cross-sectional analysis for simplicity but will eventually consider longitudinal effects in subsequent research to follow. Modelling is analysed using LS-DYNA R10.0.0 and the eight cables are modelled using SolidWorks, meshed using Altair Hypermesh, and prepared using Primer. The software packages were chosen as they are conventionally used in industry within the authors jurisdictions of engineering practice.

The material properties for the stainless steel and carbon steel are taken from Eurocode 3 – Part 1-2 [8]. The galvanized coating is ignored in the heat transfer analysis. The meshed cable cross-sections for a spiral and locked coil cable are presented in Figure 3. The outer locked wires of locked coil cables are treated as a solid mass based on the significant contact area between adjacent wires and limited presence of air voids. Heat transfer between round wires is analysed based on wire-to-wire radiation. Conduction through contact points between wires is not modelled at this stage because the cables were tested experimentally without load and as such the wire-to-wire contact area was not as significant as would be in a loaded cable. Convection in internal wire voids is not modelled based on the discussion presented by Kotosovinos et al. [6].

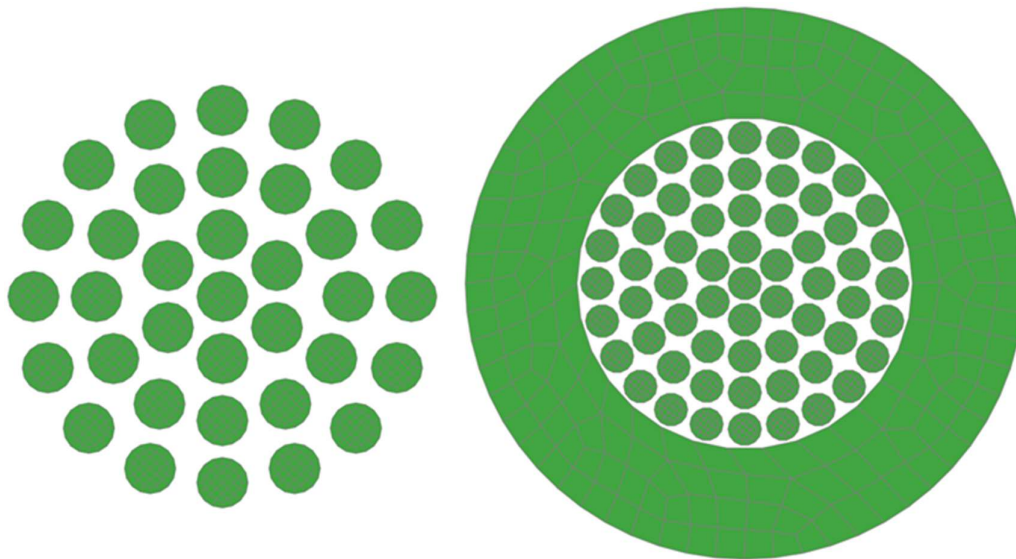


Figure 3. Mesh models of sample (left) spiral strand and (right) full locked coil cables.

The methanol pool fire boundary condition was modelled based on the surface temperatures recorded in each test. In this approach, the measured time-temperature profiles for the top and bottom cable surfaces were applied circumferentially around the outer elements. The bottom surface temperature is applied to the bottom half of the circumference while the top surface temperature is applied to the remainder. This approach was taken for simplicity instead of conducting a heat transfer analysis to the outer cable surface based on the recorded gas temperatures. As the model is two dimensional, the effects of longitudinal conduction are not included. The thermal analysis is run for the duration of both the heating and cooling phase of the experiments and therefore terminates at the same duration that temperature data recording stopped.

3 RESULTS AND DISCUSSION

3.1 Experimental Results

The average core wire temperatures measured in the fire exposed region of the cables is provided in Figure 4. Results here are distinguished based on steel type (stainless vs. carbon) and coil configuration (locked vs. spiral). It can be seen there is a consistent decrease in maximum core temperature for cables of increasing diameter with a more significant drop occurring for the largest diameter cable L-GS-140. In general, smaller diameter and stainless steel cables were able to reach a steady state temperature plateau before the fire was exhausted at approximately 30 minutes. This stabilization of temperatures is due to the small cross-sectional diameters of S-SS-22, S-SS-50, S-GS-44, and the significantly higher thermal conductivity of stainless steel. Despite similar diameters, the maximum temperatures reached between cables S-GS-74 and L-GS-70 are slightly higher in favour of the locked coil variant. This is attributed to the denser outer layer of locked wires enabling a more favourable conduction path to the core wire than the spiral strand structure in S-GS-74. Despite this difference, the general heating and cooling profiles of S-GS-74 and L-GS-70 are similar, and the maximum temperatures are within approximately 50°C.

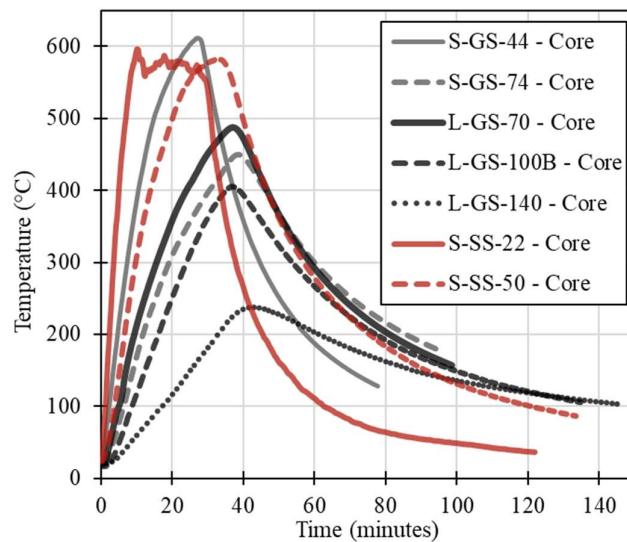


Figure 4. Time-temperature history for the core wires in the fire exposed regions of the cables.

3.2 Preliminary Numerical Modelling Results

The current state of the thermal model attempts to predict the core wire temperature profile of the eight cable studied experimentally. As described, the measured surface temperatures from the experiments are used as the thermal boundary condition to represent the heat transfer from the methanol pool fire. Table 2 presents the results from all analyses and the average maximum core temperature for each cable specimen.

Table 2. Predicted and experimental maximum core wire temperatures in the fire exposed region.

Cable	Average Experimental Temperature (°C)	LS-DYNA Prediction (°C)
S-SS-22	600 ± 5	614
S-SS-50	582 ± 5	585
S-GS-44	612 ± 5	687
S-GS-74	450 ± 4	330
L-GS-70	487 ± 4	465
L-GS-100 A	408 ± 3	360
L-GS-100 B	405 ± 3	392
L-GS-140	238 ± 3	240

Here it can be seen there is fair agreement between the model-predicted maximum core temperature and the experimental temperature for most cables however there is a relatively large discrepancy for cable S-GS-74. Figure 5 presents the time-temperature history results for cable L-GS-140.

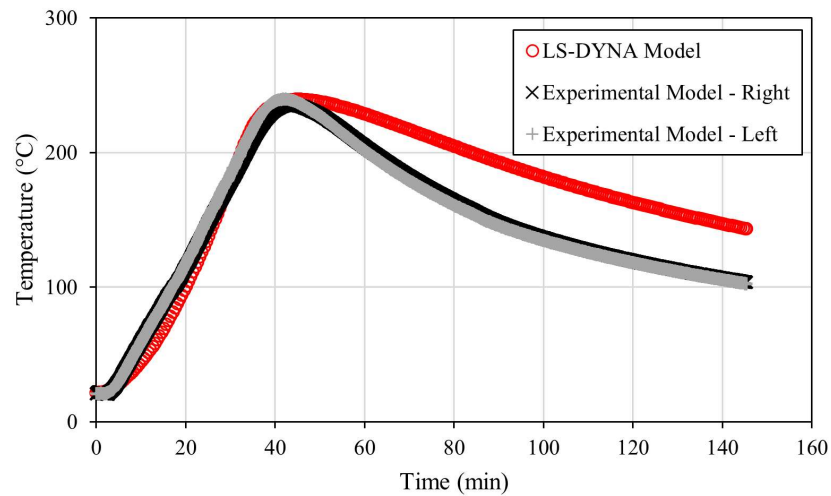


Figure 5. Experimental and predicted core wire time-temperature history in the exposed region for cable L-GS-140.

It is shown there is good agreement between experimental and analytical models during the heating phase (up to about 35 minutes) however the cooling phase is less represented. One possible cause may be the lack of longitudinal conduction in the current model which allows the experimental temperatures to cool more rapidly. This implies the assumption of an infinitely long cable may not be appropriate for the fire scenario studied herein. The overprediction of temperatures in the cooling phase is present in most model analyses with the exception of S-GS-74. In general, the model better predicted the correct time-temperature behaviour of larger diameter, locked coil cables. This may imply the outer lumped wire mass in locked coil cables may be robust when modelling the interior temperatures due to the circumferential normalization of temperatures within the locked wire layer. Therefore the interior wires may be heated more uniformly by the locked wire layer which would allow for more consistent heat transfer to the core wire. Figure 6 gives the time-temperature history for cable S-SS-50.

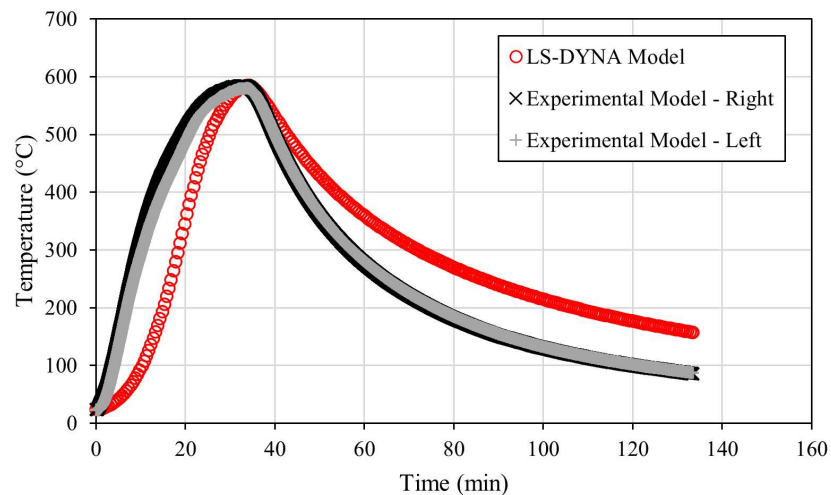


Figure 6. Experimental and predicted core wire time-temperature history in the exposed region for cable S-SS-50.

Figure 6 shows more core temperature discrepancy in the heating phase and the same overprediction of cooling temperatures during cooling. This discrepancy is more significant considering the relatively small diameter of S-SS-50 which should be more heavily informed by the top and bottom surface boundary

conditions. For example, since the temperature difference between the surface and core is greater in larger diameter cables, one would expect less error in smaller cables as the boundary condition is much closer to the expected core temperature. Therefore, this discrepancy may indicate some other inappropriate assumption in the model such as the neglect of wire-to-wire conduction in the cross-sectional plane. As this model is preliminary in nature, future work will refine the analyses presented herein.

4 FUTURE RESEARCH STEPS

The experimental program herein has yielded useful information on the thermal response of steel stay-cables in response to localised, open-air fires. While the scope of this paper was to present the current state of modelling efforts specific to the heat transfer to the cable core wires, other results from the experimental research program have shown that the use of narrow-spectrum illumination to enable deformation measurements using DIC is useful in calculating thermal strains and deflections during heating and cooling. For example, Figure 7 compares the cable thermal expansion measured during cooling by DIC to the thermal expansion predicted by the equation provided in Eurocode 2 Part 1-2 for prestressing steel [9], based on the average temperature of the top and bottom cable surface for specimen L-GS-70. It is shown there is good agreement between measured and predicted values. More detailed discussion on this research progress can be found in recent work by the authors [10]. Ultimately the data produced from the DIC analyses can be used to improve upon the thermal strain models that will arise from the thermal modelling work herein. Together, these components will be able to inform a comprehensive thermomechanical model for a robust variety of stay-cable members exposed to open-air fires.

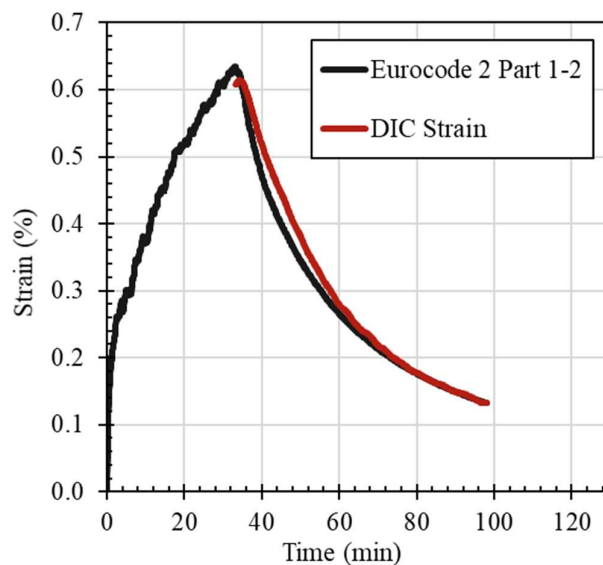


Figure 7. DIC-measured thermal contraction of L-GS-70 compared to the Eurocode equation for prestressing steel.

Future research programs by the authors aim to expand upon the application of narrow-spectrum illumination and DIC in the measurement of cable deformations and expose a larger variety of cable members to a range of fire exposures.

5 CONCLUSION

This paper shared the experimental results of multiple varieties of stay-cables exposed to a 30 minute methanol pool fire during heating and cooling. Temperature data throughout the cable structure was collected to inform computational models of the test specimens. The cables studied varied in diameter, coil configuration, and steel alloy. Experimental results demonstrated the tendency for smaller diameter cables (22-50 mm) to reach steady state temperatures for the fire scenario examined, a non-linear decrease in maximum core temperature for increasing cable diameter, and a more optimal path for conductive heat transfer in full locked coil cables versus spiral strand. The preliminary LS-DYNA computational model

was fairly accurate in predicting most maximum core temperatures with some exceptions. In general, the cooling phase temperatures are currently overpredicted by the model and the initial heating rate is slower than the experimental data. The application of a lumped mass approach for the locked wire layers of full locked coil cables may be favourable and less sensitive to boundary condition changes due to the temperature normalization in the outer layer. This model represents the authors ongoing work and as such will be improved upon in future work.

ACKNOWLEDGMENTS

The authors would like to acknowledge the contributions of ARUP U.K. in providing support as well as Bridon-Bekaert and Redaelli for supplying specimens. Stephan Labbé is also thanked for his coordination in procuring preliminary specimens. Riad Rajab, Adam McLean, Melessa Salem, Timothy Young, Danielle Alberga, Ginelle Aziz, Julia Ferri, and Yutaro Fukuhara of York University are all thanked greatly for their assistance towards this research. The Ontario Government and NSERC are acknowledged for their financial support.

REFERENCES

1. Bennetts, I., and Moinuddin, K. 2009. Evaluation of the Impact of Potential Fire Scenarios on Structural Elements of a Cable-Stayed Bridge. *J. Fire Prot. Eng.*, 19(2), 85-106. DOI: 10.1177/1042391508095091.
2. Main, J. A., and Luecke, W. E. 2010. Safety Assessment of Parallel Wire Suspension Bridge Cables under Thermal Effects. US Department of Commerce, National Institute of Standards and Technology.
3. Liu, Y. J., Ning, B., and Wang, Y. 2012. Study on Thermal and Structural Behaviour of a Cable-Stayed Bridge under Potential Tanker Truck Fires. *App. Mech. Mater.*, 238(2012), 684-688. DOI: 10.4028/www.scientific.net/AMM.238.684
4. Fontanari, V., Benedetti, M., Monelli, B.D. and Degasperri, F., 2015. Fire Behavior of Steel Wire Ropes: Experimental Investigation and Numerical Analysis. *Engineering Structures*, 84, pp.340-349.
5. Du, Y., Sun, Y.K., Jiang, J. and Li, G.Q. 2019. Effect of Cavity Radiation on Transient Temperature Distribution in Steel Cables Under ISO 834 Fire. *Fire Safety Journal*, 104, pp.79-89.
6. Kotsovinos, P., Atalioti, A., McSwiney, N., Lugaresi, F., Rein, G., and Sadowski, A. J. 2020b. Analysis of the Thermomechanical Response of Structural Cables Subject to Fire. *Fire Tech.*, 56(2), 515-543. DOI: 10.1007/s10694-019-00889-7.
7. Nicoletta, B., Panagiotis, K., Gales, J. 2019. Experimental Thermal Performance of Unloaded Steel Stay-Cables in Fire: Preliminary Progress. 15th International Conference and Exhibition on Fire Science and Engineering, Interflam. July 1st-3rd, 2019.
8. CEN (European Committee for Standardization). 2006. Design of Steel Structures—Part 1-2: General Rules. Eurocode 3, Brussels, Belgium.
9. CEN (European Committee for Standardization). 2004. Design of Concrete Structures - Part 1-2: General Rules—Structural Fire Design. Eurocode 2, Brussels, Belgium.
10. Nicoletta, B., Gales, J., Kotsovinos, P. 2020. Experimental Thermal Performance of Unloaded Steel Stay-Cables for Bridge Infrastructure Subject to Pool Fires. *Structural Engineering International*. Submitted (Manuscript No. X2526.20.08).

EXPERIMENTAL INVESTIGATION OF THE BEHAVIOR OF MARTENSITIC HIGH-STRENGTH STEELS AT ELEVATED TEMPERATURE

Xia Yan¹, Yu Xia², Hannah B. Blum³, Thomas Gernay⁴

ABSTRACT

This paper presents an experimental investigation of the mechanical properties of cold-formed martensitic (MS) steels at elevated temperature and after cooling down. Tensile specimens were cut from cold-formed martensitic steel sheets with nominal yield stress of 1030 MPa and 1200 MPa, and nominal thickness of 1.0 mm. Steady-state tests, transient-state tests, and residual tests were carried out for temperature up to 700°C. Stress-strain relationships and mechanical properties including elastic modulus, yield stress, and ultimate stress were obtained from the tests. The test results were compared with design provisions in European and American standards, as well as other test data published in the literature. The comparisons show that the cold-formed MS steels show proportionally larger reduction in stiffness and strength than lower grade steels at elevated temperature and after cooling down. Some permanent loss of strength is observed for exposure temperatures higher than 300°C. New relationships were proposed to determine the elevated temperature and post-fire mechanical properties of cold-formed MS steels with nominal yield stress up to 1200 MPa.

Keywords: Mechanical properties; cold-formed steel; martensitic alloy; predictive model

1 INTRODUCTION

Recent progress in steel manufacturing has permitted the production of Advanced High-Strength Steels (AHSS) with nominal yield stress up to 1200 MPa and ultimate stress up to 1500 MPa. AHSS refer to a new generation of steels that feature multiphase microstructure resulting from precise heating and cooling process from the austenite or austenite/ferrite phase [1]. Thus, in addition to ferrite, pearlite, or cementite, AHSS contain one or more phases such as martensite, austenite, or bainite [2]. The careful selection of chemical components and processing combination allows achievement of a wide range of strength and ductility properties. AHSS can be hot rolled or cold-formed. Given their favourable mechanical properties, AHSS have the potential to be adopted as next generation materials in structural applications, especially for structures made of cold-formed steel profiles.

However, steel structures are vulnerable to fire. To enable the structural fire design of structures made of these novel AHSS, the material behaviour needs to be characterized under and after exposure to elevated temperature. Currently, while there is some guidance related to the elevated temperature mechanical properties of cold-formed steels in design codes and standards (such as Eurocode EC3 [3], American

¹ Graduate student, Johns Hopkins University, Baltimore, MD, USA
e-mail: xyan18@jhu.edu, ORCID: <https://orcid.org/0000-0002-1263-3417>

² Graduate student, University of Wisconsin-Madison, Madison, WI, USA
e-mail: yxia44@wisc.edu, ORCID: <https://orcid.org/0000-0002-1529-0552>

³ Assistant Professor, University of Wisconsin-Madison, Madison, WI, USA
e-mail: hannah.blum@wisc.edu, ORCID: <https://orcid.org/0000-0003-4672-0903>

⁴ Assistant Professor, Johns Hopkins University, Baltimore, MD, USA
e-mail: tgernay@jhu.edu, ORCID: <https://orcid.org/0000-0002-3511-9226>

Specifications AISC [4] and AISI [5], and Australian AS 4600 standard [6]), no specification addresses cold-formed AHSS and steel grades up to 1200 MPa. Furthermore, there is no guidance related to post-fire properties in most design codes. Meanwhile, experimental investigations of the mechanical properties of cold-formed steels at elevated temperature and after cooling down are mainly focused on conventional grade steels or G550. Lee et al. [7] tested the elevated temperature mechanical properties of cold-formed G500 and G550. Chen and Young [8] investigated cold-formed G450 and G550, and Li and Young [9] tested cold-formed steels with nominal yield stress of 700 MPa and 900 MPa. For the post-fire properties, Gunalan and Mahendran [10] tested cold-formed G300, G500 and G550. Kesawan and Mahendran [11] tested cold-formed G350 and G450. Li and Young [12] tested cold-formed steels with nominal yield stress of 700 MPa and 900 MPa, and Chen et al. [13] tested cold-formed Q345 and G550. From this review, the elevated temperature and post-fire mechanical properties of cold-formed steel with steel grade greater than 550 MPa are relatively scarce.

In this study, an experimental investigation was carried out on the behavior of two types of martensitic (MS) steels with nominal yield stress of 1030 MPa and 1200 MPa at elevated temperature and after cooling down. Steady-state tests, transient-state tests, and residual tests were conducted on tensile specimens extracted from MS steel sheets with a thickness of 1.0 mm. This paper reports the stress-strain curves and mechanical properties measured from the tests, provides comparison with test data from the literature and with the EC3 and AISC 360, and formulates new equations to determine the degradation of mechanical properties of cold-formed MS steels at elevated temperature and after cooling down.

2 EXPERIMENTAL INVESTIGATION

2.1 Materials and specimens

Martensitic steel is best known for its extremely high strength. The microstructure of MS steel is mainly martensitic matrix containing small amounts of ferritic and/or bainitic phases. Almost all the austenite that exists during hot-rolling or annealing is converted into martensite by a high rate quench. The increased carbon content improves the strength and stiffness of the steel. Naming of the specimen is based on the microstructure and the nominal yield stress, namely MS-1030 and MS-1200. Nominal ultimate stresses of the two tested materials are 1300 MPa and 1500 MPa, respectively. All the specimens are uncoated, and the nominal thickness is 1.0 mm. The exact chemical composition of the two tested materials is proprietary information of the manufacturer; typical chemical composition as publicly available for MS-1030 and MS-1200 (not a specific composition from the manufacturer) is listed in Table 1.

Table 1. Chemical components of materials.

Steel type	C	Si	Mn	P	S	Al	Nb+Ti	Cr+Mo	V	B	Cu
MS-1030	0.16	0.4	1.8	0.02	0.01	0.015	0.1	1	-	0.005	0.2
MS-1200	0.28	0.4	1.3	0.02	0.01	0.015	0.1	1	-	0.01	0.2

Note: All values are the maximum percentage of steel mass (max %).

Pinned tensile test specimens were cut from two martensitic cold-formed steel sheets in the longitudinal direction. The shape and dimension of the specimens were prepared in accordance with ASTM E 21 [14] for pin-loaded tensile testing of metallic materials. The gauge length and width of the reduced parallel section are 50 mm (2 inches) and 12.7 mm (0.5 inch), as shown in Figure 1. Before testing, the true thickness and width of the specimens were measured by calliper and screw micrometre at three locations along the reduced parallel section. The averaged values were then used to calculate the mechanical properties.

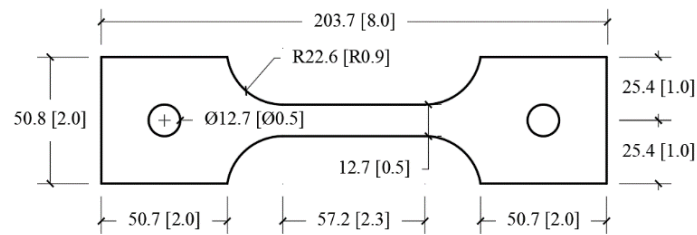
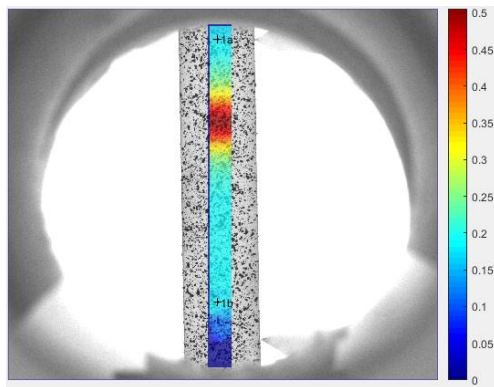


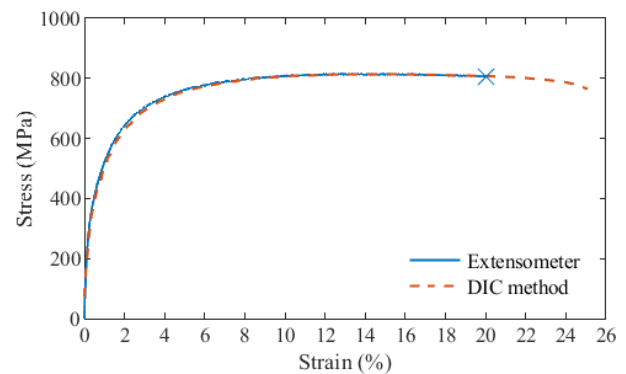
Figure 1. Dimension of the specimen (in mm [and inch]).

2.2 Test apparatus

The tests were performed in the Multi-Hazard Resilient Structures lab at Johns Hopkins University. An MTS loading frame was used to conduct the tensile tests. An ATS 3210 series high temperature furnace with three independent heating zones was used to heat up the specimens. The furnace was controlled by an ATS temperature control system which can set up the target temperature and heating rate. Three internal thermocouples, located in the middle of each heating zone, measured the furnace temperature. Three external thermocouples, located at the two ends and center of the reduced parallel section, were used to measure the steel surface temperature. The applied load was read from the load cell that had been calibrated before the test campaign. The strain was measured by a 50mm-gauge-length high-temperature extensometer (-10%/20%) and a Digital Image Correlation (DIC) method (40%) [15]. When the strain was smaller than 20%, the strain measured by the high-temperature extensometer was adopted. Once the strain exceeded 20%, the DIC measurement was adopted. The comparison of the stress-strain curves with strain measured by extensometer and the DIC method is shown in Figure 2, in which a good agreement can be observed.



(a) Strain field in *ncorr* [16].



(b) Stress-strain curves with strains measured by extensometer and DIC method.

Figure 2. Strain measurements.

For the DIC method, speckles were applied onto the surface of the specimens and an open source MATLAB-based program *ncorr* [16] was used to analyse the displacement of the speckles, which then allowed calculation of the strain. A combination of white base paint and black speckles was adopted for test temperature of 200°C-500°C. In 600°C and 700°C tests, the white base paint was not stable. Thus, only white speckles were applied (no base paint) since the specimen itself would turn dark, which made the white dots stand out and increase the contrast, as shown in Figure 3. At high temperature, the radiation from the heated specimen altered the intensity of the images captured by the DIC camera. To solve this problem, blue light illumination and blue band pass filter were used to reduce the error due to the intensity change.

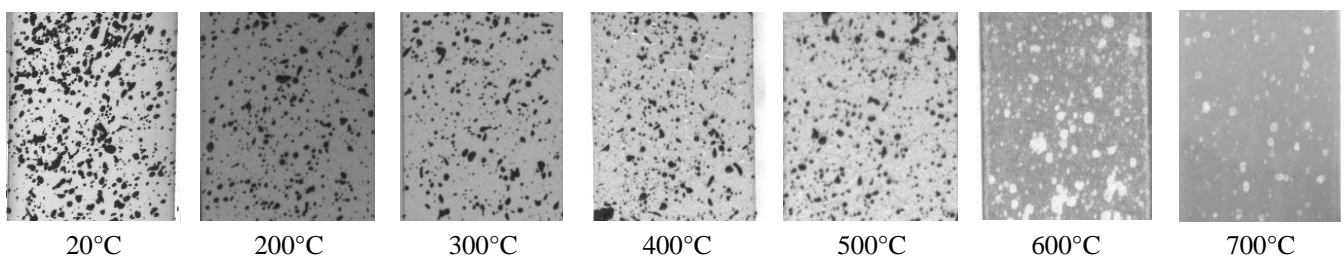


Figure 3. Speckles painted on the specimens for strain measurement by DIC method.

2.3 Tests procedures

Steady-state tests were carried out on both MS-1030 and MS-1200. The specimens were heated up to preselected target temperatures in the range of 20°C-700°C at a heating rate of 10°C/min. Heating rate has been shown to have a minor influence on the elevated temperature and post-fire mechanical properties of high-strength cold-formed steels [12,17]. The heating rates were chosen in this study to provide a reasonable representation of the real fire conditions. During heating, the upper pin was fixed, while the lower pin was manually adjusted by the test operator through a control program to allow thermal expansion. To avoid building up compression in the specimens, the displacement of the lower pin was continuously adjusted throughout the heating process to maintain the stress in the specimen between zero and a small pre-tension stress of less than 5 MPa. After the target temperature was reached, an extra 15-20 min heating was maintained to ensure the stability and uniformity of the steel temperature inside the specimens. After that, a tensile loading was applied to the specimens until fracture, while the temperature was maintained constant. The force was applied at a loading rate of 0.25mm/min (evaluated from the strain rate of 0.005/min specified in ASTM E21 [14]) in a displacement control mode. To check the repeatability of the tests, the steady-state tests were repeated for three times at selected temperatures (ambient, 300°C, and 400°C).

Transient-state tests were carried out on MS-1200. In transient-state tests, the specimens were loaded in tension to a preselected target stress state and then heated at a constant rate (while the stress state was maintained constant) until fracture. While steady-state tests are easier to carry out, transient-state tests aim at more closely capturing the sequence of loading-heating present in a loaded structure under fire. The applied stress states were based on the nominal yield stress of the tested material, ranging from 0.05 to 1.2 times the nominal yield stress. For instance, in a transient-state test of MS-1200 under 0.1 stress state, a tensile force was applied to the specimen to reach a stress state of 120 MPa ($1200 \text{ MPa} \times 0.1$) before heating. After the stress state was reached, the furnace was activated to heat the specimens with a heating rate of 5°C/min until fracture. A zero-load test was also carried out to measure the thermal strain of the tested material. The thermal strain was then subtracted from the total strain measured by the high-temperature extensometer to obtain the mechanical strain. To maintain the desired stress state, a force control mode, in which the lower pin was continuously adjusted to compensate for thermal elongation, was implemented. The temperature of the specimens was measured by the average readings of the three external thermocouples. Mechanical strain-temperature curves at several stress levels were obtained from the transient-state tests. These curves were then converted into stress-strain curves at several temperatures.

Residual tests were carried out on both MS-1030 and MS-1200 [18]. In residual tests, specimens were heated up to selected target temperatures with a heating rate of 25°C/min. During heating, the upper pin was fixed, while the lower end of the specimen was free to expand. After the target temperature was reached, an extra 15-20 min heating time was maintained to ensure the stability and uniformity of the steel temperature inside the specimens. After that, the specimen was taken out of the furnace and allowed to cool down to ambient temperature in air. Subsequently, tensile testing was performed on the specimen until fracture at ambient temperature.

3 TEST RESULTS

3.1 Steady-state tests

Test results in terms of stress-strain curves obtained from the steady-state tests are shown in Figure 4. The stress-strain curves show a gradual shape with no clear yield plateau both at ambient and elevated temperatures. Mechanical properties including elastic modulus E , 0.2% proof stress $f_{0.2}$, stress at strain levels of 0.5% $f_{0.5}$, 1.5% $f_{1.5}$, and 2.0% $f_{2.0}$, and ultimate stress f_u were obtained from the stress-strain curves. The elastic modulus is defined as the slope of the initial part of the stress-strain curves and determined by the method for calculating the steady-state elastic modulus in [1]. The 0.2% proof stress is the stress needed to impart 0.2% plastic strain. The ultimate stress is the maximum stress obtained from the stress-strain curve. Table 2 lists the mechanical properties of MS-1030 and MS-1200 obtained from steady-state tests. For the tests that were repeated three times, the mean values and coefficient of variation were

calculated. Results show that the coefficient of variation is smaller than 5%. Due to the limited materials, steady-state tests were carried out only once for the other temperatures. The mean values of the repeated tests are provided in Table 2.

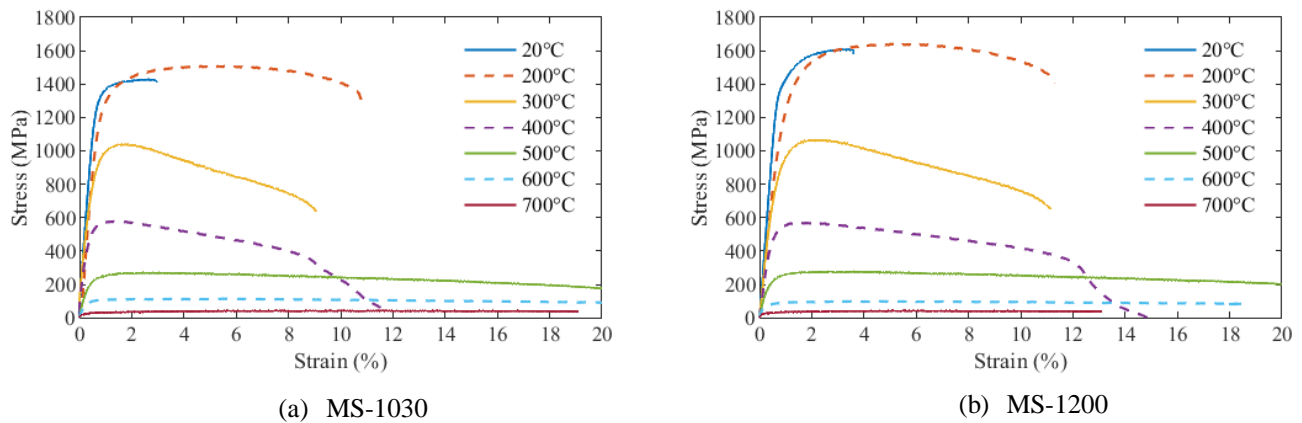


Figure 4. Stress-strain curves obtained from steady-state tests.

Table 2. Mechanical properties obtained from steady-state tests.

T (°C)	MS-1030						MS-1200					
	E (GPa)	f _{0.2} (MPa)	f _{0.5} (MPa)	f _{1.5} (MPa)	f _{2.0} (MPa)	f _u (MPa)	E (GPa)	f _{0.2} (MPa)	f _{0.5} (MPa)	f _{1.5} (MPa)	f _{2.0} (MPa)	f _u (MPa)
20	215.6	1327	1085	1406	1418	1428	208.6	1387	1030	1528	1572	1608
200	218.6	1128	863	1397	1440	1509	177.9	1222	889	1447	1524	1618
300	172.8	925	788	1037	1035	1038	152.4	887	696	1053	1066	1069
400	117.1	549	513	575	568	578	112.7	506	458	567	566	569
500	60.3	228	217	265	266	271	66.7	223	216	268	273	278
600	40.0	95	98	110	111	114	37.6	78	82	93	95	99
700	19.9	26	28	33	34	43	18.7	28	30	37	36	43

3.2 Transient-state tests

The relationship between mechanical strain and temperature is obtained under different stress states (Figure 5a), after subtracting the thermal strain from the measured total strain. Then, the strain-temperature curves are converted into stress-strain curves at several temperatures (Figure 5b). Since the number of tested stress states is limited, the stress-strain curves are described by several discrete points. Also, the ultimate stress is generally not obtained for the selected temperatures. Thus, ultimate stress cannot be obtained from the transient-state tests. In addition, stress at 1.5% and 2.0% strain may not occur in certain stress-strain curves. Table 3 lists the mechanical properties of MS-1200 obtained from transient-state tests. The elastic modulus is determined by the method for calculating the transient-state elastic modulus in [1].

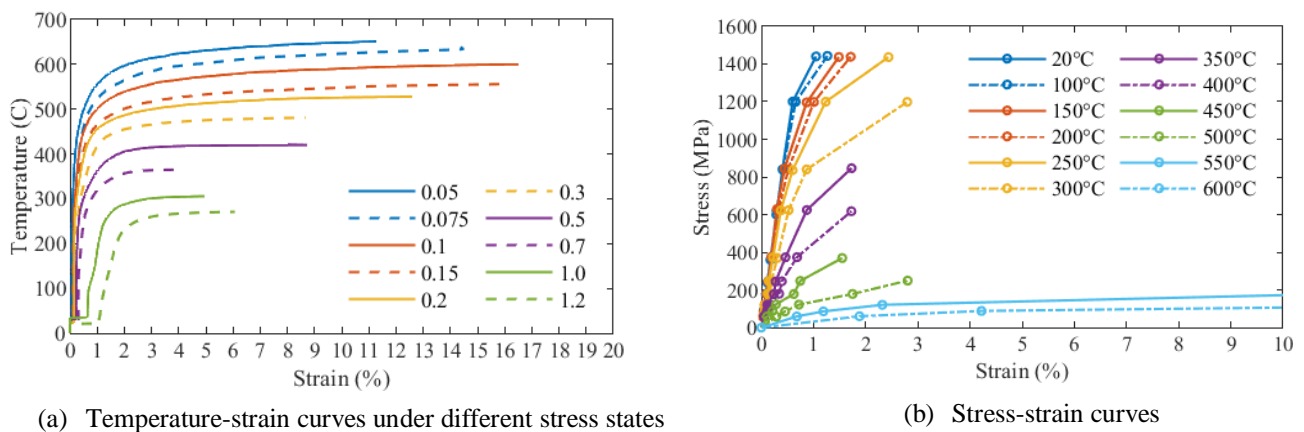


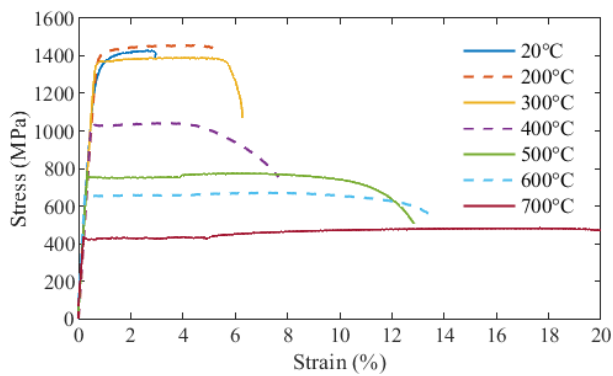
Figure 5. Temperature-strain curves and stress-strain curves obtained from transient-state tests for MS-1200.

Table 3. Mechanical properties obtained from transient-state tests for MS-1200.

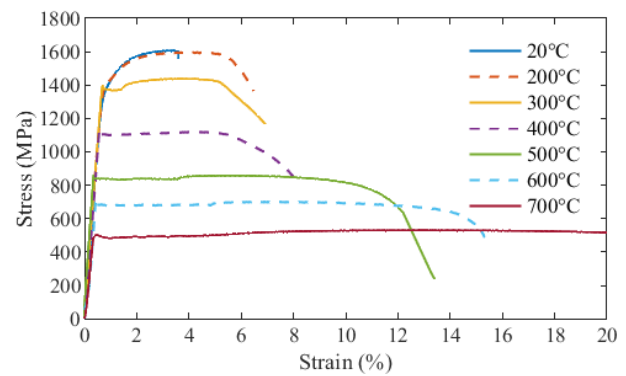
T (°C)	E (GPa)	f _{0.2} (MPa)	f _{0.5} (MPa)	f _{1.5} (MPa)	f _{2.0} (MPa)
100	227.7	1233	968	-	-
150	217.4	1034	891	-	-
200	197.7	965	821	-	-
250	183.3	879	742	-	1350
300	118.6	847	597	792	1050
350	75.7	684	396	723	-
400	48.0	508	293	677	-
450	37.0	279	159	460	-
500	20.5	128	92	255	196
550	8.8	84	44	127	111
600	3.2	65	16	70	62

3.3 Residual tests

Test results in terms of stress-strain curves obtained from residual tests are shown in Figure 6. The stress-strain curves of the two tested MS steels show a gradual shape with no clear yield plateau after exposure to 200°C, beyond which the stress-strain curves show a sharp shape with distinct yield plateau following the linear elastic regions. The mechanical properties obtained from residual tests are listed in Table 4.



(a) MS-1030



(b) MS-1200

Figure 6. Stress-strain curves obtained from residual tests.

Table 4. Mechanical properties obtained from residual tests.

T (°C)	MS-1030						MS-1200					
	E (GPa)	f _{0.2} (MPa)	f _{0.5} (MPa)	f _{1.5} (MPa)	f _{2.0} (MPa)	f _u (MPa)	E (GPa)	f _{0.2} (MPa)	f _{0.5} (MPa)	f _{1.5} (MPa)	f _{2.0} (MPa)	f _u (MPa)
200	212.3	1403	1038	1434	1445	1456	203.3	1413	1037	1515	1558	1596
300	219.9	1371	1107	1376	1381	1390	210.4	1374	1058	1389	1418	1438
400	210.1	1030	1029	1031	1036	1041	204.8	1105	997	1103	1106	1134
500	218.6	752	753	750	751	783	228.3	838	839	834	838	860
600	232.1	654	653	656	658	673	211.9	710	711	705	703	769
700	196.8	423	424	430	429	482	189.0	492	493	486	482	516

4 DISCUSSIONS

Reduction trends of mechanical properties at elevated temperature or after exposure to elevated temperature are described by retention factors. For steady-state tests and transient-state tests, the retention factors are defined as the ratio of the mechanical properties at elevated temperature to their (measured) values at ambient temperature. For residual tests, the retention factors are defined as the ratio of the mechanical properties after exposure to elevated temperature to their original values at ambient temperature. The

notation of the retention factor is k_E for elastic modulus, $k_{0.2}$ for 0.2% proof stress, and k_u for ultimate stress.

4.1 Elastic modulus

The retention factors of elastic modulus are shown in Figure 7. From steady-state tests, the elastic modulus of MS-1030 and MS-1200 show quite similar reduction trend when the temperature is higher than 400°C. At 200°C, MS-1200 shows a clear reduction in elastic modulus, while MS-1030 does not. When comparing the results from the steady-state and transient test methods, transient-state tests yield much lower elastic modulus for MS-1200 when the temperature is higher than 300°C. This discrepancy may be due to the thermal creep effect which becomes more noticeable at higher temperatures.

The retention factors obtained from steady-state tests and transient-state tests are also compared with the predictions in design codes (EC3 [3] and AISC 360 [4]) and other literature data, as shown in Figure 7(a). The predictions of elastic modulus at elevated temperature by the two codes are unconservative to predict the behaviour of the two tested MS steels. Furthermore, comparisons with other published data also highlight that the tested MS steels experience higher reduction in elastic modulus at elevated temperature than the lower grade cold-formed steels.

From residual tests, MS-1030 and MS-1200 maintain more than 97% of their original elastic modulus after exposure to temperature up to 600°C, beyond which the reduction becomes more noticeable. The test results are also compared with other literature data, as shown in Figure 7(b). The test data in this study generally agree well with other published data.

4.2 Yield stress

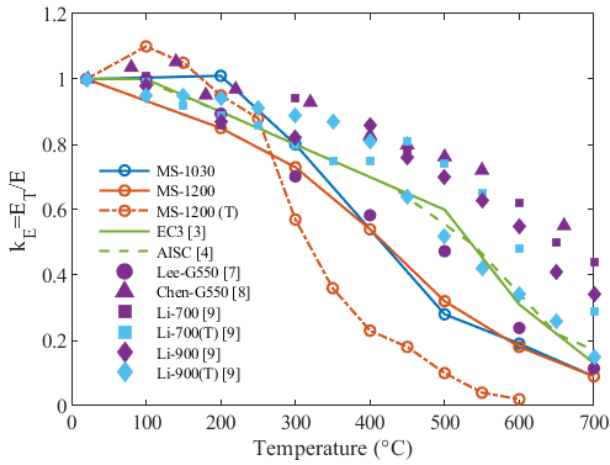
The retention factors of 0.2% proof stress are shown in Figure 8. From steady-state tests, the two MS steels show similar reduction trend at elevated temperature. When comparing the results from the steady-state and transient test methods, the two yield similar results at temperatures higher than 300°C, while a noticeable discrepancy is observed at 100°C-300°C. Overall, unlike with the elastic modulus, the test method does not have a significant influence on the retention factors of 0.2% proof stress. The results obtained from steady-state tests and transient-state tests are also compared with the predictions in EC3 [3] (Table E1 for class 4 sections giving the 0.2% proof stress, for consistency) and with other literature data, as shown in Figure 8(a). The prediction by EC3 [3] is unconservative for temperature higher than 200°C. The retention factors in other tests are generally larger than those in this study, except that the G550 by Chen and Young [8] shows similar reduction in 0.2% proof stress at 450°C-650°C.

From residual tests, the two MS steels show similar reduction trends after exposure to elevated temperature, see Figure 8(b). The 0.2% proof stress of the two MS steels starts to reduce noticeably at 300°C. Comparison with published data is also provided. The post-fire retention factors of the two MS steels are generally lower than the other published data, except the G500 and G550 by Gunalan and Mahendran [10] show similar results at 550°C-700°C.

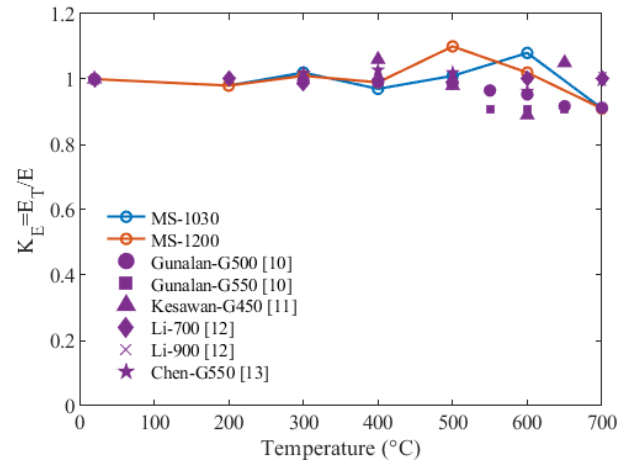
4.3 Ultimate stress

The retention factors of ultimate stress are shown in Figure 9. From steady-state tests, the two MS steels show similar reduction trend in ultimate stress at elevated temperature. The results obtained from steady-state tests in this study are also compared with the predictions in EC3 [3] and AISC [4] and other literature data, as shown in Figure 9(a). EC3 [3] predicts higher reduction in ultimate stress than AISC360 [4], but both provisions are higher than the two tested MS steels. The test results by Li and Young [9] agree well with the models in EC3, while the results by Chen and Young [8] show a similar reduction pattern with the tested MS steels at temperatures higher than 450°C.

The two MS steels show similar reduction trend in ultimate stress after exposure to elevated temperature, see Figure 9(b). They retain more than 90% of their original ultimate stress after exposure to temperature up to 300°C, and retain about 30% of their original ultimate stress after exposure to 700°C. Comparison with literature data shows that the tested MS steels generally exhibit larger reduction in ultimate stress than the lower grade cold-formed steels after exposure to elevated temperature.

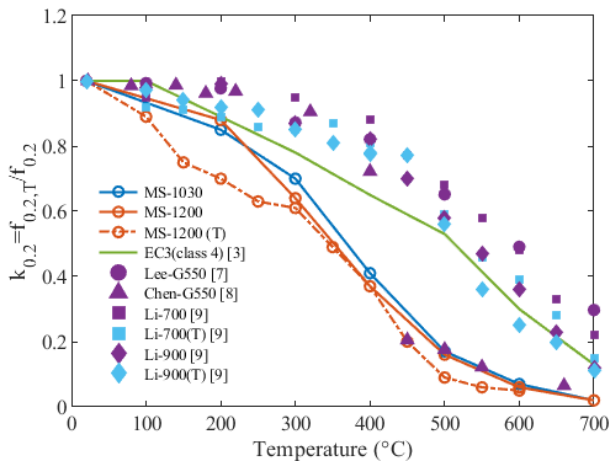


(a) Steady-state tests and transient tests

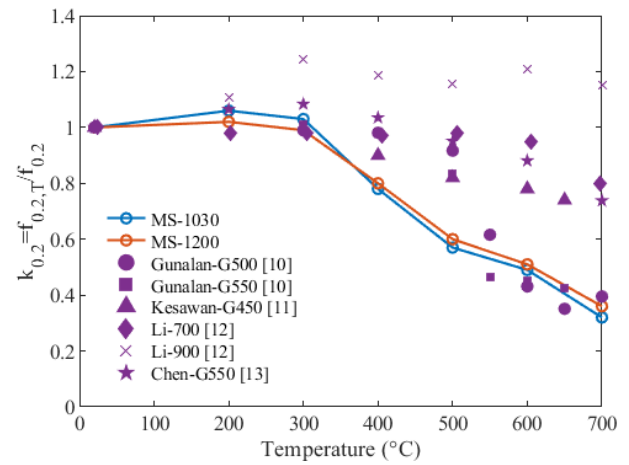


(b) Residual tests

Figure 7. Comparison of elastic modulus (transient-state test results are marked with 'T' in fig. (a)).

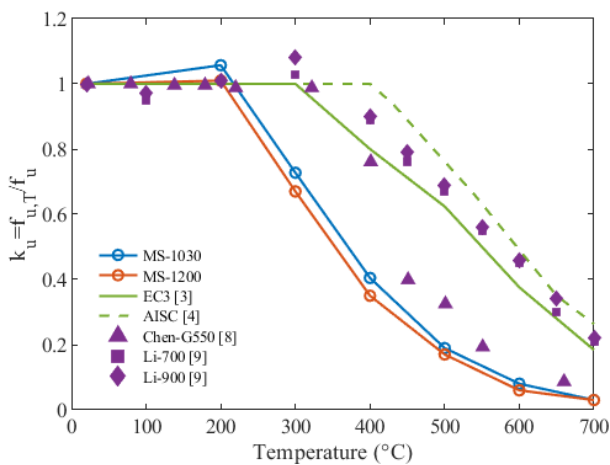


(a) Steady-state tests and transient tests

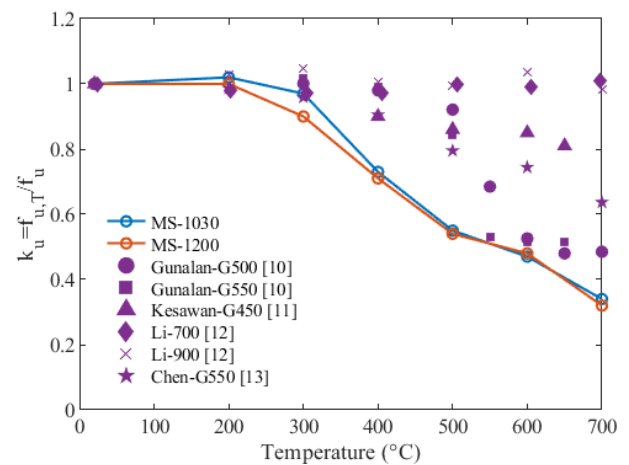


(b) Residual tests

Figure 8. Comparison of 0.2% proof stress (transient-state test results are marked with 'T' in fig. (a)).



(a) Steady-state tests



(b) Residual tests

Figure 9. Comparison of ultimate stress.

5 PROPOSED EQUATIONS

5.1 Elevated temperature mechanical properties

Comparisons in Section 4 show that the tested MS steels generally exhibit larger reduction in mechanical properties than lower grade cold-formed steels at elevated temperature, consequently the current provisions in design codes are not applicable to these new alloys. Therefore, new predictive models are proposed in this section.

For the mechanical properties of the tested MS steels at elevated temperature, a three-coefficient equation is proposed, see Eq. (1) and Eq. (2). This equation has been derived through committee work with the American Iron and Steel Institute to determine the mechanical properties of conventional grade cold-formed steels at elevated temperature [19]; the advantage of the formulation is that it can be calibrated on different materials by adjusting the coefficients. The retention factor k_x is a function of temperature normalized within the test temperature range of 20°C-700°C. The subscript x stands for the mechanical property which can be the elastic modulus, 0.2% proof stress, and ultimate stress. This format features a single continuous function with a small number of coefficients to describe the reduction trend of the mechanical properties.

$$k_x = (1 - c) \cdot \frac{1 - x^b}{1 + ax^b} + c \quad (1)$$

$$x = \frac{T - T_1}{T_2 - T_1}, T_1 = 20^\circ\text{C}, T_2 = 700^\circ\text{C} \quad (2)$$

The coefficients are calibrated based on the test results obtained in this study. For the elastic modulus of the two tested MS steels, the results from steady-state tests and transient-state tests show a marked discrepancy, thus two sets of coefficients are calibrated, with one set of coefficients calibrated based on the steady-state test data and another set calibrated based on the transient-state test data. For yield stress, the test method shows no significant influence, hence the coefficients are calibrated based on the aggregate data from both steady-state and transient-state tests. The calibrated coefficients are listed in Table 5.

Table 5. Coefficients to determine the elevated temperature retention factors of cold-formed MS steels.

Properties	Test method	a	b	c
Elastic modulus	SS	4.4	2.9	0.09
	TS	35.0	5.5	0.02
0.2% proof stress	SS+TS	9.2	3.0	0.02
Ultimate stress	SS	30.4	4.8	0.03

Note: ‘SS’ stands for steady-state test; ‘TS’ stands for transient-state test.

The proposed retention factors for the elastic modulus, 0.2% proof stress, and ultimate stress are compared with other proposed models in literature [8,9,20], as shown in Figure 10. The proposed model for the elastic modulus provides slightly higher prediction than the one by Kankanamge and Mahendran [20] and the one by Li and Young [9] when the exposure temperature is lower than 300°C, beyond which the model in this study provides lower retention factors. For the yield stress, the proposed model in this study provides lower prediction when the temperature is lower than 450°C, beyond which it agrees well with the one by Chen and Young [8]. For the ultimate stress, the proposed model provides lower prediction than the other published models.

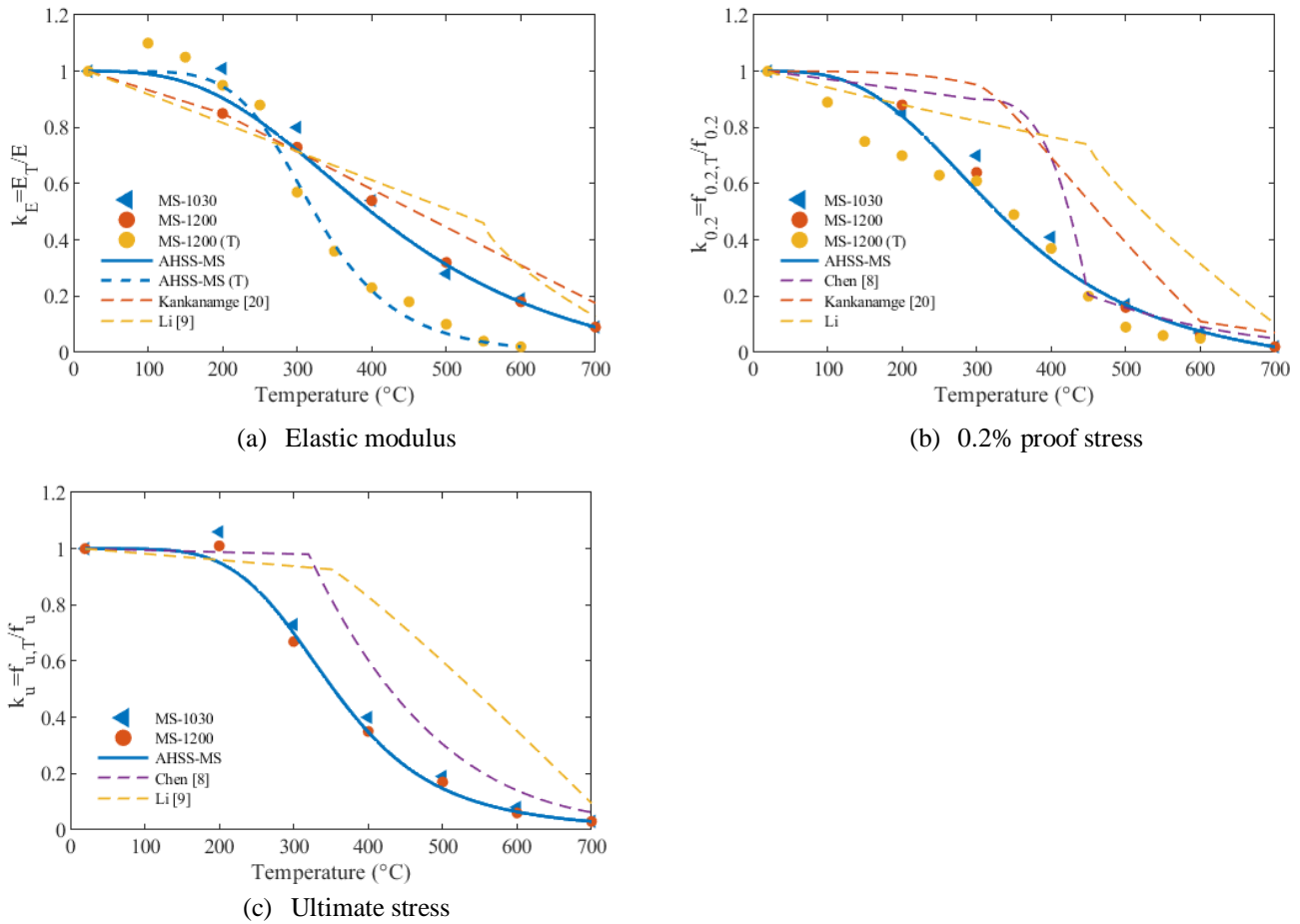


Figure 10. Retention factors for mechanical properties of cold-formed MS steels at elevated temperature. The proposed models in this study are the blue curves.

5.2 Post-fire mechanical properties

The post-fire elastic modulus of the cold-formed MS steels remains approximately unchanged after exposure up to 600°C while a more noticeable reduction is observed at 700°C. The format of piecewise linear function, as expressed in Eq. (3) and Eq. (4), proposed by Li and Young [12], is adopted in this study to describe the post-fire elastic modulus of MS steels.

$$k_E = 1, \quad 20^\circ\text{C} < T < 600^\circ\text{C} \quad (3)$$

$$k_E = 1 - \frac{T - 600}{1111}, \quad 600^\circ\text{C} < T < 700^\circ\text{C} \quad (4)$$

For the post-fire yield stress and ultimate stress, the same format of equation as expressed in Eq. (1) and Eq. (2) is adopted. The coefficients are calibrated based on the test data obtained from the residual tests in this study, as listed in Table 6.

Table 6. Coefficients to determine the post-fire retention factors of cold-formed MS steels.

Properties	a	b	c
0.2% proof stress	10	6	0.32
Ultimate stress	8	5	0.30

The proposed model in this study for the elastic modulus, 0.2% proof stress, and ultimate stress are compared with other proposed models in literature, as shown in Figure 11. The proposed model for the post-fire elastic modulus agrees with those in the published papers [10,12,13,21]. The model for 0.2% proof stress agrees with other models in temperature range of 20°C-300°C and 600°C-700°C, but provides lower

values at 300°C-600°C, indicating that MS steel residual strength is more affected than the other tested steels in the literature in the moderate exposure temperature range. For the post-fire ultimate stress, the proposed model in this study is lower than the other models in the literature.

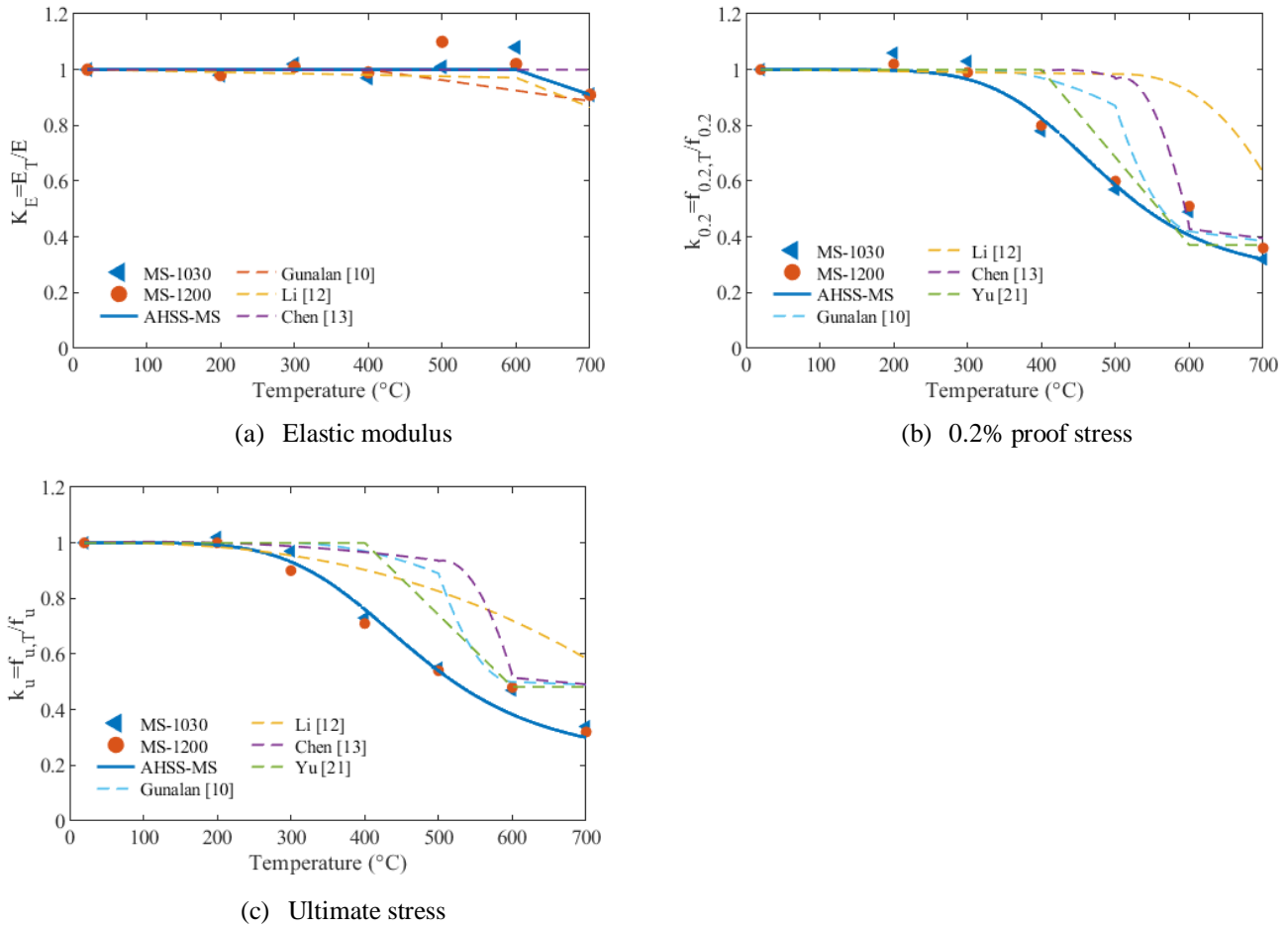


Figure 11. Retention factors for post-fire mechanical properties of cold-formed MS steels. The proposed models in this study are the blue curves.

6 CONCLUSIONS

An experimental investigation has been carried out on the mechanical properties of two cold-formed martensitic (MS) steels, with nominal yield stress of 1030 MPa and 1200 MPa, at elevated temperature and after cooling down. Three different test methods were used namely steady-state tests, transient-state tests, and residual tests. Both a DIC method and high temperature contact extensometer were used to measure strains and the two methods show good agreement. Stress-strain curves and mechanical properties of elastic modulus, yield stresses at different strain levels, and ultimate stress were obtained. Reduction trends of the mechanical properties at elevated temperature and after exposure to elevated temperature were discussed and compared with design provisions and other test data in literature.

It was found that the tested MS steels experienced proportionally larger reduction in stiffness and strength than lower grade steels at elevated temperature. After exposure to elevated temperature and cooling down, the residual retention factors for yield stress and ultimate stress were also lower than those of lower grade steels. The retention factors provided in Eurocode 3 (including those for class 4 sections relative to 0.2% proof stress) are not applicable to the tested cold-formed MS steels. New predictive equations were proposed to determine the mechanical properties of the tested MS steels at elevated temperature and after cooling down, using a continuous equation that can be calibrated based on 3 coefficients.

REFERENCES

1. X. Yan, Y. Xia, H.B. Blum, T. Gernay, Elevated temperature material properties of advanced high strength steel alloys, *J. Constr. Steel Res.* 174 (2020) 106299.
2. S. Keeler, M. Kimchi, Advanced high-strength steels application guidelines V5, WorldAutoSteel, 2015.
3. EN 1993-1-2, Eurocode 3: Design of Steel Structures - Part 1-2: General Rules – Structural Fire Design, European Committee for Standardization (CEN), Brussels, 2005.
4. AISC 360-16, Specification for Structural Steel Buildings, Chicago, 2016.
5. AISI, North American standard for cold-formed steel structural framing, 2015.
6. AS/NZS 4600, Cold-Formed Steel Structures, 2005.
7. J.H. Lee, M. Mahendran, P. Makelainen, Prediction of mechanical properties of light gauge steels at elevated temperatures, *J. Constr. Steel Res.* 59 (2003) 1517–1532. [https://doi.org/10.1016/S0143-974X\(03\)00087-7](https://doi.org/10.1016/S0143-974X(03)00087-7).
8. J. Chen, B. Young, Experimental investigation of cold-formed steel material at elevated temperatures, *Thin-Walled Struct.* 45 (2007) 96–110. <https://doi.org/10.1016/j.tws.2006.11.003>.
9. H.T. Li, B. Young, Material properties of cold-formed high strength steel at elevated temperatures, *Thin-Walled Struct.* 115 (2017) 289–299. <https://doi.org/10.1016/j.tws.2017.02.019>.
10. S. Gunalan, M. Mahendran, Experimental investigation of post-fire mechanical properties of cold-formed steels, *Thin-Walled Struct.* 84 (2014) 241–254. <https://doi.org/10.1016/j.tws.2014.06.010>.
11. S. Kesawan, M. Mahendran, Post-fire mechanical properties of cold-formed steel hollow sections, *Constr. Build. Mater.* 161 (2018) 26–36. <https://doi.org/10.1016/j.conbuildmat.2017.11.077>.
12. H.T. Li, B. Young, Residual mechanical properties of high strength steels after exposure to fire, *J. Constr. Steel Res.* 148 (2018) 562–571. <https://doi.org/10.1016/j.jcsr.2018.05.028>.
13. W. Chen, J. Ye, J. Peng, B. Liu, Experimental Investigation of Postfire Mechanical Properties of Q345 and G550 Cold-Formed Steel, *J. Mater. Civ. Eng.* 31 (2019) 1–13. [https://doi.org/10.1061/\(ASCE\)MT.1943-5533.0002791](https://doi.org/10.1061/(ASCE)MT.1943-5533.0002791).
14. ASTM E21, Standard Test Methods for Elevated Temperature Tension Tests of Metallic Materials, American Society for Testing and Materials, West Conshohocken, USA, 2009.
15. J.D.M. William Luecke, Stephen W. Banovic, High-temperature tensile constitutive data and models for structural steels in fire, NIST Tech. Note 1714. (2011) 137. <https://doi.org/10.1088/1674-1056/22/6/068503>.
16. J. Blaber, B. Adair, A. Antoniou, Ncorr: open-source 2D digital image correlation matlab software, *Exp. Mech.* 55 (2015) 1105–1122.
17. J. Outinen, P. Mäkeläinen, Mechanical properties of structural steel at elevated temperatures and after cooling down, *Fire Mater.* 28 (2004) 237–251. <https://doi.org/10.1002/fam.849>.
18. X. Yan, Y. Xia, H.B. Blum, T. Gernay, Post-fire mechanical properties of advanced high-strength cold-formed steel alloys (Under review) .
19. X. Yan, J.C. Batista Abreu, R.S. Glauz, B.W. Schafer, T. Gernay, Simple three-coefficient equation for temperature dependent mechanical properties of cold-formed steels (Under review).
20. N.D. Kankanamge, M. Mahendran, Mechanical properties of cold-formed steels at elevated temperatures, *Thin-Walled Struct.* 49 (2011) 26–44. <https://doi.org/10.1016/j.tws.2010.08.004>.
21. Y. Yu, L. Lan, F. Ding, L. Wang, Mechanical properties of hot-rolled and cold-formed steels after exposure to elevated temperature: A review, *Constr. Build. Mater.* (2019). <https://doi.org/10.1016/j.conbuildmat.2019.04.062>.

EFFECT OF TRANSIENT CREEP ON STABILITY OF STEEL COLUMNS EXPOSED TO FIRE

Venkatesh Kodur¹, Svetha Venkatachari²

ABSTRACT

This paper presents a parametric study to evaluate the influence of temperature-induced transient creep on the onset of instability in steel columns exposed to fire. A detailed finite element model is developed in ABAQUS to trace the response of a steel column under fire exposure wherein significant transient creep strains that develop in steel at elevated temperature is explicitly incorporated in the fire resistance analysis. The effect of critical parameters such as the severity of fire exposure, stress level, thermal gradients, and slenderness on the stability of steel columns as well as the extent of creep deformations that occur under fire is examined. Results from the parametric study indicate that high-temperature creep critically affects the onset of instability in a steel column under severe fire conditions. Asymmetric thermal gradients that develop in columns subjected to non-uniform fire exposure are found to have a significant influence on the extent of creep deformations.

Keywords: High-temperature creep; instability; steel columns; design fire; explicit creep

1 INTRODUCTION

Fire in steel framed buildings can cause excessive damage to structural members and in rare cases lead to local or global failure of the structure. Such fire-induced damage or failure in steel framed buildings gets initiated with the onset of instability in a single or multiple set of columns and can propagate through the system leading to failure of the respective compartment, story, or the entire structure. The onset of instability in steel columns is primarily due to temperature-induced degradation in strength and stiffness properties of steel, combined with significant levels of transient creep strain that develops at temperatures beyond 400°C [1].

In current simplified fire resistance analysis approaches the effect of temperature-induced transient creep strain is often neglected and in advanced analysis, transient creep is implicitly accounted through temperature-dependent stress-strain relations as in Eurocode 3 (EC3) [2] or ASCE [3]. However, these stress-strain relations consider only partial effects of transient creep that develops at elevated temperatures [4]. Prior studies [5–9] have shown that this implicit treatment of creep leads to unconservative fire resistance predictions of steel members and that the transient creep strain needs to be explicitly incorporated in the fire resistance analysis of steel structures.

Limited studies have been reported in the literature that explicitly accounts for the temperature-induced creep effects in the fire resistance analysis of steel columns under fire conditions [6, 7]. Li and Zhang [6] showed that neglecting high-temperature creep effects can lead to unrealistic predictions of buckling temperature in axially restrained steel columns under varying levels of axial restraint and heating rates. The

¹ University Distinguished Professor, Department of Civil and Environmental Engineering, Michigan State University, East Lansing, USA
e-mail: kodur@egr.msu.edu

² Ph.D. Candidate, Department of Civil and Environmental Engineering, Michigan State University, East Lansing, USA
e-mail: venkat28@msu.edu

experimental and numerical investigations on steel columns carried out by Morovat et al. [7] indicated that the critical buckling load depends not only on the slenderness and temperature level but also on the duration of the applied loading. In these prior studies, the influence of creep on fire response of steel columns, specifically on the onset of instability, due to the type of fire exposure, thermal gradients that develop within the column due to the number of fire-exposed faces, load levels and restraint conditions has not been evaluated.

To address the aforementioned knowledge gaps, a numerical model is built in ABAQUS to trace the effect of temperature-induced transient creep on the onset of instability in steel columns. The transient creep strain that develops under fire conditions is explicitly accounted for in the fire resistance analysis, in addition to temperature-dependent material property degradation and geometric nonlinearity effects. The developed model is applied to carry out a parametric study on steel columns to quantify the effect of high-temperature creep under varying scenarios of load levels, thermal gradients, column slenderness, and fire severity.

2 NUMERICAL MODEL

To evaluate the effect of transient creep on the evolution of temperature-induced instability in a steel column, a numerical model is developed in the finite element (FE) software ABAQUS. The analysis approach involves a sequentially coupled thermal analysis followed by structural analysis. For the thermal analysis, the cross-section of the steel column and fire insulation is discretized using 4-noded shell (S4R) elements. The interface between the steel member and fire insulation is modelled using a tie constraint such that the temperature in the interfacial nodes at the steel-insulation boundary are the same. The fire temperatures are applied on the exposed surfaces through convective and radiative boundary conditions. Convective heat transfer coefficients of 25 W/m-K and 35 W/m-K, respectively for standard and design fire exposure scenarios and an emissivity coefficient of 0.8 are used in the thermal model [10]. Temperature-dependent thermal properties are specified as per EC3 [2] recommendations. A nonlinear transient heat transfer analysis is carried out to obtain the variation of sectional temperature in the steel column as a function of fire exposure time.

For the structural analysis, the steel column is discretized using 2-noded beam (B31) elements. The end supports of the column are modelled using kinematic constraints. An initial geometric imperfection of $H/1500$ mm at mid-height of the column is assumed, where H is the height of the column (mm). The axial load on the column is applied as a vertical downward force at the top end of the column. The variation of temperature with fire exposure time obtained from the thermal analysis at critical nodes in the cross-section is applied to the column as fire load. The structural response of the steel column under fire conditions is obtained by carrying out a nonlinear transient quasi-static analysis ('Visco') in ABAQUS. The failure of the steel column is evaluated based on strength and deformation limit states as per BS-476 [11]. Temperature-dependent stress-strain relations of steel are used in the mechanical model as per EC3 [2]. As noted earlier, these stress-strain relations only account for implicit creep strain, which is only a small part of the total creep strain that develops under fire exposure. To account for the full creep effects, transient creep strain is explicitly modelled and provided as input to the numerical model in the structural analysis step.

The temperature-induced transient creep strain is modelled using the built-in CREEP power-law model in ABAQUS. The strain hardening form of power law (as shown in equation (1)) is adopted, as it is relevant for fire resistance analysis where the stress state of the material varies with time.

$$\dot{\bar{\epsilon}}^{cr} = (A\tilde{q}^n[(m+1)\bar{\epsilon}^{cr}]^m)^{\frac{1}{m+1}} \quad (1)$$

where $\dot{\bar{\epsilon}}^{cr}$ is the creep strain rate,

\tilde{q}^n is the stress,

$\bar{\epsilon}^{cr}$ is the creep strain, and

A , n , and m are temperature-dependent creep material parameters.

is *without creep*, where only partial creep effects are included implicitly through EC3 stress-strain relations. The initial stage of axial deformation response is governed by the thermal strains and much less of mechanical and transient creep strain and the column expands. During this stage, the temperatures in much of the column cross-section are lower than 400°C and hence, there is not much degradation of mechanical properties of steel and stress levels in the column are below 30%. In this stage, the trends predicted by the models *with creep* and *without creep* are similar.

As the temperatures in the cross-section rise beyond 400°C, there is larger degradation in the strength and stiffness properties of steel and stress levels rise to 40%. This results in an increase in mechanical strain and also the onset of transient creep strain which offsets some of the thermal strain. In this stage, the column continues to expand as this column is lightly loaded; however, the rate of expansion reduces. In the final stage, the temperatures increase beyond 600°C and stress levels reach 50%. Mechanical and transient creep strain dominates the response as the axial deformation of the column shifts from expansion to contraction. Instability begins to set in when the axial force in the column starts to drop to zero and the column fails at about 220 min. During this stage, the difference in the deformation and force response predicted using the models *with creep* and *without creep* becomes evident. The model without explicit creep is seen to underestimate the axial deformation and overestimate the axial force in the steel column and hence, overestimates the onset of instability (or time to failure).

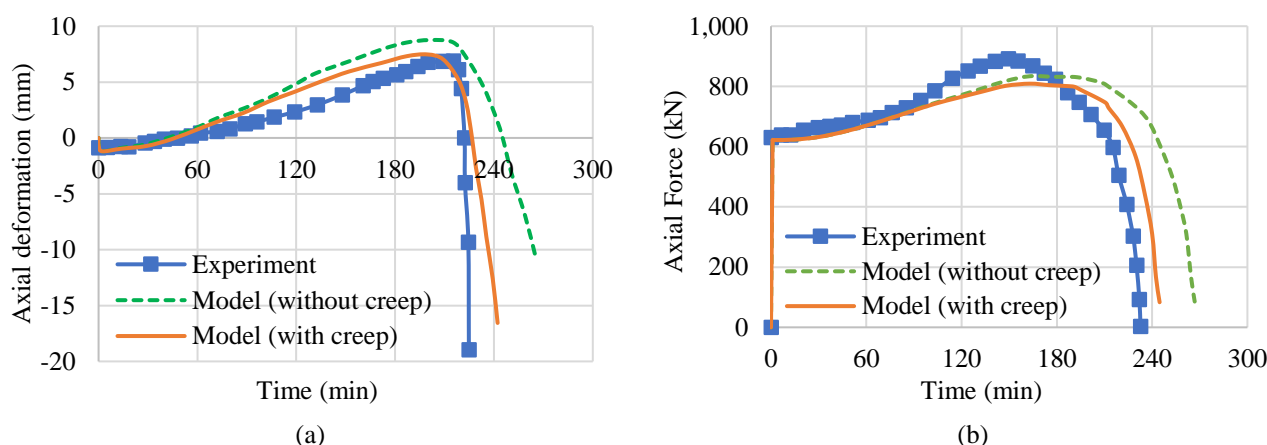


Figure 2. Comparison of measured and predicted (a) axial deformation and (b) axial force in steel column

4 PARAMETRIC STUDIES

4.1 General

To evaluate the effect of creep on the response of columns, four critical parameters, namely, load level, thermal gradients (arising from varying sides of fire-exposure), slenderness (ratio) of the column, and fire severity are considered in the analysis. The wide flange sections considered in this study are selected from commonly used gravity columns in a typical steel-framed building. The columns are assumed to be 3.05 m in height, pin supported at both ends, and made of A992 ($f_y = 345$ MPa) steel. All columns are protected using SFRM-type insulation to meet a fire rating of 2 hours. The numerical analyses are carried out using the validated FE model and the results for each case are presented for two scenarios: one *with creep*, where the high-temperature creep is explicitly incorporated, and the other *without creep*, where only partial creep effects are included implicitly in the fire resistance analysis. The different parameters considered in this study are presented in Table 2.

4.2 Load (stress) level

Load level represents the ratio of the applied axial load to the capacity of the steel column at ambient temperature. The higher the load level higher is the compressive stress on the column. Figure 3(a) shows the axial deformation plots of columns subjected to ASTM E119 fire exposure [14] under three different load levels of 30%, 40%, and 60%, with and without the inclusion of explicit creep. The results indicate

that the column deteriorates rapidly under increasing load levels, owing to the higher initial stress (load-induced) in the column. The scenario of 60% load level results in the shortest failure time of 99 min. The effect of creep is also higher in columns subjected to higher loads, as transient creep strain increases significantly with an increase in stress levels [1]. Figure 3(b) shows the deformed shape of the column for the case of 40% load level obtained using models with and without creep at 155 min of fire exposure. It is evident that the model without explicit creep underestimates the deformation of the column at stages close to failure. Although most columns are lightly loaded in typical steel framed buildings, the exposure to fire results in the degradation of strength and stiffness in steel which in turn can induce high stress levels with increasing fire exposure time, resulting in significant creep deformations and an early onset of instability in these columns.

Table 2. Transient creep effects in steel columns exposed to fire

Parameter	Column	Slenderness ratio (λ_r)	Applied Load (kN)	Load level (LL) (%)	Fire scenario	Exposed sides	Fire resistance		
							With creep	Without creep	Difference
Load level	W14x53	63	705	30	ASTM E119	4	232	241	9
	W14x53	63	940	40	ASTM E119	4	158	188	30
	W14x53	63	1410	60	ASTM E119	4	99	136	37
Thermal gradients	W14x53	63	940	40	ASTM E119	1	NF	NF	-
	W14x53	63	940	40	ASTM E119	2	NF	NF	-
	W14x53	63	940	40	ASTM E119	3	227	273	46
	W14x53	63	940	40	ASTM E119	4	158	188	30
Slenderness	W14x53	63	940	40	ASTM E119	4	158	188	30
	W14x82	48	1620	40	ASTM E119	4	186	199	13
	W14x145	30	3204	40	ASTM E119	4	200	208	8
Fire severity	W14x53	63	1175	40	DF-90	4	NF	NF	-
	W14x53	63	1175	40	DF-120	4	134	164	30

DF – Design fire; NF – No failure

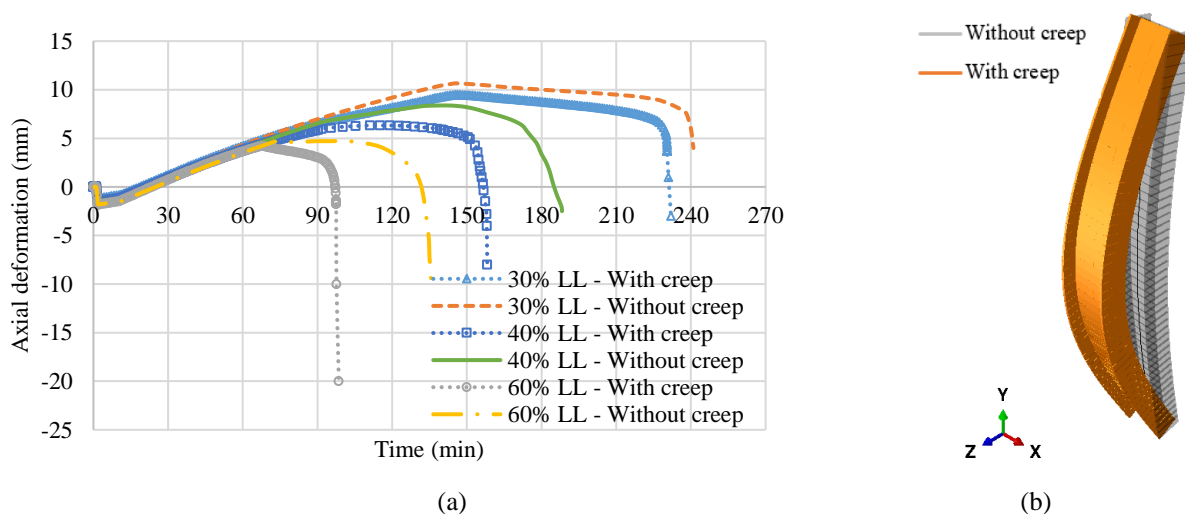


Figure 3. (a) Axial deformation response of steel columns under varying load levels (b) Deflected profile of steel column under 40% LL at a fire exposure time of 155 min

4.3 Thermal gradients

Based on the location of a column member in a building, whether in the interior, perimeter, or corner of a steel-framed building, the exposure conditions on the member can vary when subjected to fire. The axial deformation response of columns exposed to fire from 1, 2, 3 and 4 sides, from the analyses *with creep* and *without creep*, is presented in Figure 4. Under uniform fire exposure (4-sides), the column member experiences higher temperatures, which in turn leads to faster degradation of strength and stiffness of steel, resulting in an early onset of instability. The influence of high-temperature creep, on the other hand, is the highest in the case of 3-sided fire exposure, with the difference between failure times of 227 min and 273 min respectively predicted using models with and without creep being 46 min. The column experiences uniaxial bending (thermal bowing), due to the asymmetric thermal gradients that develop under 3-sided fire exposure, which gets further increased due to the differential creep strain that develops in the column section, leading to higher stresses and in turn higher creep deformations and subsequent failure.

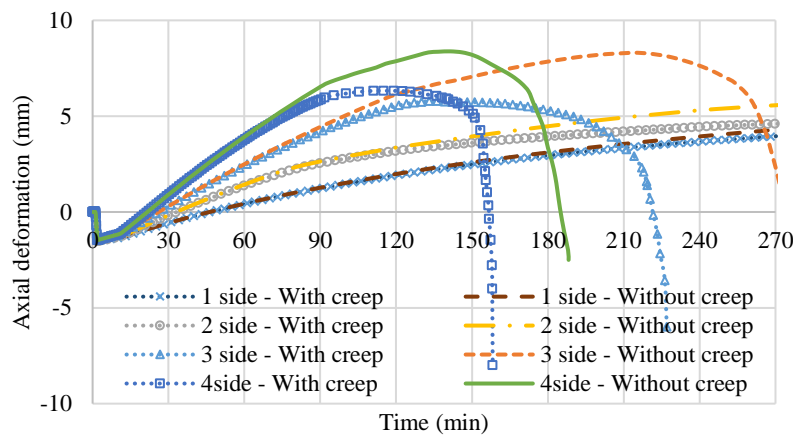


Figure 4. Axial deformation response of steel columns under varying thermal gradients

4.4 Slenderness

Three wide flange sections, W14x53, W14x82, and W14x145 with slenderness ratios of 63, 48, and 30 are considered. The slenderness values chosen are representative of those of typical columns used in the upper, middle, and lower stories of a mid-rise steel framed building. Figure 5 shows the comparison of the axial deformation response of the three columns considered, with and without incorporating explicit creep. The difference in fire resistance times is the highest (30 min) in the case of W14x53 column with the largest slenderness ratio. The column with higher slenderness experiences a faster reduction in capacity with rising temperature, which in turn leads to higher stress levels and an early onset on instability.

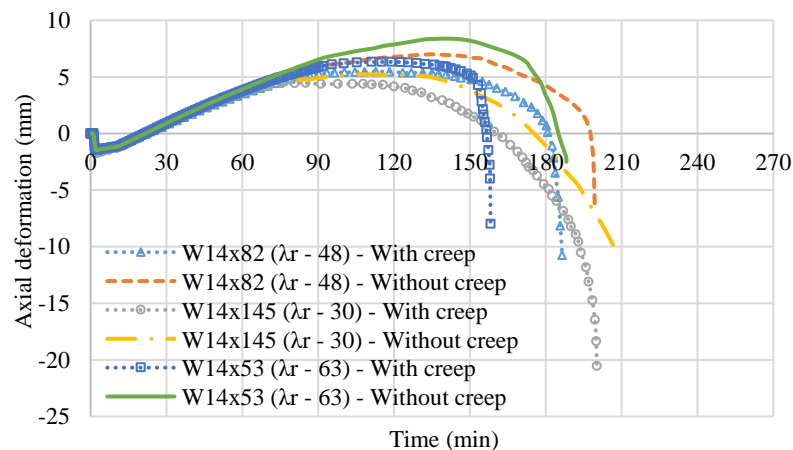


Figure 5. Axial deformation response of steel columns with varying slenderness ratios

4.5 Fire severity

To investigate the influence of the severity of fire exposure on the extent of transient creep deformations that develop in steel columns, two design fire scenarios of moderate to high severity are selected, namely, DF-90 and DF-120, as shown in Figure 6(a). The axial deformation response of the column under exposure to these design fires is presented in Figure 6(b). Under the DF-90 fire scenario, which has a burning period of 90 min, the steel temperatures in the column section are within 400°C for the entire duration of exposure and very less creep deformations develop in the member. On the other hand, exposure to the more severe DF-120 fire scenario results in high temperatures in the column member at quicker times leading to a lower failure time as compared to the standard fire scenario. The effect of creep is high in the case of DF-120 and is evident from the axial deformation response which shows a difference of 30 min in fire resistance times predicted using models with and without creep. Due to the high peak fire temperature (above 1000°C) and a long burning duration (2 hours), significant creep deformations develop in the steel column under DF-120 scenario. When exposed to severe fires, with peak temperatures above 1000°C and burning for more than 2 hours, and steel temperatures exceeding 450°C, the high level of creep strain that develops in steel can be critical to the stability of the column. In such scenarios, an explicit creep analysis is needed to realistically predict the onset of instability in the steel column.

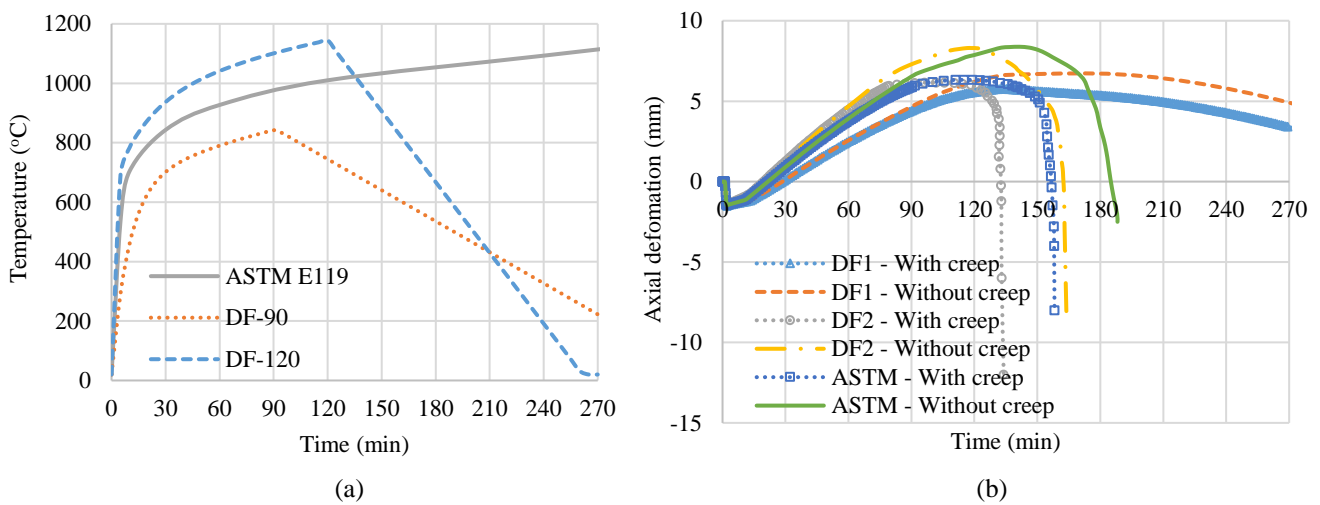


Figure 6. (a) Fire exposure scenarios considered (b) Axial deformation response of steel columns under varying fire severity

5 RESEARCH IMPLICATIONS

The focus of this study is limited to evaluating the high-temperature creep effects in steel columns subjected to fire conditions. The difference in the time of onset of instability (or fire resistance) in steel columns predicted using models with and without the inclusion of explicit creep under varying scenarios of load levels, thermal gradients, column slenderness, and fire severity is quantified. Specific attention is given to the evolution of transient creep that develops under fire exposure at a member level. Results from this study can be utilized in developing design guidelines for the treatment of transient creep in the fire resistance analysis of steel columns.

Creep deformations, however, can be more critical to the stability of a fire-exposed steel structure leading to a progressive collapse in severe cases. In a steel-framed building, columns are integral to the stability of the structure. The loss of one or more columns results in a redistribution of loads to the adjoining members leading to higher stress levels in the adjacent columns. The increased stress levels, combined with high temperature levels, produce large creep strains which can lead to an early onset of instability in the columns and this may lead to the collapse of the structure. Therefore, system level analysis approaches are to be applied to incorporate the effect of high-temperature creep on the fire-induced collapse of steel framed buildings.

6 CONCLUSIONS

Based on the results from the parametric study, the following conclusions are drawn:

1. Not accounting for full transient creep effects will lead to an underestimation of axial deformation and overestimation of axial force, thus predicting a delayed onset of instability in a steel column. Incorporating the full effects of temperature-induced transient creep strain, through an explicit analysis is critical in realistically predicting the onset of instability (or fire resistance) under fire exposure.
2. Asymmetric thermal gradients that develop in a steel column on account of 1-, 2- or 3-sided fire exposure can induce large creep deformations under sustained fire exposure. The scenario with 3-sided fire exposure produced the highest difference between the predicted fire resistance times obtained using models with and without the inclusion of explicit creep.
3. The effect of transient creep is minimal under fires with low to moderate fire severity if the temperatures in the steel section do not exceed 450°C and in such cases incorporating transient creep strain implicitly in the fire resistance analysis is sufficient. In scenarios of high fire severity (peak fire temperature above 1000°C and burning more than 2 hours and steel temperatures exceeding 450°C), the full extent of high-temperature creep needs to be included through an explicit treatment of transient creep in the fire resistance analysis.

REFERENCES

1. Kodur, V., Naser, M., Structural Fire Engineering. McGraw Hill Professional, New York; 2020.
2. EN 1993-1-2: Eurocode 3-Design of Steel Structures, Part 1-2: General Rules for Structural Fire Design. Commission of European Communities, Brussels, Belgium; 2005.
3. ANSI/AISC 360-16: Specifications for structural steel buildings. American Institute of Steel Construction, Chicago, IL; 2016.
4. Wang, W., Kodur, V., Chapter 5 - Creep behavior of steels at elevated temperatures. In: Wang, W., Kodur, V., (eds), Material Properties of Steel in Fire Conditions. Academic Press, Cambridge, MA, pp 261–343; 2020.
5. Kodur, V., Dwaikat, M., Effect of high temperature creep on the fire response of restrained steel beams. Materials and structures 43:1327–1341 (2010). <https://doi.org/10.1617/s11527-010-9583-y>.
6. Li, G-Q., Zhang, C., Creep effect on buckling of axially restrained steel columns in real fires. Journal of Constructional Steel Research 71:182–188 (2012). <https://doi.org/10.1016/j.jcsr.2011.09.006>.
7. Morovat, MA, Engelhardt, MD, Helwig, TA, Taleff, EM, High-Temperature Creep Buckling Phenomenon of Steel Columns Subjected to Fire. Journal of Structural Fire Engineering 5:189–202. (2014). <https://doi.org/10.1260/2040-2317.5.3.189>.
8. Kodur, VK, Aziz, EM, Effect of temperature on creep in ASTM A572 high-strength low-alloy steels. Materials and Structures 48:1669–1677 (2015). <https://doi.org/10.1617/s11527-014-0262-2>.
9. Hantouche, EG, Al Khatib, KK, Morovat, MA, Modeling creep of steel under transient temperature conditions of fire. Fire Safety Journal 100:67–75 (2018). <https://doi.org/10.1016/j.firesaf.2018.07.006>.
10. EN 1991-1-2: Eurocode 1: Actions on structures - Part 1-2: General actions - Actions on structures exposed to fire. Commission of European Communities, Brussels, Belgium; 2002.
11. BS 476-20: Fire tests on building materials and structures – Part 20: Method for determination of the fire resistance of elements of construction (general principles). BSI, UK; 1987.
12. Morovat, MA, Lee, JW, Engelhardt, MD, et al., Creep properties of ASTM A992 steel at elevated temperatures. Trans Tech Publ, pp 786–792 (2012).
13. Dwaikat, MMS, Kodur, VKR, Quiel, SE, Garlock, MEM, Experimental behavior of steel beam–columns subjected to fire-induced thermal gradients. Journal of Constructional Steel Research 67:30–38 (2011). <https://doi.org/10.1016/j.jcsr.2010.07.007>.
14. ASTM E119-19: Standard Test Methods for Fire Tests of Building Construction and Materials. ASTM International, West Conshohocken, PA; 2019.

COMPRESSIVE STRENGTH AND MOE OF SOLID SOFTWOOD AT ELEVATED TEMPERATURES

Abdulrahman Zaben^{*1}, David Lange², and Cristian Maluk³.

ABSTRACT

This article reports on work which was conducted to evaluate the effect of elevated temperatures on the compressive strength and modulus of elasticity (MoE) in compression of Australian Southern Pine. Sixty specimens of solid softwood were tested in a uniaxial loading system parallel to the grain after reaching a steady-state temperature condition for temperatures range between 20 and 285°C. The results present a maximum reduction in the compressive strength and elastic modulus of 83% and 57%, respectively, compared to the ambient conditions properties. The outcomes of this experimental study are valuable in order to better understand the reduction of compressive strength of timber at elevated temperatures as experienced by timber during a fire.

Keywords: Timber; compressive strength; modulus of elasticity; elevated temperature

1 INTRODUCTION

Increased adoption of timber in the construction industry as primary structural elements is sometimes limited by the perceived underperformance in the event of a fire. It is well-recognized these days that the mass timber structures can have an appropriate fire performance, as there is a sufficient mass of wood such that a char layer can form. In structural calculations, the char layer should be ignored as it has a negligible strength. Beyond the char layer, there is a zone of heated timber, typically called the ‘heat-affected zone’, with reduced mechanical properties. The designer of timber structures need to be confident that load-bearing timber elements must not fail for the full duration of a building fire, neither due to the loss of the cross-section nor the reduction of the mechanical properties of the heat-affected zone of timber [1].

Several studies tried to quantify the effect of elevated temperatures on the compressive strength of timber in order to estimate the capacity of the heat-affected zone in different heating conditions [2-9]. However, there is an apparent disagreement between the various curves represented by those studies which are likely due use of different experimental setups, different timber species, different moisture migration during the test, and other factors [1].

This work establishes a local reference for one of the popular Australian structural timber species ‘Australian Southern Pine’ that can be used to estimate the actual reduction of the timber compressive strength and modulus of elasticity due to exposure to elevated temperatures.

¹ Abdulrahman Zaben, School of Civil Engineering, The University of Queensland, Australia
e-mail: a.zaben@uq.edu.au, ORCID: <https://orcid.org/0000-0001-7229-9193>

² Dr Cristian Maluk, School of Civil Engineering, The University of Queensland, Australia
e-mail: c.maluk@uq.edu.au, ORCID: <https://orcid.org/0000-0002-1662-6943>

³ Dr David Lange, School of Civil Engineering, The University of Queensland, Australia
e-mail: d.lange@uq.edu.au, ORCID: <https://orcid.org/0000-0002-4551-1045>

2 SAMPLE PREPARATION AND TESTING METHOD

Sixty specimens of clear, defect-free, straight-grained material were cut from 35mm thickness timber planks of grade MGP15 (Machine Graded Pine) and an average density of 670 kg/m³. The specimens' dimensions were 35mm × 45mm × 140mm according to the Australian standard [AS/NZS 4063]. The specimens had a 12% moisture content at ambient temperature conditions before testing.

Eighteen specimens were tested at ambient temperature conditions, and six specimens at each of the target temperature increments of 50, 100, 150, 200, 240, 270, 285°C. The specimens were placed inside the preheated environmental chamber until a steady-state condition at the centre of each specimen was achieved, for each target temperature, before starting the loading test. The steady-state condition was defined as the instant where the centre of the specimen reached the target temperature with a temperature variation rate of less than 1°C/min. The 1°C/min variation rate was achieved for all temperature increments except the 270°C and the 285°C, where for these two temperatures an internal exothermic reaction started inside the specimens which increased the internal rate of temperature variation, this is why the loading tests for those specimens were initiated while the rate of temperature variation was about 3°C/min. More investigation is still required to identify any possible combination that caused the internal exothermic reaction at the higher temperature increments.

Conducting the tests in this way may allow us to explore the correlation between the central temperature development and the derived heating rates inside the timber, and the reduction in its mechanical properties due to elevated temperatures.

2.1 Heating conditions

A preliminary thermal characterisation study was conducted to define the thermal steady-state condition at the centre of the specimens as described previously. Once the specimens were placed inside an MTS environmental chamber, K-type thermocouples were used to measure the gas-phase temperature, the surface temperature, and the in-depth centre temperature of the specimens when they were being heated. Figure 1 shows the temperatures measured for a typical 270-280°C specimen placed inside the environmental chamber in addition to the heating rate curve of the internal temperature. Typical temperature curves inside the timber specimens and the heating rate curves for each target temperature are shown in Figure 2 and Figure 3, respectively. The vertical green dashed lines in Figure 2 present the onset of applying the compressive load which was around 55 minutes for 50, 270, 285°C increments, and around 70 minutes for the 100, 150, 200, 240°C increments.

It is important to highlight that the heating conditions during the experiments described herein are not representative of the expected heating conditions for timber during a real fire in a real building. Nevertheless, the outcomes of this experimental study are valuable in order to better understand the reduction of compressive strength of timber at elevated temperatures as experienced by timber during a fire.

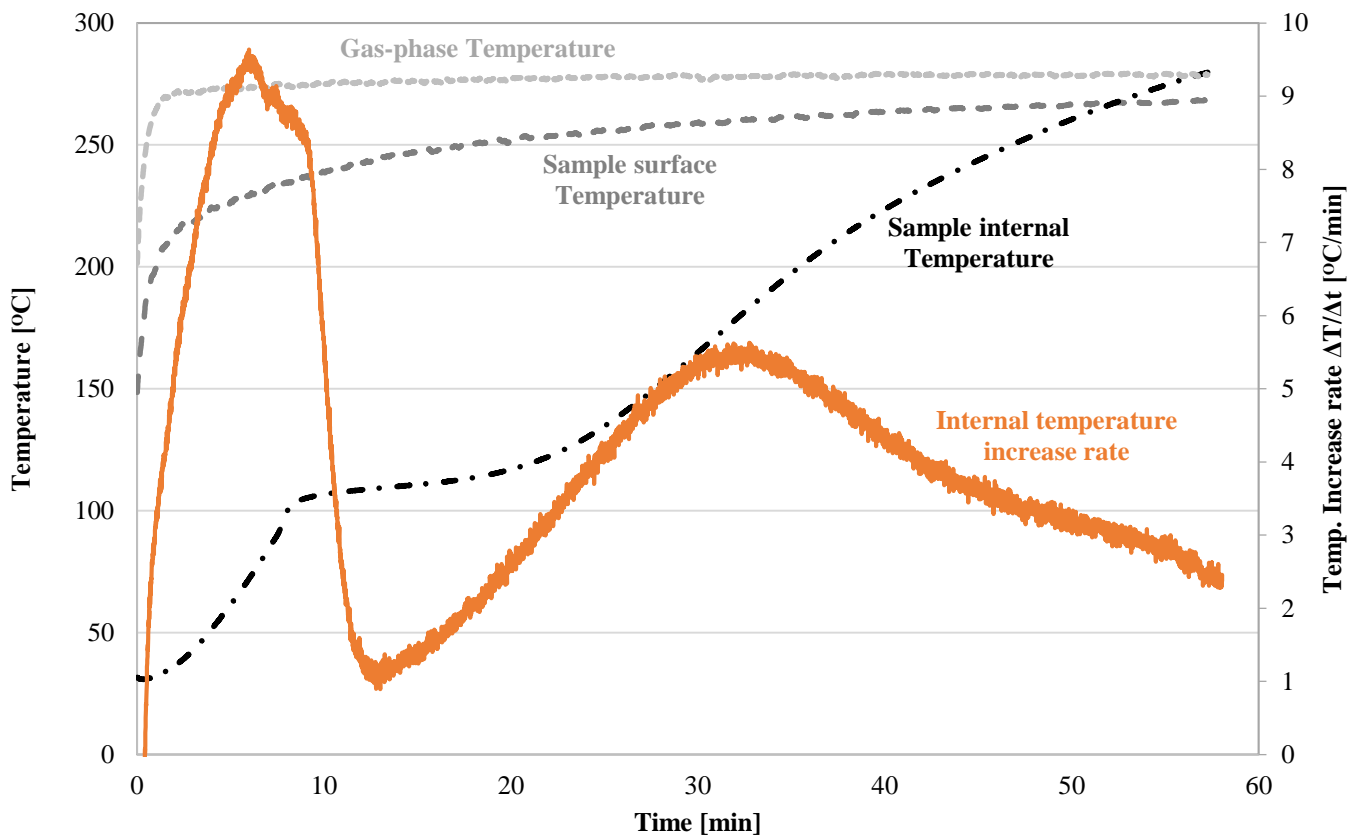


Figure 1. Temperatures measurements and heating rate curves for a typical 270-280 °C specimen

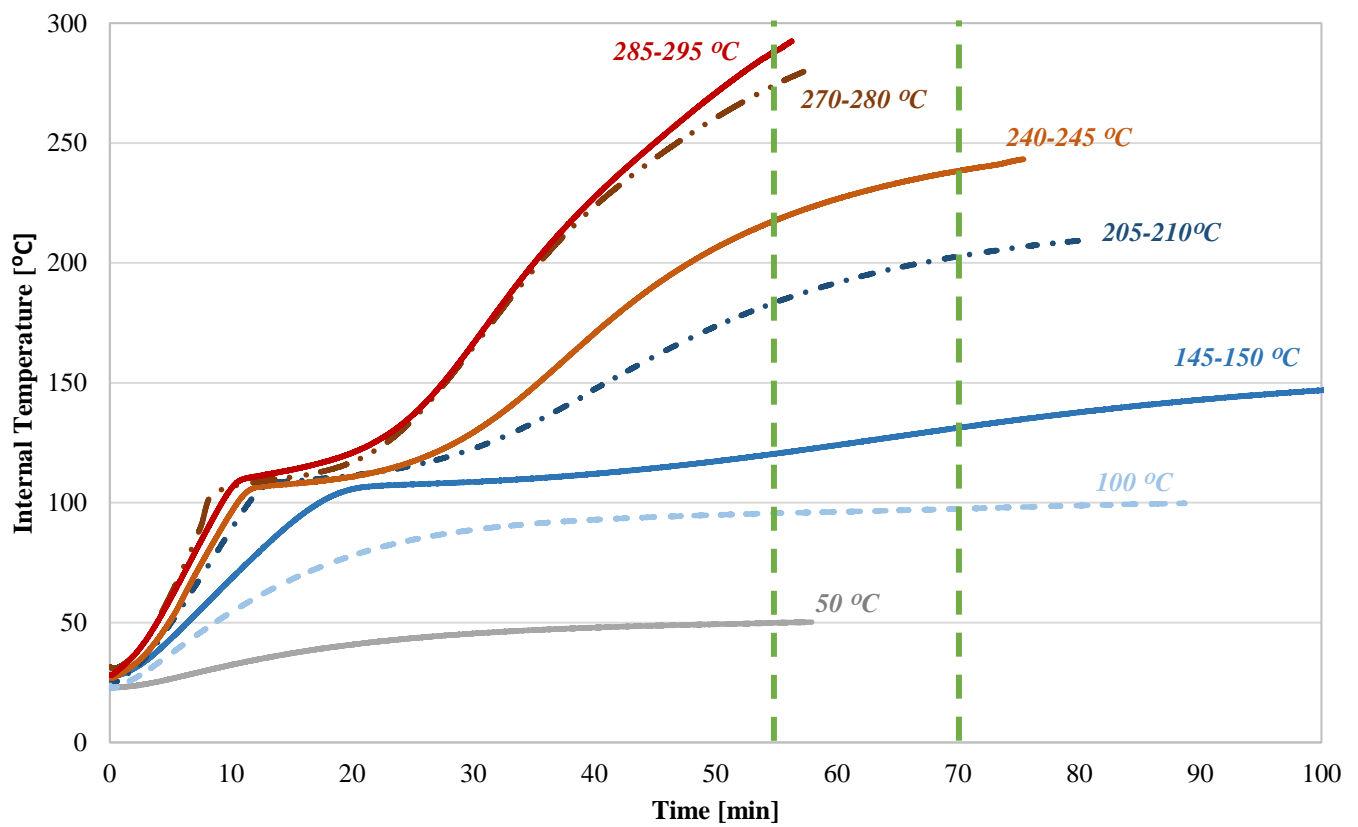


Figure 2. Typical temperature curves at the centre of the timber specimens for each target temperature

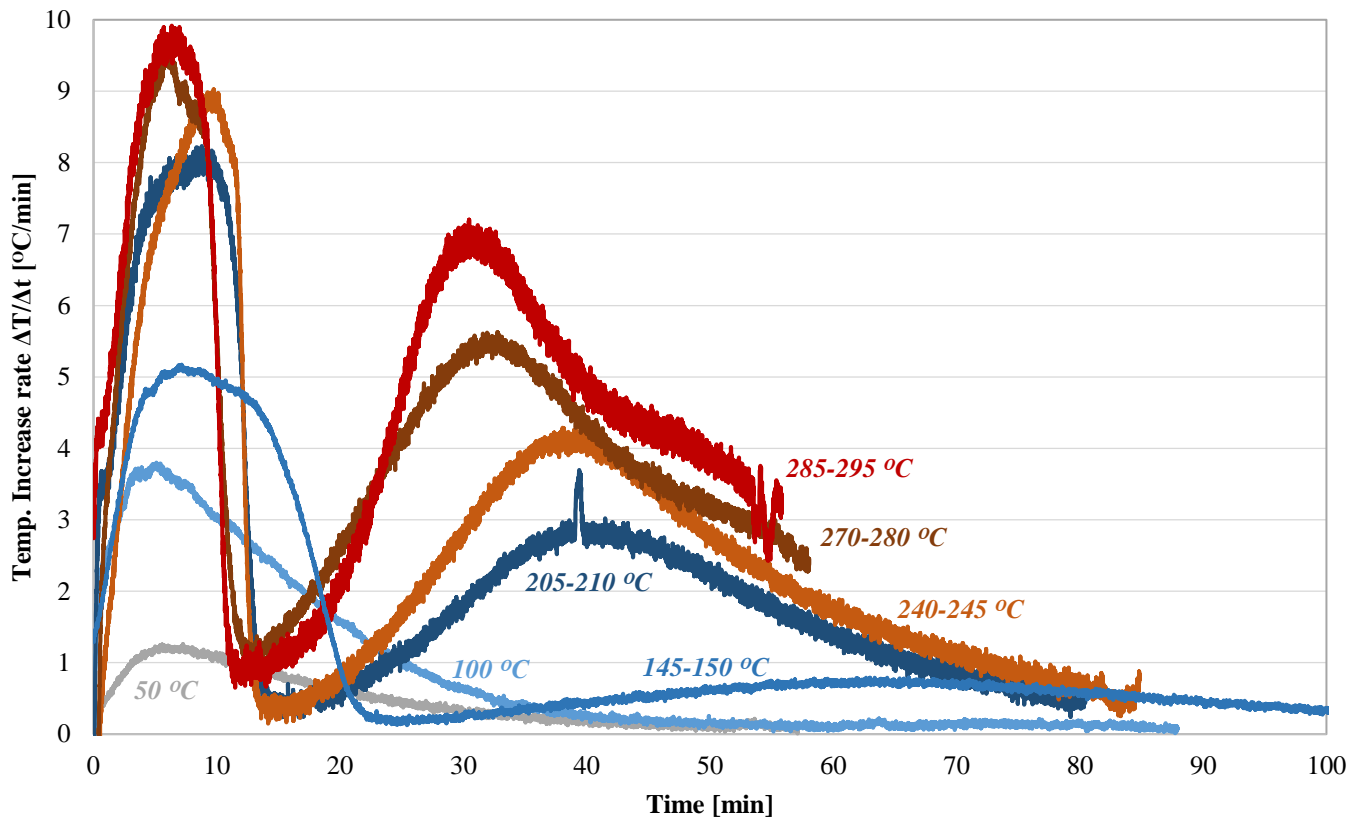


Figure 3. Typical heating rate curves at the centre of the timber specimens for each target temperature

2.2 Loading test setup

For the direct compression test, each specimen was placed in a preheated environmental chamber, refer to Figure 4, with a type K sheathed Thermocouple (TC) inserted in a 2mm hole drilled at the middle of the specimen. The loading tests were performed using a 1 MN MTS machine, and the load was applied continuously after reaching the target temperature increasing at a rate of displacement of 0.5mm/min to achieve the final failure within 3-10 minutes from the onset of loading. MoE of the timber specimens at elevated temperatures was indirectly measured using the MTS crosshead displacement. The MTS displacement was calibrated prior to testing using control specimens with strain-gauges at the ambient temperature conditions.

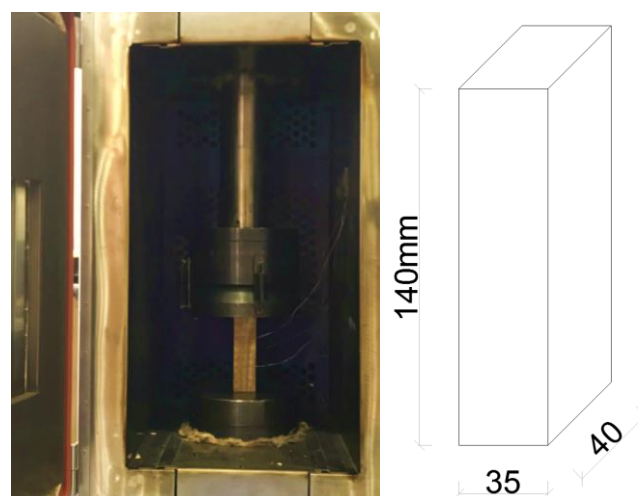


Figure 4. Test setup and specimen dimensions

3 RESULTS AND ANALYSIS

3.1 Stress-strain curves and MoE

The stress-strain curves from the compressive strength tests conducted at ambient conditions and at elevated temperatures are shown in Figure 5. The MoE was obtained from the slope of the stress-strain curves in the elastic region, when the stress is between the range of 10% and 40% of the maximum applied stress for each temperature increment. The reduction in MoE was calculated based on the difference between MoE obtained at ambient temperature conditions and at elevated temperatures for each temperature increment. The experimental results of MoE in compression are shown in Figure 6, and the normalized reduction curve with temperature are presented in Figure 7 in comparison with various curves from different studies.

Based on the average of eighteen tests at ambient temperature conditions, and the average of six tests at each target temperature, the average MoE in compression at ambient temperature conditions is 16.7 GPa, and it decreases to an average value of 7.1 GPa at 285 °C.

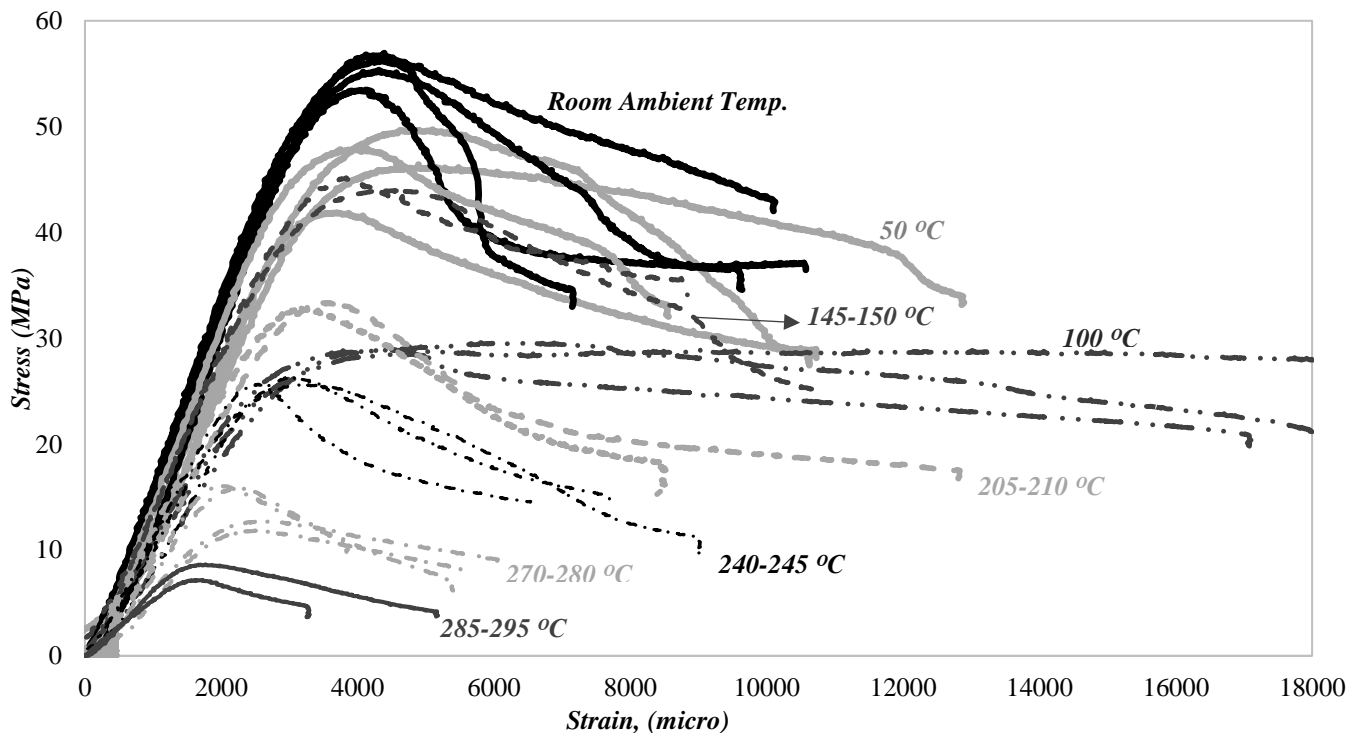


Figure 5. Stress-strain curves of timber in compression at ambient temperature conditions and at elevated temperatures

3.2 Compressive strength

The experimental results of the timber compressive strength are shown in Figure 6. The normalized reduction curves with temperature are presented in Figure 7 in comparison with various curves from different studies. Similar to the MoE, the reduction in compressive strength was calculated based on the difference between compressive strength obtained at ambient temperature conditions and at elevated temperatures for each temperature increment. The average compressive strength in compression at ambient temperature conditions is 55 MPa, and it decreases to an average value of 10 MPa at 285 °C.

Tests results show that both compressive strength and MoE in compression decrease as temperature increases from ambient temperature conditions to 100 °C. Between 100 and 150 °C, there is a significant recovery for the strength and the MoE, but above 150 °C the reduction continues. The ultimate reduction in compressive strength at 285 °C is higher than the ultimate reduction on MoE. A comparison between the outcomes of this study against outcomes from past studies is shown in Figure 7.

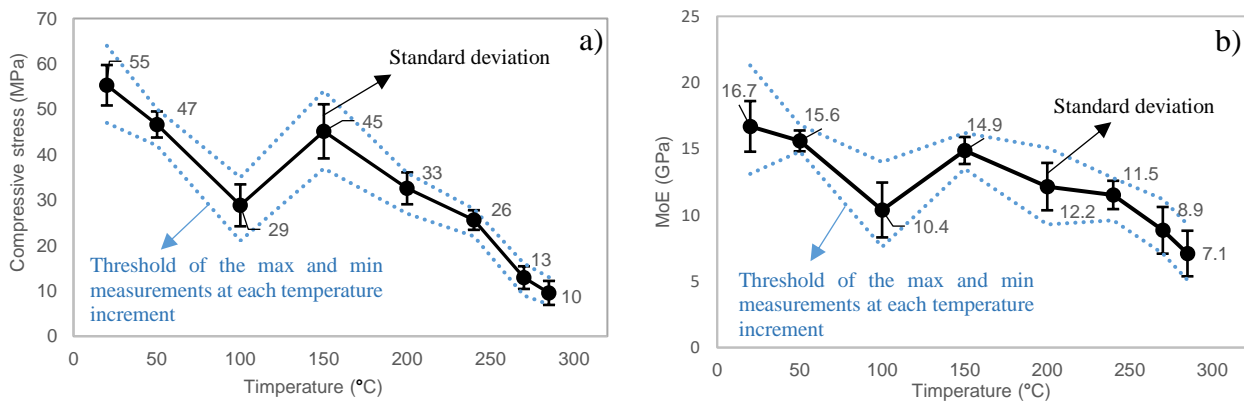


Figure 6. a) Compressive strength and b) Modulus of Elasticity (MoE) in compression parallel to grain at different temperatures

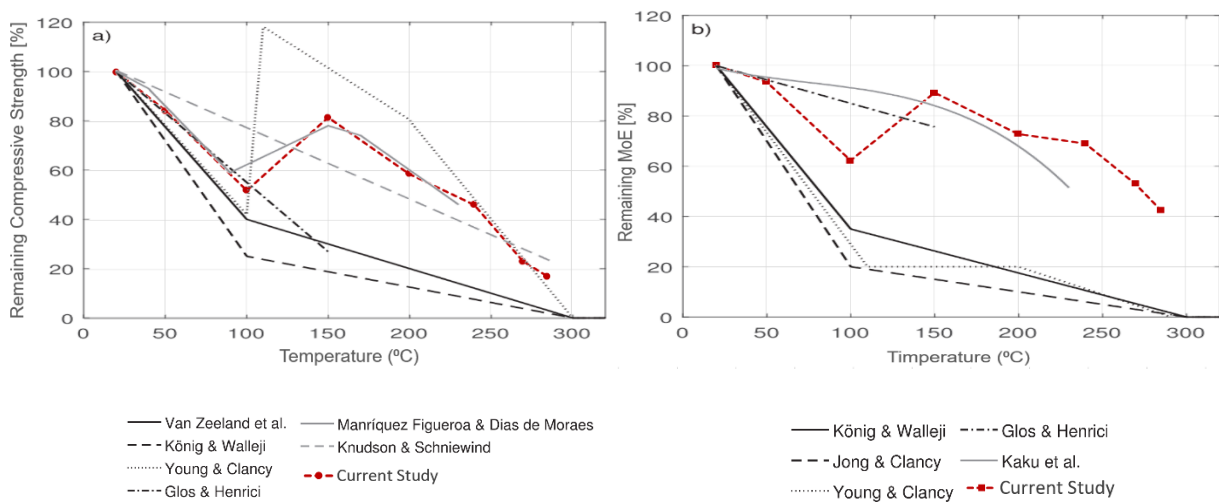


Figure 7. Normalized reduction curves with temperature compared with curves from various authors [2-9] for a) compressive strength, and b) MoE in compression of timber. (Reproduced after F. Wiesner and L. Bisby, 2018), [1].

Further analysis of the change in the failure pattern of the timber specimens, the change in the ductile behaviour with temperature increase, besides the strength and stiffness recovery process due to the drying effect during heating, could lead to a better understanding of the reduction of timber mechanical properties at elevated temperatures. It could also help in reducing the discrepancies between the different research outcomes, and to obtain more reliable results based on different material properties and different thermal boundary conditions.

4 CONCLUSIONS

The reported study is the first stage of a larger study that aims to establish a database to evaluate the reduction of the mechanical properties of Australian structural timber. The next stage of the study aims to evaluate the reduction of timber tensile strength at elevated temperatures, and the residual strength of timber in tension and compression after different thermal exposure scenarios. This database which represent the behaviour of a local Australian structural timber can be used for research purposes and by timber structures' designers to estimate the reduction of structural capacity of timber elements during fire by evaluating the mechanical properties of the 'heat-affected zone' beyond the char layer, Other key issues should be identified to be able to build a robust fire safety strategy and to predict the structural fire performance of timber structures; however, this experimental study has been mainly focused on the compressive mechanical properties of solid softwood at elevated temperatures.

The results also could be used to provide a knowledge base that could enhance the understanding of fire performance of load bearing timber structures under a compressive stress state, and from which a detailed theoretical model can be produced to predict the failure mechanisms.

Since the different heating rates within the timber can affect the moisture migration and therefore affect the timber structural capacity, it is important for further research to consider the combined effect of moisture migration and thermal profile on the structural capacity of timber.

Due to the long heating process that the timber was subjected to during this study, it is expected that the moisture profile inside the timber specimens at the onset of loading is symmetrical for all the temperature increments beyond 100 °C. Hence, the reduction in the compressive mechanical properties for those temperature increments is expected to be independent from the timber moisture profile. There could be a potential to couple these thermo-mechanical properties with a hygro-mechanical model to explain the combined effect of moisture migration and thermal profile inside the timber.

ACKNOWLEDGMENT

The authors are grateful for the financial support received from the Australian Research Council under the Industrial Transformation Hub for Advanced Solutions to Transform Tall Timber Buildings (IH150100030).

REFERENCES

1. F. Wiesner, L. Bisby, The structural capacity of laminated timber compression elements in fire: A meta-analysis, *Fire Safety Journal*, 2018.
2. J. König, L. Walleij, Timber Frame Assemblies Exposed to Standard and Parametric Fires: Part 2: a Design Model for Standard Fire Exposure, 2000.
3. P. Glos, D. Henrici, Festigkeit von Bauholz bei hohen Temperaturen, Abschlussbericht 87505, 1990.
4. R.M. Knudson, A. Schniewind, Performance of Structural Wood Members Exposed to Fire, 1975.
5. M.J. Manriquez Figueroa, P. Dias de Moraes, Temperature Reduction Factor for Compressive Strength Parallel to the Grain, 2016.
6. I. Van Zeeland, J. Salinas, J. Mehaffey, Compressive strength of lumber at high temperatures, *Fire Mater.* 29 (2005) 71–90.
7. S.A. Young, P. Clancy, Compression Mechanical Properties of Wood at Temperatures Simulating Fire Conditions, 2001.
8. F. Jong, P. Clancy, Compression Properties of Wood as Functions of Moisture, Stress and Temperature, 2004.
9. C. Kaku, Y. Hasemi, N. Yasui, M. Yasukawa, D. Kamikawa, N. Kameyama, T. Ono, M. Koshihara, H. Nagao, Influence of Fire Exposure on the Mechanical Properties of Wood, 2014.
10. F. Wiesner, T. Daniel, L. Bisby, The effect of adhesive type and ply number on the compressive strength retention of CLT at elevated temperatures, *Construction and Building Materials*, 2021.

A METHOD FOR DETERMINING TIME EQUIVALENCE FOR COMPARTMENTS WITH EXPOSED MASS TIMBER, USING ITERATIVE PARAMETRIC FIRE CURVES

David Barber¹, Robert Dixon², Egle Rackauskaite³, Khai Looi⁴

ABSTRACT

High-rise mass timber buildings using cross laminated timber and glulam are being designed and constructed globally at an increasing rate. For mass timber buildings, there are a limited number of methodologies for the structural fire assessment, when the mass timber is exposed. To determine an acceptable area of exposed load-bearing timber, such that the minimum period of fire resistance of the structure can be met in a fully developed fire, a method has been developed using an iterative approach to the Eurocode parametric fire exposure. The natural fire model can be adapted to account for the contribution of the burning timber that is exposed, with the parametric fire used to determine heat flux within the compartment, from which the time and heat flux dependant char rate can be calculated, and the charred mass of timber added into the fuel load. The overall char depth calculated can then be used to determine the equivalent fire resistance period the time at which the char depth under a realistic design fire equals the char depth resulting from exposure to the standard fire (time equivalence). This paper also presents how the iterative parametric method has been validated against available compartment fire tests and is being improved through addressing the decay period further.

Keywords: Timber; fire resistance; time-equivalence; parametric fires; cross laminated timber

1 INTRODUCTION

Multi-story buildings utilising engineered timber (“mass timber”), such as glulam and cross laminated timber (CLT) are becoming globally prevalent given they are aesthetically different and achieve sustainability goals of reduced embodied carbon [1, 2]. Mass timber buildings typically use a combination of glulam for the structural frame with CLT floors and walls. While combustible, engineered timbers have fire resistance ratings for standard fire exposures that have been well researched and understood [3, 4]. To date, the design of multi-story mass timber buildings has been predominantly based on protecting timber elements with gypsum board products to improve their required fire resistance rating (FRR). The protective board performs the function of either delaying or altogether preventing combustion of the mass timber [5]. Accompanying the movement for taller mass timber buildings is a significant interest in exposing some, or all the timber structure.

For high-rise buildings, a key issue to be addressed is the requirement for the building to withstand the full developed of a fire, including decay to such a level where the structure ceases to retain structural resistance.

¹ Arup, 1120 Connecticut Avenue, Washington DC 20036, USA, david.barber@arup.com

² Arup, 699 Collins Street, Docklands Vic3008, Australia robert.dixon@arup.com

³ Arup, 13 Fitzroy Street London W1T4BQ United Kingdom, egle.rackauskaite@arup.com

⁴ Arup, 182 Cecil Street, Frasers Tower, Singapore 069547 khai.looi@arup.com

This is a complex problem, particularly when the load-bearing timber is exposed to a fire source. To date, fire testing for buildings with exposed timber has been limited in building size but has been very informative. A common finding is the impact of large areas of exposed timber to the fire, with the heat release rate (HRR) increasing and the fire decay period prolonged. This affect is exacerbated by configuring timber over multiple adjacent surfaces, which can create radiation feedback between the surfaces [6]. Hence traditional methods of calculating fire resistance should be approached with caution. Therefore, it is important to consider the effect of timber on the compartment fire dynamics.

For fire safety engineers involved with high-rise mass timber buildings, the impact of exposed mass timber is not covered in detail, or at all, within available guidance. To determine the acceptable area of exposed load-bearing timber such that the minimum period of fire resistance of the structure and fire compartment floors and walls can be met, a method to assess the compartment design fire, impacted by the exposed timber, is required. This paper presents a relatively straight-forward method for evaluating the impact of exposed mass timber on the compartment fire, using adapted existing calculation methods.

1.1 High Rise Buildings and Code Required Fire Safety Goals

Building and fire safety codes have traditionally not been written to include for high-rise mass timber buildings. Codes increase the required fire safety measures with building height and high-rise buildings are required to have improved structural performance in fire, often over and above the inclusion of automatic sprinkler protection. This is to account for longer evacuation times, to support more complex firefighting intervention and to maintain structural stability, in the unlikely situation of the sprinkler protection failing to control a fire and / or severe delay in fire brigade activities. Building codes require a high-rise building to remain structurally stable, such that the fire decays, before the structure can fail due to the heat energy released by the fire [7].

2 PRESCRIPTIVE OR PERFORMANCE-BASED DESIGN?

To determine the structural resistance of a building in fire, a prescriptive or performance-based approach can be used by engineers. A building following a prescriptive approach uses the requirements of the applicable building code and is based on the building elements achieving an FRR (i.e. under exposure to a standard fire). A building following a performance-based approach will deviate from the applicable code for the structural fire resistance and the fundamentals of fire behaviour and structural response to a range of design fires is assessed [7]. For a performance-based approach applied to a high-rise building, regardless of structural material, must maintain structural stability through fire growth and decay, for several reasonable worst case ‘natural’ design fires.

For a high-rise building that includes an exposed mass timber, the structure needs to have a proven stability through to fire decay, a prescriptive approach to the structural fire safety cannot apply and only a performance-based approach can be used to determine the fire resistance. This is best understood by considering how structural capacity for mass timber is determined.

Traditionally, the structural design for timber members exposed to fire has been based on sizing sections by applying a prescribed char for a period of standard fire exposure, to calculate a residual section and then determining structural capacity for that residual section. This methodology is generally referred to as the ‘reduced cross section’ method and is codified in Eurocode 5 (EN 1995-1-2) [8], Australian Standard AS1720.4-2019 [9] and others. These reduced cross section methods are only appropriate when assessing standard fires, given the char rate to be used has been determined from a large number of existing standard fire tests [10]. A standard fire derived char rate cannot be used directly (i.e. without robust justification) when assessing natural design fires expected in exposed timber structures, which will have a variable char

rate throughout the fire growth, peak and decay cycle. Also, as the exposed timber pyrolyses it changes the compartment fire dynamics, prolonging the heat release and impacting fire spread. Hence the design fires chosen also needs to be based on the feedback and interaction caused by the exposed timber itself. Therefore, when a high-rise structure has mass timber exposed, a performance-based approach to the design fires, char rates and structural capacity must be utilised to capture the variable char rates, and the influence of the exposed timber on the design fire. The fire safety design must address the fire growth, HRR, fire duration and fire decay.

The aim of a performance-based design is to demonstrate, with a reasonable degree of confidence, that the building will maintain structural stability, under exposure from a realistic fire for an appropriate period of time. In most cases, this cannot be extrapolated from standard furnace testing, due to the nature of the material and furnace exposure. The prescriptive FRR is an example of a code requirement which is developed on assumptions that are not applicable to timber, due to the combustibility of the material. As such, a prescriptive FRR cannot be directly applied to timber structures, particularly in a large or complex building.

In practice, a performance-based design can encompass both natural and standard fires, given that building construction requires the specification of constructions based on an achieved FRR, with exposure to a standard fire. Building construction is reliant on elements of construction achieving an FRR so that code compliance can be shown to be achieved, construction elements can be priced accurately, procured in a competitive manner, delivered on time and most importantly, obtain a final building certification. Hence, the construction industry relies on standard fire testing and mass timber structures need to work within this framework to enable successful project completions. However, evidence from standard fire testing must be considered within the limitations of the tests, and cannot be solely relied upon as evidence of, for example, structural stability within a real building scenario.

2.1 STANDARD FIRE TESTING AND MASS TIMBER

The applicability of standard fire testing (hence ‘code compliant’ solutions) for combustible building elements needs to be considered with caution, given that a combustible building element such as mass timber, will release its own energy within a furnace, resulting in the input energy required to maintain the standard fire temperature time curve being less than required for a non-combustible element [11]. Also relevant is the combustion efficiency of timber in that it is very dependent on the presence of atmospheric oxygen. Oxygen concentrations within a furnace have been measured to be relatively constant, peaking at a maximum of around 5% [12] at the specimen surface, which is significantly lower than within a typical building fire. For a relatively small timber compartment, oxygen concentrations are expected fluctuate throughout fire development phases, being significantly higher (than 5%) during fire growth and decay phases. This is likely to be further exacerbated when considering a fire in a large, open well-ventilated compartment. This may result in more onerous (oxygen rich) combustion efficiency and, importantly, char development within the timber of a real building, when comparing standard fire test results.

3 TIME EQUIVALENCE FOR PERFORMANCE-BASED DESIGN

Generalised prescriptive code requirements, in the current form, are simply not intended to be applied to buildings which contain exposed timber structure. For such buildings a performance-based design approach must be adopted. Time-equivalence is a commonly used engineering approach developed to compare the severity of fire exposure under a defined real (natural) fire back to the exposure of structural member in the standard fire used for compliance fire testing. The time equivalence concept was first introduced by Ingberg [13]. As described by Law [14], *“The term time-equivalence is usually taken to be the exposure time in the standard fire resistance test which gives the same heating effect on a structure as a given compartment fire.”* This concept allows a simple comparison of the response of a structure under different ‘natural’ fire

scenarios which can account for more realistic fuel load and ventilation conditions and classification of the structure in relation to a standard fire, i.e. prescriptive framework.

The time-equivalence method enables and facilitates discussions with other designers, contractors, and approving authorities as construction products available in the market and design requirements set out in codes are based on the standard fire exposure. Thus, knowing the ‘equivalent’ fire resistance of the timber structure when subjected to ‘natural’ fires enables the selection of appropriate fire rated elements for the building, construction products, and compare it against prescriptive requirements.

4 CONSIDERATIONS FOR FIRE RESISTANCE OF A TIMBER STRUCTURE

Structural fire resistance for an exposed timber structure is assessed based on the residual (or reduced) cross section and determining structural capacity for that residual section required to sustain fire limit state structural loads for an appropriate period. For a performance-based design approach, the residual cross section (or conversely the heat affected timber depth) must be determined via exposure to a range of natural design fires. The factors that influence natural design fires are discussed below, in the context of the time-equivalence methodology presented.

For a compartment with exposed mass timber, there can be three possible types of HRR. As Figure 1 shows, if there is a large proportion of timber exposed, then the fire may not decay (shown indicatively as curve ‘3’). In some situations, there can be fire decay, but then fire regrowth, due to the type of CLT used or the failure of any protective encapsulation (shown indicatively as curve ‘2’). The type of HRR profile required for fire safety design, is where the growth is followed by a steady and predictable decay (curve ‘1’). The full growth, development and decay phases impact the final assessed char depth and hence, the structural capacity.

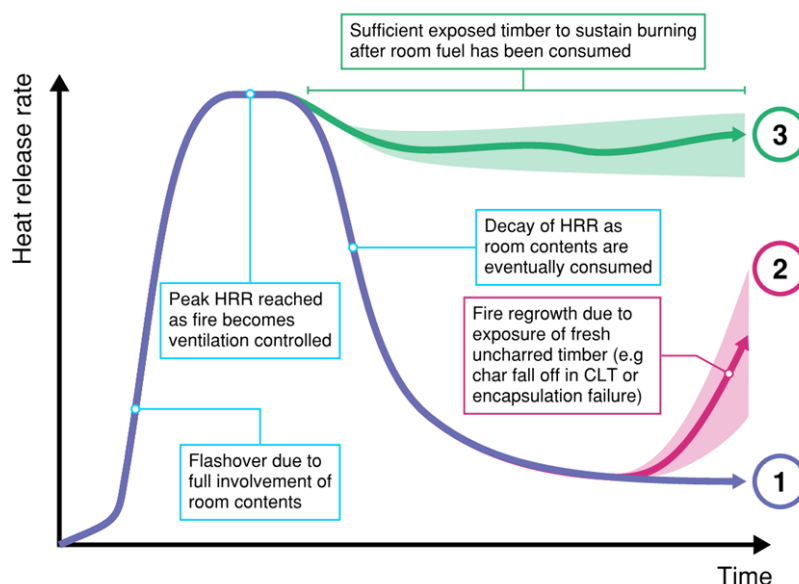


Figure 1. Time temperature curves for a compartment fire with exposed mass timber structure (Image: Arup)

4.1 Fire Decay

Fire decay is an area of influence for exposed mass timber buildings that needs to be considered carefully, as a requirement of a performance-based fire safety design is to demonstrate structural stability once all the compartment contents have been consumed by the fire. Compartment fire testing with exposed CLT has

shown that the decay is slower than for non-combustible construction, with compartment heat flux and temperature sufficient to support smouldering combustion of the exposed timber can continue for a number of hours, once all the fixtures and furnishings have been consumed [6, 15, 16]. Designing for fire decay is often referred to as designing for ‘burnout’ [17]. This is traditionally a term associated with non-combustible construction, whereby the structure is designed to survive burnout of the fuel load provided by the compartment contents. Where the structure itself is combustible and contributes to the overall fuel load, this definition of burnout becomes somewhat blurred, and may be difficult to predict with a high degree of confidence.

To accurately determine fire decay within exposed timber compartments, the structural response is best determined based on a well-defined limit of fire decay, rather than designing for complete burnout. Fire testing has shown that where there is a large areas of exposed mass timber, smouldering may continue within the structure for many hours after the main fuel load has been consumed. As such this could extend the time for burnout to many hours. By considering a well-defined acceptance criterion for decay, either based on compartment temperature, fire heat release or received heat flux at the exposed timber, structural stability can be demonstrated, avoiding uncertainty regarding how and when burnout occurs. Ultimately a fire within a timber compartment, like all structures that have a fully developed fire occurring, will rely on fire brigade intervention to extinguish smouldering flames. This approach allows for a reasonable worst credible fire scenario that includes significant fire brigade intervention delay, potentially multiple hours, before any firefighting water is applied to the building.

4.2 The Role of the Char Layer

A stable char layer forming over the surface of the timber structure is a critical component in controlling fire decay, fire duration, the fire dynamics within the compartment and the mechanical properties of the residual, load-carrying timber. All of which share a strong interdependence and must be considered as part of the performance-based design. A stable char layer will influence the final assessed char depth and loadbearing capacity of the structure.

A stable char layer may not be present in some forms of CLT where the panel does not have glue line integrity under heating [6, 18]. Under exposure to fire as the char line moves towards the adhesive, excessive amounts of char may dislodge due to thermal degradation of the adhesive. This weakening of the char can have a detrimental impact on the compartment fire, including increased combustion of the freshly exposed timber affecting fire spread and fire duration, and increased thermal penetration into the fresh timber (affecting mechanical properties of load-carrying timber). A more reliable (and hence stable) char layer can be provided in CLT by using heat resistance adhesives.

The benefit of using CLT with a heat resisting adhesive has been demonstrated by compartment fire testing by NRC, Canada [16]. The tests carried out included exposed CLT and exposed glulam beams and columns and were conducted to show the difference in overall HRR when the CLT is changed from one that is susceptible to glue line integrity failure and CLT that is not. The test compartments were set up with CLT that meet with the latest edition of PRG-320 [19], that requires CLT adhesives to not be susceptible to glue line integrity failure and char debonding. The results show that a fully developed fire will more reliably decay where the CLT has predictable performance under long-exposure heating, compared to CLT with adhesives that result in glue line integrity failure. Further recent fire testing by the American Wood Council and RISE have provided more evidence of the beneficial characteristics of heat resistance adhesives, in terms of producing favourable conditions for fire decay, consistent char rates through bonded glue lines and char layer stability.

5 DETERMINING TIME-EQUIVALENCE FOR EXPOSED MASS TIMBER

Load bearing mass timber can be exposed in parts of the building, as columns, beams, walls and the soffit to the underside of floor. When timber is exposed (not protected or encapsulated) and is exposed to fire, the timber mass is converted to heat that will increase the fire size and more importantly, the fire duration.

5.1 Timber Time Equivalence - Fundamentals

For a mass timber structural element, strength is a function of the size of the cross section. As the exposed timber surfaces char in fire due to incident heat flux, the cross section reduces, which reduces the ability of the element to resist the applied loads. For mass timber exposed to fire, the reduced cross section of ambient temperature material (i.e. full strength) must be sufficient to resist the design loads at the required minimum period of fire resistance.

Time equivalence for exposed timber is char related rather than temperature related (as for steel), hence the mismatch in the traditional approach to time-equivalence. For mass timber, the equivalent period for a natural fire is the time at which the maximum char depth under a natural fire equals the char depth resulting from exposure to the standard fire, as shown in Figure 2. This method ensures that the same cross section of strong un-charred timber remains to sustain loads under both heating regimes (hence equivalency, by strength). The maximum char depth results from an assessment method (such as the iterative parametric methodology described in the next sections) can be compared to the char depth under the standard fire. This approach provides a means by which to determine the time equivalence fire resistance period for a timber member, based on an approximate natural fire determined from compartment characteristics, initial fuel, exposed timber and available ventilation.

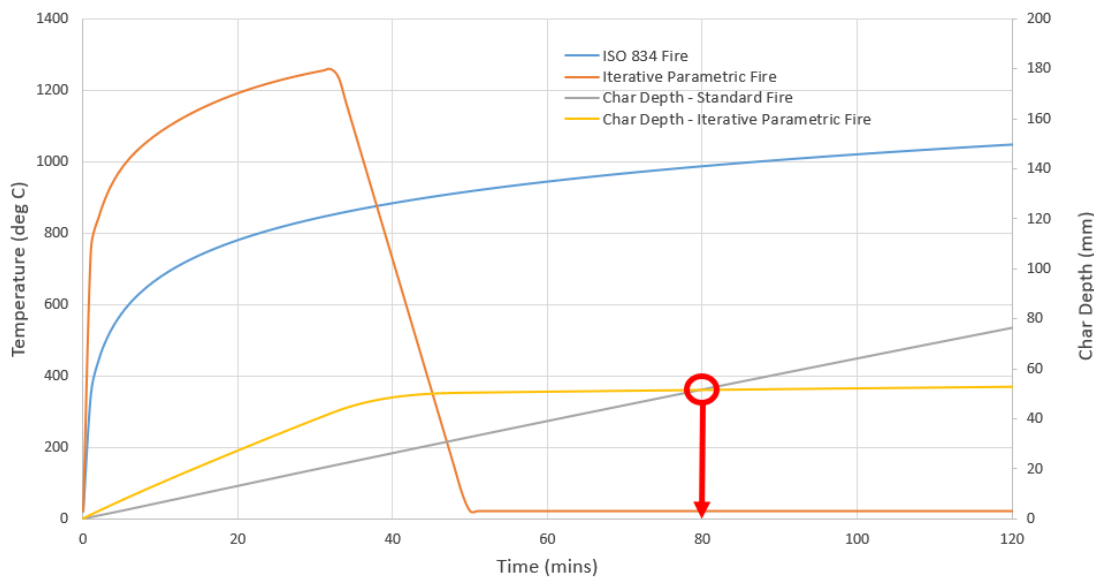


Figure 2. Concept sketch for time equivalence based on char depth under standard and natural fires

It should be noted that comparison to underpredicted standard fire char depths (as discussed previously in Section 2.1) results in conservativity for the assessment methodology presented within i.e. this comparison presented yields a longer equivalent time, than for accelerated charring as would be expected under more natural conditions. To determine the time-equivalence for timber, the complete char depth must be determined, which includes the charring during the decay phase and, any charring that occurs with smouldering, i.e. complete char depth through to full consumption of the calculated fuel load and any impact due to smouldering and thermal penetration. Thus, to determine time-equivalence for a mass timber

structure, the HRR decay phase is critical. This differs from the assessment that occurs for a steel structure, where peak temperature is important.

5.2 Total Char Depth - Iterative Parametric Temperature-Time Curve Methodology

For a mass timber structure, an approach based on exposure to a standard fire is not accurate given the feedback that occurs between the exposed mass timber and the compartment fire, which is not accounted for in standard testing. The assessment of char depth and hence, reduced cross section for member capacity needs to be based on the area of exposed mass timber structure; and the resultant char depth being proportional to the received heat flux, which is dependent on compartment temperature and fire duration, governed by the area of timber exposed. Hence, the char depth for the mass timber structure needs to be analysed more fundamentally, to account for the impact on the compartment fire dynamics, that will occur as a result of the exposed mass timber, and the feedback loop.

To determine the total char depth within a timber member exposed to a natural fire, to then determine the time-equivalence, a methodology has been developed based on making transparent and easily understood changes to an existing and well-accepted compartment modelling method, being the Eurocode 1 EN 1991-2-2 Annex A Parametric temperature-time curves ('Parametric curves') [20]. The approach follows the framework set out within the SFPE Handbook for Fire Protection Engineering [21].

The traditional parametric curve methodology does not consider the exposed timber as an additional fuel. Hence, the method cannot be used to assess a compartment with exposed mass timber unless they are amended to account for the additional fuel mass of the timber structure. An iterative method is used to account for the exposed timber that is converted to energy within the compartment, given the timber the combusts will influence the temperature-time curve. The parametric fire relationship is initially used to determine heat flux within the compartment, assuming that all surfaces are non-combustible and calculating a temperature-time curve. A second iteration then uses this initial temperature-time curve as the basis for calculating char rate at every time step, from the heat flux, at the exposed timber surface. The timber surfaces are aggregated into a single exposed surface, whereby the timber that will be consumed by the fire is "lumped" together as one fuel load item and assumed to be consumed by the fire over the duration. The exposed timber will start to influence the fire when there is enough source of heat applied, such that charring occurs (heat flux is more than 12kW/m^2) [22]. It is assumed that once the heat flux is below 5kW/m^2 , the exposed timber will stop charring and contributing to the fire [23], with an additional char depth included for smouldering. The incident heat flux is based on a single compartment value of temperature and hence is conservative.

From this initial input, a heat flux dependent char rate can be calculated. The total char depth is the sum of char rates over the given temperature-time curve and a total char depth is determined through the growing, fully developed and decay phase for the fire. The charred mass of timber from this iteration can then be converted to fire load density (MJ/m^2) using the calorific value for the timber and added into the fuel load for the next iteration. Thus, fire severity is increased due to the increased fuel in subsequent iterations, as are the exposed timber properties (timber to char) and new char rates, mass of timber and resultant fuel energy density are calculated for that iteration. This is repeated until convergence, when a total char depth can be assessed [24]. The approach allows for sensitivity assessments and variations in compartment dimensions, bounding materials (including timber), ventilation conditions and initial fire load density. Most importantly, changes to the total area of exposed load-bearing timber can be easily made and the results can be viewed quickly. When convergence does not occur, less timber must be exposed. If the proportion of exposed timber is too high, then the minimum period of fire resistance provided within the compartment may be insufficient and encapsulation to reduce the amount of exposed timber is required. Where the timber forming part of the primary structural frame is not designed to be exposed, it is required to be protected by

non-combustible encapsulation that prevents the timber becoming exposed and charring, or charring behind the fire protection system, for the duration of the expected fire.

The resultant total char depth, from ignition through the complete decay, can then be used to determine the fire severity time-equivalence, a design value that is required for the building design, approval and construction. Other models to predict the impact of exposed timber on compartment fires and total char depth are also in development and have been published [25, 26].

5.3 Decay Phase Modelling

The Eurocode Parametric fires allow for specific thermal properties of compartment bounding materials, but the time temperature computations are not able to account for time dependant thermal inertia variations within the bounding materials, such as is the case with an exposed timber structure. This is particularly significant in the decay phase of a fire, given the propensity for slower decay within a timber compartment, the importance of fire duration on the structural resistance of a timber building and the prediction of burnout required for some performance-based designs. For time-equivalence to be accurately determined, the total char depth needs to be assessed, including all charring during decay.

As a method to capture prolonged combustion due to combustible bounding materials (therefore impact on structural resistance), the parametric temperature time decay phase computation has been modified to reflect experimental data from timber fire tests. This modification was then tested against independent fire tests to assess appropriateness. The average decay rate for the FPRF [6] Test 4 (exposed timber ceiling, beam and column) was measured as approximately $5.1^{\circ}\text{C} / \text{minute}$. This can be considered a lower bound decay rate (most onerous) for compartments larger than those burned in the FPRF tests ($\sim 11\text{m}^2$), due to decreased re-radiative feedback within larger compartments. The cooling rate for a larger compartment lies between the unmodified parametric temperature time decay rate and that recorded in the FPRF test (for similar exposure configurations). By introducing a ‘test factor’ parameter i.e. a proportional measure of how closely the tests represent a specific fire compartment, a realistic decay rate can be determined. The test factor was initially chosen as 50%, then tested against the several independent fire test data (by applying the assessment methodology to the test configurations). Through trial and error, a test factor of 60% provided reasonable correlation to the independent tests, with generally conservative outcomes. Examples of comparisons against the USFS-ICC tests [15] are shown in Figures 3 and 4. This approach is still being validated against other compartment tests, with the aim of ensuring total char depth is captured.

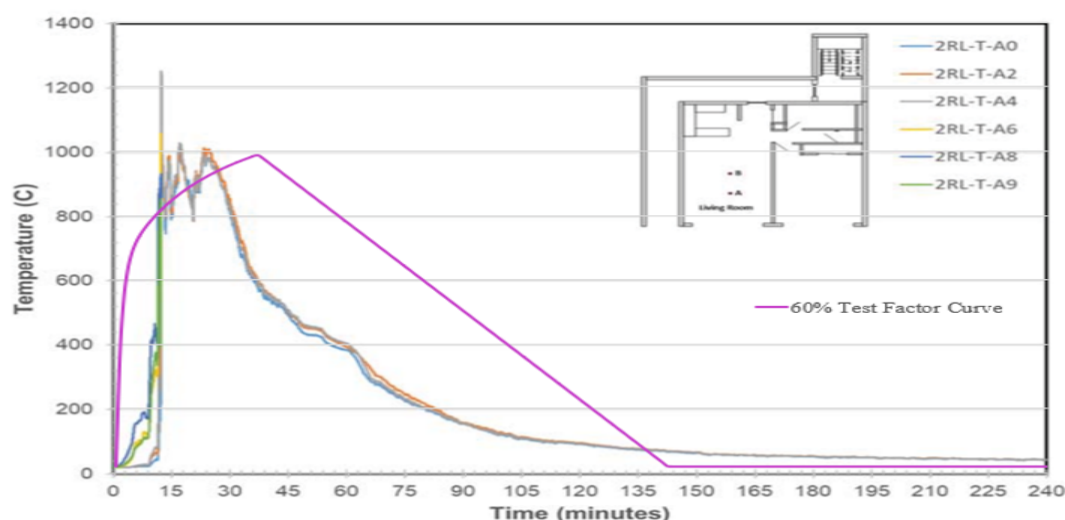


Figure 3. Test Factor Validation – USFS ICC Test 2 Living Room – with Modified Decay Definition

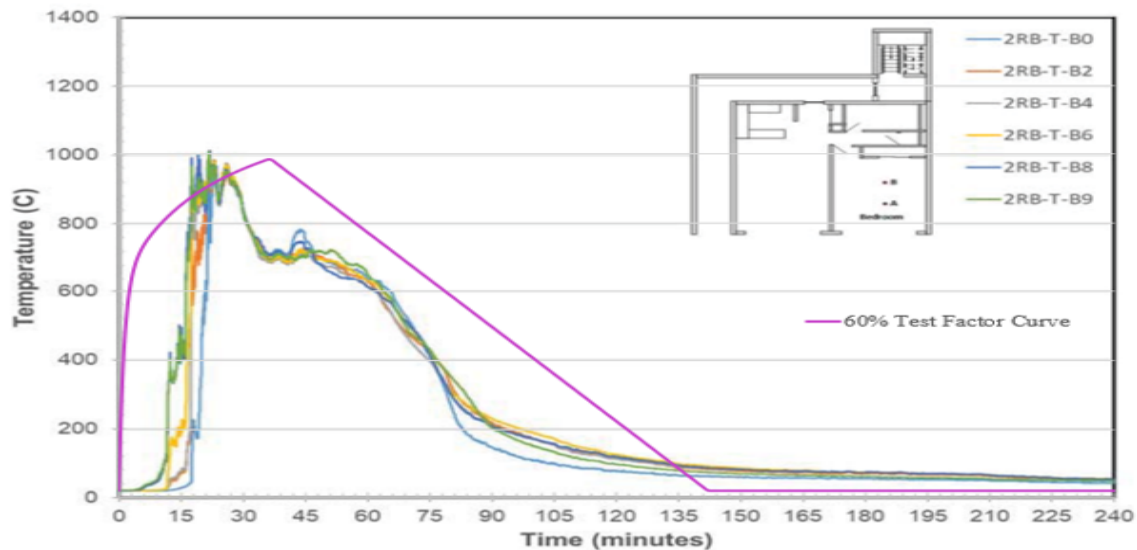


Figure 4. Test Factor Validation – USFS ICC Test 2 Living Room – with Modified Decay Definition

A comparison of results was made without the decay phase modelling adjustment for a large compartment (~500 m² floor area). The decay phase modelling included the test factor described above. The comparison showed that the both the time-equivalence and maximum char depth are significantly increased when HRR decay assessment is further improved. For a short ‘hot’ fire the increase with the decay factor is approximately 25% greater in final char depth than without the decay factor. For a long ‘cool’ fire the increase in overall char depth is approximately 22%. These increases are more pronounced for smaller compartments, as expected. This comparison provides a clear numerical indication of the importance of considering the decay phase and utilising a modified fire decay definition, based on real fire test results, to assess the impact on fire resistance.

5.4 Methodology Limitations and Further Work

This calculation approach requires several assumptions and, in turn, contains several limitations. As with any analysis methodology, it must be applied appropriately. The methodology is intended to be used to facilitate discussions with developers, architects and approval authorities about safe proportions of exposed timber structure.

5.4.1 Compartment Area

The limitations on Eurocode 1 Parametric approach are also applicable to this methodology, in that it cannot be used for multi-level interconnected compartments, compartments over 500m² and 4m tall. The values for certain parameters should also follow the recommended range given in Eurocode 1, including the thermal absorptivity of enclosure (*b* value), opening factor and fire load density. The methodology presented does however allow for sensitivity studies to be carried out to quickly ascertain if the outcomes for larger compartments (with similar internal area to opening ratios) to determine conservativity against the floor area limitations described in Eurocode 1.

5.4.2 Glue line integrity (Char debonding)

The methodology assumes that the CLT that is exposed is not susceptible to issues with glue line integrity and char debonding. The method relies on consistency in char rate across the exposed timber and no issues of potential fire re-growth. The methodology cannot be used for compartments with CLT that is susceptible to char debonding, as the char rate changes cannot be accurately predicted, nor can the potential compartment fire regrowth be predicted.

5.4.3 Mass timber protection

The areas of mass timber that are not exposed to the fire must have non-combustible protection that remains in place for the full duration of the fire and does not allow the mass timber to reach a charred state (temperature below 300°C). If the non-combustible protection allows the timber to char, then this will add to the fuel load and fire duration and can also lead to complete non-combustible protection failure, causing fire re-growth.

5.4.4 Char rate correlation

Timber char rate has been shown to be directly linked with incident heat flux by a number of researchers over many decades [27, 28], but based on relatively low heat fluxes (20kW/m² to 50kW/m²). Compartment fires have heat fluxes that are in excess of 150kW/m² and there is limited research or calculation approaches to determine char rates for these high heat fluxes at present. The method is therefore limited given the lack of experimental data to validate high heat flux charring.

5.4.5 Char depth approximation

The char depth determined using the methodology is applied uniformly on all the timber members in the compartment. It does not consider the possible effect of different char rates on vertical members (walls) and horizontal members (ceilings) or different char rates due to different timber products (CLT, glulam, etc.). Conservatively, it is assumed that all members char at the same rate, based on the highest incident heat flux.

5.4.6 Estimation of thermal penetration depth

As previously discussed, formulation of a stable insulating char layer on the exposed timber surfaces will provide protection to the load-carrying timber within the structural members. This has yet to be quantitatively demonstrated as part of this study, however, this is identified as further work to develop this methodology. Heat transfer analyses through the char layer into the protected timber within, will be undertaken to gain understanding of the potential changes in mechanical properties (hence fire resistance) of the load-carrying timber within the char layer. The heat transfer assessment can be included in the current methodology, which will utilise the iterative parametric design fires as an input boundary condition. The heat transfer element of the assessment will be validated against measured through temperatures recorded during real fire tests. This work may also assist to inform the impact of smouldering surface combustion on the mechanical properties of load-carrying timber and the magnitude of heat affected zero (or reduced) strength layers.

5.5 Impact on Compartment Area on Fire Dynamics and Decay

Fire testing to date with exposed mass timber compartments has been based on under-ventilated compartments, with varying areas of exposed mass timber. Flashover within these room size compartments always occurs and the decay period that follows the fully developed phase once all the moveable fuel (fixtures, fittings etc) is influenced by the extent of mass timber, CLT glue-line integrity and encapsulation reliability. For larger compartments, such as office floors over 2000m², where the fire is fuel controlled due to the high availability of ventilation, flashover may not occur and there is a longer period of full development. Peak compartment temperatures differ between smaller compartments with ventilation-controlled fires, compared with larger compartments with fuel-controlled fires. The Cardington large compartment test with floor area 378m², was in the fuel-controlled region and exhibited the lower temperatures associated with this burning behaviour (peak of 760°C) [29]. Given the relationship between compartment temperature and char depth, a lower overall compartment temperature should be positive for structural capacity.

Of interest for larger compartments is the lack of a flashover period will result in an uncertain decay phase, as more moveable fuel is available during fire decay. For a large compartment, the fire decay period after

a peak temperature is reached will be influenced by not just the exposed mass timber (and glue line integrity and encapsulation reliability), but also by the unburnt contents that will continue to form part of the compartment fuel. Thus, the current understanding of fire decay influenced by exposed timber informed by numerous small compartment ventilation-controlled fire tests, may not be valid for larger compartments with fuel-controlled fires that do not achieve flashover.

For models that aim to predict fire decay with exposed mass timber, there will need to be a clear connection between compartment size and ventilation, which is best achieved through the use of the “opening factor” [22] as this provides a means by which to have ‘classic’ pre and post flashover compartment behaviour. Opening factors of approximately $8\text{-}10\text{ m}^{-1/2}$ and above correspond to ventilation-controlled fires where typical flashover conditions will occur. To be confident that flashover conditions will occur, that will result in all moveable fuel (including fixtures and fittings) being consumed before fire decay occurs, as would be expected in a flashed over compartment, then decay of the HRR is dependent on the exposed mass timber only (assuming no issues with CLT glue line integrity and encapsulation). Fire testing has informed us the expected conditions and provides a means by which to assess decay. Where the opening factor is below approximately $8\text{-}10\text{ m}^{-1/2}$, modelling the fire decay period will need to be based on not just the exposed timber but will also have to include the moveable fuel within the compartment. With no large-scale fire testing to inform this fire decay behaviour, estimates will need to be very conservative. A lower ventilation factor (fuel controlled) may result in overall lower temperatures in the compartment, but given that flashover may not occur, the impact of the moveable fuel continuing to be involved in the fire decay period may result in a further prolonged and slower decay for exposed timber compartments and potentially greater overall char depths.

6 CONCLUSIONS

High-rise buildings that are constructed with mass timber as the primary structure are in demand, because of sustainability benefits, the increased speed of construction and the potentially higher financial returns they offer. Where timber is exposed as part of the load-bearing structure, it influences the fire dynamics and requires iterative analysis methods and careful control of contributing parameters to achieve convergent results. Research to date shows that exposing mass timber could result in a fire that releases more energy than the structural elements can resist where influencing parameters are not properly controlled. Designing fire safe high-rise mass timber structures is possible, with careful design and material selection, to avoid unpredictable behaviour such as issues with glue line integrity in CLT and protective gypsum board failure in long duration fires. This helps to achieve predictable decaying fires that are required by fire safety engineers. Calculation methods are being developed that address the impact of exposed timber, but these are validated only for smaller compartments. Data for large compartments is urgently needed to validate models for larger compartments typical of office buildings. Further, efforts in mass timber research continue and more work is required in both research and guidance to enable robust designs and to assure approval authorities that performance-based assessment methods for high-rise buildings with large areas of exposed mass timber structure are safely engineered.

REFERENCES

1. Waugh Thistleton architects, 2018 “100 Projects – UK CLT”, published by Waugh Thistleton Architects for the Softwood Lumber Board and Forest Innovation Investment
2. Jones, S., 2018 “Mass Timber: Design and Research”, ORO Editions
3. White R., 2016 “Analytical Methods for Determining Fire Resistance of Timber Members”, SFPE Handbook of Fire Protection Engineering, 5th Edition, Gaithersburg
4. United States Department of Agriculture, Forest Service, Forest Products Laboratory, 2010, “Wood Handbook: Wood as an Engineering Material”. Madison, U.S. Dept. of Agriculture, Forest Service, Forest Products Laboratory
5. Barber, D., Gerard, R., 2015 “Summary of the Fire Protection Foundation Report - Fire Safety Challenges of Tall Wood Buildings” Fire Science Reviews, 4:5, DOI 10.1186/s40038-015-0009-3

6. Su, J., LaFrance, P., Hoehler, M., Bundy, M., 2018, "Fire Safety Challenges of Tall Wood Buildings – Phase 2: Task 2 & 3 Cross Laminated Timber Compartment Fire Tests" Fire Protection Research Foundation, Report No. FPRF-2018-01
7. Buchanan, A., Abu, A., 2016 "Structural Design for Fire Safety", second edition, John Wiley and Sons
8. CEN, 2009, "Eurocode 5: Design of Timber Structures – Part 1-2: General – Structural Fire Design", EN 1995-1-2
9. Australian Standards, 2019, "AS1720.4 - Timber structures Fire resistance for structural adequacy of timber members"
10. American Wood Council, 2015, "Calculating the Fire Resistance of Exposed Wood Members, Technical Report No. 10", Leesburg, Virginia
11. Lange, D., Hidalgo, J., Sjöström, J., Brandon, D., Schmid J., 2020, "A Comparison of the Conditions in a Fire Resistance Furnace When Testing Combustible and Non-combustible Construction", Fire Technology 56, pages 1621–1654
12. Schmid, J., Lange, D., Sjöström, J., Brandon, D., Klippel, M., Frangi, A., 2018, "The Use of Furnace Tests to Describe Real Fires of Timber Structures", Proceedings, World Conference on Timber Engineering, Seoul
13. Ingberg, S.H., 1928, "Tests of the Severity of Fires", Quarterly NFPA, 22, 43-61.
14. Law, M.A., 1997, "Review of formulae for T-equivalent", Proceedings of the Fourth International Symposium on Fire Safety Science, Melbourne, Australia, pp. 985-996.
15. Zelinka, S., Hasburgh, L., Bourne, K., Tucholski, D., Ouellette, J., 2018, "Compartment Fire Testing of a Two-Story Mass Timber Building" General Technical Report FPL–GTR–247, May 2018
16. Su, J., Leroux, P., Lafrance, P., Berzins, R., Gratton, K., Gibbs, E., Weinfurter, M., 2018, "Fire Testing of Rooms with Exposed Wood Surfaces in Encapsulated Mass Timber Construction", National Research Council, Canada Report No. A1-012710.
17. Deeny, S., Lane, B., Hadden, R., and Lawrence, A., 2018, "Fire safety design in modern timber buildings," The Structural Engineer, Vol. 96, No. 1, Jan-2018, pp. 48–53
18. McGregor, C., 2013 "Contribution of cross laminated timber panels to room fires", Carleton University, Masters Thesis
19. ANSI / APA, 2018 "PRG-320 Standard for Performance-Rated Cross-Laminated Timber"
20. EN 1991-1-2, 2002 "Eurocode 1: Actions on structures - Part 1-2: General actions - Actions on Structures Exposed to Fire"
21. Franssen, J., Iwankiw, N., 2016, "Structural Fire Engineering of Building Assemblies and Frames", SFPE Handbook of Fire Protection Engineering, 5th Edition, Gaithersburg.
22. Drysdale, D., 2011 "An Introduction to Fire Dynamics, Third Edition", Wiley
23. Crielaard, R., 2015 "Self-Extinguishment of Cross-Laminated Timber" Master's Thesis report, Faculty of Civil Engineering and Geosciences, Delft University of Technology
24. Barber, D., 2016, "Fire Safety Engineering of Tall Timber Buildings in the USA", Proceedings of World Conference on Timber Engineering
25. Brandon, D., 2018, "Fire Safety Challenges of Tall Wood Buildings – Phase 2: Task 4 – Engineering Methods", Final report, RISE Research Institutes of Sweden.
26. Wade, C., Spearpaint, M., Fleischmann, C., Baker, G., Abu, A., 2018, "Predicting the Fire Dynamics of Exposed Timber Surfaces in Compartments Using a Two-Zone Model," Fire Technology, Vol. 54, No. 4, pp. 893–920
27. Butler, C.P., 1971, "Notes on Charring Rates in Wood", Fire Research Note No, 896.
28. Babrauskas V. (2004) "Wood Char Depth: Interpretation in Fire Investigations"
29. Building Research Establishment, "Cardington Steel Framed Building Fire Tests," BRE, Watford, 1997.

CALIBRATION OF A COUPLED POST-FLASHOVER FIRE AND PYROLYSIS MODEL FOR DETERMINING CHAR DEPTH IN MASS TIMBER ENCLOSURES

Colleen Wade¹, Danny Hopkin², Michael Spearpoint³, Charles Fleischmann⁴

ABSTRACT

This paper describes the continued development of a coupled post-flashover fire zone model including pyrolysis of exposed timber surfaces intended for predicting the fire gas temperatures and the depth of charring in exposed timber surfaces for small enclosures. A new flame heat flux term for the burning timber surfaces has been included and a calibration factor investigated to modify the thermal conductivity of non-char elements to compensate for phenomena not addressed. The pyrolysis and fire models were decoupled to aid in the calibration of the pyrolysis model using both furnace and constant heat flux experiments. The coupled model is compared with full-scale enclosure experiments in which the impact of the calibration on the enclosure gas temperature and char depths are examined. While the model enhancements and calibration appear to provide predictions that are closer to the measured values, it is concluded that further work is needed to provide sufficient confidence for design purposes.

Keywords: Structures; zone modelling; compartment fires; mass timber; fire dynamics; pyrolysis

1 INTRODUCTION

There is an increasing realisation that standard fire resistance test results for mass timber structural elements do not necessarily ensure design objectives such as structural stability or fire containment will be achieved in practice.

An alternative is to undertake a performance based assessment, which typically involves analysis assuming time-temperature histories that reflect the expected growth, steady burning and decay stages of a fire as determined from the available ventilation, fuel load and enclosure materials and their properties. This decouples the thermal assault from the structure's response. In the case of timber structures, when the combustible surfaces are directly exposed to the fire (i.e. unprotected) or have the potential to become exposed (e.g. due to protective lining failure) the structure can contribute fuel to the fire creating a feedback loop between the amount or depth of char and the fire severity. This effect is likely to be more significant where exposed timber is in the form of large panels rather than isolated elements such as beams or columns, as the exposed surface area of the additional fuel is much larger.

This paper investigates the calibration of a timber pyrolysis and charring sub model for mass timber panels coupled with an enclosure zone fire model. The combined model is intended to provide structural fire engineers with a convenient tool to determine the expected depth of char within mass timber panels due to fire in a small enclosure where the enclosure dimensions, area of openings, and fuel load energy density

¹ Dr Colleen Wade, Fire Research Group Ltd,
e-mail: colleen.wade@fireresearchgroup.com, ORCID: <https://orcid.org/0000-0001-7959-9295>

² Dr Danny Hopkin, OFR Consultants
e-mail: danny.hopkin@ofrconsultants.com, ORCID: <https://orcid.org/0000-0002-2559-3581>

³ Dr Michael Spearpoint, OFR Consultants
e-mail: michael.spearpoint@ofrconsultants.com, ORCID: <https://orcid.org/0000-0002-3632-4870>

⁴ Dr Charles Fleischmann, University of Canterbury
e-mail: charles.fleischmann@canterbury.ac.nz, ORCID: <https://orcid.org/0000-0001-6914-7885>

are known along with the expected density, thickness, moisture content and exposed surface area of the mass timber panels.

2 BACKGROUND

Design methods have been developed over recent years that attempt to predict the gas temperatures over the course of a fire that also include the contribution from the mass timber surfaces such as exposed cross-laminated timber (CLT) panels, as well as the incident heat flux to bounding surfaces and depth of char within such surfaces. Simpler methods include hand/spreadsheet calculations using parametric fire temperature equations and involve iterative processes to balance the char depth with the additional fuel contributed, such as the methods proposed by Barber et al. [1] and Brandon [2].

As a first step, Wade et al. [3] developed a post-flashover fire zone model based on energy and mass conservation within an enclosure bounded by mass timber elements by adapting the existing fire zone model B-RISK to include a simple wood pyrolysis model. This assumed a moveable fire load represented as wood cribs with the added contribution of fuel from the exposed timber surfaces incrementally added to the fire load at each time step. This was based on a one-dimensional heat transfer calculation for the timber surfaces to determine the depth of the 300 °C isotherm assuming constant thermal properties. Wade et al. [4] then developed a more advanced model with the timber surface pyrolysis determined from a four component (lignin, cellulose, hemicellulose and water) kinetic sub model where the thermal properties in the solid phase heat transfer analysis considered the different components of char and wood for each element considered.

Subsequently Wade [5] made further improvements by including modified thermal properties, dehydration and desorption effects, dimensional changes, and alternative kinetic properties. In all three model variations, a finite difference scheme was used to calculate heat transfer and internal temperatures within the exposed timber surfaces bounding the enclosure. This paper is a continuation of the model development introducing an additional flame heat flux term for the burning timber surfaces that accounts for the oxygen mass fraction of the enclosure gases along with a critical mass loss rate for flaming combustion which better describes the thermal boundary conditions during the decay phase, especially as the enclosure oxygen levels return to their ambient value. However, it is apparent that a calibration of the pyrolysis model to compensate for phenomena not otherwise addressed is still required in order to produce char depth predictions that are appropriate for design and ultimately to provide structural fire engineers with a more useful model to inform the fire design of mass timber buildings.

3 THEORY

3.1 Two zone model

The governing equations for the zone model are described elsewhere [6] but are similar to other two-zone models where the conservation of mass and energy are represented by a set of first order differential equations which when solved provide solutions advancing in time for the upper layer volume, upper and lower layer temperatures, and pressure. The ceiling, upper wall, lower wall and floor transfer radiation independently to each of the other surfaces with the fire treated as point source of radiation intercepted by each surface. Soot particles are assumed to emit radiation, and carbon dioxide and water vapour are assumed to absorb radiation. The boundary between the upper and lower wall is distinguished by the position of the interface between the two gas layer control volumes, which changes with time as each volume expands or contracts in response to the gas entrainment into the fire plume and the air entering the enclosure. The radiation exchange sub model calculates the net radiant heat flux emitted or absorbed by the enclosure surfaces, and along with the convective heat flux at the surface, is used to determine the boundary conditions for the heat transfer into the enclosure surfaces.

3.2 Flame heat flux for burning surfaces

In this paper, an additional term is introduced to the boundary conditions for the heat transfer to the enclosure surface being a flame heat flux term for burning timber wall and ceiling surfaces where the heat flux from the flames is estimated from Equation 1 after Rasbash et al. [7], where \dot{m}'' is the mass loss rate per unit area from the burning timber surface (calculated from the pyrolysis model described later), $\Delta H_{c,n}$ is the heat of combustion of the timber (taken as 17.5 MJ/kg) and ϕ is the proportion of energy from the flames transferred back to the surface and estimated from Equation 2 [7] where h_c is the convective heat transfer coefficient (in W/m²K), $c_{p,air}$ is the specific heat of air (1.01 J/gK), Y_{ox} is the oxygen mass fraction (0.23 at ambient) but calculated by the zone model for the upper layer gases in the enclosure fire and r is the stoichiometric ratio of oxygen to fuel taken as 3.43 for timber [7].

$$\dot{q}_f'' = \phi \Delta H_{c,n} \dot{m}'' \quad (1)$$

$$\dot{m}_{cr}'' = \frac{h_c}{c_{p,air}} \ln \left(1 + \frac{Y_{ox}}{r\phi} \right) \quad (2)$$

Taking the critical mass loss rate (\dot{m}_{cr}'') for timber as 3.5 g/m²s from Bartlett [8] and combining Equations (1) and (2) gives the following expression for the flame heat flux:

$$\dot{q}_f'' = \frac{Y_{ox} \Delta H_{c,n} \dot{m}''}{r \left[\exp \left(\frac{c_{p,air}}{h_c} \dot{m}_{cr}'' \right) - 1 \right]} \quad (3)$$

Bartlett [8] conducted bench scale experiments using the Fire Propagation Apparatus (FPA) and evaluated $c_{p,air}/h_c$ to be 9 g/m²s for a flat plate while Rasbash et al. assumed 10 g/m²s. EN 1991-1-2 gives the convective heat transfer coefficient for the standard fire resistance test exposure as 25 W/m²K. Veloo and Quintiere [9] studied the convective heat transfer coefficient in fully developed fire experiments, using a heated plate heat flux gauge and a water-cooled gauge, in which the convective heat transfer coefficient was measured and correlated over a range of temperatures in flaming and cooling periods for enclosure fires. They found the heat flux could attain levels between 100 and 200 kW/m² where convection accounted for up to 25%, with an order of magnitude for the convective heat transfer coefficient given as 50 W/m²K. Higher convective heat flux values are attributed due to high local velocities disturbing the flow field [10]. Given the findings by Veloo and Quintiere [9] and also by Gorska et al. [11], who observed higher velocities at the opening that they attributed to the burning timber surfaces producing stronger buoyant gas flows inside the enclosure, in the present paper, a constant post-flashover convective heat transfer coefficient of 50 W/m²K has been used both for the zone model calculations and for evaluating the flame flux for burning timber surfaces from Equation (3). This was found to provide higher predictions of the gas phase enclosure temperatures, in particular during the decay phase of the fire. Previously, a calculated convective heat transfer coefficient based on natural convection was used in the zone model.

3.3 Pyrolysis model

The pyrolysis and charring of mass timber panels is calculated from a one-dimensional, four-component (including moisture) kinetic sub model for the pyrolysis of the wood. The decomposition of the wood is described by an Arrhenius equation that gives a relationship between the reaction rate and temperature of the solid. This requires the kinetic properties (activation energy, E_i , pre-exponential factor, A_i , and reaction order, n_i) to be specified. A multiple-component scheme is used that assumes a solid material is composed of several components, with each component undergoing a single independent reaction to generate products. The constituent components of solid wood included in the model are cellulose, hemicellulose, lignin and water.

The reaction rate for each component can be described with a first order differential equation where $Y_{i,j}$ is the mass fraction ($m_i/m_{i,0}$) of component i at time j , m_i is the mass of component i and $m_{i,0}$ is the initial

mass of component i . For each component, the initial mass fraction is $Y_{i,o} = 1$ at the start of the simulation. c_i is the initial fraction of the overall unheated composite solid represented by component i i.e. $(m_{i,o}/m_o)$ and T_j is the temperature of the solid. Equation (1) is solved using a Runge Kutta numerical method to give the residual mass fraction value for each component (Y_i) at each time step for each element comprising the enclosure wall or ceiling surface. The model uses the parameters given in Table 1 from Matala et al. [12], based on thermogravimetric experiments and a genetic algorithm.

$$\frac{dY_{i,j}}{dt} = c_i A_i \exp\left(-\frac{E_i}{RT_j}\right) (Y_{i,j})^{n_i} \quad (4)$$

Table 1. Kinetic parameters of wood estimated using a genetic algorithm [12].

Component	E_i (J/mol)	A_i (s ⁻¹)	n_i	$(\rho_{i,o}/\rho_o)$	Char Yield (-)
Hemicellulose	1.64×10^5	5.78×10^{13}	4.166	0.28	0.268
Cellulose	1.95×10^5	2.68×10^{14}	0.85	0.37	0.100
Lignin	1.38×10^5	2.18×10^{10}	7.0	0.25	0.567
Water	1.62×10^5	1.00×10^{20}	1.0	0.10	-

Janssens and Douglas [13] provide detailed equations for the thermal conductivity of wood, char and partially charred wood at ambient and elevated temperature. These are used along with an adjustment to the thermal conductivity for char contraction as proposed by Parker [14]. The specific heat of wood depends on the temperature and moisture content. The specific heat of dry wood given by Tenwolde et al. [15] is used with the latent heat of vaporisation and heat of wetting effects as described by Janssens and Douglas [13] included over the temperature range 100 to 120 °C. The specific heat of char is also taken from Janssens and Douglas [13]. From Table 1, the initial proportions by mass of hemicellulose, cellulose, lignin and water within the solid wood are taken as 28%, 37%, 25% and 10% respectively.

3.4 Heat transfer model

The boundary surfaces within the enclosure are represented by an implicit finite difference scheme where temperatures within each bounding surface of the enclosure (ceiling, walls, floor) are determined by advancing the calculation at each time step. The temperature at each internal node throughout the depth of each bounding surface is calculated by solving a set of simultaneous equations at each time step using the finite difference approximation. A timestep of 0.5 – 1.0 s and element thickness of 1 mm have generally been used in the calculations. The temperature for each element in the bounding surface that comprises exposed timber drives the rate of decomposition of the cellulose, hemicellulose, lignin and evaporation of water as determined by the kinetic pyrolysis sub model. At each time step, a weighted average for the thermal properties of each element is calculated based on the residual mass fractions of the cellulose, hemicellulose, lignin, water and char. The mass loss rate per unit area assumed to be released from the exposed surface is determined by summing the mass loss from each element over the full depth of the bounding surface.

The char depth for the bounding surface is calculated based the position of the 300°C isotherm. However, it is noted that the user has the option of extracting the corresponding depth based on any other temperature isotherm or residual chemical composition that could be more informative regarding the residual strength or threshold for non-reversible damage to the timber at depth. Furthermore, the mass loss rate prediction per unit area from the exposed timber surfaces allows the potential for self-extinguishment to be evaluated based on the mass loss rate from the burning surfaces that is also calculated as a function of time.

3.5 Model limitations

Despite addressing a wide range of phenomena in the pyrolysis model, not all those that may be important are captured, leading to the ultimate char depth predictions generally being underestimated. The most significant phenomena or other effects not addressed in the pyrolysis sub model are:

- Oxidation of the char.
- Cracking and continued degradation or erosion of the wood char during the decay phase such that in reality the maximum char depth tends to a constant value rather than continuously increasing.
- Water vapour within the timber panels evaporating but then condensing again deeper into the enclosure surfaces.

Furthermore, the zone model formulation may also not correctly capture effects such as:

- The actual mass loss rate for the wood cribs (representing the moveable fire load) may differ from the assumed burning rate given by correlations rate due to the enclosure heating and ventilation effects, collapsing cribs or other reasons.
- Representing actual fuel packages and materials as wood cribs may not be realistic.
- Not accurately representing the conduction heat losses within the enclosure due to the thermal properties applying to the partial areas protected with gypsum plasterboard being represented by the properties of wood/char.

As previously found by Wade [5], the coupled pyrolysis and zone model tends to overpredict the rate of decline of gas temperatures in the decay phase of the fire and tends to underpredict the ultimate depth of char within the timber surface. In this paper, we investigate a calibration of the pyrolysis model to help compensate for these limitations and consequently provide char depth predictions that are closer to the experimentally derived values.

4 CALIBRATION OF THE CHARRING SUB-MODEL

Calibration of thermal properties for the purpose of improving agreement between measured and predicted char rates in timber members has been discussed previously in the literature. For example, König and Walleij [16] carried out calculations using thermal properties that were calibrated to assess results using the standard fire resistance test with good success. The advanced thermo-physical properties in the EN 1995-1-2 are based on the work of König and Walleij [16]. The effective thermal conductivity is increased at high temperatures to compensate for increased heat transfer due to shrinkage cracks above about 500 °C as well as the consumption of the char layer at about 1000 °C. However, they also found the charring rate when the rate of temperature rise is greater than the standard fire resistance test was overpredicted whereas it was underpredicted when the rate of temperature rise was slower. Thus, the same set of calibrated properties did not lead to good agreement for non-standard fire exposures. This subject has also been discussed previously by Hopkin [17]. The EN 1995-1-2 properties are therefore recommended only for standard fire exposure and not parametric or natural fires that include a decay phase.

While investigating a coupled pyrolysis, heat transfer and fire model for enclosure fires, Wade et al. [4] also found that using the EN 1995-1-2 effective thermal conductivity relationship for wood resulted in significantly lower predicted peak gas temperatures in the enclosure compared to the measured gas temperatures, and attributed this to the higher predicted heat losses due to the much higher assumed thermal conductivity for the exposed char layers nearest the surface where the temperatures were the highest. They concluded that the EN 1995-1-2 approach to calibrating the thermal properties was not appropriate in coupled enclosure fire models that solve energy conservation equations.

In this paper, a calibration factor is proposed as a multiplier to the calculated thermal conductivity applicable to each non-char element where the temperature of that element is higher than 50 °C. This effectively corresponds to the pyrolysis region and a heated zone that extends deeper within the section. The multiplier is based on a simple trial and error procedure. The calibration process first involves isolating the pyrolysis model from the fire model and supplying defined boundary conditions to the pyrolysis model

i.e. a time temperature curve or heat flux value along with the oxygen mass fraction, and then comparing the char depth (based on the 300 °C isotherm) with experiments where the boundary conditions are clearly defined. The pyrolysis and charring sub model is benchmarked against constant heat flux experiments by Pope et al. [18] and furnace experiments by König and Walleij [16] as described in Sections 4.1 and 4.2. These experiments are used to inform the selection of a suitable calibration factor. Results are then given in Section 5 using the coupled fire and pyrolysis model for simulations of three full-scale fire experiments in CLT enclosures where the resulting gas phase enclosure temperatures and solid phase char depths are compared with and without calibration.

4.1 Constant heat flux experiment

As part of an investigation into the measurement errors associated with thermocouples inserted perpendicular to a thermal wave in a charring material, Pope et al. [18] carried out experiments using the FPA that exposed laminated bamboo blocks to a constant heat flux. The specimens had dimensions $120 \times 120 \times 100$ mm thick and the lamellae were bonded together with a phenol-formaldehyde resin. The density of the bamboo was given as 675 kg/m^3 and moisture content was found to be approximately 6.5–7%. The ambient temperature was 25 °C.

Simulations using the pyrolysis and charring sub model are made, where the ambient oxygen mass fraction is taken as 0.23, the convective heat transfer coefficient as $10 \text{ W/m}^2\text{K}$ and the heat of combustion as 17.5 kJ/kg . Figure 1 was adapted from Pope et al. [18] and shows the measured depth of the 60 °C (blue lines) and 300 °C (orange lines) isotherms based on thermocouples installed from the side and from the back of the specimen. The plot has been overlaid with the predicted char depths versus time without calibration (the dashed lines) and with a calibration factor of 1.6 applied to the wood thermal conductivity (the solid lines), as previously described. The uncalibrated simulations provide reasonable agreement in the first 20–30 minutes of the experiment but underpredict for longer times. The calibration factor of 1.6 provides a reasonable correction though may have still underpredicted the char depth if the experiment had continued beyond 60 minutes.

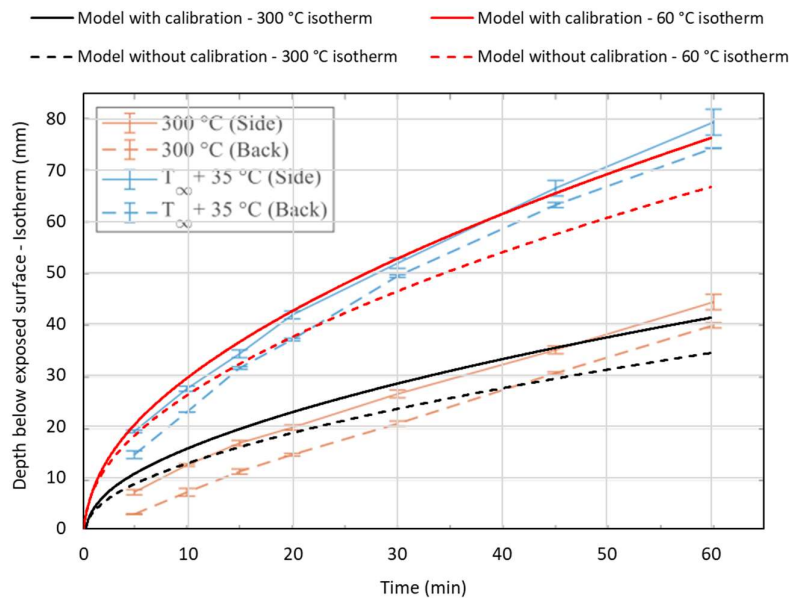


Figure 1. Laminated bamboo exposed to 60 kW/m^2 [18] with and without calibration.

4.2 Furnace experiments

Three experiments using a fire resistance test furnace were carried out by König and Walleij [16] to measure the depth of char in timber sections 95 mm deep. The timber species used was a spruce with a dry density of $420 - 430 \text{ kg/m}^3$ conditioned at 20 °C and 65% RH. For the present calculations, a wet density of 470

kg/m³ and moisture content of 10% are used. The furnace thermal exposures represented a standard time temperature curve and two parametric curves that both included decay phases as shown in Figure 2 from ref. [16]. Oxygen concentration in the furnace was not recorded but it is assumed in the present analysis to be no more than 10% by mass for the heating phases returning to ambient level (23% by mass) for the decay phase. Figure 3 shows the char depth versus time based on the thermocouple measurements and 300 °C isotherm measured by König and Walleij [16] for the standard fire resistance curves labelled SFE in Figure 2. The char depths predicted from the pyrolysis and charring sub model are overlaid on the plot and show the uncalibrated pyrolysis and charring model gives good agreement for the first 40 minutes or so but thereafter the char rate decreases in comparison with the experimental values. The calibrated curve using a calibration factor of 1.6 provides more conservative predictions but the difference between the measured and predicted values is seen to reduce with time.

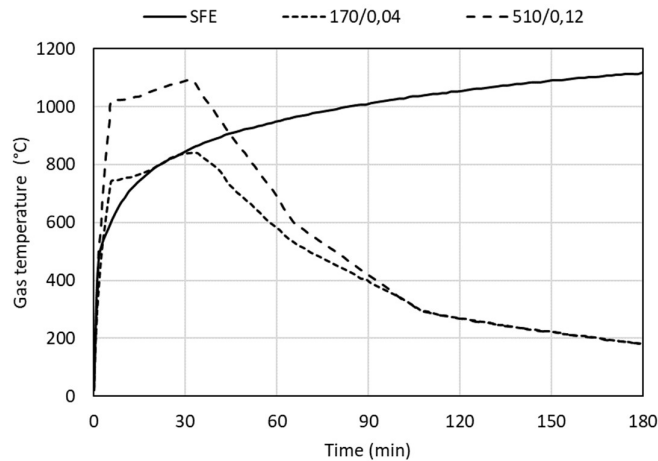


Figure 2. Furnace time-temperature histories for experiments (from König and Walleij [16]).

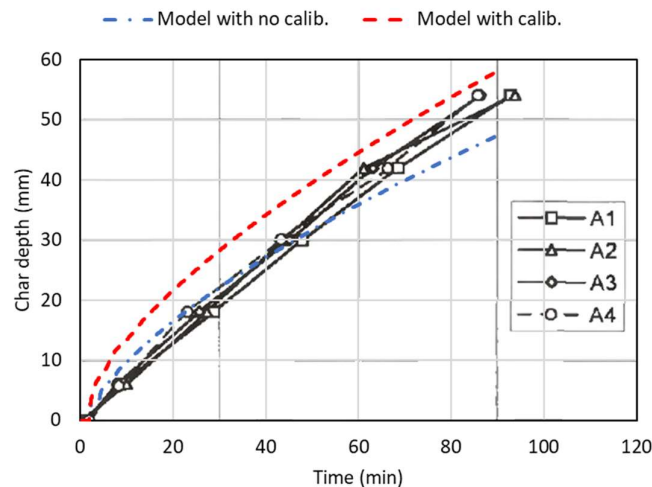


Figure 3. Depth of char due to standard fire resistance test exposure (König and Walleij [16] – SFE Test Series A) compared with model prediction.

Figure 4 shows the char depth versus time based on the thermocouple measurements and 300 °C isotherm for the Test Series C1 to C3. This is the curve labelled 510/0,12 in Figure 2. The predicted char depths with and without calibration are overlaid on Figure 4. Again, the uncalibrated prediction shows good agreement only in the early period and underpredicts the ultimate char depth. While the prediction using a calibration factor of 1.6 provides good prediction of the ultimate char depth it tends to overpredict the char depth at earlier times. Figure 5 shows the char depth versus time for the second parametric curve labelled 170/0,04 in Figure 2. Again, the predicted char depths with and without calibration are overlaid on Figure 5 with

similar trends shown, however the calibration factor of 1.6 produces an ultimate char depth that may still be considered too low.

5 BENCHMARKING WITH FULL-SIZED CLT ENCLOSURE EXPERIMENTS

The performance of the coupled fire and pyrolysis model is now considered with and without the calibration included by benchmarking the results against three full-scale experiments in enclosures constructed from CLT, where in each case different areas of CLT were exposed.

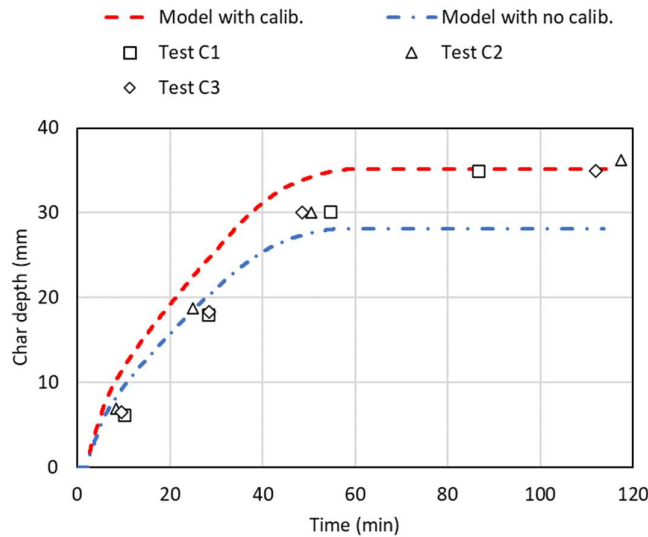


Figure 4. Depth of char due to standard fire resistance test exposure (König and Walleij [16] – Test Series C1 to C3) compared with model prediction.

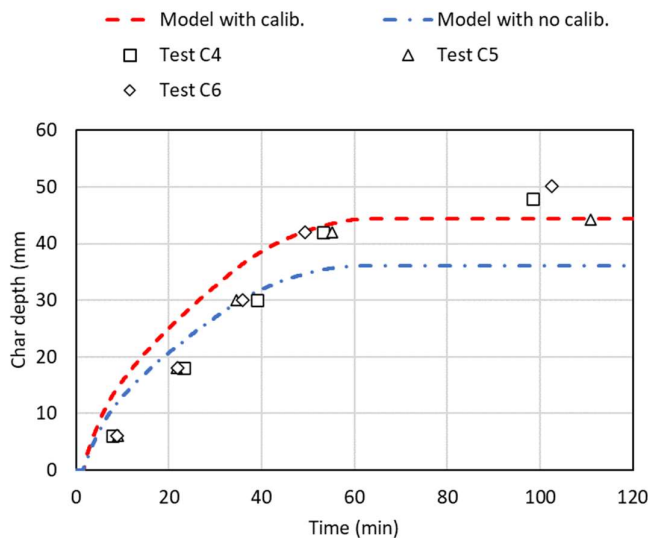


Figure 5. Depth of char due to standard fire resistance test exposure (König and Walleij [16] – Test Series C4 to C6) compared with model prediction.

5.1 NRCC room fire experiments

Su et al. [19] at the National Research Council of Canada conducted five full-scale fire experiments burning wood cribs within a CLT enclosure with an opening. The CLT was 175 mm thick CLT manufactured using

five lamellae, each 35 mm thick and bonded together with a thermal resistive polyurethane adhesive. The enclosure measured 4.5 m long \times 2.4 m wide \times 2.7 m high with a single doorway opening in one of the longer walls measuring 0.76 m wide \times 2.0 m high. The fuel contents in each experiment comprised three wood cribs each weighing 120 kg providing a nominal fire load of 467 MJ/m² (assuming an effective heat of combustion of 14 MJ/kg). Encapsulation was provided, where required, by 2–3 layers of 15.9 mm thick Type X gypsum board. Two of the experiments are considered here which only involved areas of exposed wall and ceiling. Experiment 2 had 33% of the wall and 10% of the ceiling area exposed (or unprotected) and Experiment 5 had 35% of the wall and 100% of the ceiling exposed.

Figure 6 shows the gas temperature versus time measured inside the enclosure and in the doorway for Experiment 2. The maximum char depths measured in the upper wall ranged from 50 – 70 mm (mean 55.6 mm) and the maximum char depth in the ceiling ranged from 45 – 63 mm (mean 52.5 mm). Figure 6 also shows the predicted gas temperature from the coupled fire and pyrolysis sub models with several different calibration factors used as well as with no calibration (i.e. $k = 1.0$).

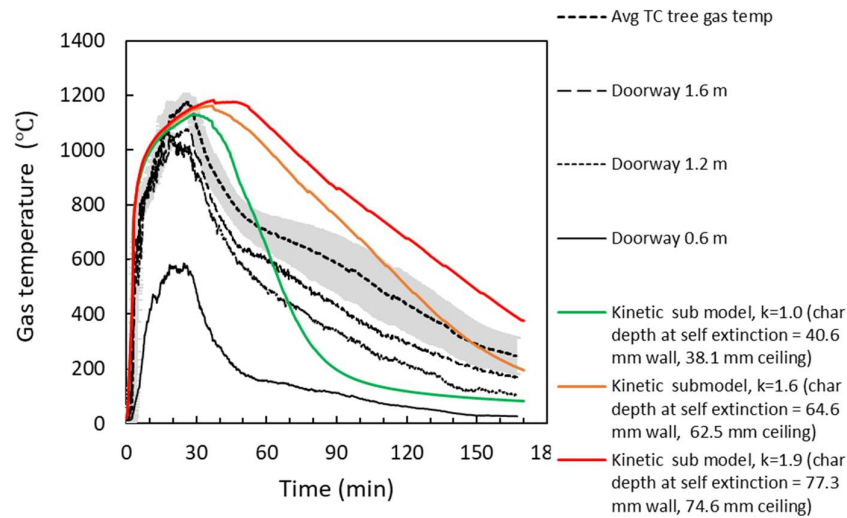


Figure 6. Enclosure Test 2 (33% walls and 10% ceiling exposed).

Figure 7 shows the corresponding graph for Experiment 5. The maximum char depths measured in the upper wall ranged from 81 – 109 mm (mean 88.6 mm) and the maximum char depth in the ceiling ranged from 70 – 90 mm (mean 77.5 mm).

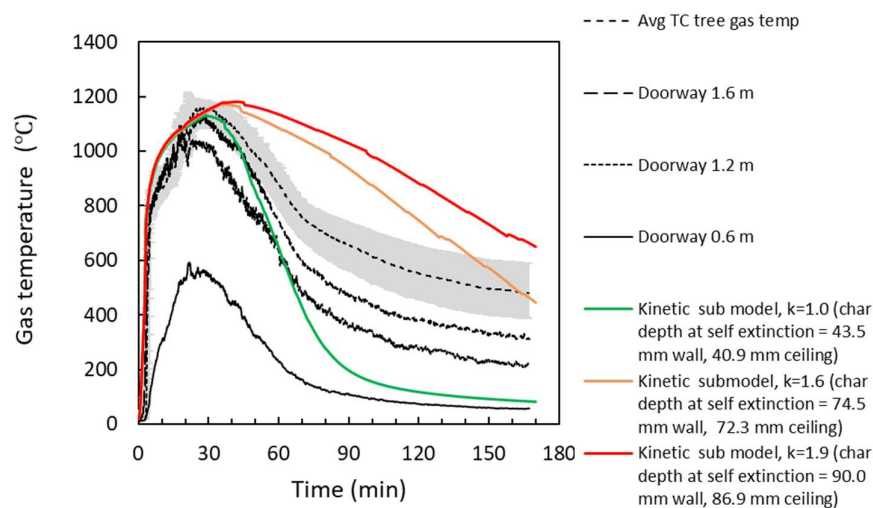


Figure 7. Enclosure Test 5 (35% walls and 100% ceiling exposed).

5.2 NRCC/NIST room fire experiment

Su et al. [20] conducted a series of full-scale enclosure experiments in a CLT enclosures with various amounts of exposed wall and ceiling areas. The CLT was 175 mm thick with five lamellae each 35 mm thick. The lamellae were adhered with a polyurethane adhesive. One of these experiments is included here – referred to as Test 1-4. The enclosure measured $9.1 \times 4.6 \times 2.7$ m high with an opening 2.0 m high and 1.8 m wide. The ceiling was fully exposed with all walls protected with gypsum plasterboard. Figure 8 shows the gas temperature versus time measured inside the enclosure. The increase in gas temperature after 120 minutes is due to delamination of CLT that allowed the fire to grow again upon exposing fresh fuel. For the current analysis, delamination is ignored on the assumption that it can be avoided by using a thermally resistive adhesive to bond the CLT lamellae together or through improved consideration of the CLT lay-up, e.g. increasing the thickness of the room facing lamellae. Brandon [21] conducted additional intermediate scale experiments and estimated the char depth for this experiment as 50 mm in the absence of any delamination.

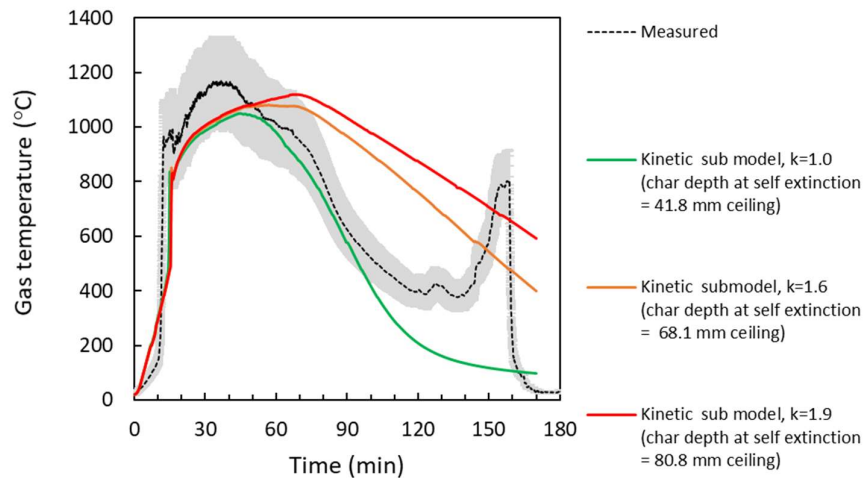


Figure 8. Enclosure Test 1-4 (100% ceiling only exposed).

6 DISCUSSION AND CONCLUSIONS

Considering the enclosure fires in the previous section, the measured and predicted char depths are shown in Figure 9 (a) to (c) with and without calibration. A calibration factor of at least 1.6 is found to be successful in providing better prediction of both the gas temperature during the decay phase and of the ultimate char depth. The error bars shown represent the range of char depth measured by a resistograph.

Previously, Wade [5] compared the coupled B-RISK enclosure fire model with pyrolysis of mass timber surfaces with 19 enclosure fire experiments with and without exposed CLT surfaces and found it predicted the peak gas temperature within experimental error. However, the predictions of gas temperatures in the decay phase of the fire showed a more rapid rate of decline compared to the measured data. The thermal environment during the decay stage has a great influence on the char depth predictions and therefore it is important that the coupled fire and pyrolysis sub model is able to reasonably describe the gas temperatures and heat fluxes to surfaces during the decay period. Including a flame heat flux term to the heat transfer boundary conditions and incorporating a calibration factor as described in this paper is helpful in slowing the predicted rate of temperature decline during the decay phase and in providing predictions of char depth at self-extinction that better reflect the available experimental data. However, the investigation described here should only be considered ‘work in progress’ and it may not be appropriate to conclude that the suggested calibration factors are sufficient for design purposes. It is necessary that further benchmarking and analysis be conducted, including by potential end users, to increase confidence in char depth predictions.

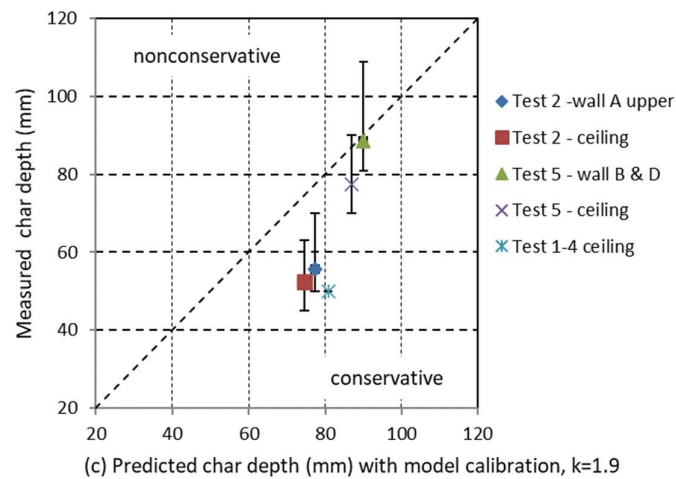
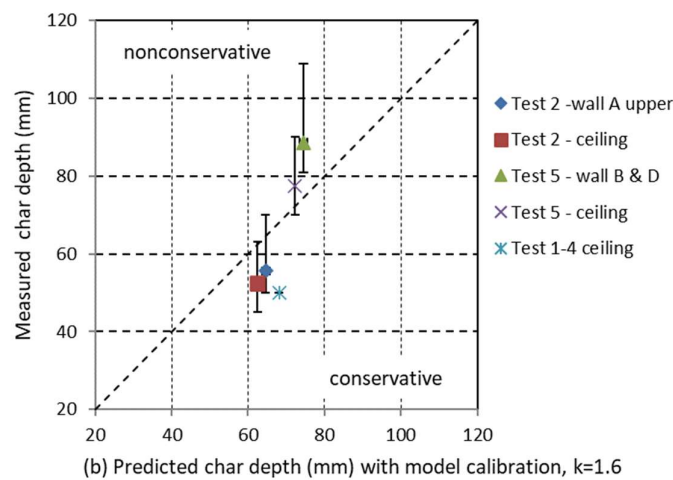
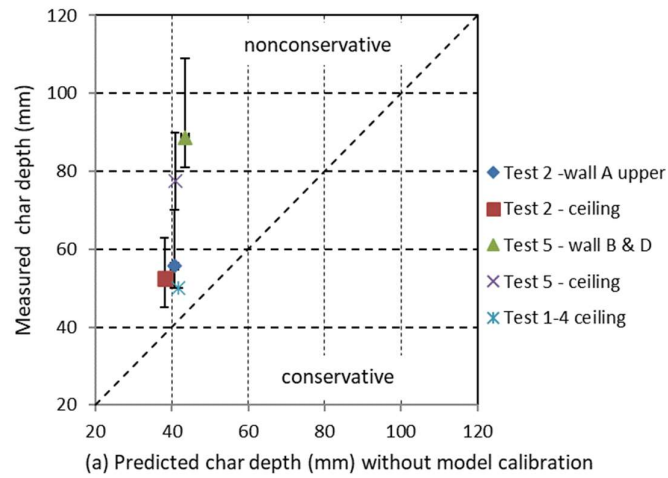


Figure 9. Predicted versus measured final char depth in CLT enclosure fires (a) without model calibration $k = 1.0$ (b) with calibration $k = 1.6$ (c) with calibration $k = 1.9$.

ACKNOWLEDGMENTS

The Building Research Levy NZ has provided financial support for the research described in this paper.

REFERENCES

1. Barber D, Crielaard R, Li X (2016) Towards fire safety design of exposed timber in tall timber buildings. In: Proceedings of WCTE 2016 World Conference on Timber Engineering. Vienna Austria
2. Brandon D (2018) Fire safety challenges of tall wood buildings – Phase 2: Task 4 Engineering methods. Fire Protection Research Foundation, Quincy, MA
3. Wade CA, Spearpoint MJ, Fleischmann CM, et al (2018) Predicting the fire dynamics of exposed timber surfaces in compartments using a two-zone model. *Fire Technol* 54:893–920. <https://doi.org/10.1007/s10694-018-0714-2>
4. Wade CA, Hopkin D, Su J, et al (2019) Enclosure fire model for mass timber construction - benchmarking with a kinetic pyrolysis submodel. In: Interflam 2019: 15th International Conference on Fire Science and Engineering. InterScience Communications Limited, Royal Holloway College, Nr Windsor, UK
5. Wade CA (2019) A theoretical model of fully developed fire in mass timber enclosures. PhD Thesis, University of Canterbury, Department of Civil and Natural Resources Engineering
6. Wade CA, Baker GB, Frank K, et al (2016) B-RISK 2016 User guide and technical manual. BRANZ, Porirua, New Zealand
7. Rasbash DJ, Drysdale DD, Deepak D (1986) Critical heat and mass transfer at pilot ignition and extinction of a material. *Fire Safety Journal* 10:1–10. [https://doi.org/10.1016/0379-7112\(86\)90026-3](https://doi.org/10.1016/0379-7112(86)90026-3)
8. Bartlett AI (2018) Auto-extinction of engineered timber. PhD Thesis, The University of Edinburgh
9. Veloo PS, Quintiere JG (2013) Convective heat transfer coefficient in compartment fires. *Journal of Fire Sciences* 31:410–423. <https://doi.org/10.1177/0734904113479001>
10. Inghelbrecht A (2014) Evaluation of the burning behaviour of wood products in the context of structural fire design. International Master of Science in Fire Safety Engineering, The University of Queensland and Ghent University
11. Gorska C, Hidalgo JP, Torero JL (2020) Fire dynamics in mass timber compartments. *Fire Safety Journal* 103098. <https://doi.org/10.1016/j.firesaf.2020.103098>
12. Matala A, Hostikka S, Mangs J (2008) Estimation of pyrolysis model parameters for solid materials using thermogravimetric data. In: Fire Safety Science - Proceedings of the 9th International Symposium. International Association for Fire Safety Science, Karlsruhe, Germany, pp 1213–1224
13. Janssens ML, Douglas B (2004) Wood and wood products. In: Harper CA (ed) Handbook of building materials for fire protection. McGraw-Hill
14. Parker WJ (1989) Prediction of the Heat Release Rate of Douglas Fir. In: Fire Safety Science - Proceedings of the Second International Symposium. Hemisphere Publishing Corporation
15. TenWolde A, McNatt JD, Krahn L (1988) Thermal Properties of Wood Panel Products Buildings. USDA, Forest Products Laboratory, Madison, Wisconsin
16. König J, Walleij L (1999) One-dimensional charring of timber exposed to standard and parametric fires in initially unprotected and postprotection situations. Swedish Institute for Wood Technology Research, Stockholm, Sweden
17. Hopkin D (2013) Predicting the thermal response of timber structures in natural fires using computational “heat of hydration” principles. *Fire and Materials* 37:311–327. <https://doi.org/10.1002/fam.213>
18. Pope I, Hidalgo JP, Torero JL (2020) A correction method for thermal disturbances induced by thermocouples in a low-conductivity charring material. *Fire Safety Journal* 103077. <https://doi.org/10.1016/j.firesaf.2020.103077>
19. Su J, Leroux P, Lafrance P, et al (2018) Fire testing of rooms with exposed wood surfaces in encapsulated mass timber construction. National Research Council of Canada, Ottawa, Canada
20. Su J, Lafrance P, Hoehler M, Bundy M (2018) Fire safety challenges of tall wood buildings – Phase 2: Task 2 & 3 – Cross Laminated Timber Compartment Fire Tests. Fire Protection Research Foundation, Quincy, MA
21. Brandon D, Schmid J, Su J, et al (2018) Experimental fire simulator for post-flashover compartment fires. In: Proceedings of the 10th International Conference on Structures in Fire. Belfast, UK

THE BEHAVIOUR OF TIMBER IN FIRE INCLUDING THE DECAY PHASE - CHARRING RATES, CHAR RECESSION AND SMOULDERING

Joachim Schmid¹, Antonio Totaro², Andrea Frangi³

ABSTRACT

For the assessment of the fire resistance of timber members, the depth of the virgin wood has been documented as crucial parameter in numerous scientific experiments in the past; results have been used primarily for the load-bearing resistance verification. An excessive number of tests with timber members have been performed with various products (e.g. glulam, cross-laminated timber) in furnace environments showing a consistent one-dimensional charring rate of $0.65 \text{ mm/min} \pm 0.1$ for standard fire exposure. More severe fire exposure (e.g. hydrocarbon fire) showed a moderate increase of the charring rates to about 1.4 mm/min . The interest for performance-based design (PBD) moved the focus away from the fully developed fire phase and included other conditions, where further parameters are relevant. In furnaces, mainly the charring rate has been observed while in oxygen rich environments further a reduction of the char layer can be observed. This paper presents results from a novel charring investigation apparatus where exposure levels up to 120 kW/m^2 and gas velocities up to 8 m/s (heated gas) in moderately and highly turbulent conditions were investigated. Typically, the prediction of the charring rate is done using the external heat flux, which resulted in poor fit for the observed charring rates up to 2.4 mm/min . The predictions could be significantly improved if further characteristics were considered. The most significant characteristic was the smouldering combustion of the char layer. Findings of the experimental campaign can describe the contribution of the timber to the fire dynamics and are expected to be used in future calculation models.

Keywords: Fire; Timber; Charring; Cooling phase; Oxygen; Turbulence; Heat Release Rate

1 INTRODUCTION

The fire resistance and its verification is of high importance regardless the structural material. The use of timber structures has been limited in many countries due to its combustibility. Improved products, the request for sustainable buildings and new boundary conditions such as improved fire service performance, fire safety systems and the increased reliability of heating systems led to an opening of building regulations for timber structures. The recently introduced cross-laminated timber elements stimulated the marked and further raised questions about the fire safety of these structures and the validity of the fire resistance framework for combustible members in general.

A performance based design (PBD) has been requested of structures with a significant share of combustible surfaces contributing to the fire development, see e.g. Su et al. [1]. To allow for PBD, further knowledge is

¹ MSc, ETH Zürich,
e-mail: schmid@ibk.baug.ethz.ch, ORCID: <https://orcid.org/0000-0002-4460-8638>

² MSC, Gruner AG,
e-mail antonio.totaro@gruner.ch

³ Prof, IBK, ETH Zürich,
e-mail: frangi@ibk.baug.ethz.ch, ORCID: <https://orcid.org/0000-0002-2735-1260>

needed exceeding the well-documented behaviour of timber structures in the fully developed fire phase, see e.g. Buchanan et al. [2].

From numerous compartment experiments documented in the literature, it is apparent that the contribution of exposed timber to the compartment fire cannot be described with actual design models. In earlier work, the authors investigated the influence of the gas velocity and the oxygen concentration on the charring behaviour [3,4] and proposed how the heat release rate (HRR) of structural timber can be determined, i.e. 5.4 MJ/m² per mm charring. Here it should be noted that the actual 2nd draft for the revision of Eurocode 5 contains rules for the consideration of structural timber as part of the total fire load. Comparing HRR measurements of compartment experiments with calculations for the particular compartment, Brandon [5] proposed a fitting factor to consider the apparent contribution of the structural timber in the fully developed fire phase. In a recent study, Schmid et al. [6], showed that the afore mentioned fitting factor can be traced back to (a) the combustion efficiency and (b) the combustion behaviour of structural timber. The latter is understood by the authors as the pyrolysis of the virgin wood releasing a limited amount of combustible volatiles and the modification of the virgin wood to a new material, the char layer. Apparently, this thermal modification from wood to char goes along with a significant reduction of the density and increase of the heat content. The char layer is involved in the following in the compartment fire.

So far, the charring rate has been the only input parameter for the description of the combustion of structural timber in compartment fires. Traditionally, the charring rate is correlated with a fire temperature, e.g. the EN/ISO standard fire exposure [7.8] or an external heat flux, typically done for cone calorimeter tests. In this paper, it is shown that the description of the charring rate can be significantly improved by considering further parameters. Those additional parameters can be used to describe the contribution of structural timber in a fire.

2 METHOD

In this Section, the background of the experimental campaign is presented resulting in a novel test method. In the context of a research study at ETH Zürich, several existing methods were analysed with respect to the suitability for the analysis of the behaviour of structural timber representative for compartment fires. Model- or bench scale setups were preferred as they allow to isolate characteristics and their cost efficiency allows for the performance of a large number of experiments. Contrary to the post-flashover environments where the oxygen concentration is limited, it was aimed for an oxygen rich experimental environment with controlled gas flow.

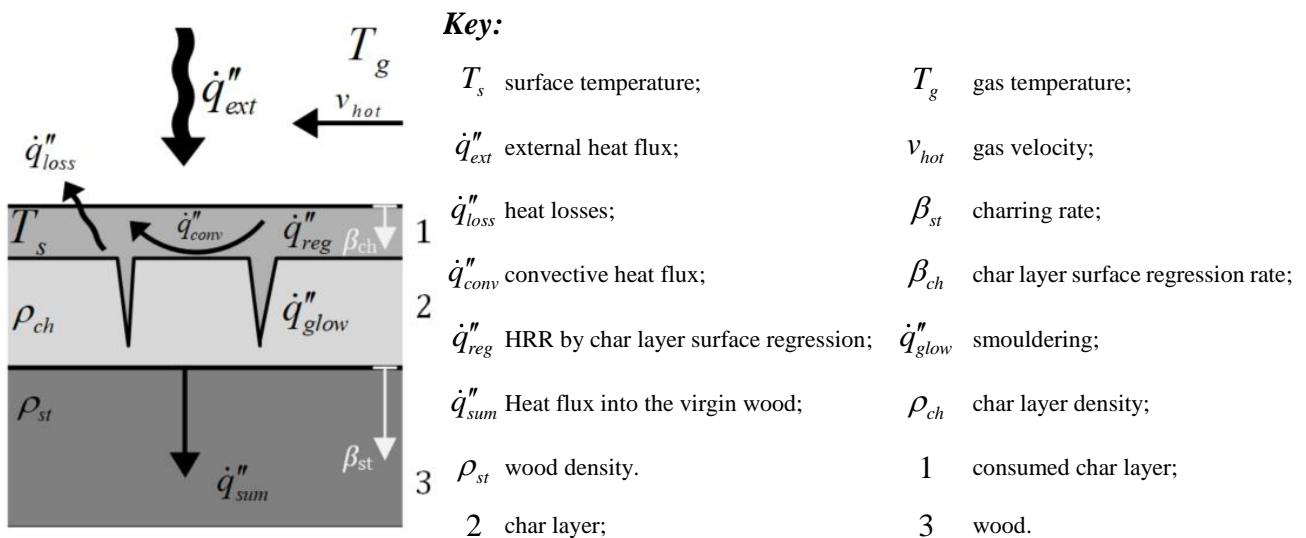
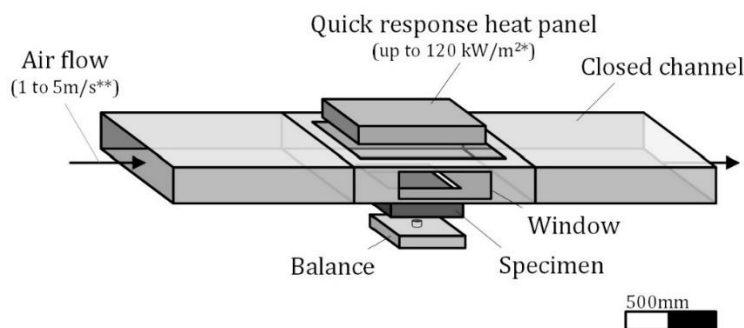


Figure 1. Characteristics to describe the general charring behaviour of timer in fire.

The study presented in this paper included various requirements for the experimental setup to allow the measurement of (i) the mass loss (rate), (ii) the charring (rate), (iii) the char layer surface regression (rate), (iv) the temperature distribution in the specimen and (v) the char layer density. Furthermore, the criteria for the description of the environment were (vi) the exposure with a potentially variable external heat flux exceeding 100 kW/m^2 and (vii) the controlled gas flow with gas velocities up to 5 m/s (reference velocity at normal temperature). After a review of the characteristics and available methods, the cone calorimeter according to ISO 5660 [9], the fire propagation apparatus according to ASTM E2058 [10], fire resistance furnaces according to EN 1363-1 [7] and the fire tunnel presented by Schmid et al. [3,4] were found unsuitable. Thus, a novel Fire Apparatus for Non-standard heating and Charring Investigation (FANCI) was developed at ETH Zürich.

3 EQUIPMENT AND MATERIAL

A custom-made experimental setup, shown in Figure 2, the Fire Apparatus for Non-standard heating and Charring Investigation (FANCI-setup), was developed to systematically investigate characteristics, which were found to appear as variables in experiments in large, medium and small-scale experiments when timber members were heated or fire exposed. Contrary to existing methods, the experimental apparatus should be able to simulate realistic conditions by the environment with respect to the fire exposure of the member. The *fire exposure* is understood by the authors as the *thermal exposure* (gas and radiation temperature) and the *gas characteristics* (oxygen concentration and movement of the hot gas), compare Schmid et al. [3,4]. Existing setups show limitations with respect to the specimen dimensions, which should allow for the investigation of the one-dimensional heat transfer and the one-dimensional charring in the specimen. Furthermore, the energy supply power, its modification during the experiment, the applicable gas velocities and its control, the measurement possibilities of the char layer recession and the mass loss of the specimen experience typically limitations.



* variable external heat flux

** reference velocity at normal temperature

Figure 2. Experimental setup developed in this study to investigate the charring behaviour of timber under realistic fire conditions. Schematic view (left) and photo of the setup at ETH Zürich (right).

In the developed FANCI-setup, a specimen with an area of about $250 \text{ mm} \times 250 \text{ mm}$ surface area is installed on a load-cell-supported lab platform. The adjustable specimen support allows to keep the surface of the specimen flush with the closed channel and in constant distance to the radiation source. This allowed the estimation of the char recession during the experiment. The char recession is described by the char layer surface regression, i.e. the reduction of the char layer thickness. Previously, this characteristic was observed for environments with oxygen concentrations above about 15% (Schmid et al. 2018).

As fires produce a severe incident heat flux in the range of about 120 kW/m^2 (rough equivalent for the incident heat flux for standard fire exposure at 60 min) and exceeding 200 kW/m^2 (rough equivalent for real compartment fires at its maximum) an electric quick response radiation panel was installed. The device

induces an external heat flux exceeding 120 kW/m^2 considered representative for real fires. The actual setup allows the control of the actual power, which was initially checked with several heat flux sensors (HFS). Among others, for the calibration measurements of the incident heat flux, a novel device was used which allows the exclusion of the convective heat transfer. The HFS was a modified water-cooled HFS of Schmidt-Boelter-type. The modification concern the protection of the sensor by a glazing to prevent any disturbing influence of the measurement by convection, see Figure 3. The convective heat transfer is highly dependent on the surface temperature of the specimen when the surface temperature and the gas temperature would be significantly different.

The FANCI-setup, was fed with ambient air using two types of fans producing (i) moderately or (ii) highly turbulent conditions at the specimen's surface. The degree of turbulence, understood by the authors as standard deviation of the velocity vector in the combustion chamber, was measured using a dynamic pressure device at ambient conditions in the calibration runs and three Pitot tubes in the combustion chamber above the specimen during the experiments, see Figure 4.

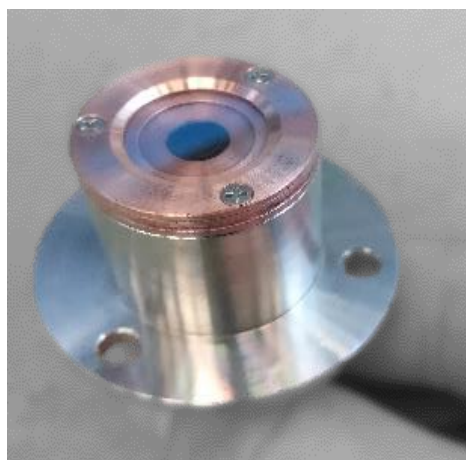


Figure 3. Novel heat flux sensor for the exclusion of the convective heat transfer.



Figure 4. Installed specimen (FH03) during the exposure with surface thermocouples and the three fixed installed Pitot-tubes to measure the static pressure changes near the specimen surface.

Except some calibration runs, all experiments were performed with clear wood specimens, see Figure 6, produced from wood from five trees with annual rings perpendicular to the default heat flux. The specimens were assembled from five beams (width ca. 45 mm). The beams were arranged edgewise to simulate an infinitely wide solid timber panel (STP), see Figure 5. The arrangement with vertical bond lines (one-component adhesive) was chosen to exclude any potential influence of the adhesive with respect to the bond line integrity in fire (sometimes referred to as debonding in fire). The specimens' density was determined based on the mass measurements. The material for assembling the specimens and the specimens were conditioned to 12% equilibrium moisture content and 20°C . In total, about 80 experiments were conducted including calibration and test runs. Finally, 67 specimens were produced; about 50% were instrumented with thermocouples arranged in a way to minimize the measurement error (Fahrni et al. 2018).

4 EXPERIMENTS

The experiments were conducted in ten series between 2015 and 2020. The horizontally arranged laminate specimens, see Figure 6, were exposed on their upper side. Some comparative experiments were conducted with fitting mineral insulation between the incombustible lower surface in the combustion unit while for most of the experiments a gap of 1 mm to 2 mm was designed between the specimen and the setup to allow for undisturbed horizontal movement of the specimen. The experimental series had different objectives and can be grouped to experiments A, B and C as follows:

A. ISO fire temperature at the exposed surface;

- B. Constant exposure levels (i.e. constant energy supply from the heat panel) between 50 kW/m² and 120 kW/m²;
- C. Multi-level exposure: initially exposure at 100 kW/m², subsequently a lower limit to investigate smouldering combustion including self-extinguishment.

The measurements taken during and after an experiment included the gas temperature in the combustion chamber, the gas velocity of the supplied air and in the combustion chamber above the specimen, the time to ignition, the surface temperature by means of indicative measurements using sheathed thermocouples and the mass loss (rates). Experiments lasted between 15 min and 40 min. After an experiment, the specimen was removed from the FANCI-setup, its final mass was checked by a lab balance and the specimen was extinguished with water. This procedure took less than 90 sec. Subsequently, the specimen was dried, its geometry was 3D-scanned before and after the removal of the char layer. The difference between the geometries was used to determine the char layer thickness and the residual virgin section. The procedure of the 3D-scanning was always checked with manual measurements. The mass of the char layer was determined using the bulk volume of the char layer. The following analysis of the char layer comprised the heat content of the char layer material. Corresponding results including the comparison to data of char layer originating from furnace and compartment experiments and including the density profile of the char layer are presented in another paper by the author (Schmid et al. 2020).

5 EXPERIMENTAL RESULTS

Results are the rates for (a1) the char layer surface regression, (a2) the charring, (b) the heating within the solid and at the surface of the specimen and the (c) the mass loss.

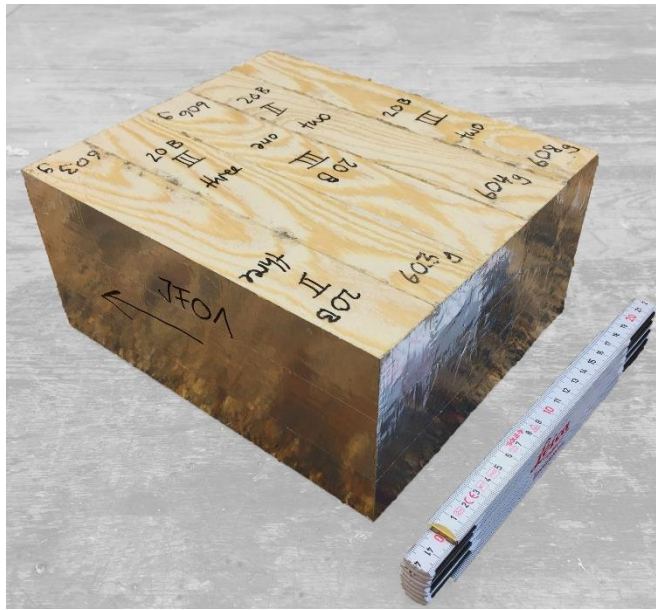


Figure 5. Specimen JF01 before exposure.

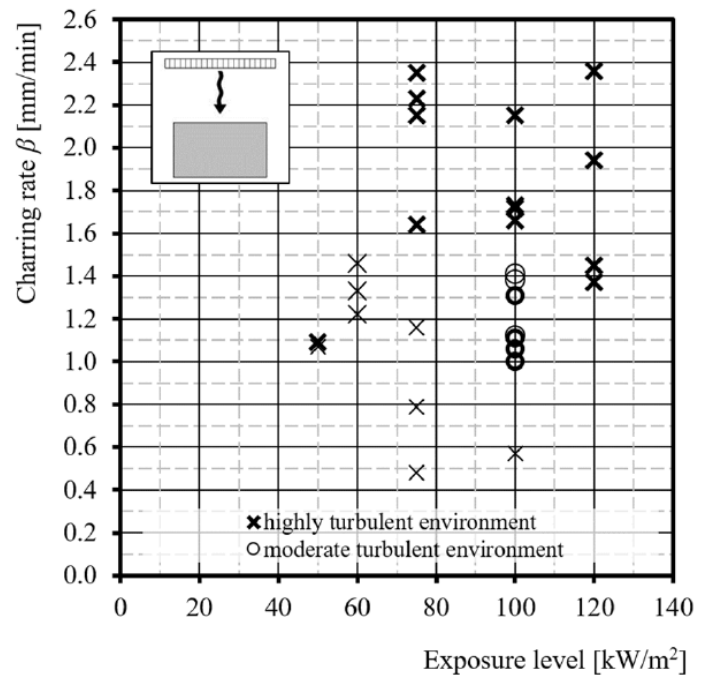


Figure 6. Results for the charring rates in oxygen rich environments. Highly turbulent (crosses) and moderate turbulent gas flow (circles).

In Figure 6, the charring rates are plotted for Series B (constant exposure level) for highly turbulent (ht) and moderate turbulent (mt) gas flow. The scatter of the results is significant. In general, the trend shows that results for the charring rates exceed the charring rates typically observed in furnace tests. Results are further dependent on the degree of turbulence, which is apparently responsible for the intensity of the contact of the char layer and the moving gas (ambient oxygen concentration). The results from the mass loss measurements (e.g. equivalent to 37 kg/m²h for 100 kW/m² and about 5 m/s) exceed known values from furnace tests in various scales of about 14 kg/m²h ± 1, see Klippel et al. [11] and Lange et al. [12].

The mass loss measurement were used to detect the ending of the smouldering combustion. Dependent on the gas velocity, mass consistency (no further mass loss) was observed between about 4 kW/m² (1 m/s) and about 2 kW/m² (5 m/s) incident radiant heat flux.

Further characteristics measured were the char layer surface regression up to 1.8 mm/min and the density of the char layer between about 220 kg/m³. and 40 kg/m³. The density of the char layer is understood as the bulk density of the char layer including visible and invisible cracks and voids. The density was determined using the dry mass of the char layer (0% MC), the surface area of the specimen and the difference between the virgin wood thickness after the exposure and the total thickness of the specimen after exposure. Exemplarily, results with respect to the change of the geometry for two experiments (MH14 and LA17) are given in Table 1.

Table 1. Examples of results of FANCI-experiments with respect to the charring and char recession. Characteristics in line with Figure 1.

#	β_{st} [mm/min]	β_{ch} [mm/min]	ρ_{ch} [kg/m ³]	\dot{q}_{ext}'' [kW/m ²]	v_{hot} [m/s]
MH14	1.5	0.7	74.2	47.2	2.5
LA17	2.0	1.5	70.8	120.0	5.0

6 ANALYSIS

In Figure 7, the charring rates of all experiments regardless the degree of turbulence are plotted against the external heat flux as typically done in the literature, see e.g. Tran et al. [11]. A moderate fit can be observed quantified by $R^2 \sim 0.5$ (method of least squares). Tran et al. [11] showed that the fit can be improved for their experimental results from a cone-calorimeter, when the density of the timber is considered. For the presented correlation in Figure 8, no influence of the density has been considered. In the analysis presented in this paper, the fit was improved considering further elements contributing to the heat flux \dot{q}_{sum}'' at the char line, see Figure 8.

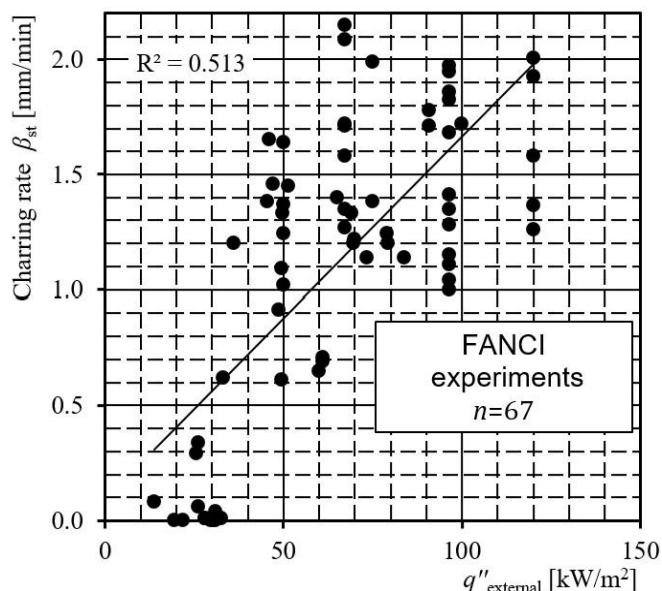


Figure 7. Analysis of charring rate observed in the FANCI-experiments; correlation with the external heat flux.

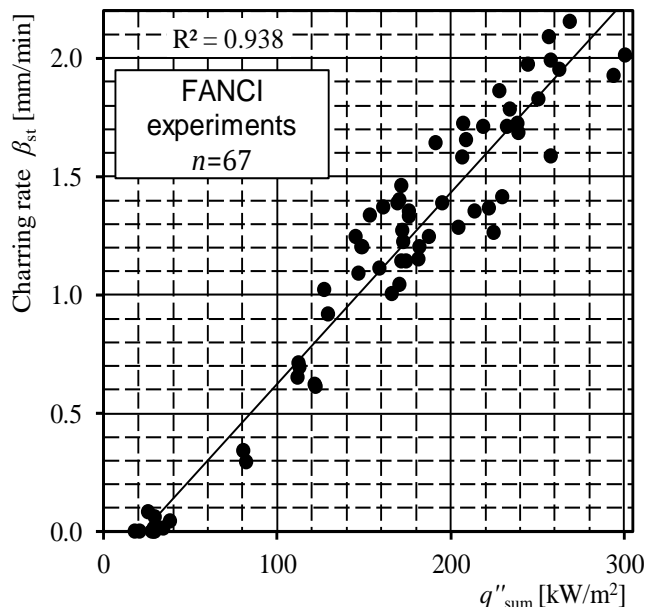


Figure 8. Analysis of charring rate observed in the FANCI-experiments; correlation with the superimposed heat flux at the char line.

6.1 Conversion and combustion behaviour of timber and the char layer

In the following, the elements are described which contribute to the charring. It is assumed that the heat flux \dot{q}_{sum}'' at the char line can be estimated by superimposing the contributions, which appear in the experiments.

6.1.1 Initially available amount of energy

The initial energy amount to consider is the heat content of structural timber, which deviates slightly from the dry wood heat content, usually referred to 17.5 MJ/kg. Schmid et al. [14] proposed a modification factor for considering the water stored in moist wood and proposed to consider structural timber in heated indoor climates with 10% MC. This is slightly deviating from the MC in the FANCI-experiments, i.e. 12%.

6.1.2 Release of combustible volatiles during thermal modification of the virgin wood

The first part for the improvement of the correlation is the consideration of flaming combustion. In the experiments, flaming was apparent in the initial phases but for external heat fluxes greater than 75 kW/m² difficult to detect, by a HFS (fluctuation and location appeared to be challenging) and visual observations (radiation of the radiant panel outscored the flames). It was assumed that the oxygen concentration in the ambient air (21%) allows for flaming combustion as observed by Jervis [15]. Subsequently, after the ignition, recorded for all experiments, the combustible volatiles are met by favourable conditions for flaming combustion. Thus, it can be assumed that the volatiles created during the thermal modification process of the virgin wood (pyrolysis) were combusted in the combustion chamber near the surface, contributing to the radiation received at the specimen's surface (radiative feedback). It is assumed that the combustible volatiles consist mainly from hydrocarbons. The amount of appearing volatiles can be estimated by the corresponding losses described for the char production, quantified to 6% of the energy available in the source material [16]. This part of the heat release considered for the superimposition is indicated as \dot{q}_{vol}'' . It should be highlighted that the combustion process requires oxygen while the creation of the volatiles is assumed temperature dependent only.

6.1.3 Smouldering combustion during the combustion of the char layer

After the char layer has been created in parallel to energy losses due to the conversion of the material and the release of combustible volatiles (see Section 6.1.2), the char layer gets consumed. It should be noted that the char layer represents a new material with different characteristics. It appears to be relevant to refer to the significantly different decreased density (about 50% to 10% of the source material) and the significantly increased heat content (about 200% of the source material). Schmid et al. [6] have observed the robustness of the heat content provided by the char layer material. Consequently, the energy of the char layer is released as heat dependent on the mass loss of the char layer. Apparently, the latter can be observed as density loss determined in the FANCI-experiments. From the experimental data, this part of the heat release considered for the superimposition, indicated as \dot{q}_{glow}'' , is the most relevant parameter, partly superior of the external heat flux.

6.1.4 Consumption of the char layer

From tests in cone-calorimeters and also from the experimental series conducted by Schmid et al. [3,4] it is known that the char layer can be reduced in its thickness. Friquin [17] summarized the documentation available in the literature with respect to this characteristic, sometimes referred to as char oxidation or char contraction. In this paper, the char layer surface regression is understood as part of the smouldering combustion of the char layer but described separately. In the experiments, it was observed that the char layer was reduced in its depth, in general, dependent on the fire exposure and, in particular, dependent on the description of the gas movement at the specimen's surface. The analysis of the dependency of the characteristic will be content of a future paper and is not further discussed here. In the FANCI-experiments,

this characteristic was directly measured with values up to 1.8 mm/min, understood as char layer surface regression rate. This part of the heat release is considered for the superimposition, indicated as \dot{q}_{reg}'' .

6.1.5 Heat losses

The heat losses of the char layer were considered for the improvement of the correlation presented originally in Figure 8. These losses are the heat transfer from the hot surface of the char layer to the environment of the combustion chamber. For the FANCI-experiments, this is possible as (indicative) surface temperature measurements were done with two surface thermocouples. The mean of both were used together with the estimated compartment gas temperature (mean of the in- and outflow gas temperature) to derive a film temperature. Furthermore, the hot gas velocity was used to calculate the losses according to well-known heat transfer methodologies, see e.g. Wickström [18]. In general, for the FANCI-experiments, the losses were of minor magnitude and are indicated as \dot{q}_{loss}'' , for the superimposition.

6.2 Heat flux at the char line

The heat flux at the char line, describing the conductive heat transfer into the solid virgin wood, is indicated as \dot{q}_{sum}'' in Figure 1. It is considered as relevant parameter to describe the reaction of the wood, i.e. the conversation to the char layer material (pyrolysis). It is determined calculating the sum of the energy stored and heat released as described in the Sections 6.1.1 to 6.1.5. For the exemplarily presented results in Table 1, the elements are specified in Table 2. After the consideration of the aforementioned characteristics, a significantly increased fit can be observed quantified by $R^2 \sim 0.94$ (method of least squares), see Figure 9.

Table 2. Elements shown in Figure 1 used for the superimposition of the heat flux at the char line for two experiments in the FANCI-setup. Heat flux in kW/m².

#	\dot{q}_{ext}''	\dot{q}_{vol}''	\dot{q}_{glow}''	\dot{q}_{reg}''	\dot{q}_{loss}''	\dot{q}_{sum}''
MH14	47.2	10.2	90.0	33.4	8.7	172.0
LA17	120.0	14.0	127.3	55.9	16.1	301.0

7 DISCUSSION

The FANCI-setup allowed for the measurements of additional parameters, which are often not available. However, the non-availability can be traced back to the limited interest in the field of fire science when it comes to structural timber engineering.

From the literature review, the experimental campaign and the analysis of the experimental results it became apparent that the overall combustion behaviour of structural timber can be solved only if the combustion of the char layer is understood. In the analysed, it was shown that the heat flux at the char line exceeds 300 kW/m². Also for lower exposure levels, see Table 2, the smouldering combustion reaches significant values exceeding the external heat flux. In the FANCI-experiments, the smouldering combustion was found as the most relevant contribution to determine the heat flux at the level of the virgin wood. However, the heat, which is made available by smouldering combustion, affects significantly the compartment of a testing unit or a compartment. As observed in the experiments, the contribution by the char layer combustion, subdivided in (a) smouldering combustion measured as the density loss of the char layer and (b) the complete consumption of the char layer, the char layer surface regression. Both elements are needed to improve the description of the heating of the timber section. The char layer surface regression appeared to be a function of the gas flow. By trend, for more homogeneous gas flows (moderately turbulent environment), the char layer surface regression was significantly limited.

8 CONCLUSIONS

It appears that the charring rate, considered essential for the description of the general behaviour of structural timber elements, cannot be explained only with the applied external heat flux. The FANCI-setup allowed for further measurements, typically left unconsidered when experiments or tests are performed. Although e.g. the cone-calorimeter as the standard setup for the investigation of the reaction to fire properties is often used to determine a total mass-loss, the contribution by the combustion of the char layer has been often neglected. From the presented improvement of the fit, it can be concluded that the smouldering combustion is of superior influence and can not be neglected.

In the past, the combustion behaviour of timber in standard fire and deviating fires have been described by only the charring rate. Among others, this value has been used to verify the load-bearing capacity of structural timber members in fire the charring rates are considered as essential input parameters. When it comes to the assessment of the fire dynamics in compartment fires, the description of the contribution to the fire by the structural timber is needed. This can be done by the determination of the structural fire load as addition to the movable fire load corresponding to the charring depth. However, recent observations comparing the charring of timber panels with large exposed surfaces showed that the only use of the charring rate is sufficient. Thus, for description of the general behaviour of structural timber, further parameters are needed.

Unfortunately, measurement of the overall mass-loss is not sufficient to describe the combustion behaviour. This is as the loss of one unit mass may indicate the complete combustion of this unit mass or the conversion of e.g. two units mass to one unit mass of a new material, i.e. the char layer material. Consequently, the char layer mass has to be estimated separately. Thus, for future experimental series and tests it is highly recommended to measure the relevant characteristics (gas velocity) and density of the char layer.

Available literature results with respect to burnout and self-extinguishment could be improved and extended with the data provided here. It should be highlighted that both, the condition for self-extinguishment and the contribution by the char layer to the compartment heating are dependent on the external or incident radiant heat flux and the gas characteristics describing the movement of the gas. From a designers point of view, it should be highlighted that, in general, currently available tools neglect the gas movement and its impact on burnout and self-extinguishment. Using data and techniques presented in this study, the calculation tools can be improved.

REFERENCES

1. Su J, Lafrance PS, Hoehler MS, Bundy MF. Fire Safety Challenges of Tall Wood Buildings–Phase 2: Task 3-Cross Laminated Timber Compartment Fire Tests. 2018 Feb 14.
2. Buchanan, Andrew, et al. (2014) White Paper on Fire Resistance of Timber Structures. US Department of Commerce, National Institute of Standards and Technology.
3. Schmid J, Santomaso A, Brandon D, Wickström U, Frangi A (2016) Timber under real fire conditions - the influence of oxygen content and gas velocity on the charring behavior. SIF'16, Structures in Fire 2016, Princeton, U.S.A.
4. Schmid, J., Santomaso, A., Brandon, D., Wickström, U., Frangi, A. (2018). Timber under real fire conditions—the influence of oxygen content and gas velocity on the charring behavior. *Journal of Structural Fire Engineering*, 9(3), 222-236.
5. Brandon, D. (2018). Engineering methods for structural fire design of wood buildings: Structural integrity during a full natural fire. *Brandforsk Report 2018:2*.
6. Schmid, J., Richter, F., Werther, N., Frangi, A. (2020). Combustion characteristics of structural timber compartments in the steady-state fire phase, Under review at *Fire Technology*.
7. EN 1363-1 (2012) -1: Fire resistance tests - Part 1: General requirements. European Committee for Standardization, Brussels.
8. ISO 834-1 (1999) Fire-Resistance Tests - Elements of Building Construction - Part 1: General Requirements. International Organization for Standardization. Geneva, Switzerland.

9. ISO 5660-1 (2015) Reaction-to-fire tests--heat release, smoke production and mass loss rate--Part 1: heat release rate (cone calorimeter method) and smoke production rate (dynamic measurement). International Organization for Standardization. Geneva, Switzerland.
10. ASTM E 2058-13, Standard Test Methods for Measurement of Synthetic Polymer Material Flammability Using a Fire Propagation Apparatus (FPA). ASTM International, West Conshohocken, 2013.
11. Klippel, M., Schmid, J., Fahrni, R., & Frangi, A. (2018). Assessing the adhesive performance in CLT exposed to fire.
12. Lange, D., Sjöström, J., Schmid, J., Brandon, D., Hidalgo, J. (2019) A Comparison of the Conditions in a Fire Resistance Furnace When Testing Combustible and Non-combustible Construction, *Fire Technology*.
13. Tran, H.C. and White, R. H. (1992), "Burning rate of solid wood measured in a heat release rate calorimeter", *Fire and materials* 16, 4 (1992), pp. 197--206.
14. Schmid, J., Fahrni, R., Frangi, A., Werther, N., Brandon, D., Just, A. (2019). Determination of design fires in compartments with combustible structure - modification of existing design equations. *Proceedings INTER International Network on Timber Engineering Research*, 52, 509-511.
15. Jervis, C. (2012). Application of fire calorimetry to understand factors affecting flammability of cellulosic material: Pine needles, tree leaves and chipboard. PhD Thesis. The University of Edinburgh, UK.
16. Bunbury, H. M. (1925). *Die bei der trockenen Destillation des Holzes erhaltenen Handelsprodukte*, Springer.
17. Friquin, K. L. (2010). Charring rates of heavy timber structures for Fire Safety Design: A study of the charring rates under various fire exposures and the influencing factors.
18. Wickström, U. (2016). *Temperature calculation in fire safety engineering*. Cham, Switzerland: Springer.
19. Fahrni, R., Schmid, J., Klippel, M., & Frangi, A. (2018). Investigation of different temperature measurement designs and installations in timber members as low conductive material. In *Structures in Fire (SiF 2018)* (pp. 257-264). Belfast, United Kingdom.

DESIGN OF TIMBER-CONCRETE COMPOSITE FLOORS FOR FIRE

Erica C. Fischer¹, Annabel B. Shephard², Arijit Sinha³, Andre R. Barbosa⁴

ABSTRACT

The popularity of mass timber is occurring at the same time as code developments in the field of structural fire engineering. Due to this synchronism, benchmarked analytical models are needed to design timber-concrete composite floors throughout a fire exposure. Existing analytical models were developed for cross-laminated timber or glue-laminated timber-concrete composite floors with dowel-type fasteners. These models have not been benchmarked against nail-laminated timber (NLT) or screw-laminated timber (SLT)-concrete composite floors with truss plate shear connectors. Data on the experimental behaviour of truss plate shear connectors under direct shear load are presented and compared with typical dowel-type shear connectors. Data on truss plate shear connectors along with experimental data from literature on fire tests of NLT- and SLT-concrete composite floors was used to benchmark analytical modelling techniques for calculating the strength and effective stiffness of the timber-concrete composite floors throughout a fire exposure. The results presented herein can be used to design NLT- and SLT-concrete composite floors for improved fire performance.

Keywords: Mass timber; fire tests; timber-concrete composite floors

1 INTRODUCTION

Mass timber products are becoming increasingly popular around the world. Future codes and standards will permit taller mass timber buildings (ICC 2021), and current codes allow for alternative fire protection design as an option other than using the prescriptive approach. However, there is limited research and limited resources available to design and evaluate the behaviour of timber-concrete composite floors in a fire exposure. Nail-laminated timber (NLT) is a mass timber product in which dimensional lumber is placed on edge and connected with nails. Screw-laminated timber (SLT) is similar, except screws are utilised instead of nails. NLT was popular at the beginning of the 20th century and has recently had a renaissance in buildings such as the M3 building in Milwaukee (Figure 1). This type of floor system is a one-way floor spanning between glue-laminated beams and uses commonly used construction materials to develop a diaphragm. However, NLT and SLT are not effective or efficient in resisting lateral force demands or adhering to code-required vibration requirements [1, 2]. Therefore, to ameliorate this in modern buildings, engineers have utilised concrete toppings with NLT and SLT diaphragms. Through the use of shear connectors, the NLT or SLT floors can be composite with these concrete toppings, thereby increasing the

¹ Assistant Professor, Oregon State University,

e-mail: erica.fischer@oregonstate.edu, ORCID: <https://orcid.org/0000-0002-7653-2068>

² Design Engineer, PCS Structural Solutions

e-mail: ashephard@pcs-structural.com, ORCID: <https://orcid.org/0000-0001-6415-4947>

³ Associate Professor, Oregon State University

e-mail: arijit.sinha@oregonstate.edu ORCID: <https://orcid.org/0000-0003-3718-5910>

⁴ Associate Professor, Oregon State University

e-mail: andre.barbosa@oregonstate.edu, ORCID: <https://orcid.org/0000-0003-4547-531X>

load-carrying capacity of these floors (both for gravity and lateral forces) and improving the fire performance.

Previous researchers have studied timber-concrete composite floors and developed analytical models to evaluate these floors under gravity, seismic, and fire demands [3-5]. However, these analytical models were developed for dowel-type fasteners commonly used in CLT-concrete composite floors or glue-laminated beam-concrete composite floors, such as fully-threaded screws. Due to the construction of NLT and SLT, typical shear connectors used are truss plate shear connectors that are embedded into the timber during construction.

The objectives of this paper are to: (1) summarize previous research on shear connectors utilised in NLT- and SLT-concrete composite floors, (2) discuss the issues with using this data within the existing frameworks to calculate the strength and stiffness of NLT- and SLT-concrete composite floors during a fire, and (3) demonstrate how existing analytical models with adjustments can predict the strength and stiffness of NLT- and SLT-concrete composite floors throughout a standard fire exposure.



Figure 1. Photo of the M3 building in Milwaukee, Wisconsin (US) with NLT floors [6]

2 SHEAR CONNECTORS

Shear connectors provide composite action between two materials through the transfer of transverse shear along the length of the member. For NLT- and SLT-concrete composite floors, a limited number of shear connectors have been tested. The most common being MiTek MT20 truss plates [7, 8]. In both instances, the truss plates were utilised as shear connectors between the timber and the concrete to develop composite action. A hydraulic press was used to embed the truss plates in the NLT as specified by the manufacturer's standard (ICC-ES 2016). In both cases (as shown in Figure 2), 76.2 mm of the truss plate was embedded in the NLT, and the remainder 51 mm was embedded in the concrete topping.

Both, Dagenais et al. [7] and Shephard et al. [8] performed direct shear tests on SLT-concrete and NLT-concrete composite specimens, respectively, using the MiTek MT20 truss plates. Details of the tests, including material properties and specimen dimensions, are discussed by the researchers [7, 8]. Shephard et al. [8] concluded that the truss plates have significant ductility and that the peak load on the specimens was controlled by yielding of the shear connector. Splitting of the wood or significant cracking of the concrete was not observed in either set of experiments.

Figure 2a is the resulting force-slip behaviour of the tests performed by Shephard et al. [8]. These tests followed the loading protocol per ISO 6891 [9], modified such that the loading was controlled through the displacement of the crosshead at 0.5 mm/min (0.02 inches/min). The measured force-slip behaviour shown in Figure 2a shows a yield plateau between 2 mm and 8 mm of slip between the timber and the concrete. This behaviour is different than dowel-type shear connectors tested by others [7, 8], which do not have a yield plateau. After the experiments, the shear connectors exhibited signs of yielding at the timber-concrete interface after the test (see Figure 2b and 2c). This was evident by the elongations of the slots in the truss plate, fracture of the truss plates themselves, and large deformations of the plates.

The direct shear test results are discussed in detail in Shephard et al. [8] and summarised in Table 1. The maximum force, F_{max} , is the peak load measured during the direct shear tests. Per ISO 6891 [9], F_{max} corresponds to the peak load at 15 mm of slip. Because this peak load occurred prior to 15 mm of slip, the F_{max} shown in Table 1 also corresponds to the F_{max} in ISO 6891 [9]. The displacement corresponding to the maximum load, F_{max} , is δ_u . The slip modulus, k_s , was calculated using ISO 6891 [9]. Although there was high variability in the calculation of the slip moduli between the experiments, there was little variability in the maximum load resisted by the specimens. The peak load and the slip modulus calculated from the experiments are used to calculate strength and stiffness.

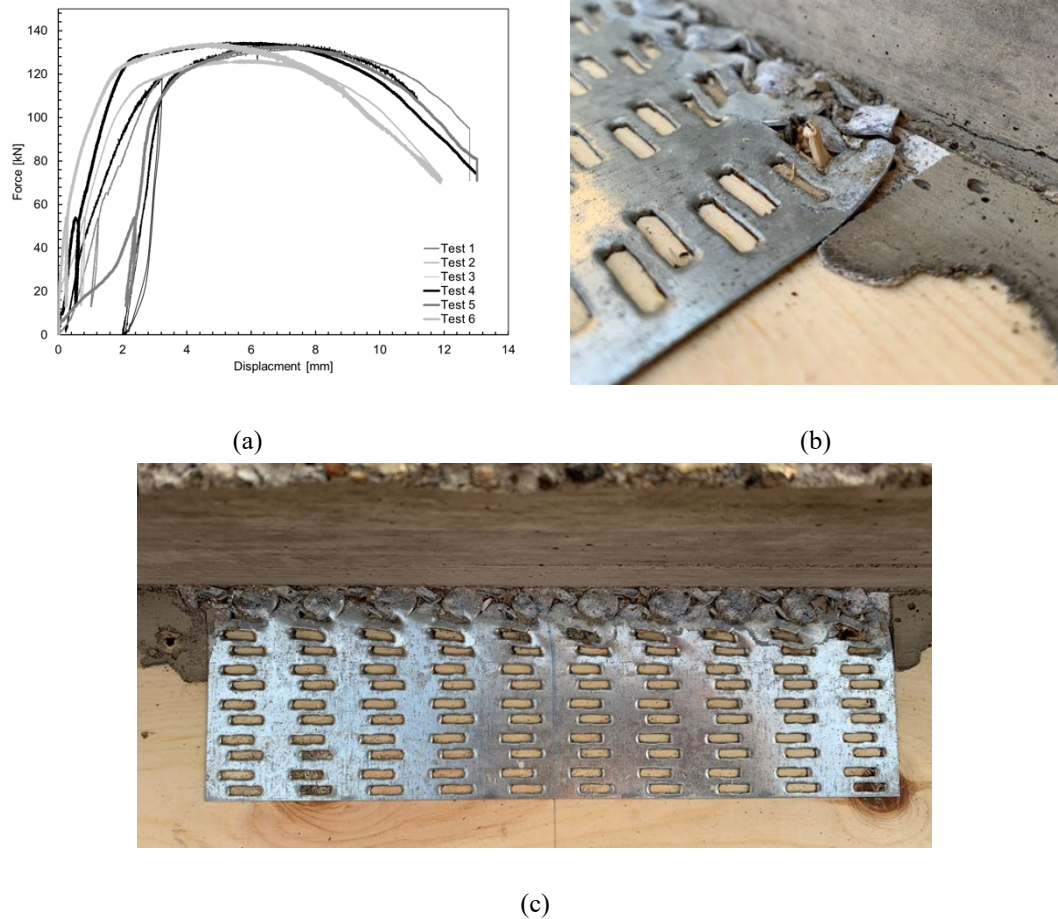


Figure 2. Direct shear test results on truss plate shear connectors (a) measured force-slip behaviour, (b) close up image of the shear connector after the experiments, and (c) overall image of the shear connector after the experiments

Table 1. NLT-concrete composite direct shear test results

	F_{max}	δ_u	k_s
	kN	mm	kN/mm
average	132	6.50	87.0
standard deviation	2.99	1.56	90.0

3 USING TESTING RESULTS TO BENCHMARK ANALYTICAL MODELS

Existing analytical models can be utilised to predict the behaviour of NLT- and SLT-concrete composite floors with truss plate shear connectors [3, 5]. The elasto-plastic model with the reduced cross-section method (RCSM) [3, 10] is commonly used to calculate the stress distribution through the cross-section of a timber-concrete composite floor. However, because this methodology was developed for dowel-type

shear connectors, adjustments are required to adapt this methodology to timber-concrete composite floors with truss plate shear connectors. The γ -method is commonly utilised to calculate the effective stiffness of timber composite sections (timber-timber composite and timber-concrete composite). This method has demonstrated the ability to calculate the deflection of timber-concrete composite floors using dowel-type shear connectors; however, it has not been applied to timber-concrete composite floors with truss plate shear connectors.

3.1 Large-scale test overview

3.1.1 *Dagenais et al. [7]*

The SLT-concrete composite floor tested was constructed from 38 mm x 184 mm solid sawn Grade No. 2 Spruce-Pine-Fir (SPF). The screws joining the timber laminations were self-tapping and 180 mm in length. The lamination screw pattern was two rows of nails spaced 610 mm staggered by 305 mm inclined at a 45° angle. The concrete was 89 mm in depth with a design compressive strength of 30 MPa at 28 days and steel mesh for shrinkage reinforcement. The floor was 1715 mm wide and 4800 mm in length. MiTek MT20 truss plates were used as shear connectors between the timber and concrete to develop composite action. The truss plates were embedded in the timber by a hydraulic press every fifth lamination and spaced 610 mm on centre. 76.2 mm of the truss plate depth was embedded in the timber, while the remainder was embedded in the concrete topping. The edge distance of the truss plates in the longitudinal direction is 38 mm.

The SLT-concrete composite floor was exposed to the CAN/ULC-S101 fire curve (similar exposure to the ASTM E119 standard fire) and loaded with a distributed service live load of 2.4 kPa. Testing stopped at 214 minutes, and the SLT-concrete composite floor did not reach failure at the end of the test.

3.1.2 *Shephard et al. [8]*

The NLT-concrete composite floor tested was constructed from 38 mm x 140 mm solid sawn Grade No. 2 SPF. The nail pattern joining the timber laminations followed the guidelines of NLT Design Guide [11] with nails staggered at 127 mm on centre. The nails had a smooth shank of 76.2 mm in length and a diameter of 3.05 mm. The concrete topping was 76.2 mm with a design compressive strength of 34.5 MPa at 28 days and used steel mesh for shrinkage reinforcement. The floor was 1200 mm wide and 4800 mm in length. MiTek MT20 truss plates were used as shear connectors between the timber and concrete, just as in the SLT-concrete composite specimen tested by Dagenais et al. [7]. The NLT-concrete specimen used the same embedment depth into the timber as the specimen tested by Dagenais et al. [7]. The truss plates were installed using a hydraulic press and were placed every third lamination at 610 mm on centre along the length of the specimen. The edge distance of the truss plates in the longitudinal direction is 140 mm.

The NLT-concrete composite floor was exposed to the ASTM E119 [12] fire curve and loaded with a distributed service live load of 3.83 kPa. Testing stopped at 185 minutes, and the NLT-concrete composite floor did not reach failure at the end of the test, although it was approaching runaway deflection and the average remaining uncharred depth was 38.1 mm.

3.2 Strength calculations

Shephard et al. [8] summarises modifications to apply the elasto-plastic model with the RSCM to NLT-concrete composite floors. The elasto-plastic model is an analytical model used to calculate the stress distribution through the cross-section of a timber-concrete composite member with ductile dowel-type shear connectors [3]. The model was initially developed for glue-laminated-concrete composite beams and has been benchmarked against experimental tests conducted at ambient temperature and when the beams are exposed to a standard fire exposure [13]. The elasto-plastic model has five assumptions: (1) a linear-elastic concrete model is used because the timber portion of the timber-concrete composite floor fails prior to the concrete exhibiting plastic behaviour, (2) a linear-elastic model is used for the timber because the timber is subjected to combined tension and bending resulting in brittle behaviour, (3) shear connectors in a fully-

composite section are rigid, (4) shear connectors are rigid-perfectly plastic, (5) concrete strength in tension is neglected. The RCSM, as defined in Eurocode 5 [10], assumes the mechanical properties of uncharred timber do not change with temperature, the section size is reduced through charring, and the charred timber is assigned zero-strength.

Shephard et al. [8] showed that the elasto-plastic model with RCSM greatly underestimates the strength of NLT-concrete composite floors throughout a standard fire exposure. Figure 3a is a plot of the elasto-plastic model with RCSM without any modifications. This plot shows that the NLT-concrete composite floor strength is greatly underestimated, predicting loss of load-carrying capacity at about 100 minutes. The truss plate yielding during the direct shear tests indicates that the truss plates are reinforcing the timber in tension and contributing to the flexural capacity. To account for this, yielding of the truss plates is considered in calculating the stress distribution through the cross section, as shown in Figure 4.

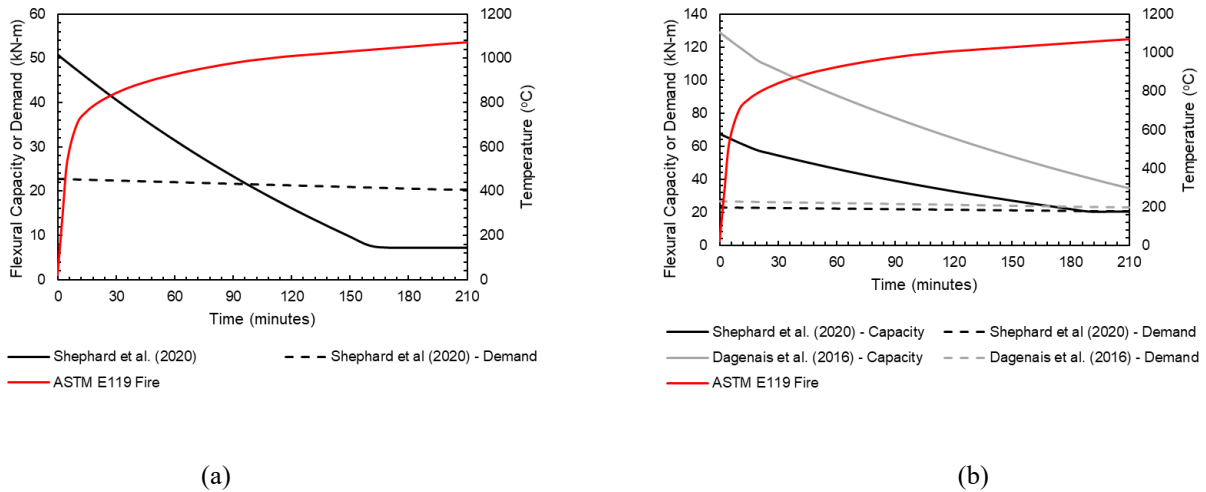


Figure 3. (a) Flexural capacity and demand of the NLT-concrete composite floor using the elasto-plastic model with RCSM [3, 10] and (b) Flexural capacity and demand of the NLT- and SLT-concrete composite floors throughout a fire exposure using the modified elasto-plastic model with RCSM [3, 10]

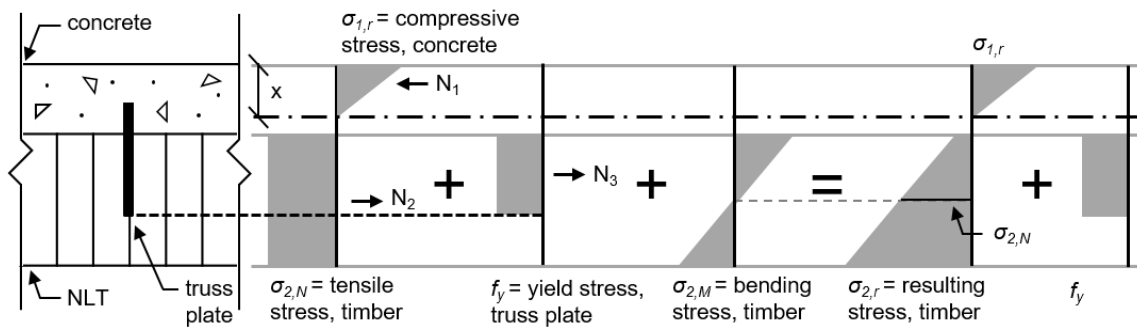


Figure 4. Stress distribution through an NLT-concrete composite floor with truss plate shear connectors

The authors applied the modifications to the elasto-plastic model with the RCSM described in Shephard et al. [8] and shown in Figure 4 to the NLT- and SLT-concrete composite floors described previously. The calculations used prescribed char rates from Eurocode 5 [10]. The results of this analysis, shown in Figure 3b, agree with the observations throughout the two tests. The NLT-concrete composite floor was nearing loss of load-carrying capacity when the test was stopped at 185 minutes. Figure 3b shows that the capacity of the NLT-concrete composite floor (solid black line) intersects with the flexural demand in the floor due to the imposed live load and self-weight. The intersection of the two lines occurs at 190 minutes, which aligns with the observations during the experiment. The SLT-concrete composite floor did not fail during the test, which was stopped at 214 minutes. Figure 3b reflects this observation, where the SLT-concrete composite floor (solid grey line) does not intersect with the flexural demand in the floor (dashed grey line) before the end of the test.

3.3 Serviceability calculations

The deflection of timber-concrete composite floors can be calculated using the effective bending stiffness, $(EI)_{eff}$. The γ -method can be used to calculate the effective bending stiffness of the composite section. Per Eurocode 5, the initial assumptions of the γ -method are: (1) design method based on the theory of linear elasticity, (2) beams are simply supported with a span l , (3) individual parts span the full length l and are wood or wood-based panels, (4) the individual parts are joined by mechanical fasteners, (5) spacing between the fasteners is constant or varies per [14], (6) applied load is acting in the z -direction (perpendicular to the span) giving a moment varying sinusoidally or parabolically [14]. Cuerrier-Auclair [5] recently further developed the γ -method such that the concrete was assumed to have negligible tensile capacity. The RCSM is utilised in conjunction with the γ -method to account for the loss of timber height due to the formation of a char layer.

Unlike the strength calculations, the truss plates do not contribute to the timber-concrete composite section stiffness. Figure 5a is a plot of the experimentally measured deflections throughout the NLT-concrete composite floor fire test with the calculated deflections with (dash-dot line) and without (solid line) the consideration of the truss plates. This plot shows that there is a negligible difference between the two calculation methods.

Figure 5 shows the measured deflections from both of the tests compared with the calculated deflections throughout the standard fire exposure. The calculations used prescribed char rates from Eurocode 5 [10]. For both the NLT- and SLT-concrete composite floors, the experimentally measured and the calculated deflections align well. For the NLT-concrete composite floor (Figure 5a), the calculated deflection follows the same trend as the experimental data from the beginning of the test to about 150 minutes. Thus, the calculated deflections are less than the measured deflections. At 150 minutes, the experimental deflection is 5.7 cm, and the calculated deflection is 6.1 cm (+7.5% difference). After 150 minutes, the difference between the calculated and experimental deflection increases. During testing, the NLT-concrete composite floor was observed to approach failure at about 187 minutes, indicated by runaway deflection [12]. The calculated deflection demonstrates similar behaviour indicative of failure. At 180 minutes the experimental deflection is 10.0 cm and the calculated deflection is 15.2 cm (+51% difference).

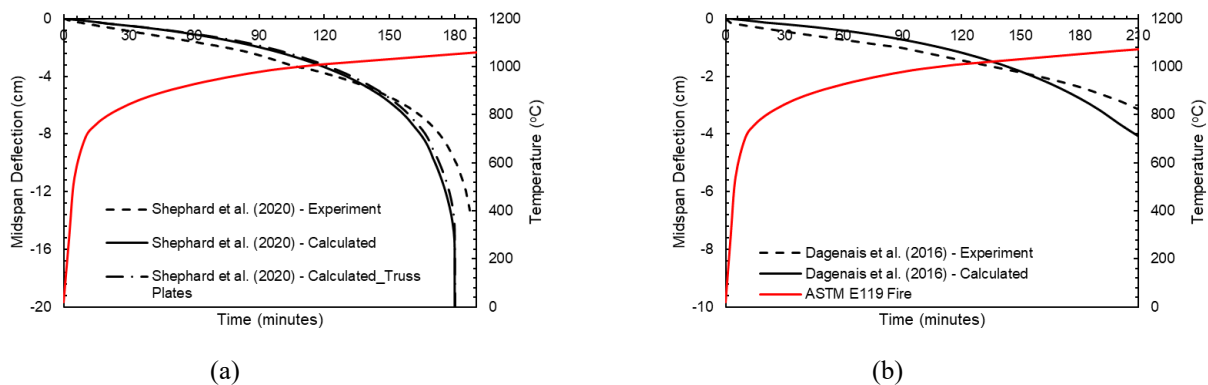


Figure 5. Deflection of the tested NLT- and SLT-concrete composite floors as a function of temperature computed using the γ -method with the RCSM [10, 14] (a) NLT-concrete composite floor and (b) SLT-concrete composite floor

For the SLT-concrete composite floor, the calculated deflection (solid black line, Figure 5b) follows the trend of the experimental deflection consistently throughout the test. The difference between the experimental data and the calculated deflection remains less than half a centimetre until 180 minutes. At 180 minutes, the difference between the experimental data (dashed black line, Figure 5b) and the calculated deflection (solid black line, Figure 5b) begins to increase. At the end of the test, the experimental deflection is 3.25 cm. The calculated deflection is 4.56 cm, which is a +40% difference from the experimental deflection.

4 DISCUSSION AND CONCLUSIONS

The experimental data from the large-scale timber-concrete composite floor fire tests was used to benchmark strength and stiffness analytical models for NLT- and SLT-concrete composite floors with truss plate shear connectors. The observational data from the tests were used to benchmark the modified elasto-plastic model [3, 8] with the RSCM [10] for the flexural capacity of both NLT- and SLT-concrete composite floors exposed to a standard fire curve [12]. The experimental deflection data was used to benchmark the γ -method [14] and the RSCM [10]. The deflection of NLT- and SLT-concrete composite floors exposed to a standard fire [12, 13] was reasonably estimated using the γ -method [14] and the RSCM [10]. Both the strength and deflection calculations assumed the concrete in tension did not contribute to the composite section stiffness, which is consistent with the state-of-practice [5]. In addition, these methodologies demonstrated that while the truss plates used as shear connectors in the NLT- and SLT-concrete composite floor contributed to the strength of the floor, they did not contribute to the stiffness throughout a fire.

ACKNOWLEDGMENT

This work is in collaboration with many industry partners that are actively working on mass timber buildings. The authors would like to thank Holmes Structures, Skidmore Owings & Merrill, Kattera, Arup, Forest Products Laboratory, and WoodWorks for their participation in technical advisory committees. Agricultural Research Service along with TallWood Design Institute funded the research presented in this paper through the US Department of Agriculture, award number 58-0204-6-002.

REFERENCES

1. American Society of Civil Engineers (ASCE). Minimum Design Loads for Buildings and Other Structures (ASCE 7-16). ASCE, Reston, VA. 2016.
2. International Code Council (ICC). International Building Code (IBC). ICC, Washington, D.C. 2018
3. Frangi, A., Fontana, M. Elasto-Plastic Model for Timber-Concrete Composite Beams with Ductile Connection. *Structural Engineering International*. 13(1), 47-57 (2003).
4. Frangi, A., Knobloch, M., Fontana, M. Fire Design of Timber-Concrete Composite Slabs with Screwed Connections." *Journal of Structural Engineering*, 136(2), 219-228 (2010).
5. Cuerrier-Auclair, S. Design Guide for Timber-Concrete Composite Floors in Canada. FPIInnovations, Canada. 2020.
6. Hilburg, J. North America's tallest timber tower wins city support in Milwaukee. *Architect's Newspaper*. 2019: <https://www.archpaper.com/2019/01/north-america-tallest-timber-tower-milwaukee-ascent/>
7. Dagenais, C., Ranger, L., Cuerrier-Auclair, S. Understanding Fire Performance of Wood-Concrete Composite Floor Systems. *World Conference on Timber Engineering*, Vienna, Austria. 2016.
8. Shephard, A.B., Fischer, E.C., Barbosa, A.R., & Sinha, A. Fundamental behavior of timber concrete composite floors in fire. *Journal of Structural Engineering*. (2020). In Production.
9. International Organization for Standardization (ISO). Timber structures – Joints made with mechanical fasteners – General principles for the determination of strength and deformation characteristics. ISO 6891, Geneva, Switzerland. 1983.
10. European Committee for Standardization (CEN). Design of timber structures – Part 1-2: General – Structural fire design. EN 1995-1-2, Brussels, Belgium. 2004.
11. Binational Softwood Lumber Board (BSLB). Nail-laminated Timber: US Design & Construction Guide 1.0. Binational Softwood Lumber Board, Surrey, BC. 2017
12. American Society for Testing and Materials (ASTM). ASTM E119-16a Standard Test Methods for Fire Tests of Building Construction and Materials. ASTM International, West Conshohocken, PA. 2018.
13. Underwriters Laboratories of Canada (ULC). CAN/ULC S101 - Standard Method of Fire Endurance Tests of Building Construction Materials. ULC, Toronto, Ont., Canada. 2014
14. European Committee for Standardization (CEN). Design of timber structures – Part 1-1: General –Common rules and rules for buildings. EN 1995-1-1, Brussels, Belgium. 2004.

PROPOSAL FOR STRESS-STRAIN CONSTITUTIVE MODELS FOR LAMINATED BAMBOO AT ELEVATED TEMPERATURES

Mateo Gutierrez Gonzalez¹ and Cristian Maluk²

ABSTRACT

Due to the negative impacts of global warming and climate change, there is a growing demand for sustainable load-carrying materials that can offer an alternative to other traditional construction materials such as concrete and steel. Laminated bamboo is a material with outstanding physical and mechanical properties, in addition to producing a minimum carbon footprint. However, extensive research is needed on the load-bearing behaviour of bamboo during and after fire before engineered bamboo can be used with confidence in higher and larger bamboo-based structures. This paper describes the outcomes of a comprehensive study conducted to understand the mechanical behaviour of bamboo (*Phyllostachys pubescens* species) at elevated temperatures; more specifically investigating the reduction of compressive and tensile strength, as well as the Modulus of Elasticity (*MoE*) up to 250°C. Findings from this work show that at 200°C, bamboo retains 20%, 42% and 70% of the compressive strength, tensile strength and modulus of elasticity at ambient, respectively. The results presented herein, which provide a thorough understanding of strength and elasticity reduction at elevated temperatures, enable the development of stress-strain constitutive models that will constitute the basis for designing fire-safe bamboo structures.

Keywords: laminated bamboo, fire performance, compressive strength, tensile strength, modulus of elasticity, structural fire engineering

1 INTRODUCTION

In recent years bamboo has gained popularity in the built environment, mainly due to its low cost, excellent mechanical performance, appealing aesthetics, and positive environmental impact. Bamboo has one of the highest renewable rates when compared with other natural construction materials. The ability to sequester high amounts of CO₂, makes bamboo an attractive alternative for the construction industry [1]. Traditionally, bamboo has been used as a primary load-bearing material for low-rise constructions. However, there is a real need for building in highly populated urban areas where fire safety is a governing design consideration. In that sense, bamboo has risen concerns about its mechanical behaviour when subjected to elevated temperatures. Understanding the mechanical performance of bamboo during a fire is essential to develop a sound fire safety strategy, which is critical for mid- and high-rise buildings [2]. Similar to other natural grown materials like timber, bamboo experiences a thermo-chemical degradation at temperatures above 150°C. Between ambient and 150°C, dehydration and phase changes are known to influence the mechanical response of bamboo [3], and a reduction on the strength, elasticity, and ductility has been observed. Prior researchers have studied the reduction in the mechanical properties of some bamboo products at elevated temperatures [4]; however, few studies have reported how the reduction of such properties can influence the development of constitutive stress-strain models that can be used to analyse structural load-bearing member under fire conditions. This work aims to investigate the reduction in the compressive strength, tensile strength, and Modulus of Elasticity (*MoE*) for bamboo at elevated temperatures. These findings would provide the required inputs to build constitutive stress-strain models

¹ PhD Candidate, The University of Queensland,

e-mail: m.gutierrezgonzalez@uq.edu.au, ORCID: <https://orcid.org/0000-0002-5147-3575>

² Senior Lecturer, The University of Queensland

e-mail: c.maluk@uq.edu.au, ORCID: <https://orcid.org/0000-0002-1662-6943>

for bamboo as a function of temperature. Outcomes of this study will establish the basis to conduct structural fire engineering analysis and design of load-bearing bamboo structures exposed to fires based on the reduction of the mechanical properties and the constitutive models of bamboo at elevated temperatures.

2 MATERIALS AND METHODS

2.1 Materials

Compressive strength samples were fabricated using *Phyllostachys pubescens*, bamboo species with a measured density between 580-651 kg/m³ and moisture content between 4.6-7.6%. Laminated bamboo was manufactured using phenol resorcinol formaldehyde glue. Sample dimensions were chosen based on recommendations presented in the European standard EN 408 for testing the mechanical properties of laminated timber products. Direct tensile strength test samples were fabricated using the same bamboo species, and they presented a density ranging from 841 to 914 kg/m³ and an average moisture content of 9.1%. Dimensions were chosen based on recommendations shown in ASTM D143-94 and ISO 22157.

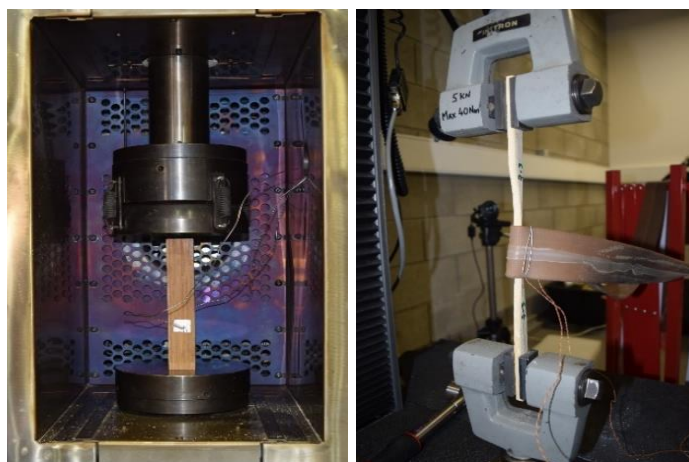


Figure 1. Experimental set-up

2.2 Thermal exposure and mechanical tests at elevated temperature

The specimens for the compressive tests were placed inside an environmental chamber and heated to a rate of 5°C /min until reaching a steady-state for temperatures between ambient and 250°C. The internal temperature was obtained through correlations with the temperature on the surface of the sample measured with K-type thermocouples. Tensile specimens were heated to a rate of 25°C /min thanks to the use of a heating blanket and a PID controller. The compressive and tensile strength tests were conducted following the procedures established in the EN 408 and ASTM D143-94, respectively, as can be seen from Figure 1. Once the sample had achieved a constant temperature along the whole cross-section, the test was conducted loading the sample with a constant deformation rate of 0.6 mm/min.

3 MECHANICAL PROPERTIES AT ELEVATED TEMPERATURES

3.1 Compressive and tensile strength reduction

Figure 2 presents the normalised compressive strength and the normalised tensile strength of bamboo for temperatures between ambient and 250°C. The average compressive strength of laminated bamboo at ambient temperature was measured to be at 51.7 MPa (SD = 5.6 MPa). The results show that bamboo suffers a decrease in its compressive strength for temperatures between ambient and 100°C. Between 100 and 150°C, there is no apparent reduction, but above 150°C, the drop continues until the compressive strength is practically lost when temperatures are above 250°C.

Bamboo tensile strength at ambient temperature was 123.8 MPa (SD=13.81 MPa), but once the temperatures rise, the tensile strength has a continuous fall between ambient temperature and 150°C, where the reduction is about 30%. For temperatures above 150°C, bamboo experiences a steeper fall until reaching a 60% reduction at 200°C.

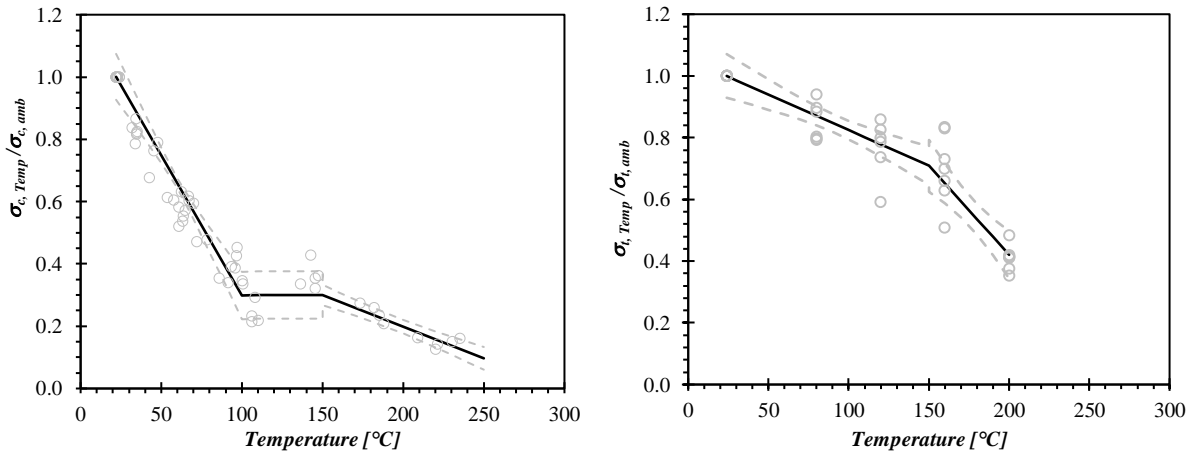


Figure 2. Normalised compressive (left) and tensile (right) strength of bamboo at elevated temperatures

Equations (1) and (2) presents a mathematical model for obtaining the reduction for the compressive and tensile strength of bamboo at elevated temperatures, respectively.

$$\frac{\sigma_{c,Temp}}{\sigma_{c,amb}} = \begin{cases} -9.0 \times 10^{-3} \cdot T + 1.20 & 20^{\circ}C \leq T < 100^{\circ}C \\ 0.3 & 100^{\circ}C \leq T < 150^{\circ}C \\ -2.0 \times 10^{-3} \cdot T + 0.60 & 150^{\circ}C \leq T < 250^{\circ}C \end{cases} \quad (1)$$

$$\frac{\sigma_{t,Temp}}{\sigma_{t,amb}} = \begin{cases} -2.3 \times 10^{-3} \cdot T + 1.06 & 20^{\circ}C \leq T < 150^{\circ}C \\ -5.8 \times 10^{-3} \cdot T + 1.58 & 150^{\circ}C \leq T < 200^{\circ}C \end{cases} \quad (2)$$

Further analysis in the reduction of the mechanical properties of bamboo at elevated temperatures can be investigated in other publications presented by the authors [5, 6].

3.2 Elastic modulus reduction

Figure 3 shows the normalised values of *MoE* at elevated temperatures. As it can be observed from this graph, the stiffness is reduced in a lower magnitude than strength. At 100°C, the reduction in *MoE* is only 5%, whereas at 200°C the reduction is about 20%. Equation (3) presents the model proposed with a 95 % confidence to predict the normalised *MoE* of bamboo at elevated temperatures. The average *MoE* at ambient temperature obtained for laminated bamboo in compression was 10429 MPa (SD=193 MPa), whereas in tension, the average *MoE* was 15455 MPa (SD=1341 MPa).

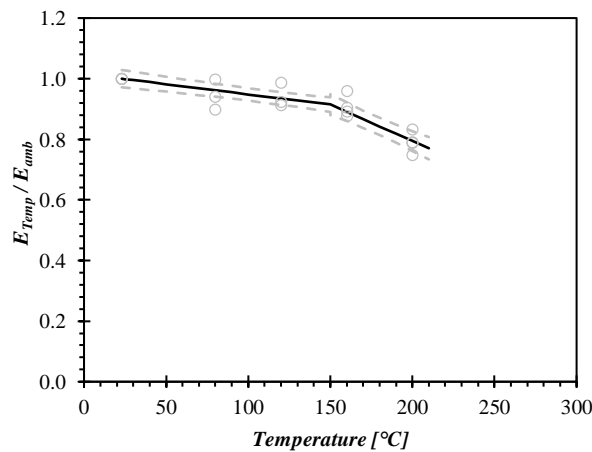


Figure 3. Normalised modulus of elasticity at elevated temperatures

$$\frac{E_{Temp}}{E_{amb}} = \begin{cases} -6.7 \times 10^{-4} \cdot T + 1.02 & 20^{\circ}C \leq T < 150^{\circ}C \\ -2.4 \times 10^{-3} \cdot T + 1.27 & 150^{\circ}C \leq T < 250^{\circ}C \end{cases} \quad (3)$$

3.3 Dynamic mechanical analysis

Figure 4 shows the results of a dynamic mechanical analysis performed in for four different specimens tested in a temperature range between ambient and 250°C. Results

are compared against the results presented in figure 3 for bench-scale tests presented in section 3.2. It can be observed that when the temperature rises to 100°C the reduction in the MoE is not larger than 10%, from 100°C to 150°C the reduction is still below 20%, however, after 150°C there is a significant loss of stiffness. The reduction in the MoE is higher than 40% when the temperature is above 200°C. Between 220°C and 240°C the plot falls drastically and the sample stiffness can be neglected.

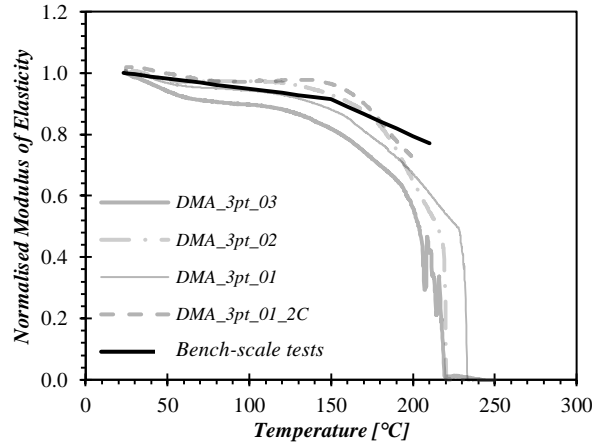


Figure 4. Normalised elastic modulus at elevated temperatures obtained from DMA and bench-scale tests.

4 CONSTITUTIVE STRESS-STRAIN MODELS

Results of the experimental studies on the mechanical properties of bamboo demonstrate that there is an inverse correlation between temperature and the compressive and tensile strength and stiffness of bamboo. The relevance of the study not only resides in the possibility of determining the strength and stiffness reduction, but it also enables understanding the effect of temperature over the element's maximum allowable stress and yielding strain, as well as the impact on its failure modes and final capacity. Other researchers such as Li et al. [7, 8], or Dongsheng et al. [9, 10] have already investigated the constitutive stress-strain models of bamboo at ambient temperatures to predict the response of axially loaded members or to calculate the bending capacity of bamboo beams. Indeed, they agree that bamboo behaves as a perfect linear elastic material in tension, where the stress-strain relationship can be described as a linear function until reaching the failure, with the slope of that line defined as the MoE . Nevertheless, several approaches have been developed to describe the compressive behaviour of bamboo, since under that loading condition bamboo behaves as an elastoplastic material. At low-stress levels, the bamboo compressive behaviour is linearly elastic, and Hooke's law can be applied. However, there is a point where the stress-strain curve flattens, and a non-linear correlation is observed until reaching the maximum compressive stress. After that point, the material experiences a large deformation before ultimate failure. In some cases, the exact point of failure is hard to localise, as the material can sustain load for considerably high axial deformations. Regardless, in most cases, lateral deformation is so high that it eventually leads to the collapse of the specimen.

4.1 Compressive stress-strain model

Previous research [7, 11] on the compressive behaviour of bamboo has established that the stress-strain relationship can be defined as a bi-linear function. At the beginning of the loading process, a linear elastic zone can be identified before reaching the maximum compressive stress. Afterwards, the plastic zone is characterised by a straight line with slope equal to zero until reaching the failure strain.

Considering the results presented in section 3, a bilinear model as a function of temperature relates the compressive stress and strain, as stated in equation (4). Both the modulus of elasticity E_c and the maximum compressive stress $\sigma_{c,max}$ vary as a function of temperature ($E_c(T)$ and $\sigma_c(T)$), as it was presented in equations (1) and (3).

$$\sigma_c = \begin{cases} E_c \varepsilon & , 0 \leq \varepsilon < \varepsilon_{c,max} \\ \sigma_{c,max} & , \varepsilon_{c,max} \leq \varepsilon < \varepsilon_{c,u} \end{cases} \quad (4)$$

As explained before, the compressive stress can be obtained following Hooke's law where the stress is directly proportional to the strain, with the *MoE* as the slope of that line. As the *MoE* varies as a function of temperature, as well as the strain at failure, the strain at the maximum stress, $\varepsilon_{c,max}$, can be calculated as the ratio between the maximum stress and the *MoE* at each temperature, as it can be seen in equation (5). The compressive strength and the *MoE* at elevated temperatures can be calculated from the equations (1) and (3). According to equations (6) and (7), the compressive strength and the *MoE* of bamboo at ambient temperature should be factorised by the normalised strength and the *MoE* obtained from the results of the tests presented in section 3.

$$\varepsilon_{c,max} = \frac{\sigma_{c,max}}{E_c} \quad (5)$$

$$\sigma_{c,max} = 51.7 \text{ MPa} \frac{\sigma_{c,Temp}}{\sigma_{c,amb}} \quad (6)$$

$$E_c = 10429 \text{ MPa} \frac{E_{Temp}}{E_{amb}} \quad (7)$$

4.2 Tensile stress-strain model

Tensile behaviour of bamboo remains linearly elastic until the strength is entirely lost for temperatures above 250°C. According to section 3 results, there is a reduction in the tensile strength and *MoE* as temperature increases, but the failure mechanism remains the same. Tensile failures are brittle and explosive, with cracks starting at the inner side of the bamboo culm, with all the failures happening at the node location. The crack propagates along the rest of the cross-sectional area until total failure occurs.

Since the stress-strain relationship is linearly proportional, Hooke's law can be applied until failure is reached, which considerably simplifies the problem. Equation (8) describes the tensile stress-strain model of bamboo as a function of temperature.

$$\sigma_t = E_t \varepsilon \quad , 0 \leq \varepsilon < \varepsilon_{t,u} \quad (8)$$

Where the *MoE* in tension, E_t , can be obtained using the equation (3) and (9). The limits of the model are defined by the strain at failure, which is also defined by the reduction in the tensile strength. Same as for the *MoE*, the maximum tensile strength can be obtained using the equation (2) and the average tensile strength at ambient temperature. Therefore, the tensile strength at elevated temperatures is presented in the equation (10), and the strain at failure can be obtained thanks to Hook's law and it is given by the equation (11).

$$E_t = 15455 \text{ MPa} \frac{E_{Temp}}{E_{amb}} \quad (9)$$

$$\sigma_{t,u} = 123.8 \text{ MPa} \frac{\sigma_{t,Temp}}{\sigma_{t,amb}} \quad (10)$$

$$\varepsilon_{t,u} = \sigma_{t,u} / E \quad (11)$$

Figure 5 illustrates the bi-linear compressive stress-strain model and tensile stress-strain model based on the reduction of the mechanical properties presented in the previous section. Other researchers have proposed similar models for timber at elevated temperatures [12]. Thermo-mechanical stress-strain models can be applied in situations when the temperature distribution in elements exposed to fire loads is known as it has been already proven in other research [13, 14].

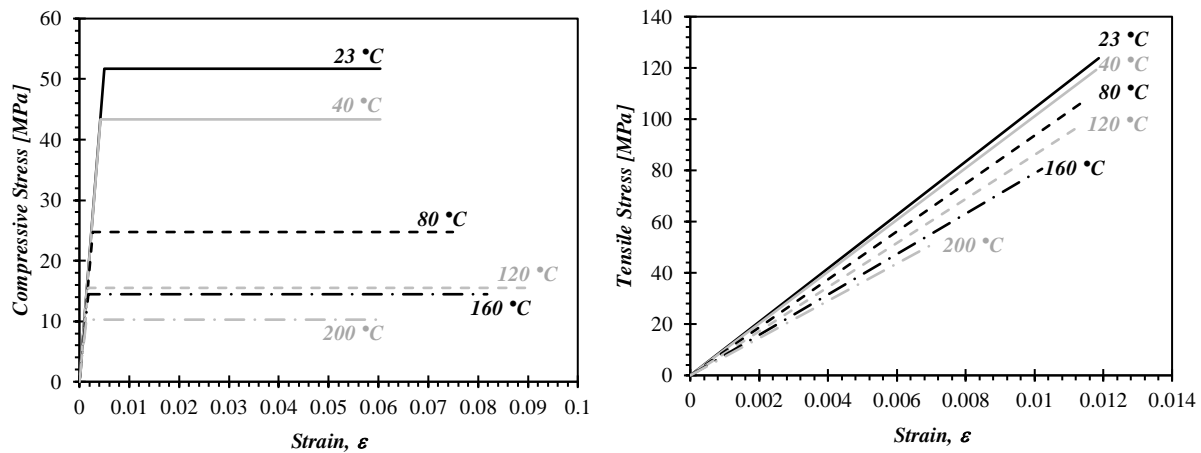


Figure 5. Compressive (left) and tensile (right) stress-strain model at elevated temperatures

5 CONCLUSIONS

The outcomes of the experimental studies described in this study define the variation on the compressive and tensile mechanical properties of bamboo at elevated temperatures. The study of the compressive stress-strain models has shown that bamboo behaves as a linear elastic material below the proportional limit. Hooke's law can be used to correlate stress and strain, but the maximum compressive strength, tensile strength and *MoE* would change as a function of temperature to account for the effects of elevated temperature. These models provide valuable information to predict the structural performance of members under axial forces, and flexural loads in members exposed to fire.

ACKNOWLEDGMENTS

The authors would like to thank Moso International BV for providing the laminated bamboo for this project. The authors are also grateful for the assistance of Van Thuan Nguyen, Angela Solarte, Ian Pope, and the technical support from staff in the Structures and Fire Laboratories at The University of Queensland.

REFERENCES

1. Vogtlander, J.G., and Van der Lugt, P. The Environmental Impact of Industrial Bamboo Products: Life-cycle Assessment and Carbon Sequestration, INBAR Technical Report No. 35, 2014
2. Buchanan, A., Ostman, B., and Frangi, A. Fire resistance of timber structures (National Institute of Standards and Technology Gaithersburg, 2014. 2014).
3. Guan, M., and Zhang, Q. Hygrothermal effect of bamboo by dynamic mechanical analysis, *Frontiers of Forestry in China*, 2006, 1, (3), pp. 353-356. 10.1007/s11461-006-0040-6
4. Xu, M., Cui, Z., Chen, Z., and Xiang, J. Experimental study on compressive and tensile properties of a bamboo scrimber at elevated temperatures, *Construction and Building Materials*, 2017, 151, pp. 732-741. 10.1016/j.conbuildmat.2017.06.128
5. Gutierrez, M., and Maluk, C. Mechanical behaviour of bamboo at elevated temperatures – Experimental studies, *Engineering Structures*, 2020, 220, pp. 110997. <https://doi.org/10.1016/j.engstruct.2020.110997>
6. Gutierrez Gonzalez, M., Madden, J., and Maluk, C. Experimental study on compressive and tensile strength of bamboo at elevated temperatures, in Editor (Ed.)^(Eds.): *Book Experimental study on compressive and tensile strength of bamboo at elevated temperatures* (2018, edn.), pp.
7. Li, H., Zhang, Q., Huang, D., and Deeks, A.J. Compressive performance of laminated bamboo, *Composites Part B: Engineering*, 2013, 54, pp. 319-328. <https://doi.org/10.1016/j.compositesb.2013.05.035>
8. Li, H., Su, J., Zhang, Q., Deeks, A.J., and Hui, D. Mechanical performance of laminated bamboo column under axial compression, *Composites Part B: Engineering*, 2015, 79, pp. 3174-382. <https://doi.org/10.1016/j.compositesb.2015.04.027>

9. Dongsheng, H., Aiping, Z., and Yuling, B. Experimental and analytical study on the nonlinear bending of parallel strand bamboobeams, *Construction and Building Materials*, 2013, 44, pp. 585-592. <https://doi.org/10.1016/j.conbuildmat.2013.03.050>
10. Shen, Y., Huang, D., Zhou, A., and Hui, D. An inelastic model for ultimate state analysis of CFRP reinforced PSB beams, *Composites Part B: Engineering*, 2017, 115, pp. 266-274. <https://doi.org/10.1016/j.compositesb.2016.09.089>
11. Sharma, B., Gatóo, A., and Ramage, M.H. Effect of processing methods on the mechanical properties of engineered bamboo, *Construction and Building Materials*, 2015, 83, pp. 95-101. <https://doi.org/10.1016/j.conbuildmat.2015.02.048>
12. Buchanan, A. Fire performance of timber construction, *Progress in Structural Engineering and Materials*, 2000, 2, (3), pp. 278-289. 10.1002/1528-2716(200007/09)2:3<278::aid-pse33>3.0.co;2-p
13. Fragiocomo, M., Menis, A., Clemente, I., Bochicchio, G., and Ceccotti, A. Fire Resistance of Cross-Laminated Timber Panels Loaded Out of Plane, *Journal of Structural Engineering*, 2013, 139, (12), pp. 04013018. doi:10.1061/(ASCE)ST.1943-541X.0000787
14. Pope, I., Hidalgo, J.P., Osorio, A., Maluk, C., and Torero, J.L. Thermal behaviour of laminated bamboo structures under fire conditions, *Fire and Materials*, 2019, n/a, (n/a)10.1002/fam.2791

THE USE OF RESEARCH FOR THE EXPLICIT CONSIDERATION OF SELF-EXTINCTION IN THE DESIGN OF TIMBER STRUCTURES

Juan Cuevas¹ and Cristian Maluk²

ABSTRACT

Fire safety stands as the real handicap regarding the realisation of timber structures. Currently, there is an increasing demand for load-bearing ETPs to remain exposed. Thus, a compromise is commonly made, and sacrificial protection due to charring of the exposed layer is considered as a fire safety design tool. Unfortunately, the means available for this task are not ideal; standardised tools have been proven to be inadequate, and performance-based approaches usually recur to research outcomes that present a high degree of discrepancy. This work offers a potential use of bench-scale fire testing to support a proposed design methodology to allow the construction of exposed timber structures.

Keywords: Timber; fire; self-extinction; fire tests

1 INTRODUCTION

Our current fire resistance regulations are based on the fundamental premise that a structure must survive the burning of the initial fuel load in a compartment. This concept is known as design for burnout. For a combustible material as timber, this poses a fundamental issue. In the event of a fire, the exposed timber elements inside of a compartment will contribute to the growth, intensity, and overall duration of the fire. The only way that we can satisfy the design-for-burnout requirement in timber construction by ensuring the self-extinction of the exposed timber elements after the complete consumption of the initial fuel load of the compartment. Furthermore, for the particular case of Engineered Timber Products (ETPs), the time required to achieve self-extinction must be lower than the time available for the occurrence of encapsulation failure (if present) and/or delamination.

The challenge of designing fire-safe exposed timber structures is commonly addressed through a performance-based approach, in which the exposed layer of a timber element is considered as sacrificial, and its charring is considered as a fire safety design tool. In this scenario, the application of the concept of self-extinction is critical. However, the means available for this task are not ideal. Standardised tools like the Eurocode's reduced cross-section method combined with a constant one-dimensional charring rate have been proven to be inadequate [1], and fail to address the complexities of the burning behaviour of timber elements. In an attempt to improve the tools available, research outcomes are used to support the design process. Many times, this is done without considering the context and current level of maturity of the results produced. Furthermore, there is a significant level of discrepancy between the values found in the scientific literature.

For engineering purposes, the use of a single deterministic value derived from these outcomes can lead to under- or over-sized timber elements. In the first scenario, this translates into an insufficient level of safety

¹ Juan Cuevas, The University of Queensland, Brisbane, Australia
e-mail: j.cuevas@uq.edu.au, ORCID: <https://orcid.org/0000-0002-0732-6252>

² Cristian Maluk, The University of Queensland, Brisbane, Australia
e-mail: c.maluk@uq.edu.au, ORCID: <https://orcid.org/0000-0002-1662-6943>

the potential collapse of the structure. The second scenario leads to an unnecessary increase in the production and construction costs of a building.

The work presented herein discusses some of the challenges that must be addressed to use research outcomes to support the use of self-extinction as a design methodology to enable fire-safe timber structures.

2 BURNING BEHAVIOUR AND SELF-EXTINCTION OF TIMBER

When exposed to heat, timber undergoes different thermal and chemical processes that propagate through the material. A simplified scenario of this phenomenon is presented in Figure 1.

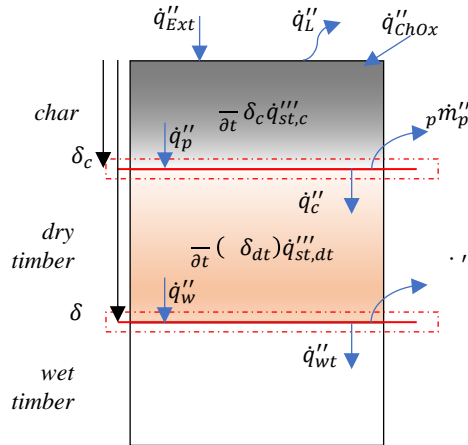


Figure 1. Simplified schematic of the burning of timber.

The first reaction occurs at temperatures of approximately 100°C and corresponds to the migration of moisture (free water) contained within the material. Some of the moisture will evaporate and diffuse out of the solid, while the rest will migrate inwards, inducing a localised pressure and moisture build-up region [2]. The proportion of water that diffuses into the material has been found to depend on the orientation of the fibres relative to the direction of the application of heat [3].

If heating continues and the temperature inside of the material is sufficiently high, the onset of the thermal decomposition of timber into flammable gases (pyrolysis) begins. This decomposition reaction is endothermic (requires energy) and generates two different products; a carbon-rich solid residue known as char, and a flammable gas mixture.

As the pyrolysis reaction front progresses, the flammable gases diffuse out of the, leaving only a growing char layer. Even though char is not inert, has a thermal conductivity that is considerably lower than the one from the virgin timber. This allows char to act as a natural insulation layer, regulating the amount of heat that reaches the pyrolysis front.

When temperatures in the range of 400°C [4] are reached in the vicinity of the burning surface of the material, a final reaction, char oxidation, takes place. This reaction provides additional heat into the solid, leaving behind a low-density residue known as ash.

The processes just described can be represented through the following energy balance,

$$\frac{\partial}{\partial t} \delta_c q'''_{st,c} = \dot{q}''_{Ext} - \dot{q}''_L + \dot{q}''_{Chox} - \dot{q}''_p \quad (1)$$

where the energy stored at the char layer is equal to the sum of the total heat flux at the exposed surface (per unit area) of the burning material \dot{q}''_{Ext} , the heat flux provided by the char oxidation reaction \dot{q}''_{Chox} , the heat losses at the surface of the solid \dot{q}''_L , and the flow of heat that leaves the char layer and is conducted inwards, reaching the pyrolysis front \dot{q}''_p .

At the pyrolysis front (located at a depth δ_c), only a fraction of the energy available is used to generate pyrolysis gases, as described in the following energy balance,

$$\dot{q}_p'' = \dot{q}_p'' + \dot{q}_{con}'' \quad (2)$$

where ΔH_p is the heat of pyrolysis of timber, \dot{m}_p'' is the mass flow per unit of area of pyrolysis gases being generated, and \dot{q}_{con}'' represents the unused energy that is conducted further into the material. This following section of the material corresponds to dry timber (as the moisture migration front has already passed), and in it, the next energy balance can be established,

$$\frac{\partial}{\partial t} \delta_{dt} q_{st,dt}''' = \dot{q}_{con}'' - \dot{q}_w'' \quad (3)$$

where now the energy stored in the dry portion of the material of thickness $\Delta\delta_{dt}$ (expressed as the difference between the position of the pyrolysis and moisture migration fronts), is be equal to the difference between the heat flux that penetrates this portion of the material \dot{q}_{con}'' , and the heat flux that reaches the moisture migration front \dot{q}_w'' , located at δ_c .

Finally, at the moisture migration front, it is found that,

$$\dot{q}_w'' = \dot{q}_w'' + \dot{q}_{wt}'' \quad (4)$$

that is, the energy that reaches this reaction front \dot{q}_w'' , will be partially used in evaporating moisture (represented through the heat of vaporisation ΔH_w , and the mass flow of water vapour \dot{m}_w''), and the other part will be conducted into the “wet” portion of the material.

Finally, combining Eqs. (2)-(4) into Eq.(1) and solving for \dot{m}_p'' leads to the following expression that describes the mass flow of pyrolysis gases in terms of the participating heat fluxes and ongoing reactions,

$$\dot{m}_p'' = \frac{1}{p} \left[\dot{q}_{Ext}'' + \dot{q}_{ChOx}'' - \dot{q}_L'' - \frac{\partial}{\partial t} (\delta_c q_{st,c}''' + \Delta\delta_{dt} q_{st,dt}''') - \dot{q}_w'' - \dot{q}_{wt}'' \right] \quad (5)$$

The flow of pyrolysis gases that leaves the solid is found to be at its maximum when the last three subtracting terms are at its minimum. In other words, the flow of energy that leaves the moisture migration front unused and the amount of energy used in evaporating the moisture out of the solid are minimal, and no energy is spent in heating the char and dry timber layers. This last part can be translated as reaching a thermal steady-state within the timber element.

The arrival to this steady-state, as described by Emberley et al. [6], is a two-stage process; the first stage is transient, and it is characterised by the occurrence of a peak in the sample's decomposition rate, right after ignition. This peak is due to a thin (but growing) char layer that can retain only a small fraction of the heat that reaches the exposed surface and transfer the rest of it into the pyrolysis front.

As the depth of the char layer increases, its capacity to store heat increases as well; hence, the amount of heat that reaches the pyrolysis front diminishes, reducing the amount of pyrolysis gases being generated. After a certain time, a thermal steady-state characterised by a constant-thickness char layer is reached.

At this stage, flaming may be sustained, but if the flow of pyrolysis gases generated drops below a critical value, flame extinction would occur.

From this analysis, the self-extinction of timber can be studied in terms of a worst-case-scenario analysis. If critical conditions that lead to flame extinction are identified when the flow of pyrolysis gases is at its highest (maximum achievable from Eq. (5)), then these conditions will induce flame extinction for every other scenario that is less severe as well.

3 EXPLICIT CONSIDERATION OF SELF-EXTINCTION IN THE DESIGN OF TIMBER STRUCTURES

3.1 The design methodology

As an example, let us consider the design methodology proposed by Bartlett et al. [7] for the evaluation of the potential self-extinction of the exposed timber surfaces in a compartment fire (Table 1).

Table 1. Proposed steps for incorporating auto-extinction into design methodology. Reproduced from [7].

Step	Action
1	Determine the time to burnout of the original fuel load of the compartment
2	Based on the amount of exposed timber after burnout, estimate the re-radiation heat flux between the exposed timber surfaces.
3	Estimate the surface temperature of the exposed timber elements
4	Evaluate the heat losses on the compartment geometry using these surface temperatures
5	Solve Eq.(5) to estimate the mass loss rate of each exposed timber surface and determine if it is less than the critical mass-loss rate for self-extinction.
6	Repeat steps 2-6 for the next timestep (re-radiation is time-dependent) until: <ul style="list-style-type: none"> a) Self-extinction occurs b) Pre-defined failure criteria are met c) A steady-state is achieved

As highlighted by Bartlett et al., these steps need to be performed as a time-dependent analysis, as the surface temperature of the exposed timber surfaces will vary in time. It is important to notice that the three possible outcomes of this analysis consider no firefighter intervention, and only the first outcome can be deemed as acceptable from a fire safety design perspective. The last two outcomes will require the modification of the design to reach a scenario in which self-extinction is reached.

The crucial element in this design approach is the use of a benchmark critical mass-loss rate for self-extinction. There is an important level of discrepancy in the critical conditions that lead to the self-extinction of timber. This generates a significant challenge that practitioners need to overcome when using experimental outcomes to aid performance-based design.

In the following section, an extensive review of the research conducted on the topic of self-extinction is presented to illustrate the beforementioned challenge.

3.2 The state of the art

The occurrence of self-extinction of timber has been reported by several researchers in the past, mainly as an event observed in studies focused on understanding the different phenomena related to the burning of timber. In the early '40s, Bamford et al. [8] conducted a series of experimental and numerical studies to determine the decomposition rates of timber given a set of boundary and initial conditions. The experimental studies were conducted using 23 cm^2 deal samples of different thicknesses that varied from two to four centimetres, positioned in a vertical orientation and heated from both sides through gas burners, it was observed that flaming combustion could be sustained when the mass loss rate of the test samples was above 2.5 g/m^2s . Furthermore, it was observed that a minimum radiation intensity of 46 kW/m^2 was required to sustain flaming combustion for more than 12.5 minutes.

In the late 70s, Tewarson & Pion [9] presented a comprehensive experimental study focused on investigating burning characteristics for a range of commercially available plastics, timber (Douglas Fir), plywood, and liquid fuels. In their research, they concluded that for a range of materials -timber among them- the heat losses from the exposed surface are equivalent or greater than the heat provided from the

flames at the exposed surface. This formally introduced the fundamental concept that the heat flux supplied by the flame of a burning timber element is not sufficient to overcome the heat losses at the exposed surface, if the additional heat provided is not enough, timber will undergo into self-extinction. A couple of years later, Petrella [10] showed the existence of a defined functionality between a sample's mass burning rate and Spalding's mass transfer number B . Later on, Rangwala [11] concluded that a critical B -number of approximately 0.5 is required to sustain flaming combustion on Douglas Fir pine, that can be translated into a critical mass loss rate of $4.0 \text{ g/m}^2\text{s}$.

With the arrival of Engineered Timber Products, new failure modes like delamination changed the way we approached the self-extinction potential of timber structures, and our knowledge in the area had to be revisited. Inghelbrecht [12], proposed a design framework that aimed at demonstrating that a better understanding of the fire behaviour of timber structures can lead to a safe, explicit structural design. Experiments conducted within the scope of this work involved bench-scale testing of Cross-Laminated Timber (CLT), Glue-laminated Timber (Glulam), a conventional solid wood material (Hoop pine). It was found that the charring rate tends to an asymptotic value of 0.6 mm/min , in agreement with the expected value found in the literature. Additionally, it was found that significant charring and mass loss is only achievable if flaming combustion is sustained. Finally, a critical mass loss rate to support flaming combustion of approximately $4.0 \text{ g/m}^2\text{s}$ was identified.

Emberley et al., have done extensive work on the study of the self-extinguishment capabilities of CLT, across different scales. An experimental study conducted using bench-scale samples of different timber species and products and a vertically-oriented Mass-loss Calorimeter (MLC), found that regardless of the heating time and imposed heat flux, the steady-state mass loss rate tends asymptotically to a maximum value [6]. Furthermore, a critical mass loss rate for self-extinction of $4.0 \text{ g/m}^2\text{s}$ was established experimentally and is consistent with previously reported literature values. Self-extinction was found to occur after the mass loss rate decreased below this value independent of the heating history. A following bench-scale study by the same author identified the conditions that lead to the self-extinction of six types of timber (European Spruce, Radiata Pine, Red Ironbark, Balsa, Kumaru, and Blackbutt). The critical mass-loss rate for self-extinction was found to range from 2.7 to $8.3 \text{ g/m}^2\text{s}$ across the different type of species tested, while the critical incident heat flux for self-extinction ranged from 24 to 57 kW/m^2 [13]. Later on, a large-scale test conducted using a compartment of Radiata Pine CLT with only two exposed timber surfaces (ceiling and lateral wall) [14]. From the test, it was found that both surfaces reached extinction when the maximum incident heat flux over them decreased below 45 kW/m^2 .

Bartlett et al. also explored the idea of self-extinguishment in CLT through the fire-point theory developed by Rasbash [15]. In a series of bench-scale experiments conducted using horizontally-oriented Radiata Pine CLT samples the critical mass-loss rate for self-extinction was evaluated to be of $3.5 \text{ g/m}^2\text{s}$, and the critical external incident heat flux was found to be of 31 kW/m^2 [16]. In later work [17], a series of large-scale tests were conducted to evaluate the effectiveness of the fire-point theory to predict self-extinction at large scales. These tests were conducted using compartments with two exposed timber surfaces (back wall and ceiling). From the three tests conducted under the same thermal load, two failed to reach self-extinction due to the occurrence of progressive delamination of the exposed CLT layers. In the test that reached self-extinction, the magnitude of the mass-loss rate at the moment of its occurrence agreed with the previous bench-scale outcomes.

Crielaard et al. [18] defined the self-extinguishment of CLT as the complete cease of combustion (both flaming and smouldering) and investigated its occurrence across scales; First, a numerical model was implemented to identify the conditions at which self-extinguishment should be achieved. Secondly, two series of tests were conducted to quantify these conditions. The tests were performed in a Cone Calorimeter in two different series. In the first tier, bench-scale ($100 \times 100 \text{ mm}^2$) five-ply CLT samples of different thicknesses were exposed to a 75 kW/m^2 heat flux representative of a fully developed fire. After a certain level of charring, the heat flux was dropped to heat fluxes lower than 10 kW/m^2 where samples were expected to self-extinguish if this second heat flux was lower than the critical value to sustain flameless combustion. The second series of tests aimed to understand the complete model of self-extinguishment, including delamination and char fall-off. For this, medium-scale ($0.5 \times 0.5 \text{ m}^2$) CLT samples were

assembled into small compartments that were imposed to a constant 41 kW/m^2 and decay design fire. From this work, it was concluded that CLT has the potential of reaching self-extinguishment if the external heat flux over the burning surface drops below 5 to 6 kW/m^2 (to cease smouldering combustion), and the flow of oxidiser is limited to 0.5 m/s for this critical heat flux values.

Arnórsson et al. [19] conducted an experimental study to evaluate the variability in the magnitude of the critical mass loss rate for self-extinction, based mainly on the bench-scale experiments conducted previously by Emberley et al. and Bartlett et al. Using an experimental configuration almost identical to Emberley's study (smaller samples), the critical mass loss rate for self-extinction was found to be of $3.2 \text{ g/m}^2\text{s}$. Furthermore, the critical mass loss rate at self-extinction was found to increase up to approximately $9 \text{ g/m}^2\text{s}$ when a forced flow of 2.3 m/s was included. No critical incident heat flux for self-extinction was identified in this study.

3.3 The difficulties of using currently available data

The previous section has left in evidence the wide range of scattering in the information available regarding the potential self-extinction of timber. In an attempt to simplify the decision process for the selection of this benchmark value, one might be tempted to group the available scientific data into two main categories; large-scale, and bench-scale results.

Large-scale experiments represent, in theory, the most realistic scenarios as they are meant to represent the full-scale phenomena and response of the structure. Nevertheless, the number of experiments that fit in this category is minimal, and the few tests available have been intended as demonstrators of the concept of self-extinction. Moreover, self-extinction was only achieved in large-scale experiments when delamination did not occur, whether this was planned or not. When taking this into account, the use of experimental outcomes obtained from large-scale experiments does not seem ideal.

Bench-scale experiments are commonly posed as an attractive alternative to large-scale testing not only in terms of cost and time but also as they allow for the study of simplified scenarios whose results should be, in theory, extrapolatable across scales. Unfortunately, the research outcomes available at the moment have a significant discrepancy as well, despite being based on similar theoretical frameworks, in general terms. On this basis, one might validly question if these bench-scale experiments are reproducing accurately the theory in which they are based. Furthermore, could be this discrepancy between experiments and theory one of the sources of uncertainty?

3.4 Addressing the challenges in the use of bench-scale outcomes in design.

In the previous section, some questions were raised that are related to the use of bench-scale testing outcomes, and the potential to scale these results into larger configurations. With these ideas in mind, the following questions need to be addressed before confidently using bench-scale outcomes in design:

3.4.1 How reliable are the results obtained from bench-scale experiments?

Several studies have reported the difficulty on the scaling of the burning behaviour of different materials across scales. Some researchers have attributed this challenge to the differences in the boundary conditions that each type of test and scale imposes over the test sample [20].

In addition to these effects, the natural inhomogeneity of timber and the presence of natural defects [22] increases the complexity of a potential multi-scale approach. Edge effects due to the scale of the test [20] and the natural imperfections of the material will increase the degree of uncertainty in the results obtained from the bench-scale testing of timber products.

To overcome this, repeats of the same experiment are usually conducted. Reszka [22] determined that three repetitions of each one of his experiments were sufficient to obtain a confidence interval smaller than the standard deviation of the temperature measurements obtained. For his calculations, the author considered a standard deviation of 15 K and a confidence interval of 95%.

The use of this number of repetitions became a common denominator in most of the experimental works centred about the potential self-extinction of timber [6,16,18]. Nevertheless, none of these works verified

that this amount of repetitions was sufficient to achieve the performance criteria presented by Reszka, even though the experiments were different (different materials, sample preparation, and equipment).

With this in mind, the following question arises; how many repetitions of a bench-scale experiment are necessary to reduce the uncertainty of the results, make them independent of the number of repetitions that are performed, and most importantly, genuinely representative of the material response?

To answer this question, a sufficiently large number of repetitions of the bench-scale experiment described in Table 2 were conducted using the Fire Propagation Apparatus (FPA).

Table 2. Experimental parameters used to generate the sampling universe

Parameter	Value
Thermal exposure	50 kW/m ² (constant) during 60 min
Sample dimensions	90x90x150 (LxWxD)
Material	Cross-laminated Timber (Radiata Pine)
Sample insulation	(1) Inner layer of 9 mm thick Ceramic Paper; (2) Outer lining of reflective material
Diagnostics	Mass loss
Repetitions	10

The results of this series of experiments are presented in Figure 2(a). From the figure, it can be seen that the mass-loss rate reaches a peak briefly after ignition, and rapidly decays to a somewhat steady-state value. To enable comparison, the steady-state mass loss rate (*SS – MLR*) is defined as the control parameter. This parameter was obtained as the average of the data collected within a 30 min window that started 15 min after ignition. The average of the *SS – MLR*s of each repetition was defined as the benchmark parameter. The steady-state mass loss rate for each one of the repetitions, along with the reference value is presented in Figure 2(b).

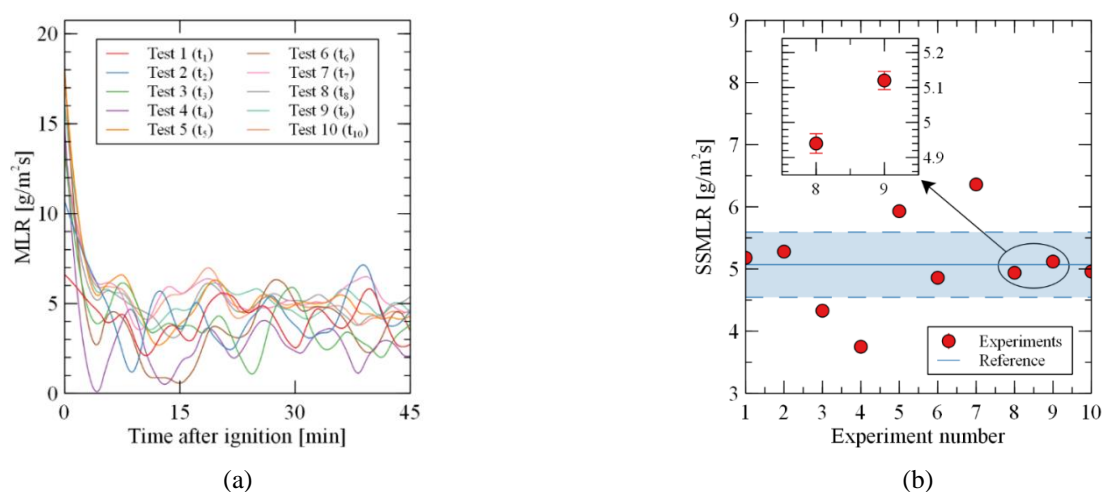


Figure 2: Data used for the study; (a) MLR of the ten experiments conducted; (b) SS-MLR retrieved for each experiment, and the reference value; (c) MAD of the uncertainty in the MLR.

For the following step, random sets of data were generated by combining the ten repetitions that constitute our entire database. These sets were assembled by picking, in a random fashion, from three to nine of the ten tests available. The amount of sets generated is therefore defined by combinatorial probabilities, and it ranged from 120 to 10 for the groups formed with only three and up to nine experiments, respectively.

Following, the steady-state mass loss rate was calculated for each set of each group, and it was found that as the number of repetitions considered in each set is increased, the estimates obtained become more precise and accurate.

To provide a quantitative measure of the improvement generated, the mean absolute difference (MAD) was used. The mean absolute difference is defined as the average difference between each estimate and a target/reference value, and it, therefore, provides information about the variability of a parameter. The mean absolute difference was calculated for the uncertainty in the estimation of the steady-state mass-loss rate, and the result of this calculation is shown in Figure 3. It was found that increasing the number of repetitions decreases the uncertainty of the estimate exponentially. Furthermore, it was found that after increasing the repetitions beyond a certain point, the mean absolute difference of the uncertainty reaches a steady value. This is more evident when looking at the derivative of the mean absolute difference over the number of repetitions; it can be seen that after increasing the number of repetitions beyond six, the improvement to the precision of the estimate is no longer significant. Therefore, it is concluded that six is the ideal number of times that a given experiment should be conducted within the scope of this study.

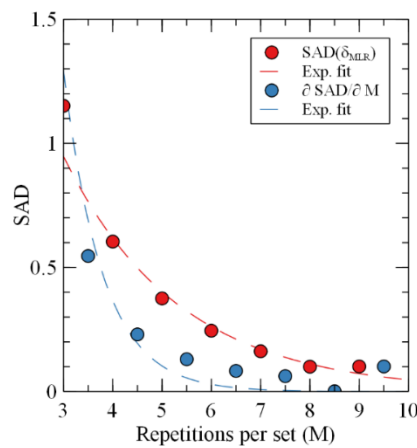


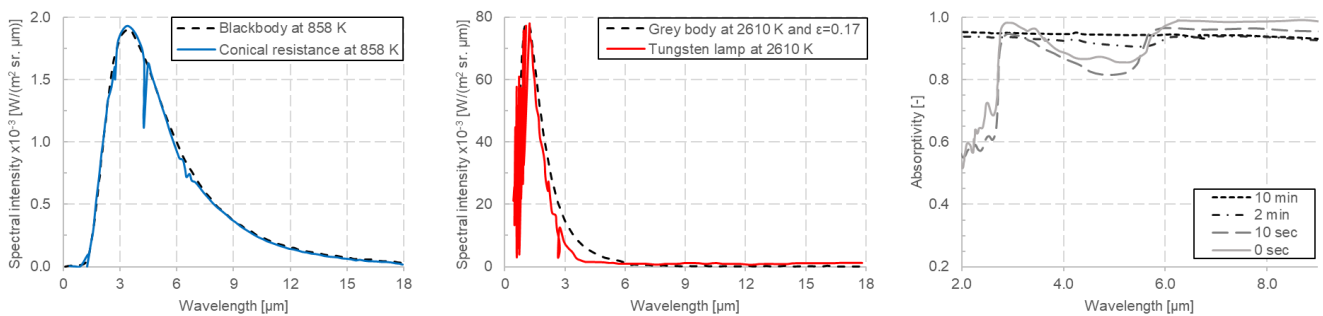
Figure 3. Mean average difference of the uncertainty in the MLR as a function of the number of repetitions conducted.

3.4.2 What do these tests truly represent?

With this question, what we intend to address is if there is an agreement between the conditions that the experiment itself imposes over the sample, and what the intended scenario that we want to replicate is.

To check this, we need to focus on the way heat is applied to the test sample. This involves understanding how the heating element emits radiation and how good the material being tested at absorbing this radiation.

Figure 4 presents the spectral distribution of the emissivity of two different types of heating elements commonly used in bench-scale fire testing; a conical resistance (cone calorimeter), and a tungsten lamp (FPA), along with the spectral absorptivity of a reference timber species (plywood).



(a) Conical resistance from [23]

(b) Tungsten lamp from [23]

(c) Plywood exposed to 50 kW/m^2 from [24]

Figure 4. Spectral characteristics of heating elements and timber

From the figure, it can be seen that there is an important difference in the way both of these heating elements will impose heat over the test sample. The conical resistance follows a spectral distribution equivalent to the one of a black-body emitter, and it is usually considered as the closest one to the spectral distribution of a real fire [23]. The tungsten lamp on the other hand concentrates most of the intensity of its radiant emission in the infrared side of the spectrum and it can be described as a grey-body emitter up to a certain extent. Furthermore, when we take these different emission spectrums and we compare it to the way timber (plywood used as a surrogate) absorbs radiation, it becomes clear how this can be a source of uncertainty; during the initial heating of a timber sample, its absorptivity is considerably lower in the lower end of the spectrum, matching the peak of the emission distribution of the tungsten lamp. This means that it will absorb less of the radiation received when compared to the scenario in which a conical heater provides heat. This effect can partially explain the discrepancies that exist in the times-to-ignition reported by several researchers for common materials. It is also interesting to notice how this effect diminishes as the exposed surface of the timber sample becomes charred, and it reaches an almost constant absorptivity across the whole spectrum.

Now that the effect of the nature of the radiation being imposed over the test sample has been discussed, it is necessary to analyse the impact of how the radiation is being applied.

Previous experimental results presented in [25] showed the distribution of the incident heat over a complete test sample when testing in the FPA (Figure 5(a)). Through a numerical model, it was found that the magnitude of the incident heat flux over the target surface of the sample was a 2% deviation when compared to the average (and 6% difference between the minimum and maximum values), but also that additional heat is being delivered to the sides of the sample, reaching values of up to 40% in average of the maximum magnitude found at the top surface. Furthermore, a short experimental campaign was conducted in order to quantify the impact of this lateral heating. The results of this campaign are presented in Figure 5(b). It was found that a test sample without any form of lateral insulation will lose approximately 35% of its original mass after being exposed to a constant incident heat flux of 50 kW/m^2 during 15 minutes, while a sample protected with the lateral insulation described in Table 2 will only lose 15% of its mass during the same conditions.

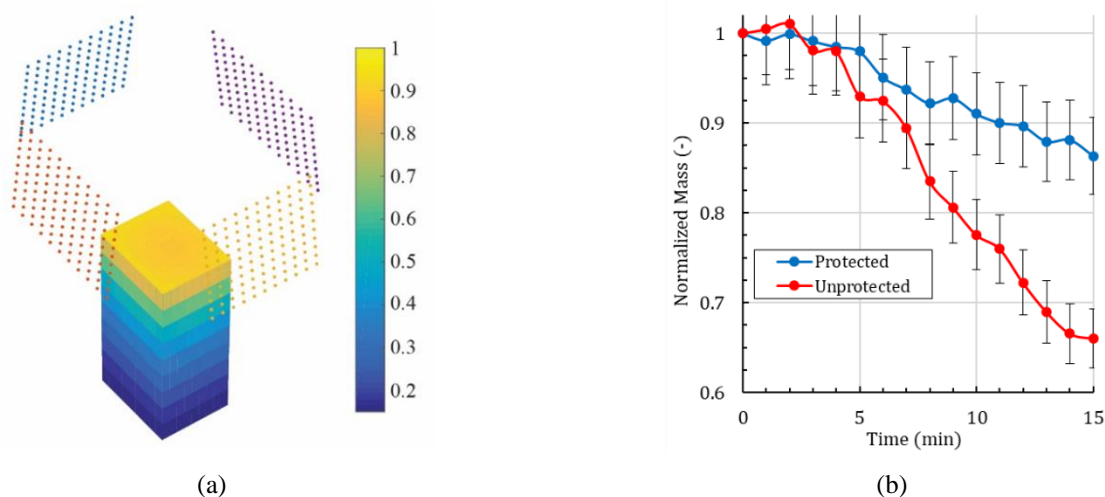


Figure 5. Effect of the external incident heat flux over the sample; (a) Normalized distribution of the incident radiation over the sample; (b) Normalised mass loss of protected and unprotected samples.

From this study, it becomes evident that the neglect of this undesired effect leads to an inaccurate determination of the thermal conditions imposed over the test sample. This partially explains the discrepancy that exists in the determination of the critical conditions for the self-extinction of timber; especially when looking at the bench-scale studies conducted by Ingelbrecht [12], Crielaard et al. [18], Emberley et al. [6], and Bartlett et al. [16].

3.5 Case study: a non-deterministic approach to the self-extinction of timber through bench-scale testing.

Considering all of the information previously discussed, Cuevas et al. [26] conducted a bench-scale experimental campaign to determine the critical conditions that lead to the self-extinction of timber.

The experimental campaign considered CLT Radiata Pine prepared according to the parameters presented in Table 2, and involved the variation of the incident heat flux over the sample from 50 to 30 kW/m^2 in order to determine the minimum conditions required to sustain flaming combustion, conducting six repetitions for each condition tested. Moreover, the experimental campaign considered the measurements of mass-loss and in-depth temperature, but only the mass-loss rate results will be presented herein.

Figure 6(a) shows the average mass-loss rate from the experiments conducted using secondary thermal exposures of 40, 30, and 35 kW/m^2 . For all conditions, there is a clear drop in the mass loss when the heat flux is decreased at ≈ 1200 s. After this point, the behaviour showed by the curves is no longer uniform. The samples exposed at 35 and 40 kW/m^2 reached a secondary steady-state condition, characterised by a steady-state mass loss rate slightly lower than 4.5 $\text{g/m}^2\text{s}$. On the other hand, the samples exposed to a 30 kW/m^2 self-extinguished just a few seconds after decreasing the incident heat flux.

To improve the accuracy of the determined critical mass-loss rate for extinction, additional experimental campaigns were conducted using secondary incident heat fluxes of 32.5 and 33.8 kW/m^2 . In these scenarios, the occurrence of self-extinction was not observed as an absolute condition and therefore, it is necessary to decouple the scenarios that self-extinguished from the ones that did not. Figure 7(b) shows the results obtained for the samples tested at 32.5 and 33.8 kW/m^2 that did not achieve self-extinction. After the reduction in the incident heat flux, there is a decrease in the mass-loss rate, reaching a new steady-state value slightly lower than 4.5 $\text{g/m}^2\text{s}$. Figure 7(c) shows the average mass-loss rate curves of the samples that reached self-extinction under incident heat fluxes of 32.5 and 33.8 kW/m^2 . Again, in both scenarios self-extinction was achieved briefly after decreasing the incident heat flux. When considering the totality of the experiments conducted, the critical mass-loss rate for self-extinction was found to be of $3.6 \pm 0.6 \text{ g/m}^2\text{s}$.

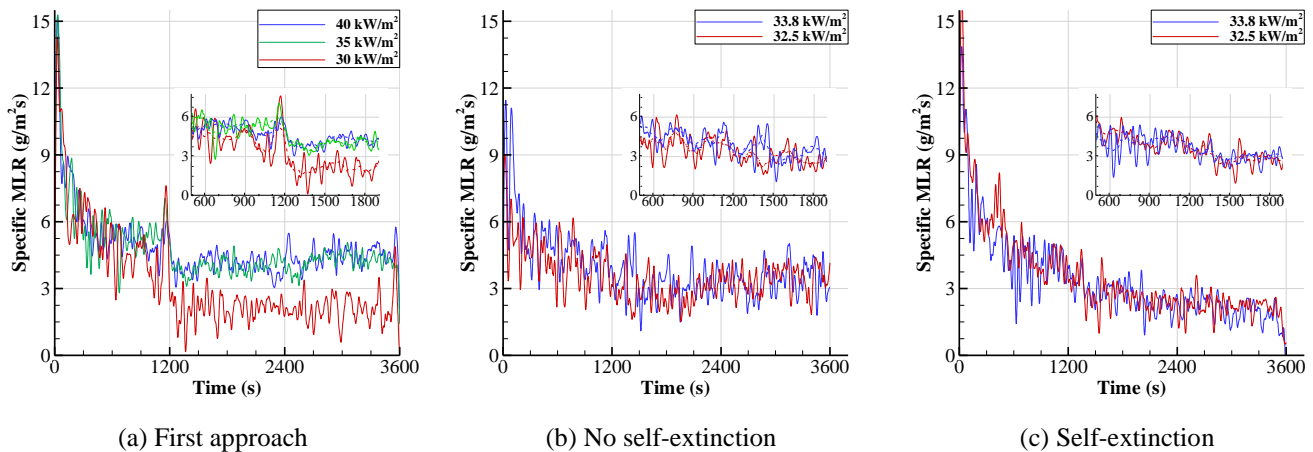


Figure 6. Mass-loss rate results for different incident heat fluxes

Finally, when considering the totality of the experiments conducted within the scope of this experimental campaign (12, six for mass-loss measurements, and six for in-depth temperature) it is found that the occurrence of self-extinction in bench-scale tests should not be treated as a binary phenomenon, but a probabilistic one, greatly affected by testing conditions, sample preparation, and most importantly, the inherent heterogeneity of the material. As shown in Figure 7, a secondary incident heat flux of 30 kW/m^2 lead to the extinction of the 12 samples tested. As the heat flux was increased, the number of samples that self-extinguished decreased almost linearly. For a secondary incident heat flux of 35 kW/m^2 , no samples self-extinguished when tested under an ambient atmosphere.

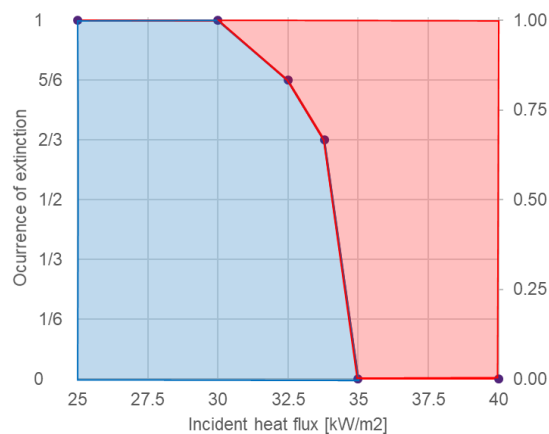


Figure 7. Occurrence of self-extinction for different incident heat fluxes.

4 CONCLUSIONS

The work presented herein highlighted the significant challenge that practitioners face when attempting to use research outcomes to support the performance-based design of exposed timber structures by relying on the self-extinction potential of timber. This main difficulty comes from the large degree of dispersion in the results available in research. Furthermore, a series of experimental results were presented to identify and understand these sources of uncertainty. Finally, a case study based on an experimental study that incorporated the knowledge presented is showcased.

From this experimental campaign, a critical mass-loss rate for the self-extinction of timber was presented, and more importantly, it was found that the occurrence of self-extinction should not be addressed as a deterministic phenomenon. The authors have chosen this to approach to account for the uncertainty when performing bench-scale experiments in a material as intrinsically variable as timber.

REFERENCES

1. Schmid J, Just A, Klippel M, Fragiaco M. The Reduced Cross-Section Method for Evaluation of the Fire Resistance of Timber Members: Discussion and Determination of the Zero-Strength Layer. *Fire Technol* 2015;51:1285–309. <https://doi.org/10.1007/s10694-014-0421-6>.
2. Browne F. Theories of the combustion of wood and its control. United States Dep Agric For Serv Rep No 2136 1958:1–72.
3. Ross RJ, USDA Forest Service. FPL. Wood handbook: wood as an engineering material. Madison, Wisconsin: 2010. <https://doi.org/10.2737/FPL-GTR-190>.
4. Roberts AF, Clough G. Thermal decomposition of wood in an inert atmosphere. *Symp. Combust.*, vol. 9, 1963, p. 158–66. [https://doi.org/10.1016/S0082-0784\(63\)80022-3](https://doi.org/10.1016/S0082-0784(63)80022-3).
5. Bartlett A, Hadden R, Bisby L. A Review of Factors Affecting the Burning Behaviour of Wood for Application to Tall Timber Construction. *Fire Technol* 2019;55. <https://doi.org/10.1007/s10694-018-0787-y>.
6. Emberley R, Inghelbrecht A, Yu Z, Torero JL. Self-extinction of timber. *Proc Combust Inst* 2017;36:3055–62. <https://doi.org/10.1016/j.proci.2016.07.077>.
7. Bartlett A, Hadden R, Bisby L, Lane B. Auto-Extinction of Engineered Timber As a Design Methodology. WCTE 2016 - World Conf. Timber Eng., 2016.
8. Bamford CH, Crank J, Malan DH, Wilson AH. The combustion of wood. Part I. *Math Proc Cambridge Philos Soc* 1945;42:166–82. <https://doi.org/10.1017/S030500410002288X>.
9. Tewarson A, Pion RF. Flammability of plastics-I. Burning intensity. *Combust Flame* 1976;26:85–103. [https://doi.org/10.1016/0010-2180\(76\)90059-6](https://doi.org/10.1016/0010-2180(76)90059-6).
10. Petrella R V. The Mass Burning Rate and Mass Transfer Number of Selected Polymers, Wood, and Organic Liquids. *Polym Plast Technol Eng* 1979;13:83–103. <https://doi.org/10.1080/03602557908067676>.

11. Rangwala A. Flame Spread Analysis Using a Variable B-Number. *Fire Saf Sci* 2008;9:243–54. <https://doi.org/10.3801/IAFSS.FSS.9-243>.
12. Inghelbrecht A. Evaluation of the burning behaviour of wood products in the context of structural fire design. The University of Queensland, Ghent University, n.d.
13. Emberley R, Do T, Yim J, Torero JL. Critical heat flux and mass loss rate for extinction of flaming combustion of timber. *Fire Saf J* 2017;91:252–8. <https://doi.org/10.1016/j.firesaf.2017.03.008>.
14. Emberley R, Gorska Putynska C, Bolanos A, Lucherini A, Solarte A, Soriguer D, et al. Description of small and large-scale cross laminated timber fire tests. *Fire Saf J* 2017;91:327–35. <https://doi.org/10.1016/j.firesaf.2017.03.024>.
15. Rasbash DJ, Drysdale DD, Deepak D. Critical Heat and Mass Transfer at Pilot Ignition and Extinction of a Material *. *Fire Saf J* 1986;10:1–10.
16. Bartlett A, Hadden R, Bisby L, Lane B. Auto-extinction of engineered timber: the application of firepoint theory. Interflam, 2016.
17. Bartlett A, Hadden R, Hidalgo JP, Santamaria S, Wiesner F, Bisby L, et al. Auto-extinction of engineered timber: Application to compartment fires with exposed timber surfaces. *Fire Saf J* 2017;91:407–13. <https://doi.org/10.1016/j.firesaf.2017.03.050>.
18. Crielaard R, van de Kuilen JW, Terwel K, Ravenshorst G, Steenbakkers P. Self-extinguishment of cross-laminated timber. *Fire Saf J* 2019;105:244–60. <https://doi.org/10.1016/j.firesaf.2019.01.008>.
19. Arnórsson SM, Hadden RM, Law A. The Variability of Critical Mass Loss Rate at Auto-Extinction. *Fire Technol* 2020. <https://doi.org/10.1007/s10694-020-01002-z>.
20. Zhou A, Yu Z. Validating thermal response models using bench-scale and intermediate-scale fire experiment data. *Mech Adv Mater Struct* 2014;21:412–21. <https://doi.org/10.1080/15376494.2012.697603>.
21. Lautenberger C, Torero JL, Fernandez-Pello AC. Understanding materials flammability. In: Apte Transport and Mining VBBT-FT of MU in C, editor. *Flammabl. testing of Mater. used Constr. Min.*, Cambridge: Woodhead Publishing; 2006, p. 1–21. <https://doi.org/10.1533/9781845691042.1>.
22. Reszka P. In-Depth Temperature Profiles in Pyrolyzing Wood 2008.
23. Bal N, Raynard J, Rein G, Torero JL, Försth M, Boulet P, et al. Experimental study of radiative heat transfer in a translucent fuel sample exposed to different spectral sources. *Int J Heat Mass Transf* 2013;61:742–8. <https://doi.org/10.1016/j.ijheatmasstransfer.2013.02.017>.
24. Boulet P, Brissinger D, Collin A, Acem Z, Parent G. On the influence of the sample absorptivity when studying the thermal degradation of materials. *Materials (Basel)* 2015;8:5398–413. <https://doi.org/10.3390/ma8085251>.
25. Cuevas J, Hidalgo JP, Torero JL, Maluk C. Complexities of the Thermal Boundary Conditions when Testing Timber using the Fire Propagation Apparatus. *Proc. Ninth Int. Semin. Fire Explos. Hazards*, St. Petersburg, Russia: 2019, p. 959–69. <https://doi.org/10.18720/spbpu/2/k19-88>.
26. Cuevas J, Torero JL, Maluk C. Flame extinction and burning behaviour of timber under varied oxygen concentrations. *Fire Saf J* 2020.

FIRE PERFORMANCE OF MOMENT-RESISTING CONCEALED TIMBER CONNECTIONS REINFORCED WITH SELF-TAPPING SCREWS

Oluwamuyiwa Okunroumu¹, Osama (Sam) Salem², George Hadjisophocleous³

ABSTRACT

Recent research shows that the two predominant failure modes encountered in concealed wood-steel-wood bolted connections at ambient temperature are perpendicular-to-grain tensile splitting and row shear out [1]. The study presented in this paper aims to investigate the fire performance of these connections but with self-tapping screws (STS) acting as perpendicular-to-wood grain reinforcement along with applying fire protection to the metal components, e.g., head and nut of steel bolts and connecting steel plates, of the connections. Two full-size glulam beam end connections were tested experimentally at elevated temperatures while being loaded perpendicular to wood grain to develop bending moment on the connection. Two connection configurations, each involved four steel bolts arranged in two different patterns, were examined. In both fire tests, the connection assemblies were exposed to elevated temperatures that followed the CAN/ULC S101 standard time-temperature curve [2] and each connection configuration was loaded to 100% of the ultimate design load of the weakest connection configuration. The experimental results showed that the influence of the self-tapping screws was significant as it helped in avoiding the occurrence of wood splitting or row shear out, and thus resulted in increased time to failure of the connections in standard fire condition.

Keywords: Fire resistance; wood-steel-wood connection; fire protection; concealed timber connection; self-tapping screws.

1 INTRODUCTION

Wood is one of the long-established materials used in constructions for thousands of years, ever since the existence of mankind. The usage of wood has significantly increased over the last few decades owing to its sustainability, renewability and availability of innovative, high quality engineered products such as glued-laminated timber (glulam). Timber construction can be categorized as either heavy timber or light wood frame. Heavy timber members are known to have a good passive fire resistance when exposed to fire directly due to their large size resulting in a relatively lower average charring rate over fire duration (the rate of advance of char into the wood) as compared to members used in light frame construction that can be burn out in a few minutes [3]. The charred layer formed on the exposed surface insulates the core wood underneath from exposure to fire and impedes oxygen penetration as well as heat propagation.

Fire occurrence in buildings is unpredictable and its effects on structural elements can be very destructive, especially in timber structures. Under fire exposure, timber connections are often the weakest component of any timber structure.

¹ MSc Candidate, Carleton University, Dept. of Civil and Environmental Engineering, Ottawa, Canada.
e-mail: oluwamuyiwa.okunroumu@carleton.ca

² Associate Professor, Lakehead University, Dept. of Civil Engineering, Ontario, Canada.
e-mail: sam.salem@lakeheadu.ca,

³ Professor, Carleton University, Dept. of Civil and Environmental Engineering, Ottawa, Canada.
e-mail: george.hadjisophocleous@carleton.ca

The most common types of connections used in mass timber construction are: exposed (steel-wood-steel); seated; and concealed connections (wood-steel-wood). The concealed connections are preferably used owing to their ease of assembling in multi-storey buildings and their aesthetic appearance. Nevertheless, the strength and fire resistance of those concealed connections are significantly impaired due to the reduction in the cross-section of the member due to existence of notches and slotted cuts needed to accommodate the steel connecting components. Furthermore, the presence of metal fasteners along with the middle steel connecting plate transmitting heat to the core of the wood increases the charring rate and thus, decreases the fire resistance of such connections [4]. As a result, concealed connections perform less favourably under fire exposure than exposed or seated connections [5].

One of the significant technical challenges faced in timber construction is the analysis and safe design of timber connections in fire due to the many parameters involved, such as the different thermo-physical and thermo-mechanical properties of the materials (steel and wood), variety of wood species, applied load ratios and fire protections, the geometry of the connection, fastener types and their layout [6]. Thus, the behaviour of a timber connection subjected to fire is complex and not easily predictable. To fully understand and assess the fire performance of such connections, more research needs to be conducted.

In recent years, reasonable number of experimental and numerical studies have been conducted to investigate the fire performance of timber connections [7–18]. Peng et al. [19] published research work on the fire resistance of bolted wood-steel-wood (WSW) and steel-wood-steel (SWS) connections, all subjected to direct tension. In that study, 22 specimens comprising of 16 wood-steel-wood and 6 steel-wood-steel connections were exposed to elevated temperatures that followed the CAN/ULC-S101 standard time-temperature curve [2]. The test assemblies were subjected to a monotonic tensile load parallel to wood grain. Factors that affect fire performance of connections, such as wood thickness, fastener diameter, number of fasteners, end distance, load ratio and fire protection were all examined. The result shows that a single layer of 15.9 mm Type X gypsum board increased the fire resistance by about 30 minutes, while as a double layer of 12.7 mm plywood improved the fire resistance by only 15 minutes. The fire resistance of both WSW and SWS connections were less than 51 and 25 minutes, respectively. It was also reported that the average charring rates for WSW connections were found to be approximately 0.78 mm/min and 0.71 mm/min for the two cross-sections used, i.e., 2@80 x 190 mm and 130 x 190 mm. In addition, it was found that decreasing the applied load ratio increased the fire resistance of the connections in particular those of thicker wood members. However, it was found that the difference in the fire resistance of the specimens with bolts of 12.7 mm diameter is almost negligible compared to that of specimens with bolts of 19.1 mm diameter (about 1-3 minutes time difference). Overall, the governing failure mode of the specimens was mostly bolt hole elongation followed by splitting of the wood members [19].

Owusu et al. [20] investigated the performance of unprotected and fully protected concealed glulam beam end connections exposed to elevated temperatures of standard fire. In that study, four large-scale tests were conducted on 1600 mm long glulam black spruce-pine grade 24f-EX beam with cross-sectional dimensions of 184 x 362 mm at both ambient and elevated temperatures. The first stage of that study involved experimental testing of two specimens at ambient temperature to investigate the failure modes, failure load and the maximum moment-resisting capacity of the beam end connections. While the second stage involved testing two specimens identical to those tested at ambient temperature but subjected to elevated temperatures of CAN/ULC-S101 standard fire [2] to determine the average charring rate, failure modes and time to failure. The two test assemblies exposed to standard fire were also subjected to constant load equal to 100% of the ultimate design load capacity of the weakest connection throughout the fire tests. The steel connecting components, i.e., steel bolt head and nut and steel plate, in one of the two specimens tested in fire were protected with same-species wood plugs and strips. Tests results revealed that the two predominant failure modes of concealed (wood-steel-wood) bolted connections at both ambient and elevated temperatures are perpendicular-to-grain tensile splitting and row shear (both identified as brittle failures). These failure modes play a major role in reducing the moment-resisting capacity that can be attained in concealed (wood-steel-wood) bolted connections. At ambient temperature, the unprotected connection configuration tested in that study exerted a maximum moment of approximately 7% more than that of similar but protected configuration. While at elevated temperatures, the time to failure of the fire

protected connection configuration was 23 minutes more than that of similar but unprotected configuration. It was also observed that splitting of wood occurred along the glue-line plane aligned with the top row of bolts in the glulam beam section, and thus this further shortened the time to failure of the unprotected connection configuration [20].

To strengthen timber connections against brittle failure modes, a few studies [21–25] were conducted experimentally by employing various forms of reinforcements at ambient temperature. A study conducted at ambient temperature by Zhang et al. [26] showed that self-tapping screws can be used to enhance the bending strength, control crack propagation and significantly prevent splitting failure in dowel-type moment-resisting connections. In another study [27], experimental tests were conducted at ambient temperature to evaluate the performance of moment-resisting bolted timber connections with self-tapping wood screws acting as perpendicular-to-grain reinforcement. In that study, it was observed that employing self-tapping screws as reinforcements greatly increased the ductility and overall performance of the connections. However, at elevated temperatures, Palma et al. [28] reported that self-tapping screws used as perpendicular-to-grain reinforcement in connections can significantly increase the charring rate of the wood if prematurely exposed to fire as a result of being too long and hence, reduces the fire resistance of the connections. In contrast, another study conducted recently by Petrycki and Salem [29] on the fire performance of concealed wood-steel-wood bolted connections with and without perpendicular-to-wood grain reinforcements revealed that employing self-tapping screws as perpendicular-to-grain reinforcement considerably increased the time-to-failure of the connections [29]. Therefore, further studies need to be conducted on the influence of self-tapping screws on the fire performance of timber connections as very limited data are available and virtually none exists on fully-protected concealed connections reinforced with self-tapping screws.

In the study presented in this paper, only two full-size fire tests that are part of a larger experimental campaign are included to investigate the influence of self-tapping screws on the structural performance of fully protected concealed glulam beam end connections subjected to standard fire.

2 EXPERIMENTAL PROGRAM

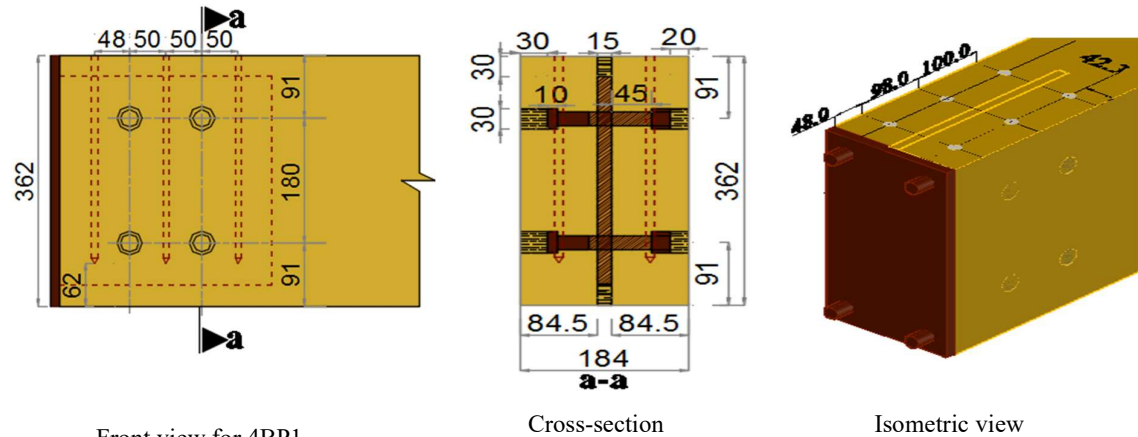
2.1 Materials

The glulam beam sections used in this study were produced from Canadian black spruce-pine (S-P), with a stress grade of 24f-EX. The wood members were conditioned indoor at 20°C and approximately 50% relative humidity (RH). The beam sections experienced minimal shrinkage due to the reduction of moisture content that was recorded at an average value of about 12 %. The steel T-stub connectors were manufactured from a 12.7-mm thick steel plate of grade 300W, and all the fasteners used were made of 19.1-mm diameter A325M high-strength structural steel bolts. The reinforcements used to strengthen the test specimens were self-tapping screws (STS) made of carbon steel and had a yield strength of 1,015 MPa and a shear strength of 641 MPa [30]. The self-tapping screws were fully threaded of 300 mm in length and 8 mm in outer thread diameter.

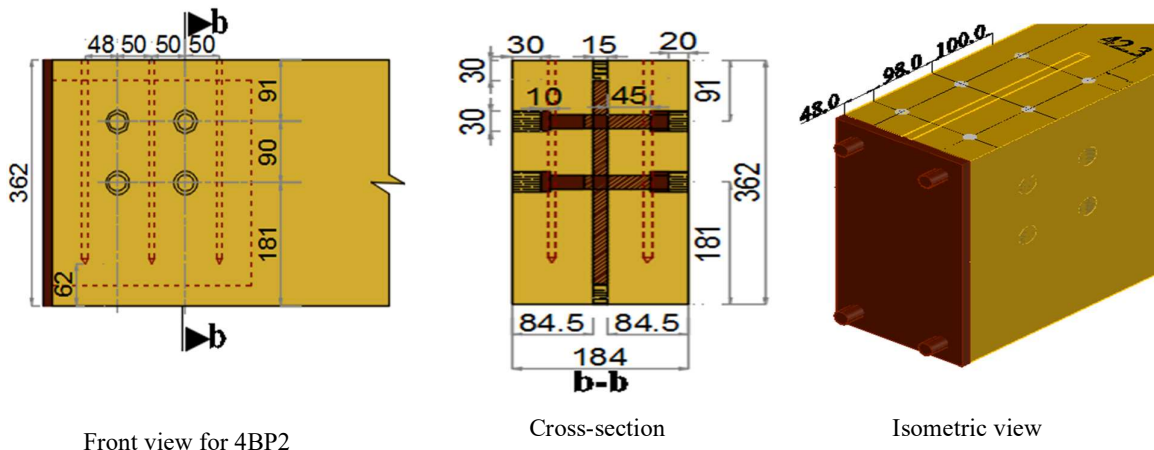
2.2 Test specimens

The glulam beam sections were 1600 mm in length and had a rectangular cross-sectional dimensions of 184 mm x 362 mm. For each test specimen, a T-stub steel connector was used to connect the glulam beam to a supporting steel column. A slotted cut to accommodate the 12.7-mm thick T-stub steel connector was prepared at one end of the beam with approximately 15 mm width to allow for a fabrication tolerance of 1 to 2 mm as required in CAN/CSA O86-14 standard [31], and also to reduce friction in the connection. Circular holes were drilled into the glulam beam face with the use of a 30-mm diameter spade bit to embed the bolt heads and nuts, as well as to accommodate the wood plugs used as fire protection to the heads and nuts of the bolts. The inner 19.1-mm diameter bolt holes were drilled using a 20-mm diameter drill bit to allow for approximately 1 mm fabrication tolerance as specified in CAN/CSA O86-14 design standard [31]. In each connection configuration, the T-stub steel connector was sandwiched between two wood side sections each with thickness of approximately 84.5 mm and fastened together with four steel bolts. The

spacings of the fasteners, i.e., end and edge distances, and row spacings, used in the glulam beam end connections were designed to meet the spacing requirements as per CAN/CSA O86-14 design standard [31]. Thereafter, the glulam beam section was connected to the supporting steel column via the T-stub connector using another four short 19.1-mm diameter structural steel bolts. The heads and nuts of the four steel bolts and the T-stub connector in each test specimen were fire protected using glued-in wood plugs and strips made of the same wood material as that of the glulam beam. Figures 1a and 1b show the geometrical configurations of the tested concealed glulam connections with two different bolt patterns, P1 and P2, respectively, along with the cross-section of each connection configuration showing the installed STS as reinforcements.



(a) Four-bolt pattern P1 (4BP1) and connection cross-section



(b) Four-bolt pattern P2 (4BP2) and connection cross-section

Figure 1. The two-glulam beam end connection configurations with cross-sections showing STS (all dimensions in mm)

The two rows of bolts in the connection configuration with the first bolt pattern (P1) were symmetrically positioned near the top and bottom sides of the beam cross-section. While in the connection configuration with the second bolt pattern (P2), the bottom row shifted upward to the mid-height of the beam section to further contribute to the moment-resisting capacity of the connection. The dimensions of the steel T-stub connectors used with the two connection configurations are depicted in Figure 2.

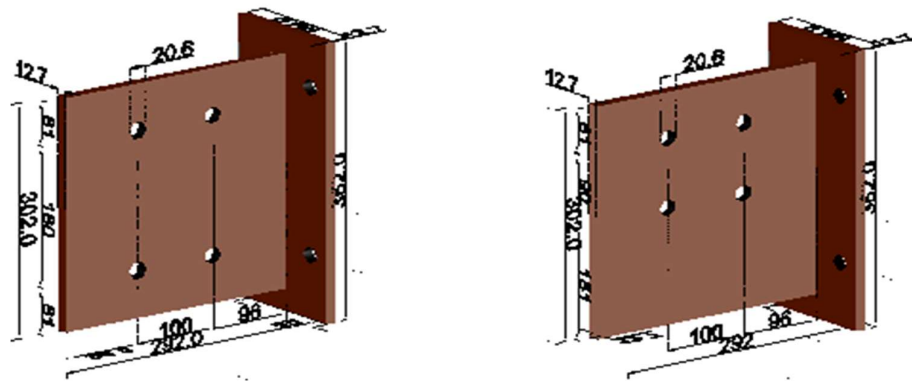
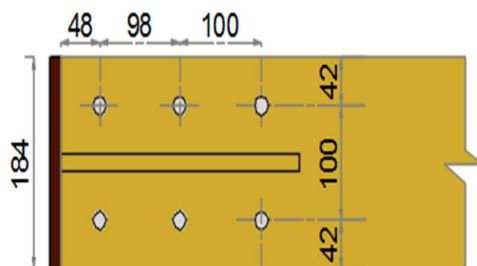
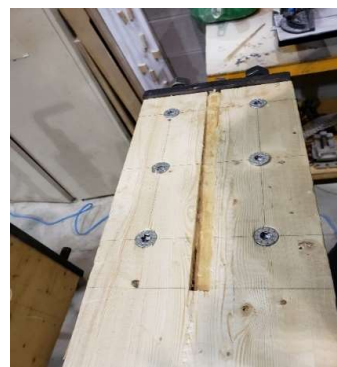


Figure 2. Dimensions of the steel T-Stub connectors with two different bolt patterns: Bolt pattern P1 (left); and bolt pattern P2 (right).

Before each connection was assembled for testing, fully threaded self-tapping screws were installed perpendicular-to-wood grain and parallel to the embedded steel plate through most of the full depth of the beam section to strengthen the connection and prevent splitting failure. During the installation of the fully threaded long self-tapping screws, it is a common practice to pre-drill small pilot holes for the self-tapping screws to avoid either splitting in the wood section or damage of the screw which could be caused due to large friction forces that might be generated while driving in the screws. The pilot holes were pre-drilled with the aid of a 3-mm diameter drill bit to about 280 mm depth into the beam to aid the precision of the screw positioning and also minimize the development of friction forces. Six reinforcing screws were installed from the top to near the bottom of each beam section near its end where the connection is located. Screws were concealed at the centre of the wood side sections and arranged in two rows, each of three screws, on each side of the embedded steel plate. In the beam longitudinal direction, one pair of screws was centred between the beam end and the first column of bolts; the second pair of screws was centred between the first and second column of bolts; and the last pair was placed at a distance of 50 mm beyond the second column of bolts into the beam length. As previously discussed, Palma et al. [28] found that significant increase of the charring rate in the wood connections can be attributed to the use of reinforcing screws that run almost the full depth of the wood beam (with only 30 mm wood cover from the bottom side of the beam). Therefore, the screws used in this study for the two connection configurations were 300 mm in length to allow for slightly more than 60 mm wood cover from the bottom of the beam. The screw characteristics and strength parameters can be found in CCMC [30]. The self-tapping screws layout as installed within the connection area for the connection configuration with the first pattern of bolts (P1) is shown in Figure 3.



(a) Plan view of the STS layout



(b) Self-tapping screws layout

Figure 3. Self-tapping screws layout for the connection with the first bolt pattern (P1) installed from the top side of the beam.

2.3 Instrumentation

Temperatures were measured within the connection area from both front and back faces of the beam. These thermal measurements were taken by twelve (12) metal-shielded Type K thermocouples (TC) that were placed at different locations and depths inside the glulam beam. Thermocouples were inserted into 1-mm diameter pre-drilled holes at depths of 20 mm, 30 mm, 40 mm, 60 mm, and 85.7 mm from the fire exposed surface. Eight (8) thermocouples were placed at the front face of the beam and four thermocouples from the back face of the beam, as shown in Figure 4. The location of, and the depth at which each thermocouple was inserted inside the wood section are also shown in Figure 4. At the beam front face, two thermocouples (TC1 and TC8) were installed to measure the temperatures of the bolt heads under 30-mm thick wood plugs, while another two thermocouples (TC2 and TC6) were installed at 85.7 mm depth to measure the temperature of the steel plate. At the beam back face, thermocouples (TC11 and TC12) measured the temperatures of the bolt nuts under 20-mm thick wood plugs. Thermocouples (TC4 and TC5) were used to measure the temperatures at 60 mm depth inside the beam section; thermocouples (TC3 and TC7) were installed at 40 mm depth; and thermocouples (TC9 and TC10) were installed at only 20 mm depth to measure the internal temperatures of wood so that the calculations for the actual charring rates can be executed. Figures 4a and 4b illustrate the thermocouples layout for both the front and back faces of the beam, respectively. Table 1 shows a summary of the test matrix details.

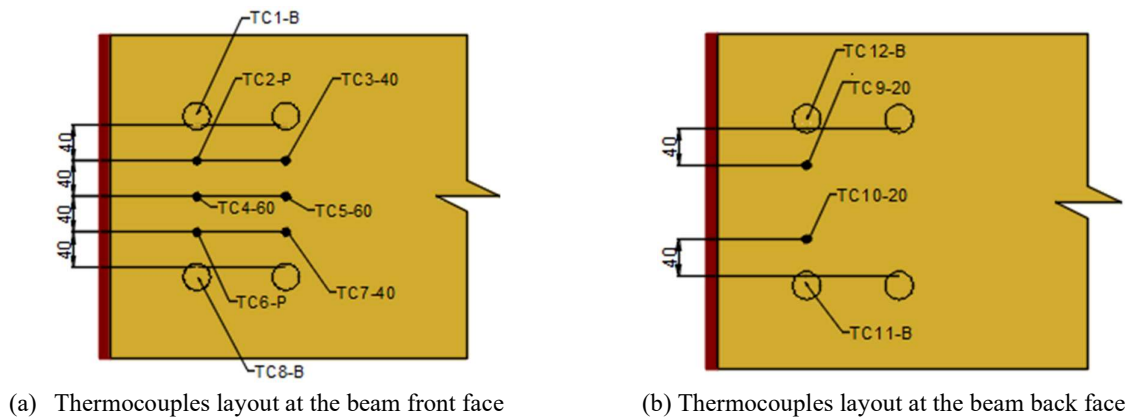


Figure 4. Thermocouples layout for the connection configuration with the first bolt pattern (P1).

Table 1. Test matrix details

Connection ID	Bolt pattern	Load ratio (%)	Number of bolts	Number of self-tapping screws	Beam unloaded depth below the bottom row of bolts (mm)
4BP1LR100	P1	100	4	6	91
4BP2LR100	P2	100	4	6	181

Notes: 4B for four bolts; P1 and P2 for the first and second patterns of bolts, respectively; LR100 for 100% load ratio.

2.4 Test Setup and Procedure

The fire tests were conducted in a large-size horizontal natural gas-fuelled furnace located at Lakehead University's Fire Testing and Research Laboratory (LUFTRL), Thunder Bay, Ontario, Canada. Two high capacity burners are installed in opposite corners of the furnace to allow uniform circulation of the hot gases throughout the furnace volume. Gas input into the furnace is regulated via automatic gas actuator that is controlled by computer system and logic circuits that are built in an advanced control panel connected to the furnace. Through the touch screen Human-Machine Interface (HMI) that is integrated in the furnace control panel, the CAN/ULC-S101 [2] standard time-temperature curve was programmed and precisely followed (with $\pm 2\%$ deviation from the standard time-temperature curve). In order to apply the transverse load at the free end of the cantilevered glulam beam, a hydraulic cylinder mounted above the furnace to a

strong steel loading frame was utilized. A distance of 1400 mm was measured between where the transverse load was applied on the beam and the beam end attached to the supporting column.

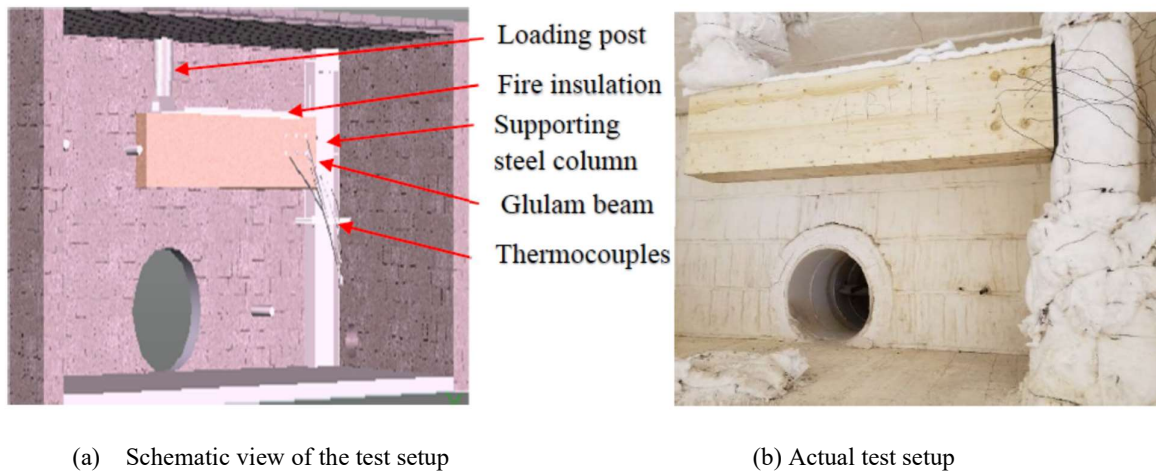


Figure 5. Test setup of the specimen with the connection of the first pattern of bolts (P1) installed inside the furnace.

Each specimen was gradually pre-loaded in four increments each of 25% to allow for stabilization of deflection after each load increment. The fire tests were conducted in accordance with CAN/ULC-S101 fire endurance testing standard [2]. This standard prescribes the procedure for loading the specimen before as well as during the test as well as the failure criteria. The test commenced 30 minutes after the full load was applied as per standard. During the test, the load level applied on the specimen was measured and maintained constant with the aid of a load cell and a hydraulic cylinder connected to a manually-controlled hydraulic pump. A linear variable differential transducer (LVDT) installed outside the furnace was used to continuously measure the beam vertical displacement throughout the tests. The measured vertical deflections of the beam were then used to calculate the connection rotations with respect to time.

In both fire tests, the specimen was exposed to elevated temperatures that followed the CAN/ULC-S101 standard time-temperature curve [2] on all sides except the top one simulating the existence of a slab on top of the beam. The top side of the beam, the loading post and the supporting steel column were all fire protected using a 1.0-inch thick ceramic-fibre blanket. The two test assemblies with different bolt patterns were loaded to 100% of the ultimate design load capacity of the weakest connection configuration. The failure criterion for the connection was assumed to occur when the vertical deflection of the beam corresponds with a rotational limit of the magnitude of 0.1 radians. However, both fire tests continued beyond this point until the test assembly could not sustain the applied load and a significant drop in the load was measured by the installed load cell with no recovery was observed. Thereafter, the test was terminated and the cooling phase of the furnace commenced. The time to failure and the thermal measurements of each test specimen were recorded and in a subsequent phase the recorded temperatures were used to calculate the average charring rate of the wood at the connection location.

3 TEST RESULTS AND DISCUSSION

The experimental results presented in this paper describe the effects of the bolt patterns and self-tapping screws utilization on the time to failure, failure mode, and rotations of the two glulam beam end concealed connections with their metal components fire protected using same-species wood plugs and strips.

3.1 Charring rate and char depth

The charring rates for the two specimens were calculated from equation (1) using the thermal measurements recorded from the thermocouples during the fire tests. The char front for the specimens was set at 300°C isotherm, which implies that the charring rates for the connections were calculated from the times at which

the temperatures of the four thermocouples (TC3, TC7, TC9 and TC10) at different locations reached 300°C. The charring rates were calculated by dividing the depth of the char layer, which is essentially the depth at which each thermocouple was installed, by the time to reach 300°C. This was the only method that could be used to estimate the charring rate since the beam sections were burnt out completely during the cooling phase of the furnace.

$$C = \beta t \quad (1)$$

Where C is the depth of char front (mm)
 β is the rate of charring (mm/min)
 t is the time difference for thermocouples at depths 20 and 40 mm to reach 300°C (min).

The times to reach 300°C at the two fixed depths, i.e., 20 and 40 mm, from the fire exposed surface of the beam section were analysed to calculate the charring rates for the connections and the values are summarized in Table 2. At the termination of both tests, it was found that the protection of the metal components of the connection played very significant role as it delayed the heat to penetrate to the wood core and thus resulted in less charring rate. However, the wood around the bolts showed more charring due to more heat transferred through the bolts, which led to the elongation of the bolt holes that was observed by the end of the fire test through the furnace observation port.

Table 2. Charring rates estimated for the two connections tested in fire

Connection ID	0 – 20 mm		20 – 40 mm		0 – 40 mm	
	TC10	TC9	TC10 & TC3	TC9 & TC7	TC3	TC7
4BPILR100	-	1.58	-	0.87	1.12	0.85
Average	1.58		0.87		0.99	
4BP2LR100	1.21	1.32	0.80	0.72	0.97	0.93
Average	1.27		0.76		0.95	

Notes: 4B for four bolts; P1 and P2 for the first and second patterns of bolts, respectively; LR100 for 100% load ratio.

3.2 Time to failure and failure mode

The main results of the fire tests are summarized in Table 3. Based on the obtained results, the time to failure of both connections exceeded 50 minutes which is higher than the minimum fire resistance rating specified as 45 minutes in the current National Building code of Canada (NBCC) [32] for combustible construction. From Table 3, it was observed that the time to failure of the connection with the second bolt pattern (P2) was recorded as 57 minutes which is 5 minutes (about 10.0%) greater than that of the connection with the first bolt pattern (P1). Therefore, there is a considerable effect of the bolt pattern on the time to failure of the connections. Furthermore, the self-tapping screws were very effective in increasing the time to failure of the connections when compared to the results for same connections, but unreinforced that were obtained by Owusu [33]. Owusu et al. [1, 20] reported shorter time to failure of same connections but without the use of self-tapping screws as reinforcement mainly due to earlier wood splitting and row shear out failures encountered during their fire tests. It was also found that the time to failure for the connections depends considerably on the actual charring rate of the wood in the location of the connection where the metal connecting components exist. Also, the connections were assumed to fail in deflection when the deflection of the beam corresponds with a rotational limit of the magnitude of 0.1 radians. This occurred mainly as a result of the excessive wood charring surrounding the bolts, which caused elongation in the bolt holes that further contributed to the increase of the rotation values of the connection as the beam exhibited considerable losses in its cross-sectional dimensions through charring.

Table 3. Summary of fire tests results.

Connection Configuration ID	Load ratio (%)	Applied Moment (kN.m)	Time to failure (min)	Failure Mode
4BP1	100	14.8	52	Deflection
4BP2	100	14.8	57	Deflection

3.3 Effect of bolt pattern on the connection rotations

The vertical displacements of the beam measured throughout the duration of the two fire tests were used to calculate the rotations of the connections. Figure 6 shows the connection rotations versus time for the two fire tests. The figure shows that both connections experienced similar trends of increased rotation values with time. At the early stage of the fire tests (about 7 minutes), the time-rotation curves for both connections exhibited a slight linear increase until about 30 minutes into fire tests, and thereafter experienced a relatively linear increase but at higher rates until about 40 and 50 minutes into fire tests for the connections with the first and second bolt patterns (P1 and P2), respectively. Afterwards, the time-rotation curves took exponential increase trend in both fire tests until the connection deemed to reach the set failure criterion. Figure 6 illustrates the effects of bolt pattern on the rotations of the connections subjected to the same load ratio, i.e., 100%. As shown in the figure, it was found that the bolt pattern has a considerable effect on the rotational capacity of the connections, as the rotational capacity of the connection with the second bolt pattern (P2) was noticeably greater than that of the connection with the first bolt pattern (P1) by approximately 10%. This higher stiffness of the connection resulted in an increase of 5 minutes in the time to failure for the connection with the second bolt pattern (P2).

Overall, the rotational capacity of the connection is regarded as a measure of the ductility of the connection and hence, the degree of ductility of the connections presented in this study was considerably higher when compared to that of identical connections, but unreinforced tested by Owusu et al. [20]

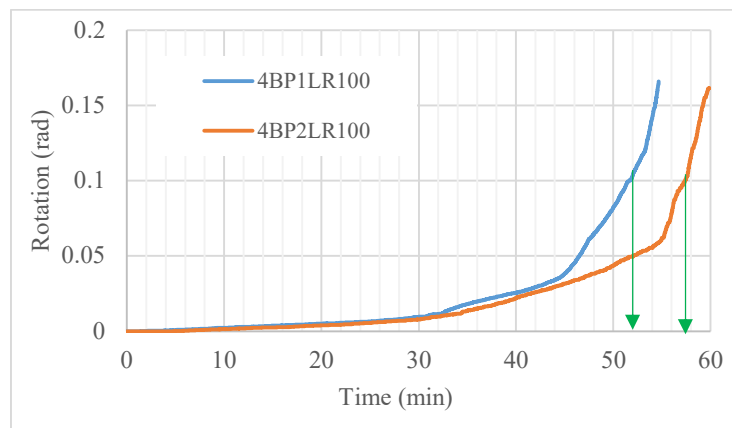


Figure 6. Time-rotation relationships developed to illustrate the effect of bolt patterns

Figures 7a and 7b show a slight increase in the rotation of the connections with the first and second bolt patterns (P1 and P2), respectively, at about 30 minutes into standard fire exposure.



(a) Connection with the first bolt pattern (P1)

(b) Connection with the second bolt pattern (P2)

Figure 7. Connections with the two different bolt patterns underwent slight rotations at 30 minutes into standard fire exposure.

3.4 Time-temperature curves

Thermal measurements recorded with the use of the twelve (12) metal-shielded Type K thermocouples installed at different locations within the beam end connection were used to plot the time-temperature curves as illustrated in Figure 8. At the early stage of the fire test of the connection with four-bolt pattern (P1), thermocouples (TC9 and TC10) inserted at 20 mm depth from the fire exposed face of the beam recorded a temperature of 100°C after about 4 minutes into standard fire exposure. As the temperature continues to increase above 100°C, the moisture in the wood begins to evaporate from the surface and as a result, between 180°C and 200°C the wood starts to decompose and subsequently char when wood temperature reached 300°C at approximately 13 minutes from the start of the fire test. In both fire tests, it was observed that the temperature of the steel plate as well as that of thermocouples (TC4 and TC5) installed at a depth of 60 mm into the beam section were considerably below the 300°C. This indicates that the char layer depth of the beam section did not reach the 60 mm depth from the fire exposed surface and that the steel plate embedded at the centre of the beam cross-section and fire protected with the glued-in wood strips did not contribute to the charring of the wood section. However, at about 30 minutes it was found that the temperatures of the steel bolts had risen above 300°C, which caused noticeable charring around the bolt holes. This led to the elongation of the bolt holes, that further increased the connection rotation values. At about 40 minutes, thermocouples (TC3 and TC7) installed at a depth of 40 mm from the beam face measured temperatures that correspond with the wood charring temperature, i.e., 300°C, and a few minutes after, the char layer progressed to the location of the STS. At the failure time of the connection it was found that thermocouples (TC9 and TC10) installed at a depth of 20 mm had measured a temperature of approximately 940 °C which is close to the furnace temperature, while thermocouples (TC2 and TC6) installed deep in the wood section at the face of the embedded steel plate measured a temperature of approximately 200°C.

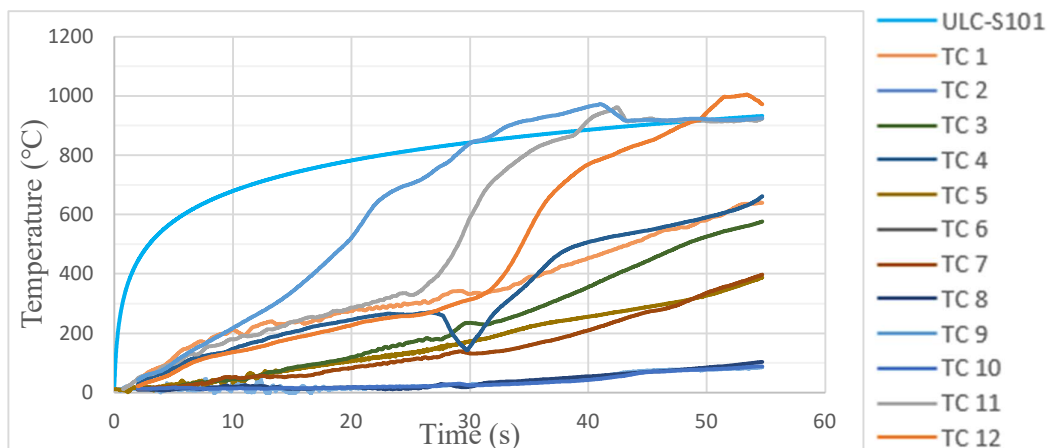


Figure 8. Time-temperature curves developed from the thermal measurements recorded during the fire test of the connection with the four-bolt pattern (P1).

4 CONCLUSIONS

In this paper, the fire test results for two full-size glulam beam end concealed connections that were fully protected and reinforced with self-tapping screws are analysed and presented. The main objective of the conducted two fire tests was to investigate the effect of bolt pattern and self-tapping screws utilization on the rotation, charring rate, time to failure and failure modes of this type of concealed (wood-steel-wood) connection. Based on the unique experimental results obtained in this study, the following conclusions can be drawn.

- The time to failure of both connections tested in this study exceeded the minimum fire-resistance rating specified in the NBCC [32] as 45 minutes for combustible construction.
- It was found that the behaviour of the connections in fire significantly depends on the actual charring rates exhibited by the wood surrounding the metal connecting components of the connection. Hence, there is a noticeable reduction in the time to failure of the connections as the actual charring rate within the connection locations is more than the nominal wood charring rate.
- Based on the experimental observations, the tendency of brittle failure modes, i.e., wood splitting and row shear out, usually encountered in concealed (wood-steel-wood) connections were sufficiently prevented in the connections tested in this study due to the utilization of the self-tapping screws as internal reinforcement for the connections, which in turn significantly increased the time to failure of the two connection configurations tested under standard fire exposure in this study.
- Also, it was observed that the STS reinforcement enhanced the ductility of the tested connections and consequently, improved the rotational behaviour of the connections.

REFERENCES

1. Owusu, A., Salem, O., Hadjisophocleous, G., Fire performance of concealed timber connections with varying bolt patterns, in: *Proceedings of the 6th International Conference on Applications of Structural Fire Engineering*, Singapore 2019.
2. CAN/ULC-S101-14, Standard methods of fire endurance tests of building construction and materials, Fifth edition, Canada, 2014.
3. Buchanan, A.H., Abu, A.K., Structural Design for Fire Safety, 2nd ed., John Wiley & Sons, Ltd, Chichester, UK 2017.
4. Peng, L., Hadjisophocleous, G., Mehaffey, J., Mohammad, M., Fire resistance performance of unprotected wood-wood-wood and wood-steel-wood connections: A literature review and new data correlations. *Fire Safety Journal* 2010, 45, 392–399.
5. Akotuah, A.O., Ali, S.G., Erochko, J., Zhang, X., et al., Study of the fire performance of hybrid steel-timber connections with full-scale tests and finite element modelling. *Applications of Structural Fire Engineering* 2016.
6. Buchanan, A.H., Fire performance of timber construction. *Progress in Structural Engineering and Materials* 2000, 2, 278–289.
7. Erchinger, C., Frangi, A., Fontana, M., Fire design of steel-to-timber dowelled connections. *Engineering Structures* 2010, 32, 580–589.
8. Palma, P., Frangi, A., Hugi, E., Cachim, P., et al., Fire resistance tests on timber beam-to-column shear connections. *Fire Engineering* 2016, 7, 41–57.
9. Maraveas, C., Miamis, K., Matthaiou, Ch.E., Performance of Timber Connections Exposed to Fire: A Review. *Fire Technology* 2015, 51, 1401–1432.
10. Audebert, M., Dhima, D., Taazount, M., Bouchaïr, A., Behavior of dowelled and bolted steel-to-timber connections exposed to fire. *Engineering Structures* 2012, 39, 116–125.
11. Barber, D., Determination of fire resistance ratings for glulam connectors within US high rise timber buildings. *Fire Safety Journal* 2017, 91, 579–585.
12. Audebert, M., Dhima, D., Taazount, M., Bouchaïr, A., Experimental and numerical analysis of timber connections in tension perpendicular to grain in fire. *Fire Safety Journal* 2014, 63, 125–137.
13. Akotuah Ohene, A., Modelling the Fire Performance of Hybrid Steel-Timber Connections, Master of Applied Science, Carleton University, 2014.

14. Moss, P., Buchanan, A., Fragiaco, M., Austruy, C., Experimental Testing and Analytical Prediction of the Behaviour of Timber Bolted Connections Subjected to Fire. *Fire Technology* 2010, 46, 129–148.
15. Fragiaco, M., Menis, A., Moss, P.J., Clemente, I., et al., Predicting the fire resistance of timber members loaded in tension. *Fire and Materials* 2013, 37, 114–129.
16. Palma, P., Frangi, A., Modelling the fire resistance of steel-to-timber dowelled connections loaded perpendicularly to the grain. *Fire Safety Journal* 2017, 107, 54–74.
17. Petrycki, A.R., Salem, O. (Sam), Experimental fire testing of concealed steel-glulam timber semi-rigid bolted connections, in: Proceeding of the 6th International Conference on Engineering Mechanics and Materials, Vancouver, Canada 2017, pp. EMM546-1–10.
18. Peng, L., Hadjisophocleus, G., Mehaffey, J., Mohammad, M., Predicting the Fire Resistance of Wood–Steel–Wood Timber Connections. *Fire Technology* 2009, 47, 1101–1119.
19. Peng, L., Hadjisophocleus, G., Mehaffey, J., Mohammad, M., Fire Performance of Timber Connections, Part 1: Fire Resistance Tests on Bolted Wood-Steel-Wood and Steel-Wood-Steel Connections. *Journal of Structural Fire Engineering* 2012, 3, 107–132.
20. Owusu, A., Salem, O., Hadjisophocleus, G., Fire performance of protected and unprotected concealed timber connections, in: Proceedings of the 3rd International Fire Safety Symposium (IFireSS), Ottawa, Ontario, Canada, 2019, pp. 370–378.
21. Lam, F., Schulte-Wrede, M., Yao, C.C., Moment resistance of bolted timber connections with perpendicular to grain reinforcements. 2008, 8.
22. Awaludin, A., Sasaki, Y., Oikawa, A., Hirai, T., et al., Moment resisting timber joints with high- strength steel dowels: natural fiber reinforcements, in: *World Conference of Timber Engineering*, 2010, pp. 1–6.
23. Yeh, M.-C., Lin, Y.-L., Huang, G.-P., Investigation of the structural performance of glulam beam connections using self-tapping screws. *Journal of Wood Science* 2014, 60, 39–48.
24. Lathuillière, D., Bléron, L., Descamps, T., Bocquet, J.-F., Reinforcement of dowel type connections. *Construction and Building Materials* 2015, 97, 48–54.
25. Gehloff, M., Cloßen, M., Lam, F., Reduced edge distances in bolted timber moment connections with perpendicular to grain reinforcements. *World Conference on Timber Engineering* 2010, 1–8.
26. Zhang, C., Guo, H., Jung, K., Harris, R., et al., Screw reinforcement on dowel-type moment-resisting connections with cracks. *Construction and Building Materials* 2019, 215, 59–72.
27. Lam, F., Gehloff, M., Cloßen, M., Moment-resisting bolted timber connections. Proceedings of the Institution of Civil Engineers - Structures and Buildings 2010, 163, 267–274.
28. Palma, P., Fire resistance tests on steel-to-timber dowelled connections reinforced with self drilling screws, in: 2nd CILASCI-Ibero-Latin-American Congress in Fire Safety Engineering, ETH Library, Coimbra, Portugal 2013, p. 12.
29. Petrycki, A.R., Salem, O. (Sam), Structural fire performance of wood-steel-wood bolted connections with and without perpendicular-to-wood grain reinforcement. *Journal of Structural Fire Engineering* 2019, ahead-of-print.
30. CCMC, Evaluation Report: SWG ASSY VG Plus and SWG ASSY 3.0 Self-Tapping Wood Screws, Canadian Construction Materials Centre Report No. CCMC 13677-R. <http://www.swg-produktion.de/fileadmin/Zulassungen/13677eCCMCEvaluationReportASSY30ASSYplusVG.pdf>, 2014.
31. CAN/CSA-O86-14, Engineering design in wood, Canadian Standards Association, Rexdale, ON, Canada 2014.
32. NBCC, The National Building Code of Canada. Commission on Building and Fire Codes, National Research Council of Canada, Ottawa, Canada, 2015.
33. Owusu, A., Structural Performance of Hybrid Timber Connections with Varying Bolt Patterns at Ambient and Elevated Temperatures, Master of Applied Science Thesis, Carleton University, 2019.

DEFORMATION BEHAVIOUR AND FAILURE TIME OF GLUED LAMINATED TIMBER COLUMNS IN FIRE

Takeo Hirashima¹, Heisuke Yamashita², Shungo Ishi³, Tatsuki Igarashi⁴, Shigeaki Baba⁵,
Tomoyuki Someya⁶

ABSTRACT

This paper reports on results of load-bearing fire tests of large cross-section structural glued laminated timber columns made of Japanese larch and cedar. The purpose of the tests was to investigate the properties of charring, the temperature distribution in the cross-section, the deformation behaviour and the failure time of the glulam columns exposed to standard fire heating not only during the heating phase but also during the cooling decay phase. Furthermore, numerical analyses of the tests were carried out, and the results of both were compared. The analysis results using the thermal and high temperature mechanical properties model of soften wood in accordance with Eurocode5 approximately agreed with the tests result of the temperature, the deformation behaviour and the failure time.

Keywords: Glulam timber; column; deformation behaviour; load-bearing fire test; numerical analysis

1 INTRODUCTION

In recent years, request of the use of timber structures for large and multi-story buildings has increased. Timber elements, unlike other structural elements, have a characteristic problem in that the load-bearing capacity decreases due to self-burning in the case of a fire, and self-combustion may continue even after all other fuel in the room has been consumed. Timber columns may fail with global buckling because the cross-sectional secondary moment decrease considerably in fire. The failure of columns may induce collapse of the building and may occur not during the heating phase but during the cooling decay phase. Some previous researches with load bearing fire test of timber columns were carried out in order to investigate the fire resistance during the heating phase [1, 2]. However, there is few research focused on the behaviours during the cooling decay phase after fire heating stop [3]. Therefore, load-bearing fire tests of unprotected glued laminated timber columns with large cross-section made of Japanese larch and cedar were carried out in order to investigate the properties of charring, the temperature distribution in the cross-section, the deformation behaviour and the failure time of the glulam columns exposed to standard fire heating not only the during heating phase but also during the cooling decay phase. Furthermore, numerical analyses of the test were carried out, and the results of both were compared. This paper reports on results of the tests and its numerical analysis.

¹ Professor, Chiba University

e-mail: hirashima@faculty.chiba-u.jp, ORCID: <https://researchmap.jp/read0071161?lang=en>

² Researcher, Japan Testing Center For Construction Materials

e-mail: yheisuke@jtccm.or.jp

³ Structural Engineer, Kozo Keikaku Engineering Inc. (Former Graduate Student, Chiba University)

e-mail: shungo-ishii@kke.co.jp

⁴ Researcher, Fujita Corporation (Former Graduate Student, Chiba University)

e-mail: tatsuki.igarashi@fujita.co.jp

⁵ Senior Research Engineer, Taisei Corporation

e-mail: shigeaki.baba@sakura.taisei.co.jp

⁶ Engineering Director, Nikken Sekkei

e-mail: someya@nikken.jp

2 TEST SETUP

2.1 Test parameters and specimens

The test parameters of the load-bearing fire tests for glulam columns were tree species (Japanese larch and cedar), cross-sectional dimension (300 x 300 and 450 x 450 mm), Heating duration for standard time/temperature fire curve (30, 60 and 90 min) and constant axial load ratio on the basis of the design allowable stress for the permanent action (1, 2/3, 1/3) as shown in Table 1. Number of column specimens was twenty. Length of the all specimens was 3,300 mm. Thermocouples were installed in the cross section at the mid-span of some specimens as shown in Figures 3 (a) and (b) in order to obtain the cross-section temperatures. Table 2 shows the specifications of the specimen. These tree species and strength grade are widely used for timber buildings in Japan.

2.2 Loading, heating and measurements

The load-bearing fire tests were carried out with the furnace for columns in Japan Testing Center for Construction Materials as shown in Figure 1 (a). The length of heating was 3,000 mm. Both ends of the columns were pins, and the load was applied from the column base side as shown in Figure 1 (b). Axial displacement and rotational angle at the column base, cross-section temperatures (mainly non-charring area) and residual cross-sections after the test were measured.

Table 1. Test parameters

Heating time (ISO 834-1)	Ratio of load to long-term allowable load	Tree species, cross-sectional dimension and specimen name			
		Japanese Larch (<i>Larix leptolepis</i>)		Japanese Cedar (<i>Cryptomeria japonica</i>)	
		300 x 300 mm	450 x 450 mm	300 x 300 mm	450 x 450 mm
30 min	1	L300-30-1	(none)	C300-30-1	(none)
	2/3	L300-30-2/3		C300-30-2/3	
60 min	1	L300-60-1	L450-60-1	C300-60-1	C450-60-1
	2/3	L300-60-2/3	(none)	C300-60-2/3	(none)
	1/3	L300-60-1/3	L450-60-1/3	C300-60-1/3	C450-60-1/3
90 min	1	(none)	L450-90-1	(none)	C450-90-1
	2/3		L450-90-2/3		C450-90-2/3
	1/3		L450-90-1/3		C450-90-1/3

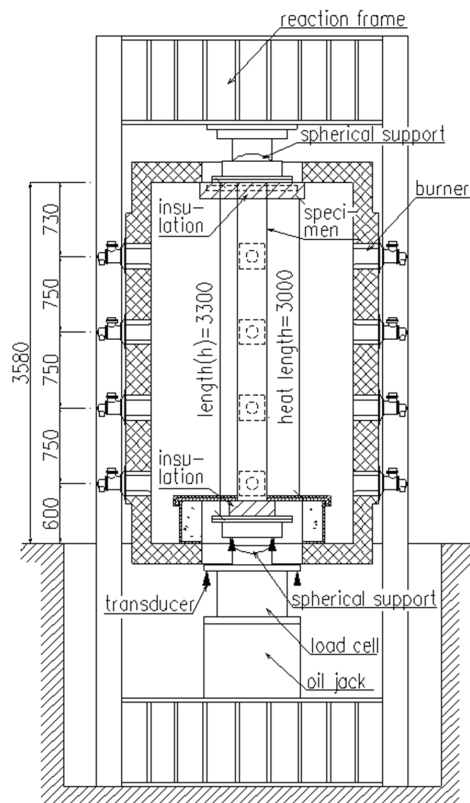
Table 2. Specifications of specimens

Tree species	Japanese Larch	Japanese Cedar
Strength grade	E95-F315	E65-F255
Length	3,300 mm	
Lamination	Thickness 30 mm	
Lamination grade	L100	L70
Adhesive	Resorcinol phenol resin	
Compressive strength from the material tests [N/mm ²]	48.5	34.0
Oven-dry density [g/cm ³]	300 x 300: 0.520, 0.505 - 0.539	300 x 300: 0.371, 0.330 - 0.400
Cross-section: Average value, Min. - Max.	450 x 450: 0.534, 0.513 - 0.563	450 x 450: 0.347, 0.331 - 0.370
Moisture content [%]	300 x 300: 11.6, 10.5 - 12.2	300 x 300: 11.3, 11.1 - 11.7
Cross-section: Average value, Min. -Max.	450 x 450: 10.4 , 9.9 - 11.0	450 x 450: 11.5, 11.3 - 11.9

Figure 2 shows the results of average gas temperature in the furnace. The test specimens were heated based on the standard time/temperature curve in accordance with ISO 834-1. During the post-heat cooling decay phase, the furnace cover was left in place and air was supplied to facilitate smoke extraction. As shown in Figure 2, the furnace temperature during the decay phase tended to be higher for the cedar than for the larch. In addition, from the results of 60 minutes heating test, at the column width of 450 mm, the furnace temperature during the decay phase tended to be slightly higher than that of the column width of 300 mm. In the heat transfer analysis on the cross-section temperature of the columns, the furnace temperatures during the decay phase were given based on these experimental results.



(a) Furnace and specimen



(b) Loading frame and specimen

Figure 1. Test setup

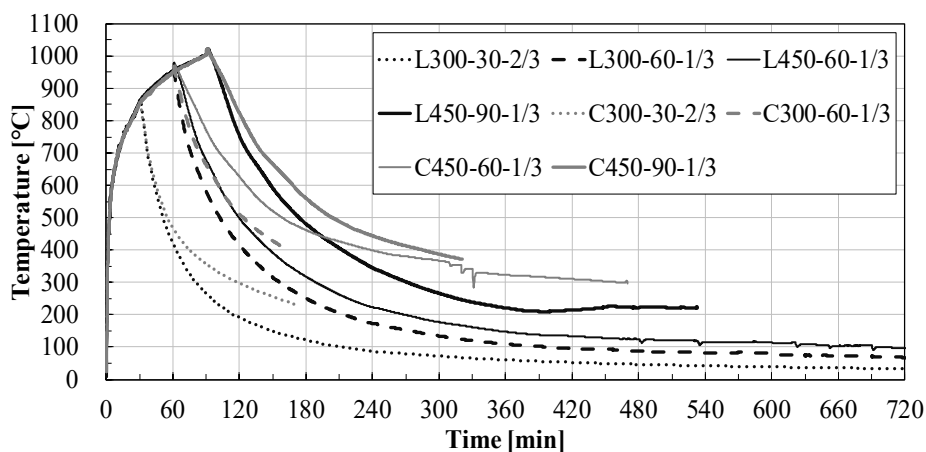


Figure 2. Average gas temperatures in the furnace

3 NUMERICAL ANALYSIS

3.1 Heat transfer analysis

Heat transfer analysis using finite element method was carried out in order to obtain the temperature distribution in the cross section of the columns for input data of the structural analysis of the load-bearing fire tests. The heat transfer analysis program was developed in the Fire Safety Engineering Laboratory at Chiba University. The thermal properties (thermal conductivity, specific heat and density) of the timber specimens were given as values of softwood in accordance with Eurocode5 [4]. However, only the thermal conductivity of Japanese larch was 1.4 times the Eurocode5 value in order to match the analysis results and the test results. The convective heat transfer coefficient was $23 \text{ W/m}^2 \text{ K}$ and the total emissivity was 0.9. In this analysis, the heat due to the heat release of the wood itself was considered because the self-combustion of the timber columns continued for a while even after the heating. The increment of the heat due to the self-combustion of the wood was given by Equation (1).

$$\Delta Q_{SI} = -eS \Delta \rho H_W B_{SI} \quad (1)$$

Where ΔQ_{SI} is the increment of heat to the node due to the self-combustion of the wood [J],

eS is the area covered by the node multiply unit thickness [m^3],

$\Delta \rho$ is the change in density due to the temperature rise (negative value) [kg/m^3],

H_W is the heat release per unit weight of the wood ($18.3 \times 10^6 \text{ J/kg}$),

B_{SI} is the efficiency of heat due to the self-combustion: larch (4.0×10^{-6}), cedar (6.0×10^{-6}).

The heat increment due to the self-combustion was assumed to be generated when the temperature of wood was 400°C or higher during only cooling decay phase. The self-combustion efficiencies depended on the tree species and were determined to be agreed with the test results of the cross-section temperatures. Figures 3 (a) and (b) show the mesh model of the column cross section. The minimum width of the mesh was 7.5 mm. The temperatures around the columns during the cooling decay phase were given based on the test results of the furnace temperature shown in Fig. 2. In order to confirm the validity of the structural analysis model, it is necessary to give the temperature distribution to be input to the structural analysis data as accurately as possible. Therefore, in the heat transfer analysis, the heat model was set so as to match the cross-section temperatures of the test results.

3.2 Structural analysis

Structural analysis was carried out in order to predict the deformation behaviour and failure time of the columns exposed to standard fire heating. The structural analysis program used originates in a report by Becker and Bresler at the University of California, Berkeley [5], and had been amended at Chiba University. This is a finite element analysis (FEA) using Bernoulli-Euler beam elements, which is capable of modelling the deflection behaviour of steel and concrete frames subjected to fire, and includes geometrical non-linearity and material non-linearity. In this study, the mechanical models for the timber elements at elevated temperatures was incorporated in this FEA program. Figures 3 (c) shows the divided model of the beam element. In this study, the analysis considering eccentricity was also carried out separately. However, in the analysis of these tests with large-section column specimens, the deformation behaviour could be sufficiently traced by the analysis without considering the eccentricity. Therefore, this report introduces the analysis results which did not consider the eccentricity of loading.

The properties of the timber were given on the basis of reduction factor for strength and modulus of elasticity of softwood in accordance with EN 1995-1-2:2004 Annex B [4]. The compressive strength of the larch and cedar was determined from the material test results at ambient temperature. Its strength was 1.6 to 1.9 times the compressive strength for the structural design. Stress-strain relationships for use in calculation were represented by Equations (2) and (3) [6].

$$\sigma = \frac{\{E(T) - E_t(T)\} \times \varepsilon}{\left\{1.0 + \left|\frac{\varepsilon}{\varepsilon_1(T)}\right|^n\right\}^{\frac{1}{n}}} \quad (2)$$

$$\varepsilon_1(T) = \frac{F(T) - 0.01E_t(T)}{E(T) - E_t(T)} \quad (3)$$

Where σ is the stress [N/mm²],

$E(T)$ is the Modulus of elasticity at elevated temperature T °C [N/mm²],

$E_t(T)$ is the strain hardening coefficient at elevated temperature ($=E(T)/1000$) [N/mm²],

ε is the strain,

$\varepsilon_1(T)$ is the strain at the intersection of two asymptotes or the yield strain,

n is the shape factor of the stress-strain curve (20°C: 4.0, 60°C: 3.0, 100°C or more: 2.0),

$F(T)$ is the compressive strength at elevated temperature T °C [N/mm²].

Figures 4 (a) and (b) show the Stress-strain curves of the larch and the cedar for compression at elevated temperatures. The shape factor n was determined by the load-displacement relationships based on the compression tests.

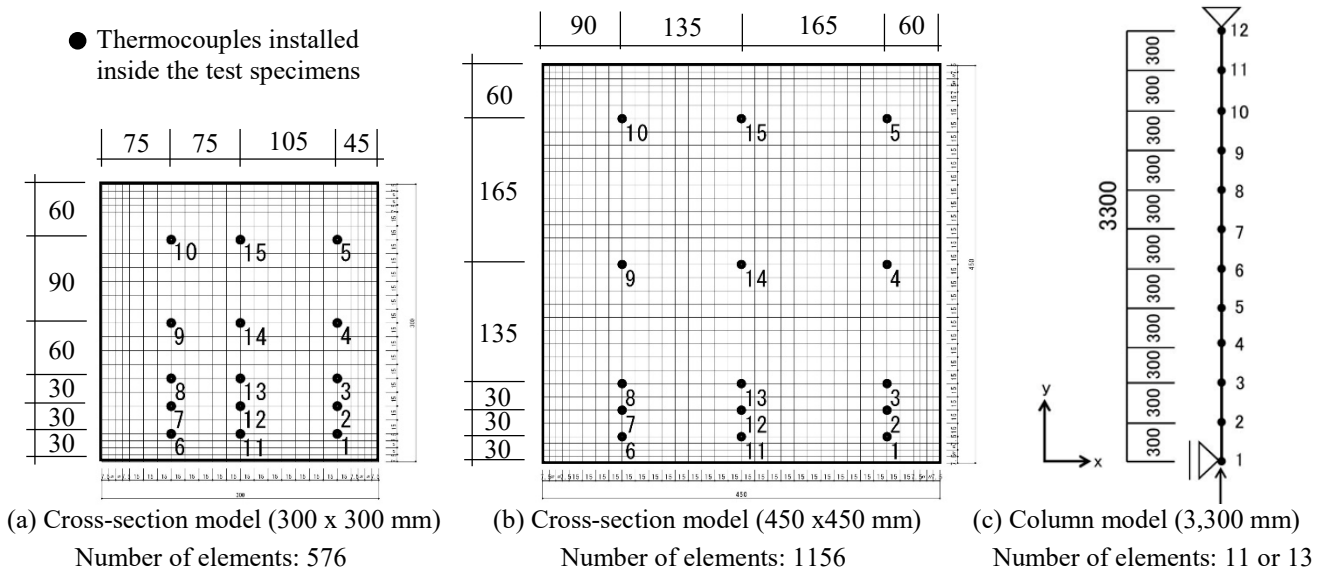


Figure 3. Finite element model of thermal and structural analysis

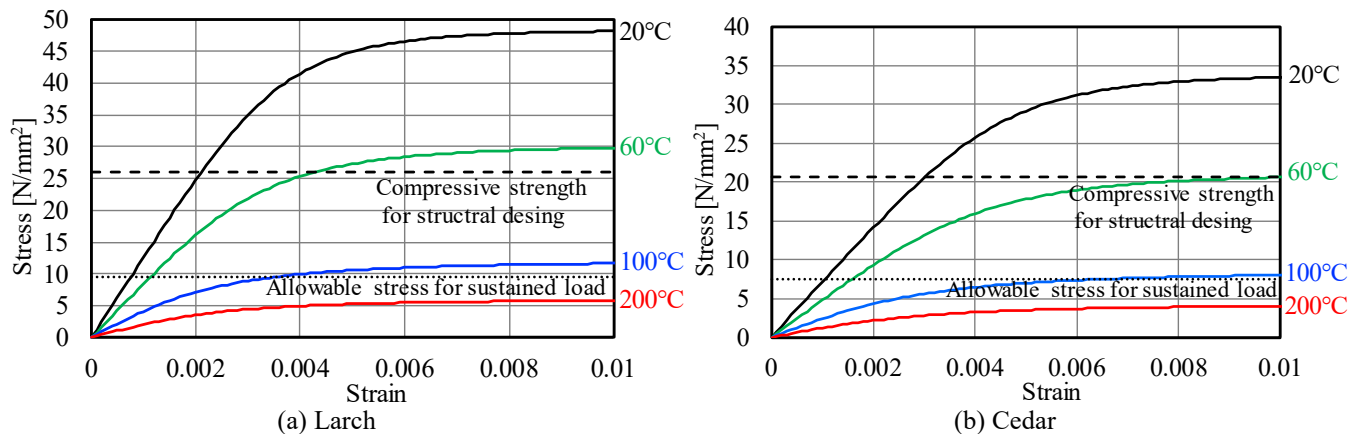


Figure 4. Stress-strain curves for compression at elevated temperatures

4 RESULTS AND DISCUSSIONS

4.1 Outlines of the test results

Table 3 shows outlines of the test results. All the specimens loaded with the load corresponding to allowable stress for sustained load did not fail during the heating phase. The failure time was longer when the load ratio was smaller and when the cross-sectional dimension was larger. The three larch specimens continued to support the load for up to 720 minutes. Their load bearing capacities (or compressive resistances) were obtained by increasing the applied loading after 720 minutes. The failure time of the cedar column was shorter than that of larch column under the same condition. The failure mode of buckling or crushing was determined based on the observation of the specimen after the test and the amount of rotation of the column ends. Many specimens with a column width of 300 mm observed failure due to buckling. All specimens which exceeded a slenderness ratio at the time of failure by 51 resulted in buckling failure. Since the cross sections of these specimens were large, the slenderness ratios at the time of failure were relatively small. Therefore, the influence of eccentric buckling may be not considerable. When the load ratio was less and the failure time was longer even though the heating duration was the same, the residual cross-sectional area of the column after the test was smaller.

Figures 5 (a) to (c) show examples of the global aspect of the specimen immediately after opening the door of the furnace. In case of the cedar, self-combustion continued for a long time even during the cooling decay phase. In addition, in the specimen that failed due to buckling, it can be confirmed that it is slightly bent as show in Figures 5 (b) and (c). Figures 5 (d) to (g) show examples of the cross section of the specimen cut after the test. Even if the heating duration was the same, 90 minutes, the charring area was larger, and the charring of the corners was particularly remarkable in the specimen with the less load ratio because it took a long time from the end of heating. In the case of C450-90-1/3, the cross-sectional secondary moment after the test was less than 1/10 of that before the test. The reason was that the charring area expanded due to the self-combustion of the wood during the cooling decay phase.

4.2 Cross-section temperatures

Figures 6 (a) to (h) show the temperatures on the centroid axis of the cross-section of the columns exposed to the standard fire heating. For discussing the failure time of columns in case of a fire, it is necessary to grasp the temperature distribution of the non-charring area more accurately. Therefore, in this report, the temperatures of the non-charring area were focused on. More information about the test results of the temperatures at the measurement position shown in Figures 3 (a) and (b) was shown in the previous report [7].

Focusing on the temperatures in the non-charring area, the temperatures does not rise so much during the heating duration. However, as the time passed from the end of the heating, the internal temperatures gradually increased, and finally the temperature at the centroid (point 14) of the cross-section reached nearly 100 °C. This phenomenon was similar to the fire test results of the glulam larch beams [3]. Comparing the results of the larch and the cedar with the same cross section and the same heating duration, the internal temperature of the cedar is higher. The cedar, which had a lower density, was more combustible, so the temperature of the cedar during the cooling decay phase was higher. Meanwhile, in case of the larch, self-combustion decreased as the time passed from the end of heating, and four test specimens (L300-30-2/3, L300-60-1/3 and L450-60-1/3) finally extinguished the fire.

Regarding the cross-section temperatures of the glulam columns, the analysis results and the test results were in good agreement because in the heat transfer analysis, the values of thermal properties were adjusted to agree with the test results. For example, the thermal conductivity of the larch at elevated temperature was 1.4 times the value of Eurocode5. Meanwhile, in the case of the cedar, the internal temperature could be predicted accurately by using the thermal properties of Eurocode5. The cross-section temperatures during the decay phase greatly affects the self-combustion of the wood. In this heat transfer analysis, the effect was taken into consideration by adjusting the value of the efficiency of heat due to the self-combustion in Equation (1). It is the difficult issue in the future work how to determine this value in the case of real fire situation.

Table 3. Outlines of the test results

Specimen Name *1	Failure Time [min]	Failure mode *2	Load bearing capacity [kN]	Residual ratio in cross-sectional area [%]	Residual ratio in cross-sectional secondary moment [%]	Slenderness ratio at failure
L300-30-1	257	C	788.4	61.4	35.1	50.4
L300-30-2/3	(720)	B	(1662.4)	61.7	35.3	50.4
L300-60-1	95	B	788.4	41.8	16.0	61.7
L300-60-2/3	169	B	525.6	41.4	15.4	62.6
L300-60-1/3	(720)	B	(379.5)	33.4	10.6	67.7
L450-60-1	283	C	1929.8	50.0	22.9	37.5
L450-60-1/3	(720)	C	(1014.9)	44.5	18.1	39.8
L450-90-1	185	B	1929.8	40.6	15.4	41.2
L450-90-2/3	281	B	1286.5	33.8	10.4	45.7
L450-90-1/3	532	B	643.3	30.8	8.6	48.1
C300-30-1	120	B	624.6	59.4	33.2	51.0
C300-30-2/3	169	B	416.4	56.8	29.9	52.5
C300-60-1	66	B	624.6	37.7	13.2	64.5
C300-60-2/3	95	B	416.4	36.3	12.0	66.2
C300-60-1/3	158	B	208.2	31.5	9.2	70.6
C450-60-1	164	B	1528.9	47.2	20.9	38.2
C450-60-1/3	465	C	509.6	30.5	8.6	47.7
C450-90-1	125	C	1528.9	36.9	12.9	43.0
C450-90-2/3	166	B	1019.3	28.4	7.5	49.5
C450-90-1/3	320	B	509.6	30.4	8.5	48.2

*1: Width [mm] - Heating duration [min]- Load ratio. *2: B: Buckling, C: Crushing.

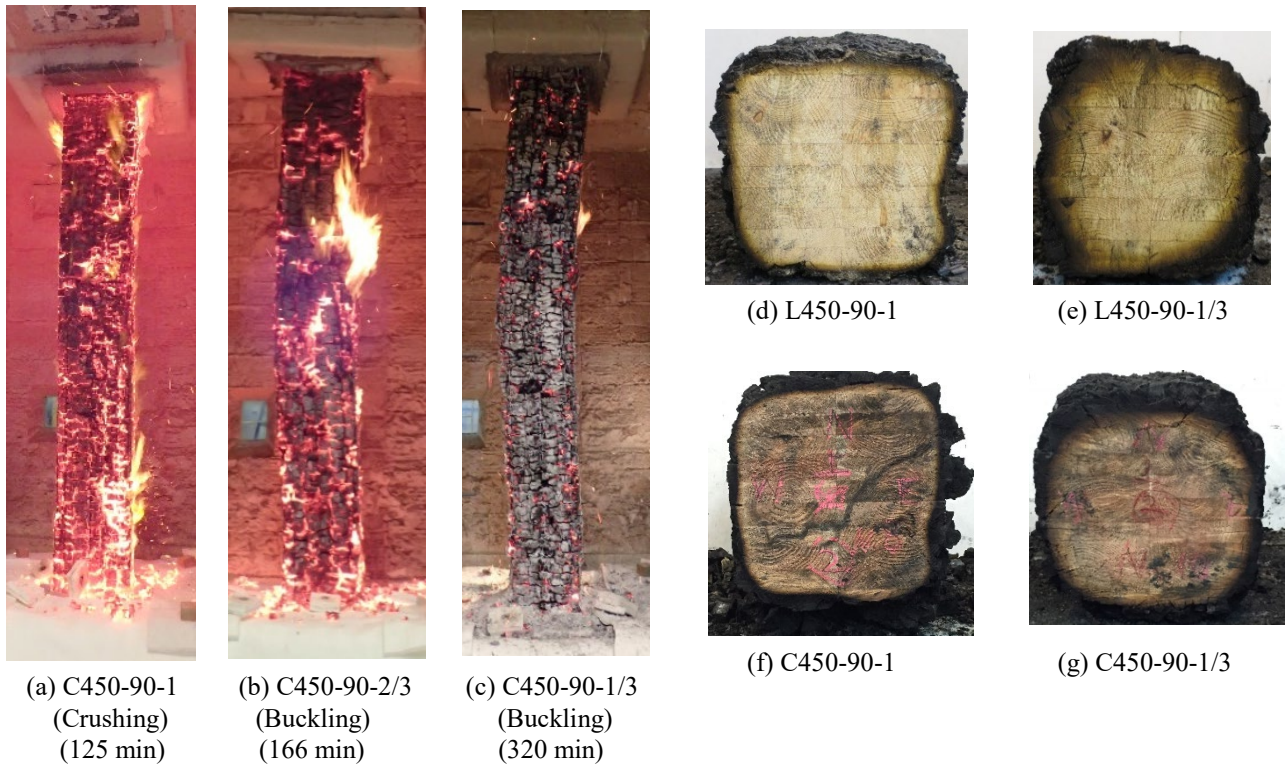
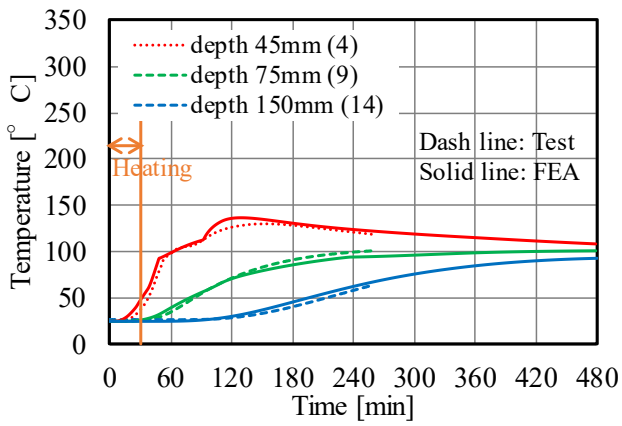
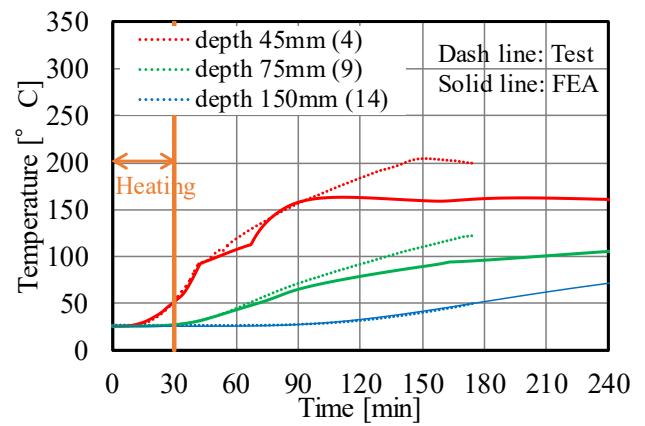


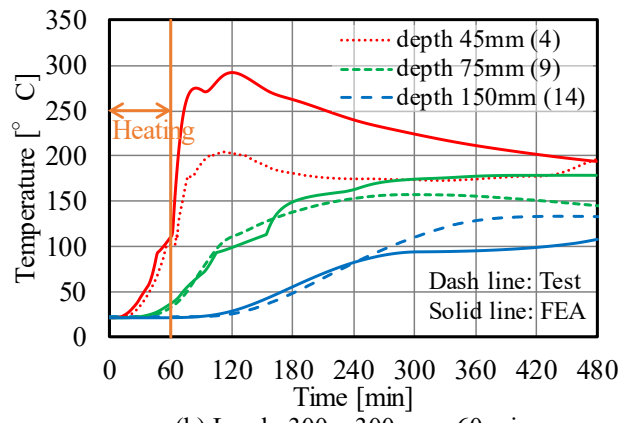
Figure 5. Global aspects of the column specimen and the cross-section after the test (450 x 450 mm, heating time: 90 min)



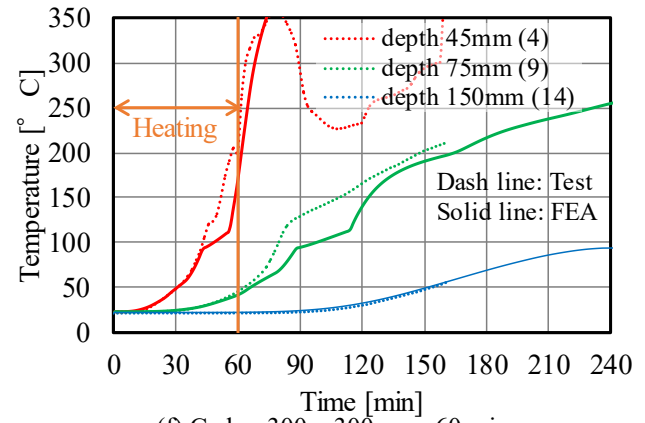
(a) Larch, 300 x 300 mm, 30 min



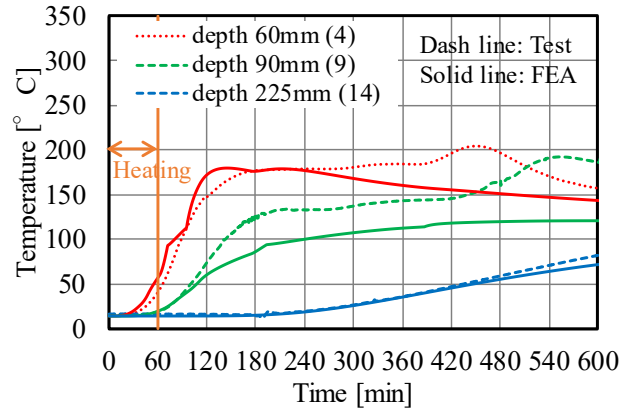
(e) Cedar, 300 x 300 mm, 30 min



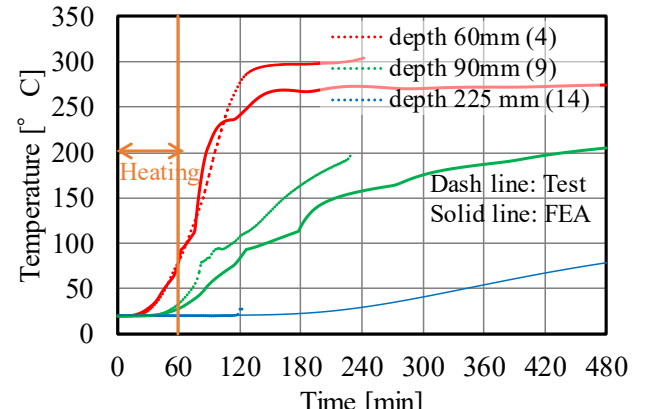
(b) Larch, 300 x 300 mm, 60 min



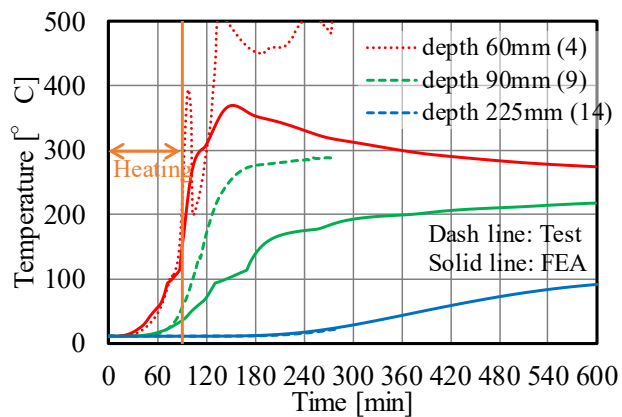
(f) Cedar, 300 x 300 mm, 60 min



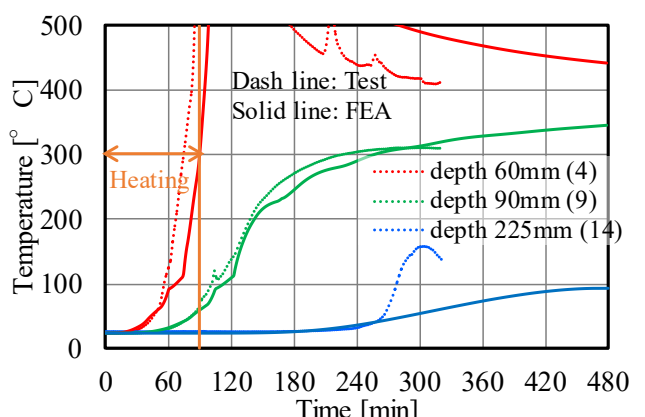
(c) Larch, 450 x 450 mm, 60min



(g) Cedar, 450 x 450 mm, 60 min



(d) Larch, 450 x 450 mm, 90min



(h) Cedar, 450 x 450 mm, 90 min

Figure 6. Temperatures on the centroid axis of the cross section

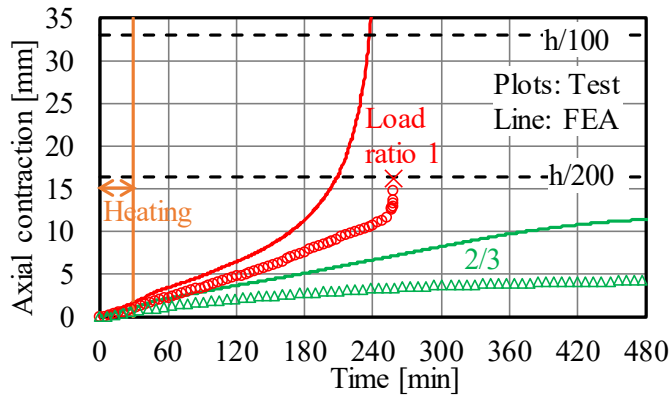
4.3 Deformation behaviour and failure time

Figures 7 (a) to (h) show the compressive deformation behaviour of the columns with large cross-section exposed to the standard fire heating. In case the heating duration was 30 minutes, the columns with width of 300 mm could support the load corresponding to allowable stress for sustained load for 2 hours for cedar and 4 hours or more for larch as shown in Figures 7 (a) and (e). As a matter of course, for the column with width of 300 mm, the failure time was shorter in the case of heating for 60 minutes than in the case of heating for 30 minutes as shown in Figures 7 (a), (b), (e) and (f). From the result of the same heating time of 60 minutes, the amount of axial contraction of the column with width of 300 mm was considerably larger than that of the column with width of 450 mm. In addition, even if the load ratio was the same, the failure time of the both columns with different cross-sectional dimensions was more than doubled as shown in Figures 7 (b), (c), (f) and (g). In case the heating duration was 90 minutes, the columns with width of 450 mm could support the load corresponding to allowable stress for sustained load for 2 hours for cedar and 3 hours for larch as shown in Figures 7 (d) and (h). In the 90 minutes heating test, even in the case of the larch, the combustion of the column in the cooling decay phase did not stop, and the column of the load ratio 1/3 failed after about 9 hours from the ignition. The deformation behaviour and the failure time considerably depended on the axial load ratio. The axial contractions at the failure were between 1/200 of and 1/100 of the column length.

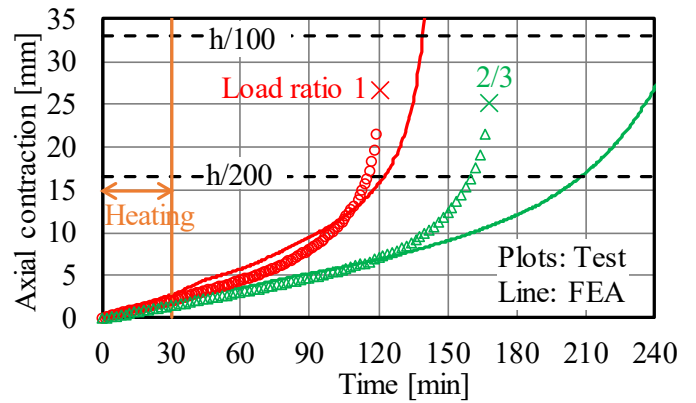
In all the results, the axial contraction during heating phase was relatively small, and the axial contraction increased during the decay phase from the end of the heating. This phenomenon was related to the change in the cross-section temperatures of the non-charring area as shown in Figures 6 (a) to (h). The compressive strength of softwood may decrease considerably while the cross-section temperatures rose to 100 °C, and may be strongly affected by moisture contained in the wood [8]. In consideration of these factors, Eurocode5 reduces the compressive strength of softwood at 100 °C to 1/4 of that at ambient temperature [9]. Figures 7 (a) to (h) indicated that the compressive deformation behaviour of the glulam columns during the post-heating decay phase was also considerably influenced by the decrease in compressive strength and elastic modulus of the wood up to 100 °C. Therefore, information of the reduction factors for strength and elastic modulus at elevated temperature by Eurocode5 would be particularly effective for calculating the deformation behaviour during the cooling decay phase.

The structural FEA results based on the reduction factor of mechanical properties at elevated temperature in accordance with Eurocode5 approximately agreed with the test results on deformation behaviour of the both larch and cedar columns not only during heating phase but also during cooling decay phase. One of the reasons why the analysis results and the experimental results were in good agreement is probably that the variation in the strength of the glulam timber used for this test specimen was relatively small. Meanwhile, in case the load ratio was less and the failure time was longer, it is more difficult to accurately predict the failure time by this analysis. For example, in case of L300-60-1/3, L450-90-1/3 and C300-30-2/3, the difference between the test result and the analysis result increased as the time passed. The axial contractions at the failure were between 1/200 and 1/100 of the column length from the load-bearing fire test results. In case the limit of axial contraction of the column was assumed to be 1/200 of the column length, the failure time by the analysis was close to the failure time from the experimental results. In this analysis, the deformation behaviour could be sufficiently traced by the analysis without considering the eccentricity in case the column had a cross-section with width of 300 mm or more. The failure time by the analysis considering the eccentric load was much shorter than the test result. However, if the column width is smaller or the heating duration is longer, it may be necessary to conduct on the analysis that takes into account the effects of the eccentricity of load.

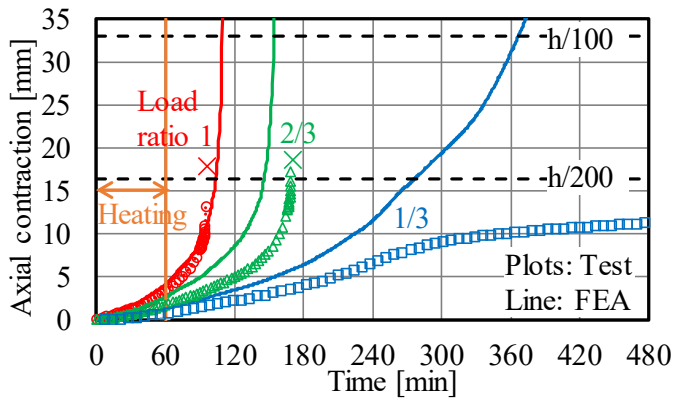
From the above results on deformation behaviour, it was indicated that columns with a large cross section did not fail for a while even if it received standard fire heating for up to about 90 minutes, and that the approximate failure time can be predicted by the analysis using the Eurocode5 model. It is a future work to investigate whether the behaviours of timber elements exposed to actual fire heating of large scale fire tests can be predicted by this analysis.



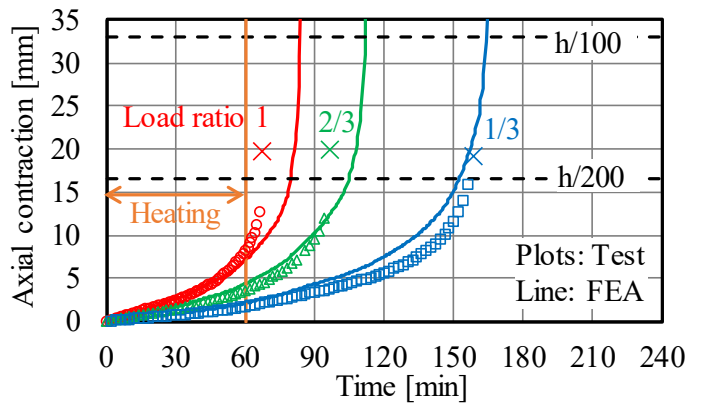
(a) Larch, 300 x 300 mm, 30 min



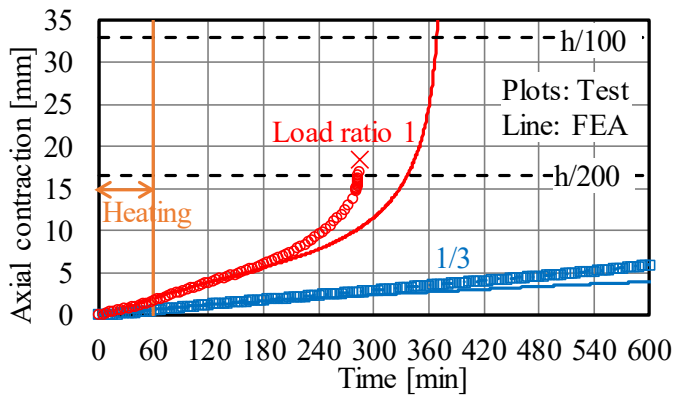
(e) Cedar, 300 x 300 mm, 30 min



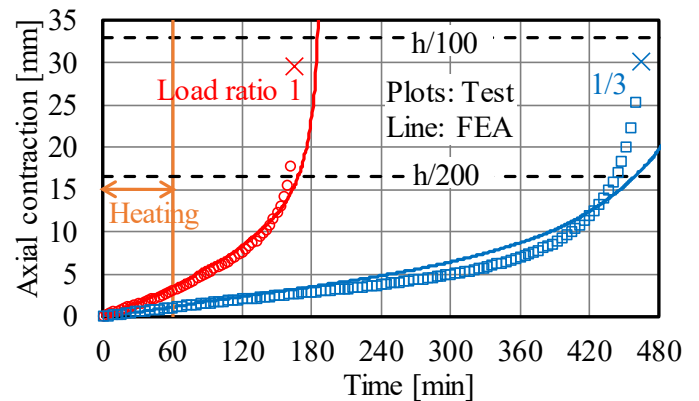
(b) Larch, 300 x 300 mm, 60 min



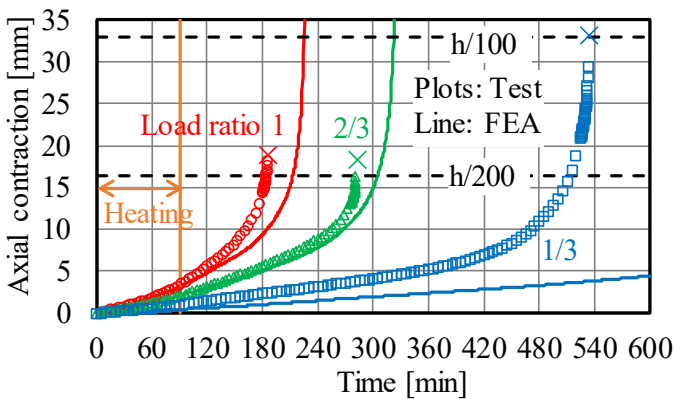
(f) Cedar, 300 x 300 mm, 60 min



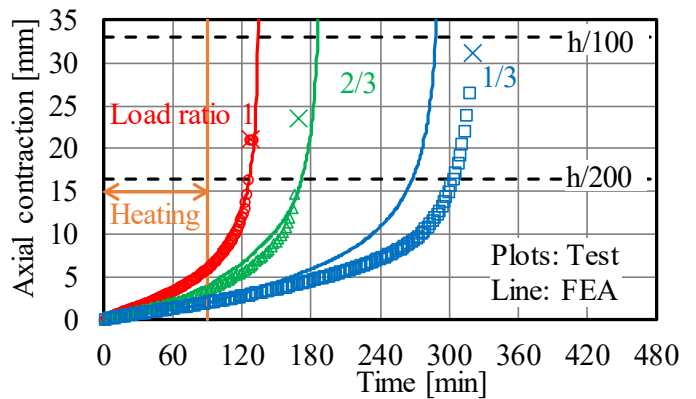
(c) Larch, 450 x 450 mm, 60 min



(g) Cedar, 450 x 450 mm, 60 min



(d) Larch, 450 x 450 mm, 90 min



(h) Cedar, 450 x 450 mm, 90 min

Figure 7. Deformation behaviour of the columns

5 CONCLUSIONS

Load-bearing fire test and its numerical analysis of the glulam column with large cross sections were carried out, and the following results were obtained.

- (1) Focusing on the cross-section temperatures in the non-charring area, the temperatures did not rise so much during the heating duration. Meanwhile, as the time passed from the end of the heating, the cross-section temperatures gradually increased, and finally the temperature at the centroid of the cross-section reached nearly 100 °C.
- (2) The cedar, which had a lower density, was more combustible, so the cross-section temperatures of the cedar during the cooling decay phase was considerably higher than that of the larch.
- (3) Regarding the cross-section temperatures in the non-charring area of the glulam columns, the heat transfer analysis results and the test results were in good agreement not only during heating phase but also during cooling decay phase by considering the effect of heat due to the self-combustion of the wood.
- (4) The compressive deformation behaviour and the failure time of the columns exposed to fire heating considerably depended on the tree species, the cross-sectional dimensions and the load ratio.
- (5) The axial contractions at the failure were between 1/200 of and 1/100 of the column length.
- (6) In all the results, the axial contraction during heating phase was relatively small, and the axial contraction increased during the decay phase because the compressive strength of softwood may decrease considerably while the cross-section temperature rose to 100 °C.
- (7) The structural FEA results based on the reduction factors of mechanical properties at elevated temperature in accordance with Eurocode5 approximately agreed with the test results on deformation behaviour of the glulam columns not only during heating phase but also during cooling decay phase.

It is a future work to investigate whether the behaviours of timber elements exposed to actual fire heating of large scale fire tests can be predicted by this analysis.

ACKNOWLEDGMENT

This research was carried out as a joint research between Chiba University, Taisei Corporation, Japan Laminated Wood Products Association and Nikken Sekkei. This research project was supported by the Ministry of Land, Infrastructure, Transport and Tourism.

REFERENCES

1. Malhotra, H. L. and Rogowski, B. F., Fire resistance of laminated timber columns, Fire Research Note No. 671, 1967.
2. Stanke, J., Klement, E., and Rudolphi, R., Das Brandverhalten von Holzstutzen unter Druckbeanspruchung, BAM- BERICHT Nr. 24, 1973.
3. Kinjo, H., Katakura, Y., Hirashima, T., Yusa, S. and Saito, K., Deflection behaviour and load-bearing period Fire performance of structural glued laminated timber beams in fire including the cooling phase, Journal of Structural Fire Engineering Vol. 9 Issue: 4, 2018, pp .287-299. <https://doi.org/10.1108/JSFE-01-2017-0009>
4. EN 1995-1-2, Eurocode 5: Design of timber structures –Part 1-2: General-Structural fire design, 2004.
5. Becker, J. and Bresler, B., FIRES-RC, A Computer Program for the Fire Response of Structure, Reinforced Concrete Frames, Report No. UCB FRG 74-3, University of California Berkeley, 1974.
6. Richard, R.M and Abbott, B.J., Versatile Elastic-Plastic Stress-Strain Formula, EM4 Technical Note, 1975, pp. 511 - 515.
7. Igarashi, T., Ishii, S., Yamashita, H., Baba, S., Someya, T. and Hirashima, T., Buckling strength and failure time of Japanese cedar and larch glued laminated timber columns exposed to fire, J. Struct. Constr. Eng., AIJ, Vol. 85 No. 770, 639-649, (2020). <http://doi.org/10.3130/aijs.85.639>
8. Gerhards, C. C., Effect of Moisture Content and Temperature of the Mechanical Properties of Wood: An Analysis of Immediate Effects, Wood and Fiber, 14 (1), pp. 4-36, 1982
9. Konig, J., Structural Fire Design According to Eurocode 5 -Design Rules and Their Background, Fire and Materials, 29, pp.147-163 (2005). <https://doi.org/10.1002/fam.873>

COMPARATIVE STUDY ON THE FIRE BEHAVIOUR OF FIRE-RATED GYPSUM PLASTERBOARDS VS. THIN INTUMESCENT COATINGS USED IN MASS TIMBER STRUCTURES

Ambrosine Hartl¹, Qazi Samia Razzaque², Andrea Lucherini³, and Cristian Maluk⁴

ABSTRACT

The experimental study presented herein describes a comparative investigation on the fire performance of fire-rated gypsum plasterboards and thin intumescent coatings used in mass timber structures. Timber samples, (1) unprotected, (2) encapsulated with fire-rated gypsum plasterboard(s), or (3) coated with a thin intumescent coating, were fire tested using the H-TRIS (Heat-Transfer Rate Inducing System) test method. Samples were tested until the heated surface of protected timber had reach a 300°C threshold (or for at least 1 hour of heating) under a constant incident radiant heat flux of 50 or 100 kW/m². As expected, unprotected samples quickly ignited, while samples with plasterboards or thin intumescent coating showed a delay on the onset of timber charring and a reduction of the average charring rate after initiation of charring. The intumescent coating demonstrated a high dependency on the heating conditions. This experimental study offers an interesting comparison between the fire behaviour of timber protected with plasterboard vs. protected with intumescent coating. At the start of the heating exposure, the coating rapidly swelled up to a quasi-steady thickness. The number of plasterboards and Dry Film Thicknesses (DFT) of the intumescent coating was varied for enabling a comparative analysis between the fire behaviour of the two protective methods.

Keywords: Intumescent coatings; timber; charring rate; fire testing; H-TRIS

1 INTRODUCTION AND BACKGROUND

Engineering advances in the space of timber being used for construction of load-bearing assemblies has stimulated the design of timber structures where fire could be a problem [1]. However, demonstrating and ensuring that the timber structure will perform appropriately during (and even after) a fire is a challenge [2]. In the event of a fire, timber ignites and chars, resulting in an exothermic reaction that (1) may provide additional fuel to the fire and (2) result in a reduction of the load-bearing cross-section for structural timber elements. Consequently, timber structures must fulfil fire safety functional requirements to ensure structural integrity and stability during and after a fire [3].

¹ Ms Ambrosine Harl, The University of Queensland, Australia
e-mail: a.hartl@uq.edu.au

² Ms Qazi Samia Razzaque, Remedial Building Services Australia, Australia
e-mail: samia@permax.com.au

³ Dr Andrea Lucherini, The University of Queensland, Australia
e-mail: a.lucherini@uq.edu.au, ORCID: <https://orcid.org/0000-0001-8738-1018>

⁴ Dr Cristian Maluk, The University of Queensland, Australia
e-mail: firstname.lastname@address, ORCID: <https://orcid.org/0000-0002-1662-6943>

The use of encapsulating thermal barriers (e.g. fire-rated boards) is a common solution used for minimizing or even preventing the burning of timber during a fire [4]. Thin intumescent coatings, typically used in the steel industry, are thermally reactive materials that when exposed to heat swell to form a thick porous carbonaceous layer characterized by low density and low thermal conductivity [4]. Usually, thin intumescent are applied to a thickness of only a few millimetres; swelling up to 100 times its original thickness [5]. The potential mainstream use of intumescent coatings for the protection of load-bearing timber is new; the advantages over conventional fire-rated plasterboard systems can be for example: intumescent coatings can be applied onsite or offsite, the application can be compared to the application of a common paint, and can even provide coating formulations which are transparent [6].

Most of the experimental fire studies available in the literature have been performed using a cone calorimeter under heat fluxes included between 35 and 50 kW/m² [6,7]. Particularly, researchers have found that intumescent compositions based on amino-resins can be successfully applied on wooden substrates [6]. However, in the available literature there are limited research studies that have performed detailed characterization and quantification of the overall effectiveness of thin intumescent coatings applied to timber. Since the practitioners charged with the design and construction of fire safe timber structures have reservations and only a few research studies focused on this topic have been published so far, there are several challenges that must be investigated before thin intumescent coatings become a mainstream solution [8]. For instance, the adherence of the coating to the wooden substrate, the potential for delamination of burnt timber lamellas and the influence on time-to-ignition and charring rate are matters of great debate.

The experimental study presented herein describes a comparative investigation on the fire performance of fire-rated gypsum plasterboards and thin intumescent coatings used in mass timber structures. Timber samples, (1) unprotected timber, (2) timber encapsulated with fire-rated gypsum plasterboard(s), or (3) timber coated with a thin intumescent coating, were fire tested using the H-TRIS (Heat-Transfer Rate Inducing System) test method. Samples were tested until the heated surface of protected timber had reach a 300°C threshold (or for at least 1 hour of heating) under a constant incident radiant heat flux of 50 or 100 kW/m².

2 METHODOLOGY, MATERIALS, AND INSTRUMENTATION

2.1 Experimental fire test setup

The fire testing method used in this experimental study is based on a test procedure known as Heat-Transfer Rate Inducing System (H-TRIS) [9]. The method uses high-performance radiant panels and it enables the accurate control of the heating conditions imposed on the test samples with high repeatability and low costs [9]. Using a computer-controlled linear motion system, H-TRIS controls the relative position between the target exposed surface of the test sample and an array of radiant panels. In this way, within the limits of minimum proximity to the exposed surface, test samples can be exposed to any specified time-history of incident radiant heat flux. The test setup used within the scope of this work was assembled by combining four high-performance natural-gas-fired radiant heater mounted on a supporting frame, forming a 300x400 mm² radiant heat source and able to impose incident radiant heat fluxes up to 100 kW/m² (see Figure 1). Moreover, the fire test method enables the visual inspection of the test samples during testing (e.g. for gauging the rate of coating swelling), technically challenging during a conventional standard furnace test. The test setup and experimental procedure is similar to that described by the authors in Lucherini et al. [10].



Figure 1. Photograph of the H-TRIS method experimental test setup and of the three types of test samples during testing: (left) unprotected timber, (centre) timber encapsulated with plasterboard, and (right) timber coated with intumescent coating.

2.2 Test samples and instrumentation

Test samples were made from Cross Laminated Timber (CLT) with a depth of 150 mm and a cross-section of 90 x 90 mm. The wood used in all samples is Austrian radiata pine, consisting of five lamellae of thicknesses 45, 20, 20, 20, 45 mm (see Figure 2). Thermocouple holes were drilled at various depths along the side of the sample, perpendicular to the principal direction of heat penetration during testing. Holes were placed staggered to minimise the impact downstream. The array seen in Figure 2 was used for all control experiments and initial plasterboard experiments.

Samples with intumescent coating were prepared with coating thicknesses of 1, 1.5, or 2mm DFT. The intumescent used was A90H Pro (manufactured by Aithon Ricerche International), a water-based intumescent. The primer used was a two-part water-based zinc phosphate epoxy. Aiming to obtain precise temperature measurements at the interface between timber and coating, two 2 mm grooves were hammered in a triangle shape, meeting at the centre of the sample (Figure 3). The thermocouple wire was wire sit in the grooves and was held in place until application of the primer and intumescent coating.

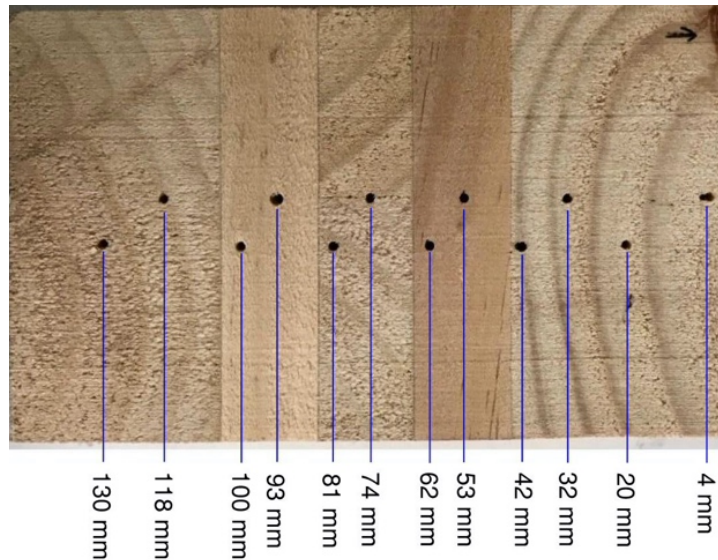


Figure 2. Distribution of thermocouples position at the side of the sample (surface shown at the right is heated surface).

After the surface thermocouple was attached, the perimeter of the sample closest to the exposed surface were covered in masking tape, to prevent any drips from the intumescent application from touching the timber. The surface of the timber was wiped and allowed to dry. The primer and the intumescent coating were applied individually to each of the samples by weighing the mass of the sample during each coating. A thin layer of primer was first applied with minimal pressure using a flat paintbrush. This was allowed to dry for at least 48 hours. When the primer was dried, the samples were weighed again. The intumescent coating was then applied in several layers, using a different paintbrush, and allowed to dry for at least 6 hours between coatings. Figure 3 shows the samples after the primer was applied and after the layers of the intumescent coating were applied. Once the final layer of the intumescent coating had dried, the masking tape was removed.

Plasterboard samples were prepared with one, two, or three layers of 13 mm thick fire-rated gypsum plasterboard. To obtain a temperature measurement at the interface between plasterboards and the interface between plasterboard and timber, grooves were done using a similar procedure to that for timber samples protected with intumescent coatings (but using shielded thermocouples). It was assumed that this would have minimal impact in temperature measurements. The location of the groove in the plasterboard was offset from the groove at the surface of the timber to further minimise the impact of compacting the material on the heat transfer through the sample.

All unprotected and protected samples with plasterboard or intumescent coating were surrounded by a layer of ceramic insulation in order to minimise the heat losses with the surrounding sample holder (see Figure 4). The insulation layer was attached using Aluminium tape, with small holes at the positions where the thermocouple insertion points were (refer to Figure 2).

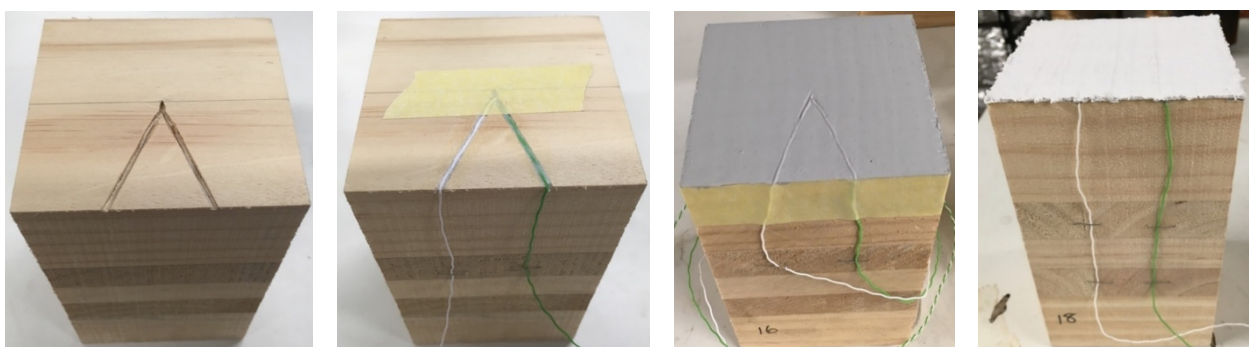


Figure 3. Process by which a thermocouple was placed at the interface between coating and timber: groove was made, the thermocouple was positioned, the primer was applied, and the intumescent coating was applied (left-to-right).

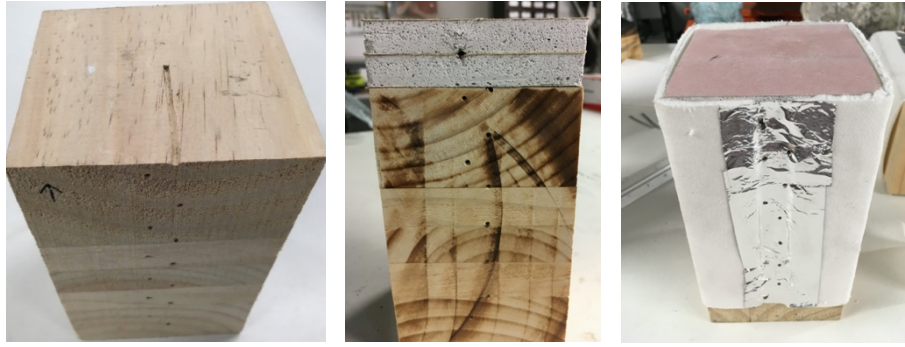


Figure 4. Process by which thermocouple were placed at the interface in-between each plasterboard and between timber and plasterboard, and also photograph of a sample with plasterboard showing side insulation prior to testing.

3 RESULTS AND ANALYSIS

This section shows the results and analysis for all experiments performed within the scope of this work. Figure 7 shows a time-lapse for exemplar experiment for timber samples coated with a DFT of 1 mm and heated at 50 kW/m². Experiments were conducted until a threshold critical temperature of 300°C measured at a depth of 4 mm from the heated surface of timber samples, or for at least one hour from the start of heating. Experiments were conducted at heating conditions of 50 or 100 kW/m².

- **Unprotected timber** – The threshold critical temperature of 300°C measured at a depth of 4 mm from the heated surface of timber was reached in about 4 min and 1 min, for timber tested at 50 or 100 kW/m², respectively (see Figure 5 and 6).
- **Timber protected with plasterboards** – The results shown in Figure 5 shows the temperature at a depth of 4 mm for all timber samples protected with one, two or three 13 mm fire-rated plasterboards.
- **Timber protected intumescent coatings** – The results shown in Figure 6 shows the temperature at a depth of 4 mm for all timber samples protected with a DFT of 1.0, 1.5, or 2.0 mm.

Results from this experimental study may be summarised in the following domains:

- **Influence of number of boards for timber protected with plasterboard(s)** – outcomes demonstrated that the applied number of fire-rated plasterboards has a positive influence in the time-to-reach a critical temperature of 300°C near the heated surface of timber. The time-to-reach a critical temperature of 300°C at 4 mm from the heated surface of timber was about:
 - 25, 60, 100 min for one, two, or three plasterboards, respectively at 50 kW/m².
 - 17, 38, 70 min for one, two, or three plasterboards, respectively at 100 kW/m².
- **Influence of heating conditions for timber protected with plasterboard(s)** – outcomes demonstrated that the heating conditions (50 or 100 kW/m²) has a negative influence in the time-to-reach a critical temperature of 300°C near the heated surface of timber. The time-to-reach a critical temperature of 300°C at 4 mm from the heated surface of timber protected with intumescent was about:
 - 25 and 17 min one plasterboards, at 50 or 100 kW/m², respectively.
 - 60 and 38 min for two plasterboards, at 50 or 100 kW/m², respectively.
 - 100 and 70 min for three plasterboards, at 50 or 100 kW/m², respectively.

- ***Influence of initial DFT for timber protected with intumescent coating*** – outcomes demonstrated that the applied coating thickness (i.e. DFT) has a **positive** influence in the time-to-reach a critical temperature of 300°C near the heated surface of timber. The time-to-reach a critical temperature of 300°C at 4 mm from the heated surface of timber was about:
 - 50 min for a DFT of 1.0 mm and between 100-160 min for DFTs of 1.5 and 2.0 mm (refer to Figure 6) at 50 kW/m².
 - 10, 12, 18 min for a DFT of 1.0, 1.5, and 2.0 mm, respectively at 100 kW/m².
- ***Influence of heating conditions for timber protected with intumescent coating*** – outcomes demonstrated that the heating conditions (50 or 100 kW/m²) has a **negative** influence in the time-to-reach a critical temperature of 300°C near the heated surface of timber. The time-to-reach a critical temperature of 300°C at 4 mm from the heated surface of timber protected with intumescent was about:
 - 50 and 10 min for a DFT of 1.0 mm, at 50 or 100 kW/m², respectively.
 - 100-160 and 12 min for a DFT of 1.5 mm, at 50 or 100 kW/m², respectively.
 - 120-160 and 18 min for a DFT of 1.0 mm, at 50 or 100 kW/m², respectively.

3.1 Comparative analysis between intumescent coating and plasterboard

This section details a comparison between the heating behaviour for timber protected with fire-rated plasterboard against timber protected with intumescent coating. The comparative method uses the time-to-reach a critical temperature of 300°C measured at a depth of 4 mm from the heated surface of timber, shown in Figure 5 and Figure 6. Explicit formulations were derived to correlate DFT or total thickness of fire-rated plasterboard to directly estimate the time-to-reach a critical temperature of 300°C at a depth of 4 mm from the heated surface of timber heated 50 and 100 kW/m² (refer to Figure 8). These formulations were estimated using trend straight lines (i.e. one-degree polynomial equation) and were arranged to intersect the vertical axis (i.e. the scenario with no protection) at the time-to-reach 300°C measured at a depth of 4 mm based on experiments where timber was left unprotected (see Figure 5 or 6); 3.45 and 0.95 minutes for 50 and 100 kW/m², respectively.

These formulations are valid within the range of heating conditions, and DFTs, and number of fire-rated plasterboards for the experiments shown herein. Figure 9 shows a function that correlates the amount of DFT of intumescent coating required to achieve an equivalent behaviour to that achieved with fire-rated plasterboard(s). Due to the relatively poor swelling for the timber samples protected with intumescent 100 kW/m², the formulations for 50 or 100 kW/m² are vastly different under the two different heating conditions. On the other hand, the behaviour for timber samples protected with plasterboard is not negatively influenced at high heating conditions (i.e. 100 kW/m²).

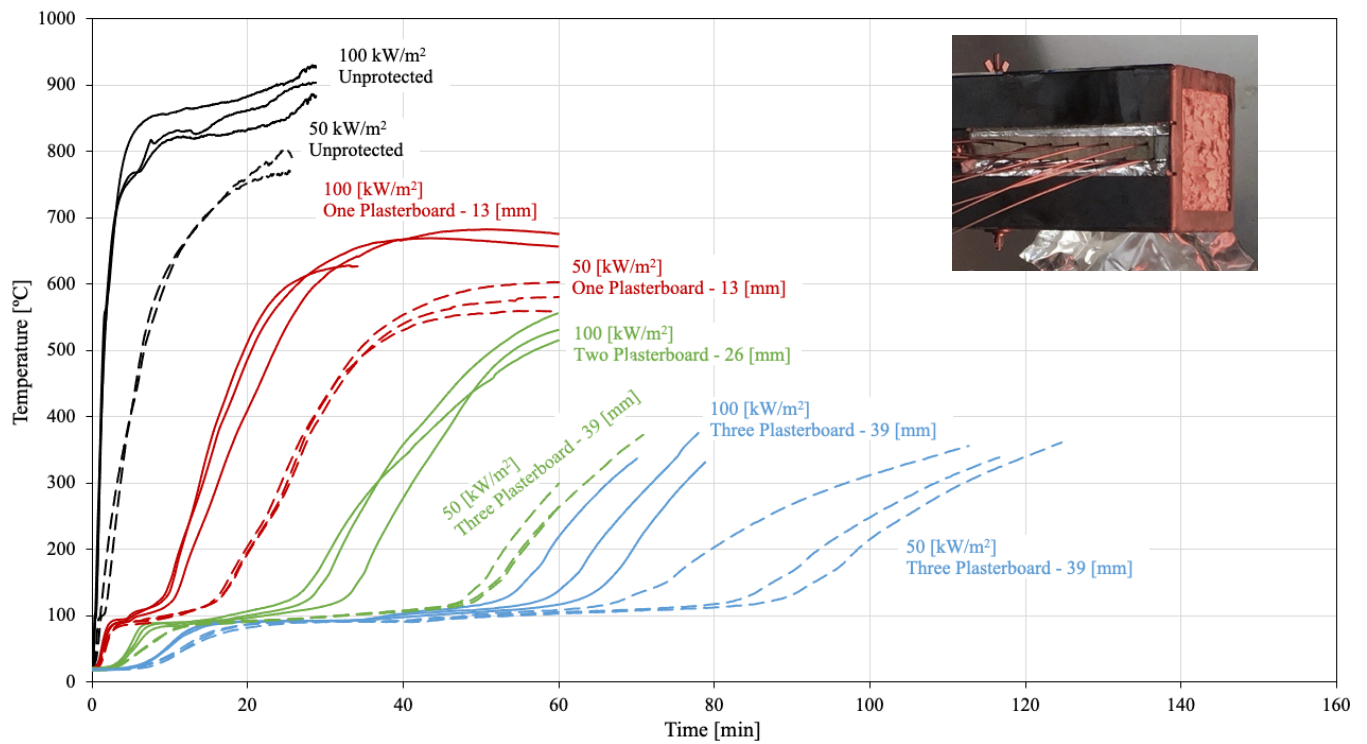


Figure 5. Temperature (measured 4 mm from the heated surface of timber) vs. time for samples protected with plasterboard(s) at 50 or 100 kW/m² and also for unprotected timber.

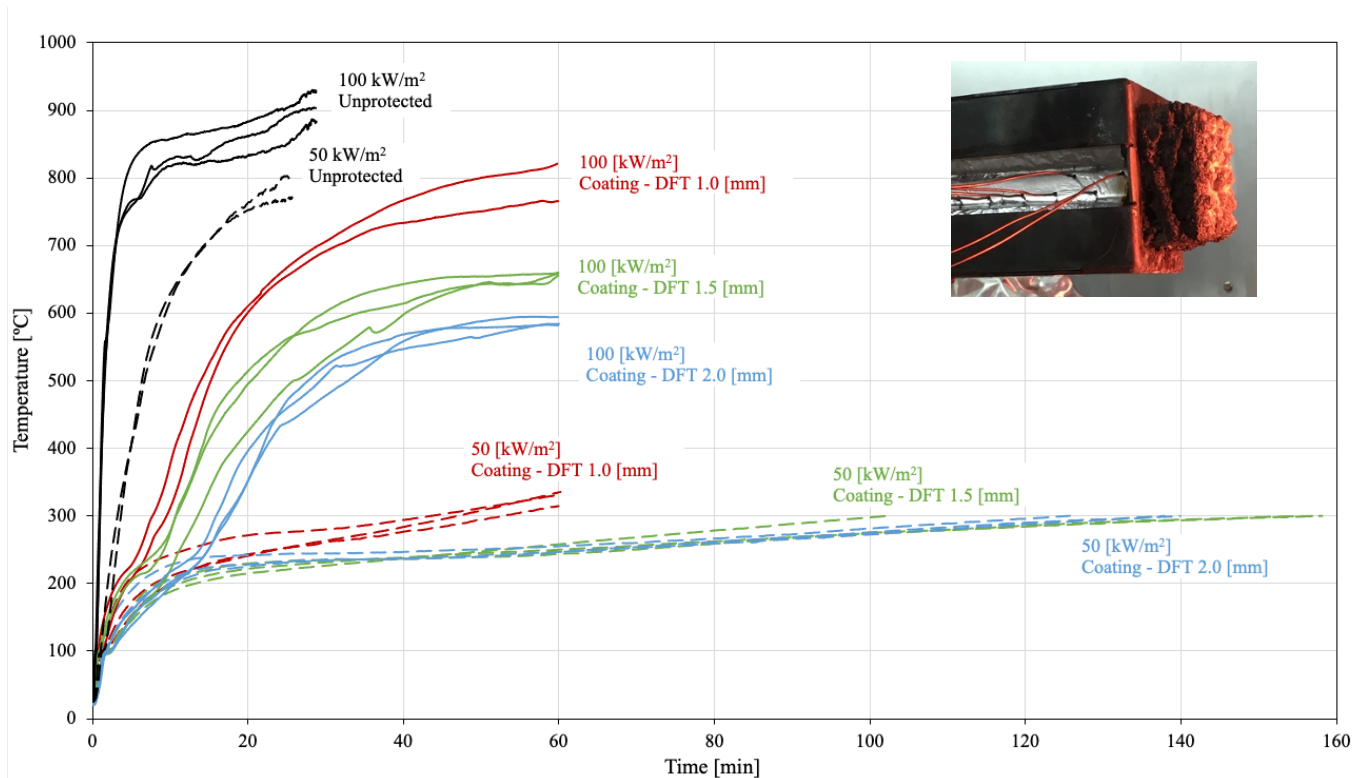


Figure 6. Temperature (measured 4 mm from the heated surface of timber) vs. time for samples protected with intumescent at 50 or 100 kW/m² and also for unprotected timber.

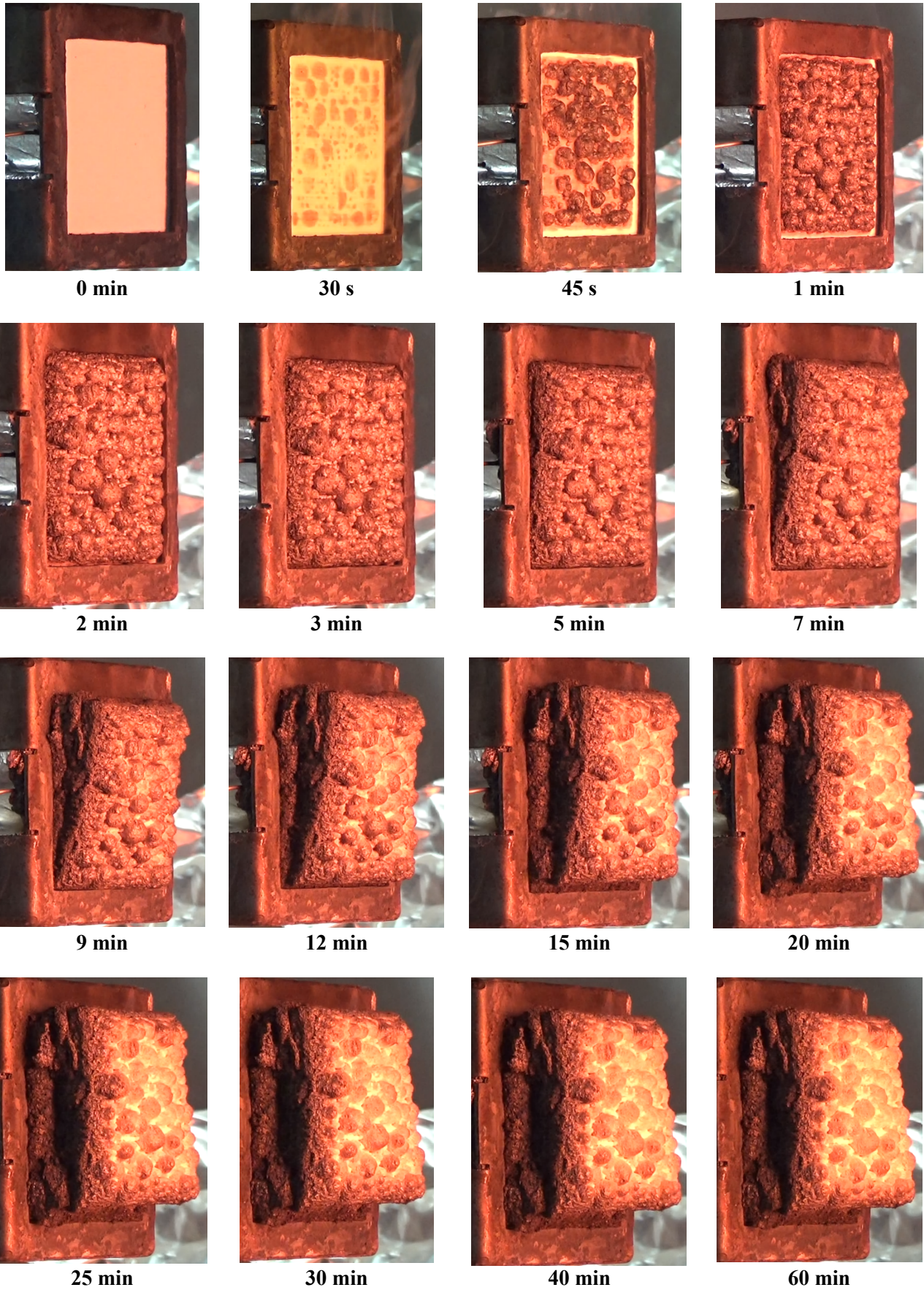


Figure 7. Time-lapse for exemplar experiment for timber samples coated with a DFT of 1.0 mm and heated at 50 kW/m².

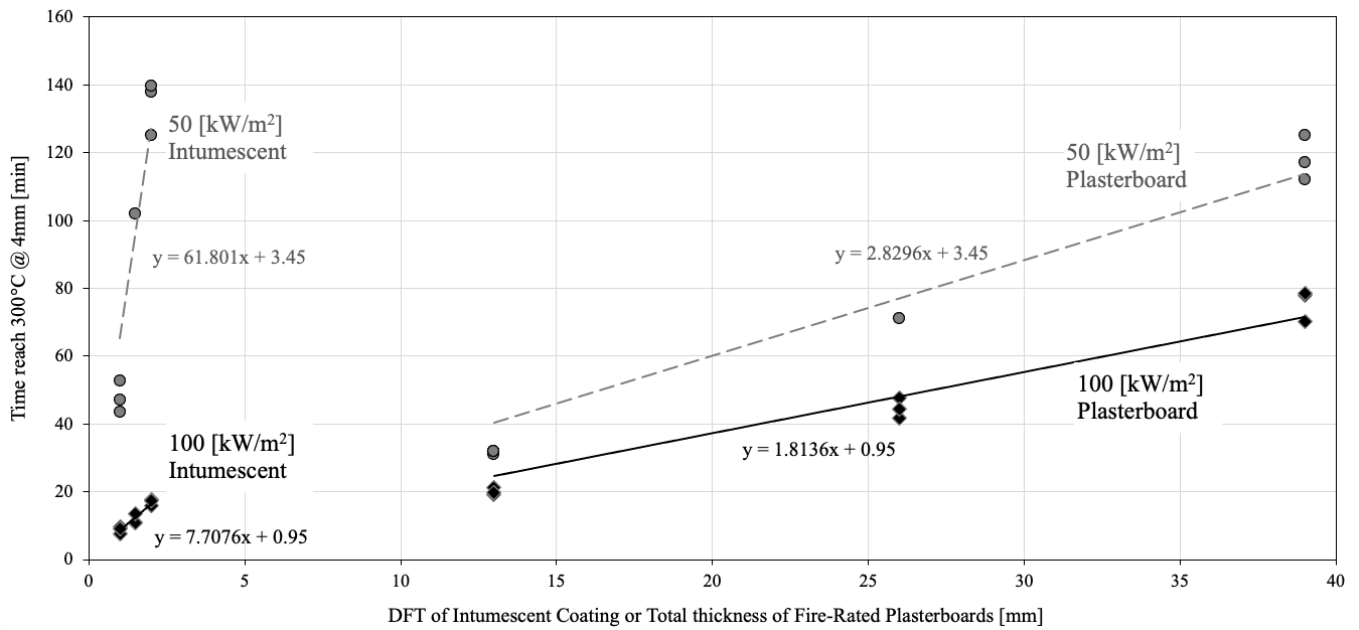


Figure 8. Time-to-reach a critical temperature of 300°C measured at a depth of 4 mm vs. DFT of intumescent coating or total thickness of fire-rated plasterboard for timber tested at 50 or 100 kW/m².

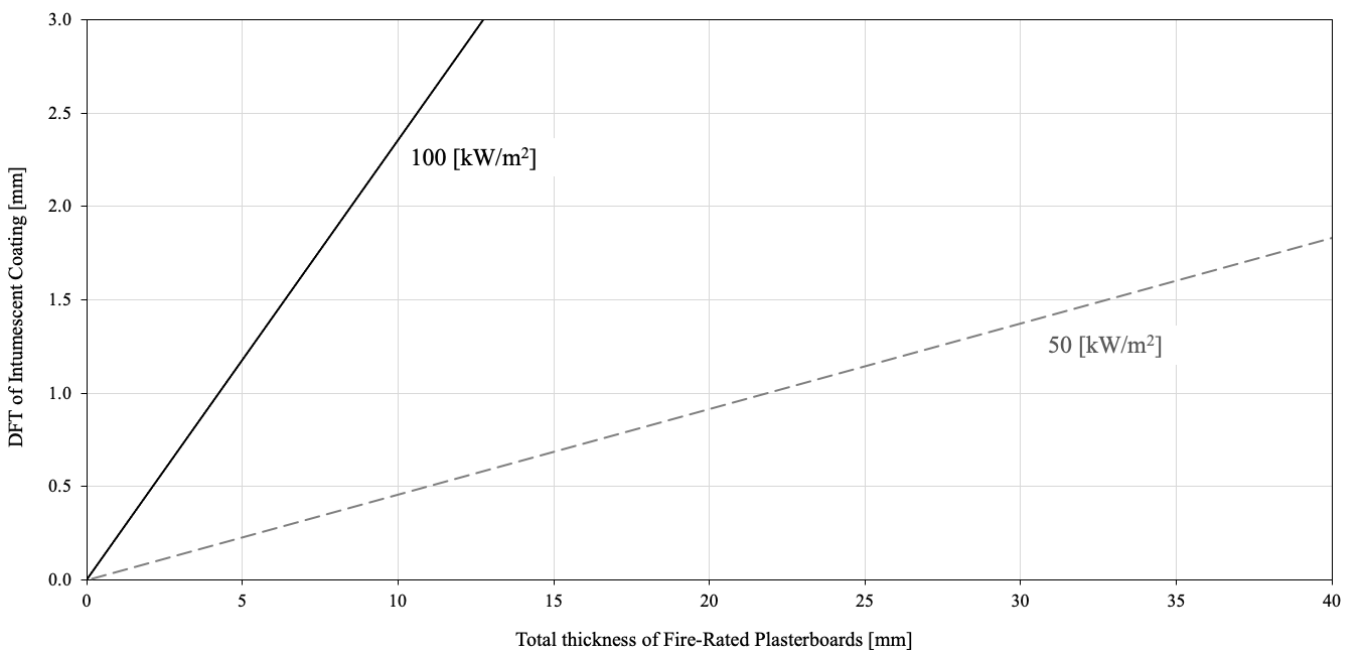


Figure 9. Time-to-reach a critical temperature of 300°C measured at a depth of 4 mm vs. DFT of intumescent coating or total thickness of fire-rated plasterboard for timber tested at 50 or 100 kW/m².

4 CONCLUDING REMARKS

The study presented herein describes a comparative investigation on the fire performance of fire-rated gypsum plasterboards and thin intumescent coatings used in mass timber structures. The outcomes of the experimental study and analysis can be summarized as follows:

- Timber encapsulated with one or more plasterboards** shows that temperature of timber near the heated surface plateaus (i.e. remains constant over time) at about 300°C, for a period of time that is proportional to the number of plasterboards used for encapsulations. Following this plateau, the temperature near the

heated surface continues to increase at rates which are comparable to those observed for unprotected timber. The influence of heating conditions (between 50 and 100 kW/m²) was as expected.

- **Timber coated with intumescent coating** shows that temperature of timber near the heated surface is continuously increasing during heating. The influence of heating conditions (between 50 and 100 kW/m²) is detrimental to the behaviour of the intumescent coating. The intumescent evidence a relatively diminished swelling behaviour when heated at an incident radiant heat of 100 kW/m².
- **Comparative analysis between plasterboard and intumescent coating** – formulations were derived to correlate the amount of DFT of intumescent coating required to achieve an equivalent behaviour to that achieved with fire-rated plasterboard(s); refer to Figure 9.

ACKNOWLEDGMENT

The authors gratefully acknowledge the support of Remedial Building Services Australia and the Philanthropic Grants for Early Career Engineering Researchers (The University of Queensland – SE12015). More specifically, the authors are grateful to Massimo Falzone (Aithon Ricerche International) and Andrew Abrahams (Remedial Building Services Australia) for their technical support and valuable contributions during the research project.

REFERENCES

1. Barber D. 2015. Tall Timber Buildings: What's Next in Fire Safety?. *Fire Technology*, vol. 51, no. 6, pp. 1279-1284.
2. White RH and Dietsberger MA. 2010. *Wood Handbook: Wood as an Engineering Material – Chapter 18: Fire Safety of Wood Construction*. General Technical Report FPL–GTR–190, Centennial Edition, Forest Products Laboratory, United States Department of Agriculture Forest Service, Madison, Wisconsin.
3. Comité Européen de Normalization (CEN). 2004. *EN 1995-1-2:2004 Eurocode 5: Design of timber structures - Part 1-2: General rules - Structural fire design*. Brussels, Belgium.
4. Puri EG and Khanna AS. 2017. Intumescent coatings: a review on recent progress. *Journal of Coatings Technology and Research*, vol. 14, pp.1-20.
5. Taylor AP and Sall FR 1992. Thermal analysis of intumescent coatings. *European Polymer Paint Colour Journal*, vol. 182, no. 4301, pp. 122-130.
6. Yan L, Xu Z, and Liu D 2019. Synthesis and application of novel magnesium phosphate ester flame retardants for transparent intumescent fire-retardant coatings applied on wood substrates. *Progress in Organic Coatings*, vol. 129, pp. 327–337.
7. Hakkarainen T. 2010. *Thin thermal barriers for wood based products to improve fire resistance*. Research Report VTT-R-07061-09, VTT Technical Research Centre of Finland, Finland.
8. Xu Q, Wang Y, Chen L, Gao R, and Li X. 2016. Comparative experimental study of fire-resistance ratings of timber assemblies with different fire protection measures”. *Advances in Structural Engineering*, vol. 19, no. 3, pp. 500–512.
9. Maluk C, Bisby L, Krajcovic M, and Torero JL. 2019. A Heat-Transfer Inducing System (H-TRIS) Test Method. *Fire Safety Journal*, vol. 105, pp. 307-319.
<https://doi.org/10.1016/j.firesaf.2016.05.001>
10. Lucherini, A, Razzaque QS, and Maluk, Cristian. 2019. Exploring the fire behaviour of thin intumescent coatings used on timber. *Fire Safety Journal*, vol. 109 102887 102887.
<https://doi.org/10.1016/j.firesaf.2019.102887>

THE RESPONSE OF EXPOSED TIMBER IN OPEN PLAN COMPARTMENT FIRES AND ITS IMPACT ON THE FIRE DYNAMICS

Sam Nothard¹, David Lange², Juan P. Hidalgo³, Vinny Gupta⁴, Martyn S. McLaggan⁵

ABSTRACT

Fires in open plan compartments have been the subject of much research over the past decade. The impact of exposed CLT on the fire dynamics in such compartments is also receiving a great deal of interest as trends in timber buildings include also open plan buildings. This article presents some initial results from an experimental study which was conducted to explore the role of a timber ceiling as well as ceiling intrusions on the flame spread rate of the fuel-bed on the floor. The reduced scale testing methodology is validated by contrasting observed fire behaviour with large-scale compartment fire experiments reported in the literature. The reduced-scale experiments highlight the complexity of the fire dynamics, with ceiling intrusions dramatically increasing spread rates. Spread rates of the fuel-bed with a timber ceiling are initially slower than configurations without a timber ceiling. Once ignition of the timber ceiling occurs, flames spread across the ceiling almost instantaneously. The additional feedback from the flames, smoke layer, and charring timber surface induces a very rapid flame spread across the fuel-bed. Self-extinction of the timber is obtained in all cases once the complete burn-out of the fuel-bed is attained. The results demonstrate that idealisations of a travelling fire for open-plan compartments may not be valid when considering complexities such as ceiling intrusions or combustible timber ceilings.

Keywords: Timber, open plan compartments, compartment fire dynamics, CLT

1 INTRODUCTION

Timber as a construction material is experiencing rapid growth in its use at the moment. This is a result of strong environmental credentials and a drive for an improved end user experience in offices and residential developments. This growth has been enabled by the development of both engineered timber products and the structural engineering knowledge required to build taller timber buildings or new structural forms from timber.

International House Sydney (IHS) was Australia's first engineered timber building constructed using only CLT floor plates and walls and Glulam beams. The IHS is only one example of the many designs being produced, which include even taller and more complex buildings in excess of 100 m high. It was identified

¹ Firecheck consultants PTY and The University of Queensland,
e-mail: nothard.sam@gmail.com

² Senior Lecturer in Structural Engineering, The University of Queensland
e-mail: d.lange@uq.edu.au, ORCID: <https://orcid.org/0000-0002-4551-1045>

³ Senior Lecturer in Timber Engineering, The University of Queensland
e-mail: j.hidalgo@uq.edu.au, ORCID: <https://orcid.org/0000-0002-2972-5238>

⁴ PhD student, The University of Queensland
e-mail: v.gupta@uq.edu.au, ORCID: <https://orcid.org/0000-0003-0514-5834>

⁵ Research fellow, The University of Queensland
e-mail: m.mclaggan@uq.edu.au, ORCID: <https://orcid.org/0000-0002-4173-5615>

by Lend Lease (the developer of IHS) that there were risks associated with the building design methodology and sole use of cross laminated timber (CLT). This is because technical advances and research in the building industry tend to be very sluggish in making their way to market as contractors struggle to quantify and price the risks presented by using new construction materials such as CLT. One of the major obstacles to the realisation of exposed timber in buildings is the necessity to meet fire safety requirements which otherwise often result in fully encapsulated timber buildings.

Much of the work ongoing to understand the behaviour of timber in compartment fires originates in small cubic compartments where post-flashover fire conditions are guaranteed. This has led to the demonstration of the concept of self-extinction of burning timber in fires and the identification of criteria for this [1] and to further work studying the impact of timber on the existing compartment fire framework [2]. The evolution of contemporary structures, particularly those including exposed timber has seen a rise in open-plan spaces with large interconnected compartments. In such large spaces with a distributed fuel load over the floor plate, it is often unlikely for the compartment to reach post-flashover conditions, but rather the fire can “travel” across the floor plate. Methodologies to approximate the thermal conditions of such fires for the purposes of structural design are described by Stern-Gottfried et al. [3,4] and other researchers [5,6]. While there have been attempts at developing theoretical frameworks to define the fire dynamics and fire spread in open-plan compartments, these theories have not been extended to compartments with exposed timber surfaces [7, 8].

There is therefore a need to understand the impact that exposed timber surfaces in a large open plan compartment have on the fire dynamics and if the fire evolution in open plan timber compartments can be idealised as travelling fires or if modifications to this concept are needed.

This paper summarises part of a research project aiming to evaluate travelling fires for structural design in open plan compartments at reduced-scales. Here, the influence of ceiling intrusions, such as beams, and the addition of exposed cross laminated timber (CLT) as a structural material on the fire dynamics are investigated.

A reduced-scale compartment geometry was employed in this study. Three different compartment configurations were selected, including a flat ceiling and a combination of an edge and middle beam at the opening and across the ceiling. Using these configurations, a wood crib fuel load was used to carry out baseline tests with non-combustible boundaries followed by CLT tests with a CLT ceiling. The test setup is shown in Figure 1 during one of the CLT tests. This paper summarises some of the results from these tests, including the impact of the exposed CLT on the development of the fire and reports on the response of the timber ceiling to the conditions inside of the compartment. Specifically, the charring rate as a function of the varying exposure during the development of the fire. Other results from this study will be presented in future publications.



Figure 1. External view of the test setup during flat ceiling exposed CLT test.

2 METHODOLOGY

Scale testing is implemented in this work as a means of systematically exploring specific behaviour for the identification of phenomenon which may need to be explored in more detail at a large scale. The problem discussed in this article requires geometric scaling as well as consideration of the scaling of the relevant fire dynamics. Quintiere identifies that scaling fire phenomena requires preservation of too many non-dimensional groups to encapsulate similarity between the model and prototype [9]. Since complete scaling is not viable, partial scaling is required and the modelling prerequisite is that the physical model is ‘similar’ to the prototype (full scale) in the sense that there is a direct correlation between the general response of the two systems to equivalent stimuli events [10].

For the series of tests reported in this paper, the fire source (heat release rate) and the compartment geometry are both scaled. Other aspects of the fire dynamics, such as time, momentum, etc. are considered to be phenomenologically similar in the scaled test, but not preserved in the scaling analysis.

Geometric scaling is typically straight forward and uses a length scale (l) to define the geometrical relationship between the full-scale prototype and scale model. Scaling the compartment fire requires a selected fuel load to model the energy released. Thought must be given to the application of the model and the desired outcome and effects of the fuel used such as the combustion products which can influence factors in the model. For example, a high soot yielding material is likely to have a greater effect on radiative heat gain and loss between the smoke layer and compartment lining compared to a low soot yielding fuel material. The consideration of the type of fuel used links back to the art of partial scaling and requires consideration based on the governing scaling laws.

Typically, compartment fire tests (both scale and prototype) have used fuel loads of wood cribs or liquid pool fires. Different fuel loads require varied scaling to ensure the HRR is scaled correctly. Li and Ingason provide a detailed approach on the requirements for scaling wood cribs for model testing [11]. The fuel source scaling requirements for this are summarised in detail below.

The three parameters considered for scaling combustible material are geometry, heat release rate and energy content. Li and Ingason found the maximum mass burning rate for wood cribs approaches a constant for well ventilated fires.

The HRR of a wood crib is defined by Eq. 1, where the effective heat of combustion for pine wood sticks used is about 12 kJ/g [9].

$$\dot{Q} = \dot{m}\Delta H_c \quad (\text{Eq. 1})$$

The selection of a peak HRR provides the ability to then scale a wood crib fuel load by selecting the scaled number of sticks (n) and length of stick (l). The mass loss rate (\dot{m}) is calculated by Eq. 2, where C is the crib constant and taken to be 1 mg/cm^{1.5} for pine [12] and b is the thickness of a stick.

$$\dot{m} = Cn(4lb^{0.5}) \quad (\text{Eq. 2})$$

The spacing size of the sticks in the crib is selected to ensure that the crib porosity is sufficiently large to guarantee that crib burning rate is not controlled by the porosity of the crib [13], but instead by the crib geometry and thermal feedback from the compartment [14]. The relationship between stick spacing and porosity are presented in Eq. 3 and 4, respectively, where A_v is the total open area of vertical shafts and A_s is the total surface area of sticks exposed to air.

$$s = \frac{l - \left(\frac{\#sticks}{\#layers}\right)b}{\left(\frac{\#sticks}{\#layers}\right) - 1} \quad (\text{Eq. 3})$$

$$\varphi = s^{0.5}b^{0.5}\frac{A_v}{A_s} \quad (\text{Eq. 4})$$

2.1 Compartment geometry

The experimental compartment was designed to approximate a 1/8 reduced scale configuration of large-scale experiments in the literature, namely the Malveira Fire Test [15], ETFT experimental campaign [16] and the Guttasjön Fire Tests [8,17]. The aspect ratio is also similar in configuration to that of the floor plate of International House. Table 1 outlines the compartment geometry in comparison to previous full-scale test open plan floor plate compartments.

Table 1 – Scaled compartment geometry comparison with full scale tests.

Compartment	Length [m]	Depth [m]	Height [m]
Scaled 1/8 test compartment	2.22	0.8	0.4
Full scale equivalent compartment	17.8	6.4	3.12
Malveira Fire Test	21	4.7	2.85
Edinburgh Tall Building Fire Tests (ETFT)	17.8	4.9	2
Guttasjön Fire Tests (GFT)	18.0	6.0	3.0

The experimental compartment had a single large opening for ventilation along the front of the compartment to simulate an open plan compartment. The opening and ceiling characteristics were varied to assess the influence of intrusions on the formation of smoke and how these influence the fire dynamics within the compartment. These intrusions comprised a beam inserted along the top of the opening of the compartment (an edge beam); and a beam inserted along the short axis centreline of the compartment (middle beam). Both of these intrusions had a depth of 70 mm. Table 2 provides a comparison of the opening and ceiling characteristics for each test configuration.

Table 2 – Compartment opening characteristics.

Test Configuration	Test 1	Test 2	Test 3
Description	No edge beam	Edge beam	Edge & middle beam
Opening Width [m]	2.2	2.2	2.2
Opening Height [m]	0.4	0.33	0.33
Opening Area [m ²]	0.88	0.726	0.726
Smoke Reservoir Volume [m ³]	0	0.126	2 x 0.062

The material used for the compartment floor and walls was vermiculite board (density 375 kg/m³). The ceiling lining was varied between the different tests, as shown in Figure 2. The three baseline tests were conducted using a non-combustible ceiling constructed with plasterboard covered in Superwool (ceramic wool) Paper Insulation. The ceiling was then substituted for three further tests with an Xlam Radiata Pine CLT ceiling with three lamellae. Dimensions for the ceiling linings are shown in Figure 2.



Figure 2 – Compartment with varied ceiling lining: non-combustible (left) and combustible (right).

To achieve the experimental objectives a series of six (6) experiments were carried out. Test variables included altering the ceiling material and adding intrusions such as ceiling beams. Ignition of the fuel bed was at the left-hand side in the orientation shown in Figure 2. To achieve ignition of the wood cribs a small pan of Kerosene placed underneath both of the left most cribs in Figure 2 and was ignited first. The fire was allowed to freely propagate from the ignition point along the fuel-bed. Table 3 provides an overview of the experimental program.

Table 3 – Testing matrix.

Test No.	Floor and Wall Lining	Ignition Source	Fuel-bed Mass*	Ceiling Lining	Edge Beam	Middle Beam
Baseline Tests						
B1	Vermiculite Board	30 mL Kerosene	14.2 ± 0.5 kg	non-combustible	-	-
B2				non-combustible	x	-
B3				non-combustible	x	x
CLT Tests						
C1	Vermiculite Board	30 mL Kerosene	14.2 ± 0.5 kg	CLT	-	-
C2				CLT	x	-
C3				CLT	x	x
* Fuel is pine wood sticks with a cross section of 25 x 25 mm.						
x indicates the test includes the variable						

Data obtained during the experimental work includes the heat release rate (obtained by oxygen consumption calorimetry), total mass loss rate, flame spread velocity and burnout front velocity, gas-phase temperatures, solid-phase (in-depth) temperatures and incident heat flux at the ceiling and adjacent to the surface of the fuel-bed. This article presents the timeline of events from the different tests and discusses the influence of the CLT ceiling and the ceiling intrusions on the overall behaviour. The charring behaviour of the CLT slab is also discussed. Other results will be discussed in future publications.

3 RESULTS

This section presents the characteristic results associated with the experiments outlined in the test matrix. The results from each test allow conclusions to be drawn regarding the following factors.

1. The influence of compartment configurations – indexed by 1 (flat ceiling), 2 (edge beam) and 3 (edge and middle beam); and

2. The different ceiling linings that are non-combustible (Baseline) and combustible (CLT) – indexed by B and C respectively.

The aim of the 6 tests was to quantify the effects of the above factors on the overall behaviour of the system in fire and to provide input to potential expected behaviour for future large-scale testing.

3.1 Validation of the experimental approach

As a means of validating the experimental approach, the observed fire spread modes identified in other full-scale fire tests of similar configuration compartments are identified in the reduced-scale experiments. The flame and burnout fronts are determined for each test in this series to obtain the characteristic modes of the fire in correspondence with large-scale travelling fire tests in the ETFT, Malveira, and Guttasjön Fire Tests, all of which had similarity in the compartment and fuel geometries [8]. The flame and burnout front location and propagation velocity was determined through analysis of the video footage. The resulting flame (X_f) and burnout (X_b) front locations for the first of the baseline tests are shown in Figure 3. Based on the measured average spread rates of the flame and burnout fronts, three modes of fire spread are identified and shown in Table 5. The vertical steps seen in the data are a result of the spread of fire between wood cribs resulting from the discrete package nature of the fuel load. All three modes are identified in this data, which supports the use of this scaled testing approach for further study of the effect of ceiling intrusions and the inclusion of combustible linings. During the travelling fire mode, the flame and burnout fronts are constant across the width of the fuel. The transition from Mode 3 (travelling, i.e. $V_s \approx V_{BO}$) to Mode 2 (growing, i.e. $V_s > V_{BO}$) and then to Mode 1 (rapid flame spread, i.e. $V_s \rightarrow \infty$) is demonstrated by the flame front location departing from the parallel trend. This departure signifies the length of the burning area increasing as the flame front propagates significantly faster than the burnout front.

Table 5 – Characteristic flame spread modes.

Characteristic Mode	Fire Behaviour Description	Value
Mode 1	Extremely rapid to instantaneous increase in flame front	$V_s \rightarrow \infty$
Mode 2	The flame front increases faster than the burnout front	$V_s > V_{BO}$
Mode 3	The flame front and burnout front are constant at the same rate	$V_s \approx V_{BO}$

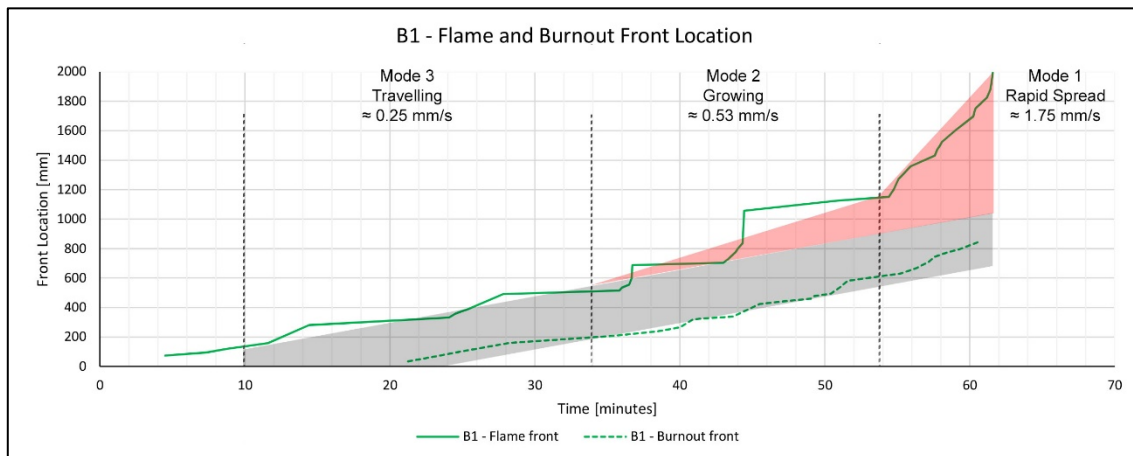


Figure 3 – Flame and burnout front location showing modes of flame spread during baseline tests with no ceiling intrusion.

3.2 Effect of combustible ceiling lining

Figure 4 shows the impact of the combustible ceiling on the flame spread and burnout front locations in the fire test with a CLT lining and without ceiling intrusions. The constant burning length during Mode 3 is highlighted in both Figures 3 and 4 by the grey shaded area with constant parallel width. In comparison, the growing burning length during Mode 2 and 1 has been shaded red, which illustrates the departure from the constant burning region length of Mode 3. The data shows the presence of all three fire spread modes

regardless of the ceiling lining, however spread rates in the case of the CLT ceiling are always slower during Mode 3, and increase significantly compared with the non-combustible ceiling cases for Mode 2 and Mode 1. In both tests, the slow transition from Mode 3 to Mode 2 is induced by increased preheating of the fuel-bed ahead of the flame front as the smoke layer evolves [8]. Ignition of the ceiling occurs at approximately 50 minutes and flames rapidly propagate along the ceiling. Despite the presence of a flaming ceiling, there is a delay of approximately 2.5 minutes prior to the onset of rapid flame spread, indicating a time delay to raise the remaining wood crib fuel-bed to an ignition temperature. It is worth noting that the burnout time of the wood crib fuel bed with the CLT ceiling is only marginally shorter than in the baseline test with this configuration indicating that the radiative feedback from the ceiling may not significantly alter the burning rates.

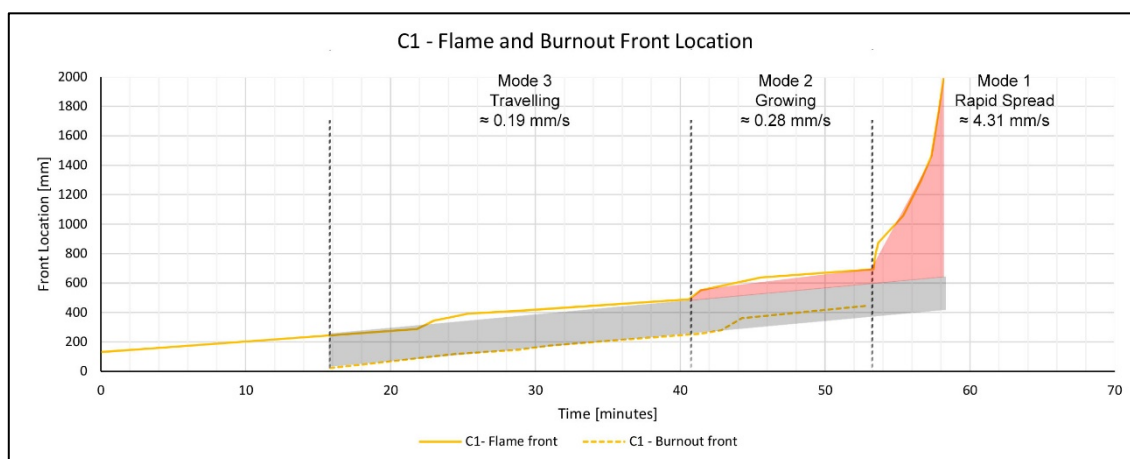


Figure 4 – Flame and burnout front location showing modes of flame spread during CLT test with no ceiling intrusion

3.3 Description of Events

The graphs in Figure 3 and Figure 4 show similarities in flame spread during the initial establishment of the fire followed by variations in each test as a result of the presence of the CLT ceiling. The addition of a flaming ceiling is shown to induce rapid flame spread, however there is little effect on the propagation of the burnout front velocity. The ceiling appears to marginally increase the total burnout time of the fuel-bed. Under both the combustible and non-combustible ceiling configuration, the presence of the ceiling intrusions, in particularly the combination of both the edge and ceiling beams dramatically increases the flame spread rate, but has a moderate effect on the burnout front velocity, with a maximum increase of 20% (Table 4). These results are consistent with the results of large-scale compartment fire experiments as reported in Gupta *et al.* [8]. The insensitivity the burnout front velocity is likely attributed to the fact that the crib burns a regime where the geometry and characteristics of the fuel-bed controls the burning rate, thus radiative feedback can be simply treated as a small correction to the crib burning rate [14].

3.4 Behaviour of CLT in Scaled Compartment Tests

3.4.1 Ignition

The ignition of the CLT was piloted by flame impingement on the visible pyrolyzates diffusing from the ceiling (Figure 1). Ignition can be defined by a critical heat flux for ignition $\dot{q}''_{0,ig}$, which is the minimum incident heat flux necessary to raise the surface temperature of the solid to an ignition temperature, T_{ig} ; a review of the fundamentals is provided by Torero [18]. Under standard testing conditions, this critical heat flux and surface ignition temperature ranges within 10 to 13 kW/m² and 296 to 355 °C, respectively [19]. This value is strongly dependent on the material properties and the environmental conditions, which greatly differ when comparing the experimental compartment to standard testing apparatus. Material parameters controlling the ignition temperature include the ceiling orientation (i.e. inverted or downward), the heat transfer modes such as radiation and convection, moisture content, density and thickness of the material. Environmental variables will include the flow fields and the oxygen concentration at the surface of the fuel. The profile of incident heat flux to the timber surface in the first of the 3 CLT tests is shown in Figure 5.

Table 4 – Description and timeline of events.

Test Configuration	B1	B2	B3	C1	C2	C3
Ignition & Growth Phase Events	Time of Event [minutes]					
Ignition (row 1)	0.0	0.0	0.0	0.0	0.0	0.0
Pool fire extinguished	3.5	2.8	2.7	2.8	2.9	2.9
Row 1 fully flaming	13.2	15.3	16.1	15.3	12.6	11.5
Row 2 fully flaming	26.5	27.9	23.4	32.3	32.8	29.5
Row 3 fully flaming	35.4	32.3	28.9	47.9	50.1	39.7
Ignition of CLT ceiling	N/A	N/A	N/A	52.3	50.8	39.4
Row 4 fully flaming	43.1	35.3	30.5	54.0	52.0	40.3
Row 5 fully flaming	49.5	36.2	31.3	55.5	52.6	40.8
CLT ceiling fully flaming	N/A	N/A	N/A	56.2	52.3	40.8
Row 6 fully flaming	54.6	36.7	32.1	56.6	53.0	41.3
Row 7 fully flaming	57.7	36.9	32.5	57.3	53.2	41.5
Row 8 fully flaming	59.1	37.3	32.8	57.8	53.5	41.7
Row 9 fully flaming	60.4	37.5	32.9	58.1	53.8	41.8
Flashover [#]	60.4	37.5	32.9	58.1	53.8	41.8
Decay Phase Events	Time of Event [minutes]					
Row 1 burnout	37.2	33.7	30.2	35.5	30.4	33.8
Row 2 burnout	47.7	40.5	36.1	52.6	51.5	43.8
Row 3 burnout	53.9	44.7	42.8	60.3	59.7	53.0
Row 4 burnout	59.3	46.8	44.3	67.1	64.8	52.4
Initial self-extinction (left side)	N/A	N/A	N/A	67.4	64.8	49.7
Row 5 burnout	67.1	46.5	44.1	67.9	64.8	53.3
Row 6 burnout	67.8	48.1	44.1	68.7	65.4	53.4
Row 7 burnout	70.6	50.3	45.3	69.7	64.4	53.0
Row 8 burnout	72.9	50.1	46.2	69.3	65.8	53.8
Row 9 burnout	72.3	48.3	44.8	68.9	65.4	53.8
Wood crib total burnout	72.9	50.3	46.2	69.7	65.8	53.8
CLT self-extinction	N/A	N/A	N/A	81.5	75.8	69.0
[#] time to flashover is here defined as the time at which ignition of all remaining fuel occurs, which was always accompanied by external flaming.						

Figure 5 shows that ignition occurred when the average incident heat flux to the ceiling reached 30 kW/m^2 . These values are considerably larger than experimentally determined values for $\dot{q}_{0,ig}''$.

However, for ignition to occur a flammable gas mixture must exist somewhere in the gas-phase which was then required to be elevated in temperature for the combustion reaction to occur. Once pyrolysis of the CLT had occurred, the correct mixture (of volatiles and oxygen) and environmental conditions were required for the combustion reaction to occur. This can only be attained when chemical timescale of the pyrolysis had occurs faster than the residence time of the reactants within the control volume at the CLT surface.

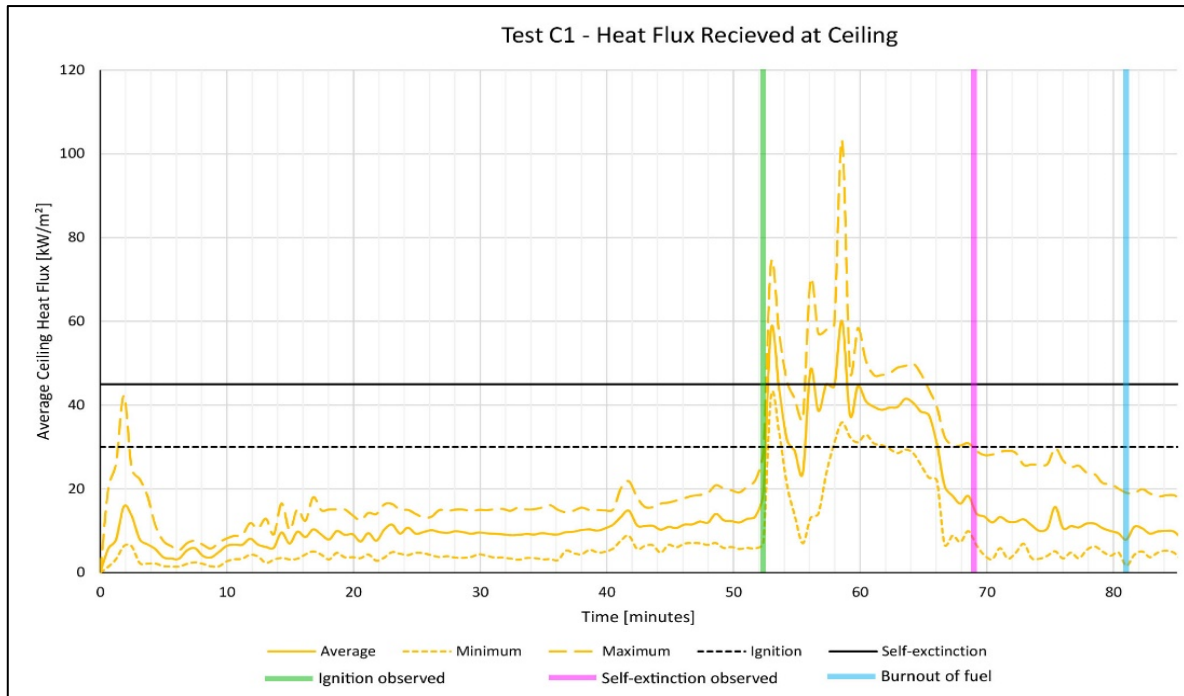


Figure 5 – Average incident heat flux to the ceiling of configuration 1.

To understand why higher incident heat fluxes were required for ignition, the following key points are highlighted:

1. As the CLT began to heat, initial thermal decomposition of the timber surface likely induces formation of a char layer. Due to the insulating properties and presence of char, the CLT would have required a higher surface temperature to provide the necessary heat flux to virgin timber to produce sufficient pyrolysis gases for the combustion reaction.
2. The large size of the openings enables the hot gases to leave the compartment as fast as air is entrained in. Therefore, the flow fields are dominated by the thermal gradient of the fire source and entrained air, thus the flow field is largely momentum-driven [7]. Experimental observations show the gases leaving the compartment without any smoke layer build-up. Thus, it is likely that the flows increased the convective losses and also increased the required external heat flux for ignition. Additionally, the flow characteristics changed when the ceiling intrusions were introduced, resulting in the volatiles being contained for longer within a thicker hot gas layer. This is thought to have altered the residence time of the pyrolysis gases leading to a faster time to ignition, summarised in Table 4, for the cases with different ceiling intrusions. This was most notable when the middle beam was introduced in configuration 3 which contained the pyrolysis gases in the near field region of the compartment, increasing the residence time and enabling a flammable mixture to form faster. These factors will be discussed in a future publication.
3. Despite piloted ignition occurring, continuous flame impingement was not observed during the experiments. Therefore, although pyrolysis gases were mixing at the ceiling surface, the absence of a constant flame is also a likely reason for the higher than expected heat flux required for the piloted ignition.

3.4.2 Self-extinction

Self-extinction is the process whereby the exposed CLT ceiling ceases to continue burning upon the burnout of the fuel-bed on the floor. It is important to define the potential for self-extinction to occur with regards to fire safety of a building to ensure the compartment does not continue to burn and lead to potential structural failure.

Self-extinction was observed during each CLT test after the wood crib fuel load was consumed. The phenomenon was found to occur when the incident heat flux to the boundary reached between 10 to 20 kW/m². Comparatively, Emberley [1] suggests that self-extinction should occur during the fire decay phase

once the incident heat flux falls below 45 kW/m². However, the empirical value of 45 kW/m² was determined using a cone heater test configuration over a range of constant exposed heat fluxes which then defines the critical heat flux for self-extinction under the worst-case scenario. Cuevas *et al.* [20] has more recently identified a range of heat fluxes over which self-extinction is a stochastic process and below which (30 kW/m²) it will always occur and above which it will never occur (40 kW/m²). Additionally, the empirical value does not necessarily represent the variations in time scales due to the changes in temperature and heat flux inside the compartment compared to the bench scale experiments and also as a result of the temperature gradient developed inside the solid-phase of the timber. Therefore, the suggested value of 45 kW/m² is merely an indication of the possibility for self-extinction behaviour to occur during the decay phase of a fire and this critical value will be dependent on the environmental conditions in the compartment (such as the flow fields), similar to ignition.

3.4.3 Charring rate

Based on the duration of CLT burning, the average char depth measured after the test was compared to values outlined in design standards. Char depth, averaged over the entire ceiling was estimated based on in-depth temperature measurements in the CLT slab and on visual inspections made after the test. Both of these methods are prone to significant errors as a result of conduction along the thermocouple [21] and continued progression of the char front after the external heat flux has been removed. The CLT burning duration, average experimental char depths and average char depths based on BS EN 1995-1-2:2004 [22] and on AS 1720.4-2006 [23] are presented in Table 5.

Table 5 – Comparison of experimental and theoretical char depths.

Test	Duration of CLT Burning [min]	Observed [mm]	300 °C Isotherm position[mm]	Expected char depth from standards	
				Eurocode [mm]	Australian Standard [mm]
C1	27.5	29	17*	17.9	20.6
C2	23.8	28	11.5*	15.5	17.9
C3	28.7	26	11.5*	18.7	21.5

Note: *Data used for the 300 °C isotherm does not accurately define the char depth due to the arrangement of the in-depth thermocouples. Inserted from the back, their orientation conducts heat away from the thermocouple and provides inaccurate measurements. [23]

It was observed after each experiment that the char surface had regressed significantly, resulting in a thin char layer. It is proposed that this is associated to large concentrations of oxygen close to the ceiling enabling diffusion of oxygen into the char layer facilitating the oxidation. The insulating char layer would therefore be thinner than would be expected in an under ventilated fire with a large availability of oxygen. As a result, the char rate would be expected to remain high throughout the combustion process leading to the larger char depths reported in Table 5.

Given the above experimental char depths and duration of burning, the average experimental charring rate was found to be between 0.91 and 1.18 mm/min. Research has been carried out by many [18] to define the charring rate as a function of external (or incident) heat flux to the boundary, Eq. 5. It must be noted that char rates during low incident heat fluxes are not included in this correlation.

$$\beta = 0.02014\dot{q}_e'' \quad (\text{Eq. 5})$$

Using Eq. 5 the charring rate of the ceiling was estimated for each of the CLT tests by considering the average incident heat flux levels along the ceiling shown in Figure 5. The results, outlined in Figure 7, show very low char rates were expected during the initial stages of the fire which were then followed by high charring rates sustained over the duration of the fully-developed fire ranging between 0.8 and 1.2 mm/min.

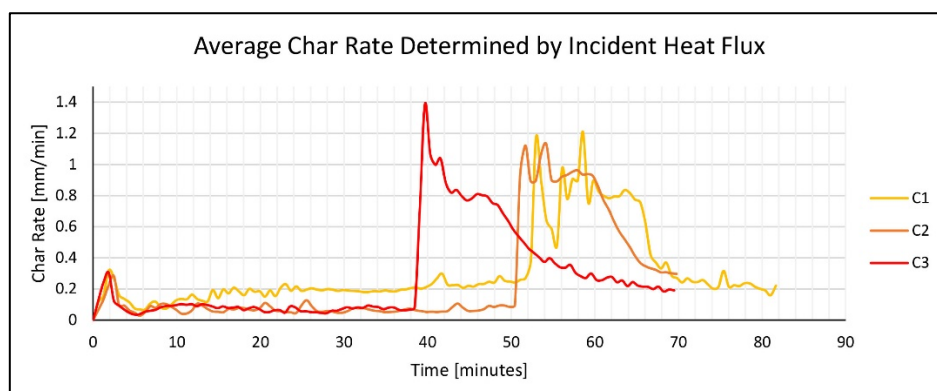


Figure 7 – Theoretical char rate determined by the average incident heat flux exposed to the ceiling.

Following the analysis of char rate as a function of incident heat flux, the total expected char depth in the CLT was calculated using the average char rate during the fully-developed phase of the fire. The resulting char depths are shown in Table 6, compared with the char rate calculated based on observations of char depth made after the experiments. Whilst this appears favourable, as noted the existing correlation does present limitations at low heat fluxes and requires further studies to accurately define the char rate as a function of imposed incident heat flux. The impact of oxygen concentration on the charring rate is also a likely key contributing factor to the char rate which is not reflected in Eq. 5.

Table 6 – Comparison of theoretical char depth using incident heat flux data and experimental results.

Test	Average Char Rate During Fully-Development Phase	Theoretical Char Depth (Using Average Heat Flux)	Average Char Depth Observed from Experiment
C1	0.83 mm/min	22.8 mm	29 mm
C2	0.95 mm/min	22.6 mm	28 mm
C3	0.91 mm/min	26.1 mm	26 mm

4 CONCLUSIONS

This article has given an overview of a number of tests which were conducted to determine the influence of an exposed timber ceiling and ceiling intrusions on the fire dynamics in an open plan compartment. The tests were conducted at reduced scale and were shown to exhibit similarity in the fire dynamics when contrasted to data from large scale fire tests of similar aspect ratios and configurations in the literature.

Conclusions from the work include:

- The CLT ceiling leads to a significant increase in the spread rate of the fire in the compartment once ignition of the ceiling occurs. Once this happens, the compartment transitions to a fully developed fire. Again, in the case of the CLT ceiling, this transition is substantially more rapid.
- That the orientation of the ceiling and thus the residence time of the reactants is critical in understanding or predicting the ignition of the CLT ceiling.
- That self-extinction of the timber occurs under similar conditions as is reported in the literature. Although not discussed in this paper there was no delamination in the tests reported.
- The charring rate of timber is shown, as expected, to be significantly different from values reported for standard fire exposure in codes and standards. In these tests it is affected by the rate of regression of the exposed surface, and thus the low char layer thickness, which is in turn impacted on by a relatively high availability of oxygen in large open plan compartments.

Of importance for design, we have shown the fact that ceiling intrusions have an influence on spread and burnout rates in open plan compartments. The edge beam and the middle beam in the compartment help establish a smoke layer as per classic compartment fire dynamics, inducing pre-heating of the fuel bed and CLT. The middle beam concentrates the energy to a smaller localised area which further increases local spread rates. The compartment geometry acts as a feedback loop which reduces the time required to

transition to rapid flame spread and ignition of the CLT. Once a CLT ceiling ignites, the enhanced radiative feedback onto the fuel bed will rapidly initiate a transition of the fire spread mode from a travelling fire into a growing or fully-developed fire.

5 REFERENCES

- [1] R. Emberley, T. Do, J. Yim, J.L. Torero, Critical heat flux and mass loss rate for extinction of flaming combustion of timber, *Fire Saf. J.* 91 (2017) 252-258. <https://doi.org/10.1016/j.firesaf.2017.03.008>.
- [2] Hadden, R., Bartlett, I., Hidalgo, J., Santamaria, S., Wiesner, F., Bisby, L., Deeny, S., Lane, B., Effects of exposed cross laminated timber on compartment fire dynamics, *Fire Saf. J.* 91 (2017) 480-489. <https://doi.org/10.1016/j.firesaf.2017.03.074>.
- [3] J. Stern-Gottfried and G. Rein, Travelling fires for structural design–Part I: Literature review, *Fire Saf. J.* 54 (2012) 74–85. <https://doi.org/10.1016/j.firesaf.2012.06.003>.
- [4] J. Stern-Gottfried and G. Rein, Travelling fires for structural design–Part II: Design methodology, *Fire Saf. J.* 54 (2012) 96–112. <https://doi.org/10.1016/j.firesaf.2012.06.011>.
- [5] E. Rackauskaite, C. Hamel, A. Law, and G. Rein, Improved formulation of travelling fires and application to concrete and steel structures, *Structures* 3 (2015) 250–260. <https://doi.org/10.1016/j.istruc.2015.06.001>.
- [6] X. Dai, S. Welch, O. Vassart, K. Cábová, L. Jiang, J. Maclean, G. Clifton, A. Usmani, An extended travelling fire method framework for performance based structural design, *Fire Mat.* 44 (2018) 437-457.
- [7] V. Gupta, J.P. Hidalgo, A. Cowlard, C. Abecassis-Empis, A.H. Majdalani, C. Maluk, J.L. Torero, 2020. Ventilation effects on the thermal characteristics of fire spread modes in open-plan compartment fires. *Fire Saf. J.* 103072. <https://doi.org/10.1016/j.firesaf.2020.103072>.
- [8] V. Gupta, A.F Osorio, J.L. Torero, J.P. Hidalgo, Mechanisms of flame spread and burnout in large enclosure fires, *Proc. Comb. Inst.* 38 (2020). <https://doi.org/10.1016/j.proci.2020.07.074>
- [9] J.G. Quintiere, *Fundamentals of Fire Phenomena*, 1st Ed., John Wiley & Sons, Ltd, Chichester, UK, 2006.
- [10] D. Drysdale, *An introduction to fire dynamics*, 3rd Ed., John Wiley & Sons, Ltd, Chichester, UK, 2011.
- [11] Y.Z. Li and H. Ingason, Scaling of wood pallet fires. *Fire Saf. J.* 88 (2017) 96–103. <https://doi.org/10.1016/j.firesaf.2017.01.004>.
- [12] J.A. Block. A theoretical and experimental study of nonpropagating free-burning fires. *Symp. (Int.) Combust.* 13 (1971) 971-978. [https://doi.org/10.1016/S0082-0784\(71\)80097-8](https://doi.org/10.1016/S0082-0784(71)80097-8).
- [13] Gross, D. (1962). Experiments on the burning of cross piles of wood. *Journal of Research, J. Res. Natl. Bur. Stand.* 66 (1962) 99–105. <https://doi.org/10.6028/JRES.066C.010>.
- [14] V. Gupta, J.L. Torero, J.P. Hidalgo, Burning dynamics and in-depth flame spread of wood cribs in large compartment fires. Under-review. *Combustion and Flame*.
- [15] J.P. Hidalgo, T. Goode, V. Gupta, A. Cowlard, C. Abecassis-Empis, C. Maluk, J.M. Montalvá, J. Maclean, A. Bartlett, A.F. Osorio, J.L. Torero, The Malveira Fire Test: Full-scale demonstration of fire modes in open-floor plan compartments, *Fire Saf. J.* 108 (2019) 102827, <https://doi.org/10.1016/j.firesaf.2019.102827>.
- [16] J.P. Hidalgo, A. Cowlard, C. Abecassis-Empis, C. Maluk, A.H. Majdalani, S. Kahrmann, R. Hilditch, M. Krajcovic, J.L. Torero, An experimental study of a full-scale open floor plan enclosure fires, *Fire Saf. J.* 89 (2017) 20-40. <https://doi.org/10.1016/j.firesaf.2017.02.002>.
- [17] J. Sjöström, E. Hallberg, F. Kahl, A. Temple, J. Andersson, S. Welch, X. Dai, V. Gupta, D. Lange, J.P. Hidalgo, Characterization of TRAvelling FIREs in large compartments, TRAFIR Deliverable Report 2.2, Research Institutes of Sweden, Borås, Sweden, 2019.
- [18] J.L. Torero, Flaming ignition of solids, in: M.J. Hurley et al. (eds) *SFPE Handbook of Fire Protection Engineering*, Springer, New York, 2011, pp. 633-661.
- [19] A.I. Bartlett, R.M. Hadden, L.A. Bibby, A review of factors affecting the burning behaviour of wood. *Fire Technol.* 55 (2019) 1-49. <https://doi.org/10.1007/s10694-018-0787-y>
- [20] J. Cuevas, J. L. Torero, and C. Maluk, 2020. Flame extinction and burning behaviour of timber under varied oxygen concentrations, *Fire Saf. J.* 103087. <https://doi.org/10.1016/j.firesaf.2020.103087>.
- [21] I. Pope, J.P. Hidalgo, J.L. Torero, 2020, A correction method for thermal disturbances induced by thermocouples in a low-conductivity charring material, *Fire Saf. J.* 103077. <https://doi.org/10.1016/j.firesaf.2020.103077>
- [22] EN 1995-1-2: 2004 Eurocode 5: design of timber structures - Part 1-2: General 0 Structural fire design
- [23] AS 1720.4-2006 Timber structures – Fire resistance for structural adequacy of timber members

UQ Fire



THE UNIVERSITY
OF QUEENSLAND
AUSTRALIA

CREATE CHANGE